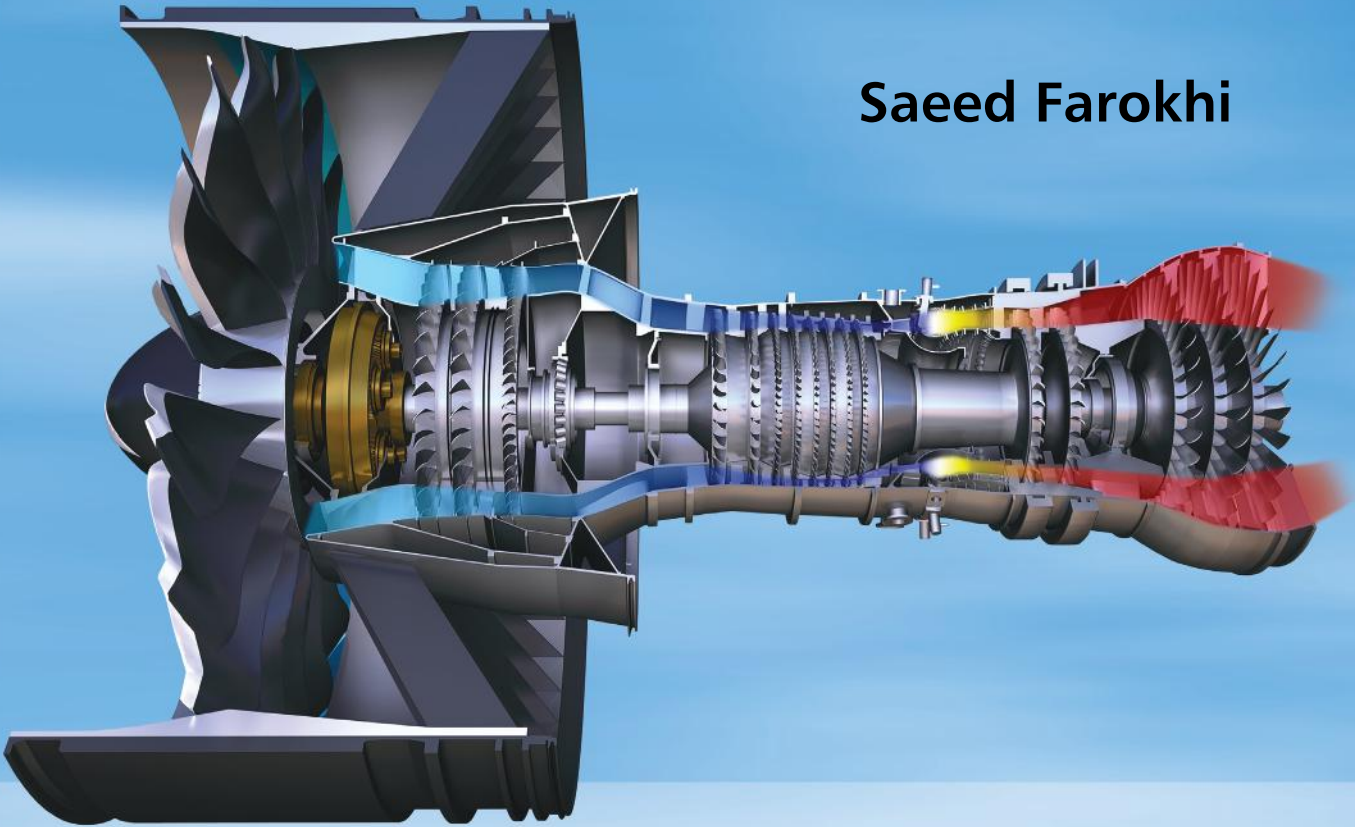


Aircraft Propulsion

Second Edition

Saeed Farokhi



WILEY

Aircraft Propulsion

Aircraft Propulsion

Second Edition

SAEED FAROKHI, PhD

Professor

Aerospace Engineering Department

The University of Kansas, USA

WILEY

This edition first published 2014
© 2014 John Wiley & Sons Ltd

Registered office

John Wiley & Sons Ltd, The Atrium, Southern Gate, Chichester, West Sussex, PO19 8SQ, United Kingdom

For details of our global editorial offices, for customer services and for information about how to apply for permission to reuse the copyright material in this book please see our website at www.wiley.com.

The right of the author to be identified as the author of this work has been asserted in accordance with the Copyright, Designs and Patents Act 1988.

All rights reserved. No part of this publication may be reproduced, stored in a retrieval system, or transmitted, in any form or by any means, electronic, mechanical, photocopying, recording or otherwise, except as permitted by the UK Copyright, Designs and Patents Act 1988, without the prior permission of the publisher.

Wiley also publishes its books in a variety of electronic formats. Some content that appears in print may not be available in electronic books.

Designations used by companies to distinguish their products are often claimed as trademarks. All brand names and product names used in this book are trade names, service marks, trademarks or registered trademarks of their respective owners. The publisher is not associated with any product or vendor mentioned in this book.

Limit of Liability/Disclaimer of Warranty: While the publisher and author have used their best efforts in preparing this book, they make no representations or warranties with respect to the accuracy or completeness of the contents of this book and specifically disclaim any implied warranties of merchantability or fitness for a particular purpose. It is sold on the understanding that the publisher is not engaged in rendering professional services and neither the publisher nor the author shall be liable for damages arising herefrom. If professional advice or other expert assistance is required, the services of a competent professional should be sought.

Library of Congress Cataloging-in-Publication Data

Farokhi, Saeed.

Aircraft propulsion / Saeed Farokhi. – Second edition.

pages cm

Includes bibliographical references and index.

ISBN 978-1-118-80677-7 (hardback)

1. Airplanes–Jet propulsion. 2. Airplanes–Motors–Design and construction. I. Title.

TL709.F34 2014

629.134'35–dc23

2014001461

A catalogue record for this book is available from the British Library.

ISBN 9781118806777

Set in 10/12pt Times by Aptara Inc., New Delhi, India

I dedicate this book to my lovely grandchildren:

Sophia

Sasha

Sydney

Melody

Table of Contents

<i>Preface to the Second Edition</i>	<i>xvii</i>
<i>Preface</i>	<i>xix</i>
<i>Nomenclature</i>	<i>xxiii</i>
1	
<i>Introduction</i>	1
1.1 History of the Airbreathing Jet Engine, a Twentieth-Century Invention—The Beginning	1
1.2 Innovations in Aircraft Gas Turbine Engines	4
1.2.1 Multispool Configuration	4
1.2.2 Variable Stator	5
1.2.3 Transonic Compressor	5
1.2.4 Low-Emission Combustor	6
1.2.5 Turbine Cooling	7
1.2.6 Exhaust Nozzles	8
1.2.7 Modern Materials and Manufacturing Techniques	8
1.3 New Engine Concepts	10
1.3.1 Advanced Turboprop (ATP) and Geared Turbofan (GTF)	10
1.3.2 Advanced Airbreathing Rocket Technology	11
1.3.3 Wave Rotor Topping Cycle	12
1.3.3.1 Humphrey Cycle versus Brayton Cycle	12
1.3.4 Pulse Detonation Engine (PDE)	14
1.3.5 Millimeter-Scale Gas Turbine Engines: Triumph of MEMS and Digital Fabrication	14
1.3.6 Combined Cycle Propulsion: Engines from Takeoff to Space	15
1.4 New Vehicles	16
1.5 Summary	16
1.6 Roadmap for the Second Edition	18
References	19
Problems	20

2***Compressible Flow with Friction and Heat: A Review*** **21**

2.1	Introduction	21
2.2	A Brief Review of Thermodynamics	22
2.3	Isentropic Process and Isentropic Flow	27
2.4	Conservation Principles for Systems and Control Volumes	28
2.5	Speed of Sound & Mach Number	35
2.6	Stagnation State	38
2.7	Quasi-One-Dimensional Flow	41
2.8	Area–Mach Number Relationship	44
2.9	Sonic Throat	45
2.10	Waves in Supersonic Flow	49
2.11	Normal Shocks	50
2.12	Oblique Shocks	54
2.13	Conical Shocks	60
2.14	Expansion Waves	63
2.15	Frictionless, Constant-Area Duct Flow with Heat Transfer	67
2.16	Adiabatic Flow of a Calorically Perfect Gas in a Constant-Area Duct with Friction	77
2.17	Friction (Drag) Coefficient C_f and D'Arcy Friction Factor f_D	91
2.18	Dimensionless Parameters	91
2.19	Fluid Impulse	95
2.20	Summary of Fluid Impulse	102
	References	103
	Problems	103

3***Engine Thrust and Performance Parameters*** **113**

3.1	Introduction	113
3.1.1	Takeoff Thrust	119
3.2	Installed Thrust—Some Bookkeeping Issues on Thrust and Drag	119
3.3	Engine Thrust Based on the Sum of Component Impulse	124
3.4	Rocket Thrust	128
3.5	Airbreathing Engine Performance Parameters	129
3.5.1	Specific Thrust	129
3.5.2	Specific Fuel Consumption and Specific Impulse	130
3.5.3	Thermal Efficiency	131
3.5.4	Propulsive Efficiency	134
3.5.5	Engine Overall Efficiency and Its Impact on Aircraft Range and Endurance	137
3.6	Modern Engines, Their Architecture and Some Performance Characteristics	140
3.7	Summary	143
	References	144
	Problems	144

4		
	Gas Turbine Engine Cycle Analysis	151
4.1	Introduction	151
4.2	The Gas Generator	151
4.3	Aircraft Gas Turbine Engines	152
4.3.1	The Turbojet Engine	152
4.3.1.1	The Inlet	153
4.3.1.2	The Compressor	157
4.3.1.3	The Burner	164
4.3.1.4	The Turbine	168
4.3.1.5	The Nozzle	177
4.3.1.6	Thermal Efficiency of a Turbojet Engine	185
4.3.1.7	Propulsive Efficiency of a Turbojet Engine	194
4.3.1.8	The Overall Efficiency of a Turbojet Engine	196
4.3.1.9	Performance Evaluation of a Turbojet Engine	196
4.3.2	The Turbojet Engine with an Afterburner	197
4.3.2.1	Introduction	197
4.3.2.2	Analysis	200
4.3.2.3	Optimum Compressor Pressure Ratio for Maximum (Ideal) Thrust Turbojet Engine with Afterburner	203
4.3.3	The Turbofan Engine	209
4.3.3.1	Introduction	209
4.3.3.2	Analysis of a Separate-Exhaust Turbofan Engine	210
4.3.3.3	Thermal Efficiency of a Turbofan Engine	215
4.3.3.4	Propulsive Efficiency of a Turbofan Engine	216
4.3.4	Ultra-High Bypass (UHB) Turbofan Engines	221
4.4	Analysis of a Mixed-Exhaust Turbofan Engine with an Afterburner	225
4.4.1	Mixer	226
4.4.2	Cycle Analysis	229
4.4.2.1	Solution Procedure	229
4.5	The Turboprop Engine	241
4.5.1	Introduction	241
4.5.2	Propeller Theory	242
4.5.2.1	Momentum Theory	242
4.5.2.2	Blade Element Theory	247
4.5.3	Turboprop Cycle Analysis	249
4.5.3.1	The New Parameters	249
4.5.3.2	Design Point Analysis	250
4.5.3.3	Optimum Power Split Between the Propeller and the Jet	254
4.6	Summary	260
	References	261
	Problems	261
5		
	General Aviation and Uninhabited Aerial Vehicle Propulsion System	283
5.1	Introduction	283

5.2	Cycle Analysis	284
5.2.1	Otto Cycle	284
5.2.2	Real Engine Cycles	284
5.2.2.1	Four-Stroke Cycle Engines	284
5.2.2.2	Diesel Engines	286
5.2.2.3	Two-Stroke Cycle Engines	288
5.2.2.4	Rotary (Wankel) Engines	290
5.3	Power and Efficiency	293
5.4	Engine Components and Classifications	295
5.4.1	Engine Components	295
5.4.2	Reciprocating Engine Classifications	296
5.4.2.1	Classification by Cylinder Arrangement	296
5.4.2.2	Classification by Cooling Arrangement	299
5.4.2.3	Classification by Operating Cycle	299
5.4.2.4	Classification by Ignition Type	300
5.5	Scaling of Aircraft Reciprocating Engines	300
5.5.1	Scaling of Aircraft Diesel Engines	306
5.6	Aircraft Engine Systems	308
5.6.1	Aviation Fuels and Engine Knock	308
5.6.2	Carburetion and Fuel Injection Systems	310
5.6.2.1	Float-Type Carburetors	310
5.6.2.2	Pressure Injection Carburetors	311
5.6.2.3	Fuel Injection Systems	311
5.6.2.4	Full Authority Digital Engine Control (FADEC)	311
5.6.3	Ignition Systems	311
5.6.3.1	Battery Ignition Systems	312
5.6.3.2	High Tension Ignition System	312
5.6.3.3	Low Tension Ignition System	312
5.6.3.4	Full Authority Digital Engine Control (FADEC)	312
5.6.3.5	Ignition Boosters	312
5.6.3.6	Spark Plugs	313
5.6.4	Lubrication Systems	313
5.6.5	Supercharging	314
5.7	Electric Engines	314
5.7.1	Electric Motors	315
5.7.2	Solar cells	316
5.7.3	Advanced Batteries	316
5.7.4	Fuel cells	318
5.7.5	State of the Art for Electric Propulsion – Future Technology	319
5.8	Propellers and Reduction Gears	319
	References	322
	Problems	324

6

Aircraft Engine Inlets and Nozzles **327**

6.1	Introduction	327
6.2	The Flight Mach Number and Its Impact on Inlet Duct Geometry	328

6.3	Diffusers	329
6.4	An Ideal Diffuser	330
6.5	Real Diffusers and Their Stall Characteristics	331
6.6	Subsonic Diffuser Performance	333
6.7	Subsonic Cruise Inlet	338
6.8	Transition Ducts	348
6.9	An Interim Summary for Subsonic Inlets	349
6.10	Supersonic Inlets	350
6.10.1	Isentropic Convergent–Divergent Inlets	350
6.10.2	Methods to Start a Supersonic Convergent–Divergent Inlet	353
6.10.2.1	Overspeeding	355
6.10.2.2	Kantrowitz–Donaldson Inlet	356
6.10.2.3	Variable-Throat Isentropic C–D Inlet	358
6.11	Normal Shock Inlets	359
6.12	External Compression Inlets	362
6.12.1	Optimum Ramp Angles	365
6.12.2	Design and Off-Design Operation	366
6.13	Variable Geometry—External Compression Inlets	368
6.13.1	Variable Ramps	368
6.14	Mixed-Compression Inlets	368
6.15	Supersonic Inlet Types and Their Performance—A Review	370
6.16	Standards for Supersonic Inlet Recovery	371
6.17	Exhaust Nozzle	373
6.18	Gross Thrust	373
6.19	Nozzle Adiabatic Efficiency	373
6.20	Nozzle Total Pressure Ratio	374
6.21	Nozzle Pressure Ratio (NPR) and Critical Nozzle Pressure Ratio ($NPR_{crit.}$)	374
6.22	Relation Between Nozzle Figures of Merit, η_n and π_n	376
6.23	A Convergent Nozzle or a De Laval?	376
6.24	The Effect of Boundary Layer Formation on Nozzle Internal Performance	379
6.25	Nozzle Exit Flow Velocity Coefficient	379
6.26	Effect of Flow Angularity on Gross Thrust	381
6.27	Nozzle Gross Thrust Coefficient C_{fg}	385
6.28	Overexpanded Nozzle Flow—Shock Losses	386
6.29	Nozzle Area Scheduling, A_8 and A_9/A_8	389
6.30	Nozzle Exit Area Scheduling, A_9/A_8	391
6.31	Nozzle Cooling	394
6.32	Thrust Reverser and Thrust Vectoring	396
6.33	Hypersonic Nozzle	401
6.34	Exhaust Mixer and Gross Thrust Gain in a Mixed-Flow Turbofan Engine	404
6.35	Noise	406
6.35.1	Jet Noise	407
6.35.2	Chevron Nozzle	408
6.36	Nozzle-Turbine (Structural) Integration	409
6.37	Summary of Exhaust Systems	410
	References	411
	Problems	413

7		
	Combustion Chambers and Afterburners	429
7.1	Introduction	429
7.2	Laws Governing Mixture of Gases	431
7.3	Chemical Reaction and Flame Temperature	434
7.4	Chemical Equilibrium and Chemical Composition	445
	7.4.1 The Law of Mass Action	446
	7.4.2 Equilibrium Constant K_p	448
7.5	Chemical Kinetics	459
	7.5.1 Ignition and Relight Envelope	460
	7.5.2 Reaction Timescale	461
	7.5.3 Flammability Limits	461
	7.5.4 Flame Speed	464
	7.5.5 Flame Stability	466
	7.5.6 Spontaneous Ignition Delay Time	470
	7.5.7 Combustion-Generated Pollutants	472
7.6	Combustion Chamber	473
	7.6.1 Combustion Chamber Total Pressure Loss	474
	7.6.2 Combustor Flow Pattern and Temperature Profile	483
	7.6.3 Combustor Liner and Its Cooling Methods	485
	7.6.4 Combustion Efficiency	488
	7.6.5 Some Combustor Sizing and Scaling Laws	489
	7.6.6 Afterburner	493
7.7	Combustion-Generated Pollutants	498
	7.7.1 Greenhouse Gases, CO_2 and H_2O	498
	7.7.2 Carbon Monoxide, CO , and Unburned Hydrocarbons, UHC	499
	7.7.3 Oxides of Nitrogen, NO and NO_2	500
	7.7.4 Smoke	501
	7.7.5 Engine Emission Standards	502
	7.7.6 Low-Emission Combustors	503
	7.7.7 Impact of NO on the Ozone Layer	507
7.8	Aviation Fuels	509
7.9	Alternative “Drop-In” Jet Fuels (AJFs)	513
7.10	Combustion Instability: Screech and Rumble	515
	7.10.1 Screech Damper	515
7.11	Summary	516
	References	516
	Problems	518

8		
	Axial Compressor Aerodynamics	525
8.1	Introduction	525
8.2	The Geometry	525
8.3	Rotor and Stator Frames of Reference	526
8.4	The Euler Turbine Equation	529

8.5	Axial-Flow Versus Radial-Flow Machines	530
8.6	Axial-Flow Compressors and Fans	532
8.6.1	Definition of Flow Angles	534
8.6.2	Stage Parameters	536
8.6.3	Cascade Aerodynamics	549
8.6.4	Aerodynamic Forces on Compressor Blades	563
8.6.5	Three-Dimensional Flow	571
8.6.5.1	Blade Vortex Design	573
8.6.5.2	Three-Dimensional Losses	585
8.6.5.3	Reynolds Number Effect	590
8.7	Compressor Performance Map	593
8.8	Compressor Instability – Stall and Surge	595
8.9	Multistage Compressors and Their Operating Line	599
8.10	Multistage Compressor Stalling Pressure Rise and Stall Margin	604
8.11	Multistage Compressor Starting Problem	612
8.12	The Effect of Inlet Flow Condition on Compressor Performance	615
8.13	Isometric and Cutaway Views of Axial-Flow Compressor Hardware	620
8.14	Compressor Design Parameters and Principles	620
8.14.1	Blade Design – Blade Selection	626
8.14.2	Compressor Annulus Design	627
8.14.3	Compressor Stall Margin	628
8.15	Summary	636
	References	638
	Problems	640

9

Centrifugal Compressor Aerodynamics **651**

9.1	Introduction	651
9.2	Centrifugal Compressors	652
9.3	Radial Diffuser	666
9.4	Inducer	670
9.5	Inlet Guide Vanes (IGVs) and Inducer-Less Impellers	673
9.6	Impeller Exit Flow and Blockage Effects	673
9.7	Efficiency and Performance	674
9.8	Summary	677
	References	678
	Problems	678

10

Aerothermo-dynamics of Gas Turbines **685**

10.1	Introduction	685
10.2	Axial-Flow Turbines	685
10.2.1	Optimal Nozzle Exit Swirl Mach Number $M_{\theta 2}$	698
10.2.2	Turbine Blade Losses	702
10.2.2.1	Blade Profile Loss	703

10.2.2.2	Secondary Flow Losses	703
10.2.2.3	Annulus Losses	705
10.2.3	Optimum Solidity	714
10.2.4	Turbine Cooling	718
10.2.4.1	Convective Cooling	723
10.2.4.2	Impingement Cooling	728
10.2.4.3	Film Cooling	729
10.2.4.4	Transpiration Cooling	732
10.3	Turbine Performance Map	733
10.4	The Effect of Cooling on Turbine Efficiency	734
10.5	Turbine Blade Profile Design	735
10.5.1	Angles	736
10.5.2	Other Blade Geometrical Parameters	737
10.5.3	Throat Sizing	737
10.5.4	Throat Reynolds Number Re_o	738
10.5.5	Turbine Blade Profile Design	738
10.5.6	Blade Vibration and Campbell Diagram	739
10.5.7	Turbine Blade and Disk Material Selection and Design Criteria	740
10.6	Stresses in Turbine Blades and Disks and Useful Life Estimation	743
10.7	Axial-Flow Turbine Design and Practices	746
10.8	Gas Turbine Design Summary	754
10.9	Summary	755
	References	757
	Problems	759

11

Aircraft Engine Component Matching and Off-Design Analysis **767**

11.1	Introduction	767
11.2	Engine (Steady-State) Component Matching	768
11.2.1	Engine Corrected Parameters	769
11.2.2	Inlet-Compressor Matching	769
11.2.3	Compressor-Combustor Matching	771
11.2.4	Combustor-Turbine Matching	773
11.2.5	Compressor-Turbine Matching and Gas Generator Pumping Characteristics	774
11.2.5.1	Gas Generator Pumping Characteristics	777
11.2.6	Turbine-Afterburner-(Variable-Geometry) Nozzle Matching	783
11.2.6.1	Fixed-Geometry Convergent Nozzle Matching	784
11.3	Engine Off-Design Analysis	785
11.3.1	Off-Design Analysis of a Turbojet Engine	786
11.3.2	Off-Design Analysis of an Afterburning Turbojet Engine	789
11.3.3	Off-Design Analysis of a Separate-Flow Turbofan (Two-Spool) Engine	793
11.4	Unchoked Nozzles and Other Off-Design Iteration Strategies	798
11.4.1	Unchoked Exhaust Nozzle	799
11.4.2	Unchoked Turbine Nozzle	800

11.4.3	Turbine Efficiency at Off-Design	801
11.4.4	Variable Gas Properties	801
11.5	Principles of Engine Performance Testing	802
11.5.1	Force of Inlet Bellmouth on Engine Thrust Stand	804
11.5.1.1	Bellmouth Instrumentation	804
11.5.1.2	The Effect of Fluid Viscosity	805
11.5.1.3	The Force of Inlet Bellmouth on Engine Thrust Stand	806
11.6	Summary	810
	References	812
	Problems	813

12

Chemical Rocket and Hypersonic Propulsion **821**

12.1	Introduction	821
12.2	From Takeoff to Earth Orbit	823
12.3	Chemical Rockets	824
12.4	Chemical Rocket Applications	826
12.4.1	Launch Engines	826
12.4.2	Boost Engines	826
12.4.3	Space Maneuver Engines	827
12.4.4	Attitude Control Rockets	827
12.5	New Parameters in Rocket Propulsion	827
12.6	Thrust Coefficient, C_F	830
12.7	Characteristic Velocity, c^*	833
12.8	Flight Performance	835
12.9	Multistage Rockets	845
12.10	Propulsive and Overall Efficiencies	847
12.11	Chemical Rocket Combustion Chamber	849
12.11.1	Liquid Propellant Combustion Chambers	849
12.11.1.1	Some Design Guidelines for Injector Plate	854
12.11.1.2	Combustion Instabilities	855
12.11.2	Solid Propellant Combustion Chambers	855
12.12	Thrust Chamber Cooling	862
12.12.1	Liquid Propellant Thrust Chambers	862
12.12.2	Cooling of Solid Propellant Thrust Chambers	868
12.13	Combustor Volume and Shape	869
12.14	Rocket Nozzles	870
12.14.1	Multiphase Flow in Rocket Nozzles	874
12.14.2	Flow Expansion in Rocket Nozzles	883
12.14.3	Thrust Vectoring Nozzles	884
12.15	High-Speed Airbreathing Engines	884
12.15.1	Supersonic Combustion Ramjet	891
12.15.1.1	Inlet Analysis	892
12.15.1.2	Scramjet Combustor	892
12.15.1.3	Scramjet Nozzle	895

12.16 Rocket-Based Airbreathing Propulsion	895
12.17 Summary	897
References	898
Problems	899
A. U.S. Standard Atmosphere	903
B. Isentropic Table	907
C. Normal Shock Table	924
D. Rayleigh Flow	937
E. Fanno Flow	946
F. Prandtl–Meyer Function and Mach Angle	955
G. Oblique Shock Charts	958
H. Conical Shock Charts	963
I. Cascade Data	966
J. Websites	972
K. 10-Minute Quiz	973
L. Some “ <i>Rules of Thumb</i> ” and <i>Trends</i> in Aircraft Propulsion	991
Index	999

Preface to the Second Edition

Since the first edition of this book appeared in 2008, the Uninhabited Aerial Vehicle (UAV) has gained wider interest and market share in aircraft industry. As a result, the second edition has a new chapter dedicated to *General Aviation and UAV Propulsion Systems*. The remaining changes to the second edition stem from technological advances in propulsion in recent years. For example in the commercial transport sector, we have witnessed the development of *Ultra-High Bypass (UHB)* turbofan engines with bypass ratio above 12. An enabling technology to UHB is the *Geared Turbofan*, which has also received an introductory coverage in the second edition. Other technological advances include *Chevron Nozzle*, *Alternative “drop-in” Jet Fuels (AJF)* and *advanced heat exchanger in airbreathing rocket engine* for single-stage-to-orbit application, which are introduced in the new edition.

Some of the reviewers and readers suggested an introductory presentation on *propeller theory* could well be integrated with the presentation of the turboprop engines. In response, I have added a section on propeller theory prior to the turboprop cycle analysis section. The instructors often wrote and asked for *more problems* at the end of chapters and as a result the new edition has about 50% more end-of-chapter problems than the first edition (i.e., 446 in 2E vs. 305 in 1E). There is an increased interest in Aerospace Engineering (AE) programs to offer propulsion system design as one of the capstone design options in AE curriculum. Towards that goal, additional *design guidelines* are added to each component chapter in 2E. A new section on aircraft engines *performance testing and basic instrumentation* in ground facilities is added to Chapter 11: Aircraft Engine Component Matching and Off-Design Analysis.

Two new appendices are created in the second edition. The first one is an assembly of 45 *Ten-Minute Quizzes* that I had given to my propulsion students at KU in the past three decades. These 10-minute closed books/notes quizzes were given to students at the beginning of my class and concentrated on recent materials. The goal is to show the importance of fundamental concepts, governing laws, important definitions to students and hopefully develop an engineering sense for “ballpark” numbers in propulsion system engineering. The quizzes may be used as an assessment tool by the instructors or the learners themselves. To help the students with the *“Rules of Thumb” and Trends* in

aircraft propulsion, a second new appendix is created. Students of propulsion and practicing system engineers should find the new appendix on “Rules of Thumb” and Trends particularly useful.

Acknowledgments

I express my sincere appreciation to my friend and colleague at KU-Aerospace, Professor Ray Taghavi, who wrote the invited chapter on General Aviation and UAV Propulsion in the second edition. I received extensive support from Pratt & Whitney on engine data, many engine cutaways, including their new geared turbofan engine, PW1000G, and others. For these, I express my sincere appreciation to Dr. Alan Epstein, Vice President of Engineering Technology and Environment at P&W and Mr. Steve O’Flarity who helped immensely with data and approvals’ gathering at P&W. The copyright permissions from GE Aviation, Boeing and other industry help enrich the presentation and content of this book and are greatly appreciated.

To many colleagues who had adopted my book and sent corrections and helpful suggestions, I express my heartfelt appreciation. I have tried to adopt their suggestions and numerous corrections in the second edition. Since the last edition, I have been assisted by my new doctoral students, Seung-Jae Hwang (2011), Leslie Smith, Amool Raina and Dhaval Mysore who continue to improve my understanding of the advanced concepts in aircraft propulsion and (green) power generation. I am also indebted to many graduate students in the MS level who have helped me in research and provided solutions to the end-of-chapter problems that appear in the solution manual, as an instructor resource.

Finally, my wife Mariam and our growing family continue to be the real inspiration behind this work and I owe my peace of mind and productivity to their love and support.

Saeed Farokhi
Lawrence, Kansas
November 12, 2013

Preface

Intended Audience

This book is intended to provide a foundation for the analysis and design of aircraft engines. The target audience for this book is upper classmen, undergraduates, and first-year graduate students in aerospace and mechanical engineering. The practicing engineers in the gas turbine and aircraft industry will also benefit from the integration and system discussions in the book. Background in thermodynamics and fluid mechanics at a fundamental level is assumed.

Motivation

In teaching under graduate and graduate propulsion courses for the past 23 years, I accumulated supplemental notes on topics that were not covered in most of our adopted textbooks. The supplemental materials ranged from issues related to the propulsion system integration into aircraft to the technological advances that were spawned by research centers around the world. I could have continued handing out supplemental materials to the textbooks to my classes, except that I learned that the presentation style to undergraduate students had to be (pedagogically) different than for the graduate students. For example, leaving out many steps in derivations of engineering principles can lead to confusion for most undergraduate students. Although it is more important to grasp the underlying principles than the mechanics of some derivations, but if we lose the students in the derivation phase, they may lose sight of the underlying principles as well. Another motivation for attention to details in analysis is my conviction that going back to basics and showing how the end results are obtained demystifies the subject and promotes students' confidence in their own abilities.

Mathematical Level

The mathematics in the present book is intentionally kept at the calculus and basic differential equations level, which makes the book readily accessible to undergraduate engineering students. Physical interpretations of mathematical relations are always offered in the text to help students grasp the physics that is hidden and inherent in the formulas.

This approach will take the mystery out of formulas and let engineering students go beyond symbols and into understanding concepts.

Chapter Organization and Topical Coverage

The first chapter is an introduction to airbreathing aircraft engines and is divided in two parts. The first part reviews the history of gas turbine engine development, and the second part highlights modern concepts in aircraft engine and vehicle design. Young engineering students are excited to learn about the new opportunities and directions in aircraft engine design that are afforded by advances in materials, manufacturing, cooling technology, computational methods, sensors, actuators, and controls. Renewed interest in hypersonic air breathing engines in general and supersonic combustion ramjets in particular as well as a sprawling interest in Uninhabited Aerial Vehicles (UAVs) has revitalized the ever-popular X-planes. The goal of Chapter 1 is first to inform students about the history, but more importantly to excite them about the future of aerospace engineering.

Chapter 2 is a review of compressible flow with heat and friction. The conservation principles are reviewed and then applied to normal and oblique shocks, conical shocks, and expansion waves, quasi-one-dimensional flows in ducts as well as Rayleigh and Fanno flows. At the closing of Chapter 2, the impulse concept and its application to gas turbine engine components are introduced.

Chapter 3 is on engine thrust and performance parameters. Here, we introduce internal and external performance of aircraft engines and their installation effect.

Chapter 4 describes aircraft gas turbine engine cycles. The real and ideal behaviors of engine components are described simultaneously in this chapter. Efficiencies, losses, and figures of merit are defined both physically and mathematically for each engine component in Chapter 4. Once we define the real behavior of all components in a cycle, we then proceed to calculate engine performance parameters, such as specific thrust, specific fuel consumption and thermal and propulsive efficiencies. The ideal cycle thus becomes a special case of a real cycle when all of its component efficiencies are equal to one.

The next five chapters treat aircraft engine components. Chapter 5 deals with aircraft inlets and nozzles. Although the emphasis throughout the book is on internal performance of engine components, the impact of external or installation effects is always presented for a balanced view on aircraft propulsion. As a building block of aircraft inlet aerodynamics, we have thoroughly reviewed two-dimensional and conical diffuser performance. Some design guidelines, both internal and external to inlet cowl, are presented. Transition duct aero-dynamics also plays an important role in design and understanding of aircraft inlets and is thus included in the treatment. Supersonic and hypersonic inlets with their attendant shock losses, boundary layer management, and instabilities such as buzz and starting problem are included in the inlet section of Chapter 5. The study of aircraft exhaust systems comprises the latter part of Chapter 5. Besides figures of merit, the performance of a convergent nozzle is compared with the de Laval or a convergent–divergent nozzle. The requirements of reverse- and vector thrust are studied in the context of thrust reversers and modern thrust vectoring nozzles. In the hypersonic limit, the exhaust nozzle is fully integrated with the vehicle and introductory design concepts and off-design issues are presented. Nozzle cooling is introduced for high-performance military aircraft engine exhaust systems and the attendant performance penalties and limitations are considered.

Plug nozzle and its on-and off-design performances are introduced. Since mixers are an integral part of long-duct turbo fan engines, their effect on gross thrust enhancement is formulated and presented in the nozzle section in Chapter 5.

Chemical reaction is studied on a fundamental basis in Chapter 6. The principles of chemical equilibrium and kinetics are used to calculate the composition of the products of combustion in a chemical reaction. These principles allow the calculation of flame temperature and pollutant formations that drive the design of modern aircraft gas turbine combustors. Further details of flame speed, stability, and flame holding are presented in the context of combustion chamber and afterburner design. Pollutant formation and its harmful impact on ozone layer as well as the greenhouse gases in the exhaust are presented to give students an appreciation for the design issues in modern combustors. Aviation fuels and their properties and a brief discussion of combustion instability known as screech are included in Chapter 6.

Turbomachinery is introduced in three chapters. Chapter 7 deals with axial-flow compressors in two and three dimensions. The aerodynamics of axial-flow compressors and stage performance parameters are derived. The role of cascade data in two-dimensional design is presented. Emphasis throughout this chapter is in describing the physical phenomena that lead to losses in compressors. Shock losses and transonic fans are introduced. The physics of compressor instability in stall and surge is described. A simple model by Greitzer that teaches the value of characteristic timescales and their relation to compressor instability is outlined. Chapter 8 discusses the aerodynamics and performance of centrifugal compressors. Distinctive characters of centrifugal compressors are highlighted and compared with axial-flow compressors. Turbine aerodynamics and cooling are presented in Chapter 9. Component matching and engine parametric study is discussed in Chapter 10. Finally, chemical rocket and hypersonic propulsion is presented in Chapter 11.

Instructor Resources

The following resources are available to instructors who adopt this book for their course. Please visit the website at www.wiley.com/go/farokhi to request a password and access these resources.

- Solutions Manual
- Image Gallery

Acknowledgments

I express my sincere appreciation and gratitude to all those who have contributed to my understanding of fluid mechanics and propulsion. Notable among these are my professors in Illinois and MIT. Hermann Krier, Jack Kerrebrock, James McCune, William Hawthorne, and Ed Greitzer contributed the most. The fellow graduate students in the Gas Turbine Lab were also instrumental in my education. Choon Tan, Maher El-Masri, Alan Epstein, Arun Sehra, Mohammad Durali, Wai Cheng, Segun Adebayo, James Fabunmi, and Anthony Nebo discussed their dissertations with me and helped me understand my own. In the Gas Turbine Division of Brown, Boveri and Co. in Baden, Switzerland, I learned the value

of hardware engineering and testing, advanced product development, and component research. My colleagues, Meinhard Schobeiri, Konrad Voegeler, Hans Jakob Graf, Peter Boenzli, and Horst Stoff, helped me understand how industry works and how it engineers new products. At the University of Kansas, my graduate students were my partners in research and we jointly advanced our understanding of fluid mechanics and propulsion. My doctoral students, Ray Taghavi, Gary Cheng, Charley Wu, Ron Barrett, and Kyle Wetzell, taught me the most. I appreciate the contributions of 30 M.S. students whom I chaired their theses to our ongoing research. The colleagues at NASA-Lewis (now Glenn) who sponsored my research and provided insightful discussions and hospitality over the summer months in Cleveland are Ed Rice, Khairul Zaman, Ganesh Raman, Bernie Anderson, Reda Mankbadi, James Scott, and Charlie Towne who welcomed me into their laboratory (and their homes), and we enjoyed some fruitful research together. The faculty and staff in the Aerospace Engineering Department of the University of Kansas have been very supportive for the past 23 years, and I would like to express my sincere appreciation to all of them. Vince Muirhead, Jan Roskam, Eddie Lan, Dave Downing, Howard Smith, Dave Ellis, Tae Lim, John Ogg, James Locke, Mark Ewing, Rick Hale, and Trevor Sorenson taught me an appreciation for their disciplines in aerospace engineering. I joined my colleagues in GE-Aircraft Engines in teaching propulsion system design and integration short courses to engineers in industry, FAA, and NASA for many years. I learned from Don Dusa and Jim Youngmans from GE and Bill Schweikhard of KSR some intricate aspects of propulsion engineering and flight-testing.

I would like to thank the following colleagues who reviewed the draft manuscript:

David Benson, Kettering University
Kirby S. Chapman, Kansas State University
Mohamed Gad-el-Hak, Virginia Commonwealth University
Knox Millsaps, Naval Postgraduate School
Alex Moutsoglou, South Dakota State University
Norbert Mueller, Michigan State University
Meinhard T. Schobeiri, Texas A&M University
Ali R. Ahmadi, California State University and Polytechnic—Pomona
Ganesh Raman, Illinois Institute of Technology

Finally, I express my special appreciation to my wife of 36 years, Mariam, and our three lovely daughters, Kamelia, Parisa, and Farima (Fallon) who were the real inspiration behind this effort. I could not have contemplated such a huge project without their love, understanding, encouragement, and support. I owe it all to them.

Saeed Farokhi
Lawrence, Kansas
March 16, 2007

Nomenclature

Latin	Definition	Unit
a	Local speed of sound	m/s, ft/s
a	Semimajor axis of inlet elliptic lip (internal)	m, ft
a	Swirl profile parameter	—
a_t	Speed sound based on total temperature	m/s, ft/s
A	Area	m ² , ft ²
A_n	Projection of area in the normal direction	m ² , ft ²
A_9	Nozzle exit flow area	m ² , ft ²
A_{ref}	Reference area	m ² , ft ²
A_o	Inlet (freestream) capture area	m ² , ft ²
A_1	Inlet capture area	m ² , ft ²
A_8, A_{8geo}	Nozzle throat area (geometrical area)	m ² , ft ²
A_{8eff}	Effective nozzle throat area	m ² , ft ²
A_B	Blocked area (due to boundary layer)	m ² , ft ²
A_b	Burning area of grain in solid rocket motors	m ² , ft ²
A_E	Effective area	m ² , ft ²
A_{HL}	Inlet highlight area	m ² , ft ²
A_M	Maximum nacelle area	m ² , ft ²
A_{th}	Inlet throat area	m ² , ft ²
A^*	Sonic throat, choked area	m ² , ft ²
b	Semiminor axis of inlet elliptic lip (internal)	m, ft
b	Swirl profile parameter	—
B	Blockage	—
B	Compressor instability parameter due to Greitzer	—
\vec{C}	Absolute velocity vector in turbomachinery	m/s, ft/s
C	Absolute flow speed, i.e., $\sqrt{C_r^2 + C_\theta^2 + C_z^2}$	m/s, ft/s
c	Chord length	m, ft
c	Effective exhaust velocity in rockets	m/s, ft/s
c^*	Characteristic velocity in rockets	m/s, ft/s
C_r, C_θ, C_z	Radial, tangential, axial velocity components in the absolute frame of reference	m/s, ft/s
C_D	drag coefficient, discharge coefficient	—
C_f	Friction drag coefficient	—

XXIV Nomenclature

c_f	Local skin friction coefficient	—
C_F	Force coefficient	—
C_P	Pressure coefficient	—
C_{PR}	Diffuser static pressure recovery coefficient	—
C_A	Nozzle flow angularity loss coefficient	—
C_{D8}	Nozzle (throat) discharge coefficient	—
C_{fg}	Nozzle gross thrust coefficient	—
C_V	Nozzle exit velocity coefficient	—
C_d	Sectional profile drag coefficient	—
C_{Di}	Induced drag coefficient	—
C_l	Sectional lift coefficient	—
C_h	Enthalpy-equivalent of the static pressure rise coefficient due to Koch	—
c_p	Specific heat at constant pressure	J/kg · K
c_v	Specific heat at constant volume	J/kg · K
\bar{c}_p	Molar specific heat at constant pressure	J/kmol · K
d	Flameholder width	m, ft
D	Diameter, drag	m, N
D	Liquid fuel droplet diameter	micron
$D_{\text{flameholder}}$	Flameholder drag	N, lbf
D_{add}	Additive drag	N, lbf
D_{nacelle}	Nacelle drag	N, lbf
D_{pylon}	Pylon drag	N, lbf
D_r	Ram drag	N, lbf
D_{spillage}	Spillage drag	N, lbf
$D_{\text{aft-end}}$	Nozzle aft-end drag	N, lbf
D_{boattail}	Nozzle boattail drag	N, lbf
$D_{\text{plug-friction}}$	Friction drag on the plug nozzle	N, lbf
D	Diffusion factor in turbomachinery	—
D'	Two-dimensional or sectional profile drag	N/m
\hat{e}	Unit vector	—
e	Specific internal energy	J/kg
e_c, e_t	Polytropic efficiency of compressor or turbine	—
E	Internal energy	J
E_a	Activation energy	kcal/mol
f	Fuel-to-air ratio	—
f_{stoich}	Stoichiometric fuel-to-air ratio	—
F_g	Gross thrust	N, lbf
F_{lip}	Lip suction force	N, lbf
F_{plug}	Axial force on the nozzle plug	N, lbf
F_n	Net thrust	N, lbf
F	Force	N, lbf
F_θ, F_z	Tangential force, axial force	N, lbf
f_D	D'Arcy (pipe) friction factor	—
g	Staggered spacing (s.cos β in a rotor and s.cos α in a stator)	m
g_0	Gravitational acceleration on the surface of the earth	m/s ² , ft/s ²
h	Specific enthalpy	J/kg
h_t	Specific total enthalpy	J/kg

h	Heat transfer rate per unit area per unit temp. difference	W/m ² K
h	Altitude above a planet	km, kft
h_t	Specific total (or stagnation) enthalpy in the absolute frame; $h + C^2/2$	J/kg
h_{tr}	Specific total enthalpy in relative frame of reference; $h + W^2/2$	J/kg
h_{lg}	Latent heat of vaporization	J/kg
HHV	Higher heating value	J/kg, BTU/lbm
H	Enthalpy	J, ft-lbf
H	Afterburner duct height	m, ft
i	Blade section incidence angle	deg
i_{opt}	Optimum incidence angle	deg
I_s	Specific impulse	s
I_t	Total impulse	N · s, lbf · s
I	Impulse	N, lbf
K_p	Equilibrium constant based on partial pressure	(bar) ^x
K_n	Equilibrium constant based on molar concentration	—
L	Length	m, ft
L	Lift	N, lbf
L	Flameholder length of recirculation zone	m, ft
L	Diffuser wall length	m, ft
L	Diffusion length scale in a blade row	m, ft
LHV	Lower heating value	J/kg, BTU/lbm
L/D	Aircraft lift-to-drag ratio	—
M_b	Blowing parameter in film cooling, $\rho_c u_c / \rho_g u_g$	—
M_T	Blade tangential Mach number U/a	—
M_z	Axial Mach number, C_z/a	—
M_r	Relative Mach number (in turbomachinery); $(M_z^2 + M_T^2)^{1/2}$	—
M	Mach number	—
M^*	Characteristic Mach number	—
M_s	Gas Mach number upstream of a shock inside a nozzle	—
m	Parameter in Carter's rule for deviation angle	—
m	Mass	kg, lbm
\dot{m}	Mass flow rate	kg/s, lbm/s
\dot{m}_c	Corrected mass flow rate	kg/s, lbm/s
\dot{m}_0	Air mass flow rate	kg/s, lbm/s
\dot{m}_f	Fuel mass flow rate	kg/s, lbm/s
\dot{m}_p	Propellant (oxidizer and fuel) mass flow rate	kg/s, lbm/s
\dot{m}_s	Mass flow rate through the side of the control volume	kg/s, lbm/s
\dot{m}_c	Coolant flow rate	kg/s, lbm/s
MW	Molecular weight	kg/kmol
n	Exponent of superellipse	—
n	Polytropic exponent; parameter in general swirl distribution	—
N	Number of blades; shaft rotational frequency; number of stages	—
N	Number of bluff bodies in a flameholder	—
N	Diffuser axial length	m, ft
N_a	Avagadro's number (6.023×10^{23} molecules per gmole)	—
N_B	Inlet lip bluntness parameter	—
N_c	Corrected shaft speed	rad/s, rpm

XXVI Nomenclature

\hat{n}	Unit normal vector (pointing out of a surface)	—
Nu	Nusselt number	—
Pr	Prandtl number	—
p	Static pressure	bar, Pa, psia
p_t	Total pressure	bar, Pa, psia
p_s	Static pressure upstream of a shock (in nozzle)	bar, Pa, psia
$\dot{\mathcal{P}}$	Power	W, hp
$\dot{\mathcal{P}}_s$	Shaft power	W, BTU/s
PF	Pattern factor	—
P_f	Profile factor	—
Q	Heat exchange	J, BTU
q	Dynamic pressure	bar, atm
q	Heat transfer rate per unit area (heat flux)	W/m ² , BTU/s.ft ²
q	Heat transfer rate per unit mass flow rate	J/kg, BTU/lbm
Q_R	Fuel heating value	kJ/kg, BTU/lbm
\dot{Q}	Heat transfer rate	W, BTU/s
\mathfrak{R}	Aircraft range	nm
Re	Reynolds number	—
R	Gas constant	J/kg · K, BTU/lbm-°R
$R_{l.e.}$	Blade leading-edge radius	m, in
\bar{R}	Universal gas constant	J/kmol · K
r	Mixture ratio (oxidizer to fuel) in liquid propellant rockets	—
r	Burning rate in solid propellant rockets	cm/s, in/s
r	Radius	m, ft
r	Cylindrical or spherical coordinate	—
r_h	Hub radius	m, ft
r_t	Tip radius	m, ft
r_m	Pitchline or mean radius $(r_h+r_t)/2$	m, ft
°R	Stage degree of reaction in turbomachinery	—
S	Entropy	J/K
S_L	Laminar flame speed	m/s, ft/s
S_T	Turbulent flame speed	m/s, ft/s
St	Stanton number	—
SN	Smoke number	—
s	Specific entropy	J/kg · K
s	Blade spacing	m, ft
t	Blade thickness	m, ft
t	Time	s, hr
t_{max}	Maximum blade thickness	m, ft
$t_{reaction}$	Reaction time scale in a combustor	ms
t_i	Ignition delay time	ms
t_e	Evaporation time scale in a combustor	ms
T	Static temperature	K, °R, °C, °F
T_t	Total temperature	K, °R, °C, °F
T_f	Reference temperature, 298.16 K	K, °R, °C, °F
T_g	Gas temperature	K, °R, °C, °F
T_c	Coolant temperature	K, °R, °C, °F

T_{af}	Adiabatic flame temperature	K, °R, °C, °F
T_{aw}	Adiabatic wall temperature	K, °R, °C, °F
Tu	Turbulence intensity, $[(u'^2 + v'^2 + w'^2)/3]^{1/2}/V_m$	—
u	Speed, velocity normal to a shock	m/s, ft/s
u	Gas speed	m/s, ft/s
u'_{rms}	Turbulent fluctuating speed (root mean square)	m/s, ft/s
\vec{U}	Rotational velocity vector of rotor; v-reg	m/s, ft/s
U_T	Blade tip rotational speed, ωr_t	m/s, ft/s
u', v', w'	Root mean square of fluctuating velocities in 3 spatial directions	m/s, ft/s
\bar{v}	Average gas speed in the mixing layer	m/s, ft/s
V	Volume	m^3, ft^3
V	Speed	m/s, ft/s
V_m	Mean speed (used in stall margin or turbulence intensity)	m/s, ft/s
V'	Relative speed used in the stall margin analysis	m/s, ft/s
V_c	Compressor or chamber volume	m^3, ft^3
V_p	Plenum volume	m^3, ft^3
W	Weight	N, lbf
W	Flame width in afterburner	m, ft
W	Width	m, ft
\vec{W}, W	Relative velocity vector, relative flow speed	m/s, ft/s
W_r, W_θ, W_z	Radial, tangential and axial velocity components in relative frame of reference	m/s, ft/s
w_c	Rotor specific work (rotor power per unit mass flow rate; ϕ/\dot{m})	J/kg, BTU/lbm
w	Specific work	J/kg, BTU/lbm
w	Tangential speed to an oblique shock	m/s, ft/s
w_p	Propellant weight	N, lbf
$W_{visc.}$	Rate of work done by the viscous force	W, BTU/s
X	Solid flow fraction in a rocket nozzle	—
X	Semimajor axis of an elliptic external cowl	m, ft
Y	Semiminor axis of an elliptic external cowl	m, ft
z	Axial coordinate in the cylindrical coordinate system	—
z	Airfoil camber	m, ft
z_{max}	Maximum airfoil camber	m, ft
x, y, z	Cartesian coordinates	—

Greek	Definition	Unit
α	Bypass ratio in a turbofan engine	—
α	Angle of attack	deg
α	Absolute flow angle with respect to the axial direction in turbomachinery	deg
$\Delta\alpha$	Flow turning angle across a stator blade section	deg
Δp	Pressure drop	Pa, psi
β	Plane oblique shock wave angle	deg
β	Relative flow angle with respect to the axial direction in turbomachinery	deg
β_m	Mean flow angle corresponding to an average swirl across a blade row	deg
$\Delta\beta$	Flow turning angle across a rotor blade section	deg
δ	Boundary layer thickness	m, ft
δ^*	Boundary layer displacement thickness	m, ft
δ	Ratio of total pressure to reference (standard sea level) pressure; p/p_{ref}	—

δ_T	Thermal boundary layer thickness	m, ft
δ^*	Deviation angle defined at the blade trailing edge, a cascade parameter	deg
$\Delta \bar{h}_f^0$	(Standard) molar heat of formation	J/kmol
Δh_f^0	(Standard) specific heat of formation	J/kg
ε	Tip clearance; slip factor in turbomachinery	—
ε	A small quantity ($\ll 1$)	—
ε_g	Emissivity of gas	—
κ	Coefficient of thermal conductivity	W/m · K
κ_1	Blade leading-edge angle in turbomachinery	deg
κ_2	Blade trailing-edge angle in turbomachinery	deg
π	Total pressure ratio	—
ω	Angular speed	rad / s, rpm
ϖ	Total pressure loss parameter in a cascade; $\Delta p_t/q_r$	—
ϕ	Spherical coordinate	—
ϕ	Equivalence ratio	—
ϕ	Diffuser wall divergence angle	deg
ϕ	Flow coefficient; C_z/U	—
φ	Camber angle, $\kappa_1 - \kappa_2$	deg
Φ	Cooling effectiveness parameter	—
γ	Ratio of specific heats	—
Γ	Circulation (of a vortex filament), blade circulation	m ² /s, ft ² /s
γ°	Cascade stagger angle or blade setting angle	deg
ρ	Fluid density	kg/m ³ , lbf/ft ³
μ	Coefficient of viscosity	N · s/m ²
μ	Mach angle	degree
ν	Kinematic viscosity $\equiv \mu/\rho$	m ² /s, ft ² /s
ν	Prandtl-Meyer angle	radians, degree
π_c	Compressor total pressure ratio	—
π_b	Burner total pressure ratio	—
π_d	Inlet total pressure recovery	—
π_n	Nozzle total pressure ratio	—
π_K	Temperature sensitivity of chamber pressure in solid rockets	%/K, %/F
Π_M	Mach index $\equiv U_T/a_{t1}$	—
θ	Flow angle, cylindrical or spherical coordinate	deg
θ	Nozzle exit flow angle (from axial direction)	deg
θ	Ratio of total temperature to the reference (standard sea level) temperature; T/T_{ref}	—
θ	Circumferential extent of the inlet spoiled or distortion sector	deg
θ^*	Momentum deficit thickness in the boundary layer	m
σ	Cascade or blade solidity; c/s , in turbomachinery	—
σ	Stefan–Boltzmann constant	W/m ² K ⁴
σ_p	Temperature sensitivity of burning rate in solid propellant grain	%/K, %/F
τ	Shear stress	Pa, lbf/ft ² , psi
τ	Total temperature ratio	—
τ	Characteristic timescale	s
τ_r, τ_s	Rotor torque, stator torque in turbomachinery	N · m, ft-lbf
τ_t	Turbine total temperature ratio, T_{t5}/T_{t4}	—
τ_λ	Cycle limit enthalpy ratio, $c_{pt}T_{t4}/c_{pc}T_0$	—
$\tau_{\lambda AB}$	Limit enthalpy ratio with afterburner, $c_{pAB}T_{t7}/c_{pc}T_0$	—
τ_{resident}	Resident timescale	ms

η_b	Burner efficiency	—
η_o	Overall efficiency	—
η_p	Propulsive efficiency	—
η_{prop}	Propeller Efficiency	—
η_L	Ideal Propeller Efficiency	—
η_{th}	Cycle or engine Thermal efficiency	—
η_d	Adiabatic efficiency of a diffuser	—
η_n	Adiabatic efficiency of a nozzle	—
ξ	Coordinate along the vortex sheet	—
ψ	Stage loading parameter; $\Delta h_t/U^2$	—
ψ	stream function	m ² /s, ft ² /s
∇	Vector operator, Del	m ⁻¹
∇p	Pressure gradient	bar/m
χ	Mole fraction	—
ζ	Propellant mass fraction	—

Subscripts

1, 2	Stations up- and downstream of a shock, or inlet and exit of a duct
C.S.	Control surface
C.V.	Control volume
e	Boundary layer edge
h	Hydraulic (in hydraulic diameter)
max	Maximum
n	Normal to an oblique shock
net	Net
r	Rotor, relative
rev	Reversible
s	Shock, shaft, stator
s	Isentropic
t	Total or stagnation
w	Wall
∞	Free stream

Superscripts

*	Sonic or critical state
---	-------------------------

Abbreviations and acronyms

ADEN	Augmented-Deflector Exhaust Nozzle
AGARD	Advisory Group for Aeronautical Research and Development
AGT	Allison Gas Turbine
AIAA	American Institute of Aeronautics and Astronautics
AR	Blade aspect ratio
AR	Diffuser area ratio
ASME	American Society of Mechanical Engineers
ATF	Altitude Testing Facility
ATP	Advanced Turboprop
AVGAS	Aviation Gasoline
BDC	Bottom Dead Center
BLING	Bladed ring

XXX Nomenclature

BLISK	Bladed disk
BMEP	Brake Mean Effective Pressure
BPR	Bypass ratio
BTDC	Before Top Dead Center
C–D	Convergent–divergent
CEV	Crew Exploration Vehicle
C.G.	Center of gravity
CFD	Computational fluid dynamics
CHT	Cylinder Head Temperature
CLP	Combustor Loading Parameter
CO	Carbon monoxide
C.V.	Control volume
C.S.	Control surface
CDA	Controlled-diffusion airfoil
CDP	Compressor Discharge Pressure
CR	Compression Ratio
DCA	Double-circular arc blade
DOC	Direct Operating Cost
E ³	Energy efficient engine
EGT	Exhaust Gas Temperature
EPA	Environmental Protection Agency
EPNL	Effective Perceived Noise Level
ET	External tank
FADEC	Full-Authority Digital Electronic (or Engine) Control
FMEP	Friction Mean Effective Pressure
GE	General Electric company
GNC	Guidance–navigation–control
GTF	Geared Turbofan
HPC	High-pressure compressor
HPT	High-pressure turbine
IC	Internal Combustion
IGV	Inlet guide vane
ICAO	International Civil Aviation Organization
IMEP	Indicated Mean Effective Pressure
IPC	Intermediate Pressure Compressor
ITAR	International Traffic in Arms Regulation
K–D	Kantrowitz–Donaldson inlet
LCA	Life Cycle Assessment
LE	Leading edge
LEO	Low-Earth Orbit
LHS	Left-hand side
LOX	Liquid oxygen
LPC	Low-pressure compressor
LPT	Low-pressure turbine
MAP	Manifold Absolute Pressure
MEP	Mean Effective Pressure
MFR	Inlet mass flow ratio
MCA	Multiple-circular arc blade
MEMS	Micro-electro-mechanical systems

MIT	Massachusetts Institute of Technology
MR	Mass ratio
NACA	National Advisory Committee on Aeronautics
NASA	National Aeronautics and Space Administration
NPR	Nozzle pressure ratio
NO _x	Nitric oxide(s)
N.S.	Normal shock
OPR	Overall pressure ratio
O.S.	Oblique shock
PDE	Pulse detonation engine
PR	Pressure ratio
PS	Pressure surface
P&W	Pratt & Whitney
P&WC	Pratt & Whitney Canada
RBCC	Rocket-based combined cycle
RJ	Ramjet
RMS	Root mean square (of a fluctuating signal, e.g. turbulence or total pressure distortion)
RR	Rolls-Royce
RAE	Royal Aeronautical Establishment
RHS	Right-hand side
RPV	Remotely Piloted Vehicle
SABRE	Synergetic Air Breathing Rocket Engine
SCRJ	Scramjet
SERN	Single Expansion Ramp Nozzle
Sfc	Specific fuel consumption (same as TSFC)
SM	Stall margin
SPL	Sound Pressure Level
SS	Suction surface
SSTO	Single-Stage to Orbit
STOL	Short Takeoff and Landing
SSME	Space Shuttle Main Engine
TBC	Thermal Barrier Coating
TDC	Top Dead Center
TE	Trailing edge
TF	Turbofan
TJ	Turbojet
TP	Turboprop
TPC	Thermal protection coating
TO	Takeoff
TSFC	Thrust specific fuel consumption
UAS	Uninhabited Aerial System
UAV	Uninhabited aerial vehicles
UCAV	Uninhabited combat air vehicle
UDF	Unducted fan
UHB	Ultra-high bypass
UHC	Unburned hydrocarbons
VCE	Variable Cycle Engine
VTOL	Vertical takeoff and landing

CHAPTER 1

Introduction



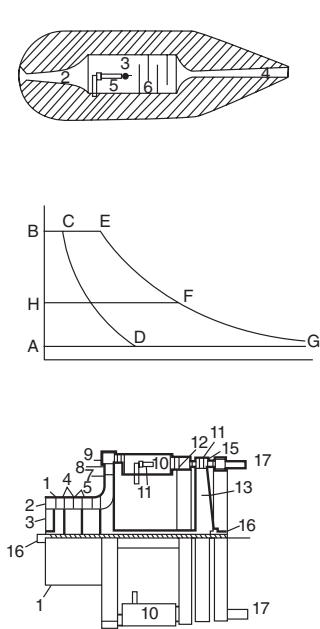
NASA Dryden Flight Research Center Photo Collection
<http://www.dfrc.nasa.gov/gallery/photo/index.html>
NASA Photo: EC99-44921-1 Date: 1999 (X-33 artist
concept - 1999)

1.1 History of the Airbreathing Jet Engine, a Twentieth-Century Invention—The Beginning

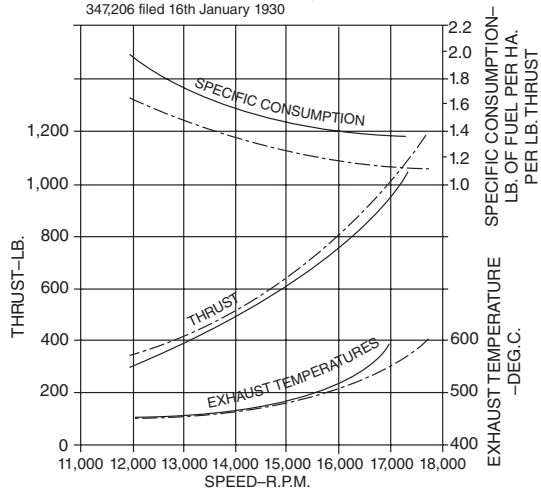
Powered flight is a twentieth-century invention. The era of powered flight began on December 17, 1903 with the Wright brothers who designed, fabricated, and flew “The Flyer” in Kitty Hawk, North Carolina. The power onboard The Flyer was a gas powered, 12-hp reciprocating intermittent combustion engine. This type of engine, with a propeller, provided power to all (manned) aircraft until late 1930s. The history of aircraft gas turbine engine started in January 1930 with a patent issued to Frank Whittle in Great Britain. Figure 1.1 shows a p - v diagram and components of the Whittle engine as they appeared in the patent application. The flow pattern and engine assembly are shown in Figure 1.2. The performance of the W1 engine and the aircraft that flew it are shown in Figure 1.3. An engineer at work, Sir Frank Whittle, the inventor of jet engine, with a slide rule is shown in Figure 1.4. For more details on the Whittle turbojet see Meher-Homji (1997).

The gas turbine engine of Figure 1.1 is based on the Brayton cycle. The compression in the Whittle engine is achieved via a double-sided centrifugal compressor. The axial compressor had not been developed due to aerodynamic stability complications. The combustion takes place in a reverse-flow burner that is very large relative to other engine components. The straight through-flow burner had posed problems with stable combustion and thus a reverse-flow combustor provided the needed flame stability in the burner. The compressor shaft power is delivered from a single-stage axial flow turbine.

■ **FIGURE 1.1**
Patent drawings of Sir Frank Whittle jet engine



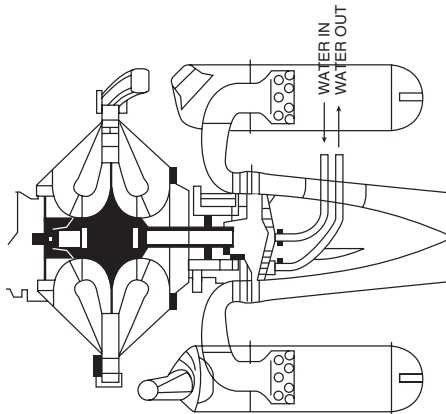
Reproduction of Drawings Illustrating British Patent No. 347,206 filed 16th January 1930



The W1 Engine: Curves of Thrust, Specific Fuel Consumption, and Exhaust Temperatures plotted against speed.

————— Test results
- - - - - "Desing" performance

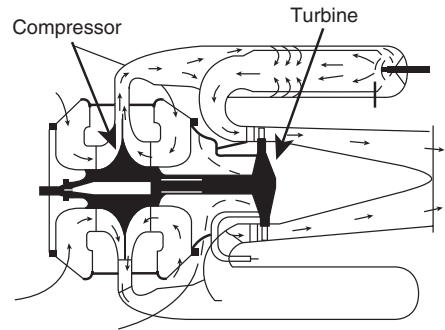
■ **FIGURE 1.2**
The assembly and flow pattern in Whittle jet engine



Assembly of W1 Engine. (Combustion chamber details not shown)

PROGRESS IN JET PROPULSION

The company formed by Whittle, known as Power Jets Ltd. produced the W.2.B. engine which was a classic of its type. It had the reverse flow combustion system which was typical of the Whittle designs. It was eventually developed to give nearly three times the thrust of the W.1 without occupying more space.



■ **FIGURE 1.3**
Performance testing of Whittle jet engine, known as W1, and the experimental aircraft, Gloster E28/39 that flew it in 1941. Source: Crown Publications



Gloster Experimental Aeroplane E28/39 at Takeoff. (Royal Aerospace Establishment, Crown Copyright.)

■ **FIGURE 1.4**
Sir Frank Whittle with a slide rule. Source: Crown Publications



■ **FIGURE 1.5**
The first historic meeting between the two inventors of the jet engine took place in WPAFB on May 3, 1978. Source: AFRL/AFMC



In an independent effort, Hans-Joachim Pabst von Ohain invented a turbojet engine in Germany that was granted a patent in 1936. In 1937, von Ohain's engine designated as the He S-1 turbojet engine with hydrogen fuel was tested and produced a thrust of 250 pounds at 10,000 rpm. Von Ohain's engine was the first to be developed ahead of the Whittle engine and flew on the first jet-powered aircraft, Heinkel 178, in 1939. Both Whittle and von Ohain are credited as the coinventors of airbreathing gas turbine engine. Figure 1.5 shows the two inventors of the jet engine, a historical meeting on May 3, 1978.

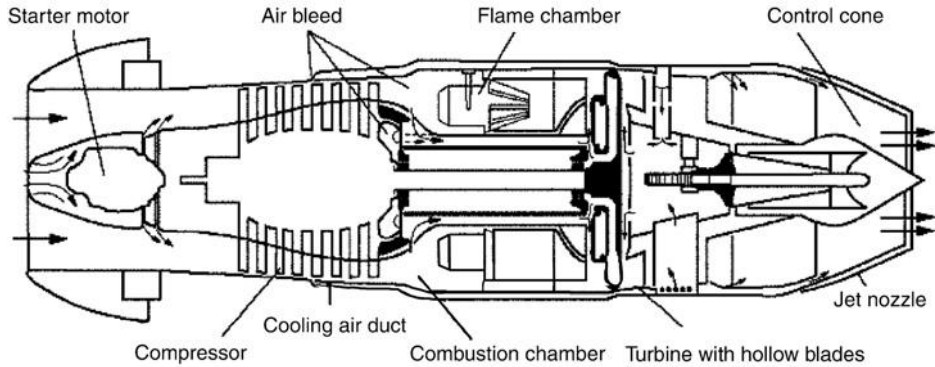
The first production jet aircraft was Messerschmitt Me 262, shown in Figure 1.6. Two Jumo 004B turbojet engines powered the Messerschmitt Me 262 jet fighter. The Me 262 first-flight was on July 18, 1942. Dr. Anselm Franz of the Junkers Engine Company designed the Jumo 004, which was based on von Ohain's patent. The Jumo 004B engine cutaway is shown in Figure 1.7. This engine has many modern gas turbine features such as axial-flow compressor and a straight throughflow combustor with air-cooling of the turbine and the nozzle. For more details see Meher-Homji (1996).

The drawing of the Jumo 004B turbojet engine in Figure 1.7 shows an air-cooling system that bleeds air from the compressor and cools the turbine and the exhaust nozzle. The engine produces ~2000 lb of thrust at an airflow of 46.6 lb/s. The engine pressure ratio is 3.14, turbine inlet temperature is 1427°F, and the specific fuel consumption is 1.4 lbm/h/lbf-thrust. The engine dry weight is ~1650 lb, its diameter and length are ~30 and 152 in., respectively. Engine component efficiencies are reported to be 78%

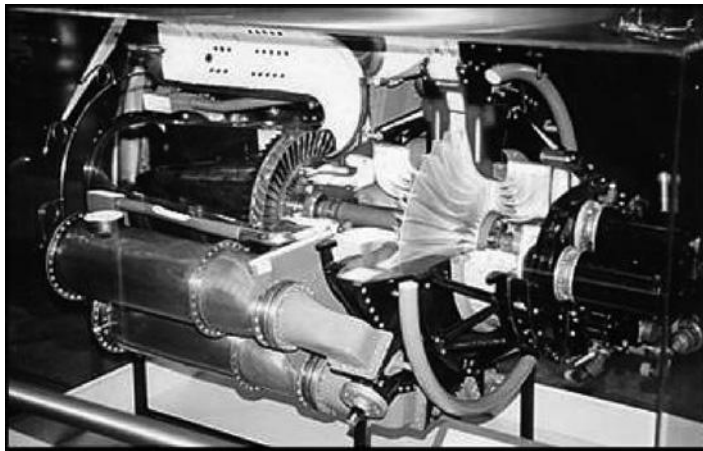
■ **FIGURE 1.6**
The first production jet aircraft, Me 262



■ **FIGURE 1.7** Jumo 004B engine cutaway features an axial-flow compressor, a straight throughflow combustor, an air-cooled axial turbine, and an exhaust nozzle



■ **FIGURE 1.8** The first U.S. produced aircraft gas turbine engine. Source: Courtesy of US Air Force Museum



compressor, 95% combustor, and 79.5% turbine. We will put these numbers in perspective when we compare them with their modern counterparts.

The jet engine came from Great Britain to the United States in 1941. The J-31 (also known by its company designation, I-16) was the first turbojet engine produced in quantity in the United States. It was developed from the General Electric I-A, which was a copy of the highly secret British “Whittle” engine. Figure 1.8 shows the J-31 gas turbine engine (courtesy of Air Force Museum).

1.2 Innovations in Aircraft Gas Turbine Engines

In this section, we introduce the most significant innovations in gas turbine industry since the introduction of aircraft jet engine by Whittle and von Ohain. Dawson (1991) and Wallace (1996) as well as the NASA websites (references 5 and 7) and publication (reference 8) should be consulted for further reading/information.

1.2.1 Multispool Configuration

In order to achieve a high-pressure compression system, two distinct and complementary approaches were invented in the United States. One is the multispool concept (developed

■ **FIGURE 1.9**
 Three-spool gas turbine engine as developed by Rolls-Royce. Source: *The Jet Engine*, 2005. Reproduced by permission from *The Jet Engine*, Copyright Rolls-Royce plc 2005



by Pratt & Whitney) and the second is variable stator (developed by GE). The multispool concept groups a number of compressor stages together in two or three groups, known as the low-pressure compressor (LPC), intermediate-pressure compressor (IPC), and high-pressure compressor (HPC). A different shaft that spins at different rotational speed drives each group. Figure 1.9 shows the Trent 1000, a modern Rolls-Royce engine that employs three spools.

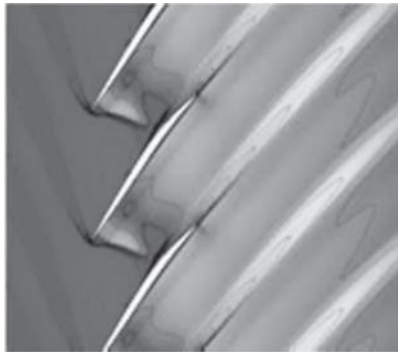
1.2.2 Variable Stator

The need to adjust the flow direction in a multistage high-pressure ratio compressor (in starting and off-design) prompted Gerhard Neumann of GE to invent variable stator. By allowing the stators to rotate in pitch, compressors can operate at higher pressure ratios and away from stall. Modern gas turbine engines use variable stators in their LPC and IPC. The high-temperature environment of HPC has not been hospitable to variable stators.

1.2.3 Transonic Compressor

Better understanding of supersonic flow and the development of high strength-to-weight ratio titanium alloy allowed the development of supersonic tip fan blades. The transonic fan is born at a high shaft speed that creates a relative supersonic flow at the tip and a subsonic flow at the hub. A modern transonic fan stage produces a stage pressure ratio of ~ 1.6 . The Jumo 004B produced a cycle pressure ratio of 3.14 with eight stages, which means an average stage pressure ratio of ~ 1.15 . Therefore to achieve a pressure ratio of 3.14, we need only two transonic fan stages instead of eight. The higher compression per stage has allowed a reduction in engine weight, size, and part-count and has improved reliability. The advances in computational fluid dynamics (CFD) and nonintrusive testing techniques have paved the way for a better understanding of supersonic flow in compressors. A compressor flow simulation is shown in Figure 1.10(a). The rotor passage shock, boundary layer interaction, and flow separation are clearly visualized in Figure 1.10(a). An advanced transonic fan is shown in Figure 1.10(b) from Rolls-Royce.

■ **FIGURE 1.10**
 (a) CFD in transonic compressor rotor flowfield. Source: Courtesy of NASA;
 (b) advanced transonic fan. Source: Reproduced with permission from Rolls-Royce plc



(a)



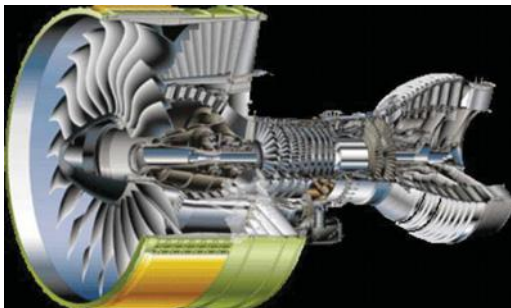
(b)

1.2.4 Low-Emission Combustor

The gas turbine combustor has perhaps seen the most dramatic innovations/changes since the Whittle reverse-flow burner. A better understanding of the combustion process, from atomization and vaporization of the fuel to mixing with air and chemical reaction, has allowed efficient combustion to take place in small spaces. For example, compare the relative length and volume of the combustor in GP7000, shown in Figure 1.11, to the Whittle engine or Jumo 004B.

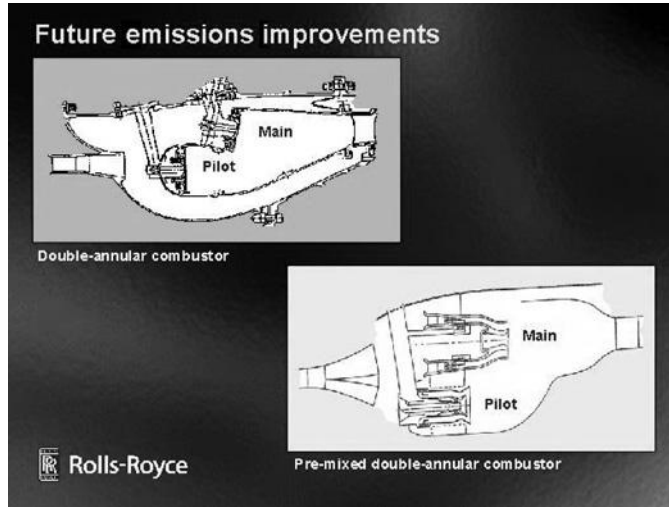
In the textbox of Figure 1.11, we note that the combustor emissions are characterized by their nitric oxide formation, the so-called NO_x , the unburned hydrocarbon (UHC) emission, and finally carbon monoxide formation in the exhaust nozzle flow. In order to achieve low levels of pollutant emissions, different concepts in “staged combustion” are developed by aircraft engine manufacturers (as shown in Figure 1.12).

■ **FIGURE 1.11**
 Engine Alliance engine GP7000. Source: Reproduced with permission from the Engine Alliance. [Note: Engine Alliance is a 50/50 joint venture between GE Aviation and Pratt & Whitney]



Engine Alliance engine: GP7000
T.O. Thrust: 76,500 lbs/340 kN
OPR: 36 ⁺ (on GP7200)
BPR (cruise): 8.7
Fan Diameter: 116.7 in.
Emissions:
NO_x : 59.7 g/kN
UHC: 3.9 g/kN
CO: 33.8 g/kN
Noise: 22.9 dB Margin to Stage 3

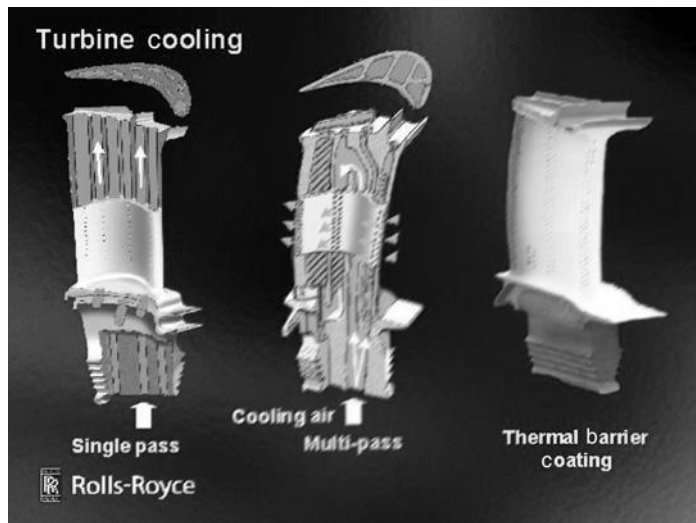
■ FIGURE 1.12 Concepts in low-emission combustor design. Source: Reproduced with permission from Rolls-Royce plc



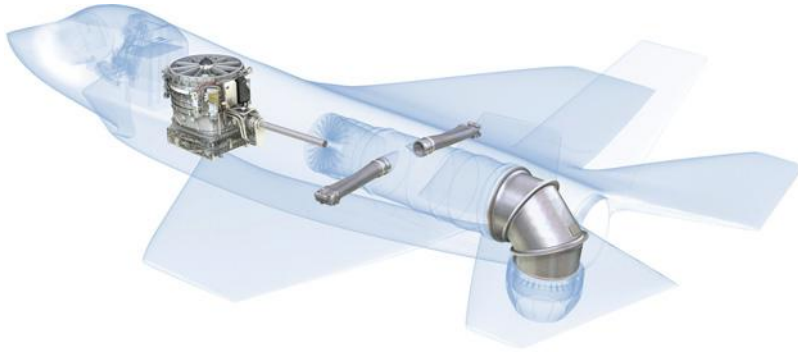
1.2.5 Turbine Cooling

The need to cool the turbine stems from being able to operate the combustor at higher temperature (to produce more thrust) and to achieve turbine durability, that is, an improved component life. The first production turbojet engine, Jumo 004B, utilized internal cooling for the turbine blades. So, the concept is as old as the turbojet engine itself. Improved manufacturing techniques and better understanding of the flow physics involved in coolant ejection, mixing with hot gas, and three-dimensional flow in turbines have allowed for a rationed approach to coolant usage as well as component life enhancement. Figure 1.13 shows a single-and a multipass internal cooling of a turbine blade that incorporates film cooling as well as the thermal protection (or barrier) coating (TPC or TBC) to reduce the heat transfer to turbine blades.

■ FIGURE 1.13 Turbine blade cooling. Source: Reproduced with permission from Rolls-Royce plc



■ **FIGURE 1.14**
 Propulsion layout for
 vertical landing and
 stability of F-35 Joint
 Strike Fighter. Source:
 Reproduced with
 permission from
 Rolls-Royce plc



1.2.6 Exhaust Nozzles

The concept of an exhaust nozzle for aircraft jet engine has changed from a simple convergent duct that was used to propel the hot exhaust gases to a variable-geometry and multitasked component in modern designs. The new tasks involve thrust reversing, thrust vectoring, noise suppression, and dynamic stability enhancement of maneuvering aircraft. To achieve these goals, advancements in nozzle cooling, actuation, and manufacturing had to be realized. Figure 1.14 shows a sophisticated propulsion layout (and nozzle system) in F-35 aircraft that has vertical takeoff/landing (VTOL) capability as well as roll control in hover. Figure 1.15 shows a $\pm 20^\circ$ vector thrust in F119 engine developed by Pratt & Whitney for F-22 “supercruise” aircraft.

1.2.7 Modern Materials and Manufacturing Techniques

Nonmetallics and composite materials represent a sizable change in modern material usage in aircraft and jet engines. Metal matrix composites technology offers a high strength-to-weight ratio relative to titanium and nickel superalloys suitable for fan blades. Single crystal turbine blades offer more resistance to vibration and thus fatigue failure. A manufacturing technique that utilizes a honeycomb core with a composite skin offers weight and stress reductions in fan blades. Compressor weight savings are derived from bladed disk “Blisk” and bladed ring “Bling” manufacturing technology. All these are shown in Figure 1.16.

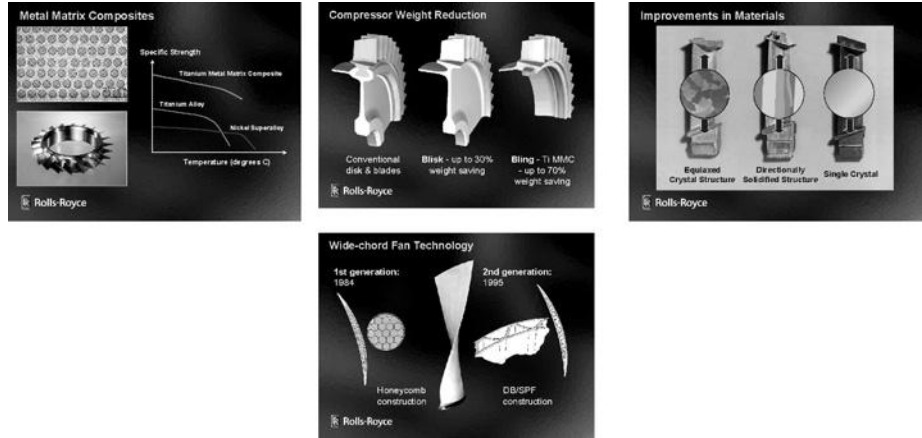
An example of a modern engine is EJ200, which powers the “Eurofighter” Typhoon (shown in Figure 1.17). Its design features are tabulated in Table 1.1.

The modern materials and the manufacturing techniques that we have discussed are described in Table 1.1. Compare the turbine inlet temperature (T_{14}) in EJ200 and Jumo 004B, or thrust-to-weight ratio.

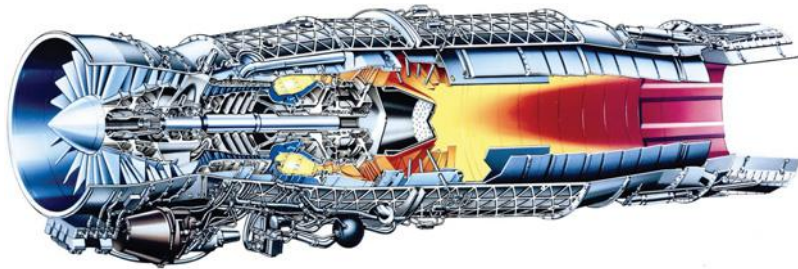
■ **FIGURE 1.15**
 F119 engine that
 powers F-22 Raptor is
 shown in vector thrust.
 Source: Reproduced
 with permission of
 United Technologies
 Corporation, Pratt &
 Whitney



■ **FIGURE 1.16**
Advanced materials and manufacturing techniques. Source: Reproduced with permission from Rolls-Royce plc



■ **FIGURE 1.17**
Cutaway of EJ200, an afterburning turbofan engine designed for the Eurofighter. Source: Reproduced with permission from Rolls-Royce plc



■ **TABLE 1.1**
EJ200 Specifications

Two-spool configuration		Fan/compressor stages	1/3/5
Fan technology		LPT/HPT	1/1
Wide chord		Max. diameter	29 in.
Single-crystal “Blisk” (Bladed Disk)		OPR	26:1
No IGV		BPR	0.4
Three-stage LPC:	4.2 PR	Length	157 in.
Mass flow:	77 kg/s or 170 lbm/s	Dry weight	2,286 lbf
HPC:	Single crystal Blisk	Sfc (max. power)	0.81 lbm/h/lbf
T_{t4} :	1800 K (or 2780°F)	Sfc w. AB	1.75 lbm/h/lbf
HPT:	Air-cooled + TPC (two-layers)	Thrust (SL)	13,500 lbf
C-D nozzle:	Titanium alloy	Thrust w. AB	20,250–22,250 lbf
		Thrust/weight (Dry)	5.92
		Thrust/weight (AB)	9.1
		Thrust vectoring:	23° any direction
		Engine management	FADEC + monitoring unit

1.3 New Engine Concepts

In this section, we examine a few modern concepts in aircraft propulsion. The first one deals with advanced turboprop (ATP) and geared turbofan (GTF) engines. The ATP pushes the frontier of turboprops from low speed flight into high subsonic cruise Mach numbers ($M_0 \sim 0.8$) and GTF allows turbofan engines to use a gearbox and achieve high-efficiency ultra-high bypass ratio capability, the so-called UHB (for ultra-high bypass). Next, we present an exciting airbreathing rocket, the Single-Stage to Orbit (SSTO) engine that is under promising development in the United Kingdom. The next two concepts harness unsteadiness as a means of thrust production. The fourth is a triumph of microelectromechanical (MEM) device manufacturing. The rest are combined cycles.

1.3.1 Advanced Turboprop (ATP) and Geared Turbofan (GTF)

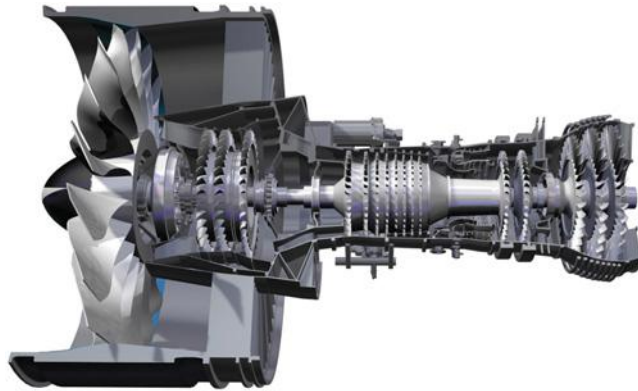
Conventional propellers lose their thrust production capability when their tip operates in supersonic flow and stalls. In the United States, Pratt & Whitney/Allison Gas Turbine, GE Aviation and NASA collaborated in developing the technology of advanced turboprop engines in the 1970s and 1980s. These engines are generally called Propfan, while GE's gearless, direct-drive ATP is called the Unducted Fan (UDF). The advanced propellers operate with relative supersonic tip Mach number ($M_T \sim 1.1-1.15$) without stalling! With increasing capability in relative tip Mach number of the propeller, the cruise flight Mach number is increased to $M_0 \sim 0.8-0.82$. Several configurations in co- and counterrotating propeller sets and pusher versus tractor configurations were developed and tested. The advanced propellers are highly swept at the tip (between $30-40^\circ$) to improve tip efficiency at high relative Mach numbers. Figure 1.18 shows an ATP. Courtesy of GE Aviation and NASA.

The technology of the ultra-high bypass (UHB) turbofan engine developed at Pratt & Whitney utilizes an advanced gear system that improves low-pressure spool operating efficiency. The fan pressure ratio in UHB engines is reduced to accommodate bypass ratios of 12^+ , which improves propulsive efficiency, cuts down on fuel consumption, and

■ **FIGURE 1.18**
GE Unducted Fan
(UDF) or GE-36.
Source: Reproduced
with permission from
General Electric
Company



■ **FIGURE 1.19**
Cutaway view of the
PW1000G UHB geared
turbofan engine.
Source: Reproduced by
permission of United
Technologies
Corporation, Pratt &
Whitney



reduces jet noise and engine emissions. The first single-aisle transport aircraft equipped with GTF entered service in 2013. The engine architecture is readily scalable to include widebody aircraft thrust levels as well. Figure 1.19 shows the cutaway of the P&W GTF engine, that is, the PW1000G geared turbofan engine family. The advanced fan gear system on the low-pressure spool is visible in Figure 1.19 (trimetric view).

1.3.2 Advanced Airbreathing Rocket Technology

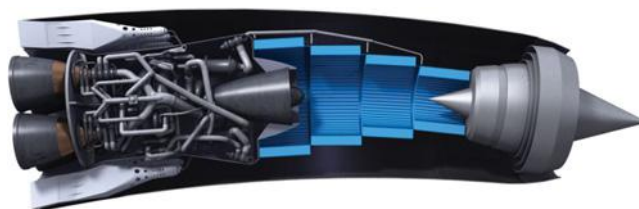
An ultra-light weight precooler heat exchanger uses a closed-cycle Helium loop to cool the air from 1000 to -150°C in a fraction of a second (actually in 10 ms). This innovative counterflow precooler/heat exchanger technology is at the heart of an innovative airbreathing rocket engine that is capable of horizontal takeoff, climb, acceleration to Mach 5⁺ using subcooled air in its rocket engines and then transition to pure rocket mode above 20⁺ km altitude. The air intake system uses a translating cone which completely closes the inlet in the pure rocket mode. Due to its versatility, this combined cycle engine is dubbed *SABRE*—Synergetic Air Breathing Rocket Engine—and is being developed by Reaction Engines Ltd. in the United Kingdom (Figure 1.20). At the time of this writing, the critical components of SABRE are undergoing testing and with promising results.

The reusable SSTO winged aerospace plane that is designed around SABRE technology is in its early development phase; it is called SKYLON. The configuration of

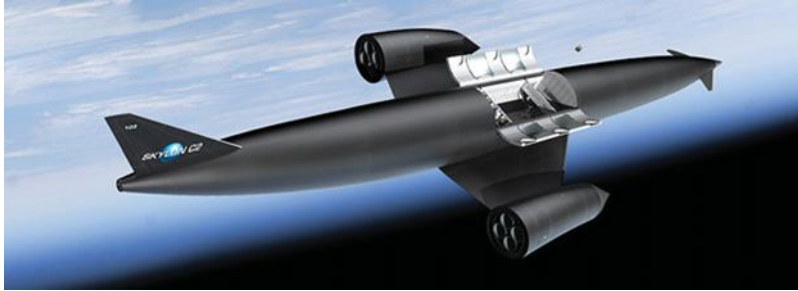
■ **FIGURE 1.20**
Cutaway of SABRE
shows the counterflow
heat exchanger
integrated in the air
intake system. Source:
Reproduced by
permission of Reaction
Engines

Pure rocket mode to Mach 25 orbital
speeds and 300 km circular orbit

Airbreathing rocket mode up to
Mach 5.5 at 20+ km altitude



■ **FIGURE 1.21**
SKYLON in
Low-Earth Orbit, with
open payload bay.
Source: Reproduced by
permission of Reaction
Engines



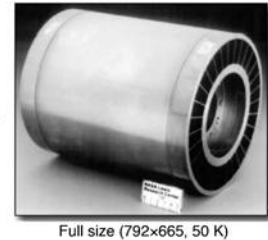
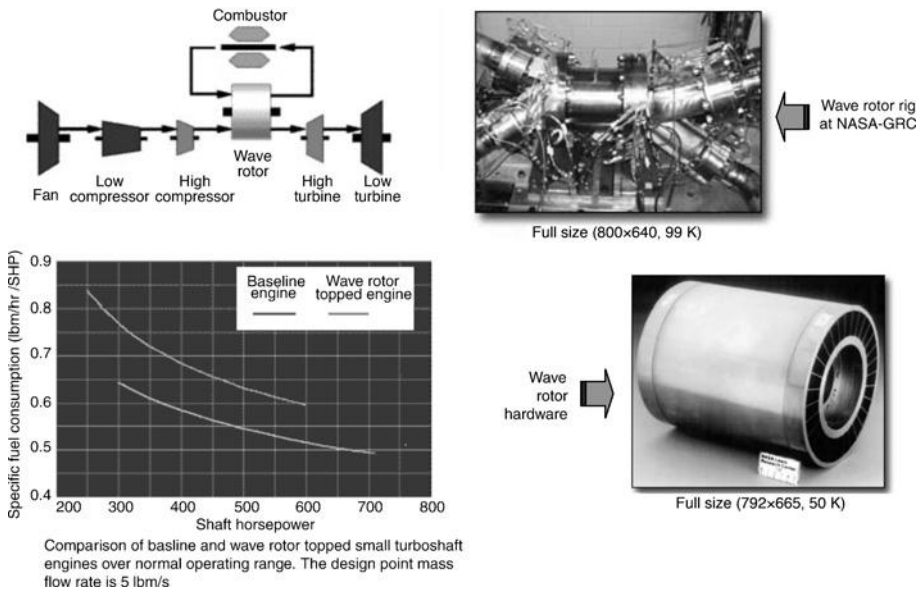
this vehicle is shown in Figure 1.21. Extensive technical information on SABRE and SKYLON can be found on the Reaction Engines website.

1.3.3 Wave Rotor Topping Cycle

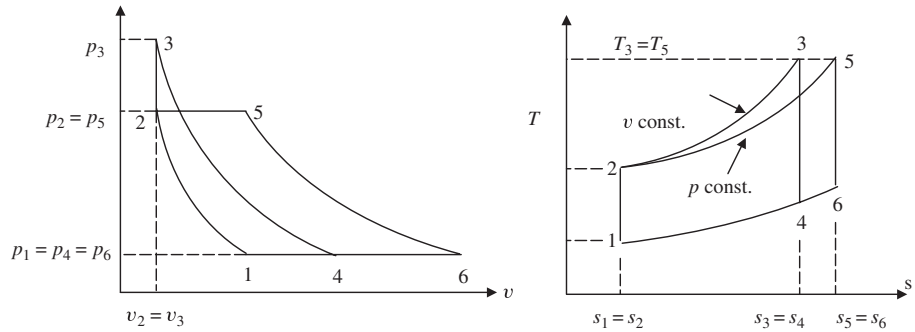
Wave rotor creates a pressure gain in the combustor, instead of the baseline pressure drop, thereby enhances cycle efficiency. As a simple example of a higher efficiency cycle that takes advantage of constant-volume combustion, we may examine the Humphrey cycle. Schematics of the wave rotor topping cycle concept, a wave rotor hardware, and a test rig at NASA-Glenn Research Center are shown in Figure 1.22. A performance chart of the wave rotor topping cycle for small turboshaft engines, also in Figure 1.22, shows nearly 10% fuel savings compared with a baseline engine.

1.3.3.1 Humphrey Cycle versus Brayton Cycle. An ideal Humphrey cycle is shown in Figure 1.23 in a pressure–volume and temperature–entropy diagrams. Combustion takes place at constant volume in a Humphrey cycle, whereas it takes place at

■ **FIGURE 1.22**
Schematics of the wave
rotor topping cycle wave
rotor hardware and a
test rig at NASA.
Source: Courtesy of
NASA



■ **FIGURE 1.23**
Constant-volume and
constant-pressure
combustion cycles



constant pressure in an ideal Brayton cycle. We utilize the definition of cycle efficiency and thermodynamic principles to get Brayton and Humphrey cycle efficiencies.

Cycle efficiency of a constant-pressure combustion (Brayton) cycle: 1–2–5–6–1, is:

$$\eta_{th} = 1 - \frac{T_1}{T_2}$$

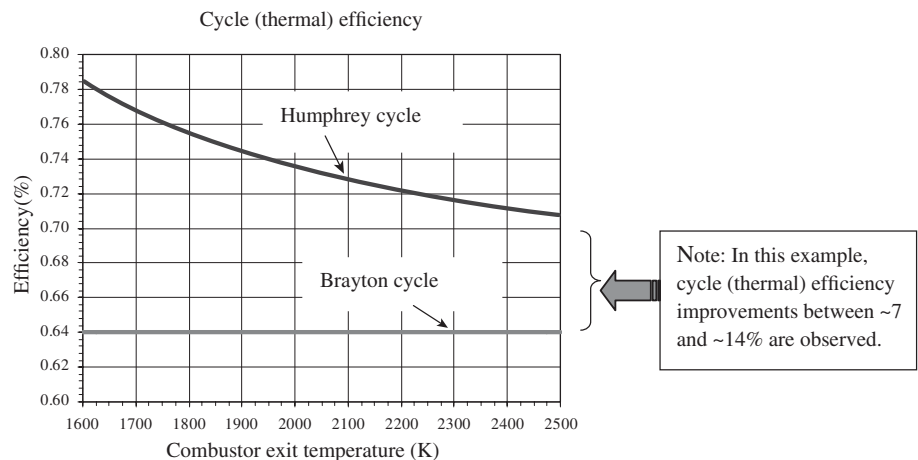
The cycle efficiency of a constant-volume combustion (Humphrey cycle: 1–2–3–4–1) is:

$$\eta_{th} = \frac{1 - \gamma \frac{T_1}{T_2} \left[\left(\frac{T_3}{T_2} \right)^{\frac{1}{\gamma}} - 1 \right]}{\left[\frac{T_3}{T_2} - 1 \right]}$$

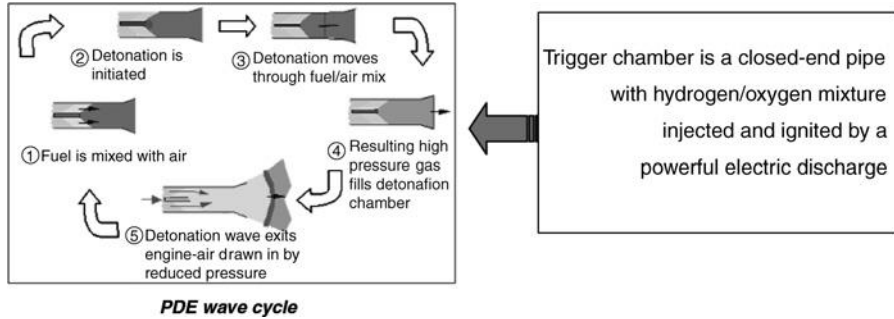
where γ is the ratio of specific heats.

Cycle efficiency in Humphrey cycle depends on T_1/T_2 and on the temperature ratio T_3/T_2 (in effect p_3/p_2). Figure 1.24 shows the ideal cycle thermal efficiency of a Brayton

■ **FIGURE 1.24**
Ideal thermal
efficiency of Humphrey
and Brayton cycles for
 $\gamma = 1.4$, and $T_1 = 288$ K,
 $T_2 = 800$ K, and T_3
that varies between
1600 and 2500 K



■ **FIGURE 1.25**
The Pulse Detonation engine with a trigger chamber. Source: Courtesy of NASA



and a Humphrey cycle for $T_1 = 288$ K, $T_2 = 800$ K, and T_3 that varies between 1600 and 2500 K, for $\gamma = 1.4$.

Note: In this example, cycle (thermal) efficiency improvements between ~7% and ~14% are observed.

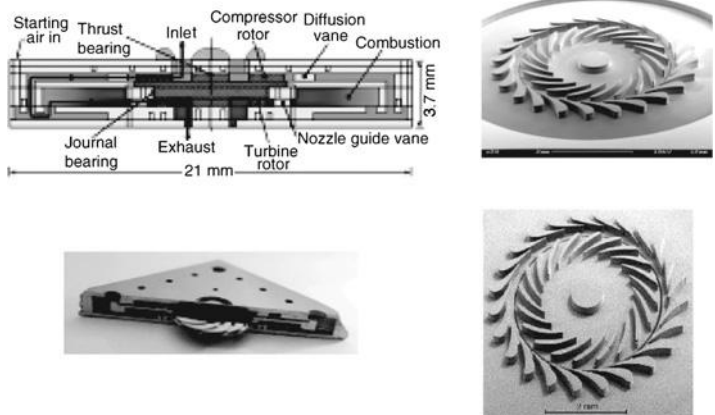
1.3.4 Pulse Detonation Engine (PDE)

The Pulse Detonation Engine (PDE) is a constant-volume combustion ramjet that is capable of producing static thrust. The operation of a PDE is similar to a pulsejet except combustion in a pulsejet is based on the principle of deflagration that is a slow wave front with low-pressure ratio. The PDE creates a detonation wave, which is akin to an explosion that creates high-pressure shock waves. To get a feel for how often these explosions occur, we note the frequency of these explosions that is ~60 detonations per second. The PDE wave cycle is shown in Figure 1.25.

1.3.5 Millimeter-Scale Gas Turbine Engines: Triumph of MEMS and Digital Fabrication

Microchip manufacturing techniques and some vivid imaginations have given birth to millimeter-scale gas turbine engines. Figure 1.26 shows a “button” size gas turbine engine

■ **FIGURE 1.26**
Millimeter-scale gas turbine engine with the rotor and external shell. Source: Courtesy of MIT Gas Turbine Laboratory

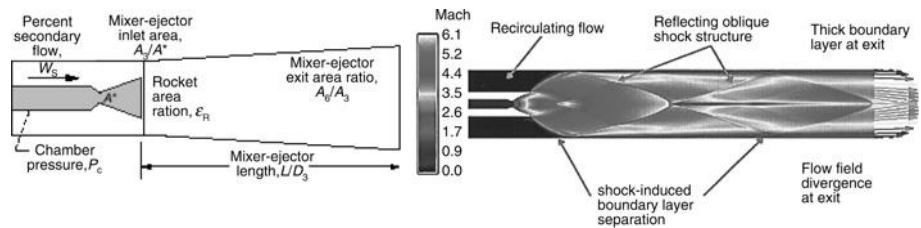


that is designed, manufactured, and tested at MIT. At these scales, the rotor has to spin at $\sim 1,000,000$ rpm to achieve the needed compression for the cycle. The process of fuel injection, atomization, vaporization, and combustion is a challenge among the myriad of other mechanical challenges in the manufacturing of millimeter-scale gas turbine engine.

1.3.6 Combined Cycle Propulsion: Engines from Takeoff to Space

We have examined the SABRE technology in SSTO in a previous section (1.3.2). In this section, we examine other concepts in single-stage to orbit propulsion systems. There are several developments that address combined cycles as a means of producing efficient propulsion over a wide range of flight speeds, typically from takeoff to hypersonic Mach numbers. An example of this approach is found in the airbreathing rocket engine, which is a Rocket-Based Combined Cycle (RBCC) engine. At takeoff where conventional ramjets are incapable of producing thrust, a rocket is fired (with an ejector nozzle configuration to get a thrust boost) that accelerates the vehicle to, say, Mach 2. At Mach 2, the rocket is turned off and air intakes are opened to start a subsonic ramjet engine operation. The airbreathing engine switches from the subsonic to supersonic combustion ramjet (scramjet) near Mach 5. The scramjet will accelerate the vehicle to, say, Mach 15. The air intakes close at Mach 15 and rocket operation resumes accelerating the vehicle to orbital speeds (\sim Mach 25 or higher). The rocket with the ejector nozzle and computational results of Mach contours are shown in Figure 1.27. An RBCC engine is capable of reducing launch costs by two orders of magnitude. An artist's concept of the vehicle is shown in Figure 1.28. An RBCC flight weight engine system test was conducted in 2006. Figure 1.29 shows the test firing of the airbreathing rocket.

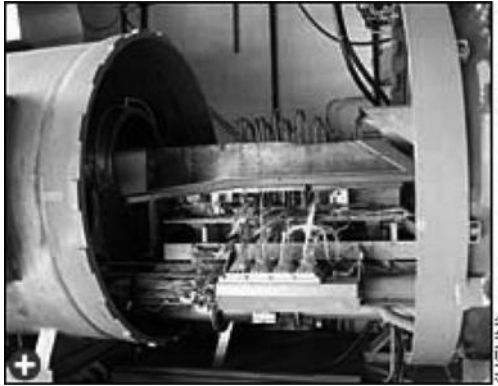
■ **FIGURE 1.27**
An RBCC
air-augmented rocket
with an ejector nozzle
(with Mach contours
computed). Source:
Courtesy of NASA



■ **FIGURE 1.28**
Artist's drawing of an
advanced launch
vehicle using RBCC
propulsion. Source:
Courtesy of NASA



■ **FIGURE 1.29**
 Testing of an
 airbreathing rocket at
 NASA. Source:
 Courtesy of NASA



1.4 New Vehicles

There are exciting new vehicles on the drawing board for many different missions at many different speeds. The interest in uninhabited aerial vehicles (UAVs) has prompted new configurations such as the Northrop–Grumman X-47 “Pegasus,” or the tailless agility aircraft X-36 from Boeing, or the X-45A Unmanned Combat Air Vehicle (UCAV), or the X-48 using Blended Wing-Body technology. NASA’s interest in hypersonic flight and scramjet propulsion has prompted the X-43 series of technology demonstrator vehicles. Some of these aircraft are shown in Figure 1.30.

1.5 Summary

There are exciting developments in aerospace propulsion and vehicle design:

- Physics-based computer simulation/design
- Advanced composite materials
- Digital fabrication and manufacturing will take unprecedented precision from nano-scale up, including 3-D printing and digital assembly
- Exciting new vehicles on the horizon
- Hybrid and electric propulsion for light aircraft, e.g., UAVs
- NASA X-planes are back!
- Harnessing unsteadiness as a means of propulsion
- Synergetic Airbreathing Rocket Engine (SABRE) technology
- High-efficiency, low-emission, quiet engines for transport aircraft, e.g., PW1000G, geared ultra-high bypass turbofan engine
- Rocket-based combined cycle propulsion: from takeoff to orbit!
- New lunch vehicles and missions for hypersonic aircraft and space exploration

■ **FIGURE 1.30**
Uninhabited aerial
vehicles and NASA
X43 technology
demonstrators. Source:
Boeing and NASA.
Reproduced with
permission.



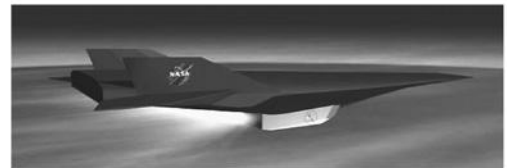
Boeing X-45A UCAV



Boeing X-36



Boeing X-48B



NASA X43-A Mach 10 airbreathing
technology demonstrator



NASA X43-B technology demonstrator



NASA X43-C technology demonstrator

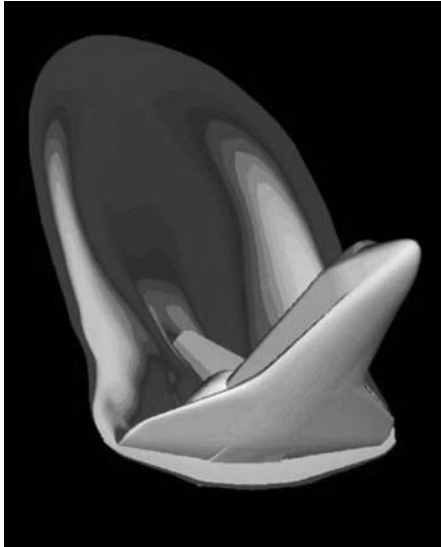


Boeing X-48A

- “There’s a lot of room at the bottom” Richard Feynman said. Enter MEMS-GT engines!
- Manned-mission to Mars
- US-Europe-China-Russia active in commercial space race!

An additional example of computational flow simulation is shown in Figure 1.31.

■ **FIGURE 1.31**
Flowfield simulations
around the Space
Shuttle in reentry
using computational
fluid dynamics.
Source: Courtesy of
NASA

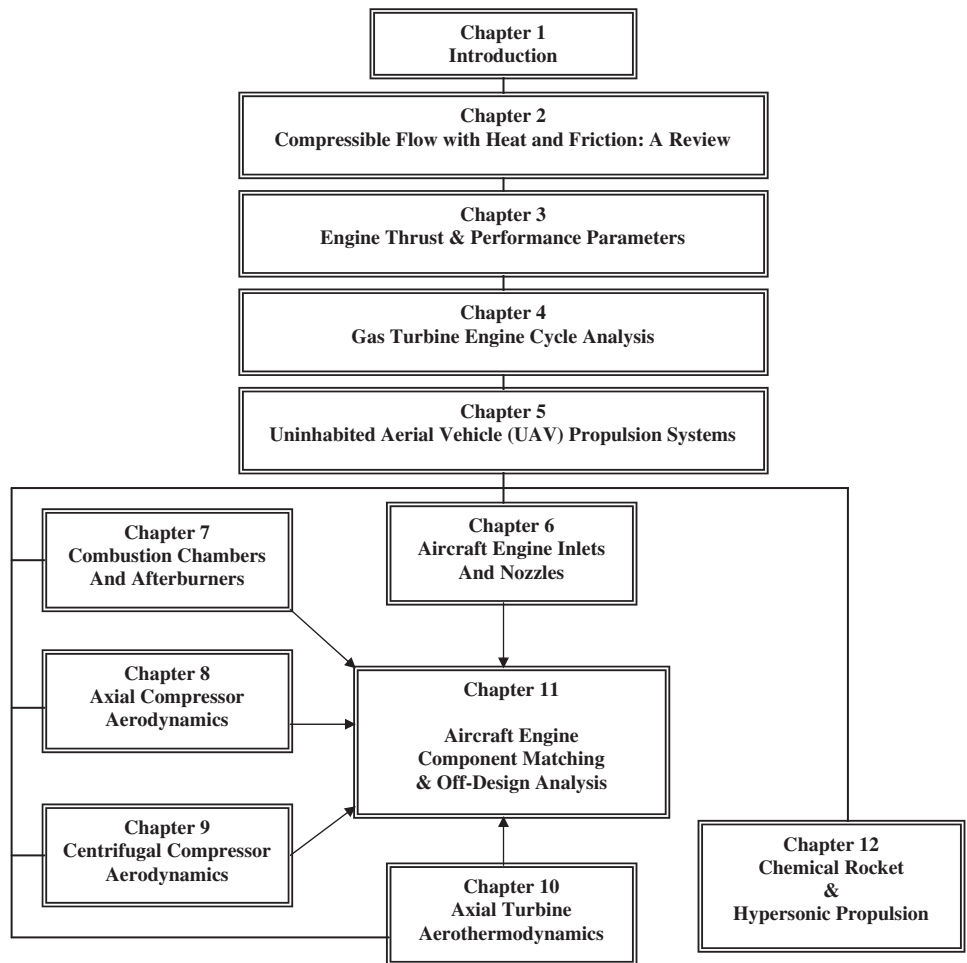


1.6 Roadmap for the Second Edition

We begin our studies in propulsion with a review of compressible flow that involves friction and heat transfer in Chapter 2. Engine thrust and performance parameters are discussed in Chapter 3 where rigorous derivation of uninstalled thrust and installation effects are presented. Gas turbine engine cycle analysis both for ideal and real components are studied in Chapter 4, including a new section on propeller theory and a section on Ultra-High Bypass (UHB) engines. The Uninhabited Aerial Vehicle (UAV) propulsion system is new to the second edition and is presented in Chapter 5. Aircraft engine inlets and nozzles, over a wide speed range, are analyzed in Chapter 6. A new section on jet noise and the Chevron Nozzle is added to Chapter 6. The principles of combustion are detailed in Chapter 7. The specific characteristics of the primary and afterburners, as in flameholding, are discussed in the same chapter. A discussion of alternative jet fuels from renewable sources is also included in Chapter 7. The turbomachinery principles and their application to axial-flow compressor, centrifugal compressor and the axial-flow turbine are extensively derived and discussed in Chapters 8 through 10. Additional design guidelines are added to turbomachinery chapters. Chapter 11 aims to integrate all the gas turbine engine components into a unified system, from component matching to engine off-design analysis. The new material in this chapter includes the principles of engine performance testing. Chapter 12 is dedicated to chemical rocket and hypersonic propulsion where rockets, ramjets, scramjet and combined cycles are discussed. An overview of available computational and online resources and links, related to propulsion, is also assembled in a separate appendix. Two new appendices are added to the book, namely Appendix K, where 45 ten-minute quizzes are listed for use by the instructors and the students, and Appendix L, where aircraft propulsion “Rules of Thumb” and trends are listed for information and quick reference.

Aircraft Propulsion

Roadmap to the Second Edition



References

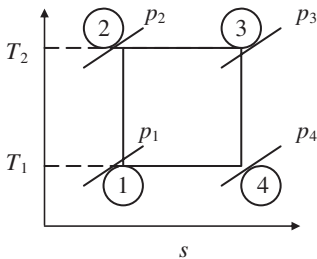
1. Dawson, V.P., *Engines and Innovation: Lewis Laboratory and American Propulsion Technology*, NASA SP-4306, 1991.
2. Meher-Homji, C.B., "The Development of Junkers Jumo 004B—The World's First Production Turbojet," ASME Paper No. 96-GT-457, 1996.
3. Meher-Homji, C.B., "The Development of Whittle Turbojet," ASME Paper No. 97-GT-528, 1997.
4. Meher-Homji, C.B., "Pioneering Turbojet Developments of Dr. Hans von Ohain—From HeS 01 to HeS 011," ASME Paper No. 99-GT-228, 1999.
5. NASA History Division's website: <http://history.nasa.gov/> (last accessed 16 November 2013).
6. Wallace, L.E., *Flights of Discovery: Fifty Years at the NASA Dryden Flight Research Center*, National Aeronautics and Space Administration, Washington, DC, 1996.
7. <http://www.nasa.gov/centers/dryden/news/FactSheets> (last accessed 16 November 2013).
8. "Celebrating a Century of Flight," NASA Publication SP-2002-09-511-HQ.
9. The website of Reaction Engines Ltd is www.reactionengines.co.uk (last accessed 16 November 2013).

Problems

1.1 The Carnot cycle sets the limit on thermal efficiency of a heat engine operating between two temperature limits. Show that ideal Carnot efficiency is

$$\eta_{th} = 1 - \frac{T_1}{T_2}$$

What is the thermal efficiency if $T_1 = 288 \text{ K}$ and $T_2 = 2000 \text{ K}$?

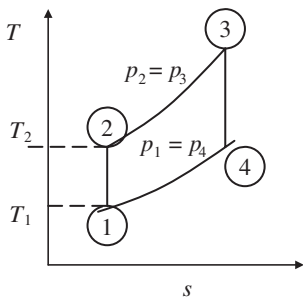


■ FIGURE P1.1

1.2 The ideal Brayton cycle operates between two pressure limits as shown. It is the model of an airbreathing jet engine, such as a turbojet or ramjet engine. Show that ideal Brayton cycle efficiency is

$$\eta_{th} = 1 - \frac{T_1}{T_2}$$

What is the thermal efficiency of the Brayton that has $T_1 = 288 \text{ K}$ and $T_2 = 864 \text{ K}$? Note that maximum cycle temperature T_3 has no effect on cycle thermal efficiency.



■ FIGURE P1.2

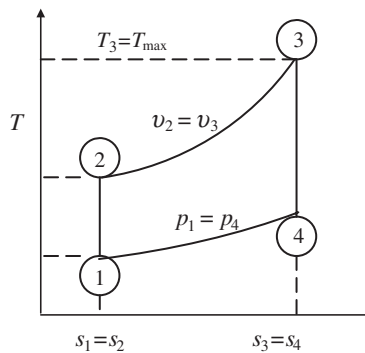
1.3 The Humphrey cycle operates a constant-volume combustor instead of a constant-pressure cycle like the Brayton cycle. Show that

$$\eta_{th} = 1 - \gamma \frac{T_1}{T_2} \left[\left(\frac{T_3}{T_2} \right)^{\frac{1}{\gamma}} - 1 \right] \bigg/ \left[\frac{T_3}{T_2} - 1 \right]$$

is the thermal efficiency of an ideal Humphrey cycle (as shown).

Let us use the same T_1 as in Problems 1.1 and 1.2, that is, $T_1 = 288 \text{ K}$. Let us use the same temperature T_2 as in Problem 1.2, that is, $T_2 = 864 \text{ K}$.

Finally, let us use the same maximum cycle temperature as in Carnot (Problem 1.1), that is, $T_{max} = 2000 \text{ K}$. With the ratio of specific heats $\gamma = 1.4$, calculate the thermal efficiency of the Humphrey cycle. Compare the answer with Brayton cycle efficiency.



■ FIGURE P1.3

1.4 The rotor of a millimeter-scale gas turbine engine has a radius of 1 mm. It has to reach a tip, or rim speed of nearly the speed of sound for an effective compression. Assuming that the speed of sound is 340 m/s, calculate the rotor rotational speed in revolutions per minute (rpm).

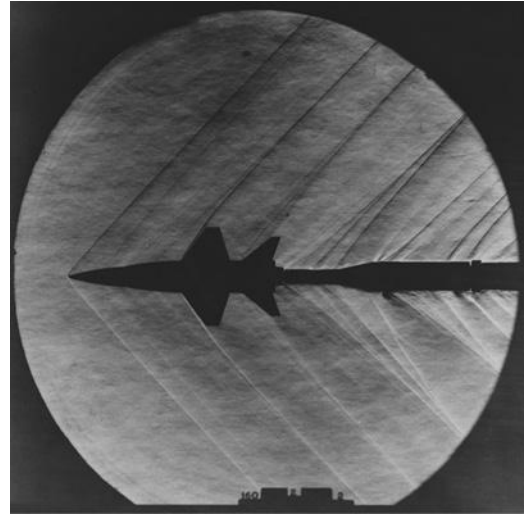
1.5 Specific fuel consumption (sfc) projects the fuel economy of an engine, that is, it measures the fuel flow rate (say in pound-mass per hour or g/s) that leads to a production of a unit thrust (say 1 pound-force or 1 Newton). Two sets of numbers are copied from Table 1.1 (from EJ200 specification), which are

Sfc (max. power)	0.81 lbm/h/lbf
Sfc w. AB	1.75 lbm/h/lbf
Thrust (SL)	13,500 lbf
Thrust w. AB	20,250–22,250 lbf

First note that afterburner (AB) use more than doubles the fuel consumption while boosting the thrust by only ~50%. This explains the sparse use of an afterburner in aircraft mission. Now to quantify, calculate the amount of additional fuel burned in 30 min of afterburner use (producing 21,000 lbf thrust) as compared with 30 min of no afterburner use (producing 13,500 lbf thrust).

CHAPTER 2

Compressible Flow with Friction and Heat: A Review



Schlieren visualization of waves around an X-15 model in a supersonic wind tunnel. Source: Courtesy of NASA

2.1 Introduction

The study of propulsion is intimately linked to the understanding of internal fluid mechanics. This means that duct flows are of prime interest to propulsion. The physical phenomena in a real duct include the following effects:

- Friction
- Heat transfer through the walls
- Chemical reaction within the duct
- Area variation of the duct
- Compressibility effects, e.g. appearance of shocks

The laws of thermodynamics govern the relationship between the state variables of the gas, namely density ρ , pressure p , absolute temperature T , entropy s , internal energy e , and derived properties such as enthalpy h and specific heats at constant pressure and volume, c_p and c_v , respectively. In addition to the laws of thermodynamics, the fluid flow problems need to obey other conservation principles that were introduced in Newtonian mechanics. These are conservation of mass and momentum as described in classical mechanics. Since the study of gas turbine engines and propulsion in undergraduate curricula in mechanical and aerospace engineering follows the introductory courses in thermo-fluid dynamics, we shall review only the principles that have a direct impact on our study of jet engines.

The purpose of this chapter is thus to provide a review of the working principles in aerothermodynamics, which serve as the foundation of propulsion. The reader should consult textbooks on thermodynamics, such as the classical work of Sonntag, Borgnakke, and Van Wylen (2003), and modern fluid mechanics books, such as Munson, Young, and Okiishi (2006) or John Anderson's books on aerodynamics (2005). For detailed exposition of compressible flow, the two volumes written by Shapiro (1953) should be consulted.

2.2 A Brief Review of Thermodynamics

To get started, we need to characterize the medium that flows through the duct. In gas turbine engines the medium is a perfect gas, often air. The perfect gas law that relates the pressure, density, and the absolute temperature of the gas may be derived rigorously from the kinetic theory of gases. Prominent assumptions in its formulation are (1) intermolecular forces between the molecules are negligibly small and (2) the volume of molecules that occupy a space is negligibly small and may be ignored. These two assumptions lead us to

$$p = \rho RT \quad (2.1)$$

where R is known as the gas constant, which is inversely proportional to the molecular weight of the gas, i.e.,

$$R \equiv \frac{\bar{R}}{MW} \quad (2.2a)$$

where \bar{R} is the universal gas constant expressed in two systems of units as

$$\bar{R} = 8314 \frac{\text{J}}{\text{kmol} \cdot \text{K}} \quad (2.2b)$$

$$\bar{R} = 4.97 \times 10^4 \frac{\text{ft} \cdot \text{lbf}}{\text{slug} \cdot \text{mol} \cdot ^\circ\text{R}} \quad (2.2c)$$

The thermodynamic relations for a perfect gas in terms of specific heats at constant pressure and volume are

$$dh \equiv c_p dT \quad (2.3)$$

$$de \equiv c_v dT \quad (2.4)$$

In general, the specific heats at constant pressure and volume are functions of gas temperature,

$$c_p = c_p(T) \quad (2.5)$$

$$c_v = c_v(T) \quad (2.6)$$

The gas is then called a *thermally perfect* gas. There is often a simplifying assumption of constant specific heats, which is a valid approximation to gas behavior in a narrow

temperature range. In this case,

$$c_p = \text{Constant} \tag{2.5a}$$

$$c_v = \text{Constant} \tag{2.6a}$$

The gas is referred to as a *calorically perfect* gas.

EXAMPLE 2.1

Calculate the density of (dry) air where its static pressure and temperature are 3.0 MPa and 25°C, respectively.

First express the static temperature in absolute scale, $T = 25 + 273 = 298 \text{ K}$.

The gas constant for air is calculated from Equation 2.2a based on its (average) molecular weight of 29 kg/kmol, i.e.,

$$\begin{aligned} R &= \frac{\bar{R}}{MW} = \frac{8,314 \text{ J/kmol} \cdot \text{K}}{29 \text{ kg/kmol}} \\ &= 286.69 \text{ J/kg} \cdot \text{K} \cong 287 \text{ J/kg} \cdot \text{K} \end{aligned}$$

We use the perfect gas law (Equation 2.1) to get the density, i.e.,

$$\begin{aligned} \rho &= \frac{p}{RT} = \frac{3 \times 10^6 \text{ N/m}^2}{287 \frac{\text{J}}{\text{kg} \cdot \text{K}} (298 \text{ K})} \\ &\cong 35.08 \frac{\text{kg}}{\text{m}^3} \end{aligned}$$

$\rho \cong 35.08 \frac{\text{kg}}{\text{m}^3}$

The first law of thermodynamics is the statement of conservation of energy for a system of fixed mass m , namely,

$$\delta q = de + \delta w \tag{2.7}$$

where the element of heat transferred to the system from the surrounding is considered positive and on a per-unit-mass basis is δq with a unit of energy/mass, e.g., J/kg. The element of work done by the gas on the surrounding is considered positive and per-unit-mass of the gas is depicted by δw . The difference in the convention for positive heat and work interaction with the system explains the opposite sides of equation where the two energy exchange terms are located in Equation 2.7, otherwise they both represent energy exchange with the system. The net energy interaction with the system results in a change of energy of the system; where again on a per-unit-mass basis is referred to as de . The three terms of the first law of thermodynamics have dimensions of energy per mass. The elemental heat and work exchange are shown by a delta “ δ ” symbol instead of an exact differential “ d ” as in “ de .” This is in recognition of *path-dependent* nature of heat and work exchange, which differ from the thermodynamic property of the gas “ e ,” which is independent of the path, i.e.,

$$\int_1^2 \delta q \neq q_2 - q_1 \tag{2.8}$$

rather

$$\int_1^2 \delta q = q_2 - q_1 \tag{2.9}$$

Whereas in the case of internal energy (or any other thermodynamic property),

$$\int_1^2 de = e_2 - e_1 \quad (2.10)$$

Note that in the eyes of the first law of thermodynamics, there is no distinction between heat and mechanical work exchange with the system. It is their “net” interaction with the system that needs to be accounted for in the energy balance. The application of the first law to a closed cycle is of importance to engineering and represents a balance between the heat and work exchange in a cyclic process, i.e.,

$$\oint \delta q = \oint \delta w \quad (2.11)$$

Also, for an adiabatic process, i.e., $\delta q = 0$, with no mechanical exchange of work, i.e., $\delta w = 0$, the energy of a system remains constant, namely $e_1 = e_2 = \text{constant}$. We are going to use this principle in conjunction with a control volume approach in the study of inlet and exhaust systems of an aircraft engine.

The second law of thermodynamics introduces the absolute temperature scale and a new thermodynamic variable s , the entropy. It is a statement of impossibility of a heat engine exchanging heat with a single reservoir and producing mechanical work continuously. It calls for a second reservoir at a lower temperature where heat is rejected to by the heat engine. In this sense, the second law of thermodynamics distinguishes between heat and work. It asserts that all mechanical work may be converted into system energy whereas not all heat transfer to a system may be converted into system energy continuously. A corollary to the second law incorporates the new thermodynamic variable s and the absolute temperature T into an inequality, known as the Clausius inequality,

$$Tds \geq \delta q \quad (2.12)$$

where the equal sign holds for a reversible process. The concept of irreversibility ties in closely with frictional losses, viscous dissipation, and the appearance of shock waves in supersonic flow. The pressure forces within the fluid perform reversible work, and the viscous stresses account for dissipated energy of the system (into heat). Hence the reversible work done by a system per unit mass is

$$\delta w_{\text{rev}} = pdv \quad (2.13)$$

where v is the specific volume, which is the inverse of fluid density ρ . A combined first and second law of thermodynamics is known as the Gibbs equation, which relates entropy to other thermodynamic properties, namely

$$Tds = de + pdv \quad (2.14)$$

Although it looks as if we have substituted the reversible forms of heat and work into the first law to obtain the Gibbs equation, it is applicable to irreversible processes as well. Note that in an irreversible process, all the frictional forces that contribute to *lost work*

are dissipated into heat. Now, we introduce a derived thermodynamic property known as enthalpy, h , as

$$h \equiv e + pv \quad (2.15)$$

This derived property, that is, h , combines two forms of fluid energy, namely internal energy (or thermal energy) and what is known as the flow work, pv , or the pressure energy. The other forms of energy such as kinetic energy and potential energy are still unaccounted by the enthalpy h . We shall account for the other forms of energy by a new variable called the *total enthalpy* later in this chapter.

Now, let us differentiate Equation 2.15 and substitute it in the Gibbs equation, to get

$$Tds = dh - vdp \quad (2.16)$$

By expressing enthalpy in terms of specific heat at constant pressure, via Equation 2.3, and dividing both sides of Equation 2.16 by temperature T , we get

$$ds = c_p \frac{dT}{T} - \frac{v}{T} dp = c_p \frac{dT}{T} - R \frac{dp}{p} \quad (2.17)$$

We incorporated the perfect gas law in the last term of Equation 2.17. We may now integrate this equation between states 1 and 2 to arrive at

$$s_2 - s_1 \equiv \Delta s = \int_1^2 c_p \frac{dT}{T} - R \ln \frac{p_2}{p_1} \quad (2.18)$$

An assumption of a calorically perfect gas will enable us to integrate the first term on the right-hand side of Equation 2.18, i.e.,

$$\Delta s = c_p \ln \frac{T_2}{T_1} - R \ln \frac{p_2}{p_1} \quad (2.19)$$

Otherwise, we need to refer to a tabulated thermodynamic function ϕ defined as

$$\int_1^2 c_p \frac{dT}{T} \equiv \phi_2 - \phi_1 \quad (2.20)$$

From the definition of enthalpy, let us replace the flow work, pv , term by its equivalent from the perfect gas law, i.e., RT , and then differentiate the equation as

$$dh \equiv c_p dT = de + RdT = c_v dT + RdT \quad (2.21)$$

Dividing through by the temperature differential dT , we get

$$c_p = c_v + R \quad (2.22a)$$

$$\frac{c_p}{R} = \frac{c_v}{R} + 1 \quad (2.22b)$$

This provides valuable relations among the gas constant and the specific heats at constant pressure and volume. The ratio of specific heats is given by a special symbol γ due to its frequency of appearance in compressible flow analysis, i.e.,

$$\gamma \equiv \frac{c_p}{c_v} = \frac{c_v + R}{c_v} = 1 + \frac{1}{c_v/R} \quad (2.23)$$

In terms of the ratio of specific heats γ and R , we express c_p and c_v as

$$c_p = \frac{\gamma}{\gamma - 1} R \quad (2.24a)$$

$$c_v = \frac{1}{\gamma - 1} R \quad (2.24b)$$

The ratio of specific heats is related to the degrees of freedom of the gas molecules, n , via

$$\gamma = \frac{n + 2}{n} \quad (2.25)$$

The degrees of freedom of a molecule are represented by the sum of the energy states that a molecule possesses. For example, atoms or molecules possess kinetic energy in three spatial directions. If they rotate as well, they have kinetic energy associated with their rotation. In a molecule, the atoms may vibrate with respect to each other, which then creates kinetic energy of vibration as well as the potential energy of intermolecular forces. Finally, the electrons in an atom or molecule are described by their own energy levels (both kinetic energy and potential) that depend on their position around the nucleus. As the temperature of the gas increases, the successively higher energy states are excited; thus the degrees of freedom increases. A monatomic gas, which may be modeled as a sphere, has at least three degrees of freedom, which represent translational motion in three spatial directions. Hence, for a monatomic gas, under “normal” temperatures the ratio of specific heats is

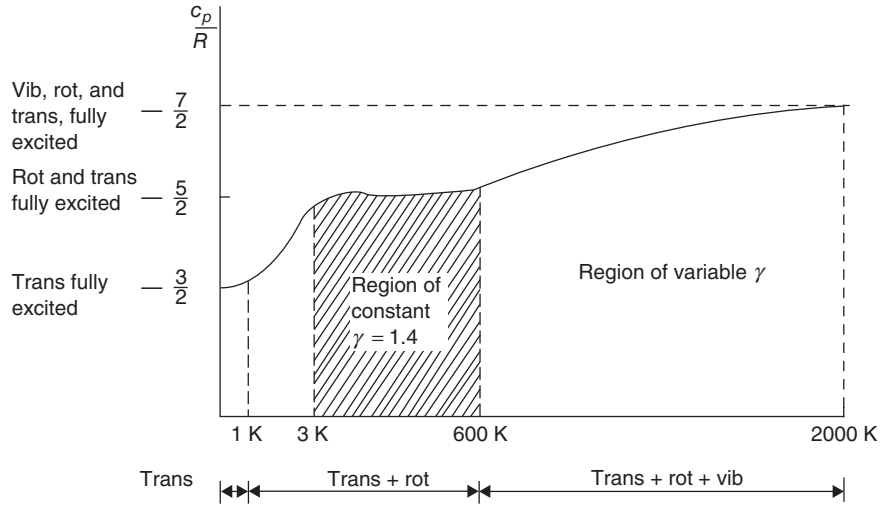
$$\gamma = \frac{5}{3} \cong 1.667 \quad \text{Monatomic gas at “normal” temperatures} \quad (2.26)$$

A monatomic gas has negligible rotational energy about the axes that pass through the atom due to its negligible moment of inertia. A monatomic gas will not experience a vibrational energy, as vibrational mode requires at least two atoms. At higher temperatures, the electronic energy state of the gas is affected, which eventually leads to ionization of the gas. For a diatomic gas, which may be modeled as a dumbbell, there are five degrees of freedom under “normal” temperature conditions, three of which are in translational motion and two of which are in rotational motion. The third rotational motion along the intermolecular axis of the dumbbell is negligibly small. Hence for a diatomic gas such as air (near room temperature), hydrogen, nitrogen, and so on, the ratio of specific heats is

$$\gamma = \frac{7}{5} = 1.4 \quad \text{Diatomic gas at “normal” temperatures} \quad (2.27a)$$

At high temperatures, molecular vibrational modes and the excitation of electrons add to the degrees of freedom and that lowers γ . For example, at ~ 600 K vibrational modes in air are excited, thus the degrees of freedom of diatomic gasses are initially increased

■ **FIGURE 2.1**
Temperature
dependence of specific
heat for a diatomic gas.
Source: Anderson
2003, Fig. 16.11, p. 613.
Reproduced with
permission from
McGraw Hill



by 1, that is, it becomes $5 + 1 = 6$, when the vibrational mode is excited. Therefore, the ratio of specific heats for diatomic gases at elevated temperatures becomes

$$\gamma = \frac{8}{6} \approx 1.33 \quad \text{Diatomic gas at elevated temperatures} \quad (2.27b)$$

The vibrational mode represents two energy states corresponding to the kinetic energy of vibration and the potential energy associated with the intermolecular forces. When fully excited, the vibrational mode in a diatomic gas, such as air, adds 2 to the degrees of freedom, that is, it becomes 7. Therefore, the ratio of specific heats becomes

$$\gamma = \frac{9}{7} \approx 1.29 \quad \text{Diatomic gas at higher temperatures} \quad (2.27c)$$

For example, air at 2000 K has its translational, rotational, and vibrational energy states fully excited. This temperature level describes the combustor or afterburner environment. Gases with a more complex structure than a diatomic gas have more degrees of freedom, and thus their ratio of specific heats is less than 1.4. Figure 2.1 (from Anderson, 2003) shows the behavior of a diatomic gas from 0 to 2000 K. The nearly constant specific heat ratio between 3 and 600 K represents the calorically perfect gas behavior of a diatomic gas such as air with $\gamma = 1.4$. Note that near absolute zero (0 K), $c_p/R \rightarrow 3/2$; therefore, a diatomic gas ceases to rotate and thus behaves like a monatomic gas, that is, it exhibits the same degrees of freedom as a monatomic gas, that is, $n = 3$, $\gamma = 5/3$.

2.3 Isentropic Process and Isentropic Flow

For an isentropic process, where entropy remains constant, the Gibbs equation relates the pressure and temperature ratios by an isentropic exponent:

$$\frac{p_2}{p_1} = \left(\frac{T_2}{T_1} \right)^{\frac{c_p}{R}} = \left(\frac{T_2}{T_1} \right)^{\frac{\gamma}{\gamma-1}} \quad (\text{valid for a calorically perfect gas}) \quad (2.28)$$

Now, using the perfect gas law by replacing the temperature ratio by pressure and density ratios in Equation 2.28 and simplifying the exponents, we get

$$\frac{p_2}{p_1} = \left(\frac{\rho_2}{\rho_1} \right)^\gamma \quad (\text{valid for a calorically perfect gas}) \quad (2.29)$$

EXAMPLE 2.2

Air is compressed from $p_1 = 100$ kPa, $T_1 = 15^\circ\text{C}$ to $p_2 = 1.0$ MPa isentropically. Calculate the exit temperature and density of air. Assume $\gamma = 1.4$, $R = 287$ J/Kg · K, and the gas is calorically perfect.

First convert the temperature to absolute scale, i.e., $T_1 = 15 + 273 = 288$ K.

From the isentropic relation (2.28), we get the exit temperature according to

$$T_2 = T_1 \left(\frac{p_2}{p_1} \right)^{\frac{\gamma-1}{\gamma}} = (288 \text{ K})(10)^{0.4/1.4} \cong 556 \text{ K}$$

There are two ways that we can calculate the exit density. The first method calls for the application of the perfect gas law at the exit, that is,

$$\rho_2 = \frac{p_2}{RT_2} = \frac{10^6 \text{ Pa}}{(287 \text{ J/kg} \cdot \text{K})(556 \text{ K})} \cong 6.267 \text{ kg/m}^3$$

The second method uses the isentropic relation between the inlet and exit density, i.e., Equation 2.29. We need to calculate the inlet density first,

$$\rho_1 = \frac{p_1}{RT_1} = \frac{100 \text{ kPa}}{(287 \text{ J/kg} \cdot \text{K})(288 \text{ K})} \cong 1.2098 \text{ kg/m}^3$$

Now, we may use the isentropic relation 2.29 to get the exit density ρ_2

$$\rho_2 = \rho_1 \left(\frac{p_2}{p_1} \right)^{\frac{1}{\gamma}} = (1.2098 \text{ kg/m}^3)(10)^{1/1.4} \cong 6.267 \text{ kg/m}^3$$

2.4 Conservation Principles for Systems and Control Volumes

A system is a collection of matter of fixed identity, hence fixed mass, whereas a control volume is a fixed region in space with fluid crossing its boundaries. A control volume approach seems to be a more practical method of treating the fluid flow problems in gas turbine engines. However, all the classical laws of Newtonian physics are written for a matter of fixed mass, i.e., the system approach. For example, the mass of an object (in our case a collection of matter described by a system) does not change with time, is a Newtonian mechanics principle. The counterpart of that expressed for a control volume is known as the continuity equation and is derived as follows. The starting point is the system expression, namely

$$\left. \frac{dm}{dt} \right|_{\text{system}} = 0 \quad (2.30)$$

We now express mass as the integral of density over volume

$$\frac{d}{dt} \iiint_{V(t)} \rho dV = 0 \quad (2.31)$$

where $V(t)$ is the volume of the system at any time t . Note that to encompass the entire original mass of the gas in the system, the boundaries of the system become a function of time. Expression 2.31 is a derivative with respect to time of an integral with time-dependent limits. The Leibnitz rule of differentiating such integrals is the bridge between the system and the control volume approach, namely

$$\frac{d}{dt} \iiint_{V(t)} \rho dV = \iiint_{V(t_0)} \frac{\partial \rho}{\partial t} dV + \iint_{S(t_0)} \rho \vec{V} \cdot \hat{n} dS \quad (2.32)$$

The limits of the integrals on the right-hand side (RHS) of Equation 2.32 describe a volume $V(t_0)$ and a closed surface $S(t_0)$, which represents the boundaries of the system at time t_0 . We choose our control volume to coincide with the boundaries of the system at time t_0 . Since the time t_0 is arbitrary, the above equation represents the control volume formulation for the medium, namely our continuity equation or law of conservation of mass for a control volume is written as

$$\iiint_{C.V.} \frac{\partial \rho}{\partial t} dV + \iint_{C.S.} \rho \vec{V} \cdot \hat{n} dS = 0 \quad (2.33)$$

The fluid velocity vector is \vec{V} and \hat{n} represents a unit vector normal to the control surface and pointing outward. The first integral in Equation 2.33 accounts for unsteady accumulation (or depletion) of mass within the control volume and, of course, vanishes for steady flows. We may demonstrate this by switching the order of integration and differentiation for the first integral, that is,

$$\iiint_{C.V.} \frac{\partial \rho}{\partial t} dV = \frac{\partial}{\partial t} \iiint_{C.V.} \rho dV = \frac{\partial}{\partial t} (m)_{C.V.} \quad (2.34)$$

A positive value depicts mass accumulation in the control volume and a negative value shows mass depletion. The second integral takes the scalar product of the fluid velocity vector and the unit normal to the control surface. Therefore, it represents the net crossing of the mass through the control surface per unit time. Flow enters a control volume through one or more inlets and exits the control volume through one or more exits. There is no mass crossing the boundaries of a control volume at any other sections besides the “inlets” and “outlets.” Since the dot product of the velocity vector and the unit normal vector vanishes on all surfaces of the control volume where mass does not cross the boundaries, the second integral makes a contribution to the continuity equation through its inlets and outlets, namely

$$\iint_{C.S.} \rho \vec{V} \cdot \hat{n} dS = \iint_{\text{Outlets}} \rho \vec{V} \cdot \hat{n} dS + \iint_{\text{Inlets}} \rho \vec{V} \cdot \hat{n} dS \quad (2.35)$$

We also note that a unit normal at an inlet points in the opposite direction to the incoming velocity vector, therefore the mass flux at an inlet contributes a negative value to the

mass balance across the control volume (through a negative dot product). An outlet has a unit normal pointing in the same direction as the velocity vector, hence contributes positively to the mass balance in the continuity equation. In general, the inlet and exit faces of a control surface are not normal to the flow, but still the angle between the normal and the velocity vector is obtuse for inlets and acute for exits, hence a negative and a positive dot product over the inlets and outlets, respectively. Therefore, the net flux of mass crossing the boundaries of a control volume, in a steady flow, is zero. We may assume a uniform flow over the inlet and exits of the control volume, to simplify the integrals of Equation 2.35, to

$$\sum (\rho VA)_{\text{out}} = \sum (\rho VA)_{\text{in}} \quad (2.36)$$

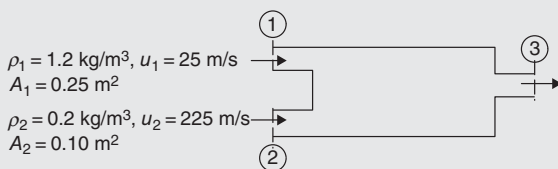
The product VA in the above equation is more accurately written as $V_n A$ or VA_n where a normal component of velocity through an area A contributes to the mass flow through the area, or equivalently, the product of velocity and a normal projection of the area to the flow contributes to the mass flow through the boundary. Often the subscript “ n ” is omitted in the continuity equation for convenience; however, it is always implied in writing the mass flow through a boundary. To write the conservation of mass for a control volume, let us combine the unsteady term and the net flux terms as

$$\frac{d}{dt}(m)_{C.V.} + \dot{m}_{\text{out}} - \dot{m}_{\text{in}} = 0 \quad (2.37)$$

where the mass flow rate is now given the symbol \dot{m} (with units of kg/s, lbm/s, or slugs/s). We note that the difference between a positive outgoing mass and a negative incoming mass appears as a mass accumulation or depletion in the control volume. If the exit mass flow rate is higher than the inlet mass flow rate, then mass depletes within the control volume and vice versa.

EXAMPLE 2.3

Consider the control volume shown. There are two inlet boundaries and one exit boundary where flow crosses the control volume. Assuming the flow is steady and uniform, calculate the exit flow rate from the known inlet conditions.



The mass flow rate entering boundary 1, is

$$\dot{m}_1 = \rho_1 A_1 u_1 = (1.2 \text{ kg/m}^3)(0.25 \text{ m}^2)(25 \text{ m/s}) = 7.5 \text{ kg/s}$$

The mass flow rate entering boundary 2, is

$$\dot{m}_2 = \rho_2 A_2 u_2 = (0.2 \text{ kg/m}^3)(0.10 \text{ m}^2)(225 \text{ m/s}) = 4.5 \text{ kg/s}$$

Therefore, the mass flow rate out of boundary 3 is the sum of the mass flow rate into the box, i.e.,

$$\dot{m}_3 = \dot{m}_1 + \dot{m}_2 = (7.5 + 4.5) \text{ kg/s} = 12 \text{ kg/s}$$

The momentum equation, according to the Newtonian mechanics, relates the time rate of change of linear momentum of an object of fixed mass to the net external forces that act

on the object. We may write this law as

$$\frac{d}{dt}(m\vec{V}) = \vec{F}_{\text{net}} \quad (2.38)$$

Again, we propose to write the mass as the volume integral of the density within the system as

$$\frac{d}{dt} \iiint_{V(t)} \rho \vec{V} dV = \vec{F}_{\text{net}} \quad (2.39)$$

Equation 2.39 is suitable for a system. We apply Leibnitz's rule to the momentum equation to arrive at the control volume formulation, namely

$$\iiint_{C.V.} \frac{\partial}{\partial t} (\rho \vec{V}) dV + \iint_{C.S.} \rho \vec{V} (\vec{V} \cdot \hat{n}) dS = \vec{F}_{\text{net}} \quad (2.40)$$

The first integral measures the unsteady momentum within the control volume and vanishes identically for a steady flow. The second integral is the net flux of momentum in and out of the control surface. Assuming uniform flow at the boundaries of the control surface inlets and outlets, we may simplify the momentum equation to a very useful engineering form, namely

$$(\dot{m}\vec{V})_{\text{out}} - (\dot{m}\vec{V})_{\text{in}} = \vec{F}_{\text{net}} \quad (2.40a)$$

Note that momentum equation (2.40a) is a vector equation and a shorthand notation for the momentum balance in three spatial directions. For example, in Cartesian coordinates, we have

$$(\dot{m}V_x)_{\text{out}} - (\dot{m}V_x)_{\text{in}} = F_{\text{net},x} \quad (2.41a)$$

$$(\dot{m}V_y)_{\text{out}} - (\dot{m}V_y)_{\text{in}} = F_{\text{net},y} \quad (2.41b)$$

$$(\dot{m}V_z)_{\text{out}} - (\dot{m}V_z)_{\text{in}} = F_{\text{net},z} \quad (2.41c)$$

In cylindrical coordinates (r, θ, z) , we may write the momentum equation as

$$(\dot{m}V_r)_{\text{out}} - (\dot{m}V_r)_{\text{in}} = F_{\text{net},r} \quad (2.42a)$$

$$(\dot{m}V_\theta)_{\text{out}} - (\dot{m}V_\theta)_{\text{in}} = F_{\text{net},\theta} \quad (2.42b)$$

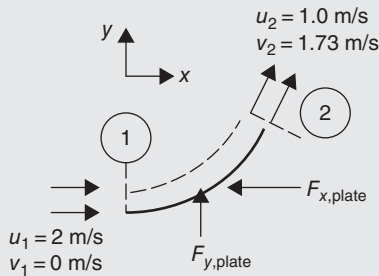
$$(\dot{m}V_z)_{\text{out}} - (\dot{m}V_z)_{\text{in}} = F_{\text{net},z} \quad (2.42c)$$

We may write these equations in spherical coordinates (r, θ, ϕ) as well. The force terms in the momentum equation represent the net external forces exerted on the fluid at its boundaries and any volume forces, known as body forces, such as gravitational force. If the control volume contains/envelopes an object, then the force acting on the fluid is equal and opposite to the force experienced by the body. For example a body that experiences a drag force D imparts on the fluid a force equal to $-D$.

EXAMPLE 2.4

In placing a curved plate in front of a garden hose with a water flow rate of 0.1 kg/s, we have to exert an axial force on the plate, as shown, to hold it in place. Estimate the axial and lateral forces, F_x and F_y , respectively, that are needed to support the plate.

(Note: u and v are x - and y -component of velocity, respectively.)



For a quick estimation of the axial force, we assume the flow is uniform and steady. Then, we may apply Equation 2.41a

to get

$$\begin{aligned} F_{x,\text{fluid}} &= \dot{m}_2 u_2 - \dot{m}_1 u_1 = \dot{m}(u_2 - u_1) \\ &= 0.1 \text{ kg/s}(-1 \text{ m/s}) = -0.1 \text{ N} \end{aligned}$$

The axial force acting on the curved plate is equal and opposite to $F_{x,\text{fluid}}$. Therefore, the external force needed to hold the plate horizontally is -0.1 N (that is in the negative x -direction, as shown). Also, the lateral force on the fluid is calculated from the lateral momentum balance, i.e.,

$$\begin{aligned} F_{y,\text{fluid}} &= \dot{m}_2 v_2 - \dot{m}_1 v_1 = \dot{m}(v_2 - v_1) \\ &= 0.1 \text{ kg/s}(1.73 \text{ m/s}) = 0.173 \text{ N} \end{aligned}$$

The lateral force on the plate is in the opposite direction (i.e., in the $-y$ direction), and thus the external force to hold the plate laterally is $+0.173 \text{ N}$, as shown.

The law of conservation of energy for a control volume starts with the first law of thermodynamics applied to a system. Let us divide the differential form of the first law by an element of time dt to get the rate of energy transfer, namely

$$\dot{Q} = \frac{dE}{dt} + \dot{W} \quad (2.43)$$

where the equation is written for the entire mass of the system. The energy E is now represented by the internal energy e times mass, as well as the kinetic energy of the gas in the system and the potential energy of the system. The contribution of changing potential energy in gas turbine engines or most other aerodynamic applications is negligibly small and often ignored. We write the energy as the mass integral of specific energy over the volume of the system, and apply Leibnitz's rule of integration to get the control volume version, namely

$$\frac{dE}{dt} = \frac{d}{dt} \iiint_{V(t)} \rho \left(e + \frac{V^2}{2} \right) dV = \iiint_{C.V.} \frac{\partial}{\partial t} \left[\rho \left(e + \frac{V^2}{2} \right) \right] dV + \iint_{C.S.} \rho \left(e + \frac{V^2}{2} \right) \vec{V} \cdot \hat{n} dS \quad (2.44)$$

The first term on the RHS of Equation 2.44 is the time rate of change of energy within the control volume, which identically vanishes for a steady flow. The second integral represents the net flux of fluid power (i.e., the *rate* of energy) crossing the boundaries of the control surface. The rates of heat transfer to the control volume and the rate of

mechanical energy transfer by the gases inside the control volume on the surrounding are represented by \dot{Q} and \dot{W} terms in the energy equation (2.43). Now, let us examine the forces at the boundary that contribute to the rate of energy transfer. These surface forces are due to pressure and shear acting on the boundary. The pressure forces act normal to the boundary and point inward, that is, opposite to \hat{n} ,

$$-p\hat{n}dS \quad (2.45)$$

To calculate the rate of work done by a force, we take the scalar product of the force and the velocity vector, namely

$$-p\vec{V} \cdot \hat{n}dS \quad (2.46)$$

Now, we need to sum this elemental rate of energy transfer by pressure forces over the surface, via a surface integral, that is,

$$\oint_{C.S.} -p\vec{V} \cdot \hat{n}dS \quad (2.47)$$

Since the convention on the rate of work done in the first law is positive when it is performed “on” the surroundings, and Equation 2.46 represents the rate of work done by the surroundings on the control volume, we need to incorporate an additional negative factor for this term in the energy equation. The rate of energy transfer by the shear forces is divided into a shaft power \mathcal{G}_s that crosses the control surface in the form of shaft shear and the viscous shear stresses on the boundary of the control volume. Hence,

$$\dot{W} = \oint_{C.S.} p\vec{V} \cdot \hat{n}dS + \mathcal{G}_s + \dot{W}_{\text{viscous-shear}} \quad (2.48)$$

Let us combine the expression 2.48 with Equations 2.44 and 2.43 to arrive at a useful form of the energy equation for a control volume, that is,

$$\oint_{C.V.} \frac{\partial}{\partial t} \left[\rho \left(e + \frac{V^2}{2} \right) \right] dV + \oint_{C.S.} \rho \left(e + \frac{V^2}{2} \right) \vec{V} \cdot \hat{n}dS + \oint_{C.S.} p\vec{V} \cdot \hat{n}dS = \dot{Q} - \mathcal{G}_s - \dot{W}_{\text{visc}} \quad (2.49)$$

The closed surface integrals on the left-hand side (LHS) may be combined and simplified to

$$\oint_{C.V.} \frac{\partial}{\partial t} \left[\rho \left(e + \frac{V^2}{2} \right) \right] dV + \oint_{C.S.} \rho \left(e + \frac{V^2}{2} + \frac{p}{\rho} \right) \vec{V} \cdot \hat{n}dS = \dot{Q} - \mathcal{G}_s - \dot{W}_{\text{visc}} \quad (2.50)$$

We may replace the internal energy and the flow work terms in Equation 2.50 by enthalpy h and define the sum of the enthalpy and the kinetic energy as the total or stagnation enthalpy, to get

$$\oint_{C.V.} \frac{\partial}{\partial t} \left[\rho \left(e + \frac{V^2}{2} \right) \right] dV + \oint_{C.S.} \rho h_t \vec{V} \cdot \hat{n}dS = \dot{Q} - \mathcal{G}_s - \dot{W}_{\text{visc}} \quad (2.51)$$

where the total enthalpy h_t is defined as

$$h_t \equiv h + \frac{V^2}{2} \quad (2.52)$$

In steady flows the volume integral that involves a time derivative vanishes. The second integral represents the net flux of fluid power across the control volume. The terms on the RHS are the external energy interaction terms, which serve as the *drivers* of the energy flow through the control volume. In adiabatic flows, the rate of heat transfer through the walls of the control volume vanishes. In the absence of shaft work, as in inlets and nozzles of a jet engine, the second term on the RHS vanishes. The rate of energy transfer via the viscous shear stresses is zero on solid boundaries (since velocity on solid walls obeys the no slip boundary condition) and nonzero at the inlet and exit planes. The contribution of this term over the inlet and exit planes is, however, small compared with the net energy flow in the fluid, hence neglected.

The integrated form of the energy equation for a control volume, assuming uniform flow over the inlets and outlets, yields a practical solution for quick engineering calculations

$$\sum (\dot{m}h_t)_{\text{out}} - \sum (\dot{m}h_t)_{\text{in}} = \dot{Q} - \dot{\phi}_s \quad (2.53)$$

The summations in Equation 2.53 account for multiple inlets and outlets of a general control volume. In flows that are adiabatic and involve no shaft work, the energy equation simplifies to

$$\sum (\dot{m}h_t)_{\text{out}} = \sum (\dot{m}h_t)_{\text{in}} \quad (2.54)$$

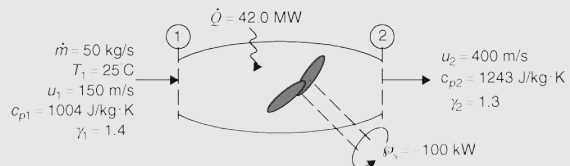
For a single inlet and a single outlet, the energy equation is even further simplified, as the mass flow rate also cancels out, to yield

$$h_{t-\text{exit}} = h_{t-\text{inlet}} \quad (2.55)$$

Total or stagnation enthalpy then remains constant for adiabatic flows with no shaft power, such as inlets and nozzles or across shock waves.

EXAMPLE 2.5

Let us consider a control volume with heat transfer rate and mechanical power (i.e., shaft power) exchange specified at its boundaries. There is a single inlet and a single outlet where mass crosses the boundary in a steady and uniform flow, as shown. Calculate the exit total and static temperatures T_{t2} and T_2 , respectively (note that the gas is not calorically perfect).



First, we conclude that the exit mass flow rate is 50 kg/s, to satisfy the continuity equation for steady flow. Second, we cast the inlet static temperature in the absolute scale, i.e.,

$$T_1 = 25 + 273 = 298 \text{ K}$$

Third, we apply the conservation of energy equation (2.53) to this problem, which requires the knowledge of total enthalpy at the inlet. We use the definition of total enthalpy:

$$\begin{aligned} h_{t1} &= h_1 + u_1^2/2 = c_{p1}T_1 + u_1^2/2 = (1004 \text{ J/kg} \cdot \text{K})(298 \text{ K}) \\ &\quad + (150)^2/2 \text{ J/kg} \\ &= 310,442 \text{ J/kg} \end{aligned}$$

Now, Equation 2.53 gives the exit total enthalpy as

$$\begin{aligned} h_{t2} &= h_{t1} + \left(\frac{\dot{Q} - \dot{\phi}_s}{\dot{m}} \right) = 310.442 \text{ kJ/kg} \\ &\quad + \left(\frac{(42,000 + 100) \times 1000 \text{ W}}{50 \text{ kg/s}} \right) \cong 1,152.4 \text{ kJ/kg} \end{aligned}$$

$$T_{t2} = \frac{h_{t2}}{c_{p2}} = \frac{1,152.4 \text{ kJ/kg}}{1.243 \text{ kJ/kg} \cdot \text{K}} \cong 927 \text{ K}$$

$$\begin{aligned} T_2 &= T_{t2} - u_2^2/2c_{p2} \\ &= 927 \text{ K} - (400)^2/(2 \times 1243 \text{ J/kg} \cdot \text{K}) \cong 863 \text{ K} \end{aligned}$$

2.5 Speed of Sound & Mach Number

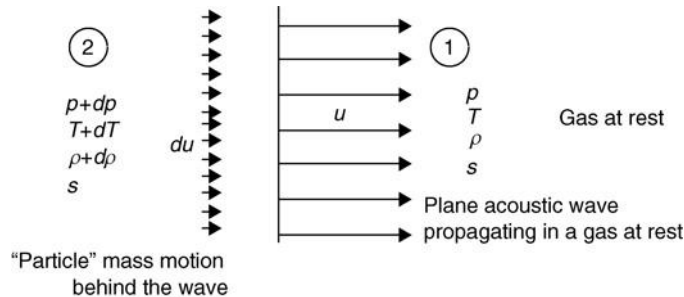
Sound waves are infinitesimal pressure waves propagating in a medium. The propagation of sound waves, or acoustic waves, is reversible and adiabatic, hence isentropic. Since sound propagates through collision of fluid molecules, the speed of sound is higher in liquids than gas. The derivation of the speed of sound is very simple and instructive. Assume a plane sound wave propagates in a medium at rest with speed u . The fluid behind the wave is infinitesimally set in motion at the speed du with an infinitesimal change of pressure, temperature, and density. The fluid ahead of the wave is at rest and yet unaffected by the approaching wave. A schematic drawing of this wave and fluid properties are shown in Figure 2.2.

By switching observers from the gas at rest to an observer that moves with the wave at the wave speed u , we change the unsteady wave propagation problem into a steady one. This is known as the Lorentz transformation. The transformed problem is shown in Figure 2.3.

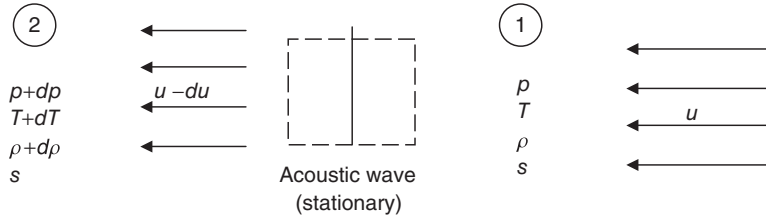
The fluid static properties, pressure, density, and temperature are independent of the motion of an observer; hence they remain unaffected by the observer transformation. We may now apply steady conservation principles to a control volume, as shown in Figure 2.3. The control volume is a box with its sides parallel to the flow, an inlet and an exit area normal to the flow. We may choose the entrance and exit areas of the box to be unity. The continuity demands

$$\rho u = (\rho + d\rho)(u + du) \quad (2.56)$$

■ **FIGURE 2.2**
Propagation of a plane acoustic wave in a gas at rest (an unsteady but isentropic problem)



■ **FIGURE 2.3**
Flow as seen by an
observer fixed at the
wave (a steady
problem)



which simplifies to

$$\rho du = -u d\rho \tag{2.57}$$

The momentum equation for this one-dimensional wave problem is

$$(\rho u)(u + du) - (\rho u)u = p - (p + dp) \tag{2.58}$$

The change of momentum from inlet to exit is shown on the LHS of Equation 2.58. The first parenthesis of each momentum term is the mass flow rate, which is multiplied by the respective flow speeds at the exit and inlet. The driving forces on the RHS of Equation 2.58 are the pressure-area terms in the direction and opposite to the fluid motion, acting on areas that were chosen to be unity. The momentum equation simplifies to

$$\rho u du = dp \tag{2.59}$$

Now, let us substitute the continuity equation (2.57) in the momentum equation (2.59), to get an expression for the square of the acoustic wave propagation in terms of pressure and density changes that occur as a result of wave propagation in a medium at rest

$$u^2 d\rho = dp \tag{2.60}$$

or

$$u^2 = \frac{dp}{d\rho} = \left(\frac{\partial p}{\partial \rho} \right)_s \tag{2.61}$$

Since, for isentropic flow, $p = \text{const} \cdot \rho^\gamma$, Equation 2.61 reduces to

$$u^2 = \frac{\gamma p}{\rho} = \gamma RT \tag{2.62}$$

We replaced the ratio of pressure to density by RT from the perfect gas law in Equation 2.62. The symbol we use in this book for the speed of sound is “ a ,” hence, local speed of sound in a gas is

$$a = \sqrt{\frac{\gamma p}{\rho}} = \sqrt{\gamma RT} = \sqrt{(\gamma - 1) c_p T} \tag{2.63}$$

The speed of sound is a *local* parameter, which depends on the local absolute temperature of the gas. Its value changes with gas temperature, hence it drops when fluid accelerates (or *expands*) and increases when gas decelerates (or *compresses*). The speed of sound in air at standard sea level conditions is ~ 340 m/s or ~ 1100 ft/s. The type of gas also affects the speed of propagation of sound through its molecular weight. We may observe this behavior by the following substitution:

$$a = \sqrt{\gamma RT} = \sqrt{\gamma \left(\frac{\bar{R}}{MW} \right) T} \quad (2.64)$$

A light gas, like hydrogen (H_2) with a molecular weight of 2, causes an acoustic wave to propagate *faster* than a heavier gas, such as air with (a mean) molecular weight of 29. If we substitute these molecular weights in Equation 2.64, we note that sound propagates in gaseous hydrogen *nearly four times faster* than air. Since both hydrogen and air are diatomic gases, the ratio of specific heats remains (nearly) the same for both gases at the same temperature.

The equation for the speed of propagation of sound that we derived is for a gas at rest. Let us superimpose a uniform collective gas speed in a particular direction to the wave front, then the wave propagates as the vector sum of the two, namely, $\vec{V} + \vec{a}$. For waves propagating normal to a gas flow, we get either $(V + a)$ or $(V - a)$ as the propagation speed of sound. It is the $(V - a)$ behavior that is of interest here. In case the flow is sonic, then $(a - a = 0)$, which will not allow the sound to travel upstream and hence creates a zone of silence upstream of the disturbance. In case the flow speed is even faster than the local speed of sound, that is, known as supersonic flow, the acoustic wave will be confined to a cone. These two behaviors for small disturbances are shown in Figure 2.4.

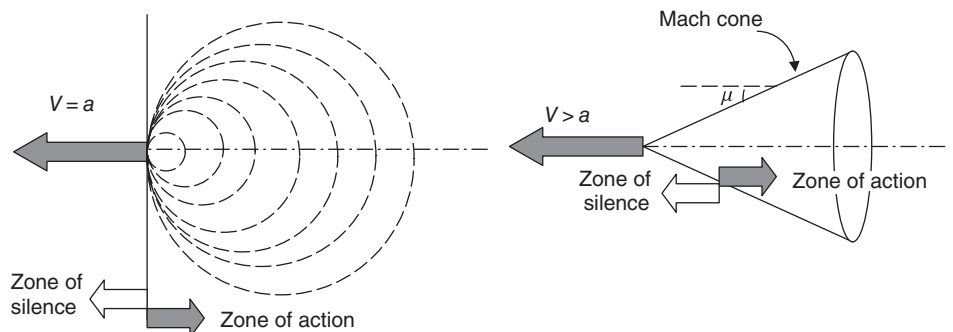
The ratio of local gas speed to the speed of sound is called Mach number, M

$$M \equiv \frac{V}{a} \quad (2.65)$$

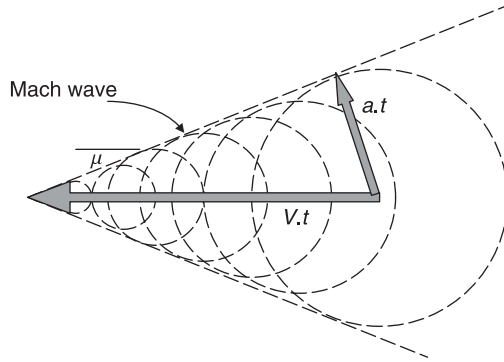
The envelope of the waves that create the zones of action and silence is the Mach wave. It makes a local wave angle with respect to the flow μ , which from the geometry of wave propagation, as shown in Figure 2.5, is

$$\mu = \sin^{-1} \left(\frac{a \cdot t}{V \cdot t} \right) = \sin^{-1} \left(\frac{1}{M} \right) \quad (2.66)$$

■ **FIGURE 2.4**
Acoustic wave propagation in sonic and supersonic flows (or the case of a moving source)



■ **FIGURE 2.5**
Wave front created by a *small disturbance* moving at a supersonic speed



2.6 Stagnation State

We define the stagnation state of a gas as the state reached in decelerating a flow to rest reversibly and adiabatically and without any external work. Thus, the stagnation state is reached isentropically. This state is also referred to as the *total* state of the gas. The symbols for the stagnation state in this book use a subscript “t” for total. The total pressure is p_t , the total temperature is T_t , and the total density is ρ_t . Since the stagnation state is reached isentropically, the static and total entropy of the gas are the same, that is, $s_t = s$. Based on the definition of stagnation state, the total energy of the gas does not change in the deceleration process, hence the stagnation enthalpy h_t takes on the form

$$h_t \equiv h + \frac{V^2}{2} \tag{2.52}$$

which we defined earlier in this chapter. Assuming a *calorically perfect gas*, we may simplify the total enthalpy relation 2.52 by dividing through by c_p to get an expression for total temperature according to

$$T_t = T + \frac{V^2}{2c_p} \quad (\text{valid for a calorically perfect gas}) \tag{2.67}$$

This equation is very useful in converting the local static temperature and gas speed into the local stagnation temperature. To nondimensionalize Equation 2.67, we divide both sides by the static temperature, that is,

$$\frac{T_t}{T} = 1 + \frac{V^2}{2c_p T} \tag{2.68}$$

The denominator of the kinetic energy term on the RHS is proportional to the square of the local speed of sound a^2 according to Eq 2.63, which simplifies to

$$\frac{T_t}{T} = 1 + \left(\frac{\gamma - 1}{2}\right) \frac{V^2}{a^2} = 1 + \left(\frac{\gamma - 1}{2}\right) M^2 \tag{2.69}$$

Therefore to arrive at the stagnation temperature of the gas, we need to have its static temperature as well as either the gas speed V or the local Mach number of the gas M to substitute in Equations 2.68 or 2.69, respectively. The ratio of stagnation to static temperature of a (calorically perfect) gas is a unique function of local Mach number, according to Equation 2.69. We may also use a spreadsheet tabulation of this function for later use for any gas characterized by its ratio of specific heats γ . From isentropic relations between the pressure and temperature ratio that we derived earlier based on Gibbs equation of thermodynamics, we may now relate the ratio of stagnation to static pressure and the local Mach number via

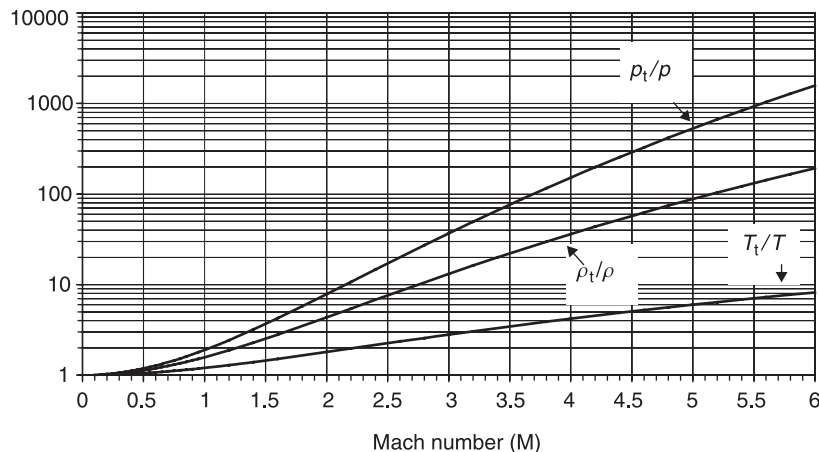
$$\frac{p_t}{p} = \left(\frac{T_t}{T}\right)^{\frac{\gamma}{\gamma-1}} = \left[1 + \left(\frac{\gamma-1}{2}\right)M^2\right]^{\frac{\gamma}{\gamma-1}} \quad (\text{valid for a calorically perfect gas}) \quad (2.70)$$

We used the isentropic relation between the stagnation and static states based on the definition of the stagnation state that is reached isentropically. Also, the stagnation density is higher than the static density according to

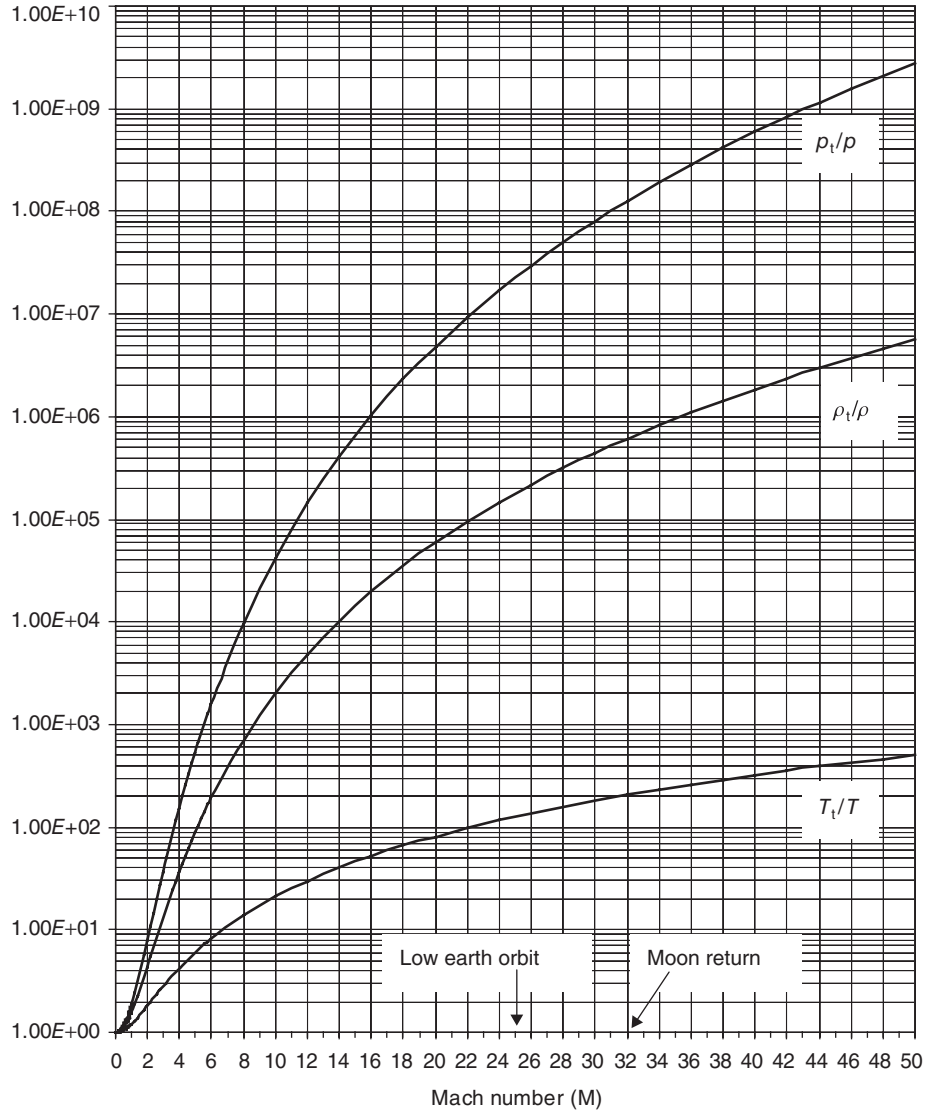
$$\frac{\rho_t}{\rho} = \left(\frac{p_t}{p}\right)^{\frac{1}{\gamma}} = \left[1 + \left(\frac{\gamma-1}{2}\right)M^2\right]^{\frac{1}{\gamma-1}} \quad (\text{Valid for a calorically perfect gas}) \quad (2.71)$$

We note that the ratio of stagnation-to-static state of a gas is totally described by the local Mach number and the type of gas γ . The tabulation of these functions, that is, p_t/p , T_t/T , and ρ_t/ρ are made in isentropic tables for a gas described by its ratio of specific heats γ . Figure 2.6 shows the variation of the stagnation state with Mach number for a diatomic gas, such as air ($\gamma = 1.4$). The least variation is noted for the stagnation temperature, followed by the density and pressure. To graph these variations (up to Mach 6), we had to use a logarithmic scale, as the total pressure rise with Mach number reaches above one thousand (times the static pressure) while the stagnation temperature stays below ten (times the static temperature). We may examine higher Mach numbers in Figure 2.7. The assumption in arriving at the stagnation state properties relative to the static properties was a *calorically perfect gas*. The impact of high-speed flight on

■ **FIGURE 2.6**
Variation of the stagnation state with Mach number for a diatomic gas, $\gamma = 1.4$ (For a calorically perfect gas, i.e., c_p , c_v , and γ are constants)



■ **FIGURE 2.7**
 Variation of stagnation state of gas with flight Mach number for $\gamma = 1.4$ (for a calorically perfect gas)

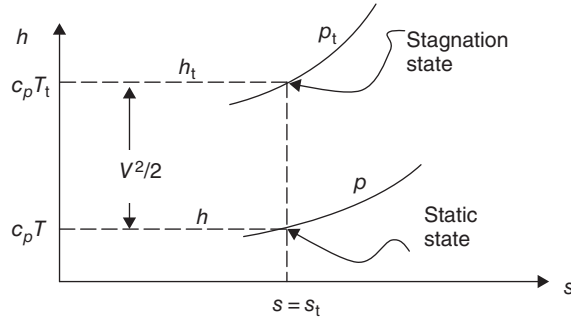


the atmosphere is to cause molecular dissociation, followed by ionization of the oxygen and nitrogen molecules. A host of other chemical reactions takes place, which result in a violation of our initial assumption. In reality, both the specific heats (c_p and c_v) are functions of temperature as well as the pressure at hypersonic Mach numbers, that is, $M > 5$. There are two lessons to be learned here. The first is to always examine the validity of your assumptions; the other is to be cautious about data extrapolations!

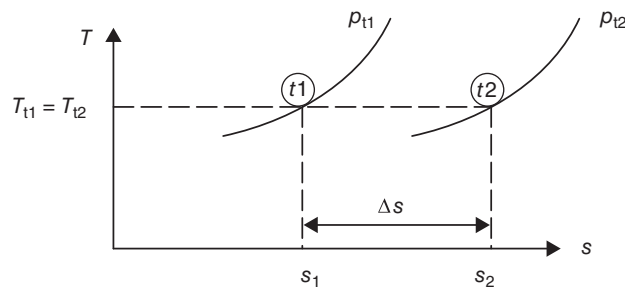
Although the pressure ratio (p_t/p) is relieved through real gas effects due to a high-speed flight, it still remains high. Consequently, the high-speed flight has to be scheduled at a high altitude where the static pressure is low. For example, the static pressure at 25 km is only $\sim 2.5\%$ and at 50 km altitude is 0.07% of the sea level pressure.

To identify the local static and stagnation states of a gas in a Mollier ($h-s$) diagram is important in studying propulsion. We use the stagnation enthalpy definition to identify

■ **FIGURE 2.8**
Stagnation and static states of a gas in motion shown on an h - s diagram



■ **FIGURE 2.9**
Adiabatic flow that shows total pressure loss Δp_t , e.g., flows containing shocks



the local stagnation properties of a gas, for example, we start with the static state and then build up a kinetic energy, as in Figure 2.8.

We may also apply the Gibbs equation to the stagnation state of the gas to get

$$\Delta s = c_p \ell n(T_{t2}/T_{t1}) - R \ell n(p_{t2}/p_{t1}) \quad (2.72)$$

For adiabatic flows the first term on the RHS identically vanishes, since the total temperature remains constant. Hence, the total pressure for adiabatic flows with losses, for example, due to frictional losses, always decreases, since the entropy change has to be positive. The exponential relationship between the total pressure ratio and the entropy rise in an adiabatic flow is very useful to propulsion studies and we write it in Equation 2.73

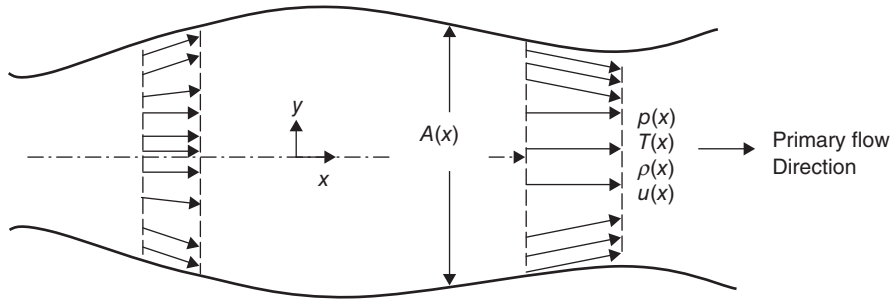
$$p_{t2}/p_{t1} = e^{-\frac{\Delta s}{R}} \quad (2.73)$$

All adiabatic flows with loss result in a drop of total pressure. For example, in a supersonic inlet with shocks and frictional losses in the boundary layer, we encounter a total pressure loss. Since, the total pressure is now cast as a measure of loss via Equation 2.73, it serves as a commodity that propulsion engineers try to preserve as much as possible. The T - s diagram of an adiabatic flow with loss is shown in Figure 2.9.

2.7 Quasi-One-Dimensional Flow

In duct flows with area variations, such as a diffuser or a nozzle, where the boundary layers are completely attached, the streamwise variation of flow variables dominate the lateral variations. In essence, the flow behaves as a uniform flow with pressure gradient

■ **FIGURE 2.10**
Schematic drawing of a variable-area duct with attached boundary layers

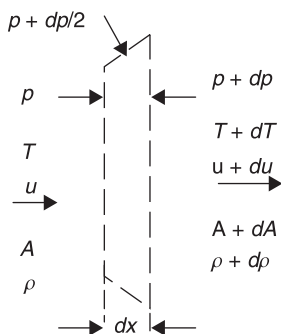


in a variable-area duct. A schematic drawing of a duct with area variation is shown in Figure 2.10. The primary flow direction is labeled as “ x ” and the lateral direction is “ y .” Although the flow next to the wall assumes the same slope as the wall, the cross-sectional flow properties are based on uniform parallel flow at the cross-section. The flow area at a cross-section enters the conservation laws, but the variation in the cross-section from the centerline to the wall is neglected. Such flows are called quasi-one-dimensional flows.

For high Reynolds number flows where the boundary layer is thin compared with lateral dimensions of a duct and assuming an attached boundary layer, the assumption of an *inviscid* fluid leads to a reasonable approximation of the duct flow. This means that an inviscid fluid model accurately estimates the pressure, temperature, and flow development along the duct axis. Attached boundary layers require a slow variation in the duct area, which is almost invariably the case in propulsion engineering. Inviscid flow analysis also produces a limit performance capability of a component when boundary layers are infinitely thin. In a practical sense, ducts with boundary layer suction approach an inviscid flow model. To develop the quasi-one-dimensional flow equations in a variable-area duct with inviscid fluid, we examine a slice, known as a *slab*, of the flow and apply the Taylor series approximation to the two sides of the slab. Figure 2.11 shows a thin slice of a duct flow with streamwise length dx separating the two sides of the slab.

We assume general parameters on one side and step in the x -direction using the Taylor series approximation of an analytical function expanded in the neighborhood of a point. Since the step size dx is small, we may truncate the infinite Taylor series after the first derivative. Note that the walls exert one-half of the incremental pressure ($dp/2$) over the upstream pressure p , since we take only one-half the step size ($dx/2$) to reach

■ **FIGURE 2.11**
Slab of inviscid fluid in a variable-area duct (walls exert pressure on the fluid)



its center. Now, let us apply the conservation principles to this thin slice of the flow. Continuity demands

$$\rho u A = (\rho + d\rho)(u + du)(A + dA) \quad (2.74)$$

Ignoring higher order terms involving the products of two small parameters, such as $du \cdot dA$, we get

$$\rho u dA + u A d\rho + \rho A du = 0 \quad (2.75)$$

Now dividing both sides by a nonzero constant, namely $\rho u A$, we get the continuity equation in differential form

$$\frac{dA}{A} + \frac{d\rho}{\rho} + \frac{du}{u} = 0 \quad (2.76)$$

This is also known as the *logarithmic derivative* of the local mass flow rate, $\rho u A = \text{constant}$. Since we use the logarithmic derivative often in our analysis, let us examine it now. From the continuity equation

$$\rho u A = \text{Constant} \quad (2.77)$$

We take the natural logarithm of both sides, to get the sum

$$\ell n(\rho) + \ell n(u) + \ell n(A) = \text{Constant} \quad (2.78)$$

Now, if we take the differential of both sides we get Equation 2.76, which is called the logarithmic derivative of the continuity equation.

The momentum balance in the streamwise direction gives

$$(\rho u A)(u + du) - (\rho u A)u = pA - (p + dp)(A + dA) + (p + dp/2)dA \quad (2.79)$$

The first term on the LHS is the rate of momentum out of the slab, which is the mass flow rate times the velocity out of the box. The second term on the LHS is the rate of momentum into the box. The first term on the RHS is the pressure force pushing the fluid out. The second term on the RHS is the pressure force in the opposite direction to the flow, hence negative. The last term on the RHS is the pressure force contribution of the walls. First, we note that its direction is in the flow direction, hence positive. Second, we note that the projection of the sidewalls in the flow direction is dA , which serves as the *effective* area for the wall pressure to push the fluid out of the box. We may simplify this equation by canceling terms and neglecting higher order quantities to get

$$\rho u A du = -A dp \quad (2.80)$$

The flow area term is cancelled from Equation 2.80 (as expected) to yield

$$\rho u du = -dp \quad (2.81)$$

The energy equation for an adiabatic (non heat-conducting) flow with no shaft work is the statement of conservation of total enthalpy, which differentiates into

$$dh_t = dh + u du = 0 \quad (2.82)$$

The equation of state for a perfect gas may be written in logarithmic derivative form as

$$dp/p = d\rho/\rho + dT/T \quad (2.83)$$

Also, as we stipulated an isentropic flow through the duct, that is, $ds = 0$, the pressure–density relationship follows the isentropic rule, namely $p/\rho^\gamma = \text{constant}$, which has the following logarithmic derivative:

$$\frac{dp}{p} - \gamma \frac{d\rho}{\rho} = 0 \quad (2.84)$$

The set of governing equations for an isentropic flow through a duct of variable area are summarized as:

$$\begin{aligned} d\rho/\rho + du/u + dA/A &= 0 \\ \rho u du &= -dp \\ dh + u du &= 0 \\ dp/p &= d\rho/\rho + dT/T \end{aligned}$$

The unknowns are the pressure p , density ρ , temperature T , and velocity u . The enthalpy for a perfect gas follows $dh = c_p dT$, hence we need to know the specific heat at constant pressure of the gas as well. The entropy remains constant, hence the static pressure is related to the speed of sound and density according to:

$$p = \rho a^2 / \gamma \quad (2.85)$$

throughout the flow. We shall apply these governing equations in the following sections to fluid flow problems of interest to propulsion.

2.8 Area–Mach Number Relationship

Let us divide the momentum equation by $d\rho$, to get

$$\frac{\rho}{d\rho} u du = -\frac{dp}{d\rho} = -a^2 \quad (2.86)$$

which yields

$$\frac{dp}{\rho} = -\frac{u du}{a^2} \quad (2.87)$$

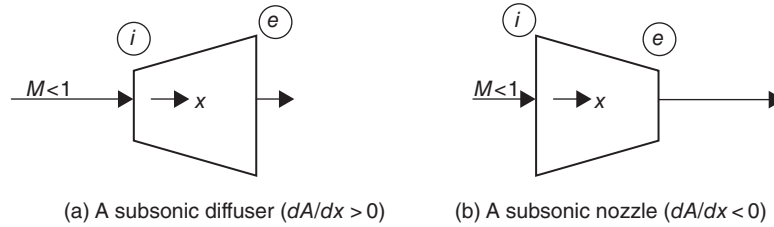
Now, let us substitute the density ratio in the continuity equation to relate the area variation to Mach number according to

$$-\frac{u du}{a^2} + \frac{du}{u} + \frac{dA}{A} = 0 \quad (2.88a)$$

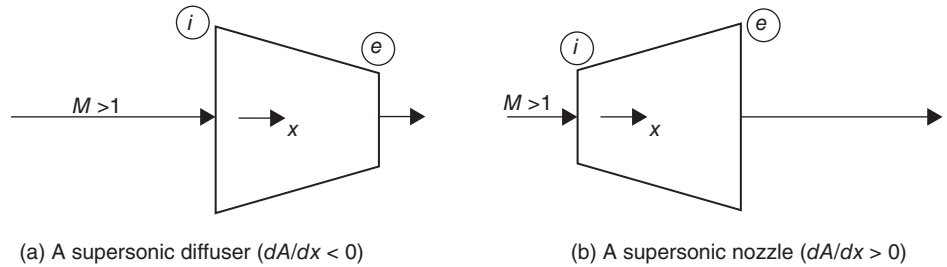
This simplifies to

$$(M^2 - 1) \frac{du}{u} = \frac{dA}{A} \quad (2.88b)$$

■ FIGURE 2.12
Area variations for a
subsonic diffuser and a
nozzle



■ FIGURE 2.13
Area variations for a
supersonic diffuser and
nozzle



This equation relates area variation to speed variation for the subsonic and supersonic flows. Assuming a subsonic flow, the parenthesis involving Mach number becomes a negative quantity. Hence, an area increase in a duct, that is, $dA > 0$, results in $du < 0$, to make the signs of both sides of Equation 2.88b consistent. A negative du means flow deceleration. Hence, a subsonic diffuser requires a duct with $dA/dx > 0$. A subsonic nozzle with $du > 0$ demands $dA < 0$. These two duct geometries for a subsonic flow are shown in Figure 2.12.

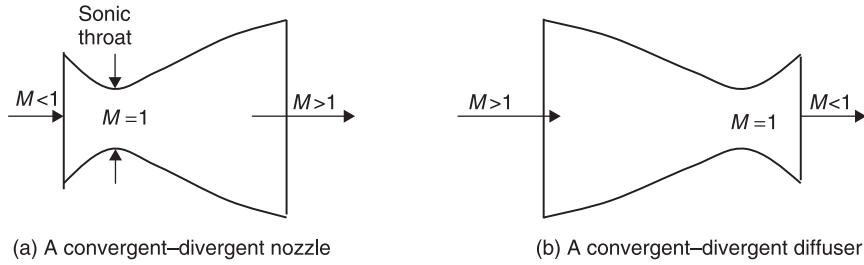
For a supersonic flow, the parenthesis that involves Mach number in Equation 2.88b is positive. Hence, an area increase results in flow acceleration and vice versa. These geometric relationships between area variation and flow speed for supersonic flow are shown in Figure 2.13.

We note that the geometric requirements for a desired fluid acceleration or deceleration in a duct are opposite to each other in subsonic and supersonic flow regimes. This dual behavior is seen repeatedly in aerodynamics. We shall encounter several examples of this in this chapter.

2.9 Sonic Throat

A unique flow condition separates the subsonic from supersonic flow. It is the sonic flow that marks the boundary between the two flows. In a subsonic flow, we learned that area reduction accelerates the gas and, ultimately, could reach a sonic state at the exit of the subsonic nozzle. A sonic flow may accelerate to supersonic Mach numbers if the area of the duct increases in the streamwise direction. This initial contraction and later expansion of the duct is capable of accelerating a subsonic flow to supersonic exit flow. This is called a convergent–divergent duct, with an internal throat, that is, the sonic throat. Conversely, a convergent–divergent duct with a supersonic entrance condition has the capability of decelerating the flow to subsonic exit conditions through a sonic throat. These duct geometries are shown in Figure 2.14.

■ **FIGURE 2.14**
Convergent–divergent
duct with an internal
sonic throat



The sonic state where the gas speed and the local speed of sound are equal is distinguished with an asterisk. For example, the pressure at the sonic point is p^* and the temperature is T^* , the speed of sound is a^* , and so on. Since the flow is isentropic throughout the duct, the stagnation pressure remains constant and as a consequence of adiabatic duct flow the stagnation temperature remains constant. By writing the stagnation temperature in terms of the local static temperature and local Mach number, we may relate the local static temperature to sonic temperature according to

$$T_t = T \left[1 + \left(\frac{\gamma - 1}{2} \right) M^2 \right] = T^* \left[1 + \left(\frac{\gamma - 1}{2} \right) (1) \right] = T^* \left(\frac{\gamma + 1}{2} \right) \quad (2.89)$$

Taken in ratio, the above equation yields

$$\frac{T}{T^*} = \frac{\frac{\gamma + 1}{2}}{1 + \left(\frac{\gamma - 1}{2} \right) M^2} \quad (2.90)$$

We may apply the isentropic relationship between temperature ratio and pressure ratio (Equation 2.24) to get an expression for p/p^* .

$$\frac{p}{p^*} = \left[\frac{\frac{\gamma + 1}{2}}{1 + \left(\frac{\gamma - 1}{2} \right) M^2} \right]^{\frac{\gamma}{\gamma - 1}} \quad (2.91)$$

From perfect gas law and the two expressions for temperature and pressure ratio, (2.90) and (2.91), we get an expression for the density ratio

$$\frac{\rho}{\rho^*} = \frac{p}{p^*} / \frac{T}{T^*} = \left[\frac{\frac{\gamma + 1}{2}}{1 + \left(\frac{\gamma - 1}{2} \right) M^2} \right]^{\frac{1}{\gamma - 1}} \quad (2.92)$$

The above expressions for the sonic ratios describe the properties of a section of the duct where flow Mach number is M to the flow properties at the sonic point. The mass flow rate balance between any section of the duct and the sonic throat yields an expression for the area ratio A/A^* . First, let us write the continuity equation for a uniform flow in terms

of the total gas properties, p_t and T_t .

$$\dot{m} = \rho AV = \frac{\gamma P}{a^2} AV = \frac{\gamma p AM}{a} = \sqrt{\frac{\gamma}{R}} \frac{p}{\sqrt{T}} AM \quad (2.93a)$$

We replaced the density with speed of sound and pressure to get Equation 2.93a. Now, we may substitute the total pressure and temperature for the static pressure and temperature of Equation 2.93a and their respective functions of Mach number to get Equation 2.93b.

$$\dot{m} = \sqrt{\frac{\gamma}{R}} \frac{p_t}{\sqrt{T_t}} A \cdot M \left(\frac{1}{1 + \frac{\gamma-1}{2} M^2} \right)^{\frac{\gamma+1}{2(\gamma-1)}} \quad (2.93b)$$

According to Equation 2.93b, we need the local flow area A , the local Mach number M , the local total pressure and temperature p_t and T_t , respectively, and the type of gas, γ , R , to calculate the mass flow rate. The total temperature remains constant in adiabatic flows with no shaft work and the total pressure remains constant for isentropic flows with no shaft work, hence they are convenient parameters in Equation 2.93b. Since the mass flow rate between any two sections of a duct in steady flow has to be equal, Equation 2.93b is a Mach number–area relationship. We use the sonic flow area A^* , with $M = 1$, to express a nondimensional area ratio.

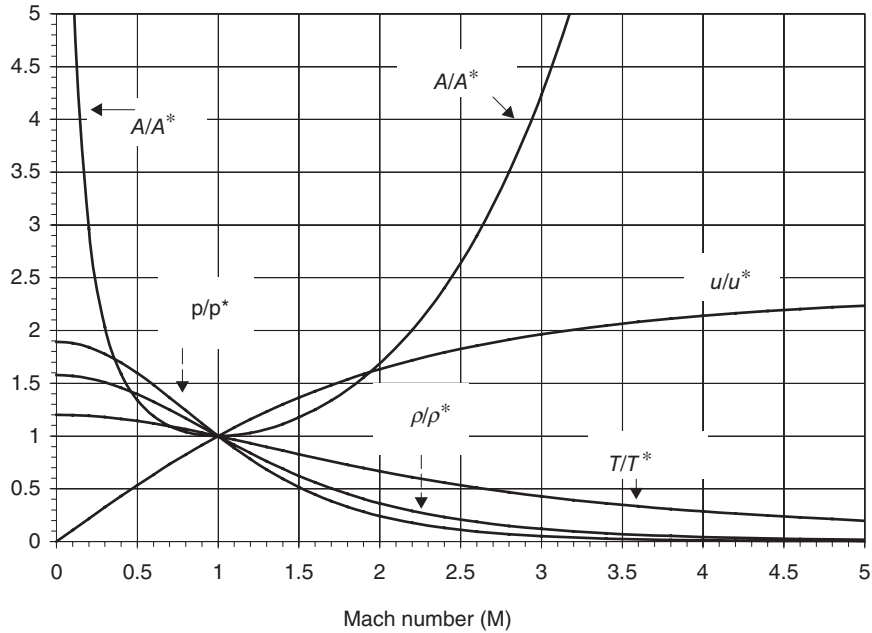
$$\frac{A}{A^*} = \frac{1}{M} \left(\frac{1 + \frac{\gamma-1}{2} M^2}{\frac{\gamma+1}{2}} \right)^{\frac{\gamma+1}{2(\gamma-1)}} \quad (2.94)$$

We may tabulate the functions p/p^* , T/T^* , and A/A^* in addition to p_t/p , T_t/T in an isentropic table for a specific gas, that is, $\gamma = \text{constant}$. Figure 2.15 shows the isentropic flow parameters as a function of Mach number for a diatomic gas, such as air.

At the minimum-area section, the ratio of mass flow rate to the cross-sectional area becomes maximum. Therefore, to demonstrate that $M = 1$ maximizes the mass flow per unit area, we differentiate the following equation and set it equal to zero,

$$\begin{aligned} \frac{\dot{m}}{A} &= \text{const} \cdot M \cdot \left(\frac{1}{1 + \frac{\gamma-1}{2} M^2} \right)^{\frac{\gamma+1}{2(\gamma-1)}} \\ \frac{d}{dM} \left(\frac{\dot{m}}{A} \right) &= \text{const} \cdot \left[\left(\frac{1}{1 + \frac{\gamma-1}{2} M^2} \right)^{\frac{\gamma+1}{2(\gamma-1)}} \right. \\ &\quad \left. + M \left(\frac{-\gamma+1}{2(\gamma-1)} \right) ((\gamma-1)M) \left(\frac{1}{1 + \frac{\gamma-1}{2} M^2} \right)^{\frac{\gamma+1}{2(\gamma-1)}+1} \right] = 0 \end{aligned} \quad (2.95)$$

■ **FIGURE 2.15**
Isentropic flow parameters for a diatomic (calorically perfect) gas, $\gamma = 1.4$



After some minor simplifications we get

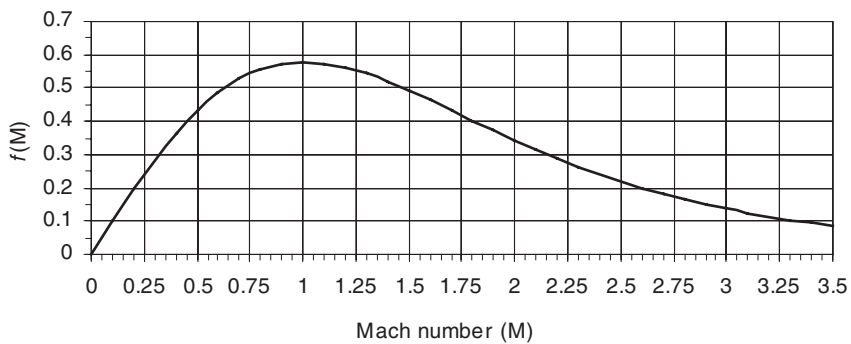
$$1 - \left(\frac{\gamma + 1}{2} M^2 \right) / \left(1 + \frac{\gamma - 1}{2} M^2 \right) = 0 \tag{2.96}$$

Equation 2.96 is identically satisfied by $M = 1$. We may also demonstrate this principle graphically by plotting the function $f(M)$ (from Equation 2.93b):

$$f(M) = M / \left(1 + \frac{\gamma - 1}{2} M^2 \right)^{\frac{\gamma + 1}{2(\gamma - 1)}} \tag{2.97}$$

Figure 2.16 is a graph of the nondimensional mass flow rate per unit area, that is, Equation 2.97.

■ **FIGURE 2.16**
Nondimensional mass flow parameter variation with Mach number shows a sonic condition at the minimum-area section, i.e., the throat



2.10 Waves in Supersonic Flow

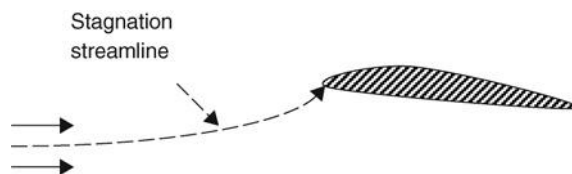
In a subsonic flow, a disturbance travels upstream to alert the flow of an upcoming object, say an airfoil. The streamlines in the flow make the necessary adjustments prior to reaching the obstacle to “make room” for the body that has a thickness. Figure 2.17 shows the phenomenon of “upwash” ahead of a subsonic wing, as evidence of subsonic flow adjustment before reaching the body.

In contrast to a subsonic flow, the flowfield in a supersonic flow has to make adjustment for a body abruptly and within the zone of action. For small disturbances, the zone of action is the Mach cone, as shown in Figure 2.4. Larger disturbances, as in thick bodies or bodies at an angle of attack, create a system of compression and expansion waves that turn the supersonic flow around the body. The finite compression waves in aerodynamics are called shock waves due to their abrupt nature. A diamond airfoil in a supersonic flow shows the wave pattern about the body in Figure 2.18.

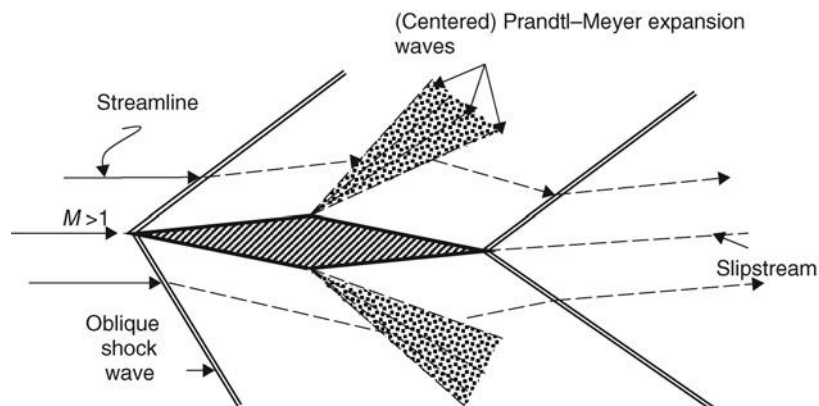
The attached oblique shocks at the leading edge turn the flow parallel to the surface and the expansion waves, known as the Prandtl–Meyer waves, cause the flow to turn at the airfoil shoulders. The trailing-edge waves turn the flow parallel to each other and the slipstream. The flow downstream of the tail waves, in general, is not parallel to the upstream flow. This is also in contrast to the subsonic flow that recovers the upstream flow direction further downstream of the trailing edge. The slipstream in supersonic flow allows for parallel flows and a continuous static pressure across the upper and lower parts of the trailing flowfield. It is the latter boundary condition that determines the slipstream inclination angle.

A special case of an oblique shock wave is the normal shock. This wave is normal to the flow and causes a sudden deceleration; static pressure, temperature, density, and

■ FIGURE 2.17
“Upwash” ahead of a subsonic wing section



■ FIGURE 2.18
Sketch of waves about a diamond airfoil at an angle of attack in supersonic flow



entropy rise; Mach number and total pressure drop across the wave. We derive the *jump conditions* across a normal shock in the following section.

2.11 Normal Shocks

We apply the conservation principles to a normal shock flow, as shown in Figure 2.19. The shape of the control volume is chosen to simplify the applications of the conservation laws. The frame of reference is placed (with an observer) at the shock wave for a steady flow.

To avoid writing the flow area of our arbitrary control volume, we choose it to be unity. The continuity equation of a steady flow through the control volume demands

$$\rho_1 u_1 = \rho_2 u_2 \tag{2.98}$$

The momentum equation in the x -direction is

$$\rho_2 u_2^2 - \rho_1 u_1^2 = p_1 - p_2 \tag{2.99a}$$

Now separating the flow conditions on the two sides of the shock, we get

$$p_1 + \rho_1 u_1^2 = p_2 + \rho_2 u_2^2 \tag{2.99b}$$

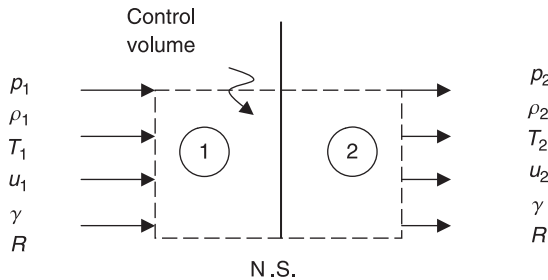
Each side of Equation 2.99b is called fluid impulse per unit area, I/A . Since the flow area is constant across a normal shock, we conclude that *impulse* is conserved across the shock. We will return to impulse later in this chapter. By factoring the static pressure and introducing the speed of sound in Equation 2.99b, we get an alternative form of the conservation of momentum across the shock that involves Mach number and pressure, namely

$$p_1 (1 + \gamma M_1^2) = p_2 (1 + \gamma M_2^2) \tag{2.100}$$

The energy equation for an adiabatic flow with no shaft work demands the conservation of the total enthalpy, that is,

$$c_p T_1 + \frac{u_1^2}{2} = c_p T_2 + \frac{u_2^2}{2} \quad (\text{assuming } c_p = \text{constant}) \tag{2.101}$$

■ **FIGURE 2.19**
Control volume for a normal shock (for an observer fixed at the shock)



The essential unknowns in a normal shock flow are p_2 , ρ_2 , T_2 , and u_2 . The other unknowns are derivable from these basic parameters. For example, from the static temperature, T_2 , we calculate the local speed of sound, a_2 , and then the Mach number downstream of the shock, M_2 . Also, with the Mach number known, we may calculate the total pressure, p_{t2} , and temperature, T_{t2} , downstream of a shock. The three conservation laws and an equation of state for the gas provide the four equations needed to solve for the four basic unknowns, that is, gas properties and the speed. These governing equations are coupled, however, and not immediately separable. We introduce the steps to the derivation of a normal shock flow in the following section.

We may relate the enthalpy to speed of sound, via Equation 2.61a, and derive alternative forms of the energy equation

$$\frac{a^2}{\gamma - 1} + \frac{u^2}{2} = \frac{a^{*2}}{\gamma - 1} + \frac{a^{*2}}{2} = \frac{\gamma + 1}{2(\gamma - 1)} a^{*2} = \frac{a_t^2}{\gamma - 1} = \text{Constant} \quad (2.102a)$$

Divide through by u^2 , and multiply by $(\gamma - 1)$, to get

$$\frac{1}{M^2} + \frac{\gamma - 1}{2} = \frac{\gamma + 1}{2} \cdot \frac{1}{M^{*2}} \quad (2.102b)$$

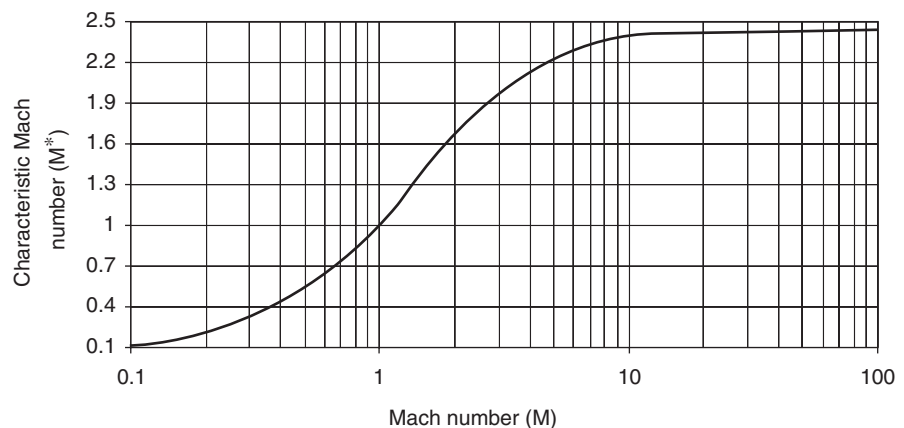
Here, we have introduced a new parameter M^* , which is called the characteristic Mach number and has a definition

$$M^* \equiv \frac{u}{a^*} \quad (2.103)$$

The characteristic Mach number is the ratio of local gas speed to the speed of sound at the sonic point. Hence, it is the ratio of two speeds at two different points in the flow. It is related to the local Mach number, M , through Equation 2.102b. If we solve for M^{*2} in terms of M^2 , we get the expression 2.104, which is plotted in Figure 2.20.

$$M^{*2} = \frac{(\gamma + 1)M^2}{2 + (\gamma - 1)M^2} \quad (2.104)$$

■ **FIGURE 2.20**
Variation of the
characteristic Mach
 M^* , with Mach
number M , $\gamma = 1.4$



We note that for $M < 1$, M^* is less than 1, for $M = 1$, M^* is equal to 1, and for $M > 1$, M^* is greater than 1. The characteristic Mach number is finite, however, as the Mach number M approaches infinity, M^* approaches a finite value, that is,

$$M^* \rightarrow \sqrt{\frac{\gamma + 1}{\gamma - 1}} \quad \text{as } M \rightarrow \infty. \quad (2.105)$$

For $\gamma = 1.4$, the limiting value of M^* is $\sqrt{6} = 2.449$.

The momentum balance across the shock may be written as

$$\rho_1 u_1 \left(\frac{p_1}{\rho_1 u_1} + u_1 \right) = \rho_2 u_2 \left(\frac{p_2}{\rho_2 u_2} + u_2 \right) \quad (2.106)$$

From the continuity equation, we note that the product of density–velocity is a constant of motion, that is, $\rho_1 u_1 = \rho_2 u_2$, hence it may be cancelled from Equation 2.106. Also, we recognize that the ratio of static pressure to density is proportional to the speed of sound squared according to

$$p/\rho = a^2/\gamma$$

Hence, the modified form of the momentum equation is

$$\frac{a_1^2}{\gamma u_1} + u_1 = \frac{a_2^2}{\gamma u_2} + u_2 \quad (2.107)$$

From energy Equation 2.101, we may replace the local speed of sound a by the local speed u and the speed of sound at the sonic point a^* to get an equation in terms of the gas speeds across the shock and the speed of sound at the sonic point.

$$\frac{1}{\gamma u_1} \left[\frac{\gamma + 1}{2} a^{*2} - \frac{\gamma - 1}{2} u_1^2 \right] + u_1 = \frac{1}{\gamma u_2} \left[\frac{\gamma + 1}{2} a^{*2} - \frac{\gamma - 1}{2} u_2^2 \right] + u_2 \quad (2.108)$$

This equation simplifies to the Prandtl relation for a normal shock, that is,

$$u_1 u_2 = a^{*2} \quad (2.109)$$

Prandtl relation states that the product of gas speeds on two sides of a normal shock is a constant and that is the square of the speed of sound at the sonic point. This powerful expression relates the characteristic Mach number upstream and downstream of a normal shock via an inverse relationship, namely

$$M_2^* = 1/M_1^* \quad (2.110)$$

We may also conclude from this equation that the flow downstream of a normal shock is subsonic, since the characteristic Mach number upstream of the shock is greater

than 1. From Equation 2.104, we replace the characteristic Mach number by the local Mach number to get

$$M_2^{*2} = \frac{1}{M_1^{*2}} = \frac{2 + (\gamma - 1)M_1^2}{(\gamma + 1)M_1^2} = \frac{(\gamma + 1)M_2^2}{2 + (\gamma - 1)M_2^2} \quad (2.111a)$$

This equation contains M_2^2 as the only unknown and thus gives:

$$M_2^2 = \frac{2 + (\gamma - 1)M_1^2}{2\gamma M_1^2 - (\gamma - 1)} \quad (2.111b)$$

The downstream Mach number of a normal shock is finite even for $M_1 \rightarrow \infty$, which results in

$$M_2 \rightarrow \sqrt{\frac{\gamma - 1}{2\gamma}} \quad \text{as } M_1 \rightarrow \infty \quad (2.111c)$$

The density ratio across the shock is inversely proportional to the gas speed ratio via the continuity equation, which is related to the upstream Mach number according to

$$\frac{\rho_2}{\rho_1} = \frac{u_1}{u_2} = \frac{M_1^*}{M_2^*} = M_1^{*2} = \frac{(\gamma + 1)M_1^2}{2 + (\gamma - 1)M_1^2} \quad (2.112a)$$

We note that the density ratio is also finite as $M_1 \rightarrow \infty$, that is,

$$\frac{\rho_2}{\rho_1} \rightarrow \frac{\gamma + 1}{\gamma - 1} \quad \text{as } M_1 \rightarrow \infty \quad (2.112b)$$

To derive the static pressure ratio across a shock, we start with the gas momentum equation. We may regroup the pressure and momentum terms in Equation 2.99b according to

$$p_2 - p_1 = \rho_1 u_1^2 \left(1 - \frac{\rho_2}{\rho_1} \cdot \frac{u_2^2}{u_1^2} \right) = \rho_1 u_1^2 \left(1 - \frac{\rho_1}{\rho_2} \right) \quad (2.113)$$

Now, we may divide both sides by p_1 and substitute for the density ratio from Equation 2.112, and simplify to get

$$\frac{p_2}{p_1} = 1 + \frac{2\gamma}{\gamma + 1} (M_1^2 - 1) \quad (2.114)$$

From the perfect gas law, we establish the static temperature ratio across the shock in terms of the static pressure and density ratios in terms M_1 :

$$\frac{T_2}{T_1} = \frac{p_2}{p_1} \frac{\rho_1}{\rho_2} = \left[1 + \frac{2\gamma}{\gamma + 1} (M_1^2 - 1) \right] \left[\frac{2 + (\gamma - 1)M_1^2}{(\gamma + 1)M_1^2} \right] \quad (2.115)$$

The stagnation pressure ratio across a normal shock may be written as the static pressure ratio and the function of local Mach numbers according to

$$\begin{aligned} \frac{p_{t2}}{p_{t1}} &= \frac{p_2}{p_1} \left[\frac{1 + \frac{\gamma - 1}{2} M_2^2}{1 + \frac{\gamma - 1}{2} M_1^2} \right]^{\frac{\gamma}{\gamma - 1}} \\ &= \left[1 + \frac{2\gamma}{\gamma + 1} (M_1^2 - 1) \right] \left[\frac{1 + \frac{\gamma - 1}{2} \left(\frac{2 + (\gamma - 1)M_1^2}{2\gamma M_1^2 - (\gamma - 1)} \right)}{1 + \frac{\gamma - 1}{2} M_1^2} \right]^{\frac{\gamma}{\gamma - 1}} \end{aligned} \quad (2.116)$$

The entropy rise across a shock is related to the stagnation pressure loss following Equation 2.73,

$$\Delta s/R = -\ell n(p_{t2}/p_{t1}) \quad (2.117)$$

In summary, we established the downstream Mach number in terms of the upstream Mach number and all the jump conditions across a normal shock, that is, p_2/p_1 , T_2/T_1 , ρ_2/ρ_1 , p_{t2}/p_{t1} , $\Delta s/R$, as well as identifying the constants of motion, namely:

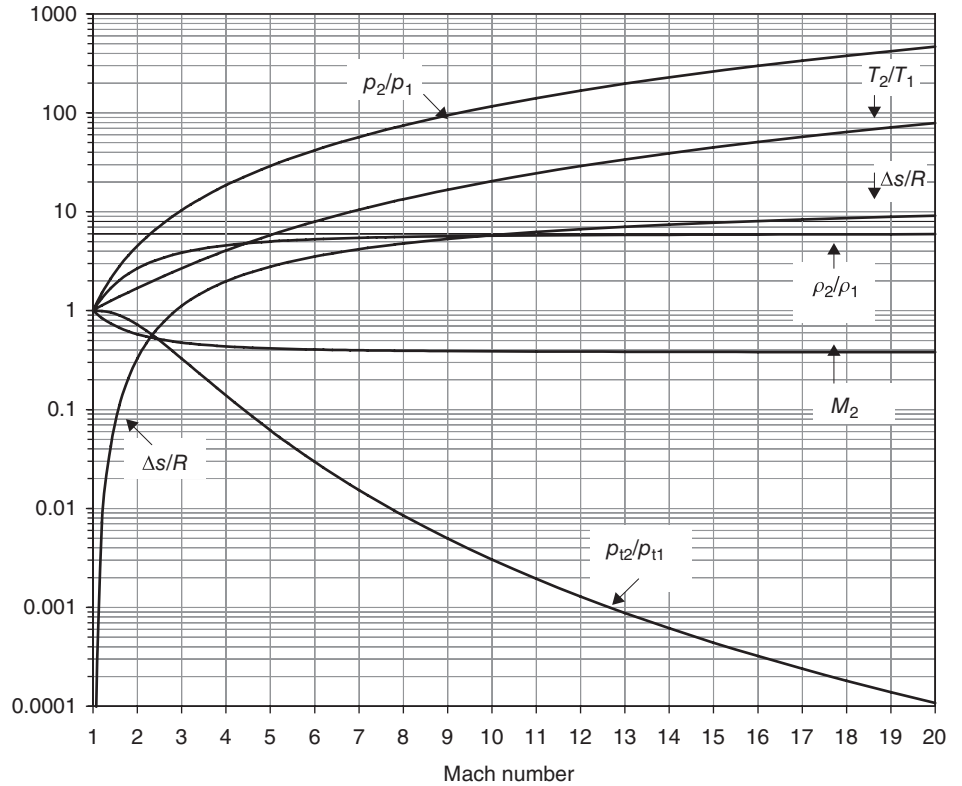
$$\begin{aligned} \rho u &= \text{Constant} \\ p + \rho u^2 &= p(1 + \gamma M^2) = \text{Constant} \\ h + \frac{u^2}{2} &= \frac{a^2}{\gamma - 1} + \frac{u^2}{2} = \frac{(\gamma + 1)}{2(\gamma - 1)} a^{*2} = \frac{a_t^2}{\gamma - 1} = \text{Constant} \\ u_1 u_2 &= a^{*2} = \text{Constant} \end{aligned}$$

Figure 2.21 shows the normal shock parameters for $\gamma = 1.4$ on a log-linear scale. Note that the density ratio as well as the Mach number downstream of the shock approach constant values as the Mach number increases.

2.12 Oblique Shocks

Compression Mach waves may coalesce to form an oblique shock wave. A normal shock is a special case of an oblique shock with a wave angle of 90° . Figure 2.22 shows a schematic drawing of an oblique shock flow with a representative streamline that abruptly changes direction across the shock. The shock wave angle with respect to upstream flow is called β and the flow-turning angle (again with respect to the upstream flow) is θ . A representative control volume is also shown in Figure 2.22. The flow is resolved into a normal and a tangential direction to the shock wave. The velocity components are u and w (normal and tangential to the shock wave front, respectively). Two velocity triangles are shown upstream and downstream of the shock with vertex angles β and $(\beta - \theta)$, respectively. The control volume is confined between a pair of streamlines and the entrance, and exit

■ **FIGURE 2.21**
Normal shock parameters for a calorically perfect gas, $\gamma = 1.4$

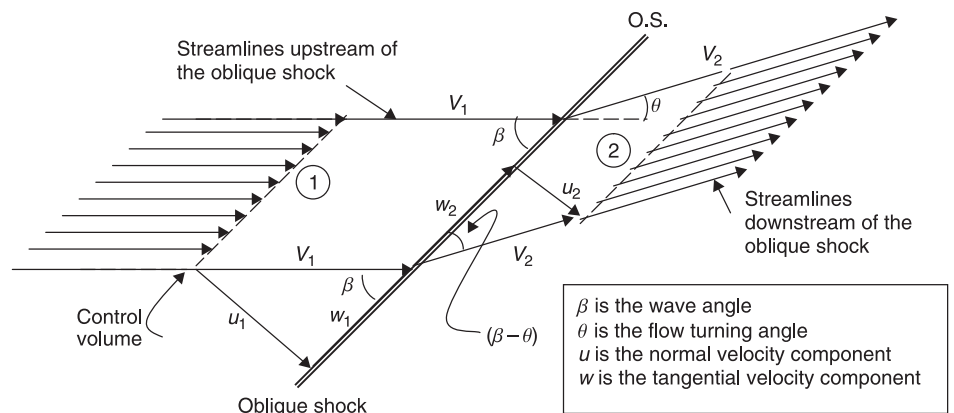


planes are parallel to the shock. We choose the area of the entrance and exit to be one for simplicity.

To arrive at the shock jump conditions across the shock, we satisfy the conservation of mass, momentum normal and tangential to the shock, and the energy across the oblique shock. The continuity equation demands

$$\rho_1 u_1 = \rho_2 u_2 \tag{2.118}$$

■ **FIGURE 2.22**
Definition sketch of velocity components normal and parallel to an oblique shock, with the wave angle and flow turning angle definitions



The conservation of normal momentum requires the momentum change normal to the shock to be balanced by the fluid forces acting in the normal direction on the control volume. The only forces acting normal to the shock are the pressure forces acting on the entrance and the exit planes of the control surface.

$$\rho_2 u_2^2 - \rho_1 u_1^2 = p_1 - p_2 \quad (2.119)$$

The conservation of momentum along the shock front, that is, tangential to the shock, requires

$$\rho_2 u_2 w_2 - \rho_1 u_1 w_1 = 0 \quad (2.120)$$

The net pressure forces in the tangential direction are zero, hence the tangential momentum is conserved. We may cancel the continuity portion of Equation 2.120 to arrive at the simple result of the conservation of tangential velocity across an oblique shock, namely

$$w_1 = w_2 \quad (2.121)$$

The energy equation demands the conservation of total enthalpy, therefore

$$h_1 + \frac{u_1^2 + w_1^2}{2} = h_2 + \frac{u_2^2 + w_2^2}{2} \quad (2.122)$$

Since the tangential velocity is conserved across the shock the energy equation is simplified to

$$h_1 + \frac{u_1^2}{2} = h_2 + \frac{u_2^2}{2} \quad (2.123)$$

Now, we note that the conservation equations normal to the shock take on the exact form of the normal shock equations that we solved earlier to arrive at the shock jump conditions. Consequently, all the jump conditions across an oblique shock are established uniquely by the normal component of the flow to the oblique shock, that is, M_{1n} .

From the wave angle β , we get

$$M_{1n} = M_1 \sin \beta \quad (2.124)$$

The normal shock relation Equation 2.111b establishes the normal component of the Mach number downstream of an oblique shock, according to

$$M_{2n}^2 = \frac{2 + (\gamma - 1)M_{1n}^2}{2\gamma M_{1n}^2 - (\gamma - 1)} = \frac{2 + (\gamma - 1)M_1^2 \sin^2 \beta}{2\gamma M_1^2 \sin^2 \beta - (\gamma - 1)} \quad (2.125)$$

From the velocity triangle downstream of the oblique shock, we have

$$M_2 = \frac{M_{2n}}{\sin(\beta - \theta)} \quad (2.126)$$

To summarize, an oblique shock jump conditions are established by the normal component of the flow and the downstream Mach number follows Equation 2.126. To establish a relationship between the flow turning angle and the oblique shock wave angle, we use the velocity triangles upstream and downstream of the shock,

$$\tan \beta = \frac{u_1}{w_1} \quad (2.127)$$

$$\tan(\beta - \theta) = \frac{u_2}{w_2} \quad (2.128)$$

The ratio of these two equations relates the angles and the normal velocity ratio according to

$$\frac{\tan \beta}{\tan(\beta - \theta)} = \frac{u_1}{u_2} = \frac{\rho_2}{\rho_1}$$

Now substituting for the density ratio from the normal shock relations, we get

$$\frac{\tan \beta}{\tan(\beta - \theta)} = \frac{(\gamma + 1)M_1^2 \sin^2 \beta}{2 + (\gamma - 1)M_1^2 \sin^2 \beta} \quad (2.129)$$

Expression 2.129 is called “ θ - β - M ” equation and a graph of the oblique shock angle versus the turning angle is plotted for a constant upstream Mach number to create oblique shock charts. In the limit of zero turning angle, that is, as $\theta \rightarrow 0$,

$$(\gamma + 1)M_1^2 \sin^2 \beta = 2 + (\gamma - 1)M_1^2 \sin^2 \beta \quad (2.130)$$

There are two solutions to Equation 2.130. The first is

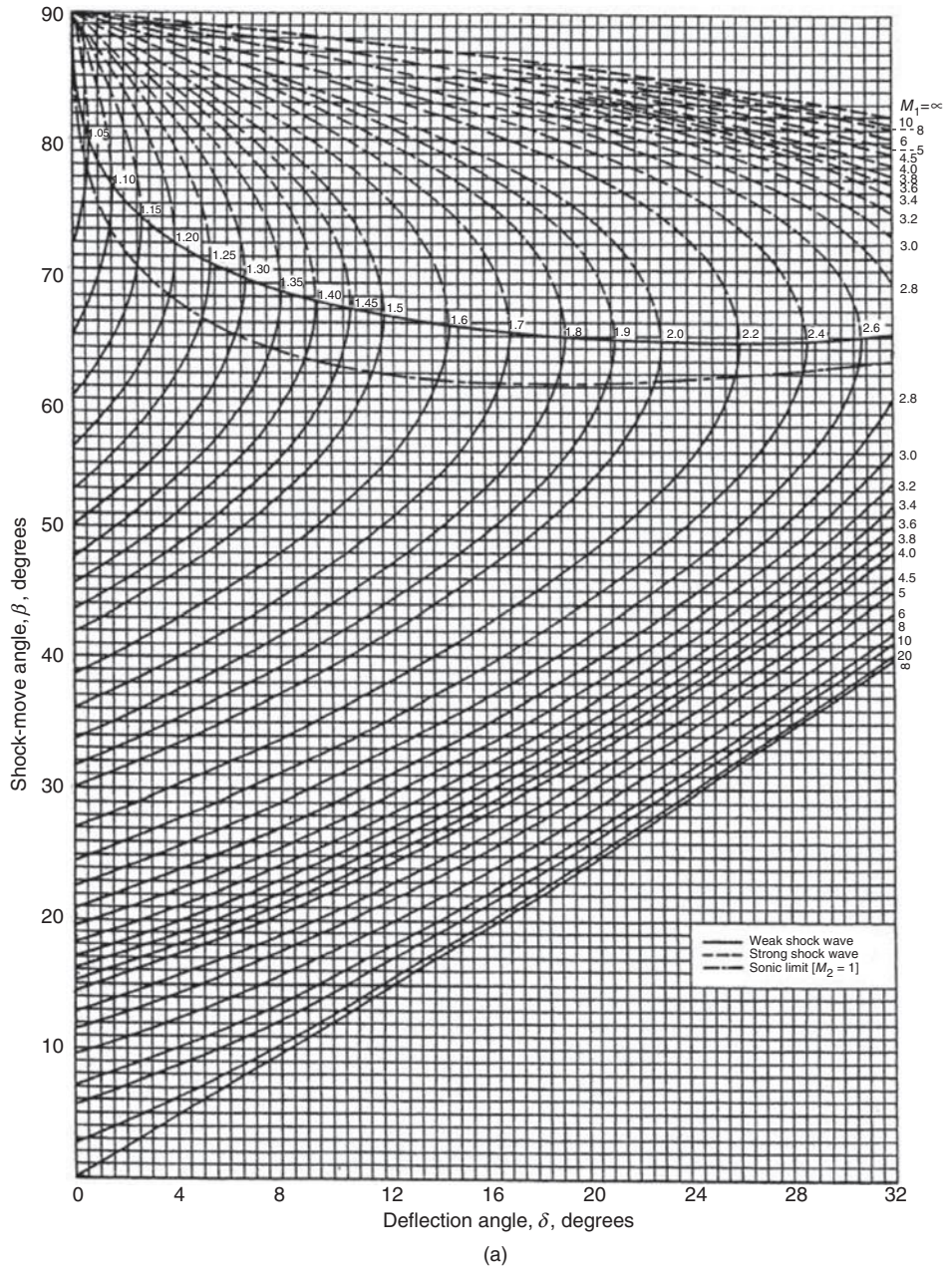
$$\beta = \sin^{-1} \left(\frac{1}{M} \right) \equiv \mu \quad (2.131)$$

which identifies an infinitesimal strength shock wave as a Mach wave, and the second is $\beta = 90^\circ$, which identifies a normal shock as the strongest oblique shock. Thus, the weakest oblique shock is a Mach wave and the strongest oblique shock is a normal shock. Since the strength of the wave depends on $M \cdot \sin \beta_s$, an oblique shock wave angle is larger than the Mach angle, that is,

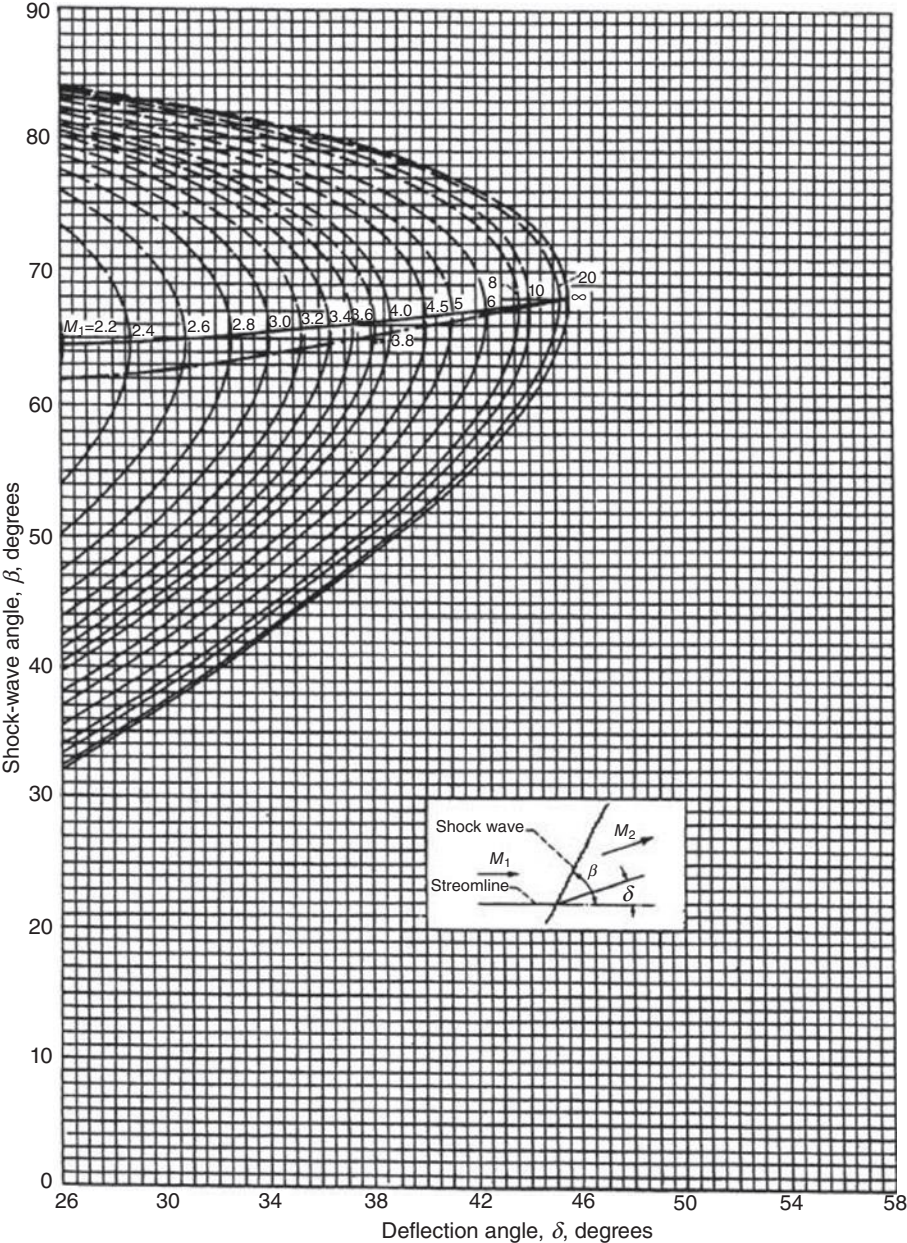
$$\mu \leq \beta \leq 90^\circ \quad (2.132)$$

Figure 2.23 is a graph of Equation 2.129 with Mach number as a running parameter (from NACA Report 1135, 1953). There are two solutions for the wave angle β for each turning angle θ . The high wave angle is referred to as the strong solution, and the lower wave angle is called the weak solution. A continuous line and a broken line distinguish the weak and strong solutions in Figure 2.23, respectively. Also, there is a maximum turning angle, θ_{\max} , for any supersonic Mach number. For example, a Mach 2 flow can turn only $\sim 23^\circ$ via an attached plane oblique shock wave. For higher turning angles than θ_{\max} , a

■ **FIGURE 2.23**
 (a) The plane oblique shock chart for $\gamma = 1.4$ (from NACA Report 1135, 1953); (b) The plane oblique shock chart continued (from NACA Report 1135, 1953)



■ FIGURE 2.23
(Continued)



(b)

detached shock will form upstream of the body. This shock, due to its shape, is referred to as the bow shock.

The SR-71 at Mach 3+ is a marvel in supersonic aerodynamic and propulsion system design. Courtesy of NASA

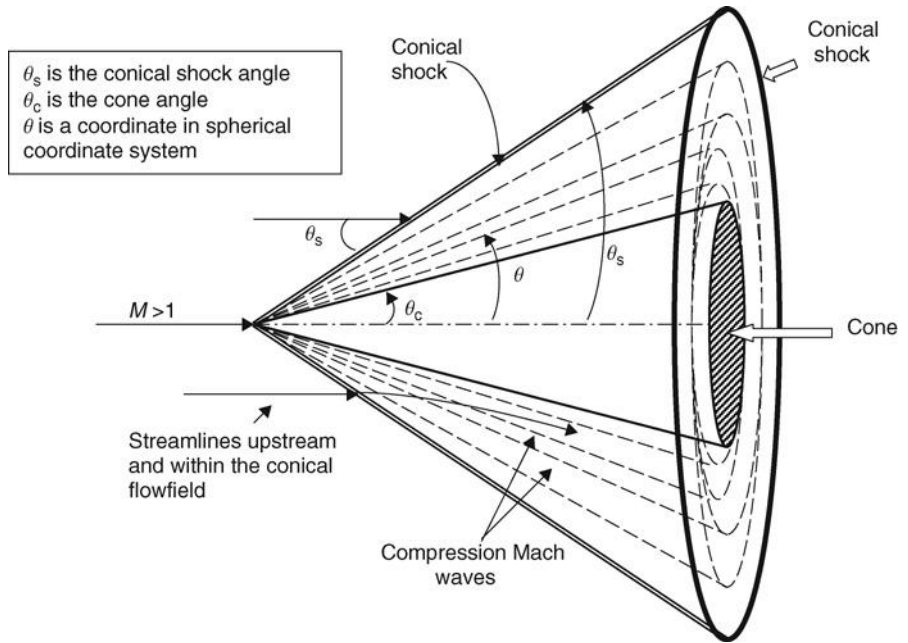


2.13 Conical Shocks

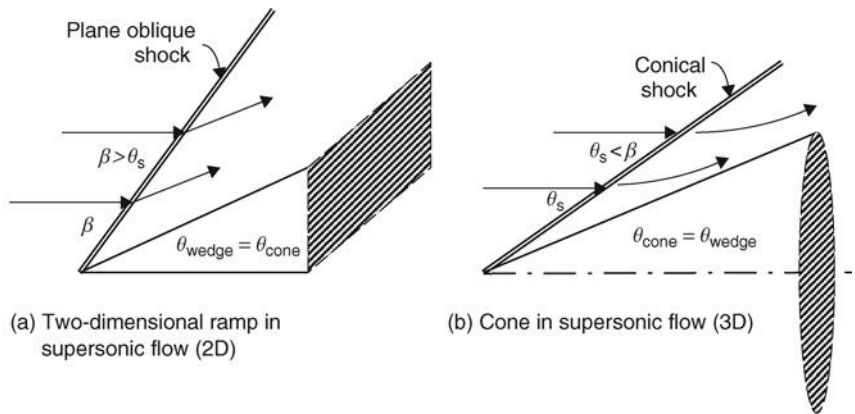
A cone in supersonic flow creates a conical shock. In the case of zero angle of attack, the flowfield is axisymmetric and the cone axis and the conical shock axis coincide. The jump conditions at the shock are, however, established by the (local) normal component of Mach number to the shock front. The flowfield behind a conical shock continues to vary from the shock surface to the cone surface. In a plane oblique shock case, the flowfield undergoes a single jump at the shock and then its flow properties remain constant. The mechanism for a continuous change behind a conical shock is the compression Mach waves emanating from the cone vertex. These are the rays along which flow properties remain constant. Note that an axisymmetric conical shock flow lacks a length scale and hence θ becomes the only variable of the problem. Figure 2.24 shows a definition sketch of an axisymmetric conical shock flow.

All the jump conditions across the conical shock depend on $M \cdot \sin\theta_s$, as we derived earlier in this section. The flow properties downstream of the shock, for example, p , T , ρ , V , are a function of the conical angle θ , that is, $p(\theta)$, etc. Therefore, all the rays emanating from the cone vertex have different flow properties. The cone surface is a ray itself and thus experiences constant flow properties, such as pressure, temperature, density, velocity, and Mach number. The streamlines downstream of a conical shock continue to turn in their interaction with the compression Mach waves. The flowfield downstream of the conical shock remains reversible, however, as the compression Mach waves are each of infinitesimal strength. The flowfield downstream of an axisymmetric conical shock is irrotational since the shock is straight, hence of constant strength. We apply conservation principles to arrive at the detail flowfield downstream of a conical shock. In addition, we utilize the irrotationality condition to numerically integrate the governing conical flowfield equation, known as the Taylor–Maccoll equation. A cone of semivertex angle θ_c would create a conical shock wave of angle θ_s , which is smaller than a corresponding plane oblique shock on a two-dimensional ramp of the same vertex angle. This results in a weaker shock in three-dimensional space as compared with a corresponding two-dimensional space. This important flow behavior is referred to as the *3D relieving effect* in aerodynamics. Figure 2.25 shows a two-dimensional compression ramp and a conical ramp of equal vertex angle in supersonic flow.

■ FIGURE 2.24
Definition sketch of a
conical shock flowfield

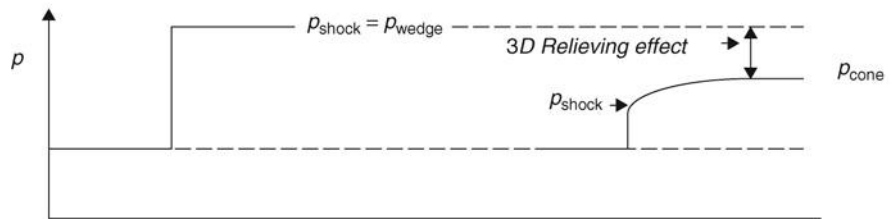


■ FIGURE 2.25
Three-dimensional
relieving effect on a
cone



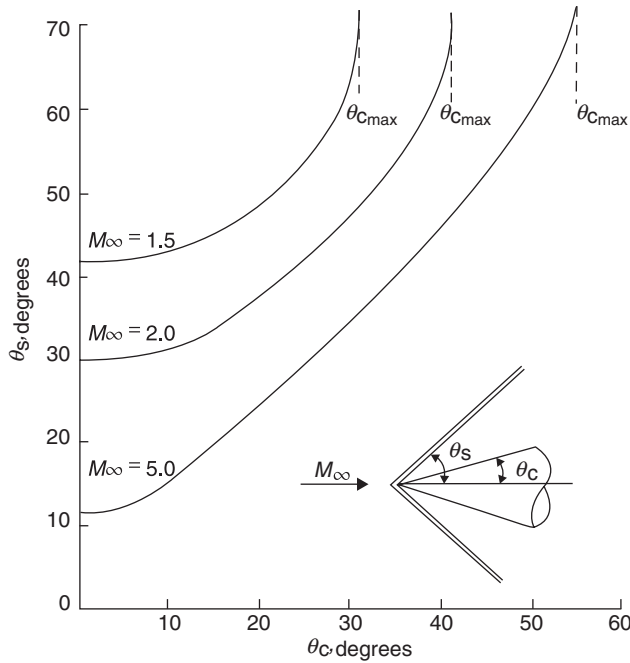
(a) Two-dimensional ramp in
supersonic flow (2D)

(b) Cone in supersonic flow (3D)



(c) Static pressure jump and variation across a plane oblique shock and a conical shock

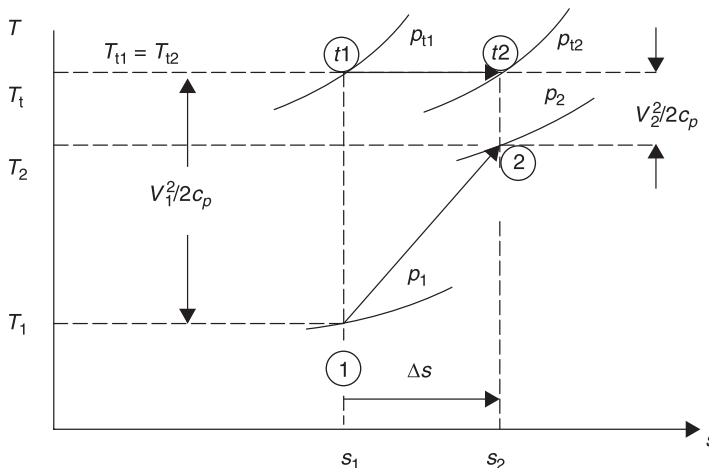
■ **FIGURE 2.26**
 Conical shock chart for a calorically perfect gas, $\gamma = 1.4$. Source: Anderson 2003, Fig. 10.5, p. 373. Reproduced with permission from McGraw Hill



A conical shock chart for three Mach numbers is shown in Figure 2.26 (from Anderson, 2003). This figure contains only the weak solution. Note that the maximum turning angle for a given Mach number is larger for a cone than a two-dimensional ramp of the same nose angle. This, too, is related to the well-known *3D relieving effect*.

Finally, we graph a shock wave static and stagnation states on a T - s diagram (Figure 2.27). All shocks are irreversible and, hence, suffer an entropy rise, as graphically demonstrated in Figure 2.27. The static path connects points 1 and 2 across the shock wave. The stagnation path connects “t1” to “t2.” The constant-pressure lines indicate a static pressure rise and a stagnation pressure drop between the two sides of a shock. The

■ **FIGURE 2.27**
 Static and stagnation states of a (calorically perfect) gas across a shock wave



static temperature rises and the stagnation temperature remains constant (assuming c_p is constant as in a calorically perfect gas). We also note a drop in the kinetic energy of the gas, which is converted into heat through viscous dissipation within the shock. Shocks are generally thin and are of the order of the mean free path of the molecules in the gas. Thus, shocks are often modeled as having a zero thickness, unless the gas is in near vacuum of upper atmosphere where the mean free path is of the order of centimeters.

2.14 Expansion Waves

The oblique shocks are compression waves in a supersonic flow that abruptly turn the flow and compress the gas in the process. An expansion wave causes a supersonic flow to turn and the static pressure to drop. The expansion waves are Mach waves that make a Mach angle with respect to the local flow. The flow through expansion waves is inherently isentropic, as the Mach waves are of infinitesimal strength and hence reversible. An expansion Mach wave is capable of only turning the flow incrementally and accelerates the flow incrementally. Such a flow turning and flow acceleration is shown in Figure 2.28 with exaggeration of the turning angle and the flow acceleration increment. The local wave angle with respect to upstream flow is at the Mach angle μ . The incremental turning angle is labeled as $d\theta$. The change of velocity is shown by a magnitude of dV and a direction $d\theta$ with respect to upstream flow. Since the velocity downstream of the Mach wave has to have the same tangential component as the upstream flow, the right triangles that share the same tangential velocity are labeled with V and $V + dV$ vectors in Figure 2.28.

We may apply the law of sines to the triangle with sides V and $V + dV$ to relate the turning angle and incremental speed change,

$$\frac{V + dV}{\sin\left(\frac{\pi}{2} - \mu\right)} = \frac{V}{\sin\left(\frac{\pi}{2} - \mu - d\theta\right)} \quad (2.133)$$

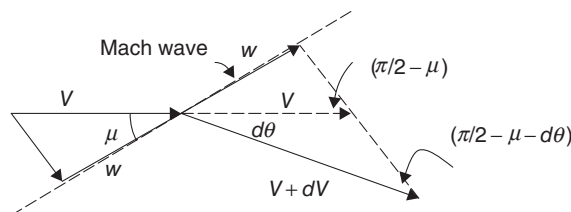
Let us simplify the sines and isolate the velocity terms, such as

$$1 + \frac{dV}{V} = \frac{\cos \mu}{\cos(\mu + d\theta)} \cong \frac{\cos \mu}{\cos \mu - d\theta \cdot \sin \mu} = \frac{1}{1 - d\theta \cdot \tan \mu} \approx 1 + d\theta \cdot \tan \mu \quad (2.134)$$

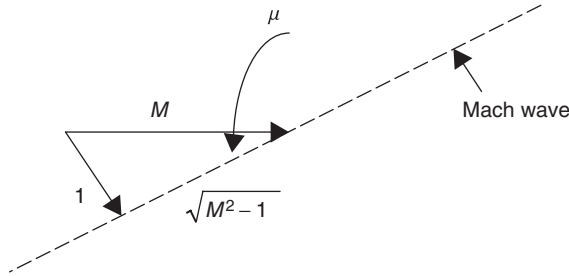
We applied a small angle approximation to sine and cosine $d\theta$, and in the last approximation on the RHS we used a binomial expansion and truncation at the linear term for a small ε :

$$\frac{1}{1 \pm \varepsilon} \approx 1 \mp \varepsilon \quad (2.135)$$

■ FIGURE 2.28
Incremental turning
across a Mach wave



■ **FIGURE 2.29**
Sketch of a Mach wave
and its right triangle



Now from the Mach triangle shown in Figure 2.29, we deduce that

$$\tan \mu = \frac{1}{\sqrt{M^2 - 1}} \quad (2.136)$$

Substitute this expression in Equation 2.134 to get a simple relationship between the flow turning and the incremental acceleration across a Mach wave in a supersonic flow, that is,

$$d\theta = \sqrt{M^2 - 1} \frac{dV}{V} \quad (2.137)$$

We first express the incremental velocity ratio in terms of Mach number and then proceed to integrate Equation 2.137. Now, we employ logarithmic derivative as a tool to derive the functions of Mach number. We start with a basic definition and then build on that, for example:

$$V = M \cdot a = \text{constant} \cdot M \cdot T^{1/2} \quad (2.138)$$

The logarithmic derivative of Equation 2.138 is

$$\frac{dV}{V} = \frac{dM}{M} + \frac{1}{2} \frac{dT}{T} \quad (2.139)$$

To express the temperature ratio in terms of Mach number, we use

$$T = \text{constant} \cdot \left(1 + \frac{\gamma - 1}{2} M^2 \right)^{-1} \quad (2.140)$$

Note that the constant in Equation 2.140 is the total temperature, which remains constant across the supersonic waves. Now, we may logarithmically differentiate Equation 2.140 to get

$$\frac{dT}{T} = \frac{-(\gamma - 1) M dM}{1 + \frac{\gamma - 1}{2} M^2} \quad (2.141)$$

We substitute Equation 2.141 into 2.139 and the result into 2.137 to get

$$d\theta = \frac{\sqrt{M^2 - 1}}{1 + \frac{\gamma - 1}{2}M^2} \frac{dM}{M} \quad (2.142)$$

Now, this equation may be integrated, as we have isolated a single variable M on the RHS of Equation 2.142. The limits of integral are set at zero angle for $M = 1$ and $\nu(M)$ at Mach M . The angle $\nu(M)$ is called the Prandtl–Meyer function.

$$\int_0^{\nu(M)} d\theta = \nu(M) = \int_1^M \frac{\sqrt{M^2 - 1}}{1 + \frac{\gamma - 1}{2}M^2} \frac{dM}{M} \quad (2.143a)$$

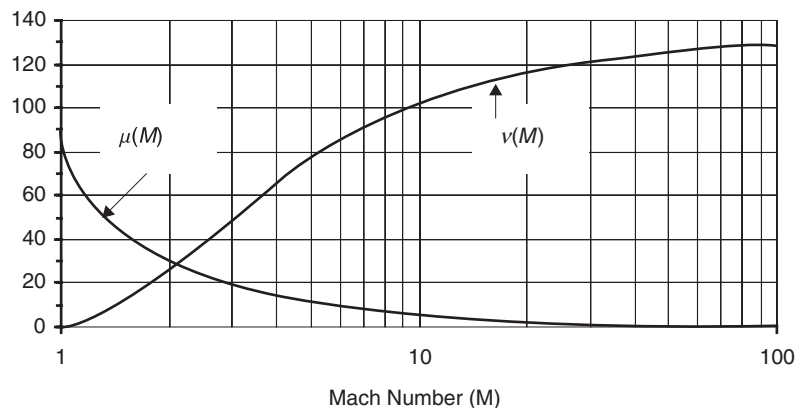
The definite integral on the RHS of Equation 2.143a is integrable in closed form by partial fraction and simple change of variables to cast the integrand in the form of the derivative of an inverse tangent function. The result of integration is

$$\nu(M) = \sqrt{\frac{\gamma + 1}{\gamma - 1}} \tan^{-1} \sqrt{\frac{\gamma - 1}{\gamma + 1}}(M^2 - 1) - \tan^{-1} \sqrt{M^2 - 1} \quad (2.143b)$$

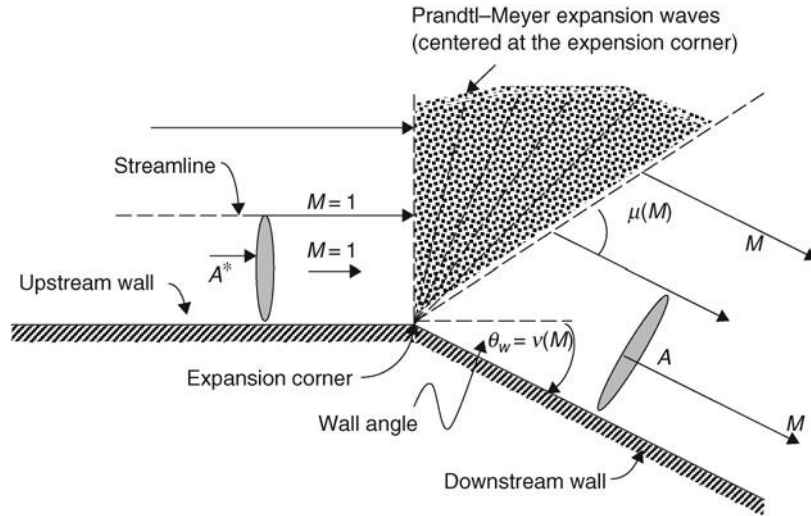
Figure 2.30 shows the Prandtl–Meyer function and the Mach angle as a function of Mach number for $\gamma = 1.4$.

We may tabulate this function in terms of Mach number for any gas, described by its specific heat ratio γ . A physical interpretation of the Prandtl–Meyer angle at Mach M is the turning angle needed to turn a sonic flow into a supersonic flow at Mach M . A schematic drawing of an expanding flow around a sharp corner is shown in Figure 2.31. The wall turning angle is $\nu(M)$ and the downstream flow is at M . Note that the streamlines expand through Prandtl–Meyer waves to allow for a higher Mach number (thus lower density) downstream. Since the flow in an expansion wave is isentropic, the area between streamlines follows the A/A^* rule, derived earlier.

FIGURE 2.30
Prandtl–Meyer
function and Mach
angle (in degrees) for a
diatomic gas, $\gamma = 1.4$



■ **FIGURE 2.31**
Sonic flow turns to
expand into a
supersonic flow
downstream of a sharp
corner



The limiting values of the Prandtl–Meyer angle are zero at Mach 1 and in the limit of Mach number approaching infinity, the turning angle is

$$v(M_2 \rightarrow \infty) = \left(\sqrt{\frac{\gamma + 1}{\gamma - 1}} - 1 \right) \frac{\pi}{2} \quad (2.144)$$

For a ratio of specific heats of $\gamma = 1.4$, the maximum wall angle leading to infinite Mach number is $\sim 130.5^\circ$, as also shown in Figure 2.31. The lead Mach wave in Figure 2.31 is normal to the sonic flow and the tail Mach wave makes an angle $\mu(M)$ with the downstream velocity vector. In general, the wall-turning angle for any upstream flow ($M_1 > 1$) is the difference between the Prandtl–Meyer angles downstream and upstream of the corner,

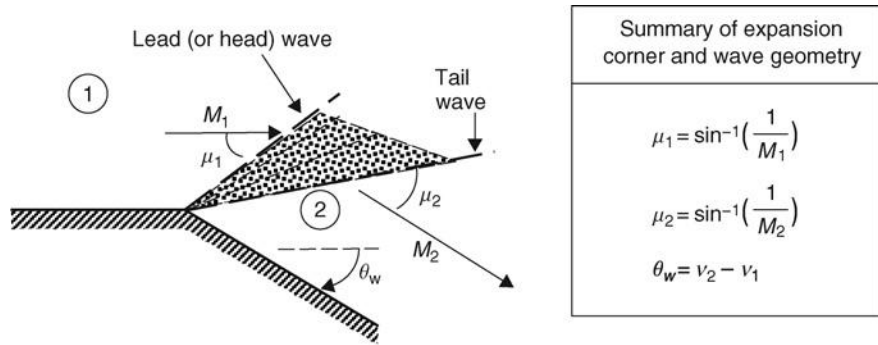
$$\Delta\theta = \theta_{\text{wall}} = \nu_2 - \nu_1 \quad (2.145)$$

The wall-turning angle in a supersonic flow uniquely determines the flow Mach number downstream of the corner. The wave structure at the sharp corner in a supersonic flow is the same as that shown in Figure 2.31, except the lead Mach wave is now at the local Mach angle $\sin^{-1}(1/M_1)$ instead of 90° for the sonic flow, and the wave envelope is rotated in the direction of wall-turning angle (Figure 2.32). The ratio of flow parameters follows the isentropic relation, namely,

$$\frac{T_2}{T_1} = \frac{1 + \frac{\gamma - 1}{2} M_1^2}{1 + \frac{\gamma - 1}{2} M_2^2} \quad (2.146)$$

$$\frac{p_2}{p_1} = \left(\frac{1 + \frac{\gamma - 1}{2} M_1^2}{1 + \frac{\gamma - 1}{2} M_2^2} \right)^{\frac{\gamma}{\gamma - 1}} \quad (2.147)$$

■ **FIGURE 2.32**
An expansion corner in a supersonic flow



2.15 Frictionless, Constant-Area Duct Flow with Heat Transfer

The class of one-dimensional compressible flow problems includes the effects of heat transfer and friction. These two effects have been traditionally separated to make the analysis simple and the effects of friction and heat transfer individually and separately studied. We first examine the effect of heat transfer on a compressible flow in a constant-area duct without friction. This fluid problem is called the Rayleigh flow.

We first define the geometry and the boundary conditions of the problem in a schematic drawing (Figure 2.33) to assist with the application of conservation principles.

The boundary conditions are uniform flow, zero wall friction, a known inlet flow condition, that is, \dot{m}, p_1, T_1 , and heat transfer rate \dot{Q} . The unknowns are the flow parameters at the exit of the duct, namely, M_2, p_2, T_2 , and so on. The medium is a perfect gas.

The continuity equation demands

$$\rho_1 u_1 = \rho_2 u_2 \tag{2.148}$$

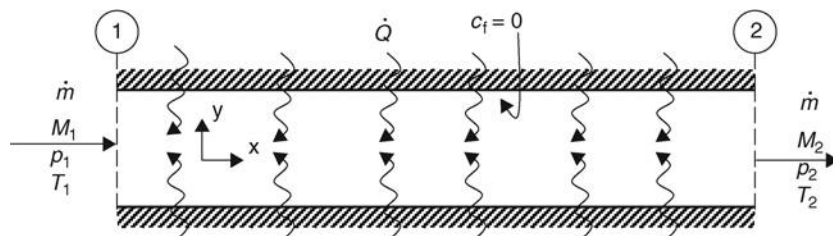
The momentum equation along the flow direction is

$$\rho_2 u_2^2 - \rho_1 u_1^2 = p_1 - p_2 \tag{2.149a}$$

$$p_1 + \rho_1 u_1^2 = p_2 + \rho_2 u_2^2 \Rightarrow I_1 = I_2 \tag{2.149b}$$

Again, we note that due to our frictionless flow assumption in Rayleigh flow, the fluid impulse, I , remains constant.

■ **FIGURE 2.33**
Uniform frictionless flow in a constant-area duct with heat transfer



The energy equation that accounts for the heat transfer through the walls is

$$\dot{m}(h_{t2} - h_{t1}) = \dot{Q} \quad (2.150a)$$

The mass flow rate is the size parameter and may be divided out of the energy equation and the heat transfer rate per unit mass flow rate is called q , to get

$$h_{t2} = h_{t1} + q \quad (2.150b)$$

The exit total enthalpy is immediately calculated based on the inlet condition h_{t1} and the known heat transfer per unit mass flow rate q . The governing equations, that is, the mass flow rate and the momentum equation, are identical to a normal shock flow, except for the energy equation of the Rayleigh flow that includes heat transfer.

The momentum equation is written in terms of pressure and Mach number as in the normal shock flow,

$$p_2/p_1 = (1 + \gamma M_1^2) / (1 + \gamma M_2^2) \quad (2.151)$$

The continuity equation leads us to the density ratio in terms of the Mach numbers and temperature ratio following a simple manipulation,

$$\frac{\rho_2}{\rho_1} = \frac{u_1}{u_2} = \frac{M_1 a_1}{M_2 a_2} = \frac{M_1}{M_2} \sqrt{\frac{T_1}{T_2}} \quad (2.152)$$

Now, let us use the perfect gas law for the density ratio in favor of the pressure and temperature ratio to simplify Equation 2.152 according to

$$\frac{p_2}{p_1} \cdot \frac{T_1}{T_2} = \frac{1 + \gamma M_1^2}{1 + \gamma M_2^2} \cdot \frac{T_1}{T_2} = \frac{M_1}{M_2} \sqrt{\frac{T_1}{T_2}} \quad (2.153a)$$

This equation simplifies to

$$\frac{T_2}{T_1} = \frac{M_2^2}{M_1^2} \left(\frac{1 + \gamma M_1^2}{1 + \gamma M_2^2} \right)^2 \quad (2.153b)$$

The density ratio is the ratio of pressure ratio to the temperature ratio, therefore

$$\frac{\rho_2}{\rho_1} = \frac{\frac{1 + \gamma M_1^2}{1 + \gamma M_2^2}}{\frac{M_2^2}{M_1^2} \left(\frac{1 + \gamma M_1^2}{1 + \gamma M_2^2} \right)^2} = \frac{M_1^2}{M_2^2} \left(\frac{1 + \gamma M_2^2}{1 + \gamma M_1^2} \right) \quad (2.154)$$

All the exit conditions are expressed in terms of the inlet and the exit Mach numbers. The exit Mach number is determined from the energy equation according to Equation 2.155.

The only unknown in this equation is the exit Mach number M_2 . To facilitate numerical calculations, we take the exit flow condition to be sonic and tabulate functions, p/p^* , T/T^* , ρ/ρ^* , p_t/p_t^* , T_t/T_t^* .

$$\frac{T_{t2}}{T_{t1}} = \frac{T_2}{T_1} \left(\frac{1 + \frac{\gamma-1}{2} M_2^2}{1 + \frac{\gamma-1}{2} M_1^2} \right) = \frac{M_2^2}{M_1^2} \left(\frac{1 + \gamma M_1^2}{1 + \gamma M_2^2} \right)^2 \left(\frac{1 + \frac{\gamma-1}{2} M_2^2}{1 + \frac{\gamma-1}{2} M_1^2} \right) = 1 + \frac{q}{c_p T_{t1}} \quad (2.155)$$

These functions are written for a general inlet condition M and an exit Mach number of 1. A flow that reaches a sonic state is said to be *choked*, and the effect of heat transfer may lead to an exit choking condition, which is referred to as a *thermally choked* flow. The sonic, that is, choked condition is used as a reference state in compressible flow problems. The Rayleigh flow functions are

$$\frac{p}{p^*} = \frac{\gamma + 1}{1 + \gamma M^2} \quad (2.156)$$

$$\frac{T}{T^*} = M^2 \left(\frac{\gamma + 1}{1 + \gamma M^2} \right)^2 \quad (2.157)$$

$$\frac{\rho}{\rho^*} = \frac{1}{M^2} \left(\frac{1 + \gamma M^2}{\gamma + 1} \right) \quad (2.158)$$

$$\frac{T_t}{T_t^*} = M^2 \left(\frac{\gamma + 1}{1 + \gamma M^2} \right)^2 \left(\frac{1 + \frac{\gamma-1}{2} M^2}{\frac{\gamma + 1}{2}} \right) \quad (2.159)$$

$$\frac{p_t}{p_t^*} = \left(\frac{\gamma + 1}{1 + \gamma M^2} \right) \left(\frac{1 + \frac{\gamma-1}{2} M^2}{\frac{\gamma + 1}{2}} \right)^{\frac{\gamma}{\gamma-1}} \quad (2.160)$$

Now, let us examine the thermodynamics of this flow on a T - s diagram, which is called a Rayleigh line. The Gibbs equation is

$$ds = c_p dT/T - R dp/p \quad (2.161)$$

The momentum equation in terms of pressure and Mach number is

$$p(1 + \gamma M^2) = \text{constant} \quad (2.162)$$

The logarithmic derivative of the momentum equation relates incremental pressure change to the Mach number variation, that is,

$$\frac{dp}{p} + \frac{2\gamma M dM}{1 + \gamma M^2} = 0 \quad (2.163)$$

We may substitute the incremental pressure ratio in terms of dM/M in Equation 2.161,

$$ds = c_p dT/T + R[2\gamma M^2/(1 + \gamma M^2)]dM/M \quad (2.164)$$

Now, we use continuity equation

$$d\rho/\rho + du/u = 0 \quad (2.165)$$

We may now substitute for the density ratio in terms of the pressure and temperature ratio following the perfect gas law,

$$dp/p - dT/T + dM/M + dT/2dT = dp/p - dT/2dT + dM/M = 0 \quad (2.166)$$

Let us substitute for the incremental pressure from the momentum equation (2.163) to relate the Mach increment to static temperature change dT ,

$$dM/M = \frac{1}{2}dT/T + [2\gamma M^2/(1 + \gamma M^2)]dM/M \quad (2.167a)$$

This equation simplifies to

$$dM/M = (dT/2T)[(1 + \gamma M^2)/(1 - \gamma M^2)] \quad (2.167b)$$

Substitute the incremental Mach number expression in the Gibbs equation (2.164) to get

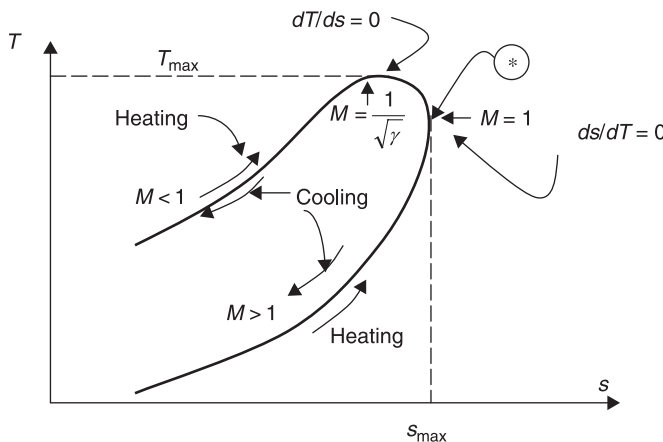
$$ds = c_p \frac{dT}{T} + R \frac{2\gamma M^2}{1 + \gamma M^2} \left(\frac{1}{2} \frac{dT}{T} \frac{(1 + \gamma M^2)}{(1 - \gamma M^2)} \right) = c_p \frac{dT}{T} \left[1 + (\gamma - 1) \left(\frac{M^2}{1 - \gamma M^2} \right) \right] \quad (2.168)$$

This equation simplifies to $s(T, M)$ for a Rayleigh line that may be graphed on a T - s diagram where the parameter along the T - s curve is the local Mach number M .

$$ds = c_p [(1 - M^2)/(1 - \gamma M^2)]dT/T \quad (2.169)$$

A graph of this function is shown in Figure 2.34. Critical points of this function are at $ds/dT = 0$ and $dT/ds = 0$. These points represent the maximum entropy and the maximum temperature on the Rayleigh line, respectively. The point of maximum entropy

■ FIGURE 2.34 Static states of a gas in a frictionless, one-dimensional flow in constant-area duct with heat transfer



occurs at $ds/dT = 0$, which Equation 2.169 indicates the sonic condition at this point, that is,

$$ds/dT = 0 \text{ at } M = 1 \tag{2.170}$$

and the maximum temperature point is at $dT/ds = 0$, which again Equation 2.169 requires

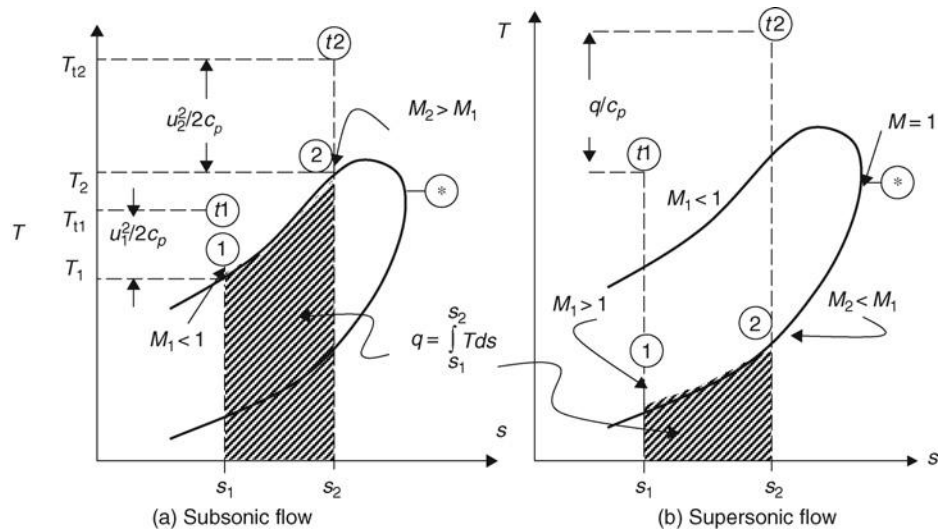
$$dT/ds = 0 \text{ at } M = 1/\sqrt{\gamma} \tag{2.171}$$

There are two branches of the Rayleigh line, namely a subsonic and a supersonic branch. These two branches are separated at the sonic point, labeled (*) in Figure 2.34. Also, the path of heating tends to choke both the subsonic and supersonic flows and the cooling path drives the flow Mach number down in subsonic flows and up in supersonic flows. Interestingly, the point of maximum temperature occurs at a subsonic Mach number of $(1/\gamma)^{1/2}$ and further heating actually reduces the static temperature toward the exit sonic condition. The stagnation temperature continues to increase, however, with heating. The heating that leads to a choked exit condition is called the critical heating q^* . Since the point of s_{\max} occurs at the sonic point, the sonic condition has to occur at the exit of the duct.

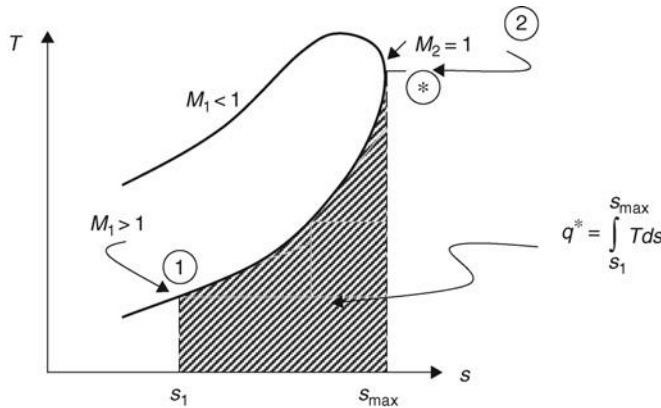
The Rayleigh line, as shown in Figure 2.34, is the loci of all the points with a constant mass flow rate ρuA . Since the area of the duct is constant, the product of density and velocity remains constant, that is, mass flow rate per unit area. The momentum equation of the Rayleigh line and a normal shock are the same. In deriving the functional form of the Rayleigh line in the T - s diagram, we did not use the energy equation. Therefore, this flow at least at one point represents a normal shock. We will establish this point when we study an adiabatic flow in a constant-area duct with friction in the next section.

The Rayleigh line does not involve any frictional dissipation, hence the heating/cooling of the gas is reversible. Therefore, the area under the T - s curve represents the heat transfer per unit mass of the fluid, as in $\delta q_{\text{rev}} = Tds$. This is graphically shown in Figure 2.35 for a subsonic inlet condition and a supersonic case. The gas at point 1 is in a subsonic flow (in part (a) of Figure 2.35) and upon heating it reaches a higher Mach

■ FIGURE 2.35 Heating of a frictionless flow in a constant-area duct (Rayleigh line)



■ **FIGURE 2.36**
Thermally choking a supersonic flow in a constant-area frictionless duct (model of a scramjet combustor)



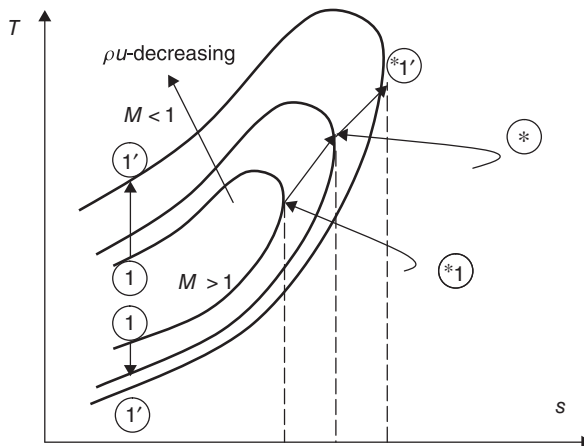
number represented by point 2 and a higher static temperature. For a supersonic case, we refer to part (b) of Figure 2.35. The heating decelerates the gas from Mach number M_1 to a lower supersonic flow Mach number with $M_2 < M_1$. The stagnation enthalpy difference between points 1 and 2 is equal to q following the energy equation.

The critical heating q^* will cause the exit of the duct to be choked. The heat transfer to a supersonic flow decelerates the gas and we deduce that in a supersonic combustion (as in a scramjet) there must be a critical fuel flow rate that causes the combustion chamber flow to choke at its exit. This is shown in Figure 2.36. We shall examine supersonic combustion further in this book.

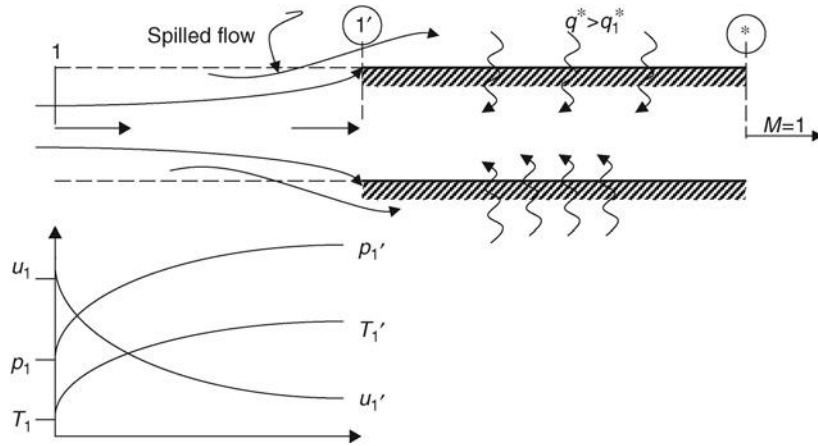
The critical heating q^* is a function of the inlet condition, as evident from Figure 2.36. Any additional heating beyond q^* can be accommodated only by a reset inlet condition, through a reduced mass flow rate. A family of Rayleigh lines is shown in Figure 2.37 with successively reduced mass flow rate.

The inlet flow condition shifts from state 1 to state 1', as shown in Figure 2.37, for a reduced flow rate in the duct. The physical inlet flow may be depicted as an inlet with flow spillage, as shown in Figure 2.38. A subsonic inlet flow is shown with a curved streamline that allows for mass spillage. The diverging area of the streamtube in subsonic flow decelerates the gas to a lower speed as it increases the gas static pressure and temperature. These features are shown on the lower half of Figure 2.39. For a supersonic throughflow

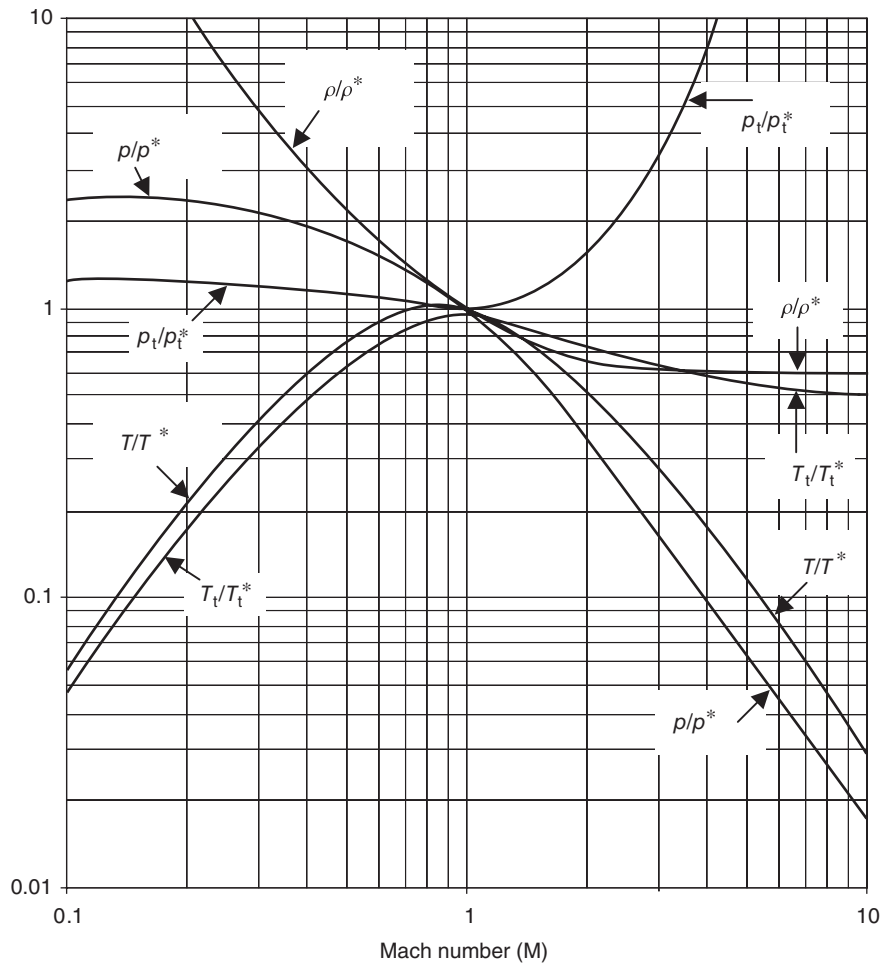
■ **FIGURE 2.37**
Family of Rayleigh lines with a decreasing flow rate in the duct caused by $q > q_1^*$



■ **FIGURE 2.38**
Excessive heating of a gas in constant-area frictionless duct causes the inlet flow to spill and a new inlet state 1' to be established



■ **FIGURE 2.39**
Rayleigh flow parameters for a calorically perfect gas, $\gamma = 1.4$



with $q^* > q_1^*$, the inlet is in the zone of silence and hence it may not be reset. However, the boundary layers that form on solid surfaces are partially subsonic and serve as the communication line, or a wave-guide, between the exit and the inlet planes; hence the inlet may be reset to accommodate a higher heating rate. Since our assumption of one-dimensional flow could not allow for a boundary layer formation, in the strictest sense of this theory, a reset supersonic Rayleigh flow is not possible.

EXAMPLE 2.6

Air enters a constant-area duct of circular cross-section with diameter $D = 20$ cm. The inlet conditions are Mach number $M_1 = 0.2$, $p_{t1} = 100$ kPa, and $T_{t1} = 288$ K. There is a heat transfer to the fluid at the rate of $\dot{Q} = 100$ kW. Assuming the fluid is inviscid that allows us to neglect the frictional drag force on the fluid, calculate

- (a) Mass flow rate through the duct
- (b) The critical heat flux that would choke the duct for the given M_1

- (c) The exit Mach number M_2
- (d) The percentage total pressure loss
- (e) The entropy rise $\Delta s/R$
- (f) The static pressure drop Δp
- (g) Label the inlet and exit states on a Rayleigh line on a T - s diagram

Assume $R = 287$ J/kg · K and $\gamma = 1.4$.

SOLUTION

The inlet mass flow rate, assuming the inlet conditions prevail, is

$$\begin{aligned} \dot{m} &= \sqrt{\frac{\gamma}{R}} \frac{p_{t1}}{\sqrt{T_{t1}}} \cdot A \cdot \frac{M_1}{\left(1 + \frac{\gamma - 1}{2} M_1^2\right)^{\frac{\gamma + 1}{2(\gamma - 1)}}} \\ &= \sqrt{\frac{1.4}{287(\text{J/kg} \cdot \text{K})}} \frac{100 \times 1000(\text{N/m}^2)}{\sqrt{288(\text{K})}} \\ &\quad \times (0.1)^2 \cdot \pi(\text{m}^2) \cdot \frac{(0.2)}{(1 + 0.2 \times 0.04)^3} \approx 2.525 \text{ kg/s} \end{aligned}$$

The heat per unit mass q is the ratio of heat flow rate to the fluid mass flow rate

$$q \equiv \frac{\dot{Q}}{\dot{m}} = \frac{100 \text{ kW}}{2.525 \text{ kg/s}} \approx 39.61 \text{ kJ/kg}$$

Now, let us compare the actual heat flux q to the critical heat flux q^* by going through the Rayleigh tables,

$$\begin{aligned} M_1 = 0.2 \xrightarrow[\gamma = 1.4]{\text{Rayleigh table}} T_{t1}/T_t^* &= 0.1736 \\ p_{t1}/p_{t1}^* &= 1.2346 \\ (\Delta s/R)_1 &= 6.3402 \\ p_1/p^* &= 2.2727 \end{aligned}$$



$$T_t^* = 288 \text{ K}/0.1736 \approx 1,659 \text{ K}$$

$$p^* = 100 \text{ kPa}/2.2727 = 44 \text{ kPa}$$

From energy equation, we have

$$\begin{aligned} T_{t2} &= T_{t1} + q/c_p \\ &= 288 \text{ K} + (39.61 \text{ kJ/kg})/(1.004 \text{ kJ/kg} \cdot \text{K}) \\ &= 327.4 \text{ K} \end{aligned}$$

Where c_p was calculated from γ and R via

$$c_p = \frac{\gamma}{\gamma - 1} R = 1004 \text{ J/kg} \cdot \text{K}$$

Since the exit total temperature is less than T_t^* , the heat flux is less than the critical value and thus the exit is unchoked. The critical heat flux is calculated from energy equation, for an exit total temperature of T_t^* , namely,

$$\begin{aligned} q_1^* &= c_p (T_t^* - T_{t1}) \\ &\approx 1.004(1659 - 288) \text{ kJ/kg} \approx 1,376.5 \text{ kJ/kg} \end{aligned}$$

For the exit Mach number, we form the ratio T_{t2}/T_t^*

$$T_{t2}/T_t^* = (327.4 \text{ K})/(1659 \text{ K}) = 0.1973 \xrightarrow{\text{Rayleigh Table}}$$

$$M_2 \cong 0.22$$

$$p_{t2}/p_t^* \cong 1.2281$$

$$(\Delta s/R)_2 \cong 5.7395$$

$$p_2/p^* \cong 2.2477$$



The percentage total pressure drop is

$$\frac{(p_{t1}/p_t^*) - (p_{t2}/p_t^*)}{(p_{t1}/p_t^*)} \times 100$$

$$\cong \frac{1.2346 - 1.2281}{1.2346} \times 100 \approx 0.526\%$$

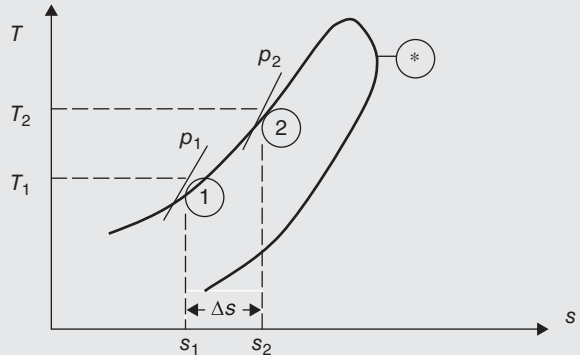
The entropy rise is the difference between $(\Delta s/R)_1$ and $(\Delta s/R)_2$

$$\Delta s/R \approx 6.3402 - 5.7395 = 0.6007$$

The static pressure drop in the duct due to heat transfer is

$$\Delta p = [(p_1/p^*) - (p_2/p^*)] \times p^*$$

$$= [2.2727 - 2.2477](44 \text{ kPa}) = 1.1 \text{ kPa}$$



EXAMPLE 2.7

Air enters a constant-area combustion chamber at Mach 3.0 at a pressure and temperature of $p_{t1} = 45 \text{ kPa}$ and $T_{t1} = 1,800 \text{ K}$, respectively. Hydrogen is the fuel with a lower heating value of $120,000 \text{ kJ/kg}$. Calculate

- (a) Exit total temperature T_{t2} (K) if the exit is choked
- (b) The maximum heat release per unit mass of air, q^*

- (c) The fuel-to-air ratio f to thermally choke the combustor exit
- (d) The total pressure loss in the supersonic combustor

Assume the gas mixture in the combustor is a perfect gas and has the following properties: $\gamma = 1.3$ and $R = 0.287 \text{ kJ/kg} \cdot \text{K}$.

SOLUTION

As a first approximation, we may neglect the wall friction and thus treat the fluid as inviscid. In addition, we will make a uniform flow approximation to enable us to use the Rayleigh flow theory. The mass addition in the combustor due to fuel flow rate is assumed to be small compared with the inlet airflow rate. Finally, we assume a 100% burner efficiency that allows all of the fuel heating value to be released as thermal energy to the fluid.

From the Rayleigh flow table (for $\gamma = 1.3$), we get

$$M_1 = 3.0 \xrightarrow[\gamma = 1.3]{\text{Rayleigh table}} T_{t1}/T_t^* = 0.6032$$

$$p_{t1}/p_t^* = 4.0073$$

Therefore the exit total temperature is $T_{t2}/T_t^* = 1800 \text{ K}/0.6032 \approx 2,984 \text{ K}$

$$c_p = \gamma R / (\gamma - 1)$$

$$= 1.3(0.287 \text{ kJ/kg} \cdot \text{K}) / 0.3 \cong 1.2437 \text{ kJ/kg} \cdot \text{K}$$

From the energy balance across the burner, we get

$$q_1^* = c_p(T_t^* - T_{t1}) = c_p T_{t1} \left(\frac{T_t^*}{T_{t1}} - 1 \right)$$

$$= 1.2437(1800) \left(\frac{1}{0.6032} - 1 \right) \text{ kJ/kg}$$

$$q_1^* \cong 1472.6 \text{ kJ/kg (of air)}$$

Therefore the fuel-to-air ratio f is derived from

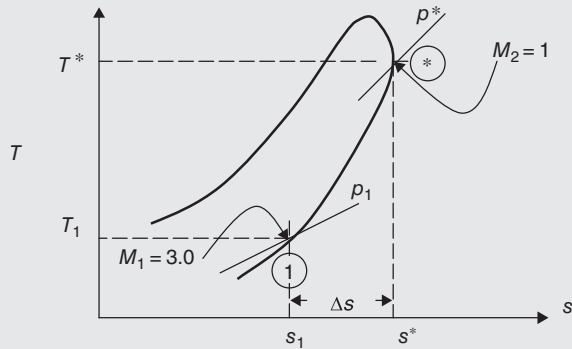
$$f(120,000 \text{ kJ/kg}) = q_1^* = 1472.6 \text{ kJ/kg} \rightarrow f \approx 1.23\%$$

The total pressure loss is $\Delta p_t/p_{t1}$ or $1 - p_1^*/p_{t1}$

Therefore, Total pressure loss = $1 - (1/4.0073) \approx 75\%$

REMARKS Solving a scramjet problem using a simple Rayleigh flow approximation produces a quick estimation of the *ballpark* values of the fuel flow rate and the stagnation pressure losses. We may add wall friction to our analysis without major difficulty, as we shall see in the next section. The effect of duct area variation may also be modeled. Some of the most complex elements of the analysis deal with the chemical reaction in the burner. We face the issues of flame stability, reaction rates, and, finally,

the combustion efficiency. These fundamental issues are addressed in an introductory manner in the chapter called combustion chambers and afterburners in this book.



EXAMPLE 2.8

A subsonic flow in a constant-area duct is subjected to heat transfer. For the inlet flow parameters

$$M_1 = 0.5, p_{t1} = 14.7 \text{ psia},$$

$$T_{t1} = 50^\circ\text{F}, \gamma = 1.4 \text{ and } R = 53.34 \text{ ft} \cdot \text{lbf}/\text{lbm} \cdot ^\circ\text{R}$$

Neglecting the wall friction, calculate

- (a) The new inlet Mach number $M_{1'}$, if $q = 1.2 q_1^*$
- (b) The percentage spilled flow at the inlet

SOLUTION

We first convert the inlet total temperature to the absolute scale, i.e.,

$$T_{t1} = (50 + 460)^\circ\text{R} = 510^\circ\text{R}$$

Next, we refer to the Rayleigh table (for $\gamma = 1.4$) to calculate the critical heat flux q_1^*

$$M_1 = 0.5 \xrightarrow[\gamma = 1.4]{\text{Rayleigh table}} T_{t1}/T_t^* = 0.69136$$

The energy equation establishes q_1^* according to

$$q_1^* = c_p (T_t^* - T_{t1})$$

From γ and R , we calculate the specific heat at constant pressure c_p

$$c_p = \gamma R / (\gamma - 1) = 1.4(53.34) / 0.4 \text{ ft} \cdot \text{lbf}/\text{lbm} \cdot ^\circ\text{R} \\ = 186.69 \text{ ft} \cdot \text{lbf}/\text{lbm} \cdot ^\circ\text{R}$$

Therefore,

$$q_1^* = (186.69)(510^\circ\text{R})(1/0.69136 - 1) \text{ ft} \cdot \text{lbf}/\text{lbm} \cdot ^\circ\text{R} \\ \cong 42,505 \text{ ft} \cdot \text{lbf}/\text{lbm}$$

The heat flux is specified to be $1.2 q_1^* = 1.2(42,505) = 51,006 \text{ ft} \cdot \text{lbf}/\text{lbm}$.

From this value of heat flux and the energy equation, we calculate the new exit total temperature T_{t1}' , which reflects the additional q , according to

$$q_{1'}^* = c_p (T_{t1}' - T_{t1})$$

Therefore the new exit total temperature is

$$T_{t1}' = T_{t1} + \frac{q_{1'}^*}{c_p} = 510 + \frac{51,006}{186.69} \approx 783^\circ\text{R}$$

The ratio of the T_{t1}/T_{t1}' may now be calculated as

$$\begin{aligned}
 T_{t1}/T_{t1}' &= 510/783 \\
 &= 0.65116 \xrightarrow[\gamma = 1.4]{\text{Rayleigh table}} \\
 M_{1'} &\cong 0.473 \text{ (via inter polation)}
 \end{aligned}$$

The percentage spilled mass flow rate is

$$\frac{\dot{m}_1 - \dot{m}_{1'}}{\dot{m}_1} \times 100$$

Since the total pressure and temperature remain constant between the states 1 and 1', the mass flow in both cases is proportional to the mass flow parameter $f(M)$,

$$f(M) = M \left/ \left(1 + \frac{\gamma - 1}{2} M^2 \right)^{\frac{\gamma + 1}{2(\gamma - 1)}} \right.$$

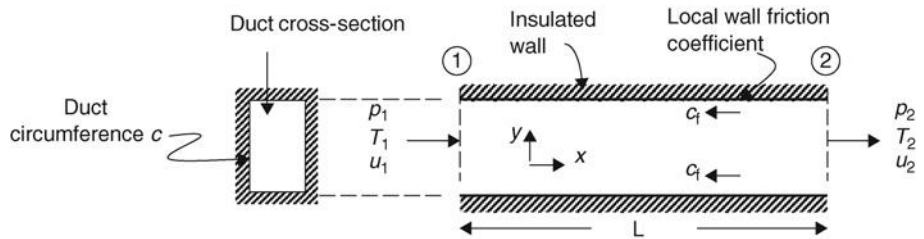
Hence, $f(M_1) = 0.4319$ and $f(M_{1'}) = 0.4148$
 Therefore, % inlet flow spillage = $3.966\% \approx 4\%$

2.16 Adiabatic Flow of a Calorically Perfect Gas in a Constant-Area Duct with Friction

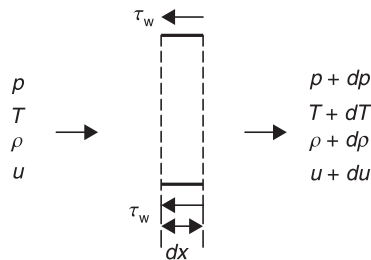
In this section, a compressible flow in a constant-area duct is subjected to the effect of friction. The walls are insulated to heat transfer and thus the flow is assumed to be adiabatic. The medium is a perfect gas and the flow is steady. This flow is called the *Fanno* flow in fluid mechanics. The governing equations are the conservation principles applied to a control volume with specified boundary conditions. Let us first define the geometry of the problem/control volume and identify its boundary conditions. Figure 2.40 shows the schematic drawing of this problem.

To apply the conservation principles to this problem, we choose an elemental slab of fluid, of incremental length, dx . The derivation involves differential equations of motion and is very useful as a practice drill in fundamentals. Figure 2.41 shows a representative slab of a fluid in an adiabatic constant-area duct flow with friction.

■ FIGURE 2.40
 Geometry of an adiabatic flow in a duct with friction



■ FIGURE 2.41
 Slab of fluid in a constant-area insulated duct with friction



The continuity equation demands

$$\rho u = (\rho + d\rho)(u + du) \quad (2.172)$$

It simplifies to the following differential forms:

$$\rho du = -u d\rho \quad (2.173a)$$

or

$$\frac{d\rho}{\rho} = -\frac{du}{u} \quad (2.173b)$$

The momentum equation per unit area of the flow, in the x -direction, is

$$\rho u(u + du) - \rho u^2 = p - (p + dp) - \tau_w \cdot c \cdot dx/A \quad (2.174)$$

We may introduce the hydraulic diameter ($D_h \equiv 4A/c$) in Equation 2.174 and simplify it to

$$\rho u du = -dp - 4\tau_w dx/D_h \quad (2.175)$$

Note that the fluid impulse is not conserved in Fanno flow due to wall friction. The fluid impulse is reduced along the flow direction (note the minus sign in front of wall shear in Equation 2.175).

The energy equation for the slab is

$$dh + u du = c_p dT + u du = 0 \quad (2.176)$$

The energy equation may be divided by u^2 to get

$$c_p \frac{dT}{u^2} + \frac{du}{u} = \frac{\gamma}{\gamma - 1} \frac{RT}{u^2} \frac{dT}{T} + \frac{du}{u} = \frac{1}{(\gamma - 1)M^2} \frac{dT}{T} + \frac{du}{u} = 0 \quad (2.177a)$$

We may isolate du/u and express it in terms of dT/T , as

$$\frac{du}{u} = -\frac{1}{(\gamma - 1)M^2} \frac{dT}{T} \quad (2.177b)$$

The momentum equation may be nondimensionalized by dividing through by ρu^2 and writing the local skin friction coefficient c_f as the ratio of wall shear stress divided by the local dynamic pressure in Equation 2.174; this yields

$$\frac{du}{u} = -\frac{p}{\rho u^2} \frac{dp}{p} - 2c_f \frac{dx}{D_h} \quad (2.178)$$

where

$$c_f \equiv \frac{\tau_w}{\rho u^2/2} \quad (2.179)$$

The skin friction coefficient is a function of Reynolds number based on duct diameter and the surface roughness of the wall. In supersonic flow, the skin friction coefficient is a function of the local Mach number as well. To simplify the Fanno flow problem,

we introduce an average wall friction coefficient C_f (also known as the friction drag coefficient), which is defined as

$$C_f \equiv \frac{1}{L} \int_0^L c_f dx \quad (2.180)$$

We use Equation 2.177b to replace the incremental speed ratio du/u in the momentum equation. The ratio of static pressure to density on the RHS of Equation 2.178 is the product of $1/\gamma$ and the square of the local speed of sound a^2 , and we may replace the incremental pressure ratio with density and temperature ratio following the perfect gas law, according to

$$\frac{1}{(\gamma - 1)M^2} \frac{dT}{T} = \frac{1}{\gamma M^2} \left(\frac{d\rho}{\rho} + \frac{dT}{T} \right) + 2c_f \frac{dx}{D_h} \quad (2.181)$$

We replace the density ratio from the continuity equation and then substitute for the Mach temperature via the logarithmic derivatives to get

$$\frac{1}{(\gamma - 1)M^2} \frac{dT}{T} = \frac{1}{\gamma M^2} \left(\frac{1}{(\gamma - 1)M^2} \frac{dT}{T} + \frac{dT}{T} \right) + 2c_f \frac{dx}{D_h} \quad (2.182a)$$

$$\frac{M^2 - 1}{\gamma M^2 \cdot (\gamma - 1)M^2} \frac{dT}{T} = 2c_f \frac{dx}{D_h} \quad (2.182b)$$

Since the stagnation temperature T_t remains constant, we may use the logarithmic derivative to represent dT/T in terms of dM/M following:

$$T_t = T \left(1 + \frac{\gamma - 1}{2} M^2 \right) \quad (2.183a)$$

$$\frac{dT_t}{T_t} = \frac{dT}{T} + \frac{(\gamma - 1)M dM}{1 + \frac{\gamma - 1}{2} M^2} = \frac{dT}{T} + \frac{(\gamma - 1)M^2}{1 + \frac{\gamma - 1}{2} M^2} \frac{dM}{M} = 0 \quad (2.183b)$$

Now, let us combine Equations 2.183b and 2.182b to get

$$\left[\frac{1 - M^2}{\gamma M^2 \left(1 + \frac{\gamma - 1}{2} M^2 \right)} \right] \frac{dM}{M} = 2c_f \frac{dx}{D_h} \quad (2.184a)$$

Since the terms in the bracket involve M^2 , we may express dM/M as $(1/2)dM^2/M^2$, which produces

$$4c_f \frac{dx}{D_h} = \left[\frac{1 - M^2}{\gamma M^2 \left(1 + \frac{\gamma - 1}{2} M^2 \right)} \right] \frac{dM^2}{M^2} \quad (2.184b)$$

The LHS of this equation is always positive. The RHS should also be positive for any M . Therefore, for a subsonic flow, that is, $M < 1$, dM^2 has to be positive, and for supersonic flow, where $M > 1$, then dM^2 has to be negative. This suggests that the effect of friction on a subsonic flow is to accelerate it toward the sonic state. Also, a supersonic flow is decelerated toward the sonic point by friction. This impact of friction on compressible flow is similar to the Rayleigh flow, where heating causes the flow to approach a choking condition. In both cases, friction and heating act like a *valve*, or in effect a flow area reduction. Now, we may integrate this equation from $x = 0$ to L^* while M^2 varies from M^2 to 1, to get an expression for the Fanno parameter $4C_f L^*/D_h$,

$$\frac{4}{D_h} \int_0^{L^*} c_f dx = 4C_f \frac{L^*}{D_h} = \int_{M^2}^1 f(M^2, \gamma) dM^2 = \frac{1 - M^2}{\gamma M^2} + \frac{\gamma + 1}{2\gamma} \ell n \left[\frac{(\gamma + 1) M^2}{2 \left(1 + \frac{\gamma - 1}{2} M^2\right)} \right] \quad (2.185)$$

We have selected the choking condition to represent a reference state, as in Rayleigh flow. The energy equation for Fanno flow maintains a constant total temperature, therefore,

$$\frac{T}{T^*} = \frac{\gamma + 1}{2 \left(1 + \frac{\gamma - 1}{2} M^2\right)} \quad (2.186)$$

The density ratio from the continuity equation may be written as

$$\frac{\rho}{\rho^*} = \frac{u^*}{u} = \frac{1}{M} \sqrt{\frac{T^*}{T}} = \frac{1}{M} \sqrt{\frac{2 \left(1 + \frac{\gamma - 1}{2} M^2\right)}{\gamma + 1}} \quad (2.187)$$

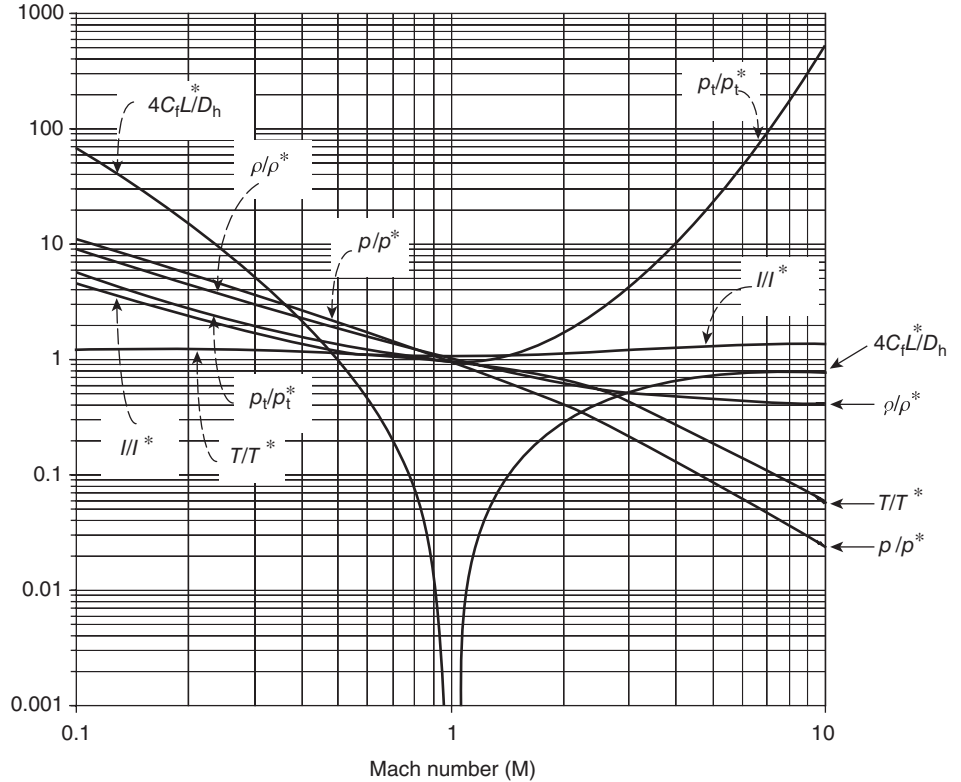
The pressure ratio is the product of the density and temperature ratio, therefore,

$$\frac{p}{p^*} = \frac{1}{M} \sqrt{\frac{\gamma + 1}{2 \left(1 + \frac{\gamma - 1}{2} M^2\right)}} \quad (2.188a)$$

The fluid impulse ratio I/I^* is related to the static pressure ratio and Mach number following

$$\frac{I}{I^*} = \frac{p(1 + \gamma M^2)}{p^*(1 + \gamma)} = \left(\frac{p}{p^*}\right) \frac{1 + \gamma M^2}{\gamma + 1} = \frac{1}{M} \sqrt{\frac{\gamma + 1}{2[1 + (\gamma - 1)M^2/2]}} \left(\frac{1 + \gamma M^2}{\gamma + 1}\right) \quad (2.188b)$$

■ FIGURE 2.42
Fanno flow parameters
for a calorically perfect
diatomic gas with
 $\gamma = 1.4$



The stagnation pressure ratio is expressed in terms of the static pressure ratio and Mach number as

$$\frac{p_t}{p_t^*} = \frac{p}{p^*} \left(\frac{1 + \frac{\gamma - 1}{2} M^2}{\frac{\gamma + 1}{2}} \right)^{\frac{\gamma}{\gamma - 1}} = \frac{1}{M} \left(\frac{1 + \frac{\gamma - 1}{2} M^2}{\frac{\gamma + 1}{2}} \right)^{\frac{\gamma + 1}{2(\gamma - 1)}} \quad (2.189)$$

Figure 2.42 shows a log–log graph of the Fanno flow parameters for a diatomic gas ($\gamma = 1.4$).

To interpret the parameter variations properly in Figure 2.42, we need to remember that the movement is toward the sonic point on both sides of the $M = 1$ axis. For example, the static pressure, temperature, and density drop in subsonic flow and all increase in a supersonic flow with friction. The total pressure drops in both cases.

To graph the thermodynamic state variation of this flow on a T - s diagram, which is referred to as the Fanno line, we need to derive the fluid entropy in terms of temperature and local Mach number. We start with the Gibbs equation,

$$ds = c_p dT/T - R dp/p \quad (2.190)$$

We replace the logarithmic derivative of pressure by the logarithmic derivatives of density and temperature using the perfect gas law, namely

$$dp/p = d\rho/\rho + dT/T \quad (2.191a)$$

The density ratio is related to the incremental speed ratio via the continuity equation, therefore

$$dp/p = -du/u + dT/T \quad (2.191b)$$

Now, replace the logarithmic derivative of gas speed by the logarithmic derivatives of Mach number and temperature via the definition of Mach number, that is,

$$\frac{dp}{p} = -\left(\frac{dM}{M} + \frac{1}{2} \frac{dT}{T}\right) + \frac{dT}{T} = \frac{1}{2} \frac{dT}{T} - \frac{dM}{M} \quad (2.191c)$$

Substituting Equation 2.191c in the Gibbs equation, we get

$$ds = c_p dT/T - R(dT/2dT - dM/M) \quad (2.192)$$

From the energy equation for an adiabatic flow, we may write the following logarithmic derivative:

$$dT/T + [(\gamma - 1)M dM] / \left[1 + \frac{\gamma - 1}{2} M^2\right] = 0 \quad (2.193a)$$

Now, we isolate dM/M in terms of dT/T according to

$$\frac{dM}{M} = -\left(\frac{1 + \frac{\gamma - 1}{2} M^2}{(\gamma - 1)M^2}\right) \frac{dT}{T} \quad (2.193b)$$

Substituting Equation 2.193b into Equation 2.192 gives

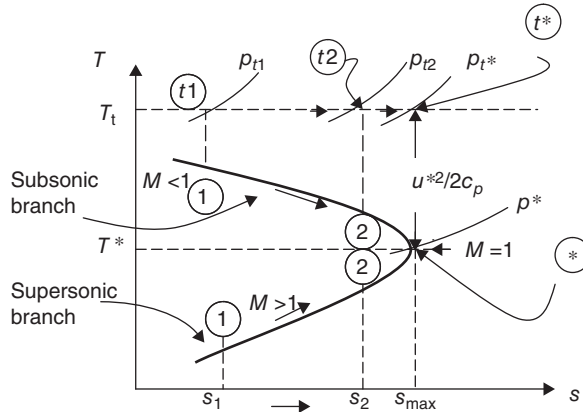
$$\frac{ds}{R} = \left[\frac{\gamma}{\gamma - 1} - \frac{1}{2} - \left(\frac{1 + \frac{\gamma - 1}{2} M^2}{(\gamma - 1)M^2} \right) \right] \frac{dT}{T} \quad (2.194)$$

The bracket may be simplified to get the final form of $s(T, M)$ as

$$ds/R = [(M^2 - 1) / ((\gamma - 1)M^2)] dT/T \quad (2.195)$$

The critical point of this function is at $ds/dT = 0$, which occurs at the sonic condition, that is, when the numerator of the bracket in 2.195 vanishes. A graph of this function in a T - s diagram is shown in Figure 2.43. There is a subsonic and a supersonic branch separated by the sonic point (designated by *). An arrow on these branches shows

■ **FIGURE 2.43**
The path of a one-dimensional adiabatic flow with friction on a T - s diagram



the direction of the thermodynamic states in a compressible, adiabatic one-dimensional flow with friction on a T - s diagram. The effect of friction is seen to increase the entropy of the gas as expected, and hence to push a subsonic or supersonic flow toward the sonic point. This phenomenon is referred to as the *frictional choking* effect in a duct with compressible flow.

In arriving at the $s(T, M)$ for the Fanno flow, we did not use the momentum equation, which contained the friction term. The continuity and the energy equations that we used in the derivation of $s(T, M)$ are identical to a normal shock flow equations. Hence, a transition from a supersonic flow to a subsonic flow, with an associated entropy rise, may depict a normal shock on a Fanno line. This is similar to a Rayleigh flow that shares the momentum and mass conservation with a normal shock. A Fanno line shares the mass and energy conservation with a normal shock flow. Hence, the intersection of a Rayleigh line and a Fanno flow with the same mass flow rate per unit area, that is, ρu , satisfies the mass, momentum, and the energy conservation principles across a normal shock. Figure 2.44 shows a possible normal shock at the intersection of a Fanno and a Rayleigh line.

For a duct longer than the choking length of the inlet Mach number, that is, $L > L_1^*$, a subsonic flow will reset itself with a lower mass flow rate at its inlet, similar to a Rayleigh line flow spillage at the inlet due to excessive heating, $q > q^*$. In the case of a supersonic

■ **FIGURE 2.44**
The intersection of Rayleigh and Fanno lines with the same mass flow rate satisfying the conservation principles across a normal shock

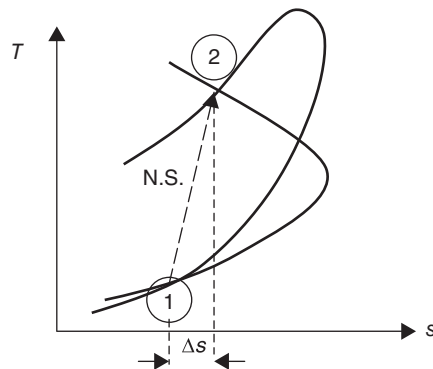
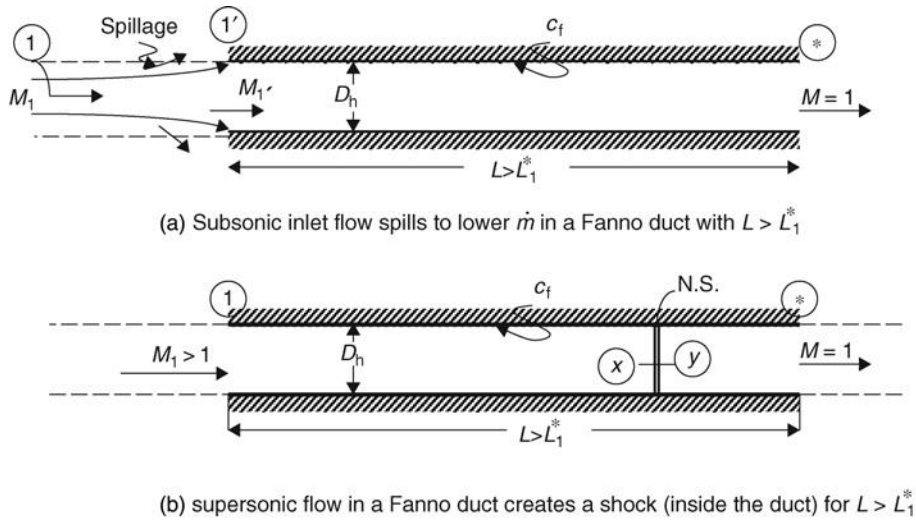


FIGURE 2.45
Adjustment mechanisms for a Fanno flow with $L > L_1^*$ for subsonic and supersonic throughflow cases



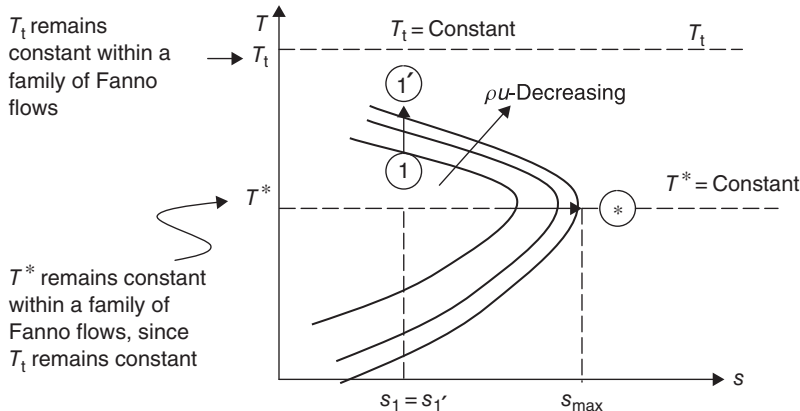
flow in the duct with friction, a normal shock appears in the duct that transitions the flow to subsonic. The schematic drawing of these two cases is shown in Figure 2.45. We introduce a family of Fanno lines, each representing a mass flow rate (per unit area) on a T - s diagram, similar to the Rayleigh line family. The inlet flow is reset to a lower mass flow rate, hence a reduced inlet Mach number when the throughflow is subsonic. The exit remains choked. Figure 2.46 shows a Fanno line family.

To show the case of supersonic inlet flow and a shock in the duct, we use a schematic drawing on a T - s diagram. Figure 2.47 shows the shock formation for $L > L_1^*$ in a supersonic Fanno flow.

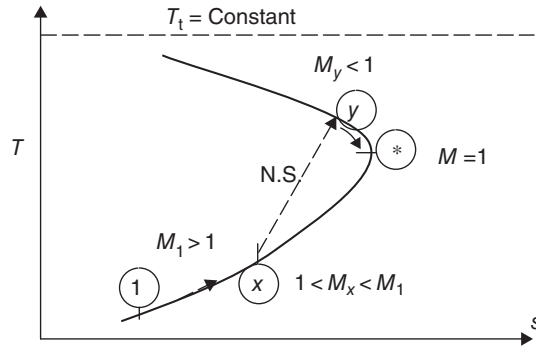
To establish the exit flow conditions in a Fanno line problem, we may use the tabulated functions according to the following steps:

- Given: $M_1, L, \text{Cross-sectional shape of the duct, } C_f \text{ and } \gamma$
 Calculate: $M_2, p_2/p_1, T_2/T_1, \rho_2/\rho_1, p_{t2}/p_{t1}, \Delta s/R, u_2/u_1, \text{ etc.}$

FIGURE 2.46
Family of Fanno lines on a T - s diagram with decreasing mass flow rate



■ FIGURE 2.47 Frictional choking with a normal shock in the duct



Solution: We first calculate the hydraulic diameter of the duct from the cross-sectional shape according to

$$D_h \equiv 4A/c$$

Next, we look up the choking length of the duct for its inlet Mach number from the tabulated functions, that is,

$$M_1, \gamma \rightarrow 4C_f L_1^*/D_h$$

Then, we compare the choking length L_1^* and the physical length of the duct, L . Let us examine the three possible cases:

Case 1: $L < L_1^*$

We conclude that the exit is not choked, the inlet flow remains unaffected by the length of the duct and there is no normal shock in the duct. Figure 2.48 shows this case.

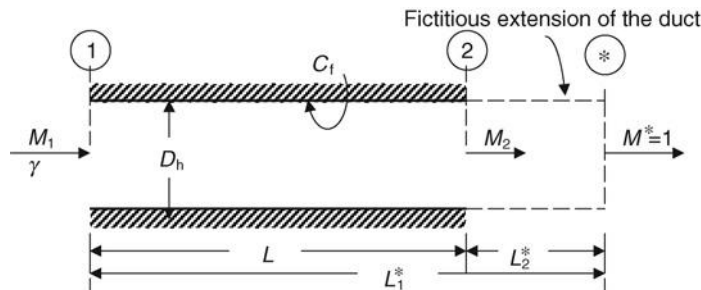
The length of the fictitious duct is $L_1^* - L$, which is the choking length for the exit Mach number, M_2 . Hence, we calculate L_2^* according to

$$L_2^* = L_1^* - L$$

We form the Fanno parameter at the exit of the duct, which results in M_2 from the tabulated functions:

$$4C_f L_2^*/D_h \rightarrow M_2$$

■ FIGURE 2.48 Length of a duct that does not choke the exit



We read the parameters p_1/p^* , T_1/T^* , and so on from the M_1 value of the table and p_2/p^* , T_1/T^* , and so on from the M_2 value of the Fanno table. Since the choking condition is unique, the ratio of these parameters reveals the duct ratios, namely

$$\frac{p_2}{p_1} = \frac{p_2/p^*}{p_1/p^*}$$

Case 2: $L = L_1^*$

This case is the easiest of the three, since the exit is choked and all exit conditions are sonic, namely, $M_2 = 1$, $p_2 = p^*$, and so on.

Case 3: $L > L_1^*$

The length of the duct is longer than the choking length based on the inlet Mach number M_1 . In the case of subsonic flow, then the inlet flow is reset to a lower mass flow rate (i.e., Mach number), such that the physical length of the duct is now the choking length for the new inlet condition ($1'$). We immediately conclude that the exit is choked, that is,

$$M_2 = 1, p_2 = p^*, T_2 = T^*, \text{ etc.}$$

Since the length of the duct is the choking length for the new inlet condition, the Fanno parameter $4C_f L_{1'}^*/D$ is actually $4C_f L/D$, from the Fanno table, we get $M_{1'}$ according to

$$4C_f L_{1'}^*/D_h = 4C_f L/D_h \rightarrow M_{1'}$$

The inlet static pressure and temperature are now increased due to spillage, while the stagnation pressure and temperature at the inlet are preserved, that is,

$$p_{t1'} = p_{t1} \text{ and } T_{t1'} = T_{t1}$$

With the new Mach number at the inlet, $M_{1'}$, we may calculate the new inlet static pressure and temperature, $p_{1'}$ and $T_{1'}$, using the fundamental relations we derived earlier, namely

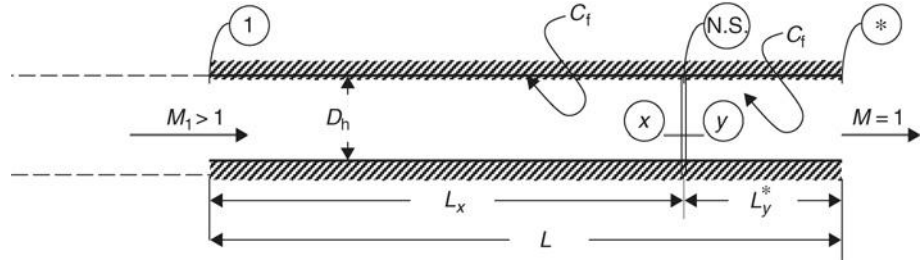
$$p_{1'} = \frac{p_{t1'}}{\left(1 + \frac{\gamma-1}{2} M_{1'}^2\right)^{\frac{\gamma}{\gamma-1}}} = \frac{p_{t1}}{\left(1 + \frac{\gamma-1}{2} M_{1'}^2\right)^{\frac{\gamma}{\gamma-1}}}$$

$$T_{1'} = \frac{T_{t1'}}{\left(1 + \frac{\gamma-1}{2} M_{1'}^2\right)} = \frac{T_{t1}}{\left(1 + \frac{\gamma-1}{2} M_{1'}^2\right)}$$

From $M_{1'}$ and the Fanno table, we read p/p^* , and so on; the (*) represents the exit state and the p , T , and so on are the newly calculated $p_{1'}$, $T_{1'}$, and so on.

Now, we address the case of supersonic flow with $L > L_1^*$. The inlet flow is unchanged and the exit flow Mach number is also known to be sonic. The key unknown is the location of a normal shock that splits the length of the duct into a supersonic Fanno

■ FIGURE 2.49
Normal shock in an
insulated duct with
friction



and a subsonic Fanno flows. The physical constraint is the length of the duct and the governing equations on both sides of the shock.

We may solve this problem iteratively by guessing the normal shock Mach number M_x and check if the length constraint of the duct is satisfied. Figure 2.49 shows the relationship between the shock position and its associated length scales along the duct.

The solution procedure is as follows:

Guess an M_x (less than M_1 obviously) then use the table of Fanno functions,

$$M_x \rightarrow 4C_f L_x^* / D_h$$

Then, we establish the length, L_x according to

$$L_x = L_1^* - L_x^*$$

Now, we are ready to tackle the shock jump and the remaining portion of the duct, first by using the normal shock table to get M_y , then the Fanno table to get $4C_f L_y^* / D_h$, that is,

$$\begin{aligned} M_x &\rightarrow M_y \\ M_y &\rightarrow 4C_f L_y^* / D_h \end{aligned}$$

Does the length L_y^* and the L_x add up to the physical duct length L ? If yes, then our initial guess of M_x was correct and if not, then we need to guess again. To know whether to guess higher or lower depends on the relative magnitude of the sum $(L_x + L_y^*)$ and L .

- If $(L_x + L_y^*) > L$, then our shock was too strong, and we need to lower the shock Mach number, M_x .
- If $(L_x + L_y^*) < L$, then our initial guess of the shock Mach number was not strong enough, hence we need to increase M_x .

An iteration process has a *target* value that needs to be met. The target value is a *constraint* imposed by the geometry and/or physics of the problem. We need to specify the level of accuracy that we demand of our final iterated solution. For example, we may expect/specify that the target value to be met should be within 0.1% of the last iteration value.

EXAMPLE 2.9

Air enters a constant-area duct of circular cross-section with diameter $D = 10$ cm. The length of the duct is $L = 20$ m. The duct is insulated hence the flow inside the duct is assumed to be adiabatic. The average wall friction coefficient is $C_f = 0.005$. The inlet Mach number is $M_1 = 0.24$. Calculate

- The choking length of the duct, L_1^*
- The exit Mach number M_2
- The percentage total pressure loss
- The static pressure drop
- Loss of fluid impulse due to friction

Assume $\gamma = 1.4$.

SOLUTION

From the Fanno table, we get the Fanno friction parameter based on the inlet Mach number, i.e.,

$$M_1 = 0.24 \xrightarrow{\text{Fanno table}} 4C_f L_1^*/D_h = 9.3866$$

$$p_{t1}/p_t^* = 2.4956$$

$$p_1/p^* = 4.5383 \text{ and}$$

$$I_1/I^* = 2.043$$

Now, we calculate the choking length of the duct, L_1^* (note that $D = 0.1$ m)

$$L_1^* = [9.3866(0.1 \text{ m})]/[4(0.005)] = 46.933 \text{ m}$$

Therefore, $L_1^* \approx 46.933 \text{ m}$

We note that the physical length of the duct is less than the choking length; therefore the exit Mach number will be less than 1. To arrive at the exit Mach number, we form the Fanno parameter $4C_f L_2^*/D_h$

$$L_2^* = L_1^* - L = 46.933 \text{ m} - 20 \text{ m} = 26.933 \text{ m}$$

$$4C_f L_2^*/D_h = [4(0.005)(26.933 \text{ m})]/0.1 \text{ m} = 5.3866$$

$$4C_f L_2^*/D_h = 5.3866 \xrightarrow{\text{Fanno table}} M_2 \approx 0.3$$

$$p_{t2}/p_t^* = 2.0351$$

$$p_2/p^* = 3.6191$$

$$\text{and } I_2/I^* = 1.698.$$

Therefore the percentage total pressure drop due to friction is

$$\frac{p_{t1} - p_{t2}}{p_{t1}} \times 100 = \frac{(p_{t1}/p_t^*) - (p_{t2}/p_t^*)}{(p_{t1}/p_t^*)} \times 100$$

$$= \frac{2.4956 - 2.0351}{2.4956} \times 100$$

$$\frac{\Delta p_t}{p_{t1}} \times 100 \approx 18.45\%$$

Similarly, the static pressure drop is $(4.5383 - 3.6191)/4.5383 = 20.25\%$

The loss of fluid impulse due to friction is

$$I_2 - I_1 \approx (1.698 - 2.043)I^* \approx -0.345I^*$$

EXAMPLE 2.10

Air flows in a duct with a rectangular cross-section of 1×2 cm. The average skin friction coefficient is 0.005. Assuming the walls of this duct are insulated and the entrance Mach number is 0.5, calculate

- The maximum length of the duct that will support its inlet condition
- The new inlet condition M_1' , if $L = 2.16 L_{\max}$
- The percentage inlet mass flow drop due to the longer length of the duct

SOLUTION

The maximum length with the inlet flow remaining intact is L_1^* . From the Fanno table we have

$$M_1 = 0.5 \xrightarrow{\text{Fanno table}} 4C_f L_1^*/D_h = 1.0691$$

The hydraulic diameter is

$$D_h = 4A/c = 4(2 \times 1)/[2(2 + 1)]\text{cm} = 4/3 \text{ cm}$$

$$L_{\max} = L_1^* \cong 71.27 \text{ cm}$$

Therefore, $L_1^* = 1.069(4/3 \text{ cm})/[4(0.005)] = 71.27 \text{ cm}$

The longer duct is still choked, however, with a reduced flow rate. Since the duct is choked, its physical length is the choking length for its new inlet flow condition, namely the inlet Mach number $M_{1'}$.

$$4C_f L_{1'}/D_h = 4(0.005)[2.16(71.27 \text{ cm})]/(4/3 \text{ cm}) = 2.309$$

$$4C_f L_{1'}/D_h = 2.309 \xrightarrow{\text{Fanno table}} M_{1'} = 0.4$$

$$M_{1'} = 0.4$$

The inlet total pressure and temperature remain the same, therefore the mass flow rate in the duct is proportional to

$$f(M) = \frac{M}{\left(1 + \frac{\gamma - 1}{2} M^2\right)^{\frac{\gamma + 1}{2(\gamma - 1)}}$$

via the continuity equation. We evaluate this mass flow parameter at two inlet Mach numbers M_1 and $M_{1'}$ to get

$$f(M_1) = \frac{0.5}{(1 + 0.2 \times 0.25)^3} = 0.4319$$

$$f(M_{1'}) = \frac{0.4}{(1 + 0.2 \times 0.16)^3} = 0.3639$$

Therefore the mass flow drop is:

$$\frac{\Delta \dot{m}}{\dot{m}_1} = \frac{0.4319 - 0.3639}{0.4319} = 0.1574 \therefore \frac{\Delta \dot{m}}{\dot{m}_1} \cong 15.74\%$$

EXAMPLE 2.11

Consider a supersonic flow of air in a long duct with friction but with negligible heat transfer. The duct length-to-diameter ratio is 40. The inlet Mach number is $M_1 = 2.6$ and an average wall skin friction coefficient is 0.005. First demonstrate that a normal shock will appear in the duct and then calculate

- The location of the normal shock in the duct
- The T - s diagram for this flow

SOLUTION

From the Fanno table, we find the Fanno friction parameter $4C_f L_1^*/D_h$, i.e.,

$$M_1 = 2.6 \xrightarrow{\text{Fanno table}} 4C_f L_1^*/D_h = 0.45253$$

Therefore, $L_1^*/D_h = 0.45253/[4(0.005)] = 22.62$. Since $L_1^*/D_h > L/D_h$, a normal shock will appear in the duct

to support a choked exit flow, as shown in Figure 2.45(b) or Figure 2.46.

Guess M_x to be 1.5

$$M_x = 1.5 \xrightarrow{\text{Fanno table}} 4C_f L_x^*/D_h = 0.13602$$

$$4C_f L_x/D_h = (4C_f L_1^*/D_h) - (4C_f L_x^*/D_h) = 0.45253 - 0.13602 = 0.31651$$

Then, we establish the shock jump conditions, namely

$$M_x = 1.5 \xrightarrow{\text{Normal shock table}} M_y = 0.7011$$

$$M_y = 0.70 \xrightarrow{\text{Fanno table}} 4C_f L_y^*/D_h \cong 0.2081$$

Now, we check the criterion: $L_x + L_y^* = L$ or equivalently

$$4C_f L_x/D_h + 4C_f L_y^*/D_h = 0.31651 + 0.2081 = 0.5246$$

$4C_f L/D_h = 4(0.005)(40) = 0.8 \neq 0.5246$, therefore our initial guess on M_x was incorrect. Do we need to guess a higher or a lower M_x ? Since the sum of L_x and L_y^* was less than the physical length of the duct, L , our shock was not strong enough to choke the exit flow. Hence, we need to guess a higher M_x , namely, let

$$M_x = 2.0 \xrightarrow{\text{Fanno table}} 4C_f L_x^*/D_h = 0.30495$$

$$4C_f L_x/D_h = (4C_f L_1^*/D_h) - (4C_f L_x^*/D_h) = 0.45253 - 0.30495 = 0.14758$$

$$M_x = 2.0 \xrightarrow{\text{Normal shock table}} M_y = 0.5774$$

$$M_y = 0.5774 \approx 0.58 \xrightarrow{\text{Fanno table}} 4C_f L_y^*/D_h \cong 0.57572$$

$$4C_f L_x/D_h + 4C_f L_y^*/D_h = 0.14758 + 0.57572 = 0.7233$$

$$4C_f L/D_h = 0.8 \neq 0.7233$$

Our shock Mach number of 2.0 was slightly weaker than it should be. Hence, we choose a new shock Mach number, namely,

$$M_x = 2.1 \xrightarrow{\text{Fanno table}} 4C_f L_x^*/D_h = 0.33381$$

$$4C_f L_x/D_h = (4C_f L_1^*/D_h) - (4C_f L_x^*/D_h) = 0.45253 - 0.33381 = 0.11872$$

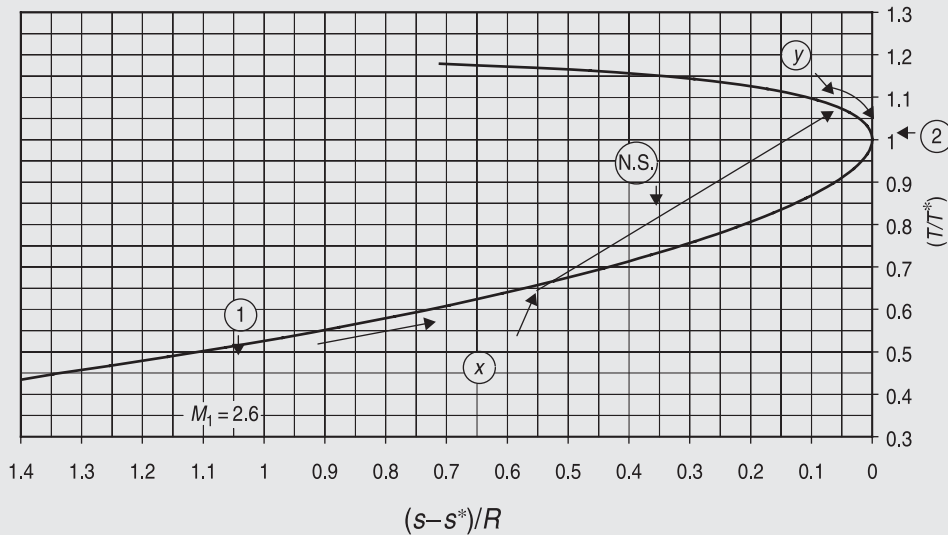
$$M_x = 2.1 \xrightarrow{\text{Normal shock table}} M_y = 0.5613$$

$$M_y = 0.5613 \approx 0.56 \xrightarrow{\text{Fanno table}} 4C_f L_y^*/D_h \cong 0.67362$$

$$4C_f L_x/D_h + 4C_f L_y^*/D_h = 0.11872 + 0.67362 = 0.7923$$

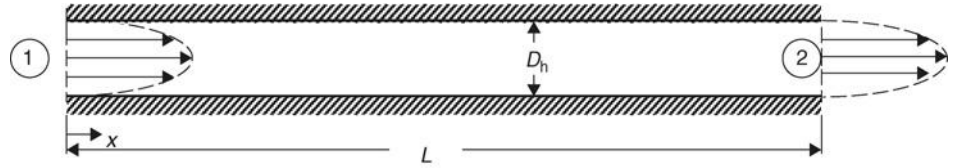
Although we are close to our target value of 0.8, we need to slightly increase the shock Mach number (to perhaps 2.12). Also, instead of using the nearest values from the tables, we may use the Fanno flow equations to improve accuracy. However, we have demonstrated the principles and we stop at this value of $M_x \sim 2.1$. Figure 2.50 shows the T - s diagram for this problem.

Fanno flow with a normal shock



■ FIGURE 2.50 Thermodynamic states of a calorically perfect gas on the Fanno line ($\gamma = 1.4$)

■ FIGURE 2.51
Schematic drawing of a
fully developed pipe
flow



2.17 Friction (Drag) Coefficient C_f and D'Arcy Friction Factor f_D

Let us consider a fully developed pipe flow, where the velocity profile remains constant, that is, preserved, along the length of the pipe, as shown in Figure 2.51.

Since the momentum of the fluid remains constant along the length of the pipe, the frictional drag on the fluid has to be in balance with the pressure forces acting on the fluid. Therefore,

$$\int_0^L \tau_w \cdot c \cdot dx = (p_1 - p_2)A = \Delta p \cdot A \quad (2.196)$$

where c is the circumference of the pipe. Dividing both sides by the dynamic pressure and introducing the friction drag coefficient C_f , we get

$$C_f \cdot L \cdot c = \frac{\Delta p}{\rho V^2 / 2} \cdot A \quad (2.197)$$

Rearranging Equation 2.197 and using the definition of hydraulic diameter D_h , we get

$$4 \cdot C_f = \left(\frac{\Delta p}{(\rho V^2 / 2) (L / D_h)} \right) \quad (2.198a)$$

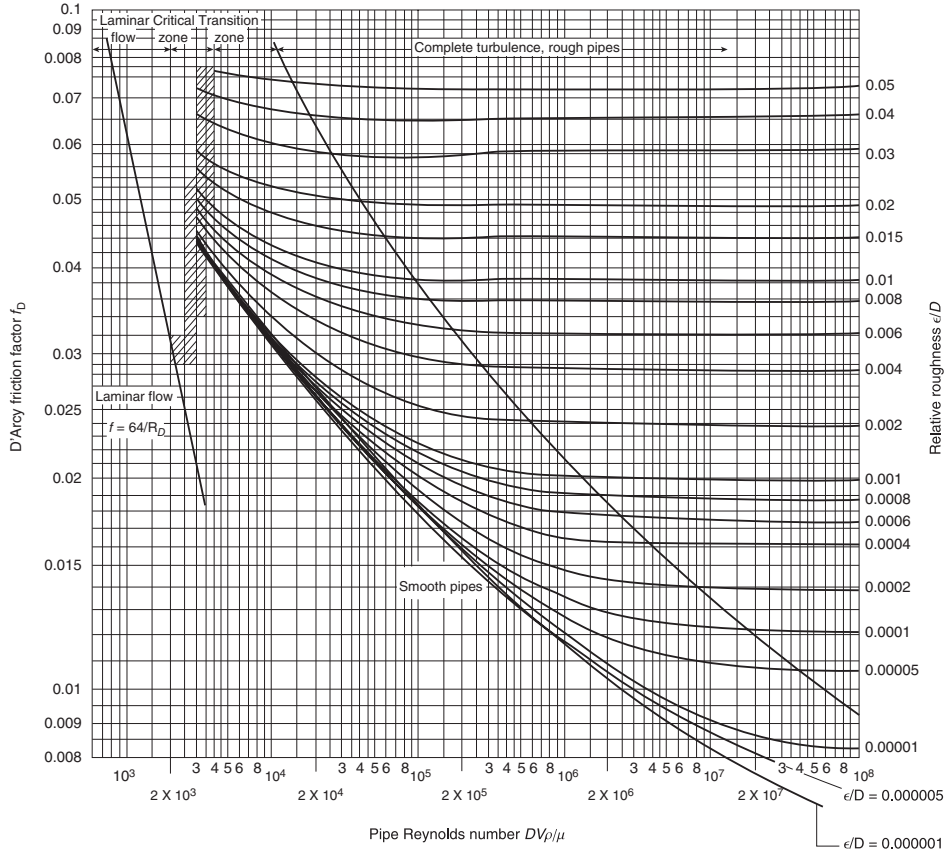
The nondimensional term in the bracket on the RHS of Equation 2.198a is referred to as the D'Arcy friction factor, f_D . Moody (1944) developed the functional dependence of the friction factor on pipe Reynolds number for incompressible flow. A graphic presentation of the friction factor f_D due to Moody is shown in Figure 2.52. The Fanno flow calculations that need the friction coefficient C_f need to take 1/4 of the friction factor data presented in the Moody diagram (Figure 2.52).

$$C_f = f_D / 4 \quad (2.198b)$$

2.18 Dimensionless Parameters

Following the Buckingham Π theorem, a group of independent dimensionless parameters appear in fluid mechanics that govern its behavior and hence introduce dynamic similarity between flows that share these parameters. The major dimensionless groups that are relevant to our studies are

■ **FIGURE 2.52**
Moody diagram for the friction factor f_C , in terms of pipe Reynolds number and the relative roughness of a pipe with an incompressible fluid flow. Source: Moody 1944, Fig. 1, p. 672. Reproduced with permission from ASME



- Mach number $M \equiv V/a$
- Reynolds number $Re_l \equiv \rho V l / \mu$
- Prandtl number $Pr \equiv \mu \cdot c_p / k$
- Nusselt number $Nu_l = h \cdot l / k$, where h is the rate of heat transfer per unit area per unit temperature difference

$$h \equiv \frac{\dot{Q}/A}{T_w - T_e}$$

where T_w and T_e are the wall and thermal boundary layer edge temperatures, respectively.

- Stanton number, $St \equiv Nu / Pr \cdot Re$
- Pressure coefficient $C_p \equiv (p - p_\infty) / (\rho_\infty V_\infty^2 / 2)$
- Force coefficient $C_F \equiv F / \left[\left(\frac{\rho_\infty V_\infty^2}{2} \right) A \right]$
- Knudsen number $Kn \equiv \lambda / l$, where λ is the mean-free path of the molecules in the gas.

The pressure coefficient, C_p , may be written in terms of Mach number and static pressure ratio, such as

$$\dot{C}_p \equiv \frac{p - p_\infty}{\rho_\infty V_\infty^2 / 2} = \frac{2p_\infty}{\rho_\infty V_\infty^2} \left(\frac{p}{p_\infty} - 1 \right) = \frac{2}{\gamma V_\infty^2} \cdot \frac{\gamma p_\infty}{\rho_\infty} \left(\frac{p}{p_\infty} - 1 \right) = \frac{2}{\gamma M_\infty^2} \left(\frac{p}{p_\infty} - 1 \right) \tag{2.199}$$

There are no approximations in expressing the pressure coefficient in terms of the Mach number and the pressure ratio, as shown in Equation 2.199. We may use the Bernoulli equation

$$p_t = p + \rho V^2 / 2 \tag{2.200}$$

which is valid for a low-speed flow, to get the low-speed approximation of the pressure coefficient, such as

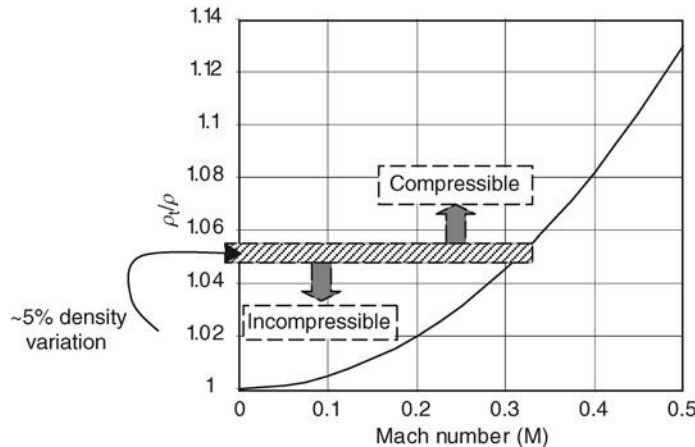
$$C_p \approx 1 - V^2 / V_\infty^2 \tag{2.201}$$

The low-speed range of validity for the Bernoulli equation or the pressure coefficient representation, as in Equation 2.201, is for flows with $M < 0.3$. From the compressible flow equation for the total and static densities we have

$$\frac{\rho_t}{\rho} = \left(1 + \frac{\gamma - 1}{2} M^2 \right)^{\frac{1}{\gamma - 1}} \tag{2.202}$$

For a Mach number of 0.3 or below, the maximum density variation, that is, between the total and static densities, is less than ~5%. A density variation with Mach number is shown in Figure 2.53.

■ FIGURE 2.53
Maximum density ratio
at low subsonic Mach
numbers for $\gamma = 1.4$



Now, let us compare the ratio of total-to-static pressure a low speed and at compressible levels. The low-speed version, which is based on the Bernoulli equation, is a special case of the general expression,

$$p_t/p = [1 + (\gamma - 1)M^2/2]^{\frac{\gamma}{\gamma-1}} \tag{2.203}$$

We may use binomial expansion of Equation 2.203 for a low Mach number and keep the first term in the expansion, such as

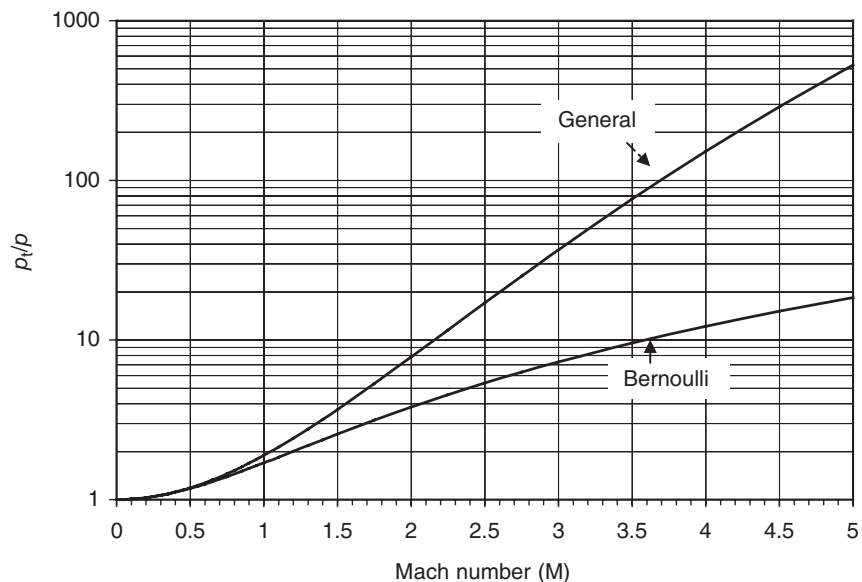
$$\frac{p_t}{p} \cong 1 + \left(\frac{\gamma - 1}{2}\right) \left(\frac{\gamma}{\gamma - 1}\right) M^2 = 1 + \frac{\gamma}{2} M^2 \tag{2.204}$$

By replacing the Mach number in Equation 2.204 with the gas speed and the speed of sound, we show that Equation 2.204 is the Bernoulli equation,

$$\frac{p_t}{p} \cong 1 + \frac{\gamma}{2} \frac{V^2}{a^2} = 1 + \frac{1}{RT} \cdot \frac{V^2}{2} = 1 + \frac{\rho}{p} \cdot \frac{V^2}{2} \tag{2.205}$$

We have demonstrated that the Bernoulli equation is only a special case of the general equation relating stagnation and static pressure via Mach number. Hence, the Bernoulli equation should be used only at low speeds. Let us graph the general and the special case of total pressure equation as a function of Mach number in Figure 2.54 to appreciate the shortcomings of Bernoulli at compressible speeds. To capture the discrepancy between the Bernoulli and the general expression at high Mach numbers, we use a logarithmic scale on the ordinate of Figure 2.54.

■ **FIGURE 2.54**
Comparison between the Bernoulli and the general equation for total pressure as a function of local Mach number ($\gamma = 1.4$)



2.19 Fluid Impulse

Let us consider a duct, or device, where fluid enters at certain inlet conditions, for example, mass flow rate, speed, static pressure, and temperature, and exits the duct or device at a different state. A definition sketch is shown in Figure 2.55.

Note that in Figure 2.55b, p_w represents the pressure exerted *on the fluid* from the wall, and the term τ_w is the shear stress acting *on the fluid*, that is, exerted by the wall on the fluid. The pressure and shear felt at the wall is the opposite in direction and equal in magnitude to the ones acting on the fluid. Assuming that the flow is uniform at the inlet and exit planes, we may write the momentum equation for the fluid (in the x -direction) as

$$\dot{m}V_2 - \dot{m}V_1 = p_1A_1 - p_2A_2 + F_x|_{\text{fluid}} \quad (2.206)$$

where $F_{x,\text{fluid}}$ is the integral of pressure and shear forces exerted on the fluid by the wall, in the $+x$ -direction. Now, we can isolate this force exerted by the wall on the fluid and express it in terms of fluid impulse I , which is defined as

$$I \equiv pA + \dot{m}V = pA(1 + \gamma M^2) \quad (2.207)$$

at the inlet and exit planes of the duct, namely,

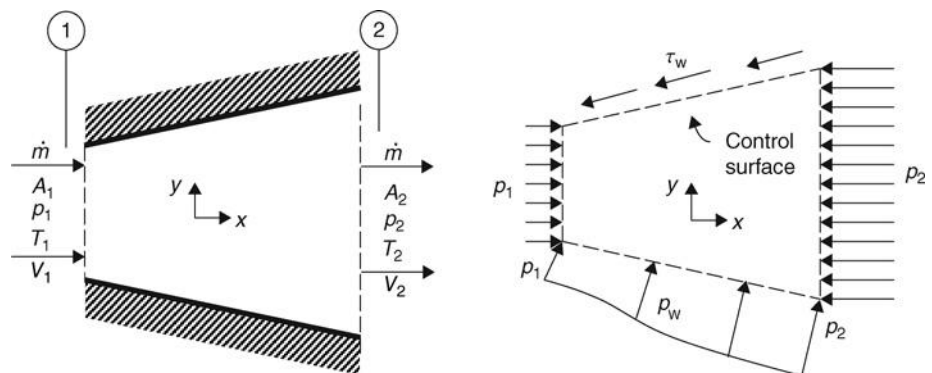
$$F_x|_{\text{fluid}} = (\dot{m}V_2 + p_2A_2) - (\dot{m}V_1 + p_1A_1) = I_2 - I_1 \quad (2.208)$$

In turn, the force felt by the duct (in the x -direction), in reaction to fluid flow through it, is equal and opposite to $F_{x,\text{fluid}}$, that is,

$$F_x|_{\text{walls}} = -F_x|_{\text{fluid}} = I_1 - I_2 \quad (2.209)$$

There are three lessons here. One, we may arrive at the integrated wall force, as in $F_{x,\text{wall}}$ above, by simply balancing the fluid impulse at the inlet and exit of a duct. Two, depending on the change of fluid impulse from inlet to exit, $I_1 - I_2$, the force acting on the wall will be in the thrust or drag direction, that is, in the $-x$ or $+x$ -direction. Finally, the force that we call $F_{x,\text{wall}}$ is force on the *inner wall* and thus accounts for no external drag contribution.

■ **FIGURE 2.55**
Definition sketch for a duct flow and its corresponding (closed) control surface



(a) Duct geometry and flow parameters

(b) Forces acting on the *fluid* (control surface)

In a diffuser where $I_2 > I_1$, the duct will experience a thrust (i.e., $-x$) force. In air-breathing jet engines, the inlet is responsible for a percentage of net thrust production. The percentage of inlet contribution to thrust increases with flight Mach number. In hypersonic flight, the inlet is responsible for more than 50% of thrust production of the engine. Note that we are addressing the *internal performance* of an inlet. The external aerodynamic drag plays a dominant role in inlet selection and airframe integration and contributes to the net *installed thrust*.

EXAMPLE 2.12 (Subsonic Diffuser)

Consider a diffusing duct of the following geometrical and flow characteristics:

A_1 is the inlet area

$$M_1 = 0.7$$

Total pressure loss in the diffuser is 1% of the inlet total pressure, i.e., $p_{t2}/p_{t1} = 0.99$

The exit area is $A_2 = 1.237 A_1$

Assume that the flow in the diffuser is adiabatic and unseparated and the exit flow is uniform, calculate

- (a) the exit Mach number M_2
- (b) the static pressure recovery in the diffuser C_{PR}
- (c) the force acting on the diffuser inner wall, i.e., $F_{x,wall}$, nondimensionalized by the inlet static pressure and area, i.e., $p_1 A_1$

SOLUTION

Expressing the continuity equation in terms of fluid total or stagnation state and Mach number, we can calculate the exit Mach number M_2 via

$$\begin{aligned} \sqrt{\frac{\gamma}{R}} \frac{p_{t1}}{\sqrt{T_{t1}}} A_1 M_1 \left(\frac{1}{1 + \frac{\gamma-1}{2} M_1^2} \right)^{\frac{\gamma+1}{2(\gamma-1)}} \\ = \sqrt{\frac{\gamma}{R}} \frac{p_{t2}}{\sqrt{T_{t2}}} A_2 M_2 \left(\frac{1}{1 + \frac{\gamma-1}{2} M_2^2} \right)^{\frac{\gamma+1}{2(\gamma-1)}} \end{aligned}$$

which simplifies to:

$$\begin{aligned} \frac{M_2}{(1 + 0.2M_2^2)^3} &= \left(\frac{p_{t1}}{p_{t2}} \right) \frac{A_1}{A_2} \frac{M_1}{(1 + 0.2M_1^2)^3} \\ &= \left(\frac{1}{0.99} \right) \left(\frac{1}{1.237} \right) \frac{0.7}{1.3237} = 0.4318 \end{aligned}$$

The (subsonic) solution to the above equation for M_2 is

$$M_2 \approx 0.50$$

The static pressure recovery in a diffuser is defined as

$$C_{pr} \equiv \frac{p_2 - p_1}{q_1} = \frac{1}{\gamma M_1^2} \left(\frac{p_2}{p_1} - 1 \right)$$

We may write the static pressure ratio in terms of total pressure ratio and a function of Mach number as

$$\begin{aligned} \frac{p_2}{p_1} &= \frac{p_{t2}}{p_{t1}} \left(\frac{1 + \frac{\gamma-1}{2} M_1^2}{1 + \frac{\gamma-1}{2} M_2^2} \right)^{\frac{\gamma}{\gamma-1}} = (0.99) \left(\frac{1.098}{1.05} \right)^{3.5} \\ &= 1.169353 \end{aligned}$$

Therefore, the static pressure recovery is

$$C_{PR} \approx 0.4937$$

$$C_{PR} = \frac{2}{(1.4)(0.7)^2} (0.169353) = 0.4937$$

The physical interpretation of the value of C_{PR} that we calculated is that the diffuser has converted $\sim 49.4\%$ of its inlet dynamic pressure into static pressure rise. We note the flow deceleration in the diffuser, from Mach 0.7 at the inlet to 0.5 at the exit.

What is the internal force that the diffuser feels? To answer this question, we look at the change in fluid impulse, $I_1 - I_2$, according to Equation 2.209:

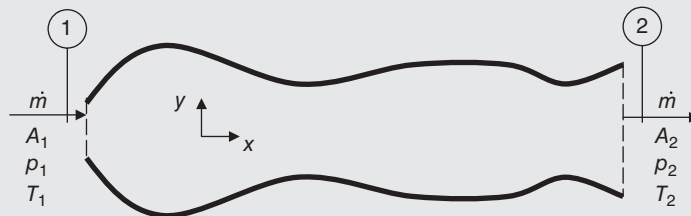
$$F_x|_{\text{walls}} = I_1 - I_2 = A_1 p_1 (1 + \gamma M_1^2) - A_2 p_2 (1 + \gamma M_2^2)$$

As suggested in the problem statement, we may use inlet static pressure and area as the nondimensionalizing force (although we could have used inlet dynamic pressure and the area, instead), therefore,

$$\frac{F_x|_{\text{walls}}}{p_1 A_1} = 1 + \gamma M_1^2 - \left(\frac{A_2}{A_1}\right) \left(\frac{p_2}{p_1}\right) (1 + \gamma M_2^2)$$

Upon substitution of the values that we calculated and were given in the problem statement, in the above expression, we get

$$\frac{F_x|_{\text{walls}}}{p_1 A_1} = -0.26676$$



■ FIGURE 2.56 Diffuser with different cross-section and longitudinal shapes as that shown in Figure 2.55 (with the same inlet and exit flow conditions)

COMMENTS The negative sign on the force acting on the diffuser inner wall identifies the force as acting in the $-x$ -direction, i.e., in the *thrust* direction. Note that we calculated the force acting on the inner wall, including the viscous force (that caused the total pressure drop in the diffuser), without the knowledge of either the wall static pressure distribution or the viscous shear stress distribution on the wall. The balance of fluid impulse is, therefore, a powerful tool that we use to calculate forces on the engine components.

Also, note that the shape of the duct (cross-section or in longitudinal direction) did not enter the problem, in other words, for the same flow conditions at the inlet, area ratio, and the total pressure loss, the duct shape could have been as drawn in Figure 2.56.

However, one manifestation of different cross-sections and longitudinal shapes is in the extent of total pressure loss that is created in the duct. Boundary layer development is sensitive to both streamwise and *transverse pressure gradients* and therefore potential flow separation as well as extensive secondary flow losses will be different in ducts of different geometries.

EXAMPLE 2.13 (Supersonic Nozzle)

Consider a convergent–divergent nozzle as shown in Figure 2.57. The flow conditions are

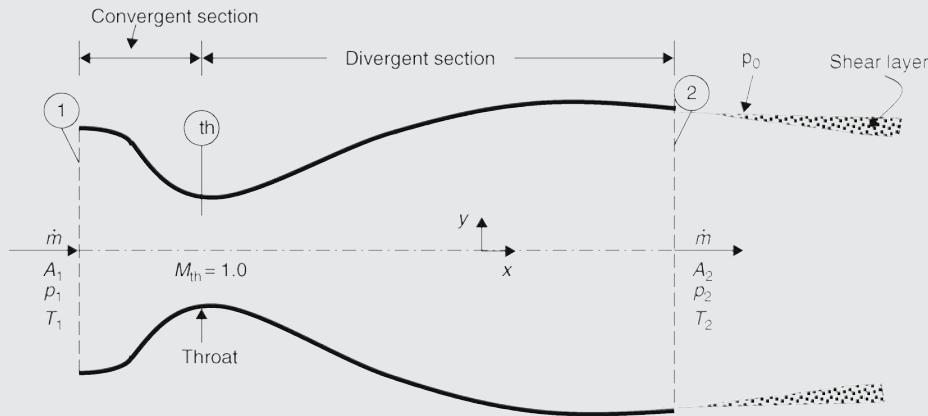
- inlet Mach number $M_1 = 0.5$
- inlet nozzle total pressure is $p_{t1} = 10 p_0$, where p_0 is the ambient pressure
- total pressure loss in the convergent section of the nozzle is 1%, i.e. $(p_{t1} - p_{t,th})/p_{t1} = 0.01$
- total pressure loss in the divergent section of the nozzle is 2%, i.e. $(p_{t,th} - p_{t2})/p_{t,th} = 0.02$
- nozzle area expansion ratio is $A_2/A_{th} = 2.0$

In addition, we assume that the gas is perfect and its properties remain unchanged throughout the nozzle. The gas is characterized by

- $\gamma = 1.4$
- $R = 287 \text{ J/kg} \cdot \text{K}$

The flow in the nozzle is assumed to be steady and adiabatic, therefore the total enthalpy remains constant, i.e.,

- $h_{t2} = h_{t1}$



■ FIGURE 2.57 Sketch of a convergent–divergent nozzle with choked throat and the free shear layer

Calculate

- the exit Mach number M_2
- the exit static pressure in terms of ambient pressure p_2/p_0
- the nondimensional axial force acting on the convergent nozzle $F_{x, \text{con.-wall}}/A_{\text{th}} p_{t1}$
- the nondimensional axial force acting on the divergent nozzle $F_{x, \text{div.-wall}}/A_{\text{th}} p_{t1}$
- the total (nondimensional) axial force acting on the nozzle $F_{x, \text{nozzle}}/A_{\text{th}} p_{t1}$

SOLUTION

By setting the mass flow rate at the exit and throat equal to each other, we calculate the exit Mach number M_2 . We used the same approach in the previous example on subsonic diffusers.

$$\begin{aligned} \sqrt{\frac{\gamma}{R}} \frac{p_{t, \text{th}}}{\sqrt{T_{t, \text{th}}}} A_{\text{th}} M_{\text{th}} \left(\frac{1}{1 + \frac{\gamma-1}{2} M_{\text{th}}^2} \right)^{\frac{\gamma+1}{2(\gamma-1)}} \\ = \sqrt{\frac{\gamma}{R}} \frac{p_{t2}}{\sqrt{T_{t2}}} A_2 M_2 \left(\frac{1}{1 + \frac{\gamma-1}{2} M_2^2} \right)^{\frac{\gamma+1}{2(\gamma-1)}} \end{aligned}$$

“Frozen” gas properties along the nozzle will cause the elimination of similar terms on both sides of the continuity equation. We will cancel the total temperature and substitute $M_{\text{th}} = 1.0$ for the throat Mach number, to get

$$\begin{aligned} \frac{M_2}{(1 + 0.2M_2^2)^3} &= \left(\frac{p_{t, \text{th}}}{p_{t2}} \right) \frac{A_{\text{th}}}{A_2} \frac{M_{\text{th}}}{(1 + 0.2M_{\text{th}}^2)^3} \\ &= \left(\frac{1}{0.98} \right) \left(\frac{1}{2} \right) \frac{1.0}{1.728} = 0.295257 \end{aligned}$$

There are two solutions to the above equation. One is subsonic, i.e., $M_2 = 0.313$, which is unacceptable in light of a large nozzle pressure ratio ($p_{t1}/p_0 = 10$) and the second solution is $M_2 = 2.174$.

Therefore, the acceptable solution for exit Mach number is

$$M_2 = 2.174$$

The nozzle exit static pressure is related to the exit total pressure and the exit Mach number via

$$p_2 = \frac{p_{t2}}{\left(1 + \frac{\gamma-1}{2} M_2^2 \right)^{\frac{\gamma}{\gamma-1}}}$$

The nozzle exit total pressure is calculated based on nozzle losses, e.g.,

$$p_{t2} = \frac{p_{t2}}{p_{t, \text{th}}} \frac{p_{t, \text{th}}}{p_{t1}} \frac{p_{t1}}{p_0} p_0$$

Therefore, the nozzle exit static pressure is related to ambient static pressure by

$$\frac{p_2}{p_0} = \frac{(0.98)(0.99)(10)}{[1 + 0.2(2.174)^2]^{3.5}} = 0.9450$$

$$p_2/p_0 \cong 0.945$$

Since $p_2 < p_0$, the (nozzle) flow is overexpanded (but just slightly). A weak oblique shock at the nozzle lip will appear to balance the static pressure across the jet shear layer. Let us apply Equation 2.209 to calculate the force acting on the wall, i.e.,

$$F_x|_{\text{wall}} = -F_x|_{\text{fluid}} = I_1 - I_2$$

Therefore, the force on the convergent section of the nozzle is

$$F_{x,\text{con-wall}} = p_1 A_1 (1 + \gamma M_1^2) - p_{\text{th}} A_{\text{th}} (1 + \gamma M_{\text{th}}^2)$$

and the nondimensional force is

$$\frac{F_{x,\text{con-wall}}}{A_{\text{th}} p_{\text{t1}}} = \left(\frac{p_1}{p_{\text{t1}}} \right) \left(\frac{A_1}{A_{\text{th}}} \right) (1 + 1.4(0.5)^2) - \left(\frac{p_{\text{th}}}{p_{\text{t1}}} \right) \quad (2.4)$$

We may calculate the inlet area ratio A_1/A_{th} using the continuity equation,

$$\begin{aligned} \sqrt{\frac{\gamma}{R}} \frac{p_{\text{t1}}}{\sqrt{T_{\text{t1}}}} A_1 M_1 \left(\frac{1}{1 + \frac{\gamma-1}{2} M_1^2} \right)^{\frac{\gamma+1}{2(\gamma-1)}} \\ = \sqrt{\frac{\gamma}{R}} \frac{p_{\text{t,th}}}{\sqrt{T_{\text{t,th}}}} A_{\text{th}} M_{\text{th}} \left(\frac{1}{1 + \frac{\gamma-1}{2} M_{\text{th}}^2} \right)^{\frac{\gamma+1}{2(\gamma-1)}} \end{aligned}$$

Which simplifies to

$$\begin{aligned} \frac{A_1}{A_{\text{th}}} &= \frac{p_{\text{t,th}}}{p_{\text{t1}}} \frac{1}{M_1} \left(\frac{1 + \frac{\gamma-1}{2} M_1^2}{\frac{\gamma+1}{2}} \right)^{\frac{\gamma+1}{2(\gamma-1)}} \\ &= (0.99)(1/0.5) \left(\frac{1 + 0.2(0.25)^2}{1.2} \right)^3 = 1.326445 \end{aligned}$$

We can calculate the throat static pressure, p_{th} in terms of the inlet total pressure p_{t1} according to

$$p_{\text{th}} = \frac{p_{\text{t,th}}}{\left(\frac{\gamma+1}{2} \right)^{\frac{\gamma}{\gamma-1}}} = \frac{0.99 p_{\text{t1}}}{(1.2)^{3.5}} = 0.523 p_{\text{t1}}$$

The static pressure at the inlet is written in terms of the inlet total pressure and the Mach number,

$$p_1 = \frac{p_{\text{t1}}}{\left(1 + \frac{\gamma-1}{2} M_1^2 \right)^{\frac{\gamma}{\gamma-1}}} = \frac{p_{\text{t1}}}{[1 + 0.2(0.25)^2]^{3.5}} = 0.84302$$

Now, we are ready to calculate the nondimensional force on the convergent section of the nozzle wall,

$$\frac{F_{x,\text{con-wall}}}{A_{\text{th}} p_{\text{t1}}} = (0.84302)(1.326445)(1.35) - (0.523)$$

$$(2.4) \cong 0.2544$$

$$F_{x,\text{con-wall}}/A_{\text{th}} \cdot p_{\text{t1}} \cong 0.2544$$

The force on the divergent section of the nozzle is

$$F_{x,\text{div-wall}} = p_{\text{th}} A_{\text{th}} (1 + \gamma M_{\text{th}}^2) - p_2 A_2 (1 + \gamma M_2^2)$$

The non-dimensional force on the nozzle divergent section is

$$\frac{F_{x,\text{div-wall}}}{A_{\text{th}} p_{\text{t1}}} = \left(\frac{p_{\text{th}}}{p_{\text{t1}}} \right) (2.4) - \left(\frac{p_2}{p_{\text{t1}}} \right) \left(\frac{A_2}{A_{\text{th}}} \right) (1 + \gamma M_2^2)$$

The ratio of exit static pressure to inlet total pressure is

$$\frac{p_2}{p_{\text{t1}}} = \frac{p_2}{p_0} \frac{p_0}{p_{\text{t1}}} = (0.945)(1/10) = 0.0945$$

Now, we may substitute for all the parameters in the non-dimensional axial force acting on the divergent section of the nozzle

$$\begin{aligned} \frac{F_{x,\text{div-wall}}}{A_{\text{th}} p_{\text{t1}}} &= (0.523)(2.4) - (0.0945)(2)[1 + 1.4(2.174)^2] \\ &= -0.18437 \end{aligned}$$

$$F_{x,\text{div-wall}}/A_{\text{th}} p_{\text{t1}} \cong -0.1844$$

The total axial force acting on the nozzle wall is the sum of the convergent and divergent sections, namely

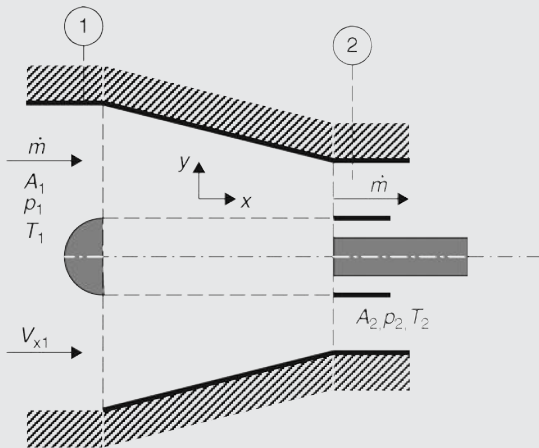
$$\frac{F_{x,\text{nozzle}}}{A_{\text{th}}p_{t1}} \cong 0.2544 - 0.1844 = 0.07$$

$$F_{x,\text{nozzle}}/A_{\text{th}} \cdot p_{t1} \cong 0.07$$

The net positive sign on the axial force acting on the convergent–divergent nozzle wall shows the C–D nozzle as a drag-producing component of an airbreathing engine.

EXAMPLE 2.14 (Axial-Flow Compressor)

Let us apply the fluid impulse principle to an axial-flow compressor, as shown in Figure 2.58.



■ FIGURE 2.58 Axial-flow compressor with its inlet and exit flow parameters identified

For a constant axial velocity through the compressor, as a design choice, we note that flow cross-sectional area shrinks inversely as the density rise, i.e., (steady-flow) continuity demands

$$\frac{A_2}{A_1} = \frac{\rho_1}{\rho_2}$$

To simplify the analysis, we may relate the density ratio to the pressure ratio using an isentropic relation. Therefore, for a compressor pressure ratio of say, 20,

$$\frac{\rho_2}{\rho_1} = 20$$

the density ratio is

$$\frac{\rho_2}{\rho_1} = \left(\frac{p_2}{p_1}\right)^{1/\gamma} = (20)^{1/1.4} \cong 8.4978$$

Therefore, the area ratio is the inverse of 8.4978, i.e.,

$$\frac{A_2}{A_1} \cong \frac{1}{8.4978} \approx 0.1177$$

Guided by these basic principles, we choose the following parameters for our compressor:

$$\begin{aligned} p_2/p_1 &= 20 \\ V_{x1} &= V_{x2} \\ A_2/A_1 &= 0.12 \end{aligned}$$

The application of the impulse principle, Equation 2.209, produces the net axial force experienced by all the surfaces interacting with the flow between stations 1 and 2, i.e.,

$$\begin{aligned} F_{x,walls} &= -F_x|_{\text{fluid}} = I_1 - I_2 \\ &= p_1A_1 + \dot{m}V_{x1} - (p_2A_2 + \dot{m}V_{x2}) = p_1A_1 - p_2A_2 \end{aligned}$$

Note that by our (constant axial velocity) design choice, the axial momentum across the compressor remained constant. The nondimensional axial force $F_{x,walls}/p_1A_1$ is therefore

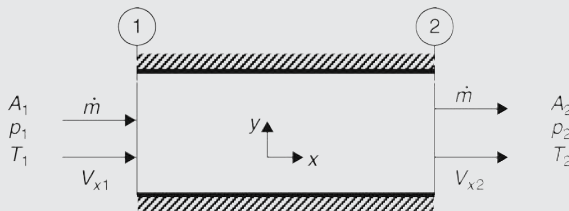
$$\frac{F_{x,walls}}{p_1A_1} = 1 - \left(\frac{p_2}{p_1}\right) \left(\frac{A_2}{A_1}\right) = 1 - (20)(0.12) = -1.4$$

$$F_{x,walls}/p_1A_1 = -1.4$$

The negative sign on the axial force experienced by the compressor structure signifies a thrust production by this component.

EXAMPLE 2.15 (Combustor)

A combustor represents a complex problem for a simple application of the impulse principle. A typical combustor has several ports that carry two different fluids, i.e., fuel and the compressed air, into a reaction chamber. The compressed air itself is introduced at different levels along the combustor length. Let us simplify the problem by assuming a constant-area duct, which takes all the fluid at its entrance (in gaseous form) at certain pressure and temperature conditions and allow a heated fluid (as a result of chemical reaction) to leave the combustor at nearly the same pressure as the inlet, i.e., $p_1 \cong p_2$. Since the pressure is assumed constant, the density drops inversely proportional to the rising temperature. Also with a constant-area duct assumption, the axial velocity rises inversely proportional to the fluid density drop, which in turn is inversely proportional to the static temperature rise. All of these assumptions and trends are simplifications to the real and complex process; however, by making these simplifications, we can apply the simple impulse principle and examine the direction of axial force on the combustor. Let us assume that Figure 2.59 is a simple model of a combustor.



■ FIGURE 2.59 Simple model of a combustor flow

Therefore, let the combustor be modeled as a duct with

$$\begin{aligned} A_2 &= A_1 \\ p_2 &\approx p_1 \\ T_2 &= 1.8T_1 \end{aligned}$$

The density ratio will be the inverse of 1.8, i.e., $\rho_2/\rho_1 \approx 1/1.8 = 0.5556$.

The axial velocity ratio will be equal to the temperature ratio (or inverse of the density ratio),

$$V_{x2}/V_{x1} = 1.8$$

Now the impulse equation written for this simple duct yields

$$\begin{aligned} F_x|_{\text{wall}} &= -F_x|_{\text{fluid}} = I_1 - I_2 \\ &= p_1A_1 + \dot{m}V_{x1} - (p_2A_2 + \dot{m}V_{x2}) = \dot{m}(V_{x1} - V_{x2}) \end{aligned}$$

The nondimensional axial force acting on the combustor walls (according to our model) is

$$\frac{F_x|_{\text{wall}}}{\dot{m}V_{x1}} = 1 - \frac{V_{x2}}{V_{x1}} = -0.8$$

$$F_x|_{\text{wall}}/\dot{m}V_{x1} = -0.8$$

The negative sign of the axial force again signifies a thrust production by the device, i.e., in this case, our model of a combustor.

EXAMPLE 2.16 (Axial-Flow Turbine)

We anticipate the opposite behavior from the turbine compared with a compressor. To quantify that, we model an uncooled turbine flow as a reversible and adiabatic expansion of a perfect gas. Figure 2.60 shows the schematics of an axial-flow turbine.

Assuming the turbine is designed for a constant axial velocity $V_{x1} = V_{x2}$ similar to the compressor, the area ratio will be inversely proportional to the density ratio, i.e.,

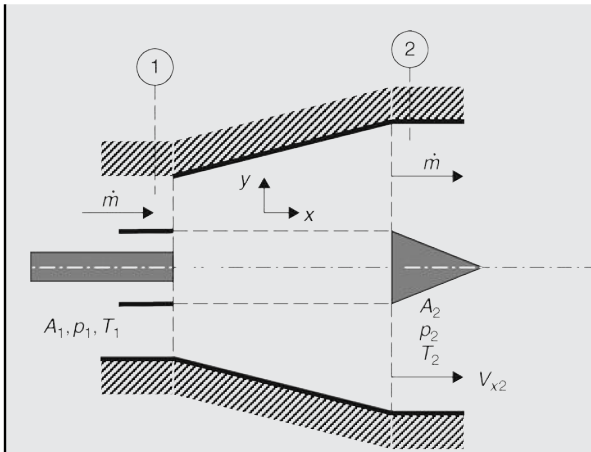
$$A_2/A_1 = \rho_1/\rho_2$$

The density ratio is then related to the temperature ratio isentropically, namely

$$\rho_2/\rho_1 = (T_2/T_1)^{1/\gamma-1}$$

The turbine temperature ratio is calculated from the power balance between the compressor/fan and the turbine, as discussed in the cycle analysis. For now, we assume the turbine expansion is known to be

$$T_2/T_1 \cong 0.79$$



■ FIGURE 2.60 Schematic drawing of an uncooled axial-flow turbine

Therefore, the density ratio will be $\rho_2/\rho_1 = (0.79)^{2.5} = 0.5547$

The area ratio is the inverse of the density ratio, i.e., $A_2/A_1 = 1.803$

And the pressure ratio is related to density ratio according to

$$p_2/p_1 = (\rho_2/\rho_1)^{\gamma} = (0.5547)^{1.4} = 0.4382$$

The impulse equation will again simplify to

$$\begin{aligned} F_y|_{\text{walls}} &= -F_x|_{\text{fluid}} = I_1 - I_2 \\ &= p_1A_1 + \dot{m}V_{x1} - (p_2A_2 + \dot{m}V_{x2}) = p_1A_1 - p_2A_2 \end{aligned}$$

and the nondimensional axial force is

$$\frac{F_{x,\text{walls}}}{p_1A_1} = 1 - \left(\frac{p_2}{p_1}\right) \left(\frac{A_2}{A_1}\right) = 1 - (0.4382)(1.803) \approx 0.210$$

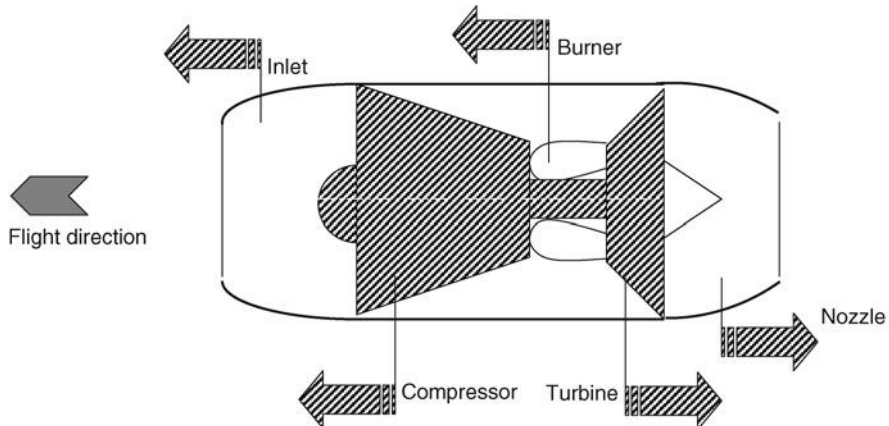
$$F_{x,\text{walls}}/p_1A_1 \approx 0.210$$

As expected, the turbine behavior is opposite to the compressor, i.e., the turbine walls experience an axial force in the drag direction.

2.20 Summary of Fluid Impulse

We have applied fluid impulse principle to various aircraft engine components. Figure 2.61 represents a schematic drawing of a turbojet engine and the (axial) forces internally developed by each component. The vectors indicate the direction and are not drawn to scale. The vector sum of these component forces is transmitted to the aircraft as engine (internal) force. There are external forces (both in the drag and thrust directions) that act on the nacelle that we have not accounted for through our treatment of *internal flow* in engine components. We shall discuss *external flow* effects in Chapter 5.

■ FIGURE 2.61 Turbojet engine shown with its component's (internal) axial force (not to scale) contributing to engine force



References

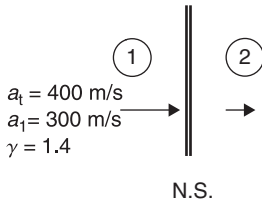
- Anderson, J.D., Jr., *Modern Compressible Flow*, 3rd edition, McGraw-Hill, New York, 2003.
- Anderson, J.D., Jr., *Fundamentals of Aerodynamics*, 4th edition, McGraw-Hill, New York, 2005.
- Moody, L.F., "Friction Factors for Pipe Flow," Transactions of ASME, November 1944.
- Munson, B.R., Young, D.F., and Okiishi, T.H., *Fundamentals of Fluid Mechanics*, 5th edition, John Wiley & Sons, Inc., New York, 2006.
- NACA Report 1135, Ames Research Staff, "Equations, Tables and Charts for Compressible Flow," 1953.
- Shapiro, A.H., *The Dynamics and Thermodynamics of Compressible Fluid Flow*, Vol. I and II, The Ronald Press, New York, 1953.
- Sonntag, R.E., Borgnakke, C., and Van Wylen, G.J., *Fundamentals of Thermodynamics*, 6th edition, John Wiley & Sons, Inc., New York, 2003.

Problems

ASSUME ALL GASES ARE CALORICALLY PERFECT, UNLESS OTHERWISE SPECIFIED.

2.1 A normal shock flow is characterized by stagnation speed of sound a_t and speed of sound a as shown. Calculate

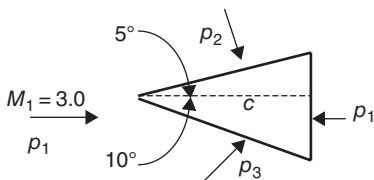
- M_1
- M_2^*



■ **FIGURE P2.1**

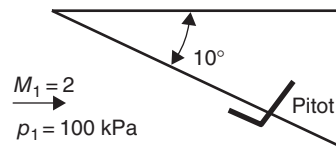
2.2 A two-dimensional projectile with a sharp nose is exposed to a Mach 3 flow, as shown. Assuming the base pressure is p_1 , calculate

- p_2/p_1
- p_3/p_1
- $C_d \equiv D'/q_1 \cdot c$



■ **FIGURE P2.2**

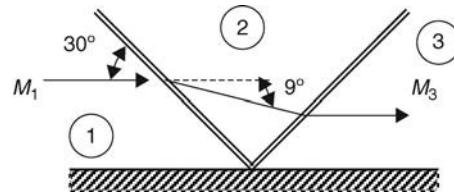
2.3 Calculate the stagnation pressure measured by a Pitot tube on an inclined ramp in a supersonic flow, as shown.



■ **FIGURE P2.3**

2.4 A reflected oblique shock has the following geometry. Calculate

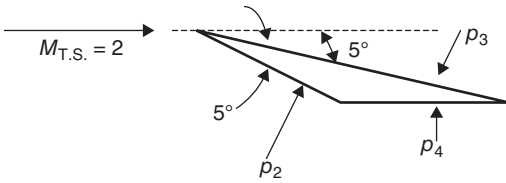
- M_1
- M_2
- M_3



■ **FIGURE P2.4**

2.5 A symmetrical half-diamond airfoil has a leading-edge angle of 5° . This airfoil is set at 5° angle of attack, as shown, and is placed in a wind tunnel with $M_{T.S.} = 2.0$, $p_{t.T.S.} = 100$ kPa, $T_{t.T.S.} = 25^\circ\text{C}$. Assume $\gamma = 1.4$, $c_p = 1.004$ kJ/kg \cdot K. Calculate

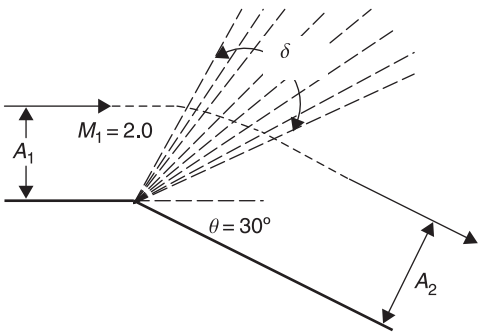
- p_2 (kPa)
- p_3 (kPa)
- p_4 (kPa)



■ FIGURE P2.5

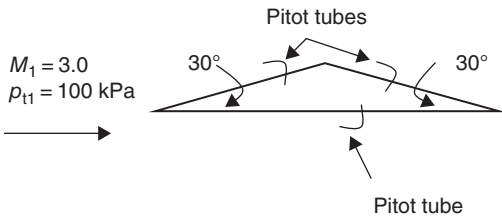
2.6 A supersonic flow expands around a sharp corner, as shown. Calculate the following parameters:

- (a) M_2
- (b) A_2/A_1
- (c) The angle of Prandtl–Meyer fan envelope δ



■ FIGURE P2.6

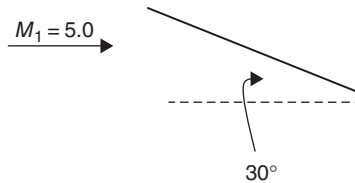
2.7 A symmetrical half-diamond airfoil has a nose angle $\theta_{\text{nose}} = 30^\circ$ and is exposed to a supersonic flow. A pitot tube is installed on each of the three surfaces, as shown. Calculate the pitot tube readings on the airfoil surfaces at zero angle of attack.



■ FIGURE P2.7

2.8 A flat plate is in a Mach 5 flow at 30° angle-of-attack. Calculate

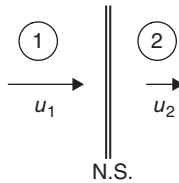
- (a) lift-to-drag ratio, L'/D'
- (b) pitching moment coefficient about the L.E.



■ FIGURE P2.8

2.9 A normal shock is in a Mach 2.0 flow. Upstream gas temperature is $T_1 = 15^\circ\text{C}$, the gas constant is $R = 287 \text{ J/kg} \cdot \text{K}$ and $\gamma = 1.4$. Calculate

- (a) a^* in m/s
- (b) u_2 in m/s (use Prandtl's relation)
- (c) a_1 in m/s
- (d) h_2 in kJ/kg

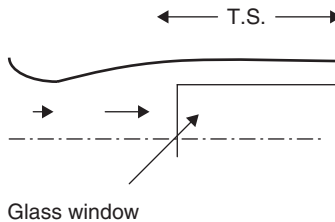


■ FIGURE P2.9

2.10 A supersonic tunnel has a test section (T.S.) Mach number of $M_{\text{T.S.}} = 2.0$. The reservoir for this tunnel is the room with $T_{\text{room}} = 15^\circ\text{C}$ and $p_{\text{room}} = 100 \text{ kPa}$. The test section has two windows (each $10 \times 20 \text{ cm}$). Calculate

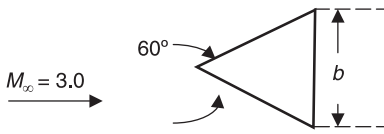
- (a) the speed of sound in the test section
- (b) the force on each glass window

Assume $R = 287 \text{ J/kg} \cdot \text{K}$, $\gamma = 1.4$.



■ FIGURE P2.10

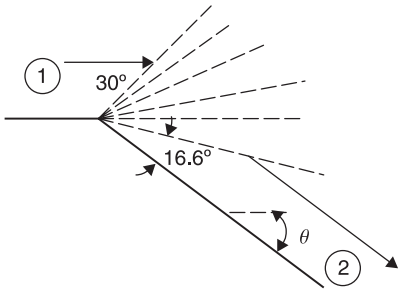
2.11 Calculate the wave drag coefficient of a 2D sharp-nosed projectile, as shown, assuming the base pressure is ambient, i.e., $p_{\text{base}} = p_\infty$. The 2D wave drag coefficient is defined based on b . Assume the angle of attack is zero.



■ FIGURE P2.11

2.12 A Prandtl–Meyer centered expansion wave is visualized with the wave angles as shown. Calculate

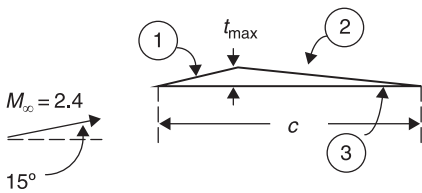
- (a) the flow turning angle, i.e., wall angle θ
- (b) velocity ratio across the expansion wave V_2/V_1



■ FIGURE P2.12

2.13 A diamond airfoil with a nose angle of 15° and a thickness-to-chord ratio of 10% is in a supersonic flow, as shown. Calculate

- (a) the chordwise location of the max thickness point (in % c)
- (b) the trailing-edge angle
- (c) the nondimensional pressure on the three surfaces, $p_1/p_\infty, p_2/p_\infty, p_3/p_\infty$



■ FIGURE P2.13

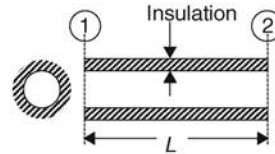
2.14 A blunt-nosed vehicle is in supersonic flight at an altitude where static pressure is $p_\infty = 20$ kPa. Calculate the stagnation pressure on the vehicle.



■ FIGURE P2.14

2.15 An adiabatic constant-area duct has an inlet flow of $M_1 = 0.5$, $T_1 = 260^\circ\text{C}$, $p_1 = 1$ MPa. The average skin friction coefficient, $C_f = 0.005$ and the duct cross-section is circular with inner diameter $d = 10$ cm. Assuming the gas is perfect and has properties $\gamma = 1.4$ and $R = 286.8$ J/kg · K, calculate

- (a) mass flow rate \dot{m}
- (b) L_{\max} to choke this duct at the exit
- (c) p_1 loss in the duct at $L = L_{\max}$



■ FIGURE P2.15

2.16 Calculate the critical heat flux q^* to a frictionless, constant-area duct with an inlet Mach number $M_1 = 2.0$ and an inlet temperature $T_1 = -15^\circ\text{C}$. Assume $\gamma = 1.4$ and $c_p = 1,004$ J/kg · K.

2.17 A constant-area duct has an L/D of 100 and is frictionally choked. For an entrance Mach number of 0.5, calculate

- (a) average wall friction coefficient C_f
- (b) percent static pressure drop in the flow

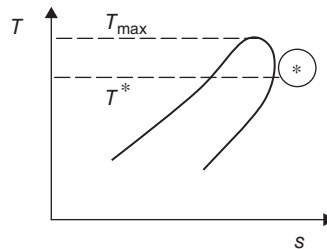
Assume the fluid is air, with $\gamma = 1.4$.

2.18 A frictionless, constant-area duct flow of a perfect gas is heated to a choking condition. The rate of heat transfer per unit mass flow rate is 500 kJ/kg. Assuming inlet Mach number is $M_1 = 3.0$ and $c_p = 1.004$ kJ/kg · K, calculate

- (a) inlet total temperature T_{t1}
- (b) percentage static pressure rise in the flow

2.19 In a Rayleigh flow, as shown, the maximum temperature T_{\max} is reached on the subsonic branch. The sonic condition is shown as * on the T - s diagram. Assuming the medium is air, with $\gamma = 1.4$, calculate

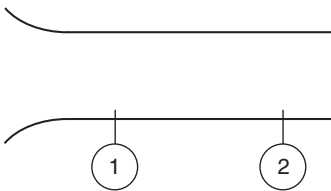
- (a) T_{\max}/T^*
- (b) $p_{@T-\max}/p^*$



■ FIGURE P2.19

2.20 In an adiabatic, constant-area flow of a perfect gas, the inlet conditions are $p_1 = 100$ kPa, $\rho_1 = 1$ kg/m³, and $u_1 = 100$ m/s. At a downstream station the gas is at 200 m/s. Assuming the medium is air, calculate the corresponding static pressure and density, p_2 and ρ_2 , respectively.

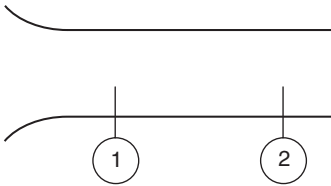
$$[R_{\text{air}} = 287 \text{ J/kg} \cdot \text{K}, \gamma_{\text{air}} = 1.4]$$



■ FIGURE P 2.20

2.21 In a frictionless, constant-area flow of a perfect gas, the inlet conditions are $p_1 = 100$ kPa, $\rho_1 = 1$ kg/m³, and $u_1 = 100$ m/s. At a downstream station the gas is at 200 m/s. Assuming the medium is air, calculate the corresponding static pressure and density, p_2 and ρ_2 , respectively.

$$[R_{\text{air}} = 287 \text{ J/kg} \cdot \text{K}, \gamma_{\text{air}} = 1.4]$$



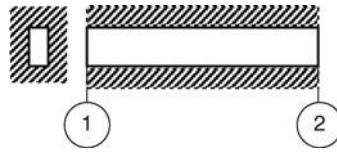
■ FIGURE P 2.21

2.22 Consider a one-dimensional adiabatic flow of a perfect gas with friction. Air enters a circular duct of 20-cm diameter at Mach 0.5 and an average wall friction coefficient of $C_f = 0.005$. If the exit total pressure drops to 85% of the inlet value, i.e., $p_{t2} = 0.85 P_{t1}$, calculate the length of the duct, L .

2.23 A perfect gas flows in a well-insulated, constant-area pipe with friction at $M_1 = 2.0$. For an average wall friction coefficient of $C_f = 0.004$, calculate

- (a) the maximum length of the pipe that can transmit the flow
- (b) total pressure loss at this length

Assume the pipe cross-section is rectangular and has the dimensions of 10×20 cm.



■ FIGURE P 2.23

2.24 Air enters a frictionless, constant-area pipe at $p_1 = 60$ psia., $T_1 = 500$ °R/ and $M_1 = 0.6$. If heat is transferred to the air in the pipe at $q = 300$ BTU/lbm of air, calculate

- (a) the exit Mach number
- (b) static and total pressure and temperature at the exit, p_2, T_2, P_{t2}, T_{t2}
- (c) the critical heat flux q^* that will thermally choke the pipe.

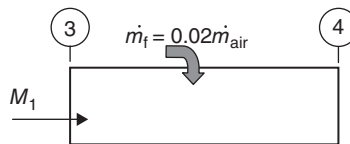
$$c_p = 0.24 \text{ BTU/lbm} \cdot \text{°R}, \gamma = 1.4$$

2.25 A constant-area frictionless pipe is thermally choked. The inlet total temperature and the heat flux are $T_{t1} = 650$ °R and $q^* = 500$ BTU/lbm, respectively. Calculate

- (a) the inlet Mach number M_1
- (b) exit total temperature T_{t2}

$$c_p = 0.24 \text{ BTU/lbm} \cdot \text{°R}, \gamma = 1.4$$

2.26 If we neglect the friction in a jet engine combustion chamber and assume the flow through the burner may be modeled as a Rayleigh line flow, calculate the combustor exit Mach number if $M_3 = 0.2$, $T_{t3} = 900$ °R. The fuel heating value is 18,400 BTU/lbm (of fuel) and the fuel-to-air ratio is 2%. Assume $\gamma = 1.33$ and $c_p = 0.27$ BTU/lbm·°R and neglect the added mass of the fuel.



■ FIGURE P 2.26

2.27 A perfect gas flows in a constant-area tube with no heat interaction with the surroundings. The inlet Mach number is $M_1 = 0.5$. The average wall friction coefficient is $C_f = 0.005$. Calculate

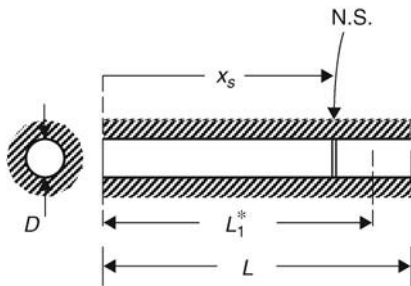
- (a) the choking L/D of the pipe
- (b) the new inlet Mach number M_1' , if the pipe is 20% longer than part (a)

Assume $\gamma = 1.4$.

2.28 Air enters an insulated duct with a constant area with an average wall friction coefficient of $C_f = 0.004$. The inlet Mach number is $M_1 = 2.0$. There is a choking length L_1^* , for this duct that corresponds to the inlet Mach number M_1 . For any duct longer than the choking length L_1^* , a normal shock appears in the duct. Assuming the length of the duct is 10% longer than L_1^* , i.e., $L = 1.1 L_1^*$, calculate

- (a) the shock location along the duct x_s/D
- (b) percentage total pressure loss in the longer duct
- (c) percentage loss of fluid impulse

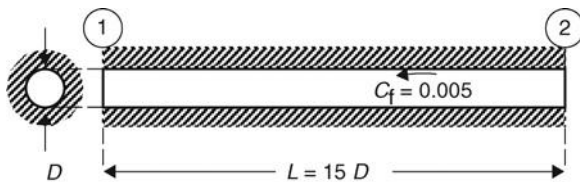
Assume $\gamma = 1.4$.



■ FIGURE P2.28

2.29 Consider an adiabatic flow of a perfect gas in a duct with friction. The geometry of the duct is shown. Assuming $\gamma = 1.4$ and the exit flow is choked, calculate

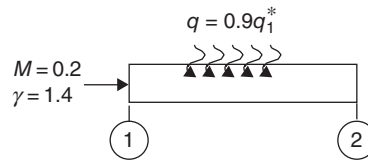
- (a) two possible inlet Mach numbers M_1 , one subsonic and the second supersonic
- (b) the static pressure drop in the subsonic case between the inlet and exit, i.e., $\Delta p/p_1$
- (c) the static pressure rise in the supersonic case, i.e., $\Delta p/p_1$
- (d) the loss of fluid impulse due to friction



■ FIGURE P2.29

2.30 A frictionless flow in a constant-area duct encounters heat transfer through the sidewall as shown. Calculate

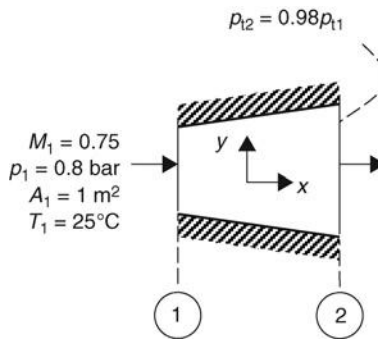
- (a) the exit Mach number
- (b) the static temperature ratio T_2/T_1
- (c) the percentage total pressure loss in the duct, $\Delta p_t/p_{t1} (\times 100)$



■ FIGURE P2.30

2.31 The inlet and exit flow conditions of a subsonic diffuser are shown. The diffuser has an area ratio of $A_2/A_1 = 1.25$. Assuming the fluid is air and is treated as a calorically perfect gas with $\gamma = 1.4$ and $R = 287 \text{ J/Kg} \cdot \text{K}$, calculate

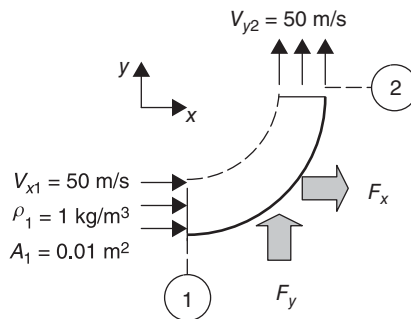
- (a) the mass flow rate in kg/s
- (b) the exit Mach number M_2
- (c) the diffuser static pressure recovery $C_{PR} \equiv (p_2 - p_1)/q_1$
- (d) the axial force exerted on the diffuser wall by the fluid in kN



■ FIGURE P2.31

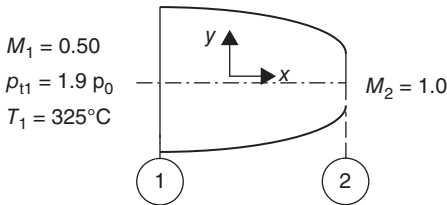
2.32 Consider the flow of perfect gas (air) on a vane, as shown. Apply momentum principles to the fluid to calculate the components of force F_x and F_y that act on the vane.

Assume the flow is uniform, and due to low speeds, $p_1 = p_2 = p_0$, where p_0 is the ambient pressure.



■ FIGURE P2.32

2.33 A subsonic nozzle is choked, i.e., $M_2 = 1.0$. Also the exit static pressure is equal to the ambient pressure p_0 . Calculate the axial force that is experienced by the nozzle, i.e., $F_{x, \text{noz}}$, nondimensionalized by $p_1 A_1$. Assume $\gamma = 1.4$.



■ FIGURE P 2.33

2.34 A scramjet combustor has a supersonic inlet condition and a choked exit. The combustor flow area increases linearly in the flow direction, as shown. The inlet and exit flow conditions are

- $M_1 = 3.0$
- $p_1 = 1 \text{ bar}$
- $T_1 = 1000 \text{ K}$
- $A_1 = 1 \text{ m}^2$
- $M_2 = 1.0$
- $A_2 = 1.4 \text{ m}^2$
- $\gamma = 1.4, R = 287 \text{ J/kg} \cdot \text{K}$

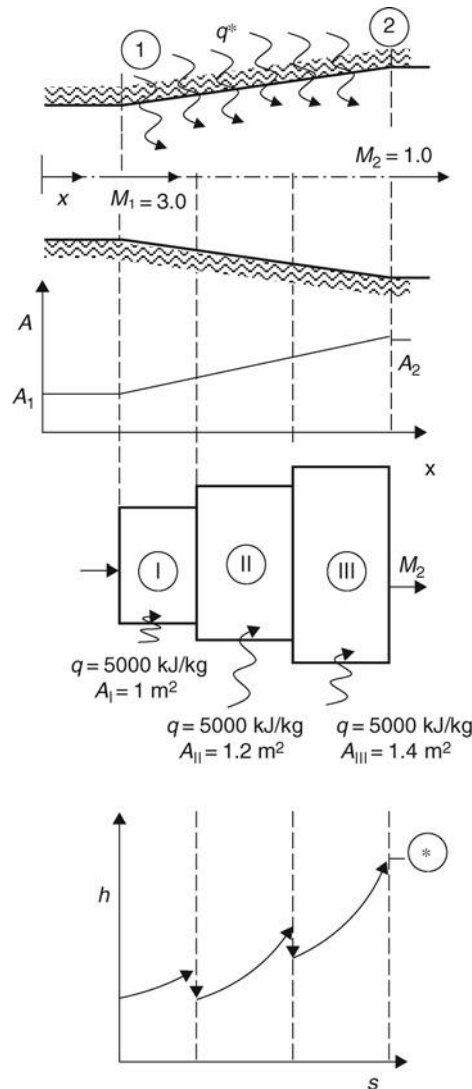
The total heat release due to combustion, per unit flow rate in the duct, is initially assumed to be 15 MJ/kg. If we divide the combustor into three constant-area sections, with stepwise jumps in the duct area, we may apply Rayleigh flow principles to each segment, as shown. The heat release per segment is then 1/3 of the total heat release in the duct, i.e., 5,000 kJ/kg. As the exit condition of a segment needs to be matched to the inlet condition of the following segment, we propose to satisfy continuity equation at the boundary through an isentropic step area expansion, i.e., p_t, T_t remain the same and only the Mach number jumps isentropically through area expansion.

If we march from the inlet condition toward the exit with the assumed heat release rates, we calculate the exit Mach number M_2 . Since the exit flow is specified to be choked, then we need to adjust the total heat release in order to get a choked exit. Calculate the critical heat release in the above duct that leads to thermal choking of the flow.

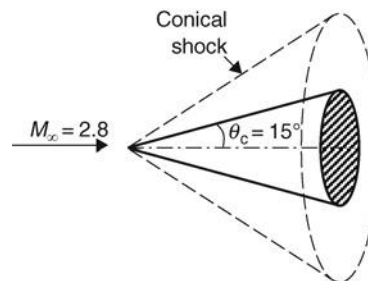
2.35 The center spike of an external-compression inlet is a cone. Use conical shock charts in appendix to calculate

- (a) surface Mach number M_{cone}
- (b) surface pressure coefficient $C_{p, \text{cone}}$
- (c) cone pressure drag (also known as wave drag) coefficient $C_{D, \text{cone}}$.

Assume the cone base pressure is p_∞ .



■ FIGURE P 2.34

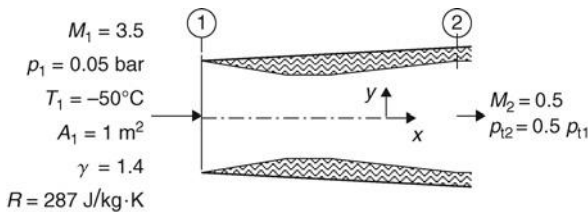


■ FIGURE P 2.35

2.36 A supersonic inlet is shown. Based on the flow conditions specified, calculate

- (a) the inlet mass flow rate \dot{m} in kg/s
- (b) exit area A_2 in m^2
- (c) exit static pressure p_2 in bar
- (d) fluid impulse at the inlet I_1
- (e) fluid impulse at the exit I_2
- (f) the (internal) axial force on the inlet F_x in kN

Assume the flow in the inlet is adiabatic as well as the inlet and exit flows are uniform.



■ FIGURE P 2.36

2.37 A steady-adiabatic flow in a convergent–divergent nozzle (as shown in Figure 2.57) is characterized by

- (a) inlet Mach number $M_1 = 0.55$
- (b) inlet nozzle total pressure is $p_{t1} = 6 p_0$, where p_0 is the ambient pressure
- (c) total pressure loss in the convergent section of the nozzle is 1%, i.e. $(p_{t1} - p_{t,th})/p_{t1} = 0.01$
- (d) total pressure loss in the divergent section of the nozzle is 2%, i.e. $(p_{t,th} - p_{t2})/p_{t,th} = 0.02$
- (e) nozzle area expansion ratio is $A_2/A_{th} = 1.50$

Assuming that the gas is perfect and its properties remain unchanged throughout the nozzle with

$$\begin{aligned} \gamma &= 1.4 \\ R &= 287 \text{ J/kg} \cdot \text{K} \end{aligned}$$

Calculate

- (a) the exit Mach number M_2
- (b) the exit static pressure in terms of ambient pressure p_2/p_0
- (c) the nondimensional (internal) axial force acting on the convergent nozzle, $F_{x,con.-wall}/A_{th}p_{t1}$
- (d) the nondimensional (internal) axial force acting on the divergent nozzle, $F_{x,div.-wall}/A_{th}p_{t1}$
- (e) the total (nondimensional) axial force acting on the nozzle, $F_{x,nozzle}/A_{th}p_{t1}$

2.38 A subsonic diffuser flow is steady and adiabatic with inlet Mach number $M_1 = 0.6$. Total pressure loss in the diffuser is 2% of the inlet total pressure, i.e., $p_{t2}/p_{t1} = 0.98$. The diffuser area ratio is $A_2/A_1 = 1.50$.

Assuming that the flow in the diffuser has a uniform exit flow, calculate

- (a) the exit Mach number M_2
- (b) the static pressure recovery in the diffuser C_{PR}
- (c) the (internal) force acting on the diffuser, i.e., $F_{x,wall}$, nondimensionalized by the inlet static pressure and area, i.e., $p_1 A_1$

2.39 An axial-flow compressor (as shown in Figure 2.58) has a pressure ratio $p_2/p_1 = 15$. In addition, we have

$$\begin{aligned} V_{x1} &= V_{x2} \\ A_2/A_1 &= 0.155 \end{aligned}$$

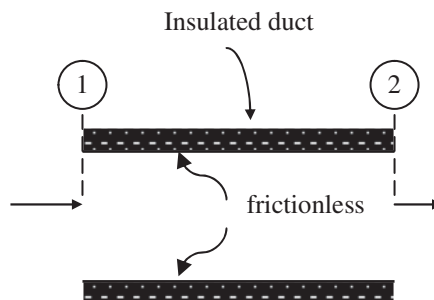
Calculate the nondimensional internal force that acts in the axial direction on the compressor, $F_{x,wall}/A_1 p_1$ if the flow is assumed to be steady and uniform at the compressor inlet and exit.

2.40 An axial-flow turbine (as shown in Figure 2.60) is designed for constant axial velocity, $V_{x1} = V_{x2}$. Turbine pressure ratio is measured to be $p_2/p_1 = 0.36$. The turbine area ratio is $A_2/A_1 = 2.1$. Assuming the flow is steady and uniform at the inlet and exit of the turbine, calculate the nondimensional internal force that acts in the axial direction on the turbine, $F_{x,wall}/A_1 p_1$

2.41 A supersonic combustion is modeled as Rayleigh flow. The inlet Mach number is $M_1 = 3.0$, the total temperature and pressure at the inlet are $T_{t1} = 1,500 \text{ K}$ and $p_{t1} = 100 \text{ kPa}$, respectively. Calculate

- (a) minimum q to choke the flow at the exit
- (b) exit temperature, T_2
- (c) if the fuel is hydrogen with a heating value of 120,000 kJ/kg, calculate the fuel-to-air ratio, f .

Assume $\gamma = 1.4$ and $c_p = 1,004 \text{ J/kg} \cdot \text{K}$



■ FIGURE P 2.37

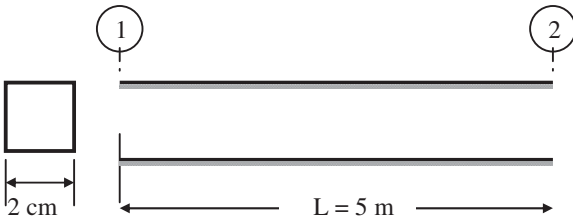
2.42 A scramjet combustor is modeled as a frictionless flow of a perfect gas in a constant-area duct with heating (Rayleigh flow). The inlet Mach number to the burner is $M_1 = 2.8$ with $\gamma = 1.4$. Critical heating of the gas (i.e., by

burning fuel) in the combustor achieves a sonic exit state. Assuming the gas is calorically perfect, calculate

- (a) the nondimensional critical heat flux, $q_1^*/c_p T_{t1}$, to achieve thermal choking of the flow
- (b) the percentage static pressure rise, $\Delta p/p_1$

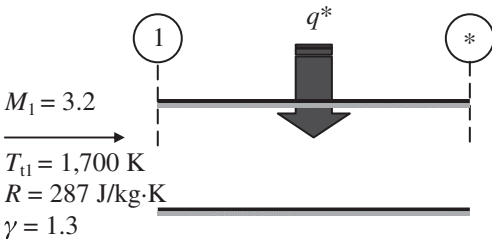
2.43 A duct with square cross-section is shown. The inlet flow conditions are known to be: $M_1 = 0.3$, $p_1 = 150$ kPa, $T_1 = 300$ K, $\gamma = 1.4$, $R = 287$ J/kg · K. The duct is insulated but the flow is frictional, with the wall friction coefficient $C_f = 0.005$. Assuming the flow is steady, calculate

- (a) the mass flow rate, \dot{m} in kg/s and lbm/s
- (b) the hydraulic diameter of the duct in centimeter and feet
- (c) the exit Mach number, M_2
- (d) the percentage total pressure loss, $(\Delta p_t/p_{t1}) \times 100$, across the duct



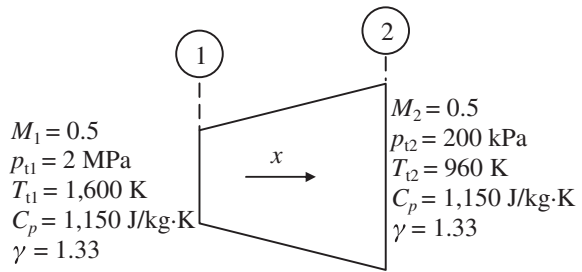
■ FIGURE P2.43

2.44 Air enters a constant-area scramjet combustor at Mach 3.2. Assuming the flow is frictionless and the combustion is simulated as external heating of air, use Rayleigh flow to calculate q^* and the fuel-air ratio that is needed to thermally choke the scramjet combustor. The fuel heating value is assumed to be 118,500 kJ/kg of fuel.



■ FIGURE P2.44

2.45 Calculate the axial force that is exerted by the fluid on the wall of a gas turbine engine component with uniform inlet and exit flow conditions, as shown. Assume the flow is adiabatic and the mass flow rate is $\dot{m} = 200$ kg/s. Also, by checking the power in the flow at the entrance and the exit of this unit, identify this engine component.



■ FIGURE P2.45

2.46 Consider an insulated constant-area duct. The average wall friction coefficient is $C_f = 0.005$. Assuming the length-to-(hydraulic) diameter ratio for the duct is $L/D_h = 9.9$, the gas is perfect with $\gamma = 1.4$ and $R = 287$ J/kg · K, and the inlet flow conditions are: $M_1 = 2.0$, $p_1 = 20$ kPa and $T_1 = 650$ K.

Calculate

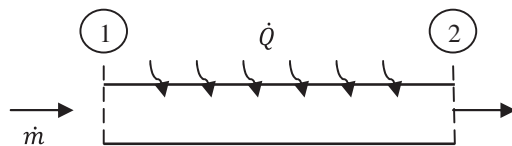
- (a) inlet total temperature in K
- (b) inlet total pressure in kPa
- (c) exit Mach number, M_2
- (d) percentage total pressure drop in the duct
- (e) the minimum L/D_h for this duct to choke (keep inlet at Mach 2.0)
- (f) nondimensional entropy rise, $\Delta s/R$



■ FIGURE P2.46

2.47 An inviscid perfect gas flows through a constant-area duct that is subject to heat transfer. The ratio of heat transfer to mass flow rate is $q = 250$ kJ/kg. The inlet condition to the duct is: $M_1 = 0.5$, $p_1 = 100$ kPa and $T_1 = 600$ K. Assuming that gas properties are: $\gamma = 1.4$ and $R = 287$ J/kg · K, calculate

- (a) inlet total pressure, p_{t1} in kPa
- (b) inlet gas speed, u_1 in m/s
- (c) exit Mach number, M_2
- (d) percentage total pressure drop in the duct



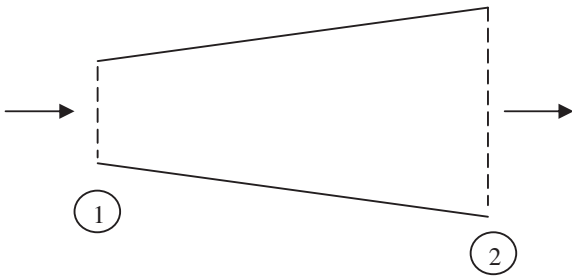
■ FIGURE P2.47

2.48 In an adiabatic flow of a perfect gas in a constant-area duct with friction, we have the inlet condition as $M_1 = 2.0$, $p_1 = 25 \text{ kPa}$, $T_1 = 250 \text{ K}$. The duct length-to-(hydraulic) diameter ratio is $L/D_h = 10.262$ and the average friction coefficient at the wall is $C_f = 0.005$. Assuming gas properties are $\gamma = 1.4$ and $R = 287 \text{ J/kg} \cdot \text{K}$, calculate

- (a) exit Mach number, M_2
- (b) total temperature of the gas at the exit, T_{t2} in K
- (c) total pressure of the gas at the exit, p_{t2} in kPa

2.49 Consider the flow of perfect gas in a duct with $T_2/T_1 = 1.01$, $p_2/p_1 = 1.038$ and $M_2/M_1 = 0.88$. Assuming gas properties are $\gamma = 1.4$ and $R = 287 \text{ J/kg} \cdot \text{K}$, calculate

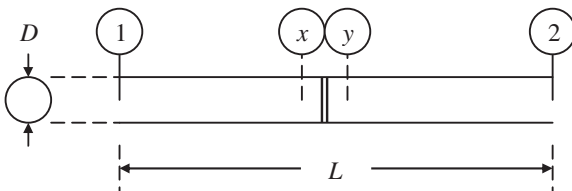
- (a) the density ratio, ρ_2/ρ_1
- (b) the velocity ratio, V_2/V_1
- (c) the duct area ratio, A_2/A_1



■ FIGURE P 2.49

2.50 In a Fanno flow problem with a supersonic inlet Mach number of $M_1 = 2.0$, a normal shock appears at $M_x = 1.2$. Assuming the average friction coefficient in the pipe is $C_f = 0.005$ and $\gamma = 1.4$, calculate

- (a) L_x/D
- (b) L/D
- (c) percentage total pressure loss, $\Delta p_t/p_{t1}$

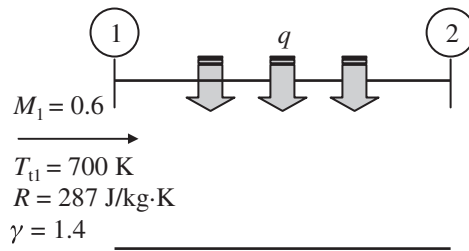


■ FIGURE P 2.50

2.51 Air enters a constant-area duct with heat transfer q per unit mass flow rate through the duct. Assuming the flow is frictionless, calculate

- (a) the external heat transfer, q_1^* , that will choke the duct

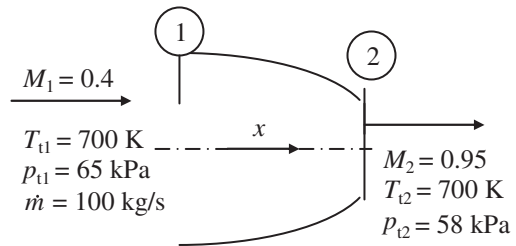
- (b) the reset inlet Mach number, $M_{1'}$, if $q = 3q_1^*$
- (c) percentage mass flow rate reduction if $q = 3q_1^*$



■ FIGURE P 2.51

2.52 The inlet and exit flow conditions of a convergent nozzle are known. The flow inside the nozzle is frictional. Assuming the ratio of specific heats is $\gamma = 1.40$ and $c_p = 1,004 \text{ J/kg} \cdot \text{K}$, calculate

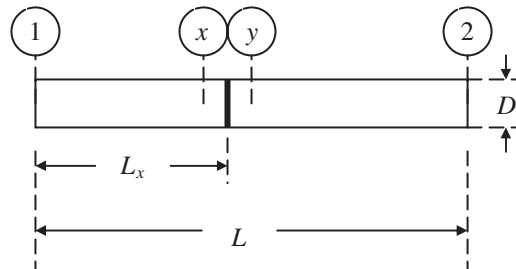
- (a) the inlet and exit areas, A_1 and A_2 in m^2
- (b) the axial force acting on the nozzle in kN



■ FIGURE P 2.52

2.53 In an adiabatic flow of perfect gas in a constant-area duct with friction, the inlet is supersonic with Mach number $M_1 = 2.0$. A normal shock appears in the duct where local Mach number is $M_x = 1.5$. Assuming the average friction coefficient in the duct is $C_f = 0.005$ and $\gamma = 1.4$, calculate

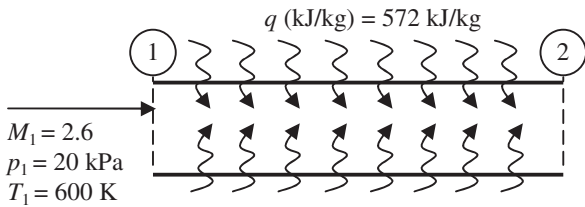
- (a) L_x/D
- (b) L/D
- (c) L_x/L
- (d) total pressure loss, $\Delta p_t/p_{t1}$ (%)



■ FIGURE P 2.53

2.54 Consider the flow of air (perfect gas) in a constant-area duct with heat transfer. Air enters the duct at a supersonic Mach number, $M_1 = 2.6$. The gas properties are: $\gamma = 1.4 = \text{constant}$ and $c_p = 1004 \text{ J/kg} \cdot \text{K}$. Assuming the fluid is inviscid, and the rate of heat transfer per unit mass flow rate is $q = 572 \text{ kJ/kg}$, calculate

- (a) exit total temperature, T_{t2} (K)
- (b) exit Mach number, M_2
- (c) exit static pressure, p_2 , in kPa
- (d) total pressure loss, $\Delta p_t/p_{t1}$ (%)
- (e) critical heat transfer rate to choke the inlet flow, i.e., q^* , in kJ/kg

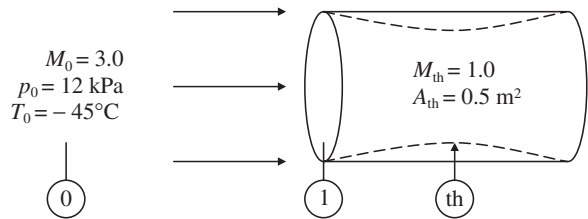


■ FIGURE P2.54

2.55 A convergent–divergent inlet duct is placed in a supersonic stream, as shown. Assuming the gas constant is $R = 287 \text{ J/kg} \cdot \text{K}$ and $\gamma = 1.4$, calculate

- (a) the flow dynamic pressure, q_0 , in kPa
- (b) the inlet duct area ratio, A_1/A_{th}
- (c) the mass flow rate in the duct, \dot{m} , in kg/s

Assume the flow in the duct is steady and isentropic.



■ FIGURE P2.55

CHAPTER 3

Engine Thrust and Performance Parameters

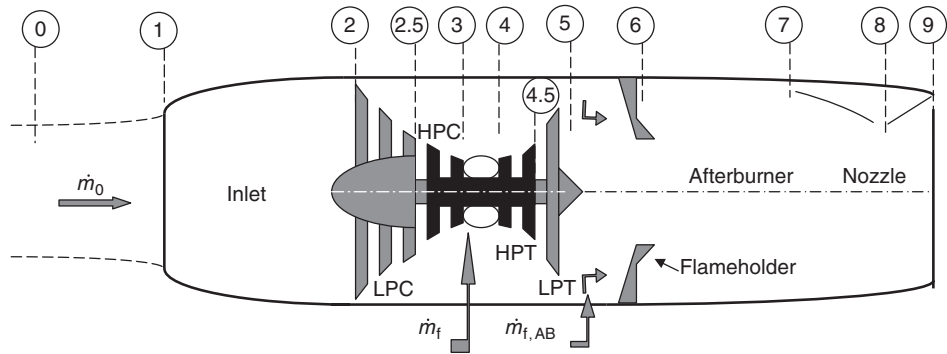


Trent 1000 Turbofan Engine. Source: Reproduced with permission from Rolls-Royce plc

3.1 Introduction

An aircraft engine is designed to produce thrust F (or sometimes lift in VTOL/STOL aircraft, e.g., the lift fan in the Joint Strike Fighter, F-35). In an airbreathing engine, a mass flow rate of air \dot{m}_0 and fuel \dot{m}_f are responsible for creating that thrust. In a liquid rocket engine, the air is replaced with an onboard oxidizer \dot{m}_{ox} , which then reacts with an onboard fuel \dot{m}_f to produce thrust. Although we will discuss the internal characteristics of a gas turbine engine in Chapter 4, it is instructive to show the station numbers in a two-spool turbojet engine with an afterburner. Figure 3.1 is schematic drawing of such engine. The air is brought in through the air intake, or inlet, system, where station 0 designates the unperturbed flight condition, station 1 is at the inlet (or cowl) lip, and station 2 is at the exit of the air intake system, which corresponds to the inlet of the compressor (or fan). The compression process from stations 2 to 3 is divided into a low-pressure compressor (LPC) spool and a high-pressure compressor (HPC) spool. The exit of the LPC is designated by station 2.5 and the exit of the HPC is station 3. The HPC is designed to operate at a higher shaft rotational speed than the LPC spool. The compressed gas enters the main or primary burner at 3 and is combusted with the fuel to produce hot high-pressure gas at 4 to enter the high-pressure turbine (HPT). Flow expansion through the HPT and the low-pressure turbine (LPT) produces the shaft power for the HPC and LPC, respectively. An afterburner is designated between stations 5 and 7, where an additional

■ FIGURE 3.1 Station numbers for an afterburning turbojet engine

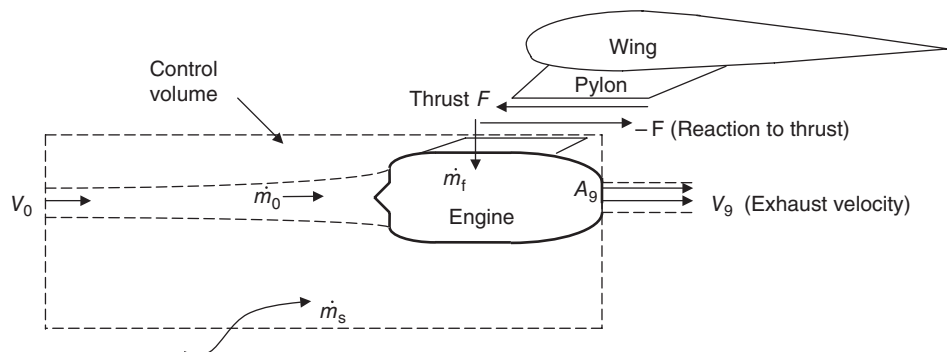


fuel is combusted with the turbine discharge flow before it expands in the exhaust nozzle. Station 8 is at the throat of the nozzle and station 9 designates the nozzle exit.

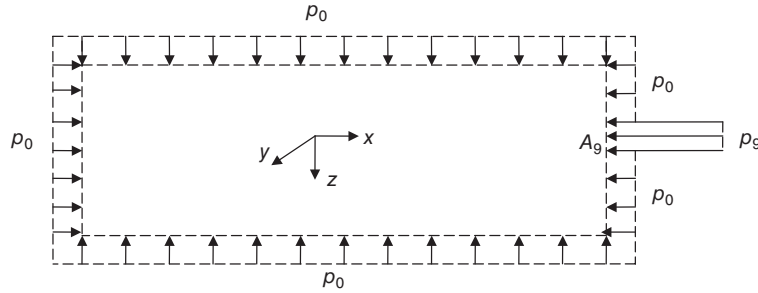
To derive an expression for the engine thrust, it is most convenient to describe a control volume surrounding the engine and apply momentum principles to the fluid flow crossing the boundaries of the control volume. Let us first consider an airbreathing engine. From a variety of choices that we have in describing the control volume, we may choose one that shares the same exit plane as the engine nozzle, and its inlet is far removed from the engine inlet so not to be disturbed by the nacelle lip. These choices are made for convenience. As for the sides of the control volume, we may choose either stream surfaces, with the advantage of no flow crossing the sides, or a constant-area box, which has a simple geometry but fluid flow crosses the sides. Regardless of our choice of the control volume, however, the physical expression derived for the engine thrust has to produce the same force in either method. Figure 3.2 depicts a control volume in the shape of a box around the engine.

The pylon, by necessity, is cut by the control volume, which is enclosing the engine. The thrust force F and its reaction are shown in Figure 3.2. We may assume the sides of the control volume are not affected by the flowfield around the nacelle, that is, the static pressure distribution on the sides is nearly the same as the ambient static pressure p_0 . In the same spirit, we may assume that the exit plane also sees an ambient pressure of p_0 with an exception of the plane of the jet exhaust, where a static pressure p_9 may prevail. To help us balance momentum flux and net forces acting on the fluid crossing the control surface, we show the external pressure distributions as in Figure 3.3.

■ FIGURE 3.2 Schematic drawing of an airbreathing engine with a box-like control volume positioned around the engine (Note the flow of air to the engine, through the sides, and the fuel flow rate)



■ **FIGURE 3.3**
Simplified model of static pressure distribution on the surface of the control volume



From our study of fluid mechanics, we know that the closed surface integral of a constant pressure results in a zero net force acting on the closed surface, that is,

$$\oiint -p\hat{n}ds = 0 \quad (\text{for constant } p) \quad (3.1)$$

where \hat{n} is the unit normal vector pointing out of the control surface, ds is the elemental surface area, and the negative sign shows that the direction of the pressure is in the inward normal direction to the closed surface. The equivalence of the closed surface integral and the volume integral via the gradient theorem may be used to prove the above principle, namely;

$$\oiint p\hat{n}ds = \iiint \nabla p dv \quad (3.2)$$

where dv is the element of volume and ∇p is the pressure gradient vector. Note that $\nabla p \equiv 0$ for a constant p . Now, let us subtract the constant ambient pressure p_0 from all sides of the closed surface of the control volume shown in Figure 3.4, to get a net pressure force acting on the control surface.

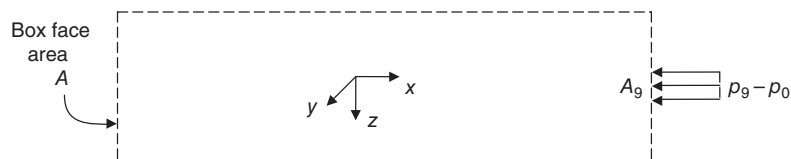
As we are interested in deriving an expression for a force, namely thrust, we have to use the momentum conservation principles, namely, we need to balance the fluid momentum in the x -direction and the resultant external forces *acting on the fluid* in the x -direction. Before doing that, we must establish the fluid flow rates in and out of the control volume. This is achieved by applying the law of conservation of mass to the control volume. In its simplest form, that is, steady flow case, we have

$$\sum \dot{m}_{\text{in}} = \sum \dot{m}_{\text{out}} \quad (3.3)$$

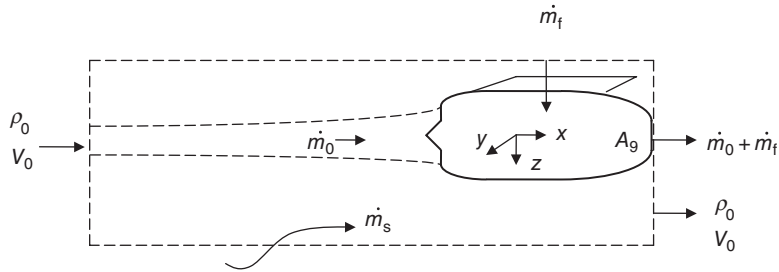
Applying Equation 3.3 to the control volume surrounding our engine (Figure 3.5) gives the following bookkeeping expression on the mass flow rates in and out of the box, namely,

$$\rho_0 V_0 A + \dot{m}_s + \dot{m}_f = (\dot{m}_0 + \dot{m}_f) + \rho_0 V_0 (A - A_g) \quad (3.4)$$

■ **FIGURE 3.4**
Simplified model of the static pressure force acting on the control surface



■ FIGURE 3.5
Control volume and
the mass flow rates in
and out of its
boundaries



which simplifies to:

$$\dot{m}_s = \dot{m}_0 - \rho_0 V_0 A_9 \quad (3.5)$$

Now, we are ready to apply the momentum balance to the fluid entering and leaving our control volume. Again assuming steady, uniform flow, we may use the simplest form of the momentum equation, that is,

$$\sum (\dot{m}V_x)_{\text{out}} - \sum (\dot{m}V_x)_{\text{in}} = \sum (F_x)_{\text{fluid}} \quad (3.6)$$

which states that the difference between the fluid (time rate of change of) momentum out of the box and into the box is equal to the net forces acting on the fluid in the x -direction on the boundaries and within the box. Now, let us spell out each of the contributions to the momentum balance of Equation 3.6, that is,

$$\sum (\dot{m}V_x)_{\text{out}} = (\dot{m}_0 + \dot{m}_f)V_9 + [\rho_0 V_0(A - A_9)]V_0 \quad (3.7)$$

$$\sum (\dot{m}V_x)_{\text{in}} = (\rho_0 V_0 A)V_0 + \dot{m}_s V_0 \quad (3.8)$$

$$\sum (F_x)_{\text{fluid}} = (-F)_{\text{fluid}} - (p_9 - p_0)A_9 \quad (3.9)$$

Substituting Equations 3.7, 3.8, and 3.9 into Equation 3.6 and for \dot{m}_s from Equation 3.5, we get

$$\begin{aligned} & (\dot{m}_0 + \dot{m}_f)V_9 + \rho_0 V_0(A - A_9)V_0 - \rho_0 V_0 A V_0 - (\dot{m}_0 - \rho_0 V_0 A_9)V_0 \\ & = (-F_x)_{\text{fluid}} - (p_9 - p_0)A_9 \end{aligned} \quad (3.10)$$

which simplifies to

$$(\dot{m}_0 + \dot{m}_f)V_9 - \dot{m}_0 V_0 = (-F_x)_{\text{fluid}} - (p_9 - p_0)A_9 \quad (3.11)$$

Now, through the action–reaction principle of the Newtonian mechanics, we know that an equal and opposite axial force is exerted on the engine, by the fluid, that is,

$$-F_x)_{\text{fluid}} = F_x)_{\text{pylon}} = F_x)_{\text{engine}} \quad (3.12)$$

Therefore, calling the axial force of the engine “thrust,” or simply F , we get the following expression for the engine thrust

$$F = (\dot{m}_0 + \dot{m}_f)V_9 - \dot{m}_0V_0 + (p_9 - p_0)A_9 \quad (3.13)$$

This expression for the thrust is referred to as the “net uninstalled thrust” and sometimes a subscript “n” is placed on F to signify the “net” thrust. Therefore, the thrust expression of Equation 3.13 is better written as

$$F_n^{\text{uninstalled}} = (\dot{m}_0 + \dot{m}_f)V_9 - \dot{m}_0V_0 + (p_9 - p_0)A_9 \quad (3.14)$$

Now, we attribute a physical meaning to the three terms on the right-hand side (RHS) of Equation 3.14, which contribute to the engine net (uninstalled) thrust. We first note that the RHS of Equation 3.14 is composed of two momentum terms and one pressure–area term. The first momentum term is the exhaust momentum through the nozzle contributing positively to the engine thrust. The second momentum term is the inlet momentum, which contributes negatively to the engine thrust in effect it represents a drag term. This drag term is called “ram drag,” or simply the penalty of bringing air in the engine with a finite momentum. It is often given the symbol of D_{ram} and expressed as

$$D_{\text{ram}} = \dot{m}_0V_0 \quad (3.15)$$

The last term in Equation 3.14 is a pressure–area term, which acts over the nozzle exit plane, that is, area A_9 , and will contribute to the engine thrust only if there is an imbalance of static pressure between the ambient and the exhaust jet. As we remember from our aerodynamic studies, a nozzle with a subsonic jet will always expand the gases to the same static pressure as the ambient condition, and a sonic or supersonic exhaust jet may or may not have the same static pressure in its exit plane as the ambient static pressure. Depending on the “mismatch” of the static pressures, we categorized the nozzle flow as

if $p_9 < p_0$, the nozzle is *overexpanded*
which can happen in supersonic jets only (i.e., in convergent–divergent nozzles
with area ratio *larger* than needed for perfect expansion)

if $p_9 = p_0$, the nozzle is *perfectly expanded*
which is the case for *all subsonic jets* and sometimes in sonic or supersonic jets
(i.e., with the “right” nozzle area ratio)

if $p_9 > p_0$, the nozzle is *underexpanded*
which can happen in sonic or supersonic jets only
(i.e., with inadequate nozzle area ratio)

EXAMPLE 3.1

An airbreathing engine has a flight Mach number of $M_0 = 0.85$ at an altitude where the speed of sound is 300 m/s. The air mass flow rate into the engine is 50 kg/s. Calculate the ram drag (in kN) for this engine.

SOLUTION

The flight speed is $V_0 = M_0 \cdot a_0 = (0.85)(300 \text{ m/s}) = 255 \text{ m/s}$

The ram drag is given in Equation 3.15, therefore,

$$D_{\text{ram}} = (50 \text{ kg/s})(255 \text{ m/s}) = 12.75 \text{ kN}$$

Examining the various contributions from Equation 3.14 to the net engine (uninstalled) thrust, we note that the thrust is the difference between the nozzle contributions (both momentum and pressure–area terms) and the inlet contribution (the momentum term). The nozzle contribution to thrust is called *gross thrust* and is given a symbol F_g , that is,

$$F_g \equiv (\dot{m}_0 + \dot{m}_f)V_9 + (p_9 - p_0)A_9 \quad (3.16)$$

and, as explained earlier, the inlet contribution was negative and was called “ram drag” D_{ram} , therefore

$$F_{\text{n}})_{\text{uninstalled}} = F_g - D_{\text{ram}} \quad (3.17)$$

Now, we can generalize the result expressed in Equation 3.17 to aircraft engines with more than a single stream, as, for example, the turbofan engine with separate exhausts. This task is very simple as we account for all gross thrusts produced by all the exhaust nozzles and subtract all the ram drag produced by all the air inlets to arrive at the engine uninstalled thrust, that is,

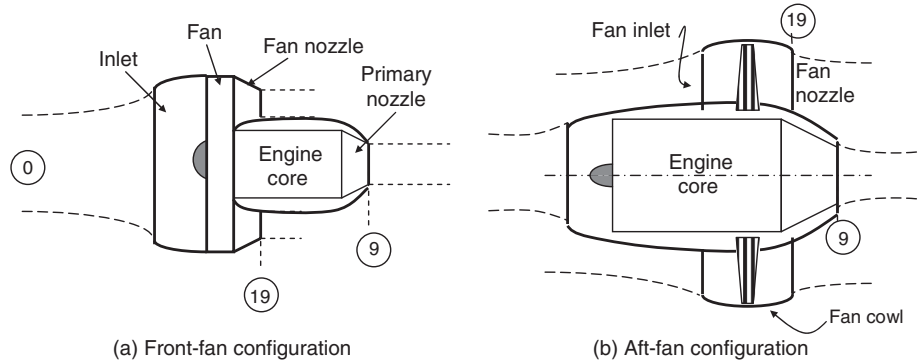
$$F_{\text{n}})_{\text{uninstalled}} = \sum (F_g)_{\text{nozzles}} - \sum (D_{\text{ram}})_{\text{inlets}} \quad (3.18)$$

Another way of looking at this is to balance the momentum of the exhaust stream and the inlet momentum with the pressure thrust at the nozzle exit planes and the net uninstalled thrust of the engine. In a turbofan engine, the captured airflow is typically divided into a “core” flow, where the combustion takes place, and a fan flow, where the so-called “bypass” stream of air is compressed through a fan and later expelled through a fan exhaust nozzle. This type of arrangement, that is, bypass configuration, leads to a higher overall efficiency of the engine and lower fuel consumption. A schematic drawing of the engine is shown in Figure 3.6.

In this example, the inlet consists of a single (or dual) stream, and the exhaust streams are split into a primary and a fan nozzle. We may readily write the uninstalled thrust produced by the engine following the momentum principle, namely,

$$F_{\text{n}})_{\text{uninstalled}} = \dot{m}_9 V_9 + \dot{m}_{19} V_{19} + (p_9 - p_0)A_9 + (p_{19} - p_0)A_{19} - \dot{m}_0 V_0 \quad (3.19)$$

■ **FIGURE 3.6**
Schematic drawing of a
turbofan engine with
separate exhausts



The first four terms account for the momentum and pressure thrusts of the two nozzles (what is known as gross thrust) and the last term represents the inlet ram drag.

EXAMPLE 3.2

A separate flow turbofan engine develops exhaust velocities of 450 m/s and 350 m/s in the core and fan nozzles, respectively. The nozzles are perfectly expanded. The mass

flow rate through the core nozzle is 50 kg/s and through the fan nozzle is 350 kg/s. Calculate the gross thrust of the core and the fan nozzles.

SOLUTION

Since the core and fan nozzles are both perfectly expanded, the gross thrust is simply the momentum thrust at the nozzle exit, i.e.,

$$F_{g,\text{core}} = \dot{m}_9 V_9 = (50 \text{ kg/s})(450 \text{ m/s}) = 22.5 \text{ kN}$$

$$F_{g,\text{fan}} = \dot{m}_{19} V_{19} = (350 \text{ kg/s})(350 \text{ m/s}) = 122.5 \text{ kN}$$

3.1.1 Takeoff Thrust

At takeoff, the air speed V_0 (“flight” speed) is often ignored in the thrust calculation, therefore the ram drag contribution to engine thrust is neglected, that is,

$$F_{\text{takeoff}} \approx F_g = (\dot{m}_0 + \dot{m}_f)V_9 + (p_9 - p_0)A_9 \quad (3.20)$$

For a perfectly expanded nozzle, the pressure thrust term vanishes to give

$$F_{\text{takeoff}} \approx (\dot{m}_0 + \dot{m}_f)V_9 \approx \dot{m}_0 V_9 \quad (3.21)$$

Therefore, the takeoff thrust is proportional to the captured airflow.

3.2 Installed Thrust—Some Bookkeeping Issues on Thrust and Drag

As indicated by the description of the terms “installed thrust” and “uninstalled thrust,” they refer to the *actual propulsive force* transmitted to the aircraft by the engine and the thrust produced by the engine if it had zero external losses, respectively. Therefore, for

the installed thrust, we need to account for the installation losses to the thrust such as the nacelle skin friction and pressure drags that are to be included in the propulsion side of the drag bookkeeping. On the contrary, the pylon and the engine installation that affects the wing aerodynamics (in podded nacelle, wing-mounted configurations), namely by altering its “clean” drag polar characteristics, causes an “interference” drag that is accounted for in the aircraft drag polar. In the study of propulsion, we often concentrate on the engine “internal” performance, that is, the uninstalled characteristics, rather than the installed performance because the external drag of the engine installation depends not only on the engine nacelle geometry but also on the engine–airframe integration. Therefore, accurate installation drag accounting will require computational fluid dynamics (CFD) analysis and wind tunnel testing at various flight Mach numbers and engine *throttle settings*. In its simplest form, we can relate the installed and uninstalled thrust according to

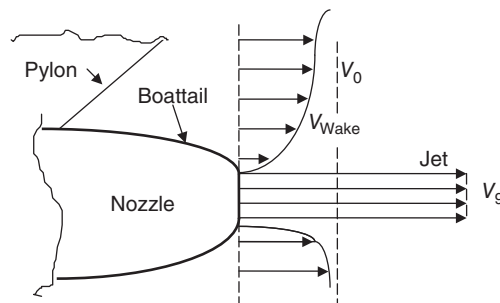
$$F_{\text{installed}} = F_{\text{uninstalled}} - D_{\text{nacelle}} \tag{3.22}$$

In our choice of the control volume as depicted in Figure 3.2, we made certain assumptions about the exit boundary condition imposed on the aft surface of the control volume. We made assumptions about the pressure boundary condition as well as the velocity boundary condition. About the pressure boundary condition, we stipulated that the static pressure of flight p_0 imposed on the exit plane, except at the nozzle exit area of A_9 , therefore we allowed for an under- or overexpanded nozzle. With regard to the velocity boundary condition at the exit plane, we stipulated that the flight velocity V_0 prevailed, except at the nozzle exit where the jet velocity of V_9 prevails. In reality, the aft surface of the control volume is, by necessity, downstream of the nacelle and pylon, and therefore it is in the middle of the wake generated by the nacelle and the pylon. This implies that there would be a momentum deficit in the wake and the static pressure nearly equals the free stream pressure. The velocity profile in the exit plane, that is, the wake of the nacelle and pylon, is more likely to be represented by the schematic drawing in Figure 3.7.

However, the force transmitted through the pylon to the aircraft is not the “uninstalled” thrust, as we called it in our earlier derivation, rather the *installed* thrust and pylon drag. But the integral of momentum deficit and the pressure imbalance in the wake is exactly equal to the nacelle and pylon drag contributions, that is, we have

$$D_{\text{nacelle}} + D_{\text{pylon}} = \iint \rho V(V_0 - V)dA + \iint (p_0 - p)dA \tag{3.23}$$

■ **FIGURE 3.7**
Velocity profile in the nacelle and pylon wake showing a momentum deficit region



where the surface integral is taken over the exit plane downstream of the nacelle and pylon.

Now, let us go back and correct for the wake contributions noted in Equation 3.21 as well as the *actual* force transmitted through the pylon, namely,

$$F_{\text{uninstalled}} - D_{\text{nacelle}} - D_{\text{pylon}} = (\dot{m}_0 + \dot{m}_f)V_9 - \dot{m}_0V_0 + (p_9 - p_0)A_9 - \iint \rho V(V_0 - V)dA - \iint (p_0 - p)dA \quad (3.24)$$

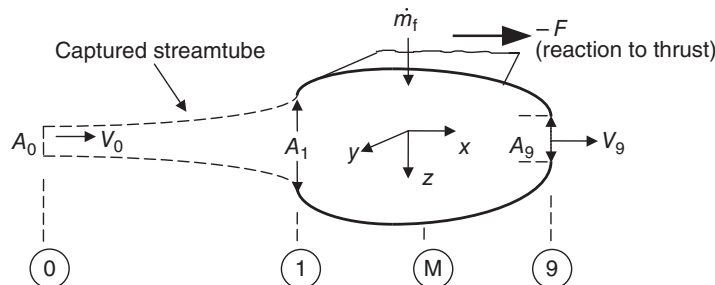
After canceling the integrals on the RHS with the drag terms of the left-hand side (LHS) in Equation 3.24, we recover Equation 3.14 that we derived earlier for the *uninstalled thrust*, that is

$$F_{n\text{uninstalled}} = (\dot{m}_0 + \dot{m}_f)V_9 - \dot{m}_0V_0 + (p_9 - p_0)A_9$$

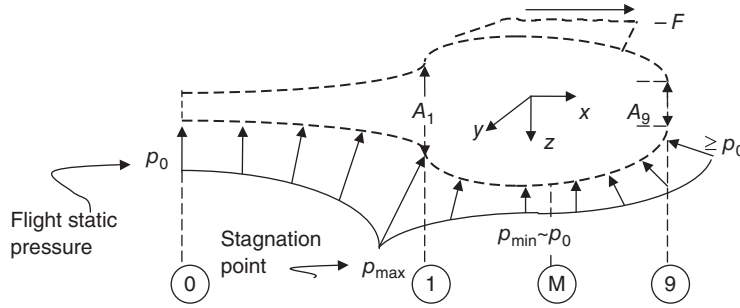
As noted earlier, we are not limited to the choice of the control volume that we made in the form of a box wrapped around the engine and cutting through the pylon (Figure 3.2). Let us examine other logical choices that we could have made. For example, we could use the inlet-captured streamtube as the upstream portion of the control volume and allow the nacelle external surface to serve as the remaining portion of the control volume, and then truncate the control volume at the nozzle exit plane. This choice of control volume is schematically shown in Figure 3.8.

The choice of the control volume depicted in Figure 3.8 offers the advantage of no airflow crossing the sides of the control surface. There is, of course, the fuel flow rate through the pylon and the airflow rates through the inlet-captured streamtube (station 0) and the nozzle exit plane (station 9), as expected. The penalty of using this control volume is in the more complicated force balance terms, which appear in the momentum equation. The pressure distribution on the captured streamtube, for example, will correspond to a diffusing stream pattern, from station 0 to 1, therefore, the static pressure increases along the captured streamtube. Then, the static pressure is decreased to the point of maximum nacelle diameter (station labeled M) as the flow accelerates from the inlet lip stagnation point. From the position of minimum static pressure at M, the flow is diffused on the aft end of the nacelle and will recover most of the static pressure and almost reach the flight ambient pressure p_0 . The static pressure distribution on the control surface is schematically shown in Figure 3.9.

■ **FIGURE 3.8**
Schematic drawing of an alternative control volume



■ **FIGURE 3.9**
Sketch of the static pressure distribution on the sides of the control surface, including the capture streamtube and the nacelle



Following Newton’s second law of motion, we stipulate that the change of momentum of fluid crossing the boundaries of the control volume (Figure 3.8) in the x -direction, say, is balanced by the net forces acting on the fluid in the x -direction. Therefore,

$$(\dot{m}_0 + \dot{m}_f)V_9 - \dot{m}_0V_0 = \sum (F_{x\text{-external}})_{\text{control-surface}} \quad (3.25)$$

where the LHS is the net gain in x -momentum, which is created by the net forces in the positive x -direction acting on the fluid, that is, the RHS terms of Equation 3.25.

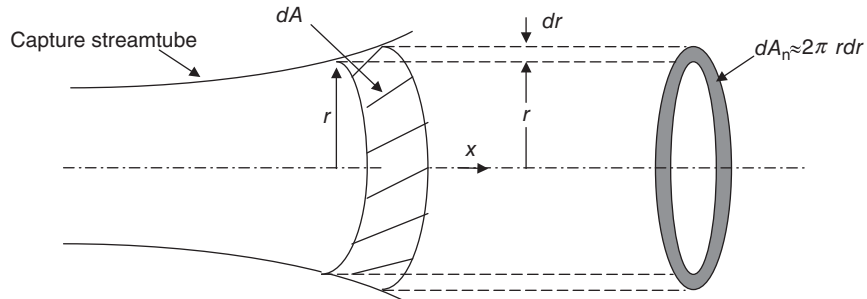
The external forces are due to pressure and frictional stresses acting on the control surface in the x -direction. In the x -balance of momentum, the reader notes that the gravitational force does not enter the calculation at any case and in general we do not include the effect of gravitational force, as it represents a negligible contribution to the force balance involving aircraft jet propulsion. Now, let us breakdown the elements of external force, which act on the control surface. First, the pressure integral over the captured streamtube acting on the fluid in the x -direction can be written

$$(F_x)_{\text{pressure},0-1} = \iint (p - p_0)dA_n \quad (3.26)$$

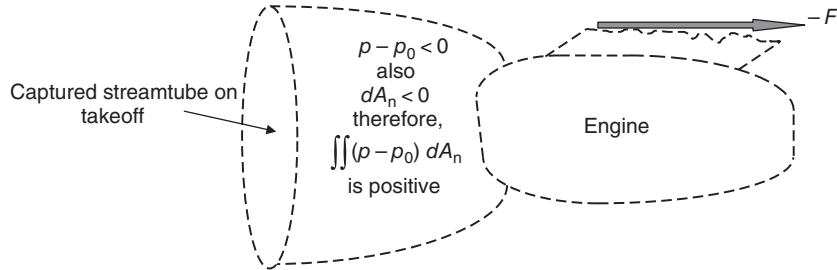
where the element of area dA_n is the change of the area of the captured streamtube normal to the x -direction, that is, varying from A_0 at the inlet to A_1 at the exit, therefore experiencing $(A_1 - A_0)$ change over the length of the captured streamtube. We can use the Figure 3.10 as an aid in demonstrating what is meant by dA_n .

On the captured streamtube depicted in Figure 3.8 (or 3.9), the local pressure p is greater than the ambient pressure p_0 , and dA_n is also positive, as the captured streamtube

■ **FIGURE 3.10**
Definition sketch for dA and its projection normal to the x -axis dA_n



■ FIGURE 3.11
Captured streamtube at takeoff



widens ($dA > 0$), hence the pressure integral of Equation 3.26 is positive. This means that the flow deceleration outside the inlet will contribute a positive force in the x -direction on the control surface, which represents a drag for the engine installation. This drag term is called *pre-entry drag* or *additive drag*. It is interesting to note that if the captured streamtube were inverted, that is, it caused external flow acceleration instead of deceleration, a typical scenario for takeoff and climb or the engine static testing, then the local static pressure would drop below ambient pressure, which causes the integrand $(p - p_0)$ to be negative. Despite this, we still encounter a pre-entry drag, as we note that dA_n is also negative for a shrinking streamtube, hence the pre-entry momentum contribution remains as a penalty, that is, a drag term. This is schematically shown in Figure 3.11.

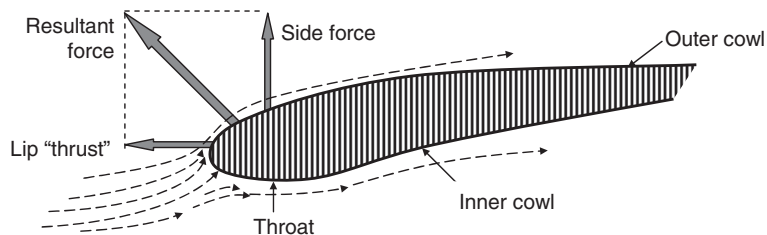
The axial force due to static pressure distribution over the cowl lip from station 1 to M (Figure 3.9) can be written as the integral:

$$(F_x)_{\text{pressure},1-M} = \iint (p - p_0) dA_n \tag{3.27}$$

where the element of area is again represented by the change of area normal to the x -direction. The integral of pressure over the inlet cowl (i.e., from 1 to M) represents a thrust contribution, as the wall static pressure on the forward region of the cowl is below the ambient pressure, that is, $p - p_0 < 0$, and dA_n is positive, therefore the pressure integral of Equation 3.27 is negative. A negative force in the x -direction represents a thrust term. This force may be thought of as the suction force on a *circular wing* (to represent the inlet cowl lip) projected in the x -direction. To demonstrate this point, we examine the following schematic drawing (Figure 3.12).

For an axisymmetric inlet, the aerodynamic side force created on the nacelle integrates to zero, but as most engine nacelles are asymmetrical for either ground clearance or accessibility of the engine accessories reasons, a net side force is created on the nacelle, as well.

■ FIGURE 3.12
Flow detail near a blunt cowl lip showing a lip thrust component and a side force



The inlet additive drag is thus for the most part balanced by the cowl lip thrust and the difference is called the *spillage drag*, that is,

$$D_{\text{spillage}} = \iint_{0-1} (p - p_0) dA_n - \iint_{1-M} (p - p_0) dA_n \quad (3.28)$$

In general, for well-rounded cowl lips of subsonic inlets, the spillage drag is rather small and it becomes significant for only supersonic, sharp-lipped inlets. The nacelle frictional drag also contributes to the external force as well as the aft-end pressure drag of the boattail, which may be written as

$$\begin{aligned} \sum (F_{x\text{-external}})_{\text{control-surface}} = & D_{\text{spillage}} + \iint_{M-9} (p - p_0) dA_n + \iint_{1-9} \tau_w dA_x + D_{\text{pylon}} - F_{x,\text{fluid}} \\ & \text{(I)} \qquad \qquad \text{(II)} \qquad \qquad \text{(III)} \qquad \qquad \text{(IV)} \qquad \qquad \text{(V)} \\ & - (p_9 - p_0)A_9 \qquad \qquad \qquad \qquad \qquad \qquad \qquad \qquad \qquad \text{(3.29)} \\ & \text{(VI)} \end{aligned}$$

The first term on the RHS, that is, (I), is the spillage drag that we discussed earlier, the second term (II) is the pressure drag on the nacelle aft end or boat tail pressure drag, the third term (III) is the nacelle viscous drag, the fourth term (IV) is the pylon drag, the fifth term (V) is the reaction to the installed thrust force and pylon drag acting on the fluid, and the last term (VI) is the pressure thrust due to imperfect nozzle expansion. To summarize

- Terms I + II + III are propulsion system installation drag losses
- Term IV is accounted for in the aircraft drag polar
- Terms V and VI combine with I, II, III, and IV to produce the uninstalled thrust.

Therefore, we recover the expression for the uninstalled thrust that we had derived using another control volume for an airbreathing engine, namely

$$F_n)_{\text{uninstalled}} = (\dot{m}_0 + \dot{m}_f)V_9 - \dot{m}_0V_0 + (p_9 - p_0)A_9$$

Figure 3.13 shows the elements of force that contribute to installed net thrust.

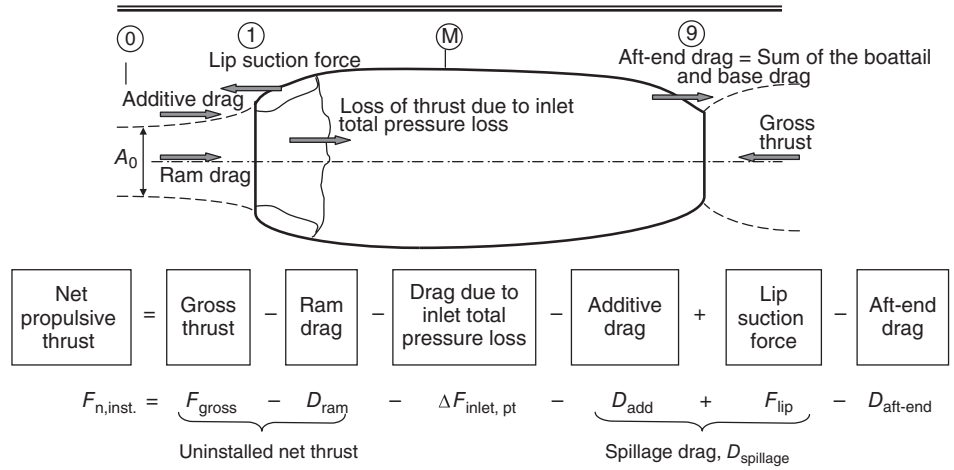
3.3 Engine Thrust Based on the Sum of Component Impulse

We have derived an expression for a component internal force based on the fluid impulse at its inlet and exit in Chapter 2. We wish to demonstrate the relationship between the sum of the component forces and the engine thrust.

The axial component of force felt by the inner walls of the diffuser (from 1 to 2), see Figure 3.14, is

$$F_{x,\text{diffuser}} = I_1 - I_2 \quad (3.30)$$

■ **FIGURE 3.13**
 Definition of *installed net thrust* in terms of internal and external parameters of an engine nacelle (adapted from Lotter, 1977)



The axial component force felt by the inner walls of the compressor (from 2 to 3) is

$$F_{x,compressor} = I_2 - I_3 \tag{3.31}$$

The axial component force felt by the inner walls of the combustor (from 3 to 4) is

$$F_{x,burner} = I_3 - I_4 \tag{3.32}$$

The axial component force felt by the inner walls of the turbine (from 4 to 5) is

$$F_{x,turbine} = I_4 - I_5 \tag{3.33}$$

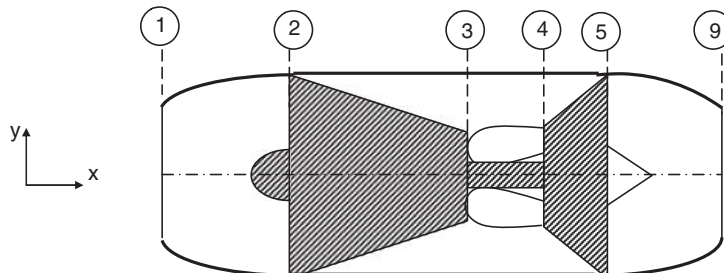
The axial component force felt by the inner walls of the nozzle (from 5 to 9) is

$$F_{x,nozzle} = I_5 - I_9 \tag{3.34}$$

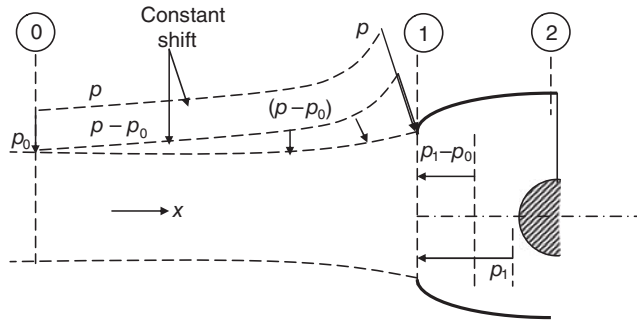
Therefore, the total internal axial force acting on the inner walls of the engine is

$$\begin{aligned} F_{x,engine} &= F_{x,diffuser} + F_{x,compressor} + F_{x,burner} + F_{x,turbine} + F_{x,nozzle} \\ &= I_1 - I_2 + I_2 - I_3 + I_3 - I_4 + I_4 - I_5 + I_5 - I_9 = I_1 - I_9 \\ &= \dot{m}_1 V_1 + p_1 A_1 - (\dot{m}_9 V_9 + p_9 A_9) \end{aligned} \tag{3.35}$$

■ **FIGURE 3.14**
 Definition sketch used in engine thrust calculation based on component impulse



■ **FIGURE 3.15**
Pressure distribution
on the captured
streamtube



The thrust acts in the $-x$ -direction, therefore the engine internal thrust is (minus the above)

$$\text{Internal Thrust} = \dot{m}_0 V_0 - \dot{m}_1 V_1 + p_0 A_0 - p_1 A_1 \quad (3.36)$$

However, in flight we neither know V_1 nor p_1 . To connect the inlet flow to the flight condition, we examine the captured streamtube, as shown in Figure 3.15.

We have subtracted a constant pressure p_0 from all sides, as shown in Figure 3.15. The momentum balance in the x -direction gives

$$\dot{m}_1 V_1 - \dot{m}_0 V_0 = \int_0^1 (p - p_0) dA_n - (p_1 - p_0) A_1 \quad (3.37)$$

The integral on the RHS is called the *additive drag* D_{add} , therefore,

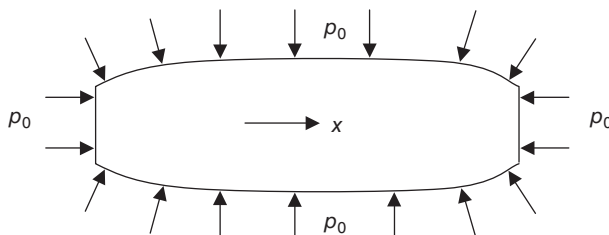
$$\dot{m}_1 V_1 + p_1 A_1 = \dot{m}_0 V_0 + p_0 A_1 + D_{\text{add}} \quad (3.38)$$

$$\text{Internal - Thrust} = \dot{m}_0 V_0 - \dot{m}_0 V_0 + p_0 A_0 - p_0 A_1 + D_{\text{add}} \quad (3.39)$$

The integral of constant pressure distribution p_0 around the nacelle, as in Figure 3.16, leads to

$$\oint p_0 dA_n = p_0 A_1 - p_0 A_0 + \int_{\text{sides}} p_0 dA_n = 0 \quad (3.40)$$

■ **FIGURE 3.16**
Nacelle under a
constant pressure
distribution



Therefore, we may replace p_0A_1 by p_0A_9 and the integral on the sides to get

$$\text{Internal Thrust} = \dot{m}_9 V_9 - \dot{m}_0 V_0 + p_9 A_9 - p_0 A_9 + D_{\text{add}} - \int_{\text{sides}} p_0 dA_n \quad (3.41)$$

The external forces acting on the nacelle (in the x -direction) arise from pressure and shear integrals, namely

$$F_{x\text{-nacelle}} = \int_{\text{sides}} p dA_n + F_{x\text{-viscous}} \quad (3.42)$$

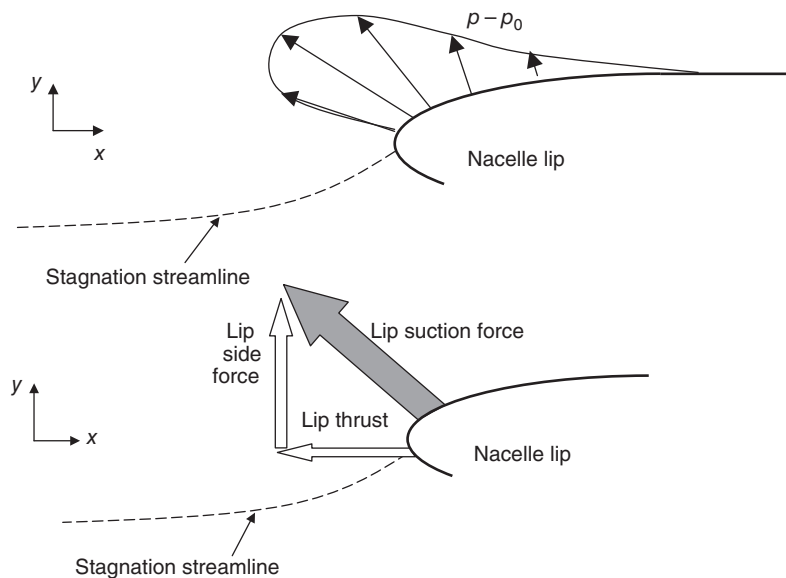
The integral of pressure on the nacelle lip produces a lip thrust force, which almost cancels the inlet additive drag (Figure 3.17), that is,

$$\int_{\text{nacelle-lip}} (p - p_0) dA_n = \text{lip - thrust} \approx -D_{\text{add}} \quad (3.43)$$

Therefore, the *net installed thrust*, after canceling inlet additive drag with the lip suction force, is

$$\text{Installed - Thrust} = \underbrace{\dot{m}_9 V_9 - \dot{m}_0 V_0 + p_9 A_9 - p_0 A_9}_{\text{Uninstalled thrust}} - \int_{\text{sides-lip}} \underbrace{(p - p_0) dA_n - F_{x\text{-viscous}}}_{\text{Installation drag}} \quad (3.44)$$

■ **FIGURE 3.17**
Nacelle lip pressure distribution and the resulting force



The uninstalled thrust thus connects the free stream to the nozzle exit, after we account for the additive drag and the nacelle lip suction force to cancel each other. The leftover external pressure and shear integral are then attributed to installation drag.

$$\text{Uninstalled thrust} = \dot{m}_9 V_9 - \dot{m}_0 V_0 + (p_9 - p_0)A_9 \quad (3.45)$$

3.4 Rocket Thrust

Although our primary effort in this book is to study airbreathing propulsion, the subject of rocket propulsion has been presented in Chapter 12. For now, we may think of the rocket thrust as a special case of an airbreathing engine with a “sealed inlet”! It is simply too tempting to ignore this special case of jet propulsion with no inlet penalty. Figure 3.18 shows a schematic drawing of a rocket engine where all the propellant, that is, fuel and oxidizer, is stored in specialized tanks onboard the rocket.

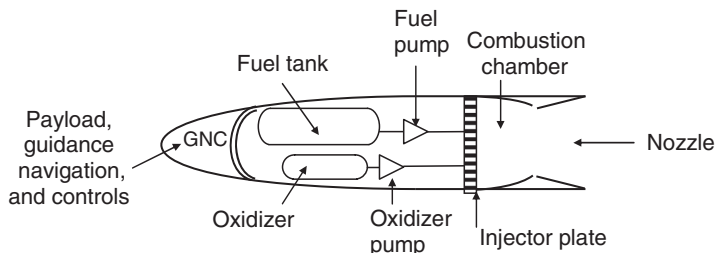
The thrust produced by a rocket engine amounts to only the *gross thrust* produced by an airbreathing engine. We remember that the gross thrust was the *nozzle* contribution to thrust, which a rocket also possesses to accelerate the combustion gas. The air intake system is missing in a rocket, and therefore the inlet ram drag contribution is also absent from the rocket thrust equation. Consequently, we can express the rocket thrust as

$$F_{\text{rocket}} = (\dot{m}_{\text{ox}} + \dot{m}_{\text{f}})V_9 + (p_9 - p_0)A_9 \quad (3.46)$$

It is interesting to note that the rocket thrust is independent of flight speed V_0 , as Equation 3.46 does not explicitly involve V_0 . However, if the flight trajectory has a vertical component to it, then the ambient pressure p_0 changes with altitude, and therefore the pressure thrust term of Equation 3.46 will then affect the thrust magnitude. For example, the space shuttle main engine produces about 25% more thrust in “vacuum” than at sea level, mainly due to the pressure thrust difference between sea level p_0 of 14.7 psia (or 1 atm) and p_0 of zero corresponding to “vacuum” in near earth orbit.

Again, for the net propulsive force acting on the rocket, we need to account for the vehicle external drag. Although, the Equation 3.46 is not explicitly referred to as “uninstalled” thrust in rocket propulsion literature, the reader should view it as the *internal performance* of a rocket engine. The external aerodynamic analysis will produce control forces and vehicle external drag contributions.

■ **FIGURE 3.18**
Schematic drawing of liquid propellant rocket engine internal components



EXAMPLE 3.3

A liquid propellant rocket engine consumes 200 kg/s of oxidizer and 50 kg/s of fuel. After the combustion, the gas is accelerated in a convergent–divergent nozzle where it attains $V_9 = 4000$ m/s and $p_9 = 200$ kPa. The rocket engine

is at sea level where $p_0 = 100$ kPa. If the exit diameter of the nozzle is 2 m, calculate

- (a) the pressure thrust
- (b) the rocket gross thrust

SOLUTION

The pressure thrust is $(p_e - p_0)A_e$. The nozzle exit area is

$$A_9 = \pi D_e^2/4 \approx 3.1416 \text{ m}^2$$

The pressure thrust is

$$(p_9 - p_0)A_9 = (200 - 100)\text{kPa} \cdot (3.1416 \text{ m}^2) \approx 314.16 \text{ kN}$$

The momentum thrust is $\dot{m}_9 V_9 = (250 \text{ kg/s})(4000 \text{ m/s}) = 1 \text{ MN}$

$$F_g = 1000 \text{ kN} + 314.16 \text{ kN} \approx 1314 \text{ kN}$$

3.5 Airbreathing Engine Performance Parameters

The engine thrust, mass flow rates of air and fuel, the rate of kinetic energy production across the engine or the mechanical power/shaft output, and engine dry weight, among other parameters, are combined to form a series of important performance parameters, known as the propulsion system figures of merit.

3.5.1 Specific Thrust

The size of the air intake system is a design parameter that establishes the flow rate of air, \dot{m}_0 . Accordingly, the fuel pump is responsible for setting the fuel flow rate in the engine, \dot{m}_f . Therefore, in producing thrust in a “macroengine,” the engine size seems to be a “scaleable” parameter. The only exception in scaling the jet engines is the “microengines” where the component losses do not scale. In general, the magnitude of the thrust produced is directly proportional to the mass flow rates of the fluid flow through the engine. Then, it is logical to study thrust per unit mass flow rate as a figure of merit of a candidate propulsion system. In case of an airbreathing engine, the ratio of thrust to air mass flow rate is called *specific thrust* and is considered to be an engine performance parameter, that is,

Airbreathing engine performance parameter # 1:

$$\frac{F}{\dot{m}_0} \text{ “specific thrust” with a metric unit of [N} \cdot \text{s/kg]} \text{ and a British unit of [lbf} \cdot \text{s/lbm]}$$

The target for this parameter, that is, specific thrust, in a cycle analysis is usually to be maximized, that is, to produce thrust with the least quantity of air flow rate, or equivalently to produce thrust with a minimum of engine frontal area. However, with subsonic cruise

Mach numbers, the drag penalty for engine frontal area is far less severe than their counterparts in supersonic flight. Consequently, the specific thrust as a figure of merit in a commercial transport aircraft (e.g., Boeing 777 or Airbus A-340) takes a back seat to the lower fuel consumption achieved in a very large bypass ratio turbofan engine at subsonic speeds. As noted, specific thrust is a dimensional quantity with the unit of force per unit mass flow rate. A nondimensional form of the specific thrust, which is useful for graphing purposes and engine comparisons, is (following Kerrebrock, 1992)

$$\text{Nondimensional specific thrust} \equiv \frac{F}{\dot{m}_0 a_0} \quad (3.47)$$

where a_0 is the ambient speed of sound taken as the reference velocity.

3.5.2 Specific Fuel Consumption and Specific Impulse

The ability to produce thrust with a minimum of fuel expenditure is another parameter that is considered to be a performance parameter in an engine. In the commercial world, for example, the airline business, specific fuel consumption represents perhaps the most important parameter of the engine. After all, the money spent on fuel is a major expenditure in operating an airline, for example. However, the reader is quickly reminded of the unspoken parameters of *reliability and maintainability* that have a direct impact on the cost of operating commercial engines and, therefore, they are at least as important, if not more important, as the engine-specific fuel consumption. In the military world, the engine fuel consumption parameter takes a decidedly secondary role to other aircraft performance parameters, such as stealth, agility, maneuverability, and survivability. For an airbreathing engine, the ratio of fuel flow rate per unit thrust force produced is called thrust-specific fuel consumption (TSFC), or sometimes just the specific fuel consumption (sfc) and is defined as

<p>Airbreathing engine performance parameter # 2:</p> $\frac{\dot{m}_f}{F} \text{ “thrust-specific fuel consumption”}$ <p>(TSFC) with a metric unit of [mg/s/N] and a British unit of : [lbm/h/lbf]</p>

The target for this parameter, that is, TSFC, in a cycle analysis is to be minimized, that is, to produce thrust with a minimum of fuel expenditure. This parameter, too, is dimensional. For a rocket, on the contrary, the oxidizer as well as the fuel both contribute to the “expenditure” in the engine to produce thrust, and as such the oxidizer flow rate \dot{m}_{ox} needs to be accounted for as well. The word “propellant” is used to reflect the combination of oxidizer and fuel in a liquid propellant rocket engine or a solid propellant rocket motor. It is customary to define a corresponding performance parameter in a rocket as thrust per unit propellant weight flow rate. This parameter is called *specific impulse* I_s , that is,

$$I_s \equiv \frac{F}{\dot{m}_p g_0} \quad (3.48)$$

where

$$\dot{m}_p \equiv \dot{m}_f + \dot{m}_{ox} \quad (3.49)$$

and g_0 is the gravitational acceleration on the surface of the earth, that is 9.8 m/s^2 or 32.2 ft/s^2 . The dimension of $\dot{m}_p g_0$ in the denominator of Equation 3.48 is then the *weight flow rate* of the propellant based on earth's gravity, or force per unit time. Consequently, the dimension of specific impulse is "Force/Force/second" which simplifies to just the "second." All propulsors, rockets, and airbreathers, then could be compared using a unifying figure of merit, namely their specific impulse in seconds. An added benefit of the specific impulse is that regardless of the units of measurement used in the analysis, that is, either metric or the British on both sides of the Atlantic, specific impulse comes out as seconds in both systems. The use of specific impulse as a unifying figure of merit is further justified in the twenty-first century as we attempt to commercialize space with potentially reusable rocket-based combined cycle (RBCC) power plants in propelling a variety of single-stage-to-orbit (SSTO) vehicles. To study advanced propulsion concepts where the mission calls for multimode propulsion units, as in air-ducted rockets, ramjets, and scramjets, all combined into a single "package," the use of specific impulse becomes even more obvious. In summary,

Specific impulse : $I_s \equiv \frac{F}{\dot{m}_f g_0} [\text{s}]$ for an airbreathing engine Specific impulse : $I_s \equiv \frac{F}{\dot{m}_p g_0} [\text{s}]$ for a rocket
--

An important goal in an engine cycle design is to maximize this parameter, that is, the ability to produce thrust with the least amount of fuel or propellant consumption in the engine.

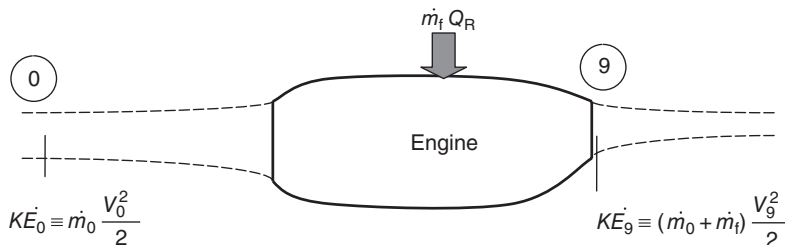
3.5.3 Thermal Efficiency

The ability of an engine to convert the thermal energy inherent in the fuel (which is unleashed in a chemical reaction) to a net kinetic energy gain of the working medium is called the engine thermal efficiency, η_{th} . Symbolically, thermal efficiency is expressed as

$$\eta_{th} \equiv \frac{\Delta K\dot{E}}{\mathcal{P}_{thermal}} = \frac{\dot{m}_9 \frac{V_9^2}{2} - \dot{m}_0 \frac{V_0^2}{2}}{\dot{m}_f Q_R} = \frac{(\dot{m}_0 + \dot{m}_f)V_9^2 - \dot{m}_0 V_0^2}{2\dot{m}_f Q_R} \quad (3.50)$$

where \dot{m} signifies mass flow rate corresponding to stations 0 and 9, subscript "f" signifies fuel, and Q_R is the fuel heating value. The unit of Q_R is energy per unit mass of the fuel (e.g., kJ/kg or BTU/lbm) and is tabulated as a fuel property. Equation 3.50 compares the *mechanical power* production in the engine to the *thermal power* investment in the engine. Figure 3.19 is a definition sketch, which is a useful tool to help remember thermal efficiency definition, as it graphically depicts the energy sources in an airbreathing engine. The rate of thermal energy consumption in the engine and the rate of mechanical power

■ **FIGURE 3.19**
Thermal power input
and the mechanical
power production
(output)



production by the engine are not equal. Yet, we are not violating the law of conservation of energy. The thermal energy production in an engine is not actually “lost,” as it shows up in the hot jet exhaust stream, rather this energy is “wasted” and we were unable to convert it to a “useful” power. It is important to know, that is, to quantify, this inefficiency in our engine.

EXAMPLE 3.4

Consider an aircraft engine (a turbojet) in takeoff condition with the following parameters:

- $\dot{m}_0 = 100 \text{ kg/s}$ (this is equivalent to about 220 lbm/s of air flow rate)
- $V_0 \approx 0 \text{ m/s}$ (this is a typical takeoff assumption that ignores low takeoff speeds)
- $\dot{m}_f = 2 \text{ kg/s}$ (this represents a 2% fuel-to-air ratio)
- $Q_R = 42,000 \text{ kJ/kg}$ (this is the heating value of a typical hydrocarbon fuel)
- $V_9 = 900 \text{ m/s}$ (this represents a high speed exhaust jet)

If we substitute these numbers in Equation 3.34, we get

$$\eta_{th} = \frac{(102)(900)^2}{2(2)(42000)(1000)} \cong 49.2\%$$

The engine thrust at takeoff is

$$F_n \approx F_g \approx \dot{m}_9 V_9 = 102(900) \text{ N} = 91.8 \text{ kN} \\ = (91,800/4.448) \text{ lbf} \approx 20,640 \text{ lbf}$$

Equation 3.50, which defines thermal efficiency, is simply the ratio of “net mechanical output” to the “thermal input,” as we had learned in thermodynamics.

Example 3.4 shows a turbojet engine (with the specified parameters) is only about 49.2% thermally efficient! What happened to the rest of the fuel (thermal) energy? We know that ~49.2% of it was converted to a net mechanical output and the remaining 51.8% then must have been untapped and left in the exhaust gas as *thermal energy*. The thermal energy in the exhaust gas is of no use to the vehicle and, in fact, in many applications, costs an additional weight that needs to be considered for cooling/thermal protection of the exhaust nozzle and nearby structures. The thermal energy in the exhaust gas of an aircraft engine basically goes to waste. Therefore, the lower the exhaust gas temperature, the more useful energy is extracted from the combustion gases and, hence, the cycle is more efficient in the thermal context. Now, you may wonder what other context is there, besides the thermal efficiency context in a heat engine? The answer is found in the *application* of the engine. The purpose of an aircraft engine is to provide propulsive power to the aircraft. In simple terms, the engine has to produce a thrust force that can accelerate the vehicle to a desired speed, for example, from takeoff to cruise condition, or maintain the vehicle

speed, that is, just to overcome vehicle drag in cruise. Of course, one may add the hover and lifting applications to an aircraft engine purpose as, for example, in helicopters and short takeoff and landing (STOL) aircraft, respectively. Therefore, there is another context other than the thermal efficiency for an aircraft engine, namely the *propulsive efficiency*. Before leaving our treatment of the thermal efficiency of the jet engines and investigating their propulsive efficiency, let us explore various ways of improving the thermal efficiency for an aircraft engine.

To lower the exhaust gas temperature, we can place an additional turbine wheel in the high pressure, hot gas stream and produce shaft power. This shaft power can then be used to power a propeller, a fan, or a helicopter rotor, for example. The concept of additional turbine stages to extract thermal energy from the combustion gases and powering a fan in a jet engine has led to the development of more efficient two- or three-spool turboprop engines. Therefore, the mechanical output of these engines is enhanced by the additional shaft power. The thermal efficiency of a cycle that produces a shaft power can therefore be written as

$$\eta_{th} = \frac{\dot{\mathcal{P}}_{shaft} + \Delta K\dot{E}}{\dot{m}_f Q_R} \tag{3.51}$$

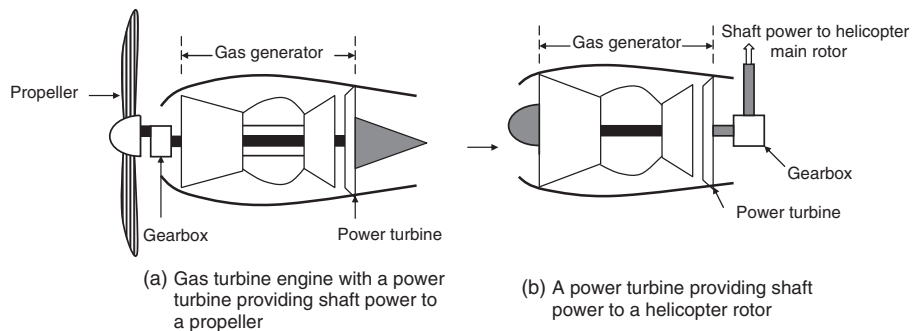
A schematic drawing of an aircraft gas turbine engine, which is configured to produce shaft power, is shown in Figure 3.20. In Figure 3.20a, the “power turbine” provides shaft power to a propeller, whereas in Figure 3.20b, the power turbine provides the shaft power to a helicopter main rotor.

The gas generator in Figure 3.20 refers to the compressor, burner, and the turbine combination, which are detailed in the next chapter. In turboprops and turboshaft engines, the mechanical output of the engine is dominated by the shaft power; therefore, in the definition of the thermal efficiency of such cycles the rate of kinetic energy increase is neglected, that is,

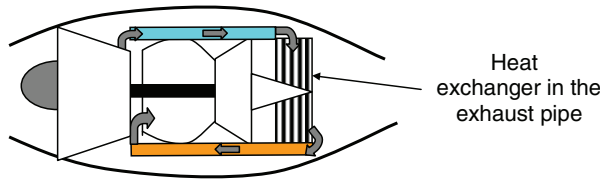
$$\eta_{th} \equiv \frac{\dot{\mathcal{P}}_s}{\dot{m}_f Q_R} \quad \text{in turboprop and turboshaft engines} \tag{3.52}$$

In addition to a shaft-power turbine concept, we can lower the exhaust gas temperatures by placing a heat exchanger in the exhaust stream to preheat the compressor air prior to combustion. The exhaust gas stream is cooled as it heats the cooler compressor gas and the less fuel need be burnt to achieve a desired turbine entry temperature. This scheme is referred to as *regenerative cycle* and is shown in Figure 3.21.

■ FIGURE 3.20
Schematic drawing of a power turbine placed in the exhaust of a gas turbine engine



■ **FIGURE 3.21**
Schematic drawing of a gas turbine engine with a regenerative scheme



All of the cycles shown in Figures 3.20 and 3.21 produce less wasted heat in the exhaust nozzle; consequently, they achieve a higher thermal efficiency than their counterparts without the extra shaft power or the heat exchanger. However, we engineers need to examine a *bottom line question* all the time, that is, “will our gains outweigh our losses?” Obviously we gain in thermal efficiency but our systems in all instances require more complexity and weight. System complexity ties in with the issues of reliability and maintenance and the system weight ties in with the added cost and thus market acceptability. Therefore, we note that a successful engine does not necessarily have the highest thermal efficiency, but rather its *overall system performance and cost* is designed to meet the *customer’s requirements* in an optimum manner. And in fact, its thermal efficiency is definitely compromised by the engine designers within the propulsion system design optimization loop/process. We will return to the issues surrounding thermal efficiency in every cycle we study in the next chapter.

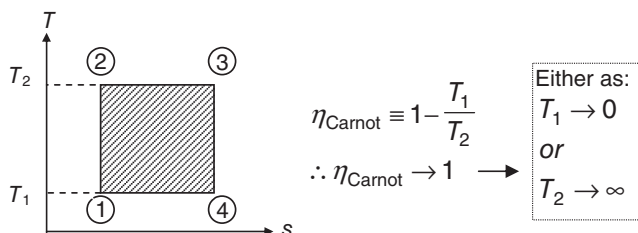
Finally, one last question before we leave this subject is that “is it possible to achieve a 100% thermal efficiency in an aircraft engine?” This was actually a trick question to see who remembered his/her thermo! The answer is obviously no! We cannot violate the second law of thermodynamics. We remember that the highest thermal efficiency attainable in a heat engine operating between two temperature limits was that of a Carnot cycle operating between those temperatures. Figure 3.22 shows the Carnot cycle on a T - s diagram.

As noted in Figure 3.22, both heat rejection at absolute zero ($T_1 = 0$) and heating to infinite temperatures ($T_2 = \infty$) are impossibilities, therefore we are thermodynamically bound by the Carnot thermal efficiency as the maximum (<100%). A Brayton cycle, which gas turbine engines are represented by, experiences a lower thermal efficiency than the Carnot cycle and this subject is presented in the cycle analysis (Chapter 4) in more detail.

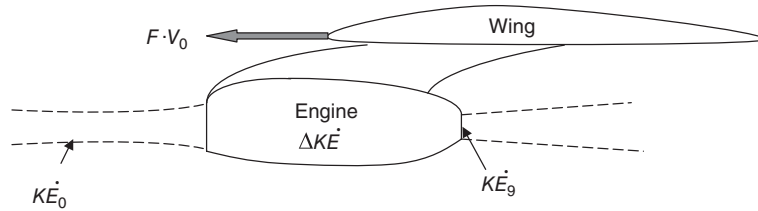
3.5.4 Propulsive Efficiency

The fraction of the net mechanical output of the engine which is converted into thrust power is called the propulsive efficiency. The net mechanical output of the engine is $\Delta K\dot{E}$

■ **FIGURE 3.22**
 T - s diagram of a Carnot cycle



■ **FIGURE 3.23**
Schematic drawing of
an engine installation
showing the
mechanical and thrust
power



for perfectly expanded nozzle and the thrust power is $F \cdot V_0$, therefore, the propulsive efficiency is defined as their ratio:

$$\eta_p \equiv \frac{F \cdot V_0}{\Delta K\dot{E}} \quad (3.53)$$

A graphical depiction of propulsive efficiency is shown in Figure 3.23 to help the reader to remember the definition of propulsive efficiency.

Although the thrust power represented by $F \cdot V_0$ in Equation 3.53 is based on the *installed* thrust, for simplicity, it is often taken as the *uninstalled* thrust power to highlight a very important, and at first astonishing, result about the propulsive efficiency. Now, let us substitute the *uninstalled* thrust of a perfectly expanded jet in the above definition to get

$$\eta_p \approx \frac{[(\dot{m}_0 + \dot{m}_f)V_9 - \dot{m}_0 V_0]V_0}{(\dot{m}_0 + \dot{m}_f)\frac{V_9^2}{2} - \dot{m}_0 \frac{V_0^2}{2}} \quad (3.54)$$

We recognize that the fuel flow rate is but a small fraction ($\sim 2\%$) of the air flow rate and thus can be ignored relative to the air flow rate; thus Equation 3.54 can be simplified to

$$\eta_p \approx \frac{(V_9 - V_0)V_0}{\frac{1}{2}(V_9^2 - V_0^2)} = \frac{2V_0}{V_9 + V_0} = \frac{2}{1 + \frac{V_9}{V_0}} \quad (3.55)$$

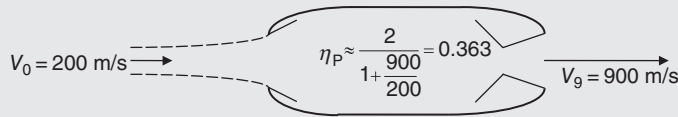
Equation 3.55 as an approximate expression for the propulsive efficiency of a jet engine is cast in terms of a single parameter, namely the jet-to-flight velocity ratio V_9 / V_0 . We further note that 100% propulsive efficiency (within the context of approximation presented in the derivation) is mathematically possible and will be achieved by engines whose exhaust velocity is as fast as the flight velocity, that is, $V_9 = V_0$. But a practical question poses itself, “how can we produce thrust in an airbreathing jet engine if the jet velocity is not *faster* than the flight velocity?” The short answer is that we cannot! Therefore, we conclude that some overspeeding in the jet, compared with flight speed, is definitely needed to produce reaction thrust in an airbreathing jet engine. Therefore for practical reasons, a 100% propulsive efficiency is not possible, just as the thermal efficiency of 100% was not possible. However, the smaller the increment of velocity rises across the engine, the higher its propulsive efficiency will be. In order to achieve a small velocity increment across a gas turbine engine for a given fuel flow rate, we need to drain the thermal energy in the combustion gas further and convert it to additional shaft power that in turn can act on a larger mass flow rate of air, in a secondary or a bypass stream, for example, a fan or a propeller, to produce the desired level of thrust.

EXAMPLE 3.5

A turbojet engine is flying at 200 m/s. The products of combustion achieve an exhaust velocity of 900 m/s. Estimate the engine propulsive efficiency.

SOLUTION

Equation 3.55 is used to estimate the propulsive efficiency of ~36.3% (Figure 3.24).

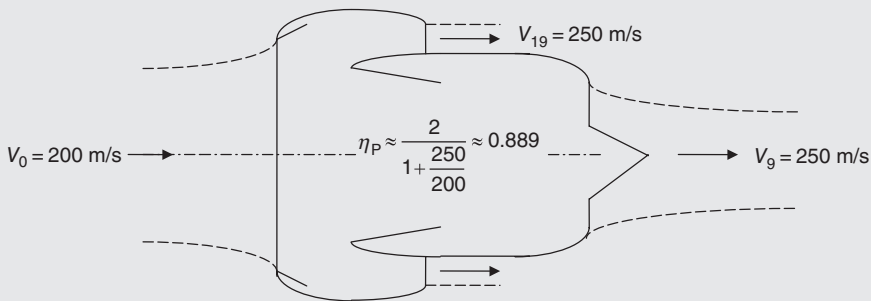


■ FIGURE 3.24 Schematic drawing of a turbojet engine in flight with a velocity ratio of 4.5

EXAMPLE 3.6

Consider a turbofan engine flying at the same speed as the previous example turbojet engine (Figure 3.25), that is, 200 m/s. Now, the exhaust velocity is significantly reduced as

more airflow rate is accelerated. For simplicity, assume that the exhaust velocity in the primary and fan exhaust nozzles is 250 m/s. Estimate the engine's propulsive efficiency.



■ FIGURE 3.25 Schematic drawing of a turbofan engine in flight with a velocity ratio of 1.25

SOLUTION

As the exhaust velocities are the same in the primary and fan nozzles, this engine becomes equivalent to a single stream engine with a reduced velocity ratio of $250/200 = 1.25$. Therefore using Equation 3.55, we arrive at a propulsive

efficiency of 88.9%. In comparison to the previous turbojet engine with a velocity ratio of 4.5, our turbofan engine has achieved a 52.6% increase in propulsive efficiency.

Propulsive efficiency of a turboprop engine is defined as the fraction of mechanical power that is converted to the total thrust (i.e., the sum of propeller and engine nozzle thrust) power, namely

$$\eta_p \equiv \frac{F \cdot V_0}{\dot{\mathcal{Q}}_s + \Delta K\dot{E}} \approx \frac{F \cdot V_0}{\dot{\mathcal{Q}}_s} \quad [\text{turboprop}] \quad (3.56)$$

Again, this definition compares the propulsive *output* ($F \cdot V_0$) to the mechanical power *input* (shaft and jet kinetic energy change) in an aircraft engine. The fraction of shaft power delivered to the propeller that is converted to the propeller thrust is called *propeller efficiency* η_{prop}

$$\eta_{\text{prop}} \equiv \frac{F_{\text{prop}} \cdot V_0}{\dot{\mathcal{Q}}_{s,\text{prop}}} \quad (3.57)$$

Due to large diameters of propellers, it is necessary to reduce their rotational speed to avoid severe tip shock-induced losses. Consequently, the power turbine rotational speed is mechanically reduced in a reduction gearbox and a small fraction of shaft power is lost in the gearbox, which is referred to as gear box efficiency, that is,

$$\eta_{\text{gb}} \equiv \frac{\dot{\mathcal{Q}}_{s,\text{prop}}}{\dot{\mathcal{Q}}_{s,\text{turbine}}} \quad (3.58)$$

We will address turboprop performance in Chapter 4.

3.5.5 Engine Overall Efficiency and Its Impact on Aircraft Range and Endurance

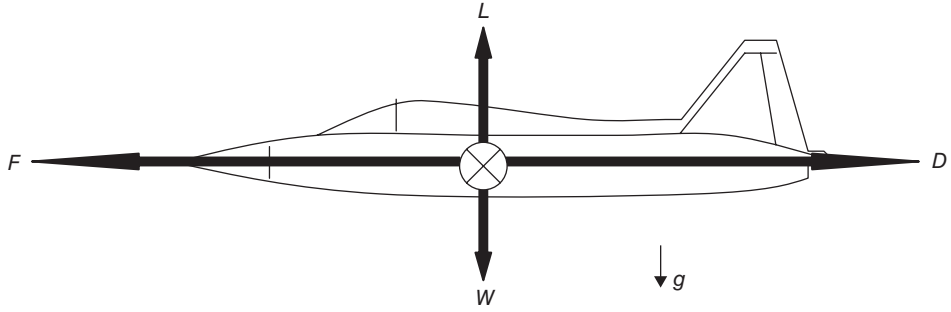
The product of the engine thermal and propulsive efficiency is called the engine overall efficiency

$$\eta_0 \equiv \eta_{\text{th}} \cdot \eta_p = \frac{\Delta K\dot{E}}{\dot{m}_f Q_R} \frac{F \cdot V_0}{\Delta K\dot{E}} = \frac{F \cdot V_0}{\dot{m}_f Q_R} \quad (3.59)$$

The overall efficiency of an aircraft engine is therefore the fraction of the fuel thermal power that is converted into the thrust power of the aircraft. Again a useful output is compared with the input investment in this efficiency definition. In an aircraft performance course that typically precedes the aircraft propulsion class, the engine overall efficiency is tied with the aircraft range through the Breguet range equation. The derivation of the Breguet range equation is both fundamental to our studies and surprisingly simple enough for us to repeat it here for review purposes. An aircraft in level flight cruising at the speed of V_0 (Figure 3.26) experiences a drag force that is entirely balanced by the engine thrust (for no acceleration), that is,

$$F_{\text{engine}} = D_{\text{aircraft}} \quad (3.60)$$

■ **FIGURE 3.26**
Aircraft in an un-accelerated level flight



The aircraft lift L is also balanced by the aircraft weight to maintain level flight, that is,

$$L = W \tag{3.61}$$

We can multiply Equation 3.60 by the flight speed V_0 and then replace the resulting thrust power, $F \cdot V_0$, by $\eta_0 \dot{m}_f Q_R$, via the definition of the engine overall efficiency, to get

$$F \cdot V_0 = \eta_0 \dot{m}_f Q_R = D \cdot V_0 \tag{3.62}$$

Now, let us divide the RHS term in Equation 3.62 by lift L and the middle term of Equation 3.62 by aircraft weight (which is the same as lift), to get

$$\frac{\eta_0 \dot{m}_f Q_R}{W} = \frac{D}{L} \cdot V_0 \tag{3.63}$$

Noting that the fuel flow rate, $\dot{m}_f = -\frac{1}{g_0} \frac{dW}{dt}$, that is, the rate at which the aircraft is losing mass (thus the negative sign), we can substitute this expression in Equation 3.63 and rearrange to get

$$-\frac{\eta_0 Q_R}{g_0} \frac{dW}{W} = \frac{D}{L} \cdot V_0 dt = \frac{dR}{L/D} \tag{3.64}$$

where g_0 is the Earth’s gravitational acceleration and $V_0 dt$ is interpreted as the aircraft elemental range dR , which is the distance traveled in time dt by the aircraft at speed V_0 . Now, we can proceed to integrate Equation 3.64 by making the assumptions of constant lift-to-drag ratio and constant engine overall efficiency, over the cruise period, to derive the Breguet range equation as

$$R = \eta_0 \cdot \frac{Q_R}{g_0} \cdot \frac{L}{D} \cdot \ell n \frac{W_i}{W_f} \tag{3.65}$$

where W_i is the aircraft initial weight and W_f is the aircraft final weight (note that the initial weight is larger than the final weight by the weight of the fuel burned in flight). Equation 3.65 is known as the Breguet range equation, which owes its simplicity and elegance to our assumptions of (1) unaccelerated level flight and (2) constant lift-to-drag ratio and engine overall efficiency. Also note that the range segment contributed by the takeoff, climb and approach and landing distances is not accounted for in the Breguet

range equation. The direct proportionality of the engine overall efficiency and the aircraft range is demonstrated by the Breguet range equation, that is,

$$\text{Aircraft range } R \propto \eta_0$$

Now, let us replace the overall efficiency of the engine in the range equation by the ratio of thrust power to the thermal power in the fuel according to

$$R = \frac{F_n V_0}{\dot{m}_f Q_R} \frac{Q_R}{g_0} \frac{L}{D} \ell n \frac{W_i}{W_f} \quad (3.66)$$

We may express the flight speed in terms of a product of flight Mach number and the speed of sound; in addition, we may substitute the thrust specific fuel consumption for the ratio of fuel flow rate to the engine net thrust, to get

$$R = \left(M_0 \frac{L}{D} \right) \frac{a_0/g_0}{\text{TSFC}} \ell n \frac{W_i}{W_f} \quad (3.67)$$

The result of this representation of the aircraft range is the emergence of (ML/D) as the aerodynamic figure of merit for aircraft range optimization, known as the *range factor*,

$$\text{Aircraft range } R \propto M_0 \frac{L}{D} \quad (3.68)$$

$$\text{Aircraft range } R \propto \frac{1}{\text{TSFC}} \quad (3.69)$$

Now, if we use a more energetic fuel than the current jet aviation fuel, for example hydrogen, we will be able to reduce the thrust specific fuel consumption, or we can see the effect of fuel energy content on the range following Equation 3.65, which shows

$$\text{Aircraft range } R \propto Q_R \quad (3.70)$$

Equivalently, we may seek out the effect of engine overall efficiency, or the specific fuel consumption on aircraft endurance, which for our purposes is the ratio of aircraft range to the flight speed,

$$\text{Aircraft endurance} = \frac{R}{V_0} = \frac{\eta_0}{V_0} \cdot \frac{Q_R}{g_0} \cdot \frac{L}{D} \cdot \ell n \frac{W_i}{W_f} \quad (3.71)$$

This again points out the importance of engine overall efficiency on aircraft performance parameters such as endurance. Now, let us substitute for engine overall efficiency and recast this equation in terms of TSFC, to get

$$\text{Aircraft endurance} = \left(\frac{L}{D} \right) \frac{1/g_0}{\text{TSFC}} \ell n \frac{W_i}{W_f} \quad (3.72)$$

The engine thrust-specific-fuel consumption appears in the denominator as in the engine impact on the range equation, and this time the aerodynamic figure of merit is L/D , instead

of ML/D , as expected for the aircraft endurance.

$$\text{Aircraft endurance} \propto \frac{1}{\text{TSFC}} \quad (3.73)$$

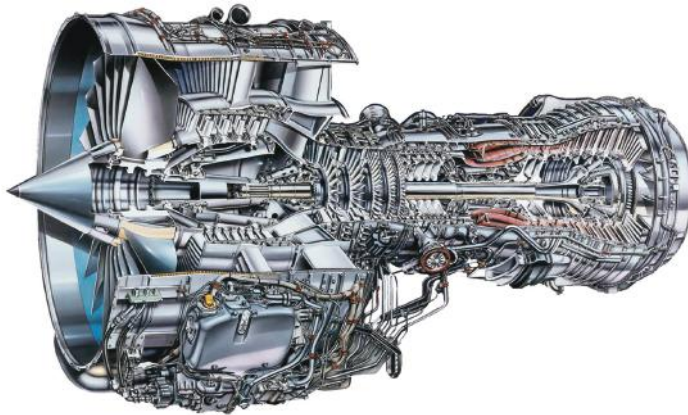
$$\text{Aircraft endurance} \propto \frac{L}{D} \quad (3.74)$$

For additional reading on the subject, Anderson (1999), Newman (2002) and Pratt & Whitney operations manual 200 (1988) are recommended.

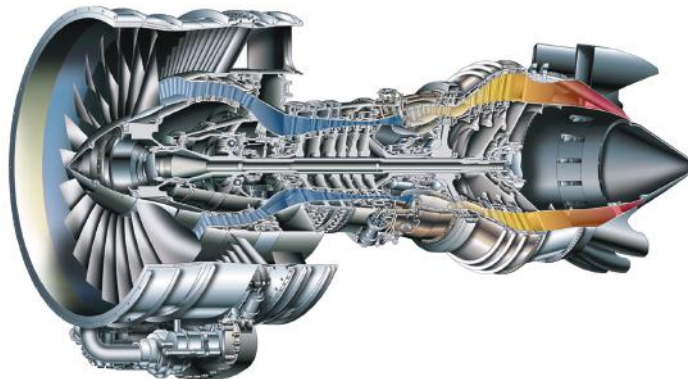
3.6 Modern Engines, Their Architecture and Some Performance Characteristics

At the time of this writing, the science/engineering community is facing very strict compliance requirements in the United States on ITAR (International Traffic in Arms Regulation). This limits the availability of some engine performance parameters and data. With gratitude, I acknowledge the receipt of modern engine cutaways (Figures 3.27 to 3.33)

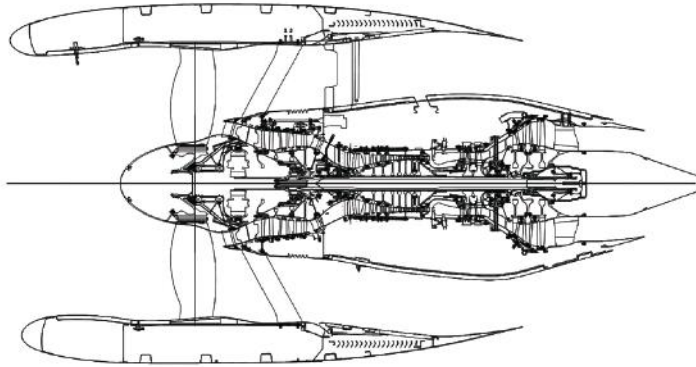
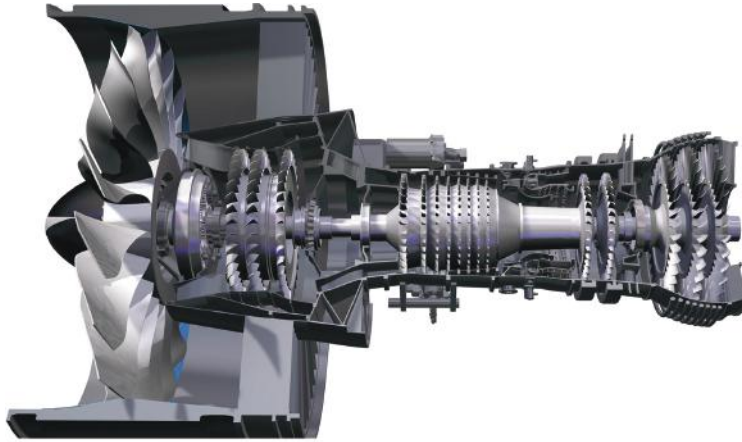
■ **FIGURE 3.27**
V2500 engine cutaway. Source: Reproduced by permission of United Technologies Corporation, Pratt & Whitney



■ **FIGURE 3.28**
PW6000 engine cutaway. Source: Reproduced by permission of United Technologies Corporation, Pratt & Whitney



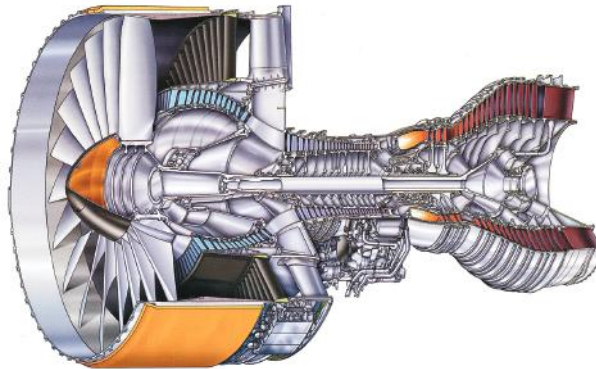
■ **FIGURE 3.29**
The PW1000G engine.
Source: Reproduced by
permission of United
Technologies
Corporation, Pratt &
Whitney



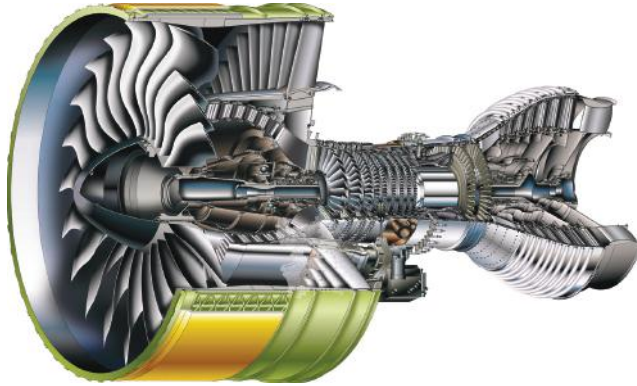
THIS DOCUMENT HAS BEEN PUBLICLY RELEASED
© UNITED TECHNOLOGIES CORPORATION

■ **FIGURE 3.30**
The PW4000 112-inch
fan engine. Source:
Reproduced by
permission of United
Technologies
Corporation, Pratt &
Whitney

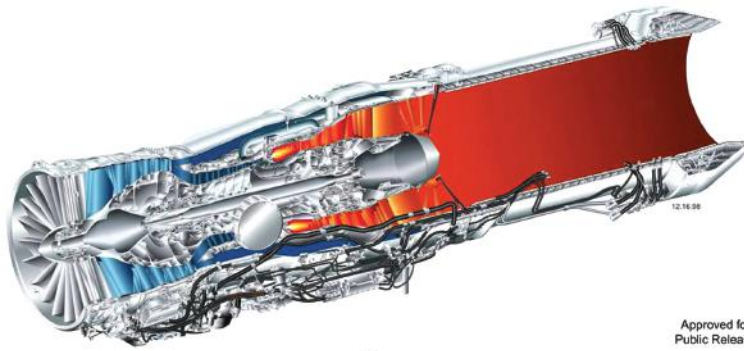
PW4000 112-INCH FAN ENGINE



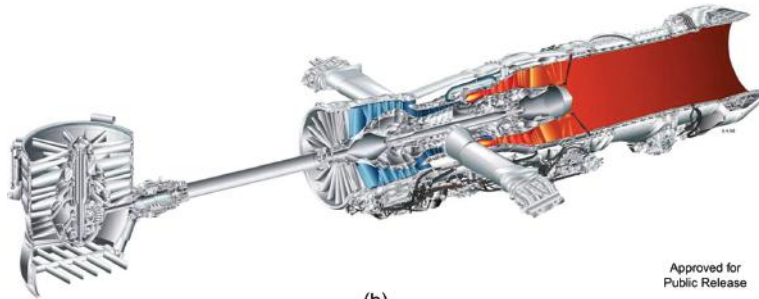
■ **FIGURE 3.31**
GP7000 engine cutaway. Source: Reproduced by permission of United Technologies Corporation, Pratt & Whitney



■ **FIGURE 3.32**
F135 engine cutaway:
(a) conventional takeoff and landing;
(b) short takeoff, vertical landing.
Source: Reproduced by permission of United Technologies Corporation, Pratt & Whitney



(a)



(b)

■ **FIGURE 3.33**
F119 engine cutaway. Source: Reproduced by permission of United Technologies Corporation, Pratt & Whitney



■ TABLE 3.1

Pratt & Whitney engine characteristics (courtesy United Technology Corporation, Pratt & Whitney)

PRATT & WHITNEY ENGINE CHARACTERISTICS

Feature v	Model >	V2533-A5	PW4098	PW6122A	GP7270	PW1524G	F119-PW-100	F135-PW-100
Engine Type		High Bypass Turbofan	High Bypass Turbofan	High Bypass Turbofan	Very High Bypass Turbofan	Ultra High Bypass Turbofan	Augmented Turbofan	Augmented Turbofan
Number of fan / LPC / HPC stages		1 / 4 / 10	1 / 7 / 11	1 / 4 / 6	1 / 5 / 9	1 / Gear / 3 / 8	3 / 0 / 6	3 / 0 / 6
Number of HP / LP turbine stages		2 / 5	2 / 7	1 / 3	2 / 6	2 / 3	1 / 1	1 / 2
Combustor type		Annular	Annular	Annular	Annular	Annular	Annular	Annular
Maximum Std Day thrust at sea level (lbs)		31,600	99,040	22,100	74,735	23,300	35,000 class	43,000 class
Specific fuel consumption at takeoff power		0.355	0.358	0.383				
Overall pressure ratio at max. power		33.4	42.8	26.6	36.1			28
Bypass Ratio		4.5	5.8	5.0	8.7			
Fan Pressure Ratio		1.8	1.8	1.7	1.6			
Diameter (inches)		64	120	62	124	79		46
Length, flange to flange (inches)		126	192	108	187	120		220
Weight, bare engine (lbs)		5,300	16,260	5,041	14,798			
Application for this model		Airbus A321-200	Boeing 777-300	Airbus A318-100	Airbus A380-800	Bombardier CS100, CS300	Lockheed F-22	Lockheed F-35A (CTOL)
Other Applications for the engine family		Airbus A319, A320, Boeing MD-90	Boeing 777-200			Embraer E190, E195 Second Generation		Lockheed F-35B (STOVL), F-35C (CTOL Carrier Variant)
Takeoff TT4 (degC)		1550	1748	1582				
Cruise TT4 (degC)		1139	1197	1235				
Takeoff EGT (degC)		670	675	760				
Max Continuous EGT (degC)		610	617	727				



THIS DOCUMENT HAS BEEN PUBLICLY RELEASED

© UNITED TECHNOLOGIES 2013

Source: Reproduced by permission of United Technologies Corporation, Pratt & Whitney.

and a table of engine data (Table 3.1) from United Technology Corporation, Pratt & Whitney. These are reproduced here with permission. The students in propulsion shall enjoy every single frame and data.

3.7 Summary

In this chapter, we defined engine thrust and the factors outside the engine that influenced its “installed” performance. We noted that the specific fuel consumption is a “fuel economy” parameter and is thus very critical to the direct operating expenses of an aircraft. We also used component impulse formulation to demonstrate the thrust equation for an airbreathing engine. Thermal and propulsive efficiencies each measured the internal performance and thrust production efficiency of an engine in flight, respectively. The overall

efficiency of the engine, as the product of thermal and propulsive efficiencies, is tied to both the fuel economy as well as aircraft range. A unifying figure of merit for airbreathing engines and rockets is “specific impulse” with units of seconds.

Airbreathing engines incur *ram drag*, which is the product of air mass flow rate and the flight speed. The exhaust nozzle produces *gross thrust*, which is the sum of the momentum thrust and a pressure force contribution that occurs for a nozzle with imperfect expansion. The gross thrust is maximized for a *perfectly expanded nozzle* where $p_9 = p_0$. The sum of the gross thrust and the ram drag is the engine uninstalled thrust. The installation effects are primarily due to inlet and nacelle aft-end drag contributions.

Propulsive efficiency improves when the exhaust and flight speeds are closer to each other in magnitude, as in a turbofan engine. The parameter that brings the exhaust and flight speeds closer to each other in a turbofan engine is the *bypass ratio*. The trend in subsonic engine development/manufacturing is in developing ultra-high bypass (UHB) engines, with bypass ratio in 12–15 range. Pratt & Whitney has developed a geared UHB Turbofan engine, PW1000G, that represents the future of commercial aviation (shown in Section 3.6). Current conventional turbofan engines offer a bypass ratio of ~ 8 . Since the turboprop affects a much larger airflow at an incrementally smaller speed increase, it offers the highest propulsive efficiency for a low-speed (i.e., subsonic) aircraft. Advanced turboprops may utilize counterrotating propellers and may include a *slimline nacelle*, as in a ducted fan configuration.

Thermal efficiency is a cycle-dependent parameter. The highest thermal efficiency of a heat engine operating between two temperature limits corresponds to the Carnot cycle. Consequently, a higher compression (Brayton) cycle, still bound by two temperature limits, offers a higher thermal efficiency. The trend in improving engine thermal efficiency is in developing high-pressure ratio compressors. The current maximum (compressor pressure ratio in aircraft gas turbine engines) is ~ 45 –50.

References

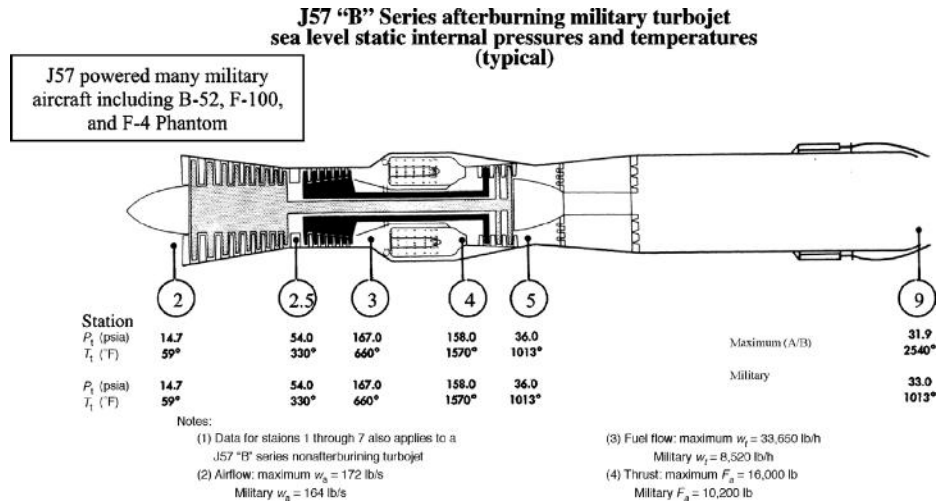
1. Anderson, J.D., A, *Aircraft Performance and Design*, McGraw-Hill, New York, 1999.
2. Kerrebrock, J.L., *Aircraft Engines and Gas Turbines*, 2nd edition, MIT Press, Cambridge, Massachusetts, 1992.
3. Lotter, K., “Aerodynamische Probleme der Integration von Triebwerk und Zelle beim Kampfflugzeugen,” *Proceedings of the 85th Wehrtechnischen Symposium*, Mannheim, Germany, 1977.
4. Newman, D., *Interactive Aerospace Engineering and Design*, McGraw-Hill, New York, 2002.
5. Pratt & Whitney *Aircraft Gas Turbine Engine and Its Operation*, P&W Operations Manual 200, 1988.

Problems

3.1 The total pressures and temperatures of the gas in an afterburning turbojet engine are shown (J57 “B” from Pratt & Whitney, 1988). The mass flow rates for the air and fuel are also indicated at two engine settings, the Maximum Power and the Military Power. Use the numbers specified in this engine to calculate

- (a) the fuel-to-air ratio f in the primary burner and the afterburner, at both power settings
- (b) the low- and high-pressure spool compressor pressure ratios and the turbine pressure ratio (note that these remain constant with the two power settings)
- (c) the exhaust velocity V_9 for both power settings by assuming the specified thrust is based on the nozzle gross thrust (because of sea level static) and neglecting any pressure thrust at the nozzle exit
- (d) the thermal efficiency of this engine for both power settings (at the sea level static operation),

■ **FIGURE P3.1**
 Source: Reproduced by permission of United Technologies Corporation, Pratt & Whitney



- assuming the fuel heating value is 18,600 BTU/lbm and $c_p = 0.24$ BTU/lbm · °R. Explain the lower thermal efficiency of the Maximum power setting
- (e) the thrust specific fuel consumption in lbm/h/lbf in both power settings
 - (f) the Carnot efficiency of a corresponding engine, i.e., operating at the same temperature limits, in both settings
 - (g) the comparison of percent thrust increase to percent fuel flow rate increase when we turn the afterburner on
 - (h) why don't we get proportional thrust increase with fuel flow increase (when it is introduced in the afterburner), i.e., doubling the fuel flow in the engine (through afterburner use) does not double the thrust

3.2 The total pressures and temperatures of the gas are specified for a turbofan engine with separate exhaust streams (JT3D-3B from Pratt & Whitney, 1974). The mass flow rates in the engine core (or primary) and the engine fan are also specified for the sea level static operation. Calculate

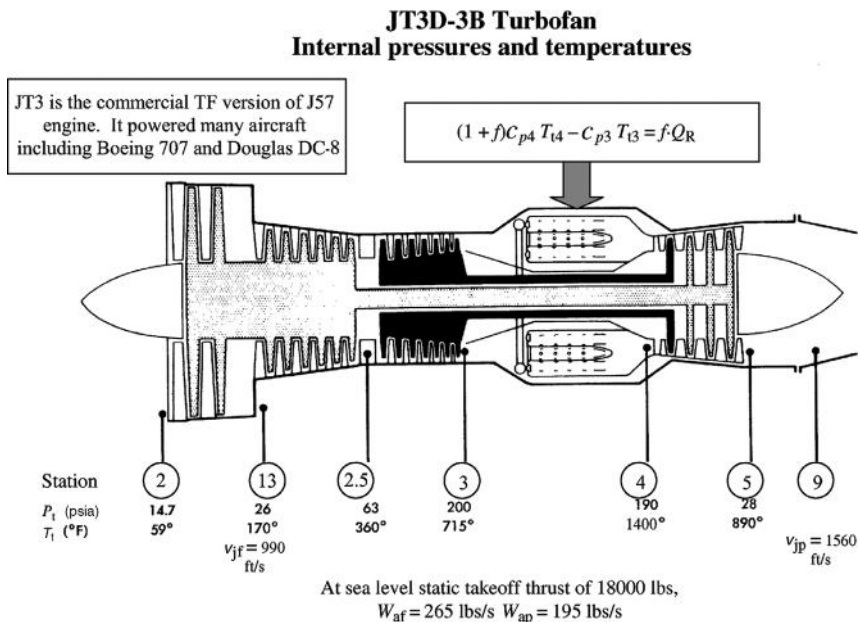
- (a) the engine bypass ratio α defined as the ratio of fan-to-core flow rate
- (b) from the total temperature rise across the burner, estimate the fuel-to-air ratio and the fuel flow rate in lbm/h, assuming the fuel heating value is $Q_R \sim 18,600$ BTU/lbm and the specific heat at constant pressure is 0.24 and 0.26 BTU/lbm · °R at the entrance and exit of the burner, respectively
- (c) the engine static thrust based on the exhaust velocities and the mass flow rates *assuming perfectly expanded nozzles* and compare your answer to the specified thrust of 18,000 lbs
- (d) the engine thermal efficiency η_{th}

- (e) the thermal efficiency of this engine compared to the afterburning turbojet of Problem 1. Explain the major contributors to the differences in η_{th} in these two engines
- (f) the engine thrust specific fuel consumption in lbm/h/lbf
- (g) the nondimensional engine specific thrust
- (h) the Carnot efficiency corresponding to this engine
- (i) the engine overall pressure ratio p_{t3} / p_{t2}
- (j) fan nozzle exit Mach number [use $T_t = T + V^2/2c_p$ to calculate local static temperature at the nozzle exit, then local speed of sound $a = (\gamma RT)^{1/2}$]

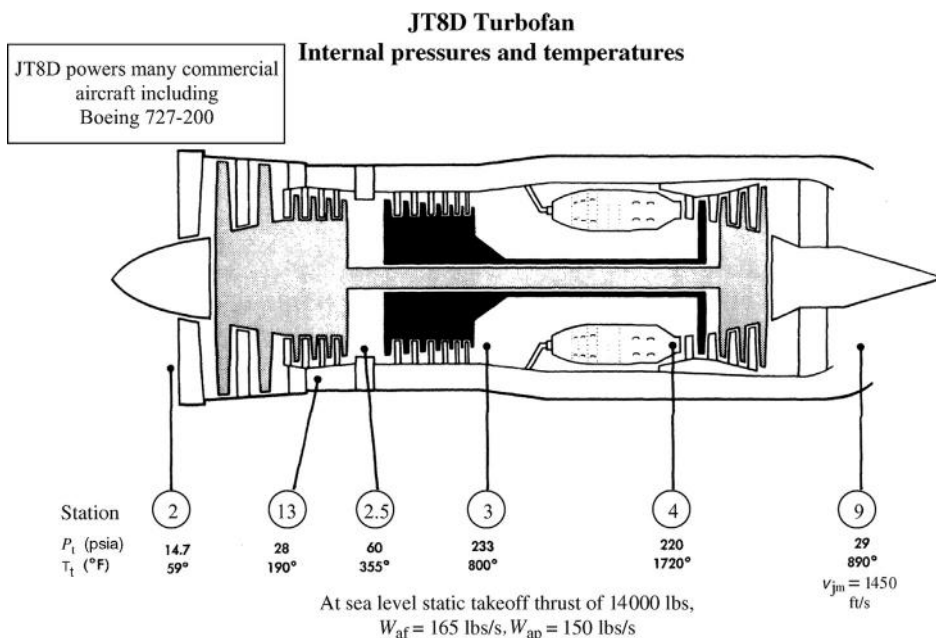
3.3 A mixed exhaust turbofan engine (JT8D from Pratt and Whitney, 1974) is described by its internal pressures and temperature, as well as air mass flow rates and the mixed jet (exhaust) velocity. Let us examine a few parameters for this engine, for a ballpark approximation.

- (a) Estimate the fuel flow rate from the total temperature rise across the burner assuming the fuel heating value is $\sim 18,600$ BTU/lbm and the specific heat at constant pressure is 0.24 and 0.26 BTU/lbm · °R at the entrance and exit of the burner, respectively
- (b) Calculate the momentum thrust at the exhaust nozzle and compare it to the specified thrust of 14,000 lbs
- (c) Estimate the thermal efficiency of this engine and compare it to Problems 3.1 and 3.2 as well as a Carnot cycle operating between the temperature extremes of this engine. Explain the differences
- (d) Estimate the specific fuel consumption for this engine in lbm/h/lbf
- (e) The overall pressure ratio (of the fan-compressor section) p_{t3} / p_{t2}

■ **FIGURE P3.2**
 Source: Reproduced by permission of United Technologies Corporation, Pratt & Whitney



■ **FIGURE P3.3**
 Source: Reproduced by permission of United Technologies Corporation, Pratt & Whitney



- (f) What is the bypass ratio α for this engine at takeoff
- (g) What is the Carnot efficiency corresponding to this engine
- (h) Estimate nozzle exit Mach number [look at part (j) in Problem 3.2]
- (i) What is the low-pressure compressor (LPC) pressure ratio $p_{2.5}/p_{12}$
- (j) What is the high-pressure compressor (HPC) pressure ratio $p_{13}/p_{2.5}$

3.4 A large bypass ratio turbofan engine (JT9D engine from Pratt and Whitney, 1974) is described by its fan and core engine gas flow properties.

- (a) What is the overall pressure ratio (OPR) of this engine
- (b) Estimate the fan gross thrust $F_{g, fan}$ in lbf
- (c) Estimate the fuel-to-air ratio based on the energy balance across the burner, assuming the fuel heating value is $\sim 18,600$ BTU/lbm and the specific heat at constant pressure is 0.24 and 0.26 BTU/lbm \cdot $^{\circ}$ R at the entrance and exit of the burner, respectively
- (d) Calculate the core gross thrust and compare the sum of the fan and the core thrusts to the specified engine thrust of 43,500 lbf
- (e) Calculate the engine thermal efficiency and compare it to Problems 3.1–3.3. Explain the differences
- (f) Estimate the thrust-specific fuel consumption (TSFC), in lbm/h/lbf
- (g) What is the bypass ratio of this turbofan engine

- (h) What is the Carnot efficiency η_{Carnot} corresponding to this engine
- (i) What is the LPC pressure ratio $p_{2.5}/p_{12}$
- (j) What is the HPC pressure ratio $p_{13}/p_{2.5}$
- (k) Estimate the fan nozzle exit Mach number [see part (j) in Problem 3.2]
- (l) Estimate the primary nozzle exit Mach number

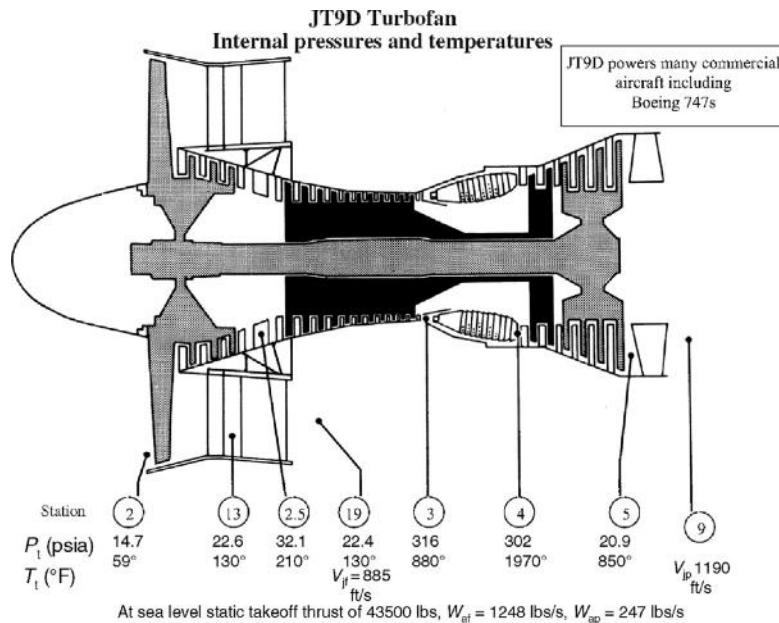
3.5 An airbreathing engine flies at Mach $M_0 = 2.0$ at an altitude where the ambient temperature is $T_0 = -50^{\circ}$ C and ambient pressure is $p_0 = 10$ kPa. The airflow rate to the engine is 25 kg/s. The fuel flow rate is 3% of airflow rate and has a heating value of 42,800 kJ/kg. Assuming the exhaust speed is $V_9 = 1050$ m/s, and the nozzle is perfectly expanded, i.e., $p_9 = p_0$, calculate

- (a) ram drag in kN
- (b) gross thrust in kN
- (c) net (uninstalled) thrust in kN
- (d) thrust-specific fuel consumption in kg/h/N
- (e) engine thermal efficiency η_{th}
- (f) propulsive efficiency η_p
- (g) engine overall efficiency η_o

3.6 A turbo-propeller-driven aircraft is flying at $V_0 = 150$ m/s and has a propeller efficiency of $\eta_{pr} = 0.75$. The propeller thrust is $F_{prop} = 5000$ N and the airflow rate through the engine is 5 kg/s. The nozzle is perfectly expanded and produces 1000 N of gross thrust. Calculate

- (a) the shaft power delivered to the propeller in kW

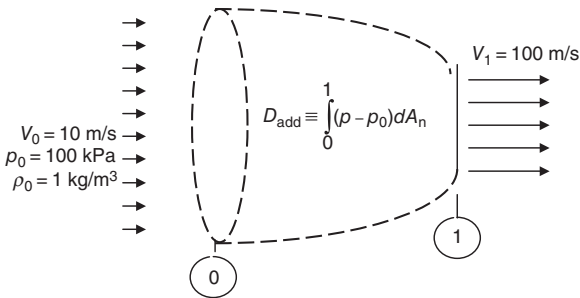
FIGURE P3.4
Source: Reproduced by permission of United Technologies Corporation, Pratt & Whitney



- (b) the nozzle exit velocity in m/s (neglect fuel flow rate in comparison to the air flow rate)
- (c) in using Equation 3.56, $\eta_p \equiv \frac{F \cdot V_0}{\dot{\varphi}_s + \Delta KE}$, first show that the contribution of the net kinetic power produced by the engine ΔKE is small compared to the shaft power $\dot{\varphi}_s$ in denominator of Equation 3.56. Second, estimate the propulsive efficiency η_p for the turboprop engine from this equation.

3.7 Let us consider the control volume shown to represent the capture streamtube for an airbreathing engine at takeoff. The air speed is 10 m/s in area A_0 and 100 m/s in A_1 .

- (a) Use incompressible flow assumption to estimate capture area ratio A_0/A_1
- (b) Use the Bernoulli equation to estimate p_1/p_0
- (c) Use momentum balance to estimate nondimensional additive drag $D_{add}/A_1 p_0$



■ FIGURE P3.7

3.8 A rocket motor burns propellant at a rate of 50 kg/s. The exhaust speed is 3500 m/s and the nozzle is perfectly expanded. Calculate

- (a) the rocket thrust in kN
- (b) the rocket motor specific impulse I_s (s).

3.9 For the turbofan engine shown, calculate

- (a) ram drag D_{ram} in kN
- (b) primary nozzle gross thrust F_{g_9} in kN
- (c) fan nozzle gross thrust $F_{g_{19}}$ in kN
- (d) the engine net thrust F_n in kN
- (e) the propulsive efficiency η_p (-)

Hint: To calculate the pressure thrust for the primary and fan nozzles, you may calculate the flow areas at A_9 and A_{19} using the mass flow rate information as well as the density that you may calculate from pressure and temperature (via the speed of sound) using perfect gas law.

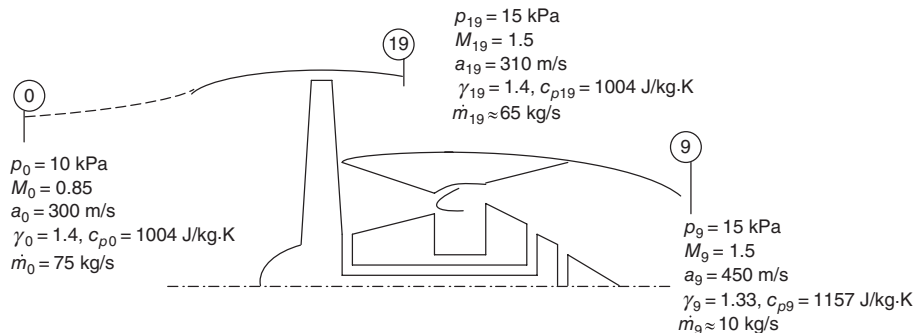
3.10 A ramjet is flying at Mach 2.0 at an altitude where $T_0 = -50^\circ\text{C}$ and the engine airflow rate is 10 kg/s. If the exhaust Mach number of the ramjet is equal to the flight Mach number, i.e., $M_9 = M_0$, with perfectly expanded nozzle and T_{19} 2500 K, calculate

- (a) the engine ram drag D_{ram} in kN
- (b) the nozzle gross thrust F_g in kN
- (c) the engine net thrust F_n in kN
- (d) the engine propulsive efficiency η_p

Assume gas properties remain the same throughout the engine, i.e., assume $\gamma = 1.4$ and $c_p = 1004 \text{ J/kg} \cdot \text{K}$. Also, assume that the fuel flow rate is 4% of airflow rate.

3.11 A turbojet-powered aircraft cruises at $V_0 = 300 \text{ m/s}$ while the engine produces an exhaust speed of 600 m/s. The air mass flow rate is 100 kg/s and the fuel mass flow rate is 2.5 kg/s. The fuel heating value is $Q_R = 42,000 \text{ kJ/kg}$. Assuming that the nozzle is perfectly expanded, calculate

- (a) engine ram drag in kN
- (b) engine gross thrust in kN
- (c) engine net thrust in kN
- (d) engine thrust-specific fuel consumption (TSFC) in mg/s/kN



■ FIGURE P3.9

- (e) engine thermal efficiency
- (f) engine propulsive efficiency
- (g) aircraft range R for L/D of 10 and the W_i / W_f of 1.25
- (h) if this aircraft make it across the Atlantic Ocean?

3.12 We wish to investigate the range of a slender supersonic aircraft where its lift-to-drag ratio as a function of flight Mach number is described by

$$\frac{L}{D} \approx 3 \frac{M_0 + 3}{M_0}$$

Using Equation 3.67, i.e.,

$$R = \left(M_0 \frac{L}{D} \right) \frac{a_0/g_0}{\text{TSFC}} \epsilon n \frac{W_i}{W_f}$$

for range equation, vary the thrust specific fuel consumption TSFC between 1.0 and 2.0 lbm/h/lbf to graph R for flight Mach number ranging between 2.0 and 4.0. You may assume a_0 is 1000 ft/s and the aircraft initial-to-final weight ratio is $W_i/W_f = 2.0$.

3.13 A turboshaft engine consumes fuel with a heating value of 42,000 kJ/kg at the rate of 1 kg/s. Assuming the thermal efficiency is 0.333, calculate the shaft power that this engine produces.

3.14 A rocket engine consumes propellants at the rate of 1000 kg/s and achieves a specific impulse of $I_s = 400$ s. Assuming the nozzle is perfectly expanded, calculate

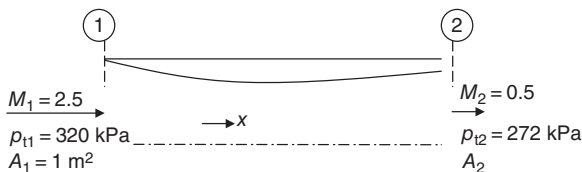
- (a) the rocket exhaust speed V_9 in m/s
- (b) the rocket thrust in MN

3.15 A rocket engine has a nozzle exit diameter of $D_9 = 2$ m. It is perfectly expanded at sea level. Calculate the rocket pressure thrust in vacuum.

3.16 A ramjet engine is in supersonic flight. Its inlet flow parameters are shown.

Assuming the flow is adiabatic and $\gamma = 1.4$, calculate

- (a) the diffuser exit area A_2 in m^2
- (b) impulse (in kN) in stations 1 and 2, I_1 and I_2
- (c) internal force exerted (by the fluid) on the inlet in flight (or $-x$) direction

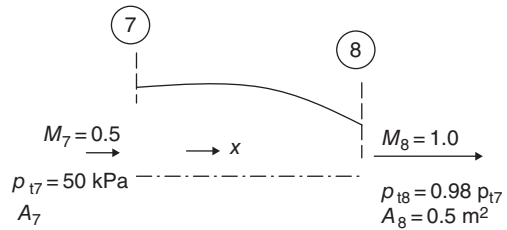


■ FIGURE P3.16

3.17 A convergent nozzle is perfectly expanded with exit Mach number $M_8 = 1.0$. The exit total pressure is 98% of the inlet total pressure. The nozzle inlet Mach number is $M_7 = 0.5$ and the nozzle area at the exit is $A_8 = 0.5 \text{ m}^2$.

Assuming the gas ratio of specific heats is $\gamma = 1.33$, and the flow is adiabatic, calculate

- (a) nozzle inlet area A_7 in m^2
- (b) nozzle inlet impulse I_7 in kN
- (c) nozzle exit impulse I_8 in kN
- (d) the axial force (i.e., in the x -direction) exerted by the fluid on the nozzle



■ FIGURE P3.17

3.18 A turboprop engine flies at $V_0 = 200$ m/s and produces a propeller thrust of $F_{\text{prop}} = 40$ kN and a core thrust of $F_{\text{core}} = 10$ kN. Engine propulsive efficiency η_p is 85%. Calculate

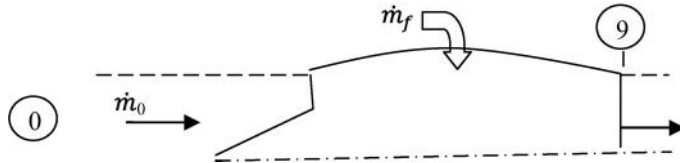
- (a) total thrust produced by the turboprop in kN
- (b) thrust power in MW
- (c) shaft power produced by the engine ϕ_s in MW

3.19 A turbojet engine produces a net thrust of 40,000 N at the flight speed of V_0 of 300 m/s. For a propulsive efficiency of $\eta_p = 0.40$, estimate the turbojet exhaust speed V_9 in m/s.

3.20 Calculate the engine specific impulse in seconds for Problem 3.19. Also, assuming the fuel heating value is 42,000 kJ/kg and the thermal efficiency is 45%, estimate the fuel-to-air ratio consumed in the burner.

3.21 A turbojet engine is shown in cruise condition. The flight condition is known to be: $M_0 = 2.0$, $p_0 = 20$ kPa, $T_0 = -35^\circ\text{C}$ with $\gamma = 1.4$ and $R = 287$ J/kg.K. The air mass flow rate into the engine is known to be $\dot{m}_0 = 110$ kg/s. The fuel flow rate to the combustor is $\dot{m}_f = 4.2$ kg/s with heating value $Q_R = 42,800$ kJ/kg. If the nozzle is perfectly expanded and the exhaust velocity is $V_9 = 1,200$ m/s, calculate:

- (a) Ram drag, D_r , in kN and lbf
- (b) Gross thrust, F_g , in kN and lbf
- (c) Net un-installed thrust in kN
- (d) TSFC in mg/s/N and lbm/hr/lbf
- (e) Engine thermal efficiency, η_{th}
- (f) Propulsive efficiency, η_p

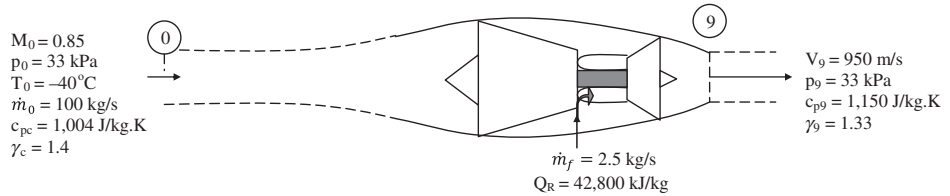


■ FIGURE P3.21

3.22 An aircraft gas turbine engine is shown in flight. Calculate:

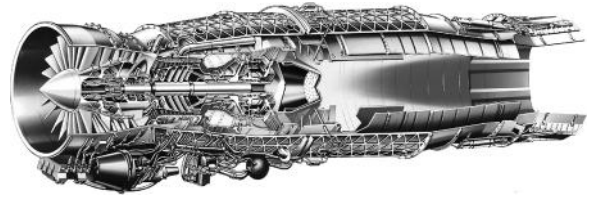
- (a) ram drag in kN and lbf
- (b) gross thrust in kN and lbf

- (c) specific fuel consumption in mg/s/N and lbm/hr/lbf
- (d) thermal efficiency, η_{th}
- (e) propulsive efficiency, η_p



■ FIGURE P3.22

CHAPTER 4



Source: Reproduced with permission from Rolls-Royce plc

Gas Turbine Engine Cycle Analysis

4.1 Introduction

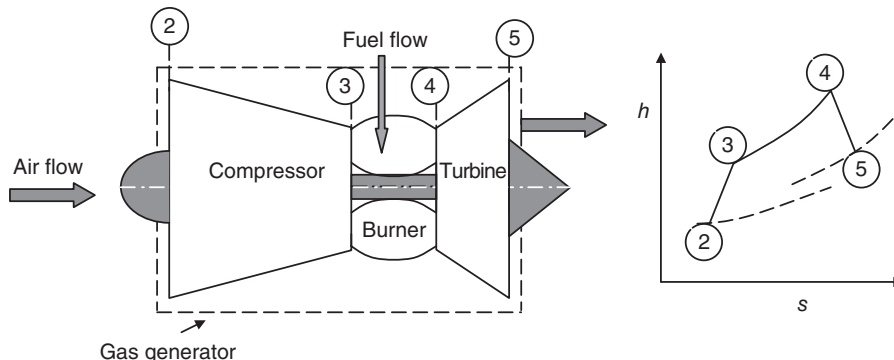
In this chapter, we examine the aerothermodynamics of aircraft gas turbine engines. We first start our analysis with the basic building block or the common features of any gas turbine engine, namely the gas generator. We will then *construct* a variety of aircraft engines employing the gas generator. These include the turbojet, the afterburning turbojet, the separate and mixed-exhaust turbofan, and the turboprop engines.

4.2 The Gas Generator

At the heart of an aircraft gas turbine engine is a *gas generator*. It is composed of three major components, a compressor, a burner (sometimes referred to as combustor or combustion chamber), followed by a turbine. The schematics of a gas generator and station numbers are shown in Figure 4.1. The parameters that define the physical characteristics of a gas generator are noted in Table 4.1.

Compressor total pressure ratio π_c is a design parameter. An aircraft engine designer has the design choice of the compressor staging, that is, the number and the type of compressor stages. That choice is a strong function of flight Mach number, or what we will refer to as *ram pressure ratio*. As a rule of thumb, the higher the flight Mach number, the lower the compressor pressure ratio the cycle requires to operate efficiently. In fact at the upper supersonic Mach numbers, that is, $M_0 \geq 3$, an airbreathing engine will not even require *any* mechanical compression, that is, the compressor is totally unneeded. Such engines work on the principle of ram compression and are called *ramjets*. We will refer

■ FIGURE 4.1
Schematic drawing of a
gas generator



■ TABLE 4.1
The Parameters in a Gas Generator

1.	Compressor pressure ratio $\pi_c \equiv \frac{p_{13}}{p_{12}}$	(“design” parameter)
2.	Compressor air mass flow rate \dot{m}_0	(“size” parameter)
3.	Combustor fuel flow rate \dot{m}_f or turbine entry temperature T_{14}	(“temperature limit” parameter)
4.	Fuel heating value Q_R	(“ideal fuel energy” parameter)
5.	Component efficiency	(“irreversibility” or loss parameter)

to this later on in our analysis. The compressor air mass flow rate is the sizing parameter, which basically scales the engine face diameter. The takeoff gross weight of the aircraft is the primary parameter that most often *sizes* the engine. Other parameters that contribute to engine sizing are the engine-out rate of climb requirements, the transonic acceleration, and the allowable use of afterburner, among other mission specification parameters. The burner fuel flow rate is the fuel energy release rate parameter, which may be replaced by the turbine entry temperature T_{14} . Both of these parameters establish a *thermal limit* identity for the engine, which dictates the material and the cooling technologies to be employed in the engine *hot section* (i.e., the turbine and nozzle) at the design stage. Fuel heating value, or heat of reaction Q_R , represents the (ideal) fuel energy density, that is, the fuel thermal energy per unit mass of fuel. Finally, the component efficiencies are needed to describe the extent of losses or stated in thermodynamic language “irreversibility” in each component.

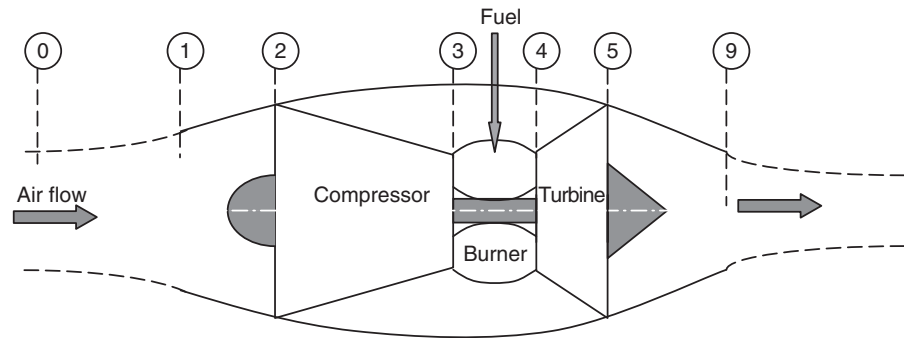
4.3 Aircraft Gas Turbine Engines

In this section, we examine the variety of aircraft gas turbine engines that are possible around the basic theme of a gas generator. The simplest example is the turbojet engine.

4.3.1 The Turbojet Engine

An aircraft turbojet (TJ) engine is basically a gas generator fitted with an inlet and exhaust system. A schematic drawing of a TJ-engine is shown in Figure 4.2.

■ **FIGURE 4.2**
Schematic drawing of a
turbojet engine



The additional parameters that are needed to calculate the performance of a turbojet engine are the inlet and exhaust component efficiencies. These parameters will be defined in the next section. The station numbers in a turbojet engine are defined at the unperturbed flight condition, 0, inlet lip, 1, compressor face, 2, compressor exit, 3, burner exit, 4, turbine exit, 5, and the nozzle exit plane, 9.

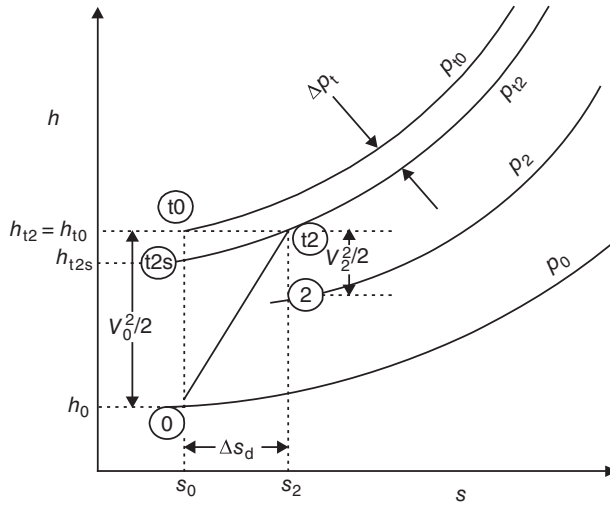
4.3.1.1 The Inlet. The *basic* function of the inlet is to deliver the air to the compressor at the *right* Mach number M_2 and the *right* quality, that is, low distortion. The subsonic compressors are designed for an axial Mach number of $M_2 = 0.5\text{--}0.6$. Therefore, if the flight Mach number is higher than 0.5 or 0.6, which includes all commercial (fixed wing) transports and military (fixed wing) aircraft, then the inlet is required to *decelerate* the air efficiently. Therefore, the main function of an inlet is to *diffuse or decelerate* the flow, and hence it is also called a diffuser. Flow deceleration is accompanied by the static pressure rise or what is known as the *adverse pressure gradient* in fluid dynamics. As one of the first principles of fluid mechanics, we learned that the boundary layers, being of a low-energy and momentum-deficit zone, facing an adverse pressure gradient environment tend to separate. Therefore, one of the challenges facing an inlet designer is to prevent inlet boundary layer separation. One can achieve this by tailoring the geometry of the inlet to avoid rapid diffusion or possibly through variable geometry inlet design. Now, it becomes obvious why an aircraft inlet designer faces a bigger challenge if the inlet has to decelerate a Mach 2 or 3 stream to the compressor face Mach number of 0.5 than an aircraft that flies at Mach 0.8 or 0.9. In the present section, we will examine the *thermodynamics* of an aircraft inlet. This exciting area of propulsion, that is, inlet aerodynamics, will be treated in more detail in Chapter 6.

An ideal inlet is considered to provide a *reversible and adiabatic*, that is, isentropic, compression of the captured flow to the engine. The adiabatic aspect is actually met in real inlets as well. This requirement says that there is no heat exchange between the captured stream and the ambient air, through the diffuser walls. We remember (from the Fourier law of heat conduction) that for heat transfer to take place through the inlet wall, we need to set up a *temperature gradient* across the wall, such that

$$q_n \equiv \frac{\dot{Q}_n}{A} = -k \frac{\partial T}{\partial n} \quad (4.1)$$

where n denotes the direction of heat conduction, k the thermal conductivity of the wall, and q_n the heat flux, which is defined as the heat transfer rate \dot{Q}_n per unit area A .

■ FIGURE 4.3
h-s diagram of an aircraft engine inlet flow under real and ideal conditions



Equation 4.1 signifies the importance of a *gradient* to set up the heat transfer. The temperature gradient across the inlet wall (i.e., nacelle) is negligibly small, and consequently the inlet aerodynamics is considered to be *adiabatic*, even in a real flow. Therefore, it is only the *reversible* aspect of our ideal inlet flow assumption that negates the realities of wall friction and any shocks, which are invariably present in *real* supersonic flows. The process of compression in a real inlet can be shown on the *h-s* diagram of Figure 4.3.

Now, let us describe the information we observe in Figure 4.3. First, four isobars are shown on the *h-s* diagram. From the lowest to the highest value, these are p_0 , the static pressure at the flight altitude, p_2 , the static pressure at the engine face, p_{t2} , the total pressure at the inlet discharge (or compressor face), and p_{t0} , the flight total pressure. We also note five thermodynamic states identified, as the flight static (0), the flight total (t0), the compressor face or inlet discharge static (2), and total (t2) and a stagnation state (t2s) that does not actually exist! Note, that the first four states, that is, 0, t0, 2, and t2, do all in reality exist and are measured. The states 0 and t0 are measured by a pitot-static tube on an aircraft, and the static and total pressures at the engine face are measured by a pressure rake or inlet pitot tubes. We note that the state (t2s) is at the intersection of s_0 and p_{t2} , which is arrived at isentropically from state (0) to a state that shares the same total pressure as that of a real inlet (t2). We note an entropy rise Δs_d across the inlet as well. The total enthalpy of the real inlet h_{t2} is identified to be the same as the total enthalpy of flight h_{t0} . This is based on the earlier assertion that a *real* inlet flow may be considered to be *adiabatic*. It is to be noted that although the total energy of the fluid in a real inlet is not changing, there is an *energy conversion* that takes place in the inlet. The inlet kinetic energy is partially converted to the static pressure (rise) and partially it is dissipated into heat. It is the latter portion, that is, the dissipation, which renders the process irreversible and cause the entropy to rise. The entropy rise in an adiabatic process leads to a total pressure loss Δp_t following the combined first and second law of thermodynamics, that is, Gibbs equation, according to

$$\frac{p_{t2}}{p_{t0}} = e^{-\frac{s_2 - s_0}{R}} = e^{-\frac{\Delta s}{R}} \quad (4.2)$$

From Figure 4.3, we also note that the states (t0) and (0) are separated *isentropically* by the amount of $V_0^2/2$, as expected from the definition of stagnation state and its relation to the static state. The states (t2s) and (0) are separated isentropically by a kinetic energy amount, which produces p_{t2} as its stagnation state and obviously the rest of the kinetic energy, that is, the gap between the states (t0) and (t2s), represents the amount of dissipated kinetic energy into heat. Therefore, the smaller the gap between the states (t2s) and (t0), the more efficient will the diffuser flow process be. Consequently, we use the fictitious state (t2s) in a definition of inlet efficiency (or a figure of merit) known as the *inlet adiabatic efficiency*. Symbolically, the inlet adiabatic efficiency is defined as

$$\eta_d \equiv \frac{h_{t2s} - h_0}{h_{t2} - h_0} = \frac{(V^2/2)_{\text{ideal}}}{V_0^2/2} \quad (4.3)$$

The practical form of the above definition is derived when we divide the numerator and denominator by h_0 to get

$$\eta_d = \frac{\frac{h_{t2s}}{h_0} - 1}{\frac{h_{t2}}{h_0} - 1} = \frac{\frac{T_{t2s}}{T_0} - 1}{\frac{h_{t0}}{h_0} - 1} = \frac{\left(\frac{p_{t2}}{p_0}\right)^{\frac{\gamma-1}{\gamma}} - 1}{\frac{\gamma-1}{2}M_0^2} = \frac{\left(\frac{p_{t2}}{p_0}\right)^{\frac{\gamma-1}{\gamma}} - 1}{\tau_r - 1} \quad (4.4)$$

where we have used the isentropic relation between the states (t2s) and (0). Note that the only unknown in Equation 4.4 is p_{t2} for a given flight altitude p_0 , flight Mach number M_0 , and an inlet adiabatic efficiency η_d . We can separate the unknown term p_{t2} and write the following expression:

$$\frac{p_{t2}}{p_0} = \left\{ 1 + \eta_d \frac{\gamma-1}{2} M_0^2 \right\}^{\frac{\gamma}{\gamma-1}} \quad (4.5)$$

It is interesting to note that Equation 4.5 recovers the isentropic relation for a 100% efficient inlet or $\eta_d = 1.0$. Another parameter, or a *figure of merit*, that describes the inlet performance is the total pressure ratio between the compressor face and the (total) flight condition. This is given a symbol π_d and is often referred to as the *inlet total pressure recovery*:

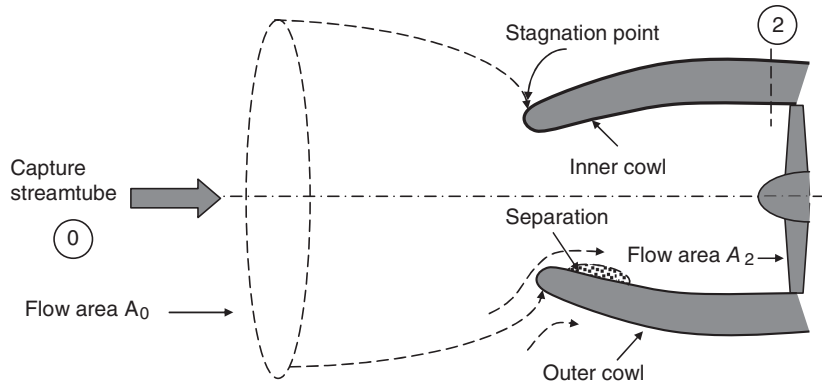
$$\pi_d \equiv \frac{p_{t2}}{p_{t0}} \quad (4.6)$$

As expected, the two figures of merit for an inlet, that is, η_d or π_d , are not independent from each other and we can derive a relationship between η_d and π_d working the left-hand side of Equation 4.5, as follows:

$$\frac{p_{t2}}{p_0} = \frac{p_{t2} p_{t0}}{p_{t0} p_0} = \left\{ 1 + \eta_d \frac{\gamma-1}{2} M_0^2 \right\}^{\frac{\gamma}{\gamma-1}} \quad (4.6a)$$

$$\pi_d = \frac{\left\{ 1 + \eta_d \frac{\gamma-1}{2} M_0^2 \right\}^{\frac{\gamma}{\gamma-1}}}{\frac{p_{t0}}{p_0}} = \left\{ \frac{1 + \eta_d \frac{\gamma-1}{2} M_0^2}{1 + \frac{\gamma-1}{2} M_0^2} \right\}^{\frac{\gamma}{\gamma-1}} = \frac{\left[1 + \eta_d \frac{\gamma-1}{2} M_0 \right]^{\frac{\gamma}{\gamma-1}}}{\pi_r} \quad (4.6b)$$

■ **FIGURE 4.4**
Schematic drawing of an inlet flow at low-speed and/or takeoff flight condition (note: $A_0 > A_2$)

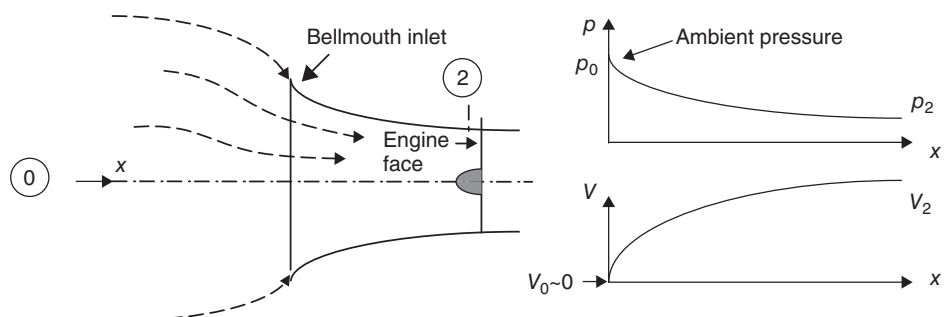


Therefore, Equation 4.6b relates the inlet total pressure recovery π_d to the inlet adiabatic efficiency η_d at any flight Mach number M_0 . We note that Equation 4.6b as $\eta_d \rightarrow 1$, then $\pi_d \rightarrow 1$ as well, as expected. Figure 4.3 also shows the static state 2, which shares the same entropy as the total state t2 and lies below it by the amount of kinetic energy at 2, namely, $V_2^2/2$. Compare the kinetic energy at 2 and at 0, shown in Figure 4.3, and then justify the static pressure rise achieved in the inlet (diffuser), $p_2 - p_0$.

So far, we have considered the cruise condition or the high-speed end of the flight envelope and have thought of inlets as diffusers. Under low-speed or takeoff conditions, the captured stream tube will instead undergo acceleration to the engine face and as such the inlet acts like a nozzle! In Figure 4.4, the schematics of a captured stream tube, under a low-speed flight condition, are shown. Note that the stagnation point is on the outer cowl and flow accelerates to the engine face ($A_0 > A_2$). The aerodynamics of the outer nacelle geometry affects the drag divergence of the inlet and plays a major role in the propulsion system integration studies of engine installation. However, the cycle analysis phase usually disregards the external performance and concentrates on the internal evaluation of the propulsion system.

The nature of the flow path into the inlet at low forward speed or under static engine testing conditions requires the inlet to act as a nozzle; therefore, it explains the use of a bellmouth in static test rigs. Figure 4.5 shows the schematic drawing of an inlet configuration in a static test rig. In Figure 4.5, we note that the static pressure along the stream lines drop from the ambient p_0 to the engine face pressure of p_2 . Also, we note

■ **FIGURE 4.5**
Bellmouth inlet guides the flow smoothly into the engine on a static test rig



that the gas speed starts at almost zero, since the captured flow area A_0 is fairly large, and continues to grow to the engine face speed of V_2 .

In summary, we have learned that

- the inlet flow may be considered to be adiabatic, that is, $h_{t2} = h_{t0}$
- the inlet flow is always irreversible, that is, $p_{t2} < p_{t0}$, with viscous dissipation in the boundary layer and in a shock as the sources of irreversibility ($s_2 > s_0$)
- there are two figures of merit that describe the extent of *losses* in the inlet and these are η_d and π_d
- the two figures of merit are related (via Equation 4.6b)
- in cruise, $A_0 < A_2$ and hence a diffusing passage and at low speed or takeoff, $A_0 > A_2$, that is, a nozzle
- the outer nacelle geometry of an inlet dictates the drag divergence and high angle of attack characteristics of the inlet and is crucial for the installed performance.

EXAMPLE 4.1

An aircraft is flying at an altitude where the ambient static pressure is $p_0 = 10$ kPa and the flight Mach number is $M_0 = 0.85$. The total pressure at the engine face is measured to be $p_{t2} = 15.88$ kPa. Assuming the inlet is adiabatic and $\gamma = 1.4$, calculate

- (a) the inlet total pressure recovery π_d
- (b) the inlet adiabatic efficiency η_d
- (c) the nondimensional entropy rise caused by the inlet $\Delta s_d/R$

SOLUTION

We first calculate the flight total pressure p_{t0} , and from definition of π_d (i.e., Equation 4.6), the inlet total pressure recovery.

$$p_{t0} = p_0 [1 + (\gamma - 1)M_0^2/2]^{\frac{\gamma}{\gamma-1}} = 10 \text{ kPa} [1 + 0.2(0.85)^2]^{3.5} = 16.04 \text{ kPa}$$

$$\pi_d \equiv p_{t2}/p_{t0} = 15.88/16.04 = 0.990$$

Inlet adiabatic efficiency η_d is calculated from Equation 4.4

$$\eta_d = \left[\left(\frac{p_{t2}}{p_0} \right)^{\frac{\gamma-1}{\gamma}} - 1 \right] / \left[\left(\frac{\gamma-1}{2} M_0^2 \right) \right] = [(15.88/10)^{0.2857} - 1] / [0.2(0.85)^2] \cong 0.9775$$

The entropy rise is linked to the inlet total pressure loss parameter π_d via Equation 4.2,

$$\Delta s_d/R = -\ln(\pi_d) = -\ln(0.99) \cong 0.010$$

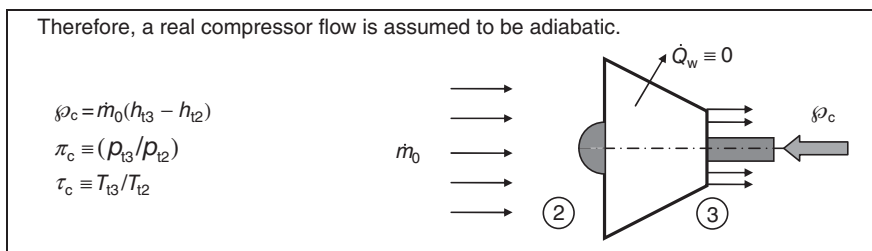
4.3.1.2 The Compressor. The thermodynamic process in a gas generator begins with the mechanical compression of air in the compressor. As the compressor discharge contains higher energy gas, that is, the compressed air, it requires *external power* to operate. The power comes from the turbine via a shaft, as shown in Figure 4.1 in case of an operating gas turbine engine. Other sources of external power may be used to *start* the engine, which are in the form of electric motor, air turbine, and hydraulic starters. The flow of air in a compressor is considered to be an essentially adiabatic process, which suggests that only a *negligible* amount of heat transfer takes place between the air inside and the ambient air outside the engine. Therefore, even in a real compressor analysis, we will

still treat the flow as adiabatic. Perhaps a more physical argument in favor of neglecting the heat transfer in a compressor can be made by examining the order of magnitude of the energy transfer sources in a compressor. The power delivered to the medium in a compressor is achieved by one or more rows of rotating blades (called rotors) attached to one or more spinning shafts (typically referred to as *spools*). Each rotor blade, which changes the *spin* (or swirl) of a medium, will experience a countertorque as a reaction to its own action on the fluid. If we denote the rotor torque as τ , then the power delivered to the medium by the rotor spinning at the angular speed ω follows Newtonian mechanics, that is,

$$\dot{\varphi}_c = \tau \cdot \omega \tag{4.7}$$

A typical axial-flow compressor contains hundreds of rotor blades (distributed over several stages), which interact with the medium according to the above equation. Therefore, the rate of mechanical energy transfer in a typical modern compressor is usually measured in mega-Watt (MW) and is several orders of magnitude larger than heat transfer through the compressor wall. Symbolically, we may present this as

$$\dot{\varphi}_c \gg \dot{Q}_w \tag{4.8}$$



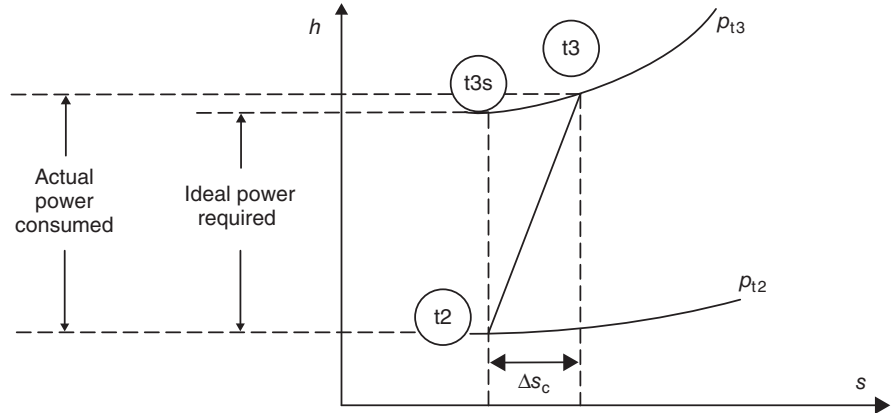
As a real process, however, the presence of wall friction acting on the medium through the boundary layer and shock waves caused by the relative supersonic flow through compressor blades will render the process irreversible. Therefore, the sources of irreversibility in a compressor are due to the viscosity of the medium and its consequences (boundary layer formation, wakes, vortex shedding) and the shock formation in relative supersonic passages.

The measure of irreversibility in a compressor may be thermodynamically defined through some form of compressor efficiency. There are two methods of compressor efficiency definitions. These are

- compressor adiabatic efficiency η_c
- compressor polytropic efficiency e_c .

To define the compressor adiabatic efficiency η_c , we depict a “real” compression process on an h - s diagram, as shown in Figure 4.6 and compare it to an ideal, that is, isentropic process. The state “t2” represents the *total* (or stagnation) state of the gas entering the compressor, typically designated by p_{t2} and T_{t2} . An actual flow in a

■ **FIGURE 4.6**
Enthalpy–entropy
(h – s) diagram of an
actual and ideal
compression process
(note Δs_c)



compressor will follow the solid line from “t2” to “t3”, thereby experiencing an entropy rise in the process, Δs_c . The actual total state of the gas is designated by “t3” in Figure 4.6. The ratio p_{t3}/p_{t2} is known as the compressor pressure ratio, with a shorthand notation π_c . The compressor total temperature ratio is depicted by, the shorthand notation, $\tau_c \equiv T_{t3}/T_{t2}$. Since the state “t3” is the actual state of the gas at the exit of the compressor and is not achieved via an isentropic process, we cannot expect the isentropic relation between τ_c and π_c , to hold, that is,

$$\tau_c \neq \pi_c^{\frac{\gamma-1}{\gamma}} \quad (4.9)$$

It can be seen from Figure 4.6 that the actual τ_c is larger than the ideal, that is, isentropic τ_c , which is denoted by the end state T_{t3s} . This fact actually helps with the exponent memorization in a real compression process. The compressor adiabatic efficiency is the ratio of the ideal power required to the power consumed by the compressor, that is,

$$\eta_c \equiv \frac{h_{t3s} - h_{t2}}{h_{t3} - h_{t2}} = \frac{\Delta h_{t,\text{isentropic}}}{\Delta h_{t,\text{actual}}} \quad (4.10)$$

The numerator in Equation 4.10 is the power-per-unit mass flow rate in an *ideal compressor* and the denominator is the power-per-unit mass flow rate in the actual compressor. If we divide the numerator and denominator of Equation 4.10 by h_{t2} , we get

$$\eta_c = \frac{T_{t3s}/T_{t2} - 1}{T_{t3}/T_{t2} - 1} \quad (4.11)$$

Since the thermodynamic states “t3s” and “t2” are on the same isentrope, the temperature and pressure ratios are then related via the isentropic formula, that is,

$$\frac{T_{t3s}}{T_{t2}} = \left(\frac{p_{t3s}}{p_{t2}} \right)^{\frac{\gamma-1}{\gamma}} = \left(\frac{p_{t3}}{p_{t2}} \right)^{\frac{\gamma-1}{\gamma}} = \pi_c^{\frac{\gamma-1}{\gamma}} \quad (4.12)$$

Therefore, compressor adiabatic efficiency may be expressed in terms of compressor pressure and temperature ratios as

$$\eta_c = \frac{\pi_c^{\frac{\gamma-1}{\gamma}} - 1}{\tau_c - 1} \quad (4.13)$$

Equation 4.13 involves three parameters, η_c , π_c , and τ_c . It can be used to calculate τ_c for a given compressor pressure ratio and adiabatic efficiency. As compressor pressure ratio and efficiency are typically known and assumed quantities in a gas turbine cycle analysis, the only unknown in Equation 4.13 is τ_c .

A second efficiency parameter in a compressor is *polytropic efficiency* e_c . As might be expected, compressor adiabatic and polytropic efficiencies are related. The definition of compressor polytropic efficiency is

$$e_c \equiv \frac{dh_{ts}}{dh_t} \quad (4.14)$$

It is interesting to compare the definition of compressor adiabatic efficiency, involving finite jumps (Δh_t), and the polytropic efficiency, which takes infinitesimal steps (dh_t). The conclusion can be reached that the polytropic efficiency is actually the adiabatic efficiency of a compressor with *small* pressure ratio. Consequently, compressor polytropic efficiency is also called *small stage efficiency*. From the combined first and second law of thermodynamics, we have

$$T_t ds = dh_t - \frac{dp_t}{\rho_t} \quad (4.15)$$

We deduce that for an isentropic process, that is, $ds = 0$, $dh_t = dh_{ts}$ and, therefore,

$$dh_{ts} = \frac{dp_t}{\rho_t} \quad (4.16)$$

If we substitute Equation 4.16 in 4.14 and replace density with pressure and temperature from the perfect gas law, we get

$$e_c = \frac{\frac{dp_t}{p_t}}{\frac{dh_t}{RT_t}} = \frac{\frac{dp_t}{p_t}}{\frac{C_p dT_t}{RT_t}} = \frac{\frac{dp_t}{p_t}}{\frac{\gamma}{\gamma-1} \frac{dT_t}{T_t}} \quad (4.17)$$

$$\frac{dp_t}{p_t} = \frac{\gamma e_c}{\gamma-1} \frac{dT_t}{T_t} \quad (4.18)$$

which can now be integrated between the inlet and exit of the compressor to yield

$$\frac{p_{t3}}{p_{t2}} = \pi_c = \left(\frac{T_{t3}}{T_{t2}} \right)^{\frac{\gamma e_c}{\gamma-1}} = (\tau_c)^{\frac{\gamma e_c}{\gamma-1}} \quad (4.19)$$

To express the compressor total temperature ratio in terms of compressor pressure ratio and polytropic efficiency, Equation 4.19 can be rewritten as

$$\tau_c = \pi_c^{\frac{\gamma-1}{\gamma e_c}} \quad (4.20)$$

The presence of e_c in the denominator of the above exponent (Equation 4.20) causes the exponent of π_c to be greater than its isentropic exponent (which is $(\gamma - 1)/\gamma$), therefore,

$$\tau_{c,\text{real}} > \tau_{c,\text{isentropic}} \quad \text{or} \quad T_{t3} > T_{t3s} \quad (4.21)$$

as noted earlier (Figure 4.6). The physical argument for higher actual T_t than the isentropic T_t (to achieve the same compressor pressure ratio) can be made on the grounds that *lost work* to overcome the irreversibility in the real process (friction, shock) is converted into heat, a higher exit T_t is reached in a real machine due to dissipation. On the contrary, for a given compressor pressure ratio π_c , an ideal compressor consumes less power than an actual compressor (the factor being η_c , as defined earlier). Again, the absence of dissipative mechanisms, leading to lost work, is cited as the reason for a reversible flow machine to require less power to run.

Now, to relate the two types of compressor efficiency description, e_c and η_c , we may substitute Equation 4.20 into Equation 4.13, to get

$$\eta_c = \frac{\pi_c^{\frac{\gamma-1}{\gamma}} - 1}{\tau_c - 1} = \frac{\pi_c^{\frac{\gamma-1}{\gamma}} - 1}{\pi_c^{\frac{\gamma-1}{\gamma e_c}} - 1} \quad (4.22)$$

Equation 4.22 is plotted in Figure 4.7.

The compressor adiabatic efficiency η_c is a function of compressor pressure ratio, while the polytropic efficiency is independent of it. Consequently, in a cycle analysis, we usually assume the polytropic efficiency e_c as the figure of merit for a compressor (and turbine) and then we can maintain e_c as constant in our engine off-design analysis. Typical values for the polytropic efficiency in modern compressors are in the range 88–92%.

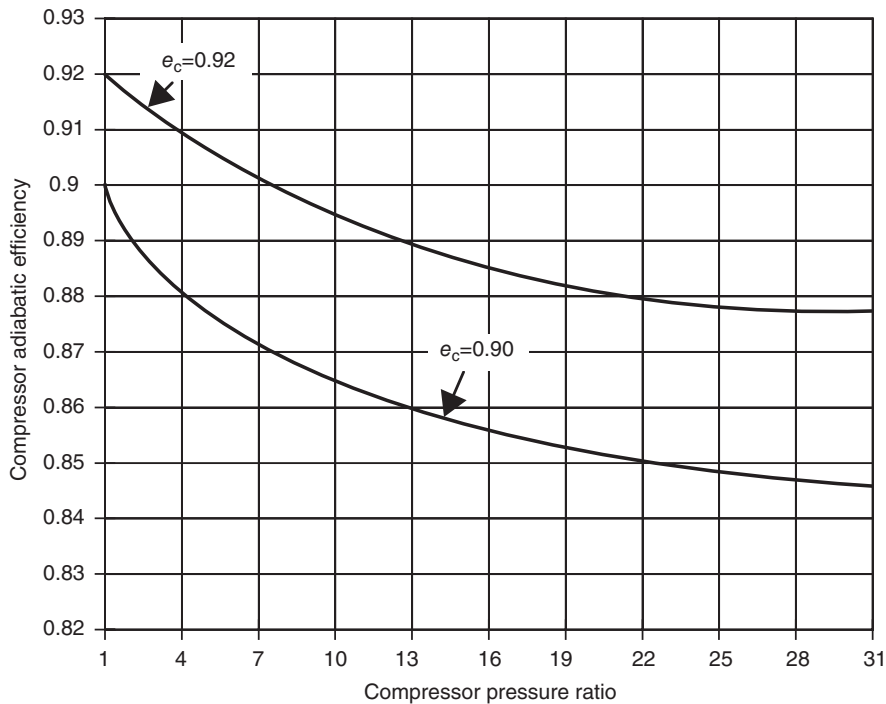
So far, we have studied the thermodynamics of the mechanical compression through the stagnation states of the working medium. It is also instructive to examine the static states of the gas in a compressor as well. The mental connection between these states will help us with the fluid dynamics of the compressors. Figure 4.8 is basically an elaborate version of the earlier Figure 4.6, to which we have added the static states of the gas at the inlet and exit of the compressor. These states, that is, the local stagnation and static states, when plotted on the h - s diagram, are distanced from each other only by the amount of local (specific) kinetic energy $V^2/2$ and on the same isentrope.

The flow velocity at the compressor inlet, V_2 , is nearly the same as the fluid velocity at the compressor exit, V_3 , by design. This explains why the vertical gap shown in Figure 4.8, between the static and stagnation states at 2 and 3 is nearly the same, that is,

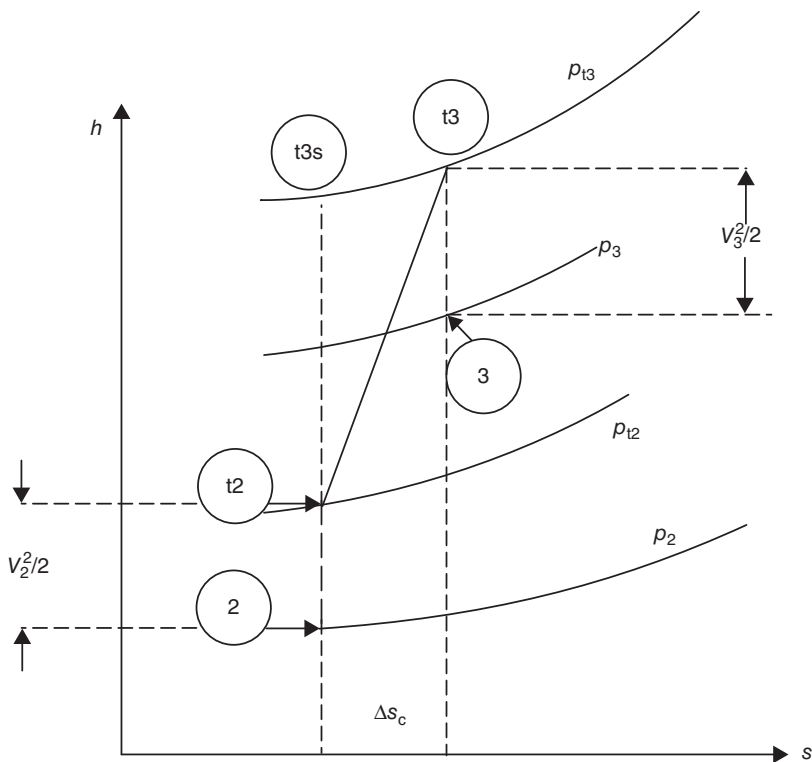
$$V_2^2/2 \approx V_3^2/2 \quad (4.23)$$

This design philosophy, that is, $V_2 = V_3$, is a part of the so-called constant through flow assumption often used in compressor aerodynamics. We will return to this topic, in detail, in Chapter 8.

■ FIGURE 4.7
Variation of
compressor adiabatic
efficiency with the
pressure ratio and
polytropic efficiency



■ FIGURE 4.8
Static and stagnation
states at the
compressor inlet and
exit on an $h-s$ diagram



In summary, we have learned that

- a real compressor flow may be considered adiabatic, that is, $Q_{\text{compressor}} \approx 0$
- the energy transfer to the fluid due to the shaft in a compressor is several orders of magnitude higher than any heat transfer that takes place through the casing, thus heat transfer is neglected
- viscous dissipation in the wall boundary layer and shocks account for the sources of irreversibility in a compressor
- there are two figures of merit that describe the compressor efficiency, one is the adiabatic compressor efficiency η_c (sometimes referred to as “isentropic” efficiency) and the second is the polytropic or small-stage efficiency e_c
- the two compressor efficiencies are interrelated, that is, $\eta_c = \eta_c(\pi_c, e_c)$
- the compressor polytropic efficiency is independent of compressor pressure ratio π_c
- the compressor adiabatic efficiency is a function of π_c and decreases with increasing pressure ratio
- to achieve a high-pressure ratio in a compressor, multistage and multispool configurations are needed
- in a gas turbine engine, the compressor power is derived from a shaft that is connected to a turbine.

EXAMPLE 4.2

A multistage axial-flow compressor has a mass flow rate of 50 kg/s and a total pressure ratio of 35. The compressor polytropic efficiency is $e_c = 0.90$. The inlet flow condition to the compressor is described by $T_{12} = 288$ K and $p_{12} = 100$ kPa. Assuming the flow in the compressor is adiabatic, and constant gas properties throughout the com-

pressor are assumed, i.e., $\gamma = 1.4$ and $c_p = 1004$ J/kg · K, calculate

- (a) compressor exit total temperature T_{13} in K
- (b) compressor adiabatic efficiency η_c
- (c) compressor shaft power $\dot{\varphi}_c$ in MW

SOLUTION

Following Equation 4.20, we relate compressor total temperature and pressure ratio via polytropic efficiency,

$$\tau_c = \pi_c^{\frac{\gamma-1}{\gamma e_c}} = (35)^{0.31746} \cong 3.0916$$

Therefore, the exit total temperature is $T_{13} = 3.0916 T_{12} = 3.0916(288 \text{ K}) \cong 890.4 \text{ K}$.

Compressor adiabatic efficiency is related to the polytropic efficiency and compressor pressure ratio, via Equation 4.13

$$\eta_c = \frac{\pi_c^{\frac{\gamma-1}{\gamma}} - 1}{\tau_c - 1} = \frac{35^{0.2857} - 1}{3.0916 - 1} \approx 0.8422$$

Therefore, compressor adiabatic efficiency is $\eta_c \cong 84.22\%$.

Compressor shaft power is proportional to the mass flow rate (i.e., the size of the compressor) as well as the total enthalpy rise across the compressor, according to

$$\begin{aligned} \dot{\varphi}_c &= \dot{m}(h_{13} - h_{12}) = \dot{m}c_p(T_{13} - T_{12}) \\ &= (50 \text{ kg/s})(1004 \text{ J/kg} \cdot \text{K})(890.4 - 288) \text{ K} \\ &\approx 30.24 \text{ MW} \end{aligned}$$

Therefore the shaft power delivered to the compressor is $\dot{\varphi}_c \approx 30.24 \text{ MW}$

4.3.1.3 The Burner. In the combustor, the air is mixed with the fuel and a chemical reaction ensues which is *exothermic*, that is, it results in a heat release. The ideal burner is considered to behave like a reversible heater, which in the combustion context, means very slow burning, $M_b \approx 0$, and with no friction acting on its walls. Under such circumstances, the total pressure remains conserved.

In a real combustor, due to wall friction, turbulent mixing and chemical reaction at finite Mach number, the total pressure drops, that is,

$$\pi_b = \frac{P_{t4}}{P_{t3}} < 1 \quad \text{“real combustion chamber”} \quad (4.24)$$

$$\pi_b = 1 \quad \text{“ideal combustion chamber”} \quad (4.25)$$

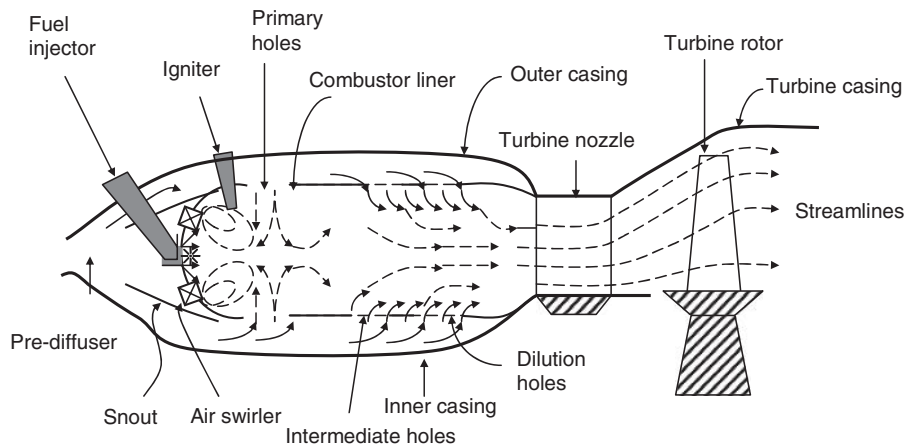
Kerrebrock gives an approximate expression for π_b in terms of the average Mach number of the gas in the burner, M_b , as

$$\pi_b \approx 1 - \epsilon \frac{\gamma}{2} M_b^2 \quad \text{where } 1 < \epsilon < 2 \quad (4.26)$$

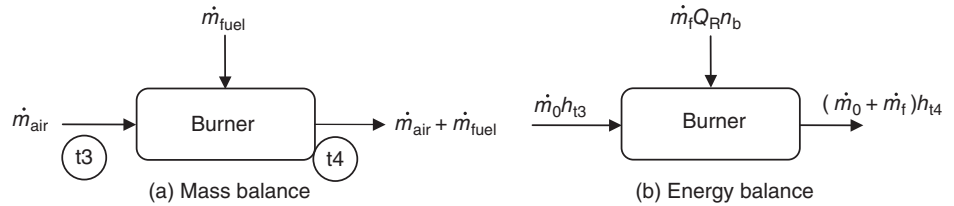
The total pressure loss in a burner is then proportional to the average dynamic pressure of the gases inside the burner, that is, $\propto \gamma/2 M_b^2$, where the proportionality coefficient is ϵ . Assuming an average Mach number of gases of 0.2 and $\epsilon = 2$, we get $\pi_b \approx 0.95$ (for a $\gamma \approx 1.33$). This formula is obviously not valid for supersonic combustion throughflows, rather it points out the merits of *slow* combustion in a conventional burner. A schematic diagram of a combustion chamber, and its essential components, is shown in Figure 4.9.

A preliminary discussion of the components of the combustion chamber is useful at this time. The inlet diffuser decelerates the compressor discharge flow to a Mach number of about 0.2–0.3. The low-speed flow will provide an efficient burning environment in the combustor. Mixing improvement with the fuel in the combustor primary zone is achieved via the air swirler. A recirculation zone is created that provides the necessary stability in the primary combustion zone. To create a fuel-rich environment in the primary zone to sustain combustion, a large percentage of air is diverted around a dome-like structure. The

■ **FIGURE 4.9**
Components of a conventional combustion chamber and the first turbine stage



■ FIGURE 4.10
Block diagram of a
burner with mass and
energy balance



airflow that has bypassed the burner primary zone will enter the combustor as the cooling flow through a series of cooling holes (as shown). The fuel-air mixture is ignited in the combustor primary zone via an igniter properly positioned in the dome area.

For the purposes of *cycle analysis*, a combustor flow is analyzed only at its inlet and outlet. Thus, we will not consider the details of combustion processes such as atomization, vaporization, mixing, chemical reaction, and dilution in the cycle analysis phase. Also, we do not consider pollutant formation and the means of reducing it in this chapter. We will address these issues in a later chapter dealing with combustor flow and design considerations. Obviously, with the details of flow and reaction omitted, we need to make assumptions regarding the loss of total pressure and burner efficiency in the cycle analysis only. A block diagram representation of a combustor, useful in cycle analysis, is shown in Figure 4.10. Figures 4.10a and 4.10b are the steady-state mass and the energy balance applied to the combustion chamber, that is,

$$\dot{m}_4 = \dot{m}_0 + \dot{m}_f = \dot{m}_0(1 + f) \quad (4.27)$$

where, f is the fuel-to-air ratio and $f \equiv \frac{\dot{m}_f}{\dot{m}_0}$. Using the energy balance in Figure 4.10b gives

$$\dot{m}_0 h_{t3} + \dot{m}_f Q_R \eta_b = (\dot{m}_0 + \dot{m}_f) h_{t4} = \dot{m}_0(1 + f) h_{t4} \quad (4.28)$$

The fuel is characterized by its *energy content per unit mass*, that is, the amount of thermal energy inherent in the fuel, capable of being released in a chemical reaction. This parameter is heat of reaction and is given the symbol Q_R . The unit for this parameter is energy/mass, which in the metric system is kJ/kg and in the British system of units is BTU/lbm. In an actual combustion chamber, primarily due to volume limitations, the entirety of the Q_R cannot be realized. The fraction that can be realized is called *burner efficiency* and is given the symbol η_b . Therefore,

$$\eta_b \equiv \frac{Q_{R, \text{Actual}}}{Q_{R, \text{Ideal}}} \quad (4.29)$$

The ideal heat of reaction, or heating value of typical hydrocarbon fuels, to be used in our cycle analysis is

$$Q_R = 42,000 \text{ kJ/kg} \quad (4.30a)$$

or

$$Q_R = 18,000 \text{ BTU/lbm} \quad (4.30b)$$

However, the most energetic fuel is the hydrogen, which is capable of releasing roughly three times the energy of typical hydrocarbon fuels per unit mass, that is,

$$Q_R = 127,500 \text{ kJ/kg} \quad (4.30c)$$

or

$$Q_R = 55,400 \text{ BTU/lbm} \quad (4.30d)$$

Consistent with the theory of *no free lunch*, we need to note the drawbacks of a fuel such as hydrogen. The low-molecular weight of hydrogen makes it the lightest fuel (with a density ratio of about 1/10 of typical hydrocarbon fuels, such as octane). This implies a comparatively very large volume requirement for the hydrogen fuel. We may want to think of this as *volumetric efficiency* of the hydrogen is the lowest of all fuels. Secondly, hydrogen in liquid form is cryogenic, which means a very low boiling point temperature, that is, -423°F or 20 K at ambient pressure. The cryogenic aspect of hydrogen requires thermally insulated fuel tanks, fuel lines, valves, and the associated weight penalty. Therefore, due to space limitations and system requirement weight penalties on board conventional atmospheric-flight aircraft, conventional hydrocarbon fuels are preferred over hydrogen. An exception to this is found in rocketry and hypersonic airbreathing propulsion where the regenerative cooling of the engine components requires a cryogenic fuel such as hydrogen to withstand the thermal loads of aerodynamic heating.

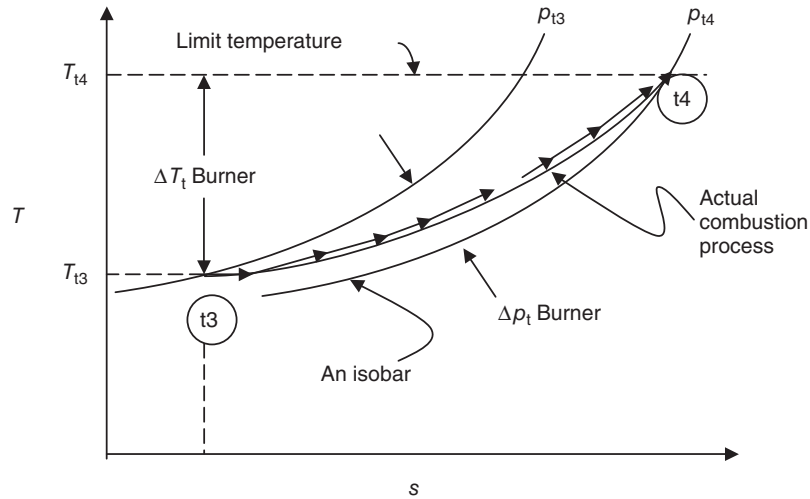
Typically in modern gas turbine engines, the burner efficiency can be as high as 98–99%. In a cycle analysis, we need to make assumptions about the loss parameters in every component, which in a combustion chamber are $\pi_b < 1$ and $\eta_b < 1$. The real and ideal combustion process can be depicted on a T - s diagram, which later will be used to perform cycle analysis. Figure 4.11 shows the burner thermodynamic process on a T - s diagram.

The isobars p_{t3} and p_{t4} drawn at the entrance and exit of the combustor in Figure 4.11, clearly show a total pressure drop in the burner, $\Delta p_{t, \text{burner}}$. The maximum temperature limit T_{t4} is governed by the level of cooling technology, material selection, and the protective thermal coating used in the turbine. Typical current values for the maximum T_{t4} are about 3200 – $3,600^\circ\text{R}$ or 1775 – $2,000 \text{ K}$. Another burner parameter is the temperature rise ΔT_t across the combustion chamber, as shown in Figure 4.11. The thermal power invested in the engine (by the fuel) is proportional to the temperature rise across the combustor, that is, it is nearly equal to $\dot{m}_0 c_p (\Delta T_t)_{\text{burner}}$.

The application of energy balance across the burner, that is, Equation 4.28, will yield the fuel-to-air ratio f as the only unknown parameter. To derive an expression for the fuel-to-air ratio, we will divide Equation 4.28 by \dot{m}_0 , the air mass flow rate, to get

$$h_{t3} + fQ_R\eta_b = (1 + f)h_{t4} \quad (4.31)$$

■ **FIGURE 4.11**
Actual flow process in
a burner (note total
pressure loss Δp_t across
the burner)



The unknown parameter f can be isolated and expressed as

$$f = \frac{h_{t4} - h_{t3}}{Q_R \eta_b - h_{t4}} \quad (4.32)$$

Knowing the fuel property Q_R , assuming burner efficiency η_b , and having specified a turbine inlet temperature T_{t4} , the denominator of Equation 4.32 is fully known. The compressor discharge temperature T_{t3} is established via compressor pressure ratio, efficiency, and inlet condition, as described in the compressor section and in Equation 4.19, which renders the numerator of Equation 4.32 fully known as well. Therefore, application of energy balance to a burner usually results in the establishment of fuel-to-air ratio parameter f . It is customary to express Equation 4.32 in terms of nondimensional parameters, by dividing each term in the numerator and denominator by the flight static enthalpy h_0 to get

$$f = \frac{\frac{h_{t4}}{h_0} - \frac{h_{t3}}{h_0}}{\frac{Q_R \eta_b}{h_0} - \frac{h_{t4}}{h_0}} = \frac{\tau_\lambda - \tau_r \tau_c}{\frac{Q_R \eta_b}{h_0} - \tau_\lambda} \quad (4.33)$$

where we recognize the product $\tau_r \tau_c$ as h_{t3}/h_0 , and τ_λ as the cycle thermal limit parameter h_{t4}/h_0 .

In summary, we learned that

- the fuel is characterized by its heating value Q_R (maximum releasable thermal energy per unit mass)
- the burner is characterized by its efficiency η_b , and its total pressure ratio π_b
- burning at finite Mach number, frictional losses on the walls and turbulent mixing are identified as the sources of irreversibility, that is, losses, in a burner

- the fuel-to-air ratio f and the burner exit temperature T_{t4} are the thrust control/engine design parameters
- the application of the energy balance across the burner yields either f or T_{t4} .

EXAMPLE 4.3

A gas turbine combustor has inlet condition $T_{t3} = 800$ K, $p_{t3} = 2$ MPa, air mass flow rate of 50 kg/s, $\gamma_3 = 1.4$, $c_{p3} = 1004$ J/kg · K.

A hydrocarbon fuel with ideal heating value $Q_R = 42,000$ kJ/kg is injected in the combustor at a rate of 1 kg/s. The burner efficiency is $\eta_b = 0.995$ and the total pressure at the combustor exit is 96% of the inlet total pressure,

i.e., combustion causes a 4% loss in total pressure. The gas properties at the combustor exit are $\gamma_4 = 1.33$ and $c_{p4} = 1156$ J/kg · K. Calculate

- fuel-to-air ratio f
- combustor exit temperature T_{t4} in K and p_{t4} in MPa

SOLUTION

The air and fuel flow rates are specified at 50 and 1 kg/s, respectively, in the problem, therefore, $f = 1/50 = 0.02$ or 2%.

We calculate combustor exit temperature by energy balance,

$$\dot{m}_0 h_{t3} + \dot{m}_f Q_R \eta_b = (\dot{m}_0 + \dot{m}_f) h_{t4} = \dot{m}_0 (1 + f) h_{t4}$$

Therefore

$$h_{t3} + f Q_R \eta_b = (1 + f) h_{t4}$$

$$T_{t4} = \frac{(c_{p3}/c_{p4})T_{t3} + f Q_R \eta_b / c_{p4}}{1 + f}$$

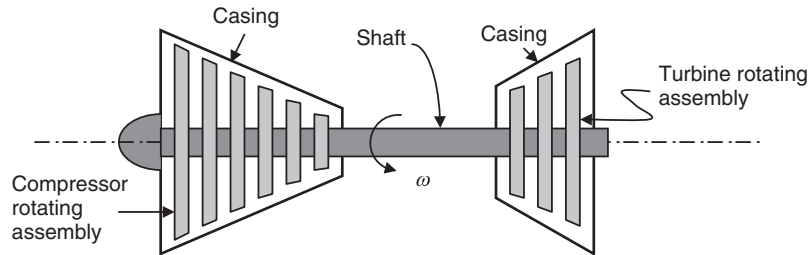
$$= \frac{(1004/1156) 800 \text{ K} + 0.02 (42000 \text{ kJ/kg}) (0.995) / 1.156 \text{ kJ/kg} \cdot \text{K}}{1.02}$$

Therefore, combustor exit temperature is $T_{t4} \cong 1390$ K and $p_{t4} = 0.96(2 \text{ MPa}) = 1.92 \text{ MPa}$

4.3.1.4 The Turbine. The high pressure and temperature gas that leaves the combustor is directed into a turbine. The turbine may be thought of as a *valve* because on one side it has a high-pressure gas and on the other side it has a low-pressure gas of the exhaust nozzle or the tailpipe. Therefore, the first *valve*, that is, the throttle station, in a gas turbine engine is at the turbine. The throat of an exhaust nozzle in a supersonic aircraft is the second and final throttle station in an engine. Thus, the flow process in a turbine (and exhaust nozzle) involves significant (static) pressure drop and, in harmony with it, the (static) temperature drop, which is called *flow expansion*. The flow expansion produces the necessary power for the compressor and the propulsive power for the aircraft. The turbine is connected to the compressor via a common shaft, which provides the shaft power to the compressor (Figure 4.12). In drawing an analogy, we can think of the expansion process in a gas turbine engine as the counterpart of *power stroke* in an intermittent combustion engine. However, in a turbine, the power transmittal is continuous.

Due to high temperatures of the combustor exit flow, the first few stages of the turbine, that is, the high-pressure turbine (HPT), need to be cooled. The coolant is the air bleed from the compressor, which may be bled from different compression stages, for example, between the low- and high-pressure compressor and at the compressor exit. It has been customary, however, to analyze an *uncooled* turbine in the preliminary cycle analysis, followed by an analysis of the cycle with cooling effects in the turbine and

■ **FIGURE 4.12**
Common shaft in a gas generator connects the compressor and turbine (ω is the shaft rotational speed)

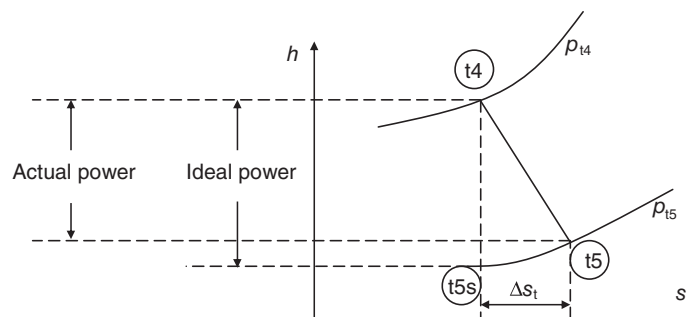


the exhaust nozzle. Other cooling media, such as water, have been used in stationary gas turbine power plants. However, in the design-to-weight environment of an aircraft carrying extra water to cool the turbine blades is not feasible. A cooling solution, which uses the engine cryogenic fuel, such as hydrogen or methane, as the coolant to cool the engine and aircraft components is called *regenerative cooling* and has proven its effectiveness in liquid propellant chemical rocket engines for decades.

A real flow process in an uncooled turbine involves irreversibilities such as frictional losses in the boundary layer, tip clearance flows, and shock losses in transonic turbine stages. The viscous dominated losses, that is, boundary layer separation, reattachment, and tip vortex flows, are concentrated near the end walls, thus a special attention in turbine flow optimization is made on the *end-wall* regions. We will address the end wall losses and treatments in the turbomachinery chapters. Another source of irreversibility in a real turbine flow is related to the cooling losses. Coolant is typically injected from the blade attachment (to the hub or casing) into the blade, which provides internal convective cooling and usually external film cooling on the blades. The turbulent mixing associated with the coolant stream and the hot gases is the primary mechanism for (the turbine stage) cooling losses. We will examine the question of turbine cooling and cycle thermal efficiency later in this chapter.

The thermodynamic process for an uncooled turbine flow may be shown in an h - s diagram (Figure 4.13). The actual expansion process in the turbine is depicted by the solid line connecting the total (or stagnation) states t_4 and t_5 (Figure 4.13). The isentropically reached exit state t_{5s} represents the ideal, loss-free flow expansion in the turbine to the same backpressure p_{t5} . The relative height, on the enthalpy scale in Figure 4.13, between the inlet total and outlet total condition of the turbine represents the power production

■ **FIGURE 4.13**
Expansion process in an uncooled turbine (note the entropy rise across the turbine, Δs_t)



potential (i.e., ideal) and the actual power produced in a turbine. The ratio of these two heights is called the turbine adiabatic efficiency η_t , that is,

$$\mathcal{P}_{t,\text{actual}} = \dot{m}_t(h_{t4} - h_{t5}) = \dot{m}_t \Delta h_{t,\text{actual}} \quad (4.34)$$

$$\mathcal{P}_{t,\text{ideal}} = \dot{m}_t(h_{t4} - h_{t5s}) = \dot{m}_t \Delta h_{t,\text{isentropic}} \quad (4.35)$$

$$\eta_t \equiv \frac{h_{t4} - h_{t5}}{h_{t4} - h_{t5s}} = \frac{\Delta h_{t,\text{actual}}}{\Delta h_{t,\text{isentropic}}} \quad (4.36)$$

In Equations 4.34 and 4.35, the turbine mass flow rate is identified as \dot{m}_t , which accounts for the air and fuel mass flow rate that emerge from the combustor and expand through the turbine, that is,

$$\dot{m}_t = \dot{m}_0 + \dot{m}_f = (1 + f)\dot{m}_0 \quad (4.37)$$

The numerator in Equation 4.36 is the actual power produced in a *real uncooled turbine*, and the denominator is the *ideal* power that in a reversible and adiabatic turbine could be produced. If we divide the numerator and denominator of Equation 4.36 by h_{t4} , we get

$$\eta_t = \frac{1 - T_{t5}/T_{t4}}{1 - T_{t5s}/T_{t4}} \quad (4.38)$$

Since the thermodynamic states “t5s” and “t4” are on the same isentrope, the temperature and pressure ratios are then related via the isentropic formula, that is,

$$\frac{T_{t5s}}{T_{t4}} = \left(\frac{p_{t5s}}{p_{t4}} \right)^{\frac{\gamma-1}{\gamma}} = \left(\frac{p_{t5}}{p_{t4}} \right)^{\frac{\gamma-1}{\gamma}} = \pi_t^{\frac{\gamma-1}{\gamma}} \quad (4.39)$$

Therefore, turbine adiabatic efficiency may be expressed in terms of the turbine total pressure and temperature ratios as

$$\eta_t = \frac{1 - \tau_t}{1 - \pi_t^{\frac{\gamma-1}{\gamma}}} \quad (4.40)$$

We may also define a *small-stage* efficiency for a turbine, as we did in a compressor, and call it the turbine polytropic efficiency e_t . For a small expansion, representing a small stage, we can replace the finite jumps, that is, Δs , with incremental step d in Equation 4.36 and write

$$e_t \equiv \frac{dh_t}{dh_{ts}} = \frac{dh_t}{\frac{dp_t}{\rho_t}} \quad (4.41)$$

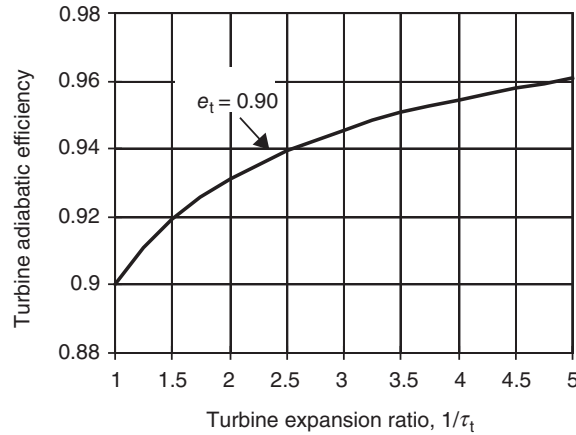
Expressing enthalpy in terms of temperature and specific heat at constant pressure as $dh_t = c_p dT_t$, which is suitable for a perfect gas, and simplifying Equation 4.41 similar to the compressor section, we get

$$\tau_t = \pi_t^{\frac{(\gamma-1)e_t}{\gamma}} \quad \text{or} \quad \pi_t = \tau_t^{\frac{\gamma}{(\gamma-1)e_t}} \quad (4.42)$$

$$\tau_t \equiv T_{t5}/T_{t4} \quad (4.43)$$

$$\pi_t \equiv p_{t5}/p_{t4} \quad (4.44)$$

■ **FIGURE 4.14**
Variation of turbine
adiabatic efficiency η_t
with the inverse of
turbine expansion ratio
 $1/\tau_t$



We note that in Equation 4.42, in the limit of e_t approaching 1, that is, isentropic expansion, we will recover the isentropic relationship between the temperature and pressure ratio, as expected. Replacing π_t in Equation 4.39 by its equivalent expression (from Equation 4.42), we derive a relation between the two types of turbine efficiencies, η_t and e_t , as

$$\eta_t = \frac{1 - \tau_t}{1 - \tau_t^{1/e_t}} \quad (4.45)$$

Equation 4.45 is plotted in Figure 4.14. For a small-stage efficiency of 90%, that is, $e_t = 0.90$, the turbine adiabatic efficiency η_t grows with the inverse of turbine expansion parameter $1/\tau_t$. This may initially defy logic that how is it possible to become more efficient if we *add* more stages to the turbine? Wouldn't it add to losses? The opposite of this trend occurred in the compressor, that is, compressor adiabatic efficiency for a finite-size compressor *was* lower than the efficiency of a small-stage compressor (Figure 4.7). The explanation is that the energy transfer occurs from the fluid to the rotor in the turbine; therefore, more stages offer more opportunities to convert fluid energy into shaft power. The opposite happens in a compressor, that is, the compressor stages *consume* power, which means that the additional stages add losses to the process. In simple terms, the turbine stages may be thought of as *opportunities* and compressor stages as the *burden*.

The temperature ratio parameter τ_t across the turbine is established via a power balance between the turbine, compressor, and other shaft power extraction (e.g., electric generator) on the gas generator. Let us first consider the power balance between the turbine and compressor in its simplest form and then try to build on the added parameters. Ideally, the compressor absorbs all the turbine shaft power, that is,

$$\dot{\varphi}_t = \dot{\varphi}_c \quad (4.46a)$$

$$\dot{m}_0(1+f)(h_{t4} - h_{t5}) = \dot{m}_0(h_{t3} - h_{t2}) \quad (4.46b)$$

which simplifies to the following nondimensional form

$$(1+f)\tau_\lambda(1 - \tau_t) = \tau_t(\tau_c - 1) \quad (4.46c)$$

The only unknown in the above equation is τ_t , as all other parameters either flow from upstream components, for example, the combustor will provide f , the compressor produces τ_c , and so on, or are design parameters such as τ_λ or τ_r . Hence, the turbine expansion parameter τ_t can be written as

$$\tau_t = 1 - \frac{\tau_r(\tau_c - 1)}{(1 + f)\tau_\lambda} \quad (4.46d)$$

Next, we consider the practical issue of hydrodynamic (frictional) losses in (radial) bearings holding the shaft in place and provide dynamic stability under operating conditions to the rotating assemblies of turbine and compressor. Therefore, a small fraction of the turbine power output is dissipated through viscous losses in the bearings, that is,

$$\wp_t = \wp_c + \Delta\wp_{\text{bearings}} \quad (4.47)$$

where $\Delta\wp_{\text{bearings}}$ is the power loss due to bearings. In addition, an aircraft has electrical power needs for its flight control system and other aircraft subsystems, which requires tapping into the turbine shaft power. Consequently, the power balance between the compressor and turbine should account for the electrical power extraction, which usually accompanies the gas generator, that is,

$$\wp_t = \wp_c + \Delta\wp_{\text{bearing}} + \Delta\wp_{\text{electric generator}} \quad (4.48a)$$

$$\wp_c = \wp_t - \Delta\wp_{\text{bearing}} - \Delta\wp_{\text{electric generator}} \quad (4.48b)$$

In a simple cycle analysis, it is customary to lump all power dissipation and power extraction terms into a single *mechanical efficiency* parameter η_m that is multiplied by the turbine shaft power, to derive the compressor shaft power, that is,

$$\wp_c = \eta_m \wp_t \quad (4.49)$$

where η_m is the mechanical efficiency parameter that needs to be specified a priori, for example, $\eta_m = 0.95$.

Therefore, an uncooled turbine is assumed to be adiabatic.

$$\wp_t = \dot{m}_0(1 + f)(h_{t4} - h_{t5})$$

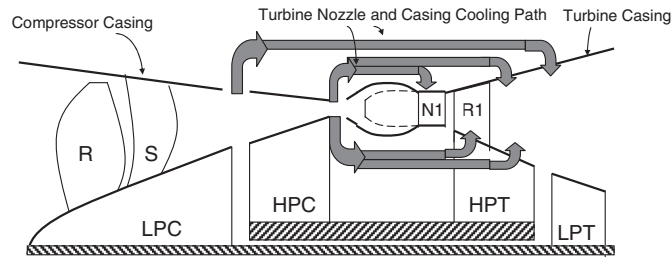
$$\pi_t \equiv (\rho_{t5} / \rho_{t4})$$

$$\tau_t \equiv T_{t5} / T_{t4}$$

$$\wp_c = \eta_m \wp_t$$

To cool the high-pressure turbine stages, a small fraction of compressor air can be diverted from various stages of the compression. Engine cooling is essentially a *pressure-driven* process, which calls for a pressure scheduling of the coolant to achieve the highest cooling efficiency. For example, to cool the first nozzle and the first rotor in a turbine,

■ **FIGURE 4.15**
Two-spool gas turbine engine with two stations of compressor bleed for cooling purposes (LPC: Low-pressure compressor, HPC: High-pressure compressor, HPT: High-pressure turbine, LPT: Low-pressure turbine, R: Rotor, S: Stator, N: Nozzle)

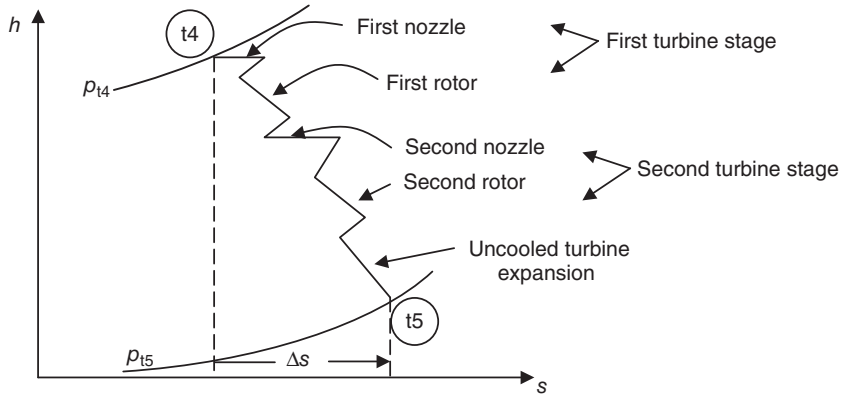


we need to tap the compressor exit air, as it has the *right* pressure. Earlier stages of the compressor have not yet developed the necessary pressure to overcome downstream pressure in the high-pressure end of a turbine. To cool the medium-pressure turbine stages, we need to divert compressor air from the medium-pressure compressor. We could use higher pressure compressor exit air as well but the extra compression work we spent compressing the gas to the exit condition is essentially a wasted effort, that is, energy loss for the cycle. Therefore, the problem of *pressure matching* between the coolant stream and the hot gas in a turbine is real and significant. The consequence of a mismatch is either inadequate cooling flow in a turbine blade with even a possibility of a *reverse flow* of hot gases into the cooling channels or the need for excessive throttling of the coolant stream and associated cycle losses. Figure 4.15 shows possible coolant extraction in the compressor for turbine cooling.

We can simplify the investigation of the thermodynamics of cooled turbine stages significantly by assuming that each blade row coolant is discharged at the blade row exit, that is, trailing edge ejection. This simplifies the thermodynamics as we consider *dumping* the entire coolant used in a given blade row at the trailing edge of the blades and then apply conservation laws to the coolant–hot gas mixing process. This approach avoids the discrete coolant–hot gas mixing, which may be distributed over the suction and pressure surfaces of the blade row, as in film-cooled blades. Application of the energy equation to the coolant–hot gas mixing process will result in a lower mixed-out temperature for the hot gas. Consequently, the hot gas stream will experience a reduced entropy state after mixing with the coolant. In return, the coolant stream, which is heated by the hot gas, will experience an entropy rise, which according to the second law of thermodynamics is greater than the entropy reduction in the hot gas stream. The expansion process in a turbine with two cooled stages followed by an uncooled low-pressure turbine is depicted in an h – s diagram in Figure 4.16. The mixing process at the exit of each blade row is identified with negative entropy production, and the cooling path is roughly drawn in as a nearly constant pressure process. In contrast, the coolant stream will undergo a heating process from the blade and then through mixing with the hot gases in the turbine. The thermodynamic state of the coolant is shown in Figure 4.16.

The h – s diagram for the hot gas (shown in Figure 4.16) shows a constant h_t process for the first and second turbine nozzle. Constant total enthalpy indicates an adiabatic process with no mechanical energy exchange. These two criteria are met in an uncooled turbine nozzle, which is stationary and consequently exchanges no mechanical energy with the fluid. Across the nozzle, due to frictional and shock losses, a total pressure drop is indicated in Figure 4.16. Regarding the blade cooling, however, we will introduce the entire blade row coolant at the blade row exit, as suggested earlier. The cooling process results in a lower total temperature of the mixture of hot and cold gas, as well as a total

■ **FIGURE 4.16**
h-s diagram for a turbine expansion with two cooled stages followed by an uncooled LPT (blade row exit mixing with the coolant is indicated by a negative Δs and a temperature drop)



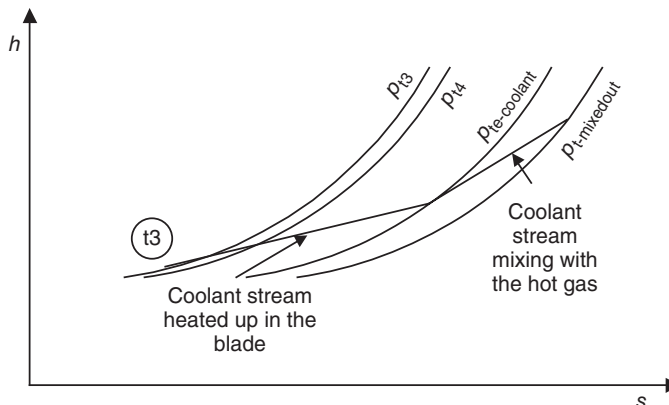
pressure drop due to turbulent mixing of the two streams. This process can be seen in Figure 4.17. The drop of total enthalpy across the rotor is proportional to the shaft power production by the rotor blade row. This shaft power may be written as

$$\dot{\mathcal{P}}_{\text{rotor}} = \tau_{\text{rotor}} \omega = \dot{m}_{\text{rotor}} \Delta h_t \quad (4.50)$$

The product of rotor torque τ and the angular speed ω of the rotor is the shaft power à la Newton. The irreversibility in the flow through the rotor is shown via a process involving entropy rise across the rotor in Figure 4.16. Again the flow expansion after the rotor is cooled off by the blade row coolant, which is injected at the blade row trailing edge and the process continues. To establish the mixed-out state of the coolant and the hot gas, we will apply the conservation principles, as noted earlier. The law of conservation of energy applied to a coolant stream of \dot{m}_c mass flow rate carrying a total enthalpy of $h_{t,c}$ mixing with a hot gas stream of \dot{m}_g with a total enthalpy of $h_{t,g}$ is written as

$$\dot{m}_c h_{t,c} + \dot{m}_g h_{t,g} = (\dot{m}_c + \dot{m}_g) h_{t,\text{mixed-out}} \quad (4.51)$$

■ **FIGURE 4.17**
h-s diagram of the coolant stream, first inside the blade then mixing with the hot turbine gas



where the only unknown is the mixed-out enthalpy state of the coolant-hot gas mixture, $h_{t,\text{mixed-out}}$. We can express the above equation in nondimensional form by dividing both sides by $\dot{m}_g h_{t,g}$, to get

$$\frac{h_{t,\text{mixed-out}}}{h_{t,g}} = \frac{1 + \frac{\dot{m}_c}{\dot{m}_g} \frac{h_{t,c}}{h_{t,g}}}{1 + \frac{\dot{m}_c}{\dot{m}_g}} \approx \left(1 - \frac{\dot{m}_c}{\dot{m}_g}\right) \left(1 + \frac{\dot{m}_c}{\dot{m}_g} \frac{h_{t,c}}{h_{t,g}}\right) \quad (4.52)$$

In Equation 4.52, two nondimensional parameters emerge that basically govern the energetics of a hot and a cold mixture. These parameters are

- $\frac{\dot{m}_c}{\dot{m}_g}$ the coolant mass fraction (typically $\ll 1$)
- $\frac{h_{t,c}}{h_{t,g}}$ cold-to-hot total enthalpy ratio.

We have also used a mathematical approximation in Equation 4.52, in the form of binomial expansion:

$$\frac{1}{1 + \varepsilon} \approx 1 - \varepsilon \quad (4.53)$$

where $\varepsilon \ll 1$ and the largest neglected term in the series is $O(\varepsilon^2)$.

The coolant stream experiences a total pressure drop in the cooling channels of the blade as a result of frictional losses and a total pressure drop as a result of turbulent mixing with the hot gas. The enthalpy-entropy diagram representing a coolant stream is depicted in Figure 4.17.

In summary we learned that

- the flow expansion in the turbine produces the needed shaft power for the compressor and other propulsion system or aircraft needs, for example, an electric generator
- there are two figures of merit in a turbine, which measure the extent of irreversibility in a turbine, η_t and e_t and they are related
- the gas expansion in an uncooled turbine is treated as adiabatic
- the frictional losses on the blades and the casing as well as any shock losses, in relative supersonic passages, are the sources of irreversibility in an uncooled turbine
- turbulent mixing losses between the coolant and the hot gas is an added source of irreversibility in a cooled turbine
- the turbine entry temperature T_{t4} is a design parameter that sets the stage for the turbine material and cooling requirements
- the power balance between the turbine, the compressor, and other known power drainage, establishes the turbine expansion ratio τ_t
- cooling of the high-pressure turbine is achieved through compressor air bleed that is injected through the blade root in the rotor and the casing for the turbine nozzle

- the turbine nozzle is choked (i.e., the throat Mach number is 1), over a wide operating range of the engine, and as such is the first *throttle station* of the engine.

EXAMPLE 4.4

Consider an uncooled gas turbine with its inlet condition the same as the exit condition of the combustor described in Example 4.3. The turbine adiabatic efficiency is 88%. The turbine produces a shaft power to drive the compressor and other accessories at $\dot{\varphi}_t = 45$ MW. Assuming that the gas properties in the turbine are the same as the burner exit in Example 4.3, calculate

- turbine exit total temperature T_{15} in K
- turbine polytropic efficiency, e_t
- turbine exit total pressure p_{15} in kPa
- turbine shaft power $\dot{\varphi}_t$ based on turbine expansion ΔT_t

SOLUTION

The turbine shaft power is proportional to the mass flow rate through the turbine, which from Example 4.3 is 51 kg/s (50 for air and 1 for fuel flow rate), as well the total enthalpy drop, i.e.,

$$\dot{\varphi}_t = \dot{m}_t(h_{t4} - h_{t5})$$

Therefore, we isolate h_{t5} from above equation to get

$$\begin{aligned} h_{t5} &= h_{t4} - \dot{\varphi}_t / \dot{m}_t = c_{p4} T_{t4} - 35 \times 10^6 / 51 \\ &= 1.156 \text{ kJ/kg} \cdot \text{K} (1390 \text{ K}) \\ &\quad - 45,000 \text{ kW} / 51 \text{ kg/s} \approx 724.5 \text{ kJ/kg} \end{aligned}$$

$$\begin{aligned} T_{15} &= h_{t5} / c_{p5} \\ &= (724.5 \text{ kJ/kg}) / (1.156 \text{ kJ/kg} \cdot \text{K}) \approx 626.7 \text{ K} \end{aligned}$$

Turbine polytropic efficiency e_t may be related to its adiabatic efficiency and τ_t via equation

$$\eta_t = \frac{1 - \tau_t}{1 - \tau_t^{1/e_t}}$$

The turbine expansion parameter $\tau_t = 626.7/1390 = 0.4509$; and if we isolate e_t from above equation we get

$$\begin{aligned} e_t &= \ln(\tau_t) / \ln[1 - (1 - \tau_t)/\eta_t] \\ &= \ln(0.4509) / \ln[1 - 0.5491/0.88] \approx 0.8144 \end{aligned}$$

We know that turbine pressure and temperature ratios are related by the polytropic efficiency via

$$\pi_t = \tau_t^{\frac{\gamma}{(\gamma-1)e_t}} = (0.4509)^{\frac{1.33}{0.33(0.8144)}} \approx 0.01941$$

The turbine exit total pressure is therefore $p_{t4} \cdot \pi_t$. We had found $p_{t4} = 1.92$ MPa in Example 4.3, therefore,

$$p_{15} = 0.01941(1.92 \text{ MPa}) = 37.26 \text{ kPa}$$

The turbine shaft power is the product of the turbine mass flow rate and the total enthalpy drop across the turbine, i.e.,

$$\begin{aligned} \dot{\varphi}_t &= \dot{m}_t c_{pt}(T_{t4} - T_{t5}) \\ &= 51 \text{ kg/s} (1156 \text{ J/kg} \cdot \text{K}) (1390 - 626.7) \text{ K} \approx 45 \text{ MW} \end{aligned}$$

EXAMPLE 4.5

Consider a turbine nozzle blade row with a hot gas mass flow rate of 50 kg/s and $h_{tg} = 1850$ kJ/kg. The nozzle blades are internally cooled with a coolant mass flow rate of 0.5 kg/s and $h_{tc} = 904$ kJ/kg as the coolant is ejected through the nozzle blades trailing edge. The coolant mixes

with the hot gas and causes a reduction in the mixed-out enthalpy of the gas. Calculate the mixed-out total enthalpy after the nozzle. Also for the $c_{p, \text{mixed-out}} = 1594$ J/kg · K, calculate the mixed-out total temperature.

SOLUTION

A simple energy balance between the mixed-out state and the hot and cold streams solves this problem, namely,

$$\begin{aligned}\dot{m}_c h_{t,c} + \dot{m}_g h_{t,g} &= (\dot{m}_c + \dot{m}_g) h_{t,\text{mixed-out}} \\ 50.5 \text{ kg/s} (h_{t,\text{mixed-out}}) &= 0.5 \text{ kg/s} (904 \text{ kJ/kg}) \\ &\quad + 50 \text{ kg/s} (1850 \text{ kJ/kg}) \\ &= 92,952 \text{ kW}\end{aligned}$$

$$\begin{aligned}h_{t,\text{mixed-out}} &= 92,952 \text{ kW}/50.5 \text{ kg/s} = 1840.6 \text{ kJ/kg} \\ T_{t,\text{mixed-out}} &= 1840.6 \text{ kJ/kg}/1.594 \text{ kJ/kg} \cdot \text{K} = 1154.7 \text{ K}\end{aligned}$$

EXAMPLE 4.6

Consider the internally cooled turbine nozzle blade row of Example 4.5. The hot gas total pressure at the entrance of the nozzle blade is $p_{t4} = 1.92 \text{ MPa}$, $c_{pg} = 1156 \text{ J/kg} \cdot \text{K}$, and $\gamma_g = 1.33$. The mixed-out total pressure at the exit of

the nozzle has suffered 2% loss due to both mixing and frictional losses in the blade row boundary layers. Calculate the entropy change $\Delta s/R$ across the turbine nozzle blade row.

SOLUTION

The hot gas total temperature is h_{tg}/c_{pg} , which for a $c_{pg} = 1156 \text{ J/kg} \cdot \text{K}$ is calculated to be $T_{tg} = [1850 \text{ kJ/kg}]/[1.156 \text{ kJ/kg} \cdot \text{K}] = 1600 \text{ K}$. This is the same temperature as T_{t4} at the entrance to the nozzle. The coolant total temperature is $T_{tc} = h_{tc}/c_{pc} = 904 \text{ kJ/kg}/1.04 \text{ kJ/kg} \cdot \text{K} = 900.4 \text{ K}$. Also, the mixed-out total pressure is 98% of the incoming (hot gas) total pressure, i.e., $p_{t,\text{mixed-out}} = 0.98 (1.92 \text{ MPa}) = 1.8816 \text{ MPa}$. We may use the Gibbs equa-

tion (assuming constant gas specific heats) to calculate the entropy change, namely,

$$\Delta s/R = \frac{\gamma_g}{\gamma_g - 1} \ln (T_{t,\text{mixed-out}}/T_{t4}) - \ln (p_{t,\text{mixed-out}}/p_{t4})$$

Upon substitution, we get

$$\Delta s/R \cong -1.297$$

The negative sign of entropy change is due to cooling.

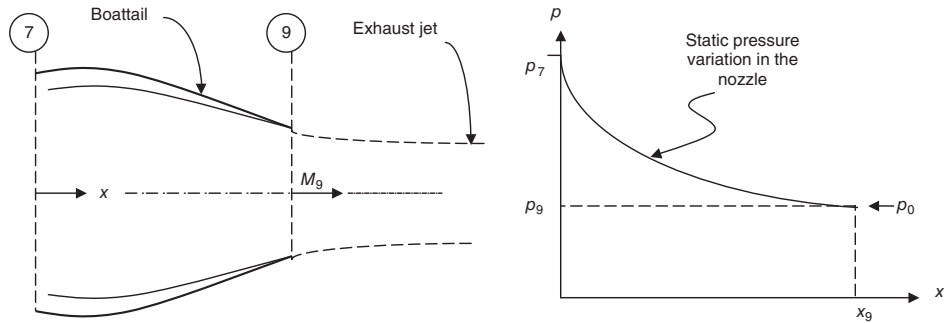
4.3.1.5 The Nozzle. The primary function of an aircraft engine exhaust system is to accelerate the gas efficiently. The nozzle parameter that is of utmost importance in *propulsion* is the gross thrust F_g . The expression we had earlier derived for the gross thrust was

$$F_g = \dot{m}_9 V_9 + (p_9 - p_0) A_9 \quad (4.54)$$

In this equation, the first term on the right-hand side is called the momentum thrust and the second term is called the pressure thrust. It is interesting to note that the nozzles produce a “signature,” typically composed of infrared radiation, thermal plume, smoke, and acoustic signatures, which are key design features of a stealth aircraft exhaust system in *addition* to the main propulsion requirement of the gross thrust.

As the fluid accelerates in a nozzle, the static pressure drops and hence a *favorable pressure gradient* environment is produced in the nozzle. This is in contrast to diffuser flows where an *adverse pressure gradient* environment prevails. Therefore, boundary layers are, by and large, well behaved in the nozzle and less cumbersome to treat than the inlet. For a subsonic exit Mach number, that is, $M_9 < 1$, the nozzle expansion process

■ FIGURE 4.18 Schematic drawing of a subsonic nozzle with its static pressure distribution



will continue all the way to the ambient pressure p_0 . This important result means that in subsonic streams, the static pressure inside and outside of the jet are the same. In fact, there is no mechanism for a pressure jump in a subsonic flow, which is in contrast to the supersonic flows where shock waves and expansion fans allow for static pressure discontinuity. We have depicted a convergent nozzle in Figure 4.18 with its exhaust stream (i.e., a jet) emerging in the ambient gas of static state (0). The outer shape of the nozzle is called a boattail, which affects the *installed performance* of the exhaust system. The external aerodynamics of the nozzle installation belongs to the propulsion system integration studies and does not usually enter the discussions of the *internal performance*, that is, the cycle analysis. However, we need to be aware that our decisions for the internal flow path optimization, for example, the nozzle exit-to-throat area ratio, could have adverse effects on the installed performance that may offset any gains that may have been accrued as a result of the internal optimization.

We have learned in aerodynamics that a convergent duct, as shown in Figure 4.18, causes flow acceleration in a subsonic stream to a maximum Mach number of 1, which can only be reached at the minimum area of the duct, namely at its exit. So we stipulate that for all subsonic jets, that is, $M_9 < 1$, there is a static pressure equilibrium in the exhaust stream and the ambient fluid, that is, $p_9 = p_0$. Let us think of this as the *Rule 1* in nozzle flow.

Rule 1 : If $M_{\text{jet}} < 1$, then $p_{\text{jet}} = p_{\text{ambient}}$

The expression “jet” in the above rule should not be confusing to the reader, as it relates to the flow that emerges from the nozzle. In that context, M_{jet} is the same as M_9 , and p_{ambient} is the same as p_0 . We recognize that not only it is entirely possible but also desirable for the sonic and supersonic jets to expand to the ambient static pressure as well. Such nozzle flows are called *perfectly expanded*. Actually, the nozzle gross thrust can be maximized if the nozzle flow is perfectly expanded. We state this principle here without proof, but we will address it again, and actually prove it, in the next chapters. Let us think of this as the *Rule 2* in nozzle flow.

Rule 2 :	If $p_{\text{jet}} = p_{\text{ambient}}$
then we have a perfectly expanded nozzle which results in $F_{g,\text{max}}$	

Here, the stipulation is only on the *static pressure match* between the jet exit and the ambient static pressure and not *perfect flow* inside the nozzle. A real nozzle flow experiences total pressure loss due to viscous dissipation in the boundary layer as well as shock waves, and yet it is possible for it to *perfectly expand* the gas to the ambient condition. Remembering compressible duct flows in aerodynamics, we are reminded that the exit pressure p_9 is a direct function of the nozzle area ratio $A_{\text{exit}}/A_{\text{throat}}$, which in our notation becomes A_9/A_8 , and the nozzle pressure ratio (NPR). Recalling the definition of NPR,

$$\text{NPR} \equiv \frac{p_{t7}}{p_0} \tag{4.55}$$

we will demonstrate a critical value of NPR will result in the choking condition at the nozzle throat, that is, $M_8 = 1.0$, when $\text{NPR} \geq (\text{NPR})_{\text{critical}}$. Let us think of this as *Rule 3* in convergent or convergent-divergent nozzle aerodynamics. These rules do not apply if the divergent section of a C–D nozzle becomes a subsonic a diffuser.

Rule 3 : If $\text{NPR} \geq (\text{NPR})_{\text{critical}}$
then the nozzle throat velocity is sonic (i.e., choked), $M_8 = 1.0$

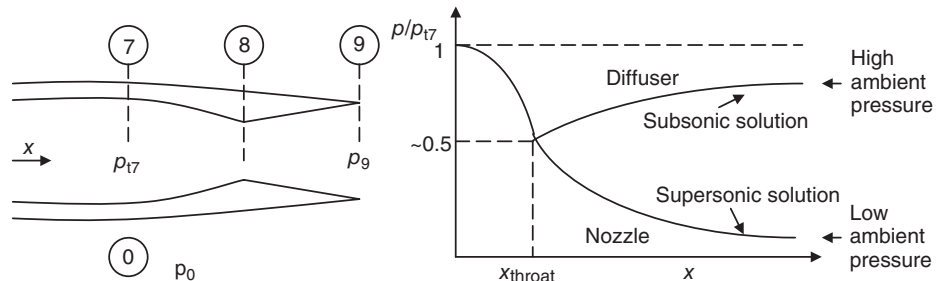
A schematic drawing of a convergent–divergent supersonic nozzle is shown in Figure 4.19.

The nozzle throat becomes choked at a static pressure of about 50% of the nozzle total pressure, that is, $p_{\text{throat}} \sim 1/2 p_{t7}$. This fact provides for an important *rule of thumb* in nozzle flows, which is definitely worth remembering. Let us consider this as *Rule 4*.

Rule 4 : If $\frac{p_{t7}}{p_0} \geq \sim 2$ then the nozzle throat can be choked, i.e., $M_8 = 1.0$

For example, a passage (or a duct) connecting a pressure vessel of about 30 psia pressure to a room of about 15 psia pressure will experience sonic speed at its minimum (orifice) area. As with any rules of thumb, Rule 4 is stated as an *approximation* and the exact value of the critical nozzle pressure ratio depends on the nozzle expansion efficiency, that is, the extent of losses in the nozzle.

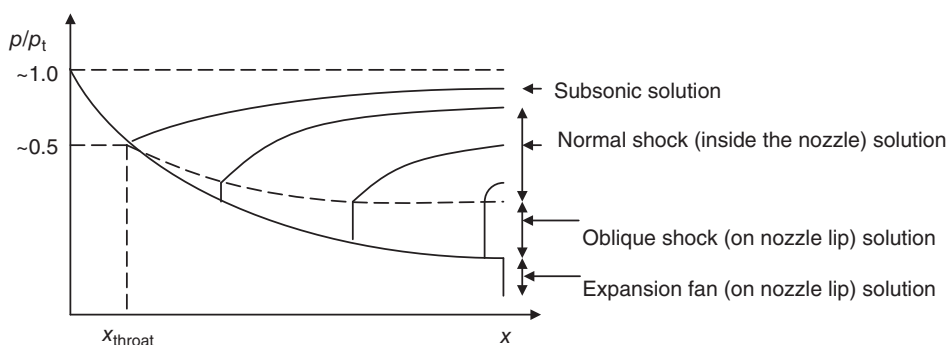
■ FIGURE 4.19
A choked convergent–divergent nozzle and the static pressure distribution along the nozzle axis



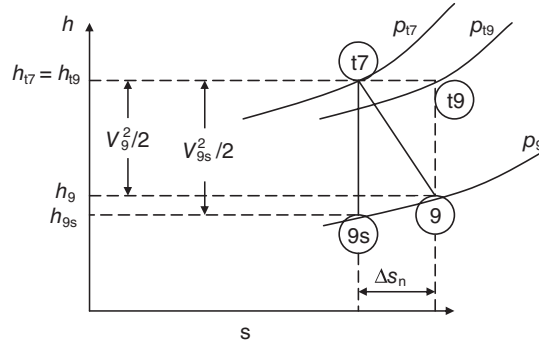
The two possible solutions in static pressure distribution along the nozzle axis are shown in Figure 4.19. One is a subsonic solution downstream of the nozzle throat and the second is a supersonic flow solution downstream of the throat. The subsonic solution is clearly a result of high backpressure, that is, p_0 , and causes a flow deceleration in the divergent duct downstream of the throat. Therefore, the divergent portion of the duct is actually a *diffuser* and not a nozzle. The supersonic solution is a result of low backpressure and, therefore, the flow continues to expand (i.e., accelerates) beyond the throat to supersonic speeds at the exit. Also note that only a perfectly expanded nozzle flow is shown as the supersonic branch of the nozzle flow in Figure 4.19. For ambient pressures in between the two pressures shown in Figure 4.19, there are a host of shock solutions, which occur as an oblique shock at the lip or normal shock inside the nozzle. The range of backpressures for a given nozzle area ratio, which lead to a normal shock solution inside the nozzle is shown in Figure 4.20. The jump in static pressure across a normal shock is shown as an abrupt (i.e., vertical) pressure rise in Figure 4.20, whereas in reality shocks have finite thickness, and, therefore, all the *jump* conditions are then *diffused* or *spread* over the scale of shock thickness. We note the diffusing nature of the flow, that is, the static pressure increasing, after the shock occurs inside the nozzle, which signifies a *diffuser environment* after the shock. For a lower range of backpressures, the oblique shock solution is possible, which indicate an oblique shock is hanging on the nozzle lip. Then we reach a unique nozzle pressure ratio, which leads to perfect expansion, as shown in Figure 4.19 and repeated in Figure 4.20. For all backpressures lower than the perfect expansion, we get the isentropic centered expansion fan solution. All these waves are the necessary mechanisms to satisfy the physical requirement of continuous static pressure across the slipstream in the jet exit flow. Let us call this important gas dynamic *boundary condition* as rule number 5 in nozzle flows. Note that this rule is not unlike the familiar Kutta condition in airfoil aerodynamics, where we prevented a static pressure jump at the sharp trailing edge of an airfoil.

To examine the efficiency of a nozzle in expanding the gas to an exit (static) pressure p_9 , we create an enthalpy–entropy diagram, very similar to an inlet. In the inlet studies, we took the ambient static condition 0 and compressed it to the total intake exit condition t2. But since a nozzle may be treated as a reverse-flow diffuser (and vice versa), we take the nozzle inlet gas, at the total state t7, and expand it to the exit static condition 9. This process is shown in Figure 4.21. The analogy in the thermodynamic analysis of a nozzle and a diffuser is helpful in better learning both components. The actual nozzle expansion process is shown by a solid line connecting the gas total state t7 to the exit static state 9.

■ FIGURE 4.20
Schematic drawing of possible static pressure distributions inside a choked supersonic nozzle



■ FIGURE 4.21
Enthalpy–entropy
diagram of nozzle flow
expansion



As the real nozzle flows may still be treated as adiabatic, the total enthalpy h_t , remains constant in a nozzle.

Rule 5 : Static pressure must be continuous across the slipstream of a jet exhaust plume.

$$h_{t7} = h_{t9} \quad (4.56)$$

We remember that the inlet flow was also considered to be adiabatic. An ideal exit state 9s is reached isentropically from the total state t7 to the same exit pressure p_9 , in Figure 4.21. The vertical gap between a total and static enthalpy states, in an h - s diagram, represents the kinetic energy of the gas, $V^2/2$, which is also shown in Figure 4.21. Due to frictional and shock losses in a nozzle, the flow will suffer a total pressure drop, that is,

$$p_{t9} < p_{t7} \quad (4.57)$$

as depicted in Figure 4.21. Again, this behavior is quite analogous to a diffuser. We can immediately define the total pressure ratio across a nozzle as its figure of merit, similar to the total pressure recovery of an inlet, namely,

$$\pi_n \equiv \frac{p_{t9}}{p_{t7}} \quad (4.58)$$

Now we can quantify the entropy rise in an adiabatic nozzle, as a result of total pressure losses, using the combined first and second law of thermodynamics,

$$\frac{\Delta s_n}{R} = -\ln \pi_n \quad (4.59)$$

We may also define a nozzle adiabatic efficiency η_n very similar to the inlet adiabatic efficiency, as

$$\eta_n \equiv \frac{h_{t7} - h_9}{h_{t7} - h_{9s}} = \frac{V_9^2/2}{V_{9s}^2/2} \quad (4.60)$$

Let us interpret the above definition in physical terms. The fraction of an ideal nozzle exit kinetic energy $V_{9s}^2/2$, which is realized in a real nozzle $V_9^2/2$, is called the nozzle adiabatic efficiency. The loss in total pressure in a nozzle manifests itself as a loss of kinetic energy. Consequently, the adiabatic efficiency η_n , which deals with the loss of kinetic energy in a nozzle, has to be related to the nozzle total pressure ratio π_n . Again, in a very similar manner as in the inlet, let us divide the numerator and denominator of Equation 4.60 by h_{t7} , to get

$$\eta_n = \frac{1 - \frac{h_9}{h_{t7}}}{1 - \frac{h_{9s}}{h_{t7}}} = \frac{1 - \frac{h_9}{h_{t7}}}{1 - \left(\frac{p_9}{p_{t7}}\right)^{\frac{\gamma-1}{\gamma}}} = \frac{1 - \left(\frac{p_9}{p_{t9}}\right)^{\frac{\gamma-1}{\gamma}}}{1 - \left(\frac{p_9}{p_{t7}}\right)^{\frac{\gamma-1}{\gamma}}} \quad (4.61)$$

where we used $h_{t7} = h_{t9}$ in the numerator and the isentropic relation between the temperature and pressure ratios in both numerator and denominator. It is interesting to note that as the nozzle exit total pressure p_{t9} approaches the value of the nozzle inlet total pressure p_{t7} , the nozzle adiabatic efficiency will approach 1. We may treat Equation 4.61 as containing only one unknown and that is p_{t9} . Therefore, for a given nozzle exit static pressure p_9 and the nozzle inlet total pressure p_{t7} , the nozzle adiabatic efficiency η_n will result in a knowledge of the total pressure at the exit of the nozzle, p_{t9} . Now, if we multiply the numerator and denominator of the right-hand side of Equation 4.61 by $(p_{t7}/p_9)^{\frac{\gamma-1}{\gamma}}$, we will reach our goal of relating the two figures of merit in a nozzle, that is,

$$\eta_n = \frac{\left(\frac{p_{t7}}{p_9}\right)^{\frac{\gamma-1}{\gamma}} - \pi_n^{-\frac{\gamma-1}{\gamma}}}{\left(\frac{p_{t7}}{p_9}\right)^{\frac{\gamma-1}{\gamma}} - 1} \quad (4.62)$$

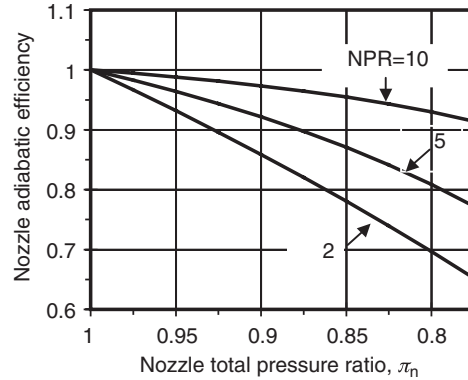
There are three parameters in Equation 4.62. The two figures of merit, η_n and π_n , and the ratio of nozzle inlet total pressure to the nozzle exit static pressure, p_{t7}/p_9 . The last parameter is a known quantity, as we know the nozzle inlet total pressure p_{t7} from the upstream component analysis (in a turbojet, it is the turbine, $p_{t7} = p_{t5}$), and the nozzle exit pressure p_9 is a direct function of the nozzle area ratio A_9/A_8 . To express Equation 4.62 in terms of the NPR, we may split p_{t7}/p_9 into

$$\frac{p_{t7}}{p_9} = \frac{p_{t7}}{p_0} \frac{p_0}{p_9} = \text{NPR} \cdot \left(\frac{p_0}{p_9}\right) \quad (4.63)$$

Now, substituting the above expression in Equation 4.62, we get

$$\eta_n = \frac{\left\{ \text{NPR} \left(\frac{p_0}{p_9}\right) \right\}^{\frac{\gamma-1}{\gamma}} - \pi_n^{-\frac{\gamma-1}{\gamma}}}{\left\{ \text{NPR} \left(\frac{p_0}{p_9}\right) \right\}^{\frac{\gamma-1}{\gamma}} - 1} \quad (4.64)$$

■ **FIGURE 4.22**
Two figures of merit in
a nozzle plotted as a
function of NPR
($\gamma = 1.33$)



A plot of Equation 4.64 is shown in Figure 4.22 for a perfectly expanded nozzle, that is, $p_9 = p_0$.

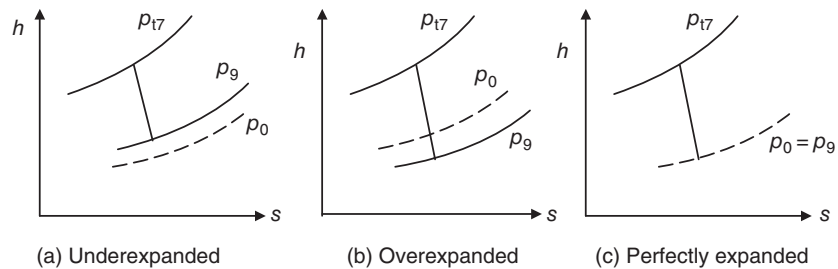
It is comforting to note that in Equation 4.64, the nozzle adiabatic efficiency will approach 1, as the nozzle total pressure ratio approaches 1. The parameter p_0/p_9 represents a measure of mismatch between the nozzle exit static pressure and the ambient static pressure. For $p_9 > p_0$, the flow is considered to be *underexpanded*. For $p_9 < p_0$, the flow is defined as *overexpanded*. In the under-expanded scenario, the nozzle area ratio is not adequate, that is, not large enough, to expand the gas to the desired ambient static pressure. In the overexpanded nozzle flow case, the nozzle area ratio is too large for perfect expansion. As noted earlier, a perfectly expanded nozzle will have $p_0 = p_9$, therefore, the above equation is further simplified to

$$\eta_n = \frac{\{\text{NPR}\}^{\frac{\gamma-1}{\gamma}} - \pi_n^{-\frac{\gamma-1}{\gamma}}}{\{\text{NPR}\}^{\frac{\gamma-1}{\gamma}} - 1} \quad (4.65)$$

for a perfectly expanded nozzle. It is instructive to show the three cases of nozzle expansion, that is, under-, over-, and perfectly expanded cases, on an h - s diagram (Figure 4.23).

In Figure 4.23a, the nozzle area ratio is smaller than necessary for perfect expansion and that explains the high exit pressure p_9 . However, an expansion fan at the nozzle

■ **FIGURE 4.23**
The h - s diagram for
the three possible
nozzle expansions



exit plane will adjust the pressure down to the ambient level, after the jet leaves the nozzle, in accordance to Rule 5. After all, the slipstream cannot take a (static) pressure jump. In Figure 4.23b, the nozzle area ratio is too large for this altitude, which explains a lower-than-ambient static pressure at the nozzle exit. To adjust the low exit pressure up to the ambient level, a shock wave is formed on the nozzle exit lip, which for mild overexpansion will be an oblique shock. Higher levels of over expansion will strengthen the shock to a normal position and, eventually, cause the shock to enter the nozzle. Figure 4.23c shows a perfect expansion scenario, which implies the nozzle area ratio is perfectly matched to the altitude requirements of ambient pressure. Again, as noted in Figure 4.23, all nozzle expansions are depicted as irreversible processes with an associated entropy rise; therefore, *perfect expansion* is not to be mistaken as *perfect (isentropic) flow*.

In summary, we learned that:

- the primary function of a nozzle is to accelerate the gas efficiently
- the gross thrust parameter F_g signifies nozzle's contribution to the thrust production
- the gross thrust reaches a maximum when the nozzle is perfectly expanded; that is, $p_9 = p_0$
- real nozzle flows may still be considered as adiabatic
- a nozzle pressure ratio (NPR) that causes a Mach-1 flow at the throat (i.e., choking condition) is called the *critical nozzle pressure ratio*, and as a rule of thumb, we may remember an $(\text{NPR})_{\text{crit}}$ of ~ 2
- there are two efficiency parameters that quantify losses or the degree of irreversibility in a nozzle and they are related
- nozzle losses manifest themselves as the total pressure loss
- all subsonic exhaust streams have $p_{\text{jet}} = p_{\text{ambient}}$
- a perfect nozzle expansion means that the nozzle exit (static) pressure and the ambient pressure are equal
- an imperfect nozzle expansion is caused by a mismatch between the nozzle area ratio and the altitude of operation
- underexpansion is caused by smaller-than-necessary nozzle area ratio, leading to $p_9 > p_0$
- overexpansion is caused by larger-than-necessary nozzle area ratio, leading to $p_9 < p_0$.

EXAMPLE 4.7

Consider a convergent–divergent nozzle with a pressure ratio $\text{NPR} = 10$. The gas properties are $\gamma = 1.33$ and $c_p = 1,156 \text{ J/kg} \cdot \text{K}$ and remain constant in the nozzle. The nozzle adiabatic efficiency is $\eta_n = 0.94$. Calculate

- (a) nozzle total pressure ratio π_n
- (b) nozzle area ratio A_9/A_8 for a perfectly expanded nozzle
- (c) nozzle exit Mach number M_9 (perfectly expanded)

SOLUTION

We may use Equation 4.64 that relates the figures of merit of a nozzle (η_n and π_n) with NPR,

$$\eta_n = \frac{\left\{ \text{NPR} \left(\frac{p_0}{p_9} \right) \right\}^{\frac{\gamma-1}{\gamma}} - \pi_n^{-\frac{\gamma-1}{\gamma}}}{\left\{ \text{NPR} \left(\frac{p_0}{p_9} \right) \right\}^{\frac{\gamma-1}{\gamma}} - 1}$$

For a perfectly expanded nozzle, $p_0 = p_9$, therefore, we get the following expression for π_n

$$\pi_n = \left[\text{NPR}^{\frac{\gamma-1}{\gamma}} - \eta_n \left(\text{NPR}^{\frac{\gamma-1}{\gamma}} - 1 \right) \right]^{\frac{\gamma}{\gamma-1}} \cong 0.8335$$

The entropy rise in an adiabatic nozzle is a function of the total pressure ratio π_n , according to (Equation 4.59)

$$\Delta s_n/R = -\ell n \pi_n \cong -\ell n(0.8335) \approx 0.1822$$

We can calculate the local Mach number M_9 if we know the total and static pressures p_{t9} and p_9 simultaneously. From the NPR and the total pressure ratio, we may write

$$\begin{aligned} p_{t9}/p_9 &= (p_{t9}/p_{t7})(p_{t7}/p_0)(p_0/p_9) = 0.8335(10)(1) \\ &= 8.335 \end{aligned}$$

From the general expression for total pressure and Mach number

$$p_t/p = (1 + (\gamma - 1)M^2/2)^{\frac{\gamma}{\gamma-1}}$$

We can isolate Mach number as follows

$$\begin{aligned} M_9 &= \sqrt{\frac{2}{\gamma-1} \left[(p_{t9}/p_9)^{\frac{\gamma-1}{\gamma}} - 1 \right]} \\ &= \sqrt{\frac{2}{0.33} \left[(8.335)^{0.3/1.33} - 1 \right]} \cong 2.05 \end{aligned}$$

Using continuity, we calculate $A_9/A_8 \sim 1.8242$

4.3.1.6 Thermal Efficiency of a Turbojet Engine. An ideal turbojet engine (with the components of inlet, gas generator, and the nozzle) is the same as an ideal Brayton cycle that we learned in thermodynamics. We remember the Brayton cycle efficiency as

$$\eta_{th} = 1 - \frac{T_0}{T_3} \quad (4.66)$$

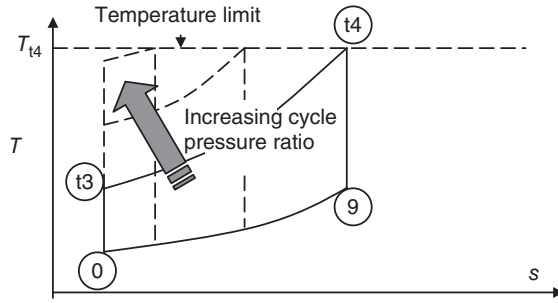
where T_3 is the compressor discharge temperature and T_0 is the inlet temperature, we note that the Brayton cycle thermal efficiency improves with increasing T_3 . We can recast Equation 4.66 in terms of the compressor pressure ratio and the ram temperature ratio, as follows:

$$\eta_{th} = 1 - \frac{1}{\frac{T_3}{T_0}} = 1 - \frac{1}{\frac{T_{t3}}{T_{t2}} \frac{T_{t2}}{T_0}} = 1 - \frac{1}{\tau_c \tau_r} = 1 - \frac{1}{\pi_c^{\frac{\gamma-1}{\gamma}} \left(1 + \frac{\gamma-1}{2} M_0^2 \right)} \quad (4.67)$$

From Equation 4.67, we note that for a given flight Mach number M_0 , that is, for a constant ram temperature ratio τ_r , the cycle thermal efficiency increases with the compressor temperature ratio τ_c . However, the higher the cycle pressure ratio, the higher the compressor discharge temperature will be, which implies the following attributes for the high-pressure compressor:

- using turbine material in HPC
- cooling needs of the HPC (potentially regenerative fuel cooling)
- narrow passage (vanishing flow annulus) in HPC with large secondary flow losses.

■ FIGURE 4.24 Simple Brayton cycle with increasing cycle pressure ratio



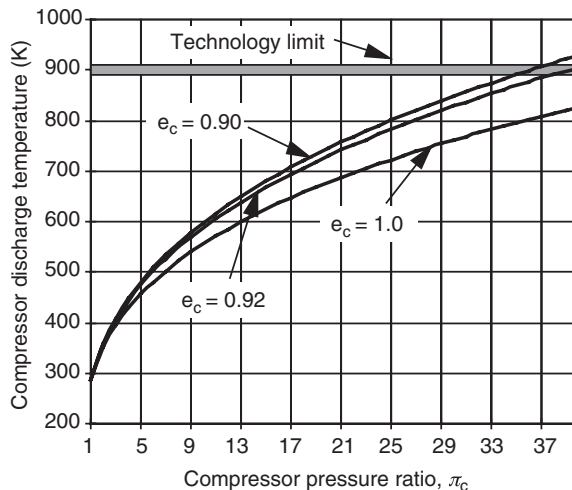
Furthermore, for a constant turbine inlet temperature T_{t4} , the cycle work output w_{cycle} will eventually vanish in the limit of $T_{t3} = T_{t4}$. It is also interesting to note the emergence of Carnot-looking cycles with successively higher cycle pressure ratios (Figure 4.24). We remember from basic thermodynamics that a Carnot cycle operating between the temperature limits T_0 and T_4 will attain a thermal efficiency of

$$\eta_{\text{th-Carnot}} = 1 - \frac{T_0}{T_4} \quad (4.68)$$

which is the highest thermal efficiency of any heat engine operating between the temperature limits T_0 and T_4 . The technology limit on compressor discharge temperature is shown in Figure 4.24 for the standard sea level condition at takeoff, that is, $M_0 \approx 0$.

The information presented in Figure 4.25 identifies a limitation on the compressor pressure ratio π_c . Based on the practical limits of the compressor materials and potential cooling requirements, a compressor pressure ratio of $\sim 40\text{--}45$ seems to represent the upper

■ FIGURE 4.25 Influence of compressor pressure ratio on the discharge temperature T_{t3} ($M_0 = 0$, standard sea level condition)



limit of the current technology for the subsonic commercial aircraft gas turbine engines. The useful portion of Equation 4.67 is repeated here for the purpose of discussion.

$$\eta_{\text{th}} = 1 - \frac{1}{\pi_c^{\frac{\gamma-1}{\gamma}} \left(1 + \frac{\gamma-1}{2} M_0^2 \right)} \quad (4.67)$$

The effect of flight Mach number on the thermal efficiency of an ideal turbojet engine can be discerned from Equation 4.67. For a given compressor pressure ratio π_c , the thermal efficiency of an ideal turbojet engine increases with an increasing flight Mach number. The rationale for this behavior is that the higher flight stagnation temperature T_{12} , combined with a constant compressor pressure ratio, leads to higher T_{13} s. Going back to Equations 4.66 or 4.67, we observe that a high compressor discharge temperature T_{13} leads to a high thermal efficiency. On the contrary, aircraft engines experience their lowest thermal efficiency at takeoff. Although the fact that thermal efficiency improves with flight Mach number is important to know, it is of little practical value, because the flight Mach number (e.g., at cruise) is established by the mission requirements and not the engine thermal efficiency requirement. A family of thermal efficiency curves with the flight Mach number is plotted in Figure 4.26, for different compressor pressure ratios.

The thermal efficiency shown above, for the most part, is not realized in a turbojet engine for the following reasons

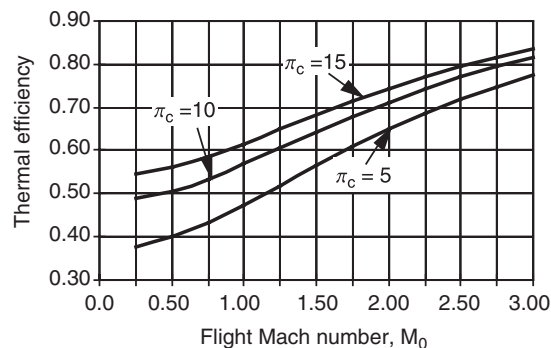
1. the engine components are not *ideal*
2. for a high flight Mach number, for example, $M_0 = 3$, there is no need for a compressor!

To appreciate item number 2, we need to examine the cycle output w_c more closely. For an ideal turbojet engine, neglecting a small mass flow contribution due to the fuel, the cycle specific work can be written as

$$w_c \cong (h_{t4} - h_9) - (h_{13} - h_0) \quad (4.68)$$

where the first parenthesis contains the turbine and nozzle output (per unit mass flow rate) and the second parenthesis contains the inlet and compressor input (per unit mass flow rate). Therefore, the difference between the *expansion leg* and the *compression leg* in a

■ **FIGURE 4.26**
The effect of flight Mach number on the thermal efficiency of an ideal turbojet engine



Brayton cycle is the net output of the cycle. To put it differently, in an ideal cycle, the difference between the power production and consumption can be entirely converted into useful cycle power output. Now, let us manipulate Equation 4.68 in order to cast it in terms of useful nondimensional quantities, that is,

$$\begin{aligned} w_c &\cong h_{t4} \left(1 - \frac{T_9}{T_{t4}} \right) - h_{t3} \left(1 - \frac{T_0}{T_{t3}} \right) \\ &= h_{t4} \left\{ 1 - \left(\frac{p_9}{p_{t4}} \right)^{\frac{\gamma-1}{\gamma}} \right\} - h_{t3} \left\{ 1 - \left(\frac{p_0}{p_{t3}} \right)^{\frac{\gamma-1}{\gamma}} \right\} \end{aligned} \quad (4.69)$$

But since $p_9 = p_0$ and $p_{t4} = p_{t3}$ in an ideal cycle with a perfectly expanded nozzle, we can rewrite Equation 4.69 in the following form;

$$\begin{aligned} w_c &\cong (h_{t4} - h_{t3}) \left(1 - \frac{T_0}{T_{t3}} \right) = h_0 (\tau_\lambda - \tau_c \tau_r) \left(1 - \frac{1}{\tau_c \tau_r} \right) \\ &= h_0 \left(\tau_\lambda - \frac{\tau_\lambda}{\tau_r \tau_c} - \tau_r \tau_c + 1 \right) \end{aligned} \quad (4.70)$$

where $\tau_\lambda \equiv h_{t4}/h_0$ is the engine thermal limit parameter, $\tau_r \equiv T_{t0}/T_0 = 1 + \gamma - 1/2 M_0^2$ is the ram temperature ratio, and $\tau_c \equiv T_{t3}/T_{t2}$ is the compressor temperature ratio. To find a maximum value for the specific work of the cycle, for a constant turbine inlet temperature, that is, τ_λ , we may treat the product $\tau_r \tau_c$ as one and only variable in Equation 4.70. Therefore, we can differentiate w_c/h_0 with respect to $\tau_r \tau_c$ and set it equal to zero,

$$\frac{d \left(\frac{w_c}{h_0} \right)}{d(\tau_r \tau_c)} = \frac{\tau_\lambda}{(\tau_r \tau_c)^2} - 1 = 0 \quad (4.71)$$

which implies that

$$\tau_r \tau_c = \sqrt{\tau_\lambda} \quad (4.72)$$

Therefore, the product $\tau_r \tau_c$, which satisfies Equation 4.72, yields the *largest area under the curve* in the T - s diagram of the Brayton cycle. The area within the cycle walls, on a T - s diagram, we learned in thermodynamics that represents the net cycle specific work. We can isolate the compressor contribution to the temperature ratio as

$$\tau_c = \frac{\sqrt{\tau_\lambda}}{\tau_r} = \frac{\sqrt{\tau_\lambda}}{1 + \frac{\gamma-1}{2} M_0^2} \quad (4.73)$$

Equation 4.73 is useful in telling us that for a given burner temperature, the compressor pressure ratio requirement for the maximum cycle output (i.e., the *optimum* compressor

pressure ratio) goes down with the flight Mach number. We can recast Equation 4.73 in terms of the (optimum) compressor pressure ratio as

$$\pi_{c \text{ Optimum}} = \tau_c^{\frac{\gamma}{\gamma-1}} = \left(\frac{\sqrt{\tau_\lambda}}{1 + \frac{\gamma-1}{2} M_0^2} \right)^{\frac{\gamma}{\gamma-1}} \quad \text{For maximum thrust} \quad (4.74)$$

Before plotting Equation 4.74, we recognize that the lowest compressor pressure ratio is 1, which basically states that there is no need for a compressor, that is, in this limit we reach a *ramjet*. Setting $\pi_c = 1$, in Equation 4.74 and isolating the flight Mach number M_0 , we arrive at the following expression for the maximum flight Mach number, which renders a compressor in an aircraft engine as useless, that is,

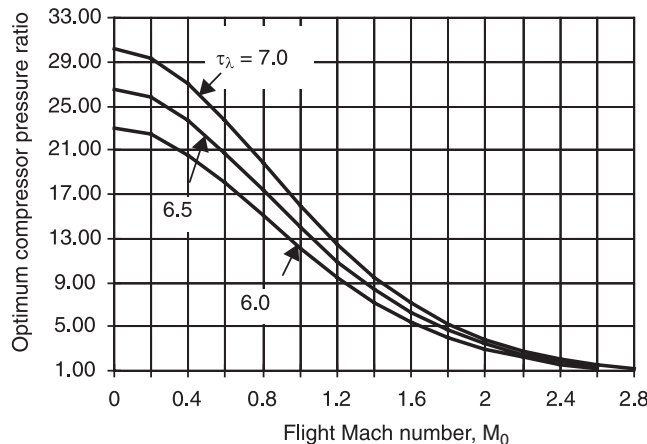
$$M_{0 \text{ max}} = \sqrt{\frac{2}{\gamma-1} (\sqrt{\tau_\lambda} - 1)} \quad (4.75)$$

Now, let us plot Equation 4.75 for a gas specific heat ratio of 1.4 ($\gamma = 1.4$).

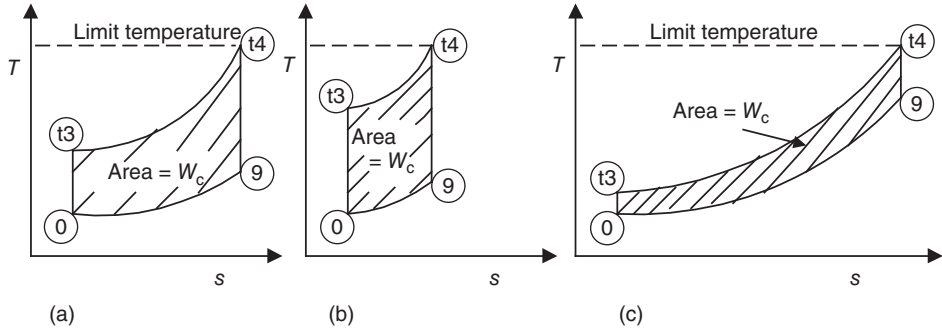
Although we chose a turbine inlet temperature corresponding to a $\tau_\gamma = 6.5$ or 7 in plotting Equation 4.74, the physical principle remains the same for other turbine inlet temperatures. The optimum compressor pressure ratio drops nonlinearly with the flight Mach number. In this case, substituting $\tau_\gamma = 6.5$ in Equation 4.75 yields a maximum flight

Mach number of $M_{0, \text{max}} = \sqrt{5(\sqrt{6.5} - 1)} = 2.783$, which corresponds to a compressor pressure ratio of 1, in Figure 4.27, and $\tau_\gamma = 7.0$ yields a maximum M_0 of 2.868. Reexamining Equation 4.72 can reveal an interesting relationship between the states t3 and 9, that is, the compressor discharge and the nozzle exit, for a cycle with maximum (specific) work output capability. Figure 4.28 shows an ideal turbojet cycle with a fixed limit temperature T_{t4} but varying compressor discharge temperatures T_{t3} . We remember that the state t3 is reached through ram compression, as well as the mechanical compression. The shaded area represents the cycle (specific energy) output, which is maximized by Equation 4.72.

■ **FIGURE 4.27**
Optimum compressor pressure ratio variation with the flight Mach number (for $\tau_\lambda = 6.0-7.0$)



■ FIGURE 4.28
T-s diagram of an ideal turbojet cycle with varying T_{t3} , or cycle pressure ratio



We will proceed to demonstrate that the maximum cycle area, which is guaranteed by the following equation, requires T_{t3} to be equal to the nozzle exit temperature T_9 .

$$\tau_r \tau_c = \sqrt{\tau_\lambda} \tag{4.72}$$

but

$$\tau_r \tau_c = \frac{T_{t0} T_{t3}}{T_0 T_{t2}} = \frac{T_{t3}}{T_0} \tag{4.76}$$

which is set equal to $\sqrt{\tau_\gamma}$ and manipulated as follows:

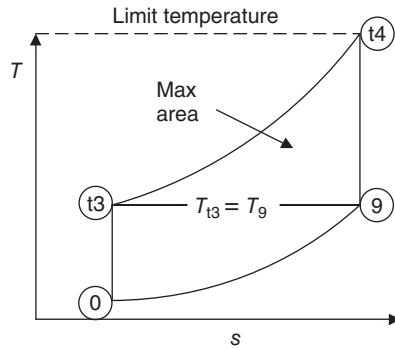
$$\frac{T_{t3}}{T_0} = \sqrt{\frac{T_{t4}}{T_0}} = \sqrt{\frac{T_{t4} T_9}{T_9 T_0}} = \sqrt{\frac{T_{t3} T_9}{T_0 T_0}} = \frac{\sqrt{T_{t3} T_9}}{T_0} \tag{4.77}$$

where we used the fact that $T_{t4}/T_9 = T_{t3}/T_0$, as they are isentropically bound by a pair of isobars, that is, $p_9 = p_0$ and $p_{t4} = p_{t3}$. Now, we can simplify Equation 4.77, to get the desired result:

$$\boxed{T_{t3} = T_9 \quad Q.E.D.} \tag{4.78}$$

None of the cycles drawn in Figure 4.28 satisfy the above requirement and, as such, have not created the largest area in the *T-s* diagram. Figure 4.29 shows the optimum compression for a Brayton cycle. We need to remember that the optimum work cycle, as shown in Figure 4.29, is not achieved at the highest cycle thermal efficiency. The highest cycle thermal efficiency is achieved in the limit of $T_{t3} = T_{t4}$, which corresponds to Carnot cycle efficiency ($\eta_{th,max} = 1 - T_0/T_{t4}$), and then the work output vanishes! Here, we learned an important lesson in propulsion, namely, a *single parameter optimization* approach in an engine may lead to impractical results for the engine performance (e.g., the highest thermal efficiency in a Brayton cycle will lead to no work output!). An engine, in reality, is a multiparameter system and an *overall optimum* is, by necessity, a mix of compromises between the component efficiencies, performance output, and the issues of reliability, maintainability, operating cost, and other market-driven practical limitations based on *customer* input/demands.

■ **FIGURE 4.29**
 T - s diagram of an optimum compression Brayton cycle shows $T_{t3} = T_9$



We may examine the description of aircraft engine thermal efficiency from another perspective. From the energy standpoint, the function of an airbreathing engine is to increase the kinetic energy of the medium per unit time, that is, $\Delta K\dot{E}$. This may be thought as the *mechanical output* of the engine with a perfectly expanded nozzle. The thermal investment in the engine is through the fuel flow rate, liberating a thermal energy equal to the heating value of the fuel per unit mass, per unit time. Graphically, we may present the change in kinetic power of the stream and the thermal investment through the fuel as in Figure 4.30.

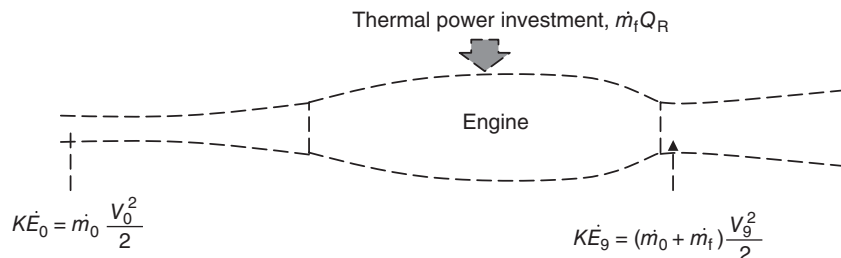
Now, it is entirely reasonable to think that the thermal efficiency of this engine is the fraction of the thermal power investment that is converted into useful mechanical power output, that is,

$$\eta_{\text{th}} \equiv \frac{\Delta K\dot{E}}{\dot{m}_f Q_R} = \frac{\frac{\dot{m}_0}{2} \{(1+f)V_9^2 - V_0^2\}}{\dot{m}_f Q_R} = \frac{(1+f)V_9^2 - V_0^2}{2fQ_R} \quad (4.79)$$

Is this expression for thermal efficiency the same as $\eta_{\text{th}} = 1 - \frac{T_0}{T_{t3}}$? The answer is obviously affirmative, as we will demonstrate that Equation 4.79 can, under some simplifying assumptions, reduce to the thermodynamic efficiency of the Brayton cycle, described earlier. First, let us ignore the fuel-to-air ratio f in favor of 1 in the numerator of Equation 4.79, that is, since $f \ll 1$, $1 + f \approx 1$

$$\eta_{\text{th}} \approx \frac{V_9^2 - V_0^2}{2fQ_R} \approx \frac{(h_{t9} - h_9) - (h_{t0} - h_0)}{h_{t4} - h_{t3}} \quad (4.80)$$

■ **FIGURE 4.30**
Schematic drawing of an aircraft engine with fuel thermal power as input and $\Delta K\dot{E}$ as output



We had replaced the kinetic energy term by the difference between the total and static enthalpy in Equation 4.80, as well as the burner input by the total enthalpy rise across it. In the approximation made to the denominator of Equation 4.80, we again neglected the small contribution of fuel-to-air ratio, as compared to one (Equation 4.31, for example). Second, let us replace h_{t9} by h_{t5} and h_{t0} by h_{t2} , as the nozzle and inlets are treated as adiabatic ducts, therefore, total enthalpy is conserved, that is,

$$\eta_{th} \approx \frac{(h_{t5} - h_9) - (h_{t2} - h_0)}{h_{t4} - h_{t3}} \quad (4.81)$$

From the power balance between the compressor and turbine, again neglecting f in favor of one, we can replace h_{t5} by $[h_{t4} - (h_{t3} - h_{t2})]$ in Equation 4.81, to get

$$\eta_{th} \approx \frac{h_{t4} - h_{t3} + h_{t2} - h_9 - h_{t2} + h_0}{h_{t4} - h_{t3}} = \frac{(h_{t4} - h_9) - (h_{t3} - h_0)}{h_{t4} - h_{t3}} \quad (4.82)$$

The thermodynamic states $t4$ and 9 and $t3$ and 0 are grouped together in Equation 4.82, as they are on the same isentrope, respectively. The temperature ratio T_{t4}/T_9 and the pressure ratio p_{t4}/p_9 are then linked via isentropic exponent. Using these simple steps in Equation 4.82 yields

$$\eta_{th} \approx \frac{h_{t4} \left(1 - \frac{T_9}{T_{t4}}\right) - h_{t3} \left(1 - \frac{T_0}{T_{t3}}\right)}{h_{t4} - h_{t3}} = \frac{h_{t4} \left\{1 - \left(\frac{p_9}{p_{t4}}\right)^{\frac{\gamma-1}{\gamma}}\right\} - h_{t3} \left\{1 - \left(\frac{p_0}{p_{t3}}\right)^{\frac{\gamma-1}{\gamma}}\right\}}{h_{t4} - h_{t3}} \quad (4.83)$$

We realize that the two parenthesis in Equation 4.83 are the same, as $p_9 = p_0$, that is, a perfectly expanded nozzle, and $p_{t4} = p_{t3}$, as a perfect combustion, consequently, we can further simplify the above equation to get the desired result, that is,

$$\eta_{th} \approx \frac{(h_{t4} - h_{t3}) \left(1 - \frac{T_0}{T_{t3}}\right)}{h_{t4} - h_{t3}} = 1 - \frac{T_0}{T_{t3}} \quad Q.E.D. \quad (4.84)$$

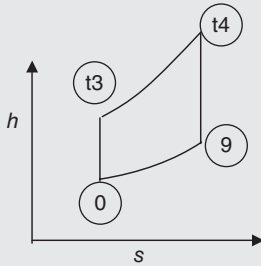
Therefore, we demonstrated that our general definition of an airbreathing engine thermal efficiency (Equation 4.79), under the assumptions of perfect nozzle expansion, ideal components, and negligible fuel flow rate as compared to the air flow rate, reduces to the ideal Brayton cycle efficiency that we learned in thermodynamics.

EXAMPLE 4.8

Prove the ideal thermal efficiency for the Brayton cycle, as shown, is $\eta_{th} = 1 - T_0/T_{t3}$

SOLUTION

From the first (and second) law of thermodynamics, we have



$$\oint \delta w = \oint \delta q = \oint T ds$$

$T ds = dh - v dp = dh$, for constant pressure processes, therefore the closed cycle integral gives

$$\oint \delta w = (h_{t4} - h_{t3}) + (h_0 - h_9) = (h_{t4} - h_9) - (h_{t3} - h_0)$$

The (specific) thermal power investment in the cycle, comes from a constant-pressure heating between t_3 and t_4 , i.e.

$$\int_{t_3}^{t_4} T ds = \int_{t_3}^{t_4} dh = h_{t4} - h_{t3}$$

The cycle thermal efficiency is the ratio of net work produced by the cycle to the net thermal investment in the cycle, i.e.,

$$\eta_{th} = \frac{h_{t4} - h_{t3} + h_0 - h_9}{h_{t4} - h_{t3}} = 1 - \frac{h_9 - h_0}{h_{t4} - h_{t3}}$$

For a constant c_p , we may replace the enthalpies with temperatures,

$$\eta_{th} = 1 - \frac{T_9 - T_0}{T_{t4} - T_{t3}} = 1 - \frac{T_0}{T_{t3}} [(T_9/T_0 - 1)/(T_{t4}/T_{t3} - 1)]$$

If we show that the last bracket is unity, then we have proven what we set out to demonstrate. Is $T_9/T_0 = T_{t4}/T_{t3}$? The answer becomes obvious when we switch the terms in the equality, to get.

Is $T_9/T_{t4} = T_0/T_{t3}$? Now, since the temperature ratios, T_9/T_{t4} and T_0/T_{t3} , are represented by isentropic processes, they may be expressed in terms of the pressure ratios raised to isentropic exponent, i.e.,

$$T_9/T_{t4} = (p_9/p_{t4})^{(\gamma-1)/\gamma}$$

$$T_0/T_{t3} = (p_0/p_{t3})^{(\gamma-1)/\gamma}$$

But since $p_0 = p_9$ and $p_{t3} = p_{t4}$, the temperature ratios are equal to each other and we have proven the last bracket in the thermal efficiency expression is unity.

$$\text{Therefore, } \eta_{th} = 1 - \frac{T_0}{T_{t3}}$$

EXAMPLE 4.9

Prove the thermal efficiency of an ideal Carnot cycle is $\eta_{th} = 1 - T_0/T_{t4}$.

SOLUTION

The net specific work of the cycle is

$$\oint \delta w = \oint \delta q = \oint T ds$$

Therefore the net specific work is

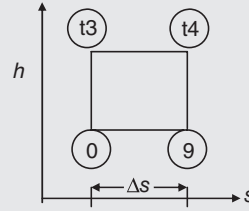
$$w = (T_{t3} - T_0) \Delta s$$

The constant temperature heating from t_3 to t_4 represents the specific thermal investment in the cycle, i.e.,

$$\int_{t_3}^{t_4} T ds = T_{t_3} \cdot \Delta s$$

The thermal efficiency of the Carnot cycle is the fraction of the thermal investment that is converted into mechanical work, namely,

$$\eta_{th} = \frac{(T_{t_3} - T_0) \Delta s}{T_{t_3} \Delta s} = 1 - \frac{T_0}{T_{t_3}}$$



4.3.1.7 Propulsive Efficiency of a Turbojet Engine. The fraction of the net kinetic power created by the engine, which is converted into thrust power delivered to the vehicle, is called the propulsive efficiency of the engine. Symbolically, we may represent this as

$$\eta_p \equiv \frac{F \cdot V_0}{\Delta KE} = \frac{F \cdot V_0}{\dot{m}_9 \frac{V_9^2}{2} - \dot{m}_0 \frac{V_0^2}{2}} \quad (4.85)$$

For the thrust power expression in the numerator, we have an option of using the net *uninstalled* thrust, or include the effect of installations on the thrust and calculate the *installed* thrust power. The latter is more difficult, as it includes the throttle-dependent inlet and exhaust system drag and the engine-airframe integration. In order to simplify the calculations, the general form of the net uninstalled thrust is

$$F_{n_{uninstalled}} = \dot{m}_9 V_9 - \dot{m}_0 V_0 + (p_9 - p_0) A_9 \quad (4.86)$$

However, if we assume a perfectly expanded nozzle, then the pressure thrust, that is, the last term in Equation 4.86, vanishes identically. Furthermore, if we neglect the small contribution of the fuel flow rate in the exhaust momentum term, the mass flow rate in the exit plane is nearly equated to the air mass flow rate, therefore,

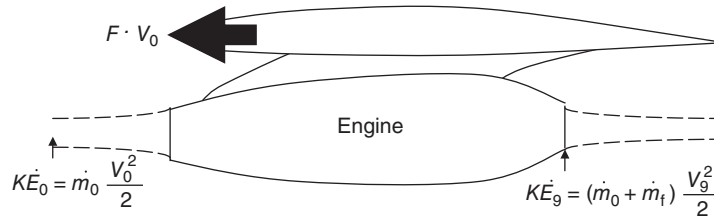
$$F_{n_{uninstalled}} \approx \dot{m}_0 (V_9 - V_0) \quad (4.87)$$

Now, if we substitute Equation 4.87 into Equation 4.85 and simplify, we get

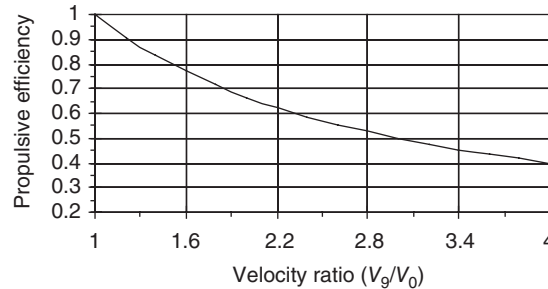
$$\eta_p \cong \frac{2(V_9 - V_0)V_0}{V_9^2 - V_0^2} \cong \frac{2V_0}{V_9 + V_0} \cong \frac{2}{1 + (V_9/V_0)} \quad (4.88)$$

Figure 4.31 is a useful tool in the definition of the propulsive efficiency.

■ **FIGURE 4.31**
Definition sketch used in defining propulsive efficiency (nozzle is perfectly expanded)



■ **FIGURE 4.32**
Propulsive efficiency variation with the velocity ratio V_9/V_0



The propulsive efficiency expressed in Equation 4.88 is an approximation. It is cast in terms of only one variable, V_9/V_0 , which is the ratio of the (exhaust) jet speed to the flight speed of the aircraft. The propulsive efficiency of an airbreathing aircraft engine drops inversely proportional to this velocity ratio. Also, we note that, in the limit of this velocity ratio approaching 1, the propulsive efficiency reaches 100%, that is, for $V_9/V_0 = 1$, then $\eta_p \approx 100\%$. The dilemma here is that an engine, which operates near 100% propulsive efficiency, that is, $V_9 = V_0$, cannot produce significant momentum thrust! The solution seems to be an engine that captures, that is, interacts with, large quantities of air and only imparts a small velocity jump to the flow. A turboprop or a large bypass ratio turbofan engine fit this description. The point is made, however, that for improved propulsive efficiency, the ratio of exhaust stream to flight speed needs to be slightly larger than 1. A plot of Equation 4.88 is a useful reminder of this fact and hence is shown in Figure 4.32.

EXAMPLE 4.10

Calculate the propulsive efficiency of a turbojet engine under the following two flight conditions that represent takeoff and cruise, namely:

1. $V_0 = 160$ km/h and $V_9 = 1000$ km/h
2. $V_0 = 800$ km/h and $V_9 = 1000$ km/h

SOLUTION

We may use the approximation $\eta_p \cong 2/(1 + V_9/V_0)$ to estimate engine propulsive efficiencies,

$$\eta_p \cong 2/(1 + 1000/160) \cong 0.2759$$

$$\eta_p \cong 2/(1 + 1000/800) = 0.8889$$

4.3.1.8 The Overall Efficiency of a Turbojet Engine. The overall efficiency of a turbojet engine is defined as the product of the thermal and the propulsive efficiency of the engine, namely,

$$\eta_o \equiv \eta_{th} \cdot \eta_p = \frac{F \cdot V_0}{\dot{m}_f Q_R} \quad (4.89)$$

which states that the fraction of thermal power invested in the engine by the fuel, which is converted into thrust power, is called the engine overall efficiency. The above equation for the overall efficiency, Equation 4.89, can be expressed in terms of specific thrust by dividing the numerator and denominator by the air mass flow rate through the engine, that is,

$$\eta_o = \frac{(F/\dot{m}_0)V_0}{fQ_R} \quad (4.90)$$

4.3.1.9 Performance Evaluation of a Turbojet Engine. As outlined in the engine performance chapter, the performance parameters for an aircraft engine are

- (a) specific thrust F/\dot{m}
- (b) thrust specific fuel consumption (TSFC) or specific impulse I_s
- (c) thermal, propulsive, and overall efficiencies.

Our approach to calculating the performance parameters of an aircraft engine is to *march through* an engine, component by component, until we calculate the target parameters, which are

- (a) fuel-to-air ratio f
- (b) exhaust velocity V_9 .

Once we established these unknowns, that is, V_0 , f , and V_9 , the specific thrust, as a figure of merit for an aircraft engine, may be written as

$$\frac{F_n}{\dot{m}_0} = (1+f)V_9 - V_0 + \frac{(p_9 - p_0)A_9}{\dot{m}_0} \quad (4.91)$$

which can be expressed in terms of the calculated parameters by recognizing that the air mass flow rate is only a factor $(1+f)$ away from the exhaust mass flow rate, that is,

$$\dot{m}_0 = \frac{\dot{m}_9}{1+f} = \frac{\rho_9 A_9 V_9}{1+f} = \frac{p_9 A_9 V_9}{RT_9(1+f)} \quad (4.92)$$

Now, substituting Equation 4.92 into Equation 4.90, we can get

$$\frac{F_n}{\dot{m}_0} = (1+f)V_9 - V_0 + \frac{(p_9 - p_0)A_9}{\frac{p_9 A_9 V_9}{RT_9(1+f)}} = (1+f)V_9 - V_0 + \frac{RT_9(1+f)}{V_9} \left(1 - \frac{p_0}{p_9}\right) \quad (4.93a)$$

Note that we have calculated all the terms on the right-hand side of the Equation 4.93a, namely, f , V_9 ; V_0 , and T_9 . Therefore,

$$\frac{F_n}{\dot{m}_0} = (1+f)V_9 - V_0 + \frac{RT_9(1+f)}{V_9} \left(1 - \frac{p_0}{p_9}\right) \quad (4.93b)$$

The primary contribution to the specific thrust in an airbreathing engine comes from the first two terms in Equation 4.93b, that is, the momentum contribution. The last term would identically vanish if the nozzle is perfectly expanded, that is, $p_9 = p_0$. Otherwise, its contribution is small compared with the momentum thrust. It is very tempting to insert a γ in the numerator and denominator of the last term in Equation 4.93b, and identify the γRT_9 as the a_9^2 to recast the above equation in a more elegant form, as

$$\frac{F_n}{\dot{m}_0} = (1+f)V_9 \left(1 + \frac{1}{\gamma M_9^2} \left(1 - \frac{p_0}{p_9}\right)\right) - V_0 \quad (4.93c)$$

Thrust specific fuel consumption was defined as

$$\text{TSFC} \equiv \frac{\dot{m}_f}{F_n} = \frac{f}{F_n/\dot{m}_0} \quad (4.94)$$

and we have calculated the fuel-to-air ratio and the specific thrust that are combined as in Equation 4.94 to create the fuel efficiency parameter, or figure of merit, of the engine.

The overall efficiency, which was derived earlier in Equation 4.90, can be recast in terms of the TSFC as

$$\eta_0 = \frac{(F_n/\dot{m}_0)V_0}{fQ_R} = \frac{V_0/Q_R}{\text{TSFC}} \quad (4.95a)$$

The inverse proportionality between the engine overall efficiency and the thrust specific fuel consumption, that is, the lower the specific fuel consumption, the higher the engine overall efficiency, is noted in Equation 4.95a, that is,

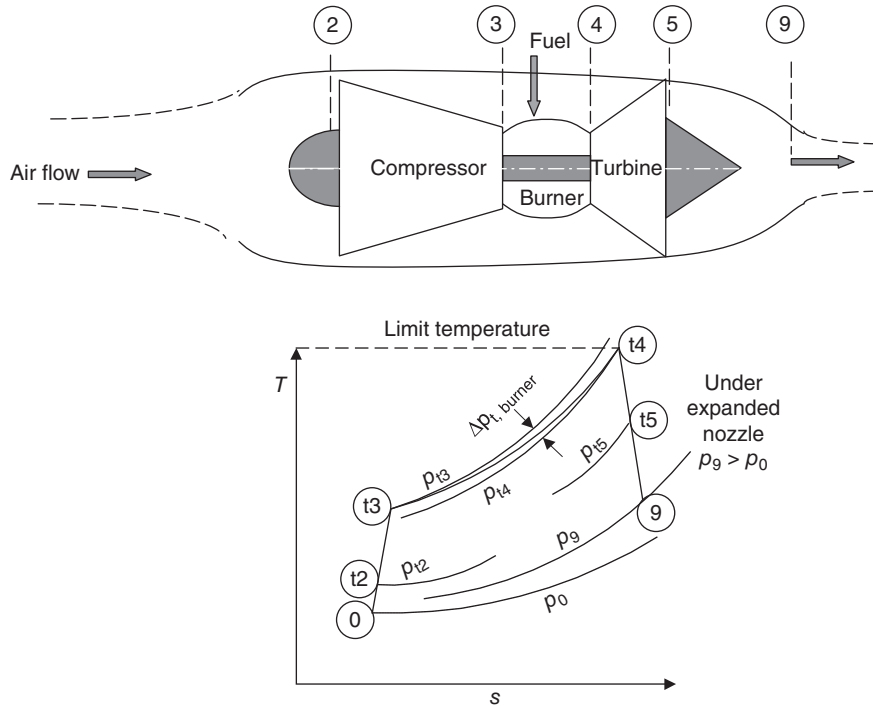
$$\eta_0 \propto \frac{1}{\text{TSFC}} \quad (4.95b)$$

In concluding the section on turbojet engines, it is appropriate to show a *real cycle* depicted on a T - s diagram. This is shown in Figure 4.33.

4.3.2 The Turbojet Engine with an Afterburner

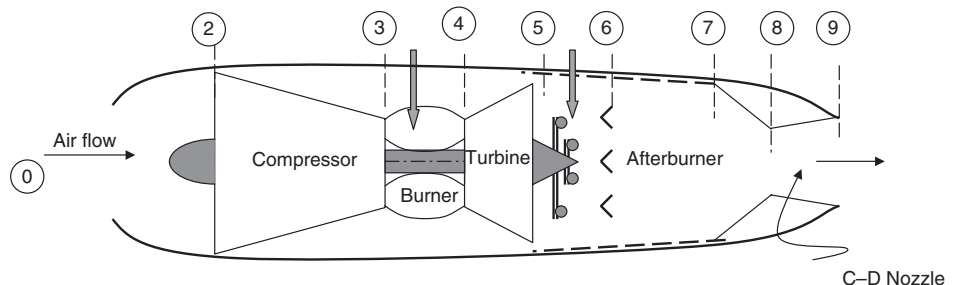
4.3.2.1 Introduction. To augment the thrust of an aircraft gas turbine engine, an afterburner can be used. This solution is often sought in military aircraft, primarily due to its simplicity and effectiveness. It is interesting to note that an afterburner has the potential of nearly doubling the thrust produced in an aircraft gas turbine engine while in the process the engine fuel consumption rate is more than quadrupled. Figure 4.34 shows

■ FIGURE 4.33 *T-s* diagram of a turbojet engine with component losses and imperfect expansion in the nozzle



the schematics of an afterburning turbojet (AB-TJ) engine. The new station numbers 7 and 8 refer to the exit of the afterburner and the nozzle throat, respectively. Suitable nozzle geometry for an afterburning turbojet (or turbofan) engine is a *supersonic nozzle* with a convergent–divergent (C–D) geometry, that is, a nozzle with a well-defined throat before a divergent cone or ramp. The throat Mach number is 1, over a wide range of operating conditions, which is referred to as the *choked* throat. As the afterburner operation causes the gas temperature to rise, the gas density decreases in harmony with the temperature rise. Consequently, to accommodate the lower density gas at the sonic condition prevailing at the nozzle throat and satisfy continuity equation, the throat area needs to be opened. This is referred to as a *variable-geometry* nozzle requirement of the exhaust system. The continuity equation for a steady flow of a perfect gas is rewritten here to demonstrate

■ FIGURE 4.34 Schematic drawing of an afterburning turbojet engine



the extent of the nozzle throat-opening requirement in a variable-geometry, convergent–divergent nozzle.

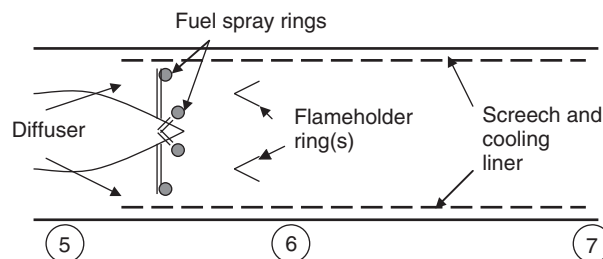
$$\dot{m} = \sqrt{\frac{\gamma}{R}} \cdot \frac{P_t}{\sqrt{T_t}} A.M. \left(\frac{1}{1 + \frac{\gamma-1}{2} M^2} \right)^{\frac{\gamma+1}{2(\gamma-1)}} \quad (4.96)$$

Let us examine the various terms in Equation 4.96, as a result of the afterburner operation. First, the mass flow rate increases slightly by the amount of $\dot{m}_{f,AB}$, which is but a small percentage of the gas flow with the afterburner-off condition, say 3–4%. The total pressure p_t drops with the afterburner operation, but this too is a small percentage, say 5–8%. The throat Mach number will remain as 1; therefore, except for the gas property variation, the last parentheses in Equation 4.96 will remain unchanged as a result of afterburner operation. Now, again neglecting small variations in the gas properties γ and R , which are in reality a function of the gas temperature, the first term under the square root in Equation 4.96 will be unchanged. This brings us to the main driver for the nozzle throat area increase requirement when the afterburner is in operation, namely the gas total temperature T_t . Therefore, the nozzle throat area needs to be opened directly proportional to the square root of the gas total temperature in the nozzle throat. This is symbolically expressed as

$$\frac{A_{8,AB-ON}}{A_{8,AB-OFF}} \approx \sqrt{\frac{T_{t8,AB-ON}}{T_{t8,AB-OFF}}} \quad (4.97)$$

The afterburner is composed of an inlet diffuser, a fuel spray bar, and a flameholder to stabilize the combustion, as shown in Figures 4.34 and 4.35. The inlet diffuser decelerates the gas to allow for higher efficiency combustion in the afterburner. A similar prediffuser is found at the entrance to the primary burner. The fuel spray bar is typically composed of one or more rings with distinct fuel injection heads circumferentially distributed around the ring. The V-shaped flame holder ring(s) create a fuel–air mixture recirculation region in its turbulent wake, which allows for a stable flame front to be established. There is also a perforated liner, which serves two functions. One, it serves as a cooling conduit that blankets, that is, protects, the outer casing from the hot combustion gases. Two, it serves as an acoustic liner that dampens the high frequency noise, that is, screech, which is generated as a result of combustion instability.

■ FIGURE 4.35
Schematic drawing of
an afterburner



An afterburner is considered to be an adiabatic duct with insulated walls, which neglects the small heat transfer through the casing, that is,

$${}_5(\dot{Q}_{\text{wall}})_7 \cong 0 \tag{4.98}$$

We notice in Figure 4.34 that the basic building block of an afterburning turbojet engine is again a simple gas generator.

Additional parameters (beyond the simple turbojet engine) are needed to analyze the performance of an afterburning turbojet engine. These are related to the physical characteristics of the afterburning system, for example, the type of fuel used in the afterburner (which is typically the same as the fuel in the primary burner), either the fuel flow setting of the afterburner fuel pump, or the exit total temperature of the afterburner, the afterburner efficiency and the afterburner total pressure loss.

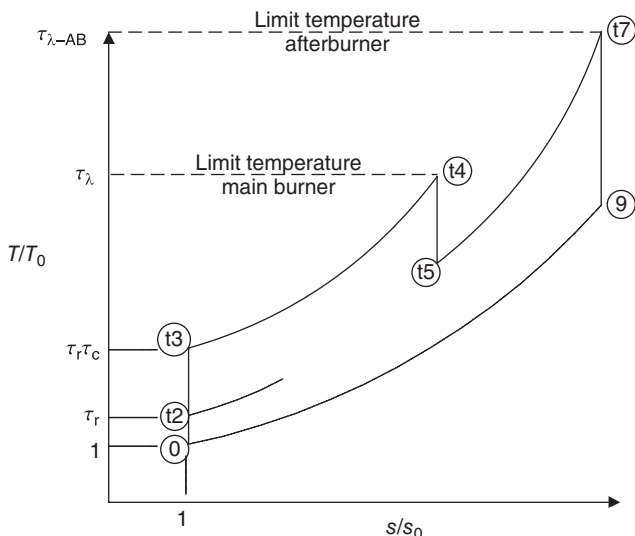
Symbolically, we represent the new parameters as

New parameters in an afterburner

-
1. $Q_{R,AB}$ (ideal) heating value of the fuel in the afterburner
 2. $\dot{m}_{f,AB}$ or T_{t7} or $\tau_{\lambda-AB} \equiv \frac{c_{pAB}T_{t7}}{c_{pc}T_0}$ fuel flow rate or the exit temperature
 3. $\eta_{AB} \equiv \frac{(Q_{R,AB})_{\text{actual}}}{(Q_{R,AB})_{\text{ideal}}}$ afterburner efficiency (<1)
 4. $\pi_{AB} \equiv \frac{p_{t7}}{p_{t5}}$ total pressure ratio across the afterburner (<1)
-

4.3.2.2 Analysis. A nondimensional T - s diagram for an ideal afterburning turbojet engine is shown in Figure 4.36. It is interesting to note the appearance of τ parameters

■ **FIGURE 4.36**
Nondimensional T - s
diagram for an ideal
afterburning turbojet
engine



on the nondimensional temperature axis. Also, we note that the thermodynamic process from the flight static 0 to the turbine exit, that is, t_5 , is unaffected by the afterburner. Although, the T - s diagram depicts an ideal afterburning turbojet engine in Figure 4.36, the real engine afterburner is to operate with no *back influence* on the upstream components as well. We will continue using the *marching technique* in establishing the stagnation flow properties throughout the engine as we used in the turbojet section. The above stipulation, that the operation of an afterburner does not affect the upstream components, will bring our analysis, unchanged, to station t_5 . We will take up the analysis from station t_5 and establish exit conditions at t_7 .

To allow marching through the afterburner, we need to know or estimate its losses in total pressure and its inefficiency in heat release in the confines of the finite volume of the afterburner. These are π_{AB} and η_{AB} , respectively. So far the afterburner loss depiction through the total pressure and heat release capability is the same as the primary or main burner. However, unlike the primary burner, an afterburner may or may not be in operation and this has a large influence on the total pressure loss characteristics of the afterburner. It is only obvious to expect that the operating total pressure loss in the afterburner to be larger than the afterburner-off total pressure loss. One may think of it as the *compounding* of the burning losses as well as the frictional losses on the walls and the flameholder, which add up to the total pressure loss in an operating afterburner. Thus, we distinguish between π_{AB-OFF} and π_{AB-ON} by

$$\pi_{AB-OFF} > \pi_{AB-ON} \quad (4.99)$$

We perform an energy balance across the afterburner to establish the afterburner fuel-to-air ratio f_{AB} .

$$(\dot{m}_0 + \dot{m}_f + \dot{m}_{f,AB})h_{t7} - (\dot{m}_0 + \dot{m}_f)h_{t5} = \dot{m}_{f,AB}Q_{R,AB}\eta_{AB} \quad (4.100)$$

Divide both sides by the air mass flow rate \dot{m}_0 to get

$$(1 + f + f_{AB})h_{t7} - (1 + f)h_{t5} = f_{AB}Q_{R,AB}\eta_{AB} \quad (4.101)$$

Now, we can isolate f_{AB} as

$$f_{AB} = \frac{(1 + f)(h_{t7} - h_{t5})}{Q_{R,AB}\eta_{AB} - h_{t7}} \approx \frac{(1 + f)(T_{t7} - T_{t5})}{\frac{Q_{R,AB}\eta_{AB}}{c_{pAB}} - T_{t7}} \quad (4.102)$$

where c_{pAB} represents an average specific heat at constant pressure between the temperatures T_{t5} and T_{t7} .

The only unknown in Equation 4.102 is the fuel-to-air ratio in the afterburner, as we had calculated all the upstream parameters, for example, f , T_{t5} , values and the afterburner fuel heating value and the efficiency as well as the exit temperature are all specified. The total pressure at the afterburner exit, p_{t7} , is

$$p_{t7} = \pi_{AB} \cdot p_{t5} \quad (4.103)$$

The operation of the afterburner changes the inlet conditions to the nozzle in so far as the mass flow rate, total pressure, and temperature are concerned. The mass flow rate due to the fuel in the afterburner is calculated via Equation 4.102, the total pressure is calculated via Equation 4.103, and the total temperature at the exit of the afterburner constitutes another thermal limit, which is often specified. The analysis of the nozzle, therefore, remains unchanged, except the nozzle inlet values are different as a result of the afterburner operation.

The fundamental definitions of the cycle thermal and propulsive efficiency as given earlier in the turbojet section remain the same for an afterburning turbojet engine as well, that is,

$$\eta_{\text{th}} \equiv \frac{\Delta K \dot{E}}{\dot{Q}_{\text{thermal}}} = \frac{\Delta K \dot{E}}{\dot{m}_f \cdot Q_R + \dot{m}_{f,AB} \cdot Q_{R,AB}} \quad (4.104a)$$

$$\eta_{\text{th}} = \frac{(\dot{m}_0 + \dot{m}_f + \dot{m}_{f,AB}) \frac{V_9^2}{2} - \dot{m}_0 \frac{V_0^2}{2}}{\dot{m}_f \cdot Q_R + \dot{m}_{f,AB} \cdot Q_{R,AB}} \quad (4.104b)$$

$$\eta_p \equiv \frac{F \cdot V_0}{\Delta K \dot{E}} \quad (4.105a)$$

$$\eta_p = \frac{(F_n / \dot{m}_0) V_0}{(1 + f + f_{AB}) \frac{V_9^2}{2} - \frac{V_0^2}{2}} \quad (4.105b)$$

The only term that has been added to the denominator of Equation 4.104 (as compared with the turbojet) is the afterburner contribution to the thermal power investment in the engine. We can expand on the nondimensional form of the nozzle total pressure ratio for a turbojet, that is,

$$\pi_n = \left\{ \left(\pi_t \pi_b \pi_c \pi_d \pi_r \frac{p_0}{p_9} \right)^{\frac{\gamma-1}{\gamma}} - \eta_n \left[\left(\pi_t \pi_b \pi_c \pi_d \pi_r \frac{p_0}{p_9} \right)^{\frac{\gamma-1}{\gamma}} - 1 \right] \right\}^{\frac{-\gamma}{\gamma-1}} \quad (\text{Turbojet}) \quad (4.106)$$

by inserting the π_{AB} in the total pressure chain, to get the afterburning version of the equation, namely,

$$\pi_n = \left\{ \left(\pi_{AB} \pi_t \pi_b \pi_c \pi_d \pi_r \frac{p_0}{p_9} \right)^{\frac{\gamma-1}{\gamma}} - \eta_n \left[\left(\pi_{AB} \pi_t \pi_b \pi_c \pi_d \pi_r \frac{p_0}{p_9} \right)^{\frac{\gamma-1}{\gamma}} - 1 \right] \right\}^{\frac{-\gamma}{\gamma-1}} \quad (\text{AB-TJ}) \quad (4.107)$$

Now, we insert π_{AB} in the expression for the nozzle exit Mach number M_9 that we had derived for a turbojet, that is,

$$M_9 = \sqrt{\frac{2}{\gamma - 1} \left[\left(\pi_n \pi_{AB} \pi_t \pi_b \pi_c \pi_d \pi_r \frac{p_0}{p_9} \right)^{\frac{\gamma-1}{\gamma}} - 1 \right]} \quad (\text{AB-TJ}) \quad (4.108)$$

The exhaust velocity will remain as the product of the exit Mach number and the speed of sound in station 9,

$$\begin{aligned} V_9 &= M_9 \cdot a_9 = M_9 \sqrt{\gamma R \frac{T_{t9}}{1 + \frac{\gamma-1}{2} M_9^2}} \\ &= M_9 \sqrt{\gamma R \frac{T_0 \tau_{\lambda,AB}}{1 + \frac{\gamma-1}{2} M_9^2}} = a_0 M_9 \sqrt{\frac{\tau_{\lambda,AB}}{1 + \frac{\gamma-1}{2} M_9^2}} \end{aligned} \quad (\text{AB-TJ}) \quad (4.109)$$

The specific thrust for an afterburning turbojet engine is defined as

$$\begin{aligned} \frac{F_n}{\dot{m}_0} &\equiv \frac{(\dot{m}_0 + \dot{m}_f + \dot{m}_{f,AB})V_9 - \dot{m}_0 V_0 + (p_9 - p_0)A_9}{\dot{m}_0} \\ &= (1 + f + f_{AB})V_9 - V_0 + \frac{(1 + f + f_{AB})p_9 \left(1 - \frac{p_0}{p_9}\right) A_9}{\rho_9 V_9 A_9} \\ &= (1 + f + f_{AB})V_9 - V_0 + (1 + f + f_{AB}) \frac{RT_9 \left(1 - \frac{p_0}{p_9}\right)}{V_9} \\ &= (1 + f + f_{AB})V_9 \left(1 + \frac{1 - \frac{p_0}{p_9}}{\gamma M_9^2}\right) - V_0 \end{aligned} \quad (\text{AB-TJ}) \quad (4.110)$$

The thrust specific fuel consumption for an afterburning turbojet engine is defined as

$$\text{TSFC} \equiv \frac{\dot{m}_f + \dot{m}_{f,AB}}{F_n} = \frac{f + f_{AB}}{F_n/\dot{m}_0} \quad (4.111)$$

4.3.2.3 Optimum Compressor Pressure Ratio for Maximum (Ideal) Thrust Turbojet Engine with Afterburner. In an ideal turbojet engine with an afterburner where the thermal limit parameters τ_λ and $\tau_{\lambda,AB}$ are specified and remain fixed, we search for a compressor pressure ratio, which would maximize the performance of the engine. The desired performance parameter to be maximized is the specific thrust, F_n/\dot{m}_0 . To

simplify the analysis, let us assume the nozzle is perfectly expanded and thus there is no pressure thrust contribution. Thus, the specific thrust becomes

$$\frac{F_n}{\dot{m}_0} \approx (1 + f + f_{AB})V_9 - V_0 \approx V_9 - V_0 \quad (4.112)$$

Now, if we multiply both sides by the *average* flight and exhaust speed, that is, $1/2(V_0 + V_9)$, we get the cycle specific work, namely,

$$w_c \approx \frac{V_9^2}{2} - \frac{V_0^2}{2} \quad (4.113)$$

Therefore, to maximize the specific work of the cycle at a given flight speed, we need to maximize the exhaust kinetic energy. The exhaust kinetic energy is the difference between the stagnation and static enthalpies at the nozzle exit, that is,

$$\frac{V_9^2}{2} \equiv h_{t9} - h_9 = h_{t9} \left(1 - \frac{T_9}{T_{t9}} \right) = h_0 \cdot \tau_{\lambda,AB} \left(1 - \frac{1}{1 + \frac{\gamma-1}{2} M_9^2} \right) \quad (4.114)$$

Therefore, to maximize the exit kinetic energy for a given $\tau_{\lambda,AB}$ and h_0 , we need to maximize the exit Mach number M_9 , or M_9^2 . We can express the exit Mach number in terms of the total and static pressures at the nozzle exit, as in the turbojet section, as

$$M_9^2 = \frac{2}{\gamma - 1} \left[\left(\frac{P_{t9}}{P_9} \right)^{\frac{\gamma-1}{\gamma}} - 1 \right] \quad (4.115)$$

The exit Mach number could then be maximized if the ratio of total-to-static pressure at the exit is maximized, namely,

$$\begin{aligned} \frac{P_{t9}}{P_9} &= \frac{P_{t9}}{P_{t7}} \frac{P_{t7}}{P_{t5}} \frac{P_{t5}}{P_{t4}} \frac{P_{t4}}{P_{t3}} \frac{P_{t3}}{P_{t2}} \frac{P_{t2}}{P_{t0}} \frac{P_{t0}}{P_9} \\ &= \pi_n \pi_{AB} \pi_t \pi_b \pi_c \pi_d \pi_r \frac{P_0}{P_9} \end{aligned} \quad (4.116)$$

Assuming ideal components and perfect expansion and substitute for the turbine pressure ratio, we get

$$\frac{P_{t9}}{P_9} = 1 \cdot 1 \cdot \tau_t^{\frac{\gamma}{\gamma-1}} \cdot 1 \cdot \tau_c^{\frac{\gamma}{\gamma-1}} \cdot 1 \cdot \tau_r^{\frac{\gamma}{\gamma-1}} \cdot 1 = \left[\tau_r \tau_c \left(1 - \frac{\tau_r(\tau_c - 1)}{\tau_\lambda} \right) \right]^{\frac{\gamma}{\gamma-1}} \quad (4.117)$$

Note the exponent in Equation 4.117 is the inverse of the pressure exponent in Equation 4.115, therefore, we differentiate the terms in the bracket with respect to τ_c and set it equal to zero, namely,

$$\frac{d}{d\tau_c} \left[\tau_r \tau_c \left(1 - \frac{\tau_r(\tau_c - 1)}{\tau_\lambda} \right) \right] = \tau_r - \frac{2\tau_r^2 \tau_c}{\tau_\lambda} + \frac{\tau_r^2}{\tau_\lambda} = 0 \quad (4.118)$$

which simplifies to

$$\tau_\lambda - 2\tau_r \tau_c + \tau_r = 0 \quad (4.119a)$$

$$\tau_c = \frac{\tau_r + \tau_\lambda}{2\tau_r} \quad (4.119b)$$

$$\pi_{c, \text{Optimum}} = \left(\frac{\tau_r + \tau_\lambda}{2\tau_r} \right)^{\frac{\gamma}{\gamma-1}} \quad \text{For maximum (ideal) thrust} \quad (4.120)$$

We have plotted Equation 4.120 in Figure 4.37 for a $\tau_\lambda = 6.0$, in terms of the flight Mach number M_0 . It is interesting to note that the optimum compressor pressure ratio in an afterburning turbojet engine is independent of the afterburner temperature limit $\tau_{\lambda, AB}$. Also, by comparing the compressor pressure ratio for a maximum thrust nonafterburning turbojet (Figure 4.27) with the afterburning engine (Figure 4.37), we note that at low speed, very large compressor pressure ratios are required for the afterburning engine. In fact, at subsonic flight Mach numbers, the optimum compressor pressure ratios depicted in Figure 4.37 are unreasonably high. Figure 4.38 shows a comparison between the optimum compressor pressure ratio for a maximum-thrust turbojet with and without afterburning.

■ FIGURE 4.37
Optimum compressor pressure ratio for a maximum-thrust turbojet engine with afterburner

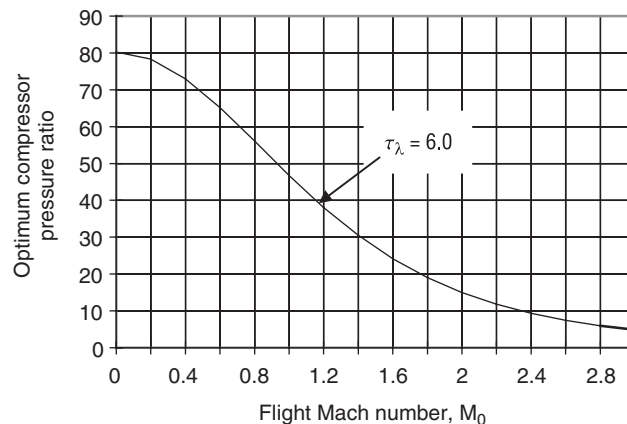
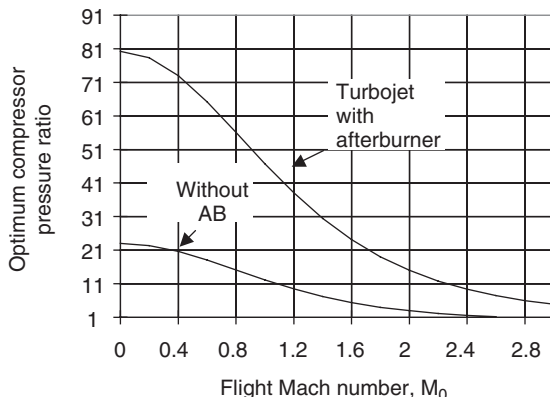


FIGURE 4.38
Compressor pressure ratio for a maximum-thrust turbojet engine with and without afterburner ($\tau_\lambda = 6.0$)



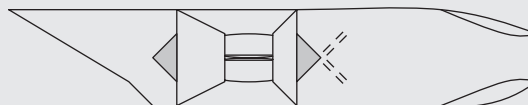
EXAMPLE 4.11

An afterburning turbojet engine operates at

- $M_0 = 2.0, p_0 = 10 \text{ kPa}, T_0 = -45^\circ\text{C}, \gamma_c = 1.4,$
- $c_{pc} = 1004 \text{ J/kg} \cdot \text{K}, \pi_d = 0.88$
- $\pi_c = 12, e_c = 0.90$
- $\tau_\lambda = 8.0, Q_R = 42,000 \text{ kJ/kg},$
- $\eta_b = 0.98, \pi_b = 0.95$
- $\gamma_t = 1.33, c_{pt} = 1156 \text{ J/kg} \cdot \text{K},$
- $e_t = 0.82, \eta_m = 0.995$
- $\tau_{\lambda AB} = 11, Q_{RAB} = 42,000 \text{ kJ/kg},$
- $\eta_{AB} = 0.98, \pi_{AB} = 0.93$
- $\gamma_{AB} = 1.30, c_{pAB} = 1,243 \text{ J/kg} \cdot \text{K}$
- $\pi_n = 0.93, p_9 = p_0$

Calculate

- (a) total pressure and temperature throughout the engine as well as fuel-to-air ratio f and f_{AB}
- (b) nondimensional specific thrust $F_n/\dot{m}a_0$
- (c) thrust specific fuel consumption (TSFC) in mg/s/N
- (d) thermal and propulsive efficiencies η_{th} and η_p , respectively



SOLUTION

We first convert the ambient temperature into absolute scale, $T_0 = -45 + 273 = 228 \text{ K}$. The corresponding speed of sound and flight speeds are

$$a_0 = \sqrt{(\gamma_c - 1)c_{pc}T_0} = \sqrt{0.4(1004)(228)} \text{ m/s} \cong 302.6 \text{ m/s}$$

$$V_0 = M_0 \cdot a_0 = (2)(302.6 \text{ m/s}) \cong 605.2 \text{ m/s}$$

Flight total pressure and temperature are

$$\left. \begin{aligned} p_{t0} &= p_0 \left[1 + (\gamma_c - 1)M_0^2/2 \right]^{\gamma_c/(\gamma_c - 1)} = 10 \text{ kPa}(1.8)^{3.5} \cong 78.24 \text{ kPa} \\ T_{t0} &= T_0 \left[1 + (\gamma_c - 1)M_0^2/2 \right] = 228 \text{ K}(1.8) \cong 410.4 \text{ K} \end{aligned} \right\} \text{Flight Total pressure and temperature} \quad \textcircled{1}$$

$$\left. \begin{aligned} \text{Since inlets are adiabatic, } T_{t2} &= T_{t0} = 410.4 \text{ K} \\ p_{t2} &= p_{t0} \cdot \pi_d(78.24 \text{ kPa})(0.88) \cong 68.85 \text{ kPa} \end{aligned} \right\} \text{total pressure and temperature at} \quad \textcircled{2}$$

$$\left. \begin{aligned} \text{Compressor exit total pressure is } p_{t3} &= p_{t2} \cdot \pi_c = 68.85 \text{ kPa} \cdot (12) \cong 826.26 \text{ kPa} \\ \text{Compressor temperature ratio is related to pressure ratio via} & \end{aligned} \right\} \text{Compressor exit} \quad \textcircled{3}$$

$$\tau_c = \pi_c^{\frac{\gamma_c}{e_c(\gamma_c - 1)}} = (12)^{1.4/0.4/0.9} \cong 2.201$$

Therefore, $T_{13} = T_{12} \cdot \tau_c = (410.4 \text{ K})(2.201) \cong 903.24 \text{ K}$

$$\left. \begin{aligned} \text{Compressor exit temperature is } \tau_\lambda &\equiv p_t T_{t4} / c_{pc} T_0, \text{ therefore,} \\ T_{t4} &= c_{pc} T_0 \tau_\lambda / c_{pt} = (1004)(228 \text{ K})(8) / 1156 \cong 1,584.2 \text{ K} \\ p_{t4} &= p_{13} \times \pi_b = 826.26 \text{ kPa}(0.95) \cong 784.95 \text{ kPa} \end{aligned} \right\} \text{Burner exit} \quad (4)$$

For fuel-to-air ratio in the burner, we use the energy balance $c_{pc} T_{13} + f Q_R \eta_b = (1+f) c_{pt} T_{t4}$

$$\text{Where } f = \frac{c_{pt} T_{t4} - c_{pc} T_{13}}{Q_R \eta_b - c_{pt} T_{t4}} = \frac{(1156)(1584.2) - (1004)(903.24)}{42000(1000)(0.98) - 1156(1584.2)} \cong 0.02351$$

For the turbine exit temperature, we use the power balance between the compressor and turbine:

$$\left. \begin{aligned} c_{pc}(T_{13} - T_{12}) &= \eta_m(1+f)c_{pt}(T_{t4} - T_{t5}) \\ \text{Therefore} \\ T_{t5} &= T_{t4} - c_{pc}(T_{13} - T_{12}) / c_{pt}\eta_m(1+f) \\ &= 1584.2 - 1004(903.24 - 410.4) / 1156(0.995)(1 + 0.02351) \cong 1,163.85 \text{ K} \end{aligned} \right\} \text{Turbine exit} \quad (5)$$

$$\pi_t = \tau_t^{\frac{\gamma_t}{(\gamma_t - 1)\epsilon_t}} = (1163.85 / 1584.2)^{1.33 / 0.33 / 0.82} \cong 0.2197$$

$$p_{t5} = p_{t4} \cdot \pi_t = 784.95 \text{ kPa}(0.2197) \cong 172.47 \text{ kPa}$$

The afterburner exit total pressure is $p_{t7} = p_{t5} \cdot \pi_{AB} = (172.47 \text{ kPa})(0.93) = 160.4 \text{ kPa}$

$$\left. \begin{aligned} \text{The afterburner exit total temperature is } T_{t7} &= c_{pc} T_0 \tau_{\lambda AB} / c_{pAB} = (1004)(228)(11) / (1243) \cong 2025.8 \text{ K} \\ f_{AB} &= \frac{(1+f)(h_{t7} - h_{t5})}{Q_{R,AB}\eta_{AB} - h_{t7}} = \frac{(1+0.02351)[1243(2025.8) - 1156(1163.85)]}{42000(1000)(0.98) - 1243(2025.8)} \cong 0.0311 \end{aligned} \right\} \text{Afterburner exit} \quad (7)$$

The nozzle exit total pressure is $p_{t9} = p_{t7} \cdot \pi_n = (160.4 \text{ kPa})(0.93) \cong 149.17 \text{ kPa}$

Since the flow in the nozzle is adiabatic, $T_{t9} = T_{t7} = 2025.8 \text{ K}$

Since $p_9 = p_0 = 10 \text{ kPa}$, we can calculate M_9 from

$$M_9 = \sqrt{\frac{2}{\gamma_{AB} - 1} \left[\left(\frac{p_{t9}}{p_9} \right)^{\frac{\gamma_{AB} - 1}{\gamma_{AB}}} - 1 \right]} = \sqrt{\frac{2}{0.3} [(14.917)^{0.3/1.3} - 1]} \cong 2.402 \quad \left. \vphantom{M_9} \right\} \text{Nozzle exit} \quad (9)$$

$$T_9 = \frac{T_{t9}}{1 + (\gamma_{AB} - 1)M_9^2/2} = \frac{2025.8 \text{ K}}{1 + 0.15(2.402)^2} \cong 1,085.8 \text{ K}$$

$$a_9 = \sqrt{(\gamma_{AB} - 1)c_{pAB}T_9} = \sqrt{0.3(1243)(1,085.8)} \cong 636.3 \text{ m/s}$$

$$V_9 = M_9 \cdot a_9 = 2.402(636.3 \text{ m/s}) = 1,528.67 \text{ m/s}$$

The specific thrust when the nozzle is perfectly expanded as in this problem is

$$F_n / \dot{m}_0 = (1 + f + f_{AB})V_9 - V_0$$

The nondimensional specific thrust is

$$F_n / \dot{m}_0 a_0 = (1 + f + f_{AB})V_9 / a_0 - M_0 = (1 + 0.02351 + 0.0311)(1528.67) / 302.6 - 2.0 \cong 3.3275$$

Also, the thrust specific fuel consumption is

$$\text{TSFC} = \frac{f + f_{AB}}{F_n / \dot{m}_0} = \frac{0.02351 + 0.0311}{3.3275(302.6)} (\text{kg/s/N})(10^6 \text{ mg/kg}) \cong 54.2 \text{ mg/s/N}$$

The cycle thermal efficiency is:

$$\eta_{th} = \frac{(1 + f + f_{AB}) \frac{V_9^2}{2} - \frac{V_0^2}{2}}{f \cdot Q_R + f_{AB} \cdot Q_{R,AB}} = \frac{(1 + 0.02351 + 0.0311)(1528.67)^2 - (605.2)^2}{2[0.02351(42000)(1000) + 0.0311(42000)(1000)]} \cong 0.4578 \quad \left. \vphantom{\eta_{th}} \right\} \text{Performance parameters}$$

The cycle propulsive efficiency in the exact form is:

$$\eta_p = \frac{(F_n/\dot{m}_0)V_0}{(1 + f + f_{AB})\frac{V_9^2}{2} - \frac{V_0^2}{2}} = \frac{3.3275(302.6)(605.2)}{(1 + 0.02351 + 0.0311)(1528.67)^2/2 - (605.2)^2/2} \cong 0.5809$$

The approximate form of propulsive efficiency is:

$$\eta_p \approx \frac{2}{1 + V_9/V_0} = 2/(1 + 1528.67/605.2) \approx 0.5672$$

EXAMPLE 4.12

Use a spreadsheet or write a computer program (e.g., MATLAB) to study the effect of the compressor pressure ratio on an afterburning turbojet engine. Use compressor pressure ratio range from 1 to 24, and the remaining engine parameters from Example 4.11. Our choice of the start-

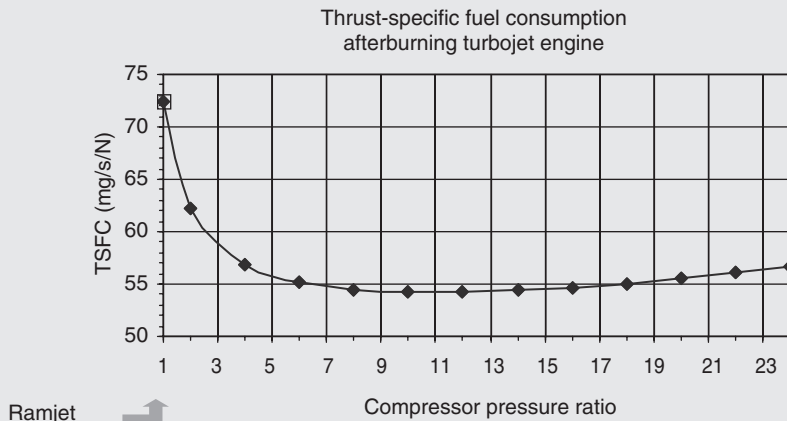
ing compressor pressure ratio of 1 allows us to simulate a ramjet. We are interested in TSFC in mg/s/N, nondimensional specific thrust, thermal, propulsive, and overall efficiency. Offer physical explanations for the behavior observed.

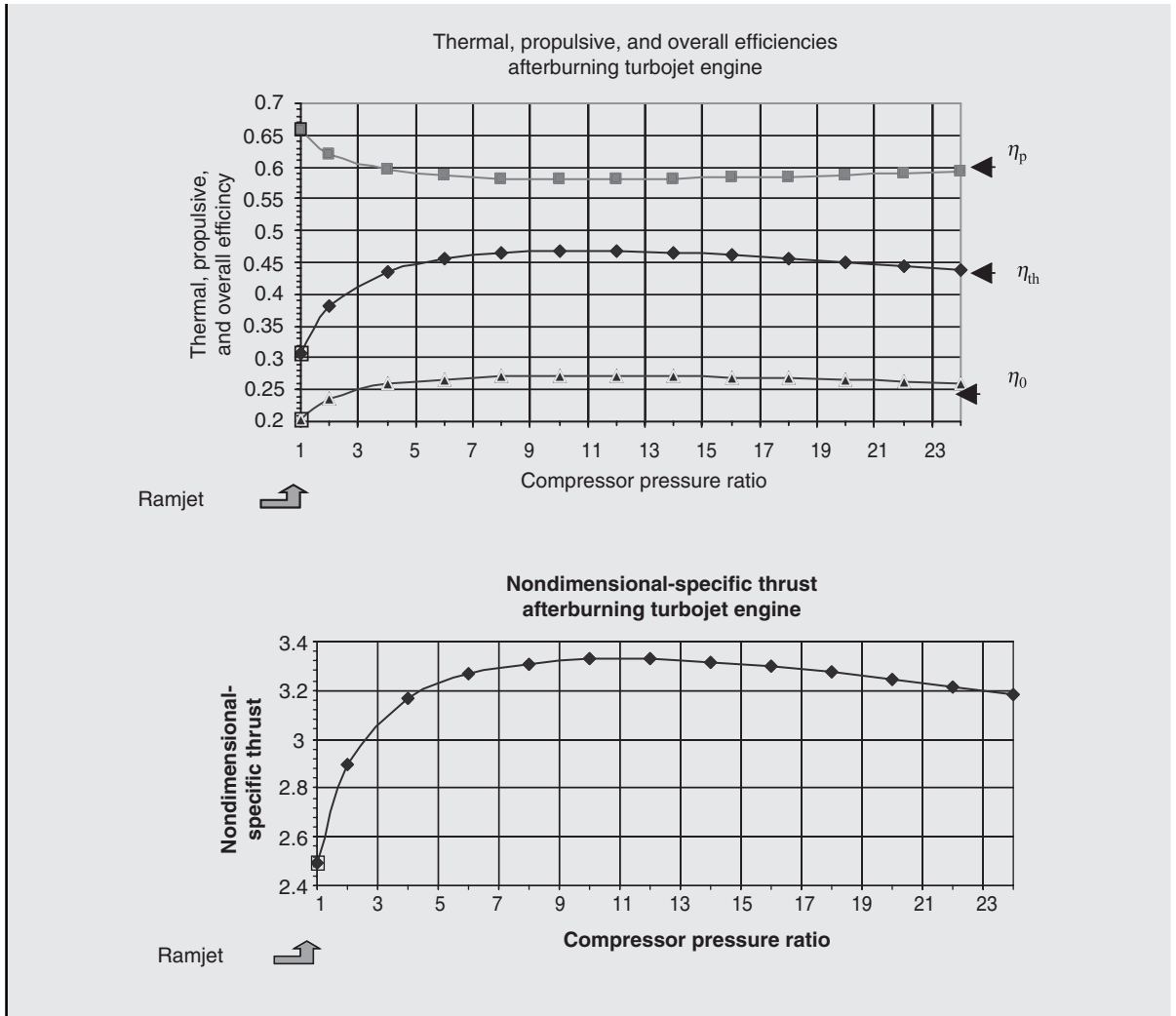
SOLUTION

Spreadsheet calculations are performed, and tables of performance parameters are produced. The graph of TSFC as a function of compressor pressure ratio is shown first.

We observe that the engine consumes the highest amount of fuel if the compressor is eliminated, i.e., in the ramjet mode, $\pi_c = 1.0$. That corresponds to a very low cycle thermal efficiency (of ~30%), as observed in the following graph. Also, we observe that there is an optimum pressure ratio (of ~12) that minimizes the fuel consumption. This behavior is also observed in specific

thrust figure, which shows a maximum thrust is produced for an optimum compressor pressure ratio. Propulsive efficiency is less profoundly affected than the cycle thermal efficiency. A decrease in propulsive efficiency with increasing cycle pressure ratio is due to an increase in exhaust velocity. The minimum exhaust velocity that occurs in a ramjet mode is $V_9 \approx 1288$ m/s. The maximum exhaust velocity occurs at the optimum compressor pressure ratio (since the cycle produces maximum work) and is $V_9 \approx 1,588$ m/s.

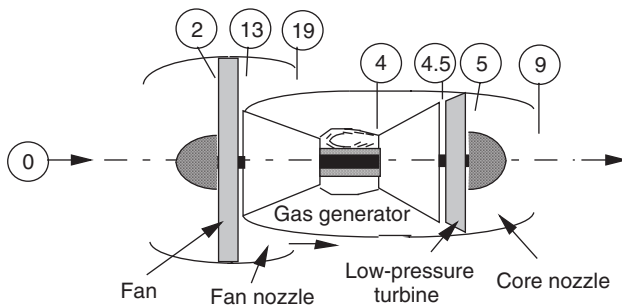




4.3.3 The Turbofan Engine

4.3.3.1 Introduction. To create a turbofan engine, a basic gas generator is followed by an additional turbine stage(s), which tap into the exhaust stream thermal energy to provide shaft power to a fan. This arrangement of multiple loading demands on the turbine stages leads to a multiple shaft arrangement, referred to as *spools*. The fan stages and potentially several (low-pressure) compressor stages may be driven by a shaft, which is connected to the low-pressure turbine. The high-pressure compressor stages are driven by the high-pressure turbine stage(s). The rotational speeds of the two shafts are called N_1 and N_2 , respectively, for the low- and high-pressure spools. An additional two new parameters enter our gas turbine vocabulary when we consider turbofan engines. The first is the *bypass ratio* and the second is the *fan pressure ratio*. The ratio of the flow rate in the fan *bypass duct* to that of the gas generator (i.e., the *core*) is called the bypass ratio α .

■ FIGURE 4.39 Schematic drawing of a separate-exhaust turbofan engine with two spools



The fan pressure ratio is the ratio of total pressure at the fan exit to that of the fan inlet. It is given a symbol π_f .

$$\alpha \equiv \dot{m}_{\text{fan-bypass}} / \dot{m}_{\text{core}} \tag{4.121}$$

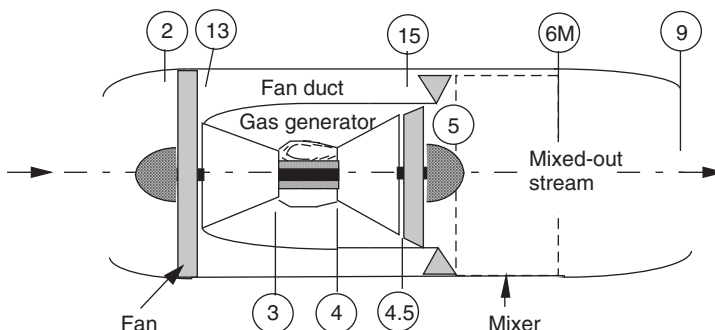
$$\pi_f \equiv p_{t13} / p_{t2} \tag{4.122}$$

The principle behind the turbofan concept comes from sharing the power with a larger mass flow rate of air at a smaller velocity increment pays dividend at low-speed flight. As we have seen earlier, the smaller the velocity increment across the engine, the higher the propulsive efficiency will be. This principle is Mach number independent; however, for supersonic flight the *installation drag* of large bypass ratio turbofan engines becomes excessive and, consequently, *small-frontal-area engines* are more suitable to high-speed flight. The fan exhaust stream may be separate from the so-called *core stream*, which is then referred to as *separate exhaust turbofan engine*. Figure 4.39 shows the schematic drawing of a two-spool, separate-exhaust turbofan engine. Note that the gas generator is still the heart of this engine.

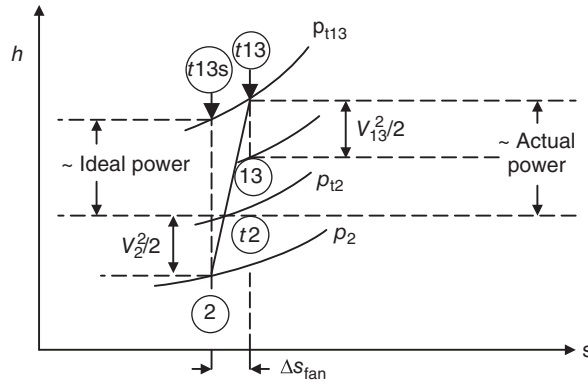
It is possible to extend the fan duct and provide mixing of the fan and the core stream in a common exhaust nozzle. The weight penalty of the long-duct turbofan engine needs to be assessed against the thrust enhancement potential of mixing a cold and hot stream in a mixer before the exhaust nozzle. The schematic drawing of this configuration is shown in Figure 4.40.

4.3.3.2 Analysis of a Separate-Exhaust Turbofan Engine. In applying our marching technique developed in the analysis of a turbojet engine to a turbofan engine,

■ FIGURE 4.40 Schematic of a long-duct turbofan engine with a mixer



■ FIGURE 4.41
h-s diagram
 representing the flow
 process in an
 (adiabatic) fan



we are confronted with the fan. Therefore, the logical question is “how do we treat the thermodynamics of a fan?” The short answer is “it is treated the same way as a compressor.” This short answer should suffice and it enables us to proceed with the analysis of a turbofan engine for now. The long answer is postponed to the chapter on turbomachinery. As in a compressor, a fan is characterized by its pressure ratio and efficiency. We may define, in an analogous manner to the compressor, an adiabatic fan efficiency η_f or a fan polytropic efficiency e_f . Let us depict the fan compression process on an *h-s* diagram, as in Figure 4.41.

The fan adiabatic efficiency is defined as

$$\eta_f \equiv \frac{h_{t13s} - h_{t2}}{h_{t13} - h_{t2}} = \frac{\Delta h_{t, \text{isentropic}}}{\Delta h_{t, \text{actual}}} = \frac{\text{ideal power}}{\text{actual power}} \quad (4.123)$$

Upon dividing the numerator and denominator of Equation 4.123 by h_{t2} , we get

$$\eta_f = \frac{T_{t13s}/T_{t2} - 1}{T_{t13}/T_{t2} - 1} = \frac{\pi_f^{\frac{\gamma-1}{\gamma}} - 1}{\tau_f - 1} \quad (4.124)$$

which relates the fan pressure and temperature ratio through adiabatic fan efficiency, that is,

$$\tau_f = 1 + \frac{1}{\eta_f} \left(\pi_f^{\frac{\gamma-1}{\gamma}} - 1 \right) \quad (4.125)$$

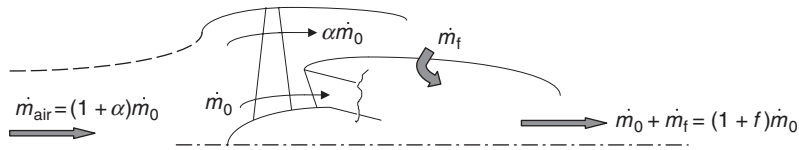
$$\pi_f = \{1 + \eta_f(\tau_f - 1)\}^{\frac{\gamma}{\gamma-1}} \quad (4.126)$$

Except for the subscript “*f*,” the above expressions for the fan are identical to those we derived for the compressor (Equation 4.13, for example).

The power balance between the turbine and compressor now includes the fan, that is, we have to write

$$\eta_m \dot{m}_0 (1 + f)(h_{t4} - h_{t5}) = \dot{m}_0 (h_{t3} - h_{t2}) + a \dot{m}_0 (h_{t13} - h_{t2}) \quad (4.127)$$

■ **FIGURE 4.42**
 Definition sketch for various mass flow rates in a separate-exhaust turbofan engine



Note that the mass flow rates in a turbofan engine are

- \dot{m}_0 air mass flow rate through the engine core
- $\alpha\dot{m}_0$ air mass flow rate through the fan duct
- $(1 + \alpha)\dot{m}_0$ air mass flow rate through the inlet (which later splits into core and the fan duct flow rates)
- \dot{m}_f the fuel flow rate in the main burner and the fuel-to-air ratio f is defined as \dot{m}_f/\dot{m}_0 ; as logically expected

This is depicted graphically in Figure 4.42.

From the power balance equation (4.127), the core mass flow rate \dot{m}_0 cancels out and if we divide both sides by flight static enthalpy h_0 to nondimensionalize the equation, we get

$$\eta_m(1 + f)\frac{h_{t4}}{h_0}(1 - \tau_t) = \frac{h_{t2}}{h_0}[(\tau_c - 1) + \alpha(\tau_f - 1)] \tag{4.128}$$

We recognize the ratio of total enthalpy at the turbine inlet to the flight static enthalpy as τ_λ and the ratio h_{t2}/h_0 as τ_r , and we proceed to isolate τ_t and express it in terms of all the known quantities, namely

$$\tau_t = 1 - \frac{\tau_r[(\tau_c - 1) + \alpha(\tau_f - 1)]}{\eta_m(1 + f)\tau_\lambda} \tag{4.129}$$

In the above equation, all the terms on the right-hand side (RHS) are either directly specified, for example, α , η_m , or τ_λ , or easily calculated from the given engine design parameters. For example, flight Mach number M_0 will produce τ_r , or compressor pressure ratio π_c and efficiency e_c will produce τ_c and similarly, fan pressure ratio π_f and efficiency e_f produce τ_f . The parameter fuel-to-air ratio f in Equation 4.129 is calculated by applying a power balance *across the burner*, which makes it independent of the bypass ratio and dependent only on the flight condition, compressor exit temperature, the specified turbine inlet temperature, and the fuel heating value and burner efficiency. The fuel-to-air ratio in a turbofan engine is thus expressed the same way as the fuel-to-air ratio in a turbojet engine, that is,

$$f = \frac{\tau_\lambda - \tau_r\tau_c}{\frac{Q_R\eta_b}{h_0} - \tau_\lambda} \tag{4.130}$$

The only point of caution about the above expression is that the fuel flow rate is referenced to the airflow rate *in the core* of a turbofan engine and not the entire airflow rate through the inlet that partially goes through the fan.

Now, let us examine Equation 4.129 more closely. We immediately note that the turbine expansion parameter τ_t is a strong function of fan bypass ratio and the compressor pressure ratio, as fully expected. After all, the power to compress the air in the fan and compressor comes directly from the turbine. However, we note that under certain conditions of, say, large fan pressure ratio or the engine bypass ratio, we may end up in a negative turbine expansion!! To see this, let us split Equation 4.129 into its rational constituents, namely,

$$\tau_t = 1 - \frac{\tau_r(\tau_c - 1)}{\eta_m(1+f)\tau_\lambda} - \frac{\tau_r\alpha(\tau_f - 1)}{\eta_m(1+f)\tau_\lambda} = 1 - A - B \tag{4.131}$$

where A and B are the second and third terms on the RHS of Equation 4.131. Let us further rearrange Equation 4.131 as follows:

$$1 - \tau_t = A + B \tag{4.132}$$

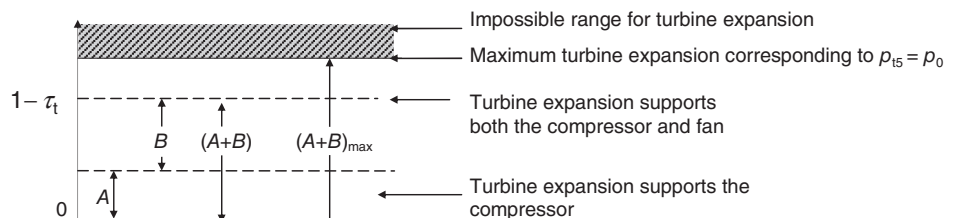
We note that $(1 - \tau_t)$ term that appears on the left-hand side of Equation 4.132 is a nondimensional expression for the turbine power output, as may be seen in Equation 4.133,

$$1 - \tau_t = \frac{T_{t4} - T_{t5}}{T_{t4}} = \frac{\wp_t}{\dot{m}_t c_{pt} T_{t4}} \tag{4.133}$$

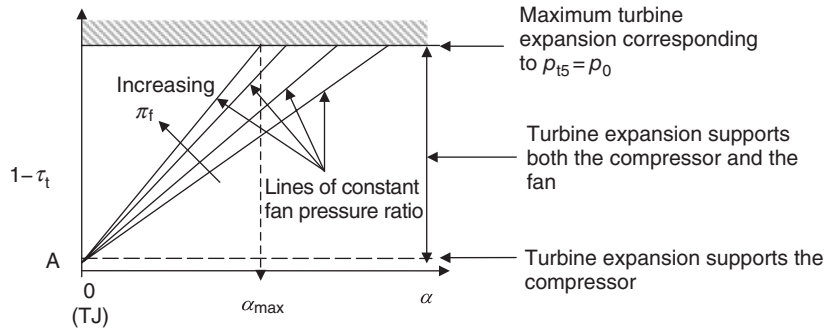
The quantity “ A ” represents the turbine expansion needed to power the compressor, as in the turbojet analysis (see, for example, Equation 4.46d). The magnitude of A is therefore independent of the fan bypass and pressure ratio. The last term in Equation 4.131, namely the B term, represents the additional turbine expansion of gases needed to run the fan. Now, this is the term that could render Equation 4.131 physically meaningless, that is, lead to a negative τ_t ! We further note that the maximum expansion in an aircraft gas turbine engine is produced when the turbine exit pressure is equal to the ambient pressure, that is, $p_{t5} = p_0$. This assumes that there is no *exhaust diffuser* downstream of the turbine (in place of the exhaust nozzle) as it is customary in stationary gas turbine power plants. Therefore, not only is a negative τ_t impossible but also a $1 - \tau_t > \wp_{t,max} / \dot{m}_t c_{pt} T_{t4}$, based on the expansion beyond the ambient pressure, is impossible. All of these arguments are presented graphically in Figure 4.43.

We can also present the impact of the engine bypass ratio as well as the fan pressure ratio on the power balance equation (4.132) graphically, for example, by noting the linear dependence of turbine expansion and bypass ratio and plotting that in Figure 4.44.

■ FIGURE 4.43
Various turbine expansion possibilities including the impossible range



■ FIGURE 4.44
Variation of turbine power parameter $(1 - \tau_t)$ with the fan bypass and pressure ratios



We learn from Figure 4.44 that for a desired fan pressure ratio π_f , the bypass ratio is limited by the maximum turbine expansion corresponding to $p_{t5} = p_0$. Also, we note that with an increasing fan pressure ratio, the bypass ratio needs to be reduced for a given turbine power output. In essence, what is graphically depicted in Figure 4.44 is intuitive.

We are now ready to develop the thrust and performance parameters for a separate-exhaust turbofan engine. The question of thrust developed in a turbofan engine is best answered if we apply the momentum principles learned in the turbojet section to two separate streams and write the gross thrust for two nozzles and account for the entire ram drag through the inlet, namely,

$$F_n = \dot{m}_0(1 + f)V_9 + \alpha\dot{m}_0V_{19} - (1 + \alpha)\dot{m}_0V_0 + (p_9 - p_0)A_9 + (p_{19} - p_0)A_{19} \quad (4.133)$$

We recognize the terms on the RHS of Equation 4.133 as the two nozzle momentum thrusts followed by the ram drag and then the pressure thrust of the primary and the fan nozzles. Once we learn the principles of thrust development of a single-stream engine, as in a turbojet, the generalization to a two-stream engine, as in the separate-exhaust turbofan engine, is very simple and straightforward. The specific thrust for a turbofan engine is the ratio of the net (uninstalled) thrust divided by the entire airflow rate through the inlet, that is, specific thrust is

$$\frac{F_n}{(1 + \alpha)\dot{m}_0} = \frac{1 + f}{1 + \alpha}V_9 + \frac{\alpha}{1 + \alpha}V_{19} - V_0 + \frac{(p_9 - p_0)A_9}{(1 + \alpha)\dot{m}_0} + \frac{(p_{19} - p_0)A_{19}}{(1 + \alpha)\dot{m}_0} \quad (4.134)$$

We immediately note that the specific thrust drops for a turbofan engine (see $1 + \alpha$ in the denominator of the left-hand side of Equation 4.134), in comparison to a turbojet engine that has zero bypass ratio, as more air is handled to produce the thrust in a bypass configuration. Therefore, this observation of lower specific thrust for a turbofan engine leads to the conclusion that bypass engines have, by necessity, larger frontal areas, again in comparison to a turbojet engine producing the same thrust. Now, we know that the larger frontal areas will result in a higher level of nacelle and installation drag. Therefore, the benefit of higher propulsive efficiency promised in a bypass engine should be carefully weighed against the penalties of higher installation drag for such configurations. The general conclusions are that for subsonic applications, the external drag penalty of a turbofan engine installation is significantly smaller than the benefits of higher engine propulsive efficiency. As a result, in a subsonic cruise civil transport, for example, the trend has been and continues to be in developing higher bypass ratio engines in order to

save on fuel consumption. Ground clearance for an under wing installation poses the main constraint on the bypass ratio/engine envelope. As the flight Mach number increases into supersonic regime, the optimum bypass ratio is then reduced. For a perfectly expanded primary and fan nozzles, Equation 4.134 simplifies to

$$\frac{F_n}{(1 + \alpha)\dot{m}_0} = \frac{1 + f}{1 + \alpha} V_9 + \frac{\alpha}{1 + \alpha} V_{19} - V_0 \quad (4.135)$$

We may divide both sides of Equation 4.134 or Equation 4.135 by the ambient speed of sound a_0 to arrive at a nondimensional expression for the specific thrust.

Applying the definition of specific fuel consumption to a turbofan engine, we get

$$\text{TSFC} = \frac{\dot{m}_f}{F_n} = \frac{f}{F_n/\dot{m}_0} = \frac{f/(1 + \alpha)}{F_n/(1 + \alpha)\dot{m}_0} \quad (4.136)$$

4.3.3.3 Thermal Efficiency of a Turbofan Engine. The ideal cycle thermal efficiency η_{th} is unaffected by the placement of a fan stage in a gas generator where the fan discharge is then expanded in a nozzle. The reason is that the power utilized to compress the gas in the fan is balanced by the power turbine and, therefore, the net energy exchange in the bypass duct comes from the balance of the fan inlet and the fan nozzle. A perfectly expanded nozzle will recover the kinetic energy exchange of the inlet diffuser, and thus the ideal thermal efficiency of a turbofan engine is unaffected. We can see this, for an ideal fan inlet and a nozzle, in the T - s diagram shown in Figure 4.45.

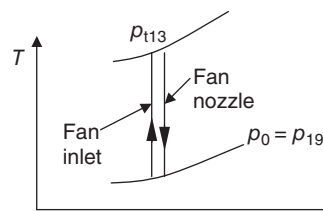
Therefore, the thermal efficiency of an ideal turbofan engine is identical to a turbojet engine with the same cycle pressure ratio, hence

$$\eta_{\text{th}} = 1 - \frac{1}{\tau_r \tau_c} = 1 - \frac{1}{\left(1 + \frac{\gamma - 1}{2} M_0^2\right) \pi_c^{\frac{\gamma - 1}{\gamma}}} \quad (4.137)$$

For the real, that is, nonideal, turbofan engine, we start from the definition of thermal efficiency:

$$\begin{aligned} \eta_{\text{th}} &\equiv \frac{\Delta K\dot{E}}{\dot{m}_f Q_R} = \frac{\alpha \dot{m}_0 \frac{V_{19}^2}{2} + (1 + f)\dot{m}_0 \frac{V_9^2}{2} - (1 + \alpha)\dot{m}_0 \frac{V_0^2}{2}}{\dot{m}_f Q_R} \\ &= \frac{\alpha V_{19}^2 + (1 + f)V_9^2 - (1 + \alpha)V_0^2}{2fQ_R} = \frac{(1 + f)V_9^2 - V_0^2}{2fQ_R} + \alpha \frac{V_{19}^2 - V_0^2}{2fQ_R} \end{aligned} \quad (4.138a)$$

■ **FIGURE 4.45**
 T - s diagram of a compression (fan) inlet stream followed by the expansion in a nozzle



The right-hand side of Equation 4.138a identifies the bypass ratio, the two exhaust velocities, the fuel-to-air ratio, the fuel heating value, and the burner efficiency as the parameters in a turbofan engine that affect the thermal efficiency of the engine. The typical unknowns, however, for the design point analysis of a turbofan engine with a given bypass ratio and a fuel type, are the two nozzle exhaust velocities and the combustor fuel-to-air ratio. We note from the last equality in Equation 4.138a that all the bypass contribution to engine cycle thermal efficiency is lumped in the last term and the core contribution is in the first term. Ideally, the lower kinetic energy of the core due to power drainage of the fan, that is, the first term, appears as the kinetic energy rise in the bypass stream, that is, the second term. Therefore, the thermal efficiency of a turbofan engine is ideally unaffected by the magnitude of the bypass stream.

Equation 4.138a is correct for a turbofan engine with perfectly expanded nozzles. In the case that the exhaust nozzles are not perfectly expanded, we have to use *effective exhaust speeds* $V_{19\text{eff}}$ and $V_{9\text{eff}}$ in place of actual exit velocities V_{19} and V_9 . We define the nozzle effective exhaust speed as

$$V_{19\text{eff}} \equiv \frac{F_{g\text{-fan}}}{\dot{m}_{19}} \quad (4.138b)$$

$$V_{9\text{eff}} \equiv \frac{F_{g\text{-core}}}{\dot{m}_9} \quad (4.138c)$$

4.3.3.4 Propulsive Efficiency of a Turbofan Engine. The propulsive efficiency of a turbofan engine, in contrast to the thermal efficiency of such engines, is a strong function of the engine bypass ratio. Starting from the definition of propulsive efficiency

$$\eta_p \equiv \frac{F_n V_0}{\Delta KE} = \frac{[(1+f)V_9 + \alpha V_{19} - (1+\alpha)V_0 + (p_9 - p_0)A_9 + (p_{19} - p_0)A_{19}]V_0}{(1+f)\frac{V_{9\text{eff}}^2}{2} + \alpha\frac{V_{19\text{eff}}^2}{2} - (1+\alpha)\frac{V_0^2}{2}} \quad (4.139)$$

and assuming the nozzles are perfectly expanded and the fuel-to-air ratio f is negligible compared to 1, the above equation may be further simplified to

$$\eta_p \approx \frac{2V_0[V_9 + \alpha V_{19} - (1+\alpha)V_0]}{V_9^2 + \alpha V_{19}^2 - (1+\alpha)V_0^2} \quad (4.140)$$

Let us recast Equation 4.140 in terms of nondimensional velocity ratios V_9/V_0 and V_{19}/V_0 , by dividing the numerator and denominator of Equation 4.140 by the square of the flight velocity V_0^2 to get

$$\eta_p \approx \frac{2 \left[\left(\frac{V_9}{V_0} \right) + \alpha \left(\frac{V_{19}}{V_0} \right) - (1+\alpha) \right]}{\left(\frac{V_9}{V_0} \right)^2 + \alpha \left(\frac{V_{19}}{V_0} \right)^2 - (1+\alpha)} \quad (4.141)$$

In a turbofan engine, the propulsive efficiency seems to be influenced by three parameters, as shown in Equation 4.141, the bypass ratio α , the primary jet-to-flight velocity ratio V_9/V_0 , and the fan jet-to-flight velocity ratio V_{19}/V_0 . In the case that the fan nozzle velocity and the primary nozzle velocity are equal, Equation 4.141 reduces to the familiar expression we derived earlier for a turbojet, namely,

$$\eta_p \approx 2/(1 + V_9/V_0) \quad (4.142)$$

which interestingly does not explicitly depend on the bypass ratio α ! The effect of bypass ratio is implicit, however, in the exhaust velocity reduction that appears in the denominator of Equation 4.142. Again as noted earlier, if the nozzles are not perfectly expanded, we have to use the effective exhaust speeds instead of the “actual” velocities. We will examine these issues in the next two examples.

EXAMPLE 4.13

A high-bypass ratio (separate-exhaust) turbofan engine powers a commercial transport. At the cruise condition, the flight and engine operating conditions are

$$\begin{aligned} M_0 &= 0.88, & p_0 &= 15 \text{ kPa}, & T_0 &= -40^\circ\text{C}, & \gamma_c &= 1.4, \\ c_{pc} &= 1004 \text{ J/kg} \cdot \text{K} \\ \pi_d &= 0.995 \\ \pi_f &= 1.6, & e_f &= 0.90, & \alpha &= 8.0 \end{aligned}$$

Fan nozzle is convergent with $\pi_{f_n} = 0.95$

$$\begin{aligned} \pi_c &= 40, & e_c &= 0.90 \\ \tau_\lambda &= 8.0, & c_{pt} &= 1,152 \text{ J/kg} \cdot \text{K}, \\ \gamma_t &= 1.33, & Q_R &= 42,000 \text{ kJ/kg}, & \pi_b &= 0.95, \\ \eta_b &= 0.992 \\ \eta_m &= 0.95, & e_t &= 0.85 \end{aligned}$$

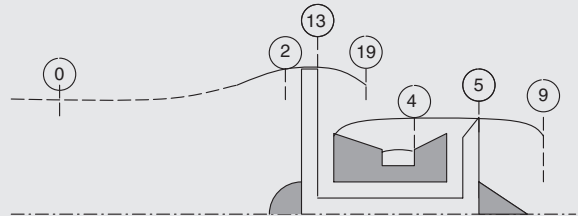
Primary nozzle is of convergent design and operates at $\pi_n = 0.98$

Calculate

- total pressures and temperatures throughout the engine and the fuel-to-air ratio
- nozzle exit static pressure p_{19} and p_9
- actual and *effective* (fan and core) nozzle exit velocities V_{19} , V_9 and $V_{19\text{eff}}$, $V_{9\text{eff}}$
- ratio of fan-to-core thrust
- nondimensional specific thrust

(f) TSFC in mg/s/N

(g) all engine efficiencies η_{th} , η_p , and η_o



Note: For (convergent) exhaust nozzles that are not perfectly expanded, the thermal and propulsive efficiencies are defined based on effective exhaust velocities:

$$\eta_{th} \equiv \frac{\Delta K \dot{E}}{\dot{m}_f Q_R} = \frac{\dot{m}_{19} V_{19\text{eff}}^2 + \dot{m}_9 V_{9\text{eff}}^2 - (\dot{m}_{19} + \dot{m}_0) V_0^2}{2 \dot{m}_f Q_R}$$

$$\eta_p \equiv \frac{2 F_\eta V_0}{\dot{m}_{19} V_{19\text{eff}}^2 + \dot{m}_9 V_{9\text{eff}}^2 - (\dot{m}_{19} + \dot{m}_0) V_0^2}$$

where the effective exhaust velocity $V_{19\text{eff}}$ is defined

$$V_{19\text{eff}} \equiv \frac{F_{g\text{-jet}}}{\dot{m}_{19}}$$

$$V_{9\text{eff}} \equiv \frac{F_{g\text{-carg}}}{\dot{m}_9}$$

SOLUTION

To practice the principles that we have learned, we march component-by-component through the engine. First, we convert ambient static temperature to absolute scale, i.e.,

$$T_0 = (-40 + 273) \text{ K} = 233 \text{ K}$$

Speed of sound at the flight altitude is $a_0 = \sqrt{(\gamma_c - 1)c_{pc}T_0} = \sqrt{0.4(1004)(233)} \text{ m/s} \cong 305.9 \text{ m/s}$

The flight speed is $V_0 = M_0 a_0 = (0.88)(305.9 \text{ m/s}) \cong 269.2 \text{ m/s}$

The total pressure of flight is $p_{t0} = p_0 \left[1 + (\gamma_c - 1) M_0^2/2\right]^{\gamma_c/(\gamma_c - 1)} = 15 \text{ kPa} \left[1 + 0.2(0.88)^2\right]^{3.5} \cong 24.83 \text{ kPa}$

The total temperature of flight is $T_{t0} = T_0 \left[1 + (\gamma_c - 1) M_0^2/2\right] = 233 \text{ K} \left[1 + 0.2(0.88)^2\right] \cong 269.1 \text{ K}$

The total pressure at the engine face is $p_{t2} = p_{t0} \cdot \pi_d = 24.83 \text{ kPa}(0.995) \cong 24.7 \text{ kPa}$

The total temperature at the engine face is equal to flight total temperature, since inlets are adiabatic, $T_{t2} = T_{t0} = 269.1 \text{ K}$

At this point, air is divided into two streams, one that goes through the fan and the second that enters the engine core.

First, let us analyze the fan stream.

The fan exit total pressure is $p_{t13} = p_{t2} \cdot \pi_f = 24.7 \text{ kPa}(1.6) \cong 39.53 \text{ kPa}$

We calculate fan exit total temperature from its efficiency, namely $\tau_f = \pi_f^{(\gamma_c - 1)/e_f \gamma_c} = 1.6^{0.4/0.90/1.4} \cong 1.1609$

The total temperature at the fan exit is $T_{t13} = T_{t2} \cdot \tau_f = (269.1 \text{ K})(1.1437) \cong 312.4 \text{ K}$

The fan nozzle exit total pressure is $p_{t19} = p_{t13} \cdot \pi_{fn} = 39.53 \text{ kPa}(0.95) \cong 37.55 \text{ kPa}$

Since the fan nozzle is of convergent design, the highest exit Mach number that it can attain is Mach 1. Let us check whether the nozzle exit reaches Mach 1. The nozzle exit static pressure for a Mach 1 exit is

$$p_{19} = p_{t19} / \left[1 + (\gamma_c - 1)/2\right]^{\gamma_c/(\gamma_c - 1)} = 37.55 \text{ kPa}/(1.2)^{3.5} \cong 19.84 \text{ kPa}$$

Since $p_{19} > p_0$, the nozzle flow is underexpanded, therefore the convergent fan nozzle has reached its peak exit velocity, i.e., sonic. Therefore, $M_{19} = 1.0$.

The fan nozzle exit static temperature is $T_{19} = T_{t13}/(1.2) = 312.4 \text{ K}/1.2 \cong 260.3 \text{ K}$

The speed of sound at the fan nozzle exit is $a_{19} = \sqrt{(\gamma_c - 1)c_{pc}T_{19}} = \sqrt{0.4(1004)(260.3)} \text{ m/s} \cong 323.3 \text{ m/s}$

Since the fan nozzle exit Mach number is 1, $V_{19} = a_{19} = 323.3 \text{ m/s}$

The fan gross thrust is $F_{g-fan} = \dot{m}_{19} V_{19} + (p_{19} - p_0)A_{19}$

The effective velocity at the fan nozzle exit is defined as $V_{19\text{eff}} \equiv F_{g-fan}/\dot{m}_{19}$

Therefore, the effective fan nozzle exit velocity is

$$V_{19\text{eff}} = V_{19} + \frac{(p_{19} - p_0)A_{19}}{\dot{m}_{19}} = V_{19} + \frac{p_{19}(1 - p_0/p_{19})A_{19}}{\rho_{19} V_{19} A_{19}} = V_{19} + \left(\frac{\gamma_c p_{19}}{\rho_{19}}\right) \frac{(1 - p_0/p_{19})}{\gamma_c V_{19}}$$

The terms in the parenthesis on the RHS of the above equation represent the speed of sound at the fan nozzle exit $(a_{19})^2$.

We have calculated all these terms, so upon substitution, we get $V_{19\text{eff}} \cong 379.7 \text{ m/s}$

Now, we are ready to calculate the core stream.

The compressor exit total pressure is $p_{t3} = p_{t2} \cdot \pi_c = 24.7 \text{ kPa}(40) \cong 988.2 \text{ kPa}$

The compressor exit total temperature is calculated via $\tau_c = \pi_c^{(\gamma_c - 1)/e_c \gamma_c} = 40^{0.4/1.4/0.90} \cong 3.225$

The exit total temperature is $T_{t3} = T_{t2} \cdot \tau_c = 269.1 \text{ K}(3 \cdot 225) \approx 868 \text{ K}$

The burner exit total pressure is $p_{t4} = p_{t3} \cdot \pi_b = 988.2 \text{ kPa}(0.95) \approx 938.8 \text{ kPa}$

The burner exit total temperature is $T_{t4} = c_{pc} T_0 \cdot t_{\lambda}/c_{pt} = 1004(233 \text{ K})(8)/1152 \approx 1,624.5 \text{ K}$

The fuel-to-air ratio is calculated from the energy balance across the burner,

$$f = (c_{pt} T_{t4} - c_{pc} T_{t3}) / (Q_R \eta_b - c_{pt} T_{t4})$$

We substitute the values in the above equation to get $f = 0.0251$

To get the total temperature at the turbine exit, we apply the power balance between the turbine and the compressor and fan, i.e., $(1 + f)c_{pt}(T_{t4} - T_{t5}) \cdot \eta_m = c_{pc}(T_{t3} - T_{t2}) + \alpha c_{pc}(T_{t13} - T_{t2})$

We have calculated all the parameters in the above equation, except T_{t5} . Upon substitution, we get $T_{t5} \approx 778.6 \text{ K}$

To calculate the turbine exit total pressure, we use the polytropic efficiency e_t in $\pi_t = \tau_t^{\gamma_t/(e_t(\gamma_t - 1))}$

The turbine $\tau_t = T_{t5}/T_{t4} = 778.6/1624.5 \approx 0.4793$

Therefore, $\pi_t = (0.4793)^{1.33/0.33/0.85} \approx 0.0306$. The turbine exit total pressure is $p_{t5} = p_{t4} \cdot \pi_t = 938.8$ kPa (0.0306) ≈ 28.72 kPa

The nozzle exit total pressure is $p_{t9} = p_{t5} \cdot \pi_n = 28.72$ kPa (0.98) ≈ 28.14 kPa

Since the maximum Mach number at the convergent nozzle exit is $M_9 = 1.0$, we examine the static pressure p_9 and compare it to p_0 . If $p_9 \geq p_0$, then the exit Mach number is 1. Otherwise, the exit Mach number is less than 1 and the exit static pressure is equal to the ambient static pressure. We calculate p_9 based on p_{t9} and the choked exit condition according to

$$p_9 = p_{t9}/[(\gamma_t + 1)/2]^{\gamma_t/(\gamma_t - 1)} = 28.14 \text{ kPa } (1.165)^{1.33/0.33} \approx 15.21 \text{ kPa}$$

Since $p_9 > p_0$, the exit Mach number is $M_9 = 1.0$ and $p_9 = 15.21$ kPa

The nozzle exit static temperature is $T_9 = T_{t5}/(\gamma_t + 1)/2 = 778.6 \text{ K}/(1.165) = 668.3 \text{ K}$

The speed of sound at the nozzle exit is $a_9 = \sqrt{(\gamma_t - 1)c_{pt}T_9} = \sqrt{0.33(1152)(668.3 \cdot 9)} \text{ m/s} \approx 504.1 \text{ m/s}$

Since $M_9 = 1$, $V_9 = a_9 = 504.1 \text{ m/s}$

The effective exhaust speed is $V_{9\text{eff}} = F_{g\text{-core}}/\dot{m}_9 = V_9 + \frac{(p_9 - p_0)A_9}{\dot{m}_9} = V_9 + \frac{a_9^2(1 - p_0/p_9)}{\gamma_t \cdot V_9} \approx 509.2 \text{ m/s}$

The fan net thrust is $F_{n\text{-fan}} = F_{g\text{-fan}} - \alpha \dot{m}_0 V_0 = \alpha \dot{m}_0 V_{19\text{eff}} - \alpha \dot{m}_0 V_0$

The nondimensional specific fan thrust (based on the inlet mass flow rate) is $\frac{F_{n\text{-fan}}}{(1 + \alpha)\dot{m}_0 \cdot a_0} = \frac{\alpha (V_{19\text{eff}} - V_0)}{(1 + \alpha) \cdot a_0}$

Upon substitution, we get $\frac{F_{n\text{-fan}}}{(1 + \alpha)\dot{m}_0 \cdot a_0} \approx 0.3210$

The net core thrust is $F_{n\text{-core}} = F_{g\text{-core}} - \dot{m}_0 V_0 = (1 + f)\dot{m}_0 V_{9\text{eff}} - \dot{m}_0 V_0$

The nondimensional specific core thrust (based on the inlet mass flow rate) is $\frac{F_{n\text{-core}}}{(1 + \alpha)\dot{m}_0 \cdot a_0} = \frac{(1 + f)V_{9\text{eff}} - V_0}{(1 + \alpha) \cdot a_0}$

Upon substitution, we get $\frac{F_{n\text{-core}}}{(1 + \alpha)\dot{m}_0 \cdot a_0} \approx 0.09184$

The ratio of fan-to-core thrust is $\frac{F_{n\text{-fan}}}{F_{n\text{-core}}} = \frac{0.3210}{0.09184} \approx 3.495$

The fan contribution to the engine net thrust is $F_{n\text{-fan}}/F_{n\text{-total}} = 0.3210/(0.3210 + 0.09184) \approx 77.75\%$

The core contribution to the total net thrust is $F_{n\text{-core}}/F_{n\text{-total}} = 0.09184/(0.3210 + 0.09184) \approx 22.25\%$

The thrust specific fuel consumption is $\text{TSFC} = \dot{m}_f/F_n$. In terms of the nondimensional specific thrust, TSFC may be written as $\text{TSFC} = \frac{f}{(1 + \alpha)a_0 F_n / [(1 + \alpha)\dot{m}_0 a_0]} = \frac{(0.0251) \cdot 10^6}{(9)(305.9)(0.4128)} \text{ mg/s/N} = 22 \cdot 11 \text{ mg/s/N}$

Note that without the 10^6 in the numerator, we would get kg/s/N. Therefore, $\text{TSFC} \approx 22.11 \text{ mg/s/N}$.

Since the fan and core nozzles were not perfectly expanded, we use the effective exhaust speeds in calculating thermal and propulsive efficiencies.

$$\eta_{\text{th}} \equiv \frac{\Delta K \dot{E}}{\dot{m}_f \dot{Q}_R} = \frac{\dot{m}_{19} V_{19\text{eff}}^2 + \dot{m}_9 V_{9\text{eff}}^2 - (\dot{m}_{19} + \dot{m}_0) V_0^2}{2 \dot{m}_f \dot{Q}_R} = \frac{\alpha V_{19\text{eff}}^2 + (1 + f) V_{9\text{eff}}^2 - (1 + \alpha) V_0^2}{2f \dot{Q}_R}$$

Upon substitution, we get $\eta_{\text{th}} \approx 36.32\%$

The propulsive efficiency is

$$\eta_p \equiv \frac{2F_n V_0}{\dot{m}_{19} V_{19\text{eff}}^2 + \dot{m}_9 V_{9\text{eff}}^2 - (\dot{m}_{19} + \dot{m}_0) V_0^2} = \frac{2 \left[\frac{F_n}{(1 + \alpha)\dot{m}_0 a_0} \right] (1 + \alpha) a_0 V_0}{\alpha V_{19\text{eff}}^2 + (1 + f) V_{9\text{eff}}^2 - (1 + \alpha) V_0^2}$$

We have calculated the terms on the RHS, upon substitution, we get $\eta_p \approx 79.80\%$

The overall efficiency is the product of the thermal and propulsive efficiency, $\eta_0 \approx (0.3632)(0.798) \approx 28.99\%$

EXAMPLE 4.14

Write a computer program or use the spreadsheet to calculate and graph the performance of the separate-exhaust turbofan engine described in Example 4.13 for a range of bypass ratios from 0 to 8. The zero bypass ratio simu-

lates a turbojet. Explain the results that you graphically depict for TSFC, nondimensional-specific thrust, and thermal, propulsive, and overall efficiencies.

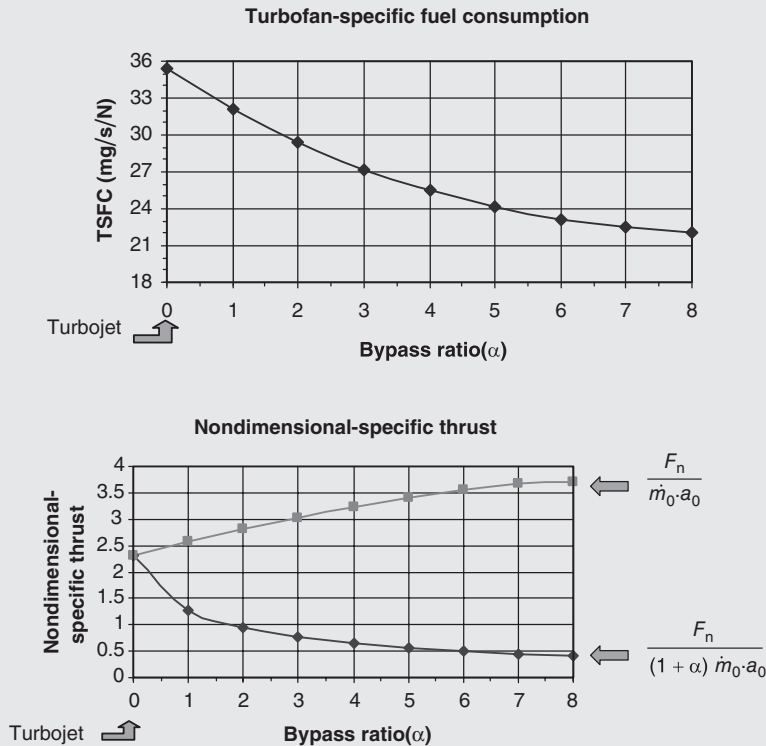
SOLUTION

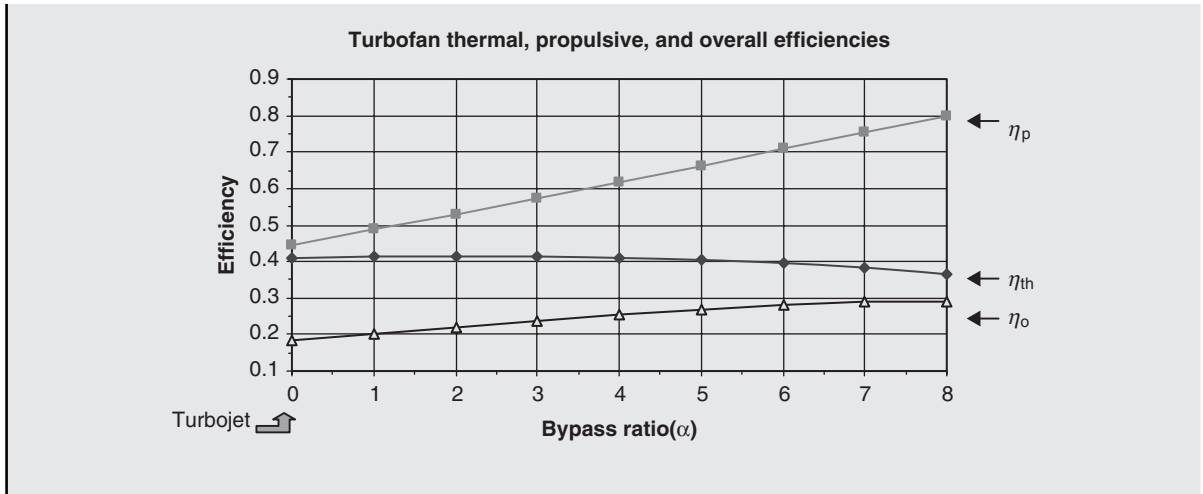
Spreadsheet calculations are performed in the range of 0–8 bypass ratio turbofan of Example 4.13. A plot of TSFC in (mg/s/N) shows continuous improvement with increasing bypass ratio. Indeed, the turbojet case of $\alpha = 0$ consumes the most fuel. The modern ultra-high bypass ratio turbofan engines in commercial aviation with a bypass ratio of ~ 8 use $\sim 40\%$ less fuel than a turbojet or $\sim 10\%$ less fuel than a bypass ratio 5 turbofan engine.

The specific thrust of the turbofan engine as a function of bypass ratio is shown in the following graph. Since a turbofan produces its thrust by acting over a large mass flow of air, its specific thrust is lower than a turbojet. We note that the engine thrust per unit *inlet mass flow rate*, nondimensionalized by the ambient speed of sound a_0 is reduced with increasing bypass ratio. However, if we graph the turbofan

engine thrust per unit core *mass flow rate* (again nondimensionalized by a_0), we note that engine thrust continuously increases with bypass ratio.

The thermal efficiency of the turbofan engine as a function of bypass ratio is graphed. As indicated in the text, the ideal thermal efficiency of a turbofan engine does not change with bypass ratio and, as seen, this point is borne out by data for the “real” turbofan engine as well. The propulsive efficiency, which was the target of improvement in a turbofan engine, shows continuous increase with bypass ratio. The lowest propulsive efficiency corresponds to the turbojet engine ($\alpha = 0$) at $\sim 44\%$ in this example. The overall efficiency improves with bypass ratio similar to the propulsive efficiency.





4.3.4 Ultra-High Bypass (UHB) Turbofan Engines

There is a new class of turbofan engines, called Ultra-High Bypass, or UHB, that promises to reduce fuel consumption (by nearly 15% compared to current TF engines, e.g., the CFM56 family of turbofan engines), cut noise (by a 20 dB margin to FAA Stage 4 Aircraft Noise Standards), and produce less pollutants/emissions. Typical bypass ratios in this class starts around 12. To make a comparison, the advanced turboprops that were developed in 1980s and 1990s had bypass ratios of 35–70 (the GE-UDF had a bypass ratio of 35 and the P&W/AGT had a bypass ratio of 70). Therefore, the UHB turbofan engines of 2010 fall between the current conventional turbofans with bypass ratios in the 6–8 range and the ATP engines with bypass ratios in the 35–70 range. We learned that propulsive efficiency improved with bypass ratio in a turbofan engine. We derived an expression for the thrust-specific fuel consumption in a jet engine that was inversely proportional to propulsive efficiency, η_p , namely from Equation 4.95a, we get

$$TSFC = \frac{V_0/Q_R}{\eta_p \eta_{th}}$$

Therefore, UHB development targets propulsive efficiency improvements to reduce fuel consumption as well as offering other attractive features (e.g., reduced noise and pollution). Airline industry and commercial cargo business/transporters are most affected by the fuel consumption performance, as it represents the lion's share of their Direct Operating Cost (DOC). So, it stands to reason to increase the bypass ratio as long as we can innovate our way through the technology challenges associated with the UHB engines. The practical problems of developing/implementing a high-efficiency large bypass ratio turbofan engine are inherent in:

- Operational disparity between a large-diameter fan and a very small engine core diameter, that is, low-pressure turbines (LPT) and intermediate pressure

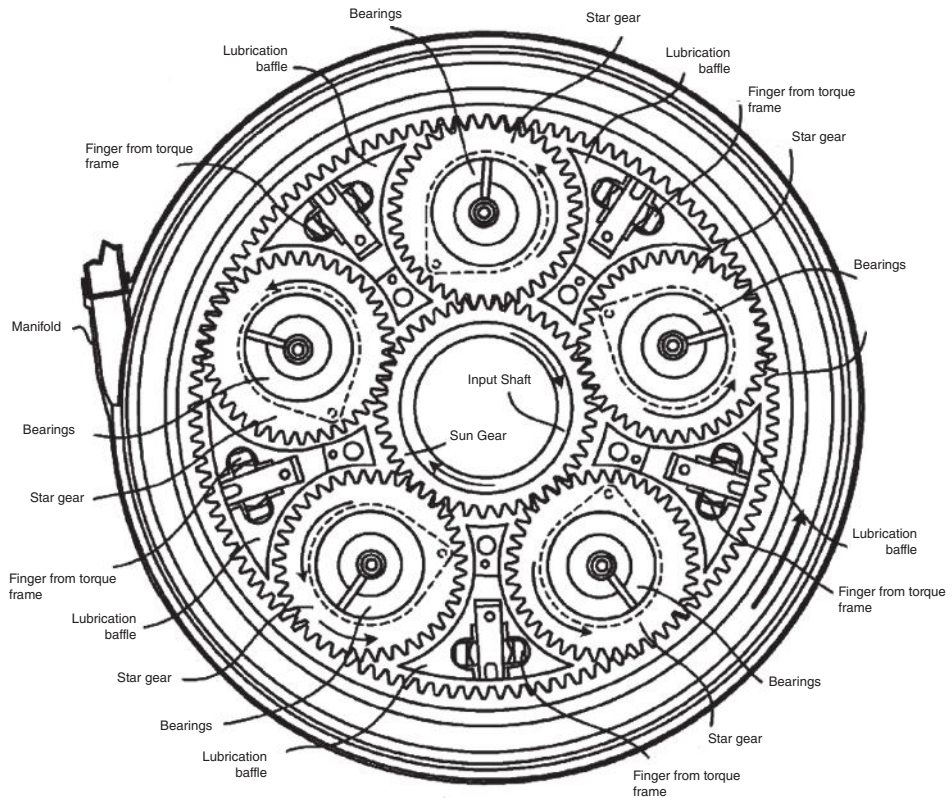
compressors (IPC) have much smaller diameters than the fan, yet are driven by the same shaft (i.e., the low-pressure spool)

- To improve the efficiency of the fan, IPC and LPT, we need a suitable (i.e., lightweight, reliable) fan drive gear system
- The UHB turbofan installation concerns on aircraft are mainly:
 - Wing/fuselage integration, clearance/envelope, limits on fan diameter
 - Transonic nacelle drag calling for a “*slim line*” nacelle design with natural laminar flow or hybrid laminar flow (i.e., with boundary layer suction)
 - Nacelle weight concerns demanding the use of advanced composite materials
 - Innovative fan reverser design and integration into nacelle.

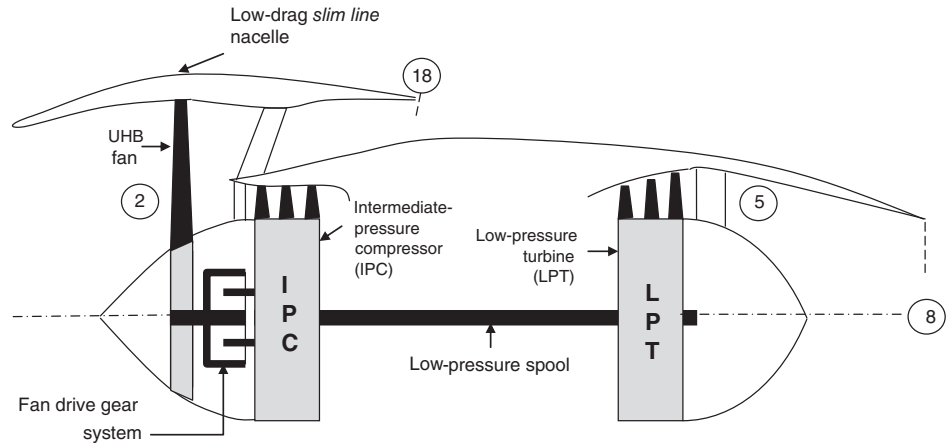
Pratt & Whitney and NASA have worked closely to develop the geared turbo-fan (GTF) engine technology in connection with the UHB requirements. The first GTF entry into service, PW1000G family, was in 2013. The engine uses a patented lightweight “floating gearbox” system that separates the fan from the IPC and LPT. The gear ratio is 3:1. Figure 4.46 shows the cross-sectional view of the star gear train used in the fan drive system (Duong *et al.*, 2009).

The weight reduction in the nacelle is accomplished through a composite fan nacelle design. The schematic drawing of the low-pressure spool in a candidate GTF engine is shown in Figure 4.47.

■ **FIGURE 4.46**
Cross-sectional view of
the star gear train
(Duong *et al.*, 2009)



■ **FIGURE 4.47**
Schematic drawing of
the low-pressure spool
in a UHB with fan
drive gear system



To appreciate the cycle parameters of typical UHB engines, for example, its fan low-pressure ratio and thrust-specific fuel consumption performance, we solve an example problem (Example 4.16).

EXAMPLE 4.15

A geared turbofan (GTF) is used in a UHB engine with a single-stage, low-pressure ratio fan. The engine design point is at the standard sea level static condition, $M_0 = 0$, $p_0 = 101 \text{ kPa}$, $T_0 = 288 \text{ K}$, $\gamma_c = 1.4$ and $c_{pc} = 1,004 \text{ J/kgK}$ and the engine at the design point is sized for the air mass flow rate (into the inlet) of 600 kg/s .

The inlet at the design point is assumed to have $\pi_d = 0.995$ total pressure recovery.

The fan bypass ratio at the design point is $\alpha = 12$, its design pressure ratio is $\pi_f = 1.36$ (which is considered low compared to 1.6 fan pressure ratio) and its polytropic efficiency, $e_f = 0.90$. The reduction gearbox is characterized by efficiency, which is the ratio of power transmission across the gearbox, namely:

$$\eta_{gb} \equiv \frac{(\varphi_{\text{gearbox}})_{\text{out}}}{(\varphi_{\text{gearbox}})_{\text{in}}}$$

We assume $\eta_{gb} = 0.998$. The core compressor pressure ratio (i.e., excluding the inner fan section) is $p_{13}/p_{12} = 22$ with polytropic efficiency, $e_c = 0.90$. Note that the overall com-

pressor pressure ratio that includes the inner fan section is then $p_{13}/p_{12} = (1.36)(22) = 29.92$.

The combustor at takeoff is characterized by: $T_{t4} = 1,600 \text{ K}$, $Q_R = 42,800 \text{ kJ/kg}$, $\eta_b = 0.99$, $\pi_b = 0.96$.

The turbine has a polytropic efficiency of $e_t = 0.85$ and power transmission (or mechanical) efficiency, $\eta_m = 0.975$. The gas in the hot section may be modeled as $\gamma_t = 1.33$, $c_{pt} = 1,156 \text{ J/kgK}$.

Both the fan and the core nozzles are of convergent design with $\pi_{fn} = 0.985$ and $\pi_{cn} = 0.990$. We simplify our analysis in this example by treating the gas properties as specified in two “cold” and “hot” zones as described.

Calculate

- total pressures and temperatures at every station inside the engine
- combustor fuel flow rate in kg/s and lbm/s
- shaft power delivered to the gearbox in MW and hp
- shaft power delivered to the fan in MW and hp
- fan nozzle exit Mach number, M_{18}
- core nozzle exit Mach number, M_8
- fan nozzle gross thrust, F_{gf} , in kN and lbf

- (h) core nozzle gross thrust, F_{gc} , in kN and lbf
 (i) thrust-specific fuel consumption (TSFC) in mg/s/N and lbf/hr/lbf

- (j) estimate the gearbox mass if its mass is proportional to the shaft horsepower according to the following gearbox mass density rule: gearbox mass density = 0.008 lbf/hp.

SOLUTION

Since $M_0 = 0$, $p_{10} = p_0 = 101$ kPa and $T_{10} = T_0 = 288$ K. The total temperature in the inlet remains constant (adiabatic flow), which gives $T_{12} = 288$ K. The total pressure in the inlet suffers some loss due to friction, which results in $p_{12} = \pi_d \cdot p_{10} = 100.5$ kPa

Based on fan total pressure ratio, we get the total pressure in station 13 as $p_{13} = \pi_f \cdot p_{12} = 136.7$ kPa. We use $\tau_c = \pi_c^{\frac{\gamma-1}{\gamma c}}$ to get $T_{13} = 317.5$ K. To march towards the fan nozzle exit, we use the fan nozzle total pressure ratio to get $p_{18} = p_{13} \cdot \pi_{fn} = 134.6$ kPa. Since the fan nozzle flow is adiabatic, the total temperature remains constant; therefore, $T_{18} = T_{13} = 317.5$ K.

We calculate the fan nozzle pressure ratio p_{13}/p_0 to check it against the “critical” NPR where the nozzle chokes. In this problem, $\text{NPR}_{fn} = 1.353$, which is far less than the critical value (of ~ 2). Therefore, we conclude that the exit of our convergent fan nozzle is unchoked, and thus subsonic. We also conclude that the static pressure at the nozzle exit is the same as the ambient pressure; therefore, $p_{18} = p_0 = 101$ kPa. From p_{18} and p_{13} we calculate M_{18} , which produces $M_{18} = 0.654$. From T_{18} and M_{18} , we calculate $T_{18} = 292.5$ K, with the corresponding speed of sound, $a_{18} = 342.7$ m/s, and fan nozzle exit velocity is $V_{18} = M_{18} \cdot a_{18} = 224.2$ m/s. Since the nozzle is perfectly expanded, $V_{18,eff} = V_{18} = 224.2$ m/s. Therefore, the fan nozzle gross thrust is $F_{gf} = \dot{m}_0 V_{18} = 124.16$ kN (or 27,913 lbf).

Now, we do the core calculations. The compressor overall pressure ratio, including the fan inner section, is the product of the fan and the core pressure ratio, i.e., $\pi_c = \pi_f \cdot \pi_{core} = 29.92$ (this is the cycle pressure ratio). Based on π_c and p_{12} , we get $p_{13} = 3006.8$ kPa. From the polytropic efficiency of the compressor, we calculate the compressor total temperature ratio, $\tau_c = 2.9414$. Therefore, the compressor exit total temperature is $T_{13} = 847$ K. The combustor exit total temperature is a given design value at takeoff of $T_{14} = 1600$ K; therefore, through energy balance across the combustor, we calculate the fuel-to-air ratio to be $f = 0.0247$. From the total pressure ratio across the burner, π_b , we get the exit total pressure, $p_{14} = 2886.5$ kPa. The turbine shaft power is delivered to the core compressor and the fan gearbox. The gearbox delivers its input power times the

efficiency of gearbox to the fan. We calculate fan power through energy balance across the fan, namely,

$$\begin{aligned} \dot{\mathcal{Q}}_f &= (1 + \alpha) \dot{m}_0 c_{pc} (T_{113} - T_{12}) \\ &= 600 \frac{\text{kg}}{\text{s}} \left(1004 \frac{\text{J}}{\text{kgK}} \right) (317.5 - 288) \text{K} \\ &= 17.789 \text{ MW (or 23,859 hp)} \end{aligned}$$

The power delivered to the gearbox is

$$\dot{\mathcal{Q}}_{\text{gb-in}} = \frac{\dot{\mathcal{Q}}_f}{\eta_{\text{gb}}} = 17.825 \text{ MW (or 23,907 hp)}$$

The core compressor shaft power is calculated from the power balance across the core compressor

$$\begin{aligned} \dot{\mathcal{Q}}_{\text{core}} &= \dot{m}_0 c_{pc} (T_{13} - T_{113}) \\ &= 46.15 \frac{\text{kg}}{\text{s}} \left(1004 \frac{\text{J}}{\text{kgK}} \right) (847 - 317.5) \text{K} \\ &= 24.54 \text{ MW} \end{aligned}$$

The turbine shaft power produced is

$$\dot{\mathcal{Q}}_t = \frac{\dot{\mathcal{Q}}_f + \dot{\mathcal{Q}}_{\text{core}}}{\eta_m} = 43.452 \text{ MW}$$

Therefore, the turbine exit total temperature is calculated from the power balance across the turbine to be: $T_{15} = 805.2$ K. From the polytropic efficiency of the turbine and its τ_t , we calculate $\pi_t = 0.0385$ and, thus, $p_{15} = 111.2$ kPa. The core nozzle exit total pressure is the product of π_{cn} and p_{15} ; therefore $p_{18} = 110.14$ kPa. The total temperature in the adiabatic nozzle remains constant; therefore, $T_{18} = T_{15} = 805.2$ K. The core nozzle pressure ratio, $\text{NPR}_{\text{core-nozzle}} = 1.10$, which is far below the critical nozzle pressure ratio of ~ 2 . Therefore, the core nozzle exit is subsonic and it is perfectly expanded, i.e., $p_8 = p_0 = 101$ kPa, and we calculate M_8 from p_{18} and p_8 to be $M_8 = 0.363$. In the core nozzle calculations we use the hot gas properties. From the

T_{t8} and M_8 , we calculate $T_8 = 788$ K and, thus, $a_8 = 548.3$ m/s and $V_8 = 199$ m/s. The core nozzle gross thrust is

$$F_{gc} = (1 + f) \dot{m}_0 V_8 = 9.411 \text{ kN (or 2116 lbf)}$$

The ratio of fan-to-core thrust is thus $27913/2116 = 13.2$

The engine thrust is the sum of the two gross thrusts (since there is no ram drag at takeoff),

$$F_{\text{total}} = 133.6 \text{ kN (or 30,000 lbf)}.$$

The thrust-specific fuel consumption (TSFC) = 8.519 mg/s/N, which is equal to 0.301 lbm/hr/lbf, which is about 20% below a conventional turbofan engine (of bypass ratio 6) that delivers a TSFC of about 0.367 lbm/hr/lbf.

When we calculate the specific impulse, I_s , for this engine, we get $I_s \approx 12,000$ s, which is again another indicator for a tremendous takeoff performance, more in line with turboprops.

The mass of the gearbox is directly proportional to the power delivered to the gearbox through this correlation: 0.008 lbm/hp (as suggested by Ian Halliwell, 2010). Consequently, since the power into the gearbox was calculated to be $23,907$ hp, the mass of the gearbox is estimated at

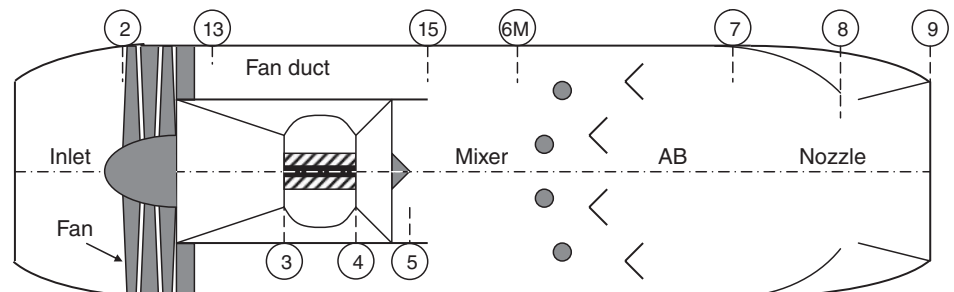
191 lbm or 86.6 kg, which is insignificant as a key component in a $30,000$ -pound thrust class engine.

In this example we performed a one-dimensional analysis with a simple gas model. Our turbine was uncooled but we specified a lower turbine efficiency to partially account for the effect of cooling. Also, we did not extract any auxiliary shaft power, as it is always done in aircraft gas turbine engines. However, more accurate engine simulators are available (Kurzke, 2013) that will properly model the gas, perform cooling bleed and power extraction, which must be used for higher accuracy. In our simple analysis, we demonstrated a 20% reduction in TSFC whereas in real engine testing a 15% reduction in TSFC is measured. Additional information on GTF can be found on the Pratt & Whitney website; Asbury and Yetter (2000) may be consulted for thrust reversers; Guynn *et al.* (2009) have treated advanced cycles for single-aisle transport aircraft. The CFM website provides performance parameters of other modern turbofan engines.

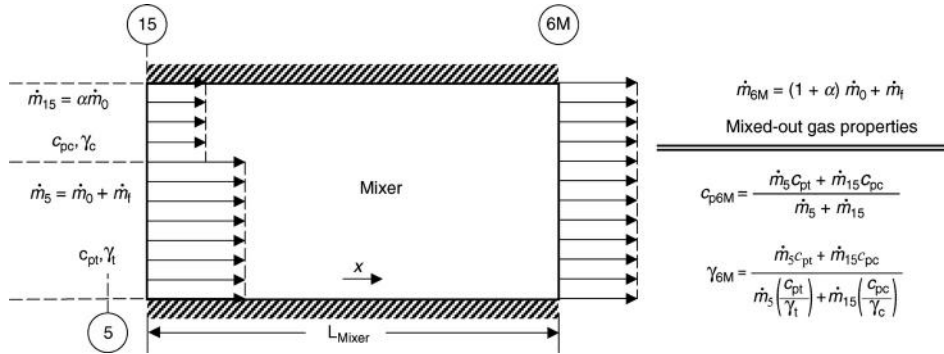
4.4 Analysis of a Mixed-Exhaust Turbofan Engine with an Afterburner

The schematic in Figure 4.48 of a mixed-exhaust turbofan engine shows the station numbers for this engine and identifies a new component, namely the mixer. The engine core discharges a hot gas into the mixer, whereas the fan duct injects a “cold” gas into the mixer. Upon mixing of the two streams, the gas will attain a “mixed-out” state at station 6M. Now, what about the pressure of the two incoming streams? On the question of pressure between the two streams, as they enter the mixer, we rely on our understanding of the Kutta trailing-edge condition applied to airfoils with a sharp trailing edge. We learned this principle in aerodynamics. In simple terms, the Kutta condition demands the continuity of static pressure at the trailing edge, that is, $p_{\text{upper}} = p_{\text{lower}}$ on an airfoil at

■ **FIGURE 4.48**
Long-duct turbofan engine with a mixer and an afterburner



■ FIGURE 4.49 Mixer control volume showing a nonuniform inlet and mixed-out exit velocity profiles



its trailing edge. It physically suggests that the two merging streams at the trailing edge of an airfoil, or fan duct and engine core streams cannot support a *static pressure jump*. Therefore, we demand

$$p_{15} = p_5 \tag{4.143}$$

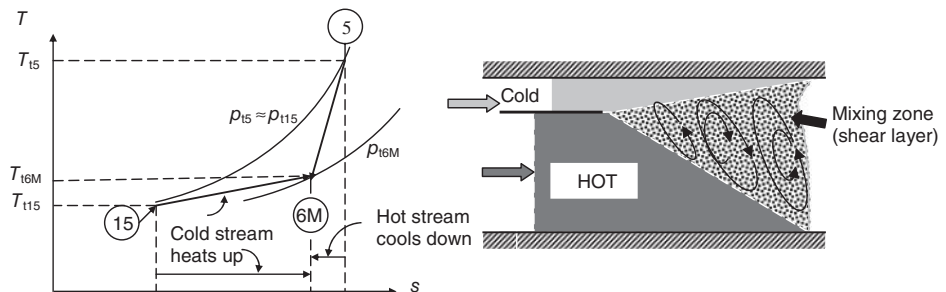
We can think of Equation 4.143 as the static pressure that is *communicated* between the core and the fan duct, which is a physical principle. Therefore, the fan pressure ratio and hence mass flow rate are basically set by the *engine backpressure*. Here, we note that the two parameters of a fan, namely its pressure ratio and the bypass ratio, cannot be independently set in this configuration. Here, we can stipulate only one parameter and the second parameter *falls out* of the common backpressure requirement.

4.4.1 Mixer

To analyze a constant-area mixer, we employ the conservation principles of mass, momentum, and energy. Also, the mixture gas laws establish the mixed-out gas properties at the mixer exit. Figure 4.49 shows a constant-area mixer where mixed-out gas properties c_{p6M} and c_{v6M} are mass averaged and γ_{6M} is the ratio of the two.

The thermodynamic state of gas before and after the mixing process is shown on a T - s diagram in Figure 4.50. The physical mixing process takes place in the shear layer where cold and hot vortices interject and mingle.

■ FIGURE 4.50 Mixing of two streams at different temperatures on a T - s diagram and in physical domain



The application of the law of conservation of energy to an insulated mixer gives

$$\dot{m}_5 h_{t5} + \dot{m}_{15} h_{t15} = \dot{m}_{6M} h_{t6M} \quad (4.144)$$

Assuming the inlet conditions are known for the mixer, the only unknown in the above equation is the mixed-out total enthalpy h_{t6M} , namely,

$$h_{t6M} = \frac{(1+f)h_{t5} + \alpha h_{t15}}{1 + \alpha + f} \quad (4.145)$$

Here we can introduce the component nondimensional parameters in the above equation as follows:

$$h_{t6M} = h_0 \cdot \frac{(1+f)\tau_t \cdot \tau_\lambda + \alpha \tau_r \cdot \tau_f}{1 + \alpha + f} \quad (4.146)$$

In order to establish the mixed-out pressure p_{6M} at the exit of the mixer, we apply the conservation of momentum in the streamwise direction, that is, x as shown in Figure 4.49. A simple expression for the x -momentum is just $\dot{m}V_x$, which holds for a steady uniform flow and may be applied to the mixer control volume as follows:

$$\dot{m}_{6M} V_{6M} - [\dot{m}_5 V_5 + \dot{m}_{15} V_{15}] = \sum F_x \quad (4.147)$$

In the above expression, the right-hand side is the sum of all external forces acting on the control volume in the x -direction. The external forces are nothing more than the integrals of pressure and wall shear over the flow and wetted areas, respectively, namely,

$$\sum F_x = p_5 A_5 + p_{15} A_{15} - p_{6M} A_{6M} - \int \tau_w dA_{\text{wetted}} \quad (4.148)$$

where the last term is the wall friction drag force acting on the mixer wall, $D_{f_{\text{mixer}}}$, associated with the mixer in the above flow condition. We also note that the static pressures at the entrance to the mixer from the core and the fan duct side are the same à la Kutta condition,

$$p_5 = p_{15} \quad (4.149)$$

and

$$A_{6M} = A_5 + A_{15} \quad (4.150)$$

for a constant-area mixer. Now, let us put all these relationships together in the x -momentum equation of the mixer, that is, Equation 4.147, and group terms to arrive at

$$(\dot{m}_{6M} V_{6M} + p_{6M} A_{6M}) - (\dot{m}_5 V_5 + p_5 A_5) - (\dot{m}_{15} V_{15} + p_{15} A_{15}) = -D_f \quad (4.151)$$

The grouped terms in the above equation are the *impulse* (given a symbol I , as we discussed in Chapter 2) in corresponding stations, namely 6M, 5, and 15, respectively. We note that the fluid impulse out of the mixer is somewhat less than the (sum of the)

fluid impulse entering the mixer and this difference or loss is caused by the friction drag on the mixer wall. Therefore, if we had assumed a frictionless flow in the mixer, we would have concluded that the impulse is conserved, that is,

$$I_{6M} = I_5 + I_{15} \quad (4.152)$$

We proceed with our analysis using the assumption of zero boundary layer frictional losses on the walls of the mixer in order to derive a closed form solution for the unknown mixer exit conditions. We then suggest a correction factor due to friction that accounts for the viscous flow losses on the total pressure.

The impulse function “ I ” attains a very simple form when we express it in terms of flow Mach number. The steps are outlined in the following equation:

$$I \equiv \dot{m}V + pA = A(\rho V^2 + p) = Ap \left(\frac{\rho V^2}{p} + 1 \right) = Ap(1 + \gamma M^2) \quad (4.153)$$

We had used the equation for the speed of sound $a^2 = \gamma p/\rho$ in the above derivation. Hence, the flow impulse at any station is the product of pressure–area term and $(1 + \gamma M^2)$ at that station. Now, in light of this expression for impulse, let us recast Equation 4.152 in terms of flow Mach number and pressure area terms as

$$p_{6M}A_{6M}(1 + \gamma_{6M}M_{6M}^2) - p_5A_5(1 + \gamma_5M_5^2) - p_{15}A_{15}(1 + \gamma_cM_{15}^2) = 0 \quad (4.154)$$

Now, if we divide the above equation by a reference area, namely turbine exit area A_5 , we will eliminate the effect of size from the above equation. Therefore, we can express Equation 4.154 as

$$p_{6M} \left[1 + \gamma_{6M}M_{6M}^2 \right] (1 + A_{15}/A_5) - p_5 \left[(1 + \gamma_5M_5^2) + (A_{15}/A_5)(1 + \gamma_cM_{15}^2) \right] = 0 \quad (4.155)$$

Equation 4.155 has two unknowns, namely p_{6M} and M_{6M} , that need to be determined. The continuity equation can be expressed in terms of pressure and Mach number according to

$$\dot{m} \equiv \rho AV = AVp/RT = \frac{\gamma pAM}{\sqrt{\gamma RT}} = \frac{\gamma pAM}{\sqrt{\gamma RT_t}} \sqrt{1 + \frac{\gamma - 1}{2} M^2} \quad (4.156)$$

Therefore, the continuity equation as expressed in terms of pressure and Mach number, applied to the mixer, can be written as

$$\begin{aligned} & \frac{p_{6M}M_{6M} \sqrt{1 + (\gamma_{6M} - 1)M_{6M}^2/2}}{\sqrt{\gamma_{6M}R_{6M}T_{t6M}}} (1 + A_{15}/A_5) \\ &= \frac{p_5M_5 \sqrt{1 + (\gamma_t - 1)M_5^2/2}}{\sqrt{\gamma_t R_t T_{t5}}} + \frac{p_{15}M_{15} \sqrt{1 + (\gamma_c - 1)M_{15}^2/2}}{\sqrt{\gamma_c R_c T_{t15}}} (A_{15}/A_5) \end{aligned} \quad (4.157)$$

The above equation and the impulse equation, 4.155 and 4.157, contain two unknowns, P_{6M} and M_{6M} . We can solve the equations in closed form as they reduce to a quadratic equation in M_{6M}^2 .

4.4.2 Cycle Analysis

To reinforce the powerful *marching technique* that we have learned so far in cycle analysis, let us apply it to a mixed-flow turbofan engine at this time.

First, we will identify a mix of *parameters* that we need to specify in order to start a cycle analysis in a mixed-flow turbofan engine.

Flight condition: We need the flight Mach number (or speed), static temperature, and pressure at the flight altitude, that is, M_0 (or V_0), T_0 , and p_0 .

Inlet: We need the inlet adiabatic efficiency or its total pressure recovery parameter, that is, η_d or π_d , only one figure-of-merit is needed.

Fan: We need the fan's pressure ratio $\pi_f \equiv (p_{t13}/p_{t2})$ or the fan bypass ratio α and its polytropic efficiency e_f or its adiabatic efficiency η_f .

Compressor: We need the compressor's total pressure ratio $\pi_c \equiv p_{t3}/p_{t2}$ and its polytropic efficiency e_c or its adiabatic efficiency η_c .

Combustor: We need the combustor's total pressure ratio π_b , combustion efficiency η_b , and fuel heating value Q_R and either the turbine inlet temperature T_{t4} or the fuel-to-air ratio f .

Turbine: We need the turbine's polytropic efficiency e_t or adiabatic efficiency η_t , mechanical efficiency η_m exit Mach number M_5 , and an extra assumption about the pressure matching condition between the core and fan ducts at their merging boundary, typically $p_{t5} = p_{t15}$ or $p_5 = p_{15}$.

Mixer: We need a viscous loss parameter that accounts for the mixer wall friction on the total pressure loss across the mixer, namely, $\pi_{M,f}$.

Afterburner: We need the afterburner efficiency η_{AB} , the maximum temperature T_{t7} (or f_{AB}), afterburner total pressure ratio π_{AB} , and the heating value of the fuel $Q_{R,AB}$ in the afterburner.

Nozzle: We need adiabatic efficiency of the nozzle η_n or its total pressure loss parameter π_n , and the nozzle exit pressure p_9 or instead of exit pressure, we may specify the nozzle's (exit-to-throat) area ratio A_9/A_8 .

4.4.2.1 Solution Procedure. Let us first map out the total temperature and pressure distribution throughout the engine. Since our analysis is limited to a (steady) one-dimensional flow study of components, we treat the fluid and flow properties as being uniform at each and every station of the engine. Therefore, we propose to follow a candidate streamline that goes through the core and a candidate streamline that goes through the fan. Once we establish the total fluid properties after each interaction along the streamline path, we have the 1D information for the core and the fan streams. Then, we allow the Kutta condition to establish the communication between the two streams before the mixer takes over and achieves a mixed-out state of the gas prior to discharge into the nozzle or afterburner.

Station 0

$$p_{t0} = p_0 \left(1 + \frac{\gamma_c - 1}{2} M_0^2 \right)^{\frac{\gamma_c}{\gamma_c - 1}}$$

$$\pi_r = \left(1 + \frac{\gamma_c - 1}{2} M_0^2 \right)^{\frac{\gamma_c}{\gamma_c - 1}} \quad (4.158)$$

$$T_{t0} = T_0 \left(1 + \frac{\gamma_c - 1}{2} M_0^2 \right)$$

$$\tau_r = \left(1 + \frac{\gamma_c - 1}{2} M_0^2 \right) \quad (4.159)$$

$$a_0 = \sqrt{\gamma_c R_c T_0}$$

$$V_0 = a_0 M_0$$

Station 2

$p_{t2} = \pi_d \cdot p_{t0}$ or in terms of adiabatic efficiency,

$$p_{t2} = p_0 \left(1 + \eta_d \frac{\gamma_c - 1}{2} M_0^2 \right)^{\frac{\gamma_c}{\gamma_c - 1}} \quad (4.160)$$

$$T_{t2} = T_{t0}$$

Now, following a streamline that enters the core, we proceed to station 3.

Station 3

$$p_{t3} = p_{t2} \cdot \pi_c$$

$$T_{t3} = T_{t2} \cdot \pi_c^{\frac{\gamma-1}{\gamma_c}}$$

$$\tau_c = \pi_c^{\frac{\gamma_c-1}{\gamma_c}}$$
(4.161)

Station 4

$$p_{t4} = p_{t3} \cdot \pi_b$$

T_{t4} is either explicitly given as the engine maximum temperature or can be calculated from the fuel-to-air ratio f according to

$$h_{t4} = C_{pt} T_{t4} = \frac{1}{1+f} (h_{t3} + f Q_R \eta_b)$$

We also calculate the fuel-to-air ratio in the burner, if only T_{t4} is specified, that is,

$$f = \frac{h_{t4} - h_{t3}}{Q_R \eta_b - h_{t4}} = \frac{\tau_\lambda - \tau_r \tau_c}{\frac{Q_R \eta_b}{h_0} - \tau_\lambda} \quad (4.162)$$

where $\tau_\lambda \equiv \frac{h_{t4}}{h_0}$

Before marching to station 5, let us follow a streamline that goes through the fan.

Station 13

$$p_{t13} = p_{t2} \cdot \pi_f$$

$$T_{t13} = T_{t2} \cdot \pi_f^{\frac{\gamma_c - 1}{\gamma_c \cdot e_f}}$$

or

$$\tau_f = \pi_f^{\frac{\gamma_c - 1}{\gamma_c \cdot e_f}} \quad (4.163)$$

Station 15

Here we assume the fan duct to be frictional but adiabatic and we characterize the frictional aspect of it by a total pressure ratio π_{fd} .

$$p_{t15} = p_{t13} \cdot \pi_{fd} \quad (4.164)$$

where π_{fd} is given. Also, our adiabatic flow assumption in the fan duct earns the following condition

$$T_{t15} = T_{t13} \quad [\text{for a calorically-perfect gas, otherwise, } h_{t15} = h_{t13}]$$

or

$$\tau_{fd} = 1$$

Now, let us proceed through the turbine by a representative “core” streamline.

Station 5

$$\eta_m(1 + f)(h_{t4} - h_{t5}) = (h_{t3} - h_{t2}) + \alpha(h_{t13} - h_{t2}) \quad (4.165)$$

We note that in the above equation there are two unknowns, namely the bypass ratio α and the turbine exit (total) enthalpy h_{t5} . Let us nondimensionalize the above equation by dividing both sides by the flight static enthalpy h_0 to get

$$\eta_m(1 + f)\tau_\lambda(1 - \tau_t) = \tau_r(\tau_c - 1) + \alpha\tau_r(\tau_f - 1) \quad (4.166)$$

Here, we still have the two unknowns in terms of the bypass ratio and the turbine expansion ratio. We can make the assumption that the turbine expansion parameter as depicted by τ_t is linked to compressor and fan pressure ratios such that

$$p_{t5} \approx p_{t15} \quad (4.167)$$

This immediately ties the turbine pressure ratio to the fan pressure ratio if we divide both sides by the engine face total pressure p_{t2} to get

$$\frac{p_{t5}}{p_{t2}} = \pi_t \cdot \pi_b \cdot \pi_c = \frac{p_{t15}}{p_{t2}} = \pi_{fd} \cdot \pi_f \quad (4.168)$$

Consequently, turbine total pressure ratio may be expressed in terms of all known parameters of the cycle as

$$\pi_t = \frac{\pi_{fd} \cdot \pi_f}{\pi_b \cdot \pi_c} \quad (4.169)$$

The turbine temperature expansion ratio τ_t may be linked to π_t via the polytropic exponent, namely,

$$\tau_t = \pi_t^{\frac{\gamma_t-1}{\gamma_t} e_t} = \left(\frac{\pi_{fd} \cdot \pi_f}{\pi_b \cdot \pi_c} \right)^{\frac{\gamma_t-1}{\gamma_t} e_t} \quad (4.170)$$

Now, we see that the power balance equation written above for the turbine (Equation 4.166), fan, and compressor contains only one unknown and that is the bypass ratio α , which is expressed as

$$\alpha = \frac{\eta_m(1+f)\tau_\lambda(1-\tau_t) - \tau_r(\tau_c - 1)}{\tau_r(\tau_f - 1)} \quad (4.171)$$

The assumption of constant total pressure at the exit of the turbine and the fan duct is a reasonable assumption for a design-point analysis. This has enabled us to calculate the turbine pressure ratio and hence the temperature ratio linked via the polytropic exponent. The power balance then gave us the bypass ratio according to Equation 4.171.

Station 6M

From the energy balance across an adiabatic mixer, we obtained

$$h_{t6M} = h_0 \cdot \frac{(1+f)\tau_t \cdot \tau_\lambda + \alpha\tau_f \cdot \tau_r}{1 + \alpha + f} \quad (4.172)$$

All parameters in the above equation are either given as design/limit parameters or have been calculated in the previous steps, thus enabling us to march through the gas turbine. Now, we are ready to calculate the flow Mach number at the fan duct exit M_{15} in terms of turbine exit Mach number M_5 according to

$$p_{t15} = p_{15} \cdot \left(1 + \frac{\gamma_c - 1}{2} M_{15}^2 \right)^{\frac{\gamma_c}{\gamma_c - 1}} = p_5 \cdot \left(1 + \frac{\gamma_t - 1}{2} M_5^2 \right)^{\frac{\gamma_t}{\gamma_t - 1}} \quad (4.173)$$

which would reduce to the trivial solution, $M_{15} = M_5$, except when we account for a different ratio of specific heats in the core and the fan duct exit, namely, γ_c and γ_t . Now, assuming a different ratio of specific heats, we can express the fan duct exit Mach number as

$$M_{15}^2 = \frac{2}{\gamma_c - 1} \left\{ \left[\left(1 + \frac{\gamma_t - 1}{2} M_5^2 \right)^{\frac{\gamma_t}{\gamma_t - 1}} \right]^{\frac{\gamma_c - 1}{\gamma_c}} - 1 \right\} \quad (4.174)$$

We can use the mass flow rate expression that utilizes the static pressure and Mach number as its variables to calculate the ratio of flow areas between the fan duct and the core flow, namely,

$$\dot{m}_{15} = \frac{\gamma_c p_{15} A_{15} M_{15}}{a_{15}} = \alpha \dot{m}_0 \quad (4.175)$$

$$\dot{m}_5 = \frac{\gamma_t p_5 A_5 M_5}{a_5} = (1 + f) \dot{m}_0 \quad (4.176)$$

Now, if we take the ratio of the above two expressions and note that static pressures are identical (à la Kutta condition), we get an expression for the unknown area ratio, that is,

$$\frac{A_{15}}{A_5} = \frac{\alpha}{1 + f} \cdot \left(\frac{\gamma_t}{\gamma_c} \right) \frac{a_{15}}{a_5} \frac{M_5}{M_{15}} \quad (4.177)$$

So far, we have established the mixed-out total enthalpy h_{t6M} and all the upstream parameters to the mixer, such as M_{15} and the area ratio A_{15}/A_5 . In the mixer analysis, we have derived two equations and two unknowns based on the continuity and the (inviscid) momentum balance across the mixer, Equations 4.155 and 4.157.

$$p_{6M} [1 + \gamma_{6M} M_{6M}^2] (1 + A_{15}/A_5) - p_5 [(1 + \gamma_t M_5^2) + (A_{15}/A_5)(1 + \gamma_c M_{15}^2)] = 0 \quad (4.178)$$

$$\begin{aligned} & \frac{\gamma_{6M} p_{6M} M_{6M} \sqrt{1 + (\gamma_{6M} - 1) M_{6M}^2 / 2}}{\sqrt{(\gamma_{6M} - 1) c_{p6M} T_{t6M}}} (1 + A_{15}/A_5) \\ &= \frac{\gamma_t p_5 M_5}{a_5} + \frac{\gamma_c p_{15} M_{15}}{a_{15}} (A_{15}/A_5) \end{aligned} \quad (4.179)$$

Let us nondimensionalize Equation 4.178 by dividing through by p_5 and rewriting it in the following form:

$$\frac{p_{6M}}{p_5} [1 + \gamma_{6M} M_{6M}^2] = [(1 + \gamma_t M_5^2) + (A_{15}/A_5)(1 + \gamma_c M_{15}^2)] / (1 + A_{15}/A_5) = C_1 \quad (4.180)$$

The right-hand side of the above equation is known and we have given it a shorthand notation of C_1 . Now, we can isolate the same unknowns in Equation 4.179 to get

$$\begin{aligned} & \frac{p_{6M}}{p_5} \left(M_{6M} \sqrt{1 + (\gamma_{6M} - 1) M_{6M}^2 / 2} \right) \\ &= \left[\left(\frac{\gamma_t}{\gamma_{6M}} \right) \frac{M_5}{a_5} + \left(\frac{\gamma_c}{\gamma_{6M}} \right) \frac{M_{15} (A_{15}/A_5)}{a_{15}} \right] \frac{\sqrt{(\gamma_{6M} - 1) c_{p6M} T_{t6M}}}{(1 + A_{15}/A_5)} = C_2 \end{aligned} \quad (4.181)$$

Again the RHS of the above equation is known and it is labeled C_2 . By dividing Equation 4.180 by Equation 4.181, we can eliminate the mixer static pressure ratio and arrive at the mixer exit Mach number M_{6M} via

$$\frac{1 + \gamma_{6M} M_{6M}^2}{M_{6M} \sqrt{1 + (\gamma_{6M} - 1) M_{6M}^2 / 2}} = \frac{C_1}{C_2} = \sqrt{C} \quad (4.182)$$

Let us cross-multiply and square both sides of Equation 4.182 to arrive at a quadratic equation in M_{6M}^2 , as follows

$$(1 + \gamma_{6M} M_{6M}^2)^2 = C \cdot M_{6M}^2 (1 + (\gamma_{6M} - 1) M_{6M}^2 / 2) \quad (4.183)$$

$$[\gamma_{6M}^2 - C(\gamma_{6M} - 1)/2] M_{6M}^4 + (2\gamma_{6M} - C) M_{6M}^2 + 1 = 0 \quad (4.184)$$

$$M_{6M}^2 = \frac{C - 2\gamma_{6M} - \sqrt{(C - 2\gamma_{6M})^2 - 4[\gamma_{6M}^2 - C(\gamma_{6M} - 1)/2]}}{2\gamma_{6M}^2 - C(\gamma_{6M} - 1)} \quad (4.185)$$

where C is defined in Equation 4.182 and is expressible in terms of earlier established parameters C_1 and C_2 . Now, the mixer static pressure ratio can be determined from

$$\frac{p_{6M}}{p_5} = \frac{C_1}{1 + \gamma_{6M} M_{6M}^2} \quad (4.186)$$

The *ideal* (i.e., inviscid) total pressure ratio across the mixer is p_{t6M}/p_{t5} , which is expressible in terms of the static pressure ratio of Equation 4.186 and a function of Mach number according to

$$\pi_{M_i} \equiv \frac{p_{t6M}}{p_{t5}} = \frac{p_{6M}}{p_5} \frac{[1 + (\gamma_{6M} - 1) M_{6M}^2 / 2]^{\frac{\gamma_{6M}}{\gamma_{6M} - 1}}}{[1 + (\gamma_t - 1) M_5^2 / 2]^{\frac{\gamma_t}{\gamma_t - 1}}} \quad (4.187)$$

The *actual* total pressure ratio across the mixer should also account for the mixer wall frictional losses, which may be expressed as a multiplicative factor of the ideal parameter, namely,

$$\pi_M \equiv \pi_{M_i} \cdot \pi_{M_f} \quad (4.188)$$

where the frictional loss parameter π_{M_f} needs to be specified.

Station 7

Application of the energy equation to the afterburner yields an expression for the fuel-to-air ratio in the afterburner in terms of known parameters as follows:

$$(\dot{m}_{6M} + \dot{m}_{fAB}) h_{t7} - \dot{m}_{6M} h_{t6M} = \dot{m}_{fAB} Q_{R,AB} \eta_{AB} \quad (4.189)$$

$$f_{AB} \equiv \frac{\dot{m}_{fAB}}{\dot{m}_{6M}} = \frac{h_{t7} - h_{t6M}}{Q_{R,AB} \eta_{AB} - h_{t7}} = \frac{\tau_{\lambda AB} - h_{t6M}/h_0}{\frac{Q_{R,AB} \eta_{AB}}{h_0} - \tau_{\lambda AB}} \quad (4.190)$$

The total pressure at the exit of the afterburner is known via the loss parameter according to

$$p_{t7} = p_{t6M} \cdot \pi_{AB} \quad (4.191)$$

Note that we need two afterburner total pressure loss parameters, one for the afterburner on and the second for the afterburner off, that is, π_{AB-On} and π_{AB-Off} .

Station 9

From adiabatic flow assumption in the nozzle, we maintain the total enthalpy in the nozzle, namely,

$$T_{t9} = T_{t7} \quad (4.192)$$

and the total pressure at the nozzle exit p_{t9} is expressible in terms of the nozzle total pressure ratio parameter, according to

$$p_{t9} = p_{t7} \cdot \pi_n \quad (4.193)$$

or in case of an adiabatic nozzle efficiency η_n , we can relate the total pressure ratio across the nozzle to this parameter according to

$$\eta_n = \left[\left(\frac{p_{t7}}{p_9} \right)^{\frac{\gamma_{AB}-1}{\gamma_{AB}}} - \pi_n^{\frac{\gamma_{AB}-1}{\gamma_{AB}}} \right] / \left[\left(\frac{p_{t7}}{p_9} \right)^{\frac{\gamma_{AB}-1}{\gamma_{AB}}} - 1 \right] \quad (4.194)$$

where the only unknown is π_n .

Now, with the total pressure calculated at the nozzle exit and the static pressure p_9 as a given in the cycle analysis, we can establish the exit Mach number, according to

$$M_9^2 = \frac{2}{\gamma_{AB} - 1} \left[\left(\frac{p_{t9}}{p_9} \right)^{\frac{\gamma_{AB}-1}{\gamma_{AB}}} - 1 \right] \quad (4.195)$$

and the exit speed of sound from the exit Mach number and total temperature, according to

$$a_9^2 = \frac{\gamma_{AB} R_{AB} T_{t9}}{1 + (\gamma_{AB} - 1) M_9^2 / 2} \quad (4.196)$$

and exit velocity, as the product of $M_9 \cdot a_9$, that is,

$$V_9 = M_9 \cdot a_9 \quad (4.197)$$

Now, we have completely established the desired parameters inside the engine, albeit a one-dimensional or an *average* value per station, the fuel-to-air ratios in the primary and the afterburner and the nozzle exhaust velocity. We can insert these parameters in the performance equations for the specific thrust, propulsive and thermal efficiencies, and specific fuel consumption parameter.

EXAMPLE 4.16

A mixed-exhaust turbofan engine with afterburner is flying at

$$M_0 = 2.0, p_0 = 10 \text{ kPa}, T_0 = 223 \text{ K}$$

The engine inlet total pressure loss is characterized by $\pi_d = 0.90$

The fan pressure ratio is $\pi_f = 1.9$ and polytropic efficiency of the fan is $e_f = 0.90$

The flow in the fan duct suffers 1% total pressure loss, i.e., $\pi_{fd} = 0.99$

The compressor pressure ratio and polytropic efficiency are $\pi_c = 13$ and $e_c = 0.90$, respectively

The combustor exit temperature is $T_{t4} = 1600 \text{ K}$, fuel heating value is $Q_R = 42,000 \text{ kJ/kg}$, total pressure ratio is $\pi_b = 0.95$, and the burner efficiency is $\eta_b = 0.98$

The turbine polytropic efficiency is $e_t = 0.80$, its mechanical efficiency is $\eta_m = 0.95$, and $M_5 = 0.5$

The constant-area mixer suffers a total pressure loss due to friction, which is characterized by $\pi_{M,f} = 0.98$

The afterburner is on with $T_{t7} = 2,000 \text{ K}$, $Q_{R,AB} = 42,000 \text{ kJ/kg}$, $\pi_{AB-On} = 0.92$, $\eta_{AB} = 0.98$

The nozzle has a total pressure ratio of $\pi_n = 0.95$ and $p_9/p_0 = 3.8$

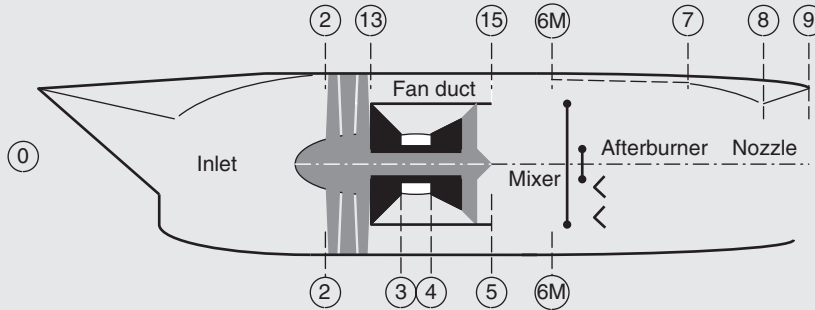
The gas behavior in the engine is dominated by temperature (in a thermally perfect gas), thus we consider four distinct temperature zones:

Inlet, fan, and compressor section: $\gamma_c = 1.4, c_{pc} = 1004 \text{ J/kg} \cdot \text{K}$

Turbine section: $\gamma_t = 1.33, c_{pt} = 1152 \text{ J/kg} \cdot \text{K}$

Mixer exit: γ_{6M}, c_{p6M} (to be calculated based on mixture of gases)

Afterburner and nozzle section: $\gamma_{AB} = 1.30, c_{p,AB} = 1241 \text{ J/kg} \cdot \text{K}$



Calculate

- (a) total pressure and temperature throughout the engine, the fan bypass ratio α , and include the con-

tributions of fuel-to-air ratio in the primary and afterburner f and f_{AB}

- (b) engine performance parameters, i.e., TSFC in mg/s/N , specific thrust, and cycle efficiencies

SOLUTION

Marching through the engine, we start with the flight condition. The remaining parameters to know in station “0” are p_{t0} and T_{t0} , the speed of sound a_0 , and flight speed V_0 .

$$p_{t0} = p_0 \left(1 + \frac{\gamma_c - 1}{2} M_0^2 \right)^{\frac{\gamma_c}{\gamma_c - 1}} = 78.24 \text{ kPa},$$

$$T_{t0} = T_0 \left(1 + \frac{\gamma_c - 1}{2} M_0^2 \right) = 401.4 \text{ K}$$

$$\pi_r = p_{t0}/p_0 = 7.824, \tau_r = T_{t0}/T_0 = 1.8$$

$$a_0 = \sqrt{(\gamma_c - 1)c_{pc}T_0} \cong 299.3 \text{ m/s}$$

$$V_0 = a_0 \cdot M_0 = 598.5 \text{ m/s}$$

The inlet is adiabatic and thus $T_{t2} = T_{t0}$. The total pressure in the inlet is reduced due to shocks and boundary layer friction, $p_{t2} = p_{t0} \cdot \pi_d \cong 70.42 \text{ kPa}$.

The fan exit pressure is $p_{13} = p_{12} \cdot \pi_f \approx 133.8$ kPa. The fan temperature and pressure ratios are related via $\tau_f = \pi_f^{\frac{\gamma_c - 1}{\gamma_c}} = 1.226$. The fan exit temperature is $T_{13} = T_{10} \cdot \tau_f \approx 492.12$ K. The fan duct is also adiabatic, which gives $T_{15} = T_{13}$. The flow in the fan duct is frictional; therefore it suffers a total pressure loss, $p_{15} = p_{13} \cdot \pi_{fd} \approx 132.46$ kPa

The compressor calculations are similar to those for the fan, which results in $p_{13} = p_{12} \cdot \pi_c = 915.46$ kPa, the temperature ratio $\tau_c = 2.2575$, and the compressor exit temperature is $T_{13} = 906.2$ K. This temperature represents an upper limit for an uncooled compressor.

The burner exit total pressure is $p_{14} = p_{13} \cdot \pi_b \approx 869.69$ kPa. We can calculate fuel-to-air ratio in the burner from

$$f = \frac{h_{t4} - h_{t3}}{Q_R \eta_b - h_{t4}} \approx 0.0237$$

We impose the same total pressure at the turbine exit as the fan duct exit (namely, we assume $p_{15} = p_{115}$) to get the turbine pressure ratio π_t

$$\pi_t = \frac{\pi_{fd} \cdot \pi_f}{\pi_b \cdot \pi_c} \approx 0.1523$$

The turbine temperature expansion ratio is related to its pressure ratio following

$$\tau_t = \pi_t^{\frac{\gamma_t - 1}{\gamma_t}} \approx 0.6883$$

The turbine exit total temperature is $T_{15} = T_{14} \cdot \tau_t \approx 1101$ K. Knowing turbine exit Mach number (given as 0.5), we can calculate T_5 and then a_5 . These are 1057.6 K and 634.1 m/s, respectively.

We can calculate the fan bypass ratio α by the energy balance between the turbine and fan/compressor,

$$\alpha = \frac{\eta_m(1+f)\tau_\lambda(1-\tau_t) - \tau_t(\tau_c - 1)}{\tau_t(\tau_f - 1)} \approx 0.5707$$

The mixer energy balance produces the mixed-out total enthalpy at the exit of the mixer,

$$h_{t6M} = h_0 \cdot \frac{(1+f)\tau_t \cdot \tau_\lambda + \alpha\tau_f \cdot \tau_t}{1 + \alpha + f}$$

where $\tau_\lambda \equiv c_{pt}T_{14}/c_{pc}T_0 \approx 8.2325$. Upon substitution, we get $h_{t6M} \approx 991.423$ kJ/kg. The gas properties c_p and c_v at the

mixer exit are related to the cold and hot streams entering the mixer according to

$$c_{p6M} = \frac{\dot{m}_5 c_{pt} + \dot{m}_{15} c_{pc}}{\dot{m}_5 + \dot{m}_{15}} \text{ and}$$

$$\gamma_{6M} = \frac{\dot{m}_5 c_{pt} + \dot{m}_{15} c_{pc}}{\dot{m}_5 \left(\frac{c_{pt}}{\gamma_t} \right) + \dot{m}_{15} \left(\frac{c_{pc}}{\gamma_c} \right)}$$

Upon substitution in the above expressions, we get, $c_{p6M} = 1099$ J/kg · K and $\gamma_{6M} \approx 1.352$, respectively.

To get the mixer exit static pressure and Mach number, we balance the mass flow and fluid impulse across the ideal mixer. Since the gas properties in the fan duct are different than the turbine exit, the gas Mach number in station “15” is derived from Equation 4.174.

$$M_{15}^2 = \frac{2}{\gamma_c - 1} \left\{ \left[\left(1 + \frac{\gamma_t - 1}{2} M_5^2 \right)^{\frac{\gamma_t}{\gamma_t - 1}} \right]^{\frac{\gamma_c - 1}{\gamma_c}} - 1 \right\}$$

which results in $M_{15} \approx 0.4881$

The gas temperature and static pressure at the fan duct exit are calculated from the total temperature and pressure and the flow Mach number M_{15} , $T_{15} = 469.74$ K and $p_{15} = 112.55$ kPa.

The gas static temperature and pressure at the turbine exit may similarly be calculated, $T_5 = 1057.64$ K and $p_5 = 112.55$ kPa. There is no discrepancy in static pressure between stations 5 and 15. Different gas properties in stations 5 and 15 resulted in a slightly lower M_{15} than M_5 . The area ratio between the fan duct and the turbine exit flow is expressed via the continuity equation in 4.177.

$$\frac{A_{15}}{A_5} = \frac{\alpha}{1+f} \cdot \left(\frac{\gamma_t}{\gamma_c} \right) \frac{a_{15}}{a_5} \frac{M_5}{M_{15}}$$

Upon substitution, we get $A_{15}/A_5 = 0.3716$.

From impulse balance across the ideal mixer, we get (Equation 4.180).

$$\frac{p_{6M}}{p_5} \left[1 + \gamma_{6M} M_{6M}^2 \right] = \left[\left(1 + \gamma_t M_5^2 \right) + (A_{15}/A_5) \right. \\ \left. \left(1 + \gamma_c M_{15}^2 \right) \right] / (1 + A_{15}/A_5) \\ = C_1 = 1.33278$$

From mass balance, we get

$$\begin{aligned} \frac{p_{6M}}{P_5} & \left(M_{6M} \sqrt{1 + (\gamma_{6M} - 1) M_{6M}^2 / 2} \right) \\ & = \left[\left(\frac{\gamma_t}{\gamma_{6M}} \right) \frac{M_5}{a_5} + \left(\frac{\gamma_c}{\gamma_{6M}} \right) \frac{M_{15} (A_{15} / A_5)}{a_{15}} \right] \\ & \frac{\sqrt{(\gamma_{6M} - 1) c_{p6M} T_{16M}}}{(1 + A_{15} / A_5)} = C_2 \end{aligned}$$

Upon substitution, we get $C_2 = 0.52037$.

Taking the ratio of the above two equations eliminates the pressure and leaves a quadratic in M_{6M}^2 , as in

$$\begin{aligned} M_{6M}^2 & = \\ \frac{C - 2\gamma_{6M} - \sqrt{(C - 2\gamma_{6M})^2 - 4[\gamma_{6M}^2 - C(\gamma_{6M} - 1)/2]}}{2\gamma_{6M}^2 - C(\gamma_{6M} - 1)} \end{aligned}$$

where $C = (C_1 / C_2)^2$

The answer to mixer exit Mach number is $M_{6M} \approx 0.5218$ and from

$$\frac{p_{6M}}{p_5} = \frac{C_1}{1 + \gamma_{6M} M_{6M}^2}$$

we get the exit static pressure $p_{6M} \approx 109.63$ kPa. Note that there is a slight static pressure drop in the mixer, i.e., from ~ 112.5 kPa to ~ 109.6 kPa. The (ideal) total pressure at the mixer exit is $p_{16Mi} = 131.23$ kPa. This results in an ideal mixer total pressure ratio of $\pi_{M,i} \approx 0.9907$ and the frictional contribution is specified in $\pi_{M,f}$ in the problem (as 0.98), therefore, $\pi_M \approx 0.9709$. The actual mixer exit total pressure is $p_{16M} = p_{16Mi} \cdot \pi_{Mf} = 128.6$ kPa

The afterburner is on with $T_{17} = 2000$ K and the total pressure loss is given by $\pi_{AB-On} = 0.92$. Therefore, $p_{17} = 118.32$ kPa. The energy balance across the afterburner yields the fuel-to-air ratio f_{AB} according to

$$f_{AB} \equiv \frac{\dot{m}_{fAB}}{\dot{m}_{6M}} = \frac{h_{17} - h_{16M}}{Q_{R,AB} \eta_{AB} - h_{17}} = 0.03854$$

The nozzle exit total pressure is $p_{19} = p_{17} \cdot \pi_n$, which gives $p_{19} = 112.40$ kPa. The exit static pressure is specified to be $p_9/p_0 = 3.8$, which gives $p_9 = 38$ kPa. Knowing total and static pressure at the nozzle exit, we calculate the local Mach number $M_9 = 1.377$. The static temperature at the nozzle exit is calculated from the total temperature and the Mach number information at the exit, i.e., we get $T_9 = 1557.2$ K. The speed of sound at “9” is $a_9 = 761.4$ m/s and the exhaust velocity at the nozzle exit is $V_9 = M_9 \cdot a_9 = 1048.4$ m/s. Since the nozzle did not achieve perfect expansion, the effective exhaust speed is

$$\begin{aligned} V_{9\text{eff}} & = F_g / \dot{m}_9 = V_9 + \frac{(p_9 - p_0) A_9}{\dot{m}_9} \\ & = V_9 + \frac{a_9^2 (1 - p_0 / p_9)}{\gamma_{AB} \cdot V_9} \cong 1,361.8 \text{ m/s} \end{aligned}$$

The nondimensional specific thrust is

$$\frac{F_n}{\dot{m}_0 (1 + \alpha) a_0} = \left(\frac{1 + \alpha + f + f_{AB}}{1 + \alpha} \right) \frac{V_{9\text{eff}}}{a_0} - M_0 \cong 2.731$$

The thrust-specific fuel consumption is

$$\text{TSFC} = \frac{(f + f_{AB}) / (1 + \alpha) a_0}{F_n / \dot{m}_0 (1 + \alpha) a_0} \times 10^6 \cong 48.515 \text{ mg/s/N}$$

The thermal efficiency is calculated from

$$\begin{aligned} \eta_{\text{th}} & \equiv \frac{\Delta K \dot{E}}{\dot{m}_f Q_R + \dot{m}_{f,AB} Q_{R,AB}} \\ & = \frac{(1 + \alpha + f + f_{AB}) V_{9\text{eff}}^2 - (1 + \alpha) V_0^2}{2(f Q_R + f_{AB} Q_{R,AB})} \cong 47.13\% \end{aligned}$$

The propulsive efficiency is calculated from

$$\eta_p \equiv \frac{2 F_n V_0}{\dot{m}_9 V_{9\text{eff}}^2 - (1 + \alpha) \dot{m}_0 V_0^2}$$

to be $\eta_p \approx 62.3\%$. Therefore, the overall efficiency is the product of the thermal and propulsive efficiencies, namely $\eta_o = 29.37\%$.

EXAMPLE 4.17

A mixed exhaust turbofan engine with afterburner has the same parameters as those specified in Example 4.16, except for the compressor pressure ratio. Write a computer

program, e.g., MATLAB, or use spreadsheet to calculate engine performance for a range of compressor pressure ratios from 6 to 16.

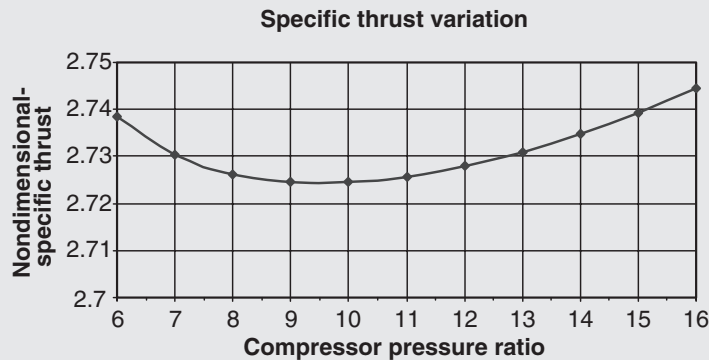
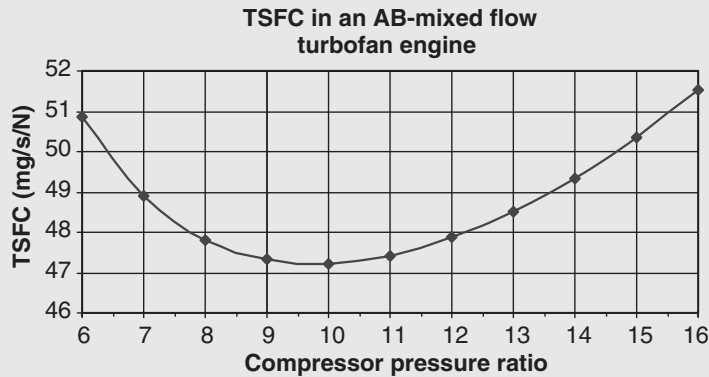
SOLUTION

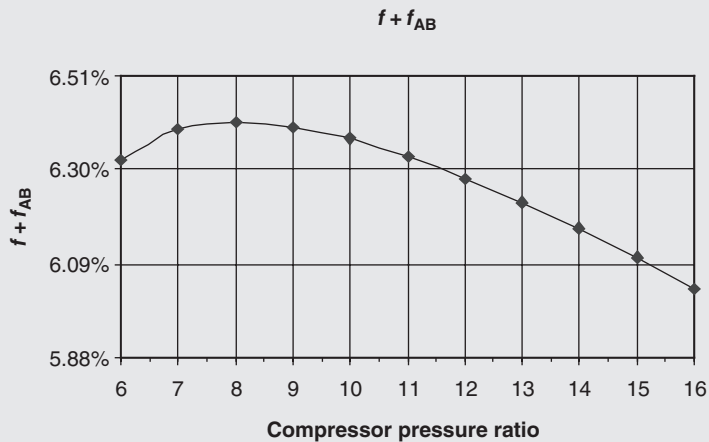
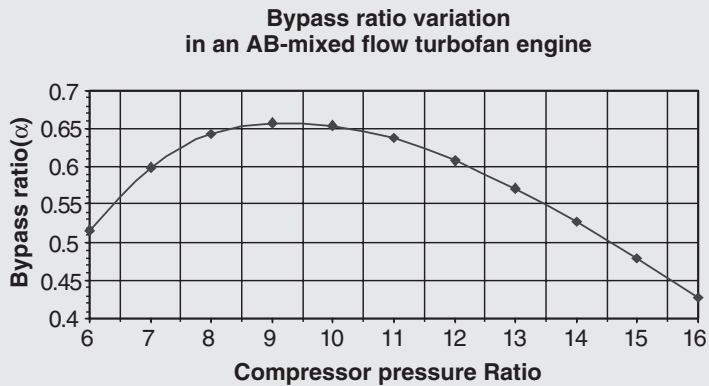
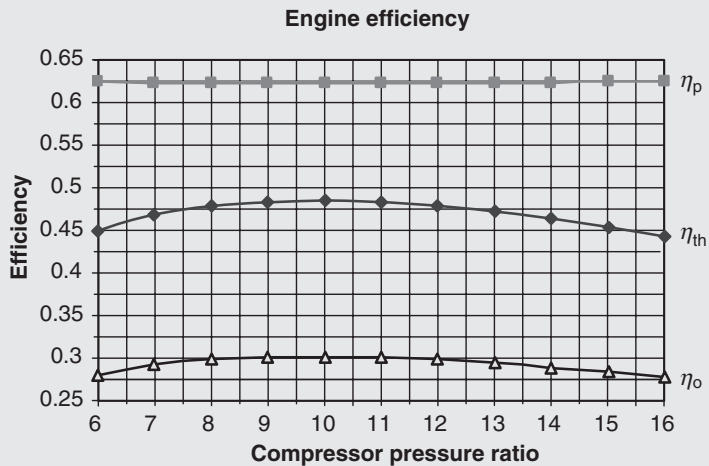
Using a spreadsheet, we calculate the engine performance parameters, summarized in the following table.

The graphical representations of these parameters are shown. In the following figure, TSFC shows the familiar bucket curve behavior as a function of compressor pressure ratio. The optimum compressor pressure ratio, in this engine and flight condition, is ~ 10 .

In addition, the variations of engine bypass ratio and total fuel to air ratio are calculated and graphed.

π_c	TSFC (mg/s/N)	Specific thrust/ a_0	η_{th}	η_p	η_o
6	50.858	2.7386	0.4491	0.6240	0.2802
7	48.902	2.7305	0.4674	0.6235	0.2914
8	47.823	2.7263	0.4782	0.6232	0.2980
9	47.316	2.7246	0.4834	0.6230	0.3012
10	47.214	2.7245	0.4845	0.6230	0.3018
11	47.416	2.7257	0.4824	0.6230	0.3005
12	47.863	2.7279	0.4779	0.6231	0.2977
13	48.515	2.7310	0.4713	0.6232	0.2937
14	49.350	2.7348	0.4632	0.6234	0.2888
15	50.352	2.7394	0.4538	0.6236	0.2830
16	51.513	2.7446	0.4434	0.6239	0.2766

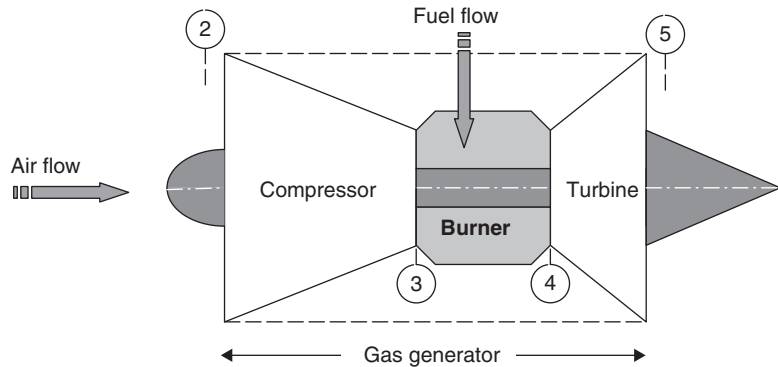




4.5 The Turboprop Engine

4.5.1 Introduction

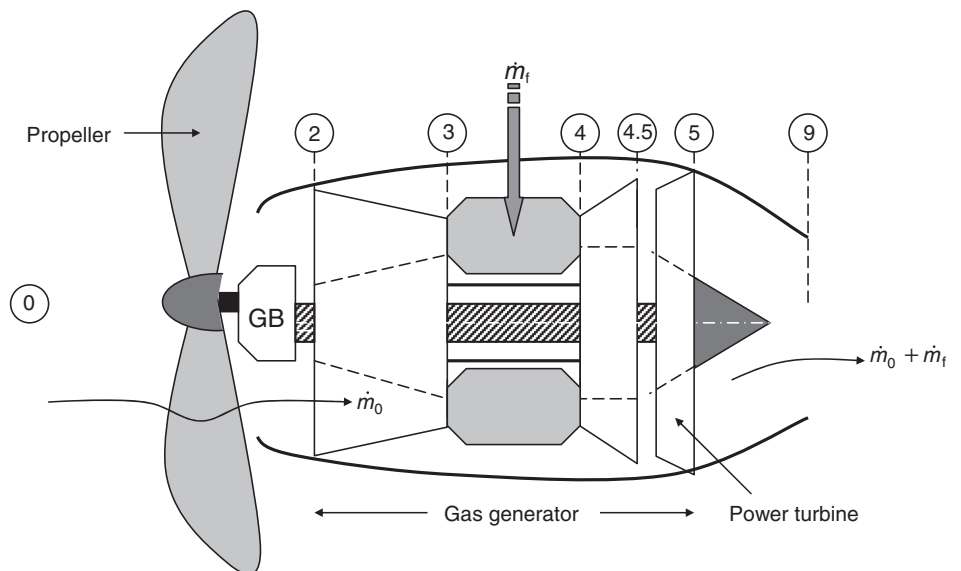
To construct a turboprop engine, we start with a gas generator.



The turbine in the gas generator provides the shaft power to the compressor. However, we recognize that the gas in station 5 is still highly energetic (i.e., high p_t and T_t) and capable of producing shaft power, similar to a turbofan engine. Once this shaft power is produced in a follow-on turbine stage that is called “power” or “free” turbine, we can supply the shaft power to a propeller. A schematic drawing of this arrangement is shown in Figure 4.51.

The attractiveness of a turbopropeller engine as compared with a turbofan engine lies in its ability to offer a very large bypass ratio, which may be between 30 and 100.

■ FIGURE 4.51 Schematic drawing of a turboprop engine with station numbers identified



The large bypass ratio, by necessity, will then cut back on the exhaust velocities of the propulsor, thereby attaining higher propulsive efficiencies for the engine. The high propulsive efficiency, however, comes at a price. The limitation on the tip Mach number of a rotating propeller, say to less than 1.3, leads to a cruise Mach number in the 0.7–0.8 range for advanced turboprops and to 0.4–0.6 for conventional propellers. We do not have *this limitation* on cruise Mach number in a turbofan engine. Also, the large diameter of the propeller often requires a reduction gearbox that adds to the engine weight and system complexity with its attendant reliability and maintainability issues.

Before we start our discussion of turboprop engines, it is appropriate to present basic concepts in propeller theory with applications to performance, sizing and selection.

4.5.2 Propeller Theory

Propellers are means of converting mechanical shaft (torque) power efficiently into forward/reverse thrust power in a vehicle. Although our application is in aircraft in this book, the same function and principles hold in a marine vehicle, that is, surface ships and submarines. There are two classical approaches to propeller theory:

1. Momentum or actuator disk theory
2. Blade element theory.

The pioneers of the momentum or actuator disk theory are Rankine (1865) and Froude (1889). The momentum theory replaces the propeller by a circular actuator disk that creates a jump in swirl, and thus angular momentum, across the disk, as well as a jump in static pressure. The product of the static pressure jump and the propeller disk area is then interpreted as the propeller thrust. The jump in the angular momentum is then related to the shaft (or torque) power that is delivered to and absorbed by the propeller. Individual blades lose their meaning in the actuator disk theory since they are *smear*ed into an axisymmetric disk. The shaft power is not delivered to individual propeller blades either, since there are no individual blades, rather a uniform disk. Therefore, the shaft power, too, is *smear*ed into a parameter that is described by power disk loading, which is the shaft power per unit disk area. In the absence of discrete propeller blades, the resulting swirling flow downstream of the actuator disk is uniformly swirling in the azimuthal direction. The flow process is further assumed to be completely steady and the fluid is treated as incompressible and inviscid. With these limitations, elegant ideal solutions are obtained that represent the *ideal* or the upper limit of the performance of a propeller.

4.5.2.1 Momentum Theory. A definition sketch is shown in Figure 4.52, which depicts a captured stream tube with free stream conditions at its entrance, an actuator disk, of area A_p corresponding to the propeller disk area and a uniformly swirling flow downstream of the actuator disk that extends to far downstream conditions.

As indicated by the definition sketch, V_0 is the forward speed of the propeller; p_0 and ρ_0 are the ambient pressure and density, which are essentially altitude dependent flight parameters. The axial velocity at the disk is V_p , which is continuous across the disk (to satisfy the continuity equation across the disk for incompressible fluid) and different from the forward speed of the propeller. We will show that the axial velocity at the propeller disk is the average of far upstream and downstream speeds, V_0 and V_1 respectively. The static pressure undergoes a jump across the disk. The disk area is A_p . Upstream flow

Note that the jump in static pressure across the disk results in propeller thrust that is in the $-z$ direction and its reaction that acts on the fluid is in the $+z$ direction. Furthermore, an approximation is made in writing Equation 4.201 that assumes the streamwise integrals of static pressure on the captured stream tube upstream and downstream of the propeller are small compared to the propeller thrust term. Von Mises (1959) offers more elaborate discussion on the assumptions that lead to Equation 4.201 for propeller thrust in momentum theory.

The power absorbed by the propeller appears as the thrust power of the propeller plus the change in the rate of kinetic energy between stations 0 and 1, namely

$$\mathcal{P}_p = F_{\text{prop}} V_0 + \dot{m}_p \left(\frac{V_1^2}{2} + \frac{V_{\theta 1}^2}{2} - \frac{V_0^2}{2} \right) \quad (4.202)$$

where

$$F_{\text{prop}} = (p_{p'} - p_p) A_p \quad (4.203)$$

Finally, the law of conservation of angular momentum applied to flow immediately downstream of the propeller disk and far downstream station, yields two equations for propeller torque, which produces shaft power when combined with propeller shaft angular speed, ω , according to:

$$\mathcal{P}_p = \omega \cdot \tau_{\text{prop}} = \omega \int_0^{r_1} (rV_{\theta}) \rho_0 V_1 (2\pi r) dr = \frac{2}{3} \dot{m}_p \omega \bar{V}_{\theta 1} r_1 \quad (4.204a)$$

$$\mathcal{P}_p = \omega \cdot \tau_{\text{prop}} = \omega \int_0^{r_p} (rV_{\theta p'}) \rho_0 V_p (2\pi r) dr = \frac{2}{3} \dot{m}_p \omega \bar{V}_{\theta p'} r_p \quad (4.204b)$$

The two swirl terms, $\bar{V}_{\theta 1}$ and $\bar{V}_{\theta p'}$, on the RHS of Equations 4.204a and 4.204b, are the (torque-based) mean swirl far downstream and immediately downstream of the propeller, respectively. Now, based on the conservation principles in fluids, we have written eight coupled nonlinear equations that involve the eight unknowns. Following Rankine, two additional approximations to the flow may be introduced that simplify our task significantly and lead to an elegant solution. The first approximation is to neglect the change in the swirl kinetic energy in Bernoulli equation (4.200) and the second approximation drops the swirl kinetic energy term in power balance equation (4.202) in favor of the propeller thrust power and the axial kinetic energy change. The approximate equations can be summarized:

$$p_{p'} + \frac{1}{2} \rho_0 V_p^2 \approx p_0 + \frac{1}{2} \rho_0 V_1^2 \quad (4.205)$$

$$\mathcal{P}_p \approx F_{\text{prop}} V_0 + \dot{m}_p \left(\frac{V_1^2}{2} - \frac{V_0^2}{2} \right) \quad (4.206)$$

$$F_{\text{prop}} \approx \rho_0 V_p A_p (V_1 - V_0) \text{ (acts in } -z, \text{ or forward thrust direction)} \quad (4.207)$$

If we subtract the two Bernoulli equations (4.199 and 4.205), we get:

$$p_{p'} - p_p \approx \frac{1}{2} \rho_0 (V_1^2 - V_0^2) = \frac{F_{\text{prop}}}{A_p} \quad (4.208)$$

Now, substitute for F_{prop}/A_p in Equation 4.208 from Equation 4.207 to get:

$$V_p \approx \frac{1}{2} (V_0 + V_1) \quad (4.209)$$

Within these approximations, the flow speed at the propeller plane is the average of the flight speed and far downstream of the propeller.

We substitute for the propeller thrust in the energy equation (4.206) from Equation 4.207 to get:

$$\mathcal{P}_p \approx \rho_0 V_p A_p (V_1 - V_0) V_0 + \rho_0 V_p A_p \left(\frac{V_1^2}{2} - \frac{V_0^2}{2} \right) \quad (4.210)$$

If we substitute for V_p from Equation 4.209, the above equation would only contain a single unknown, namely, V_1 . The resulting equation is a cubic in V_1/V_0 :

$$\frac{\mathcal{P}_p}{\left(\frac{1}{2} \rho_0 V_0^2 \right) V_0 A_p} = \frac{1}{2} \left(\frac{V_1}{V_0} \right)^3 + \frac{3}{2} \left(\frac{V_1}{V_0} \right)^2 - \frac{1}{2} \left(\frac{V_1}{V_0} \right) - \frac{3}{2} \quad (4.211)$$

The left-hand side of Equation 4.211 is nondimensional power with all terms known, which may be referred to as the propeller power loading, C_p . The RHS of Equation 4.211 is a cubic in velocity ratio, V_1/V_0 . Note that the shaft power vanishes when the velocity ratio V_1/V_0 approaches 1.

Finally, on the discussion of efficiency, we have propeller efficiency that is defined as the fraction of propeller shaft power that is converted to the propeller thrust power, namely

$$\eta_{\text{prop}} \equiv \frac{F_{\text{prop}} V_0}{\mathcal{P}_p} \quad (4.212)$$

By applying propulsive efficiency definition to the stream tube upstream and downstream of the propeller, we get:

$$\eta_p \equiv \frac{F_{\text{prop}} V_0}{\dot{m}_p \left(\frac{V_1^2}{2} - \frac{V_0^2}{2} \right)} \approx \frac{2V_0}{V_0 + V_1} \quad (4.213)$$

We note that the propeller and propulsive efficiencies in Equations 4.212 and 4.213 are related to each other and indeed propulsive efficiency is the ideal limit of the propeller efficiency, since

$$\eta_{\text{prop}} \equiv \frac{F_{\text{prop}} V_0}{\mathcal{P}_p} = \left[\frac{F_{\text{prop}} V_0}{\dot{m}_p \left(\frac{V_1^2}{2} - \frac{V_0^2}{2} \right)} \right] \left[\frac{\dot{m}_p \left(\frac{V_1^2}{2} - \frac{V_0^2}{2} \right)}{\mathcal{P}_p} \right] = \eta_p \eta_L \quad (4.214)$$

where

$$\eta_L \equiv \frac{\dot{m}_p \left(\frac{V_1^2}{2} - \frac{V_0^2}{2} \right)}{\mathcal{P}_p} \quad (4.215)$$

In Equation 4.215, η_L , is the efficiency of propeller in converting its shaft power into stream kinetic power. Since propulsive efficiency (Equation 4.213) is the maximum, or the limit, efficiency of a propeller, it is often times calculated and reported as the “ideal” propeller efficiency in literature. Further discussion on propeller and propulsive efficiencies may be found in Oates (1988) and Lan-Roskam (1997).

Let us solve two propeller problems using the momentum theory.

EXAMPLE 4.18

A propeller of diameter $d_p = 3$ m, is in forward flight with speed $V_0 = 100$ m/s in an altitude where $p_0 = 40$ kPa, and density $\rho_0 = 0.61$ kg/m³. The shaft power delivered to the propeller is 1.2 MW (equivalent to 1609 hp) and the shaft angular speed is 1000 rpm. Use momentum theory of propellers to estimate the:

- (a) air speed at the propeller, V_p , in m/s
- (b) propeller thrust, F_{prop} , in kN

- (c) air mass flow rate captured by the propeller in kg/s
- (d) propeller thrust power in MW
- (e) “ideal” propeller efficiency
- (f) propeller efficiency
- (g) mean swirl downstream of the propeller as well as far downstream station
- (h) propeller torque in kN.m.

SOLUTION

We use the cubic Equation 4.211

$$\frac{\mathcal{P}_p}{\left(\frac{1}{2} \rho_0 V_0^2 \right) V_0 A_p} \approx 0.5569 = \frac{1}{2} \left(\frac{V_1}{V_0} \right)^3 + \frac{3}{2} \left(\frac{V_1}{V_0} \right)^2 - \frac{1}{2} \left(\frac{V_1}{V_0} \right) - \frac{3}{2}$$

The only real positive root of the cubic is $V_1/V_0 = 1.127$, which makes the far downstream speed, $V_1 = 112.7$ m/s. The air speed at the propeller is the average of forward speed and the far downstream speed, that is,

$$V_p = (100 + 112.7)/2 = 106.4 \text{ m/s}$$

We use Equation 4.207 for propeller thrust to calculate:

$$F_{\text{prop}} \approx \rho_0 V_p A_p (V_1 - V_0) \approx 5.821 \text{ kN}$$

(This is about 1310 lbf)

We apply continuity at the propeller disk to get the air mass flow rate through the propeller:

$$\dot{m}_0 = \dot{m}_p \approx \rho_0 V_p A_p = 458.3 \text{ kg/s}$$

Propeller thrust power is the product of propeller thrust and the forward speed, $F_{\text{prop}} V_0 = 0.5821 \text{ MW}$

Ideal propeller efficiency is the propulsive efficiency, $\eta_p \approx (2V_0)/(V_0 + V_1) = 94\%$

Propeller efficiency is $\eta_{\text{prop}} \equiv \frac{F_{\text{prop}} V_0}{\mathcal{G}_p} \approx 48.5\%$

We may also estimate the induced mean swirl downstream of the propeller from Equation 4.204b

$$\mathcal{G}_p = \frac{2}{3} \dot{m}_p \omega \bar{V}_{\theta p'} r_p$$

which gives $\bar{V}_{\theta p'} \approx 25 \text{ m/s}$

and

$$\mathcal{G}_p = \frac{2}{3} \dot{m}_p \omega \bar{V}_{\theta 1} r_1$$

yields $\bar{V}_{\theta 1} \approx 25.8 \text{ m/s}$

We can also calculate propeller torque from the shaft power and the angular speed, namely:

$$\tau_{\text{prop}} = \frac{\mathcal{G}_p}{\omega} \approx 11.5 \text{ kN} \cdot \text{m}$$

EXAMPLE 4.19

A propeller of 1.8-m diameter (5.89 ft) produces 6.2 kN (~1400 lbf) of thrust in 75 m/s (~168 mph) flight at standard sea level conditions ($\rho_0 \approx 1.22 \text{ kg/m}^3$). Using momentum theory, estimate the:

- (a) velocity at the propeller disk, V_p , in m/s
- (b) ideal propeller efficiency.

SOLUTION

The propeller disk area is $A_p = 2.5434 \text{ m}^2$. From Equation 4.207, we relate propeller thrust to the velocity field, fluid density and disk area as:

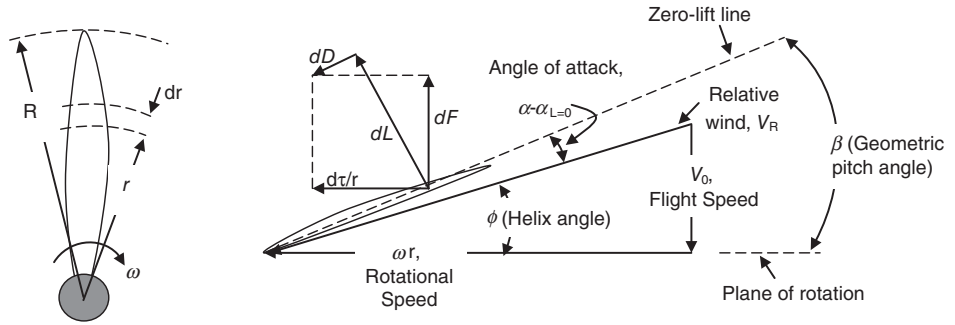
$$F_{\text{prop}} \approx \rho_0 V_p A_p (V_1 - V_0) = \rho_0 A_p \left(\frac{V_1^2}{2} - \frac{V_0^2}{2} \right)$$

which gives $V_1 \approx 98 \text{ m/s}$ and thus $V_p = (V_1 + V_0)/2 \approx 86.5 \text{ m/s}$

Also the ideal propeller efficiency is the propulsive efficiency, $\eta_p \approx \frac{2V_0}{V_0 + V_1} \approx 86.7\%$

4.5.2.2 Blade Element Theory. Another approach proposed to study the aerodynamic design and performance of propellers is blade element theory. The foundation of this theory is found in the classical airfoil and wing theory. A propeller is a spinning (twisted) wing, with angular speed $\omega = 2\pi n$, with its span-wise elements in solid-body rotation. The rotational speed increases linearly with distance from the axis of rotation, r , hence the need for twist. Therefore, by virtue of rotation, the blade sections are subjected to relative flow magnitude and angle, that is, as seen by the blade element. A propeller blade is composed of airfoil sections along its span that see the relative flow and create local aerodynamic forces and torques. The aerodynamic performance of the sections depends on the local relative flow speed, airfoil profile, and angle of attack (as seen by the section) and Reynolds number based on chord and relative speed. Figure 4.53 is a

■ **FIGURE 4.53**
 Definition sketch of a propeller and the aerodynamic forces on an airfoil element at radius r



definition sketch that shows a propeller and its sectional velocity vectors and angles with elemental aerodynamic force components.

The relative flow, or the relative wind V_R , is created as the vector sum of flight and the blade rotational speed at any element along the span. The relative flow angle is ϕ , which is also called the helix angle. The aerodynamic lift on the blade element is proportional to the local effective angle of attack, which is composed of: (i) the geometric angle of attack; (ii) the angle-of-zero lift (due to airfoil camber); and (iii) the induced angle of attack (due to the trailing vortices in the propeller wake). The basic blade element theory, however, does not account for the induced angle of attack that is caused by the 3D trailing vortices. Therefore, in the strict sense, propeller blade performance in three dimensions is constructed from the superposition of sectional 2D performance. The geometric pitch angle, β , is also shown in Figure 4.53; it is the angle that the blade element (in cambered airfoil measured from zero-lift-line) makes with respect to plane of rotation. The tangential force element multiplied by the moment arm, r , measured from the axis of rotation, creates blade element torque, $d\tau$, as shown in Figure 4.53. The propeller parameters of interest, namely thrust and torque, are the integrals of elemental thrust and torque along the blade span. In turn, the elemental torque and thrust are related to the lift and drag components, using the pitch angle, ϕ , according to:

$$dF = dL \cos \phi - dD \sin \phi \quad (4.216)$$

$$d\tau = r(dL \sin \phi + dD \cos \phi) \quad (4.217)$$

The lift and drag forces are proportional to lift and drag coefficients with the product of relative dynamic pressure and the local chord length as the proportionality constant, namely

$$dL = \frac{1}{2} \rho_0 V_R^2 \cdot c \cdot c_\ell \quad (4.218)$$

$$dD = \frac{1}{2} \rho_0 V_R^2 \cdot c \cdot c_d \quad (4.219)$$

The sectional propeller efficiency may be defined as:

$$d\eta_{\text{prop}} = \frac{V_0 dF}{\omega d\tau} \quad (4.220)$$

A major shortcoming of blade element theory in modeling 3D propellers is in lack of 3D coupling of the propeller sections along its span, which may be partially alleviated if we incorporate the induced axial and swirl velocity components from the momentum theory. Also, the compressibility effect may cause local supersonic flow near the blade tip with the subsequent shock formation, boundary layer separation and stall. Modern supersonic tip propeller designs that use sweep are introduced in advanced turboprops (ATP) by Pratt and Whitney and GE (which is called *Propfan*). Further discussions on propellers, in the context of Uninhabited Aerial Systems (UAS), related to control, type and performance are presented in Chapter 5.

4.5.3 Turboprop Cycle Analysis

4.5.3.1 The New Parameters. Let us identify the new parameters that we have introduced by inserting a propeller in the gas turbine engine. We will examine the turboprop from the power distribution point of view as well as its thrust producing capabilities namely the propeller thrust contribution to the overall thrust, which includes the core thrust.

From the standpoint of power, the low-pressure turbine power is supplied to a gearbox, which somewhat diminishes it in its frictional loss mechanism in the gearing and then delivers the remaining power to the propeller. We will call the fractional delivery of shaft power through the gearbox, the *gearbox efficiency* η_{gb} , which symbolically is defined as

$$\eta_{gb} \equiv \mathcal{P}_{prop} / (\mathcal{P}_{LPT})_{gb} \quad (4.221)$$

where the numerator is the power supplied to the propeller and the denominator is the shaft power provided by the power turbine to the gearbox. Also, we define the fraction of *propeller shaft power* that is converted in the *propeller thrust power* as the *propeller efficiency* η_{prop} as

$$\eta_{prop} \equiv F_{prop} \cdot V_0 / \mathcal{P}_{prop} \quad (4.222)$$

Now, let us examine the overall thrust picture of a turboprop engine. We recognize that the propeller and the engine core both contribute to thrust production. We can express this fact as

$$F_{total} = F_{prop} + F_{core} \quad (4.223)$$

The contribution of the engine core to the overall thrust, which we have called as the *core thrust*, takes on the familiar form of the gross thrust of the nozzle minus the ram drag of the air flow rate that enters the engine, that is,

$$F_{core} = (\dot{m}_0 + \dot{m}_f)V_9 - \dot{m}_0V_0 + (p_9 - p_0)A_9 \quad (4.224)$$

The pressure thrust contribution of the nozzle, that is, the last term in Equation 4.224, for a turboprop engine is often zero due to perfectly expended exhaust, that is, $p_9 = p_0$. So,

for all practical purposes, the engine core of a turboprop produces a thrust based solely on the momentum balance between the exhaust and the intake of the engine, namely,

$$F_{\text{core}} \cong (\dot{m}_0 + \dot{m}_f)V_9 - \dot{m}_0V_0 \quad (4.225)$$

4.5.3.2 Design Point Analysis. We require the following set of input parameters in order to estimate the performance of a turboprop engine. The following list, which sequentially proceeds from the flight condition to the nozzle exit, summarizes the input parameters per component. In this section, we will practice the powerful marching technique that we have learned so far in this book.

Station 0

The flight Mach number M_0 , the ambient pressure and temperature p_0 and T_0 , and air properties γ and R are needed to characterize the flight environment. We can calculate the flight total pressure and temperature p_{t0} and T_{t0} , the speed of sound at the flight altitude a_0 , and the flight speed V_0 , based on the input.

Station 2

At the engine face, we need to establish the total pressure and temperature P_{t2} and T_{t2} . From adiabatic flow assumption in the inlet, we conclude that

$$T_{t2} = T_{t0}$$

To account for the inlet frictional losses and its impact on the total pressure recovery of the inlet, we need to define an inlet total pressure ratio parameter π_d or adiabatic diffuser efficiency η_d . This results in establishing p_{t2} , similar to our earlier cycle analysis, for example,

$$p_{t2} = \pi_d \cdot p_{t0}$$

Station 3

To continue our march through the engine, we need to know the compressor pressure ratio π_c , which again is treated as a design choice, and the compressor polytropic efficiency e_c . This allows us to calculate the compressor temperature ratio in terms of compressor pressure ratio using the polytropic exponent, that is,

$$\tau_c = \pi_c^{\frac{\gamma_c - 1}{\gamma_c e_c}}$$

Now, we have established the compressor discharge total pressure and temperature p_{t3} and T_{t3} .

Station 4

To establish the burner exit conditions, similar to earlier analysis, we need to know the loss parameters η_b and π_b as well as the limiting temperature T_{t4} . The fuel type with its energy content, that we had called the *heating value* of the fuel, Q_R , needs to be specified. Again, we establish the fuel-to-air ratio f by energy balance across the burner and the total pressure at the exit, p_{t4} , by loss parameter π_b .

Station 4.5

For the upstream turbine, or the so-called the HPT, we need to know the mechanical efficiency η_{mHPT} , which is a power transmission efficiency, and the turbine polytropic efficiency e_{tHPT} , which measures the internal efficiency of the turbine. The power balance between the compressor and high-pressure turbine is

$$\eta_{mHPT}(1+f)(h_{t4} - h_{t4.5}) = h_{t3} - h_{t2} \tag{4.226a}$$

$$h_{t4.5} = h_{t4} - \frac{h_{t3} - h_{t2}}{\eta_{mHPT}(1+f)} \tag{4.226b}$$

leads to the only unknown in the above equation, which is $h_{t4.5}$. The total pressure at station 4.5 may be linked to the turbine total temperature ratio according to

$$\frac{p_{t4.5}}{p_{t4}} = \left(\frac{T_{t4.5}}{T_{t4}} \right)^{\frac{\gamma_t}{(\gamma_t-1)e_{tHPT}}} \tag{4.227}$$

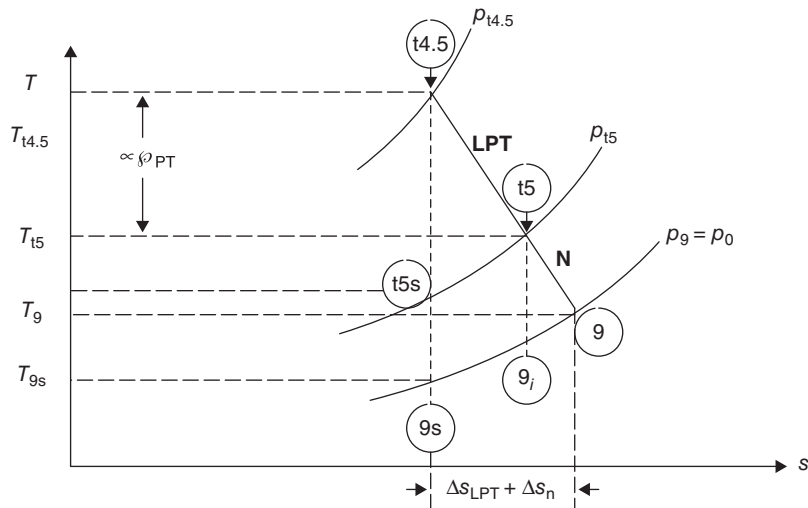
$$\pi_{HPT} = \tau_{HPT}^{\frac{\gamma_t}{(\gamma_t-1)e_{tHPT}}} \tag{4.228}$$

Stations 5 and 9

Since the power turbine drives a *load*, that is, the propeller, we need to specify the turbine expansion ratio that supports this *load*. In this sense, we consider the propeller as an external load to the cycle and hence as an input parameter to the turboprop analysis. It serves a purpose to put this and the following station, that is, 9, together, as both are responsible for the thrust production. Another view of stations 5 and 9 downstream of 4.5 points to the *power split*, decision made by the designer, between the propeller and the exhaust jet. The following T - s diagram best demonstrates this principle.

In the T - s diagram (Figure 4.54), both the actual and the ideal expansion processes are shown. We will use this diagram to define the component efficiencies as well as

■ FIGURE 4.54
Thermodynamic states of an expansion process in free turbine and nozzle of a turboprop engine



the power split choice. For example, we define the power turbine (i.e., LPT) adiabatic efficiency as

$$\eta_{LPT} \equiv \frac{h_{t4.5} - h_{t5}}{h_{t4.5} - h_{t5s}} = \frac{h_{t4.5}(1 - \tau_{LPT})}{h_{t4.5} \left[1 - \pi_{LPT}^{\frac{\gamma-1}{\gamma}} \right]} = \frac{1 - \tau_{LPT}}{1 - \pi_{LPT}^{\frac{\gamma}{\gamma-1}}} \quad (4.229)$$

Also, we may define the nozzle adiabatic efficiency η_n as

$$\eta_n \equiv \frac{h_{t5} - h_9}{h_{t5s} - h_{9s}} \quad (4.230)$$

We note that the above definition for the nozzle adiabatic efficiency deviates slightly from our earlier definition in that we have assumed

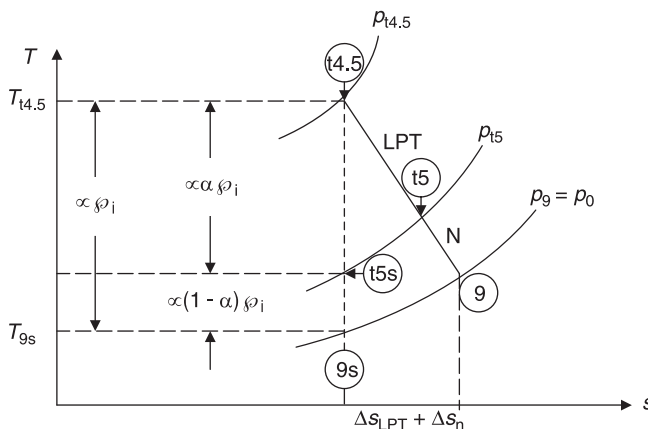
$$h_{t5} - h_{9i} \approx h_{t5s} - h_{9s} \quad (4.231)$$

which in light of small expansions in the nozzle and hence near parallel isobars, this approximation is considered reasonable. The total ideal power available at station 4.5, per unit mass flow rate, may be written as

$$\frac{\mathcal{P}}{\dot{m}_0(1+f)} = h_{t4.5} - h_{9s} = h_{t4.5} \left[1 - \left(\frac{p_9}{p_{t4.5}} \right)^{\frac{\gamma-1}{\gamma}} \right] = \mathcal{P}_{i,\text{total}}/\dot{m}_9 \quad (4.232)$$

If we examine the RHS of the above equation, we note that all terms on the RHS are known. Therefore, the total ideal power is known to us a priori. Now, let us assume that the power split between the free turbine and the nozzle is, say α and $1 - \alpha$, respectively, as shown in Figure 4.55.

■ FIGURE 4.55
Definition of power split α in a turboprop engine



We can define the power split as

$$\alpha \equiv \frac{h_{t4.5} - h_{t5s}}{h_{t4.5} - h_{9s}} = \frac{\mathcal{P}_{\text{LPT}}/\dot{m}_9}{\mathcal{P}_{i,\text{total}}/\dot{m}_9} \quad (4.233)$$

which renders the following expression for the free turbine (LPT) power in terms of a given α ,

$$\mathcal{P}_{\text{LPT}} = \dot{m}_9 \eta_{\text{LPT}} \cdot \alpha \cdot h_{t4.5} \left[1 - \left(\frac{p_9}{p_{t4.5}} \right)^{\frac{\gamma_t - 1}{\gamma_t}} \right] = \dot{m}_9 (h_{t4.5} - h_{t5}) \quad (4.234)$$

This expression for the power turbine (LPT) can be applied to the propeller through gearbox and propeller efficiency in order to arrive at the thrust power produced by the propeller, namely,

$$\begin{aligned} F_{\text{prop}} \cdot V_0 &= \eta_{\text{prop}} \cdot \eta_{\text{gb}} \cdot \eta_{\text{mLPT}} \cdot \mathcal{P}_{\text{LPT}} = \eta_{\text{prop}} \cdot \eta_{\text{gb}} (\mathcal{P}_{\text{LPT}})_{\text{gb}} \\ &= \dot{m}_0 (1 + f) [\alpha \eta_{\text{LPT}} \eta_{\text{mLPT}} \eta_{\text{gb}} \eta_{\text{prop}}] h_{t4.5} \left[1 - \left(\frac{p_9}{p_{t4.5}} \right)^{\frac{\gamma_t - 1}{\gamma_t}} \right] \end{aligned} \quad (4.235)$$

We note that the RHS of the above equation, per unit mass flow rate, is known. Now, let us examine the nozzle thrust. The kinetic energy per unit mass at the nozzle exit may be linked to

$$V_9^2/2 \cong \eta_n (h_{t5s} - h_{9s}) = \eta_n (1 - \alpha) \mathcal{P}_{i,\text{total}}/\dot{m}_9 = (1 - \alpha) \eta_n h_{t4.5} \left[1 - \left(\frac{p_9}{p_{t4.5}} \right)^{\frac{\gamma_t - 1}{\gamma_t}} \right] \quad (4.236)$$

Therefore, the exhaust velocity is now approximated by the power split parameter α and the total ideal power available after the gas generator, that is, station 4.5, according to

$$V_9 \approx \sqrt{2(1 - \alpha) \eta_n h_{t4.5} \left[1 - \left(\frac{p_9}{p_{t4.5}} \right)^{\frac{\gamma_t - 1}{\gamma_t}} \right]} \quad (4.237)$$

A more accurate expression for exhaust velocity is derived based on nozzle adiabatic efficiency that is defined based on the states t5, 9 and 9i. Example 4.20 calculates the nozzle exhaust velocity using the more accurate method.

Now, the turboprop thrust per unit air mass flow rate (through the engine) can be expressed in terms of the propeller thrust of expression 4.235 and the core thrust expression 4.225 with Equation 4.237 incorporated for the exhaust velocity.

$$\frac{F_{\text{total}}}{\dot{m}_0} = (1+f)V_9 - V_0 + \frac{(1+f)[\alpha\eta_{\text{PT}}\eta_{\text{mLPT}}\eta_{\text{gb}}\eta_{\text{prop}}]h_{\text{t4.5}} \left[1 - \left(\frac{p_9}{p_{\text{t4.5}}} \right)^{\frac{\gamma_1-1}{\gamma_1}} \right]}{V_0} \quad (4.238)$$

The fuel efficiency of a turboprop engine is often expressed in terms of the fraction of the fuel consumption in the engine to produce a unit shaft/mechanical power, according to

$$\text{PSFC} \equiv \frac{\dot{m}_f}{\mathcal{P}_{\text{prop}} + \mathcal{P}_{\text{core}}} = \frac{f}{\left(\frac{\mathcal{P}_{\text{prop}}}{\dot{m}_0} + \frac{\mathcal{P}_{\text{core}}}{\dot{m}_0} \right)} \quad (4.239)$$

$$\mathcal{P}_{\text{prop}} = \eta_{\text{gb}}\eta_{\text{mLPT}}\mathcal{P}_{\text{LPT}} = \dot{m}_0(1+f)\eta_{\text{gb}}\eta_{\text{mLPT}}\eta_{\text{LPT}} \cdot \alpha \cdot h_{\text{t4.5}} \left[1 - \left(\frac{p_9}{p_{\text{t4.5}}} \right)^{\frac{\gamma_1-1}{\gamma_1}} \right] \quad (4.240)$$

$$\mathcal{P}_{\text{core}} = \frac{\dot{m}_0}{2} [(1+f)V_9^2 - V_0^2] \text{ for a perfectly expanded nozzle, otherwise use } V_{9\text{eff}} \quad (4.241)$$

We can define the thermal efficiency of a turboprop engine as

$$\eta_{\text{th}} \equiv \frac{\mathcal{P}_{\text{prop}} + \mathcal{P}_{\text{core}}}{\dot{m}_f Q_{\text{R}}} = \frac{\left(\frac{\mathcal{P}_{\text{prop}}}{\dot{m}_0} + \frac{\mathcal{P}_{\text{core}}}{\dot{m}_0} \right)}{fQ_{\text{R}}} \quad (4.242)$$

The propulsive efficiency η_{p} may be defined as

$$\eta_{\text{p}} \equiv \frac{F_{\text{total}} \cdot V_0}{\mathcal{P}_{\text{prop}} + \mathcal{P}_{\text{core}}} = \frac{\frac{F_{\text{total}}}{\dot{m}_0} \cdot V_0}{\left(\frac{\mathcal{P}_{\text{prop}}}{\dot{m}_0} + \frac{\mathcal{P}_{\text{core}}}{\dot{m}_0} \right)} \quad (4.243)$$

where all the terms in the above efficiency definitions have been calculated in earlier steps and the overall efficiency is again the product of the thermal and propulsive efficiencies.

4.5.3.3 Optimum Power Split Between the Propeller and the Jet. For a given fuel flow rate, flight speed, compressor pressure ratio, and all internal component efficiencies, we may ask a very important question, which is “at what power split α would the total thrust be maximized?” This is a simple mathematics question. What we need first, is to express the total thrust in terms of all independent parameters, i.e., f , V_0 , π_c , and so on, and then differentiate it with respect to α and set the derivative equal to zero. From that

equation, obtain the solution(s) for α that satisfies the equation. We go to Equation 4.238 for an expression for the total thrust.

$$\frac{F_{\text{total}}}{\dot{m}_0} = (1+f)V_9 - V_0 + \frac{(1+f)[\alpha\eta_{\text{LPT}}\eta_{\text{mLPT}}\eta_{\text{gb}}\eta_{\text{prop}}]h_{t4.5} \left[1 - \left(\frac{p_9}{p_{t4.5}} \right)^{\frac{\gamma-1}{\gamma}} \right]}{V_0}$$

We express the exhaust velocity V_9 as (Equation 4.237)

$$V_9 \approx \sqrt{2(1-\alpha)\eta_{\text{n}}h_{t4.5} \left[1 - \left(\frac{p_9}{p_{t4.5}} \right)^{\frac{\gamma-1}{\gamma}} \right]}$$

We note that the bracketed term in the above equations, that is,

$$\begin{aligned} 1 - \left(\frac{p_9}{p_{t4.5}} \right)^{\frac{\gamma-1}{\gamma}} &= 1 - \left(\frac{p_9}{p_0} \frac{p_0}{p_{t0}} \frac{p_{t0}}{p_{t2}} \frac{p_{t2}}{p_{t3}} \frac{p_{t3}}{p_{t4}} \frac{p_{t4}}{p_{t4.5}} \right)^{\frac{\gamma-1}{\gamma}} \\ &= 1 - \left(\frac{p_9}{p_0} (\pi_{\text{r}} \pi_{\text{d}} \pi_{\text{c}} \pi_{\text{b}} \pi_{\text{HPT}})^{-1} \right)^{\frac{\gamma-1}{\gamma}} \end{aligned} \quad (4.244)$$

which is a constant. Also let us examine the total enthalpy at station 4.5, $h_{t4.5}$,

$$h_{t4.5} = \frac{h_{t4.5}}{h_{t4}} \frac{h_{t4}}{h_0} h_0 = \tau_{\text{HPT}} \cdot \tau_{\lambda} \cdot h_0 \quad (4.245)$$

which is a constant, as well. Therefore, the expression for the total thrust of the engine (per unit mass flow rate in the engine nozzle) is essentially composed of a series of constants and the dependence on α takes on the following simplified form:

$$\frac{F_{\text{total}}}{(1+f)\dot{m}_0} = C_1 \sqrt{1-\alpha} + C_2 \alpha + C_3 \quad (4.246)$$

where C_1 , C_2 , and C_3 are all constants. Now, let us differentiate the above function with respect to α and set the derivative equal to zero, that is,

$$\frac{d}{d\alpha} \left[\frac{F_{\text{total}}}{(1+f)\dot{m}_0} \right] = \frac{-C_1}{2\sqrt{1-\alpha}} + C_2 = 0 \quad (4.247)$$

which produces a solution for the power split parameter α that maximizes the total thrust of a turboprop engine. Hence, we may call this special value of α , the “optimum” α , namely

$$\alpha_{\text{opt}} = 1 - \left(\frac{C_1}{2C_2} \right)^2 \quad (4.248)$$

Now, upon substitution for the constants C_1 and C_2 and some simplification, we get

$$\alpha_{\text{opt}} = 1 - \frac{\eta_n}{(\eta_{\text{PT}}\eta_{\text{mLPT}}\eta_{\text{gb}}\eta_{\text{prop}})^2} \cdot \frac{\gamma_c - 1}{2} \frac{M_0^2}{\tau_{\text{HPT}}\tau_\lambda \left[1 - \left(\frac{p_9/p_0}{\pi_r\pi_d\pi_c\pi_b\pi_{\text{HPT}}} \right)^{\frac{\gamma_t-1}{\gamma_t}} \right]} \quad (4.249)$$

This expression for the optimum power split between the propeller and the jet involves all component and transmission (of power) efficiencies, as expected. However, let us assume that all efficiencies were 100% and further assume that the exhaust nozzle was perfectly expanded, that is, $p_9 = p_0$. What does the above expression tell us about the optimum power split in a perfect turboprop engine? Let us proceed with the simplifications.

$$\alpha_{\text{opt ideal}} = 1 - \frac{\frac{\gamma_c-1}{2}M_0^2}{\tau_{\text{HPT}}\tau_\lambda - \frac{\tau_\lambda}{\tau_r\tau_c}} \quad (4.250)$$

From power balance between the compressor and the high-pressure turbine, we can express the following:

$$\tau_r(\tau_c - 1) = (1+f)\tau_\lambda(1 - \tau_{\text{HPT}}) \approx \tau_\lambda(1 - \tau_{\text{HPT}}) \quad (4.251)$$

which simplifies to

$$\tau_\lambda\tau_{\text{HPT}} \cong \tau_\lambda - \tau_r(\tau_c - 1) \quad (4.252)$$

Substitute the above equation in the optimum power split in an ideal turboprop engine, Equation 4.250, to get

$$\alpha_{\text{opt ideal}} = 1 - \frac{\frac{\gamma_c-1}{2}M_0^2}{\tau_\lambda - \tau_r(\tau_c - 1) - \frac{\tau_\lambda}{\tau_r\tau_c}} = 1 - \frac{\tau_r - 1}{\tau_\lambda - \tau_r(\tau_c - 1) - \frac{\tau_\lambda}{\tau_r\tau_c}} \quad (4.253)$$

At takeoff condition and low-speed climb/descent ($\tau_r \rightarrow 1$), the optimum power split approaches 1, as expected. The propeller is the most efficient propulsor at low speeds, as it attains the highest propulsive efficiency. As flight Mach number increases, the power split term becomes less than 1.

EXAMPLE 4.20

An advanced turboprop flies at $M_0 = 0.7$ at an altitude where $p_0 = 16$ kPa and $T_0 = -45^\circ\text{C}$. The propeller efficiency is $\eta_{\text{prop}} = 0.85$. The inlet captures airflow rate at 10 kg/s and has a total pressure recovery of $\pi_d = 0.98$. The compressor pressure ratio is $\pi_c = 30$ and its polytropic efficiency is

$e_c = 0.92$. The combustor has an exit temperature $T_{t4} = 1600$ K and the fuel heating value is $Q_R = 42,000$ kJ/kg with a burner efficiency of $\eta_b = 0.99$ and the total pressure loss in the burner is $\pi_b = 0.96$. The HPT has a polytropic efficiency of $e_{t,\text{HPT}} = 0.82$, and a mechanical efficiency of

$\eta_{m,HPT} = 0.99$. The power split between the LPT and the engine nozzle is at $\alpha = 0.85$ and the mechanical efficiency of the LPT is $\eta_{m,LTP} = 0.99$, the LPT adiabatic efficiency is $\eta_{LPT} = 0.88$. A reduction gearbox is used with an efficiency of $\eta_{gb} = 0.995$. The exhaust nozzle is convergent with an adiabatic efficiency of $\eta_n = 0.95$. We will describe gas properties in the engine based only on two temperature zones (cold and hot):

Inlet and compressor sections (cold): $\gamma_c = 1.4$,
 $c_{pc} = 1004 \text{ J/kg} \cdot \text{K}$
 Turbines and Nozzle Sections (hot): $\gamma_t = 1.33$,
 $c_{pt} = 1152 \text{ J/kg} \cdot \text{K}$

SOLUTION

We start with the flight parameters p_{10} , T_{10} , a_0 , V_0 . Since all our temperature calculations are expressed in absolute scale, we convert $T_0 = (-45 + 273) \text{ K} = 228 \text{ K}$

From ambient static temperature and flight Mach number, we get $T_0 \cong 250.34 \text{ K}$

Remember $T_t = T [1 + (\gamma - 1)M^2/2]$ at any point in the flow.

From ambient static pressure and flight Mach number, we get $p_{10} \cong 22.194 \text{ kPa}$

The speed of sound at the ambient temperature condition is $a_0 \cong 302.6 \text{ m/s}$

The flight speed is $V_0 = M_0 \cdot a_0 \cong 211.8 \text{ m/s}$

Now, we march through the rest of the engine, component by component, beginning with the inlet. The exit total pressure of the inlet is $p_{12} = p_{10} \cdot \pi_d = 21.75 \text{ kPa}$. Since inlets are adiabatic, $T_{12} = T_{10} = 250.34 \text{ K}$.

The compressor exit total pressure is the product of the compressor pressure ratio π_c and p_{12} , i.e.,

$$p_{13} = 30(21.75 \text{ kPa}) \cong 652.5 \text{ kPa}$$

The compressor total temperature ratio $\tau_c = \pi_c^{(\gamma_c - 1)/e_c \gamma_c}$ therefore, $T_{13} \cong 719.9 \text{ K}$. Now, we are ready for the burner. The fuel-to-air ratio follows the energy balance across the burner, namely,

$$f = \frac{h_{14} - h_{13}}{Q_R \eta_b - h_{14}} \approx 0.0282$$

The burner exit total pressure is $p_{14} = p_{13} \cdot \pi_b$, which gives $p_{14} \cong 626.4 \text{ kPa}$.

The power balance between the HPT and the compressor follows Equation 4.226a, $\eta_{m,HPT}(1 + f)(h_{14} - h_{14.5}) =$

Calculate

- total pressure and temperature throughout the engine (include fuel-to-air ratio in mass/energy balance)
- engine core thrust in kN
- propeller thrust in kN
- power-specific fuel consumption in mg/s/kW
- thrust-specific fuel consumption in mg/s/N
- thermal and propulsive efficiencies η_{th} and η_p
- engine overall efficiency η_o

$h_{13} - h_{12}$ with the only unknown $h_{14.5}$. Upon solving for $h_{14.5}$, we get $h_{14.5} \cong 1,380.065 \text{ kJ/kg}$ and since $T_{14.5} = h_{14.5}/c_{pt}$, the HPT exit total temperature is $T_{14.5} \cong 1198 \text{ K}$.

The total pressure ratio across the HPT is related to its total temperature ratio and the HPT polytropic efficiency e_{HPT} following Equation 4.227, therefore $p_{145} \cong 151.065 \text{ kPa}$.

Since we have specified the power split between the LPT and the nozzle, we may use Equation 4.234

$$\begin{aligned} \wp_{LPT} &= \dot{m}_9 \eta_{LPT} \cdot \alpha \cdot h_{14.5} \left[1 - \left(\frac{p_9}{p_{14.5}} \right)^{\frac{\gamma_t - 1}{\gamma_t}} \right] \\ &= \dot{m}_9 (h_{14.5} - h_{15}) \end{aligned}$$

to calculate the shaft power produced by the LPT; also note that we have the mass flow rate through the engine, $\dot{m}_9 = (1 + f)\dot{m}_0 = (1 + 0.0282)(10 \text{ kg/s}) \cong 10.282 \text{ kg/s}$. The nozzle exit pressure p_9 is initially assumed to be the ambient static pressure p_0 subject to later verification. Turboprop engines typically have a subsonic exhaust ($M_9 < 1$), so the initial assumption of $p_9 = p_0$ is often borne out. Therefore,

$$\wp_{LPT} \cong 4.533 \text{ MW}$$

Also from Equation 4.234, we get the LPT exit total enthalpy h_{15} (and temperature T_{15}). These are $h_{15} = 939.16 \text{ kJ/kg}$ and $T_{15} \cong 815.24 \text{ K}$. We calculate p_{15} from $p_{14.5}$ and LPT total temperature ratio and polytropic efficiency e_{LPT} . Equation 4.45 relates polytropic and adiabatic efficiencies and turbine total temperature ratio. We get $e_t = 0.8533$ and then we use the efficiency exponent, i.e., $\pi_t = \tau_t^{\gamma_t/e_t(\gamma_t - 1)}$ to get $p_{15} = 24.53 \text{ kPa}$.

To calculate T_{9j} , we use isentropic pressure and temperature ratio rule between the two states t5 and 9i, to get $T_{9i} = 733.25$ K. From the definition of nozzle adiabatic efficiency and T_{9j} , we calculate the nozzle exit static temperature T_9 to be $T_9 = 737.35$ K. Now, we calculate nozzle exit velocity more accurately from $V_9^2 = 2c_{pt}(T_{t5} - T_9)$, which gives $V_9 = 423.65$ m/s.

From the following equation, we calculate propeller thrust

$$\begin{aligned} F_{\text{prop}} \cdot V_0 &= \eta_{\text{prop}} \cdot \eta_{\text{gb}} \cdot \eta_{\text{mLPT}} \cdot \mathcal{P}_{\text{LPT}} \\ F_{\text{prop}} &= 17.92 \text{ kN} \end{aligned}$$

From T_9 , we calculate speed of sound and the nozzle exit Mach number to be $a_9 = 529.44$ m/s and $M_9 = 0.80$.

Since $M_9 < 1$, then $p_9 = p_0$ was a valid assumption. Based on nozzle exit Mach number M_9 and static pressure, we calculate p_{t9} to be 23.98 kPa, which gives the nozzle total pressure ratio $\pi_n = p_{t9}/p_{t5} = 0.978$.

The (net) thrust produced by the engine core is

$$\begin{aligned} (F_n)_{\text{core}} &= \dot{m}_0[(1+f)V_9 - V_0] \\ &= 10 \text{ kg/s}[(1+0.0282)423.65 \text{ m/s} \\ &\quad - 211.8 \text{ m/s}] \approx 2.238 \text{ kN} \end{aligned}$$

The shaft power delivered to the propeller is

$$\begin{aligned} \mathcal{P}_{\text{prop}} &= \eta_{\text{gb}} \eta_{\text{mLPT}} \mathcal{P}_{\text{LPT}} \\ &= (0.995)(0.99)(4.533 \text{ MW}) \approx 4.465 \text{ MW} \end{aligned}$$

Also the engine total thrust is the sum of the propeller and core thrust, i.e.,

$$F_{\text{total}} = F_{\text{prop}} + F_{\text{core}} = (17.92 + 2.238) \text{ kN} = 20.16 \text{ kN}$$

The power specific fuel consumption is defined as PSFC $\equiv \dot{m}_f / \mathcal{P}_{\text{prop}} + \mathcal{P}_{\text{core}}$. The mechanical power produced by the core is $\mathcal{P}_c = \dot{m}_9 V_9^2 / 2 - \dot{m}_0 V_0^2 / 2$ for a perfectly expanded nozzle. We have calculated all the parameters in the equation, therefore, $\mathcal{P}_c \approx 698.37$ kW. Based on fuel-to-air ratio and air flow rate in the engine, $\dot{m}_f = 0.282$ kg/s, thus the power specific fuel consumption is PSFC ≈ 54.6 mg/s/kW.

The definition of thrust-specific fuel consumption is TSFC $\equiv \dot{m}_f / (F_{\text{prop}} + F_{\text{core}}) \approx 13.99$ mg/s/N

$$\eta_{\text{th}} \equiv \frac{\mathcal{P}_{\text{prop}} + \mathcal{P}_{\text{core}}}{\dot{m}_f Q_R} \approx 43.6\%$$

$$\eta_p \equiv \frac{F_{\text{total}} \cdot V_0}{\mathcal{P}_{\text{prop}} + \mathcal{P}_{\text{core}}} \approx 82.68\%$$

$$\eta_o = \eta_{\text{th}} \eta_p \approx 36.05\%$$

Note that the thermal efficiency is dominated by the cycle pressure ratio in a Brayton cycle and ideally is $\eta_{\text{th-ideal}} = 1 - (PR)^{-(\gamma-1)/\gamma}$, which in this cycle, the pressure ratio is $p_{t3}/p_0 \approx 40.8$ and the ideal Brayton cycle thermal efficiency (for $\gamma = 1.33$) is $\sim 60.1\%$. Obviously, component losses contribute to a lower thermal efficiency than that predicted by an ideal cycle. On the contrary, the real advantage of turboprop is in its increased propulsive efficiency, which in this case that represents cruise, it is $\sim 83\%$.

EXAMPLE 4.21

For the turboprop engine specified in Example 4.20, vary the power split α from 0.79 to 0.97 using a spreadsheet or write a program in MATLAB and calculate and graph engine total thrust and specific fuel consumption versus

the power split factor α . Also calculate the optimum power split based on the theory developed in the TP-section and compare the two results.

SOLUTION

First, the optimum power split is calculated to be

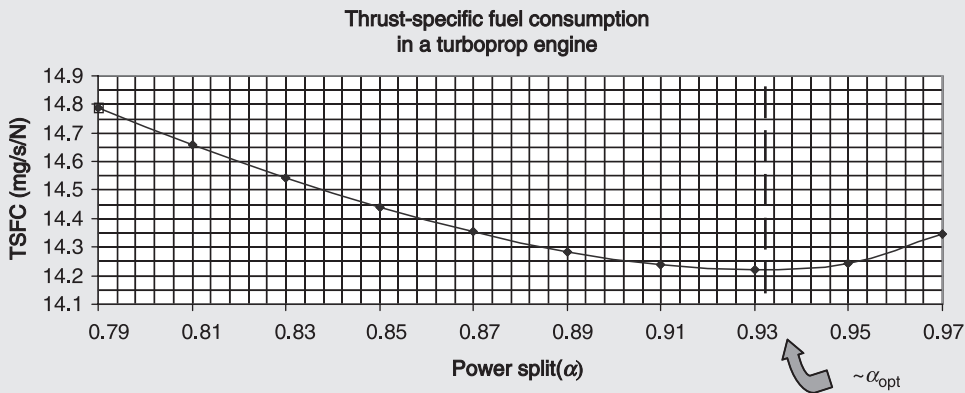
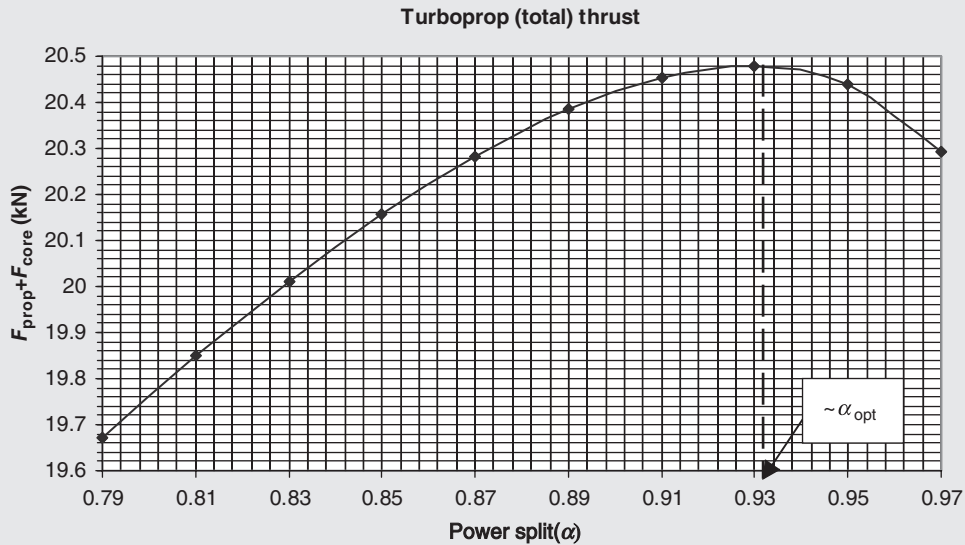
$$\begin{aligned} \alpha_{\text{opt}} &= 1 - \frac{\eta_n}{(\eta_{\text{PT}} \eta_{\text{mLPT}} \eta_{\text{gb}} \eta_{\text{prop}})^2} \cdot \frac{\gamma_c - 1}{2} \\ &\quad \times \frac{M_0^2}{\tau_{\text{HPT}} \tau_\lambda \left[1 - \left(\frac{p_9/p_0}{\pi_r \pi_d \pi_c \pi_b \pi_{\text{HPT}}} \right)^{\frac{\gamma-1}{\gamma}} \right]} \cong 0.9334 \end{aligned}$$

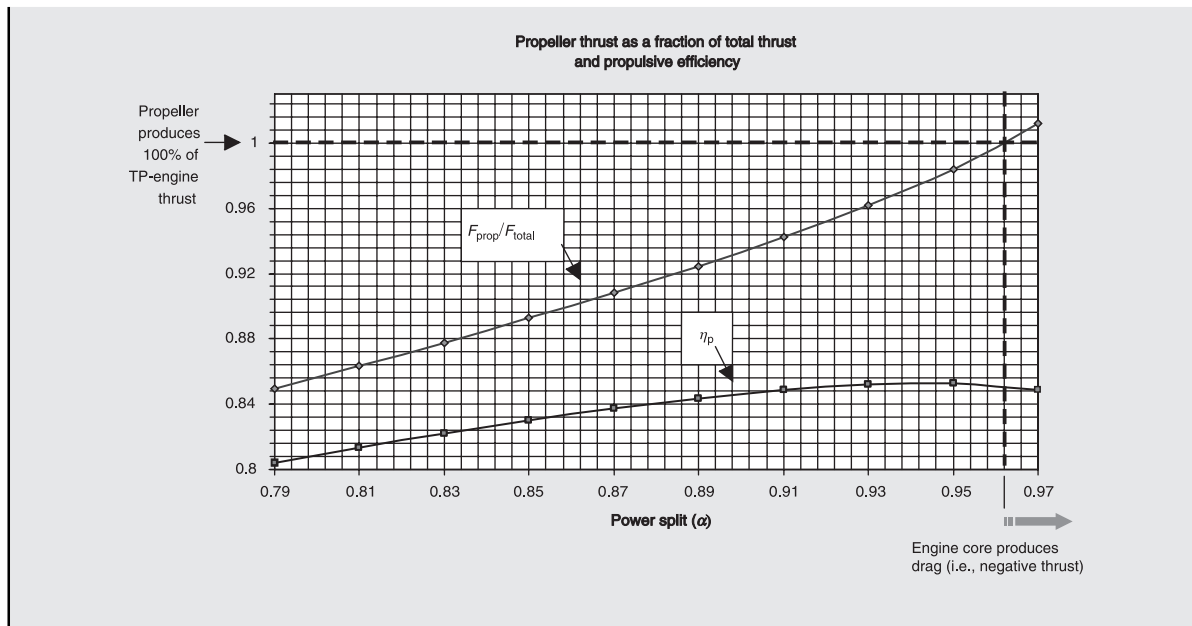
This problem is easily solved using a spreadsheet program. The important results are graphed. As expected, the total thrust produced by a TP engine reaches a maximum at the optimum power split α_{opt} .

Since fuel-to-air ratio remains constant (with α variation), the TSFC reaches a minimum at α_{opt} . As the power split increases, the propellers share of thrust production

increases as well, as shown in the last figure. At very large power split factors (e.g., ~ 0.96 in this example), the core ram drag becomes larger than its nozzle gross thrust, thus start producing drag! This is expected, as we drain more energy from exhaust (by producing more shaft power for the prop), the nozzle exhaust velocity drops below the flight speed, i.e., $V_9 < V_0$.

The engine thermal efficiency remains nearly constant with the power split factor α . This result is also expected as the thermal efficiency is dominated by the engine pressure ratio, which remains constant with α . On the contrary, engine propulsive efficiency keeps on improving, as we reduce core exhaust velocity. This behavior is also shown graphically in the last figure.





4.6 Summary

In this chapter, we learned various gas turbine engine configurations and their analysis. The performance parameters were identified to be specific thrust, specific fuel consumption, thermal, propulsive, and overall efficiencies. We had limited our approach to steady, one-dimensional flow and the “design-point” analysis. We also learned that we may analyze ramjets by setting compressor pressure ratio to one in a turbojet engine. We had essentially removed the compressor (and thus turbine) by setting its pressure ratio equal to 1. We included the effect of fluid viscosity and thermal conductivity in our cycle analysis empirically, that is, through the introduction of component efficiency. The knowledge of component efficiency at different operating conditions is critical to their design and optimization. We always treated that knowledge, that is, the component efficiency, as a “given” in our analysis. In reality, engine manufacturers, research laboratories, and universities continually measure component performance and sometimes report them in open literature. However, commercial engine manufacturers treat most competition-sensitive data as proprietary. Propeller theory is treated as a part of turboprop cycle analysis.

In the following six chapters, we will take on the propulsion system of Uninhabited Aerial Vehicles (UAV) and then follow this with engine component analysis. The nonrotating components, that is, inlets and nozzles, are treated in a single chapter (Chapter 6). An introductory study of combustion and the gas turbine burner and afterburner configurations follows in Chapter 7. The rotating components, that is, compressors and turbines, are treated in the turbomachinery Chapters 8–10. Finally, we allow components to be “matched” and integrated in a real engine where we explore its off-design analysis in Chapter 11: Component Matching and Engine Off-design Analysis.

References 1–11 provide for complementary reading on aircraft propulsion and are recommended to the reader.

References

1. Archer, R.D. and Saarlal, M., *An Introduction of Aerospace Propulsion*, Prentice Hall, New York, 1998.
2. Cumpsty, N., *Jet Propulsion: A Simple Guide to the Aerodynamic and Thermodynamic Design and Performance of Jet Engines*, 2nd edition, Cambridge University Press, Cambridge, UK, 2003.
3. Flack, R.D. and Rycroft, M.J., *Fundamentals of Jet Propulsion with Applications*, Cambridge University Press, Cambridge, UK, 2005.
4. Heiser, W.H., Pratt, D.T., Daley, D.H., and Mehta, U.B., *Hypersonic Airbreathing Propulsion*, AIAA, Washington, DC, 1993.
5. Hesse, W.J. and Mumford, N.V.S., *Jet Propulsion for Aerospace Applications*, 2nd edition, Pittman Publishing Corporation, New York, 1964.
6. Hill, P.G. and Peterson, C.R., *Mechanics and Thermodynamics of Propulsion*, 2nd edition, Addison-Wesley, Reading, Massachusetts, 1992.
7. Kerrebrock, J.L., *Aircraft Engines and Gas Turbines*, 2nd edition, MIT Press, Cambridge, Mass, 1992.
8. Mattingly, J.D., *Elements of Gas Turbine Propulsion*, McGraw-Hill, New York, 1996.
9. Mattingly, J.D., Heiser, W.H., and Pratt, D.T., *Aircraft Engine Design*, 2nd edition, AIAA, Washington, DC, 2002.
10. Oates, G.C., *Aerothermodynamics of Gas Turbine and Rocket Propulsion*, AIAA, Washington, DC, 1988.
11. Shepherd, D.G., *Aerospace Propulsion*, American Elsevier Publication, New York, 1972.
12. Asbury, S.C. and Yetter, J.A., Static Performance of Six Innovative Thrust Reverser Concepts for Subsonic Transport Applications, NASA/TM 2000-210300, National Aeronautics and Space Administration, Langley Research Center, Hampton, VA, July 2000.
13. CFM, The Power of Flight. <http://www.cfmaeroengines.com/>; last accessed 24 November 2013.
14. Duong, L., McCune, M., and Dobek, L., Method of Making Integral Sun Gear Coupling, United States Patent 2009/0293278, 3 December 2009.
15. Guynn, M.D. Berton, J.J. Fisher, K.L. *et al.*, Engine Concept Study for an Advanced Single-Aisle Transport", NASA TM 2009-215784, National Aeronautics and Space Administration, Langley Research Center, Hampton, VA, August 2009.
16. Halliwell, I., AIAA-IGTI Undergraduate Team Engine Design Competition Request for Proposal, 2010–2011; www.aiaa.org; last accessed 24 November 2013.
17. Kurzke, J., A design and off-design performance program for gas turbines, GasTurb, 2013. <http://www.gasturb.de>; last accessed 24 November 2013.
18. Lan, C.T. and Roskam, J., *Airplane Aerodynamics and Performance*, DAR Corporation, Lawrence, KA, 2008.
19. Pratt & Whitney, Geared Turbo Fan. http://www.pw.utc.com/PurePowerPW1000G_Engine; last accessed 24 November 2013.
20. Von Mises, R., *Theory of Flight*, Dover Publications, New York, 1959.

Problems

4.1 An aircraft is flying at an altitude where the ambient static pressure is $p_0 = 25$ kPa and the flight Mach number is $M_0 = 2.5$. The total pressure at the engine face is measured to be $p_{t2} = 341.7$ kPa. Assuming the inlet flow is adiabatic and $\gamma = 1.4$, calculate

- (a) the inlet total pressure recovery π_d
- (b) the inlet adiabatic efficiency η_d
- (c) the nondimensional entropy rise caused by the inlet $\Delta s_d/R$

4.2 A multistage axial-flow compressor has a mass flow rate of 100 kg/s and a total pressure ratio of 25. The compressor polytropic efficiency is $e_c = 0.90$. The inlet flow condition to the compressor is described by $T_{t2} = -35^\circ\text{C}$ and $p_{t2} = 30$ kPa. Assuming the flow in the compressor is adiabatic, and constant gas properties throughout the compressor are assumed, i.e., $\gamma = 1.4$ and $c_p = 1004$ J/kg · K, calculate

- (a) compressor exit total temperature T_{t3} , in K
- (b) compressor adiabatic efficiency η_c
- (c) compressor shaft power $\dot{\varphi}_c$ in MW

4.3 A gas turbine combustor has inlet condition $T_{t3} = 900$ K, $p_{t3} = 3.2$ Mpa, air mass flow rate of 100 kg/s, $\gamma_3 = 1.4$, $c_{p3} = 1004$ J/kg · K.

A hydrocarbon fuel with ideal heating value $Q_R = 42,800$ kJ/kg is injected in the combustor at a rate of 2 kg/s. The burner efficiency is $\eta_b = 0.99$ and the total pressure at the combustor exit is 97% of the inlet total pressure, i.e., combustion causes a 3% loss in total pressure. The gas properties at the combustor exit are $\gamma_4 = 1.33$ and $c_{p4} = 1,156$ J/kg · K. Calculate

- (a) fuel-to-air ratio f
- (b) combustor exit temperature T_{t4} in K and p_{t4} in MPa

4.4 An uncooled gas turbine has its inlet condition the same as the exit condition of the combustor described in Problem 4.3. The turbine adiabatic efficiency is 85%. The turbine produces a shaft power to drive the compressor and other accessories at $\dot{\phi}_t = 60$ MW. Assuming that the gas properties in the turbine are the same as the burner exit in Problem 4.3, calculate

- (a) turbine exit total temperature T_{t5} in K
- (b) turbine polytropic efficiency e_t
- (c) turbine exit total pressure p_{t5} in kPa
- (d) turbine shaft power $\dot{\phi}_t$ based on turbine expansion ΔT_t

4.5 In a turbine nozzle blade row, hot gas mass flow rate is 100 kg/s and $h_{t_g} = 1900$ kJ/kg. The nozzle blades are internally cooled with a coolant mass flow rate of 1.2 kg/s and $h_{t_c} = 904$ kJ/kg as the coolant is ejected through nozzle blades trailing edge. The coolant mixes with the hot gas and causes a reduction in the mixed-out enthalpy of the gas. Calculate the mixed-out total enthalpy after the nozzle. Also for the $c_{p, \text{mixed-out}} = 1594$ J/kg · K, calculate the mixed out total temperature.

4.6 Consider the internally cooled turbine nozzle blade row of Problem 4.5. The hot gas total pressure at the entrance of the nozzle blade is $p_{t4} = 2.2$ MPa, $c_{pg} = 1156$ J/kg · K, and $\gamma_g = 1.33$. The mixed-out total pressure at the exit of the

4.7 A convergent–divergent nozzle with a pressure ratio, $\text{NPR} = 12$. The gas properties are $\gamma = 1.33$ and $c_p = 1156$ J/kg · K and remain constant in the nozzle. The nozzle adiabatic efficiency is $\eta_n = 0.94$. Calculate

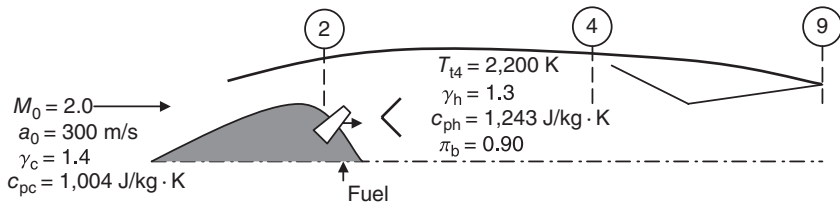
- (a) nozzle total pressure ratio π_n
- (b) nozzle area ratio A_9/A_8 for a perfectly expanded nozzle
- (c) nozzle exit Mach number M_9 (perfectly expanded)

4.8 Calculate the propulsive efficiency of a turbojet engine under the following two flight conditions that represent takeoff and cruise, namely

- (a) $V_0 = 100$ m/s and $V_9 = 2000$ m/s
- (b) $V_0 = 750$ m/s and $V_9 = 2000$ m/s

4.9 A ramjet is in supersonic flight, as shown. The inlet pressure recovery is $\pi_d = 0.90$. The combustor burns hydrogen with $Q_R = 117,400$ kJ/kg at a combustion efficiency of $\eta_b = 0.95$. The nozzle expands the gas perfectly, but suffers from a total pressure loss of $\pi_n = 0.92$. Calculate

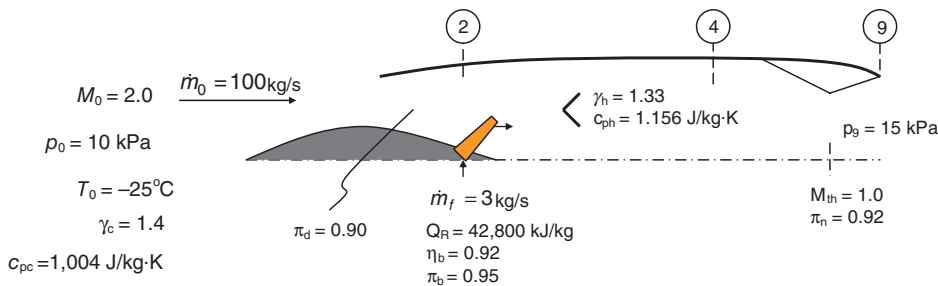
- (a) fuel-to-air ratio f
- (b) nozzle exit Mach number M_9
- (c) specific (net) thrust F_n/\dot{m}_0 (in N/kg/s)
- (d) η_{th} , engine thermal efficiency
- (e) η_p , engine propulsive efficiency



■ FIGURE P 4.9

nozzle has suffered 5% loss due to both mixing and frictional losses in the blade row boundary layers. Calculate the entropy change $\Delta s/R$ across the turbine nozzle blade row.

4.10 A ramjet takes in 100 kg/s of air at a Mach 2 flight condition at an altitude where $p_0 = 10$ kPa and $T_0 = -25^\circ\text{C}$. The engine throttle setting allows 3 kg/s of fuel flow rate



■ FIGURE P 4.10

in the combustor where a hydrocarbon fuel of 42,800 kJ/kg heating value is burned. The ramjet component efficiencies are all listed on the engine cross section. Note that the exhaust nozzle is not perfectly expanded. We intend to establish some performance parameters for this engine as well as some flow areas (i.e., physical sizes) of this engine.

Assuming the gas properties are split into a *cold* section and a hot section (perfect gas properties), namely, $\gamma_c = 1.4$ and $c_{pc} = 1.004 \text{ kJ/kg} \cdot \text{K}$ and $\gamma_h = 1.33$ and $c_{ph} = 1.156 \text{ kJ/kg} \cdot \text{K}$ (subscript “c” stands for “cold” and “h” for “hot”), calculate

- (a) ram drag in kN
- (b) the inlet capture area A_0 in m^2
- (c) p_{t4} in kPa
- (d) T_{t4} in K
- (e) p_{t9} in kPa
- (f) exit Mach number M_9
- (g) exhaust velocity V_9
- (h) nozzle exit area A_9 in m^2
- (i) gross thrust in kN
- (j) thermal efficiency η_{th}
- (k) propulsive efficiency η_p

Note:

For exhaust nozzles that are not perfectly expanded the thermal and propulsive efficiencies are defined as

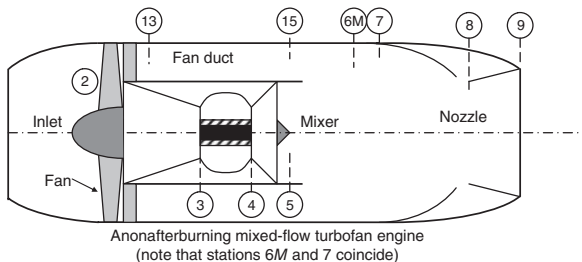
$$\eta_{th} \equiv \frac{\Delta K \dot{E}}{\dot{m}_f Q_R \eta_b} = \frac{\dot{m}_9 V_{9eff}^2 - \dot{m}_0 V_0^2}{2 \dot{m}_f Q_R \eta_b}$$

$$\eta_p \equiv \frac{2 F_n V_0}{\dot{m}_9 V_{9eff}^2 - \dot{m}_0 V_0^2}$$

where the effective exhaust velocity V_{9eff} is defined as

$$V_{9eff} \equiv \frac{F_g}{\dot{m}_0}$$

4.11 A mixed-exhaust turbofan engine is described by the following design and limit parameters:



■ FIGURE P4.11

- Flight: $M_0 = 2.2, p_0 = 10 \text{ kPa}, T_0 = -50^\circ\text{C}, R = 287 \text{ J/kg} \cdot \text{K}, \gamma = 1.4$
- Inlet mass flow rate and total pressure recovery: $(1 + \alpha) \dot{m}_0 = 25 \text{ kg/s}, \pi_d = 0.85$
- Compressor, fan: $\pi_c = 15, e_c = 0.90, \pi_f = 1.5, e_f = 0.90$
- Burner: $\pi_b = 0.95, \eta_b = 0.98, Q_R = 42,800 \text{ kJ/kg}, T_{t4} = 1400^\circ\text{C}$
- Turbine: $e_t = 0.92, \eta_m = 0.95, M_5 = 0.5$
- Mixer: $\pi_{M,f} = 0.98$
- Afterburner: None
- Nozzle: $\pi_n = 0.90, p_9/p_0 = 1.0$

Calculate

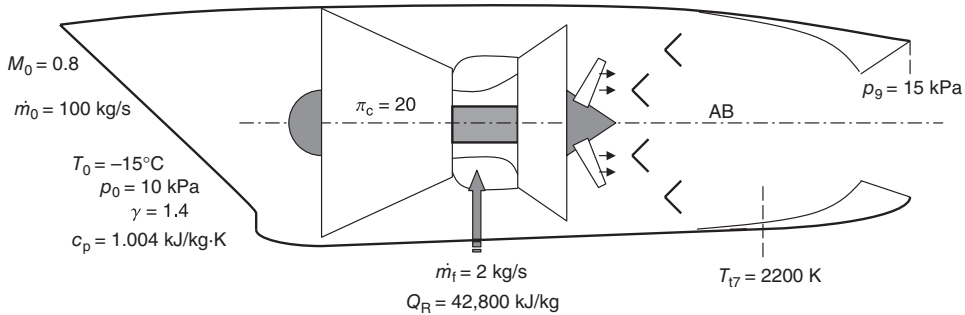
- (a) ram drag D_R in kN
- (b) p_{t2} in kPa, T_{t2} in K
- (c) p_{t3} in kPa, T_{t3} in K
- (d) p_{t13} in kPa, T_{t13} in K
- (e) p_{t4} in kPa, T_{t5} in K
- (f) fuel-to-air ratio f
- (g) bypass ratio α, \dot{m}_{core} in kg/s, and \dot{m}_{fan} in kg/s
- (h) T_{t6M} in K
- (i) p_{t9} in kPa, T_{t9} in K
- (j) M_9, V_9 in m/s
- (k) gross thrust F_g in kN
- (l) thrust-specific fuel consumption in mg/s/N

You may assume constant gas properties γ and R throughout the engine.

We may also assume that the flow in the fan duct, i.e., between stations 13 and 15, is frictionless and adiabatic.

4.12 In the afterburning turbojet engine shown, assume constant gas properties and ideal components to calculate

- (a) ram drag
- (b) compressor shaft power ϕ_c
- (c) fuel-to-air ratio in the primary burner
- (d) τ_λ , the limit enthalpy parameter in the gas generator
- (e) turbine expansion parameter τ_t
- (f) turbine shaft power ϕ_t
- (g) $\tau_{\lambda AB}$, the afterburner limit enthalpy parameter
- (h) fuel-to-air ratio in the afterburner
- (i) nozzle gross thrust
- (j) engine thrust specific fuel consumption
- (k) engine net uninstalled thrust
- (l) engine thermal efficiency
- (m) engine propulsive efficiency



■ FIGURE P4.12

4.13 An ideal separate-exhaust turbofan engine has the following design parameters:

$$T_0 = -20^\circ\text{C}, p_0 = 15 \text{ kPa}, M_0 = 0.85$$

$$\pi_c = 30$$

$$\pi_f = 1.60, \alpha = 6$$

$$\tau_\lambda = 6.5, Q_R = 42,800 \text{ kJ/kg}$$

Fan and core nozzles are convergent.

Assuming the gas is calorically perfect with $\gamma = 1.4$ and $c_p = 1.004 \text{ kJ/kg} \cdot \text{K}$, calculate

- (a) compressor exit pressure p_{13} in kPa
- (b) fan exit temperature T_{113} in K
- (c) fuel-to-air ratio f
- (d) turbine exit temperature T_{15} in K
- (e) fan nozzle exit Mach number M_{19}
- (f) core nozzle exit Mach number M_9
- (g) core nozzle exit velocity V_9 in m/s
- (h) The ratio of fan-to-core thrust $F_{\text{fan}}/F_{\text{core}}$

4.14 In a mixed-exhaust turbofan engine, we have calculated the parameters shown on the engine diagram.

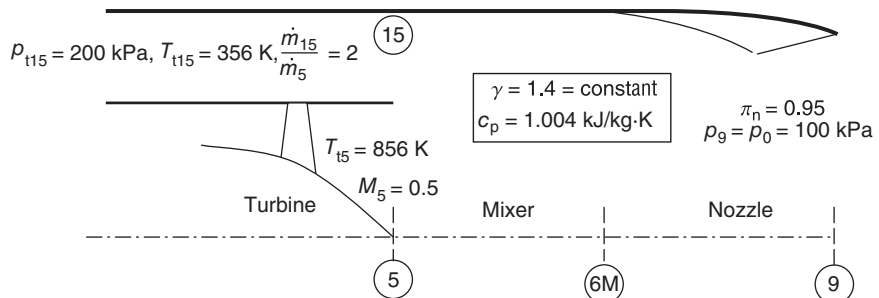
Assuming constant gas properties between the two streams and constant total pressure between the hot and cold gas streams, calculate

- (a) the mixer exit total temperature T_{16M}
- (b) M_9
- (c) V_9
- (d) $\frac{F_g}{\dot{m}_5}$

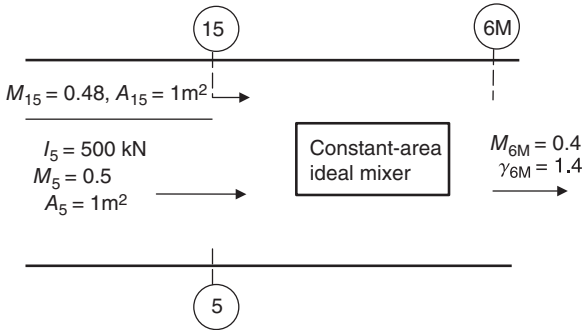
4.15 In an afterburning gas turbine engine, the exhaust nozzle is equipped with a variable area throat. Calculate percentage increase in nozzle throat area needed to accommodate the engine flow in the afterburning mode. With the afterburner on, the nozzle mass flow rate increases by 3%, the nozzle total temperature doubles, i.e. $(T_{18})_{\text{AB-ON}}/(T_{18})_{\text{AB-OFF}} = 2$, and the total pressure at the nozzle entrance is reduced by 20%. You may assume the gas properties γ and R remain constant and the nozzle throat remains choked.

4.16 For the constant-area ideal mixer shown, assuming constant gas properties, calculate

- (a) p_5 (kPa)
- (b) p_{15} (kPa)
- (c) p_{6M} (kPa)



■ FIGURE P4.14



■ FIGURE P 4.16

4.17 A turbojet engine has the following parameters at the on-design operating point:

$$M_0 = 0, p_0 = p_{STD}, T_0 = T_{STD}, \gamma = 1.4, c_p = 1.004 \text{ kJ/kg} \cdot \text{K}$$

$$\pi_d = 0.99$$

$$\pi_c = 30, e_c = 0.9$$

$$\tau_x = 6.0, \eta_b = 0.98, \pi_b = 0.95, \text{ and } Q_R = 42,800 \text{ kJ/kg}$$

$$e_t = 0.90, \eta_m = 0.95$$

$$\pi_n = 0.98 \text{ and } p_9/p_0 = 1.0$$

Calculate

- (a) p_{t3} and τ_c
- (b) fuel-to-air ratio f and p_{t4}
- (c) τ_t

Now for the following off-design condition:

$$M_0 = 0.85 \text{ at } 20 \text{ km U.S. standard altitude and throttle ratio,}$$

$$T_{t4} = 0.9 T_{t4\text{-design}}, \text{ assuming that } \tau_t \text{ remains constant}$$

between on-design and off-design, calculate

- (d) compressor pressure ratio at the off-design operation

4.18 A turbojet engine has the following design point parameters:

$$M_0 = 0, p_0 = 100 \text{ kPa}, T_0 = 15^\circ\text{C}$$

$$\pi_d = 0.98$$

$$\pi_c = 25, e_c = 0.90$$

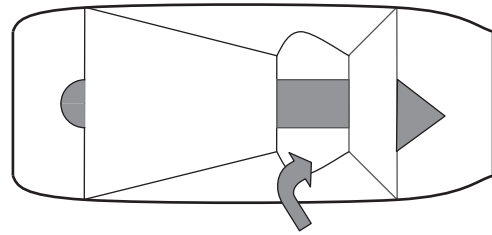
$$Q_R = 42,800 \text{ kJ/kg}, \pi_b = 0.95, \eta_b = 0.98, \tau_\lambda = 6.0$$

$$e_t = 0.85, \eta_m = 0.98$$

$$\pi_n = 0.97, p_9 = p_0$$

Calculate

- (a) fuel-to-air ratio f
- (b) turbine total temperature ratio τ_t



■ FIGURE P 4.18

For the following off-design operation:

$$M_0 = 0.85, p_0 = 10 \text{ kPa}, T_0 = -15^\circ\text{C}$$

$$\tau_\lambda = 6.5$$

Assume $\gamma = 1.4, c_p = 1004 \text{ kJ/kg} \cdot \text{K}$ and calculate

- (c) $\pi_{c\text{-Off-Design}}$ if $\tau_{t\text{-Design}} = \tau_{t\text{-Off-Design}}$

4.19 An ideal turbojet engine has the following design and limit parameters, namely,

$$M_0 = 2.0, \text{ altitude } 37 \text{ kft}$$

$$\text{compressor pressure ratio } \pi_c$$

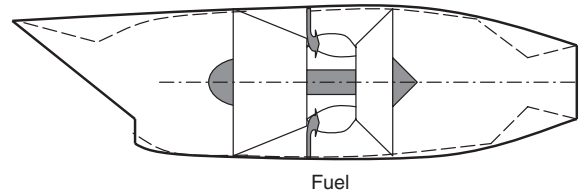
$$\text{maximum enthalpy ratio } \tau_\lambda = 7.0$$

$$\text{fuel type is hydrocarbon with } Q_R = 42,800 \text{ kJ/kg}$$

$$\text{assume constant gas properties } c_p = 1.004 \text{ kJ/kg} \cdot \text{K} \text{ and}$$

$$\gamma = 1.4.$$

For a range of compressor pressure ratios, namely, $1 \leq \pi_c \leq 40$, calculate and graph (using MATLAB or a spreadsheet)



■ FIGURE P 4.19

- (a) engine (nondimensional) specific thrust $F_n/(\dot{m} \cdot a_0)$
- (b) thrust specific fuel consumption in mg/s/N
- (c) in order to assess the effect of gas property variations with temperature on the engine performance parameters, repeat parts (a) and (b) for the following gas properties:

$$\text{Engine cold section: } \gamma_c = 1.40, c_{pc} = 1.004 \text{ kJ/kg} \cdot \text{K}$$

$$\text{Engine hot section: } \gamma_t = 1.33, c_{pt} = 1.156 \text{ kJ/kg} \cdot \text{K}$$

- (d) To assess the effect of inlet total pressure recovery on the engine performance, calculate and graph the engine specific thrust and fuel consumption for a single compressor pressure ratio of $\pi_c = 20$, but vary π_d from 0.50 to 1.0. Use gas properties of part (c)
- (e) Now, for the following component efficiencies

$$\pi_d = 0.90, e_c = 0.90, \pi_b = 0.98, \eta_b = 0.98, e_t = 0.91, \eta_m = 0.99, \pi_n = 0.95, \pi_c = 20, \tau_\lambda = 7, \text{ and } p_9 = p_0,$$

calculate the engine performance parameters

1. specific thrust (nondimensional)
2. specific fuel consumption
3. thermal efficiency
4. propulsive efficiency

4.20 For an ideal ramjet, derive an expression for the flight Mach number in terms of the cycle limit enthalpy, τ_λ that will lead to an engine thrust of zero.

4.21 Derive an expression for an optimum Mach number that maximizes the engine-specific thrust in an ideal ramjet.

4.22 For an ideal ramjet with a perfectly expanded nozzle, show that the nozzle exit Mach number M_9 is equal to the flight Mach number M_0 .

4.23 Assuming the component efficiencies in a real ramjet are

$$\pi_d = 0.90, \pi_b = 0.95, \eta_b = 0.98, \pi_n = 0.90 \text{ and } p_9/p_0 = 1.0 \text{ flying at 37 kft altitude.}$$

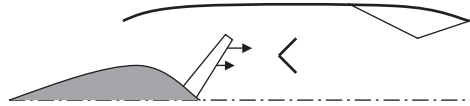
For the maximum enthalpy ratio $\tau_\lambda = 8.0$, the fuel heating value of 42,000 kJ/kg and a cold and hot section gas properties

Engine cold section: $\gamma_c = 1.40, c_{pc} = 1.004 \text{ kJ/kg} \cdot \text{K}$
 Engine hot section: $\gamma_t = 1.33, c_{pt} = 1.156 \text{ kJ/kg} \cdot \text{K}$

calculate the optimum flight Mach number corresponding to the maximum specific thrust.

4.24 A ramjet uses a hydrocarbon fuel with $Q_R = 42,800 \text{ kJ/kg}$ flying at Mach 2 (i.e., $M_0 = 2$) in an atmosphere where $a_0 = 300 \text{ m/s}$. Its exhaust is perfectly expanded and the exhaust velocity is $V_9 = 1200 \text{ m/s}$. Assuming the inlet total pressure recovery is $\pi_d = 0.90$, the burner losses are $\pi_b = 0.98$ and $\eta_b = 0.96$, the nozzle total pressure ratio is $\pi_n = 0.98$ and $\lambda = 1.4$ and $c_p = 1.004 \text{ kJ/kg} \cdot \text{K}$ are constant throughout the engine, calculate

- (a) τ_λ
- (b) fuel-to-air ratio f
- (c) nondimensional-specific thrust $F_n/(\dot{m}_0 a_0)$
- (d) propulsive efficiency
- (e) thermal efficiency



■ FIGURE P 4.24

4.25 A large bypass ratio turbofan engine has the following design and limit parameters:

$$M_0 = 0.8, \text{ altitude} = 37 \text{ kft U.S. standard atmosphere}$$

$$\pi_d = 0.995$$

$$\pi_c = 40, e_c = 0.90$$

$$\alpha = 6, \pi_f = 1.6, e_f = 0.90, \pi_{fn} = 0.98, \text{ fan nozzle is convergent}$$

$$\tau_\lambda = 7.0, Q_R = 42,800 \text{ kJ/kg}, \pi_b = 0.95, \eta_b = 0.98$$

$$e_t = 0.90, \eta_m = 0.975$$

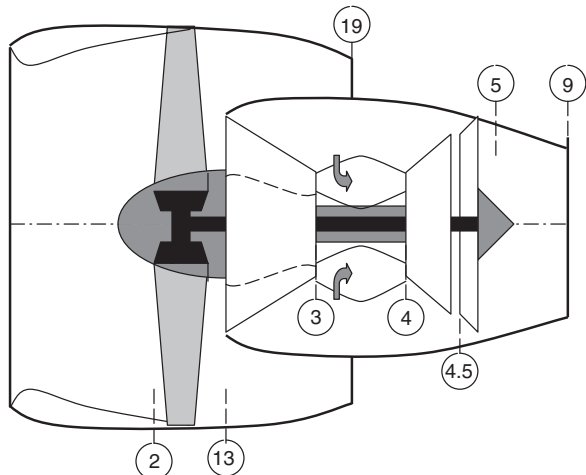
$$\pi_n = 0.98, \text{ core nozzle is convergent}$$

Assuming the gas properties may be described by two sets of parameters, namely, cold and hot stream values, i.e.,

Engine cold section: $\gamma_c = 1.40, c_{pc} = 1.004 \text{ kJ/kg} \cdot \text{K}$
 Engine hot section: $\gamma_t = 1.33, c_{pt} = 1.156 \text{ kJ/kg} \cdot \text{K}$

Calculate

- (a) the ratio of compressor to fan shaft power ϕ_c/ϕ_f
- (b) fuel-to-air ratio f
- (c) the ratio of fan nozzle exit velocity to core nozzle exit velocity V_{19}/V_9
- (d) the ratio of two gross thrusts, $F_{g,\text{fan}}/F_{g,\text{core}}$
- (e) the engine thermal efficiency and compare it to an ideal Carnot cycle operating between the same temperature limits



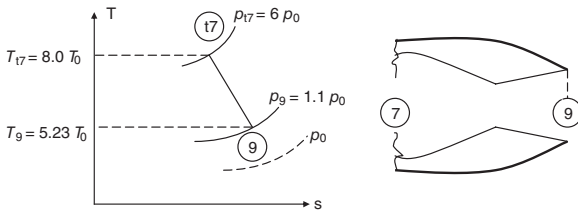
■ FIGURE P 4.25

- (f) the engine propulsive efficiency and compare it to the turbojet propulsive efficiency of Problem 4.19
- (g) engine thrust specific fuel consumption
- (h) engine (fuel)-specific impulse I_s in seconds

4.26 The flow expansion in an exhaust nozzle is shown on a $T-s$ diagram.

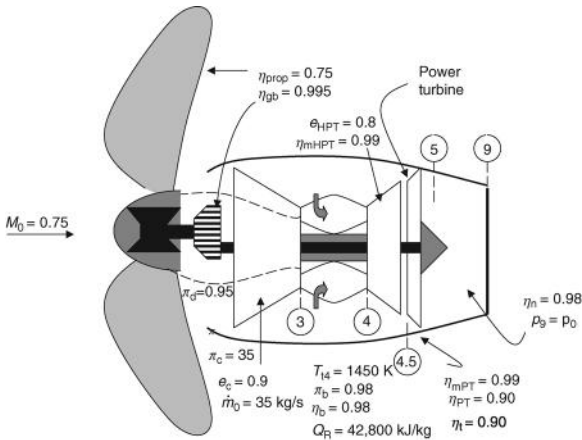
Assuming $\gamma = 1.4$, $c_p = 1.004 \text{ kJ/kg} \cdot \text{K}$, calculate

- (a) nozzle adiabatic efficiency η_n
- (b) V_9/a_0
- (c) nondimensional pressure thrust, i.e., $\frac{(p_9 - p_0)A_9}{\dot{m}_9 \cdot a_0}$



■ FIGURE P 4.26

4.27 An advanced turboprop engine is flying at $M_0 = 0.75$ at 37 kft standard altitude. The component parameters are designated on the following engine drawing.



■ FIGURE P 4.27

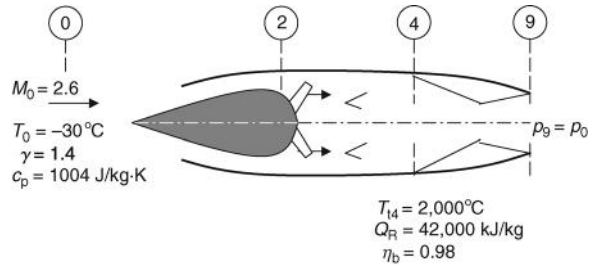
Assuming an optimum power split α_{opt} that leads to a maximum engine thrust, calculate

- (a) core thrust
- (b) propeller thrust
- (c) thrust-specific fuel consumption
- (d) engine overall efficiency

4.28 Consider a ramjet, as shown. The diffuser total pressure ratio is $\pi_d = 0.80$, the burner total pressure ratio is $\pi_b = 0.96$, and the nozzle total pressure ratio is $\pi_n = 0.90$.

Calculate

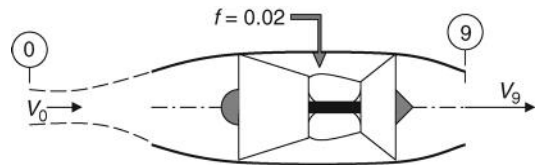
- (a) fuel-to-air ratio f
- (b) exit Mach number M_9
- (c) nondimensional-specific thrust, i.e., $F_n/\dot{m}_0 a_0$



■ FIGURE P 4.28

4.29 A turbojet engine flies at $V_0 = 250 \text{ m/s}$ with an exhaust velocity of $V_9 = 750 \text{ m/s}$. The fuel-to-air ratio is 2% and the actual fuel heating value is $Q_{R,actual} = 40,800 \text{ kJ/kg}$. Estimate the engine propulsive and thermal efficiencies, η_p and η_{th} .

Assume the nozzle is perfectly expanded.



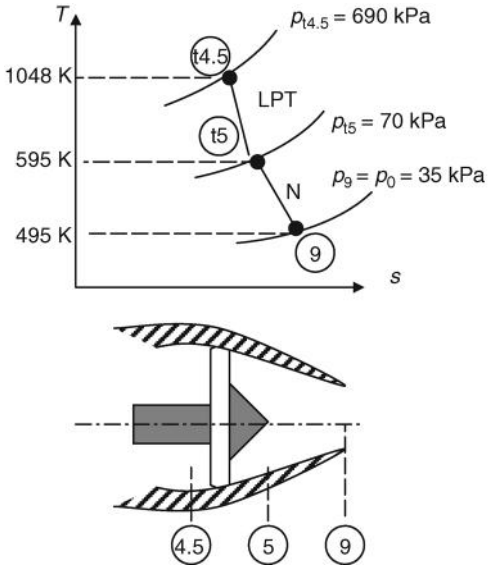
■ FIGURE P 4.29

4.30 Consider a turboprop engine with the following parameters (note that the nozzle is convergent):

- $\dot{m}_0 = 20 \text{ kg/s}$
- $V_0 = 220 \text{ m/s}$
- $\eta_{prop} = 0.80$
- $\eta_{gb} = 0.995$
- $\eta_{mLPT} = 0.99$

Calculate

- (a) propeller thrust F_{prop} in kN
- (b) nozzle gross thrust $F_{g,core}$ in kN
- (c) M_9

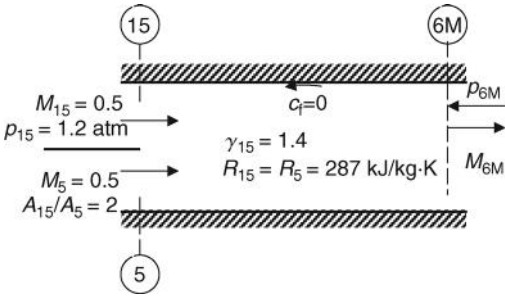


■ FIGURE P 4.30

- (d) core net thrust $F_{n,core}$ in kN, assume $f = 0.02$
- (e) nozzle adiabatic efficiency η_n
- (f) power turbine adiabatic efficiency η_{PT}

Assume $\gamma = 1.4$, $c_p = 1.004 \text{ kJ/kg} \cdot \text{K}$.

4.31 A constant-area mixer operates with the inlet conditions as shown.



■ FIGURE P 4.31

Assuming the hot stream has a total temperature of

$$T_5 = 4 T_{t15}$$

Calculate

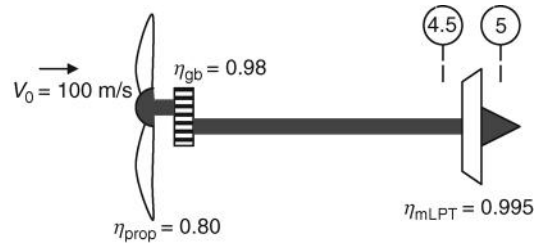
- (a) the ratio of mass flow rates \dot{m}_{15}/\dot{m}_5
- (b) A_{6M}/A_5

- (c) $p_{6M} (1 + \gamma M_{6M}^2) \dots$ from impulse
- (d) T_{t6M}/T_{t5}

4.32 Consider a turboprop engine with the power turbine driving a propeller, as shown. The power turbine inlet and exit total temperatures are $T_{t4.5} = 783 \text{ K}$ and $T_{t5} = 523 \text{ K}$. The mass flow rate through the turbine is 25 kg/s . Assuming $c_p = 1,100 \text{ J/kg} \cdot \text{K}$.

Calculate

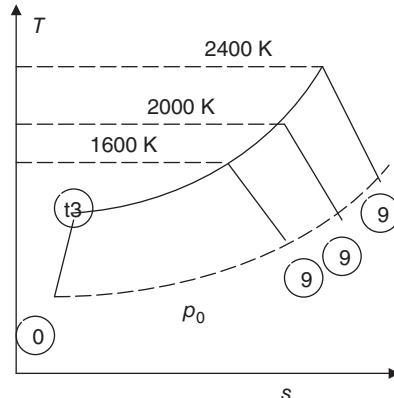
- (a) the power produced by the turbine
- (b) the power delivered to the propeller
- (c) the propeller thrust F_{prop}



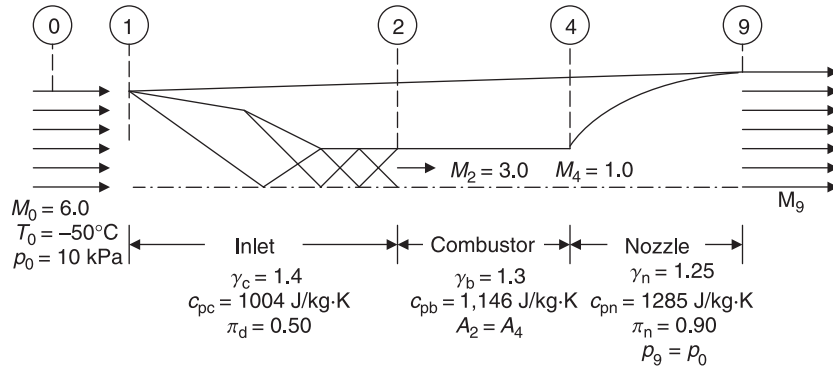
■ FIGURE P 4.32

4.33 Let us study a family of turbojet engines, all with the same component parameters except the burner, as shown on the T - s diagram. The family of turbojets are at the standard sea-level condition and stationary, i.e., $M_0 = 0$. The fixed engine parameters are

- $\pi_d = 0.995$
- $\pi_c = 20$, $e_c = 0.90$, $\gamma_c = 1.4$, $c_{pc} = 1,004 \text{ J/kg} \cdot \text{K}$
- $\pi_b = 0.95$, $\eta_b = 0.98$, $Q_R = 42,800 \text{ kJ/kg}$
- $\eta_m = 0.99$, $e_t = 0.85$, $\gamma_t = 1.33$, $c_{pt} = 1,146 \text{ J/kg} \cdot \text{K}$
- $\pi_n = 0.98$
- $p_9/p_0 = 1$



■ FIGURE P 4.33



■ FIGURE P4.35

The burner exit temperature ranges from $T_{t4} = 1600$ K to 2400 K. Calculate and graph

- (a) nondimensional-specific gross thrust $F_g/\dot{m}_0 a_0$ versus T_{t4}
- (b) specific impulse I_s (based on fuel flow rate) in seconds versus T_{t4}
- (c) T_9/T_0 versus T_{t4}
- (d) thermal efficiency, η_{th} versus T_{t4}

4.34 A ramjet is in flight at an altitude where $T_0 = -23^\circ\text{C}$, $p_0 = 10$ kPa, and the flight Mach number is M_0 . Assuming $T_{t4} = 2500$ K and the nozzle is perfectly expanded, calculate the “optimum” flight Mach number such that ramjet specific thrust is maximized. Assume that all components are ideal, with constant γ and c_p throughout the engine and $Q_R = 42,600$ kJ/kg. Would the fuel heating value affect the “optimum” flight Mach number?

4.35 Consider a scramjet in a Mach-6 flight. The fuel of choice for this engine is hydrogen with $Q_R = 120,000$ kJ/kg. The inlet uses multiple oblique shocks with a total pressure recovery of $\pi_d = 0.5$. The combustor entrance Mach number is $M_2 = 3.0$. Use Rayleigh flow approximations in the supersonic combustor to estimate the fuel-to-air ratio f for a choking exit

condition, as shown, after you calculate the combustor exit total temperature T_{t4} .

Also calculate

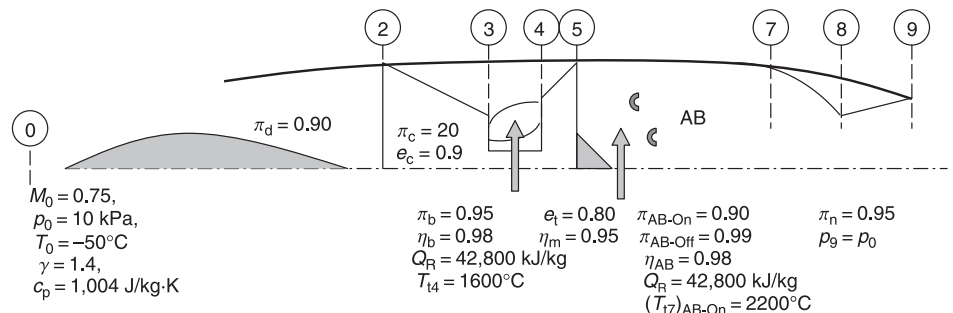
- (a) nozzle exit Mach number M_9
- (b) nondimensional ram drag $D_{ram}/p_0 A_1$ (note that $A_0 = A_1$)
- (c) nondimensional gross thrust $F_g/p_0 A_1$
- (d) fuel specific impulse I_s in seconds

4.36 We are interested in calculating the thrust boost of an afterburning turbojet engine when the afterburner is turned on. The flight condition and engine parameters are shown.

For simplicity of calculations, we assume that gas properties γ , c_p remain constant throughout the engine.

Calculate

- (a) percentage thrust gained when afterburner is turned on
- (b) percentage increase in exhaust speed with afterburner is turned on
- (c) static temperature rise at the nozzle exit when the afterburner is turned on



■ FIGURE P4.36

- (d) percentage fuel–air ratio increase when the afterburner is turned on
- (e) percentage increase in thrust specific fuel consumption with afterburner on
- (f) percentage drop in thermal efficiency when the afterburner is turned on

4.37 A separate-flow turboprop engine is designed with an aft-fan configuration, as shown. The fan and core engine nozzles are of convergent design.

For simplicity, you may assume constant gas properties in the engine, i.e., let γ be 1.4 and $c_p = 1,004 \text{ J/kg} \cdot \text{K}$.

Calculate

- (a) ram drag (in kN)
- (b) compressor adiabatic efficiency η_c
- (c) shaft power produced by the high-pressure turbine in MW
- (d) shaft power consumed by the fan in MW
- (e) core net thrust in kN
- (f) fan net thrust in kN
- (g) thrust-specific fuel consumption in mg/s/N
- (h) engine thermal efficiency η_{th}
- (i) engine propulsive efficiency η_p

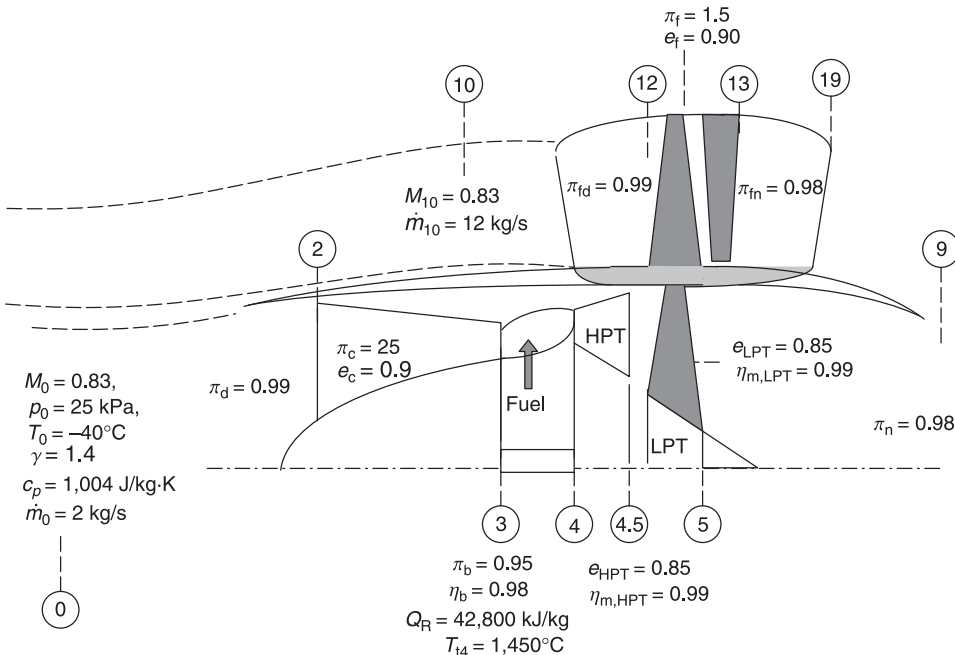
Is there an obvious advantage to an aft-fan configuration?
Is there an obvious disadvantage to this design?

4.38 An advanced turboprop flies at $M_0 = 0.82$ at an altitude where $p_0 = 30 \text{ kPa}$ and $T_0 = -15^\circ\text{C}$. The propeller efficiency is $\eta_{prop} = 0.85$. The inlet captures airflow rate at 50 kg/s and has a total pressure recovery of $\pi_d = 0.99$. The compressor pressure ratio is $\pi_c = 35$ and its polytropic efficiency is $e_c = 0.92$. The combustor has an exit temperature $T_{i4} = 1650 \text{ K}$ and the fuel heating value is $Q_R = 42,000 \text{ kJ/kg}$, with a burner efficiency of $\eta_b = 0.99$ and the total pressure loss in the burner is $\pi_b = 0.96$. The HPT has a polytropic efficiency of $e_{t,HPT} = 0.80$, and a mechanical efficiency of $\eta_{m,HPT} = 0.99$. The power split between the LPT and the engine nozzle is at $\alpha = 0.75$ and the mechanical efficiency of the LPT is $\eta_{m,LPT} = 0.99$, the LPT adiabatic efficiency is $\eta_{LPT} = 0.88$. A reduction gearbox is used with an efficiency of $\eta_{gb} = 0.995$. The exhaust nozzle is convergent with an adiabatic efficiency of $\eta_n = 0.95$. We will describe gas properties in the engine based only on two temperature zones (cold and hot):

Inlet and compressor sections (cold): $\gamma_c = 1.4$,
 $c_{pc} = 1004 \text{ J/kg} \cdot \text{K}$
Turbines and nozzle sections (hot): $\gamma_t = 1.33$,
 $c_{pt} = 1,152 \text{ J/kg} \cdot \text{K}$

Calculate

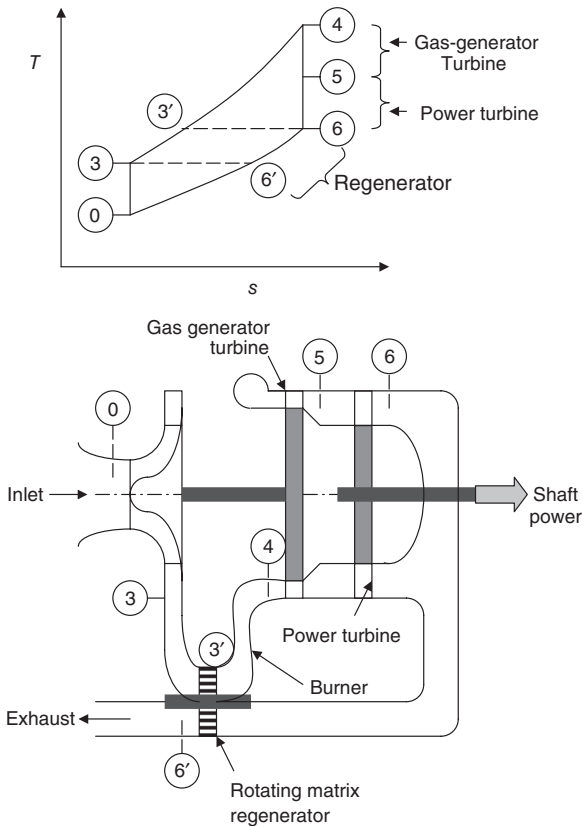
- (a) total pressure and temperature throughout the engine (include fuel-to-air ratio in mass/energy balance)
- (b) engine core thrust in kN



■ FIGURE P4.37

- (c) propeller thrust in kN
- (d) power-specific fuel consumption in mg/s/kW
- (e) thrust-specific fuel consumption in mg/s/N
- (f) thermal and propulsive efficiencies η_{th} and η_p
- (g) engine overall efficiency η_o

4.39 An ideal regenerative (Brayton) cycle is shown. The cycle compression is between states 0 and 3. The compressor discharge is preheated between states 3' and 4. The source of this thermal energy is the hot exhaust gas from the engine. The burner is responsible for the temperature rise between states 3' and 4. The expansion in the turbine is partly between states 4 and 5 that supplies the shaft power to the compressor and partly between states 5 and 6 that produces shaft power for an external load (e.g., propeller, helicopter rotor, or electric generator). The total power production as shown in the expansion process is unaffected by the heat exchanger between states 6 and 6'. Note that the turbine exit temperature T_6 has to be higher than the compressor discharge temperature T_3 for the regenerative cycle to work. Therefore low-pressure ratio cycles can benefit from this (regenerative) concept. Also note that $T_{6'} = T_3$ and $T_{3'} = T_6$.



■ FIGURE P4.39

Show that the thermal efficiency of this cycle is

$$\eta_{th} = 1 - \frac{T_3}{T_4}$$

Calculate the thermal efficiency of a Brayton cycle with cycle pressure ratio of 10, i.e., $p_3/p_0 = 10$ and the maximum cycle temperature ratio of $T_4/T_0 = 6.5$ with and without regeneration.

4.40 A mixed-exhaust turbofan engine with afterburner is flying at $M_0 = 2.5$, $p_0 = 25$ kPa, and $T_0 = -35^\circ\text{C}$. The engine inlet total pressure loss is characterized by $\pi_d = 0.85$. The fan pressure ratio is $\pi_f = 1.5$ and polytropic efficiency of the fan is $e_f = 0.90$.

The flow in the fan duct suffers 1% total pressure loss, i.e., $\pi_{fd} = 0.99$. The compressor pressure ratio and polytropic efficiency are $\pi_c = 12$ and $e_c = 0.90$, respectively. The combustor exit temperature is $T_{t4} = 1800$ K, fuel heating value is $Q_R = 42,800$ kJ/kg, total pressure ratio $\pi_b = 0.94$, and the burner efficiency is $\eta_b = 0.98$. The turbine polytropic efficiency is $e_t = 0.80$, its mechanical efficiency is $\eta_m = 0.95$, and the turbine exit Mach number is $M_5 = 0.5$. The constant-area mixer suffers a total pressure loss due to friction, which is characterized by $\pi_{M,f} = 0.95$. The afterburner is on with $T_{t7} = 2200$ K, $Q_{R,AB} = 42,800$ kJ/kg, $\pi_{AB-On} = 0.92$, and afterburner efficiency $\eta_{AB} = 0.98$. The nozzle has a total pressure ratio of $\pi_n = 0.95$ and $p_9/p_0 = 2.6$.

The gas behavior in the engine is dominated by temperature (in a thermally perfect gas), thus we consider four distinct temperature zones:

Inlet, fan, and compressor section: $\gamma_c = 1.4$,

$$c_{pc} = 1,004 \text{ J/kg} \cdot \text{K}$$

Turbine section: $\gamma_t = 1.33$, $c_{pt} = 1,152 \text{ J/kg} \cdot \text{K}$

Mixer exit: γ_{6M} , c_{p6M} (to be calculated based on mixture of gases)

Afterburner and nozzle section: $\gamma_{AB} = 1.30$,

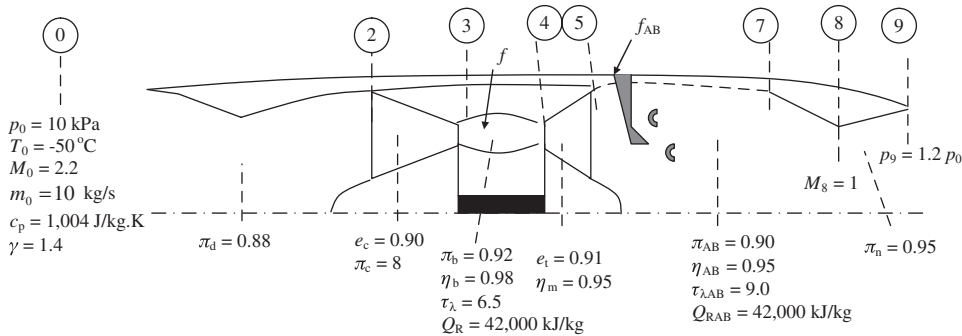
$$c_{p,AB} = 1,241 \text{ J/kg} \cdot \text{K}$$

Calculate

- (a) total pressure and temperature throughout the engine, the fan bypass ratio α , and include the contributions of fuel-to-air ratio in the primary and afterburner, f and f_{AB} and
- (b) engine performance parameters, i.e., TSFC in mg/s/N, specific thrust and cycle efficiencies

4.41 An afterburning turbojet engine is in supersonic flight, as shown. The flight condition and cycle parameters are specified. Assuming constant gas properties throughout the engine, calculate

- (a) ram drag, D_r in kN
- (b) compressor shaft power, $\dot{\phi}_c$ in MW
- (c) fuel-to-air ratio in the primary burner, f



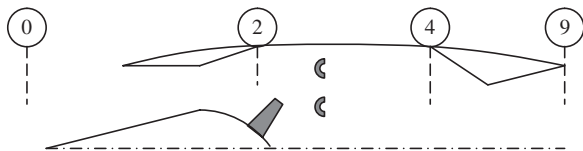
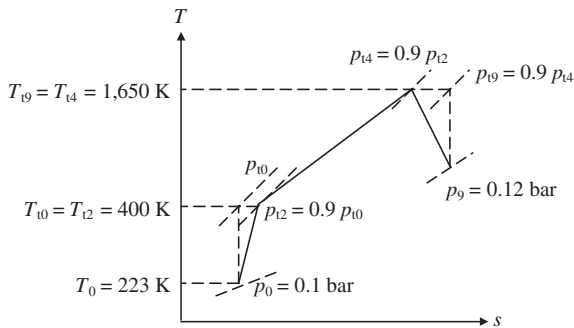
■ FIGURE P 4.41

- (d) fuel-to-air ratio in the afterburner, f_{AB}
- (e) gas speed at the nozzle throat, V_8 , in m/s
- (f) exit Mach number, M_9
- (g) exit flow area, A_9 , in m^2

For Intermediate Steps Calculate These Parameters:

$\tau_r =$	$\tau_c =$	$\tau_t =$
$\pi_r =$	$\pi_t =$	

4.42 The thermodynamic state of gas in a ramjet is shown on a T - s diagram.



■ FIGURE P 4.42

Assuming constant gas properties, $\gamma = 1.4$ and $c_p = 1,004$ J/kg · K, calculate

- (a) the flight Mach number, M_0
- (b) the exhaust Mach number, M_9
- (c) the exhaust velocity, V_9 , in m/s

4.43 The air mass flow rate in a turbojet engine at takeoff is 100 kg/s at standard sea-level conditions ($p_0 = 100$ kPa, $T_0 = 15^\circ\text{C}$). The fuel-to-air ratio is 0.035 and the nozzle exhaust speed is 1000 m/s. The nozzle is underexpanded with $p_9 = 150$ kPa. Assuming the nozzle exit temperature is $T_9 = 1,176$ K with $\gamma_9 = 1.33$ and $c_{p9} = 1,156$ J/kg · K, calculate

- (a) Nozzle exit area, A_9 , in m^2
- (b) Effective exhaust speed, $V_{9\text{eff}}$, in m/s
- (c) Takeoff thrust, $F_{T.O.}$, in kN
- (d) Fuel-specific impulse, I_s , at takeoff in seconds

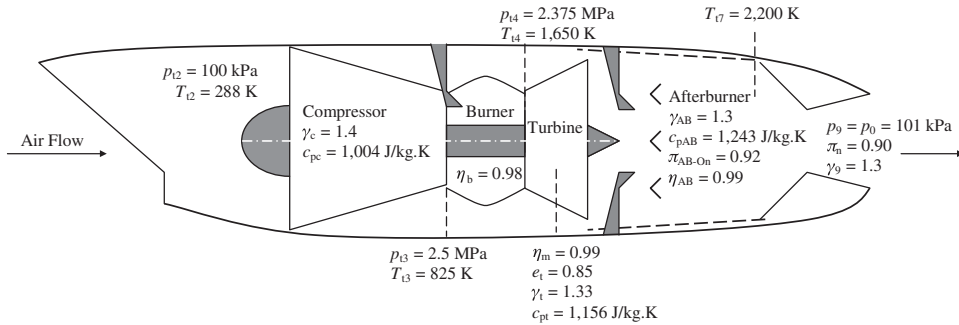
4.44 An afterburning turbojet engine is shown in “wet mode”.

Calculate

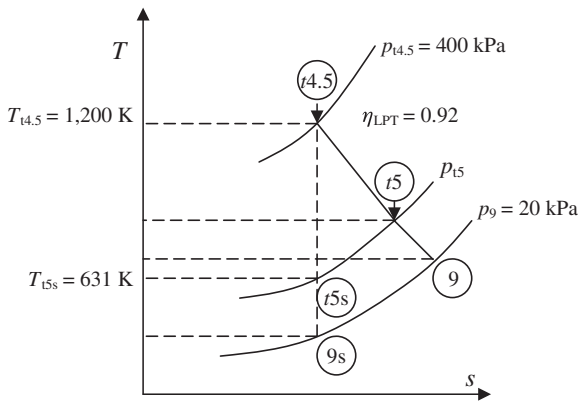
- (a) fuel-to-air ratio in the primary burner, f , for $Q_R = 42,000$ kJ/kg
- (b) turbine exit total temperature, T_{15} (K)
- (c) turbine exit total pressure, p_{15} , in kPa
- (d) fuel-to-air ratio in the afterburner, f_{AB} , for $Q_{R,AB} = 42,000$ kJ/kg
- (e) nozzle exit Mach number, M_9

4.45 The T - s diagram shows the power split between the propeller and the nozzle. Assuming the mass flow rate is $\dot{m} = 37$ kg/s with $\gamma = 1.33$ and $c_p = 1,152$ J/kg · K, calculate

- (a) ideal power available in station 4.5, ϕ_{i1} in MW
- (b) LPT exit pressure, p_{15} , in kPa
- (c) LPT exit temperature, T_{15} , in K
- (d) LPT power (actual) in MW
- (e) nozzle exit velocity, V_9 , in m/s, for $\eta_n = 0.95$



■ FIGURE P4.44



■ FIGURE P4.45

4.46 A turboprop aircraft flies at $V_0 = 150$ m/s and its engine produces 20 kN of propeller thrust and 2 kN of core thrust. For a propeller efficiency of $\eta_{prop} = 0.85$, estimate the engine propulsive efficiency, η_p . [Hint: neglect ΔKE]

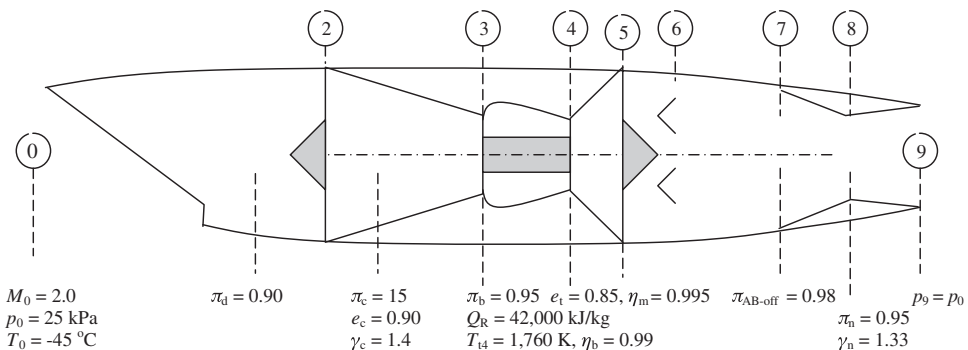
4.47 Consider an afterburning turbojet engine, with afterburner off, as shown.

The gas is thermally perfect with two zones of “cold” and “hot” described by the gas properties in the compressor and turbine sections as $\gamma_c = 1.4$, $c_{pc} = 1,004$ J/kg · K and $\gamma_t = 1.33$ and $c_{pt} = 1,156$ J/kg · K, respectively. Assuming the air flow rate is $\dot{m}_0 = 100$ kg/s, calculate

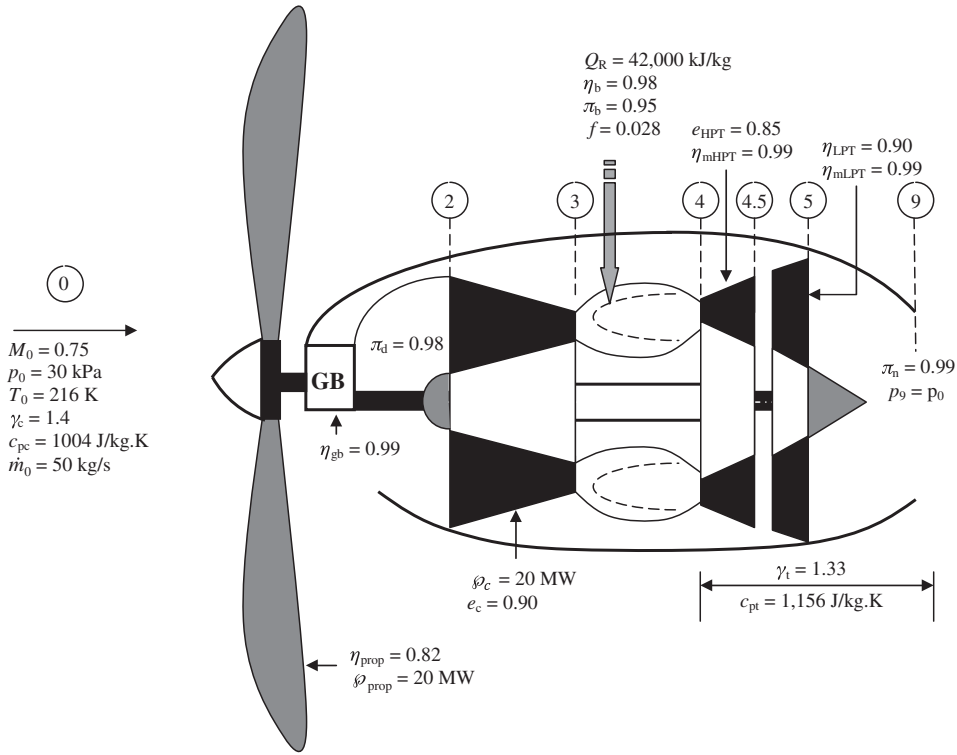
- (a) D_r , ram drag, in kN and lbf
- (b) f , fuel-to-air ratio
- (c) T_{15} in K and °R
- (d) M_9
- (e) F_n , net uninstalled thrust in kN and lbf

4.48 An exhaust nozzle has an inlet total pressure and temperature, $p_{17} = 75$ kPa and $T_{17} = 900$ K, respectively. The nozzle exit static pressure is $p_9 = 30$ kPa where the ambient pressure is $p_0 = 20$ kPa. Assuming nozzle total pressure ratio is $\pi_n = 0.95$, $\gamma_n = 1.33$ and $c_{pn} = 1,156$ J/kg · K, calculate

- (a) nozzle exhaust speed, V_9 , in m/s and fps
- (b) the nozzle exhaust speed (in m/s and fps) if the nozzle were perfectly expanded, i.e., $p_9 = 20$ kPa



■ FIGURE P4.47



■ FIGURE P 4.49

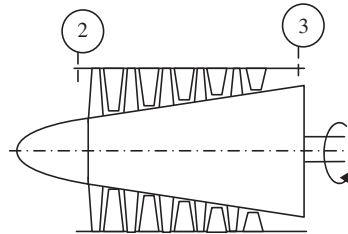
4.49 An advanced turboprop engine cruises at Mach 0.75 at an altitude where $p_0 = 30 \text{ kPa}$ and $T_0 = 216 \text{ K}$, as shown. The parameters related to each component is identified on the graph, e.g., $\pi_d = 0.98$. Also the gas constants representative of the cold and hot section are also specified. The air mass flow rate in the engine is noted to be 50 kg/s . Calculate

- total pressure and temperature at the engine face, p_{t2} and T_{t2} , in kPa and K, respectively
- total pressure and temperature, p_{t3} and T_{t3} , in kPa and K, respectively
- Compressor exit temperature and pressure, T_{t4} and p_{t4} , in K and kPa, respectively
- total temperature and pressure at the exit of HPT, $T_{t4.5}$ and $p_{t4.5}$ in K and kPa respectively
- total temperature and pressure at the exit of LPT, T_{t5} and p_{t5} , in K and kPa, respectively
- ram drag, D_r , in kN and lbf
- propeller thrust, F_{prop} , in kN and lbf
- core nozzle exit Mach number, M_9
- core thrust, F_{core} , in kN and lbf
- thrust-specific fuel consumption, TSFC, in mg/s/N (and lbm/hr/lbf)

4.50 A compressor in a turbojet engine consumes 40 MW of shaft power to handle 100 kg/s of air flow rate and create a compressor total pressure ratio of 15.4. Assuming the inlet condition to the compressor is $p_{t2} = 100 \text{ kPa}$, $T_{t2} = 288 \text{ K}$, calculate

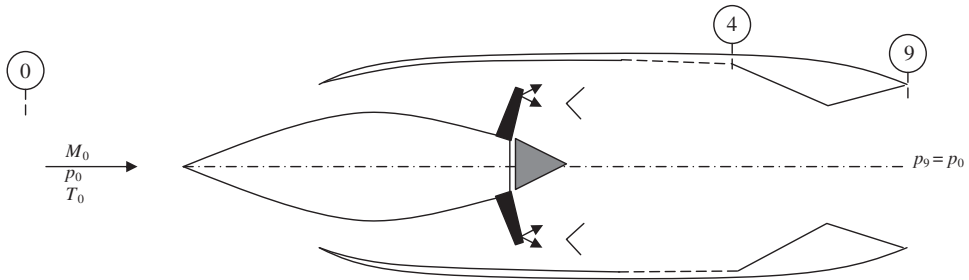
- the exit total temperature, T_{t3} , in K
- compressor polytropic efficiency, e_c

Assume $\gamma = 1.4$ and $c_{pc} = 1004 \text{ J/kg}\cdot\text{K}$

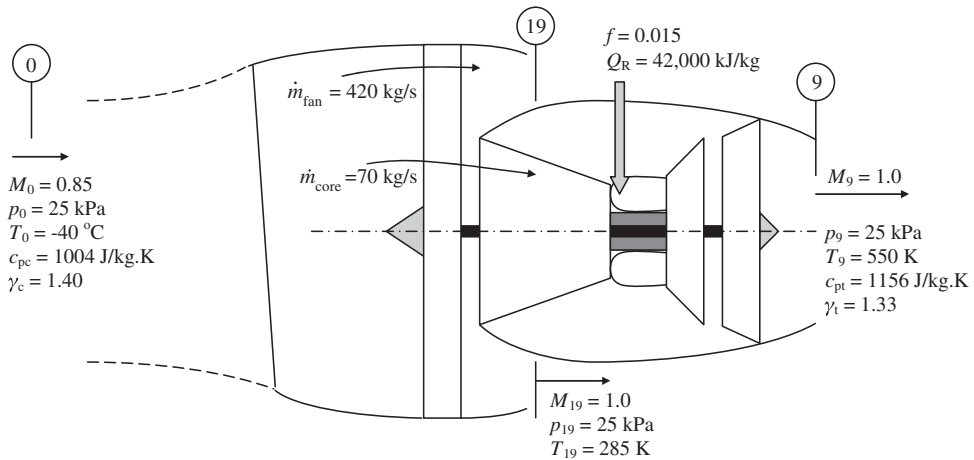


■ FIGURE P 4.50

4.51 A ramjet engine flies at Mach 2 at an altitude where $p_0 = 20 \text{ kPa}$ and $T_0 = 245 \text{ K}$.



■ FIGURE P4.51



■ FIGURE P4.52

The inlet total pressure recovery is $\pi_d = 0.90$ and the combustor exit temperature is $T_{14} = 1800$ K.

The fuel heating value is $Q_R = 42,000$ kJ/kg the burner efficiency is $\eta_b = 0.98$ and the burner total pressure ratio is $\pi_b = 0.95$. The nozzle is perfectly expanded with $\pi_n = 0.92$.

Assume constant γ of 1.4 and constant c_p of 1004 J/kg · K. Calculate

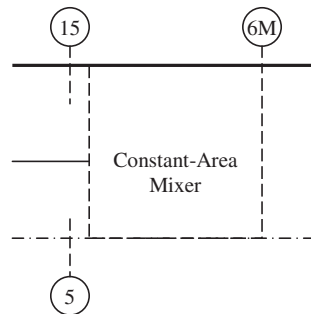
- (a) flight speed, V_0 , in m/s and fps
- (b) fuel-to-air ratio in the combustor, f
- (c) exhaust velocity, V_9 , in m/s and fps
- (d) ratio of gross thrust to ram drag, F_g/D_r

4.52 For the separate exhaust turbofan engine shown, calculate: (a) ram drag in kN, (b) fan nozzle gross thrust in kN, (c) net uninstalled thrust in kN, (d) thermal efficiency, (e) propulsive efficiency, (f) thrust specific fuel consumption in mg/s/N.

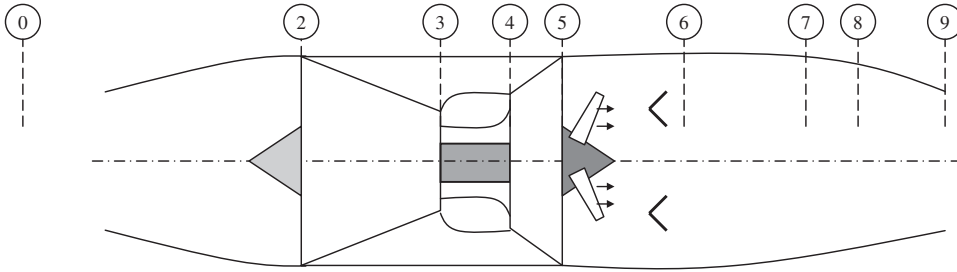
4.53 Consider a constant-area mixer, as shown. The mass flow ratio between the cold and hot streams is 3, i.e., $\frac{\dot{m}_{15}}{\dot{m}_5} = 3$. The gas properties are: $c_{p15} = 1,004$ J/kg · K, $\gamma_{15} = 1.4$ $c_{p5} =$

1,156 J/kg · K and $\gamma_5 = 1.33$. The flow conditions in the inlet to the mixer are:

$$p_{15} = p_{115} = 150 \text{ kPa}, T_{115} = 500 \text{ K} \text{ and } T_{15} = 880 \text{ K}.$$



■ FIGURE P4.53



■ FIGURE P4.54

Assuming the hot gas Mach number is $M_5 = 0.4$, calculate

- (a) gas properties at the mixed exit, c_{p6M} and γ_{6M}
- (b) Mach number of the cold stream, M_{15}
- (c) area ratio, A_{15}/A_5
- (d) total temperature at the mixed exit, T_{t6M} in K

4.54 An afterburning turbojet engine operates at an altitude where the ambient pressure and temperatures are: $p_0 = 15$ kPa and $T_0 = 223$ K, respectively. The flight Mach number is $M_0 = 2.5$ and the ambient air is characterized by $c_{pc} = 1,004$ J/kg · K and $\gamma_c = 1.4$. The engine has the following operating parameters and efficiencies: $\pi_d = 0.85$, $\pi_c = 6$, $e_c = 0.92$, $\tau_\lambda = 7.7$, $\pi_b = 0.95$, $\eta_b = 0.98$, $Q_R = 42,600$ kJ/kg, $e_t = 0.85$, $\eta_m = 0.99$, $\tau_{\lambda AB} = 10.5$, $Q_{RAB} = 42,600$ kJ/kg, $\pi_{AB} = 0.94$, $\eta_{AB} = 0.97$, $\pi_n = 0.95$ and $p_9 = 15$ kPa. Assuming the air flow rate is 50 kg/s in the engine, and gas properties in the turbine and afterburner/nozzle are described by $c_{pt} = 1,156$ J/kg · K, $\gamma_t = 1.33$, $c_{pAB} = 1,243$ J/kg · K and $\gamma_{AB} = 1.30$, respectively, calculate

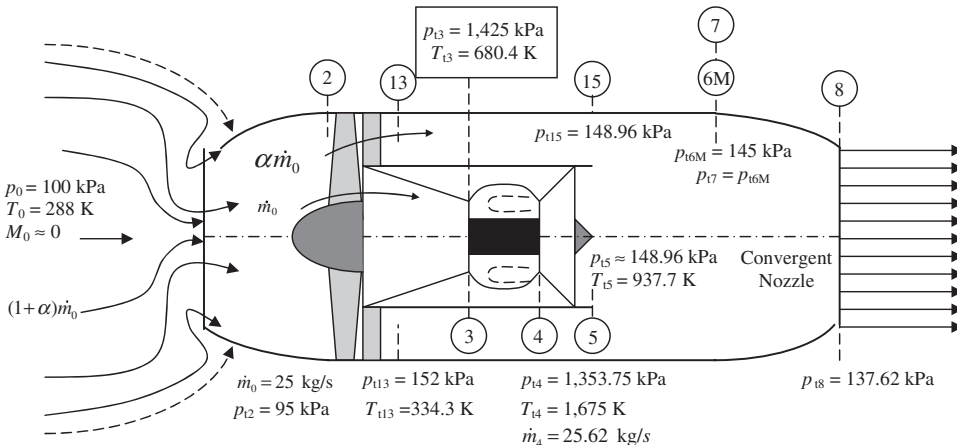
- (a) ram drag, D_r , in kN and lbf
- (b) compressor shaft power in MW and hp

- (c) fuel-to-air ratio, f , in the main burner
- (d) turbine discharge p_{t5} and T_{t5} in kPa and K, respectively
- (e) fuel-to-air-ratio in the afterburner, f_{ab}
- (f) nozzle gross thrust in kN and lbf
- (g) thrust specific fuel consumption, TSFC, in mg/s/N and lbm/hr/lbf
- (h) thermal efficiency, η_{th}
- (i) propulsive efficiency, η_p

4.55 The total pressures, temperatures and mass flow rates at some stations inside a nonafterburning, mixed-flow turbofan engine, at takeoff, are shown.

For simplicity of analysis, assume the gas is calorically perfect with constant properties ($\gamma = 1.4$ and $c_p = 1004$ J/kg · K) throughout the engine. Calculate

- (a) bypass ratio, α
- (b) fuel-to-air ratio, f
- (c) mixer exit total temperature, T_{t6M} , in K
- (d) exhaust Mach number, M_8 (note that the exhaust nozzle is of convergent type)
- (e) (un-installed) takeoff thrust, $F_{T.O.}$, in kN and lbf



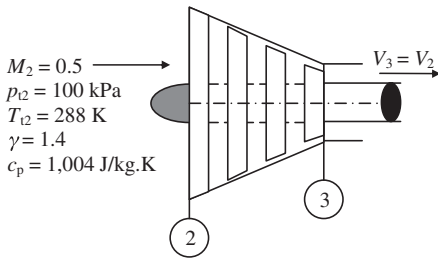
■ FIGURE P4.55

4.56 The power turbine in a turboprop engine produces a shaft power of 4.53 MW, working on a gas flow rate of 10.25 kg/s with $c_{pt} = 1,152 \text{ J/kg} \cdot \text{K}$ and $\gamma = 1.33$. Assuming $\eta_{mPT} = 0.99$, $\eta_{gb} = 0.99$ and $\eta_{prop} = 0.85$ at flight speed of 200 m/s, calculate

- (a) the total temperature drop across the power turbine in K
- (b) the shaft power delivered to propeller, ϕ_{prop} (MW)
- (c) the propeller thrust, F_{prop} , in kN

4.57 A multistage compressor develops a total pressure ratio of $\pi_c = 35$ with a polytropic efficiency of $e_c = 0.90$. The air mass flow rate through the compressor is $\dot{m} = 200 \text{ kg/s}$. Assuming γ and c_p remain constant, calculate

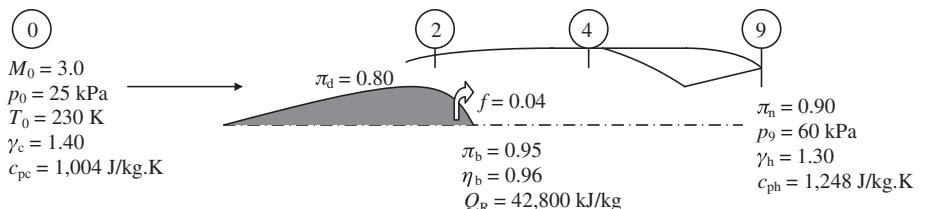
- (a) Compressor shaft power, ϕ_{c_s} , in MW
- (b) Flow area in 2, i.e., A_2 , in m^2
- (c) Density of air in station 3, ρ_3 , in kg/m^3 [note: the axial velocity at the compressor exit, $V_3 = V_2$]
- (d) The nondimensional entropy rise across the compressor, $\Delta s/R$



■ FIGURE P4.57

4.58 A ramjet in flight is shown. The inlet total pressure recovery is $\pi_d = 0.80$ and the nozzle is underexpanded. Calculate

- (a) ram temperature and pressure ratios, τ_r and π_r
- (b) the total temperature at the combustor exit, T_{t4} , in K and the corresponding τ_4
- (c) exhaust velocity, V_9 , in m/s



■ FIGURE P4.58

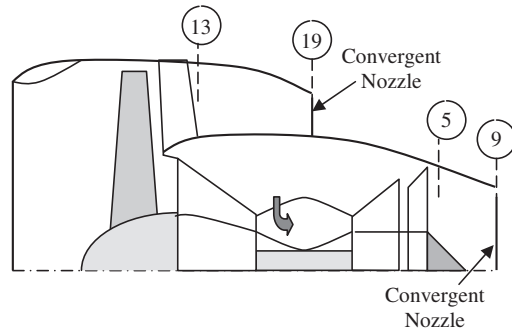
- (d) pressure thrust as a fraction of nozzle momentum thrust, i.e., $\frac{(p_9 - p_0)A_9}{\dot{m}_9 V_9}$
- (e) the propulsive efficiency of the ramjet, η_p (note that the nozzle is not perfectly expanded, so you need to calculate V_{9eff})
- (f) thrust-specific fuel consumption, TSFC, in mg/s/N and lbm/hr/lbf

4.59 A separate exhaust turbofan engine has **convergent nozzles** with the following parameters:

$M_0 = 0.85$
 $p_0 = 30 \text{ kPa}, T_0 = 240 \text{ K}, \gamma_c = 1.4, c_{pc} = 1004 \text{ J/kg} \cdot \text{K}$
 $\pi_d = 0.98$
 $\pi_f = 1.55, e_f = 0.90$
 $\pi_{fn} = 0.97$

Calculate

- (a) fan exit total pressure, p_{t13} , in kPa
- (b) fan exit total temperature, T_{t13} , in K
- (c) exit Mach number, M_{19}
- (d) nozzle exit static pressure, p_{19} (or p_{18}), in kPa
- (e) exhaust speed, V_{19} (or V_{18}), in m/s
- (f) effective exhaust velocity, V_{19eff} , in m/s



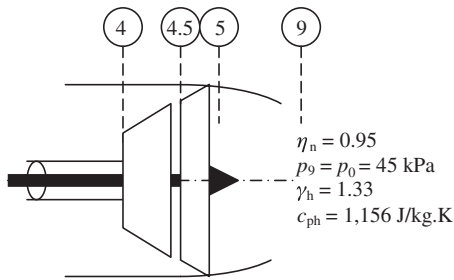
■ FIGURE P4.59

4.60 A turboprop uses a power split of 0.96 between the power turbine and the exhaust nozzle, i.e. $\alpha = 0.96$. The

adiabatic efficiency of the LPT (or power turbine) is $\eta_{LPT} = 0.88$. The flow at the inlet of the LPT has $p_{t4.5} = 99$ kPa and $T_{t4.5} = 845$ K. The nozzle adiabatic efficiency is $\eta_n = 0.95$.

Calculate

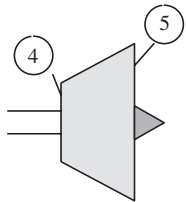
- (a) the shaft power per unit mass flow rate of the LPT in kJ/kg
- (b) the exhaust velocity, V_9 , in m/s



■ FIGURE P 4.60

4.61 An un-cooled turbine has entrance and exit flow conditions: $p_{t4} = 2.5$ MPa, $T_{t4} = 1760$ K, $T_{t5} = 1000$ K. The gas mass flow rate in the turbine is $\dot{m}_4 = 103$ kg/s and the turbine polytropic efficiency is $e_t = 0.85$. Assuming $\gamma_t = 1.33$ and $c_{pt} = 1156$ J/kg · K, calculate

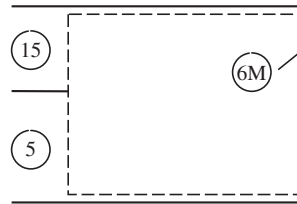
- (a) turbine exit total pressure, p_{t5} , in kPa
- (b) turbine shaft power in MW
- (c) turbine adiabatic efficiency, η_t



■ FIGURE P 4.61

4.62 The flow condition at the entrance to a constant-area mixer is that the mass flow rate from the fan side, $\dot{m}_{15} = 250$ kg/s and the mass flow rate from the core is $\dot{m}_5 = 51.5$ kg/s. The entrance total temperatures are $T_{t15} = 360$ K and $T_{t5} = 895$ K. The cold and hot streams have $\gamma_c = 1.4$, $c_{pc} = 1004$ J/kg · K, $\gamma_t = 1.33$ and $c_{pt} = 1156$ J/kg · K. Calculate

- (a) the gas properties at the mixer exit, γ_{6M} and c_{p6M}
- (b) the mixer exit total temperature, T_{t6M} , in K



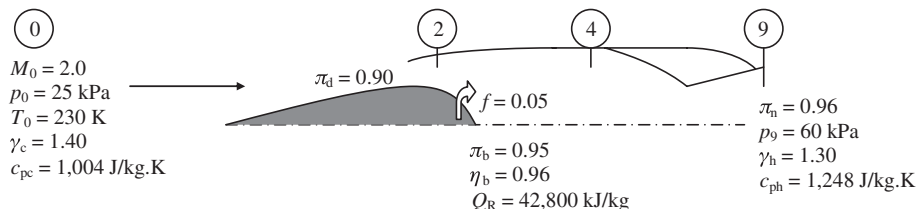
■ FIGURE P 4.62

4.63 A ramjet is shown in supersonic flight. The inlet total pressure recovery is $\pi_d = 0.90$ and the nozzle is under-expanded (note that $p_9 \neq p_0$).

Calculate

- (a) ram temperature and pressure ratios, τ_r and π_r
- (b) the total temperature at the combustor exit, T_{t4} , in K and the corresponding τ_λ
- (c) Exhaust velocity, V_9 , in m/s
- (d) pressure thrust as a fraction of nozzle momentum thrust, i.e., $\frac{(p_9 - p_0)A_9}{\dot{m}_0 V_9}$
- (e) the propulsive efficiency of the ramjet, η_p (note that the nozzle is not perfectly expanded, so you need to calculate V_{9eff})
- (f) thrust-specific fuel consumption, TSFC, in mg/s/N and lbm/hr/lbf

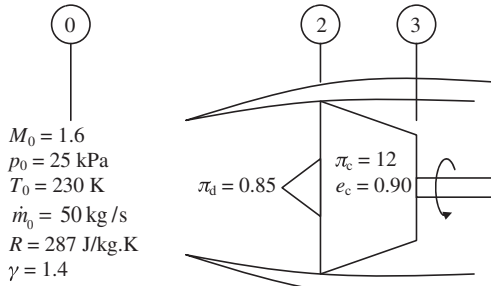
4.64 A turbojet engine is flying at Mach 1.6, with ambient pressure, $p_0 = 25$ kPa and temperature, $T_0 = 230$ K. The inlet total pressure recovery is $\pi_d = 0.85$ and the compressor pressure ratio is $\pi_c = 12$ with $e_c = 0.90$.



■ FIGURE P 4.63

Assuming the air flow rate is 50 kg/s, calculate

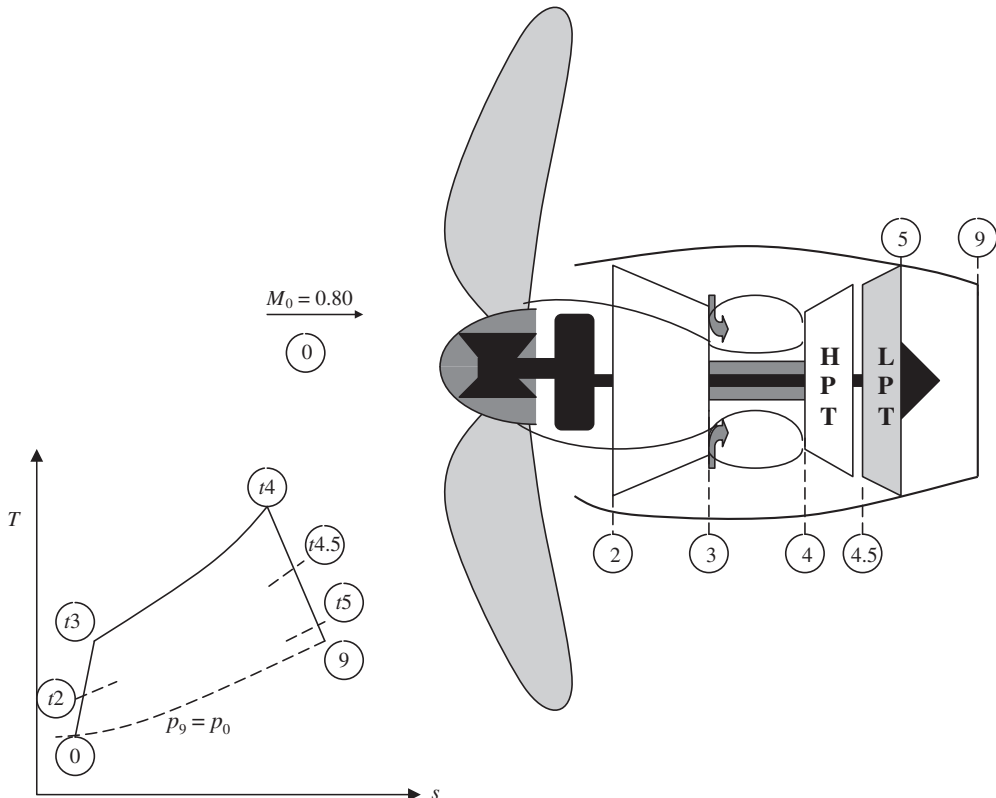
- (a) ram drag in kN
- (b) compressor exit total pressure, p_{t3} , in kPa
- (c) compressor shaft power, $\dot{\varphi}_c$, in MW
- (d) inlet adiabatic efficiency, η_d



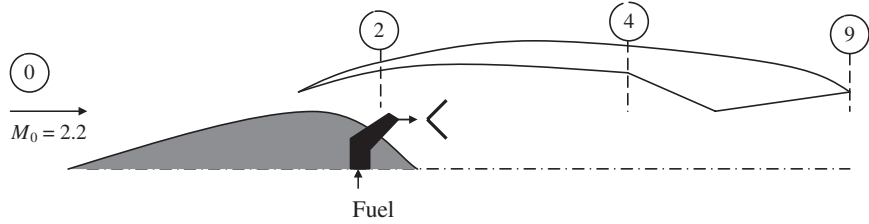
■ FIGURE P4.64

4.65 A turboprop is in a Mach 0.80 flight at an altitude where $p_0 = 22$ kPa and temperature is $T_0 = 245$ K with $\gamma_c = 1.4$ and $c_{pc} = 1004$ J/kg · K. The inlet total pressure loss is 3% of flight dynamic pressure, i.e., $p_{t0} - p_{t2} = 0.03 q_0$. The compressor pressure ratio is $\pi_c = 35$ and its polytropic efficiency is $e_c = 0.90$. The combustor achieves an exit total temperature of $T_{t4} = 1,650$ K while burning a hydrocarbon fuel with an ideal heating value of 42,000 kJ/kg, at a burner efficiency of $\eta_b = 0.99$ and a total pressure ratio $\pi_b = 0.95$. The gas in the hot section is characterized by $\gamma_t = 1.33$ and $c_{pt} = 1,152$ J/kg · K. The high-pressure turbine has $\eta_{mHPT} = 0.995$ and a polytropic efficiency of $e_{HPT} = 0.85$. The power split parameter between the low-pressure turbine and the nozzle is $\alpha = 0.85$. The low-pressure turbine has adiabatic and mechanical efficiencies of $\eta_{LPT} = 0.90$ and $\eta_{m,LPT} = 0.995$ respectively. The propeller is gearbox-driven with $\eta_{gb} = 0.995$ and the propeller efficiency is $\eta_{prop} = 0.80$. Assuming the nozzle is perfectly expanded, $p_9 = p_0$, and $\eta_n = 0.96$, calculate:

- (a) flight dynamic pressure, q_0 , in kPa
- (b) compressor discharge (total) temperature, T_{t3} in K
- (c) the fuel-to-air ratio, f , in the burner



■ FIGURE P4.65



■ FIGURE P4.66

- (d) the total pressure and temperature at the exit of HPT, i.e., $p_{t4.5}$ (in kPa) and $T_{t4.5}$ in K
- (e) the total pressure and temperature at the exit of the LPT, p_{t5} in kPa and T_{t5} in K
- (f) the nozzle exit Mach number, M_9
- (g) the nozzle exit velocity, V_9
- (h) the propeller thrust, F_{prop} in kN

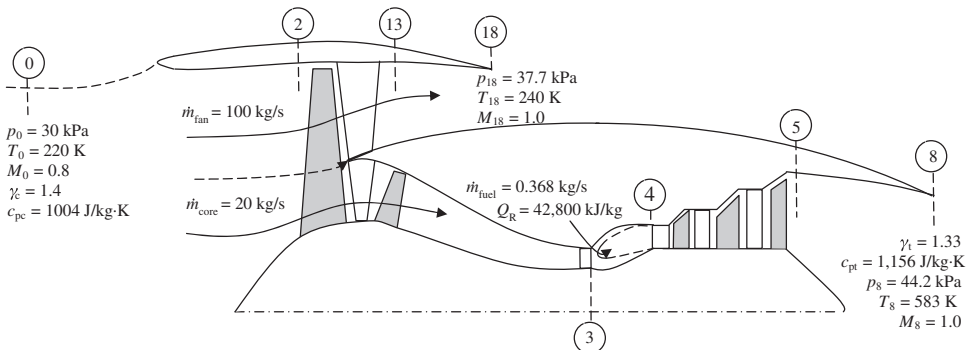
4.66 A ramjet flies at Mach 2.2 at an altitude where the speed of sound is $a_0 = 294$ m/s and the pressure is $p_0 = 20$ kPa. The air is characterized as perfect gas with $\gamma = 1.4$ and $R = 287$ J/kg · K. The inlet total pressure recovery is $\pi_d = 0.90$, combustor losses are characterized by $\pi_b = 0.92$, $\eta_b = 0.99$ and the nozzle total pressure loss parameter is $\pi_n = 0.94$. Assuming nozzle is perfectly expanded, combustor exit temperature is $T_{t4} = 2,000$ K, fuel heating value is $Q_R = 42,600$ kJ/kg, and gas properties (γ and R) remain constant in the ramjet, calculate

- (a) enthalpy ratio, τ_λ
- (b) fuel-to-air ratio, f
- (c) exhaust speed, V_9 , in m/s
- (d) non-dimensional specific thrust, $F_n/\dot{m}_0 a_0$
- (e) propulsive efficiency, η_p
- (f) thermal efficiency, η_{th}

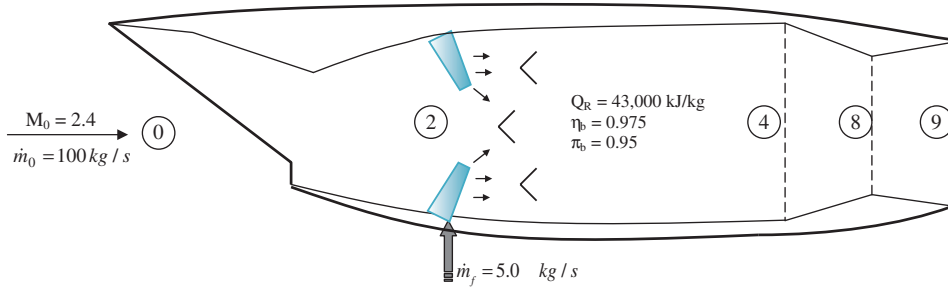
4.67 A separate-flow turbofan engine is shown at cruise condition. The flight condition, air and fuel flow rates, nozzle exit conditions and fuel properties are all labeled in the schematic drawing (Figure P4.67). The primary and fan nozzles are of *convergent* type and both are choked, as shown. Calculate

- (a) ram drag in kN and lbf
- (b) fan nozzle exit area, A_{18} , in m^2 and ft^2
- (c) fan nozzle gross thrust in kN and lbf
- (d) core nozzle exit area, A_8 , in m^2 and ft^2
- (e) core nozzle gross thrust in kN and lbf
- (f) TSFC in mg/s/N and lbfm/hr/lbf
- (g) fan total temperature ratio, τ_f
- (h) fan total pressure ratio, π_f , if the fan polytropic efficiency is $e_f = 0.90$
- (i) fan nozzle *effective exhaust speed*, $V_{18,eff}$, in m/s and fps
- (j) core nozzle *effective exhaust speed*, $V_{8,eff}$, in m/s and fps
- (k) engine propulsive efficiency, η_p (%)
- (l) engine thermal efficiency, η_{th} (%)

4.68 A ramjet is shown at Mach 2.4 flight at an altitude where $p_0 = 25$ kPa and $T_0 = 240$ K. The inlet total pressure



■ FIGURE P4.67



■ FIGURE P4.68

recovery is 90%. The air and fuel mass flow rates are 100 and 5.0 kg/s respectively, as shown.

The nozzle total pressure ratio is 95% and it is perfectly expanded. The gas properties for the cold and hot sections of the engine are: $\gamma_c = 1.4$, $c_{pc} = 1,004 \text{ J/kg}\cdot\text{K}$ and $\gamma_t = 1.3$, $c_{pt} = 1,243 \text{ J/kg}\cdot\text{K}$, respectively. Calculate

- (a) ram drag, D_r , in kN and lbf
- (b) combustor exit total pressure, p_{t4} , in kPa
- (c) combustor exit total temperature, T_{t4} , in K
- (d) nozzle exit Mach number and velocity, M_9 and V_9 , in m/s
- (e) nozzle gross thrust, F_g , in kN and lbf
- (f) thrust-specific fuel consumption, TSFC, in mg/s/N and lbm/hr/lbf
- (g) engine thermal efficiency, η_{th}
- (h) engine propulsive efficiency, η_p

CHAPTER 5

General Aviation and Uninhabited Aerial Vehicle Propulsion System*



Source: Courtesy of NASA.
[http://www.nasa.gov/centers/
glenn/about/fs01grc.html](http://www.nasa.gov/centers/glenn/about/fs01grc.html)

5.1 Introduction

The selection of an appropriate engine is critical to the performance of an aircraft or any other vehicle. However, aircraft have tighter constraints. Thus, an appropriate engine that best suits the given mission requirements must be selected. Constraints on engine selection often include size, weight, power, and specific fuel consumption. For general aviation (GA) aircraft flying at low altitudes and at low Mach numbers, reciprocating engines have proved to be the best propulsion options. Of course, electric engines are also making significant progress in small aircraft and Uninhabited Aerial Vehicle (UAV) applications. For airplanes flying at speeds up to about 500 knots and a service ceiling of about 40,000 feet, turboprops serve the best. Beyond these limits, turbojets and turbofans are the most appropriate power plants.

*This chapter is written as an invited contribution by Professor Ray Taghavi of the Aerospace Engineering Department of the University of Kansas. Ray's expert contribution is deeply appreciated.

The piston engine is an integral part of the general aviation aircraft design. The importance of the piston engine in aviation can be seen by looking at all of the small civilian aircraft that are completely reliant on piston engines as their means of propulsion. The majority of small UAVs and radio-controlled aircraft are also piston engine powered.

In this chapter; we briefly cover engines other than gas turbine engines. We concentrate primarily on reciprocating engines and their systems, due to their extensive application on GA aircraft and UAVs. The material is presented very briefly and, in some cases, in bullet form due to space limitations. However, an extensive bibliography is included at the end of the chapter for further reference.

5.2 Cycle Analysis

5.2.1 Otto Cycle

The Otto Cycle is an air standard cycle that approximates the operation of spark-ignition engines. The T–s and P–V diagrams of this cycle are shown in Figure 5.1. The ideal Otto Cycle operates on the constant-volume principle. It consists of an isentropic compression, a constant-volume heat addition, an isentropic expansion, and a constant-volume heat rejection process as shown in the above figure. It can be shown that the ideal thermal efficiency of the cycle, $\eta_{th} = 1 - \frac{T_4}{T_3} = 1 - \frac{T_1}{T_2} = 1 - \frac{1}{(CR)^{\gamma-1}}$, in which CR is the compression ratio (defined in Section 5.3). For derivation of the above equation, references 6 to 15 may be consulted. From this equation, it is clear that the cycle thermal efficiency increases with increased compression ratio. But in real engine cycles, fuel octane number has to be increased as well to prevent engine knocks (pre-ignition and detonation). Currently, only 100LL (low lead) avgas (aviation gasoline) is available at the airports. This fuel limits the compression ratio of aircraft engines and prevents a high level of supercharging. The thermal efficiency of air-cooled aircraft engines is about 30%.

5.2.2 Real Engine Cycles

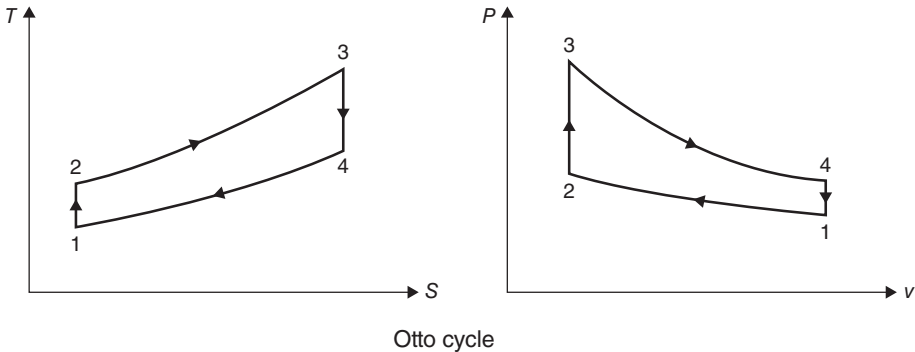
5.2.2.1 Four-Stroke Cycle Engines. Aircraft reciprocating engines operate on the four-stroke cycle known as the Otto Cycle. As shown in Figure 5.2, the four strokes are:

1. intake stroke
2. compression stroke
3. power stroke
4. exhaust stroke.

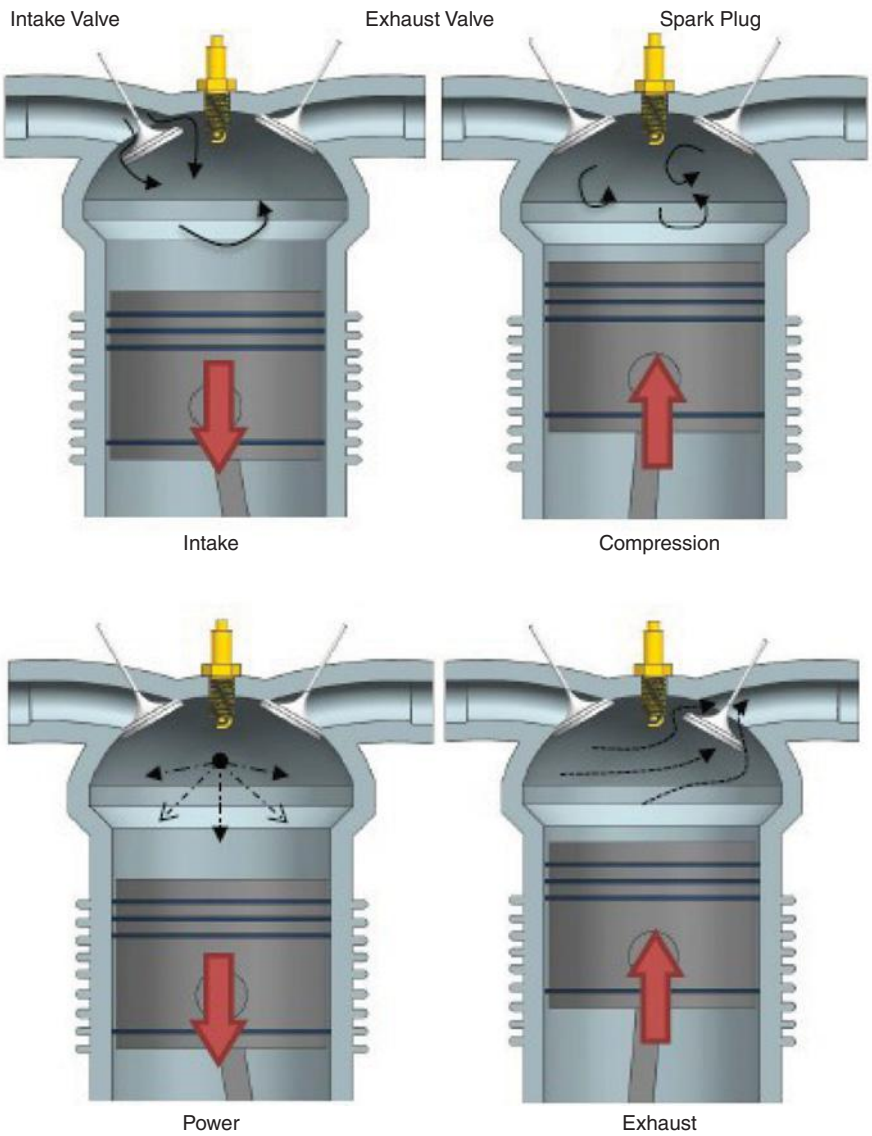
The P–V diagram of an actual four-stroke cycle engine is shown in Figure 5.3. In a four-stroke engine the valve timing is:

- (i) Intake valve opens before the top dead center of the exhaust stroke. The exhaust gases rushing out of the cylinder create suction and help in admitting more fresh charge into the cylinder. This improves the engine's volumetric efficiency.

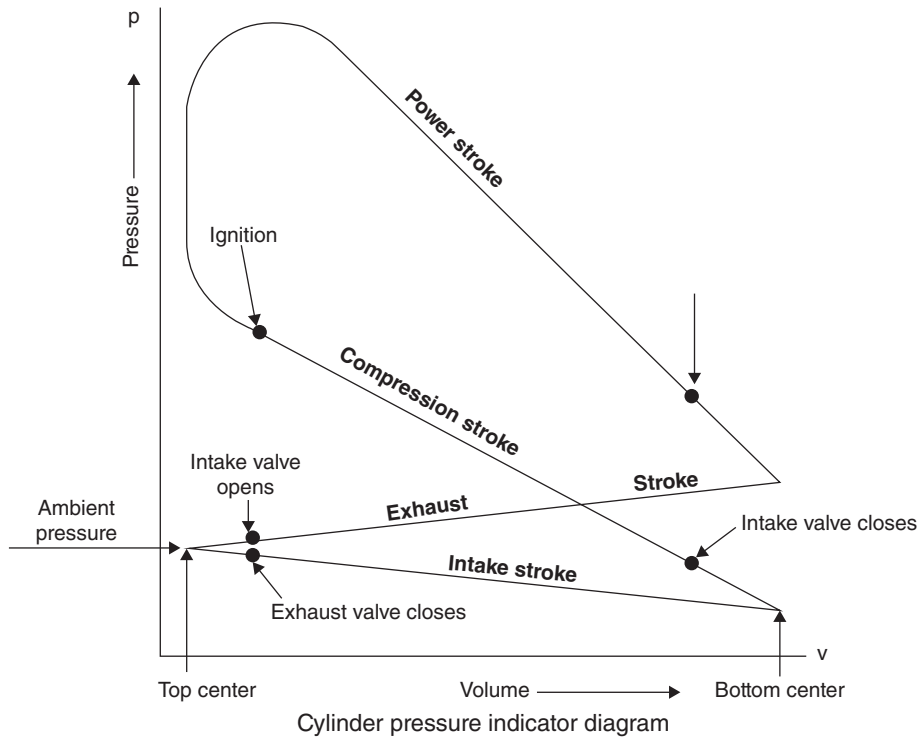
■ FIGURE 5.1
The Otto Cycle



■ FIGURE 5.2
The strokes in a
4-stroke cycle engine



■ **FIGURE 5.3**
The P-V diagram of a 4-stroke cycle engine



- (ii) Intake valve closes after bottom dead center of the compression stroke. This is to take advantage of the inertia of the incoming charge. It improves the volumetric efficiency of the engine.
- (iii) Exhaust valve opens before bottom dead center of the power stroke. This prevents overheating of the cylinders. The exhaust gases are forced out of the cylinder under their own pressure.
- (iv) Exhaust valve closes after top dead center of the intake stroke. This is to take advantage of the inertia of the exhaust gases to force more exhaust gases out and also, by creating suction in the cylinders, to help bring more fresh charge in the cylinders. This improves the volumetric efficiency of the engine.

The spark plug generates a hot spark before top dead center (BTDC) of the compression stroke. The period of time (the angular rotation of the crankshaft) during which both valves are open is called *valve overlap*.

5.2.2.2 Diesel Engines. An increasingly popular power plant for general aviation (GA) aircraft and uninhabited air vehicles (UAVs) is the diesel engine. While still not very common, advances in diesel engine research and development have led to more of these engines being available and even certified by the U.S. Federal Aviation Administration (FAA).

Diesel engines are very attractive power plants due to their low specific fuel consumption (sfc) and their ability to use a variety of available low-cost fuels. The increase in price of avgas and its limited availability, specifically at higher octane number range

has led to the additional research and increased popularity of diesel engines in aircraft application. The ability of diesel engines to run on jet fuel makes them ideal for both civilian and military applications.

Many years ago, several diesel aircraft engines built by Guiberson, Packard, Rolls-Royce, Clerget, Fiat and other manufacturers powered older aircraft. The very successful Junkers “Jumo 205” supercharged two-stroke diesel engine was used in scheduled transatlantic service between Europe and South America. It had a cruise bsfc (brake-specific fuel consumption) of 0.356 lb/bhp-hr, delivered full sea-level power up to 40,000 feet and powered aircraft flying at 50,000 feet. It was a direct drive, air-cooled, two-stroke cycle diesel with four cylinders per row. It featured two stages of supercharging and intercooling.

Although still not widespread, there are several certified and uncertified diesel engines in aviation use. Current diesel aircraft engines are comparable in size and power to the typical Continental or Lycoming engines that are common in the market. The power output ranges from 100 to 400 hp. The specific fuel consumption of these engines is as much as 0.1 lb/hp-hr, less than most spark-ignition engines.

Most of the engine applications are modifications to existing production aircraft and homebuilt aircraft. Such aircraft include the Cessna 172 and the Piper PA-28 line, of which many have been modified with Thielert Centurion brand engines. These aircraft require an STC (supplemental type certificate) to be allowed to fly. The integration of a Thielert Centurion engine on a UAV is shown in Figure 5.4. Several aircraft companies that see the advantages of diesel engines offer or are planning to offer aircraft with a diesel engine option too. Such companies include Cessna, Maule (U.S.A.), Diamond (Austria), and Socata.

Advantages of diesel engines

- Desirable fuel type: low flammability and worldwide availability of Jet-A or diesel fuel is valued in all applications.
- Fuel efficiency: the bsfc (brake-specific fuel consumption) of diesel engines is typically lower than 0.4 lb/hp/hr versus current avgas-powered aviation engine

■ **FIGURE 5.4**
Thielert aircraft diesel
engine installed on
Meridian UAV



with a bsfc of 0.59 lb/hp/hr at 75% and above. For large two-stroke marine diesels, the sfc could be as low as 0.26!!).

- Lower fuel cost and higher fuel availability: 20–30% more range per gallon. Also, cost per gallon of Jet-A is less than 100LL aviation fuel in the U.S.A. The price differential is much greater in Europe. No fuel availability problem worldwide.
- Single-lever power operation: no mixture, no alternate air, no auxiliary fuel pump, no magneto switches, no mandatory temperature, boost or power restrictions.
- Electromagnetic noise elimination: absence of an ignition system reduces interference with navigational and communication systems. For military applications, this is desirable for tactical reasons.
- Durability: inherent in diesels because diesel and jet fuels provide more lubricity and because no electrical system (magnetos or electronic ignition) is required.
- Less toxic emissions: diesel and jet fuels contain no toxic substances such as lead, benzene or scavengers.
- Dramatically reduced fire hazard: diesel fuels have much lower flammability. Exhaust manifold temperature is about few hundred degrees lower than gasoline engines.
- Good reliability and low maintenance cost: no carburetor icing, no magneto or spark-plug problems, and no vapor lock.

Disadvantages of diesel engines

- Unreliable starting at low temperatures
- Higher weight
- Higher operating temperature.

Some modern diesel engines are shown in Table 5.1.

5.2.2.3 Two-Stroke Cycle Engines. The events that occur during one cycle of operation of two-stroke cycle engines (Figure 5.5) are:

1. intake of the charge to the crankcase
2. transfer of the charge from crankcase to the combustion cylinder
3. compression
4. ignition
5. power
6. exhaust.

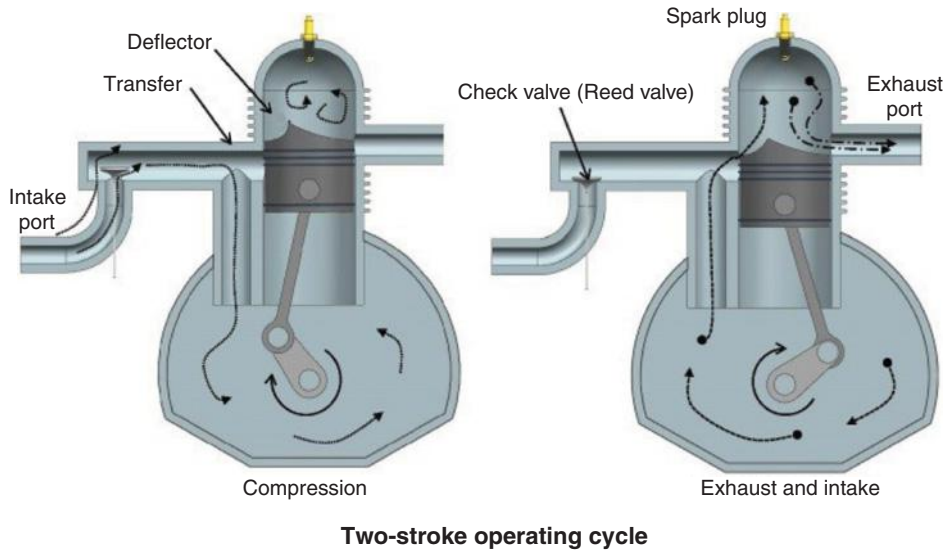
Advantages

- Mechanically simpler: fewer moving parts
- Improved reliability and durability: the two-stroke piston-ported design reduces the parts count by eliminating valves, valve train and cam shaft and therefore have no valve problems
- Weight reduction

■ **TABLE 5.1**
Modern diesel engines

Manufacturer	Country	Engine Model	# Cylinders	Type	Cooling	Capacity (in ³)	Power (hp)	sfc		Weight (lb)	Certified	Uses
								Takeoff (lb/hp-h)	Cruise (lb/hp-h)			
ATG	UK	A-Tech 100	2	Opposed	L	110.5	100	N/A	0.38	220	N	Airships
ATG	UK	A-Tech 600	4	Opposed	L	559	600	N/A	0.36	496	N	Airships
Centurion (Thielert)	Germany	Centurion 1.7	4	Inline	L	103.07	135	N/A	0.36	295.41	Y	GA
Centurion (Thielert)	Germany	Centurion 4.0	8	V	L	243.85	350	N/A	N/A	606.3	N	GA
CRM	Italy	18D/SS	18	Rotary	L	3495	1850	N/A	0.353	3745	Y	Marine, aircraft
DeltaHawk	USA	DH160V4	4	V	L	201.062	160	N/A	0.4	327	N	Homebuilt
DeltaHawk	USA	DH200V4	4	V	L	201.062	200	N/A	0.38	327	N	Homebuilt
DieselAir	UK	DAIR-100	2	Opposed	L	110.5	100	0.53	0.38	204.37	Y	Homebuilt, LTA, small aircraft
Novikov	Russia	DN-200	4	Opposed	L	270.9	148	N/A	N/A	231	N/A	N/A
Société de Motorisations Aeronautiques	France	SR 305	4	Opposed	A	305	227	N/A	0.315	423.3	Y	GA
VM	Italy	1304HF	4	Opposed	A	356.4	206	N/A	N/A	408	N	Automotive
VM	Italy	1306HF	6	Opposed	A	534.6	315	N/A	N/A	536	N	Automotive
VM	Italy	1308HF	8	Opposed	A	713	424	N/A	N/A	657	N	Automotive
Wilksch Airmotive Ltd	UK	WAM-100	3	Inline	L	N/A	100	0.49	0.43	262.35	N	Homebuilt
Wilksch Airmotive Ltd	UK	WAM-120	3	Inline	L	N/A	120	0.49	0.43	280.43	N	Homebuilt
Wilksch Airmotive Ltd	UK	WAM-160	4	Inline	L	N/A	160	0.49	0.43	337.31	N	Homebuilt
Zoche Aerodiesels	Germany	ZO 01A	4	Radial	A	162.6	150	0.365	0.346	185	N	Production singles
Zoche Aerodiesels	Germany	ZO 02A	8	Radial	A	325.3	300	0.365	0.346	271	N	Production singles
Zoche Aerodiesels	Germany	ZO 03A	2	V	A	81.3	70	0.381	0.357	121	N	Production singles

■ **FIGURE 5.5**
Operation of a two-stroke engine: (a) compression, ignition, and power events; (b) exhaust and intake events.



- Reduction of frontal area: by elimination of overhead valve mechanism
- Smoothness of operation: a two-stroke has one power stroke per cylinder per revolution.
- Very low vibration level: Torque vibration is minimal due to one power pulse per cylinder per revolution.

Disadvantages

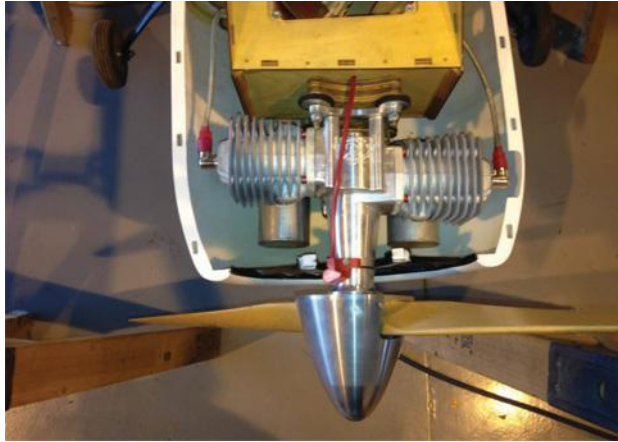
- Less efficient
 - Some of the fuel–air mixture is diluted with burned gases
 - Some of the fresh fuel–air charge is discharged through the exhaust port
- More difficult to lubricate
- More difficult to cool.

Integration of a Desert model DA-150, two-stroke cycle engine in a UAV is shown in Figure 5.6.

5.2.2.4 Rotary (Wankel) Engines. In Wankel engines, the four strokes of a typical Otto Cycle engine are arranged sequentially around the rotating rotor, unlike the piston of reciprocating engine. In the basic single-rotor Wankel engine, a single oval (technically an epitrochoid) housing surrounds a three-sided rotor (a Reuleaux triangle), which turns and moves within the housing. The sides of the rotor seal against the sides of the housing and the corners of the rotor seal against the inner periphery of the housing, dividing it into three combustion chambers. A sketch of the Wankel engine is shown in Figure 5.7.

As the rotor turns, its motion and shape and the shape of the housing cause each side of the rotor to get closer and farther from the wall of the housing, compressing and

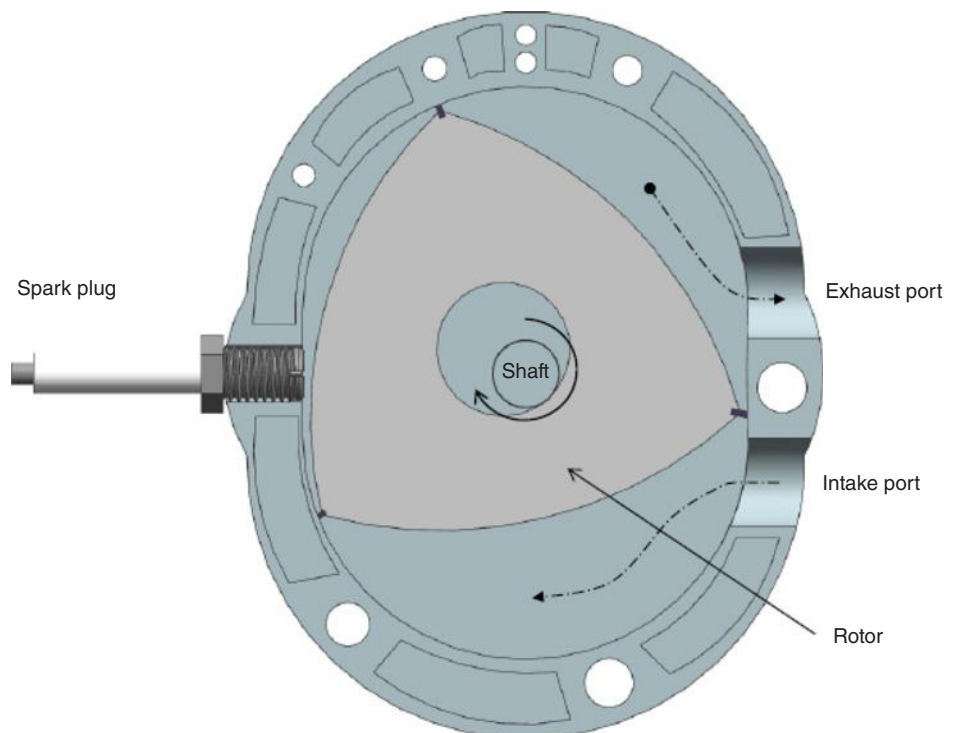
■ **FIGURE 5.6**
Desert model DA-150,
2-stroke cycle engine
installed on a UAV



expanding the charge in the combustion chamber similar to the “strokes” of a reciprocating engine. However, whereas a normal four-stroke cycle engine produces one combustion stroke per cylinder for every two revolutions (that is, one half power stroke per revolution per cylinder), each combustion chamber of each rotor in the Wankel engine generates one combustion “stroke” per revolution (that is, three power strokes per one rotor revolution).

Since the Wankel output shaft is geared to spin at three times the rotor speed, this becomes one combustion “stroke” per output shaft revolution per rotor, twice as many as

■ **FIGURE 5.7**
Rotary (Wankel)
Engine



the four-stroke piston engine, and similar to the output of a two-stroke cycle engine. Thus, power output of a Wankel engine is generally higher than that of a four-stroke piston engine of similar engine displacement in a similar state of tune, and higher than that of a four-stroke piston engine of similar physical dimension and weight.

In the Wankel engine, a triangular rotor incorporating a central ring gear is driven around a fixed pinion within an oblong chamber. The fuel–air mixture is drawn in the intake port during this phase of the rotation.

Advantages of the Wankel (Rotary) Engine. Wankel engines have several major advantages over reciprocating piston designs, in addition to having a higher output for similar displacement and physical size. Wankel engines are considerably simpler and contain far fewer moving parts. For example, because simple ports cut into the walls of the rotor housing accomplish valving, they have no valves or complex valve trains. In addition, since the rotor is geared directly to the output shaft, there is no need for crankshaft, crankshaft balance weights, and so on. The elimination of these parts not only makes a Wankel engine much lighter (typically half that of a conventional engine with equivalent power) but also completely eliminates the reciprocating mass of a piston engine with its internal strain and inherent vibration due to repetitious acceleration and deceleration, producing not only a smoother flow of power but also the ability to produce more power by running at higher rpm.

In addition to the enhanced reliability due to the elimination of this reciprocating strain on internal parts, the construction of the engine, with an iron rotor within a housing made of aluminum, which has thermal expansion, ensures that even when grossly overheated the Wankel engine will not seize-up, as an overheated piston engine is likely to do. This has substantial benefit for aircraft use.

The simplicity of design and smaller size of the Wankel engine also allow for savings in construction costs, compared to piston engines of comparable power output.

As another advantage, the shape of the Wankel combustion chamber and the turbulence induced by the moving rotor prevent localized hot spots from forming, thereby allowing the use of fuel of very low octane number without pre-ignition or detonation.

In the United States, John Deere, Inc., had a major research effort in rotary engines in collaboration with the NASA Lewis Research Center and designed a version that was capable of using a variety of fuels without changing the engine. The design was proposed as the power source for several U.S. marine combat vehicles in the late 1980s.

Disadvantages of the Wankel (Rotary) Engine. The design of the Wankel engine requires numerous sliding seals and a housing, typically built as a sandwich of cast iron and aluminum pieces that expand and contract by different degrees when exposed to heating and cooling cycles in use. These elements led to a very high incidence of loss of sealing, both between the rotor and the housing and also between the various pieces making up the housing. Hydrocarbon emission and high sfc are another two serious drawbacks of Wankel engines. Just as the shape of the Wankel combustion chamber prevents pre-ignition; it also leads to incomplete combustion of the air–fuel charge, with the remaining unburned hydrocarbon released into the exhaust.

Another disadvantage of the Wankel engine is the difficulty of expanding the engine to more than two rotors. The complex shapes of the rotor, housing, and output shaft and the way they fit together requires that engines with more than two rotors use an output shaft made of several sections assembled during the assembly of the rest of the engine.

While this technique has been used successfully in Wankel-powered racing cars, it negates a great deal of the relative simplicity and lower cost of the Wankel engine construction.

The potential drawbacks of Wankel (Rotary) engines are the only reasons for its demise in aircraft applications. However, continued engineering research on the rotary engine has resulted in performance improvements through improved seals, lean-burn combustion, fuel injection, integral electronic control, improved intake design, weight reduction, and turbocharging. This could open up the way once more for the introduction of rotary engines in aircraft applications.

5.3 Power and Efficiency

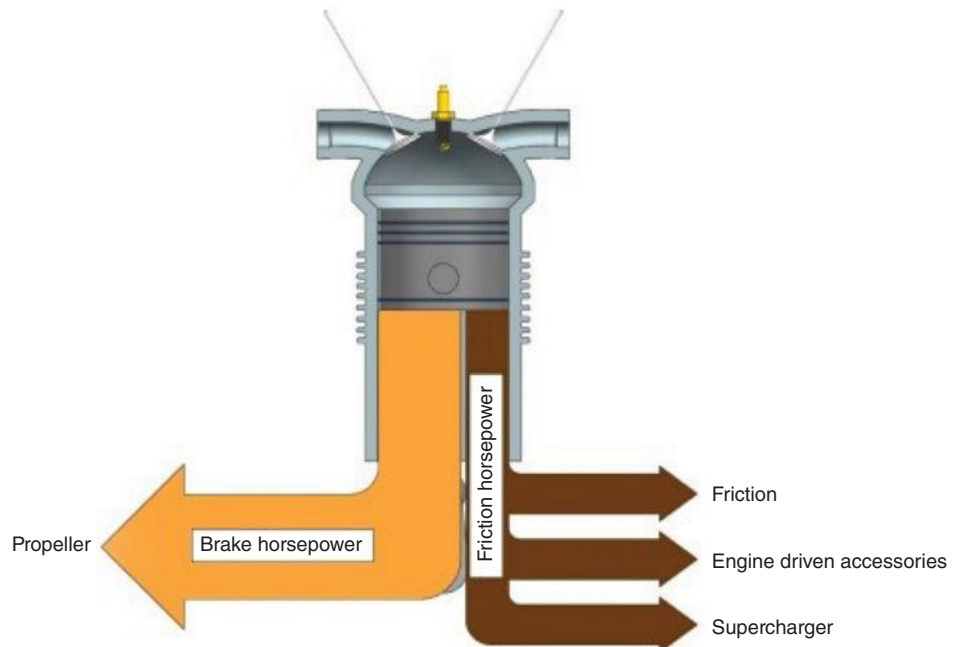
Power Definitions (Figure 5.8)

- **Indicated Horsepower (IHP).** The actual power produced in the engine cylinders. This is calculated based on the cylinder pressure, RPM, and the displacement volume.
- **Brake Horsepower (BHP).** The power output of the engine. Brake Horsepower is also sometimes called **Shaft Horsepower**.

$$BHP = \frac{(2\pi)(Torque)(rpm)}{33000} \quad \text{Torque in ft} - \text{lb}$$

- **Friction Horsepower (FHP).** Is the power loss due to friction, accessories, and superchargers. It is indicated horsepower minus brake horsepower.

■ **FIGURE 5.8**
Engine power definitions



- **Thrust Horsepower (THP).** The power delivered by the propeller. THP is calculated by $BHP \times \text{Propeller efficiency}$.

Also, $THP = (T \times V_{\infty}) / 325$, where V_{∞} is the aircraft speed in knots. The denominator will be 375 if V_{∞} is in mph and 550 if it is in fps. For a steady state flight, propeller thrust equals aircraft drag ($T = D$); therefore, if aircraft drag is known, we can solve for THP from $THP = (V_{\infty} \times D) / 325$.

- Mean Effective Pressure, MEP, is defined as the constant pressure which would have to act upon the piston for one stroke to equal the actual work output of one complete cycle. It is actually an average pressure inside of cylinders of an internal combustion engine during the power stroke. IMEP is the indicated mean effective pressure, BMEP is the brake mean effective pressure, and FMEP is the friction mean effective pressure.
- For four-stroke cycle engines: Brake horsepower, $BHP = \frac{(BMEP) \cdot L \cdot A \cdot N \cdot K}{33,000}$

BMEP = Brake mean effective pressure

L = Cylinder Stroke in ft.

A = Piston Head (top surface) area in in^2

N = $\frac{RPM}{2}$ (for four-stroke cycle engines)

K = Number of cylinders

- Indicated horsepower, $IHP = \frac{(IMEP) \cdot L \cdot A \cdot N \cdot K}{33,000}$, where IMEP is indicated mean effective pressure.
- Friction horsepower, $FHP = \frac{(FMEP) \cdot L \cdot A \cdot N \cdot K}{33,000}$, where FMEP is friction mean effective pressure

Factors Affecting Piston Engine Power

- manifold absolute pressure
- RPM
- fuel-to-air ratio
- air density (pressure, temperature, humidity)
- carburetor air intake ram pressure
- exhaust back pressure
- compression ratio
- carburetor air temperature (CAT).

Definitions and Useful Information

- $\eta_{\text{mech}} = \frac{(\text{bhp})}{(\text{ihp})}$ Mechanical efficiency;
Approximate value $\approx 90\%$
- Volumetric efficiency; $\eta_{\text{vol}} = \frac{(\text{Volume of charge (Corrected for Temperature and Pressure)})}{(\text{Total Engine Piston Displacement})}$

Approximate value $\approx 75\%$ for “naturally aspirated engines”. Could be greater than 100% for supercharged engines. Volumetric efficiency decreases as RPM increases.

- Propeller efficiency; $\eta_{pr} = \frac{(\text{Thrust horsepower})}{(\text{Brake horsepower})}$ OR $\frac{\text{THP}}{\text{BHP}}$
Approximate value $\approx 80\%$
- Brake thermal efficiency; $\eta_{th} = \frac{(\text{BHP} \times 33,000)}{(\text{Weight of fuel burned per minute}) \times (\text{Heat value of the fuel}) \times 778}$
Approximate value $\approx 30\%$
The maximum heat loss is through the exhaust gases.
- Specific fuel consumption, sfc, is defined as pounds of fuel burned per horsepower per hour; lbs/bhp-hr. For FAA certified aircraft engines, brake specific fuel consumption, bsfc, ≈ 0.4 to 0.5 lbs/bhp-hr.
- Engine weight to power ratio ≈ 1.0 to 2.0 lbs/bhp
- Compression Ratio, $\text{CR} = \frac{(\text{Cylinder volume when the piston is at bottom dead center})}{(\text{Cylinder volume when the piston is at top dead center})}$
For spark ignition engines, $\text{CR} \approx 7:1$ to $11:1$
For compression-ignition engines (diesel engines), $\text{CR} \approx 14:1$ to $21:1$
- Heat value of aviation gasoline (avgas) $\approx 20,000$ Btu/lb.
- Specific weight of avgas ≈ 6 lbs/gal.

EXAMPLE 5.1

If an engine is rated at 200 BHP:

Indicated Horsepower ≈ 222 hp (assuming mechanical efficiency of 90%)

Friction Horsepower ≈ 22 hp

Thrust Horsepower ≈ 160 hp (assuming propeller efficiency of 80%)

5.4 Engine Components and Classifications

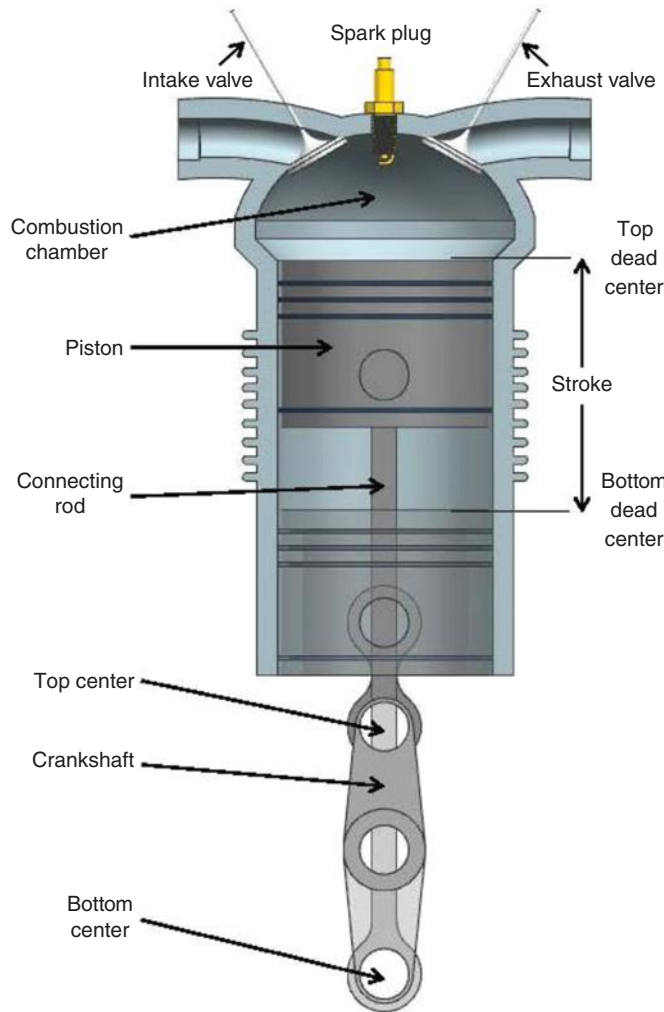
5.4.1 Engine Components

The major components of reciprocating engines (Figure 5.9) are the:

- piston
- cylinder
- connecting rod
- crankshaft.

The cylinders usually have two valves, an intake valve and an exhaust valve. The majority of aircraft engine pistons are machined from aluminum alloy forgings. Some intake and exhaust valve stems are hollow and partially filled with metallic sodium. This material is used because it is an excellent heat conductor. The sodium will melt at approximately 208°F (98°C). Some valve stems have a narrow groove below the lock ring groove for the installation of safety circllets or spring rings. The circllets are designed

■ **FIGURE 5.9**
Main Components and terminology of piston engines



Components and terminology of engine operation

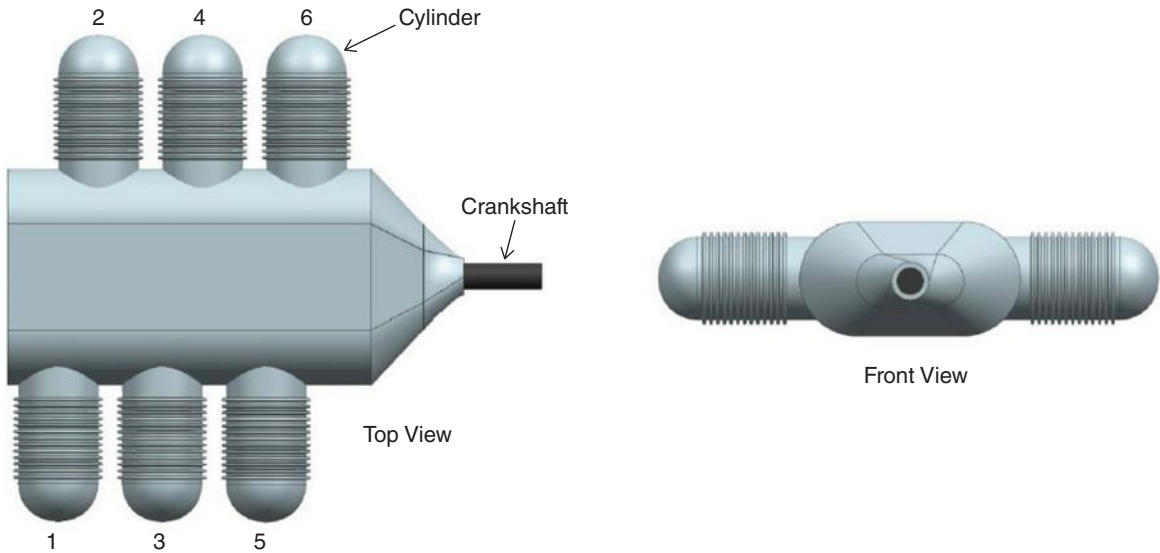
to prevent the valves from falling into the combustion chambers if the tip should break during engine operation and on the occasion of valve disassembly and assembly.

5.4.2 Reciprocating Engine Classifications

5.4.2.1 Classification by Cylinder Arrangement

Opposed. This is the most extensively used piston type engine for general aviation aircraft. A sketch of this type of cylinder arrangement is shown in Figure 5.10.

An example of this type of engine is Teledyne Continental GTSIO-520. This is a typical modern high-power, opposed-type reciprocating engine that is being extensively used on general aviation aircraft. The engine has total piston displacement of 520 cubic inches and is equipped with reduction gear, supercharger and fuel injection system.



■ **FIGURE 5.10** Opposed aircraft engine cylinder arrangement

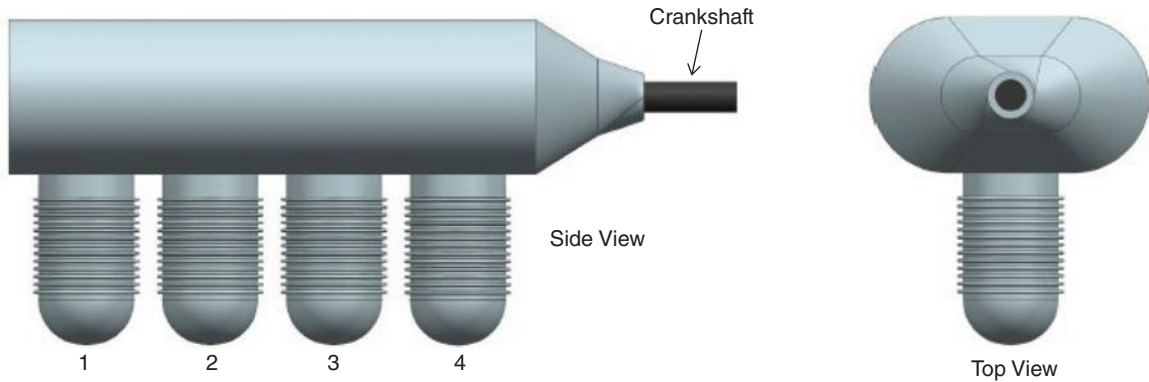
Integration of a Lycoming IO-540 opposed engine with a Cessna 182 aircraft is shown in Figure 5.11.

Inline. This type of engine has been extensively used in the past for low power ranges. Limited production continues. A sketch of this type of cylinder arrangement is shown in Figure 5.12. An example of this type of aircraft engine is the M-337b, which is a six-cylinder inline engine made by LOM PRAHA that generates 173 kW of power.

Radial. This arrangement is suitable for powerful engines having more than six cylinders. A sketch of this type of cylinder arrangement is shown in Figure 5.13. An example of

■ **FIGURE 5.11**
Lycoming IO-540
opposed engine
installation on a
Cessna 182 airplane

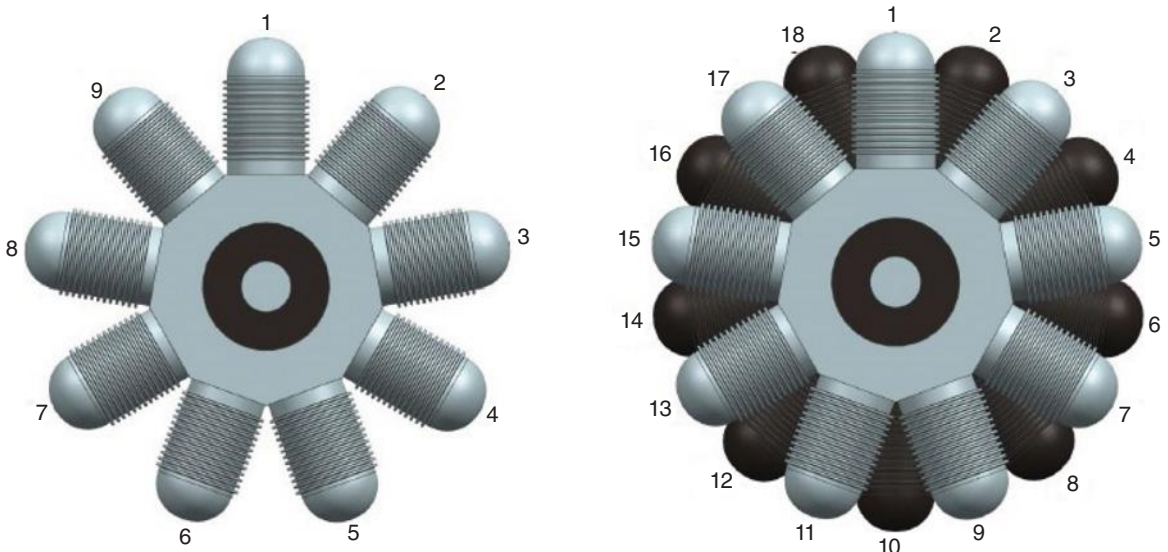




■ FIGURE 5.12 Inline aircraft engine cylinder arrangement

this type of engine is the Pratt and Whitney R-4360. This 28-cylinder radial engine, with four rows of seven cylinders in each row, has 4360 cubic inches of piston displacement. This was the largest and most powerful reciprocating engine built and used successfully in the United States.

Rotary-Radial. The cylinders of a rotary-radial engine spin around the crankshaft, which is mounted rigidly on the airframe. One end of each connecting rod rides in a groove in a cam that is offset from the center of the crankshaft. These engines have not been in actual production for a very long time.



■ FIGURE 5.13 Single-row and double-row radial aircraft engine cylinder arrangements

5.4.2.2 Classification by Cooling Arrangement

- Air cooled
- Liquid cooled.

Air-Cooled Engines. Most aircraft engines operating today are of air cooled type. Cylinders of an air-cooled engine are shown in Figures 5.11 and 5.14. Air-cooled cylinders have cooling fins around them to increase their contact surface with air. Up to about 10% of the engine's horsepower can be wasted by the cooling drag. The cooling air intake area can be 30–50% of engine frontal area. Cooling air exit should be about 30% larger. Either downdraft or cooling updraft cooling arrangements can be used. Integration of the air-cooled Lycoming O-320 engine on a Cessna 172 aircraft is shown in Figure 5.14, in which the engine cowling is removed to make the baffles and engine mount visible. The baffles guide the cooling airflow inside the engine nacelle and around the cylinders for maximum cooling effectiveness. The engine mount extends the engine forward of the firewall by about half of the engine length. In some aircraft this space is used for the battery and nose wheel steering.

Liquid-cooled engines. Liquid cooling reduces overcooling in descents from altitude. Also, reduced thermal variance in operation reduces engine component fatigue and allows tighter manufacturing tolerances, leading to increased power and fuel efficiency. Liquid-cooled engines have water passages around their crankcase and cylinders for cooling purposes. Streamlined installation would be difficult due to water hoses and radiators. The arrangement is similar to that used on most automobile engines. The Thielert Centurion diesel engine shown in Figure 5.4 is liquid cooled.

5.4.2.3 Classification by Operating Cycle

- Four-stroke cycle engines
- Two-stroke cycle engines.

The above cycles have been covered in Sections 5.2.2.1 and 5.2.2.3 respectively.

■ **FIGURE 5.14**
Integration of a
Lycoming O-320
air-cooled engine in a
Cessna 172 aircraft



5.4.2.4 *Classification by Ignition Type*

- Spark-ignition engines
- Compression-ignition engines (diesel)

The ignition systems will be covered in Section 5.6.3 and diesel engines have already been covered in Section 5.2.2.2

5.5 Scaling of Aircraft Reciprocating Engines

When considering the design of a piston engine driven aircraft, a major consideration that must be accounted for is the type and size of engine used. The amount of horsepower that an engine can produce is necessary in order to provide adequate thrust for the aircraft and allow it to lift off of the ground. However, for most cases, the more horsepower that an engine can produce, the more it will weigh.

The analysis of engine data, such as bore, stroke, capacity, horsepower, weight, and specific fuel consumption, from full size engines and Remotely Controlled (RC) engines over the past decade shows in multiple trends. These trends include a linear relationship between the weight of a piston engine and the horsepower it produces. Several scaling equations have been developed for full size engines and Remotely Controlled engines with specifically defined constants “a” and “b”. The constants and equation for which they are used is:

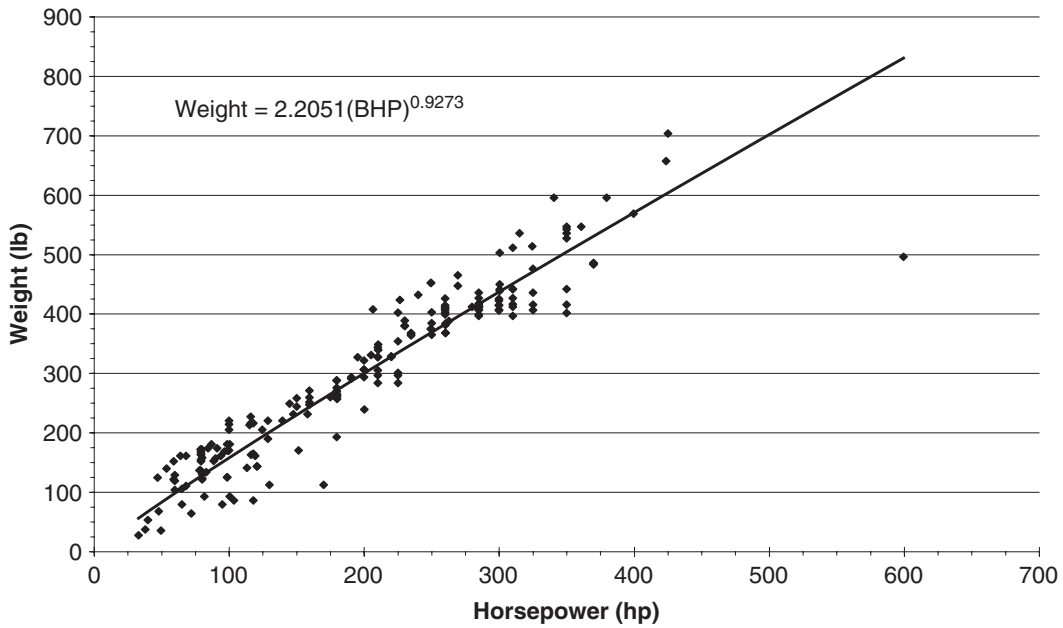
$$X = a(\text{BHP})^b \tag{5.1}$$

“X” could be any engine characteristic, for example, weight, sfc, and so on. The analytically derived results from the current analysis based on the data of many piston engines available for aircraft can be seen in Table 5.2. Figures 5.15–5.20 show the general trends in the piston engine industry when it comes to weight and corresponding horsepower. Obviously, the more horsepower that is required to produce, the higher will be the overall weight of the engine. For more coverage of the engine scaling laws references 4 and 16 may be consulted.

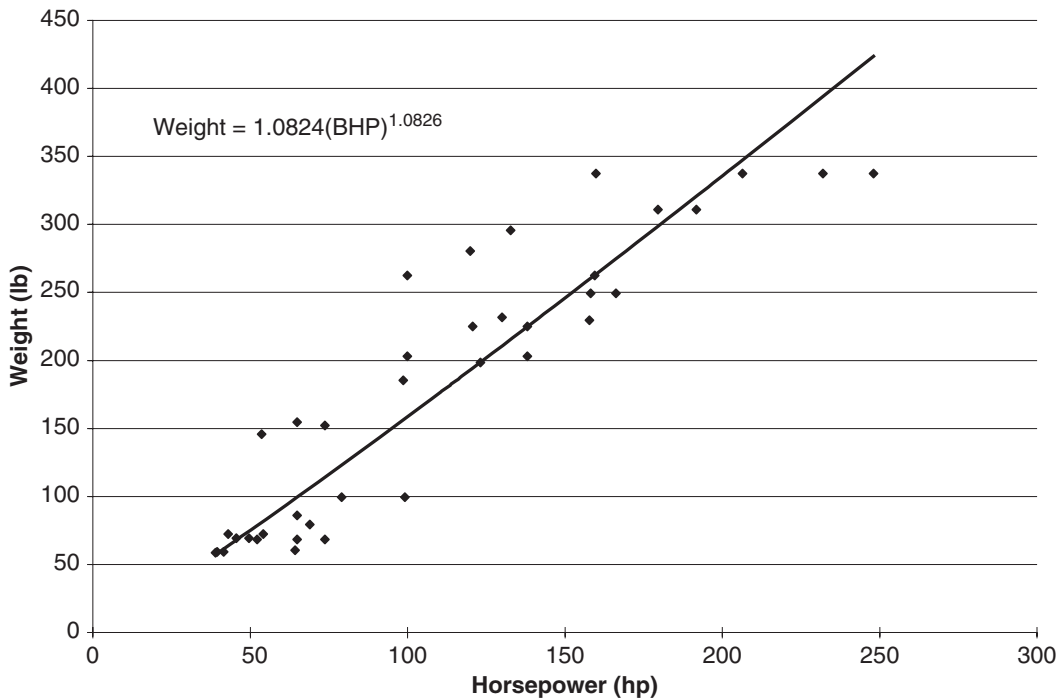
Figures 5.21 and 5.22 depict the specific fuel consumption (SFC) for some of the aircraft engines that were surveyed. This is a critical aspect of engine selection as it can determine the range and endurance of the aircraft as well as many other factors in the

■ **TABLE 5.2**
Curve fit results

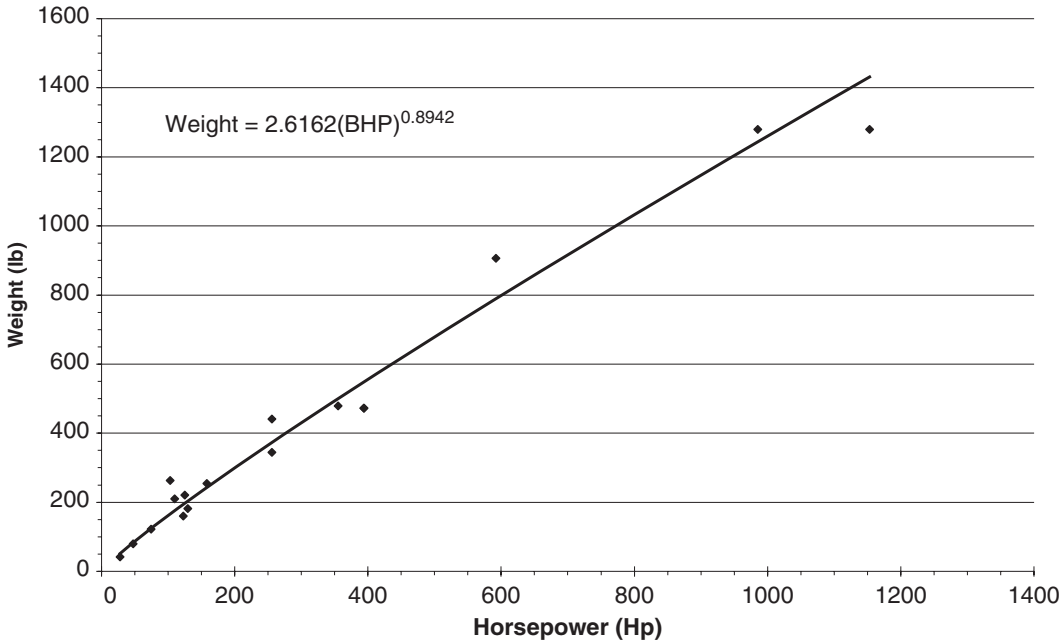
$X = a (\text{BHP})^b$ (lb or in)										
Piston Engine Cylinder Arrangement										
X	Opposed		Inline		Radial		V-Type		Rotary	
	a	b	a	b	a	b	a	b	a	b
Weight	2.205	0.927	1.082	1.083	2.616	0.894	9.259	0.667	2.274	0.891



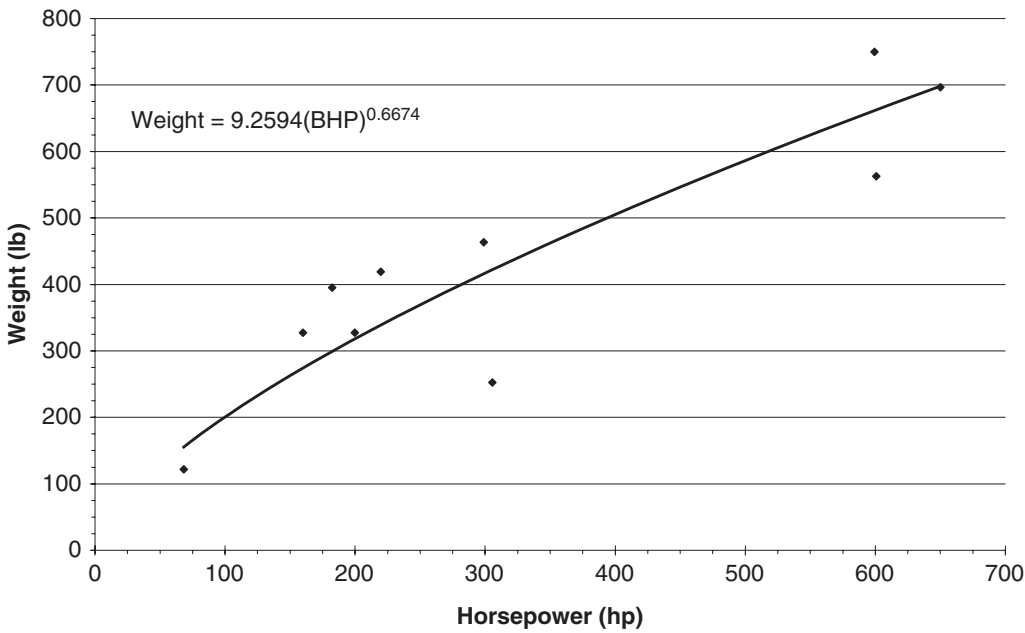
■ FIGURE 5.15 Weight versus horsepower for opposed engines



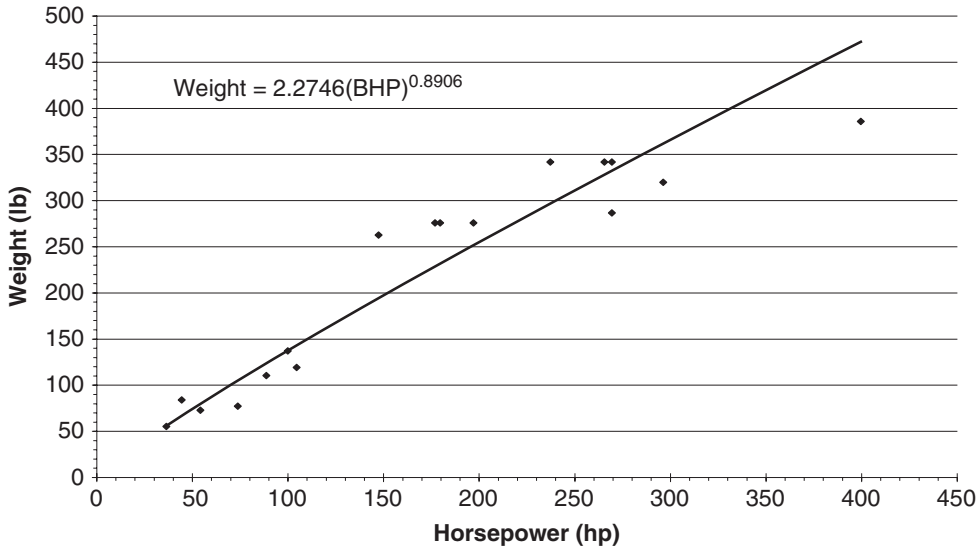
■ FIGURE 5.16 Weight versus horsepower for inline engines



■ FIGURE 5.17 Weight versus horsepower for radial engines

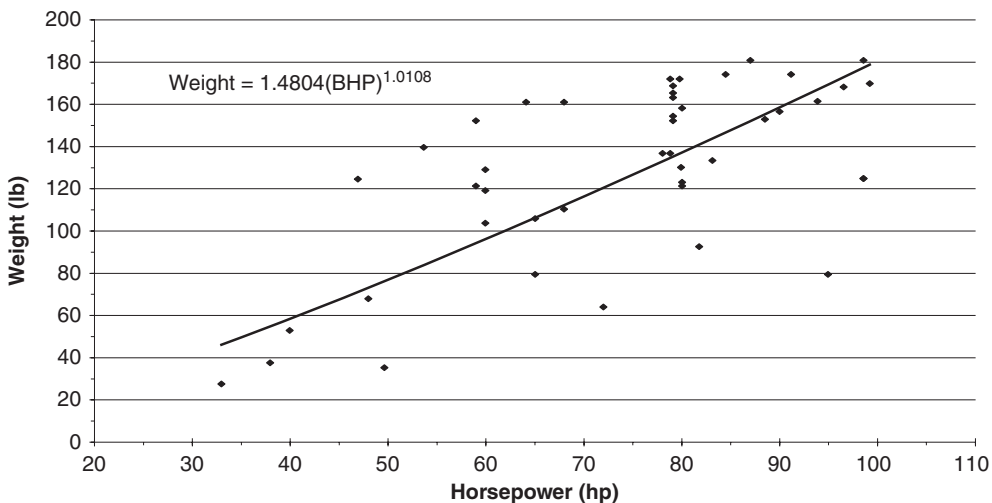


■ FIGURE 5.18 Weight versus horsepower for V-type engines

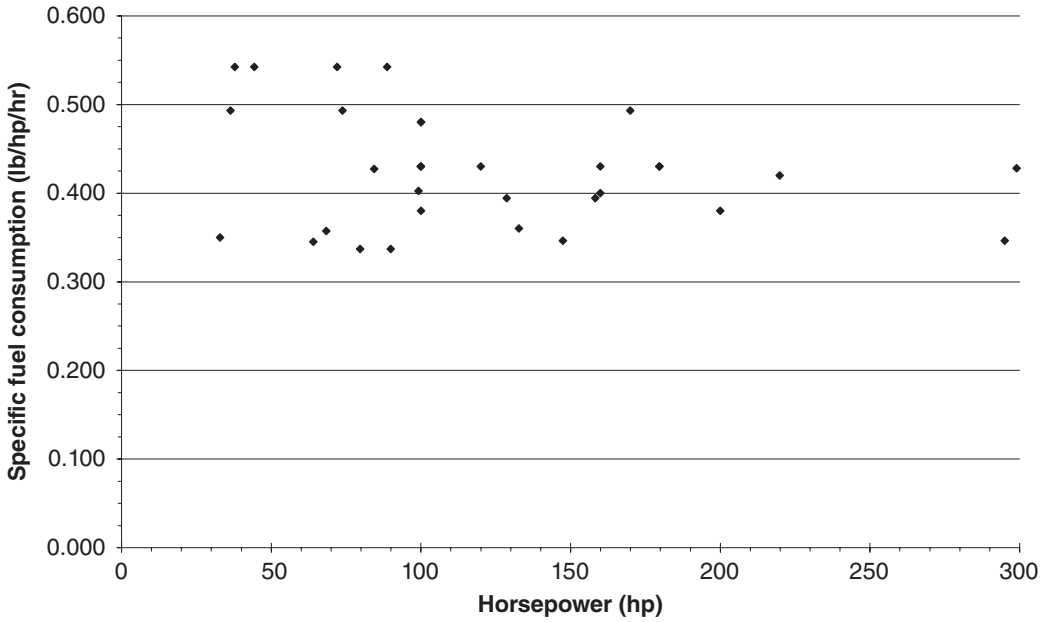


■ FIGURE 5.19 Weight versus horsepower for rotary engines

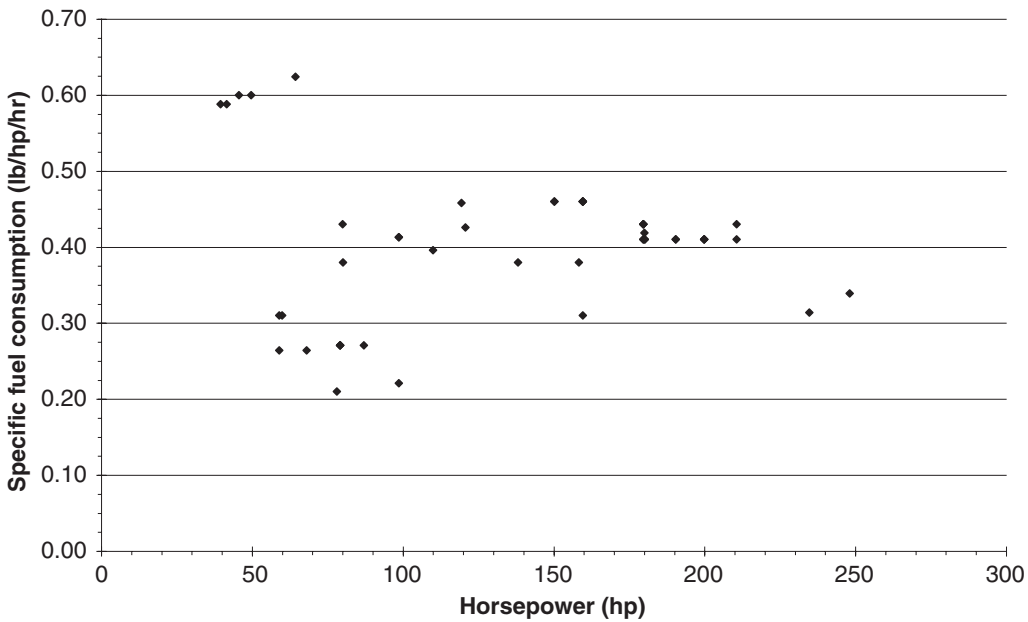
preliminary design stages. This also happens to be one of the least reported specifications for engine data. The graphs have been broken up into those in which the manufacturer listed the engine's specific fuel consumption and those who listed a fuel burn rate from which an SFC was calculated. It should be noted that the calculations are not an accurate depiction of the real engines fuel consumption, which must be determined through testing. Also, there is no discernable trend for either case. The typical numbers for an SFC are 0.4 to 0.5 lb/hp/hr. However some manufacturers are beginning to breach the 0.4 value with numbers just under 0.4 lb/hp/hr. Figure 5.23 is a graph depicting the engine total displacement volume that can be expected from an aircraft piston engine of a given horsepower. It should be noted that the trend is not as clear as the models for predicting weight.



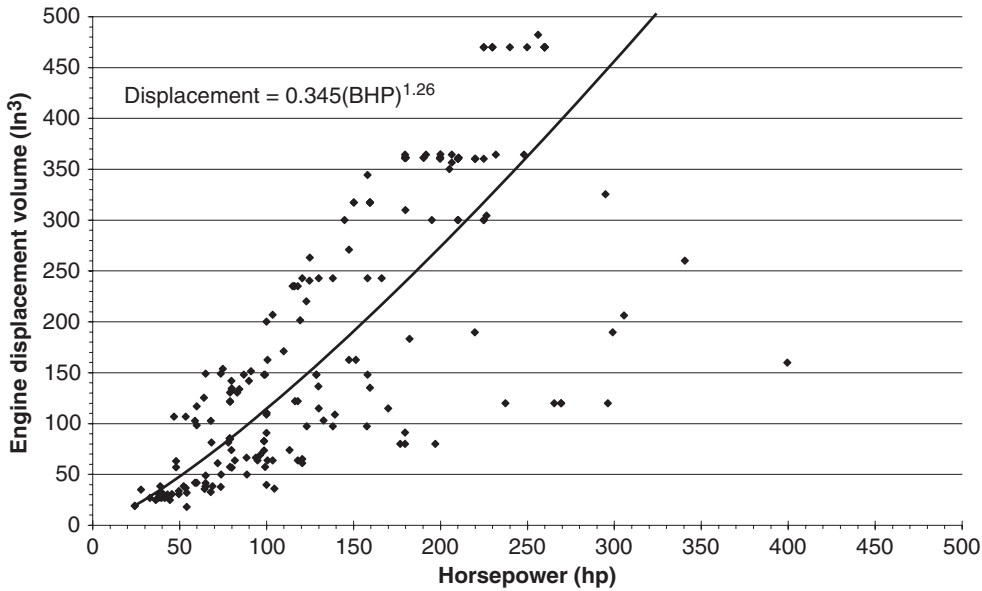
■ FIGURE 5.20 Weight versus horsepower for opposed engines of less than 100 hp output



■ FIGURE 5.21 Specific fuel consumption as posted by manufacturer



■ FIGURE 5.22 Specific fuel consumption calculated from the given engine data



■ FIGURE 5.23 Engine displacement volume versus horsepower for all aircraft engine types

EXAMPLE 5.2

Estimate the weight of the following three engine types using the derived scaling formulas and compare the results with the manufacturer's data.

- (a) Teledyne Continental Motors IO-520 six-cylinder opposed engine
- (b) LOM M332A, four-cylinder inline engine
- (c) VOKBM M-14PT, nine-cylinder radial engine

■ TABLE 5.3

Comparison of opposed engine analysis with manufacturer's data

Scaling Method	Horsepower (hp)	Weight (lb)	Percentage error (%)
Method of Reference 4	285	449.5	9.1
Current Analysis	285	416.7	1.1
IO-520	285	412	0.0

■ TABLE 5.4

Comparison of inline engine analysis with manufacturer's data

Scaling Method	Horsepower (hp)	Weight (lb)	Percentage error (%)
Method of Reference 4	138	243.7	8.3
Current Analysis	138	224.4	0.3
M332A	138	225	0.0

■ **TABLE 5.5**
Comparison of radial engine weight analysis with manufacturer's data

Scaling Method	Horsepower (hp)	Weight (lb)	Percentage error (%)
Method of Reference 4	355	566.7	18.6
Current Analysis	355	498.9	4.4
M-14PT	355	478	0.0

It is evident that the model derived from this analysis yields a closer estimate of the weight of the radial piston engines.

5.5.1 Scaling of Aircraft Diesel Engines

A study of aircraft diesel engines may be found in Reference 44. This reference also contains scaling laws for predicting diesel engine size and performance parameters. All engines for which the scaling equations were given fall into the following three categories:

- five or fewer cylinders
- six cylinders
- eight cylinders.

For each group a different set of equations should be used.

Five or fewer cylinders. The engine weight can be estimated with

$$W_{\text{wet}} = 15.17(SHP_{\text{t.o.}})^{0.610} \text{ [lb]} \quad (5.2)$$

The engine specific fuel consumption at sea level and takeoff is estimated with

$$sfc_{\text{t.o.}} = 0.541(SHP_{\text{t.o.}})^{-0.062} \text{ [lb/hp/hr]} \quad (5.3)$$

Six cylinders. The engine weight can be estimated with

$$W_{\text{wet}} = 15.17(SHP_{\text{t.o.}})^{0.610} \text{ [lb]} \quad (5.4)$$

The engine specific fuel consumption at sea level and takeoff is estimated with

$$sfc_{\text{t.o.}} = 0.541(SHP_{\text{t.o.}})^{-0.062} \text{ [lb/hp/hr]} \quad (5.5)$$

The engine length is estimated with

$$L = 1.56(SHP_{\text{t.o.}})^{0.15} \text{ [ft]} \quad (5.6)$$

The engine width can be estimated with

$$W = 1.5 + 0.00134(SHP_{t.o.}) \text{ [ft]} \quad (5.7)$$

The engine height can be estimate with

$$H = 1.7 + 0.00156(SHP_{t.o.}) \text{ [ft]} \quad (5.8)$$

Eight cylinders. The engine weight can be estimated with

$$W_{wet} = 15.17(SHP_{t.o.})^{0.610} \text{ [lb]} \quad (5.9)$$

The engine specific fuel consumption at sea level and takeoff is estimated with:

$$sfc_{t.o.} = 0.541(SHP_{t.o.})^{-0.062} \text{ [lb/hp/hr]} \quad (5.10)$$

The engine length is estimated with

$$L = 1.56(SHP_{t.o.})^{0.15} \text{ [ft]} \quad (5.11)$$

The engine width can be estimated with:

$$W = 1.9 + 0.00042(SHP_{t.o.}) \text{ [ft]} \quad (5.12)$$

The engine height can be estimate with:

$$H = 1.8 + 0.00081(SHP_{t.o.}) \text{ [ft]} \quad (5.13)$$

EXAMPLE 5.3

Using the diesel engine scaling laws, calculate and compare as much information as possible for the *Thielert* and

Zoche aircraft diesel engines and compare the results with the information in the manufacturer's data sheet.

Scaling Results

Engine	HP(t.o.)	sfc(t.o.) – sea level	sfc(t.o.) – 15,000 ft	sfc(t.o.) – 25,000 ft	W(wet) [lb]	Length [ft]	Width (6-cylinder) [ft]	Width (8-cylinder) [ft]	Height (6-cylinder) [ft]	Height (8-cylinder) [ft]
ZO 02A	300	0.380	0.3318	0.335	509.589	3.670	N/A	2.026	N/A	2.043
Centurion 4.0	135	0.399	0.347	0.356	313.098	3.256	N/A	1.9567	N/A	1.90935

Manufacturer Specifications

Engine	HP (hp)	Weight (lb)	Length (ft)	Width (ft)	Height (ft)
ZO 02A	300	271	2.375	2.125	2.125
Centurion 4.0	135	N/A	2.95	2.525	2.2

The scaling results had a tendency to overestimate the weight of the Zoche ZO 02A by a very large amount, about 232 pounds. It also overestimated the engine's length by roughly 1.3 feet but came close to the actual width and height of the engine – these two estimations were only off by 0.1 feet and 0.08 feet, respectively. One reason for the major discrepancy is that the Zoche engine has a nontraditional diesel configuration because it has radial cylinder

arrangement and is also air cooled. As for the Centurion 4.0, no data on the actual weight of the engine could be found but the length, width, and height results were compared for that engine. The estimated values for these were off by about 0.31 feet, 0.56 feet, and 0.29 feet, respectively. These results show us that the scaling laws are not very accurate but could provide us with ballpark estimates to what the actual engine specifications are.

5.6 Aircraft Engine Systems

5.6.1 Aviation Fuels and Engine Knock

Current aviation fuel for high compression engines is leaded and will soon be made unavailable by the U.S. Environmental Protection Agency (EPA), making these engines unusable. Many aircraft in the general aviation (GA) fleet require high octane fuels to avoid engine knock and subsequent damage during their operation. Leaded avgas, 100LL, contains tetraethyl lead (TEL) to boost octane for the safe operation of piston engine aircraft. While not all piston engine aircraft require 100LL avgas to run on, airports and the avgas market supply 100LL almost exclusively to the GA piston engine fleet because it meets the needs of the majority of the GA fleet. In 2008, the U.S. Environmental Protection Agency (EPA) lowered the National Ambient Air Quality Standards (NAAQS) for lead from 1.5 to 0.15 $\mu\text{g}/\text{m}^3$ to reduce lead emission impacts on human health and the environment. During the regulatory process, the EPA identified sources of lead emissions and estimated that 50% of national emissions comes from GA aircraft due to the combustion of avgas with TEL. Initial monitoring for lead at airports indicates that the latest NAAQS may be exceeded at some airports. The FAA and industry continue to explore alternatives to avgas with TEL additive, but no alternative fuel formulation has yet been found that would meet the demands of the majority of the GA fleet for safe flight operation. In the meantime, there may be practices and procedures that can reduce the impact of lead emissions at airports. Engine malfunctions due to the wrong fuel octane number or improper mixture ratios are:

Pre-ignition (surface ignition)

This could happen if any flake of carbon or a *feather-edge* on a *valve* is heated to incandescence; it will ignite the fuel–air mixture before the correct time and the mixture will burn as the piston is moving outward. This long burning period could cause the mixture to reach its critical pressure and temperature and then results in detonation. Pre-ignition is usually due to the following:

- feather-edged valves

- excessive carbon formation in cylinder heads and combustion chamber
- spark plugs thickly coated with carbon.

Detonation

Part of the fuel–air charge goes through normal combustion but the rest of the charge detonates. This will result in overheating and may cause major engine damage. Detonation is usually caused by using low octane number fuels in high compression or supercharged engines.

Backfiring

Is defined as burning of the fuel–air mixture in the induction system. This condition can be caused by an excessively lean mixture.

Afterfiring (torching)

Flame in the exhaust system caused by raw fuel flowing through the intake valve to the cylinder and out to the exhaust stack. Could also be due to an excessively rich mixture.

Leaded fuels ingredients. A lead compound in form of “tetraethyl lead (TEL)” is added to the fuel. The lead could burn to “lead oxide”, which is solid with a high boiling point. To prevent this a gasoline-soluble “bromine compound” is added. The mixture forms “lead bromide”, which has a much lower boiling point than “lead oxide” and, therefore, a large portion of it will be expelled from the cylinders with exhaust gases.

Dye is added to the lead and gasoline-soluble bromine compound to indicate that gasoline contains lead. The mixture of lead, bromine compound, and dye is known as an “antiknock compound”.

Avgas grades, colors, and lead contents

- 80: Red, max lead content 0.5 ml of tetraethyl lead (TEL) per gallon
- 100 LL (low lead): Blue, max lead content 2.0 ml of tetraethyl lead (TEL) per gallon
- 100: Green, max lead content 3.0 ml of tetraethyl lead (TEL) per gallon.

Fuel–air mixtures. The mixture ratios are the fuel-to-air ratios in terms of weight

- rich best power mixture; $1:11.5 = 0.087$
- lean best power mixture; $1:13.5 = 0.074$
- best economy; $1:15 = 0.067$
- limits of flammability; 1:8 to 1:18.

Engine problems associated with lean mixtures

- overheating
- loss of power
- detonation.

Note: Excessively lean mixtures could cause backfiring and possible complete engine stoppage.

Problems associated with rich mixtures

- loss of power
- black smoke emerging from the exhaust.

Note: Excessively rich mixtures could cause engine afterfiring (torching). Also note that rich mixtures aid in engine cooling.

5.6.2 Carburetion and Fuel Injection Systems

The aircraft engine fuel–air metering systems consist of the following types:

- float type carburetors
- pressure injection carburetors
- fuel injection systems
- full authority digital engine control (FADEC).

5.6.2.1 *Float-Type Carburetors.* Float-type carburetors consist of the following systems:

- float mechanism and its chamber
- main metering system
- idling system and idle cut-off
- accelerating system
- mixture control system
- power enrichment system (economizer system).

Main Metering System The main metering system consists of the following components

- venturi tube
- main metering jet
- main discharge nozzle
- throttle valve
- main air bleed.

Accelerating System. Between the time the idle system loses its effectiveness and the time there is sufficient airflow for the main metering system to operate, there is a tendency for the engine to develop a “flat spot” or a period of lean mixture. The same condition occurs during rapid accelerations. The accelerating system is installed to overcome this condition.

The purpose of air bleed is to keep the fuel–air mixture essentially constant as the air flow through the carburetor changes. It also aids in fuel atomization.

The economizer system enriches the mixture during high power settings to help engine cooling.

Disadvantages of Float-Type Carburetors. The main disadvantages of float type carburetors are:

- carburetor icing
- the fuel metering force in float-type carburetors is only due to the pressure differential between air in the float chamber and that at the main discharge nozzle and, therefore, it is low
- flight attitude and disturbances can affect the float level and, therefore, fuel metering to the engine
- unsuitable for aerobatics and inverted flights.

5.6.2.2 Pressure Injection Carburetors. Pressure injection carburetor design is a radical departure from float-type carburetor methodology. The float and its mechanism have been eliminated and the fuel is sprayed from the main discharge nozzle under pump pressure. This drastically improves the performance of large aircraft engines. The aircraft attitude will have no effect on carburetor operation and full aerobatic capability, including inverted flight, would be feasible. The fuel discharge nozzle has been moved to downstream of the throttle valve and, therefore, throttle icing has been eliminated.

5.6.2.3 Fuel Injection Systems. In these systems, the single large main discharge nozzle that was located inside the carburetor has been replaced by multiple small discharge nozzles for each individual cylinder. There are two types of fuel injection systems:

- direct fuel injection system
- continuous-flow injection system.

In direct fuel injection systems, fuel is directly sprayed inside the combustion chamber of each individual cylinder. Because of the requirements of the fuel spray timing, as well as higher pump pressure requirements, this system is not used on today's aircraft production engines.

In the continuous-flow injection systems, fuel is sprayed upstream of the intake valve, therefore eliminating the two key main disadvantages of direct fuel injection systems. This type of system is exclusively used in today's aircraft production engines that are fuel injected.

Engines equipped with fuel injection systems do not require separate priming systems because the injection system pumps fuel directly into the intake ports of each cylinder.

5.6.2.4 Full Authority Digital Engine Control (FADEC). As the name implies, this unit is similar to the gas turbine engine fuel controls. It measures several parameters for each individual cylinder, including manifold absolute pressure (MAP), cylinder head temperature (CHT), and exhaust gas temperature (EGT), as well as engine RPM, and adjusts the amount of fuel required for each cylinder. A pilot's command through the throttle lever is only one input to the FADEC and that will be ignored if any of the other variables is at its maximum value. Some of the advantages of FADEC are:

- demonstrated fuel saved 12–20%
- approximately 5% more takeoff power
- smoothest ride with less noise and vibration (subjective)
- simplifies operations – single lever power control (fixed pitch propellers)
- very easy restarts in-flight and hot starts on the ground
- tested on max power dives with no excessive speed and no aircraft speed limits exceeded.

5.6.3 Ignition Systems

Four types of ignition system are:

- battery ignition systems
- high tension ignition systems

- low tension ignition systems
- full authority digital engine controls (FADEC)

5.6.3.1 Battery Ignition Systems. In the battery ignition system, the battery current passes through an ignition switch, the primary of an ignition coil (consists of a few turns), and contact-breaker points. The contact-breaker points convert the battery's DC current to pulsating DC (interrupted DC). This will cause a few thousands volts to be induced in the secondary of the ignition coil, which is then distributed by the distributor among the spark plugs of the respective cylinders in the correct firing order. This system is entirely dependent on the aircraft electrical system, which could be a safety issue.

5.6.3.2 High Tension Ignition System. In this system, the high voltage is generated by the magneto and the ignition system is entirely independent of the aircraft electrical system. The aircraft battery is only used during the starting operation and is disconnected from the ignition system as soon as the engine is started. FAA certified engines are required to have two independent ignition systems and each one supplies high voltage current to one of the two spark plugs of each cylinder. The engine can operate with one system but at a lower efficiency. Both ignition systems are required to be operational before takeoff, and there is a standard procedure to conduct that test by the pilot.

5.6.3.3 Low Tension Ignition System. This system is similar to high tension ignition system, except that the magnetos generate low voltage current. The high voltage is generated by individual coils located on the top of the cylinders. The ignition harness for this system does not require heavy insulation like the high tension system, except for a very short length between the individual coils and spark plugs. This system is ideal for the aircraft flying at high altitudes.

5.6.3.4 Full Authority Digital Engine Control (FADEC). In this system, the cross-fire ignition coils located inside the FADEC produce high voltage sparks for optimum starting and better performance. This eliminates magnetos and magneto-to-engine timing. Variable ignition timing is provided to individual cylinders for better performance.

5.6.3.5 Ignition Boosters. Ignition boosters are used to provide the high voltage to the spark plugs during starting when the magneto rpm is extremely low. Below 4 kV, the engine may not start consistently. Once the engine starts, the magnetos will kick in and the ignition boosters will be disconnected from the spark plugs.

There are four types of ignition boosters:

- impulse coupling
- booster coil = booster magneto
- ignition vibrator = starting vibrator
- solid-state magneto start booster.

From the above four boosters, the first three types are used on almost all of the existing FAA certified aircraft engines. The impulse-coupled magnetos generate about 4.8 kV and the starting vibrator systems 2.2 kV during starting. FADEC equipped engines do not require an ignition booster during starting.

Advantages of the Solid-State Magneto Start Booster

- delivers over 400% more spark energy to the spark plugs (about 10.2 kV).
- overcomes poor engine priming
- reduces electrical stress to the battery and starter
- requires no maintenance.

Engine Kickback. Rotation of the crankshaft in opposite direction of normal engine operation is called engine kickback. This is caused by advance ignition during starting. Ignition should be retarded automatically by the booster to prevent kickback. FADEC will time ignition during all engine operating conditions including starting.

5.6.3.6 Spark Plugs. There are two types of spark plugs:

- shielded
- unshielded.

Certified aircraft engines all have shielded spark plugs. Considering that the magnetos and ignition harness are also shielded, they reduce the electromagnetic interference of the whole ignition system.

The firing end of the aircraft engine spark plugs are either of the fine-wire or massive-wire electrode type. Fine-wire electrodes are usually made of platinum or iridium alloys and the massive-wire electrode types are usually made of nickel alloys.

Hot and Cold Spark Plugs. The firing end of hot spark plugs is at a higher operating temperature than of cold spark plugs due to the long length of the insulator tip at the firing end. The hot spark plugs should only be installed on the engines that run cold, and the cold spark plugs should only be installed on the engines that run hot.

5.6.4 Lubrication Systems

The Purposes of a Lubrication System

- reduce friction
- to cool the engine
- to clean the engine
- to help piston rings in sealing the combustion chamber.

Types of Aircraft Engine Lubrication System

- wet sump
- dry sump

In wet sump systems, the oil reservoir is the sump located at the bottom of the engine. Lubricating oil is sucked from the sump by the oil pump, cleaned by the oil filter, cooled by the oil cooler, and then circulated through the engine. The returned oil pours by

gravity to the engine sump and the process continues. All of the production piston engines today are equipped with this system.

In dry sump engines, the lubricating oil is stored in a large external tank and pumped to the engine by a pressure pump. The returned oil is collected in small sumps and returned back to the tank by a couple of scavenge pumps. An air-cooled oil cooler is located either in the pressure line or scavenge line.

Oil Coolers. Oil coolers are either air cooled or fuel cooled. Air-cooled oil coolers are similar to the coolant radiators of automobile engines and use ram air for cooling. Fuel-cooled oil coolers use fuel as the cooling agent. They are mostly used in gas turbine engines. Both have a thermostat (vernathern) to keep the oil temperature at a constant value.

Advantages of a Fuel-Cooled Oil Cooler Compared to an Air-Cooled Oil Cooler

- increased cycle thermal efficiency
- less drag penalty
- reduced fuel system icing
- improved combustion
- can have any shape and can be installed anywhere.

5.6.5 Supercharging

Supercharging and turbocharging allow maximum power from the engine at high altitudes and boost the engine power during takeoff. In a supercharged engine, a centrifugal compressor is located in the induction system and increases MAP. The compressor could be engine driven by a crankshaft through a gear train or powered by a turbine driven by the engine exhaust gases (turbocharger or turbo-supercharger). Almost all of today's production aircraft engines that are supercharged are equipped with turbochargers. These engines are usually flat-rated (constant brake horsepower) up to a certain altitude.

When the supercharger is located between the carburetor and the cylinder intake port, it is called an internal-type supercharger. If the supercharger is located before the carburetor in the induction system, it is called an external-type supercharger. As mentioned before, turbochargers (turbo-superchargers) are designed to be externally driven devices by a turbine wheel which receives its power from the engine exhaust gases. An example of a turbocharged aircraft engine is Teledyne Continental TSIOF-550 engine, which is also fuel injected and FADEC equipped.

5.7 Electric Engines

Advantages

- reduced noise
- environmentally friendly
- reduced maintenance
- not affected by altitude

- 90–95% efficient versus 20–25% for aircraft reciprocating engines
- for low subsonic flight, electric motors are much more efficient than internal combustion engines or jet engines and have better torque-to-weight ratios as well.
- higher safety and more reliability than a reciprocating engine providing the same propulsion with fewer moving parts.
- lighter weight models can be used without having the bulk of a reciprocating engine.
- providing comparable aircraft performance for far lower cost than a reciprocating engines especially if the cost of fuel over a long time period is taken into account.

Disadvantages

- batteries and motors have low power density
- batteries are heavy and discharge fast, resulting in short flight times.

5.7.1 Electric Motors

There are two major parts: a rotor and a stator. The magnets in the rotor chase the magnets in the stator, causing rotation. The effective location of the magnets in either the rotor or the stator must be moved to keep the chase going. Magnets switch polarity by reversing the current flow. During rotation (with the motor energized), the rotor magnets are attracted to and repelled from the stator magnets in such a way to cause rotation. The commutator has segments all the way around the rotor and the stator is connected to brushes that rub against these segments to conduct the electricity.

Advantages of AC Motors

- higher torque/horsepower capabilities
- no permanent magnet
- magnetic field strength adjustable
- cost advantage.

Advantages of DC Motors

- less rotor heat
- wide spectrum of optimal power setting
- no efficiency loss due to DC to AC conversion.

Disadvantages of AC Motors

- optimal power factor: 85%
- cumbersome to control.

Disadvantages of DC Motors

- permanent magnet is expensive.

Note: The most commonly used motor today is actually the DC motor due to the optimal power setting variability a DC motor allows along with the benefit of not having to convert DC current into AC current (which can be expensive).

Future of Electric Motor Propelled Aircraft

- We are just at the beginning of the production of the electric airplane
- The electric airplane industry is clearly in its infancy, but developments are happening fast. Its future depends on the cost and energy density of batteries
- The future looks bright for the environment and the development of clean-air solutions to flight
- Even now, with the current cost of avgas nearing \$5 per gallon, the aircraft will fly virtually for free after a couple hundred hours if you don't factor the life of the battery.

5.7.2 Solar cells

Solar cells convert sunlight into electrical energy. The maximum efficiency achieved so far is 43%.

Negative Attributes

- take up a lot of space
- not efficient, absorb 10–40%
- do not produce a lot of power.

Positive Attributes

- abundant source of energy
- clean source of power
- no noise
- no moving parts.

Airplane/UAV/Model aircraft applications

- first applications on model airplanes was in 1957
- good for small aircraft, not very useful for large aircraft
- good for aircraft that requires high endurance.

5.7.3 Advanced Batteries

Li-ion Battery Basics

- electrode components: lithium and carbon primarily

- operate as most batteries with electrochemical cells containing cathode, anode, and separator of finely perforated plastic through which ions are allowed to pass; this arrangement is then submerged in an electrolyte solution
- discharge: electrons travel from anode to cathode while chemical energy is converted to electric as ions flow within the cell
- charge: an external voltage is applied to force electric current in the opposite direction and return electrical energy to chemical.

Li-ion Battery Basics (discharge of cell)

- anode is comprised of a metallic solid reducing agent while the cathode is a solid oxidant
- anode provides electrons to exterior circuit and Li^+ ions internally
- conducting electrolyte transports Li^+ ions to cathode
- Cathode ions are balanced with electrons from exterior circuit.

Advantages

- good cycling characteristics
- relatively high energy density (average 150 W-hr)
- complete discharge unnecessary: no “memory”
- high holding characteristics (charge lost $\sim 5\%$ per month)

Disadvantages

- high temperature sensitivity
- poor lifespan independent of usage (~ 3 years)
- price (temperature monitoring system, etc.)
- potentially hazardous failure characteristics

Li-ion: Aviation Battery Applications. In addition to their application in small technologies, such as cell phones, laptops, small UAVs and so on, Li-ion batteries have been integrated in large commercial aircraft.

Battery applications on large commercial aircraft are:

- provide power for on-ground (engine off) maneuvering such as refueling and towing
- Auxiliary Power Unit battery powers the APU in emergency conditions
- main battery supplies power to systems prior to engine start
- main battery also serves for redundant power to critical areas during flight.

Future Aviation Battery Demand

- increasing popularity and applications for light weight vehicles and UAVs
- greater focus on environmentally friendly aircraft

- increasing battery reliability and cycling characteristics
- significantly lighter than previous alternatives and work well in conjunction with other “green” technologies such as solar energy
- large aircraft moving away from hydraulic systems and replacing with electric, leading to increased electrical capacity demand
- easy to replace and service when compared with electric engines and so on.

5.7.4 Fuel cells

Fuel cells are a source of electrical energy somewhat similar to a battery. Both use chemical reactions to generate electricity instead of using moving parts. However, batteries just store energy, fuel cells produce it continuously as long as a fuel and oxidant are supplied.

Charge exchange occurs between the anode and cathode by means of the electrolyte in between. This gives off heat and water, while converting the chemical energy directly into electricity. The heat given off can also be used to enhance combined-cycle applications by creating even more electricity.

Different Types of Fuel Cells

- Alkaline Fuel Cell (AFC)
- Molten Carbonate Fuel Cell (MCFC)
- Phosphoric Acid Fuel Cell (PAFC)
- Proton Exchange Membrane Fuel Cell (PEMFC)
- Solid Oxide Fuel Cell (SOFC)
- direct methanol fuel cell.

First Commercially Available Fuel Cell Product

- alkaline: potassium hydroxide electrolyte solution, used in space applications
- molten carbonate: high temperature (600–700°C), high fuel-to-electricity conversion
- phosphoric acid: 100% phosphoric acid electrolyte.

Benefits of Fuel Cells

- pollution: only byproducts are heat and water
- oil independence: fuels used can all be obtained domestically
- reliability: harder to break something with no moving parts
- production: operate close to constant efficiency regardless of size or load.

Problems with Fuel Cells

- fuel: hydrogen is not readily available everywhere
- storage: some vehicles can make it as far as a gas operated car but most are still a work in progress

- durability: fuel cell systems are currently less reliable than combustion engines
- cost: vehicles with fuel cells cost more than gas running hybrid vehicles.

Aerospace Applications

- alkaline fuel cells have been used for over four decades on manned spacecraft
- UAVs: longer sustained flight, reduced weight, good for military where supplies are not readily accessible
- Airbus and Boeing are studying the replacement of auxiliary power units with fuel cells. They would reduce aircraft weight and decrease emissions.

5.7.5 State of the Art for Electric Propulsion – Future Technology

- current developments focusing on raising power density of batteries and motors
- lithium–air batteries
- state of the art lithium ion: 100–200 Wh/kg versus kerosene: 1200 Wh/kg
- Future technology (2030) for lithium–air battery is 750–2000 Wh/kg
- Superconducting motors. theoretical power output of 8–25 kW/kg.

5.8 Propellers and Reduction Gears

Thrust is the aerodynamic force exerted by an aircraft to overcome drag and other forces acting to retard that aircraft's forward motion in the air and on the ground (for example, friction).

In a propeller driven airplane, it is produced by the propeller accelerating a large mass of air rearwards. The thrust exerted is proportional to the mass and velocity of the accelerated air.

Propeller Blade Airfoils

- RAF – 6 (WW1)
- Clark Y
- Standard NACA Sections
- NACA 16 series
- Supercritical airfoils
- New generation propeller airfoils (e.g., Dowty ARA-D).

Definitions and Terminology

- Geometric Pitch: The axial distance that the propeller will move forward for one revolution if it is moving (theoretically) through a solid object.
- Effective Pitch: The axial distance that the propeller will move forward for one revolution through the air. Small blade angle results in low pitch. Large blade angle results in high pitch. Because of this, the terms propeller blade angle and pitch are used interchangeably.
- Propeller slip: The difference between geometric pitch and effective pitch.

- Resultant Velocity: The vector sum of the rotational speed at any blade cross-section and the forward speed of the aircraft.
- Blade angle: The angle between the propeller blade chord and plane of rotation at any blade cross-section. It has its maximum value around the blade hub and decreases towards the tip of propeller blade.
- Helix Angle: The angle between the resultant velocity at any blade station and the plane of rotation. It varies along the blade span.
- Angle of attack: The angle between the resultant velocity and propeller blade chord at any blade cross-section. If the axial velocity is zero, the blade angle and angle of attack will be equal and propeller thrust is maximum. As airspeed increases, the angle of attack decreases, therefore the blade produces less thrust.
- Advance ratio: Is the ratio of the aircraft speed divided by propeller revolutions per second times the propeller diameter ($J = V_{\infty}/n.D$).
- Feathering: When a propeller is feathered, its blades are turned to an angle of approximately 90° to the plane of propeller rotation. It is typically used when the engine is stopped in the air to prevent windmilling and, therefore, reducing the drag, as well as further damage to the engine if the stoppage is due to the engine failure.
- Reversing: The propeller blade angles move to a negative value and, consequently, generate negative thrust. This is typically used to help decelerating the aircraft during landing.
- Propeller efficiency = THP/BHP
- Thrust Horsepower Available (THP): This is calculated by $BHP \times \text{Propeller efficiency}$. It can also be calculated as $THP = T \times V_{\infty}/325$, where T is propeller thrust in pounds and V_{∞} is the aircraft speed in knots. The denominator will be 375 if the aircraft speed is in mph and 550 if it is given in fps.

Climb Propeller versus Cruise Propeller

- Climb propeller: Has a relatively low blade angle (low pitch). This allows the propeller to turn at a higher RPM. This allows more air to be accelerated and, therefore, translates more power from the engine to the propeller. The propeller is not very efficient.
- Cruise propeller: Has a higher blade angle (high pitch) that allows a higher efficiency at cruise speed but turns at a lower rpm due to the increased induced drag on the propeller blades. Therefore, the propeller does not develop as much power during takeoff and climbout.

Forces Acting on Propeller Blades

- centrifugal force
- thrust bending force
- torque bending force
- aerodynamic twisting force
- centrifugal twisting force.

Types of Propeller

- Fixed pitch propellers: the blade angle of the propeller is fixed and cannot be changed. A fixed pitch propeller will be most efficient in only one airspeed range.
- Ground adjustable propellers: the propeller blade angle can be adjusted on the ground when the engine is stopped. In this case, the blades are usually held in the hub by clamps that can be loosened during the blade angle adjustments and tightened before starting the engine.
- Constant speed propellers: are equipped with propeller governors that keep the engine rpm constant by automatically changing the blade angle. The pilot selects the rpm through a propeller control lever located in the cockpit which is connected to the propeller governor. The force required for the blade angle change is usually provided by oil pressure, electric power, or mechanical devices (counterweights or springs).

Propeller Governor Components

- flyweights
- speeder spring
- pilot valve.

When the centrifugal force of the flyweights balances the force of speeder spring, the pilot valve will stay in the neutral position and the engine rpm will remain constant. This condition is called “onspeed”.

If the engine rpm exceeds the selected value, the centrifugal force of the flyweights would exceed the speeder spring. This condition is called “overspeed”.

If the engine rpm is below the selected value, the centrifugal force of the flyweights will be less than that of the speeder spring. This condition is called “underspeed”.

Propeller Miscellaneous Systems

- synchronizing: allows the engine rpm of multi-engined aircraft to be equal (within a certain range). One engine will be selected as the master engine and the other engines will follow the rpm of the master engine.
- synchrophasing: allows the pilot to adjust the phase angle between the propellers on the various engines to reduce the noise and vibration to a minimum
- anti-icing system: prevents the formation of ice on the leading edges of the propeller blades
- deicing system: allows a thin layer of ice to form and then break it away; it typically uses electrically powered deicer boots.

Propeller Reduction Gears. Noise and stress limitations require that the large diameter propellers rotate at a much lower rpm than the relatively smaller diameter propellers. Hence, a rather large reduction gear unit, having a speed ratio of from 10:1 to 15:1 could be required for turboprop engines. For piston powered aircraft the reduction ratio is usually from 1.5:1 to 2:1.

Types of Reduction Gears

- spur gear type
- planetary.

Advantages of Planetary Reduction Gear Systems

- propeller shaft is in line with the crankshaft
- minimum weight
- minimum space
- propeller can turn in the same direction as the crankshaft.

References

1. Rolls-Royce, *The Jet Engine, Technical Publications Department*, Rolls-Royce, Derby, U.K., 1986.
2. Pratt & Whitney, *The Aircraft Gas Turbine Engine and its Operation*, United Technologies Corporation, Pratt & Whitney, 1988.
3. Roskam, J., *Airplane Design*, Roskam Aviation and Engineering Corp., Lawrence, KS, 1987.
4. Raymer, D.P., *Aircraft Design: A Conceptual Approach*, AIAA Education Series, Washington, DC, 1989.
5. Nikolai, L.M., *Fundamentals of Aircraft Design*, METS, Inc., San Jose, CA, 1975.
6. Taylor, C.F., *The Internal Combustion Engine in Theory and Practice*, The MIT Press, Cambridge, MA, 1985.
7. Heywood, J.B., *Internal Combustion Engine Fundamentals*, McGraw-Hill Publishing Company, 1988.
8. Hill, P. and Peterson, C., *Mechanics and Thermodynamics of Propulsion*, Addison Wesley Publishing Co., 1992.
9. Rogowski, A.R., *Elements of Internal Combustion Engines*, McGraw-Hill Publishing Company, 1953.
10. Pulkrabek, W., *Engineering Fundamentals of the Internal Combustion Engine*, Pearson Prentice Hall, 2004.
11. Archer, R. and Saarlal, M., *An Introduction to Aerospace Propulsion*, Prentice Hall, 1996.
12. Oats, G., *Aero-thermodynamics of Gas Turbine and Rocket Propulsion*, AIAA Education Series, Washington, DC, 1984.
13. Mattingly, J., *Elements of Gas Turbine Propulsion*, McGraw-Hill, Inc., 1996.
14. Mattingly, J., Heiser, W., and Pratt, D., *Aircraft Engine Design*, 2nd edition, AIAA Education Series, Washington, DC, 2002.
15. Huang, F.F., *Engineering Thermodynamics: Fundamentals and Applications*, Macmillan Publishing Company, 1988.
16. Roskam, J. and Lan, C.T., *Airplane Aerodynamics and Performance*, DAR Corporation, Lawrence, KA, 1997.
17. McKinley, J. and Bent, R., *Powerplants for Aerospace Vehicles*, 3rd edition, McGraw-Hill Book Company, 1965.
18. Casamassa, J., and Bent, R., *Jet Aircraft Power Systems*, McGraw-Hill Book Company, 1965.
19. Treager, I., *Aircraft Gas Turbine Engine Technology*, Glencoe Aviation technology Series, McGraw-Hill, 1995.
20. U.S. Department of Transportation Federal Aviation Administration, *Airframe and Powerplant Mechanics, Powerplant Handbook*, 1976.
21. Crane, D., Otis, C., and Delp, F. *Powerplant Section Textbook*, IAP, Inc., 1983.
22. Kroes, M.J., Wild, T.W., Bent, R.D., and Mckinley, J.L. *Aircraft Powerplants*, 6th Edition, Macmillan/McGraw-Hill, 1990.
23. Smith, H., *A History of Aircraft Piston Engines*, Sunflower University Press, Manhattan, KA, 1981.
24. Sweeten, B., Royer, D., and Keshmiri, S., *The Meridian UAV Flight Performance Analysis Using Analytical and Experimental Data*, AIAA Infotech@Aerospace Conference and Exhibit, 6–9 April, Seattle, WA, 2009.
25. Royer, D., Keshmiri, S., and Sweeten, B., *Modeling and Sensitivity Analysis of the Meridian Unmanned Aircraft*, AIAA Infotech@Aerospace Conference and Exhibit, 20–22 April, Atlanta, GA, 2010.
26. Garcia, G. and Keshmiri, S., *Online Artificial Neural Network Model Based Nonlinear Model Predictive Controller for the Meridian UAS*, Accepted for Publication, *International Journal of Robust and Nonlinear Control*, Vol. 23, June 2013, pp. 1657–1681.

27. Rozenkranc, M. and Ernst, J., Tactical UAV Engines Integration in IAI, 2nd AIAA “Unmanned Unlimited” Conference and Workshop & Exhibit, 15–18 September, San Diego, CA, 2003.
28. Lycoming Aircraft Engines homepage; <http://www.lycoming.com/> (last accessed 26 November 2013).
29. Continental Aircraft Engines homepage; <http://www.continentalmotors.aero/> (last accessed 26 November 2013).
30. Zoche Aero-Diesels homepage; <http://www.zoche.de/> (last accessed 26 November 2013).
31. DeltaHawk Diesel Engines homepage; <http://www.deltahawkengines.com/> (last accessed 26 November 2013).
32. Eclipse Aviation homepage; <http://www.eclipseaviation.com> (last accessed 26 November 2013).
33. Dynacam homepage; www.dynacam.com (last accessed 26 November 2013).
34. Rotax Aircraft Engines homepage; <http://www.flyrotax.com/home.aspx> (last accessed 26 November 2013).
35. LOM PRAHA Aircraft Engine homepage; <http://www.lompraha.cz/en/> (last accessed 26 November 2013).
36. FAA homepage; http://www.faa.gov/regulations_policies/faa_regulations/ (last accessed 26 November 2013).
37. European Aviation Safety Agency homepage; <http://www.easa.europa.eu/home.php> (last accessed 26 November 2013).
38. Continental Motors Training Manual; <http://www.tcmlink.com/aviationtraining.cfm> (last accessed 26 November 2013).
39. NASA TM 4331, Research and Technology, Langley Research Center, Hampton, VA, 1991.
40. NASA SP-292, “Vehicle Technology for Civil Aviation,” Proceedings of a conference held at NASA Langley Research Center, Hampton, VA, 2–4 November 1971.
41. NASA CP-10063, “Aeropropulsion 91,” Proceedings of a conference held at NASA Lewis Research Center, Cleveland, OH, 20–21 March 1991.
42. NASA CP-3049, “Aeropropulsion 87,” Proceedings of a conference held at NASA Lewis Research Center, Cleveland, OH, 17–19 November 1987.
43. 100LL Demise Expected Over the Next Decade, *Aviation Week & Space Technology*, 23 July 2001, 51–53.
44. Brouwers, A.P., Lightweight Diesel Engines for Commuter Type Aircraft, NASA CR-165470, Lewis Research Center, Cleveland, OH, 1981.
45. Gundlach, J., *Designing Unmanned Aircraft Systems: A Comprehensive Approach*, 1st edition, AIAA Education Series, Washington, DC, 1975.
46. Marshall, B., How Lithium-ion Batteries Work, *How Stuff Works* [online]; <http://electronics.howstuffworks.com/everyday-tech/lithium-ion-battery.htm> (accessed 8 September 2013).
47. Wakihara, M. and Yamamoto, O., *Lithium Ion Batteries: Fundamentals and Performance*, 1st edition, Kodansha, Tokyo, 1998.
48. Shwartz, M., Scientists Observe Lithium-Sulfur Batteries in Action, *Stanford: Precourt Institute for Energy* [online]; <https://energy.stanford.edu/news/scientists-observe-lithium-sulfur-batteries-action> (accessed 8 September 2013).
49. Lin, Z., Liu, Z., Fu, W., *et al.* (2013), Lithium polysulfidophosphates: a family of lithium-conducting sulfur-rich compounds for lithium–sulfur batteries, *Angewandte Chemie International Edition*, **52**: 7460–7463. doi: 10.1002/anie.201300680.
50. After 14 nights in the air, QinetiQ prepares to land its Zephyr solar powered unmanned aircraft, *QinetiQ* [online news article]; <http://www.qinetiq.com/news/PressReleases/Pages/zephyr-14-days.aspx> (accessed 8 September 2013).
51. The Tactical Advantages: Unmanned Aerial Vehicles, *Scion Power* [online]; <http://www.sionpower.com/unmanned.html> (accessed 1 September 2013).
52. Batteries and Advanced Airplanes: 787 Electrical System, *The Boeing Company* [online]; 2013 <http://787updates.newairplane.com/787-Electrical-Systems/Batteries-and-Advanced-Airplanes> (accessed 1 September 2013).
53. New all-solid Li-S battery from ORNL shows approximately 4x energy density of current Li-ion batteries, *Green Car Congress* [online article]; <http://www.greencarcongress.com/2013/06/new-ornl-li-sulfur-battery.html> (accessed 1 September 2013).
54. Ullman, D., The Electric-Powered Aircraft, EAA Experimenter; http://www.eaa.org/experimenter/articles/2010-05_electric.asp (last accessed 26 November 2013).
55. Electric Propulsion Systems for Manned Aircraft (19 October 2010), Propulsiontech’s Blog; <http://propulsiontech.wordpress.com/2010/10/19/electric-propulsion-systems-for-manned-aircraft/> (last accessed 26 November 2013).
56. Fehrenbacher, J., Stanley, D.L., Johnson, M.E., and Honchell, J., Electric Motor & Power Source Selection for Small Aircraft Propulsion (14 April 2011), Purdue University; <http://docs.lib.purdue.edu/techdirproj/33/> (last accessed 26 November 2013).
57. Cessna Aircraft Company, Skyhawk; <http://www.cessna.com/single-engine/skyhawk> (last accessed 26 November 2013).
58. GreenWing International, e430 Specifications; http://greenwing.aero/?page_id=2345 (last accessed 26 November 2013).

59. Electric Aircraft Corporation, ElectraFlyer-C; <http://www.electraflyer.com/electraflyerc.php> (last accessed 26 November 2013).

60. Lange Aviation GmbH, Antares 20E; http://www.lange-aviation.com/htm/english/products/antares_20e/antares_20E.html (last accessed 26 November 2013).

61. Airbus, Fuel Cells; <http://www.airbus.com/innovation/future-by-airbus/fuel-sources-of-tomorrow/fuel-cells/> (last accessed 26 November 2013).

62. NASA, Fuel Cells: A Better Energy Source for Earth and Space, NASA Glenn Research Center; http://www.nasa.gov/centers/glenn/technology/fuel_cells.html (last accessed 26 November 2013).

63. U.S. Department of Energy, Fuel Cell Vehicles; <http://www.fueleconomy.gov/feg/fuelcell.shtml> (last accessed 26 November 2013).

64. National Fuel Cell Research Center, University of California, Irvine homepage; <http://www.nfccr.uci.edu/2/Default.aspx> (last accessed 26 November 2013).

65. Ultra Electronics, Fuel Cells Create New Potential for UAVs, Other Critical Military Technologies (10 June 2013); <http://www.ultra-ami.com/2013/06/fuel-cells-create-new-potential-for-uavs-other-critical-military-technologies/> (last accessed 26 November 2013).

66. LaMonica, M. (14 April 2011), Solar Junction claims cell efficiency record; http://news.cnet.com/8301-11128_3-20053851-54.html (last accessed 26 November 2013).

67. Dimova-Malinovska, D., The state-of-the-art and future development of the photovoltaic technologies – the route from crystalline to nanostructured and new emerging materials, Central Laboratory of Solar Energy and New Energy Sources, Bulgarian Academy of Sciences, Sofia, Bulgaria, 2010.

68. Solar Cells | PV Companies List | ENF Company Directory, <http://www.enfsolar.com/directory/panel> (last accessed 9 December 2013).

69. Boucher, R.J., History of Solar Flight, AIAA/SAE/ASME 20th Joint Propulsion Conference, 11-13 June, Cincinnati, Ohio, 1984.

70. Cowley, M., Solar Challenger; http://library.propdesigner.co.uk/solar_challenger.pdf (last accessed 26 November 2013).

71. icaré 2 homepage; <http://icare2records.com/> (last accessed 26 November 2013).

Problems

5.1 The following information is available for an aircraft four-stroke reciprocating engine:

indicated mean effective pressure (IMEP) = 160 psi
 stroke = 5 in
 bore = 5 in
 engine rpm = 3000
 number of cylinders = 9
 cylinder clearance volume = 15 in³
 engine mechanical efficiency, η_{mech} = 90%
 propeller efficiency, η_{prop} = 80%

Calculate

- (a) brake horsepower (BHP)
- (b) indicated horsepower (IHP)
- (c) thrust horsepower (THP)
- (d) friction horsepower (FHP)
- (e) brake mean effective pressure (BMEP)
- (f) Compression Ratio (is your answer reasonable for a spark ignition engine?)

5.2 A four-stroke cycle reciprocating engine generates 300 ft-lb of torque at 3000 RPM. Calculate the BHP of the engine.

5.3 An aircraft four-stroke cycle reciprocating engine produces 140 brake horsepower and burns 10 gallons of aviation gasoline per hour. Calculate

- (a) the engine bsfc. Is your answer reasonable for aircraft spark-ignition engines?
- (b) the brake thermal efficiency, η_{th} , of the engine. Is your answer reasonable for aircraft spark-ignition engines?

Note: Assume the heat value of the fuel to be 20,000 Btu/lb and nominal weight of avgas = 6 lb/gal.

5.4 A nine-cylinder radial aircraft engine has a bore of 5.5 inches and a stroke of 5.5 inches and runs at 3500 rpm. Assuming that the brake horsepower of the engine is measured at 600 hp, calculate

- (a) the brake mean effective pressure (BMEP)
- (b) the indicated mean effective pressure (IMEP) (hint: assume an appropriate value for η_{mech}).

5.5 Using the following information, determine how many degrees the crankshaft will rotate with both the intake and exhaust valves closed for a four stroke cycle engine: intake valve opens 15° before top dead center.; exhaust valve opens 70° before bottom dead center; intake closes 45° after bottom dead center; exhaust closes 10° after top dead center. (answer 245°)

5.6 Ignition occurs at 28° before top dead center on a four-stroke cycle engine and the intake valve opens at 15° before top dead center. Determine how many degrees of crankshaft travel after ignition does the intake valve open. Consider one cylinder only. (answer 373°)

5.7 Estimate the weight of the following three engine types using the derived scaling formulas and compare the results with the manufacturer's data

- (a) Lycoming O-320, 4-cylinder opposed engine.
- (b) LOM M137A, 6-cylinder inline engine.

(c) P&W R-1830, 14-cylinder radial engine.

5.8 Using the diesel engine scaling laws, calculate and compare as much information as possible for a production aircraft diesel engine and compare the results with the manufacturer's data sheet.

CHAPTER 6

Aircraft Engine Inlets and Nozzles



Source: Reproduced with permission from Rolls-Royce plc

6.1 Introduction

In this chapter, we study the aerothermodynamics of aircraft engine inlets and nozzles. These two components in an aircraft engine represent “duct” flows with internal losses and hence we propose to study them in a single chapter. Despite these similarities, the inlet flowfield bears no resemblance to the exhaust flowfield. The presence of adverse pressure gradient in an inlet diffuser leads to a stalling boundary layer behavior, whereas the favorable pressure gradient in a nozzle promotes attached boundary layer flows. Another dissimilarity between these two components is in the cooling requirements of an advanced exhaust system as compared with the inlets, which remain uncooled until well into the hypersonic flight Mach numbers.

The system requirements of an aircraft intake primarily depend on the aircraft *mission specification*. In general, an aircraft intake system has to be designed to many of the following qualities, namely

1. light weight and low cost to manufacture
2. provide the engine with adequate mass flow rate at a proper Mach number at the engine face throughout the flight envelope
3. provide *spatially smooth* flow into the engine compressor, that is, low *steady-state distortion* throughout the flight envelope
4. provide *temporally smooth* flow into the engine compressor, that is, low *dynamic distortion* throughout the flight envelope

5. integrate well with the engine nacelle and/or fuselage, that is, *low installation drag*
6. provide acoustic absorption of fan/engine noise, that is, *quiet engine*
7. provide a particle separator for an engine in a vertical lift aircraft, that is, foreign object damage (FOD) *control*
8. provide low radar signature, that is, *low observables* for stealth requirement
9. provide favorable “*ilities*,” for example, accessibility, inspectability, reliability, maintainability, repairability
10. allow for engine *thrust growth*.

By a close inspection of the above “wish” list, we note several conflicting drivers that appear in the air inlet system design. Therefore, a team of engineers is tasked with seeking an “optimum compromise” for the design. The presence of conflicting requirements and seeking an optimal solution are invariably present in any commercial product development.

Our one-dimensional cycle analysis treated an aircraft engine component as a “black box,” that is, the block approach. The “block” approach linked the exit condition of a component to its inlet condition via an efficiency parameter. For example, an exit total pressure of an inlet was linked to the inlet total pressure via the inlet adiabatic efficiency parameter η_d or the total pressure recovery parameter π_d . In turn, we treated the component efficiencies as an input to our cycle analysis. Now, we propose to look inside the black box and identify design features that affect the component efficiencies. Inevitably, we will need to examine the true multidimensional aspect of the flowfield in aircraft engine components.

6.2 The Flight Mach Number and Its Impact on Inlet Duct Geometry

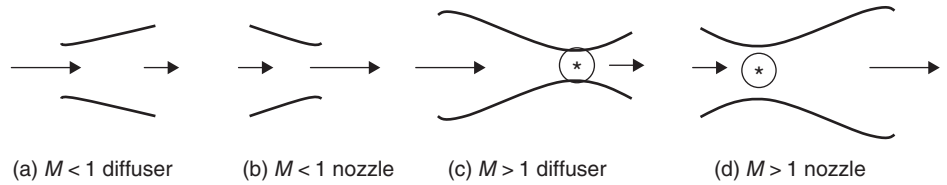
It is customary to divide the inlet flowfield into subsonic and supersonic flow regimes. The flow in the subsonic portion of an inlet is dominated by its boundary layer behavior, whereas the supersonic portion of an inlet is dominated by the appearance of shocks and their interaction with the boundary layer on the compression ramps and the nacelle or fuselage. Hence, the emphasis is different in the two flows. In this section, we will examine the geometrical requirements for subsonic and supersonic diffusers.

From one-dimensional compressible flow studies in aerodynamics (Anderson, 2005) we learned that

$$\frac{dA}{A} = (M_\infty^2 - 1) \frac{dV}{V} \quad (6.1)$$

Hence for a subsonic duct flow, where $M_\infty < 1$, the flow deceleration, that is, $dV < 0$, requires an area increase, that is, $dA > 0$, in the duct. Therefore, a cross-sectional area increase in a duct causes a subsonic flow to decelerate. On the contrary, a supersonic deceleration requires a flow area shrinkage with a turning point occurring at $M = 1$, that is, the sonic point. This suggests a converging flow in the supersonic regime to achieve a sonic condition followed by a diverging duct to decelerate the flow to the desired subsonic speeds for a supersonic diffuser. An opposite behavior is observed in accelerating flows, such as those in nozzles. A subsonic flow is accelerated through a converging duct, that

■ **FIGURE 6.1**
Geometric requirements for inlets and nozzles (* represents the sonic throat)



is, $dA < 0$, and a supersonic acceleration is achieved in a diverging duct, that is, $dA > 0$. Again, a supersonic nozzle needs to have a sonic “throat” before the diverging area begins for a supersonic acceleration. A schematic drawing of various duct geometries and flow regimes is shown in Figure 6.1.

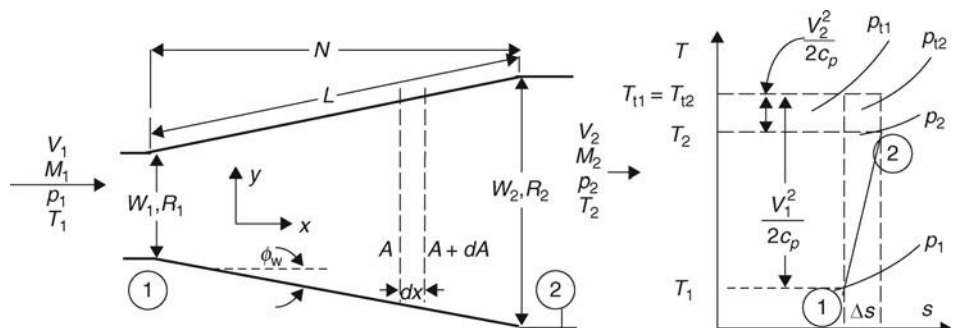
6.3 Diffusers

Now, let us introduce some preliminary nomenclature in a subsonic diffuser. A more detailed geometry of a subsonic diffusing flow is shown in Figure 6.2, where x is the primary flow direction and y is the lateral or transverse flow direction. The symbols W and R stand for the width (in the diverging direction) of a rectangular and the radius of a conical diffuser, respectively. The axial diffuser length is called N and the diffuser wall length is depicted as L , in Figure 6.2. We also note that the diffuser wall inclination or divergence angle is shown as ϕ_w .

The thermodynamic states of a diffuser flow are shown in Figure 6.2 as well. Note the static pressure rise ($p_2 > p_1$), which is accompanied by a static temperature rise in the diffuser ($T_2 > T_1$). Also, we note a large inlet kinetic energy is shown in Figure 6.2, ($V_1^2/2c_p$), which diminishes to a small kinetic energy at the exit ($V_2^2/2c_p$). The flow stagnation enthalpy remains constant in an adiabatic diffuser, which is shown in Figure 6.2 as a constant total temperature process. Finally, we note that the total pressure at the exit of diffuser is lower than the inlet, which is the basis of an entropy rise Δs .

Now, we are ready to introduce a new performance parameter in a diffuser. This new parameter accounts for the *static* pressure rise in a diffuser, which essentially characterizes the conversion of fluid kinetic energy into the fluid static pressure. Note that in a compressible flow, the kinetic energy converts into static pressure rise as well as the internal energy of the fluid, unlike an incompressible fluid where kinetic energy is

■ **FIGURE 6.2**
Definition sketch for a subsonic diffuser and a $T - s$ diagram depicting the static and stagnation states in a diffuser



converted to static pressure only. The nondimensional pressure rise parameter in a diffuser is called the static pressure recovery coefficient C_{PR} and is defined as

$$C_{PR} \equiv \frac{p_2 - p_1}{\bar{q}_1} = \frac{\Delta p}{\rho_1 \bar{V}_1^2 / 2} \quad (6.2)$$

The “bar” over q_1 in the denominator represents the mass-averaged velocity to be used in the dynamic pressure calculation. This reminds us that all internal flows contain boundary layers, which make the flow nonuniform (at least within the boundary layer). We will study this new parameter and other figures-of-merit in various diffuser environments. First, let us look at an *ideal* diffuser, where the fluid is both incompressible and inviscid.

6.4 An Ideal Diffuser

Applying the Bernoulli equation between stations 1 and 2 of a diffuser for an inviscid fluid, and using the continuity equation for a one-dimensional flow, we can relate the (ideal) diffuser performance $C_{PR,ideal}$ to the diffuser area ratio A_2/A_1 as follows:

$$C_{PR,ideal} = \frac{q_1 - q_2}{q_1} = 1 - \left(\frac{A_1}{A_2} \right)^2 = 1 - \frac{1}{AR^2} \quad (6.3)$$

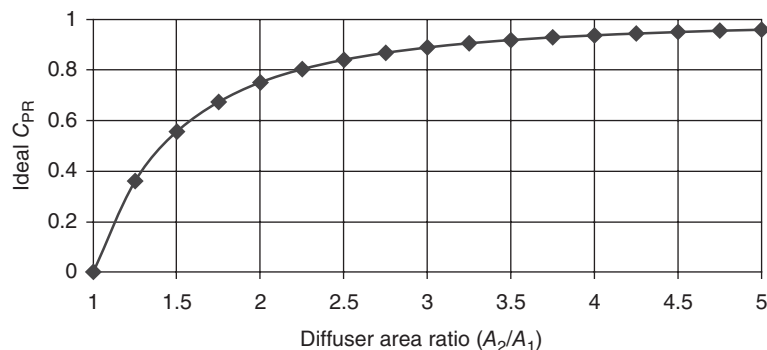
where the AR depicts the diffuser exit-to-inlet area ratio. This statement shows that for a very large area ratio diffuser, the ideal static pressure recovery will approach 1. We expected this result, which states that the inlet dynamic pressure is entirely converted into static pressure rise in a duct if the exit area is infinitely large. Let us plot the ideal static pressure recovery coefficient C_{PR} versus the diffuser area ratio (Figure 6.3).

We note from the ideal diffuser pressure recovery Equation 6.3 that the shape of the cross section of the diffuser does not enter the problem, that is,

$$C_{PR,ideal} \neq f(\text{geometry})_{\text{crosssection}} \quad (6.4)$$

This is a consequence of our oversimplified picture of a diffusing flow in a single direction, which ignores viscosity of the fluid and thus boundary layer formation. Consequently, a

■ **FIGURE 6.3**
An ideal diffuser pressure recovery as a function of diffuser area ratio



major driver in diffuser performance, namely the cross-sectional shape and the shape of the diffuser centerline influencing the wall boundary layer flow, is ignored in the *ideal* flow analysis. We also note that a high static pressure recovery requires a large diffuser area ratio. We will return to this parameter, that is, the area ratio, later in this chapter.

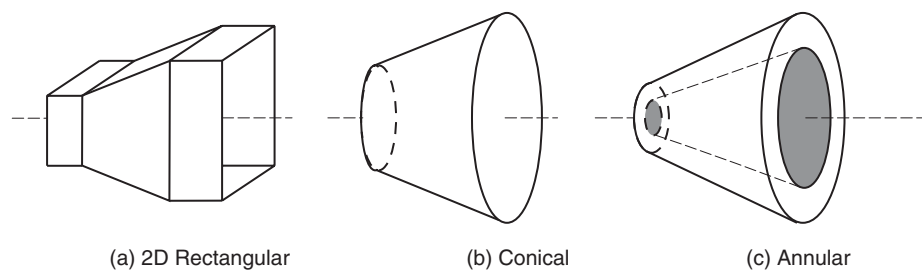
6.5 Real Diffusers and Their Stall Characteristics

We recognize that in a real flow environment, boundary layers are formed, and have a tendency to separate when exposed to a rising static pressure, known as an adverse (streamwise) pressure gradient. Therefore, we expect the behavior of a diffuser to be driven by the viscous region near its walls, that is, the state of the boundary layer as in attached, separated, or transitory (unsteady). Consequently, the performance of a real diffuser should strongly depend on its inlet boundary layer condition. In addition, the geometry of the cross-section as well as the centerline curvature of a diffuser both influence the cross-flow tendency in the boundary layer and hence affect the three-dimensional separation characteristics of the diffuser. The formation of a skewed boundary layer is in direct response to a transverse (or lateral) pressure gradient in a diffuser duct. Therefore, we expect the geometry of the diffuser in both the streamwise area variation and the cross-sectional shape (and its streamwise variation), to be of great importance in the performance of a diffuser. The three basic geometries of interest are (Figure 6.4)

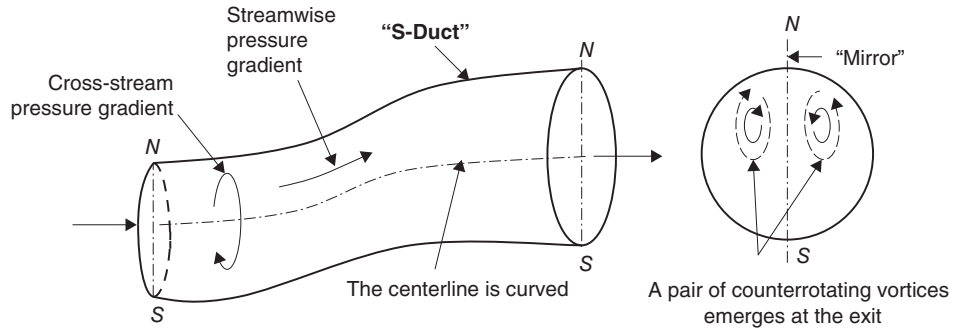
- (a) two-dimensional rectangular
- (b) axisymmetric, that is, conical
- (c) annular.

Another feature of a real diffuser is the geometrical shape of its centerline. Often the engine face is hidden from an observer looking through the inlet. The feature of a hidden engine face offers the potential of masking the radar reflections off the engine face, which is advantageous in a stealth aircraft. In addition, fighter aircraft are often designed with their engine(s) inside the fuselage to leave the wings free to carry external weapons. The so-called “buried” engine design of such aircraft requires an S-shaped subsonic diffuser duct to channel air to the engine face. From the fluid dynamics point of view, a curved duct induces a secondary flow pattern, which essentially sets up “pockets” of swirling flow at the duct exit. Often these pockets of swirling flow occur in pairs and are counterrotating. Also, since our diffuser exit is directly tied into the fan entrance duct, the pockets of swirling flow tend to locally increase or decrease (depending on their direction

■ **FIGURE 6.4**
Schematic drawing of
(subsonic) diffuser
geometries with
straight centerline



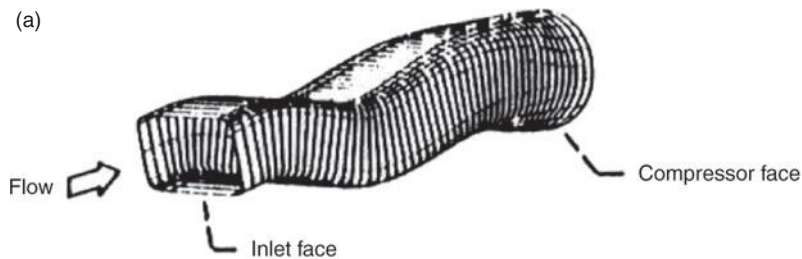
■ **FIGURE 6.5**
Schematic drawing of an S-duct with two pockets of swirling flows (known as the secondary flow pattern) generated by the bends



of rotation) the relative flow angle into the fan, which in turn can lead to cyclic loading of the fan and cause a high-cycle fatigue (HCF) problem. In severe situations, the pockets of swirling flow can produce rotating stall instability of the fan rotor. We will discuss in more detail the compressor/fan inlet flow conditions, that is, the various types of inlet distortion that affect the stability of a compressor flow in the turbomachinery chapter. In Figure 6.5, we show a schematic of a diffuser duct with an S-shaped (curved) centerline.

An aircraft inlet shape may be rectangular for integration and control purposes but it still has to tie in with an engine face, which is circular. Hence, the connecting diffuser duct should continually change its shape from, say, a rectangular to a circular geometry. Such ducts that change their cross-sectional shape are called "transition" ducts and pose interesting fluid mechanic problems due to their highly three-dimensional pressure pattern,

■ **FIGURE 6.6**
Curved-centerline (double-S) transition duct in a B1-B aircraft. Source: (a) Anderson, B.H. 1986. Reproduced with permission from AIAA. (b) Courtesy of USAF



B1-B aircraft

■ **FIGURE 6.7**
 Isometric views of various transition ducts with and without centerline curvature. *Note:* that the duct area ratio is shown as A_e/A_i and the duct aspect ratio at the exit is shown as AR . Source: Farokhi, Sheu, and Wu 1989. Reproduced with permission from Springer

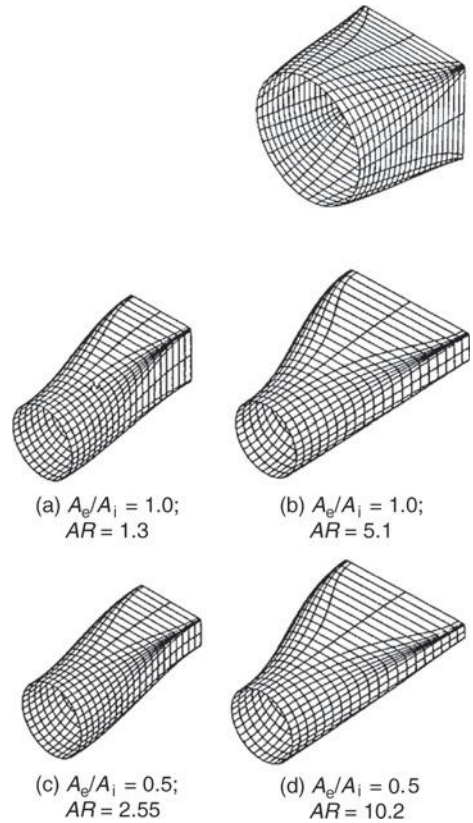
A transition duct with a straight centerline, which is suitable for an exhaust duct in an aircraft engine, is shown on the right. The ratio of length-to-diameter for this duct is 1 and represents the “shortest” transition duct without significant flow separation.

Two transition ducts with exit-to-inlet area ratio of 1, and two different exit aspect ratios are shown on the right.

The aspect ratio at the exit plane of a rectangular nozzle is defined as the ratio of the width to height of the duct.

Converging transition ducts with area ratio of 1/2 and two different nozzle exit aspect ratio rectangular nozzles are shown on the right.

All four ducts (a–d) have a curved centerline corresponding to the exit plane being one inlet radius up from the inlet plane.

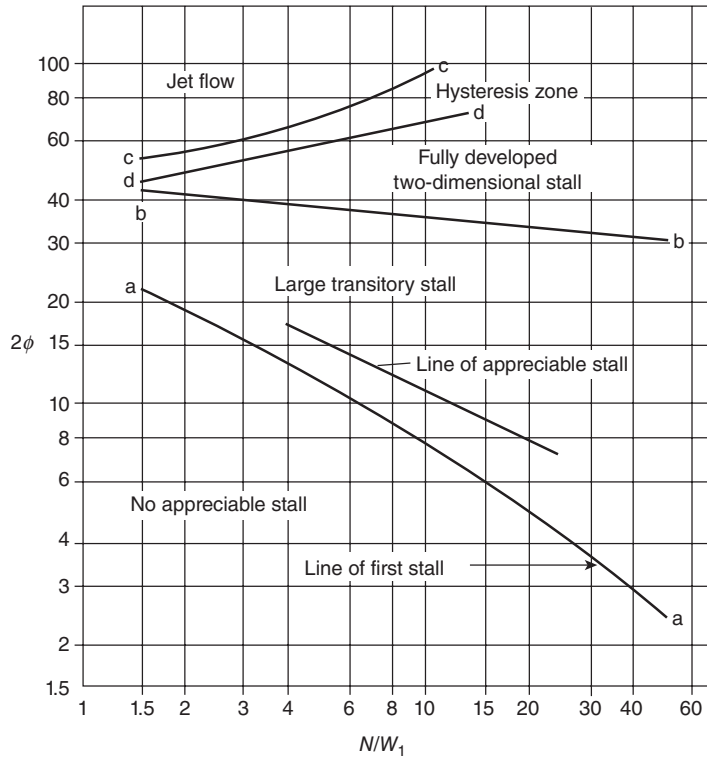


that is, the flowfield. It is interesting to note that the corners in the rectangular portion of a transition duct create, trap, and transport vortices in a complex streamwise and transverse trajectory pattern along the duct's length. Due to their prominence in modern engines, we will examine the viscous flow characteristics in transition ducts more closely in this chapter. The use of transition ducts in an aircraft engine is not limited, however, to the air inlet system. Rather, it includes circular-to-rectangular exhaust systems as well. Rectangular nozzles are useful for stealth, vector thrust, and integration purposes and will be discussed more at the end of this chapter. Figure 6.6 shows the B1-B aircraft inlet transition duct. An isometric view of rectangular nozzle transition ducts with and without curved centerline is also shown in Figure 6.7.

6.6 Subsonic Diffuser Performance

Subsonic diffusers exhibit four different flow regimes, or *stall* characteristics, as presented by Kline (1959) and Kline, Abbot, and Fox (1959). The flow regimes are tied to the quality of exit flow, that is, the state of the boundary layer at the diffuser exit. Although not all different flow regimes are of interest to an aircraft inlet designer, to present the chart and examine various features of the flowfields proves beneficial to all engineers interested in internal fluid mechanics.

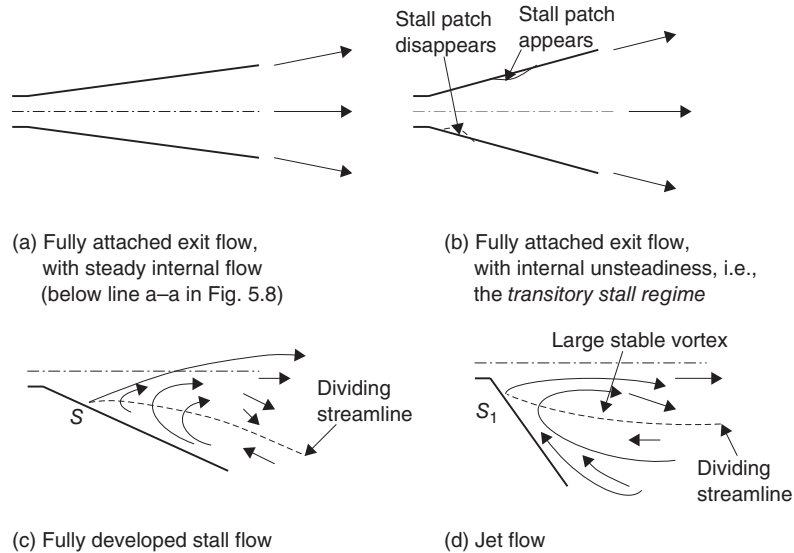
■ **FIGURE 6.8**
 Flow regimes in a
 two-dimensional
 rectangular diffuser.
 Source: Kline, Abbot
 and Fox 1959. Fig. 4. p.
 326. Reproduced with
 permission from
 ASME



Nondimensional axial length of the diffuser and the total divergence angle of the diffuser are chosen as the axes of the chart in Figure 6.8. Let us examine this chart more closely. On the lower half of the chart where the line a–a is drawn, we note a *stable flow regime*, which is identified by the “line of first stall.” Above line a–a, but below line b–b, we note that the stall phenomenon is recognized and characterized as “transitory.” This behavior embodies the *unsteadiness* associated with the first appearance of stall, that is, the transitory stall characteristics of diffuser flows. This means that a stall patch may appear and then disappear at various positions along the diffuser wall. Beyond the transitory behavior lies the fully developed stall, which is shown above line b–b and below line c–c. In this regime, a stable but separated flow is established in a diffuser. Typically, the stable separation first appears on one wall. Upon increasing the divergence angle of the diffuser, we arrive at what is known as the jet flow. In this regime, the flow emerges like a jet, with little regard for the walls of the diffuser. Two stable and large eddies appear on the walls with a central jet flow emerging in the center. Now, upon reducing the wall divergence angle, the flow exhibits a hysteresis behavior in that the stable separated flow from one wall may now appear on the other wall. This behavior is marked as hysteresis on the chart in Figure 6.8. We can try to depict these flow regimes in Figure 6.9.

Now, let us look at the hysteresis behavior in a diffuser with a fully developed stall again. In Figure 6.9(c), the lower wall is shown to support the stalled boundary layer flow. So the question is why the lower wall? Now, going back from (d) toward (c) in a reverse experiment that reduces the overall divergence angle of the diffuser, the upper wall may now separate and the flow on the lower wall remain attached. Why is it that we cannot a priori predict the wall that stalls? What else is at play that we are overlooking

■ **FIGURE 6.9**
Flow pattern in four
diffusers with an
increasing wall
divergence angle

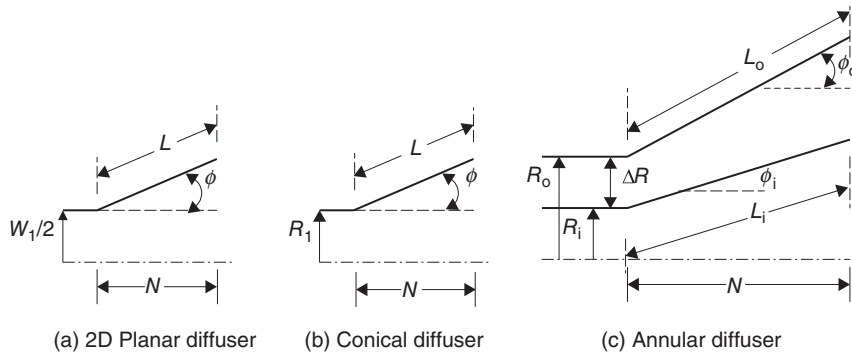


in our reverse experiment? The answer lies in the fine details of the flow (remember the saying “the devil is in the detail”?), namely the instability waves, that is, the disturbances that existed in both flows and those disturbances that are generated by the diffuser wall actuation mechanism in closing/opening of the walls in our reverse experiment. Hence, our actions or external influences disturbed/created the waves that changed the overall behavior. This leads us to a new level of understanding of the fluid behavior, namely, that a global large-scale behavior in a fluid flow must have its roots in the behavior of tiny waves, which may have found the environment in the flow ripe for interactions and growth, analogous to the environment of a mass-spring driven at its resonant frequency.

The highest static pressure recovery is achieved in a diffuser that is on the *verge* of separation, that is, when it operates in a transitory stall mode. Although maximum static pressure recovery C_{PR} is desirable, the challenge for an aircraft inlet designer lies in the *off-design* behavior of such a diffuser, namely the possibility of a massive engine face distortion that could be created due to a large-scale flow separation in the diffuser. This reminds us of an analogous situation with a pendulum. As we remember, the highest potential energy of a pendulum occurs when it is inverted, that is, top heavy. But at that point, the slightest disturbance will create a large-scale response, that is, toppling of the pendulum, and thus the situation with an inverted pendulum is called *metastable*. In a similar vein, the highest-pressure recovery diffuser is very sensitive to the inlet disturbances and thus acts in a *metastable* manner. However, we can invest in a flow control strategy in the air intake system in order to enhance the stability of fluid flow in diffusers. We have a variety of flow control devices/strategies at our disposal, which include boundary layer suction, blowing, vortex generator placement, and dynamic (excitation) devices such as a vibrating foil/tab, that we can use in a modern diffuser.

Sovran and Klomp (1963) have developed a unified way of correlating the performance of different diffuser geometries with a straight centerline. The nondimensional parameters that describe the geometry of a diffuser are chosen to be the area ratio AR for all diffusers, and the axial length ratio N/W_1 for the rectangular diffuser, N/R_1 for the conical diffuser, and $N/\Delta R_1$ for the annular diffuser (Figure 6.10 shows a definition

■ **FIGURE 6.10**
 Definition sketch for three types of diffusers, the subscripts *i* and *o* in the annular diffuser (c) represent *inner* and *outer* walls, respectively



sketch). These geometrical parameters, from a fluid mechanics point of view, establish the (adverse) pressure gradient in a diffuser. The relative thickness of the diffuser inlet boundary layer is also recognized as an important parameter. Although similar attempts could be made with different boundary layer length scales, Sovran and Klomp chose the displacement thickness in defining an area blockage parameter *B* to represent the quality of the inlet flow. Blockage is defined as the ratio of *blocked-to-geometric* area, as

$$B \equiv \frac{A_B}{A} \tag{6.5}$$

where A_B is the blocked area, with the definition

$$A_B \equiv A - A_E = A - \int_A \frac{u}{U} dA = \int_A dA - \int_A \frac{u}{U} dA = \int_A \left(1 - \frac{u}{U}\right) dA \tag{6.6}$$

The parameter A_E is an *effective area* accounting for the inlet flow nonuniformity. In terms of displacement thickness, the blockage is expressed as

$$B_1 = \frac{2\delta_1^*}{W_1} \quad \text{(2D rectangular diffuser)} \tag{6.7}$$

$$B_1 \cong \frac{2\delta_1^*}{R_1} \quad \text{(conical diffuser)} \tag{6.8}$$

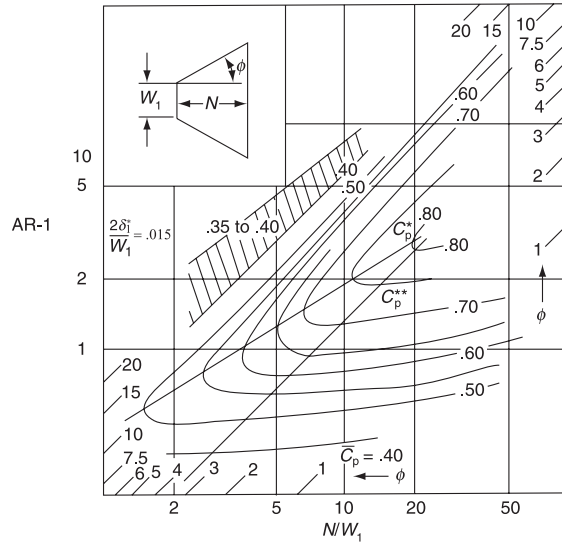
$$B_1 \cong \frac{2\bar{\delta}_1^*}{\Delta R} \quad \text{(annular diffuser)} \quad \bar{\delta}_1^* \equiv \frac{\delta_i^* + \delta_o^*}{2} \tag{6.9}$$

Here, we have defined the inlet displacement thickness δ_1^* in Equations 6.7 and 6.8 and an *average* displacement thickness over the annulus height ΔR in the annular diffuser geometry. An approximation is made in the above definitions of the inlet blockage parameter, namely, δ^{*2} terms are neglected by virtue of assuming the *inlet* boundary layer displacement thickness is reasonably thin, as compared with the channel width/radius.

The optimum performance of these rectilinear (i.e., straight centerline) diffusers, at high Reynolds numbers assuring an inlet turbulent boundary layer, and with small inlet blockage, $B < 5\%$, are correlated by Sovran and Klomp (1963), which are shown in Figure 6.11. These charts serve a useful first step in a subsonic diffuser design. More

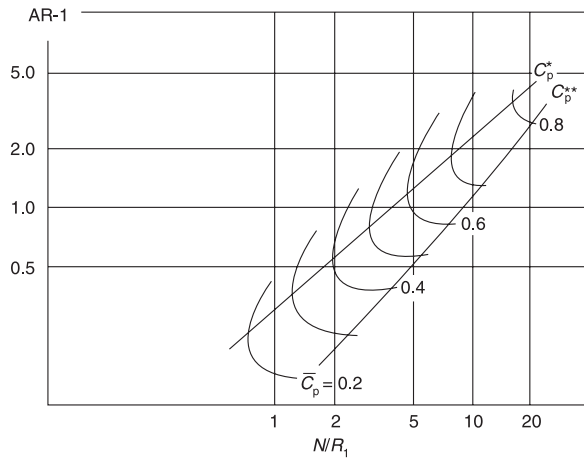
(a) Performance chart of a 2D planar diffuser with inlet blockage of $\sim 1.5\%$ is shown on the right, based on the data from Kline, Abbot, and Fox (1959). Constant C_P contours are plotted. The lines of C_p^* and C_p^{**} represent the maximum diffuser static pressure recovery for a given length ratio and for a prescribed area ratio, respectively. The tick marks on the side show the diffuser half angle ϕ .

Source: Sovran, G. and Klomp E.D. 1967. Copyright Elsevier



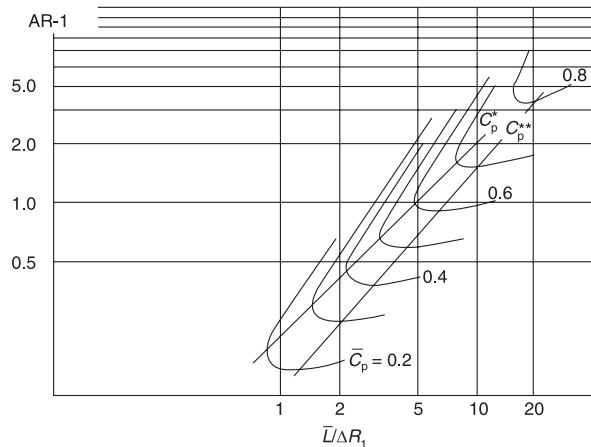
(b) Contour plots of the static pressure recovery in a conical diffuser are shown on the right, based on the data of Cockrell and Markland. The inlet blockage is $B_1 \sim 2\%$.

Source: Sovran, G. and Klomp E.D. 1967. Copyright Elsevier



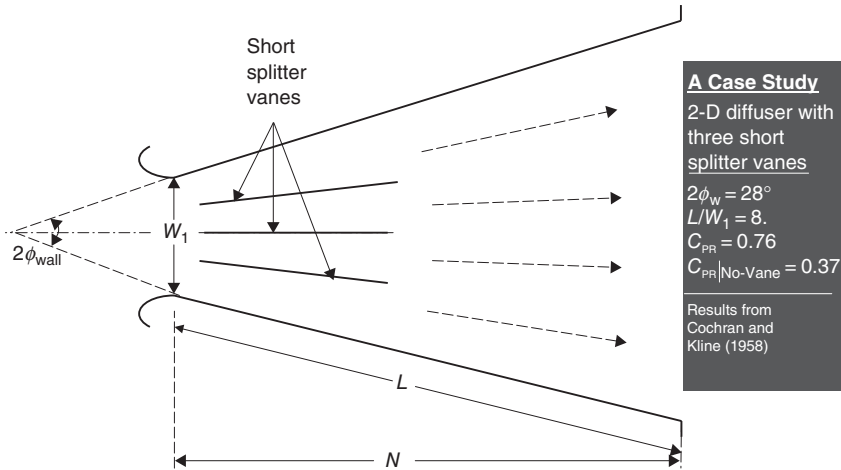
(c) Annular diffuser pressure recovery is shown on the right, based on the data of Sovran and Klomp. The inlet blockage is $\sim 2\%$. The \bar{L} , on the abscissa, represents the average wall length of the inner and outer walls, i.e., $\bar{L} \equiv (L_i + L_o)/2$.

Source: Sovran, G. and Klomp E.D. 1967. Copyright Elsevier



■ FIGURE 6.11 Diffuser performance charts. Source: Sovran and Klomp 1967. Copyright Elsevier

■ **FIGURE 6.12**
Wide-angle diffuser is fitted with three internal splitter vanes to prevent flow separation and promote mixing



advanced steps require the computational fluid dynamics (CFD) analysis involving Navier–Stokes equations. Also, at *transonic* Mach numbers, shock waves appear, and since their interaction with the boundary layer plays a dominant role in the diffuser performance, we cannot use these charts in the high subsonic Mach range with high degree of accuracy.

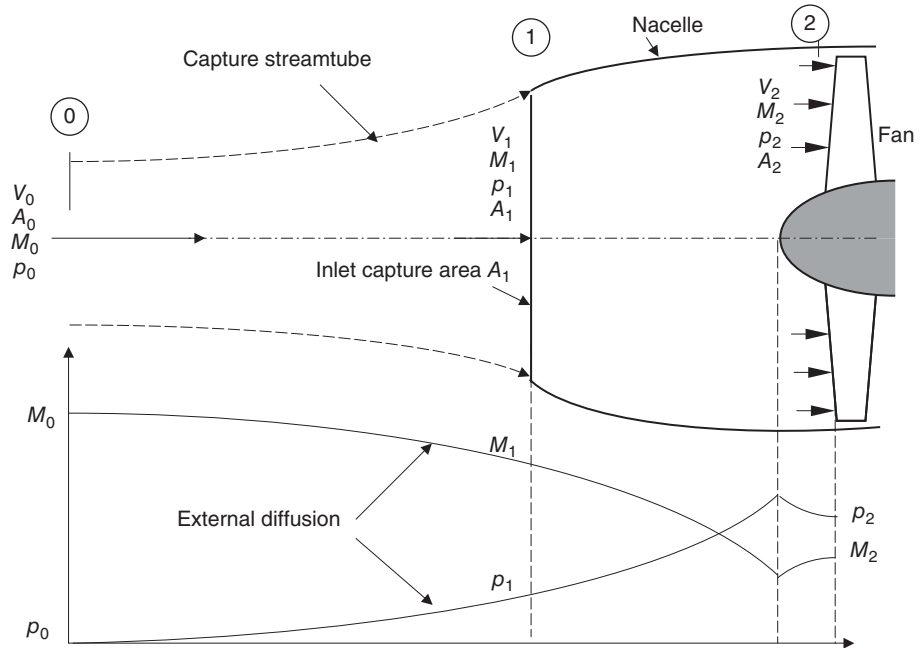
The hatched region on the top performance chart in Figure 6.11 shows a low-pressure recovery zone associated with a fully developed stall behavior in 2D planar diffusers, as also shown in Figure 6.8. Note that the hatched zone lies above the 15° half angle or above the 2ϕ of 30° in Figure 6.8. We can use these charts in several ways, namely, for a fixed area ratio diffuser, we can seek the length ratio that optimizes the static pressure recovery of that diffuser. Conversely, the area ratio of an optimum performance diffuser can be established through these charts for a prescribed diffuser length ratio. The combination of diffuser area ratio and the axial length ratio also identifies the diffuser angle and its performance. Also note that the triangular *wedge*, created between the C_p^* and C_p^{**} lines on the 2D rectilinear diffuser performance chart of the Figure 6.11, corresponds to a total diffuser divergence angle of $\sim 8^\circ$ – 10° . This leads us to the conclusion, that is, a rule of thumb, that an optimum wall inclination angle in a planar diffuser should lie in the neighborhood of $\phi_w \sim 4^\circ$. This rather shallow wall inclination angle reminds us that the (natural) diffusion is a rather slow process. Consequently, rapid diffusion requires a forcing mechanism that enhances mixing of the high- and low-energy fluid in a duct. This again suggests using either vortex generators (i.e., passive control) or devise active flow control strategies to achieve enhanced mixing in a diffuser duct.

A passive method in achieving a short diffuser of a large area ratio is to install splitter plates/cones in a 2D/conical diffuser, which in essence creates a series of parallel diffusers within the overall diffuser (Cochran and Kline, 1958). This is shown in Figure 6.12.

6.7 Subsonic Cruise Inlet

For a subsonic cruise application, the total flow deceleration is divided into external and internal segments. The external diffusion takes place outside the inlet where the design

■ **FIGURE 6.13**
Typical subsonic inlet
at cruise condition
showing external as
well as internal
diffusion (note that
flow accelerates over
the fan centerbody)



capture streamtube itself acts like a subsonic diffuser. We depict this behavior graphically in Figure 6.13. We have discussed this as a pre-entry drag earlier.

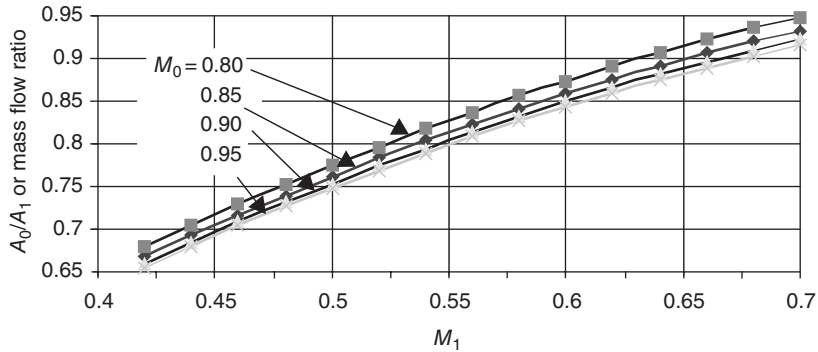
The inlet area at the lip, which is also known as the *highlight*, is called the *inlet capture area* and is sometimes given the symbol A_c . Since the external flow, in the absence of shocks and/or a centerbody that protrudes outside the inlet, is reversible and adiabatic, the ratio of parameters between the flight condition and the inlet face follow the isentropic rule. Namely,

$$\frac{A_0}{A_1} = \frac{M_1}{M_0} \left[\frac{1 + \frac{\gamma-1}{2} M_0^2}{1 + \frac{\gamma-1}{2} M_1^2} \right]^{\frac{\gamma+1}{2(\gamma-1)}} \quad (6.10)$$

Therefore, the capture (area) ratio A_0/A_1 is a function of the desired external deceleration from the cruise Mach number M_0 to the inlet lip Mach number M_1 and is called the mass flow ratio parameter or simply MFR in abbreviation. We have graphed Equation 6.10 for various cruise flight Mach numbers in the transonic regime in Figure 6.14.

Now, let us address the limitations on M_1 . The internal contour of a subsonic inlet lip, that is, near the highlight, is shown in Figure 6.15. Due to the convex shape of the inner lip contour of a subsonic inlet, as shown, the flow accelerates near the throat and thus creates a nonuniform velocity profile, somewhat similar to the profile shown in Figure 6.15. In order to control the “overshoot” in local speed at the throat to a value below the sonic speed, we should limit the one-dimensional throat Mach number, that is, the mass-averaged throat Mach number, to $\bar{M}_{th} \leq 0.75$. Therefore, it is desirable to prevent a

■ **FIGURE 6.14**
 Capture (area) ratio
 and inlet face Mach
 number



sonic bubble formation at the throat, which may terminate in a shock and possibly cause a boundary layer separation.

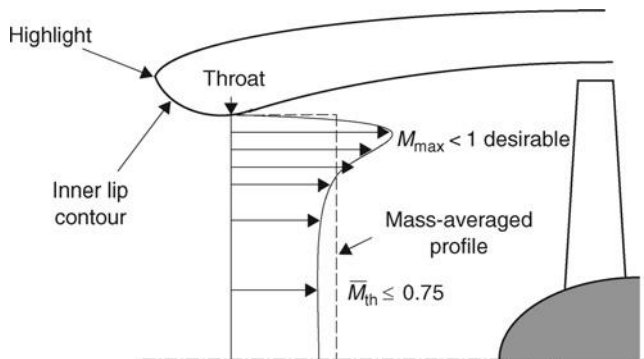
The one-dimensional throat Mach number of 0.75 represents an *upper bound* used for the throat sizing of a subsonic inlet. A lower value, say 0.6, is perhaps more desirable as it allows for the thrust growth potential of the engine, which invariably occurs. The average Mach number at the throat of 0.75 as compared with 0.6 represents a ~12% increase in mass flow rate and nearly the same increase in thrust. The same inlet can thus accommodate a 12% increase in thrust without a need for resizing the inlet.

Now that we have fixed the (mass) average throat Mach number to, say, ~0.75, applying continuity equation to the region between the highlight and the throat, and neglecting small total pressure loss due to friction on the wall, we can relate the average Mach number at highlight, M_1 , to the area ratio between the highlight and the inlet throat. Continuity equation applied to an isentropic flow demands

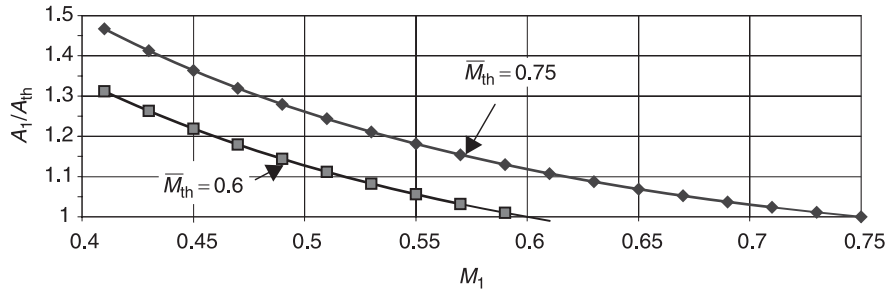
$$\frac{A_{HL}}{A_{th}} = \frac{A_1}{A_{th}} = \frac{\bar{M}_{th}}{M_1} \left[\frac{1 + \frac{\gamma - 1}{2} M_1^2}{1 + \frac{\gamma - 1}{2} \bar{M}_{th}^2} \right]^{\frac{\gamma + 1}{2(\gamma - 1)}} \tag{6.11}$$

In Figure 6.16, we plotted the inlet lip contraction ratio A_{HL}/A_{th} as a function of the inlet lip Mach number for an average throat Mach number of 0.75. There are at least

■ **FIGURE 6.15**
 Flow curvature at the
 throat causes a
 nonuniform velocity
 profile



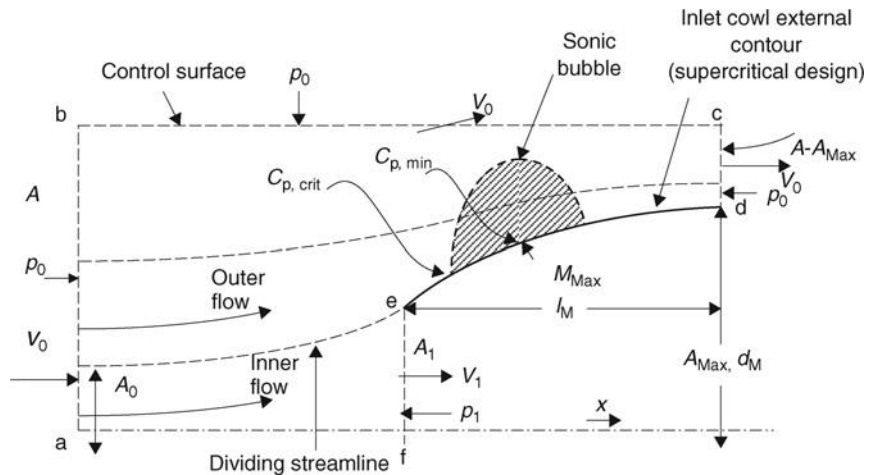
■ FIGURE 6.16
Inlet lip Mach number
variation with the lip
contraction ratio and \bar{M}_{th}



two competing effects at play near the inlet lip, namely, the conflict between the internal and the external contours of the inlet. This is to be expected, since the flow splits into an *inner* and an *outer* flow around the inlet lip that influences the diffuser performance and the external nacelle drag characteristics, respectively. For example, a large inlet lip contraction ratio contributes to a parameter known as the lip “bluntness,” which is good for low-speed, high-angle-of-attack, and side flow environments and is bad for the drag divergence characteristics of the nacelle at high speed. A low contraction ratio inlet lip offers a good high-speed characteristic for the nacelle external drag and a poor low-speed characteristic toward the engine face and flow distortion.

The high-speed performance of an air intake system is dominated by its external cowl drag behavior. The flow acceleration around the cowl external surface may exceed the local sonic speed with a potential for drag rise with shock formation and boundary layer separation. The maximum diameter of the nacelle and its axial disposition from the inlet lip (highlight) control the flow overspeed over the cowl outer surface. These parameters are denoted as A_M and l_M , respectively, for the maximum area and the length measured from the highlight to the maximum diameter. The nondimensional external cowl parameters are A_{HL}/A_M analogous to the inlet lip contraction ratio A_{HL}/A_{th} , which governed the internal performance of the inlet and l_M/d_M . Let us examine a control volume with an inlet area larger than A_M and two outlet areas, one at the capture area of the inlet and the other over the cowl maximum area, as shown in Figure 6.17. Note that at

■ FIGURE 6.17
Control volume
(a-b-c-d-e-f-a) used for
the external flow
analysis of subsonic
inlets



the first appearance of sonic speed on the cowl, we reach the critical C_p (as labeled). Also note that the sonic bubble is not terminated in a shock, thus we call the inlet nacelle outer contour a “supercritical” nacelle, similar to the supercritical airfoil. Somewhere inside the bubble, the velocity peaks to V_{\max} and at that location we noted the lowest C_p (as labeled). With the side of the control volume not coinciding with a stream surface, we allowed a flow *spillage* through the side at a speed of V_0 , which clearly is an assumption and an acceptable one.

Let us apply the continuity equation to the control surface shown in Figure 6.17, in order to quantify the (spillage) mass flow rate through the side in terms of the inlet mass flow rate and the geometrical parameters of the inlet.

$$\dot{m}_0 + \rho_0 V_0(A - A_0) = \dot{m}_1 + \dot{m}_s + \rho_0 V_0(A - A_M) \quad (6.12)$$

Upon simplification, expression 6.12 yields

$$\dot{m}_s = \rho_0 V_0(A_M - A_0) \quad (6.13)$$

Applying the (inviscid) momentum equation to the control volume in the x -direction gives

$$\dot{m}_0 V_1 + \dot{m}_s V_0 + \rho_0 V_0(A - A_M)V_0 - \rho_0 V_0 A V_0 = - \int_{A_1}^{A_M} (p - p_0) dA - (p_1 - p_0)A_1 \quad (6.14)$$

$$\dot{m}_0(V_1 - V_0) = - \int_{A_1}^{A_M} (p - p_0) dA - (p_1 - p_0)A_1 \quad (6.15)$$

We shall nondimensionalize the above equation by dividing through by the free-stream dynamic pressure, $q_0 = \rho_0 V_0^2/2 = \gamma p_0 M_0^2/2$ multiplied by the inlet lip area A_1 to get

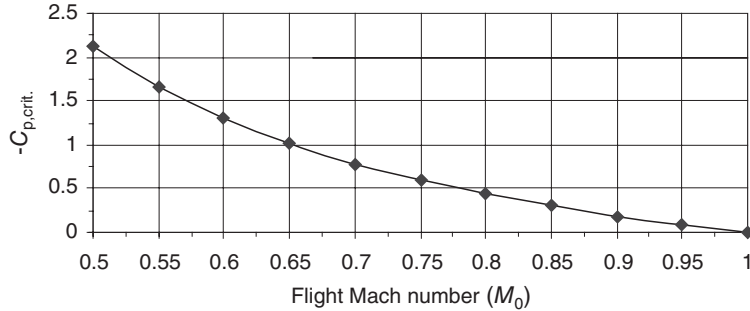
$$2 \frac{A_0}{A_1} \left(\frac{V_1}{V_0} - 1 \right) = - \int_1^{A_M/A_1} C_p dA' - \frac{2}{\gamma M_0^2} \left(\frac{p_1}{p_0} - 1 \right) \quad (6.16)$$

where the integrand in Equation 6.16 is cast in terms of surface pressure coefficient C_p in the integral and the variable of integration is now changed to A' , which is the nondimensional area A/A_1 . The inlet lip pressure ratio in Equation 6.16 may be written in terms of M_1 and M_0 , as

$$\frac{p_1}{p_0} = \left(\frac{1 + \frac{\gamma - 1}{2} M_0^2}{1 + \frac{\gamma - 1}{2} M_1^2} \right)^{\frac{\gamma}{\gamma - 1}} \quad (6.17)$$

To perform the integral on the right-hand side (RHS) of Equation 6.16, we either input a “desired” C_p distribution, which may be a constant C_p design, on the inlet external cowl or

■ **FIGURE 6.18**
The pressure coefficient at the sonic point on the nacelle forebody



we may express the integral in terms of a surface-mean C_p , as an area-averaged quantity, defined as

$$\int_1^{A_M/A_1} C_p dA' = \bar{C}_p \left(\frac{A_M}{A_1} - 1 \right) \quad (6.18)$$

We may substitute Equations 6.17 and 6.18 into Equation 6.16 and express A_M/A_1 in terms of the mean-surface C_p on the external cowl, the flight Mach number M_0 , and the capture ratio A_0/A_1 to get

$$\frac{A_M}{A_1} = 1 + \left(2 \frac{A_0}{A_1} \left[\frac{M_1}{M_0} \sqrt{\frac{1 + \frac{\gamma-1}{2} M_0^2}{1 + \frac{\gamma-1}{2} M_1^2}} - 1 \right] + \frac{2}{\gamma M_0^2} \left(\left(\frac{1 + \frac{\gamma-1}{2} M_0^2}{1 + \frac{\gamma-1}{2} M_1^2} \right)^{\frac{\gamma}{\gamma-1}} - 1 \right) \right) / (-\bar{C}_p) \quad (6.19)$$

Note that the inlet Mach number M_1 in Equation 6.19 is a function of the inlet capture ratio, as shown in Figure 6.14. We may substitute $C_{p,crit}$ (i.e., the pressure coefficient at the sonic point) for the surface-averaged pressure coefficient, in order to plot the nacelle area ratio A_M/A_1 . The critical pressure coefficient is a function of flight Mach number according to isentropic flow:

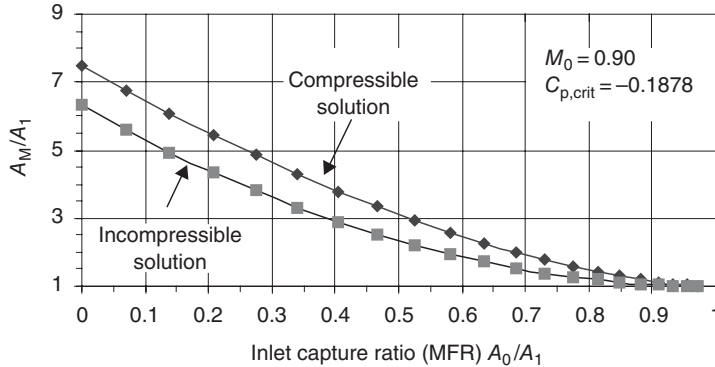
$$\bar{C}_p \approx C_{p,crit} = \frac{2}{\gamma M_0^2} \left[\left(\frac{1 + \frac{\gamma-1}{2} M_0^2}{\frac{\gamma+1}{2}} \right)^{\frac{\gamma}{\gamma-1}} - 1 \right] \quad (6.20)$$

We have graphed Equation 6.20 as a function of the flight Mach number in Figure 6.18.

Now, let us incorporate the critical pressure coefficient in Equation 6.19 and plot the external nacelle area ratio A_M/A_1 in terms of flight Mach number and the inlet capture ratio, or MFR. The result is presented in Figure 6.19.

We incorporated the incompressible solution in Figure 6.19 as well to demonstrate the effect of compressibility on the cowl frontal area requirement. Once we account for the effect of density variations in the flow, the inlet cowl area ratio requirements show a

■ **FIGURE 6.19**
The minimum inlet cowl frontal area (A_M/A_1) corresponding to the sonic flow on the cowl at the cruise Mach number of 0.90

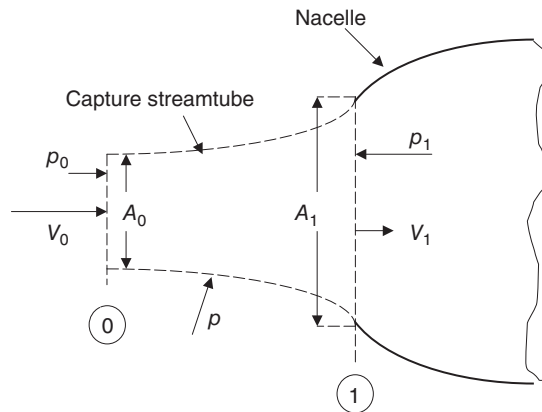


higher A_M/A_1 needed than the incompressible solution, as shown in Figure 6.19. A typical capture ratio at cruise is ~ 0.70 , which then using Figure 6.19 suggests a minimum cowl frontal area ratio of ~ 1.88 for a cruise Mach number of 0.90. This area ratio corresponds to an inlet (highlight)-to-maximum diameter ratio of ~ 0.73 . This is somewhat lower than in the large bypass ratio turbofan engine nacelles, which have their highlight-to-maximum diameter ratio at $\sim 0.80\text{--}0.90$, primarily due to ground clearance reasons, according to Seddon and Goldsmith (1985). The higher R_1/R_M in the large bypass engines leads to a *slimline* design of the fan cowls with an attendant relief on supersonic flow and the sonic bubble formation on the cowl.

Now, let us quantify the additive drag associated with the capture streamtube that we first introduced in the engine thrust and performance parameters Chapter 3. A control volume is shown in Figure 6.20, which is composed of the capture streamtube, free stream entrance, and the inlet lip, that is, highlight exit surfaces. The conservation of mass relates the area ratios to Mach numbers in an isentropic flow via

$$\frac{A_0}{A_1} = \frac{M_1}{M_0} \left(\frac{1 + \frac{\gamma - 1}{2} M_0^2}{1 + \frac{\gamma - 1}{2} M_1^2} \right)^{\frac{\gamma + 1}{2(\gamma - 1)}} \tag{6.21}$$

■ **FIGURE 6.20**
A control volume for additive drag derivation



The conservation of momentum in the streamwise direction applied to the control volume outside the inlet may be written as

$$\dot{m}_0(V_1 - V_0) = p_0 A_0 + \int_{A_0}^{A_1} p dA - p_1 A_1 \quad (6.22)$$

This expression balances the momentum change in the streamwise direction by the forces that cause the change of momentum, that is, the pressure–area terms on the RHS. By subtracting a constant pressure p_0 from all the surfaces of the control volume, we can rewrite the momentum equation as

$$\dot{m}_0(V_1 - V_0) = \int_{A_0}^{A_1} (p - p_0) dA - (p_1 - p_0) A_1 \quad (6.23)$$

As we recall from the chapter on engine thrust (Chapter 3), the pressure integral on the capture streamtube is called the pre-entry or additive drag, therefore, we may write it as

$$D_{\text{add}} \equiv \int_{A_0}^{A_1} (p - p_0) dA = \dot{m}_0(V_1 - V_0) + (p_1 - p_0) A_1 \quad (6.24)$$

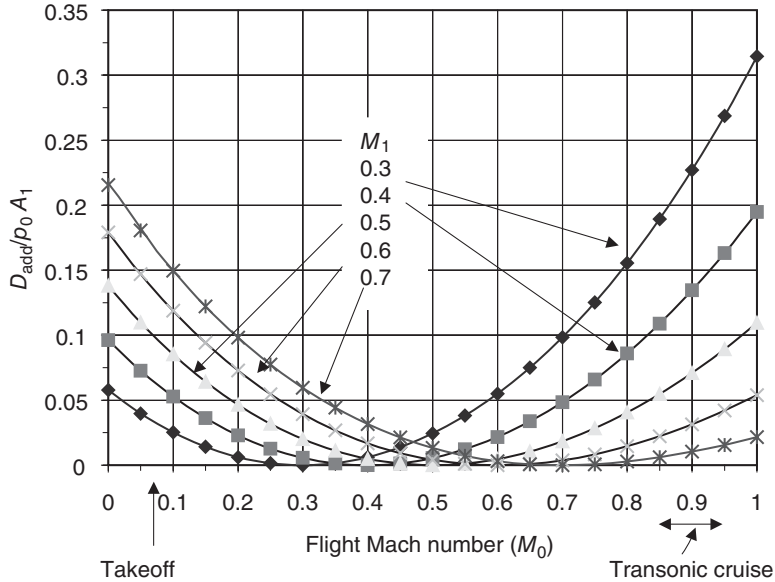
Now, let us cast this expression in terms of a nondimensional parameter, such as

$$\frac{D_{\text{add}}}{p_0 A_1} = \frac{\rho_0 A_0}{\rho_0 A_1} V_0^2 \left(\frac{V_1}{V_0} - 1 \right) + \frac{p_1}{p_0} - 1 \quad (6.25)$$

Note the logical choice of the ambient pressure p_0 and the inlet capture area A_1 as the nondimensionalizing parameters in Equation 6.25. These parameters do not change with the engine throttle setting, as say A_0 and p_1 would. We may introduce the flight Mach number on the RHS of Equation 6.25, as well as the static pressure ratio in terms of flight and the inlet Mach number M_0 and M_1 , respectively, using isentropic relations and the capture ratio via the continuity equation, to get

$$\begin{aligned} \frac{D_{\text{add}}}{p_0 A_1} = & \gamma M_1 \left(\frac{1 + \frac{\gamma-1}{2} M_0^2}{1 + \frac{\gamma-1}{2} M_1^2} \right)^{\frac{\gamma+1}{2(\gamma-1)}} \left(M_1 \sqrt{\frac{1 + \frac{\gamma-1}{2} M_0^2}{1 + \frac{\gamma-1}{2} M_1^2}} - M_0 \right) \\ & + \left(\frac{1 + \frac{\gamma-1}{2} M_0^2}{1 + \frac{\gamma-1}{2} M_1^2} \right)^{\frac{\gamma}{\gamma-1}} - 1 \end{aligned} \quad (6.26)$$

■ FIGURE 6.21
 Inlet additive drag profiles from takeoff to transonic cruise at different inlet lip Mach numbers M_1 , $\gamma = 1.4$



Note that the nondimensional additive drag is a function of the flight Mach number and the inlet lip Mach number, that is, a function of the capture streamtube shape. A cylindrical capture streamtube with $A_0 = A_1$ would experience a vanishing pre-entry drag. Let us graph this equation for a family of inlets characterized by different inlet lip Mach number designs and flight conditions (Figure 6.21).

Let us examine the family of additive drag curves in Figure 6.21 more closely. Two distinct trends become apparent. First, at takeoff or low-speed flight, since the inlet capture ratio is very large for this flight condition, it corresponds to a high-inlet lip Mach number, say $M_1 \sim 0.7$ or higher, where

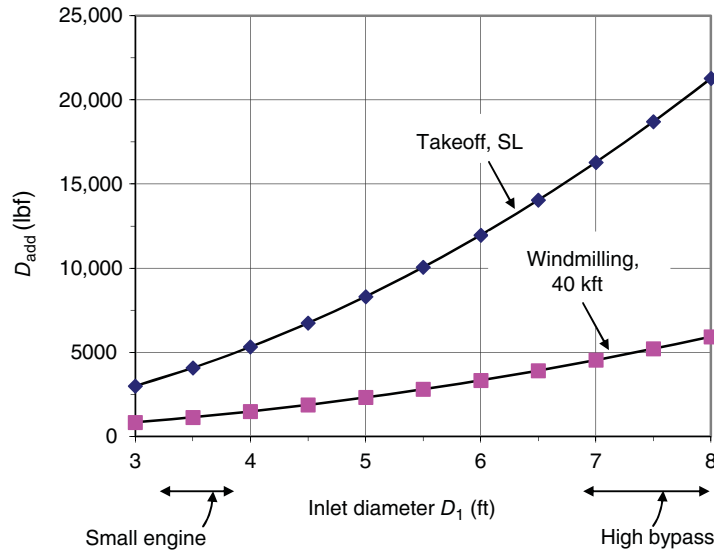
$$\left. \frac{D_{add}}{p_0 A_1} \right|_{\text{Takeoff}} \sim 0.2 \tag{6.27}$$

The second trend that we may observe from the family of nondimensional additive drag profiles, shown in Figure 6.21, is their behavior at transonic flight condition when an engine becomes inoperative. This situation is represented by a low-inlet lip Mach number corresponding to the engine “windmilling” condition, say $M_1 \sim 0.3$ (or less), hence

$$\left. \frac{D_{add}}{p_0 A_1} \right|_{\text{Windmill}} \sim 0.3 \tag{6.28}$$

To develop an appreciation for the *magnitude* of the inlet additive drag at takeoff and the engine windmilling condition at altitude, we may graph these conditions for engines of different inlet diameters. The ambient pressure at takeoff was chosen to be the standard

■ **FIGURE 6.22**
Inlet additive drag at
takeoff and at
transonic cruise with a
windmilling engine
(High bypass turbofan
engines in range 7–8)



sea level pressure of 14.7 psia (or 100 kPa) and the altitude curve was chosen at 40,000 ft with an ambient pressure of 393 lb/ft². The result is shown in Figure 6.22.

Although the magnitude of additive drag is very large, both at takeoff and altitude, the cowl lip suction force, on a blunt cowl, almost balances out the additive drag. In an engine out situation, however, there is a drag, a penalty due to a flow separation from the outer cowl, that is external nacelle drag increases due to the flow spillage from the inlet over the cowl lip. The imbalance between the additive drag and the lip suction force is called the spillage drag, as we introduced it earlier in the engine force and performance parameters Chapter 3.

$$D_{\text{spillage}} \equiv D_{\text{add}} - F_{\text{lip}} \quad (6.29)$$

A well-designed subsonic cruise inlet attains a total pressure recovery between the flight and the engine face, that is, ~ 0.995 – 0.997 . This is a remarkable feat achieved by the aircraft industry today. Although the total pressure recovery is reduced at takeoff and climb, as the throat Mach number is increased, we may still neglect the total pressure drop when we compare the captured stream area to the engine face area. Hence, we may link the engine face Mach number and area to the flight Mach number and the free stream area using the isentropic flow relation, namely,

$$\frac{A_0}{A_2} = \frac{M_2}{M_0} \left[\frac{1 + \frac{\gamma - 1}{2} M_0^2}{1 + \frac{\gamma - 1}{2} M_2^2} \right]^{\frac{\gamma + 1}{2(\gamma - 1)}} \quad (6.30)$$

Let us graph this equation for a typical engine face Mach number range of 0.4–0.6 and the flight Mach numbers ranging from 0.1 at takeoff to 0.95 at cruise

■ **FIGURE 6.23**
 Captured
 stream-to-engine face
 area ratio from takeoff
 to cruise (isentropic)

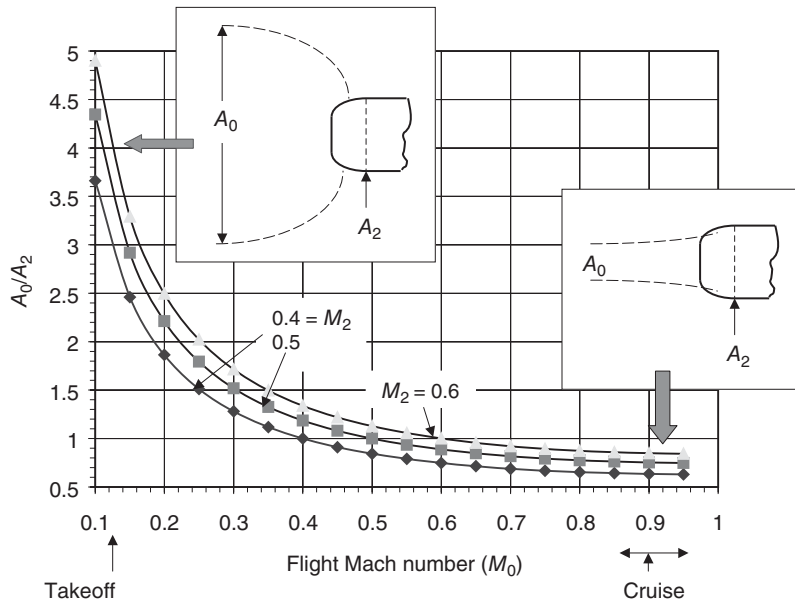
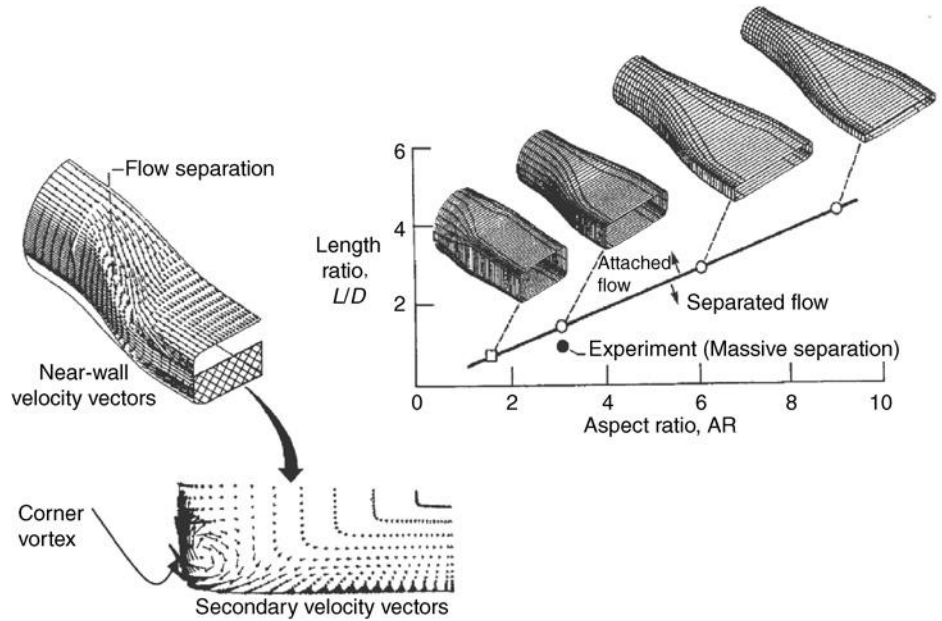


(Figure 6.23). The upper value corresponds to the proposed Sonic Cruiser commercial transport of Boeing.

6.8 Transition Ducts

A duct that changes its cross-sectional shape is called a transition duct. These ducts are prevalent in advanced propulsion systems, typically the transition from rectangular to round in the inlet and the round-to-rectangular cross-section in the exhaust systems. The fluid mechanics of transition ducts is rich with merging boundary layers at the corners of the duct, corner vortex formation, and three-dimensional pressure field setting up fascinating swirling patterns in the cross-flow, known as the *secondary flows*. Our interest in these ducts as a part of an inlet system is to be able to quantify and minimize the engine face distortion levels caused by these ducts over the entire flight envelope of the aircraft. In a rectangular exhaust system, however, the interest is in eliminating separation bubbles and minimizing corner vortices, which can *trap* the unburned fuel in the afterburner and potentially cause a burn through in the nozzle wall if combustion takes place over the wall-bounded recirculating flows. These practical concerns for the inlets and nozzles are coupled with a design-to-weight mentality, which has been the cornerstone of aircraft system development. To minimize the length of these ducts while maintaining a healthy state of boundary layer, a designer may use a computational fluid dynamics tool, which is capable of three-dimensional viscous flow solutions. Bernhard Anderson of NASA has performed numerous computational studies of transition ducts including an extensive comparison with benchmark experimental data for validation purposes. Figure 6.24 is a composite diagram of Anderson's work (Abbott, Anderson, and Rice, 1987) with transition ducts suitable for exhaust systems (round-to-rectangular).

■ **FIGURE 6.24**
Transition duct
flowfield visualized by
near-wall velocity
vectors and a
cross-stream plane and
on the upper right, a
flow regime map of
transition ducts with
area ratio equal to one.
Source: Abbott,
Anderson, and Rice
1987. Courtesy of
NASA



6.9 An Interim Summary for Subsonic Inlets

We learned that

- An inlet aerodynamic performance has an *internal* as well as an *external* component, an internal figure of merit, and an external figure of merit
- An inlet internal performance is dominated by its throat Mach number
- The one-dimensional (or average) throat Mach number should be less than 0.75
- The internal performance is governed by the *laws* of diffusers, e.g., C_{PR} (AR, N/R_1 , B), that is, area ratio, length ratio, inlet blockage, and centerline shape for offset exits
- A *cubic* is proposed for the internal diffuser contour with a maximum angle of 8.7°
- The internal performance at low speed is helped by the *lip contraction ratio*
- The captured streamtube introduces an *additive drag* with a capture ratio other than 1, which can be very large at takeoff or with a windmilling engine situation
- The capture ratio (or inlet mass flow ratio) for a subsonic cruise inlet is ~ 0.70
- The additive drag is nearly balanced out by the cowl lip suction force, that is, lip *thrust*
- The uncanceled part of the additive drag by the lip suction force is called *spillage drag*, which is a strong function of lip bluntness
- Cowl lip bluntness has an internal and an external component to it
- The internal lip contour is near elliptic (i.e., a superelliptic profile)
- “Bluntness” is quantifiable

- Large capture ratios at takeoff and climb pose a potential problem for engine face distortion
- Wing and aft fuselage-mounted inlets are exposed to flow angularity, that is, droop or toe up angles depending on their placement, that is, the wing upwash or downwash
- Nacelle external contour sets the limitation on high-speed performance of the inlet
- Drag divergence Mach number can be raised by a *supercritical* nacelle design
- Drag reduction may be achieved through a hybrid laminar flow control on the nacelle
- Transition ducts may be needed for integration purposes, sometimes with an offset
- Secondary flow patterns are introduced in ducts with a bend or transition ducts in general, a cause of distortion

There are additional discussions that are relevant to inlets and inlet-aircraft integration:

- Inlet acoustic treatment
- Inlet (cowl) lip icing detection and anti-icing strategies
- Inlet-engine matching, steady-state, and dynamic distortion

Further readings on subsonic inlets and engine installations (references 3, 16, 18, 22, 23, 27, 29, 31, 33, 34, 45 and 47) are recommended.

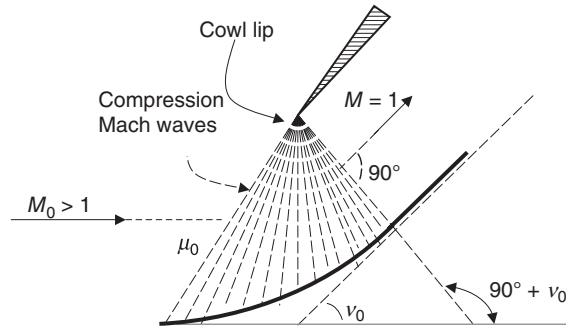
6.10 Supersonic Inlets

The function of a supersonic inlet is the same as the function of a subsonic inlet, namely, to decelerate the flow to the engine face Mach number requirements (set by the throttle), typically in the range of $M_2 \sim 0.4\text{--}0.6$, efficiently, within the entire flight envelope. In practice, flow diffusion from supersonic to subsonic flow involves shocks. Therefore, the study of supersonic inlets is very much dominated by the study of shocks intersecting, interacting, reflecting, and the shock boundary layer interaction. We will also learn that shocks pose instability problems for an inlet and learn possible approaches to stabilizing them. As in subsonic inlets, we are still concerned about the external drag characteristics of the supersonic inlets. Although, there are no supersonic inlet flows that are reversible, we still propose to study them in the limit of reversible, adiabatic flow. By studying isentropic inlets, we learn about throat sizing issues, some off-design Mach numbers, and their impact on the inlet flow behavior.

6.10.1 Isentropic Convergent–Divergent Inlets

By insisting on an isentropic compression, we propose to create an isentropic compression Mach wave system that all converge to a single point, like a fan. It is theoretically possible to machine a concave surface that can decelerate a supersonic flow to a sonic flow. The

■ **FIGURE 6.25**
An isentropic
compression ramp
decelerating a
supersonic flow to
 $M = 1$



concave surface is known as an isentropic compression ramp. The picture of the waves set up on an isentropic compression ramp looks like Figure 6.25.

Now let us remember the wave and ramp angles from aerodynamics. We remember that all Mach waves make an angle, called Mach angle, with respect to the *local* flow. Therefore, the lead Mach wave makes an angle

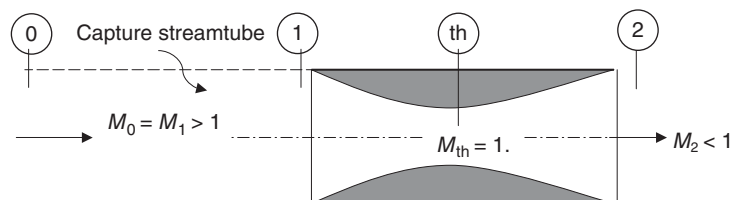
$$\mu_0 = \sin^{-1}(1/M_0) \tag{6.31}$$

The last Mach wave, that is, the tail wave, is normal to the sonic exit flow, that is, $\sin^{-1}(1) = 90^\circ$. We also remember from Prandtl–Meyer flow that the ramp angle of v_0 , which is called Prandtl–Meyer angle, corresponds to turning a *sonic* flow to achieve a supersonic Mach number M_0 . Since the process of isentropic compression is reversible, it means that a flow approaching the ramp from the top of Figure 6.25 at sonic speed (i.e., reverse flow) will *accelerate* to achieve M_0 at the bottom of the ramp, the flow turning angle is thus the Prandtl–Meyer angle v_0 corresponding to M_0 . An expression for this angle as a function of Mach number and the ratio of specific heats γ is written as Equation 6.32, which we derived in Chapter 2.

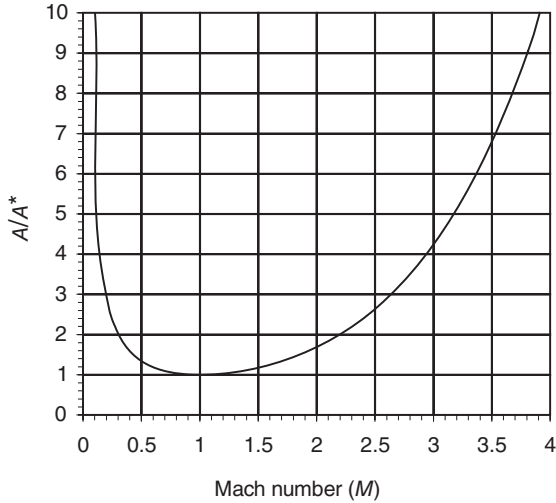
$$v(M) \equiv \sqrt{\frac{\gamma + 1}{\gamma - 1}} \tan^{-1} \sqrt{\frac{\gamma - 1}{\gamma + 1}(M^2 - 1)} - \tan^{-1} \sqrt{M^2 - 1} \tag{6.32}$$

We may decelerate the sonic exit flow from the compression ramp in a subsonic diffuser, which requires a flow area expansion, that is, a diverging duct. Now let us incorporate such isentropic compression ramps in a duct and subsonic diffusers to create a *convergent–divergent* (C–D) duct capable of decelerating a supersonic flow to a subsonic flow reversibly and adiabatically. This duct is then called an isentropic C–D inlet. The simple geometry of it is presented in Figure 6.26.

■ **FIGURE 6.26**
Schematic drawing of
an isentropic C–D inlet



■ **FIGURE 6.27** Isentropic area ratio as a function of Mach number ($\gamma = 1.4$) shows that a C–D duct exhibits choking behavior at a supersonic as well as a subsonic Mach number



Let us note that the capture streamtube in Figure 6.26 shows a capture ratio A_0/A_1 of 1, and furthermore its area ratio A_1/A_{th} is uniquely established via an isentropic A/A^* relation corresponding to M_1 . For example, the inlet-to-throat area ratio is equal to 2 for an inlet Mach number of 2.2. We can read these numbers from an isentropic table for $\gamma = 1.4$. Also, we note that since the flow deceleration in this inlet takes place entirely within the duct, we may call it an *internal-compression* inlet. The unique isentropic area ratio (A/A^*) at a supersonic speed creates problems at subsonic speeds. Namely, the same area ratio duct *chokes* at a subsonic Mach number too! This means that prior to reaching our target supersonic design Mach number of M_D , we have already choked the throat at a subsonic Mach number. Let us return to the example we used in this paragraph. For a supersonic design Mach number of 2.2, the C–D inlet should have its area ratio set at 2.0. By looking up the isentropic tables, in the subsonic portion of it, we note that area ratio 2.0 first chokes at Mach number ~ 0.3 ! In other words, each value of A/A^* is repeated twice in the isentropic table, once in the subsonic flow part and then the second time in the supersonic flow portion of the table. Now let us graphically represent the *dual* nature of choking in a compressible flow, that is, (A/A^*) is a *double-valued* function of Mach number. The continuity equation for an isentropic flow established A/A^* according to

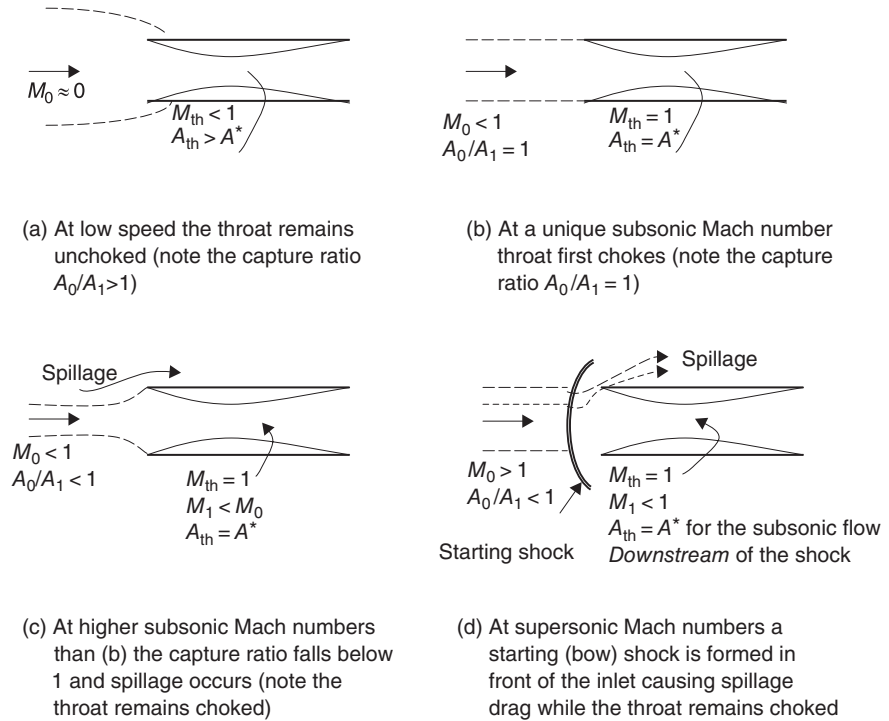
$$A/A^* = (1/M) \left[\left(1 + \frac{\gamma - 1}{2} M^2 \right) / \left(\frac{\gamma + 1}{2} \right) \right]^{\frac{\gamma + 1}{2(\gamma - 1)}} \tag{6.33}$$

We may graph this equation for a range of Mach numbers (Figure 6.27) to demonstrate that there are two Mach numbers, one subsonic and the other supersonic, for each A/A^* .

Now, let us examine the sequence of events that takes place outside and within the inlet from start to the design Mach number. The capture ratio for the inlet starts larger than 1, as in the subsonic inlet at takeoff. The capture ratio remains greater than 1 until the throat chokes at the corresponding subsonic (A/A^*). At this moment, the capture area ratio is 1, and the throat is choked.

Various flow characteristics of an isentropic C–D inlet are shown in Figure 6.28 as a function of flight Mach number. The first choking occurs at a unique subsonic Mach

■ **FIGURE 6.28**
Flow characteristics of
an isentropic C–D inlet
from low speed to
supersonic conditions



number corresponding to the “bucket” graph of (A/A^*) shown in Figure 6.27, where the capture ratio is exactly 1 and no spillage occurs. At all Mach numbers above this unique subsonic Mach number, the throat continues to remain choked and the consequence of higher flow manifests itself in a spillage over the inlet lip, as shown in parts (c) and (d) of Figure 6.28. For supersonic flow, a bow shock is formed ahead of the inlet to allow for spillage to occur. The spillage accounts for a choked throat, which is smaller than the corresponding A/A^* at M_0 . As long as the starting shock remains in front of the supersonic inlet, the spillage drag and low total pressure recovery are the consequences of this flow. This undesirable condition is called an “unstarted” inlet. We shall now examine a few methods that enable *starting* a C–D inlet.

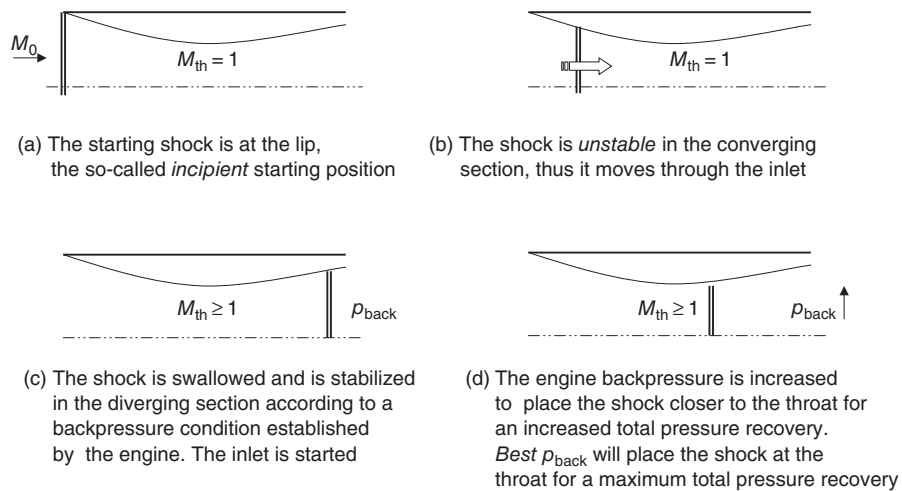
6.10.2 Methods to Start a Supersonic Convergent–Divergent Inlet

The starting process of a supersonic C–D inlet involves swallowing the starting shock. A normal shock that is brought to the inlet lip is said to be in an incipient starting position. Any disturbance that causes the starting shock to enter the inlet will then result in the shock to move through the convergent portion of the duct and be stabilized at a location in the divergent section downstream of the throat. Normal shocks are therefore said to be unstable in a converging duct. The position of a shock in a duct is dictated by the *backpressure*, which establishes the downstream condition, or outflow condition of the shock. When the backpressure increases, a shock is pushed upstream and when the backpressure decreases, the shock moves downstream. We may use the backpressure principle to explore shock stability in converging as well as diverging ducts. First let us look at a converging duct

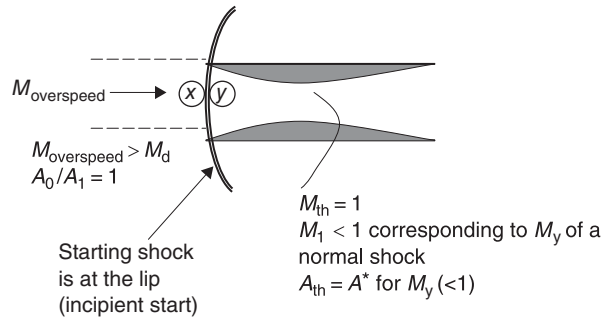
that leads to a sonic throat. The starting shock that moves in a converging duct, by virtue of flow area contraction, will experience a decrease in its upstream Mach number M_x . Therefore, the shock *weakens* as it enters a contracting duct. Consequently, the total pressure downstream of the shock in its new position is increased, as the shock is now weaker. The sonic throat, which acts as the first engine throttle, experiences an increased mass flow rate. We remember that the mass flow rate is linearly proportional to the total pressure, that is, $\dot{m} \propto p_t$. The increase in mass flow rate downstream of the shock will reduce the shock backpressure (i.e., it creates a suction), which in turn draws the shock further in the duct and toward the throat. The shock continues moving until it has passed through the throat and is stabilized in the diverging section of the duct. The process of swallowing the starting shock, from the inlet lip to beyond the throat, occurs on the order of convective time scale, namely, $t \sim l/V$, where l is the characteristic diffuser length and V is an average flow speed in the inlet. For a diffuser of ~ 10 ft or ~ 3 m length and an average flow speed of ~ 2000 ft/s or ~ 600 m/s, the starting shock should be swallowed on the order of $\sim 10/2000$ s or ~ 5 ms. This example shows the abruptness of starting and perhaps most importantly the *unstart* process of a supersonic inlet with an internal throat.

We will address the unstart phenomenon later in this chapter. Now, let us examine the movement of a normal shock downstream of the throat, that is, in the diverging section of a C–D inlet. Assuming the shock is in a position that matches the engine-imposed backpressure condition, any shock motion into the duct will cause M_x to increase, therefore p_t after the shock will drop and the mass flow rate is proportionately reduced. A reduced mass flow rate has the effect of an increased backpressure, which in turn pushes the shock back upstream. So, a displaced shock in the diverging section of a duct returns to its original position, which is the essence of a stable system. A similar argument can be applied to a shock displaced in the opposite direction, that is, closer to the throat. In this case, the upstream Mach number of the shock is reduced, therefore the total pressure downstream of the shock is increased, which causes an increase in the mass flow rate and hence a reduced backpressure, which draws the shock to its original position. Again, we demonstrate shock stability in a diverging duct. We may use Figure 6.29 to graphically depict the starting process.

■ FIGURE 6.29 Starting sequence of a C–D inlet and the role of backpressure in positioning the shock



■ **FIGURE 6.30**
The starting shock is pushed toward the inlet lip through overspeeding



We are now ready to examine different starting methods that will place the starting shock in an *incipient* position, namely, at the inlet lip. These include overspeeding, an enlarged throat, and a variable throat geometry C–D inlet.

6.10.2.1 Overspeeding. For a fixed-geometry C–D inlet, a process of *overspeeding* may start the inlet. This method is feasible for low supersonic design Mach number C–D inlets only. The proposition is to offer a reduced spillage condition on the inlet so as to attract the starting shock toward the inlet lip. Eventually, for an overspeed Mach number $M_{\text{overspeed}}$, the starting shock is at the inlet lip. This condition is shown in Figure 6.30 and is known as the incipient inlet start.

EXAMPLE 6.1

Consider an isentropic fixed-geometry C–D inlet, which is designed for $M_D = 1.5$. Calculate the overspeed Mach number that will start this inlet.

SOLUTION

We first establish the design area ratio A_1/A^{th} for a design Mach number of 1.5. From the isentropic table for $\gamma = 1.4$, we have

$$A_1/A_{\text{th}} = A_1/A^* = 1.176$$

Now, if the starting shock is at the lip, the subsonic flow at M_y will have the same A/A^* as the inlet, since the throat is still choked. Therefore we look up the isentropic table for a subsonic Mach number, which corresponds to this area ratio

$$A_y/A^* = 1.176 \xrightarrow[M < 1]{\text{Isentropic table}} M_y \approx 0.61$$

From a normal shock table, we establish a corresponding upstream Mach number M_x or $M_{\text{overspeed}}$.

$$M_y \approx 0.61 \xrightarrow{\text{Normal shock table}} M_x \approx 1.80$$

Therefore,

$$M_{\text{overspeed}} \approx 1.80$$

Now, let us examine an aerodynamic limitation of overspeeding. For this purpose, we assume an infinite overspeed is possible (although both structurally and propulsively impossible). From the normal shock (NS) table, we have

$$M_x \sim \infty \text{ yields a } M_y \rightarrow \sim 0.378$$

Now we look up the isentropic area ratio A/A^* corresponding to $M_y = 0.378$.

$$M_y \approx 0.378 \xrightarrow{\text{Isentropic table}} A_y/A^* \approx 1.666 = A_1/A_{\text{th}}$$

For this area ratio, we find a corresponding supersonic Mach number, which then represents the design Mach number M_D

$$A_1/A^* \approx 1.666 \xrightarrow[M>1]{\text{Isentropic table}} M_1 = M_D \approx 1.99$$

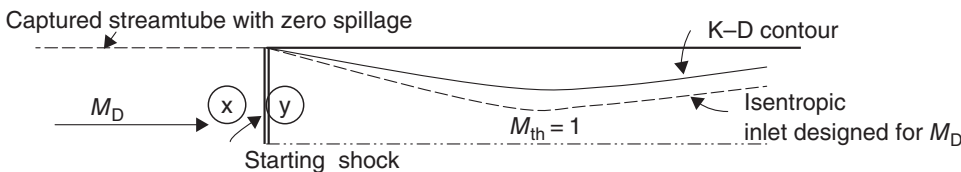
(requires infinite overspeeding)

This example shows that through overspeeding, we cannot even start a C–D inlet designed for a design Mach number of $M_D = 2$. We alluded to structural limitations, infinite loads, as well as propulsive limitations, that is infinite thrust, earlier which prevent infinite overspeeding as a means of starting an inlet. With these limitations, we examine an enlarged throat C–D inlet that is capable of self-starting at the design Mach number. This is called Kantrowitz–Donaldson inlet.

6.10.2.2 Kantrowitz–Donaldson Inlet. Consider a C–D inlet with an enlarged throat area that eliminates spillage of an isentropic C–D inlet at design Mach number. Therefore, we are interested in a C–D duct with a unique contraction ratio that places the starting shock at the inlet lip at the design Mach number. This is called a Kantrowitz–Donaldson (K–D) inlet, which has a self-starting capability (Kantrowitz and Donaldson, 1945). By virtue of having absorbed the spillage mass flow rate at the design Mach number, the throat area of a K–D inlet has to be larger than that of the corresponding isentropic inlet. Let us graph this proposition (Figure 6.31).

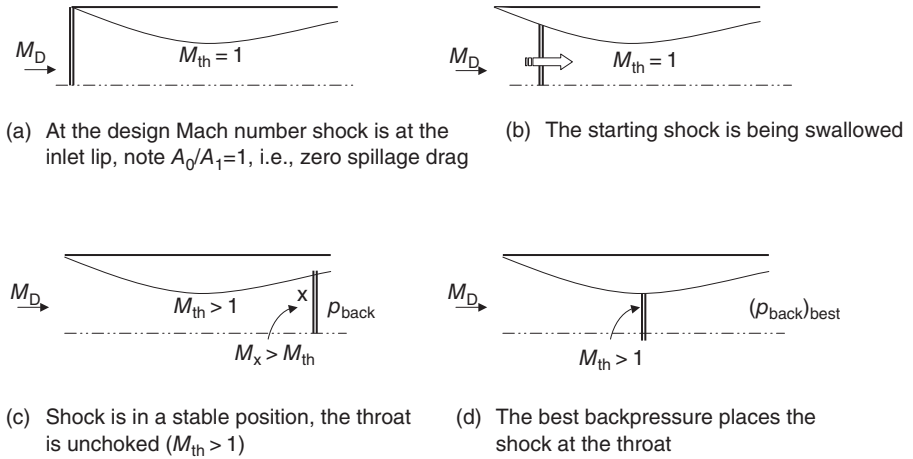
We may quantify the K–D inlet contraction ratio since from the design Mach number, we can establish M_y , which is the M_1 just downstream of the shock. Also assuming an isentropic flow downstream of the shock, we may establish the required area ratio A_1/A_{th} . Once the shock is swallowed and stabilized downstream of the throat, the throat Mach number will be greater than 1. The best backpressure will place the shock at the throat. Note that a normal shock at the throat is unstable and could lead to the phenomenon of unstart, or the shock sweeping backwards through the inlet and causing tremendous spillage drag as well as a loss of engine thrust. For this reason, all supersonic inlets with an internal throat need to actively control the position of the terminal shock in the diverging section of the duct. We will address this issue later in this chapter. Let us graphically depict the various phases of a K–D inlet flow environment from design Mach number M_D to the best backpressure (Figure 6.32a).

We now solve a problem that demonstrates the geometry and capabilities of a K–D inlet.



■ FIGURE 6.31 A K–D inlet at design Mach number (at the moment of incipient start); also note the larger throat area of a K–D inlet as compared with an isentropic inlet designed for M_D

■ **FIGURE 6.32**
The sequence of events
in a
Kantrowitz–Donaldson
inlet



EXAMPLE 6.2

Calculate the contraction ratio A_1/A_{th} , and the maximum total pressure recovery of a self-starting C–D inlet designed for $M_D = 2.65$.

SOLUTION

At the design Mach number, a self-starting inlet has its starting shock at the lip (Figure 6.32a), therefore

$$M_D = M_x = 2.65 \xrightarrow{\text{Normal shock table}} M_y = 0.4996 = M_1$$

$$M_1 = 0.4996 (\sim 0.5) \xrightarrow{\text{Isentropic table}} A_1/A^* \\ \equiv 1.34 = A_1/A_{th}$$

$$\therefore \boxed{A_1/A_{th} \equiv 1.34}$$

The best backpressure places the shock at the throat, thus we need to calculate the throat Mach number M_{th} after the inlet was started. From Figure 6.32c, we note that a supersonic flow at the design Mach number enters the inlet and assuming isentropic deceleration to the throat, we may arrive at the throat Mach number, via the following steps

$$M_D = 2.65 \xrightarrow{\text{Isentropic table}} A_1/A^* = 3.036$$

$$A_{th}/A^* = (A_1/A^*)/(A_1/A_{th}) = 3.036/1.34 \\ = 2.2656 \xrightarrow{\text{Isentropic table } M > 1} M_{th} \sim 2.35$$

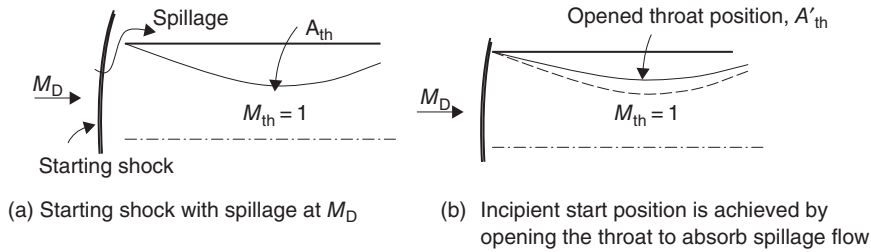
Now we need to place a shock at this Mach number, i.e.

$$(p_{ty}/p_{tx})_{\text{best backpressure}} \xrightarrow{\text{Normal shock table } M_x \sim 2.35}$$

$$\boxed{p_{ty}/p_{tx} \sim 0.5615}$$

Note that the price of a fixed-geometry self-starting C–D inlet is a high throat Mach number and subsequent large total pressure loss. We calculated the throat Mach number, i.e., the lowest Mach number in the duct, of a started K–D inlet designed for Mach 2.65 is ~ 2.35 . This performance penalty of a fixed-geometry inlet suggests the potential advantage of a variable geometry throat inlet. We shall examine such inlets next.

■ **FIGURE 6.33**
Variable-geometry C–D inlet starts by enlarging its throat area (from A_{th} to A'_{th})



6.10.2.3 Variable-Throat Isentropic C–D Inlet. To eliminate spillage flow and attract the starting shock to the inlet lip, a variable geometry inlet opens up its throat to accommodate a higher flow rate and thus begin the starting process. The two shock positions prior to the starting and at the incipient start condition are shown in Figure 6.33.

After the starting shock has swept through the opened throat in the starting process, the throat Mach number becomes supersonic. The opening size of the throat and the throat Mach number are identical to those of the Kantrowitz–Donaldson inlet. However, in this case of variable geometry, we can proceed to close the inlet throat back to its original sonic condition/dimension. The attractiveness of this method of starting a supersonic inlet with an internal throat is the potential for high total pressure recovery, that is, high performance. The price for this performance is paid through the added system weight and complexity associated with multisegmented inlet with actuators, sensors, and a controller needed to operate the inlet.

Now, let us learn, through a sample problem, the important parameters associated with a variable-geometry inlet, namely, the percentage opening of the throat needed to start the inlet, the throat Mach number after the inlet has started.

EXAMPLE 6.3

A supersonic convergent–divergent inlet is to be designed for an isentropic operation (in the started mode) at $M_D = 3.3$. Calculate the inlet design contraction ratio A_1/A_{th} , the

percentage opening of the throat $(A'_{th} - A_{th})/A_{th}$ needed to start the inlet, and the throat Mach number in the open position M'_{th} .

SOLUTION

First, the isentropic area ratio for M_D is read from the isentropic table to be

$$M_D = 3.3 \xrightarrow{\text{Isentropic table}} A_1/A^* = A_1/A_{th} = 5.629$$

Now, at the opened throat position, the starting shock is at the lip, therefore,

$$\begin{aligned} M_D = M_x = 3.3 &\xrightarrow{\text{Normal shock}} M_y = M_1 \\ &= 0.4596 \xrightarrow{\text{Isentropic table}} A_1/A'_{th} \cong 1.425 \end{aligned}$$

Now, we can calculate the percentage throat opening according to

$$\begin{aligned} \frac{A'_{th} - A_{th}}{A_{th}} \times 100 &= \left(\frac{\frac{A'_{th}}{A_1} - \frac{A_{th}}{A_1}}{\frac{A_{th}}{A_1}} \right) \times 100 \\ &= \frac{(1/1.425) - (1/5.629)}{1/5.629} \cong 295\% \end{aligned}$$

Our calculations indicate that the opened throat is roughly three times the size of the isentropic throat to start the inlet designed for Mach 3.3. We can calculate the flow Mach number at the throat, in the open position, once the shock is stabilized downstream of the throat. To get the Mach number we need A'_{th}/A^* , similar to the K–D inlet calculation,

namely,

$$\begin{aligned} A'_{th}/A^* &= (A'_{th}/A_1)/(A^*/A_1) = (1/1.425)/(1/5.629) \\ &\cong 3.950 \xrightarrow{\text{Isentropic table } M>1} M'_{th} \sim 2.95 \end{aligned}$$

We finally proceed to close the throat to achieve $M_{th} = 1$ and a near isentropic flow condition.

6.11 Normal Shock Inlets

A sharp-lipped subsonic diffuser may be used in a supersonic stream without a significant aerodynamic penalty if the free stream Mach number is below ~ 1.6 . As for all supersonic inlets, a shock is formed at or near the inlet, which decelerates the supersonic flow to subsonic. The sharp lip geometry allows for an attached shock, whereas a blunt cowl leading edge creates a bow shock with the attendant external drag penalty. This type of supersonic inlet is short, light weight, and with no movable surfaces, which is suitable for low supersonic Mach applications or low-cost weapon systems development. Let us define the geometry and salient features of a normal shock inlet in Figure 6.34.

The position of the normal shock depends on the inlet backpressure, which is established by the engine. The best backpressure, corresponding to design Mach number, places the normal shock at the lip where the best total pressure recovery coincides with zero spillage drag. This mode of operation is called the *critical* mode. In the event of higher backpressure, that is, when the engine mass flow rate drops, the shock stands outside the inlet and a spillage flow takes place. This is the so-called *subcritical* mode of operation. The shock is drawn into the inlet, beyond the lip, when the engine backpressure is lowered. This is the so-called *supercritical* mode of operation. In the supercritical mode, the shock Mach number is higher than M_0 , hence a larger total pressure drop in the inlet results. Consequently, the corrected mass flow rate at the engine face increases, which results in an increase in axial Mach number, thereby, reducing the engine face static pressure, that is, the inlet backpressure. Furthermore, the shock inside the duct may interact adversely with the wall boundary layer and cause separation and increase engine face distortion.

■ **FIGURE 6.34**
Normal shock inlet is shown with the shock at the lip

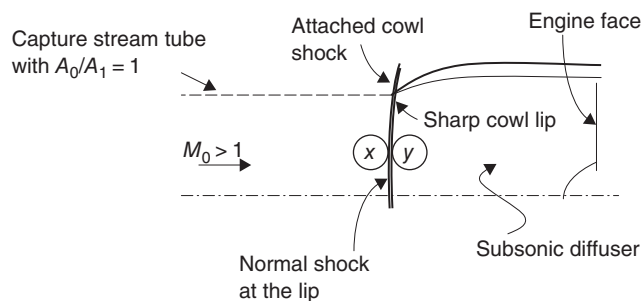
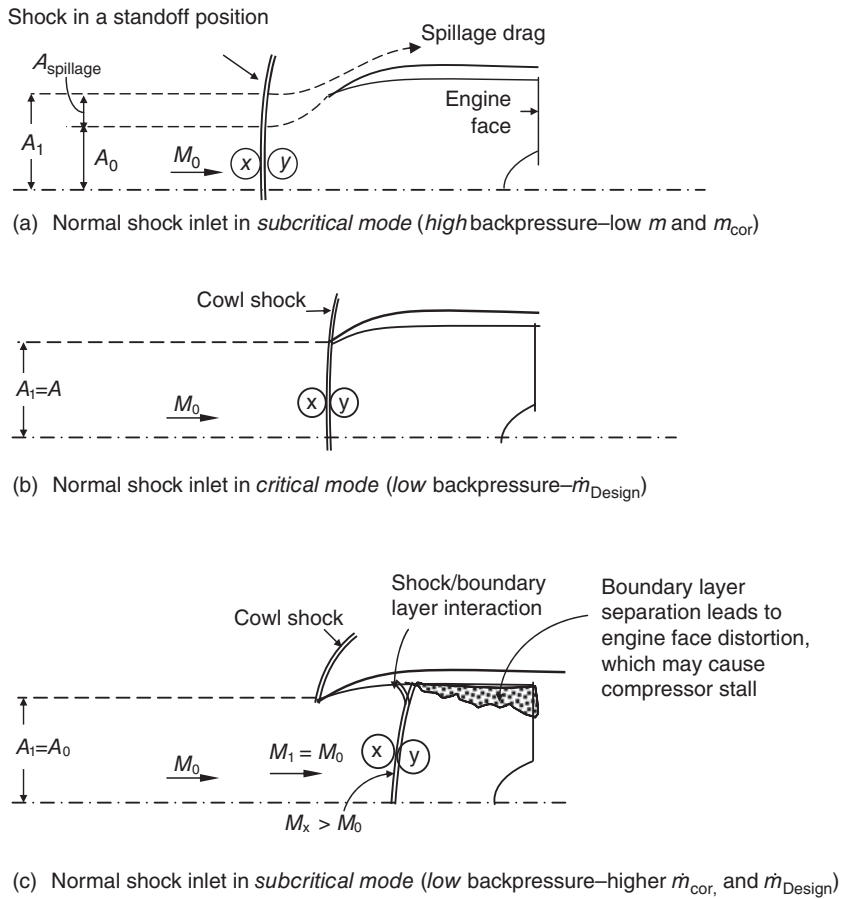
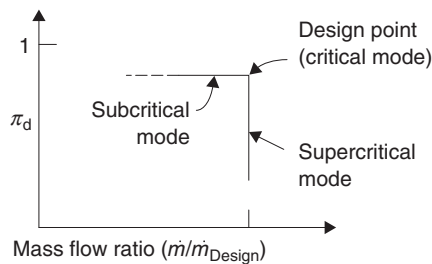


FIGURE 6.35 Three modes of operation of a normal shock inlet show the subcritical mode as an external-performance limiting and the supercritical mode as the internal performance limiting flow conditions with the best mode identified as the critical mode

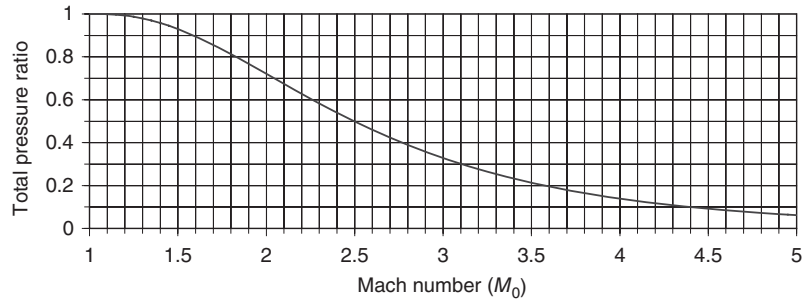


Note that a normal shock inlet has its throat at the lip and hence experiences no starting problem. Even in the sub or supercritical modes the shock is stable. The three modes of operation of a normal shock inlet are shown in Figure 6.35. It is also customary to present the off-design performance of supersonic inlets as a plot of their total pressure recovery versus the inlet mass flow ratio. The design mass flow rate is used as the reference value to create a dimensionless mass flow ratio. A typical graph of shock total pressure recovery versus the mass flow ratio for a NS-inlet is shown in Figure 6.36.

FIGURE 6.36 Typical performance plot of a normal shock inlet



■ **FIGURE 6.37**
Normal shock recovery
as a function of Mach
number ($\gamma = 1.4$)



The total pressure recovery of a normal shock rapidly deteriorates beyond Mach ~ 1.6 , where a $\sim 90\%$ total pressure recovery is achieved. The normal shock recovery as a function of Mach number is graphed in Figure 6.37.

EXAMPLE 6.4

A normal shock inlet operates in a Mach 1.4 stream. Calculate

(a) inlet total pressure recovery with the shock at the lip, i.e., the best backpressure

(b) inlet total pressure recovery when the shock is inside the duct at $A_x/A_1 = 1.1$, i.e., the supercritical mode

(c) inlet total pressure recovery in subcritical mode with 10% spillage, i.e., $A_{\text{spillage}}/A_1 = 0.1$

SOLUTION

We need to establish the shock Mach number in each mode of inlet operation. In case (a), where the shock is at the lip, representing the best backpressure, the shock Mach number is M_0 , therefore,

$$M_0 = 1.4 \xrightarrow{\text{Normal shock table}} p_{t2}/p_{t0} = 0.9582$$

To calculate the shock Mach number when the shock is inside the inlet, we note that the inlet flow may be assumed isentropic all the way to the shock. Hence, we will use A/A^* at the shock, based on upstream flow, to establish the shock Mach number M_x .

$$A_x/A^* = (A_x/A_1)(A_1/A^*)$$

The position of the shock inside the inlet is given as $A_x/A_1 = 1.1$ in the problem statement. The ratio A_1/A^* is purely a function of M_1 via isentropic flow relations, which is known to be $M_1 = M_0 = 1.4$. Therefore,

$$M_1 = 1.4 \xrightarrow{\text{Isentropic table}} A_1/A^* = 1.115$$

$$A_x/A^* = (1.1)(1.115) = 1.226 \xrightarrow{\text{Isentropic table } M > 1}$$

$$M_x \approx 1.56 \xrightarrow{\text{Normal shock table}} p_{t2}/p_{t0} \approx 0.91$$

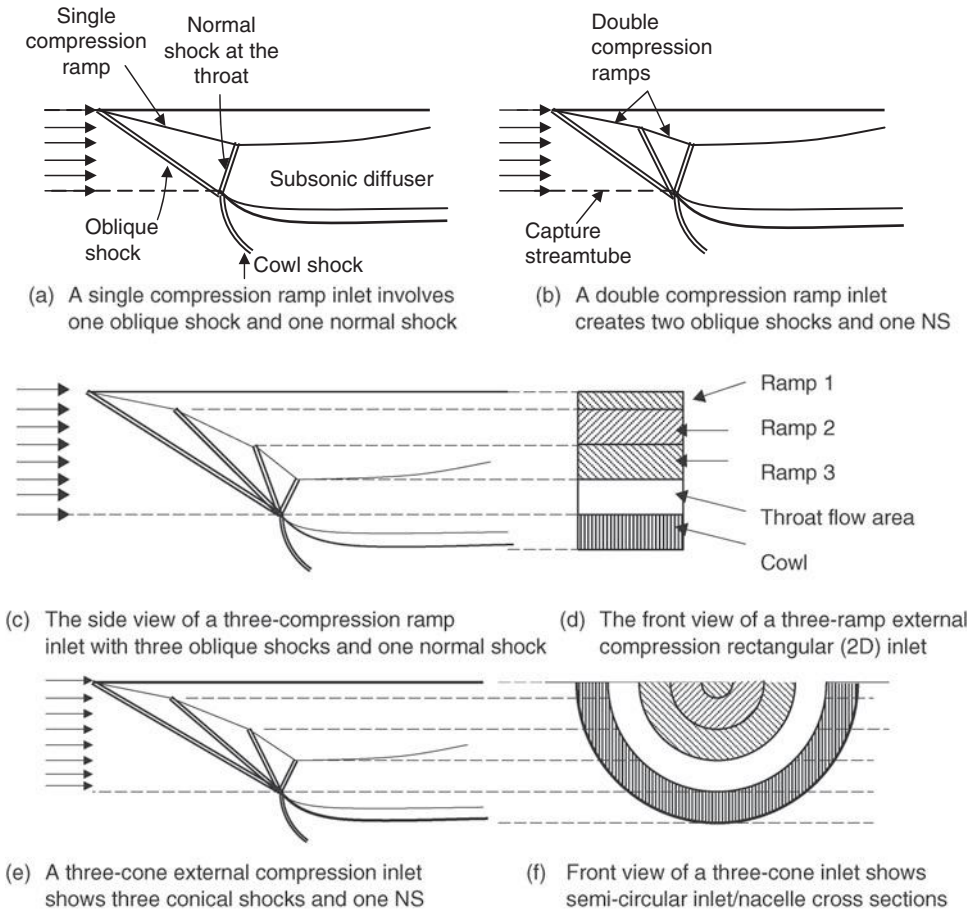
Note that the shock Mach number M_x is higher than M_0 as expected (supersonic Mach number goes up in a diverging duct, i.e., with flow area increase). Also, note that the total pressure recovery is reduced in case (b), again as expected. The other penalty of the supercritical mode of operation is the potential boundary layer separation and engine face distortion, which are complex fluid phenomena and beyond the scope of the present text.

Now, let us address the case (c), where the shock stands outside the inlet and causes spillage. It is quantified as causing a 10% spillage, which is $1 - A_0/A_1$. The shock Mach number, however, is the same as M_0 , hence the same total pressure recovery is expected, i.e.,

Since $M_x = M_0$ in subcritical mode, then

$$p_{t2}/p_{t0} = 0.9582$$

However, we note that the penalty for subcritical mode of operation is the spillage drag D_{spillage} .



■ **FIGURE 6.38** Shock systems of two-dimensional and axisymmetric external compression inlets with the best backpressure placing the terminal (normal) shock at the lip (throat)

6.12 External Compression Inlets

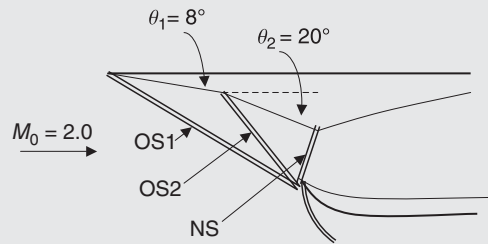
To achieve a higher total pressure recovery than a normal shock inlet, we need to design an inlet configuration that incorporates multiple shocks. Supersonic flow deceleration over multiple shocks is more efficient than the deceleration through a normal shock. Here, the efficiency of the supersonic diffusion process is defined by the total pressure recovery of the shock system. An external compression inlet is designed to maintain the shock system external to the inlet and, hence, has its throat at the cowl lip. The internal duct is hence a subsonic diffuser, which is often a transition duct with offset. Two-dimensional external compression inlets employ external compression ramps to create plane oblique shocks, whereas axisymmetric inlets employ multiple cones to create conical shocks. Single and multiple ramp external compression inlets as well as axisymmetric inlets are shown in Figure 6.38. The position of the normal shock, which is also called a *terminal shock*, is dictated by the inlet backpressure. The optimal location for the normal shock is at the throat where the flow Mach number is the least. With the normal shock at the cowl lip,

the inlet is said to operate at its critical mode, which represents the design point. Figure 6.38 shows several external compression inlets at their design point operation.

The total pressure recovery of the inlet shock system may be calculated via a straight-forward marching technique that we learned in supersonic aerodynamics. Assuming the geometry of the external compression ramp is known (the so-called *design problem*), each ramp angle represents the flow turning θ , which combined with the information on the local Mach number M , leads to a determination of the wave angle β , by using a θ - β - M oblique shock chart (or conical shock charts). The wave angle helps establish the strength of the oblique shock, which depends on the normal component of the flow to the shock, namely, $M_n = M \sin\beta$. Since the local Mach number is only a priori known in station 0, that is, the free stream condition, we need to start with the first oblique shock and continue marching downstream through multiple ramps and shocks. This method is best illustrated through an example.

EXAMPLE 6.5

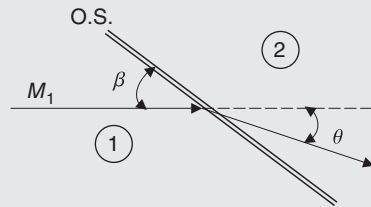
A two-ramp external compression inlet in a supersonic flow is shown. Calculate the total pressure recovery of this inlet assuming the best backpressure has placed the normal shock on the lip. Also compare this inlet to a NS-inlet at Mach 2.0



SOLUTION

The shock total pressure recovery as a function of Mach number M and the wave angle β is

$$\frac{p_{t2}}{p_{t1}} = \frac{\left(\frac{\frac{\gamma + 1}{2} M^2 \sin^2 \beta}{1 + \frac{\gamma - 1}{2} M^2 \sin^2 \beta} \right)^{\frac{\gamma}{\gamma - 1}}}{\left(\frac{2}{\gamma + 1} M^2 \sin^2 \beta - \frac{\gamma - 1}{\gamma + 1} \right)^{\frac{1}{\gamma - 1}}}$$



Therefore, we need to establish the wave angles and the local Mach numbers upstream of every shock. Using an oblique shock chart θ - β - M , any pair of values determines the third. For the first oblique shock (OS1) we know the Mach number and the flow turning angle, i.e.,

OBLIQUE SHOCK 1

$$\begin{array}{l} M_0 = 2.0 \\ \theta = 8^\circ \end{array} \rightarrow \begin{array}{l} \theta - \beta - M \text{ chart} \\ \beta_1 \approx 37^\circ \end{array} \Rightarrow M_{n1} = M_0 \sin \beta = 2 \sin 37^\circ \approx 1.20 \Rightarrow (p_{t2}/p_{t1})_{OS1} \approx 0.993$$

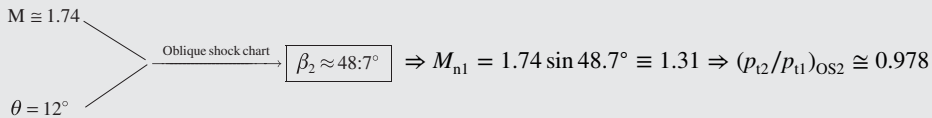
Also, from a normal shock table (or the following equation), we get M_n downstream of the first shock, i.e.,

$$M_{n2}^2 = \frac{2 + (\gamma - 1)M_{n1}^2}{2\gamma M_{n1}^2 - (\gamma - 1)}$$

$$M_{n1} \cong 1.2 \Rightarrow M_{n2} = 0.843 \Rightarrow M_2 = M_{n2} / \sin(\beta - \theta) \cong 0.843 / \sin 29^\circ \cong 1.74$$

Now, we are ready for the oblique shock 2.

OBLIQUE SHOCK 2 We need the Mach number, which was calculated from above to be 1.74 and the turning angle through the second shock. Although the ramp angle is shown to be 20° , note that the flow had already turned by 8° through the first oblique shock, therefore the net turning angle through the second shock is only 12° , hence



$$M_{n1} = 1.31 \Rightarrow M_{n2} \cong 0.782$$

$$M_2 = \frac{M_{n2}}{\sin(\beta - \theta)} \Rightarrow M_2 \cong 0.782 / \sin(36.7^\circ) \cong 1.31$$

NORMAL SHOCK We calculated the local Mach number downstream of the OS2 as $M = 1.31$. Since the flow is normal to the terminal shock, $\beta = 90^\circ$, which may be substituted in the above equation for p_{12}/p_{11} or simply use a normal shock table.

$$M \cong 1.31, \beta = 90^\circ \Rightarrow (p_{12}/p_{11})_{NS} \cong 0.977$$

Overall shock total pressure recovery

$$(p_{12}/p_{11})_{\text{overall}} \cong (p_{12}/p_{11})_{OS1} (p_{12}/p_{11})_{OS2} (p_{12}/p_{11})_{NS} \cong (0.993)(0.978)(0.977) \cong 0.949$$

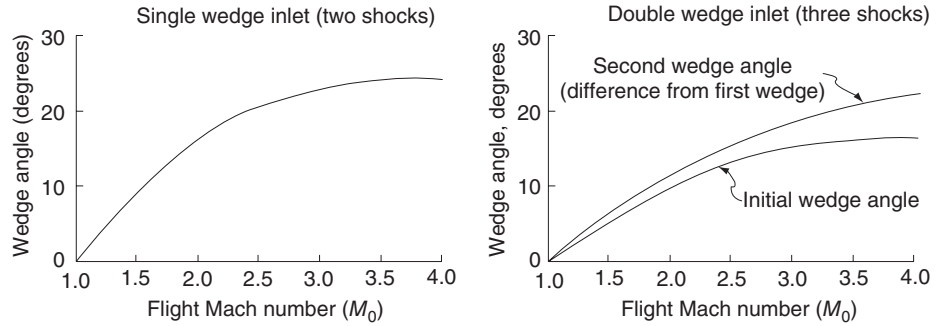
$$(p_{12}/p_{11})_{\text{overall}} \cong 0.949$$

COMPARISON TO A NORMAL SHOCK INLET A normal shock inlet at Mach 2, with the best back-pressure gives a dismal performance, i.e.,

$$(p_{12}/p_{11})_{NS} \cong 0.721$$

We see a tremendous improvement in total pressure recovery where multiple ramps are used.

■ **FIGURE 6.39**
Optimum ramp angles for a single and double-ramp external compression inlet.
 Source: Rodean 1958



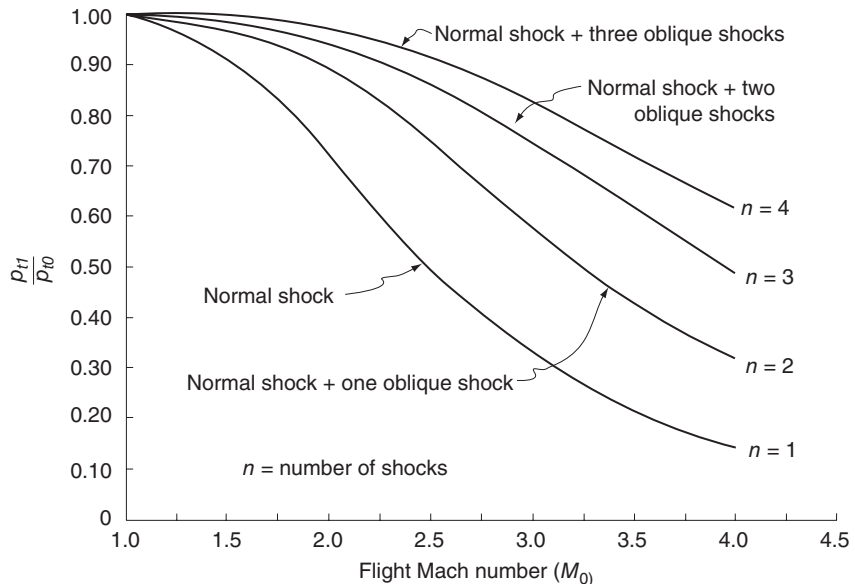
6.12.1 Optimum Ramp Angles

In the previous problem, we arbitrarily chose two ramp angles of 8° and 12° net turning, respectively, for our Mach 2.0 inlet. This design recovered nearly 95% of total pressure through the shock system. A question of optimization arises as to the optimum ramp angles, which lead to a maximum pressure recovery at a given Mach number. So, let us restate the problem in general terms as follows:

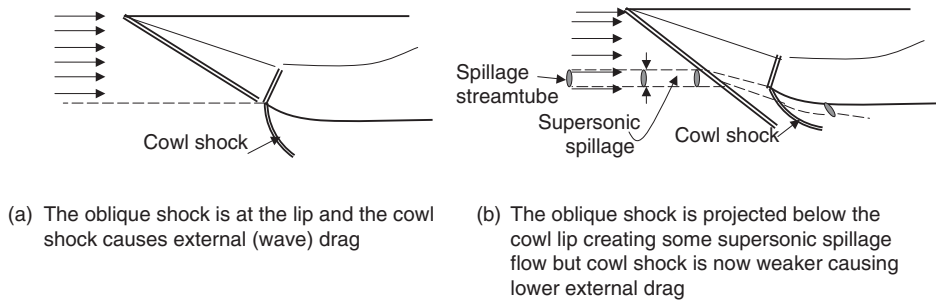
Find optimum ramp angles for a multiramp external compression inlet designed for $M_0 > 0$.

This fundamental aerodynamic question was raised and answered by Oswatitsch in a 1944 German report (translated into English in 1947 as a NACA report). The result is astonishingly simple. It states that in an optimum multishock inlet, all shocks need to be of equal strength. This speaks to the *principle of equal burden*. Hesse and Mumford (1964) in their classical propulsion textbook produced the optimum geometries for a single and double ramp external compression inlet. These are shown in Figures 6.39 and 6.40.

■ **FIGURE 6.40**
Optimum total pressure recovery of external compression inlets. Source: Rodean 1958



■ FIGURE 6.41 Shock location and nacelle wave drag issues



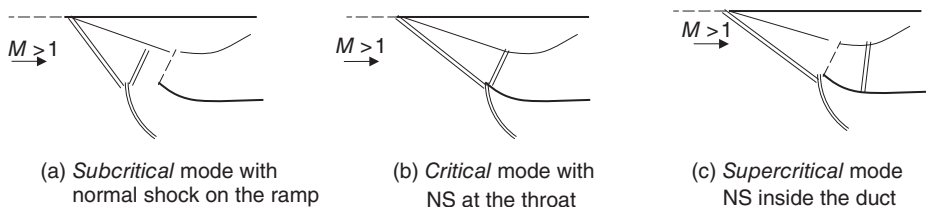
6.12.2 Design and Off-Design Operation

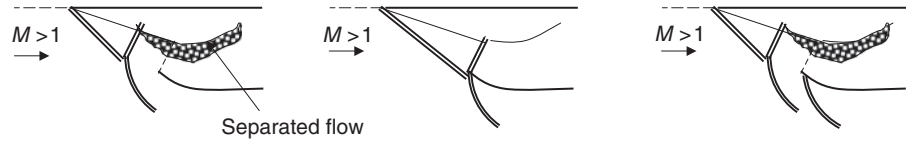
The shock system associated with an external compression inlet determines both the internal performance of the inlet through total pressure recovery as well as the external performance through inlet external drag. The design point operation focuses the oblique shocks onto or slightly below the cowl lip and places the terminal shock exactly at the throat. These two configurations of shocks are graphed (Figure 6.41) for discussion purposes.

Figure 6.41 raises an interesting issue about the spillage and the inlet wave drag. In Figure 6.41a the capture ratio A_0/A_1 is exactly 1, which eliminates any spillage drag. On the contrary, the static pressure rise on the cowl lip due to a strong cowl shock integrates into a wave drag. In Figure 6.41b the configuration of the shock system intentionally misses the cowl lip and hence incurs some spillage drag. Note that the capture ratio A_0/A_1 is less than 1. But, since the flow downstream of the oblique shock has already turned by the ramp inclination angle, any additional turning due to cowl (thickness) creates a weaker cowl shock. Hence, a weaker static pressure rise on the cowl leads to a lower wave drag penalty of the inlet. Here, we learned an important lesson about *system optimization*. Simply stated, a system is more than the sum of its isolated parts! There are interaction laws between the elements of the system that inherently affect system behavior and hence optimization.

The location of the normal shock is dictated by the inlet backpressure. The cowl lip represents the throat and hence the minimum Mach number. The normal shock placement at the throat is hence considered to represent the design point operation, the so-called *critical mode*. With an increase in the backpressure, the normal shock is pushed onto the compression ramp(s) and hence it represents a *subcritical mode* of operation. With a lowered backpressure, the shock is sucked into the inlet, that is, the subsonic diffuser, and it represents a *supercritical mode*. These are shown in Figure 6.42.

■ FIGURE 6.42 Definition sketch for external compression inlet modes of operation





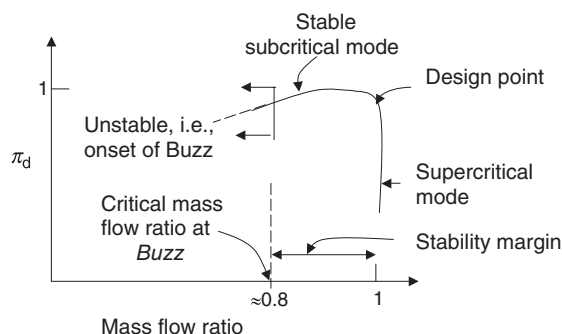
■ **FIGURE 6.43** A *Buzz instability* cycle showing (from left) a blocked throat, reduced backpressure, shock movement toward the lip, pressure buildup, pushing the shock back out sequence

The off-design operations involve subcritical and supercritical modes. The normal shock inside the subsonic diffuser, as shown in Figure 6.42c, results in a lower total pressure recovery, as well as a potential boundary layer separation, engine face distortion. The lower total pressure recovery of this mode of operation is due to a stronger normal shock inside the duct than the shock at the throat. The method of calculation of the shock strength is identical to the supercritical mode of a normal shock inlet (see example problem solved). On the shock boundary layer interaction inside the duct, we may have to employ active or passive viscous flow control techniques, for example, boundary layer suction, vortex generators, and so on. We will address the flow control schemes that may be utilized to stabilize a boundary layer later in this chapter.

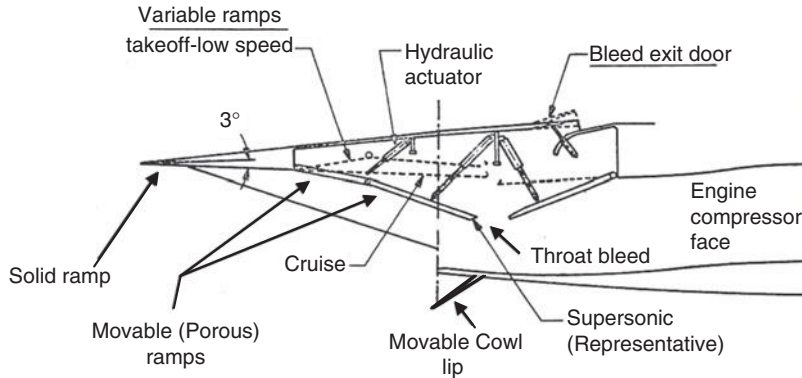
With an increasing backpressure in the inlet, the normal shock is pushed out of the inlet lip and onto the external compression ramps. There are three major penalties associated with this mode of operation. One, the spillage drag increases significantly. Two, the intersecting shocks outside the inlet create a vortex sheet (shear layer), which creates a distortion at the engine face. Three, the normal shock on the ramp could separate the boundary layer and cause a large amplitude oscillatory flow pulsation, with high levels of distortion at the engine. This oscillatory flow is called *Buzz* instability and is worth a closer examination. The separated boundary layer of the ramps partially blocks the throat. To supply the engine with its desired flow rate, the blocked throat experiences fluid acceleration and hence the shock backpressure drops. This will cause the shock to be attracted to the inlet lip. However, at the inlet lip position, the engine is supplied with more flow than it needs; therefore, the shock is pushed back out onto the ramps. An oscillatory back and forth flow is now ensued. A complete *Buzz instability* cycle is shown in Figure 6.43.

It is customary to capture the overall performance of external compression inlets in a total pressure recovery graph versus mass flow ratio. A typical example is shown in Figure 6.44.

■ **FIGURE 6.44** Typical external compression inlet performance plot



■ **FIGURE 6.45**
Variable geometry inlet shows a movable cowl lip, ramp actuation at different flight phases and a bleed exit door.
Source: Adapted from Abernethy and Roberts 1986



6.13 Variable Geometry—External Compression Inlets

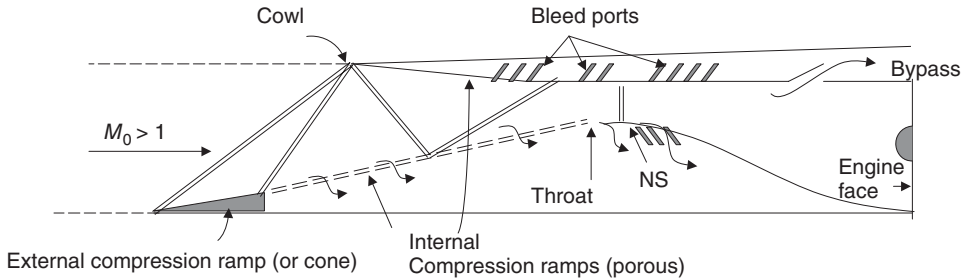
As noted earlier, the ramp angles for optimum total pressure recovery are a strong function of flight Mach number (Figures 6.39 and 6.40). In addition, the engine mass flow rate demands are different at different Mach numbers, altitudes within the flight envelope. For these reasons, the external compression ramps (or cones) need to be equipped with actuators (presently hydraulic) that control their position in various flight phases. Also, the buzz instability improvement/elimination as well as engine face distortion level control demand boundary layer management techniques that require variable geometry. Let us address these and other performance optimizing techniques used in this class of supersonic inlets. Although in our discussions, we refer to ramps, as in 2D inlets, similar statements can be made for cones and axisymmetric inlets.

6.13.1 Variable Ramps

The leading ramp, for structural reasons, is a fixed-geometry solid wedge, typically 3–5°. The following ramps may be extended into the flow or withdrawn from the flow using hydraulic actuators. The withdrawn position, which is also referred to as collapsed ramp position, allows for a larger inlet area needed for the takeoff, climb, subsonic cruise, and transonic acceleration. Figure 6.45 shows a typical 2D variable geometry external compression inlet (Abernethy and Roberts 1986).

6.14 Mixed-Compression Inlets

To achieve the entire supersonic deceleration outside an inlet, as in the external compression inlet, is only economical at flight Mach numbers below ~ 2.5 . The penalty comes from excessive cowl wave drag, as the cowl lip has almost the same inclination, with respect to the flow, as that of the last compression ramp of the inlet. A large flow deceleration needs a large supersonic flow turning and hence the cowl lip angle may exceed the θ_{\max} of the oblique shock, resulting in a bow shock formation. To alleviate this performance limitation of external compression inlets, that is, to reduce the curvature of the cowl lip, we need to allow for internal shock reflections and obviously an internal throat. An inlet with these characteristics exhibits a mixed compression behavior and hence earns the name. A schematic drawing of a mixed compression inlet is shown in Figure 6.46.



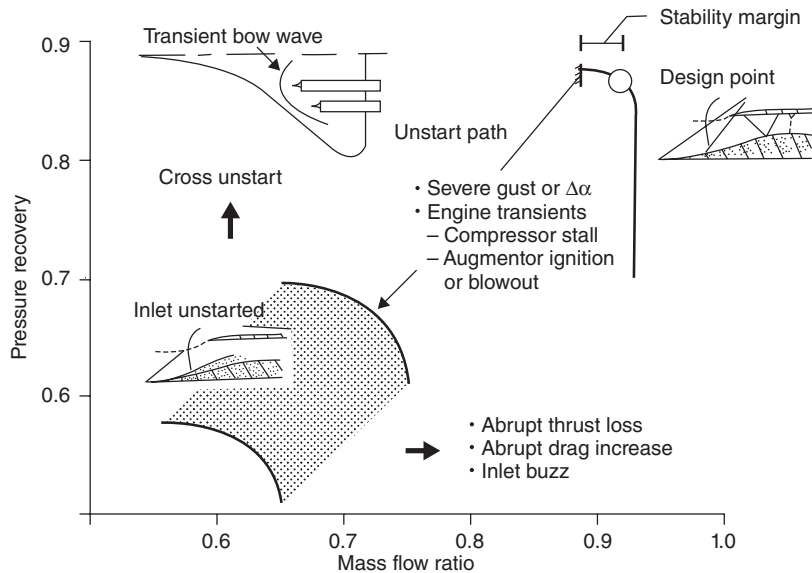
■ **FIGURE 6.46** A mixed compression inlet with external and internal shocks, an internal throat

The operational Mach number of a mixed compression inlet extends to \sim Mach 4.0–5.0. Since we can allow multiple ramps both outside and inside of the inlet without a concern on a cowl wave drag penalty, we may achieve a rather high total pressure recovery characteristic with this inlet. However, the presence of an internal throat indicates an inherent starting problem. The presence of external compression surfaces indicates a Buzz instability in the unstart mode. The shocks that are created and reflected from solid surfaces inside the duct alert us to the shock boundary layer interaction problems with flow separation and engine face distortion as serious byproducts. The sharp cowl lips or the centerbody indicate sensitivity to misaligned flow, which is expected with takeoff, climb, landing, maneuver, and side wind. Now, let us summarize the challenge areas for mixed compression inlet design/operation:

1. Starting problem
2. *Buzz* in unstart mode (subcritical instability)
3. Shock-induced separated boundary layers and distortion
4. Unstart problem, (i.e., terminal shock stability margin)
5. Sensitivity to angle of attack, sideslip

The starting problem demands a variable throat inlet for practical purposes, as discussed earlier in the internal compression inlet section. In case of axisymmetric inlets, the centerbody assumes a translational displacement to open and close the throat area. Two-dimensional compression ramps, however, may be collapsed or deployed using a hinged flap design with hydraulic actuators. The origin of Buzz in unstart mode is the boundary layer separation off of compression ramps. Consequently, boundary layer suction and throat bleed need to be employed to overcome this instability. The separated boundary layers inside the duct, as a result of shock boundary layer interaction, also dictate a boundary layer bleed strategy through porous surfaces or slots to be incorporated in critical duct areas. The unstart problem, or providing an adequate stability margin for the normal shock in the divergent portion of the inlet, demands a shock position sensor as well as fast acting valves to alleviate the backpressure problem. A shock position sensor may be a pair of pitot tubes mounted in the desired location on the wall of the diffuser downstream of the throat. The terminal shock is to remain between these two pitot tubes. In the event of increasing backpressure, where the shock is pushed toward the throat (and potentially beyond it to the unstart position), the pitot tube reading suddenly drops and indicates the shock crossing. Fast acting valves are to be opened to dump the excessive flow from the downstream position so as to relieve the backpressure and stabilize the

■ **FIGURE 6.47**
Performance plot of a
mixed-compression
inlet. Source: Strack
1987. Courtesy of
NASA



shock. Since the two pitot tubes confine the position of the shock, they are also called a *shock trap*.

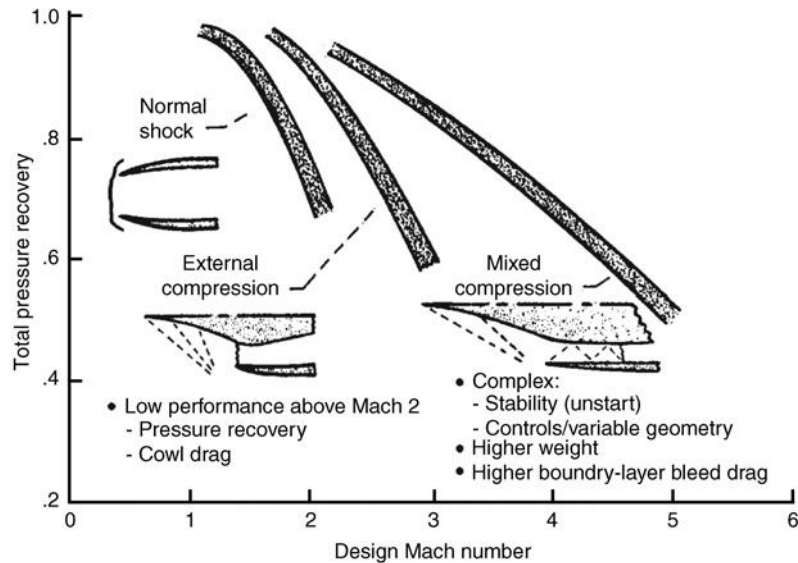
The sensitivity to flow angularity is caused by the sharp cowl and centerbody configuration of these inlets. Although supersonic design demands a sharp leading edge of the cowl, wing, and so on, the low-speed operation is hampered by flow separation off of sharp corners/edges. Hence, articulating cowl, movable lip, cowl slot, spike bleed, and other boundary layer control techniques must be used to overcome the inherently poor low-speed characteristics of these inlets. Figure 6.47 shows the performance plot of a mixed-compression inlet (from Strack, 1987).

Schweikhard and Montoya (1974) also present valuable operational information on mixed compression inlets that is recommended for further reading.

6.15 Supersonic Inlet Types and Their Performance—A Review

Supersonic inlets invariably involve shocks to decelerate the flow to subsonic engine face Mach numbers. For subsonic throughflow engines, as in all the existing conventional engines, the deceleration to subsonic Mach number implies the placement of a normal shock somewhere in the inlet stream. The simplest supersonic diffuser, therefore, utilizes a single normal shock to achieve the desired flow deceleration. This is a good and simple solution for low supersonic Mach numbers such as $M_0 \geq 1.6$. Beyond this Mach number, the normal shock deceleration becomes inefficient, as it creates excessive total pressure loss. To extend the operational Mach numbers to ~ 2.5 , a series of oblique shocks decelerate the flow through external compression ramps or cones prior to the normal shock appearance near the cowl lip. This type of inlet was called an external compression inlet and exhibited good internal and external flow qualities for up to $M_0 \sim 2.5$. The cowl wave drag was the limiting performance parameter for the external compression inlet. We also discovered that when the normal shock is pushed out onto the ramp (i.e.,

■ **FIGURE 6.48**
Performance of
supersonic inlets with
flight Mach number.
Source: Strack 1987.
Courtesy of NASA

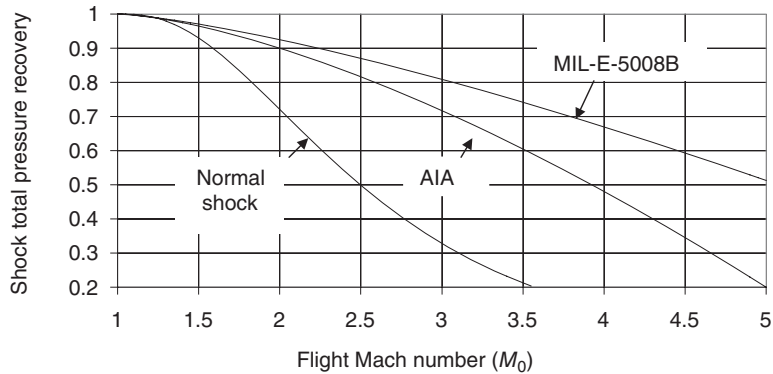


the subcritical mode), the potential flow separation could cause a shock/flow oscillation that was called *Buzz instability*. To operate without buzz or simply to widen the stability margin of external compression inlets required the boundary layer removal from the compression ramps and incorporating a throat slot for bleed purposes. To reduce the cowl wave drag at higher supersonic Mach numbers, that is, $M_0 > 2.5$, was to invite internal shock reflections and an internal throat into our design approach. Such inlets were called mixed-compression inlets, which produced the highest overall (internal and external) performance for $2.5 < M_0 < 5.0$. The internal throat created another form of instability, namely, the starting and unstarting instability of the inlet. Variable geometry throat offered a practical starting approach to mixed-compression inlets. To avoid unstart meant controlling the inlet backpressure through a shock trap with a fast acting bleed valve and a bypass secondary flow control valve integrated in the subsonic diffuser. To manage the engine face distortion levels, in the face of multiple shocks inside the duct, required excessive bleeding of the boundary layer. The thrust penalty for the boundary layer bleed was the price to pay for the mixed-compression inlet. For hypersonic Mach numbers, internal compression inlets offer the lowest engine installation wave drag. In addition, flow deceleration through multiple shocks and their reflections inside a duct is preferred over fewer shock decelerations. However, the normal shock could be eliminated altogether if the engine design allowed for supersonic throughflow. A supersonic throughflow fan and a supersonic combustion ramjet (scramjet) are examples of this kind of modern thinking in hypersonic propulsion. The performance plot of the first three supersonic inlets, as a function of flight Mach number, is shown in Figure 6.48 (from Strack, 1987).

6.16 Standards for Supersonic Inlet Recovery

Here, we introduce two standard recoveries in existence today, one according to Aircraft Industries Association (AIA) and the second one due to the Department of Defense,

■ **FIGURE 6.49**
Standards of inlet recovery compared to a normal shock inlet



known as the MIL-E-5008B standard. These standards that address the shock recovery of supersonic inlets are

$$\pi_d = 1 - 0.1(M_0 - 1)^{1.5} \quad 1 < M_0 \quad \text{AIA-Standard} \quad (6.34)$$

$$\pi_d = 1 - 0.075(M_0 - 1)^{1.35} \quad 1 < M_0 < 5 \quad \text{MIL-E-5008B} \quad (6.35)$$

$$\pi_d = 800 / (M_0^4 + 935) \quad 5 < M_0 \quad \text{MIL-E-5008B} \quad (6.36)$$

Now, let us graph the standard recoveries and compare them to a normal shock inlet (Figure 6.49).

In Figure 6.49, we intentionally stop at Mach 5, as we approach the hypersonic regime. The AIA standard is seen to be rather conservative, as compared with the MIL-E-5008B standard. The normal shock recovery, as noted earlier, loses its attractiveness around Mach 1.6. It is interesting to note that these standards date back to 1950s! With the development of smart structures and advanced flow control techniques of today, the MIL-E-5008B is deemed to be a conservative standard as well. These inlet recovery standards are reproduced here for reference and historical perspective.

Further readings on supersonic inlets and aircraft integration (references 19, 32 and 35) are recommended.



XB-70 (shown in flight) is a Mach-3 aircraft with advanced inlets.
Source: Courtesy of NASA

6.17 Exhaust Nozzle

A modern aircraft exhaust system is tasked with the following design objectives:

- Efficient expansion of the engine gases to ambient pressure
- Low installation drag
- Low noise
- Low cooling requirements
- Efficient thrust reversing capability
- Efficient thrust vectoring capability
- Low observables (radar, thermal, IR signature)
- Light weight system
- Low-cost manufacturing

In this section, we address the parameters that influence the above design goals in a realistic nozzle. First, we review nozzle performance parameters/figures of merit that we learned in our one-dimensional cycle analysis, such as gross thrust, nozzle adiabatic efficiency, and nozzle total pressure ratio. Specialized topics in nozzle cooling, thrust reversing and thrust vectoring, hypersonic nozzles, and exhaust mixers are also presented.

6.18 Gross Thrust

The nozzle contribution to engine thrust is called gross thrust. It comprises two terms, namely, the momentum thrust and the pressure thrust, as we discussed in Chapters 3 and 4.

$$F_g \equiv \dot{m}_9 V_9 + (p_9 - p_0)A_9 \quad (6.37)$$

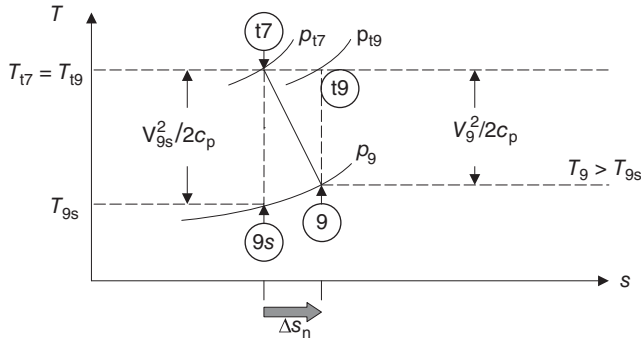
The first term on the RHS represents the momentum thrust and the second term is the pressure thrust. The gross thrust of a nozzle is maximized when it is operated as fully expanded. A nozzle is fully expanded when the static pressure in the exhaust plane and the ambient static pressure are the same, that is, $p_9 = p_0$. As we learned earlier, all subsonic jets are perfectly expanded. In choked convergent nozzles as well as supersonic and hypersonic nozzles, the exit static pressure may be different than the ambient pressure. These are referred to as the under- or overexpanded nozzles.

6.19 Nozzle Adiabatic Efficiency

The ratio of actual kinetic energy at the nozzle exit to the ideal kinetic energy that emerges from an isentropic expansion in the nozzle is defined as the nozzle adiabatic (or isentropic) efficiency, that is

$$\eta_n \equiv \frac{h_{t7} - h_9}{h_{t7} - h_{9s}} = \frac{V_9^2/2}{V_{9s}^2/2} \quad (6.38)$$

■ **FIGURE 6.50**
Adiabatic expansion
process in a nozzle with
loss



The fraction of the gas thermal energy that is not converted into directed kinetic energy at the exit plane of the nozzle is dissipated into heat in the boundary layers and across shocks. Thus, actual exhaust gas has a higher exit static temperature than the exhaust gas emerging from an isentropic nozzle, that is, $T_9 > T_{9s}$. These behaviors are best described using a T - s diagram (Figure 6.50).

6.20 Nozzle Total Pressure Ratio

We have identified nozzle total pressure ratio π_n as a figure of merit. Its definition is

$$\pi_n \equiv p_{t9}/p_{t7} \tag{6.39}$$

This parameter is a direct measure of flow irreversibility, that is, due to friction and shock, in the nozzle. Recall that the nondimensional entropy rise in an adiabatic process is negative natural logarithm of total pressure ratio, namely,

$$\frac{\Delta s}{R} = -\ln \left(\frac{p_{t9}}{p_{t7}} \right) \tag{6.40}$$

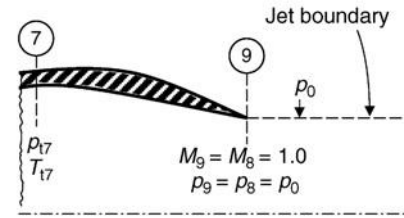
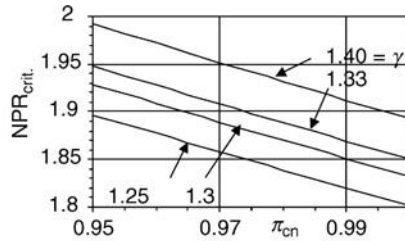
6.21 Nozzle Pressure Ratio (NPR) and Critical Nozzle Pressure Ratio (NPR_{crit.})

An important operational parameter of a nozzle is the NPR. It is defined as

$$\text{NPR} \equiv \frac{p_{t7}}{p_0} \tag{6.41}$$

This parameter signifies the nozzle flow expansion potential (i.e., from the stagnation or total state at 7 to the ambient static state at 0). Since p_0 is the ambient pressure, nozzle pressure ratio is a strong function of altitude, demanding higher area expansion ratios of the nozzle with altitude (hence, a variable geometry). The choice of a convergent or a

■ **FIGURE 6.51**
Critical nozzle pressure ratio for different gas temperature/composition and internal total pressure loss parameter (a *Rule of Thumb* is that the critical nozzle pressure ratio is ~2)



(a) Critical pressure ratio for a convergent nozzle

(b) Convergent nozzle operating at NPR_{crit}

convergent–divergent nozzle can also be guided based on the magnitude of this parameter, that is, the nozzle pressure ratio.

A critical nozzle pressure ratio leads to a sonic throat with $p_9 = p_8 = p_0$ for a convergent nozzle. It may be thought of as the minimum nozzle pressure ratio that chokes an expanding nozzle. We may write

$$p_{t8} = p_8 \left(1 + \frac{\gamma - 1}{2} M_8^2 \right)^{\frac{\gamma}{\gamma - 1}} = p_0 \left(\frac{\gamma + 1}{2} \right)^{\frac{\gamma}{\gamma - 1}} \quad (6.42)$$

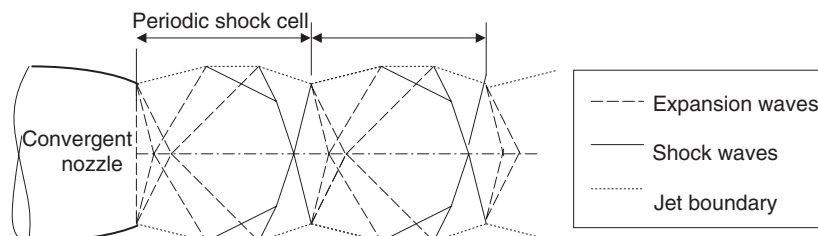
By introducing a total pressure loss from nozzle inlet to the throat, we may recast Equation 6.42 as

$$\frac{p_{t7}}{p_0} = \text{NPR}_{\text{crit}} = \frac{1}{\pi_{\text{cn}}} \left(\frac{\gamma + 1}{2} \right)^{\frac{\gamma}{\gamma - 1}} \quad (6.43)$$

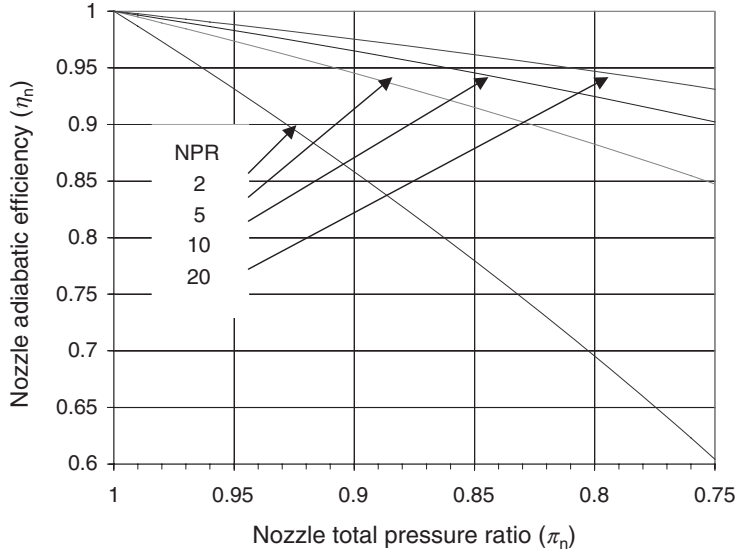
where π_{cn} is the convergent nozzle total pressure ratio. Now, let us graph this equation for different gas temperature/composition and loss parameter in Figure 6.51a (shown for a convergent nozzle).

A convergent nozzle that operates with a higher pressure ratio than the critical will still have an exit Mach number of 1, except the static pressure in the exit plane, p_9 , will be higher than the ambient static pressure p_0 . To relieve the high pressure in the jet at the exit plane, centered expansion waves at the nozzle exit cause a flow deflection with subsequent shock wave formations. The exhaust flowfield of a convergent nozzle that operates with $\text{NPR} > \text{NPR}_{\text{crit}}$ is schematically shown in Figure 6.52.

■ **FIGURE 6.52**
An underexpanded convergent nozzle with a periodic shock cell in its exhaust plume



■ **FIGURE 6.53**
Exhaust nozzle figures
of merit for a
perfectly-expanded
nozzle with $\gamma = 1.30$



6.22 Relation Between Nozzle Figures of Merit, η_n and π_n

The two figures of merit for an adiabatic nozzle flow, η_n and π_n , are related to each other, via

$$\eta_n = \frac{\left\{ \text{NPR} \left(\frac{p_0}{p_9} \right) \right\}^{\frac{\gamma-1}{\gamma}} - \pi_n^{-\frac{\gamma-1}{\gamma}}}{\left\{ \text{NPR} \left(\frac{p_0}{p_9} \right) \right\}^{\frac{\gamma-1}{\gamma}} - 1} \quad \text{or} \quad \eta_n = \frac{\{ \text{NPR} \}^{\frac{\gamma-1}{\gamma}} - \pi_n^{-\frac{\gamma-1}{\gamma}}}{\{ \text{NPR} \}^{\frac{\gamma-1}{\gamma}} - 1} \quad \text{for } p_9 = p_0 \quad (6.44)$$

Figure 6.53 is a graph of Equation 6.44 for a perfectly expanded nozzle, $p_9 = p_0$.

We note that the nozzle adiabatic efficiency improves with the nozzle pressure ratio, as expected. Furthermore, the nozzle adiabatic efficiency is diminished with a decreasing nozzle total pressure ratio, as shown in Figure 6.53. With no loss of total pressure in the nozzle (i.e., $\pi_n = 1$), the adiabatic efficiency is 100%.

6.23 A Convergent Nozzle or a De Laval?

When do we choose a convergent–divergent nozzle with its added weight and complexity over a simple, lightweight convergent nozzle? To answer this question, we need to assess the gross thrust performance gain of a De Laval nozzle over a convergent nozzle at a given nozzle pressure ratio. Alternatively, we need to assess the gross thrust penalty of a convergent nozzle operating in an underexpanded mode. Assuming an adiabatic and

reversible, that is, isentropic, expansion process in the convergent–divergent nozzle, we can write

$$V_9 = \sqrt{2h_{t8} \left(1 - \frac{T_9}{T_{t9}}\right)} = \sqrt{2h_{t8} \left[1 - \left(\frac{p_9}{p_{t9}}\right)^{\frac{\gamma-1}{\gamma}}\right]} = \sqrt{2h_{t8} \left[1 - \left(\frac{p_0}{p_{t7}}\right)^{\frac{\gamma-1}{\gamma}}\right]} \quad (6.45)$$

The gross thrust of a perfectly expanded convergent–divergent nozzle is

$$F_{g-CD} = \dot{m}_9 V_9 \quad (6.46)$$

A convergent nozzle will produce a choked exit flow with $M_9 = 1$ for all nozzle pressure ratios beyond the critical (i.e., NPR of roughly ~ 2). Therefore,

$$\begin{aligned} F_{g-Conv.} &= \dot{m}_9 V_9 + (p_9 - p_0)A_9 = \dot{m}_9 V_9 \left(1 + \frac{p_9(1 - p_0/p_9)A_9}{\rho_9 V_9^2 A_9}\right) \\ &= \dot{m}_9 V_9 \left(1 + \frac{1 - p_0/p_9}{\gamma M_9^2}\right) \end{aligned} \quad (6.47)$$

We may express the static pressure ratio p_0/p_9 in terms of the nozzle pressure ratio and exit Mach number, that is 1 (note that for a convergent nozzle stations 8 and 9 coincide, i.e., throat is at the exit).

$$\frac{p_0}{p_9} = \frac{p_0}{p_{t9}} \frac{p_{t9}}{p_9} = \frac{p_0}{p_{t9}} \left(1 + \frac{\gamma-1}{2} M_9^2\right)^{\frac{\gamma}{\gamma-1}} = \frac{p_0}{p_{t7}} \left(\frac{\gamma+1}{2}\right)^{\frac{\gamma}{\gamma-1}} \quad (6.48)$$

The exit velocity V_9 may be written in terms of total and static enthalpy according to

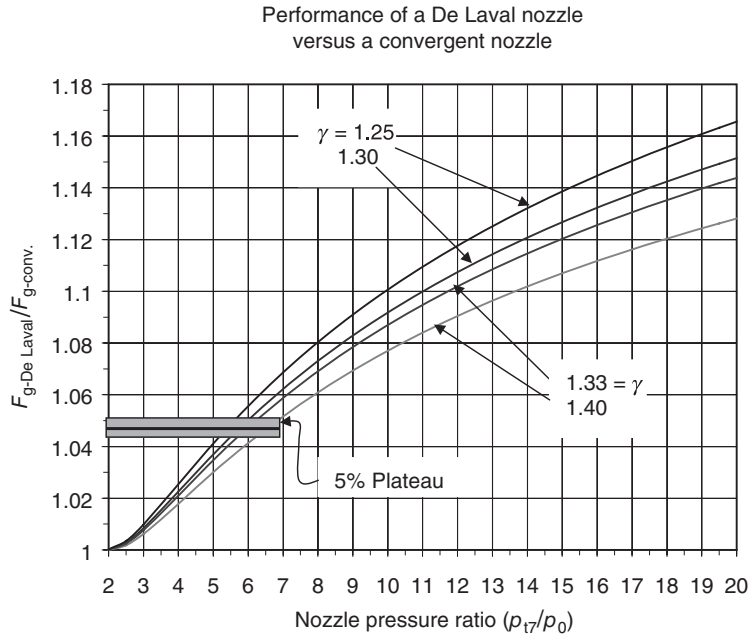
$$\begin{aligned} V_9 &= \sqrt{2h_{t9} \left(1 - \frac{T_9}{T_{t9}}\right)} = \sqrt{2h_{t9} \left(1 - \frac{1}{1 + \frac{\gamma-1}{2} M_9^2}\right)} = \sqrt{2h_{t9} \left(1 - \frac{2}{\gamma+1}\right)} \\ &= \sqrt{2h_{t9} \left(\frac{\gamma-1}{\gamma+1}\right)} \end{aligned} \quad (6.49)$$

Now, taking the ratio of the gross thrust developed by a perfectly expanded De Laval nozzle and the gross thrust produced by a convergent nozzle that is under-expanded, we have

$$\frac{F_{g-CD}}{F_{g-Conv.}} = \sqrt{\frac{1 - \text{NPR}^{-\frac{\gamma-1}{\gamma}}}{\frac{\gamma-1}{\gamma+1}}} \frac{\gamma}{\gamma + \left(1 - \left(\frac{\gamma+1}{2}\right)^{\frac{\gamma}{\gamma-1}} \cdot \text{NPR}^{-1}\right)} \quad (6.50)$$

The two parameters that affect the ratio of gross thrusts in Equation 6.50 are the nozzle pressure ratio and the gas ratio of specific heats γ . We have plotted this equation in Figure

FIGURE 6.54
Thrust producing capability of an ideal convergent–divergent nozzle in comparison to a convergent nozzle



6.54 where we note that a ~5% gross thrust gain is achieved by a De Laval nozzle over a simple convergent nozzle at nozzle pressure ratios of ~6. In the case of a hot exhaust gas, that is $\gamma \sim 1.30$, we observe that the 5% gain in nozzle thrust is achieved at a lower NPR, namely, 5.5. Hence, we may conclude that for a nozzle pressure ratio >5.5 , it *pays* (through a gross thrust enhancement of at least 5%) to choose a convergent–divergent nozzle over a convergent nozzle.

Our discussion of exhaust nozzle performance to this point was based on one-dimensional flow analysis. Now, we are ready to address the influence of multidimensionality of real fluid environments, such as the influence of fluid viscosity through boundary layer formation and the influence of nonaxial exit flow on nozzle gross thrust.

EXAMPLE 6.6

An exhaust nozzle has a pressure ratio of 8, i.e., $p_{t7}/p_0 = 8$. The ratio of specific heats for the gas is $\gamma = 1.3$. Calculate the percentage increase in gross thrust if we were to

expand the gas in an ideal convergent–divergent nozzle as compared with a convergent nozzle.

SOLUTION

The gross thrust of a perfectly expanded convergent–divergent nozzle is

$$F_{g,C-D} = \dot{m}_9 V_9$$

The ideal exhaust velocity is derived in Equation 6.45 to be

$$V_9 = \sqrt{2h_{t8} \left[1 - \left(\frac{p_0}{p_{t7}} \right)^{\frac{\gamma-1}{\gamma}} \right]} = \sqrt{2h_{t8}(0.3811)}$$

The gross thrust in a convergent nozzle is derived in Equation 6.47 to be

$$F_{g-\text{Conv.}} = \dot{m}_9 V_9 \left(1 + \frac{1 - \frac{p_0}{p_9}}{\gamma M_9^2} \right)$$

$$= \dot{m}_9 V_9 [1 + (1 - p_0/p_9)/\gamma]$$

The exit Mach number $M_9 = 1.0$ and $p_9 > p_0$. We derived an expression for the static pressure ratio p_0/p_9 in Equation 6.48 in terms of NPR to be

$$\frac{p_0}{p_9} = \frac{p_0}{p_{t7}} \left(\frac{\gamma + 1}{2} \right)^{\frac{\gamma}{\gamma-1}} \approx 0.229$$

The nozzle exit velocity V_9 is $V_9 = \sqrt{2h_{t8}(\gamma - 1)/(\gamma + 1)} = \sqrt{2h_{t8}(0.1304)}$

Therefore, the ratio of the two gross thrusts is

$$\frac{F_{g,\text{C-D}}}{F_{g-\text{Conv}}} = \frac{V_{9\text{C-D}}}{V_{9-\text{con}}[1 + (1 - 0.229)/1.3]}$$

$$\approx \sqrt{\frac{0.381}{0.1304}} \frac{1}{1.59}$$

$$\approx 1.073$$

7.3% increase in gross thrust

6.24 The Effect of Boundary Layer Formation on Nozzle Internal Performance

The presence of a boundary layer on a surface represents a displacement thickness δ^* , which act as a *blockage* of the geometric flow area. There is also a total pressure loss associated with the boundary layer formation on the wall, namely, $p_{t8}/p_{t7} < 1$. The combined effect of these parameters on the mass flow rate is represented through a discharge coefficient C_{D8} as

$$C_{D8} \equiv \frac{\dot{m}_8}{\dot{m}_{8i}} = \frac{A_{8\text{eff}}}{A_{8\text{geo}}} \cong \frac{p_{t8}}{p_{t7}} \quad (6.51)$$

where the numerator is the actual mass flow rate through the nozzle throat and the denominator is the ideal mass flow rate based on geometrical throat area.

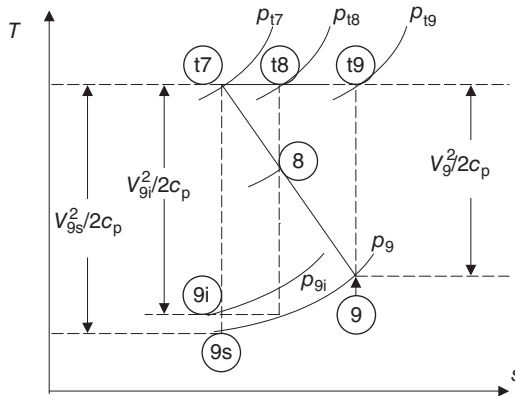
6.25 Nozzle Exit Flow Velocity Coefficient

We may define a velocity coefficient that measures the extent of viscous flow losses in the exhaust plane, that is, let us define C_V as

$$C_V \equiv \frac{V_9}{V_{9i}} \quad (6.52)$$

where the numerator is the actual exhaust velocity and the denominator is the ideal exhaust velocity with no loss of total pressure $p_{t9} = p_{t8}$. Therefore, V_{9i} is the ideal exit velocity only if the divergent section of the nozzle were isentropic. Earlier in the definition of the nozzle adiabatic efficiency, we defined a V_{9i} that was achieved if the entire nozzle were isentropic.

■ FIGURE 6.55
Definition sketch of the states of gas defined in an exhaust nozzle



A definition sketch of the three different exhaust velocities, V_9 , V_{9s} , and V_{9i} , is very helpful at this point and is shown in Figure 6.55.

After some manipulation, we may show the following expression for the velocity coefficient:

$$C_V = \sqrt{\frac{\left[1 - \left(\frac{p_9/p_0}{\text{NPR} \cdot \pi_n} \right)^{\frac{\gamma-1}{\gamma}} \right]}{\left[1 - \left(\frac{p_9/p_0}{\text{NPR} \cdot C_{D8}^2} \right)^{\frac{\gamma-1}{\gamma}} \right]}} \quad (6.53)$$

EXAMPLE 6.7

The total temperature of the gas entering a convergent–divergent nozzle is $T_{t7} = 900$ K. The ratio of specific heats of the gas is $\gamma = 1.3$ and $c_p = 1,243.7$ J/kg · K. The nozzle pressure ratio $p_{t7}/p_0 = 8.0$, the convergent portion of the nozzle has a total pressure ratio $p_{t8}/p_{t7} = 0.98$, and the divergent section total pressure ratio is $p_{t9}/p_{t8} = 0.95$. For $p_9 = p_0$, calculate

- (a) V_9 in m/s
- (b) V_{9s} in m/s
- (c) V_{9i} in m/s and
- (d) The velocity coefficient C_V

SOLUTION

The ratio of the nozzle exit total pressure to static pressure is written in a chain rule as

$$\frac{p_{t9}}{p_9} = \frac{p_{t9}}{p_{t8}} \frac{p_{t8}}{p_{t7}} \frac{p_{t7}}{p_0} \frac{p_0}{p_9} = (0.95)(0.98)(8)(1) \approx 7.448$$

The exit Mach number M_9 is related to the above ratio, following:

$$M_9 = \sqrt{\frac{2}{\gamma - 1} \left[\left(\frac{p_{t9}}{p_9} \right)^{\frac{\gamma-1}{\gamma}} - 1 \right]} \approx 1.982$$

The nozzle exit static temperature is

$$T_9 = \frac{T_{r9}}{1 + (\gamma - 1)M_9^2/2} = \frac{900 \text{ K}}{1 + 0.15(1.982)^2} \approx 566.2 \text{ K}$$

The speed of sound in the exit plane is

$$a_9 = \sqrt{(\gamma - 1)c_p T_9} = \sqrt{0.3(1243.7)(566.2)} \approx 459.6 \text{ m/s}$$

Therefore, the nozzle exit velocity is $V_9 = M_9 a_9 = 1.982(459.6 \text{ m/s})$

$$V_9 \approx 911 \text{ m/s}$$

Now, we calculate V_{9s} from the total and static enthalpy h_{t7} and h_{9s} respectively according to

$$V_{9s} = \sqrt{2(h_{t7} - h_{9s})} = \sqrt{2h_{t7} \left[1 - \left(\frac{p_9}{p_{t7}} \right)^{\frac{\gamma-1}{\gamma}} \right]}$$

$$= \sqrt{2(1243.7)(900) \left[1 - 8^{-0.3/1.3} \right]} \approx 923.7 \text{ m/s}$$

To calculate the V_{9i} , we write the ideal expansion from p_{t8} to p_9 , as shown in Figure 6.55, for which we need the ratio p_{t8}/p_9

$$\frac{p_{t8}}{p_9} = \frac{p_{t8}}{p_{t7}} \frac{p_{t7}}{p_0} \frac{p_0}{p_9} = (0.98)(8)(1) \approx 7.84$$

$$V_{9i} = \sqrt{2(h_{t8} - h_{9i})} = \sqrt{2h_{t8} \left[1 - \left(\frac{p_9}{p_{t8}} \right)^{\frac{\gamma-1}{\gamma}} \right]}$$

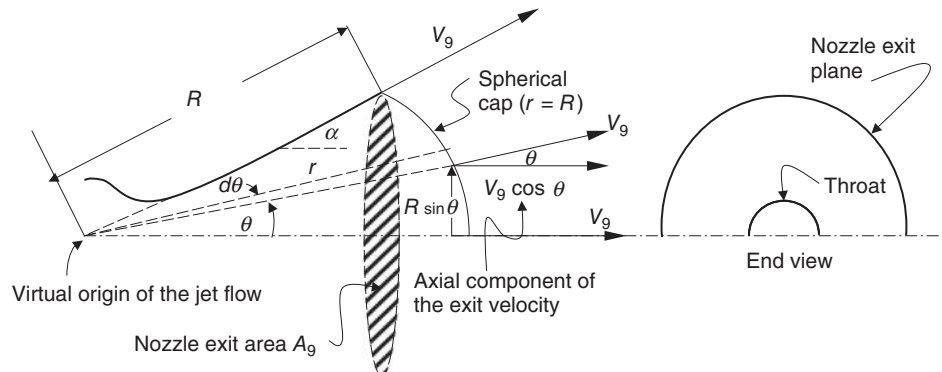
$$= \sqrt{2(1243.7)(900) \left[1 - 7.84^{-0.3/1.3} \right]} \approx 920.2 \text{ m/s}$$

The nozzle velocity coefficient, $C_V = V_9/V_{9i} = 911/920.2 \approx 0.99$

6.26 Effect of Flow Angularity on Gross Thrust

For all nozzle geometries other than a bell-shaped nozzle, the exhaust velocity field, that is, exit momentum, is nonaxial and hence it does not entirely contribute to an axial thrust. Let us examine a conical nozzle first for simplicity. The flow that emerges from a conical nozzle is a divergent jet flow, as shown in Figure 6.56. Due to its radial velocity pattern, the jet flow may be seen as that of emerging from a virtual origin, somewhat like a source flow where the velocity is constant at $r = \text{constant}$. In this case at $r = R$, $V = V_9$, therefore $V = V_9$ over a spherical dome or cap.

■ **FIGURE 6.56**
Working sketch used to derive flow angularity loss (or divergence correction factor) for a conical nozzle of half angle α in attached exit flow



We define an angularity loss coefficient as the ratio of axial (momentum) thrust to the momentum thrust of an equivalent bell-shaped nozzle:

$$F_g = C_A \dot{m}_9 V_9 + (p_9 - p_0) A_9 \quad (6.54)$$

where C_A is

$$C_A \equiv \frac{\int V_9 \cos \theta \, d\dot{m}}{\dot{m}_9 V_9} \quad (6.55)$$

For the element of mass flow rate $d\dot{m}$, we take the exit surface to be spherical in shape, such that the velocity vector V_9 is normal to it. The element of area on the dome is

$$dA = 2\pi R \sin \theta \cdot R \, d\theta \quad (6.56)$$

Hence, the element of mass flow rate at the nozzle exit is

$$d\dot{m} = \rho_9 V_9 dA = 2\pi R^2 \rho_9 V_9 \sin \theta \, d\theta \quad (6.57)$$

We integrate this equation to get the entire mass flow rate from the nozzle, namely,

$$\dot{m}_9 = \int_0^\alpha 2\pi R^2 \rho_9 V_9 \sin \theta \, d\theta = 2\pi R^2 \rho_9 V_9 (1 - \cos \alpha) \quad (6.58)$$

Now, let us evaluate the axial momentum thrust, as

$$\int V_9 \cos \theta \, d\dot{m} = \int_0^\alpha 2\pi R^2 \rho_9 V_9^2 \sin \theta \cos \theta \, d\theta = \pi R^2 \rho_9 V_9^2 \sin^2 \alpha \quad (6.59)$$

Substitute the axial momentum expression in the definition of the flow angularity or the divergence correction factor, to get

$$C_A = \frac{\sin^2 \alpha}{2(1 - \cos \alpha)} = \frac{1 + \cos \alpha}{2} \quad \boxed{C_{A\text{conical}} = \frac{1 + \cos \alpha}{2}} \quad (6.60)$$

EXAMPLE 6.8

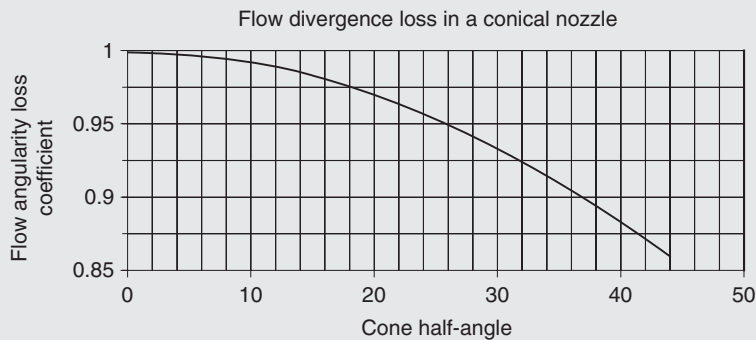
Calculate and graph the divergence correction factor C_A for a conical nozzle with the exit flow angles in the range of 0–44°.

SOLUTION

We first make a spreadsheet for C_A versus α from Equation 6.60 and then graph the resulting table. The result is shown in Figure 6.57.

For cone angles of up to $\sim 30^\circ$ (or half-cone angle of $\sim 15^\circ$), we note that the divergence loss coefficient is rather insignificant with $C_A > 0.98$. The main advantage of a

conical nozzle is in the low-cost manufacturing and for a modest cone angle the thrust penalty is less than 2%. We also note that the flow angularity correction (Equation 6.60) is purely geometrical and hence gas composition, i.e., γ , does not enter the correction process.



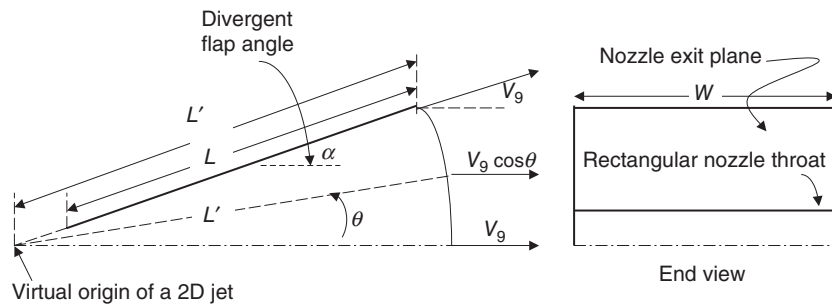
■ FIGURE 6.57 Flow angularity loss coefficient for a conical nozzle

For a two-dimensional convergent–divergent nozzle, we can derive the angularity loss factor, in a straight forward manner, using the definition sketch, Figure 6.58, as a tool.

We take the element of area at the exit to be a cylindrical surface normal to exit flow, that is

$$dA = L' d\theta \cdot W \quad (6.61)$$

■ FIGURE 6.58 Definition sketch for divergence loss factor in a 2D-CD nozzle



Therefore, the element of mass flow rate at the nozzle exit is

$$dm = \rho_9 V_9 L' d\theta \cdot W \tag{6.62}$$

The total mass flow rate is the integral of elemental mass flow rate, that is

$$\dot{m} = 2 \int_0^\alpha \rho_9 V_9 L' W d\theta = 2\rho_9 V_9 L' W \alpha \tag{6.63}$$

Hence, the correction factor C_A then becomes

$$C_A \equiv \frac{\int V_9 \cos \theta dm}{\dot{m}_9 V_9} = \frac{2 \int_0^\alpha V_9 \cos \theta \rho_9 V_9 L' W d\theta}{2\rho_9 V_9^2 L' W \alpha} = \frac{\sin \alpha}{\alpha} \quad \boxed{C_{A2D-CD} = \frac{\sin \alpha}{\alpha}} \tag{6.64}$$

Note that the α in denominator of C_A must be in *radians* (not degrees).

EXAMPLE 6.9

Calculate and graph the divergence correction factor $C_{A,2D-CD}$ for α two-dimensional nozzle with the exit flow angles in the range of 0–44°. Then, compare the angular-

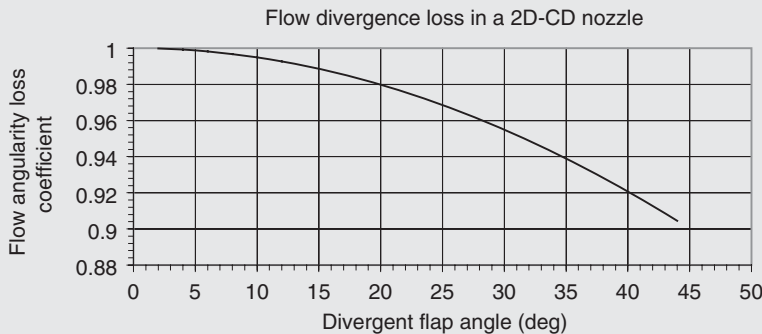
ity correction of the conical nozzle to the two-dimensional C–D nozzle.

SOLUTION

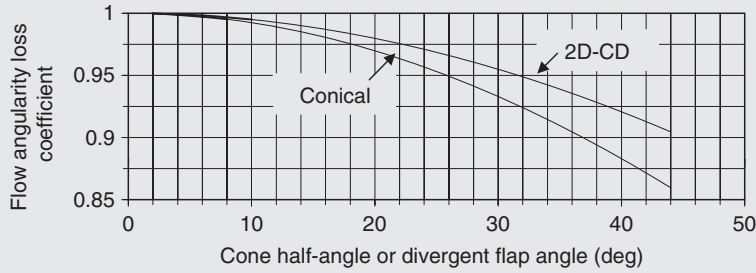
We first make a spreadsheet for $C_{A,2D-CD}$ versus α from Equation 6.64 and then graph the resulting table. The result is shown in Figure 6.59.

By comparing Figures 6.57 and 6.59, we note that a two-dimensional C–D nozzle experiences a smaller flow angularity loss than a similar conical nozzle of the same wall angle. This result was expected, as the conical nozzle

flow diverges axisymmetrically (in 3D) as opposed to a single direction in a 2D rectangular nozzle. Therefore, a conical nozzle develops less axial thrust than a 2D–C–D nozzle of the same wall divergence. Figure 6.60 shows the conical and 2D-CD nozzle performance on a same plot for comparison purposes.



■ FIGURE 6.59 Flow angularity loss coefficient for a 2-D, C–D nozzle



■ **FIGURE 6.60** Divergence loss of a conical nozzle and a 2D-CD nozzle, assuming attached exit flow

6.27 Nozzle Gross Thrust Coefficient C_{fg}

We define a nozzle gross thrust coefficient C_{fg} according to

$$C_{fg} \equiv \frac{F_{g\text{-actual}}}{F_{g\text{-ideal}}} \quad (6.65)$$

where the actual gross thrust is

$$\begin{aligned} F_{g\text{-actual}} &= C_A \dot{m}_9 V_9 + (p_9 - p_0) A_9 = \dot{m}_9 V_9 \left(C_A + \frac{p_9 A_9 (1 - p_0/p_9)}{\rho_9 A_9 V_9^2} \right) \\ &= \dot{m}_9 V_9 \left[C_A + \frac{1 - \frac{p_0}{p_9}}{\gamma M_9^2} \right] \end{aligned} \quad (6.66)$$

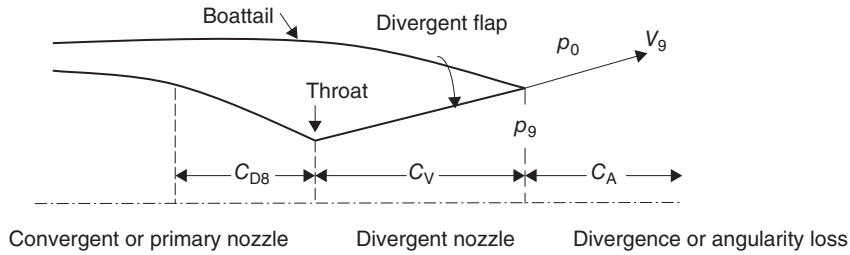
Now, by replacing the momentum thrust with the ideal thrust and introducing the loss coefficients, we get

$$F_{g\text{-actual}} = C_{D8} C_V \dot{m}_{8i} V_{9i} \left[C_A + \frac{1 - \frac{p_0}{p_9}}{\frac{2\gamma}{\gamma - 1} \left[\left(\frac{p_{t9}}{p_9} \right)^{\frac{\gamma-1}{\gamma}} - 1 \right]} \right] \quad (6.67)$$

Since the ideal gross thrust is defined as

$$F_{g\text{-ideal}} \equiv \dot{m}_{8i} V_{9s}$$

■ **FIGURE 6.61** Convergent–divergent nozzle with the primary, secondary, and exit flow, each identified with a loss parameter, C_{D8} , C_V , and C_A , respectively



where V_{9s} is the isentropic exit velocity of a perfectly expanded jet, which may be written as

$$\begin{aligned}
 V_{9s} &= \sqrt{2h_{t8} \left(1 - \frac{T_{9s}}{T_{t9}} \right)} = \sqrt{2h_{t8} \left[1 - \left(\frac{p_0}{p_{t9}} \right)^{\frac{\gamma-1}{\gamma}} \right]} = \sqrt{2h_{t8} \left[1 - \left(\frac{p_0}{p_{t7}} \right)^{\frac{\gamma-1}{\gamma}} \right]} \\
 &= \sqrt{2h_{t8} \left[1 - \text{NPR}^{-\frac{\gamma-1}{\gamma}} \right]} \tag{6.68}
 \end{aligned}$$

Hence, the gross thrust coefficient becomes

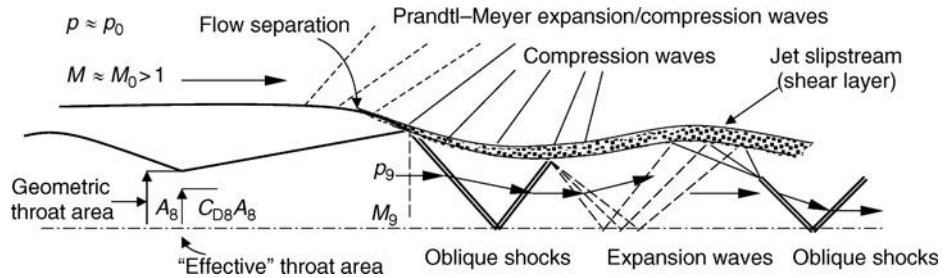
$$\begin{aligned}
 C_{fg} &= C_{D8} C_V \frac{V_{9i}}{V_{9s}} \left[C_A + \frac{\frac{\gamma-1}{2\gamma} \left(1 - \frac{p_0}{p_9} \right)}{\left[\left(\pi_n \text{NPR} \frac{p_0}{p_9} \right)^{\frac{\gamma-1}{\gamma}} - 1 \right]} \right] \\
 &= C_{D8} C_V \sqrt{\frac{1 - \left(\frac{p_9/p_0}{\text{NPR} \cdot C_{D8}^2} \right)^{\frac{\gamma-1}{\gamma}}}{1 - \text{NPR}^{-\frac{\gamma-1}{\gamma}}}} \left[C_A + \frac{\frac{\gamma-1}{2\gamma} \left(1 - \frac{p_0}{p_9} \right)}{\left(\pi_n \text{NPR} \frac{p_0}{p_9} \right)^{\frac{\gamma-1}{\gamma}} - 1} \right] \tag{6.69}
 \end{aligned}$$

Now, let us put this complex looking equation into perspective. An imperfect expansion in the nozzle where $p_9 \neq p_0$ leads to a pressure thrust term, which is essentially the last term in the bracket. The momentum thrust is affected by total pressure losses and flow angularity at the exit, which is the first term of the bracket. These losses are seen as C_{D8} , C_V , and C_A distributed throughout the nozzle, as shown in Figure 6.61.

6.28 Overexpanded Nozzle Flow—Shock Losses

There is an aspect of nozzle performance that is hampered by the presence of shocks inside the nozzle. This behavior, which is represented by a severe case of overexpansion, is not readily apparent from Equation 6.66. An overexpanded nozzle has an area expansion

■ **FIGURE 6.62**
A cartoon of the inner and outer flow of an overexpanded nozzle in supersonic flight shows a wavy jet slipstream with a varying static pressure inside the jet

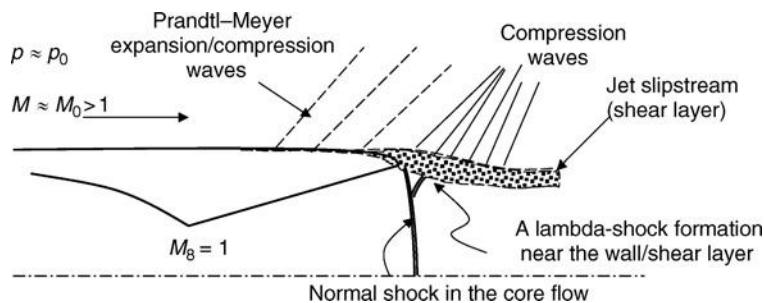


ratio A_9/A_8 in excess of that needed for a perfect expansion. This results in an exit static pressure, which falls below the ambient pressure $p_9/p_0 < 1$. The need for an abrupt adjustment of the static pressure in the emerging supersonic flow causes a shock formation on the nozzle lip. The mild cases of overexpansion are resolved through oblique shock waves on the nozzle lip. A greater mismatch between the static pressures of the jet and ambient calls for a stronger shock, which in essence increases the wave angle with respect to stream. Eventually, a normal shock is formed at the nozzle lip. In case the normal shock at the nozzle lip is found incapable of satisfying static pressure continuity across the jet slipstream, the normal shock is then brought inside the nozzle. At this time, the exit flow is subsonic and a potential boundary layer separation needs to be investigated. Let us first examine the flow environment near the exit of an overexpanded nozzle in supersonic flight. Figure 6.62 shows the external flow around a nozzle boattail and the jet geometry dominated by wave formations. The shear layer separating the inner and outer flowfields is labeled as the jet slipstream. Due to flow curvature near the nozzle exit, local static pressure is higher than ambient pressure, that is, local ambient static pressure near plane 9 is not p_0 , which we had assumed all along in our analysis.

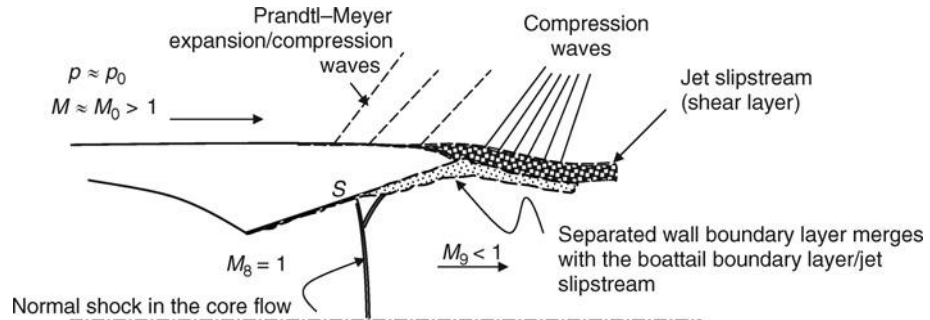
Note that we intentionally omitted a drawing of the wall boundary layers on the primary nozzle and divergent flaps to avoid further crowding of Figure 6.62. This figure was produced, with simplifications, to develop an appreciation of the flow complexities in supersonic exhaust flow. Now, let us graphically examine higher levels of overexpansion in the above nozzle. With larger area ratios, assuming an attached flow, the static pressure at the exit plane drops, demanding a normal shock at the lip. Due to the presence of the wall boundary layer and a curved free shear layer (i.e., the jet slipstream), a lambda shock is formed at the lip, which is graphically depicted in Figure 6.63.

Again for simplicity, the inner boundary layer and the vortex sheet emanating from the junction of lambda shock are not graphed in Figure 6.63. Here, we clearly see a curved

■ **FIGURE 6.63**
Overexpanded flow from a CD-nozzle shows a lambda-shock formation at the lip



■ **FIGURE 6.64**
Curved shock inside the nozzle creates a potential for boundary layer separation and produces a subsonic exit flow



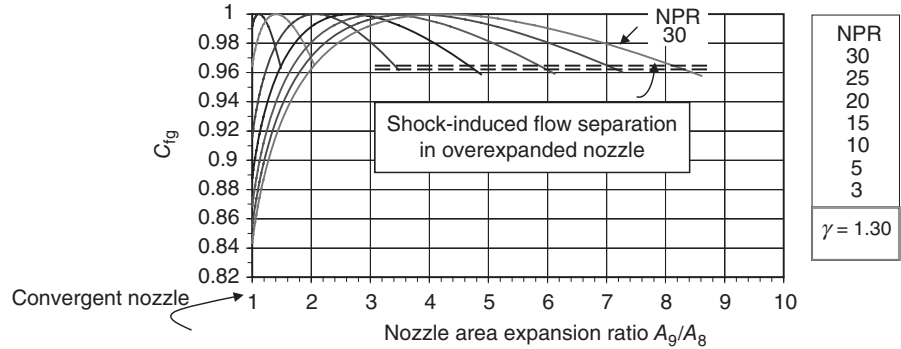
shock formation, which is predominantly normal to the core flow and dominated by a lambda-shock geometry near the wall and exit shear layer. In the case of a more severe overexpansion, the shock will be drawn inside the nozzle and a subsonic jet will emerge at the exit. Figure 6.64 examines this kind of overexpansion.

From Figure 6.64, we note that a separated boundary layer could alter the picture of exit flow, in particular with the flow direction as well as the effective exit flow area. How much of this complexity can we capture by simple one-dimensional models and correction factors? For example, in our gross thrust coefficient approach to account for viscous losses and nonaxial exit flow, are there any provisions for curved shocks or separated flows, such as demonstrated by some overexpanded nozzle flows? The short answer is no. The long answer starts with a maybe! A plausible approach calls for identifying and bracketing off zones of invalidity from our performance charts that we derived based on simple 1D loss models and assumptions. This approach relies, in part, on the experience base of the manufacturing company and other available experimental data in the literature. For example, in separated nozzle flows, the physical meaning of the velocity coefficient C_V and the angularity loss factor C_A are completely lost, based on our definitions and simplifying assumptions. Consequently, the nozzle gross thrust coefficient C_{fg} , as described by Equation 6.69, becomes at best inaccurate and at worst meaningless. Here, we need to exert judgment when dealing with overexpanded nozzle flows that include a shock inside the nozzle. Let us reproduce some of the criteria found in the literature for a passage shock that causes flow separation. In Kerrebrock (1992), a reference is made to Zukoski (1990) who suggests a separation point criterion in an overexpanded supersonic nozzle according to

$$p_s = p_0 / (1 + M_s/2) \quad (6.70)$$

where p_s is the static pressure upstream of the shock, p_0 is the ambient static pressure, and M_s is the gas Mach number upstream of the shock. Over a wide operating range of the nozzle, that is, NPR ranging between 2 and 50, the separation pressure ratio, Kerrebrock notes that p_s/p_0 ranges between 0.4 and 0.625. Mattingly (1996) recommends a $p_s/p_0 \approx 0.37$, following Summerfield, Foster, and Swan (1954) and Sutton (1992) who recommend a rough separation criterion of $p_s/p_0 \leq 0.4$. In summary, several simple or more sophisticated models for shock separation criterion are introduced, which roughly identify the zones of invalidity of our *simple* nozzle theory. Figure 6.65 shows the ideal gross thrust coefficient

■ **FIGURE 6.65**
 An ideal nozzle, i.e.,
 $p_t = \text{constant}$, $T_t = \text{constant}$, $C_{D8} = C_V = C_A = 1$, gross thrust coefficient with Zukoski separation criterion in overexpanded mode



with nozzle area ratio as a function of nozzle pressure ratio. The maximum $C_{fg} = 1$ for $p_9/p_0 = 1.0$.

Note that the nozzle overexpanded mode of operation is more prevalent for a rocket engine than an airbreathing aircraft engine. A rocket engine that operates between the ambient pressures of sea level, ~ 14.7 psia (1 atm.), and near vacuum conditions of space, requires a large nozzle area expansion ratio (A_9/A_8) to optimize its performance. A nozzle, which is optimized for high altitude, then operates in an overexpanded mode in lower altitudes. Consequently, the thrust loss and shock interactions inside the nozzle are serious realities of rocket nozzle design. However, the airbreathing engine of an aircraft invariably operates with a smaller area expansion ratio, hence it experiences less severe over-expansion problems. In the hypersonic regime, the airbreathing and a rocket nozzle attain geometric and operational similarities and thus face the same challenges for off-design operations.

Now, we are ready to address the nozzle throat size and scheduling with afterburner operation. Also, we start the discussion on the nozzle exit area scheduling within the flight envelope and its impact on external drag penalties due to boattail and base flowfield.

6.29 Nozzle Area Scheduling, A_8 and A_9/A_8

The exhaust nozzle throat of a modern aircraft engine operates in a choked mode over a wide operating range within the flight envelope. Consequently, the nozzle throat serves as the low-pressure turbine's backpressure controller or equivalently as the engine aft *throttle station*. With an afterburner in operation, the exhaust gas temperature increases significantly with a subsequent drop of density. To accommodate a lower density gas, a choked nozzle needs to *open up* its throat to pass almost the same mass flow rate as with no afterburner operation. The one-dimensional continuity equation for a choked nozzle throat may be written as

$$\dot{m}_8 = \sqrt{\frac{\gamma_8}{R_8}} \frac{p_{t8}}{\sqrt{T_{t8}}} A_8 \left(\frac{2}{\gamma_8 + 1} \right)^{\frac{\gamma_8 + 1}{2(\gamma_8 - 1)}} \quad (6.71)$$

We note from Equation 6.71 that the term that undergoes the most dramatic change with the afterburner operation is T_{t8} due to heat release in the combustion process. The other terms in the equation undergo smaller changes. For example, the mass flow rate increases by $\sim 2\text{--}4\%$, the gas constant R hardly changes as the molecular weight of the new mixture has not changed much by the addition of the fuel; the total pressure drops with the afterburner, perhaps by $2\text{--}5\%$; the specific heat ratio γ_8 changes with temperature and may go from ~ 1.33 to ~ 1.30 or 1.25 . In its simplest form, the nozzle throat scheduling with afterburner for a turbojet engine may be written as

$$\frac{A_{8\text{-AB-On}}}{A_{8\text{-AB-Off}}} \approx \sqrt{\frac{T_{t8\text{-AB-On}}}{T_{t8\text{-AB-Off}}}} = \sqrt{\frac{\tau_{\lambda\text{AB}}}{\tau_t \tau_\lambda}} \quad (6.72)$$

If the aim is to be more exact with the nozzle throat area scheduling, then one must do the bookkeeping of all the terms in the continuity equation more carefully, namely,

$$\frac{A_{8\text{-AB-On}}}{A_{8\text{-AB-Off}}} \cong \frac{1+f+f_{\text{ab}}}{1+f} \sqrt{\frac{\gamma'_8 p'_{t8}}{\gamma_8 p_{t8}}} \sqrt{\frac{\tau_{\lambda\text{AB}}}{\tau_t \tau_\lambda}} \left[\frac{\left(\frac{\gamma'_8 + 1}{2}\right)^{\frac{\gamma'_8 + 1}{2(\gamma'_8 - 1)}}}{\left(\frac{\gamma_8 + 1}{2}\right)^{\frac{\gamma_8 + 1}{2(\gamma_8 - 1)}}} \right] \quad (6.73)$$

where the primed terms are the afterburner-on quantities.

EXAMPLE 6.10

Calculate and graph the ratio of nozzle throat area with the afterburner on and off for a range of turbine expansion parameters τ_t between 0.45 and 0.65. Keep $\tau_\lambda =$

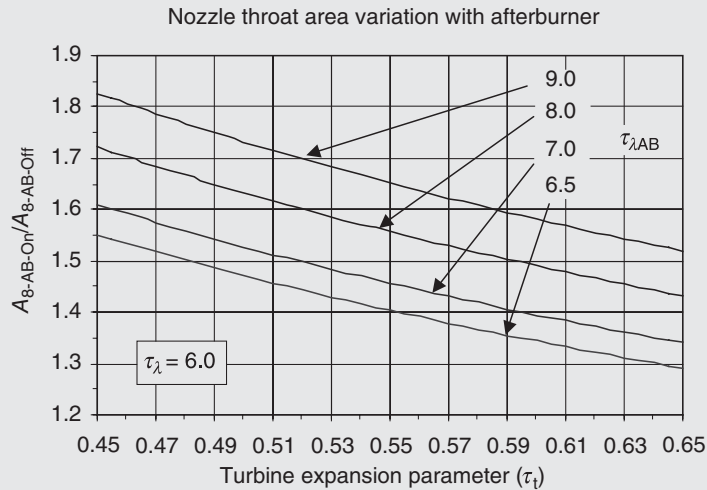
6.0 and vary $\tau_{\lambda\text{AB}}$ from 6.5 to 9.0. Also, investigate the effect of flow losses on the throat area ratio of the nozzle with/without afterburner operation.

SOLUTION

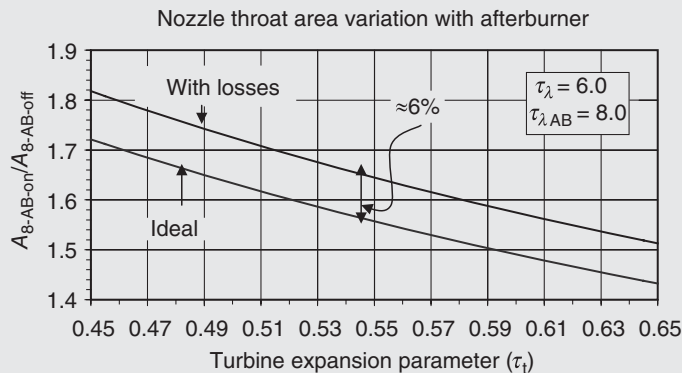
We calculate the nozzle throat area ratio from Equation 6.73, for a range of turbine expansion parameter τ_t and afterburner $\tau_{\lambda\text{AB}}$ from 6.5 to 9.0. The resulting spreadsheet is graphed in Figure 6.66.

Figure 6.66 shows that the ideal nozzle throat area must be enlarged by $\sim 30\text{--}80\%$ in order to accommodate the afterburner flow condition (of low density, high temperature gas).

To investigate the effect of flow losses and gas property variation, we examine the case of $\tau_\lambda = 6.0$, $\tau_{\lambda\text{AB}} = 8.0$. We assume that $\gamma = 1.33$ and $\gamma' = 1.30$ with and without afterburner operation, respectively. We also assume that the total pressure ratio with and without afterburner operation is $p'_{t8}/p_{t8} = 0.96$ where the primary burner fuel-to-air ratio is $f = 0.02$ and the afterburner fuel-to-air ratio is $f_{\text{ab}} = 0.04$. We apply these values to Equation 6.73 and graph the result in Figure 6.67 for a range of turbine expansion parameters.



■ **FIGURE 6.66** Ideal nozzle throat area variation for an afterburning turbojet engine

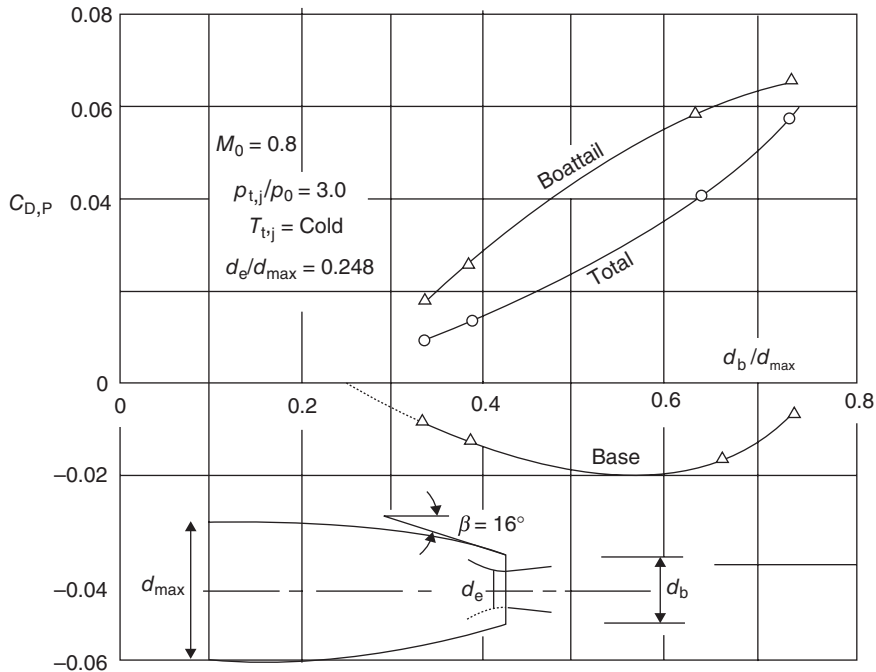


■ **FIGURE 6.67** The impact of flow losses and gas property variation with afterburner combustion on a turbojet nozzle throat area
[for $\gamma = 1.33$, $\gamma' = 1.30$, $p'_{18}/p_{18} = 0.96$, $f = 0.02$, $f_{ab} = 0.04$]

6.30 Nozzle Exit Area Scheduling, A_9/A_8

Unlike the choked nozzle throat that required scheduling with an afterburner operation (i.e., a single parameter control), the nozzle exit area scheduling involves a multiparameter optimization study. The reason for this added complexity is rather obvious. Exit area variation of the nozzle impacts external aerodynamics of the nacelle boattail and base flowfields, and hence external drag. Therefore, if we gain an increment of gross thrust due

■ **FIGURE 6.68**
 Pressure drag contribution of the boattail and base as a function of geometry of a propulsion nacelle installation.
 Source: Bowers and Tamplin 1985.
 Reproduced with permission from AIAA



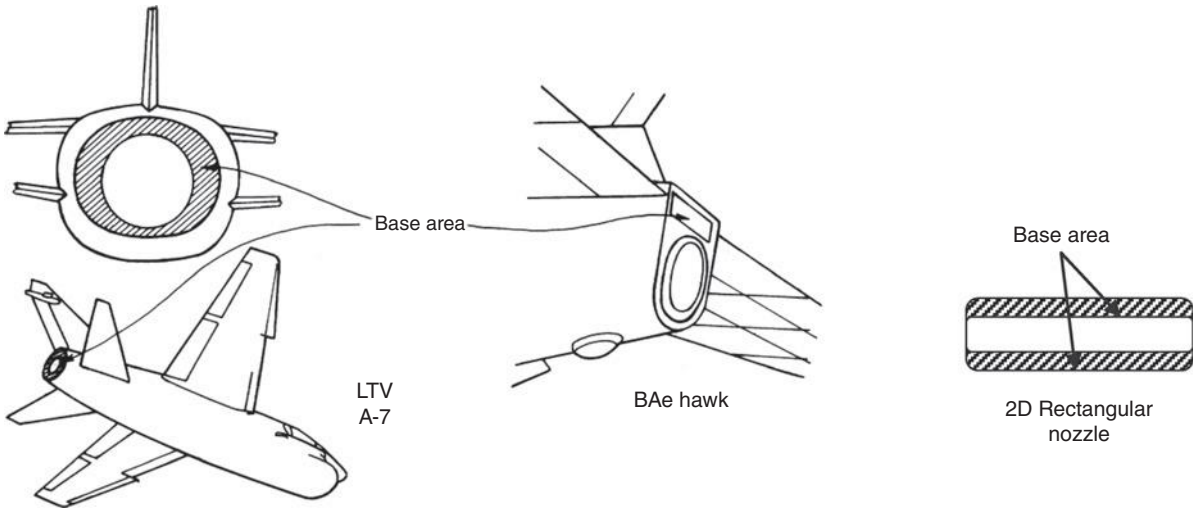
to a better nozzle expansion of say $p_9 \cong p_0$, and as a result incur an increment of drag rise due to nacelle boattail and base flow changes, then the nozzle area ratio A_9/A_8 needs to optimize the installed performance, namely,

$$\Delta F_g - (\Delta D_{\text{Boattail}} - \Delta D_{\text{Base}}) = \Delta F_g - \Delta D_{\text{Nacelle-Aftend}} \tag{6.74}$$

Here, we are again reminded that the internal optimization of an airbreathing engine inlet and exhaust system is meaningless in isolation. Rather, the *engine-installed performance* should be optimized at each flight phase within the flight envelope of the aircraft. Traditionally, the nozzle exit area of a variable geometry nozzle assumed only two positions. One closed and the other open, very similar to the nozzle throat with/without afterburner. But, the limitation of only two positions for the nozzle exit area seems unnecessary today especially in light of advanced propulsion control system of modern aircraft. Here, the goal of nozzle area scheduling control is to achieve a continuous improvement of installed performance with altitude, speed, aircraft attitude, and acceleration rather than that achieved by a bang–bang (a two-position, open-closed) controller.

The contributors to the aftbody aerodynamics on an engine installation are the contributions from the boattail and base areas of the nacelle. The geometry of nozzle boattail and base areas and their impact on aftbody drag are shown in Figure 6.68 (Bowers and Tamplin, 1985). We note that the base pressure force contribution is in the thrust direction and when integrated with the boattail drag contribution, they yield the “total” pressure drag penalty, as shown in Figure 6.68. Also, a graphic definition of base *area* is helpful and is shown in Figure 6.69 (from Whitford, 1987).

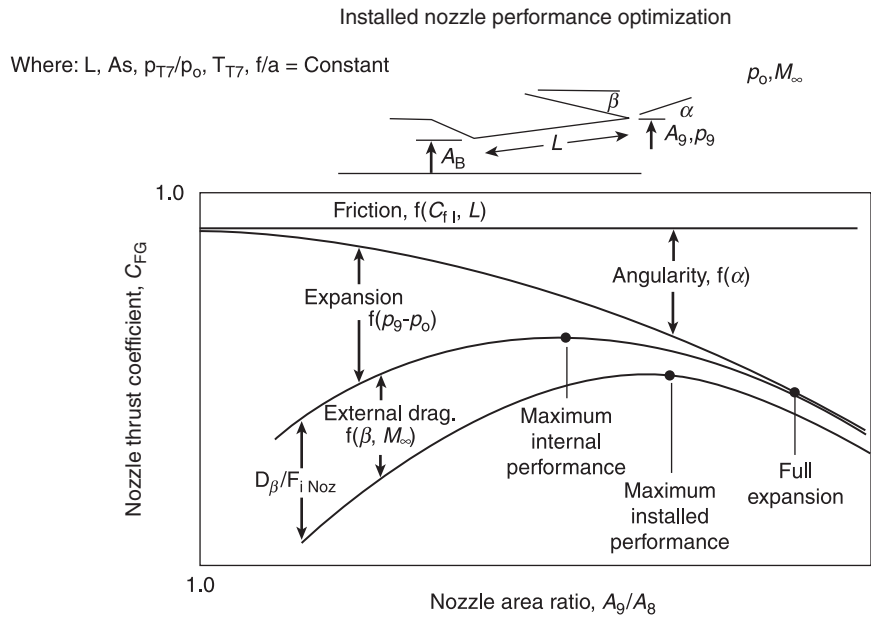
An installed nozzle performance optimization that accounts for the internal as well as external losses is reported by Younghans and Dusa (1993) and reproduced here in



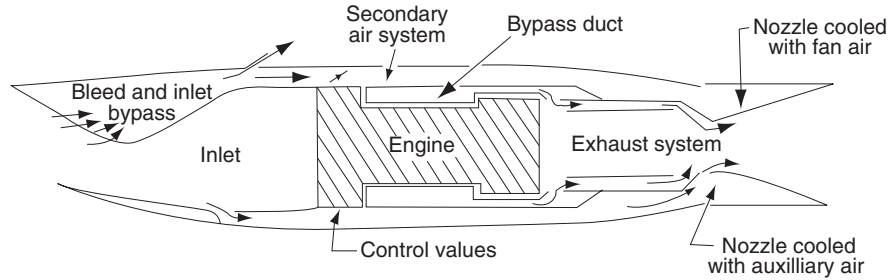
■ **FIGURE 6.69** Definition sketch of candidate nozzle/afterbody base areas. Source: Adapted from Whitford 1987

Figure 6.70. First, note that nozzle area ratio A_9/A_8 that is needed for a perfect expansion does not give the best-installed performance. Second, note that each loss parameter has a different area ratio for its optimization. For example, flow angularity loss vanishes for $A_9/A_8 = 1.0$. The expansion loss vanishes at full expansion ($p_9 = p_0$). The friction penalty holds in a somewhat steady manner across the nozzle area ratios. Finally, the internal performance curve is shifted down by the external drag penalties. This leads to a shift in the area ratio for optimized installed performance.

■ **FIGURE 6.70** Internal/external factors contributing to an optimized nozzle performance. Source: Younghans and Dusa 1993



■ **FIGURE 6.71**
Schematic drawing of an exhaust system cooling air sources in a turbofan engine. Source: Younghans and Dusa 1993

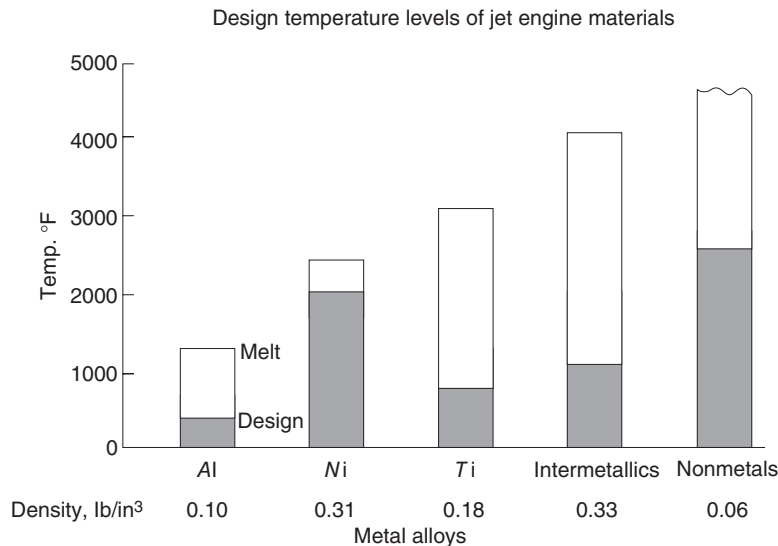


6.31 Nozzle Cooling

The operational temperatures of a modern, multitask exhaust system, with an afterburner, have required an increasing level of active nozzle cooling. In a turbofan engine, the fan stream could provide the required nozzle cooling through an engine bypass system. The supersonic inlet/engine flow match often requires an inlet excess air bypass/bleed system to be integrated into the propulsion system design. The excess air has traditionally been used for engine bay and nozzle cooling purposes. Figure 6.71 shows a schematic drawing of a flow network between an inlet and an exhaust system in a turbofan engine (from Younghans and Dusa, 1993). A typical engine airflow variation with flight Mach number and its comparison with the inlet supply are shown for a Mach 5 aircraft by Dusa (1988).

The primary goal of nozzle cooling is to operate the exhaust system components, that is, the liner, primary and secondary nozzle walls/ramps, seals, and the actuators at a temperature that allows for reliability of operation and good material life expectancy. The material operating temperature should be well below the melting point of the material. A very useful graph from Wazyniak (2000) is reproduced here in Figure 6.72; it shows the design temperature levels of jet engine materials. It is useful to examine the design versus the melting point temperature of different materials in addition to material density,

■ **FIGURE 6.72**
Melting point/design temperature characteristics of various jet engine materials. Source: Wazyniak 2000



as shown in Figure 6.72. The typical uses of the materials listed are: nickel-based alloys in turbines, titanium in compressors and fan blades, aluminum for aircraft and nacelle skin, intermetallics and nonmetals in the high-temperature environment of afterburners and exhaust systems. The acceptable operating temperature of metals (e.g., stainless steel) extends to $\sim 1700^\circ\text{F}$ (or $\sim 927^\circ\text{C}$), whereas ceramics may operate up to $\sim 2800^\circ\text{F}$ (or $\sim 1538^\circ\text{C}$). Carbon-carbon offers an extended operating temperature of up to $\sim 3400^\circ\text{F}$ (or $\sim 1870^\circ\text{C}$). There are also refractory metals, such as tungsten and molybdenum that offer higher operating temperatures than stainless steel (of up to $\sim 2880^\circ\text{F}$). However, refractory metals have exhibited manufacturing-related problems as well as operational problems with embrittlement and oxidation.

Now, let us examine the flight total temperature, or ram temperature, as it increases with flight Mach number. Assuming an adiabatic flow of a calorically perfect gas, the inlet air total temperature follows

$$T_{t0} = T_0 \left(1 + \frac{\gamma - 1}{2} M_0^2 \right) \quad (6.75)$$

Now assuming the supersonic/hypersonic flight occurs in the stratosphere (between 50 and 150 kft) where the static temperature is $\sim -60^\circ\text{F} = \text{constant}$, then the air ram temperature with flight Mach number varies parabolically according to

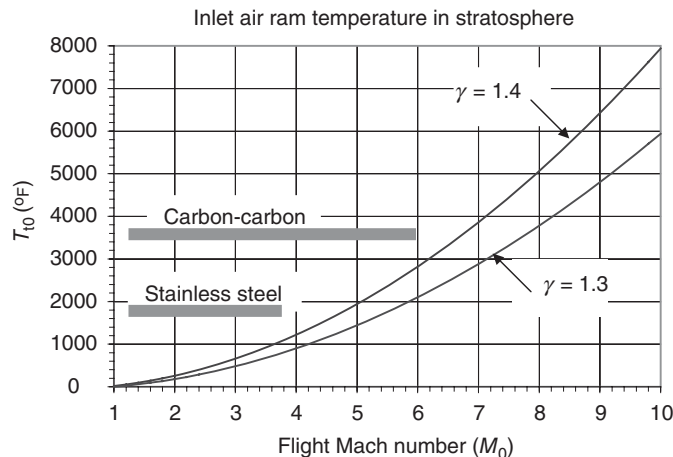
$$T_{t0} \cong 400 + 80M_0^2 \quad (\text{in } ^\circ\text{R}) \quad \gamma = 1.4 \quad (6.76a)$$

$$T_{t0} \cong 400 + 60M_0^2 \quad (\text{in } ^\circ\text{R}) \quad \gamma = 1.3 \quad (6.76b)$$

A graph of the inlet air ram temperature in stratosphere (for constant γ) is shown in Figure 6.73.

We note that the ratio of specific heats γ decreases with temperature, and hence the ram temperature calculation based on cold γ of 1.4 leads to an overestimation of the temperature. To put this in perspective, for a Mach 6 flight in stratosphere, T_{t0} calculated based on $\gamma = 1.4$ is 2820°F , where as $\gamma = 1.3$ yields T_{t0} of 2100°F . There is a $\sim 720^\circ\text{F}$ discrepancy between the two temperatures; although significant, it does not change the

■ **FIGURE 6.73**
Stagnation
temperature variation
with flight Mach
number in stratosphere
(50 kft < alt. < 150 kft)

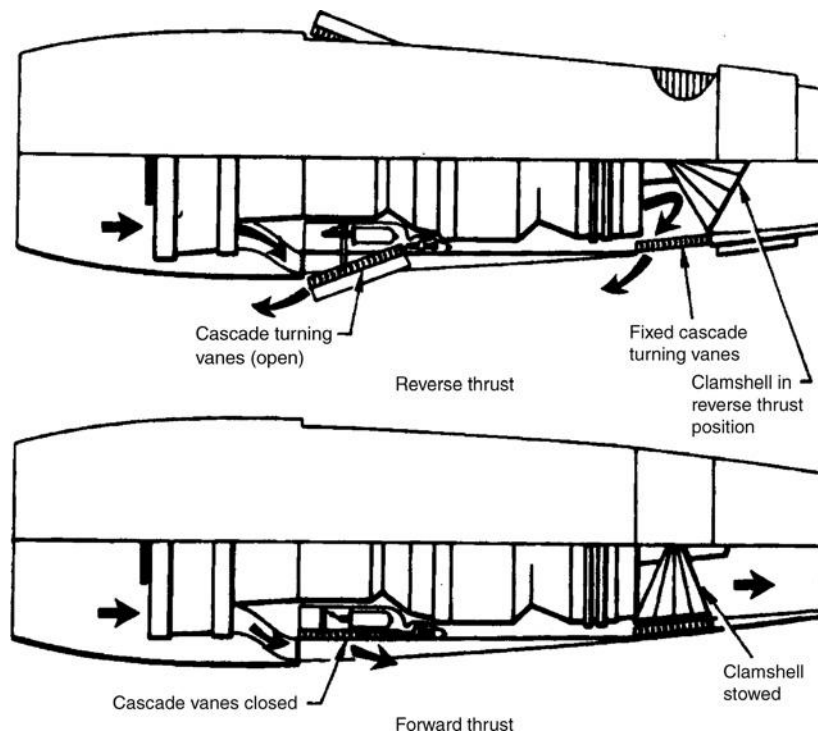


arguments about the special cooling needs of high-speed flight. Now, let us accept the goal of $\sim 3000^\circ\text{F}$ operating temperature of say carbon-carbon, the inlet air becomes too hot to be used as a coolant for flight Mach numbers $M_0 = 6^+$. Therefore, the coolant needs to be precooled in a heat exchanger, which adds weight and complexity to the engine. The other alternative is to use a cryogenic fuel that acts as a heat sink for the propulsor walls, before its injection in the combustor and reaction with air or another oxidizer, as in a rocket engine. To use a cryogenic fuel as a coolant is a common and tried approach in rocket propulsion. The method is called regenerative cooling. From the Saturn-V Apollo launch vehicle (all three stages) to the Space Shuttle Main Engine, nozzles and the thrust chambers are regeneratively cooled using fuels and sometimes oxidizers. Cryogenic fuels of interest are liquid hydrogen, H_2 , and methane, CH_4 . Both of these fuels are available in abundance in nature in various liquid and gaseous forms. The heat sink capacity of these fuels is in part quantified by their latent heat of vaporization, namely, 446 kJ/kg for liquid hydrogen and 510 kJ/kg for liquid methane.

6.32 Thrust Reverser and Thrust Vectoring

Thrust reversers are used to decelerate the aircraft upon landing (for a shorter runway), to reduce wear on the landing gear brakes upon touchdown and landing roll, and to enhance maneuverability of a fighter aircraft in flight. The goals of thrust vectoring nozzles are to enable an aircraft to takeoff and land either vertically or use a very short runway (<500 ft) as well as to achieve supermaneuverability in flight. Thrust vectoring is offered

■ **FIGURE 6.74**
The use of clamshell and cascade thrust reversers in a turbofan engine.
Source: Reproduced by permission of United Technologies Corporation, Pratt & Whitney



as a means of reducing the size or ultimately eliminating the tail (i.e., tailless aircraft), as well as to provide the aircraft with stall recovery. Additional goals of thrust vectoring are the low-speed flight control where the conventional aerodynamic control surfaces become ineffective and the high angle of attack (the so-called high-alpha) capabilities. The latter two goals fall under the supermaneuverability category. To provide some degree of reverse thrust, we need to divert the exhaust jet partially in the flight direction. This is commonly achieved through a *block and turn* mechanism designed into exhaust systems of aircraft today. Two such concepts have been the clamshell and cascade thrust reversers. The clamshell thrust reverser is often used for nonafterburning engines to reverse the turbine exhaust gases, and the cascade type is typically used as a fan exit flow reverser in turbofan engines. Schematic drawings of the two types of thrust reverser are shown in Figure 6.74 (from a Pratt & Whitney Aircraft, 1980).

EXAMPLE 6.11

Some details of thrust reversing and percentage contributions of fan and core, in a separate- and mixed-flow turbofan engine, are shown in Figure 6.75 (from Dietrich and

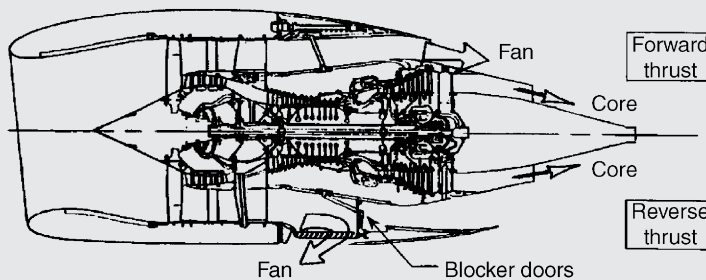
Kuchar, 2000). Compare the thrust reverser effectiveness of these two engine types.

SOLUTION

We note that in a large bypass ratio turbofan engine, the fan provides the majority of forward thrust, namely, in the example shown in Figure 6.75, 75%. The core contributes ~25% of the forward thrust. The blocker doors are deployed

in the fan duct and a translating nacelle aftbody exposes a cascade of turning vanes. The hot core flow continues to provide forward thrust, as no core flow thrust reverser is provisioned in the separate flow turbofan design. However,

Separate-flow turbofan thrust reverser



Forward thrust

- Fan ~ 75% of total thrust
- Core ~ 25%

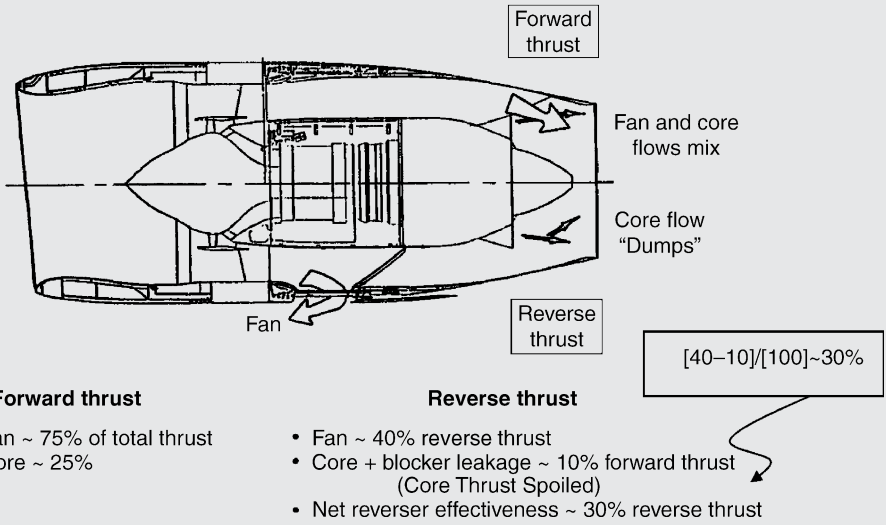
Reverse thrust

- Fan ~ 40% reverse thrust
- Blocker leakage ~ 5% forward thrust
- Core ~ 25% forward thrust
- Net reverser effectiveness ~ 10% reverse thrust

$$[40-5-25]/[100] \sim 10\%$$

■ FIGURE 6.75 The thrust reverser on a separate- and mixed-flow turbofan engine with the contributions of fan and core. Source: Dietrich and Kuchar 2000

Mixed-flow turbofan thrust reverser



■ FIGURE 6.75 (Continued)

in the mixed flow case, the core flow is “dumped,” as in a dump diffuser, with subsequent flow deceleration and a forward thrust reduction.

The long-duct turbofan engine provides significantly more thrust reversing capability than a separate-flow turbofan engine (~30% versus ~10%). The effectiveness of a

thrust reverser is defined as the fraction of forward thrust that is converted into reverse thrust. It is also customary to include the ram drag contribution to the reverse thrust in the definition of reverser effectiveness:

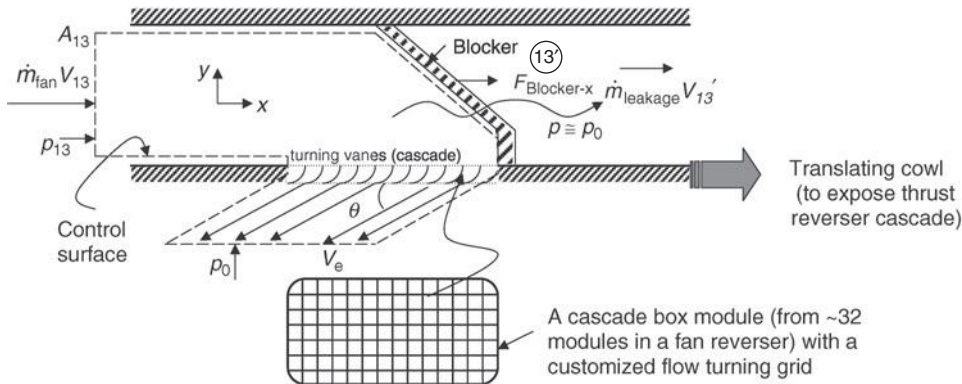
$$\text{Reverser Effectiveness} \equiv \frac{F_{\text{Reverse}} + D_{\text{Ram}}}{F_{\text{Forward}}} \quad (6.77)$$

For an elemental mass flow rate $d\dot{m}$ that attains an exit velocity from a reverser of V_e magnitude, which exits at an angle of θ with respect to the flight direction, a reverse thrust equal to $d\dot{m} V_e \cos \theta$ is created. This needs to be integrated over the exit of the turning vane cascade to evaluate the reverse thrust. A schematic diagram of a fan reverser is shown in Figure 6.76.

$$\text{Reverse thrust from the cascade reverser} = \int_{\dot{m}_e} V_e \cos \theta d\dot{m}_e \quad (6.78)$$

The actual force exerted by the fluid on the blocker and the turning vanes, that is, the reverse thrust force exerted on the aircraft, is established by a momentum balance of the fluid across the blocker and turning vanes, such as

$$\begin{aligned} F_{\text{Reverse}} &= F_{\text{blocker-x}} + F_{\text{vanes-x}} \\ &= \dot{m}_{\text{fan}} V_{13} - \dot{m}_{\text{leakage}} V'_{13} - (p_{13} - p_0)A_{13} + \int_{\dot{m}_e} V_e \cos \theta d\dot{m}_e \end{aligned} \quad (6.79)$$



■ FIGURE 6.76 A fan reverser demonstrating leakage and cascade vane angle θ

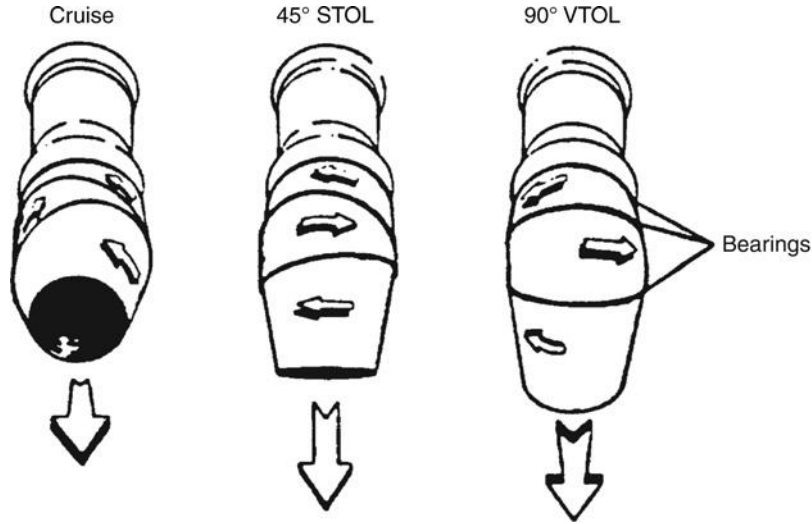
The terms of Equation 6.79 represent momentum and pressure–area terms, similar to the engine net thrust equation. The two positive terms on the RHS of Equation 6.79 dominate the bulk of reverse thrust force generation. The two negative contributions are due to leakage and pressure imbalance in the fan duct, p_{13} , and the ambient pressure p_0 . We may estimate these terms to get a feel for the reverser effectiveness. For example, the turning vane cascade can be assumed to operate with an inlet total pressure of the fan, that is, p_{t13} , and an exit pressure of the ambient air, p_0 . We may also assume an adiabatic efficiency of the expansion process in the turning vanes, similar to a nozzle. The vane angle may be assumed to be $\sim 45^\circ$, and the leakage flow may be $\sim 5\%$ of the incoming flow. To account for the boundary layer blockage in the turning vanes, we may use a discharge coefficient C_D similar to C_{D8} . We may consider the air speed through the blocker is reduced by a factor, for example, $V'_{13} \sim 1/2V_{13}$ (note that a mistake in here will not be very large as the leakage mass flow rate is a small fraction of the incoming flow). For the fan exit speed V_{13} , we may estimate that based on a fan exit Mach number of ~ 0.5 . The static pressure p_{13} may be estimated by the fan total pressure ratio and the M_{13} of ~ 0.5 .

The British Harrier, AV-8B, is the first operational fighter aircraft to achieve vertical takeoff through thrust vectoring. The Harrier's four rotating nozzles turn the engine flow to a near vertical direction to achieve hover, takeoff, and landing. A three-bearing swivel nozzle in Figure 6.77 shows the mechanism for thrust vectoring in an exhaust system (from Dusa, Speir, and Rowe, 1983). The nozzle is of convergent design, hence most suitable for low nozzle pressure ratio (i.e., $NPR < 6$) operation of a subsonic V/STOL aircraft.

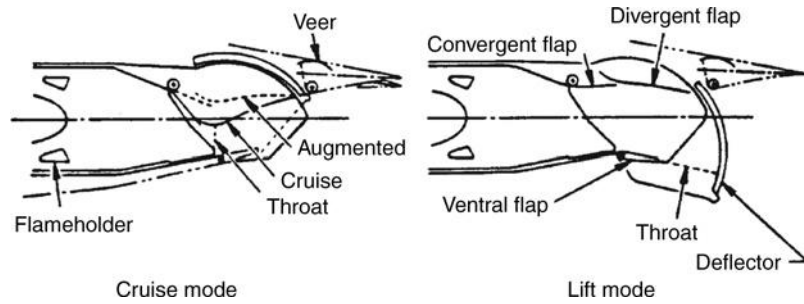
For a supersonic application, a single-expansion ramp nozzle (SERN) offers jet deflection capability through turning of the upper/lower flaps or engaging a separate deflector mechanism. The augmented-deflector exhaust nozzle (Figure 6.78) is capable of 110° thrust vectoring angle. The deflecting flap SERN nozzle is shown in Figure 6.79 (from Dusa, Speir, and Rowe, 1983). The two-dimensional geometry of these nozzles allows for low-drag, body-blended exhaust system integration.

Here, we note that the lower flap also serves as a reverser blocker in the STOL/SERN nozzle configuration, which is shown in Figure 6.79. To get a feel for the cooling requirements of an advanced thrust-vectoring nozzle with an afterburner, we look into the experimental results of ADEN tests (at flight weight, self-cooled with the fan air on a thrust

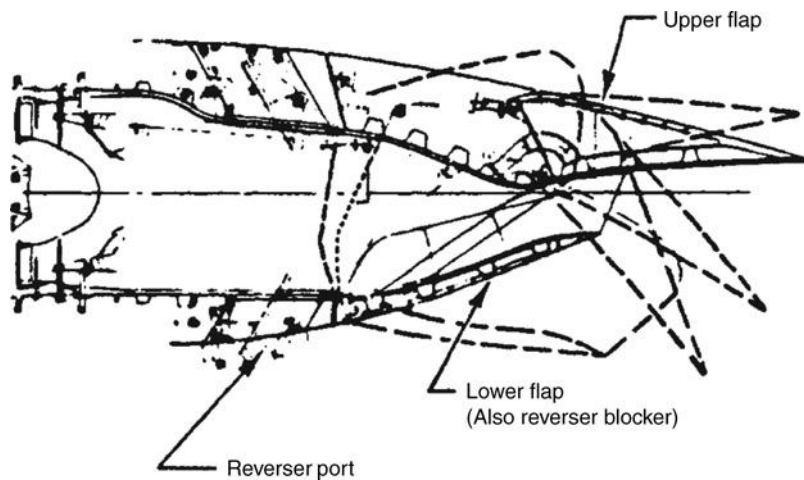
■ **FIGURE 6.77**
 Three-bearing swivel nozzle.
 Source: Dusa, Speir,
 and Rowe 1983.
 Reproduced with
 permission from AIAA



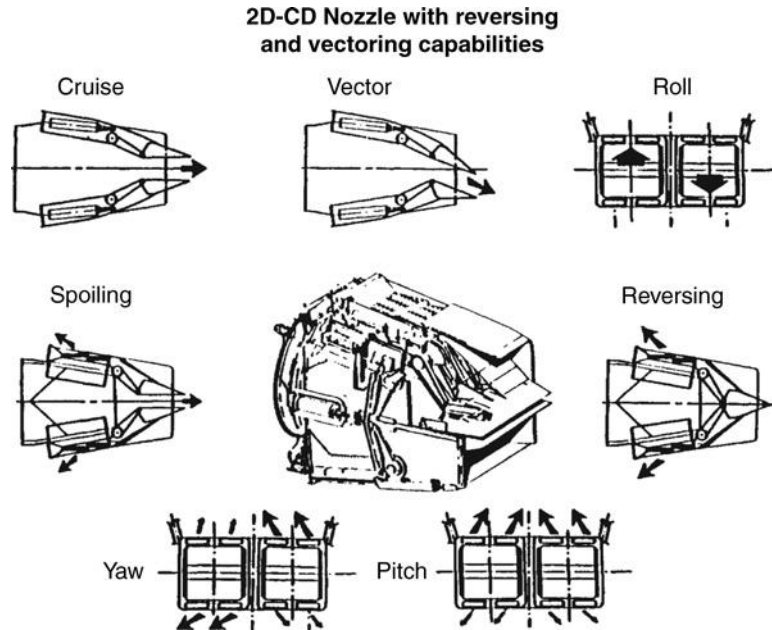
■ **FIGURE 6.78**
 Single expansion ramp
 configuration in an
 augmented-deflector
 exhaust nozzle design
 (ADEN) for V/STOL
 applications.
 Source: Dusa, Speir,
 and Rowe 1983.
 Reproduced with
 permission from AIAA



■ **FIGURE 6.79**
 Single expansion ramp
 exhaust nozzle
 configuration with
 deflecting flaps suitable
 for STOL application.
 Source: Dusa, Speir,
 and Rowe 1983.
 Reproduced with
 permission from AIAA



■ **FIGURE 6.80**
Schematic drawing of a
multifunctional 2D-CD
nozzle. Source:
Younghans and Dusa
1993



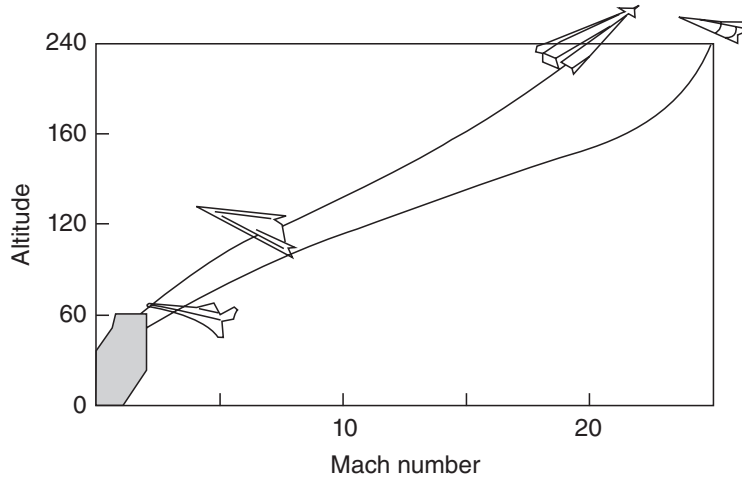
stand at NASA-Lewis). To achieve a surface temperature below the *hot streak design limit* of 2700°F, a ~5.7% cooling air was required at maximum afterburner operation of $T_{t8} = 3028^\circ\text{F}$ and the maximum nozzle pressure ratio of 15 (from Dusa and Wooten, 1984). Now, let us examine the following twin configuration (Figure 6.80).

Another concept for vector thrust–thrust reverser nozzle is shown as a multiflap 2D-CD nozzle in Figure 6.80 (from Younghans and Dusa, 1993). The twin configuration shown uses segmented, that is, split, divergent flaps, which are used to achieve pitch and roll control. The yaw control requires the use of thrust reverser, which causes a reduction in axial thrust. Note that the convergent flaps serve as the blocker in the reverse thrust mode.

6.33 Hypersonic Nozzle

In this section, we explore the challenges of a hypersonic nozzle design. There are several design conflicts in the hypersonic exhaust system that stem from the range of flight speeds, that is, from takeoff to Mach > 5 and the range of altitude, namely, from sea level takeoff to upper atmosphere, or 100^+ kft. The combination of altitude and Mach number constitutes the flight envelope of an aircraft, and in Figure 6.81 we examine such a flight envelope (from Dusa, 1988). The shaded area in the corner of Figure 6.81 represents the flight envelope of conventional commercial and military aircraft. We examine the representative nozzle pressure ratio for airbreathing hypersonic engines in Example 6.12.

■ **FIGURE 6.81**
 Flight envelope of
 hypersonic vehicles
 with altitude in kft.
 Source: Dusa 1988.
 Courtesy of NASA



EXAMPLE 6.12

Demonstrate that a hypersonic airbreathing propulsion system creates a nozzle pressure ratio of one or two orders of

magnitude higher than that of a conventional Mach 2.5 aircraft.

SOLUTION

Let us consider a Mach 6 flight for a hypersonic cruise aircraft at high altitude, say 120,000 ft. For the purpose of demonstration, let us assume that the ratio of specific heats γ is constant. For an adiabatic flow of a perfect gas, the ratio of stagnation to static pressure may write as

$$\frac{p_{t0}}{p_0} = \left(1 + \frac{\gamma - 1}{2} M_0^2 \right)^{\frac{\gamma}{\gamma - 1}} \quad (6.80)$$

Assuming a Mach 6 flight and $\gamma = 1.4$, we get

$$\frac{p_{t0}}{p_0} = [1 + 0.2(36)]^{3.5} = 1,580$$

Now, assuming the inlet total pressure recovery is between 40 and 50% at Mach 6, the ratio of total pressure at the combustor inlet of a ramjet (or scramjet) to ambient static pressure is

$$\frac{p_{t2}}{p_0} \approx 632 - 790$$

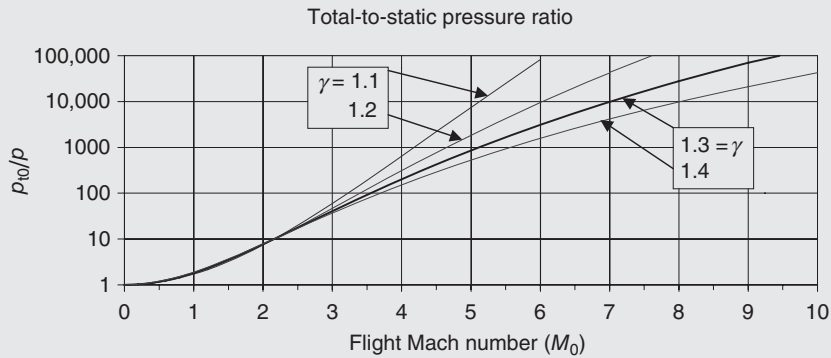
For a supersonic combustor with a Mach 3 inlet condition and a 30% total temperature rise, Kerrebrock (1992) shows that the combustor total pressure ratio is 37%, i.e.,

$$\frac{p_{t4}}{p_{t2}} \approx 0.37$$

Hence, the ratio of total pressure at the nozzle inlet to the ambient static pressure is

$$\text{NPR} = \frac{p_{t4}}{p_0} \approx 234 - 292$$

Note that this nozzle pressure ratio of two to three hundred was created in a Mach 6 hypersonic cruise aircraft. The NPR exponentially grows with the flight Mach number. There is no relief in the real gas effects at high temperatures since a reduced ratio of specific heats will only exacerbate the magnitude of stagnation pressure, as shown in Figure 6.82.

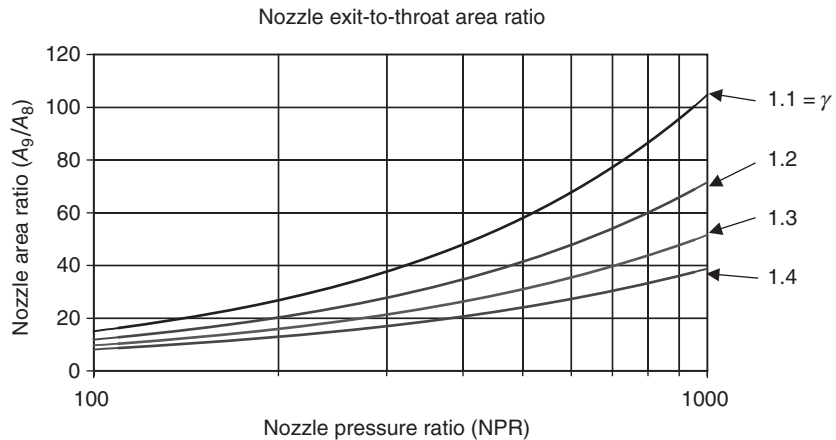


■ FIGURE 6.82 Exponential growth of stagnation pressure with Mach number

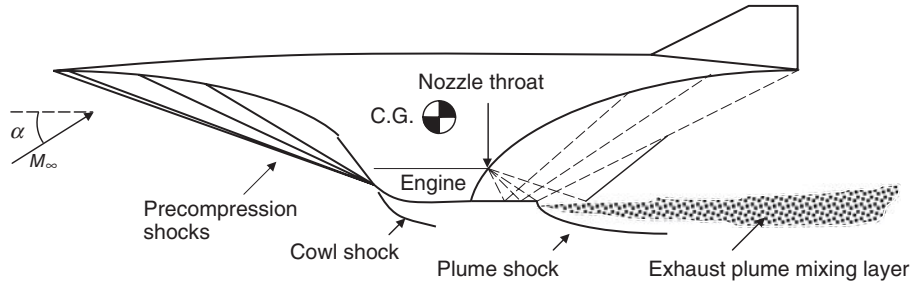
The nozzle area ratio as a function of nozzle pressure ratio is shown in Figure 6.83, using a log-linear scale. We note that a hypersonic airbreathing propulsor will require a very large nozzle area ratio, whose integration into the vehicle is the challenge number one.

To reduce the burden of excessive weight, a hypersonic nozzle will perform an external expansion of the gas, in a geometrically similar manner as a plug nozzle. However, instead of a plug, the nozzle external expansion surface may be the lower surface of the fuselage aftbody. A schematic drawing of such a nozzle is shown in Figure 6.84 where the expansion waves in the exhaust plume are shown as dashed lines and the compression waves as solid lines. Remember from supersonic aerodynamics that the wave reflection from a free boundary, as in the exhaust plume mixing layer, is in an *unlike* manner and the wave reflection from a solid boundary is in a *like* manner. Hence, a shock is reflected as an expansion wave from a free boundary and reflects as a shock from a solid surface. A similar statement may be made regarding an expansion wave reflections.

■ FIGURE 6.83
Nozzle exit-to-throat
area ratio for a
perfectly expanded
nozzle, assuming a
perfect gas with the
ratio of specific heats γ
a constant



■ **FIGURE 6.84**
Schematic drawing of a generic hypersonic vehicle powered by an airbreathing engine shows a highly integrated inlet and exhaust system with the airframe



6.34 Exhaust Mixer and Gross Thrust Gain in a Mixed-Flow Turbofan Engine

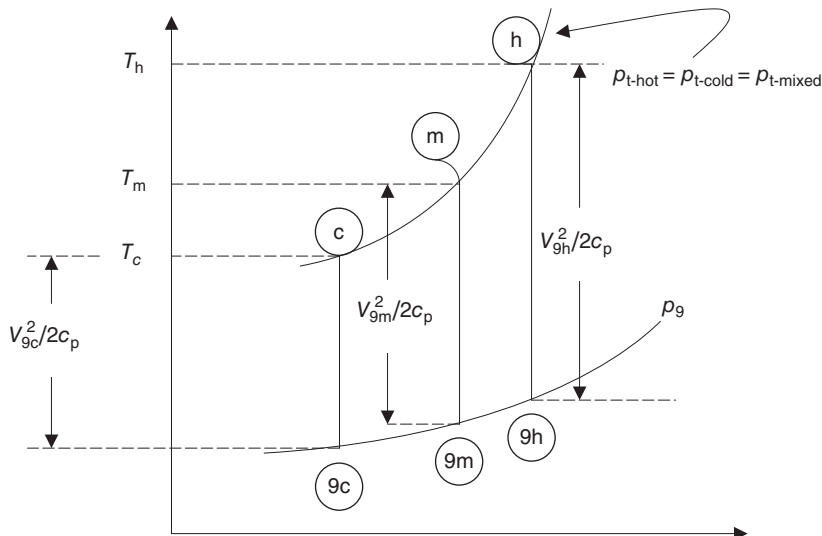
A mixed-flow turbofan engine offers the potential of gross thrust gain and a reduction in fuel consumption as compared with an optimized separate flow turbofan engine. In this section, we examine the extent of gross thrust improvements and the nondimensional parameters that impact the performance gains.

To demonstrate the gain in the gross thrust realized by mixing a cold and a hot stream, we first treat the problem by assuming an ideal mixer. Expanding the cold, hot, or mixed gases in a nozzle to an exit pressure of p_9 , we shall realize a conversion of the thermal energy into the kinetic energy in the exhaust nozzle. The thermodynamics of the expansion process for the three streams is shown in Figure 6.85.

The gross thrust for a separate exhaust turbofan engine, assuming the nozzles are perfectly expanded is

$$\frac{F_g}{\dot{m}_0} \Big|_{\text{unmixed}} \cong V_{9h} + \alpha V_{9c} = \sqrt{2c_p T_h \left(1 - \frac{T_{9h}}{T_h}\right)} + \alpha \sqrt{2c_p T_c \left(1 - \frac{T_{9c}}{T_c}\right)} \quad (6.81)$$

■ **FIGURE 6.85**
An ideal expansion of a cold, hot, and a mixed stream to the same backpressure p_9



We may write the isentropic pressure ratio for the temperature ratios in Equation 6.81 to get

$$\frac{F_g}{\dot{m}_0} \Big|_{\text{unmixed}} \cong \sqrt{2c_p T_h \left[1 - \left(\frac{p_9}{p_{th}} \right)^{\frac{\gamma-1}{\gamma}} \right]} + \alpha \cdot \sqrt{2c_p T_c \left[1 - \left(\frac{p_9}{p_{tc}} \right)^{\frac{\gamma-1}{\gamma}} \right]} \quad (6.82)$$

The mixed exhaust nozzle shall have a gross thrust of

$$\frac{F_g}{\dot{m}_0} \Big|_{\text{mixed}} \cong (1 + \alpha) V_m = (1 + \alpha) \cdot \sqrt{2c_p T_m \left[1 - \left(\frac{p_9}{p_{tm}} \right)^{\frac{\gamma-1}{\gamma}} \right]} \quad (6.83)$$

We note that the pressure terms in the brackets are identical hence they cancel when we express the ratio of gross thrusts. Assuming the same gas properties in the three streams, namely, we get

$$\frac{F_g \Big|_{\text{mixed}}}{F_g \Big|_{\text{unmixed}}} = \frac{(1 + \alpha) \sqrt{T_m}}{\sqrt{T_h} + \alpha \cdot \sqrt{T_c}} \quad (6.84)$$

$$T_m = \frac{T_h + \alpha \cdot T_c}{1 + \alpha} \quad (6.85)$$

Therefore the rise of the gross thrust as a result of mixing a cold and a hot stream may be expressed in terms of the nondimensional parameters of the respective temperature ratio T_h/T_c and the mass flow ratio, namely, the bypass ratio α . This is expressed in the following equation.

$$\frac{F_g \Big|_{\text{mixed}}}{F_g \Big|_{\text{unmixed}}} = \frac{\sqrt{1 + \alpha} \cdot \sqrt{\frac{T_h}{T_c} + \alpha}}{\sqrt{\frac{T_h}{T_c} + \alpha}} \quad (6.86)$$

EXAMPLE 6.13

For a range of hot-to-cold temperature ratios between 1.5 and 4.5 and the turbofan bypass ratio of up to 8, calcu-

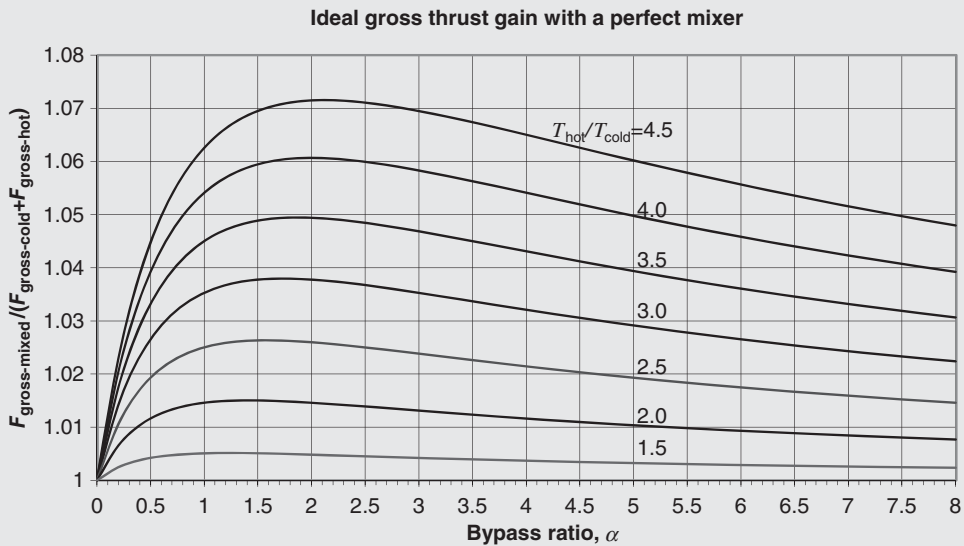
late and graph the ratio of mixed to separate-flow turbofan engines gross thrust.

SOLUTION

We use a spreadsheet for Equation 6.86 and graph the results in Figure 6.86.

As expected, the gain in gross thrust due to mixing of a cold and a hot stream vanishes as $T_h/T_c \rightarrow 1$, as well

as for $\alpha \rightarrow 0$. The gain peaks for a bypass ratio in the vicinity of 2, and the effect diminishes as the bypass ratio increases. The modest gain of ~2–3% is realizable in a real engine if the mixing losses in the mixer are kept low. This



■ FIGURE 6.86 Gain in gross thrust due to an ideal mixer

gross thrust increase of a mixed exhaust turbofan engine translates into a corresponding drop of 2–3% in the thrust-specific fuel consumption of such engines compared with a separate exhaust turbofan engines. We recognize that the real process in a mixer will result in a loss of total pressure due to

1. Turbulent mixing of the cold and hot streams
2. Frictional losses on the walls of the mixer

Therefore an effective design of a mixer is crucial to realizing the performance gains promised by the mixer.

6.35 Noise

High-performance gas turbine engines are very noisy machines, by design! Energy transfer in turbomachinery can only take place through *unsteady means*, as presented in Chapter 8. Also, to maximize energy transfer, modern engines use high-speed wheels of rotating and stationary or counterrotating blade rows. These always involve *supersonic tip* speeds, which create shocks and their associated *discrete tone noise*. Since the energy transfer is unsteady, the blade wakes are unsteady with periodic vortex shedding structure. The unsteady wakes of a blade row are then chopped by the next row of blades, as they are in relative motion. In addition, there are ample opportunities for *resonance* to occur in blade row-blade row interaction. Due to blade elasticity and aerodynamic loads, the blades *vibrate* in various modes, for example, first bending, second bending, first torsional mode, coupled bending and torsional mode, and higher order modes. The *unsteady* mechanism of energy release in a combustor creates combustion noise. Finally, the pressure fluctuation in the exhaust jet due to *turbulent structure and mixing* is the source of *broadband* jet noise.

Modern fan blades that are thin and incorporate blade sweep, and the inlet fan and core exit ducts that are treated with an acoustic liner, are successful solutions that alleviate the turbine noise problem. For example, the acoustic duct liners, which are Helmholtz resonators embedded in the wall, attenuate the dominant frequency in the transonic fans' and LPTs' noise spectra, namely the discrete tone noise at the blade passing frequency. In addition, proper selection of blade numbers in successive blade rows and blade row spacing are the solutions that alleviate, by and large, the intrablade row resonance problem.

6.35.1 Jet Noise

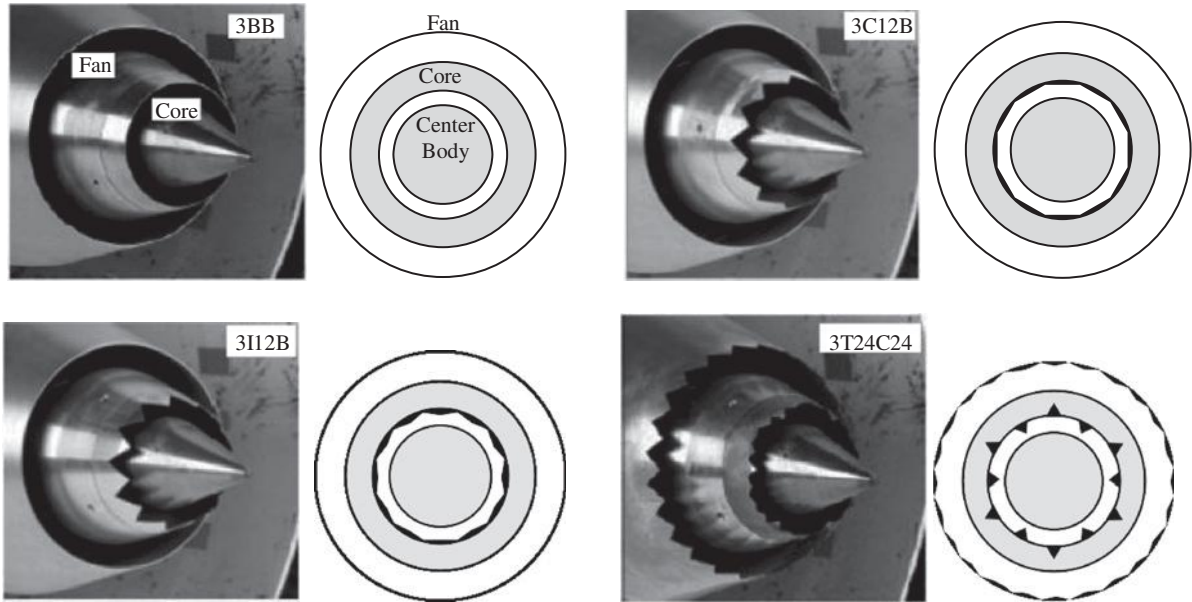
In a classical paper, Lighthill (1952) showed that the acoustic power in a subsonic turbulent jet is proportional to the eight power of the jet speed, V_j , that is,

$$\mathcal{P}_j \propto V_j^8 \quad (6.87)$$

Therefore, to reduce the broadband noise from an aircraft exhaust, the jet speed needs to be reduced. Interestingly, propulsive efficiency is also improved with reduced exhaust speed, as we discovered in the cycle analysis (Chapter 4). The development of high and ultra-high bypass ratio turbofan engines accomplish both goals, that is, higher propulsive efficiency and reduced jet noise, simultaneously. Also, the concept of Variable Cycle Engine (VCE) promises the capability of higher bypass ratio at takeoff and landing and reduced bypass ratio at cruise condition, which is advantageous in the reduction of the airport's community noise. Since the kinetic power in a jet is proportional to V_j^3 , an acoustic efficiency parameter may be defined as the ratio of the radiated acoustic to the jet kinetic power (for derivation see Kerrebrock, 1992), which is then proportional to the fifth power of the jet Mach number, M_{j0} , which in this derivation is defined as the ratio of V_j and the ambient speed of sound, a_0 , that is,

$$\eta_{jet\ noise} \propto \left(\frac{\rho_j}{\rho_0} \right) M_{j0}^5 \quad (6.88)$$

This efficiency parameter may be used to compare different noise suppression concepts. The noise suppressors of the 1950s that were developed originally for turbojets added significant weight to the engine and caused significant loss of gross thrust. The turbofan engines of the 1960s and 1970s alleviated the jet noise problem based on their reduced jet speed and their blade and duct treatments also reduced the turbine noise; but still more stringent noise regulations were on the horizon. These limitations are set by the Federal Aviation Regulation – Part 36 Stage 3 and the new FAA Stage 4 Aircraft Noise Standards (that is used for the certification of turbofan-powered transport aircraft). One thing is for certain and that is the growth in commercial aviation and its impact on society will certainly demand yet more stringent regulatory aircraft noise standards in the future. Beyond a reduction in jet speed, as in high bypass ratio turbofan engines, are there any other means of reducing jet noise without paying a severe penalty on gross thrust? The jet noise reduction depends on many parameters but predominantly on the nozzle pressure



■ FIGURE 6.87 Baseline nozzle (3BB) and examples of Chevron and tab configurations (3C12B, 3I12B and 3T24C24, respectively) in static test. Source: Saiyed, Mikkelsen, and Bridges, 2000. Courtesy of NASA

ratio (NPR) and the jet Mach number. In this section, the most promising development in transonic jet noise reduction is briefly presented.

For the past two decades, research and development by NASA' Glenn Research Center and the aircraft engine and airframe industry on jet noise reduction has led to the development of a new winning technology: the Chevron Nozzle. An excellent review article by Zaman *et al.* (2011), which chronicles the development of mixing devices, mainly tabs and chevrons, is suggested for further reading.

6.35.2 Chevron Nozzle

Chevrons are triangular serrations at the nozzle exit plane that have the potential of “calming” turbulent jets (Zaman *et al.*, 2011). The *calming* effect stems from a redistribution of azimuthal vorticity at the nozzle exit that attains certain streamwise components. For optimal redistribution of vorticity, the chevron tips have to slightly penetrate the jet. Excessive penetration gives rise to thrust loss and an insignificant dipping into the jet does not produce the desired sound pressure level (SPL) reduction. Figure 6.87 shows a baseline nozzle that is used to compare the aeroacoustic and propulsive performance of various chevron configurations on the core and/or the fan nozzles in a separate flow turbofan engine.

The most promising of the chevron configurations in static test were then flown to demonstrate takeoff, landing and the flyover noise reduction effectiveness. Naturally, on the propulsion side thrust loss coefficient at cruise conditions is the measure of viability of any noise reduction device.

■ **TABLE 6.1**
Noise benefit and cruise thrust loss data

Configuration	Noise benefit (EPN dB)	Loss in thrust coefficient at cruise (%)
3C12B	1.36	0.55
3I12B	2.18	0.32
3I12C24	2.71	0.06
3T24B	2.37	0.99
3T48B	2.09	0.77
3T24C24	—	0.43
3T48C24	—	0.51
3A12B	—	0.34
3A12C24	—	0.49

The benefits in noise reduction of chevron-equipped aircraft in flyovers, that is, community noise, is first measured (using a logarithmic scale known as the Bel or the more commonly used unit of one tenth of a Bel, i.e., the dB) in the frequency range where human ear is sensitive (i.e., between 50 and 10 kHz) and subsequently weighted towards the frequencies where the human ear is most sensitive, that is, 2–5 kHz. There are other corrections that contribute to the calculation of what is known as the *Effective Perceived Noise Level* (EPNL) in dB; this is the basis of FAR-36 certification limits. Kerrebrock (1992) offers a clear methodology to EPNL calculations and is suggested for further reading on engine noise. There is ample data that support a reduction in turbulent kinetic energy in a jet where streamwise vorticity is injected at the nozzle exit, as produced by chevrons. The significance of the chevron technology is in its light weight and negligible impact (i.e., loss) on nozzle gross thrust, which is measured at 0.25%.

At the outset, the goal of jet noise reduction was to achieve 2.5 EPNL (dB) in flyover, that is, community, noise reduction while limiting the thrust penalty in cruise to less than 0.5%. As evidenced in Table 6.1, where the noise benefit and cruise thrust loss data from Zaman *et al.* (2011) are shown, there are several chevron configurations that achieve the desired performance.

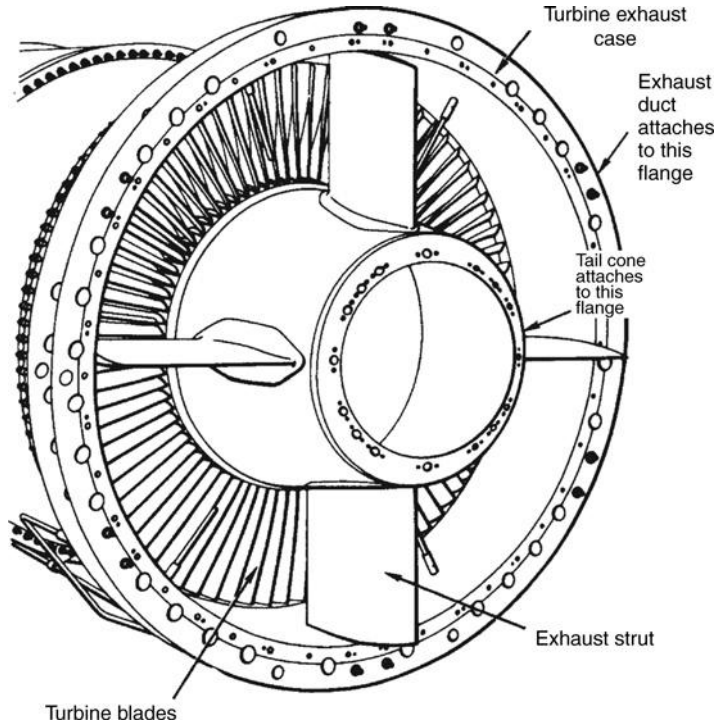
The success of the chevron nozzle has made it into a standard component on several new aircraft, such as the Boeing 787.

6.36 Nozzle-Turbine (Structural) Integration

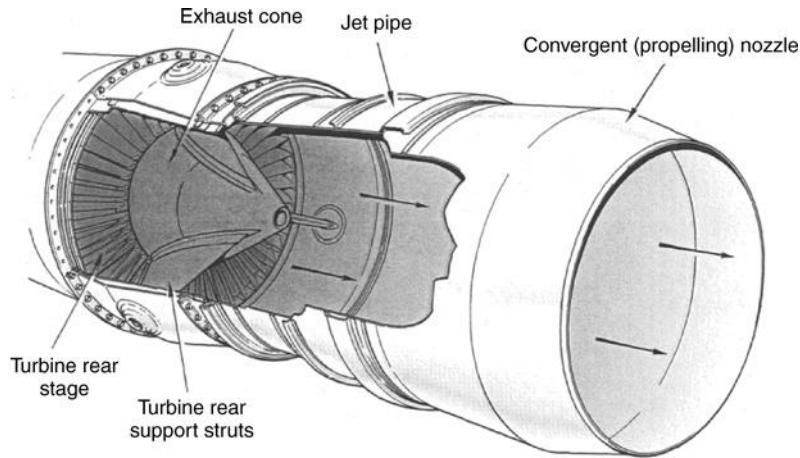
The turbine exhaust case, support struts, and a tail cone flange are shown in Figure 6.88 (from Pratt & Whitney, 1980). The turbine exhaust cone houses the turbine bearings and provides for a smooth flow to the nozzle (or afterburner).

The exhaust cone, jet pipe, and a convergent nozzle are shown schematically in Figure 6.89 (from Rolls-Royce, 2005). In this view of the exhaust system, the turbine rear support struts are also shown.

■ **FIGURE 6.88**
Turbine exhaust's case, struts, and a tail cone flange.
Source: Reproduced by permission of United Technologies Corporation, Pratt & Whitney



■ **FIGURE 6.89**
Drawing of exhaust cone, jet pipe, and a convergent nozzle.
Source: Reproduced with permission from Rolls-Royce plc



6.37 Summary of Exhaust Systems

An aircraft exhaust system is a multifunctional component whose primary mission is to convert fluid thermal energy into directed forces in any desired direction (x, y, z) efficiently. These forces are usually in vector thrust mode, including hover, as well as thrust reversing directions. The system weight (and complexity) and cooling requirements are the optimizing parameters for the design and selection of exhaust systems. Advanced

nozzle cooling requirements are in the $\sim 5\text{--}10\%$ range. Airbreathing engines with afterburner require a variable geometry nozzle to open the throat with afterburner operation. The nozzle throat scheduling with the afterburner throttle setting is to decouple the afterburner/exhaust system from the gas generator. The nozzle exit area scheduling has to include the net effect of internal performance gains as well as the external boattail drag penalties. The internal performance is optimized when the nozzle is perfectly expanded. The build up of boundary layer in the convergent or primary nozzle is accounted for by a flow (discharge) coefficient at the throat, C_{D8} . The effect of total pressure loss on the exhaust velocity in the divergent section of the nozzle is accounted for by a velocity coefficient C_V . The effect of nonaxial exhaust flow appears as a reduction in axial force produced by the nozzle. The appropriate accounting of this loss is made using the flow angularity loss coefficient C_A . Lobed mixers in a mixed-stream turbofan engines improve gross thrust by a few percentage points. Off-design operation of supersonic nozzles in overexpanded mode causes shock waves to be formed and a corresponding loss of thrust. Plug nozzles have a superior overexpanded nozzle performance over the convergent-divergent nozzles, but require additional cooling and thus system complexity and weight. In hypersonic flight, the nozzle pressure ratio reaches into several hundred level, somewhat similar to a rocket engine. The required area expansion ratio for efficient expansion of the high-pressure gas demands integration with vehicle. To achieve reduced signature, an exhaust system could employ high-aspect ratio rectangular nozzles with offset to shield the turbine as well as enhanced mixing to reduce the jet temperature. The exit plane of the nozzle placed on the upper surface of the aircraft fuselage or wing provides shielding from ground radar.

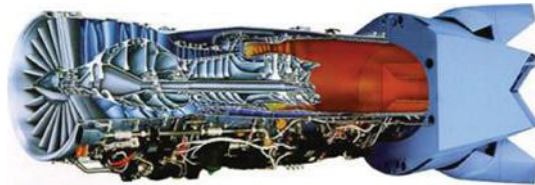
Further readings on exhaust systems and installation (references 4, 7, 8, 24 and 26) are recommended.

References

1. Abbott, J.M., Anderson, B.H., and Rice, E.J., "Inlets, Ducts and Nozzles," *Aeropropulsion '87*, NASA CP-3049, 1987.
2. Abernethy, R.B. and Roberts, J.H., *In-Flight Thrust Determination and Uncertainty*, SAE Special Publication, SP-674, 1986.
3. Albers, J.A., *et al.*, "Aerodynamic Analysis of Several High Throat Mach Number Inlets for the Quiet, Clean, Short-Haul Experimental Engine," NASA TMX-3183, 1975.
4. Aulehla, F. and Lotter, K., "Nozzle/Airframe Interference and Integration," in AGARD Lecture Series, LS-53, Paper 4, 1972.
5. Anderson, B.H., "Three-Dimensional Viscous Design Methodology of Supersonic Inlet Systems for Advanced Technology Aircraft," *Numerical Methods for Engine-Airframe Integration*, Eds. Murthy, S.N.B. and Paynter, G.C., Progress in Astronautics & Aeronautics, Vol. 102, AIAA, Washington, DC, 1986, pp. 431-480.
6. Anderson, J.D., Jr., *Fundamentals of Aerodynamics*, 4th edition, McGraw-Hill, New York, 2005.
7. Anon., Symposium on "Developments in Aircraft Propulsion," Haarlem, the Netherlands, 1987.
8. Berman, K. and Crimp, F.W., "Performance of Plug-Type Rocket Exhaust Nozzles," *ARS Journal*, Vol. 31, No. 1, January 1961.
9. Bowers, D.L. and Tamplin, G., "Throttle-Dependent Forces," Chapter 5 in *Thrust and Drag: Its Prediction and Verification*, Eds Covert, E.E. *et al.*, Progress in Astronautics and Aeronautics, Vol. 98, AIAA, New York, 1985.
10. Cochran, D.L. and Kline, S.J., "The Use of Short Flat Vanes for Producing Efficient Wide-Angle Two-Dimensional Subsonic Diffusers," NACA TN 4309, September 1958.
11. Dietrich, D.A. and Kuchar, A.P., "High Bypass Turbo-fan Nacelles for Subsonic Transports," UTISI Course notes, April 2000.

12. Dusa, D.J., "Nozzles and Turbo-Ramjet Propulsion for Mach 0 to 6 Aircraft," *Short Course Notes in Hypersonic Propulsion*, NASA-Lewis, 1988.
13. Dusa, D.J., Speir, D.W., and Rowe, R.K., "Advanced Technology Exhaust Nozzle Development," AIAA Paper No. 83-1286, 1983.
14. Dusa, D.J. and Wooten, W.H., "Single Expansion Ramp Nozzle Development Status," AIAA Paper No. 84-2455, 1984.
15. Farokhi, S., Sheu, W.L., and WU, C., "On the Design of Optimum-Length Transition Ducts with Offset: A Computational Study," *Computers and Experiments in Fluid Flow*, Eds Carlomagno, G.M. and Brebbia, C.A., Springer Verlag, Berlin 1989, pp. 215–228.
16. Hancock, J.P. and Hinson, B.L., "Inlet Development for the L-500," AIAA Paper No. 69-448, June 1969.
17. Hesse, W.J. and Mumford, N.V.S., Jr., *Jet Propulsion for Aerospace Applications*, 2nd edition, Pitman Publishing Corp., New York, 1964.
18. Holmes, B.J., "Progress in Natural Laminar Flow Research," Paper Presented at AIAA/NASA General Aviation Technology Conference, Wichita, Kansas, July 1984.
19. Johnson, C.L., "Some Development Aspects of the YF-12A Interceptor Aircraft," AIAA Paper No. 69-757, July 1969.
20. Kantrowitz, A. and Donaldson, C. du P., "Preliminary Investigation of Supersonic Diffusers," NACA ACR L5020, 1945.
21. Kerrebrock, J.L., *Aircraft Engines and Gas Turbines*, 2nd edition, MIT Press, Cambridge, Mass, 1992.
22. Kimzey, W.F., Wehofer, S., and Covert, E.E., "Gas Turbine Engine Performance Determination," *Thrust and Drag: Its Prediction and Verification*, Ed. Covert, E.E., AIAA progress in Astronautics & Aeronautics, Vol. 98, AIAA, Washington, DC, 1985, pp. 47–119.
23. Kline, S.J., Abbott, D.E., and Fox, R.W., "Optimum Design of Straight-Walled Diffusers," *Journal of Basic Engineering*, 81, Series D, No. 3, September 1959, pp. 321–331.
24. Kozlowski, H. and Larkin, M., "Energy Efficient Engine Exhaust Mixer Model Technology Report," NASA CR-165459, June 1981.
25. Kline, S.J., "On the Nature of Stall," *Journal of Basic Engineering*, 81, series D, No. 3, September 1959, pp. 305–320.
26. Kuchar, A.P., "Variable Convergent–Divergent Exhaust Nozzle Aerodynamics," Chapter in *Aircraft Propulsion System Technology and Design*, Ed. Oates, G.C., AIAA Education Series, AIAA Inc., Washington, DC, 1989.
27. Kuechemann, D. and Webber, J., *Aerodynamics of Propulsion*, McGraw-Hill, New York, 1953.
28. Mattingly, J.D., *Elements of Gas Turbine Propulsion*, McGraw-Hill, New York, 1996.
29. Mount, J.S. and Millman, V., "Development of an Active Laminar Flow Nacelle," AIAA Paper 85-1116, 1985.
30. MIL-E-5008B, "Military Specifications–Engines, Aircraft, Turbojet, Model Specifications for," January 1959.
31. Oates, G.C., *Aerothermodynamics of Gas Turbine and Rocket Propulsion*, AIAA, Washington, DC, 1988, pp. 198–199.
32. Oswatitsch, K., "Pressure Recovery for Missiles with Reaction Propulsion at High Supersonic Speeds (The Efficiency of Shock Diffusers)," NACA TM 1140, 1947.
33. Paul, D.L. and YOUNGHANS, J.L., "Inlets & Inlet Engine Integration," Chapter 13 of *The Aerothermodynamics of Aircraft Gas Turbine Engines*, AFAPL TR-78-52, Ed. Oates, G. C., 1978.
34. Potonides, H., *et al.*, "Design and Experimental Studies of a Type "A" V/STOL Inlet," AIAA Paper No. 78-956, 1978.
35. Powel, A.G., Welge, H.R., and Trefny, C.J., "Low-Speed Aerodynamic Test of an Axisymmetric Supersonic Inlet with Variable Cowl Slot," AIAA Paper 85-1210, 1985.
36. Pratt & Whitney Aircraft, *The Aircraft Gas Turbine Engine and Its Operation*, PWA Oper. Instr. 200, United Technologies Corporation, East Hartford, CT, June 1980.
37. Rodean, H.C., "Supersonic Inlet Analysis and Design," Ling-Temco-Vought Report No. 11174, January 1958.
38. Rolls-Royce, *The Jet Engine*, Rolls-Royce plc, Derby, England, 2005.
39. Schweikhard, W.G. and Montoya, E.J., "Research Instrumentation Requirements for Flight/Wind Tunnel Tests of the YF-12 Propulsion System and Related Flight Experience," in *Instrumentation for Airbreathing Propulsion*, AIAA Series, Progress in Astronautics and Aeronautics, Vol. 34, Eds Fuhs, A.E. and Kingery, M., MIT Press, Cambridge, Mass. 1974.
40. Seddon, J. and Goldsmith, E.L., *Intake Aerodynamics*, AIAA, Washington, DC, 1985.
41. Sovran, G. and Klomp, E.D., "Experimentally Determined Optimum Geometries for Rectilinear Diffusers for Rectangular, Conical or Annular Cross Section," *Fluid Mechanics of Internal Flow*, Ed. Sovran, G., Elsevier Publishing Co., Amsterdam, 1963, pp. 270–319.
42. Strack, W.C., "Propulsion Challenges and Opportunities for High-Speed Transport Aircraft," in *Aeropropulsion '87*, NASA CP-10003, 1987.
43. Summerfield, M., Foster, C.R., and Swan, W.C., "Flow Separation in Over-expanded Supersonic Exhaust Nozzles," *Jet Propulsion*, Vol. 24, September–October 1954, pp. 319–321.
44. Sutton, G.P., *Rocket Propulsion Elements*, 6th edition, John Wiley & Sons, Inc., New York, 1992.
45. Wazelt, F., Ed., "Suitable Averaging Techniques in Non-Uniform Internal Flows," AGARD Advisory Report 182, June 1983.

46. Wazyaniak, J., "Mission Adaptation & Technology Trends in Aero Propulsion," Short Course Notes in *Aero-Propulsion* at UTSI, 2000.
47. Whitcomb, R.T. and Clark, L.R., *An Airfoil Shape for Efficient Flight at Supercritical Mach Numbers*, NASA TMX-1109, July 1965.
48. Whitford, R., *Design for Air Combat*, Jane's Publishing, London, UK, 1987.
49. Youngmans, J.L. and Dusa, D.J., "Inlets and Exhaust Systems for Multi-Mission Applications (Aero-Design and Installed Performance)," Short Course Notes, The University of Kansas, 1993.
50. Brausch, J.F., Bangalore, A.J., Barter, J.W., and Hoff, G.E., "Chevron exhaust nozzle for gas turbine engine," US Patent 6360528 B1, 2002.
51. Bridges, J.E., Wernet, M., and Brown, C.A., "Control of jet noise through mixing enhancement", Noise-Con, 23–25 June 2003, Cleveland, OH (NASA TM 2003-212335).
52. Lighthill, M.J., "On Sound Generated Aerodynamically, I: General Theory," *Proceedings of the Royal Society, Series A*, Vol. 211, 1952, pp. 564–587.
53. Saiyed, N., Mikkelsen, K.L., and Bridges, J., "Acoustics and Thrust of Separate-Flow Exhaust Nozzles With Mixing Devices for High-Bypass-Ratio Engines," NASA TM 2000-209948, 2000.
54. Zaman, K.B., Bridges, J.E., and Huff, D.L., "Evolution from 'tabs' to 'chevron technology' – a review," *International Journal of Aeroacoustics*, Vol. 10, No. 5 & 6, 2011, pp. 685–710.



F119-PW-100. Source: Reproduced by permission of United Technologies Corporation, Pratt & Whitney

The advanced thrust-vectoring exhaust system



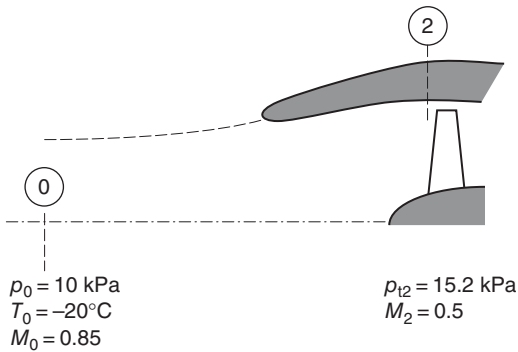
F-22 Raptor air-superiority fighter. Courtesy of USAF

Problems

In solving the following problems, assume $\gamma = 1.4$ and $c_p = 1004 \text{ J/kg K}$, unless otherwise stated.

-
- 6.1 In a real inlet, the total pressure loss is 10% of the flight dynamic pressure, i.e., $p_{t0} - p_{t2} = 0.1 q_0$ at a flight Mach number of $M_0 = 0.85$. Calculate
 - (a) inlet total pressure recovery π_d
 - (b) inlet adiabatic efficiency η_d .
 - 6.2 A subsonic inlet in cruise condition is shown. Calculate
 - (a) total pressure recovery π_d
 - (b) area ratio A_2/A_0
 - (c) static pressure ratio p_2/p_0

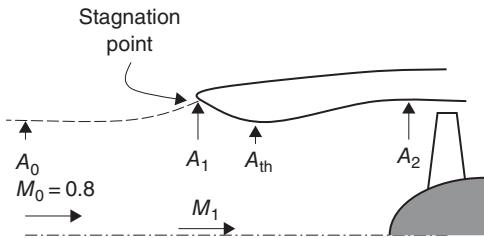
- (d) adiabatic efficiency η_d
- (e) entropy rise Δ_s/R .



■ FIGURE P6.2

6.3 Consider a subsonic inlet at a flight cruise Mach number of 0.8. The captured streamtube undergoes a prediffusion external to the inlet lip, with an area ratio $A_0/A_1 = 0.92$, as shown. Calculate

- (a) C_p (i.e., the pressure coefficient) at the stagnation point
- (b) inlet lip Mach number M_1
- (c) lip contraction ratio A_1/A_{th} for a throat Mach number $M_{th} = 0.75$ (assume $p_{t,th}/p_{t1} = 1$)
- (d) the diffuser area ratio A_2/A_{th} if $M_2 = 0.5$ and $p_{12}/p_{t,th} = 0.98$
- (e) the nondimensional inlet additive drag $D_{add}/\rho_0 A_1$.



■ FIGURE P6.3

6.4 The captured streamtube for a subsonic inlet experiences external diffusion, where flight Mach number of $M_0 = 0.85$ decelerates to M_1 of 0.65 at the inlet lip. Calculate the inlet additive drag nondimensionalized by flight static pressure p_0 and inlet area A_1 .

6.5 An aircraft flies at an altitude where p_0 is 0.1915 atm and the flight total pressure p_{t0} is 1.498 atm. The engine face total pressure is measured to be, $p_{12} = 1.348$ atm. For this inlet calculate

- (a) τ_r , ram temperature ratio

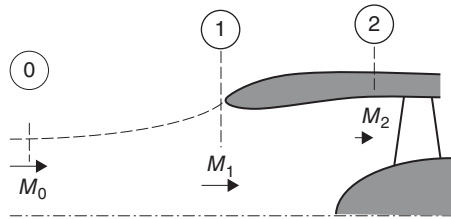
- (b) $\frac{\Delta s_d}{R}$, nondimensional entropy rise in the diffuser
- (c) η_d , inlet adiabatic efficiency

6.6 A subsonic diffuser has an area ratio of $A_2/A_1 = 1.3$. The inlet Mach number to the diffuser is $M_1 = 0.72$ and the total pressure loss in the diffuser is characterized by $\Delta p_1 = 0.1 q_1$. Assuming the flow in the diffuser is adiabatic, calculate

- (a) the diffuser exit Mach number M_2 and
- (b) diffuser static pressure recovery C_{PR}

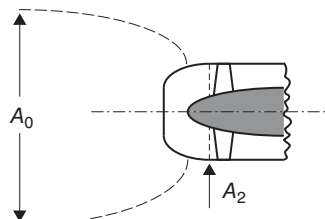
6.7 A subsonic inlet is cruising at $M_0 = 0.85$ and the capture area ratio A_0/A_1 is 0.90 (as shown). For an altitude pressure of $p_0 = 25$ kPa, the temperature of $T_0 = -25^\circ\text{C}$, and inlet area $A_1 = 3$ m², calculate

- (a) the inlet Mach number M_1
- (b) the inlet additive drag D_{add} (N)
- (c) inlet mass flow rate \dot{m} (kg/s)
- (d) the inlet ram drag D_{ram} (kN)
- (e) engine face area A_2 , if $M_2 = 0.5$ (assuming $\pi_d = 0.99$)



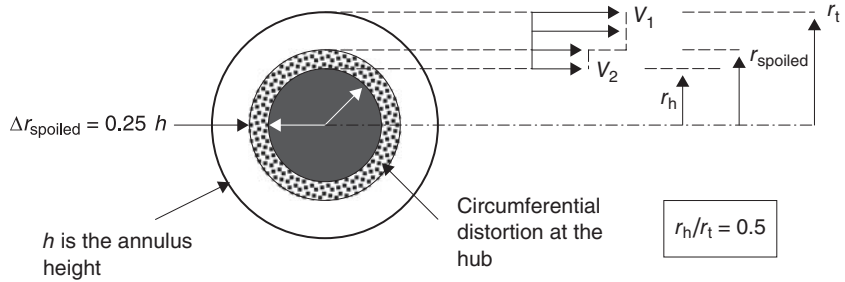
■ FIGURE P6.7

6.8 The Mach number at the compressor face is $M_2 = 0.65$ at takeoff ($M_0 \cong 0.2$). Assuming the inlet suffers a 2% total pressure loss at takeoff, calculate the capture-to-engine face area ratio A_0/A_2 .



■ FIGURE P6.8

6.9 A subsonic aircraft cruises at $M_0 = 0.85$ and its inlet operates with a capture ratio of $A_0/A_1 = 0.7$. First, calculate the lip Mach number M_1 . Second, assuming an engine becomes inoperative and the inlet lip Mach number drops to 0.3 (the so-called engine wind-milling condition), calculate the additive drag D_{add} for an inlet area of $A_1 = 4$ m² and the ambient static pressure of $p_0 = 16.6$ kPa.



■ FIGURE P6.12

6.10 A subsonic inlet is flying at Mach 0.8, with an inlet capture area ratio of $A_0/A_1 = 0.7$. The inlet lip contraction ratio A_1/A_{th} is 1.15. Calculate the 1D throat Mach number and comment on the potential shock formation, near the convex surface, at the throat.

6.11 A subsonic aircraft flies at $M_0 = 0.85$ with an inlet mass flow ratio (MFR) of 0.90. Calculate the critical pressure coefficient $C_{p,crit}$ on the nacelle. Also calculate the maximum cowl (frontal) area ratio A_M/A_1 if this inlet is to experience an average surface pressure coefficient corresponding to the critical value, i.e., $\bar{C}_p \approx C_{p,crit}$.

6.12 An inlet creates a circumferential distortion at the engine face, as shown. The hub-to-tip radius ratio is $r_h/r_t = 0.5$. The spoiled sector has a 15% mass flow deficit (per unit area) as compared with a uniform flow. Assuming the static density, temperature, and pressure are uniform at the engine face and the mass flow deficit in the spoiled sector is caused by a velocity deficit (as shown), use Bernoulli equation to estimate the total pressure deficit in the spoiled sector, i.e., $[p_t - p]_{spoiled}/[p_t - p]_{uniform}$. Also calculate

- (a) $\bar{P}_{t,area-avg}$
- (b) $\bar{P}_{t,mass-avg}$

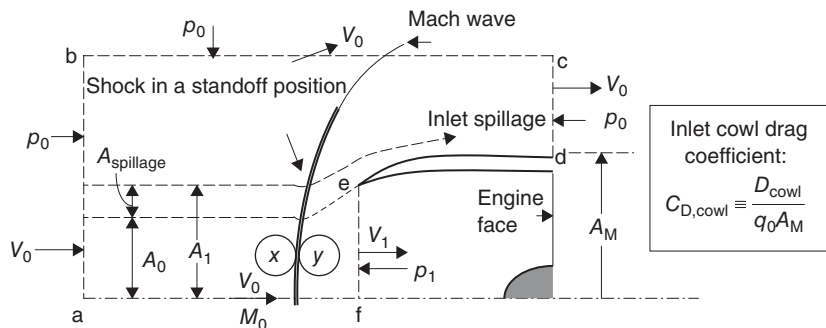
6.13 A subsonic inlet has a capture area ratio of $A_0/A_1 = 0.8$. Assuming the flight Mach number is 0.80 and the inlet area ratio is $A_2/A_1 = 1.25$, calculate

- (a) Mach number at the inlet lip M_1
- (b) diffuser exit Mach number if p_{t2}/p_{t1} is 0.95
- (c) inlet static pressure ratios p_1/p_0 and p_2/p_1 for $p_{t2}/p_{t1} = 0.95$

6.14 A normal shock inlet operates in the subcritical mode, with the shock in standoff position, as shown. The bow shock is normal to the flow at the inlet centerline and weakens into an oblique shock and eventually a Mach wave away from the inlet.

Apply conservations of mass and momentum to the control volume a-b-c-d-e-f-a, to approximate inlet cowl external drag force coefficient, in terms of the flight and inlet parameters that are shown, for example $V_0, M_0, p_0, p_1, V_1, A_1, A_M$, and $A_{spillage}$.

6.15 Consider a variable-geometry, convergent-divergent isentropic inlet that is designed for $M_D = 4.0$. To swallow the starting shock, i.e., to start the inlet, the throat needs to be opened. Calculate the percentage of throat area opening needed to start this inlet, $(\Delta A_{th}/A_{th}) \times 100$.

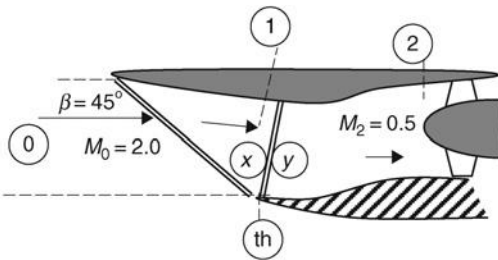


■ FIGURE P6.14

6.16 An external compression inlet is in a Mach-2 flow. The shocks are positioned according to the figure shown. Calculate

- (a) shock total pressure ratio π_s
- (b) A_2/A_{th}

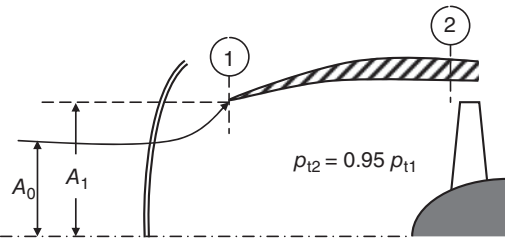
You may neglect the frictional losses in the subsonic diffuser.



■ FIGURE P6.16

6.17 A normal-shock inlet is operating in a supercritical mode, as shown. Flight Mach number is $M_0 = 1.6$. The inlet capture area ratio $A_0 = A_1 = 0.90$ and the diffuser area ratio $A_2 = A_1 = 1.2$. Calculate

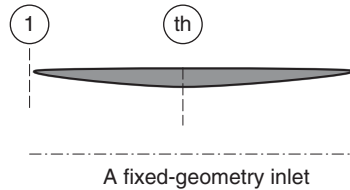
- (a) M_1
- (b) inlet total pressure recovery π_d , i.e., p_{t2}/p_{t0}



■ FIGURE P6.17

6.18 An isentropic convergent–divergent supersonic inlet is designed for $M_D = 1.6$. Calculate the inlet’s

- (a) area contraction ratio A_1/A_{th}
- (b) subsonic Mach number where the throat first chokes
- (c) percent spillage at $M_0 = 0.7$
- (d) percent spillage at $M_0 = 1.6$ (in the unstarted mode)
- (e) overspeed Mach number to start this inlet, $M_{overspeed}$
- (f) throat Mach number after the inlet was started, with still $M_{overspeed}$ as the flight Mach number



■ FIGURE P6.18

6.19 Consider an isentropic fixed-geometry C–D inlet, which is designed for $M_D = 1.75$. The inlet flies at an altitude where ambient (static) pressure is 20 kPa. Calculate

- (a) Overspeed Mach number that will start this inlet
- (b) The flight dynamic pressure corresponding to the altitude and $M_{overspeed}$

6.20 An isentropic, convergent–divergent supersonic inlet is designed for $M_D = 3.0$. Assuming that the throat area is adjustable, calculate the percentage of the design throat area that needs to be opened to swallow the starting shock, i.e., $\frac{A_{th,open} - A_{th,design}}{A_{th,design}} \times 100$

6.21 A supersonic C–D inlet is designed for a flight Mach number of $M_0 = 3.5$. This inlet starts by opening its throat (from A_{th} to A'_{th}). Neglecting wall frictional losses, calculate

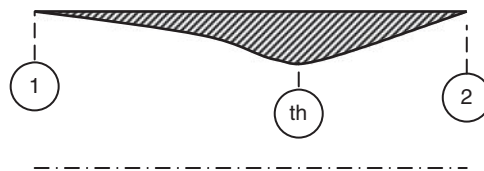
- (a) percentage throat opening required
- (b) throat Mach number after it starts (with the throat open at A'_{th})

6.22 A Kantrowitz–Donaldson inlet is designed for Mach 2.0. Calculate

- (a) the required contraction area ratio A_1/A_{th}
- (b) the inlet total pressure recovery with the best backpressure

6.23 A Kantrowitz–Donaldson inlet is designed for $M_D = 1.7$. Calculate

- (a) the inlet contraction ratio A_1/A_{th}
- (b) the throat Mach number after the inlet self started
- (c) the total pressure recovery with the best backpressure.



■ FIGURE P6.23

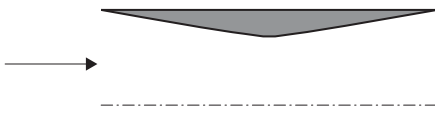
6.24 Calculate the contraction ratio A_1/A_{th} and the maximum total pressure recovery of a self-starting C–D inlet designed for $M_D = 3.2$.

6.25 A normal-shock inlet is operating in a supercritical mode, with the shock inside the inlet. If the flight Mach number is $M_0 = 1.6$ and the shock is located at $A_s/A_t = 1.2$, calculate

- (a) Mach number ahead of the shock wave, M_x
- (b) percentage total pressure gain if the inlet were to operate in the critical mode

6.26 A variable geometry isentropic supersonic inlet is designed for $M_D = 1.6$. Calculate

- (a) percentage flow spillage at $M_0 = 0.8$
- (b) percentage flow spillage at $M_D = 1.6$ before the inlet is started
- (c) percentage throat area increase needed to start this inlet
- (d) throat Mach number after the shock is swallowed, M_{th}
- (e) inlet total pressure recovery with the best backpressure (with open throat)



■ FIGURE P 6.26

6.27 An isentropic, fixed-geometry inlet, is designed for $M_D = 1.5$. If this inlet is to be started by overspeeding, calculate the necessary Mach number for overspeed.

6.28 A fixed-geometry, convergent–divergent, internal-compression inlet is designed for $M_D = 2.0$ and a self-starting capability. Calculate

- (a) A_1/A_{th}
- (b) M_{th}
- (c) inlet total pressure recovery for the “best” backpressure

6.29 A normal-shock inlet is flying at a Mach number of 1.8. However, due to a nonoptimum backpressure, the normal shock is inside the duct where $A_s/A_t = 1.15$. Calculate the percentage loss in the total pressure recovery due to this backpressure.

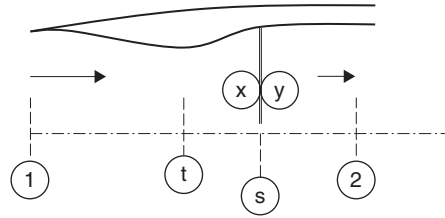
6.30 A variable-geometry supersonic convergent–divergent inlet is to be designed for an isentropic operation (in the started mode) at $M_D = 2.6$. Calculate

- (a) the inlet design contraction ratio A_1/A_{th}
- (b) the percentage opening of the throat $(A'_{th} - A_{th})/A_{th}$ needed to start the inlet
- (c) the throat Mach number in the open position, M'_{th}

6.31 A variable-geometry, internal-compression, C–D inlet is designed for $M = 2.0$. Calculate percentage opening of the throat required to swallow the starting shock.

6.32 A 2D fixed geometry convergent–divergent diffuser is shown. Mach number at the entrance is $M_1 = 3.0$ and the static pressure is $p_t = 10$ kPa. A shock occurs at an area ratio $A_s/A_{th} = 1.25$ downstream of the throat, as shown. Calculate

- (a) M_x
- (b) P_y
- (c) P_{ty}
- (d) A_2/A_1 if the exit Mach number is 0.5, i.e., $M_2 = 0.5$



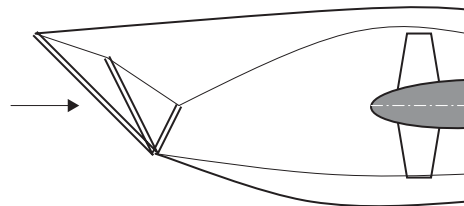
■ FIGURE P 6.32

You may assume the throat is choked and neglect wall friction.

6.33 A normal-shock inlet operates in a Mach 1.86 stream with ambient static pressure of $p_0 = 30$ kPa. Neglecting total pressure loss in the subsonic diffuser, calculate

- (a) inlet total pressure recovery with the shock at the lip, i.e., the best backpressure
- (b) inlet total pressure recovery when the shock is inside the duct at $A_x/A_t = 1.2$, i.e., the supercritical mode
- (c) inlet total pressure recovery in subcritical mode with 10% spillage, i.e., $A_{stage}/A_1 = 0.1$
- (d) flight dynamic pressure q_0

6.34 Consider an external compression inlet with two ramps operating in a Mach-2.5 stream of air. Calculate the total pressure recovery of the inlet shock system for the case of the best backpressure for the two ramp angles of 8° and 12° , respectively, and compare it to the normal-shock inlet at the same Mach number and with the best backpressure.



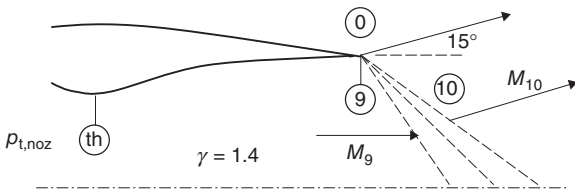
■ FIGURE P 6.34

6.35 A supersonic flow is to be decelerated over two oblique shocks and one normal shock, similar to Problem

6.34 (i.e., $M_0 = 2.5$). The Mach number downstream of the normal shock is 0.7. Assuming the maximum total pressure recovery is obtained when the first two oblique shocks are of equal strength, calculate the necessary ramp angles.

6.36 A supersonic nozzle operates in an underexpanded mode with an area ratio $A_9/A_{th} = 2$. We know that the exhaust plume turns outward by 15° , as shown. Assuming the flow inside the nozzle is isentropic and $\gamma = 1.4$, calculate

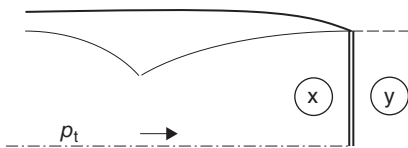
- (a) exit Mach number M_9 and
- (b) the nozzle pressure ratio $p_{t, \text{noz}}/p_0$ (note that $p_{10} = p_0$)
- (c) the Mach number after the expansion waves M_{10}
- (d) the NPR if the nozzle was perfectly expanded
- (e) the nozzle pressure ratio if a normal shock appears at the exit



■ FIGURE P6.36

6.37 A convergent–divergent nozzle discharges to ambient air and has an exit-to-throat area ratio of $A_e/A_{th} = 2.4$. The total pressure at the entrance to the nozzle is $p_t = 100$ kPa. A normal shock occurs at the nozzle exit, as shown. Calculate

- (a) the ambient pressure p_0 (note that $p_0 = p_y$)
- (b) the exhaust temperature T_y if the temperature at the throat is known $T_{th} = 350^\circ\text{C}$
- (c) mass flow rate through the nozzle if the throat area is $A_{th} = 0.25$ m²



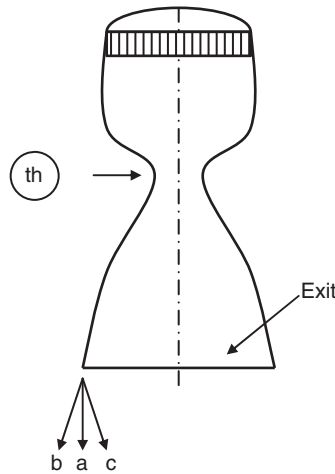
■ FIGURE P6.37

Assume the medium is air with $\gamma = 1.4$, $c_p = 1.004$ kJ/kg · K.

6.38 A supersonic nozzle has an exit-to-throat area ratio of $A_e/A_{th} = 3.5$ and an upstream stagnation pressure of $p_t = 19 \times 10^5$ Pa, which remains constant with altitude. Calculate

- (a) the altitude at which the nozzle is perfectly expanded
- (b) the altitude at which the exhaust plume is turned 10° outward

- (c) the altitude at which the exhaust flow is turned 4° inward



■ FIGURE P6.38

Assume: $\gamma = 1.4$ and $c_p = 1,004$ J/kg · K.

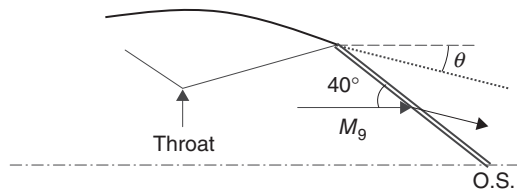
6.39 A convergent–divergent nozzle operates at a pressure altitude of $p_{\text{amb}} = 1$ kPa. The nozzle total pressure and temperature are $p_t = 101$ kPa and $T_t = 2000$ K, respectively. Calculate

- (a) nozzle area expansion ratio A_9/A_{th} , for perfect expansion
- (b) nozzle exit Mach number M_9 for perfect expansion
- (c) nozzle exit velocity V_9

Assume isentropic flow of air (with $\gamma = 1.4$ and $R = 287$ J/kg · K).

6.40 Consider an overexpanded nozzle as shown. Assuming the oblique shock at the exit makes a 40° angle with respect to the exit flow and the nozzle area ratio is 2.4, i.e., $A_9/A_{th} = 2.4$, calculate

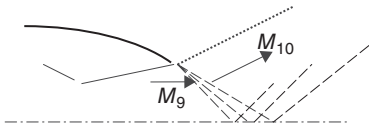
- (a) M_9
- (b) jet turning angle θ
- (c) NPR, i.e., p_t/p_{amb}



■ FIGURE P6.40

6.41 A convergent–divergent nozzle has an area ratio $A_9/A_{th} = 6.79$ and a stagnation pressure of $p_t = 38.13$ atm. First, calculate the pressure altitude (i.e., p_0) for which the nozzle is perfectly expanded. If this nozzle operated at a higher altitude, i.e., discharge to a lower backpressure atmosphere, it will operate as an *underexpanded* nozzle with an attendant expansion fan at the exit lip. Now, if the backpressure, i.e., $p_0 = 1/2 p_{0\text{-perfect-expansion}}$, calculate

- (a) Mach number after the (first) expansion fan, M_{10}
- (b) the jet turning angle θ
- (c) the tail wave angle of the first expansion fan with respect to the local flow

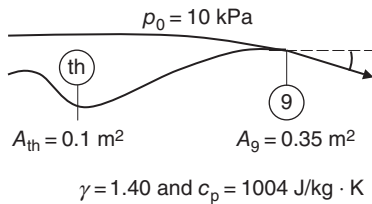


■ FIGURE P6.41

6.42 The exit flow from a two-dimensional C–D nozzle is shown to turn inward an angle of 15° . Calculate

Calculate

- (a) exit Mach number, M_9
- (b) wave angle at the nozzle exit lip
- (c) nozzle total pressure p_t (kPa)



■ FIGURE P6.42

6.43 A convergent nozzle experiences π_{cn} of 0.98, the gas ratio of specific heats $\gamma = 1.30$, and the gas constant is $R = 291$ J/kg · K. First, calculate the minimum nozzle pressure ratio that will choke the expanding nozzle, i.e., NPR_{crit} . This nozzle operates, however, at a higher NPR than the critical, namely, $NPR = 4.2$ and with an inlet stagnation temperature of $T_{t7} = 939$ K. Assuming this nozzle operates in $p_0 = 100$ kPa ambient static pressure, calculate

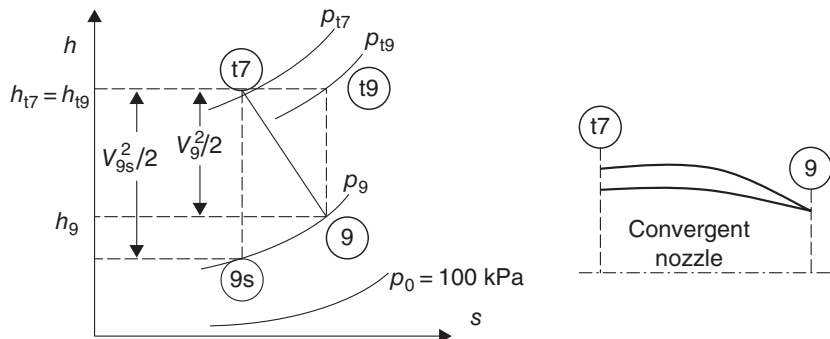
- (a) the exit static pressure and temperature p_9 and T_9 , respectively
- (b) the actual exit velocity V_9 in m/s
- (c) nozzle adiabatic efficiency η_n
- (d) the ideal exit velocity V_{9s} in m/s
- (e) percentage gross thrust gain, had we used a convergent–divergent nozzle with perfect expansion
- (f) nozzle discharge coefficient C_{D8}
- (g) draw a qualitative wave pattern in the exhaust plume

6.44 A convergent–divergent nozzle has a conical exhaust shape with the half-cone angle of $\alpha = 25^\circ$. Calculate the divergence loss C_A for this nozzle due to nonaxial exhaust flow. Assuming the same (half) divergence angle of 25° , but in a 2D rectangular nozzle, calculate the flow angularity loss and compare it to the conical case.

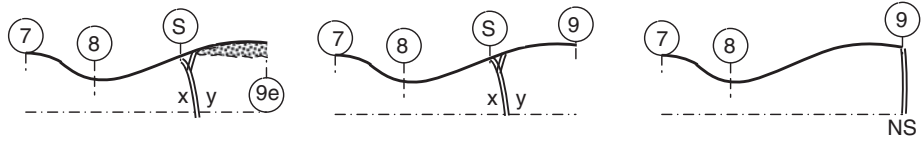
6.45 The bypass ratio in a turbofan engine is $\alpha = 3.5$. We intend to mix the cold fan and the hot core flows in a mixer to enhance the engine gross thrust. Assuming the hot core temperature of the gas is $T_h = 3 T_c$, calculate

- (a) the mixed-out temperature of the gas T_m / T_c
- (b) the percentage increase in ideal gross thrust as a result of mixing the cold and hot streams in the mixer

You may assume a reversible adiabatic mixer flow with $\gamma_h = \gamma_c = 1.4$.



■ FIGURE P6.43



■ FIGURE P6.46

6.46 Consider a fixed-geometry supersonic nozzle with the following inlet and geometrical parameters: $T_{17} = 2500$ K, $p_{17} = 233.3$ kPa, $\dot{m}_8 = 100$ kg/s, $A_9/A_8 = 7.45$, $\gamma = 1.4$, and $c_p = 1004$ J/kg · K. Assuming isentropic flow in the nozzle, calculate

- ambient pressure p_0 , if this nozzle is perfectly expanded
- ambient pressure if a normal shock appears at the nozzle exit
- nozzle throat and exit areas A_8 and A_9 , respectively, in m^2
- the nozzle gross thrust with a NS at the exit (part b)
- the nozzle gross thrust in the severely overexpanded case of the N.S. being inside the nozzle at $A_8/A_8 = 4.23$. Assume the flow remains attached after the shock
- in reality the boundary layer in part e separates and reduces the exit flow area by the amount of “blockage”.

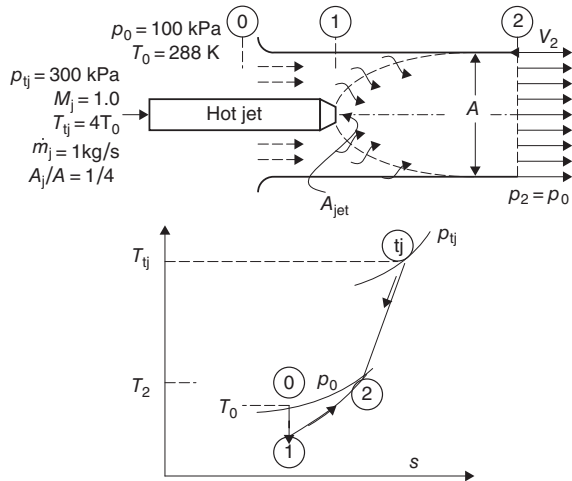
Assuming the effective exit area is $A_{9e} = A_8$ calculate the gross thrust for this more realistic scenario.

- compare the gross thrust with/without separation. Why did separation help?

6.47 A convergent nozzle discharges into an open duct, as shown (i.e., the ejector concept). Through flow entrainment in the jet, air is drawn in from the upstream open end of the duct. The two flows mix in the duct and produce a mixed-out exit flow at the ambient static pressure p_0 . Neglecting wall friction in the duct flow, calculate:

- the jet exit area A_j (in cm^2) and the ejector duct area A in cm^2
- the airflow drawn in from the duct inlet, i.e., the secondary flow rate \dot{m}_s
- the exit mixed-out gas velocity V_2
- the percentage increase in mass flow rate
- the percentage decrease in gas static temperature with the ejector
- gross thrust with and without the ejector

Hint: Apply conservation of mass, momentum, and energy to the control volume between 1 and 2. Flow between 0 and 1 is assumed to be isentropic.



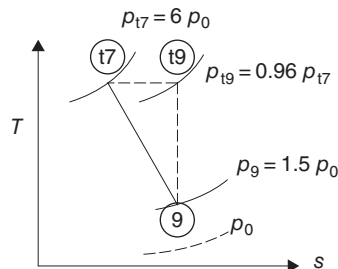
■ FIGURE P6.47

6.48 The thermodynamic states of gas in an exhaust nozzle are shown on the T - s diagram.

Calculate

- exit Mach number M_9
- nozzle adiabatic efficiency η_n

Assume $\gamma = 1.30$.

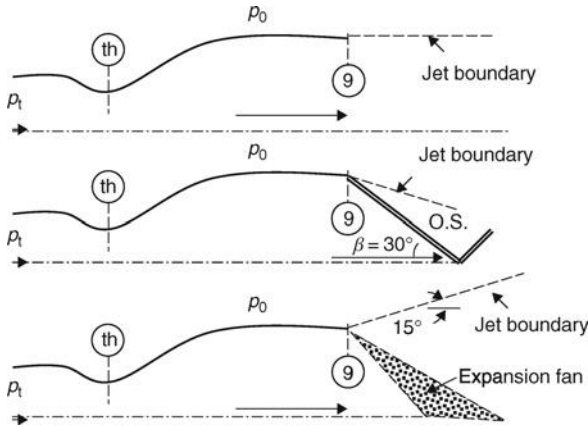


■ FIGURE P6.48

6.49 A convergent–divergent nozzle has an area ratio of $A_9/A_{th} = 5.9$. Assuming the flow is adiabatic and frictionless with $\gamma = 1.40$, calculate

- the nozzle pressure ratio p_t/p_0 for perfect expansion

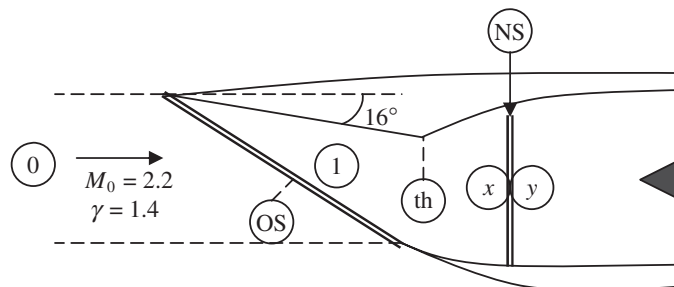
- (b) the nozzle pressure ratio p_t/p_0 if there is an oblique shock with $\beta = 30^\circ$ at the exit lip, as shown
- (c) the nozzle pressure ratio p_t/p_0 if there is an expansion wave at the lip that turns the flow 15° outward, as shown.



■ FIGURE P 6.49

- 6.50** A scramjet flies at Mach 6 with an inlet total pressure recovery of 50%. Assuming the combustor experiences a total pressure loss of 42% (from its inlet condition), calculate the NPR, assuming $\gamma = 1.30$ and is constant.
- 6.51** Calculate the ratio of gross thrust produced by a convergent–divergent nozzle to the gross thrust produced by a convergent nozzle when they both operate with the same nozzle pressure ratio of NPR = 10 and $\gamma = 1.30$.
- 6.52** An external compression inlet operates in supercritical mode, as shown. The normal shock is at $A_x/A_{th} = 1.2$. Calculate:

- (a) Throat Mach number, M_{th}
 - (b) Normal shock Mach number, M_x
 - (c) Total pressure ratio across the shock system
- (Assume losses are only due to shocks)

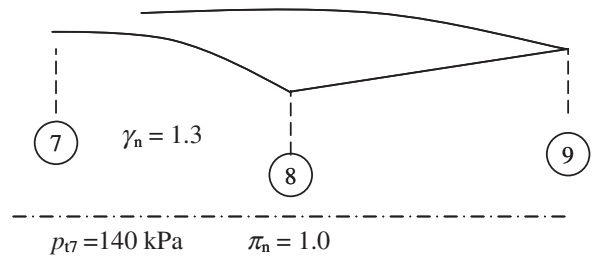


■ FIGURE P 6.52

6.53 A convergent–divergent exhaust system has an exit-to-throat area ratio, $A_9/A_8 = 3.0$.

Assuming the flow in the nozzle is isentropic, calculate:

- (a) nozzle exit Mach number, M_9
- (b) nozzle exit pressure, p_9 (kPa)
- (c) the ratio of momentum thrust to pressure thrust at the nozzle exit, for $p_0 = 5$ kPa



■ FIGURE P 6.53

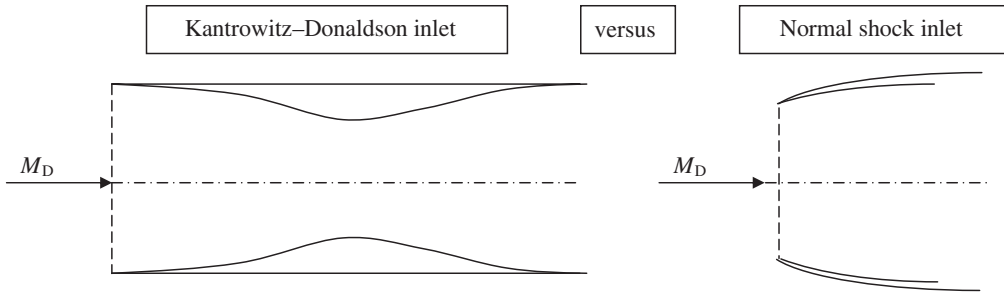
6.54 Consider two supersonic inlets, first is a self-starting (K–D) inlet, and the second is a NS inlet. Both inlets are designed for $M_D = 1.7$. Calculate:

- (a) the inlet contraction ratio, A_1/A_{th} , for the self-starting (K–D) inlet
- (b) throat Mach number in the K–D inlet after the inlet started
- (c) the total pressure recovery of K–D inlet with best back pressure
- (d) % gain in total pressure recovery in K–D versus NS inlet (both at best back pressure)

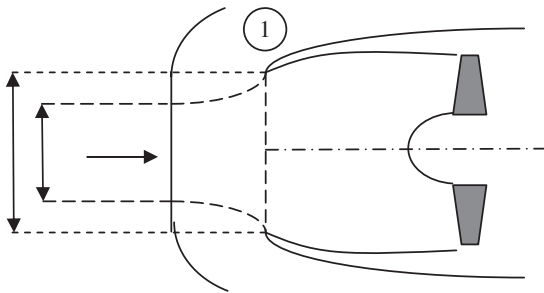
6.55 A normal-shock inlet operates in air at Mach 1.5 in subcritical mode, as shown. The Mach Number at the cowl lip is $M_1 = 0.62$.

Calculate

- (a) inlet spillage mass fraction, $\frac{\dot{m}_{spillage}}{\dot{m}_0}$
 - (b) inlet total pressure recovery, π_d
- (Neglect viscous losses in the subsonic diffuser)



■ FIGURE P6.54

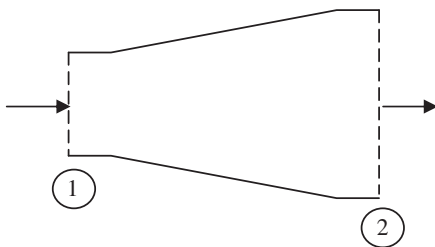


■ FIGURE P6.55

6.56 A subsonic diffuser has an area ratio, $A_2/A_1 = 2.02$ and operates in air with $\gamma_c = 1.4$ and $R = 287 \text{ J/kg}\cdot\text{K}$. Its inlet condition is measured to be: $p_{t1} = 100 \text{ kPa}$, $T_{t1} = 288 \text{ K}$ and $M_1 = 0.5$.

Assuming the flow in the diffuser is inviscid, calculate

- (a) inlet dynamic pressure, q_1 , in kPa
- (b) exit static pressure, p_2 in kPa
- (c) diffuser static pressure recovery, C_{PR}



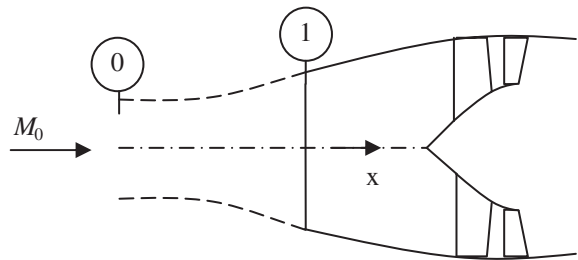
■ FIGURE P6.56

6.57 There is a subsonic inlet in cruise condition (as shown). We know the flight condition is: $M_0 = 0.8$, $p_0 = 25 \text{ kPa}$, $T_0 = 245 \text{ K}$.

The inlet mass flow rate is $\dot{m}_0 = 40 \frac{\text{kg}}{\text{s}}$ and the inlet capture ratio is $A_0/A_1 = 0.837$.

For $\gamma = 1.4$, and $R = 287 \text{ J/kg}\cdot\text{K}$, calculate

- (a) impulse at station 0, I_0 , in kN
- (b) impulse at the inlet lip, I_1 , in kN
- (c) additive drag force in kN
- (d) ram drag in kN

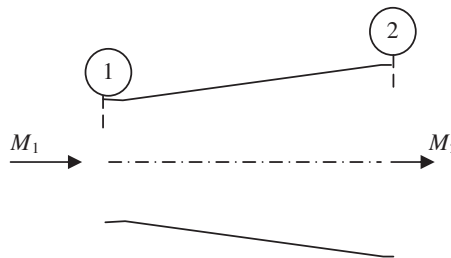


■ FIGURE P6.57

6.58 A subsonic diffuser has an inlet Mach number of $M_1 = 0.4$. The inlet pressure and temperature are $p_1 = 100 \text{ kPa}$ and $T_1 = 15^\circ\text{C}$, respectively. The diffuser static pressure recovery is $C_{PR} = 0.75$ and the exit Mach number is $M_2 = 0.1$.

For $\gamma = 1.4$, and $R = 287 \text{ J/kg}\cdot\text{K}$, calculate

- (a) inlet dynamic pressure, q_1 , in kPa
- (b) exit static pressure, p_2 , in kPa
- (c) exit total pressure, p_{t2} , in kPa
- (d) diffuser area ratio A_2/A_1



■ FIGURE P6.58

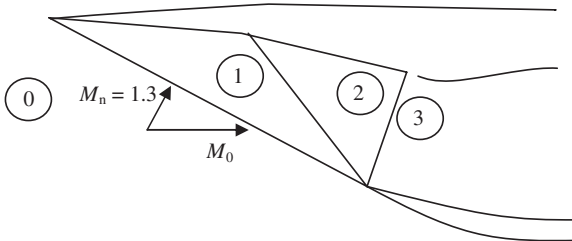
6.59 A subsonic inlet is in $M_0 = 0.86$ cruise with external diffusion characterized by the inlet mass flow ratio parameter, $MFR=0.89$, which is the same as the inlet capture area ratio, A_0/A_1 . Assume an isentropic flow with $\gamma = 1.4$ and $c_p = 1004$ J/kg.K, to calculate

- (a) the Mach number at the inlet lip, M_1
- (b) the external static pressure ratio, p_1/p_0 , i.e., as the result of external diffusion
- (c) the external velocity ratio, V_1/V_0 , i.e., as the result of external diffusion

6.60 A supersonic inlet creates two oblique shocks and a normal shock, as shown. The normal component of Mach number to these shocks is 1.3, for each of the three shocks.

For $\gamma = 1.4$, calculate

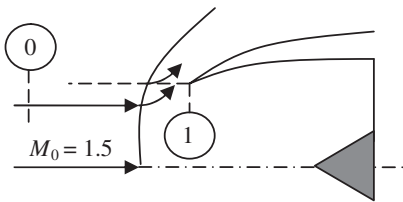
- (a) the total pressure recovery of the shock system
- (b) Mach number at the entrance to the subsonic diffuser, M_3



■ FIGURE P6.60

6.61 An isentropic C–D inlet is designed for Mach 4.0. Calculate the percentage opening of the throat area that is needed to start the inlet. Assume $\gamma = 1.4$.

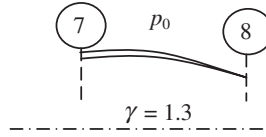
6.62 A normal shock inlet operates in subcritical mode, as shown. Calculate the percentage spillage for this inlet if $M_1 = 0.60$. Assume $\gamma = 1.4$ (Note: percentage spillage = $100 * (A_1 - A_0)/A_1$)



■ FIGURE P6.62

6.63 A convergent nozzle operates at a nozzle pressure ratio of 3.0. Assuming $\gamma = 1.3$ and $\pi_{cn} = 0.98$, Calculate

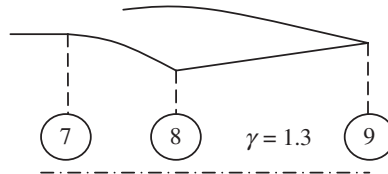
- (a) exit Mach number, M_8
- (b) ratio of exit to ambient static pressure, p_8/p_0



■ FIGURE P6.63

6.64 A convergent-divergent nozzle has an area ratio of $A_9/A_8 = 4.2$. The nozzle pressure ratio is $NPR = 20$ with $\gamma = 1.3$. Assuming that the flow in the CD nozzle is isentropic, calculate

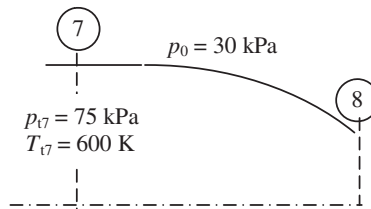
- (a) exit Mach number, M_9
- (b) ratio of exit static to inlet total pressure, p_9/p_{17}
- (c) what kind of wave will form at the nozzle exit? Why?
- (d) what is the static pressure ratio across the wave?



■ FIGURE P6.64

6.65 A convergent nozzle is shown. The ambient static pressure is $p_0 = 30$ kPa. Assuming the flow in the nozzle is isentropic with $\gamma = 1.3$ and $R \approx 287$ J/kg.K, calculate

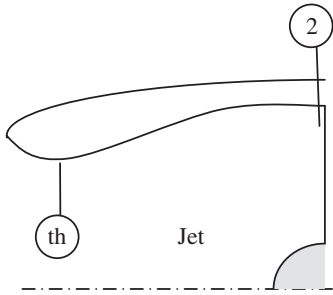
- (a) nozzle exit Mach number, M_8
- (b) exit static pressure, p_8 in kPa
- (c) exit velocity, V_8 , in m/s



■ FIGURE P6.65

6.66 A subsonic inlet has an average throat Mach number of $M_{th} = 0.70$ and an average total pressure of 75 kPa. The engine face area is 125% of the throat area, i.e., $A_2 = 1.25 A_{th}$. For the engine face Mach number of $M_2 = 0.5$, calculate

- (a) engine face total pressure, p_{12} , in kPa
- (b) static pressure at the throat, p_{th} , in kPa
- (c) dynamic pressure at the throat, q_{th} , in kPa



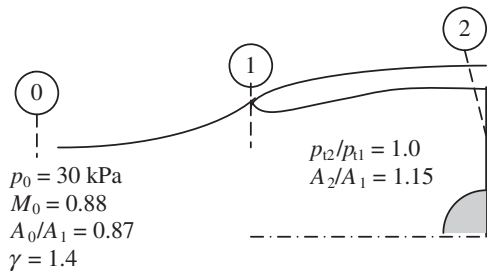
■ FIGURE P6.66

6.67 A convergent nozzle has an inlet total pressure, $p_{t7} = 150$ kPa and inlet total temperature of $T_{t7} = 660$ K with $\gamma_7 = 1.33$ and $C_{p7} = 1,156$ J/kg.K. The ambient pressure is $p_0 = 100$ kPa. Assuming that the convergent nozzle total pressure ratio is $\pi_{cn} = 0.98$, calculate

- (a) nozzle exit Mach number, M_8
- (b) nozzle exit velocity, V_8 , in m/s

6.68 A subsonic inlet is in flight, as shown. Calculate

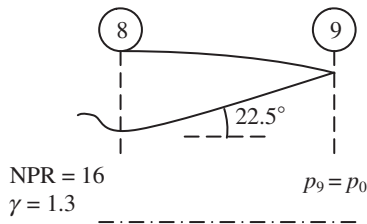
- (a) the Mach number at the inlet lip, M_1
- (b) the Mach number at the engine face, M_2



■ FIGURE P6.68

6.69 A convergent–divergent nozzle has a throat discharge coefficient of $C_{D8} = 0.98$. The velocity coefficient in the divergent section is $C_V = 0.96$.

Assuming the ratio of specific heats in the nozzle is $\gamma = 1.30$, and nozzle is of conical shape with the semi-vertex angle of $\alpha = 22.5^\circ$, calculate

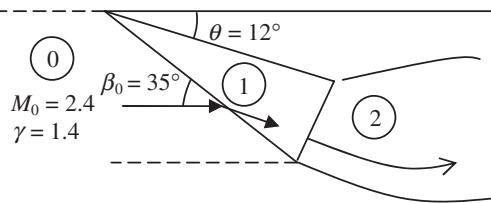


■ FIGURE P6.69

- (a) gross thrust coefficient, C_{fg}
- (b) percentage increase in gross thrust if the nozzle were bell-shaped, i.e., exhaust velocity was axial

Note that the nozzle is perfectly expanded.

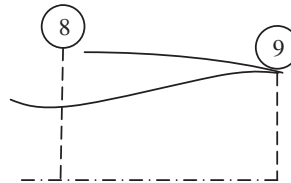
6.70 An external-compression supersonic inlet creates oblique and normal shocks in flight, as shown. Calculate the inlet total pressure recovery due to shocks.



■ FIGURE P6.70

6.71 A convergent–divergent nozzle operates at NPR of 14.86 in an altitude where the ambient pressure is $p_0 = 30$ kPa. Assuming the flow in the nozzle is isentropic with $\gamma = 1.3$, calculate

- (a) nozzle area ratio, A_9/A_8 , if the nozzle is perfectly expanded 5
- (b) exit Mach number, M_9



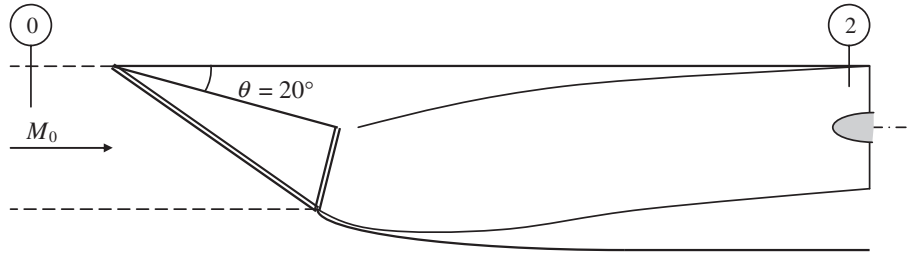
■ FIGURE P6.71

6.72 An external-compression supersonic inlet has a single ramp and it operates in critical mode, as shown. The flight speed is $V_0 = 750$ m/s where the ambient speed of sound is $a_0 = 300$ m/s and the ambient (static) pressure is 20 kPa. Assuming that the air flow rate captured by the inlet is $\dot{m}_0 = 30$ kg/s, calculate

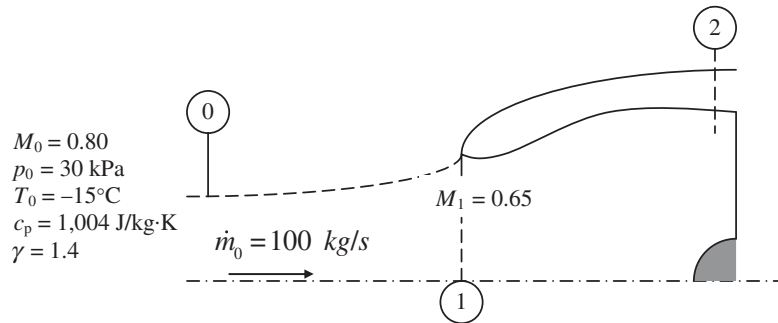
- (a) ram drag in kN
- (b) inlet total pressure recovery (due to shocks)

6.73 Consider a subsonic inlet in cruise condition as shown. Assuming the mass flow rate (of air) is 100 kg/s (as shown), calculate:

- (a) the ram drag, D_r , in kN
- (b) freestream capture area, A_0 in m^2
- (c) the static pressure at the inlet lip, p_1 in kPa
- (d) the static temperature at the inlet lip, T_1 in K



■ FIGURE P6.72

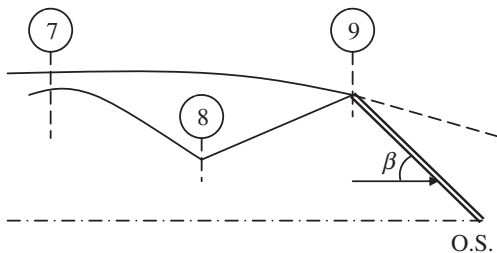


■ FIGURE P6.73

- (e) the inlet capture area, A_1 in m^2
- (f) the additive drag, D_{ad} , in N

6.74 An overexpanded supersonic convergent–divergent nozzle has an inlet total pressure of $p_{t7} = 213$ kPa and an area ratio of $A_0/A_8 = 3.02$. The ratio of specific heats is $\gamma = 1.3$ and $c_p = 1,250$ J/kg·K. Neglecting losses in the nozzle and assuming ambient static pressure is $p_0 = 25.2$ kPa, calculate

- (a) nozzle exit Mach number M_9
- (b) nozzle exit (static) pressure, p_9
- (c) the oblique shock wave angle, β in degrees

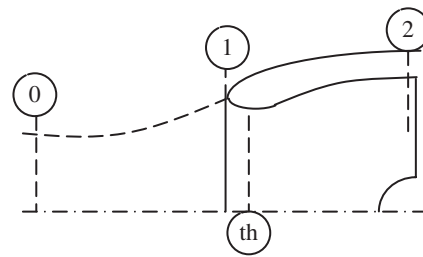


■ FIGURE P6.74

6.75 A subsonic pitot inlet is cruising at $M_0 = 0.84$ at an altitude where $p_0 = 30$ kPa and $T_0 = 240$ K. The inlet capture ratio is $A_0/A_1 = 0.88$. The inlet lip area contraction ratio

is $A_1/A_{th} = 1.05$. The area ratio between the throat and the engine face is $A_{th}/A_2 = 0.85$. Assuming the flow is reversible and adiabatic inside the inlet, and $\gamma = 1.4$, calculate

- (a) Mach number at the inlet lip, M_1
- (b) Mach number at the throat, M_{th}
- (c) Mach number at the engine face, M_2
- (d) overall static pressure recovery coefficient, C_{PR} between the engine face and flight, i.e., $C_{PR} = \frac{p_2 - p_0}{p_0}$

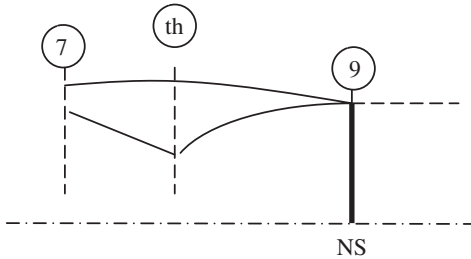


■ FIGURE P6.75

6.76 A convergent–divergent nozzle operates with a normal shock at its exit plane, as shown. The nozzle total pressure at its inlet is $p_{t7} = 200$ kPa and the nozzle area ratio is

$A_9/A_8 = 3.0$. Assuming $\gamma = 1.3$, and The flow in the nozzle is isentropic, calculate

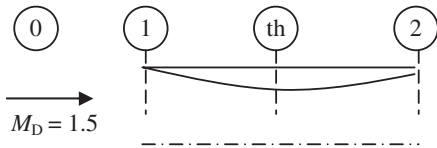
- (a) the exit Mach number, M_9 , before the NS
- (b) the ambient pressure, p_0 , in kPa



■ FIGURE P6.76

6.77 A Kantrowitz–Donaldson inlet is designed to self-start at $M_D = 1.5$. Assume the medium is air with $\gamma = 1.4$. Calculate the

- (a) inlet contraction ratio, A_1/A_{th}
- (b) Mach number at the inlet throat, M_{th} at the design Mach number when the inlet is started
- (c) best inlet total pressure recovery at $M_D = 1.5$.



■ FIGURE P6.77

6.78 A subsonic inlet has a throat area, $A_{th} = 1 \text{ m}^2$, with the average axial Mach number at the throat of $M_{th} = 0.7$. The corresponding flight condition is: $M_0 = 0.86$, $p_0 = 30 \text{ kPa}$, $T_0 = -50^\circ\text{C}$, $\gamma = 1.4$, $R = 287 \text{ J/kg}\cdot\text{K}$. Calculate

- (a) the captured stream area, A_0 , in m^2
- (b) the mass flow rate, \dot{m}_0 , in kg/s

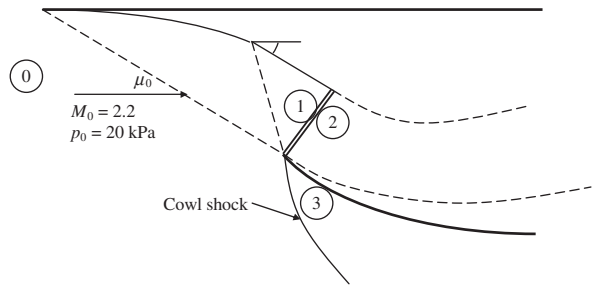
You may treat the flow to the inlet throat to be isentropic.

6.79 A supersonic inlet uses isentropic pre-compression for a total of 17° turn, as shown.

Calculate

- (a) Mach number upstream of the normal shock, M_1
- (b) inlet total pressure recovery, p_{t2}/p_{t0}
- (c) static pressure on the cowl lip after the cowl shock, p_3 in kPa (assume lip is very thin)

6.80 Calculate nondimensional additive drag, D_{add}/p_0A_1 , for a subsonic inlet at cruise condition, $M_0 = 0.8$, $A_0/A_1 = 0.835$.

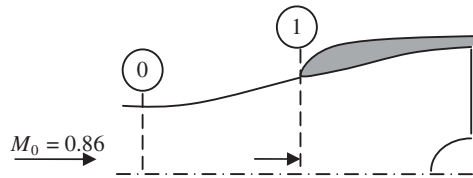


■ FIGURE P6.79

6.81 A subsonic inlet has a contraction area ratio of 1.112, i.e., $A_{HL}/A_{th} = 1.112$. The (mass) average throat Mach number is 0.74. Neglecting the frictional losses (on total pressure) between the highlight and the throat, calculate the Mach number at the highlight.

6.82 Calculate and compare the nondimensional additive drag, D_{add}/p_0A_1 , on a subsonic inlet with a cruise Mach number of $M_0 = 0.86$ that is designed with either of the two inlet capture ratios:

- Case I: $A_0/A_1 = 0.82$
- Case II: $A_0/A_1 = 0.76$



■ FIGURE P6.82

6.83 A 2D external-compression inlet is shown in super-sonic flight. The external cowl is composed of three flat panels, as shown. The Cartesian coordinates of the panels are:

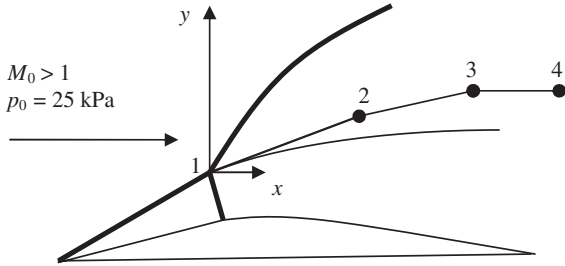
- $x_1 = 0.0 \text{ m}$, $y_1 = 0.00 \text{ m}$
- $x_2 = 1.0 \text{ m}$, $y_2 = 0.25 \text{ m}$
- $x_3 = 2.0 \text{ m}$, $y_3 = 0.35 \text{ m}$
- $x_4 = 3.0 \text{ m}$, $y_4 = 0.35 \text{ m}$

Assuming the panels' static pressure is:

- Panel #1: $p \approx 50 \text{ kPa}$
- Panel #2: $p \approx 30 \text{ kPa}$
- Panel #3: $p \approx 25 \text{ kPa}$

Calculate

- (a) cowl wave drag (per unit width of the inlet) in kN/m
- (b) can you estimate M_0 ? (Hint: static pressure doubled on panel #1 from free stream, and the flow turning angle to the first panel is also known.)



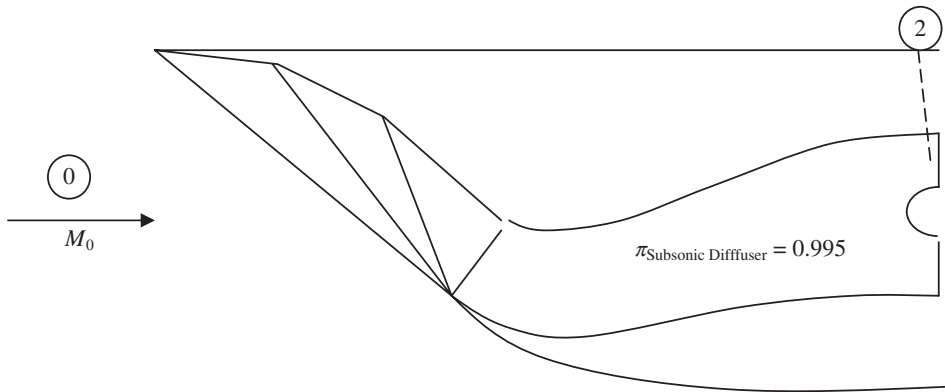
■ FIGURE P6.83

6.84 A three-ramp external compression inlet is shown. The three oblique shocks and the terminal, i.e., the normal shock, are all of equal strength. Assuming that nor-

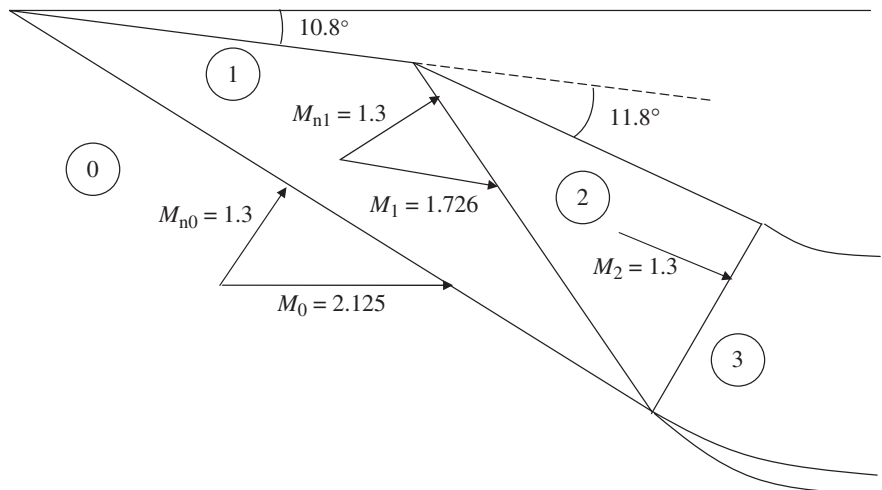
mal component of Mach number to each shock is 1.3, calculate

- (a) the total pressure recovery of the shock system
- (b) the inlet total pressure recovery
- (c) estimate the flight Mach number, M_0 , if this inlet represents “the optimum” four-shock external compression inlet.

6.85 It is desirable to design a two-ramp external compression inlet for a design-point Mach number of $M_0 = 2.125$ that creates three shocks of equal strength. We have calculated the normal components of Mach number in this design to be 1.3, as shown. Validate that the two successive ramp angles are 10.8° and 11.8° respectively. Also, calculate the (shock) total pressure recovery for this inlet at the design point. [Note that the figure is not-to-scale]



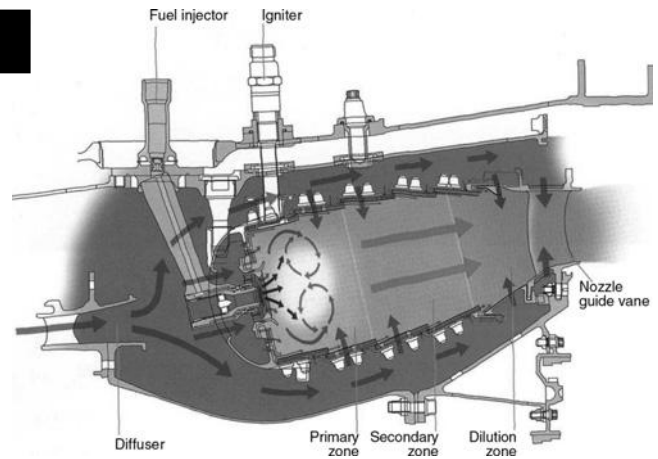
■ FIGURE P6.84



■ FIGURE P6.85

CHAPTER 7

Combustion Chambers and Afterburners



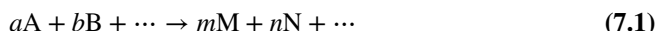
Source: Reproduced with permission from Rolls-Royce plc

7.1 Introduction

To study the *mechanism of heat release* in an aircraft gas turbine engine combustion chamber, we need to revisit the thermochemistry principles that we learned in our freshman chemistry class. As engineers, we are interested in maximizing the heat release while minimizing the space requirements for the combustion chamber of an aircraft engine. Besides the *mechanism of heat release*, we are also interested in the *rate* at which chemical reactions takes place. We may think of it as one characteristic *timescale* of the problem. The question of *rate* is governed by the *chemical kinetics*, which is a subject in thermochemistry. In addition, we hope to understand the characteristic *length scales* of the problem involved in flame stability and length, which ultimately are tied to the combustion chamber geometry and sizing. In a combustion chamber of an airbreathing engine, we bring a liquid fuel and air together and an ignition source to start off the chemical reaction. We understand that the fuel has to be first vaporized before any reaction can take place between it and the oxygen in the air. We also recognize that a reaction between the oxygen in the air and the fuel must take place upon a *collision* between the two molecules. Only very energetic collisions result in the molecular dissociation of the fuel and a reaction with the oxygen. Therefore, not only the collisions are of necessity for a chemical reaction but also the *collision energy* is of importance. We may want to think of those collisions that lead to a chemical reaction as *effective collisions* in contrast to those collisions that result in a bounce back of the molecules. The question of whether collision

energy is sufficient for a chemical reaction is answered by a chemical parameter known as the *activation energy* of the reaction. Now that we are relating to chemical reactions as energetic collisions between the oxygen and the fuel molecules, we may relate to the *rate of reaction* by the *frequency* of such collisions. We immediately recognize that these parameters, namely the characteristic time and length scales in a combustion chamber, depend on many parameters, including the vaporization rate of the atomized fuel droplets and the turbulence intensity of the mixing process. Finally, as citizen engineers, we are committed to zero pollution, which will prove to be a daunting task in the combustion of a hydrocarbon fuel in air.

Chemical reactions take place at the molecular level and are always expressed in the following form:



where a , b , m , and n are the number of *moles* of reactants A and B and the products M and N, respectively. The left-hand side of the reaction is known as the *reactants*, and the right-hand side of the reaction is known as the *products*. The number of moles of a substance is the ratio of the mass of the substance to its molecular weight, for example,

$$a \equiv \frac{m_a}{MW_a} \quad (7.2)$$

with the dimensions of

$$[a] = \frac{\text{kg}}{\text{kg/kmol}} = \text{kmol} \quad (7.3)$$

EXAMPLE 7.1

If a mixture contains 12 kg of H_2 and 8.0 kg of O_2 , determine the number of moles of hydrogen and oxygen in the mixture.

$$n_{\text{H}_2} = \frac{12 \text{ kg}}{2 \text{ kg/kmol}} = 6.0 \text{ kmol}$$

$$n_{\text{O}_2} = \frac{8 \text{ kg}}{32 \text{ kg/kmol}} = 0.25 \text{ kmol}$$

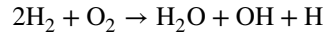
Another interpretation of the mole of a substance is the amount of the substance that contains 6.023×10^{23} molecules (in a gram. mole), which is known as the Avogadro's number N_a . Avogadro's number is defined as the number of carbon atoms in 12 g of ^{12}C , which is 6.023×10^{23} molecules/gmol, therefore,

$$n = \frac{N}{N_a} \quad (7.4)$$

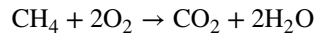
However, presenting the number of moles of a substance is easiest based on mass and molecular weight rather than the number of individual molecules and the Avogadro's

number. In an engineering combustion problem, we typically introduce a certain *mass* of fuel and oxidizer in a reaction and not (explicitly) their number of individual molecules.

An important conservation law applicable to chemical reactions is the *law of conservation of atomic species*. It simply states that the numerical count of atoms of each species on both sides of a reaction has to be the same. The following two examples illustrate this conservation principle.



There are four hydrogen atoms on the reactants side as well as the product side. Two oxygen atoms appear on both sides as well. In the following reaction, methane (CH_4) is reacting with oxygen, with C, H, and O in balance.



In dealing with the problems of reacting gases, such as the type experienced in a combustion chamber of a gas turbine engine, we are faced with a *mixture* of gases and hence we need to review the laws governing such mixtures. The most fundamental question regarding mixtures is whether we know the *mixture* properties, as a function of its *constituent* properties. The mixture properties range from the molecular weight of the mixture to the specific heats of the mixture, the specific enthalpy and entropy of the mixture. In addition, the constituent gases are assumed to obey the perfect gas law, which at sufficiently low densities, we understand that all gases behave as perfect.

7.2 Laws Governing Mixture of Gases

Imagine there is a volume V that contains several gases. The equilibrium mixture of gases has attained a mixture temperature T_m , which we now identify as being shared by all the constituents, that is, all constituents have the same random kinetic energy after numerous collisions that brought them to an equilibrium state, namely,

$$T_m = T_1 = T_2 = T_3 = \dots = T_n \quad (7.5)$$

Before we define the pressure of the mixture p_m , let us first define the *partial pressure* associated with the constituents of the mixture. A constituent of a mixture that occupies the *entire volume* of the mixture, V , and is at the mixture temperature, exerts a pressure on the vessel, which is called its partial pressure. Now, Dalton's law of additive pressures states that the mixture pressure is the sum of all its constituents' partial pressures (a direct consequence of perfect gas law), namely,

$$p_m = p_1 + p_2 + p_3 + \dots + p_n = \sum_{i=1}^n p_i \quad (7.6)$$

where p_n is the partial pressure of the n th constituent.

On the question of internal energy, enthalpy and the entropy of the mixture of gases, we have the Gibbs–Dalton law that states

$$E_m = E_1 + E_2 + E_3 + \cdots + E_n = \sum_{i=1}^n E_i \quad (7.7)$$

$$H_m = H_1 + H_2 + H_3 + \cdots + H_n = \sum_{i=1}^n H_i \quad (7.8)$$

$$S_m = S_1 + S_2 + S_3 + \cdots + S_n = \sum_{i=1}^n S_i \quad (7.9)$$

where E is the internal energy, H the enthalpy, and S is the entropy. The constituent properties in Equations 7.7 to 7.9 are all based on the assumption that a constituent occupies the entire volume and is at the mixture temperature. We can also express the intrinsic variables of state, namely, the *specific* internal energy, the *specific* enthalpy, and the *specific* entropy based on the above Equations 7.7 to 7.9, as

$$e_m = \frac{m_1 e_1 + m_2 e_2 + m_3 e_3 + \cdots + m_n e_n}{m_m} = \left[\sum_{i=1}^n m_i e_i \right] / \left[\sum_{i=1}^n m_i \right] \quad (7.10)$$

$$h_m = \frac{m_1 h_1 + m_2 h_2 + m_3 h_3 + \cdots + m_n h_n}{m_m} = \left[\sum_{i=1}^n m_i h_i \right] / \left[\sum_{i=1}^n m_i \right] \quad (7.11)$$

$$s_m = \frac{m_1 s_1 + m_2 s_2 + m_3 s_3 + \cdots + m_n s_n}{m_m} = \left[\sum_{i=1}^n m_i s_i \right] / \left[\sum_{i=1}^n m_i \right] \quad (7.12)$$

Now, the mass of the mixture m_m is obviously the sum of the individual masses m_i based on the law of conservation of mass. We can express the mass of each constituent as the product of the number of moles and the molecular weight, of that constituent, based on Equation 7.2, as

$$m_m = n_m \text{MW}_m = \sum_{i=1}^n m_i = \sum_{i=1}^n n_i \text{MW}_i \quad (7.13)$$

Therefore, the mixture molecular weight is now expressible in terms of the individual molecular weights and the *mole fraction* of each constituent, which we now define as χ

$$\chi_i \equiv \frac{n_i}{\sum n_i} = \frac{n_i}{n_m} \quad (7.14)$$

and, therefore,

$$\text{MW}_m = \frac{\sum n_i \text{MW}_i}{n_m} = \sum \chi_i \text{MW}_i \quad (7.15)$$

As an example, air is composed of nitrogen, oxygen, and traces of inert gases, such as argon. Its composition is said to be nearly 78% N_2 , 21% O_2 , and 1% Ar, by volume. Therefore, 0.78, 0.21, and 0.01 are the *volume fractions* of the nitrogen, oxygen, and argon, respectively, in air.

From perfect gas law, written for a constituent as

$$p_i V_m = n_i \bar{R} T_m \quad (7.16)$$

where \bar{R} is the universal gas constant with a value of

$$\begin{aligned} \bar{R} &= 8.3146 \frac{\text{kJ}}{\text{kmol K}} = 1.9864 \frac{\text{kcal}}{\text{kmol K}} \\ \bar{R} &= 1545.4 \frac{\text{ft} \cdot \text{lbf}}{\text{lbm} \cdot \text{mole} \cdot ^\circ\text{R}} = 1.9872 \frac{\text{BTU}}{\text{lbm} \cdot \text{mole} \cdot ^\circ\text{R}} \end{aligned}$$

We can sum Equation 7.16 for all the constituents to get

$$\sum p_i V_m = p_m V_m = n_m \bar{R} T_m = \sum n_i \bar{R} T_m \quad (7.17)$$

which suggests that the ratio of partial pressure of any constituent to the mixture pressure is equal to the mole fraction of that constituent, namely,

$$\frac{p_i}{p_m} = \frac{n_i}{n_m} \equiv \chi_i \quad (7.18)$$

Now, if we consider a mixture of gases, such as air, at a pressure, namely, p_m , and a temperature T_m , we may define a volume occupied by each constituent, V_i , such that

$$p_m V_i = n_i \bar{R} T_m \quad (7.19)$$

Dividing Equation 7.19 by Equation 7.17 yields

$$\frac{V_i}{V_m} = \frac{n_i}{n_m} = \chi_i \quad (7.20)$$

The above equation states that the volume fraction of a gas constituent in a mixture, as defined by Equation 7.19 (i.e., at T_m and p_m), is equal to the constituent's mole fraction. The same conclusion about the volume fraction and mole fraction (i.e., being equal) may be reached by remembering the Law of Equal Volumes. It states that the volume occupied by one mole of any perfect gas is the same as that of any other perfect gas at a constant pressure and temperature. Consequently, when we describe the air composition as being 0.78, 0.21, and 0.01 for N_2 , O_2 , and Ar, respectively, by volume, we are stating that the air composition on a mole fraction basis as

$$1 \text{ mole of air} = 0.78 \text{ N}_2 + 0.21 \text{ O}_2 + 0.01 \text{ Ar} \quad (7.21)$$

with 0.78, 0.21, and 0.01 as mole fractions of the constituents N_2 , O_2 , and Ar. Now, we can use Equation 7.15 to arrive at the molecular weight of air as

$$\text{MW}_{\text{air}} \cong 0.78(28) + 0.21(32) + 0.01(40) = 28.97 \approx 29 \text{ kg/kmol} \quad (7.22)$$

■ **FIGURE 7.1**
Definition sketch
 showing the volumes
 occupied by a
 constituent gas in a
 mixture of gases (with
 $V_A/V_B = n_A/n_B$)

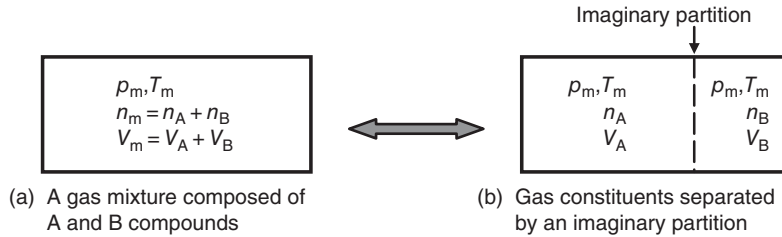


Figure 7.1 shows the meaning of the volume occupied by a constituent gas in a mixture of gases. The specific heats at constant volume and pressure follow the perfect gas law:

$$\begin{aligned} de &= c_v dT \\ dh &= c_p dT \end{aligned} \quad (7.23)$$

Now, combining these results with the mixture laws for the internal energy and enthalpy, Equations 7.10 and 7.11, respectively, we get

$$c_{v_m} = \frac{\sum m_i c_{vi}}{m_m} \quad (7.24)$$

$$c_{p_m} = \frac{\sum m_i c_{pi}}{m_m} \quad (7.25)$$

The ratio of specific heats for the mixture may now be written as

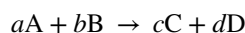
$$\gamma_m \equiv \frac{c_{p_m}}{c_{v_m}} = \frac{\sum m_i c_{pi}}{\sum m_i c_{vi}} \quad (7.26)$$

If instead of working with masses, we prefer to work with the moles and mole fractions, we can replace each constituent mass by the product of its molecular weight and its number of moles. This approach is preferred in chemical analysis where compounds reaction is on a *molar* basis rather than mass basis. For example, let us express specific heat at constant pressure of the mixture in terms of the mole fractions instead of mass fractions, as given in Equation 7.25,

$$c_{p_m} = \sum \frac{n_i MW_i c_{pi}}{n_m MW_m} = \frac{\sum \chi_i MW_i c_{pi}}{MW_m} \quad (7.27)$$

7.3 Chemical Reaction and Flame Temperature

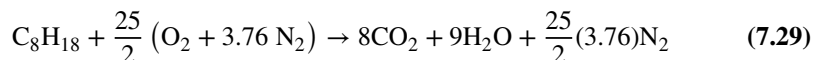
First, we define a series of terms that describe a chemical reaction, such as exothermic or endothermic. Let us assume the following chemical reaction:



If the reaction proceeds from the *reactants* A and B to the *products* C and D and the reaction produces heat as a result, we call such reactions as *exothermic*. If the opposite occurs, that is, if the reactants would not naturally react without an initial external heat input (stimulus), then such reactions are called *endothermic*. An example of an exothermic reaction is the combustion of hydrocarbon fuels and air. An example of an endothermic reaction is the phase transformation of water from liquid to vapor that requires a heat input. Our interest in chemical reaction lies primarily in the study of combustion and hence exothermic processes. In gas turbine engines, the reactants are typically hydrocarbon fuels and air. In a liquid propellant chemical rocket, the reactants are typically highly energetic fuels, such as hydrogen, and an oxidizer, such as oxygen. Let us consider octane (C_8H_{18}) as a typical hydrocarbon fuel in a gas turbine engine. Let us also describe air (by lumping argon into the nitrogen molecule) as being approximately composed of

$$\text{Air} \cong O_2 + \frac{79}{21}N_2 \cong O_2 + 3.76 N_2 \quad (7.28)$$

Now, we define a *unique* mass ratio between the fuel and oxidizer, which results in the *complete combustion* of the fuel and a *stable* product composition. This unique ratio is called the *stoichiometric* ratio and now we apply it to the combustion of octane and air, as an example.



We took a mole of octane and brought in $25/2$ moles of O_2 and $(3.76)(25/2)$ moles of N_2 . Note that the need for $25/2$ came from turning “ C_8 ” of octane into “ $8 CO_2$ ” and the “ H_{18} ” of octane into “ $9 H_2O$,” therefore $16 + 9 = 25$ oxygen atoms were needed for the complete combustion (which also means complete *oxidation*) of one mole of octane.

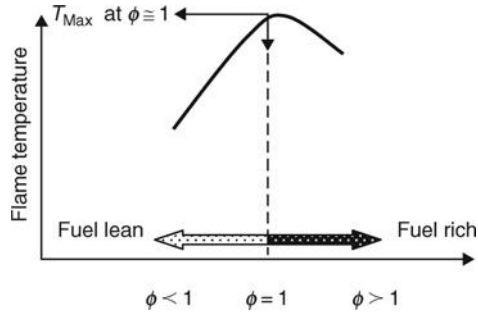
As noted, this *unique* proportion of fuel to oxidizer results in neither excess oxygen nor any excess fuel. Any more fuel would result in unburned fuel in the products of combustion and any more air would result in excess oxygen in the products of combustion. The nitrogen (molecule) (N_2) is treated as remaining unreacted (or *inert* in chemical terms) in the combustion process. Now, the stoichiometric fuel-to-air ratio for the combustion of octane in air is

$$f_{\text{stoich}} \equiv \frac{\text{mass}_{\text{fuel}}}{\text{mass}_{\text{oxidizer}}} = \frac{\dot{m}_f}{\dot{m}_{\text{air}}} \approx \frac{8(12) + 18(1)}{\frac{25}{2}[32 + 3.76(28)]} \cong \frac{114}{1716} \cong 0.0667 \quad (7.30)$$

Therefore, we say that the stoichiometric ratio for hydrocarbon fuels and air is about 6.7%. This is a number to remember. If we use proportionately less fuel than the stoichiometric ratio, the combustion is said to be on a *fuel lean* basis and the opposite is called a *fuel rich* combustion. A parameter that describes the fuel lean or rich condition of a combustor is called the *equivalence ratio* ϕ , which is defined as

$$\phi \equiv \frac{f}{f_{\text{stoich}}} \quad \text{Equivalence ratio definition} \quad (7.31)$$

■ **FIGURE 7.2**
 Flame temperature dependence on the equivalence ratio showing T_{\max} at $\phi \cong 1$



Consequently,

$$\phi > 1 \quad \text{A fuel rich combustion} \quad (7.32)$$

$$\phi = 1 \quad \text{Stoichiometric combustion} \quad (7.33)$$

$$\phi < 1 \quad \text{A fuel lean combustion} \quad (7.34)$$

It will be demonstrated in this chapter that the highest combustion temperature is achieved very near the stoichiometric ratio (proportion of the fuel to the oxidizer). This fact, which is depicted in Figure 7.2, should also be stored in memory as a useful concept. For many fuels, the maximum temperature, that is, the adiabatic flame temperature, occurs at the equivalence ratio between 1 and 1.1, since the product-specific heat is reduced with a slightly fuel rich mixture ratio.

Now, assuming that we know the composition of the products in a chemical reaction, that is, the constituents of the product and their number of moles, the fundamental question that remains is the product's temperature. How do we arrive at the product's temperature? If we treat the combustor as a black box, where the reactants enter the box at certain temperature, say T_1 , and the products leave the box at another temperature, say T_2 , and we can describe the heat transfer through the sides of the box, that is, the heat exchange with the surrounding, as say Q , we can use the law of conservation of energy to write:

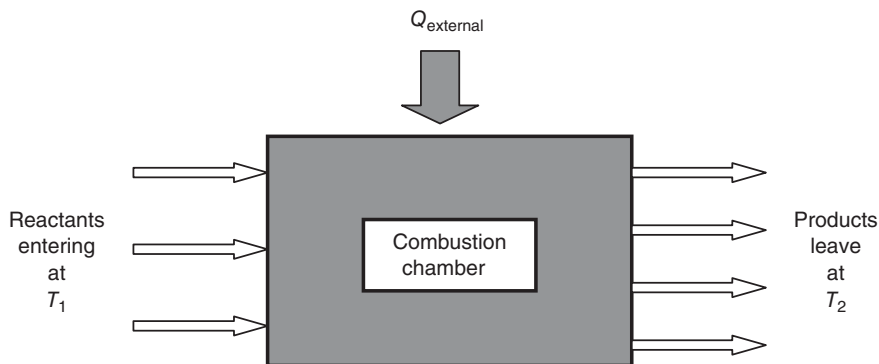
$$Q_{\text{external}} = \sum H_{\text{Products}} - \sum H_{\text{Reactants}} \quad (7.35)$$

where H is the *absolute enthalpy* and Q is the *external* heat interaction with the combustion chamber. We show this box schematically in Figure 7.3, as an aid.

Remember *absolute enthalpy* from thermodynamics that was defined as the sum of heat of formation of the substance at the reference temperature (298.16 K) and what was called the *sensible enthalpy*, which raised the enthalpy of the substance from the reference temperature to the desired temperature. Absolute enthalpy H may be written as the product of mass and the specific absolute enthalpy for a substance. The mass may be expressed as the product of the number of moles and the molecular weight of the substance. Now, for a perfect gas, if we incorporate all of the above concepts, the absolute enthalpy may be written as

$$H = m \cdot h = n \cdot MW \cdot h = n \cdot MW \left[\int_{T_f}^T c_p dT + \Delta h_f^0 \right] \quad (7.36)$$

■ **FIGURE 7.3**
Combustion chamber
is depicted at its
boundaries, through
energy exchange



where T_f is the reference temperature, Δh_f^0 is the standard heat of formation of the substance at the reference temperature per unit mass at the pressure of 1 bar. The subscript “f” refers to the reference temperature and the superscript “0” refers to the standard state of the chemical compound at the pressure of 1 bar. We define the product of the molecular weight and the specific heat at constant pressure (that appears above) as the *molar specific heat*, and give it a special symbol, namely, the \bar{c}_p with a bar, that is, let

$$\bar{c}_p \equiv MW \cdot c_p \quad (7.37)$$

The dimensions of the molar specific heat are

$$[\bar{c}_p] = \frac{\text{kg}}{\text{kmol}} \frac{\text{kJ}}{\text{kg} \cdot \text{K}} = \frac{\text{kJ}}{\text{kmol} \cdot \text{K}} \quad (7.38)$$

We also define the product of the molecular weight and the heat of formation per unit mass of a substance, as the *molar heat of formation*, and give it a special symbol (with a bar to identify the molar), as

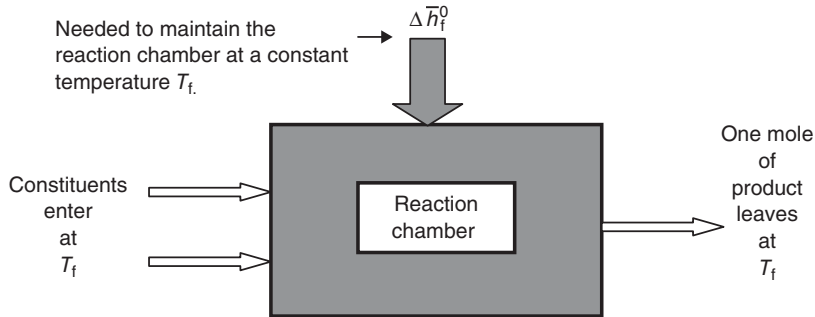
$$\Delta \bar{h}_f^0 \equiv MW \cdot \Delta h_f^0 \quad (7.39)$$

The molar heat of formation is the evolved heat in forming *one mole* of the substance from its elements in their standard states at constant temperature of $T_f = 298.16 \text{ K}$ and the constant pressure of $p_f = 1 \text{ bar}$. The dimensions of the molar heat of formation at a reference temperature are

$$[\Delta \bar{h}_f^0] = \frac{\text{kg}}{\text{kmol}} \frac{\text{kJ}}{\text{kg}} = \frac{\text{kJ}}{\text{kmol}} \quad (7.40)$$

Imagine a reaction chamber, where the basic elements of a chemical compound, at their standard state, enter at a reference temperature T_f at the pressure of 1 bar and the compound is then formed in the reaction chamber. Now, in order to maintain the temperature of the compound at the reference temperature, we need to interact with the reaction chamber through heat transfer to or from the box. The heat of formation of a chemical compound is the amount of heat exchange to (positive) or from (negative) a reaction chamber, which forms the chemical compound from its constituents, and maintains a constant (known

■ **FIGURE 7.4**
Definition sketch for
the heat of formation of
(one mole of) a
chemical compound in
an isothermal process
($p = 1$ bar)



as reference) temperature. The heat of formation of all naturally occurring elements is then, by definition, zero. The reference temperature is 298.16 K, which corresponds to a standard room temperature of 25°C (77°F) and the reference pressure of 1 bar is the standard atmospheric pressure (also very close to 1 atm). This process can be schematically shown in Figure 7.4.

The exothermic reactions from basic elements to form one mole of a chemical compound then lead to a negative heat of formation, because we need to extract heat from the reaction chamber in order to maintain a constant temperature. The opposite is true for endothermic reactions to form a compound. These concepts are best learned through a series of examples.

EXAMPLE 7.2

The standard heat of formation of the following naturally occurring elements (at $p = 1$ bar) is zero:

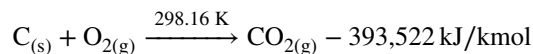
O_2 (g) Oxygen (molecule) in gaseous form, $(\Delta \bar{h}_f^0)_{\text{O}_2} = 0$

N_2 (g) Nitrogen (molecule) in gaseous form, $(\Delta \bar{h}_f^0)_{\text{N}_2} = 0$

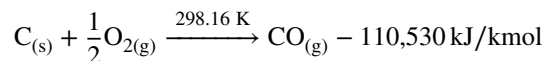
H_2 (g) Hydrogen (molecule) in gaseous form, $(\Delta \bar{h}_f^0)_{\text{H}_2} = 0$

C (s) Carbon in solid form, $(\Delta \bar{h}_f^0)_{\text{C(s)}} = 0$

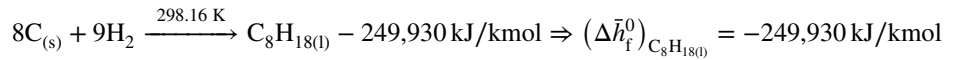
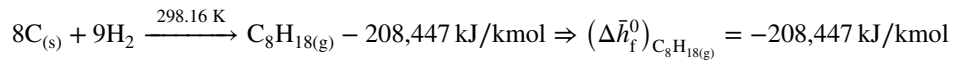
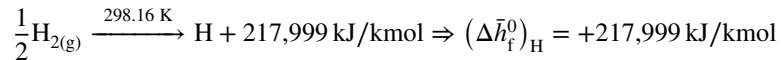
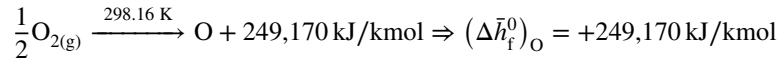
The heat of formation of carbon dioxide can be found from the following isothermal reaction at 1 bar:



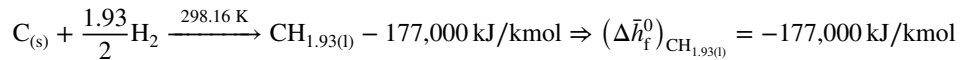
Therefore, CO_2 (g), carbon dioxide (gaseous), has a standard heat of formation of $\Delta \bar{h}_f^0 = -393,522$ kJ/kmol. We note that in the previous reaction the carbon enters the reaction as a solid and the oxygen as a gas, that is, the standard states of carbon and oxygen, to form one mole of carbon dioxide (in gaseous form).



In forming one mole of carbon monoxide in an isothermal process with $T_f = 298.16$ K and at a pressure of 1 bar, carbon and oxygen in their standard states have reacted according to the above. We note that a heat extraction of 110,530 kJ/kmol (same as J/mol) is necessary to maintain isothermal status for the reaction. Hence, we conclude that standard heat of formation of carbon monoxide, CO (g), is $\Delta\bar{h}_f^0 = -110,530$ kJ/kmol. The following four reactions serve as additional examples on the standard heat of formation.



A blended jet fuel known as JP-4 has an approximate formulation, $\text{CH}_{1.93}$ and the following isothermal reaction defines its standard heat of formation in liquid form, that is,



The energy balance equation across the burner (Equation 7.35) may now be expressed on a molar basis, to include the complete enthalpy expression. This will account for the reactants entering the combustion chamber at other than reference temperature, namely, T_1 , and the products of combustion leave the chamber at another temperature, namely, T_2 , as follows:

$$Q_{\text{external}} = \sum_j [n_j \cdot \bar{c}_{pj} (T_2 - T_f)_j]_{\text{Products}} - \sum_i [n_i \cdot \bar{c}_{pi} (T_1 - T_f)_i]_{\text{Reactants}} + \Delta H_{\text{RPf}} \quad (7.41)$$

where “P” and “R” stand for products and reactants, respectively, and the last term defined as

$$\Delta H_{\text{RPf}} = \sum_j [n_j \Delta\bar{h}_{fj}^0]_{\text{Products}} - \sum_i [n_i \Delta\bar{h}_{fi}^0]_{\text{Reactants}} \quad (7.42)$$

is the difference between the standard heats of formation of all the product constituents and the reactant constituents, at the reference temperature at the pressure of 1 bar. This quantity is also called *heat of reaction* with a symbol Q_R . Therefore, heat of reaction in a combustion process is defined as

$$Q_R \equiv \sum_P n_j \Delta\bar{h}_{fj}^0 - \sum_R n_i \Delta\bar{h}_{fi}^0 \quad (7.43)$$

We can specialize the concept of the *heat of reaction* to combustion of a fuel in pure oxygen O_2 . This will be the basis for the definition of the fuel heating value. Assuming that the fuel and the gaseous oxygen, that is, O_2 (g), enter the combustion chamber at

the reference temperature of 298.16 K and a complete combustion takes place, the heat release per unit mass of the fuel, which will return the products of combustion to the reference temperature, is called the *heating value* of the fuel. In simple terms, substitute T_f for T_1 and T_2 in Equation 7.41, which will force the summations over the products and the reactants to zero, and note that

$$Q = Q_R = \sum_P n_j \Delta \bar{h}_{f_j}^0 - \sum_R n_i \Delta \bar{h}_{f_i}^0 \quad (7.44)$$

Although the negative sign on the summations of Equation 7.43 or 7.44 shows the necessity of *removing* a quantity of heat from the combustion chamber in order to maintain an isothermal environment, it is customary to report the fuel heating value as a positive quantity. Hence, we define

$$\text{Fuel heating value} = -Q_R \quad (7.45)$$

Now, depending on the state of water in the products of combustion, that is, as a liquid or vapor, the fuel heating value is referred to as higher heating value (HHV) or lower heating value (LHV), respectively. Since the difference between the higher and lower heating values depends on the energy spent in vaporizing the condensed water in the products of combustion, the following energy balance relates the two heating values:

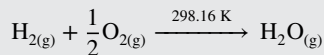
$$\text{HHV} = \text{LHV} + \frac{m_{\text{H}_2\text{O}}}{m_{\text{fuel}}} h_{1g} \quad (7.46)$$

where the last term h_{1g} is the latent heat of vaporization for water at 25°C, which is 2443 kJ/kg. Now, let us put these concepts to work and obtain a fuel heating value based on the standard heats of formation and the water/fuel mass fraction and the latent heat of vaporization of water.

EXAMPLE 7.3

Establish the lower and higher heating values of hydrogen, $\text{H}_{2(g)}$.

First consider the following chemical reaction between one mole of hydrogen and 1/2 mole of oxygen to produce one mole of water vapor:



We had identified the heat of reaction Q_R in a chemical reaction as Equation 7.43, that is,

$$\begin{aligned} Q_R &\equiv \sum_P n_j \Delta \bar{h}_{f_j}^0 - \sum_R n_i \Delta \bar{h}_{f_i}^0 \\ &= 1 \text{ kmol} \left(\Delta \bar{h}_{f}^0 \right)_{\text{H}_2\text{O}(g)} = -241,827 \text{ kJ} \end{aligned}$$

in the above equation, we used the standard heat of formation of water in gaseous form as: $-241,827 \text{ kJ/kmol}$. Since the mass of 1 kmol of hydrogen is $\sim 2 \text{ kg}$, and the water in the product is in vapor form, we conclude that the lower heating value of hydrogen is

$$\text{LHV} \approx 241,827 \text{ kJ}/(2 \text{ kg}) = 120,913 \text{ kJ/kg}$$

And the higher heating value of hydrogen is obtained from Equation 7.46, as

$$\begin{aligned} \text{HHV} &\approx 120,913 \text{ kJ/kg} + (18/2) \times (2,443 \text{ kJ/kg}) \\ &\approx 142,900 \text{ kJ/kg} \end{aligned}$$

The values listed in thermo chemical tables (or fuel property tables) are

$H_{2(g)}$	
LHV	HHV
120,000 kJ/kg	141,800 kJ/kg

Our result is within 1% of the above values, where our approximation of the molecular weights accounts for a portion of the difference, and the rest lies in the measurement accuracy.

■ **TABLE 7.1**
Standard Heats of Formation at 298.16 K

Chemical symbol	Name	State	$\Delta \bar{h}_f^0$ (kJ/gmol) [per mole basis]	Δh_f^0 (kJ/gm) [per mass basis]
C	Carbon	Solid	0	0
C	Carbon	Gas	716.67	59.72
CO ₂	Carbon dioxide	Gas	-393.522	-8.944
CO	Carbon monoxide	Gas	-110.53	-3.947
H ₂	Hydrogen	Gas	0	0
H	Hydrogen atom	Gas	217.999	217.999
OH	Hydroxyl radical	Gas	39.463	2.321
H ₂ O	Water	Gas	-241.827	-13.435
H ₂ O ₂	Hydrogen peroxide	Gas	-136.106	-4.003
N ₂	Nitrogen	Gas	0	0
N	Nitrogen atom	Gas	472.68	33.763
NO	Nitric oxide	Gas	90.291	3.010
NO ₂	Nitrogen dioxide	Gas	33.10	0.7196
N ₂ O	Nitrous oxide	Gas	82.05	1.8648
O ₂	Oxygen	Gas	0	0
O	Oxygen atom	Gas	59.56	3.723
O ₃	Ozone	Gas	34.00	0.708
CH ₄	Methane	Gas	-74.873	-4.6796
CH ₃ OH	Methyl alcohol	Gas	-201.07	-6.2834
CH ₃ OH	Methyl alcohol	Liquid	-238.66	-7.4581
C ₂ H ₅ OH	Ethyl alcohol	Gas	-235.00	-5.108
C ₂ H ₅ OH	Ethyl alcohol	Liquid	-277.20	-6.026
C ₃ H ₈	Propane	Gas	-103.90	-2.3614
C ₄ H ₁₀	Butane	Gas	-126.148	-2.175
C ₈ H ₁₈	Octane	Gas	-208.447	-1.8285
C ₈ H ₁₈	Octane	Liquid	-249.93	-2.1924
CH _{1.553}	JP-3	Liquid		-1.11
CH _{1.93}	JP-4	Liquid		-1.77

Some useful conversion factors are 1 kcal = 4.1868 kJ = 3.9684 BTU = 3,088 ft · lbf kcal/gmol = 4186.8 kJ/kmol and kJ/kmol = 1000 kJ/gmol

Tables of thermochemical data (Table 7.1) that list the standard heat of formation of numerous compounds are found in compilations, such as JANAF or the *Handbook of Chemistry and Physics*. Here, only a partial listing is reproduced for the purposes of illustration and problem solving involving chemical reactions.

Applying Equation 7.41, to a chemical reaction with a known product composition and a known heat exchange characteristics through the walls of the combustor, Q_{external} , will result in the calculation of the exit temperature of the products of combustion, T_2 . A reference boundary condition on the combustion chamber is the adiabatic assumption of zero heat exchange with the environment, that is, $Q_{\text{external}} \equiv 0$, which leads to a unique exit temperature value, known as the *adiabatic flame temperature* T_{af} . In addition, there are polynomial expressions that are developed for the molar specific heats of various chemical compounds, such as the sample produced in Table 7.2, which provide the remaining input to the enthalpy balance equation across the combustor, that is, Equation 7.41. As the polynomial expressions for specific heat are in temperature, and we do not a priori know the temperature of the products of combustion, the process of selecting a suitable molar specific heat is iterative. Otherwise an *average* specific heat may be assumed, over the expected temperature range. Also note that in a fuel-rich combustion, $\phi > 1$, the heat of reaction remains the same as that of stoichiometric reaction, whereas the flame temperature will be reduced as the heat of reaction is now used to raise the temperature of additional fuel.

Now, let us proceed with two example problems that assume the molar composition of the products of combustion.

■ TABLE 7.2
Molar Specific Heats of Various Gases

Gases at low pressures $\bar{c}_{p0} = \text{kJ/kmol} \cdot \text{K} \theta = \text{T(K)}/100$			
Gas		Range K	Max. error (%)
N ₂	$\bar{c}_{p0} = 39.060 - 512.79\theta^{-1.5} + 1072.7\theta^{-2} - 820.40\theta^{-3}$	300–3500	0.43
O ₂	$\bar{c}_{p0} = 37.432 + 0.020102\theta^{1.5} - 178.57\theta^{-1.5} + 236.88\theta^{-2}$	300–3500	0.30
H ₂	$\bar{c}_{p0} = 56.505 - 702.74\theta^{-0.75} + 1165.0\theta^{-1} - 560.70\theta^{-1.5}$	300–3500	0.60
CO	$\bar{c}_{p0} = 69.145 - 0.70463\theta^{0.75} - 200.77\theta^{-0.5} + 176.76\theta^{-0.75}$	300–3500	0.42
OH	$\bar{c}_{p0} = 81.564 - 59.350\theta^{0.25} + 17.329\theta^{0.75} - 4.2660\theta$	300–3500	0.43
HO	$\bar{c}_{p0} = 59.283 - 1.7096\theta^{0.5} - 70.613\theta^{-0.5} + 74.889\theta^{-1.5}$	300–3500	0.34
H ₂ O	$\bar{c}_{p0} = 143.05 - 183.54\theta^{0.25} + 82.751\theta^{0.5} - 3.6989\theta$	300–3500	0.43
CO ₂	$\bar{c}_{p0} = -3.7357 + 30.529\theta^{0.5} - 4.1034\theta + 0.024198\theta^2$	300–3500	0.19
NO ₂	$\bar{c}_{p0} = 46.045 + 216.10\theta^{-0.5} - 363.66\theta^{-0.75} + 232.550\theta^{-2}$	300–3500	0.26
CH ₄	$\bar{c}_{p0} = 672.87 + 439.74\theta^{0.25} - 24.875\theta^{0.75} + 323.88\theta^{-0.5}$	300–2000	0.15
C ₂ H ₄	$\bar{c}_{p0} = 95.395 + 123.15\theta^{0.5} - 35.641\theta^{0.75} + 182.77\theta^{-3}$	300–2000	0.07
C ₂ H ₆	$\bar{c}_{p0} = 6.895 + 17.26\theta - 0.6402\theta^2 + 0.00728\theta^3$	300–1500	0.83
C ₃ H ₈	$\bar{c}_{p0} = -4.042 + 30.46\theta - 1.571\theta^2 + 0.03171\theta^3$	300–1500	0.40
C ₄ H ₁₀	$\bar{c}_{p0} = 3.954 + 37.12\theta - 1.833\theta^2 + 0.03498\theta^3$	300–1500	0.54

Source: Adapted from Van Wylen and Sonntag 1985.

EXAMPLE 7.4

Consider a chemical reaction involving H_2 and O_2 in gaseous form. The reactants enter the combustion chamber at 25°C . Assuming only water vapor exits as the composition product and the molar specific heat of water vapor is $\bar{c}_{\text{PH}_2\text{O}} \cong 56.5 \text{ kJ/kmol} \cdot \text{K}$, calculate

- The ratio $n_{\text{H}_2}/n_{\text{O}_2}$ of the reactants (mole ratio)
- The fuel–oxidizer (mass) ratio
- The adiabatic flame temperature, T_{af}

SOLUTION

The problem is calling for a stoichiometric combustion of hydrogen and oxygen that goes to completion, hence the reaction takes on the following form:



The fuel–oxidizer mass ratio = $\boxed{\frac{2(1)}{1/2(32)} = \frac{1}{8} = 0.125}$

Equation 7.41 is set equal to zero for the adiabatic flame temperature calculation,

$$Q = \sum_{\text{P}} n_j \cdot \bar{c}_{pj} (T_2 - T_f)_j - \sum_{\text{R}} n_i \cdot \bar{c}_{pi} (T_1 - T_f)_i + \Delta H_{\text{RPF}} = 0$$

$$\Delta H_{\text{RPF}} = \sum_{\text{P}} n_j \Delta \bar{h}_f^0 - \sum_{\text{R}} n_i \Delta \bar{h}_f^0 = -241,827 \text{ kJ}$$

We also note that the reactants entrance temperature is the same as the reference temperature, hence the only contribution from the energy equation is:

$$\bar{c}_{\text{PH}_2\text{O}} (T_{\text{af}} - 298) = 241,827 \text{ kJ} \Rightarrow$$

$$\boxed{T_{\text{af}} = 298 \text{ K} + \frac{241,827}{56.5} \text{ K} \cong 4,578 \text{ K}}$$

REMARKS The adiabatic flame temperature of hydrogen–oxygen combustion is only *theoretically* 4578 K, as we have assumed a complete combustion. In an actual reaction, product dissociation takes place, which would reduce the energy release and hence not allow the adiabatic flame temperature to reach 4578 K. A fraction of water dissociates (back) into O_2 , H_2 , O , H and OH . A realistic analysis would allow product dissociation to take place at an unknown molar concentration levels in a final equilibrium state. The actual adiabatic flame temperature for the products of combustion (of H_2 and $1/2 \text{ O}_2$) in equilibrium is also a function of combustion pressure. We will address the methodology that allows us to calculate the equilibrium temperature and species concentration in section 7.4.

Reactants	n_j	\bar{h}_f^0	Products	n_j	\bar{h}_f^0	\bar{c}_{pj}
	kmol	kJ/kmol		kmol	kJ/kmol	kJ/kmol · K
H_2	1	0	H_2O	1	-241,827	56.5
O_2	1/2	0				

EXAMPLE 7.5

One mole of methane is burned with 120% theoretical air. Assuming that the methane and air enter the combustion chamber at 25°C and the excess oxygen and nitrogen in the reaction will not dissociate, calculate:

- (a) the fuel-to-air ratio
- (b) the equivalence ratio ϕ

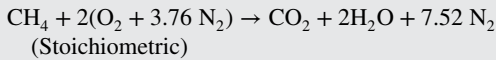
(c) the adiabatic flame temperature

Assume:

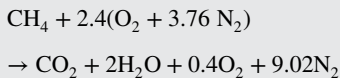
$$\begin{aligned}\bar{c}_{\text{PCO}_2} &= 61.9 \text{ kJ/kmol} \cdot \text{K}, & \bar{c}_{\text{PO}_2} &= 37.8 \text{ kJ/kmol} \cdot \text{K}, \\ \bar{c}_{\text{PN}_2} &= 33.6 \text{ kJ/kmol} \cdot \text{K}, & \bar{c}_{\text{PH}_2\text{O}} &= 52.3 \text{ kJ/kmol} \cdot \text{K},\end{aligned}$$

SOLUTION

Theoretical air is composed of oxygen and nitrogen according to $(\text{O}_2 + 3.76 \text{ N}_2)$. First, let us write the stoichiometric reaction of methane and air, to establish a reference point:



Now, let us implement the 120% factor for air, namely



Therefore, fuel-to-air ratio (based on mass) may be written as

$$\frac{m_{\text{fuel}}}{m_{\text{air}}} = \frac{12 + 4}{2.4(32 + 3.76(28))} \cong 0.048$$

For the equivalence ratio, we need the fuel-to-air ratio at stoichiometric condition as well,

$$\begin{aligned}\left(\frac{m_{\text{fuel}}}{m_{\text{air}}}\right)_{\text{Stoich.}} &= \frac{12 + 4}{2(32 + 3.76(28))} \\ &\cong 0.0583 \Rightarrow \phi = \frac{0.048}{0.0583} \approx 0.827\end{aligned}$$

For the adiabatic flame temperature, let us set up a table for the “products” and “reactants,” and calculate

$$\begin{aligned}\Delta H_{\text{RPF}} &= \sum_{\text{P}} n_j \Delta \bar{h}_{f_j}^0 - \sum_{\text{R}} n_i \Delta \bar{h}_{f_i}^0 = -877, 176 + 74,873 \\ &= -802,303 \text{ kJ and } \sum n_j \bar{c}_{pj} = 484.7 \text{ kJ}\end{aligned}$$

From Equation 7.41

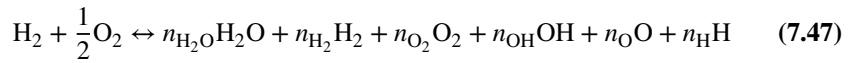
$$T_2 - T_f = \frac{-\Delta H_{\text{RPF}}}{\sum n_j \bar{c}_{pj}} = \frac{802,303}{484.7} \text{ K} \Rightarrow T_2 \cong 1,953 \text{ K},$$

REMARKS Now that we know the products’ temperature, we need to go back and check the molar specific heats that were assumed at the beginning of the problem for a combustion temperature of 1953 K. We can use the polynomial expressions from Table 7.2. As expected, an iteration process ensues. Also note that our assumption of a complete combustion and no reverse reaction was flawed. We should allow for an equilibrium mixture of unburned methane, oxygen, some NO_x formation, among other products species to be present in the products of combustion. For example, if we had allowed product dissociation to occur, the final temperature would have been reduced. We clearly need more “tools” to dig deeper!

Reactants	n_j kmol	$\Delta \bar{h}_{f_i}^0$ kJ/kmol	Products	n_j kmol	$\Delta \bar{h}_{f_i}^0$ kJ/kmol	\bar{c}_{pj} kJ/kmol · k
CH_4	1	-74,873	H_2O	2	-241,827	52.3
O_2	2.4	0	CO_2	1	-393,522	61.9
N_2	9.02	0	O_2	0.4	0	37.8
			N_2	9.02	0	33.6

7.4 Chemical Equilibrium and Chemical Composition

A chemical reaction normally continues until no more changes in molar concentration of the products occur. At that point, we say the reaction has reached an equilibrium state. We take advantage of the state of equilibrium in a chemical reaction and then try to establish the *chemical composition* of the products of combustion in that state. Take the combustion of one mole of hydrogen and one half mole of oxygen, as an example.



First, note that *forward and reverse* arrows in Equation 7.47 have replaced the forward reaction arrow of our earlier chemical reaction expressions. This simply means that a fraction of the products convert back into the reactants and as the combustion temperature increases other products may be formed and *eventually* a state of equilibrium is reached among all constituents. The word “eventually” in the previous sentence signifies a *period of time* needed to achieve the equilibrium state in a chemical reaction. Therefore, it is entirely reasonable to talk about a *rate of reaction*, and in particular the *rate of formation* of chemical species, which belong to the field of chemical kinetics. In the above equilibrium reaction of hydrogen and oxygen, we have expected/identified some water formation, some “leftover” hydrogen, some “leftover” oxygen, some hydroxyl (OH) formation, and possibly some dissociation of oxygen and hydrogen to form the atomic oxygen and hydrogen. We did not have to stop, however! Could the temperature of combustion be so high as for the oxygen and hydrogen atoms to ionize? And if so, what will the product concentrations be? These are all legitimate (and tough) questions. Now, let us stay at the level of Equation 7.47, which identifies six constituents of unknown molar concentrations. The total number of moles of products at equilibrium is n_m , where

$$n_m = n_{\text{H}_2\text{O}} + n_{\text{H}_2} + n_{\text{O}_2} + n_{\text{OH}} + n_{\text{O}} + n_{\text{H}} \quad (7.48)$$

The *molar concentration* of any species is simply the ratio of the number of moles of that species to the total number of moles of the product, that is, the same as the *mole fraction* of any given species

$$x_i \equiv \frac{n_i}{n_m}$$

We shall apply the law of conservation of atomic species to the above reaction and conclude that

$$2n_{\text{H}_2\text{O}} + 2n_{\text{H}_2} + n_{\text{OH}} + n_{\text{H}} = 2 \dots \dots \dots \text{to balance H}$$

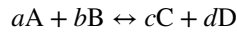
$$n_{\text{H}_2\text{O}} + 2n_{\text{O}_2} + n_{\text{OH}} + n_{\text{O}} = 1 \dots \dots \dots \text{to balance O}$$

Now, we have two equations and six unknowns. We need to produce four additional equations involving the six unknowns before we have a chance of solving for the six (unknown) molar concentrations.

In order to produce additional equations to assist with the unknown molar concentrations, we introduce a new law, which is called the *law of mass action*.

7.4.1 The Law of Mass Action

Consider a stoichiometric reaction of the type:



where a, b, c, and d are the (stoichiometric) number of moles in the reaction. The law of mass action states that the rate of disappearance of chemical species in the reactants is proportional to the concentrations of the reactants each raised to their respective stoichiometric exponent. Applied to the forward rate of reaction r_f is proportional to the products of the concentrations of the reactants raised to their stoichiometric exponents, that is,

$$r_f \propto [A]^a \cdot [B]^b \quad (7.49)$$

The bracketed terms are molar concentrations of reactants A and B. The proportionality constant in Equation 7.49 is called the forward reaction rate coefficient k_f , that is,

$$r_f = k_f [A]^a \cdot [B]^b \quad (7.50)$$

The law of mass action applied to a reverse reaction then relates the rate of formation of the products to the product of concentration of the products raised to their stoichiometric exponents, namely,

$$r_r = k_r [C]^c \cdot [D]^d \quad (7.51)$$

An equilibrium state is reached among the reactants and the product species, when the forward and reverse reaction rates are equal, namely,

$$k_f [A]^a \cdot [B]^b = k_r [C]^c \cdot [D]^d \quad (7.52)$$

Therefore the ratio of forward to reverse reaction rate coefficients in an equilibrium reaction is called the equilibrium constant K

$$K \equiv \frac{k_f}{k_r} = \frac{[C]^c \cdot [D]^d}{[A]^a \cdot [B]^b} \quad (7.53)$$

It is customary to express the concentrations of species by their partial pressures in the equilibrium mixture and the equilibrium constant is then referred to as K_p since it is based on partial pressures. Hence, in terms of the partial pressures, the law of mass action is written as

$$K_p = \frac{p_C^c \cdot p_D^d}{p_A^a \cdot p_B^b} \quad (7.54)$$

We may equivalently use the mole fractions (or molar concentrations) for species concentration in the law of mass action to arrive at an equivalent expression, namely,

$$K_n = \frac{\chi_C^c \cdot \chi_D^d}{\chi_A^a \cdot \chi_B^b} \quad (7.55)$$

The two equilibrium constants are related to each other, as we may relate the ratio of partial pressures and the mixture pressure to the mole fraction (according to Equation 7.18), hence,

$$K_P = \frac{\chi_C^c \cdot \chi_D^d}{\chi_A^a \cdot \chi_B^b} p_m^{c+d-a-b} = K_n p_m^{c+d-a-b} \quad (7.56)$$

Among the two equilibrium constants, K_P and K_n , the former is a function of temperature alone and hence independent of pressure, whereas the latter is in general a function of both temperature and pressure, that is,

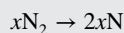
$$K_p = K_p(T_m) \quad (7.57)$$

$$K_n = K_n(T_m, p_m) \quad (7.58)$$

Based on a *single parameter* functional dependence of K_p , tables and charts of this equilibrium constant are produced as a function of temperature and used for product composition calculations. It is also interesting to note that the molar concentrations in a stoichiometric mixture are a function of the mixture pressure (if $c + d - a - b \neq 0$, according to Equation 7.56), whereas the equilibrium constant K_p is only a function of the mixture temperature. The tables of values for the equilibrium constant K_p , as a function of temperature for numerous reactions of interest to combustion, are used to setup a series of auxiliary equations for the unknown molar concentrations. Some of these tables and graphical depictions of equilibrium constant K_p for many reactions are shown at the end of this section. The following example shows a simple application of this principle.

EXAMPLE 7.6

One mole of nitrogen, $N_2(g)$, is heated to 6250 K at the pressure of p_m . A fraction of nitrogen dissociates to nitrogen atom according to

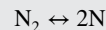


Assuming a state of equilibrium is reached in the mixture, calculate

(a) mole fraction of N_2 at equilibrium when p_m is 1 atm

(b) mole fraction of N_2 at equilibrium when p_m is 10 atm

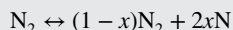
Assume the equilibrium constant for the reaction



is $K_p = 0.1$ atm at the temperature of 6250 K.

SOLUTION

If we start with a mole of N_2 and a fraction of it, say x mole, dissociates into nitrogen atoms, then our equilibrium mixture takes on the following form:



In the above reaction, the nitrogen is in balance and we still have the unknown x to contend with. First, we need to express the mole fractions of the products in equilibrium. We start with the total number of moles of the mixture in equilibrium and then divide the species number of moles by the total, according to:

Total number of moles of the mixture at equilibrium is

$$(1-x) + 2x = 1+x$$

Therefore the nitrogen *mole fraction* of the mixture at equilibrium is $\frac{1-x}{1+x} = \chi_{N_2}$

The *mole fraction* of the nitrogen atom in the mixture at equilibrium is $\frac{2x}{1+x} = \chi_N$

Writing an expression for the equilibrium constant of $N_2 \leftrightarrow 2N$, from its definition

$$\begin{aligned} K_p &\equiv \frac{p_N^2}{p_{N_2}} = \frac{\chi_N^2}{\chi_{N_2}} \cdot p_m^{2-1} \\ &= \left[\left(\frac{2\chi}{1+\chi} \right)^2 \right] / \left[\frac{1-\chi}{1+\chi} \right] \cdot p_m = 0.1 \text{ atm} \end{aligned}$$

(a) $p_m = 1 \text{ atm}$

$$\frac{4x^2}{1-x^2} = 0.1 \Rightarrow x^2 = \frac{0.1}{4.1} \Rightarrow x = 0.156$$

Therefore, $\chi_{N_2} \cong 0.73$

(b) $p_m = 10 \text{ atm}$

$$\frac{4x^2}{1-x^2} = 0.01 \Rightarrow x^2 = \frac{0.01}{4.01} \Rightarrow x \cong 0.05$$

Therefore, $\chi_{N_2} \cong 0.90$

REMARKS First, note that the sum of the mole fractions in the mixture adds up to 1, as expected. Second, the fraction of nitrogen, which dissociates into nitrogen atom, x , is suppressed by the mixture pressure, i.e., the lower mixture pressure promotes dissociation of nitrogen. Third, the mole fractions substituted in the K_p equation above were from the original reaction and not the stoichiometric reaction, $N_2 \leftrightarrow 2N$. Finally, the equilibrium constant given for the nitrogen dissociation, K_p , has a dimension of atmosphere (for this reaction) and is obtained from a table for the $N_2 \leftrightarrow 2N$ reaction at $T = 6250 \text{ K}$. We will use the tables/charts for the equilibrium constants in the following sections.

7.4.2 Equilibrium Constant K_p

A first attempt in studying the molar concentrations of the products of combustion will require knowledge of the equilibrium constants (as a function of temperature) for at least the following subreactions:

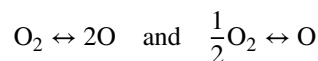
- Dissociation of oxygen, nitrogen, and hydrogen into the atoms of O, N, and H, respectively
- Formation of OH, NO, NO_2 , CO, O_3 , NH_3 from various stoichiometric reactions
- Dissociation of water into elements, O, H, and/or OH, dissociation of CO_2 .

A more elaborate analysis will require additional subreactions, which go beyond the scope of our treatment. Now, let us examine some of the more useful subreactions we encounter more often in our analysis, namely,

Reaction	Equilibrium Constant
1. $\text{CO}_2 + \text{H}_2 \leftrightarrow \text{CO} + \text{H}_2\text{O}$	$K_p = \frac{p_{\text{CO}} \cdot p_{\text{H}_2\text{O}}}{p_{\text{CO}_2} \cdot p_{\text{H}_2}} = \frac{\chi_{\text{CO}} \cdot \chi_{\text{H}_2\text{O}}}{\chi_{\text{CO}_2} \cdot \chi_{\text{H}_2}}$
2. $\text{H}_2\text{O} + \frac{1}{2}\text{N}_2 \leftrightarrow \text{H}_2 + \text{NO}$	$K_p = \frac{p_{\text{H}_2} \cdot p_{\text{NO}}}{p_{\text{H}_2\text{O}} \cdot p_{\text{N}_2}^{1/2}} = \frac{\chi_{\text{H}_2} \cdot \chi_{\text{NO}}}{\chi_{\text{H}_2\text{O}} \cdot \chi_{\text{N}_2}^{1/2}} \cdot p_m^{1/2}$
3. $2\text{H}_2\text{O} \leftrightarrow 2\text{H}_2 + \text{O}_2$	$K_p = \frac{p_{\text{H}_2}^2 \cdot p_{\text{O}_2}}{p_{\text{H}_2\text{O}}^2} = \frac{\chi_{\text{H}_2}^2 \cdot \chi_{\text{O}_2}}{\chi_{\text{H}_2\text{O}}^2} \cdot p_m$
4. $\text{H}_2\text{O} \leftrightarrow \text{H}_2 + \text{O}$	$K_p = \frac{p_{\text{H}_2} \cdot p_{\text{O}}}{p_{\text{H}_2\text{O}}} = \frac{\chi_{\text{H}_2} \cdot \chi_{\text{O}}}{\chi_{\text{H}_2\text{O}}} \cdot p_m$
5. $\frac{1}{2}\text{H}_2 \leftrightarrow \text{H}$	$K_p = \frac{p_{\text{H}}}{p_{\text{H}_2}^{1/2}} = \frac{\chi_{\text{H}}}{\chi_{\text{H}_2}^{1/2}} \cdot p_m^{1/2}$
6. $\text{H}_2\text{O} \leftrightarrow \frac{1}{2}\text{H}_2 + \text{OH}$	$K_p = \frac{p_{\text{H}_2}^{1/2} \cdot p_{\text{OH}}}{p_{\text{H}_2\text{O}}} = \frac{\chi_{\text{H}_2}^{1/2} \cdot \chi_{\text{OH}}}{\chi_{\text{H}_2\text{O}}} \cdot p_m^{1/2}$
7. $\text{N}_2 \leftrightarrow 2\text{N}$	$K_p = \frac{p_{\text{N}}^2}{p_{\text{N}_2}} = \frac{\chi_{\text{N}}^2}{\chi_{\text{N}_2}} \cdot p_m$
8. $\text{C} + \frac{1}{2}\text{O}_2 \leftrightarrow \text{CO}$	$K_p = \frac{p_{\text{CO}}}{p_{\text{C}} \cdot p_{\text{O}_2}^{1/2}} = \frac{\chi_{\text{CO}}}{\chi_{\text{C}} \cdot \chi_{\text{O}_2}^{1/2}} \cdot p_m^{-1/2}$
9. $\text{CO} + \frac{1}{2}\text{O}_2 \leftrightarrow \text{CO}_2$	$K_p = \frac{p_{\text{CO}_2}}{p_{\text{CO}} \cdot p_{\text{O}_2}^{1/2}} = \frac{\chi_{\text{CO}_2}}{\chi_{\text{CO}} \cdot \chi_{\text{O}_2}^{1/2}} \cdot p_m^{-1/2}$
10. $\frac{1}{2}\text{N}_2 + \frac{1}{2}\text{O}_2 \leftrightarrow \text{NO}$	$K_p = \frac{p_{\text{NO}}}{p_{\text{N}_2}^{1/2} \cdot p_{\text{O}_2}^{1/2}} = \frac{\chi_{\text{NO}}}{\chi_{\text{N}_2}^{1/2} \cdot \chi_{\text{O}_2}^{1/2}}$
11. $\text{O}_2 \leftrightarrow 2\text{O}$	$K_p = \frac{p_{\text{O}}^2}{p_{\text{O}_2}} = \frac{\chi_{\text{O}}^2}{\chi_{\text{O}_2}} \cdot p_m$
12. $\text{CO}_2 \leftrightarrow \text{CO} + \frac{1}{2}\text{O}_2$	$K_p = \frac{p_{\text{CO}} \cdot p_{\text{O}_2}^{1/2}}{p_{\text{CO}_2}} = \frac{\chi_{\text{CO}} \cdot \chi_{\text{O}_2}^{1/2}}{\chi_{\text{CO}_2}} \cdot p_m^{1/2}$

The equilibrium constants are depicted in graphical form in Figure 7.5 (adapted from Hill and Peterson, 1992). The equilibrium constants for additional dissociation reactions of interest are tabulated in Table 7.3 (from Strehlow, 1984).

Let us work with these equilibrium constants to deduce equilibrium constants for other reactions that may be of interest. For example, how does the equilibrium constant of the following two Stoichiometric reactions relate to each other?



$$K_p = \frac{p_{\text{O}}^2}{p_{\text{O}_2}} \quad \text{and} \quad K_p = \frac{p_{\text{O}}}{p_{\text{O}_2}^{1/2}}$$

Equilibrium Constant, K_p , for Various Stoichiometric Reactions

$$K_1 = \frac{p(\text{CO})p(\text{H}_2\text{O})}{p(\text{CO}_2)p(\text{H}_2)}$$

$$K_5 = \frac{p(\text{H})}{[p(\text{H}_2)]^{1/2}}$$

$$K_9 = \frac{p(\text{CO}_2)}{p(\text{CO})[p(\text{O}_2)]^{1/2}}$$

$$K_2 = \frac{p(\text{NO})p(\text{H}_2)}{[p(\text{N})]^{1/2}p(\text{H}_2\text{O})}$$

$$K_6 = \frac{[p(\text{H}_2)]^{1/2}p(\text{OH})}{p(\text{H}_2\text{O})}$$

$$K_{10} = \frac{p(\text{NO})}{[p(\text{N}_2)]^{1/2}[p(\text{O}_2)]^{1/2}}$$

$$K_3 = \frac{[p(\text{H}_2)]^2p(\text{O}_2)}{[p(\text{H}_2\text{O})]^2}$$

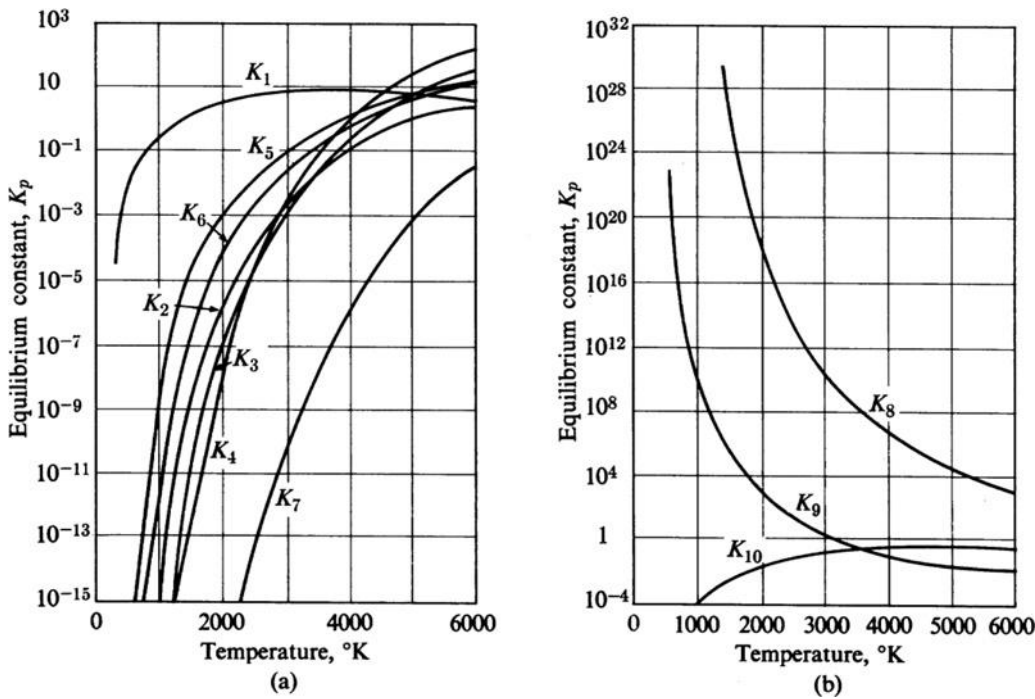
$$K_7 = \frac{p(\text{N})^2}{p(\text{N}_2)}$$

$$K_{11} = \frac{p(\text{O})}{[p(\text{O}_2)]^{1/2}}$$

$$K_4 = \frac{p(\text{H}_2)p(\text{O})}{p(\text{H}_2\text{O})}$$

$$K_8 = \frac{p(\text{CO})}{p(\text{C})[p(\text{O}_2)]^{1/2}}$$

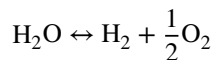
$$K_{12} = \frac{(p(\text{CO})[p(\text{O}_2)]^{1/2})}{(p(\text{CO}_2))}$$



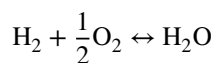
■ FIGURE 7.5 Equilibrium constants in terms of partial pressures, pressure in atmosphere. Source: Adapted from Hill and Peterson 1992

We note that the reaction on the right depicts one half of the reaction on the left, on a molar basis, therefore the equilibrium constant on the right is the square root of the reaction on the left.

As another example, let us look at a reaction where the reactants and products are switched. The first reaction dissociates water into molecular hydrogen and oxygen, such as



And the second reaction is the reverse of the first, namely,



■ TABLE 7.3

Logarithm to Base 10 of the Equilibrium Constant, K_p

Temperature K	Temperature °R	$\frac{1}{2}\text{O}_2 \leftrightarrow \text{O}$	$\frac{1}{2}\text{H}_2 \leftrightarrow \text{H}$	$\frac{1}{2}\text{N}_2 \leftrightarrow \text{N}$	$\text{H}_2 + \frac{1}{2}\text{O}_2 \leftrightarrow \text{H}_2\text{O}$	$\text{C} + \text{O}_2 \leftrightarrow \text{CO}_2$	$\text{C} + \frac{1}{2}\text{O}_2 \leftrightarrow \text{CO}$
600	1080	-18.574	-16.336	-38.081	18.633	34.405	14.318
700	1260	-15.449	-13.599	-32.177	15.583	29.506	12.946
800	1440	-13.101	-11.539	-27.744	13.289	25.830	11.914
900	1620	-11.272	-9.934	-24.292	11.498	22.970	11.108
1000	1800	-9.807	-8.646	-21.528	10.062	20.680	10.459
1100	1980	-8.606	-7.589	-19.265	8.883	18.806	9.926
1200	2160	-7.604	-6.707	-17.377	7.899	17.243	9.479
1300	2340	-6.755	-5.958	-15.778	7.064	15.920	9.099
1400	2520	-6.027	-5.315	-14.406	6.347	14.785	8.771
1500	2700	-5.395	-4.756	-13.217	5.725	13.801	8.485
1600	2880	-4.842	-4.266	-12.175	5.180	12.940	8.234
1700	3060	-4.353	-3.833	-11.256	4.699	12.180	8.011
1800	3240	-3.918	-3.448	-10.437	4.270	11.504	7.811
1900	3420	-3.529	-3.102	-9.705	3.886	10.898	7.631
2000	3600	-3.178	-2.790	-9.046	3.540	10.353	7.469
2100	3780	-2.860	-2.508	-8.449	3.227	9.860	7.321
2200	3960	-2.571	-2.251	-7.905	2.942	9.411	7.185
2300	4140	-2.307	-2.016	-7.409	2.682	9.001	7.061
2400	4320	-2.065	-1.800	-6.954	2.443	8.625	6.946
2500	4500	-1.842	-1.601	-6.535	2.224	8.280	6.840
2600	4680	-1.636	-1.417	-6.149	2.021	7.960	6.741
2700	4860	-1.446	-1.247	-5.790	1.833	7.664	6.649
2800	5040	-1.268	-1.089	-5.457	1.658	7.388	6.563
2900	5220	-1.103	-0.941	-5.147	1.495	7.132	6.483
3000	5400	-0.949	-0.803	-4.858	1.343	6.892	6.407
3100	5580	-0.805	-0.674	-4.587	1.201	6.668	6.336
3200	5760	-0.670	-0.553	-4.332	1.067	6.458	6.269
3300	5940	-0.543	-0.439	-4.093	0.942	6.260	6.206
3400	6120	-0.423	-0.332	-3.868	0.824	6.074	6.145
3500	6300	-0.310	-0.231	-3.656	0.712	5.898	6.088
3600	6480	-0.204	-0.135	-3.455	0.607	5.732	6.034
3700	6660	-0.103	-0.044	-3.265	0.507	5.574	5.982
3800	6840	-0.007	0.042	-3.086	0.413	5.425	5.933
3900	7020	0.084	0.123	-2.915	0.323	5.283	5.886
4000	7200	0.170	0.201	-2.752	0.238	5.149	5.841

(Continued)

■ TABLE 7.3

(Continued)

Temperature K	Temperature °R	$\frac{1}{2}\text{O}_2 + \frac{1}{2}\text{N}_2$ ↔ NO ₂	$\text{O}_2 + \frac{1}{2}\text{N}_2$ ↔ NO ₂	$\frac{1}{2}\text{O}_2 + \frac{1}{2}\text{H}_2$ ↔ OH	$\frac{1}{2}\text{O}_2 + \text{N}_2$ ↔ N ₂ O	$\text{C} + 2\text{H}_2$ ↔ CH ₄	$\text{C} + \frac{3}{2}\text{H}_2$ ↔ CH ₃
600	1080	-7.210	-6.111	-2.568	-11.040	2.001	-13.212
700	1260	-6.086	-5.714	-2.085	-10.021	0.951	-11.458
800	1440	-5.243	-5.417	-1.724	-9.253	0.146	-10.152
900	1620	-4.587	-5.185	-1.444	-8.654	-0.493	-9.145
1000	1800	-4.062	-5.000	-1.222	-8.171	-1.011	-8.344
1100	1980	-3.633	-4.848	-1.041	-7.774	-1.440	-7.693
1200	2160	-3.275	-4.721	-0.890	-7.442	-1.801	-7.153
1300	2340	-2.972	-4.612	-0.764	-7.158	-2.107	-6.698
1400	2520	-2.712	-4.519	-0.656	-6.914	-2.372	-6.309
1500	2700	-2.487	-4.438	-0.563	-6.701	-2.602	-5.974
1600	2880	-2.290	-4.367	-0.482	-6.514	-2.803	-5.681
1700	3060	-2.116	-4.304	-0.410	-6.347	-2.981	-5.423
1800	3240	-1.962	-4.248	-0.347	-6.198	-3.139	-5.195
1900	3420	-1.823	-4.198	-0.291	-6.065	-3.281	-4.991
2000	3600	-1.699	-4.152	-0.240	-5.943	-3.408	-4.808
2100	3780	-1.586	-4.111	-0.195	-5.833	-3.523	-4.642
2200	3960	-1.484	-4.074	-0.153	-5.732	-3.627	-4.492
2300	4140	-1.391	-4.040	-0.116	-5.639	-3.722	-4.355
2400	4320	-1.305	-4.008	-0.082	-5.554	-3.809	-4.230
2500	4500	-1.227	-3.979	-0.050	-5.475	-3.889	-4.115
2600	4680	-1.154	-3.953	-0.021	-5.401	-3.962	-4.009
2700	4860	-1.087	-3.928	0.005	-5.333	-4.030	-3.911
2800	5040	-1.025	-3.905	0.030	-5.270	-4.093	-3.820
2900	5220	-0.967	-3.884	0.053	-5.210	-4.152	-3.736
3000	5400	-0.913	-3.864	0.074	-5.154	-4.206	-3.659
3100	5580	-0.863	-3.846	0.094	-5.102	-4.257	-3.584
3200	5760	-0.815	-3.828	0.112	-5.052	-4.304	-3.515
3300	5940	-0.771	-3.812	0.129	-5.006	-4.349	-3.451
3400	6120	-0.729	-3.797	0.145	-4.962	-4.391	-3.391
3500	6300	-0.690	-3.783	0.160	-4.920	-4.430	-3.334
3600	6480	-0.653	-3.770	0.174	-4.881	-4.467	-3.280
3700	6660	-0.618	-3.757	0.188	-4.843	-4.503	-3.230
3800	6840	-0.585	-3.746	0.200	-4.807	-4.536	-3.182
3900	7020	-0.554	-3.734	0.212	-4.773	-4.568	-3.137
4000	7200	-0.524	-3.724	0.223	-4.741	-4.598	-3.095

(Continued)

■ TABLE 7.3

(Continued)

Temperature K	Temperature °R	$C + H_2$ $\leftrightarrow CH_2$	$C + \frac{1}{2}H_2$ $\leftrightarrow CH$	$2C + H_2$ $\leftrightarrow C_2H_2$	$C_2 + 2H_2$ $\leftrightarrow C_2H_4$	$\frac{1}{2}N_2 + \frac{3}{2}H_2$ $\leftrightarrow NH_3$	$\frac{1}{2}N_2 + H_2$ $\leftrightarrow NH_2$	$\frac{1}{2}N_2 + \frac{1}{2}H_2$ $\leftrightarrow NH$
600	1080	-30.678	-45.842	-16.687	-7.652	-1.377	-18.326	-31.732
700	1260	-25.898	-38.448	-13.882	-7.114	-2.023	-15.996	-27.049
800	1440	-22.319	-32.905	-11.784	-6.728	-2.518	-14.255	-23.537
900	1620	-19.540	-28.597	-10.155	-6.438	-2.910	-12.905	-20.806
1000	1800	-17.321	-25.152	-8.856	-6.213	-3.228	-11.827	-18.621
1100	1980	-15.508	-22.336	-7.795	-6.034	-3.490	-10.948	-16.834
1200	2160	-14.000	-19.991	-6.913	-5.889	-3.710	-10.216	-15.345
1300	2340	-12.726	-18.008	-6.168	-5.766	-3.897	-9.598	-14.084
1400	2520	-11.635	-16.310	-5.531	-5.664	-4.058	-9.069	-13.004
1500	2700	-10.691	-14.838	-4.979	-5.575	-4.197	-8.610	-12.068
1600	2880	-9.866	-13.551	-4.497	-5.497	-4.319	-8.210	-11.249
1700	3060	-9.139	-12.417	-4.072	-5.430	-4.426	-7.856	-10.526
1800	3240	-8.493	-11.409	-3.695	-5.369	-4.521	-7.542	-9.883
1900	3420	-7.916	-10.507	-3.358	-5.316	-4.605	-7.261	-9.308
2000	3600	-7.397	-9.696	-3.055	-5.267	-4.681	-7.009	-8.790
2100	3780	-6.929	-8.963	-2.782	-5.223	-4.749	-6.780	-8.322
2200	3960	-6.503	-8.296	-2.532	-5.183	-4.810	-6.572	-7.896
2300	4140	-6.115	-7.687	-2.306	-5.146	-4.866	-6.382	-7.507
2400	4320	-5.760	-7.130	-2.098	-5.113	-4.916	-6.208	-7.151
2500	4500	-5.433	-6.617	-1.506	-5.081	-4.963	-6.048	-6.823
2600	4680	-5.133	-6.144	-1.730	-5.052	-5.005	-5.899	-6.520
2700	4860	-4.854	-5.706	-1.566	-5.025	-5.044	-5.762	-6.240
2800	5040	-4.596	-5.300	-1.415	-5.000	-5.079	-5.635	-5.979
2900	5220	-4.356	-4.922	-1.274	-4.977	-5.112	-5.516	-5.737
3000	5400	-4.132	-4.569	-1.142	-4.955	-5.143	-5.405	-5.511
3100	5580	-3.923	-4.239	-1.019	-4.934	-5.171	-5.300	-5.299
3200	5760	-3.728	-3.930	-0.903	-4.915	-5.197	-5.203	-5.100
3300	5940	-3.544	-3.639	-0.795	-4.897	-5.221	-5.111	-4.914
3400	6120	-3.372	-3.366	-0.693	-4.880	-5.244	-5.024	-4.738
3500	6300	-3.210	-3.108	-0.597	-4.864	-5.265	-4.942	-4.572
3600	6480	-3.056	-2.865	-0.506	-4.848	-5.285	-4.865	-4.416
3700	6660	-2.912	-2.636	-0.420	-4.834	-5.304	-4.791	-4.267
3800	6840	-2.775	-2.418	-0.339	-4.821	-5.321	-4.721	-4.127
3900	7020	-2.646	-2.212	-0.262	-4.808	-5.338	-4.655	-3.994
4000	7200	-2.523	-2.016	-0.189	-4.796	-5.353	-4.592	-3.867

The equilibrium constant for the first reaction is

$$K_{P1} = \frac{\chi_{H_2} \cdot \chi_{O_2}^{1/2}}{\chi_{H_2O}} \cdot p_m^{1/2}$$

The second reaction has

$$K_{P2} = \frac{\chi_{H_2O}}{\chi_{H_2} \cdot \chi_{O_2}^{1/2}} p_m^{-1/2}$$

as its equilibrium constant.

$$\text{We note that } K_{P2} = \frac{1}{K_{P1}}$$

After these basic manipulations, we may want to add and subtract elementary reactions to form other reactions of interest. As an example, let us consider the following (water-gas) reaction in equilibrium:

$$CO_2 + H_2 \leftrightarrow CO + H_2O \quad K_P = \frac{\chi_{CO} \cdot \chi_{H_2O}}{\chi_{CO_2} \cdot \chi_{H_2}}$$

Now, if we subtract

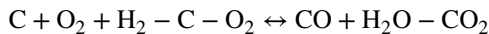
$$C + O_2 \leftrightarrow CO_2 \quad K_P = \frac{\chi_{CO_2}}{\chi_C \cdot \chi_{O_2}} p_m^{-1}$$

from the sum of the following two reactions

$$C + \frac{1}{2}O_2 \leftrightarrow CO \quad K_P = \frac{\chi_{CO}}{\chi_C \cdot \chi_{O_1}^{1/2}} p_m^{-1/2}$$

$$H_2 + \frac{1}{2}O_2 \leftrightarrow H_2O \quad K_P = \frac{\chi_{H_2O}}{\chi_{H_2} \cdot \chi_{O_2}^{1/2}} p_m^{-1/2}$$

we get



All terms on the reactant side vanish except H₂ and we may bring the negative CO₂ from the product side to the reactant side, to get the desired reaction

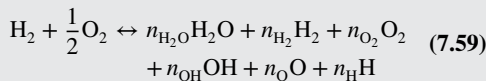
$$CO_2 + H_2 \leftrightarrow CO + H_2O \quad K_P = \frac{\chi_{CO} \cdot \chi_{H_2O}}{\chi_{CO_2} \cdot \chi_{H_2}}$$

Therefore, the equilibrium constant for this reaction is the product of the reactions that we added divided by the reaction that we subtracted to form the desired reaction, namely,

$$K_p = \frac{\frac{\chi_{\text{CO}}}{\chi_{\text{C}} \cdot \chi_{\text{O}_2}^{1/2}} p_m^{-1/2} \cdot \frac{\chi_{\text{H}_2\text{O}}}{\chi_{\text{H}_2} \cdot \chi_{\text{O}_2}^{1/2}} p_m^{-1/2}}{\frac{\chi_{\text{CO}_2}}{\chi_{\text{C}} \cdot \chi_{\text{O}_2}} p_m^{-1}} = \frac{\chi_{\text{CO}} \cdot \chi_{\text{H}_2\text{O}}}{\chi_{\text{CO}_2} \cdot \chi_{\text{H}_2}}$$

EXAMPLE 7.7

Now, let us revisit the stoichiometric combustion of hydrogen and oxygen that we started in Section 7.4. In this example, we are allowing the reaction to reach an equilibrium state, where a fraction of the fuel and oxidizer are still present, instead of the reaction going to a completion, where there is no leftover oxygen or fuel in the products of combustion.



$$2n_{\text{H}_2\text{O}} + 2n_{\text{H}_2} + n_{\text{OH}} + n_{\text{H}} = 2 \dots \dots \dots \text{to balance H}$$

$$n_{\text{H}_2\text{O}} + 2n_{\text{O}_2} + n_{\text{OH}} + n_{\text{O}} = 1 \dots \dots \dots \text{to balance O}$$

From the total of six unknowns and the two equations relating the unknowns, we are still in need of four more equations that involve the unknowns. We shall use the following four stoichiometric reactions:

$$1. \frac{1}{2}\text{O}_2 \leftrightarrow \text{O} \quad K_{p1} = \frac{\chi_{\text{O}}}{\chi_{\text{O}_2}^{1/2}} \cdot p_m^{1/2}$$

$$2. \frac{1}{2}\text{H}_2 \leftrightarrow \text{H} \quad K_{p2} = \frac{\chi_{\text{H}}}{\chi_{\text{H}_2}^{1/2}} \cdot p_m^{1/2}$$

$$3. \frac{1}{2}\text{H}_2 + \frac{1}{2}\text{O}_2 \leftrightarrow \text{OH} \quad K_{p3} = \frac{\chi_{\text{OH}}}{\chi_{\text{H}_2}^{1/2} \cdot \chi_{\text{O}_2}^{1/2}}$$

$$4. \text{H}_2 + \frac{1}{2}\text{O}_2 \leftrightarrow \text{H}_2\text{O}_{(\text{g})} \quad K_{p4} = \frac{\chi_{\text{H}_2\text{O}}}{\chi_{\text{H}_2} \chi_{\text{O}_2}^{1/2}} \cdot p_m^{-1/2}$$

The mole fractions in our equilibrium constants are

$$\chi_{\text{O}} = \frac{n_{\text{O}}}{n_{\text{H}_2\text{O}} + n_{\text{H}_2} + n_{\text{O}_2} + n_{\text{OH}} + n_{\text{O}} + n_{\text{H}}} \quad (7.60)$$

$$\chi_{\text{O}_2} = \frac{n_{\text{O}_2}}{n_{\text{H}_2\text{O}} + n_{\text{H}_2} + n_{\text{O}_2} + n_{\text{OH}} + n_{\text{O}} + n_{\text{H}}} \quad (7.61)$$

$$\chi_{\text{H}} = \frac{n_{\text{H}}}{n_{\text{H}_2\text{O}} + n_{\text{H}_2} + n_{\text{O}_2} + n_{\text{OH}} + n_{\text{O}} + n_{\text{H}}} \quad (7.62)$$

$$\chi_{\text{H}_2} = \frac{n_{\text{H}_2}}{n_{\text{H}_2\text{O}} + n_{\text{H}_2} + n_{\text{O}_2} + n_{\text{OH}} + n_{\text{O}} + n_{\text{H}}} \quad (7.63)$$

$$\chi_{\text{OH}} = \frac{n_{\text{OH}}}{n_{\text{H}_2\text{O}} + n_{\text{H}_2} + n_{\text{O}_2} + n_{\text{OH}} + n_{\text{O}} + n_{\text{H}}} \quad (7.64)$$

$$\chi_{\text{H}_2\text{O}} = \frac{n_{\text{H}_2\text{O}}}{n_{\text{H}_2\text{O}} + n_{\text{H}_2} + n_{\text{O}_2} + n_{\text{OH}} + n_{\text{O}} + n_{\text{H}}} \quad (7.65)$$

The denominator of the mole fractions is the number of moles of the equilibrium products. For a complete reaction of one mole of hydrogen and 1/2 mole of oxygen we would create one mole of water. Therefore, we may assume a number slightly bigger than one (due to high temperature dissociations) as a first approximation, say 1.1, and replace the denominator by 1.1. We then check the total number of moles of the mixture against our initial guess and iterate as necessary. This method helps arrive at the unknown number of moles of the products more quickly, albeit iteratively.

In order to utilize the equilibrium constants K_{p1}, \dots, K_{p4} , we need to know the mixture reaction pressure, i.e., the combustion pressure. In a gas turbine combustor, we may use the compressor discharge pressure p_{t3} as the combustion pressure. A typical value is between 25 and 50 atm (corresponding to $\pi_c \sim 25$ and 50) for a modern aircraft gas turbine engine at sea level takeoff condition. In a rocket application, the combustion chamber pressure is actually a design choice (typically $\sim 1\text{--}3000$ psia or $\sim 70\text{--}200$ atm). Although the equilibrium constants are not a function of

mixture pressure, the mole fractions of the species are, however, a function of the combustion pressure. Hence, combustion pressure affects the mole fractions of the species in equilibrium. We also need to have an idea of the final temperature of the products of combustion, before we can use the equilibrium constants, as they are known as a function of temperature. Here, we may assume an adiabatic combustion flame temperature and proceed to solve the six equations and six unknowns for the unknown mole fractions of the products in equilibrium. Now, we need to use the calculated composition of the products of combustion to calculate the adiabatic combustion flame temperature through an enthalpy balance. If the guessed value and the calculated value matched to within a few degrees, then we stop the calculation, otherwise, we need to assume another final combustion temperature and redo the calculations. As noted earlier, determination of the species and their concentration in an equilibrium combustion product is an iterative process. An initial guess of the total number of moles of the products also helps the calculation along and requires its own iteration.

Now, let us consider the example of hydrogen–oxygen combustion at 20 atm with the combustion temperature maintained at 3500 K. Compare the estimate proposed in the above example and the exact solution.

For this problem, we need to calculate the composition and concentration of the product species at the end of equilibrium combustion. Also, since we are maintaining the final temperature, at 3500 K, we need to calculate the heat transfer needed to achieve the final temperature. An equilibrium chemical reaction analysis results in the following composition (in number of moles):

$$\begin{aligned} n_{\text{H}_2} &\approx 0.1585 & n_{\text{O}_2} &\approx 0.0500 & n_{\text{O}} &\approx 0.0269 \\ n_{\text{H}} &\approx 0.0504 & n_{\text{OH}} &\approx 0.1166 & n_{\text{H}_2\text{O}} &\approx 0.7506 \end{aligned}$$

The total number of moles of the products is 1.153, which is slightly bigger than our initial guess of 1.1. The result of enthalpy balance applied to the chemical reaction in the combustor yields the necessary heat transfer to the reaction chamber to maintain the final temperature, i.e.,

$$Q \approx 5.8 \text{ kcal/gmol} \cdot \text{O}_2$$

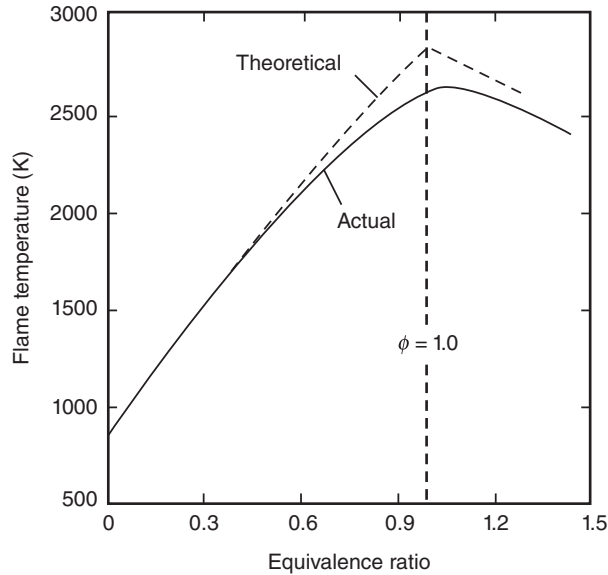
The adiabatic flame temperature of a stoichiometric combustion of hydrogen and oxygen yields a temperature of ~ 3080 K at 1 atm pressure.

The adiabatic flame temperature as a function of equivalence ratio for the Jet A fuel combustion in air at 800 K initial temperature and 25 atm initial pressure is shown in Figure 7.6 (from Blazowski, 1985). There are several noteworthy features in Figure 7.6 that are instructive to our study. First, the initial temperature and pressure were chosen to represent the combustion chamber inlet conditions in a modern aircraft gas turbine engine. Second, the *actual* flame temperature that allows for dissociation falls below the theoretical predictions (of a complete combustion). The difference between the actual curve and theoretical predictions starts around an equivalence ratio of ~ 0.4 – 0.5 , which points to a flame temperature of ~ 1650 – 1750 K, where dissociation reactions begin. Interestingly, a combustion chamber in a modern aircraft gas turbine engine operates in the 0.4 – 0.5 range of the equivalence ratio, which corresponds to a fuel-to-air ratio of ~ 2.5 – 3.5% . Third, although the figure caption identifies the initial temperature at 800 K, we could have discerned this fact from the flame temperature at zero equivalence ratio on the graph, that is, no combustion. Fourth, as noted earlier, the maximum flame temperature occurs at an equivalence ratio slightly greater than 1 (~ 1.1).

Also, note that the burner exit (or flame) temperature is a double-valued function of equivalence ratio, or fuel-to-air ratio, that is, we can reach a burner exit temperature from either the fuel-lean or the fuel-rich side of the stoichiometric point.

The effect of initial air temperature on the stoichiometric flame temperature of a Jet A fuel combustion in air is shown in Figure 7.7a. Comparing the slope of the flame temperature rise with inlet temperature to a slope = 1.0 line drawn in Figure 7.7a for

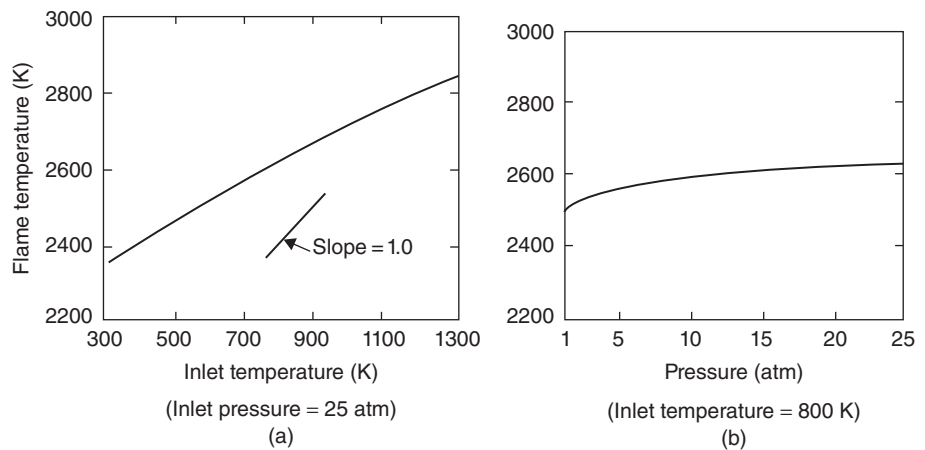
■ **FIGURE 7.6**
Adiabatic flame temperature of Jet A fuel combustion in air at 800 K initial temperature and 25 atm pressure. Source: Blazowski 1985. Reproduced with permission from AIAA



reference, we note that only $\sim 1/2$ of the inlet temperature rise appears as the rise in the final flame temperature. This behavior corresponds to higher molar concentrations of dissociated species that appear with higher temperatures. Consequently, a 100 K increase in the inlet air temperature for this reaction results in ~ 50 K final flame temperature rise. The effect of the combustion pressure on the stoichiometric flame temperature of Jet A fuel is shown in Figure 7.7b. The increasing pressure leads to a rise in the stoichiometric flame temperature. The increase is due to a suppressed dissociation levels with pressure, as shown in Example 7.4. We observed that a lower mixture pressure promoted nitrogen dissociation and it was suppressed with an increasing mixture pressure in Example 7.4.

It is instructive to examine the effect of oxidizer, as in pure oxygen or air, on the combustion of various fuels and the impact of the oxidizer on the stoichiometric flame temperature. For this purpose, Table 7.4 is reproduced from Glassman

■ **FIGURE 7.7**
Effect of inlet temperature and pressure on the stoichiometric flame temperature of a Jet-A fuel combustion in air. Source: Blazowski 1985. Reproduced with permission from AIAA



■ TABLE 7.4

Maximum Flame Temperature of Fuel–Air and Fuel–Oxygen Mixtures at 25° C Temperature and 1 or 20 atm Pressure

Approximate flame temperatures of various stoichiometric mixtures, critical temperature 298 K

Fuel	Oxidizer	Pressure (atm)	T(K)
Acetylene	Air	1	2600 ^a
Acetylene	Oxygen	1	3410 ^b
Carbon monoxide	Air	1	2400
Carbon monoxide	Oxygen	1	3220
Heptane	Air	1	2290
Heptane	Oxygen	1	3100
Hydrogen	Air	1	2400
Hydrogen	Oxygen	1	3080
Methane	Air	1	2210
Methane	Air	20	2270
Methane	Oxygen	1	3030
Methane	Oxygen	20	3460

Source: Glassman 1987. Reproduced with permission from Elsevier

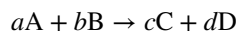
^aThis maximum exists at $\phi = 1.3$.^bThis maximum exists at $\phi = 1.7$.

(1987) that examines the maximum temperature at equivalence ratios near stoichiometric of various fuels reacting with air or pure oxygen. Moreover, the effect of pressure on combustion temperature is reported for methane, similar to Figure 7.7b. Combustion of hydrogen in air results in a stoichiometric flame temperature of ~ 2400 K at 1 atm pressure. The flame temperature for the combustion of hydrogen with pure oxygen is ~ 3080 K, at 1 atm pressure. Air contains nitrogen ($\sim 78\%$ by volume), which for the most part is inert and does not react with the fuel or oxidizer. Also, the fuel heating value remains the same whether the oxidizer is oxygen or air. For the same energy release (per unit mass of the fuel), there are more reactants in air that do not participate in the combustion but need to be heated to the final temperature. Consequently, the flame temperature will be lower when a fuel reacts with air as opposed to pure oxygen. This behavior is observed for all (five) fuels listed in Table 7.4. Now to the effect of pressure on combustion, we note that methane reacts with air at 1 atm pressure and reaches a maximum flame temperature of 2210 K. If we increase the combustion pressure to 20 atm, the flame temperature increases to ~ 2270 K. This is a rather minor increase in temperature, which is caused by a decrease in the dissociation levels of the products of combustion with pressure. At this temperature, the dissociation levels were small and hence a suppressed level of dissociation did not cause a pronounced effect in final temperature. To ascertain this point, we examine the combustion of methane with pure oxygen, which reaches a flame temperature of ~ 3030 K at 1 atm pressure. The flame temperature rises to ~ 3460 K when methane reacts with pure oxygen at 20 atm pressure. At the temperature of 3030 K, the level of dissociation is much higher, hence the effect of pressure on suppressing the product dissociation is more pronounced and leads to a flame temperature of ~ 3460 K.

7.5 Chemical Kinetics

So far our study of the chemical reactions involved an equilibrium state where the forward and reverse reaction rates were equal. However, the time it takes to reach the equilibrium state was not explicitly studied. To study the (time) rate of formation of product species in a chemical reaction, or equivalently the rate of disappearance of reactants in a reaction, is the subject of chemical kinetics. As a propulsion engineer, why should you be interested in chemical kinetics? The short answer is that it gives you an important characteristic timescale of the problem, which may affect the size and efficiency of your combustion chamber. For example, you will need to design the combustion chamber (as in a supersonic combustion ramjet) such that the residence time of species in the chamber is longer than the characteristic chemical reaction timescale for the heat of reaction to be fully realized. Also, we learn that the reaction rate depends on the pressure of the mixture, which at high altitudes (low pressures) may become too slow to effect a combustor relight. Finally, the study of chemical kinetics helps combustion engineers meet the low-pollution design objectives of low NO_x , low CO, soot, and (visible) smoke dictated by the regulatory organizations (e.g., EPA and ICAO).

The cornerstone of chemical kinetics is the law of mass action, which for the following generic reaction



may be written as

$$r_f = k_f [A]^a \cdot [B]^b$$

that depicts the forward reaction rate. The reaction rate coefficient k_f is independent of reactant's concentration (note that the concentrations are already accounted for in the law of mass action itself) and in general is a function of pressure and temperature. The temperature dependency of the rate coefficient is in the form proposed by Arrhenius to be the Boltzmann factor (from the kinetic theory of gases), which is equal to the fraction of all collisions (i.e., the number of collisions per unit time and volume) with an energy greater than, say E_a , namely,

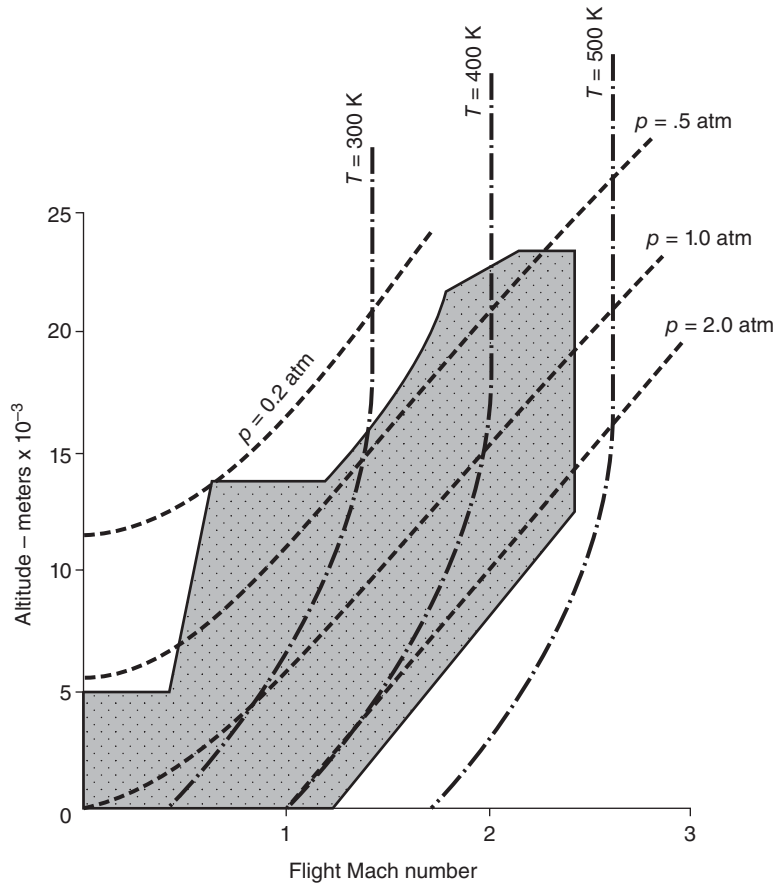
$$\text{Temperature dependence of } k_f = e^{-\frac{E_a}{RT}} \quad (7.66)$$

where E_a is the activation energy (for the reaction, which is the minimum energy to cause a chemical reaction to occur), \bar{R} is the universal gas constant, and T is the reactant's absolute temperature. The activation energy for the combustion of hydrocarbon fuel in air is in the range of 40–60 kcal/mol. The frequency of the collisions, per unit volume, contributes to the reaction rate most directly and hence the pressure dependence of the reaction rate coefficient is revealed. In general,

$$k_f = p^n f(T) e^{-\frac{E_a}{RT}} \quad (7.67)$$

which is called the Arrhenius rule, in honor of the man who first proposed the exponential dependence, the Boltzmann factor, for the chemical reaction rate. The exponent n on the

■ **FIGURE 7.8**
 The typical ignition/relight envelope shows relight capability in the shaded zone. Source: Henderson and Blazowski 1989. Reproduced with permission from AIAA



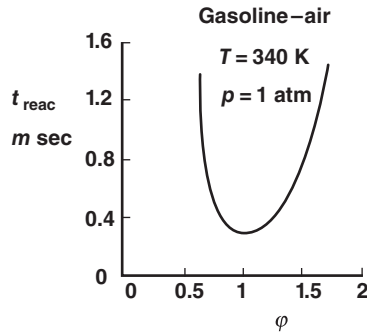
pressure term depends on the number of molecules involved in a collision to produce the chemical reaction. For example, the combustion of hydrocarbon fuels in air involves the collision of two molecules, namely, oxygen and the fuel, hence $n \approx 2$. More complex reactions involving collisions of more than two molecules in a chemical reaction lead to a higher pressure exponent n such as 3 or 4.

Now, let us examine the impact of a chemical kinetic study on a practical problem in aircraft propulsion.

7.5.1 Ignition and Relight Envelope

As noted earlier, the pressure dependence of the reaction rate coefficient may cause a relight problem at high altitude. A relight zone is plotted in Figure 7.8 in an altitude–Mach number plot (i.e., flight envelope) for the combustion of a typical hydrocarbon fuel in air (Henderson and Blazowski, 1989). We note that below 0.2 atm pressure, combustor relight is not possible at standard temperature, due to low reaction rate.

■ **FIGURE 7.9**
Reaction timescale for gasoline–air combustion as a function of equivalence ratio (Mixture at 1 atm pressure and 340 K temperature). Source: Kerrebrock 1992, Fig. 4.41. Reproduced with permission from MIT Press



7.5.2 Reaction Timescale

The reaction timescale and its relation to the residence timescale of the air–fuel vapor mixture control the combustion efficiency. We require that the two timescales to be equal, to establish a minimum length requirement of the combustor. A typical variation of reaction timescale with equivalence ratio for gasoline–air combustion is shown in Figure 7.9 (from Kerrebrock, 1992). This shows that near stoichiometric combustion, $\phi \sim 1$, the reaction time reaches a minimum of ~ 0.3 ms. The minimum reaction timescale is one of the indicators of the desirability of stoichiometric combustion. We shall see in the next section that the flammability limit of most fuels is a narrow band centered on the stoichiometric mixture ratio of $\phi = 1$.

The reaction timescale is inversely proportional to reaction rate (Equation 7.67), which may be written as

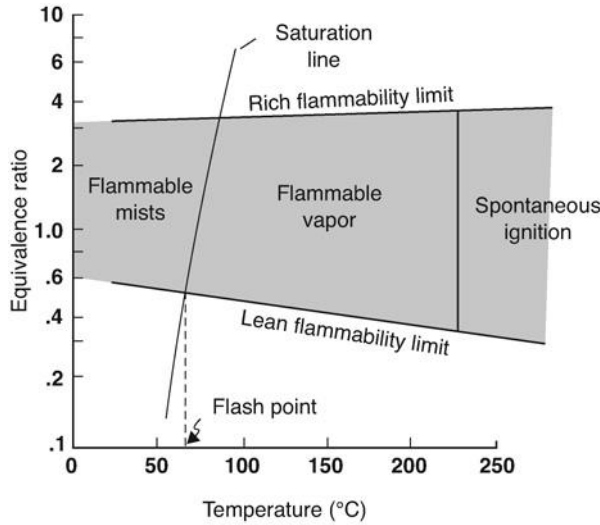
$$t_{\text{reaction}} \sim k_f^{-1} \sim p^{-n} T^{-m} e^{\frac{E_a}{RT}} \quad (7.68)$$

There are no universal rules for the pressure and temperature exponents, n and m , in a gas turbine combustor, but typical value of n is ~ 1 – 2 and m is ~ 1.5 – 2.5 (Zukoski, 1985). The aircraft gas turbine combustor or afterburner is designed for a residence timescale in the primary zone or the flameholder recirculation zone-mixing layer to be long compared with the reaction timescale. Hence, we are not reaction-time-limited in a conventional combustor or afterburner. However, in a scramjet combustor with a Mach 3 combustor inlet flow, we are *residence-time-limited*, hence reaction timescale becomes especially critical. Fortunately, the fuel of choice, hydrogen, offers not only a regenerative cooling option for the engine inlet, combustor, and nozzle but also $\sim 1/10$ of the chemical reaction timescale of hydrocarbon fuels. The pollutant formations and their dependence on the combustor characteristic timescales will be discussed in section 7.7 in this chapter.

7.5.3 Flammability Limits

A practical aspect of combustor design examines the issues of flammability limits of various fuel–air mixture ratios as a function of temperature and pressure in a quiescent environment. It is learned that a fuel–air mixture of equivalence ratio leaner than 0.6 and richer than 3.0 will not react (i.e., sustain combustion) in room temperature and pressure, as shown in Figure 7.10 (Blazowski, 1985). In reality, a narrow band around a stoichiometric fuel–air mixture ratio is our open window for a sustained combustion.

■ **FIGURE 7.10**
 Flammability limits of a kerosene-type fuel in air at atmospheric pressure. Source: Blazowski 1985. Reproduced with permission from AIAA



With the increase in temperature, the flammability limit boundary widens to $0.3 < \phi < 4.0$ in the spontaneous ignition temperature range ($T > 225^\circ\text{C}$) for a kerosene-air mixture. The flammability limits of different fuel-air mixtures, in percentage stoichiometric, are shown in Table 7.5 at the temperature of 25°C and 1 atm pressure. The most remarkable is the wide flammability limits of hydrogen. Also hydrogen, methane, and propane enjoy very large heating capacity making them suitable coolants for active cooling of the engine and airframe structure of a hypersonic aircraft.

The effect of low ambient pressure (corresponding to high altitude) on flammability limit of gasoline-air mixtures is shown in Figure 7.11 (from Olson, Childs, and Jonash, 1955). We note that the lean flammability limit at altitude approaches the stoichiometric ratio, that is, $\phi \approx 1$. We also observe that the rich flammability limit becomes much wider with the increase in pressure.

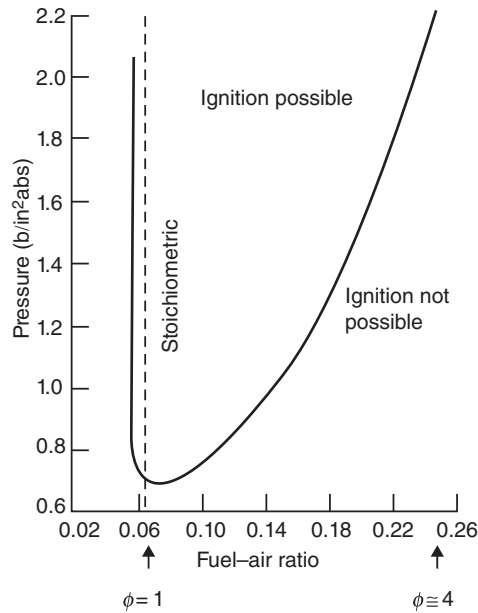
As noted earlier, the flammability limits are defined for a fuel-air (gas phase) mixture as a function of temperature and pressure in a *quiescent* environment. In the presence of flow, combustion instabilities may set in to cause a flame blowout. Hence, the presence of a flow may drive an otherwise stable combustion (in the flammable zone) into an unstable reaction where the combustion efficiency goes to zero at the point of flame blowout. In order to sustain combustion in the presence of flow, that is, to avoid blowout, we need to employ flame stabilization schemes, which are suitable for the primary combustors and the afterburners. We will address several stabilization schemes in this chapter.

A need for an external source of energy release, as provided by an electric spark discharge, is (implicitly) demonstrated in the flammability limit diagram of

■ **TABLE 7.5**
 Flammability Limits of Some Fuels (25°C and 1 atm pressure)

Fuels	Jet A kerosene	Propane C_3H_8	Methane CH_4	Hydrogen H_2
Flammability limits (percent stoichiometric)	52–400	51–280	46–164	14–250

■ **FIGURE 7.11**
 Flammability limits of
 gasoline-air mixtures
 as a function of
 combustion pressure.
 Source: Olson et al.
 1955. Fig. 1, p. 606.
 Reproduced with
 permission from
 ASME



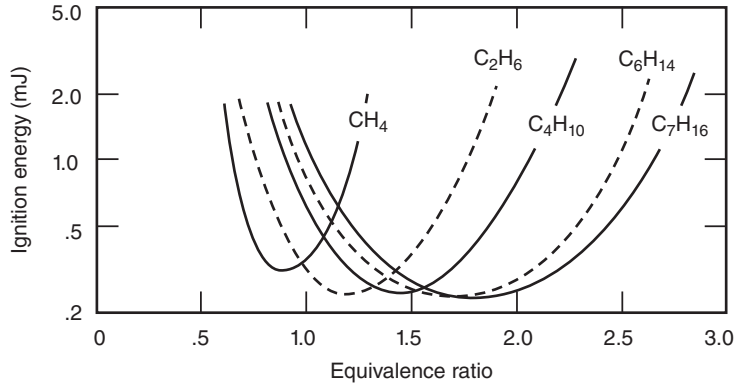
kerosene-air mixture in Figure 7.10. Note that below the spontaneous ignition temperature (SIT) of the fuel-air mixture (of $\sim 225^\circ\text{C}$), the mixture that is defined as flammable will not self-ignite. Hence, an ignition source that is an intense localized heat source is needed to initiate the reaction. The intense localized energy release will raise the temperature of a *pocket* of the vaporized fuel-air mixture to a temperature above the SIT. A flame front signifying the chemical reaction zone is then formed, which propagates in the flammable mixture at a finite speed S_T . Table 7.6 contains the spontaneous ignition temperature of some common fuels for reference (from Gouldin, 1973). A high spontaneous ignition temperature is desirable for a fuel that is to be used for its cooling capacity. For example, propane in Table 7.6 has the highest SIT at 767 K, which makes it a good candidate for cooling purposes. Since the spontaneous ignition temperature of fuel-air mixtures is a strong function of mixture pressure, the SIT information contained in Table 7.6 needs to

■ **TABLE 7.6**
 Spontaneous Ignition Temperatures of Common Fuels

Fuel	SIT (K)	Fuel	SIT (K)
Propane	767	Decane	481
Butane	678	Hexadecane	478
Pentane	558	Isooctane	691
Hexane	534	Kerosene (JP-8 or Jet A)	501
Heptane	496	JP-3	511
Octane	491	JP-4	515
Nonane	479	JP-5	506

Source: Adapted from Gouldin 1973.

■ **FIGURE 7.12**
 Minimum ignition energy of various vaporized fuel–air mixtures. Source: Lewis and von Elbe 1961. Reproduced with permission from Elsevier



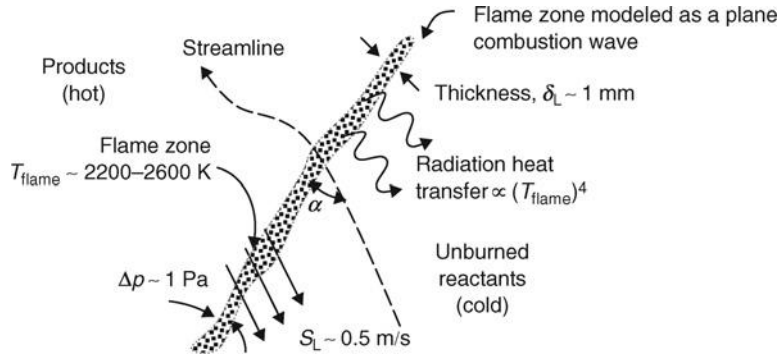
be viewed with caution and not to be used for the “general purpose” fuel system safety calculation. The minimum external energy (stimulus) needed to initiate a reaction is a function of the equivalence ratio as well as the type of fuel for vaporized fuel–air mixtures. Figure 7.12 (from Lewis and von Elbe, 1961) shows the level of ignition energy of various vaporized fuel–air mixtures as a function of equivalence ratio. The ignition energies are in the form of “bucket” shapes with the minimum ignition energy corresponding to a particular equivalence ratio.

Note that in Figure 7.11, the minimum ignition energy points on the “buckets” shifts to the right, that is, toward higher equivalence ratios, with higher molecular weight fuels. Methane, CH₄, has a molecular weight of 16 and the minimum ignition energy around the stoichiometric ratio, whereas *n*-heptane, C₇H₁₆, has a molecular weight of 100 and the minimum ignition energy occurring around an equivalence ratio of ~2. We may express this observation in terms of the specific gravity of these fuels as well where methane’s specific gravity is 0.466 (a light fuel) and *n*-heptane’s specific gravity is 0.684 (a relatively heavier fuel).

7.5.4 Flame Speed

There are two types of flames, premixed flames and diffusion flames. When the fuel and oxidizer are in gaseous form and premixed into a (stoichiometric) flammable mixture prior to combustion initiation, the resulting flame is called a premixed flame (e.g., Bunsen burner). When the fuel and oxidizer are initially separated, as in a candle burning in air, the combustion takes place within a diffusion flame zone where the vaporized fuel diffuses outward and meets an inwardly diffusing oxidizer. For an aircraft application where space is at a premium, a premixed flame combustor with a high level of turbulence intensity is the desirable choice. The effect of turbulence intensity is to promote mixing enhancement. It is the rapid and efficient mixing of the vaporized fuel–air mixture in a combustion chamber that is a performance limiting parameter, that is, limiting the energy release rate, rather than the chemical reaction timescale or flame propagation speed in conventional burners. The flame zone in a premixed combustor starts propagating initially as a laminar flame and later develops into a turbulent flame. A schematic drawing of a laminar premixed flame and its typical characteristic parameters (thickness, propagation speed, temperature range, pressure drop, and wave angle, α) are shown in Figure 7.13. The laminar flame parameters in Figure 7.13 are extracted from Borman and Ragland

■ **FIGURE 7.13**
A schematic drawing of a thin premixed laminar flame propagating in a stoichiometric mixture of a hydrocarbon fuel and air at 1 atm pressure and $T = 25^\circ\text{C}$

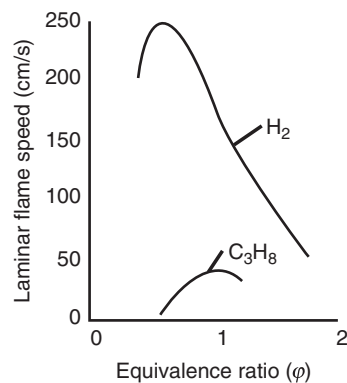


(1998). S_L is the laminar flame speed, δ_L is the flame thickness, and α is the relative flow angle.

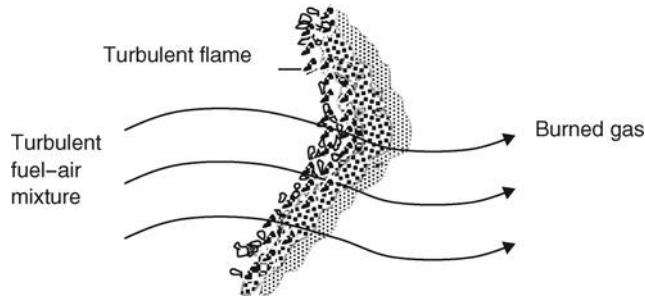
The initial mixture temperature has the most pronounced effect on laminar flame speed. The burning velocity of the laminar flame zone increases nearly fourfold when the initial mixture temperature is raised from 200 to 600 K, as reported by Dugger and Heimele (1952) for methane (CH_4), propane (C_3H_8), and ethylene (C_2H_4) combustion in air. The mixture pressure has a minor effect on the laminar flame speed as discussed by Lefebvre (1983). The experimental results of Jost (1946), shown in Figure 7.14, demonstrate the equivalence ratio of the laminar flame speed. Moreover, they confirm the typical speed of ~ 0.5 m/s for a hydrocarbon fuel, as in propane. They also show nearly an order of magnitude increase in laminar flame speed for hydrogen, which reconfirms the status of hydrogen as an ideal fuel.

The effect of turbulence on premixed flame speed is to enhance momentum transfer between the burning front and the unburned reactants. In addition, turbulence increases the total surface area of the flame and hence increases the heat transfer between the reaction zone and the unburned gas. To visualize the surface area of a flame front under the influence of turbulence, a *wrinkled* flame front is proposed. Under this scenario, large (energetic) turbulent eddies strike the flame front and *wrinkle* the surface, while small-scale turbulence changes the transport properties within the flame zone. Figure 7.15 shows a representative drawing of a wrinkled flame front with a range of turbulent eddy sizes within the flame (adapted from Ballal and Lefebvre, 1975). Consequently, the flame

■ **FIGURE 7.14**
Laminar flame speed for propane and hydrogen as a function of equivalence ratio. Source: Jost 1946



■ **FIGURE 7.15**
Graphical depiction of a wrinkled turbulent flame with a distribution of eddies within the flame.
Source: Adapted from Ballal and Lefebvre 1975. Reproduced with permission from the Royal Society



propagation speed is increased from the laminar flame speed S_L to the turbulent flame speed S_T . The first model, due to Damkohler (1947), proposes enhancing the laminar flame speed by adding the root mean square of the turbulent fluctuation speed. The increase in flame surface area due to turbulence is proportional to

$$u'_{\text{rms}} \text{ i.e.,} \quad (7.69)$$

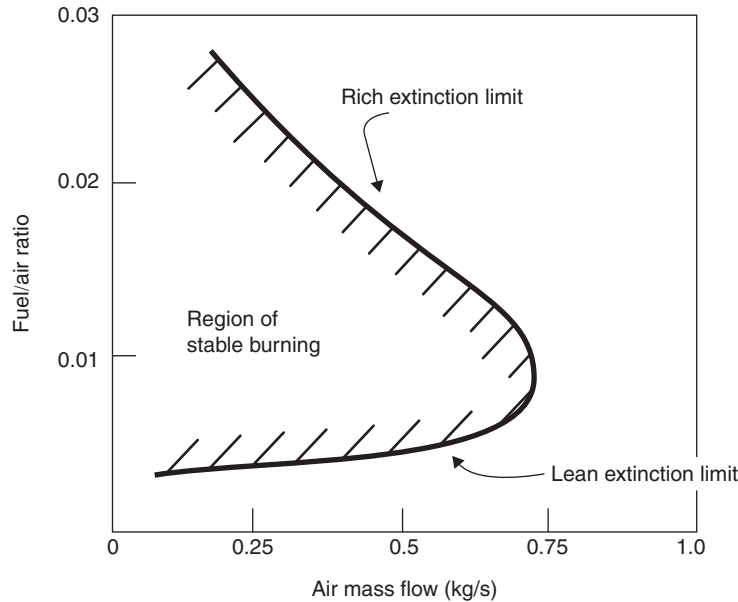
$$S_T = S_L + u'_{\text{rms}}$$

The laminar flame speed is $S_L \sim 0.5\text{--}2$ m/s (depending on the initial mixture temperature), which is now enhanced by turbulent fluctuations. A low turbulence intensity environment, of say 5%, in a (fuel-air mixture) flow of $\sim 50\text{--}100$ m/s results in a root mean square of the turbulent fluctuation speed of 2.5–5 m/s. Now, in a high turbulence intensity environment, of say 15–30%, in a flow with a mean speed of ~ 100 m/s, the turbulence contribution to flame propagation speed may be as high as 30 m/s. Although the simple model of Damkohler in Equation 7.69 does not account for turbulence scale, the thickness of the reaction zone and other effects such as flame stretching, it serves the purpose of demonstrating the attractiveness of turbulence-enhanced mixing and its impact on the reaction timescale. A review of more elaborate models is beyond the scope and intention of the present treatment. Excellent books on combustion, such as those authored by Lefebvre (1983), Kuo (1986), Glassman (1987), Borman and Ragland (1998), among others, are recommended for further reading in this fascinating field.

7.5.5 Flame Stability

Does a Bunsen burner or a candle in a laboratory produce a stable flame? The obvious answer is yes, but the correct answer should be a conditional yes or a maybe. Since we did not specify any source or intensity of airflow in the room, we could not rule out the possibility of flame extinction caused by the airflow. If we place a Bunsen burner or a candle in a duct (for measurement purposes) connected to a fan on one side, we may experimentally establish the wind speed in the duct that causes the candle flame to blowout. Similar experiments may be conducted in a premixed combustible mixture where a flame front is established and propagates in the mixture at the flame speed S . Now, if we set the premixed gas into motion at speed U in the opposite direction to S and equal to it in magnitude, we shall achieve a stationary flame front. Simply adding the velocity vectors demonstrates the principle. For a given mixture fuel-air ratio, we may repeat the experiment for different flow speeds until we achieve an extinction of the flame

■ **FIGURE 7.16**
A typical stability loop
for a combustor at $p_3 =$
constant. Source:
Lefebvre 1983.
Reproduced with
permission from
Taylor and Francis
Group LLC, a division
of Informa plc

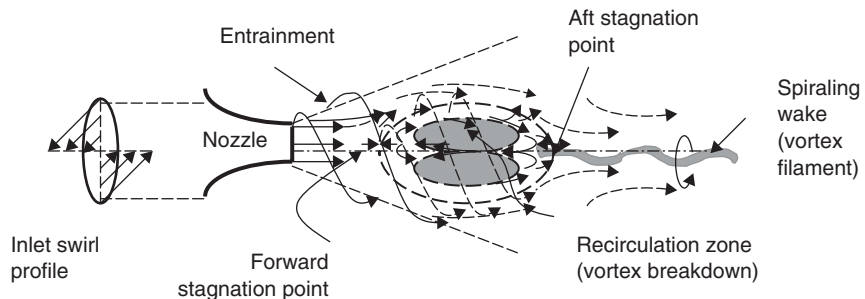


(i.e., at the blowout speed). We may subsequently vary the fuel–air mixture ratio from a lean limit where extinction occurs to a rich limit at a given flow speed. The result of this experiment may be plotted in terms of the fuel–air mixture (or equivalence ratio) and the flow speed (or air mass flow rate, which is proportional to flow speed) in what is known as a stability plot or the *stability loop*, due to its shape. Figure 7.16 shows the combustion system stability loop for a constant pressure (from Lefebvre, 1983).

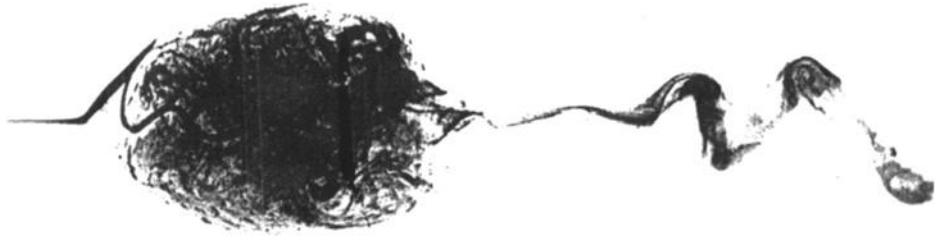
The lower branch of the stability loop is the lean extinction limit and the upper branch is the rich extinction limit of combustion chamber. The maximum blowout speed occurs at the maximum flame speed, which is usually near the stoichiometric mixture ratio. The effect of pressure on the lean stability limit is negligible and widens the rich stability limit with the increase in pressure.

A recirculation zone in the burner (with a backward flow) is needed to stabilize a premixed flame. In studying swirling jets, we learn that when the ratio of jet angular momentum to jet axial thrust times jet diameter exceeds ~ 0.5 , a recirculatory flow in the core of the swirling jet is established. This is known as a vortex breakdown. A schematic drawing of a swirling jet with vortex breakdown is shown in Figure 7.17.

■ **FIGURE 7.17**
The flow pattern of a
(bubble-type) vortex
breakdown in a
swirling jet



■ **FIGURE 7.18**
Flow visualization of a
bubble-type vortex
breakdown. Source:
Sarpkaya 1971.
Reproduced with
permission from
Cambridge University
Press



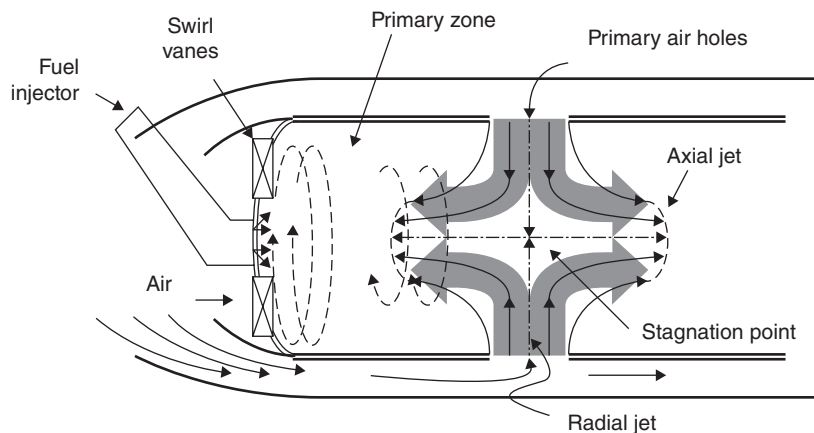
Flow visualization (via dye injection in water) of a bubble-type vortex breakdown is shown in Figure 7.18 (from Sarpkaya, 1971). The complex network of vortex filaments winding in and out of the bubble and a spiraling wake formation indicates filling and emptying of the bubble. This environment, that is, the recirculation and intense mixing of a vortex breakdown, comes close to a model of a perfectly stirred reactor that is often used in combustion studies.

To help stabilize the flame in the primary zone of a main burner, air is introduced through single or double rows of swirl vanes. Also, to create a perfectly stirred reaction zone in the main burner, part of the excess air is injected into the burner through the primary air holes as radial jets. When opposing radial jets collide, a stagnation point is created with the resultant streams directed along the axis in the upstream and downstream directions. The opposing flows of the axial jet moving upstream and the spiraling air–fuel mixture create a recirculation zone with intense mixing. The combustor primary zone may also be modeled as a perfectly stirred reactor. A schematic drawing of radial jets and subsequent axial jet formations are shown in Figure 7.19.

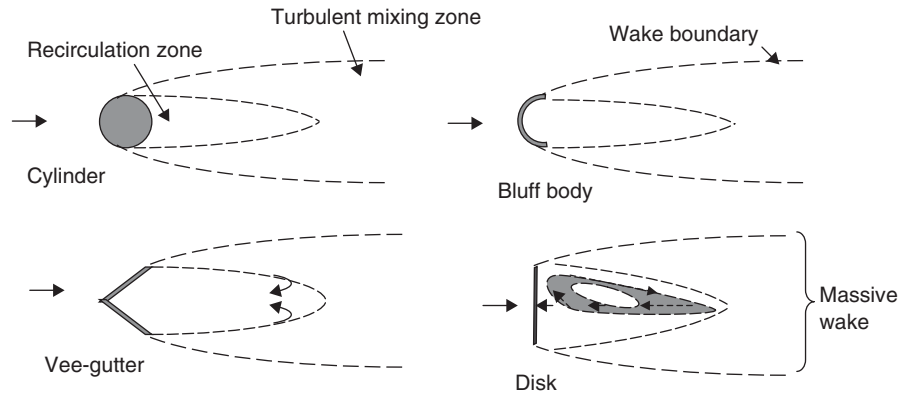
In an afterburner, the necessary recirculation zone to stabilize the premixed flame is created by the massively separated wakes of bluff bodies. Some geometric examples of bluff bodies that create massively separated wakes are produced in Figure 7.20.

The flameholding, that is, creating a reversed flow environment, in a high-speed scramjet combustor may be achieved by a direct fuel injection in the supersonic air stream, or via a backward-facing step. The former involves a bow shock, and the latter involves the corner flow separation. These flowfields are of interest in high-speed propulsion and are shown in Figure 7.21.

■ **FIGURE 7.19**
Collision of radial jets,
stagnation point, and
axial jet formation
with a reverse flow in
the primary zone of the
combustion chamber



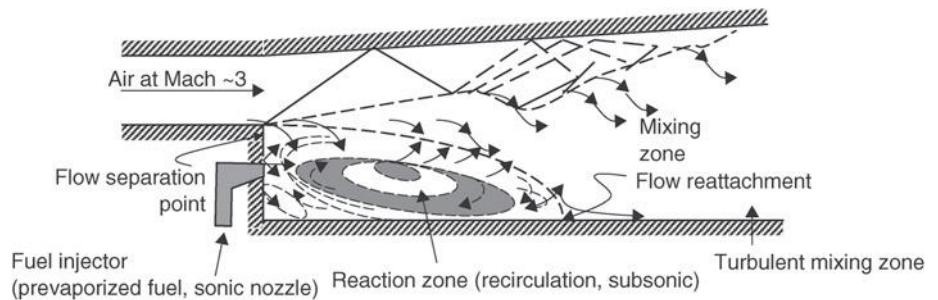
■ **FIGURE 7.20**
Bodies that create recirculation and massive wakes (suitable for subsonic flameholding)



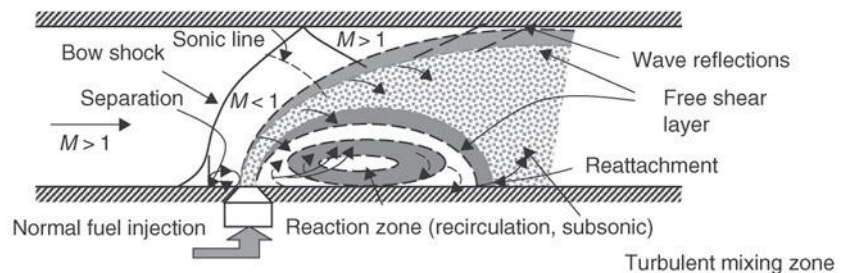
The primary zone of a burner and the wake of a bluff body in the afterburner are modeled as a *perfectly stirred reactor* where the reactants and products are mixed infinitely fast. Such an environment produces the maximum energy release (due to infinitely fast chemical reaction rates) for the given volume of the reactor and at a fixed reactor pressure. The theory of perfectly stirred reactor has many applications, among which the stability of premixed turbulent flames in a flow environment. The perfectly stirred reactor theory predicts

$$\frac{\dot{m}}{p^n V} = f(\phi) \quad (7.70)$$

■ **FIGURE 7.21**
Fuel injection schemes in high-speed flow

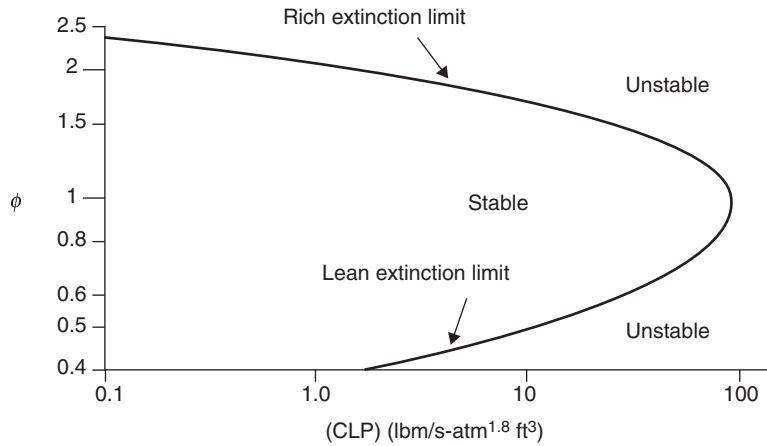


(a) Backward-facing step with base fuel injection in supersonic flow



(b) Normal fuel injection in a supersonic stream creates a bow shock and a recirculation zone, which serves as the flameholder for a scramjet combustor

■ **FIGURE 7.22**
 Combustor stability loop in terms of the loading parameter and the equivalence ratio ϕ . Source: Spalding 1979. Reproduced with permission from Elsevier



where the mass flow rate in the reactor is \dot{m} , volume of the reactor is V , pressure of the reactor is p , the exponent of pressure represents the order of reaction, which is close to 2, and ϕ is the equivalence ratio of the fuel–air mixture. The parameter on the right-hand side of Equation 7.70 is called the combustor loading parameter (CLP). A graph of Equation 7.70 is shown in Figure 7.22 (from Spalding, 1979). A lean and a rich extinction limit (i.e., when flame instability causes extinction) are observed in Figure 7.22, similar to the stability loop of Figure 7.16. The pressure exponent “ n ” is taken as 1.8 in Figure 7.22, and the dimensions of the combustor loading parameter are $\text{lbm}/(\text{s} \cdot \text{atm}^{1.8} \cdot \text{ft}^3)$ in English units.

Fundamental contributions to understanding flame stability are due to the works of Longwell, Chenevey, and Frost (1949), Haddock (1951), and Zukoski–Marble (1955). Although, we will briefly address the afterburner stability in this chapter, these references are recommended for further reading.

7.5.6 Spontaneous Ignition Delay Time

In continuing with our studies of combustion timescales and the role of chemical kinetics, we enter a new characteristic timescale, namely, the spontaneous ignition delay time. Spontaneous ignition delay time is defined as the time elapsed between the injection of a high-temperature fuel–air mixture and the appearance of a flame in the absence of an ignition source. There are two factors that contribute to an autoignition delay time. First is the rate of evaporation of fuel droplets, and the second is the chemical reaction time of the vaporized fuel and air. To promote the rate of evaporation, a liquid fuel has to be efficiently atomized to a fine spray mist. Modern aircraft engine combustors utilize spray injectors that produce an atomized fuel drop size distribution in the range of 10–400 μm . Rao and Lefebvre (1981) express the ignition delay time as

$$t_i = t_e + t_{\text{reaction}} \quad (7.71)$$

The subscript “i” stands for ignition delay, and “e” stands for evaporation timescale in Equation 7.71. Evaporation timescale in a stagnant mixture is proportional to the surface

area of the liquid fuel droplet, as the heat transfer rate to the liquid is proportional to the surface area, i.e.,

$$t_e \propto D^2 \quad \text{Re}_D = 0 \quad (\text{stagnant mixture}) \quad (7.72)$$

where D is the liquid fuel droplet diameter, and Re_D is the fuel droplet Reynolds number based on diameter of the droplet, turbulent fluctuation velocity u' (rms), and the kinematic viscosity of the gas ν_g . In the presence of a highly turbulent mixture, the evaporation time is proportional to the droplet diameter to the power three halves, that is,

$$t_e \propto D^{1.5} \quad \text{Re}_D \gg 1 \quad (7.73)$$

according to Ballal and Lefebvre (1980). The effect of turbulence is hence to increase the heat transfer and reduce the evaporation timescale. The reaction time is expressed in terms of the mixture temperature (in K), by Rao and Lefebvre (1981), as

$$t_{\text{reaction}} \propto e^{\frac{9160}{T_m}} \quad (7.74)$$

From the chemical kinetic rate Equation 7.67, we may also deduce the reaction timescale as the inverse of the rate constant based on initial temperature T_1 , namely,

$$t_{\text{reaction}} \propto e^{\frac{E_a}{RT_1}} \quad (7.75)$$

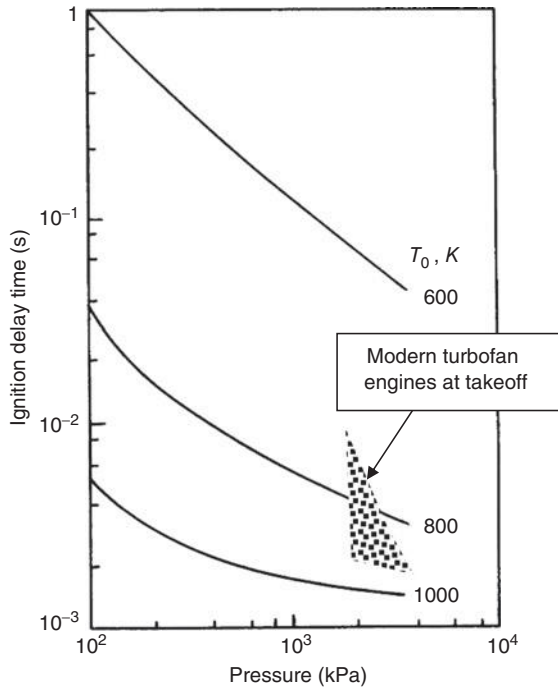
The ignition delay time for a range of initial temperatures between 600 and 1000 K and a range of pressures between 1 and 30 atm is shown in Figure 7.23 (adapted from Rao and Lefebvre, 1981).

Figure 7.23 is a log–log plot. It shows an exponential drop in ignition delay time with initial temperature, as expected from Equation 7.75. The ignition delay time is also reduced with the increase in combustion pressure. This pressure dependence becomes weaker for a high inlet temperature (1000 K) and at a high pressure (30 atm). Interestingly, the conditions of 1000 K inlet temperature and 30 atm combustion pressure are representative of a typical gas turbine engine combustor inlet conditions. Based on these, the ignition delay time is $\sim 1\text{--}2$ ms. From the reaction timescale given by Kerrebrock in Equation 7.78, we may express the pressure dependence of the ignition delay time with an inverse relation, such as

$$t_i \sim \frac{1}{p} \quad (7.76)$$

The results of autoignition delay time studies of Spadaccini (1977) for typical hydrocarbon fuels at elevated temperatures and at the pressure of 10 atm are shown in Figure 7.24 (a log–linear plot). We again observe an exponential drop in ignition time delay with temperature.

■ **FIGURE 7.23**
 Effect of pressure and initial temperature on ignition delay time for a fuel–air mixture with 50 μm mean diameter fuel droplet and $u' = 0.25$ m/s. Source: Adapted from Rao and Lefebvre 1981

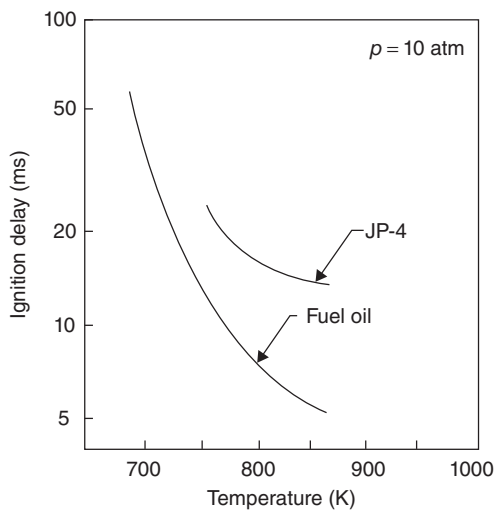


The pressure dependence follows Equation 7.76, or the trends shown by Rao and Lefebvre in Figure 7.23.

7.5.7 Combustion-Generated Pollutants

The subject of pollution is an integral part of the current section, that is, chemical kinetics. However, due to its importance, this subject is presented, in more detail, after the discussion of combustion chambers and afterburners in section 7.7.

■ **FIGURE 7.24**
 Spontaneous ignition delay time as a function of initial temperature at 10 atm pressure. Source: Spadaccini 1977, Fig. 9, p. 86. Reproduced with permission from ASME



7.6 Combustion Chamber

In this section, we explore geometric configurations of combustion chambers that are found in aircraft gas turbine engines. The flammability limits of fuel–air mixtures that we studied in the last section, required a near stoichiometric mixture ratio. To prolong the turbine life, we are forced to reduce the turbine inlet temperature to levels corresponding to an equivalence ratio of $\phi \sim 0.4\text{--}0.5$. Consequently, we have to introduce the combustor inlet air in *stages* along the combustion chamber length. The first stage admits air in a (near) stoichiometric proportion of the injected fuel flow rate. In the first stage, air and fuel mix and chemically react in what is known as the primary zone. In the second stage, air may be used to stabilize the flame of the primary zone. The subsequent stages of air are introduced along the combustor length for dilution and cooling purposes. Proper tailoring of these stages leads to a stable combustion, reduced pollutant formation as well as a combustor exit temperature profile that is reasonably uniform and devoid of hot spots. To reduce the levels of total pressure loss in a combustor, we need to decelerate the flow at the inlet to the combustion chamber. This calls for a prediffuser.

There are two combustor configurations that are in use in aircraft gas turbine engines, namely, the reversed-flow combustor and the straight through flow combustor. Figure 7.25 shows a schematic drawing of a reverse-flow combustor.

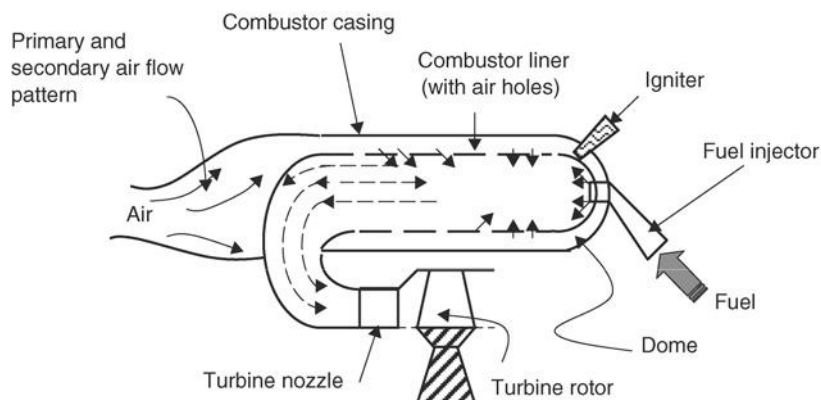
The reverse-flow combustor is best suited for application in small gas turbine engines that utilize centrifugal compressors. The flow turns nearly 180° twice and hence it suffers an added total pressure loss due to turning over a straight through flow burner. The compact design of this burner places the turbine inlet plane near the compressor discharge plane and hence results in a shorter turbine–compressor shaft. Small airbreathing engines for drone applications as well as the early engines (e.g., Whittle engines) utilized this configuration.

A second configuration, which represents most gas turbine engines today, is the straight through flow burner. A schematic drawing of this burner is shown in Figure 7.26.

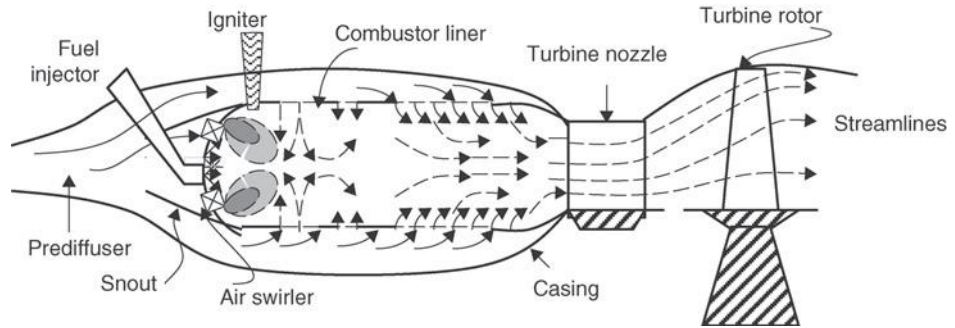
The combustion chamber may be of a single-can-type tubular design, a multican design, a can-annular design, or an annular design. These configurations are shown in Figures 7.27 and 7.28.

The single-can and the multican combustors are heavier than the latter two types of can-annular and annular combustors. The total pressure loss in these combustors is also

■ **FIGURE 7.25**
Reverse-flow
combustor



■ **FIGURE 7.26**
Schematic drawing of a straight through flow burner



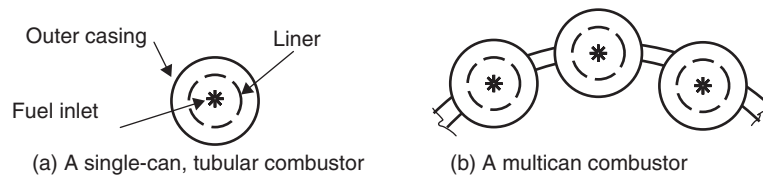
higher than the annular types due to their larger wetted area. However, the advantages of the can type are in their mechanical robustness and their good match with the fuel injector. Coupled with a lower development cost, the single and multican systems were widely used in the early jet engines. Presently, the lowest system weight and size belong to the winner, the annular combustor, which also offers the lowest total pressure drop. The annular combustor, due to its open architecture between the fuel injectors, is more susceptible to combustion and cross-coupling-related instabilities than its counterparts with their confined configurations.

It is of critical importance to combustion system designers to understand the total pressure loss mechanisms in a combustor.

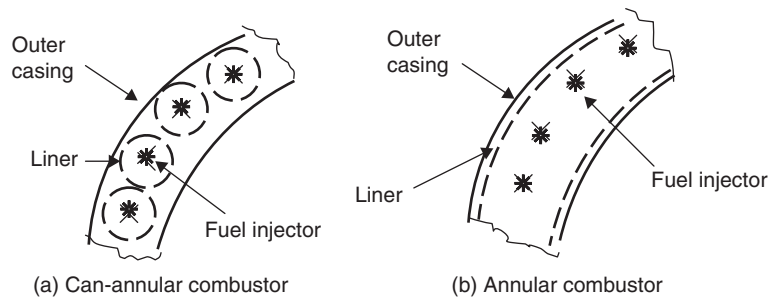
7.6.1 Combustion Chamber Total Pressure Loss

The total pressure loss in a combustor is predominantly due to two sources. The first is due to the frictional loss in the viscous layers where we can lump in the mixing loss of the fuel and air streams prior to chemical interaction. The second source is due to heat release in an exothermic chemical reaction in the burner. The first is usually modeled as the “cold” flow loss and the second is the “hot” flow loss. We recognize, however, that the subdivision of the losses into “cold” and “hot” is artificial and the two forms of

■ **FIGURE 7.27**
Single-can, tubular, and multican combustor configurations



■ **FIGURE 7.28**
Annular combustor configurations



total pressure loss occur simultaneously and interact in a complex way. But throughout the ages, engineering is practiced through the art of simplification, that is, engineers have broken down a complex problem into a series of elementary and solvable problems and then tried to predict the solution of the complex problem by devising a correlation between the elementary solutions and the observation or measurement. We intend to stay our engineering course on the topic of combustion chamber total pressure loss. There are several methods of quantifying the total pressure loss in a combustor, namely,

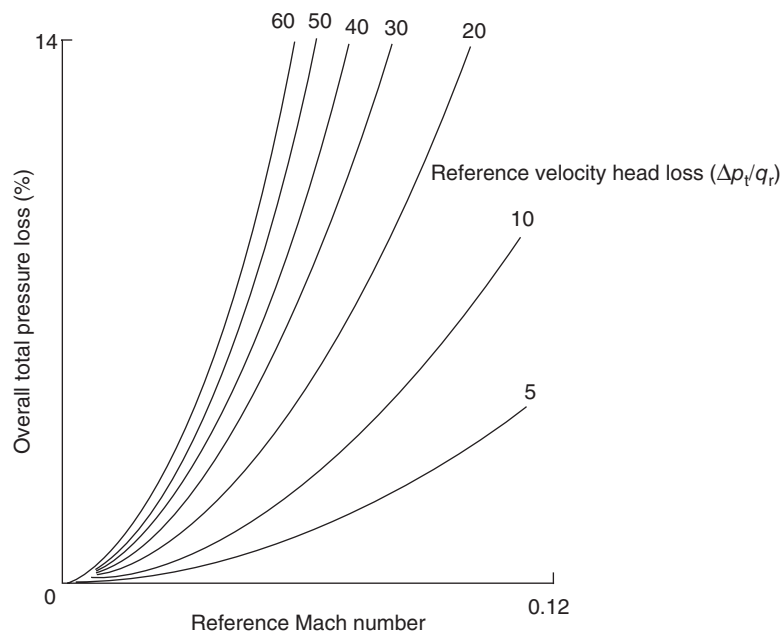
$$(a) \frac{p_{t3} - p_{t4}}{p_{t3}} \text{ (Relative to the inlet total pressure)} \quad (7.77)$$

$$(b) \frac{p_{t3} - p_{t4}}{q_3} \text{ (Relative to the inlet dynamic pressure)} \quad (7.78)$$

$$(c) \frac{p_{t3} - p_{t4}}{q_r} \text{ (Relative to a reference dynamic pressure)} \quad (7.79)$$

The first expression is the overall total pressure loss ratio, the second expression is a measure of the total pressure loss in terms of the inlet dynamic pressure, and the last expression uses a reference velocity for the dynamic pressure and measures the total pressure loss in terms of the reference dynamic pressure. The reference velocity is the mass averaged gas speed at the largest cross-section of the burner, based on the combustor inlet pressure and temperature. The reference Mach number is the ratio of the reference speed to the speed of sound at the prediffuser inlet a_3 . All the aerodynamic losses scale with reference dynamic pressure, as shown in Figure 7.29 (from Henderson and Blazowski, 1989).

■ **FIGURE 7.29**
Percentage total pressure loss in a combustor. Source: Henderson and Blazowski 1989. Reproduced with permission from AIAA



A parabolic dependence of the total pressure loss on the reference Mach number is shown in Figure 7.29. Kerrebrock suggests an empirical rule for the combustor total pressure ratio, as a fraction of reference dynamic pressure. In terms of the average Mach number of the gases in the burner, M_b , Kerrebrock's empirical rule is stated as

$$\pi_b \approx 1 - \epsilon \left(\frac{\gamma}{2} \right) M_b^2 \quad (7.80)$$

where $1 < \epsilon < 2$.

This equation states that the total pressure loss is proportional to an “average” dynamic pressure of the gases in the combustor, with the proportionality constant ϵ . We note that the total pressure loss grows as the mean flow speed increases. Now, we appreciate the role of prediffuser in a combustion chamber. The total pressure loss due to combustion that is, heat release, in the burner may be modeled by a Rayleigh flow analysis. The conservation of mass and momentum for a constant-area frictionless duct are

$$\rho_3 u_3 = \rho_4 u_4 \quad (7.81)$$

$$p_3 + \rho_3 u_3^2 = p_4 + \rho_4 u_4^2 \quad (7.82)$$

Now, instead of the compressible equation for the total pressure involving Mach number, we may use the low-speed version in an approximation, that is, the Bernoulli equation, namely,

$$p_{t3} - p_{t4} \approx p_3 + \frac{1}{2} \rho_3 u_3^2 - p_4 - \frac{1}{2} \rho_4 u_4^2 = (p_3 + \rho_3 u_3^2) - (p_4 + \rho_4 u_4^2) - \frac{1}{2} (\rho_3 u_3^2 - \rho_4 u_4^2) \quad (7.83)$$

Canceling the first two parentheses via momentum Equation 7.82, and using the continuity equation we may simplify Equation 7.83 as

$$[p_{t3} - p_{t4}] / q_3 \approx [\rho_4 u_4^2] / [\rho_3 u_3^2] - 1 = [\rho_3 / \rho_4] - 1 \quad (7.84)$$

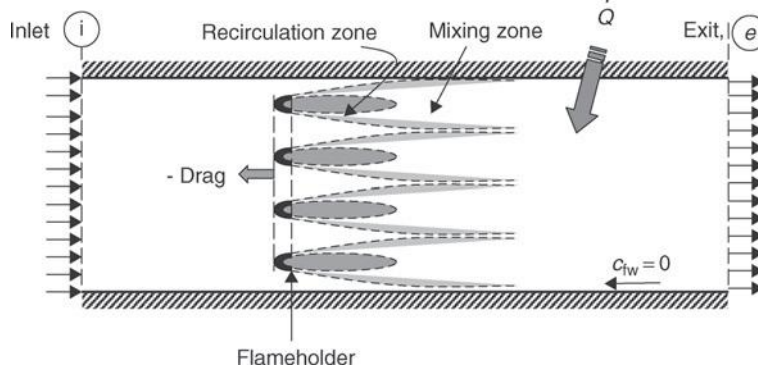
Now, using the perfect gas law for the density ratio and neglecting static pressure changes between the inlet and exit of the burner in favor of the large temperature rise across the combustor, we may write the following simple expression for the total pressure loss due to heating in a constant-area burner as

$$[p_{t3} - p_{t4}] / q_3 \approx T_4 / T_3 - 1 \quad (7.85)$$

In deriving the above expression, we made a series of approximations and simplifications. Consequently, we may use Equation 7.85 in relative terms, for example, in describing the effect of the throttle setting (T_4) on the variation of (hot) total pressure loss in a burner. Lefebvre (1983) suggests a correlation based on the Equation 7.85 that involves two unknown coefficients, K_1 and K_2 , as

$$[(\Delta p_t)_{\text{hot}}] / q_{\text{ref}} = K_1 (T_4 / T_3 - K_2) \quad (7.86)$$

■ **FIGURE 7.30**
Control volume for the
estimation of total
pressure loss in an
afterburner



The correlation coefficients K_1 and K_2 need to be established experimentally. This is another example of a simple model (Equation 7.85) that is the basis of an engineering correlation for a complex problem. The total pressure loss due to combustion is small compared with aerodynamic losses, namely,

$$[(\Delta p_t)_{\text{hot}}] / p_{t3} \approx 0.5 - 1.0\%$$

The cold total pressure loss is in the range of $\sim 4-7\%$, that is,

$$[(\Delta p_t)_{\text{cold}}] / p_{t3} \approx 4 - 7\%$$

In an afterburner, the process of flame stabilization is achieved via flameholders, as described earlier, that creates massively separated wakes and is responsible for the bulk of the total pressure loss. We model an afterburner as a constant-area duct with a series of bluff bodies in the stream with a known drag coefficient. The diagram that describes the problem is shown in Figure 7.30.

We may account for the wall friction in the momentum balance equation either directly or we may combine its overall drag contribution with the flameholder drag. The effect of combustion on total pressure loss is important and will be investigated later in this section.

First, we model the afterburner-off condition, which is known as the “dry” analysis of the engine. The “wet” mode analysis follows the “dry” mode in this section.

From continuity equation we have

$$\rho_e u_e = \rho_i u_i \quad (7.87)$$

The fluid momentum equation in the streamwise direction gives

$$\rho_e u_e^2 - \rho_i u_i^2 = p_i - p_e - \frac{D_{\text{flameholder}}}{A} \quad (7.88)$$

We define the flameholder drag in terms of the duct cross-sectional area A as

$$D_{\text{flameholder}} \equiv C_D \cdot q_i \cdot A \quad (7.89)$$

Rearranging the terms of the momentum equation, we get

$$p_e(1 + \gamma_e M_e^2) = p_i \left[1 + \gamma_i M_i^2 \left(1 - \frac{C_D}{2} \right) \right] \quad (7.90)$$

Therefore, the static pressure ratio is expressed in terms of the inlet and exit Mach numbers and the flameholder drag coefficient C_D as

$$\frac{p_e}{p_i} = \frac{1 + \gamma_i M_i^2 \left(1 - \frac{C_D}{2} \right)}{1 + \gamma_e M_e^2} \quad (7.91)$$

From the continuity equation, we express the density ratio in terms of the velocity ratio and then we replace the gas speed by the product of Mach number and the speed of sound to get

$$\frac{\rho_e}{\rho_i} = \frac{u_i}{u_e} = \frac{M_i}{M_e} \sqrt{\frac{(\gamma_i - 1)c_{pi}T_i}{(\gamma_e - 1)c_{pe}T_e}} \quad (7.92)$$

We use the energy equation for an adiabatic process, which is a statement of the conservation of total enthalpy, to get the static temperature ratio, namely,

$$\frac{c_{pe}T_e}{c_{pi}T_i} = \frac{1 + \frac{\gamma_i - 1}{2}M_i^2}{1 + \frac{\gamma_e - 1}{2}M_e^2} \quad (7.93)$$

By invoking the perfect gas law, we link the static pressure, density, and temperature ratios of the gas at the inlet and exit of the duct as

$$\frac{p_e}{p_i} = \frac{R_e}{R_i} \frac{\rho_e}{\rho_i} \frac{T_e}{T_i} \quad (7.94)$$

Now, all the ratios in Equation 7.94 are expressed in terms of the inlet and exit Mach numbers and gas properties. Hence, for a known inlet condition, we may use this equation to establish the exit Mach number M_e . Let us substitute expressions 7.91, 7.92, and 7.93 in Equation 7.94 to get the desired equation involving one unknown M_e ,

$$\frac{1 - \gamma_i M_i^2 \left(1 - \frac{C_D}{2} \right)}{1 + \gamma_e M_e^2} = \frac{R_e}{R_i} \frac{M_i}{M_e} \sqrt{\frac{(\gamma_i - 1) \left(\frac{1 + \frac{\gamma_e - 1}{2}M_e^2}{1 + \frac{\gamma_i - 1}{2}M_i^2} \right) c_{pi}}{(\gamma_e - 1) \left(\frac{1 + \frac{\gamma_i - 1}{2}M_i^2}{1 + \frac{\gamma_e - 1}{2}M_e^2} \right) c_{pe}}} \left(\frac{1 + \frac{\gamma_i - 1}{2}M_i^2}{1 + \frac{\gamma_e - 1}{2}M_e^2} \right) \quad (7.95)$$

We may simplify the above equation by combining the gas properties and the last two brackets, to get

$$\frac{1 + \gamma_i M_i^2 \left(1 - \frac{C_D}{2}\right)}{1 + \gamma_e M_e^2} = \frac{\gamma_i M_i}{\gamma_e M_e} \sqrt{\left(\frac{\gamma_e - 1}{\gamma_i - 1}\right) \left(\frac{1 + \frac{\gamma_i - 1}{2} M_i^2}{1 + \frac{\gamma_e - 1}{2} M_e^2}\right)} \quad (7.96)$$

Fortunately, Equation 7.96 is a quadratic equation for M_e with a closed form solution, that is, no iteration is needed. Therefore the exit Mach number is

$$M_e^2 = \frac{2(\gamma_e - 1) - \gamma_e A^2 + \sqrt{(\gamma_e A^2 - 2\gamma_e + 2)^2 + 2(\gamma_e - 1)^2 (A^2 - 2)}}{(\gamma_e - 1)(A^2 - 2)} \quad (7.97)$$

where

$$A = \left(\frac{1 + \gamma_i M_i^2 \left(1 - \frac{C_D}{2}\right)}{\gamma_i M_i} \right) \sqrt{\frac{\gamma_i - 1}{1 + \frac{\gamma_i - 1}{2} M_i^2}} \quad (7.98)$$

With exit Mach number known, we may substitute it in Equation 7.91 to get the static pressure ratio, and the total pressure ratio is then calculated by

$$\frac{p_{te}}{p_{ti}} = \frac{p_e}{p_i} \frac{\left(1 + \frac{\gamma_e - 1}{2} M_e^2\right)^{\frac{\gamma_e}{\gamma_e - 1}}}{\left(1 + \frac{\gamma_i - 1}{2} M_i^2\right)^{\frac{\gamma_i}{\gamma_i - 1}}} = \frac{1 + \gamma_i M_i^2 \left(1 - \frac{C_D}{2}\right)}{1 + \gamma_e M_e^2} \frac{\left(1 + \frac{\gamma_e - 1}{2} M_e^2\right)^{\frac{\gamma_e}{\gamma_e - 1}}}{\left(1 + \frac{\gamma_i - 1}{2} M_i^2\right)^{\frac{\gamma_i}{\gamma_i - 1}}} \quad (7.99)$$

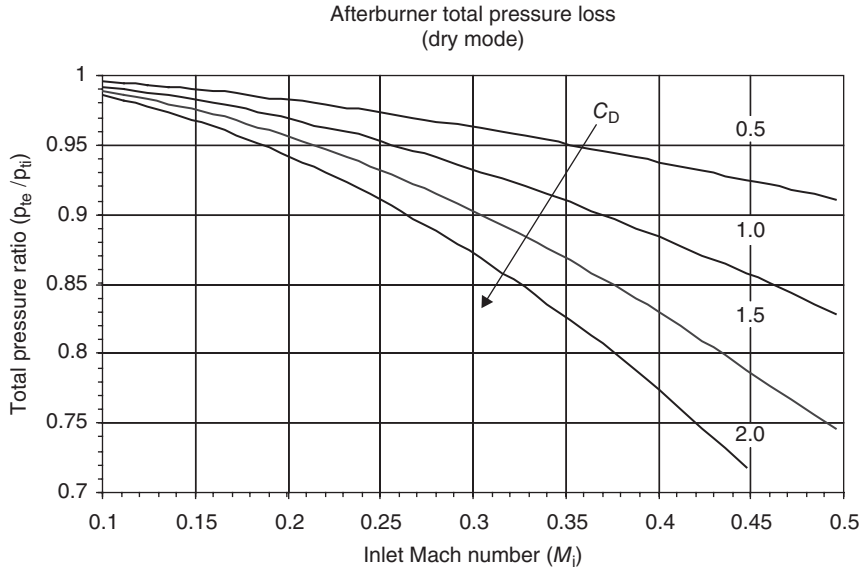
Now we may graph the total pressure loss, due to flameholder drag, across the afterburner, as a function of inlet Mach number and gas properties at the inlet and exit.

Figure 7.31 shows the aerodynamic impact of flameholder drag on afterburner total pressure loss. The importance of low inlet Mach number to the afterburner may also be discerned from this figure. The penalty for a high inlet Mach number (of say ~ 0.5) is severe and thus the necessity of a pre-diffuser becomes evident. The presence of aerodynamic drag in the afterburner causes the exit Mach number to increase and approach a choked, that is, $M_e = 1$, state. Frictional choking in the afterburner is to be avoided since combustion also tends to increase the Mach number, as in Rayleigh flow. A graph of the exit Mach number as a function of inlet Mach number and the flameholder drag coefficient is shown in Figure 7.32.

The flameholder drag coefficient in our analysis was defined based on the afterburner cross-sectional area. However, the drag coefficient of bluff bodies is defined based on the maximum cross-sectional area of the bluff body. Therefore,

$$D_{\text{afterburner}} \equiv C_D \text{ bluff-body} \cdot q_\infty A_{\text{max}} \cdot N = C_D \cdot q_i A_{\text{afterburner}} \quad (7.100)$$

■ **FIGURE 7.31**
 Afterburner total pressure loss due to flameholder drag ($\gamma_i = 1.33, \gamma_e = 1.30$)



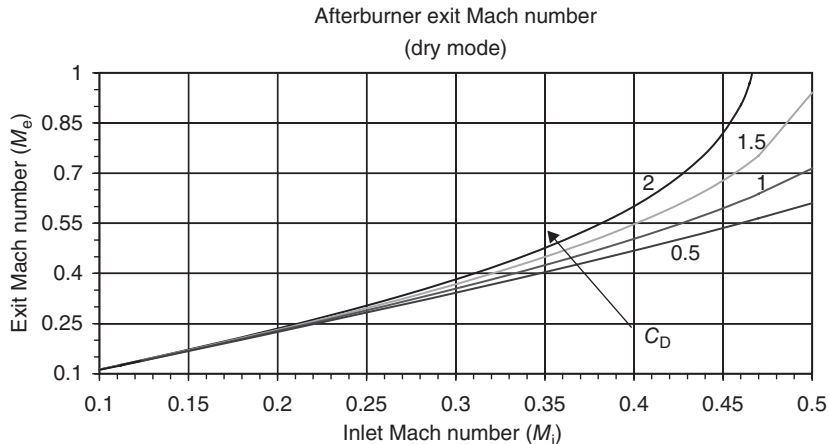
where the A_{max} is the base area of an individual bluff body and N is the number of bluff bodies used in the flameholder arrangement, typically in the form V-gutter rings and radial V-gutter connectors. We may define a flameholder blockage area ratio as

$$\text{Blockage} \equiv B \equiv \frac{N \cdot A_{max}}{A_{afterburner}} \tag{7.101}$$

Therefore, the drag coefficient used in our afterburner total pressure loss calculation is related to the individual drag coefficients via the blockage factor, that is,

$$C_D = B \cdot C_{D \text{ bluff-body}} \tag{7.102}$$

■ **FIGURE 7.32**
 Frictional choking of afterburner caused by flameholder drag ($\gamma_i = 1.33, \gamma_e = 1.30$)



■ **FIGURE 7.33**
Schematic drawing of
the afterburner duct
and the flameholder
rings

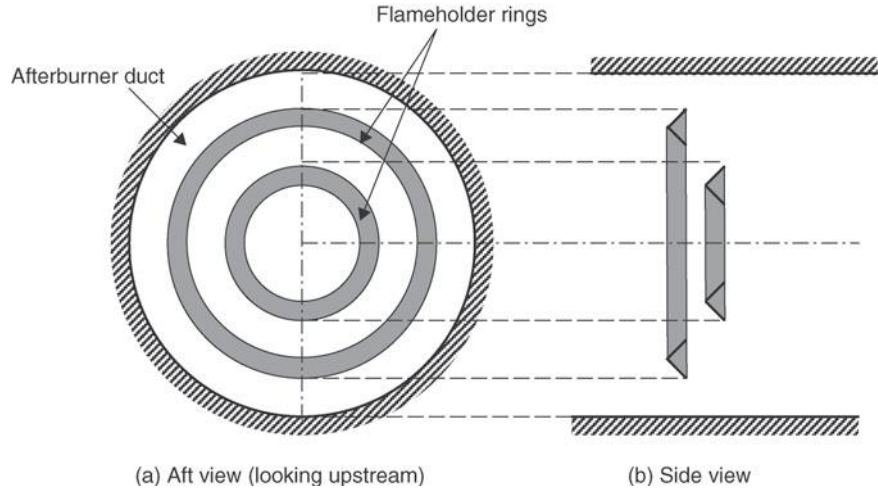


Figure 7.33 serves as a definition sketch for the afterburner duct, and the flameholder rings that contribute to the blockage parameter B . Here the radial gutters that connect the V-gutter rings to the turbine exit diffuser cone or the casing are not shown. The EJ200 of Eurojet Consortium uses radial gutters (instead of rings) for flame holding (Figure 7.47).

To account for higher flow velocities in the plane of the flameholder, due to flameholder blockage, the drag coefficient needs to be scaled by the dynamic pressure ratio, that is,

$$C_D = B \cdot \frac{\rho_{fh} V_{fh}^2}{\rho_i V_i^2} \cdot C_{D \text{ bluff-body}} \approx B \left(\frac{V_{fh}}{V_i} \right)^2 \cdot C_{D \text{ bluff-body}} \approx B \left(\frac{V_{fh}}{V_i} \right)^2 \quad (7.103)$$

where subscript “fh” identifies the plane of the flameholder and the bluff body drag coefficient (e.g., a V-gutter) was assumed to be ~ 1 . Note that a flat plate, in broadside, creates a drag coefficient of 2 and a cylinder in cross flow ~ 1.2 (both flows at a Reynolds number based on plate height or cylinder diameter of 100,000).

The analysis of an afterburner in the “wet” mode differs from the “dry” mode only in its energy balance equation, namely,

$$(1 + f_{AB})c_{pe}T_{te} - c_{pi}T_{ti} = f_{AB}Q_R\eta_{AB} \quad (7.104)$$

By neglecting the fuel-to-air ratio in the afterburner in favor of 1 on the left-hand side of the energy equation and renaming the product term on the RHS as “ q ,” we get

$$\frac{c_{pe}T_{te}}{c_{pi}T_{ti}} \cong 1 + \frac{q}{c_{pi}T_{ti}} \quad (7.105)$$

We may relate the static enthalpy ratio to the stagnation enthalpy and Mach number as

$$\frac{c_{pe}T_e}{c_{pi}T_i} = \left(1 + \frac{q}{c_{pi}T_i}\right) \frac{1 + \frac{\gamma_i - 1}{2}M_i^2}{1 + \frac{\gamma_e - 1}{2}M_e^2} \tag{7.106}$$

By replacing Equation 7.93 with the above equation, and proceeding with the substitution of the static pressure ratio and density ratio in the perfect gas law, we obtain

$$\frac{1 + \gamma_i M_i^2 \left(1 - \frac{C_D}{2}\right)}{1 + \gamma_e M_e^2} = \frac{\gamma_i M_i}{\gamma_e M_e} \sqrt{\left(\frac{\gamma_e - 1}{\gamma_i - 1}\right) \left(1 + \frac{q}{c_{pi}T_i}\right) \left(\frac{1 + \frac{\gamma_i - 1}{2}M_i^2}{1 + \frac{\gamma_e - 1}{2}M_e^2}\right)} \tag{7.107}$$

Again, the above expression involves one unknown, that is, M_e , and is fortunately a quadratic equation with the following closed form solution:

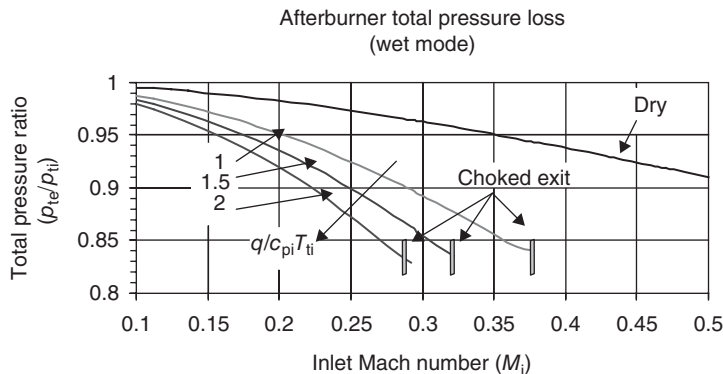
$$M_e^2 = \frac{2(\gamma_e - 1) - \gamma_e A^2 + \sqrt{(\gamma_e A^2 - 2\gamma_e + 2)^2 + 2(\gamma_e - 1)^2(A^2 - 2)}}{(\gamma_e - 1)(A^2 - 2)} \tag{7.108}$$

where

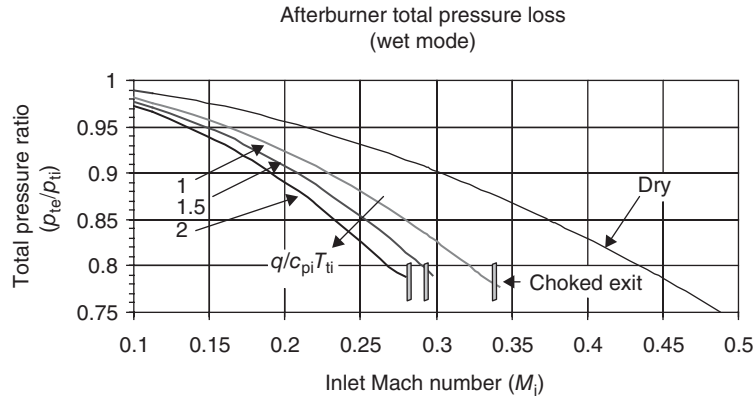
$$A = \left(\frac{1 + \gamma_i M_i^2 \left(1 - \frac{C_D}{2}\right)}{\gamma_i M_i}\right) \sqrt{\frac{\gamma_i - 1}{1 + \frac{\gamma_i - 1}{2}M_i^2} \left(\frac{1}{1 + \frac{q}{c_{pi}T_i}}\right)} \tag{7.109}$$

Now, let us graph the total pressure loss in an afterburner in the wet mode (sometimes referred to as the *reheat* mode), using the above solution for the exit Mach number. Figure 7.34 shows the afterburner total pressure loss increases with heat release in the combustor. We also note that the choked exit condition is reached at a relatively low inlet Mach number of <0.4. Higher heating levels and flameholder drag coefficients will result

■ **FIGURE 7.34**
Afterburner total pressure loss variation with inlet Mach number and heat release ($\gamma_i = 1.33$, $\gamma_e = 1.30$, $C_D = 0.5$)



■ **FIGURE 7.35**
Afterburner total pressure loss with heat release and a higher flameholder drag ($\gamma_i = 1.33$, $\gamma_e = 1.30$, $C_D = 1.5$)



in earlier choking than shown in Figure 7.34. Thus, the necessity of decelerating the flow entering an afterburner is again evident from Figure 7.34.

We produce Figure 7.35 to demonstrate the effect of higher flameholder drag coefficient on the afterburner wet mode total pressure loss, and the inlet Mach number range that leads to exit choking. Based on these results, an inlet's Mach number range of ~ 0.2 – 0.25 is desirable for an afterburner.

7.6.2 Combustor Flow Pattern and Temperature Profile

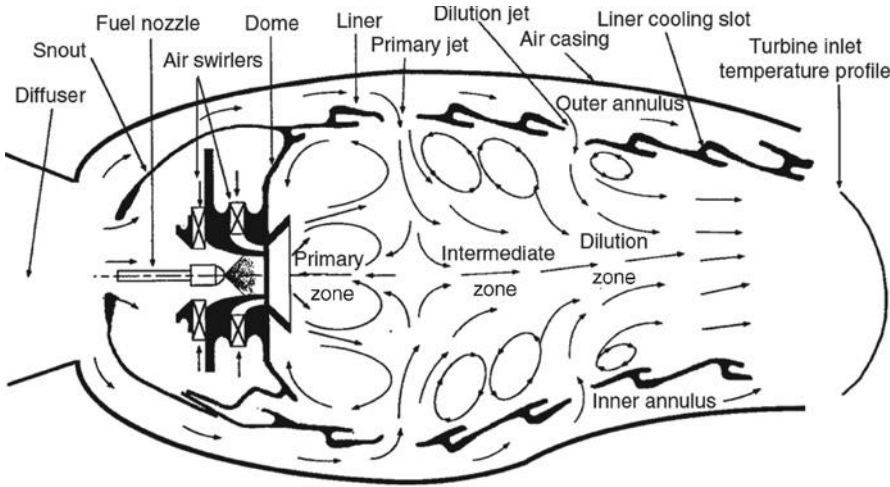
A typical flow pattern in a primary burner is demonstrated in Figure 7.36a (from Tacina, 2000), which shows the burner primary zone, intermediate zone, and the dilution zone in an annular combustor. We have already discussed the primary zone in the context of flammability, flame stability, and stoichiometry. The primary air jets in opposing radial directions are also introduced to stabilize the flame and increase combustor efficiency/heat release rate. The role of intermediate zone is seen as an extension of the primary zone in achieving a complete combustion/controlling pollutant formations, and the dilution zone is seen as producing a desired turbine inlet temperature profile, as shown in Figure 7.36a. Airflow distribution in a modern combustor is shown in Figure 7.36b.

The temperature profile at the turbine inlet exhibits nonuniformity due to the number of fuel injectors used in the circumferential direction, the nonuniformity in dilution air cooling and mixing characteristics as well as other secondary flow patterns and instabilities that are set up in the burner. These spatial nonuniformities at combustor exit are described by two nondimensional parameters, the pattern factor and the profile factor.

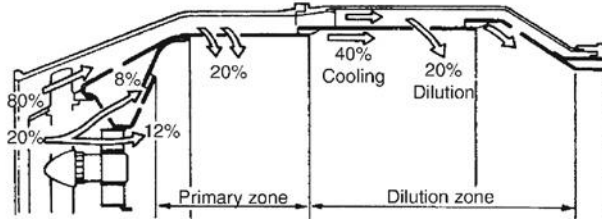
Pattern factor

$$\text{PF} \equiv \frac{T_{t-\max} - T_{t-\text{avg}}}{T_{t-\text{avg}} - T_{t-\text{in}}} \quad (7.110)$$

where $T_{t-\max}$ is the absolute maximum exit temperature in the circumferential and radial directions, $T_{t-\text{avg}}$ is the average of the exit temperature, and $T_{t-\text{in}}$ is the average inlet total temperature. Since the nonuniformity parameter in the numerator of Equation 7.110 is the absolute maximum of the exit temperature (i.e., the absolute peak), this parameter is also known as the peak temperature factor. Turbine nozzle is exposed to this nonuniformity.



(a) A representative flow pattern in an annular combustor with double air swirler.
Source: Tacina 2000



(b) Combustor flow distribution.
Source: Reproduced with permission from Rolls-Royce plc.

■ FIGURE 7.36 Flow distribution and pattern in modern combustors

The desired range of this parameter is between 0.15 and 0.25 in modern high-temperature rise combustors.

Profile factor

$$P_f \equiv \frac{T_{t-max-avg} - T_{t-in}}{T_{t-avg} - T_{t-in}} \tag{7.111}$$

where $T_{t-max-avg}$ is the circumferential average of the maximum temperature, that is, the average of all the local peaks in the circumferential direction. Since the flow acceleration in the turbine nozzle reduces the temperature distortion levels, the turbine rotor that follows the nozzle is exposed to this nonuniformity. The range of this parameter is between 1.04 and 1.08.

REMARKS Flow acceleration dampens nonuniformity in the flow, whereas flow deceleration amplifies distortion. Therefore, the temperature distortion at the turbine inlet is reduced after the nozzle. By the same token, the flow distortion in the inlet diffuser or in the compressor blades is amplified. All engineers dealing with fluid flow problems should know this principle. The proof of this principle is very simple using a parallel flow model (see Problem 7.22).

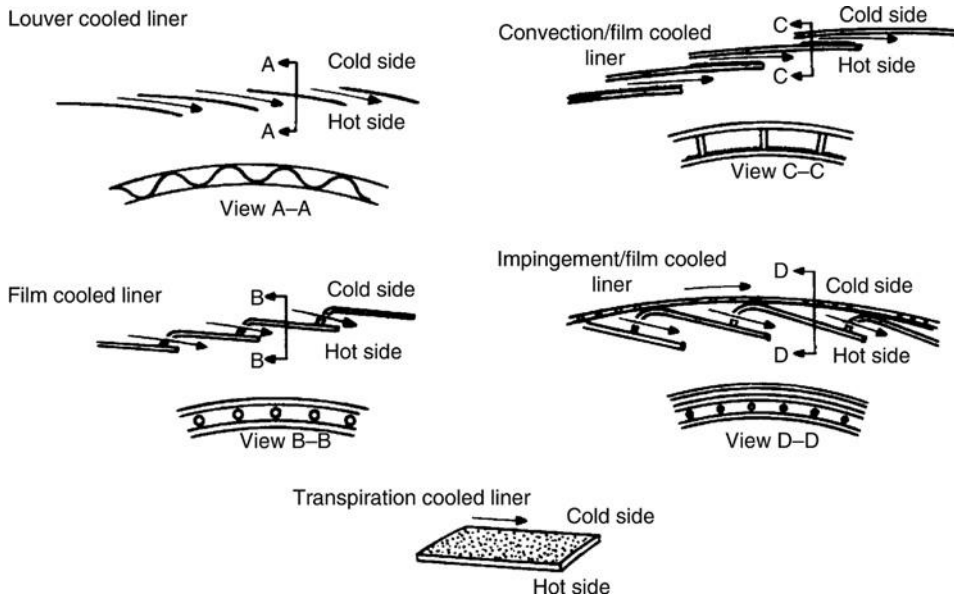
7.6.3 Combustor Liner and Its Cooling Methods

Combustion takes place inside a combustor liner. It consists of a dome in the primary zone, primary air holes for the primary (radial) jets, air holes for the intermediate zone (radial jets), and the cooling holes/slots in the dilution zone. The combustion temperature may exceed 2500 K (in the primary zone), whereas the liner temperature needs to be kept at ~ 1200 K. The heat transfer to the liner from the combustion side is in the form of radiation and convective heating by the hot combustion gases. The conventional cooling techniques used in gas turbine engines are

1. Convective cooling
2. Impingement cooling
3. Film cooling
4. Transpiration cooling
5. Radiation cooling
6. Some combination of the above.

The convective cooling method is primarily used in cooled turbine blades with the philosophy of *maximizing* the heat transfer rate from a hot wall (gas side) to the coolant inside the blade. The coolant may also impinge on a hot surface to create a stagnation point and hence enhance the heat transfer to the coolant through the wall. The impingement cooling method is often used in the leading-edge cooling of turbine blades. The film cooling method operates on the principle of *minimizing* heat transfer to the wall from the hot gases by providing a protective cool layer on the hot surface. The cool layer acts like a “blanket” that protects the surface from the hot gases. In film cooling, the coolant is injected through a series of discrete fine film holes, at a slanted angle to the flow direction, and emerges on the hot side to provide the protective cooling layer. Note that the philosophy of film cooling to minimize heat transfer to a wall is different from that of convective cooling, which maximizes the heat transfer through a wall. The transpiration cooling calls for a porous surface where the coolant emerges on the hot gas side through the pores. The cooling protection that it provides is similar to the film cooling technique, that is, by *blanketing* the surface with a coolant layer. Transpiration cooling may be viewed as the ultimate film cooling in the limit of infinitely many and continuously distributed film holes on a surface. Finally, the radiation cooling accompanies all surfaces above the absolute zero temperature. The radiation cooling of the liner to the outer casing, however, represents only a small fraction of the overall heat transfer of the liner. We shall discuss these in the context of cooled turbine blades and shrouds in more detail in Chapter 10.

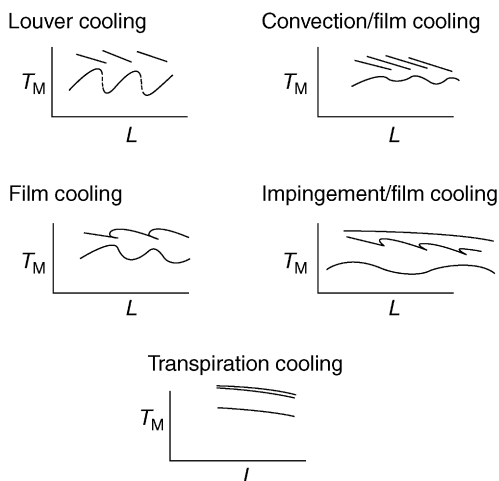
The availability of excess air at the burner inlet dominates the application of these heat transfer techniques to a combustor liner. The primary and the intermediate zone air holes are designed to provide combustion stability and maximizing the chemical reaction heat release. The remaining air, which may be about 15–30% of the combustor inlet flow, is used to provide a reliable and uniform cooling protection to the liner. A successively more sophisticated technique of liner cooling is shown in Figures 7.37 and 7.38 (from Henderson and Blazowski, 1989). Starting from the *lower* cooling with the problems of uniform coolant distribution and control that marked the early combustor development to the most sophisticated *transpiration* cooling are schematically shown in Figure 7.37.



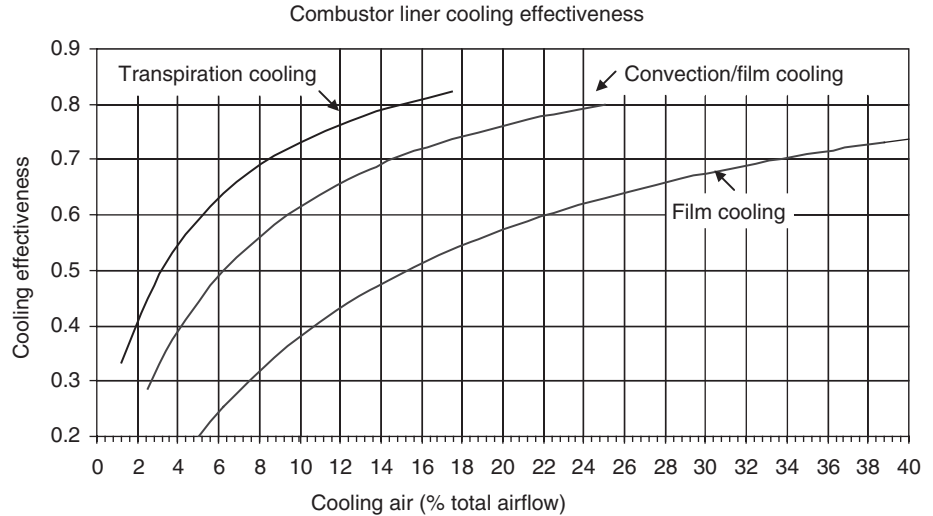
■ **FIGURE 7.37** Combustor liner cooling methods. Source: Henderson and Blazowski 1989. Reproduced with permission from AIAA

The coolant mass flow requirement is diminished with cooling effectiveness. Simple film cooling, convection/film, impingement/film, and the transpiration cooling are ranked from the highest to the lowest coolant requirement, respectively. The film cooling method eliminates the problem of coolant injection uniformity and control that was shown by louver technique. The combination convection/film and impingement/film cooling techniques offer a further enhancement of cooling effectiveness of the combustor liner. The transpiration cooling through a porous liner minimizes the coolant flow requirement and offers the most uniform wall temperature distribution (Figure 7.38). The problem of pore clogging, however, poses a challenge in transpiration cooling.

■ **FIGURE 7.38** Combustor liner cooling techniques. Source: Henderson and Blazowski 1989. Reproduced with permission from AIAA



■ **FIGURE 7.39**
Combustor liner
cooling effectiveness.
Source: Adapted from
Nealy and Reider 1980



To quantify the coolant mass flow requirement, we define a cooling effectiveness parameter Φ according to

$$\Phi \equiv \frac{T_g - T_w}{T_g - T_c} \quad (7.112)$$

The cooling effectiveness is the ratio of two temperature differentials. The numerator is the difference between the hot gas T_g and the desired (average) wall temperature T_w . The denominator represents the absolute maximum potential for wall cooling. Therefore, the cooling effectiveness Φ is the fraction of the absolute maximum cooling potential that is realized in the wall cooling process. The hot gas in this application is the combustion temperature (T_g) or sometimes referred to as the flame temperature, and the coolant is the compressor discharge temperature (T_c). The desired wall temperature T_w is dictated by the wall material properties and durability requirements (e.g., 18,000 or 20,000-hr life). The variation of cooling effectiveness with coolant flow is shown in Figure 7.39 (data from Nealy and Reider, 1980).

In future advanced gas turbine engines, the combustor temperature may reach ~ 2500 K (near the maximum adiabatic flame temperature of hydrocarbon fuels), with a desired liner temperature of ~ 1200 K and a compressor discharge temperature of 900 K, the cooling effectiveness is then 0.8125. In examining Figure 7.39, we note that a film-cooled liner may not reach this desired level of cooling effectiveness, regardless of percentage coolant available. On the contrary, this level of cooling effectiveness represents the maximum possible limit of the transpiration cooling at close to 18% coolant availability/usage. Application of a thin layer of refractory material such as a ceramic coating lowers the heat transfer to the wall and thus allows a higher operating temperature in the combustor. To tolerate a higher heat release level in an advanced combustor, the liner material needs to tolerate higher operating temperatures and require less (to no) cooling percentage. In addition to operating at high temperatures, the liner material has to be oxidation resistant. Refractory metals such as molybdenum and tungsten suffer in this regard. A promising new liner material is the ceramic matrix composite (CMC).

Development of prototype CMC combustor liner has been approached in industry by using silicon carbide fiber reinforced silicon carbide (SiC/SiC). The use of advanced composite materials as combustor liners represents a challenge in manufacturing, scaling up, life prediction, damage tolerance, reparability characteristics and cost.

7.6.4 Combustion Efficiency

Combustion efficiency measures the actual rate of heat release in a burner and compares it with the theoretical heat release rate possible. The theoretical heat of reaction of the fuel assumes a complete combustion with no unburned hydrocarbon fuel and no dissociation of the products of combustion. The actual heat release is affected by the quality of fuel atomization, vaporization, mixing, ignition, chemical kinetics, flame stabilization, intermediate air flow, liner cooling, and, in general, the aerodynamics of the combustor. Here a variety of timescales as in residence time, chemical reaction/reaction rate timescales, spontaneous ignition delay time that includes vaporization timescale, among other time constants enter the real combustion problem. The unburned hydrocarbon (UHC) and carbon monoxide (CO) that contribute to combustor inefficiency are also among the combustion-generated pollutants. The allowable levels of these pollutants in aircraft gas turbine engine emissions, regulated by the U.S. Environmental Protection Agency (EPA), place a 99% combustion efficiency demand on the combustor.

For a gas turbine combustor, when chemical kinetics is the limiting factor in combustor performance, Lefebvre (1959, 1966) introduces a combustor loading parameter (CLP) θ , which correlates well with combustion efficiency. θ parameter is defined as

$$\text{CLP} = \theta = \frac{p_{t3}^{1.75} A_{\text{ref}} H \cdot e^{\frac{T_{t3}}{b}}}{\dot{m}_3} \quad (7.113)$$

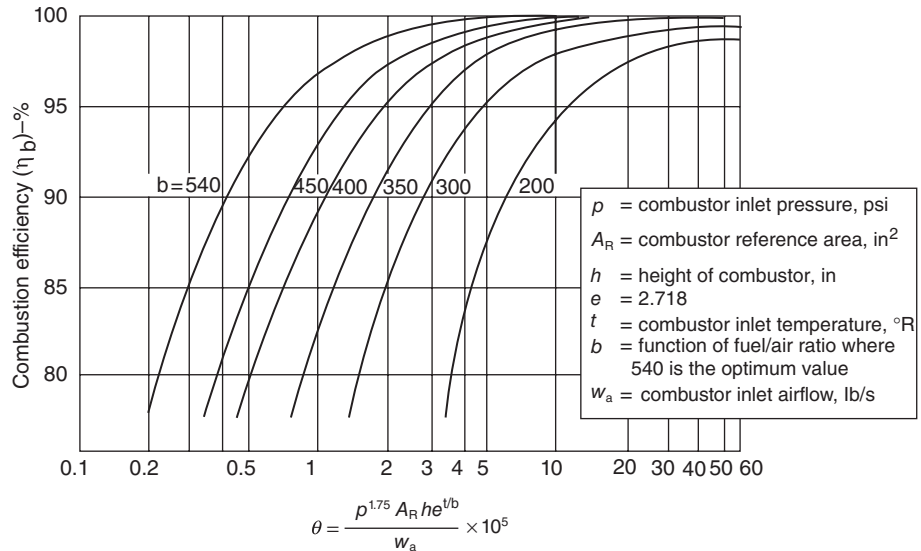
The combustor inlet pressure, temperature, and mass flow rate are p_{t3} , T_{t3} , and \dot{m}_3 , respectively, maximum cross-sectional area of the burner is defined as A_{ref} , the combustor height is H and b is a reaction rate parameter. The dependence of the reaction rate parameter b on the primary zone equivalence ratio ϕ is estimated by Herbert (1957) to be

$$b = 382 \left(\sqrt{2} \pm \ln \frac{\phi}{1.03} \right) \quad [(+) \text{ for } \phi < 1.03, (-) \text{ for } \phi > 1.03] \quad (7.114)$$

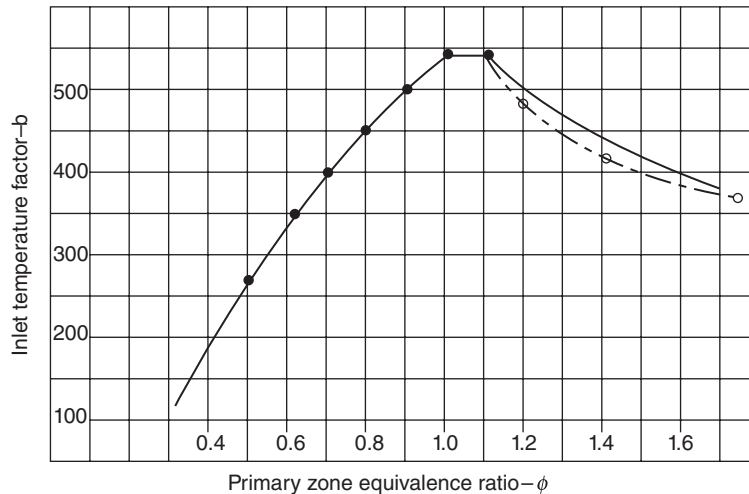
These expressions are plotted in Figure 7.40 (from Henderson and Blazowski, 1989). Note that dimensions of the parameters used in Figure 7.40a are in English units, as described in the definition box in the graph.

The lowest combustion efficiency is, of course, zero in the flameout limit. This could happen at a high altitude when the low combustor pressure in essence slows the reaction rate to a halt ($\tau_{\text{residence}} \ll \tau_{\text{reaction}}$). The graphical correlations used in the combustion efficiency Figure 7.40 are then used to size the combustor in conditions corresponding to high altitude (for a reflight requirement) assuming a combustor efficiency of 80%.

■ **FIGURE 7.40**
 Combustion efficiency correlation based on Lefebvre θ parameter.
 Source: Henderson and Blazowski 1989.
 Reproduced with permission from AIAA



(a) A correlation of combustion efficiency



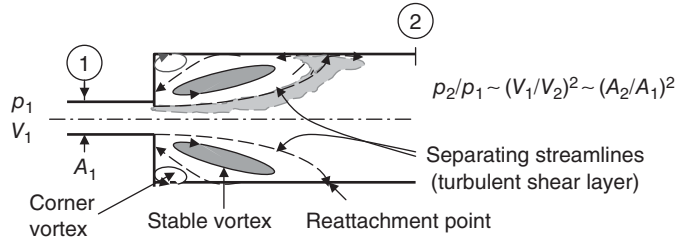
(b) Variation of reaction rate parameter b with the equivalence ratio in the primary zone

7.6.5 Some Combustor Sizing and Scaling Laws

The engine size, that is, the core (air) mass flow rate, and the compressor pressure ratio, by and large, determine the combustor inlet flow area. The flow area takes the form of an annulus, and its size is A_3 . We may calculate the flow area A_3 by a one-dimensional continuity equation such as

$$A_3 = \frac{\dot{m}_3 \sqrt{T_{t3}}}{p_{t3} \cdot M_3} \left(1 + \frac{\gamma_3 - 1}{2} M_3^2 \right)^{\frac{\gamma_3 + 1}{2(\gamma_3 - 1)}} \cdot \sqrt{\frac{R_3}{\gamma_3}} \quad (7.115)$$

■ FIGURE 7.41
Schematic drawing of a
dump diffuser



At design point, the engine (core) mass flow rate, the compressor discharge parameters p_{t3} and T_{t3} (which are a function of π_c and e_c), and our design choice for M_3 size the flow area A_3 according to Equation 7.115. A typical compressor exit Mach number is $\sim 0.4\text{--}0.5$. However, a combustor requires a prediffuser to decelerate the air from the compressor to improve combustion total pressure (loss) and combustion efficiency. A desired combustor inlet Mach number is ~ 0.2 . A conventional diffuser may be designed by using the design charts that were presented in the inlet and nozzle chapter. Diffusion is a slow and patient process, which normally takes place in a long duct of shallow wall divergence angles of $\sim 3\text{--}5^\circ$ inclination with respect to a straight centerline. To shorten the axial length of a combustor prediffuser, one may employ a

- Diffuser with splitter vanes
- Dump diffuser
- Vortex-controlled diffuser.

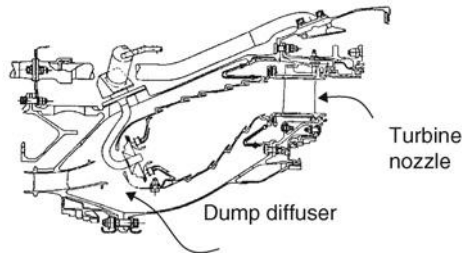
The subject of a wide-angle diffuser that employs splitter vanes was already presented in Chapter 6 (references 1 and 2 should be consulted on short and hybrid diffusers). In a dump diffuser, the flow area undergoes a sudden expansion with the attendant flow separation at the lip. Figure 7.41 shows a schematic drawing of a dump diffuser.

A curved turbulent shear layer emerges from the point of separation, which reattaches in approximately 5–7 inlet channel heights, for a two-dimensional expansion. A pair of stable vortex structures is formed (in 2D) at the separation junction. In the axisymmetric case, a stable vortex ring is formed at the separation junction. The expression used in Figure 7.41 for the static pressure ratio and velocity ratio is based on Bernoulli equation, and the last part that relates the flow speed to flow area is based on the incompressible continuity equation. The loss of total pressure between stations 1 and 2 is due to viscous/turbulent mixing and dissipation in the separated shear layer and the boundary layer formation downstream of the reattachment point. An example of an annular combustor using a dump prediffuser is shown in Figure 7.42 (from Henderson and Blazowski, 1989).

Total pressure recovery of a dump diffuser is a function of Reynolds number and the Mach number at its inlet. For Reynolds number based on the inlet diameter of $\sim 500,000$ to 10^6 , Barclay (1972) recommends the following correlation:

$$\frac{p_{t2}}{p_{t1}} \approx \exp \left\{ -\frac{\gamma M_1^2}{2} \left[\left(1 - \frac{A_1}{A_2} \right)^2 + \left(1 - \frac{A_1}{A_2} \right)^6 \right] \right\} \quad [\text{for } 1 < A_2/A_1 < 5] \quad (7.116)$$

■ **FIGURE 7.42**
F101 annular combustor with a dump (pre-) diffuser design. Source: Henderson and Blazowski 1989. Reproduced with permission from AIAA



The exit Mach number M_2 is then established using a continuity equation, according to

$$\frac{p_{t2} A_2 M_2}{\left(1 + \frac{\gamma - 1}{2} M_2^2\right)^{\frac{\gamma+1}{2(\gamma-1)}}} = \frac{p_{t1} A_1 M_1}{\left(1 + \frac{\gamma - 1}{2} M_1^2\right)^{\frac{\gamma+1}{2(\gamma-1)}}} \quad (7.117)$$

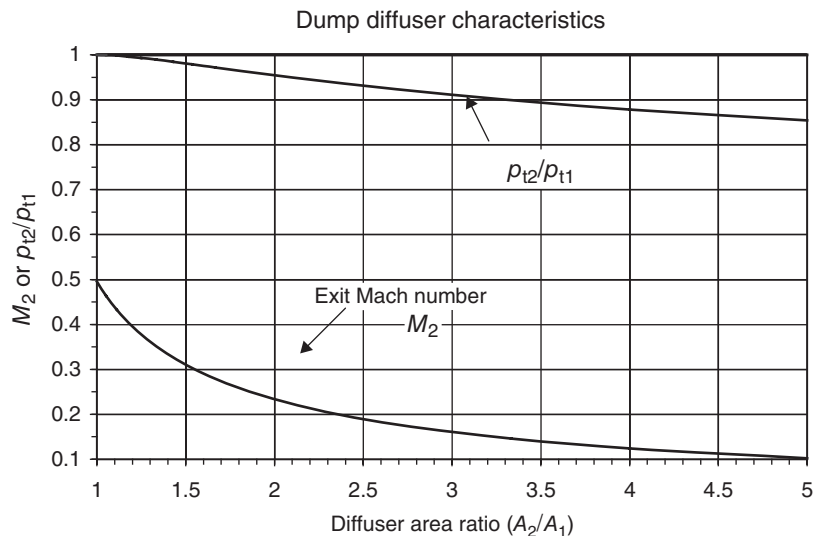
The total pressure recovery of a dump diffuser and its exit Mach number are plotted in Figure 7.43 for an inlet Mach number of $M_1 = 0.5$ and $\gamma = 1.4$.

Figure 7.43 indicates that in order to decelerate a Mach 0.5 flow to an exit Mach number of 0.2 in a dump diffuser, we need to employ an area ratio of ~ 2.35 , and the flow in the dump diffuser will recover ~ 0.935 of its inlet total pressure (i.e., it suffers $\sim 6.5\%$ loss).

To establish a length for the main combustor, we relate the residence time of the fluid in the burner to the ratio of fluid mass to the flow rate in the combustor, namely,

$$\tau_{\text{resident}} \approx \frac{m_{\text{burner-gas}}}{\dot{m}} \approx \frac{\rho_{t3} A_{\text{ref}} L}{\dot{m}_3} \quad (7.118)$$

■ **FIGURE 7.43**
Total pressure ratio and exit Mach number in a dump diffuser [$M_1 = 0.5$, $\gamma = 1.4$]



where A_{ref} is the maximum cross-sectional area of the burner, L is the burner length, and the mass flow rate through the burner is estimated as the airflow rate at the combustor entrance. Now, expressing the fluid density in terms of compressor pressure ratio via an isentropic exponent, namely,

$$\rho_{t3} \sim \rho_{t2} \cdot \pi_c^{1/\gamma}$$

We may isolate combustor length L from Equation 7.118 and express it as

$$L \propto \frac{\dot{m}_2 \cdot \tau_{\text{resident}}}{\rho_{t2} A_{\text{ref}} \pi_c^{1/\gamma}} = \left(\frac{\dot{m}_2}{\rho_{t2} A_2} \right) \cdot \left(\frac{A_2}{A_{\text{ref}}} \right) \frac{\tau_{\text{resident}}}{\pi_c^{1/\gamma}} \quad (7.119)$$

In the above expression, A_2 is the engine face area and the first parenthesis is a design parameter, which is independent of the engine size. The area ratio A_2/A_{ref} may be related via continuity equation to the engine face axial Mach number (a design choice) and the combustor exit Mach number (i.e., taken at the exit of the turbine nozzle) M_4 and the total pressure and temperature ratios according to

$$\frac{A_2}{A_{\text{ref}}} \propto \frac{p_{t4}}{p_{t2}} \sqrt{\frac{T_{t2}}{T_{t4}}} \frac{\left(1 + \frac{\gamma-1}{2} M_2^2\right)^{\frac{\gamma+1}{2(\gamma-1)}}}{M_2} f(\gamma_4, R_4) \quad (7.120)$$

In Equation 7.120, the burner exit Mach number (taken at the exit of the turbine nozzle) is set equal to 1, as the turbine nozzle remains choked over a wide range of operating conditions. We may approximate the total pressure ratio term in Equation 7.120 by the compressor pressure ratio and express the combustor length L as

$$L \propto \frac{\tau_{\text{resident}}}{\pi_c^{1/\gamma}} \frac{\pi_c}{\sqrt{T_{t4}}} \sim \frac{\pi_c^{\frac{\gamma-1}{\gamma}}}{\sqrt{T_{t4}}} \cdot \tau_{\text{resident}} \quad (7.121)$$

The fluid residence timescale and the chemical reaction timescale may be interchanged in a combustor

$$\tau_{\text{resident}} \cong \tau_{\text{reaction}} \quad (7.122)$$

The reaction timescale is inversely proportional to the reaction rate and attains the following general form,

$$\tau_{\text{reaction}} \propto p_{t3}^{-n} \cdot T_{t3}^{-m} \quad (7.123)$$

Now, substituting Equation 7.123 for the residence timescale into Equation 7.121, we get

$$L \propto \frac{\pi_c^{\frac{\gamma-1}{\gamma}}}{\sqrt{\tau_\lambda}} \pi_c^{-n} \tau_c^{-m} \quad (7.124)$$

■ **TABLE 7.7**
Data on Combustor Size, Weight, and Cost

Parameter	TF39	TF41	J79	JT9D	T63
Type	Annular	Cannular	Cannular	Annular	Can
Mass flow (design point)					
Airflow, lb/s	178	135	162	242	3.3
kg/s	81	61	74	110	1.5
Fuel flow, lb/h	12,850	9965	8350	16,100	235
kg/h	5829	4520	3788	7303	107
Size					
Length, in	20.7	16.6	19.0	17.3	9.5
cm	52.6	42.2	48.3	43.9	24.1
Diameter, in	33.3	5.3/24.1 ^a	6.5/32.0 ^a	38.0	5.4
cm	84.6	13.5/61.2	16.5/81.3	96.5	13.7
Weight, lb	202	64	92	217	2.2
kg	92	29	42	98	1.0
Cost, \$	42,000	17,000	11,300	80,000	710

Source: Henderson and Blazowski 1989. Reproduced with permission from AIAA

^aCan diameter/annulus diameter.

We may combine the exponents of the compressor pressure ratio in Equation 7.124 as

$$L \propto \frac{\pi_c^{(1-m)\left(\frac{\gamma-1}{\gamma}\right)-n}}{\sqrt{\tau_\lambda}} \quad (7.125)$$

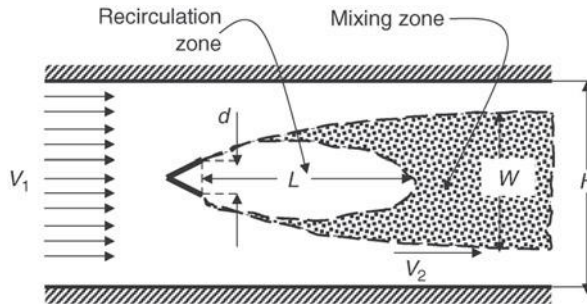
This equation relates the combustor length L to cycle parameters π_c and τ_λ , which are independent of size. Hence, a high-pressure ratio engine occupies a smaller length combustor than a comparable size engine with a lower pressure ratio. A similar argument can be made regarding the cycle thermal loading parameter τ_λ . Table 7.7 (from Henderson and Blazowski, 1989) shows some data on contemporary combustor size, weight, and cost.

7.6.6 Afterburner

So far, we have discussed the total pressure drop in an afterburner due to flameholder drag and combustion. We also alluded to the flame stability provided by a bluff-body flameholder. In this section, we quantify the parameters governed by the fluid mechanics and the chemical reaction that afford flame stability in an afterburner. We also develop a scaling parameter that connects different flameholder arrangements and duct geometries to experimental results obtained in a rectangular duct with a single flameholder. We first define a bluff body and its wake in a duct by the following length and velocity scales, as shown in Figure 7.44.

The wake of a V-gutter of height “ d ” is shown to have a central recirculation zone of length “ L ,” a wake width “ W ,” a channel height “ H ,” an upstream gas velocity V_1 , and an accelerated gas velocity, just outside the mixing layer, V_2 , known as the “edge velocity.” We had defined a blockage parameter B , which for a two-dimensional duct,

■ **FIGURE 7.44**
Length and velocity scales associated with a single flameholder in a duct



as shown in Figure 7.44, is the ratio $B = d/H$. The blockage parameter B and the wake width establish the flow acceleration V_2 . A continuous chemical reaction in the mixing layer will be supported only if the resident timescale of the fuel/air mixture in the mixing layer is longer than the reaction timescale. Hence, for flame stability, the following simple relationship should hold between the two characteristic timescales, namely,

$$\tau_{\text{resident}} > \tau_{\text{reaction}} \tag{7.126}$$

This is the basis of Zukoski-Marble (1955) characteristic time model for flame stability. The resident timescale of the unburned gas is proportional to the ratio

$$\tau_{\text{resident}} \sim \frac{L}{\bar{v}} \tag{7.127}$$

where \bar{v} is an average gas speed in the mixing layer. Hence, a dimensionless parameter $\bar{v}\tau/L$ emerges that could serve as a stability criterion. Experiments are conducted that establish the flame blowout condition in a rectangular duct with a single flameholder at the center of the duct with a range of chemical reaction parameters. The blowout condition parameters are labeled with a subscript “c” and by combining the proportionality constants in the unknown time constant τ_c , the average gas speed in the mixing layer is replaced by V_{2c} to produce

$$\left(\frac{\tau_c V_{2c}}{L} \right)_{\text{blowout}} = 1 \tag{7.128}$$

as the blowout stability criterion, or the *marginal* stability criterion. The measurements of L and V_{2c} then establish the critical timescale τ_c at the blowout condition. The ratio V_{2c}/L represents the fluid dynamic parameter in Equation 7.128, whereas τ_c represents the effect of all chemical reaction parameters lumped into a single term. The timescale τ_c , which is also referred to as ignition time, is independent of the flameholder geometry and arrangement so long as the mixing layer is turbulent. It depends, however, on a number of parameters, such as the fuel-to-air ratio, fuel type, inlet temperature, and the degree of vitiation of the afterburner gas. Experimental results of Zukoski (1985) over a range of two- and three-dimensional flame-holders indicate that the τ_c is ~ 0.3 ms at stoichiometric fuel–air ratio. This is consistent with Figure 7.9 (from Kerrebrock) that shows the reaction bucket has a minimum of ~ 0.3 ms near stoichiometric ratio and up to ~ 1.5 ms in fuel lean and rich limits of gasoline–air mixtures (see Figure 7.9). A more convenient stability

parameter may be defined using the upstream blowout velocity V_{1c} and the duct height H as a reference velocity and length scale,

$$\frac{\tau_c V_{1c}}{H} = \frac{V_{1c}}{V_{2c}} \frac{L}{W} \frac{W}{H} \left(\frac{\tau_c V_{2c}}{L} \right) = \frac{V_{1c}}{V_{2c}} \frac{L}{W} \frac{W}{H} \quad (7.129)$$

The length of recirculation zone to the wake width L/W is approximately four, over a wide range of bluff-body flameholder geometries. We may also approximate the ratio of edge velocity to the upstream velocity using the continuity equation for an incompressible fluid and neglecting the entrainment in the mixing layer as

$$\frac{V_{1c}}{V_{2c}} \approx \frac{H - W}{H} = 1 - \frac{W}{H} \quad (7.130)$$

By neglecting the entrainment in the mass flow balance of Equation 7.130; we overpredict the edge velocity V_{2c} , which makes our analysis more conservative. As a first-order approximation, we neglect the entrainment in the mass balance. Substituting Equation 7.130 in the stability parameter of Equation 7.129, we get

$$\frac{\tau_c V_{1c}}{H} \approx 4 \frac{W}{H} \left(1 - \frac{W}{H} \right) \quad (7.131)$$

The emergence of W/H as the nondimensional parameter in the flameholder stability criterion is of great significance. This ratio depends mainly on the flameholder blockage parameter B , which may now be generalized to include different number and arrangement of flameholders in a circular duct.

Table 7.8 is reproduced from Zukoski (1985), which relates the flameholder blockage to velocity ratio for a V-gutter wedge half-angle of 15° and 90° (flat plate in broadside) in a rectangular duct.

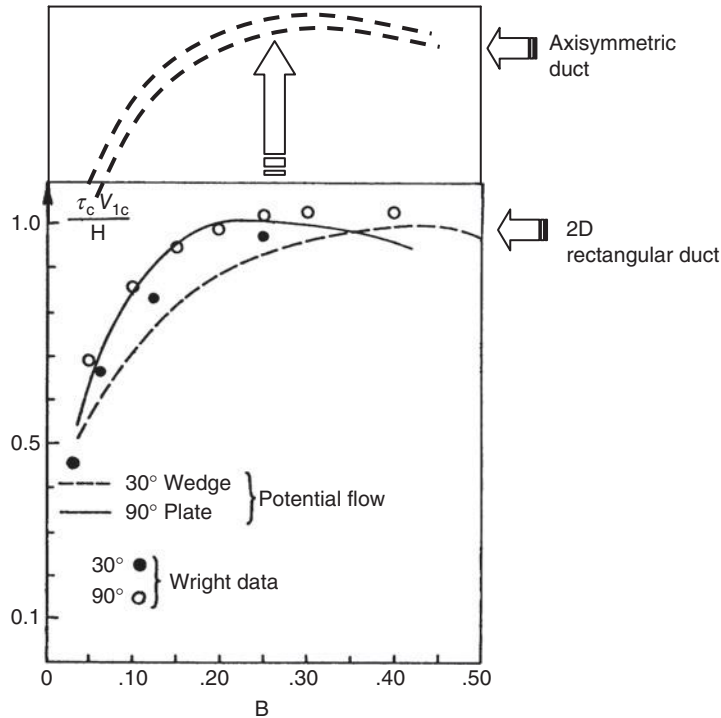
We note that stability parameter $(W/H)(V_1/V_2)$ increases with the blockage ratio and approaches a value of 0.25 for a 50% blockage. Examining the quadratic nature

TABLE 7.8
Dependence of Wake Width W , Edge Velocity V_2 , and a Stability Parameter on Blockage Ratio d/H and wedge Half-Angle α

$\frac{d}{H}$	$\alpha = 15 \text{ deg}$			$\alpha = 90 \text{ deg}$		
	$\frac{W}{d}$	$\frac{V_2}{V_1}$	$\left(\frac{W}{H}\right)\left(\frac{V_1}{V_2}\right)$	$\frac{W}{d}$	$\frac{V_2}{V_1}$	$\left(\frac{W}{H}\right)\left(\frac{V_1}{V_2}\right)$
0.05	2.6	1.15	0.11	4.0	1.25	0.16
0.10	1.9	1.23	0.15	3.0	1.43	0.21
0.20	1.5	1.42	0.20	2.2	1.75	0.248
0.30	1.3	1.62	0.23	1.7	2.09	0.250
0.40	1.2	1.90	0.25	1.6	2.50	0.248
0.50	1.2	2.3	0.25	1.4	3.16	0.22

Source: Zukoski 1985. Reproduced with permission from AIAA

■ **FIGURE 7.45**
 Comparison between theoretical stability predictions (potential flow) and the experimental data of Wright for flameholder wedge half-angles of 30° and 90° in a 2D rectangular duct. Source: Adapted from Zukoski 1985



of Equation 7.131, we deduce that W/H of 0.5 maximizes the stability parameter, for a flameholder in a rectangular duct, which states that the optimum wake width is 50% of the duct height. Substituting these values into Equation 7.131 yields a maximum blowout velocity in the approach stream of the flameholder, V_{1m}

$$\frac{\tau_c V_{1m}}{H} \approx 1 \tag{7.132}$$

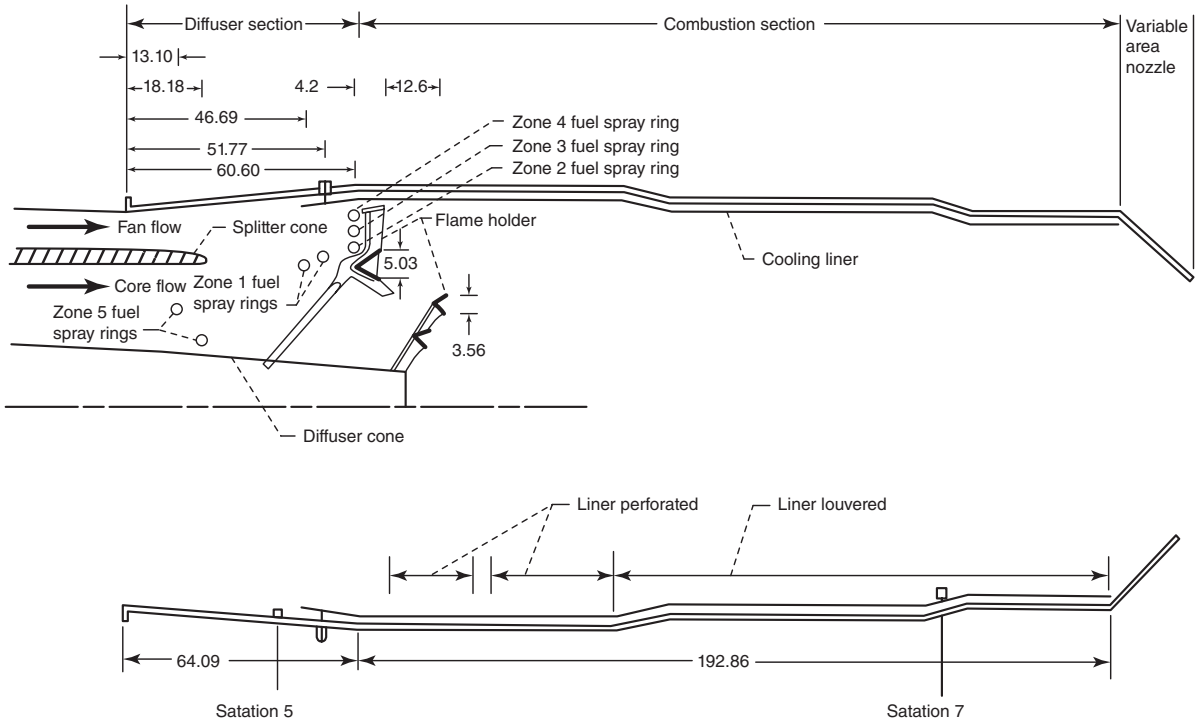
To demonstrate the validity of this approach, Zukoski (1985) compares the result of the theoretical predictions of Table 7.7 with experimental data of Wright (1959). Figure 7.45 shows this comparison.

These results confirm the method of approach proposed by Zukoski and support the stability criterion of Equation 7.132 for two-dimensional flameholder geometries in a rectangular duct.

For a general axisymmetric flameholder in a circular duct, the wake width is less than a two-dimensional counterpart, due to a three-dimensional relieving effect, that is,

$$\left(\frac{W}{d}\right)_{3D} < \left(\frac{W}{d}\right)_{2D} \tag{7.133}$$

Remember that a 3D drag coefficient is also less than a 2D drag coefficient (on a body with the same cross-section), hence the wake width in 3D is less than the wake width in 2D. Consequently, the edge velocity V_2 in 3D is less than the edge velocity on a two-dimensional wake. The lower edge speed increases the residence time of the fuel-air



■ **FIGURE 7.46** The TF30-P-3 turbofan engine with its afterburner showing the installation and scales of the flameholders, fuel injection rings and the diffuser cone (all dimensions in cm). Source: McAulay and Abdelwahab 1972. Courtesy of NASA

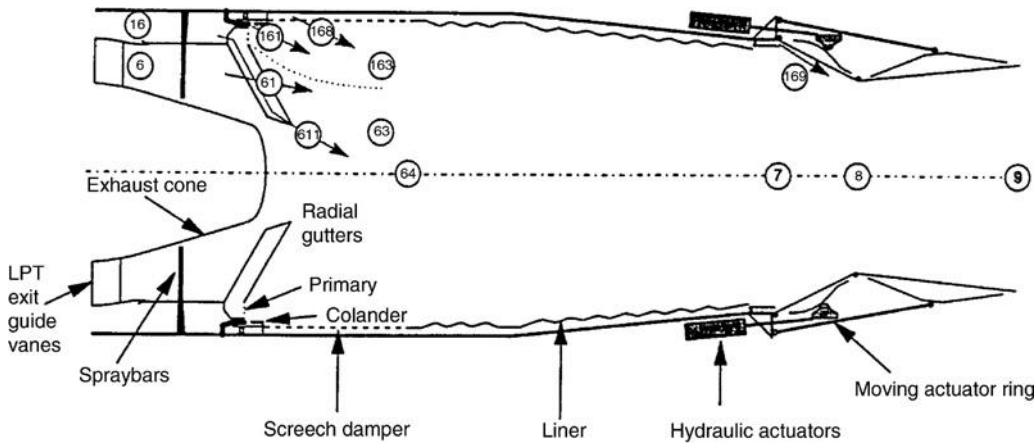
mixture in the mixing layer, therefore the velocity in the approach stream for marginal stability is higher for a 3D flameholder, that is,

$$(V_{1c})_{3D} > (V_{1c})_{2D} \tag{7.134}$$

In an axisymmetric flameholder and circular duct, the optimum wake width is $\sim 1/3$, and the approach stream velocity for marginal stability is 50% higher in 3D than 2D, according to Zukoski (1985).

Figure 7.46 shows an afterburner with three V-gutter flameholder rings attached to the turbine exit diffuser cone via radial V-gutters (from Zukoski, 1985). There are seven fuel spray rings that are divided into five zones. The fuel spray rings are upstream of the flameholders to allow for fuel evaporation and hence reduce the ignition time in the flameholder shear layer. Zone 1 is on the shear layer of the fan and core flow. Zones 2–4 are in the fan stream and zone 5 is in the core stream. The zonal approach to fuel injection in the afterburner provides for engine thrust modulation in the reheat mode. The flow to the cooling liner is supplied by the fan stream and serves two functions. First, it protects the casing through a coolant protective layer (liner louvered) and second, the liner dampens a combustion-related acoustic instability, known as screech (liner perforated). We will examine the afterburner screech issue in more detail in a later section.

A longitudinal section of Eurojet Consortium, EJ200, turbofan engine afterburner, and nozzle is shown in Figure 7.47 (from Kurzke and Riegler, 1998). Here the fuel spray



■ FIGURE 7.47 Longitudinal section of the EJ200 afterburner and nozzle. Source: Kurzke and Riegler 1998. Courtesy of U.S. Government

in the afterburner is divided into three stages, again for thrust modulation purposes. The fuel spray bars shown represent the primary zone, and the fuel spray to the radial gutter region (in the core stream) is the secondary zone. The fuel injection in the bypass stream is at the throat of the “colander” region. These constitute the three stages or burning zones associated with the fuel spray in this engine. The flameholder is of radial V-gutter configuration, instead of a multiring configuration, as in Figure 7.46. The perforated screech damper and the cooling liner are also shown in Figure 7.47.

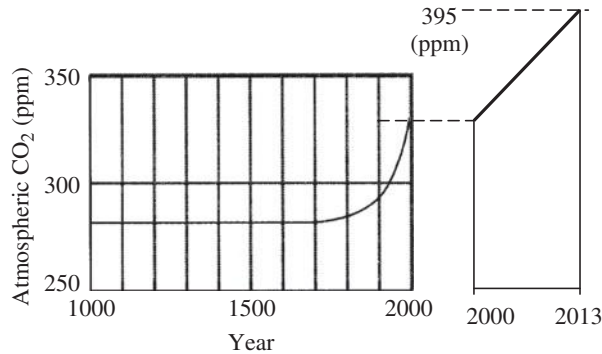
7.7 Combustion-Generated Pollutants

Smoke, oxides of carbon (CO and CO_2), oxides of nitrogen (NO_x), and unburned hydrocarbon fuel (UHC) constitute the bulk of combustor-generated pollutants. Although oxides of sulfur (SO_x) are considered engine exhaust pollutants as well, since the sulfur content of a fuel is dictated by the aviation fuel production (or the refinery) process and is not controlled by combustion, its discussion is often absent from combustion-generated pollutants. The U.S. Environmental Protection Agency (EPA) has been charged with setting the emission standards for aircraft engines operated in the United States. There are two areas of concern with air pollution. The first deals with engine emissions near airports in landing-takeoff cycle (LTO), below 3000 feet. The second area of concern examines the effect of engine emissions at cruise altitude in the stratosphere.

7.7.1 Greenhouse Gases, CO_2 and H_2O

Carbon dioxide (CO_2) and water vapor (H_2O) constitute the products of complete combustion. The large deposition of these products in stratosphere by a fleet of commercial aircraft is feared to contribute to global warming through greenhouse effect. Both of these molecules, that is, CO_2 and H_2O , absorb infrared radiation from earth and radiate it back toward earth. Earth’s atmosphere like the glass of a greenhouse is transparent to visible light from the sun but absorbs the infrared radiation, which accounts for a warmer earth

■ **FIGURE 7.48**
 Concentration of
 carbon dioxide in the
 atmosphere over the
 past 1000 years based
 on ice core data and
 direct readings since
 1958. Source: Adapted
 from Zumdahl 2000



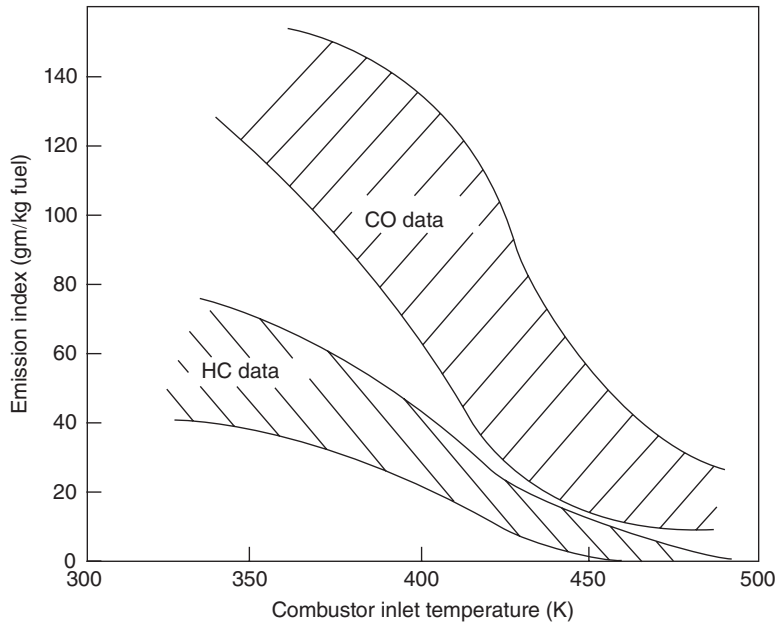
surface temperature due to a radiation absorption in its atmosphere. Now, the average temperature of the earth's surface is 298 K, whereas without the greenhouse gases in the atmosphere it would be 255 K (i.e., 43°C colder). However, a higher concentration of these greenhouse gases in the stratosphere may tilt the balance toward global warming. The impact of the additional greenhouse gases in the atmosphere is being debated. Conflicting climatic data between the Southern hemisphere and the Northern latitudes over the past century suggest a more complex dynamics than a simple infrared radiation model proposed. Figure 7.48 (adapted from Zumdahl, 2000) shows, however, the *undeniable* rapid rise in atmospheric CO₂ concentration over the past 100 years with the increase in consumption of hydrocarbon fuels for electric power generation and transportation. At the present time, there is no emission regulation for carbon dioxide and water vapor and thus no FAA engine certification requirements. The unit of concentration in Figure 7.48 is parts per million in molar concentration of CO₂, that is, equal to volume fraction of CO₂ in the atmosphere. Note the rise of the atmospheric CO₂ concentration from 2000–2013, which is also shown in Figure 7.48. Data are based on the mean values of seasonal variations.

7.7.2 Carbon Monoxide, CO, and Unburned Hydrocarbons, UHC

Carbon monoxide is formed as a result of an incomplete combustion of hydrocarbon fuels. It is a source of combustion inefficiency as well as a pollutant in the engine emissions. In combustion terms, CO is a fuel with a heating value of 2267 cal/g, which is approximately 24% of the Jet A fuel specific energy, which leaves the engine in the exhaust gases without releasing its chemical energy. Partial dissociation of carbon dioxide in the hot primary zone is also responsible for carbon monoxide formation. A fuel lean operation at low engine power setting causes a slow reaction rate in the combustor and thus carbon monoxide formation. At a low power setting, combustor inlet temperature and pressure are reduced, which directly impact the reaction rate in the combustor as discussed earlier. In the case of unburned hydrocarbons, a fraction of fuel may remain unburned due to poor atomization, vaporization, and residence time or getting trapped in the coolant film of the combustor liner. The indices of carbon monoxide and unburned hydrocarbons both drop with the engine power setting. An accumulation of aircraft engine data, which is reported in Figure 7.49 (from Henderson and Blazowski, 1989), suggests the sensitivity of CO and UHC formations to engine power setting.

It is entirely plausible to relate the combustion inefficiency, that is, $1 - \eta_b$, particularly in the idle setting, to the emission index of CO and UHC, as they are both fuels that are

■ **FIGURE 7.49**
Emission index of carbon monoxide and unburned hydrocarbons (labeled as HC Data) with engine idle setting. Source: Henderson and Blazowski 1989. Reproduced with permission from AIAA



present in the exhaust. Blazowski (1985) expresses the combustion inefficiency in terms of emission index EI (at idle) as

$$1 - \eta_b = [0.232(EI)_{CO} + (EI)_{UHC}] \times 10^{-3} \quad (7.135)$$

Note that the emission index EI is the mass ratio in grams of pollutants generated per kilogram of fuel consumed. As an example, let us take emission indices of CO and UHC to be ~ 100 and ~ 40 g/kg, respectively, (from Figure 7.49) to represent the engine idle power setting with combustor inlet temperature ~ 400 K. Substitution of these emission indices in Equation 7.135 suggests a combustor inefficiency of $\sim 6.3\%$. However, EPA standards on emissions applied to Equation 7.135 demands a combustor efficiency of 99% at idle setting.

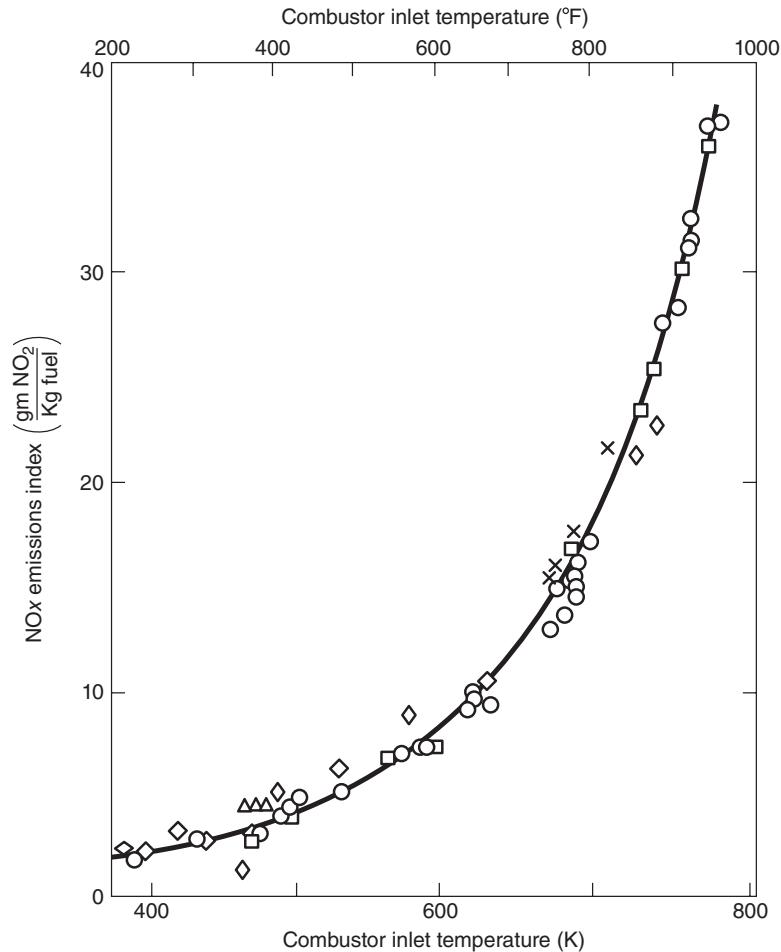
7.7.3 Oxides of Nitrogen, NO and NO₂

Nitric oxide, NO, is formed in the high temperature region of the primary zone at temperatures above 1800 K. The chemical reaction responsible for its production is



Since the reaction of nitrogen is with the oxygen atom in order to create nitric oxide, the regions within the flame where dissociated oxygen exists (in equilibrium) will produce nitric oxide. This explains the high temperature requirement for NO production (in near stoichiometric mixtures). Therefore, nitric oxide is produced at high engine power settings, in direct contrast to the carbon monoxide and UHC pollutants that are generated at the low power (idle) settings. Further oxidation of NO into NO₂ takes place at the lower

■ **FIGURE 7.50**
Correlation of current engine NO_x emissions with combustor inlet temperature. Source: Lipfert 1972, Fig. 6.50. Reproduced with permission from ASME

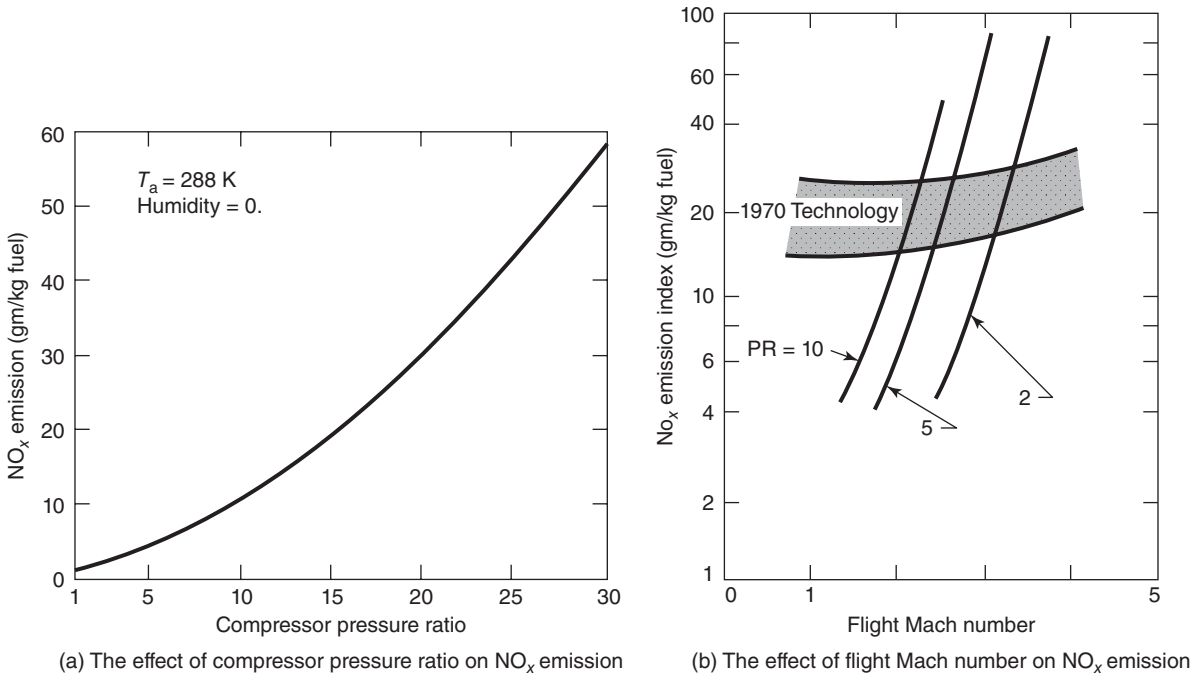


temperatures of the intermediate or dilution zones of the combustor. Both types of the oxides of nitrogen are referred to as NO_x in the context of engine emissions. Lipfert (1972) demonstrates the temperature sensitivity of NO_x formation through an excellent correlation with numerous gas turbine engine data. His results are shown in Figure 7.50.

We note that engine types, combustor types, and fuels had apparently no effect on the NO_x correlation presented by Lipfert (Figure 7.50). All engines correlated with the combustor inlet temperature T_{t3} . Combustor inlet temperature is directly related to the compressor pressure ratio π_c ; thus, we expect a similar dependence on the cycle pressure ratio, as shown in Figure 7.51 (from Henderson and Blazowski, 1989).

7.7.4 Smoke

The fuel-rich regions of the primary zone in the combustor produce carbon particulates known as soot. The soot particles are then partially consumed by the high temperature gases, that is, in the intermediate and, to a lesser, extent, in the dilution zones of the combustor. Visible exhaust smoke corresponds to a threshold of soot concentration in the



■ FIGURE 7.51 Impact of cycle pressure ratio (PR) on NO_x emission. Source: Henderson and Blazowski 1989. Reproduced with permission from AIAA

exhaust gases. Soot particles are primarily carbon (96% by weight), hydrogen, and some oxygen. An improved atomization of the fuel (using air-blast atomizers) and enhanced mixing intensity in the primary zone reduces the soot formation. The parameter that quantifies soot in the exhaust gases is called the smoke number, SN. Its measurement is based on passing a given volume of the exhaust gas through a filter for a specific time, then comparing the optical reflectance of the stained and the clean filter by using a photoelectric reflectometer. The procedure for aircraft gas turbine engines exhaust smoke measurements is detailed in a Society of Automotive Engineers (SAE) document – ARP 1179 (1970). The smoke number is defined as

$$SN \equiv 100(1 - R/R_0) \tag{7.137}$$

where R is the absolute reflectance of the stained filter, and R_0 is the absolute reflectance of the clean filter material.

7.7.5 Engine Emission Standards

The emission standards of the U.S. EPA (1973, 1978 and 1982) and the International Civil Aviation Organization (ICAO) (1981) define the limits on CO, UHC, NO_x, and smoke production of aircraft engines near airports (Table 7.9).

In the ICAO standards, the rated cycle pressure ratio π_{00} and the rated engine thrust F_{00} (in kN) are incorporated in the regulated limits.

■ **TABLE 7.9**
EPA and ICAO Engine Emission Standards

Pollutant	EPA (1979) Standards	ICAO (1981) Standards
CO	4.3 g/(kg · thrust · h)	118 g/kN F_{00}
UHC	0.8 g/(kg · thrust · h)	19.6 g/kN F_{00}
NO _x	3.0 g/(kg · thrust · h)	40 + 2(π_{00}) g/kN F_{00}
Smoke	19–20	83.6(F_{00}) ^{-0.274} use F_{00} in kN

7.7.6 Low-Emission Combustors

To combat the problems of CO and UHC production at the low engine power settings, the concept of staged combustion is introduced. This concept breaks down a conventional combustor primary zone into a pair of separately controlled combustor stages, which may be stacked (as in parallel) or in series. The stages are referred to as a pilot and a main stage, with their separate fuel injection systems. The pilot stage serves as the burner for the low power setting at peak idle combustion efficiency. The main stage is for maximum power climb and cruise condition, however, operating in a leaner mixture ratio to control NO_x emissions. Complete combustion is achieved through separate fuel scheduling as well as an efficient (air-blast atomizer) fuel atomization, vaporization, and mixing in smaller volume combustors. Two concepts developed by GE-Aircraft Engines and Pratt & Whitney Aircraft are shown in Figure 7.52.

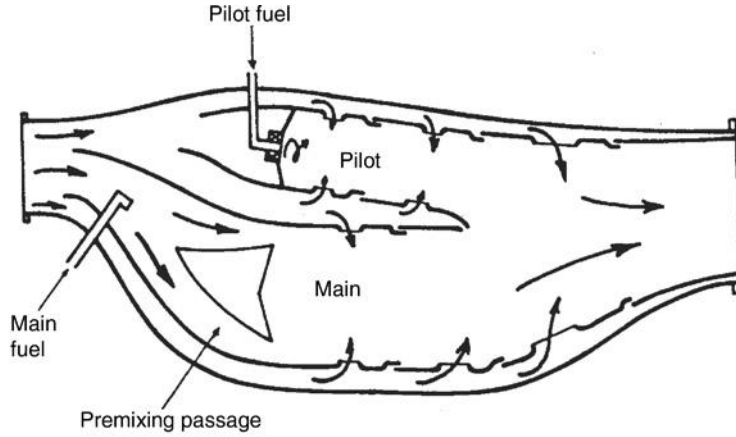
The result of application of the double annular and Vorbix combustors to CF6–50 and JT9D-7 engines, respectively, is shown in Table 7.10 (data from Lefebvre, 1983).

The staged combustion concept is very effective in overall engine emission reduction in particular with CO and UHC, whereas NO_x continues to be a challenge. To combat NO_x, we should lower the flame temperature, which requires the combustor to operate at a lower equivalence ratio, of say $\phi \sim 0.6$. The problems of combustion stability and flameout accompany lean fuel–air mixtures. To achieve a stable lean mixture ratio to support a continuous combustion, a premixing, prevaporization approach has to be implemented. Both combustors that are shown in Figure 7.52 employ this concept. Also the positive impact of employing air-blast atomizers is incorporated in both combustors. However, Table 7.10 indicates higher levels of smoke are generated by the double annular and the Vorbix low-emission combustors. This reminds us of the conflict between single parameter and system optimization problems, in which different elements of the system often have opposing requirements for their optimization.

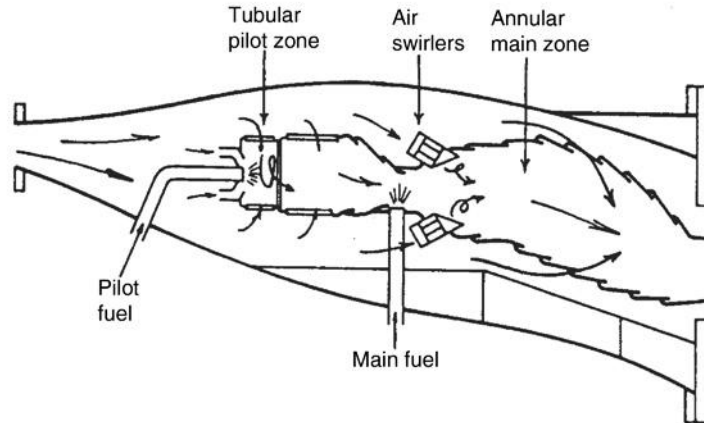
Water injection in the combustor effectively reduces the flame temperature and has demonstrated significant NO_x reduction. Figure 7.53 (from Blazowski and Henderson, 1974) shows the effect of water injection in the combustor on NO_x emission reduction. We note that the ratio of water to fuel flow is ~ 1 for a nearly 50% NO_x reduction level. This fact eliminates the potential of using water injection at the cruise altitude to lower the NO_x emissions from an aircraft gas turbine engine.

Ultralow NO_x combustors with premixed prevaporized gases are shown to operate at low equivalence ratios (below 0.6) when the combustor inlet temperature is increased. The application of this concept to automotive gas turbines has produced a very

■ **FIGURE 7.52**
Examples of staged
combustion for low
emissions



(a) GE radial two-stage (double annular) combustor for CF6-50 engine

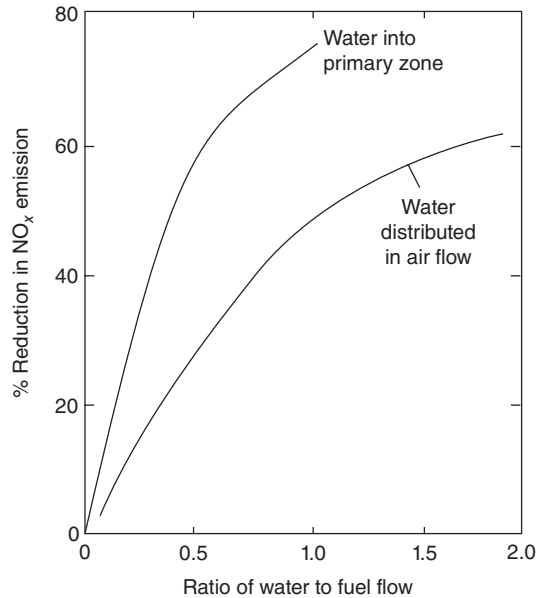


(b) Pratt & Whitney two stage series "Vorbix" combustor for JT9D-7 engine

■ **TABLE 7.10**
Engine Emissions with Staged Combustors

	Pollutant, g/(kg · thrust · hr · cycle)			
	CO	UHC	NO _x	Smoke
1979 EPA standards	4.3	0.8	3.0	20
production combustor	10.8	4.3	7.7	13
CF6-50				
Double-annular combustor	6.3	0.3	5.6	25
production combustor	10.4	4.8	6.5	4
JT9D-7				
Vorbix combustor	3.2	0.2	2.7	30

■ **FIGURE 7.53**
Water injection in the combustor reduces NO_x emission. Source: Blazowski and Henderson 1974. Reproduced with permission from AIAA

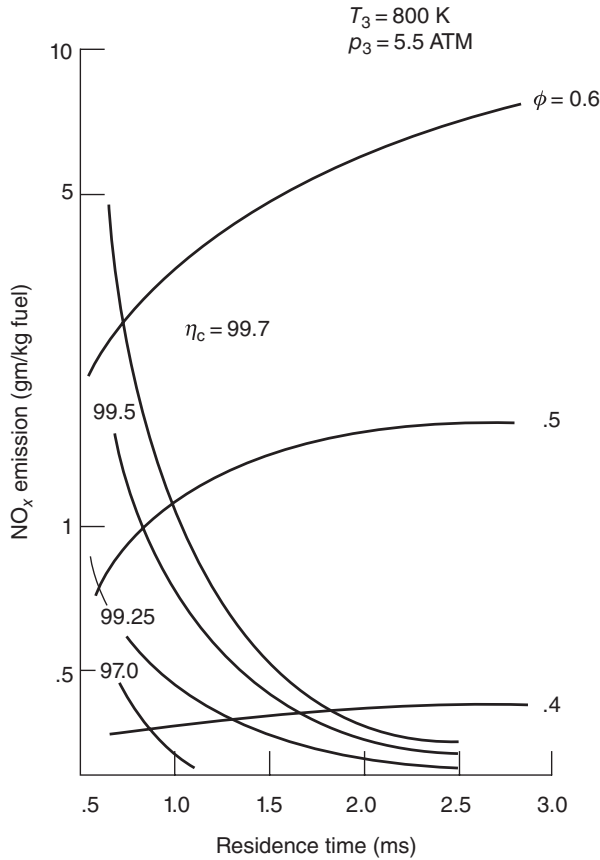


promising ultralow NO_x emission level. The burner inlet conditions of 800 K and 5.5 atm pressures in the automotive gas turbines resemble the altitude operation (or cruise operation) of an aircraft gas turbine engine. These ultralow NO_x combustor results are shown in Figure 7.54 (from Anderson, 1974).

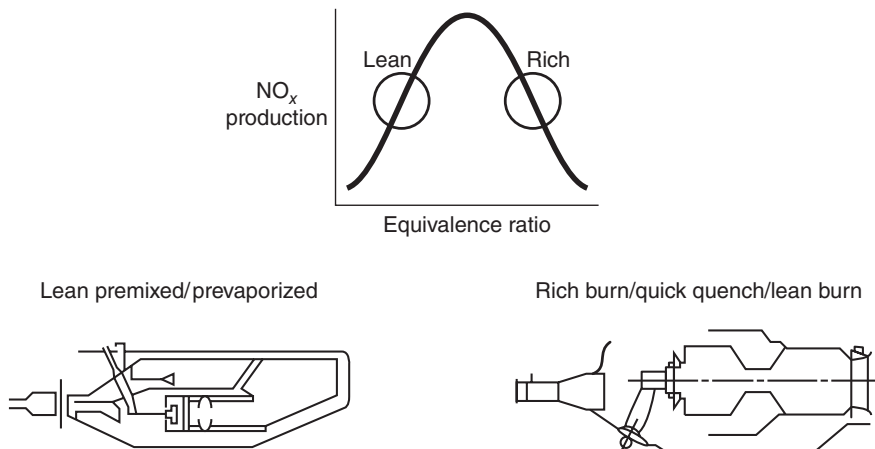
From Anderson's results in Figure 7.54, we note that a reduced residence time, which is good for NO_x production, leads to a higher level of CO and UHC emissions with an attendant combustion efficiency loss. The equivalence ratio has a large impact on NO_x emissions, as seen in Figure 7.54. The NO_x emission index of 0.3 g/kg-fuel seems to be the absolute minimum possible, as indicated by Anderson. To achieve these ultralow levels of the oxides of nitrogen in the exhaust emission, an increased burner inlet temperature is required. Incorporating a solid catalytic converter in an aircraft gas turbine engine burner may enable lean combustion and ultralow NO_x emission but at the expense of more complexity, weight, cost, and durability. The premixed/prevaporized burners also exhibit problems with autoignition and flashback for advanced aircraft engines with high-pressure ratios. Another possibility for low NO_x combustor development takes advantage of *rich burn*, which results in a reduced flame temperature, and *quick quench*, which allows for the combustion to be completed while the temperature of the combustion gases remain very near the combustor exit temperature. This approach is called *rich burn–quick quench–lean burn* and has shown promising results. These approaches are summarized in Figure 7.55, from Merkur (1996). Despite these advances, we recognize that the problem of gas turbine engine emission abatement is complex and challenging. We need to improve our understanding of the physical phenomenon in the combustor and in particular in the area of autoignition and flashback in lean combustible mixtures on the boundary of lean extinction limit.

It is instructive to compare the 1992 subsonic engine technology and the high-speed civil transport (HSCT) program goals of 2005 (from Merkur, 1996). The HSCT program is inactive at the present time (Table 7.11).

■ **FIGURE 7.54**
 Effect of residence time and ϕ on NO_x emission levels in ultralow NO_x premixed/prevaporized burners. Source: Anderson 1974. Courtesy of NASA



■ **FIGURE 7.55**
 Approaches to a low- NO_x combustor development. Source: Merkur 1996, Fig. 8, p. 8



■ TABLE 7.11

Comparison between the subsonic engine of 1992 and the design goals for the high-speed civil transport of 2005

	1992 Subsonic engine	2005 HSCT engine
Equivalence ratio	1.0 → 1.2	< 0.7 or > 1.5
Gas temperature (°F)	3700	3400 → 3750
Liner temperature (°F)	<1800	2200 → 2600
Liner material	Sheet or cast superalloys	Ceramic matrix composites (CMC)
Cooling methods	Transpiration/film	Convection
Environment	oxidizing	Oxidizing or reducing
NO _x	36–45 g/kg f	<5 g/kg f

Source: Merkur 1996. Reproduced with permission from ASME

7.7.7 Impact of NO on the Ozone Layer

Ozone, O₃, is toxic and a highly oxidizing agent, which is harmful to eyes, lungs, and other tissues. NO_x production in high-temperature combustion impacts the ozone in the lower as well as upper atmosphere. In this section, the chemical processes that lead to ozone creation in the lower atmosphere and to a depletion of ozone in the stratosphere are discussed.

Lower atmosphere

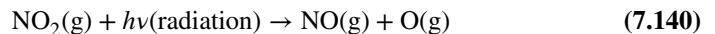
Combustion at high temperature (when local combustion temperature exceeds ~1800 K) breaks the molecular bond of N₂ and O₂ and causes NO to be formed, that is,



Nitric oxide reacts with the oxygen in the atmosphere to form nitrous oxide, NO₂, according to



NO₂ absorbs light and decomposes to



The quantity $h\nu$ in Equation 7.140 is radiation energy with h as Planck's constant and ν as the frequency of the electromagnetic wave. Oxygen atom is a highly reactive substance and among other reactions, it reacts with oxygen to create ozone, that is,



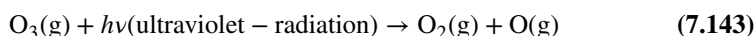
If we sum all the reactions 7.139–7.141, we get the following net result, namely,



Since NO facilitated the creation of ozone, without being consumed in the process, it is serving as a catalyst. In the lower atmosphere, nitric oxide, NO, helps generate harmful ozone in a catalyst role. The impact of NO on ozone changes as we enter the ozone layer in the stratosphere.

Upper atmosphere

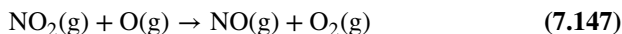
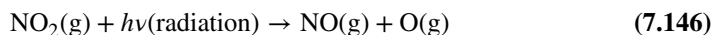
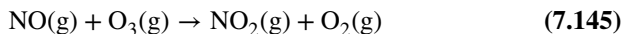
The role of ozone in the upper atmosphere is to protect the earth against harmful radiation from the sun, namely, to absorb the highly energetic rays known as the ultraviolet radiation (with wavelength between 100 and 4000 Å).



The oxygen atom is highly reactive and combines with O₂ to form ozone,



The photochemical cycle described by reactions 7.143 and 7.144 reactions results in no net change of the ozone concentration in stratosphere. Hence, ozone serves a stable protective role in upper atmosphere. Flight of commercial supersonic aircraft with large quantities of NO emissions (~30 g/kg fuel) from their high-temperature engines, over extended cruise periods, and with a large fleet promises to deplete the ozone concentration levels. Again, NO appears to be a catalyst in destroying ozone in the upper atmosphere according to



By adding reactions 7.146 and 7.147 with *twice* the reaction in 7.145 (to get the right number of moles to cancel), we get the net photochemical reaction in the stratosphere as

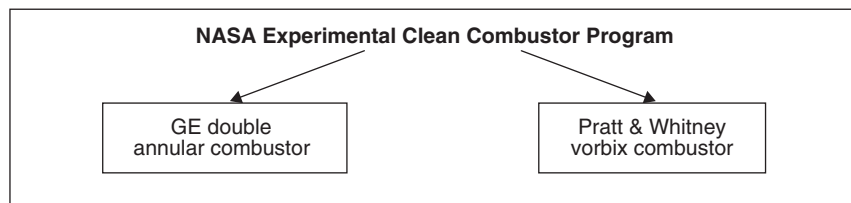
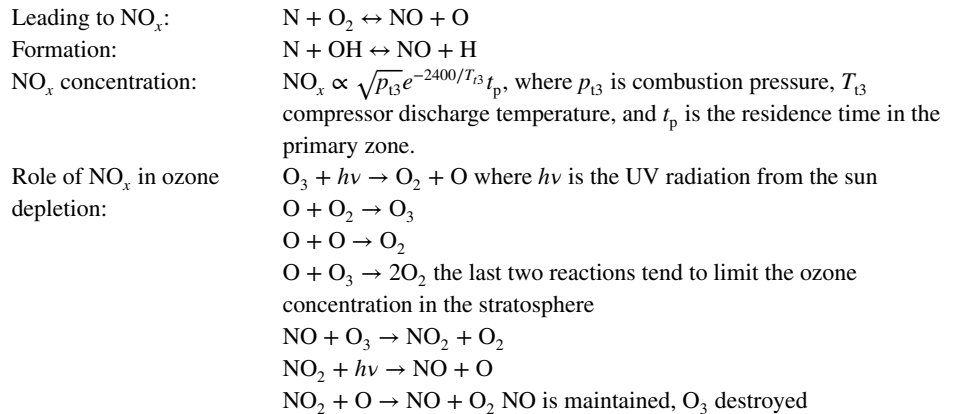
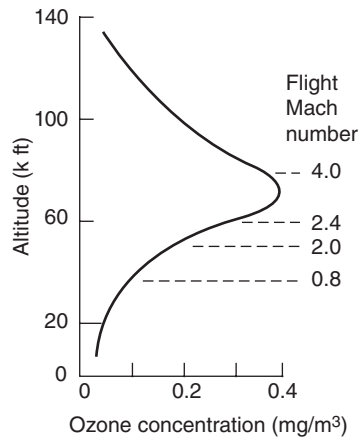


Hence, ozone is depleted through a catalytic intervention of NO. The high-energy radiation absorption in stratosphere by ozone is, by and large, the source of warmth in this layer of earth's atmosphere. Since a rise in temperature in the stratosphere with altitude is stable with respect to vertical disturbances, the ozone concentration levels should remain stable (i.e., constant) over time. A chart of ozone concentration with altitude that also depicts the best cruise altitude for the cruise Mach number of commercial aircraft is shown in Figure 7.56 (taken from Kerrebrock, 1992).

Now let us briefly summarize NO_x formation, combustor design parameters that impact its generation, and the ozone layer.

NO _x definition:	N ₂ O, NO, NO ₂
Combustor reactions:	N ₂ + O ↔ NO + N

■ **FIGURE 7.56**
 Profile of ozone concentration with altitude with a suitable cruise flight Mach number versus altitude superimposed. Source: Kerrebrock 1992. Fig. 4.46. Reproduced with permission from MIT Press

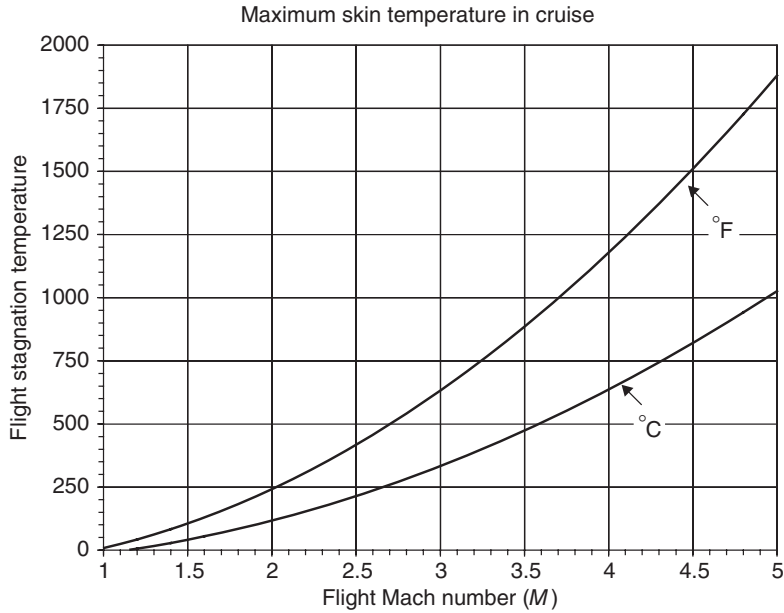


7.8 Aviation Fuels

Aircraft flight envelope, that is, altitude Mach number, establishes the operational temperature range of the aircraft and hence its desirable fuel properties. Some of the aviation fuel properties and combustion characteristics of interest are

- Specific gravity
- Viscosity
- Initial and end boiling points
- Heat capacity

■ **FIGURE 7.57**
Skin temperature rise
with flight Mach
number ($\gamma = 1.4$,
 $T_{amb} \cong -70^\circ\text{F}$ or
 -56°C)

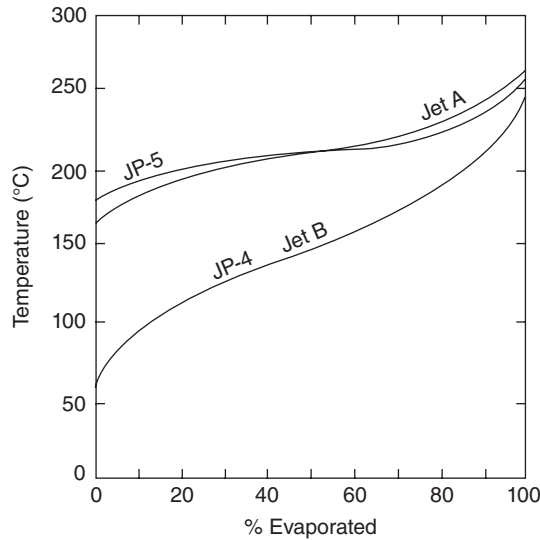


- Vapor pressure
- Volatility
- Flashpoint
- Heating value
- Freezing point
- Thermal stability
- Spontaneous ignition temperature
- Flammability limits
- Handling qualities, toxicity
- Storability
- Low fire risk
- Price/availability

Let us examine the maximum skin temperature of an aircraft in cruise and compare it to the thermal characteristics of some typical aircraft fuels. The skin temperature of an aircraft is calculated through an energy balance that accounts for aerodynamic heating, radiation cooling, regenerative wall cooling, and thermal conduction. The maximum skin temperature is, however, very near stagnation temperature of flight. Figure 7.57 shows a rapid skin temperature rise with flight Mach number, assuming the cruise is in the constant-temperature layer (i.e., tropopause, between 11 and 20 km or 36–66 kft).

At these elevated temperatures for high-speed flight, the fuel should exhibit thermal stability, which is partially addressed through its boiling point characteristics. The initial boiling point temperature begins when fuel vaporization starts. The end point is the temperature where all the fuel is vaporized. The range of the initial and end boiling points, known as the distillation curve, for several fuels is shown in Figure 7.58 (from Blazowski, 1985). The military fuels have a “JP” designation, and Jet A is the most common commercial aircraft fuel. The original gas turbine fuel was kerosene, which is used as a basis of comparison and blending with other hydrocarbon jet engine fuels. JP-4 was used primarily by the USAF and was a highly volatile fuel. A less volatile fuel, JP-5, was a gasoline–kerosene blended fuel that was used by the USN. The lower volatility of JP-5 made it more suitable for long-term storage in the ship tanks as well as the blended

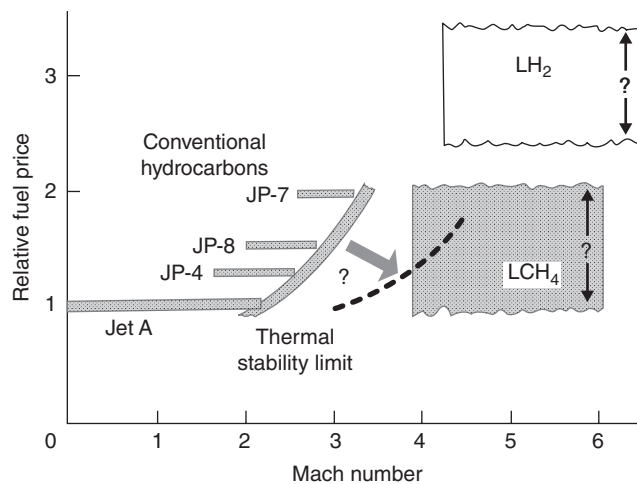
■ **FIGURE 7.58**
Distillation curve for
common jet fuels – a
measure of fuel
volatility. Source:
Blazowski 1985.
Reproduced with
permission from AIAA



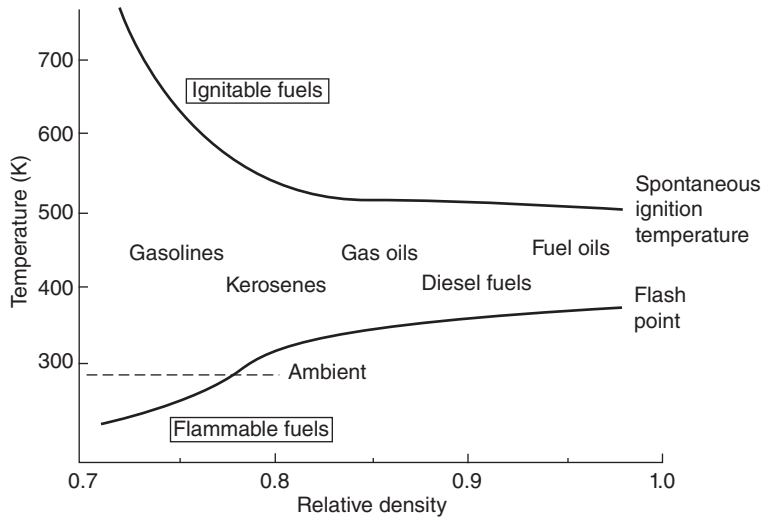
nature of the fuel allowed a wider availability on board a U.S. ship. The distillation curves of these two fuels may be seen in Figure 7.58, with JP-5 showing lower volatility and higher thermal stability. The low initial boiling point of JP-4 contributes to its volatility. We note that the fuels shown in Figure 7.58 are all evaporated at 100% when the fuels are heated to 250°C. At high temperatures, the fuels thermally decompose to form gum (coke deposits) and clog fuel filters, fuel injector, and the fuel pump. This limit corresponds to a flight Mach number of ~ 2.6 . The obvious choice for higher speed flights is the use of cryogenic fuels such as liquid methane, propane, or liquefied hydrogen. Thermal stability, flight Mach number limit, and the relative fuel cost (tentative) are shown in Figure 7.59 (from Strack, 1987).

The specific gravity is a measure of relative liquid fuel density (relative to water at 4°C), which is lowest for gasoline among petroleum fuels. The flammability limits, flash

■ **FIGURE 7.59**
Thermal stability and
relative price of
aviation fuels. Source:
Strack 1987. Courtesy
of NASA



■ **FIGURE 7.60**
 Ignition temperatures
 for petroleum fuels.
 Source: Lefebvre 1983.
 Reproduced with
 permission from
 Taylor and Francis
 Group LLC, a division
 of Informa plc



point temperature, and spontaneous ignition temperature of various fuels are shown in a graph from Lefebvre (1983) in Figure 7.60.

All hydrocarbon fuels have about the same heating value (nearly 18,600 BTU/lbm or 43.3 MJ/kg) regardless of their blends. The parameter that contributes to the heat of combustion of a fuel is the hydrogen content of the fuel. For example, the percentage hydrogen content (this is the fraction of mass of the fuel molecule contributed by the hydrogen atoms) of kerosene (~C₁₂H₂₆) is ~15.3%, JP-4 (~CH_{2.02}) is at 14.5%, propane (C₃H₈) has 18.18%, methane (CH₄) has 25%, and of course pure hydrogen is at 100% hydrogen content. It is interesting to examine the heating values of these fuels and compare them to their hydrogen content. Table 7.12 shows the impact of hydrogen content on the heat of combustion (lower heating value). The higher hydrogen content in the fuel yields a higher heat of reaction, as expected.

Ragozin (1962) presents a correlation between the fuel lower heating value and the percentage mass content of carbon, hydrogen, oxygen, sulfur, and water in the fuel. This useful and *approximate* correlation is

$$\text{LHV} = 0.339C + 1.03H - 0.109(O - S) - 0.025W \quad (7.149)$$

■ **TABLE 7.12**
 Hydrogen Content and Heating Value of Common Fuels

Fuel	JP-4	Propane	Methane	Hydrogen
Hydrogen content	14.5%	18.8%	25%	100%
Lower heating value				
kcal/g	10.39	11.07	11.95	28.65
MJ/kg	43.47	46.32	49.98	119.88
BTU/lbm	18,703	19,933	21,506	51,581

The dimensions of Equation 7.149 are MJ/kg. All parameters on the right-hand side are percent mass of carbon, hydrogen, oxygen, sulfur, and water in the fuel, respectively. The coefficient of hydrogen term is the largest and hence contributes the most to an increase in the fuel heating value. Also, it is interesting to note that oxygen in the fuel reduces its heating value, which is representative of all alcohol fuels (a typical alcohol fuel, ethanol, C_2H_5OH , has a lower heating value of $\sim 62\%$ of a hydrocarbon fuel, or methanol, CH_3OH , has only $\sim 46\%$ of the heating value). As expected, water dissolved in the fuel also lowers the heating value of the fuel. This parameter, that is, dissolved water content in the fuel, may be controlled through proper fuel handling and storage.

Fuel viscosity is an important property that determines the pressure drop in the fuel lines and the fuel pump requirements, as well as atomization of the fuel by the fuel injection system. The lower the fuel viscosity the smaller the fuel droplets, hence faster vaporization rate and the ignition timescale. Poor atomization causes a higher fraction of UHC as well as higher CO and soot formation. On the contrary, a low viscosity fuel exhibits poor lubricity, which causes an increased fuel pump wear and reduced life. Fuel viscosity is a function of temperature and increases for a liquid fuel when temperature decreases and vice versa. At low temperatures corresponding to high altitudes, a subsonic aircraft may need an antifreeze fuel additive or employ a fuel heating system integrated with its fuel tank at the propulsion system design phase.

A liquid fuel in a tank always contains a certain quantity of fuel vapor, which exerts a pressure on the liquid. This is known as the vapor pressure of the liquid at the given temperature. For example, JP-4, a highly volatile fuel, has a very high vapor pressure of ~ 0.18 atm at $38^\circ C$ (or $100^\circ F$), compared with JP-5 fuel with a corresponding low vapor pressure of 0.003 atm. Although a high vapor pressure is good in a combustor and leads to better vaporization rates, it is undesirable for its lower flash point temperature. The excessive rate of vapor production in a fuel tank or a fuel line, especially at higher temperatures of supersonic flight, could lead to an unacceptable flash point fire risk. Figure 7.60 (from Lefebvre, 1983) shows the heavier fuels have a higher flash point (therefore safer) than light fuels, such as gasoline or kerosene.

Aviation fuel is a blend of different hydrocarbons with different molecular structures and different reaction tendencies. We address two such compounds, olefins and aromatics, which are found in aviation fuels. Olefins are unsaturated hydrocarbons ($\sim C_nH_{2n}$) that are present in aviation fuel produced in the refinery process. Aromatics ($\sim C_nH_{2n-6}$) are ring compounds such as benzene (C_6H_6) that are also present in the aircraft fuel. In the case of olefins, the gum formation tendency of these compounds makes them undesirable. The aromatics have lower hydrogen content than gasoline or kerosene, which reduces the heat of reaction of the fuel mixture. Aromatic content also increases the soot formation tendencies in the combustor, which again makes them undesirable. The volume fraction of fuel containing aromatic and olefinic compounds is included in the table of fuel properties. Table 7.13 from Blazowski (1985) presents important jet fuel properties for three widely used aircraft fuels, JP-4, JP-5 and JP-8, including, their aromatic and olefinic contents.

7.9 Alternative “Drop-In” Jet Fuels (AJFs)

Conventional aircraft engine exhaust produces a range of hazardous compounds: CO, NO_x , SO_x , unburned hydrocarbons (UHC) and particulate matter (soot), in addition to greenhouse gases, most notably CO_2 . The impact of these compounds is felt locally,

■ **TABLE 7.13**
Important Jet Fuel Properties

Property	JP-4		Jet A (JP-8)		JP-5	
	Spec. req.	Typical value	Spec. req.	Typical value	Spec. req.	Typical value
Vapor pressure at 38°C (100°F), atm	0.13–0.2	0.18	—	0.007	—	0.003
Initial boiling point (°C)	—	60	—	169	—	182
End point (°C)	—	246	288	265	288	260
Flash point (°C)	—	–25	>49	52	>63	65
Aromatic content (% Vol)	<25	12	<20	16	<25	16
Olefinic content (% Vol)	<5	1	—	1	—	1
Saturates content (% Vol)	—	87	—	83	—	83
Net heat of combustion (cal/g)	>10,222	10,388	>10,222	10,333	>10,166	10,277
Specific gravity	0.751–0.802	0.758	0.755–0.830	0.810	0.788–0.845	0.818
Approximate U.S. yearly consumption (10 ⁹ gal)		3.4		13.1		0.7

Source: Blazowski 1985. Reproduced with permission from AIAA

through ambient air quality reductions at or near airports, and on regional or global scales, due both to the reaction and transport of compounds emitted in-flight and to the global climate impact of greenhouse gas release. For the aviation sector to evolve and grow, there must be reliable, diverse, cost effective, and environmentally sustainable energy sources. Many different feedstocks can be used to generate alternative jet fuels (AJFs), and the most economical and environmentally sustainable feedstock will likely differ by region. The description “drop-in” in AJF calls for the compatibility of these fuels with the current conventional petroleum fuels, namely in their equivalent safety and performance. The feedstocks of interest must all be second or third generation feedstocks that do not compete with the nation’s food supply. Renewable feedstocks utilize waste sources (algae grown using wastewater, lignocellulosic crop residues, municipal solid waste, wastewater, and renewable fats, oils, and grease) and existing infrastructure (woody biomass), or demonstrate promising new crops (oil-based plants, such as *Jatropha curcas*, and perennial grasses). For production of alternative jet fuels (AJFs) in the near term, nonconventional oil and gas supplies (oil sands, lignite coal, and natural gas) may have a lower environmental footprint than traditional jet fuels and may be easily developed with existing infrastructure. Biocoal can be produced from any carbonaceous materials and biogas can be collected from existing landfills or anaerobic digestion of waste matter from farms and wastewater treatment plants.

One key aspect of the FAA’s *Destination 2025* vision calls for air travel to be environmentally sustainable. This vision is further addressed in the FAA’s March 2012 NextGen Implementation Plan, which calls for reducing aviation’s impact on the environment. The FAA has set forth an ambitious aspirational goal of having one billion gallons of drop-in jet fuel from renewable sources in use by 2018.

Alternative jet fuels (AJFs) are currently under extensive research and development to study the impact of their use in jet engines on noise pollution, engine exhaust and air quality emissions, engine deterioration and wear and complete AJF environmental benefit analysis (through life cycle assessment, LCA). Finally, the issues of supply chain

development, refining infrastructure, scale production, cost and AJF qualification/certification for use in commercial aviation are some of the real-world challenges that face the aviation and energy industries.

Additional reading on AJF may be found at the FAA's website: www.faa.gov, as well as the website of the Commercial Aviation Alternative Fuels Initiative (CAAFI) organization: www.caafi.org. An excellent overview on near-term feasibility of AJF is presented in a 2009 technical (team) report by MIT and Rand Corp. (Hileman *et al.*, 2009). For the technical reports on the standards related to the qualification and certification of aviation fuels, the website of the American Society for Testing and Materials (ASTM), www.astm.org may be consulted.

7.10 Combustion Instability: Screech and Rumble

Acoustic waves propagate at a local speed a in a gas at rest. The acoustic waves “ride the flow,” however, when the gas is in motion. The speed of propagation of a plane acoustic wave along the axis of a duct with a mean flow speed of u is $(u + a)$ in the direction of the flow and $(u - a)$ in the opposite direction. In addition, an open end of a duct or a sudden area increase/decrease in a duct causes a *reflected* wave to propagate back in the duct. These waves contribute to what is known as the *longitudinal acoustic modes* (or organ pipe modes) of a duct. We may imagine the acoustic waves propagating in the radial or in the tangential directions due to disturbances along the axis or azimuth of the duct. For example, fuel injectors in a combustor or an afterburner are placed azimuthally and flameholders in an afterburner are placed radially in the duct. Disturbances generated by these elements predominantly attain tangential and radial characteristics, respectively. The *radial and tangential acoustic modes* have their origin in these kinds of disturbances. Now, let us superimpose a swirl component to the mean flow and observe *spinning (or tangential) modes*. Add axial velocity and we get *helical waves*. These waves interact with each other and the sources of energy in the flow such as the mean flow or pockets of reacting gas mixtures through resonance phenomenon that leads to the growth of the disturbance wave(s) amplitude. This is similar to the dynamics of a mass-spring oscillator. The maximum energy transfer from the forcing mechanism to the driven oscillator (i.e., the mass) is found (i.e., tuned) at the resonance frequency. Nonresonant interactions are not amplified. Large-amplitude pressure waves (>10–15% of the mean) are observed in combustors at frequencies ranging from 50 to 100 Hz for longitudinal modes (called “rumble”) and as high as 5000 Hz for radial and tangential modes (called “screech”). The resonant phenomena in real systems do not have unlimited growth, however, rather they reach a limit cycle. The real systems have damping and nonlinear dynamics, which lead the oscillations to a limit cycle. Due to the large amplitudes of these high-frequency disturbances, the problem of fatigue and structural failure needs to be addressed in combustors. The reflected acoustic wave from the nozzle downstream of an afterburner couples with the combustor oscillations to create a closed-loop instability wave, known as screech.

7.10.1 Screech Damper

A Helmholtz resonator is a cavity that serves as the spring to an oscillating mass, which is contained in the neck of the cavity. The damping occurs at the natural frequency of the cavity, which is a function of the geometry of the cavity and the speed of sound. An acoustic liner composed of numerous Helmholtz resonators integrated within the liner

can be designed to efficiently dampen the acoustic power near the resonant frequency of the cavity. A perforated sheet covering a honeycomb substrate is often used as an acoustic liner.

7.11 Summary

Combustion is a complex and thus challenging process. It involves chemical reactions that take place at the molecular level. The process inevitably involves fuel atomization and vaporization with subsequent mixing with an oxidizer (i.e., air in airbreathing engines) leading to a chemical reaction. We learned that the laws that govern the mixture of gases are important in a chemical reaction. To simplify our analysis, we learned and applied the concept of “chemical equilibrium” to reactions in a combustor. The wealth of experimental data on equilibrium constants allowed us to use the law of mass action to calculate the equilibrium mixture of the products of combustion. Conservation of energy principle then yielded the adiabatic flame temperature. The rate of chemical reactions identified characteristic timescales, for example, evaporation and reaction that in conjunction with the characteristic velocity scales identified a residence time, which then affected the combustor and afterburner designs.

In the combustor design section, we learned about prediffusers, flow mixing through turbulent recirculation zones that may be generated by swirl, bluff bodies, or backward-facing steps. Combustor liner cooling techniques and the use of advanced composite materials promised a lowering in the percentage coolant requirement. The nonuniformity in the combustor-exit flow was characterized by two parameters, namely, a pattern factor and a profile factor. The concern with high-altitude flameout, ignition, and relight issues were presented. Combustor pollutants in the form of UHC, CO, NO_x, and greenhouse gases were discussed, and the design choices that lead to an environmentally friendly combustor were identified.

We have scratched the surface of combustion and combustor design, only. The reader should follow up this material in specialized combustion textbooks, as cited throughout this chapter. In addition, references 16, 22, 23, and 37 provide background and supplementary material and are recommended for further reading. Finally, a new area in renewable aviation fuel, i.e., Alternative Jet Fuels (AJF), was briefly introduced. AJF holds the promise of sustainable commercial aviation in the 21st Century.

References

- Adkins, R. C., “A Short Diffuser with Low Pressure Loss,” ASME Paper, May 1974.
- Adkins, R. C., Matharu, D. S., and Yost, J. O., “The Hybrid Diffuser,” ASME Paper 80-GT-136, 1980.
- Anderson, D. N., “Effect of Equivalence Ratio and Dwell Time on Exhaust Emissions from an Experimental Pre-mixing Pre-vaporizing Burner,” NASA TM-X-71592, 1974.
- Ballal, D. R. and Lefebvre, A. H., “Flame Propagation into Heterogeneous Mixtures of Fuel Droplets, Fuel Vapor and Air,” *Eighteenth International Symposium on Combustion*, The Combustion Institute, Pittsburgh, 1980, pp. 321–328.
- Ballal, D. R. and Lefebvre, A. H., “Structure and Propagation of Turbulent Flames,” Proceedings of the Royal Society of London, Series A, Vol. 344, 1975 pp. 217–234.
- Barclay, L. P., “Pressure Losses in Dump Combustors,” AFAPL-TR-72-57 Air Force Aero-Propulsion Laboratory, Wright-Patterson AFB, OH, 1972.
- Blazowski, W. S., “Fundamentals of Combustion,” Chapter in *Aerothermodynamics of Aircraft Engine*

- Components*, Ed. Oates, G. C., AIAA Education Series, AIAA Inc. Washington, DC, 1985.
8. Blazowski, W. S. and Henderson, R. E., "Aircraft Exhaust Pollution and its Effects on a U.S. Air Force," Air Force Aero Propulsion Lab, Wright-Patterson AFB, OH, Report AFAL-TR-74-64, 1974.
 9. Borman, G. L. and Ragland, K. W., *Combustion Engineering*, McGraw-Hill, New York, 1998.
 10. Dugger, G. L. and Heimel, S., Flame Speeds of Methane-Air, Propane-Air and Ethylene-Air Mixtures at Low Initial Temperatures, NACA TN 2624, 1952.
 11. Environmental Protection Agency, Control of Air Pollution from Aircraft and Aircraft Engines, Federal Register, Vol. 38, No. 136, 1973.
 12. Environmental Protection Agency, Control of Air Pollution from Aircraft and Aircraft Engines, Federal Register, Vol. 43, No. 58, 1978.
 13. Environmental Protection Agency, Control of Air Pollution from Aircraft and Aircraft Engines, Federal Register, Vol. 47, No. 251, 1982.
 14. Glassman, I., *Combustion*, 2nd edition, Academic Press, New York, 1987.
 15. Gouldin, F. C., "Controlling Emissions from Gas Turbines—The Importance of Chemical Kinetics and Turbulent Mixing," *Combustion Science and Technology*, Vol. 7, 1973.
 16. Greenhow, V. W. and Lefebvre, A. H., "Some Application of Combustion Theory to Gas Turbine Development," *Sixth International Symposium on Combustion*, Reinhold, New York, 1957, pp. 858–869.
 17. Haddock, G. H., "Flame Blowoff Studies of Cylindrical Flameholders in Channeled Flow," Jet Propulsion Laboratory, Pasadena, California, Progress Report 3–24, May 1951.
 18. Henderson, R. E. and Blazowski, W. S., "Turbopropulsion Combustion Technology," Chapter in *Aircraft Propulsion Systems Technology and Design*, Ed. Oates, G. C., AIAA Education Series, AIAA Inc., Washington, DC, 1989.
 19. Hileman, J.I., Ortiz, D.S., Bartis, J.T., *et al.*, "Near-Term Feasibility of Alternative Jet Fuels," Technical Report, Rand Corporation, Santa Monica, CA, 2009.
 20. Herbert, J. D., "Theoretical Analysis of Reaction Rate Controlled Systems-Part I," AGARD Combustion Research and Reviews, Chapter 6, 1957.
 21. Hill, P. G. and Peterson, C. R., *Mechanics and Thermodynamics of Propulsion*, 2nd edition, Addison-Wesely, Reading, Massachusetts, 1992.
 22. Howell, J. R. and Buckius, R. O., *Fundamentals of Engineering Thermodynamics*, McGraw-Hill, New York, 1987.
 23. Jones, R. E., Diehl, L. A., Petrash, D. A., and Grobman, J., "Results and Status of the NASA Aircraft Engine Emission Reduction Technology Programs," NASA TM-79009, 1978.
 24. Jost, W., *Explosion and Combustion Processes in Gases*, McGraw-Hill, New York, 1946.
 25. Kerrebrock, J. L., *Aircraft Engines and Gas Turbines*, 2nd edition, MIT Press, Cambridge, Mass., 1992.
 26. Kuo, K. K., *Principles of Combustion*, John Wiley & Sons, Inc., New York, 1986.
 27. Kurzke, J. and Riegler, C., "A Mixed-Flow Turbofan Afterburner Simulation for the Definition of Reheat Fuel Control laws," *RTO-Applied Vehicle Technology panel, Symposium on Design Principles and Methods for Aircraft gas Turbine Engines*, Toulouse, France, 1998.
 28. Lefebvre, A. H., *Gas Turbine Combustion*, Hemisphere Publishing Corp., New York, 1983.
 29. Lefebvre, A. H., "Theoretical Aspects of Gas Turbine Combustion Performance," College of Aeronautics Note Aero 163, Cranfield Institute of Technology, Bedford, England, 1966.
 30. Lefebvre, A. H. and Halls, G. A., "Some Experiences in Combustion Scaling," AGARD Advanced Aero-Engine Testing, AGARDograph 37, Pergamon, New York, 1959, pp. 177–204.
 31. Lewis, B. and von Elbe, G., *Combustion Flames and Explosions of Gases*, Academic Press, New York, 1961.
 32. Lipfert, F. W., "Correlations of Gas Turbine Emissions Data," ASME Paper 72-GT-60, March 1972.
 33. Longwell, J. E., Chenevey, W. W., and Frost, E. E., "Flame Stabilization by Baffles in a High Velocity Gas Stream," *Third Symposium on Combustion, Flame and Explosion Phenomena*, Williams and Wilkins, Baltimore, 1949, pp. 40–44.
 34. Merkur, R. A., "Propulsion System Considerations for Future Supersonic Transports—A Global Perspective," ASME Paper 96-GT-245, 1996.
 35. Nealy, D. A. and Reider, S. B., "Evaluation of Laminated Porous Wall Materials for Combustor Liner Cooling," *Transaction of ASME Journal of Engineering for Power*, Vol. 102, No. 2, April 1980, pp. 268–276.
 36. Olson, W. K., Childs, J. H., and Jonash, E. R., "The Combustion Efficiency Problem of the Turbojet at High Altitude," *Transaction of ASME*, Vol. 77, 1955.
 37. Pinkel, B. and Karp, I. M., "A Thermodynamic Study of the Turbojet Engine," NACA Report No. 891, 1947.
 38. Ragozin, N. A., *Jet Propulsion Fuels*, Pergamon, Oxford, 1962.
 39. Rao, K. V. L. and Lefebvre, A. H., "Spontaneous Ignition Delay Times of Hydrocarbon Fuel/Air Mixtures," *First International Combustion Specialists Symposium*, Bordeaux, France, 1981, pp. 325–330.
 40. Rolls-Royce, The Jet Engine, Rolls-Royce, plc, Derby, England, 2005.

41. Sarpkaya, T., "On Stationary and Traveling Vortex Breakdown," *Journal of Fluid Mechanics*, Vol. 45, Part 3, 1971, pp. 545–559.
42. Spadaccini, L. J., "Autoignition Characteristics of Hydrocarbon Fuels at Elevated Temperatures and Pressures," *Transactions of ASME, Journal of Engineering for Power*, Vol. 99, Ser. A, No. 1, 1977, pp. 83–87 (also ASME Paper 76-GT-3, 1976).
43. Spalding, D. B., *Combustion and Mass Transfer*, Pergamon Press Inc., New York, 1979.
44. Strack, W. C., "Propulsion Challenges and Opportunities for High-Speed Transport Aircraft," Chapter in *Aeropropulsion '87*, NASA CP-3049, November 1987.
45. Strehlow, R. A., *Combustion Fundamentals*, McGraw-Hill, New York, 1984.
46. Tacina, R. R., "Combustion Technology," UTSI Short Course Notes, 2000.
47. Wright, F. H., "Bluff Body Flame Stabilization: Blockage Effects," *Combustion and Flame*, Vol. 3, 1959, p. 319.
48. Zumdahl, S. S. and Zumdahl, S. A., *Chemistry*, 5th edition, Houghton Mifflin Co., Boston, 2000.
49. Zukoski, E. E., "Afterburners," Chapter in *Aerothermodynamics of Aircraft Engine Components*, Ed. Oates, G. C., AIAA Education Series, AIAA Inc. Washington, DC, 1985.
50. Zukoski, E. E. and Marble, F. E., "The Role of Wake Transition in the Process of Flame Stabilization on Bluff Bodies," *Combustion Researches and Reviews*, 1955, Butterworths Scientific Publications, London, 1955.
51. Zukoski, E. E. and Marble, F. E., "Experiments Concerning the Mechanism of Flame Blowoff from Bluff Bodies," *Proceedings of the Gas Dynamics Symposium on Aerothermochemistry*, Northwestern University Press, Evanston, Illinois, 1955.

Problems

7.1 A mixture of gases contains 44 kg of CO₂, 112 kg of N₂, and 32 kg of O₂ at a mixture temperature of $T_m = 287$ K and the mixture pressure is $p_m = 1$ bar.

Calculate

- (a) number of moles of carbon dioxide, nitrogen, and oxygen
- (b) mole fraction of carbon dioxide
- (c) partial pressure of constituent gases, i.e., CO₂, N₂, and O₂
- (d) mixture molecular weight MW_m
- (e) volume fraction of the constituent gases

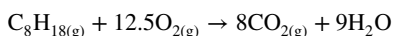
7.2 Write the chemical reaction for the combustion of hydrogen, H₂, and air then calculate the stoichiometric fuel-to-air ratio f_{stoich} .

7.3 A gas is a mixture of 22% O₂, 33% N₂, and 45% CO₂ by volume. Calculate

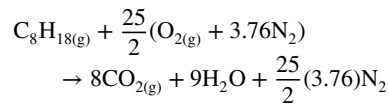
- (a) the mole fraction of the constituents in the mixture
- (b) the mixture molecular weight MW_m

7.4 Write the chemical reaction for the complete combustion of JP-4 and air. JP-4 has the formula CH_{1.93}. Also, calculate the stoichiometric fuel-to-air ratio for this blended jet fuel.

7.5 Calculate the lower and higher heating values of octane, C₈H₁₈, in the stoichiometric chemical reaction with oxygen at a reference temperature of 298.16 K and the pressure of 1 bar.



7.6 Establish the higher and lower heating values of octane, C₈H₁₈, by considering the stoichiometric reaction in air at a reference temperature of 298.16 K and at 1 bar pressure.



Compare your answer to Problem 7.5 and explain.

7.7 Adiabatic flame temperature associated with the combustion of a fuel in air depends on the temperature and pressure of air. Figure 7.6 shows the adiabatic flame temperature of Jet-A fuel in air with initial temperature of 800 K and initial pressure of 25 atm.

- (a) What is the stoichiometric flame temperature of JP-A if the initial air temperature was 1000 K at 25 atm pressure?
- (b) What is the stoichiometric flame temperature of Jet-A if the initial pressure of air was 1 atm and the initial temperature remained at 800 K?

7.8 Consider burning methane (CH₄) with 110% theoretical air. Calculate the equivalence ratio for this reaction. Assume that the nitrogen and the excess oxygen do not dissociate and/or chemically react to form new compounds.

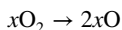
7.9 One mole of octane is burned with 120% theoretical air. Assuming that the octane and air enter the combustion chamber at 25°C and the excess oxygen and nitrogen in the reaction will not dissociate, calculate

- (a) the fuel–air ratio
- (b) the equivalence ratio ϕ
- (c) the adiabatic flame temperature T_{af}

Assume

$$\begin{aligned}\bar{c}_{p\text{CO}_2} &= 61.9 \text{ kJ/kmol} \cdot \text{K}, \quad \bar{c}_{p\text{O}_2} = 37.8 \text{ kJ/kmol} \cdot \text{K} \\ \bar{c}_{p\text{N}_2} &= 33.6 \text{ kJ/kmol} \cdot \text{K}, \quad \bar{c}_{p\text{H}_2\text{O}} = 52.3 \text{ kJ/kmol} \cdot \text{K}\end{aligned}$$

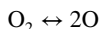
7.10 One mole of oxygen, $\text{O}_{2(\text{g})}$, is heated to 4000 K at the pressure of p_m . A fraction of the oxygen dissociates to oxygen atoms according to



Assuming a state of equilibrium is reached in the mixture, calculate

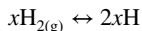
- (a) mole fraction of O_2 at equilibrium when p_m is 1 atm.
- (b) mole fraction of O_2 at equilibrium when p_m is 10 atm.

Assume the equilibrium constant for the reaction



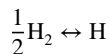
is $K_p = 2.19$ atm at the temperature of 4000 K. Explain the effect of pressure on dissociation.

7.11 One mole of gaseous hydrogen is heated to 3000 K at the pressure of p_m . Assuming a fraction of the hydrogen dissociates upon heating into atomic hydrogen, i.e.,



calculate the mole fraction of hydrogen, H_2 , in the equilibrium mixture for $p_m = 1$ atm and $p_m = 10$ atm. Does higher mixture pressure inhibit or promote the dissociation of hydrogen?

You may find the equilibrium constant K_p for the following stoichiometric reaction



at 3000 K from Table 7.3.

7.12 Mass flow rate (combined fuel and air) into a reactor of volume 2.35 ft^3 is 100 lbm/s . The equivalence ratio is 0.6. Use the combustor loading parameter (CLP)

$$\frac{\dot{m}}{p^n V} = f(\phi)$$

and the combustor stability loop (Figure 7.22) to establish the range of reactor pressure that leads to a stable combustion. Note that the scale is logarithmic.

7.13 Combustion involves many timescales. For example, a flammable mixture of fuel and air (under a spontaneous ignition temperature condition) experiences an ignition delay time t_i . The elements contributing to the ignition delay time are the fuel droplet evaporation time and a reaction timescales. The ignition delay results of the combustion of two hydrocarbon fuels at 10 atm of pressure are shown in Figure 7.24. Graph an estimated ignition delay time for the same fuels but at the pressure of 30 atm by assuming pressure dependence for the reaction timescale is For a first-order approximation, you may neglect the evaporation time dependence on the mixture pressure.

- (a) $1/p$
- (b) $1/p^{1.5}$

7.14 An afterburner uses flameholders with a drag coefficient of $C_D = 0.5$, based on the afterburner cross-sectional area. The inlet Mach number to the afterburner is $M_i = 0.2$, with $\gamma_i = 1.33$. The heat release due to combustion in the afterburner is $q/c_{p_i}T_{i_i} = 2.0$. The exhaust gas in the wet mode has a lower ratio of specific heats, namely, $\gamma_e = 1.30$. Calculate

Dry mode

- (a) exit Mach number M_e
- (b) total pressure loss as a percentage of inlet total pressure

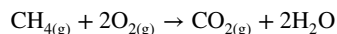
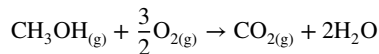
Wet mode

- (c) exit Mach number M_e
- (d) total pressure loss as a percentage of inlet total pressure

7.15 A combustion chamber uses a prediffuser with a sudden area expansion (known as a dump diffuser) to decelerate the flow of air ($\gamma = 1.4$) before entering the combustor. Assuming the inlet Mach number to the dump diffuser is $M_1 = 0.5$, the area ratio of the dump diffuser is $A_2/A_1 = 2.0$, calculate

- (a) exit Mach number M_2
- (b) the ratio of total pressures, i.e., p_{t2}/p_{t1}

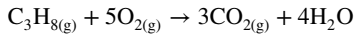
7.16 Calculate the higher and lower heating values of methyl alcohol, CH_3OH , and methane, CH_4 , by considering the following reactions at the reference temperature of 298.16 K and at 1 bar pressure.



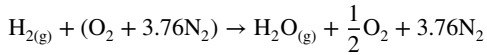
Note that the products of combustion for both reactions are the same. Explain the difference between the heating values of these two fuels that are *seemingly* so similar.

7.17 Calculate the lower and higher heating values of propane, C_3H_8 , in the following chemical reaction at a

reference temperature of 298.16 K and the pressure of 1 bar.



7.18 Gaseous hydrogen and air enter an adiabatic combustion chamber at a temperature of 298.16 K (the reference temperature) and pressure of 1 bar.



Assuming the average molar specific heats of the products are

$$\begin{aligned} \bar{c}_{pO_2} &= 37.8 \text{ kJ/kmol} \cdot \text{K}, & \bar{c}_{pN_2} &= 33.6 \text{ kJ/kmol} \cdot \text{K}, \\ \bar{c}_{pH_2O} &= 52.3 \text{ kJ/kmol} \cdot \text{K} \end{aligned}$$

Calculate

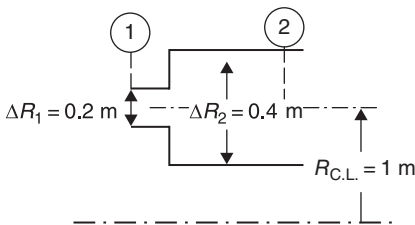
- (a) fuel-to-air ratio
- (b) the adiabatic flame temperature T_{af}

7.19 Stoichiometric flame temperature for the combustion of methane in oxygen at 1 atm pressure and at reference temperature of 298 K is listed as 3030 K in Table 7.4. The combustion of methane in air would produce the stoichiometric flame temperature of 2210 K. Explain the difference.

7.20 An annular combustor utilizes a dump prediffuser, as shown. Calculate

- (a) the diffuser area ratio A_2/A_1
- (b) the total pressure loss $\Delta p_t/p_{t1}$
- (c) exit Mach number M_2

Assume the inlet Mach number is $M_1 = 0.4$ and $\gamma = 1.4$.



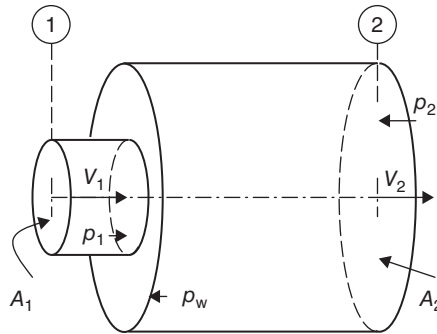
■ FIGURE P 7.20

7.21 Consider a coaxial dump diffuser with area ratio A_2/A_1 . Assuming that the static pressure acting on the sudden expansion wall p_w is the same as the inlet static pressure p_1 and wall friction may be neglected, apply the conservation principles to show that

$$\frac{\Delta p_t}{\rho V_1^2 / 2} = \left(1 - \frac{A_1}{A_2}\right)^2$$

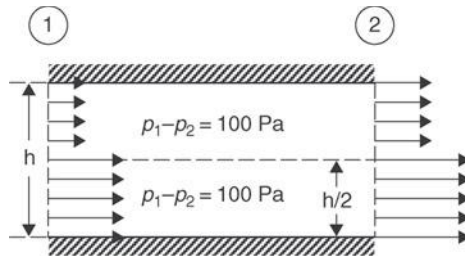
in the limit of incompressible fluid.

Assume the flow is uniform at the exit.



■ FIGURE P 7.21

7.22 Take two parallel streams with initial speeds of 20 and 30 m/s, as shown.



■ FIGURE P 7.22

Assuming the two streams do not mix and thus remain parallel, calculate

- (a) the initial distortion level
- (b) the final speed of both streams
- (c) the final distortion level
Here, we define the distortion level as $\Delta u/\bar{u}$ where \bar{u} is the area-averaged u . Assume the fluid density is constant at 1 kg/m^3 . Why did the distortion level decrease in this case?
- (d) Repeat this problem with a static pressure rise $p_1 - p_2 = -100 \text{ Pa}$, instead of a static pressure drop. Explain the distortion level behavior.

7.23 The effect of flammability limit on gasoline-air mixture as a function of combustion pressure is presented in Figure 7.11. First, what is the lowest pressure that combustion is possible? Second, at combustion pressure of 1.8 psia, what are the equivalence ratios corresponding to the flammability limits?

7.24 We model an afterburner as a constant-area duct with a series of bluff bodies in the stream with a known drag coefficient. Assuming the following inlet conditions for dry mode

Inlet Mach number $M_i = 0.3$
 $\gamma_i = \gamma_e = 1.33$ and $c_{pi} = c_{pe}$
 flameholder drag coefficient $C_D = 0.5$

Calculate

- static pressure ratio p_e/p_i
- exit Mach number M_e
- static temperature ratio T_e/T_i
- total pressure ratio p_{te}/p_{ti}

7.25 The afterburner in Problem 7.24 operates in “wet mode.” Assuming the nondimensional heat release $q/c_{pi}T_{ti} = 1.0$ and $\gamma_e = 1.25$ in wet mode, calculate

- total pressure ratio in the wet mode
- exit Mach number in the wet mode

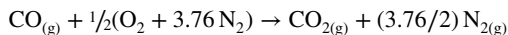
7.26 Atmospheric ozone is depleted through catalytic intervention of nitric oxide, NO. NO emissions in the upper atmosphere are estimated to be ~ 30 g/kg fuel from high-temperature engines, overextended cruise periods. A supersonic transport carries 50,000 kg of fuel at takeoff. Assuming 90% of the fuel is consumed during cruise calculate the amount of nitric oxide emissions for a round trip flight. Now, multiply that by 360 round trips per year to estimate the (NO) pollution (of one aircraft) per year. Finally, what is the environmental impact of a fleet of 100 aircraft?

7.27 Emission index (EI) of carbon monoxide and unburned hydrocarbons at idle power is shown in Figure 7.49. Assuming that the combustor inlet temperature at idle power is 425 K, read an average value of the emission index for carbon monoxide and unburned hydrocarbons from the graph. Then, calculate the combustion inefficiency from

$$1 - \eta_b = [0.232(\text{EI})_{\text{CO}} + (\text{EI})_{\text{UHC}}] \times 10^{-3}$$

and compare the combustion efficiency η_b at idle setting to EPA standards (of 99%).

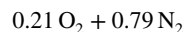
7.28 Carbon monoxide is a byproduct of incomplete combustion of hydrocarbon fuels and is considered to be a pollutant. It is also a fuel capable of reacting with air to produce an adiabatic flame temperature of ~ 2400 K at the pressure of 1 atm (Table 7.4). The stoichiometric combustion of carbon monoxide and air may be described by the following reaction:



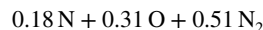
Use conservation of energy principles applied to the above stoichiometric reaction to show that the adiabatic flame temperature of carbon monoxide is indeed ~ 2400 K in a reaction with air at 1 atmospheric pressure.

You may use Table 7.1 for standard heats of formation and Table 7.2 for molar specific heats of various gases. Assume the reactants enter the combustion chamber at $T_f = 298.16$ K.

7.29 Air composition at room temperature is approximated by 21% O_2 and 79% N_2 by volume, or by mole fractions, i.e., one mole of air is composed of



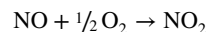
Strong shocks are, however, formed when aircraft fly at supersonic/hypersonic Mach numbers. The composition of air thus changes as a sudden compression is encountered through a shock. At 6000 K and one atmospheric pressure, one mole of air assumes the following equilibrium composition:



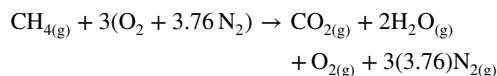
Calculate

- the molecular weight of air in the new mixture, MW_m , in kg/kmol
- the fuel-to-air ratio for the stoichiometric combustion of hydrogen in air (at 6000 K)

7.30 Unburned hydrocarbons, UHC, and nitric oxide, NO, are formed as products of combustion in aircraft gas turbine engines. They lead to burner inefficiency, as they still possess heating value. Consider the combustion of NO, at reference temperature and pressure, to estimate the heating value of NO, in the following stoichiometric reaction:



7.31 Combustion of gaseous methane with dry air is shown as:



Assuming the air entered at reference temperature of $T_f = 298.16$ K and pressure of 1 bar, calculate the

- fuel-to-air ratio, f
- equivalence ratio,
- adiabatic flame temperature, T_{af} , in K

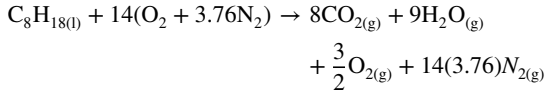
Use the chemical properties shown in the box.

$\Delta \bar{h}_f^\circ _{\text{CH}_{4(g)}} = -74,873$ kJ/kmol
$\Delta \bar{h}_f^\circ _{\text{H}_2\text{O}_{(g)}} = -241,827$ kJ/kmol
$\Delta \bar{h}_f^\circ _{\text{CO}_{2(g)}} = -393,522$ kJ/kmol
$\bar{c}_{p\text{CO}_2} = 54.31$ kJ/kmol · K $\bar{c}_{p\text{O}_2} = 34.88$ kJ/kmol · K
$\bar{c}_{p\text{N}_2} = 32.7$ kJ/kmol · K $\bar{c}_{p\text{H}_2\text{O}} = 41.22$ kJ/kmol · K

7.32 Write the stoichiometric combustion of methanol (CH_3OH) in (dry) theoretical air. If the lower heating value,

LHV, of methanol is 21.2 MJ/kg, calculate its higher heating value, HHV.

7.33 Calculate the adiabatic flame temperature in the following reaction of octane in dry air at reference temperature ($T_f = 298.16$ K) and pressure (1 bar),



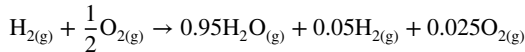
Assume the average molar specific heats of the chemical compounds at constant pressure are:

$$\begin{aligned} \bar{c}_{p\text{CO}_2} &= 54.31 \text{ kJ/kmol} \cdot \text{K} & \bar{c}_{p\text{O}_2} &= 34.88 \text{ kJ/kmol} \cdot \text{K} \\ \bar{c}_{p\text{N}_2} &= 32.7 \text{ kJ/kmol} \cdot \text{K} & \bar{c}_{p\text{H}_2\text{O}} &= 41.22 \text{ kJ/kmol} \cdot \text{K} \end{aligned}$$

The standard heats of formation in this reaction are:

$$\begin{aligned} \Delta \bar{h}_f^\circ |_{\text{C}_8\text{H}_{18(l)}} &= -249,930 \text{ kJ/kmol}, \\ \Delta \bar{h}_f^\circ |_{\text{H}_2\text{O}(g)} &= -241,827 \text{ kJ/kmol}, \\ \Delta \bar{h}_f^\circ |_{\text{CO}_2(g)} &= -393,522 \text{ kJ/kmol} \end{aligned}$$

7.34 In the combustion of gaseous hydrogen and gaseous oxygen, as described by



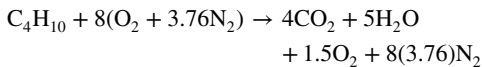
the reactants entered the combustion chamber at $T_1 = 298.16$ K and pressure of 1 atm. Assume:

$$\begin{aligned} \left(\Delta \bar{h}_f^\circ \right)_{\text{H}_2\text{O}(g)} &= -241,827 \text{ kJ/kmol} & \bar{c}_{p\text{O}_2} &= 37.8 \text{ kJ/kmol} \cdot \text{K} \\ \bar{c}_{p\text{H}_2} &= 34.18 \text{ kJ/kmol} \cdot \text{K} & \bar{c}_{p\text{H}_2\text{O}} &= 51.0 \text{ kJ/kmol} \cdot \text{K} \end{aligned}$$

Calculate the

- heat of reaction, Q_R , in kJ
- lower heating value, LHV, in kJ/kg
- adiabatic flame temperature, T_{af} , in K

7.35 Consider the combustion of butane and air according to

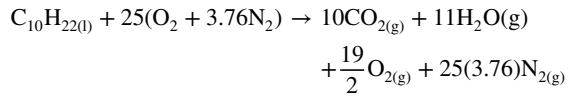


Calculate the

- fuel-to-air ratio, f
- equivalence ratio, ϕ , for this reaction

7.36 Lean combustion of liquid n -decane (from the kerosene family) and air at a reference temperature of

$T_f = 298.16$ K and pressure of 1 bar is approximated by the following chemical reaction:



Assuming the standard heats of formation in this reaction are:

$$\begin{aligned} \Delta \bar{h}_f^\circ |_{\text{C}_{10}\text{H}_{22(l)}} &= -300,900 \text{ kJ/kmol} \\ \Delta \bar{h}_f^\circ |_{\text{H}_2\text{O}(g)} &= -241,827 \text{ kJ/kmol}, \\ \Delta \bar{h}_f^\circ |_{\text{CO}_2(g)} &= -393,522 \text{ kJ/kmol} \end{aligned}$$

and average molar specific heats at constant pressure are:

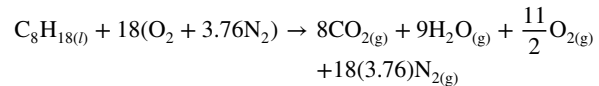
$$\begin{aligned} \bar{c}_{p\text{CO}_2} &= 54.31 \text{ kJ/kmol} \cdot \text{K} & \bar{c}_{p\text{O}_2} &= 34.88 \text{ kJ/kmol} \cdot \text{K} \\ \bar{c}_{p\text{N}_2} &= 32.7 \text{ kJ/kmol} \cdot \text{K} & \bar{c}_{p\text{H}_2\text{O}} &= 41.22 \text{ kJ/kmol} \cdot \text{K} \end{aligned}$$

Calculate

- the fuel-to-air ratio, f , for this reaction
- write the stoichiometric reaction for this fuel in air
- the equivalence ratio, ϕ
- the adiabatic flame temperature, T_{af} , in K in the first reaction
- the Lower Heating Value (LHV) of this fuel, in kJ/kg, in stoichiometric combustion in oxygen

7.37 Write the stoichiometric combustion of propane (C_3H_8) in theoretical air. If the lower heating value, LHV, of propane is 46.32 MJ/kg, calculate its higher heating value, HHV.

7.38 Calculate the adiabatic flame temperature in the combustion reaction of octane in air at reference temperature ($T_f = 298.16$ K) and pressure (1 bar),



You may assume the average molar specific heats of the compounds at constant pressure are:

$$\begin{aligned} \bar{c}_{p\text{CO}_2} &= 54.31 \text{ kJ/kmol} \cdot \text{K} & \bar{c}_{p\text{O}_2} &= 34.88 \text{ kJ/kmol} \cdot \text{K} \\ \bar{c}_{p\text{N}_2} &= 32.7 \text{ kJ/kmol} \cdot \text{K} & \bar{c}_{p\text{H}_2\text{O}} &= 41.22 \text{ kJ/kmol} \cdot \text{K} \end{aligned}$$

The standard heats of formation in this reaction are listed in Table 6.1 in the book as:

$$\Delta \bar{h}_f^\circ |_{\text{C}_8\text{H}_{18(l)}} = -249,930 \text{ kJ/kmol},$$

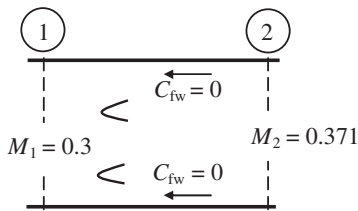
$$\Delta \bar{h}_f^o \Big|_{\text{H}_2\text{O}(\text{g})} = -241,827 \text{ kJ/kmol},$$

$$\Delta \bar{h}_f^o \Big|_{\text{CO}_2(\text{g})} = -393,522 \text{ kJ/kmol}$$

7.39 Consider the flow in an afterburner, in *dry mode*, as shown. The flow upstream of the flameholder, i.e., the afterburner inlet, is characterized by:

$$p_1 = 33 \text{ kPa}, \quad T_1 = 675 \text{ K}, \quad M_1 = 0.3, \quad \dot{m}_1 = 100 \text{ kg/s},$$

$$\gamma_1 = 1.33, \quad R_1 = 287 \text{ J/kgK}$$

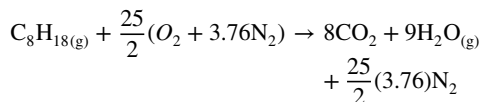


■ **FIGURE P7.39**

Assuming the flameholder drag coefficient is $C_D = 1.0$, which is based on the duct cross-sectional area, and the flow is *adiabatic*, calculate

- the duct cross sectional area, A_1 , in m^2
- flameholder drag, $D_{\text{flameholder}}$, in kN
- static pressure in station 2, where $M_2 = 0.371$, $\gamma_2 = \gamma_1 = 1.33$ and wall friction drag coefficient is neglected (i.e., $C_{fw} = 0$) as shown
- static temperature in station 2, T_2 , in K

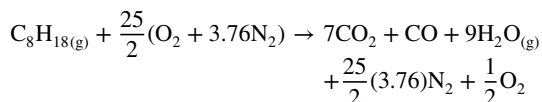
7.40 Consider the stoichiometric combustion of one mole of octane in dry air, where the carbon in fuel is completely oxidized to form eight moles of CO_2 in the products, as shown in the following reaction



Assuming the reactants entered the combustion chamber at reference temperature of 298.16 K and combustion takes place at reference pressure of 1 bar, calculate:

- adiabatic flame temperature, T_{af} (K), of octane in the above reaction

Now, consider the same reactants at the same entrance condition and pressure engage in combustion that produces seven moles of carbon dioxide and one mole of carbon monoxide in the products of combustion, following



Calculate

- the adiabatic flame temperature of octane in the second reaction
- compare the two adiabatic flame temperatures and briefly comment on the cause for the difference

$$\bar{c}_{p\text{N}_2} = 33.6 \text{ kJ/kmol} \cdot \text{K} \quad \bar{c}_{p\text{CO}_2} = 57.9 \text{ kJ/kmol} \cdot \text{K}$$

$$\bar{c}_{p\text{O}_2} = 37.8 \text{ kJ/kmol} \cdot \text{K} \quad \bar{c}_{p\text{H}_2\text{O}(\text{g})} = 42.3 \text{ kJ/kmol} \cdot \text{K}$$

$$\bar{c}_{p\text{CO}(\text{g})} = 36.27 \text{ kJ/kmol} \cdot \text{K}$$

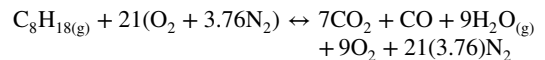
$$\left(\Delta \bar{h}_f^o\right)_{\text{C}_8\text{H}_{18(\text{g})}} = -208,447 \text{ kJ/kmol}$$

$$\left(\Delta \bar{h}_f^o\right)_{\text{H}_2\text{O}(\text{g})} = -241,827 \text{ kJ/kmol}$$

$$\left(\Delta \bar{h}_f^o\right)_{\text{CO}_2(\text{g})} = -393,522 \text{ kJ/kmol}$$

$$\left(\Delta \bar{h}_f^o\right)_{\text{CO}(\text{g})} = -110,530 \text{ kJ/kmol}$$

7.41 The chemical reaction of gaseous octane in air reaches an equilibrium state in a combustor that is described by:



Assuming the reactants entered the combustor at the reference temperature (298.16 K) and pressure (1 atm), calculate the

- fuel-to-air ratio, f
- equivalence ratio, ϕ
- adiabatic flame temperature, T_{af} , in K, at the combustor exit

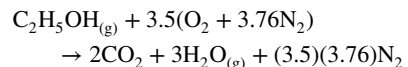
Assume the molar specific heats of the products are:

$$\bar{c}_{p\text{CO}_2} = 61.9 \text{ kJ/kmol} \cdot \text{K}, \quad \bar{c}_{p\text{O}_2} = 37.8 \text{ kJ/kmol} \cdot \text{K},$$

$$\bar{c}_{p\text{N}_2} = 33.6 \text{ kJ/kmol} \cdot \text{K},$$

$$\bar{c}_{p\text{H}_2\text{O}} = 52.3 \text{ kJ/kmol} \cdot \text{K}, \quad \bar{c}_{p\text{CO}} = 29.2 \text{ kJ/kmol} \cdot \text{K}$$

7.42 Consider the stoichiometric combustion of gaseous ethyl alcohol (or ethanol) in air, as shown:



Assuming the reactants entered the combustion chamber at reference temperature of 298.16 K and combustion takes place at reference pressure of 1 bar, calculate the

- adiabatic flame temperature, T_{af} , in K, of ethanol in stoichiometric combustion
- lower heating value (LHV) of ethanol in kJ/kg
- higher heating value (HHV) of ethanol in kJ/kg

$$\bar{c}_{pN_2} = 33.6 \text{ kJ/kmol} \cdot \text{K}$$

$$\bar{c}_{pCO_2} = 61.9 \text{ kJ/kmol} \cdot \text{K}$$

$$\left(\Delta\bar{h}_f^0\right)_{C_2H_5OH(g)} = -235,000 \text{ kJ/kmol}$$

$$\bar{c}_{pH_2O(g)} = 52.3 \text{ kJ/kmol} \cdot \text{K}$$

$$\left(\Delta\bar{h}_f^0\right)_{CO_2(g)} = -393,522 \text{ kJ/kmol}$$

$$\left(\Delta\bar{h}_f^0\right)_{H_2O(g)} = -241,827 \text{ kJ/kmol}$$

7.43 Write the stoichiometric combustion of C_6H_6 with (dry) theoretical air.

7.44 Consider the stoichiometric combustion of Jet-A fuel, $C_{12}H_{23}$, in (dry) air.

- (a) Write the chemical reaction between Jet-A fuel and air in stoichiometric combustion
- (b) Calculate stoichiometric fuel-to-air ratio in this reaction

Axial Compressor Aerodynamics



Source: Reproduced with permission from Rolls-Royce plc

8.1 Introduction

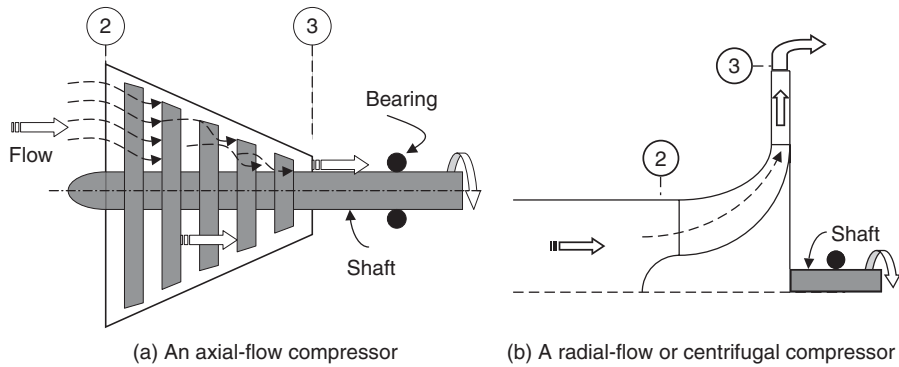
In this chapter, we address compressors and turbines in an aircraft gas turbine engine. We first present the fundamental equations that are applicable to all types of turbomachinery and then follow with the flow characteristics of each machine in subsequent Chapters 9 and 10.

Turbomachinery is at the heart of gas turbine engines. The role of mechanical compression of air in an engine is given to the compressor. The shaft power to drive the compressor typically is produced by expanding gases in the turbine. The machines that exchange energy with a fluid, called the working fluid, through shaft rotation are known as turbomachinery. The machines where the fluid path is predominantly along the axis of the shaft rotation are called axial-flow turbomachinery. In contrast to these machines, in radial-flow turbomachinery the fluid path undergoes a 90° turn from the axial direction. These machines are sometimes referred to as centrifugal machines. A mixed-flow turbomachinery is a hybrid between the axial and the radial-flow machines. In aircraft gas turbine engines, the axial-flow compressors and turbines enjoy the widest application and development (Figure 8.1). The centrifugal compressors and radial-flow turbines are used in small gas turbine engines and automotive turbocharger applications.

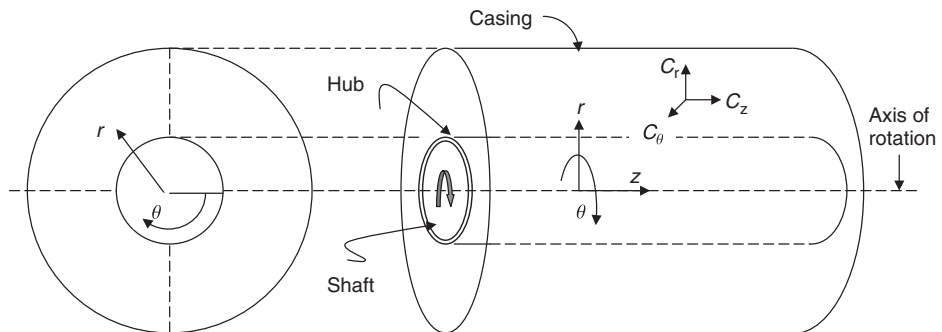
8.2 The Geometry

The geometry of rotating blades demands a cylindrical duct with a shaft centric configuration. This in turn leads to the choice of cylindrical coordinates for the analysis of flows in

■ **FIGURE 8.1**
Schematic drawing of
different types of
compressors in aircraft
gas turbine engines



■ **FIGURE 8.2**
Definition sketch for
the coordinates and the
velocity components of
the flow in cylindrical
coordinates

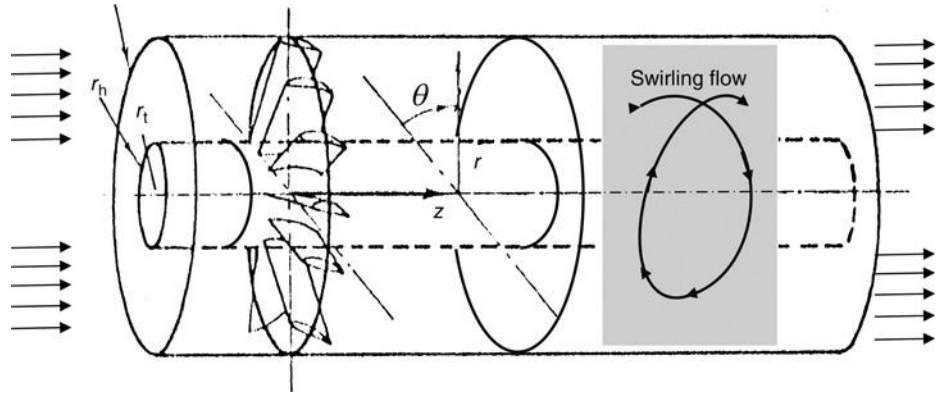


turbomachinery. The coordinates $[r, \theta, z]$ are in radial, tangential or azimuthal, and axial directions, respectively. The velocity components $[C_r, C_\theta, C_z]$ are the radial, tangential (or sometimes referred to as swirl or azimuthal velocity), and axial velocity components, respectively. These are shown in a definition sketch in Figure 8.2.

8.3 Rotor and Stator Frames of Reference

In turbomachinery, energy transfer between the blades and the fluid takes place in an inherently unsteady manner. This is achieved by a set of rotating blades, called the rotor. The rotor blades are three-dimensional aerodynamic surfaces, which experience aerodynamic forces. The rotor blades are cantilevered at the hub and thus feel a root bending moment and a torque. The reaction to the blade forces and moments is exerted on

■ **FIGURE 8.3**
Isolated rotor in a
cylinder. Source:
Adapted from Marble
1964



the fluid, via the action–reaction principle of Newton. Stationary blades called the stator follow the rotor blades in what is known as a turbomachinery *stage*. The stator blades are three-dimensional aerodynamic surfaces as well. They are cantilevered from the casing and experience forces and moments, like the rotor. The exception is that the stator forces and moments are stationary (in the laboratory frame of reference) and thus perform no work on the fluid. The energy of the fluid is, thus, expected to remain constant in passing through the stator blades. The position of the observer is, however, important in viewing the flowfield and the energy exchange in turbomachinery. An observer fixed at the casing (or laboratory) is called an *absolute* observer. If the observer is attached to the rotor blade and spins with it, then it is called a *relative* observer. The frames of reference are then called the absolute and relative frames of reference, respectively. Consider an isolated rotor in a cylindrical duct, as shown in Figure 8.3. An absolute observer sees the blades' aerodynamic forces are in motion, at an angular rate, that is, the angular velocity ω of the shaft. Hence, as measured by this observer, the total enthalpy of the fluid goes up in crossing the rotor row. On the contrary, let us put ourselves in the frame of reference of a relative observer who is spinning with the rotor. According to a relative observer, the blades are not moving! An observer fixed at the rotor measures aerodynamic forces and moments of the blades, however, as the forces are stationary, there is no work done on the fluid according to this observer. Thus, the relative observer measures the same total enthalpy across the blade row.

The flowfield as seen by a relative observer attached to an isolated rotor in a cylinder is thus steady. The absolute observer on the casing, however, sees the passing of the blades and thus experiences an unsteady flowfield. As the rotor blades pass by, a periodic pressure pulse (due to blade tip) is registered at the casing, which signifies an unsteady event with a periodicity of blade passing frequency. To be able to analyze a flowfield in a steady frame of reference offers tremendous advantages in the nature and the solution of governing equations. Consequently, in analyzing the flow within a rotor blade row, we employ the relative observer stance, while the stator flows are viewed from the standpoint of an absolute observer. We need to be mindful, however, that in practice there are no isolated rotors and thus the flowfield in rotating machinery is *inherently* unsteady. We shall present some preliminary discussions on the scale and effect of unsteadiness in axial-flow compressors later in this chapter.

The velocity components as seen by observers in the two frames of reference are related. First, we note that the radial and axial velocity components are identical in the two

frames, as the relative observer moves only in the θ , or the angular, direction. Therefore, the swirl or tangential velocity is the only component of the velocity vector field that is affected by the observer rotation. At a radial position r on the rotor, the relative observer rotates with a speed ωr and thus registers a tangential velocity, which is ωr less than the absolute swirl velocity, that is,

$$\text{Relative swirl} = \text{Absolute swirl} - \omega r \tag{8.1}$$

The fluid velocity vectors in the two frames are labeled as \vec{C} and \vec{W} for the absolute and relative observers, respectively. Therefore, the absolute velocity vector is described as

$$\vec{C} = C_r \hat{e}_r + C_\theta \hat{e}_\theta + C_z \hat{e}_z \tag{8.2}$$

The relative velocity vector is

$$\vec{W} = W_r \hat{e}_r + W_\theta \hat{e}_\theta + W_z \hat{e}_z \tag{8.3}$$

The rotor blade spins with an angular velocity ω , hence it describes a solid body rotation as

$$\vec{U} = \omega r \hat{e}_\theta \tag{8.4}$$

Comparing the velocity vectors as described by Equations 8.2–8.4, we conclude that the following vector identities hold, namely,

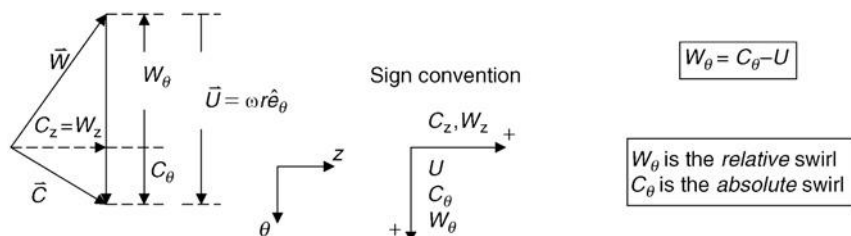
$$\vec{W} = \vec{C} - \vec{U} \tag{8.5a}$$

$$\vec{C} = \vec{W} + \vec{U} \tag{8.5b}$$

These three vectors form a triangle known as the *velocity triangle*.

Figure 8.4 shows a definition sketch of the velocity triangle and the sign convention. The positive tangential or azimuthal angle θ is in the direction of rotor rotation \vec{U} . The swirl velocity component is considered positive if in the direction of rotor rotation. For example, we note that the absolute swirl is pointing in the positive θ direction, therefore it is considered positive. The relative swirl velocity component W_θ is in the opposite direction, hence it is a negative quantity. The scalar relation given in Equation 8.1 between the two swirl components is always valid.

■ FIGURE 8.4
The velocity triangle



8.4 The Euler Turbine Equation

The Euler turbine equation is called the fundamental equation of turbomachinery. Once we derive this simple yet powerful expression, its significance becomes evident. Let us consider a streamtube that enters a turbomachinery blade row. Figure 8.5 illustrates a generic streamtube with its geometry and velocity components. In general, stream surfaces undergo a radial shift when interacting with a blade row, as depicted in Figure 8.5.

The mass flow rate in the streamtube is constant, by definition, and is labeled as \dot{m} . The angular momentum of the fluid in the streamtube is the moment of the tangential momentum of the fluid about the axis of rotation, namely,

$$(\text{Time rate of change of the}) \text{ Fluid angular momentum} = \dot{m}rC_\theta \quad (8.6)$$

The change of fluid angular momentum between the exit and inlet of the streamtube is the applied torque exerted by the blade on the fluid, that is,

$$\dot{m}(r_2C_{\theta 2} - r_1C_{\theta 1}) = \tau_{\text{fluid}} \quad (8.7a)$$

The torque is the product of blade tangential force F_θ and the moment arm r from the axis of rotation. Hence the blade torque is

$$\tau_{\text{blade}} = F_{\theta, \text{blade}} \cdot r = -\tau_{\text{fluid}} \quad (8.7b)$$

The expression 8.7a (or 8.7b) is valid for the rotor as well as the stator. In case of rotor, there is an angular motion, hence the product of the angular velocity of the blade and the torque provides the power transmitted to the fluid, namely,

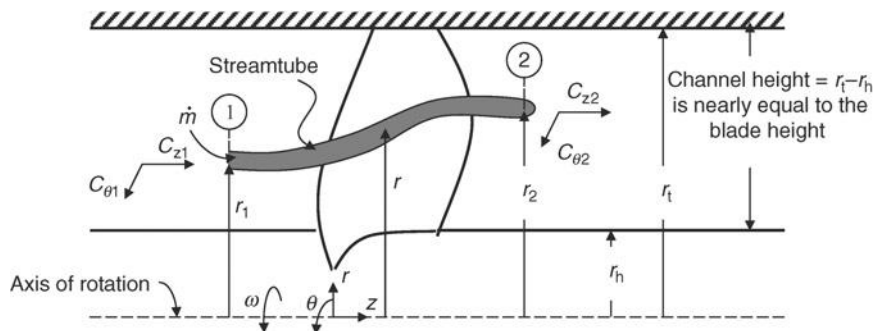
$$\dot{\mathcal{P}} = \tau_{\text{fluid}} \cdot \omega = \dot{m}\omega(r_2C_{\theta 2} - r_1C_{\theta 1}) = \dot{m}\omega\Delta(rC_\theta) \quad (8.8)$$

The ratio of shaft power to mass flow rate is called the specific work of the rotor, w_c for the compressor and w_t for the turbine, hence,

$$w_c \equiv \frac{\dot{\mathcal{P}}_c}{\dot{m}_c} = \omega\Delta(rC_\theta)_c \quad (8.9a)$$

$$w_t \equiv \frac{\dot{\mathcal{P}}_t}{\dot{m}_t} = \omega\Delta(rC_\theta)_t \quad (8.9b)$$

■ **FIGURE 8.5**
Streamtube interacting
with a turbomachinery
blade row



This is the Euler turbine equation written for the fluid interacting with a compressor or turbine rotor. As evidenced in Equation 8.9, the rotor (specific) work appears as the change in (specific) angular momentum across a blade row times the shaft speed. The rotor and stator torques are proportional to the change in angular momentum across the rotor and stator blade rows, respectively, via Equation 8.7.

The first law of thermodynamics applied to a steady and adiabatic process demands that the change of total enthalpy of the fluid across the blade row to be equal to the blade-specific work delivered to the fluid, namely,

$$h_{t2} - h_{t1} = \frac{\mathcal{G}}{\dot{m}} = w_c \quad (8.10a)$$

From the Euler turbine equation, the exit stagnation enthalpy in Equation 8.10a is related to the inlet stagnation enthalpy and the change of the angular momentum across the rotor row,

$$h_{t2} = h_{t1} + \omega \Delta(rC_\theta) \quad (8.10b)$$

The nondimensional total enthalpy change is then

$$\frac{h_{t2}}{h_{t1}} = 1 + \frac{\omega \Delta(rC_\theta)}{h_{t1}} = \frac{T_{t2}}{T_{t1}} \quad (8.10c)$$

Note that we assumed a calorically perfect gas in Equation 8.10c when we replaced the ratio of stagnation enthalpy with the ratio of total temperatures.

8.5 Axial-Flow Versus Radial-Flow Machines

In an axial-flow turbomachinery, the fluid path is predominantly along the axis of rotation. In radial-flow or centrifugal machinery, the fluid path departs from axial and attains a predominantly radial motion at the exit. As a result, the following approximation is typically made for axial-flow machines,

$$r_1 \approx r_2 \approx r \quad (8.11)$$

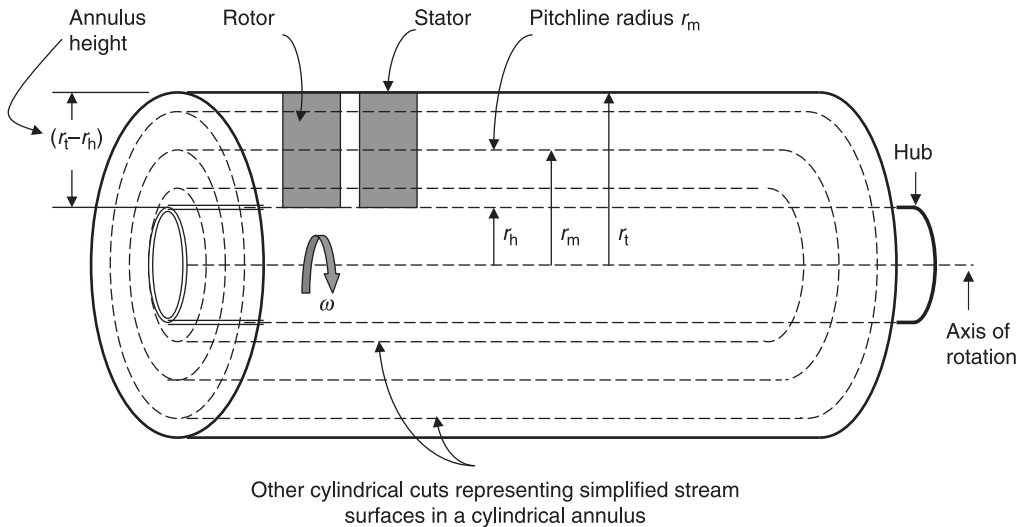
Therefore, the Euler turbine equation may be simplified to

$$w_c \cong \omega r(\Delta C_\theta) = U(C_{\theta 2} - C_{\theta 1}) \quad (8.12)$$

The assumption of constant “ r ” in axial-flow turbomachinery places the stream surfaces on cylindrical surfaces. This means that stream surfaces do not undergo significant *radial deviation*. Thus, radial deviation or radial shift of stream surfaces is often assumed negligible in axial-flow machines. The simplified flowfield in an axial turbomachinery annulus may be divided into a series of $r = \text{constant}$ cylindrical cuts, as shown in Figure 8.6.

The pitchline radius r_m is defined as the mid-radius between the hub and the casing, that is,

$$r_m \equiv \frac{r_h + r_t}{2} \quad (8.13)$$



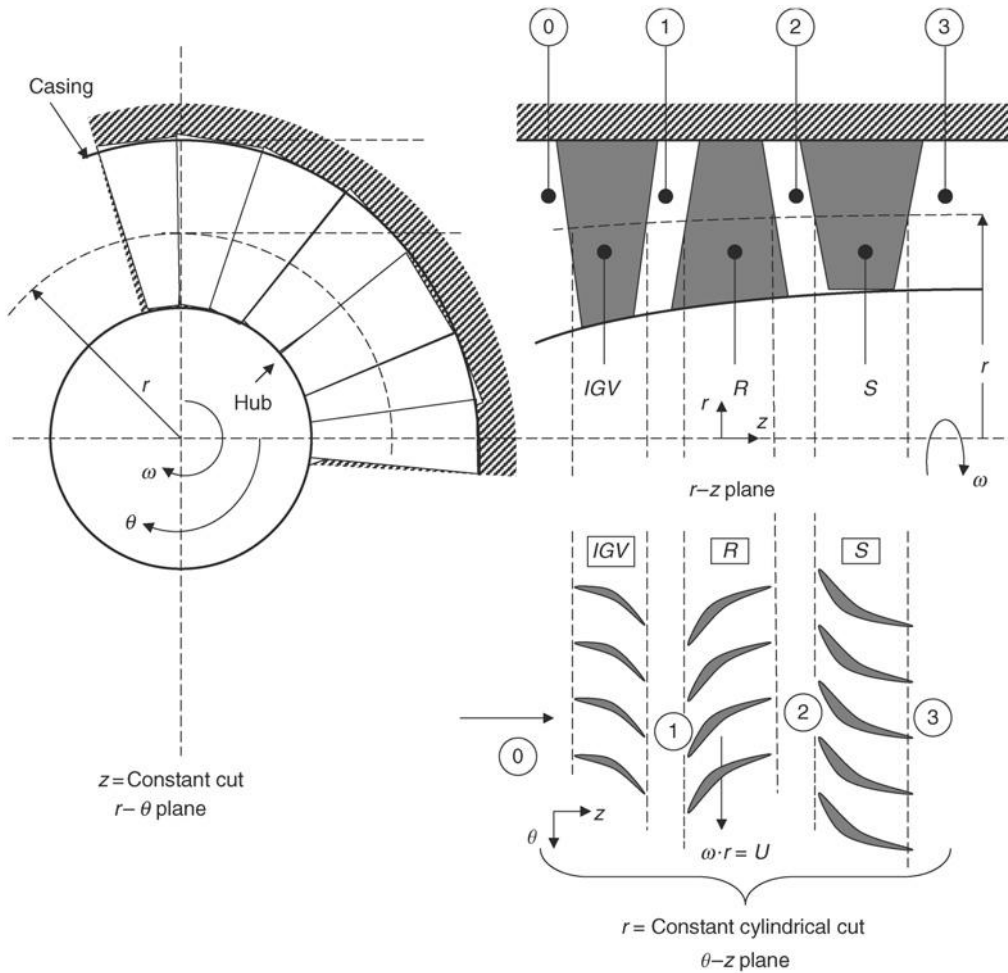
■ **FIGURE 8.6** A simple model of an axial compressor stage (rotor and stator) in a cylindrical annulus showing a mean or pitchline radius r_m along with other cylindrical cuts of the annulus representing simplified stream surfaces

Often, the pitchline radius of an axial-flow turbomachinery is assumed to represent the mean or average of the flowfield properties in the annulus and thus serves as the first line of attack in a *one-dimensional* flow analysis approach. The hub and the tip radii represent the maximum deviations from the mean and thus are analyzed next. For a more accurate analysis, other cylindrical cuts are introduced in the annulus, as shown in Figure 8.6. To further improve the accuracy of our analysis, we need to incorporate the radial disposition of the stream surfaces interacting with turbomachinery blade rows. In general, the stream surfaces undergo a radial shift interacting with a blade row and thus form *conical surfaces* in the vicinity of a blade. We need to employ a three-dimensional flow theory such as radial equilibrium theory or an actuator disc theory to approximate their exit radius r_2 of stream surfaces that have entered the blade row at the inlet radius of r_1 . We will estimate the radial shift of stream surfaces using radial equilibrium theory Section 8.6.5.

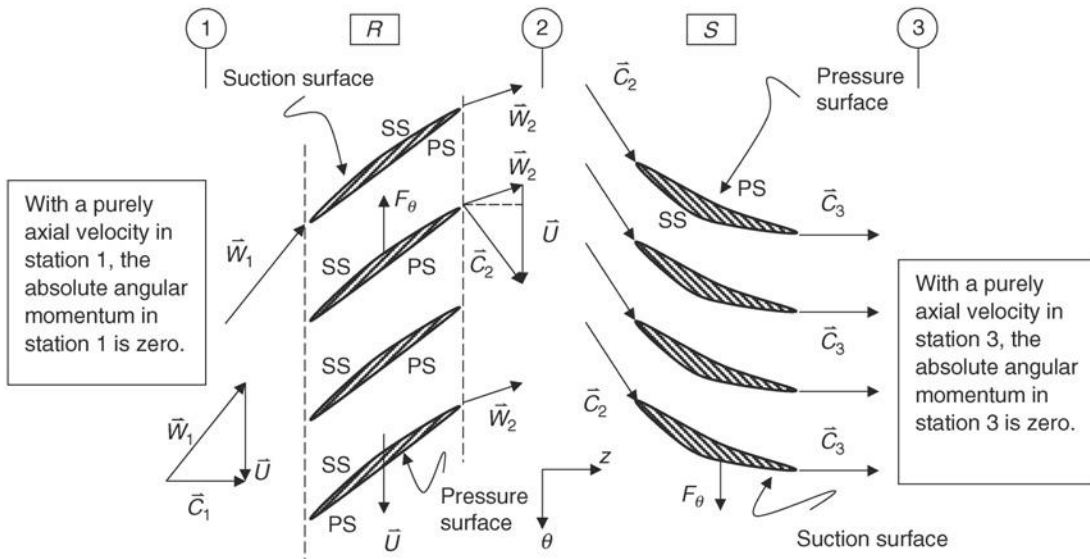
A centrifugal or radial compressor receives the fluid in the axial direction near the axis of rotation and imparts large angular momentum to the fluid by expelling the fluid at a higher radius and with a large swirl kinetic energy. The radial turbines receive the fluid at a large radius and with high swirl kinetic energy and expel the fluid near the axis of rotation with a small angular momentum. In the process of absorbing the swirl kinetic energy, a large blade torque is created, which in a rotor translates into shaft power. Hence, the radial shift of stream surfaces needs to be large for an efficient centrifugal compression/expansion and thus may not be neglected from our analysis. Fortunately, unlike axial-flow turbomachinery that we have to employ three-dimensional flow theories to predict the exit radius of an incoming stream surface, in a centrifugal machine the exit radius for all stream surfaces is fixed by the impeller geometry, that is, the impeller exit radius. We will treat centrifugal compressors in Chapter 9.

8.6 Axial-Flow Compressors and Fans

Axial-flow compressors and fans provide mechanical compression for the air stream that enters a gas turbine engine. Thermodynamically, their function is to increase the fluid pressure, efficiently. Hence, the boundary layers on the blades of compressors and fans, as well as their hub and casing, are exposed to an adverse, or rising, pressure gradient. Boundary layers exposed to an adverse pressure gradient, due to their inherently low momentum, cannot tolerate significant pressure rise. Consequently, to achieve a large pressure rise, axial-flow compressors and fans need to be staged. With this stipulation, a multistage machinery, or compression system, is born. In a stage, the rotor blade imparts angular momentum to the fluid, while the following stator blade row removes the angular momentum from the fluid. A definition sketch of a compressor stage with an inlet guide vane that imparts angular momentum to the incoming fluid is shown in Figure 8.7. A



■ FIGURE 8.7 Definition sketch for station numbers and three different planes, $r-\theta$, $r-z$, and $\theta-z$, in a compressor stage with an inlet guide vane (IGV)



■ **FIGURE 8.8** Cylindrical ($r = \text{constant}$) cut of a compressor stage with velocity triangles showing the rotor imparting and the stator removing the swirl and angular momentum to the fluid

compressor stage without an inlet guide vane is depicted in Figure 8.8. In either case, the principle of rotor increasing the fluid angular momentum and the stator blade removing the swirl (or angular momentum) is independent of any preswirl in the incoming flow to the stage. We may introduce an inlet guide vane upstream of the rotor blades that imparts a preswirl (in the direction of the rotor motion) to the incoming stream and yet the principle of rotor–stator angular momentum interactions with the fluid remains intact.

Based on the absolute velocity field in regions 1, 2, and 3, for a generic inlet condition that may include a preswirl $C_{\theta 1}$ created by an inlet guide vane, we may write the rotor and stator torques

$$\tau_{\text{rotor}} = -\tau_{\text{fluid}} = -\dot{m} \cdot r(C_{\theta 2} - C_{\theta 1}) \quad (8.14)$$

$$\tau_{\text{stator}} = -\tau_{\text{fluid}} = -\dot{m} \cdot r(C_{\theta 3} - C_{\theta 2}) \quad (8.15)$$

Assuming the absolute swirl and angular momentum across the stage remains the same, that is, $C_{\theta 1} = C_{\theta 3}$ and $r_1 = r_3$ the rotor and stator torques become equal and opposite, namely,

$$\tau_{\text{rotor}} = -\tau_{\text{stator}} \quad (8.16)$$

We observe the suction and pressure surfaces of the rotor and stator blades, as shown in Figure 8.8, and note that the blade aerodynamic forces in the θ -direction F_{θ} for the rotor and stator blades are in opposite directions. Since the moment of this tangential force, that is, $r \cdot F_{\theta}$ from the axis of rotation, is the blade torque, we conclude that the rotor and stator torques are opposite in direction and nearly equal in magnitude.

EXAMPLE 8.1

The absolute flow at the pitchline to a compressor rotor is swirl free. The exit flow from the rotor has a positive swirl, $C_{\theta 2} = 145 \text{ m/s}$. The pitchline radius is $r_m = 0.5 \text{ m}$, and the

rotor angular speed is $\omega = 5600 \text{ rpm}$. Calculate the specific work at the pitchline and the rotor torque per unit mass flow rate.

SOLUTION

Rotor tangential speed at pitchline is

$$\begin{aligned}
 U_m &= \omega r_m \\
 &= (5600 \text{ rev/min})(2\pi \text{ rad/rev})(\text{min}/60 \text{ s})(0.5 \text{ m}) \\
 &= 293.2 \text{ m/s}
 \end{aligned}$$

$$\begin{aligned}
 w_c &\cong \omega r(\Delta C_\theta) = U(C_{\theta 2} - C_{\theta 1}) = 293.2 \text{ m/s}(145 \text{ m/s}) \\
 &\approx 42.516 \text{ kJ/kg}
 \end{aligned}$$

$$\tau_{r,m}/\dot{m} = r_m(C_{\theta 2} - C_{\theta 1}) = 0.5 \text{ m}(145 \text{ m/s}) = 72.5 \text{ m}^2/\text{s}$$

8.6.1 Definition of Flow Angles

The flow angles are measured with respect to the axial direction, or axis of the machine, and are labeled as α and β , which correspond to the absolute and relative flow velocity vectors \vec{C} and \vec{W} , respectively. Figure 8.9 is a definition sketch that shows the absolute and relative flow angles in a compressor stage.

We may use these absolute and relative flow angles to express the velocity components in the axial and the swirl direction as

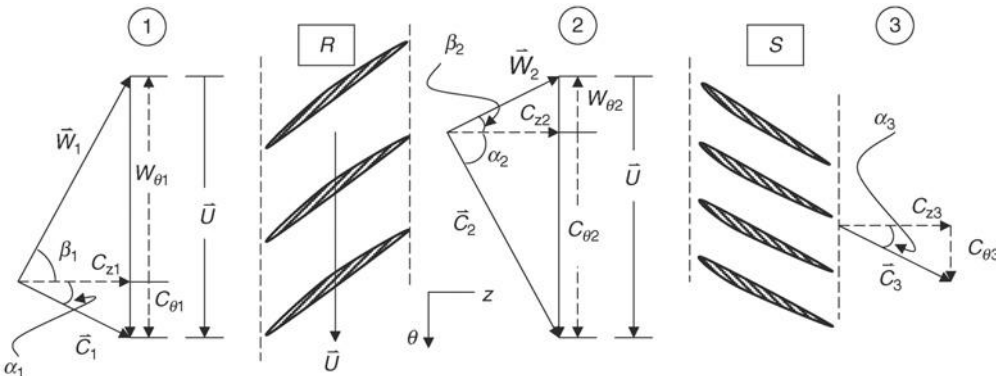
$$C_{\theta 1} = C_{z1} \cdot \tan(\alpha_1) \tag{8.17}$$

$$W_{\theta 2} = C_{z2} \cdot \tan(\beta_1) \tag{8.18}$$

$$C_{\theta 2} = C_{z2} \cdot \tan(\alpha_2) \tag{8.19}$$

$$W_{\theta 2} = C_{z2} \cdot \tan(\beta_2) \tag{8.20}$$

One method of accounting for positive and negative swirl velocities is through a convention for positive and negative flow angles. We observe that the absolute velocity vector upstream



■ FIGURE 8.9 Definition sketch for the absolute and relative flow angles in a compressor stage (a cylindrical cut of the stage, $r = \text{constant}$)

of the rotor has a swirl component in the direction of the rotor rotation. Hence, the absolute flow angle α_1 is considered positive. The opposite is true for the relative velocity vector \vec{W}_1 , which has a swirl component in the opposite direction to the rotor rotation. Both the relative flow angle β_1 and the swirl velocity facing it $W_{\theta 1}$ are thus negative.

A turbomachinery blade row is designed to maintain an attached boundary layer, under normal operating conditions. Hence, the flow angles at the exit of the blades are primarily fixed by the blade angle at the exit plane. For example, the relative velocity vector at the exit of the rotor, W_2 , should nearly be tangent to the rotor suction surface at the trailing edge. Hence, β_2 is fixed by the geometry of the rotor and remains nearly constant over a wide operating range of the compressor. The same statement may be made about α_1 or α_3 . These angles remain constant over a wide range of the operation of the compressor as well. Again, remember that the exit flow angle argument is made for an attached (boundary layer) flow. The other flow angles, as in β_1 or α_2 , change with rotor speed U (i.e., ωr). Consequently, use is made of the nearly constant exit flow angles α_1 , β_2 , and α_3 in expressing performance parameters of the compressor stage and the blade row.

The axial velocity components C_{z1} , C_{z2} , or C_{z3} contribute to the mass flow rate through the machine. A common (textbook) design approach in axial-flow compressors and fans maintains a constant axial velocity throughout the stages. We shall make use of this simplifying design approach repeatedly in this chapter. Figure 8.8 shows an example of a constant axial velocity in a compressor stage. Although a simplifying design assumption, the reader needs to be aware that the goal of constant axial velocity is nearly impossible to achieve in practice. This is due to a highly three-dimensional nature of the flowfield, set up by three-dimensional pressure gradients, in a turbomachinery stage. We will address this and other topics related to three-dimensional flow in Section 8.6.5.

A useful concept in turbomachinery design calls for a *repeated stage* (also referred to as *normal stage*). This implies that the velocity vectors at the exit and entrance to a stage are the same, that is,

$$\vec{C}_3 = \vec{C}_1 \quad (8.21a)$$

$$\alpha_3 = \alpha_1 \quad (8.21b)$$

The velocity triangles at the inlet and the exit of the stage shown in Figure 8.8 have made use of the repeated stage concept. Another concept in turbomachinery calls for a *repeated row* design, which leads to flow angle implications that are noteworthy. In a repeated row design, the exit relative flow angle has the same magnitude as the absolute inlet flow angle, and the inlet relative flow angle has the same magnitude as the exit absolute flow angle, that is,

$$|\beta_2| = |\alpha_1| \quad (8.22a)$$

$$|\alpha_2| = |\beta_1| \quad (8.22b)$$

The example of the compressor stage shown in Figure 8.9 has used the concept of repeated row. Note that a repeated row design leads to a repeated stage but the reverse is not necessarily correct. Namely, we may have a repeated stage design that does not use a repeated row concept. Figure 8.8 shows an example of a repeated stage that does not obey a repeated row design.

8.6.2 Stage Parameters

The Euler turbine equation that we derived earlier is the starting point for this section with the assumption of $r_1 \approx r_2 \approx r$,

$$\frac{T_{t2}}{T_{t1}} = 1 + \frac{U(C_{\theta 2} - C_{\theta 1})}{c_p T_{t1}}$$

We may replace the swirl velocities by the flow angles and the axial velocity components, namely,

$$\frac{T_{t2}}{T_{t1}} = 1 + \frac{U(C_{z2} \tan \alpha_2 - C_{z1} \tan \alpha_1)}{c_p T_{t1}} = 1 + \left(\frac{U^2}{c_p T_{t1}} \right) \left(\frac{C_{z1}}{U} \right) \left(\frac{C_{z2}}{C_{z1}} \tan \alpha_2 - \tan \alpha_1 \right) \quad (8.23)$$

Expression 8.23 for the total temperature rise across the rotor (or stage) involves nondimensional groups C_{z1}/U and $c_p T_{t1}/U^2$. These groups appear throughout the turbomachinery literature and deserve a special attention. Also, the axial velocity ratio C_{z2}/C_{z1} appears that is often set equal to 1, as a first-order design assumption. Equation 8.23 is expressed in terms of the absolute flow angle at the exit of the rotor, which is not, however, a good choice, since it varies with the rotor speed. A better choice for the flow angle in plane 2, that is, downstream of the rotor, is the relative flow angle β_2 . The relative exit flow angle β_2 remains nearly unchanged as long as the flow remains attached to the blades. To express the total temperature rise across the rotor to the flow angles α_1 and β_2 , we replace the absolute swirl $C_{\theta 2}$ by the relative swirl speed, namely,

$$C_{\theta 2} = U + W_{\theta 2} \quad (8.24)$$

Therefore,

$$\frac{T_{t2}}{T_{t1}} = 1 + \left(\frac{U^2}{c_p T_{t1}} \right) \left[1 + \frac{C_{z2}}{U} \tan \beta_2 - \frac{C_{z1}}{U} \tan \alpha_1 \right] \quad (8.25a)$$

If we assume a constant axial velocity design, that is, $C_{z1} = C_{z2}$, then we get

$$\frac{T_{t2}}{T_{t1}} = 1 + \left(\frac{U^2}{c_p T_{t1}} \right) \left[1 + \left(\frac{C_z}{U} \right) (\tan \beta_2 - \tan \alpha_1) \right] \quad (8.25b)$$

Here, we have expressed the stage total temperature ratio as a function of two nondimensional parameters. Note that β_2 is a negative angle and α_1 is a positive angle, according to our sign convention. Therefore, the contribution to the stage total temperature ratio falls with increasing (C_z/U) for a given wheel speed and inlet stagnation enthalpy. The ratio of axial-to-wheel speed is called the *flow coefficient* ϕ

$$\phi \equiv \frac{C_z}{U} \quad (8.26a)$$

We may divide both numerator and the denominator of Equation 8.26a by the speed of sound in plane 1, that is, a_1 , to get the ratio of axial to blade (rotational) or tangential Mach number, namely,

$$\phi = \frac{C_z/a_1}{U/a_1} = \frac{M_z}{M_T} \quad (8.26b)$$

where M_z is the axial Mach number, and M_T is the blade tangential Mach number based on U and a_1 . For example, a stream surface with an axial Mach number of 0.5 that approaches a section of a rotor that is spinning at Mach 1 has a flow coefficient of 0.5. Now, let us interpret the first nondimensional group $U^2/(c_p T_{t1})$. We may divide this expression by the square of the upstream speed of sound a_1^2 to get

$$\frac{U^2/a_1^2}{c_p T_{t1}/(\gamma R T_1)} = \frac{(\gamma - 1) M_T^2}{1 + \left(\frac{\gamma - 1}{2}\right) M_1^2} \quad (8.27)$$

Noting that the absolute Mach number M_1 is expressible in terms of the axial Mach number and a constant preswirl angle α_1 as

$$M_1 = \frac{M_z}{\cos \alpha_1} \quad (8.28)$$

We conclude that

$$\frac{U^2}{c_p T_{t1}} = \frac{(\gamma - 1) M_T^2}{1 + \left(\frac{\gamma - 1}{2}\right) \frac{M_z^2}{\cos^2 \alpha_1}} \quad (8.29)$$

Based on Equations 8.26b and 8.29, we may recast the stage stagnation temperature ratio in terms of blade tangential and axial Mach numbers as

$$\frac{T_{t2}}{T_{t1}} = 1 + \left[\frac{(\gamma - 1) M_T^2}{1 + \left(\frac{\gamma - 1}{2}\right) \frac{M_z^2}{\cos^2 \alpha_1}} \right] \left[1 + \left(\frac{M_z}{M_T}\right) (\tan \beta_2 - \tan \alpha_1) \right] \quad (8.30)$$

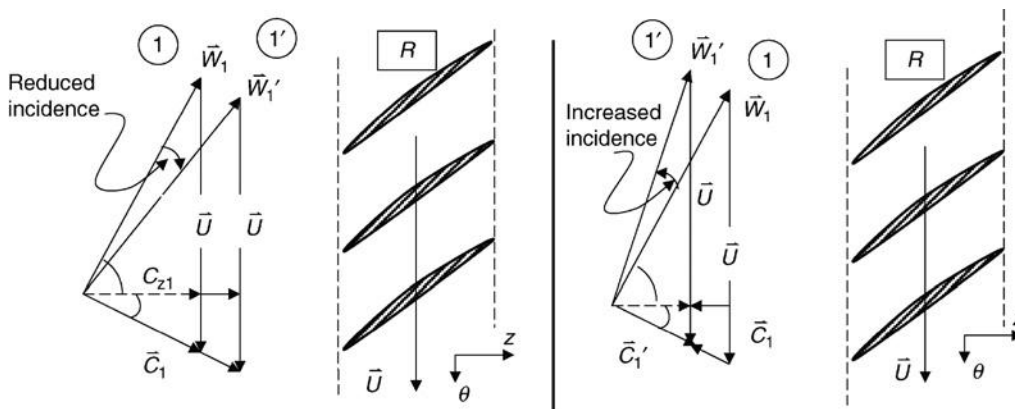
Kerrebrock (1992) offers an insightful discussion of compressor aerodynamics based on this equation. Two Mach numbers, that is, the axial and the blade tangential Mach numbers, appear to influence the stage temperature ratio in three ways, namely, via M_z , M_T , and M_z/M_T influence in Equation 8.30. However, if we divide the first bracket on

the right-hand side (RHS) of Equation 8.30 by the square of the blade tangential Mach number, we reduce this dependency to two parameters, namely,

$$\frac{T_{t2}}{T_{t1}} = 1 + \left[\frac{\gamma - 1}{\left(\frac{1}{M_T^2}\right) + \left(\frac{\gamma - 1}{2 \cos^2 \alpha_1}\right) \left(\frac{M_z}{M_T}\right)^2} \right] \left[1 + \left(\frac{M_z}{M_T}\right) (\tan \beta_2 - \tan \alpha_1) \right] \tag{8.31}$$

Consequently, two parameters govern the stage temperature ratio (or pressure ratio) and these are the blade tangential Mach number M_T and the flow coefficient or the ratio of the axial-to-tangential Mach number M_z/M_T . For given flow angles α_1 and β_2 , an increase in the flow coefficient reduces the temperature rise in the stage. We may interpret an increase in the flow coefficient as an increase in the axial Mach number or the mass flow rate through the machine. As the mass flow rate increases, keeping the blade rotational Mach number the same, the blade angle of attack, or in the language of turbomachinery the *incidence angle*, decreases, hence the total temperature ratio drops. The opposite effect is observed with a decreasing mass flow rate through the machine where the incidence angle increases and thus blade work on the fluid increases to produce higher temperature or pressure rise. To visualize the effect of throughflow on rotor work, temperature and pressure rise, a rotor blade at different axial Mach numbers (or flow rate) and the same blade tangential Mach number (or wheel speed) are shown in Figure 8.10.

A reduced flow rate leads to an increased compressor temperature (or pressure) ratio. However, there is a limitation on how low the flow rate, or axial Mach number, can sink before the blades stall, for a fixed shaft rotational speed. Consequently, at reduced flow rates we could enter a blade stall flow instability, which marks the lower limit of



(a) The effect of *increased mass flow rate* while maintaining the same rotational speed is to reduce blade incidence angle

(b) The effect of *decreased mass flow rate*, with constant U , is to expose the blades to a higher incidence

■ FIGURE 8.10 Inlet velocity triangles for a compressor rotor with a changing flow rate

the axial flow speed on the compressor map for a given shaft speed. The increased flow rate that leads to a reduction of the stage total temperature rise has its own limitation. The phenomenon of negative stall could be entered as the inlet Mach number is increased significantly.

The second parameter is the blade tangential Mach number M_T . A higher blade tangential Mach number increases the stage total temperature rise as deduced from Equation 8.31. However, the limitations on the blade tangential Mach number are the appearance of strong shock waves at the tip as well as the structural limitations under centrifugal and vibratory stresses. The rotor shock losses increase (nonlinearly) with the relative tip Mach number; however, the advantage of higher work ($\propto M_T^2$) on the fluid outweighs the negatives of such a design at modest tip Mach numbers. The relative tip Mach number is defined as

$$M_{\text{tip,r}} = \sqrt{M_z^2 + (M_{T,\text{tip}}^2)} \quad (8.32)$$

where it represents the case of zero preswirl. The general case that includes a nonzero preswirl, may be written as

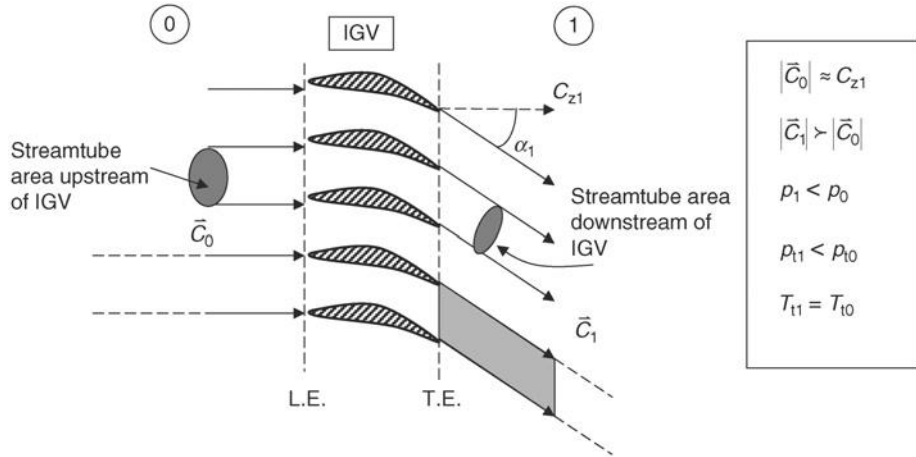
$$M_{\text{tip,r}} = \sqrt{M_z^2 + (M_{T,\text{tip}} - M_z \tan \alpha_1)^2} \quad (8.33)$$

The relative blade Mach numbers at the tip of operational fan blades have been supersonic for the past three decades. By necessity, these blade sections should be thin to avoid stronger bow shocks. A typical value for the relative tip Mach number is ~ 1.2 but may be designed as high as ~ 1.7 . The thickness-to-chord ratio of supersonic blading may be as low as $\sim 3\%$. High strength-to-weight ratio titanium alloys represented the enabling technology that allowed the production of supersonic (tip) fans in the early 1970s.

The inlet absolute flow angle to the rotor α_1 is a design choice that has the effect of reducing the rotor relative tip speed. The inlet preswirl is created by a set of inlet guide vanes, known as an IGV. To reduce the relative flow to the rotor tip, the IGV turns the flow in the direction of the rotor rotation, by α_1 . The flowfield entering an IGV is swirl-free and thus the function of the IGV is to impart positive swirl (or positive angular momentum) to the incoming fluid. This in effect reduces the rotor blade loading whose purpose is to impart angular momentum to the incoming fluid. An inlet guide vane and its flowfield are shown in Figure 8.11.

We note that the blade passages in the IGV form a subsonic nozzle (i.e., contracting area) and cause flow acceleration across the blade row. The result of the flow acceleration is found in the static pressure drop due to flow acceleration, as well as a total pressure drop due to frictional losses of the blade passages. Hence, if the compressor design could avoid the use of an IGV, then certain advantages, including cost and weight savings, are gained. The advantage of operating at higher tip speeds at times outweighs the disadvantages of an IGV. The inlet guide vane may also be actuated rapidly if a quick response in thrust modulation is needed. For example, consider a lift fan, or a deflected engine exhaust flow, to support a VTOL aircraft in hover mode. The ability to modulate the jet lift (or vertical thrust) for stability and maneuver purposes may not be achieved through a spool up or spool down throttle sequence of the engine. Due to a large moment of inertia of the rotating parts in a turbomachinery, the rapid spooling is not fast enough for the control

FIGURE 8.11
An inlet guide vane is seen to impart swirl to the fluid (note the shrinking stream tube area implies flow acceleration and static pressure drop)



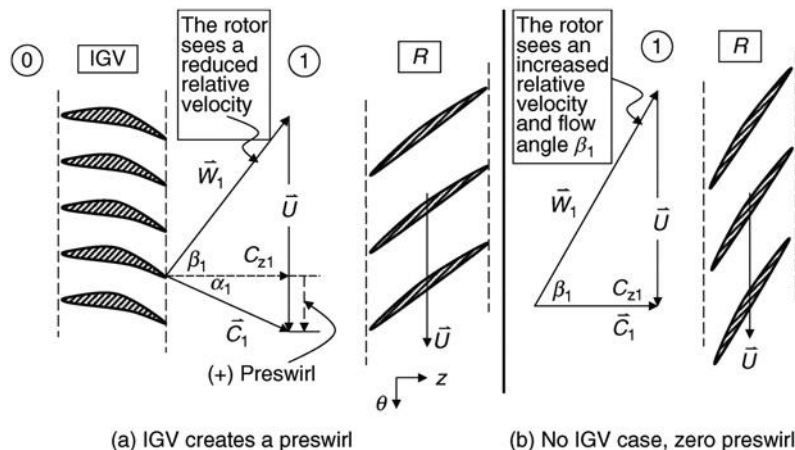
and stability purposes of a VTOL aircraft. In such applications, fast-acting IGV actuators could modulate the inlet flow to the rotor and hence the thrust/lift. An adjustable exit louver at the deflected nozzle end achieves the same goal. The inlet swirl angle α_1 may be zero or be adjustable in the range of $\pm 30^\circ$ or more using a variable geometry IGV to relieve the relative tip Mach number, improve efficiency at compressor off-design operation, and provide for rapid thrust/lift modulation in military aircraft.

An example of a velocity triangle upstream of the rotor blade with and without the inlet guide vane is shown in Figure 8.12. In both cases, we maintain the rotational speed and the mass flow rate, i.e., the axial velocity C_z constant.

The stage total pressure ratio is related to the stage total temperature ratio via a stage efficiency parameter η_s . Recalling from the chapter on cycle analysis,

$$\eta_s \equiv \frac{T_{t3s} - T_{t1}}{T_{t3} - T_{t1}} = \frac{\pi_s^{\frac{\gamma-1}{\gamma}} - 1}{\tau_s - 1} \tag{8.34}$$

FIGURE 8.12
Impact of IGV on the rotor relative flow for constant axial velocity and rotor speed



Therefore, we may calculate the stage total pressure ratio from the velocity triangles that are used in the Euler turbine equation to establish τ_s and an efficiency parameter η_s to get

$$\pi_s = [1 + \eta_s (\tau_s - 1)]^{\frac{\gamma}{\gamma-1}} \quad (8.35)$$

Since the axial flow compressor pressure ratio per stage is small (i.e., near 1), the stage adiabatic efficiency and the polytropic efficiency are nearly equal. We recall that the polytropic efficiency was also called the “small-stage” efficiency, valid for an infinitesimal stage work. Although the approximation

$$\eta_s \cong e_c \quad (8.36)$$

is valid for low-pressure ratio axial flow compressor stages. The exact relationship between these parameters is derived in the cycle analysis chapter to be

$$\eta_s = \frac{\tau_s - 1}{\frac{1}{\tau_s^{e_c}} - 1} \quad (8.37)$$

Therefore, by calculating the stage total temperature ratio from the Euler turbine equation and assuming polytropic efficiency, of say 0.90, we may calculate the stage adiabatic efficiency. Otherwise, we may calculate the stage total pressure ratio from the polytropic efficiency e_c and the stage total temperature ratio directly, via

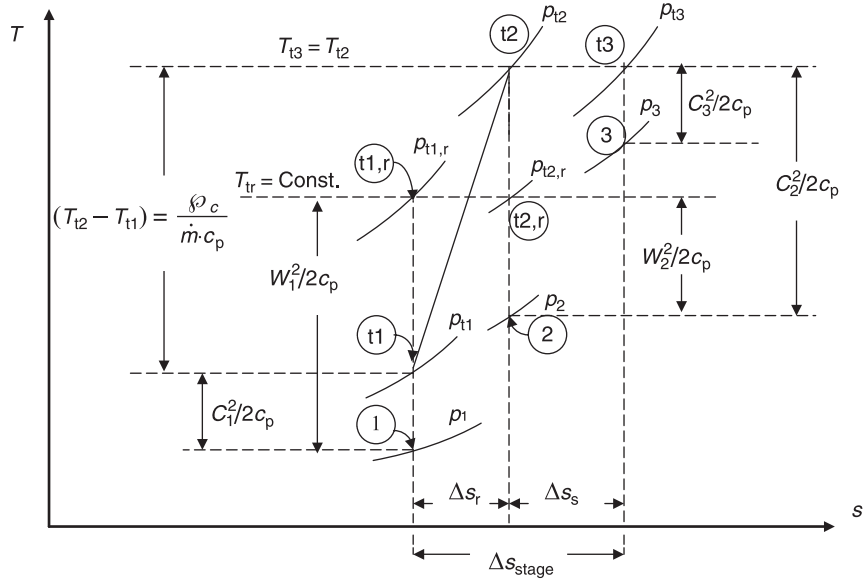
$$\pi_s = \tau_s^{\frac{\gamma e_c}{\gamma-1}} \quad (8.38)$$

The frictional and shock losses are the main contributors to a total pressure loss in the relative frame of reference. We note that in a relative frame of reference, the blade passage is stationary and thus blade aerodynamic forces perform no work. Examining the fluid total pressure across the blade through the eyes of a relative observer, there are only losses to report. As noted, these losses stem from the viscous and turbulent dissipation of mechanical (kinetic) energy into heat as well as the flow losses associated with a shock. From the vantage point of an absolute observer, the blades are rotating and doing work on the fluid, thus increasing the fluid total temperature and pressure in the absolute frame of reference. These processes may be shown on a T - s diagram (Figure 8.13) that is instructive to review. For example, follow the static state of gas across the stage then follow the stagnation states in the absolute and relative frames. Explain the behavior of kinetic energy of gas as the fluid encounters the stationary and rotating blade rows, as seen by absolute and relative observers.

The *relative* total enthalpy is constant across the rotor along a stream surface (in steady flow without a radial shift in the stream surface),

$$h_{t,r} = h_1 + \frac{W_1^2}{2} = h_2 + \frac{W_2^2}{2} \quad (8.39)$$

■ **FIGURE 8.13**
Absolute and relative states of gas across a compressor rotor and stator



We may replace the total kinetic energy terms in Equation 8.39 by the sum of the kinetic energy of the component velocities, namely,

$$h_1 + W_{z1}^2/2 + W_{\theta1}^2/2 = h_2 + W_{z2}^2/2 + W_{\theta2}^2/2 \quad (8.40)$$

Let us substitute the absolute swirl minus the wheel speed ($C_\theta - U$) for the relative swirl in Equation 8.40, to get

$$h_1 + C_{z1}^2/2 + C_{\theta1}^2/2 - C_{\theta1} \cdot U = h_2 + C_{z2}^2/2 + C_{\theta2}^2/2 - C_{\theta2}U \quad (8.41)$$

The sum of the first three terms is the absolute total enthalpy on each side of the above equality, therefore,

$$h_{t1} - UC_{\theta1} = h_{t2} - UC_{\theta2} \quad (8.42)$$

This enthalpy constant in the rotor frame is known as “rothalpy,” which may be rearranged to help us arrive at the Euler turbine equation, that is,

$$h_{t2} - h_{t1} = \frac{\phi}{\dot{m}} = w_c = U(C_{\theta2} - C_{\theta1}) \quad (8.43)$$

The rotor specific work on the fluid in nondimensional form is written as

$$\psi \equiv \frac{\Delta h_t}{U^2} = \frac{C_{\theta2}}{U} - \frac{C_{\theta1}}{U} = \frac{W_{\theta2} + U}{U} - \frac{C_{\theta1}}{U} = 1 + \left(\frac{C_z}{U}\right) (\tan \beta_2 - \tan \alpha_1) \quad (8.44)$$

The function ψ is the nondimensional stage work parameter, which is called the *stage-loading factor or parameter* defined in Equation 8.44. The ratio of axial-to-wheel speed

was called the flow coefficient ϕ , which forms another two-parameter family for the stage characteristics, namely,

$$\psi = 1 + \phi (\tan \beta_2 - \tan \alpha_1) \tag{8.45}$$

We note that the rotor exit relative flow angle is a negative quantity that leads to a stage-loading factor that is less than 1. In the case of zero preswirl, or no inlet guide vane, the stage loading factor increases with a decreasing rotor exit flow angle β_2 . In the limit of zero relative swirl at the rotor exit and no inlet guide vane, the stage loading factor approaches unity. However, a rotor relative exit flow angle of zero implies significant turning in the rotor blade passage, which may lead to flow separation. The stage-loading factor is an alternate form of expressing the stage characteristics and, in essence, takes the place of the rotor tangential Mach number M_T , which was presented earlier. Horlock (1973) takes advantage of the linear dependence of the stage loading and the flow coefficient in Equation 8.45 to explore the off-design behavior of ideal turbomachinery stages. We shall discuss the off-design behavior of turbomachinery later in this chapter but for now show the linear dependence of the two parameters in Figure 8.14 (adapted from Horlock, 1973).

We define a stage *degree of reaction* ${}^\circ R$ as the fraction of static enthalpy rise across the stage that is accomplished by the rotor. Although the stator does no work on the fluid, it still acts as a diffuser that decelerates the fluid and thus causes an increase in fluid temperature, or static enthalpy. The stator takes out the swirl (kinetic energy) put in by the rotor and thus converts it to a static pressure rise. The degree of reaction measures the rotor share of the stage enthalpy rise as compared with the burden on the stator. This process is shown in an h - s diagram for the static states in a compressor stage. Remember that the static states are independent of the motion of the observer, hence they carry no subscript labels besides the station number (Figure 8.15).

$${}^\circ R \equiv \frac{h_2 - h_1}{h_3 - h_1} = \frac{h_{t2} - h_{t1} - (C_2^2 - C_1^2)/2}{h_{t3} - h_{t1} - (C_3^2 - C_1^2)/2} \tag{8.46a}$$

FIGURE 8.14
 Linear dependence of stage loading and flow coefficient parameters in ideal turbomachinery stages. Source: Adapted from Horlock 1973

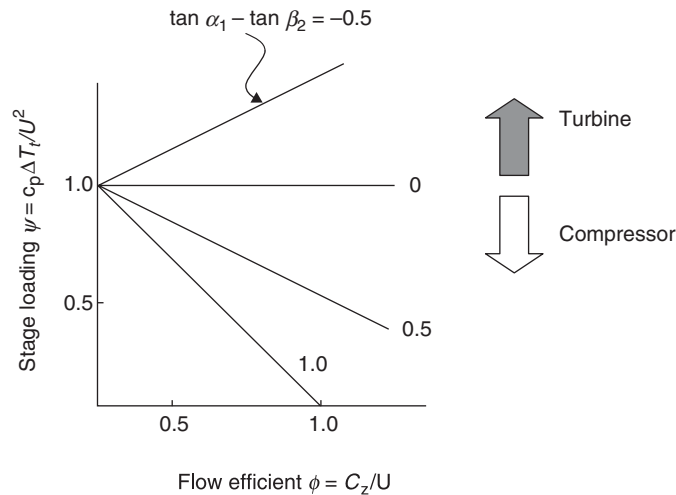
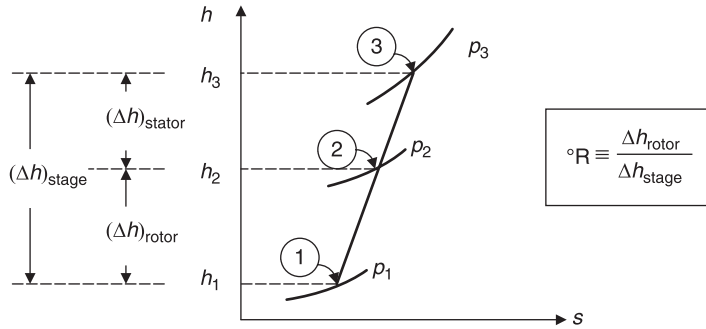


FIGURE 8.15
 Static states of gas in a
 compressor stage and a
 definition sketch for
 the stage degree of
 reaction °R



The stagnation enthalpy across the stator remains constant as the stator blades do no work on the fluid, hence $h_{t3} = h_{t2}$ and if we assume a repeated stage, with $C_1 = C_3$, we simplify the above expression to get

$$\text{°R} \cong 1 - \frac{C_2^2 - C_1^2}{2(h_{t2} - h_{t1})} = 1 - \frac{C_{z2}^2 + C_{\theta 2}^2 - C_{z1}^2 + C_{\theta 1}^2}{2U(C_{\theta 2} - C_{\theta 1})} \quad (8.46b)$$

Now, for a constant axial velocity across the rotor, $C_{z2} = C_{z1}$, we get a simple expression for the stage degree of reaction, as

$$\text{°R} \cong 1 - \frac{C_{\theta 2} + C_{\theta 1}}{2U} = 1 - \frac{C_{\theta, \text{mean}}}{U} \quad (8.46c)$$

where $C_{\theta, \text{mean}}$ is the average swirl across the rotor. Since the flow has to fight an uphill battle with an adverse pressure gradient throughout a compressor stage, it stands to reason to expect/design an equal burden of the static pressure rise in the rotor as that of a stator. Consequently, a 50% degree of reaction stage may be thought of as desirable. We may express the swirl velocity components across the rotor in terms of the absolute in flow and relative exit flow angles, α_1 and β_2 , respectively,

$$\text{°R} = 1 - \frac{W_{\theta 2} + U + C_{\theta 1}}{2U} = \frac{1}{2} - \frac{C_z \tan \beta_2 + C_z \tan \alpha_1}{2U} = \frac{1}{2} - \left(\frac{C_z}{U} \right) \left(\frac{\tan \beta_2 + \tan \alpha_1}{2} \right) \quad (8.47)$$

For a 50% degree of reaction stage (at some spanwise radius r), the rotor exit flow angle has to be equal in magnitude and opposite to the inlet absolute flow angle, which is dictated by an IGV, namely,

$$\beta_2 = -\alpha_1$$

This is the condition for a repeated row design, as noted in Equations 8.22a and 8.22b. Therefore a purely axial inflow (with no inlet guide vane) demands a purely axial relative outflow in order to produce a 50% degree of reaction. Again, we need to examine the net turning angle across the blade and assess the potential for flow separation. We shall introduce another parameter that will shed light on the state of the boundary layer at the blade exit and that is the diffusion factor.

On the degree of reaction, there is a body of experimental results that support the proposal that a boundary layer on a spinning blade, that is, the rotor, is more *stable* than a corresponding boundary layer on a stationary blade, that is, the stator, hence allocating a slightly higher burden of static pressure rise to the rotor. Here the word *stable* is used in the context of resistant to adverse pressure gradient or higher stalling pressure rise. Based on this, a degree of reaction of 60% may be a desirable split between the two blade rows in a compressor stage. As we shall see in the three-dimensional flow section in this chapter, the desirable degree of reaction is often compromised at different radii along a blade span to satisfy other requirements, namely, a healthy state of boundary layer flow.

EXAMPLE 8.2

An axial-flow compressor stage has a pitchline radius of $r_m = 0.5$ m. The rotational speed of the rotor at pitchline is $U_m = 212$ m/s. The absolute inlet flow to the rotor is described by $C_{zm} = 155$ m/s and $C_{\theta 1m} = 28$ m/s. The stage degree of reaction at pitchline is ${}^\circ R_m = 0.60$, $\alpha_3 = \alpha_1$, and C_{zm} remains constant. Calculate

(a) rotor angular speed ω in rpm

(b) rotor exit swirl $C_{\theta 2m}$

(c) rotor specific work at pitchline w_{cm}

(d) relative velocity vector at the rotor exit

(e) rotor and stator torque per unit mass flow rate

(f) stage loading parameter at pitchline ψ_m

(g) flow coefficient ϕ_m .

SOLUTION

$\omega = U_m/r_m = (212 \text{ m/s})/0.5 \text{ m} = (424 \text{ rad/s}) (\text{rev}/2\pi \text{ rad})$
 $(60 \text{ s/min}) \approx 4,049 \text{ rpm}$

From Equation 8.46c, written at the pitchline

$${}^\circ R_m \cong 1 - \frac{C_{\theta 2m} + C_{\theta 1m}}{2U_m}$$

We isolate $C_{\theta 2m}$ to be

$$\begin{aligned} C_{\theta 2m} &= 2U_m(1 - {}^\circ R_m) - C_{\theta 1m} \\ &= 2(212 \text{ m/s})(0.4) - 28 \text{ m/s} \approx 141.6 \text{ m/s} \end{aligned}$$

Euler turbine equation describes the rotor specific work,

$$w_c \equiv \frac{\mathcal{G}_c}{\dot{m}_c} = \omega \Delta (rC_\theta)_c, \quad \text{therefore,}$$

$$\begin{aligned} w_{cm} &= U_m(C_{\theta 2m} - C_{\theta 1m}) \\ &= 212 \text{ m/s} (141.6 - 28) \text{ m/s} \approx 24.08 \text{ kJ/kg} \end{aligned}$$

Rotor relative swirl at the exit is

$$W_{\theta 2m} = C_{\theta 2m} - U_m = (141.6 - 212) \text{ m/s} = -71 \text{ m/s}$$

Since the axial component of velocity remains constant, we can write the vector

$$\vec{W}_{2m} = 155\hat{k} - 71\hat{e}_\theta$$

Since $\alpha_3 = \alpha_1$, the rotor and stator torques are equal and opposite to each other, i.e.,

$$\begin{aligned} \tau_{rm}/\dot{m} &= r_m(C_{\theta 2m} - C_{\theta 1m}) = 0.5\text{m}(141.6 - 28) \text{ m/s} \\ &= 56.8 \text{ m}^2/\text{s} = -\tau_{sm}/\dot{m} \end{aligned}$$

The stage loading parameter and flow coefficients are

$$\begin{aligned} \psi_m &= \Delta C_\theta / U_m = (141.6 - 28)/212 \approx 0.5358 \\ \phi_m &= C_{zm} / U_m = 155/212 = 0.731 \end{aligned}$$

Another figure of merit for a compressor blade section that addresses the health of a boundary layer is, as noted earlier, the *Diffusion Factor*, or the *D-factor*. Its definitions for

rotor and stator blades are, respectively

$$D_r \equiv 1 - \frac{W_2}{W_1} + \frac{|W_{\theta 2} - W_{\theta 1}|}{2\sigma_r W_1} \quad (\text{rotor } D\text{-Factor}) \quad (8.48)$$

$$D_s \equiv 1 - \frac{C_3}{C_2} + \frac{|C_{\theta 3} - C_{\theta 2}|}{2\sigma_s C_2} \quad (\text{stator } D\text{-Factor}) \quad (8.49)$$

where σ defines the blade solidity, that is, the ratio of blade chord c to spacing s

$$\sigma_r \equiv \frac{c_r}{s_r} \quad (\text{rotor solidity}) \quad (8.50)$$

$$\sigma_s \equiv \frac{c_s}{s_s} \quad (\text{stator solidity}) \quad (8.51)$$

Modern compressor design utilizes a high solidity ($\sigma_m \geq 1$) blading at the pitchline radius (i.e., r_m). Since the blade spacing increases linearly with radius, the solidity of a constant chord blade also decreases linearly with the blade span, that is,

$$s(r) = \frac{2\pi \cdot r}{N_b} \quad (\text{blade spacing}) \quad (8.52)$$

where the N_b is the number of blades in the rotor or the stator row. We can see the variation of blade row solidity with blade span by substituting Equation 8.52 for the blade spacing, as

$$\sigma(r) = \frac{N_b \cdot c}{2\pi \cdot r} \quad (\text{blade solidity}) \quad (8.53)$$

The hub section (r_h) has thus the highest solidity and the tip section (r_t) the lowest. The rationale for the definition of D -factor and its link to blade stall is made by Lieblein (1953, 1959, 1965). We review it here for its physical importance. First note that the definition of rotor diffusion factor is the same as the stator D -factor, except the parameters for the rotor are all in relative frame of reference. Next note that the change in swirl velocity across the rotor is the same regardless of the frame of reference, that is, the change in absolute swirl is the same in magnitude as the change in relative swirl, namely,

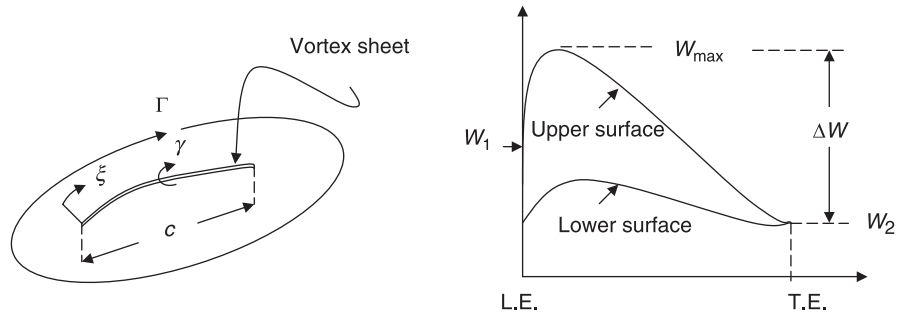
$$|W_{\theta 2} - W_{\theta 1}| = |C_{\theta 2} - C_{\theta 1}| \quad (8.54)$$

The blade circulation Γ is the integral of the vortex sheet strength γ over the chord, namely,

$$\Gamma \equiv \int_0^c \gamma(\xi) d\xi \approx \bar{\gamma} \cdot c \quad (8.55)$$

Figure 8.16 shows an element of a blade section represented by a vortex sheet of local strength $\gamma(\xi)$. The local strength is equal to the local tangential velocity jump across the

■ **FIGURE 8.16**
Blade airfoil section is represented by a vortex sheet and a velocity distribution



blade. The average vortex sheet strength is thus the average velocity jump across the sheet, namely,

$$\bar{\gamma} \approx (\Delta W)_{\text{avg}} \approx \frac{W_{\text{max}} - W_1}{2} \tag{8.56}$$

Therefore, the average (positive) circulation around the blade section is

$$\Gamma_{\text{avg}} \approx \frac{c}{2} (W_{\text{max}} - W_1) \tag{8.57}$$

Now, let us consider a control volume symmetrically wrapped around a blade section, as shown in Figure 8.17.

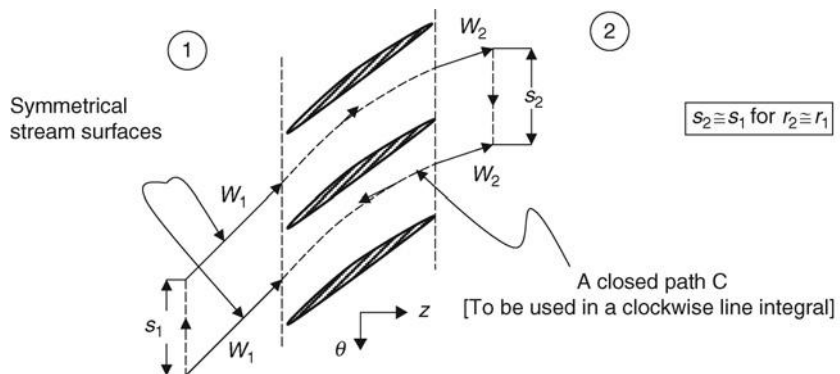
By performing a closed line integral in the clockwise direction around the path *C* (Figure 8.18), we calculate the magnitude of blade circulation Γ as

$$\Gamma = s |W_{\theta 1} - W_{\theta 2}| \tag{8.58}$$

Therefore equating the two expressions for the (magnitude of) blade circulation, we get

$$W_{\text{max}} \approx W_1 + \frac{|W_{\theta 2} - W_{\theta 1}|}{2\sigma} \tag{8.59}$$

■ **FIGURE 8.17**
Control volume for determining the blade circulation Γ along a stream surface



The maximum adverse pressure gradient on the blade suction surface leads to a maximum flow diffusion, which may be measured by the following parameter

$$\text{Maximum flow diffusion} \approx \frac{W_{\max} - W_2}{W_2} \approx \frac{W_{\max} - W_2}{W_1} \quad (8.60)$$

This parameter is called the *Diffusion Factor D*

$$D \equiv \frac{W_{\max} - W_2}{W_1} = \frac{W_1 + (|\Delta C_\theta|/2\sigma) - W_2}{W_1} = 1 - \frac{W_2}{W_1} + \frac{|\Delta C_\theta|}{2\sigma W_1} \quad (8.61)$$

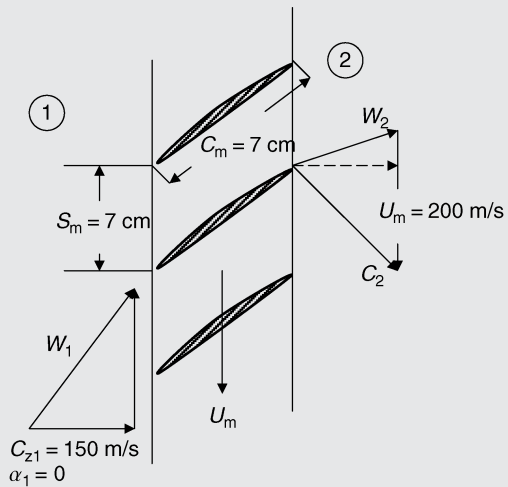
EXAMPLE 8.3

A rotor blade row is cut at pitchline, r_m . The velocity vectors at the inlet and exit of the rotor are shown.

Assuming that $U_{m1} = U_{m2} = 200$ m/s and $C_{z1} = C_{z2} = 150$ m/s

And $\beta_2 = -35^\circ$, calculate

- (a) W_{1m} and W_{2m}
- (b) D -factor D_{rm}
- (c) circulation Γ_m



SOLUTION

$$W_{1m} = [(150)^2 + (200)^2]^{1/2} = 250 \text{ m/s}$$

$$W_{\theta 2m} = C_{z2} \tan \beta_2 = (150 \text{ m/s}) \tan(-35^\circ)$$

$$W_{\theta 2m} \approx -105 \text{ m/s}$$

$$W_{2m} = [(150)^2 + (105)^2]^{1/2} = 183.1 \text{ m/s}$$

The D -factor for the rotor at the pitchline is

$$D_{rm} \equiv 1 - \frac{W_{2m}}{W_{1m}} + \frac{|W_{\theta 2m} - W_{\theta 1m}|}{2\sigma_{rm} W_{1m}}$$

The rotor solidity at the pitchline is $\sigma_{rm} = c/s = 7/7 = 1.0$
 The relative tangential speed at the inlet to the rotor is equal in magnitude to the rotor speed U_m , but it has a negative

value, as it points in the opposite direction to the rotor rotation

$$W_{\theta 1m} = -200 \text{ m/s}$$

Therefore, we have

$$D_{rm} = 1 - (183.1/250) + |(-105 + 200)|/(2.1.250) \approx 0.457$$

Since D -factor is less than ~ 0.5 , the rotor boundary layer at the pitchline is expected to be attached.

Circulation around the rotor at pitchline is

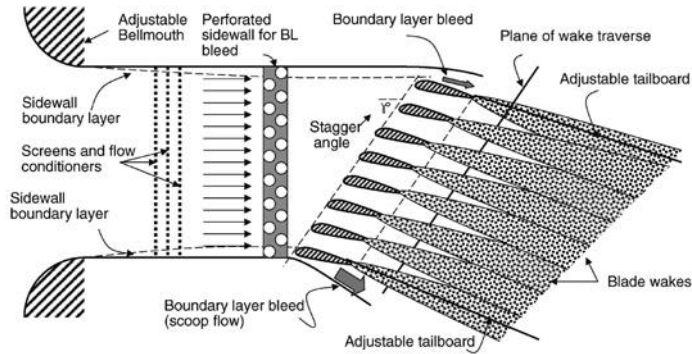
$$\Gamma_m = s_m |W_{\theta 1m} - W_{\theta 2m}| = (0.07\text{m})|(-200 + 105)| \approx 6.65 \text{ m}^2/\text{s}$$

8.6.3 Cascade Aerodynamics

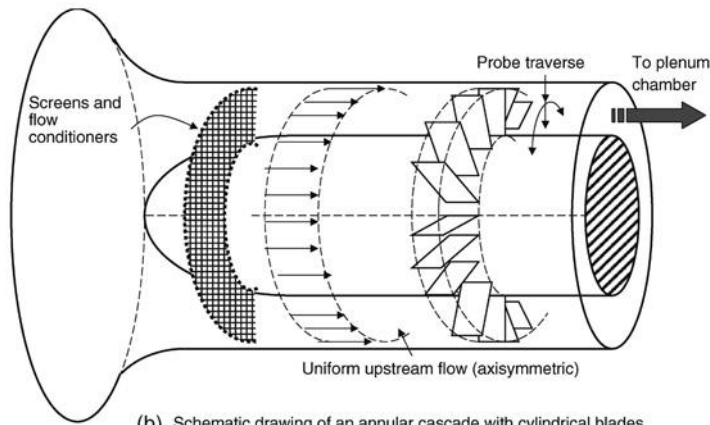
A large body of experimental data supports a correlation between the blade stall and the diffusion factor. Let us first examine the attributes of a stalled flow in a compressor blade row. A separated boundary layer will create a thick wake, which may be characterized by its momentum deficit length scale θ^* . Equivalently, a wake is a region of deficit total pressure, hence in the blade frame of reference stall creates a rapid rise in the total pressure loss across the blade row. In either case, we need to examine the wake profile downstream of a blade row to quantify momentum and total pressure loss. To concentrate on the study of compressor blades, NACA (the predecessor of NASA) developed the so-called 65 series of airfoil profiles in early 1950s. To test the aerodynamic behavior of the newly developed blade shapes, NACA performed an extensive series of cascade experiments, concentrating on the impact of the 65-series compressor airfoil shapes on two-dimensional compressor loss and stall characteristics. Airfoil shapes are defined around a mean camber line, typically of circular arc or parabolic shape and a prescribed thickness distribution. A cascade is composed of a series of two-dimensional or cylindrical blades placed in a uniform flow to simulate the two-dimensional flowfield about a *spanwise section* of a compressor blade row. The goal of the investigation is to quantify the profile loss of two-dimensional blade elements as a function of the profile geometry and cascade parameters such as blade chord-to-spacing ratio, blade stagger angle, and other parameters. To construct the three-dimensional loss characteristics of compressor blades, two-dimensional cascade loss data are *stacked up* to represent the 3D picture. This approach neglects the cross interaction of the stream surfaces that is created through 3D pressure gradients. We learned in wing theory that three-dimensional pressure gradients lead to the formation of the streamwise vortices in the wake, which causes a 3D induced velocity (and induced drag) along the blade span. We shall address three-dimensional losses that are overlooked by the cascade data later in this chapter. Let us return to two-dimensional cascade studies performed at NACA. The wake profile with its momentum deficit and total pressure loss holds the key to characterizing the behavior of a compressor blade section. Figure 8.18a shows a rectilinear cascade, Figure 8.18b an annular cascade, and Figure 8.18c defines the geometric parameters of the blade section and the cascade. Figure 8.19 shows periodic blade wakes downstream of a cascade where the momentum deficit and the total pressure loss are concentrated. The thickness of the wake is exaggerated in Figure 8.19 for visualization purposes, but a thicker suction surface boundary layer than the pressure surface is intentionally graphed to show the behavior of these boundary layers that merge to form the blade wake in turbomachinery.

Let us review the cascade parameters as shown in Figure 8.18c. An important geometrical cascade parameter is the solidity σ , which is defined as the ratio of chord-to-spacing. A high solidity blading is capable of a higher net turning angle than a low solidity blading. Consequently, a high solidity cascade is less susceptible to stall. Experimental evidence to support this assertion will be presented as cascade test results. As noted earlier, the modern compressor and fan design utilizes a high solidity blading ($\sigma_t \cong 1$). The angle of the mean camber line at the leading and trailing edge is used as a reference where we measure the inlet flow incidence angle i and the exit deviation angle δ^* . The incidence angle is defined as the flow angle between the tangent to the mean camber line and relative velocity vector at the inlet. In compressors, incidence angle takes the place of angle of attack in external aerodynamics. An optimum, incidence angle is defined as the incidence that causes minimum (total pressure) loss across a given cascade. A

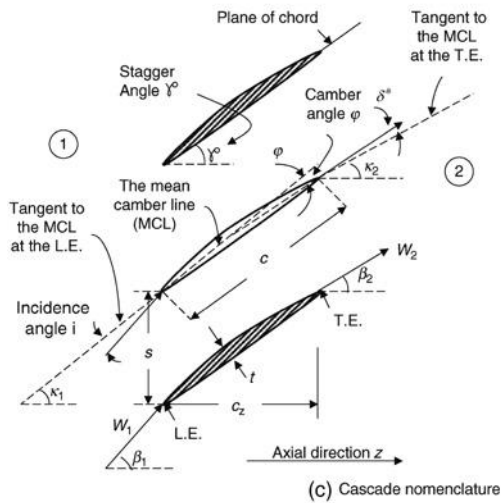
■ FIGURE 8.18 Cascade types and nomenclature



(a) Schematic drawing of a rectilinear cascade test rig with cylindrical blades



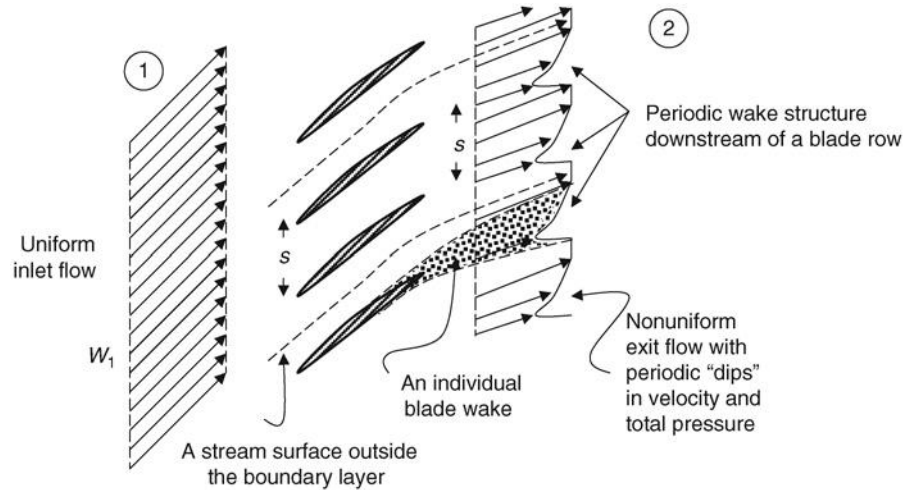
(b) Schematic drawing of an annular cascade with cylindrical blades



(c) Cascade nomenclature

Cascade parameters	
Solidity	$\sigma = c/s$
Stagger angle	γ°
Camber angle	$\phi = \kappa_1 - \kappa_2$
Incidence angle	$i = \beta_1 - \kappa_1$
Deviation angle	$\delta^* = \beta_2 - \kappa_2$
Net turning angle	$\Delta\beta = \beta_1 - \beta_2 = \phi + i - \delta^*$
Angle of attack	$\beta_1 - \gamma^\circ$
Thickness-to-chord ratio	t/c

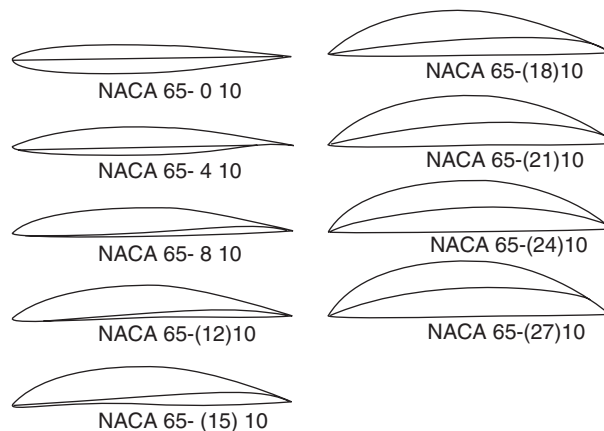
■ **FIGURE 8.19**
Survey of the
wake-velocity profile
downstream of a
cascade



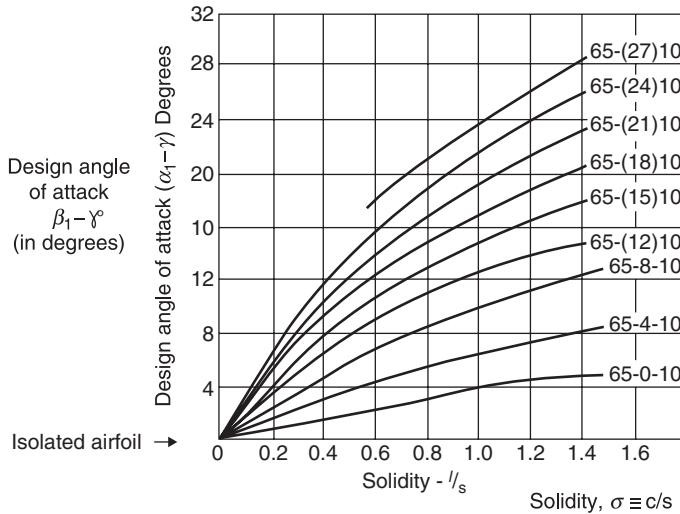
typical value of the optimum incidence angle for a subsonic flow cascade is $i_{\text{opt}} \sim 2^\circ$. Cascade experimental results support this rule of thumb. The camber angle ϕ is defined as the angle formed at the intersection of the two tangents to the mean camber line at the leading and trailing edges, as shown. A large camber means a large flow turning, which may lead to flow separation. Hence, compressor blade camber is small compared with a turbine blade, which is capable of large turning due to a favorable pressure gradient. The stagger angle γ° is sometimes referred to as the *blade-setting angle* is the blade chord angle with respect to the axial direction. The stagger angle increases with radius as the blade rotational speed (ωr) increases linearly with radius. The difference between the stagger angle and the relative inflow angle is called the angle of attack, as in external aerodynamics. Finally, the net turning angle refers to the difference between the inlet and exit flow angles, respectively.

The 65-series compressor cascade airfoil shapes are shown in Figure 8.20. The design (theoretical) lift coefficient for an isolated airfoil shape (at zero angle of attack) is listed in parenthesis (times ten) following the 65-series designation. Note that the lift

■ **FIGURE 8.20**
The 65-series cascade
airfoil shapes with
10% thickness. Source:
Herrig, Emery, and
Erwin 1951



■ **FIGURE 8.21**
 Design angle of attack, $\beta_1 - \gamma^\circ$, for the 65-series airfoils with 10% thickness as a function of solidity. Source: Herrig, Emery, and Erwin 1951



coefficient at zero angle of attack is entirely due to camber. The *isolated* means that the airfoil is not in a cascade configuration, that is, solidity is zero. The thickness-to-chord ratio (in percent) comprises the last two digits of the series designation.

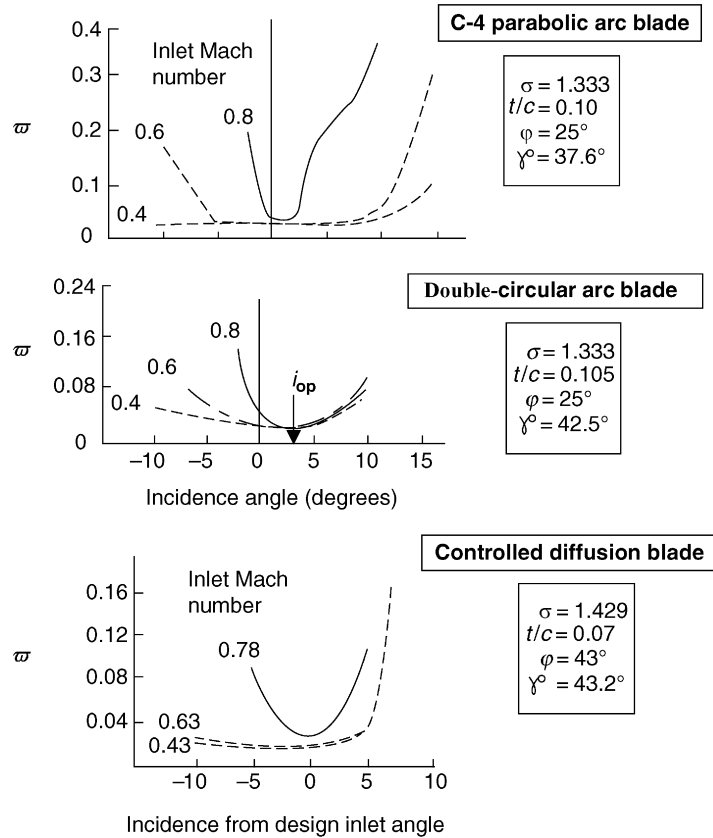
For example, a NACA 65-(18)10 represents the 65-series camber shape that produces an isolated theoretical (i.e., inviscid) lift coefficient of 1.8 (at zero angle of attack) and has a 10% thickness-to-chord ratio. The cascade parameters, namely, solidity and stagger, are included in the individual loss characteristic (bucket) curves that are produced for different cascades. NACA defined a design angle of attack for the 65-series airfoils based on the smoothness of the pressure distributions on the airfoils. Figure 8.21 shows the design angle of attack for the 65-series airfoils arranged in a cascade of varying solidity. The zero solidity refers to an isolated airfoil case. Note that the combination of high solidity and high camber that leads to a high angle of attack (Figure 8.21) does not mean that the incidence angle is very large too. The blade inlet angle κ_1 makes a large angle with respect to the blade chord for highly cambered airfoils (see Figure 8.20 for airfoil shapes with high camber). The message from Figure 8.21 is that higher solidity allows for larger turning, which translates into an increase in inlet flow angle (keeping the exit angle \sim fixed).

A survey of total pressure downstream of cascade reveals the presence of periodic wakes. Defining an *average* total pressure loss parameter for a cascade as

$$\varpi \equiv \frac{p_{t1} - \bar{p}_{t2}}{\rho_1 W_1^2 / 2} \tag{8.62}$$

where the average downstream total pressure may be taken as the area-average of the total pressure survey. The denominator of Equation 8.62 is the familiar dynamic pressure ($\rho_1 W_1^2 / 2$) in the cascade frame of reference. The cascade loss “bucket curves” are shown in Figure 8.22 for a parabolic arc, a double-circular arc, and a controlled diffusion blading at different inlet Mach numbers (adapted from Kerrebrock, 1992). The works of Hobbs and Weingold (1984) and Hechert, Steinert and Lehmann (1985) on development of

■ **FIGURE 8.22**
Variation of cascade total pressure loss parameter with inlet Mach number and flow incidence angle.
Source: Adapted from Kerrebroch 1992



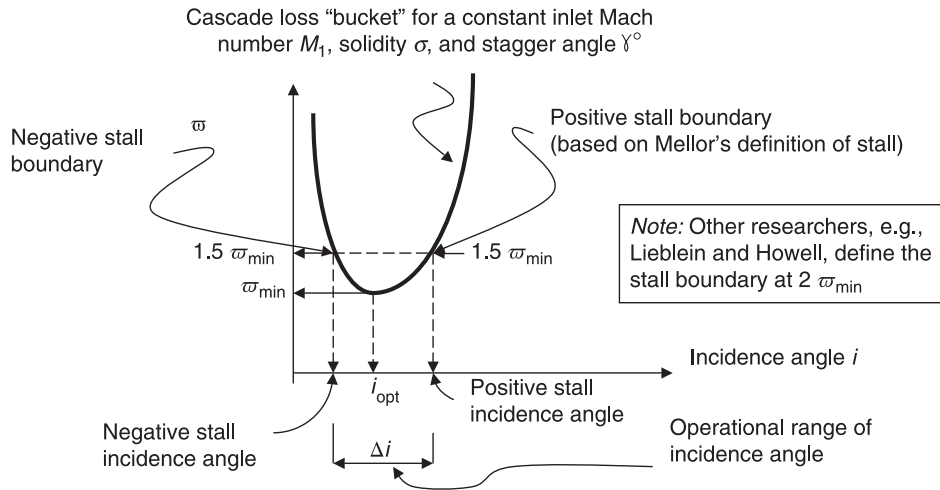
controlled diffusion airfoils and their comparison to NACA-65 airfoils for compressors should be consulted for further reading.

The minimum loss incidence angle is referred to as w_{\min} that corresponds to the optimum incidence angle i_{opt} . We further define an acceptable operational range for the incidence angle that corresponds to 150% of the minimum loss w_{\min} , which Mellor referred to as the positive and negative stall boundaries. A definition sketch is shown in Figure 8.23.

Mellor presents the operational range of each 65-series airfoils in various cascade arrangements that are very useful for preliminary design purposes. Mellor's unpublished graphical correlations (originated at MIT Gas Turbine Laboratory) were published by Horlock (1973), Hill and Peterson (1992), among others.

The correlation between the diffusion factor and the wake momentum deficit thickness θ^* is presented in Figure 8.24 (Lieblein, 1965). The cascade data of Lieblein present 10% thick blades with the mean camber line shapes described by the NACA 65-series profiles and the British C-4 parabolic arc profiles, as shown in Figure 8.24. The Reynolds number for the cascade tests is $\sim 250,000$. Blade stall leads to a thickening of the wake that results in a rapid increase in profile drag and hence momentum deficit thickness. From Figure 8.24, we note this behavior occurs around a D -factor of 0.6. Hence, the maximum

■ **FIGURE 8.23**
Definition sketch for the stall boundaries based on the cascade loss curve

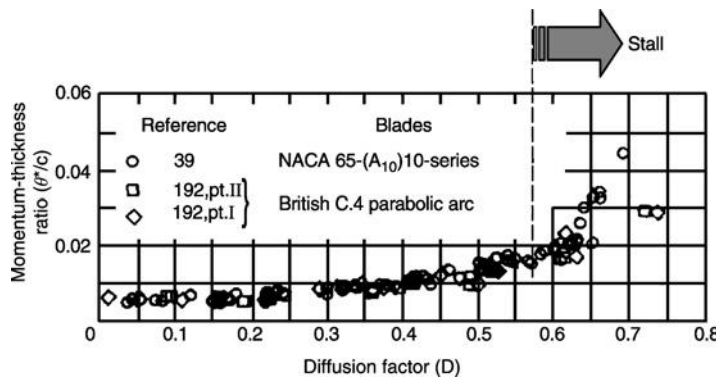


diffusion factor associated with a well-behaved boundary layer on these classical blade profiles is $D_{max} \sim 0.6$. A higher D -factor (of ~ 0.7) may be achieved in cascades of modern controlled-diffusion profiles.

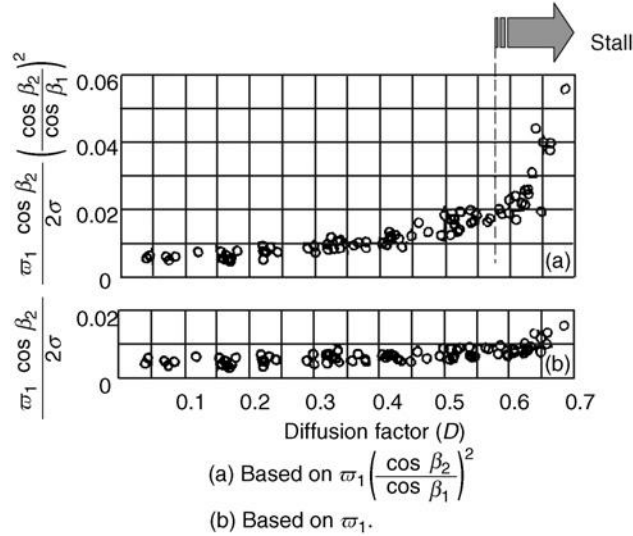
How does the momentum deficit thickness θ^*/c relate to the total pressure loss parameter w in a cascade? By averaging the total pressure downstream of the cascade assuming a periodic momentum deficit thickness with zero momentum, we can correlate these two parameters. Figure 8.25 (Lieblein, 1965) shows two total pressure loss functions and their correlation with D -factor.

To demonstrate the functional form of the correlation (see the ordinate of Figure 8.25), we approximate the cascade exit flow as being composed of uniform flow with periodic gaps of zero momentum, each with θ^*/c thickness corresponding to wakes. The static pressure is assumed to be uniform in the measuring station downstream of the cascade. Figure 8.26 shows a definition sketch of this simplified cascade exit flow model. Although the original contribution to this derivation is due to Lieblein-Roudebush (1956), this author has benefited from Kerrebrock's (1992) treatment of this and other turbomachinery subjects.

■ **FIGURE 8.24**
Correlation between the diffusion factor and the wake momentum deficit thickness.
 Source: Lieblein 1965 (reference numbers are in Lieblein). Courtesy of NASA



■ **FIGURE 8.25**
 Total pressure loss correlation with *D*-factor. Source: Lieblein 1965. Courtesy of NASA



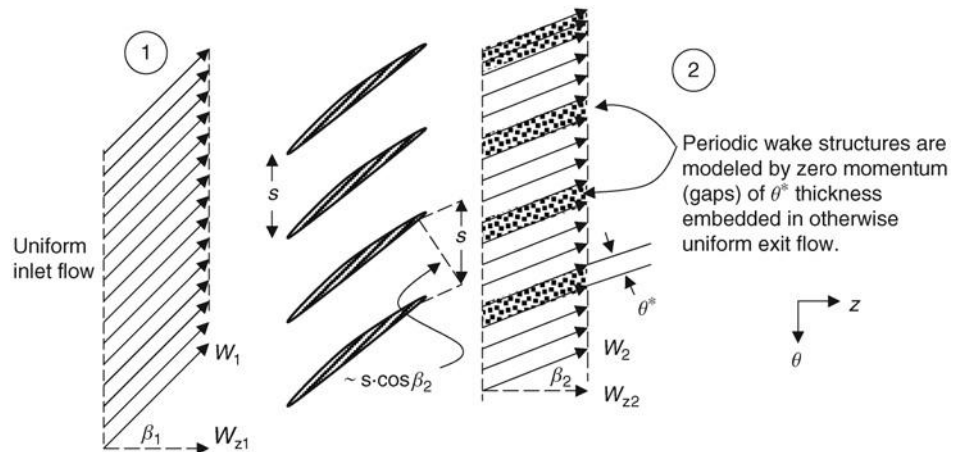
The total pressure downstream of the cascade is the sum of static and dynamic pressures, according to (incompressible) Bernoulli equation. The dynamic pressure is zero in the wake region of θ^* thickness. We may area-average the total pressure in the downstream region according to

$$p_{t2} \cdot (s \cdot \cos \beta_2 - \theta^*) + p_2 \cdot \theta^* = \bar{p}_{t2} \cdot s \cdot \cos \beta_2 \tag{8.63a}$$

$$\bar{p}_{t2} = p_{t1} - \frac{p_{t2} - p_2}{s \cdot \cos \beta_2} \cdot \theta^* = p_{t1} - \frac{\rho \cdot W_2^2}{2s \cdot \cos \beta_2} \cdot \theta^* \tag{8.63b}$$

Note that we have used the concept of constant total pressure in an inviscid fluid by using $p_{t1} = p_{t2}$ outside the wake region. Therefore, in the blade frame of reference, the total pressure remains conserved in the inviscid limit, assuming there are no shocks in

■ **FIGURE 8.26**
 Definition sketch for a cascade exit flow model with periodic wakes



the blade passage. In this context, we have applied the Bernoulli equation, which strictly speaking holds for an incompressible fluid. All these approximations are reasonable for our purposes here of demonstrating subsonic cascade data correlation of total pressure loss with D -factor. Now, in terms of the total pressure loss parameter ϖ we get

$$\varpi = \frac{p_{t1} - \bar{p}_{t2}}{\rho_1 W_1^2 / 2} \approx \frac{\rho \left(\frac{W_z^2}{\cos^2 \beta_2} \right) \cdot \theta^*}{2s \cdot \cos \beta_2 \cdot \rho \left(\frac{W_z^2}{\cos^2 \beta_1} \right) / 2} = \left(\frac{\cos \beta_1}{\cos \beta_2} \right)^2 \frac{\sigma}{\cos \beta_2} \left(\frac{\theta^*}{c} \right) \quad (8.64)$$

Here we made a simple approximation of constant axial flow across the cascade. Finally, we conclude that since θ^*/c correlated with the diffusion factor, then the RHS of

$$\frac{\theta^*}{c} = \varpi \cdot \left(\frac{\cos \beta_2}{\sigma} \right) \left(\frac{\cos \beta_2}{\cos \beta_1} \right)^2 = f(D, t/c, Re_c, M, \sigma, \text{camber shape}) \quad (8.65)$$

correlates with the D -factor as well, keeping other cascade parameters constant. This functional dependence of the total pressure loss parameter on D -factor is demonstrated in Figure 8.25.

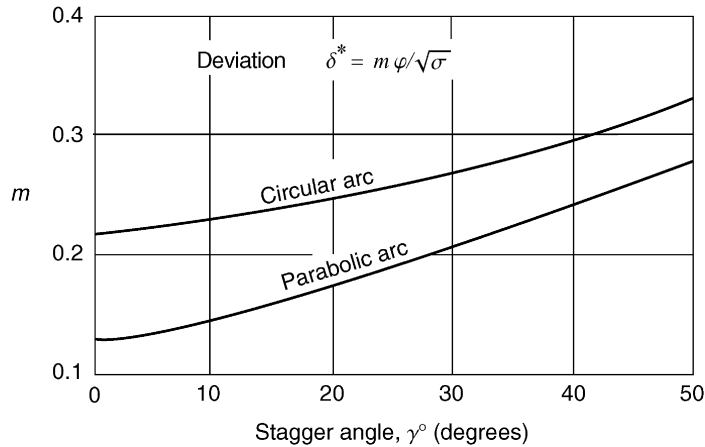
The exit flow angle deviates from the exit blade angle by what is called a deviation angle δ^* due to boundary layer buildup at the trailing edge. Cascade experiments have revealed a correlation between the deviation angle and the geometric parameters of a cascade, namely, the camber angle, the solidity, and the stagger angle. The following correlation is due to Carter (1955).

$$\delta^* = \frac{m\varphi}{\sigma^n} \quad (\text{Carter's rule for deviation angle}) \quad (8.66)$$

where φ is the camber angle, σ is the solidity, m is a function of cascade stagger angle, and n is $1/2$ for a compressor cascade and 1 for an inlet guide vane (or an accelerating passage such as turbines). The higher exponent of solidity for a turbine ($n = 1$) than the compressor ($n = 1/2$) leads to higher exit deviation angles in a compressor, as expected. The boundary layer build up in a compressor in adverse pressure gradient is greater than its counterpart in the turbine. The dependence of m on stagger angle and the profile shape is presented in Figure 8.27, following Carter (1955).

The double-circular arc blade has a circular arc mean camber line shape where the point of maximum camber and thickness occur at mid-chord. The parabolic arc mean camber line blade that is shown in Figure 8.27 has a maximum camber location at 40% chord. The location of the maximum camber and even the thickness affect the pressure distribution about the blade and hence the exit flow deviation angle. It is instructive to know that in turbomachinery blading the chordwise location of the maximum camber moves farther aft with an increasing inlet relative Mach number. For example, a multiple-circular arc blade may be used in the supersonic section of a transonic compressor with the maximum camber placed at 75% chord. We shall discuss multiple-circular arc and other profile shapes of suitable blades for supersonic applications later in this chapter.

■ **FIGURE 8.27**
Compressor cascade
deviation angle rule
following Carter
(1955). Source:
Reproduced with
permission from
Elsevier



A more general definition of the diffusion factor should involve the radial shift of stream surfaces across compressor blade rows. The constant radius, cylindrical cut approximation of the flowfield is rather restrictive. The method allows for a “pitchline,” one-dimensional analysis of a compressor, but falls short of a realistic “mean” flow modeling. A general D -factor is defined as

$$D \equiv 1 - \frac{W_2}{W_1} + \frac{|r_2 W_{\theta 2} - r_1 W_{\theta 1}|}{2\sigma r_m \cdot W_1} = 1 - \frac{W_2}{W_1} + \frac{|r_2 W_{\theta 2} - r_1 W_{\theta 1}|}{(r_1 + r_2) \sigma \cdot W_1} \quad (8.67)$$

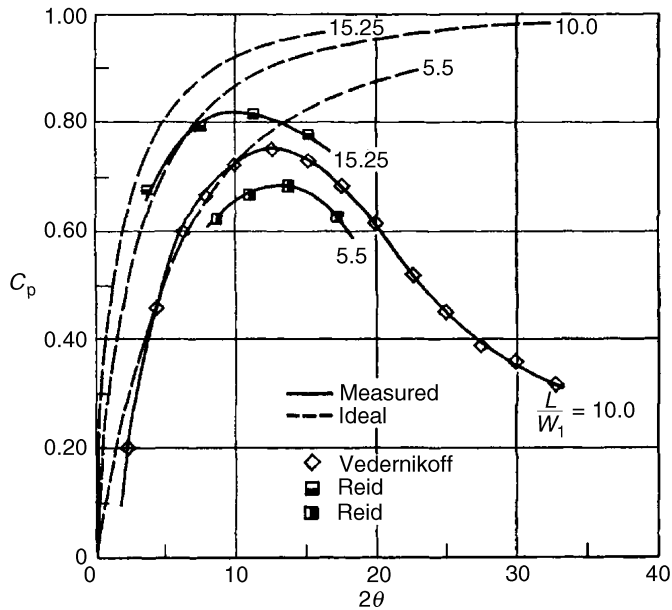
Note that the change in angular momentum has replaced the change in tangential momentum in the definition of a general D -factor. We will address the general diffusion factor in the three-dimensional flow section in this chapter.

Another performance limiting parameter in a compressor in addition to the D -factor is the static pressure rise coefficient, as in a diffuser. The pressure rise coefficient and the D -factor are two different ways of measuring the same thing, namely, the tendency of the boundary layer to stall. However, the D -factor examines the stall behavior of a compressor blade suction surface, whereas the stalling pressure rise coefficient analogy with a diffuser examines the end wall stall that dominates the multistage compressor aerodynamics. The new limiting parameter is defined as

$$C_p \equiv (p_2 - p_1) / (\rho_1 W_1^2 / 2) \quad (8.68)$$

The static pressure rise across a blade row, in the numerator of Equation 8.68, is independent of the observer frame of reference. The dynamic pressure at the inlet to the blade row is in the relative frame, that is, as in a cascade parameter. From our studies of boundary layers in adverse pressure gradient we have learned that $C_{p,\max} \approx 0.6$. Interestingly, the numerical values of $C_{p,\max}$ and the limiting D -factor are both ~ 0.6 , a coincidence. The nature of the compressor end wall boundary layer and its stalling characteristics is more complicated than a simple diffuser. Figure 8.28 shows the pressure rise data for a two-dimensional diffuser, where a working range of C_p within ~ 0.4 to ~ 0.8 is observed (from Kline *et al.*, 1959).

■ **FIGURE 8.28**
 Static pressure rise limitation in a 2D diffuser (data from Kline, Abbott and Fox 1959). Source: Kline, Abbott and Fox 1959, Fig. 4, p. 326. Reproduced with permission from ASME



The main differences between a diffuser flow and a flow in a compressor blade row are

- (a) Compressor boundary layer is highly skewed due to large streamwise and radial pressure gradients, that is, leading to (a highly) three-dimensional flow separation
- (b) Inherent unsteadiness in turbomachinery due to relative motion of neighboring blade rows are absent in a diffuser
- (c) Compressibility effects through the passage shock interaction with the boundary layer is absent in diffuser performance charts such as Figure 8.28
- (d) Upstream wake transport in downstream blade rows is also absent in diffusers
- (e) Blade tip clearance flow is unique to turbomachinery
- (f) End wall regions create secondary vortex formations as in corner and scraping vortex structures in compressors with no counterpart in a diffuser

In light of these complicating factors, to suggest a single value for the maximum (sometimes called *stalling*) pressure rise coefficient for all compressor blade sections is oversimplistic. For example, the stalling pressure rise coefficient near the end walls may be ~ 0.48 (first stipulated by de Haller, 1953) and at the pitchline radius ~ 0.6 . A stalling pressure rise correlation for multistage axial-flow compressors is successfully derived by Koch (1981). We will present Koch's correlation in the context of compressor stall margin later in this chapter. A simple application of de Haller pressure rise criterion in the incompressible limit restricts the maximum flow deceleration (W_2/W_1) in a blade row to 0.72. The shock in passage also changes the abruptness of the static pressure rise, hence the boundary layer separation. Despite these shortcomings, the concept of a stalling

pressure rise in a compressor blade row is very attractive and useful. We shall examine some limiting features of stalling pressure rise coefficient in a compressor blade. First, let us use Bernoulli equation in recasting the static pressure rise coefficient C_p as

$$C_p = 1 - \frac{W_2^2}{W_1^2} - \frac{\Delta p_t}{(\rho_1 W_1^2/2)} = 1 - \frac{W_2^2}{W_1^2} - \varpi_{\text{cascade}} \tag{8.69}$$

The cascade total pressure loss parameter ϖ_{min} is $\sim 2\%$ for unstalled blades (Figure 8.21). For a maximum pressure rise coefficient of ~ 0.6 , the maximum flow deceleration (expressed in terms of W_2/W_1) is

$$W_2 \geq 0.62 W_1$$

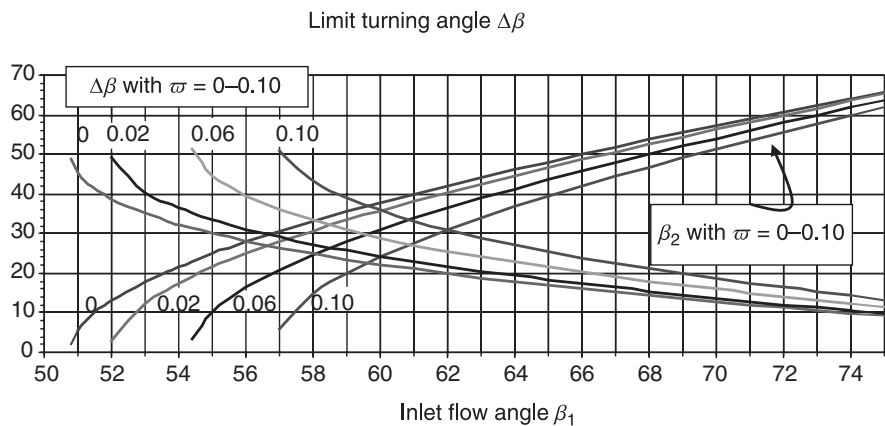
The implication of this (maximum) flow deceleration may be found in the turning angle limitation, namely, for a constant axial velocity W_z , we have $W_1 = W_z/\cos\beta_1$ and $W_2 = W_z/\cos\beta_2$,

$$C_p = 1 - (\cos^2 \beta_1 / \cos^2 \beta_2) - \varpi_{\text{cascade}} \tag{8.70}$$

We may solve Equation 8.20 for the exit flow angle β_2 for a given cascade total pressure loss parameter, inlet flow angle, and the maximum pressure rise coefficient. The maximum turning angle ($\Delta\beta$) associated with a limiting pressure rise coefficient is graphed in Figure 8.29. The cases of zero total pressure loss, that is, ideal flow, and a cascade with a total pressure loss parameter of 2, 6, and 10% are shown. The effect of total pressure loss increase is seen in Figure 8.29 as a reduction in exit flow angle and thus an increase in flow turning in a compressor blade row. Also, from Equation 8.70, we observe that the maximum static pressure rise coefficient $C_{p,\text{max}}$ for a given inlet flow angle β_1 and total pressure loss occurs at the exit flow angle $\beta_2 = 0$, or axial flow direction at the exit, as expected.

Another aspect of the pressure rise coefficient may be found in its relation to the relative inlet Mach number M_{1r} . From the definition of the static pressure rise coefficient,

■ **FIGURE 8.29**
The exit flow and the limit turning angles (in degrees) based on a $C_{p,\text{max}}$ of 0.6



we may express the dynamic pressure in terms of the inlet static pressure and the inlet relative Mach number, as

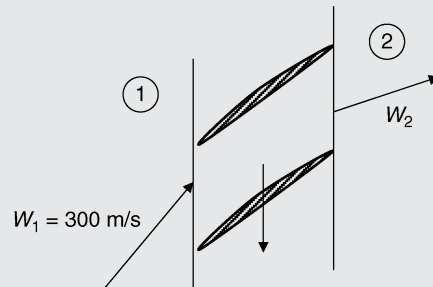
$$C_p = \frac{p_2 - p_1}{\gamma \cdot p_1 M_{1r}^2 / 2} \quad (8.71a)$$

$$\frac{p_2}{p_1} = 1 + C_p \cdot \gamma \cdot M_{1r}^2 / 2 \quad (8.71b)$$

EXAMPLE 8.4

A rotor blade row at pitchline radius is shown. The rotor total pressure loss coefficient at this radius is $\varpi_{rm} = 0.03$.

- How much deceleration is allowed in the rotor under de Haller criterion? i.e., What is the minimum W_2 ?
- What is the static pressure rise coefficient, assuming incompressible flow and W_{2min} from de Haller criterion?



SOLUTION

de Haller criterion states that W_2/W_1 should be >0.72 . Therefore, the minimum W_2 is $0.72 W_1$ or

$$W_{2min} = 216 \text{ m/s}$$

The incompressible flow static pressure rise is given by Equation 8.69

$$C_p = 1 - \frac{W_2^2}{W_1^2} - \varpi_{cascade} = 1 - (0.72)^2 - 0.03 \approx 0.4516$$

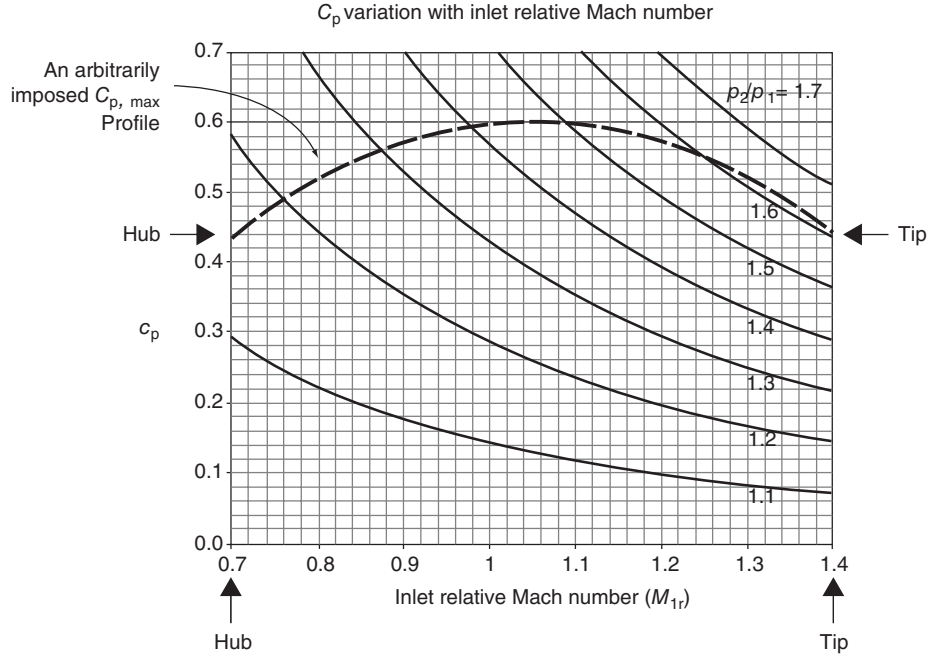
In a modern transonic fan or compressor stage, the relative Mach number to the rotor varies from hub-to-tip of ~ 0.7 to ~ 1.4 , respectively. The variation of feasible static pressure ratio along the blade span with relative Mach number is shown in Figure 8.30.

We observe that the static pressure ratio p_2/p_1 is nearly limited by ~ 1.15 near the hub and may increase to ~ 1.6 for a supersonic relative tip Mach number for a $C_{p,max}$ of ~ 0.45 near the tip. The static pressure distribution downstream of a turbomachinery blade row strongly depends on the swirl distribution and the axial velocity profile in the spanwise direction. The most common approach in preliminary analysis of three-dimensional flows in turbomachinery is the radial equilibrium theory that we shall discuss in this chapter.

It is useful to correlate the compressor stage efficiency, at a given radius, with the cascade loss coefficients at the corresponding radius. Let us consider the cascade total pressure loss coefficients of ϖ_r and ϖ_s to represent the relative total pressure loss in the rotor and the stator blade sections, respectively, nondimensionalized with respect to the inlet dynamic pressure.

$$\varpi_r \equiv \frac{p_{t1r} - \bar{p}_{t2r}}{\rho_1 W_1^2 / 2} = \frac{2p_{t1r}}{\rho_1 W_1^2} \left(1 - \frac{\bar{p}_{t2r}}{p_{t1r}} \right) = \frac{2p_1 \left(1 + \frac{\gamma - 1}{2} M_{1r}^2 \right)^{\frac{\gamma}{\gamma - 1}}}{\rho_1 W_1^2} \left(1 - \frac{\bar{p}_{t2r}}{p_{t1r}} \right) \quad (8.72)$$

■ **FIGURE 8.30**
Variation of static pressure rise coefficient C_p with inlet relative Mach number (for constant pressure ratio p_2/p_1) with an arbitrarily imposed $C_{p,max}$ profile



We may also express the ratio of static pressure to dynamic pressure in terms of the relative Mach number to simplify the above expression as

$$\frac{\bar{p}_{t2r}}{p_{t1r}} = 1 - \omega_r \left[\frac{\gamma M_{1r}^2 / 2}{\left(1 + \frac{\gamma - 1}{2} M_{1r}^2\right)^{\frac{\gamma}{\gamma - 1}}} \right] \tag{8.73}$$

The stagnation pressure ratio across the stator blade sections may be written in an analogous manner to Equation 8.73, as

$$\frac{\bar{p}_{t3}}{p_{t2}} = 1 - \omega_s \left[\frac{\gamma M_2^2 / 2}{\left(1 + \frac{\gamma - 1}{2} M_2^2\right)^{\frac{\gamma}{\gamma - 1}}} \right] \tag{8.74}$$

The compressor stage adiabatic efficiency η_s is

$$\eta_s = \frac{\pi_s^{\frac{\gamma - 1}{\gamma}} - 1}{\tau_s - 1} \tag{8.75}$$

We may use the following chain rule to express the stage total pressure ratio as

$$\pi_s \equiv \frac{p_{t3}}{p_{t1}} = \left(\frac{p_{t3}}{p_{t2}}\right) \left(\frac{p_{t2}}{p_{t2r}}\right) \left(\frac{p_{t2r}}{p_{t1r}}\right) \left(\frac{p_{t1r}}{p_{t1}}\right) \tag{8.76}$$

Equations 8.73 and 8.74 describe two of the parentheses in Equation 8.76, and we may relate the remaining two expressions to flow Mach numbers in the absolute and relative frame, namely

$$\frac{p_{t1r}}{p_{t1}} = \left[\frac{1 + \frac{\gamma - 1}{2} M_{1r}^2}{1 + \frac{\gamma - 1}{2} M_1^2} \right]^{\frac{\gamma}{\gamma - 1}} \quad (8.77)$$

$$\frac{p_{t2}}{p_{t2r}} = \left[\frac{1 + \frac{\gamma - 1}{2} M_2^2}{1 + \frac{\gamma - 1}{2} M_{2r}^2} \right]^{\frac{\gamma}{\gamma - 1}} \quad (8.78)$$

From the inlet conditions, we can calculate M_1 and M_{1r} that are needed in Equation 8.77. The absolute and relative Mach numbers in station 2, that is, downstream of the rotor, may be calculated from the velocities C_2 and W_2 from the velocity triangles and the speed of sound a_2 . The speed of sound may be related to fluid total enthalpy and kinetic energy according to

$$h_t = a^2 / (\gamma - 1) + C^2 / 2 \quad (8.79)$$

Therefore,

$$a_2^2 = (\gamma - 1) \left[h_{t2} - \frac{C_2^2}{2} \right] = (\gamma - 1) \left\{ [h_{t1} + \omega (r_2 C_{\theta 2} - r_1 C_{\theta 1})] - \frac{(C_{z2}^2 + C_{\theta 2}^2)}{2} \right\} \quad (8.80)$$

Hence, the absolute Mach number downstream of the rotor, in terms of known quantities, is

$$M_2 = \sqrt{\frac{(C_{z2}^2 + C_{\theta 2}^2)}{(\gamma - 1) [h_{t1} + \omega (r_2 C_{\theta 2} - r_1 C_{\theta 1}) - (C_{z2}^2 + C_{\theta 2}^2) / 2]}} \quad (8.81)$$

The relative Mach number M_{2r} is

$$M_{2r} = \sqrt{\frac{[C_{z2}^2 + (C_{\theta 2} - \omega \cdot r_2)^2]}{(\gamma - 1) [h_{t1} + \omega (r_2 C_{\theta 2} - r_1 C_{\theta 1}) - (C_{z2}^2 + C_{\theta 2}^2) / 2]}} \quad (8.82)$$

Now, we have established all the parameters that enter the stage adiabatic efficiency Equation 8.75 in terms of the basic velocity triangles and the cascade total pressure loss coefficients. Our analysis is valid for compressible flows in turbomachinery. However, by

limiting the analysis to incompressible fluids, we may relate the stage efficiency to the stagnation pressure loss in the rotor and stator blade rows, via

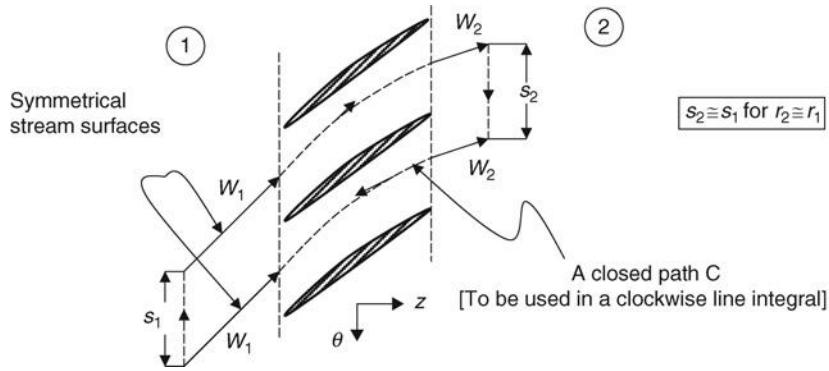
$$\eta_s \approx 1 - \frac{\Delta p_{t-\text{Rotor}} + \Delta p_{t-\text{Stator}}}{\rho (h_{t2} - h_{t1})} \quad (8.83)$$

The derivation of Equation 8.83 is straightforward and is shown in Hill and Peterson (1992). The cascade total pressure loss data directly feed into Equation 8.83 for the stage efficiency estimation. In general, we have to supplement the cascade total pressure loss coefficient by shock losses in supersonic flow. In addition, we need to account for the effect of the shock-boundary layer interaction, which increases the blade profile losses. These effects belong to what is known as the *compressibility effects*. A host of other losses in a turbomachinery stage occur that are not usually simulated in a cascade experiment. For example, the end-wall effects, including the tip clearance flow, the streamwise vortices in the blades' wakes due to spanwise variation of blade circulation, as well as flow unsteadiness that result in vortex shedding in the wakes, are not simulated in a typical cascade experiment. The cascade total pressure loss parameter ϖ describes the profile loss of a two-dimensional blade in a steady flow. We will use it as a foundation to construct a more elaborate blade loss model, only.

8.6.4 Aerodynamic Forces on Compressor Blades

The conservation principles that we learned and applied to wings and bodies in external aerodynamics apply to internal aerodynamics as well. There are some complicating factors in a turbomachinery flow that are absent in external aerodynamics. The most dominant feature is the presence of strong swirl in turbomachinery that is either completely absent or weak in external flows. Second, the net turning in the flow is large in turbomachinery and zero in external aerodynamics. We may characterize the flow in a turbomachinery as lacking a unique flow direction, unlike external aerodynamics. As an example, the Kutta–Joukowski theorem on lift predicts a magnitude for an ideal two-dimensional lift (on a body that creates circulation, Γ) as $\rho_\infty V_\infty \Gamma$ and a direction for the lift that is normal to V_∞ . In turbomachinery blading, there are two distinct flow speeds, one upstream and the other downstream of the blade, that is, W_1 and W_2 and not just a single V_∞ . Also, on the question of the direction of this force, is it normal to W_1 or W_2 ? In turbomachinery, we will define a “mean” flow angle and a “mean” velocity that help us describe the blade lift and its direction. There are other complicating factors in internal flows that deal with flow distortion (e.g., upstream wake transport and interaction with downstream blades) and unsteadiness (i.e., from neighboring blade rows in relative rotation) that are inherent in a turbomachinery stage and have either no or weak counterparts in external aerodynamics. In a compressor, the flow is continually subjected to an adverse pressure gradient, as the static pressure rises along the flow direction. On the contrary, in external aerodynamics the flow is only *locally* subjected to adverse pressure gradient. Therefore, we may distinguish the two adverse pressure gradients experienced by the internal and external flows as one having a “global” and the second a “local” character, respectively. Another subtle, yet important, difference between external aerodynamics and internal flows with swirl (as in turbomachinery) deals with the stability of such flows to external disturbances. The distinguishing feature of having a mean swirl profile in a compressor leads to centrifugal instability waves that may grow and cause compressor stall. The

■ **FIGURE 8.17**
 Suitable control surface surrounding a blade along a stream surface for the application of conservation laws



closest external aerodynamic experience to a centrifugal instability comes from the vortex breakdown on a delta wing at high angle of attack. Kerrebrock (1977) has illuminated the behavior of instabilities in a swirling flow (in an annulus) that provides for a new understanding of disturbances in swirling flows in turbomachinery.

Figure 8.17 is reproduced here to help with the control surface definition and the application of conservation principles to the flow in a compressor blade row.

Continuity demands:

$$\rho_1 W_{z1} s_1 = \rho_2 W_{z2} s_2 \tag{8.84}$$

Making an assumption of negligible radial shift in the stream surface from entrance to exit of the blade, we may conclude that $r_2 \approx r_1$ and therefore $s_2 \approx s_1$, hence,

$$\rho_1 W_{z1} \cong \rho_2 W_{z2} \tag{8.85}$$

The momentum equation in the axial (or z -) direction demands

$$\dot{m}(W_{z2} - W_{z1}) = (p_1 - p_2) \cdot s + F_z|_{\text{fluid}} \tag{8.86}$$

Assuming a constant axial throughflow speed, that is, $W_{z1} = W_{z2}$, we get

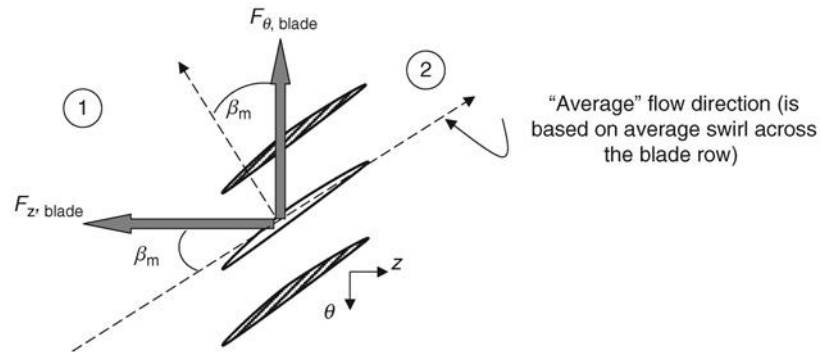
$$F_z|_{\text{fluid}} = -F_z|_{\text{blade}} = (p_2 - p_1)s \tag{8.87}$$

Therefore, we conclude that the axial force *acting on the blade* is in negative z -direction, that is, it points in the upstream direction. The conservation of tangential momentum requires

$$\dot{m}(W_{\theta 2} - W_{\theta 1}) = F_{\theta}|_{\text{fluid}} = -F_{\theta}|_{\text{blade}} \tag{8.88}$$

Therefore, we conclude that the tangential force on the blade is also in the negative θ -direction. These two blade forces are shown in Figure 8.31.

■ **FIGURE 8.31**
The axial and tangential blade forces acting on a compressor blade



We may resolve the axial and tangential blade forces into a lift and drag components but first we have to define an average flow direction through the blade row. We define a mean flow direction β_m based on the average swirl in the blade row, namely,

$$\tan \beta_m \equiv W_{\theta m} / W_z \quad (8.89)$$

where the average swirl, $W_{\theta m}$ is defined as

$$W_{\theta m} \equiv (W_{\theta 1} + W_{\theta 2}) / 2 \quad (8.90)$$

The lift is the sum of the projections of the axial and tangential forces in a direction normal to the “average” flow direction defined in Figure 8.31, that is,

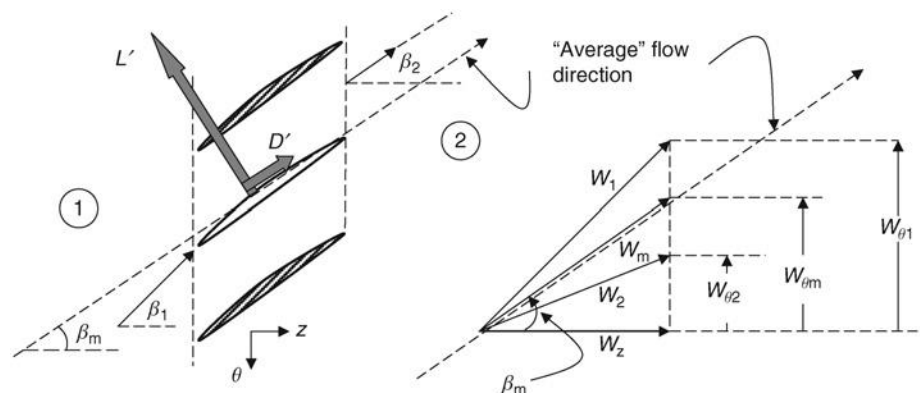
$$L' = F_{\theta, \text{blade}} \cos \beta_m + F_{z, \text{blade}} \sin \beta_m \quad (8.91)$$

Also the drag is the sum of the projections of the two forces in the direction of “average” flow, namely,

$$D' = F_{\theta, \text{blade}} \sin \beta_m - F_{z, \text{blade}} \cos \beta_m \quad (8.92)$$

The lift and drag forces acting on a compressor blade are shown in Figure 8.32.

■ **FIGURE 8.32**
Blade lift and drag forces based on a definition of average flow direction β_m



Therefore the lift force (per unit span) is

$$L' = \rho \cdot W_z \cdot s(W_{\theta 1} - W_{\theta 2}) \cos \beta_m + (p_2 - p_1)s \cdot \sin \beta_m \quad (8.93)$$

Assuming an incompressible fluid and applying the Bernoulli equation to the static pressure rise term in Equation 8.93, we get

$$L' = \rho \cdot W_z \cdot s(W_{\theta 1} - W_{\theta 2}) \left(\frac{W_z}{W_m} \right) + (p_{t2} - \rho \cdot W_2^2/2 - p_{t1} + \rho \cdot W_1^2/2) \cdot s \cdot \left(\frac{W_{\theta m}}{W_m} \right) \quad (8.94a)$$

This equation simplifies to

$$L' = \rho \cdot s(W_{\theta 1} - W_{\theta 2}) \left(\frac{W_z^2}{W_m} \right) + \frac{\rho \cdot s}{2} \left(\frac{W_{\theta m}}{W_m} \right) (W_z^2 + W_{\theta 1}^2 - W_z^2 - W_{\theta 2}^2) - \Delta p_t \cdot s \cdot \left(\frac{W_{\theta m}}{W_m} \right) \quad (8.94b)$$

$$L' = \rho \cdot s(W_{\theta 1} - W_{\theta 2}) \left(\frac{W_z^2}{W_m} \right) + \rho \cdot s \left(\frac{W_{\theta m}}{W_m} \right) \left(\frac{W_{\theta 1} + W_{\theta 2}}{2} \right) (W_{\theta 1} - W_{\theta 2}) - s \cdot \Delta p_t \left(\frac{W_{\theta m}}{W_m} \right) \quad (8.94c)$$

Finally, the blade sectional lift force is expressed as

$$L' = \rho \cdot W_m \cdot s(W_{\theta 1} - W_{\theta 2}) - s \cdot \Delta p_t \left(\frac{W_{\theta m}}{W_m} \right) \quad (8.94d)$$

From Equation 8.58, we may replace the product of blade spacing and the change in swirl velocity by the blade circulation Γ , i.e. $\Gamma \equiv s(W_{\theta 1} - W_{\theta 2})$, to get the familiar Kutta–Joukowski theorem counterpart in turbo-machinery flow, namely,

$$L' = \rho \cdot W_m \cdot \Gamma - s \cdot \Delta p_t (W_{\theta m}/W_m) \quad (8.95)$$

The first term is the familiar Kutta–Joukowski lift, and the second term is the effect of boundary layer formation and viscous losses on lift.

From Equation 8.92, we may write the blade drag force per unit span as

$$D' = \rho \cdot W_z \cdot s(W_{\theta 1} - W_{\theta 2}) \left(\frac{W_{\theta m}}{W_m} \right) - \rho \cdot s \cdot W_{\theta m}(W_{\theta 1} - W_{\theta 2}) \left(\frac{W_z}{W_m} \right) + s \cdot \Delta p_t \cdot \left(\frac{W_z}{W_m} \right) \quad (8.96a)$$

Upon cancellation of the first two terms, we get a simple expression, entirely based on profile losses, for the blade drag force as

$$D' = s \cdot \Delta p_t (W_z/W_m) \quad (8.96b)$$

The lift and drag coefficients are

$$C_l \equiv \frac{L'}{\left(\frac{\rho \cdot W_m^2}{2}\right) \cdot c} = \frac{2\Gamma}{W_m \cdot c} - \frac{\varpi}{\sigma} \cdot \sin \beta_m \quad (8.97)$$

where the cascade total pressure loss is nondimensionalized based on the inlet relative dynamic pressure and the σ is the blade solidity.

$$C_d \equiv \frac{D'}{\left(\frac{\rho \cdot W_m^2}{2}\right) \cdot c} = \frac{\varpi}{\sigma} \cdot \cos \beta_m \quad (8.98)$$

As expected, the blade two-dimensional drag coefficient in the limit of low-speed flow is related to the total pressure loss in the cascade, that is, the momentum deficit thickness in the blade wake. Furthermore, the drag coefficient is *linearly* proportional to the cascade total pressure loss measured in the wake, as expected.

We note that the wake-related loss in lift, in Equation 8.97, is proportional to the blade drag coefficient, Equation 8.98, therefore, the relation between the two-dimensional lift and drag coefficients may be written as

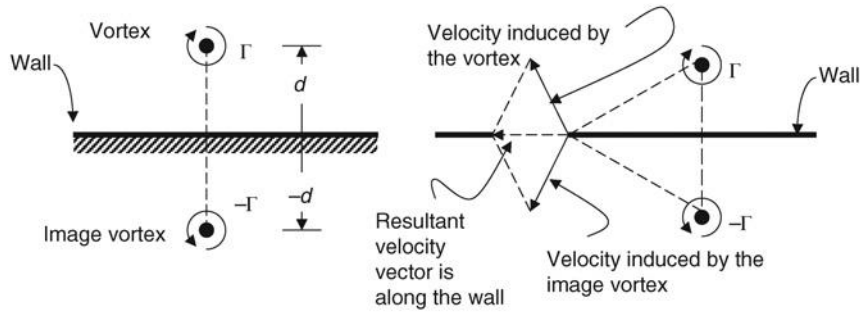
$$C_l = \frac{2\Gamma}{W_m \cdot c} - C_d \cdot \tan \beta_m \quad (8.99)$$

The first term in Equation 8.98 is the ideal lift coefficient, following the thin airfoil theory, and the second term accounts for the loss of lift due to boundary layer/wake formation. These expressions for the lift and drag coefficients, however, lack compressibility effects, three-dimensional or spanwise effects, and the end wall effects as in a real compressor. In addition, we remember that the actual flow is unsteady and involves wake transport and vortex shedding, which are not modeled here. However, we may take additional steps in correcting for some of the cited shortcomings. From Prandtl's classical wing theory, we remember that the drag due to lift, or expressed as the induced drag coefficient C_{Di} , was related to the wing lift coefficient following

$$C_{Di} = \frac{C_L^2}{\pi \cdot e \cdot AR} \quad (8.100)$$

where the span efficiency factor e in the denominator represents the nonelliptic lift contribution/penalty and the term AR represents the wing aspect ratio. A distinguishing feature of the turbomachinery wake is its spiral shape rather than the flat wake of the Prandtl's lifting line theory, where Equation 8.100 is derived. Second, the presence of solid walls acts as mirrors for the vortices (i.e., they create images), and the total induced flow has to account for the image vortices as well. A simple diagram of a vortex next to a wall and its image that renders the wall a stream surface (i.e., flow tangency condition on the wall is satisfied) is shown in Figure 8.33. The vortex strength is shown as Γ and the image vortex strength is, thus $(-\Gamma)$ and is equally disposed on the opposite side of the wall. If we calculate the induced velocity at the wall due to these two vortices, the normal component

■ **FIGURE 8.33**
Solid wall near a vortex is modeled by an image vortex, which helps satisfy the flow tangency condition on the wall



(a) A vortex and its image near a wall (b) The induced flow at the wall

to the wall vanishes, due to symmetry and the tangential component to the wall is doubled, again due to symmetry (Figure 8.33b).

The presence of the *image vortex* with a *counter swirl* is to reduce the effective induced velocity at the blades, as compared with a vortex filament in an unbounded space. Therefore, the simple expression for the drag polar for a wing, which is the sum of the profile drag and the induced drag

$$C_D = C_{d,2D} + \frac{C_L^2}{\pi \cdot e \cdot AR} \tag{8.101}$$

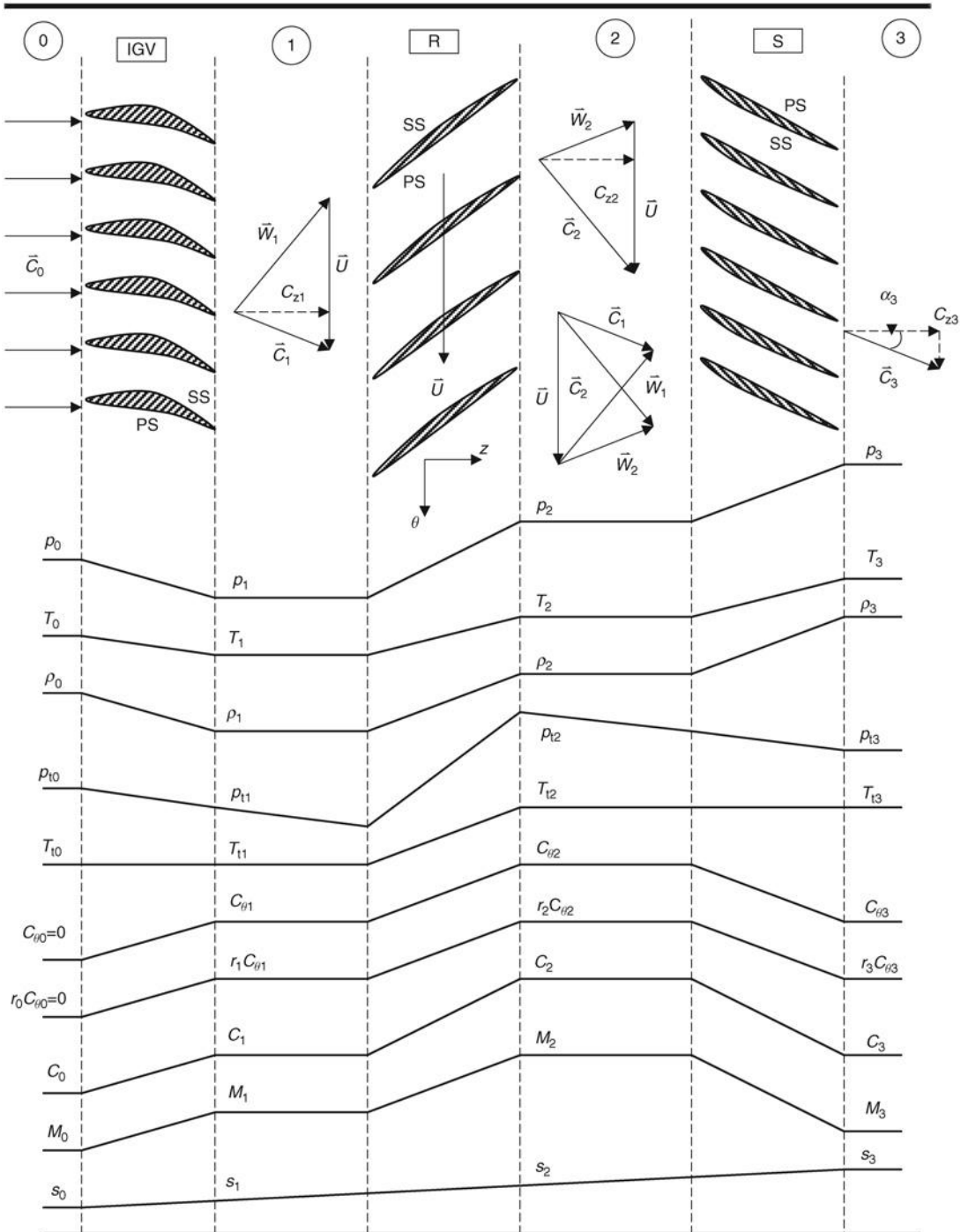
should be replaced by a more complex structure in a turbomachinery blading such as

$$C_D = \underbrace{C_{d,cascade}}_{2D} + \underbrace{\kappa \cdot \left(\frac{C_L^2}{AR} \right) + C_{D,End\ Wall} + C_{D,shock} + C_{D,turbulent-mixing} + C_{D,rms,Vortex-shedding}}_{3D} \tag{8.102}$$

In Equation 8.102, κ represents the influence factor on the induced drag due to the presence of solid walls (i.e., the annulus) and helical wakes, the end wall drag coefficient is due to viscous losses and the vortex formation (tip clearance and scraping vortex) near the wall, the drag due to shock is accounted for through $C_{D,shock}$. Turbulent mixing and the unsteady drag due to vortex shedding (the root-mean square) are reflected in the last term of Equation 8.102. Despite its rather complete look, Equation 8.102 is just an *empirical model*, which requires an extensive experimental database in order to be useful as a predictive tool. However, breaking down the blade loss to its basic constituent levels helps our understanding of the complex flow phenomena in turbo-machinery. We will address three-dimensional losses, compressibility effects, and unsteadiness further in this chapter.

Our discussion of compressor aerodynamics has been limited to 2D flows. The behavior trend of thermodynamic and flow variables in a compressor stage with an IGV in two dimensions are reviewed in Figure 8.34. For additional reading on cascade aerodynamics, Gostelow (1984) should be consulted.

Parameter trends: A study guide



■ FIGURE 8.34 Behavior trend of thermodynamic and flow variables (along a streamsurface) in a compressor stage with an IGV

EXAMPLE 8.5

A compressor stage develops a total pressure ratio of $\pi_s = 1.5$. Its stage adiabatic efficiency is $\eta_s = 0.90$. Calculate the stage total temperature ratio τ_s and compressor polytropic efficiency e_c . Assume $\gamma = 1.4$.

SOLUTION

Stage pressure and temperature ratio are related to stage adiabatic efficiency via

$$\eta_s = \frac{\pi_s^{\frac{\gamma-1}{\gamma}} - 1}{\tau_s - 1}$$

Therefore,

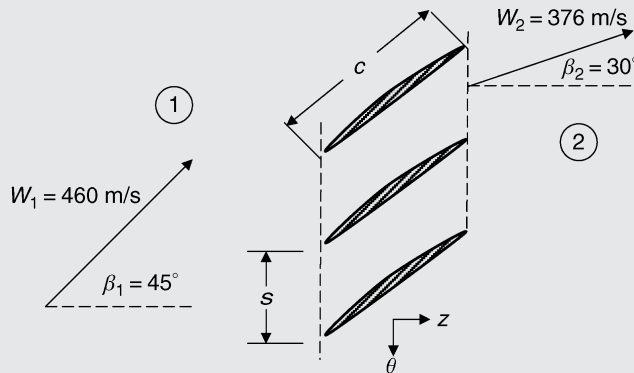
$$\tau_s = 1 + \frac{1}{\eta_s} \left(\pi_s^{\frac{\gamma-1}{\gamma}} - 1 \right) = 1 + [1.5^{0.2857} - 1]/0.90 \approx 1.1365$$

Since $\pi_s = \tau_s^{\frac{\gamma e_c}{\gamma-1}}$, $e_c = \frac{\gamma-1}{\gamma} \frac{\ln \pi_s}{\ln \tau_s} = 0.2857 \frac{\ln(1.5)}{\ln(1.1365)} \approx 0.905$

EXAMPLE 8.6

The profile loss parameter for a compressor blade rotor section is $\varpi = 0.05$. The rotor blade chord and spacing at this section are $c = 5.25$ cm and $s = 3.5$ cm, respectively. The relative velocity vectors up- and downstream of the rotor are shown. Calculate

- (a) mean relative flow angle β_m
- (b) the rotor sectional (2D) drag coefficient C_d and
- (c) the rotor circulation Γ
- (d) the rotor sectional (2D) lift coefficient



SOLUTION

The inlet swirl is $W_{\theta 1} = W_1 \cdot \sin(45^\circ) = 3253 \text{ m/s}$

The exit swirl is $W_{\theta 2} = W_2 \cdot \sin(30^\circ) = 188 \text{ m/s}$

Therefore the average swirl across the rotor is $W_{\theta m} = (W_{\theta 1} + W_{\theta 2})/2 = 256.6 \text{ m/s}$

Based on the definition of the mean flow angle β_m we have

$$\beta_m \equiv \tan^{-1} \left(\frac{W_{\theta m}}{W_z} \right)$$

The axial velocity upstream of the rotor blade is $W_{z1} = W_1 \cdot \cos(45^\circ) = 325.4 \text{ m/s}$

The axial velocity downstream of the rotor is $W_{z2} = W_2 \cdot \cos(30^\circ) = 325.6 \text{ m/s}$

Therefore, $\beta_m \approx \tan^{-1}(256.6/325.5) \approx 38.2^\circ$

The rotor blade solidity at this radius is $\sigma = c/s = 5.25/3.5 = 1.5$

The drag coefficient is related to profile loss, solidity, and mean relative flow angle according to

$$C_d = \frac{\varpi}{\sigma} \cdot \cos \beta_m = \frac{0.05}{1.5} \cos(38.2^\circ) \approx 0.026$$

The magnitude of circulation is

$$\Gamma = s |W_{\theta 1} - W_{\theta 2}| = (3.5 \times 10^{-2} \text{ m})(325.3 - 188) \text{ m/s} \approx 4.8 \text{ m}^2/\text{s}$$

To calculate the sectional lift coefficient, we need to calculate $W_m = (W_z^2 + W_{\theta m}^2)^{0.5}$ $W_m \approx 414.5 \text{ m/s}$

$$C_l = \frac{2\Gamma}{W_m \cdot c} - C_d \cdot \tan \beta_m \approx 0.4416 - 0.0206 \approx 0.4209$$

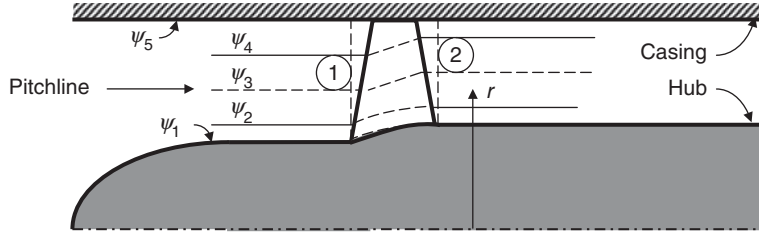
8.6.5 Three-Dimensional Flow

Our discussion of the flowfield so far has been limited to two-dimensional flows represented by the “pitchline” radius. The next level of complexity brings us to the three-dimensional flow analysis with a host of simplifying assumptions. These assumptions are necessary to render the analysis tenable. To relieve any of the assumptions requires numerical integration of the governing equations, which are coupled and nonlinear. The method of approach, in that case, is the computational fluid dynamics applied to a single or multiple stages in a compressor. Simplifying assumptions for our three-dimensional flow analysis are

1. Flow is steady, that is, $\partial/\partial t \rightarrow 0$
2. Flow is axisymmetric, that is, $\partial/\partial \theta \rightarrow 0$
3. Flow is adiabatic, that is, $q_{\text{wall}} = 0$
4. Fluid is inviscid and nonheat conducting, that is, $\mu = 0$ and $\kappa = 0$, respectively
5. Blade geometry has zero tip clearance, that is, blades stretch between hub and casing

In addition, we may choose to limit the radial shift of the stream surfaces to within the blade rows and hence require *radial equilibrium* both upstream and downstream of the blade rows. By limiting the radial shift of the stream surfaces to within the blade rows, we are thus creating cylindrical stream surfaces outside the blade rows, that is, $C_r = 0$ both upstream and downstream of the blade row. By assuming an axisymmetric flow, we are smearing out the blade-to-blade flow and thus lose blade periodicity for a finite number of blades. This is akin to having infinitely many blades. For the steady flow, we are placing the

■ FIGURE 8.35
Isolated blade row with
cylindrical stream
surfaces ψ_1 to ψ_5



coordinate system with the blade row that operates in isolation in a cylindrical duct. The implication is that having a neighboring blade row in relative rotation with respect to the blade row of interest would render the flowfield unsteady. In the limit of adiabatic flow, the only mechanism for energy transfer to/from the fluid is the mechanical shaft power. The assumption of inviscid and nonheat conducting fluid eliminates viscous and thermal boundary layer formations. In essence, the only mechanism for energy exchange and momentum transfer is the fluid pressure and not the fluid molecular viscosity and thermal conductivity. The combination of adiabatic and inviscid flow creates a fictitious isentropic environment for the flow interaction with the blades. Figure 8.35 shows cylindrical stream surfaces entering and leaving an isolated blade row in a cylindrical duct.

All parameters in this problem become a function of r only. Note that by taking a cylindrical duct downstream of the blade row, we are in essence decoupling the flow in the vicinity of the blade row from axial pressure gradients. As noted earlier, the axisymmetric flow takes out the θ -dependency; therefore the only independent parameter left is the radial position r . The velocity field in station 2, that is, downstream of the rotor, has zero radial velocity and a general swirl distribution $C_\theta(r)$, as well as an axial velocity distribution $C_z(r)$ that needs to be determined from the conservation laws. It is customary to specify a desired swirl distribution downstream of a blade row and calculate the corresponding axial velocity distribution that is supported by the swirl profile. This method of approach is called the vortex design of turbomachinery blades. The pressure distribution $p(r)$ is established by imposing a radial equilibrium condition on the stream surfaces, which simplifies to a balance of pressure gradient and the centrifugal force on a swirling fluid stream, that is,

$$\frac{\partial p}{\partial r} = \frac{dp}{dr} = \rho \frac{C_\theta^2}{r} \tag{8.103}$$

From a known swirl distribution $C_\theta(r)$, we get the spanwise blade work distribution following the Euler turbine equation, namely,

$$w_c = h_{t2} - h_{t1} = \omega (r_2 C_{\theta 2} - r_1 C_{\theta 1}) \tag{8.104}$$

However, the only unknown in the Equation 8.104 is the downstream radius r_2 corresponding to an upstream stream surface radius r_1 . This is the crux of the problem of radial shift within the blade row, which needs to be determined. To establish the radial shift of the stream surfaces, Δr , we need to satisfy the continuity equation between the stream surfaces, from hub to tip or in our case from ψ_1 to ψ_5 upstream and downstream of the blade row. For swirl profiles that produce a constant axial velocity downstream of a blade row, the problem becomes very simple. In other cases, we need to integrate a nonuniform

axial velocity and density profile in the spanwise direction to calculate the mass flow rates between the stream surfaces and thus establish the radial shift Δr .

8.6.5.1 Blade Vortex Design. The swirl velocity downstream of a blade at a given radius, namely pitchline, may be defined via a two-dimensional approach, as outlined in the previous sections. Anchoring the swirl profile at the pitchline, we may describe a variety of swirl profiles in the spanwise direction that could be analyzed and assessed for their practicality and utility. Some common swirl profiles assume a combination of a potential vortex, a solid body rotation, or, in general, a power profile for the swirl distribution, $C_\theta(r)$. The stagnation enthalpy in the absolute frame of reference may be written as

$$h_t \equiv h + \frac{C_z^2}{2} + \frac{C_\theta^2}{2} \quad (8.105)$$

The radial derivative of the above equation yields,

$$\frac{dh_t}{dr} = \frac{dh}{dr} + C_z \frac{dC_z}{dr} + C_\theta \frac{dC_\theta}{dr} \quad (8.106)$$

Also, from Gibbs equation we relate the enthalpy gradient to pressure and entropy gradients as

$$T \frac{ds}{dr} = \frac{dh}{dr} - \frac{1}{\rho} \frac{dp}{dr} \quad (8.107)$$

Now, let us substitute Equation 8.107 into Equation 8.106, to get an interim result, that is,

$$\underbrace{\frac{dh_t}{dr}}_{\text{blade-work-profile}} = \underbrace{T \frac{ds}{dr}}_{\text{blade-loss-profile}} + \underbrace{\frac{1}{\rho} \frac{dp}{dr}}_{\text{static-pressure-profile}} + \underbrace{C_z \frac{dC_z}{dr}}_{\text{axial-velocity-profile}} + \underbrace{C_\theta \frac{dC_\theta}{dr}}_{\text{swirl-profile}} \quad (8.108)$$

A constant-work blade will have the first term in Equation 8.108 vanish, otherwise the work distribution along the blade depends on the angular momentum distribution upstream and downstream of the blade according to Euler turbine equation. The entropy gradient term on the RHS of Equation 8.108 is the blade loss profile in the radial direction. This parameter has to be an input to the problem based on the accumulated loss data published in the literature or the proprietary data of the industry. It is common to ignore the radial loss profiles for the first attempt in establishing the density, velocity gradients downstream of a blade row. The static pressure gradient follows the radial equilibrium theory, namely, Equation 8.103. The axial velocity profile is the third term on the RHS of Equation 8.108, which is the goal of our analysis. The last term is the swirl profile that we consider an assumed function of radial position. Therefore, to establish an axial velocity profile $C_z(r)$, we need to integrate

$$\frac{1}{2} \frac{dC_z^2}{dr} = \frac{dh_t}{dr} - T \frac{ds}{dr} - \frac{C_\theta^2}{r} - C_\theta \frac{dC_\theta}{dr} \quad (8.109)$$

The last two terms in Equation 8.109 may be combined into a single derivative involving angular momentum to get

$$\frac{1}{2} \frac{d}{dr} (C_z^2) = \frac{dh_t}{dr} - T \frac{ds}{dr} - \frac{C_\theta}{r} \frac{d(rC_\theta)}{dr} \quad (8.110)$$

The special cases of swirl profile that are considered in compressor blade design are described in the next section.

Case 1: Free-vortex design

$$rC_\theta = \text{constant} \quad (8.111)$$

This is known as the *potential vortex* or *free-vortex* design. The name association “potential vortex” is due to the similarity between this swirl profile and that of a vortex filament ($C_\theta \sim 1/r$). We also remember that the flowfield about a vortex filament is irrotational, hence a *potential* vortex. The irrotational flow around a vortex filament has zero vorticity, hence the name *free-vortex* design.

Let us consider two scenarios here. First, consider the case of zero preswirl upstream of the rotor, that is, the case of no inlet guide vane, and the second scenario with an inlet guide vane that induces a solid-body rotation swirl profile of its own upstream of the rotor.

With no IGV, the flow upstream of the rotor is swirl free, that is,

$$C_{\theta 1} = 0 \quad (8.112)$$

The rotor inducing a free vortex swirl distribution in plane 2, gives

$$(rC_\theta)_2 = \text{constant} \quad (8.113)$$

The Euler turbine equation demands

$$h_{t2} - h_{t1} = \omega [(rC_\theta)_2 - (rC_\theta)_1] = \omega (rC_\theta)_2 = \text{constant} \quad (8.114)$$

The swirl profile associated with a free-vortex design blade produces a constant work along the blade span. This is known as a *constant-work* rotor. Therefore, the blade work profile and the angular momentum profile terms in Equation 8.110 vanish, that is,

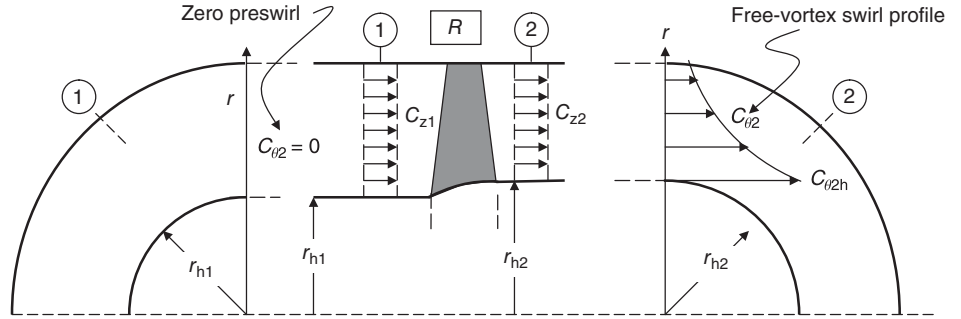
$$\frac{dh_t}{dr} = \frac{d(rC_\theta)}{dr} = 0 \quad (8.115)$$

The axial velocity profile equation reduces to

$$\frac{d}{dr} (C_z^2/2) = -T \frac{ds}{dr} \quad (8.116)$$

Here, we have a choice and that is to either specify a radial loss profile from the available data in the literature or neglect the loss term in this preliminary phase of establishing an axial velocity profile. Here, we take the second route, although we shall present

■ **FIGURE 8.36**
Velocity field across a rotor blade row with zero preswirl (i.e., no IGV) and free-vortex design for the rotor blade



and discuss radial distribution of losses associated with modern fan blades later in the chapter.

In the limit of a loss-free rotor and the free-vortex design, we conclude that the axial velocity C_z remains constant, that is, Equation 8.116 yields,

$$C_{z2} = \text{constant} \tag{8.117}$$

Figure 8.36 shows the velocity pattern across the rotor.

In Figure 8.36, we have kept the casing radius constant and have increased the hub radius to account for the density rise across the blade row. There are other choices that we could take, for example, the casing could have been tapered and the hub remained cylindrical or both hub and casing could have been tapered. Since the calculation method is identical, we shall stay with our choice of constant tip radius and an increasing hub radius. It is also customary to design turbomachinery blades based on a constant throughflow speed, that is, axial velocity remains constant. Therefore, based on the continuity equation, the channel area develops inversely proportional to density ratio, assuming a uniform density profile upstream and downstream of the rotor, that is,

$$A_2/A_1 = \rho_1/\rho_2 \tag{8.118a}$$

Therefore, the ratio of r_{h2} to r_t is related to the density ratio and the inlet hub-to-tip radius ratio,

$$\frac{r_{h2}}{r_t} = \sqrt{1 - \frac{\rho_1}{\rho_2} \left[1 - \left(\frac{r_{h1}}{r_t} \right)^2 \right]} \tag{8.118b}$$

We tackle the density ratio problem after we examine other swirl profiles of interest. The swirl put in by the rotor needs to be taken out by the stator; therefore, we demand

$$C_{\theta 3} = 0 \tag{8.119}$$

which may be expressed in the shorthand form

$$C_{\theta} = \pm a/r \tag{8.120}$$

where a is a constant and the plus sign describes the rotor swirl input to the flow and the minus sign designates the stator withdrawal of the swirl put in by the rotor. The exit flow in station 3 downstream of the stator is thus swirl free just as in the flow entering the stage.

The degree of reaction for this design is rewritten from Equation 8.46c, with a free vortex swirl distribution substituted for rotor exit swirl as

$$\circ R = 1 - \frac{C_{\theta 1} + C_{\theta 2}}{2\omega \cdot r} = 1 - \frac{0 + a/r}{2\omega \cdot r} = 1 - \frac{a/\omega}{2r^2} \quad (8.121)$$

To cast this equation relative to the pitchline radius, we divide and multiply the second term in Equation 8.121 by r_m^2 to get

$$\circ R(r) = 1 - \frac{(a/r_m) / (\omega \cdot r_m)}{2(r/r_m)^2} \quad (8.122)$$

The term a/r_m is the rotor exit swirl velocity at the pitchline radius and the second term, that is, ωr_m , is the wheel speed at the pitchline radius. From Equation 8.122, we conclude that the product of these two terms is related to the degree of reaction at the pitchline via

$$\left(\frac{a}{r_m}\right) / (\omega \cdot r_m) = 2(1 - \circ R_m) \quad (8.123)$$

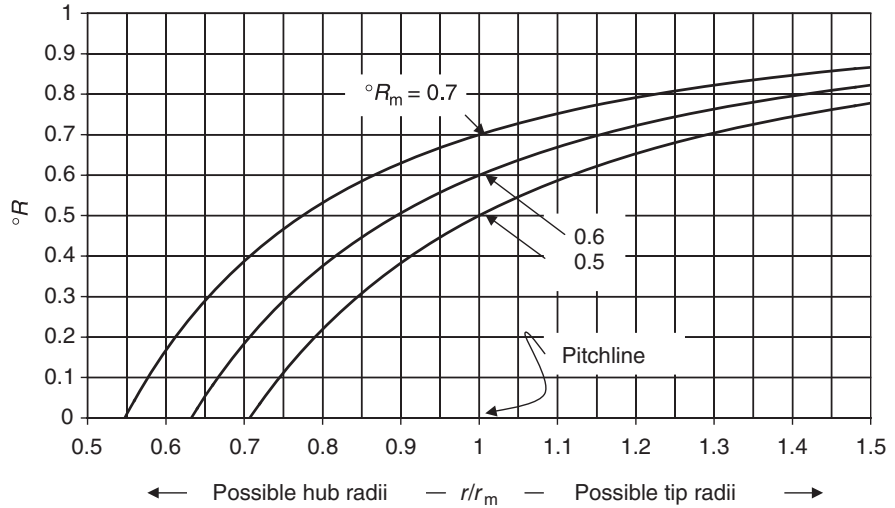
Therefore, the degree of reaction for a compressor stage with no inlet guide vane and a free vortex swirl distribution produced by its rotor is

$$\circ R(r) = 1 - \frac{1 - \circ R_m}{(r/r_m)^2} \quad (8.124)$$

We have graphed this equation for three stage designs with values of pitchline degree of reaction specified at 0.5, 0.6, or 0.7. We immediately note that the rotor hub is in danger of very low degrees of reaction. Since a negative degree of reaction implies that the flow in that section is not compressing (i.e., that section behaves like a turbine!), we have limited our graphical presentation in Figure 8.37 to positive degree of reaction cases at the hub. For example, in the case of 50% degree of reaction at the pitchline the hub radius should be at $\sim 0.71 r_m$, which calls for a minimum rotor with hub-to-tip radius ratio of ~ 0.55 . Any lower hub-to-tip radius ratio leads to a negative hub degree of reaction. For a typical value of a modern fan hub-tip radius ratio of ~ 0.5 , we need to raise the pitchline degree or reaction beyond 50%. A second source of concern is the rotor tip region, which is being asked to bear an unusually high share of the stage pressure rise.

The hub section of the rotor is to produce the highest swirl according to Figure 8.36. The tip section is imparting the lowest swirl. Thus, the free vortex swirl profile demands excessive turning of the flow near the hub and very small turning at the tip, which causes the free-vortex blades to be highly twisted. The attractiveness of the free-vortex design is in its simplicity of analysis, which leads to a constant-work rotor and constant axial velocity distribution downstream of blade rows.

■ **FIGURE 8.37**
Spanwise variation of
the stage degree of
reaction for a
free-vortex rotor
design and no inlet
guide vane



Now, let us study the case of a compressor stage *with an IGV* that induces a preswirl of solid body rotation upstream of the rotor. The purpose of an inlet guide vane is to reduce the relative Mach number at the tip; hence, a free-vortex design that attains the lowest swirl velocity at the tip would make less sense than a solid body rotation type swirl distribution downstream of the IGV.

Therefore,

$$C_{\theta 1} = b \cdot r \quad (\text{swirl profile}) \quad (8.125)$$

where b is a constant. Combining this swirl profile with a free-vortex distribution of the rotor, we get

$$C_{\theta 2} = \frac{a}{r} + b \cdot r \quad (8.126)$$

The rotor work distribution is

$$h_{t2} - h_{t1} = \omega [(rC_{\theta})_2 - (rC_{\theta})_1] \quad (8.127a)$$

Substitute swirl profiles 8.125 and 8.126 in the rotor work input (Equation 8.127a) to get

$$h_{t2} - h_{t1} = \omega [a + br^2 - br^2] = \omega \cdot a = \text{constant} \quad (8.127b)$$

We conclude that the rotor work distribution along the rotor span is constant.

Now, let us substitute the swirl profile downstream of the rotor and the constant work distribution in Equation 8.110 to get an equation involving the axial velocity distribution,

$$\frac{1}{2} \frac{d}{dr}(C_z^2) = \frac{dh_t}{dr} - T \frac{ds}{dr} - \frac{C_\theta}{r} \frac{d(rC_\theta)}{dr} = 0 - 0 - \left(\frac{a}{r^2} + b\right) \frac{d}{dr}(a + br^2) \quad (8.128)$$

This equation simplifies to

$$\frac{d}{dr}(C_z^2/2) = -\frac{2ab}{r} - 2b^2r \quad (8.129)$$

We may integrate this equation from a reference radius, for example, the pitchline radius r_m , where the axial velocity is known as C_{zm} , to any radius r to get

$$C_z^2 - C_{zm}^2 = 2 \left[-2ab \ln \frac{r}{r_m} + b^2 r_m^2 \left(1 - \frac{r^2}{r_m^2} \right) \right] \quad (8.130)$$

or in nondimensional form the axial velocity profile downstream of the rotor is

$$\frac{C_z(r)}{C_{zm}} = \sqrt{1 + 2 \left(\frac{br_m}{C_{zm}} \right)^2 \left(1 - \frac{r^2}{r_m^2} \right) - \left(\frac{4ab}{C_{zm}^2} \right) \ln \left(\frac{r}{r_m} \right)} \quad (8.131)$$

In order to calculate the downstream hub radius after the rotor, we need to integrate the product of density and axial velocity over the inlet and exit planes of the rotor, which are set equal via continuity equation. We need to ask whether the axial velocity downstream of the IGV, which is the rotor upstream, is uniform. We may use the same equation of radial equilibrium theory that we applied to the rotor and note that the IGV does no work on the fluid, hence the fluid total enthalpy remains constant. Consistent with our assumption of no radial loss in the preliminary stage of our blade row calculations, Equation 8.110 simplifies to

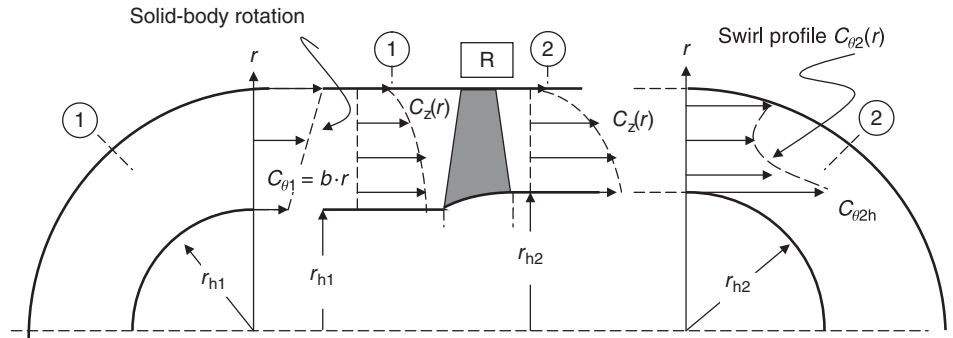
$$\frac{d}{dr}(C_z^2/2) = -\frac{C_\theta}{r} \frac{d(rC_\theta)}{dr} = -b \frac{d}{dr}(br^2) = -\frac{d}{dr}(b^2r^2) \quad (8.132)$$

Upon integration, we get a parabolic axial velocity distribution upstream of the rotor, that is,

$$\frac{C_z(r)}{C_{zm}} = \sqrt{1 + 2 \left(\frac{br_m}{C_{zm}} \right)^2 \left(1 - \frac{r^2}{r_m^2} \right)} \quad (\text{axial velocity profile}) \quad (8.133)$$

Let us compare the two axial velocity profiles upstream and downstream of the rotor by examining Equations 8.131 and 8.133. The axial velocity profile upstream of the rotor is parabolic, as noted and the profile downstream of the rotor has an extra logarithmic term, which tends to exacerbate the nonuniformity in the axial profile. This

■ **FIGURE 8.38**
A schematic drawing of axial and swirl profiles across a compressor rotor with an IGV that induces a solid-body rotation and the rotor is of free-vortex design



implies that the axial velocity at the tip is further reduced downstream of the rotor as compared with the upstream value. In contrast, the axial velocity near the hub shows an increase downstream of the rotor, hence an increased nonuniformity of the axial velocity profile. The swirl and axial velocity profiles across a compressor rotor that induces a free-vortex swirl distribution to an IGV flowfield with a solid-body rotation swirl profile are shown in Figure 8.38. The choice of solid-body rotation for the inlet guide vane is consistent with the desire to reduce the rotor tip Mach number; however, combining it with a free-vortex rotor leads to a highly nonuniform axial velocity profile, which is undesirable. What happens to the spanwise distribution of the degree of reaction in this case?

To answer this question, we recall that the swirl profiles across the rotor are

$$C_{\theta 1}(r) = b \cdot r$$

and

$$C_{\theta 2}(r) = b \cdot r + \frac{a}{r}$$

The equation for the degree of reaction is

$${}^{\circ}R = 1 - \frac{C_{\theta 1} + C_{\theta 2}}{2\omega \cdot r} = 1 - \frac{1}{2} \left[(2b/\omega) + \left(\frac{a/\omega}{r^2} \right) \right] \quad (8.134)$$

We may cast this equation in terms of the pitchline radius, similar to Equation 8.124 as

$${}^{\circ}R = \left(1 - \frac{b}{\omega} \right) - \frac{(a/r_m)/(\omega \cdot r_m)}{2(r/r_m)^2} \quad (8.135)$$

In terms of the degree of reaction at the pitchline, ${}^{\circ}R_m$, we may write Equation 8.135 as

$${}^{\circ}R = (1 - b/\omega) - \frac{(1 - b/\omega) - {}^{\circ}R_m}{(r/r_m)^2} \quad ({}^{\circ}R \text{ profile}) \quad (8.136)$$

EXAMPLE 8.7

Compare the degree-of-reaction profile of a compressor stage with and without an IGV for a range of hub-tip radii that result in a positive degree of reaction.

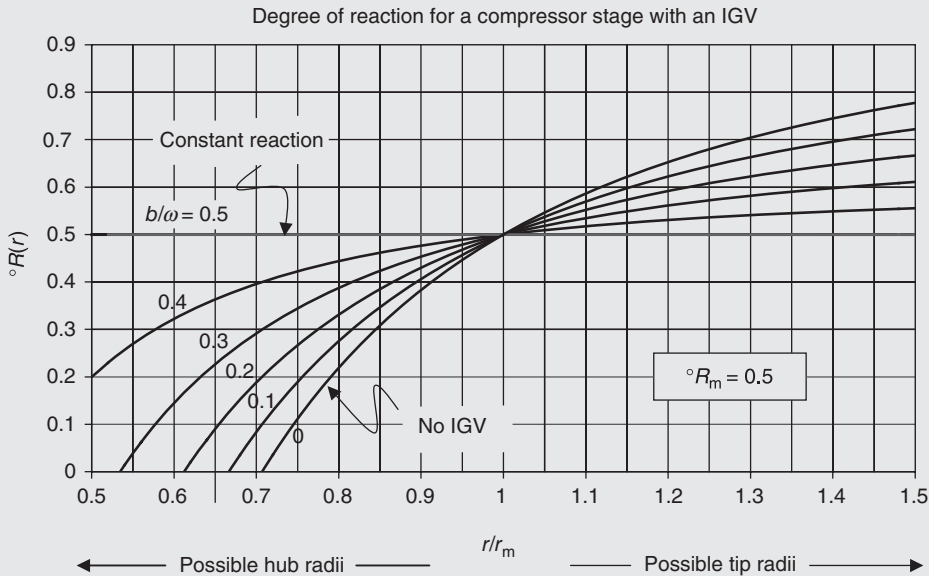
SOLUTION

We make a spreadsheet based on Equations 8.136 and 8.124 for a 50% degree of reaction at the pitchline radius, with varying IGV solid-body rotation swirl profile b/ω . The graph of the spreadsheet table is shown in Figure 8.39. We note that a positive solid-body rotation (i.e., $b > 0$) causes a change in the degree of reaction in the positive direction. The case of $b = 0$ recovers the no IGV stage of Figure 8.37.

We also note that for a special case of

$$1 - \frac{b}{\omega} = \circ R_m \quad (8.137)$$

the reaction along the blade span becomes constant. This view is shown for the case of $b/\omega = 0.5$ in Figure 8.39, which is plotted for a 50% degree of reaction at the pitchline.



■ FIGURE 8.39 IGV with solid-body rotation helps a free-vortex rotor in $\circ R(r)$

To get the density profile downstream of an IGV, we differentiate the perfect gas law in the radial direction and substitute the centrifugal force for the radial pressure gradient to get

$$\frac{dp}{dr} = R \frac{d}{dr} (\rho \cdot T) = \rho \frac{C_\theta^2}{r} \quad (8.138)$$

This equation may be solved for the density variation as

$$RTd\rho + R\rho \cdot dT = \rho \frac{C_\theta^2}{r} dr \quad (8.139)$$

We may isolate $d\rho/\rho$ in terms of the known functions of r , namely

$$\frac{d\rho}{\rho} = \left(\frac{1}{RT} \right) \frac{C_\theta^2}{r} dr - \frac{dT}{T} \quad (8.140)$$

Now, we need to use the conservation of total enthalpy to write an expression for the static temperature distribution downstream of the IGV, that is,

$$T(r) = T_{t0} - \frac{C_z^2 + C_\theta^2}{2c_p} \quad (8.141)$$

The RHS of Equation 8.141 is a known function of the radial coordinate r via Equations 8.126 and 8.133. The differential of the static temperature may be written as

$$c_p dT = -d(C_z^2/2) - d(C_\theta^2/2) = 2b^2 r dr - b^2 r dr = b^2 r dr \quad (8.142)$$

The logarithmic derivative of the static temperature is the combination of Equations 8.141 and 8.142 as

$$\frac{dT}{T} = \frac{b^2 r dr}{c_p T_{t0} - (C_z^2 + C_\theta^2)} \quad (8.143)$$

Substituting Equation 8.143 in 8.140, we may calculate the static density profile downstream of the IGV. This process is more accurate, but rather tedious, and is often simplified by making the following assumptions, namely,

$$C_{z1}(r) = C_{zm} = \text{constant} \quad (8.144)$$

$$\rho_1(r) = \rho_m = \text{constant} \quad (8.145)$$

Thus, to establish the hub radius downstream of the rotor, we satisfy the continuity equation via

$$\rho_m C_z \cdot \pi \cdot r_t^2 \left(1 - \left(\frac{r_{h1}}{r_t} \right)^2 \right) = \int_{r_{h2}}^{r_t} \rho_2(r) \cdot C_{z2}(r) \cdot 2\pi \cdot r dr \quad (8.146)$$

The density profile downstream of the rotor is a function of temperature and velocity profile using the total enthalpy expression, similar to Equation 8.141. Again, the process is rather tedious and a simplification is in order. We know that the density and temperature are related via a polytropic exponent, namely,

$$\rho \sim T^{\frac{1}{n-1}} \quad (8.147)$$

where n is the polytropic exponent. For an isentropic flow, $n = \gamma$, and for irreversible adiabatic flows, which are encountered in turbomachinery $n < \gamma$. The density distribution is a function of the temperature distribution and the polytropic exponent, that is,

$$\frac{\rho}{\rho_m} = \left(\frac{T}{T_m} \right)^{\frac{1}{n-1}} \quad (8.148)$$

We may use the small stage or polytropic efficiency in a compressor, e_c , to relate pressure and density ratio to temperature ratio across a blade row as

$$\frac{p_2}{p_1} = \left(\frac{T_2}{T_1} \right)^{\frac{\gamma e_c}{\gamma-1}} \quad (8.149)$$

$$\frac{\rho_2}{\rho_1} = \left(\frac{T_2}{T_1} \right)^{\frac{1-\gamma(1-e_c)}{\gamma-1}} \quad (8.150)$$

Therefore the strategy is as follows. We first establish all parameters at the pitchline and then expand the results to other radii by using a blade vortex design choice, for example, free vortex. Therefore, we first establish the swirl at the pitchline using a criterion based on the diffusion factor or the degree of reaction at the pitchline. Then by using the Euler turbine equation, we get the absolute total temperature at the pitchline radius, T_{t2m} . The definition of total temperature at the pitchline and the velocity components leads to the static temperature downstream of the rotor at r_m , that is, T_{2m} . By using a value for compressor polytropic efficiency (say 0.90 or 0.91), we determine the static pressure and the density at r_m , that is, p_{2m} and ρ_{2m} . Now, all parameters are established at the pitchline radius. We are now ready to expand our results to other radii. We choose a blade vortex design type, which fits a swirl profile along the rotor span to the pitchline swirl, $C_{\theta m}$. Therefore, the blade vortex design choice establishes the radial distribution of swirl, that is, $C_{\theta}(r)$. With the knowledge of swirl downstream of the rotor, we repeat the above procedure at other radii to establish all thermodynamic and flow parameters. It is customary to repeat the procedure for an odd number of stream surfaces (5 or 7), which yield a pitchline stream surface as well. The minimum is thus three, that is, the hub, pitchline, and the tip stream surfaces. We calculate the axial velocity distribution downstream of the rotor, using Equation 8.110. With assumed compressor polytropic efficiency, say 0.91, we calculate the density ratio across the blade row using Equation 8.150. Finally, we conserve the mass flow rate on the two sides of the rotor to establish the annulus area downstream of the rotor. Repeat the same process for the stator. As the process of design is iterative by nature, we need to return to our initial choices of vortex design, D -factor at the pitchline, the degree of reaction at the pitchline, or simply the blade hub-to-tip radius ratio in order to achieve an acceptable preliminary design for the stage. For the choice of blades that produce the desired flow turning at a given radius without flow separation and with an adequate margin of safety, we need to rely on cascade data presented in Figure 8.22.

Case 2: Rotor with forced vortex design (no IGV)

The rotor induced swirl increases linearly with the radius, that is, of solid-body rotation type, hence,

$$C_{\theta 2} = b \cdot r \quad (8.151)$$

The stator removes the swirl put in by the rotor, hence the stator exit plane is swirl free, that is, $C_{\theta 1} = C_{\theta 3} = 0$.

The work distribution along the rotor span is

$$w_c(r) = \omega [(rC_{\theta})_2 - (rC_{\theta})_1] = \omega \cdot b \cdot r^2 \quad (8.152)$$

Therefore, the rotor loading increases proportional to r^2 , that is, the rotor tip is overworked and the hub is not sufficiently loaded. The overloading of the rotor tip could result in flow separation at the tip with excessive flow turning and high diffusion. Usually, the tip region in a modern fan operates in the supersonic range, which limits the amount of flow turning and the appearance of shocks at the blade trailing edge. We shall address the issues of supersonic blade sections in a transonic compressor in a later section of this chapter. The degree of reaction for this vortex profile is

$$\circ R(r) = 1 - \frac{C_{\theta 1} + C_{\theta 2}}{2\omega \cdot r} = 1 - \frac{b}{2\omega} = \text{constant} \tag{8.153}$$

The axial velocity profile may be derived from Equation 8.110 as

$$\frac{1}{2} \frac{d}{dr} (C_z^2) = \frac{dh_t}{dr} - T \frac{ds}{dr} - \frac{C_\theta}{r} \frac{d(rC_\theta)}{dr} = 2\omega br - 0 - b \frac{d}{dr} (br^2) = 2\omega br - 2b^2 \cdot r \tag{8.154}$$

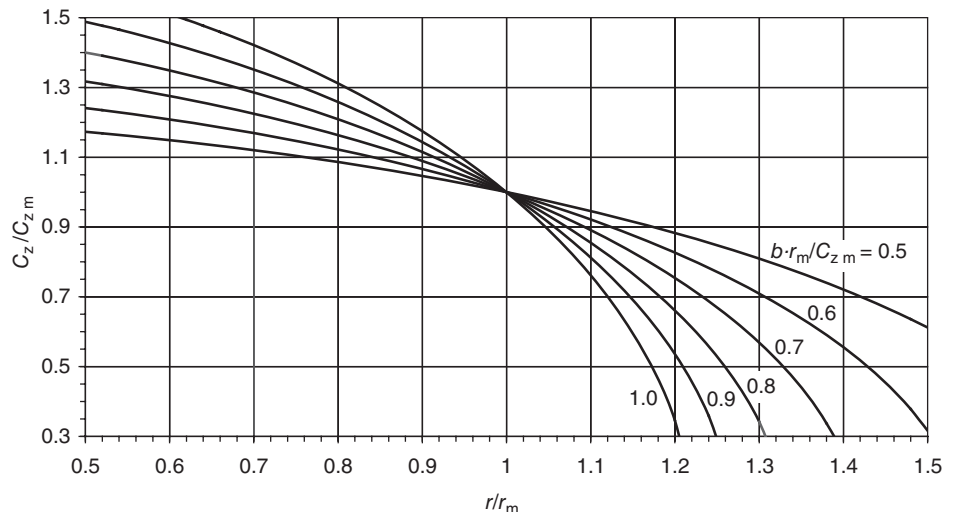
This equation is integrated with reference to the pitchline to produce

$$\frac{C_z(r)}{C_{zm}} = \sqrt{1 + 2 \left(1 - \frac{\omega}{b}\right) \left(\frac{b \cdot r_m}{C_{zm}}\right)^2 \left[1 - \left(\frac{r}{r_m}\right)^2\right]} \tag{8.155}$$

For $\omega = b$, $\circ R = 0.5$ and the axial velocity remains uniform.

Figure 8.40 shows the spanwise distribution of the axial velocity downstream of the inlet guide vane with a solid-body rotation swirl profile. The spanwise maldistribution of axial velocity is of concern for the same reason as with the excessive tip flow turning, namely, large flow deceleration at the tip could exceed allowable diffusion limits (either through D -factor or C_p) and lead to stall.

■ **FIGURE 8.40**
Axial velocity distribution downstream of an inlet guide vane, which induces a solid-body rotation swirl



Case 3: A general stage vortex design (with IGV)

Let us consider a blend of the free and forced vortex swirl distributions that may be generalized by

$$C_{\theta 1} = C_{\theta 3} = -\frac{a}{r} + br^n \tag{8.156}$$

$$C_{\theta 2} = \frac{a}{r} + br^n \tag{8.157}$$

For $n = 1$, a combination of solid body rotation and a free-vortex swirl distribution are superimposed upstream and downstream of a compressor rotor. The function of stator, which is stated as to remove the swirl put in by the rotor, is seen from Equations 8.156 and 8.157.

The degree of reaction variation along the span may be written as

$${}^\circ R(r) = 1 - \frac{C_{\theta 1} + C_{\theta 2}}{2\omega \cdot r} = 1 - \frac{br^n}{\omega \cdot r} \quad ({}^\circ R \text{ profile}) \tag{8.158}$$

Obviously, the reaction distribution depends on the exponent n . For $n = 1$, the reaction along the stage height remains constant. This is desirable since the pressure rise along the blade becomes constant. For $n > 1$, the reaction decreases with span and for $n < 1$, the reaction increases with span. Any desired variation, including a constant, may be tailored through our choice of exponent, n of the swirl profile.

The rotor work distribution is

$$w_c(r) = \omega [(rC_\theta)_2 - (rC_\theta)_1] = \omega \cdot [(a + br^{n+1}) - (-a + br^{n+1})] = 2\omega \cdot a = \text{constant} \tag{8.159}$$

This result is independent of the exponent n in Equation 8.156. Therefore, we create a constant work rotor by the above swirl distribution, which is desirable. The combination of constant work, which means the total enthalpy rise across the rotor is uniform, and the constant reaction (for $n = 1$), which implies a constant static enthalpy rise across the rotor, leads to a constant kinetic energy downstream of the rotor. Since swirl profile is a function of r , then the axial velocity has to attain a profile with the spanwise direction. We made this argument to show that the axial velocity may not be uniform in this case.

The axial velocity profile follows the same approach as the previous cases, namely,

$$\frac{1}{2} \frac{d}{dr} (C_z^2) = \frac{dh_t}{dr} - T \frac{ds}{dr} - \frac{C_\theta}{r} \frac{d(rC_\theta)}{dr} = 0 - 0 - \frac{(br^n \mp \frac{a}{r})}{r} \frac{d(br^{n+1} \mp a)}{dr} \tag{8.160}$$

$$\frac{1}{2} \frac{d}{dr} (C_z^2) = -(n+1) \cdot r^{n-1} \cdot (b^2 r^n \mp \frac{ab}{r}) \tag{8.161}$$

The case of $n = 1$ is of particular interest since it leads to a constant reaction. The axial velocity profile, for $n = 1$, is

$$C_z(r) = \sqrt{C_{zm}^2 - 2b^2 r_m^2 \left(\frac{r^2}{r_m^2} - 1 \right) \pm 4ab \ln \left(\frac{r}{r_m} \right)} \tag{8.162}$$

The plus and minus in Equation 8.162 signify the upstream and downstream of the rotor, respectively. In general, the axial velocity decreases with radius with this choice of swirl profile.

8.6.5.2 Three-Dimensional Losses. The factors that render the flow process in a turbomachinery stage irreversible are

- End wall losses
 - Secondary flow losses
 - Tip clearance loss
 - Labyrinth seal and leakage flow losses
- Shock losses
 - Total pressure loss
 - Shock-boundary layer interaction
- Blade wake losses
 - Viscous profile drag (from cascade experiments)
 - Induced drag losses
 - Radial flow losses
- Unsteady flow losses
 - Upstream wake interaction
 - Vortex shedding in the wake
- Turbulent mixing.

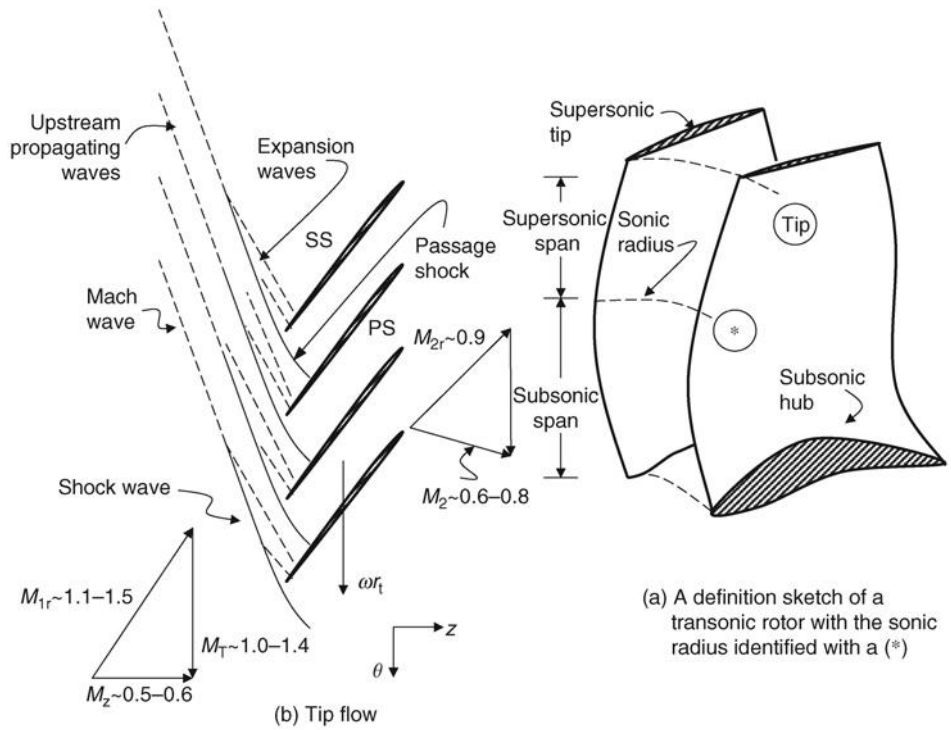
Although the above list seems like a formidable assortment of flow losses, how many of them are totally decoupled from the rest? In a practical sense, the answer has to be none. Is there the possibility of duplication, that is, double bookkeeping, in the above list? The answer is, of course, there is a possibility of counting a loss (or a part of it) twice or three times. Therefore, we conclude that any broken down list of factors contributing to loss is artificial at best and needs to be viewed with caution. The “list” is made only as a tool to help our understanding of complex flow phenomena in broad categories, such as

- Compressibility effects
- Viscous and turbulent dissipation
- Unsteadiness
- Three dimensionality.

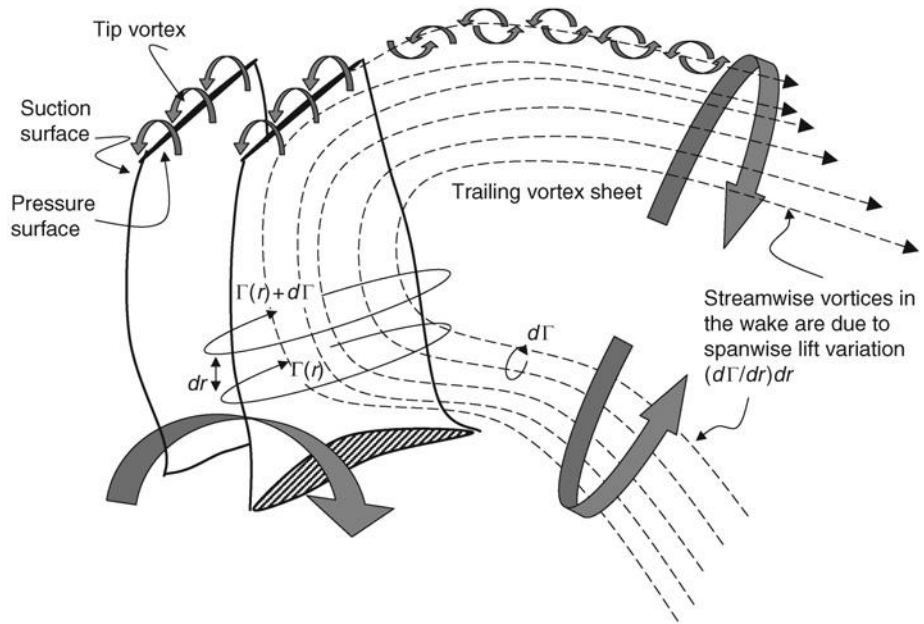
A transonic rotor creates a shock, which is weakened by suction surface expansion Mach waves and propagates upstream of the rotor row (Kerrebrock, 1981). Note that since the upstream flow is subsonic in the absolute frame of reference, there is no zone of silence preventing the propagation of the rotor created waves. Figure 8.41 shows a typical flowfield.

The broad category of “end wall” losses encompasses the annulus boundary layer, corner vortex, tip clearance flow, and the seal leakage flow. The tip clearance flow is a pressure-driven phenomenon that relieves the fluid on the pressure side towards the suction surface, as shown in Figure 8.42.

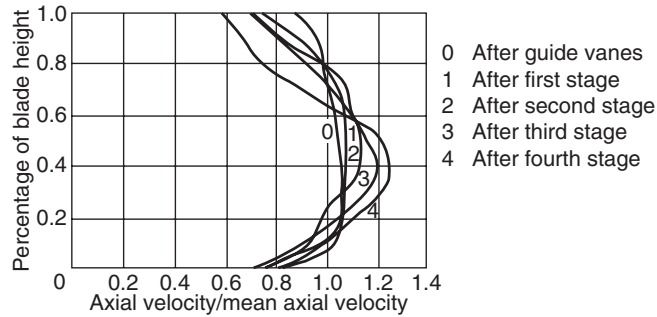
■ **FIGURE 8.41**
 Typical transonic rotor
 and its tip
 flowfield/wave pattern
 (bow shock and
 expansion waves)



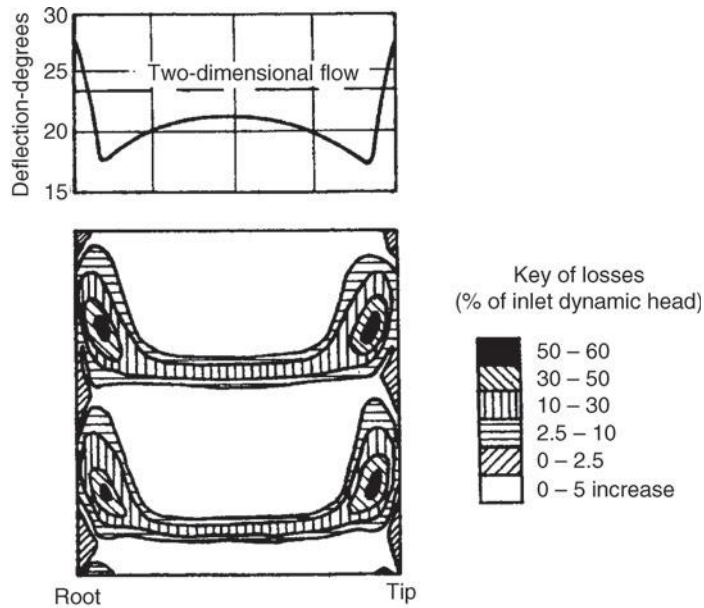
■ **FIGURE 8.42**
 Schematic drawing of
 tip vortex rollup and
 the inviscid wake
 composed of
 streamwise vortices
 due to spanwise lift
 variation on the blade



■ **FIGURE 8.43**
An aspect of end wall
flow losses studied by.
Source: Howell 1945.
Reproduced with
permission from SAGE



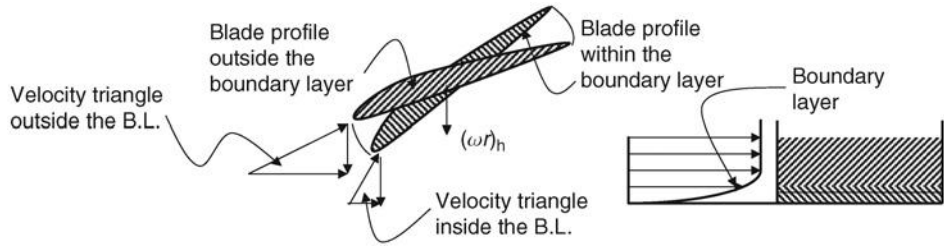
(a) The evolution of axial velocity profile with successive blade rows in a multistage compressor



(b) Total pressure loss distribution with blade height in a cascade

The boundary layer formation on the annulus is expected to grow with distance and in response to an adverse pressure gradient. The growth of the boundary layer with the number of stages is demonstrated by the data of Howell (1945), where the axial velocity distribution continually deforms and by the exit of the second stage there is no resemblance to a “potential core,” that is, flat top profile, that the inlet flowfield characterizes. The formation of corner vortices and the associated total pressure loss may be discerned from Howell data, as shown in Figure 8.43. Note that the flow deflection angle near the hub and the tip of the cascade, in the boundary layer, is in excess of data outside the annulus boundary layer as seen in Figure 8.43b. Modern blade design accounts for this difference in the relative flow angle in the boundary layer and *bends* the blade ends (*end-benders*) to minimize incidence loss. A schematic drawing of an end-bender blade is shown in Figure 8.44. Howell (1945) proposes a simple model for end wall losses

■ **FIGURE 8.44**
Schematic drawing of a bent tip blade to account for a larger boundary layer incidence due to a streamwise momentum deficit



that relates an annulus drag coefficient C_{Da} to the ratio of blade spacing to blade height, that is,

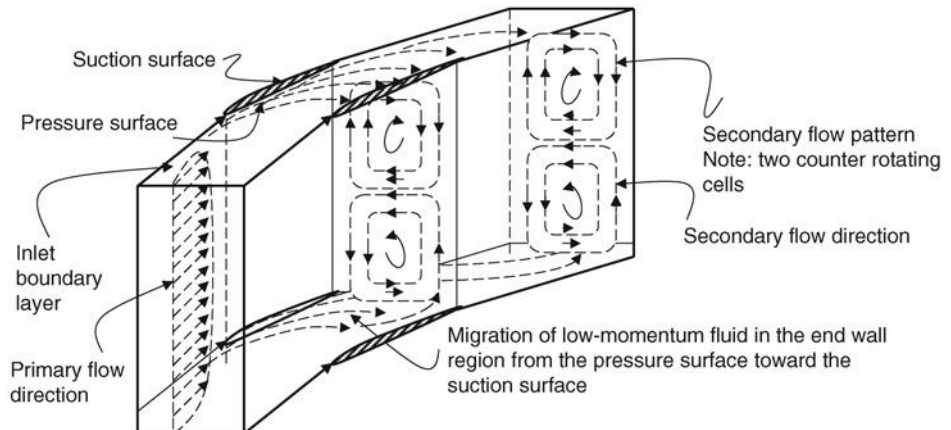
$$C_{Da} = 0.02(s/h) \tag{8.163}$$

A comparison paper by Howell (1945) on fluid dynamics of axial compressors should also be consulted. A secondary flow pattern is developed in a duct with a bend. The flow turning within the blade passages of a compressor then leads to a migration of the boundary layer fluid from the pressure surface toward the low-pressure side, that is, the suction surface. A flow pattern normal to the primary flow direction is then set up, which is called a secondary flow. A schematic drawing of a secondary flow generation and pattern is shown in Figure 8.45. Pioneering work on the formulation of secondary flows is due to Hawthorne (1951) and a simplified engineering formulation is due to Squire and Winter (1951). A simple secondary flow loss model is proposed by Howell (1945) and is expressed in terms of secondary (or induced) drag coefficient C_{Ds} ,

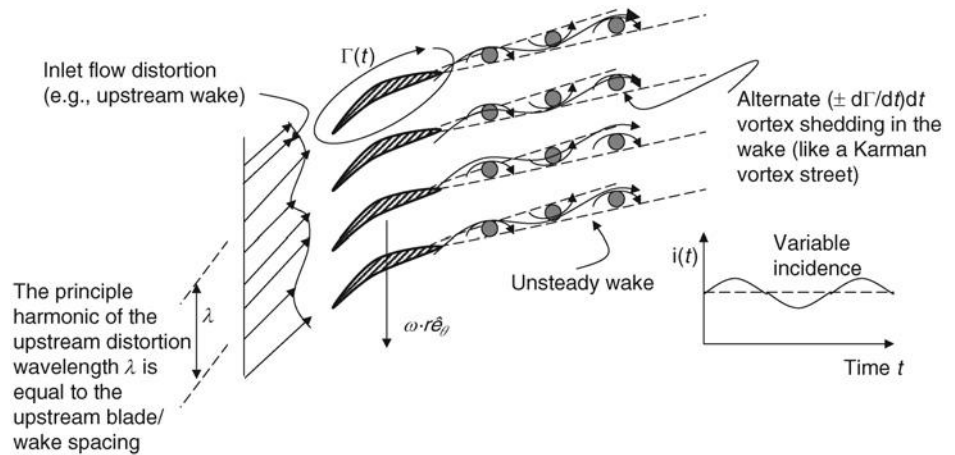
$$C_{Ds} = 0.018C_L^2 \tag{8.164}$$

The unsteadiness is an inherent mechanism for energy transfer between a rotating blade row and the fluid in turbomachinery. The upstream wake interaction with the following blade row is one source of unsteadiness (Kerrebrock and Mikolajczek, 1970). This *wake chopping* interaction leads to unsteady lift, which, following Kelvin’s circulation theorem,

■ **FIGURE 8.45**
Viscous flow in a bend creates a pair of counterrotating streamwise vortices, which set up a secondary flow pattern

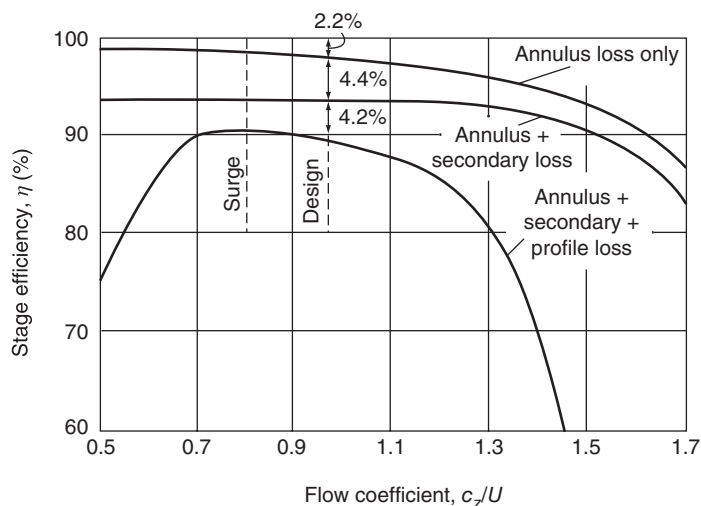


■ **FIGURE 8.46**
Unsteady flow interaction with a blade row causes periodic vortex shedding in the wake



results in a shed vortex of opposite spin in the wake. Another source of unsteadiness to a blade row is its relative motion with respect to a downstream blade row. Although, the blade is not engaged in a viscous wake chopping activity, as in the previous case, it is operating in an unsteady pressure field created by the downstream blade row. Operating in the unsteady pressure field is then referred to as unsteady *potential* interaction. Blade vibration in bending, twist or combined bending, and torsion is inevitable for elastic cantilevered structures. Therefore, blade vibration induces a spanwise variation of the incidence angle, hence an unsteady lift with a subsequent vortex shedding in the wake. The unsteady vortex shedding phenomenon is schematically shown in Figure 8.46. Kotidis and Epstein (1991) have measured unsteady radial transport in the rotor wake of a transonic fan. They have related unsteady losses to the radial transport in the spanwise vortex cores as well as turbulent mixing. The individual losses and their contributions to the overall loss are depicted in Figure 8.47 (from Howell, 1945). We note that at the design point the

■ **FIGURE 8.47**
Contributions of different losses in a compressor stage.
Source: Howell 1945.
Reproduced with permission from SAGE



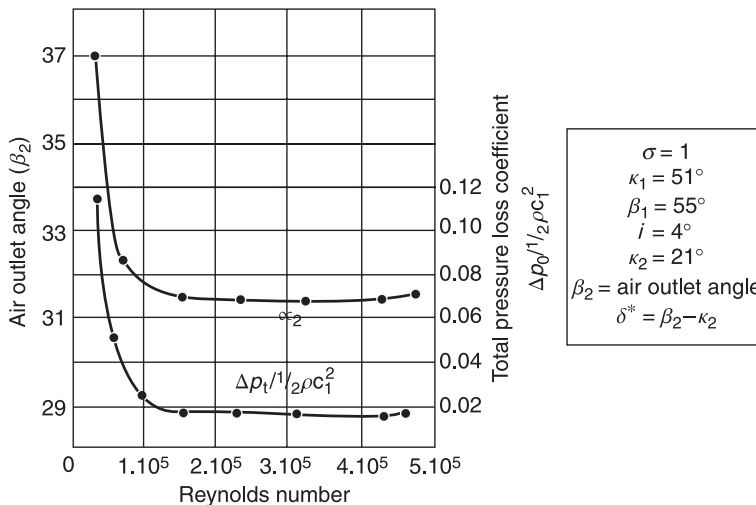
overall losses are near minimum and in low flow, the compressor enters surge and at the high flow rates profile losses dominate due to flow separation.

8.6.5.3 Reynolds Number Effect. The flow environment in a compressor, due to adverse pressure gradient, is sensitive to the state of a boundary layer. A laminar boundary layer readily separates in an adverse pressure gradient environment whereas a turbulent boundary layer may sustain a large pressure rise without separation or stall. The blade chord length, c , represents a suitable length scale for the Reynolds number evaluation as well as the relative velocity to the blade, W . Due to nearly flat compressor blade surfaces, we may borrow concepts from the flat plate boundary layer theory to predict the behavior of the boundary layer in adverse pressure gradient on a compressor blade. The effects of unsteadiness inherent in a turbomachinery as well as higher levels of turbulence in the core flow tend to provide for a higher mixing at the boundary layer and thus enhance its ability to withstand pressure rise. A more accurate approach should also include the effect of the blade curvature and its destabilizing (on a concave surface) or stabilizing (on a convex surface, such as the suction surface of a blade) effect on the boundary layer development. A simple statement can be made regarding the state of the boundary layer and its relation to compressor loss and that is to postpone/avoid flow separation, the boundary layer on a compressor blade has to be turbulent. This poses a rough minimum Reynolds number based on the blade chord of $\sim 200,000$ that serves as a rule of thumb, that is,

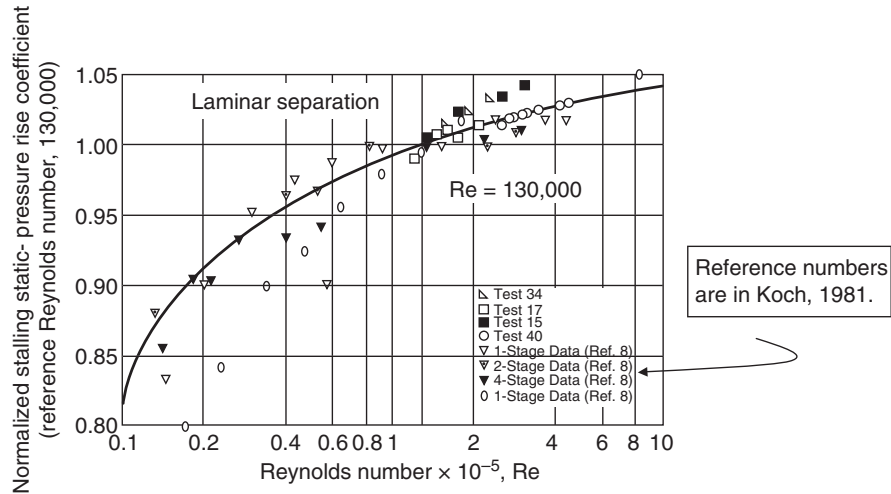
$$Re_c \equiv \rho \cdot W \cdot c / \mu \geq 200,000$$

The Reynolds number trend on the cascade exit flow angle and total pressure loss may be seen from cascade test data of Rhoden (1956) in Figure 8.48. We note that below $Re_c \sim 100,000$ the cascade suffers from a rapid increase in total pressure loss and large exit flow angle deviation, which is due to the phenomenon of laminar separation. This represents a *lower critical Reynolds number*. Koch (1981) examined the stalling pressure rise capability of axial-flow compressor stages, which indicated a much-reduced sensitivity to Reynolds

■ **FIGURE 8.48**
Cascade test results for the effect of Reynolds number on exit flow angle and the total pressure loss. Source: Rhoden 1956. Courtesy of U.K. Government



■ **FIGURE 8.49**
Variation of
normalized stalling
pressure rise coefficient
with Reynolds number
in single and
multistage compressor
tests. Source: Koch
1981. Reproduced with
permission from
ASME

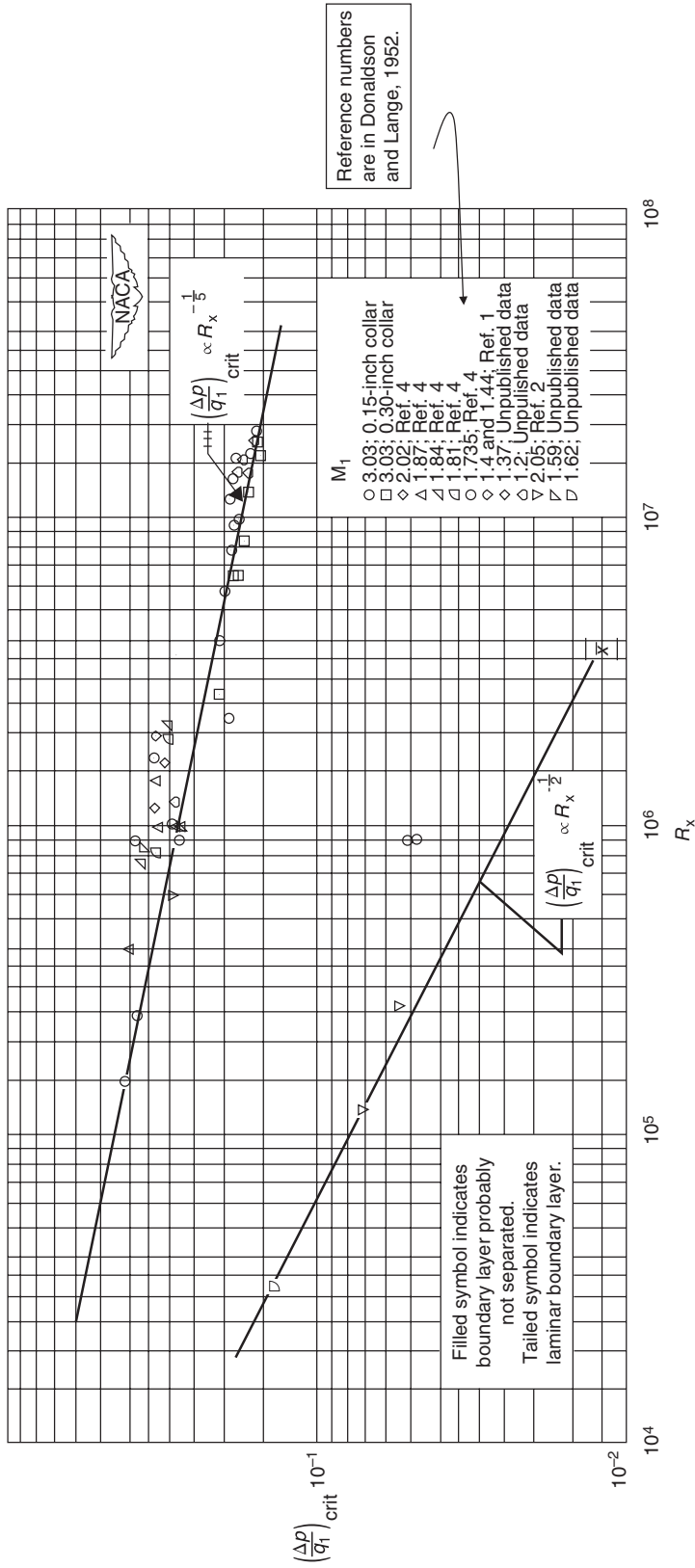


number below 200,000. The source of reduced sensitivity is found in higher turbulence levels and the unsteadiness inherent in a compressor stage. Koch's data normalized to $Re = 130,000$ is shown in Figure 8.49.

The boundary layers in transonic compressors readily reach the turbulent regime due to a high relative velocity W . For example, the Reynolds number on a fan blade operating at (relative) Mach 1.5 at the tip and 0.75 at the hub with a 1-ft (30.5 cm) chord at standard sea level conditions ranges from $\sim 5 \times 10^6$ to $\sim 10^7$. For $Re_c \sim > 500,000$ the compressor efficiency remains nearly constant, which marks the *upper critical Reynolds number*. The blade surfaces behave as hydraulically rough and thus independent of Reynolds number for $Re_c > 500,000$. At high altitudes, where the air density is low, and for a slow aircraft (e.g., a long-endurance observation platform), a suitable compressor blade should be designed with a much wider chord to combat the perils of laminar separation.

The effect of Reynolds number is expected to be minimal on secondary flow losses as the secondary flows are predominantly pressure-driven. Conventional, that is, steady, low turbulence, cascade tests do not reproduce compressor test rig results due to higher turbulence levels that promote mixing and the effect of unsteadiness with similar impact on the boundary layer. Finally, for the effect of Reynolds number on shock-boundary layer interaction, we may examine the work of Donaldson and Lange (1952). Figure 8.50 is a log-log graph of critical pressure rise across a shock that leads to boundary layer separation as a function of Reynolds number (from Donaldson and Lange). The two branches that appear on the graph correspond to the familiar laminar and turbulent boundary layers on a flat plate. We note that a turbulent boundary layer sustains nearly an order of magnitude (~ 10 times) higher stalling pressure rise across the shock than a corresponding laminar boundary layer in a supersonic flow, as pointed out earlier in this section. Also note that the Reynolds number dependence for the stalling pressure rise in a turbulent flow $\sim Re^{-0.2}$ and for the laminar boundary layer is inversely proportional to the square root of Reynolds number, that is, $\sim Re^{-0.5}$, which is identical to the Reynolds number behavior of momentum deficit thickness or friction drag coefficient on flat plates.

Shock-boundary layer interaction



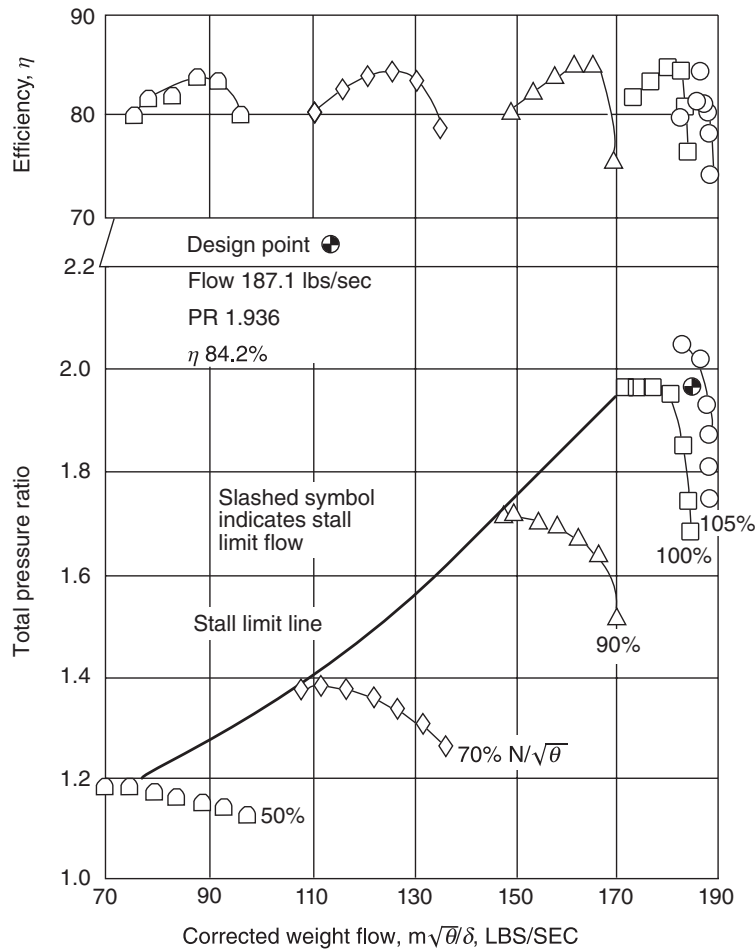
■ **FIGURE 8.50** Reynolds number dependence of the critical pressure rise across a shock that leads to boundary layer separation. Source: Donaldson, Du, and Lange 1952. Courtesy of NASA

8.7 Compressor Performance Map

Compressor pressure ratio plotted against the mass flow rate through the compressor is the compressor performance map. It is customary to graph the constant rpm lines on the performance chart as well as the adiabatic efficiency. The performance map of a single-stage transonic compressor is shown in Figure 8.51 (from Sulam, Keenan, and Flynn, 1970). The relative tip speed of the rotor is 1600 ft/s (488 m/s), and it represents a high-pressure ratio compressor stage ($\pi_s = 1.92$) with an adiabatic efficiency of 84.2% at the design point. The mass flow rate is corrected to the standard reference conditions, namely, the standard sea level pressure and temperature. The corrected mass flow rate is defined as

$$\dot{m}_{c_2} = \frac{\dot{m}_2 \sqrt{\theta_2}}{\delta_2} \tag{8.165}$$

■ **FIGURE 8.51**
Performance map of a
transonic compressor
stage. Source: Sulam,
Keenan, and Flynn
1970. Courtesy of
NASA



where

$$\theta_2 \equiv \frac{T_{t2}}{T_{\text{ref}}} \quad (8.166)$$

$$\delta_2 \equiv \frac{p_{t2}}{p_{\text{ref}}} \quad (8.167)$$

The reference pressure and temperature are the standard sea level conditions, namely, $p_{\text{ref}} = 1.01 \text{ bar}$ (or 101.33 kPa) and $T_{\text{ref}} = 288.2 \text{ K}$.

The corrected mass flow rate in a compressor is a pure function of the axial Mach number operating at the standard pressure and temperature. We can easily demonstrate this by writing the continuity equation of one-dimensional flow in terms of total pressure and temperature, the axial Mach number M_z , and the flow area A , namely,

$$\dot{m} = \sqrt{\frac{\gamma}{R}} \frac{p_t}{\sqrt{T_t}} \cdot A \cdot M_z \left(\frac{1}{1 + (\gamma - 1)M_z^2/2} \right)^{\frac{\gamma+1}{2(\gamma-1)}} \quad (8.168)$$

$$\frac{\dot{m}\sqrt{T_t}}{p_t} = \sqrt{\frac{\gamma}{R}} A \cdot M_z \left(\frac{1}{1 + (\gamma - 1)M_z^2/2} \right)^{\frac{\gamma+1}{2(\gamma-1)}} \quad (8.169)$$

Now, we may multiply both sides by the standard pressure and divide by the square root of the standard temperature to get the “corrected mass flow rate,”

$$\frac{\dot{m}\sqrt{\theta}}{\delta} = \sqrt{\frac{\gamma}{R}} \frac{p_{\text{ref}}}{\sqrt{T_{\text{ref}}}} A \cdot M_z \left(\frac{1}{1 + (\gamma - 1)M_z^2/2} \right)^{\frac{\gamma+1}{2(\gamma-1)}} = f(\gamma, R, M_z) \quad (8.170)$$

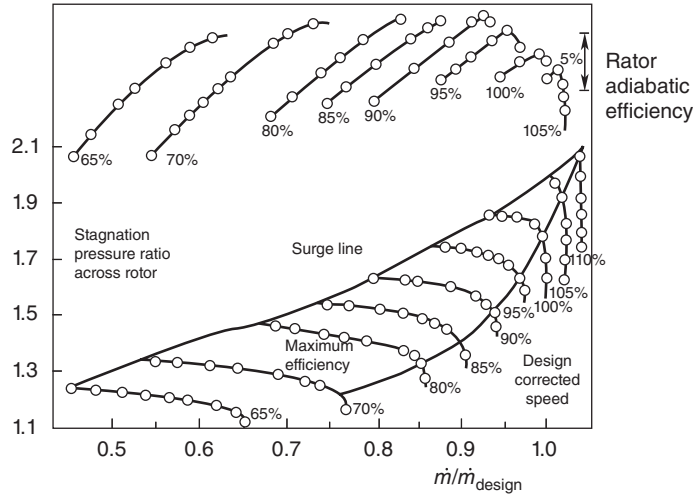
The performance of a compressor depends on the axial and blade tangential Mach numbers M_z and M_T as discussed earlier. The corrected mass flow rate is a unique function of the axial Mach number and in addition it represents the mass flow rate into the compressor at the standard day pressure and temperature. By defining a corrected mass flow rate, we have basically taken out the effect of nonstandard atmospheric conditions of engine static testing or flight operation. The blade tangential Mach number M_T is proportional to the shaft rotational speed (or angular frequency N) divided by the local speed of sound or the square root of static temperature, namely,

$$M_T \propto \frac{N}{\sqrt{T}} \propto \frac{N}{\sqrt{\theta}} \quad (8.171)$$

The RHS of Equation 8.171 is called the *corrected shaft speed*,

$$N_c \equiv \frac{N}{\sqrt{\theta}}$$

■ **FIGURE 8.52**
Performance map of a
modern fan rotor.
Source: Cumpsty 1997.
Reproduced with
permission from
Cambridge University
Press



The corrected shaft speed is a unique function of the blade tangential Mach number, which along with the axial Mach number determines the performance of a compressor or fan, that is,

$$\pi_c = \pi_c(\gamma, R, M_z, M_T) = \pi_c(\gamma, R, \dot{m}_c, N_c) \quad (8.172)$$

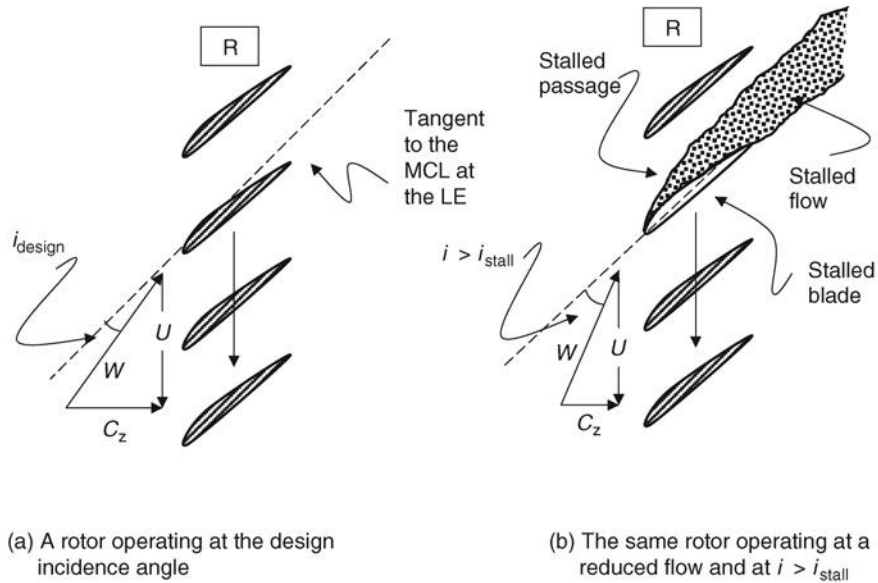
$$\eta_c = \eta_c(\gamma, R, \dot{m}_c, N_c) \quad (8.173)$$

It is also customary to nondimensionalize the corrected mass flow rate by the “design mass flow rate,” and the corrected shaft speed is nondimensionalized by the “design shaft speed” in the compressor performance map. An example of this is shown in Figure 8.52 (from Cumpsty, 1997).

8.8 Compressor Instability – Stall and Surge

The phenomenon of stall in a compressor has its roots in the aerodynamics of lifting surfaces in a high angle of attack. Therefore, from aerodynamics we understand stall as flow separation from the suction or pressure surfaces of an airfoil with large positive and negative angles of attack, respectively. In a compressor operating at a constant rotational (shaft) speed when the mass flow rate drops, the axial velocity decreases, hence the incidence angle increases. We remember from cascade data a parameter that was called “optimum incidence” angle, at which the blade losses were at a minimum. Large deviation from this minimum-loss incidence angle causes a rapid rise in total pressure loss, which signifies boundary layer separation. The positive and negative stall boundaries were then defined for a cascade of a given blade profile shape, solidity, stagger angle, and Mach number. Therefore, when the flow rate in a compressor drops while operating at constant shaft speed, the danger of stall lurks in the background. A stalled compressor flow is unsteady and, hence, offers a means of driving the naturally occurring blade vibrations into resonance. This is the mechanism for energy flow from the fluid into the blade vibration

■ **FIGURE 8.53**
 A rotor blade operating at its best incidence angle and at a reduced mass flow leading to a stalling incidence angle

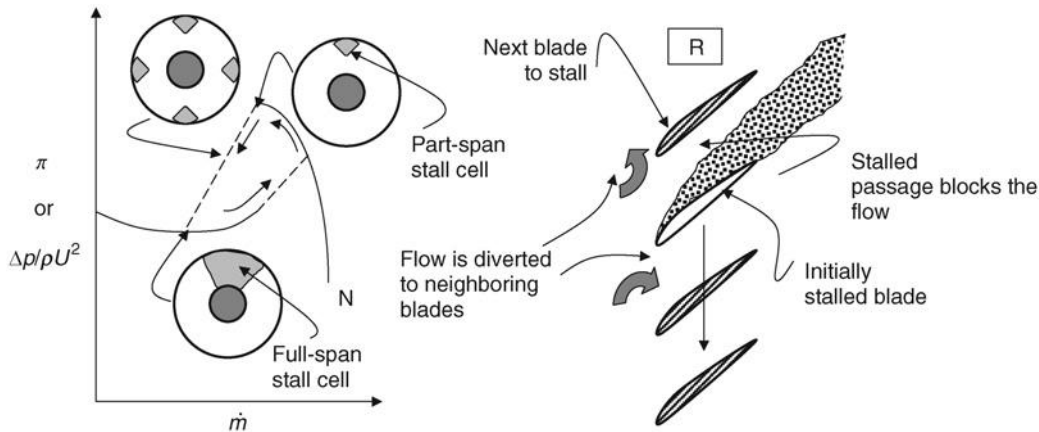


(a) A rotor operating at the design incidence angle

(b) The same rotor operating at a reduced flow and at $i > i_{\text{stall}}$

that causes *flutter*. Flutter is the *self-excited* aeroelastic instability of an aerodynamic lifting surface. In contrast, *buffet* (or *buffeting*) is a *forced vibration* of an aerodynamic surface that is in the turbulent wake of an upstream wing/fuselage, for example, horizontal tail buffet. Figure 8.53 shows schematic drawing of a compressor rotor with two velocity triangles, one representing its design point operation and the second corresponding to a stalled flow.

The stalled flow in a compressor rotor may be initiated with a single blade at a certain radius. The stalled blade passage acts as a “blocker” and diverts the flow to the neighboring (as yet unstalled) blades. Following the drawing in Figure 8.53b, we note that the flow diversion from the stalled passage to the one above the stalled blade causes an increase in that blade’s incidence angle, pushing it toward stall. Similarly, the blade below the stalled passage gets a diverted flow, which causes a reduction of the flow incidence angle to the blade below. Therefore, it moves away from stall. We note that the stalled flow in a passage is moving in the opposite direction to the blade rotation, hence it is given the name *rotating stall*. The angular speed of rotating stall propagation is $\sim 1/2$ of rotor angular speed, that is, $\omega/2$, and in the opposite direction to the rotor rotation. Hence, in the laboratory (i.e., absolute) frame of reference, a rotating stall *patch* spins with the rotor (i.e., the same direction as the rotor) but at half the speed. To get a feel for the frequency of the rotating stall cells, for example, in a large turbofan engine with a shaft speed of ~ 50 Hz, a single stall cell has half the frequency or 25 Hz. Now for a two-to-four stall cells circumferentially arranged around the compressor rotor, the stall cell frequency becomes 50–100 Hz. The rotating stall starts with a single cell and develops into a number of cells with a partial span extent (known as the part-span stall) and may grow into a full-span stalled flow with subsequent reduction in the mass flow rate. This behavior is shown schematically in Figure 8.54. The first appearance of stall is limited to a single cell with subsequent reduction of the flow the average pressure rise drops and the cells multiply into a periodic arrangement, as shown in Figure 8.54. The recovery from



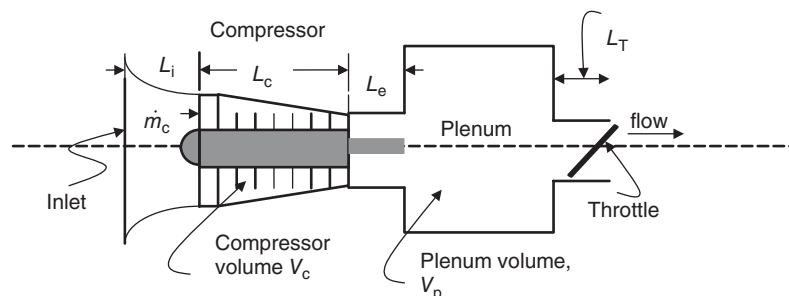
■ **FIGURE 8.54** Schematic drawing of the mechanism of rotating stall, part and full-span stall cells and a hysteresis loop in stall recovery

the stalled operation in a compressor exhibits a hysteresis behavior, which accompanies systems governed by *nonlinear dynamics*.

The coupling between the compressor stall instability and the combustion chamber resonant characteristics could lead to an overall breakdown of the flow, or flow oscillation, in the compressor and combustor. The overall flow breakdown in the “system” composed of compressor and combustor is called *surge*. In a fully developed stage, surge is an axisymmetric oscillation of the flow with a characteristic timescale dictated by the plenum chamber time to empty and fill. In the initial transient stage, surge is asymmetric and thus creates transverse loads on the blades, which may rub on the casing and lead to structural damage and system breakdown. Early contributions to understanding compressor stall and surge and their distinction were made in the United States at NACA (e.g., Bullock and Finger, 1951) and by Emmons, Pearson, and Grant at Harvard (1955).

A unifying approach to treat the compression system instability was first presented by Greitzer (1976). Greitzer developed a successful one-dimensional theory for the onset of surge in a compressor coupled to a plenum chamber cavity, which may serve as a model of the combustor in a gas turbine engine. The elements of the compression system model are shown in Figure 8.55 to be composed of an inlet duct, a compressor, an exit duct connecting to a plenum chamber followed by a throttle that sets the backpressure, and the mass flow rate through the compressor.

■ **FIGURE 8.55** Compression system model that is used to study *local* (rotating stall) and *global* (surge) system instabilities



Greitzer proposes the ratio of two characteristic timescales as the parameter that governs the dynamics of this system. One characteristic timescale is the compressor throughflow, which may be written as

$$\tau_{\text{throughflow}} \sim \frac{\rho \cdot V_c}{\dot{m}_c} \tag{8.174}$$

The second characteristic timescale is that of the plenum chamber, which is the time to charge the plenum chamber to a critical pressure rise condition for a stable compressor operation Δp_c ,

$$\tau_{\text{charge}} \sim \frac{\left(\frac{\Delta p_c}{RT}\right) \cdot V_P}{\dot{m}_c} \tag{8.175}$$

Expressing the pressure rise in the plenum as the square of the wheel speed,

$$\Delta p_c \sim \rho (\omega \cdot r)^2 \tag{8.176}$$

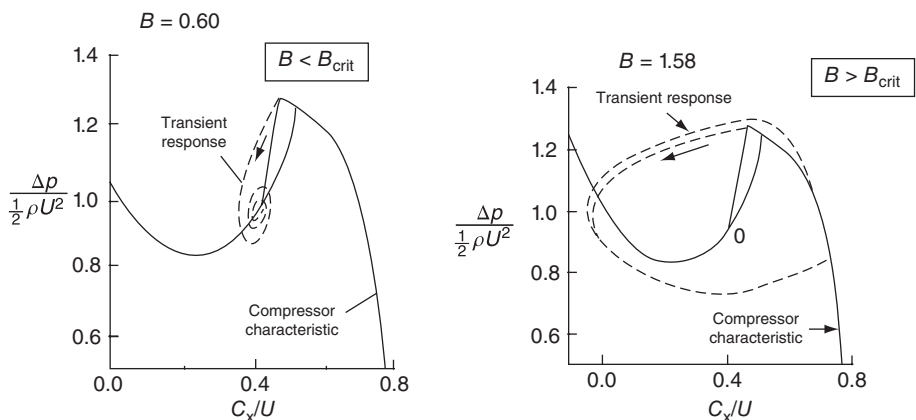
$$T \sim a^2 \tag{8.177}$$

and the temperature as the speed of sound squared, Greitzer has shown that the ratio of the two timescales is the square of a parameter B that dictates the fate of disturbances in a compressor, that is,

$$B \equiv \frac{\omega \cdot r}{2a} \sqrt{\frac{V_P}{V_c}} \sim \left(\frac{\tau_{\text{charge}}}{\tau_{\text{throughflow}}}\right)^{0.5} \tag{8.178}$$

The critical value of the B -parameter, which causes compressor instability to grow into a surge instead of a localized rotating stall, is shown to be $\sim 0.7-0.8$ by Greitzer. Experimental investigations of compression system instability have supported the proposed model. Figure 8.56 (from Greitzer, 1976) shows the computed results of a transient behavior of

■ **FIGURE 8.56**
 Transient response of a compressor to instabilities showing the appearance of a rotating stall (left) and the emergence of surge (right). Source: Greitzer 1976, Fig. 7.56, p. 190. Reproduced with permission from ASME



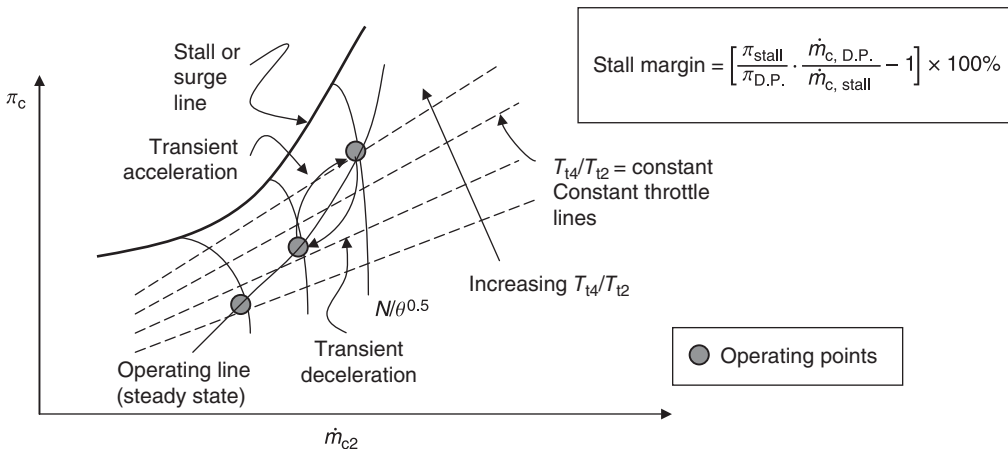
a compressor instability that settles into a rotating stall for low B -parameter and surge instability for a B -parameter of 0.6 and 1.58, respectively.

Current understanding of the compressor system instability has allowed strategies to be developed in its active control. Fast detection and cancellation of early oscillations are the keys to a successful active control system design. A review article by Paduano, Greitzer, and Epstein (2001) provides a rich exposition to the subject.

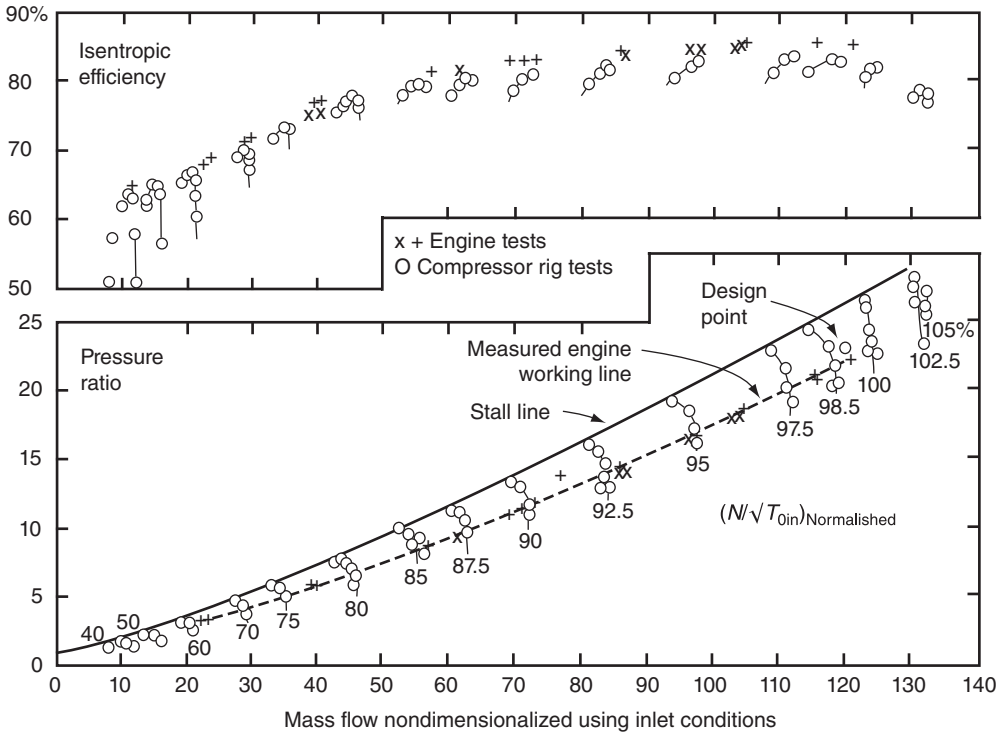
8.9 Multistage Compressors and Their Operating Line

The throttle in a gas turbine engine is the fuel flow control to the combustor. Constant throttle lines are, therefore, the lines of constant T_{t4}/T_{t2} . The path of steady-state operation of the compressor with the throttle setting is called the operating or working line in a compressor. It is often superimposed on the compressor performance map, as shown schematically in Figure 8.57. The transient behavior of “spool up” is shown in Figure 8.57 as well. In the context of the stall margin defined as the percentage stall pressure rise divided by the corresponding percentage drop in the mass flow rate, the transient engine operation deviates from the steady-state operating line and approaches the stall or surge line. The level and type of inlet flow distortion also affects the stall margin. We shall discuss inlet distortion and compressor stall later in this chapter.

Compressor performance map for the GE Energy Efficient Engine (E^3) is shown in Figure 8.58 (from Cumpsty, 1997). Compressor test rig data as well as the engine test data are superimposed for comparison. Engine measurements are limited to the data points along the engine working line, whereas the compressor rig offers the versatility to produce the entire map. As a point of reference, E^3 program was initiated by NASA in 1973 (sparked by the oil embargo) with the goal of 12% reduction in specific fuel consumption over then current commercial aircraft engines of the day. Both GE and Pratt & Whitney developed technology demonstrator engines under this program that exceeded NASA’s goal. A book by Garvin (1998) presents a history of aircraft engine development in the United States with a particular emphasis on GE’s achievements in the commercial



■ FIGURE 8.57 Constant throttle lines and a steady-state operating line are superimposed on a typical compressor performance map (D.P. is the design point)



■ FIGURE 8.58 Compressor performance map from GE E³ program with a design point pressure ratio of 23 achieved in 10 stages with variable stators in the first six stages. Source: Cumpsty 1997. Reproduced with permission from Cambridge University Press

engine market. The lead taken by the military needs and the lag of the commercial side in aircraft engine development are presented in the context of the cold war, and the impact of business and strategic teaming/partnerships that have led to a business success. Propulsion engineers need to look at the business side of engineering to appreciate issues of cost, markets, customer service, and product support. For additional reading on the history of aircraft gas turbine engine development in the United States, the book by James St. Peter (1999) is recommended.

Let us do a simple and quick calculation of this compressor’s polytropic efficiency e_c based on its design point pressure ratio and adiabatic efficiency. We estimate the compressor adiabatic efficiency of ~ 0.86 from Figure 8.58 at the design point and for the compressor pressure ratio of 23 we substitute these in the modified form of Equation 4.22:

$$e_c = \frac{\gamma - 1}{\gamma} \left[\frac{\ln \pi_c}{\ln \left\{ 1 + \frac{1}{\eta_c} \left[\pi_c^{\frac{\gamma-1}{\gamma}} - 1 \right] \right\}} \right]$$

to get an $e_c \approx 0.907$. An average stage pressure ratio in 10 stages is

$$(\pi_s)_{\text{Avg}} \approx (\pi_c)^{\frac{1}{N}} = (23)^{\frac{1}{10}} \cong 1.368$$

This represents just an *average* of the stage pressure ratios and we recognize that the front stages operate at a higher loading (front stage pressure ratio of ~ 1.6) than the aft stages (pressure ratio ~ 1.15) due to a higher blade tangential Mach number M_T .

Now, we shall demonstrate that a throttle position T_{t4}/T_{t2} establishes the compressor pressure ratio, the mass flow rate, and the corresponding shaft speed. From the chapter on cycle analysis and off-design considerations, we argued that the turbine nozzle and the exhaust nozzle throat remain choked over a wide operating range of the engine. As we recall the turbine expansion parameter,

$$\tau_{t\text{-off-design}} = \tau_{t\text{-design}} = \text{constant}$$

The compressor–turbine power balance demands

$$\dot{m}_0(h_{t3} - h_{t2}) = \dot{m}_0(1 + f)(h_{t4} - h_{t5})$$

To simplify the equation, assume the gas is calorically perfect and neglect the small contribution of fuel-to-air ratio in favor of 1 on the RHS of the above equation, to get

$$T_{t2}(\tau_c - 1) \approx T_{t4}(1 - \tau_t)$$

Therefore, the compressor temperature ratio is related to the throttle setting and a constant turbine expansion parameter τ_t via

$$\tau_c \approx 1 + (1 - \tau_t) \frac{T_{t4}}{T_{t2}} \quad (8.179)$$

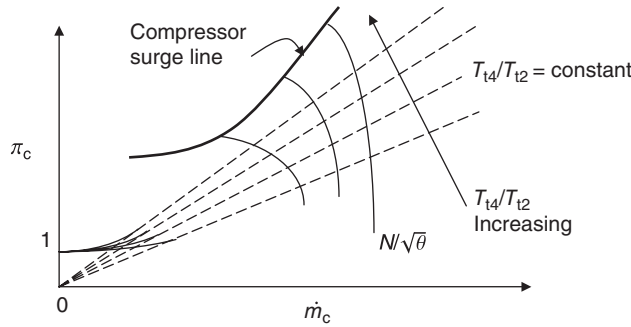
Here, we see that the compressor temperature ratio increases linearly with the throttle setting. The compressor pressure ratio is related to the temperature ratio via the polytropic efficiency; therefore, the compressor pressure ratio is established by the throttle setting as

$$\pi_c \approx \left[1 + (1 - \tau_t) \frac{T_{t4}}{T_{t2}} \right]^{\frac{\gamma_c}{\gamma - 1}} \quad (8.180)$$

The continuity equation at stations 2 and 4, that is, the compressor face and the combustor/turbine nozzle exit connects the axial Mach number at the engine face to the throttle setting according to

$$\begin{aligned} \dot{m}_2 &= \sqrt{\frac{\gamma_2}{R_2}} \frac{P_{t2}}{\sqrt{T_{t2}}} A_2 \cdot M_{z2} \left(1 + \frac{\gamma_2 - 1}{2} M_{z2}^2 \right)^{-\frac{(\gamma_2+1)}{2(\gamma_2-1)}} \\ &\approx \dot{m}_4 = \sqrt{\frac{\gamma_4}{R_4}} \frac{P_{t4}}{\sqrt{T_{t4}}} A_4 \left(\frac{\gamma_4 + 1}{2} \right)^{-\frac{(\gamma_4+1)}{2(\gamma_4-1)}} \end{aligned} \quad (8.181)$$

■ **FIGURE 8.59**
Constant throttle lines
on a compressor
performance map



By neglecting the combustor total pressure loss, we may replace the combustor exit total pressure p_{t4} with the compressor exit pressure p_{t3} to rewrite Equation 8.181 as

$$M_{z2} \left(1 + \frac{\gamma - 1}{2} M_{z2}^2 \right)^{-\frac{(\gamma+1)}{2(\gamma-1)}} \approx \text{constant} \frac{\pi_c}{\sqrt{T_{t4}/T_{t2}}} \quad (8.182)$$

We assumed the flow areas A_2 and A_4 remain constant in deriving Equation 8.182 as well as all the gas property variations included in the proportionality constant on the RHS of Equation 8.182. The left-hand side (LHS) of Equation 8.182 is proportional to the corrected mass flow rate \dot{m}_{c2} , hence

$$\dot{m}_{c2} \propto \frac{\pi_c}{\sqrt{T_{t4}/T_{t2}}} \quad (8.183)$$

Therefore, constant throttle lines, $T_{t4}/T_{t2} = \text{constant}$, are straight lines on the compressor performance map π_c versus \dot{m}_{c2} , as shown schematically in Figure 8.59. Also higher throttle constants attain higher slopes, as shown in Figure 8.59, which get the compressor operating point closer to the compressor surge line. Figure 8.59 shows the constant throttle lines and their convergence on compressor pressure ratio of 1, corresponding to a mass flow rate of zero.

The engine face axial Mach number is established by the throttle setting via Equation 8.182 and the compressor pressure ratio was related to the throttle setting via Equation 8.180, therefore,

$$M_{z2} \left(1 + \frac{\gamma - 1}{2} M_{z2}^2 \right)^{-\frac{(\gamma+1)}{2(\gamma-1)}} \approx \text{constant} \frac{[1 + (1 - \tau_t)(T_{t4}/T_{t2})]^{\frac{\gamma \epsilon_c}{\gamma-1}}}{\sqrt{T_{t4}/T_{t2}}} \quad (8.184)$$

We may solve Equation 8.184 for the engine face axial Mach number for a given throttle setting. We may also simplify the LHS somewhat by recognizing that the second term in the parenthesis involving axial Mach number is small compared to one, hence applying binomial expansion yields,

$$M_{z2} \left(1 - \frac{\gamma + 1}{4} M_{z2}^2 \right) \approx \text{constant} \frac{[1 + (1 - \tau_t)(T_{t4}/T_{t2})]^{\frac{\gamma \epsilon_c}{\gamma-1}}}{\sqrt{T_{t4}/T_{t2}}} \quad (8.185)$$

Now, let us demonstrate the dependence of wheel speed on the throttle setting. The compressor power is consumed by the rotor blades that experience a torque τ_r and spin at the angular rate of ω . The stator blades do not contribute to the power transfer. We need to sum overall the rotor blade rows in a multistage compressor to calculate the compressor power, namely,

$$\mathcal{P}_c = \omega \cdot \sum_{j=1}^N \tau_{r_j} \quad (8.186)$$

where N is the number of stages. The rotor torque is the integral of angular momentum increase across the blade row and may be expressed as

$$\tau_r = \int_{r_{h2}}^{r_{l2}} r \cdot C_{\theta 2}(r) \cdot \rho_2(r) \cdot C_{z2}(r) \cdot 2\pi r \, dr - \int_{r_{h1}}^{r_{l1}} r \cdot C_{\theta 1}(r) \cdot \rho_1(r) \cdot C_{z1}(r) \cdot 2\pi r \, dr \quad (8.187)$$

The geometrical parameters are sketched in Figure 8.60. In their simplest form the integrals are expressed as an average angular momentum at the pitchline radius r_m namely,

$$\tau_r = \dot{m} [(r_{m2} C_{\theta 2m}) - (r_{m1} C_{\theta 1m})] \quad (8.188)$$

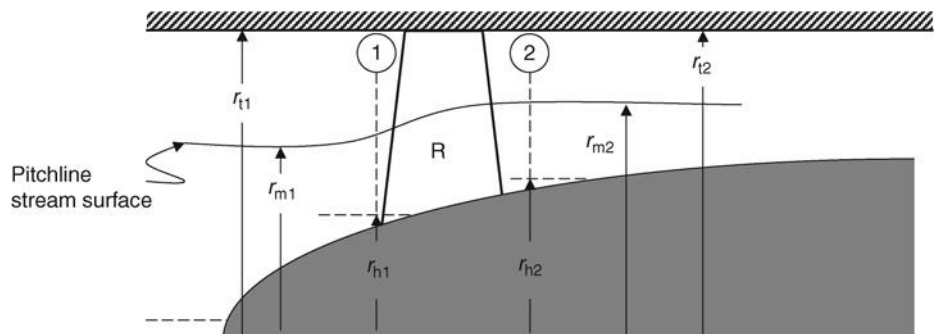
The rotor torque, however, is a function of the shaft speed as the absolute swirl downstream of the rotor changes with shaft speed according to

$$C_{\theta 2} = C_{z2} \tan \alpha_2 = U + W_{\theta 2} = U + C_{z2} \tan \beta_2 \quad (8.189)$$

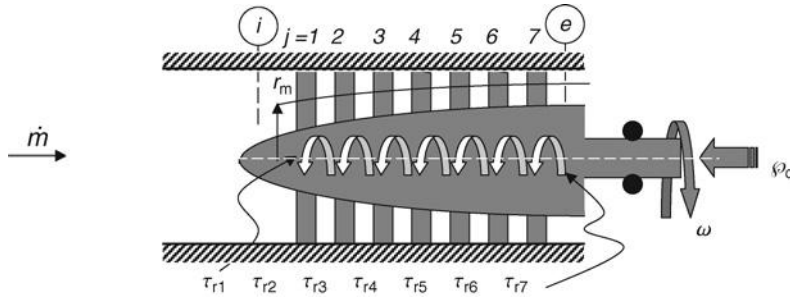
The rotor relative exit flow angle β_2 remains nearly constant with the shaft speed over a wide operating range of the compressor, that is, for attached boundary layer flow to the blades. Substituting Equation 8.189 into Equation 8.188, we get

$$\tau_r = \dot{m} [r_{m2} (\omega \cdot r_{m2} + C_{z2} \tan \beta_2) - r_{m1} C_{z1} \tan \alpha_1] \quad (8.190)$$

■ **FIGURE 8.60**
Definition sketch of the geometrical parameters



■ **FIGURE 8.61**
 Seven-stage
 compressor consuming
 power $\dot{\varphi}_c$ at the shaft
 speed of ω and the
 individual rotor
 torques $\tau_{r1}, \tau_{r2}, \dots, \tau_{r7}$



Expressing the shaft power in terms of the total enthalpy rise and the mass flow rate, we get

$$\dot{\varphi}_c = \dot{m} (h_{te} - h_{ti}) = \dot{m} h_{ti} (\tau_c - 1) = \omega \cdot \sum_{j=1}^N \tau_{rj} \quad (8.191a)$$

Figure 8.61 shows the parameters in Equation 8.191a.

By substituting for the rotor torque from Equation 8.190 to Equation 8.191a, for the compressor temperature ratio from Equation 8.179, and canceling the mass flow rate, we get

$$h_{t2}(1 - \tau_t) \frac{T_{t4}}{T_{t2}} = \omega \sum_{j=1}^N [r_{me}(\omega \cdot r_{me} + C_{ze} \tan \beta_e) - r_{mi} C_{zi} \tan \alpha_i]_j \quad (8.191b)$$

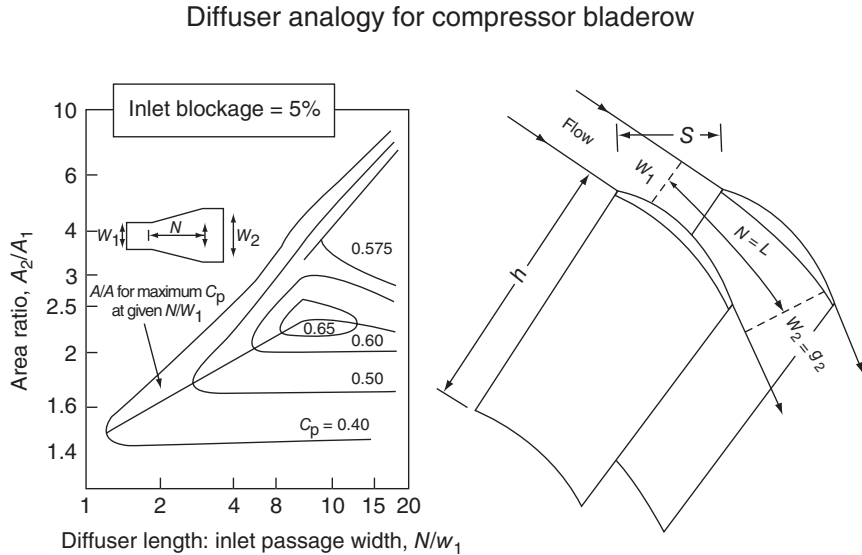
This is a quadratic equation in ω in terms of the throttle setting T_{t4}/T_{t2} , flow angles α_1 and β_2 that remain nearly constant, axial velocities across the rotor, and the radial position of the pitchline stream surface. In practice at a given throttle setting, the shaft finds its own speed consistent with the compressor power consumption and mass flow rate through the machine. We have thus established the interdependence of compressor pressure ratio, corrected mass flow rate, and shaft speed on the throttle setting.

The simplifications introduced in the above discussions may be removed one by one, if we are willing to iterate to find a consistent set of compressor performance parameters. For example, the choking condition in stations 4 and 8 may be relaxed in the case that the nozzle pressure ratio is below critical (i.e., necessary for choking). The subsonic throat Mach number may be found through application of continuity equation using a trial and error approach.

8.10 Multistage Compressor Stalling Pressure Rise and Stall Margin

Koch (1981) developed an analogy between the stalling pressure rise capability of an axial-flow compressor stage and two-dimensional diffusers. Classical diffuser data of Reneau, Johnston, and Kline (1966) and Sovran and Klomp (1967) for a straight centerline, 2D diffuser serve as the point of analogy. The pitchline radius of the compressor stage is taken as the reference point in developing the stall analogy with the diffuser. This approach is

■ **FIGURE 8.62**
 (Left) Diffuser performance chart.
 Source: Reneau et al. 1967. Reproduced with permission from ASME. (Right) The analogy to a compressor blade row.
 Source: Wisler 2000.



useful in the preliminary design phase of an axial-flow compressor in estimating the maximum pressure rise potential as well as the stall margin for a given design point operation. Figure 8.62 shows the diffuser performance data of Reneau, Johnston, and Kline for an inlet boundary layer blockage of 5%. The length of the diffuser is N , which is analogous to L , as shown on the definition sketch on the right (from Wisler, 2000), to represent a diffusion length scale of a compressor blade passage at the pitchline.

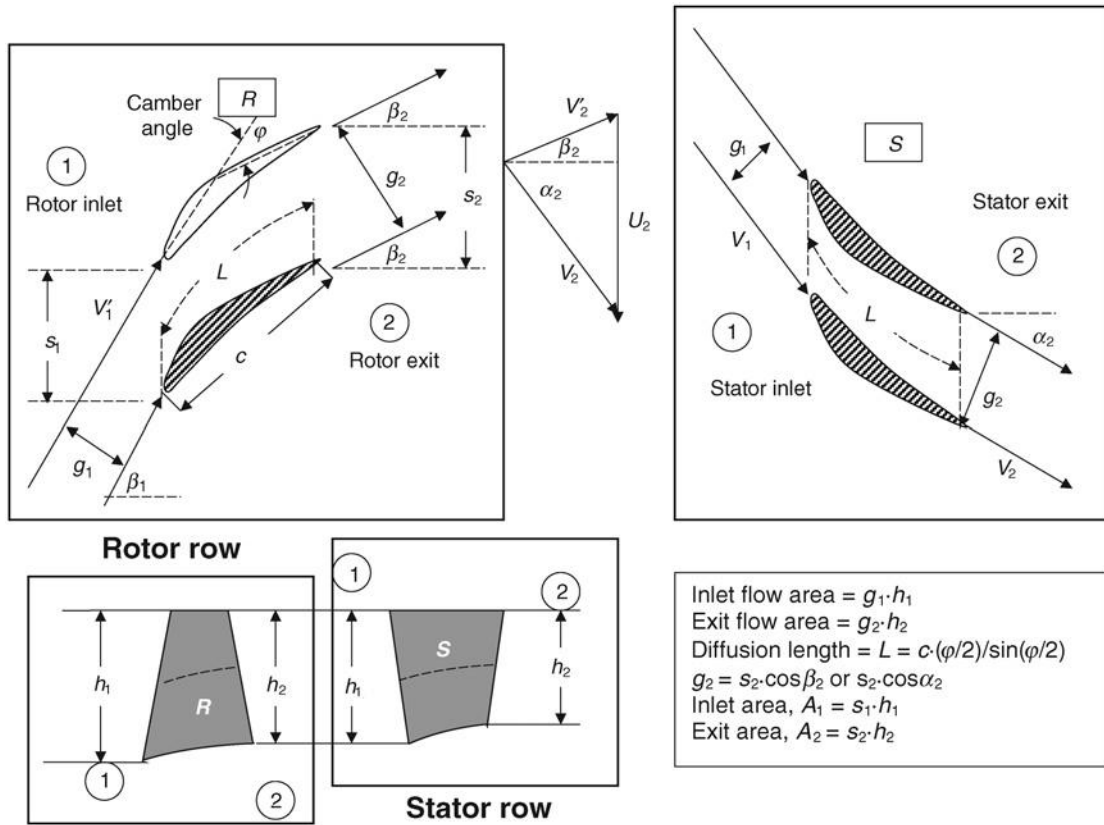
As a first approximation, the diffusion length L is represented by the arc length of the mean camber line of the airfoil at the pitchline. Assuming a circular arc for the mean camber line, the length L is related to the camber angle φ and the chord length c via

$$L \approx c \cdot \frac{\varphi/2}{\sin(\varphi/2)} \tag{8.192}$$

Although the area ratio of a diffuser, A_2/A_1 , is fixed by the geometry of the diffuser, its counterpart in a cascade depends on the blade incidence, that is, the staggered spacing of the streamtube that enters and exits the blade row. The exit flow area of the blade channel is, however, fixed over a wide operating range of the compressor flow and, therefore, it serves as the reference area in the correlation development by Koch. The inlet flow area is a function of the operating point (i.e., the throttle setting) and decreases with an increasing incidence angle. Figure 8.63 shows the staggered spacing g_1 and g_2 and the flow areas at the inlet and outlet of a compressor blade row.

Here, we have adopted the terminology of Koch in representing the rotor relative velocity as V' and the absolute velocity as V . A nondimensional diffusion parameter is the ratio of the diffusion length L to the staggered spacing at the exit of the blade row, that is, L/g_2 ,

$$\frac{L}{g_2} = \sigma_1 \cdot \frac{\varphi/2}{\sin(\varphi/2)} \cdot \frac{s_1}{s_2} \frac{1}{\cos \beta_2} = \sigma_1 \cdot \frac{\varphi/2}{\sin(\varphi/2)} \cdot \frac{A_1}{A_2} \cdot \frac{h_2}{h_1 \cdot \cos \beta_2} \tag{8.193}$$



■ FIGURE 8.63 Definition sketch of the staggered inlet and outlet spacing and area ratio for a compressor stage (V'_1 and V'_2 are relative velocities W_1 and W_2)

where the camber angle φ is in radians and the blade inlet solidity is represented by σ_1 at the pitchline. The blade solidity, the camber angle, and the exit flow angle are all reflected in the nondimensional diffusion length ratio in a compressor blade row. The stator blade row diffusion length is calculated in a similar manner using the stator inlet solidity at the pitchline, camber angle, area ratios, and the exit absolute flow angle. The effect of higher camber angle is seen as an increase in diffusion, hence static pressure rise. The effects of blade aspect ratio, tip clearance gap, and Reynolds number are accounted for through the end wall boundary layer thickness. In a diffuser, the inlet boundary layer blockage is a key parameter in the performance and stalling characteristics of diffusers, and hence the end wall boundary layer thickness in a compressor stage serves the same principle.

A stage average approach is adopted in developing a correlation between the stalling pressure rise of a diffuser and a compressor stage. For example, the diffusion length ratio L/g_2 of the stage is the weighted average of the rotor and the stator values with blade row inlet dynamic head used as the weighting factor, that is,

$$\left. \frac{L}{g_2} \right|_{\text{Stage}} = \left[\frac{(L/g_2)_{\text{Rotor}} \cdot q'_1 + (L/g_2)_{\text{Stator}} \cdot q_1}{q'_1 + q_1} \right] \quad (8.194)$$

where q'_1 is the rotor inlet dynamic head (relative) and q_1 is the stator inlet dynamic head. Koch (1981) defines an enthalpy equivalent of the static pressure rise in a compressor stage according to

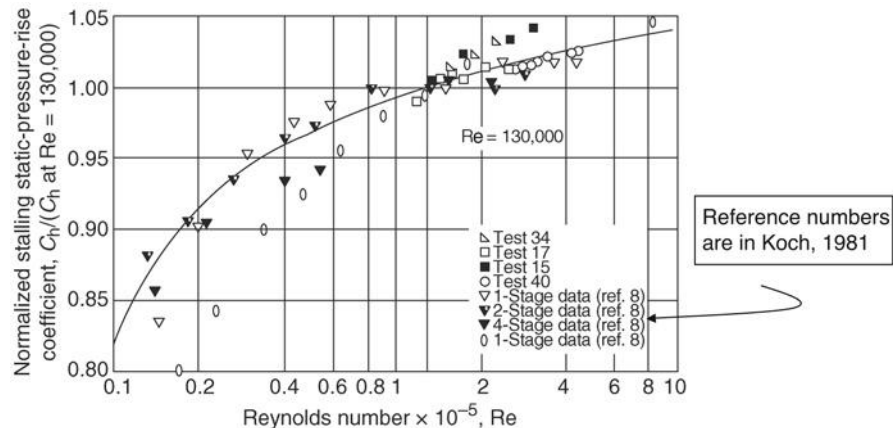
$$C_h \equiv \frac{c_p T_1 \left[\left(\frac{p_2}{p_1} \Big|_{\text{Stage}} \right)^{\frac{\gamma-1}{\gamma}} - 1 \right] - \frac{(U_2^2 - U_1^2)_{\text{Rotor}}}{2}}{\left[\frac{V_1^2 \Big|_{\text{Rotor}} + V_1^2 \Big|_{\text{Stator}}}{2} \right]} \quad (8.195)$$

The numerator of Equation 8.195 is the stage static enthalpy rise based on the isentropic stage temperature ratio, which is corrected for the radial shift across the rotor at the pitchline radius. To be comparable, the rotor *free work contribution* associated with the radial shift needs to be corrected for in the pressure rise comparisons of diffusers and compressor stages. The denominator is the sum of the free stream dynamic heads to the rotor and stator. There are *two* dynamic heads in the denominator, corresponding to *two* static enthalpy rises across the rotor and stator in the numerator.

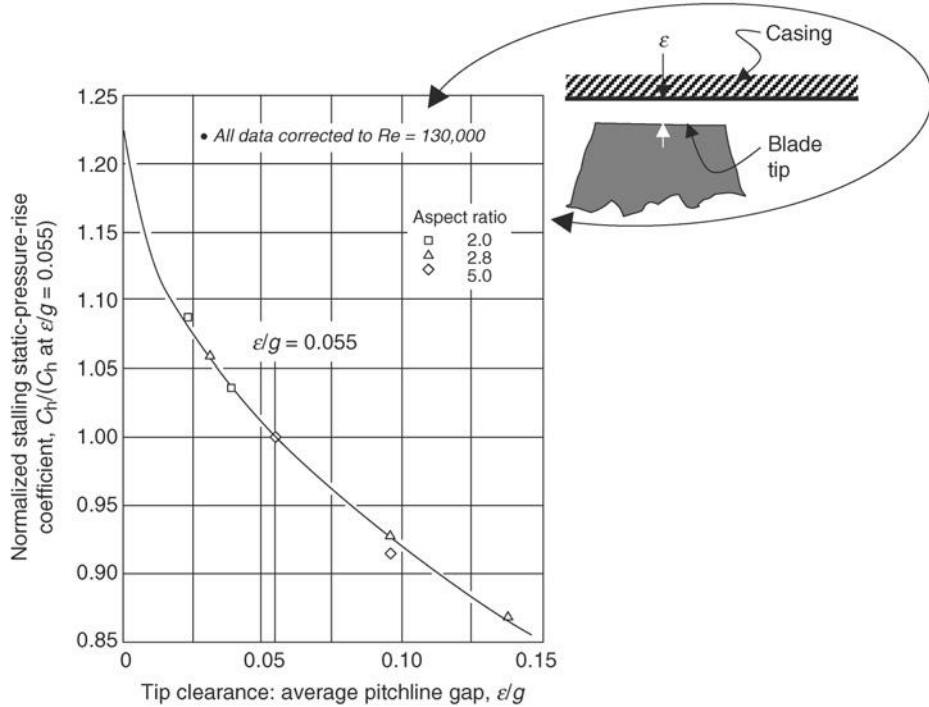
The contributions of Reynolds number, tip clearance, and the axial spacing between the rotor and the stator rows to the stalling pressure rise coefficient are represented in Figures 8.64 to 8.66, respectively (from Koch, 1981). Normalizing values for Reynolds number, ratio of tip clearance to gap, and the ratio of axial distance to the blade spacing are used in presenting the stalling pressure rise coefficient. These are Reynolds number = 130,000, the average tip (radial) clearance-to-gap ratio $\epsilon/g = 0.055$, and the ratio of axial clearance to the blade spacing $\Delta z/s = 0.38$. The Reynolds number is calculated based on the blade row inlet relative velocity and the chord length at the pitchline radius. The gap g and the blade spacing s represent a stage average at the pitchline radius in Figures 8.65 and 8.66.

Note that a higher stalling pressure rise is achieved in a compressor stage with a decreasing tip clearance as well as a decreasing axial spacing between the blade rows. The effect of blade stagger was significant on the stalling pressure rise capability of axial-flow compressor stages according to Koch (1981). The effect of stagger is related to a recovery potential of a total pressure deficit region (e.g., upstream wake) interacting with the stator

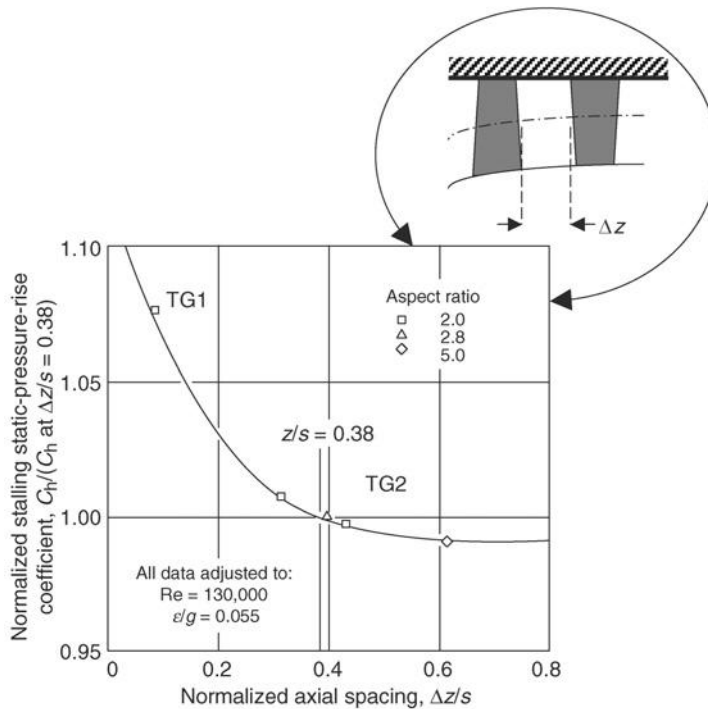
■ **FIGURE 8.64**
The effect of Reynolds number on stalling pressure rise coefficient of an axial-flow compressor stage (normalized by Reynolds number of 130,000). Source: Koch 1981. Reproduced with permission from ASME



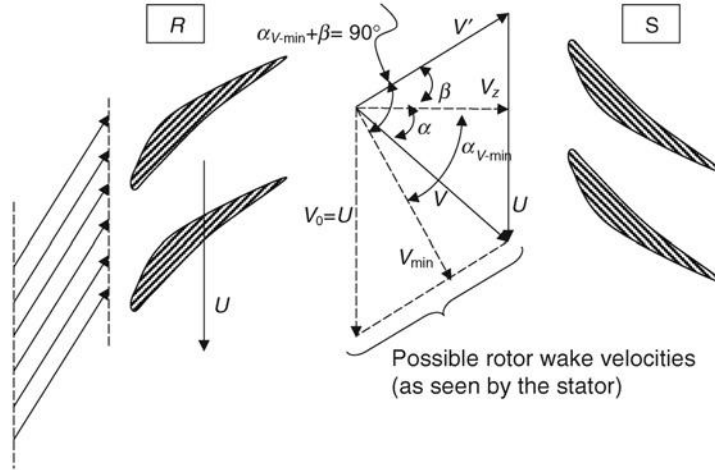
■ **FIGURE 8.65**
 The effect of tip clearance on the stalling pressure rise coefficient. Source: Koch 1981. Reproduced with permission from ASME



■ **FIGURE 8.66**
 The effect of axial spacing between rotor and stator blade rows on stalling pressure rise coefficient. Source: Koch 1981. Reproduced with permission from ASME



■ **FIGURE 8.67**
Velocity vector diagram upstream of the stator with possible upstream wake velocity vectors. Source: Adapted from Koch 1981. Reproduced with permission from ASME



blade row. Leroy Smith first identified this phenomenon in 1958. The velocity vector diagrams upstream of the stator are shown in Figure 8.67. Note that the minimum wake velocity as seen by the stator occurs when the angle between the relative velocity vector V' and the wake velocity vector is 90° . In case of zero wake velocity in the relative frame, the wake as seen by the stator is equal to U and is in the tangential direction. This point is shown as $V_0 = U$ in Figure 8.67.

The effect of low stagger (i.e., high flow coefficient) is seen in the small included angle between the relative and absolute velocity vectors $\alpha + \beta$, which will result in a low momentum wake velocity $V_{\min} \ll V$. With a low dynamic head associated with this flow, the low stagger stages seem more prone to stall than a high stagger counterpart. In a high stagger stage, that is, a low flow coefficient case, $\alpha + \beta > 90^\circ$; therefore, the upstream wake enters the stator with $V_{\text{wake}} > V$, hence a higher dynamic pressure fluid is less prone to stall. The observations of $\alpha + \beta$ and 90° and their impact on the loss recovery were made by Ashby in a discussion of Smith's (1958) paper. Here, we are alerted to the importance of the vector diagram in a compressor stage and its impact on its stall margin. Koch devised an *effective dynamic pressure factor* F_{ef} that accounts for the rotor wake interaction with the stator, that is, the effect of stagger on pressure recovery. The formulation of F_{ef} is presented by Koch to be

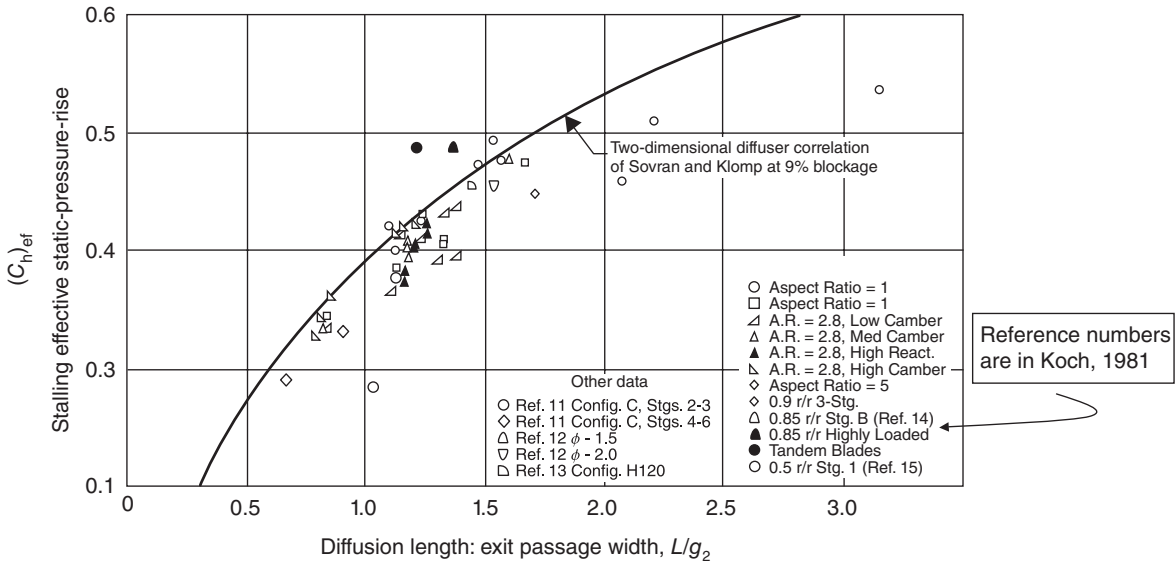
$$F_{\text{ef}} = \frac{V_{\text{ef}}^2}{V^2} = \frac{V^2 + 2.5V_{\min}^2 + 0.5V_0^2}{4V^2} \quad (8.196)$$

The minimum dynamic head is related to the included angle $(\alpha + \beta)$ of the stage vector diagram according to

$$\frac{V_{\min}^2}{V^2} = \sin^2(\alpha + \beta), \quad \text{if } (\alpha + \beta) \leq 90^\circ \text{ and } \beta \geq 0^\circ \quad (8.197a)$$

$$\frac{V_{\min}^2}{V^2} = 1.0, \quad \text{if } (\alpha + \beta) > 90^\circ \quad \text{High Stagger} \quad (8.197b)$$

$$\frac{V_{\min}^2}{V^2} = \frac{V_0^2}{V^2}, \quad \text{if } \beta < 0^\circ \quad \text{Low Stagger} \quad (8.197c)$$

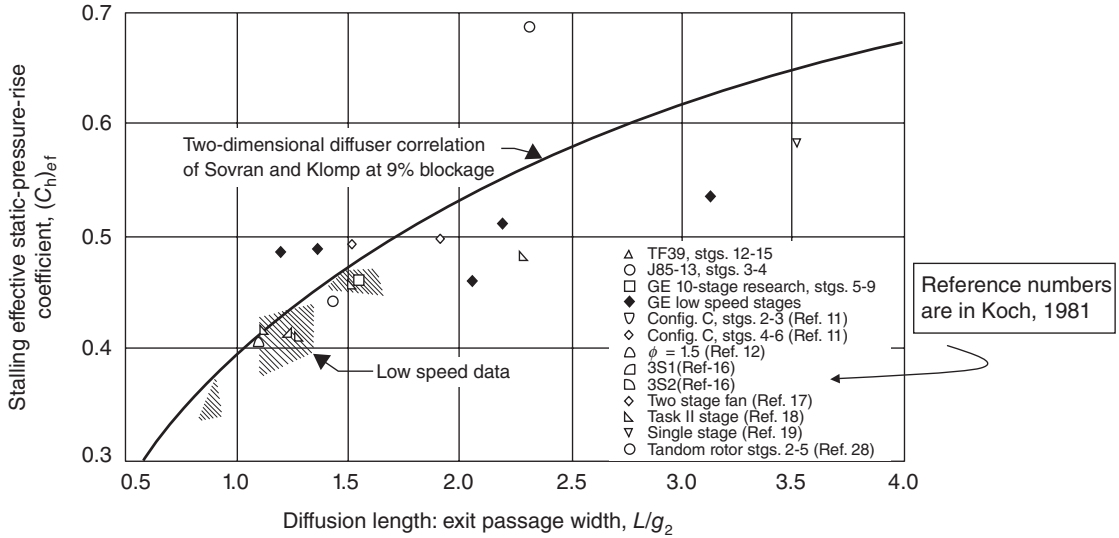


■ FIGURE 8.68 Correlation of effective static pressure rise coefficient at stall for low-speed compressor stages. Source: Koch 1981. Reproduced with permission from ASME

The procedure to account for the effects of Reynolds number, tip clearance, axial spacing, and stagger on stalling static pressure rise coefficient in a compressor stage is to first *adjust* the stalling pressure rise for Reynolds number other than 130,000 (via Figure 8.63), the tip clearance (to gap ratio) other than 5.5% (via Figure 8.64), and the axial spacing (to blade spacing) other than 0.38 (via Figure 8.65). Therefore, we first calculate the $(C_h)_{adj}$. The effect of stagger and the velocity vector diagram is now introduced through the *effective dynamic head factor* F_{ef} , which is multiplied by the free stream dynamic head of the stator, that is,

$$(C_h)_{ef} = (C_h)_{adj} \left[\frac{V_1'^2|_{Rotor} + V_1'^2|_{Stator}}{V_1'^2|_{Rotor} + F_{ef} \cdot V_1'^2|_{Stator}} \right] \quad (8.198)$$

Koch's stalling effective pressure rise correlation for low- and high-speed axial-flow compressor stages is shown in Figures 8.68 and 8.69, respectively. The maximum recovery of the two-dimensional diffuser for an inlet blockage of 9% of Sovran and Klomp (1967) marks the upper limit in Figures 8.68 and 8.69, which serves as an approximate stalling boundary for axial-flow compressor stages. We note that the stall margin correlation for the low-speed compressor predicts typically below 0.5 of static pressure recovery at stall. The high-speed compressor stages produce a higher effective stalling static pressure rise coefficient of up to ~ 0.55 . The case of a tandem rotor compressor with an L/g_2 of 2.33 poses the highest stalling static pressure recovery, that is, $\sim 23\%$ above the diffuser stall curve, as shown in Figure 8.69. The tandem blading serves as a means of flow control in a compressor rotor and the simple diffuser performance underpredicts the stall behavior of a compressor stage that employs flow control. An analogy of a tandem rotor compressor



■ **FIGURE 8.69** Correlation of effective static pressure rise coefficient at stall for high-speed compressor stages. Source: Koch 1981. Reproduced with permission from ASME

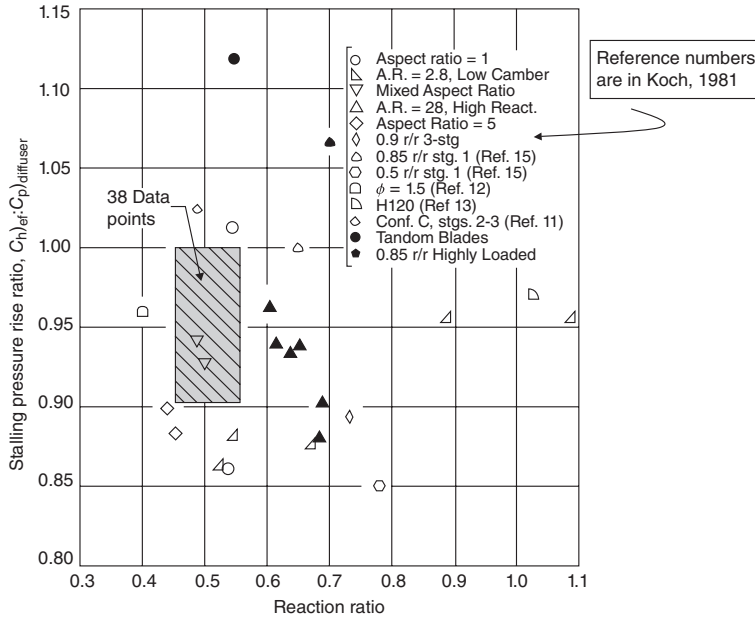
stage should be made with a wide-angle diffuser that employs splitter plates as a means of high static pressure recovery.

Koch demonstrates that effect of the stage reaction on the stalling pressure rise in axial-flow compressor is well predicted by the diffuser stall margin correlation of Figure 8.68 or 8.69. The range of stage reactions from 0.39 to 1.09 (where the stator accelerates the flow, like a turbine) is shown in Figure 8.70. It is surprising that over such a wide range of stage reaction, the stalling pressure rise in a compressor correlates with the diffuser predictions.

In a multistage high-speed compressor, the stagewise distribution of the static pressure rise at stall is compared with the stall margin correlation of Figure 8.71 (from Koch).

Figure 8.71 shows that in a multistage compressor, there is at least one or a group of stages that rises to the predicted level of stalling pressure according to the diffuser correlation. For example, the 10-stage research compressor operating at 95% speed at stall had its eighth stage reach/exceed the stall boundary as predicted by the correlation of Figure 8.69. The 16-stage TF39, at 97% speed, had stages 12 and 15 exceed the stall boundary and stages 13 and 14 operate within 96 percentile of the stall boundary. Note that we are not looking for a perfect match between the correlation and the stall pressure rise of every stage in a multistage compressor. We are rather interested in the trends and behavior of individual and groups of stages and their stall margin. In this context, the shaded symbols in Figure 8.71 represent the “critical” stages, which lie above 95 percentile of the stall boundary. These stages are likely to stall first and cause a breakdown of the flow in the rest of the compressor. The stalling pressure rise data in Figure 8.71 represent *actual* high-speed multistage compressor tests, which validate Koch’s semiempirical correlation presented in this section. The stall margin correlation based on the diffuser analogy has proven to be a valuable tool in the preliminary design stage of axial-flow compressors.

■ **FIGURE 8.70**
Effect of stage reaction on the ratio of the stalling pressure rise to a 2D diffuser pressure recovery. Source: Koch 1981. Reproduced with permission from ASME



We have taken the stalling effective pressure rise coefficient of Figures 8.68 and 8.69 and graphed a family of curves with 95%, 90%, . . . , 70% of the stall correlation (Figure 8.72). We have thus created a chart with 5% stall margin increments as a function of the stage-averaged diffusion length ratio L/g_2 . We note that increasing the diffusion length ratio L/g_2 , which points to either higher solidity or lower aspect ratio blading, helps with the stall margin. Wide chord blades also operate at a higher Reynolds number, which is beneficial to boundary layer stability, as evidenced in Figure 8.64. The minimum operational tip clearance of $\sim 1\%$ blade height and the minimum axial spacing between blade rows of ~ 0.25 axial chord also create higher static pressure rise in a compressor stage. Stage vector diagram affects the loss recovery ($\alpha + \beta \geq 90^\circ$) and thus stall static pressure rise.

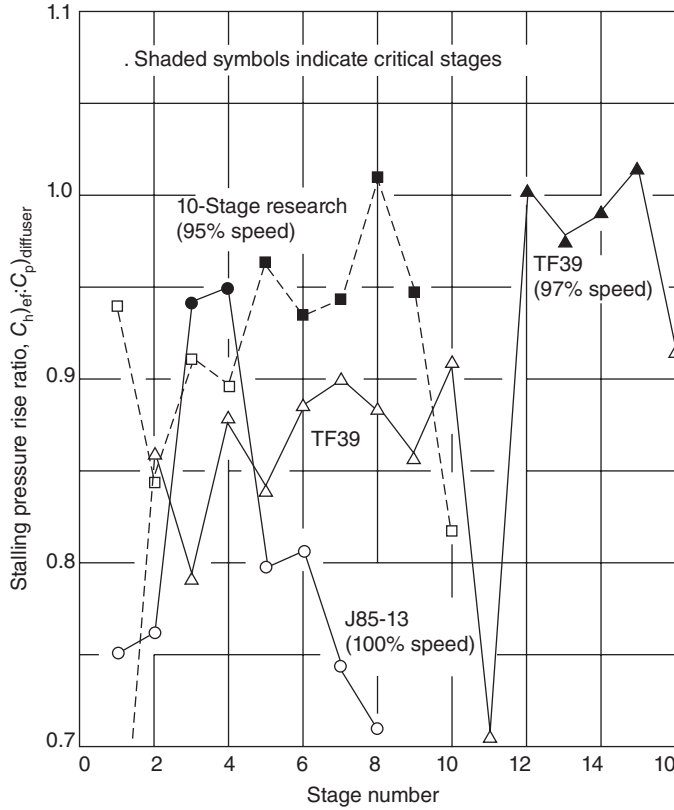
8.11 Multistage Compressor Starting Problem

The annulus flow area in a multistage compressor is designed based on the calculated density rise along the axis of the machine operating at the design point. The assumption of constant axial velocity, for example, implies that the channel area shrinks inversely proportional to the density rise, to conserve mass, namely,

$$\frac{A(z)}{A_1} = \frac{\rho_1}{\rho(z)} \tag{8.199}$$

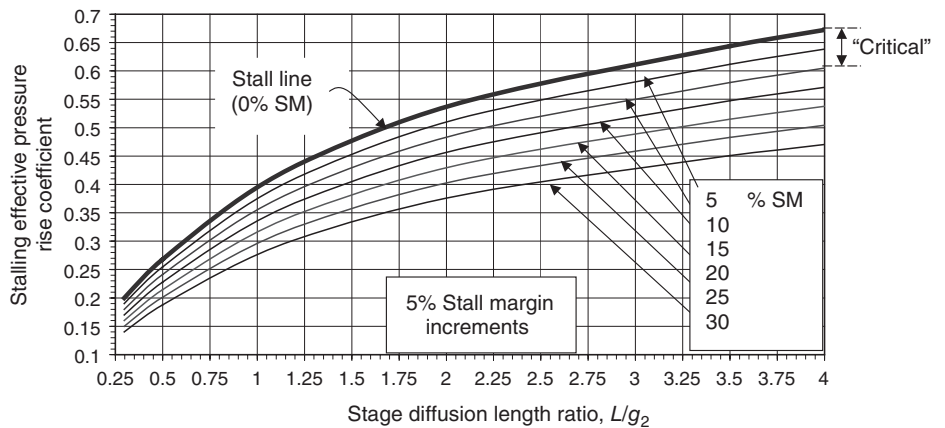
This behavior is schematically shown in Figure 8.73.

■ **FIGURE 8.71**
 Stall pressure rise, per stage, in a multistage compressor at high speed. Source: Koch 1981. Reproduced with permission from ASME

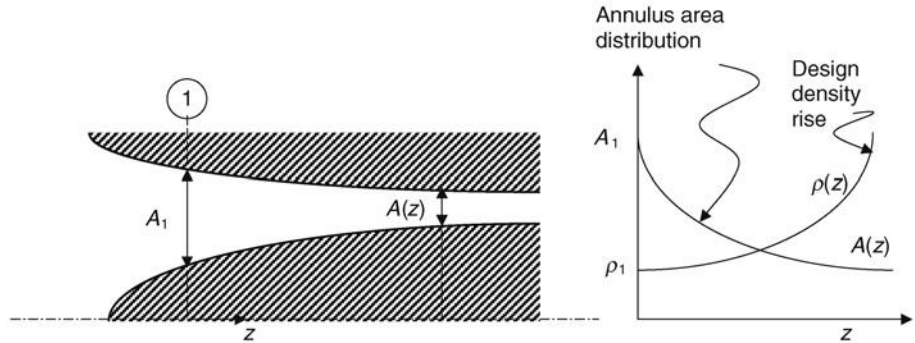


In the starting phase of a compressor, the mass flow rate is initially small, which means a higher loading for the front stages. The picture for the aft high-pressure stages is just the opposite of the front low-pressure stages. Initially, the compressor does not develop the density rise that it was designed to produce, hence with lower than design densities in the aft stages the axial velocity is increased to satisfy the continuity equation. Higher than the design axial velocity leads to a lower loading of the aft stages. Actually

■ **FIGURE 8.72**
 Axial-flow compressor stage stall margin (SM) chart with 5% stall margin increments

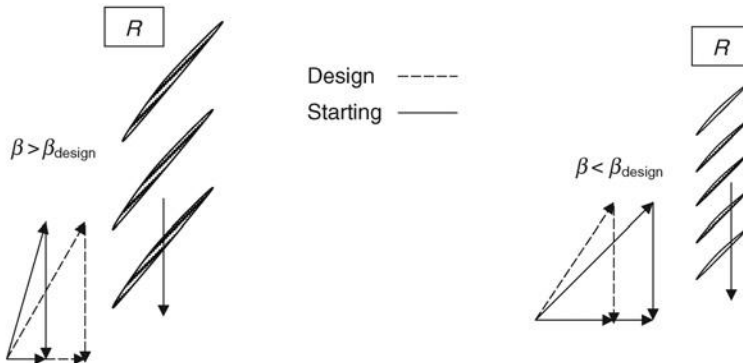


■ **FIGURE 8.73**
Flow annulus area and the density rise are inversely proportional in a multistage axial compressor



the aft stages would be *windmilling* and their blades operating in a separated flow. A comparison of the velocity triangles in the starting phase and the design point will help us understand the (starting) problem in a high-pressure compressor. Figure 8.74 shows the velocity triangles for the front and aft stages of a compressor. Note that the flow coefficient is lower than the design value for the front stages, and the flow coefficient is higher for the aft stages. We remember from the compressor performance map that with a reduction of flow coefficient the compressor can go into stall for a given shaft speed. With front stages not producing the design density ratio, the axial flow in the aft stages accelerates to conserve mass. Hence, the two ends of the compressor see the opposite flow fields and are subjected to opposite flow coefficients, that is, lower and higher than the design, respectively. However, the tendency for both front and aft stages is to stall in the starting phase of a high-pressure compressor.

The loading mismatch between the front and aft stages in the starting phase of a high-pressure axial compressor may be solved in several ways. Here we introduce three distinct approaches to the starting problem.



(a) Front stages see a higher incidence (loading), i.e., a lower flow coefficient ϕ

(b) Aft stages see a lower incidence (loading), i.e., a higher flow coefficient ϕ

■ **FIGURE 8.74** Velocity triangles at design and starting phases of a high-pressure compressor (a) Front stages see a higher incidence (loading), i.e., a lower flow coefficient ϕ (b) Aft stages see a lower incidence (loading), i.e., a higher flow coefficient ϕ

Proposition 1: Split shaft (or multispool shaft system)

Let the aft stages operate at a higher rotational speed than the front stages. This proposition aims at matching the relative flow angle to the rotor blades in the aft stages. Pratt & Whitney spearheaded the development of the split shaft concept in the United States in the 1950s. Today, all modern high-pressure compressors employ a two-to-three spool or shaft configuration to alleviate the problem of starting and improve compressor efficiency and stability. This method primarily attacks the aft stages, which would have been windmilling without a higher shaft speed, as in a single-shaft gas turbine engine. Rolls-Royce is the only engine company that has manufactured a production three-spool commercial engine, known as the RB 211, with several successful derivatives.

Proposition 2: Variable stators

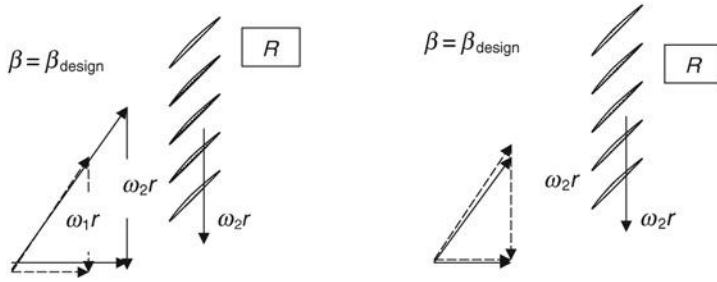
This proposition aims at adjusting the absolute flow angle (α) through a stator variable setting to improve the mismatch between the flow and the rotor relative flow angle β . GE-Aircraft Engines spearheaded the development of high-pressure compressors with the variable stator approach in the United States, also in 1950s. Today, modern high-pressure compressors use variable stators for the front several stages to help with the starting/off-design operation efficiency. This method primarily attacks the front stages. Although a variable stator benefits all stages of a compressor, its use is limited to the front few (say six) low-pressure stages as the sealing of hot gases through the variable stator seal poses an operational and maintenance problem on the high-pressure end of the compressor.

Proposition 3: Intercompressor bleed

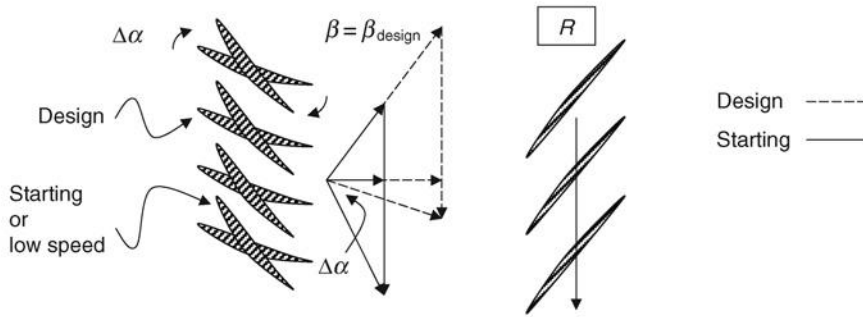
The windmilling operation of the aft stages is the result of high axial velocities through those stages. To cut down on excessive axial velocities, we may bleed off some mass flow in the intermediate stages of the compressor, the so-called intercompressor bleed. Therefore in the starting phase, bleed ports need to be opened to help the high-pressure end of the compressor to operate properly. This proposition represents a relatively low-cost method of starting compressors that does not employ either a split shaft or the variable stators. Stationary gas turbine power plants employ the intermediate bleed solution as a method of starting the compressor. This method attacks the aft as well as the front stages, as the bleed ports are located in the middle. Therefore, mass withdrawal causes a reduction in the axial velocity to the aft stages as well as lowering the backpressure for the front stages, hence increasing the flow speed in the machine. The ability to *tailor* the flow through the engine to improve overall efficiency, component stability, and provide cooling to accessories and engine components all speak in favor of intercompressor bleed. In fact, all modern gas turbine engines today employ intercompressor bleed/flow control. These methods are summarized in Figure 8.75.

8.12 The Effect of Inlet Flow Condition on Compressor Performance

Aircraft gas turbine engines operate downstream of an air intake system. The level of *distortion* that an inlet creates at the compressor face affects the performance and the stability of the compressor. First, what do we mean by *distortion*? In simple terms, distortion represents nonuniformity in the flow. The nonuniformity in total pressure as in boundary layers and wakes, the nonuniformity in temperature as in gun gas ingestion or thrust reverser flow ingestion and the nonuniformity in density, as created by hot gas ingestion are some of the different types of distortion. The common feature of all



(a) Multiple shaft allows for a higher rotational speed N_2 (b) Bleed allows for a reduced axial velocity



(c) A variable stator turns the flow in the direction of the rotor in the starting or low-speed operation

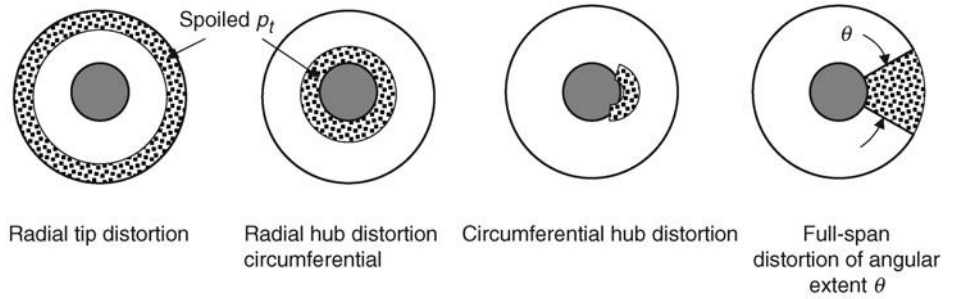
■ FIGURE 8.75 Three propositions on how to start a high-pressure compressor

different types of distortion is found in their destabilizing impact on the compressor performance. This means that all distortions reduce the stability margin of a compressor or fan, potentially to the level of compressor stall or the engine surge. The types of distortion are

1. Total pressure distortion $p_t(r, \theta)$
2. Total temperature distortion $T_t(r, \theta)$
3. Flow angle distortion $\alpha(r, \theta)$
4. Secondary flow – swirl at the engine face $C_{\theta 1}(r, \theta)$
5. Entropy distortion $s(r, \theta)$
6. Combinations of some or all of the above distortions.

The most common type of inlet distortion is the total pressure distortion that is caused by separated boundary layers in the inlet. Under normal operating conditions, the boundary layers in the inlet are well behaved and remain attached. However, if the boundary layer

■ **FIGURE 8.76**
Different types of total pressure distortion



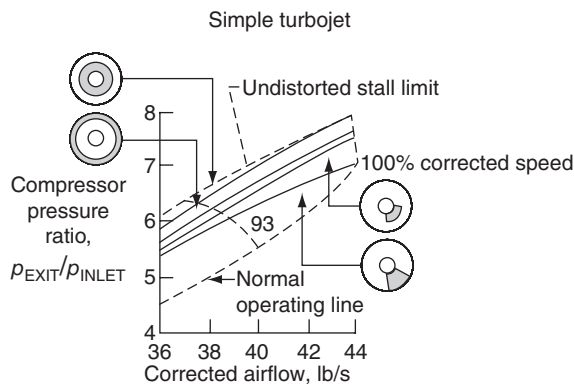
management system in a supersonic inlet, as in the bleed system, fails to react to an abrupt change in the flight operation (potentially due to a rapid combat maneuver), the flowfield at the engine face will contain large patches of low-energy, low-momentum flow that could cause flow separation in the front stage(s) of the fan or compressor. In describing the total pressure distortion and its impact on compressor performance, we divide the spatial extent of the spoiled flow according to its radial and circumferential extent, as shown in Figure 8.76.

These inlet total pressure distortion patterns may be simulated by installing screens of varying porosity upstream of the compressor or fan (typically one diameter upstream) in propulsion system ground test facilities. The distortion patterns generated by screens in a test set up in ground facilities represent the “steady-state” component of the distortion and thus lack the “dynamic” or transitory nature of the distortion encountered in real flight environment. The full description of distortion requires both the steady-state and the dynamic components, as in the study of turbulent flow requiring a mean and an rms level of the fluctuation.

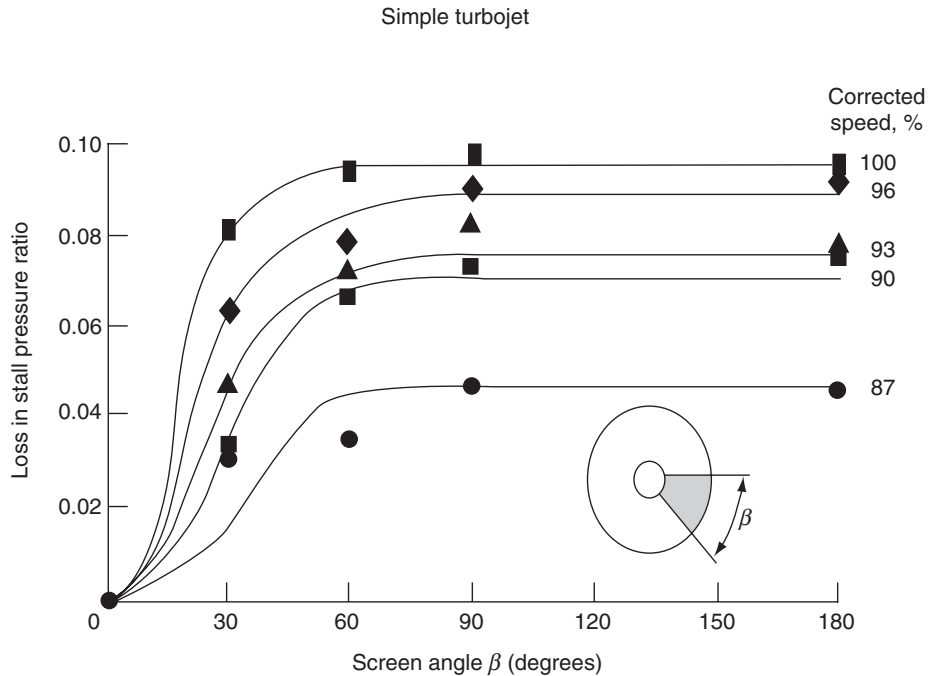
The results of a NASA-Glenn 10×10 supersonic wind tunnel study on the response of a simple turbojet engine (J-85) to steady-state inlet total pressure distortion are shown in Figure 8.77 (from Povolny *et al.*, 1970).

The normal operating line, the undistorted stall boundary, and two corrected shaft speeds of 100% and 93% design are shown in dashed lines. Four solid lines correspond to the stall boundaries of the four distortion patterns simulated at the compressor face

■ **FIGURE 8.77**
Effect of inlet total pressure distortion on compressor stability. Source: Povolny *et al.* 1970. Courtesy of NASA



■ **FIGURE 8.78**
Effect of the extent of circumferential spoiling on compressor performance. Source: Povolny et al. 1970. Courtesy of NASA

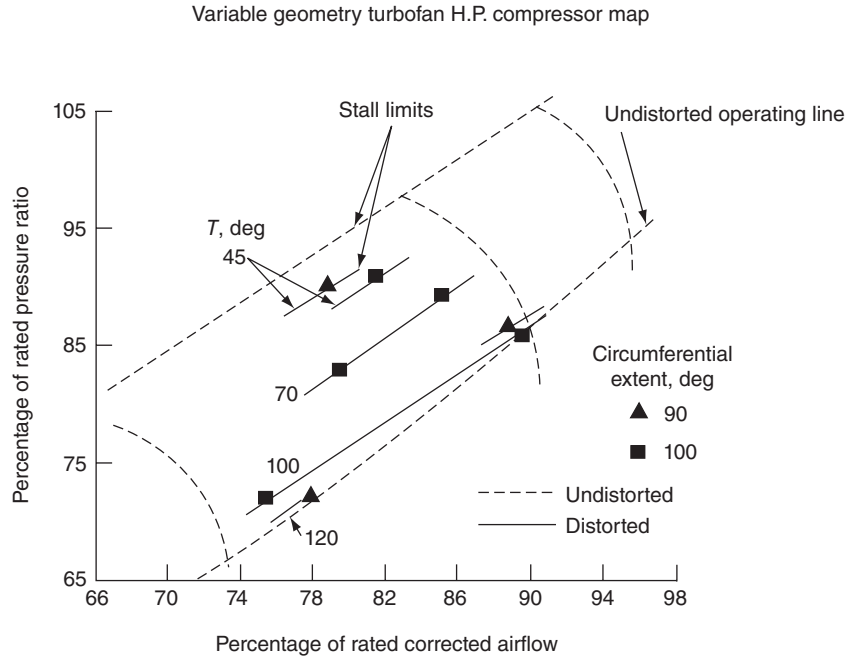


via screens. From having the least to the most impact on the stall margin deterioration, we identify the culprits as (1) radial hub, (2) radial tip, (3) circumferential hub, and (4) the full-span circumferential distortion, respectively. We also note that the full-span distortion at the 100% corrected speed operates at the stall boundary, that is, zero-stall margin! Further research identified a critical circumferential extent of the spoiled sector that causes the maximum loss in the stall pressure ratio of a compressor is at nearly 60° , as evidenced in Figure 8.78 (from Povolny *et al.*, 1970).

The loss in stall pressure ratio with circumferential inlet distortion reaches to $\sim 10\%$ at 100% corrected speed, as shown in Figure 8.78. At higher shaft speeds, the incidence angle in the spoiled sector is larger than at the lower shaft speed, thus the trend of higher loss of the stalling pressure ratio at higher shaft speeds becomes evident using simple velocity triangle arguments.

The temperature distortion also leads to a reduction in stall margin. In general, static temperature distortion in a flow brings about density nonuniformity, which creates a nonuniform velocity field. Consequently, it is impossible to create a static temperature distortion without creating other forms of nonuniformity, for example, density, velocity, total pressure, in the flow. To quantify the impact of a spatial temperature distortion on engine stall behavior, NASA researchers have conducted experiments with representative data shown in Figure 8.79 (from Povolny *et al.*, 1970). The undistorted operating line, stall limit, and different shaft speeds are shown in dashed lines. Data points corresponding to the effect of temperature distortions of $45\text{--}120^\circ\text{F}$ on the stall behavior of a variable geometry turbofan engine high-pressure compressor are plotted in solid lines. The circumferential extents of the temperature distortions were 90 and 100° in different tests. A 100°F distortion of $\sim 90\text{--}100^\circ$ circumferential extent is seen to stall the high-pressure compressor operating at its 90% corrected flow.

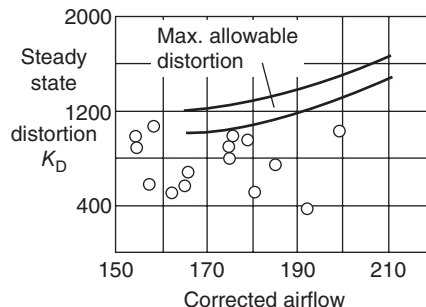
■ **FIGURE 8.79**
Effect of spatial
temperature
distortions on engine
stall. Source: Povolny
et al. 1970. Courtesy of
NASA



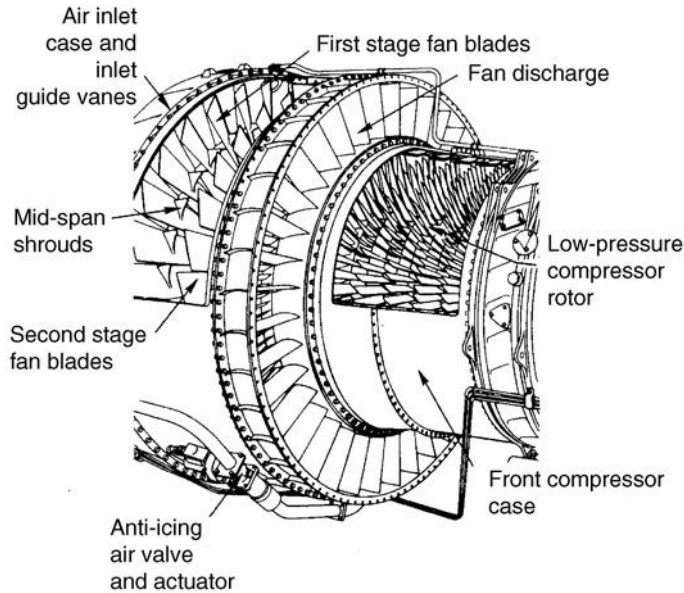
The inadequacy of steady-state distortion simulation in a wind tunnel is best seen in Figure 8.80 showing F-111 flight test data of compressor stall with TF-30 engine. A steady-state distortion parameter K_D is graphed at different corrected airflows through the engine, and a band of maximum allowable distortion based on previous wind tunnel tests is shown to miss the mark of in-flight compressor stall data by a large margin (from Seddon and Goldsmith, 1985). The culprit is identified as the *dynamic distortion*.

The steady-state distortion parameter K_D expresses a weighted average of engine face total pressure distortion pattern (circumferential and radial) recorded by an engine face rake system composed of several radial pitot tube measurements. For a mathematical description of K_D and other distortion parameters, Hercock and Williams (1974) may be consulted. In addition, Farr and Schumacher (1974) present evaluation methods of dynamic distortion in F-15 aircraft. Schweikhand and Montoya (1974) treat research instrumentation and operational aspects in YF-12. These references are recommended for further reading.

■ **FIGURE 8.80**
In-flight measurements
of engine surge.
Source: Seddon and
Goldsmith 1985.
Reproduced by
permission from AIAA



■ **FIGURE 8.81**
Dual-compressor rotor
with two front fan
stages. Source:
Reproduced by
permission of United
Technologies
Corporation, Pratt &
Whitney



8.13 Isometric and Cutaway Views of Axial-Flow Compressor Hardware

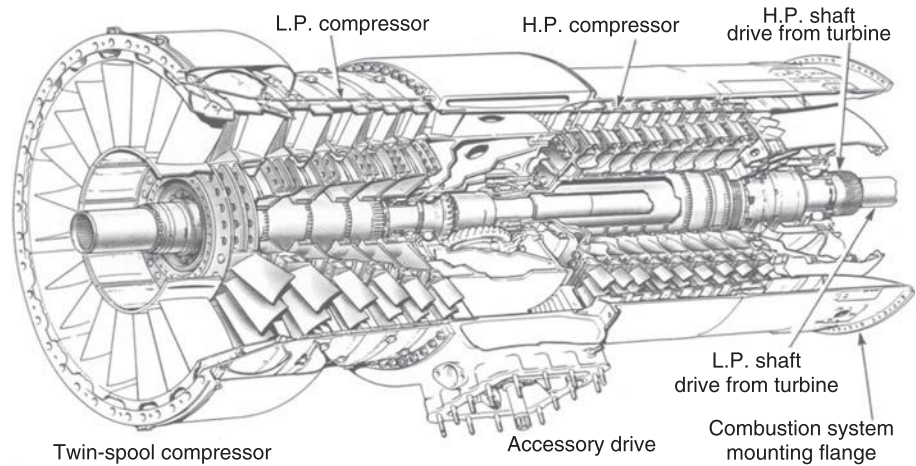
To meet the real world, engineers need to spend time with the real hardware. Isometric and cutaway views of the hardware provide for a three-dimensional feel but may not be a substitute for the cutaway of a real engine (or its components) in the laboratory. The real engine, albeit old and surplus, shows real fasteners, components assembly, manufacturing tolerances; some operational degradation, for example, wear, on the rotor blade tips, shows labyrinth seals between rotating and stationary parts; it shows signs of erosion in the compressor and turbine and perhaps corrosion in the hot section. A visual inspection and a feel of the compressor and turbine blades show the turbine blades receive heavy deposits from the combustor (and its fuel additives) and give a new meaning to “surface roughness,” which will not feel “hydraulically smooth.”

Having pointed out some of the advantages of real hardware, let us examine some isometric and cutaway views of axial-flow compressors, designed, built, tested, and flown on aircraft in this section. Figure 8.81 is taken from a manual by Pratt & Whitney Aircraft (1980), whereas Figures 8.82–8.84 are taken from Rolls-Royce’s *The Jet Engine* (2005). Figure 8.81 shows a two-stage fan and the low-pressure compressor rotor. Mid-span shrouds prevent the first bending mode of the first fan rotor blades. The anti-icing air valve and the actuator point to an operational need of the aircraft (i.e., flight under icing condition) and demands on the compressor air.

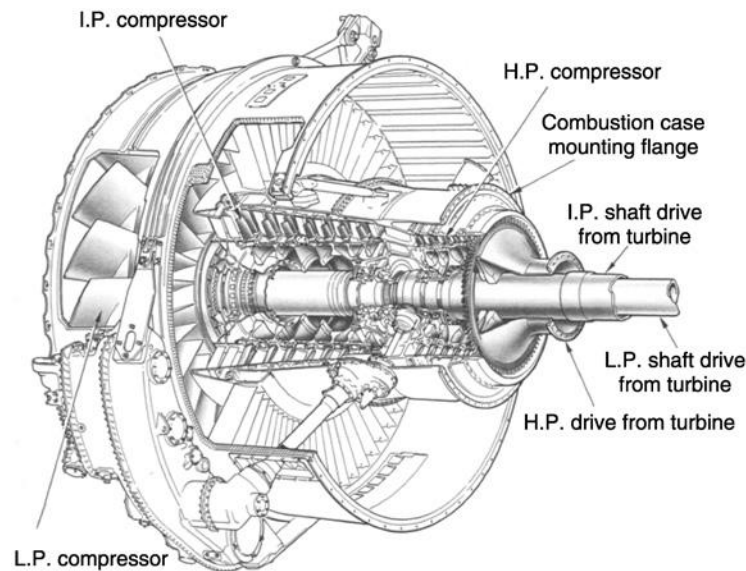
8.14 Compressor Design Parameters and Principles

In this section, we present design guidelines that are useful in the preliminary design of axial-flow compressors. The approach to turbomachinery design in textbooks is neither unique nor exact. In general, we use the lessons learned from our predecessors and the

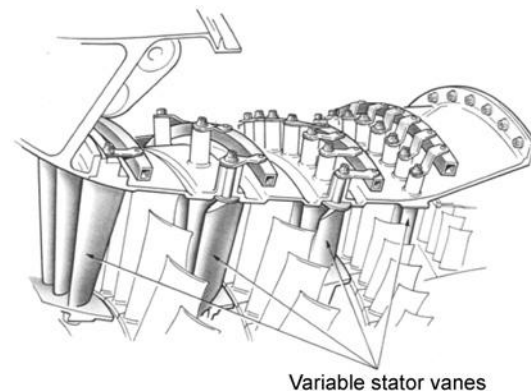
■ **FIGURE 8.82**
A twin-spool
compressor. Source:
The Jet Engine, 2005.
Reproduced by
permission from The
Jet Engine, Copyright
Rolls-Royce plc 2005



■ **FIGURE 8.83**
A triple-spool
compressor. Source:
The Jet Engine, 2005.
Reproduced by
permission from The
Jet Engine, Copyright
Rolls-Royce plc 2005



■ **FIGURE 8.84**
Typical variable-stator
vanes. Source: The Jet
Engine, 2005.
Reproduced by
permission from The
Jet Engine, Copyright
Rolls-Royce plc 2005

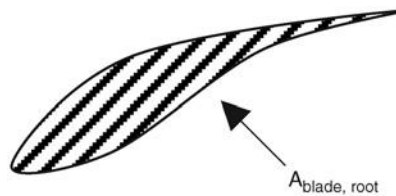


invaluable contributions of NASA and open literature, which often come from academia and industry. One possible approach to compressor design is outlined in steps that are particularly useful for students who want to learn and practice their turbomachinery design skills.

We propose to design an axial-flow compressor for a design-point mass flow rate and pressure ratio. Here, we first review the steps and in the next section we design an axial compressor at the pitchline. We start the design process by choosing

1. Axial Mach number at the compressor/fan face is $M_{z1} \sim 0.5$
2. Flow area at the compressor face is $A_1 = \pi r_{t1}^2 - (r_{h1}/r_{t1})^2$ that sizes the engine and thus establishes the mass flow rate
3. Typical hub-to-tip radius ratio, r_{h1}/r_{t1} is ~ 0.4 , a little less or more (may be up to ~ 0.5 or as low as ~ 0.3). The relative tip Mach number M_{T1} establishes the tip radius
4. $M_{T1} = \sqrt{M_{z1}^2 + M_{T1}^2}$
 - M_{T1} , tip tangential Mach number, that is, $(\omega r_t)/a_1$ is in excess of sonic
 - M_{T1} is supersonic, ~ 1.2 to ~ 1.5 (remember that $M_z \sim 0.5$)
5. Thickness-to-chord ratio varies from $\sim 10\%$ in the subsonic hub region to $\sim 3\%$ in the supersonic tip region, linearly varying in between
6. The Reynolds number based on chord has to be $> 300,000$ (in relative frame), at altitude. This establishes the minimum chord length for turbulent boundary layer at all altitudes, the other parameter contributing to the chord length is the blade aspect ratio and bending stresses. Often chord length is several times bigger than that required for the 300,000 Reynolds number at altitude
7. Centrifugal stress at the blade root (i.e., the hub) is calculated based on the simple formula

$$\sigma_{c,root} \equiv \frac{F_{c, root}}{A_{blade-root}} \tag{8.200}$$



The centrifugal force is the integral of mv^2/r , which is $m\omega^2 r$, that is,

$$F_{c, root} = \int_{r_h}^{r_t} \rho_{blade} \cdot A(r) \omega^2 r dr \tag{8.201}$$

where ρ_{blade} is blade material density and $A(r)$ is the blade cross-sectional area as a function of span.

$$\sigma_c = \frac{1}{A_h} \int_{r_h}^{r_t} \rho_{\text{blade}} \cdot A_b(r) \omega^2 r dr \quad (8.202)$$

$$\frac{\sigma_c}{\rho_{\text{blade}}} = \frac{\omega^2}{A_h} \int_{r_h}^{r_t} A_b(r) r dr = \omega^2 \int_{r_h}^{r_t} \frac{A_b}{A_h} r dr \quad (8.203)$$

$$\frac{\sigma_c}{\rho_{\text{blade}}} = \omega^2 \int_{r_h}^{r_t} \frac{A_b}{A_h} r dr \quad (8.204)$$

The blade area distribution along the span, $A_b(r)/A_h$, is known as *taper* and is often approximated to be a linear function of the span. Therefore, it may be written as

$$A_b = A_h - \frac{r - r_h}{r_t - r_h} (A_h - A_t) \rightarrow \frac{A_b}{A_h} = 1 - \frac{r - r_h}{r_t - r_h} \left(1 - \frac{A_t}{A_h} \right) \quad (8.205)$$

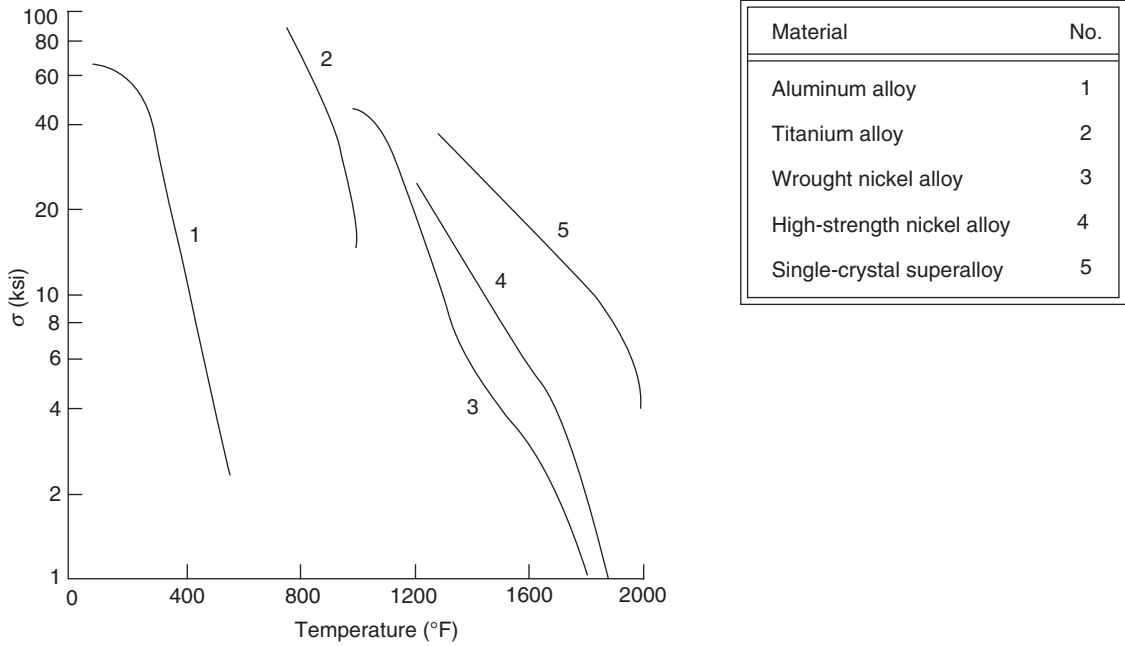
We may substitute $A_b(r)/A$ in the integral and proceed to integrate; however, a customary approximation is often introduced that replaces the variable r by the pitchline radius r_m . The result is

$$\frac{\sigma_c}{\rho_{\text{blade}}} = \frac{\omega^2 A}{4\pi} \left(1 + \frac{A_t}{A_h} \right) \quad (8.206)$$

The taper ratio A_t/A_r is ~ 0.8 – 1.0 . Therefore, the ratio of centrifugal stress to the material density is related to the square of the angular speed, the taper ratio, and the flow area, $A = 2\pi r_m (r_t - r_h)$. Equation 8.206 is the basis of the so-called AN^2 rule, where the RHS is related to the size (i.e., A) of the machine and the square of the angular speed (i.e., N^2), and the LHS is related to material property known as specific strength.

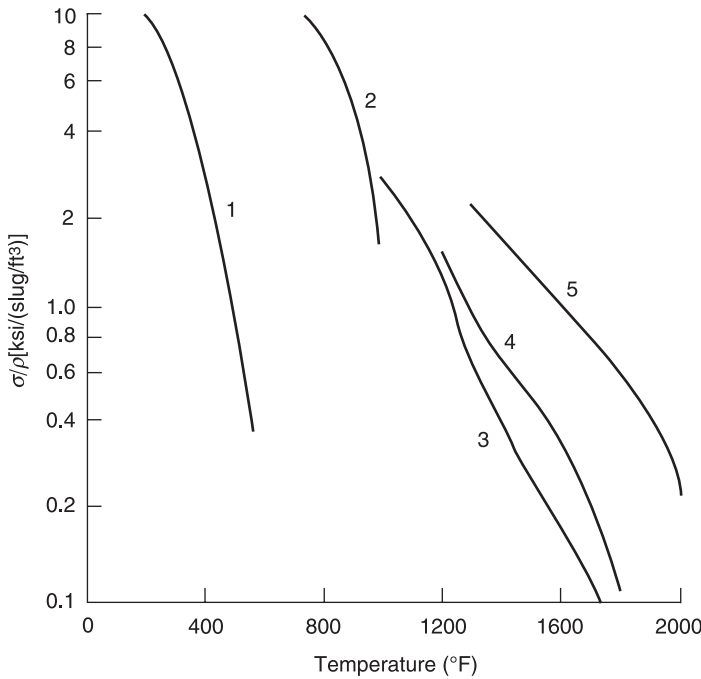
The material parameter of interest in a rotor is the *creep rupture strength*, which identifies the maximum tensile stress tolerated by the material for a given period of time at a specified operating temperature. Based on the 80% value of the allowable 0.2% creep in 1000 h for aluminum alloys and the 50% value of the allowable 0.1% creep in 1000 h for other materials, Mattingly, Heiser, and Pratt (2002) have graphed Figures 8.85 and 8.86. They show the allowable stress and the allowable specific strength of different engine materials as a function of temperature

8. The solidity at the pitchline $\sigma_m \sim 1$ to 2
9. The degree of reaction at the pitchline may be chosen to be ${}^\circ R_m \sim 0.5$ or 0.6 for subsonic sections and considerably higher (e.g., 0.8) for the supersonic portion of the blade. This choice specifies the $C_{\theta 2,m}$. We can use this information along with Euler turbine equation to establish the rotor-specific work at the pitchline



■ FIGURE 8.85 Allowable stress versus temperature for typical engine materials. Source: Mattingly, Heiser, and Pratt 2002. Reproduced with permission from AIAA

■ FIGURE 8.86 Allowable strength-to-weight ratio for typical engine materials. Source: Mattingly, Heiser, and Pratt 2002. Reproduced with permission from AIAA



as well as the stagnation temperature rise, that is, we get T_{12m} . The choice of $^\circ R$ is less critical than D -factor or de Haller criterion

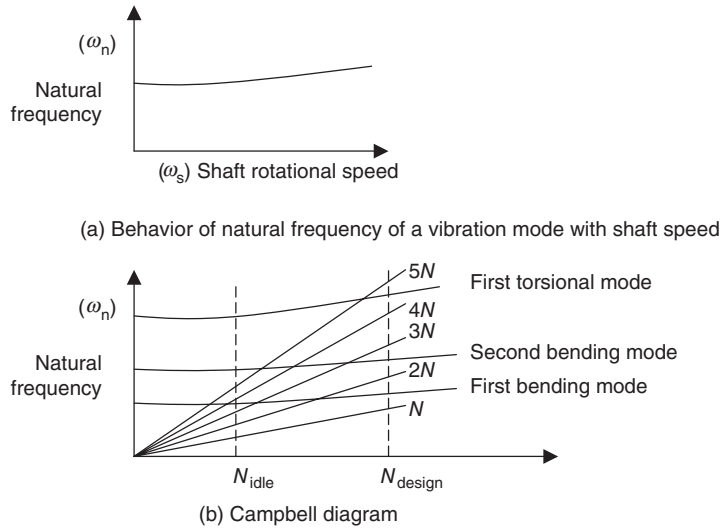
10. The D -factor at the pitchline should be ≤ 0.5 or 0.55 , often a quick check on the acceptable level of diffusion is made using the de Haller criterion that limits diffusion to a level corresponding to $W_2/W_1 \geq 0.72$
11. The choice of the vortex design, that is, $C_\theta(r)$, establishes the degree of reaction and D -factor at other radii, which we examine closely. It is acceptable for the degree of reaction to deviate from 0.5 , but we do not want it to become negative in a compressor (i.e., it then behaves like a turbine!). The D -factor has to remain below the critical value of ~ 0.5 (or 0.55). We may iterate on the vortex design choice in order to get these parameters right
12. The polytropic efficiency is assumed to be ~ 0.90 , that is, $e_c \sim 0.90$, which in combination with T_1 ratio gives p_t ratio, that is, we get total pressure at the pitchline at station 2, downstream of the rotor
13. To get the flow parameters downstream of the stator, we preserve T_1 and calculate p_{t3} based on an assumed ϖ_s of ~ 0.04 – 0.05 ; also the idea of repeated stage gives us the α_3
14. We assume the axial velocity remains constant throughout the compressor (at the design radius, i.e., the pitchline). This is a preliminary design choice
15. Bending stresses on a cantilevered blade, under aerodynamic loading, is estimated (by Kerrebrock, 1992) to be

$$\frac{\sigma_{\text{bending}}}{p} \approx \left(\frac{C_z}{U_t}\right) (\tau_s - 1) \left(\frac{s}{2c}\right) \left(\frac{r_t}{t_{\text{max}}}\right)^2 \quad (8.207)$$

Bending stress is, therefore, proportional to gas pressure, flow coefficient at the tip, stage total temperature ratio, and to the square of tip radius-to-thickness ratio. Bending stress is also inversely proportional to solidity

16. Thermal stresses are often small in axial-flow compressors and fans; however, they are significant in the turbine section. Also, the aft stages of high-pressure compressors in modern gas turbine engines operate at high gas temperatures, such as $T_{\text{gas}} \sim 850$ – 900 K, which require special attention to thermal strains and tip clearance, as well as total stress (i.e., the sum of centrifugal, bending, and thermal) at the hub
17. Blades as cantilevered structures attain diverse mode shapes, such as first bending, second bending, first torsional, coupled first bending and torsional, as well as higher modes of vibration. Each mode shape has its own natural frequency ω_n . The effect of blade rotation is to *stiffen* the structure and thus raise these natural frequencies. The shaft and the discs also exhibit their natural vibrational mode shapes and frequencies. To avoid resonance between these frequencies and the shaft rotational speed (and its multiples), a frequency diagram, known as *Campbell diagram* (Figure 8.87), is generated to examine possible match points between these frequencies inherent in the compressor, that is, in the natural modes and rotor shaft frequency. Kerrebrock (1992), Wilson and Korakianitis (1998), and Mattingley, Heiser, and Pratt (2002) provide a detailed account of engine structure.

■ **FIGURE 8.87**
Frequency diagram
showing possible
resonance condition
between the dominant
vibration modes and
multiples of shaft
frequency



8.14.1 Blade Design – Blade Selection

For blade design, we need to estimate the following angles:

1. Incidence angle i
2. Deviation angle δ^* $\delta^* = m\varphi/\sqrt{\sigma}$

The incidence angle is estimated at the location of minimum loss, from cascade data that is known as $i_{optimum}$. Typically, optimum incidence angle is $\sim -5^\circ$ to $+5^\circ$.

Iteration loop

The deviation angle is first estimated from the simple Carter’s rule:

$$\delta^* \approx \frac{\Delta\beta}{4\sqrt{\sigma}} \tag{8.208}$$

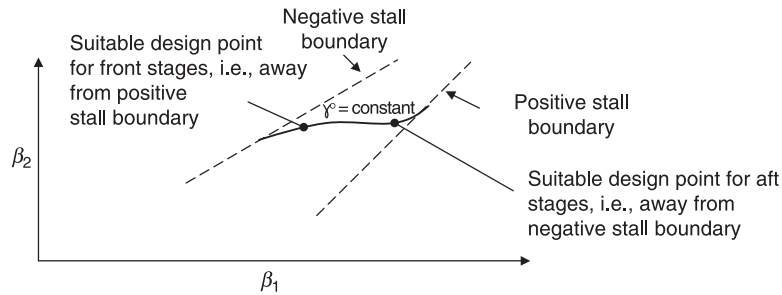
which is based on the net flow turning and the coefficient “ m ” in Carter’s formula is taken to be 0.25.

Also, based on the inlet and exit flow angles, we may use the (NACA 65-series) cascade correlation data of Mellor (Appendix I) to identify a suitable 65-series cascade geometry that gives an adequate stall margin. Note that the front and aft stages of a multistage compressor or fan face different stall challenges; for example, the front stages are more susceptible to positive stall and the aft stages are more susceptible to negative stall. Therefore, we may choose the design point to be farther away from the two stall boundaries for front and aft stages. Figure 8.88 is a definition sketch for the design point selection.

The optimum incidence angle is defined (by Mellor) to be at the point of lowest profile loss, although some authors prefer the optimum incidence to correspond to the angle where lift-to-drag ratio is at its maximum. Here, we adopt Mellor’s definition, due to its ease of use. The cascade loss data, as shown in Figure 8.22, can be used to arrive at the i_{opt} .

Johnsen and Bullock (1965) in NASA SP-36 outline optimum incidence estimation based on cascade data correlations for different profile types and profile thicknesses. This reference may be used for more accurate estimation of the incidence angle. From the inlet flow and an estimate of the optimum incidence angle, we calculate the leading-edge

■ **FIGURE 8.88**
Definition sketch for suitable design points for the front and aft stages of a multistage compressor or fan



angle on the mean camber line (MCL), κ_1 , and from the exit flow angle and deviation we calculate the blade angle at the T.E.

$$i \equiv \beta_1 - \kappa_1 \quad \longrightarrow \quad \kappa_1 \equiv \beta_1 - i$$

$$\delta^* \equiv \beta_2 - \kappa_2 \quad \longrightarrow \quad \kappa_2 \equiv \beta_2 - \delta^* \quad \longrightarrow \quad \varphi \equiv \kappa_1 - \kappa_2$$

The iteration loop on the deviation angle may be initiated at this point, since we have calculated a camber angle and we may now use the expanded version of the Carter's rule:

$$\delta^* = m\varphi / \sqrt{\sigma}$$

Although we have introduced a possible iteration loop on the deviation angle, in the preliminary stage of the compressor design it is acceptable to use the simple formula of Carter for deviation.

The supersonic section is designed based on

- Double-circular arc (DCA) blades
- J-profile design
- Multiple-circular arc design (MCA).

These designs are described in Cumpsty (1989), Schobeiri (2004), and Wilson and Korakianitis (1998).

8.14.2 Compressor Annulus Design

The annulus flow area shrinks inversely proportional to the rising fluid density for a constant axial velocity, that is,

$$A(z)/A_1 = \rho_1 / \rho(z) \quad \text{for} \quad C_z = \text{constant} (\text{say } \sim 500 \text{ ft/s or } 150 \text{ m/s})$$

We can calculate density rise per stage (at the pitchline) from the pressure and temperature rise and the use of the perfect gas law. This is an approximate method, but is adequate for the preliminary design purposes.

Common practices are

- Keep the casing, that is, the tip, radius constant, therefore the information about the annulus area gives the hub radius
- Keep the hub radius constant and thus calculate the tip radius from the annulus area
- Keep the pitchline radius constant, which then shrinks the tip and hub equally, and we can calculate those from the annulus area

- Keep the axial gap between the rotor and stator blade rows to approximately $0.23\text{--}0.25 c_z$ (i.e., about one quarter axial chord length gap between blade rows).

8.14.3 Compressor Stall Margin

Compressor stall margin may be established based on the use of Koch equivalent diffuser model of the compressor blade passage. This is rather laborious, but produces good results. We start with the equivalent enthalpy rise coefficient C_h (for notation, see section 8.10).

Note that the difference between U_1 and U_2 across the rotor (in the numerator) is due to streamline shift in the radial direction. We further correct for Reynolds number, tip clearance gap, and the axial blade spacing other than the nominal values that are used in Koch’s stall margin correlations. The correction factors are in Figures 8.64–8.66. Finally, we correct the adjusted enthalpy rise coefficient for the effect of stagger and the velocity vector diagram (wake effect) to arrive at the *effective* static enthalpy rise coefficient according to

$$(C_h)_{ef} = (C_h)_{adj} \left[\frac{V_1'^2|_{Rotor} + V_1^2|_{Stator}}{V_1'^2|_{Rotor} + F_{ef} \cdot V_1^2|_{Stator}} \right]$$

The critical stalling pressure rise is shown in Figure 8.72 as “stall line” or the case of 0% stall margin.

Guidelines on the Range of Compressor Parameters		
Parameter	Range of values	Typical value
Flow coefficient ϕ	$0.3 \leq \phi \leq 0.9$	0.6
D-Factor	$D \leq 0.6$	0.45
Axial Mach number M_z	$0.3 \leq M_z \leq 0.6$	0.55
Tip Tangential Mach Number, M_T	1.0–1.5	1.3
Degree of reaction	$0.1 \leq \circ R \leq 0.90$	0.5 (for $M < 1$)
Reynolds number based on chord	$300,000 \leq Re_c$	>500,000
Tip relative Mach number (1st Rotor)	$(M_{1r})_{tip} \leq 1.7$	1.3–1.5
Stage average solidity	$1.0 \leq \sigma \leq 2.0$	1.4
Stage average aspect ratio	$1.0 \leq AR \leq 4.0$	<2.0
Polytropic efficiency	$0.85 \leq e_c \leq 0.92$	0.90
Hub rotational speed	$\omega r_h \leq 380 \text{ m/s}$	300 m/s
Tip rotational speed	$\omega r_t \sim 450\text{--}550 \text{ m/s}$	500 m/s
Loading coefficient	$0.2 \leq \psi \leq 0.5$	0.35
DCA blade (range)	$0.8 \leq M \leq 1.2$	Same
NACA-65 series (range)	$M \leq 0.8$	Same
De Haller criterion	$W_2/W_1 \geq 0.72$	0.75
Blade leading-edge radius	$r_{L.E.} \sim 5\text{--}10\% \text{ of } t_{max}$	5% t_{max}
Compressor pressure ratio per spool	$\pi_c < 20$	up to 20
Axial gap between blade rows	$0.23 c_z \text{ to } 0.25 c_z$	$0.25 c_z$
Aspect ratio, fan	$\sim 2\text{--}5$	<1.5
Aspect ratio, compressor	$\sim 1\text{--}4$	~ 2
Taper ratio	$\sim 0.8\text{--}1.0$	0.8

EXAMPLE 8.8

Design an axial-flow compressor with the following design point parameters:

1. Takeoff at ambient condition

$$T_0 = 25^\circ\text{C} (298 \text{ K}), \quad p_0 = 101 \text{ kPa},$$

$$\gamma = 1.4, \quad c_p = 1004 \text{ J/kg} \cdot \text{K}, \quad M_0 = 0$$

2. Overall compressor pressure ratio is 20
3. Polytropic efficiency is assumed constant along the compressor, $e_c = 0.90$
4. Mass flow rate is 100 kg/s

Design Choices

No IGV
Repeated stage
Constant axial velocity C_z

Calculate

Compressor

annulus geometry at the inlet and exit
number of stages and stage pressure ratio

First Stage

Reynolds number based on chord
blade section design at the pitchline

SOLUTION

The design axial Mach number at the compressor face is assumed to be

$$M_{z1} = 0.5$$

The static temperature at the engine face is

$$T_1 = T_{t1} / [1 + (\gamma - 1)M_1^2 / 2]$$

$$= 298 \text{ K} [1 + 0.2(0.5)^2] \cong 283.8 \text{ K}$$

$$a_1 = \sqrt{(\gamma - 1)c_p T_1} = 337.6 \text{ m/s}$$

Therefore, the axial velocity is $C_{z1} \cong 168.8 \text{ m/s}$.

The static pressure at the engine face is

$$p_1 = p_{t1} / [1 + (\gamma - 1)M_1^2 / 2]^{\gamma/(\gamma-1)}$$

$$= 101 \text{ kPa} / [1 + 0.2(0.5)^2]^{3.5} \cong 85.14 \text{ kPa}$$

The static density at engine face is

$$\rho_1 = p_1 / RT_1$$

The gas constant $R = (\gamma - 1)c_p / \gamma$, which gives $R = 286.86 \text{ J/kg} \cdot \text{K}$ and the static density at the engine face is

$$\rho_1 \cong 1.046 \text{ kg/m}^3$$

The continuity equation for steady, uniform flow is

$$\dot{m} = \rho AV = \rho_1 A_1 C_{z1}$$

We calculate the flow area at the engine face

$$A_1 = (100 \text{ kg/s}) / (1.046 \text{ kg/m}^3) / (168.8 \text{ m/s})$$

$$\cong 0.56644 \text{ m}^2$$

The flow area at the engine face may be written in terms of the tip radius and hub-to-tip radius ratio, according to

$$A_1 = \pi r_{t1}^2 \left[1 - \left(\frac{r_{h1}}{r_{t1}} \right)^2 \right]$$

Here, we enter our next assumption, i.e., we choose the hub-to-tip radius ratio at the first stage to be

$$\frac{r_{h1}}{r_{t1}} = 0.5$$

This assumption along with the area A_1 gives the tip radius r_{t1} from the above equation, i.e., we calculate tip radius at the engine face to be

$$r_{t1} = \sqrt{A_1 / \pi \left[1 - \left(\frac{r_{h1}}{r_{t1}} \right)^2 \right]} \cong 0.49 \text{ m}$$

Obviously, our hub radius is half the tip radius by design choice, i.e.,

$$r_{h1} \cong 0.245 \text{ m}$$

Now, let us calculate the compressor discharge condition. The exit total pressure is 20 times the inlet total pressure therefore,

$$p_{t,exit} = 20(101 \text{ kPa}) = 2,020 \text{ kPa}$$

The compressor temperature and pressure ratio are related via the polytropic efficiency following

$$\tau_c = \pi_c^{(\gamma-1)/e_c\gamma}$$

Therefore, $\tau_c \approx 2.5884$, which gives the discharge total temperature to be

$$T_{t,exit} = 771.3 \text{ K}$$

We assume the compressor discharge is swirl free and since we had also assumed the axial velocity to be constant along the compressor, we know that

$$C_{exit} = C_{z,exit} = \text{Constant} = 168.8 \text{ m/s}$$

We calculate the static temperature of the gas at compressor discharge, T_{exit} , according to

$$T_{exit} = T_{t,exit} - C_{exit}^2 / 2c_{p,exit}$$

Assuming a calorically perfect gas, $c_p = 1004 \text{ J/kg} \cdot \text{K} = \text{constant}$ and, therefore,

$$T_{exit} = 757.14 \text{ K}$$

The speed of sound at the exit is

$$a_{exit} = \sqrt{(\gamma - 1)c_p T_{exit}} \approx 551.4 \text{ m/s}$$

Thus, the exit Mach number at the compressor discharge is

$$M_{exit} = 168.8 / 551.4 \approx 0.306$$

Note that our choice of constant axial velocity led to a reduction of flow Mach number at the compressor

discharge, since the gas temperature and thus speed of sound increases along the compressor, which cause the Mach number to drop. This is a good situation for the burner, since we have to decelerate the compressor discharge gas to around Mach 0.2 for efficient combustion. The prediffuser in the burner has to decelerate the gas from Mach ~ 0.3 to ~ 0.2 .

From M_{exit} and $p_{t,exit}$ we get p_{exit}

$$\begin{aligned} p_{exit} &= p_{t,exit} / [1 + (\gamma - 1)M_{exit}^2 / 2]^{\gamma/(\gamma-1)} \\ &= 2020 \text{ kPa} / [1 + 0.2(0.306)^2]^{3.5} \approx 1,892.9 \text{ kPa} \end{aligned}$$

We calculate the exit density ρ_{exit} from the exit temperature and pressure, from perfect gas law

$$\begin{aligned} \rho_{exit} &\approx 1892.9 \text{ kPa} / [(286.86 \text{ J/kg} \cdot \text{K})(757.14 \text{ K})] \\ \rho_{exit} &\approx 8.715 \text{ kg/m}^3 \end{aligned}$$

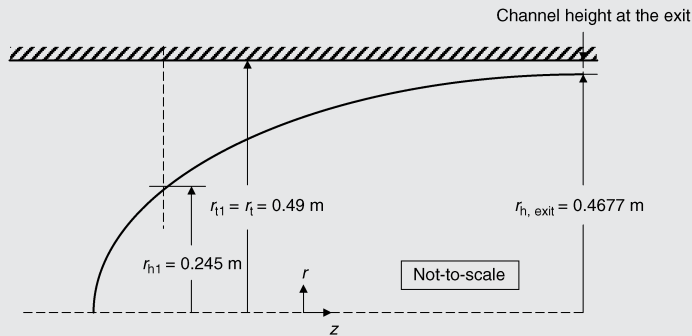
From continuity equation, we get the exit flow area,

$$A_{exit} = \frac{\dot{m}}{\rho_{exit} C_z} = \frac{100 \text{ kg/s}}{8.715 \text{ kg/m}^3 (168.8 \text{ m/s})} \approx 0.06797 \text{ m}^2$$

Assuming a constant tip radius $r_t = \text{constant}$, we calculate the hub radius at the compressor exit to be

$$\begin{aligned} r_{h,exit} &= \sqrt{r_t^2 - A_{exit} / \pi} \\ &= \sqrt{(0.49)^2 - (0.06797) / 3.14159265} \approx 0.4677 \text{ m} \end{aligned}$$

Note that the channel height (or blade height) at the compressor exit is $0.02258 \text{ m} \sim 2.2 \text{ cm}$. If we had shrunk the casing, i.e., the tip radius, instead of keeping it constant, the blade height at the exit would increase.



Here, we may do a quick trade study of the effect of outer casing shrinkage on the blade height in the last stage. The annulus area may be written in terms of the pitchline radius and the channel height as

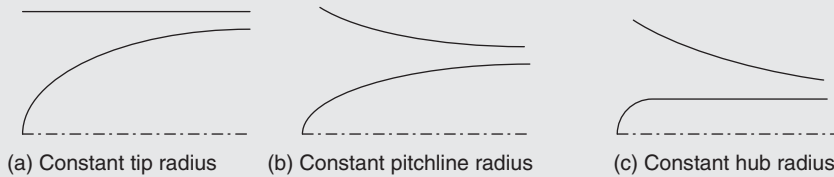
$$A = 2\pi r_m (r_t - r_h)$$

For the exit flow area of 0.06797 m², we have the product of pitchline radius and the blade height as

$$\begin{aligned} r_m \cdot h_{\text{blade}} &\cong 0.010818 \text{ m}^2 \\ h_{\text{blade}} &\cong 0.010818 \text{ m}^2 / r_m \end{aligned}$$

Therefore, the blade or channel height is inversely proportional to the pitchline radius. Here we examine three common choices:

- (a) the constant tip radius, which resulted in h_{blade} of ~2.2 cm
- (b) the constant pitchline radius $r_m = (r_h + r_t)/2 = 0.3677$ m, which gives h_{blade} of ~2.94 cm



- (c) the constant hub radius, gives an exit channel/blade height of $h_{\text{blade}} \sim 4.07$ cm

We note that the increase in blade height between cases (a) and (b) is small, whereas the blade height nearly doubles in case (c) as compared to (a).

Pitchline calculations

Pitchline radius at the compressor face is at $r_{m1} = (r_{h1} + r_{t1})/2 \cong 0.3677$ m

The shaft rpm is selected to give $U_{\text{tip}} = 450$ m/s, which is very desirable for transonic compressor pressure ratio. The choice of shaft rpm and the blade geometry will be tested against the centrifugal stress calculations at the blade root.

But, for now we choose U_{tip} and then establish shaft rpm.

$$U_{\text{tip}} = \omega r_t, \text{ which gives}$$

$$\omega = 450 \text{ m/s} / 0.49 \text{ m} = 918.4 \text{ rad/s} \cong 8,770 \text{ rpm}$$

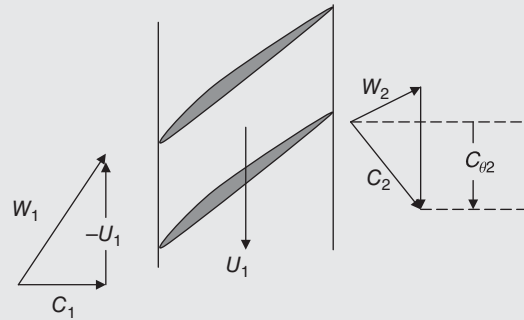
Therefore, the rotor speed at pitchline is

$$\begin{aligned} U_m &= U_{\text{tip}} (r_m / r_t) = (450 \text{ m/s})(0.3677 / 0.49) \\ &\approx 337.5 \text{ m/s.} \end{aligned}$$

The flow angles at the inlet to the rotor blade are

$$\alpha_1 = 0 \quad \text{no IGV (design choice)}$$

$$\beta_1 = \tan^{-1}(337.5 / 168.8) \approx 63.43^\circ$$



The relative velocity is $W_{m1} \approx 377.4$ m/s, which also gives the relative inlet Mach number at the pitchline of

$$M_{1,r,m} = 377.4 / 337.6 = 1.12 \quad [\text{pitchline is supersonic}]$$

In order to establish the flow angles at the rotor exit, we may choose the degree of reaction at the pitchline to be 0.5, i.e.,

$${}^\circ R_m = 0.5 \quad \text{1}^{\text{st}} \text{ Design choice on } {}^\circ R_m$$

This choice immediately gives $C_{\theta 2m}$, since

$${}^\circ R_m = 1 - \frac{C_{\theta 1,m} + C_{\theta 2,m}}{2U}$$

The choice of degree of reaction of 1/2 will make $C_{\theta 2,m} = U_m$ and thus we are asking the rotor relative exit flow to be purely axial, i.e., $\beta_{2m} = 0$.

The problem with this choice is that the net flow turning at the pitchline is ~63°, which means the blade needs too much camber and thus the excessive diffusion will cause

boundary layer to separate. This should be evident from our calculation of the D -factor. Let us see if that fact is borne by our D -factor calculation.

$$D_{r,m} = 1 - \frac{W_{2m}}{W_{1m}} + \frac{|\Delta C_\theta|}{2\sigma_m W_{1m}}$$

$$W_{2m} = C_z = 168.8 \text{ m/s}$$

$$W_{1m} = [(168.8)^2 + (337.5)^2]^{1/2} = 377.4 \text{ m/s}$$

$$\Delta C_\theta = 337.5 \text{ m/s}$$

Let the solidity at the pitchline be $\sigma_m = 1$ (design choice), therefore we calculate the D -factor at the pitchline to be

$$D_{r,m} = 1.053 \quad [\text{Unacceptable}]$$

As we suspected, the amount of turning is not tolerable by the boundary layer and it will stall. The D -factors above 0.55 indicate that the boundary layer is on the verge of stall. We are also guided by de Haller criterion that limits the amount of diffusion in the blade, i.e.,

$$\text{De Haller criterion is } \frac{W_2}{W_1} \geq 0.72$$

Using de Haller criterion, we arrive at the exit relative velocity at the pitchline of

$$W_{2m} = 271.7 \text{ m/s}$$

Therefore, $\beta_2 = \cos^{-1}(168.8/271.7) \cong 51.6^\circ$

The relative swirl at the rotor exit is

$$W_{\theta 2m} = C_{z2} \tan \beta_{2m} \cong 212.9 \text{ m/s}$$

The loading parameter at the pitchline is

$$\psi_m = 124.6/337.5 \approx 0.369$$

The absolute swirl is $C_{\theta 2m} \approx (337.5 - 212.9) \text{ m/s} = 124.6 \text{ m/s}$,

The absolute flow angle at the rotor exit at the pitchline radius is

$$\alpha_{2m} = \tan^{-1}(124.6/168.8) \approx 36.4^\circ$$

The absolute velocity at the rotor exit is $C_{2m} = (C_z^2 + C_{\theta 2m}^2)^{1/2} = 209.8 \text{ m/s}$

The stator thus has to turn the flow 36.4° and decelerate the flow to the axial velocity of 168.8 m/s if we are to

achieve a repeated stage design. Where does this deceleration fall with respect to the de Haller criterion?

$$C_3/C_2 = 168.8/209.8 = 0.805$$

This clearly meets the De Haller criterion. Now, let us supplement our knowledge of rotor and stator diffusion by calculating their D -factors.

$$D_{r,m} = 1 - \frac{W_{2m}}{W_{1m}} + \frac{|\Delta C_\theta|}{2\sigma_{r,m} W_{1m}} \cong 1 - \frac{271.7}{377.4} + \frac{124.6}{2(1)(377.4)} \cong 0.445$$

$$D_{s,m} = 1 - \frac{C_{3m}}{C_{2m}} + \frac{|\Delta C_\theta|}{2\sigma_{s,m} C_{2m}} \cong 1 - \frac{168.8}{209.8} + \frac{124.6}{2(1.5)(209.8)} \cong 0.433$$

In the rotor calculation we chose the pitchline solidity of $\sigma_{r,m} = 1$, whereas for the stator we chose a pitchline solidity of $\sigma_{s,m} = 1.25$ (see the stator blade design section where this choice becomes clear). These are the kind of design choices that we can make in early stages of compressor preliminary design. We may revisit them at any point in our design process.

The pitchline degree of reaction is ${}^\circ R_m = 1 - (C_{\theta 1m} + C_{\theta 2m})/2U_m = 1 - 124.6/2(337.5) = 0.815$

Rotor blade design at pitchline

We choose a double-circular arc blade for the supersonic section at the pitchline. The relative flow in supersonic blade sections is tangent to the upper surface. Also, we have to choose a blade thickness-to-chord ratio at the pitchline. The minimum t/c is at the tip, and for structural reasons it is limited to 3%. The hub, which operates in the subsonic relative flow, may be given a t/c of 10%. If we choose these t/cs as our design choices, and then impose a linear variation of the t/c along span, we arrive at the pitchline t/c of 6.5%.

Before we embark on the blade section design, we may establish the minimum chord length that is required for the turbulent boundary layer formation on the blade. The criterion of $Re_c > 300,000$ is clearly a useful guideline, but we have to satisfy that at all altitudes. In the low-density flight associated with the highest flight altitude in the flight envelope, we calculate the required chord length.

At 16-km altitude; the air density is ~ 0.136 times the sea level density. Therefore, at the engine face we will have

$$\rho_1 \approx (0.136)(1.046 \text{ kg/m}^3) \cong 0.142 \text{ kg/m}^3$$

Also, the kinematic viscosity ν at 16-km altitude is ~ 5.849 times the kinematic viscosity of air at sea level.

$$Re_c = \frac{W_{1m} \cdot c_m}{\nu_1} = \frac{377.4 \text{ (m/s)} \cdot c_m}{8.54 \times 10^{-5} \text{ m}^2/\text{s}}$$

$$\geq 300,000 \implies c_m > 6.8 \text{ cm}$$

We may expand the chord length beyond this minimum for the following reasons:

- blade structural calculations (demanding a wider chord)
- blade aspect ratio (pointing to the advantages of a wide-chord design in stall margin)
- blade vibrational modes (from Campbell diagram)

The relative inlet flow is aligned with the upper surface, therefore, the incidence angle may be written as

$$i \approx \frac{\theta_{L.E.}}{2} \approx \left(\frac{t_{max}}{c} \right) \implies i \approx 3.7^\circ$$

The deviation angle may be estimated from the Carter's basic rule and then supplemented by 2° , since the effect of shock boundary layer interaction is to thicken the boundary layer on the suction surface, thus, causing a higher deviation angle, i.e.,

$$\delta^* \approx \frac{\Delta\beta}{4\sqrt{\sigma}} + 2^\circ \implies \delta^* \approx 5^\circ$$

The blade leading edge angle $\kappa_{1,m} = \beta_{1,m} - i$

The blade trailing-edge angle $\kappa_{2,m} = \beta_{2,m} - \delta^*$

Therefore, the camber angle is $\varphi_m = \kappa_{1,m} - \kappa_{2,m}$

The stagger angle, for a double-circular arc blade, is related to the inlet flow angle, camber, and incidence angle according to

$$\beta_1 = \gamma^\circ + \frac{\varphi}{2} + i \implies \gamma^\circ \approx 60.6^\circ$$

The number of rotor blades may now be calculated since we have chosen the solidity at the pitchline and selected the chord length. The blade spacing at the pitchline is

$$s_{r1,m} = \frac{2\pi r_{m1}}{N_{R1}}$$

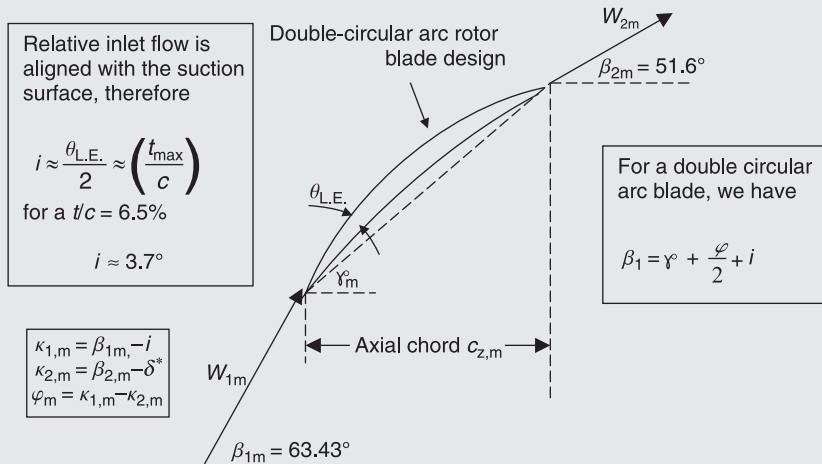
We also chose the rotor solidity of 1 at the pitchline, which gives

$$\sigma_{r1,m} = \frac{c_{r1,m}}{s_{r1,m}} = 1.0$$

Therefore, the number of rotor blades is $N_{R1} = 2\pi r_{m1} / c_{r1,m}$

For a rotor chord length of 7 cm (or 0.07 m) and the pitchline radius of 0.3677 m, we get the number of rotor blades in the first stage to be

$$N_{R1} = 33$$



Stator blade design at pitchline

The design of the stator blade at the pitchline follows the flow angles and Mach numbers in the absolute frame, i.e., we know that

$$\alpha_2 = 36.4^\circ$$

$$\alpha_3 = 0^\circ \quad [\text{repeated stage}]$$

To calculate the Mach number at the entrance to the stator, we need to calculate the static temperature and speed of sound at the pitchline radius downstream of the rotor.

From Euler turbine equation $T_{t2,m} = T_{t1} + U_m(C_{\theta 2} - C_{\theta 1})/c_p$

We made the assumption of no radial shift across the rotor and a calorically perfect gas. These assumptions or approximations are reasonable at the preliminary stage of design.

$$T_{t1} = 298 \text{ K}, U_m = 337.5 \text{ m/s}, C_{\theta 1} = 0,$$

$$C_{\theta 2} = 124.6 \text{ m/s}, c_p = 1,004 \text{ J/kg} \cdot \text{K}$$

Substitute these values in the Euler equation to get $T_{t2,m} = 339.9 \text{ K}$

Since the static temperature and total temperature are related via $T = T_t - C^2/2c_p$, we calculate the static temperature upstream of the stator at the pitchline radius

$$T_{2,m} \approx 318 \text{ K with a corresponding } \alpha_{2,m} = 357.3 \text{ m/s}$$

$$M_{2,m} = 209.8/357.3 \approx 0.587 \text{ (subsonic stator flow)}$$

$$C_{2,m} = 209.8 \text{ m/s}$$

The stator blade at the pitchline is a subsonic section. Therefore, we may choose NACA-65 series cascade profiles from the data of Mellor (see Appendix I for a complete description) that

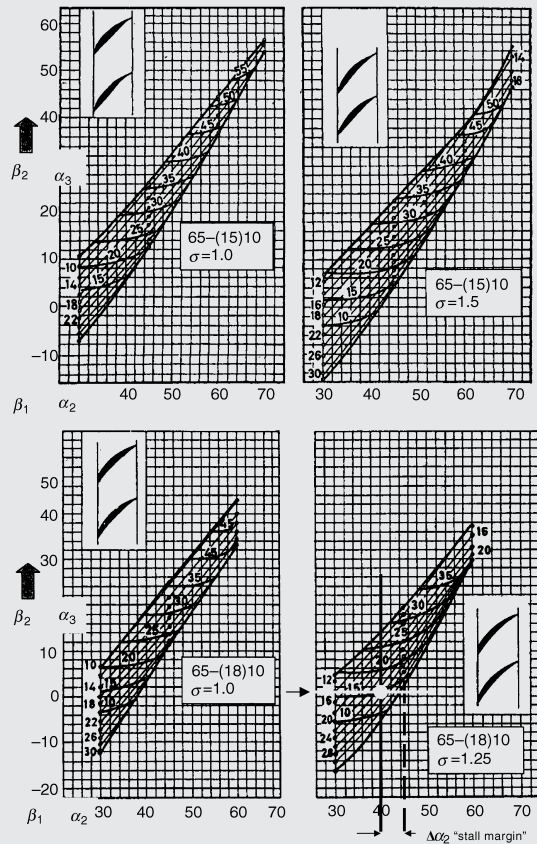
- (a) best match the inlet and exit flow angles
- (b) provide for a reasonable “stall margin”

We choose the **65-(18)10** cascade with a solidity of $\sigma = 1.25$, where the intersection of the inlet and exit flow angles yield (note that the inlet and exit angles to the stator are α_2 and α_3 respectively)

$$\gamma^\circ \approx 15^\circ$$

Angle of attack, $\alpha_2 - \gamma^\circ \approx 22^\circ$ [which is consistent with our $\alpha_2 = 36.7^\circ$ and the stagger of 15°]

We note a tolerance to inlet flow angle variation of $\sim 6.5^\circ$ margin to the positive stall boundary. We may use this range



of inlet flow angle variation to arrive at an approximate “stall margin” for the stator blade section at the pitchline in the first stage. A more accurate approach to stall margin calculation is based on Koch’s method that we have detailed in this chapter.

Stage pressure ratio and number of stages

The total temperature rise across the first stage, at the pitchline, is

$$\Delta T_t = 41.9 \text{ K}$$

For a repeated stage and assuming the blade rotational speed U remains nearly constant at the pitchline of subsequent stages, we conclude that every stage achieves $\Delta T_t = 41.9 \text{ K}$.

The total stagnation temperature rise for the compressor was calculated to be

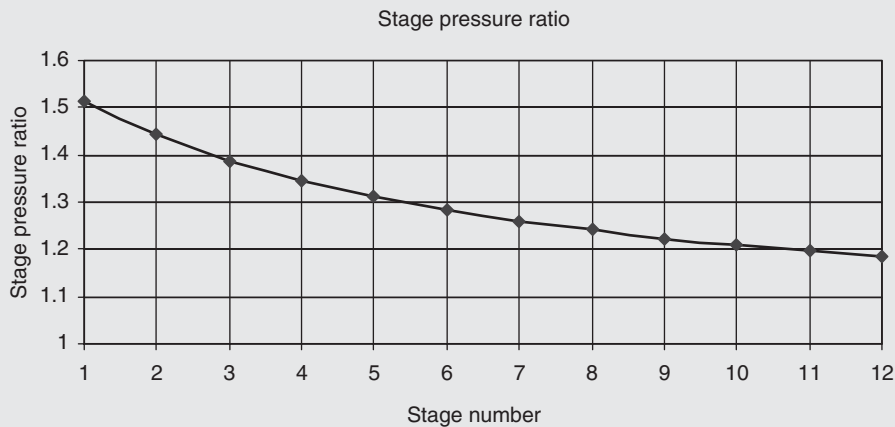
$$\Delta T_{t, \text{compressor}} = 771.3 \text{ K} - 298 \text{ K} = 473.3 \text{ K}$$

(assuming a calorically-perfect gas)

If each stage produces 41.9 K total temperature rise, we need 11.29 stages to achieve the needed total temperature rise for the compressor (at the pitchline). Based on the approximations that we have made, e.g., calorically perfect gas and representing the 3D behavior of the compressor by its pitchline, we choose 12 stages for the compressor.

$$N_{\text{stages}} = 12$$

We calculate the stage pressure ratio π_s for each stage, and graph it in the following figure.



Note that the compressor pressure ratio at the pitchline, after 12 stages will be 22.5 (which is >20 , the compressor design pressure ratio). The pitchline however does not represent the “average” of the stage pressure ratio. The main reason is that the pitchline is away from the end walls where losses are predominant. Therefore, we expect lower total pressure ratio per stage as that represented by our pitchline calculation. Another note is that the polytropic efficiency e_c should not be treated as constant along a multistage compressor. As compression progresses, the end wall losses grow and thus the slope of ideal-to-actual work (for small stage) drops. The polytropic efficiency may be as high as 0.90 (or even 0.92) for early stages, and as low as 0.85 in the aft stages.

Rotor blade stress calculations

The rotor blade is subject to centrifugal as well as bending, vibrational and thermal stresses. The dominant stress in a rotor however is the centrifugal stress σ_c .

$$\sigma_c \equiv \frac{F_c}{A_{\text{hub}}}$$

$$F_c = \int_{r_h}^{r_t} \rho_{\text{blade}} \cdot A_b(r) \omega^2 r dr$$

$$\sigma_c = \frac{1}{A_h} \int_{r_h}^{r_t} \rho_{\text{blade}} \cdot A_b(r) \omega^2 r dr$$

$$\frac{\sigma_c}{\rho_{\text{blade}}} = \frac{\omega^2}{A_h} \int_{r_h}^{r_t} A_b(r) r dr = \omega^2 \int_{r_h}^{r_t} \frac{A_b}{A_h} r dr$$

$$\frac{\sigma_c}{\rho_{\text{blade}}} = \omega^2 \int_{r_h}^{r_t} \frac{A_b}{A_h} r dr$$

The blade area distribution along the span, $A_b(r)/A_h$, is known as *taper* and is often approximated to be a linear function of the span. Therefore, it may be written as

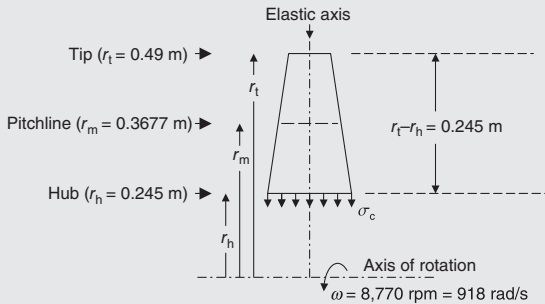
$$A_b = A_h - \frac{r - r_h}{r_t - r_h} (A_h - A_t) \longrightarrow$$

$$\frac{A_b}{A_h} = 1 - \frac{r - r_h}{r_t - r_h} \left(1 - \frac{A_t}{A_h} \right)$$

We may substitute $A_b(r)/A_h$ in the integral and proceed to integrate; however a customary approximation is often introduced that replaces the variable r by the pitchline radius r_m . The result is

$$\frac{\sigma_c}{\rho_{\text{blade}}} = \frac{\omega^2 A}{4\pi} \left(1 + \frac{A_t}{A_h} \right)$$

Therefore, the ratio of centrifugal stress to the material density is related to the square of the angular speed, the taper ratio, and the flow area $A = 2\pi r_m(r_t - r_h)$.



Titanium alloy is suitable for compressor/fan rotor blades, due to its low density, high strength characteristics, which makes it a high strength-to-weight ratio, or high specific-

strength material of choice for rotor blades in a compressor or fan. The density of Titanium alloy is

$$\rho_{\text{titanium}} = 4,680 \text{ kg/m}^3$$

The material parameter of interest in a rotor is the *creep rupture strength*, which identifies the maximum tensile stress tolerated by the material for a given period of time at a specified operating temperature. Based on the 80% value of the allowable 0.2% creep in 1000 h, for aluminum alloys and the 50% value of the allowable 0.1% creep in 1000 h for other materials, Mattingly, Heiser and Pratt (2002) have graphed Figures 8.85 and 8.86. They show the allowable specific strength of different engine materials as a function of temperature.

The allowable strength-to-weight ratio for the titanium alloy is noted to be $\sim 9 \text{ ksi/slug/ft}^3$, which is equivalent to

Allowable creep	120,560 m^2/s^2 (or $\sim 120 \text{ kPa/kg/m}^3$)
rupture strength	
Required strength	68,326 m^2/s^2 (or $\sim 68 \text{ kPa/kg/m}^3$)

8.15 Summary

Axial-flow compressors are highly evolved machines that provide efficient mechanical compression (of the gas) in a gas turbine engine. The mechanical work is delivered to the medium by a set of rotating blade rows. The rotor blades impart swirl to the flow, thereby, increasing the total pressure of the fluid. In between the rotor blade rows are the stator blade rows that remove the swirl from the fluid, thereby increasing the static pressure of the fluid. The combination of one rotor row and one stator blade row is called a compressor stage. Since the primary flow direction is along the axis of the machine, staging the axial-flow compressor is easy. The flow in an axial-flow compressor is exposed to an *adverse pressure gradient* environment, that is, a climbing pressure hill that tends to stall the boundary layer. Therefore, the phenomenon of *stall* is experienced in a compressor. The stalled compressor flow is inherently unsteady and thus may cause a system-wide instability (between the compressor and combustor) known as *surge*.

In analyzing the flow in the rotor, it is most convenient to use the rotating frame of reference that spins with the rotor, which is known as the *relative frame of reference*. The flow in stator blade row is best analyzed by a stationary observer (i.e., a frame of reference that is fixed with respect to the casing) known as the *absolute frame of reference*. The velocity vectors in the two frames of reference form a triangle, described by

$$\vec{C} - \omega r \hat{e}_\theta = \vec{W}$$

The *Euler turbine equation* is known as the fundamental equation in turbomachinery that relates the change of angular momentum $\Delta(rC_\theta)$ across a rotor blade row to the rotor specific work via

$$w_c \equiv \frac{\mathcal{G}_c}{\dot{m}} = \omega \Delta(rC_\theta) \quad (8.9a)$$

If we express the jump in swirl across a rotor in terms of the (rotor) inlet absolute and exit relative flow angles (that remain constant over a wide operating range of the compressor), we deduce from Equation 8.25a that

$$\tau_c - 1 = \left(\frac{U^2}{c_p T_{t1}} \right) \left[1 + \frac{C_{z2}}{U} \tan \beta_2 - \frac{C_{z1}}{U} \tan \alpha_1 \right]$$

The significance of this equation is the appearance of U^2 in front of the bracket on the RHS, which indicates that the total temperature rise across a rotor is proportional to the square of the wheel speed U^2 . Therefore a high blade Mach number is desirable, which is exactly the argument for the development of *transonic compressors*. A rule of thumb is that the blade tangential Mach number at the tip is slightly supersonic, $M_T \sim 1.2$ – 1.3 . The structural limitations currently limit the blade tip Mach number to ~ 1.5 in conventional (subsonic throughflow) compressors. A high strength-to-weight ratio material, such as titanium, is desirable for fan blade construction.

Since we have to limit the level and extent of the flow diffusion in a compressor blade row, we define a *diffusion factor* D for the rotor and stator blade rows according to

$$D_r \equiv 1 - \frac{W_2}{W_1} + \frac{|W_{\theta 2} - W_{\theta 1}|}{2\sigma_r W_1} \quad (\text{rotor } D\text{-Factor})$$

$$D_s \equiv 1 - \frac{C_3}{C_2} + \frac{|C_{\theta 3} - C_{\theta 2}|}{2\sigma_s C_2} \quad (\text{stator } D\text{-Factor})$$

The experience shows that diffusion factor is to be limited to ~ 0.6 about the mid-span of a blade row and to ~ 0.4 near the hub or the tip. The lower diffusion imposed on the hub and the tip is due to a complex hub boundary layer/corner vortex formation and the tip clearance flows that dominate the two ends of a blade row. We may view the diffusion factor as a blade-row-specific figure of merit. We define a stage-based figure of merit as well, which is called the *degree of reaction* ${}^\circ R$,

$${}^\circ R \equiv \frac{h_2 - h_1}{h_3 - h_1}$$

Degree of reaction is the ratio of the rise of the static enthalpy across the rotor to that of the stage. In essence, it speaks to the rotor's share of the static pressure rise to that of the stator. Therefore, a 50% degree of reaction stage equally divides the burden of the pressure rise to the rotor and the stator. Although 50% sounds desirable for equal burden, since the rotor blades spin their boundary layers are more stable and thus can withstand higher static pressure rise than the stationary stator blades. Consequently, a 60% degree of reaction may be more optimal than the 50%.

Cascade aerodynamics provides a rich background for a two-dimensional (subsonic) blade design. The minimum-loss incidence angle i_{opt} and the cascade (total pressure) loss

bucket are used for the preliminary 2D design of compressor blade sections as well as identifying the *positive and negative stall boundaries*. The limited supersonic cascade data make the preliminary design of the supersonic sections of transonic fans less grounded. The general rules are based in gas dynamics, which indicate the selection of the thinnest possible sections in order to minimize the wave drag. The thinnest (structurally feasible) section is $\sim 3\%$ thick and the subsonic root is often $\sim 10\%$ thick.

Three-dimensional design of blades, in the preliminary stage, is achieved by the so-called *vortex design* approach. Here we introduce a catalog of swirl profiles, such as free-vortex, solid-body rotation, and others that will be anchored at the pitchline and then give us a swirl profile along the span. We applied radial equilibrium theory to calculate an axial velocity profile. Three-dimensional losses are due to secondary flows, tip clearance, and the blade junction corner vortex. The unsteady flow losses are related to upstream wake chopping (by the downstream blade row) and the subsequent vortex shedding in the wake. Losses due to compressibility are minimized by thin profile designs that form the sections of swept blades.

A single-spool compressor is of limited capability in high-pressure compressor applications. The primary reason for that is the differing rotational requirement of the front versus the aft stages. This is the crux of the classical *starting problem* for a high-pressure ratio compressor. Multistage compressors are often driven by different shafts in order to spin the high-pressure stages faster than the low-pressure compressor. Variable stators in the front stages are always adjustable to help with the starting problem as well as the off-design operation of the compressor. A fraction of airflow in the compressor is bled at the intermediate and exit sections to cool the HPT, the casing, and the exhaust nozzle. The cooling fraction is $\sim 10\text{--}15\%$ in modern engines.

As an upper bound, multispool, high-pressure ratio compressors can achieve a pressure ratio of $\sim 45\text{--}50$. The exit temperature of $\sim 900\text{ K}$ is the limit of current materials for an uncooled compressor, which limit the compressor pressure ratio. The advances in computational fluid dynamics, parallel processing, and computer memory have elevated the design of compressors to be based on flow physics and with less reliance on empiricism and cascade data. The result has been the appearance of high-efficiency unconventional transonic blades and stages with *forward and aft swept blades* and *lean*. The advances in integrated manufacturing technology that involve super plastic forming and diffusion bonding (SPF/DB) are used for the manufacturing of modern (composite) wide-chord fan blades. New materials and manufacturing technology, e.g., BLISK, offer weight savings in compressors with the subsequent improvement on the engine thrust-to-weight ratio.

Dixon [7], Cheng *et al.* [2], Prince, Wisler and Hilvers [41], Whitcomb and Clark [53] are recommended for additional reading.

References

1. Bullock, R.O. and Finger, H.B., "Compressor Surge Investigated by NACA," *SAE Journal*, Vol. 59, September 1951, pp. 42–45.
2. Cheng, P., Prell, M.E., Greitzer, E.M., and Tan, C.S., "Effects of Compressor Hub Treatment on Stator Stall and Pressure Rise," *AIAA Journal*, Vol. 21, No. 7, July 1984.
3. Carter, A.D.S., "The Axial Compressor," in *Gas Turbine Principles and Practice*, Ed., Cox, H.R., Newnes Ltd., London, UK, 1955.
4. Cumpsty, N., *Compressor Aerodynamics*, Cambridge University Press, UK, 1989.
5. Cumpsty, N., *Jet Propulsion*, Cambridge University Press, Cambridge, UK, 1997.

6. De Haller, P., "Das Verhalten von Tragfluegelgittern in Axialverdichtern und im Windkanal," *Brennstoff und Waermekraft*, Vol. 5, 1953.
7. Dixon, S.L., *Fluid Mechanics, Thermodynamics of Turbomachinery*, 2nd edition, Pergamon Press, Oxford, UK, 1975.
8. Donaldson, C., Du, P., and Lange, R.H., "Study of Pressure Rise Across Shock Waves Required to Separate Laminar and Turbulent Boundary Layers," NACA Technical Note 2770, 1952.
9. Emmons, H.W., Pearson, C.E., and Grant, H.P., "Compressor Surge and Stall Propagation," *Transactions of the ASME*, Vol. 79, May 1955, pp. 455–467.
10. Farr, A.P. and Schumacher, G.A., "System for Evaluation of F-15 Inlet Dynamic Distortion," Paper in *Instrumentation for Airbreathing Propulsion*, Progress in Astronautics and Aeronautics, Vol. 34, Eds. Fuhs, A.E. and Kingery, M., MIT Press, Cambridge, MA, 1974.
11. Garvin, R.V., *Starting Something Big: The Commercial Emergence of GE Aircraft Engines*, AIAA, Inc., Reston, VA, 1998.
12. Greitzer, E.M., "Surge and Rotating Stall in Axial Flow Compressors," *ASME Journal of Engineering for Power*, Vol. 98, No. 2, 1976, p. 190.
13. Gostelow, J.P., *Cascade Aerodynamics*, Pergamon Press, Oxford, UK, 1984.
14. Hawthorne, W.R., "Secondary Circulation in Fluid Flow," *Proceedings of Royal Society*, London, Vol. 206, 374, 1951.
15. Hechert, H., Steinert, W., and Lehmann, K., "Comparison of Controlled Diffusion Airfoils with Conventional NACA-65 Airfoils Developed for Stator Blade Application in a Multistage Axial Compressor," *Transactions of the ASME, Journal of Engineering for Gas Turbines and Power*, Vol. 107, April 1985, pp. 494–498.
16. Hercock, R.G. and Williams, D.D., "Distortion-Induced Engine Instability: Aerodynamic Response," AGARD, LS72-Paper No. 3, 1974.
17. Herrig, L.J., Emery, J.C., and Erwin, J.R., "Systematic Two-Dimensional Cascade Tests of NACA 65-Series Compressor Blades at Low Speeds," NACA-RM L51G31, 1951.
18. Hill, P.G. and Peterson, C.R., "Mechanics and Thermodynamics of Propulsion," 2nd edition, Addison-Wesely, Reading, MA, 1992.
19. Hobbs, D.E. and Weingold, H.D., "Development of Controlled Diffusion Airfoils for Multistage Compressor Applications," *Transactions of ASME, Journal of Engineering for Gas Turbines and Power*, Vol. 106, April 1984, pp. 271–278.
20. Horlock, J.H., *Axial Flow Compressors*, Krieger Publishing Company, Huntington, NY, 1973.
21. Howell, A.R., "Design of Axial Compressors", *Proceedings of Institution of Mechanical Engineers*, London, Vol. 153, 1945.
22. Howell, A.R., "Fluid Dynamics of Axial Compressors", *Proceedings of Institution of Mechanical Engineers*, London, Vol. 153, 1945.
23. Johnsen, I.A. and Bullock, R.O., "Aerodynamic Design of Axial-Flow Compressors," NASA SP-36, Washington, D.C., 1965.
24. Kerrebrock, J.L., "Flow in Transonic Compressors," *AIAA Journal*, Vol. 19, No. 1, 1981, pp. 4–19.
25. Kerrebrock, J.L., *Aircraft Engines and Gas Turbines*, 2nd edition, MIT Press, Cambridge, MA, 1992.
26. Kerrebrock, J.L., "Small Disturbances in Turbomachine Annuli with Swirl," *AIAA Journal*, Vol. 15, June 1977, pp. 794–803.
27. Kerrebrock, J.L. and Mikolajczak, A.A., "Intra-Stator Transport of Rotor Wakes and Its Effect on Compressor Performance," *ASME Journal of Engineering for Power*, October 1970, p. 359.
28. Kline, S.J., Abbott, D.E., and Fox, R.W., "Optimum Design of Straight-Walled Diffusers," *Journal of Basic Engineering*, Vol. 81, series, D, No. 3, September 1959, pp. 321–331.
29. Koch, C.C., "Stalling Pressure Rise Capability of Axial Flow Compressor Stages," *Transactions of the ASME, Journal of Engineering for Power*, Vol. 103, October 1981, pp. 645–656.
30. Kotidis, P.A. and Epstein, A.H., "Unsteady Radial Transport in a Transonic Compressor Stage," *Transactions of ASME, Journal of Turbomachinery*, Vol. 113, April 1991, pp. 207–218.
31. Lieblein, S., Schwenk, F.D., and Broderick, R.L., "Diffusion Factor for Estimating Losses and Limiting Blade loadings in Axial-Flow Compressor Blade Element," NACA RM E53D01, June 1953.
32. Lieblein, S., "Loss and Stall Analysis of Compressor Cascades," *Transactions of the ASME, Journal of Basic Engineering*, September 1959, pp. 387–400.
33. Lieblein, S., "Experimental Flow in Two-Dimensional Cascades," in *Aerodynamic Design of Axial Flow Compressors*, NASA SP-36, 1965.
34. Lieblein, S. and Roudebush, W.H., "Theoretical Loss Correlation for Low-Speed Two-Dimensional Cascade Flow," NACA TN 3662, 1956.
35. Marble, F.E., Three-Dimensional Flow in Turbomachines, in *Aerodynamics of Turbines and Compressors* Vol. X, Ed. Hawthorne, W.R., Princeton Series on High Speed Aerodynamics and Jet Propulsion, Princeton University Press, Princeton, NJ, 1964.
36. Mattingly, J.D., Heiser, W.H., and Pratt, D.T., *Aircraft Engine Design*, 2nd edition, AIAA Education Series, AIAA, Reston, VA, 2002.
37. Oyama, A., Liou, M.-S., and Obayashi, S., "Transonic Axial-Flow Blade Shape Optimization using

- Evolutionary Algorithm and Three-Dimensional Navier-Stokes Solver," AIAA Paper Number 2002-642, 2002.
38. Paduano, J.D., Greitzer, E.M., and Epstein, A.H., "Compression System Stability and Active Control," *Annual Review of Fluid Mechanics*, Vol. 33, 2001, pp. 491-517.
 39. Povolny, J.H., Burcham, F.W., Calogeras, J.E., et al., "Effects of Engine Inlet Disturbances on Engine Stall Performance," Paper in NASA-SP 259, Aircraft Propulsion, 1970, pp. 313-351.
 40. Pratt and Whitney, *Aircraft Gas Turbine Engines and Its Operation*, P&W Operations Manual 200, 1980.
 41. Prince, D.C., Jr., Wisler, D.C., and Hilvers, D.E., "Study of Casing Treatment Stall Margin Improvement Phenomena," ASME Paper No. 75-GT-60, 1975.
 42. Reneau, L.R., Johnston, J.P. and Kline, S.J., "Performance and Design of Straight, Two-Dimensional Diffusers," *Journal of Basic Engineering*, ASME Transactions, Series D, Vol. 89, 1967, pp. 141-150.
 43. Rolls-Royce, *The Jet Engine*, Rolls-Royce plc, Derby, UK, 2005.
 44. Rhoden, H.G., "Effects of Reynolds Number on the Flow of Air through a Cascade of Compressor Blades," ARC R&M 2919, 1956.
 45. Schobeiri, M.T., *Turbomachinery Flow Physics and Dynamic Performance*, Springer Verlag, Berlin, 2004.
 46. Schweikhard, W.G. and Montoya, E.J., "Research Instrumentation Requirements for Flight Wind Tunnel Tests of the YF-12 Propulsion System and Related Flight Experience," Paper in *Instrumentation for Airbreathing Propulsion*, Progress in Astronautics and Aeronautics, Vol. 34, Eds. Fuhs, A.E. and Kingery, M., MIT Press, Cambridge, MA, 1974.
 47. Seddon, J. and Goldsmith, E.L., *Intake Aerodynamics*, American Institute of Aeronautics and Astronautics, Inc., Washington, D.C., 1985, pp. 292-319.
 48. Smith, L.H., "Recovery Ratio—A Measure of the Loss Recovery Potential of Compressor Stages," *Transactions of the ASME*, Vol. 80, No. 3, April 1958, pp. 517-524.
 49. Sovran, G. and Klomp, E.D., "Experimentally Determined Optimum Geometries for Rectilinear Diffusers with Rectangular, Conical or Annular Cross Section," *Fluid Mechanics of Internal Flow*, Elsevier Publishing, Amsterdam, The Netherlands, 1967.
 50. Squire, H.B. and Winter, K.G., "The Secondary Flow in a Cascade of Airfoils in a Non-Uniform Stream," *Journal of Aeronautical Sciences*, Vol. 18, No. 271, 1951.
 51. St. Peter, J., *The History of Aircraft gas Turbine Engine Development in the United States*, International Gas Turbine Institute, Atlanta, 1999.
 52. Sulam, D.H., Keenan, M.J., and Flynn, J.T., "Data and Performance of a Multiple Circular Arc Rotor," *Single-Stage Evaluation of a Highly-Loaded High-Mach-Number Compressor Stages*, Vol. II, NASA CR-72694, 1970.
 53. Whitcomb, R.T. and Clark, L.R., "An Airfoil Shape for Efficient Flight at Supercritical Mach Numbers," NASA TMX-1109, July 1965.
 54. Wisler, D.C., "Advanced Compressor and Fan Systems," *UTSI Short course notes on Aero-Propulsion Systems*, April 2000.

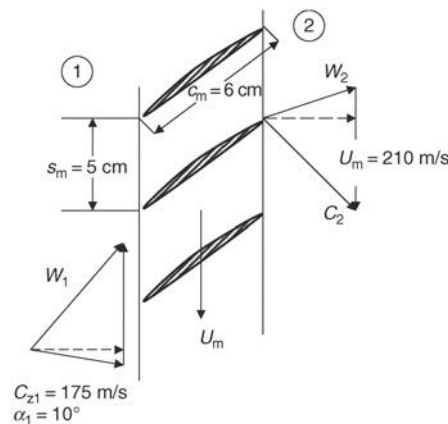
Problems

8.1 The absolute flow at the pitchline to a compressor rotor has a swirl with $C_{\theta 1} = 78$ m/s. The exit flow from the rotor has a positive swirl, $C_{\theta 2} = 172$ m/s. The pitchline radius is at $r_m = 0.6$ m and the rotor angular speed is $\omega = 5220$ rpm. Calculate the specific work at the pitchline and the rotor torque per unit mass flow rate.

8.2 An axial-flow compressor stage has a pitchline radius of $r_m = 0.6$ m. The rotational speed of the rotor at pitchline is $U_m = 256$ m/s. The absolute inlet flow to the rotor is described by $C_{z1} = 155$ m/s and $C_{\theta 1m} = 28$ m/s. Assuming that the stage degree of reaction at pitchline is $\alpha_3 = \alpha_1$, and C_{zm} remains constant, calculate

- (a) rotor angular speed ω in rpm
- (b) rotor exit swirl $C_{\theta 2m}$
- (c) rotor specific work at pitchline, w_{cm}
- (d) relative velocity vector at the rotor exit
- (e) rotor and stator torques per unit mass flow rate
- (f) stage loading parameter at pitchline, ψ_m
- (g) flow coefficient ϕ_m

8.3 A rotor blade row is cut at pitchline, r_m . The velocity vectors at the inlet and exit of the rotor are shown.



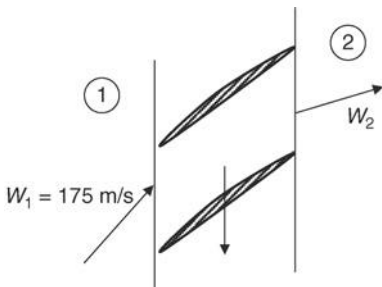
■ FIGURE P 8.3

Assuming that $U_{m1} = U_{m2} = 210$ m/s and $C_{z1} = C_{z2} = 175$ m/s, $\rho_1 = 1$ g/m³, $\beta_2 = -25^\circ$, and $\varpi_r = 0.03$, calculate

- (a) $W_{\theta 1}$ and $W_{\theta 2}$
- (b) W_{1m} and W_{2m}
- (c) D -factor D_{rm}
- (d) Circulation Γ_m
- (e) rotor lift at pitchline per unit span
- (f) lift coefficient at pitchline
- (g) rotor-specific work at r_m
- (h) loading coefficient ψ_m
- (i) degree of reaction ${}^\circ R_m$

8.4 A rotor blade row at the hub radius is shown. The rotor total pressure loss coefficient at this radius is $\varpi_{rm} = 0.04$.

- (a) How much deceleration is allowed in the rotor under de Haller criterion? i.e., What is the minimum W_2 ?
- (b) What is the static pressure rise coefficient, assuming incompressible flow and W_{2min} from de Haller criterion?
- (c) Compare the C_p in part (b) to the Arbitrary C_{pmax} shown in Figure 8.30 at the hub.



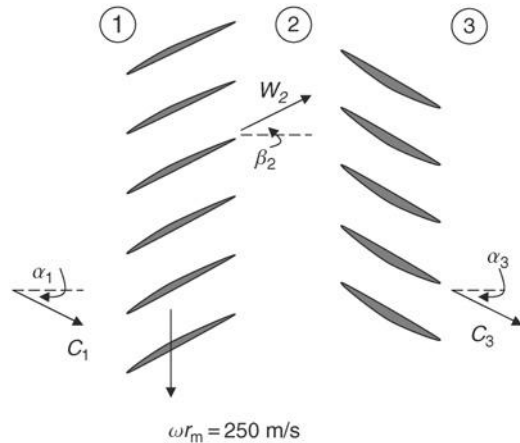
■ FIGURE P8.4

8.5 A compressor stage develops a pressure ratio of $\pi_s = 1.6$. Its polytropic efficiency is $e_c = 0.90$. Calculate the stage total temperature ratio τ_s and compressor stage adiabatic efficiency η_s . Assume $\gamma = 1.4$.

8.6 An axial-flow compressor stage is shown at the pitchline. Assuming

- $\alpha_1 = \alpha_3$
- $\beta_2 = -30^\circ$ $p_{t1} = 10^5$ Pa
- $C_{z1} \cong C_{z2} \cong C_{z3}$ $T_{t1} = 290$ K
- $r_1 \cong r_2 \cong r_3$ $M_1 = 0.5$
- $\varpi_r = 0.03$ $\alpha_1 = 30^\circ$
- $\varpi_s = 0.02$ $\gamma = 1.4$
- Calculate $c_p = 1,004$ J/kg · K

- (a) w_c (in kJ/kg)
- (b) T_{t3}/T_{t1}
- (c) M_{2r}
- (d) p_{t2}/p_{t1}
- (e) p_{t3}/p_{t2}
- (f) η_s
- (g) ${}^\circ R_m$



■ FIGURE P8.6

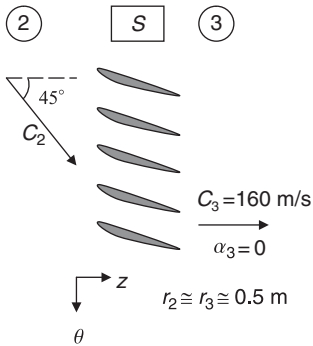
8.7 The flow at the entrance to an axial-flow compressor rotor has zero preswirl and an axial velocity of 175 m/s. The shaft angular speed is 5000 rpm. If at a radius of 0.5 m, the rotor exit flow has zero relative swirl, calculate at this radius

- (a) rotor specific work w_c in kJ/kg
- (b) degree of reaction ${}^\circ R$

8.8 The absolute flow angle at the inlet of a stator blade in a compressor is $\alpha_2 = 45^\circ$, as shown. The absolute total pressure and temperature in station 2 are $p_{t2} = 150$ kPa and $T_{t2} = 300$ K, respectively. The total pressure loss coefficient for this section of the the stator blade is $\varpi_s = 0.02$. Assuming the axial velocity remains constant and gas properties are $\gamma = 1.4$ and $c_p = 1.004$ kJ/kg · K, calculate

- (a) entrance Mach number M_2
- (b) exit total pressure p_{t3}
- (c) exit Mach number M_3
- (d) stator torque for a mass flow rate of $\dot{m} = 100$ kg/s
- (e) static pressure rise, $\Delta p = p_3 - p_2$
- (f) static temperature rise $\Delta T = T_3 - T_2$
- (g) entropy rise $(s_3 - s_2)/R$

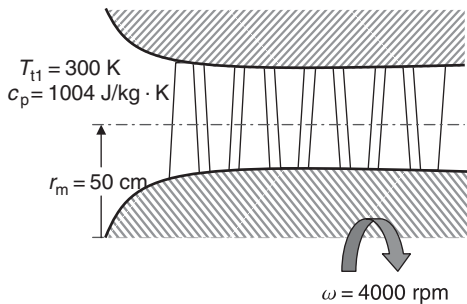
Note that the radius of this cut (section) is at $r \cong 0.5$ m from the axis of rotation, as shown in the diagram.



■ FIGURE P8.8

8.9 An axial-flow compressor with four stages is shown. Assuming a repeated stage design, with constant throughflow speed, $C_z = 150$ m/s, and 50% degree of reaction at the pitch-line with zero preswirl, calculate

- (a) rotor specific work at the pitchline (kJ/kg)
- (b) stage pressure ratio for an $\eta_s = 0.90$
- (c) compressor pressure ratio π_c
- (d) shaft power (in MW) for a mass flow rate of $\dot{m}_0 = 100$ kg/s
- (e) D -factor for the first rotor at the pitchline for $\sigma_r = 2.0$



■ FIGURE P8.9

8.10 An axial-flow compressor stage is designed on the principle of constant through flow speed. The flow at the entrance to the rotor has 100 m/s of positive swirl and 180 m/s of axial velocity. Assuming we are at the pitchline radius $r_m = 0.5$ m, where the rotor rotational speed is $U_m = 230$ m/s, the degree of reaction $\circ R_m = 0.5$, the radial shift in the streamtube is negligible, i.e., $r_{1m} \approx r_{2m} \approx r_{3m}$, and also assuming a repeated stage design principle is implemented, calculate

- (a) α_{1m} and β_{1m}
- (b) α_{2m} and β_{2m}
- (c) rotor specific work at the pitchline w_{cm} in kJ/kg
- (d) stator torque at the pitchline per unit mass flow rate, τ_s/\dot{m}

8.11 In an axial-flow compressor test rig with no inlet guide vanes, a 1-m diameter fan rotor blade spins with a sonic tip speed, i.e., $U_{tip}/a_1 = 1.0$. If the speed of sound in the laboratory is $a_0 = 300$ m/s, and the axial velocity to the fan is $C_{z1} = 150$ m/s, calculate the fan rotational speed ω in rpm.

$$R = 287 \text{ J/kg} \cdot \text{K} \text{ and } \gamma = 1.4$$

8.12 An axial-flow compressor rotor has an angular velocity of $\omega = 5000$ rpm. The flow entering the compressor rotor has zero preswirl and an axial velocity of $C_{z1} = 150$ m/s. Assuming the axial velocity is constant throughout the stage, and the rotor specific work at the radius $r = 0.5$ m is $w_c = 62$ kJ/kg ($\gamma = 1.4$ and $R = 287$ J/kg \cdot K) calculate

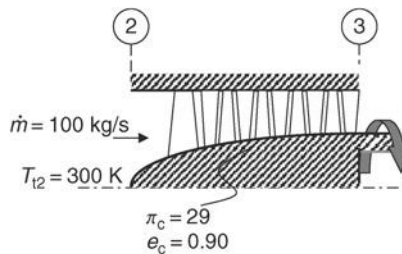
- (a) stage degree of reaction, $\circ R$, at this radius
- (b) total pressure ratio across the rotor, p_{t2}/p_{t1} , at this radius, assuming a polytropic efficiency of 90% and $T_1 = 20^\circ \text{C}$.

8.13 An axial-flow compressor rotor at the pitchline has a radius of $r_m = 0.35$ m. The shaft rotational speed is $\omega = 5000$ rpm. The inlet flow to the rotor has zero preswirl and the axial velocity is $C_{z1} = C_{z2} = C_{z3} = 175$ m/s. The rotor has a 50% degree of reaction at the pitchline. The stage adiabatic efficiency is nearly equal to the polytropic efficiency $\eta_s \cong e_c = 0.92$. Assuming the inlet total temperature is $T_{t1} = 288$ K and $c_p = 1.004$ kJ/kg \cdot K, calculate

- (a) rotor specific work at $r = r_m$
- (b) stage loading ψ at $r = r_m$
- (c) flow coefficient at $r = r_m$
- (d) rotor relative Mach number at the pitchline, $M_{1,r,m}$
- (e) stage total pressure ratio at the pitchline

8.14 For the multistage compressor, as shown, calculate

- (a) compressor adiabatic efficiency η_c
- (b) shaft power \dot{W}_e
- (c) exit total temperature T_{t3}
- (d) average π_s for ten stages, i.e., $N = 10$
Assume $\gamma = 1.4$ and $c_p = 1004$ J/kg \cdot K.



■ FIGURE P8.14

8.15 A compressor test rig operates in a laboratory where $\theta_2 = 0.95$ and $\delta_2 = 0.95$. The mass flow rate is measured

at the compressor face to be $\dot{m} = 100 \text{ kg/s}$ and the shaft power is measured to be $\dot{\varphi}_c = 50 \text{ MW}$. Assuming compressor poly-tropic efficiency is $e_c = 0.90$, calculate

- (a) compressor (total) pressure ratio π_c
- (b) compressor corrected mass flow rate \dot{m}_{c2}
- (c) compressor adiabatic efficiency η_c

8.16 A compressor adiabatic efficiency is measured to be $\eta_c = 0.85$ for a compressor total pressure ratio of $\pi_c = 20$. What is the “small-stage” efficiency for this compressor?

8.17 A compressor has a polytropic efficiency of $e_c = 0.92$ and a pressure ratio, $\pi_c = 25$ for an inlet condition of $T_{t1} = 520 \text{ }^\circ\text{R}$ and $c_p = 0.24 \text{ BTU/lbm} \cdot \text{ }^\circ\text{R}$, calculate

- (a) exit total temperature T_{t2}
- (b) compressor adiabatic efficiency η_c
- (c) compressor specific work w_c
- (d) shaft power $\dot{\varphi}_s$ for a 100 lbm/s flow rate

8.18 A multistage compressor develops a total pressure ratio $\pi_c = 25$, and is designed with eight identical (i.e., “repeated”) stages. The compressor polytropic efficiency is $e_c = 0.92$. Calculate

- (a) average stage total pressure ratio π_s
- (b) stage adiabatic efficiency η_s
- (c) compressor total temperature ratio τ_c

8.19 Plot compressor adiabatic efficiency η_c versus π_c ranging from 1.0 to 50, for the following polytropic efficiencies $e_c = 0.95, 0.90, \text{ and } 0.85$ as the running parameter.

8.20 A rotor blade row has a solidity of 1.0 at its pitchline. The absolute flow enters the rotor with no preswirl at $C_{z1m} = 500 \text{ fps}$, and the rotor rotational speed is $U_m = 1200 \text{ fps}$ (at the pitchline). If the rotor exit flow angle at r_m is $\beta_{2m} = -30^\circ$, calculate

- (a) exit swirl velocities $W_{\theta 2m}$ and $C_{\theta 2m}$
- (b) blade torque (per unit mass flow rate) at the pitchline assuming $r_m = 1.0 \text{ ft}$
- (c) the nondimensional total temperature rise across the rotor $\Delta T_t / T_{t1}$
- (d) exit speed of sound a_2 assuming inlet speed of sound is $a_1 = 1100 \text{ fps}$

- (e) exit absolute Mach number M_{2m}
- (f) inlet static pressure p_1 for an inlet total pressure of $p_{t1} = 14.7 \text{ psia}$
- (g) exit total pressure, assuming rotor adiabatic efficiency is 0.9
- (h) rotor static pressure rise, $C_{p_m} = \Delta p_m / (1/2 \rho W_{1m}^2)$
- (i) shaft rotational speed ω (rpm)
- (j) rotor torque at r_m per unit mass flow rate
- (k) the axial force on the blades at r_m , assuming the mean chord $c_m = 4 \text{ in.}$
- (l) tangential force on the blade at r_m
- (m) sectional lift-to-drag ratio, L'/D'
- (n) rotor specific work at r_m

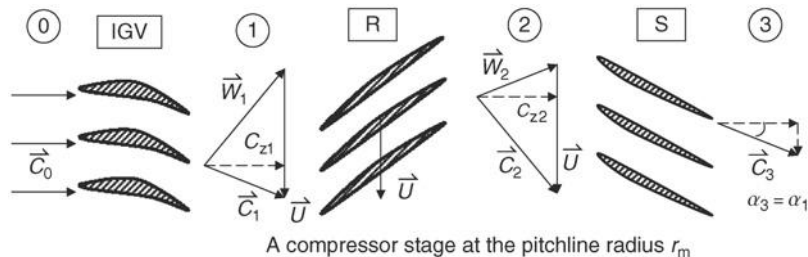
8.21 Calculate the Reynolds number based on chord at the pitchline for the rotor blade described in Problem 8.20, assuming fluid coefficient of viscosity is $\mu = 1.8 \times 10^{-5} \text{ kg/m} \cdot \text{s}$. Compare the Reynolds number that you calculate to the upper critical Reynolds number in a compressor.

8.22 Calculate the circulation at the pitchline for the rotor blade row described in Problem 8.20. Also calculate the fraction of “ideal” lift that was destroyed by the total pressure losses in the blade row. Is there any indication of shock losses at the pitchline?

8.23 A rotor blade row has a hub-to-tip radius ratio of 0.5, solidity at the pitchline of 1.0, the axial velocity is 160 m/s , and zero preswirl. The mean section has a design diffusion factor of $D_m = 0.5$. Calculate and plot where appropriate

- (a) exit swirl at the pitchline assuming the shaft rpm of 6000 and $r_m = 1.0 \text{ ft}$ (0.3 m)
- (b) downstream swirl distribution $C_{\theta 2}(r)$ assuming a freevortex design rotor
- (c) the radial distribution of degree of reaction ${}^\circ\text{R}$ along the blade span
- (d) radial distribution of diffusion factor $D_r(r)$.

8.24 An axial-flow compressor stage is downstream of an IGV that turns the flow 15° in the direction of the rotor rotation, as shown. The axial velocity component remains constant throughout the stage at $C_z = 150 \text{ m/s}$. The rotor rotational speed is $\omega = 3000 \text{ rpm}$ and the pitchline radius is $r_m = 0.5 \text{ m}$. The rotor relative exit flow angle is $\beta_2 = -15^\circ$.



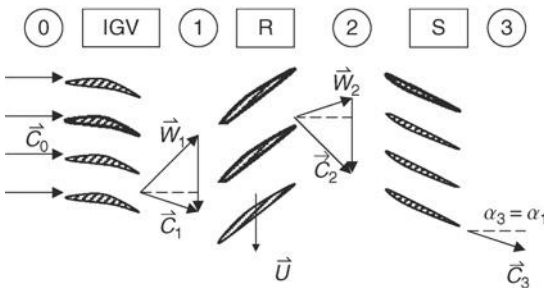
■ FIGURE P8.24

The static temperature and pressure of air upstream of the rotor are $T_1 = 20^\circ\text{C}$ and $p_1 = 10^5$ Pa, respectively. Assuming $c_p = 1.004$ kJ/kg · K and $\gamma = 1.4$, calculate

- (a) relative Mach number to the rotor, M_{1r}
- (b) absolute total temperature T_{t1}
- (c) rotor specific work w_c in kJ/kg
- (d) total temperature downstream of the rotor, T_{t2}
- (e) relative Mach number downstream of the rotor, M_{2r}
- (f) stage total pressure ratio at the pitchline radius for $e_c = 0.92$
- (g) stage degree of reaction ${}^\circ R_m$ at the pitchline

8.25 A compressor stage with an inlet guide vane is shown at its pitchline radius $r_m = 0.5$ m. The rotor angular speed is $\omega = 4000$ rpm. The axial velocity is constant throughout at $C_z = 150$ m/s and the IGW imparts a preswirl of 75 m/s in the direction of rotor rotation, as shown. Assuming the inlet flow to IGW has $p_{t0} = 100$ kPa and $T_{t0} = 25^\circ\text{C}$, calculate

- (a) T_0, M_0, p_0
Assuming the IGW has a total pressure loss coefficient of $\varpi_{IGW} = 0.02$, calculate
- (b) $p_{t1}, T_{t1}, T_1, M_1, p_1, M_{1r}$ and p_{t1r}
Knowing that the compressor stage has a degree of reaction of ${}^\circ R = 0.5$ at the pitchline, calculate
- (c) $C_{\theta 2}, T_{t2}, T_2, M_2, M_{2r}$
For a rotor total pressure loss coefficient of $\bar{\omega}_r = 0.03$ at the pitchline, calculate
- (d) p_{t2}
Assume: $\gamma = 1.4$ and $c_p = 1004$ J/kg · K throughout the stage.



■ FIGURE P8.25

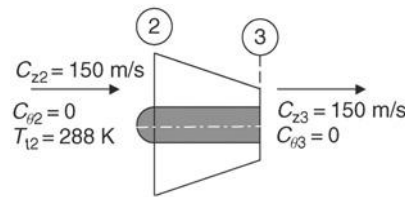
8.26 Apply Euler turbine equation to a streamtube that enters a compressor rotor blade row at $r = 2.5$ ft with zero preswirl and exits the row at $r = 2.7$ ft and attains 1000 ft/s of swirl velocity in the absolute frame. Assume that the shaft rotational speed is 5000 rpm.

8.27 Assume that we can analyze a 3D compressor rotor by stacking up its 2D flowfield, what is known as the “strip theory.” Now, let us consider one such section. The inlet flow approaches the rotor blade at $\beta_1 = -45^\circ$. The relative exit

flow angle is $\beta_2 = -30^\circ$ for a net 15° turning. The solidity of the rotor at this section is 1.5. Identify the most suitable NACA 65-series profile for this section that could produce the largest positive stall tolerance. Estimate the stagger angle that the blades need to be set at this section. To solve this problem, you have to use the cascade data. What is the safe operating range of the incidence angle (or equivalently the inlet flow angles), in degrees, for this section?

8.28 A simple method to establish the annulus geometry in a multistage compressor is to assume a constant through-flow (i.e., axial) speed C_z . Calculate

- (a) the density ratio ρ_3/ρ_2
- (b) the exit-to-inlet area ratio A_3/A_2



■ FIGURE P8.28

for

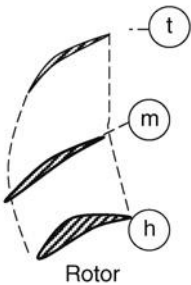
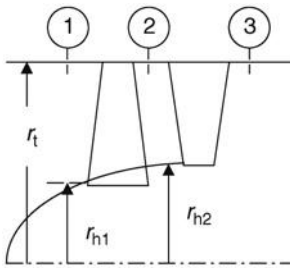
- $\pi_c = 35$
- $e_c = 0.90$
- $C_z = \text{constant}$
- $\gamma = 1.4, c_p = 1,004$ J/kg · K

Also, if the hub radius is constant and for a mass flow rate of 100 kg/s and the inlet total pressure of $p_{t2} = 100$ kPa, calculate the tip-to-tip radius ratio $(r_3/r_2)_{tip}$

8.29 Consider a compressor stage with no inlet guide vane. The hub-to-tip radius ratio for the rotor is $r_{h1}/r_{t1} = 0.5$ and the mass flow rate (of air) in the compressor is 100 kg/s, at the standard sea level condition, $p_{t1} = 100$ kPa and $T_{t1} = 288$ K. For an axial Mach number of $M_z = 0.5$, calculate

- (a) the rotor hub and casing radii r_{h1} and r_{t1} (in meters)
To achieve a relative tip Mach number of $(M_{1r})_{tip} = 1.4$, calculate
- (b) the rotor rotational speed ω (in radians per second)
For a design pitchline degree of reaction of ${}^\circ R_m = 0.5$, and constant axial velocity, calculate
- (c) the rotor exit swirl at the pitchline radius $C_{\theta 2m}$ (in m/s)
- (d) the total temperature T_{t2m} (in K) using Euler equation
- (e) the total pressure p_{t2m} (in kPa), assuming $\varpi_{rm} = 0.005$
- (f) the fluid density ρ_{2m} in kg/m³

Now, assume that we chose a free-vortex design for the rotor.



■ FIGURE P8.29

Calculate

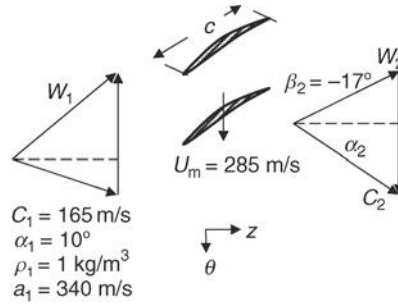
- (g) the degree of reaction for the rotor hub and tip ${}^\circ R_h$ and ${}^\circ R_t$
- (h) the diffusion factor at the pitchline D_m
- (i) the hub radius in station 2, r_{h2} , from continuity equation.

8.30 A compressor rotor velocity triangles at the pitchline are shown. The compressor hub-to-tip radius ratio is $r_h/r_t = 0.4$. The rotor solidity at the pitchline is $\sigma_m = 1.0$. Assuming constant axial velocity across the rotor at pitchline, calculate

- (a) solidity at the tip for $c_t = c_m$
- (b) solidity at the hub for $c_h = c_m$
- (c) degree of reaction ${}^\circ R_m$
- (d) diffusion factor D_m
- (e) de Haller criterion
- (f) rotor loading coefficient ψ_m
- (g) flow coefficient φ_m

Assuming that the rotor has a free-vortex design, calculate

- (h) diffusion factor at the tip D_t
- (i) the degree of reaction at the hub, ${}^\circ R_h$
- (j) the axial velocity distribution downstream of the rotor (assuming radial equilibrium)

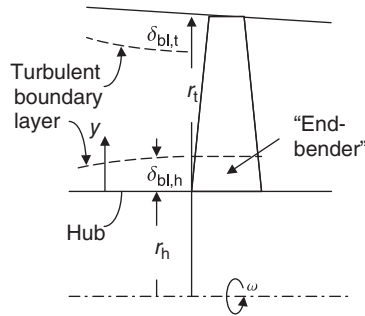


■ FIGURE P8.30

8.31 The flow coefficient to a rotor at pitchline is $\varphi_m = 0.8$, its loading coefficient is $C_m = 1.0$. The inlet flow to the rotor has zero swirl in the absolute frame of reference. Assuming axial velocity $C_{zm} = \text{constant}$ across the rotor, calculate

- (a) the relative inlet flow angle β_{1m}
- (b) the relative exit flow angle β_{2m}
- (c) the degree of reaction ${}^\circ R_m$

8.32 The end wall boundary layers and a rotor blade are shown. The hub radius is $r_h = 0.5$ m and the shaft speed is $\omega = 4000$ rpm. The rotor inlet flow has zero preswirl, i.e., $\alpha_1 = 0$. The rotor blade is twisted to meet the flow at zero incidence within the boundary layer. Calculate the blade stagger angle at the hub and its change within the boundary layer if $\delta_{bl,h} = 10$ cm and it has a 1/7th power law profile. $C_z(y)/C_{zm} = (y/\delta)^{1/7}$ and $C_{zm} = 150$ m/s. [Assume blade stagger angle is \approx relative flow angle, β_1]



■ FIGURE P8.32

8.33 A multistage compressor has 12 repeated stages. Each stage produce a constant total temperature rise of $\Delta T_t = 25^\circ\text{C}$. The inlet total temperature is $T_{t1} = 288$ K, and stage adiabatic efficiency is $\eta_s = 0.90$ and is assumed constant for the 12 stages. Calculate and graph the stage total pressure ratio for all 12 stages. What is the compressor overall total pressure ratio?

8.34 A compressor stage has 37 rotor blades and 41 stator blades. The shaft rotational speed is 5000 rpm. Calculate

- (a) the rotor blade passing frequency as seen by the stator blades
- (b) the stator blade passing frequency as seen by the rotor blades

8.35 The absolute flow to a compressor rotor has a coswirl with $\alpha_1 = 15^\circ$. The exit flow from the rotor has an absolute flow angle $\alpha_2 = 35^\circ$. The pitchline radius is at $r_m = 0.6$ m and the rotor angular speed is $\omega = 5220$ rpm. Assuming the axial velocity is $C_{zm} = 150$ m/s and is constant across the rotor, calculate

- (a) the specific work at the pitchline
- (b) the rotor torque per unit mass flow rate
- (c) the degree of reaction

8.36 A rotor blade row has a hub-to-tip radius ratio of 0.4, solidity at the pitchline of 1.2, the axial Mach number of 0.6, and zero preswirl. The mean section has a design diffusion factor of $D_m = 0.5$. Assuming $a_1 = 330$ m/s, calculate and plot where appropriate

- (a) exit swirl at the pitchline assuming the shaft rpm of 5000 and $r_m = 0.4$ m
- (b) downstream swirl distribution $C_{\theta 2}(r)$, assuming a solid-body rotation vortex design rotor
- (c) the radial distribution of degree of reaction $R(r)$, along the blade span
- (d) radial distribution of diffusion factor $D_r(r)$.

8.37 Bending stresses on a cantilevered blade, under aerodynamic loading, is estimated (by Kerrebrock, 1992) to be

$$\frac{\sigma_{\text{bending}}}{p} \approx \left(\frac{C_z}{U_1} \right) (\tau_s - 1) \left(\frac{s}{2c} \right) \left(\frac{r_t}{t_{\text{max}}} \right)^2$$

Estimate the ratio of bending stress to inlet pressure ($\sigma_{\text{bending}}/p$) in a rotor with axial velocity 165 m/s, the rotor tip radius is $r_t = 0.75$ m, the mean solidity of 1.5, angular speed is $\omega = 4000$ rpm. The maximum blade thickness is $t_{\text{max}} = 1$ cm. The stage total pressure ratio is 1.6 and the stage adiabatic efficiency is 0.88.

8.38 Centrifugal stress is proportional to AN^2 as we discussed in the compressor design section. It follows

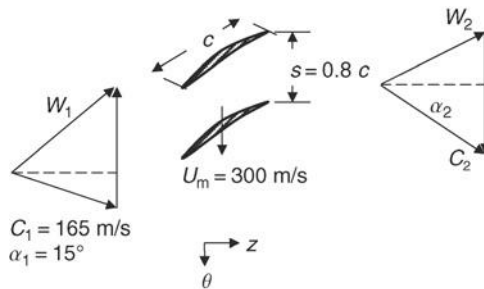
$$\frac{\sigma_c}{\rho_{\text{blade}}} = \frac{\omega^2 A}{4\pi} \left(1 + \frac{A_t}{A_h} \right)$$

for a linear taper ratio. For a titanium rotor blade of $r_h = 0.4$ m, $r_t = 0.8$ m, and taper ratio $A_t/A_h = 0.8$, calculate the

acceptable shaft speed ω if the allowable strength-to-weight ratio is ~ 9 ksi/slug/ft³, which is equivalent to

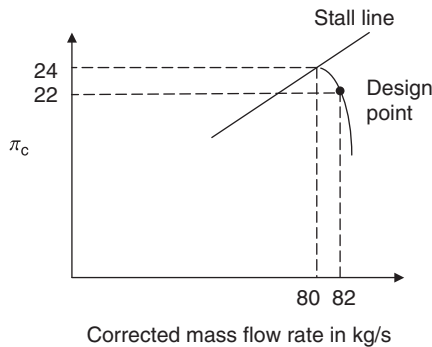
allowable creep rupture strength	120,560 m ² /s ² (or ~ 120 kPa/kg/m ³)
required strength	68,326 m ² /s ² (or ~ 68 kPa/kg/m ³)

8.39 A rotor section has de Haller criterion $W_2/W_1 = 0.75$. Assuming the axial velocity remains constant across the rotor and the velocity triangles are as shown, calculate the corresponding D -factor and degree of reaction for the rotor section.



■ FIGURE P8.39

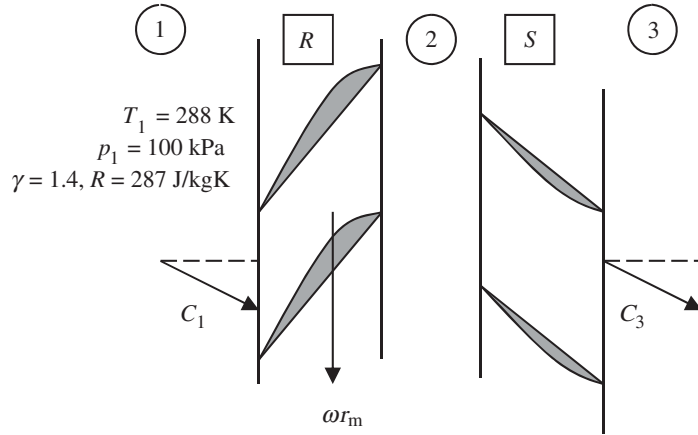
8.40 A portion of a compressor map surrounding the design point is shown.



■ FIGURE P8.40

Calculate this compressor's stall margin.

8.41 A compressor stage at the pitchline, $r_m = 0.5$ m, is shown. The inlet flow to the rotor has a preswirl with $\alpha_1 = 22^\circ$. The axial velocity is $C_{z1} = C_{z2} = C_{z3} = 170$ m/s, i.e. constant throughout the stage. The stage is of repeated design, with $\alpha_3 = \alpha_1$. Rotor and stator solidities at pitchline are 1.2 and 1.0 respectively. The rotor inlet relative velocity at pitchline is sonic, i.e., $W_1 = a_1$ and the rotor relative exit velocity, following de Haller criterion, is $W_2 = 0.75 W_1$.



■ FIGURE P8.41

Calculate:

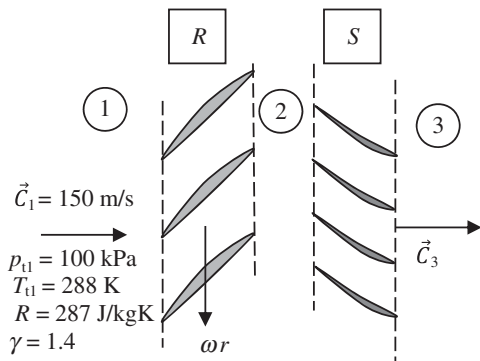
- (a) shaft rotational speed, ω , in rpm
- (b) rotor exit (absolute) swirl, $C_{\theta 2}$ in m/s
- (c) stage degree of reaction, ${}^\circ R_m$
- (d) rotor D-factor, D_r
- (e) stage total temperature ratio
- (f) stage total pressure ratio for $e_c = 0.9$

8.42 An axial-flow compressor stage at its pitchline radius ($r_m = 0.50$ m) has zero preswirl, an axial velocity of 150 m/s. Its degree of reaction is ${}^\circ R_m = 0.50$, and the shaft angular speed is 5,200 rpm. Assuming constant throughflow speed, i.e., $C_z = \text{const.}$, and repeated stage design at the pitchline, calculate:

- (d) absolute Mach number downstream of the rotor, M_2
- (e) absolute Mach number downstream of the stator, M_3
- (f) stage total temperature ratio, τ_s
- (g) stage total pressure ratio if $\eta_s = 0.90$

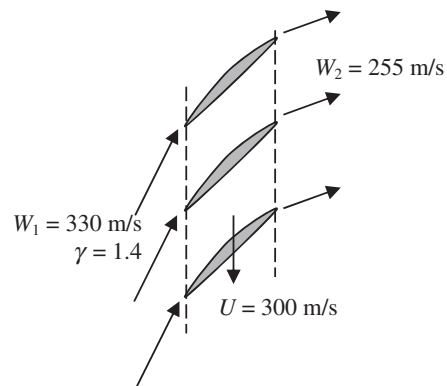
8.43 The relative flow across a compressor rotor is shown. The rotor rotational speed is $U = 300$ m/s. The axial velocity is $C_z = 165$ m/s and it remains constant across the rotor. Assuming the rotor solidity is $\sigma_r = 0.8$, calculate:

- (a) de Haller criterion
- (b) rotor degree of reaction (for a repeated stage)
- (c) rotor specific work (in kJ/kg)
- (d) rotor D-factor



■ FIGURE P8.42

- (a) relative Mach number at rotor inlet, M_{1r}
- (b) rotor exit relative velocity, W_2 (m/s)
- (c) static temperature downstream of the rotor, T_2 (K)

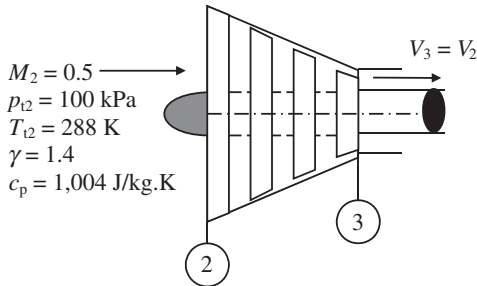


■ FIGURE P8.43

8.44 A multistage compressor develops a total pressure ratio of $\pi_c = 35$ with a polytropic efficiency of $e_c = 0.90$. The

air mass flow rate through the compressor is $\dot{m} = 200$ kg/s. Assuming γ and c_p remain constant, calculate:

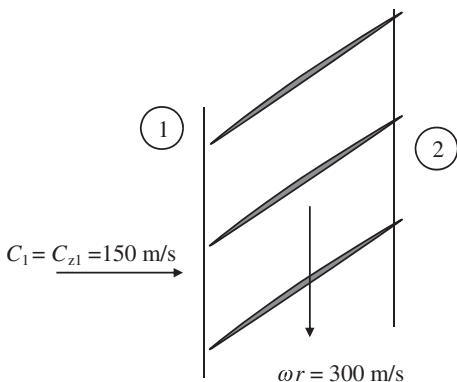
- (a) compressor shaft power, $\dot{\varphi}_c$, in MW
- (b) flow area in 2, i.e., A_2 in m^2
- (c) density of air in station 3, ρ_3 , in kg/m^3
[note: the axial velocity at the compressor exit, $V_3 = V_2$]
- (d) The nondimensional entropy rise across the compressor, $\Delta s/R$



■ FIGURE P8.44

8.45 A cylindrical cut of the rotor in an axial flow compressor is shown. The rotor uses constant-axial velocity design, $C_{z1} = C_{z2}$. Assuming diffusion in the rotor, based on de Haller criterion is described by $W_2/W_1 = 0.75$, calculate:

- (a) relative flow angle at the rotor inlet, β_1 in degrees
- (b) relative flow angle at the rotor exit, β_2 in degrees
- (c) rotor exit swirl, $C_{\theta 2}$, in m/s
- (d) stage loading parameter, ψ

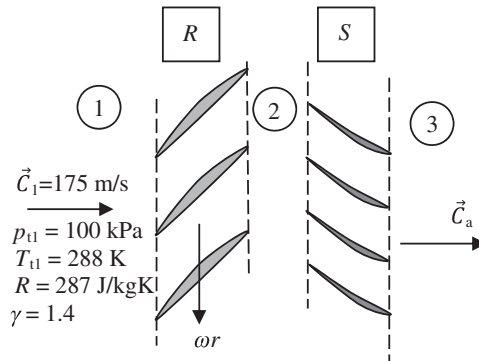


■ FIGURE P8.45

8.46 An axial-flow compressor stage at its pitchline radius ($r_m = 0.40$ m) has zero preswirl, an axial velocity of 175 m/s, a degree of reaction of ${}^\circ R_m = 0.65$, with the shaft angular speed of 6450 rpm. Assuming constant throughflow speed,

i.e., $C_z = \text{const.}$, and a repeated-stage design at the pitchline, calculate:

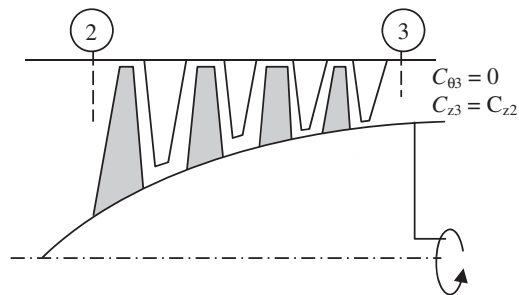
- (a) relative Mach number at rotor inlet, M_{1r}
- (b) rotor exit relative velocity, W_2 (m/s)
- (c) static temperature downstream of the rotor, T_2 in K
- (d) absolute Mach number downstream of the rotor, M_2
- (e) absolute Mach number downstream of the stator, M_3
- (f) stage total temperature ratio, τ_s
- (g) stage total pressure ratio if $\eta_s = 0.88$



■ FIGURE P8.46

8.47 A multistage compressor has a total pressure ratio of $\pi_c = 15$, a polytropic efficiency of $e_c = 0.90$ and the inlet condition: $C_2 = C_{z2} = 160$ m/s, $T_{12} = 288$ K, $p_{12} = 100$ kPa. Assuming constant gas properties $\gamma = 1.4$ and $c_p = 1004$ J/kgK and C_z remains constant with compressor exit purely in the axial direction (i.e., no exit swirl), calculate:

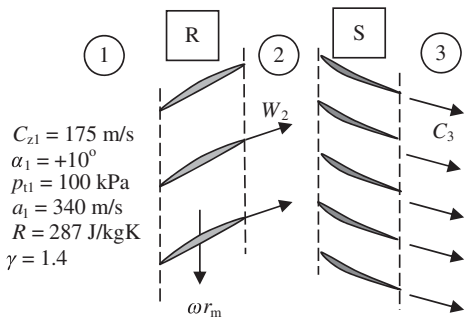
- (a) compressor exit total temperature, T_{13} in K
- (b) compressor inlet Mach number, M_2
- (c) compressor exit Mach number, $M_3 = M_{z3}$
- (d) compressor Density ratio, ρ_3/ρ_2
- (e) compressor area ratio, A_3/A_2



■ FIGURE P8.47

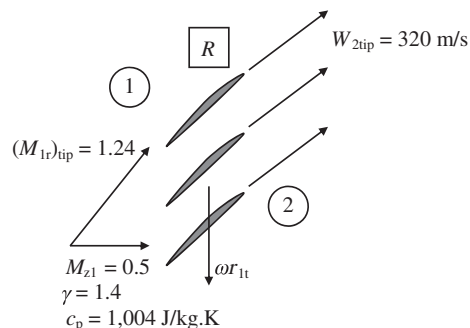
8.48 An axial-flow compressor stage is shown at its pitchline radius ($r_m = 0.30$ m). The axial velocity is 175 m/s and is constant. The rotor exit relative flow angle is $\beta_2 = -15^\circ$. Assuming the inlet *preswirl exists* with $\alpha_1 = +10^\circ$ and shaft angular speed is 7600 rpm, calculate:

- (a) absolute Mach number at the inlet, M_1
- (b) relative Mach number at the inlet, M_{1r}
- (c) static pressure at the inlet, p_1 (kPa)
- (d) total temperature at the inlet, T_{t1} (K)
- (e) rotor exit absolute swirl, $C_{\theta 2}$ (m/s)
- (f) stage degree of reaction, ${}^\circ R_m$ (assume repeated stage)
- (g) rotor specific work at pitchline, w_m in kJ/kg
- (h) static temperature downstream of the rotor, T_2 (K)
- (i) absolute Mach number downstream of the rotor, M_2
- (j) speed of sound downstream of the stator, a_3 (m/s)
- (k) absolute Mach number downstream of the stator, M_3



■ FIGURE P 8.48

8.49 An axial-flow compressor rotor has a tip relative Mach number (at the inlet) of 1.24, as shown. The tip radius is $r_{t1} = 0.73$ m and the inlet speed of sound is $a_1 = 337$ m/s. The rotor inlet flow has zero preswirl and has an axial Mach number of $M_{z1} = 0.5$. The rotor exit has a relative velocity, $W_{2tip} = 320$ m/s. Assuming C_z is constant, calculate:



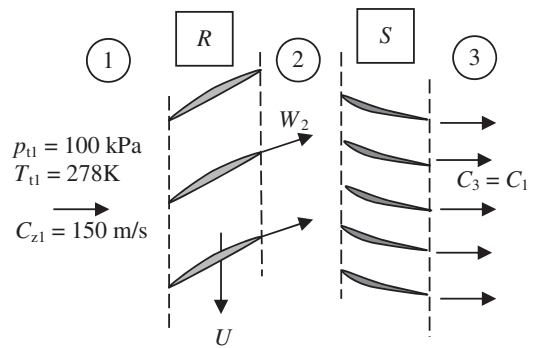
■ FIGURE P 8.49

- (a) the shaft angular speed, ω in rpm
- (b) the rotor specific work, w_c , at the tip in kJ/kg
- (c) rotor exit absolute Mach number, M_2

8.50 An axial flow compressor stage at $r = 0.4$ m is shown. The inlet flow is purely axial with $C_{z1} = 150$ m/s, which remains constant across the rotor and stator. The rotor solidity at this radius is $\sigma_r = 1.5$. The rotor angular speed is $\omega = 7400$ rpm. The stage degree of reaction at this radius is ${}^\circ R = 0.75$. The rotor total pressure loss parameter (in relative frame) is $\varpi_r = 0.05$.

The gas properties are: $\gamma = 1.4$ and $R = 287$ J/kgK. Calculate:

- (a) absolute swirl at rotor exit, $C_{\theta 2}$ in m/s
- (b) rotor exit (absolute) total temperature, T_{t2} in K
- (c) static temperature at the rotor exit, T_2 in K
- (d) rotor exit absolute Mach number, M_2
- (e) rotor exit relative Mach number, M_{2r}
- (f) relative dynamic pressure at rotor inlet, q_{1r} , in kPa
- (g) inlet relative total pressure, p_{t1r} , in kPa
- (h) static pressure at rotor exit, p_2 , in kPa
- (i) rotor exit (absolute) total pressure, p_{t2} , in kPa
- (j) rotor D-factor, D_r , at this radius



■ FIGURE P 8.50

8.51 The pitchline radius of a compressor rotor is at $r_m = 0.3$ m. The degree of reaction is ${}^\circ R_m = 0.75$. The axial velocity to the rotor is $C_{z1} = 175$ m/s = constant across the blade row. The flow to the rotor has zero preswirl and the rotor angular speed is $\omega = 6500$ rpm. The solidity of the rotor at the pitchline is $\sigma_m = 1.0$. Calculate:

- (a) absolute swirl velocity downstream of the rotor, i.e., $C_{\theta 2m}$, in m/s
- (b) relative swirl upstream and downstream of the rotor, i.e., $W_{\theta 1}$ and $W_{\theta 2}$ in m/s
- (c) de Haller parameter, W_2/W_1
- (d) diffusion factor at the pitchline radius, D_{fm}

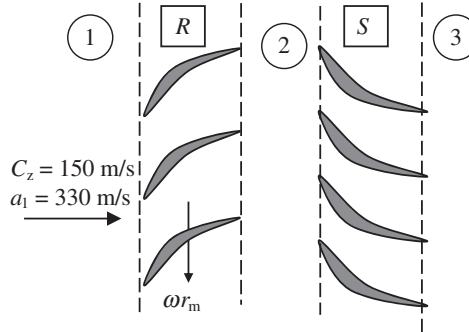
8.52 An axial-flow compressor rotor at the pitchline has a radius of $r_m = 0.5$ m. The shaft rotational speed is $\omega = 6000$ rpm. The inlet flow to the rotor has zero preswirl and the axial velocity is constant, with $C_z = 150$ m/s. The stage has a 80% degree-of-reaction at the pitchline where the solidity is $\sigma_m = 1.2$. The stage adiabatic efficiency is equal to the polytropic efficiency, $e_c = 0.92$.

Assuming that the inlet total temperature is $T_{t1} = 288$ K, $\gamma = 1.4$ and $c_p = 1.004$ kJ/kg·K, calculate:

- (a) rotor specific work at $r = r_m$ in kJ/kg
- (b) stage loading, ψ , at $r = r_m$
- (c) flow coefficient, ϕ , at $r = r_m$
- (d) rotor relative Mach number at the pitchline, $M_{1r,m}$
- (e) stage total pressure ratio at the pitchline
- (f) rotor diffusion factor at the pitchline
- (g) is the de Haller criterion satisfied?

8.53 A compressor stage at its pitchline radius ($r_m = 0.25$) has $\sigma_m = 0.73$. The axial velocity is constant at $C_{zm} = 150$ m/s. The flow entering the compressor is swirl free, i.e., $\alpha_1 = 0$. The flow exiting the stage at pitchline is also swirl free, i.e., $\alpha_3 = 0$. The compressor angular speed is $\omega = 7500$ rpm. The speed of sound at the entrance to the stage is $a_1 = 330$ m/s and rotor solidity at the pitchline radius is $\sigma_m = 0.80$. Assuming the gas constant is $R = 287$ J/kg·K and $\gamma = 1.4$, calculate:

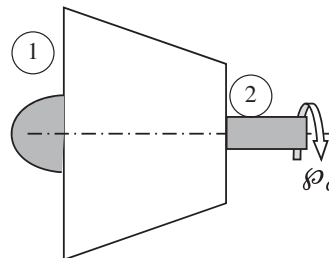
- (a) absolute swirl downstream of the rotor, $C_{\theta 2m}$, in m/s
- (b) rotor specific work at pitchline radius, w_c , in kJ/kg
- (c) total temperature downstream of the rotor, T_{t2m} , in K
- (d) de Haller criterion for the rotor at pitchline
- (e) the rotor diffusion factor at the pitchline radius, D_m



■ FIGURE P8.53

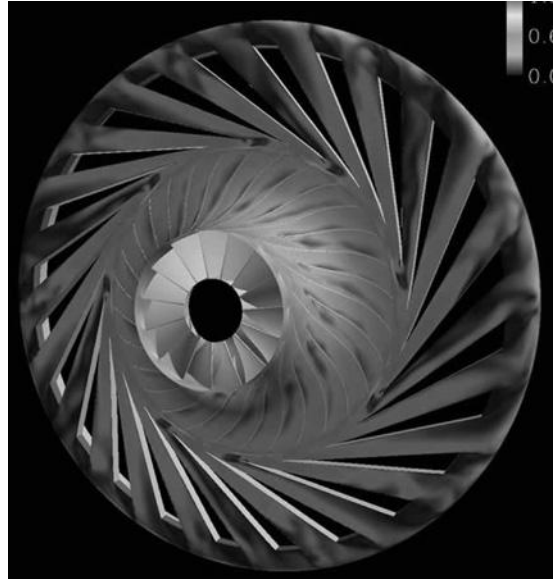
8.54 An axial-flow compressor has no IGV. Its inlet conditions are: $p_{t1} = 100$ kPa, $T_{t1} = 288$ K and the mass flow rate $\dot{m} = 100$ kg/s. The compressor pressure ratio is $\pi_c = 15$ and the polytropic efficiency is $e_c = 0.90$. The axial flow in the compressor is designed to be constant at $C_z = 166$ m/s. Assuming the gas constant is $R = 287$ J/kg·K and $\gamma = 1.4$, calculate:

- (a) absolute Mach number at the inlet to the compressor, M_1
- (b) compressor shaft power, ϕ_c , in MW
- (c) compressor inlet flow area, A_1 in m^2
- (d) exit Mach number, M_2 (assume the exit flow is swirl free)
- (e) compressor exit area, A_2 in m^2



■ FIGURE P8.54

Centrifugal Compressor Aerodynamics

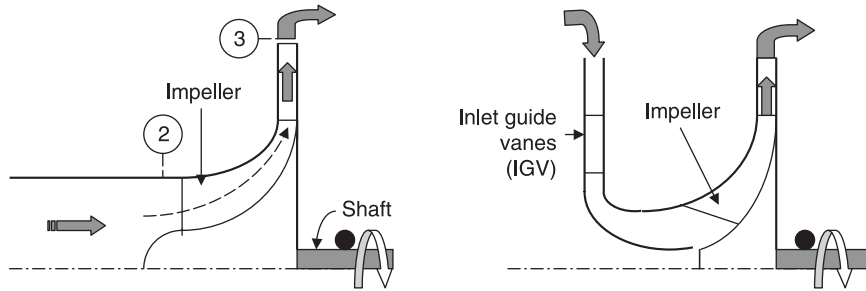


*CFD results shown in a centrifugal compressor.
Source: Courtesy of NASA*

9.1 Introduction

Centrifugal compressors belong to the general category of turbomachines. The flow may enter a centrifugal compressor in the axial direction. The rotor, which is known as the impeller, imparts energy to the fluid by the rotation of its aerodynamic surfaces (i.e., blades or impeller vanes) that are highly curved and twisted. The initial curvature and twist in the impeller, known as the inducer section, has the function of meeting the incoming flow at its relative flow angle. The second function of the inducer is to turn the relative flow toward the axial direction before it begins its journey in the radial direction. The third function of the inducer is to increase the fluid static pressure in the passage by decelerating the gas. The inducer exit flow is then further decelerated radially outward, by virtue of centrifugal force acting on the fluid in the spinning impeller (vaned) passages. Since the pressure rise in this type of configuration is primarily produced by centrifugal compression/force, this kind of turbomachinery is known as a centrifugal compressor. In contrast to axial-flow compressors where the flow deviation in the radial direction is negligible, the principle of operation of the centrifugal compressor is based on large radial shift between the inlet and exit of the impeller (Figure 9.1). Since the impeller exit radius is by design much larger than the impeller inlet radius, the centrifugal compressors have a lower mass flow rate per frontal area than the axial-flow compressors. A low mass flow per frontal area is of critical concern to aircraft propulsion system designers, since it translates into an increased drag count. However, in low-speed applications where the drag penalty is less significant, centrifugal compressors offer the advantage of high-pressure ratio per stage and robustness of construction that is less prone to structural failure. There are other

■ **FIGURE 9.1**
Schematic drawing of a first (left) and a second stage (right) centrifugal compressor



applications for small gas generators on board aircraft that are suitable for centrifugal compressor application. For example, APUs (auxiliary power units) are used to start the engines and provide power to aircraft, which are entirely embedded in the fuselage; therefore, there are no concerns of external drag penalties for their use. Industrial and automotive turbocharging applications also use centrifugal compressors.

The radially pumped flow from the impeller first needs to be decelerated through a radial and vaned diffuser, and then it needs to turn back toward the axis of rotation for either the next compressor stage or the combustion chamber. Since any ducting that involves turns is a source of (total pressure) loss, multistage centrifugal compressors are considered cumbersome (and with lower efficiency) as compared with axial-flow compressors. However, the total pressure ratio of a single-stage centrifugal compressor may be as high as 10–12, whereas an axial-flow compressor stage produces a high of ~ 1.6 –2.0 in advanced transonic fan stages.

9.2 Centrifugal Compressors

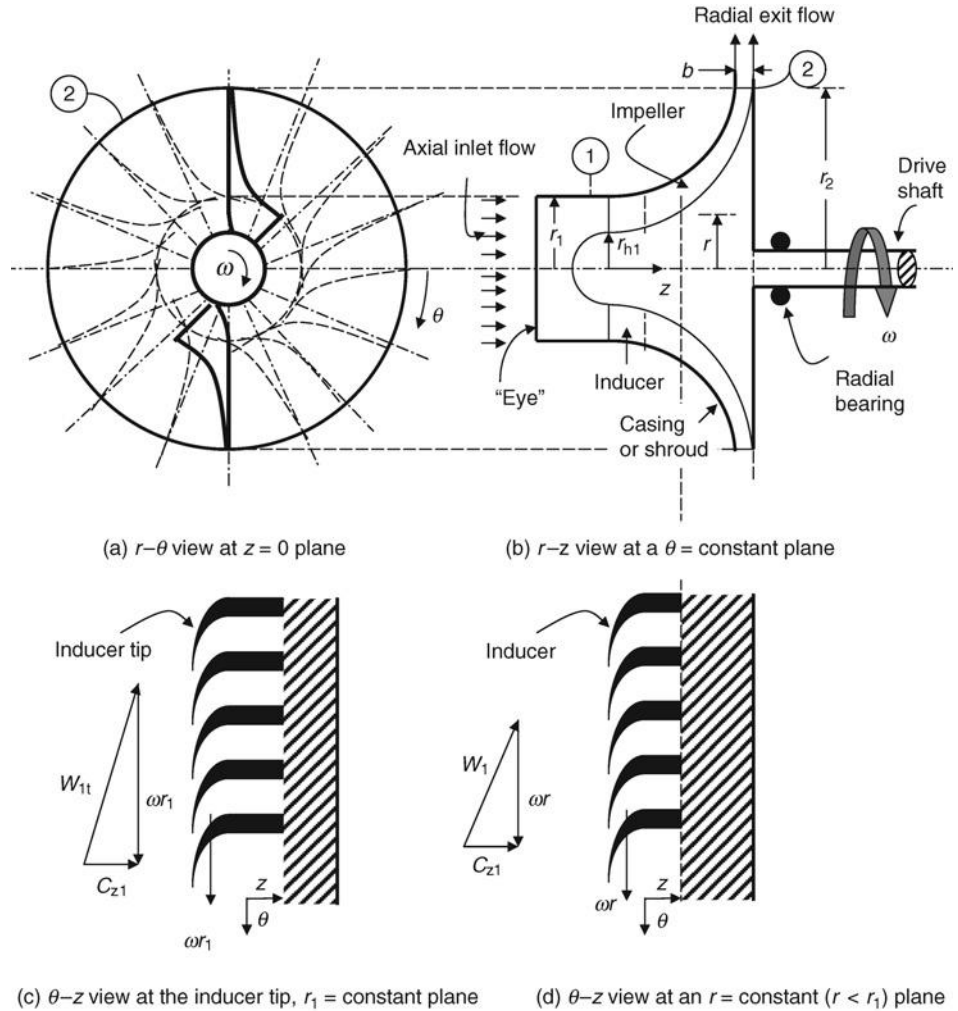
A centrifugal compressor is a robust mechanical compression system that pumps the gas from primarily an axial inlet condition to a radial exit direction. The elements of a centrifugal compressor rotor, known as the impeller, are shown in Figure 9.2.

The inlet section of an impeller is called the inducer, which is turned in the direction of impeller rotation to meet the flow at a small incidence angle. The radial displacement of the fluid in the inducer is small but the flow turning is rather large. The inducer turns the fluid from the inlet relative flow direction β_1 to the axial direction. The static pressure rise in the inducer is due to the conversion of relative swirl kinetic energy in a curved diffuser. The outer portion of the impeller is responsible for turning the flow in the radial direction and accelerating the fluid in the tangential direction. The torque acting on the fluid causes the angular momentum to change across the rotor blade following Euler turbine equation:

$$\tau_{\text{fluid}} = -\tau_{\text{blade}} = \dot{m}(r_2 C_{\theta 2} - r_1 C_{\theta 1})$$

As in the axial-flow compressors, we note that the torque acting on the fluid is positive across the rotor (as $r_2 C_{\theta 2} > r_1 C_{\theta 1}$) and thus the rotor torque being equal and opposite is negative. Then multiplying the rotor torque with the angular speed of the shaft, ω , we get a negative shaft power that is delivered to the rotor. This is consistent with the thermodynamic convention employed in the first law that considers the work done *on the surrounding* as positive. Therefore, the work done *by the surrounding* (as needed by

■ **FIGURE 9.2**
Definition sketch of a
centrifugal compressor
impeller with an
inducer



compressors) is then negative. The torque acting on the fluid crossing the stator, as in the axial-flow compressors, is negative. Therefore, the stator vanes experience a positive torque. There will not be any contribution to the fluid power by the stator blades as they are stationary and thus perform no work on the medium. The shaft power delivered to the fluid is converted into total enthalpy rise according to

$$\dot{\varphi} = \dot{m}\omega(r_2 C_{\theta 2} - r_1 C_{\theta 1}) = \dot{m}(h_{t2} - h_{t1}) \tag{9.1}$$

The rotor total temperature ratio is deduced from Equation 9.1, that is,

$$\frac{T_{t2}}{T_{t1}} = 1 + \frac{\omega \cdot r_2}{c_p T_{t1}} \left[C_{\theta 2} - \left(\frac{r_1}{r_2} \right) C_{\theta 1} \right] \tag{9.2}$$

In Equation 9.1, the impeller radius ratio (r_1/r_2) is small, which makes the second term in the bracket negligible compared with the first term. In addition, either due to a lack of

inlet guide vanes, which results in $C_{\theta 1}$ to be identically zero, or the fact that $C_{\theta 2} \gg C_{\theta 1}$ in a centrifugal compressor, we often neglect the second term in the bracket in Equation 9.2 in favor of the first term, that is,

$$\frac{T_{t2}}{T_{t1}} \cong 1 + \frac{\omega \cdot r_2 \cdot C_{\theta 2}}{c_p T_{t1}} = 1 + \frac{U_2^2}{c_p T_{t1}} \left(\frac{C_{\theta 2}}{U_2} \right) \quad (9.3)$$

However, note that we do not *have to* neglect the second term in Equation 9.2, as the inlet swirl $C_{\theta 1}$ may be treated as a known input to the problem.

There are three types of impeller geometry:

- Radial impeller
- Forward-leaning impeller
- Backward-leaning (or backswept) impeller.

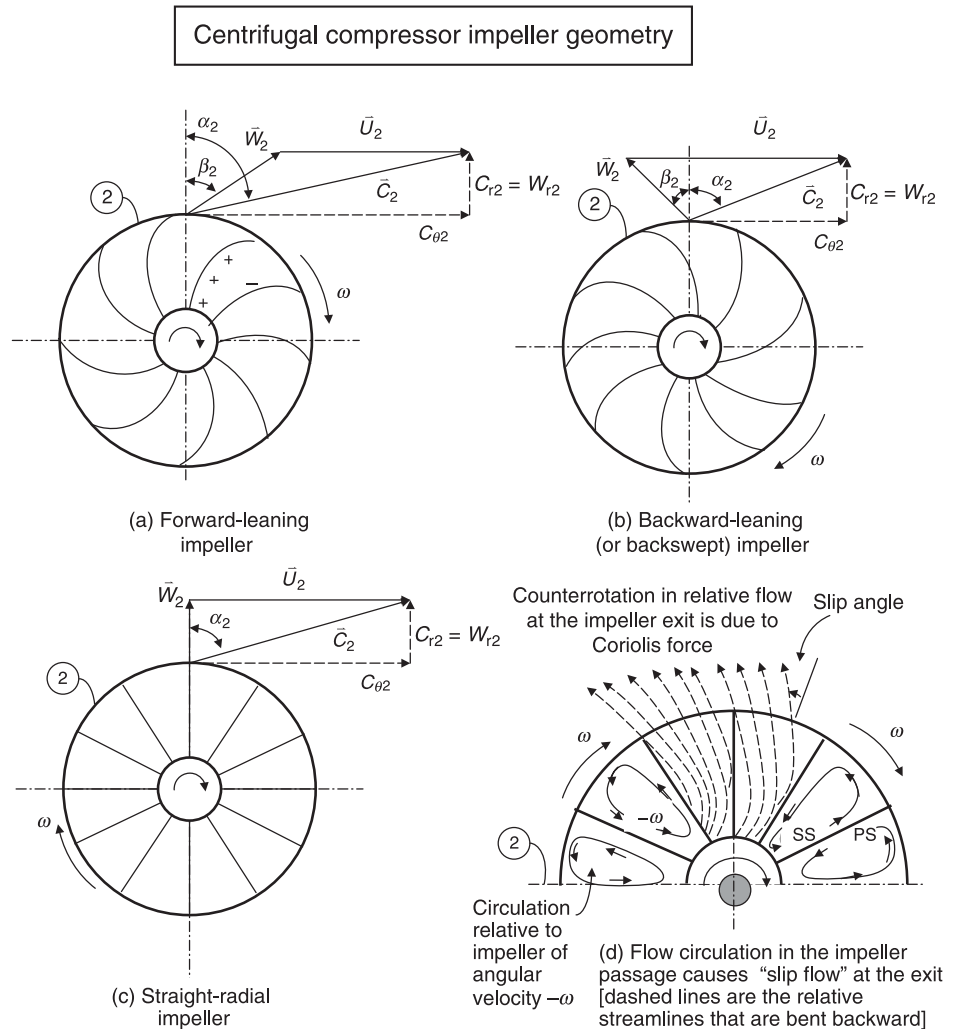
A schematic drawing of impeller geometries and their corresponding velocity triangles are shown in Figure 9.3.

The radial impeller offers radial passages to accelerate the fluid in the rotor and ideally attain a radial exit flow. The forward-leaning impeller geometry accelerates the fluid in a spiral passage leaning in the direction of the rotor rotation. The backswept impeller is composed of spiral passages that direct the relative flow in the opposite direction to rotor rotation. The geometry of the impeller dictates the exit flow angle β_2 and thus strongly impacts the magnitude of the exit swirl velocity $C_{\theta 2}$. The three types of impeller geometry are shown in Figure 9.3, with the flow angles at the impeller exit now measured with respect to the radial direction, as shown. The velocity triangles at the impeller exit show that the absolute swirl is increased when the impeller geometry is forward leaning (with $\beta_2 < 0$). For the case of the straight radial impeller, the exit absolute swirl should theoretically be the same as the wheel speed U_2 . The backward-leaning or backswept impeller geometry turns the relative flow in the opposite direction to the wheel rotation (with $\beta_2 > 0$), therefore the absolute swirl in the exit plane is reduced. All these arguments are the results of simple interpretation of the velocity triangles (Figure 9.3).

The Euler turbine equation suggests that the forward-leaning blades produce the highest total enthalpy rise and, hence, absorb the maximum shaft power. The impeller exit Mach number is the highest of the three designs and thus limits the static pressure recovery and efficiency of the radial diffuser. Also, the blades are under severe structural loads in bending due to their curvature. Similarly, the blades of a backward-leaning impeller are under high structural loading and the shaft power absorption is reduced. The exit Mach number of the backward-leaning impeller is the lowest of the three designs and will be explored as an alternative to radial impeller design. The lower exit Mach number of the backward-leaning impeller is attractive in achieving higher efficiency diffusion in the radial diffuser. The optimum geometry from structural standpoint seems to be the straight radial impeller with good power absorption, acceptable stability characteristics, and a low level of structural loading (in bending) due to purely radial design. However, the pressure rise in the compressor increases with the wheel speed, hence a backward-leaning impeller design could operate at higher U_T once the structural design issues are resolved.

In the rotor frame of reference, the flow in the impeller is primarily in the radial direction, which bends in the opposite direction to the wheel rotation due to a Coriolis

■ **FIGURE 9.3**
Definition sketch of the
impeller blade shapes,
flow angles, ideal
velocity triangles at the
impeller exit, and the
phenomenon of slip



force, that is, $\propto 2\omega W_r$. The presence of tangential pressure gradients in addition to the Coriolis effect combine to create a countercirculation in impeller blade passages toward the trailing edge. The counterrotation in the impeller exit flow causes a reduction in the absolute swirl, therefore a reduction in the power absorption and thus leads to a reduced pressure ratio. This phenomenon is known as *slip* in centrifugal compressors. An example of the slip in a straight radial impeller is shown in Figure 9.3d. The other two examples of impeller configurations, that is, the forward- and the backward-leaning types, are subject to the phenomenon of slip in their respective passages. We define a slip factor for radial impellers as the ratio of absolute swirl to the exit wheel speed, which represents the *ideal* swirl had the fluid attained the same tangential velocity as the disk, namely,

$$\epsilon \equiv \frac{C_{\theta 2}}{U_2} \quad (\text{slip factor}) \quad (9.4)$$

Hence, the total temperature rise across the straight radial impeller is related to the wheel speed and the slip factor ϵ following the Euler turbine equation, that is,

$$T_{t2} = T_{t1} + \frac{\epsilon \cdot U_2^2}{c_p} \tag{9.5a}$$

From Equation 9.5a, the impeller loading coefficient $\Delta h_t/U_2^2$ gives a simple expression for the radial impeller, which is independent of mass flow rate, assuming constant slip factor, that is,

$$\Delta h_t/U_2^2 = \epsilon \tag{9.5b}$$

In general, the slip factor is defined as

$$\epsilon \equiv \frac{(C_{\theta 2})_{\text{actual}}}{(C_{\theta 2})_{\text{ideal}}} \quad (\text{slip factor}) \tag{9.6}$$

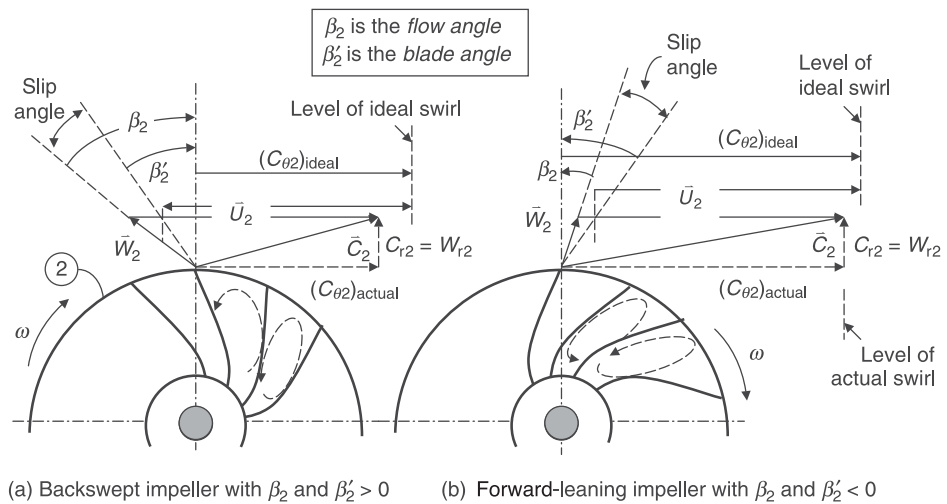
where the ideal exit swirl is calculated based on the *impeller blade exit angle* β'_2 , and the actual exit swirl is based on the *actual exit flow angle* β_2 . Figure 9.4 shows a definition sketch of these angles for the backward and forward-leaning impellers.

If we adopt the sign convention that the impeller exit angle is measured from the vane position to the radial direction and is positive in the direction of the rotor rotation, we note that a backswept impeller has a positive β'_2 and a forward-leaning impeller has a negative vane exit angle β'_2 . With a similar sign convention for the exit flow angle, we may write the ideal and actual exit swirl velocities in terms of the impeller exit angle β'_2 , flow angle β_2 as

$$C_{\theta 2, \text{ideal}} = U_2 - C_{r2} \cdot \tan \beta'_2 \tag{9.7a}$$

$$C_{\theta 2, \text{actual}} = U_2 - C_{r2} \cdot \tan \beta_2 \tag{9.7b}$$

■ **FIGURE 9.4**
Definition sketch for the slip flow in a backswept and forward-leaning impeller



From Equation. 9.7a, we note that a backswept impeller, with a positive exit vane angle, reduces the absolute (ideal) swirl, whereas a forward-leaning impeller with a negative vane angle increases the exit absolute swirl. Similar argument can be made regarding the exit swirl velocity in the actual flow as described in Equation. 9.7b. We define the slip factor as the ratio of actual to the ideal exit swirl as

$$\epsilon \equiv \frac{C_{\theta 2, \text{actual}}}{C_{\theta 2, \text{ideal}}} = \frac{U_2 - C_{r2} \cdot \tan \beta_2}{U_2 - C_{r2} \cdot \tan \beta'_2} \tag{9.8}$$

The impeller specific work and the loading are written as

$$\Delta h_t = U_2 C_{\theta 2} = U_2(U_2 - C_{r2} \tan \beta_2) = U_2^2 \left[1 - \frac{C_{r2}}{U_2} \tan \beta_2 \right] \tag{9.9a}$$

$$\Psi \equiv \frac{\Delta h_t}{U_2^2} = 1 - \left(\frac{C_{r2}}{U_2} \right) \tan \beta_2 \tag{9.9b}$$

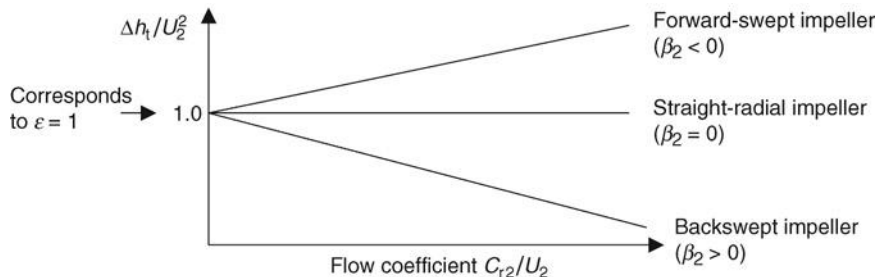
We may graph Equation 9.7b, that is, the variation of the nondimensional work, or the impeller-loading coefficient $\Delta h_t/U_2^2$, with flow coefficient C_{r2}/U_2 (which is similar to C_z/U in axial-flow compressors), for different impellers. Figure 9.5 shows the impeller loading variation with flow coefficient for the three impeller types (with a constant slip factor ϵ).

There are several correlations between the slip factor ϵ and the number of the impeller vanes N in radial impellers, which are proposed by Stodola (1927), Busemann (1928), and Stanitz–Ellis (1949). The Stanitz–Ellis model, which is similar to Stodola’s, is considered a reasonable approximation for the slip factor in straight-radial impellers (and a first-order approximation for other impeller types),

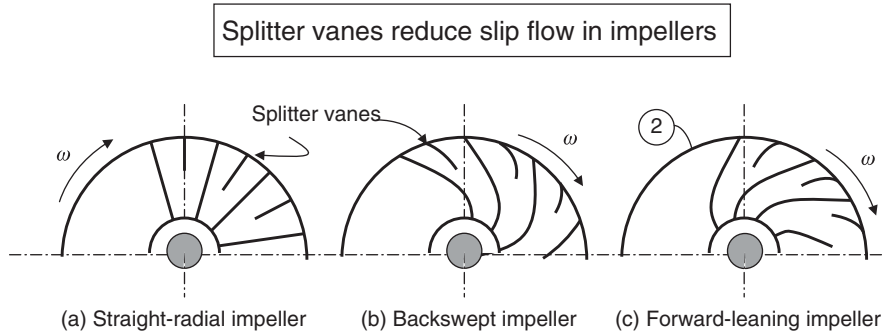
$$\epsilon = 1 - \frac{1.98}{N} \tag{9.10}$$

A 20-bladed impeller, for example, will experience a slip factor of ~ 0.9 in its energy transfer to the fluid. For radial impellers, the slip factor (as expressed in Equation 9.10) is independent of the mass flow rate. However, slip factor in reality is a function of the mass flow rate for all three configurations, that is, radial, forward- and backward-leaning impellers. Increasing the number of the impeller blades reduces the effect of slip, which in turn increases the weight. To achieve the effect of higher blade count without investing heavily in the system weight increase, a compromise solution is found by incorporating splitter vanes in the outer half of an impeller disk. The presence of splitter vanes acts as

■ **FIGURE 9.5**
Centrifugal compressor impeller loading variation with flow coefficient or mass flow rate



■ **FIGURE 9.6**
Schematic drawing of
splitter vanes on the
impeller disk of a
centrifugal compressor



an inhibitor of countercurl produced in the outer portion of an impeller disk and possible reduction of flow separation in the impeller. Figure 9.6 shows the splitter vanes concept in a centrifugal turbomachinery. A parallel argument in the creation of slip is worthy of discussion. The flow at the exit of the inducer is turned parallel to the axis and is starting its journey in the radial direction. Therefore, the rotor flow is purely radial at the exit of the inducer. This resembles a source flow, which is irrotational. For the flow to remain irrotational (in the absence of external forces, i.e., in rotor frame of reference), counter eddies of the same angular speed need to be set up in the impeller blade passages. The counter eddies thus lead to an exit flow that is rotated in the opposite direction to the wheel rotation, by an angle known as the slip angle.

The stage total temperature ratio is the same as the impeller total temperature ratio, since the stationary blades are adiabatic and do no work on the fluid; therefore, we may write Equation 9.3 as

$$\tau_{\text{stage}} = \frac{T_{t2}}{T_{t1}} = 1 + \epsilon \frac{U_2^2}{\left(\frac{\gamma R T_{t1}}{\gamma - 1}\right)} = 1 + (\gamma - 1) \epsilon \frac{U_2^2}{a_{t1}^2} \quad (9.11)$$

The stagnation speed of sound at the inlet condition is a_{t1} in Equation 9.11. The ratio of wheel speed at the impeller exit to the stagnation speed of sound at the inlet is a non-dimensional parameter that is called the Mach index Π_M in the centrifugal compressor literature. In terms of the Mach index, we may write the stage total temperature ratio for a straight-radial impeller with zero preswirl as

$$\tau_s = 1 + (\gamma - 1) \epsilon \cdot \Pi_M^2 \quad (9.12)$$

Upon closer examination of this parameter, that is, Mach index, we note that it is directly proportional to the impeller tangential Mach number at the exit and inversely proportional to the axial Mach number at the inlet of the compressor. This relation is shown in Equation 9.13.

$$\Pi_M^2 = \frac{U_2^2}{\gamma \cdot R \cdot T_{t1}} = \frac{U_2^2}{\gamma \cdot R \cdot T_1 \left(1 + \frac{\gamma - 1}{2} M_1^2\right)} = \frac{M_{T2}^2}{1 + \frac{\gamma - 1}{2} M_1^2} \approx M_{T2}^2 \quad (9.13)$$

where $M_{T2} = \frac{U_2}{a_1}$.

EXAMPLE 9.1

Use a spreadsheet to calculate and graph the ratio of Mach index to the impeller tip tangential Mach number (from

Equation 9.13) for a range of inlet Mach numbers from 0.2 to 0.6.

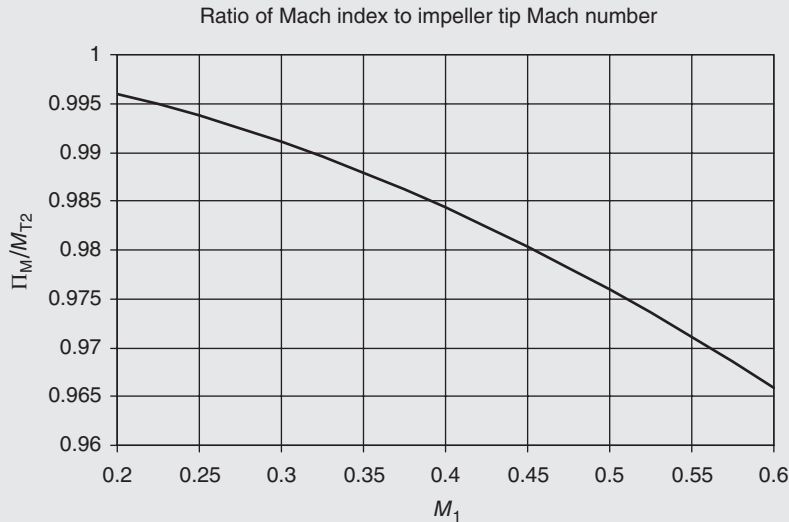
SOLUTION

The ratio of the Mach index and the impeller tip tangential Mach number M_{T2} is

$$\frac{\Pi_M}{M_{T2}} = \left(1 + \frac{\gamma - 1}{2} M_1^2 \right)^{-0.5} \quad (9.14)$$

At inlet axial Mach number of ~ 0.45 , the Mach index is $\sim 98\%$ of the rotor tip tangential Mach number. The impeller tip tangential Mach number is thus the dominant parameter that determines the stage temperature ratio and pressure ratio, similar to the axial-flow compressor.

The result of spreadsheet calculation of Equation 9.14 is graphed in Figure 9.7.



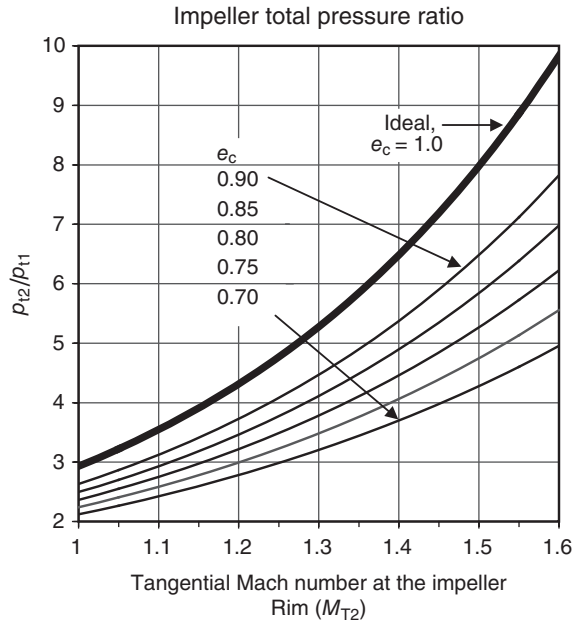
■ **FIGURE 9.7** Comparison between the Mach index and impeller tip Mach number M_{T2}

The impeller total pressure ratio is related to the impeller total temperature ratio via polytropic efficiency according to

$$\frac{p_{t2}}{p_{t1}} = \left(\frac{T_{t2}}{T_{t1}} \right)^{\frac{\gamma \cdot \epsilon_c}{\gamma - 1}} \cong \left[1 + (\gamma - 1) \epsilon_c \cdot M_{T2}^2 \right]^{\frac{\gamma \cdot \epsilon_c}{\gamma - 1}} \quad (9.15)$$

where we replaced the Mach index with the tip tangential Mach number. Now, let us graph this equation for different tip tangential Mach numbers. Figure 9.8 shows the functional dependence of pressure ratio and tip Mach number. We note an exponential growth of the

■ **FIGURE 9.8**
 Variation of impeller pressure ratio with tip tangential Mach number (based on the inlet speed of sound, a_1) for a straight-radial impeller with slip factor $\epsilon = 0.9$



impeller total pressure ratio with the tangential Mach number at the impeller tip. There are two limitations to the exponential growth performance of centrifugal compressors with tip tangential Mach number depicted in Figure 9.8. One limiting factor is due to excessive centrifugal stresses and the structural loads; the second limiting factor is due to a drop in efficiency of the diffusion process in the radial diffuser at high inlet supersonic Mach numbers. To tackle the structural problem, a high strength-to-weight ratio material is desirable for the rotor application. Titanium alloys are thus suitable, and the lighter, lower cost aluminum is still considered a material of choice for small centrifugal compressor applications. The impeller rim speed of ~ 1700 ft/s (or ~ 520 m/s) represents the state-of-the-art in centrifugal compressors. The corresponding tangential rim Mach number defined as the ratio of rim speed to the inlet speed of sound a_1 at standard sea level inlet condition, that is, a_1 of 1100 ft/s or 340 m/s, is limited to $M_{T2} \sim 1.55$. From the three possible impeller geometries, the forward-leaning design would create a higher exit Mach number than the rim tangential Mach number, based on the velocity triangle depicted in Figure 9.3a. Therefore the inlet Mach number to the diffuser will be even higher than 1.55, based on the inlet speed of sound (a_1). The straight-radial impeller would roughly achieve the same diffuser inlet Mach number as the impeller tangential rim Mach number. Note that the radial flow Mach number is small compared with a supersonic tip. To reduce the diffuser inlet Mach number to lower than 1.55 (based on a_1), we may lean the impeller blades backward, known as backsweep. The main disadvantage of curved impellers, that is, both the forward- and backward-leaning types, is in their higher (bending) stress levels than the radial vanes. The curved impellers experience large bending stresses due to the centrifugal force, whereas the radial impellers theoretically experience no bending stresses due to centrifugal loads. The higher cost of manufacturing attributed to curved impellers is considered their second disadvantage as compared with straight-radial impellers. Despite higher manufacturing costs and higher stresses, the trend is to maximize the wheel speed

for efficient centrifugal compression while reducing the diffuser entrance Mach number by backward-leaning the impeller blades. The backswept impellers of $\sim 45^\circ$ exit sweep represent the state of the art in high performance centrifugal compressors.

So far we have referenced impeller exit velocity components to the inlet speed of sound. The behavior of actual flow in the diffuser depends, however, on the Mach number based on the local speed of sound at the impeller exit, a_2 . The Euler turbine equation applied to an impeller with zero inlet swirl (or preswirl) is the starting point of our calculation of T_2 , or a_2 , that is,

$$\frac{T_{t2}}{T_{t1}} - 1 \cong \frac{U_2^2}{c_p T_{t1}} \left(\frac{C_{\theta 2}}{U_2} \right)$$

From the definition of slip factor, Equation 9.8, we will substitute for the ratio of exit absolute swirl to the wheel speed in the above equation to get

$$\frac{T_{t2}}{T_{t1}} - 1 \cong (\gamma - 1) \Pi_M^2 \cdot \varepsilon \cdot \left[1 - \left(\frac{C_{r2}}{U_2} \right) \tan \beta'_2 \right] \quad (9.16)$$

Now, the total temperature ratio may be related to the static temperatures and the fluid kinetic energy following the definition of total enthalpy, that is,

$$\frac{T_{t2}}{T_{t1}} = \frac{T_2 + C_2^2/2c_p}{T_1 + C_1^2/2c_p} \quad (9.17)$$

The contribution of kinetic energy at the entrance to the centrifugal compressor may be neglected in favor of the static temperature and thus Equation 9.17 may be approximated as

$$\frac{T_{t2}}{T_{t1}} \cong \frac{T_2 + C_2^2/2c_p}{T_1} = \frac{T_2}{T_1} + \frac{C_2^2}{2c_p T_1} \quad (9.18)$$

The right-hand side of Equation 9.18 may be simplified if we replace the absolute kinetic energy with the swirl kinetic energy, which essentially neglects small contribution of the exit radial kinetic energy. We may solve for the static temperature ratio as

$$\frac{T_2}{T_1} \cong \frac{T_{t2}}{T_{t1}} - \frac{C_{\theta 2}^2}{2c_p T_1} = \frac{T_{t2}}{T_{t1}} - \frac{\gamma - 1}{2} \Pi_M^2 \left(\frac{C_{\theta 2}}{U_2} \right)^2 \quad (9.19)$$

By substituting for the total temperature ratio from Equation 9.16 and the ratio of exit swirl to the wheel speed from Equation 9.8, we get the impeller static temperature ratio as

$$\frac{T_2}{T_1} - 1 \cong (\gamma - 1) \Pi_M^2 \cdot \varepsilon \cdot \left[1 - \left(\frac{C_{r2}}{U_2} \right) \tan \beta'_2 \right] \left\{ 1 - \frac{1}{2} \cdot \varepsilon \cdot \left[1 - \left(\frac{C_{r2}}{U_2} \right) \tan \beta'_2 \right] \right\} \quad (9.20)$$

The parameters on the right-hand side of Equation 9.20 are all nondimensional design parameters. In its simplest form, where we set radial velocity nearly equal to zero for

curved impellers or in the case of straight-radial blades, $\beta'_2 = 0$, and neglect slip, that is, $\varepsilon = 1$, the static temperature ratio reduces to

$$\frac{T_2}{T_1} - 1 \approx \left(\frac{\gamma - 1}{2} \right) \Pi_M^2 = \frac{1}{2} \left(\frac{T_{t2}}{T_{t1}} - 1 \right) \tag{9.21}$$

Since the total temperature through the stator remains constant, the impeller static temperature rise is half of the stage total temperature rise, which for low speed at the exit of the diffuser becomes one half of the stage static temperature rise ($T_3/T_1 - 1$). Therefore, under these conditions, the rotor and the stator produce the same static temperature rise, or what was called a 50% degree of reaction. The ratio of the speed of sound at the impeller exit to the inlet speed of sound is the square root of the static temperature ratio as

$$\frac{a_2}{a_1} \approx \sqrt{1 + \left(\frac{\gamma - 1}{2} \right) \Pi_M^2} \tag{9.22}$$

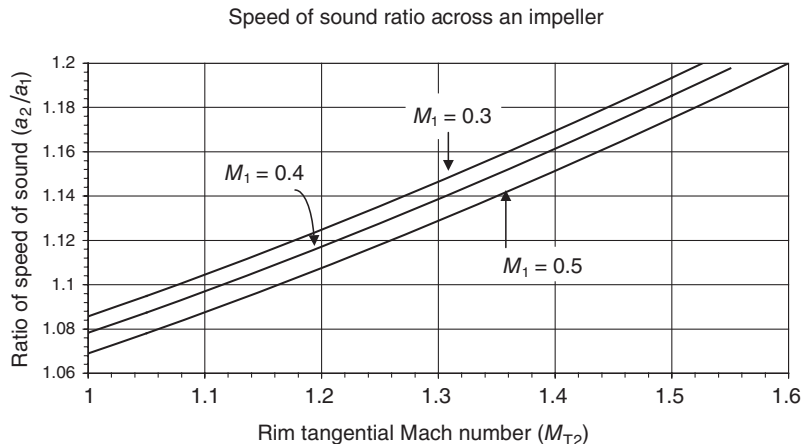
From Equation 9.14, we may substitute for the Mach index in terms of the wheel tangential Mach number M_{T2} and the inlet Mach number M_1 to write the ratio of the speeds of sound across the impeller as

$$\frac{a_2}{a_1} \approx \sqrt{1 + \frac{\left(\frac{\gamma - 1}{2} \right) M_{T2}^2}{1 + \left(\frac{\gamma - 1}{2} \right) M_1^2}} \tag{9.23}$$

We may now graph this expression to examine the rise of speed of sound across the impeller. Figure 9.9 shows the ratio of speed of sound across the impeller.

In the limiting case of $M_{T2} \sim 1.55$, the ratio of speed sounds across the impeller a_2/a_1 is ~ 1.2 . Therefore, all the local Mach numbers at the impeller exit that we had referenced to the inlet speed of sound are $\sim 20\%$ smaller when we use local speed of sound a_2 instead of a_1 . Now, let us recap, through an example, the impeller exit Mach numbers as viewed by a radial diffuser that follows the impeller.

■ **FIGURE 9.9**
The ratio of speed of sound across the impeller for three inlet Mach numbers of $M_1 = 0.3, 0.4, \text{ and } 0.5$ and zero preswirl ($\gamma = 1.4$)



EXAMPLE 9.2

Consider a centrifugal compressor impeller with the following inlet and design parameters:

Known/design inlet conditions

- Inlet absolute stagnation temperature and pressure are 288 K and 1.01×10^5 Pa, respectively, i.e., our design point operation is at the standard sea level static condition
- $C_1 = C_{z1} = 150$ m/s, this gives an axial inlet Mach number of ~ 0.5 , no preswirl, which is our design choice
- Hub-to-tip radius ratio is $r_{h1}/r_1 = 0.5$, this too is a design choice
- Limit the relative Mach number at the eye radius to 1.0, to avoid shock losses in the inducer
- Compressor adiabatic efficiency $\eta_c = 0.72$ estimated based on similar machines
- Compressor mass flow rate is $\dot{m} = 5$ kg/s
- Gas properties are $c_p = 1004$ J/kg · K and $\gamma = 1.4$

Known/design exit conditions

- $C_{r2} = C_{z2} = 150$ m/s, this could be our design choice, which sizes the impeller exit area

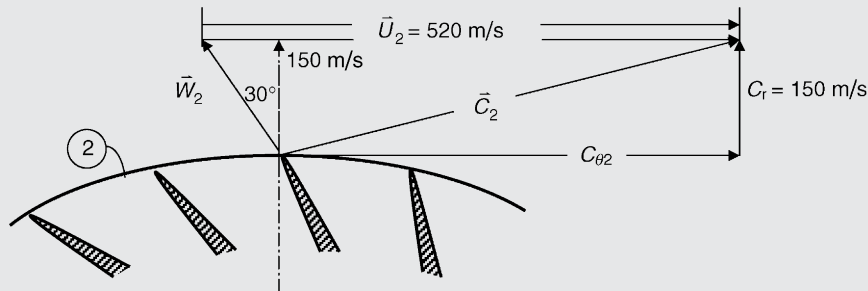
- Impeller rim speed is $U_2 = 520$ m/s, we chose the maximum rim speed in this example
- Impeller exit vane angle $\beta'_2 = 20^\circ$, i.e., we chose a backsweep design to reduce M_2
- Allow for a 10° slip angle, which makes the exit relative flow angle $\beta_2 = 30^\circ$.
- Assume equal total pressure loss parameter ω in the impeller and the radial diffuser

Calculate

- (a) the absolute Mach number entering the radial diffuser, M_2 , and its components, i.e., radial and tangential M_{r2} and $M_{\theta 2}$
- (b) the relative Mach number at the impeller exit, M_{2r}
- (c) the compressor pressure ratio π_c and its polytropic efficiency e_c
- (d) the inlet flow area and the “eye” radius r_1
- (e) the shaft angular speed ω
- (f) the impeller exit radius r_2
- (g) the impeller exit width b
- (h) the shaft power

SOLUTION

We first draw the impeller exit velocity triangle as an aid in calculating the velocity components.



The static temperature at the impeller inlet is

$$T_1 = T_{t1} - C_1^2 / 2c_p = 288 \text{ K} - (150)^2 / [2(1004)]$$

$$K = 276.8 \text{ K} \quad \Rightarrow \quad T_1 = 267.8 \text{ K}$$

$$a_1 = \sqrt{(\gamma - 1)c_p T_1} \quad \Rightarrow \quad a_1 = [0.4(1004)(267.8)]^{1/2}$$

$$= 333.4 \text{ m/s} \quad \Rightarrow \quad a_1 = 333.4 \text{ m/s}$$

The absolute Mach number in the inlet is $M_1 =$

$$150 / 333.4 \cong 0.45 \quad \Rightarrow \quad M_1 \cong 0.45$$

The absolute exit swirl velocity is the difference between the rim speed and the relative swirl velocity $W_{\theta 2}$, which from the velocity triangle, it is

$$C_{\theta 2} = 520(\text{m/s}) - 150 \cdot \tan 30^\circ(\text{m/s})$$

$$= 433.4 \text{ m/s} \quad \Rightarrow \quad C_{\theta 2} = 433.4 \text{ m/s}$$

Therefore, the absolute velocity at the exit has a magnitude of

$$C_2 = [(433.4)^2 + (150)^2]^{1/2} \text{ m/s}$$

$$= 458.6 \text{ m/s} \Rightarrow \boxed{C_2 = 458.6 \text{ m/s}}$$

We need the speed of sound at the exit, a_2 , in order to establish the absolute exit Mach numbers. We may use the approximate form of the ratio of speeds of sound as expressed in Equation 9.22, i.e.,

$$\frac{a_2}{a_1} \approx \sqrt{1 + \frac{\left(\frac{\gamma-1}{2}\right) M_{T2}^2}{1 + \left(\frac{\gamma-1}{2}\right) M_1^2}}$$

The impeller tip tangential Mach number is $M_{T2} = U_2/a_1 = 520/333.4 = 1.560$

The inlet absolute Mach number is $M_1 = C_1/a_1 = 150/333.4 = 0.450$

$$\frac{a_2}{a_1} \approx \sqrt{1 + \frac{(0.2)(1.560)^2}{1 + (0.2)(0.45)^2}}$$

$$\cong 1.212 \Rightarrow \boxed{a_2 \cong 1.212(333.4) \text{ m/s} = 404.1 \text{ m/s}}$$

We may decide to use the more accurate Equation 9.16 to calculate the exit temperature and the speed of sound, i.e.,

$$\frac{T_{t2}}{T_{t1}} = \frac{T_2 + C_2^2/2c_p}{T_1 + C_1^2/2c_p}$$

We will use the Euler turbine equation to calculate the total temperature ratio across the impeller as

$$\frac{T_{t2}}{T_{t1}} \cong 1 + \frac{\omega \cdot r_2 \cdot C_{\theta 2}}{c_p T_{t1}} = 1 + \frac{U_2^2}{c_p T_{t1}} \left(\frac{C_{\theta 2}}{U_2} \right)$$

Substituting in the above equation for total temperature ratio, we get

$$\frac{T_{t2}}{T_{t1}} = 1 + \frac{(520)^2}{(1004)(288)} \left(\frac{433.4}{520} \right)$$

$$\cong 1.7794 \Rightarrow \boxed{T_{t2} \cong 512.5 \text{ K}}$$

The static temperature is related to total temperature via

$$T_2 = T_{t2} - C_2^2/2c_p \cong 512.47 \text{ K} - (458.6)^2/2(1004)$$

$$\text{K} \cong 407.7 \text{ K} \Rightarrow \boxed{T_2 \cong 407.7 \text{ K}}$$

The speed of sound at the impeller exit is

$$a_2 = \sqrt{\gamma \cdot RT_2} = \sqrt{(\gamma-1)c_p T_2}$$

$$= \sqrt{(0.4)(1004)(407.7)}$$

$$\cong 404.7 \text{ m/s} \Rightarrow \boxed{a_2 = 404.7 \text{ m/s}}$$

The difference between the approximate and the more exact formulation of the speed of sound at the impeller exit, as we calculated, is negligible (404.1 m/s versus 404.7 m/s).

Now we can calculate the impeller exit Mach numbers, based on the local speed of sound, namely,

$$M_{\theta 2} \equiv C_{\theta 2}/a_2 = 433.4/404.7 \cong 1.071$$

$$M_{r2} \equiv C_r/a_2 = 150/404.7 \cong 0.371 \Rightarrow \boxed{\begin{matrix} M_{\theta 2} = 1.071 \\ M_{r2} = 0.371 \\ M_2 = 1.133 \end{matrix}}$$

$$M_2 \equiv C_2/a_2 = 458.6/404.7 \cong 1.133$$

The impeller exit Mach number is W_2/a_2 and $W_2 = 150 \text{ m/s} / \cos 30^\circ = 173.2 \text{ m/s}$

Therefore, the impeller exit relative Mach number is $173.2/404.7 \cong 0.428$ $\boxed{M_{r2} \cong 0.428}$

Note that our design choices have led to a slightly supersonic inlet condition to the radial diffuser that follows the impeller. To calculate the compressor total pressure ratio, we use the adiabatic efficiency η_c and the compressor total temperature ratio T_{t2}/T_{t1} as we derived earlier

$$\pi_c = [1 + \eta_c(\tau_c - 1)]^{1/\gamma} = [1 + 0.72(1.7794 - 1)]^{3.5}$$

$$\cong 4.75 \Rightarrow \boxed{\pi_c = p_{t2}/p_{t1} = 4.75}$$

Compressor polytropic and adiabatic efficiencies are related via

$$\eta_c = \left[\frac{\pi_c^{1/\gamma} - 1}{\pi_c^{1/\gamma - e_c} - 1} \right]$$

Solving the above equation for e_c , we get

$$e_c = \frac{\left(\frac{\gamma-1}{\gamma}\right) \ln(\pi_c)}{\ln \left[1 + \frac{\pi_c^{1/\gamma} - 1}{\eta_c} \right]} = \frac{0.2857 \ln(4.75)}{\ln \left[1 + \frac{(4.75)^{0.2857} - 1}{0.72} \right]}$$

$$\cong 0.773 \Rightarrow \boxed{e_c = 0.773}$$

Now let us size the inlet flow area and the eye radius r_1 for the mass flow rate of 5 kg/s, under standard sea level static condition at the inlet. First, we need to calculate the fluid density at the inlet, ρ_1 . We can calculate the density from the perfect gas law, which needs a gas constant R , or from the speed of sound, which requires γ . We calculate the static pressure at the inlet, i.e.,

$$p_1 = \frac{P_{t1}}{\left[1 + \frac{\gamma-1}{2} M_1^2\right]^{\frac{\gamma}{\gamma-1}}} = \frac{1.01 \times 10^5 \text{ Pa}}{[1 + 0.2(0.45)^2]^{3.5}} \cong 8.7897 \times 10^4 \text{ Pa}$$

$$a_1^2 = \frac{\gamma \cdot p_1}{\rho_1} \Rightarrow$$

$$\rho_1 = (1.4)(8.7897 \times 10^4)/(333.4)^2 \text{ kg/m}^3 \cong 1.107 \text{ kg/m}^3$$

$$\dot{m} = \rho_1 A_1 C_{z1} \Rightarrow$$

$$A_1 = (5 \text{ kg/s})/[(1.107 \text{ kg/m}^3)(150 \text{ m/s})] = 0.03011 \text{ m}^2 = 301.1 \text{ cm}^2$$

$$A_1 = \pi(r_1^2 - r_{h1}^2) = \pi \cdot r_1^2 \left[1 - \left(\frac{r_{h1}}{r_1}\right)^2\right] \Rightarrow$$

$$r_1 = [(301.1 \text{ cm}^2)/\pi(1 - 0.25)]^{1/2} \cong 11.30 \text{ cm or } r_1 \sim 4.466 \text{ inches}$$

$$\boxed{r_e = r_1 \cong 11.30 \text{ cm}}$$

From the inlet relative Mach number of 1.0 at the eye radius r_e , we establish the angular speed of the shaft ω ,

$$C_{z1}^2 + (\omega \cdot r_1)^2 = a_1^2 \cdot M_{r1}^2 = (333.4)^2(1.0)^2 = 111,156 \text{ m}^2/\text{s}^2$$

Therefore,

$$(\omega r_1)^2 = [111,156 - (150)^2] \text{ m}^2/\text{s}^2 = 88,656 \text{ m}^2/\text{s}^2, \text{ or } \omega r_1 \cong 297.7 \text{ m/s},$$

$$\text{or } \omega \cong 2635 \text{ rad/s}$$

$$\text{or } \omega \cong 25,160 \text{ rpm}$$

$$\Rightarrow \boxed{\omega \cong 2635 \text{ rad/s} \cong 25,160 \text{ rpm}}$$

The impeller exit radius r_2 is established by the rim speed of 520 m/s specified in the problem according to

$$r_2 = U_2/\omega = [520 \text{ m/s}]/[2635 \text{ rad/s}]$$

$$\Rightarrow \boxed{r_2 \cong 19.73 \text{ cm}}$$

This gives a radius ratio of ~ 0.572 for the eye to exit, i.e., $r_e/r_2 \sim 0.572$. We shall examine the effect of this parameter on the inducer diffusion factor in the next section. The impeller exit width (or blade axial span at the exit) b is established from continuity equation and our design choice for the exit radial velocity $C_{r2} = W_{r2} = 150 \text{ m/s}$, i.e.,

$$A_2 = \frac{\dot{m}}{\rho_2 \cdot C_{r2}} = 2\pi \cdot r_2 \cdot b$$

In this preliminary stage, note that we made a first order approximation in the flow area by not accounting for the blade thickness multiplied by the number of blades that reduces the exit flow area. There are two unknowns in the above equation. One is the blade axial span at the exit, b , and the other is the gas density at the impeller exit, ρ_2 . To calculate the gas density at the impeller exit, we first proceed to calculate the static pressure at the impeller exit p_2 . Then by using a perfect gas law at station 2, we calculate the density of the gas, ρ_2 . The exit static pressure p_2 is calculated from our assumption of equal total pressure loss parameter ω across the rotor and the diffuser. From the definition of ω_{imp} , we have

$$\omega_{\text{imp}} \equiv \frac{P_{t1r} - P_{t2r}}{q_{1r}} = \frac{p_1 \left[1 + \frac{\gamma-1}{2} M_{r1}^2\right]^{\frac{\gamma}{\gamma-1}} - p_2 \left[1 + \frac{\gamma-1}{2} M_{r2}^2\right]^{\frac{\gamma}{\gamma-1}}}{\frac{\gamma}{2} p_1 M_{r1}^2}$$

Also, the diffuser total pressure loss parameter is

$$\omega_{\text{dif}} \equiv \frac{P_{t2} - P_{t3}}{q_2} = \frac{p_2 \left[1 + \frac{\gamma-1}{2} M_2^2\right]^{\frac{\gamma}{\gamma-1}} - \pi_s \cdot p_1 \left[1 + \frac{\gamma-1}{2} M_1^2\right]^{\frac{\gamma}{\gamma-1}}}{\frac{\gamma}{2} p_2 M_2^2}$$

We replaced the exit total pressure p_{t3} by the product of the stage total pressure ratio π_s and the inlet absolute total pressure. By setting the above two total pressure loss parameters equal to each other, we calculate the impeller exit static pressure p_2 , namely,

$$p_2/p_1 \cong 1.795 \text{ or } p_2 \cong 1.578 \times 10^5 \text{ Pa}$$

$$\Rightarrow \boxed{p_2 \cong 1.578 \times 10^5 \text{ Pa}}$$

Therefore, the impeller exit density is $\rho_2 = \gamma p_2 / (a_2)^2$, which is

$$\rho_2 = (1.4) (1.578 \times 10^5 \text{ Pa}) / (404.7 \text{ m/s})^2 \cong 1.3487 \text{ kg/m}^3$$

$$\rho_2 \cong 1.3487 \text{ kg/m}^3$$

The impeller exit width b is now estimated from the continuity equation,

$$b \approx \frac{\dot{m}}{2\pi \cdot r_2 \rho_2 \cdot C_{r2}}$$

$$= \frac{5 \text{ kg/s}}{2\pi \cdot (0.1973 \text{ m})(1.3487 \text{ kg/m}^3)(150 \text{ m/s})}$$

$$\cong 0.01994 \text{ m} \rightarrow b \cong 2.0 \text{ cm}$$

The shaft power is the product of the mass flow rate and the total enthalpy rise across the rotor,

$$\dot{\mathcal{Q}}_s = \dot{m} c_p (T_{t2} - T_{t1}) = 5 \text{ kg/s} (1004 \text{ J/kg} \cdot \text{K}) (512.5 - 288)$$

$$K \cong 1,127 \text{ kW} \rightarrow \dot{\mathcal{Q}}_s \cong 1127 \text{ kW} = 1.127 \text{ MW}$$

9.3 Radial Diffuser

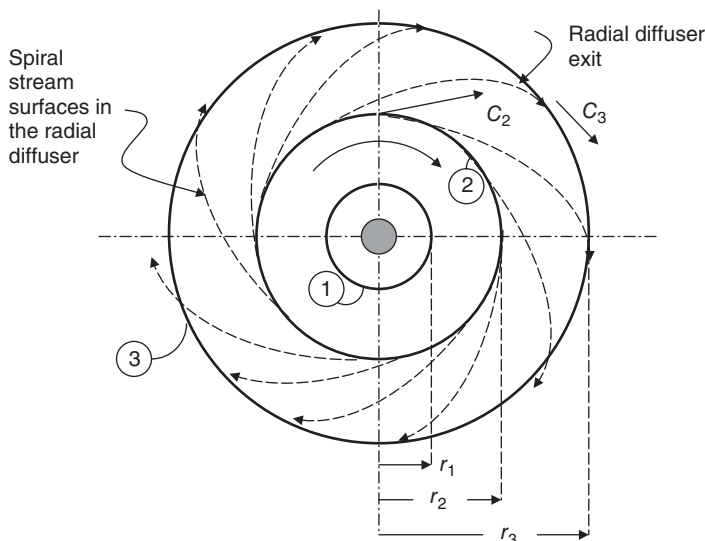
The flow that leaves the impeller of a centrifugal compressor enters a radial diffuser. As the absolute flow at the impeller exit has swirl, the streamlines in the radial diffuser are spirals in shape. A definition sketch of a radial diffuser with its spiral streamlines and the station numbers is shown in Figure 9.10.

The discharge of the centrifugal impeller enters a vaneless radial diffuser at first, which may be followed by a vaned diffuser. The function of the radial diffuser, as in all diffusers, is to decelerate the flow and convert the kinetic energy to static pressure rise.

The diffuser in a centrifugal compressor lies between parallel walls with a spiraling flow that moves outward in the radial direction. Due to the parallel sidewalls, the diffuser area increases monotonically with radius according to

$$\frac{A(r)}{A_2} = \frac{r}{r_2} \tag{9.24}$$

■ FIGURE 9.10 Definition sketch of the flow in the radial diffuser



The swirl component of the flow in the radial diffuser decays as a result of

1. The conservation of angular momentum reduces the swirl inversely proportional to an increasing radius in the radial diffuser, and
2. The external torque on the fluid applied by the wall (due to fluid viscosity) is in the opposite direction to the fluid angular momentum, thus it acts to retard the fluid swirl as it moves outward in spirals.

The conservation of angular momentum, in the absence of external torque, requires

$$rC_\theta = r_2C_{\theta 2} \tag{9.25a}$$

$$\frac{C_\theta(r)}{C_{\theta 2}} = \frac{r_2}{r} \tag{9.25b}$$

The ideal fluid path whose angular momentum is conserved results in a *logarithmic spiral*, as schematically shown in Figure 9.11. The effect of external retarding torque is

$$(\tau_{\text{ext}})_f = \dot{m}(r_3C_{\theta 3} - r_2C_{\theta 2}) = -\tau_w \tag{9.26a}$$

Therefore, in the presence of a retarding torque (due to friction), the angular momentum is reduced and swirl diminish even faster than a logarithmic spiral, namely,

$$\frac{rC_\theta}{r_2C_{\theta 2}} = 1 - \frac{\tau_{\text{wall}}}{\dot{m}(r_2C_{\theta 2})} \tag{9.26b}$$

where the (external) wall torque is written as negative, which applies a retarding influence on the fluid angular momentum. The fluid path with friction *unwinds* faster than the inviscid solution. A schematic drawing of the two stream patterns in a radial diffuser with/without friction is shown in Figure 9.11.

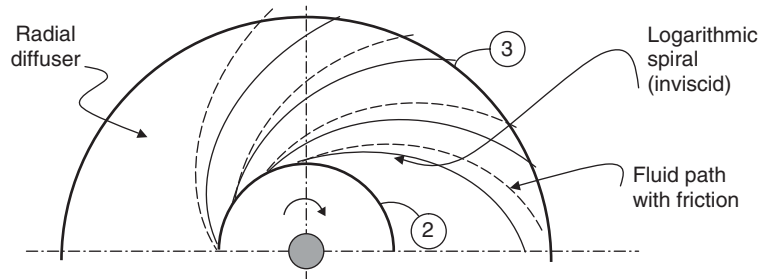
The inlet Mach number M_2 to the radial diffuser may be calculated using the velocity triangle at the impeller exit.

$$C_2 = \sqrt{C_{r2}^2 + C_\theta^2} = \sqrt{C_{r2}^2 + (U_T - C_{r2} \tan \beta_2)^2} \tag{9.27}$$

The speed of sound at the impeller exit is based on T_2 , for which we derived a simple expression,

$$\frac{T_2}{T_1} \approx 1 + \left(\frac{\gamma - 1}{2}\right) M_T^2 \tag{9.28a}$$

■ **FIGURE 9.11**
Schematic drawing of the fluid path in a radial diffuser with and without the effect of wall friction



Therefore, the speed of sound at the impeller exit is related to the speed of sound at the inlet according to

$$\frac{a_2}{a_1} \approx \sqrt{1 + \left(\frac{\gamma - 1}{2}\right) M_T^2} \tag{9.28b}$$

The combination of the exit speed to the local speed of sound is the Mach number, therefore,

$$M_2 \approx \frac{\sqrt{M_{z1}^2 + (M_T - M_{z1} \tan \beta_2)^2}}{\sqrt{1 + \left(\frac{\gamma - 1}{2}\right) M_T^2}} \tag{9.29}$$

In expression 9.29, we approximated the radial velocity at the impeller exit by the inlet axial velocity C_{z1} . We may use this as a design choice to approximate the blade axial span at the impeller exit b .

The effect of backward-leaning design (i.e., $\beta_2 > 0$) on the impeller exit Mach number is seen from Equation 9.28 to be reducing the exit velocity, thus the Mach number. A reduced impeller exit Mach number then relieves the requirements on the radial diffuser and improve its performance. Despite the choice of backward-leaning designs in reducing the exit velocity, our desire to achieve higher pressure ratios has pushed the exit Mach number of the impeller, that is, the diffuser inlet Mach number into supersonic regime. The radial diffuser is then divided into a supersonic diffuser followed by a subsonic diffuser. The dividing line between the two parts is the invisible sonic circle, as shown in Figure 9.12. The subsonic diffuser may be bladed (vanes) to improve the pressure recovery.

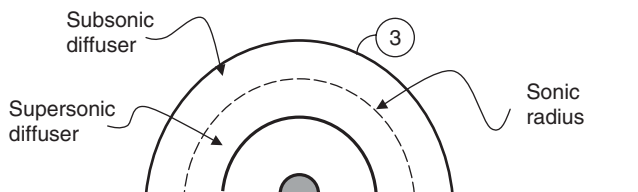
For the conversion of the entire kinetic energy to the fluid static enthalpy rise, we get

$$h_3 - h_2 = \frac{C_2^2}{2} \approx \frac{U_T^2}{2} \tag{9.30}$$

Therefore, the static temperature ratio across the compressor stage is related to the square of the impeller exit Mach number, according to

$$\frac{T_3}{T_1} = \frac{T_2}{T_1} + \left(\frac{\gamma - 1}{2}\right) M_T^2 \tag{9.31}$$

■ FIGURE 9.12 Radial diffuser with supersonic inlet flow and a sonic radius



Now, substituting for the static temperature ratio for the rotor from Equation 9.28a, we get

$$\frac{T_3}{T_1} \approx 1 + (\gamma - 1)M_T^2 \tag{9.32}$$

The static pressure ratio in the limit of reversible and adiabatic flow for the stage is

$$\frac{p_3}{p_1} \approx [1 + (\gamma - 1)M_T^2]^{\frac{\gamma}{\gamma-1}} \tag{9.33}$$

In this model, we note that the static temperature rise across the diffuser is the same as the rotor, which produces the other half of the static temperature rise. In the context of the degree of reaction, the stage that we defined is a 50% degree of reaction type.

EXAMPLE 9.3

For an impeller tip Mach number of 1.2, and equal static pressure rise across the rotor and diffuser, calculate

- the static pressure ratio across the rotor and diffuser, p_3/p_1

- the static pressure ratio across the diffuser, p_3/p_2
- estimate diffuser static pressure rise (assume $M_2 \approx M_T$)

SOLUTION

In the limit of reversible adiabatic flow, we may use Equation 9.33 to get

$$\frac{p_3}{p_1} \approx [1 + 0.4(1.2)^2]^{3.5} \cong 4.9$$

The static pressure ratio across the diffuser is square root of the stage pressure ratio, namely,

$$\frac{p_3}{p_2} \approx \sqrt{4.9} \approx 2.2$$

The static pressure rise coefficient for the diffuser is

$$C_p \equiv \frac{p_3 - p_2}{q_2} = \frac{p_3 - p_2}{\gamma \cdot p_2 M_2^2 / 2} = \frac{2}{\gamma \cdot M_2^2} \left(\frac{p_3}{p_2} - 1 \right) \tag{9.34}$$

The Mach number at the impeller exit is

$$M_2^2 = M_{r2}^2 + M_{\theta2}^2 \tag{9.35}$$

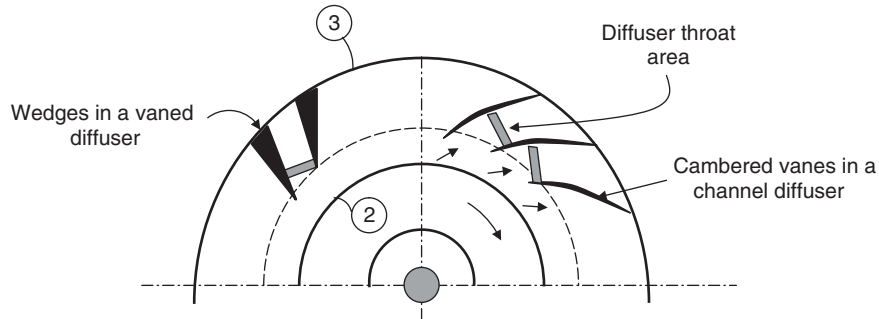
We need to analyze the velocity triangle at the impeller tip to evaluate these terms, i.e., the radial and tangential Mach numbers. For the sake of discussion, let us take M_2 to be nearly the same as M_T , which forces the static pressure rise coefficient in the radial diffuser to be

$$C_p \approx \frac{2}{(1.4)(1.2)^2} (2.2 - 1) \approx 1.19$$

From our earlier diffuser studies we know that this level of static pressure rise is not tolerable in a practical diffuser. In the axial-flow compressor Chapter 8, we set a maximum value of $C_{p,max}$ of ~0.6, which in this case is nearly twice the maximum value. We conclude that the diffuser section needs to be more lightly loaded than the rotor if the boundary layer is to remain attached in the diffuser. This is not surprising that in centrifugal compressors the rotor tip Mach number plays such a dominant role in establishing the performance of the machine. We experienced a similar behavior in axial-flow machinery.

The placement of cambered vanes in radial diffusers similar to the splitter plates in axial diffusers significantly improves the static pressure recovery of radial diffusers. The vane leading edge needs to be aligned with the local relative flow in order to avoid lip

■ **FIGURE 9.13**
Schematic drawing of
cambered vanes or
wedges in a radial
diffuser



separation. A schematic drawing of cambered vanes or wedges in a centrifugal compressor diffuser is shown in Figure 9.13.

The guiding hands of the vanes' sidewalls assist the flow in remaining attached to diffuser walls. This is another example of three-dimensional flow separation being delayed by taking one spatial degree of freedom away from the flow, that is, turning a 3D flow into an effective 2D flow. The diffuser throat blockage, as presented earlier in the inlet chapter, dominates the performance of the cambered vane diffusers. Pratt & Whitney has introduced "pipe" diffusers, which have produced a superior performance to the cambered vane or channel diffusers (Kenny, 1984).

9.4 Inducer

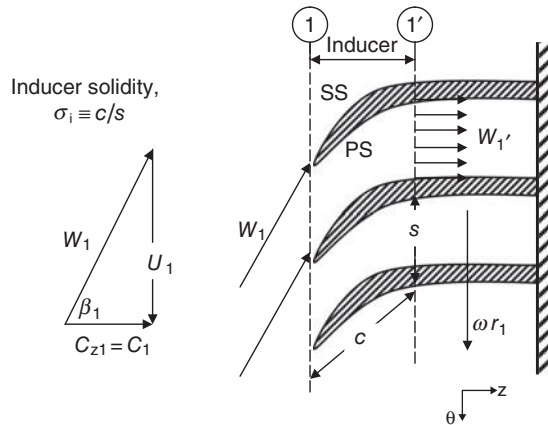
The inducer is the part of the impeller that meets the flow at the compressor inlet at the relative flow angle β_1 . Its primary function is to turn the flow toward the axial direction, as shown in Figure 9.13, thereby increasing its static pressure. In this context, the function of inducer is very similar to the rotor blades in an axial-flow compressor. There are some differences, though, that we need to consider. One is that the rotor blades in an axial-flow compressor do not need to turn the relative flow completely in the axial direction, whereas the inducer has to turn the flow completely in the axial direction. This causes a higher loading, that is, turning demand, on the inducer. The second difference is subtler than the first. The difference arises from the trailing edge of the blades. Namely, the inducer trailing edge is not free, that is, it is connected to the rest of the impeller. The axial-flow compressor rotor trailing edge is free and thus obeys the Kutta condition, which influences the trailing edge flow and the wake pattern. For example, the axial-flow compressor rotor immediately adjusts to the incoming flow disturbances by vortex shedding in the wake or adjusting the wake vortex strength in the spanwise direction. Despite these differences, we still proceed to analyze the inducer blades using the same tools we developed in the axial-flow compressors.

Let us identify station 1' as the exit of the inducer, as shown in Figure 9.14. We may define the diffusion factor for the inducer as

$$D_{\text{inducer}} \equiv 1 - \frac{W_{1'}}{W_1} + \frac{|\Delta C_\theta|}{2\sigma_1 W_1} \quad [\text{inducer } D - \text{factor}] \quad (9.36)$$

The change of swirl across the inducer is approximately the wheel speed U_1 , since the inlet flow to the inducer is swirl free (in the absolute frame) and the exit flow is nearly

■ **FIGURE 9.14**
Definition sketch of the inducer geometry and relative flow (in θ - z plane)



axial in the relative frame. Now, if we assume that the axial velocity in the inducer remains constant, i.e.,

$$C_{z1} \cong W_{1'} \tag{9.37}$$

We may write the diffusion factor in terms of axial flow Mach number at the inlet and the impeller tip Mach number M_T , according to

$$D_{\text{inducer}} \cong 1 - \frac{C_{z1}}{\sqrt{C_{z1}^2 + U_1^2}} + \frac{U_1}{2\sigma_i \sqrt{C_{z1}^2 + U_1^2}} \tag{9.38}$$

$$D_{\text{inducer}} \cong 1 - \frac{1}{\sqrt{1 + \left(\frac{U_1}{U_2}\right)^2 \left(\frac{U_2}{C_{z1}}\right)^2}} + \frac{U_1/C_{z1}}{2\sigma_i \sqrt{1 + \left(\frac{U_1}{U_2}\right)^2 \left(\frac{U_2}{C_{z1}}\right)^2}} \tag{9.39a}$$

$$D_{\text{inducer}} \cong 1 - \frac{1}{\sqrt{1 + \left(\frac{r_1}{r_2}\right)^2 \left(\frac{M_T}{M_{z1}}\right)^2}} + \frac{(M_T/M_{z1})(r_1/r_2)}{2\sigma_i \sqrt{1 + \left(\frac{r_1}{r_2}\right)^2 \left(\frac{M_T}{M_{z1}}\right)^2}} \tag{9.39b}$$

Here, we note that the geometric parameters such as the impeller radius ratio and the inducer solidity are tied together with the choices of the tangential and axial flow Mach numbers to arrive at a reasonable inducer diffusion factor D_{inducer} , that is, $D_{\text{inducer}} < 0.6$. The axial Mach number varies in the range of $M_{z1} \sim 0.4$ – 0.6 and the impeller tip Mach number $M_t \sim 1$ – 1.5 , the radius ratio, and the solidity may be plotted as a function of inducer diffusion factor.

EXAMPLE 9.4

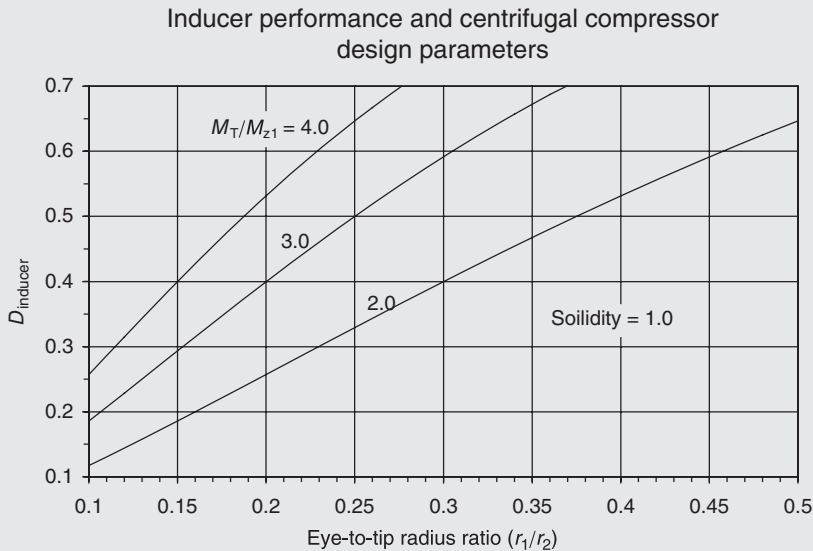
Calculate and graph the inducer D -factor for solidity of one and over a range of impeller tip Mach numbers and radius ratios.

SOLUTION

A spreadsheet is produced based on Equation 9.39b for solidity of 1. The eye-to-tip radius ratio varied from 0.1 to 0.5, and the tip-to-axial Mach number ratio varied from 2 to 4.0. The graph of the tabulated spreadsheet is shown in Figure 9.15. The parameter M_T/M_{z1} is chosen as a running parameter in Figure 9.15, as it determines the compressor pressure ratio. We observe that for a given solidity, e.g., $\sigma_i = 1$, and a maximum diffusion factor, of say 0.6, a high-pressure ratio compressor impeller requires a low eye-to-tip radius ratio (~ 0.22). But since the mass flow rate through the machine is proportional to the inlet area, for a high-pressure ratio impeller, the mass flow per unit

frontal area (i.e., A_2 or A_3) drops. This inverse relationship between the radius ratio and the pressure ratio limits the practical designs of centrifugal compressors to a compromise between these conflicting requirements.

The advances in transonic rotor design in axial-flow compressors have prompted maximum relative Mach numbers approaching the inducer tip to be as high as ~ 1.5 . The supersonic relative tip Mach number creates shocks, which demand extensive inducer geometric tailoring via viscous CFD analysis to minimize shock boundary layer interaction losses.



■ FIGURE 9.15 Inducer design parameters (for an inducer solidity of one)

EXAMPLE 9.5

In Example 9.1, we calculated an eye-to-tip radius ratio of 0.57, an axial Mach number of $M_{z1} \sim 0.45$ and $M_t \sim 1.56$. Calculate the inducer diffusion factor in terms of its solid-

ity. Is there any solidity that allows acceptable diffusion in the inducer?

SOLUTION

Upon substitution of the Mach numbers and radius ratio in Equation 9.39b that relates the diffusion factor to the impeller solidity, we get

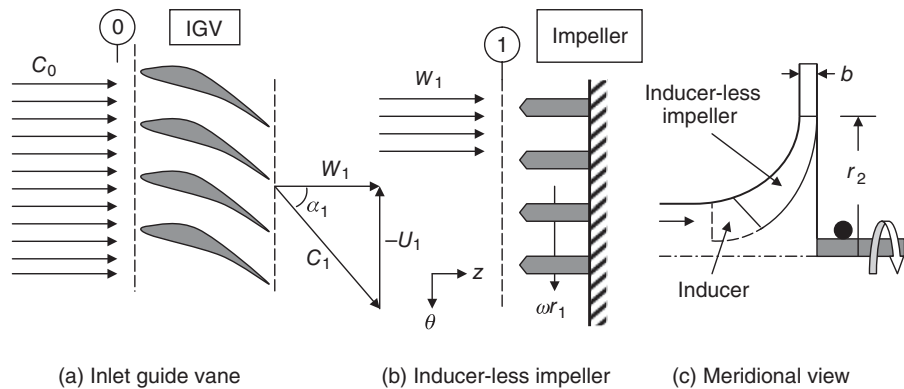
$$D_i \cong 0.79 + \frac{0.446}{\sigma_i}$$

As suspected, the diffusion is too large and there is no choice of solidity (σ_i) that can decrease the inducer diffusion factor to below 0.79. Therefore, we are prompted to change our design parameters in order to reduce the inducer (diffusion) loading.

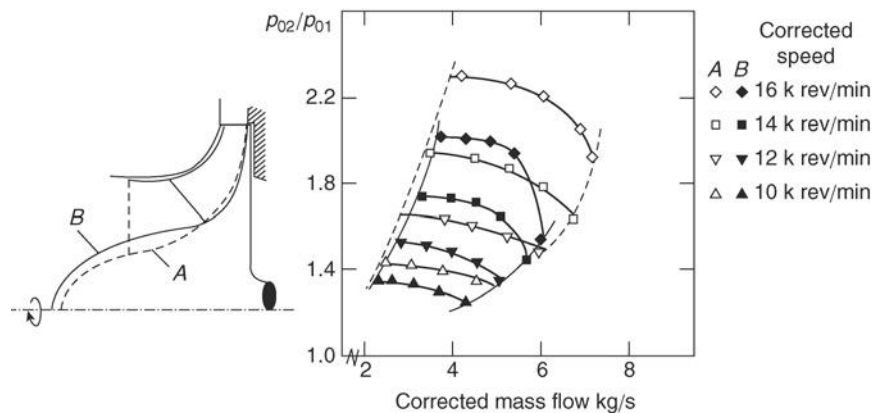
9.5 Inlet Guide Vanes (IGVs) and Inducer-Less Impellers

By incorporating inlet guide vanes in the incoming flow, we may impart a preswirl to the fluid, which is in the direction of impeller rotation. Therefore, it is possible to eliminate the need for an inducer if the relative flow to the impeller is already in the axial direction. Figure 9.16 shows the IGV exit flow and the impeller inlet relative flow, which is purely in the axial direction. In Figure 9.16c, we are comparing an impeller with inducer to an inducer-less impeller in the meridional plane. The presence of inducer offers a larger throat area than the inducer-less impeller. This geometrical influence causes the centrifugal compressor with an inducer-less impeller reach choking condition before a geometrically comparable centrifugal compressor with an inducer section. This may be seen from the data of Eckardt (1977). Figure 9.17 shows Eckardt's comparison of two centrifugal compressors with the same exit radius r_2 and width b . The "A" compressor has inducer and backsweep of 40° , whereas the "B" impeller is inducer-less and has 30° backsweep blades. The "A" impeller reaches a higher mass flow rate before choking.

■ **FIGURE 9.16**
IGV-coupled
inducer-less impeller
and geometrical
comparison of two
impellers



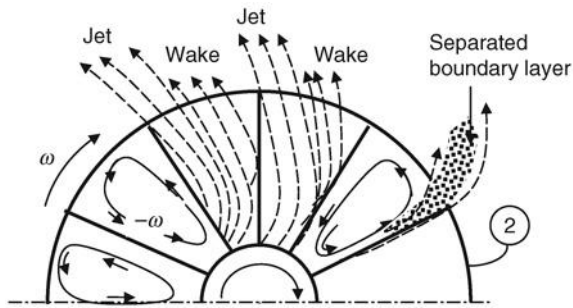
■ **FIGURE 9.17**
Performance maps of
two impellers (A) with
and (B) without
inducer. Source:
Eckhardt 1977.
Courtesy of German
Government



9.6 Impeller Exit Flow and Blockage Effects

We have introduced the phenomenon of slip at the impeller exit. The turning of the relative flow in the opposite direction to that of the rotor starts inside the impeller passage.

■ **FIGURE 9.18**
The exit flow pattern from an impeller shows a “jetwake” profile



We have graphically depicted the relative streamlines in the impeller in Figure 9.3d. The accumulation of the flow on the pressure side results in a jet-like behavior and the sparse low-momentum flow on the suction side of the impeller vanes gives an appearance of the wake (or deficit momentum) flow. This behavior at the exit of the centrifugal compressor impellers is known as the *jet-wake flow*, first described by Dean and Senoo (1960). Figure 9.18 shows the jet-wake exit flow behavior in a radial impeller. The first observation is that the impeller exit flow is highly nonuniform. Therefore, the one-dimensional approximations that we often make need to be modified to reflect the nonuniform flow behavior. The second implication is that the boundary layer on the suction surface near the impeller exit is likely separated, as schematically shown in Figure 9.18. The combined effects of jet-wake velocity profile and separated flow gives rise to a high level of *blockage* at the exit.

Through the concept of blockage, we define an effective flow area $A_{2\text{eff}}$. The definition of blockage from diffuser studies in Chapter 6 is repeated here, where effective and geometrical areas are applied to the impeller exit:

$$B_2 \equiv 1 - \frac{A_{2\text{eff}}}{A_2}$$

where A_2 is the geometric flow area that may be written as

$$A_2 = (2\pi r_2 b - Ntb) \cos \beta'_2 \quad (9.40)$$

In Equation 9.40, N is the number of the impeller vanes, t is thickness of the blades at the exit, b is the axial span of vanes at 2, and β'_2 is the blade sweep angle at the exit (measured from the radial direction). The cosine term in Equation 9.40 gives a projection of the exit area that is in the radial direction. The conclusions from this section are

- (a) One-dimensional flow analysis is totally inadequate and gives erroneous results
- (b) Jet-wake profile and flow separation have to be accounted for by a suitable averaging technique and an estimate of blockage B_2 , respectively. In either case, more experimental data are needed.

9.7 Efficiency and Performance

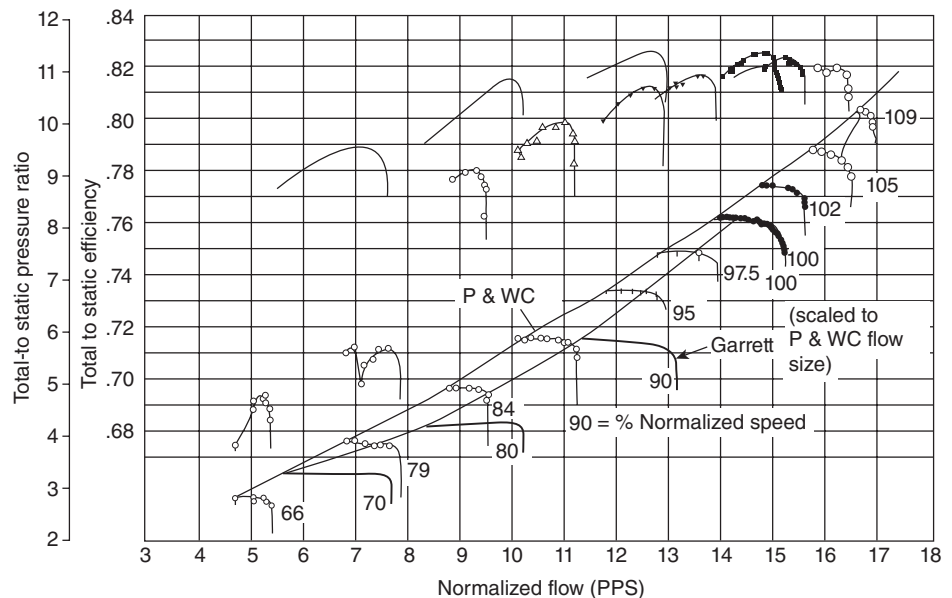
Centrifugal compressor efficiency has always lagged its counterpart, the axial-flow compressor, for the same pressure ratio. The flow path is rather torturous as it twists from one

plane to another in a centrifugal compressor, thus massive secondary flow and separation losses become imminent. In addition, for high-pressure ratio centrifugal compressors, the flow in the diffuser becomes supersonic and its efficient diffusion rather complex. In a historical perspective presented by Kenny (1984), different loss sources, future design trends, and limitations of centrifugal compressors are discussed. Although it is very difficult, if not impossible, to separate losses in turbomachinery into their components without overlapping, which is double/triple accounting, it is still instructive to expose general loss sources in turbomachinery. In a centrifugal compressor, the losses are attributed to

1. Tip clearance loss in an unshrouded impeller
2. Secondary flow losses due to flow turning
3. Disk friction losses
4. Losses due to compressibility effects in the inducer due to shocks and flow separation
5. Jet-wake mixing flow losses in the diffuser
6. Diffuser compressibility losses due to high absolute Mach numbers
7. Flow unsteadiness and vortex shedding in the impeller wake.

Also a comparison of two centrifugal compressors designed for an 8:1 total-to-static pressure ratio and their efficiencies at off-design are shown in Figure 9.19 (also from Kenny). Note that the efficiencies are listed for total exit-to-static inlet state of the gas, as well as the pressure ratio. For a Mach 0.5 (absolute inlet) flow, the ratio of total-to-static pressure is $[1 + (0.2)(0.5)^2]^{3.5} \cong 1.186$, therefore an 8:1 design total-static pressure ratio means a total-to-total pressure ratio of $\pi_s \cong 6.74$. Although centrifugal compressors are less efficient; they can produce stage pressure ratios outside the reach of the axial-flow compressors. The centrifugal compressors represent the compressor of choice for small

■ **FIGURE 9.19**
The performance map for two centrifugal compressors with an 8:1 total-static design pressure ratio. Source: Kenny 1984. Reproduced with permission from SAE International



EXAMPLE 9.6

The inlet flow to a centrifugal compressor is described by

$$C_1 = 200 \text{ m/s}$$

$$p_{t1} = 101 \text{ kPa}$$

$$T_{t1} = 288 \text{ K}$$

The compressor pressure ratio at the design point is $p_{t3}/p_{t1} = 6.8$ with a total-to-total adiabatic efficiency of $\eta_{TT} = 0.80$. Calculate the compressor total-to-static efficiency. Assume $\gamma = 1.4$ and $c_p = 1004 \text{ J/Kg} \cdot \text{K}$.

SOLUTION

From the definition of total-to-total adiabatic efficiency, we calculate T_{t3} following

$$T_{t3} = T_{t1} \left\{ 1 + \frac{1}{\eta_{TT}} \left[\left(\frac{p_{t3}}{p_{t1}} \right)^{\frac{\gamma-1}{\gamma}} - 1 \right] \right\} \approx 550.5 \text{ K}$$

Also, T_{t2s} is related to T_{t1} and compressor pressure ratio isentropically, i.e.,

$$T_{t2s} = T_{t1} \left(\frac{p_{t3}}{p_{t1}} \right)^{\frac{\gamma-1}{\gamma}} \approx 498 \text{ K}$$

The static temperature of the inlet gas is calculated from

$$T_1 = T_{t1} - \frac{C_1^2}{2c_p} \approx 288 \text{ K} - (200)^2/2/1004 \approx 268.1 \text{ K}$$

The definition of total-to-static efficiency is $\eta_{TS} \equiv \frac{h_{t3s} - h_1}{h_{t3} - h_1}$ and we have calculated all the parameters in this equation, therefore, $\eta_{TS} \approx 0.814$

9.8 Summary

Centrifugal compressors achieve high compression per stage that is predominantly produced by centrifugal force with a large exit-to-inlet impeller radius ratio. The flow area through the inlet is thus a small fraction of the frontal area of the machine. Therefore, the mass flow rate per frontal area is lower in centrifugal than the axial-flow compressors.

The pressure ratio per stage is high, however, with lower adiabatic efficiency than the axial counterpart. The flow path from the inlet to the exit twists and turns, thus secondary flow losses are significant. The phenomenon of slip creates a jet-wake nonuniform velocity profile at the impeller exit. The geometry of the impeller blade passages is characterized by a large wetted perimeter and a small flow area, which makes for an equivalently small hydraulic diameter with large frictional losses. The radial flow from the impeller is decelerated in radial and vaned diffusers. The diffuser exit flow is turned 90° for a follow up combustor or even 180° degrees for the next centrifugal compressor stage. Therefore, staging centrifugal compressors involve turnaround ducts, which make them more cumbersome than axial compressors.

The robust construction of the centrifugal compressors and their high pressure ratio per stage capability make them ideal for small gas turbine engines, auxiliary power units, automotive turbo-chargers, and other industrial uses. The inducer-less and shrouded impellers are used in industrial applications, whereas the unshrouded impellers with inducers that offer lower weight and higher mass flow capability are suitable for aerospace applications.

Classical literature on turbomachinery is found in Stodola's text (1924, 1927) as well as Traupel's book (1977). Taylor (1964), Marble (1964), Kerrebrock (1992), Cumpsty (2004) and Dixon (1975) have treated compressors in detail and are recommended for further reading. Historical perspectives presented by Garvin (1998) and St. Peter (1999) compliment the subject. Hill and Peterson's book (1992) as well as Paduano, Greitzer and Epstein's review paper (2001) on compression system stability are recommended to the reader.

References

1. Busemann, A., "Das Foerderhuehenverhaeltnis radialer Kreiselpumpen mit Logarithmisch-spiraligen Schaufeln," *Zeitschrift angewandete Mathematik und Mechanik*, Vol. 8, No. 5, 1928.
2. Cumpsty, N.A., *Compressor Aerodynamics*, Krieger Publishing Co., Malabar, FL, 2004.
3. Dean, R.C. and Senoo, Y., "Rotating Wakes in Vaneless Diffusers," Transactions of ASME, *Journal of Basic Engineering*, Vol. 82, 1960, pp. 563–574.
4. Dixon, S.L., *Fluid Mechanics, Thermodynamics of Turbomachinery*, 2nd edition, Pergamon Press, Oxford, UK, 1975.
5. Eckhardt, D., Vergleichende Stroemungsuntersuchungen an drei Radiaverdichter-Laufraden mit konventionellen Messverfahren, Forschungsbericht Verbrennungskraftmaschinen, *Vorhaben* 182, Vol. 237, 1977.
6. Garvin, R.V., *Starting Something Big: The Commercial Emergence of GE Aircraft Engines*, AIAA, Inc., Reston, VA, 1998.
7. Hill, P.G. and Peterson, C.R., *Mechanics and Thermodynamics of Propulsion*, 2nd edition, Addison-Wesely, Reading, MA, 1992.
8. Kenny, D.P., "The History and Future of the Centrifugal Compressor in Aviation Gas Turbines," SAE Paper No. 841635, 1984.
9. Kerrebrock, J.L., *Aircraft Engines and Gas Turbines*, 2nd edition, MIT Press, Cambridge, MA, 1992.
10. Marble, F.E., "Three-Dimensional Flow in Turbomachines," in *Aerodynamics of Turbines and Compressors*, Vol. X, Ed. Hawthorne, W.R., Princeton Series on High Speed Aerodynamics and Jet Propulsion, Princeton University Press, Princeton, NJ, 1964.
11. Paduano, J.D., Greitzer, E.M., and Epstein, A.H., "Compression System Stability and Active Control," *Annual Review of Fluid Mechanics*, Vol. 33, 2001, pp. 491–517.
12. Stanitz, J.D. and Ellis, G.O., "Two-Dimensional Compressible Flow in Centrifugal Compressors with Straight Blades," NACA Technical Note 1932, 1949.
13. St. Peter, J., *The History of Aircraft gas Turbine Engine Development in the United States*, International Gas Turbine Institute, Atlanta, GA, 1999.
14. Stodola, A., *Dampf- und Gasturbinen*, Springer Verlag, 1924.
15. Stodola, A., *Steam and Gas Turbines*, Vos. 1 and 2, McGraw-Hill, New York, 1927.
16. Taylor, E.S., "The Centrifugal Compressor", in *Aerodynamics of Turbines and Compressors*, Ed. Hawthorne, W.R., Princeton Series in High-Speed Aerodynamics and Jet Propulsion, Vol. X, Princeton University Press, Princeton, NJ, 1964.
17. Traupel, W., *Thermische Turbomaschinen*, 3rd edition, Springer Verlag, 1977.

Problems

9.1 A centrifugal compressor has 22 radial impellers with an (impeller) exit radius of $r_2 = 0.25$ m. Assuming the mass flow rate through the compressor is $\dot{m} = 10$ kg/s, the shaft speed is $\omega = 10,000$ rpm, and the inlet flow is swirl free, calculate

- (a) the shaft power, $\dot{\phi}_s$, in kW
- (b) the total temperature rise in the compressor (assume $\gamma = 1.4$ and $c_p = 1004$ J/kg · K)

9.2 Size the exit radius of a centrifugal compressor impeller, r_2 , that is to reach a tangential Mach number of $M_T = 1.5$. The shaft rotational speed is 25,000 rpm and the inlet flow condition is characterized by

$$\begin{aligned} p_1 &= 100 \text{ kPa} \\ T_1 &= 288 \text{ K} \\ M_1 &= 0.5 \\ \gamma &= 1.4 \text{ and } c_p = 1,004 \text{ J/kg} \cdot \text{K} \end{aligned}$$

9.3 We are interested in a parametric study of the diffusion factor for an inducer section of an impeller. We know from Equation 9.39b that

$$D_{\text{inducer}} \cong 1 - \frac{1}{\sqrt{1 + \left(\frac{r_1}{r_2}\right)^2 \left(\frac{M_{T2}}{M_{z1}}\right)^2}} + \frac{(M_{T2}/M_{z1})(r_1/r_2)}{2\sigma_1 \sqrt{1 + \left(\frac{r_1}{r_2}\right)^2 \left(\frac{M_{T2}}{M_{z1}}\right)^2}}$$

There are three nondimensional groups that appear in the above equation.

- (a) impeller radius ratio r_1/r_2
- (b) ratio of impeller tip Mach number to the inlet axial Mach number M_{T2}/M_{z1}
- (c) inducer solidity σ_1

Graph D_{inducer} versus one of the three nondimensional groups while keeping the other two groups constant.

9.4 A centrifugal compressor has no inlet guide vanes and thus zero preswirl. The axial Mach number is $M_1 = 0.5$ and is uniform at the impeller face. The inlet condition is entirely known, $p_1 = 100$ kPa, $T_1 = 288$ K, and the geometry of the inlet, $r_{1h} = 10$ cm and $r_{1t} = 25$ cm. The exit radius is $r_2 = 0.35$ cm and shaft rotational speed is 10,000 rpm. The centrifugal compressor has 20 radial impeller blades.

Assuming the compressor polytropic efficiency $e_c = 0.85$, calculate

- (a) mass flow rate \dot{m}_1 (in kg/s)
- (b) absolute swirl velocity at the impeller exit, $C_{\theta 2}$, in m/s
- (c) compressor specific work, at the pitchline, w_c , in kJ/kg
- (d) compressor shaft power in kW
- (e) compressor pressure ratio π_s
- (f) exit (absolute) Mach number at 2, M_2 , assuming $C_{r2} = C_{z1}$
- (g) swirl velocity at the exit of the radial vaneless diffuser

(assuming zero frictional losses in the diffuser) and radius of 45 cm

9.5 A centrifugal compressor has 25 impeller blades of radial design. The rotor exit diameter is $r_2 = 0.4$ m, and its rotational speed is $\omega = 8000$ rpm. Assuming the inlet to rotor flow is purely axial and the air mass flow rate is $\dot{m} = 25$ kg/s through the compressor, calculate

- (a) compressor shaft power, $\dot{\phi}_c$ in, MW
- (b) (time rate of change of) angular momentum at the rotor exit

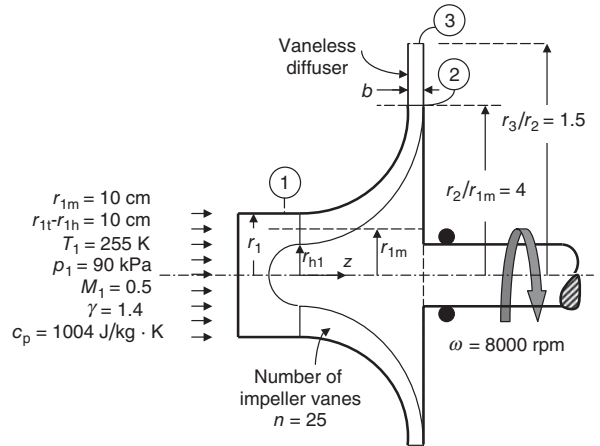


FIGURE P9.5

9.6 The inlet flow to a radial (vaneless) diffuser has a swirl component of $C_{\theta 2} = 200$ m/s and a radial component of $C_{r2} = 100$ m/s. The impeller exit radius $r_2 = 25$ cm and the flow static pressure and temperature are

$$p_2 = 300 \text{ kPa}$$

$$T_2 = 425 \text{ K}$$

Assuming inviscid flow in the radial diffuser, with $\gamma = 1.4$ and $R = 287$ J/Kg · K, calculate

- (a) $C_r(r)$
- (b) $C_\theta(r)$

9.7 A centrifugal compressor discharge pressure and temperature are measured to be

$$P_{t3} = 303 \text{ kPa}$$

$$T_{t3} = 408 \text{ K}$$

The inlet flow is purely axial with $C_{z1} = 100$ m/s and the inlet total pressure and temperature are

$$p_{t1} = 101 \text{ kPa}$$

$$T_{t1} = 288 \text{ K}$$

Calculate

- (a) total-to-static pressure ratio p_{t3}/p_1
- (b) total-to-total pressure ratio
- (c) total-to-static adiabatic efficiency η_{TS}
- (d) total-to-total adiabatic efficiency η_{TT}
- (e) polytropic efficiency e_c for total-static and total-total processes

9.8 To eliminate the inducer from a centrifugal compressor impeller, we need to induce a swirl profile in the incoming flow (known as preswirl) that is in the direction of the rotor and its relative flow to the impeller is purely axial. This task is done through an IGV.

For an inducer-less impeller of

$$\begin{aligned} r_{1h} &= 5 \text{ cm} \\ r_{1t} &= 10 \text{ cm} \\ \omega &= 11,500 \text{ rpm} \\ C_{z1} &= 100 \text{ m/s} \end{aligned}$$

Calculate

- (a) swirl profile $C_{\theta 1}(r)$
- (b) absolute flow angle $\alpha_1(r)$
- (c) the IGV twist from hub-to-tip, assuming a constant deviation angle with span

9.9 The inlet static pressure to an impeller is $p_1 = 100$ kPa and its exit static pressure is $p_2 = 200$ kPa with inlet relative dynamic pressure $q_{1r} = 140$ kPa. Treating the impeller as a diffuser, assuming $\gamma = 1.4$, calculate

- (a) inlet relative Mach number M_{1r}
- (b) static pressure recovery coefficient C_{PR}

9.10 A radial diffuser has an exit-to-inlet radius ratio r_3/r_2 of 4. Assume the flow is incompressible and the fluid is inviscid. Calculate

- (a) the diffuser area ratio A_3/A_2
- (b) exit-to-inlet radial velocity ratio C_{r3}/C_{r2}
- (c) exit-to-inlet swirl ratio $C_{\theta 3}/C_{\theta 2}$
- (d) static pressure rise coefficient or static pressure recovery C_{PR}

9.11 A centrifugal compressor has a total pressure ratio of $p_{t3}/p_{t1} = 8$. Calculate and graph this compressor's total-to-static pressure ratio p_{t3}/p_1 for a range of inlet Mach numbers M_1 from 0.25 to 0.75 in steps of 0.05. Assume $\gamma = 1.4$.

9.12 The total-to-total compressor adiabatic efficiency for a centrifugal compressor is $\eta_{TT} = 0.78$. The compressor total pressure ratio is $p_{t3}/p_{t1} = 7$. Assuming the inlet Mach number is $M_1 = 0.4$ and $\gamma = 1.4$, calculate

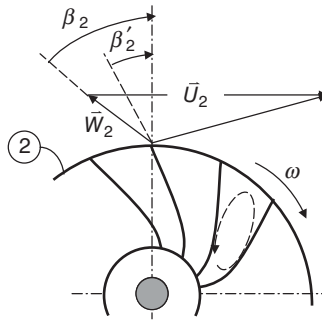
- (a) total-to-static pressure ratio
- (b) total temperature ratio T_{t3}/T_{t1}
- (c) total-to-static adiabatic efficiency η_{TS} .

9.13 A backswept impeller has a tip speed of $U_2 = 366$ m/s and the impeller blade exit angle is $\beta'_2 = 30^\circ$. The radial velocity at the impeller exit is $C_{r2} = 125$ m/s. Stagnation speed of sound at the impeller inlet is $a_{t1} = 340$ m/s, assuming the inlet flow is purely axial, and the slip angle at the impeller exit is 6° , i.e., $\beta_2 - \beta'_2 = 6^\circ$, calculate

- (a) slip factor ϵ
- (b) Mach index Π_M

- (c) Impeller specific work, w_c , in kJ/kg
- (d) stage total temperature ratio τ_{stage}
- (e) stage total pressure ratio if $e_c = 0.89$

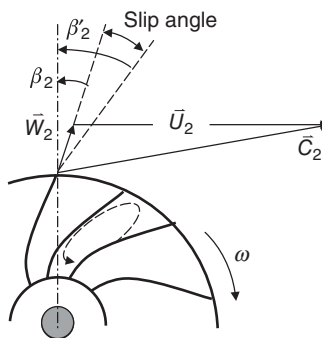
Assume $\gamma = 1.4$ and $c_p = 1004$ J/Kg · K.



■ FIGURE P9.13

9.14 A forward-swept impeller has a tip speed of $U_2 = 400$ m/s and the impeller blade exit angle is $\beta'_2 = -30^\circ$. The radial velocity at the impeller exit is $C_{r2} = 100$ m/s. Stagnation speed of sound at the impeller inlet is $a_{t1} = 330$ m/s, assuming the inlet flow is purely axial and the slip angle at the impeller exit is -6° , i.e., $\beta_2 - \beta'_2 = -6^\circ$, calculate

- (a) slip factor ϵ
- (b) Mach index Π_M
- (c) impeller specific work, w_c , in kJ/kg
- (d) stage total temperature ratio τ_{stage}
- (e) stage total pressure ratio if $e_c = 0.89$.



■ FIGURE P9.14

9.15 A 19-bladed radial impeller has an exit radius $r_2 = 25$ cm. The impeller width at the exit is $b = 1$ cm. We wish

to calculate and compare some impeller exit flow areas with successive levels of detail.

Case 1

Assume the individual trailing edge thickness of impeller blades is zero, i.e., $t = 0$, and calculate the geometric flow area.

Case 2

Assume the individual trailing edge thickness is $t = 2$ mm (per blade), and calculate the geometric flow area at the impeller exit.

Case 3

Assume the impeller exit blockage is 10% and now calculate the effective flow area.

Assuming the same slip factor between the three cases, relate the average radial velocity C_{r2} in cases 1, 2, and 3.

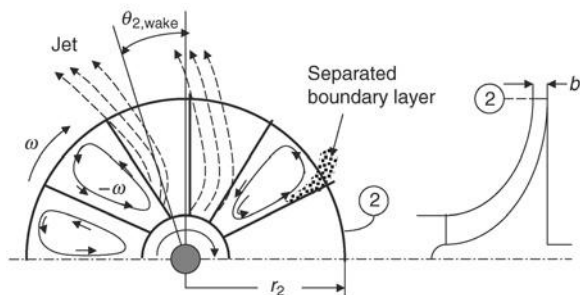
9.16 Air enters a centrifugal compressor at $p_{t1} = 101$ kPa, $T_{t1} = 288$ K, and purely in an axial direction with $M_z = 0.4$. Assuming the impeller radius at the exit is $r_2 = 25$ cm and the impeller is of radial design with slip factor $\epsilon = 0.9$ and $M_{T2} = 1.5$, calculate

- (a) U_2 in m/s
- (b) specific work, w_c , in kJ/kg
- (c) impeller exit total temperature, T_{t2} , in K
- (d) shaft rotational speed, ω , in rpm

9.17 The flow pattern at the exit of a radial centrifugal compressor impeller shows a jet-wake behavior, as shown in Figure 9.18, which is reproduced here with additional descriptions. In order to estimate the blockage, we assume that the wake region has zero momentum and is of angular extent $\theta_{2, \text{wake}}$ (per passage) at the impeller exit, as shown. The number of impeller blades is N , and the blade thickness at the exit is t (note the blade sweep angle is zero).

Calculate

- (a) the geometric flow area at 2 in terms of r_2 , t , N , and b
- (b) the effective flow area in terms of $\theta_{2, \text{wake}}$
- (c) the blockage B_2

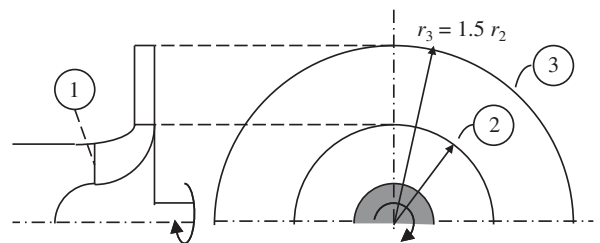


■ FIGURE P9.17

9.18 Consider a radial diffuser in a centrifugal compressor with straight radial impeller, as shown. The radial velocity at the impeller exit is $C_{r2} = 150$ m/s, the tangential velocity $C_{\theta 2} = 250$ m/s and the slip factor is $\epsilon = 0.90$. The stagnation temperature at the inlet to the impeller is $T_{t1} = 298$ K.

Assuming inlet flow to the centrifugal compressor is swirl free, i.e., $C_{\theta 1} = 0$, calculate

- (a) absolute Mach number, M_2
- (b) swirl at the exit of the radial diffuser, $C_{\theta 3}$, assuming inviscid flow
- (c) exit swirl, $C_{\theta 3}$, if the average retarding torque acting on the fluid by the wall is 5% of (time rate of change of the) fluid angular momentum at 2.

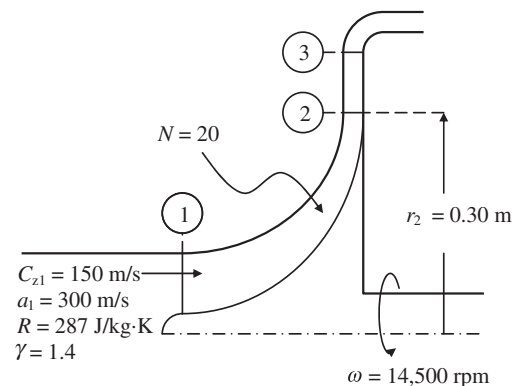


■ FIGURE P9.18

9.19 A centrifugal compressor impeller has 20 straight blades. The exit radius of the impeller is $r_2 = 0.30$ m and the angular speed is $\omega = 14,500$ rpm. The inlet flow to the compressor has zero preswirl and the axial velocity is $C_{z1} = 150$ m/s. The impeller exit has the radial velocity component C_{r2} that is equal to C_{z1} .

Assuming the speed of sound at the inlet to compressor is $a_1 = 300$ m/s, calculate

- (a) Mach index, Π_M
- (b) impeller exit absolute swirl, $C_{\theta 2}$, in m/s

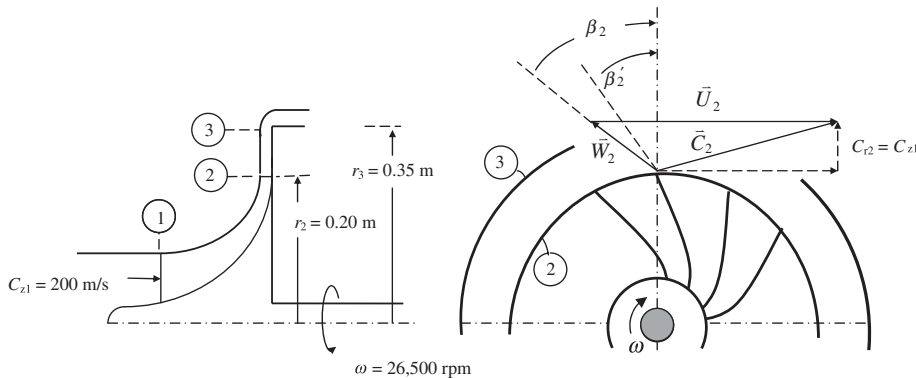


■ FIGURE P9.19

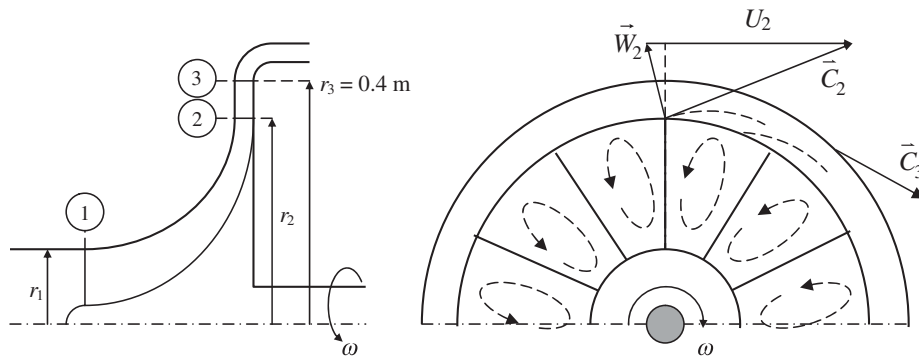
- (c) specific work of the rotor, w_c , in kJ/kg
- (d) impeller exit absolute Mach number, M_2
- (e) compressor total temperature ratio, τ_c

9.20 A centrifugal compressor impeller has 30 backswept blades with $\beta'_2 = 20^\circ$. The inlet flow condition to the compressor is purely axial with $C_{z1} = 200$ m/s and its total pressure and temperature are: $p_{t1} = 100$ kPa and $T_{t1} = 288$ K, respectively. The impeller rim is at a radius of $r_2 = 0.2$ m and the shaft rotational speed is $\omega = 26,500$ rpm. The radial velocity at the impeller exit is equal to the inlet axial velocity, as shown. Assuming the vaneless radial diffuser has an exit radius of $r_3 = 0.35$ m and further assuming that the flow in the radial diffuser is inviscid with gas properties $\gamma = 1.4$ and $R = 287$ J/kgK, calculate

- (a) impeller rim speed, U_2 , in m/s
- (b) impeller (actual) exit swirl, $C_{\theta 2}$, in m/s
- (c) specific work of the compressor, w_c , in kJ/kg
- (d) impeller absolute exit Mach number, M_2
- (e) swirl velocity at the diffuser exit, $C_{\theta 3}$, in m/s
- (f) radial velocity at the diffuser exit, C_{r3} , in m/s (neglecting density variations in the diffuser)



■ FIGURE P9.20



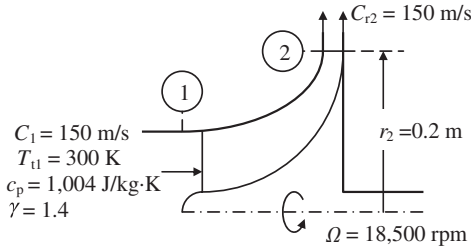
■ FIGURE P9.21

9.21 A centrifugal compressor impeller is of radial design and has 18 blades. The impeller exit radius is at $r_2 = 0.30$ m. The wheel rim speed is $U_2 = 400$ m/s. Assuming that flow in compressor inlet is swirl free, the axial velocity at the inlet and the radial velocity at the exit of the impeller are equal, i.e., $C_{z1} = C_{r2} = 150$ m/s, with $T_{t1} = 288$ K, $p_{t1} = 100$ kPa, $\gamma = 1.4$ and $c_p = 1004$ J/kg · K, calculate

- (a) absolute swirl at the impeller exit, $C_{\theta 2}$, in m/s
- (b) absolute Mach number at the impeller exit, M_2
- (c) absolute radial and tangential velocities at the radial diffuser exit, C_{r3} and $C_{\theta 3}$, in m/s (Assume the fluid is incompressible and inviscid in the radial diffuser)

9.22 A centrifugal compressor has 20 radial impeller blades that rotate at $\omega = 18,500$ rpm. The impeller exit radius is $r_2 = 0.20$ m. Assuming that the inlet flow is swirl free, calculate

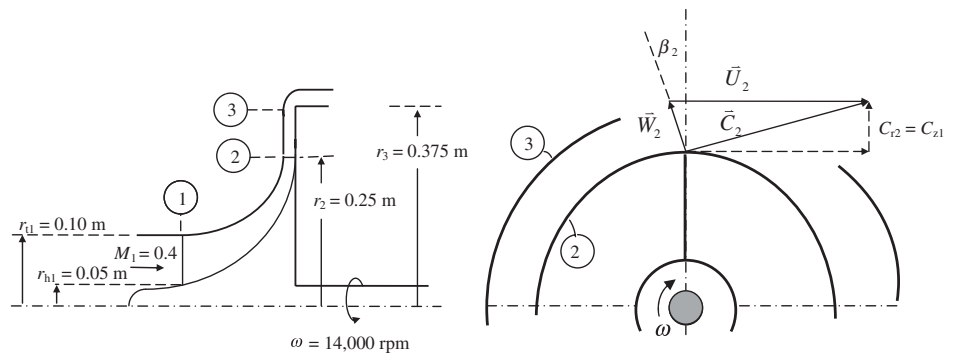
- (a) impeller exit (absolute) swirl, $C_{\theta 2}$, in m/s
- (b) impeller rim tangential Mach number, $M_T = \omega r_2 / a_1$
- (c) speed of sound, a_2 , in m/s at the impeller exit



■ FIGURE P9.22

9.23 A centrifugal compressor impeller has 20 straight impeller blades. The inlet flow condition to the compressor is purely axial with $M_1 = 0.4$. The geometric parameters of the centrifugal compressor are: $r_{h1} = 0.05$ m, $r_{t1} = 0.1$ m, $r_2 = 0.25$ m and $r_3 = 0.375$ m. The shaft rotational speed is $\omega = 14,000$ rpm. The static pressure and temperature at the inlet are $p_1 = 90$ kPa and $T_1 = 255$ K, respectively. The radial velocity at the impeller exit is equal to the inlet axial velocity, i.e., $C_{r2} = C_{z1}$ and the compressor polytropic efficiency is $e_c = 0.85$. Assuming the radial diffuser is vaneless and the flow in the radial diffuser is inviscid with gas properties $\gamma = 1.4$ and $R = 287$ J/kg · K, calculate

- (a) flow area at the inlet to the centrifugal compressor, A , in m^2
- (b) inlet axial velocity, C_{z1} , in m/s
- (c) inlet density, ρ_1 , in kg/m^3
- (d) the mass flow rate, \dot{m} , in kg/s
- (e) impeller rim speed, U_2 , in m/s



■ FIGURE P9.23

- (f) impeller (actual) exit swirl, $C_{\theta 2}$, in m/s
- (g) compressor shaft power, $\dot{\varphi}_c$, in kW
- (h) impeller absolute exit Mach number, M_2
- (i) swirl velocity at the diffuser exit, $C_{\theta 3}$, in m/s
- (j) stage total pressure ratio, π_c

9.24 The corrected mass flow rate at the inlet to a centrifugal compressor is $\dot{m}_{c1} = 20 \frac{kg}{s}$ and the axial Mach number at the compressor face is $M_{z1} = 0.5$. For the hub-to-tip radius ratio of the impeller equal to 0.1, i.e., $r_{h1}/r_{t1} = 0.1$, calculate

- (a) inlet area, A_1 , in m^2
- (b) hub and tip radii, r_{h1} and r_{t1} , in cm
- (c) shaft speed, ω , for the impeller inlet relative tip Mach number to be 0.8, i.e., $(M_{1r})_{tip}$

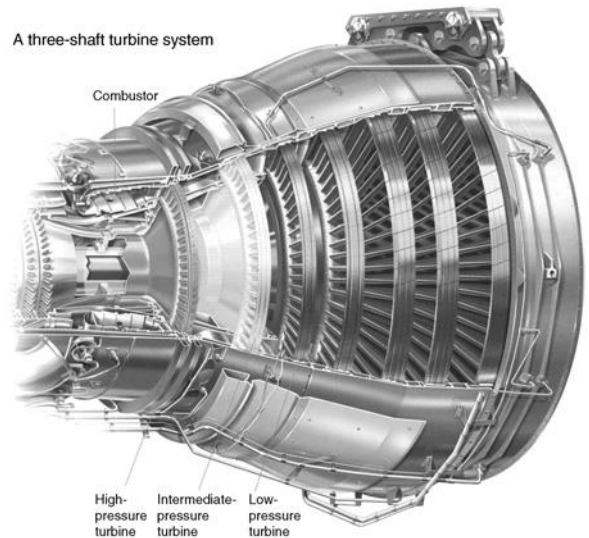
Assume gas total temperature at the impeller inlet is 288 K, $\gamma = 1.4$ and $R = 287$ J/kgK

9.25 A centrifugal compressor discharge static pressure is $p_3 = 352$ kPa and its total temperature is $T_{t3} = 444$ K. The flow at the impeller inlet has an axial component with $C_{z1} = 150$ m/s and a preswirl component with $C_{\theta 1} = 56$ m/s. The inlet total pressure and temperature are the standard sea-level conditions, i.e., $p_{t1} = 101$ kPa and $T_{t1} = 288$ K, respectively. Assuming the compressor polytropic efficiency is $e_c = 0.88$, calculate

- (a) compressor total pressure ratio, p_{t3}/p_{t1}
- (b) static pressure ratio, p_3/p_1 , across the compressor
- (c) exit Mach number, M_3
- (d) compressor specific work, w_c , in kJ/kg

Assume fluid properties are: $\gamma = 1.4$ and $c_p = 1004$ J/kgK

Aerothermodynamics of Gas Turbines



Source: Reproduced with permission from Rolls-Royce plc

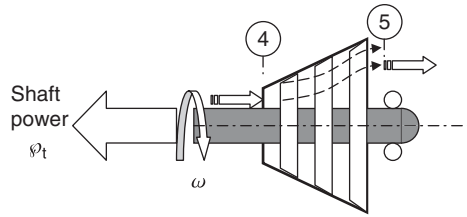
10.1 Introduction

Gas turbines produce shaft power for the compressor in the gas generator as well as other external loads, such as the fan in a turbofan, propeller in a turboprop, helicopter rotor in a turboshaft, and electric generator. The high pressure and temperature gas from the combustor enters the gas turbine first through a stationary blade row, known as the nozzle. The first nozzle is thus exposed to the highest gas temperatures in the engine ($T_{t4} \sim 1750\text{--}2000\text{ K}$). However, the stationary nature of gas turbine nozzle saves it from an additional centrifugal stress that rotor blades face. Since the gas path temperature is $400\text{--}800\text{ K}$ higher than the blade service temperature, all modern gas turbines are cooled. The coolant, which is bled from compressor accounts for $\sim 10\text{--}15\%$ of the airflow rate in the gas generator. A reduction of $\sim 3\%$ turbine efficiency per 1% cooling flow is attributed to cooling losses. In this chapter, we will introduce aerodynamics of turbine blades, optimal nozzle exit tangential Mach number, optimum solidity, turbine losses, and cooling. We conclude the chapter with axial-flow turbine design and practices and an example. Figure 10.1 shows a schematic drawing of a gas turbine.

10.2 Axial-Flow Turbines

The flowfield in a turbine is dominated by favorable pressure gradients unlike the compressor flow. The boundary layers in a turbine are thus less susceptible to stall than their counterparts in a compressor. The notion that a turbine is a “mirror image” of a compressor

■ FIGURE 10.1
Schematic drawing of
an axial-flow turbine



is therefore misleading. The evidence of many compressor stages (~ 5 in modern gas turbine engines of the same mass flow rate) being driven by a single turbine stage is a compelling reason for the inherent differences in the fluid mechanics of the two devices. The challenges in a turbine are primarily in the cooling techniques and their effectiveness; tip clearance control, blade life, and material characteristics suitable for a high-temperature environment and corrosion. In the compressor, the flow stability (rotating stall and surge) and efficiency are highly critical to the design.

The aerodynamics of turbine stages is governed by the conservation principles of mass, momentum, and energy. The conservation of angular momentum is expressed by the Euler turbine equation, which we derived in the early part of Chapter 8. It states that the time-rate-of-change of the fluid angular momentum is balanced by a net external torque that acts on the fluid, namely,

$$\tau_{\text{fluid}} = \dot{m}(r_2 C_{\theta 2} - r_1 C_{\theta 1}) \quad (10.1)$$

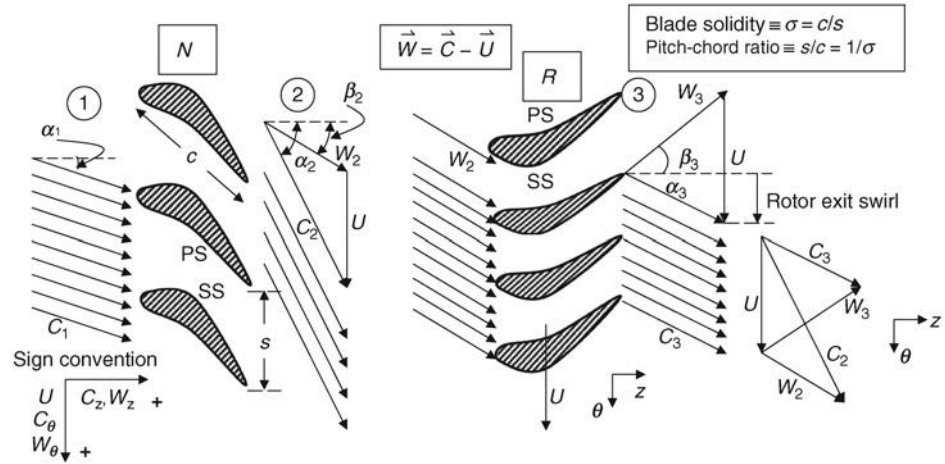
Let us show a schematic drawing of a turbine stage, assign station numbers, and show the velocity triangles in the stage. A turbine stage begins with a stationary blade row, known as the nozzle, followed by a rotating blade row, known as the rotor or sometimes bucket. The combustor exit flow is expanded, that is, accelerated, in a turbine nozzle, which converts the fluid thermal energy into the fluid kinetic energy. The inlet flow to the nozzle is typically swirl free and thus the nozzle imparts swirl to the flow. This behavior is opposite to a compressor stator, which removes the swirl from the flow. The nozzle flow is choked over a wide operating range of the engine, and the exit of the nozzle may also operate in the supersonic regime. The rotor blade row follows the nozzle and exchanges energy with the fluid. The rotor thus removes the swirl put in by the nozzle, again an opposite behavior to the compressor rotor. An examination of velocity triangles in a turbine stage (Figure 10.2) reveals the swirl deposition and extraction of the nozzle and the rotor rows in a turbine, respectively.

The sign convention on the swirl velocity component is the same as the compressors, namely, the swirl is considered positive in the direction of the rotor rotation. For example, the inlet swirl upstream of the turbine nozzle is shown in the positive direction in Figure 10.2. The absolute and relative swirls downstream of the nozzle are both in the positive direction, as also shown in Figure 10.2. The relative swirl downstream of the rotor blade has a negative swirl velocity, whereas the absolute swirl is shown in the positive direction.

The power exchange between the rotor and the fluid may be observed in Figure 10.2 as the rotor rotation is in the same direction as the aerodynamic force acting on it in the tangential direction. We may express the rotor shaft power in thermodynamic terms as

$$\mathcal{P}_{\text{rotor}} = -\mathcal{P}_{\text{fluid}} = \dot{m}(h_{t2} - h_{t3}) \quad (10.2)$$

■ **FIGURE 10.2**
Schematic drawing of a turbine stage with velocity triangles, sign convention flow angle definitions, and blade solidity



We may express the rotor power in mechanical terms via the Euler turbine equation as

$$\mathcal{P}_{\text{rotor}} = -\mathcal{P}_{\text{fluid}} = \dot{m}\omega[(r_2 C_{\theta 2}) - (r_3 C_{\theta 3})] \quad (10.3)$$

Since the stator or nozzle puts in swirl, i.e., angular momentum, in the flow and the rotor or bucket removes the angular momentum in a turbine, the bracket on the right-hand side of Equation 10.3 is positive. The implication is that the turbine rotor produces power and the power of the fluid is thus drained or diminished. These are all consistent with our expectations. The turbine nozzle imparts a positive torque on the fluid and thus feels an equal and opposite torque in reaction. We may express the nozzle torque as

$$\tau_n = -\tau_{\text{fluid}} = \dot{m}[(r_1 C_{\theta 1}) - (r_2 C_{\theta 2})] \quad (10.4)$$

From the magnitude of the angular momentum up- and downstream of the nozzle, we note that the fluid torque is positive and the nozzle torque is negative. The rotor torque is

$$\tau_r = -\tau_{\text{fluid}} = \dot{m}[(r_2 C_{\theta 2}) - (r_3 C_{\theta 3})] \quad (10.5)$$

Since the bracket on the right-hand side of Equation 10.5 is positive, as the fluid angular momentum is higher upstream of the rotor than downstream, we may conclude that the torque acting on the fluid is negative and the blade torque is in the positive direction. In case of repeated stages, we have the rotor exit angular momentum equal to the nozzle entrance angular momentum, that is,

$$r_3 C_{\theta 3} = r_1 C_{\theta 1} \quad (10.6)$$

Then the rotor torque becomes equal and opposite the nozzle torque. Consequently, a turbine stage, as a whole, does not impart a net torque on the engine structure.

In axial-flow turbines, as in axial-flow compressors, the radial shift of the stream surfaces is small and usually neglected in a first approximation. A second approximation is made about the constant axial velocity through the stage or the density-velocity ratio

across blade rows in a stage. The choice of the degree of reaction in a turbine ranges from zero to upward of 50%. A zero degree of reaction turbine stage, known as the impulse stage, produces the entire static enthalpy drop of the stage across the nozzle. The rotor produces no static enthalpy drop. The degree of reaction in a turbine is defined as the ratio of static enthalpy drop in the rotor to that of the stage, namely,

$$\circ R \equiv \frac{h_2 - h_3}{h_1 - h_3} \tag{10.7}$$

Let us rewrite Equation 10.7 in terms of the stagnation states and the fluid kinetic energy,

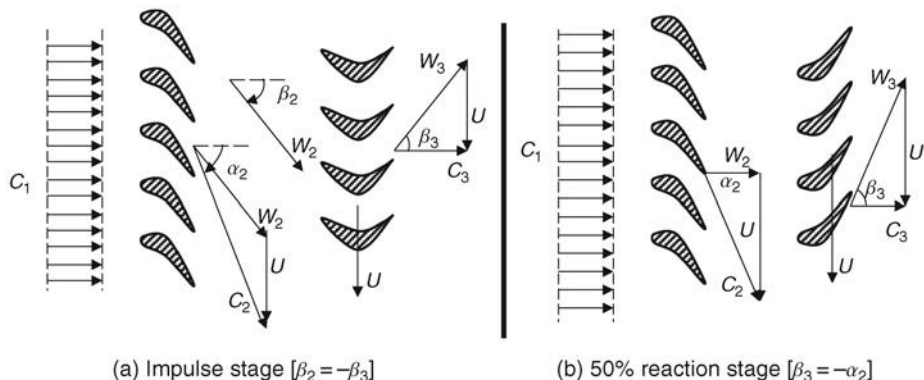
$$\circ R = \frac{h_{t2} - h_{t3} - C_2^2/2 + C_3^2/2}{h_{t1} - h_{t3} - C_1^2/2 + C_3^2/2}$$

Assuming the inlet and exit kinetic energies of the stage are equal, the above expression is simplified to

$$\circ R = 1 - \frac{C_2^2 - C_3^2}{2(h_{t2} - h_{t3})} = 1 - \frac{C_{\theta 2}^2 - C_{\theta 3}^2}{2U(C_{\theta 2} - C_{\theta 3})} = 1 - \frac{C_{\theta 2} + C_{\theta 3}}{2U} = 1 - \frac{C_{\theta \text{mean}}}{U} \tag{10.8}$$

where we have further assumed that the axial velocity remains constant and the radial shift of stream surfaces is small. The form of the degree of reaction, as expressed in Equation 10.8, is identical to the formulation of the compressor degree of reaction. It is the nondimensional average swirl velocity ($C_{\theta \text{mean}}/U$) in the rotor that establishes the degree of reaction at a given radius. Thus, the 50% degree of reaction demands the average swirl in the rotor to be one half of the rotational speed, which suggests a symmetrical velocity triangle across the rotor and nozzle (stator). This behavior is identical to the compressor. The zero degree of reaction, known as the impulse turbine, demands the average swirl in the rotor to be the same as the rotor speed. The velocity triangles and the blade row geometry for an axial exit flow are shown in Figure 10.3.

■ FIGURE 10.3
An Impulse and a 50%
reaction stage with
swirl-free exit flow



For a 50% degree of reaction turbine stage and a swirl-free exit flow condition, that is, $C_{\theta 3} = 0$, we have

$$C_{\theta m} = \frac{U}{2} = \frac{C_{\theta 2}}{2} \quad \text{or} \quad C_{\theta 2} = U \tag{10.9}$$

The rotor specific work, via the Euler turbine equation, is

$$w_t \equiv \frac{\mathcal{P}_t}{\dot{m}_t} \cong U \Delta C_\theta = U^2 \tag{10.10}$$

or stage loading coefficient ψ is

$$\psi \equiv w_t / U^2 = 1$$

The zero degree of reaction of an impulse turbine stage requires

$$C_{\theta m} = U = \frac{C_{\theta 2}}{2} \quad \text{or} \quad C_{\theta 2} = 2U \tag{10.11}$$

The rotor specific work for an impulse turbine is, therefore,

$$w_t \equiv \frac{\mathcal{P}_t}{\dot{m}_t} \cong U \Delta C_\theta = 2U^2 \tag{10.12}$$

or stage loading coefficient ψ is

$$\psi \equiv w_t / U^2 = 2$$

Comparing the specific work of the rotors from Equations 10.10 and 10.12, we note that the impulse design produces twice as much shaft power per unit mass flow rate than the 50% reaction turbine for the same rotor speed U . Although the impulse turbine designs have the potential of producing large specific works, they are less efficient than the reaction type turbines. The primary reason is in the rotor where the relative flow speed remains constant and, hence, the viscous flow losses are larger than reaction turbines where the flow continuously accelerates. It is also instructive to show the thermodynamic states of the gas in both types of turbine stages on a T - s diagram. Figure 10.4 shows the static and total (or stagnation) states of the fluid in a reaction turbine stage, that is, $^{\circ}R > 0$.

We note that the static temperature drop occurred across the nozzle as well as the rotor. Therefore, the turbine stage that is shown in Figure 10.4 is a reaction turbine.

■ **FIGURE 10.4**
T-*s* diagram of thermodynamic states of gas in a reaction turbine stage

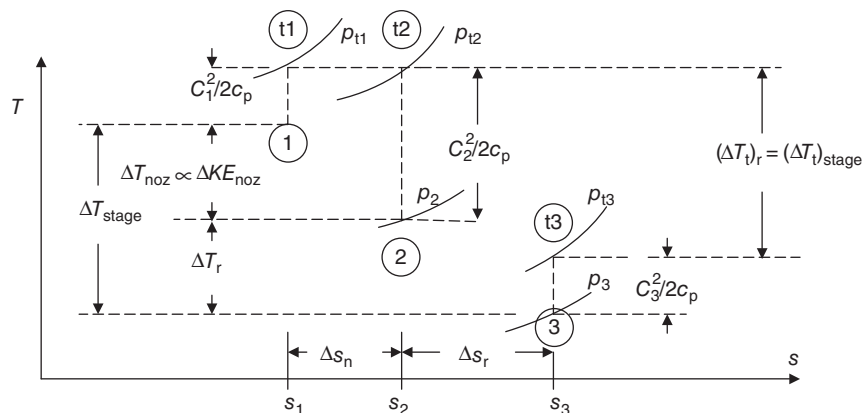
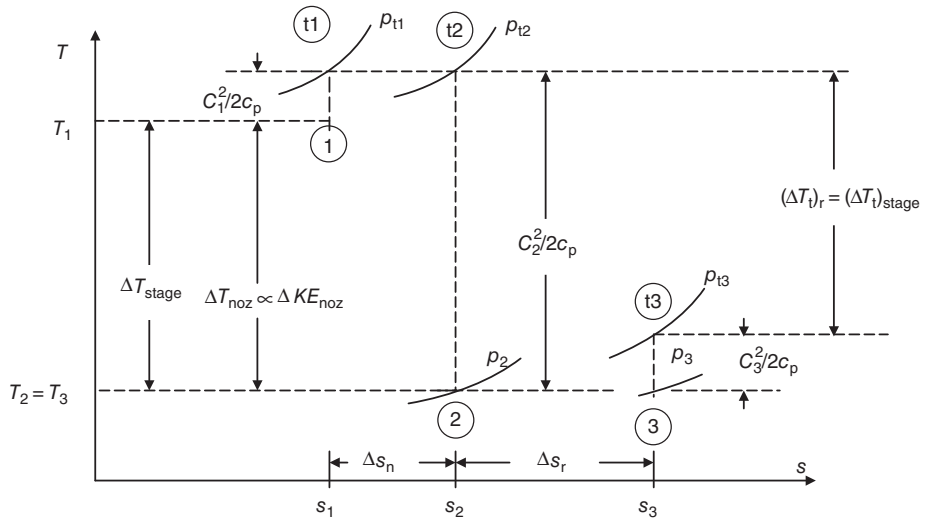


FIGURE 10.5
 Thermodynamic states of gas in an impulse turbine stage ($\gamma R = 0$) show a large power production capability, $\propto (\Delta T)_\text{stage}$



The stage work may also be noted in Figure 10.4 as proportional to the stage total temperature drop. The nozzle suffers some total pressure loss $p_{t1} - p_{t2}$ due to viscous effects in the boundary layer and possible shock losses. The rotor loss may be observed in the entropy rise Δs_r in Figure 10.4. The thermodynamic states of gas in an impulse turbine stage, for comparison purposes, are shown in Figure 10.5.

Similar observations to the reaction turbine may also be made on the impulse stage, as shown in Figure 10.5. One exception is that the static temperature change across the rotor is zero in the impulse turbine. Consequently, the static temperature drop ΔT_stage occurs solely across the nozzle. Also, we note a large expansion across the nozzle, as evidenced by a large ΔT_noz , as compared with the reaction type turbine. The entropy rise in an impulse stage is intentionally depicted as larger than the corresponding entropy rise in the reaction turbine stage to signify higher losses. We also note that the rotor specific work, which is proportional to the total temperature drop across the rotor, is depicted roughly twice as much (in Figure 10.5) as the reaction turbine stage of Figure 10.5 to reflect Equations 10.10 and 10.12. In some texts (e.g., Dixon, 1975), an impulse stage is defined as having zero static pressure drop across the rotor. In this case, then a zero-reaction turbine, which has its static enthalpy constant across the rotor, is not strictly speaking an impulse stage. In a zero-reaction turbine, there is still some static pressure drop due to frictional losses within the blade. Thus, an impulse turbine would have a slightly negative degree of reaction. In this book, the words impulse and zero reaction are interchangeably used, albeit more loosely than the strict classical definition.

The turbine specific work could be expressed in terms of the nozzle exit flow angle α_2 and the condition of zero swirl at the rotor exit as

$$w_t = U(C_{\theta 2} - C_{\theta 3}) \approx UC_{\theta 2} = UC_{z2} \tan \alpha_2 \tag{10.13}$$

For a constant axial flow velocity C_z , we note that the rotor work per unit mass flow rate increases linearly with the increase in wheel speed U and (nonlinearly with) the flow turning angle α_2 through the tangent of α_2 term in Equation 10.13. For practical reasons,

the flow angle at the nozzle exit is limited to $\sim 70^\circ$, otherwise flow losses become excessive, that is,

$$\alpha_{2,\max} \approx 70^\circ \quad (10.14)$$

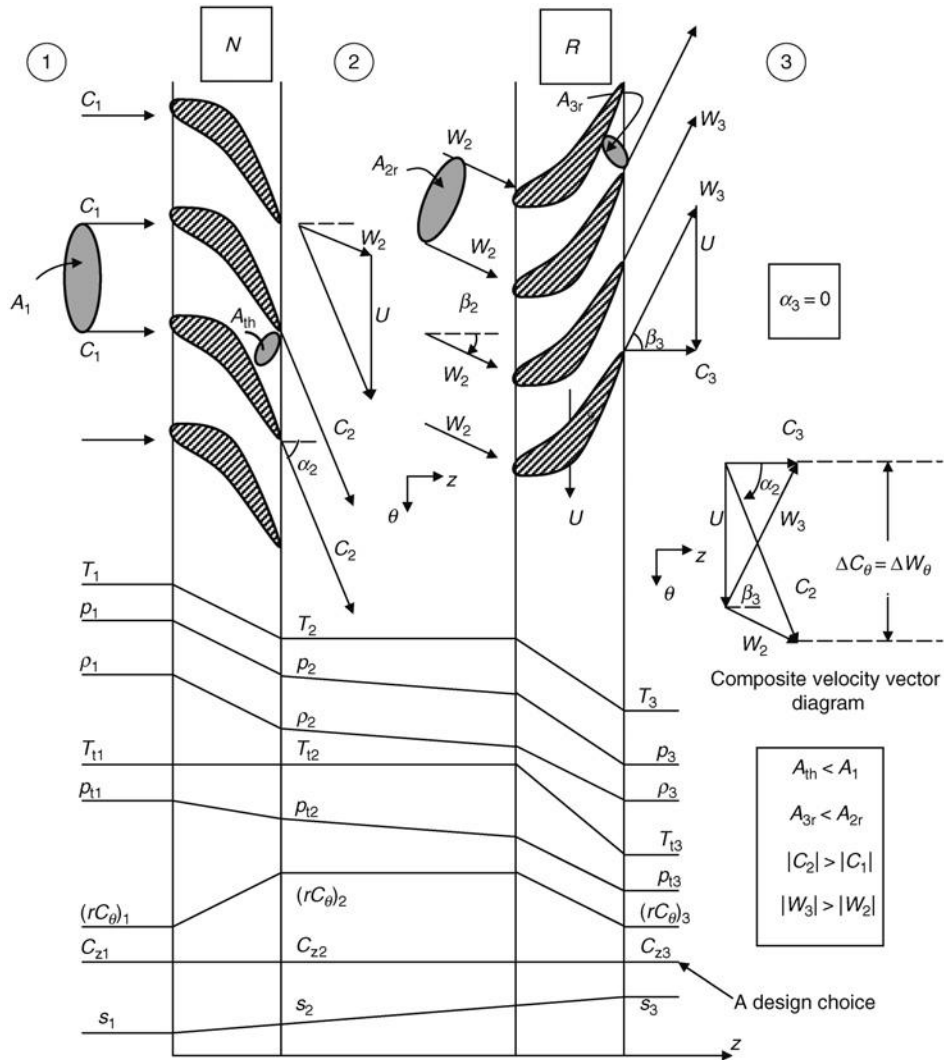
The wheel speed U is a quadratic contributor to the blade centrifugal stresses σ_c ; hence, it is limited by the structural stresses and the blade life requirements. To gain further insight, we may cast the above equation in terms of the blade tangential and the flow Mach numbers downstream of the nozzle as

$$w_t = UC_2 \sin \alpha_2 = a_2^2 M_T M_2 \cdot \sin \alpha_2 = a_{t2}^2 \cdot M_T M_2 \sin \alpha_2 \left/ \left[1 + \left(\frac{\gamma - 1}{2} \right) M_2^2 \right] \right. \quad (10.15)$$

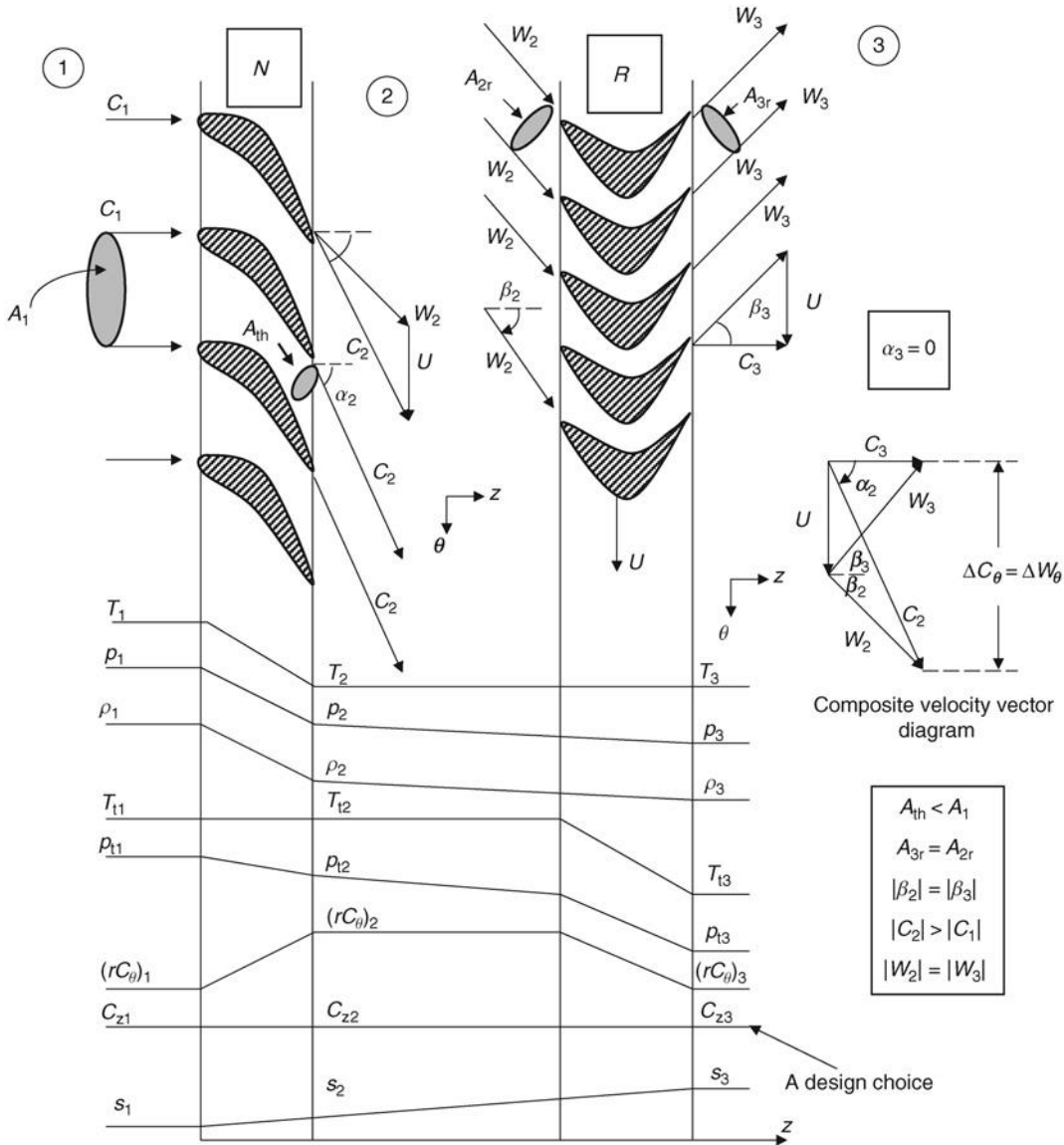
Since the stagnation temperature does not change across the nozzle, the stagnation speed of sound at 2 is the same as 1, hence proportional to the combustor exit total temperature T_{t4} , a cycle parameter. We may conclude from Equation 10.15 that to maximize the rotor specific work, we need to have high inlet stagnation temperatures, T_{t1} (or T_{t4} from our cycle analysis notation), a high tangential Mach number of the blade, M_T , a high swirl Mach number at the nozzle exit, $M_2 \sin \alpha_2$. The blade tangential Mach number M_T has a maximum at the rotor blade tip radius $M_T(r_t)$. The high gas temperatures in the high-pressure turbine (HPT) demand internal cooling of the rotor blades. A cooled rotor blade leading edge needs to be blunt to allow for sufficient surface area to cool, as it represents the stagnation point of the blade with the attendant high heat flux. A blunt leading edge is best suited for a subsonic relative flow, which then limits the maximum M_T parameter in the HPT. In the low-pressure turbine (LPT), the gas temperature is significantly reduced, hence internal cooling of the blades may not be required at all. Therefore, the rotor tip in the LPT may operate with a sharp leading edge, which is then suitable for a supersonic operation. In addition, the speed of sound for the first rotor is about $\sim \sqrt{1/\tau_t}$ higher than the speed of sound in the last rotor. This means that for the same tip speeds, ωr_t , the blade tangential Mach number is higher in the LPT than the HPT, that is, inversely proportional to the local speed of sound. These arguments are made to show the conflicting requirements of internal cooling (due to high gas temperatures) and centrifugal stresses with the desire to operate the turbine rotors with a supersonic tip to maximize the rotor work output. Let us summarize the parameter trends in reaction and impulse turbine stages graphically in Figures 10.6 and 10.7, respectively.

We have examined parameter trends in turbine stages with *zero exit swirl* in Figures 10.6 and 10.7. Let us provide a rationale for that. The swirl in the exit flow does not contribute to the thrust production, which is the function of our engine, and even increases the total pressure loss in the nozzle. Consequently, it is desirable to design a turbine stage with zero exit swirl. Also, we have depicted the streamtubes upstream and downstream of the turbine blades with corresponding flow areas A_1 and A_2 for the nozzle and A_{2r} and A_{3r} in the rotor frame of reference for the rotor. In a reaction turbine, the streamtube flow areas continually shrink, as flow continually accelerates in the blade rows. In the impulse stage, the relative flow in the rotor attains a constant speed and thus the relative streamtube does not shrink. Thus, the static temperature remains constant and the static pressure remains unchanged in the limit of inviscid flow and drops with frictional losses in the boundary layers. The relative flow downstream of the rotor in an impulse stage is the mirror image of the relative flow upstream of the rotor (Figure 10.7). Also note that the choice of constant

■ **FIGURE 10.6** Parameter trends in a reaction turbine stage with zero exit swirl and designed for constant axial velocity (in an uncooled stage)



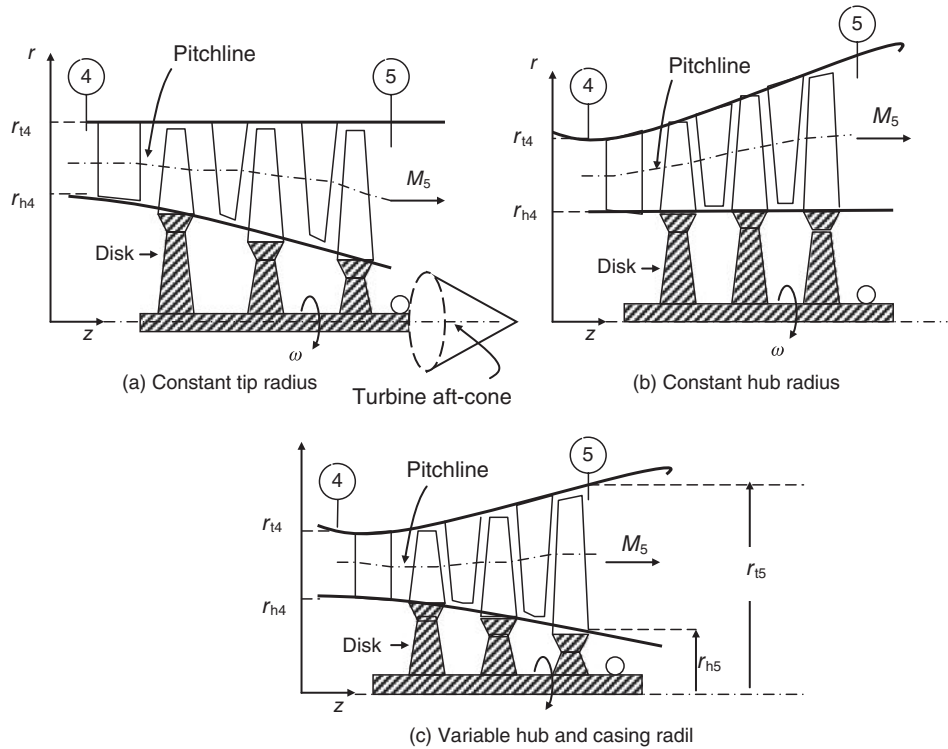
axial velocity C_z , as shown in Figures 10.6 and 10.7, is depicted as a design choice, similar to a compressor. The annulus sizing and the geometry are directly affected by our choice of the axial velocity and the mass flow rate through continuity equation. With a constant axial velocity and a decrease in gas density in the flow direction, the annulus flow area needs to grow inversely proportional to the density drop. In the case of a cooled turbine, the coolant mass flow rate needs to be added to the hot gas flow rate in establishing the annulus flow area, via continuity equation. Now, let us examine the design parameters that affect the mass flow rate in a turbine stage, the power production, and the turbine efficiency. Three turbine annuli are shown in Figure 10.8 and the station numbers at the entrance and exit correspond to our cycle analysis notation, stations 4 and 5, respectively. In this example, we show three types of annuli: the first has a constant tip radius, i.e., the casing is of cylindrical shape, and a variable hub radius for the annulus geometry (Figure 10.8a);



■ FIGURE 10.7 Parameter trends in an impulse turbine stage with zero exit swirl and designed for constant axial velocity (in an uncooled stage)

the second has constant hub radius (Figure 10.8b); and the third has a varying hub and casing radii (Figure 10.8c). In a mixed-stream turbopfan engine, the choice of constant tip radius for the outer casing of the turbine annulus leads to a better integration of the cold and hot streams in a forced mixer. The second advantage of a constant outer radius is in lower centrifugal stresses of the rotor blades, simply by the virtue of a smaller moment arm. The third advantage is in engine frontal area and weight. Integration with the turbine aft-cone in aircraft gas turbine engines will also benefit from a tapered hub radius, as shown schematically in Figure 10.8a. In some applications, for example, stationary gas

■ FIGURE 10.8 Schematic drawing of the geometry of three turbine annuli



turbine power plants, the choice of constant hub radius is considered advantageous, as it integrates with an annular exhaust diffuser as well as reduces manufacturing costs of the turbine rotor disks (i.e., all with the same diameter). The varying hub and tip case shown schematically in Figure 10.8c offers a constant radius pitchline advantage, but at an increased manufacturing costs and, potentially, an increased weight over the first two designs. In general, a turbine annulus with an increasing tip radius adds weight to the rotor disks and turbine overall weight.

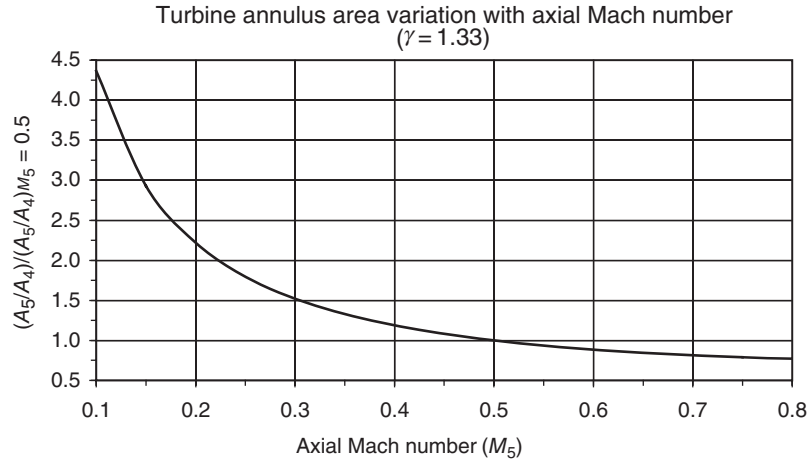
Our one-dimensional continuity equation written between stations 4 and 5 yields

$$\begin{aligned} \dot{m}_4 &= \sqrt{\frac{\gamma_4}{R_4}} \frac{p_{t4}}{\sqrt{T_{t4}}} A_4 M_4 \left(1 + \left(\frac{\gamma_4 - 1}{2} \right) M_4^2 \right)^{-\frac{\gamma_4 + 1}{2(\gamma_4 - 1)}} = \dot{m}_5 \\ &= \sqrt{\frac{\gamma_5}{R_5}} \frac{p_{t5}}{\sqrt{T_{t5}}} A_5 M_5 \left(1 + \left(\frac{\gamma_5 - 1}{2} \right) M_5^2 \right)^{-\frac{\gamma_5 + 1}{2(\gamma_5 - 1)}} \end{aligned} \quad (10.16)$$

Since the exit of the nozzle remains choked over a wide operating range of the engine, it is more convenient to use $M_4 = 1$ and A_4 as the choked throat area of the turbine nozzle. Therefore, the annulus area ratio A_5/A_4 becomes

$$\frac{A_5}{A_4} = \sqrt{\frac{\gamma_4/\gamma_5}{R_4/R_5}} \frac{1}{M_5} \frac{\sqrt{\tau_t}}{\pi_t} \frac{\left(1 + \left(\frac{\gamma_5 - 1}{2} \right) M_5^2 \right)^{\frac{\gamma_5 + 1}{2(\gamma_5 - 1)}}}{(2/(\gamma_4 + 1))^{\frac{\gamma_4 + 1}{2(\gamma_4 - 1)}}} \quad (10.17)$$

■ **FIGURE 10.9**
The effect of axial Mach number on the annulus area of a turbine (normalized for $M_5 = 0.5$, $\tau_t = \text{constant}$)



We have presented the turbine total pressure and temperature ratios as π_t and τ_t , respectively, which we used as a convention in the cycle analysis chapter. For a zero exit swirl, the flow Mach number M_5 represents the axial Mach number that we treat as a design choice. To minimize the flow area, we need to choose an axial Mach number that is not too low, for example, $M_5 = M_{z5} = 0.50$ seems to be reasonable. To show the functional dependence of the area ratio on the choice of axial Mach number, we plot Equation 10.17, keeping the turbine expansion parameters π_t and τ_t fixed as well as the gas properties. The normalized area ratio as a function of the axial Mach number is shown in Figure 10.9, for a $\gamma_5 = 1.33$ and a normalizing axial Mach number of 0.5. We note a rapid rise in the required area ratio with a decrease in axial Mach number. For example, at $M_5 = 0.3$, the required exit is 50% larger than the exit area corresponding to a design axial Mach number of 0.5. For the Mach number of 0.7, the exit area shrinks to 81.5% of that of a Mach 0.5 case. Now, let us explore the effect of turbine expansion parameters π_t and τ_t on the annulus area ratio. For this exercise, we keep the axial Mach number fixed and the gas properties constant, as we vary the turbine expansion parameters. First, let us simplify the functional dependence of the annulus area ratio to a single expansion parameter, for example, τ_t . We relate the pressure and temperature ratios across the turbine via polytropic efficiency e_t as in the cycle analysis chapter, that is,

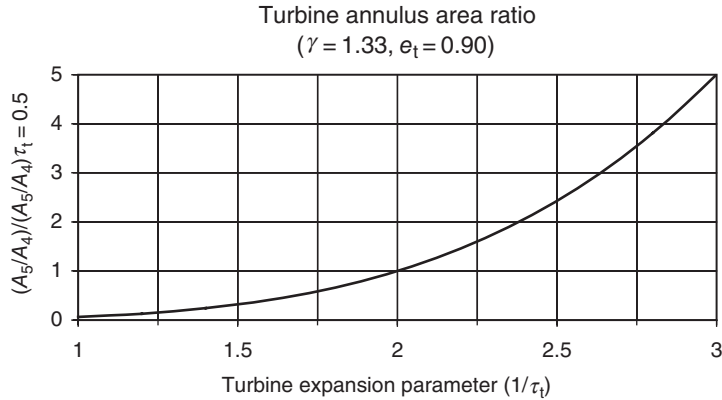
$$\pi_t = \tau_t^{\frac{\gamma}{(\gamma-1)e_t}}$$

Therefore, the functional dependence of the turbine annulus area ratio and the turbine expansion parameter τ_t is

$$A_5/A_4 \sim (1/\tau_t)^{3.978} \quad (10.18)$$

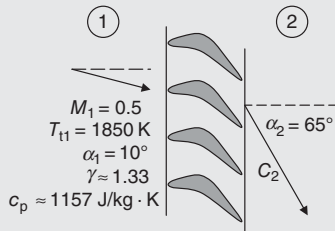
where we chose $\gamma_5 = 1.33$ and $e_t = 0.9$. A graph of this function normalized with respect to a turbine expansion parameter, $(1/\tau_t)$, of 2.0 is shown in Figure 10.10. We observe that the annulus area ratio is a strong function of the turbine expansion parameter, as expected. The exponential growth in the flow area is in response to the exponential decay in the gas density with the temperature ratio, while maintaining the constant axial Mach number.

FIGURE 10.10
Turbine annulus area as a function of the turbine expansion parameter ($1/\tau_t$) (normalized for $\tau_t = 0.5, M_5 = \text{constant}$)



EXAMPLE 10.1

The combustor discharge into a turbine nozzle has a total temperature of 1800 K and axial Mach number of 0.55, as shown.



Assuming that the nozzle is uncooled, the axial velocity remains constant across the nozzle, and the absolute flow angle at the nozzle exit is $\alpha_2 = 60^\circ$, calculate:

- (a) inlet velocity C_1 in m/s
- (b) the exit absolute Mach number M_2
- (c) nozzle torque per unit mass flow rate for $r_1 \approx r_2 = 0.35 \text{ m}$

SOLUTION

We use total temperature and Mach number at the nozzle inlet to calculate the static temperature T_1 according to

$$T_1 = \frac{T_{t1}}{1 + (\gamma - 1)M_1^2/2} \approx 1714 \text{ K}$$

The speed of sound is

$$a_1 = \sqrt{(\gamma - 1)c_p T_1} \approx 809 \text{ m/s}$$

Therefore, the absolute gas velocity into the turbine nozzle has a magnitude of

$$C_1 = M_1 a_1 \approx 445 \text{ m/s}$$

Downstream of the nozzle, we know the axial component of the velocity and the flow angle. Therefore, we calculate C_2 from

$$C_2 = C_{2z} / \cos \alpha_2 \approx 445 / \cos(60^\circ) \text{ m/s} \approx 889.2 \text{ m/s}$$

To calculate speed of sound downstream of the nozzle, we need to know the static temperature of the gas, T_2 . We know the total temperature of the gas T_{t2} since (for a calorically perfect gas) is the same as T_{t1} for an uncooled turbine, therefore, we may use the following equation to calculate T_2

$$T_2 = T_{t2} - C_2^2/2c_p = 1800 \text{ K} - (889.2)^2/2/1157 \approx 1458.3 \text{ K}$$

The speed of sound, a_2 is $a_2 = \sqrt{(\gamma - 1)c_p T_2} \approx 746.2 \text{ m/s}$

Therefore, $M_2 = C_2/a_2 \Rightarrow M_2 \approx 1.19$

The nozzle torque is equal to the change of angular momentum across the nozzle according to Equation 10.4, i.e.,

$$\tau_n/\dot{m} = r_1 C_{\theta 1} - r_2 C_{\theta 2}$$

The nozzle exit swirl is related to axial velocity C_{z2} and the swirl angle, $\alpha_2 C_{\theta 2} = C_{z2} \tan \alpha_2 \approx 445 \tan(60^\circ) \approx 769.8 \text{ m/s}$.

Therefore, the nozzle torque per unit mass flow rate is

$$\tau_n/\dot{m} = r_1 C_{\theta 1} - r_2 C_{\theta 2} \approx -269.4 \text{ m}^2/\text{s}$$

EXAMPLE 10.2

The turbine nozzle in Example 10.1 produced a slightly supersonic exit flow with $M_2 \approx 1.19$. If we turn the flow to a reduced α_2 level, we may reduce the exit Mach number

M_2 . Calculate the nozzle exit flow angle α_2 if we wish the exit Mach number to be $M_2 \approx 1.0$, i.e., choked.

SOLUTION

In this case we know M_2 , which we use with T_{t2} to calculate T_2 from

$$T_2 = T_{t2}/[1 + (\gamma - 1)M_2^2/2] = 1800 \text{ K}/[1 + 0.33/2] \\ \approx 1545 \text{ K}$$

Now, we calculate the speed of sound, a_2 to be $\Rightarrow a_2 \approx 768.1 \text{ m/s}$

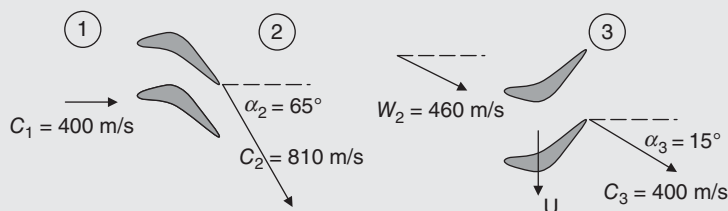
Therefore $C_2 = M_2 a_2 = a_2$

The exit flow angle is related to the axial velocity according to

$$\cos \alpha_2 = \frac{C_{z2}}{C_2} = \frac{445}{768.1} \approx 0.5794 \Rightarrow \alpha_2 \approx 54.6^\circ$$

EXAMPLE 10.3

A turbine stage at pitchline has the following velocity vectors, as shown.



Calculate

- the axial velocities up- and downstream of the rotor
- the rotor velocity U_m
- the degree of reaction at this radius.

SOLUTION

From the flow condition downstream of the nozzle, we may calculate C_{z2} to be

$$C_{z2} = C_2 \cos(60^\circ) = 400 \text{ m/s}$$

From the flow condition downstream of the rotor, we may calculate C_{z3} to be

$$C_{z3} = C_3 \cos(13^\circ) \approx 400 \text{ m/s}$$

The rotor velocity $U_m = C_{\theta 2m} - W_{\theta 2m}$

$$C_{\theta 2m} = 400 \tan 60^\circ \approx 693 \text{ m/s and}$$

$$W_{\theta 2m} = [(450)^2 - (400)^2]^{0.5} \approx 206 \text{ m/s}$$

Therefore, $U_m \approx 693 - 206 \approx 487 \text{ m/s}$

Also $C_{\theta 3} = C_3 \sin(13^\circ) \approx 92.4 \text{ m/s}$

For the degree of reaction, since $C_1 = C_3$, we use Equation 10.8 to get

$$\begin{aligned} \circ R_m &= 1 - \frac{C_{\theta 2m} + C_{\theta 3m}}{2U_m} \\ &= 1 - (693 + 92.4)/2/487 \approx 0.194 \end{aligned}$$

10.2.1 Optimal Nozzle Exit Swirl Mach Number $M_{\theta 2}$

The effect of the degree of reaction on the mass flow rate and optimal swirl in a turbine stage, for a given blade tangential Mach number M_T , is considered in this section. For simplicity of the expressions, we assume that the exit flow from the rotor is swirlfree, that is, $C_{\theta 3} = 0$. The degree of reaction may be successively written as

$$\circ R = 1 - \frac{C_{\theta m}}{U} = 1 - \frac{C_{\theta 2}}{2U} = 1 - \frac{C_2 \sin \alpha_2}{2U} = 1 - \frac{M_2 \sin \alpha_2}{2M_T} \quad (10.19)$$

This reduces to

$$M_2 \sin \alpha_2 = M_{\theta 2} = 2M_T(1 - \circ R) \quad (10.20)$$

Assuming the total temperature, total pressure, and flow area remain constant across a turbine nozzle, the continuity demands (keeping gas properties constant)

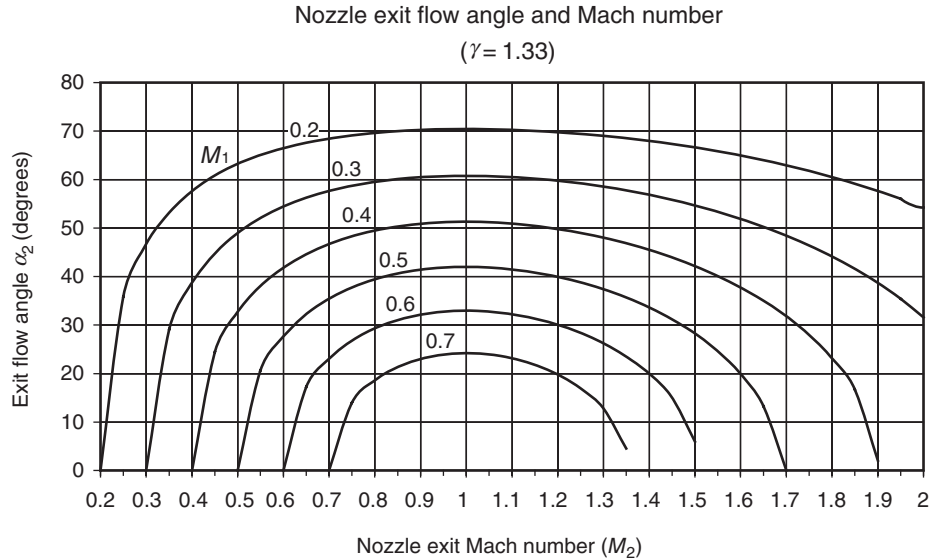
$$M_1 \left[1 + \left(\frac{\gamma - 1}{2} \right) M_1^2 \right]^{-\frac{\gamma+1}{2(\gamma-1)}} = M_2 \cos \alpha_2 \left[1 + \left(\frac{\gamma - 1}{2} \right) M_2^2 \right]^{-\frac{\gamma+1}{2(\gamma-1)}} \quad (10.21)$$

Therefore,

$$\cos \alpha_2 = \frac{M_1}{M_2} \left[\frac{1 + (\gamma - 1)M_2^2/2}{1 + (\gamma - 1)M_1^2/2} \right]^{\frac{\gamma+1}{2(\gamma-1)}} \quad (10.22)$$

Let us graph nozzle exit flow angle α_2 from Equation 10.22 for a given nozzle inlet Mach number M_1 . Figure 10.11 shows the nozzle exit flow angle for inlet Mach numbers of 0.2–0.7 in increments of 0.1, as a function of the exit Mach number M_2 . The nozzle exit flow angle α_2 reaches a maximum for the exit Mach number of 1.

■ **FIGURE 10.11**
Nozzle exit flow
variation with inlet
Mach number



Although we can discern the maximum nozzle exit flow angle from Figure 10.11, it is the product of $M_2 \sin \alpha_2$ that contributes to the specific work output of the stage. Hence, to maximize the nozzle exit swirl Mach number $M_{\theta 2}$ for a given inlet Mach number M_1 , we may rewrite Equation 10.22 as

$$(M_2 \sin \alpha_2)^2 = M_2^2 - M_1^2 \left[\frac{1 + (\gamma - 1)M_2^2/2}{1 + (\gamma - 1)M_1^2/2} \right]^{\frac{\gamma+1}{\gamma-1}} \tag{10.23}$$

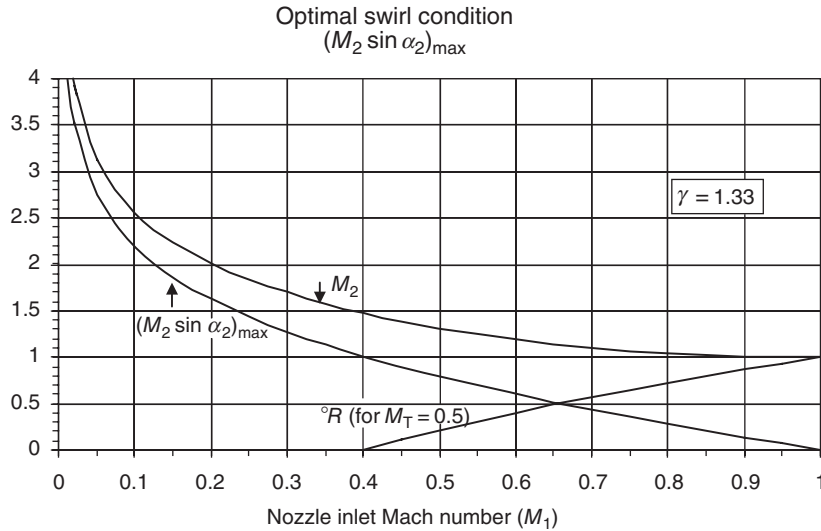
Now, let us find the exit Mach number M_2 , which maximizes the above function, that is, the square of the swirl Mach number. We differentiate the right-hand side of Equation 10.23 with respect to M_2 and set it equal to zero to find

$$M_2 = \sqrt{\frac{2}{\gamma - 1} \left\{ \left[\left(\frac{2}{\gamma + 1} \right) \frac{(1 + (\gamma - 1)M_1^2/2)^{\frac{\gamma+1}{\gamma-1}}}{M_1^2} \right]^{\frac{\gamma-1}{2}} - 1 \right\}} \tag{10.24}$$

Figure 10.12 shows nozzle flow parameters for a turbine stage that produces maximum work per unit mass flow rate, as a function of turbine inlet Mach number and the stage degree of reaction. The maximum specific work is produced at the condition of maximum nozzle exit swirl, assuming the rotor exit is swirl-free. The degree of reaction, from Equation 10.20 is also plotted in Figure 10.12 for the conditions of optimal swirl and a blade tangential Mach number of $M_T = 0.5$. The ratio of specific heat was assumed to be $\gamma = 1.33$ to represent gas in the turbine environment.

Under these optimal conditions, a choice of the stage degree of reaction establishes a turbine inlet Mach number, M_1 . An impulse turbine stage, with $^{\circ}R = 0$, demands a nozzle inlet Mach number of ~ 0.4 and a 50% reaction stage corresponds to an inlet

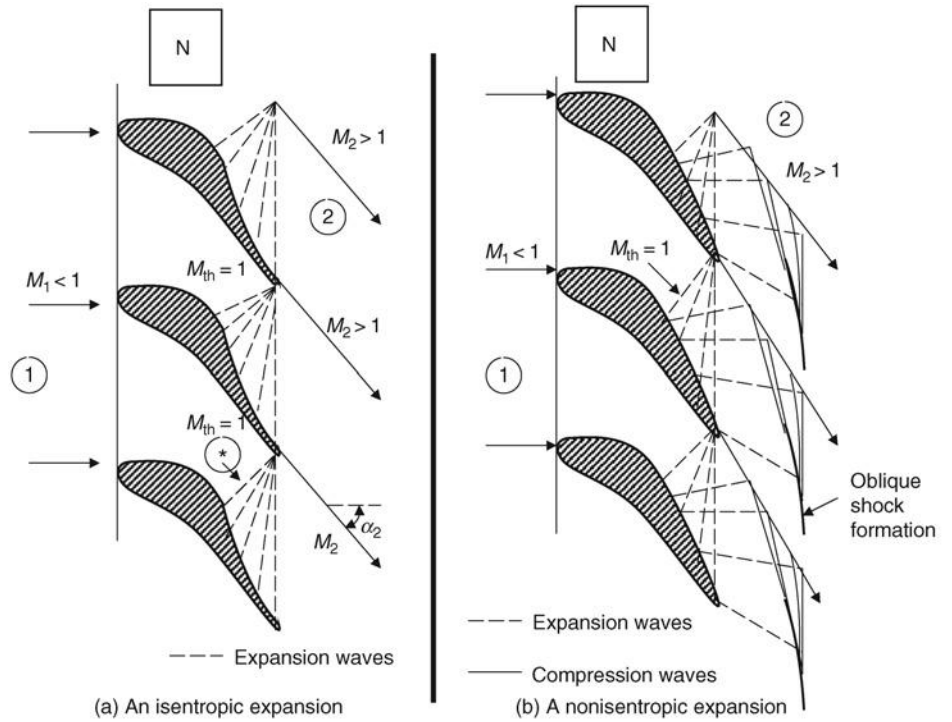
■ FIGURE 10.12
The variation of nozzle parameters for maximum swirl Mach number and the stage degree of reaction for a given inlet Mach number



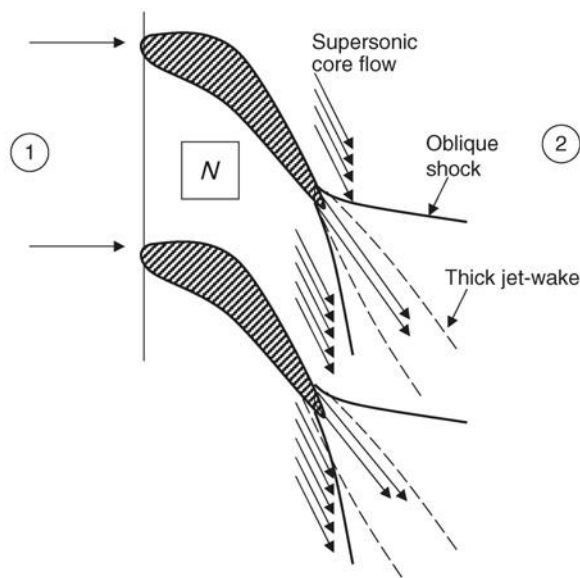
Mach number ~ 0.65 . We thus observe that with the increase in reaction, the mass flow rate per unit area increases and vice versa. An impulse stage is thus capable of producing maximum specific work, but at a reduced mass flow density. The optimal exit Mach number M_2 that maximizes the swirl and stage work, then varies between 1.2 and 1.5 for a stage reaction that varies between 50% and 0, respectively. A supersonic exit flow from the nozzle, that is, $M_2 > 1$, demands a convergent–divergent blade passage geometry, with an ideal (i.e., isentropic) area ratio of A/A^* in the range of 1.03–1.18 (for a $\gamma = 1.33$). Since the nozzle area ratios are small, the nozzle throat may be placed at the exit plane and the suction surface of the blade downstream of the throat to serve as the supersonic expansion ramp, as in a plug nozzle. By necessity, the portion of the suction surface downstream of the throat then has to be concave to cancel the expansion waves emanating from the blade trailing edge. The external aerodynamic shape of the nozzle with an isentropic expansion is depicted in Figure 10.13(a) (note the curvature reversal on the suction surface from convex to concave). In the case of a continuously convex suction surface, the expansion waves are reflected from the blade and the wake to form oblique shocks, as schematically shown in Figure 10.13(b). At off-design points, an isentropic expansion nozzle will also create wave reflections and shock formations. In addition, the curvature reversal from convex to concave on the suction surface causes an increased heat transfer to the blade (due to Goertler instability), thus the on-design advantage of an isentropic expansion nozzle is completely wiped out by its disadvantages at off-design.

In the HPT, the blades are internally cooled and their trailing edge often serves as the orifice for the coolant ejection. The resultant coolant jet is then mixed with the merging blade boundary layers downstream of the trailing edge. This gives us a picture of a thick jetwake flow under rapid mixing conditions introduced by large shear and the combustor-generated turbulence levels that are high. Consequently, the supersonic flow in the exit is confronted with a thick and growing shear layer, which then causes oblique shock waves to form at the trailing edge, as depicted in Figure 10.14. These waves are in response to wake formation and are in addition to the ones shown in Figure 10.15. A

■ FIGURE 10.13
Aerodynamic shapes of turbine nozzle blades with supersonic exit flow



■ FIGURE 10.14
Nozzle trailing-edge flow with coolant ejection and “fishtail” shock formation



■ **FIGURE 10.15**
Schlieren photograph
of a turbine nozzle
cascade showing
expansion waves and
shock formations
downstream of an
uncooled turbine
nozzle. Source:
Gostelow 1984.
Reproduced with
permission from
Elsevier



turbine nozzle flow is visualized using schlieren optics in Figure 10.15 (from Gostelow 1984). The expansion waves and their reflections as well as shock formations and the wakes are visible (note, there is no trailing-edge blowing).

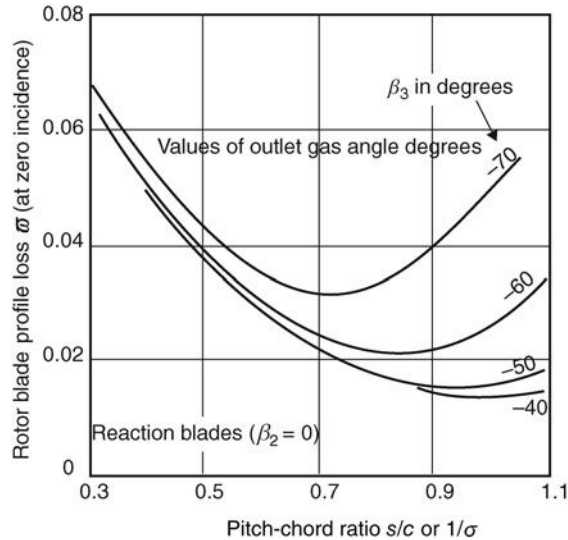
10.2.2 Turbine Blade Losses

We may categorize the losses in a turbine blade row as having their origins in

1. Profile loss, which is established based on 2D cascade studies
2. Secondary flow losses, which may be estimated using secondary flow theory of Hawthorne or the approximate version by Squire and Winter
3. Annulus losses, which includes tip clearance loss, (seal) leakage loss, casing boundary layer loss, corner vortex loss
4. Coolant-related losses, including mixing loss, induced separation loss
5. Shock and shock-boundary layer interaction losses in transonic stages of LPT
6. Unsteady flow loss causing shock oscillation and vortex shedding in the wake

Again, a reminder is in order that these losses are not all independent of each other rather they are, in most part, coupled. It is impossible to separate these losses, that is, decouple them from each other, with high degree of certainty. We may concentrate on any one aspect of these losses and proceed to study the isolated effect of that loss contributor, for example, 2D profile loss. However, the overall loss is by no means the linear sum of the elementary losses that we studied or considered.

■ **FIGURE 10.16**
 Profile loss coefficient
 for reaction (rotor)
 blades at zero
 incidence
 $Re_c = 2 \times 10^5$,
 $M < 0.6, t/c = 0.20$.
 Source: Adapted from
 Ainley 1950



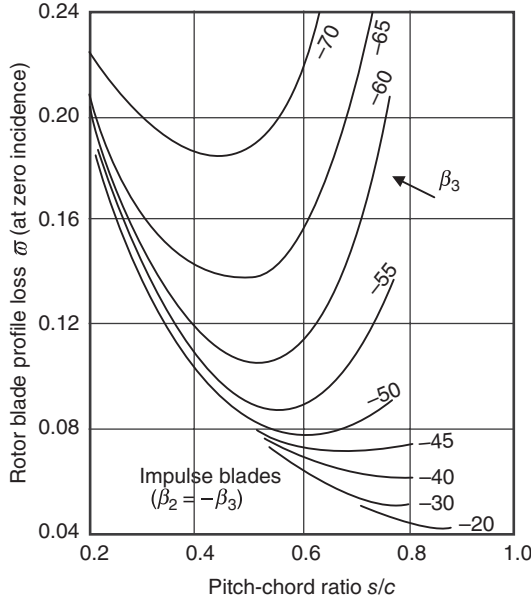
10.2.2.1 Blade Profile Loss. Ainley (1950) has assembled and presented cascade test data for rotor and nozzle blades in a turbine with limited compressibility and thickness-to-chord ratio variations. Figure 10.16 shows the profile loss of a reaction rotor blade with blade solidity (inverse of pitch-chord ratio) and the exit flow angle β_3 .

The loss “buckets” identify an optimum solidity for a given exit flow angle. The higher turning blades (e.g., $\beta_3 = -70^\circ$) require a higher solidity (lower pitch-chord ratio) than the rotor blades with lower turning, as expected. The blade thickness (20%) is high, which is typical of HPTs and is needed for internal cooling and for stress considerations. The Reynolds number based on chord of $\sim 200,000$ seems to be transitional on a flat plate, but remember that the turbine blades are highly cambered and thus flat plate transition criterion does not directly apply. Figure 10.17 shows the profile loss coefficient of an impulse rotor at zero incidence and the same flow conditions as the reaction rotor of Figure 10.16. Here, we note that the impulse blade profile losses are significantly higher than their counterparts in a reaction rotor (compare the levels of Figures 10.16 and 10.17). We expected the extra losses in an impulse rotor because the flow remains nearly at constant speed within the rotor as opposed to a continuously accelerating flow in a reaction rotor. Here again an optimum solidity is observed as a function of the exit flow angle. We will address the issue of optimum solidity in a turbine blade row in the next section.

Nozzle profile loss coefficient is presented in Figure 10.18 (from Ainley and Mathieson, 1951). The levels are comparable to the reaction rotor of Figure 10.16. We observe that the level of loss increases as the exit flow angle increases, as expected. The 70° exit angle is considered the upper limit of acceptable loss, as the 80° exit flow nozzle represents nearly doubling the profile loss of say 60° exit flow angle nozzle. Here too, we note an optimum solidity represented by the loss buckets.

10.2.2.2 Secondary Flow Losses. As we discussed earlier in the axial-flow compressor section, the secondary flows are set up in a curved channel. The mechanism for the secondary flow generation is the creation of streamwise vorticity in a bend as a result

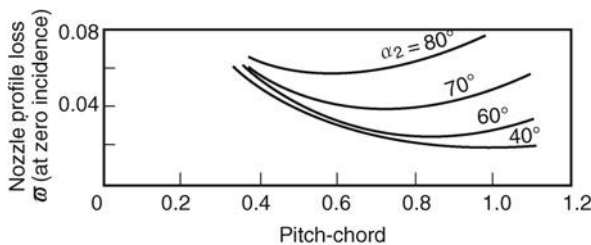
■ **FIGURE 10.17**
 Profile loss coefficient for impulse blades at zero incidence
 $Re_c = 2 \times 10^5$,
 $M < 0.6$, $t/c = 0.20$.
 Source: Adapted from Ainley 1950



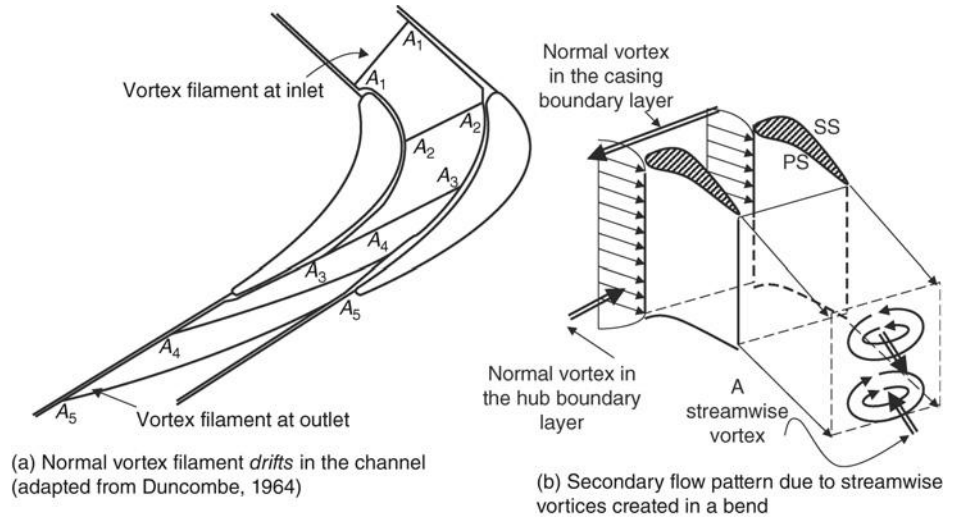
of different convection speeds on the concave and the convex sides of the channel. Take, for example, the vortex filament in the boundary layer entering a blade passage, as shown in Figure 10.19(a) (from Duncombe, 1964). The vortex filament “ A_1A_1 ” in the boundary layer is normal to the flow as depicted in Figure 10.19. Its subsequent motion in the passage is frozen at four time intervals resulting in A_2A_2 , A_3A_3 , and so on. Note that the normal filament A_1A_1 develops a streamwise component as it moves in the curved passage (Hawthorne 1951).

In Figure 10.19(b), we note a pair of counterrotating vortex filaments are generated at the exit of the curved passage (e.g., a turbine nozzle). The orientations of the normal vorticity vectors at the hub and the casing are in opposite directions, thus the streamwise vortex that they create will also be in the opposite directions, as shown. The right-hand rule applied to the streamwise vortices identifies the direction of the secondary stream pattern, that is, the circulatory flow in the clockwise or counterclockwise direction. To calculate the loss associated with the secondary flow, we need to integrate the kinetic energy trapped in the induced (secondary) flow field. The procedure and the associated uncertainties in the strength of the normal vorticity make this approach cumbersome. There are empirical models in the literature that are useful in preliminary design. One

■ **FIGURE 10.18**
 Nozzle profile loss coefficient at zero incidence
 $Re_c = 2 \times 10^5$,
 $M < 0.6$, $t/c = 0.20$.
 Source: Adapted from Ainley and Mathieson 1951



■ **FIGURE 10.19**
A normal vortex filament at the entrance to a curved channel develops a streamwise component and thus creates secondary flow



such model is that of Dunham and Came (1970), which relates the secondary flow loss to the blade aspect ratio (h/c), exit flow angle β_2 , the blade inlet angle κ_1 , blade pitch-chord ratio, lift coefficient C_L , and the mean flow angle β_m . The secondary loss correlation is

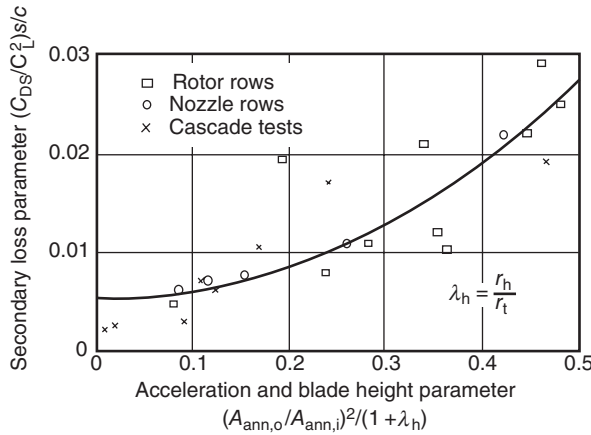
$$Y_s \equiv \frac{\bar{p}_{t1,rel} - \bar{p}_{t2,rel}}{\bar{p}_{t1,rel} - p_1} = 0.0334 \left(\frac{c}{h} \right) \left(\frac{\cos \beta_2}{\cos \kappa_1} \right) \left(\frac{C_L}{s/c} \right)^2 \left(\frac{\cos^2 \beta_2}{\cos^3 \beta_m} \right) \quad (10.25)$$

The total pressure terms in the secondary flow loss coefficient are the mass average of the inlet and exit flowfields, representing a mean spanwise average quantity at the inlet and exit planes. Note that the correlation in Equation 10.25 scales with C_L^2/AR , which is proportional to induced drag from finite wing theory of Prandtl. The product of the last two brackets in Equation 10.25 is known as the Ainley loading parameter, which was initially proposed by Ainley. In reality, separation of the secondary flow from end wall losses is impractical. The two are so intertwined, that is, strongly coupled, that any dissection results in a mutilated picture of the flowfield. However, we can observe trends and obtain rough estimates of the secondary loss from models such as Dunham and Came (1970). A graph of secondary loss parameter in Ainley's model in Figure 10.20 (from Ainley and Mathieson, 1951) confirms the trend and also indicates a large data scatter.

Separation of 2D profile loss from overall loss in a turbine nozzle is shown in Figure 10.21 (from Johnston, 1953). From this figure, we discern an optimum (mean) spacing that results in a minimum overall loss in three-dimensional nozzle blades. Also note that for the mean outlet angle of 52.8° , for a pitch-chord ratio of ~ 1.22 , the overall loss is nearly twice the minimum. The minimum loss occurs at an average pitch/chord ratio of ~ 0.9 with a mean outlet angle of $\sim 60^\circ$.

10.2.2.3 Annulus Losses. The growth of annulus boundary layer and its interactions with blade tip clearance flow at the tip, the corner vortex at the junction of the blade, and the hub (for rotor) and casing (for the nozzle) and any seal leakage flow combine to

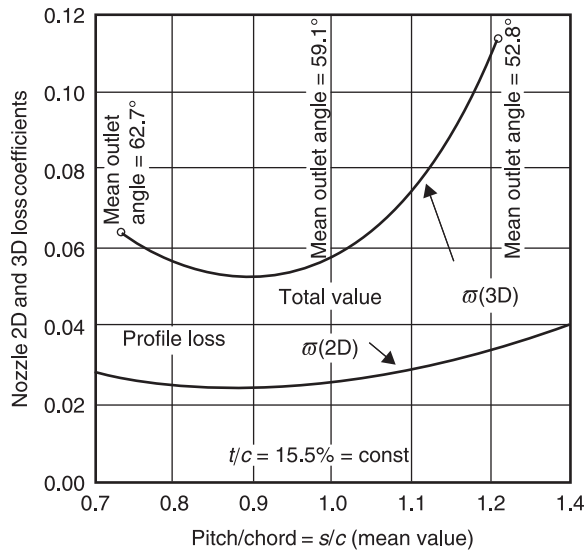
■ **FIGURE 10.20**
 Correlation of secondary loss with flow acceleration and blade height. Source: Ainley and Mathieson 1951. Courtesy of U.S. Government



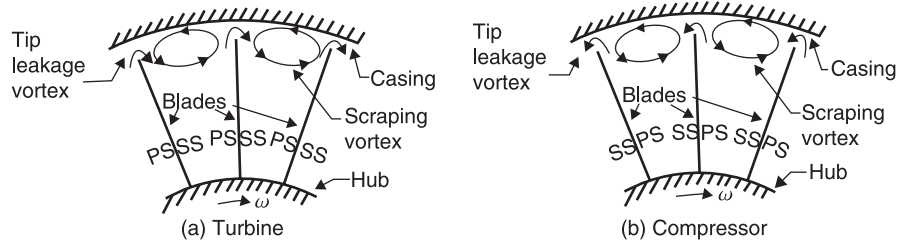
form this category of loss. It is a smorgasbord of *all the remaining* losses that dominate the annulus region. We may examine the tip clearance loss portion of the turbine annulus loss in more detail.

Turbine Rotor Tip Clearance Loss. A free-tip rotor experiences an over-the-tip flow from the pressure side toward the suction surface. With the blade tip operating very close to the casing to minimize tip leakage flow, the boundary layer on the annulus wall is scraped, rolled, and formed into a vortex, known as the scraping vortex. Schematic drawing of the scraping vortex in both a turbine and a compressor rotor is shown in Figure 10.22 (from Farokhi, 1986, 1988). The formation of passage scraping vortex is seen to modify the tip loading to reduce the pressure difference at the rotor tip in a turbine, therefore reduce the tip leakage loss. The counterpart of this effect is observed in a compressor where the scraping vortex circulation leads to an increased tip clearance flow due to higher tip loading.

■ **FIGURE 10.21**
 Profile and overall loss coefficients for a turbine nozzle (profile loss was estimated from Ainley, 1950). Source: Adapted from Johnston 1953



■ **FIGURE 10.22**
Schematic drawing of the tip vortex and the passage scraping vortex interaction in turbomachinery free-tip rotors. Source: Farokhi 1988. Reproduced with permission from AIAA



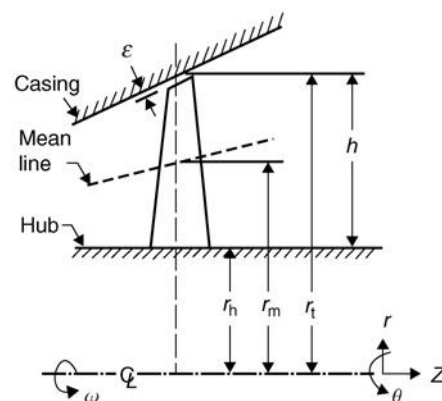
The geometrical parameters of a turbine rotor are shown in Figure 10.23 to include the hub, tip and pitchline radii, and the tip clearance gap ϵ . The nondimensional tip clearance may be expressed as a fraction of the blade height h or the local chord length c_{tip} and is referred to as *relative clearance height*.

There are several other nondimensional parameters that are of interest in the study of tip clearance loss and directly impact/measure its magnitude. These parameters are

- A_ϵ/A_0 , which is the ratio of tip clearance area to the zero-clearance annulus flow area downstream of the turbine rotor
- $\dot{m}_\epsilon/\dot{m}_0$, which is the fraction of the mass flow rate in the tip clearance region to the zero-clearance annulus mass flow rate
- $\Delta\eta/\eta_0$, which is the ratio of the turbine efficiency loss due to tip clearance to the zero-clearance turbine efficiency
- $\Delta\phi_t/\phi_{t0}$, which is the fraction of turbine power loss due to tip clearance to the turbine power with zero tip clearance.

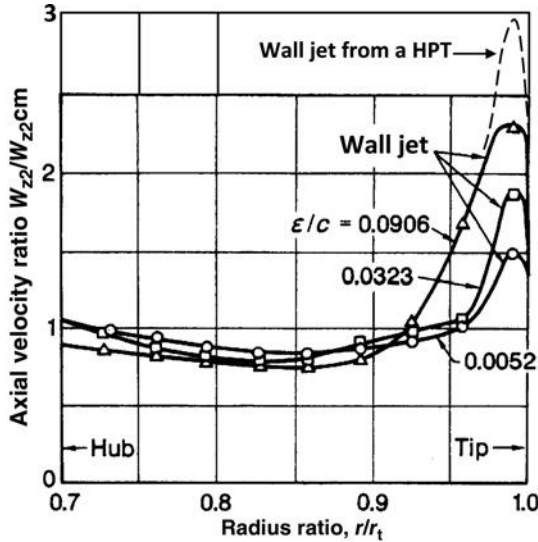
We note that the above parameters are not independent of each other. For example, the clearance area ratio and the clearance mass flow ratio are proportional to each other, or the loss of power in the turbine due to clearance must be proportional to the fraction of the mass flow rate. Also, the loss of efficiency and the loss of power are not independent. The earliest attempt in understanding/modeling the tip clearance loss in a turbine is due to

■ **FIGURE 10.23**
Geometry of a free-tip turbine rotor



■ FIGURE 10.24

Axial velocity distribution at the rotor exit. Adapted from Bammert, Klauekens, and Hartmann 1968



Anderhub (1912) who performed experimental measurements in a steam turbine. Stodola (1924, 1927) used Anderhub’s data to present a tip clearance loss efficiency model,

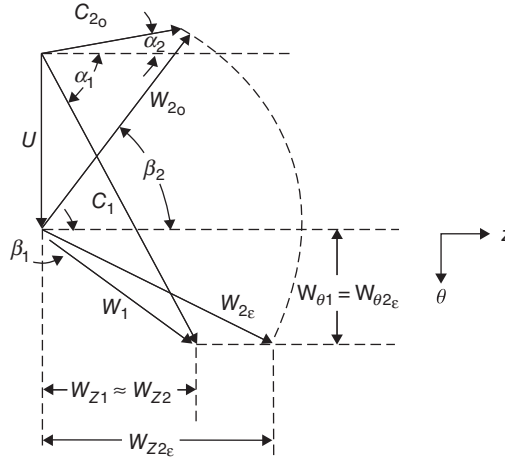
$$\frac{\Delta\eta}{\eta_0} = (1 - \alpha^*) \cdot 2 \cdot \frac{A_\epsilon}{A_0} \quad (\text{Stodola's model}) \quad (10.26)$$

where α^* is the energy recovery factor for the tip clearance flow and the factor 2 in Stodola’s model is based on Anderhub’s observations that the axial velocity of the gas emerging from the tip clearance region is nearly twice as large as the axial velocity in the core flow. In effect, the tip clearance flow emerges as a wall jet with no loss of energy, especially in light of no power interaction with the rotor. The experimental evidence of the wall jet emergence in the rotor tip clearance region is seen in Figure 10.24 (from Bammert, Klauekens, and Hartmann, 1968).

The tip clearance is presented as a fraction of the tip chord length in Figure 10.24. The axial velocity in the tip clearance region has exceeded twice the core value for a clearance-to-chord ratio of ~9%. Interestingly, the emergence of the wall jet due to tip clearance in the turbine exit flow if coupled with an axial exhaust diffuser (typical of stationary gas turbine power plants) is rather beneficial in the exhaust diffuser performance. Farokhi (1986, 1987) has investigated the effect of the rotor tip clearance flow on the axial exhaust diffuser and the turbine performance in a trade-off study. The analysis shows that turbine power loss due to rotor tip clearance is partially or completely offset by the enhanced axial diffuser pressure recovery due to the presence of a highly energetic wall jet.

Traupel (1958) proposes a tip clearance loss that is proportional to the clearance area ratio with the proportionality constant a function of the net flow turning (i.e., $\Delta\beta$) in the blade tip region. Bammert, Klauekens, and Hartmann (1968, 1987) propose an efficiency loss model that is proportional to the clearance mass flow ratio. To derive an expression for the axial velocities in the tip clearance and the core, Bammert assumes the conservation of angular momentum in the clearance flow and equal expansion of the tip

■ FIGURE 10.25 Velocity triangles in the clearance gap and the core



and the core flow. These two assumptions are clearly plausible and the velocity triangles inside the core and the blade tip region are shown in Figure 10.25, following Bammert, Klaukens, and Hartmann (1968).

Equal expansion causes the relative velocity magnitude to be preserved, as shown by the circular arc in Figure 10.25, and the conservation of angular momentum has kept the relative swirl in the upstream flow unchanged in the clearance flow downstream of the rotor, that is, $W_{\theta\epsilon} = W_{\theta 1}$. We can deduce the mass flow ratio from Figure 10.25, to be

$$\frac{\dot{m}_\epsilon}{\dot{m}_0} = \frac{A_\epsilon}{A_0} \left[1 + \tan^2 \beta_2 - \left(\frac{W_{z1}}{W_{z2}} \tan \beta_1 \right)^2 \right]^{1/2} \quad (10.27)$$

Lakshminarayana (1970) derives a semiempirical expression for the decrease in turbomachinery stage efficiency due to clearance, which is based on the induced flowfield of a potential vortex on the blades and the radial motion of the fluid in the blade boundary layer near the tip. Lakshminarayana's expression for $\Delta\eta$ is

$$\Delta\eta = \frac{0.7\tau \cdot \psi}{\cos \beta_m} \left[1 + 10 \left(\frac{\phi \cdot \tau \cdot A}{\psi \cdot \cos \beta_m} \right)^{1/2} \right] \quad (\text{Lakshminarayana's model}) \quad (10.28)$$

Lakshminarayana's model is derived for both types of turbomachinery, namely, compressors and turbines. However, as it lacks the effect of tip loading in compressors and unloading in turbines due to relative wall motion, as shown schematically in Figure 10.24, it cannot enjoy a general applicability. The effect of blade tip configurations (other than flat) on tip clearance flow is not accounted for in Lakshminarayana's model.

The fraction of turbine power loss due to rotor tip clearance is proportional to the fraction of tip leakage flow, that is,

$$\frac{\Delta\mathcal{P}_t}{\mathcal{P}_{t0}} \propto \frac{\dot{m}_\epsilon}{\dot{m}_0} \quad (10.29)$$

The zero-clearance turbine power is defined as

$$\mathcal{P}_{t0} \equiv \eta_0 \cdot \mathcal{P}_{t,\text{ideal}} \quad (10.30)$$

The turbine power output with tip clearance is

$$\mathcal{P}_{t\epsilon} = \eta_\epsilon \cdot \mathcal{P}_{t,\text{ideal}} \quad (10.31)$$

Now, defining incremental efficiency and power due to clearance as

$$\Delta\mathcal{P}_t \equiv \mathcal{P}_{t0} - \mathcal{P}_{t\epsilon} \quad (10.32)$$

$$\Delta\eta \equiv \eta_0 - \eta_\epsilon \quad (10.33)$$

We get

$$\frac{\Delta\mathcal{P}_t}{\mathcal{P}_t} = \frac{\Delta\eta}{\eta_0} \propto \frac{\dot{m}_\epsilon}{\dot{m}_0} \quad (10.34)$$

We expect the proportionality factor that emerges in Equation 10.34 between the incremental efficiency loss and the clearance mass fraction to include the following effects:

- The effect of tip shape
- Relative wall motion
- Clearance gap Reynolds number
- Clearance-to-blade height ratio $\tau \equiv \epsilon/h$.

Farokhi (1988) suggests that the proportionality function in Equation 10.34 is the blade tip discharge coefficient C_D where the discharge coefficient is in general a function of

$$C_D = C_D \left(\frac{\epsilon}{h}, \frac{\epsilon}{c}, \text{Re}_\epsilon, \phi_{\text{tip}}, \psi_{\text{tip}}, \frac{\delta_w^*}{h}, \frac{\theta_w}{h} \right) \quad (10.35)$$

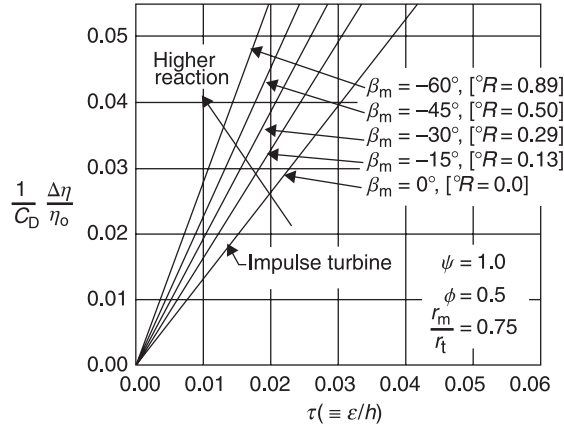
Therefore, the turbine efficiency loss due to rotor tip clearance is (from Farokhi, 1988)

$$\frac{\Delta\eta}{\eta_0} = C_D \frac{A_\epsilon}{A_0} \left[1 + \tan^2 \beta_2 - \left(\frac{W_{z1}}{W_{z2}} \tan \beta_1 \right)^2 \right]^{1/2} \quad (10.36)$$

We may simplify the above equation by assuming the axial velocity remains nearly constant across the rotor, that is, $W_{z1} \cong W_{z2}$, and by recasting it in terms of the flow coefficient and the stage loading factor, and the mean flow angle in the rotor as β_m ,

$$\frac{\Delta\eta}{\eta_0} \cong C_D \frac{A_\epsilon}{A_0} \left(1 - \frac{\psi}{\phi} \tan \beta_m \right)^{1/2} \quad (10.37)$$

■ **FIGURE 10.26**
Variation of turbine
efficiency loss
parameter with tip
clearance. Source:
Farokhi 1988.
Reproduced with
permission from AIAA



The area ratio term may also be simplified as

$$\frac{A_\varepsilon}{A_0} \approx \left(\frac{r_t}{r_m} \right) \left(\frac{\varepsilon}{h} \right) = \left(\frac{r_t}{r_m} \right) \cdot \tau \quad (10.38)$$

when we neglect the $(h\tau^2/2r_m)$. Therefore, the decrease in turbine stage efficiency is expressed as

$$\Delta\eta \cong \eta_0 C_D \cdot \tau \cdot \left(\frac{r_t}{r_m} \right) \left(1 - \frac{\psi}{\phi} \tan \beta_m \right)^{1/2} \quad (10.39)$$

Note that the mean flow angle β_m is either a negative angle (for reaction stages) or zero for an impulse stage. Therefore, the square root term in Equation 10.39 is always positive. The functional dependence of efficiency loss and the clearance height fraction is seen from the model to be linear. This behavior is shown in Figure 10.26 for a constant stage loading, flow coefficient, and pitchline radius ratio (from Farokhi, 1988).

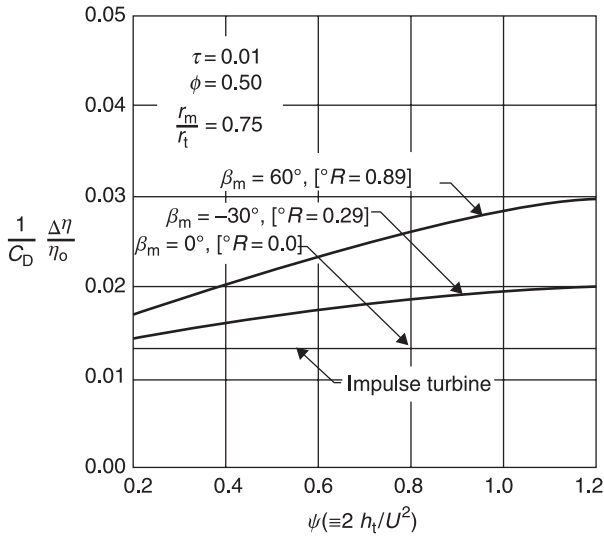
The behavior of turbine efficiency loss with stage loading and with flow coefficient is examined in Figures 10.27 and 10.28 (from Farokhi, 1988).

In a series of cascade experiments conducted in a water table, Booth, Dodge, and Hepworth (1982) measured leakage discharge coefficients over blade tips of various shapes. The baseline blade tip shape selected was that of a Garrett low-aspect ratio turbine. The variety of tip shapes included squealer, winglet, flat, knife, and grooved modifications to the baseline. These tip configurations are shown in Figure 10.29 (from Booth, Dodge, and Hepworth, 1982).

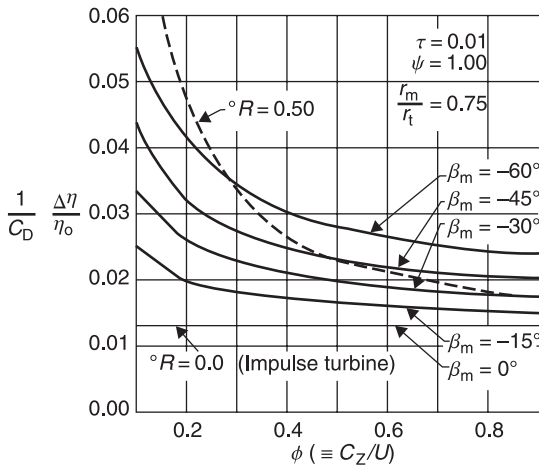
Relative tip discharge coefficients for advanced blade tip configurations are presented in Figure 10.30 (from Booth, Dodge, and Hepworth, 1982).

The flat tip discharge coefficient is reported by Booth, Dodge, and Hepworth to be ~ 0.81 – 0.83 , which may be used to estimate the discharge coefficients for tip configurations shown in Figure 10.30. The use of squealer and knife tip geometries has a potential of reducing the tip leakage flow by $\sim 30\%$. As the experiments of Booth, Dodge, and Hepworth did not include the effect of relative wall motion on tip unloading, their results need to be modified for the relative wall motion effect. The relative wall motion causes

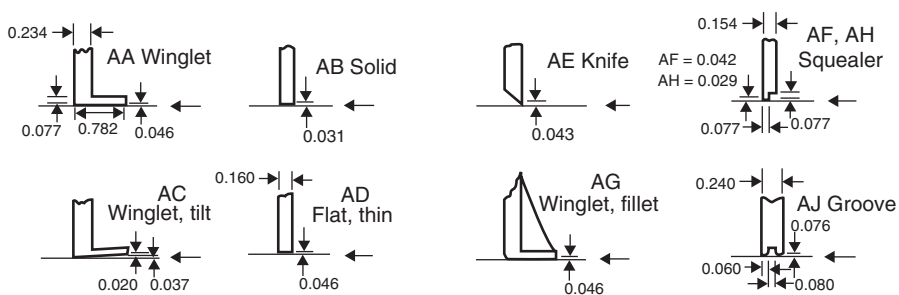
■ **FIGURE 10.27**
 Turbine efficiency loss due to tip clearance increases with the stage loading for reaction turbines and remains unchanged for an impulse turbine stage (for $\tau = 0.01$, $\phi = 0.50$, and $r_m/r_t = 0.75$). Source: Farokhi 1988. Reproduced with permission from AIAA



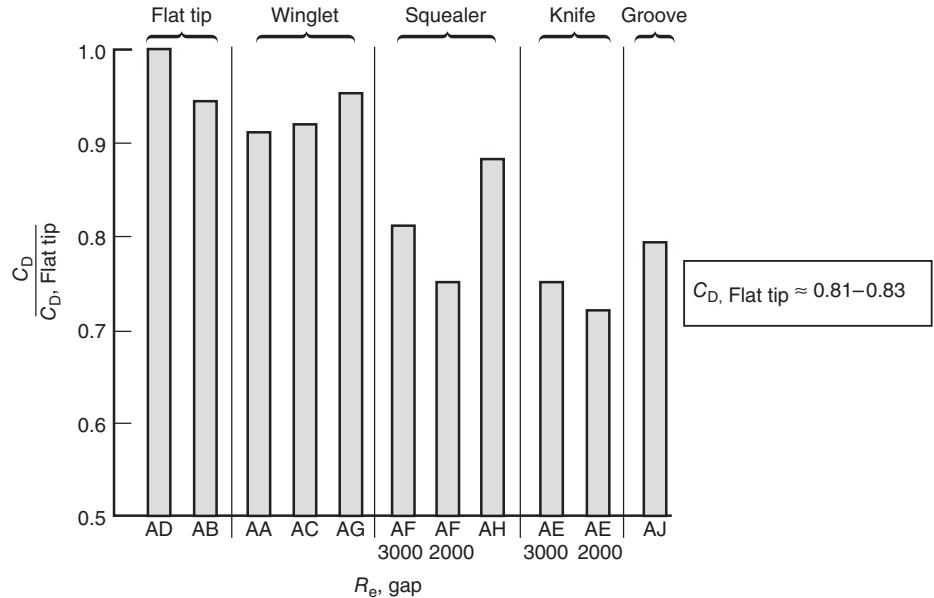
■ **FIGURE 10.28**
 Turbine efficiency loss due to tip clearance decreases with the flow coefficient for reaction turbines and remains unchanged for an impulse turbine stage (for $\tau = 0.01$, $\psi = 1.00$, and $r_m/r_t = 0.75$). Source: Farokhi 1988. Reproduced with permission from AIAA



■ **FIGURE 10.29**
 Turbine rotor blade tip configurations. Source: Booth et al. 1982. Reproduced with permission from ASME



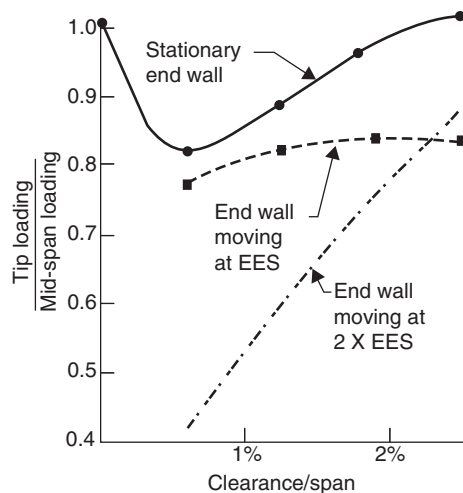
■ **FIGURE 10.30**
Relative rotor tip
discharge coefficient.
Source: Booth et al.
1982. Reproduced with
permission from
ASME



the scraping passage vortex, which in a turbine causes the tip unloading (as seen in Figure 10.22) or equivalently, a reduced tip clearance flow. Graham (1986) has verified the reduction of tip loading by virtue of rotation in a turbine blade row. Graham measured the static pressure distribution around the tip- and mid-span profiles of turbine blades in an experimental rig with relative wall motion. Figure 10.31 shows the ratio of tip- to the mid-span loading at different tip clearance fractions.

The stationary end wall case in Figure 10.31 serves as the basis to judge the effect of relative wall motion on tip loading. The experimental data range on tip clearance starts at $\sim 1/2\%$ clearance-to-span ratio and stretches to $\sim 2.5\%$. It is clearly evident that the relative wall motion causes tip unloading and at higher engine equivalent speeds ($2 \times \text{EES}$), the tip unloading is exacerbated. Since the tip clearance flow is predominantly a

■ **FIGURE 10.31**
Ratio of loading at tip
to mid-span. Source:
Graham et al. 1986.
Reproduced with
permission from
ASME. (EES stands
for engine equivalent
speed)



pressure-driven phenomenon and the effect of blade rotation is reducing the pressure difference or loading at the tip section, Farokhi (1988) proposes the following simple model for the tip discharge coefficient that accounts for blade rotation,

$$C_{D\omega} \sim C_{D,\omega=0} \left(\frac{\Delta p_\omega}{\Delta p_{\omega=0}} \right)^{1/2} \tag{10.40}$$

The subscript ω stands for the rotation in Equation 10.40. The basis for the model is the Bernoulli equation, which sets velocity proportional to the square root of static pressure drop through an orifice. In light of Graham’s data on tip unloading, we note that the magnitude of the pressure unloading term in Equation 10.40 is between 5 and 15%. This leads to a reduction in tip discharge coefficient by ~4–10% over the measurements of Booth, Dodge, and Hepworth, for example, that did not include relative wall motion.

EXAMPLE 10.4

A turbine stage is characterized by a loading coefficient ψ of 1.0 and a flow coefficient of ϕ of 0.5. The rotor is unshrouded and has a tip clearance gap-to-blade height ratio of 2%. The ratio of the tip to pitchline radius is

$r_t/r_m = 1.25$. The rotor blade tip has a knife configuration with a tip discharge coefficient of 0.5. The mean relative flow angle in the turbine rotor is $\beta_m = -20^\circ$. Calculate the loss of turbine efficiency due to the tip clearance.

SOLUTION

According to Equation 10.39, the loss of turbine efficiency is

$$\Delta\eta \cong \eta_0 C_D \cdot \tau \cdot \left(\frac{r_t}{r_m} \right) \left(1 - \frac{\psi}{\phi} \tan \beta_m \right)^{1/2} \approx 0.013 \eta_0$$

10.2.3 Optimum Solidity

Although the flow in turbines is characterized as having favorable pressure gradient, the flow acceleration on the suction surface of a turbine blade has to face an adverse pressure gradient toward the trailing edge. This behavior is typical of all lifting surfaces whether a compressor or a turbine blade. A typical pressure distribution on a turbine blade is shown in Figure 10.32, where the flow angles and velocity vectors are relative to the blade.

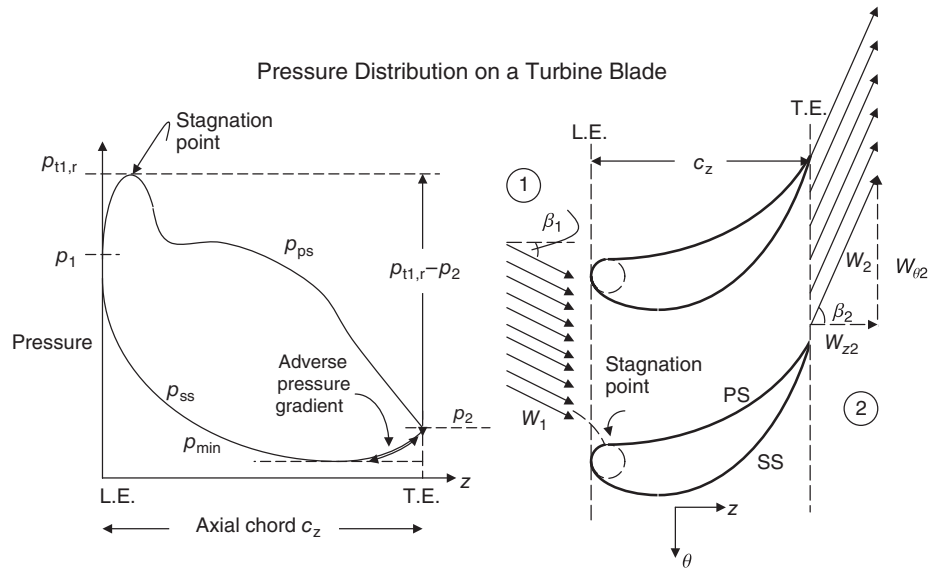
The blade loading per unit span is the integral of the pressure difference on the pressure and suction surfaces, which produces the blade tangential force F_θ , per unit span

$$F_\theta = c_z \int_0^1 (p_p - p_s) d(z/c_z) \tag{10.41}$$

Also from the momentum balance across the blade row in the tangential direction, we get the blade tangential force as

$$F_\theta = \rho_2 s \cdot W_{z2} (W_{\theta 1} - W_{\theta 2}) \quad \text{note} \quad W_{\theta 1} - W_{\theta 2} = C_{\theta 1} - C_{\theta 2} \tag{10.42}$$

■ **FIGURE 10.32**
A typical pressure distribution on a turbine blade



We note from this equation that the blade tangential force increases with blade spacing s for a given velocity vector diagram, that is, swirl distribution and through flow. With an increase in tangential blade force the integral of the pressure jump across the blade increases, according to Equation 10.41. With higher loading, the adverse pressure gradient on the suction surface may cause the boundary layer separation and a higher blade profile loss. On the contrary, keeping the blade spacing (relative to chord) small to reduce the blade loading will increase the wetted area and thus the frictional losses of the blade row. Hence, we expect that optimum blade solidity exists, which produces the lowest profile and wetted surface losses for a blade row. Zweifel (1945) has addressed the issue of optimum solidity in turbomachinery by introducing a loading parameter and a criterion that is widely accepted. Here we present Zweifel's methodology.

Equating the two expressions for the blade tangential force (per unit span) and isolating axial solidity c_z/s yields

$$\sigma_z \equiv \frac{c_z}{s} = \frac{\rho_2 W_{z2} (W_{\theta 1} - W_{\theta 2})}{\int_0^1 (p_p - p_s) d(z/c_z)} \quad (10.43)$$

Zweifel (1945) has defined a blade loading parameter ψ_z as the ratio of the blade tangential force per unit span and axial chord to the difference of inlet stagnation pressure and the exit static pressure, that is,

$$\psi_z \equiv \frac{\int_0^1 (p_p - p_s) d(z/c_z)}{p_{t1,r} - p_2} \quad (10.44)$$

Now, in terms of the Zweifel loading parameter, we may cast Equation 10.43 into the following form,

$$\sigma_z \equiv \frac{\rho_2 W_{z2}(W_{\theta 1} - W_{\theta 2})}{(p_{t1,r} - p_2)\psi_Z} \quad (10.45)$$

The axial and tangential velocities may be replaced by

$$\begin{aligned} W_{z2} &= W_2 \cos \beta_2 \\ W_{\theta 2} &= W_2 \sin \beta_2 \end{aligned}$$

We may substitute these expressions in Equation 10.45 and with some minor manipulations we get

$$\sigma_z \equiv \left(\frac{\rho_2 W_2^2 / 2}{p_{t1,r} - p_2} \right) \frac{\left(\frac{W_{\theta 1}}{W_{\theta 2}} - 1 \right) \sin(2\beta_2)}{\psi_Z} \quad (10.46)$$

If we ignore the total pressure loss between the inlet and blade exit, we may cast the pressure difference term in Equation 10.46 as

$$p_{t1,r} - p_2 \approx p_{t2,r} - p_2 = p_2 \left[\left(1 + \frac{\gamma - 1}{2} M_{2r}^2 \right)^{\frac{\gamma}{\gamma - 1}} - 1 \right] \quad (10.47)$$

The dynamic pressure term in Equation 10.46 may be written in terms of static pressure and local Mach number as

$$\rho_2 W_2^2 / 2 = \gamma \cdot p_2 M_{2r}^2 / 2 \quad (10.48)$$

Therefore, the axial solidity may be expressed as

$$\sigma_z \equiv \left(\frac{(\gamma / 2) M_{2r}^2}{\left(1 + \frac{\gamma - 1}{2} M_{2r}^2 \right)^{\frac{\gamma}{\gamma - 1}} - 1} \right) \frac{\left(\frac{W_{\theta 1}}{W_{\theta 2}} - 1 \right) \sin(2\beta_2)}{\psi_Z} \quad (10.49)$$

In the incompressible limit (i.e., $M_{2r} \rightarrow 0$), the above expression simplifies to

$$\sigma_z \equiv \frac{\left(\frac{W_{\theta 1}}{W_{\theta 2}} - 1 \right) \sin(2\beta_2)}{\psi_Z} \quad (10.50)$$

Zweifel recommended a value of 0.8 (to ~ 1) for the loading parameter ψ_z . Hence, based on the exit flow angle and swirl ratio across the blade row, an optimum solidity is obtained

from Equation 10.49 or 10.50. Equation 10.50 has a maximum for β_2 of 45° for a blade row with a fixed swirl ratio. To express the blade solidity purely in terms of the flow angles, we write the swirl velocity components in terms of the axial flow and the tangent of the flow angle as

$$W_{\theta 1} = W_{z1} \tan \beta_1$$

$$W_{\theta 2} = W_{z2} \tan \beta_2$$

By substituting these expressions in Equation 10.50 and assuming constant axial velocity, we get

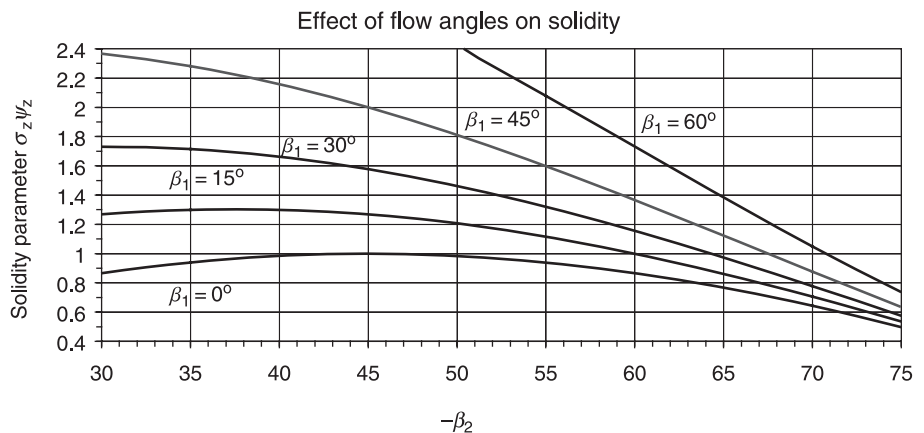
$$\sigma_z \psi_Z = \left(\frac{\tan \beta_1}{\tan \beta_2} - 1 \right) \sin(2\beta_2) \tag{10.51}$$

After some minor trigonometric manipulations, we express Equation 10.51 in terms of flow turning angle in the blade row as

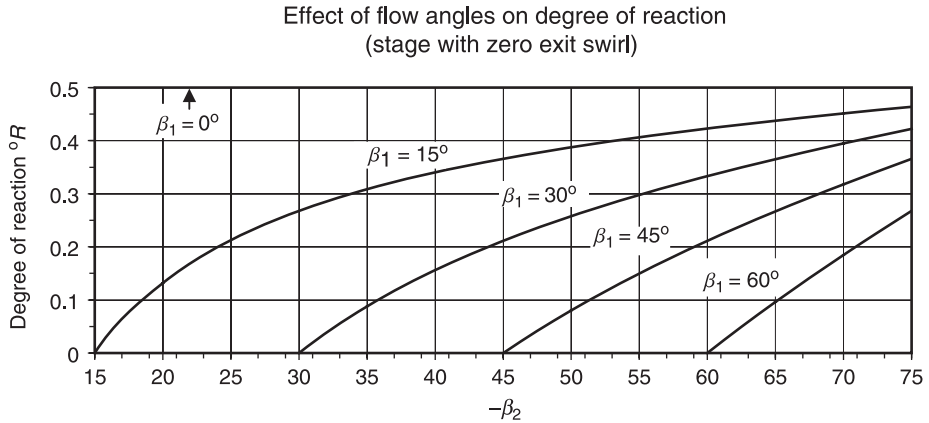
$$\sigma_z \psi_Z = \frac{2 \cos \beta_2}{\cos \beta_1} \sin(\beta_1 - \beta_2) \tag{10.52}$$

Figure 10.33 is a plot of the axial solidity parameter with turbine flow angles. In the region of interest in a turbine, that is, for the exit flow angles between -45° and -75° , we observe that the solidity parameter decreases with the decrease in exit flow angle for a given inlet flow angle. In order to interpret this result, we take the Zweifel loading parameter as a constant, namely, ~ 0.8 . Therefore, a decrease in exit flow angle, for a fixed inlet flow angle, increases the stage reaction, which tends to reduce the blade loading. However, to maintain the blade loading fixed, the solidity has to be reduced, which inversely affects the blade loading. Also, for a given exit flow angle $-\beta_2$, the increase in the inlet flow angle causes a lower stage reaction (i.e., moving toward impulse stage) and thus an increase in blade loading. To maintain the loading as described by a constant value of Zweifel parameter, the blade solidity has to increase, which has a tendency to reduce the blade

■ **FIGURE 10.33**
Effect of flow angles in a turbine blade row on the solidity parameter $\sigma_z \cdot \psi_z$



■ **FIGURE 10.34**
 The effect of flow angles on a turbine stage with zero exit swirl (β_1 and β_2 are the rotor relative inlet and exit flow angles, respectively)



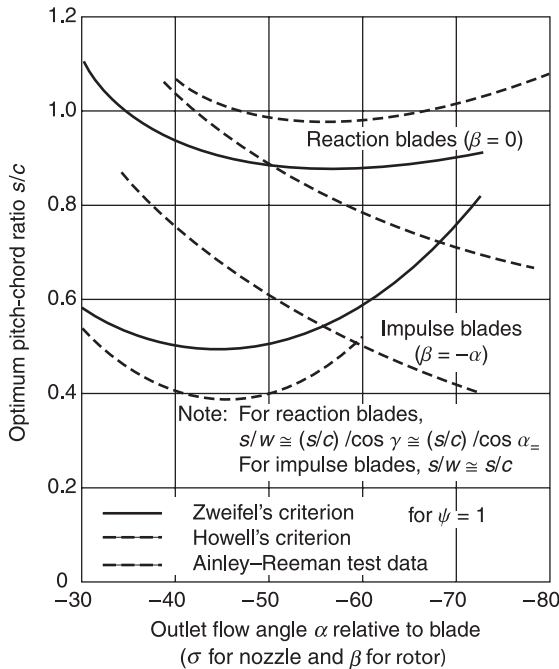
loading. The variation of stage reaction with the flow angles is depicted in Figure 10.34 for a turbine stage with zero exit swirl.

A summary of the results of the optimum pitch-chord ratio for reaction and impulse turbines as a function of blade relative exit flow angle is shown in Figure 10.35 (after Duncombe, 1964). The two criteria for optimum solidity, that is, Zweifel's and Howell's, show a very limited range of agreement with the test data, as depicted in Figure 10.35.

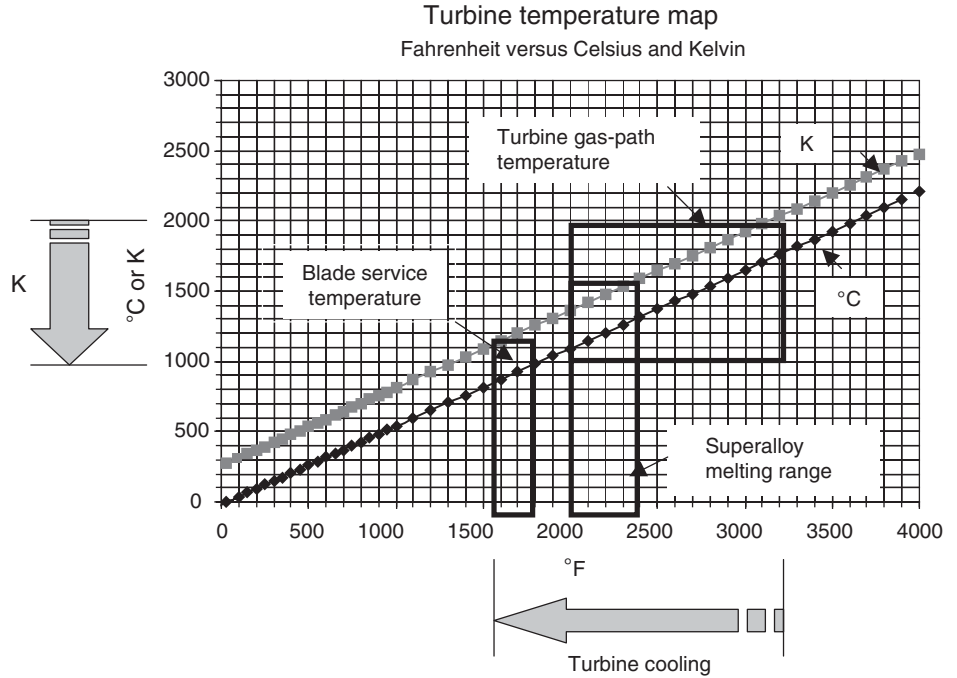
10.2.4 Turbine Cooling

The entrance flow to a turbine nozzle is the combustor exit flow with its spatially nonuniform characteristics, such as the hot spots. The average combustor exit

■ **FIGURE 10.35**
 Optimum pitch-chord ratio. Source: Adapted from Duncombe 1964



■ **FIGURE 10.36**
Turbine temperature map shows the need and the extent of turbine cooling in a modern GT-engine



temperature in modern gas turbine engines at takeoff is ~1750–2000 K and the temperature nonuniformity or “hot spots” may expose the nozzle to an additional temperature of 100–200 K. This is clearly beyond the temperature limits of metals, including the nickel-based alloys used in turbines. Figure 10.36 shows a turbine temperature map with three distinct temperature ranges. Turbine *gas-path temperature* is the hot gas temperature, which is typical of modern gas turbine combustor exit conditions. The *superalloy melting range* identifies the melting temperature for (nickel-based) superalloys that are used in turbine manufacturing. The *blade service temperature* represents the blade surface operating temperature, which is about 80% of the melting temperature of the superalloy.

Therefore, the need arises to cool the first and possibly the second and the third stages of a high-pressure turbine. The source of turbine cooling fluid is in the compressor. The compressor discharge achieves the highest pressure in the cycle, therefore it is best suited to cool the nozzle, the rotor, and the casing of the first stage of high-pressure turbine. As the gas pressure drops in subsequent turbine stages, a lower pressure coolant supply may be tapped for cooling purposes. Intercompressor bleed may thus be used to cool the lower pressure regions (i.e., blades and casing) in a turbine.

The gas is characterized by its static temperature T_g , which is independent of the motion of the observer. Then by virtue of its motion, it attains a total or stagnation temperature T_t , which is observer dependent. For example, the turbine nozzle, which is stationary, is exposed to the total temperature

$$T_t = T_g + \frac{C^2}{2c_p} \quad \text{total temperature in the absolute frame} \quad (10.53)$$

where C is the absolute gas speed and for simplicity we assumed a calorically perfect gas with constant c_p . On the contrary, the rotor that follows the nozzle attributes a relative gas speed to the incoming flow, therefore the total temperature as measured by a rotor is

$$T_{t,r} = T_g + \frac{W^2}{2c_p} \quad \text{total temperature in the rotor frame of reference} \quad (10.54)$$

The kinetic energy contribution to the gas total temperature, that is, the second term on the RHS of Equations 10.53 and 10.54, may be significant and thus affects the cooling requirements of nozzle and rotor blades. The coolant temperature T_c represents another temperature that we work with in a turbine-cooling problem. Unless we cool the coolant, T_c is the compressor discharge (static) temperature. The wall temperature T_w represents the actual wall temperature that (along with the state of stress) determines the material life. The temperature of the wall on the hot gas side is T_{wg} and the wall temperature on the coolant side is T_{wc} . In case the wall is insulated, the flow of a thermally conducting fluid over the wall creates a wall temperature, T_{aw} . A cooling effectiveness parameter η may be defined as:

$$\eta \equiv \frac{T_{tg} - T_{wg}}{T_{tg} - T_c} \quad (10.55)$$

which may be used as a figure of merit in modern gas turbine engines where it attains a value between 0.6 and 0.7.

In summary, we deal with several temperatures in a cooled turbine, these are

1. T_g , which is the gas static temperature
2. T_{aw} is the adiabatic wall temperature, that is, the temperature of the insulated wall
3. T_t , the total gas temperature in the absolute frame, for example, in the nozzle or casing frame of reference
4. $T_{t,r}$, the total gas temperature as seen by the turbine rotor
5. T_{wg} is the wall temperature on the hot gas side (i.e., actual or desired surface temperature)
6. T_{wc} is the wall temperature on the coolant side
7. T_c is the coolant temperature,

The adiabatic wall temperature in gas turbine is very nearly equal to the total or stagnation temperature of the gas. For a flat plate, the adiabatic wall temperature is

$$T_{aw} = T_g + r \frac{C^2}{2c_p} \quad \text{for a stator} \quad (10.56)$$

$$T_{aw,r} = T_g + r \frac{W^2}{2c_p} \quad \text{for a rotor} \quad (10.57)$$

The coefficient r in the above equations is known as the *recovery factor*. The recovery factor is a function of gas property, known as Prandtl number, and the state of the boundary layer, following

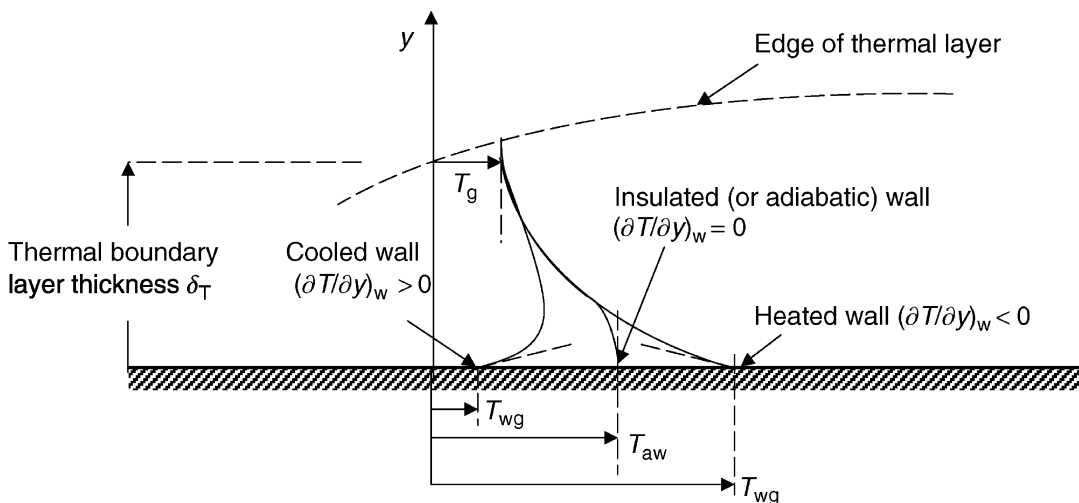
$$r = \sqrt{\text{Pr}} \quad \text{for (flat plate) laminar boundary layers} \quad (10.58)$$

$$r = \sqrt[3]{\text{Pr}} \quad \text{for a flat plate turbulent boundary layer} \quad (10.59)$$

where Pr is the gas Prandtl number, which is a fluid property, defined as

$$\text{Pr} \equiv \frac{\mu c_p}{k} \quad (10.60)$$

where μ is the fluid viscosity, c_p is the specific heat at constant pressure, and k is the fluid thermal conductivity. The Prandtl number for air is ~ 0.71 (for a wide range of temperatures), therefore the recovery factor r is either ~ 0.8426 for a laminar boundary layer or ~ 0.8921 for a turbulent boundary layer. The turbine boundary layers are predominantly turbulent, as a result of high free-stream turbulence intensity that is produced in the combustor ($\sim 10\text{--}20\%$). Therefore, the adiabatic wall temperature and the gas total temperature are very nearly equal. The implication is that unless we cool the blade (or casing), the surface metal temperature reaches nearly that of the stagnation temperature of the gas (in the appropriate frame of reference, for example, the nozzle will see Equation 10.56 and the rotor will see Equation 10.57). The static temperature distribution in a thermal boundary layer varies according to the wall boundary condition, as shown in Figure 10.37. The edge of the thermal layer is depicted by δ_T thickness, analogous to the viscous boundary layer thickness δ .



■ FIGURE 10.37 Static temperature distribution $T(y)$ within the thermal boundary layer subjected to different wall boundary conditions (i.e., cooled, adiabatic, or heated)

EXAMPLE 10.5

The total gas temperature at the exit of a turbine nozzle is $T_g = 1700$ K and the local gas Mach number is $M_2 = 1.0$. The gas ratio of specific heats is $\gamma = 1.33$, $c_p = 1157$ J/kg · K, and Prandtl number is $Pr = 0.71$. First calculate:

- (a) the gas static temperature T_g
- (b) the adiabatic wall temperature T_{aw} on the nozzle for a turbulent boundary layer

- (c) the adiabatic wall temperature on the nozzle for a laminar boundary layer

Assuming that the gas speed relative to the rotor is $W_2 = 455$ m/s, calculate

- (d) the total temperature of the gas on the rotor, i.e., as measured in the rotor frame of reference, T_{tr} .

SOLUTION

The static temperature is related to the total temperature and Mach number $T = T_t/[1 + (\gamma - 1)M^2/2]$, therefore,

$$T_g = 1700 \text{ K}/[1 + 0.165] \approx 1459.2 \text{ K}$$

The local speed of sound is $a_2 = [(\gamma - 1)c_p T_2]^{0.5} \approx 746.4$ m/s

Therefore the gas speed is the product of local Mach number and the speed of sound, i.e., $C_2 = a_2 = 746.4$ m/s.

The adiabatic wall temperature is given by Equation 10.56 (for a stator)

$$T_{aw} = T_g + r \frac{C_2^2}{2c_p} \text{ where } r = \sqrt{Pr} \text{ for laminar and } r = \sqrt[3]{Pr} \text{ for turbulent BL.}$$

$$T_{aw} = 1459.2 \text{ K} + (0.71)^{1/3}(746.4)^2/1157 \approx 1889 \text{ K} \quad (\text{for turbulent boundary layer})$$

$$T_{aw} = 1459.2 \text{ K} + (0.71)^{1/2}(746.4)^2/1157 \approx 1865 \text{ K} \quad (\text{for laminar boundary layer})$$

In the rotor frame of reference, the contribution of gas kinetic energy is based on W_2 , therefore,

$$T_{tr} = T_g + W_2^2/2c_p = 1459.2 \text{ K} + (455)^2/2/1157 \approx 1549 \text{ K}$$

The rotor feels a lower stagnation gas temperature than the stator by about 150 K.

The temperature distribution in the thermal layer is created as a result of fluid thermal conductivity and is governed by the Fourier's law of heat conduction, that is,

$$q_y = \frac{\dot{Q}}{A} = -k \frac{\partial T}{\partial y} \quad (10.61)$$

where q_y is the heat transfer per unit area (i.e., the heat flux), due to conduction, in the y -direction, k is the thermal conductivity of the fluid (or solid), and the last term is the temperature gradient in the y -direction. The negative sign indicates the flow of heat is in the opposite direction to that of the temperature gradient, which forces heat to flow from hot to cold. The dimensions of thermal conductivity are discerned from Equation 10.61 to be $W/m \cdot K$.

In the case of adiabatic wall, heat transfer rate is zero, therefore the temperature gradient at the insulated wall becomes zero, that is,

$$\left. \frac{\partial T}{\partial y} \right|_{y=0} = 0 \quad \text{for an insulated, or adiabatic, wall} \quad (10.62)$$

The flow of heat from the wall to the fluid makes q_y positive (for the fluid), thus the temperature gradient negative at the wall

$$\left. \frac{\partial T}{\partial y} \right|_{y=0} < 0 \quad \text{for a heated wall} \quad (10.63)$$

The cooled wall case will pose a negative heat transfer condition to the fluid, thus the temperature gradient will attain a positive slope at the wall.

$$\left. \frac{\partial T}{\partial y} \right|_{y=0} > 0 \quad \text{for a cooled wall} \quad (10.64)$$

All these boundary conditions on the slope of static temperature distribution at the wall are shown in Figure 10.37.

The cooling of a surface may be achieved in different ways, for example,

1. We may coat the surface with a low-thermal conductivity layer, that is, a protective layer like a ceramic coating, which reduces the heat transfer through a surface
2. Radiation cooling, which is natural to all surfaces above absolute zero temperature
3. We may increase the heat transfer through the wall by internal cooling, that is, convective cooling or impingement cooling
4. We may decrease heat transfer by *blanketing* the wall with a layer of coolant, as in film cooling
5. We may *blanket* the entire wall by transpiration cooling through a porous skin
6. Combination of the above methods.

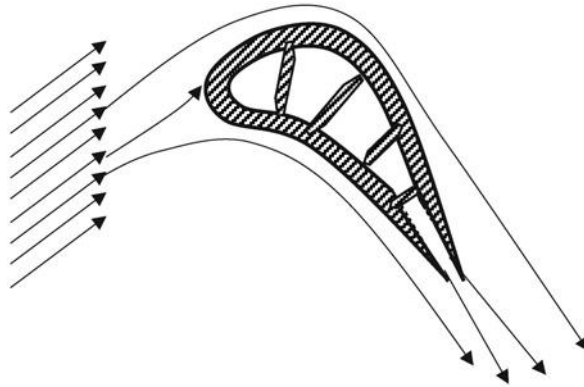
The first two methods are *passive* thermal protection system and surface radiation, whereas methods 3–6 involve *active* cooling of the surface. The radiation cooling in a gas turbine is only a small contributor to the total heat transfer and thus often neglected. The active cooling methods are divided into *internal* versus *external* cooling schemes.

10.2.4.1 Convective Cooling. Convective heat transfer is governed by the Newton's Law of Cooling, according to

$$q \equiv \frac{\dot{Q}_c}{A} = h\Delta T \quad (10.65)$$

where h is the coefficient of heat transfer and the temperature difference ΔT is the *driving* term for heat transfer. This means that heat transfer is proportional to area as well as the temperature difference. For example, $(T_{aw} - T_{wg})$ drives the heat transfer to the wall on the gas side of a cooled turbine blade. Similarly, $(T_{wc} - T_c)$ is the driver for heat transfer on the coolant side of the same blade. The dimensions of the heat transfer coefficient h are (as seen from Equation 10.65) W/m^2K . A convectively cooled turbine blade is shown in Figure 10.38. The internal passage is divided into a nose (or leading edge)

■ **FIGURE 10.38**
An internally cooled turbine blade is shown with separate cooling channels and trailing-edge ejection



section, three central sections, and one trailing-edge passage. The arrangement of these internal cooling passages meters the amount of coolant to the desired section of the blade. For example, the stagnation point heating is very critical in turbine blade heat transfer and cooling therefore the leading-edge region has its own separate nose channel. The options with the nose channel include impingement cooling that we will discuss in the next section.

The static temperature distribution on the hot gas side, across the turbine wall and in the coolant side, is shown on an internally cooled turbine blade in Figure 10.39.

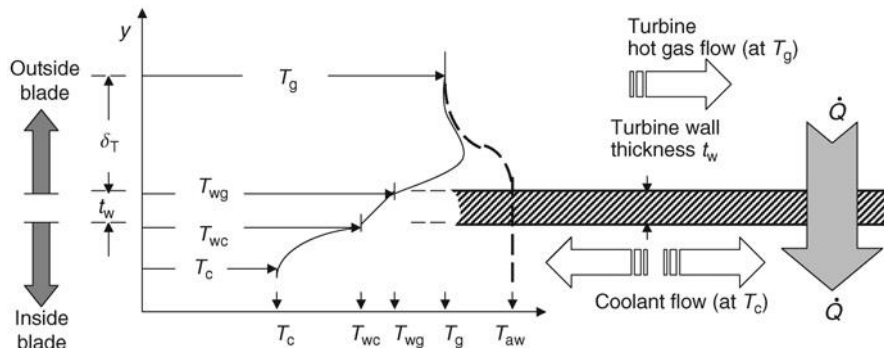
The steady-state heat transfer rate from the hot gas to the coolant suggests a balance

$$\dot{Q}_c = A_g h_g (T_{aw} - T_{wg}) = A_w k_w \frac{T_{wg} - T_{wc}}{t_w} = A_c h_c (T_{wc} - T_c) \quad (10.66)$$

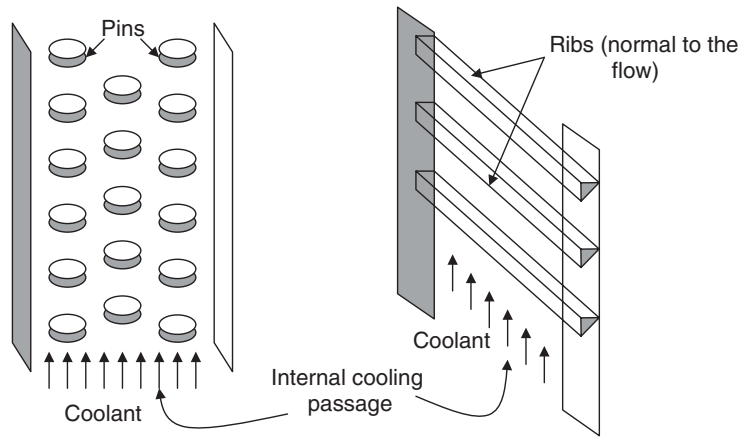
To see a correlation between the film coefficients h_g and/or h_c and the flow Reynolds number, Prandtl number, and so on, we may write the heat transfer rate from the hot gas using Stanton number according to

$$\dot{Q}_g = A_g \cdot St_g \cdot \rho_g u_g c_{pg} (T_{aw} - T_{wg}) \quad (10.67)$$

■ **FIGURE 10.39**
Static temperature distribution on a turbine blade with internal cooling (the dashed line shows the temperature distribution for an uncooled/insulated wall)



■ **FIGURE 10.40**
Pins and ribs inside turbine blade cooling passages create turbulent wakes, which enhance heat transfer to the coolant



where ρ_g is the gas density, u_g is the gas speed, c_{pg} is the specific heat at constant pressure on the gas side, and St is the Stanton number and is nondimensional. Therefore, by equating the wall heat transfer rate and the convective heat transfer to the wall in Equations 10.66 and 10.67, we note

$$h_g = \rho_g u_g c_{pg} \cdot St_g \quad (10.68)$$

The simplest expression for Reynolds analogy between the skin friction and heat transfer is derived for a gas of Prandtl number unity, that is, for $Pr = 1$, we can show that

$$St = \frac{c_f}{2} \quad (10.69)$$

where c_f is the local skin friction coefficient. We remember that local skin friction coefficient is a function of Reynolds number, and it jumps through the transition from laminar to turbulent state of the boundary layer. In boundary layer theory we learned that

$$c_f \propto Re^{-1/2} \quad (\text{Laminar}) \quad (10.70)$$

and

$$c_f \propto Re^{-1/5} \quad (\text{Turbulent}) \quad (10.71)$$

Therefore, the higher heat transfer rates for turbulent flow suggest that we should “stir up” the coolant flow inside the cooling passages as much as possible. The practical approach has been through introducing a staggered array of pins in the cooling channel (or ribs normal to the coolant flow direction), as shown in Figure 10.40. A limitation to the extent of flow resistance that we introduce inside a cooling channel is the loss of total pressure, which is a “commodity” of value for film-cooled blades.

Let us substitute Equation 10.68 into 10.66 to express the heat transfer rate to the blade in terms of gas mass flow rate, i.e.,

$$\dot{Q} = A_g \rho_g u_g c_{pg} \cdot St_g \cdot (T_{aw} - T_{wg}) = \dot{m}_g c_{pg} \cdot St_g \cdot (T_{aw} - T_{wg}) \quad (10.72)$$

The equivalent form of heat transfer on the coolant side may be written as

$$\dot{Q} = A_c \rho_c u_c c_{pc} \cdot St_c \cdot (T_{wc} - T_c) = \dot{m}_c c_{pc} \cdot St_c \cdot (T_{wc} - T_c) \quad (10.73)$$

Setting the heat transfer rate on the gas side and the coolant side equal to each other and expressing the ratio of the coolant-to-gas flow rate as ϵ , we get an expression for the coolant (mass) fraction, namely,

$$\epsilon \equiv \frac{\dot{m}_c}{\dot{m}_g} = \frac{c_{pg} St_g}{c_{pc} St_c} \left(\frac{T_{aw} - T_{wg}}{T_{wc} - T_c} \right) \quad (10.74)$$

From the heat conduction equation through the wall, we express

$$T_{wc} = T_{wg} - \frac{\dot{Q} \cdot t_w}{A_w k_w} = T_{wg} - \left(\frac{t_w}{k_w} \right) \left(\frac{A_g}{A_w} \right) \rho_g u_g c_{pg} St_g (T_{aw} - T_{wg}) \quad (10.75)$$

We note that the gas flow area is proportional to the blade passage spacing s and the wall area of the blade is proportional to twice the blade chord $2c$; therefore, the area ratio of the gas to blade is nearly the inverse of twice the solidity, $1/2\sigma$, that is,

$$T_{wc} = T_{wg} - \left(\frac{t_w}{k_w} \right) \frac{1}{2\sigma} \rho_g u_g c_{pg} St_g (T_{aw} - T_{wg}) \quad (10.76)$$

We may also cast the gas mass density, that is, $\rho_g u_g$, in terms of the pressure, temperature, and Mach number of the gas following continuity equation

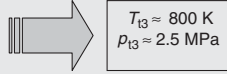
$$\rho_g u_g = \frac{\dot{m}_g}{A_g} = \sqrt{\frac{\gamma_g}{R_g}} \frac{p_{tg}}{\sqrt{T_{tg}}} M_g \left(1 + \frac{\gamma - 1}{2} M_g^2 \right)^{-\frac{\gamma+1}{2(\gamma-1)}} \quad (10.77)$$

We recognize that the gas total pressure (in the high-pressure turbine) is $\sim p_{t4} \sim p_{t3} = \sim p_{t2} \cdot \pi_c$. The gas total temperature is $\sim T_{t4}$. The average gas Mach number is ~ 0.75 . Therefore, we may substitute these parameters from our cycle analysis to estimate the coolant mass fraction in a high-pressure turbine. The example 10.6 highlights the method for estimating the coolant fraction.

EXAMPLE 10.6

Let us consider a gas turbine engine with the following cycle parameters at the sea level static condition, i.e., take-off

$$\begin{aligned} T_0 &= 288 \text{ K} \\ p_0 &= 100 \text{ kPa} \\ \gamma &= 1.4, c_{pc} = 1004.5 \text{ J/kg}\cdot\text{K} \\ \pi_c &= 25, e_c = 0.90 \\ T_{t4} &= 2000 \text{ K} \\ \gamma_g &= 1.33, c_{pg} = 1188 \text{ J/kg}\cdot\text{K} \end{aligned}$$



$$\begin{aligned} T_{t3} &\approx 800 \text{ K} \\ p_{t3} &\approx 2.5 \text{ MPa} \end{aligned}$$

Therefore, assuming the gas-side Stanton number is $St_g \approx 0.005$, the adiabatic wall temperature is nearly the gas stagnation temperature, i.e., $T_{aw} = 2000 \text{ K}$, the gas total pressure is nearly the compressor discharge total pressure, $p_{t3} \approx 2.5 \text{ MPa}$, and the desired gas-side wall temperature is $T_{wg} = 1200 \text{ K}$, the thickness of the internally cooled wall is $\sim 2 \text{ mm}$, the blade mean solidity in the HPT is ~ 2 , the ther-

mal conductivity of nickel-based alloy is $k_w = 14.9 \text{ W/m}\cdot\text{K}$, we get

$$T_{wc} \cong T_{wg} - 330 = 870 \text{ K}$$

$$\frac{1}{\varepsilon} = \left(\frac{1.0045}{1.188} \right) \frac{St_c}{St_g} \left(\frac{870 - 800}{2000 - 1200} \right) \cong 0.074 \frac{St_c}{St_g}$$

For a cooling passage to the gas-side Stanton number ratio of $St_c/St_g \sim 1/2$, we estimate the cooling fraction for the first blade row in a HPT, to be:

$$\frac{1}{\varepsilon} \approx \frac{0.074}{2} = 0.037, \quad \therefore \varepsilon \approx 26.4$$

This level of ε is impractical and points to the inadequacy of purely internal cooling in modern HPT nozzles.

Now, let us address some of the assumptions and uncertainties that entered our coolant fraction estimation. First, the cooling passage modeling with the roughness elements and turbulators (as in pins and ribs), which is also rotating (as in a rotor), is a complex matter and very difficult. It does not lend itself to a simple “rough pipe” modeling approach. Therefore, our assumed ratio of the coolant-to-gas side Stanton number of half is purely an estimate. In our heat flow balance from the gas to the coolant, we neglected the heat transfer (through conduction) to the disk as well as radiation heat transfer. This may impact the heat flux by upward of 5%. Also, the Stanton number is in general a function of the Prandtl number, Mach number, surface roughness, and rotation parameter, that is,

$$St = f(Re_x, Pr, M, \text{roughness}, \text{rotation}) \quad (10.78)$$

which we did not include in our estimation. Most convective heat transfer correlations have their origin in flat plate studies and thus are in the form of

$$St = \text{constant} Pr^{-n} \cdot Re_x^{-m} \quad (10.79)$$

An example is the Eckert-Livingood (1953) correlation (subscript “g” stands for the gas) for a turbulent boundary layer on a flat plate with constant wall temperature

$$St_g = 0.0296 Pr_g^{-2/3} Re_x^{-1/5} \quad (10.80a)$$

and for a laminar boundary layer on a flat plate with constant wall temperature

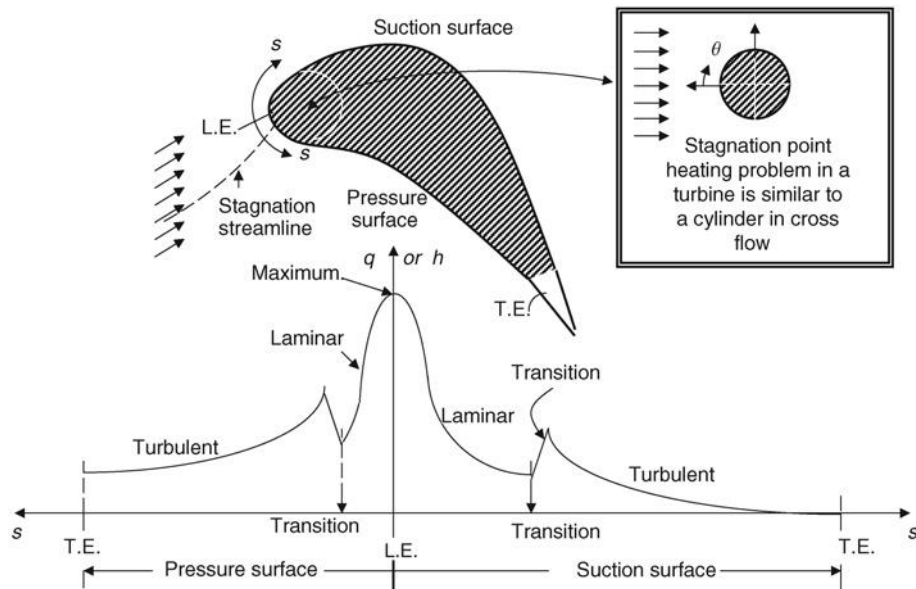
$$St_g = 0.332 Pr_g^{-2/3} Re_x^{-1/2} \quad (10.80b)$$

The blade leading edge, or stagnation point heating, is modeled as a cylinder in cross-flow. We will discuss a suitable correlation for leading-edge heating/cooling in the next section. In addition, blade rotation has a strong influence on the turbine blade heat transfer and thus deserves special attention. There are specialized heat transfer texts and reference books that should be consulted for accurate correlations of heat transfer functions of the type expressed in Equation 10.78. Eckert (1971), Rohsenow, Hartnett, and Cho (1998), and Incropera-DeWitt (2001) are among the recommended references.

10.2.4.2 Impingement Cooling. The turbine blade stagnation point, near the leading edge, represents the highest heat flux area of the blade. A typical heat flux distribution on a turbine blade (for a given free-stream turbulence intensity) is presented in Figure 10.41. “s” is a natural coordinate measuring the surface length from the leading edge on the suction and pressure surfaces. Due to longer length of the suction surface, as compared with the pressure surface, and a different location of the transition point on the two sides of the blade, the heat flux graph looks lob-sided.

An important observation (from Figure 10.41) is that the highest heat flux occurs at the leading edge, or the stagnation point heating in a turbine blade is the most critical. The second message is the rapid rise of heat transfer due to boundary layer transition from laminar to turbulent. The third observation is the *curvature switch* from convex to concave on the suction and pressure surfaces, respectively, thus affecting the transition point on the blade. In the theory of curved viscous flows, a convex curvature has a stabilizing effect on the flow, whereas a concave curvature has a destabilizing effect. The concave curvature case leads to the appearance of streamwise Goertler vortices that

■ **FIGURE 10.41**
Schematic drawing of heat flux q (or heat transfer coefficient h) distribution on an uncooled turbine blade (for a free-stream turbulence intensity)



cause an enhanced mixing of the flow at the surface. The free-stream turbulence intensity Tu also enhances the heat transfer to a surface in two ways; (1) it promotes earlier transition and (2) it enhances mixing at the surface. An accepted correlation for leading-edge heat transfer finds its roots in a cylinder in cross flow problem (Colladay, 1975), which is

$$h_{g,le} = a \left[1.14 \frac{k_g}{D} Re_D^{1/2} Pr^{0.4} \left(1 - \left| \frac{\Phi}{90} \right|^3 \right) \right] \quad -80^\circ < \Phi < 80^\circ \quad (10.81)$$

where

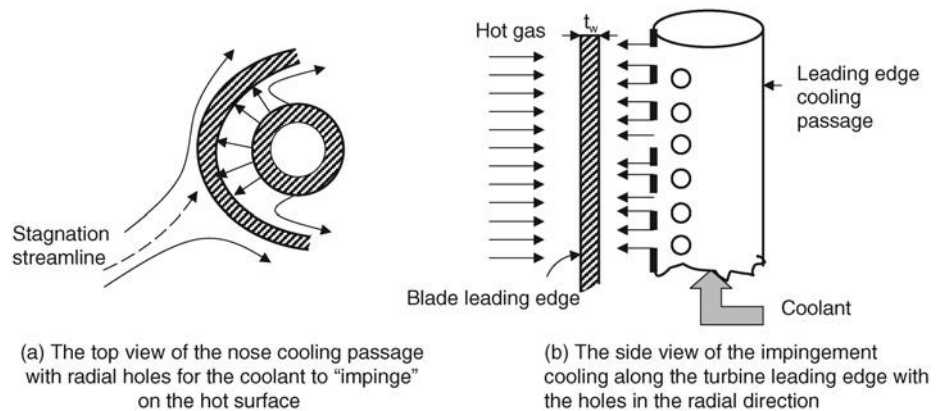
- a augmentation factor (from 1.2 to 1.8, based on free-stream turbulence)
- D diameter of leading-edge circle
- Φ angular distance from the leading-edge stagnation point, in degrees

To effectively cool the leading edge of a turbine blade, the internal cooling passage at the nose “showers” the leading edge with the coolant through a series of holes, as shown in Figure 10.42. Since the angle of impact between the coolant and the surface is nearly normal, the name “impingement” is attributed to this type of cooling. Some of the coolant that enters the leading-edge channel may discharge through the blade tip or it may be confined to within the blade. The example shown in Figure 10.42b has sealed off the nose channel exit, thus the entire coolant is used in the impingement cooling of the blade leading edge. To study heat transfer correlations with impingement cooling, Kercher and Tabakoff (1970) may be consulted.

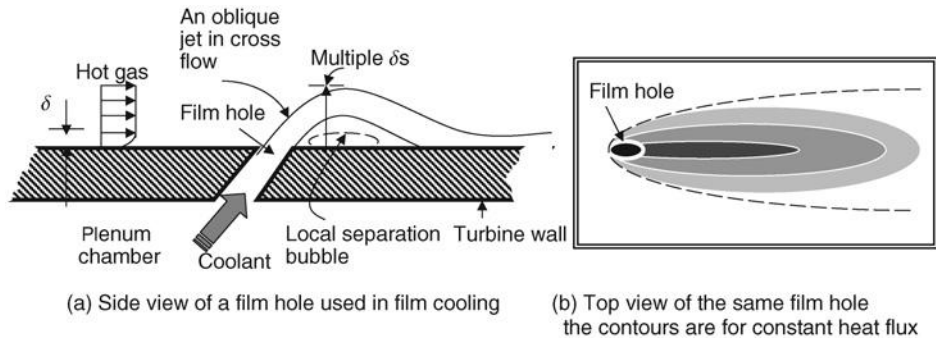
10.2.4.3 Film Cooling. The most critical areas of a turbine blade may be film cooled through a row of film-cooling holes. The coolant is ejected through a hole at an angle with respect to the flow, which in turn bend and cover a portion of the surface with a “blanket” of coolant.

Figure 10.43a shows a slanted jet emerging from a surface at an angle. Note the scale of the gas boundary layer thickness δ as depicted in Figure 10.43a, and compare it to the penetration of the coolant jet in the hot gas flow. The coolant jet penetrates the hot gas free stream (i.e., inviscid core) and is deflected by the external forces in the free

■ **FIGURE 10.42**
Schematic drawing of an impingement cooling scheme suitable for the leading edge of a turbine blade



■ **FIGURE 10.43**
Coolant ejection from
a film hole on a turbine
blade

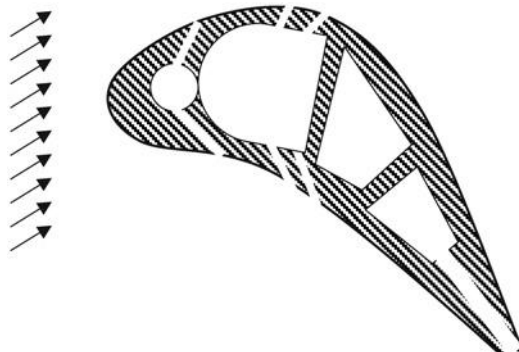


stream. The penetration of the slanted film columns in the free stream and the associated local flow separation immediately downstream of the film hole causes the profile drag of turbine blades to increase. Therefore, the film cooling of turbine blades is more disruptive to the external aerodynamics of the blades, as compared with internal cooling scheme. The contours of constant heat flux are shown in Figure 10.43b.

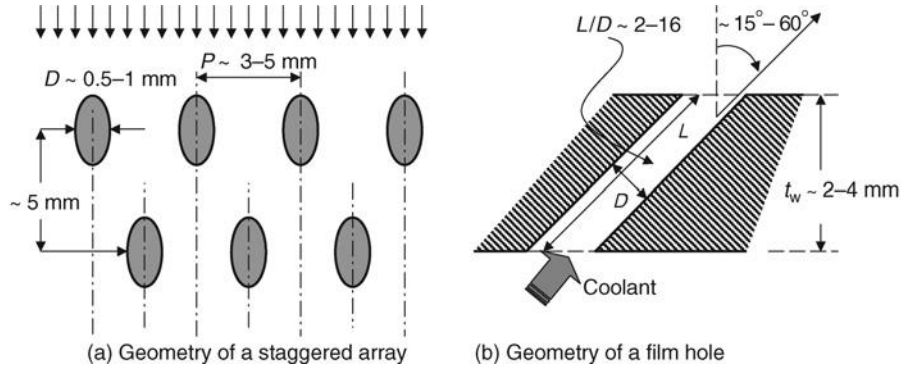
The cooling effect of the ejected jet that emerges from the film hole covers only a small region in the immediate vicinity of the ejection hole. For this reason, practical film cooling in gas turbines involves numerous film holes in one or multiple (staggered) rows to cover a significant portion of a surface. Figure 10.45 shows a staggered array of two rows of film holes with *typical* length scales, that is, hole diameter D and spacing (or pitch P) that are noted on the graph.

The diameter of the film holes range $\sim 0.5\text{--}1$ mm. Although it is possible to reduce the film-hole diameter to below 0.5 mm using advanced manufacturing techniques (e.g., using electron beam), in practice such small holes are prone to clogging, especially in the gas turbine environment. The products of combustion include particulates and by-products that *cling* to surface and clog the film holes. It is intuitively expected that the nondimensional pitch-to-diameter ratio of the film hole P/D to be an important parameter in heat transfer, thus film-cooling effectiveness. Also, the length-to-diameter ratio L/D for the film hole is important in the lateral spread of the film, and the size of the local separation bubble immediately downstream of the film hole. To add to the complexity of the film cooling, we note that the shape of the coolant plenum chamber

■ **FIGURE 10.44**
Schematic drawing of a
film-cooled turbine
blade (with six film
holes)



■ **FIGURE 10.45**
Definition sketch used
in film cooling and
some typical scales



also impacts the coolant jet velocity distribution and its mixing with the free stream and thus important to the film-cooling effectiveness. A specialized reference on the fundamentals of film cooling and gas turbine heat transfer is the von Karman Lecture Series (VKI-LS 1982).

A film-cooling effectiveness parameter η_f may be defined as

$$\eta_f \equiv \frac{T_g - T_{aw-f}}{T_g - T_c} \quad (10.82)$$

where the only new temperature in the equation, that is, T_{aw-f} , is the adiabatic wall temperature in the presence of the film and excluding other cooling effects. Note that the true adiabatic wall temperature with film cooling, T_{aw-f} , is a very difficult parameter to measure. Therefore, it is possible (and preferable) to define a film-cooling effectiveness parameter that utilizes a different and more easily measured temperature in the experiment, for example, the actual wall temperature, in the presence of film cooling. The Stanton number for a film-cooled blade involves an additional “blowing parameter” M_b with typical values for low and high blowing rates are 0.5 and 1.0, respectively. The blowing parameter is defined as

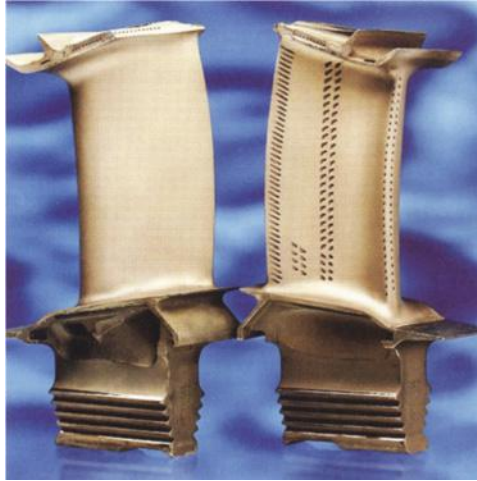
$$M_b \equiv \frac{\rho_c u_c}{\rho_g u_g} \quad (10.83)$$

Considering all of the arguments presented above, we expect the functional form of the Stanton number for a film-cooled surface (or film-cooling effectiveness) to be represented by (at least) the following parameters:

$$St = f(\text{Re}_x, \text{Pr}, M, M_b, \frac{P}{D}, \frac{L}{D}, \text{Tu, roughness, rotation, plenum - geometry}) \quad (10.84)$$

Research on film-cooling effectiveness is actively pursued in the laboratory and in the computational field. The NASA-Glenn Research Center conducts film-cooling research in-house, works with universities as collaborators as well as industry. Its website (www.nasa.gov/centers/glenn/home/index.html) should be used as a resource for the

■ **FIGURE 10.46**
Film-cooled rotor blades in high-pressure turbine. Source: Reproduced with permission from Rolls-Royce plc

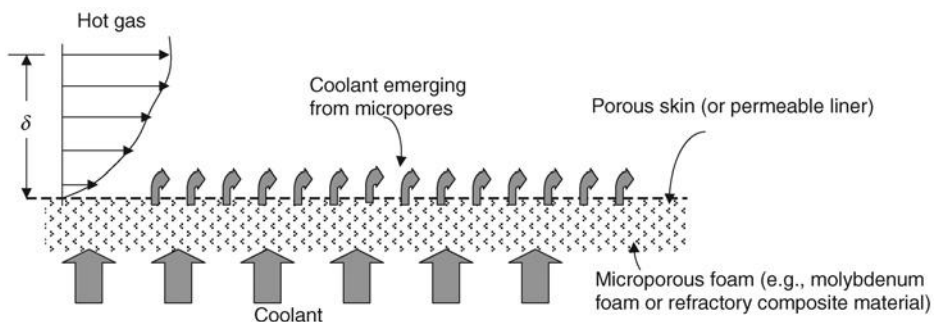


latest research in aircraft gas turbine engines. Figure 10.46 shows an advanced film-cooled rotor blade in a high-pressure turbine (courtesy of Rolls-Royce, plc.)

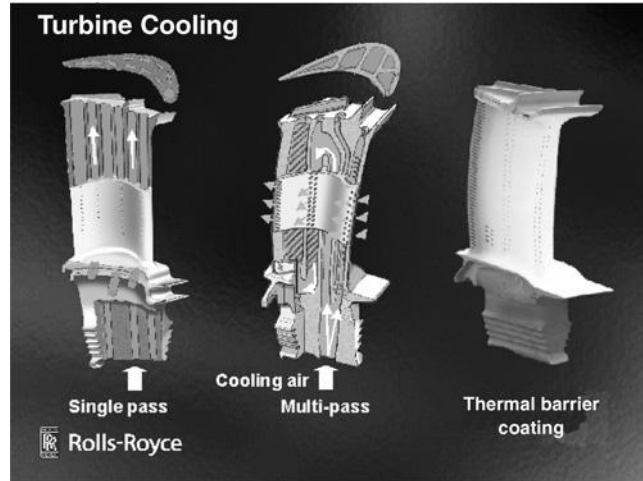
10.2.4.4 Transpiration Cooling. The coolant may emerge from very small pores ($\sim 10\text{--}100\ \mu\text{m}$) of a porous surface and thus be embedded entirely within the viscous boundary layer of the gas turbine blade. This is analogous to human perspiration as a means of cooling and is known as *transpiration cooling*. The technique involves pumping a coolant through microporous foam, which is bonded to a porous outer skin, as shown in Figure 10.47.

The appeal of transpiration cooling is in its effectiveness with minimal coolant mass flux requirement (Wang, Messner, and Stetter, 2004). The disadvantage of the scheme is in its impracticality of keeping the micropores unclogged in a gas turbine environment. Other material characteristics such as oxidation resistance, material life, and manufacturing costs all impact the practicality of transpiration cooling for an aircraft gas turbine engine. From fluid mechanics point of view, the static pressure drop across the porous foam is large (per unit mass flux); hence, the pressurized coolant requirement is more stringent for a transpiration-cooled surface as compared with film cooling. Figure 10.48 shows different cooling schemes from Rolls-Royce.

■ **FIGURE 10.47**
Definition sketch for the transpiration cooling scheme

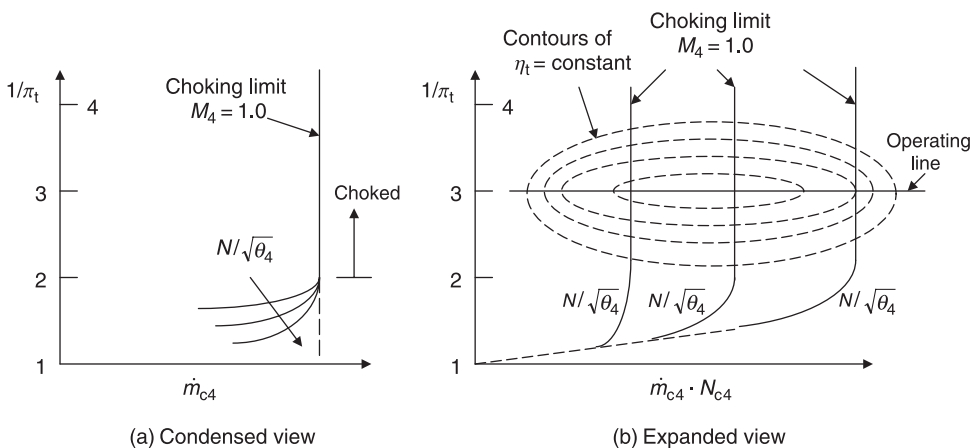


■ **FIGURE 10.48**
Turbine cooling
schemes from
Rolls-Royce. Source:
Reproduced with
permission from
Rolls-Royce plc



10.3 Turbine Performance Map

As demonstrated in the earlier part of this chapter, the performance of a turbomachinery stage is fully determined by two parameters; (1) the axial Mach number or equivalently the corrected mass flow rate and (2) the tangential blade Mach number, or equivalently the corrected shaft speed. The turbine performance map is thus a graph of $1/\pi_t$ versus the corrected mass flow rate \dot{m}_{c4} for the corrected shaft speeds N_{c4} . Typical turbine performance maps are shown in Figure 10.49. In Figure 10.49a, the choking limit (i.e., $M_4 = 1.0$) is approached with the increase in corrected shaft speed. In Figure 10.49b, however, we may graph the product of the corrected mass flow rate and the corrected shaft speed in order to (graphically) separate the individual choking limits. In addition, the contours of constant turbine adiabatic efficiency are superimposed (dashed lines).



■ **FIGURE 10.49** Typical turbine performance map

10.4 The Effect of Cooling on Turbine Efficiency

The impact of cooling on turbine efficiency may be attributed to the following effects:

1. The coolant mass flow rate does not participate in turbine power production; therefore, per 1% cooling fraction there is ~1% loss in power production (due to loss of working fluid)
2. The coolant injection in the hot gas stream causes mixing losses of two streams as well as an increase in profile drag loss on the blades (for disruption of flow on the blades, as in film holes)
3. The coolant suffers a total pressure drop inside the cooling passages due to friction, turbulators, pins, and other roughness elements inside the cooled turbine blades. The reduced total pressure on the part of the coolant then causes the stage total pressure ratio π_t to drop
4. The heat transfer between the hot gas and the coolant causes an entropy rise for the mixed-out gas.

The turbine efficiency may be defined as the ratio of actual turbine work per total airflow (that includes the coolant fraction) and the ideal turbine work, achieved isentropically, across the actual turbine expansion, $(p_{t5}/p_{t4})_{\text{actual}}$.

The actual turbine work (per unit mass flow) for the two streams is the sum of individual streams reaching the same exit total temperature T_{t5}

$$w_{t,\text{actual}} = (1 - \varepsilon)c_{pt}(T_{t4} - T_{t5}) + \varepsilon c_{pc}(T_{tc} - T_{t5}) \quad (10.85)$$

The ideal (i.e., isentropic) turbine work for the two streams expanding through the actual pressure ratio is

$$w_{t,\text{ideal}} = (1 - \varepsilon)c_{pt}T_{t4} \left[1 - (p_{t5}/p_{t4})^{(\gamma_t-1)/\gamma_t} \right] + \varepsilon c_{pc}T_{tc} \left[1 - (p_{t5}/p_{t4})^{(\gamma_t-1)/\gamma_t} \right] \quad (10.86)$$

Therefore, the cooled turbine efficiency may be written as

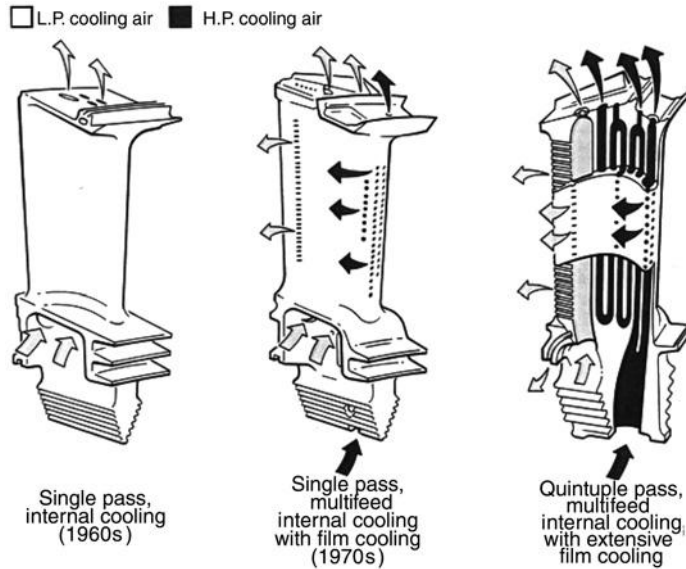
$$\eta_t = \frac{(1 - \varepsilon)c_{pt}(T_{t4} - T_{t5}) + \varepsilon c_{pc}(T_{tc} - T_{t5})}{\left[(1 - \varepsilon)c_{pt}T_{t4} + \varepsilon c_{pc}T_{tc} \right] \left[1 - (p_{t5}/p_{t4})^{(\gamma_t-1)/\gamma_t} \right]} \quad (10.87)$$

Kerrebrock (1992) shows that turbine efficiency in Equation 10.87 may be approximated by

$$\eta_t \approx 1 - \left(\frac{\tau_t}{1 - \tau_t} \right) \left[2\sigma \text{St} \left(\frac{T_{t4}}{T_{tc}} - 1 \right) \left(1 - \frac{T_w}{T_{t4}} \right) + \left(\frac{\gamma}{\gamma - 1} \right) \varepsilon \left(\frac{\Delta p_f}{p_{t4}} \right) \right] \quad (10.88)$$

Where σ is the blade solidity, Stanton number is St, and Δp_f is the total pressure loss due to friction inside the blade cooling passages. Kerrebrock estimates the loss of turbine efficiency to be ~2.7% per percent of cooling flow for a typical gas turbine, based on Equation 10.88. Accounting for other sources of loss as in kinetic energy loss in film-cooled blades, Kerrebrock estimates an additional 1/2% to be added to the 2.7% to get an estimated 3.2% turbine efficiency loss per percent of cooling flow. More experimental

■ **FIGURE 10.50**
The evolution of
turbine blade cooling.
Source: Reproduced
with permission from
Rolls-Royce plc

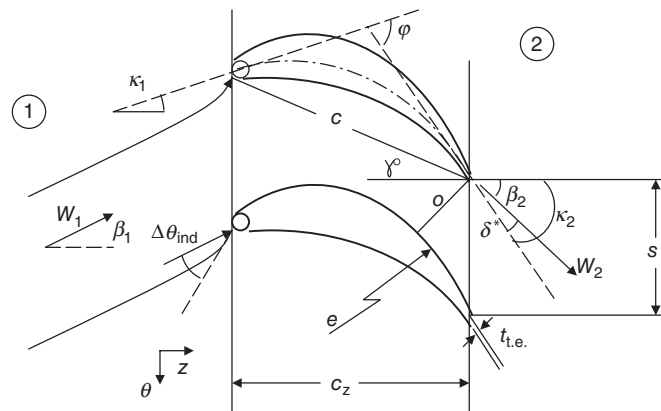


data and validation are needed to cover a wide array of internal cooling configurations and internal/external loss estimation. Figure 10.50 shows the evolution of turbine blade cooling (courtesy of Rolls-Royce plc, 2005).

10.5 Turbine Blade Profile Design

A definition sketch of a turbine cascade is shown in Figure 10.51. The basic parameters are the same as the compressor cascade. For example, the net flow turning is the difference between the inlet and exit flow angles (β_1 and β_2), or the camber angle (φ) is defined as the sum of the angles of the tangent to the mean camber line at the leading and trailing edge (κ_1 and κ_2). Also note that the deviation angle is the flow angle beyond the tangent to the mean camber line at the trailing edge (δ^*). The blade setting or stagger angle is

■ **FIGURE 10.51**
Definition sketch of a
turbine cascade



defined the same way as in a compressor cascade γ° . The blade chord and spacing are the same as c and s , respectively. Now, let us examine some of the distinguishing features in a turbine cascade, such as an inlet induced flow angle $\Delta\theta_{\text{ind}}$, or throat opening σ , or the suction surface curvature e , downstream of the throat, and finally the trailing-edge thickness $t_{\text{t.e}}$.

10.5.1 Angles

In order to construct a suitable turbine blade profile, we need to estimate the inlet and exit blade angles and their relation to the actual incidence and deviation angles. The incidence angle in a turbine cascade accounts for the flow curvature near the leading edge, called the *induced turning*, $\Delta\theta_{\text{ind}}$ and is called *actual incidence* i_{ac} . The correlation between the induced angle, inlet flow angle, and blade solidity is (from Wilson and Korakianitis, 1998)

$$\Delta\theta_{\text{ind}} = 14 \left(1 - \frac{\beta_1}{70^\circ} \right) + 9(1.8 - \sigma) \quad 0 \leq \beta_1 \leq 70^\circ \quad (10.89)$$

The actual incidence and flow angles are corrected by the induced angle according to

$$i_{\text{ac}} = i + \Delta\theta_{\text{ind}} \quad (10.90)$$

$$\beta_{\text{ac}} = \beta_1 + \Delta\theta_{\text{ind}} \quad (10.91)$$

The flow and turbine blade angles at the leading edge follow the same relation as the compressor, that is,

$$i = \beta_1 - \kappa_1 \quad (10.92)$$

The deviation angle is also important to the turbine profile design, as it *adds* to the blade camber, and if it is underpredicted, the exit swirl will be less than the design value and thus blade torque and in case of rotor, power, will be less than expected. Carter’s rule for deviation angle in a turbine, although not the most accurate, is adequate for the preliminary design purposes,

$$\delta^* = \frac{m\Delta\varphi}{\sigma} \approx \frac{\Delta\varphi}{8\sigma} \approx \frac{\Delta\beta}{8\sigma} \quad (10.93)$$

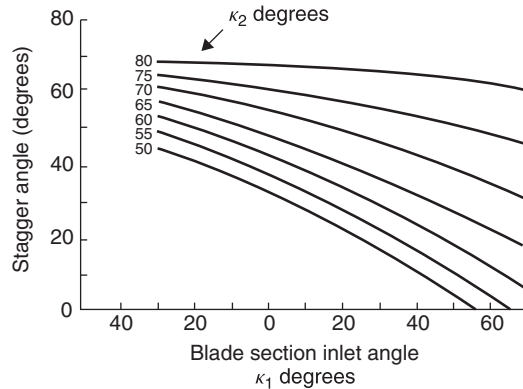
Stagger, or blade setting, angle is critical to the *smoothness* of turbine flow passage (area distribution) design. The simple approximation equates the stagger to the mean flow angle in a blade row, that is,

$$\gamma^\circ \approx \beta_m \approx \tan^{-1}(W_{\theta m}/C_z) \quad (\text{rotor}) \quad (10.94a)$$

$$\gamma^\circ \approx \alpha_m \approx \tan^{-1}(C_{\theta m}/C_z) \quad (\text{nozzle}) \quad (10.94b)$$

A more accurate determination of the stagger angle, based on the blade leading and trailing-edge angles, κ_1 and κ_2 is shown in Figure 10.52 (from Kacker and Okapuu, 1981).

■ **FIGURE 10.52**
Turbine blades stagger
in relation to blade
leading and
trailing-edge angles.
Source: Kacker and
Okapuu 1981.
Reproduced with
permission from
ASME



10.5.2 Other Blade Geometrical Parameters

Conventional turbine blade passages have their throat at the exit, as shown in Figure 10.51. It is desirable to expand the flow beyond the throat on the suction surface, that is, provide a convex curvature beyond the throat. This geometrical feature is advantageous to favorable pressure gradient and thus smaller deviation angle. The nondimensional radius of curvature s/e characterizes the convex curvature. The upper value for the convex curvature parameter s/e is 0.75 with typical range corresponding to $0.25 \leq s/e \leq 0.625$. Also note that the pressure surface at the trailing edge assumes a concave curvature of radius $\sim (e + o)$.

In a turbine, the blade leading-edge radius $r_{l.e.}$ is critical to effective cooling and thus blade life. The value of nondimensional leading-edge radius $r_{l.e.}/s$ is between 0.05 and 0.10.

The trailing-edge thickness, $t_{t.e.}$, in a turbine is finite. The main reasons are structural integrity as well as trailing-edge coolant slots. The trailing-edge thickness adversely impacts the flow blockage and blade profile losses. Thus, we wish to minimize the trailing-edge thickness consistent with the blade structural and cooling requirements. The typical non-dimensional values of $t_{t.e.}/c$ fall between 0.015 and 0.05.

10.5.3 Throat Sizing

The throat sizing in a turbine nozzle (or rotor) is very important both for choked and unchoked nozzles. The geometry that is shown in the following definition sketch (Figure 10.53) is used to relate the throat width or opening o to the blade spacing s .

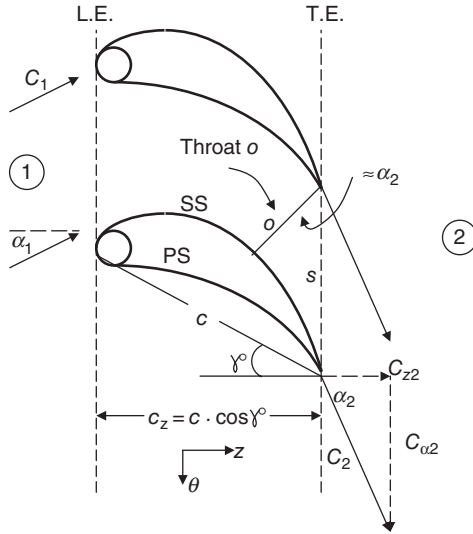
The throat opening o is related to the spacing and cosine of the exit flow angle α_2 in nozzle and β_2 in rotor, following

$$o \approx s \cdot \cos \alpha_2 \quad (10.95)$$

This approximation is acceptable for the subsonic exit flow, however, for the supersonic exit Mach numbers (but below 1.3), we correct the throat opening by the inverse of A/A^* corresponding to the supersonic exit Mach number, that is,

$$\frac{o}{s} \approx \frac{\cos \alpha_2}{(A/A^*)_{M_2}} \quad (10.96)$$

■ FIGURE 10.53
Definition sketch used
for a turbine nozzle
throat sizing



The design exit Mach number for the first turbine nozzle should slightly exceed 1, that is, $M_2 > 1$, and is commonly taken to be ~ 1.1 . The exit Mach numbers from the subsequent blades (in relative-to-blade frame of reference) in a turbine should remain below 1, that is, unchoked. For example, the design Mach number at the first rotor exit M_{3r} is chosen to be as high as 0.90, but never 1 or above. Also, all subsequent blades in a multistage turbine, on the same spool, remain unchoked. For multispool gas turbines, the first nozzle, on all spools, is choked and its design exit Mach number is ~ 1.1 .

10.5.4 Throat Reynolds Number Re_o

The throat Reynolds number should preferably be in the range of 10^5 – 10^6 . Experimental data demonstrate a strong correlation between blade profile loss and the throat Reynolds number. The definition of throat Reynolds number uses the relative exit flow velocity from the blade and the static conditions at the throat, that is,

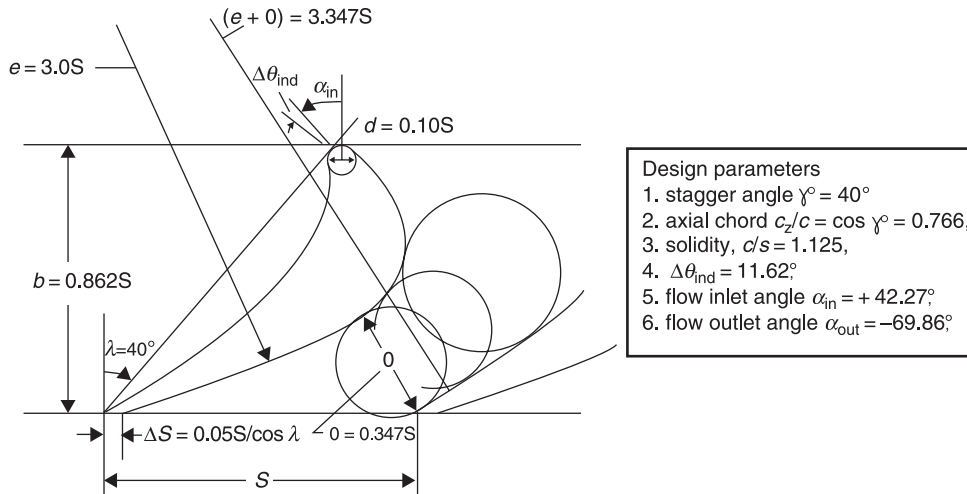
$$Re_o \equiv \rho_{th} C_2 o_n / \mu_{th} \quad (\text{Nozzle}) \quad 10^5 \leq Re_o \leq 10^6 \quad (10.97a)$$

$$Re_o \equiv \rho_{th} W_3 o_r / \mu_{th} \quad (\text{Rotor}) \quad 10^5 \leq Re_o \leq 10^6 \quad (10.97b)$$

The throat opening o is given a subscript n and r in the above definitions, to signify the nozzle and rotor throat openings, respectively.

10.5.5 Turbine Blade Profile Design

We have identified some definite structure for the turbine profile at and beyond the throat. For example, we have the throat opening o/s related to exit flow angle and Mach number, or we have a range for the trailing-edge thickness, also a curvature on the suction side and a curvature on the pressure side, all near the trailing edge. At the leading edge, we have some design guidelines for the leading-edge radius, and some correlations for the



■ **FIGURE 10.54** Example of a turbine blade profile design. Source: Wilson and Korakianitis 1998. Reproduced with permission from the authors

induced flow turning, besides the flow angles at the inlet and exit. The stagger angle is also estimated using Equation 10.94 or Figure 10.51.

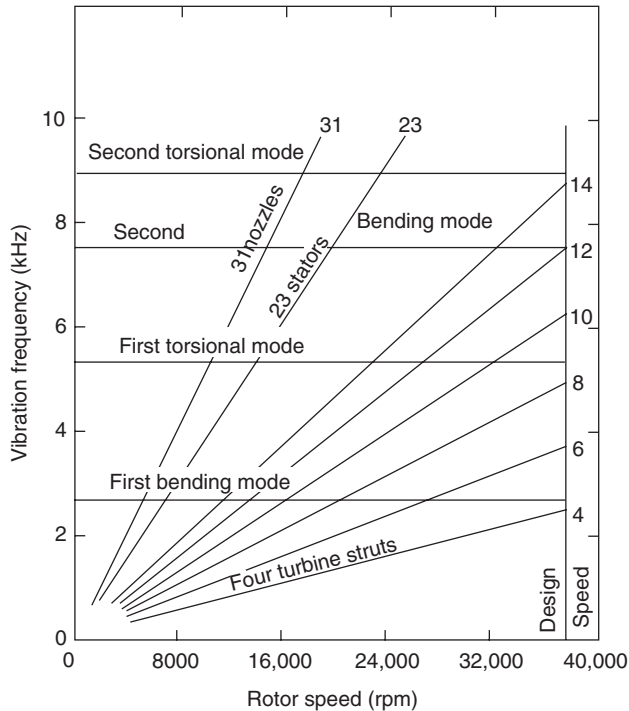
Once the trailing-edge passage beyond the throat is constructed and the leading-edge radius (or a range of radii) is chosen, the trial-and-error phase of curve fitting to the upper and lower surfaces begins. The goal is to produce a flow passage that *smoothly and uniformly* contracts to the throat section. Therefore, beyond the trailing-edge construction of the turbine blade profile, the rest of the approach deals with flow passage design (i.e., with a smooth area contraction).

Wilson and Korakianitis (1998) constructed the following turbine profile (Figure 10.54) based on the input shown in the box and the methodology of this section. Schobeiri (2004) also provides details in the construction of turbine profiles and is recommended for further reading.

10.5.6 Blade Vibration and Campbell Diagram

The Campbell diagram is of interest because it shows possible matches between blade vibrational mode frequency and multiples of shaft rotational speed. The multiples of shaft rotational speeds are caused by the struts and blades (wakes) in neighboring rows and they serve as the source of *excitation*. In essence, the blade passing frequency, which is the product of the number of blades times the shaft frequency, is the source of excitation for the blades in the next/previous row. Vibration frequency in kilohertz for the first two bending and the first two torsional modes is shown in Figure 10.55 (from Wilson and Korakianitis, 1998) to vary with rotor shaft speed (in rpm), due to the so-called stiffening effect that rotation has on a structure. The design shaft speed is also identified on the chart (to be $\sim 37,000$ rpm). The straight lines corresponding to multiple shaft speeds are drawn. The first or fundamental bending mode, known as the *first-flap* mode, has a natural frequency that lies between the fourth and sixth multiples of shaft rpm at design speed. Since the fifth multiple of shaft speed lies halfway between the fourth and sixth, we

■ **FIGURE 10.55**
Campbell frequency
diagram for a turbine
blade. Source: Wilson
and Korakianitis 1998.
Reproduced with
permission from the
authors



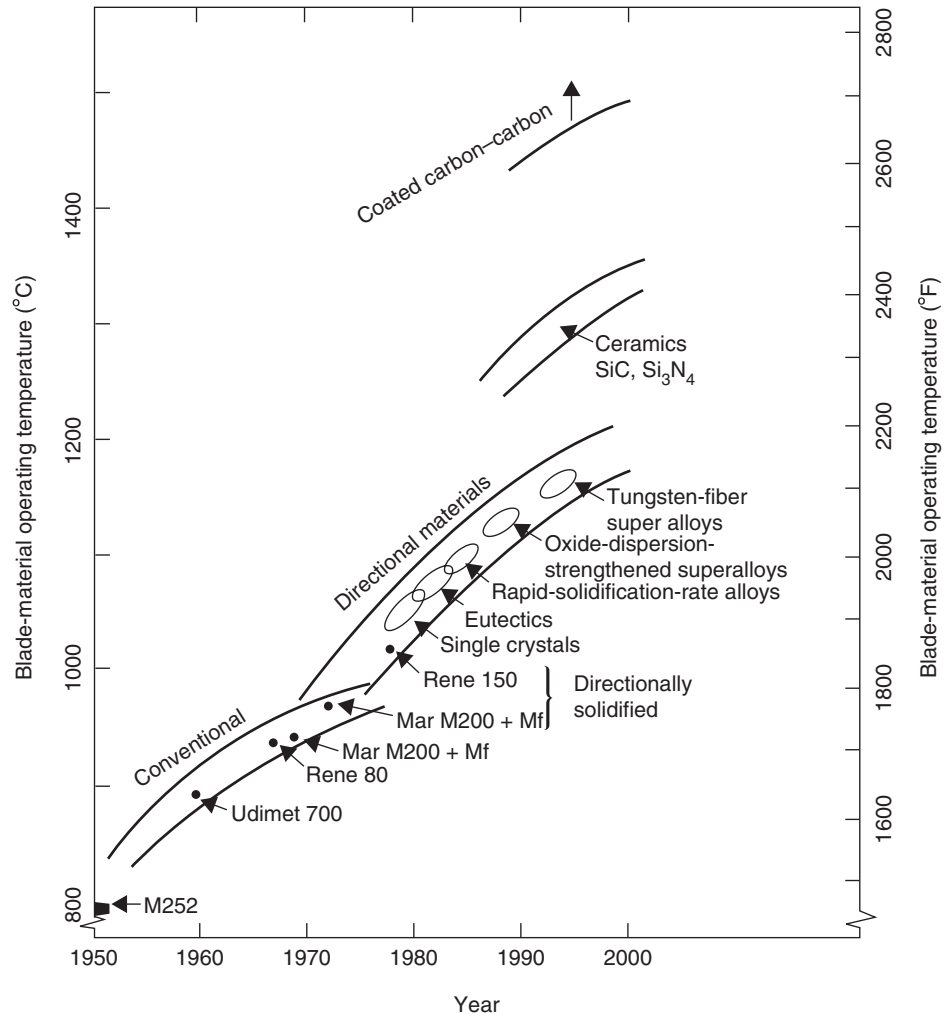
note that the first bending mode is below the fifth multiple of shaft speed at design rpm. Closer examination of Figure 10.54 also indicates that 4, 23, and 31 multiples of shaft speeds have a special significance in this turbine (rotor) blade row. These correspond to the number of struts and stator or nozzle blades that serve as the excitation source for the rotor through blade passing frequency of wakes and mutual interference effects of their rotating pressure fields.

The structural design of blades should clearly indicate a resonance-free operating condition at the design speed, idle speed, and other operational speeds where significant time is spent. However, it is impossible to avoid all resonant frequencies as we speed up to the design, or other operational shaft speeds. Therefore, spool-up speed/acceleration, or the spool-down speed/deceleration are important to the cyclic loads and fatigue life of blades, struts, disks, and other engine components.

10.5.7 Turbine Blade and Disk Material Selection and Design Criteria

Turbine blade and disk materials and the year of development are shown in Figure 10.56 (from Wilson and Korakianitis, 1998). These, by necessity, are high-temperature materials. Some have high thermal conductivity, as in nickel-based alloys for the blades and disks thermal stress alleviation, and some are low thermal conductivity materials, such as ceramics, that reduce heat transfer to the blades. All materials, especially for turbine blades, use a thermal protection coating to reduce the surface operating temperature and thus in effect increase component life.

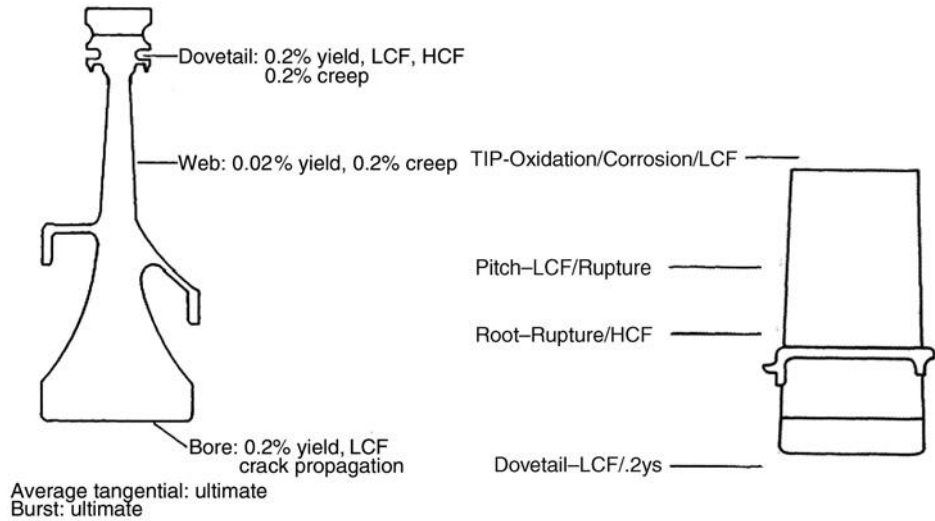
■ **FIGURE 10.56**
Turbine materials
development. Source:
Wilson and
Korakianitis 1998.
Reproduced with
permission from the
authors



There are four clusters of materials that are labeled in Figure 10.56. The *conventional* alloys exhibit the lowest operating temperature capability, whereas *directional materials* that include single crystals, rapid solidification rate alloys, oxide-dispersion-strengthened superalloys, and Tungsten-fiber superalloys achieve high temperature capability. The ceramics as in silicon carbide offer an additional tolerance to high temperature. The *coated carbon-carbon* composite material offers the highest temperature capability but the issues of cost, damage tolerance, inspectability, and reliability hamper its use in large operational gas turbine engines. The turbine design example at the end of this chapter uses a design blade surface temperature of 1400 K, which based on Figure 10.56 implies the use of directionally solidified material.

Different parts of turbine blade and disk are subject to different mechanical design criteria, as shown in Figure 10.57 (from Wilson and Korakianitis, 1998). Mechanical designs of turbine components address low- and high-cycle fatigue, oxidation/corrosion, and creep rupture problems.

■ **FIGURE 10.57**
 Different design criteria for turbine blade and disk (LCF: low-cycle fatigue HCF: high-cycle fatigue, YS: yield strength). Source: Wilson and Korakianitis 1998. Reproduced with permission from the authors



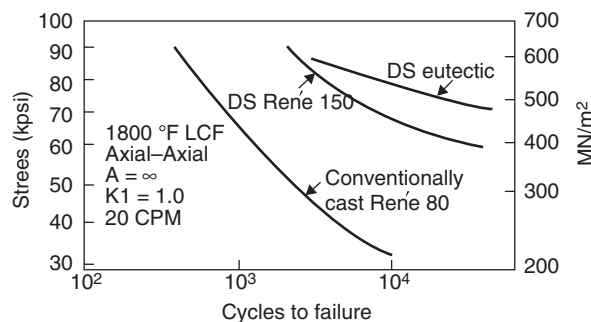
The number of cycles to failure for conventionally cast and directionally solidified material shows the fatigue strength of Rene 80, directionally solidified Rene 150, and directionally solidified Eutectic material (that are typically used in turbine blades) in Figure 10.58 (from Wilson and Korakianitis, 1998). We note that directional solidification improves fatigue strength by a factor of 2 or 5 over conventionally cast Rene 80 as shown in Figure 10.58.

Another material characteristic of interest to turbine designers is the *creep rupture strength*. It is the maximum tensile stress that material tolerates without failure over a time period at a given temperature. The 0.2% creep design criterion is listed for the turbine disk web, blade slot in the hub, blade pitchline, and root. This 0.2% creep rupture strength is plotted for three materials that are used in turbine disks in Figure 10.59 (from Wilson and Korakianitis, 1998). The temperature (in Kelvin) and time (in hours) are combined in the Larson-Miller parameter on the abscissa of Figure 10.59. The Larson-Miller parameter is defined as

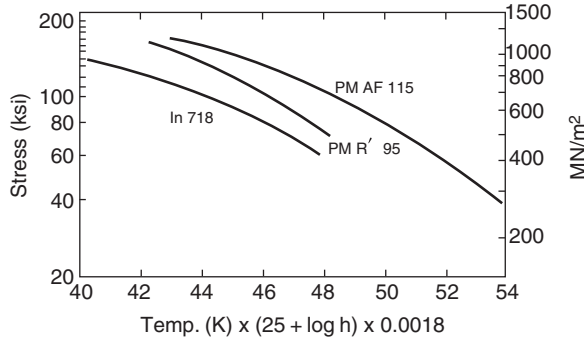
$$T(K) \cdot [C + \log t(\text{hours})] \tag{10.98}$$

Where C is constant for a material (in this case, 25).

■ **FIGURE 10.58**
 Fatigue strength of turbine blade material. Source: Wilson and Korakianitis 1998. Reproduced with permission from the authors



■ **FIGURE 10.59**
0.2% Creep strength of turbine disk alloys.
Source: Wilson and Korakianitis 1998.
Reproduced with permission from the authors



The treatment of the turbine material selection and design criteria in this section has been by necessity very brief. We have not even scratched the surface of the vast and specialized field of gas turbine high-temperature materials and mechanical design. The reader is to refer to specialized texts and references on the subject.

10.6 Stresses in Turbine Blades and Disks and Useful Life Estimation

Turbine blades and disks are subjected to centrifugal stresses due to shaft rotation as well as thermal stresses due to temperature differentials in the material due to cooling, gas bending stresses due to gas loads, and vibratory stresses due to cyclic loading and blade vibration. The centrifugal stresses take on the same form as the one developed in the compressor section.

The dominant stress in a rotor and disk is the centrifugal stress σ_c . At the blade hub, the ratio of the centrifugal force F_c to the blade area at the hub A_h is the centrifugal stress, σ_c ,

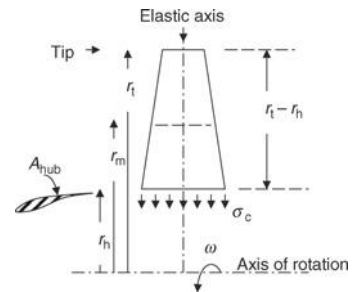
$$\sigma_c \equiv \frac{F_c}{A_{hub}} \tag{10.99}$$

$$F_c = \int_{r_h}^{r_t} \rho_{blade} \cdot A_b(r) \omega^2 r dr \tag{10.100}$$

$$\sigma_c = \frac{1}{A_h} \int_{r_h}^{r_t} \rho_{blade} \cdot A_b(r) \omega^2 r dr \tag{10.101}$$

$$\frac{\sigma_c}{\rho_{blade}} = \frac{\omega^2}{A_h} \int_{r_h}^{r_t} A_b(r) r dr = \omega^2 \int_{r_h}^{r_t} \frac{A_b}{A_h} r dr \tag{10.102}$$

$$\frac{\sigma_c}{\rho_{blade}} = \omega^2 \int_{r_h}^{r_t} \frac{A_b}{A_h} r dr \tag{10.103}$$



The blade area distribution along the span $A_b(r)/A_h$ is known as *taper* and is often approximated to be a linear function of the span. Therefore, it may be written as

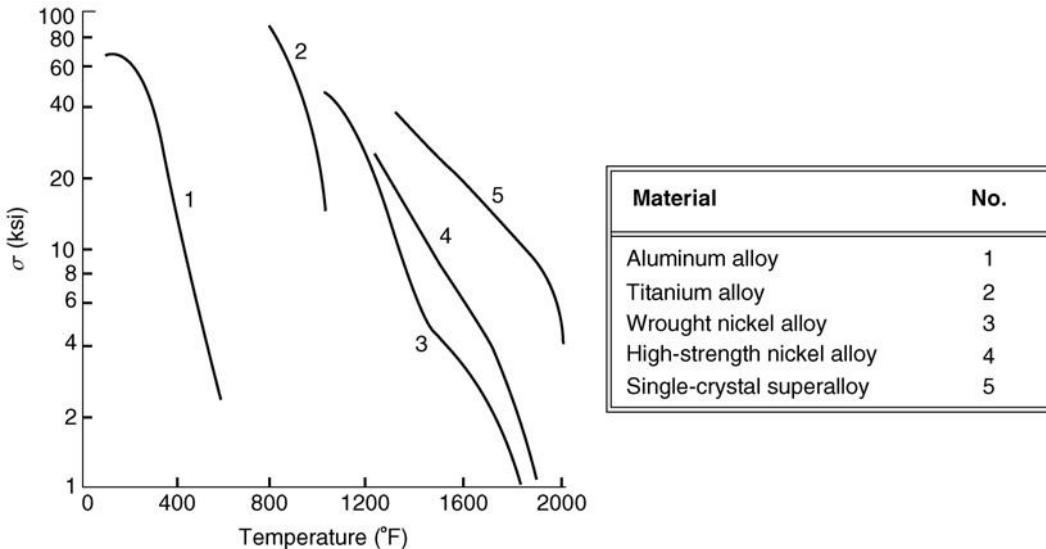
$$A_b = A_h - \frac{r - r_h}{r_t - r_h}(A_h - A_t) \implies \frac{A_b}{A_h} = 1 - \frac{r - r_h}{r_t - r_h} \left(1 - \frac{A_t}{A_h}\right) \quad (10.104)$$

We may substitute $A_b(r)/A$ in the integral and proceed to integrate; however, a customary approximation is often introduced that replaces the variable r by the pitchline radius r_m . The result is

$$\frac{\sigma_c}{\rho_{blade}} = \frac{\omega^2 A}{4\pi} \left(1 + \frac{A_t}{A_h}\right) \quad (10.105)$$

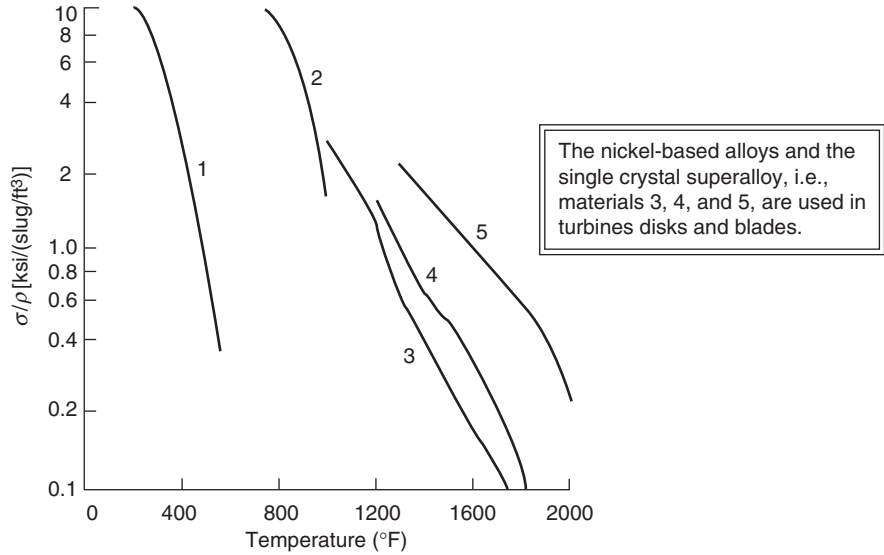
Therefore, the ratio of centrifugal stress to the material density is related to the square of the angular speed, the taper ratio, and the flow area, $A = 2\pi r_m(r_t - r_h)$. This equation is the basis of the so-called AN^2 rule, that is, where A is the flow area and N is the shaft angular speed, often expressed in the customary unit of rpm. The right-hand side of Equation 10.105 incorporates turbomachinery size (throughflow area) and the impact of angular speed, whereas the left-hand side of Equation 10.105 is a material property known as the (tensile) specific strength.

The material parameter of interest in a rotor is the *creep rupture strength*, which identifies the maximum tensile stress tolerated by the material for a given period of time at a specified operating temperature. Based on the 80% value of the allowable 0.2% creep in 1000 h, for aluminum alloys and the 50% value of the allowable 0.1% creep in 1000 h for other materials, Mattingly, Heiser, and Pratt [28] have graphed Figures 10.60 and 10.61. They show the allowable stress and the allowable specific strength of different



■ FIGURE 10.60 Allowable stress versus temperature for typical engine materials. Source: Mattingly, Heiser, and Pratt 2002. Reproduced with permission from AIAA

■ **FIGURE 10.61**
 Allowable strength-to-weight ratio for typical engine materials. Source: Mattingly, Heiser, and Pratt 2002. Reproduced with permission from AIAA



engine materials as a function of temperature. Note that the unit of stress in the following two figures is ksi, which is 1000 lb per square inch (i.e., 1000 psi) and the temperatures are expressed in degree Fahrenheit.

Thermal stresses are calculated based on thermal strains that are set up in a material with differential temperature ΔT from

$$\epsilon_t = \alpha \Delta T \tag{10.106}$$

where ϵ_t is thermal strain (i.e., elongation per unit length) and α is the coefficient of (linear) thermal expansion, which is a material property. The linear stress–strain relationship demands

$$\sigma_t = E \epsilon_t = \alpha E \Delta T \tag{10.107}$$

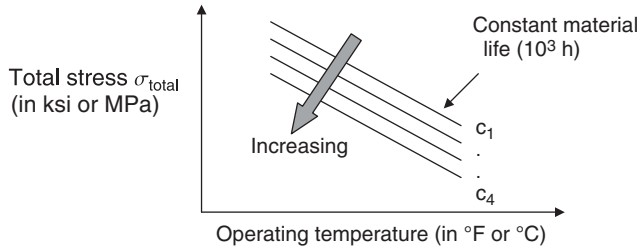
where E is the modulus of elasticity. The thermal stresses in a disk of constant thickness with no center hole and with the radius r_h is a simple model of a turbine disk. If the disk has a linear temperature distribution in the radial direction, the thermal stresses in radial and tangential directions are shown (by Mattingly, Heiser, and Pratt, 2002) to be

$$\sigma_{tr} = \frac{\alpha E \Delta T}{3} \left(1 - \frac{r}{r_h} \right) \tag{10.108a}$$

$$\sigma_{t\theta} = \frac{\alpha E \Delta T}{3} \left(1 - 2 \frac{r}{r_h} \right) \tag{10.108b}$$

The maximum of both stresses occur at the center of the disk, that is, $r = 0$, and for typical values of coefficient of thermal expansion of nickel-based alloys, $\alpha \sim 10.2 \times 10^{-6}$ in/in.°F at 1400 °F (that corresponds to gas turbine temperatures), as well as the modulus of elasticity E for nickel alloys (at 1400 °F) is $\sim 20.5 \times 10^6$ psi, which for a 100 °F temperature differential gives thermal stresses in the radial and tangential directions of

■ **FIGURE 10.62**
Material (useful) life curves



about ~ 6970 psi (equivalent to 1011 kPa). This example illustrates the need for special attention to the thermal stresses in turbine disks and material property that is of utmost interest is the thermal conductivity. The transient operations of the gas turbine that expose the turbine disk to high temperatures at the rim while the center of the disk is still at a low temperature pose the highest levels of thermal stress. Nickel alloys have the highest levels of thermal conductivity, in metals, at high temperatures, which are suitable for use in turbine disks and blades.

The total stress in the material, σ_{total} , which is the sum of the centrifugal, bending (i.e., gas loads), thermal and vibratory stresses, and the material operating temperature combine to estimate material (useful) life. There are stress–temperature–material life curves, for a variety of materials, in gas turbine industrial practice. Figure 10.62 shows an example of a family of stress–temperature–life curves for any given material, for example, nickel alloys.

10.7 Axial-Flow Turbine Design and Practices

In this section, we apply some of the concepts that we learned in the chapter to the preliminary design of a cooled gas turbine. The approach to turbine design is as varied and diverse as the textbooks written on the subject. Therefore, there is no *unique* approach to turbine design, rather the author’s preference in applying a set of guidelines to turbine design.

EXAMPLE 10.7

We intend to design an axial-flow turbine to drive a particular compressor (or other external loads, such as an electric generator. Therefore, the mass flow rate (at the design point) through the machine is established by the compressor–combustor in the gas turbine engine. Also, the shaft connecting the compressor to the turbine, on a given spool, rotates at the same speed. In addition to these two constraints, we have the third input to the turbine design problem, which is the combustor exit temperature, T_{t4} . The fourth input is the combustor exit (total) pressure, which is dictated by the compressor, i.e., cycle, pressure ratio.

Therefore, at a minimum, we have the following problem statement:

Design an axial-flow turbine for a gas generator with

- $\dot{m}_1 = 93$ kg/s ← Turbine inlet mass flow rate
- $\omega = 8770$ rpm ← Shaft rpm
- $T_{t1} = 1500$ K ← Turbine inlet (total) temperature and pressure
- $p_{t1} = 1500$ kPa
- $r_{m1} = 0.4$ m ← Pitchline radius at the compressor inlet

In addition, there is a specification that 10 kg/s of air was bled off at the compressor exit to provide turbine cooling. The coolant information is thus

$$\begin{aligned} \dot{m}_c &= 10 \text{ kg/s} \\ T_{tc} &= 704 \text{ K} \\ p_{tc} &= 1500 \text{ kPa} \end{aligned} \quad \leftarrow \text{Coolant characterization} \quad \text{(bled at the compressor exit)}$$

The design ambient pressure and temperature and flight Mach number are also known, i.e., we have

$$\begin{aligned} M_0 &= 0 \\ p_0 &= 101 \text{ kPa} \\ T_0 &= 25^\circ\text{C} \end{aligned} \quad \leftarrow \text{Design altitude and Mach number}$$

Finally, we have (or assume) gas characteristics (γ , c_p) at each station in the turbine. For the starters, we choose

$$\begin{aligned} c_{pc} &= 1004.5 \text{ J/kg} \cdot \text{K}, \gamma_c = 1.40 \\ c_{pt} &= 1243.67 \text{ J/kg} \cdot \text{K}, \gamma_t = 1.30 \end{aligned} \quad \leftarrow \text{Gas properties}$$

SOLUTION

Preliminary design of a cooled turbine

We start with the turbine shaft power that is consumed by the compressor, bearings, and other external loads. Let us assume that turbine provides shaft power only to the compressor.

$$\varphi_t = \frac{\varphi_c}{\eta_m}$$

The role of mechanical efficiency η_m term in the power balance equation is to account for power loss in bearings and other external sources, e.g., electric generator, requiring turbine shaft power. Here we assume that the mechanical efficiency is ~ 0.995 . Also from the compressor side, we calculate the shaft power absorbed by the compressor (based on cycle station numbers),

$$\varphi_c \cong \dot{m}_0 c_{pc} (T_{t3} - T_{t2})$$

The air mass flow rate in the compressor is ~ 100 kg/s with an inlet and exit total temperatures of 298 and 771 K, respectively (i.e., for a compressor pressure ratio of 20 and polytropic efficiency of $e_c = 0.90$). The shaft power consumed by the compressor is

$$\varphi_c = 40.784 \text{ MW}$$

Therefore, the turbine shaft power required is

$$\varphi_t \cong 40.989 \text{ MW}$$

The turbine power is related to the hot gas and coolant expansion to the same exit temperature $T_{t5\text{-cooled}}$ as dis-

cussed in this chapter (and based on cycle station numbers), we had

$$\begin{aligned} \varphi_{t,\text{actual}} &= \dot{m}_0 [(1 - \epsilon)c_{pt}(T_{t4} - T_{t5\text{-cooled}}) \\ &\quad + \epsilon c_{pc}(T_{tc} - T_{t5\text{-cooled}})] \end{aligned}$$

The compressor airflow rate \dot{m}_0 and ϵ (as coolant mass fraction) are known to be 100 kg/s and $\sim 10\%$ (i.e., 0.01), respectively. We solve the turbine power equation for the unknown, $T_{t5\text{-cooled}}$, to get

$$T_{t5\text{-cooled}} \approx 1098 \text{ K}$$

The total temperature drop across the turbine is $\Delta T_t = 402$ K. The question that we ask is how many stages of turbine expansion will it take to create a 402 K total temperature drop?

The answer depends on our stage degree of reaction design choice. We have seen that an impulse turbine produces (theoretically) twice as much power per stage than a 50% reaction turbine (for the case of swirl-free turbine exit flow). But we also noted that efficiency of the impulse turbine is lower than the reaction type. In addition, note that the desire to reach a zero exit swirl condition at the turbine exit is one of the goals that we will try to match at the turbine exit but it may be nonzero for intermediate stages. In this sense, the turbine stages will not be repeated. The only repetition from one stage to another seems to be in the constant axial velocity assumption that we introduce in our design strategy. Also, our calculations are limited to the turbine pitchline radius.

First turbine nozzle pitchline design (C_z – constant design)

The maximum turning angle α_2 appears at the nozzle exit Mach number of ~ 1 . Since the first turbine nozzle has to operate in a choked state (over a wide operating range), we choose the first nozzle exit Mach number slightly supersonic, i.e.,

$$M_2 = 1.1 \text{ (design choice for the 1st turbine nozzle)}$$

From the stagnation temperature $T_{11} = 1500 \text{ K}$ and the exit Mach number $M_2 = 1.1$, we calculate the static temperature at the nozzle exit,

$$T_2 = 1500 \text{ K} / [1 + 0.15(1.1)^2] \approx 1270 \text{ K}$$

The speed of sound in station 2 is

$$a_2 = 688.4 \text{ m/s}$$

Therefore, the absolute gas speed at the nozzle exit is

$$C_2 = 757.1 \text{ m/s}$$

For the first nozzle exit angle of $\sim 60^\circ$, we calculate the nozzle exit swirl and axial velocity components,

$$\text{For } \alpha_2 \approx 60^\circ, C_{\theta 2} \approx 655.6 \text{ m/s} \text{ and } C_{z2} \approx 378.5 \text{ m/s}$$

Since we adopted a constant axial velocity design approach, the nozzle inlet velocity is assumed to be purely in the axial direction as well as being equal to the nozzle exit axial velocity, i.e.,

$$C_1 = C_{z1} = C_{z2} = 378.5 \text{ m/s}$$

Now, we may calculate the nozzle inlet static temperature T_1 and speed of sound a_1

$$T_1 = T_{11} - C_1^2 / 2c_{pt} = 1500 \text{ K} - (378.5)^2 / 2 / 1243.67 = 1442.4 \text{ K} \implies a_1 = 733.6 \text{ m/s}$$

Therefore, the gas Mach number at the nozzle entrance is:

$$M_1 = M_{z1} = 0.516$$

First turbine nozzle optimal solidity

Zweifel related optimal (axial) solidity to a loading parameter ψ_z and relative flow angles β_1 and β_2 according to

$$\sigma_z \psi_z = \frac{2 \cos \beta_2}{\cos \beta_1} \sin(\beta_1 - \beta_2)$$

The graph of the optimal solidity parameter $\sigma_z \cdot \psi_z$ is shown in Figure 10.33. In the first nozzle, the inlet flow is axial, i.e., $\alpha_1 = 0$, and the exit flow angle was assumed to be $\alpha_2 \sim 60^\circ$.

From Figure 10.33, we read an optimum solidity parameter of $\sigma_z \cdot \psi_z \approx 0.85$. Therefore, following the recommended loading parameter of $\psi_z \approx 1.0$, we get the axial solidity of the first nozzle to be

$$\sigma_z \approx 0.85 \text{ (optimum axial solidity according to Zweifel)}$$

The actual solidity is $\sigma = \sigma_z / \cos \gamma^0$, where γ^0 is the stagger angle. A first approximation to stagger angle in a nozzle is the average flow angle α_m (based on the mean swirl) and in the rotor is the mean relative flow angle. The mean swirl across the nozzle is $C_{\theta m}$ and the mean flow angle is

$$\alpha_{2m} \approx \tan^{-1}(C_{\theta m} / C_z) \approx 40.9^\circ. \text{ Therefore, the stagger } \gamma^0 \approx 40.9^\circ \text{ and the actual optimum solidity is } \sigma = \sigma_z / \cos \gamma^0 \implies \sigma_n \approx 1.125.$$

Although, we estimated optimum nozzle solidity from Zweifel's method in this instance, we will not hesitate to change it to meet other blade row constraints, as in cooling requirements. The lack of overwhelming experimental support for the optimum solidity as formulated by Zweifel makes this choice an obvious one to change in subsequent turbine design iterations. We have chosen $\sigma_n \approx 2$ (for nozzle cooling considerations) although Zweifel's optimum value suggests 1.125.

First turbine nozzle deviation angle

The turbine blades, by the virtue of their predominantly favorable pressure gradient, have lower deviation angles than compressor blades (of comparable camber). Carter's rule for deviation angle in turbines (with subsonic exit flow) may be written as

$$\delta^* = \frac{m \Delta \varphi}{\sigma} \approx \frac{\Delta \varphi}{8\sigma} \approx \frac{\Delta \beta}{8\sigma} \text{ (subsonic exit)}$$

However, for sonic or supersonic exit flows, the deviation angle becomes negligibly small since the flow continues to accelerate beyond the throat and thus boundary layers remain very thin,

$$\delta^* \approx 0 \text{ (supersonic exit)}$$

Since, the first nozzle exit Mach number was chosen to be 1.1 we neglect the deviation angle at the first nozzle exit.

First turbine nozzle throat sizing

The throat sizing in a turbine nozzle (or rotor) is very important both for choked and unchoked nozzles. The geometry that is shown in the definition sketch (Figure 10.53) is used

to relate the throat width or opening o to the blade spacing s .

The throat opening o is related to the spacing and cosine of the exit flow angle α_2 following

$$o \approx s \cdot \cos \alpha_2$$

This approximation is acceptable for the subsonic exit flow; however, for the supersonic exit Mach numbers (but below 1.3), we correct the throat opening by the inverse of A/A^* corresponding to the supersonic exit Mach number, i.e.,

$$\frac{o}{s} \approx \frac{\cos \alpha_2}{(A/A^*)_{M_2}}$$

The size of correction is small (for low supersonic exit Mach numbers) and to demonstrate we use the current example for $\alpha_2 = 60^\circ$ and $M_2 = 1.1$, for which the A/A^* is ≈ 1.008 , i.e.,

$$\begin{aligned} \frac{o}{s} &\approx \cos \alpha_2 = 0.5 \quad M_2 \leq 1 \\ \frac{o}{s} &\approx \frac{\cos \alpha_2}{(A/A^*)_{M_2}} \approx 0.496 \quad M_2 = 1.1 \end{aligned}$$

First turbine nozzle cooling

We had related the cooling mass fraction in a blade row to the gas and wall temperatures and Stanton numbers on the coolant and gas side following the steady-state heat transfer equation:

$$\epsilon \equiv \frac{\dot{m}_c}{\dot{m}_g} = \frac{c_{pg}}{c_{pc}} \frac{St_g}{St_c} \left(\frac{T_{aw} - T_{wg}}{T_{wc} - T_c} \right) \quad (10.74)$$

The wall temperature on the coolant side was related to the wall temperature on the gas side, wall thickness, blade solidity, gas mass density, and thermal conductivity of the wall according to the Fourier heat conduction and steady-state heat transfer from the gas through the solid and to the coolant:

$$T_{wc} = T_{wg} - \left(\frac{t_w}{k_w} \right) \frac{1}{2\sigma} \rho_g u_g c_{pg} St_g (T_{aw} - T_{wg}) \quad (10.75)$$

Note that the blade solidity σ has entered blade cooling problem through Equation 10.76. Finally, the gas mass den-

sity is related to *average flow passage Mach number*, total pressure, and temperature following continuity equation:

$$\begin{aligned} \rho_g u_g &= \frac{\dot{m}_g}{A_g} \\ &= \sqrt{\frac{\gamma_g}{R_g}} \frac{P_{tg}}{\sqrt{T_{tg}}} M_g \left(1 + \frac{\gamma - 1}{2} M_g^2 \right)^{-\frac{\gamma+1}{2(\gamma-1)}} \quad (10.76) \end{aligned}$$

The average flow passage Mach number is simply taken to be the mean of the inlet and exit Mach numbers, i.e.,

$$M_g \approx (M_1 + M_2)/2$$

Therefore, if we approximate gas mass density in the nozzle based on

$$\begin{aligned} P_{tg} &\approx 1500 \text{ kPa} \\ T_{tg} &\approx 1500 \text{ K} \\ M_g &\approx (M_2 + M_1)/2 = 0.808 \end{aligned}$$

we get the mass density in the nozzle to be $\rho_g u_g \approx 1472.1 \text{ kg/m}^2\text{s}$

Now, we calculate the wall temperature on the coolant side, T_{wc} using the estimated gas mass density and the following parameters:

$$\begin{aligned} T_{wg} &= 1400 \text{ K} && \text{(desired gas wall temperature, a design choice that impacts life)} \\ t_w &= 1.5 \text{ mm} && \text{(1st design choice on the wall thickness)} \\ k_w &= 14.9 \text{ W/mK} && \text{(wall thermal conductivity, nickel-based alloys used in turbines)} \\ S_{tg} &\approx 0.005 && \text{(gas side Stanton number, an estimate based on } C_f) \\ T_{aw} &\approx T_{tg} = 1500 \text{ K} && \text{(adiabatic wall temperature } \approx \text{ the gas total temperature)} \end{aligned}$$

We calculate the wall temperature on the coolant side to be

$$T_{wc} \approx 1376.9 \text{ K.}$$

We may now estimate, using Equation 10.74, the coolant mass fraction that is needed in the first nozzle to maintain the gasside surface temperature on the nozzle at the desired level (of 1400 K). In addition, we have approximated the ratio of coolant-to-gas side Stanton numbers, St_c/St_g , to be

~2.0 with micro fins in internal cooling passage which gives

$$\epsilon_{N1} \approx 0.092 \text{ (nozzle-1 coolant mass fraction)}$$

Here, we have estimated the first nozzle internal cooling fraction of 9.2%, which leaves another 0.8% internal cooling for the first rotor, the casing and the second nozzle and the rotor, if needed. In case the amount of coolant fraction (of 10%) is insufficient (for internal cooling purposes), we have to go back and bleed a higher coolant fraction from the compressor.

First turbine rotor pitchline design (C_z-constant design)
The first rotor rotational speed at the pitchline is

$$U_m = \omega r_m = (8770 \text{ rpm})(2\pi \text{ rad/rev})(\text{min}/60 \text{ s})(0.4 \text{ m}) \approx 367.4 \text{ m/s}$$

Here, we have used the pitchline radius from the compressor (inlet) side as a first estimate of pitchline radius in the turbine. However, we can change the pitchline radius in the turbine to accomplish our design goals in power production and stage-by-stage load variations. Therefore, the pitchline radius in the turbine is clearly a design variable, but as a first approximation, the compressor inlet value may be used to start off the turbine design iteration cycle.

The rotor (relative) exit Mach number M_{3r} impacts the power production in the rotor as well as the turbine performance and is a design choice. The performance improves with the increase in relative exit Mach number. For starters, we choose $M_{3r} \sim 0.8$ but we will be willing to change M_{3r} up to 0.9 and even go below 0.8, if necessary. Note that the first turbine rotor is to remain unchoked. The relative Mach number is written in terms of axial and tangential velocities and speed of sound as

$$M_{3r} = \frac{1}{a_3} [C_{z3}^2 + W_{\theta 3}^2]^{1/2} = 0.80$$

(rotor relative exit Mach number design choice)

And from the conservation of energy in the relative frame, we write

$$\frac{a_3^2}{\gamma_t - 1} + \frac{W_3^2}{2} = \frac{a_2^2}{\gamma_t - 1} + \frac{W_2^2}{2}$$

We may combine the above two equations and use constant axial velocity to write

$$W_{\theta 3}^2 = \frac{M_{3r}^2 [a_2^2 + (\gamma_t - 1)W_{\theta 2}^2/2] - C_z^2}{1 + (\gamma_t - 1)M_{3r}^2/2}$$

The relative swirl downstream of the first rotor is in opposite direction to the rotor rotation, therefore it is negative. We take the minus solution of the above equation, i.e.,

$$W_{\theta 3} = -\sqrt{\frac{M_{3r}^2 [a_2^2 + (\gamma_t - 1)W_{\theta 2}^2/2] - C_z^2}{1 + (\gamma_t - 1)M_{3r}^2/2}} \Rightarrow W_{\theta 3} = -391 \text{ m/s}$$

From relative exit swirl, we calculate the absolute exit swirl $C_{\theta 3} = -24 \text{ m/s}$ and thus the degree of reaction

$$\circ R_m = 1 - \frac{C_{\theta m}}{U_m} = 1 - \frac{C_{\theta 2} + C_{\theta 3}}{2U_m} \Rightarrow \circ R_m \approx 0.14$$

Based on the velocity components across the rotor, we have all the flow angles at the rotor exit, i.e., α_3 and β_3 . Therefore, the first rotor velocity components, flow angles, and Mach number at the pitchline are

$$\begin{aligned} W_{\theta 2} &= C_{\theta 2} - U_m = 288.3 \text{ m/s} && \Rightarrow \beta_2 \approx +37.3^\circ \\ W_{\theta 3} &= -391 \text{ m/s} && \Rightarrow \beta_3 \approx -45.9^\circ \\ C_{\theta 3} &= W_{\theta 3} + U_m = -24 \text{ m/s} && \Rightarrow \alpha_3 \approx -3.6^\circ \\ W_2 &= [C_{z2}^2 + W_{\theta 2}^2]^{0.5} = 475.8 \text{ m/s} && \Rightarrow M_{2r} = 475.8/688 = 0.691 \end{aligned}$$

The total pressure and temperature of the gas depends on the motion of the observer. Therefore, the rotor sees p_{12r} and T_{12r} , and not the absolute p_{12} and T_{12} . In order to calculate the relative total pressure and temperature, we first determine the static pressure and temperature in station 2 and then use relative Mach number M_{2r} , or relative kinetic energy to calculate the relative total pressure and temperature as seen by the rotor. The static temperature of the gas in station 2 is

$$T_2 = T_{12} - C_2^2/2c_{pt} = 1500 - (757)^2/2/1243.67 = 1269.6 \text{ K}$$

Therefore, the relative total temperature is \Rightarrow

$$T_{12r} = T_2 + W_2^2/2c_{pt} \approx 1350.6 \text{ K}$$

Note that the rotor sees a stagnation temperature of 1350.6 K instead of 1500 K that the nozzle feels. The rotor operates in a ~150 K cooler gas, by virtue of its rotation!

To calculate the static pressure at nozzle exit plane, we need to estimate a total pressure loss factor that the flow in the nozzle suffers due to profile loss, secondary flow loss, other (than secondary flow) three-dimensional losses,

as well as shock losses in a supersonic nozzle. Using Figure 10.21, we estimate the total pressure loss factor in the nozzle to be $\varpi_n \sim 0.06$. Here again, we may assign a higher loss coefficient to the blade row in our design based on the relevant cascade loss data available. From the definition of total pressure loss parameter,

$$\varpi_n \equiv \frac{p_{t1} - \bar{p}_{t2}}{p_{t1} - p_1}$$

We first calculate the static pressure p_1 from p_{t1} and M_1 (0.516) that we had calculated earlier,

$$p_1 \approx 1266 \text{ kPa}$$

Therefore, the total pressure at the nozzle exit is

$$p_{t2} \approx 1486 \text{ kPa}$$

The static pressure p_2 may be calculated from p_{t2} and $M_2 = 1.1$ to be

$$p_2 \approx 721.3 \text{ kPa}$$

Since we calculated M_{2r} to be 0.691, we may now calculate p_{t2r}

$$p_{t2r} \approx 973.7 \text{ kPa}$$

To complete our first stage calculations of pressure and temperature, we should calculate the rotor exit conditions as well. The total temperature T_{t3} may be calculated from the Euler turbine equation and the known velocity triangles, i.e.,

$$T_{t3} = 1299.2 \text{ K}$$

The static temperature T_3 is calculated from $T_3 = T_{t3} - C_3^2/2c_{pt}$ to be $T_3 = 1241.4 \text{ K}$

The corresponding speed of sound is $a_3 = 680.6 \text{ m/s}$. The absolute Mach number at the exit of the rotor is $M_3 = 0.557$

If we assume a relative total pressure loss coefficient in the rotor $\varpi_r \sim 0.08$ (note that we chose a higher loss in the rotor than the nozzle to account for tip clearance flow in the rotor), we can calculate the rotor exit relative total pressure p_{t3r}

$$p_{t3r} = 953.5 \text{ kPa}$$

Since we had chosen an M_{3r} as a design choice (we took 0.8), we can calculate p_3

$$p_3 = 640.9 \text{ kPa}$$

From the optimum solidity approach of Zweifel we estimate the axial solidity parameter for the first turbine rotor to be

$$\sigma_z \psi_z \approx 1.8$$

Based on the recommended value of $\psi_z \approx 1.0$, we get the optimum axial solidity of the first rotor, $\sigma_r = 1.8$. The stagger angle at the pitchline is estimated to be at the mean swirl angle in the rotor, i.e.,

$$\beta_m \approx \tan^{-1}(W_{\theta m}/C_z) = \tan^{-1}\{[(-391.3 + 288.3)/2]/378.5\} \approx -7.75^\circ$$

Therefore the optimum rotor solidity is calculated to be $1.8/\cos(7.75^\circ) \approx 1.82$

In the spreadsheet calculation, we started with this value of solidity, but since the rotor is uncooled, we continue with the optimal rotor solidity. The value of first rotor solidity is $\sigma_{r1} \approx 1.82$.

Rotor deviation angle

Using Carter's rule for a turbine, we estimate the first rotor deviation angle δ^*

$$\delta^* \approx \frac{\Delta\beta}{8\sigma_r} \approx \frac{83^\circ}{8(1.82)} \approx 5.2^\circ$$

Note that the relatively large deviation angle of $\sim 5.2^\circ$ is caused by a very large flow turning in the rotor of $\sim 83^\circ$. With a reduced camber, or net flow turning angle, the deviation angle drops.

First turbine rotor blade cooling

In turbine rotor cooling calculations, we encounter the heat transfer in *relative frame of reference*. Consequently, the stagnation temperature becomes *as observed by the rotor*.

We calculated the relative frame stagnation pressure and temperature to be 973 kPa and 1360 K, respectively. Since $T_{t2r} < T_{wg}$ the first turbine rotor is uncooled. Indeed there will be no turbine component cooling beyond the first nozzle in our example.

First stage loading parameter and shaft power

$$w_t = U_m(C_{\theta 2} - C_{\theta 3}) = 249,622 \text{ J/kg}$$

$$\psi = w_t/u_m^2 = 1.85$$

The shaft power that the first stage (rotor) produces is

$$\dot{\mathcal{P}}_{\text{Stage-1}} = \dot{m}_{\text{Stage-1}} \cdot (w_t)_{\text{Stage-1}} = 93 \text{ kg/s}(249,622 \text{ J/kg}) \approx 23.22 \text{ MW}$$

By comparing the power that is produced by the first stage (rotor) to that of the entire turbine, i.e., 40.99 MW, we note that the second stage is needed and it needs to produce ~18 MW of power.

Second turbine nozzle pitchline design (C_z —constant design)

To begin the second stage nozzle design, we start by listing the inlet conditions to the second stage, i.e.,

$$\begin{aligned} T_{13} &= 1299.3 \text{ K} \\ p_{13} &= 780.7 \text{ kPa} \\ C_3 &= 379.3 \text{ m/s} \\ \alpha_3 &= -3.6^\circ \end{aligned}$$

Now, we are ready to choose some of the second stage design variables, e.g., either the nozzle exit Mach number M_4 or the nozzle exit flow angle α_4 , here we chose the exit flow angle and calculated the exit Mach number based on the constant axial velocity design principle, i.e.,

$\alpha_4 = 53^\circ$ (design choice, which can be adjusted up to 70° or down to $\sim 40^\circ$) leads to the nozzle exit Mach number (that has to be subsonic, or unchoked), $M_4 = 0.964$

Here, we have an additional choice about the pitchline radius for the second stage, i.e., r_{m3} does not have to be the same as r_{m1} . We started our calculations (in the spreadsheet) with the same value and then increased it to produce more shaft power. Finally, we arrived at the pitchline radius for the second stage:

$r_{m3} = 0.42 \text{ m}$ (an increase of 2 cm of radial shift for the pitchline in stage 2 over stage 1)

With these choices, we calculate the second nozzle exit flow conditions, and with an assumed total pressure loss parameter $\varpi_{n2} \sim 0.06$, we calculate the total pressure as well,

$$\begin{aligned} U_3 &= 385.7 \text{ m/s} \\ W_{\theta 4} &= 116.6 \text{ m/s} \\ \beta_4 &= 17.1^\circ \\ W_4 &= 396 \text{ m/s} \\ M_{4r} &= 0.607 \\ p_{t4} &= 772.4 \text{ kPa} \\ p_{t4r} &= 553.8 \text{ kPa} \end{aligned}$$

Our choice of the second nozzle solidity $\sigma_{n2} = 0.2$ yields a deviation angle of $\delta^* = 3.54^\circ$.

The throat sizing of the second nozzle gives $(o/s)_{N2} = 0.602$

Second turbine rotor pitchline design (C_z —constant design)

The second rotor exit Mach number is a design choice for which we have chosen

$$M_{5r} = 0.85 \text{ (a design choice, always less than 1)}$$

The second rotor exit flow conditions are

$$\begin{aligned} C_5 &= 378.5 \text{ m/s} \\ C_{\theta 5} &= -0.74 \text{ m/s} \\ \alpha_5 &= -0.1^\circ \text{ (nearly swirl-free exit, as we aimed)} \\ M_5 &= 0.594 \text{ (a reasonable exit Mach number)} \end{aligned}$$

The second stage degree of reaction is

$${}^\circ R = 0.350$$

Second stage loading parameter and shaft power

$$\begin{aligned} w_t &= U_m(C_{\theta 4} - C_{\theta 5}) = 194,048 \text{ J/kg} \\ \psi &= w_t/U_m^2 = 1.304 \end{aligned}$$

Shaft power for the second stage (rotor),

$$\begin{aligned} \wp_{\text{Stage2}} &= \dot{m}_{\text{Stage2}} \cdot (w_t)_{\text{Stage2}} = 93 \text{ kg/s}(194,048 \text{ J/kg}) \\ &\approx 18.05 \text{ MW} \end{aligned}$$

Impact of cooling on turbine exit temperature and pressure

It is important to note that we treated the blade-cooling problem completely *internally* to achieve a desired blade surface temperature T_{wg} . By this technique, we estimated the coolant fraction for internal blade cooling purposes. We did not inject the coolant in the gas stream per blade row, as it is commonly done in a real cooled gas turbine blade. The coolant is always discharged through film holes, trailing-edge slots, and other discharge orifices.

Therefore, there are at least three effects that we ignored by our internal cooling approach. First, the mass flow rate through the next blade row increases by the amount of coolant injected in the gas path. Second, the temperature of the gas is not reduced due to the injection of coolant per blade row. Finally, the total pressure of the gas is not reduced due to turbulent mixing losses of the hot and cold gas streams. There are other important details that accompany mixing of two streams with relative flow angle with

respect to each other, as in coolant flow emerging from film holes. For example, the flow angle associated with the *mixed-out state* is not exactly the same as the gas path angle that we calculate in the absence of cooling. There are two approaches that we can take to remedy the cooling problem. The first approach will correct the turbine exit total temperature and pressure for all the coolant suddenly *dumped* at the turbine exit. The second approach will do a stepwise calculation per blade row as the coolant is injected in the gas path and achieves a mixed-out state with the hot gas. The level of detail in the second approach is slightly above the scope of the present book, but definitely feasible and straightforward. Here we adopt the first approach for simplicity.

A corrective action on the temperature and pressure may be taken by first performing an energy balance between the turbine discharge total temperature where coolant was not introduced in the gas path and the coolant flow at the coolant temperature T_{ic} . The conservation of energy yields

$$T_{t5-cooled} = \frac{\dot{m}_g c_{pt} T_{t5} + \dot{m}_c c_{pc} T_{ic}}{(\dot{m}_g + \dot{m}_c) \bar{c}_p}$$

where the mean specific heat at constant pressure for the mixture is

$$\bar{c}_p = \frac{\dot{m}_g c_{pt} + \dot{m}_c c_{pc}}{\dot{m}_g + \dot{m}_c}$$

First, the average specific heat is calculated to be $\bar{c}_p \approx 1220.4 \text{ J/kg} \cdot \text{K}$

The mixed-out total temperature is then $T_{t5-cooled} \approx 1108 \text{ K}$

Our power balance at the beginning of the turbine design had indicated that the exit total temperature of the cooled turbine will be $T_{t5-cooled} \approx 1098.4 \text{ K}$

As expected, these estimations are based on the same principles and are thus very close, i.e., within 1% of each other.

To estimate the turbine total pressure at the exit, we approximate the adiabatic efficiency of a cooled turbine and then use the efficiency and temperature ratio to get the turbine pressure ratio. The adiabatic efficiency of a cooled turbine was estimated to suffer $\sim 2.5\%$ per 1% coolant mass fraction. Therefore, a 9.2% coolant mass fraction causes the turbine adiabatic efficiency to be $\eta_t \sim 77\%$. In terms of the adiabatic efficiency, we may express the turbine total pressure ratio according to

$$\pi_t = \left[1 - \frac{1}{\eta_t} (1 - \tau_t) \right]^{\frac{\gamma_t}{\gamma_t - 1}}$$

We may substitute for $\tau_t = 1108/1500 = 0.7387$ and 0.7 for the adiabatic efficiency of our cooled turbine to get the turbine pressure ratio and exit total pressure of the cooled turbine:

$$\pi_t = 0.166 \implies p_{t5-cooled} \approx 249 \text{ kPa}$$

Interim summary

In this section, we recapitulate the outcomes of our design so far in meeting the required shaft power, the target cooling mass fraction (albeit for internal cooling), and the condition of zero exit swirl that we wish to impose on the turbine exit flow.

Total shaft power

Total power produced by the internally cooled turbine is the sum of the two stages, i.e., 23.22 MW and 18.05 MW, which is 41.27 MW. The required power was calculated to be 40.99 MW. There is a match with 0.67% excess power margin.

Cooling mass fraction

We started with a 10% coolant mass fraction, which we have nearly totally consumed in the first nozzle. However, the casing needs to be cooled as well as the exhaust nozzle. Therefore we need to demand a higher level of compressor bleed for turbine and nozzle cooling purposes. But for the present (turbine preliminary design) purposes, we have achieved our internal cooling target.

Turbine exit swirl

The goal of zero turbine exit swirl is achieved. We ended up with a -0.1° of swirl angle at the exit of the second stage rotor, which in terms of absolute swirl velocity is $\sim -0.74 \text{ m/s}$.

Turbine annulus sizing

The nozzle inlet Mach number $M_1 \approx 0.516$ and the mass flow rate will be used to size the nozzle inlet flow area (A_1) around a pitchline radius of 0.40 m,

$$\dot{m}_1 = \sqrt{\frac{\gamma_t}{R_t}} \frac{p_{t1}}{\sqrt{T_{t1}}} A_1 M_{z1} \left(1 + \left(\frac{\gamma_t - 1}{2} \right) M_{z1}^2 \right)^{-\frac{\gamma_t + 1}{2(\gamma_t - 1)}} \implies A_1 = 0.08.3 \text{ m}^2$$

We calculate the first nozzle blade height h_1 , i.e., $(r_{t1} - r_{h1})$ from the flow area and the mean radius r_m , i.e.,

$$r_{t1} - r_{h1} = \frac{A_1}{2\pi r_m} \approx 3.197 \text{ cm} \implies h_1 \approx 3.197 \text{ cm}$$

Now, we can calculate the turbine exit flow area A_5 from the one-dimensional continuity equation based on the cooled turbine exit total pressure and temperature

$$\dot{m}_5 = \dot{m}_4 + \dot{m}_c$$

$$= \sqrt{\frac{\gamma_t}{R_t} \frac{P_{t5-\text{cooled}}}{\sqrt{T_{t5-\text{cooled}}}}} A_5 M_{z5} \left(1 + \left(\frac{\gamma_t - 1}{2} \right) M_{z5}^2 \right)^{-\frac{\gamma_t + 1}{2(\gamma_t - 1)}}$$

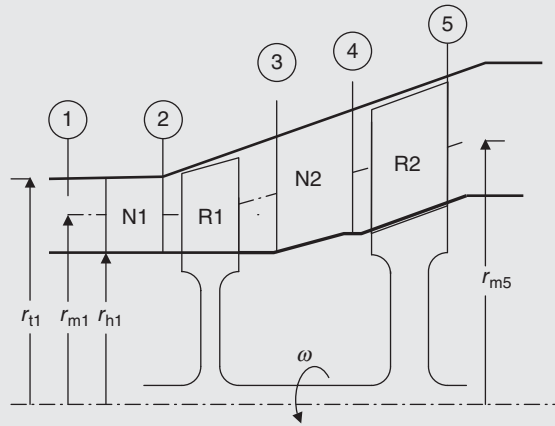
We calculate the turbine exit flow area,

$$A_5 \implies A_5 \approx 0.4184 \text{ m}^2$$

The blade/channel height at the turbine exit, h_5 , assuming the pitchline radius is $r_{m5} = r_{m4} = 0.42 \text{ m}$ is

$$r_{t5} - r_{h5} = \frac{A_5}{2\pi r_{m5}} \approx 15.85 \text{ cm} \implies h_5 \approx 15.85 \text{ cm}$$

Figure 10.63 is a schematic drawing of a two-stage turbine with its corresponding station numbers.



■ FIGURE 10.63 Definition sketch of a two-stage turbine and its station numbers

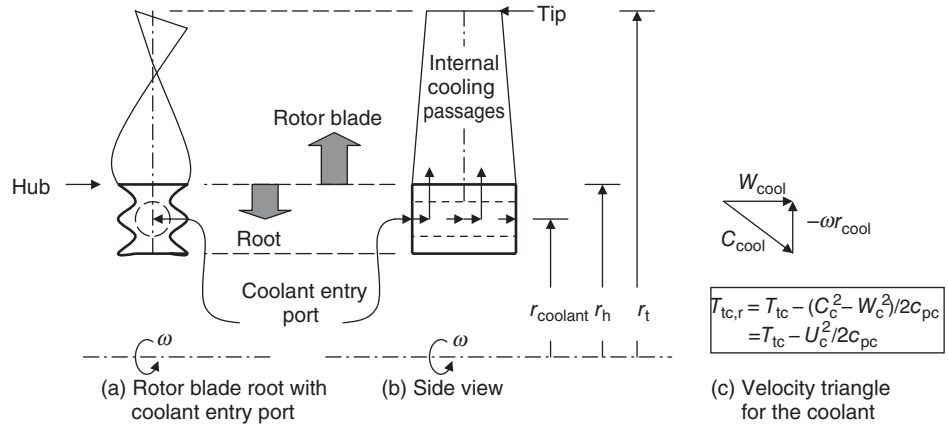
10.8 Gas Turbine Design Summary

We used some commonly accepted design practices, for example, constant axial velocity, to design suitable velocity triangles at the pitchline. In the process, we encountered some *hard* and *soft* design constraints. Some examples of hard and soft design constraints are summarized below:

<i>Hard design constraints</i>		<i>Soft design constraints</i>	
$M_2 > 1$	(choked first nozzle)	$\sigma \neq \sigma_{opt}$	(solidity other than the optimum)
$M_{3r} < 1$	(unchoked rotor exit flow)	$r_m \neq \text{constant}$	(pitchline radius is variable)
$M_{5r} < 1$	(unchoked rotor exit flow)	$\alpha_{exit} \neq 0$	(turbine exit swirl not zero)
T_{wg}	(maximum wall temperature)	$t_{wall} = 2 \text{ mm}$	(wall thickness other than nominal)
$^\circ R > 0$	(positive degree of reaction)	$0 \leq R \leq 1$	(wide-ranging choice of $^\circ R$)
		$T_{wg} = 1400 \text{ K}$	(a function of material selection)
		$\psi > 1$	(higher loading than 1 is acceptable)
		$C_z \neq \text{constant}$	(acceptable)
		$\eta \approx 0.6-0.7$	(cooling effectiveness for film + conv. cooling)
		$\eta < 0.4$	(cooling effectiveness for internal conv. cooling)
		$T_c < 900 \text{ K}$	(limited by comp. discharge)

The design process requires iteration. To facilitate successive calculations, a spreadsheet was developed. It is important to recognize the approximations that were used in the analysis. For example, we used the same T_c in our internal cooling calculations for the nozzle *and* the rotor. The coolant temperature that we used in the nozzle was the

■ FIGURE 10.64
 Definition sketch for
 coolant entry at the
 rotor blade root and
 coolant total
 temperature in the
 rotor frame of
 reference



compressor discharge temperature. However, when the coolant is injected in the hub of a rotating blade row, as in the rotor, the *relative* stagnation temperature is different than the absolute total temperature. But, we did not distinguish between the two. In practice, the coolant is injected at an angle in the direction of rotor rotation with the resultant relative stream in the axial direction. The schematic drawing of a cooled turbine rotor blade and the coolant velocity triangle is shown in Figure 10.64. The correction for the coolant relative total temperature is shown to be $\sim U_c^2/2c_{pc}$. Therefore, the coolant entering the blade root *feels cooler* to the rotor than the coolant in the nozzle. Here, the emphasis in the summary is not on the extent of correction to the stagnation temperature, rather on the awareness of the two frames of reference.

Figure 10.65 shows a flowchart in turbine design based on the methodology presented in this chapter. The flowchart shows a two-stage turbine with cooling fractions, ϵ_{N1} , ϵ_{R1} , and so on, shown in the right-hand column. The middle column shows the design input parameters in uncooled turbine blade rows as the exit Mach number and flow angles. The left-hand column shows the flow cross-sectional area sizing based on continuity.

10.9 Summary

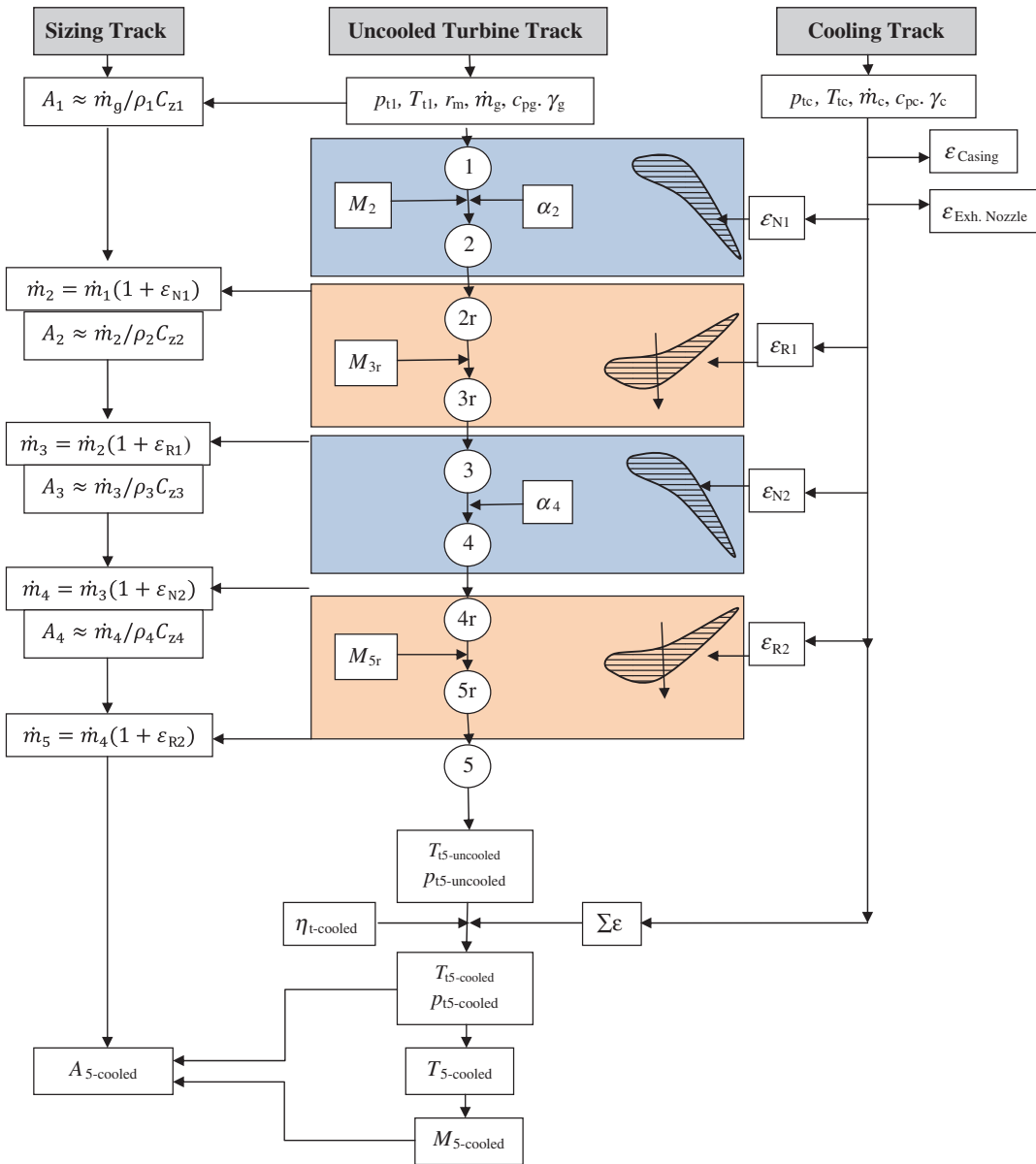
Modern gas turbines truly represent the most technologically challenging component in an aircraft engine. Critical technologies in the development of gas turbines are (single crystal) material, internal/external cooling, thermal protection coating, aerodynamics, active tip clearance control, and manufacturing.

Degree of reaction in a turbine influences power production, efficiency, and stage mass flow density (i.e., mass flow rate per unit area). For example, a 50% reaction turbine stage produces (for a swirl-free rotor exit flow)

$$w_t \equiv \frac{\dot{\mathcal{P}}_t}{\dot{m}_t} \cong U \Delta C_\theta = U^2$$

And an impulse turbine (with 0% reaction) stage produces (for a swirl-free rotor exit flow)

$$w_t \equiv \frac{\dot{\mathcal{P}}_t}{\dot{m}_t} \cong U \Delta C_\theta = 2U^2$$



■ FIGURE 10.65 Flowchart for a cooled two-stage turbine calculation strategy and sizing procedure

The choice of nozzle optimal exit swirl Mach number coupled with axial flow from the rotor demonstrated that the choice of degree of reaction establishes a turbine inlet Mach number M_1 . An impulse turbine stage, with $^{\circ}R = 0$, demands a nozzle inlet Mach number of ~ 0.4 and a 50% reaction stage corresponds to an inlet Mach number ~ 0.65 . With the increase in reaction, the mass flow rate per unit area increases and vice versa. Although an impulse stage is capable of producing maximum specific work, it also reduces the mass flow density. The optimal nozzle exit Mach number M_2 that maximizes the swirl

and stage work varies between 1.2 and 1.5 for a stage reaction that varies between 50% and 0, respectively. The practical maximum exit flow angle in a nozzle is $\alpha_{2,\max} \approx 70^\circ$.

Turbine losses are attributed to the following sources:

1. Profile loss, which is established based on 2D cascade studies
2. Secondary flow losses, which may be estimated using secondary flow theory of Hawthorne or the approximate version by Squire and Winter
3. Annulus losses, which includes tip clearance loss, (seal) leakage loss, casing boundary layer loss, corner vortex loss
4. Coolant-related losses, including mixing loss, induced separation loss, and internal passage coolant total pressure loss
5. Shock and shock-boundary layer interaction losses in transonic stages of LPT
6. Unsteady flow loss causing shock oscillation and vortex shedding in the wake.

In examining blade profile losses, we have noted that the impulse blade profile losses are significantly higher than their counterparts in a reaction rotor. This contributes to lower stage efficiency in an impulse type versus a reaction turbine. Tip clearance is a major contributor to turbine losses, and consequently the active control of tip clearance is an adopted/practiced strategy. The other option is to shroud the turbine rotor blades (at the tip) to eliminate the tip clearance loss. The added weight and centrifugal stresses in shrouded rotors are the penalty paid for such a relief.

We introduced the concept of optimal solidity in turbine aerodynamics. However, the two criteria for optimum solidity, that is, Zweifel's and Howell's, showed a very limited range of agreement with the test data.

Turbine cooling relies on internal and external cooling schemes as well as thermal protection coating. Leading-edge impingement and internal convective cooling are practiced internally. Either film or transpiration cooling achieves the external cooling. The role of the thermal protection coating is to reduce the heat transfer to the blade by coating the blades with a very low thermal conductivity layer (as in silicon-based paint, or ceramic coating).

Glassman (1973), Hill and Peterson (1992), Marble (1964) and Schobeiri (2004) are recommended for additional reading on gas turbines. VKI Lecture series (1982) and Glass, Dilley and Kelly (1999) provide valuable discussions on advanced turbine cooling. The contributions of Garvin (1998) and St. Peter (1999) on the history of gas turbine development in the United States are also recommended.

References

1. Ainley, D.G., "An Approximate Method for Estimation of the Design Point Efficiency of Axial Flow Turbines," British Aeronautical Research Council Current Paper 30, 1950.
2. Ainley, D.G. and Mathieson, G.C.R. "A Method for Performance Estimation for Axial Flow Turbines," Aeronautical Research Council, Research and Memorandum No. 2974, 1951.
3. Anderhub, W., "Untersuchungen ueber die Dampfstromung im radialen Schaufelspalts bei Ueberdruckturbinen," Doctoral Dissertation, Swiss Federal Institute of Technology, Zurich, Switzerland, 1912.
4. Bammert, K., Klaukens, H., and Hartmann, D., "Der Einfluss des radialen Schaufelspalts auf den Wirkungsgrad mehrstufige Turbinen," *VDI-Zeitschrift*, Vol. 110, No. 10, April 1968, pp. 390–395.

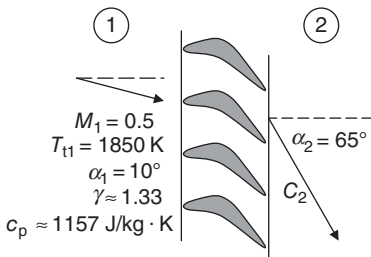
5. Booth, T.C., Dodge, P.R., and Hepworth, H.K., "Rotor Tip Leakage: Part I-Basic Methodology," *Transactions of ASME, Journal of Engineering for power*, Vol. 104, January 1982, pp. 154–161.
6. Colladay, R.S., "Turbine Cooling," A Chapter in *Turbine Design and Applications*, Glassman, A.J. (Ed.), NASA SP-290, Washington, DC, 1975.
7. Dixon, S.L., *Fluid Mechanics, Thermodynamics of Turbomachinery*, 2nd edition, Pergamon Press, Oxford, UK, 1975.
8. Duncombe, E., "Aerodynamic Design of Axial Flow Turbines," Section H, in *Aerodynamics of Turbines and Compressors*, Vol. X, Hawthorne, W. R. (Ed.), Princeton Series on High Speed Aerodynamics and Jet Propulsion, Princeton University Press, Princeton, NJ, 1964.
9. Dunham, J. and Came, P., "Improvements to the Ainley-Mathieson Method of Turbine Performance Prediction," *Transactions of the ASME, Series A*, Vol. 92, 1970.
10. Eckert, E.R.G., *Analysis of Heat and Mass Transfer* McGraw-Hill, New York, 1971.
11. Eckert, E.R.G. and Livingood, N.B., "Comparison of the Effectiveness of Convection-, Transpiration-, and Film-Cooling Methods with Air as Coolant," NACA Report 1182, 1953.
12. Farokhi, S., "The Effect of Rotor Tip Clearance Flow on the Axial Exhaust Diffuser and the Turbine Performance," *Proceedings of the First International Power Conference in Beijing-China*, October 1986, pp. 348–353.
13. Farokhi, S., "A Trade-Off Study of Rotor Tip Clearance Flow in a Turbine/Exhaust Diffuser System," ASME Paper No. 87-GT-229, June 1987.
14. Farokhi, S., "Analysis of Rotor Tip-Clearance Loss in Axial Flow Turbines," *AIAA Journal of Propulsion and Power*, Vol. 4, No. 5, September–October 1988, pp. 452–457.
15. Garvin, R.V., *Starting Something Big: The Commercial Emergence of GE Aircraft Engines*, AIAA, Inc., Reston, VA, 1998.
16. Glass, D.E., Dille, A.D., and Kelly, H.N., "Numerical Analysis of Convection/Transpiration Cooling," NASA/TM-1999-209828, 1999.
17. Glassman, A.J. (Ed.), *Turbine Design and Application*, 3 volumes, NASA SP-290, 1973.
18. Graham, J.A.H., "Investigation of Tip Clearance Cascade in a Water Analogy Rig," *Transactions of ASME, Journal of Engineering for Gas Turbines and Power*, Vol. 108, January 1986, pp. 38–46.
19. Gostelow, J.P., *Cascade Aerodynamics*, Pergamon Press, Oxford, UK, 1984.
20. Hawthorne, W.R., "Secondary Circulation in Fluid Flow," *Proceedings of Royal Society*, London, Vol. 206, 374, 1951.
21. Hill, P.G. and Peterson, C.R., *Mechanics and Thermodynamics of Propulsion*, 2nd edition, Addison-Wesely, Reading, MA, 1992.
22. Incropera, F.P. and DeWitt, D.P., *Fundamentals of Heat and Mass Transfer*, 5th edition, John Wiley & Sons, Inc., New York, 2001.
23. Johnston, I.H., "An Analysis of Air Flow Through the Nozzle Blades of a Single Stage Turbine," ARC Current Paper 131, 1953.
24. Kacker, S.C. and Okapuu, U., "A mean-line prediction method for axial-flow-turbine efficiency," Paper no. 81-GT-58, ASME, New York, 1981.
25. Kercher, D.M. and Tabakoff, W., "Heat Transfer by a Square Array of Round Air Jets Impinging Perpendicular to a Flat Surface Including the Effect of Spent Air," *ASME Journal of Engineering for Power*, Vol. 92, No. 1, January 1970, pp. 73–82.
26. Kerrebrock, J.L., *Aircraft Engines and Gas Turbines*, 2nd Edition, MIT Press, Cambridge, MA, 1992.
27. Lakshminarayana, B., "Methods of Predicting the Tip Clearance Effects in Axial Flow Turbomachinery," *Transactions of ASME, Journal of Basic Engineering*, Vol. 92, September 1970, pp. 467–482.
28. Mattingly, J.D., Heiser, W.H., and Pratt, D. T., *Aircraft Engine Design*, 2nd Edition, AIAA Education Series, AIAA, Reston, VA, 2002.
29. Marble, F.E., "Three-Dimensional Flow in Turbomachines, in *Aerodynamics of Turbines and Compressors*, Vol. X, Hawthorne W.R. (Ed.), Princeton Series on High Speed Aerodynamics and Jet Propulsion, Princeton University Press, Princeton, NJ, 1964.
30. Rohsenow, W.M., Hartnett, J.P., and Cho, Y.I., *Handbook of Heat Transfer*, 3rd edition, McGraw-Hill, New York, 1998.
31. Rolls-Royce, *The Jet Engine*, Rolls-Royce plc, Derby, UK, 2005.
32. Schobeiri, M., *Turbomachinery Flow Physics and Dynamic Performance*. Springer Verlag, Berlin, 2004.
33. St. Peter, J., *The History of Aircraft gas Turbine Engine Development in the United States*, International Gas Turbine Institute, Atlanta, GA, 1999.
34. Stodola, A., *Dampf- und Gasturbinen*, Springer Verlag, 1924.
35. Stodola, A., *Steam and Gas Turbines*, Vols. 1 and 2, McGraw-Hill, New York, 1927.
36. Traupel, W., *Thermische Turbomaschinen*, Vol. 1, Springer Verlag, 1958, pp. 295–296.
37. VKI-Lecture Series, "Film Cooling and Turbine Blade Heat Transfer," VKI-LS 82-02, 1982.
38. Wang, J.H., Messner, J., and Stetter, H., "An Experimental Investigation on Transpiration Cooling Part II: Comparison of Cooling Methods and Media," *International Journal of Rotating Machinery*, Vol. 10, No. 5, 2004, pp. 355–363.

39. Wilson, D.G. and Korakianitis, T. *The Design of High-Efficiency Turbomachinery and Gas Turbines*, 2nd edition, Prentice Hall, New York, 1998.

40. Zweifel, O., "The Spacing of Turbomachine Blading, Especially with Large Angular Deflection," *Brown Boveri Review*, Vol. 32, No. 12, December 1945, pp. 436-444.

Problems

10.1 The combustor discharge into a turbine nozzle has a total temperature of 1850 K and inlet Mach number of 0.50, as shown.



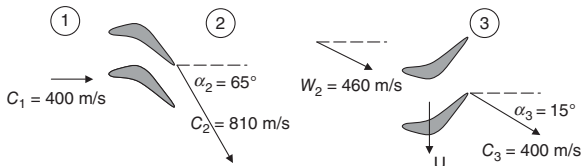
■ FIGURE P10.1

Assuming that the nozzle is uncooled, the axial velocity remains constant across the nozzle and the absolute flow angle at the nozzle exit is $\alpha_2 = 65^\circ$, calculate

- (a) inlet velocity C_1 in m/s
- (b) the exit absolute Mach number M_2 and
- (c) nozzle torque per unit mass flow rate for $r_1 \approx r_2 = 0.40$ m

10.2 Calculate the nozzle exit flow angle α_2 in Problem 10.1, if we wish the exit Mach number to be $M_2 = 1.0$, i.e., choked.

10.3 A turbine stage at pitchline has the following velocity vectors, as shown.



■ FIGURE P10.3

Calculate:

- (a) the axial velocities up- and downstream of the rotor
- (b) relative flow angle β_2 in degrees
- (c) the rotor velocity U_m
- (d) the degree of reaction at this radius
- (e) rotor specific work, w_m in kJ/kg

10.4 A turbine stage is designed with a constant axial velocity of 250 m/s and zero exit swirl. For a rotor rotational speed U_m at the pitchline of 600 m/s.

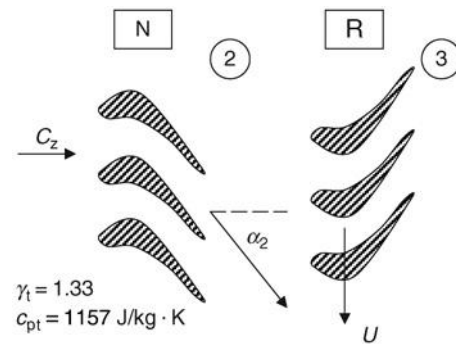
Calculate

- (a) the nozzle exit flow angle, α_2 in degrees for ${}^\circ R_m = 0.50$
- (b) the nozzle exit flow angle, α_2 in degrees for ${}^\circ R_m = 0.0$
- (c) the rotor specific work at the pitchline radius, for ${}^\circ R_m = 0.50$ and ${}^\circ R_m = 0.0$

10.5 An axial-flow turbine nozzle turns the flow from an axial direction in the inlet to an exit flow angle of $\alpha_2 = 70^\circ$. The rotor wheel speed is $U = 400$ m/s at the pitchline. The rotor is of impulse design and the exit flow from the rotor has zero swirl, i.e., $\alpha_3 = 0$. Calculate

- (a) the rotor-specific work
- (b) the stage loading at the pitchline

10.6 An axial-flow turbine stage at the pitchline is shown. The flow entering and exiting the turbine stage is axial, i.e., $\alpha_1 = \alpha_3 = 0$



■ FIGURE P10.6

The nozzle exit flow is $\alpha_2 = 65^\circ$. The shaft speed is $\omega = 5500$ rpm and the pitchline radius is $r_m = 50$ cm. Assuming $C_z = 250$ m/s = constant.

Calculate

- (a) turbine-specific work w_t (kJ/kg)
- (b) β_3 (degrees)
- (c) ${}^\circ R_m$

10.7 The combustor discharge total temperature and pressure are $T_{t1} = 2000$ K and $p_{t1} = 2$ MPa, respectively, with $\gamma_t = 1.30$ and $c_{pt} = 1244$ J/kg · K. The flow speed is 400 m/s and is in the axial direction. Calculate

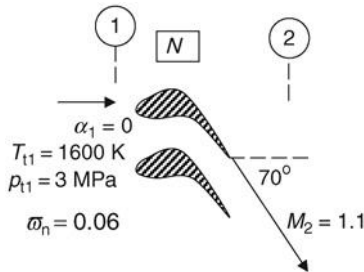
- (a) the combustor exit static temperature T_1 in K
- (b) the Mach number M_1
- (c) the combustor exit static pressure p_1 (in kPa)

10.8 The inlet flow condition to a turbine nozzle is characterized by $T_{t1} = 1800$ K and $p_{t1} = 2.4$ MPa, $M_1 = 0.5$, $\alpha = 5^\circ$, with $\gamma_t = 1.30$ and $c_{pt} = 1244$ J/kg · K. Assuming the nozzle is designed for constant axial velocity, i.e., $C_z = \text{constant}$, calculate the nozzle exit flow angle α_2 that will produce the exit Mach number of $M_2 = 1.1$.

10.9 For the flow condition across a nozzle as shown, calculate

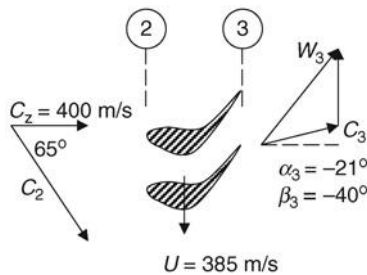
- (a) T_2 in K
- (b) C_{z2} in m/s
- (c) $C_{\theta 2}$ in m/s
- (d) M_1
- (e) p_{t2} in MPa
- (f) p_2 in kPa

Assume $C_z = \text{constant}$, $\gamma_t = 1.30$, and $c_{pt} = 1244$ J/kg · K.



■ FIGURE P10.9

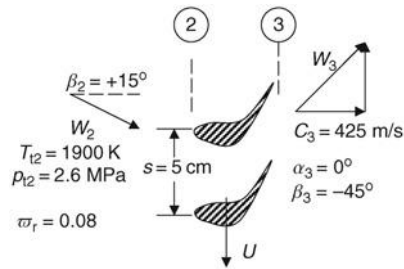
10.10 The velocity triangles across a turbine rotor are shown. The axial velocity remains constant across the rotor. If the total temperature at the rotor inlet is 1850 K with $\gamma_t = 1.30$ and $c_{pt} = 1244$ J/kg · K, calculate



■ FIGURE P10.10

- (a) inlet absolute Mach number M_2
- (b) inlet relative Mach number M_{2r}
- (c) the degree of reaction $\circ R$
- (d) rotor specific work w_t in kJ/kg
- (e) exit static temperature T_3 (K)
- (f) exit relative Mach number M_{3r} .

10.11 A rotor is designed for constant axial velocity. The velocity triangles are as shown. The rotor total pressure loss coefficient is known to be 0.08 with $\gamma_t = 1.30$ and $R_t = 287$ J/kg · K.



■ FIGURE P10.11

Calculate

- (a) rotor speed U in m/s
- (b) rotor specific work w_t in kJ/kg
- (c) stage degree of reaction $\circ R$
- (d) rotor circulation Γ in m^2/s
- (e) inlet absolute Mach number M_2
- (f) inlet gas static density ρ_2 in kg/m^3
- (g) exit relative Mach number M_{3r}
- (h) exit total pressure p_{t3} in MPa
- (i) exit static density ρ_3 in kg/m^3 .

10.12 Coolant air is bled from a compressor exit at $T_{tc} = 800$ K with $c_{pc} = 1004$ J/kg · K. The coolant is given a (positive) preswirl before it enters the rotor blade root in the direction of the rotor rotation. Assuming the port of coolant entry into the rotor is at $r_c = 42$ cm with rotor angular speed $\omega = 12000$ rpm, and the coolant enters the rotor blade root axially, as shown in Figure 10.64, calculate the coolant relative total temperature as it enters the rotor blade.

10.13 A multistage turbine is to be designed with constant axial velocity. The total temperature ratio across the entire turbine is $\tau_t = 0.72$ and the turbine polytropic efficiency is $e_t = 0.85$ with $\gamma_t = 1.30$ and $c_{pt} = 1244$ J/kg · K. Calculate

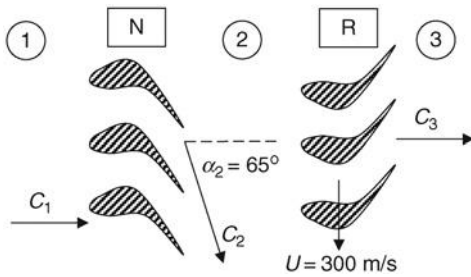
- (a) The turbine total pressure ratio π_t
- (b) the turbine adiabatic efficiency η_t
- (c) turbine area ratio, A_3/A_4 , for choked inlet, i.e., $M_4 = 1.0$, $T_{t4} = 1675$ K and $C_z = 445$ m/s and swirl-free exit flow

Assume γ and R remain constant across the turbine.

10.14 A 50% degree of reaction turbine stage is shown. The nozzle turns the flow 65° and the rotor exit flow is swirl-free. Assuming axial velocity remains constant throughout the stage, calculate

- (a) axial velocity C_z m/s
- (b) rotor specific work w_1 kJ/kg
- (c) stage loading ψ
- (d) flow coefficient ϕ
- (e) static temperature drop $\Delta T = T_1 - T_2$
- (f) static temperature drop $\Delta T = T_2 - T_3$

Assume $c_{pt} = 1.156$ kJ/kg · K.



■ FIGURE P 10.14

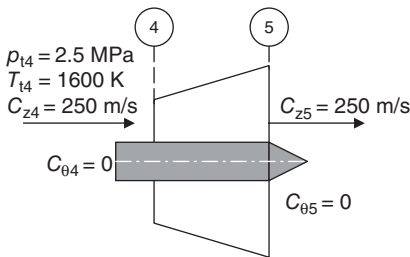
10.15 A simple method to establish the annulus geometry in a multistage turbine is to assume a constant throughflow (i.e., axial) speed C_z . Calculate

- (a) the density ratio ρ_5/ρ_4
- (b) the exit-to-inlet area ratio A_5/A_4

for

$$\begin{aligned} 1/\pi_1 &= 3.5 \\ e_t &= 0.80 \\ C_z &= \text{const.} \\ \gamma_1 &= 1.33, c_{pt} = 1156 \text{ J/kg} \cdot \text{K} \end{aligned}$$

Also, if the hub radius is constant, calculate the tip-to-tip radius ratio $(r_5/r_4)_{\text{tip}}$ for $(r_h/r_4)_4 = 0.80$

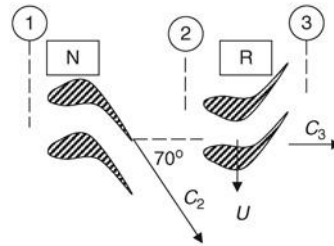


■ FIGURE P 10.15

10.16 A turbine stage has an inlet total temperature T_{t1} of 2000 K. If the rotational speed of the rotor at the pitchline is 200 m/s and the axial velocity component is $C_z = 250$ m/s, calculate

- (a) the stagnation temperature as seen by the rotor, $T_{t2,r}$
- (b) the gas static temperature upstream of the rotor, T_2
- (c) the adiabatic wall temperature for the rotor, $T_{aw,r}$ assuming a turbulent boundary layer

Assume $\gamma = 1.33, c_p = 1156$ J/kg · K and $Pr = 0.71$.



■ FIGURE P 10.16

10.17 A turbine stage is characterized by a loading coefficient, ψ of 0.8, and a flow coefficient of ϕ of 0.6. The rotor is unshrouded and has a tip clearance gap-to-blade height ratio of 2.5%. The ratio of the tip to pitchline radius is $r_t/r_m = 1.50$. The rotor blade tip has a knife configuration with a tip discharge coefficient of 0.60. The mean relative flow angle in the turbine rotor is $\beta_m = -30^\circ$. Calculate the loss of turbine efficiency due to the tip clearance.

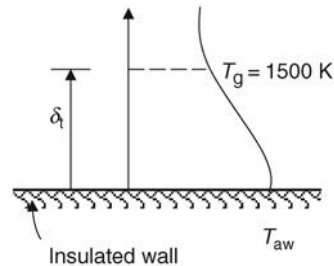
10.18 The relative flow angles in a turbine rotor are $\beta_2 = 25^\circ$ and $\beta_3 = -45^\circ$.

Calculate

- (a) optimum axial solidity parameter
- (b) the axial solidity σ_z based on the recommended value of the loading coefficient ψ_z

10.19 The thermal boundary layer associated with the flow of a hot gas over an insulated flat plate is shown.

Assume that the gas Prandtl number is $Pr = 0.71$, the ratio of specific heats is $\gamma = 1.33$, the gas Mach number is $M_g = 0.75$.



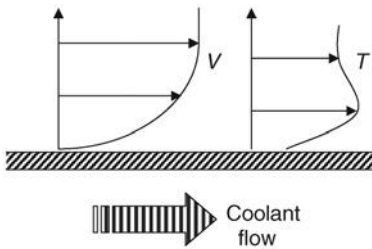
■ FIGURE P 10.19

Calculate

- (a) the adiabatic wall temperature T_{aw} in K
- (b) the gas stagnation temperature T_{tg} in K

First assume that the viscous boundary layer is laminar and then solve the problem for a turbulent boundary layer.

10.20 Consider the flow of high-temperature, high Mach number gas over a flat wall, ($M_g = 1.0, \gamma_g = 1.33, c_{pg} = 1156 \text{ J/kg} \cdot \text{K}, T_g = 1420 \text{ K}, p_g = 12 \text{ kPa}, Pr_g = 0.70$). We intend to internally cool the wall to achieve a wall temperature of $T_{wg} = 1200 \text{ K}$.



■ FIGURE P 10.20

Assuming the gas-side Stanton number is $St_g = 0.005$, calculate

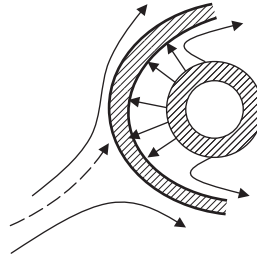
- (a) the gas stagnation temperature T_{tg} K
- (b) the adiabatic wall temperature T_{aw} K for a turbulent boundary layer
- (c) the gas-side film coefficient h_g $\text{W/m}^2 \text{ K}$
- (d) the heat flux to the wall q_w kW/m^2

For a wall thickness of $t_w = 3 \text{ mm}$, and a thermal conductivity, $k_w = 14.9 \text{ W/m} \cdot \text{K}$, calculate

- (e) the wall temperature on the coolant side T_{wc} K

10.21 The leading edge on a turbine nozzle is to be internally cooled using an impingement cooling technique, as shown. The leading-edge diameter is 8 mm. Calculate the heat transfer coefficient h_g at the leading edge, assuming an augmentation factor $a = 1.5$ due to a high-intensity turbulent flow in the turbine (use Equation 10.81 for a cylinder in cross-flow).

$$\begin{aligned}
 M_g &= 0.5, \\
 \gamma_g &= 1.33, \\
 c_{pg} &= 1156 \text{ J/kg} \cdot \text{K} \\
 k_g &= 0.082 \text{ W/m} \cdot \text{K} \\
 T_g &= 1500 \text{ K} \\
 p_g &= 1.0 \text{ MPa} \\
 Pr_g &= 0.70 \\
 \mu_g &= 4.9 \times 10^{-5} \text{ kg/m} \cdot \text{s}
 \end{aligned}$$



■ FIGURE P 10.21

10.22 The exit flow angle in a turbine nozzle at the pitch-line is 70° . The blade spacing is $s = 6 \text{ cm}$. The total pressure and temperature at the nozzle throat are 2.6 MPa and 1700 K, respectively. Assuming the nozzle throat is choked calculate the mass flow rate (per unit span) through a single nozzle blade passage. The gas properties may be assumed to be $\gamma_t = 1.30$ and $c_{pt} = 1244 \text{ J/kg} \cdot \text{K}$.

10.23 A turbine blade row is cooled with a coolant mass fraction of 3% and the coolant inlet temperature of $T_{tc} = 775 \text{ K}$. The coolant is ejected at the blade trailing edge at a temperature of 825 K as it mixes with the hot gas at the temperature of 1825 K. Assuming gas properties for the coolant and hot gas are $\gamma_c = 1.40, c_{pc} = 1004 \text{ J/kg} \cdot \text{K}$ and $\gamma_t = 1.30$ and $c_{pt} = 1244 \text{ J/kg} \cdot \text{K}$ and the coolant flow rate is 3 kg/s, calculate

- (a) the rate of heat transfer to the coolant from the blade in kW
- (b) the mixed-out specific heat (of the coolant and the hot gas after mixing)
- (c) the mixed-out temperature (of the coolant and the hot gas after mixing)

10.24 The total temperature and pressure at the entrance to a rotor are known to be 1850 K and 3.0 MPa, respectively. The rotor is of constant axial velocity design with $C_z = 442 \text{ m/s}$. The rotor relative velocity at the inlet is $W_2 = 562 \text{ m/s}$. The rotor relative exit Mach number is to be $M_{3r} = 0.90$. Assuming $\alpha_2 = 60^\circ, \gamma = 1.33$ and $c_p = 1156 \text{ J/kg} \cdot \text{K}$ calculate

- (a) the relative inlet Mach number M_{2r}
- (b) the relative flow angle at the exit β_3 (degrees)
- (c) the absolute exit flow angle α_3 (degrees)
- (d) stage degree of reaction $^\circ R$

10.25 A turbine rotor has a tip clearance height of 1% compared with blade height. The loading coefficient is $\psi = 2.5$ and the flow coefficient is $\phi = 0.6$. The turbine efficiency for zero tip clearance is $\eta_0 = 0.85$. The tip-to-mean radius ratio is $r_t/r_m = 1.25$, and the mean flow angle in the rotor is $\beta_m = -15^\circ$. Using the following tip clearance efficiency loss model,

$$\Delta\eta \cong \eta_0 C_D \cdot \tau \cdot \left(\frac{r_t}{r_m} \right) \left(1 - \frac{\psi}{\phi} \tan \beta_m \right)^{1/2}$$

calculate the turbine efficiency loss due to 1% tip clearance for the following rotor tip shapes

- (a) *knife* with gap Reynolds number of 2000
- (b) *groove*

Assuming the rotor with a flat-tip has a discharge coefficient of $C_{D,flat-tip} = 0.83$.

10.26 The free-stream gas temperature is $T_\infty = 1600$ K and the free-stream gas speed is $V_\infty = 850$ m/s. The gas properties are $\gamma_t = 1.30$, $c_{pt} = 1244$ J/kg · K and Prandtl number $Pr = 0.73$. Consider the flow of this gas over a flat plate at a high Reynolds number corresponding to turbulent flow. Calculate

- (a) the gas total temperature $T_{t\infty}$ in K in the freestream
- (b) the adiabatic wall temperature T_{aw} in K
- (c) percent error if we assume adiabatic wall temperature is the same as total temperature of the gas

10.27 A gas turbine is to provide a shaft power of 50 MW to a compressor with mass flow rate of 100 kg/s. The compressor bleeds 10 kg/s at its exit for turbine internal cooling purposes. The combustor exit mass flow rate is 93 kg/s, which accounts for 3 kg/s of fuel flow rate in the combustor. The turbine inlet temperature is $T_{t4} = 1850$ K and $p_{t4} = 2.0$ MPa with $\gamma_t = 1.30$, $c_{pt} = 1244$ J/kg · K. Assuming the coolant total temperature is $T_{tc} = 785$ K and the gas properties are $\gamma_c = 1.40$, $c_{pc} = 1004$ J/kg · K, calculate

- (a) the turbine exit total temperature $T_{t5-cooled}$
- (b) the turbine exit total pressure $p_{t5-cooled}$.

You may assume that the effect of cooling on turbine adiabatic efficiency is about ~2.8% loss (of efficiency) per 1% cooling.

10.28 The Stanton number is in general a function of Prandtl and Reynolds numbers, among other nondimensional parameters such as Mach number, roughness, curvature, free-stream turbulence intensity, etc. Eckert–Livingood model for a flat plate with constant wall temperature, excluding all other effects except Prandtl number and the Reynolds number, is

$$St_g = 0.0296 Pr_g^{-2/3} Re_x^{-1/5}$$

for a turbulent boundary layer. The Prandtl number for the gas is 0.704 and remains constant along the plate. Make a spreadsheet calculation of Stanton number St_g with respect to Reynolds number in the range of $200,000 \leq Re_x \leq 500,000$. Graph the Stanton number versus Reynolds number. Also, calculate the wall-averaged Stanton number.

10.29 The nozzle throat opening o is to be sized for a throat Reynolds number of $Re_o = 500,000$. The throat is choked with $T_{t-throat} = 2000$ K, $p_{t-throat} = 2.1$ MPa, and the gas properties at the throat are $\gamma_t = 1.30$, $c_{pt} = 1244$ J/kg · K, $\mu_{throat} = 6.5 \times 10^{-5}$ kg/m · s. Calculate the nozzle throat opening o in centimeters.

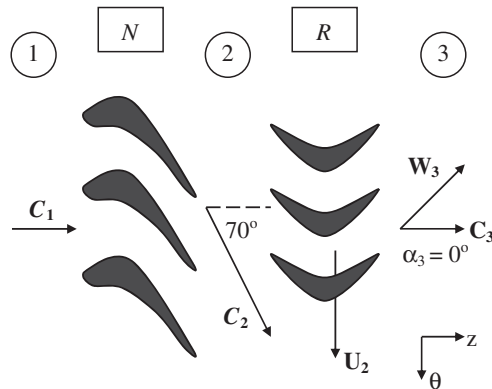
10.30 A turbine rotor has a hub and tip radii

$$\begin{aligned} r_h &= 35 \text{ cm} \\ r_t &= 45 \text{ cm} \end{aligned}$$

The rotor angular speed is $\omega = 2500$ rpm. The rotor blade taper ratio A_t/A_h is 0.75. Estimate the ratio of blade centrifugal stress at the hub to blade material density, σ_c/ρ_{blade} . If this rotor operates at 1200°F, what are the suitable materials for this rotor? (*Hint*: Use Figure 10.61 as a guide)

10.31 An uncooled turbine stage is of impulse design with $\circ R = 0$. The rotor exit is swirl free, i.e., $C_{\theta 3} = 0$. The nozzle exit absolute flow angle is $\alpha_2 = 70^\circ$. The axial velocity is constant throughout the stage and is equal to $C_z = 252$ m/s. The gas properties are: $\gamma_t = 1.33$ and $c_{pt} = 1,156$ J/kg · K. The turbine inlet total temperature is $T_{t1} = 1650$ K. Calculate

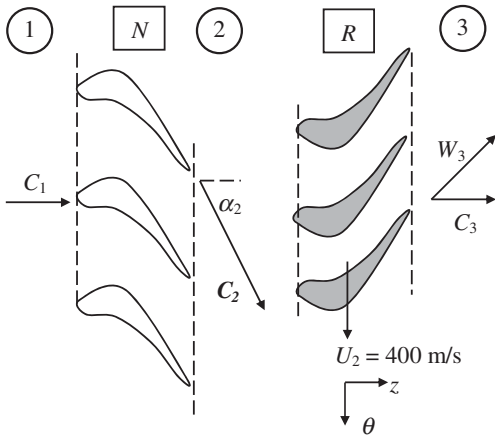
- (a) rotor (rotational) speed, U_2 , in m/s
- (b) total temperature drop in the stage, ΔT_t , in K
- (c) speed of sound, a_2 , in m/s
- (d) speed of sound, a_3 , in m/s
- (e) absolute Mach number, M_2
- (f) relative rotor exit Mach number, M_{t3}



■ FIGURE P10.31

10.32 An axial-flow turbine stage, at its pitchline radius, is shown. The rotor exit is swirl free, i.e., $C_{\theta 3} = 0$. The axial velocity is constant throughout the stage and is equal to $C_z = 300$ m/s. The flow to the turbine stage is purely axial, i.e., $C_1 = C_{z1}$ and the gas total temperature is $T_{t1} = 1500$ K with $\gamma_t = 1.33$ and $c_{pt} = 1,156$ J/kg · K. Assume that the turbine is uncooled and the stage degree of reaction is 20%. Calculate

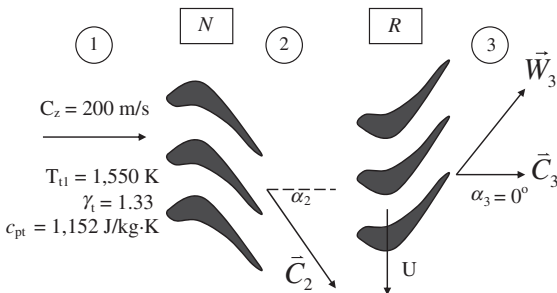
- (a) the nozzle exit flow angle, α_2 , in degrees
- (b) the stage specific work in kJ/kg
- (c) total temperature relative to the rotor, $T_{t2,r}$, in K
- (d) absolute Mach number at nozzle exit, M_2
- (e) speed of sound, a_3 , in m/s
- (f) relative rotor exit Mach number, M_{3r}



■ FIGURE P10.32

10.33 A turbine stage at the pitchline is designed with 15% degree of reaction and zero exit swirl, as shown. The pitchline radius is at $r_m = 0.60$ m and shaft rotational speed is $\omega = 6500$ rpm. Assuming the axial velocity is constant; calculate the following parameters at the pitchline:

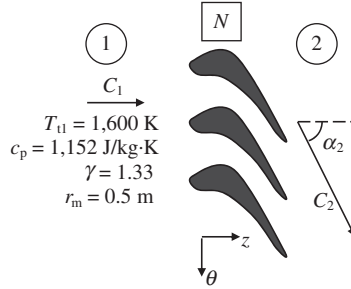
- (a) nozzle exit absolute swirl, $C_{\theta 2}$, in m/s
- (b) nozzle exit Mach number, M_2
- (c) rotor exit relative Mach number, M_{3r}
- (d) the stage loading at pitchline, ψ_m



■ FIGURE P10.33

10.34 A turbine stage is designed with constant axial velocity of $C_z = 200$ m/s. The absolute flow angle at the nozzle entrance is zero, i.e., $\alpha_1 = 0^\circ$, and at the nozzle exit is $\alpha_2 = 70^\circ$. Assuming the mass flow rate through the nozzle (blade row) is $\dot{m} = 100$ kg/s, and $r_m = 0.5$ m, calculate

- (a) (mean) torque acting on the nozzle blades in kN-m
- (b) static temperature at the nozzle exit, T_2 , in K



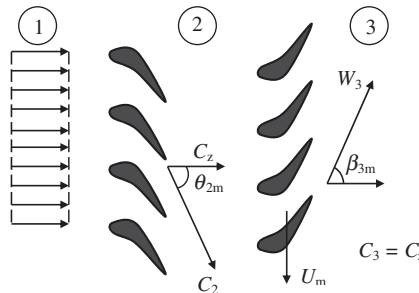
■ FIGURE P10.34

10.35 An axial-flow turbine nozzle turns the flow from an axial direction in the inlet to an exit flow angle of $\alpha_2 = 70^\circ$. The rotational speed of the rotor at the pitchline is $U = 400$ m/s. The exit flow from the stage is swirl free, i.e., $\alpha_3 = 0$. Assuming that the axial velocity is constant in the stage, $C_z = 265$ m/s, and the turbine inlet conditions are: $T_{t1} = 1750$ K, $p_{t1} = 2$ MPa, $\gamma_t = 1.33$ and $c_{pt} = 1156$ J/kg · K, calculate

- (a) absolute swirl at the nozzle exit, $C_{\theta 2}$, in m/s
- (b) absolute Mach number at the nozzle exit, M_2
- (c) relative flow angle at the rotor entrance, β_2 (deg)
- (d) the rotor-specific work, w_t
- (e) the stage loading, ψ , at the pitchline
- (f) stage degree of reaction at the pitchline
- (g) the relative exit Mach number, M_{3r}

10.36 The combustor discharges gas into a turbine with total pressure and temperature of 1.5 MPa and 1650 K, respectively. The turbine nozzle turns the purely axial flow at its entrance to 62° while maintaining a constant axial velocity of $C_z = 360$ m/s. The rotor blade rotational speed at the pitchline is $U_m = 400$ m/s. For an uncooled turbine stage with $\gamma = 1.33$ and $c_p = 1157$ J/kg · K, calculate

- (a) Mach number downstream of the nozzle, M_2
- (b) relative flow angle to the rotor, β_{2m} , in degrees
- (c) total temperature sensed by the rotor, T_{t2r} , in K
- (d) degree of reaction at pitchline (note $\alpha_3 = 0$)



■ FIGURE P10.36

10.37 In a cooled turbine nozzle, the temperature of the gas is $T_g = 1500$ K, the gas (mean) speed is $u_g = 800$ m/s. The Prandtl number for the gas is $Pr_g = 0.8$ and $c_{pg} = 1160$ J/kg · K. Estimate

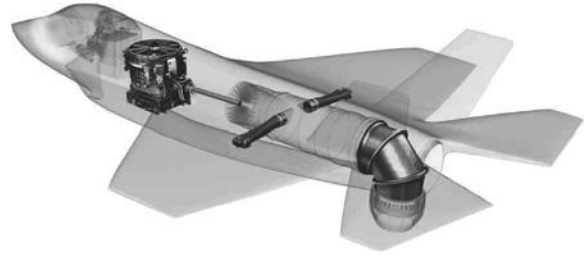
- (a) adiabatic wall temperature, T_{aw} , in K, for a laminar BL
- (b) adiabatic wall temperature, T_{aw} , in K, for a turbulent BL
- (c) gas stagnation temperature, T_{tg} , in K

10.38 An (internal) convectively-cooled turbine rotor blade has a low cooling effectiveness parameter, i.e., $\eta \equiv \frac{T_{tg} - T_{wg}}{T_{tg} - T_c} = 0.12$, where T_{tg} is in rotor (relative) frame of reference. The rotor inlet total temperature (relative to the rotor) is 1510 K and the coolant is bled from the compressor discharge with the temperature of 715 K. Assuming that the ratio of the gas-to-coolant side Stanton numbers is 0.25, i.e.,

$St_g/St_c = 0.25$, and the wall temperature on the coolant side is calculated as, $T_{wc} = 1350$ K, estimate the cooling mass fraction that is needed in the rotor blade row. Assume $c_{pg} = 1150$ J/kg · K and $c_{pc} = 1004$ J/kg · K.

10.39 The inlet flow angle to a turbine nozzle is $\alpha_1 = 5^\circ$. Using correlation 10.88, estimate the induced angle, $\Delta\theta_{ind}$, at the nozzle leading edge due to local flow curvature for a range of nozzle blade solidities from 1.0 to 2.0. Graph the induced flow angle versus the blade solidity.

10.40 The number of cycles to failure is an important design parameter in turbine blade material selection. Fatigue strength of conventionally cast and two directionally solidified materials are shown in Figure 10.58. Assuming a turbine blade root experiences a stress of 80 kpsi, and the same operating condition as shown in Figure 10.58, estimate the number of cycles to failure for the three materials shown. Note that the x-axis is in logarithmic scale.



Source: Reproduced with permission from Rolls-Royce plc

Aircraft Engine Component Matching and Off-Design Analysis

11.1 Introduction

How does an existing engine behave in an off-design operating condition? For an existing engine, we know its geometry and design-point parameters, such as compressor pressure ratio or turbine entry temperature. All the parameters that we used in the cycle analysis were in effect “design-point” parameters. For example, take compressor pressure ratio; it may be designed into a number of stages, each with a certain design pressure ratio. Although we cannot change the number of stages after the engine is manufactured, we may operate the compressor at a different shaft speed than its design speed, or, equivalently, we may operate the engine at a different throttle setting than its design. In general, the independent parameters that may be set and create an off-design flight condition for an airbreathing jet engine are

- Altitude of flight, which may include nonstandard ambient pressure and temperature, for example, arctic flight or seasonal effects
- Flight Mach number, from takeoff, climb, cruise, dash, approach, landing

- Throttle setting, that is, turbine entry temperature
- Afterburner setting, for example, -on, -off, or partial setting
- Nozzle area ratio setting, for example, to optimize installed thrust.

We will first consider individual component matching in a jet engine. Then we will examine the entire system from the gas generator to the whole aircraft engine at on- and off-designs.

11.2 Engine (Steady-State) Component Matching

What are the physical laws that need to be satisfied by engine components that interact with each other regardless of their mode of operation? In steady-state operation, the physical mass flow rate (e.g., in kg/s) through a component should be delivered in its entirety to the next component(s). For example, the air mass flow rate through the inlet must be equal to the fan mass flow rate, unless some air was bypassed in the inlet before getting to the fan, in an inlet flow stability scheme. This satisfies the law of conservation of mass.

The next conservation law that applies to the components that interact is the conservation of energy. For example, the low-pressure spool connecting the low-pressure turbine to the low-pressure compressor/fan via a shaft must deliver turbine shaft power output (e.g., in MW) to the low-pressure compressor allowing for possible power extraction for electric generator and frictional losses (i.e., energy dissipation) in the bearings supporting the rotating machinery. In addition, the compressor and turbine stages on the same shaft are constrained by the same physical shaft (angular) speed, that is, $N_{LPC} = N_{LPT}$ and $N_{HPC} = N_{HPT}$ for a two-spool machine.

There is also the law of conservation of atomic species. We studied this topic in Chapter 7 for a mixture of gases that were chemically reacting. In this chapter, we allow for a variable gas composition through a component, but we will not do an equilibrium chemical analysis of gas mixtures, except for the combustor. For example, the chemical reaction in a combustor produces a certain gas composition at the turbine entry. The flow expansion in the turbine, that is, the temperature drop, however, causes the gas composition to change. Applying the equilibrium gas chemistry principles will establish the gas composition at every operating condition. To simplify the process, that is, to avoid running the equilibrium gas chemistry codes (see, for example, Gordon and McBride, 1994) for every component, we choose to specify “appropriate” gas constants, γ , R or γ , and c_p , per component entrance and exit condition (or cold and hot). In cycle analysis, we used three levels of gas constants, (1) inlet and compressor (or cold section), (2) turbine (or hot section), and (3) the afterburner and nozzle (or very hot section). Although the principle variable in establishing gas constants is the gas temperature, the fraction of hydrocarbon fuel content in the gas also impacts these variables.

A remark about the law of conservation of momentum is also in order, as it appears that it is omitted from our component matching discussions. In reality, we still use the law of conservation of momentum to calculate the force magnitude and direction that each component produces in the propulsion system (remember the section on fluid impulse in Chapter 2). However, in the steady-state component matching case, it is the mass and energy that dictate the interaction.

Finally, a brief review of engine corrected parameters is in order, as the component performance maps are often presented in these coordinates. There are five component and

engine corrected parameters. These are (1) Corrected mass flow rate, (2) Corrected shaft speed, (3) Corrected fuel flow rate, (4) Corrected thrust, and (5) Corrected thrust-specific fuel consumption.

11.2.1 Engine Corrected Parameters

We studied in Chapters 8–10 that the corrected mass flow rate and corrected shaft speed are the parameters that fully describe the behavior of a compressor or turbine. These parameters are related to the axial and tangential Mach numbers in turbomachines, respectively. We had defined reference pressure and temperature, $p_{\text{ref}} = 101.33 \text{ kPa}$ and $T_{\text{ref}} = 288.2 \text{ K}$, respectively. Based on these reference conditions, we defined a δ and a θ parameter, for station i , according to

$$\delta_i \equiv p_{ti}/p_{\text{ref}} \quad (11.1)$$

$$\theta_i \equiv T_{ti}/T_{\text{ref}} \quad (11.2)$$

The corrected mass flow rate at station i is the mass flow rate through station i at the reference pressure and temperature:

$$\dot{m}_{ci} \equiv \frac{\dot{m}_i \sqrt{\theta_i}}{\delta_i} = \sqrt{\frac{\gamma_i}{R_i}} \frac{p_{\text{ref}}}{\sqrt{T_{\text{ref}}}} A_i M_i \left(1 + \frac{\gamma_i - 1}{2} M_i^2 \right)^{-\frac{\gamma_i + 1}{2(\gamma_i - 1)}} \quad (11.3)$$

The corrected shaft speed is

$$N_{ci} \equiv \frac{N}{\sqrt{\theta_i}} \quad (11.4)$$

We may define a corrected fuel flow rate according to

$$\dot{m}_{fc} \equiv \frac{\dot{m}_f}{\delta_2 \sqrt{\theta_2}} \quad (11.5)$$

Corrected thrust and thrust-specific fuel consumption, are

$$F_c \equiv F/\delta_0 \quad (11.6)$$

$$\text{TSFC}_c \equiv \frac{\text{TSFC}}{\sqrt{\theta_0}} \quad (11.7a)$$

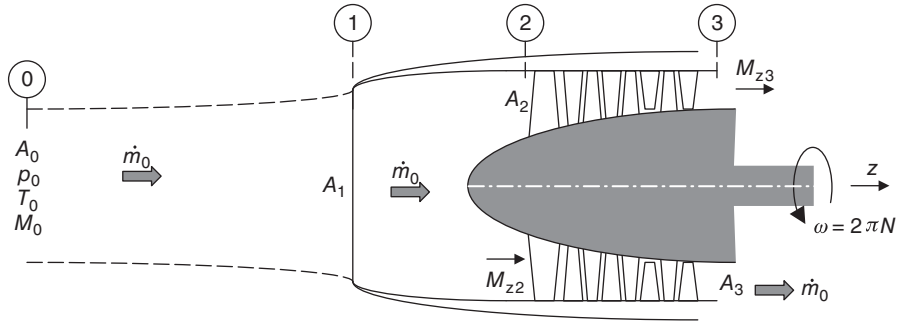
By taking the ratio of Equations 11.5 and 11.6, we relate three corrected parameters according to

$$\text{TSFC}_c = \pi_d \frac{\dot{m}_{fc}}{F_c} \quad (11.7b)$$

11.2.2 Inlet-Compressor Matching

A simple schematic drawing of an inlet coupled to a fan (or compressor) is shown as a guide to discussion in Figure 11.1. The fixed areas are the inlet lip A_1 , engine face area

■ FIGURE 11.1
Schematic
representation of the
inlet-compressor
matching



A_2 , and compressor exit area A_3 . The variable is the free stream capture area A_0 , which is a strong function of flight condition, for example, takeoff, climb, or cruise.

The ambient static pressure and temperature p_0 and T_0 and flight Mach number are independent variables as well. We may establish flight total pressure and temperature p_{t0} and T_{t0} using the static values and flight Mach number M_0 . We will use the flight Mach number and total gas properties in the cycle component matching and off-design analysis.

The physical mass flow rate through an area A is tied to axial Mach number M_z , local p_t , and T_t . The expression for the mass flow rate in terms of these variables is

$$\dot{m} = \sqrt{\frac{\gamma}{R} \frac{p_t}{\sqrt{T_t}}} \cdot A \cdot M_z \left(1 + \frac{\gamma - 1}{2} M_z^2 \right)^{\frac{-(\gamma+1)}{2(\gamma-1)}} \quad (11.8)$$

The engine face (physical) mass flow rate (e.g., in kg/s or lbm/s) is

$$\dot{m}_2 = \sqrt{\frac{\gamma}{R} \frac{p_{t2}}{\sqrt{T_{t2}}}} \cdot A_2 \cdot M_{z2} \left(1 + \frac{\gamma - 1}{2} M_{z2}^2 \right)^{\frac{-(\gamma+1)}{2(\gamma-1)}} \quad (11.9)$$

The inlet mass flow rate is

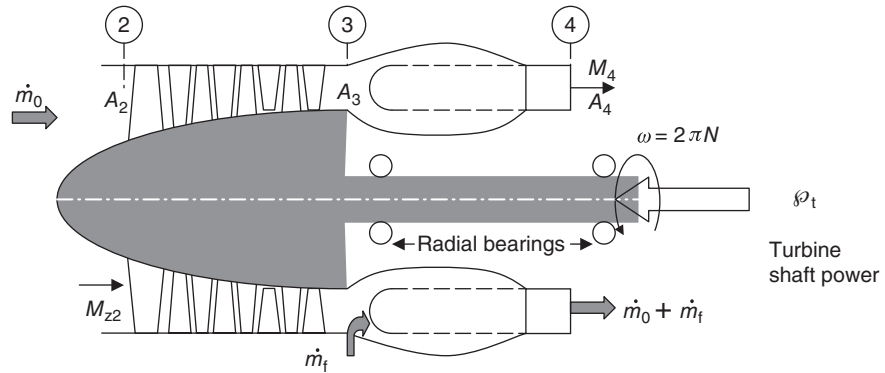
$$\dot{m}_0 = \sqrt{\frac{\gamma}{R} \frac{p_{t0}}{\sqrt{T_{t0}}}} \cdot A_0 \cdot M_0 \left(1 + \frac{\gamma - 1}{2} M_0^2 \right)^{\frac{-(\gamma+1)}{2(\gamma-1)}} \quad (11.10)$$

The law of conservation of mass demands that the inlet flow rate and the airflow rate into the engine to be equal (assuming there is no inlet bleed), that is,

$$\sqrt{\frac{\gamma}{R} \frac{p_{t2}}{\sqrt{T_{t2}}}} \cdot A_2 \cdot M_{z2} \left(1 + \frac{\gamma - 1}{2} M_{z2}^2 \right)^{\frac{-(\gamma+1)}{2(\gamma-1)}} = \sqrt{\frac{\gamma}{R} \frac{p_{t0}}{\sqrt{T_{t0}}}} \cdot A_0 \cdot M_0 \left(1 + \frac{\gamma - 1}{2} M_0^2 \right)^{\frac{-(\gamma+1)}{2(\gamma-1)}} \quad (11.11)$$

The conservation of energy, along with the assumption of the adiabatic flow in the inlet, identifies a constant total enthalpy flow or equivalently constant total temperature, if we

■ **FIGURE 11.2**
Compressor–
combustor matching
with their respective
mass flow rates, areas,
and Mach numbers



assume constant c_p . Therefore, eliminating the terms that remain unchanged between the flight condition and engine face in Equation 11.11, we get

$$\pi_d \frac{A_2}{A_0} \cdot M_{z2} \left(1 + \frac{\gamma - 1}{2} M_{z2}^2 \right)^{\frac{-(\gamma+1)}{2(\gamma-1)}} = M_0 \left(1 + \frac{\gamma - 1}{2} M_0^2 \right)^{\frac{-(\gamma+1)}{2(\gamma-1)}} \quad (11.12)$$

The right-hand side (RHS) in Equation 11.12 is completely known for a given flight Mach number M_0 . The left-hand side (LHS) contains three unknowns, (1) inlet total pressure recovery π_d , (2) the free stream capture area A_0 (or the ratio A_2/A_0), and (3) the axial Mach number at the engine face, M_{z2} . A typical inlet performance map contains the inlet recovery variation with flight Mach number, that is, $\pi_d = f(M_0)$, or we may use the AIA or MIL-E 5008-B standards that we presented in Chapter 6. Therefore, the mass and energy balance for the inlet/compressor results in two unknowns A_0 and M_{z2} for any flight Mach number M_0 .

The main area of concern in inlet-compressor matching is, however, tied to the inlet distortion problem. We have addressed both the inlet steady state and dynamic distortion effects on compressor performance extensively in Chapter 8. The ensued unsteadiness and instability in a compressor/fan, that is, stall and surge, find their roots often in inlet distortion.

11.2.3 Compressor–Combustor Matching

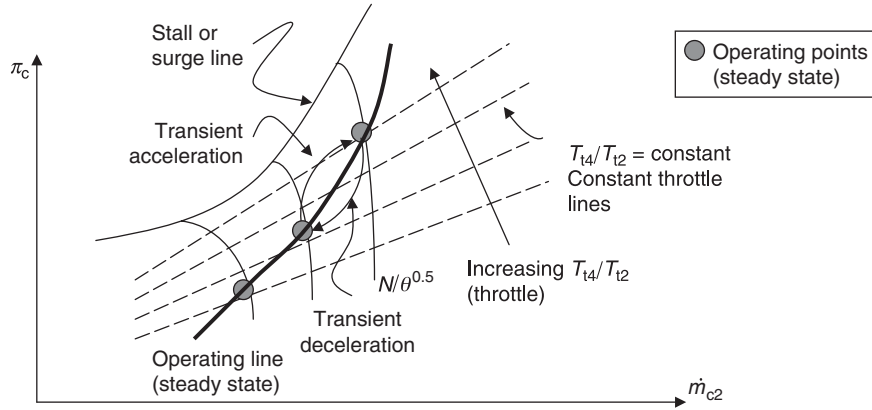
In a steady-state operation, the compressor (air) mass flow rate combines with the fuel flow rate in the combustor to form the exit mass flow rate at the entrance to the turbine. Figure 11.2 shows the combination of the compressor and burner and the three stations that connects them.

The mass flow rate at the burner exit is

$$\dot{m}_4 = \dot{m}_3 + \dot{m}_f = (1 + f)\dot{m}_0 = (1 + f)\dot{m}_2 \quad (11.13)$$

The unknowns on the RHS of Equation 11.13 are the fuel-to-air ratio f and the axial Mach number at the engine face, M_{z2} . The fuel-to-air ratio is set by the throttle, which is an independent parameter. Therefore, we consider the throttle setting as known in an off-design operating condition. We can also write the burner exit mass flow rate in terms

■ FIGURE 11.3
Operating line (or compressor-combustor matching) on a compressor map



of total pressure p_{t4} and temperature T_{t4} , flow area A_4 , and the local Mach number M_4 , namely,

$$\dot{m}_4 = \sqrt{\frac{\gamma_t}{R_t}} \frac{p_{t4}}{\sqrt{T_{t4}}} \cdot A_4 \cdot M_4 \left(1 + \frac{\gamma_t - 1}{2} M_4^2 \right)^{\frac{-(\gamma_t+1)}{2(\gamma_t-1)}} \quad (11.14)$$

Now, let us examine the RHS of Equation 11.14. If we take the station 4 as the exit of the first turbine nozzle, then over a wide operating condition, it remains choked, that is, $M_4 = 1$. The combustor exit total pressure $p_{t4} = \pi_b \cdot p_{t3}$, which for an assumed combustor total pressure loss π_b is the compressor discharge total pressure p_{t3} , which may be written as

$$p_{t4} = \pi_b p_{t3} = \pi_b \pi_c p_{t2} = \pi_d \pi_b \pi_c p_{t0} \quad (11.15)$$

The combustor exit total temperature T_{t4} is throttle setting dependent and is thus treated as known. In light of Equation 11.15, let us recast Equation 11.13 in the following form:

$$\sqrt{\frac{\gamma_t}{R_t}} \frac{\pi_b \pi_c}{\sqrt{T_{t4}/T_{t2}}} \cdot A_4 \left(\frac{\gamma_t + 1}{2} \right)^{\frac{-(\gamma_t+1)}{2(\gamma_t-1)}} = (1 + f) \sqrt{\frac{\gamma_c}{R_c}} A_2 \cdot M_{z2} \left(1 + \frac{\gamma_c - 1}{2} M_{z2}^2 \right)^{\frac{-(\gamma_c+1)}{2(\gamma_c-1)}} \quad (11.16)$$

The RHS of Equation 11.16 is a function of axial flow Mach number at the engine face, M_{z2} and throttle setting. Also, we note that the RHS of Equation 11.16 is proportional to the corrected mass flow rate at the compressor face. Therefore, we conclude that for a given compressor corrected mass flow rate and engine throttle setting, T_{t4}/T_{t2} and f , we can establish a unique compressor pressure ratio π_c . This is consistent with our earlier studies of turbomachinery as depicted in Figure 11.3 (reproduced from Figure 8.57), where a compressor performance map shows the throttle lines ($T_{t4}/T_{t2} = \text{constant}$, or nominal operating line) and the engine corrected speed lines N_c . The path of steady-state engine operation is shown as the engine “operating line” in Figure 11.3. An alternative view of Equation 11.16 is that for a given compressor pressure ratio and the throttle setting, there is a unique corrected compressor mass flow rate, which is a pure function of the axial Mach number into the engine, M_{z2} . We may use Equation 11.16 with the design choices

for π_c , M_{z2} , T_{t4}/T_{t2} , and f (and an assumed π_b) to calculate A_4/A_2 . This area ratio remains constant (for the fixed-area turbines) at off-design.

The energy balance across the combustor reveals the fuel-to-air ratio f as

$$f = \frac{h_{t4} - h_{t3}}{Q_R \eta_b - h_{t4}} \quad (11.17a)$$

The unknowns on the RHS of Equation 11.17a are h_{t3} and η_b , assuming that the throttle setting has specified T_{t4} in the off-design condition. Once we establish a compressor pressure ratio at the off-design operation, h_{t3} becomes known. We may use either a burner efficiency correlation for η_b (e.g., from Figure 7.40) or an assumed value to proceed with the calculation of the new fuel-to-air ratio f at off-design. In terms of the constant-throttle-line parameter T_{t4}/T_{t2} , as shown in Figure 11.3, and compressor temperature ratio, we can rewrite Equation 11.17a by dividing its numerator and denominator by the total enthalpy at the engine face, h_{t2} , to get

$$f Q_R \eta_b / h_{t2} \approx \frac{c_{pt}}{c_{pc}} \left(\frac{T_{t4}}{T_{t2}} \right) - \tau_c \quad (11.17b)$$

Finally, the compressor power is matched to the shaft power produced by the turbine when we account for any external (electric) power extraction and bearing frictional losses. The physical shaft rotational speed N is the same for the compressor–turbine stages on the same spool (i.e., shaft). We will address these matching requirements in the compressor–turbine matching section.

11.2.4 Combustor–Turbine Matching

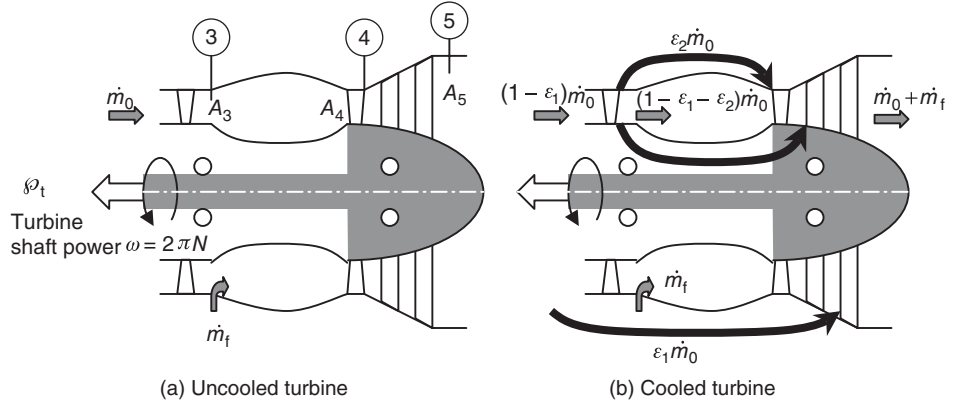
The steady-state combustor–turbine interaction is dominated by (1) choked turbine nozzle (i.e., $M_4 = 1$, which acts as the first throttle station in the gas turbine engine), (2) turbine cooling requirements, (3) hot spots in turbine entry, and (4) loss of turbine efficiency due to cooling. The latter three issues relate to either combustor design or turbine cooling and its impact on efficiency. Our goal in turbine off-design analysis is primarily to calculate turbine expansion parameter (i.e., its power production capability). The effect of cooling on turbine aerodynamics is often modeled as an equivalent uncooled turbine operating at a lower adiabatic efficiency, for example, $\eta_t = 0.75$ – 0.85 . Figure 11.4 shows the schematic drawing of a combustor–turbine with part (a) showing an uncooled turbine and part (b) showing a cooled turbine. The two epsilons ϵ_1 and ϵ_2 in Figure 11.4(b) depict air-cooling mass flow fractions that are bled from the compressor at an intermediate pressure point and at the compressor exit, respectively.

The physical mass flow rates at stations 4 and 5 are equal, if the turbine is uncooled. Therefore, by writing the corrected mass flow rates in both stations as

$$\dot{m}_{c4} = \dot{m}_4 \sqrt{\theta_4} / \delta_4 \quad (11.18a)$$

$$\dot{m}_{c5} = \dot{m}_5 \sqrt{\theta_5} / \delta_5 \quad (11.18b)$$

■ FIGURE 11.4
 Combustor–turbine
 matching



And taking the ratio of the above two expressions, we relate the corrected mass flow rates at turbine entrance and turbine exit according to

$$\frac{\dot{m}_{c4}}{\dot{m}_{c5}} = \frac{\pi_t}{\sqrt{\tau_t}} \tag{11.19}$$

The RHS of Equation 11.19 relates to turbine expansion, and it is this parameter that controls the axial Mach numbers, that is, mass flow rate, through the turbine. We will encounter this parameter again in this chapter. In the cooled turbine case, we need to account for the mass flow rate of the coolant, which is injected between stations 4 and 5 in the turbine. Therefore,

$$\dot{m}_4 = (1 + f - \epsilon_1 - \epsilon_2)\dot{m}_0 \tag{11.20a}$$

$$\dot{m}_5 = (1 + f)\dot{m}_0 \tag{11.20b}$$

The corrected mass flow rates, in the cooled turbine case, are related by cooling fractions according to

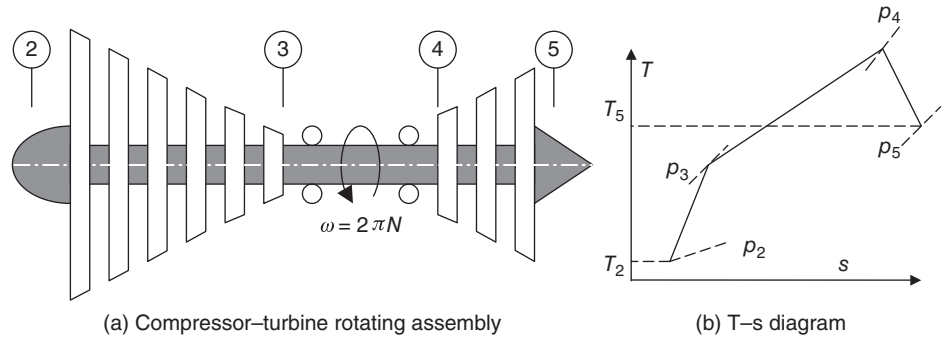
$$\frac{\dot{m}_{c4}}{\dot{m}_{c5}} = \left(\frac{1 + f - \epsilon_1 - \epsilon_2}{1 + f} \right) \frac{\pi_t}{\sqrt{\tau_t}} = \left(1 - \frac{\epsilon_1 + \epsilon_2}{1 + f} \right) \frac{\pi_t}{\sqrt{\tau_t}} \tag{11.21}$$

One last comment about τ_t is that in a cooled turbine case, T_{t5} is reduced as a result of coolant injection in the hot gas stream. Therefore τ_t (cooled turbine) is reduced compared with τ_t in an uncooled turbine. Another impact of cooling the turbine is on π_t , which is also reduced as the turbulent mixing of the coolant injection into the hot gas causes a total pressure drop in the turbine.

11.2.5 Compressor–Turbine Matching and Gas Generator Pumping Characteristics

The law of conservation of energy is applied to a compressor that is driven by a turbine on the same shaft. The schematic drawing of a compressor–turbine rotating assembly is shown in Figure 11.5. We may account for power dissipation in bearings through

■ **FIGURE 11.5**
Schematic drawing of a
compressor–turbine
rotating assembly on
the same shaft



mechanical efficiency η_m , which results in the following form of law of conservation of energy:

$$\dot{\mathcal{G}}_c = \dot{m}_0(h_{t3} - h_{t2}) = \eta_m \dot{\mathcal{G}}_t = \eta_m (\dot{m}_0 + \dot{m}_f)(h_{t4} - h_{t5}) \quad (11.22a)$$

Dividing Equation 11.22a by the air mass flow rate and the total enthalpy at the engine face (which is the same as the flight total enthalpy), we get

$$\tau_c - 1 = \eta_m (1 + f) \frac{c_{pt} T_{t4}}{c_{pc} T_{t2}} (1 - \tau_t) \quad (11.22b)$$

We shall demonstrate that the turbine expansion parameter τ_t remains constant over a wide operating range in the engine off-design condition; therefore, we may conclude from Equation 11.22b that the compression parameter $(\tau_c - 1)$ varies linearly with the throttle parameter T_{t4}/T_{t2} in off-design. Ignoring the variation of $\eta_m(1 + f)$ in on- and off-designs, we get

$$\frac{\tau_{c,O-D} - 1}{\tau_{c,D} - 1} \cong \frac{(T_{t4}/T_{t2})_{O-D}}{(T_{t4}/T_{t2})_D} \quad (11.23)$$

From Equation 11.23, we arrive at the off-design compressor pressure ratio based on either compressor polytropic or the adiabatic efficiency according to

$$\begin{aligned} \pi_c &= \tau_c^{e_c \gamma_c / (\gamma_c - 1)} \\ \pi_c &= [1 + \eta_c (\tau_c - 1)]^{\gamma_c / (\gamma_c - 1)} \end{aligned}$$

In terms of the throttle ratio T_{t4} / T_{t2} and adiabatic efficiency, the compressor off-design pressure ratio is

$$\pi_{c,O-D} \cong \left[1 + \eta_c (\tau_{c,D} - 1) \frac{(T_{t4}/T_{t2})_{O-D}}{(T_{t4}/T_{t2})_D} \right]^{\gamma_c / (\gamma_c - 1)} \quad (11.24)$$

Since compressor and turbine performance maps are always shown in terms of the corrected parameters, that is, corrected mass flow rate and the corrected shaft speed, we express the off-design performance of the gas generator in corrected terms as well.

The common shaft between the compressor and turbine has the same angular speed $\omega = 2\pi N$. Therefore, the corrected shaft speeds of the compressor and turbine, which are defined as

$$N_{c2} \equiv N/\sqrt{\theta_2} \tag{11.25a}$$

$$N_{c4} \equiv N/\sqrt{\theta_4} \tag{11.25b}$$

are related to each other by the throttle parameter, that is,

$$N_{c2} \equiv N_{c4} \sqrt{T_{t4}/T_{t2}} \tag{11.25c}$$

Since we had demonstrated in Chapter 8 that compressor (specific) work is proportional to the square of shaft speed (through turbine Euler equation), that is,

$$w_c \propto T_{t2}(\tau_c - 1) \propto N^2 \tag{11.26}$$

Divide Equation 11.26 by T_{t2} to arrive at the corrected shaft speed, that is,

$$\tau_c - 1 \propto N_{c2}^2 \tag{11.27}$$

Now, by comparing Equation 11.27 with Equation 11.25c, we conclude that for $\tau_t =$ constant, the corrected shaft speed N_{c4} remains constant, and N_{c2} is proportional to the square root of the throttle parameter T_{t4}/T_{t2} , that is,

$$N_{c4,O-D} \approx N_{c4,D} \approx \text{constant} \tag{11.28a}$$

$$\frac{N_{c2,O-D}}{N_{c2,D}} \approx \frac{\sqrt{(T_{t4}/T_{t2})_{O-D}}}{\sqrt{(T_{t4}/T_{t2})_D}} \tag{11.28b}$$

Again, the corrected mass flow rates in compressors and turbines are

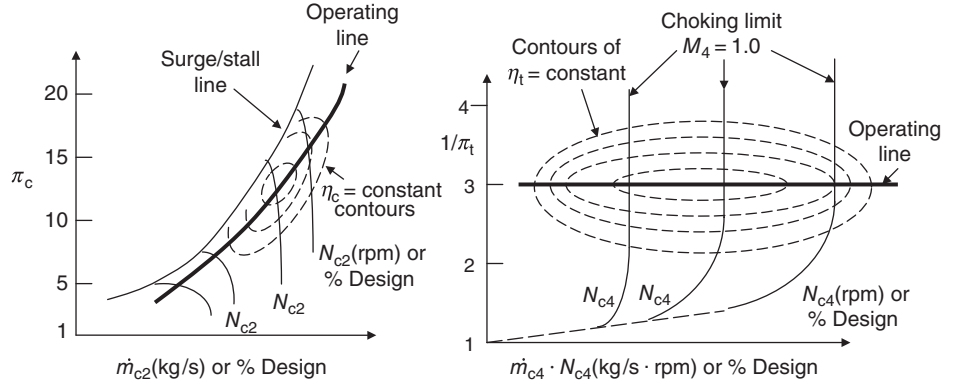
$$\dot{m}_{c2} = \dot{m}_2 \sqrt{\theta_2}/\delta_2 \tag{11.29a}$$

$$\dot{m}_{c4} = \dot{m}_4 \sqrt{\theta_4}/\delta_4 \tag{11.29b}$$

The physical mass flow rates in compressors and turbines are different only by the amount of fuel that we consume in the burner, therefore, Equations 11.29a and 11.29b yield

$$(1 + f)\dot{m}_{c2}\delta_2/\sqrt{\theta_2} = \dot{m}_{c4}\delta_4/\sqrt{\theta_4}$$

■ **FIGURE 11.6**
Typical compressor
and turbine
performance maps
used in component
matching studies



Since the flow in station 4 is choked (over a wide operating range), the corrected mass flow rate is constant at 4 and we thus conclude that

$$\dot{m}_{c2} = \frac{\dot{m}_{c4} p_{t4}}{1+f p_{t2}} \sqrt{\frac{T_{t4}}{T_{t2}}} = \frac{\dot{m}_{c4} \pi_b \pi_c}{(1+f) \sqrt{T_{t4}/T_{t2}}} \quad (11.30a)$$

$$\frac{\dot{m}_{c2,O-D}}{\dot{m}_{c2,D}} \cong \frac{\pi_{c,O-D}}{\pi_{c,D}} \frac{\sqrt{(T_{t4}/T_{t2})_D}}{\sqrt{(T_{t4}/T_{t2})_{O-D}}} \quad (11.30b)$$

Figure 11.6 shows typical compressor and turbine performance maps in corrected parameters, with constant adiabatic efficiency contours and the respective operating lines.

11.2.5.1 Gas Generator Pumping Characteristics. In the previous sections, we studied the component matching at on- and off-designs for an “on-paper” aircraft engine with a chosen set of design parameters. However, in the case of an existing gas generator where component performance maps are available, we can study all its possible operating conditions by establishing its so-called *pumping characteristics*. They are (1) the corrected airflow rate \dot{m}_{c2} , (2) the pressure ratio of the gas generator, p_{t5}/p_{t2} , (3) the temperature ratio of the gas generator, T_{t5}/T_{t2} , and (4) the fuel flow parameter, $f Q_R \eta_b / c_p T_{t2}$ or the corrected fuel flow rate \dot{m}_{fc} . The pumping characteristics are often expressed as a function of percent corrected shaft speed $\%N_{c2}$ and the throttle parameter T_{t4}/T_{t2} .

From Equation 11.30a, we have

$$\dot{m}_{c2} = \frac{\dot{m}_{c4} p_{t4}}{1+f p_{t2}} \sqrt{\frac{T_{t4}}{T_{t2}}} = \frac{\dot{m}_{c4} \pi_b \pi_c}{(1+f) \sqrt{T_{t4}/T_{t2}}} \quad (11.31)$$

$$\pi_c = \frac{(1+f) A_2 \dot{m}_{c2}/A_2}{\pi_b A_4 \dot{m}_{c4}/A_4} \sqrt{\frac{T_{t4}}{T_{t2}}} \quad (11.32)$$

There are two corrected mass flow rates per unit area in Equation 11.32. These are pure functions of axial Mach number and gas constants. Since the turbine nozzle remains choked at design and over a wide operating range of the engine, its corrected mass flow rate is

$$\begin{aligned} \dot{m}_{c4}/A_4 &= \sqrt{\frac{\gamma_t}{R_t} \frac{p_{\text{ref}}}{\sqrt{T_{\text{ref}}}}} \left(\frac{\gamma_t + 1}{2} \right)^{\frac{-(\gamma_t+1)}{2(\gamma_t-1)}} \\ &= f(\gamma_t, R_t) \quad [\approx 237(\text{kg/s})/\text{m}^2 \text{ for } \gamma_t = 1.33, R_t = 286.8 \text{ J/kg} \cdot \text{K}] \end{aligned}$$

The corrected mass flow rate at the engine face, per unit area, is

$$\dot{m}_{c2}/A_2 = \sqrt{\frac{\gamma_c}{R_c} \frac{p_{\text{ref}}}{\sqrt{T_{\text{ref}}}}} M_{z2} \left(1 + \frac{\gamma_c - 1}{2} M_{z2}^2 \right)^{\frac{-(\gamma_c+1)}{2(\gamma_c-1)}} = f(M_{z2}, \gamma_c, R_c) \quad (11.33)$$

Figure 11.7a shows a graph of Equation 11.33. A general graph of the corrected mass flow rate per unit area is shown in Figure 11.7b. The typical compressor and turbine entry (Mach number) range are identified.

As stated earlier, from the engine design point, we calculate A_2/A_4 from Equation 11.25 to be

$$\frac{A_4}{A_2} = \frac{(1+f)}{\pi_b \dot{m}_{c4}/A_4} \frac{\dot{m}_{c2}/A_2}{\pi_c} \sqrt{\frac{T_{t4}}{T_{t2}}} \quad (11.34)$$

The RHS of Equation 11.34 involves known parameters at the design point, for example, we may have chosen the following design values:

$$\begin{aligned} M_{z2} &= 0.5, \\ \pi_c &= 25, e_c = 0.90, \gamma_c = 1.4, c_{pc} = 1004 \text{ J/kg} \cdot \text{K} \\ T_{t4}/T_{t2} &= 6 \\ M_4 &= 1.0, \text{ therefore, } \dot{m}_{c4}/A_4 \cong 237 \text{ kg/s/m}^2 \\ Q_R &= 42,000 \text{ kJ/kg, } \eta_b = 0.995, \gamma_t = 1.33, c_{pt} = 1156 \text{ J/kg} \cdot \text{K} \end{aligned}$$

The fuel-to-air ratio is

$$f = \frac{c_{pt}T_{t4} - c_{pc}T_{t3}}{Q_R \eta_b - c_{pt}T_{t4}} = \frac{(c_{pt}/c_{pc})T_{t4}/T_{t2} - \tau_c}{Q_R \eta_b / c_{pc} T_{t2} - (c_{pt}/c_{pc})T_{t4}/T_{t2}} \approx 0.030$$

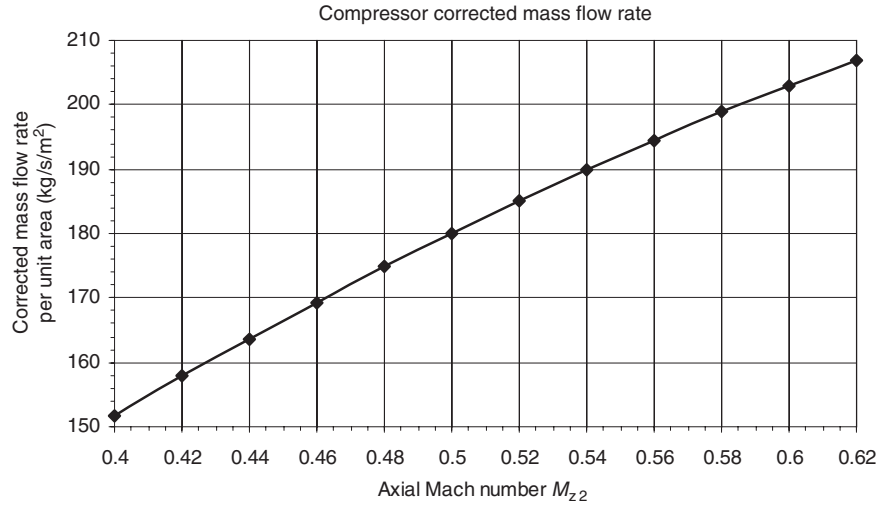
If we substitute these values and $\pi_b \approx 0.97$, in Equation 11.34, we get the area ratio $A_4/A_2 \approx 0.08$.

Now, we have the constants in Equation 11.34, that is,

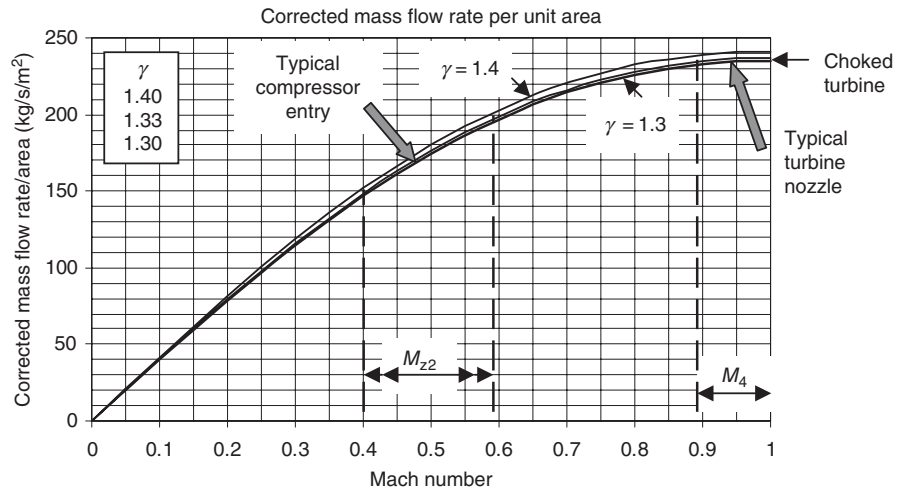
$$\pi_c = \frac{(1+f) A_2 \dot{m}_{c2}/A_2}{\pi_b A_4 \dot{m}_{c4}/A_4} \sqrt{\frac{T_{t4}}{T_{t2}}} \approx 0.0560 \sqrt{\frac{T_{t4}}{T_{t2}}} (\dot{m}_{c2}/A_2) \quad (11.35)$$

Let us graph Equation 11.35 for the compressor pressure ratio versus the corrected mass flow rate for different throttle parameters. Figure 11.8 shows the compressor map based on Equation 11.35.

■ **FIGURE 11.7**
Corrected mass flow rate per unit area A



(a) Corrected flow rate at the compressor face (per unit area A_2) for $\gamma = 1.4$



(b) General variation of corrected mass flow rate with Mach number and different γ

An exploded view of the compressor map at low-pressure ratios is shown in Figure 11.9. The power balance between the compressor and turbine yields an equation for τ_t according to

$$c_{pc}(T_{t3} - T_{t2}) = \eta_m(1 + f)c_{pt}(T_{t4} - T_{t5}) \tag{11.36a}$$

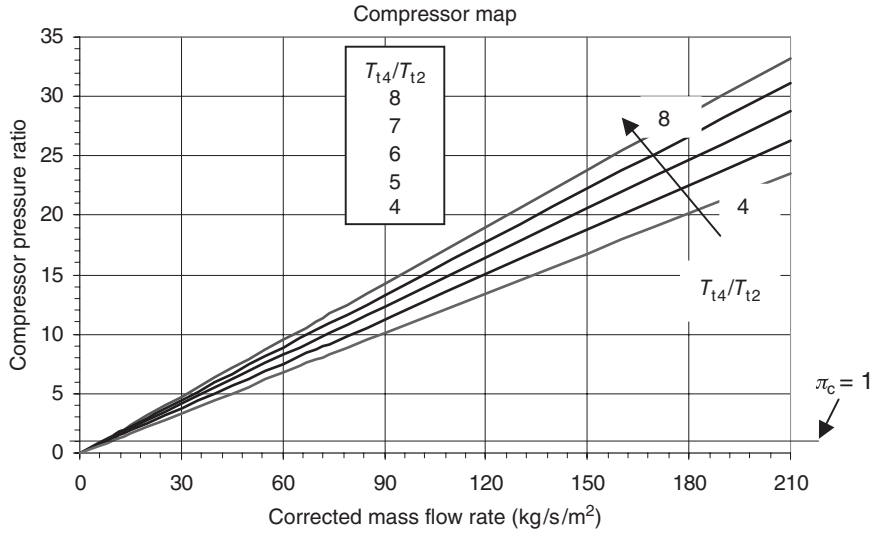
$$c_{pc}(T_{t3}/T_{t2} - 1) = \eta_m(1 + f)c_{pt}T_{t4}/T_{t2}(1 - T_{t5}/T_{t4}) \tag{11.36b}$$

$$\tau_t = 1 - \left(\frac{c_{pc}}{c_{pt}}\right) \frac{\tau_c - 1}{\eta_m(1 + f)(T_{t4}/T_{t2})} \tag{11.36c}$$

Also for the gas generator pumping characteristics, T_{t5}/T_{t2} , we write

$$\frac{T_{t5}}{T_{t2}} = \tau_t \frac{T_{t4}}{T_{t2}} = \frac{T_{t4}}{T_{t2}} - \left(\frac{c_{pc}}{c_{pt}}\right) \frac{\tau_c - 1}{\eta_m(1 + f)} \Rightarrow \frac{T_{t5}}{T_{t2}} = \frac{T_{t4}}{T_{t2}} - \left(\frac{c_{pc}}{c_{pt}}\right) \frac{\tau_c - 1}{\eta_m(1 + f)} \tag{11.37}$$

■ **FIGURE 11.8**
Compressor map (note that the graph is valid for $\pi_c > 1$)



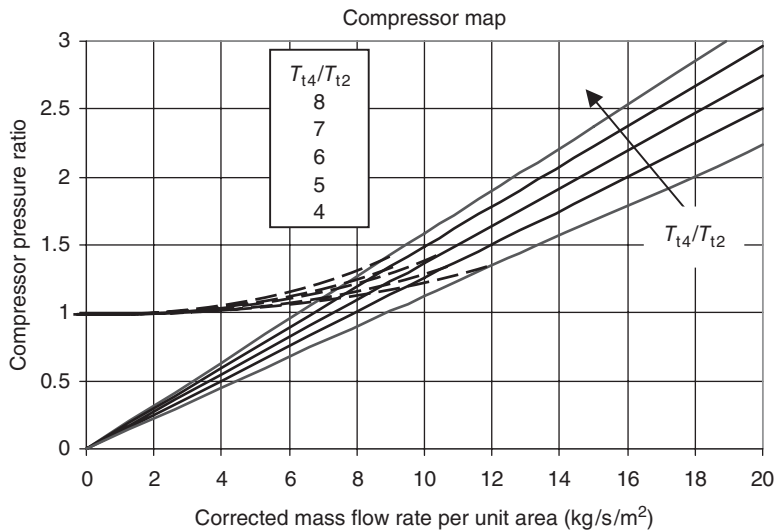
Another pumping characteristic is p_{t5}/p_{t2} , which is the product of component pressure ratios according to

$$\frac{p_{t5}}{p_{t2}} = \pi_t \pi_b \pi_c \tag{11.38}$$

The turbine pressure ratio π_t is related to turbine temperature ratio τ_t and adiabatic efficiency η_t according to

$$\pi_t = [1 - (1 - \tau_t)/\eta_t]^{\gamma_t/(\gamma_t - 1)} \Rightarrow \frac{p_{t5}}{p_{t2}} = \pi_b \pi_c [1 - (1 - \tau_t)/\eta_t]^{\gamma_t/(\gamma_t - 1)} \tag{11.39}$$

■ **FIGURE 11.9**
An exploded view of compressor map at low-pressure ratio



The fuel flow parameter in the gas generator is

$$\frac{fQ_R \eta_b}{\bar{c}_p T_{t2}} \approx \frac{T_{t4}}{T_{t2}} - \frac{T_{t3}}{T_{t2}} \Rightarrow \boxed{\frac{fQ_R \eta_b}{\bar{c}_p T_{t2}} \approx \frac{T_{t4}}{T_{t2}} - \tau_c} \quad (11.40)$$

The \bar{c}_p in Equation 11.40 is the “average” of the cold and hot c_p . The turbine corrected shaft speed is related to the compressor corrected shaft speed via Equation 11.25c. It is rewritten and boxed for the gas generator matching.

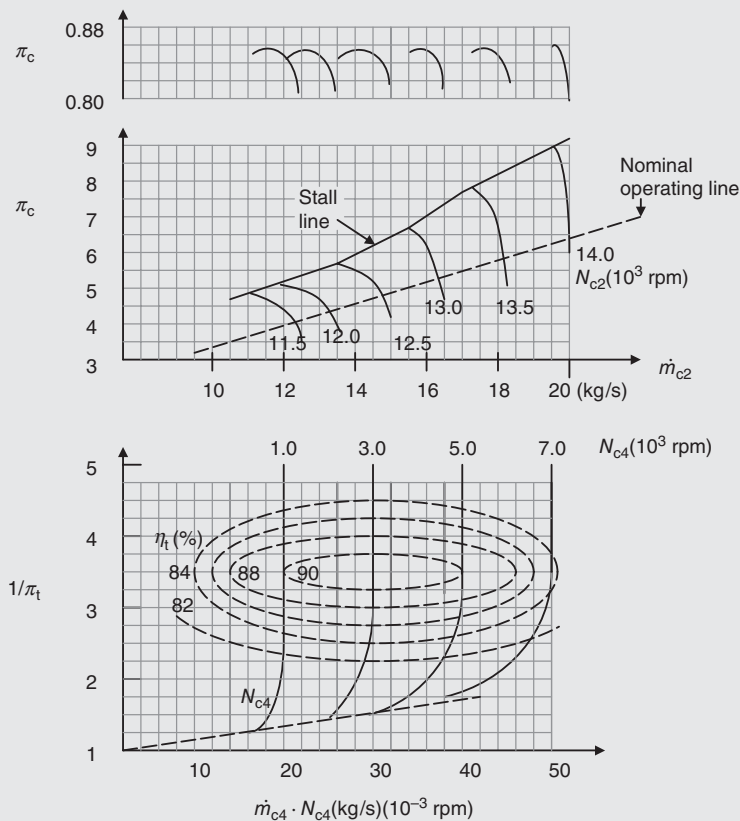
$$N_{c2} \equiv N_{c4} \sqrt{T_{t4}/T_{t2}} \Rightarrow \boxed{N_{c4} = N_{c2} / \sqrt{T_{t4}/T_{t2}}} \quad (11.41)$$

An example illustrates the calculation technique for gas generator pumping characteristics over a range of corrected shaft speeds for a constant throttle parameter T_{t4}/T_{t2} .

EXAMPLE 11.1

A compressor performance map is shown. The nominal operating line (which is a straight line) corresponds to $T_{t4}/T_{t2} = 6.0$. A turbine performance map is also shown.

Calculate and graph the gas generator pumping characteristics as a function of $N_{c2}/N_{c2,D}$ for $N_{c2,D} = 14,000$ rpm.



SOLUTION

First, we read compressor pressure ratio, corrected mass flow rate, and the adiabatic efficiency as a function of corrected shaft speed from the compressor performance map (on the nominal operating line). The compressor map data are summarized in the following table:

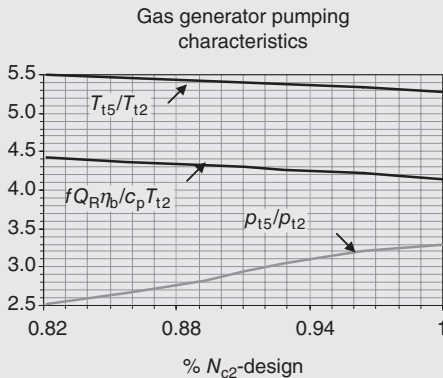
N_{c2} (1,000 rpm)	p_{t3}/p_{t2} (or π_c)	\dot{m}_{c2} (kg/s)	η_c
14.0	6.50	20.0	0.82
13.5	5.88	18.1	0.84
13.0	5.32	16.4	0.83
12.5	4.81	14.8	0.83
12.0	4.36	13.4	0.83
11.5	4.00	12.2	0.84

We may now calculate T_{t3}/T_{t2} or τ_c at each corrected shaft speed, following the definition of compressor adiabatic efficiency, i.e.,

$$\tau_c = 1 + \frac{1}{\eta_c} \left[\pi_c^{(\gamma_c - 1)/\gamma_c} - 1 \right]$$

using a spreadsheet program. Also, the fuel flow parameter from Equation 11.40

$$\frac{f Q_R \eta_b}{\dot{c}_p T_{t2}} \approx \frac{T_{t4}}{T_{t2}} - \frac{T_{t3}}{T_{t2}} = 6 - \tau_c$$



is readily calculated for each N_{c2} . From Equation 11.36c

$$\tau_t = 1 - \left(\frac{c_{pc}}{c_{pt}} \right) \frac{\tau_c - 1}{\eta_m (1 + f) (T_{t4}/T_{t2})}$$

we calculate τ_t (we estimate $f \approx 0.03$, $\eta_m \approx 0.995$, $c_{pc} = 1004 \text{ J/kg} \cdot \text{K}$ and $c_{pt} = 1156 \text{ J/kg} \cdot \text{K}$).

From Equation 11.41,

$$N_{c4} = N_{c2} / \sqrt{T_{t4}/T_{t2}}$$

we calculate N_{c4} (since T_{t4}/T_{t2} is known to be 6.0).

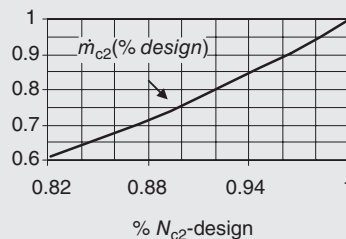
From Equation 11.31

$$\dot{m}_{c2} = \frac{\dot{m}_{c4} \pi_b \pi_c}{(1 + f) \sqrt{T_{t4}/T_{t2}}}$$

we calculate the turbine corrected mass flow rate \dot{m}_{c4} (we estimate $\pi_b \approx 0.95$).

From the product of $\dot{m}_{c4} N_{c4}$ and N_{c4} , we refer to the turbine performance map to estimate the turbine adiabatic efficiency η_t . From turbine adiabatic efficiency and temperature ratio, we use $\pi_t = [1 - (1 - \tau_t)/\eta_t]^{\gamma_t/(\gamma_t - 1)}$ to calculate turbine pressure ratio p_{t5}/p_{t4} (we use $\gamma_t = 1.33$).

We are now ready to calculate the pumping characteristics p_{t5}/p_{t2} and T_{t5}/T_{t2} . Finally, we use the table of data that we generated (in the spreadsheet) to graph the gas generator pumping characteristics, as shown in the following graphs. The gas generator pumping characteristics at other values of throttle parameter T_{t4}/T_{t2} will be needed to complete the operating range of the gas generator.



$$T_{t4}/T_{t2} = 6.0$$

11.2.6 Turbine–Afterburner–(Variable-Geometry) Nozzle Matching

As we are marching along the components of a gas turbine engine, the turbine may be followed by an afterburner, as in fighter/military aircraft, or a variable-geometry exhaust nozzle. It is thus convenient to analyze all three components in this section. What is the role of afterburner in matching with the turbine and the exhaust nozzle? The afterburner-off mode, which is referred to as the “dry” mode, is just a duct with total pressure loss associated with the viscous effects in an adiabatic flow (i.e., the afterburner-off case). The afterburner-on mode, which is referred to as the “wet” mode, impacts the mass flow rate in the exhaust nozzle in two major ways: (1) the hot gas in the afterburner has a much reduced density and (2) the mass flow rate in the nozzle is increased by the amount of fuel burned in the afterburner. There is also an additional total pressure loss due to combustion in the afterburner that we discussed in Chapter 7. The choked exhaust nozzle throat adjusts itself with afterburner operation, that is, it opens, to accommodate the extra mass flow rate at a reduced density with higher p_t -losses, but it still remains choked. Figure 11.10 shows the turbine matched to an afterburner and an exhaust nozzle with afterburner-off (top portion) and -on mode (bottom portion).

The exhaust nozzle throat, as indicated in Figure 11.10, remains choked in both dry and wet modes. In the dry mode, the total temperature at the turbine exit remains constant throughout the afterburner and the nozzle. The law of conservation of mass for stations 4 and 8 reveal

$$\dot{m}_4 = \sqrt{\frac{\gamma_4}{R_4}} \frac{p_{t4}}{\sqrt{T_{t4}}} \cdot A_4 \cdot M_{z4} \left(1 + \frac{\gamma_4 - 1}{2} M_{z4}^2 \right)^{\frac{-(\gamma_4+1)}{2(\gamma_4-1)}} = \dot{m}_8 \quad (11.42)$$

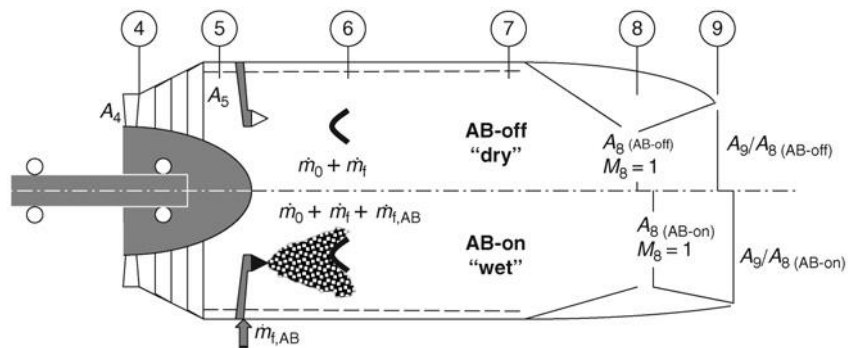
$$\dot{m}_8 = \sqrt{\frac{\gamma_8}{R_8}} \frac{p_{t8}}{\sqrt{T_{t8}}} \cdot A_{8,\text{dry}} \cdot M_{z8} \left(1 + \frac{\gamma_8 - 1}{2} M_{z8}^2 \right)^{\frac{-(\gamma_8+1)}{2(\gamma_8-1)}}$$

Since both stations 4 and 8 are choked, $M_4 = M_8 = 1$, we may rewrite Equation 11.42 as

$$\frac{p_{t8}/p_{t4}}{\sqrt{T_{t8}/T_{t4}}} = \sqrt{\frac{\gamma_4/\gamma_8}{R_4/R_8}} \frac{A_4}{A_{8,\text{dry}}} \left(\frac{2}{\gamma_4 + 1} \right)^{\frac{\gamma_4+1}{2(\gamma_4-1)}} \bigg/ \left(\frac{2}{\gamma_8 + 1} \right)^{\frac{\gamma_8+1}{2(\gamma_8-1)}} \quad (11.43)$$

$$= f(\gamma_4, \gamma_8, R_4/R_8, A_4/A_{8,\text{dry}})$$

■ **FIGURE 11.10**
Schematic drawing of turbine–afterburner–nozzle matching in “dry” and “wet” modes



The stagnation pressure at the nozzle throat is $(p_{t5})\pi_{AB-off}$ and $T_{t8} = T_{t5}$; therefore, Equation 11.43 yields

$$\frac{\pi_t}{\sqrt{\tau_t}} = f(\pi_{AB,dry}, \gamma_4, R_4, \gamma_8, R_8, A_4/A_{8,dry}) \quad (11.44)$$

The RHS of Equation 11.44 remains nearly constant between on- and off-design operations of the engine. This result is very important in engine off-design analysis, that is,

$$\boxed{\pi_t / \sqrt{\tau_t} \approx \text{constant (AB-off)}} \quad (11.45)$$

With the afterburner-on or wet mode, the continuity equation written for the two choked stations 4 and 8 gives

$$\begin{aligned} \frac{p_{t8}/p_{t4}}{\sqrt{T_{t8}/T_{t4}}} &= \sqrt{\frac{\gamma_4/\gamma_8}{R_4/R_8}} \left(\frac{1+f}{1+f+f_{AB}} \right) \frac{A_4}{A_{8,wet}} \left(\frac{2}{\gamma_4+1} \right)^{\frac{\gamma_4+1}{2(\gamma_4-1)}} \bigg/ \left(\frac{2}{\gamma_8+1} \right)^{\frac{\gamma_8+1}{2(\gamma_8-1)}} \\ &= f(\gamma_4, \gamma_8, R_4/R_8, A_4/A_{8,wet}) \end{aligned} \quad (11.46)$$

$$\frac{\pi_{AB,wet}}{\sqrt{\tau_{AB,wet}}} \frac{\pi_t}{\sqrt{\tau_t}} \cong f(\gamma_4, R_4, \gamma_8, R_8, A_4/A_{8,wet}, f_{AB}) \quad (11.47)$$

The nozzle throat in the AB-on mode is actuated to pass through the afterburner flow with sonic condition without affecting the backpressure of the turbine. In essence, the exhaust nozzle throat is just a valve. Therefore, since $A_{8(AB-on)}$ is inversely proportional to $\pi_{AB,wet}$ and directly proportional to the square root of $\tau_{AB,wet}$ and is sized to accept the additional mass flow rate due to the afterburner (i.e., f_{AB}), we conclude that

$$\boxed{\pi_t / \sqrt{\tau_t} \approx \text{constant (AB-on)}} \quad (11.48)$$

Note that the two constants on the RHS of Equations 11.45 and 11.48 are only different as the gas properties vary with afterburner operation, otherwise, turbine expansion remains unaffected with/without afterburner operation in on- and off-design modes when the gas generator is coupled to a variable-area nozzle.

Theoretically, the nozzle exit area A_9 variation is an independent parameter, which is intended to *optimize the installed thrust* with afterburner in operation. We will thus treat the nozzle area ratio A_9/A_8 as a given or prescribed parameter in our off-design analysis. The ideal value of the nozzle area ratio A_9/A_8 corresponds to the perfect expansion, that is, $p_9 = p_0$, which maximizes the nozzle gross thrust. In practice, however, there is an $A_{9,max}$ that is dictated by the nacelle aft-end geometry/envelope. In selection/scheduling of A_9/A_8 with flight Mach number, altitude, and afterburner operation, A_8 is dictated by the afterburner operation and $A_{9,Max}$ by the engine envelope.

11.2.6.1 Fixed-Geometry Convergent Nozzle Matching. In fixed-geometry convergent nozzles, the turbine is no longer decoupled from the exhaust nozzle. The turbine backpressure is continually affected by the (mass flow rate in the) nozzle, which in turn sets the turbine shaft power delivered to compressor, and thus the compressor

pressure ratio. The compressor pressure ratio and the corrected mass flow rate then establish the shaft speed. The only independent variable is thus the fuel flow rate (or throttle setting), which finds a consistent shaft speed with the gas generator pumping characteristics and the mass flow rate through a constant-area convergent nozzle. From continuity equation written between station 8 and 2, we have

$$\frac{A_8}{A_2} = \frac{(1+f) \dot{m}_{c2}/A_2}{\dot{m}_{c8}/A_8 (p_{t5}/p_{t2})} \sqrt{\frac{T_{t5}}{T_{t2}}} \quad (11.49)$$

Equation 11.49 contains, for the most part, gas generator pumping characteristics. A corrected shaft speed N_{c2} gives us p_{t5}/p_{t2} , T_{t5}/T_{t2} and \dot{m}_{c2} for a throttle setting T_{t4}/T_{t2} . Also, the nozzle corrected mass flow rate per unit area is either the maximum value corresponding to a choked exit (i.e., $M_8 = 1.0$), or it may be calculated based on the nozzle pressure ratio p_{t7}/p_0 . In either case, there is a unique relationship between the pumping characteristics variables in Equation 11.49 that is dictated by $A_8/A_2 = \text{constant}$, which corresponds to a certain throttle setting. Therefore, we may not specify both the corrected shaft speed and the throttle parameter simultaneously in a gas turbine engine with a fixed-area convergent exhaust nozzle. In general, a given throttle setting T_{t4}/T_{t2} finds a corrected shaft speed N_{c2} that provides for the mass flow and the (shaft) power balance between all the components in the engine.

11.3 Engine Off-Design Analysis

We may now apply the principles learned in steady-state component matching to engine off-design analysis. We first start with a simple (i.e., nonafterburning) turbojet engine. The known set of design parameters is

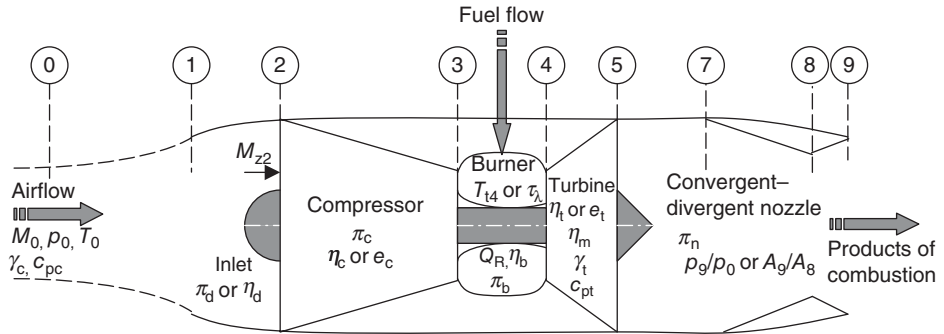
1. Design flight condition	M_0, p_0, T_0
2. Design compressor pressure ratio	π_c
3. Ideal heating value of the fuel	Q_R
4. Design turbine inlet temperature	T_{t4} (or expressed as τ_λ)
5. Design component efficiencies	$\pi_d, e_c, \pi_b, \eta_b, e_t, \eta_m, \pi_n$
6. Design nozzle exit pressure or area ratio	p_9/p_0 or A_9/A_8
7. Gas properties at design point	$\gamma_c, c_{pc}, \gamma_t, c_{pt}$
8. Design corrected mass flow rate	\dot{m}_{c2}
9. Design corrected shaft speed	N_{c2}
10. Design axial Mach number at 2	M_{z2}

Then, we subject the turbojet engine to off-design conditions, namely,

1. Off-design flight conditions (specified)	M_0, p_0, T_0
2. Off-design turbine inlet temperature (specified)	T_{t4} or τ_λ

If we assume that the component efficiencies remain the same (between on- and off-designs), the only cycle parameter that needs to be established in off-design condition is the compressor pressure ratio τ_c , which in turn establishes the off-design corrected mass flow rate and corrected shaft speed. We may also choose to specify component efficiencies at off-design based on the component performance map or empirical data.

■ FIGURE 11.11 Schematic diagram of a turbojet engine, its station numbers, and design parameters



To aid with the analysis, a schematic drawing of a simple turbojet engine and its station numbers is shown in Figure 11.11. Note that the combination of the axial Mach number and the corrected mass flow rate at any station determines the flow area in that station. The corrected mass flow rate at the compressor face and the design Mach number M_{z2} sizes the fan/compressor face area A_2 .

11.3.1 Off-Design Analysis of a Turbojet Engine

To simplify the task of engine off-design analysis, we make two assumptions:

1. Turbine inlet is choked at both design and off-design operations, that is, $M_4 = 1.0$
2. Exhaust nozzle is choked at both design and off-design operations, that is, $M_8 = 1.0$

Assuming the same gas properties between the on- and off-design conditions as well as fixed areas A_4 and A_8 , we had shown (in Equation 11.44) that

$$\frac{\pi_t}{\sqrt{\tau_t}} \approx \text{constant} \quad (11.50)$$

But, we also remember that π_t and τ_t are related via turbine polytropic efficiency e_t according to

$$\pi_t = \tau_t^{\frac{\gamma_t}{e_t(\gamma_t - 1)}}$$

Therefore, if we assume that the turbine polytropic efficiency remains constant between the on- and off-design operations, we may conclude that the turbine expansion parameter τ_t remains constant, that is,

$$\tau_t \approx \text{constant} \quad (11.51)$$

Based on this conclusion, the key to solving for the unknown compressor pressure ratio at off-design is

1. establishing τ_t from the design-mode operation
2. use power balance between the compressor and known turbine expansion parameter τ_t to calculate the off-design compressor pressure ratio
3. calculate the new corrected mass flow rate and shaft speed at off-design

The best way to demonstrate the approach to engine off-design analysis is to solve an example problem.

EXAMPLE 11.2

Assume a turbojet engine has the following design-point parameters:

$$M_0 = 0, p_0 = 0.1 \text{ MPa}, T_0 = 15^\circ\text{C}$$

$$\pi_d = 0.98$$

$$\pi_c = 25, e_c = 0.90$$

$$Q_R = 42,800 \text{ kJ/kg}, \pi_b = 0.98, \eta_b = 0.99, T_{t4} = 1500^\circ\text{C}$$

$$e_t = 0.85, \eta_m = 0.995$$

$$\dot{m}_{c2} = 73 \text{ kg/s}$$

$$N_{c2} \text{ (rpm)} = 6000$$

$$M_{z2} = 0.6$$

$$\pi_n = 0.97, p_9/p_0 = 1.0$$

If this engine is operating in the following off-design condition

$$M_0 = 0.8, p_0 = 33 \text{ kPa}, T_0 = -15^\circ\text{C}$$

$$T_{t4} = 1375^\circ\text{C}$$

$$\pi_d = 0.995$$

$$p_9/p_0 = 1.0$$

assuming all other component efficiencies (except π_d that is specified) remain the same (as design) at off-design and gas properties are $\gamma_c = \gamma_t = 1.4$ and $c_{pc} = c_{pt} = 1104 \text{ J/kg} \cdot \text{K}$, calculate

(a) $\pi_{c,O-D}$

(b) $\dot{m}_{c2,O-D}$ (in kg/s)

(c) $N_{c2,O-D}$ (in rpm)

(d) $M_{z2,O-D}$

SOLUTION

Power balance between the compressor and turbine at design point yields

$$T_{t2}(\tau_c - 1) = (1 + f)\eta_m T_{t4}(1 - \tau_t)$$

Therefore, we may isolate the turbine expansion ratio τ_t to get

$$\tau_t = 1 - \frac{1}{(1 + f)\eta_m} \frac{T_{t2}}{T_{t4}} (\tau_c - 1) = 1 - \frac{1}{(1 + f)\eta_m} \frac{\tau_r}{\tau_\lambda} (\tau_c - 1)$$

The same turbine expansion τ_t between the on- and off-design operations (as derived earlier), as well as assuming nearly constant $(1 + f)\eta_m$ between the on- and off-design modes, suggest that

$$\left. \frac{\tau_r}{\tau_\lambda} (\tau_c - 1) \right|_{\text{off-design}} \approx \left. \frac{\tau_r}{\tau_\lambda} (\tau_c - 1) \right|_{\text{design}}$$

The off-design compressor temperature ratio is

$$\tau_{c,O-D} \approx 1 + \frac{(\tau_r/\tau_\lambda)_D}{(\tau_r/\tau_\lambda)_{O-D}} (\tau_c - 1)_D$$

Now, let us calculate the parameters and substitute in the above equation

$$\begin{aligned}
 (\tau_r/\tau_\lambda)_D &= \left(\frac{T_{t2}}{T_{t4}}\right)_D = \left(\frac{T_0}{T_{t4}}\right)_D = \frac{273 + 15}{273 + 1500} \cong 0.16244 \\
 (\tau_c)_D &= (\pi_c)_D^{\frac{\gamma-1}{\gamma}} = (25)^{\frac{0.4}{(0.9)(1.4)}} \cong 2.7784 \\
 (\tau_r/\tau_\lambda)_{O-D} &= \left(\frac{T_{t2}}{T_{t4}}\right)_{O-D} = \left(\frac{T_0[1 + (\gamma - 1)M_0^2/2]}{T_{t4}}\right)_{O-D} = \frac{(273 - 15)[1 + 0.2(0.64)]}{273 + 1375} \cong 0.1766
 \end{aligned}$$

Therefore,

$$\tau_{c,O-D} \approx 1 + \frac{0.1624}{0.1766}(2.7784 - 1) \cong 2.6354$$

Hence, the compressor pressure ratio at off-design is

$$\pi_{c,O-D} = [(\tau_c)_{O-D}]^{\frac{\gamma_c}{\gamma-1}} = (2.6354)^{0.9(3.5)} \cong 21.2 \quad \Rightarrow \quad \boxed{\begin{array}{c} \text{Off-design} \\ \pi_c \approx 21.2 \end{array}}$$

With the compressor pressure ratio calculated at off-design, we may proceed to calculate engine performance parameters and figures of merit, such as specific thrust, specific fuel consumption, and thermal and propulsive efficiencies. The corrected mass flow rate at off-design is related to the design value by Equation 11.31.

$$\begin{aligned}
 \frac{\dot{m}_{c2,O-D}}{\dot{m}_{c2,D}} &\cong \frac{\pi_{c,O-D}}{\pi_{c,D}} \frac{\sqrt{(T_{t4}/T_{t2})_D}}{\sqrt{(T_{t4}/T_{t2})_{O-D}}} = \frac{21.2}{25} \sqrt{\frac{0.1766}{0.16244}} \approx 0.8842 \\
 \dot{m}_{c2,O-D} &\approx 0.8842(73 \text{ kg/s}) \approx 64.5 \text{ kg/s} \quad \Rightarrow \quad \boxed{\begin{array}{c} \text{Off-design} \\ \dot{m}_{c2} \approx 64.5 \text{ kg/s} \end{array}}
 \end{aligned}$$

The off-design corrected shaft speed is related to the design value via Equation 11.28b,

$$\begin{aligned}
 \frac{N_{c2,O-D}}{N_{c2,D}} &= \frac{\sqrt{(T_{t4}/T_{t2})_{O-D}}}{\sqrt{(T_{t4}/T_{t2})_D}} = \sqrt{\frac{0.16244}{0.1766}} \approx 0.959 \\
 N_{c2,O-D} \text{ (rpm)} &\approx 0.9591 (6000) \approx 5754 \quad \Rightarrow \quad \boxed{\begin{array}{c} \text{Off-design} \\ N_{c2} \approx 5754 \text{ rpm} \end{array}}
 \end{aligned}$$

In addition to the corrected mass flow rate at off-design, we can calculate the physical mass flow rate at off-design as well. For that purpose, Equation 8.10 may be written as

$$\begin{aligned}
 \dot{m}_2 &= \dot{m}_{c2} \delta_2 / \sqrt{\theta_2} \\
 \delta_2 &\equiv p_{t2}/p_{ref} \text{ where } p_{ref} = 101.33 \text{ kPa}
 \end{aligned}$$

$$p_{t0} = p_0(1 + 0.2M_0^2)^{3.5} = 33 \text{ kPa}[1 + 0.2(0.64)]^{3.5} \approx 50.3 \text{ kPa}$$

$$p_{t2} = \pi_d p_{t0} = (0.995)(50.3 \text{ kPa}) = 50.05 \text{ kPa}, \text{ therefore } \delta_2 = 50.05 \text{ kPa}/101.33 \text{ kPa} = 0.4939$$

$$\theta_2 \equiv T_{t2}/T_{ref} \text{ where } T_{ref} = 288.2 \text{ K}$$

$$T_{t2} = T_0(1 + 0.2M_0^2) = 258 \text{ K}[1 + 0.2(0.64)] \approx 291 \text{ K}, \text{ therefore } \theta_2 = 291 \text{ K}/288.2 \text{ K} \approx 1.01$$

We may substitute these values in the mass flow rate equation, to get

$$\dot{m}_2 = \dot{m}_{c2} \delta_2 / \sqrt{\theta_2} = 64.5 \text{ kg/s} (0.4939) / \sqrt{1.01} \approx 31.7 \text{ kg/s} \Rightarrow$$

Off-design $\dot{m}_2 \approx 31.7 \text{ kg/s}$

Now, we can calculate the off-design axial Mach number at the engine face, M_{z2} .

From the definition of corrected mass flow rate

$$\dot{m}_{c2} = \frac{\dot{m}_2 \sqrt{\theta_2}}{\delta_2} = \sqrt{\frac{\gamma_2}{R_2} \frac{P_{\text{ref}}}{\sqrt{T_{\text{ref}}}}} \cdot A_2 \cdot M_{z2} \left(1 + \frac{\gamma_2 - 1}{2} M_{z2}^2 \right)^{\frac{-(\gamma_2 + 1)}{2(\gamma_2 - 1)}} = f(\gamma_2, R_2, M_{z2})$$

we conclude that

$$\frac{\dot{m}_{c2,D}}{\dot{m}_{c2,O-D}} = \frac{M_{c2,D}}{M_{c2,O-D}} \left[\frac{1 + (\gamma_2 - 1) M_{z2,D}^2 / 2}{1 + (\gamma_2 - 1) M_{z2,O-D}^2 / 2} \right]^{\frac{-(\gamma_2 + 1)}{2(\gamma_2 - 1)}} = \frac{73}{64.5} = \frac{0.6}{M_{z2,O-D}} \left[\frac{1 + 0.2 M_{z2,O-D}^2}{1 + 0.2(0.6)^2} \right]^3$$

Solving for the only unknown in the above equation yields

$$M_{z2,O-D} = 0.4975 \Rightarrow$$

Off-design $M_{z2} \approx 0.4975$

Note that although the physical mass flow rate dropped by more than half, the axial Mach number at the engine face dropped from 0.6 to ~0.5.

11.3.2 Off-Design Analysis of an Afterburning Turbojet Engine

As we learned in the cycle analysis in Chapter 4, the design parameters for an afterburning turbojet engine are

1. M_0, p_0, T_0, γ_c , and c_{pc}
2. π_d
3. π_c and e_c
4. $Q_R, \pi_b, \eta_b, T_{t4}$
5. $e_t, \eta_m, \gamma_t, c_{pt}$
6. $Q_{RAB}, \pi_{AB}, \eta_{AB}, T_{t7}, \gamma_{AB}, c_{pAB}$
7. p_9/p_0
8. $\dot{m}_{c2}, N_{c2}, M_{z2}$

Assuming that the first turbine nozzle and the throat of the exhaust nozzle are choked at design point, that is, $M_4 = M_8 = 1.0$, and remain choked for off-design operation, we have shown in the previous section that

$$\pi_t / \sqrt{\tau_t} \approx \text{constant for both AB-on and AB-off modes of operation at on- and off-designs.}$$

We may also conclude that τ_t remains constant as π_t is related to τ_t by the polytropic efficiency of the turbine, e_t and γ_t . Again, the strategy is to calculate the turbine expansion

parameter τ_t at design point and use it to calculate the compressor pressure ratio at off-design operation. The approach is identical to the simple turbojet that we studied in the previous section.

At off-design, the following flight, throttle, and efficiency parameters are specified or assumed:

1. M_0, p_0 , and T_0, γ_c, c_{pc}
2. π_d
3. e_c
4. $Q_R, \pi_b, \eta_b, T_{t4}$
5. $e_t, \eta_m, \gamma_t, c_{pt}$
6. $Q_{RAB}, \pi_{AB}, \eta_{AB}, T_{t7}, \gamma_{AB}, c_{pAB}$
7. p_9/p_0

Comparing the two lists, we note that the only missing parameter at off-design is the compressor pressure ratio π_{c-o-D} , which in turn determines the corrected mass flow rate and the shaft speed at off-design. The enabling concept that bridges the two modes (i.e., on- and off-designs) is

$$\tau_t \approx \text{constant}$$

Now, let us solve an example problem.

EXAMPLE 11.3

An afterburning turbojet engine has the following design-point parameters:

$$\begin{aligned} M_0 &= 0, p_0 = 111.33 \text{ kPa}, T_0 = 288.2 \text{ K}, \\ \gamma_c &= 1.4, c_{pc} = 1004 \text{ J/kg} \cdot \text{K} \\ \pi_d &= 0.95 \\ \pi_c &= 20, e_c = 0.90 \\ \dot{m}_{c2} &= 33 \text{ kg/s} \\ N_{c2} &= 7120 \text{ rpm} \\ M_{c2} &= 0.6 \\ Q_R &= 42,800 \text{ kJ/kg}, \pi_b = 0.98, \eta_b = 0.97, T_{t4} = 1850 \text{ K} \\ \gamma_t &= 1.33, c_{pt} = 1156 \text{ J/kg} \cdot \text{K} \\ e_t &= 0.80, \eta_m = 0.995 \\ Q_{R,AB} &= 42,800 \text{ kJ/kg}, \pi_{AB} = 0.95, \eta_{AB} = 0.98, T_{t7} = 2450 \text{ K} \\ \gamma_{AB} &= 1.3, c_{pc} = 1243 \text{ J/kg} \cdot \text{K} \\ \pi_n &= 0.93, p_9/p_0 = 1.0 \end{aligned}$$

We wish to calculate the engine off-design performance characteristics that correspond to the supersonic flight condition of the aircraft at high altitude. The off-design conditions are

$$\begin{aligned} M_0 &= 2.0, p_0 = 20 \text{ kPa}, T_0 = 223 \text{ K}, \gamma_c = 1.4, \\ c_{pc} &= 1004 \text{ J/kg} \cdot \text{K} \\ \pi_d &= 0.80 \\ e_c &= 0.90 \\ Q_R &= 42,800 \text{ kJ/kg}, \pi_b = 0.98, \eta_b = 0.97, \\ T_{t4} &= 1,850 \text{ K} \\ \gamma_t &= 1.33, c_{pt} = 1156 \text{ J/kg} \cdot \text{K} \\ e_t &= 0.80, \eta_m = 0.995 \\ Q_{R,AB} &= 42,800 \text{ kJ/kg}, \pi_{AB} = 0.95, \eta_{AB} = 0.98, \\ T_{t7} &= 2450 \text{ K} \\ \gamma_{AB} &= 1.3, c_{pc} = 1243 \text{ J/kg} \cdot \text{K} \\ \pi_n &= 0.93, p_9/p_0 = 1.0 \end{aligned}$$

SOLUTION

DESIGN-POINT ANALYSIS Our first goal is to calculate the turbine expansion parameter, τ_t at the design condition. The power balance between the compressor and turbine gives

$$\tau_t = 1 - \frac{1}{(1+f)\eta_m} \frac{c_{pc} T_{t2}}{c_{pt} T_{t4}} (\tau_c - 1)$$

We start calculating the parameters in the above equation.

Since the design point corresponds to takeoff or $M_0 = 0$ condition, $T_{t2} = T_0 = 288.2$ K

Also, we know that the compressor pressure and temperature ratios are related via

$$\tau_c = \pi_c^{(\gamma_c - 1)/\gamma_c e_c} = 20^{0.4/1.4/0.9} \approx 2.5884$$

The compressor discharge temperature is $T_{t3} = 2.5884(288.2 \text{ K}) = 745.97$ K

The last unknown in the above equation for τ_t is the fuel-to-air ratio f

$$f = \frac{c_{pt} T_{t4} - c_{pc} T_{t3}}{Q_R \eta_b - c_{pt} T_{t4}} = \frac{1156(1850) - 1004(745.97)}{42800(1000)(0.97) - 1156(1850)} \approx 0.0360$$

Now, we have calculated all the terms in τ_t , therefore,

$$\tau_t = 1 - \frac{1004(288.2)(2.5884 - 1)}{1.036(0.995)(1156)(1850)} \approx 0.7915 \quad \Rightarrow \quad \tau_t \approx 0.7915 \text{ at on-and-off-design}$$

OFF-DESIGN ANALYSIS With $\tau_t = 0.7915$ at off-design, we are now ready to calculate the new compressor pressure ratio. Again, the power balance between the compressor and turbine holds the key, i.e.,

$$\tau_{c,O-D} = 1 + (1+f)\eta_m \left. \frac{c_{pt} T_{t4}}{c_{pc} T_{t2}} \right|_{O-D} (1 - \tau_t)$$

The total temperature at the engine face, T_{t2} , is equal to the flight total temperature T_{t0} , which is

$$T_{t2} = T_{t0} = (223 \text{ K})[1 + 0.2(2.0)^2] \approx 401.4 \text{ K}$$

We may first use the same fuel-to-air ratio in off-design as design in the above equation to calculate $\tau_{c,O-D}$ and after we calculate the off-design T_{t3} , we can recalculate the fuel-to-air ratio in the burner. We may repeat the calculation loop, until we arrive at the off-design $\tau_{c,O-D}$ to within 11^{-4} (i.e., 1/100 of 1%) accuracy. In this example, we will check the accuracy of using $(1+f)_D$ and $(1+f)_{O-D}$ on $\tau_{c,O-D}$.

$$\tau_{c,O-D} = 1 + (1.036)(0.995) \left. \frac{1156(1850)}{1004(401.4)} \right|_{O-D} (1 - 0.7915) \approx 2.1405 \quad \Rightarrow \quad \frac{\text{Off-design}}{\pi_c \approx 10.994}$$

$$\pi_{c,O-D} = (\tau_{c,O-D})^{\gamma_c e_c / (\gamma_c - 1)} = 2.1405^{3.5(0.9)} \approx 10.994$$

With the calculated compressor pressure ratio at off-design, we may proceed to calculate all other parameters of interest, namely,

$$\frac{\dot{m}_{c2,O-D}}{\dot{m}_{c2,D}} \cong \frac{\pi_{c,O-D}}{\pi_{c,D}} \frac{\sqrt{(T_{t4}/T_{t2})_D}}{\sqrt{(T_{t4}/T_{t2})_{O-D}}} = \frac{10.994}{20} \sqrt{\frac{1850/288.2}{1850/401.4}} \approx 0.6487 \quad \Rightarrow \quad \boxed{\begin{array}{c} \text{Off-design} \\ \dot{m}_{c2} \approx 21.41 \text{ kg/s} \end{array}}$$

$$\dot{m}_{c2,O-D} = 0.6487(33 \text{ kg/s}) \approx 21.41 \text{ kg/s}$$

$$\frac{N_{c2,O-D}}{N_{c2,D}} = \frac{\sqrt{(T_{t4}/T_{t2})_{O-D}}}{\sqrt{(T_{t4}/T_{t2})_D}} = \frac{\sqrt{1850/401.4}}{\sqrt{1850/288.2}} \approx 0.8473 \quad \Rightarrow \quad \boxed{\begin{array}{c} \text{Off-design} \\ N_{c2} \approx 6033 \text{ rpm} \end{array}}$$

$$N_{c2,O-D} \approx 0.8473(7120 \text{ rpm}) \approx 6033 \text{ rpm}$$

$$\delta_2 \equiv p_{t2}/p_{\text{ref}} \text{ where } p_{\text{ref}} = 101.33 \text{ kPa}$$

$$p_{t0} = p_0(1 + 0.2M_0^2)^{3.5} = 20 \text{ kPa}[1 + 0.2(2.0)^2]^{3.5} \approx 156.5 \text{ kPa}$$

$$p_{t2} = \pi_d p_{t0} = (0.8)(156.5 \text{ kPa}) = 125.2 \text{ kPa}, \text{ therefore } \delta_2 = 125.2 \text{ kPa}/101.33 \text{ kPa} = 1.2356$$

$$\theta_2 \equiv T_{t2}/T_{\text{ref}} \text{ where } T_{\text{ref}} = 288.2 \text{ K}$$

$$\theta_2 = 401.4/288.2 \approx 1.3928$$

$$\dot{m}_2 = \dot{m}_{c2} \delta_2 / \sqrt{\theta_2} = 21.41 \text{ kg/s} / (1.2356 / \sqrt{1.3928}) \approx 22.41 \text{ kg/s} \quad \Rightarrow \quad \boxed{\begin{array}{c} \text{Off-design} \\ \dot{m}_2 \approx 22.41 \text{ kg/s} \end{array}}$$

We calculate compressor discharge temperature $T_{t3} \approx 859.2 \text{ K}$, and with $T_{t4} = 1850 \text{ K}$ specified, we calculate the fuel-to-air ratio at off-design, in the combustor to be

$$f_{O-D} = 0.03305$$

We had used $f = 0.0360$ in calculating $\tau_{c,O-D}$. What is the impact of this inaccuracy (in f) on τ_c ? We note from the following compressor–turbine power balance equation

$$\tau_{c,O-D} = 1 + (1 + f)\eta_m \left. \frac{c_{pt} T_{t4}}{c_{pc} T_{t2}} \right|_{O-D} (1 - \tau_t)$$

that $(\tau_{c,O-D} - 1)$ is proportional to $(1 + f)$, therefore,

$$\frac{(\tau_{c,O-D} - 1)_{\text{new}}}{(\tau_{c,O-D} - 1)_{\text{old}}} = \frac{(1 + f_{O-D})_{\text{new}}}{(1 + f_{O-D})_{\text{old}}} = \frac{1.03305}{1.0360} \approx 0.99715$$

If we substitute for the old $\tau_{c,O-D}$, we calculate the new $\tau_{c,O-D}$ from above, which is within 1/10 of 1% of the old value. For higher accuracy, we can repeat the off-design calculations with the new value of $\tau_{c,O-D}$ and proceed to calculate a new value for the fuel-to-air ratio f . However, in this example, we are satisfied with the level of accuracy as it falls well within all the other approximations that we have introduced in the problem, namely, a priori specified gas properties and component efficiencies in off-design.

We continue to march through the engine (at off-design conditions) and calculate

$$p_{15} = 413.7 \text{ kPa}, p_{17} = 393.04 \text{ kPa}, f_{AB} \approx 0.0367, p_{19} = 365.52 \text{ kPa}, M_9 = 2.524, T_9 = 1253 \text{ K}, \\ V_9 = 1725 \text{ m/s. The nondimensional specific thrust and specific fuel consumptions are}$$

$$\frac{F_n}{\dot{m}_0 a_0} \approx 4.166 \text{ and TSFC} = 55.94 \text{ mg/s/N}$$

The cycle thermal efficiency, the engine propulsive efficiency, and the overall efficiency are

$$\eta_{th} = 0.4822, \eta_p = 0.5283, \text{ and } \eta_o = 0.2547$$

11.3.3 Off-Design Analysis of a Separate-Flow Turbofan (Two-Spool) Engine

We will approach the off-design analysis problem of separate-flow turbofan engines the same way we did in the turbojet problem, that is, we assume the first nozzle choking stations in the turbine as well as the exhaust nozzle throat in off-design engine operation. Then we set the mass flow rates between the choked stations equal to each other and establish the constants of gas turbine engine operation.

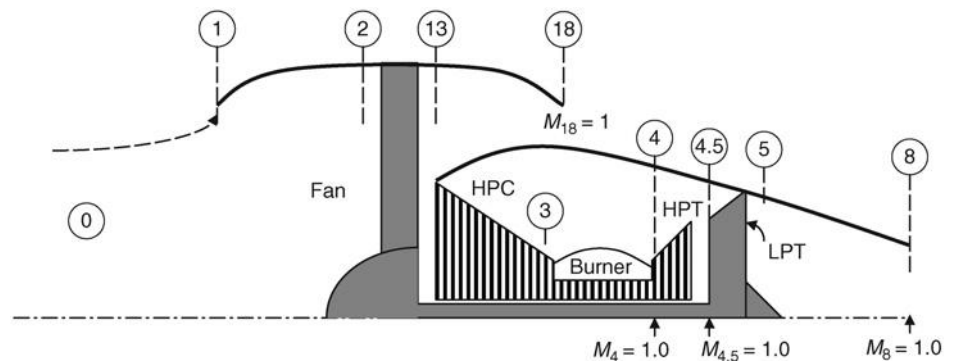
Figure 11.12 shows a definition sketch of a two-spool separate-flow turbofan engine. The fan is driven by the low-pressure turbine (LPT), and the high-pressure compressor (HPC) is driven by the high-pressure turbine (HPT). Again, we assume that the first turbine nozzles of the HPT and LPT are choked at design point and remain choked in off-design operation, that is,

$$M_4 = M_{4.5} = 1.0 \quad (11.52a)$$

The second assumption deals with the exhaust nozzle throats, that is,

$$M_8 = M_{18} = 1.0 \quad (11.52b)$$

■ **FIGURE 11.12**
Two-spool
separate-flow turbofan
engine with choked
convergent nozzles



The known design parameters for this turbofan engine are

- | | |
|--|--|
| 1. Design flight condition | M_0, p_0, T_0 |
| 2. Design compressor and fan pressure ratios | π_c, π_f |
| 3. Design bypass ratio | α |
| 4. Ideal heating value of the fuel | Q_R |
| 5. Design turbine inlet temperature | T_{t4} (or expressed as τ_λ) |
| 6. Design component efficiencies | $\pi_d, e_c, e_f, \pi_b, \eta_b, e_t, \eta_m, \pi_n, \pi_{nf},$
$p_8/p_0, p_{18}/p_0$ |
| 7. Gas properties at design point | $\gamma_c, c_{pc}, \gamma_t, c_{pt}$ |
| 8. Design choked stations | $M_4 = M_{4.5} = M_8 = M_{18} = 1.0$ |

In off-design condition, we may have a different throttle setting and fly at a different altitude Mach number, that is, we subject the turbofan engine to

1. Off-design flight conditions (specified) M_0, p_0, T_0
2. Off-design turbine inlet temperature (specified) T_{t4} or τ_λ

And off-design inlet losses.

The primary unknowns, in the off-design operation, are three cycle parameters, namely,

1. $\pi_{c,O-D}$
2. $\pi_{f,O-D}$
3. α_{O-D}

The mass flow rates between the stations 4.5 and the nozzle throat are nearly the same, therefore,

$$\dot{m}_{4.5} = \sqrt{\frac{\gamma_{4.5}}{R_{4.5}}} \frac{p_{t4.5}}{\sqrt{T_{t4.5}}} A_{4.5} \left(\frac{2}{\gamma_{4.5} + 1} \right)^{\frac{\gamma_{4.5} + 1}{2(\gamma_{4.5} - 1)}} \cong \dot{m}_8 = \sqrt{\frac{\gamma_8}{R_8}} \frac{p_{t8}}{\sqrt{T_{t8}}} A_8 \left(\frac{2}{\gamma_8 + 1} \right)^{\frac{\gamma_8 + 1}{2(\gamma_8 - 1)}}$$

Using similar arguments as in the turbojet section, for example, constant areas, constant gas properties, and so on, we conclude that,

$$\boxed{\pi_{tL} / \sqrt{\tau_{tL}} \approx \text{constant}} \quad (11.53a)$$

or assuming the same polytropic efficiency that relates pressure and temperature ratios in the turbine, we conclude that the first constant of operation in our separate-flow turbofan engine is

$$\tau_{tL} \approx \text{constant} \quad (11.53b)$$

Now let us consider the mass flow rates between two other stations, namely, station 4 and 4.5, that is,

$$\dot{m}_4 = \sqrt{\frac{\gamma_4}{R_4}} \frac{p_{t4}}{\sqrt{T_{t4}}} A_4 \left(\frac{2}{\gamma_4 + 1} \right)^{\frac{\gamma_4 + 1}{2(\gamma_4 - 1)}} \cong \dot{m}_{4.5} = \sqrt{\frac{\gamma_{4.5}}{R_{4.5}}} \frac{p_{t4.5}}{\sqrt{T_{t4.5}}} A_{4.5} \left(\frac{2}{\gamma_{4.5} + 1} \right)^{\frac{\gamma_{4.5} + 1}{2(\gamma_{4.5} - 1)}}$$

For fixed area turbines, A_4 and $A_{4.5}$ remain constant, that is, they are not adjustable, and assuming the gas properties do not appreciably change between the on- and off-design conditions, we may conclude that the second constant of engine operation is

$$\boxed{\pi_{tH}/\sqrt{\tau_{tH}} \approx \text{constant}} \quad (11.54a)$$

and similarly, assuming constant e_{tH} between on- and off-designs, we conclude that

$$\tau_{tH} \approx \text{constant} \quad (11.54b)$$

Note that the combination of Equations 11.53b and 11.54b results in the constant overall expansion across the turbine, that is,

$$\tau_t = \tau_{tH} \cdot \tau_{tL} \approx \text{constant}$$

The fan nozzle is assumed to remain choked in off-design as well as on-design operation, which states that its mass flow rate is

$$\dot{m}_{18} = \sqrt{\frac{\gamma_{18}}{R_{18}}} \frac{p_{t18}}{\sqrt{T_{t18}}} A_{18} \left(\frac{2}{\gamma_{18} + 1} \right)^{\frac{\gamma_{18} + 1}{2(\gamma_{18} - 1)}} = \alpha \cdot \dot{m}_0 \quad (11.55)$$

The main nozzle mass flow rate may be written as

$$\dot{m}_8 = \sqrt{\frac{\gamma_8}{R_8}} \frac{p_{t8}}{\sqrt{T_{t8}}} A_8 \left(\frac{2}{\gamma_8 + 1} \right)^{\frac{\gamma_8 + 1}{2(\gamma_8 - 1)}} = (1 + f) \dot{m}_0 \quad (11.56)$$

Taking the ratio of the two mass flow rates in Equations 11.55 and 11.56 and assuming the gas properties and the flow nozzle throat areas do not change between the on- and off-designs, we get

$$\frac{\alpha}{1 + f} = \text{constant} \frac{p_{t18}/\sqrt{T_{t18}}}{p_{t8}/\sqrt{T_{t8}}} = \text{constant} \frac{p_{t13}/\sqrt{T_{t13}}}{p_{t5}/\sqrt{T_{t5}}}$$

We may divide the numerator and denominator by $p_{t2}/(T_{t2})^{1/2}$ to get

$$\alpha \approx \text{constant} \frac{\left(\frac{p_{t13}}{p_{t2}} \right) / \sqrt{\frac{T_{t13}}{T_{t2}}}}{\left(\frac{p_{t5} p_{t4}}{p_{t3}} \cdot \frac{p_{t3} p_{t13}}{p_{t13} p_{t2}} \right) / \sqrt{\frac{T_{t5} T_{t4} T_0}{T_{t4} T_0 T_{t2}}}} \approx \text{constant} \frac{\sqrt{\tau_\lambda / \tau_r \cdot \tau_f}}{\pi_{cH}} \quad (11.57)$$

Note that all the constants were combined in the coefficient in front of the RHS, for example, turbine pressure ratio or temperature ratio, which do not change were lumped

in the constant of the above equation. Since the turbine expansion parameters τ_t and π_t remain constant in off-design, we may further simplify Equation 11.57 to get

$$\boxed{\alpha \pi_{cH} \sqrt{\frac{\tau_r \tau_f}{\tau_\lambda}} \approx \text{constant}} \quad (11.58)$$

The last equation, that is, Equation 11.58 constitutes the third constant of turbofan operation, within the approximations that we introduced. We use these three constants of operation between the on-and off-design modes to establish the three unknowns at off-design, namely, the fan and the compressor pressure ratio as well as the bypass ratio.

Off-design analysis

The power balance between the HPT and HPC yields

$$T_{t13}(\tau_{cH} - 1) = \eta_{mH}(1 + f)T_{t4}(1 - \tau_{tH})$$

We may divide both sides by T_{t2} to get the nondimensional expression

$$\tau_f(\tau_{cH} - 1) = \eta_{mH}(1 + f)(1 - \tau_{tH}) \frac{\tau_\lambda}{\tau_r} \approx \text{constant} \frac{\tau_\lambda}{\tau_r} \quad (11.59)$$

Note that this has only two unknowns and they are τ_{cH} and τ_f since we specify the throttle setting at off-design, T_{t4} (or τ_λ) as well as flight Mach number produces τ_r information. We may cast Equation 11.59 as

$$\frac{\tau_r \tau_f}{\tau_\lambda} (\tau_{cH} - 1) \approx \text{constant} = C_1 \quad (11.60)$$

The power balance between the fan and the LPT yields

$$(1 + \alpha)T_{t2}(\tau_f - 1) = \eta_{mL}(1 + f)T_{t4.5}(1 - \tau_{tL}) = \eta_{mL}(1 + f)T_{t4}\tau_{tH}(1 - \tau_{tL}) \quad (11.61)$$

We note that the RHS of the above equation is completely known, either from the design point calculations as in τ_{tH} and τ_{tL} or from the off-design throttle setting T_{t4} . The LHS of Equation 11.61 contains two unknowns, namely, the off-design bypass ratio and the off-design fan temperature ratio. The Equation 11.61 simplifies to

$$(1 + \alpha)(\tau_f - 1) \frac{\tau_r}{\tau_\lambda} \approx \text{constant} = C_2 \quad (11.62)$$

Now, we use the third constant, that is, Equation 11.58, to establish a third equation involving the three unknowns, α and τ_f , and π_{cH} at off-design.

$$\alpha \cdot \pi_{cH} \sqrt{\frac{\tau_r \cdot \tau_f}{\tau_\lambda}} \approx \text{constant} = C_3 \quad (11.63)$$

Is there a closed form solution for the three unknowns in terms of the three constants C_1 , C_2 , and C_3 ? The answer is no, since these equations are coupled and involve unknowns with the following exponent:

$$\pi_{cH} = \tau_{cH}^{\frac{\gamma \cdot \epsilon_{cH}}{\gamma - 1}} \quad (11.64)$$

Off-design solution strategy

From the on-design cycle analysis, calculate the three constants, C_1 , C_2 , and C_3 . Then solve Equations 11.60, 11.62 and 11.63 iteratively to arrive at the unknowns α , τ_{cH} , and τ_f . We may eliminate the bypass ratio α from Equations 11.62 and 11.63, and after some minor simplification, we get

$$\left(\frac{\tau_r}{\tau_\lambda} + \frac{C_3}{\pi_{cH}} \sqrt{\frac{\tau_r}{\tau_\lambda \tau_f}} \right) (\tau_f - 1) = C_2 \quad (11.65)$$

From Equation 11.60, we isolate τ_f , to get

$$\tau_f = \frac{C_1 \tau_\lambda}{\tau_r (\tau_{cH} - 1)} \quad (11.66)$$

We introduce expression 11.66 into Equation 11.65 and replace pressure ratio by the temperature ratio via Equation 11.64 will result in a one equation, one unknown expression,

$$\left(\frac{\tau_r}{\tau_\lambda} + \frac{C_3}{(\tau_{cH})^{\frac{\gamma \cdot e_{cH}}{\gamma - 1}}} \sqrt{\frac{\tau_r}{\tau_\lambda \left[\frac{C_1 \tau_\lambda}{\tau_r (\tau_{cH} - 1)} \right]}} \right) \left[\frac{C_1 \tau_\lambda}{\tau_r (\tau_{cH} - 1)} - 1 \right] = C_2 \quad (11.67)$$

Finally, we need to iterate for τ_{cH} in Equation 11.67. Then introducing it in Equation 11.66 yields τ_f and substituting them in Equation 11.63, we get the off-design bypass ratio α .

The corrected mass flow rate at off-design is related to the design value via:

$$\dot{m}_{c2-OD} = \dot{m}_{c2-D} \left[\frac{(1 + \alpha)_{OD}}{(1 + \alpha)_D} \right] \left[\frac{\pi_{c-OD}}{\pi_{c-D}} \right] \sqrt{\frac{(\tau_r/\tau_\lambda)_{OD}}{(\tau_r/\tau_\lambda)_D}} \quad (11.68)$$

Where π_c is the engine overall pressure ratio, namely $\pi_f \cdot \pi_{cH}$.

To demonstrate the methodology, we solve an example.

EXAMPLE 11.4

Consider a separate-flow turbofan engine (as in Figure 11.12) with the following design-point parameters:

1. $M_0 = 0$, $p_0 = 0.1$ MPa, $T_0 = 15^\circ\text{C}$
2. $\pi_d = 0.98$
3. $\pi_f = 2.0$, $e_f = 0.90$
4. $\alpha = 6.0$
5. $\pi_{cH} = 15$, $e_{cH} = 0.90$
6. $T_{t4} = 1700^\circ\text{C}$, $Q_R = 42,800$ kJ/kg, $\eta_b = 0.99$, $\pi_b = 0.95$
7. $e_{tH} = 0.85$, $\eta_{mH} = 0.995$
8. $e_{tL} = 0.89$, $\eta_{mL} = 0.995$
9. $\pi_n = \pi_{nf} = 0.98$, $p_8 = p_{18} = p_0$
10. $\gamma_c = 1.4$, $c_{pc} = 1004$ J/kg · K

11. $\gamma_t = 1.33$, $c_{pt} = 1146$ J/kg · K

12. $M_4 = M_{4.5} = M_8 = M_{18} = 1.0$

The off-design operation of this engine is represented by a cruise altitude flight such as

$$M_0 = 0.85, p_0 = 11 \text{ kPa}, T_0 = -15^\circ\text{C}$$

$$T_{t4} = 1500^\circ\text{C}$$

$$\pi_d = 0.995$$

All other efficiencies and gas properties remain constant. Calculate the following parameters at off-design condition:

- (a) Fan pressure ratio π_f
- (b) High-pressure compressor pressure ratio π_{cH}
- (c) Bypass ratio α

SOLUTION

We first calculate the design values for τ_r , τ_f , τ_{cH} and τ_λ

$$\begin{aligned}\tau_r &= 1 + 0.2(0) = 1 \\ \tau_f &= \pi_f^{0.2857/0.90} = (2)^{0.31746} = 1.2461 \\ \tau_{cH} &= \pi_{cH}^{0.2857/0.90} = (15)^{0.31746} = 2.3624 \\ \tau_\lambda &= \frac{c_{pt}T_{t4}}{c_{pc}T_0} = \left(\frac{1146}{1004}\right) \left(\frac{1700 + 273}{15 + 273}\right) \cong 7.82\end{aligned}$$

Now, we can calculate the first constant C_1

$$C_1 = \frac{\tau_r \tau_f}{\tau_\lambda} (\tau_{cH} - 1) = \frac{1.2461}{7.82} (1.3624) \cong 0.2171$$

Constants C_2 and C_3 are

$$C_2 = (1 + \alpha)(\tau_f - 1) \frac{\tau_r}{\tau_\lambda} = 7(0.2461)(1/7.82) \cong 0.2203$$

$$C_3 = \alpha \cdot \pi_{cH} \sqrt{\frac{\tau_r \cdot \tau_f}{\tau_\lambda}} = 6(15) \sqrt{\frac{1.2461}{7.82}} \cong 35.927$$

Let us calculate τ_r and τ_λ for the off-design operation

$$\begin{aligned}\tau_{r,O-D} &= 1 + 0.2(0.85)^2 = 1.1445 \\ \tau_{\lambda,O-D} &= \frac{c_{pt}T_{t4}}{c_{pc}T_0} = \left(\frac{1146}{1004}\right) \left(\frac{1500 + 273}{273 - 15}\right) \cong 7.8440\end{aligned}$$

Now, let us substitute all the parameters in Equation 11.67

$$\left(\frac{\tau_r}{\tau_\lambda} + \frac{C_3}{(\tau_{cH})^{\frac{\gamma_{cH}}{\gamma-1}}} \sqrt{\frac{\tau_r}{\tau_\lambda \left[\frac{C_1 \tau_\lambda}{\tau_r (\tau_{cH} - 1)} \right]}} \right) \left[\frac{C_1 \tau_\lambda}{\tau_r (\tau_{cH} - 1)} - 1 \right] = C_2$$

$$\left(\frac{1.1445}{7.844} + \frac{35.927}{\tau_{cH}^{3.15}} \sqrt{\frac{1.1445}{7.844 \left[\frac{0.2171(7.844)}{1.1445(\tau_{cH} - 1)} \right]}} \right) \left[\frac{0.2171(7.844)}{1.1445(\tau_{cH} - 1)} \right] = 0.2203$$

The solution to this equation is found using an Excel spreadsheet to be

$$\tau_{cH} \approx 2.1184$$

Therefore, the high-pressure compressor pressure ratio at off design is

$$\pi_{cH} = \tau_{cH}^{\gamma_e/(\gamma-1)} = (2.1184)^{3.15} \approx 10.64 \Rightarrow \text{Off-design } \pi_{cH} \approx 10.64$$

The fan pressure ratio at off-design is calculated from

$$\tau_f = \frac{C_1 \tau_\lambda}{\tau_r (\tau_{cH} - 1)} = 1.3304 \Rightarrow \text{Off-design } \pi_f \approx 2.458$$

$$\pi_f = \tau_f^{3.15} = 1.3304^{3.15} \approx 2.458$$

The off-design bypass ratio is calculated from

$$\alpha \cdot \pi_{cH} \sqrt{\frac{\tau_r \cdot \tau_f}{\tau_\lambda}} \approx \text{constant} = C_3 \Rightarrow \text{Off-design } \alpha \approx 7.66$$

$$\alpha \approx 7.66$$

11.4 Unchoked Nozzles and Other Off-Design Iteration Strategies

Let us reexamine the assumptions that we made in component matching and engine off-design analysis, in particular, choked flow condition at stations: 4,4.5, and 8, that is, the

HPT entrance, the LPT entrance, and the exhaust nozzle throat. These choked stations simplified our solution methodology, as the corrected mass flow rate in those stations remained fixed. However, what if those stations were not choked, that is, what if $M_4 \neq 1.0$, $M_{4.5} \neq 1$, and $M_8 \neq 1$, in some off-design operations? How do we know our assumption was correct?

11.4.1 Unchoked Exhaust Nozzle

We may start our off-design analysis with the assumption of choked stations at 4, 4.5, and 8, as described earlier. With these assumptions, we may calculate the missing off-design cycle parameters, namely, the compressor and fan pressure ratios and bypass ratio (if a turbofan engine). Then, we can march through the engine and calculate all the total pressures and temperatures in the engine including p_{t9} if a convergent–divergent (C–D) nozzle or p_{t8} if the nozzle was convergent. Now, we apply the nozzle-choking criterion, or what we called critical nozzle pressure ratio $(NPR)_{crit}$, for a choked throat in a C–D nozzle we must have

$$\frac{p_{t9}}{p_0} \geq \left(\frac{\gamma_9 + 1}{2} \right)^{\gamma_9/(\gamma_9-1)} \quad (11.69a)$$

For a choked throat in a convergent nozzle we must have

$$\frac{p_{t8}}{p_0} \geq \left(\frac{\gamma_8 + 1}{2} \right)^{\gamma_8/(\gamma_8-1)} \quad (11.69b)$$

With these conditions met, we had made correct assumptions (i.e., $M_8 = 1.0$). Otherwise, the nozzle throat Mach number is less than 1 and its value is

$$M_8 = \sqrt{\frac{2}{\gamma_8 - 1} \left[\left(\frac{p_{t8}}{p_0} \right)^{(\gamma_8-1)/\gamma_8} - 1 \right]} \quad (11.70)$$

With a reduced Mach number at the throat, the corrected mass flow rate through the nozzle throat drops.

$$\dot{m}_{c8} = \frac{\dot{m}_8 \sqrt{\theta_8}}{\delta_8} = \sqrt{\frac{\gamma_8}{R_8}} \frac{p_{ref}}{\sqrt{T_{ref}}} \cdot A_8 \cdot M_8 \left(1 + \frac{\gamma_8 - 1}{2} M_8^2 \right)^{\frac{-(\gamma_8+1)}{2(\gamma_8-1)}} \quad (11.71)$$

If we write the corrected mass flow rate at the turbine inlet as

$$\dot{m}_{c4} = \frac{\dot{m}_4 \sqrt{\theta_4}}{\delta_4} = \sqrt{\frac{\gamma_4}{R_4}} \frac{p_{ref}}{\sqrt{T_{ref}}} \cdot A_4 \cdot M_4 \left(1 + \frac{\gamma_4 - 1}{2} M_4^2 \right)^{\frac{-(\gamma_4+1)}{2(\gamma_4-1)}} \quad (11.72)$$

And take the ratio of the two corrected mass flow rates while ignoring variation of gas constants, we get

$$\frac{\dot{m}_{c4}}{\dot{m}_{c8}} = \frac{p_{t8}/p_{t4}}{\sqrt{T_{t8}/T_{t4}}} = \frac{\pi_t}{\sqrt{\tau_t}} \quad (\text{AB-Off}) \quad (11.73)$$

Note that although the corrected mass flow rate at 8 has dropped (to below critical), it may not have caused the turbine nozzle to unchoke. Therefore, we continue with the

assumption that turbine nozzle is choked, that is, $M_4 = 1.0$ or $\dot{m}_{c4} = \text{constant}$, and our new turbine expansion equation becomes

$$\boxed{\frac{\pi_t}{\sqrt{\tau_t}} = \frac{\text{constant}}{\dot{m}_{c8}}} \quad (11.74)$$

Compare this equation with Equation 11.45, when we had made the assumption of choked flow at 8, that is,

$$\boxed{\pi_t / \sqrt{\tau_t} \approx \text{constant}} \quad (11.45)$$

Equation 11.74 indicates that turbine expansion is no longer constant when the throat unchokes, rather it is inversely proportional to the nozzle corrected mass flow rate at the nozzle throat. A reduction in the corrected mass flow rate at the nozzle throat then causes the turbine pressure ratio π_t or backpressure p_{t5} to increase, which in turn reduces the turbine shaft power, which causes the compressor pressure ratio and mass flow rate to drop, in a domino effect.

In summary, the iteration strategy for an unchoked exhaust nozzle throat is

1. Calculate the nozzle throat Mach number from Equation 11.70 (using p_{t8}/p_0 from round 1)
2. Calculate the corrected mass flow rate at 8 from Equation 11.71
3. Calculate a new turbine expansion parameter from Equation 11.74
4. Calculate the new cycle pressure ratio, bypass ratio, fan pressure ratio, and so on
5. Calculate the new p_{t8}/p_0 from the new cycle parameters
6. Calculate the new nozzle throat Mach number from Equation 11.70 (from round 2)
7. Compare the two throat Mach numbers (from round 1 and 2)
8. Repeat the process until the two nozzle throat Mach numbers are within say $\sim 1\%$.

11.4.2 Unchoked Turbine Nozzle

In certain low mass flow rate conditions, it is possible for the turbine nozzle to operate in an unchoked mode. Typically, an inverse turbine pressure ratio ($1/\pi_t$) of ~ 2 is the boundary between choked and unchoked turbine operation at low mass flow rates. The following rule of thumb is thus of interest:

$$\boxed{\text{Rule of thumb: For } 1/\pi_t \approx 2 \text{ or less } \quad \text{turbine unchokes, i.e., } M_4 < 1}$$

When the turbine unchokes (mainly due to low mass flow rate conditions), its corrected mass flow rate at station 4 drops (to below critical corresponding to Mach 1 condition). The new turbine expansion parameter, from Equation 11.73 then follows the more general rule of

$$\boxed{\frac{\pi_t}{\sqrt{\tau_t}} = \frac{\dot{m}_{c4}}{\dot{m}_{c8}}} \quad (11.75)$$

Here we have fixed the exhaust nozzle corrected flow \dot{m}_{c8} as in the previous section, but we now have to iterate on the turbine corrected flow \dot{m}_{c4} . The strategy here is that for a given exhaust nozzle corrected mass flow rate \dot{m}_{c8} that we calculate from Equation 11.71, we assume a new (and lower) \dot{m}_{c4} , and then using Equation 11.75, we calculate a new turbine expansion parameter. The new cycle parameters at off-design are then calculated, which lead to a test of M_8 as in step #7 in the iteration strategy of Section 11.4.1.

11.4.3 Turbine Efficiency at Off-Design

So far we have considered the turbine pressure and temperature ratios that are related via constant polytropic efficiency e_t according to

$$\pi_t = \tau_t^{\frac{\gamma_t}{e_t(\gamma_t-1)}} \quad (11.76)$$

Alternatively, we have turbine adiabatic efficiency η_t that connects the turbine pressure and temperature ratios following

$$\tau_t = 1 - \eta_t \left(1 - \pi_t^{(\gamma_t-1)/\gamma_t} \right) \quad (11.77)$$

In reality, turbine efficiency, either e_t or η_t , changes with operating condition and the turbine expansion parameter that was kept constant between the on- and off-design was

$$\frac{\pi_{t,O-D}}{\sqrt{\tau_{t,O-D}}} = \frac{\pi_{t,D}}{\sqrt{\tau_{t,D}}} = C_1 \quad (11.78)$$

From our design analysis, we determine the RHS of the above equation (constant C_1), then we have two equations and two unknowns, for τ_t and π_t , if we know (or can estimate) the off-design efficiency η_t . For example, we have to numerically solve the following equation for τ_t .

$$\tau_t = 1 - \eta_t \left[1 - \left(C_1 \tau_t^{1/2} \right)^{(\gamma_t-1)/\gamma_t} \right] \quad (11.79)$$

11.4.4 Variable Gas Properties

Up to this point in our analysis, we have prescribed gas properties at both design and off-design conditions. In the off-design analysis, the compressor pressure ratio and, therefore, its exit temperature T_{13} are both unknown. Since for a thermally perfect gas we have

$$\begin{aligned} \gamma &= \gamma(T) \\ c_p &= c_p(T) \end{aligned}$$

we need to recalculate all gas properties based on our cycle temperatures and, in fact, we have to include the effect of fuel-to-air ratio on the gas constants after the burner. Based on the recalculated gas properties, we have to repeat the cycle analysis and continue the loop until certain level of accuracy (in, for example, τ_t) is achieved. Every one of these steps represents a higher level of refinement in engine performance simulation. The complexities of the iteration loops and gas modeling have prompted the creation

of computer codes. One example is the NNEP, which stands for Navy/NASA Engine Program, which also interfaces with CEC (complex chemical equilibrium composition).

11.5 Principles of Engine Performance Testing

Full-scale (prototype) engine performance testing is of vital importance to propulsion industry before a commitment can be made for their production. Prior to full engine performance testing, each component is extensively tested in component test rigs. For example, a compressor test rig tests and develops the compressor performance map, including its stall and choke boundaries. The impact of inlet flow distortion on compressor stall characteristics/deterioration would also be assessed. Once the component performance maps are completely determined, the full-scale engine testing program begins. Some of the key parameters of interest in an engine performance testing are shown in the following list:

1. Engine thrust
2. Engine air mass flow rate
3. Engine fuel consumption
4. Engine controls effectiveness, for example, in acceleration/deceleration and engine stability
5. Engine, that is, shaft, vibration levels
6. Engine noise and exhaust gas emissions.

The instrumentation used in engine performance testing is calibrated to measure the steady state and transient characteristics of pressure (via low and high frequency response pressure transducers), temperature (via thermocouples), shaft speed (via magnetic transducer or tacho-generator), shaft vibration level (via accelerometer), turbomachinery blade tip clearance (via capacitive sensors or optical probes), air flow (via instrumented bellmouth or venturi meter), fuel flow (via flow meters) and thrust (via load cells). The location of measurement stations and the respective parameters in a single-spool turbojet engine are shown in Figure 11.13.

The air temperature and pressure, p_0 and T_0 , are used to correct for the nonstandard testing conditions. Namely, engine thrust, F , air mass flow rate and thrust-specific fuel consumption, TSFC, are first corrected according to:

$$F_c \equiv F/\delta_0$$

$$\dot{m}_{c2} = \frac{\dot{m}\sqrt{\theta_2}}{\delta_2}$$

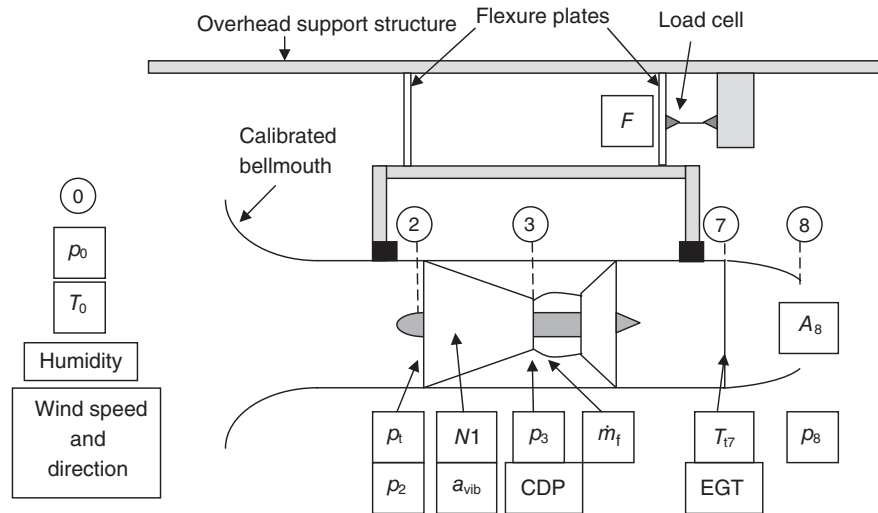
$$TSFC_c \equiv \frac{TSFC}{\sqrt{\theta_0}}$$

and then expressed as a function of corrected shaft speed

$$N_{c2} \equiv \frac{N1}{\sqrt{\theta_2}}$$

The air humidity impacts gas properties, namely its density, ρ , the ratio of specific heats, γ , and gas constant, R . Since water vapor has a molecular weight of 18 as compared to 29 for air, their mixture, that is, humidity in atmospheric air, lowers the ambient density. For

■ **FIGURE 11.13**
Schematic drawing of
an instrumented
turbojet engine in an
open-air testing facility



N1: Single-spool shaft rotational speed (rpm)

F: Thrust-stand force measured by a calibrated load cell

EGT: Exhaust gas (total) temperature measured by calibrated thermocouples

CDP: Compressor discharge pressure measured by calibrated pressure transducers

a_{vib} : Shaft vibration acceleration as measured by calibrated accelerometer (in g's)

the same reason, the gas constant, R , c_p and c_v for humid air are higher than for dry air. Also, since the humid air is partially composed of a tri-atomic gas (H_2O) versus air, which is primarily composed of diatomic gas (N_2 , O_2), the ratio of specific heats, γ , is lower for humid air. Consequently, the mass flow rate and, thus, thrust need to be corrected for the effect of humidity in atmospheric air.

The effect of wind speed and direction in open air installations is in creating ram drag and side-force, which impacts the accuracy of gross thrust measurement. Consequently, only *head wind* of less than 10 knots is the accepted limit in open-air testing practice. The engine noise is measured by an array of microphones placed at various distances and angular positions with respect to the engine centerline. The exhaust emissions (UHC, CO, NO_x , CO_2 and H_2O) are measured by gas analyzer probe (mass spectrometer), which is inserted in the exhaust nozzle and measures the mole fractions of the constituent gas.

Engine performance testing is conducted in different environments and facilities. The following group represents the ground facilities:

- open-air ground testing facility (GTF)
- engine test cell
- altitude testing facility (ATF)
- ram air facility.

In addition to these, there are certification facilities for icing and bird ingestion that are also conducted in ground test facilities. Finally, flying test bed aircraft are used to calibrate the engine thrust and aircraft drag data in flight and correlate the flight and ground test data. The consistent and corrected set of data is then used in the development

■ **FIGURE 11.14** PW1524G engine in ground testing at the Pratt & Whitney West Palm Beach, FL, test facility. Source: Reproduced by permission of United Technologies Corporation, Pratt & Whitney



of the control laws for the engine, namely through the development of the full-authority digital electronic controller (FADEC). Figures 11.14–11.17 show ground test facilities and flight test bed aircraft (courtesy of Pratt & Whitney). For additional reading on engine testing and thrust determination, Abernethy and Roberts (1986) and Covert *et al.* (1985) should be consulted.

11.5.1 Force of Inlet Bellmouth on Engine Thrust Stand

An inlet bellmouth is a bell-shaped converging duct (i.e., a nozzle) that provides for smooth flow acceleration into an airbreathing engine on a static thrust stand (Figure 11.18). The bellmouth is characterized by its contraction area ratio, A_1/A_2 , and its length ratios, L_1/D_2 and L_2/D_2 . The length ratio, L_1/D_2 , in the contraction section and the length of the constant-area throat section, L_2/D_2 , provide for a uniform, low-distortion flow into the engine. The test cell pressure, temperature and humidity are recorded prior to engine testing. Since the engine is stationary, the test cell pressure and temperature serve as the stagnation, or total, values of pressure and temperature respectively for the engine.

11.5.1.1 Bellmouth Instrumentation. The static pressure is measured at the bellmouth throat at four azimuthal locations, as shown in Figure 11.19. A certain amount of asymmetry in the flow is to be expected, even in the most controlled environment

■ **FIGURE 11.15**
PW1524G engine
conducting natural
icing tests at the
GLACIER facility in
Thompson, Manitoba,
Canada. Source:
Reproduced by
permission of United
Technologies
Corporation, Pratt &
Whitney



of axisymmetric installations. The throat pressure is the average of the four measured wall static pressures. The average throat pressure is used to calculate the air mass flow rate into the engine. In addition to throat static pressure measurements, the bellmouth may be equipped with other wall static pressure taps that are distributed both axially and azimuthally from the lip to the throat. In essence the static pressure distribution on the bellmouth can be used to estimate the resultant axial pressure force on the thrust stand (exerted by the bellmouth).

■ **FIGURE 11.16**
PW1217G flight testing
on one of the two P&W
B747SP Flying Test
Beds. Source:
Reproduced by
permission of United
Technologies
Corporation, Pratt &
Whitney



■ **FIGURE 11.17**
 PW1133G first flight
 on P&W B747SP
 Flying Test Bed.
 Source: Reproduced by
 permission of United
 Technologies
 Corporation, Pratt &
 Whitney



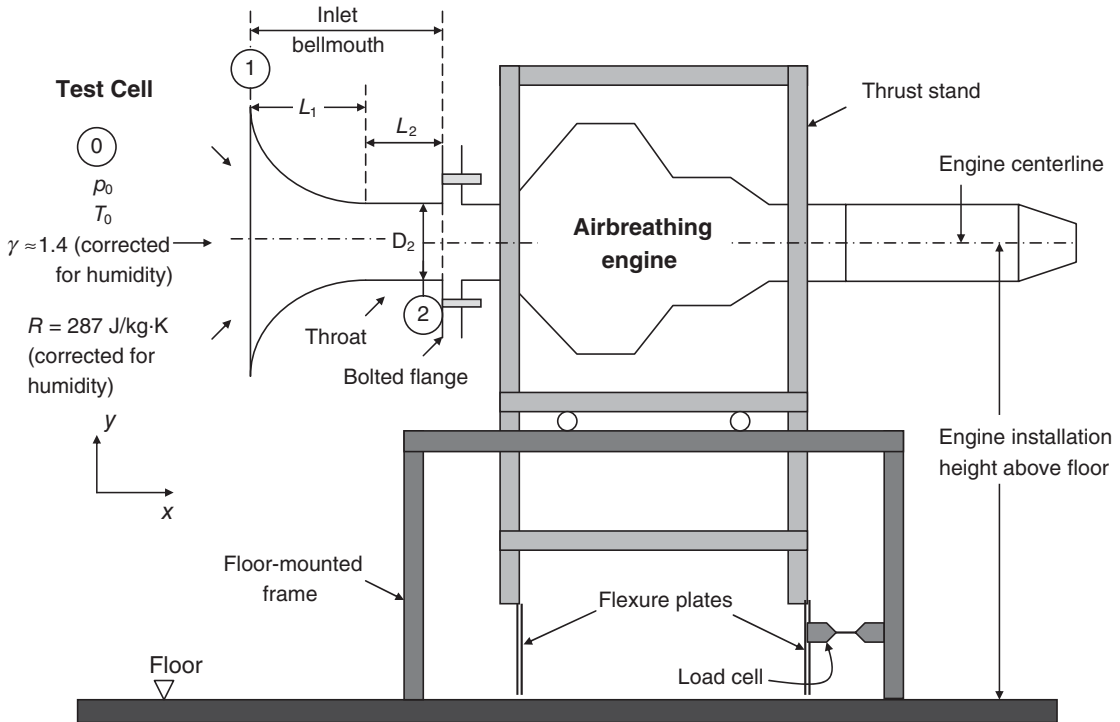
11.5.1.2 The Effect of Fluid Viscosity. The effect of fluid viscosity is to form boundary layer on the bellmouth wall. As the fluid is accelerating along the wall, the boundary layer is facing a “favorable” pressure gradient and thus remains attached (and thin). The boundary layer formation creates blockage and an *effective* flow area as well as resulting in a reduction in total pressure. The boundary layer displacement thickness at the bellmouth exit, which causes a reduction in the flow area (in A_2), is described by a discharge coefficient, C_{d2} ; typically, 0.990–0.995 is a reasonable approximation.

$$A_{2,eff} = C_{d2}A_{2,geo} \tag{11.80}$$

11.5.1.3 The Force of Inlet Bellmouth on Engine Thrust Stand. We may numerically integrate the measured wall static pressure distribution on the bellmouth to get the axial force due to pressure. According to the pressure difference on the outer and inner walls (Figure 11.20a), we can write

$$F_{x,bellmouth} = - \iint_{wall} (p - p_0) dA_n \quad dA_n = 2\pi r dr \tag{11.81}$$

Note that the integrand, that is, $(p - p_0)$ in Equation 11.81 is negative and dA_y is also negative (for a converging duct), which produces an axial force in the $-x$ direction.



■ FIGURE 11.18 Inlet bellmouth and a jet engine on a static thrust stand in a ground testing facility

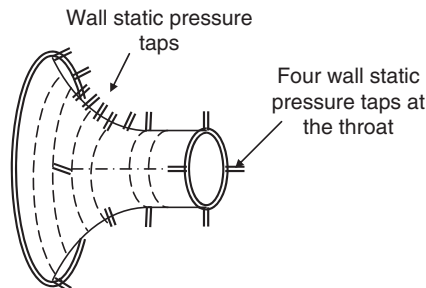
Therefore, we conclude that the bellmouth experiences a thrust force and thus “pulls” on the thrust stand.

The flow acceleration inside the bellmouth causes a static pressure drop whereas the test cell static pressure acts on the outside wall, as shown in Figure 11.20. The static pressure and velocity distribution are nonuniform at the bellmouth inlet (as shown in Figure 11.21) due to flow curvature near the convex wall.

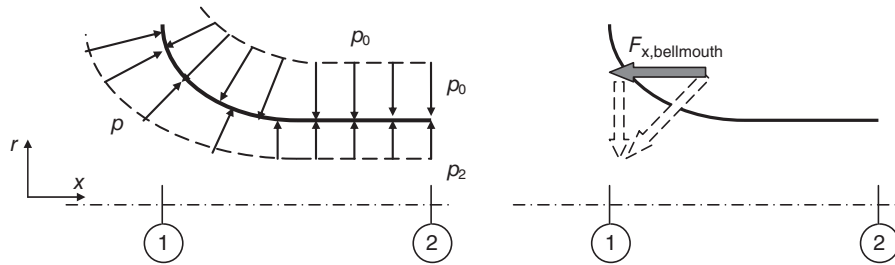
Based on (four) measured static pressures at 2, we define an average static pressure,

$$\bar{p}_2 = \sum_{i=1}^4 p_{2i}/4 \tag{11.82}$$

■ FIGURE 11.19 Schematic drawing of an inlet bellmouth with its wall static pressure taps



■ **FIGURE 11.20**
Pressure distribution
on the inner and outer
wall of a bellmouth



The ideal exit Mach number, based on the average throat static pressure is:

$$M_{2i} = \sqrt{\frac{2}{\gamma - 1} \left[\left(\frac{p_0}{\bar{p}_2} \right)^{\frac{\gamma - 1}{\gamma}} - 1 \right]} \quad (11.83)$$

Assuming an adiabatic flow inside the bellmouth, the test cell static temperature is the stagnation temperature inside the bellmouth, namely at its exit, that is, and the static temperature at 2 is thus

$$T_2 = T_0 / [1 + (\gamma - 1)M_{2i}^2 / 2] \quad (11.84)$$

The speed of sound and the average flow speed at the bellmouth exit are respectively:

$$a_2 = \sqrt{\gamma RT_2} \quad (11.85)$$

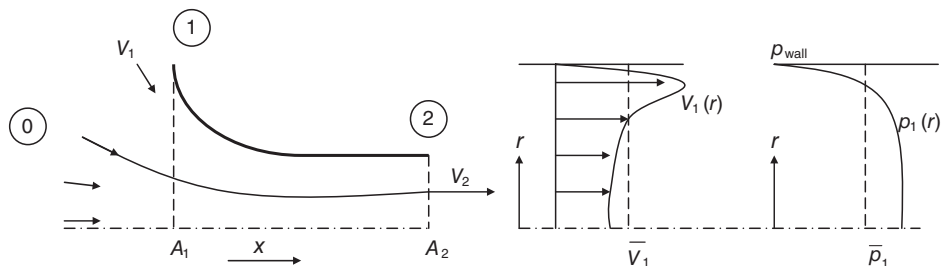
$$\bar{V}_{2i} = M_{2i} a_2 \quad (11.86)$$

From the average pressure and temperature at 2, we use perfect gas law to get the fluid density at 2, that is,

$$\rho_2 = \bar{p}_2 / RT_2 \quad (11.87)$$

Note that the assumption of incompressible flow could have been made, since the flow Mach numbers inside the bellmouth are small. The mass flow rate through the bellmouth

■ **FIGURE 11.21**
The bellmouth inlet
flow nonuniformity
shows overspeed and
suction near the convex
wall (\bar{V}_1 is the
mass-averaged inlet
velocity and \bar{p}_1 is the
average static pressure
at the bellmouth inlet)



may now be calculated based on exit values of fluid density, velocity and “effective” flow area, $A_{2\text{eff}}$, which is related to the discharge coefficient that was introduced earlier, C_{d2} ,

$$\dot{m}_2 \cong C_{d2} \rho_2 \bar{V}_{2i} A_2 \quad (11.88)$$

In general, the flow speed in the bellmouth is in low subsonic range, which makes the assumption of incompressible flow reasonable. The one-dimensional gas speed at the inlet follows the continuity equation and assuming constant density, that is,

$$\bar{V}_1 = \bar{V}_{2i} (A_2/A_1) \quad (11.89)$$

The use of the Bernoulli equation at the bellmouth inlet gives a one-dimensional estimation of p_1 , namely

$$\bar{p}_1 \approx p_0 - \rho_0 \bar{V}_1^2 / 2 \quad (11.90)$$

The one-dimensional momentum balance in the x-direction on the captured streamtube (control volume), based on the fluid impulse, gives an estimate of the bellmouth **internal** axial force that acts on the fluid, that is,

$$F_{x,BM,int})_{fluid} = I_2 - I_1 = \dot{m} (\bar{V}_2 - \bar{V}_1) + \bar{p}_2 A_2 - \bar{p}_1 A_1 \quad (11.91)$$

The bellmouth (inner wall) feels an equal and opposite force of that felt by the fluid, that is,

$$F_{x,int})_{BM} = -\dot{m} (\bar{V}_2 - \bar{V}_1) - \bar{p}_2 A_2 + \bar{p}_1 A_1 \quad (11.92)$$

The bellmouth outer wall is soaked in ambient static pressure, p_0 , which integrates into the following axial force in the $-x$ -direction, that is, the bellmouth **external** axial force,

$$F_{x,ext})_{BM} = -p_0 (A_1 - A_2) \quad (11.93)$$

Therefore, the net force acting on the bellmouth in the x-direction is the **sum of internal and external** components, namely

$$F_{x,total})_{BM} = -\dot{m} (\bar{V}_2 - \bar{V}_1) - (\bar{p}_2 - p_0) A_2 + (\bar{p}_1 - p_0) A_1 \quad (11.94)$$

We have either measured or calculated all the terms in Equation 11.94, thus we may estimate the axial force that is introduced by the installation of the inlet bellmouth on the thrust stand. Since the value of the bellmouth axial force will be negative, we conclude that ‘the bellmouth is *pulling* on the thrust stand, that is, it produces its own thrust. The load cell measures the entire “pull” on the frame, which has a contribution from the bellmouth as well. The engine thrust measurement using the load cell is thus to be corrected for the bellmouth-induced thrust.

A closer examination of Figure 11.20b also reveals that the integral of pressure on the bellmouth will produce a force in the thrust (i.e., $-x$) direction.

The bellmouth axial force may be nondimensionalized by the product of test cell static pressure, p_0 , and the bellmouth exit area, A_2 , that is,

$$F_{x,total})_{BM} / p_0 A_2 = -\dot{m} (\bar{V}_2 - \bar{V}_1) / p_0 A_2 - (\bar{p}_2 / p_0 - 1) + (\bar{p}_1 / p_0 - 1) A_1 / A_2 \quad (11.95)$$

EXAMPLE 11.5

A small airbreathing drone engine is on a thrust stand. The inlet bellmouth has an area ratio of 4 and an exit geometric area of 0.1 ft². The discharge coefficient at the bellmouth exit is assumed to be $C_{d2} = 0.995$. The test cell pressure and temperature are 14.7 psia and 59°F, respectively. At 60,000 rpm, the average static pressure at the bellmouth throat is measured to be 13.96 psia. Calculate the force that bellmouth exerts on the thrust stand.

Data summary:

$$\begin{aligned} A_1/A_2 &= 4, C_{d2} = 0.995, A_2 = 0.1 \text{ ft}^2 \\ p_0 &= 14.7 \text{ psia}, T_0 = (59^\circ\text{F}) = 519^\circ\text{R} \\ R &= 1716 \text{ ft}^2/\text{s}^2\text{R and } \gamma = 1.4 \\ \bar{p}_2 &= 13.96 \text{ psia (at 60,000 rpm shaft speed)} \end{aligned}$$

SOLUTION

$$M_{2i} = \sqrt{\frac{2}{\gamma - 1} \left[\left(\frac{p_0}{\bar{p}_2} \right)^{\frac{\gamma - 1}{\gamma}} - 1 \right]} \approx 0.2726$$

$$T_2 = T_0 / [1 + (\gamma - 1)M_{2i}^2/2] \approx 511.4^\circ\text{R}$$

$$a_2 = \sqrt{\gamma RT_2} \approx 1108 \text{ ft/s, therefore } u_2 = M_{2i} a_2 = 0.2726(1,108 \text{ ft/s}), u_2 \approx 302.2 \text{ ft/s}$$

$$\dot{m}_2 = C_{d2} \rho_2 A_2 V_2 = C_{d2} \frac{p_2}{RT_2} A_2 V_2 \approx 2.218 \text{ lbm/s}$$

$$V_1/V_2 = A_2/A_1, \dots V_1 = V_2/4$$

$$\rho_0 = p_0/RT_0 \approx 0.07653 \text{ lbm/ft}^3$$

$$p_1 = p_0 - 1/2 \rho_0 V_1^2 \dots p_1 = 14.653 \text{ psia}$$

$$\begin{aligned} F_{x,total})_{BM} &= -\dot{m} (\bar{V}_2 - \bar{V}_1) - (\bar{p}_2 - p_0)A_2 + (\bar{p}_1 - p_0)A_1 = -2.218(302.2 - 302.2/4)/32.2 - (13.96 - 14.7)(0.1)(144) \\ &+ (14.653 - 14.7)(0.4)(144) = -15.612 + 10.656 - 2.707 = -7.663 \text{ lbf} \end{aligned}$$

$$(F_{x,total})_{BM} \approx -7.66 \text{ lbf}$$

There is nearly a 7.66 lbf of thrust exerted on the bellmouth, which is transferred to the load cell. Therefore, the load cell reading for engine static thrust has to be **lowered** by the amount of the bellmouth thrust.

For example, for a thrust reading of 120 lbf by the load cell at this rpm, we conclude that the engine gross thrust is only ~112.3 lbf at 60,000 rpm.

11.6 Summary

The purpose of this chapter was to integrate our individual component studies into a complete propulsion system. We asked and answered the question of how an aircraft gas

turbine engine (that was designed for certain operating conditions) behaved in off-design. We started with a review of the five corrected parameters in an engine:

1. $\dot{m}_{ci} \equiv \frac{\dot{m}_i \sqrt{\theta_i}}{\delta_i} = \sqrt{\frac{\gamma_i}{R_i}} \frac{p_{ref}}{\sqrt{T_{ref}}} A_i M_i \left(1 + \frac{\gamma_i - 1}{2} M_i^2 \right)^{-\frac{\gamma_i + 1}{2(\gamma_i - 1)}}$
2. $N_{ci} \equiv \frac{N}{\sqrt{\theta_i}}$
3. $\dot{m}_{fc} \equiv \frac{\dot{m}_f}{\delta_2 \sqrt{\theta_2}}$
4. $F_c \equiv F / \delta_0$
5. $TSFC_c \equiv \frac{TSFC}{\sqrt{\theta_0}}$

We learned about the individual component interaction in a steady-state mode of operation. The conservation principles of mass and energy provided the link, that is, the match, between the components. In case the compressor and turbine performance maps were available, we used them to calculate the gas generator pumping characteristics for a given throttle setting. Pumping characteristics are

1. the corrected air/flow rate \dot{m}_{c2}
2. the pressure ratio p_{t5} / p_{t2}
3. the temperature ratio T_{t5} / T_{t2}
4. the fuel flow parameter $f Q_R \eta_b / c_p T_{t2}$ or the corrected fuel flow rate \dot{m}_{fc}

If the component performance maps were not available, we relied on the persistence of certain choking stations in the engine (as in stations 4 and 8 in a single-spool engine and 4,4.5, and 8 in a two-spool engine) in on- and off-designs to calculate the off-design performance of the engine. The highest level of simplifications, as in constant component efficiencies, gas properties, negligible fuel-to-air ratio variation, and so on, resulted in a constant turbine expansion parameter in a *single-spool turbojet* engine

$$\pi_t / \sqrt{\tau_t} = \text{constant}$$

between the on- and off-designs. We used the same principles in a *two-spool turbofan* engine that resulted in three constants between the on- and off-design turbine expansion parameters and one involving bypass ratio

$$\pi_{tL} / \sqrt{\tau_{tL}} \approx \text{constant}$$

$$\pi_{tH} / \sqrt{\tau_{tH}} \approx \text{constant}$$

$$\alpha \pi_{cH} \sqrt{\frac{\tau_t \tau_f}{\tau_\lambda}} \approx \text{constant}$$

In the case that the exhaust nozzle throat was unchoked, the corrected mass flow rate at the nozzle throat was reduced and the turbine expansion parameter τ_t was no longer constant, that is,

$$\frac{\pi_t}{\sqrt{\tau_t}} = \frac{\text{constant}}{\dot{m}_{c8}}$$

An iteration strategy to arrive at a consistent operating condition of the engine in off-design was outlined in Section 11.4.1. Other iteration strategies were presented for unchoked turbine and variable gas properties.

The most critical and perhaps interesting part of the engine component matching is in the study of engine transients and unsteady interactions. For example, stall and surge are unsteady behavior of the compression–combustor system. The phenomenon of inlet unstart and upstream propagation of “hammer shock” finds its root in supersonic mixed-compression inlet instability. External compression inlets may initiate “buzz” instability and subsequent compressor stall. The acceleration and deceleration paths (i.e., spool up and down) in an engine are transients that too may cause compressor instability. In general, the question that we need to ask is what happens if we disturb the steady state? Would the oscillations in the system decay or grow? What is the impact of the rate of change that we introduce in the dynamic system, as in the rate of fuel addition, spool up or spool down, or rapid actuation of (stator) blades? Kerrebrock’s paper (1977) on small disturbance theory examines the growth/decay characteristics of pressure, entropy, and vorticity perturbations in swirling flows in turbomachinery. Schobeiri (2005) has treated the time-dependent, dynamic performance of turbomachinery and gas turbine systems extensively in his book.

Finally, there are many aircraft engine simulation codes, for example, NNEP that provide for an accurate estimation of the engine performance characteristics over a wide operating range of the engine/aircraft. Also, a major new initiative on propulsion system simulation is NASA-Glenn’s “Numerical Propulsion System Simulation” (NPSS) Program (Lytle, 1999) that promises to bring high fidelity to fully three-dimensional transient simulation of complex aircraft engine configurations.

The principles that we learned in this chapter help us to (1) produce engine off-design performance for preliminary design purposes, (2) use compressor and turbine performance maps to calculate the gas generator pumping characteristics, and (3) understand and interpret the results of engine simulation codes, if they are available and used.

Additional references (e.g., 2, 3, 5–7, 9–12, and 15–19) on gas turbine and aircraft propulsion compliment the subject of this chapter and are recommended for further reading.

References

1. Abernethy, R.B. and Roberts, J.H., In-Flight Thrust Determination and Uncertainty, SAE Special Publication 64, 1986.
2. Archer, R.D. and Saarlal, M., *An Introduction of Aerospace Propulsion*, Prentice Hall, New York, 1998.
3. Bathie, W., *Fundamentals of Gas Turbines*, 2nd edition, John Wiley & Sons, Inc., New York, 1995.
4. Covert, E.E., James, C.R., Richey, G.K., and Rooney, E.C., Thrust and Drag: Its Prediction and Verification, AIAA Progress Series, Vol. 98, AIAA, New York, 1985.
5. Cumpsty, N., *Jet Propulsion: A Simple Guide to the Aerodynamic and Thermodynamic Design and Performance of Jet Engines*, 2nd edition, Cambridge University Press, Cambridge, UK, 2003.

6. Flack, R.D., *Fundamentals of Jet Propulsion with Applications*, Cambridge University Press, Cambridge, UK, 2005.
7. Gordon, S. and McBride, B.J., "Computer Program for Computation of Complex Chemical Equilibrium Compositions, Rocket Performance, Incident and Reflected Shocks, and Chapman-Jouguet Detonations," NASA SP-273, 1976.
8. Gordon, S. and McBride, B.J., "Computer Program for Calculation of Complex Chemical Equilibrium Compositions and Applications I. Analysis", NASA RP-1311, 1994.
9. Heiser, W.H., Pratt, D.T., Daley, D.H., and Mehta, U.B., *Hypersonic Airbreathing Propulsion*, AIAA, Washington, DC, 1993.
10. Hesse, W.J. and Mumford, N.V.S., *Jet Propulsion for Aerospace Applications*, 2nd edition, Pittman Publishing Corporation, New York, 1964.
11. Hill, P.G. and Peterson, C.R., *Mechanics and Thermodynamics of Propulsion*, 2nd edition, Addison-Wesley, Reading, MA, 1992.
12. Kerrebrock, J.L., *Aircraft Engines and Gas Turbines*, 2nd edition, MIT Press, Cambridge, MA, 1992.
13. Kerrebrock, J.L., "Small Disturbances in Turbomachine Annuli with Swirl," *AIAA Journal*, Vol. 15, June 1977, pp. 794–803.
14. Lytle, J.K., "The Numerical Propulsion System Simulation: A Multidisciplinary Design System for Aerospace Vehicles," NASA TM-1999-209194.
15. Mattingly, J.D., *Elements of Gas Turbine Propulsion*, McGraw-Hill, New York, 1996.
16. Mattingly, J.D., Heiser, W.H., and Pratt, D.T., *Aircraft Engine Design*, 2nd edition, AIAA, Washington, DC, 2002.
17. Oates, G.C., *Aerothermodynamics of Gas Turbine and Rocket Propulsion*, AIAA, Washington, DC, 1988.
18. Schobeiri, M.T., *Turbomachinery Performance and Flow Physics*, Springer Verlag, New York, 2005.
19. Shepherd, D.G., *Aerospace Propulsion*, American Elsevier Publication, New York, 1972.

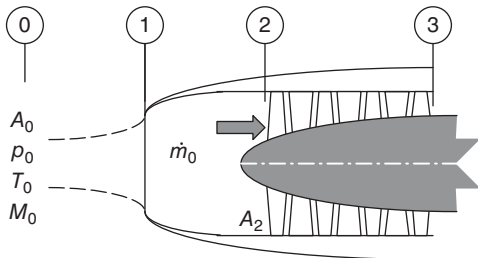
Problems

11.1 In a turbojet engine, the compressor face total pressure and temperature are 112 kPa and 268 K, respectively. The shaft speed is 6400 rpm. The air mass flow rate is 125 kg/s and the fuel mass flow rate is 2.5 kg/s. The fuel heating value is 42,000 kJ/kg and the engine produces 145 kN of thrust. Express the following engine corrected parameters:

- (a) the corrected (air) mass flow rate \dot{m}_{c2} in kg/s assuming $p_{t2} = 0.99 p_{t0}$
- (b) the corrected shaft speed N_{c2} in rpm
- (c) the corrected fuel flow rate, \dot{m}_{fc} , in kg/s
- (d) the corrected thrust F_c in kN
- (e) the corrected thrust-specific fuel consumption TSFC_c in mg/s/N.

Note: $p_{ref} = 101.33$ kPa and $T_{ref} = 288.2$ K

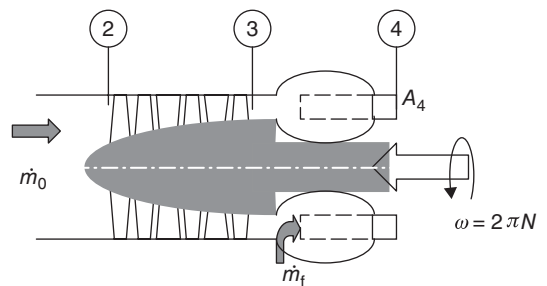
11.2 The corrected mass flow rate at the engine face is $\dot{m}_{c2} = 180$ kg/s. Calculate the axial Mach number M_{z2} at the



■ FIGURE P11.2

engine face for $A_2 = 1$ m². Also calculate the capture area A_0 for a flight Mach number of $M_0 = 0.85$ and assume an inlet total pressure recovery $\pi_d = 0.995$. Assume $\gamma_c = 1.4$. $R_c = 287$ J/kg · K, $p_0 = 30$ kPa and $T_0 = 250$ K.

11.3 A compressor has an air mass flow rate of 180 kg/s. The fuel flow rate in the burner is 6 kg/s. The flow areas are $A_2 = 1$ m², $A_3 = 0.14$ m². Compressor total pressure ratio is $\pi_c = 11$ and $e_c = 0.9$. The fuel heating value is $Q_R = 42,000$ kJ/kg, burner efficiency and total pressure ratio are $\eta_b = 0.99$ and $\pi_b = 0.95$, respectively.



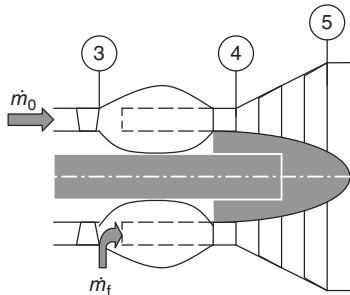
■ FIGURE P11.3

Assuming $M_{z2} = 0.5$, $T_{t2} = 300$ K and $M_{z4} = 1.0$, Calculate

- (a) T_{t4}/T_{t2}
- (b) p_{t4}/p_{t2}
- (c) A_4 in m²

- (d) the physical and corrected mass flow rates at 4, i.e., \dot{m}_4 and \dot{m}_{c4} . Gas properties are $\gamma_c = 1.4$, $c_{pc} = 1004 \text{ J/kg} \cdot \text{K}$, $\gamma_t = 1.33$, $c_{pt} = 1156 \text{ J/kg} \cdot \text{K}$

11.4 A gas turbine operates with a choked nozzle $M_4 = 1.0$ with $\gamma_t = 1.33$, and $c_{pt} = 1156 \text{ J/kg} \cdot \text{K}$. Turbine expansion parameter $\tau_t = 0.80$ and turbine adiabatic efficiency is $\eta_t = 0.86$. The burner total pressure ratio is $\pi_b = 0.95$ and the burner total temperature ratio is $\tau_b = 1.80$.

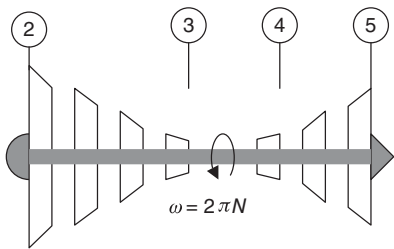


■ FIGURE P11.4

Calculate

- (a) the ratio of corrected mass flow rates $\dot{m}_{c4}/\dot{m}_{c5}$
 (b) the ratio of corrected mass flow rates $\dot{m}_{c4}/\dot{m}_{c3}$, assuming $f = 0.03$.

11.5 A multistage compressor is connected to a multistage turbine on the same shaft. The shaft speed is $N = 8000 \text{ rpm}$. The throttle parameter is $T_{t4}/T_{t2} = 6.0$. The compressor inlet flow has a $p_{t2} = p_{ref}$ and $T_{t2} = T_{ref}$. Compressor discharge temperature is $T_{t3} = 872 \text{ K}$. The engine corrected mass flow rate is $\dot{m}_{c2} = 360 \text{ kg/s}$.



$\gamma_c = 1.4$ $\gamma_t = 1.33$
 $c_{pc} = 1004 \text{ J/kg} \cdot \text{K}$ $c_{pt} = 1156 \text{ J/kg} \cdot \text{K}$

■ FIGURE P11.5

Calculate

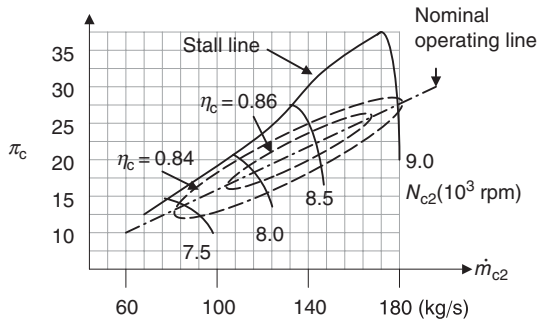
- (a) the corrected shaft speed N_{c2} (rpm)
 (b) the corrected shaft speed N_{c4} (rpm)
 (c) the compressor pressure ratio π_c assuming $e_c = 0.90$

- (d) the compressor shaft power in MW
 (e) the fuel-to-air ratio assuming $\pi_b = 0.94$, $\eta_b = 0.99$, and $Q_R = 42,000 \text{ kJ/kg}$
 (f) turbine expansion parameters T_{t5}/T_{t4} and p_{t5}/p_{t4} for $\eta_t = 0.85$ and $\eta_m = 0.99$
 (g) gas generator pumping characteristics p_{t5}/p_{t2} and T_{t5}/T_{t2}

11.6 A high-pressure ratio compressor performance map is shown. The nominal operating line corresponds to $T_{t4}/T_{t2} = 6.5$. Assuming a constant turbine adiabatic efficiency of $\eta_t = 0.88$ at on- and off-designs, calculate and plot the pumping characteristics of the gas generator similar to Example 11.1. The design corrected mass flow rate is 180 kg/s , with $\pi_{c, design} = 27.5$.

Assume

$\gamma_c = 1.4$, $c_{pc} = 1004 \text{ J/kg} \cdot \text{K}$
 $\gamma_t = 1.4$, $c_{pt} = 1156 \text{ J/kg} \cdot \text{K}$
 $f \approx 0.03$
 $\eta_m = 0.995$
 $\pi_b = 0.95$



■ FIGURE P11.6

11.7 An afterburner on- or off-mode should not affect the turbine back pressure. This requirement is often met by a variable throat convergent–divergent exhaust nozzle. The “dry” mode is characterized by a lower total pressure loss and an adiabatic flow:

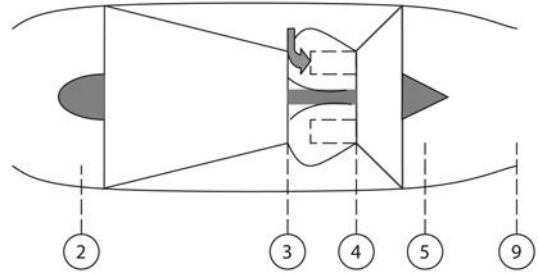
$\pi_{AB-dry} = 0.96$, $\tau_{AB-dry} = T_{t7}/T_{t5} = 1.0$,
 $\gamma_{AB-dry} = 1.33$, $c_{pAB-dry} = 1156 \text{ J/kg} \cdot \text{K}$

The “wet” mode is characterized by a higher total pressure loss and chemical energy release

$\pi_{AB-wet} = 0.90$, $\tau_{AB-wet} = T_{t7}/T_{t5} = 2.0$,
 $\gamma_{AB-wet} = 1.30$, $c_{pAB-wet} = 1243 \text{ J/kg} \cdot \text{K}$,
 $Q_{R,AB} = 42,000 \text{ kJ/kg}$, $\eta_{AB} = 0.95$

The turbine entry temperature (TET) is $T_{t4} = 1760 \text{ K}$ and $p_{t4} = 2.0 \text{ MPa}$ (in both dry and wet modes) and the turbine expansion parameter $\tau_t = 0.80$ and $\eta_t = 0.85$. The gas properties in the turbine are $\gamma_t = 1.33$ and $c_{p,t} = 1156 \text{ J/kg} \cdot \text{K}$. The corrected mass flow rate at turbine entry is $\dot{m}_{c4} = 80 \text{ kg/s}$ and turbine nozzle is choked, $M_4 = 1.0$.

The exhaust nozzle in dry and wet modes is choked, i.e., $M_8 = 1.0$. The total pressure ratio in the convergent (part of the) nozzle is $p_{t8}/p_{t7} = 0.98$ for dry and 0.95 for wet mode. The nozzle divergent section has a total pressure ratio of $p_9/p_{t8} = 0.99$ for dry and 0.95 for wet operation.



■ FIGURE P11.8

For the following off-design operation

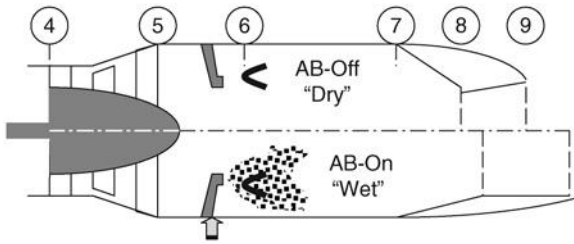
$$M_0 = 0.85, p_0 = 20 \text{ kPa}, T_0 = -15^\circ\text{C}$$

$$\tau_\lambda = 6.5$$

$$e_t = 0.80, \eta_m = 0.98, \pi_n = 0.97, p_9 = p_0$$

Assume a calorically perfect gas with $\gamma = 1.4$ and $c_p = 1004 \text{ kJ/kg} \cdot \text{K}$ constant throughout the engine, and calculate

- (c) $\pi_{c\text{-off-design}}$
- (d) the ratio of corrected shaft speeds $N_{c2, O-D}/N_{c2, D}$
- (e) the corrected mass flow rate at off-design (kg/s)
- (f) the axial Mach number at the engine face, $M_{z2, \text{atoff-design}}$
- (g) thrust-specific fuel consumption at design and off-design in mg/s/N



■ FIGURE P11.7

Calculate

- (a) $A_4 \text{ (m}^2\text{)}$
- (b) $A_5 \text{ (m}^2\text{)}$ for $M_5 = 0.5$
- (c) f_{AB}
- (d) $A_g \text{ (m}^2\text{)}$ “dry”
- (e) $A_g \text{ (m}^2\text{)}$ “wet”
- (f) A_9/A_8 “dry” for $p_9 = p_0 = 100 \text{ kPa}$
- (g) A_9/A_8 “wet” for $p_9 = p_0 = 100 \text{ kPa}$
- (h) nozzle gross thrust (kN) “dry”
- (i) nozzle gross thrust (kN) “wet”

11.8 A turbojet engine has the following design-point parameters:

$$M_0 = 0, p_0 = 101.33 \text{ kPa}, T_0 = 15.2^\circ\text{C}$$

$$\pi_d = 0.98$$

$$\pi_c = 25, e_c = 0.90$$

$$M_4 = 1.0$$

$$Q_R = 42,800 \text{ kJ/kg}, \pi_b = 0.95, \eta_b = 0.98, \tau_\lambda = 6.0$$

$$e_t = 0.85, \eta_m = 0.98$$

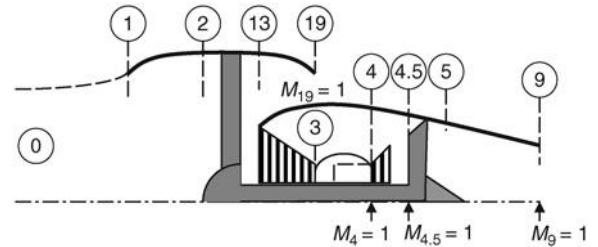
$$\pi_n = 0.97, p_9 = p_0$$

$$\dot{m}_{c2} = 80 \text{ kg/s}, M_{z2} = 0.50$$

Calculate

- (a) fuel-to-air ratio f
- (b) turbine total temperature ratio τ_t

11.9 A separate-flow turbofan engine has a dual spool configuration, as shown. Fan and core nozzles are convergent and choked.



■ FIGURE P11.9

The design parameters for this engine are:

- 1. $M_0 = 0, p_0 = 101.33 \text{ kPa}, T_0 = 15.2^\circ\text{C}$
- 2. $\pi_d = 0.98$
- 3. $\pi_f = 1.8, e_f = 0.90$
- 4. $\alpha = 5.0$
- 5. $\pi_{cH} = 14, e_{cH} = 0.90$
- 6. $T_{t4} = 1600^\circ\text{C}, Q_R = 42,800 \text{ kJ/kg}, \eta_b = 0.99, \pi_b = 0.95$
- 7. $e_{tH} = 0.85, \eta_{mH} = 0.995$

- 8. $e_{tL} = 0.89, \eta_{mL} = 0.995$
- 9. $\pi_n = \pi_{nt} = 0.98, p_8 = p_{18} = p_0$
- 10. $\gamma_c = 1.4, c_{pc} = 1004 \text{ J/kg} \cdot \text{K}$
- 11. $\gamma_t = 1.33, c_{pt} = 1146 \text{ J/kg} \cdot \text{K}$
- 12. $M_4 = M_{4.5} = M_9 = M_{19} = 1.0$

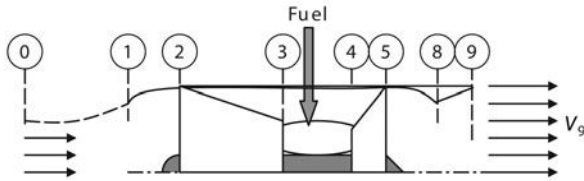
An off-design operating condition is described by

- (a) $M_0 = 0.90, p_0 = 20 \text{ kPa}, T_0 = -20^\circ\text{C}$
- (b) $T_{t4} = 1300^\circ\text{C}$

Assuming all component efficiencies remain constant, calculate

- (a) fan pressure ratio π_f
- (b) high-pressure compressor pressure ratio π_{cH}
- (c) the bypass ratio α

11.10 A turbojet engine has the following design parameters (which is at takeoff):



■ FIGURE P 11.10

- $M_0 = 0$
- $p_0 = 101.33 \text{ kPa}, T_0 = 15.2^\circ\text{C}, \gamma_c = 1.4,$
- $c_{pc} = 1004 \text{ J/kg} \cdot \text{K}$
- $\pi_d = 0.95$
- $\pi_c = 30, e_c = 0.90$
- $Q_R = 42,600 \text{ kJ/kg}, \pi_b = 0.95, \eta_b = 0.98, T_{t4} = 1700^\circ\text{C}$
- $\eta_m = 0.98, e_t = 0.85, \gamma_t = 1.33, c_{pt} = 1156 \text{ J/kg} \cdot \text{K}$
- $\pi_n = 0.90$
- $p_9 = p_0$

This engine powers an aircraft that cruises at $M_0 = 0.80$ at an altitude where $T_0 = -35^\circ\text{C}, p_0 = 20 \text{ kPa}$. The turbine entry temperature at cruise is $T_{t4} = 1500^\circ\text{C}$. Assume that the engine has the same component efficiencies at cruise and takeoff, and the nozzle is perfectly expanded at cruise, as well.

Calculate

- (a) the exhaust velocity V_9 (in m/s) at the design point, i.e., at takeoff
- (b) the thermal efficiency η_{th} at the design point
- (c) thrust-specific fuel consumption at the design point
- (d) the compressor pressure ratio at cruise
- (e) the exhaust velocity V_9 (in m/s) at cruise
- (f) the thermal efficiency η_{th} at cruise
- (g) the propulsive efficiency η_p at cruise
- (h) the thrust-specific fuel consumption at cruise

11.11 In a gas generator, the compressor and burner performance maps are shown. The turbine adiabatic efficiency is assumed nearly constant at $\eta_t = 0.85$. The nominal operating line on the compressor performance map represents the $T_{t4}/T_{t2} = 7.0$ throttle line.

The design corrected shaft speed is $N_{c2} = 10,000 \text{ rpm}$ and the compressor pressure ratio at design is $\pi_{c,D} = 13.5$ (note that the corrected mass flow rate at the compressor face is 89 kg/sat design).

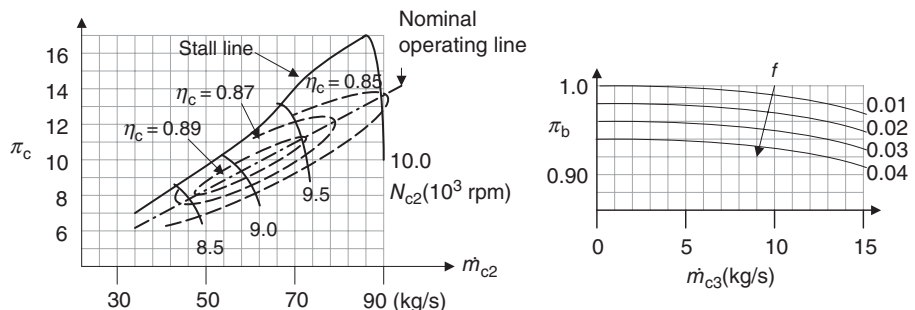
Assuming

- $\gamma_c = 1.4, c_{pc} = 1004 \text{ J/kg} \cdot \text{K}$
- $\gamma_t = 1.33, c_{pt} = 1156 \text{ J/kg} \cdot \text{K}$
- $f \approx 0.03$
- $\eta_m = 0.995$

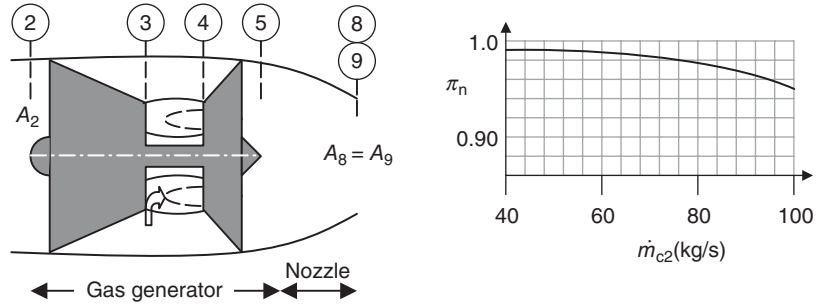
Calculate and graph the gas generator pumping characteristics, as percent corrected shaft speed N_{c2} (% design).

11.12 The gas generator in Problem 11.11 is to be matched to a variable-throat area convergent nozzle, as shown.

The nozzle performance map is also shown here as a graph of π_n versus the corrected mass flow rate (at the engine face). First, by matching the mass flow rate at station 8 (or 9) to that



■ FIGURE P 11.11



■ FIGURE P11.12

of 2, show that the corrected mass flow rates at 8 (or 9) and 2 are related to pumping characteristics according to

$$\dot{m}_{c,9} = (1 + f) \frac{\sqrt{T_{t5}/T_{t2}}}{\pi_n (p_{t5}/p_{t2})} \dot{m}_{c,2}$$

Assuming the nozzle throat remains choked, i.e., $M_8 = 1.0$, graph A_8 variation (or percentage $A_8/A_{8,D}$ variation) as a function of the percent-design corrected shaft speed N_{c2} (% design).

11.13 A separate-flow turbofan engine has the following design-point parameters:

1. $M_0 = 0, p_0 = 0.1 \text{ MPa}, T_0 = 15^\circ\text{C}$
2. $\pi_d = 0.98$
3. $\pi_f = 1.65, e_f = 0.90$
4. $\alpha = 7.0$
5. $\pi_{cH} = 20, e_{cH} = 0.90$
6. $T_{t4} = 1650^\circ\text{C}, Q_R = 42,800 \text{ kJ/kg}, \eta_b = 0.99, \pi_b = 0.95$
7. $e_{tH} = 0.85, \eta_{mH} = 0.995$
8. $e_{tL} = 0.89, \eta_{mL} = 0.995$
9. $\pi_n = \pi_{nf} = 0.98, p_8 = p_{18} = p_0$
10. $\gamma_c = 1.4, c_{pc} = 1004 \text{ J/kg} \cdot \text{K}$
11. $\gamma_t = 1.33, c_{pt} = 1146 \text{ J/kg} \cdot \text{K}$
12. $M_4 = M_{4.5} = M_8 = M_{18} = 1.0$

The off-design operation of this engine is represented by a cruise altitude flight such as

$$\begin{aligned} M_0 &= 0.85, p_0 = 11 \text{ kPa}, T_0 = -15^\circ\text{C} \\ T_{t4} &= 1,500^\circ\text{C} \\ \pi_d &= 0.995 \end{aligned}$$

Assuming all other efficiencies and gas properties remaining constant, calculate the following parameters at off-design condition:

- (a) fan pressure ratio π_f
- (b) high-pressure compressor pressure ratio π_{cH}
- (c) bypass ratio α

11.14 A turbojet engine has the following design-point parameters:

1. $M_0 = 0, p_0 = 0.1 \text{ MPa}, T_0 = 15^\circ\text{C}$
2. $\pi_d = 0.98$
3. $\pi_c = 15, e_c = 0.90$
4. $Q_R = 42,800 \text{ kJ/kg}, \pi_b = 0.97, \eta_b = 0.98, T_{t4} = 1485^\circ\text{C}$
5. $e_t = 0.80, \eta_m = 0.995$
6. $\dot{m}_{c,2} = 24 \text{ kg/s}$
7. $N_{c,2} \text{ (rpm)} = 6,000$
8. $M_{z,2} = 0.6$
9. $\pi_n = 0.97, p_9/p_0 = 1.0$

The off-design flight condition is described by

$$\begin{aligned} M_0 &= 2.0, p_0 = 18 \text{ kPa}, T_0 = -15^\circ\text{C} \\ T_{t4} &= 1475^\circ\text{C} \\ \pi_d &= 0.88 \\ p_9/p_0 &= 1.0 \end{aligned}$$

Assuming all other component efficiencies (except π_d that is specified) remain the same (as design) at off-design and gas properties are $\gamma_c = \gamma_t = 1.4$ and $c_{pc} = c_{pt} = 1004 \text{ J/kg} \cdot \text{K}$, calculate

- (a) $\pi_{c,O-D}$
- (b) $\dot{m}_{c,2,O-D}$ (in kg/s)
- (c) $N_{c,2,O-D}$ (in rpm)
- (d) $M_{z,2,O-D}$

11.15 An afterburning turbojet engine's design-point parameters are

1. $M_0 = 0, p_0 = 101.33 \text{ kPa}, T_0 = 288.2 \text{ K}, \gamma_c = 1.4, c_{pc} = 1004 \text{ J/kg} \cdot \text{K}$
2. $\pi_d = 0.95$
3. $\pi_c = 18, e_c = 0.90$
4. $\dot{m}_{c,2} = 67 \text{ kg/s}$
5. $N_{c,2} = 7120 \text{ rpm}$
6. $M_{z,2} = 0.5$

7. $Q_R = 42,800 \text{ kJ/kg}$, $\pi_b = 0.98$, $\eta_b = 0.97$, $T_{t4} = 1773 \text{ K}$
8. $\gamma_t = 1.33$, $c_{pt} = 1156 \text{ J/kg} \cdot \text{K}$
9. $e_t = 0.80$, $\eta_m = 0.995$
10. $Q_{R,AB} = 42,800 \text{ kJ/kg}$, $\pi_{AB} = 0.95$, $\eta_{AB} = 0.98$, $T_{t7} = 2250 \text{ K}$
11. $\gamma_{AB} = 1.3$, $c_{pc} = 1243 \text{ J/kg} \cdot \text{K}$
12. $\pi_n = 0.90$, $p_9/p_0 = 1.0$

The off-design conditions correspond to supersonic flight at high altitude

$$M_0 = 2.5, p_0 = 15 \text{ kPa}, T_0 = 223 \text{ K}, \gamma_c = 1.4,$$

$$c_{pc} = 1004 \text{ J/kg} \cdot \text{K}$$

$$\pi_d = 0.82$$

$$e_c = 0.90$$

$$Q_R = 42,800 \text{ kJ/kg}, \pi_b = 0.98, \eta_b = 0.97, T_{t4} = 1850 \text{ K}$$

$$\gamma_t = 1.33, c_{pt} = 1156 \text{ J/kg} \cdot \text{K}$$

$$e_t = 0.80, \eta_m = 0.995$$

$$Q_{R,AB} = 42,800 \text{ kJ/kg}, \pi_{AB} = 0.95, \eta_{AB} = 0.98,$$

$$T_{t7} = 2450 \text{ K}$$

$$\gamma_{AB} = 1.3, c_{pc} = 1243 \text{ J/kg} \cdot \text{K}$$

$$\pi_n = 0.88, p_9/p_0 = 1.0$$

Calculate

- (a) compressor pressure ratio at off-design
- (b) the corrected and physical mass flow rates at the compressor face at off-design in kg/s
- (c) the fuel-to-air ratio at off-design
- (d) the exhaust speed at off-design in m/s
- (e) thrust specific fuel consumption in mg/s/N at on- and off-design

11.16 A turbojet engine has a design corrected mass flow rate of $\dot{m}_{c2} = 100 \text{ kg/s}$ at the standard sea level static condition. The design axial Mach number at the engine face is $M_{z2} = 0.5$. Calculate the engine face flow area, A_2 , in m^2 ($\gamma = 1.4$, $R = 287 \text{ J/kg} \cdot \text{K}$, $p_{SL} = 101 \text{ kPa}$ and $T_{SL} = 288 \text{ K}$).

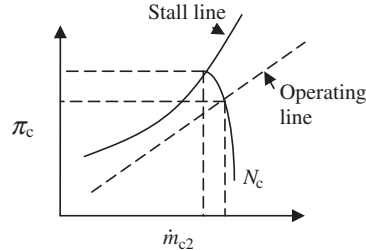
11.17 A turbojet engine has choked nozzles both in turbine as well as exhaust. Its design point is at the standard sea level static condition ($p_{SL} = 101 \text{ kPa}$ and $T_{SL} = 288 \text{ K}$) and the design calculations yield a turbine expansion parameter of $\tau_t = 0.70$. Assuming design parameters are: $T_{t4-D} = 1950 \text{ K}$, $f = 0.023$, $\eta_m = 0.993$ and $e_c = 0.9$, estimate:

- (a) compressor pressure ratio at design, π_{c-D}
- (b) compressor pressure ratio at off-design, π_{c-OD}

Where the off-design condition is described by: $M_0 = 2.0$, $p_0 = 25 \text{ kPa}$, $T_0 = 223 \text{ K}$, $T_{t4,OD} = 1650 \text{ K}$.

Assume the same component efficiencies and fuel-to-air ratio in on- and off-design and constant gas properties, i.e., assume $\gamma_c = \gamma_t = 1.4$, $c_{pc} = c_{pt} = 1004 \text{ J/kg} \cdot \text{K}$.

11.18 In a compressor performance map, the design corrected mass flow rate is $\dot{m}_{c2} = 250 \text{ kg/s}$ and the design compressor pressure ratio is $\pi_{c-D} = 30$. The mass flow rate at stall drops to 238.1 kg/s and the corresponding compressor pressure ratio at stall rises to 31.5 . Calculate



■ FIGURE P11.18

- (a) the compressor stall margin, SM (%)
- (b) estimate the drop in axial Mach number between the design point and stall, i.e., $M_{z2-D} - M_{z2-Stall}$, assuming $M_{z2-D} = 0.5$.

11.19 A high bypass ratio separate-flow turbofan engine with convergent nozzles has the following design point parameters (at takeoff, standard sea-level conditions):

$$M_0 = 0, p_0 = 101.33 \text{ kPa}, T_0 = 288.2 \text{ K}, \gamma_c = 1.4,$$

$$c_{pc} = 1004 \text{ J/kg} \cdot \text{K}$$

$$\pi_d = 0.98, \dot{m}_{c2} = 600 \text{ kg/s}, M_{z2} = 0.5$$

$$\pi_f = 1.8, e_f = 0.90, \alpha = 5.0$$

$$\pi_{cH} = 14, e_{cH} = 0.90$$

$$T_{t4} = 1873 \text{ K}, Q_R = 42800 \text{ kJ/kg} \cdot \text{K}, \pi_b = 0.95, \eta_b = 0.99$$

$$e_{tH} = 0.85, \eta_{mH} = 0.995, e_{tL} = 0.89, \eta_{mL} = 0.995, \gamma_t = 1.33,$$

$$c_{pt} = 1.1464 \text{ kJ/kg} \cdot \text{K}$$

$$\pi_n = 0.98, \pi_{nf} = 0.98, p_8 = p_{18} = p_0, M_8 = M_{18} = 1$$

The off-design point is the cruise condition described by:

$$M_0 = 0.84, p_0 = 20 \text{ kPa}, T_0 = 253 \text{ K}$$

$$T_{t4} = 1573 \text{ K}$$

Calculate C_1 , C_2 and C_3 parameters at the design point. Then use Equation 11.67 to solve, i.e., to iterate for, τ_{cH-OD} . Then, calculate τ_{f-OD} and α_{OD} . Use polytropic efficiencies to get π_f and π_{cH} at off-design.

For a turbofan engine, the corrected mass flow rate at the engine face relates to off-design condition according to:

$$\dot{m}_{c2-OD} = \dot{m}_{c2-D} \left[\frac{(1 + \alpha)_{OD}}{(1 + \alpha)_D} \right] \left[\frac{\pi_{c-OD}}{\pi_{c-D}} \right] \sqrt{\frac{(\tau_r/\tau_\lambda)_{OD}}{(\tau_r/\tau_\lambda)_D}}$$

where π_c is the overall pressure ratio, namely $\pi_f \cdot \pi_{cH}$.

Then use the corrected mass flow rate at the engine face to calculate the physical mass flow rate at cruise.

11.20 Cruise flight condition is: $M_0 = 0.85$, altitude is 12 km (U.S. standard atmosphere), with $\dot{m}_{c2} = 200$ kg/s. Assuming that the inlet total pressure recovery at cruise is 0.995, calculate

- (a) corrected mass flow rate, \dot{m}_{c0} , in kg/s
- (b) captured stream area, A_0 , in m^2
- (c) physical mass flow rate of air, \dot{m}_0 , in kg/s
- (d) inlet throat area (assume $\bar{M}_{th} = 0.70$), neglecting the total pressure loss from highlight to throat
- (e) ram drag in kN

Chemical Rocket and Hypersonic Propulsion



Source: Courtesy of NASA (Constellation Program)

12.1 Introduction

A chemical rocket is a self-contained jet engine that carries both the fuel and oxidizer that are needed for combustion. The fuel and oxidizer are jointly called the *propellant*. Since the rocket carries its own oxidizer, it does not need an air inlet to provide oxygen for combustion, as in a gas turbine engine. It is this independence of rocket operation from atmospheric air that makes it a good candidate for space propulsion. The relative simplicity and manufacturing cost of a rocket engine as compared with an airbreathing jet engine have made rockets the propulsor of choice for low-cost weapons and aerospace vehicle boost applications. For example, the Space Shuttle uses two solid rocket boosters (known as SRBs) to help achieve liftoff and vehicle acceleration to orbit. The Space Shuttle also uses a liquid propellant rocket engine as its main engine, dubbed SSME or Space Shuttle Main Engine. Depending on the form of propellant that is used in combustion, a chemical rocket may be called a *liquid propellant*, a *solid propellant*, a *gaseous propellant* rocket or, if the fuel is in solid form and the oxidizer is in liquid (or gaseous) form, the rocket is called a *hybrid*. For a liquid propellant rocket, the fuel and oxidizer are stored in separate tanks in liquid form. The solid propellant rocket has the fuel and oxidizer in solid form, packed or cast in the rocket case, in the form of a paste. Since rockets operate on the principle of jet propulsion, which is achieved when a fluid is ejected through a nozzle at finite speed, the fluid and the form of acceleration opens new

categories of rocket propulsion devices. For example, if the fluid is made up of ions (of an atom, say cesium) that are accelerated in an electric field (in lieu of a nozzle), the rocket achieves a thrust and this class of rocket propulsion belongs to electric or ion propulsion. For the case of fluid (like hydrogen) that is heated by a nuclear reactor before ejection through a nozzle, the category of engine is called a nuclear rocket propulsion device. For atmospheric applications that require stringent emissions standards, only the liquid and solid propellant rockets are suitable. These belong to the general category of *chemical rocket propulsion*. Forward (1995) presented intriguing advanced propulsion concepts (other than pure rockets) that are thought provoking and thus recommended for reading.

The main drawback of rocket engines operating in the Earth's atmosphere is their high propellant consumption rate per unit thrust produced as compared to the fuel consumption rate in airbreathing engines. The figure of merit that compares rockets to airbreathing engines is the specific impulse I_s (in seconds) that we defined in Chapter 3, repeated here for convenience:

$$I_s \equiv \frac{F}{\dot{m}_p g_0} \quad (\text{s}) \quad (3.48)$$

where

$$\dot{m}_p \equiv \dot{m}_f + \dot{m}_o \quad (3.49)$$

The numerator in specific impulse is the net (uninstalled) thrust produced, which for an airbreathing engine we derived to be (Equation 3.14)

$$F_n)_{\text{uninstalled}} = (\dot{m}_o + \dot{m}_f)V_9 - \dot{m}_o V_0 + (p_9 - p_0)A_9 \quad (3.14)$$

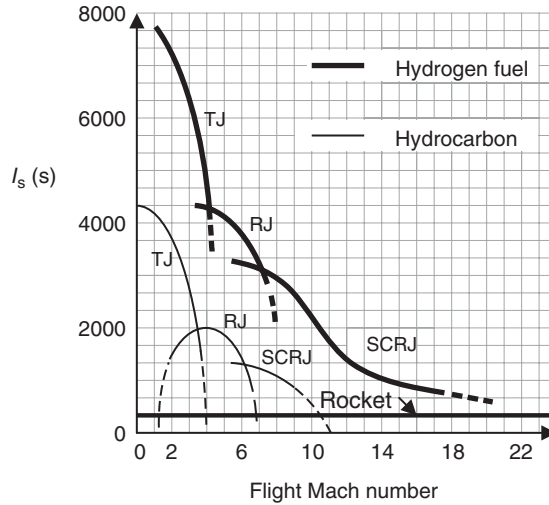
Since, conventional rockets do not suffer from any ram drag, they produce thrust according to (Equation 3.46):

$$F_{\text{rocket}} = (\dot{m}_o + \dot{m}_f)V_9 + (p_9 - p_0)A_9 \quad (3.46)$$

The denominator of specific impulse is the propellant weight flow rate for a rocket (i.e., the sum of oxidizer and fuel weight flow rates) and only the fuel weight flow rate for an airbreathing engine. The use of a more energetic fuel like hydrogen leads to directly higher specific impulse, since a smaller, that is, nearly two and half times lower, consumption of hydrogen is needed to achieve the same temperature in the combustor. Now, if we graph representative values for the specific impulse of typical airbreathing and rocket engines (Figure 12.1, also Kerrebrock, 1992) for a hydrocarbon and hydrogen fuel as a function of flight Mach number, we note the following important features:

- rocket-specific impulse is independent of vehicle speed, as it does not suffer from any ram drag penalty, nor is its combustion is affected by the stagnation temperature rise in intake
- the specific impulse for a chemical rocket is about 250–450 s
- the specific impulse for airbreathing engines is shifted upward when hydrogen is used as fuel in comparison to hydrocarbon fuels

■ **FIGURE 12.1**
Approximate variation
of specific impulse with
flight Mach number for
different airbreathing
engines (TJ: turbojet,
RJ: ramjet, and SCRJ:
scramjet) and a typical
chemical rocket



- a gas turbine engine achieves takeoff thrust and the best low-speed performance, as depicted by a specific impulse of between ~ 4000 and 8000 s for a turbojet and (not shown) higher than $10,000$ s for a turbofan
- the specific impulse of gas turbine engines drop with flight Mach number
- the rapid fall of a gas turbine engine performance with forward speed is broken up if we switch to the ramjet family of airbreathing engines, for example, near Mach 3, a conventional ramjet starts to outperform a turbojet
- the rapid fall of a conventional ramjet engine performance with flight Mach number is halted if we switch to the supersonic combustion ramjet (or scramjet)
- the flight Mach number of ~ 6 is where scramjet outperforms other airbreathing engines
- deterioration of scramjet performance with forward speed is inevitable as the flight stagnation temperature increases and components losses mount
- although the upper operational Mach number of scramjets is unknown, it is suspected that for high flight Mach numbers, for example, Mach ~ 10 – 15 , scramjet performance may begin to fall below a chemical rocket.

12.2 From Takeoff to Earth Orbit

A vehicle requires a flight Mach number of ~ 25 to achieve a circular low Earth orbit (LEO). The proof of that is very simple. On a circular orbit of radius r (which for LEO is ≥ 100 km above the Earth of ~ 6000 km radius), a vehicle of mass m experiences a centrifugal force of magnitude mV^2/r . The gravitational pull on the vehicle toward the Earth is *roughly* $\sim mg_0$. These two forces are in balance if the vehicle is to maintain its circular orbit, therefore,

$$V \approx \sqrt{rg_0} \approx \sqrt{6000 \text{ km} (9.8 \text{ m/s}^2)} \approx 7668 \text{ m/s}$$

Which for a speed of sound of ~ 300 m/s (at high altitude), we get a flight (or orbital) Mach number of ~ 25.5 . The purpose of this simple demonstration was to get a *rough order of magnitude* for the Mach number required at LEO to maintain a circular orbit. We recognize that we made several approximations, for example, in the gravitational force on the vehicle when we applied g_0 on the Earth's surface, instead of a reduced gravitational acceleration that corresponds to an altitude of 100 km, or when we did not account for any atmospheric drag at 100 km, or when we used an “average” Earth radius (of 6000 km) as in a homogeneous spherical earth.

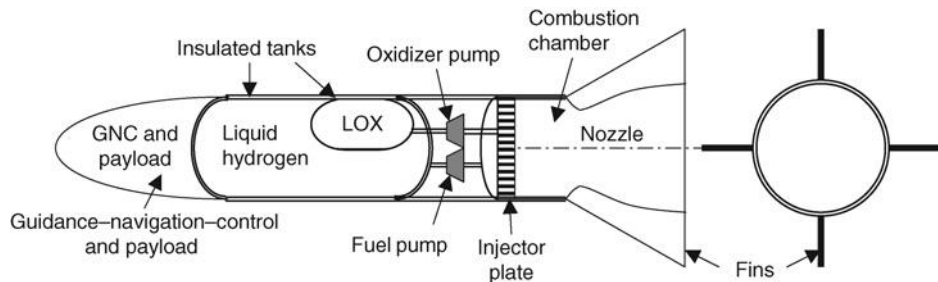
To reach LEO and maintain a circular orbit, we need to fly about Mach 25. For a single-stage to orbit aircraft (what is known as SSTO), the engine(s) have to produce takeoff thrust, maintain climb rate, and acceleration until the vehicle has achieved Mach 25. If we wish to use the most efficient means of reaching Mach 25 from takeoff, we have to employ a variety of engines, as depicted by the specific impulse chart of Figure 12.1. At takeoff, we could use a turbofan engine and gradually reduce its bypass ratio (as in a variable-bypass TF engine) with flight Mach number until it operates as a turbojet. Then, we should be able to shut down the gas generator all together near Mach 3 and switch over to a conventional (or subsonic combustion) ramjet for up to \sim Mach 6. The scramjet is to take over beyond Mach 6 and accelerate the vehicle through Mach 10–15, depending on the hydrocarbon or hydrogen fuel, respectively. At these Mach numbers, we are still too slow to maintain a circular orbit at LEO. Therefore, chemical rocket engines have to be fired for the last leg of our launch, which should take the vehicle to Mach 25 and low Earth orbit. The main challenge for such a *combination propulsion system* (CPS) is complex system integration into a vehicle and the mechanical complexities involved in transition from one set or class of engines to another.

12.3 Chemical Rockets

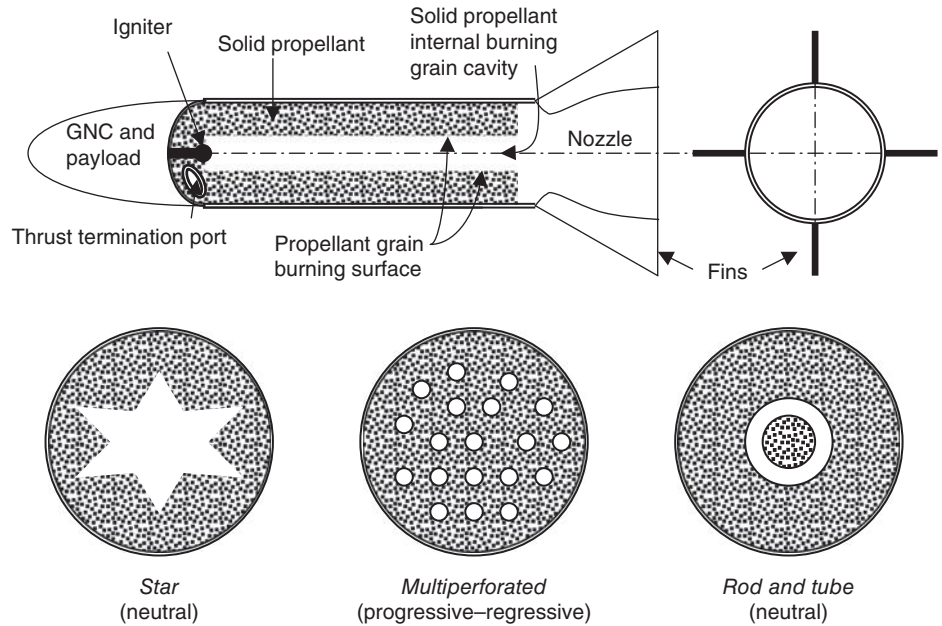
Various components of a chemical rocket are shown in a schematic drawing in Figure 12.2.

The example shown in Figure 12.2 uses liquid fuel and oxidizer as propellant. The fuel and oxidizer are stored in insulated tanks in liquid state to reduce the volumetric requirements of the propellant. The fuel and oxidizer pumps provide the propellant feed system into the combustion chamber. The pumps are driven by a turbine (not shown in the schematic drawing), therefore the name *turbopump* system. The propellant is fed into the combustion chamber through an injector plate. The pressure in the combustion chamber is $\sim 20\%$ lower than the feed pressure to avoid pressure oscillation instability known as chugging. The combustion temperature is governed by the heat of reaction of the fuel and

■ **FIGURE 12.2**
Schematic diagram of a (simplified) chemical rocket with liquid hydrogen as fuel and liquid oxygen (LO_2) as the oxidizer (with turbopump feed system)



■ **FIGURE 12.3**
Schematic drawing of a
solid-propellant
chemical rocket with
internal burning grain
(grain designs referred to
neutral, progressive,
and regressive describe
thrust-time behavior)

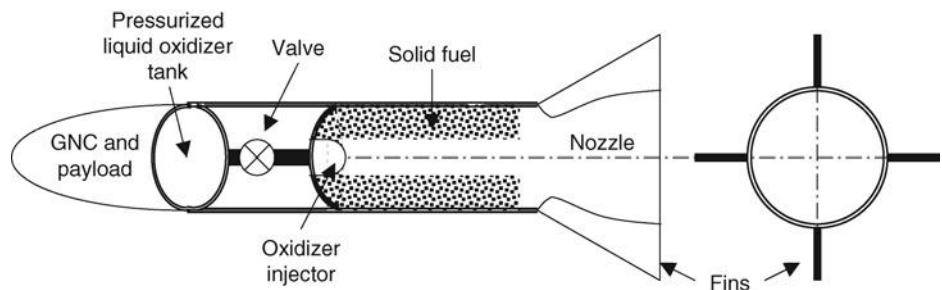


oxidizer. The products of combustion are then accelerated through an exhaust nozzle. The thrust may be controlled (to the point of shutting down and restarting) by the fuel and oxidizer pumps. The guidance, navigation, control, and payload are shown in the nose chamber. The fins provide aerodynamic control and stability of the rocket.

Elements of a solid rocket motor are shown in Figure 12.3. The propellant is in solid form and is called the grain or charge. Propellant is bonded to the rocket motor case, which typically has an internal burning grain cavity, as shown. The igniter initiates the burning of the solid grain. Once burning is initiated and hot gases are expelled through an exhaust nozzle, the thrust of the solid motor is established by the burning grain surface area and the propellant-burning rate. Since solid rocket motors have no pumps or valves to control the amount of propellant engaged in the combustion process, the thrust cannot be fully controlled. We can, however, terminate the operation of a solid rocket motor by opening thrust termination ports to cancel the thrust, as shown.

A hybrid rocket typically uses a solid fuel and a liquid oxidizer, as shown in Figure 12.4. The oxidizer flow is regulated by the pressurized tank and a valve and injects the stream of oxidizer through a solid fuel port. The chemical reaction may be initiated

■ **FIGURE 12.4**
Schematic drawing of a
hybrid rocket showing
solid fuel and gaseous
oxidizer propellant



by an igniter, similar to a solid propellant rocket motor. The hot combustion gases are expelled through the exhaust nozzle to produce thrust.

12.4 Chemical Rocket Applications

Chemical rockets are capable of producing large thrust and operate at any altitude, including space. They also lend themselves to *staging* for increased flight efficiency. These diverse capabilities in addition to the low cost of manufacturing put rockets on many flight vehicle applications, including as strap-on boosters. Some of the main examples are listed here.

12.4.1 Launch Engines

Saturn V was a three-stage liquid propellant rocket that was successfully used to launch Apollo spacecraft towards the moon. In a multistage rocket, each stage is self-contained and operates autonomously. All three stages of Saturn V used liquid oxygen (LO_2) as their oxidizer in the combustion chamber. The first stage used RP-1 (a hydrocarbon fuel), whereas the second and third stages used liquid hydrogen (LH_2) for fuel. The low density of hydrogen makes it less than optimal for use in the first stage of launch where a large volume of fuel is required to produce the launch thrust. The three stages of Saturn V produced 7,570,000 lb, 1,125,000 lb, and 230,000 lb of thrust, respectively. The launch weight of the vehicle that included the payload was 6,262,000 lb. Note that the thrust-to-weight ratio for Saturn at launch is the thrust produced by its first stage engine divided by the initial weight of the rocket, i.e., $7570/6262 = 1.209$. The first stage produces a modest thrust level of $\sim 20\%$ over the initial weight (to accelerate the vehicle), that is, it imparts $0.2 g_0$ initial acceleration to the vehicle.

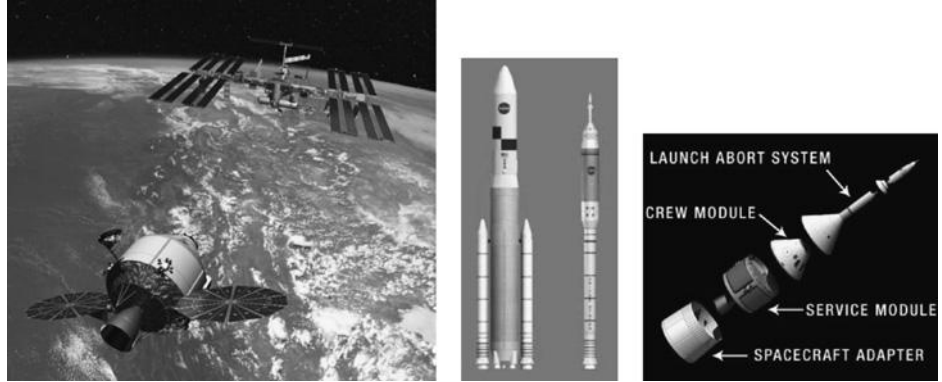
Another example is the Space Shuttle Main Engine that uses LO_2/LH_2 as propellant. There are three SSMEs and each produces 375,000 lb at sea level and 470,000 lb at altitude. The SSME starts at launch and operates for ~ 8.5 min. The use of liquid hydrogen in the SSME for launch has required an external (propellant) tank that is jettisoned after the liquid hydrogen and oxygen are consumed. The external tank (ET) is the only expendable component of the Space Shuttle.

The new generation of launch and human exploration vehicles, post Space Shuttle, were the Ares I launch vehicle and the Orion Crew Exploration Vehicle (CEV). Orion's first flight with astronauts onboard was planned for 2014 to the International Space Station (ISS). Orion's first flight to the moon was planned for 2020. However, budgetary issues have halted/postponed these programs at NASA. Figure 12.5 shows artist's concepts and models of the new family of human space exploration launch and crew exploration vehicle (courtesy of NASA). In light of recent developments, the future of cost-effective space launch services lies entirely in the private/commercial sector. Noteworthy among these is SpaceX Corporation that has developed, manufactured and successfully launched advanced rockets to LEO, including a mission to the ISS with the Dragon spacecraft.

12.4.2 Boost Engines

Boosters are capable of providing thrust, often as a simple add-on or strap-on propulsion system. For example, there are two solid rocket boosters on the Space Shuttle launch

■ **FIGURE 12.5**
Artist's concept of the Orion Crew Exploration Vehicle (CEV) approaching the International Space Station, the Ares I launch vehicle, and components of the CEV. Source: Courtesy of NASA



vehicle. Each is capable of producing 2,700,000 lb of thrust. The solid rocket boosters start at launch and operate for 123 s. The empty boosters are then jettisoned and recovered at sea for reuse.

12.4.3 Space Maneuver Engines

The Space Shuttle is equipped with two orbital maneuver systems, which are responsible for the orbiter reentry and orbit correction maneuvers.

12.4.4 Attitude Control Rockets

The Space Shuttle has 38 primary thrusters and 6 vernier thrusters that are used to impart small velocity corrections to the orbiter. The duration of operation of these reaction control thrusters (known as *pulses*) is between a few milliseconds and a few seconds.

12.5 New Parameters in Rocket Propulsion

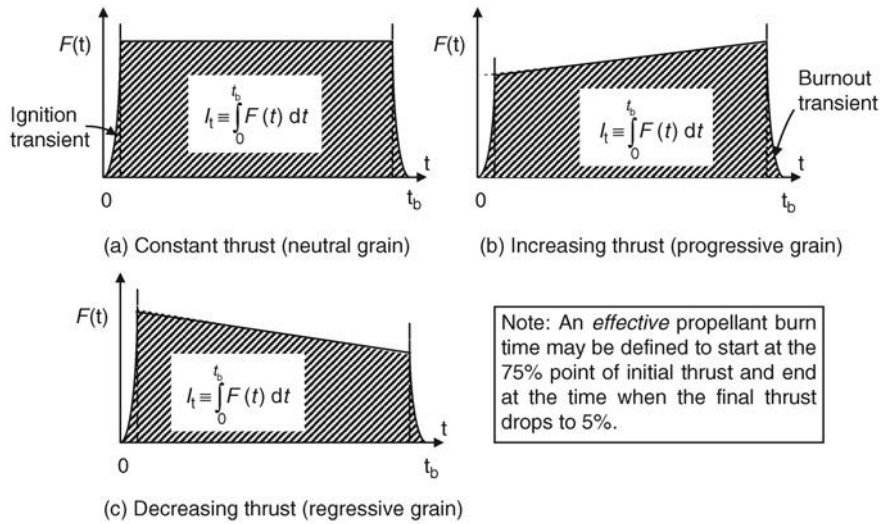
Rocket propulsion, as a self-contained system, introduces new parameters to our propulsion vocabulary. For example, thrust-time behavior, as in neutral, progressive or regressive, or total impulse I_t , which is defined as the integral of the thrust over time, have no counterparts in airbreathing engines. The total impulse is a parameter that is directly measured in rockets on thrust stand and used to estimate the engine-specific impulse I_s . The total impulse is defined as

$$I_t \equiv \int_0^{t_b} F(t) dt \quad (12.1)$$

The time at burnout is t_b . The weight of the propellant is

$$w_p = g_0 \int_0^{t_b} \dot{m}_p dt \quad (12.2)$$

■ FIGURE 12.6 Total impulse for three different grain designs in solid rocket motors



and the specific impulse is the ratio of total impulse to propellant weight, namely,

$$I_s \equiv \frac{\int_0^{t_b} F(t) dt}{g_0 \int_0^{t_b} \dot{m}_p dt} = \frac{I_t}{m_p g_0} \quad (12.3)$$

Figure 12.6 shows three different thrust-time behaviors for solid propellant rockets where the shape of the propellant grain dictates the burning surface area (variation with time) and thus thrust production. The initial (ignition delay) transient to produce thrust and the burnout transient are nearly parabolic in shape and are also shown in Figure 12.6.

The flight performance of rockets strongly depends on vehicle design through the use of stages, and the efficiency of components. For example, the rocket initial mass is m_0 , and the final mass, that is, after propellant burnout, is m_f . The ratio of final-to-initial mass is an important parameter, and a figure-of-merit in rocket design, which is known as the *mass ratio*, MR,

$$MR \equiv \frac{m_f}{m_0} \quad (12.4)$$

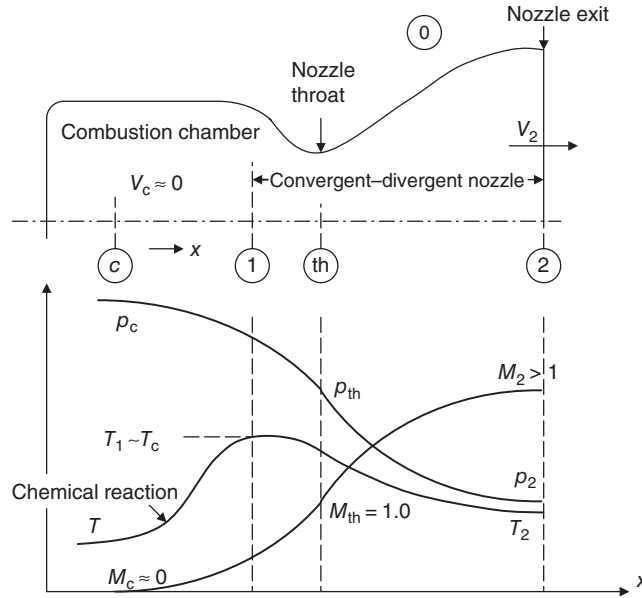
Propellant mass m_p is the difference between the initial and final masses, for a given stage, that is,

$$m_p = m_0 - m_f \quad (12.5)$$

The ratio of propellant-to-initial mass is known as the *propellant mass fraction* ζ ,

$$\zeta \equiv \frac{m_p}{m_0} = 1 - MR \quad (12.6)$$

■ **FIGURE 12.7**
Rocket engine (thrust chamber) stations and corresponding static pressure, temperature, and Mach number variations



A large value of propellant mass fraction is desirable as it indicates an efficient use of *system mass* on the rocket that is directly responsible for thrust production.

Finally, an effective exhaust velocity c is defined as, in effect, the mass-averaged nozzle gross thrust, namely,

$$c \equiv F/\dot{m}_p \quad (12.7)$$

Using Equation 3.32, at the beginning of this chapter, we relate the effective exhaust velocity c to the specific impulse,

$$c = \dot{m}_p g_0 I_s / \dot{m}_p = g_0 I_s \quad (12.8)$$

We may also relate the effective exhaust velocity to the actual exhaust velocity and pressure thrust through

$$c = V_2 + \frac{(p_2 - p_0)A_2}{\dot{m}_p} \quad (12.9)$$

Station numbers in a rocket engine are defined in Figure 12.7. Station c refers to the combustion chamber, station 1 is at the inlet to the convergent–divergent nozzle, station th at the nozzle throat, and station 2 is at the nozzle exit plane. The ambient state is identified by station 0. For most applications, there is no distinction between stations c and 1, but in reality the mixture of gases in the combustion chamber is chemically reacting, whereas at station 1 it is assumed that combustion is complete and the mixture has reached a chemical equilibrium state. Also, we usually associate a near stagnant gas state in the combustion chamber with $V_c \approx 0$, but we attribute certain finite gas speed V_1

at the nozzle inlet that follows from the area ratio A_1 / A_{th} based on the choked throat $M_{th} = 1.0$ condition. Note the parameter trends inside a rocket engine shown in Figure 12.7.

EXAMPLE 12.1

The Space Shuttle Main Engine (SSME) produces 375,000 lb of thrust at sea level and 470,000 lb at altitude. Assum-

ing constant momentum thrust with altitude, estimate the diameter D_2 of the SSME nozzle exit area A_2 .

SOLUTION

The difference between the sea level and altitude thrust is primarily caused by the difference between the pressure thrusts, i.e.,

$$F_{\text{vacuum}} - F_{\text{sea level}} \equiv (p_{sl} - 0)A_2$$

Therefore, $A_2 \approx 95,000 \text{ lb}/(14.7 \text{ lb/in}^2)/(144 \text{ in}^2/\text{ft}^2) \approx 44.88 \text{ ft}^2$

$$\text{Diameter } D_2 = (4A_2/\pi)^{1/2} \approx 7.56 \text{ ft or } 90.7 \text{ in.}$$

The actual (SSME nozzle) exit diameter is listed at 94 in. There is a small discrepancy (i.e., $\sim 3.5\%$) due to our simplified approach, e.g., assuming identical momentum thrust at sea level and altitude or neglecting pressure at altitude.

EXAMPLE 12.2

A rocket engine has a propellant mass flow rate of 1000 kg/s and the specific impulse is $I_s = 340$ s. Calculate

- (a) rocket thrust F
- (b) effective exhaust velocity c

SOLUTION

From the definition of specific impulse, we get

$$F = \dot{m}_p g_0 I_s = (1000 \text{ kg/s})(9.8 \text{ m/s}^2)(340 \text{ s}) \\ \approx 3.332 \times 10^6 \text{ N}$$

The effective exhaust velocity is the ratio of thrust to propellant mass flow rate, $c = F/\dot{m}_p \approx 3332 \text{ m/s}$

12.6 Thrust Coefficient, C_F

It is customary to express the rocket thrust as a product of chamber pressure p_c , the throat area A_{th} , and a coefficient C_F , known as the *thrust coefficient*, that is,

$$F \equiv C_F p_c A_{th} \quad (12.10)$$

In this section, we will demonstrate that thrust coefficient is a function of the nozzle area expansion ratio A_2/A_{th} , the pressure ratio p_2/p_c , and the ratio of specific heats γ . Therefore, the thrust coefficient is explicitly independent of combustion temperature (thus propellant

combination) and is treated as a nozzle-related parameter. The ratio of specific heats γ is the only link between thrust coefficient and the propellant combination or combustion temperature.

The mass flow rate through the nozzle may be written at the sonic throat, through the use of the continuity equation:

$$\dot{m}_p = \sqrt{\frac{\gamma}{R}} \frac{p_c}{\sqrt{T_c}} A_{th} \left(\frac{2}{\gamma + 1} \right)^{\frac{\gamma+1}{2(\gamma-1)}} \quad (12.11)$$

The exhaust velocity V_2 is written based on the isentropic expansion through the nozzle from the stagnation pressure of p_c to the exit static pressure p_2 through these simple steps:

$$\begin{aligned} T_c &= T_2 + V_2^2/2c_p \\ V_2 &= \sqrt{2c_p(T_c - T_2)} = \sqrt{2c_p T_c \left[1 - \left(\frac{p_2}{p_c} \right)^{\frac{\gamma-1}{\gamma}} \right]} \end{aligned} \quad (12.12)$$

Since the momentum thrust is the product of mass flow rate and the exhaust velocity (Equations 12.11 and 12.12), we may write the following expression for the thrust coefficient

$$C_F = \frac{\dot{m}_p V_2 + (p_2 - p_0)A_2}{p_c A_{th}} \quad (12.13a)$$

$$C_F = \sqrt{\left(\frac{2\gamma^2}{\gamma - 1} \right) \left(\frac{2}{\gamma + 1} \right)^{\frac{\gamma+1}{\gamma-1}} \left[1 - \left(\frac{p_2}{p_c} \right)^{\frac{\gamma-1}{\gamma}} \right]} + \frac{p_2 - p_0}{p_c} \left(\frac{A_2}{A_{th}} \right) \quad (12.13b)$$

A perfectly expanded nozzle meets the condition of static pressure match $p_2 = p_0$, therefore the maximum thrust coefficient is a function of p_2/p_c and the ratio of specific heat γ . We may graph the optimum thrust coefficient, that is, C_F for a perfectly expanded nozzle with isentropic expansion using an Excel spreadsheet calculation and graph of the function.

$$C_{F,opt} = \sqrt{\left(\frac{2\gamma^2}{\gamma - 1} \right) \left(\frac{2}{\gamma + 1} \right)^{\frac{\gamma+1}{\gamma-1}} \left[1 - \left(\frac{p_2}{p_c} \right)^{\frac{\gamma-1}{\gamma}} \right]} \quad (12.13c)$$

Figure 12.8 (with abscissa in logarithmic scale).

Before leaving the subject of thrust coefficient, we recognize the bracket term under the square root in Equations 12.13b or 12.13c as the ideal thermal efficiency of a Brayton cycle operating between the two pressures p_c and p_2 , that is,

$$\eta_{th} = 1 - \left(\frac{p_2}{p_c} \right)^{\frac{\gamma-1}{\gamma}} \quad (12.14)$$

FIGURE 12.8
 Variation of optimum thrust coefficient for different gas ratio of specific heats (note that p_c/p_2 is the familiar nozzle pressure ratio (NPR) for a perfectly expanded nozzle)

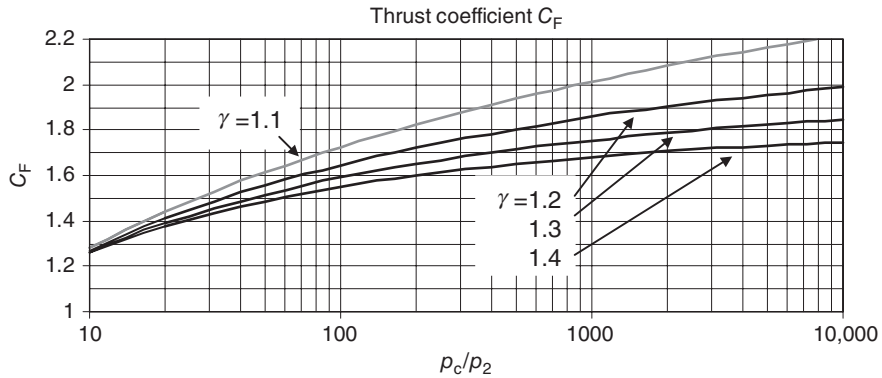
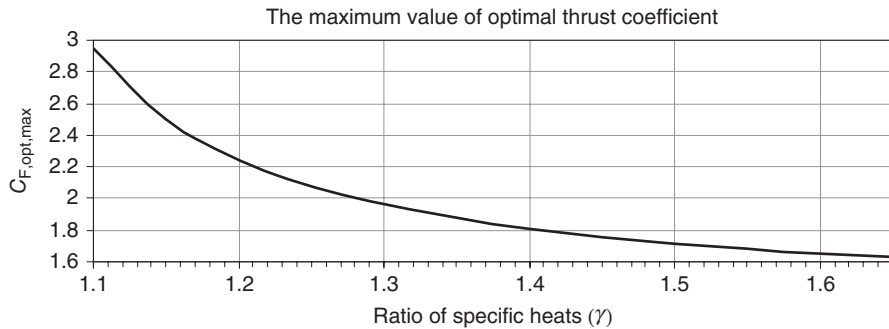


FIGURE 12.9
 The variation of maximum, optimal thrust coefficient with ratio of specific heats γ



For very large chamber pressures p_c and very large area ratio nozzles where the exit static pressure p_2 is low, the thermal efficiency approaches 1, which then points to the maximum attainable thrust coefficient $C_{F,opt,Max}$, that is,

$$C_{F,opt,Max} = \sqrt{\left(\frac{2\gamma^2}{\gamma-1}\right) \left(\frac{2}{\gamma+1}\right)^{\frac{\gamma+1}{\gamma-1}}} \quad (12.15)$$

The maximum value of thrust coefficient is a pure function of γ and is shown in Figure 12.9.

EXAMPLE 12.3

A rocket engine has a chamber pressure of $p_c = 200$ atm and the throat area is $A_{th} = 0.25$ m². Assuming that the nozzle is perfectly expanded with the gas ratio of specific heats $\gamma = 1.3$ and the ambient pressure of $p_0 = 1$ atm, calculate

- optimum thrust coefficient $C_{F,opt}$
- thrust F in N or lbf
- nozzle exit Mach number M_2
- nozzle area expansion ratio A_2/A_{th}

SOLUTION

We substitute for p_c/p_2 of 200/1 and $\gamma = 1.3$ in Equation 12.13c, to get

$$C_{F,\text{opt}} = 1.650$$

Therefore, thrust is the product of thrust coefficient, chamber pressure, and throat area. The chamber pressure is first converted to N/m² (or Pa),

$$p_c = 200 \text{ atm} = 200(101 \text{ kPa}) = 20.2 \text{ MPa}$$

$$F = 8.332 \times 10^6 \text{ N} \quad (\text{or } 1.873 \times 10^6 \text{ lbf})$$

The nozzle exit Mach number for an isentropic flow in a nozzle is related to the ratio of p_c/p_2 , according to

$$p_c/p_2 \approx p_{t2}/p_2 = \left[1 + (\gamma - 1)M_2^2/2\right]^{\gamma/(\gamma-1)}$$

Therefore, the exit Mach number is

$$M_2 = \sqrt{\frac{2}{\gamma - 1} \left[\left(\frac{p_c}{p_2} \right)^{\frac{\gamma-1}{\gamma}} - 1 \right]} \approx 4.0$$

From the continuity equation written between the exit and the throat, taking throat Mach number as unity, we express A_2/A^* , which is the same as A_2/A_{th} in terms of exit Mach number M_2 and a function of γ , according to

$$\frac{A_2}{A_{\text{th}}} = \frac{1}{M_2} \left[\frac{2}{\gamma + 1} \left(1 + \frac{\gamma - 1}{2} M_2^2 \right) \right]^{\frac{\gamma+1}{2(\gamma-1)}} \approx 15.89$$

12.7 Characteristic Velocity, c^*

A velocity parameter that is linked to the combustion chamber is called characteristic velocity c^* . We expect this velocity to be related to the speed of sound in the combustion chamber, as the characteristic speed. But, first its definition

$$c^* \equiv \frac{p_c A_{\text{th}}}{\dot{m}_p} \quad (12.16)$$

In terms of specific impulse and thrust coefficient, or effective exhaust speed and thrust coefficient, the characteristic velocity may be written as

$$c^* = I_{s0} g_0 / C_F = c / C_F \quad (12.17)$$

Returning to the definition of c^* in Equation 12.16, we may express the propellant mass flow rate for the sonic flow at the throat and gas total pressure and temperature, to get

$$c^* = \frac{\sqrt{\gamma R T_c}}{\gamma \left[\frac{2}{\gamma + 1} \right]^{\frac{\gamma+1}{2(\gamma-1)}}} \quad (12.18)$$

As expected, the numerator in Equation 12.18 is the speed of sound in the combustion chamber. The propellant combination of fuel and oxidizer and their proportions establish the equivalence ratio, the products of combustion, and the mixture temperature for a

■ TABLE 12.1

Theoretical Performance of Liquid Propellant Combinations (data from Sutton and Biblarz, 2001)

Oxidizer	Fuel	Mixture ratio (Mass)	Chamber temperature (K)	Chamber c^* (m/s)
Oxygen	Methane	3.2	3526	1835
		3.0	3526	1853
	Hydrazine	0.74	3285	1871
		0.90	3404	1892
		3.40	2959	2428
	RP-1	4.02	2999	2432
		2.24	3571	1774
2.56		3677	1800	
Fluorine	Hydrazine	1.83	4553	2128
		2.30	4713	2208
	Hydrogen	4.54	3080	2534
		7.60	3900	2549

combustion pressure p_c , as we studied in Chapter 7. From Equation 12.16, we note that the experimental estimation of characteristic velocity is rather straightforward, since the chamber pressure and propellant flow rate are easily measured and the throat area is a geometric parameter. The Table 12.1 shows some liquid propellant combinations and the characteristic speed c^* , also known as *chamber c^** (from Sutton and Biblarz, 2001). The mixture ratio is the *oxidizer-to-fuel* mass ratio. The chamber pressure for the ideal performance values in Table 12.1 is taken to be 1000 psia (this corresponds to ~ 6.87 MPa). The 1000 psia chamber pressure is often taken as a reference value in rocket propulsion. RP-1 is a hydrocarbon fuel [$\text{CH}_{1.953}$] similar to kerosene.

A few examples of solid propellant combinations and the corresponding chamber c^* values are shown in Table 12.2 (from Sutton and Biblarz, 2001). Again, the reference chamber pressure is taken to be 1000 psia. The composition of solid propellant is characterized by the amount of binder (i.e., glue or epoxy), additives, and aluminum, which enhance combustion chamber temperature and chamber c^* .

■ TABLE 12.2

Theoretical Performance of Solid Propellant Combinations (data from Sutton and Biblarz, 2001)

Oxidizer	Fuel	Chamber temperature	
		(K)	Chamber c^* (m/s)
Ammonium nitrate	11% binder and 7% additive	1282	1209
Ammonium	18% organic polymer		
Perchlorate 78–66%	binder and 4–20% Al	2816	1590
Ammonium	12% polymer		
Perchlorate 84–68%	binder and 4–20% Al	3371	1577

EXAMPLE 12.4

A liquid propellant rocket uses hydrogen fuel and oxygen for combustion. The oxidizer-to-fuel mass ratio is 4.02. The ratio of specific heats of the combustion gas is $\gamma = 1.26$ and

the chamber pressure is 1000 psia. Use Equation 12.18 to estimate combustion gas constant R as well as the molecular weight of the mixture, MW.

SOLUTION

From Table 12.1, we read $T_c = 2999$ K and $c^* = 2432$ m/s corresponding to the liquid propellant described above.

By substituting for γ and T_c , we estimate $R \approx 858.9$ J/kg · K and since the universal gas constant is $\bar{R} = 8.3146$ kJ/kmol · K,

$$c^* = \frac{\sqrt{\gamma RT_c}}{\gamma \left[\frac{2}{\gamma + 1} \right]^{\frac{\gamma+1}{2(\gamma-1)}}} = 2432 \text{ m/s} \Rightarrow \sqrt{\gamma RT_c} = 1801.5 \text{ m/s}$$

$$\text{MW} = \frac{\bar{R}}{R} \approx 9.68 \frac{\text{kg}}{\text{kmol}}$$

EXAMPLE 12.5

Consider a fuel-rich combustion of hydrogen and oxygen in a liquid propellant rocket according to



Calculate

- (a) the oxidizer-to-fuel mixture ratio
- (b) the molecular weight of the mixture of gases in the products of combustion

SOLUTION

The oxidizer-to-fuel mass ratio is (32/8), which is 4, very close to the mixture ratio in Example 12.4.

The mixture molecular weight is

$$\text{MW} = \frac{2(18) + 2(2)}{4} = 10 \frac{\text{kg}}{\text{kmol}}$$

This simple calculation of chemical reaction and the mixture of gases in the combustion products support our earlier calculations of molecular weight in Example 12.4 where we found that the average molecular weight of products of combustion was ~ 9.68 kg/kmol.

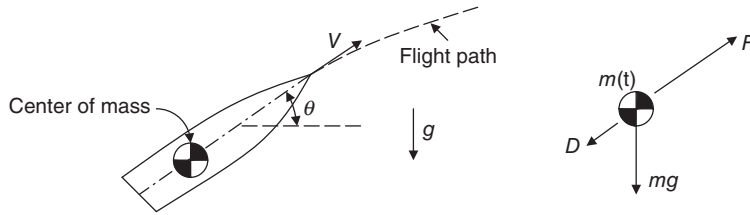
12.8 Flight Performance

Consider a rocket of instantaneous mass $m(t)$ flying at the instantaneous speed V . The flight path angle with respect to horizon is θ , where vertical is the direction of the gravitational force, as shown in Figure 12.10. The atmospheric drag D acts along the vehicle axis, as shown.

We may relate the net forces along the vehicle axis to the vehicle instantaneous acceleration according to

$$m \frac{dV}{dt} = F - D - mg \sin \theta \quad (12.19)$$

■ **FIGURE 12.10**
 Definition sketch of a rocket in flight and the forces that act on the vehicle



Case 1 Zero gravitational force and atmospheric drag

This case is of interest as it produces a simple closed-form solution, since

$$m \frac{dV}{dt} = F = \dot{m}_p c \tag{12.20}$$

We recognize that propellant flow rate is the rate at which the vehicle loses mass, therefore substituting

$$\dot{m}_p = -\frac{dm}{dt}$$

in Equation 12.20, we have

$$m \frac{dV}{dt} = \dot{m}_p c = -\frac{dm}{dt} c \tag{12.21a}$$

which separates to the following form that is suitable for integration

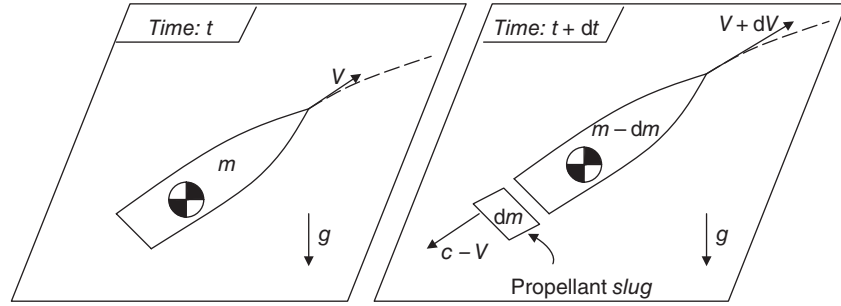
$$dV = -c \frac{dm}{m} \tag{12.21b}$$

The vehicle attains an incremental speed change ΔV as natural logarithm of inverse mass ratio, and proportional to the nozzle effective exhaust velocity c , that is,

$$\Delta V = -\bar{c} \ln \left(\frac{m_f}{m_0} \right) = \bar{c} \ln \left(\frac{1}{MR} \right) \tag{12.22}$$

This is known as the *fundamental equation of rocketry*. For a rocket designed to have a final mass of 5% of its initial mass, the inverse mass ratio is 20 and the natural logarithm of 20 is 2.9957. Therefore, the rocket may be gaining speed of $\sim 3c$, and as shown in Equation 12.8, the effective exhaust velocity is $\sim g_0 I_s$. For an average specific impulse I_s of ~ 400 s and the (earth) gravitational acceleration of ~ 10 m/s², we have an effective exhaust speed of ~ 4000 m/s. Thus, the rocket terminal speed, without accounting for gravity and drag, is $\sim 3c$, which is nearly 12,000 m/s. However, we need to correct for the effects of gravitational force and aerodynamic drag that we neglected in case 1. Both of these effects cause a reduction in the terminal speed or the attained incremental speed ΔV .

■ **FIGURE 12.11**
The rocket as observed
by a stationary frame
of reference before and
after a propellant *slug*
is ejected from the
nozzle



Before we embark on case 2, let us show the fundamental equation of rocketry derived from a stationary observer frame of reference outside the rocket. The rocket speed V is measured relative to the stationary observer. The effective exhaust speed c is relative to the rocket, which translates into $(c - V)$ in the stationary observer frame of reference. At time t , the vehicle mass is m and the instantaneous speed V . At an incremental time later, that is, $t + dt$, the vehicle has a reduced mass $(m - dm)$ and has attained an incremental speed change $(V + dV)$. During the same dt time period, the propellant of mass dm is ejected through the nozzle backward and has attained a speed $(c - V)$ with respect to the stationary observer. The external forces acting on the rocket for the observer are only the aerodynamic drag and the gravitational force. The thrust produced by the rocket motor is an internal force to the vehicle, thus the observer will not record that as external force acting on the vehicle. The graphical depiction of the two snapshots of the rocket is shown in Figure 12.11.

The change of momentum along the rocket axis for the vehicle and propellant *slug* between times t and $t + dt$ (with positive taken to be in the flight direction) is

$$[(m - dm)(V + dV) - (c - V) dm] - mV \cong mdV - cdm \quad (12.23)$$

We neglected $(dm)(dV)$ in Equation 12.23 as a second order effect. The change of momentum along the vehicle axis is equal to the impulse of external forces (along the vehicle axis and in the flight direction) in time dt , namely,

$$(-D - mg \sin \theta) dt \quad (12.24)$$

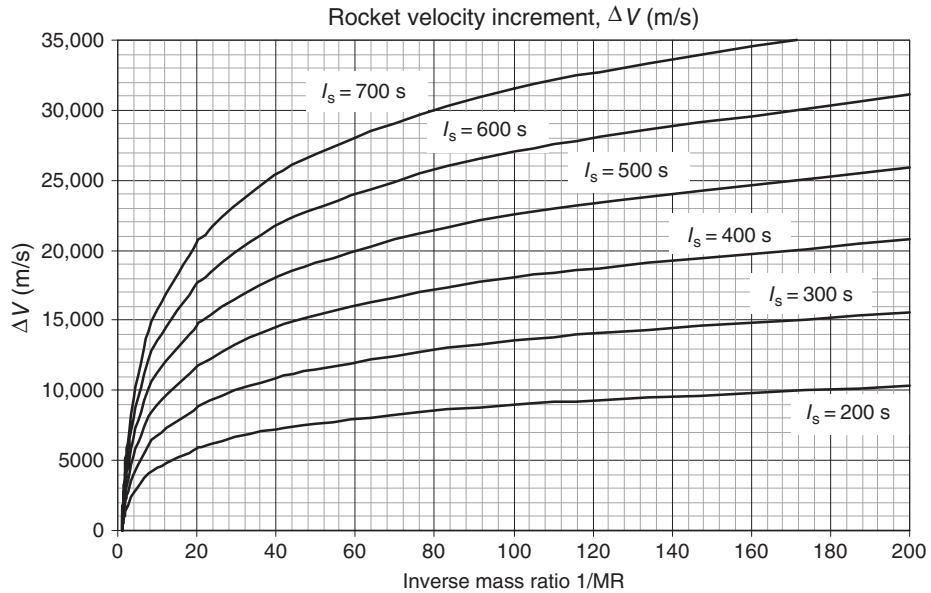
Set Equation 12.23 equal to Equation 12.24 and divide by dt to get

$$m \frac{dV}{dt} - c \frac{dm}{dt} = -D - mg \sin \theta \quad (12.25)$$

We recognize the second term on the left-hand side (LHS) of Equation 12.25 as the rocket thrust force, which then reproduces Equation 12.19, that is,

$$m \frac{dV}{dt} = F - D - mg \sin \theta$$

■ **FIGURE 12.12**
Velocity increment for
a rocket in zero gravity,
zero drag environment
(with $g_0 = 9.8 \text{ m/s}^2$)



The fundamental equation of rocketry, Equation 12.22 is expressed in terms of specific impulse and earth's surface gravitational acceleration as

$$\Delta V = g_0 \bar{I}_s \ln \left(\frac{1}{MR} \right) \quad (12.26)$$

The graph of velocity increment for different specific impulse and vehicle mass ratio is shown in Figure 12.12. We note that as mass ratio is reduced (or inverse of mass ratio is increased), velocity increment grows logarithmically. The impact of specific impulse on velocity increment may also be discerned from Figure 12.12. For a mass ratio of 5%, the velocity increment varies between 6000 and 20,000 m/s, when the specific impulse varies between 200 and 700 s. The mass ratio of 5% indicates a rocket vehicle design that has 95% of its initial mass occupied by its propellant and only 5% devoted to structure, skin, payload, navigation, and control. This value, that is, MR of 0.05, represents the best of a single-stage rocket design today. It is, however, possible to improve the rocket performance in attaining a higher terminal velocity by discarding of empty propellant tanks. This introduces the concept of a multistage rocket. Each rocket stage is completely self-contained, that is, it has its own motor, propellant tanks, and feed system.

EXAMPLE 12.6

The specific impulse of a chemical rocket is 400 s. The rocket is in a zero gravity vacuum flight. If we could improve the propellant fraction ζ from 0.90 to 0.95, cal-

culate the percentage improvement in ΔV that can be achieved.

SOLUTION

Since the propellant mass fraction is $\zeta = 1 - MR$, therefore, the mass ratio changes from 0.1 to 0.05 as ζ varies between 0.9 and 0.95. We substitute, 0.1 and 0.05 in Equation 12.24, to get

$$\begin{aligned}\Delta V &= (9.8 \text{ m/s}^2)(400 \text{ s}) \ln(1/0.10) = 9026 \text{ m/s for } \zeta = 0.90 \\ \Delta V &= (9.8 \text{ m/s}^2)(400 \text{ s}) \ln(1/0.05) = 11,743 \text{ m/s for } \zeta = 0.95\end{aligned}$$

We may realize a 30% increase in ΔV , or equivalently ~ 2700 m/s increase in the terminal velocity of the rocket.

Case 2 Rocket performance including the effect of gravity

From Equation 12.19, we keep the gravity term on the right-hand side (RHS) as we neglect the aerodynamic drag,

$$m \frac{dV}{dt} = F - mg \sin \theta = -c \frac{dm}{dt} - mg \sin \theta \quad (12.27)$$

Divide both sides by m/dt , to get

$$dV = -c \frac{dm}{m} - g \sin \theta dt \quad (12.28)$$

If we integrate Equation 12.28 and use the time-averaged value of $g \cdot \sin \theta$ (denoted by subscript, m), we get

$$\Delta V = -\bar{c} \ln(MR) - (g \sin \theta)_m t_b \quad (12.29)$$

Gravitational acceleration g is governed by Newton's law of gravitation, that is,

$$F_g = G \frac{Mm}{r^2} \quad (12.30)$$

It is customary to combine the product of universal gravitational constant G , the mass of the planet M , and inverse of planet radius squared, into a single term, called the gravitational acceleration on the planet's surface, that is,

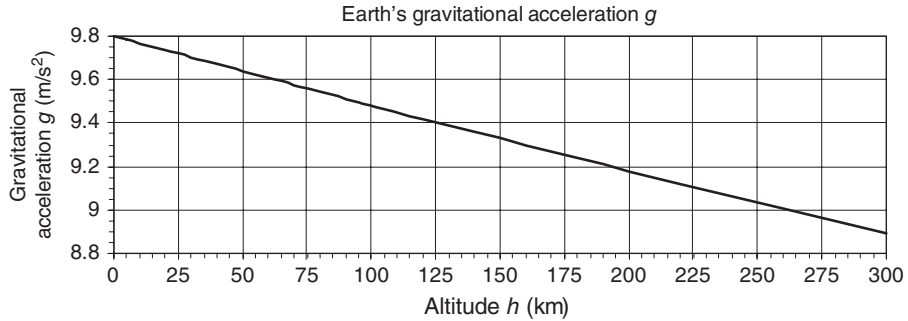
$$g_0 \equiv \frac{Gm}{R^2} \quad (12.31)$$

Therefore, gravitational acceleration g as a function of altitude h above a planet of radius R is related to the acceleration on the surface of the planet by

$$g = \frac{g_0}{(1 + h/R)^2} \quad (12.32)$$

The mean radius of earth is 6000 km and the gravitational acceleration on earth's surface is 9.8 m/s^2 , therefore, at 100 km altitude, where low Earth orbit starts, gravitational

■ **FIGURE 12.13**
Variation of earth's gravitational acceleration with altitude h (in km)



acceleration is $\approx 9.48 \text{ m/s}^2$ or $\sim 97\%$ of its sea level value. Figure 12.13 shows the variation of gravitational acceleration with altitude for up to 300 km. We note that since $h \ll R$ (in this graph), the variation is nearly linear, that is, if we apply binomial expansion to Equation 12.32 for $h/R \ll 1$, we get

$$g \approx g_0(1 - 2h/R) \quad \text{for } h \ll R \tag{12.33}$$

EXAMPLE 12.7

A rocket is vertically launched and operates for 30 s and has a mass ratio of 0.10. The (mean) rocket-specific impulse is 420 s. Assuming the average gravitational acceleration over

the burn period is 9.65 m/s^2 , calculate the terminal velocity of the rocket with and without gravitational effects. Neglect the effect of aerodynamic drag in both cases.

SOLUTION

We use Equation 12.29 with effective exhaust velocity replaced with the product of specific impulse and gravitational acceleration on earth's surface

$$\begin{aligned} \Delta V &= -(9.8)(420) \ln(0.1) \text{ m/s} - 9.65(30) \text{ m/s} \\ &\approx 9188 \text{ m/s (with gravity)} \end{aligned}$$

$$\Delta V = -g_0 \bar{I}_s \ln(MR) - (g \sin \theta)_m t_b$$

Note that the gravitational effect/deceleration caused $\sim 3\%$ reduction in terminal speed.

The vertical launch gives $\theta = 90^\circ$ and the average gravitational acceleration is also given to be 9.65 m/s^2 , therefore,

$$\begin{aligned} \Delta V &= -(9.8)(420) \ln(0.1) \text{ m/s} \approx 9477 \text{ m/s} \\ &\text{(without gravity)} \end{aligned}$$

Case 3 Rocket flight performance including the effects of gravity and aerodynamic drag
The motion of the rocket in a gravitational field including atmospheric drag was derived in Equation 12.19, to be

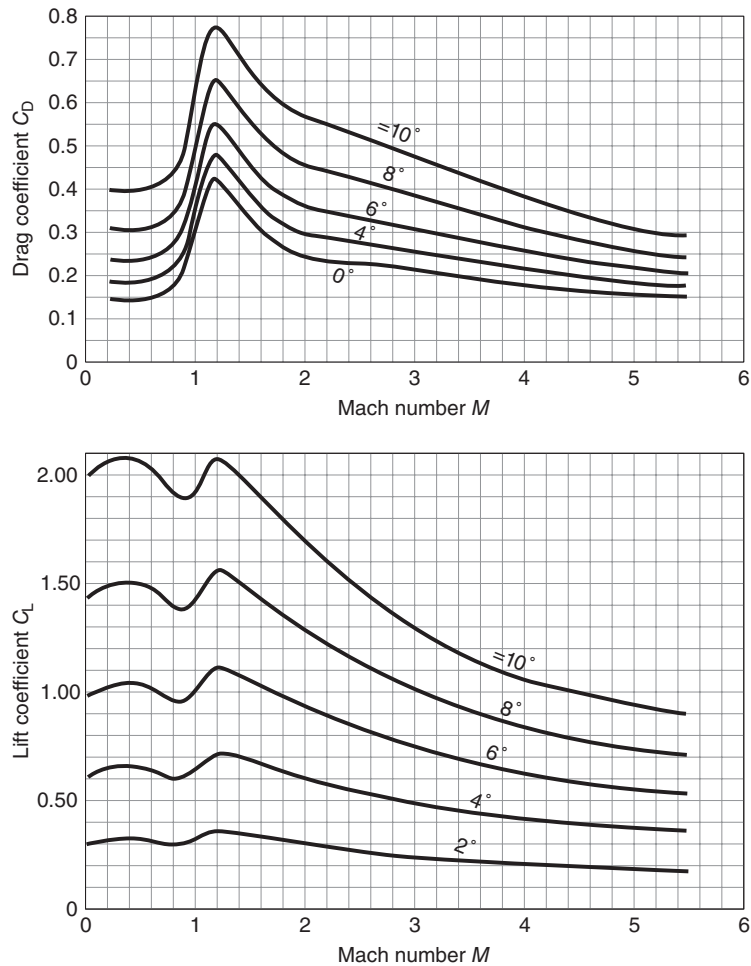
$$m \frac{dV}{dt} = F - D - mg \sin \theta$$

The thrust is again represented by $-(dm/dt) \cdot c$ and the rocket drag is proportional to the flight dynamic pressure and the frontal (cross-sectional) area of the rocket A_f , with the proportionality constant called drag coefficient C_D according to

$$D = C_D \left(\frac{\rho V^2}{2} \right) A_f \tag{12.34}$$

The variation of drag coefficient with flight Mach number may be modeled based on wind tunnel data, computational fluid dynamics codes, or design charts that are developed by industry (proprietary). In general, the presence and the shape of the exhaust plume affect the pressure distribution on the rocket and thus vehicle drag. Therefore, it is customary to depict the baseline drag coefficient in the absence of the exhaust jet. Also, a winged rocket experiences aerodynamic lift; thus we need to model the lift coefficient C_L as a function of Mach number and angle of attack. Some typical aerodynamic data, including lift variation with flight Mach number and angle of attack α , are shown in Figure 12.14 for a V-2 rocket, without the jet and exhaust plume effect (from Sutton and Biblarz, 2001).

■ FIGURE 12.14
Aerodynamic data for a V-2 rocket as a function of angle of attack, with no jet or exhaust plume effect. Source: Sutton and Biblarz 2001. Reproduced with permission from Wiley



In Figure 12.14, we note that the drag coefficient exhibits a transonic drag rise behavior as well as a *plateau* region at high supersonic Mach numbers. This behavior is indeed known as the *hypersonic Mach independence principle*.

The equation of motion of the rocket is rewritten as

$$m \frac{dV}{dt} = -c \frac{dm}{dt} - C_D \rho V^2 A_f / 2 - mg \sin \theta \quad (12.35a)$$

And by dividing both sides by m/dt , we get

$$dV = -c \frac{dm}{m} - \frac{C_D \rho V^2 A_f}{2m} dt - g \sin \theta dt \quad (12.35b)$$

We may integrate Equation 12.35b, to get

$$\int_{V_0}^{V_f} dV = - \int_{m_0}^{m_f} c \frac{dm}{m} - \int_0^{t_b} \frac{C_D \rho V^2 A_f}{2m} dt - \int_0^{t_b} g \sin \theta dt \quad (12.35c)$$

$$\Delta V = -\bar{c} \ln(MR) - (g \sin \theta)_m t_b - \int_0^{t_b} \frac{C_D \rho V^2 A_f}{2m} dt \quad (12.35d)$$

We may write the rocket instantaneous mass m in terms of initial mass, propellant mass, and burn time, as

$$m(t) = m_0 - \frac{m_p}{t_b} t = m_0 \left[1 - \zeta \left(\frac{t}{t_b} \right) \right] \quad (12.36)$$

where ζ is the propellant mass fraction. The last integral in Equation 12.35d may now be expressed as

$$\int_0^{t_b} \frac{C_D \rho V^2 A_f}{2m} dt = \frac{A_f}{2m_0} \int_0^{t_b} \frac{C_D \rho V^2}{(1 - \zeta t/t_b)} dt \quad (12.37)$$

Note that the integrand in Equation 12.37 is an *implicit* function of time, since time is related to altitude and density is a function of altitude; also, time implies rocket speed V , which is related to the Mach number at the altitude and drag coefficient is a function of flight Mach number. Therefore, we may proceed in time, in a stepwise fashion, from zero to the burnout time t_b . The governing equation is thus

$$\Delta V = -\bar{c} \ln(MR) - (g \sin \theta)_m t_b - \frac{A_f}{2m_0} \int_0^{t_b} \frac{C_D \rho V^2}{1 - \zeta t/t_b} dt \quad (12.38)$$

Note that the flight path angle, in this nonlifting case, denoted by θ , is changing with time. Therefore, rocket undergoes *gravity turn* as evidenced by the trio of forces shown in

■ **FIGURE 12.15**
Definition sketch of
velocity components
and the rocket flight
path in a *gravity turn*

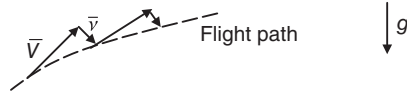


Figure 12.10. Hence, at each time step we need to calculate the new flight path angle θ . The incremental change of flight path direction is dictated by the component of gravitational force *normal* to the rocket axis, namely,

$$m \frac{dv}{dt} = -mg \cos \theta \quad (12.39)$$

which integrates to

$$\Delta v = -(g \cos \theta)_m t \quad (12.40)$$

The rocket moves to a new position along its axis Δx and normal to its axis Δy according to

$$\Delta x = \bar{V} \Delta t \quad (12.41a)$$

and

$$\Delta y = \bar{v} \Delta t \quad (12.41b)$$

Figure 12.15 shows the velocities along the vehicle axis and the turning speed due to the component of gravitational force normal to the axis. The incremental step Δx is taken along vehicle axis and the step Δy is normal to that direction.

An interesting case in hypersonic propulsion involves integrating rockets and air-breathing propulsion in an aircraft. Under those circumstances, the airbreathing engines rather than the rocket primarily drive the choice of the flight trajectory. The structural loads limit the upper bounds of acceptable flight dynamic pressure, and the lower bounds of the dynamic pressure are limited by the mass flow rate per unit area at a given altitude (i.e., thrust requirement). Hence, the flight trajectory for an airbreathing hypersonic aircraft falls within a constant dynamic pressure band, as shown in Figure 12.16 (from Heiser *et al.*, 1994). Mach number versus altitude for three constant dynamic pressures (an upper, a lower, and a mean) is shown in Figure 12.16.

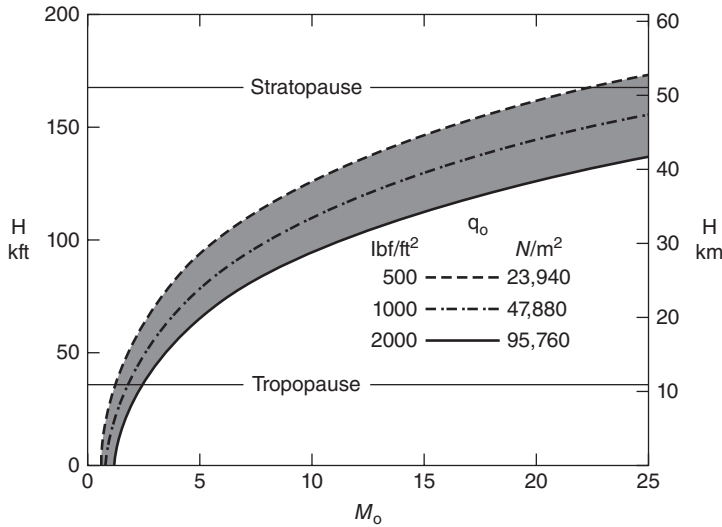
Assuming a constant dynamic pressure trajectory, we may integrate Equation 12.38 to get

$$\Delta V = -\bar{c} \ln(MR) - (g \sin \theta)_m t_b + \left(\frac{A_f}{m_0} \right) \left(\frac{\rho V^2}{2} \right) \left(\frac{t_b}{\varsigma} \right) \bar{C}_D \ln(1 - \varsigma) \quad 12.42a$$

where the drag coefficient is replaced by a suitable average C_D (shown with a bar). By combining the first and last terms on the RHS of Equation 12.42a, we obtain an interesting form for terminal velocity, namely,

$$\Delta V = -\ln(1 - \varsigma) \left[g_0 \bar{I}_s - \left(\frac{A_f}{m_0} \right) \left(\frac{\rho V^2}{2} \right) \left(\frac{t_b}{\varsigma} \right) \bar{C}_D \right] - (g \sin \theta)_m t_b \quad 12.42b$$

■ **FIGURE 12.16**
Standard day
geometric altitude
flight trajectory for
constant dynamic
pressure. Source:
Heiser, Pratt, Daley,
and Mehta 1994.
Reproduced with
permission from AIAA



The bracket on the RHS of Equation 12.42b contains the contribution of thrust and the penalty of aerodynamic drag. We note that a low dynamic pressure trajectory reduces the drag penalty as well as a high initial mass per unit frontal area, that is, m_0/A_f . This requirement tends to produce long slender vehicles for low frontal cross-sectional area and large mass. Also, low drag coefficient C_D is desirable in achieving high terminal speeds, which implies a slender conical nose or tangent ogive to reduce the vehicle drag coefficient.

EXAMPLE 12.8

A rocket plane has a propellant mass fraction of $\zeta = 0.80$ and a mean specific impulse of 345 s. The flight trajectory is described by a constant dynamic pressure of $q_0 = 100$ kPa. The mean drag coefficient is approximated to be 0.3,

the vehicle initial mass is $m_0 = 500,000$ kg, and the vehicle frontal cross-sectional area is $A_f = 20$ m². For a burn time of 60 s, calculate the rocket terminal speed while neglecting gravitational effect.

SOLUTION

The contribution of rocket thrust to terminal speed is

$$\begin{aligned}
 (\Delta V)_{\text{thrust}} &= -\ln(1 - \zeta)g_0\bar{I}_s \\
 &= -(9.8 \text{ m/s}^2)(345 \text{ s})\ln(0.2) \approx 5442 \text{ m/s}
 \end{aligned}$$

The penalty of drag on terminal speed is

$$(\Delta V)_{\text{drag}} = \ln(1 - \zeta) \left(\frac{A_f}{m_0} \right) \left(\frac{\rho V^2}{2} \right) \left(\frac{t_b}{\zeta} \right) \bar{C}_D$$

The initial rocket mass per unit cross-sectional area is, $m_0/A_f = 25,000$ kg/m². The penalty for vehicle drag on terminal speed is thus

$$(\Delta V)_{\text{drag}} \approx -580 \text{ m/s}$$

Therefore, the rocket vehicle will attain a terminal speed (excluding gravitational effect) of

$$\Delta V = (\Delta V)_{\text{thrust}} + (\Delta V)_{\text{drag}} \approx 4862 \text{ m/s}$$

12.9 Multistage Rockets

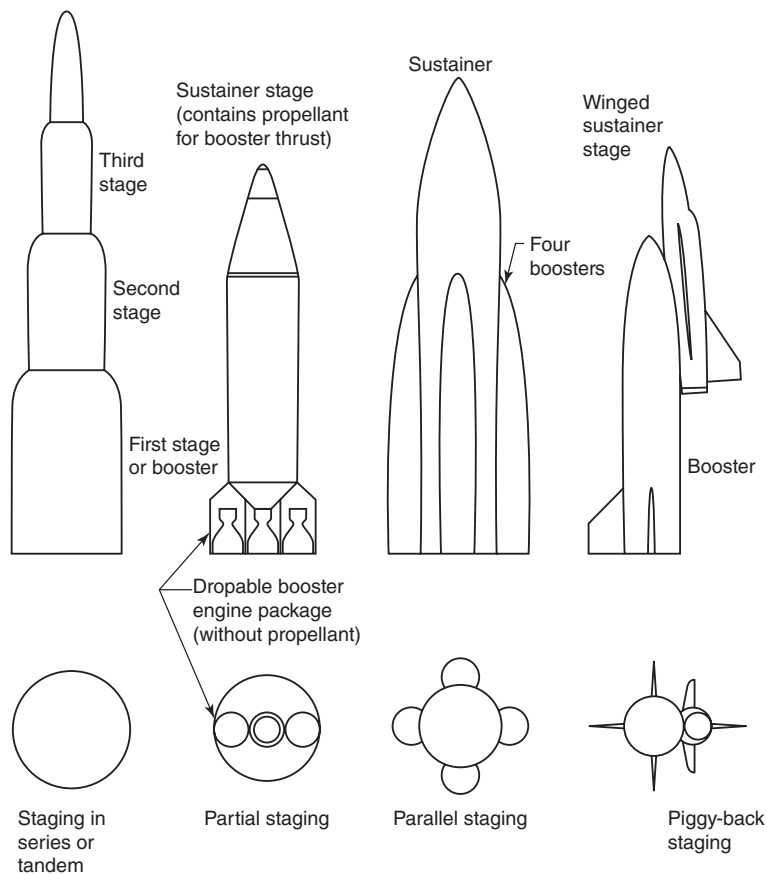
A multiple-stage rocket has the capability to improve the flight performance of a single-stage rocket. There have been many forms of staging used in rocket launch systems to date. An example of various staging concepts is shown in Figure 12.17 (from Sutton and Biblarz, 2001).

Strap-on boosters that jettison after their propellant is depleted are examples of staging that are widely used in launch systems. For example, the space shuttle has two solid rocket boosters that separate after their propellant is fully consumed (i.e., 123 s after launch). Also, the external tank that carries liquid hydrogen and liquid oxygen for launch is separated after ~8.5 min. Figure 12.18a shows the space shuttle orbiter with solid rocket boosters (SRB) and the external tank (ET). The internal compartments of the external tank are shown in Figure 12.18b from Isakowitz (1995).

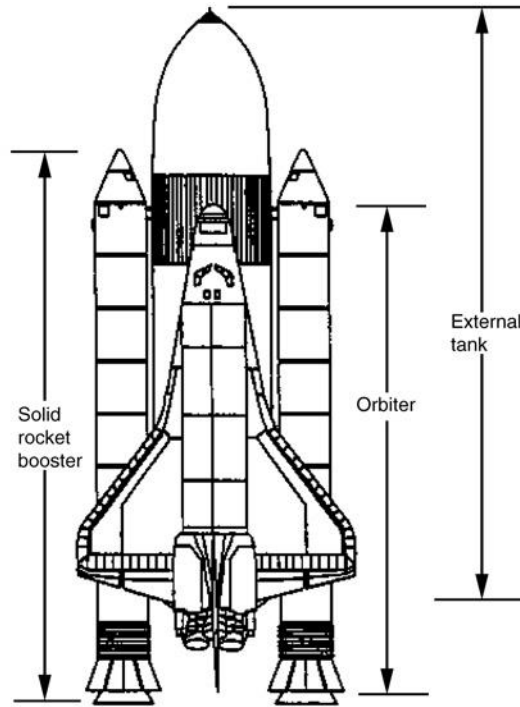
The terminal speed of a multistage rocket (with n stages) is the sum of the terminal speeds of its individual stages, namely,

$$\Delta V = \sum_{i=1}^n \Delta V_i \tag{12.43}$$

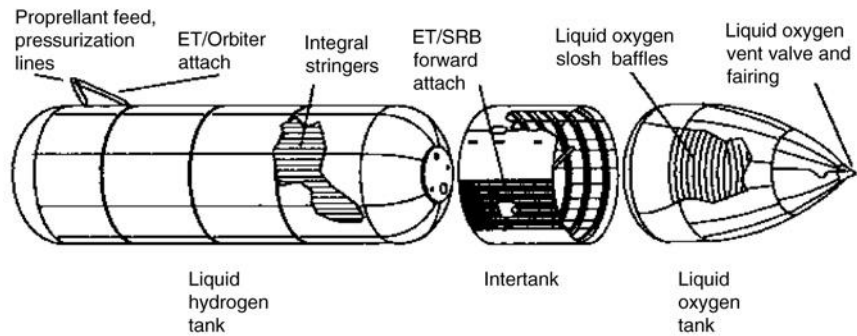
■ **FIGURE 12.17** Concepts in rocket staging. Source: Sutton and Biblarz 2001. Reproduced with permission from Wiley



■ **FIGURE 12.18**
 Space shuttle orbiter launch. Source: Isakowitz 1995. Reproduced with permission from AIAA



(a) Space shuttle orbiter with SRB and ET



(b) The internal compartments of the external tank (ET)

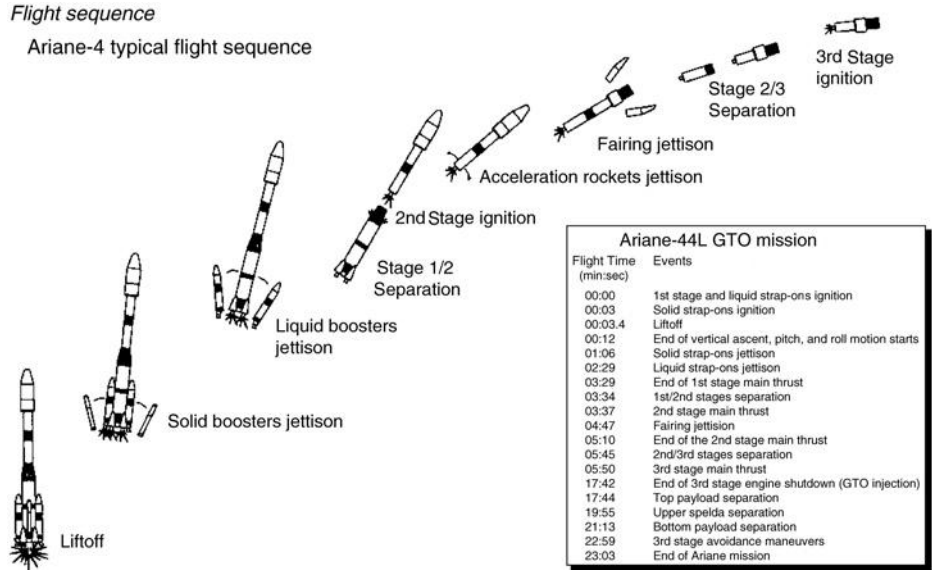
In the absence of gravity and atmospheric drag, the individual stage incremental speed is

$$\Delta V_i = -c_i \ln(MR)_i \tag{12.44}$$

Assuming that all stages have the same effective exhaust speed, for simplicity, we may express the terminal speed of a multistage rocket by

$$\Delta V = -c \ln(MR_1 \cdot MR_2 \cdot MR_3 \cdots MR_n) \tag{12.45}$$

■ **FIGURE 12.19** Typical flight sequence of Ariane-4. Source: Isakowitz 1995. Reproduced with permission from AIAA



Since the final mass of stage 1 is the initial mass of stage 2 and the final mass of stage 2 is the initial mass of stage 3, the product of n stage mass ratios in Equation 12.45 simplifies to the payload or final mass (of the n^{th} stage) divided by the initial rocket (or launch) mass. Here, we have called the final mass of the last stage as the *payload* mass m_L . Therefore,

$$\Delta V = -c \ln (m_L / m_0) \tag{12.46}$$

As noted earlier, the ratio of final-to-initial mass for a single-stage rocket is at best 0.05, or its inverse mass ratio is 20. For a multistage rocket, however, the ratio of payload to initial mass may be ~ 0.01 or even lower. This gives an inverse mass ratio in excess of 100. Therefore, the flight performance shown in Figure 12.12 where the inverse mass ratio varies from 1 to 300 should be viewed in the context of possible single or multistage rocket vehicles.

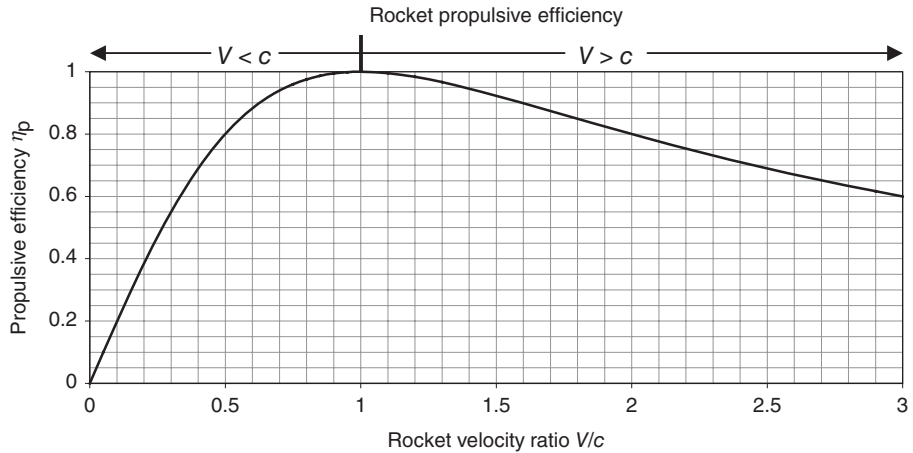
It is instructive to view the flight sequence of a multistage rocket. Figure 12.19 shows the flight sequence of Ariane-4 with the table to the right listing the flight times (from Isakowitz, 1995).

12.10 Propulsive and Overall Efficiencies

The fraction of the thrust power and the residual kinetic power in the jet that is converted to thrust power is called the propulsive efficiency of a rocket. The residual kinetic power in the jet is the kinetic power as observed by a stationary observer, that is,

$$\text{Residual kinetic power in the jet} \equiv \dot{m}_p (c - V)^2 / 2 \tag{12.47}$$

■ **FIGURE 12.20**
 Rocket propulsive efficiency η_p stretches from $V/c < 1$ to $V/c > 1$



Therefore, the propulsive efficiency is

$$\eta_p \equiv \frac{F \cdot V}{F \cdot V + \dot{m}_p(c - V)^2/2} \tag{12.48}$$

Replacing thrust by the product of propellant flow rate and the effective exhaust speed and simplifying, we get

$$\eta_p \equiv \frac{c \cdot V}{c \cdot V + (c - V)^2/2} = \frac{2cV}{c^2 + V^2} = \frac{2(V/c)}{1 + (V/c)^2} \tag{12.49}$$

The propulsive efficiency will reach its peak (of 100%) when the ratio V/c approaches unity. A graph of the rocket propulsive efficiency is shown in Figure 12.20.

A distinction between a rocket and an airbreathing engine is that a rocket may operate in $V/c > 1$, whereas an airbreathing engine has to operate with an exhaust velocity that is higher than the flight speed, since there is a ram drag penalty for the captured airstream. As a result, the range of $V/c > 1$ is unique to rockets.

Similar to an airbreathing engine, the overall efficiency of a chemical rocket engine is defined by the fraction of the chemical power invested in the combustor that is converted to the vehicle thrust power, that is,

$$\eta_o \equiv \frac{F \cdot V}{\dot{m}_p Q_R + \dot{m}_p v_{inj}^2/2} \approx \frac{c \cdot V}{Q_R} \tag{12.50}$$

The second term in the denominator of Equation 12.50 is the kinetic power of the propellant at the injector plate, that is, inlet to the thrust chamber. Often, the contribution of the injected propellant kinetic power is often small and thus neglected as compared with the chemical power of combustion.

EXAMPLE 12.9

A liquid propellant rocket uses hydrogen and oxygen as propellant. The heat of reaction for the combustion is $Q_R = 13.3$ MJ/kg. The specific impulse is 421 s and the flight speed is 2000 m/s. Neglecting the propellant kinetic power at the injector plate, calculate

(a) effective exhaust speed c in m/s

(b) propulsive efficiency

(c) overall efficiency

SOLUTION

Effective exhaust speed is $c = g_0 I_s$, therefore, $c \approx 4126$ m/s. Propulsive efficiency is $\eta_p = 2(2000/4126)/[1 + (2000/4126)^2] \approx 0.785$

Overall efficiency $\eta_o \approx c \cdot V/Q_R \approx 0.620$

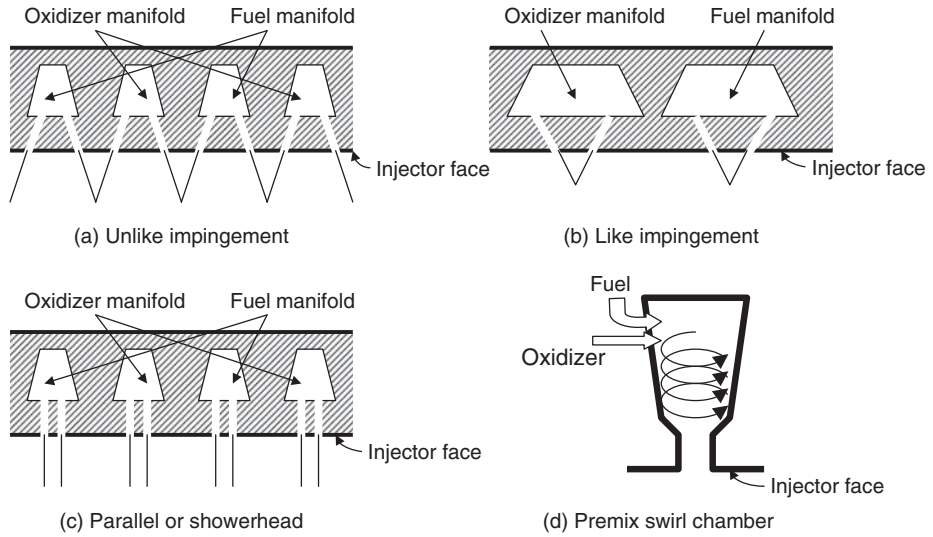
12.11 Chemical Rocket Combustion Chamber

The liquid propellant rocket thrust chamber is composed of an injector plate, a combustion chamber, and an exhaust nozzle. The injector plate serves the function of an atomizer and mixer of the fuel and oxidizer streams. Since the thrust chamber needs to be cooled, the choice of propellant often calls for cryogenic propellants such as hydrogen and oxygen. To minimize storage volume, propellant is stored in liquid form in insulated tanks. The fuel and oxidizer latent heats of vaporization and subsequent heating of the gaseous form of the propellant provide cooling of the thrust chamber walls. Vaporizing and preheating of the propellant is actually advantageous to combustion efficiency and allows the products of combustion to attain higher temperatures in the combustor. The solid propellant combustion chamber houses the propellant and uses liners, insulators, and inhibitors to protect the walls from excessive heating. The period of operation of solid motors is thus limited by the amount of propellant that is carried inside the combustion chamber, which typically lasts from a few seconds to about 2 minutes for boosters.

12.11.1 Liquid Propellant Combustion Chambers

The design of injector plate is critical to stable combustion of the liquid propellant and high combustion efficiency. The stability of combustion is achieved through a large static pressure drop across the injector plate. The conventional design rule calls for 20% drop across the injector plate, that is, the chamber pressure p_c is 20% less than the feed pressure of propellant upstream of the injector plate. This relatively large static pressure drop decouples small pressure isolations in the combustor from the propellant pressure feed oscillations. This instability is called chugging and is the easiest to be avoided. To achieve high efficiency in chemical reaction of the fuel and oxidizer streams, the injector plate design plays a critical role. The precombustion processes of atomization, vaporization, and mixing need to be efficiently accomplished through the injector plate. There are several design approaches to the injector plate, namely, fuel–oxidizer (or unlike stream impingement type), fuel–fuel and oxidizer–oxidizer (or like stream impingement

■ FIGURE 12.21 Schematic drawing of some injector plate design concepts



type), parallel stream or showerhead nozzle type, and premix swirl chamber nozzle type. These injector plate design types are schematically shown in Figure 12.21.

Precision in manufacturing of injector plates ensures proper mixture ratio of fuel and oxidizer that is brought together at a desired distance from the injector plate and at proper angle with respect to combustion chamber axis. Any misalignment in the orifice geometry and angle will cause inefficient mixing, poor combustion efficiency, and possibly chemical reaction that takes place at the wall with subsequent structural failure due to inadequate cooling. On the contrary, proper injector plate design will reduce the amount of backsplash and heat transfer to the thrust chamber walls and produce stable combustion with high efficiency. In sizing the orifice areas for the fuel and oxidizer, we use the Bernoulli equation corrected for viscous fluid effects, according to,

$$v_f = C_{df} \sqrt{\frac{2(\Delta p)_f}{\rho_f}} \tag{12.51a}$$

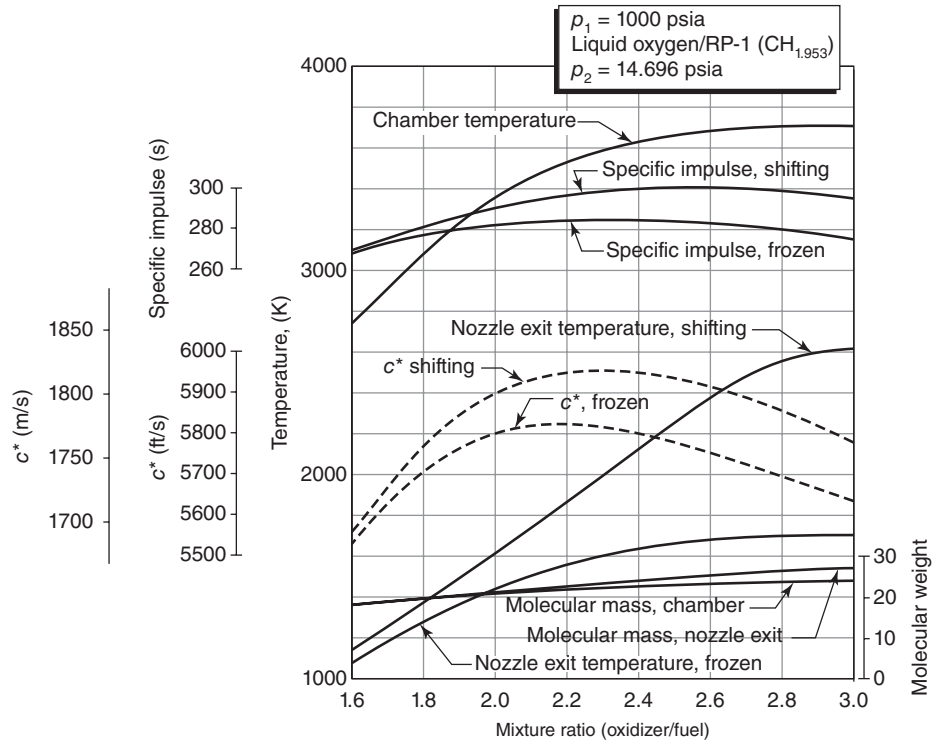
$$v_o = C_{do} \sqrt{\frac{2(\Delta p)_o}{\rho_o}} \tag{12.51b}$$

where C_d is the discharge coefficient, which is a function of the orifice geometry and Reynolds number. The mass flow rate per orifice opening follows the continuity equation, that is,

$$\dot{m}_f = \rho_f v_f A_f = C_{df} A_f \sqrt{2\Delta p_f \cdot \rho_f} \tag{12.52a}$$

$$\dot{m}_o = \rho_o v_o A_o = C_{do} A_o \sqrt{2\Delta p_o \cdot \rho_o} \tag{12.52b}$$

■ **FIGURE 12.22**
Thermochemical
calculations for
oxygen-RP-1
combustion with $p_c =$
1000 psia, $p_2 = p_0 =$
14.7 psia. Source:
Sutton and Biblarz
2001. Reproduced with
permission from Wiley

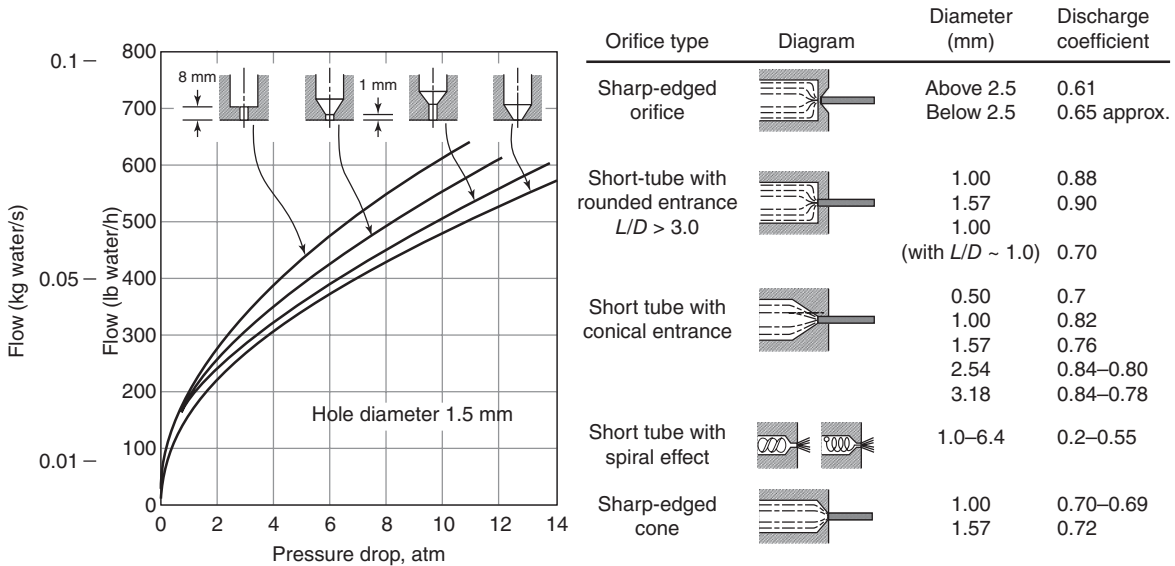


The ratio of the oxidizer-to-fuel mass flow rates is known as the *mixture ratio* r

$$r \equiv \frac{\dot{m}_o}{\dot{m}_f} = \left(\frac{C_{do}}{C_{df}} \right) \left(\frac{A_o}{A_f} \right) \sqrt{\left(\frac{\Delta p_o}{\Delta p_f} \right) \left(\frac{\rho_o}{\rho_f} \right)} \quad (12.53)$$

From our studies of combustion (Chapter 12), we remember that for stoichiometric mixture ratio, the products of combustion reach nearly their maximum temperature. However, for a hydrogen (fuel) rich mixture ratio, $r < r_{\text{stoich}}$, the products of combustion will have a lower mixture molecular weight and thus higher specific impulse. As a result, mixture ratio is often less than the stoichiometric value. Figure 12.22 (from Sutton and Biblarz, 2001) shows the result of thermochemical calculations for oxygen and a hydrocarbon fuel, known as RP-1, in a combustion chamber of 1000 psia pressure and perfect expansion to sea level ambient condition in the nozzle.

Note that there are two sets of nozzle calculations shown in Figure 12.22. The *frozen equilibrium* calculation assumes constant combustion product composition in the nozzle, that is, the equilibrium mole fractions of the products of combustion remain unchanged as the result of flow expansion (i.e., cooling) in the nozzle. Frozen equilibrium calculations are simple but not very accurate in predicting rocket thrust chamber performance. The *shifting equilibrium* calculation, however, allows for chemical reaction in the nozzle as a result of flow expansion, thus it represents a more accurate description of the rocket thrust chamber performance. In either case, we note that the specific thrust has reached maximum



■ FIGURE 12.23 Discharge coefficients for typical injector orifice geometries, based on water tests. Source: Sutton and Biblarz 2001. Reproduced with permission from Wiley

at either the mixture ratio of ~ 2.3 for frozen equilibrium or 2.5 for the shifting equilibrium calculations. Based on the chemical formula for RP-1, that is, $\text{CH}_{1.953}$, stoichiometric oxidizer-to-fuel ratio is 3.413. Thus, the choice of the mixture ratio r is based on maximum specific thrust I_s rather than maximum chamber temperature T_c . Also note that a fuel-rich rocket nozzle exit flow is advantageous to a ram-rocket configuration since the excess fuel may be used as the fuel in the ramjet/scramjet combustor.

Figure 12.23 (from Sutton and Biblarz, 2001) shows injector discharge coefficients for different orifice geometries that are suitable for rocket propulsion applications.

For preliminary injector plate calculation purposes, we use the law of conservation of momentum applied to two colliding jets. Here, we assume that the resultant jet has the same mass flow rate as the sum of individual jets' mass flow rates. Figure 12.24 is a definition sketch of two impinging jets, their angles γ_f and γ_o , and collision distance d from the wall. The *real* impingement jets, however, exhibit some backsplash as well as complex turbulent interactions, as schematically indicated in Figure 12.24b.

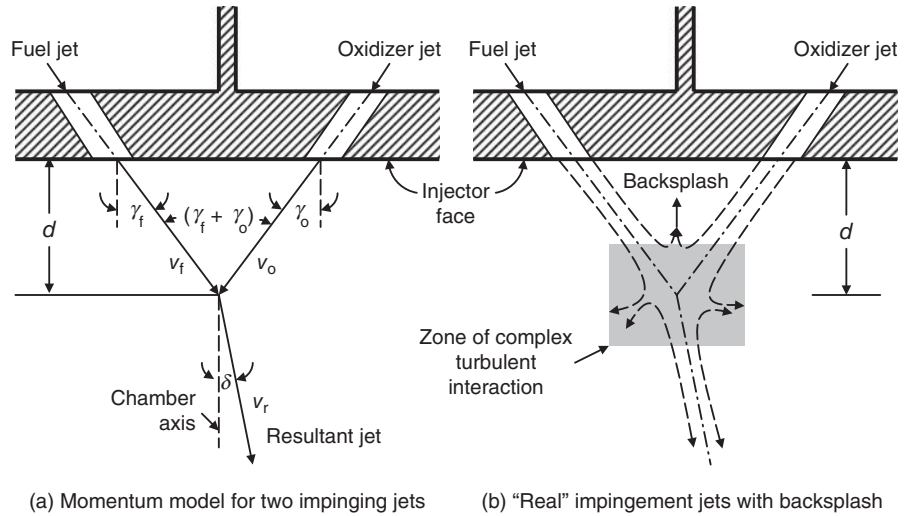
The resultant jet is assumed to emerge at angle δ with respect to chamber axis, as shown. The momentum balance in the chamber axis direction is

$$\dot{m}_f v_f \cos \gamma_f + \dot{m}_o v_o \cos \gamma_o = (\dot{m}_f + \dot{m}_o) v_r \cos \delta \tag{12.54}$$

The momentum balance normal to the chamber axis direction is

$$\dot{m}_f v_f \sin \gamma_f - \dot{m}_o v_o \sin \gamma_o = (\dot{m}_f + \dot{m}_o) v_r \sin \delta \tag{12.55}$$

■ FIGURE 12.24
Definition sketch of two impinging jets



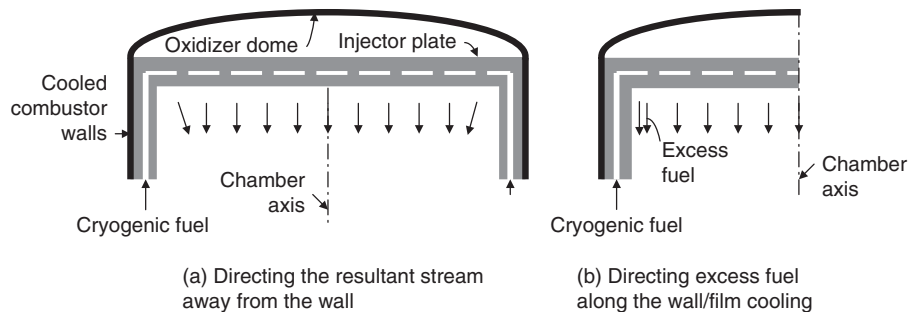
The ratio of the two momentum equations will isolate the resultant jet flow angle δ

$$\tan \delta = \frac{\dot{m}_f v_f \sin \gamma_f - \dot{m}_o v_o \sin \gamma_o}{\dot{m}_f v_f \cos \gamma_f + \dot{m}_o v_o \cos \gamma_o} \tag{12.56}$$

The resultant jet may be designed to emerge in the axial direction near the center of the combustion chamber and toward the center near the chamber walls. The schematic drawing of the resultant propellant stream is shown in Figure 12.25a. The chamber wall is regeneratively cooled by cryogenic propellant. Since rocket combustion often involves a fuel-rich mixture of the propellant, we may inject the extra fuel adjacent to the combustor wall as a means of thermal protection for the wall (Figure 12.25b)

The total included angle at the impingement point is the sum of the two angles $\gamma_o + \gamma_f$. The total impingement angle impacts the extent of backslash and potential chemical reaction and heating at the injector plate.

■ FIGURE 12.25
Schematic drawing of possible propellant injection pattern in the combustion chamber



EXAMPLE 12.10

A liquid propellant rocket injector plate uses an unlike impingement design. The fuel and oxidizer orifice discharge coefficients are $C_{df} = 0.82$ and $C_{do} = 0.65$, respectively.

The static pressure drop across the injector plate for both oxidizer and fuel jets is the same, $\Delta p_f = \Delta p_o = 200$ kPa. The fuel and oxidizer densities are $\rho_f = 85 \text{ kg/m}^3$

and $\rho_o = 1350 \text{ kg/m}^3$. The mixture ratio is $r = 2.50$. Calculate

- oxidizer-to-fuel orifice area ratio A_o/A_f
- oxidizer and fuel jet velocities v_o and v_f
- graph injection angle γ_f versus γ_o for axial resultant stream $\delta = 0$ and different mixture ratios, i.e., for $r = 2.5, 3.5,$ and 4.5

SOLUTION

The orifice area ratio follows Equation 12.53

$$r \equiv \frac{\dot{m}_o}{\dot{m}_f} = \left(\frac{C_{do}}{C_{df}} \right) \left(\frac{A_o}{A_f} \right) \sqrt{\left(\frac{\Delta p_o}{\Delta p_f} \right) \left(\frac{\rho_o}{\rho_f} \right)} \Rightarrow A_o/A_f \approx 0.791$$

From Equation 12.51 we get the fuel and oxidizer orifice discharge speed:

$$v_f = C_{df} \sqrt{2(\Delta p)_f / \rho_f} \Rightarrow v_f \approx 56.2 \text{ m/s}$$

$$v_o = C_{do} \sqrt{2(\Delta p)_o / \rho_o} \Rightarrow v_o \approx 11.2 \text{ m/s}$$

The momentum balance normal to the axis must be zero to get a purely axial resultant flow, i.e.,

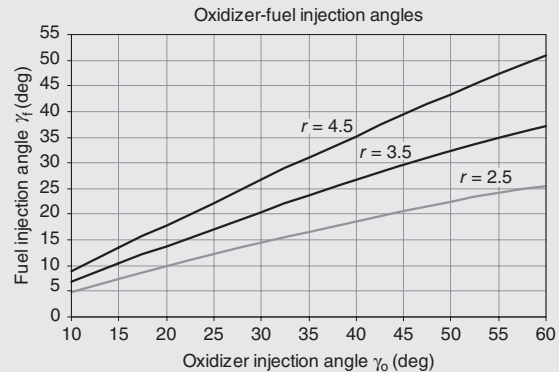
$$\dot{m}_f v_f \sin \gamma_f - \dot{m}_o v_o \sin \gamma_o = 0$$

Therefore, the flow angles are related to each other and the mixture ratio according to

$$\sin \gamma_f = r \left(\frac{v_o}{v_f} \right) \sin \gamma_o$$

$$= r \cdot (11.2/56.2) \sin \gamma_o \approx 0.199 \cdot r \cdot \sin \gamma_o$$

The graph of this function is produced using an Excel spreadsheet program.



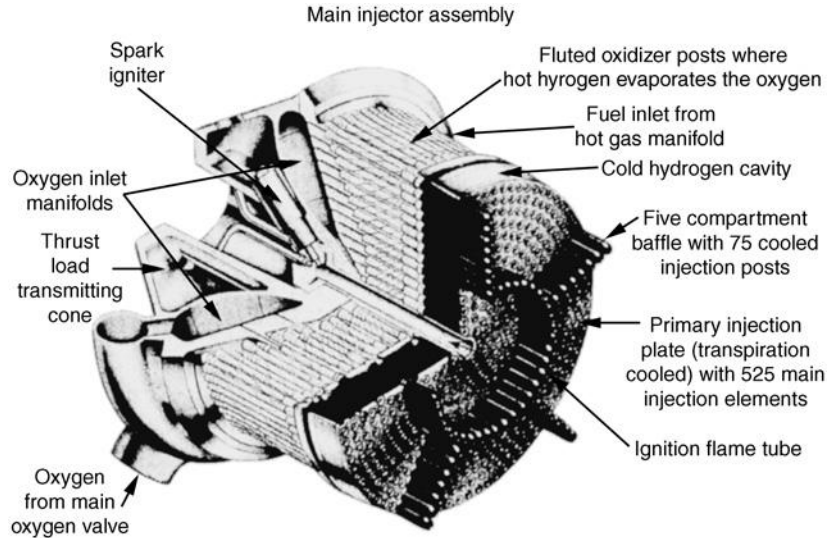
12.11.1.1 Some Design Guidelines for Injector Plate. Backsplash for impingement-type injectors, as noted earlier, can bring the propellant back toward the injector plate, where it may lead to chemical reaction and heat release with subsequent injector plate structural failure. To control backsplash, we place design limitations on impingement distance d and the total included (impingement) angle $(\gamma_o + \gamma_f)$, namely,

$$d \sim 5 \text{ to } 7 (d_o + d_f) / 2 \quad (12.57)$$

$$(\gamma_o + \gamma_f) < 60^\circ \quad (12.58)$$

To control chugging instability, we build in a large pressure drop across the injector plate, that is, $(\Delta p)_{inj} \approx 0.2 p_c$. This is a *ballpark* rule as the actual pressure drop depends on the

■ **FIGURE 12.26**
Main injector assembly
of Space Shuttle Main
Engine showing baffle
with five outer
compartments. Source:
Sutton and Biblarz
2001. Reproduced with
permission from Wiley



injector design, for example, unlike impingement, like-impingement, and others. Orifice diameters are to be small ($\sim 0.4\text{--}2.4$ mm) for good atomization. Smaller orifice diameters are prone to plugging. The orifice diameter ratio $d_o/d_f \sim 1.22$ is recommended for unlike impingement. NASA publications (e.g., NASA SP-8089 and NASA SP-8120) on injectors and rocket nozzles are sources for additional reading that are highly recommended.

12.11.1.2 Combustion Instabilities. There are three main types of instabilities associated with chemical rockets. These are categorized based on their frequency range. The first type, which is the low frequency disturbance, is known as *chugging*. Its frequency range is between 10 and 200 Hz. The source is instability is the coupling between the pressure feed oscillations and the combustion chamber pressure oscillations. This form of longitudinal instability appears as pogo instability on the vehicle's motion. The *fix* for this instability is in designing large static pressure drop ($\sim 20\%$ p_c) across the injector plate as well as stiffening the coupling between the components of propellant feed system and the thrust chamber. The second mid-range instability is known as acoustical, buzzing, or entropy instability. The frequency range for this instability is 200–1000 Hz. The source of this intermediate frequency instability is the mechanical vibration of the propulsion system and possible coupling between the injector plate spray pattern and the turbulent eddies in the combustor. Acoustic coupling between the combustion and the injector plate propellant spray pattern is also deemed responsible for this instability. The third instability is of high frequency, that is, higher than 1000 Hz, known as the *screeching or screaming* instability. This type has its roots in the energy release pattern in the combustion chamber and resonant behavior with the combustor cavity. Injector face baffles, as shown in Figure 12.26 (from Sutton and Biblarz, 2001), have proven effective in control of screaming instability in liquid propellant rockets.

12.11.2 Solid Propellant Combustion Chambers

Solid propellants embody oxidizer, fuel, and a binder in solid or rubbery form. Solid propellants are categorized based on their composition. They are known as double-base

(DB), composite, and composite modified double-base (CMDB). The double-base solid propellant is a *homogeneous* mixture of oxidizer, fuel, binder, and some additives (e.g., metal oxides and metal particles). The composite propellant is the *heterogeneous* mixture of fuel, oxidizer, binder, and additives. The composite modified double-base propellant is the combination of the first two types. As noted, the additives are often metal oxides and metal particles that enhance burning rates. Examples of solid propellants and their characteristics are shown in Table 12.3 (from Sutton and Biblarz, 2001). The U.S. Department of Defense (DOD) gives solid propellants (referred to as “explosives”) a hazard classification of 1.1 or 1.3, which regulates their manufacturing, handling, storage, labeling, and shipping (Explosive Hazard Classification Procedure, 1989).

The solid propellant burning rate r is defined as the speed of chemical reaction, that is, combustion, that progresses normal to a propellant grain surface. Therefore, the gaseous mass flow rate that emerges from a burning solid propellant grain surface is proportional to the surface burning area, the speed of propellant surface recession, and the grain density according to continuity equation

$$\dot{m} = \rho_p r A_b \quad (12.59)$$

where ρ_p is the (solid) propellant grain density, in kg/m^3 (or slugs/ft^3), r is the surface recession or burning rate in cm/s (or in/s), and A_b is the surface area of solid propellant grain that is burning. An empirical formula that relates the burning rate to combustion chamber conditions, for an end-burning grain, is

$$r = a p_c^n \quad (12.60)$$

where p_c is the combustion chamber pressure, a and n are indices of combustion that are constant for different propellants. The constant a is a function of the propellant grain temperature and n is the pressure exponent, thus the burning rate is dependent on the combustion chamber pressure as well. We can demonstrate that for stable operation, n has to be less than 1. Note that the mass flow rate through the nozzle is proportional to chamber pressure p_c , and if the chamber pressure drops the mass flow rate through the nozzle decreases. With a decrease in chamber pressure, the burning rate drops to a lesser extent if $n < 1$, thus causing the pressure to build up in the combustion chamber. However, if $n > 1$, the burning rate drops faster than the flow rate in the nozzle, thus leading to a further drop in the chamber pressure. This is clearly an unstable situation. Therefore, based on stability arguments, we conclude that the pressure exponent n in solid propellant grain burning rate has to be less than 1. Figure 12.27 shows the burning rate dependence on chamber pressure and initial grain temperature for several solid propellants. We note that the burning rate varies between ~ 0.04 and 3 in/s or ~ 0.1 and 7.5 cm/s . Also, the linear variation in the log–log plot supports the empirical formula 12.60. The indices a and n may be determined from the data in Figure 12.27. Note that there is a “Plateau DB” propellant that shows a constant burning rate with chamber pressure, thus it must have its pressure exponent, $n = 0$.

Assuming a steady-state flow, we may equate the gasification of the solid propellant to the mass flow rate through a choked nozzle throat to get the area ratio A_b/A_{th}

$$\dot{m} = \rho_p r A_b = p_1 A_{\text{th}} \sqrt{\frac{\gamma}{RT_1} \left[\frac{2}{\gamma + 1} \right]^{\frac{\gamma+1}{\gamma-1}}} \quad (12.61)$$

TABLE 12.3
Characteristics of Some Solid Propellants (from Sutton and Biblarz, 2001)

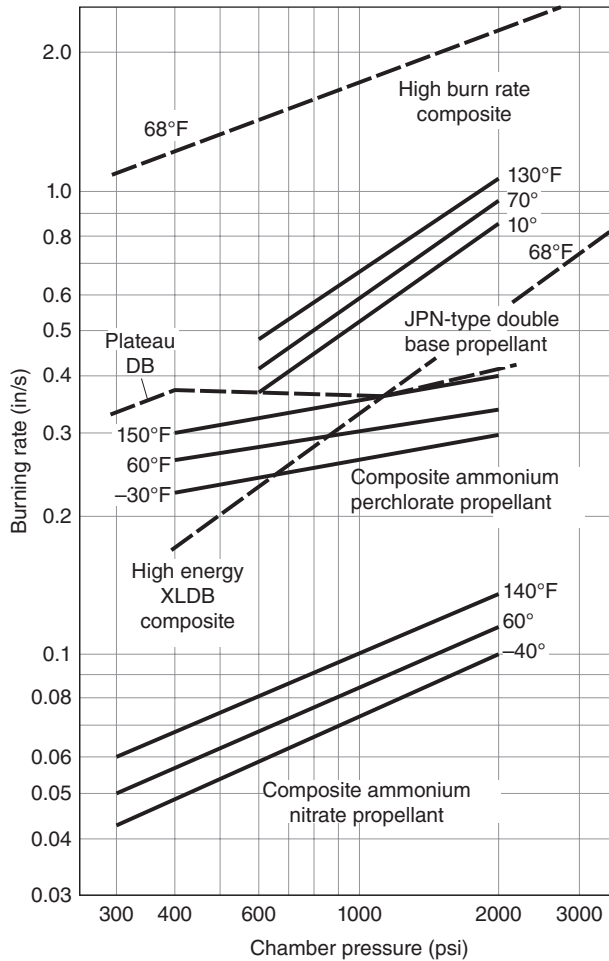
Propellant type ^c	I_s Range (sec) ^b	Flame temperature ^e		Density or specific gravity ^e	Metal content (wt %)	Burning rate ^{c,e} (in/s)	Pressure exponent ^e n	Hazard classification	Stress (psi)/Strain(%)		Processing method
		(°F)	(K)						(lb/in ³)	(sp.gr.)	
DB	220-230	4100	2550	0.058	1.61	0.05-1.2	0.30	1.1	4600/2	490/60	Extruded
DB/AP/Al	260-265	6500	3880	0.065	1.80	0.2-1.0	0.40	1.3	2750/5	120/50	Extruded
DB/AP-HMX/Al	265-270	6700	4000	0.065	1.80	0.2-1.2	0.49	1.1	2375/3	50/33	Solvent cast
PVC/AP/Al	260-265	5600	3380	0.064	1.78	0.3-0.9	0.35	1.3	369/150	38/220	Cast or extruded
PU/AP/Al	260-265	5700	3440	0.064	1.78	0.2-0.9	0.15	1.3	1170/6	75/33	Cast
PBAN/AP/Al	260-263	5800	3500	0.064	1.78	0.25-1.0	0.33	1.3	520/16	71/28	Cast
CTPB/AP/Al	260-265	5700	3440	0.064	1.78	0.25-2.0	0.40	1.3	(at -10°F)	88/75	Cast
HTPB/AP/Al	260-265	5700	3440	0.067	1.86	0.25-3.0	0.40	1.3	325/26	90/33	Cast
PBA/AP/Al	260-265	5700	3440	0.064	1.78	0.25-1.3	0.35	1.3	500/13	41/31	Cast
AN/Polymer	180-190	2300	1550	0.053	1.47	0.06-0.5	0.60	1.3	200/5	NA	Cast

^a Al, aluminum; AN, ammonium nitrate; AP, ammonium perchlorate; CTPB, carboxy-terminated polybutadiene; DB, double-base; HMX, cyclotetramethylene tetranitramine; HTPB, hydroxyl-terminated polybutadiene; PBAA, polybutadiene-acrylic acid polymer; PBAN, polybutadiene-acrylic acid-acrylonitrile terpolymer; PU, polyurethane; PVC, polyvinyl chloride.

^b At 1000 psia expanding to 14.7 psia, ideal or theoretical value at reference conditions.

^c At 1000 psia.

■ FIGURE 12.27 Dependence of burning rate of typical solid rocket propellants on chamber pressure and initial grain temperature. Source: Sutton and Biblarz 2001. Reproduced with permission from Wiley



Therefore, the ratio of burning-to-throat area is expressed as

$$\frac{A_b}{A_{th}} = \frac{p_1}{\rho_p r} \sqrt{\frac{\gamma}{RT_1} \left[\frac{2}{\gamma + 1} \right]^{\frac{\gamma+1}{\gamma-1}}} = \frac{p_1^{1-n}}{\rho_p a \sqrt{RT_1}} \sqrt{\gamma \left[\frac{2}{\gamma + 1} \right]^{\frac{\gamma+1}{\gamma-1}}} \quad (12.62)$$

Note that the RHS of Equation 12.62 is composed of three groups; the first is the combustor pressure dependence, the second is the combustion temperature dependence (in the denominator), and the last term is a function of gas property γ . For a given propellant, we note that chamber pressure is related to the area ratio A_b/A_{th} following

$$p_1 \propto \left(\frac{A_b}{A_{th}} \right)^{\frac{1}{1-n}} \quad (12.63)$$

Since n is less than 1, the exponent of Equation 12.63 shows the amplification of the chamber pressure with a change in burning surface area increase. Therefore, a sudden appearance of a crack in the grain has the potential of creating a large chamber pressure rise, which may lead to a structural failure. This parameter, that is, the burning-to-throat area ratio, is an *internal ballistic parameter* to solid rocket motors and is given a symbol K . The temperature sensitivity of the grain burning rate for a constant chamber pressure and the temperature sensitivity of chamber pressure for a constant K are known as σ_p and π_K , respectively. These are defined as

$$\sigma_p \equiv \left(\frac{\delta \ln r}{\delta T} \right)_p = \frac{1}{r} \left(\frac{\delta r}{\delta T} \right)_p \quad (12.64)$$

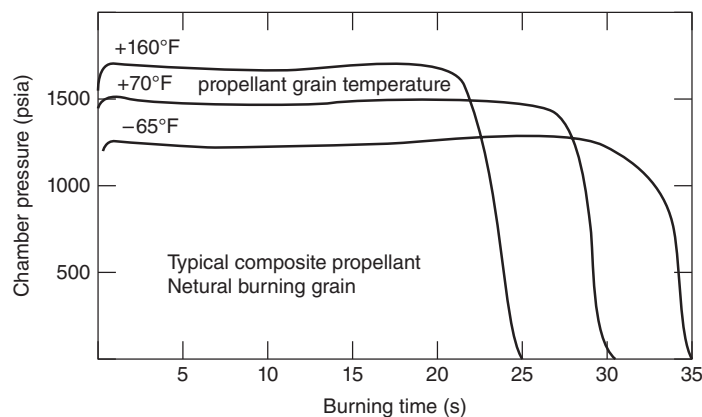
$$\pi_K \equiv \left(\frac{\delta \ln p}{\delta T} \right)_K = \frac{1}{p_1} \left(\frac{\delta p}{\delta T} \right)_K \quad (12.65a)$$

σ_p represents percentage change in burning rate r per degree change in initial grain temperature T while keeping the chamber pressure constant. π_K represents the percentage change in chamber pressure per degree change in initial grain temperature for the same burning to throat area ratio K . These initial grain temperature sensitivities form the remaining *internal ballistic parameters* for a solid rocket motor. According to Kubota (1984), typical values for σ_p range from 0.002 to 0.008/K (or per °C) and the range of π_K is related to σ_p via pressure index n according to

$$\pi_K = \frac{\sigma_p}{1 - n} \quad 12.65b$$

Since σ_p is the parameter that sizes the burning rate enhancement due to initial temperature of grain and n leads to the growth of chamber pressure, a solid propellant of low σ_p and n is desirable. Both burning rate and chamber pressure increase with initial grain temperature; therefore, the propellant is consumed at a faster rate and, thus, the burn time will be reduced. Since thrust is proportional to propellant mass flow rate, it is, therefore, inversely proportional to the burn time for a given propellant mass. But the burn time is reduced inversely proportional to the mass flow rate. Therefore, the integral of thrust over time, that is, the total impulse, remains constant. Figure 12.28 shows the effect of initial

■ **FIGURE 12.28**
Thrust-time behavior for different initial grain temperatures for a neutral solid propellant rocket conserves the total impulse. Source: Sutton and Biblarz 2001. Reproduced with permission from Wiley



grain temperature on the thrust-time behavior of a solid rocket motor (from Sutton and Biblarz, 2001).

EXAMPLE 12.11

A solid rocket motor has a design chamber pressure of 7 MPa, an end-burning grain with $n = 0.5$ and $r = 5$ cm/s at the design chamber pressure, and design grain temperature of 15°C. The temperature sensitivity of the burning rate is $\sigma_p = 0.002$ per °C and chamber pressure sensitivity to initial grain temperature is $\pi_k = 0.004$ per °C. The nomi-

nal effective burn time for the rocket is 60 s, i.e., at design conditions. Calculate

- the new chamber pressure and burning rate when the initial grain temperature is 45°C
- the corresponding reduction in burn time Δt_b in seconds

SOLUTION

The change in initial grain temperature is $\Delta T = 30^\circ\text{C}$, therefore the new chamber pressure is

$$p_c = 7 \text{ MPa}[1 + 0.004(30)] \approx 7.84 \text{ MPa}$$

We first calculate the burning rate at the new chamber pressure of 7.84 MPa while maintaining the same exponent n and coefficient a according to

$$r = ap_1^n$$

$$r = (5 \text{ cm/s}) \left(\frac{7.84}{7} \right)^{0.5} \approx 5.29 \text{ cm/s}$$

Now, we are ready to correct for the effect of the grain temperature on burning rate, which keeps the chamber pressure constant, i.e., through σ_p ,

$$r = 5.29 \text{ cm/s} [1 + 0.002(30)] \approx 5.61 \text{ cm/s}$$

The length of the end-burning grain that was designed to be burned at 5 cm/s for 60 s is approximately

$$L \approx 5 \text{ cm/s} (60 \text{ s}) = 3 \text{ m}$$

The time to burn 3 m of end-burning grain at 5.61 cm/s is therefore

$$t_b \approx 300 \text{ cm} / 5.61 \text{ cm/s} \approx 53.5 \text{ s}$$

We may also note that thrust is proportional to chamber pressure, therefore the burn time is inversely proportional to the chamber pressure (for a constant total impulse), i.e.,

$$t_b \approx 60 \text{ s} (7 \text{ MPa} / 7.84 \text{ MPa}) \approx 53.6 \text{ s}$$

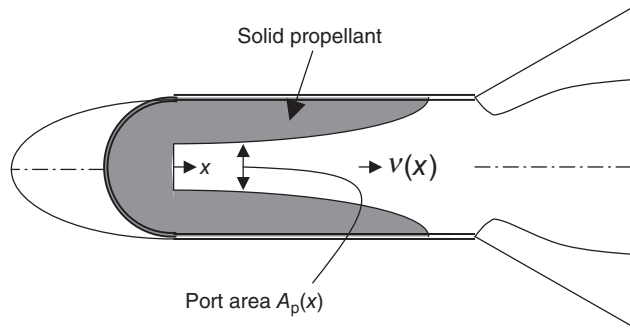
Therefore, a reduction in burn time of $\Delta t_b \approx 6.5$ s is caused by a higher grain temperature.

Solid propellant grain designs that incorporate a port area A_p experience an enhanced burning rate, known as *erosive burning*. For erosive-burning grains, heat transfer to the grain is increased due to the flow of hot combustion gases over the grain surface. The empirical rule for the burning rate thus includes the effect of gas speed. For example, we may express the erosive burning grain rate as

$$r = r_0(1 + kv) \quad (12.66)$$

where r_0 is the reference burning rate for an end burning grain and the parenthesis represents the erosive burning *augmentation factor* due to gas speed v , and the coefficient k is an empirical parameter. Figure 12.29 shows a definition sketch for a solid rocket grain that experiences erosive burning. The port area A_p varies along the length of the grain,

■ **FIGURE 12.29**
Schematic drawing of
an erosive burning
solid propellant grain

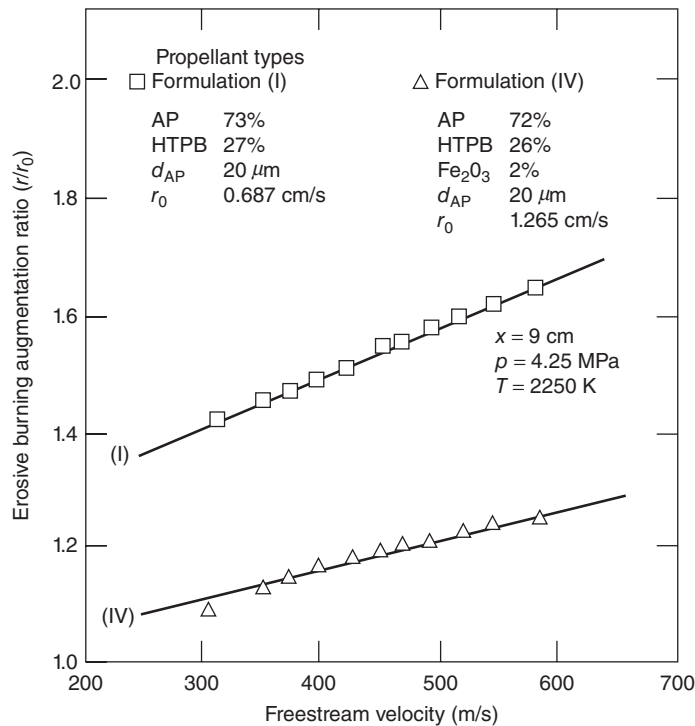


as the enhanced burning rate consumes the propellant at a faster rate toward the nozzle throat, as shown.

Figure 12.30 shows the erosive burning augmentation ratio, r/r_0 , from Razdan and Kuo (1984). The linear relationship between the augmented burning rate and the freestream velocity is clearly demonstrated in Figure 12.30. We may extract the proportionality factor k from the experimental data of Figure 12.30. This task is left to a problem at the end of this chapter. Also note that erosive burning rate may be enhanced by nearly 50% or more (depending on the propellant type and gas speed) as compared with an end burning grain. This will clearly impact the burn time and rocket flight performance as well as pose special design issues for the casing thermal protection.

There are other factors that contribute to burning rate enhancement besides erosive burning. For example, longitudinal and lateral vehicle accelerations that are encountered

■ **FIGURE 12.30**
Erosive burning
augmentation ratio.
Source: Razdan and
Kuo 1984. Reproduced
with permission from
AIAA



in rapid maneuvers or for stability purposes can amplify the rate of gasification in a solid rocket motor. Spin-stabilized platforms and antimissile rockets experience large lateral and longitudinal accelerations. These longitudinal and lateral loads may also cause stress buildup and crack development in the grain. Cracks are structural failures that will impact the performance of the rocket. Due to the random, that is, unpredictable, nature of crack initiation and development with subsequent burning along the crack and with a potential compromise of the integrity of the liner, inhibitor, or the insulator, the mechanical aspects of grain design, processing, and installation are of critical importance to solid rocket motors.

Solid propellant motors encounter combustion instabilities that often involve pressure oscillations in the combustion chamber that are due to coupling between the combustion gas, the combustor cavity, and the flowfield in the combustor. The treatment of these complex interactions and the phenomenological behavior of the instabilities are beyond the scope of the present text. Price (1984), however, has addressed solid propellant combustion instabilities in detail; this is recommended for further reading.

12.12 Thrust Chamber Cooling

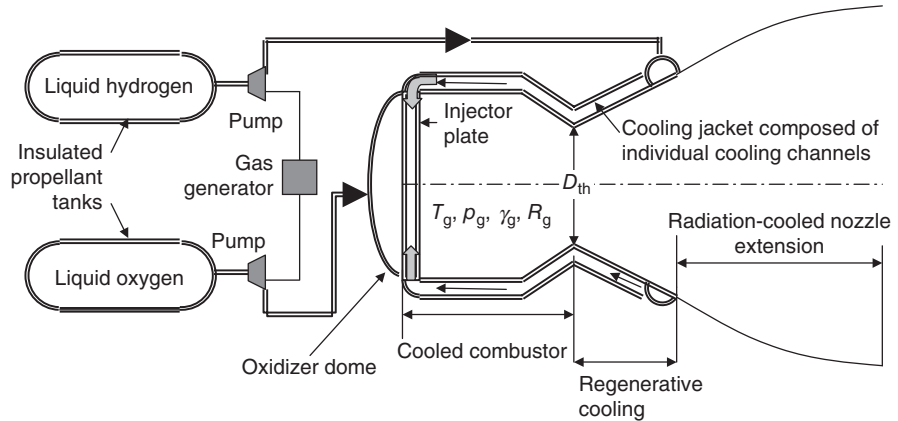
In this section, we examine the cooling requirements and challenges in liquid and solid propellant rocket thrust chambers.

12.12.1 Liquid Propellant Thrust Chambers

Liquid propellant rockets usually operate for extended periods, that is, typically for several minutes, and thus expose the combustion chamber walls to intense heating. The combustion products reach (near stoichiometric level) temperatures of $\sim 3000\text{--}4700$ K depending on the propellant combination (Table 12.1). All modes of heat transfer, that is, convection, conduction, and radiation exist in a rocket combustor and contribute to the combustor wall heating. The products of combustion then expand in a convergent–divergent nozzle to produce thrust. Although expansion of the combustion gases in the nozzle convert their thermal energy into kinetic energy, extended sections of the nozzle downstream of the throat are still exposed to excessive gas temperatures and thus need to be cooled. Fortunately, the liquid propellant onboard offers a cooling capacity that is tapped for the so-called *regenerative cooling* purposes of the thrust chamber walls. The cooling capacity is due to the phase change, that is, from liquid to vapor, known as latent heat of vaporization. Figure 12.31 shows a definition sketch of the regenerative cooling scheme in a liquid propellant rocket. Note that we switched the chamber designation of temperature, pressure, and so on from using the subscript “c” (for chamber) to “g” for (hot) gas. Since we are cooling the walls of the thrust chamber, we need the subscript “c” for the coolant.

As we discussed heat transfer in Chapter 10 for turbine cooling, the steady-state heat transfer from the hot combustion gases to the coolant takes place convectively over the combustor inner wall, across a hot gas film, radiatively due to the volume of hot combustion gases to the wall, conductively through the combustor wall, and convectively over a coolant film on the coolant channel side. The net one-dimensional heat flux to the

■ FIGURE 12.31
Definition sketch of a
regeneratively cooled
rocket thrust chamber
[subscript “g” stands
for (hot) gas]



thrust chamber wall is the sum of the convection as well as the radiative heat transfer according to

$$\dot{q}_w = \dot{q}_c + \dot{q}_r \quad (12.67)$$

The radiative heat transfer from the volume of hot gas to the solid wall in the combustor is governed by

$$\dot{q}_r = \varepsilon_g \sigma T_g^4 \quad (12.68)$$

where ε_g is the emissivity of the gas (equal to 1 for blackbody radiation and less than 1 for graybody radiation), σ is the Stefan-Boltzmann constant, which is $5.67 \times 10^{-8} \text{ W/m}^2\text{K}^4$ and T_g is the absolute gas temperature. Although the Stefan-Boltzmann constant is very small (due to 10^{-8} term), the temperature contribution to radiation heat transfer grows exponentially with temperature, that is, T_g^4 . Therefore, according to Sutton and Biblarz (2001), radiation accounts for 3–40% of the combustion chamber heat flux for the gas temperature range of 1900–3900 K. This is a reminder that we may not neglect radiative heat transfer unless the gas temperature is low, namely, ~ 700 K. The presence of solid particles in the rocket combustion chamber increases the emissivity ε_g in Equation 12.68. The upper value of 1, that is, blackbody radiation, may be chosen for high concentration of solid particles in the gas stream. The convective heat transfer is governed by the Newton's law of cooling according to

$$\dot{q}_c = h_g(T_{aw} - T_{wg}) \quad (12.69)$$

where h_g is the gas-side film coefficient, T_{aw} is the adiabatic wall temperature (on the gas side), and T_{wg} is the gas-side wall temperature. Fourier's law of heat conduction governs the heat conduction through the wall,

$$\dot{q}_{\text{cond}} = k_w \left(\frac{T_{wg} - T_{wc}}{t_w} \right) \quad (12.70)$$

where k_w is the thermal conductivity of the wall material (a property of the wall), T_{wc} is the wall temperature on the coolant side, and t_w is the wall thickness (a design parameter). Note that the minus in Fourier heat conduction law is absorbed in the parenthesis, that is, the heat transfer is from the combustor toward the coolant side. Now, combining these sources of heat flow in a steady-state (one-dimensional) rocket thrust chamber-cooling problem, we can write

$$\dot{q}_w = \underbrace{h_g(T_{aw} - T_{wg}) + \epsilon_g \sigma T_g^4}_{\text{Combustion chamber}} = \underbrace{k_w \left(\frac{T_{wg} - T_{wc}}{t_w} \right)}_{\text{Wall}} = \underbrace{h_c(T_{wc} - T_c)}_{\text{Coolant}} \quad (12.71)$$

We may eliminate the gas and coolant sidewall temperatures, T_{wg} and T_{wc} , from the heat flux equation to get

$$\dot{q}_w = \frac{T_{aw} - T_c + (\epsilon_g \sigma T_g^4 / h_g)}{(1/h_g) + (t_w/k_w) + (1/h_c)} \quad (12.72)$$

Let us examine the parameters in Equation 12.72. The stagnation temperature of the gas often approximates the adiabatic wall temperature T_{aw} as we encountered in turbine cooling section. This approximation, that is, $T_{aw} \approx T_{tg}$, is appropriate in applying to the rocket thrust chamber cooling problem as well due to the approximations that are inherent in heat transfer solutions. Coolant temperature T_c is also known since the stored liquid temperature in the insulated tank is known and is adjusted for the transmission line connecting the pump and the thrust chamber heat transfer. Approximate expressions for film coefficients h_g and h_c are also known from the heat transfer literature related to the long tubes/channels. The emissivity of gas ϵ_g in the presence of (high concentration of) solid particles may be approximated as 1, that is, treating the particle-laden gas as a perfect blackbody radiator. Again this approximation, in the context of other heat transfer approximations, is acceptable in the preliminary design phase. The thickness of the combustor wall t_w and wall thermal conductivity k_w are design choices.

The film coefficient on the gas side h_g is empirically estimated for heat transfer in tubes and is related to Reynolds number and Prandtl number according to

$$\frac{h_g D_g}{k_g} = 0.026 \left(\frac{\rho_g v_g D_g}{\mu_g} \right)^{0.8} \left(\frac{\mu_g c_{pg}}{k_g} \right)^{0.4} \quad (12.73)$$

where D_g is the (local) diameter of the thrust chamber, k_g is the gas thermal conductivity, $\rho_g v_g$ is the average gas mass flow rate per unit area in the combustion chamber, μ_g is the gas coefficient of viscosity, and c_{pg} is the specific heat of the gas at constant pressure. The left-hand side of Equation 12.73 is the Nusselt number; the parentheses on the RHS are Reynolds and Prandtl numbers, respectively. Since the fluid density and properties μ_g , k_g , and c_{pg} are functions of gas temperature, the question of “which gas temperature” in the combustion chamber should we use to estimate these parameters arise. There is

no unique answer to this question; however, for engineering approximations an “average film” temperature T_f is used as an acceptable reference temperature, that is,

$$T_f \equiv \frac{T_g + T_{wg}}{2} \quad (12.74)$$

The coolant side film coefficient (for the coolant in the liquid state) is related to the Reynolds and Prandtl numbers on the coolant side following

$$\frac{h_c D_c}{k_c} = 0.023 \left(\frac{\rho_c v_c D_c}{\mu_c} \right)^{0.8} \left(\frac{\mu_c \bar{c}_c}{k_c} \right)^{0.33} \quad (12.75)$$

where \bar{c}_c is the coolant average specific heat and D_c is the coolant passage hydraulic diameter. We may express the film coefficient on the coolant side in terms of on coolant mass flux, $\rho_c v_c$, and specific heat:

$$\frac{h_c}{(\rho_c v_c) \bar{c}_c} = 0.023 \left(\frac{\rho_c v_c D_c}{\mu_c} \right)^{-0.2} \left(\frac{\mu_c \bar{c}_c}{k_c} \right)^{-0.67} \quad (12.76)$$

This expression clearly shows that for a given coolant Reynolds number and Prandtl number, the coolant film coefficient h_c increases with coolant mass flux and the coolant specific heat. We may thus tailor the cross section of the coolant passage in critical areas such as the nozzle throat to increase the local mass flux, $\rho_c v_c$. Also, we may choose a liquid fuel with high specific heat. For example, hydrogen has a very high specific heat compared with other rocket fuels and is thus a coolant of choice for regeneratively cooling rocket thrust chambers. Table 12.4 from Sutton and Biblarz (2001) show some physical properties of some liquid propellants.

In general, we have to integrate the steady-state heat transfer Equation 12.71 along the thrust chamber (axis). We may divide the thrust chamber into cylindrical sections of small axial length Δx where all the heat transfer parameters are assumed constant. By further assuming axisymmetric condition per cylindrical sections, we can march along the axis from the combustion chamber out toward the nozzle exit. The overall heat transfer to an axisymmetric thrust chamber is the integral of the heat flux along the wall, which is thus the sum of the segments according to

$$\dot{Q} = \int \dot{q} \, dA \cong \sum_{i=1}^N 2\pi r_i \dot{q}_i \Delta x_i \quad (12.76)$$

The overall heat transfer causes the temperature of the coolant to rise according to

$$\dot{Q} = \dot{m}_c \bar{c}_c (T_2 - T_1)_c \quad (12.77)$$

where T_1 represents the entrance temperature of the coolant into the jacket, and T_2 is the bulk coolant temperature as it (leaves the cooling jacket and) enters the injector. As a design choice, we may limit the bulk coolant exit temperature to below the boiling point, that is, $T_2 < T_{\text{boiling-point}}$. Table 12.5 lists the heat transfer characteristics of some liquid propellants (from Sutton and Biblarz, 2001). The pressure in the cooling jacket has

■ TABLE 12.4
Physical Properties of Some Liquid Propellants (from Sutton and Biblarz, 2001)

Propellant	Chemical formula	Liquid				Nitric acid ^c				Unsymmetrical dimethylhydrazine (UDMH)			
		fluorine	Hydrazine	hydrogen	Methane	Monomethylhydrazine	HNO ₃	Nitrogen tetroxide	Liquid oxygen	Rocket fuel RP-1	Hydrocarbon	(CH ₃) ₂ NNH ₂	Water
		F ₂	N ₂ H ₄	H ₂	CH ₄	CH ₃ NHNH ₂	HNO ₃	N ₂ O ₄	O ₂	Hydrocarbon	(CH ₃) ₂ NNH ₂	H ₂ O	
Molecular mass	38.0	32.05	2.016	16.03	16.03	46.072	63.016	92.016	32.00	CH _{1.97} ~175	60.10	18.02	
Melting or freezing point (K)	53.54	274.69	14.0	90.5	90.5	220.7	231.6	261.95	54.4	225	216	273.15	
Boiling point (K)	85.02	386.66	20.4	111.6	111.6	360.6	355.7	294.3	90.0	460–540	336	373.15	
Heat of vaporization (KJ/kg)	1.66.26 ^b	44.7 ^b	446	510 ^b	510 ^b	875	480	413 ^b	213	246 ^b	542 (298 K)	2253 ^b	
Specific heat (kcal/ kg-K)	0.368 (85 K)	0.736 (293 K)	1.75 ^b (20.4 K)	0.835 ^b	0.698 (293 K)	0.735 (393 K)	0.042 (311 K)	0.374 (290 K)	0.4 (65 K)	0.45 (298 K)	0.672 (298 K)	1.008 (273.15 K)	
Specific gravity ^c	0.357 (69.3 K)	0.758 (338 K)	—	0.424 (111.5 K)	0.8788 (293 K)	0.857 (311 K)	0.163 (373 K)	0.447 (360 K)	1.14 (90.4 K)	0.58 (422 K)	0.856 (340 K)	1.002 (373.15 K)	
	1.636 (66 K)	1.005 (293 K)	0.071 (20.4 K)	0.12 (111.6 K)	0.8788 (293 K)	0.855 (311 K)	1.549 (273.15 K)	1.447 (293 K)	1.23 (77.6 K)	0.807 (289 K)	0.784 (244 K)	1.00 (293.4 K)	
	1.440 (93 K)	0.952 (350 K)	0.076 (14 K)	0.12 (111.6 K)	0.857 (311 K)	0.855 (293 K)	1.476 (313.15 K)	1.38 (322 K)	0.87 (53.7 K)	0.75 (289 K)	4.4 (220 K)	0.284 (373.15 K)	
Viscosity (centipoise)	0.305 (77.6 K)	0.97 (298 K)	0.024 (14.3 K)	0.12 (111.6 K)	0.855 (293 K)	0.40 (344 K)	1.45 (273 K)	0.47 (293 K)	0.19 (366 K)	0.21 (366 K)	0.48 (300 K)	1.000 (277 K)	
	0.397 (70 K)	0.913 (330 K)	0.013 (20.4 K)	0.22 (90.5 K)	0.40 (344 K)	0.0073 (300 K)	0.0027 (273.15 K)	0.33 (315 K)	0.052 (90.4 K)	0.002 (344 K)	0.0384 (289 K)	0.00689 (312 K)	
Vapor pressure (MPa)	0.0087 (100 K)	0.0014 (293 K)	0.2026 (23 K)	0.033 (100 K)	0.0073 (300 K)	0.0073 (300 K)	0.0027 (273.15 K)	0.01014 (293 K)	0.0052 (88.7 K)	0.023 (422 K)	0.1093 (339 K)	0.03447 (345 K)	
	0.00012 (66.5 K)	0.016 (340 K)	0.87 (30 K)	0.101 (117 K)	0.638 (428 K)	0.638 (428 K)	0.605 (343 K)	0.2013 (328 K)	0.0023 (422 K)				

^aRed fuming nitric acid (RFNA) has 5–20% dissolved NO₂ with an average molecular weight of about 60, and a density and vapor pressure somewhat higher than those of pure nitric acid.

^bAt boiling point.

^cReference for specific gravity ratio: 10³ kg/m³ or 62.42 lbm/ft³.

■ **TABLE 12.5**
Heat Transfer Characteristics of Some Liquid Propellants

Liquid coolant	Boiling characteristics			Nucleate boiling characteristics				
	Pressure (MPa)	Boiling Temp. (K)	Critical Temp. (K)	Critical Pressure (MPa)	Temp. (K)	Pressure (MPa)	Velocity (m/sec)	q_{\max} (MW/m ²)
Hydrazine	0.101	387	652	14.7	322.2	4.13	10	22.1
	0.689	455					20	29.4
	3.45	540			405.6	4.13	10	14.2
	6.89	588					20	21.2
Kerosene	0.101	490	678	2.0	297.2	0.689	1	2.4
	0.689	603					8.5	6.4
	1.38	651			297.2	1.38	1	2.3
	1.38	651					8.5	6.2
Nitrogen tetroxide	0.101	294	431	10.1	288.9	4.13	20	12.4
	0.689	342			322.2			9.3
	4.13	394			366.7			6.2
Unsymmetrical dimethyl hydrazine	0.101	336	522	6.06	300	2.07	10	4.9
	1.01	400					20	7.2
	3.45	489			300	5.52	10	4.7

Source: Sutton and Biblarz 2001. Reproduced with permission from Wiley.

a strong influence on the boiling point temperature of the fuel. For example, hydrazine boils at 387 K for a pressure of 0.101 MPa (i.e., 1 atm), whereas it boils at 588 K (an increase of 201 K) if the pressure is raised to 6.89 MPa. The cooling jacket pressure is to be provided by a turbopump (or a pressure) feed system and the higher pressure ratio will then require multistage pumps and very heavy turbopump feed system.

Also note that the critical heat flux, that is, the maximum heat transfer rate per unit area, in the thrust chamber theoretically occurs at the throat where the flow passage area is at a minimum. Experimental evidence of the peak heat flux *near* the throat is well documented in the literature, for example, Witte and Harper (1962). To lower the wall temperature on the gas side, we have to increase the coolant side film coefficient h_c , which according to Equation 12.76 behaves as

$$h_c \propto (\rho_c v_c)^{0.8} / D_c^{0.2} \quad (12.78)$$

The design requirement on T_{wg} at the throat dictates the following characteristics on the coolant passage side:

- High mass flux $\rho_c v_c$ or since the liquid density is nearly constant, high coolant speed v_c
- Small diameter D_c cooling tubes.

The coolant speed at the throat may be as high as $\sim 15\text{--}20$ m/s. The hydraulic diameter of the cooling tubes near the throat scales in millimeters. The most effective throat cooling in regeneratively cooled thrust chambers combines these two effects. Therefore, the cooling jacket is composed of small-diameter tubes with a tapered cross-sectional area at the throat with relatively high coolant speed.

In very small liquid propellant thrust chambers, where either insufficient coolant flow is available or insufficient (throat) surface area is available for cooling, ablative materials are used. Also, in cases where the motor is pulsed as in vernier rockets, passive cooling technique, such as ablative cooling, is used. An ablative material directly transitions from the solid-to-gaseous phase while absorbing latent heat of vaporization in the process. Additionally, the emergence (and the flow) of the (ablative) gas on the surface acts as a cooling layer that protects the surface.

12.12.2 Cooling of Solid Propellant Thrust Chambers

Solid propellant rockets may use several (nonregenerative) methods to protect the thrust chamber walls (or motorcase) against the heat loads in the combustor. The purpose of an *inhibitor* is to inhibit grain burning where the designer wishes to protect the thrust chamber walls (or as a means of controlling thrust-time or vehicle dynamic behavior). The purpose of an insulating layer, that is, the one with low thermal conductivity, next to the wall is also to protect the wall from excessive heating. In addition to these two techniques, solid propellant grain designer may place a cooler burning grain in the outer shell next to the wall to protect the motorcase. However, this is an expensive manufacturing proposition seldom used. Since ablative materials have been extensively used for thermal protection with success during the Apollo era, and graphite has emerged as a viable high temperature material, designers use ablative materials and graphite as throat inserts (or for motorcase insulation) in solid propellant rockets today with confidence. The use of graphite offers the added advantage of erosion resistance (as compared with ablative materials that decompose), thus maintaining the throat (cross-sectional flow) area nearly constant as a function of burn time. Detailed engineering design considerations in solid rocket motors, including practical thermal management approaches are presented by Heister (1995), which is suggested for further reading.

EXAMPLE 12.12

A liquid propellant rocket combustor is regeneratively cooled and is characterized by

The gas static and stagnation temperatures are nearly equal, with $T_g \approx T_{tg} = 2750$ K

The coolant bulk temperature is 300 K

The wall thickness is $t_w = 2$ mm

The thermal conductivity of the wall is $k_w = 43$ W/m \cdot °C

The gas side film coefficient $h_g = 657$ W/m²K

The coolant side film coefficient $h_c = 26,000$ W/m²K
The emissivity of the hot gas is given by $\epsilon_g = 0.05$

Calculate

- the heat flux due to radiation in kW/m²
- the total heat flux in kW/m²
- the convection heat flux in kW/m²
- wall temperature on the gas side T_{wg} in K
- wall temperature on the coolant side T_{wc} in K

SOLUTION

The radiation heat flux is governed by

$$\begin{aligned}\dot{Q}_r &= \epsilon_g \sigma T_g^4 \\ &= 0.05(5.67 \times 10^{-8} \text{ W/m}^2 \text{ K}^4)(2750)^4 \text{ K}^4 \\ &\approx 1.621 \text{ kW/m}^2\end{aligned}$$

We will use Equation 12.72 for the total heat flux and approximate adiabatic wall temperature by the gas stagnation temperature, to get

$$\begin{aligned}\dot{q}_w &\approx \frac{T_{\text{tg}} - T_c + (\epsilon_g \sigma T_g^4 / h_g)}{(1/h_g) + (t_w/k_w) + (1/h_c)} \\ &= [2750 - 300 + 1.621(10^3)/657] / [(1/657) \\ &\quad + (0.002/43) + (1/26000)] \approx 1.678 \text{ MW/m}^2\end{aligned}$$

The heat flux due to convection is the difference between the total and radiative heat flux, i.e.,

$$\begin{aligned}\dot{q}_c &= \dot{q}_w - \dot{q}_r = (1.678 - 10^3 - 162.1) \text{ kW/m}^2 \\ &= 1.516 \text{ MW/m}^2\end{aligned}$$

The wall temperature on the gas side is calculated from Equation 12.69 to be

$$\dot{q}_c = h_g(T_{\text{aw}} - T_{\text{wg}}) \Rightarrow T_{\text{wg}} \approx 443 \text{ K}$$

The liquid-side wall temperature is

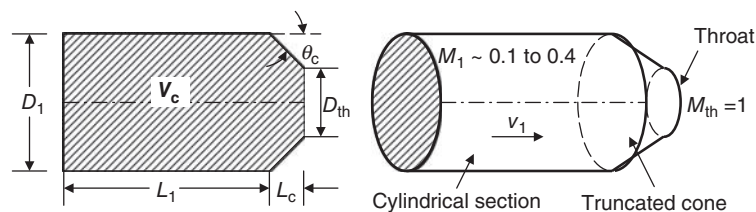
$$\dot{q}_w = h_c(T_{\text{wc}} - T_c) \Rightarrow T_{\text{wc}} \approx 364.5 \text{ K}$$

12.13 Combustor Volume and Shape

Chemical rocket combustion chambers are cylindrical in shape, characterized by a length L_1 , diameter D_1 , an area contraction ratio A_1/A_{th} , (toward the nozzle throat), and a contraction length L_c (or a contraction angle θ_c). Figure 12.32 shows a definition sketch of a combustor volume. The combustor volume V_c includes the convergent section to the throat.

Chamber diameter D_1 is primarily governed by the vehicle size or thrust magnitude. In the flight performance section, we desired a low cross-sectional area for the vehicle (through m_0/A), that is, our goal is to minimize D_1 , consistent with thrust production. The area contraction A_1/A_{th} sets the gas speed in the chamber. Remember that the throat is sonic and area ratio (A/A^*) establishes the upstream Mach number M_1 . The desire is toward large area ratio, yet limited by minimum A_1 . The contraction angle θ_c provides for a smooth flow at the throat with high discharge coefficient. The desire is to have a large angle consistent with high efficiency, which translates to about 30° or less (typically in the range of $20\text{--}30^\circ$). The chamber length L_1 is the minimum length needed for a complete combustion in liquid propellant rockets. Therefore, chamber length is directly

■ **FIGURE 12.32**
Definition sketch of a rocket combustion chamber geometry



■ **TABLE 12.6**
Combustor Characteristic Length L^*

Propellants	L^* (m), low	L^* (m), high
Liquid fluorine/hydrazine	0.61	0.71
Liquid fluorine/gaseous H_2	0.56	0.66
Liquid fluorine/liquid H_2	0.64	0.76
Nitric acid/hydrazine	0.76	0.89
N_2O_4 /hydrazine	0.60	0.89
Liquid O_2 /ammonia	0.76	1.02
Liquid O_2 /gaseous H_2	0.56	0.71
Liquid O_2 /liquid H_2	0.76	1.02
Liquid O_2 /RP-1	1.02	1.27
H_2O_2 /RP-1 (including catalyst)	1.52	1.78

Source: Huzel and Huang 1992.

proportional to the product of mean speed of the propellant in the combustor and the propellant *residence time*, that is,

$$L_1 \approx v_1 \cdot t_{\text{res}} \quad (12.79)$$

Residence time depends on the evaporation, mixing, and reaction timescales, which are a strong function of the propellant combination. Residence time is also a function of the injector plate design through the atomization scale. Therefore, chamber length is affected by the injector design and the propellant choice. Residence or stay time range between 1 and 40 ms for different propellants. It is customary to define a characteristic length scale L^* based on the combustor (total) volume that includes the convergent section to the throat area, namely,

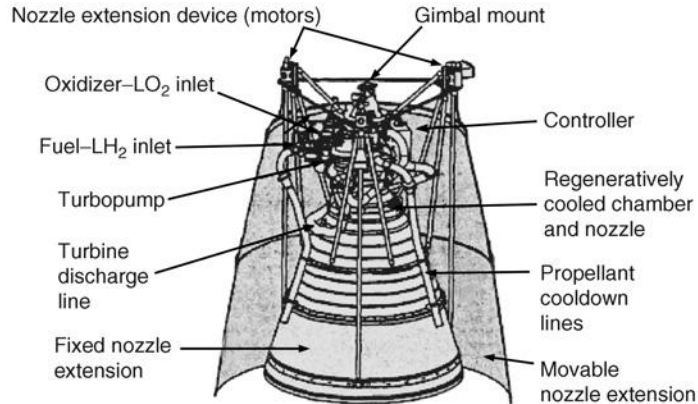
$$L^* \equiv \frac{V_c}{A_{\text{th}}} \quad (12.80)$$

Huzel and Huang (1992) present historical numbers for L^* for different propellants. As these numbers are not based on fundamental physics, they should be used for comparative purposes only. Table 12.6 shows the historical data from Huzel and Huang (1992).

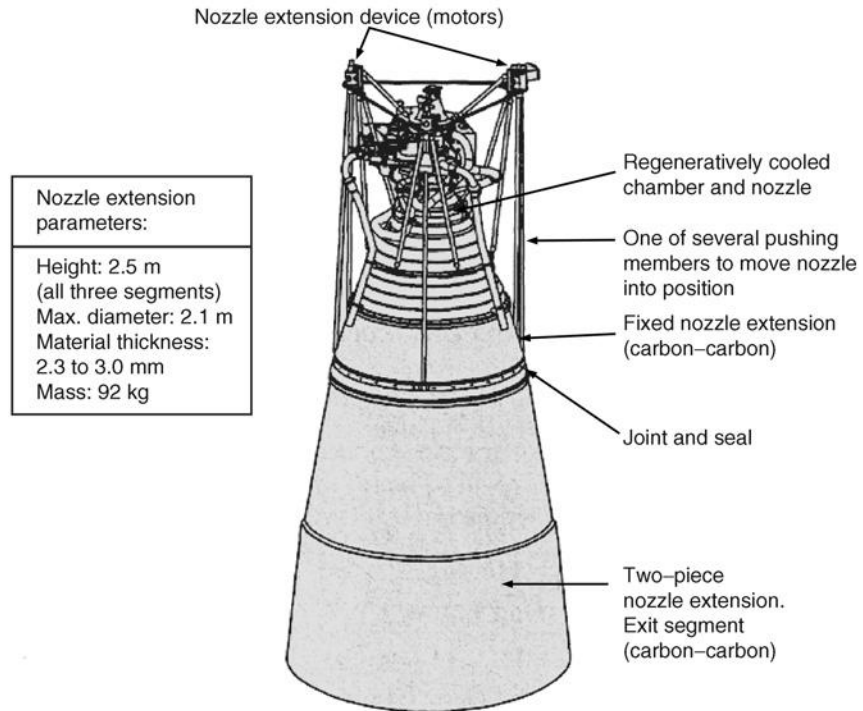
12.14 Rocket Nozzles

The aerodynamic principles of exhaust nozzles and their design considerations are presented in Chapter 6. The range of operation of the rocket nozzles, however, is vastly different than airbreathing engines. A rocket may operate in ambient conditions ranging from sea level to vacuum in space. Therefore, the nozzle pressure ratio (NPR) in a rocket may range from ~ 50 at sea level to infinity (assuming ambient pressure at orbit is zero) in space. Consequently, chemical rockets with such large pressure ratios require very large expansion area ratios, that is, $A_2/A_{\text{th}} \gg 1$, in order to maximize their thrust production. Area expansion ratios of 100 or more are designed for rocket nozzles for space

■ **FIGURE 12.33**
The RL-10B-2 rocket engine with extendable nozzle skirt. Source: Reproduced by permission of United Technologies Corporation, Pratt & Whitney



(a) Half section of nozzle extension in stowed position



(b) Nozzle extension in deployed position

applications. It is a challenge to design a variable-area rocket nozzle due to mechanical complexity and weight penalty. A successful example is shown in Figure 12.33 where the RL-10B-2 rocket engine uses a two-piece extendable nozzle skirt.

Possible rocket nozzle configurations are shown in Table 12.7 (from Sutton and Biblarz, 2001). The nozzles are divided into two categories, (1) the ones with and (2) the ones without a centerbody. The second category of exhaust nozzles, without a centerbody,

■ TABLE 12.7
 Rocket Nozzle Configurations and their Altitude Performance

	Cone (15° half angle)	Contoured or bell, full length	Contoured or bell shape, shortened	Plug or aerospike, full length	Plug or aerospike, truncated or cut off	Expansion- deflection
Shape						
Flow with underexpansion at altitude						
Flow with overexpansion (sea level)						
Mass flow distribution at exit or tip						

Source: Sutton and Biblarz 2001. Reproduced with permission from Wiley.

is the conventional conical, bell-shaped, and partial-bell configurations. All nozzles with an exit flow component that is not purely in the axial direction suffer the so-called (momentum) angularity loss. We have addressed and quantified this loss in Chapter 6. For example, the conical nozzle that offers a simple geometry for manufacturing; it introduces an angularity loss factor to the momentum thrust that is given by Equation 6.60 and is repeated here for convenience

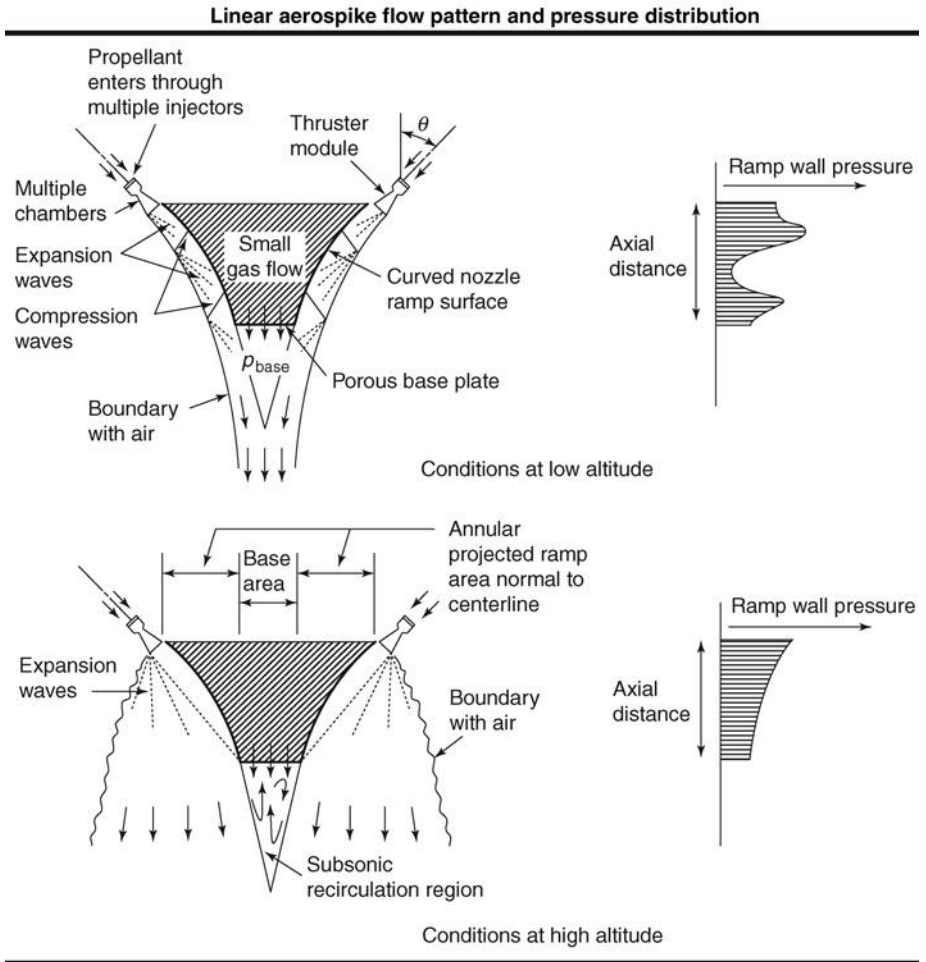
$$C_{A_{\text{Conical}}} = \frac{1 + \cos \alpha}{2}$$

where α is the half-cone angle. The two-dimensional nozzles with exit flow angle α , suffered the following momentum angularity loss, as derived in Chapter 6.

$$C_{A_{2D-CD}} = \frac{\sin \alpha}{\alpha}$$

A conical nozzle with 15° half-cone angle creates an angularity momentum loss of only 1.7%. However, the low-altitude, that is, overexpanded, operation of conical nozzles

■ **FIGURE 12.34**
Flow pattern and pressure distribution in a linear aerospike nozzle at low and high altitudes. Source: Sutton and Biblarz 2001. Reproduced with permission from Wiley



involves shock formations (inside the nozzle) that cause flow separation, as shown in Table 12.7. The bell-shaped nozzles, either full bell or partial bell, are contoured and are more complex to manufacture but, by virtue of smaller exit angularity, the nozzle momentum thrust efficiency can be better than a conical nozzle of the same area ratio, or length. We note that the sea-level performance of bell-shaped nozzles (as shown in Table 12.7) tends to create a full exit flow with oblique shocks hanging at the lip. The category of nozzles that use a centerbody, as in a plug (or aerospike) nozzle or the expansion-deflection nozzle, tends to produce better off-design performance, both at the low and high altitudes, than the ones without centerbody. We may note the flow distribution at the nozzle exit, in Table 12.7, shows a fully attached flow, that is, without any shock-induced separations. The off-design performance of aerospike and other nozzles with a centerbody is thus superior to conical and bell-shaped nozzles, but the system penalty is paid by the centerbody needs to be cooled. More details of the flow pattern for a linear (truncated) aerospike are shown in Figure 12.34. This concept is used in the XRS-2200 aerospike linear rocket engine that uses 20 individual thrust cells or modules and two concave

regeneratively (fuel) cooled (external) expansion ramps. The truncated base is porous where the gas generator flow (from the turbo pump system) fills the base and provides for a continuous and smooth expansion. The pressure distribution on the ramp shows the presence of (periodic) compression and expansion waves. The local compression (or shock) waves are followed by the reflected expansion waves from the jet boundary (or shear layer) and thus do not cause boundary layer separation. However, the presence of the compression waves on the ramp will cause an increase in the wall heat transfer; thus a more conservative fuel-cooling approach needs to be employed. The two-dimensional aspect of the linear aerospike offers better integration potential with a winged aircraft than the axisymmetric configuration. In addition, the action of (20) individual thrusters may be used for stability and control purposes of the aircraft.

The radius of curvature upstream and downstream of the nozzle throat, the initial and exit angles of the bell nozzles, and the angularity loss parameter of conical and bell-shaped nozzles are presented and compared in Figure 12.35 (adapted from Huzel and Huang, 1992). These curves that relate the geometry and performance of various nozzles may be used in preliminary design trade studies. The nozzle length comparisons in Figure 12.35 are suitable for weight estimation studies.

12.14.1 Multiphase Flow in Rocket Nozzles

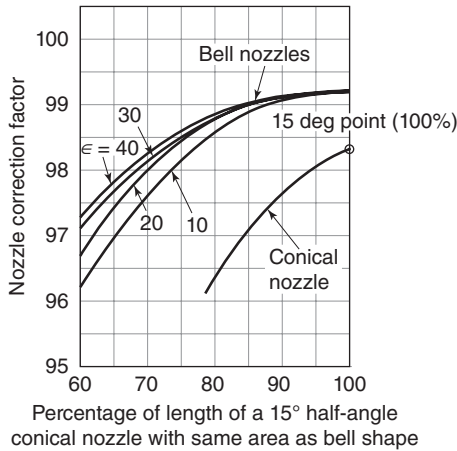
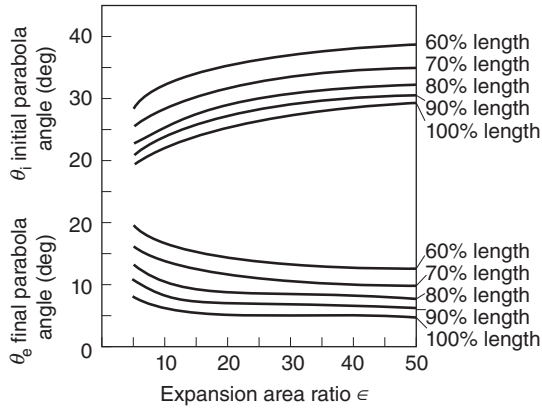
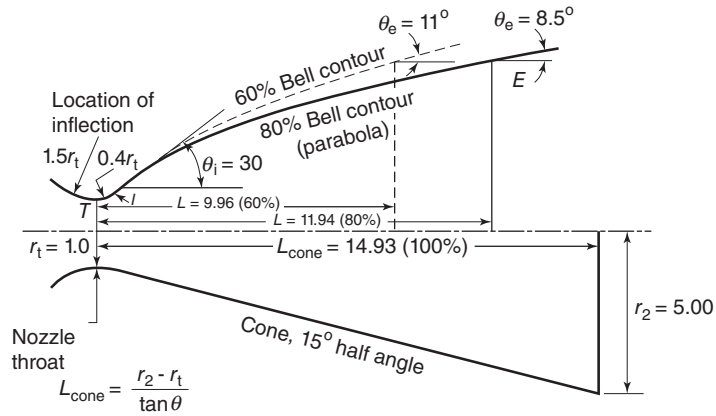
In our analysis so far, we have treated the nozzle fluid to be in the gaseous state. There are at least three sources for liquid or solid particle presence in a rocket nozzle flow. The first is the propellant itself, where solid particles are intentionally embedded or dispersed to increase the rocket performance through higher specific impulse. The second source is the combustion, which may lead to soot and particulate formation in the products of combustion. The third source is the appearance of liquid droplets, that is, condensation, in the exhaust stream due to static temperature drop in the gases. The very large area expansion ratios bring about very large temperature and pressure expansion ratios, which result in the condensation of a fraction of the exhaust stream. It is the impact of these solid or liquid fractions (present in the nozzle gases) on rocket performance that we address in this section.

The thermal and dynamic interaction of the two phases in a fluid, say solid and gas, pose complex fluid mechanics and heat transfer problems. However, in four limiting cases, we may arrive at closed-form solutions and shed light on the effects of multiphase flow on rocket performance.

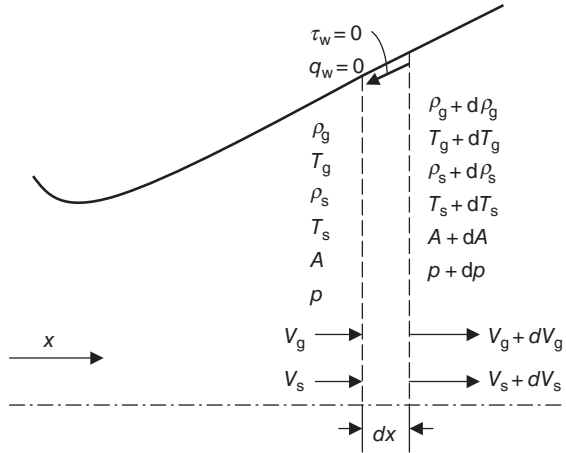
These four limiting cases are:

1. Solid particles reach the same temperature as the gas at the nozzle exit, the so-called thermal equilibrium case
2. Solid particles are fully accelerated and reach the same speed as the gas at the nozzle exit, that is, they reach momentum equilibrium
3. Solid particles maintain their temperatures, that is, the case of zero thermal interaction or heat transfer between the two phases
4. Solid particles are not accelerated by the gas and thus maintain their negligible momentum at the nozzle exit.

■ **FIGURE 12.35**
Conical, bell and partial bell nozzle design, and performance comparison. Source: Adapted from Huzel and Huang 1992



■ FIGURE 12.36
Definition sketch of a slab in a two-phase flow in a nozzle



Note that an underlying assumption in these four limiting cases is that the solid fraction present at the nozzle inlet remains unchanged, that is, *frozen*, in the nozzle and appear in whole at the nozzle exit. The four cases noted above address only the fate of these particles in heat and momentum transfer with the gas. To derive the fundamental equations of two-phase flow, we return to a *slab* concept where we apply the (one-dimensional) conservation principles to a slab of fluid. The fluid and flow parameters on the two sides of the slab are related to each other via a linear relationship using the Taylor series expansion of a continuous function. Figure 12.36 shows the definition sketch of a *slab* in a two-phase fluid flow with zero friction and heat transfer (i.e., reversible and adiabatic condition) at the wall.

By stipulating a constant mass flow rate for the gas and the solid phases in the fluid, we get

$$\dot{m}_g = \rho_g V_g A = (\rho_g + d\rho_g)(V_g + dV_g)(A + dA) \tag{12.81}$$

$$\dot{m}_s = \rho_s V_s A = (\rho_s + d\rho_s)(V_s + dV_s)(A + dA) \tag{12.82}$$

Note that the density of the solid is the mass of the solid contained in a unit volume of the gas–solid mixture and is not to be confused by the density of the solid itself. The gas density is the mass of the gas per unit volume of the mixture, as expected. By conserving the mass flow rate of solid and gas individually, through Equations 12.81 and 12.82, we conserve the collective mass flow rate in the nozzle. The conservation of momentum applied to the slab gives

$$\begin{aligned} & \underbrace{\dot{m}_g(V_g + dV_g) + \dot{m}_s(V_s + dV_s)}_{\text{“Momentum” out}} - \underbrace{(\dot{m}_g V_g - \dot{m}_s V_s)}_{\text{“Momentum” in}} \\ & = pA - \underbrace{(p + dp)(A + dA) - (p + dp/2)dA}_{\text{Net pressure force in the flow direction}} \end{aligned} \tag{12.83}$$

Note that the last term on the RHS of the Equation 12.83 is the pressure force exerted by the sidewall on the fluid (in the *x*-direction). Also the “momentum” in quotation mark

is used as the shorthand for “time rate of change of momentum.” Momentum equation simplifies to

$$\dot{m}_g dV_g + \dot{m}_s dV_s = -Adp \quad (12.84)$$

We may divide both sides of Equation 12.84 by the flow area A to get

$$\rho_g V_g dV_g + \rho_s V_s dV_s = -dp \quad (12.85)$$

The steady energy equation written for a (calorically) perfect gas and solid phases in a flow is the balance between the net flux of power (in fluid and solid phases) and the rate of the external energy exchange through heat transfer and mechanical shaft power, that is,

$$\underbrace{\left[\dot{m}_g [c_{pg}(T_g + dT_g) + (V_g + dV_g)^2/2] + \dot{m}_s [c_s(T_s + dT_s) + (V_s + dV_s)^2/2] \right]}_{\text{Fluid and solid power out}} - \underbrace{\left[\dot{m}_g [c_{pg}T_g + V_g^2/2] + \dot{m}_s [c_sT_s + V_s^2/2] \right]}_{\text{Fluid and solid power in}} = \underbrace{\dot{Q}_w - \dot{\phi}_s}_{\text{Net power exchange w/surrounding}} \equiv 0 \quad (12.86)$$

The energy equation simplifies to

$$\dot{m}_g (c_{pg} dT_g + V_g dV_g) + \dot{m}_s (c_s dT_s + V_s dV_s) = 0 \quad (12.87)$$

The fraction of solid particles in the mixture of two-phase flow may be given a symbol X defined as

$$X \equiv \frac{\dot{m}_s}{\dot{m}_g + \dot{m}_s} = \frac{\rho_s V_s}{\rho_g V_g + \rho_s V_s} \quad (12.88)$$

In terms of this parameter, that is, solid mass fraction X that constitutes a constant in our problem based on our frozen-phase assumption, we may write the energy equation as

$$(1 - X)(c_{pg} dT_g + V_g dV_g) + X(c_s dT_s + V_s dV_s) = 0 \quad (12.89)$$

We replace the solid particle density–velocity term $\rho_s V_s$ by

$$\rho_s V_s = \frac{X}{1 - X} \rho_g V_g$$

in the momentum equation to get

$$V_g dV_g = -\frac{dp}{\rho_g} - \frac{X}{1 - X} V_g dV_s \quad (12.90)$$

If we divide Equation 12.89 by $(1 - X)$ and substitute Equation 12.90 for $\rho_g dV_g$, we get

$$c_{pg}dT_g + \frac{X}{1-X}c_s dT_s + \frac{X}{1-X}(V_s - V_g)dV_s = \frac{dp}{\rho_g} \quad (12.91)$$

Case 1

The solid and gas are in thermal equilibrium, that is, $dT_s = dT_g = dT$, therefore, Equation 12.91 reduces to

$$\left(c_{pg} + \frac{X}{1-X}c_s\right)dT + \frac{X}{1-X}(V_s - V_g)dV_s = \frac{dp}{\rho_g} \quad (12.92)$$

We may consider two scenarios for the solid particles momentum behavior in the nozzle flow. First, if the solid particles are accelerated by the gas to achieve the same speed as the gas, we get $V_s = V_g$, therefore, Equation 12.92 simplifies to

$$\left(c_{pg} + \frac{X}{1-X}c_s\right)dT = \frac{dp}{\rho_g} \quad (12.93a)$$

This equation readily integrates for a perfect gas where $\rho_g = p/R_g T$ to the following form:

$$\frac{p_2}{p_c} = \left(\frac{T_2}{T_c}\right)^{\left(c_{pg} + \frac{X}{1-X}c_s\right)/R_g} \quad \text{or} \quad \frac{T_2}{T_c} = \left(\frac{p_2}{p_c}\right)^{R_g/\left(c_{pg} + \frac{X}{1-X}c_s\right)} \quad (12.93b)$$

Also Equation 12.89 for $V_s = V_g = V$ and $T_s = T_g = T$ gives

$$[(1 - X)c_{pg} + Xc_s]dT + VdV = 0 \quad (12.94)$$

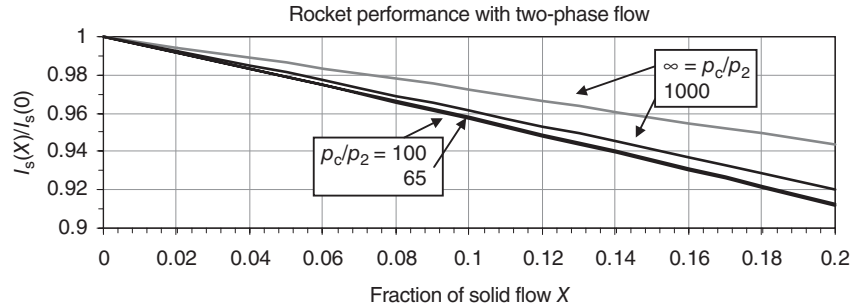
which may be integrated from the chamber condition (with $V_c \approx 0$) to the nozzle exit, V_2

$$V_2 = \sqrt{2[(1 - X)c_{pg} + Xc_s]T_c(1 - T_2/T_c)} \quad (12.95)$$

In terms of pressure ratio, nozzle exit velocity is

$$V_2 = \sqrt{2[(1 - X)c_{pg} + Xc_s]T_c \left[1 - \left(\frac{p_2}{p_c}\right)^{R_g/\left(c_{pg} + \frac{X}{1-X}c_s\right)}\right]} \quad (12.96)$$

■ **FIGURE 12.37**
The effect of solid particles on rocket performance
 (assuming $T_s = T_g$, $V_s = V_g$ and constant T_c)



Since solid particles have attained the same speed as the gas, the ratio of specific impulse with and without solid particulate flow is the ratio of the two exhaust speeds, namely,

$$\frac{I_s(X)}{I_s(0)} = \sqrt{(1 - X + Xc_s/c_{pg}) \left[\frac{1 - \left(\frac{p_2}{p_c}\right)^{R_g/(c_{pg} + \frac{X}{1-X}c_s)}}{1 - \left(\frac{p_2}{p_c}\right)^{R_g/c_{pg}}} \right]} \quad (12.97)$$

For a gas molecular weight of 20.1 kg/kmol, the ratio of specific heats $\gamma = 1.26$, and specific heat of the solid (aluminum) particles = 903 J/kg · K, we calculate and graph Equation 12.97 in Figure 12.37.

Figure 12.37 shows a drop in rocket performance with increasing fraction of the solid flow. The impact of cycle pressure ratio is small, as expected. The presence of solid particles in the propellant is, however, to enhance the burning rate and combustion temperature T_c , which was assumed constant in this calculation. The effect of higher burning rate and combustion temperature due to solids should, therefore, outweigh the penalty of the two-phase flow in the nozzle, as depicted in Figure 12.37.

The second scenario for the particle momentum/acceleration is to assume the solid particles are not accelerated by the gas, that is, $dV_s = 0$ while their temperature has reached that of the gas. The temperature–pressure relation remains the same as Equation 12.93b. However, the energy equation gives the variation of the gas speed with temperature drop of the mixture, that is,

$$[(1 - X)c_{pg} + Xc_s]dT + (1 - X)V_g dV_g = 0 \quad (12.98a)$$

The solution of the above equation is

$$V_{g2} = \sqrt{2 \left[c_{pg} + \frac{X}{1-X}c_s \right] T_c \left[1 - \left(\frac{p_2}{p_c}\right)^{R_g/(c_{pg} + \frac{X}{1-X}c_s)} \right]} \quad (12.98b)$$

The thrust of the two streams of gas and solid, one moving at speed V_{g2} and the second moving at speed V_s , is

$$F = \dot{m}_g V_{g2} + \dot{m}_s V_s + (p_2 - p_0)A_2 \quad (12.99)$$

Therefore, the stream-thrust-averaged speed at the nozzle exit (for a perfectly expanded nozzle) is

$$\bar{V}_2 = \frac{\dot{m}_g V_{g2} + \dot{m}_s V_s}{\dot{m}_g + \dot{m}_s} = (1 - X)V_{g2} + XV_{s2} \tag{12.100a}$$

Since the second term on the RHS of Equation 12.100a is the product of two small numbers (remember that the solid was assumed to be unaccelerated and X is the small solid fraction), therefore, the thrust-averaged exit velocity is

$$\bar{V}_2 \approx (1 - X)V_{g2} \tag{12.100b}$$

and the specific thrust is expressed in terms of the thrust-averaged exit velocity as

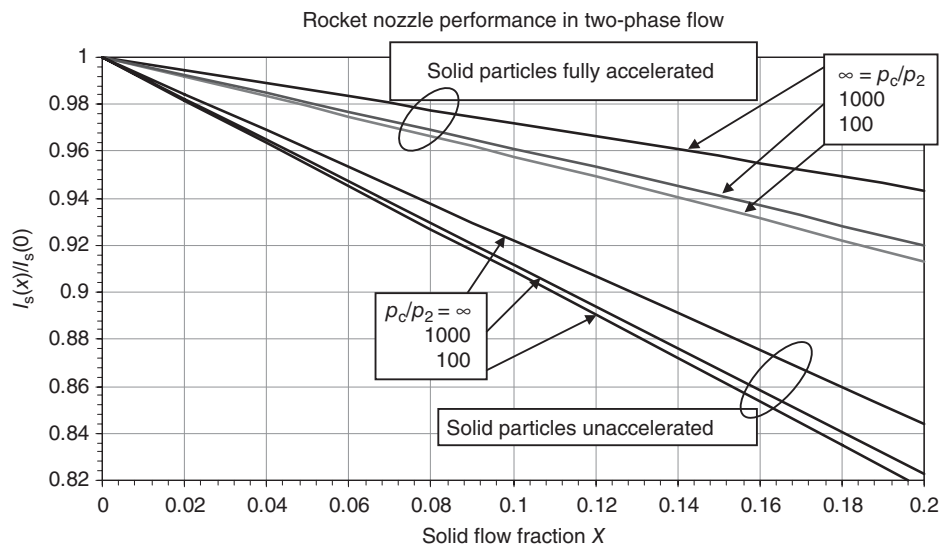
$$I_s = \bar{V}_2/g_0 \approx (1 - X)V_{g2}/g_0 \tag{12.101}$$

The ratio of specific impulse with/without solid particles that are in thermal equilibrium with the gas, but are not accelerated by the gas, is

$$\frac{I_s(X)}{I_s(0)} = (1 - X) \sqrt{\left(1 + \frac{X}{1 - X} \frac{c_s}{c_{pg}}\right) \left[\frac{1 - \left(\frac{p_2}{p_c}\right)^{R_g/(c_{pg} + \frac{X}{1-X}c_s)}}{1 - \left(\frac{p_2}{p_c}\right)^{R_g/c_{pg}}}\right]} \tag{12.102}$$

The graph of Equation 12.102 superimposed on the rocket performance chart of Figure 12.37 is shown in Figure 12.38. Note that the specific impulse is further degraded when the solid particles are not accelerated by the gas (i.e., the case of small particle drag).

■ FIGURE 12.38 Variation of specific impulse with solid flow fraction in the gaseous exhaust nozzle (assuming $T_s = T_g$, and constant T_c)



Case 2

The solid and gas are not in thermal equilibrium, that is, when the solid temperature remains constant, $dT_s = 0$ as a result of negligible heat transfer with the gas. In this case, Equation 12.91 reduces to

$$c_{pg}dT_g + \frac{X}{1-X}(V_s - V_g)dV_s = \frac{dp}{\rho_g} \quad (12.103)$$

In addition to $T_s = \text{constant}$, either for full acceleration where $V_s = V_g$ or when the solid particle remains unaccelerated, that is, when $dV_s = 0$, Equation 12.103 gives

$$c_{pg}dT_g = \frac{dp}{\rho_g} \quad \text{or} \quad \frac{T_2}{T_c} = \left(\frac{p_2}{p_c}\right)^{c_{pg}/R_g} \quad (12.104)$$

The energy Equation 12.89 reduces to the following form for $V_s = V_g$, that is, full acceleration case,

$$(1-X)c_{pg}dT_g + V_gdV_g = 0 \quad \text{or} \quad V_{g2} = \sqrt{2(1-X)c_{pg}T_c \left[1 - \left(\frac{p_2}{p_c}\right)^{c_{pg}/R_g}\right]} \quad (12.105)$$

Therefore, the specific impulse ratio is

$$\frac{I_s(X)}{I_s(0)} = \sqrt{1-X} \quad (12.106)$$

The energy Equation 12.89 for the case of constant V_s , that is, unaccelerated solid particles in the two-phase flow reduces to

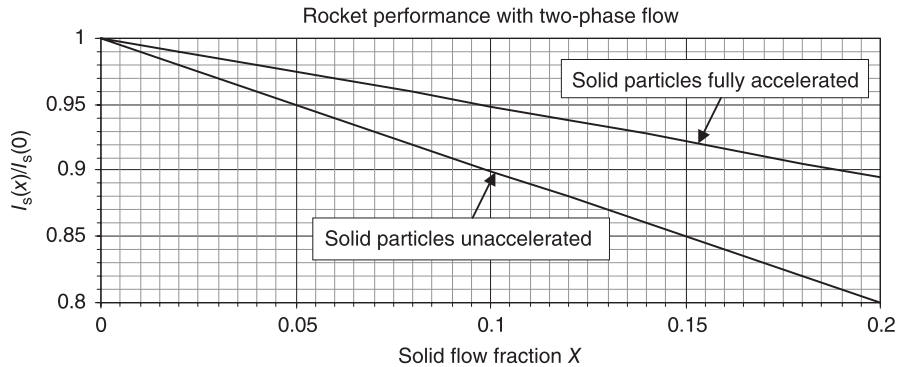
$$c_{pg}dT_g + V_gdV_g = 0 \quad (12.107)$$

which has a solution following

$$V_{g2} = \sqrt{2c_{pg}T_c \left[1 - \left(\frac{p_2}{p_c}\right)^{c_{pg}/R_g}\right]} \quad (12.108)$$

Although the gas phase seems to be unaffected by the presence of the solid particles, the thrust is affected since the two phases of the flow have different momentums at the nozzle

FIGURE 12.39
Rocket performance with solid particles in the exhaust stream
 (assumed $T_s =$
 constant)



exit. The thrust averaged exit velocity is

$$\bar{V}_2 = \frac{\dot{m}_g V_{g2} + \dot{m}_s V_s}{\dot{m}_g + \dot{m}_s} = (1 - X)V_{g2} + XV_s \quad (12.109)$$

which again for negligible solid velocity V_s in the exhaust plane, the ratio of the specific impulse will be

$$\frac{I_s(X)}{I_s(0)} \approx 1 - X \quad (12.110)$$

Now, let us graph Equations 12.106 and 12.110 in Figure 12.39. The specific impulse diminishes with solid flow fraction, as in the previous cases. The nozzle (or cycle) pressure ratio has no effect on specific impulse ratio if the solid particles are not heated to the gas temperature, that is, when they are not in thermal equilibrium with the gas. The unaccelerated solid particles cause a larger reduction in specific impulse than the fully accelerated ones. The reason is that the fully accelerated solid particles contribute to momentum, whereas the unaccelerated particles with negligible exit momentum cause a reduction in thrust. Therefore, the solid particle drag causes the particles to accelerate and contribute to thrust. The case studies in this section are useful only in establishing a range for the impact that multiphase flow makes on rocket performance. In reality, multiphase flow is more complex and accurate simulation needs computational approach.

EXAMPLE 12.13

A solid propellant rocket motor uses a composite propellant with 16% aluminum. The same propellant with 18% aluminum enhances the combustion temperature by 5.7%. Assuming in both cases that the solid particles are fully accelerated (i.e., $V_s = V_g$) in the nozzle and are in thermal

equilibrium with the gas (i.e., $T_s = T_g$), calculate the ratio of specific impulse in the two cases. Aluminum specific heat is $c_s = 903 \text{ J/kg} \cdot \text{K}$ and the specific heat at constant pressure for the gas is $c_{pg} = 2006 \text{ J/kg} \cdot \text{K}$.

SOLUTION

Equation 12.96, which is repeated here, is derived precisely for the two-phase flow case at hand, namely, $V_s = V_g$ and $T_s = T_g$. In the limit of large pressure ratio (p_c/p_2) and small variations in X , the pressure bracket will not contribute to the ratio of specific impulse significantly; hence, the exhaust speed may be approximated by

$$V_2 = \sqrt{2[(1-X)c_{pg} + Xc_s]T_c \left[1 - \left(\frac{p_2}{p_c} \right) R_g / \left(c_{pg} + \frac{X}{1-X} c_s \right) \right]}$$

$$\approx \sqrt{2[(1-X)c_{pg} + Xc_s]T_c}$$

Based on this approximation, we get the ratio of specific impulse in the two cases to be

$$\frac{I_s(X=0.18)}{I_s(X=0.16)} \approx \sqrt{\frac{[(1-0.18)2006 + 0.18(903)]}{[(1-0.16)2006 + 0.16(903)]}} (1.057)$$

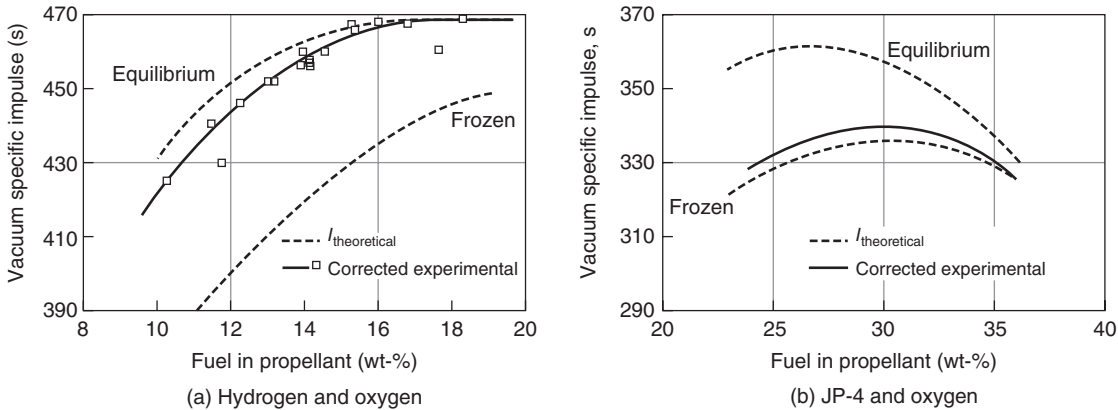
$$\approx 1.022$$

This gives an improvement of $\sim 2.2\%$ in specific impulse because the higher combustion temperature of 5.7% more than compensated for the loss due to higher levels of solid flow rate (i.e., 18% vs. 16%) in the nozzle. The higher specific impulse means higher effective exhaust velocity and thrust.

12.14.2 Flow Expansion in Rocket Nozzles

The products of combustion do not in reality stop reacting once they enter the nozzle. Actually, the conversion of thermal to kinetic energy in the nozzle causes a *cooling down effect* of the gases as well as the pressure drop, which impact the reaction rates of some of the products of combustion. Therefore, chemical reaction takes place continually from the combustor through the nozzle. Sometimes the nozzle reverses some of the reactions that took place in the combustor. For example, dissociation in the combustor, which is a direct result of high combustion temperature, may reverse, through the recombination process, to some extent in the nozzle when the temperature of the mixture drops. In addition, chemical reactions between the constituents are often considered to be in equilibrium. However, that too is an assumption that leads to major simplifications in the analysis and may be questioned. Whether chemical equilibrium is reached in a mixture depends on the chemical kinetics and the reaction rates in the mixture. In a rocket expansion process where the timescales are very short (in milliseconds) due to high (convection) speeds, chemical equilibrium may be questioned legitimately in such environments. Computational approaches to complex chemical reactions are fortunately available, for example, Gordon and McBride (1996), which may be used for an accurate analysis of chemically reacting mixtures of gases in different thermal environments.

However, the choice of *frozen (concentration of) species* of gas mixture in the nozzle (known as the *frozen chemistry* model) is often made for preliminary rocket design calculations. As evidenced from the computational results of Olson (1962), shown in Figure 12.40 (or Figure 12.22 from Sutton and Biblarz, 2001), the *corrected* specific impulses for hydrogen–oxygen and JP4–oxygen are both indicated to be higher with chemical reactions in the nozzle. Also, the corrected experimental results in Olson show that the equilibrium model gives an overestimation of the actual performance. This important result points to the frozen chemistry model as a *conservative* estimation of the rocket



■ FIGURE 12.40 Comparison of specific impulse between experimental and computational models. Source: Olson 1962. Reproduced with permission from AIAA

performance. A conservative estimation is precisely what is needed in a preliminary design stage.

12.14.3 Thrust Vectoring Nozzles

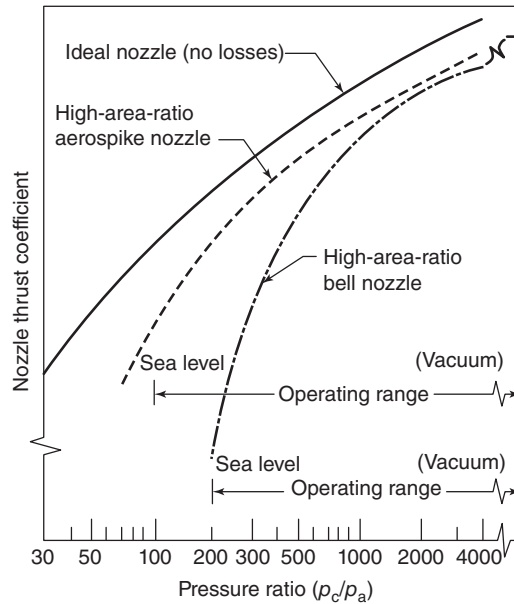
Conventional gimbals with hydraulic or electromechanical actuators may be used to swivel the entire rocket thrust chamber. The range of control authority using this approach is $\sim \pm 7^\circ$. Injection of a fluid, that is, either a propellant or an inert gas, in the nozzle, known as the secondary injection, causes an oblique shock formation and thus secondary injection thrust vector control (SITVC). The range of control authority using secondary injection is $\sim \pm 5^\circ$. The use of rocket clusters in the vehicle design opens the opportunity to differential operation of the opposite rockets in the cluster to achieve control. The use of jet deflectors, as in jet tabs or jet vanes, offers a limited-duration thrust vector control (in short burn-time rockets) since they are exposed to the hot exhaust gases. The control authority offered in this scheme is $\sim \pm 10^\circ$. Humble *et al.* (1995) present a practical engineering approach to rocket thrust vector control and is recommended for further reading.

A modern approach to (an old) nozzle design has produced linear aerospike configuration that uses many (e.g., 20) rocket engine cells. Figure 12.41 and 12.42 show aerospike nozzle thrust coefficient variation with nozzle pressure ratio; RS-2200 is a linear aerospike rocket engine on a test stand (from Stennis Space Center; courtesy of NASA). The linear aerospike nozzles have superior off-design performance over a bell nozzle as well as having a vector control capability.

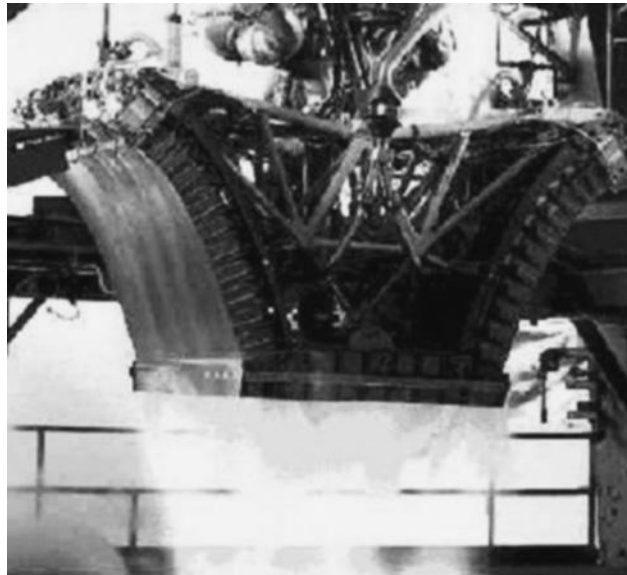
12.15 High-Speed Airbreathing Engines

Ramjets offer the highest (fuel) specific impulse at flight Mach numbers above ~ 4 , as depicted in Figure 12.1. However, they produce no static thrust. The analysis of conventional, that is, subsonic combustion, ramjets is the same as other airbreathing engines such as turbojets. A typical flow path in a conventional ramjet engine is shown in Figure 12.43.

■ **FIGURE 12.41**
Nozzle thrust coefficient for
aerospike. Source:
Huzel and Huang 1992.
Reproduced with
permission from AIAA

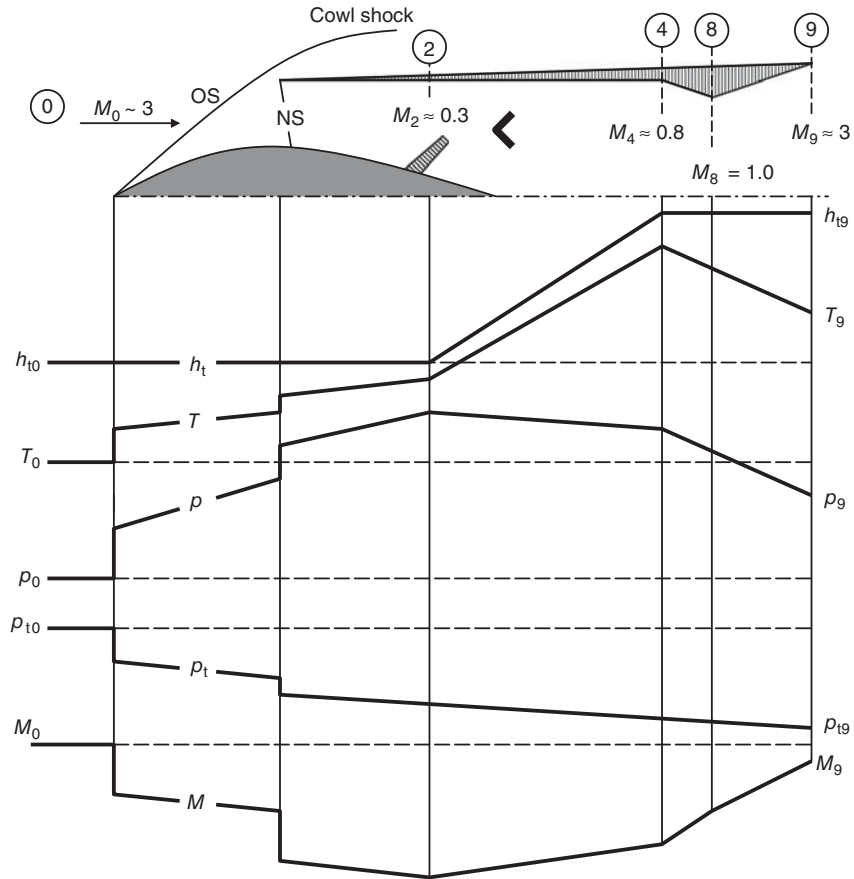


■ **FIGURE 12.42**
RS-2200 Linear
aerospike rocket
engine test. Source:
Courtesy of NASA

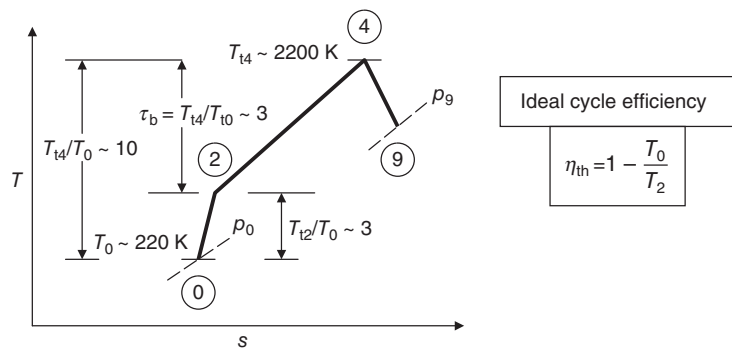


The T - s diagram of the ramjet cycle is shown in Figure 12.44. The ram compression in supersonic-hypersonic flow includes shock compression that causes an increase in gas temperature and a reduction in the Mach number. In the conventional ramjet, there is a normal shock in the inlet that transitions the flow into subsonic regime. The typical combustor Mach numbers in a conventional ramjet is ~ 0.2 – 0.3 . The combustor exit temperature T_{t4} may reach stoichiometric levels of ~ 2000 – 2500 K.

■ FIGURE 12.43
Flow parameter trends
in a typical
conventional ramjet



■ FIGURE 12.44
Conventional ramjet
cycle and its ideal
thermal efficiency



The equations that are used in the calculation of conventional ramjet performance are listed in Tables 12.8 and 12.9. The equations in these tables are listed sequentially; therefore, they are useful in computer-based calculations/simulation of ramjets. These are the same equations as in turbojets that we derived in Chapter 4, except we have set $\pi_c = 1$ to simulate a ramjet.

■ TABLE 12.8

Summary of Ramjet Equations in Terms of Dimensional Parameters (for calorically perfect gas)

Given

 M_0, p_0, T_0 (or altitude), γ , and R η_d or π_d π_d, η_d, Q_R , and T_{t4} or τ_λ π_n or η_n and p_9 Calculate $f, F_n/\dot{m}_0$, TSFC, I_s, η_{th}, η_p and η_o

$$T_{t0} = T_0 \left(1 + \frac{\gamma-1}{2} M_0^2 \right) = T_{t2} \quad \text{get flight total temperature}$$

$$p_{t0} = p_0 \left(1 + \frac{\gamma-1}{2} M_0^2 \right)^{\frac{\gamma}{\gamma-1}} \quad \text{get flight total pressure}$$

$$V_0 \equiv M_0 \cdot a_0 = M_0 \sqrt{\gamma R T_0} \quad \text{get flight velocity}$$

$$\frac{p_{t2}}{p_0} = \left\{ 1 + \eta_d \frac{\gamma-1}{2} M_0^2 \right\}^{\frac{\gamma}{\gamma-1}} \quad \text{or} \quad p_{t2} = \pi_d \cdot p_0 \quad \text{get total pressure at diffuser exit}$$

$$p_{t4} = p_{t2} \cdot \pi_b \quad \text{get burner exit total pressure}$$

$$f = \frac{h_{t4} - h_{t0}}{Q_R \eta_b - h_{t4}} = \frac{T_{t4} - T_{t0}}{Q_R \eta_b / c_p - T_{t4}} \quad \text{get fuel-to-air ratio in the burner}$$

$$\pi_n = \left\{ \left(\frac{p_{t4}}{p_9} \right)^{\frac{\gamma-1}{\gamma}} - \eta_n \left[\left(\frac{p_{t4}}{p_9} \right)^{\frac{\gamma-1}{\gamma}} - 1 \right] \right\}^{\frac{\gamma}{\gamma-1}} \quad \text{get nozzle total pressure ratio}$$

$$p_{t9} = p_{t4} \cdot \pi_n \quad \text{get total pressure at nozzle exit}$$

$$M_9 = \sqrt{\frac{2}{\gamma-1} \left[\left(\frac{p_{t9}}{p_9} \right)^{\frac{\gamma-1}{\gamma}} - 1 \right]} \quad \text{get nozzle exit Mach number}$$

$$T_9 = \frac{T_{t9}}{1 + \frac{\gamma-1}{2} M_9^2} \quad \text{get nozzle exit static temperature}$$

$$a_9 = \sqrt{\gamma R T_9} \quad \text{get speed of sound at nozzle exit}$$

$$V_9 = a_9 \cdot M_9 \quad \text{get nozzle exit velocity}$$

$$\frac{F_n}{\dot{m}_0} = (1+f) V_9 \left(1 + \frac{1}{\gamma M_9^2} \left(1 - \frac{p_0}{p_9} \right) \right) - V_0 \quad \text{get specific thrust}$$

$$\text{TSFC} \equiv \frac{\dot{m}_f}{F_n} = \frac{f}{F_n/\dot{m}_0} \quad \text{get thrust-specific fuel consumption}$$

$$I_s = 1/(g_0 \cdot \text{TSFC}) \quad \text{get (fuel)-specific impulse}$$

$$\eta_p = \frac{2 (F_n/\dot{m}_0) V_0}{(1+f) V_9^2 - V_0^2} \quad \text{get propulsive efficiency}$$

$$\eta_{th} = \frac{(1+f) V_9^2 - V_0^2}{2f Q_R \eta_b} \quad \text{get cycle thermal efficiency}$$

$$\eta_o = \eta_p \cdot \eta_{th} = \frac{(F_n/\dot{m}_0) V_0}{f Q_R \eta_b} = \frac{V_0 / Q_R \eta_b}{\text{TSFC}} \quad \text{get overall efficiency}$$

■ TABLE 12.9

Summary of Ramjet Equations in Terms of Nondimensional Parameters (for calorically perfect gas)

Given

M_0, p_0, T_0 (or altitude), γ , and R

η_d or π_d

π_d, η_d, Q_R , and T_{t4} or τ_λ

π_n or η_n , and p_9

Calculate $f, F_n/\dot{m}_0, \text{TSFC}, I_s, \eta_{th}, \eta_p$ and η_o

$$\tau_r = 1 + \frac{\gamma - 1}{2} M_0^2 \quad \text{get ram temperature ratio}$$

$$\pi_r = \left(1 + \frac{\gamma - 1}{2} M_0^2 \right)^{\frac{\gamma}{\gamma - 1}} = \tau_r^{\frac{\gamma}{\gamma - 1}} \quad \text{get ram pressure ratio}$$

$$\pi_d = \frac{p_{t2}}{p_{t0}} = \left(\frac{1 + \eta_d \frac{\gamma - 1}{2} M_0^2}{1 + \frac{\gamma - 1}{2} M_0^2} \right)^{\frac{\gamma}{\gamma - 1}} \quad \text{get inlet total pressure ratio}$$

$$f = \frac{\tau_\lambda - \tau_r}{\frac{Q_R \eta_b}{c_p T_0} - \tau_\lambda} \quad \text{get fuel-to-air ratio}$$

$$\pi_n = \left\{ \left(\pi_b \pi_d \pi_r \frac{p_0}{p_9} \right)^{\frac{\gamma - 1}{\gamma}} - \eta_n \left[\left(\pi_b \pi_d \pi_r \frac{p_0}{p_9} \right)^{\frac{\gamma - 1}{\gamma}} - 1 \right] \right\}^{\frac{\gamma}{\gamma - 1}} \quad \text{get nozzle pressure ratio}$$

$$M_9 = \sqrt{\frac{2}{\gamma - 1} \left[\left(\pi_n \pi_b \pi_d \pi_r \frac{p_0}{p_9} \right)^{\frac{\gamma - 1}{\gamma}} - 1 \right]} \quad \text{get nozzle exit Mach number}$$

$$V_9 = M_9 \sqrt{\frac{\gamma R T_0 \tau_\lambda}{1 + \frac{\gamma - 1}{2} M_9^2}} = a_0 M_9 \sqrt{\frac{\tau_\lambda}{1 + \frac{\gamma - 1}{2} M_9^2}} \quad \text{get exhaust velocity}$$

$$\frac{F_n}{\dot{m}_0} = (1 + f) V_9 \left(1 + \frac{1}{\gamma M_9^2} \left(1 - \frac{p_0}{p_9} \right) \right) - V_0 \quad \text{get specific thrust}$$

$$\text{TSFC} \equiv \frac{\dot{m}_f}{F_n} = \frac{f}{F_n/\dot{m}_0} \quad \text{get thrust-specific fuel consumption}$$

$$I_s = 1/(g_0 \cdot \text{TSFC}) \quad \text{get fuel specific impulse}$$

$$\eta_p = \frac{2 (F_n/\dot{m}_0) V_0}{(1 + f) V_9^2 - V_0^2} \quad \text{get propulsive efficiency } \eta_p$$

$$\eta_{th} = \frac{(1 + f) V_9^2 - V_0^2}{2fQ_R \eta_b} \quad \text{get thermal efficiency } \eta_{th}$$

$$\eta_o = \eta_p \cdot \eta_{th} = \frac{(F_n/\dot{m}_0) V_0}{fQ_R \eta_b} = \frac{V_0/Q_R \eta_b}{\text{TSFC}} \quad \text{get overall efficiency } \eta_o$$

EXAMPLE 12.13

A conventional ramjet has a maximum temperature $T_{t4} = 2000$ K that is set constant for all flight Mach numbers. The inlet total pressure recovery π_d varies with flight Mach number according to

$$\pi_d = 1 - 0.075(M_0 - 1)^{1.35}$$

Ramjet burns a hydrocarbon fuel with $Q_r = 42,800$ kJ/kg, and combustor efficiency and total pressure ratio are $\eta_b =$

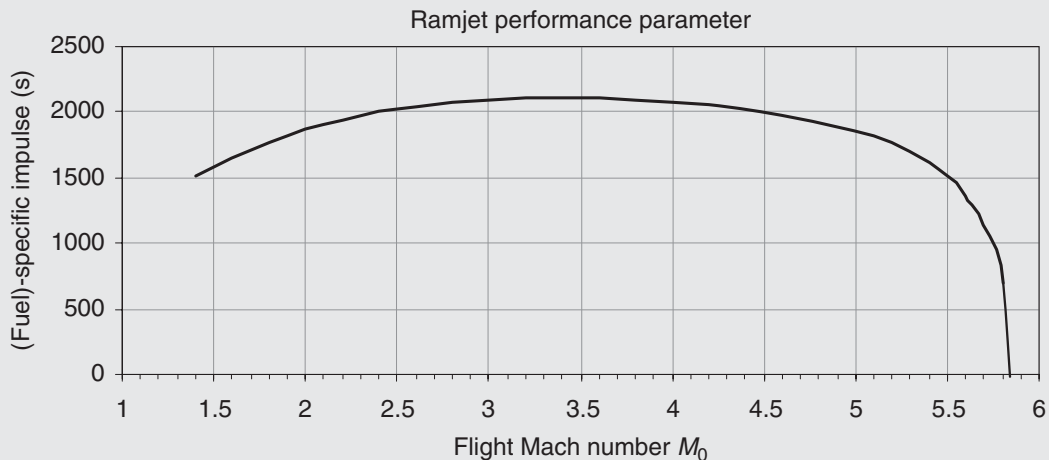
0.98 and $\pi_b = 0.95$, respectively. The nozzle is perfectly expanded and has a total pressure ratio $\pi_n = 0.95$. Assuming a calorically perfect gas with $\gamma = 1.4$ and $R = 287$ J/kg · K, use a spreadsheet to calculate the ramjet (fuel)-specific impulse, propulsive, thermal, and overall efficiencies over a range of flight Mach number starting at $M_0 = 1.4$ up until ramjet ceases to produce any thrust. Altitude pressure and temperature are 10 kPa and 240 K, respectively.

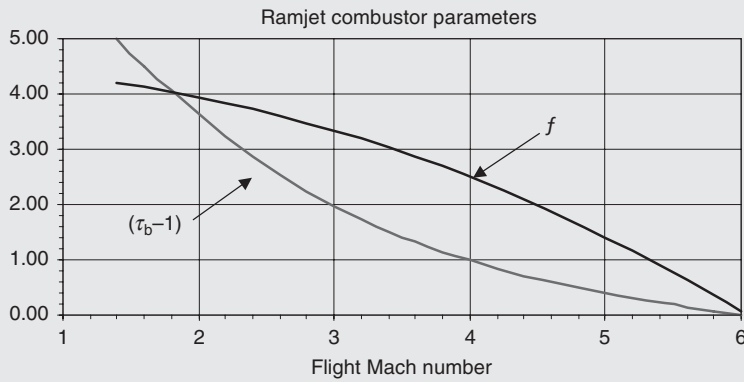
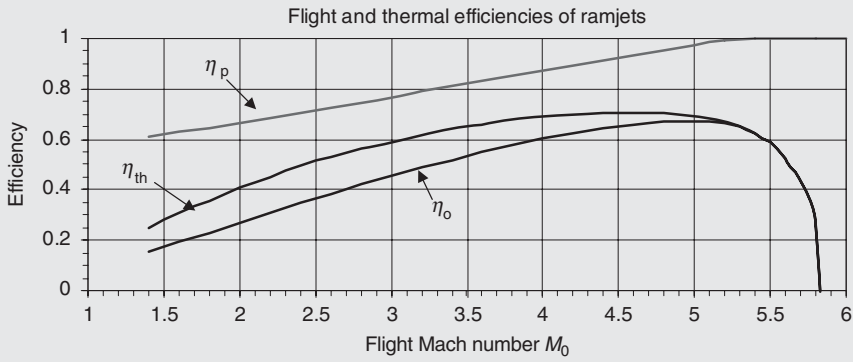
SOLUTION

A spreadsheet based on sequential equations in Table 12.8 is constructed. Graphs of specific impulse and efficiencies are generated in the spreadsheet program. There are many interesting trends/features that we observe. For example, specific impulse increases at first, peaks around Mach 3.5, then drops to zero as flight Mach number reaches ~ 5.7 . This behavior of specific impulse is first attributed to the improvements of cycle efficiency (as calculated and graphed) and later drops as flight stagnation temperature increase would allow less fuel to be burned in the combustor (to reach T_{\max} in the cycle). Consequently, thrust production capability diminishes with increase in flight speed. Eventually, we reach a point that flight stagnation tempera-

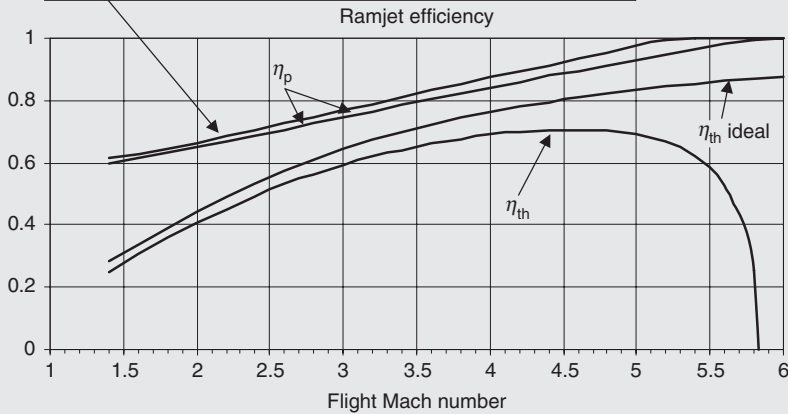
ture and cycle maximum temperature are equal. Before we reach this flight Mach number, exhaust speed V_9 falls to the levels of flight speed V_0 , which creates a zero net thrust. We may also calculate and graph burner total temperature ratio τ_b as well as fuel-to-air ratio in the burner to observe the effect of flight Mach number on these parameters. The fuel-to-air ratio and $(\tau_b - 1)$ both approach zero, as flight Mach number approaches 6.

The propulsive efficiency of a ramjet continually improves with flight Mach number, since nozzle exit velocity drops. We recall that $\eta_p \approx 2/(1 + V_9/V_0)$, which approaches 1 as V_9/V_0 approaches 1.

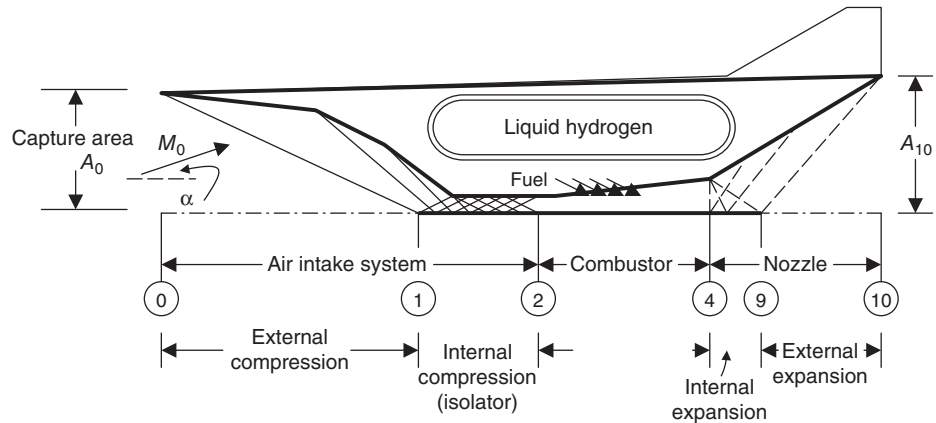




Note: The *approximate* expression for propulsive efficiency $\eta_p \approx 2/(1 + V_g/V_0)$ is very close to the full definition of η_p , since the nozzle was perfectly expanded (approximation is lower)



■ FIGURE 12.45
Typical arrangement
of a generic scramjet
engine on a hypersonic
aircraft



12.15.1 Supersonic Combustion Ramjet

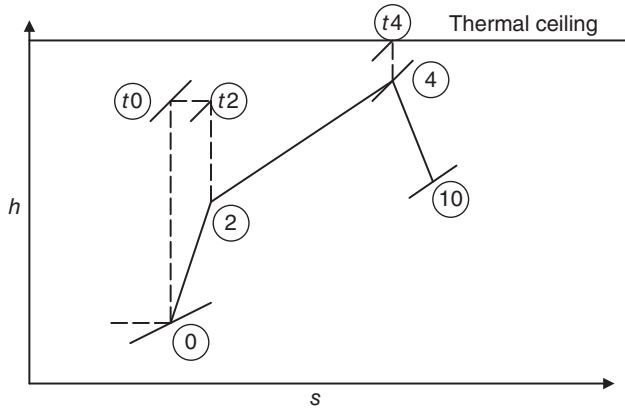
Conventional ramjets cannot produce static thrust. They require ram compression, that is, some forward flight speed, before these simple airbreathing engines (or “ducts with burners”) can produce thrust. It is seemingly ironic that the same engines (i.e., ramjets) *cease* to produce thrust at very high ram compressions! There are two aspects of ram compression that, at high speeds, are detrimental to thrust production. We studied them in Example 12.13. These are

1. the inlet total pressure recovery that exponentially deteriorates with flight Mach number, and
2. the rising gas temperature in the inlet that cuts back $(\Delta T_t)_{\text{burner}}$ to eventually zero.

The worst offender in total pressure recovery of supersonic/hypersonic inlets is the normal shock, which incidentally is also responsible for the rising gas temperatures in the burner. Therefore, if we could only do away with the normal shock in the inlet, we should be getting a super efficient ramjet. But the flow in a supersonic inlet without a (terminal) normal shock would still be supersonic! How do we burn fuel in an airstream that is moving supersonically? The short answer is *not very efficiently!* Despite the obvious challenges, supersonic combustion ramjets, or scramjets, are born out of necessity. Scramjets hold out the promise of being the most efficient airbreathing engines, that is, with the highest (fuel)-specific impulse, at flight Mach numbers above ~ 6 to suborbital Mach numbers; although the upper limit in scramjet operational Mach number is still unknown.

Scramjet engines, more than any other airbreathing engine, need to be integrated with the aircraft. The need for integration stems from a long forebody that is needed at hypersonic Mach numbers to efficiently compress the air. In addition, a long forebody offers the largest capture area possible for the engine, A_0 . Aft integration with the aircraft allows for a large area ratio nozzle suitable for high altitude hypersonic vehicles. Figure 12.45 shows a generic scramjet engine that is integrated in a hypersonic aircraft. The inlet achieves compression both externally and internally through oblique shocks. The series of oblique shock reflections inside the inlet create a shock train, known as the *isolator*. The flow that emerges from the isolator is supersonic, say Mach

■ FIGURE 12.46
Static and stagnation
states of gas in a
scramjet engine



3.0, as it enters the combustor. Achieving efficient combustion at supersonic speeds is a challenge.

Fuel injection, atomization, vaporization, mixing, and chemical reaction timescales should, by necessity, be short. If air is moving at Mach 3, where the speed of sound is ~ 333 m/s, it traverses 1 m in ~ 1 ms. This is just an indication of the convective or residence timescale in the combustor. Hydrogen offers these qualities. For example, hydrogen offers $\sim 1/10$ of the chemical reaction timescale of hydrocarbon fuels, as discussed in Chapter 7. Additionally, hydrogen is in a cryogenic state as a liquid; therefore, it offers aircraft and engine structure regenerative cooling opportunities.

By accepting high Mach numbers inside the scramjet engine, the static temperature of the gas will be lower throughout the engine and thus the burner is allowed to release heat in the combustor that is needed for propulsion. The $h-s$ diagram of the scramjet cycle is shown in Figure 12.46.

12.15.1.1 Inlet Analysis. Scramjet inlets are integrated with the aircraft forebody, involving several external and internal oblique shocks. In addition, the vehicle's angle of attack, α , impacts the inlet recovery through oblique shock waves' angles. For a given forebody shape, we may use shock-expansion theory (discussed in Chapter 2) to calculate the waves' orientations and the associated total pressure recovery. In the absence of the detailed aircraft forebody geometry, or in the preliminary phase, we may assume an inlet recovery or resort to standards such as AIA or MIL-E-5008B. We listed these in Chapter 6; they are repeated here for convenience.

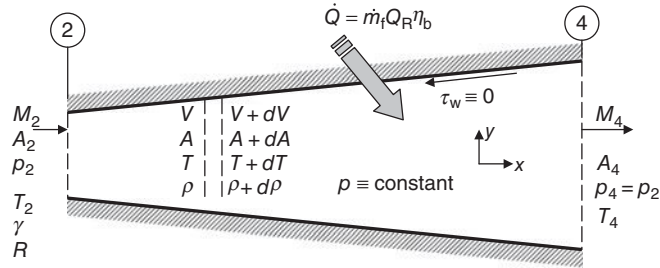
$$\pi_d = 1 - 0.1(M_0 - 1)^{1.5} \quad 1 < M_0 \quad \text{AIA-Standard} \quad (6.34)$$

$$\pi_d = 1 - 0.075(M_0 - 1)^{1.35} \quad 1 < M_0 < 5 \quad \text{MIL-E5008B} \quad (6.35)$$

$$\pi_d = 800/(M_0^4 + 935) \quad 5 < M_0 \quad \text{MIL - E - 5008 B} \quad (6.36)$$

12.15.1.2 Scramjet Combustor. Although the detailed design and analysis of supersonic combustion is beyond the scope of this book, we can still present global models and approaches that are amenable to closed-form solution. Supersonic branch of Rayleigh flow, that is, a frictionless, constant-area duct with heating is a possible (and the simplest) model for a scramjet combustor. The fact that the analysis was derived for a constant-area duct is not a major limitation, since we can divide a combustor with area

■ FIGURE 12.47
A frictionless,
constant-pressure
combustor



change into a series of combustors with constant areas. Rayleigh flow has been detailed in Chapter 2 and we will not review it here. However, we may offer to analyze a variable-area combustor that maintains a constant pressure. From a cycle analysis viewpoint, constant-pressure combustion is advantageous to cycle efficiency and thus we consider it here further. Figure 12.47 shows a frictionless duct with heat exchange, but with constant static pressure. We assume the gas is calorically perfect and the flow is steady and one-dimensional. The contribution of fuel mass flow rate to the gas in the duct is small; therefore, combustion is treated as heat transfer through the wall. The problem statement specifies the inlet condition and heat transfer rate (or fuel flow rate or fuel-to-air ratio) and assumes a constant static pressure in a duct with a variable area. The purpose of the analysis is to calculate the duct exit flow condition as well as the area A_4 .

We apply conservation principles to the slab of fluid, as shown. The continuity requires

$$\rho AV = (\rho + d\rho)(V + dV)(A + dA) \Rightarrow \frac{dV}{V} + \frac{d\rho}{\rho} + \frac{dA}{A} = 0 \quad (12.111)$$

The balance of x -momentum gives

$$\dot{m}(V + dV) - \dot{m}V = pA - p(A + dA) + pdA \equiv 0 \Rightarrow dV = 0 \quad (12.112)$$

Equation 12.112 signifies a constant-velocity flow, that is,

$$V_4 = V_2 \quad (12.113)$$

Therefore, the continuity Equation 12.111 demands $\rho A = \text{constant}$, or area is inversely proportional to density.

The energy balance written for the duct gives

$$h_{t4} - h_{t2} = \frac{\dot{Q}}{\dot{m}} = q = fQ_R\eta_b \quad (12.114a)$$

Since with constant velocity, the kinetic energy (per unit mass) remains constant, then

$$h_{T4} - h_{T2} = h_4 - h_2 \quad (12.114b)$$

$$T_4 = T_2 + q/c_p = T_2 + fQ_R\eta_b/c_p \quad (12.115)$$

The RHS of Equation 12.115 is known (as an input to the problem), which then establishes the exit static temperature T_4 . Since static pressure is constant, we can calculate the exit density ρ_4 . Also, the area ratio follows the inverse of the density ratio, that is,

$$A_4 = A_2(\rho_2/\rho_4) \quad (12.116)$$

which establishes the exit flow area. The exit static temperature calculates the exit speed of sound and Mach number (since $V = \text{constant}$).

We may calculate a critical heat flux q^* (or critical fuel-to-air ratio f^*) that will choke the duct at its exit. Equation 12.115 is written as

$$\frac{T_4}{T_2} = 1 + \frac{q}{c_p T_2} \quad (12.117)$$

Also, Mach number ratio M_4/M_2 is related to the ratio of speeds of sound following

$$\frac{M_4}{M_2} = \frac{V_4 a_2}{V_2 a_4} = \frac{a_2}{a_4} = \sqrt{\frac{T_2}{T_4}} = \frac{1}{\sqrt{1 + \frac{q}{c_p T_2}}} \quad (12.118)$$

For a choked exit, $M_4 = 1$; therefore, the critical heat flux q^* in terms of duct inlet flow conditions is expressed as

$$\frac{q^*}{c_p T_2} = M_2^2 - 1 \quad (12.118\text{-a})$$

In terms of fuel-to-air ratio, we may express q^* as $f^* QR \eta_b$ to get

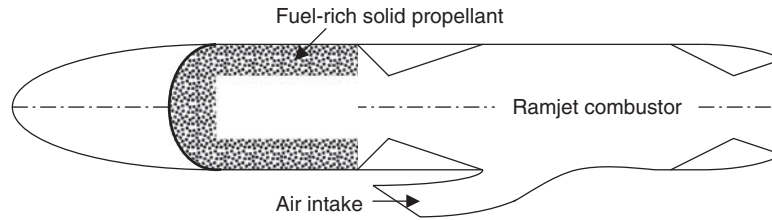
$$f^* \approx \frac{c_p T_2}{QR \eta_b} (M_2^2 - 1) \quad (12.118\text{-b})$$

With calculated exit Mach number, we may arrive at the total pressure at the exit, following

$$p_{t4} = p_2 \left(1 + \frac{\gamma - 1}{2} M_4^2 \right)^{\frac{\gamma}{\gamma - 1}}$$

An input to this analysis is the burner efficiency η_b . However, combustion efficiency in supersonic streams is not as well established or understood as the conventional low-speed burners. Mixing efficiency in supersonic shear layers, without chemical reaction, forms the foundation of scramjet combustion efficiency. A supersonic stream mixes with a lower speed stream (in our case the fuel) along a shear layer by vortex formations and supersonic wave interactions. These interactions require space along the shear layer or flow direction. Consequently, burner efficiency is a function of the combustor length and continually grows with distance along the scramjet combustor. Burrows and Kurkov (1973) may be consulted for some data and analysis related to supersonic combustion of hydrogen in vitiated air. Heiser *et al.* (1994) should be consulted for detailed discussion of hypersonic airbreathing propulsion.

■ **FIGURE 12.48**
Schematic drawing of a
gas generator
ram-rocket



12.15.1.3 Scramjet Nozzle. We have discussed hypersonic nozzles, to some extent, in Chapter 6. The large area ratios needed for high-speed, high-altitude flight prompted the use of aircraft aft-underbody as the expansion ramp for the scramjet nozzle (shown in Figure 12.45). For perfect expansion, we may approximate the area ratio requirements, A_{10}/A_9 , by one-dimensional gas dynamic equations. Severe overexpansion at lower altitudes causes a shock to appear on the aft underbody of the vehicle. The complicating factors in the analysis of hypersonic airbreathing nozzles are similar to those in the rocket nozzles, that is, continuing chemical reaction in the nozzle, flow separation, cooling, and flow unsteadiness, among others. Simple nozzle design based on the method of characteristics is a classical approach that students in gas dynamics learn. However, developing robust, high-fidelity computational fluid dynamics codes for direct numerical simulation of viscous reacting flows is the most powerful tool that researchers and industry are undertaking.

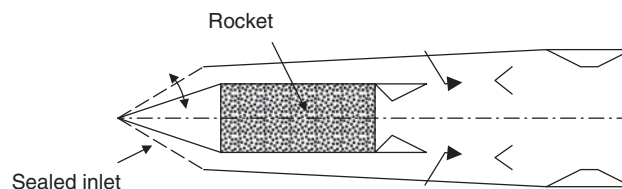
12.16 Rocket-Based Airbreathing Propulsion

Integrating rockets with ramjets has long been the solution of overcoming ramjets lack of takeoff capability. A ram-rocket may be a configuration similar to the one shown in Figure 12.48.

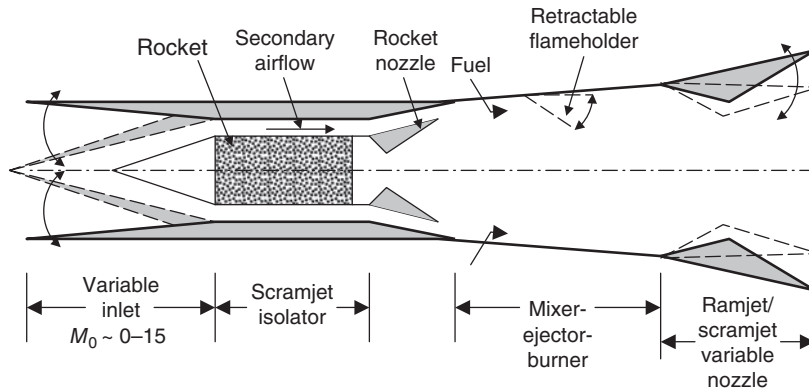
A fuel-rich solid propellant rocket provides the takeoff thrust. The air intake is sealed off until forward speed of the aircraft can produce the needed ram compression for the ramjet combustor. The rocket motor serves as the gas generator for the ramjet, that is, combustion gases from the fuel-rich solid propellant in the rocket motor mix with the air and the mixture is combusted in the ramjet burner to produce thrust. Variations of this scheme, such as a separate ramjet fuel, may be used in a gas generator ram-rocket. There is no new theory to be presented here, at least at the preliminary level, that is, we have developed the tools in this book to analyze both components individually and combined. A ram-rocket configuration where the rocket provides takeoff thrust is shown in Figure 12.49. The ramjet fuel is injected in the airstream for sustained thrust, as shown.

A rocket placed in a duct will draw air in, and through mixing of the cold and hot gases will enhance its thrust level. This is the ejector principle. Since the propulsion is

■ **FIGURE 12.49**
A ram-rocket
configuration



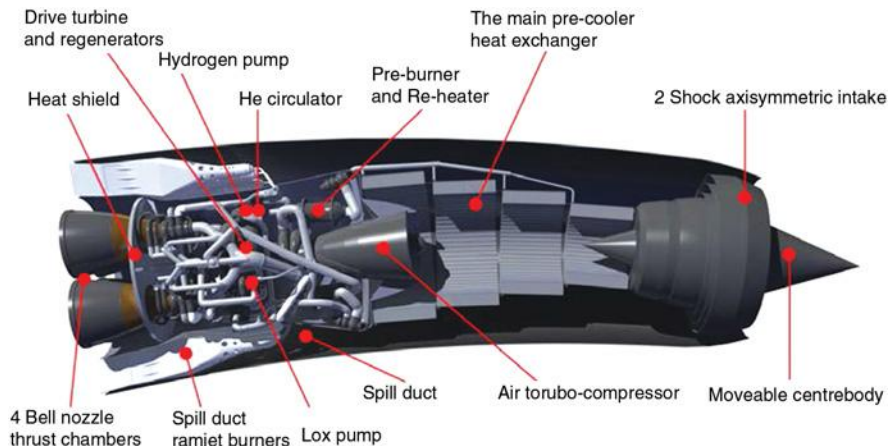
■ **FIGURE 12.50**
Concept in RBCC propulsion

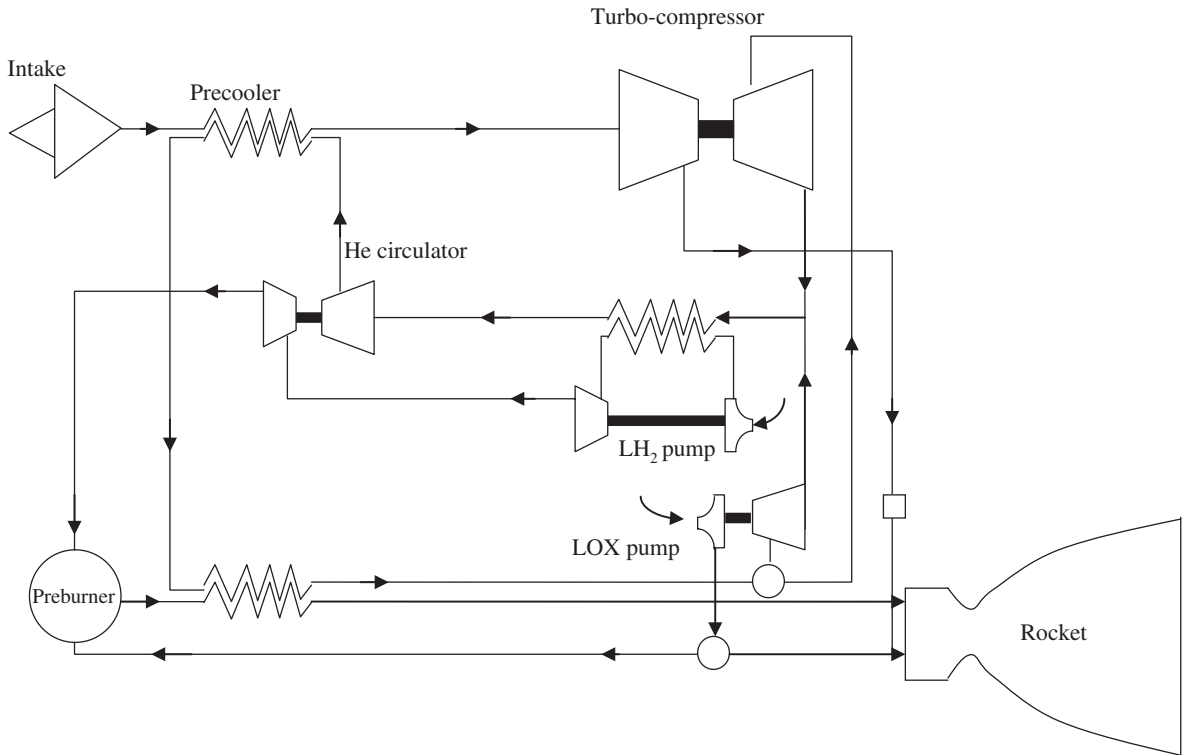


based on the rocket and is assisted by the secondary air mixing through an inlet, this may be referred to as an *airbreathing rocket*. The duct that follows the rocket nozzle is then the mixer-ejector, which may also serve as the combustor of a conventional or scramjet engine for combined operation. Now, we have clearly passed the airbreathing and rocket propulsion boundaries and entered into the realm of rocket-based combined cycle (RBCC) propulsion (Figure 12.50). This is the future of hypersonic flight from takeoff to orbit. It clearly is an exciting time to be a propulsion engineer/researcher.

Since the writing of the first edition, we have witnessed continued development and a breakthrough in airbreathing rocket technology called the *Synergetic Air Breathing Rocket Engine* (SABRE) from Reaction Engines Ltd in the United Kingdom. The breakthrough is in the thermal management of air in the airbreathing phase of the combined cycle that starts at takeoff and ends in Mach 5.5+ and at 26 km altitude. A closed-loop cryogenic helium cycle pre-cools the inlet air to -150°C in an ultra-light weight heat exchanger. Liquid hydrogen is used as the fuel in the common-core rocket thrust chamber, which is preheated prior to injection in the rocket combustion chamber by cooling down the helium in the helium cycle. The pure rocket mode uses onboard liquid oxygen in a LOX/LH₂ rocket thrust chamber. Figure 12.51 shows the components in the SABRE (courtesy of Reaction Engines Ltd). Figure 12.52 shows the closed-loop heat exchanger systems in the SABRE, which include helium for the air intake system and hydrogen for

■ **FIGURE 12.51**
Critical components in SABRE engine.
Source: Reproduced by permission of Reaction Engines





■ FIGURE 12.52 SABRE cycle showing its closed-loop helium pre-cooler and the engine system

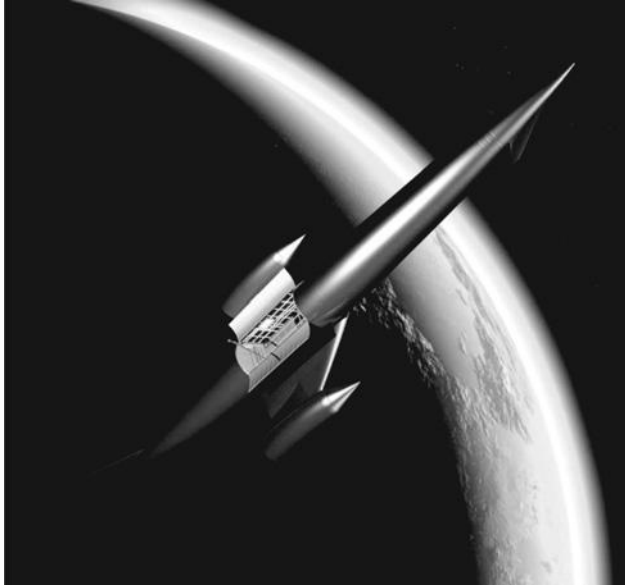
the helium loop heat exchanger and injection into the rocket thrust chamber. Figure 12.53 shows the aerospace plane *SKYLON* that is designed around the SABRE for reusable SSTO capability. A comparison of propulsion concepts for SSTO reusable launchers is presented by Varvill and Bond (2003); the is recommended for further reading.

12.17 Summary

High-speed atmospheric flight benefits from airbreathing engines. The oxygen in the air is the *infinite* oxidizer supply that combustion engines need. Requirements of takeoff to earth orbit necessitate a multitude of airbreathing and rocket engines. Interestingly, the synergy of the rocket-based combined cycle brings about the promise of efficient, cost-effective, and reliable hypersonic propulsion.

The unifying figure of merit in propulsion systems is the specific impulse. Although chemical rockets' specific impulse is in the range of 200–500 s and airbreathing engines an order of magnitude higher (i.e., ~2000–10,000 s), chemical rockets produce thrust that is independent of vehicle speed. The airbreathing engines lose their advantage as flight Mach number increases into the hypersonic regime. Chemical rockets come with liquid, solid, hybrid, or gaseous propellants. Liquid propellant rockets require a feed system that involves either a pressurized feed system with regulators and valves or a gas generator-driven turbopump system. These systems are heavy and add to the propulsion mass fraction and cost. In contrast, solid propellant rockets have no feed system and are, thus, lightweight

■ **FIGURE 12.53**
SKYLON in orbit with
payload bay doors
open. Source:
Reproduced by
permission of Reaction
Engines



and low cost and often are used as strap-on boosters. The controllability of thrust in a liquid rocket engine is the clear advantage that it has over a solid rocket motor. The ejector concept of airbreathing rockets combined with the dual-mode subsonic/supersonic combustion ramjets or the airbreathing rockets in a dual-cycle engine with precooler (as in SABRE) form the foundation of promising new engines that is suitable for continuous operation from runway to orbit.

Finally, a new era in commercial launch services, space explorations and space tourism has begun. The success of private sector in this new arena will promise the 21st century to bring space closer to mankind.

References

1. Burrows, M.C. and Kurkov, A.P., "Analytical and Experimental Study of Supersonic Combustion of Hydrogen in a Vitiated Airstream," NASA TMX-2628, 1973.
2. "Explosive Hazard Classification Procedures," DOD, U.S. Army Technical Bulletin TB 700-2, 1989.
3. Forward, R.L., "Advanced Propulsion Systems," Chapter 11 in *Space Propulsion Analysis and Design*, Humble, R.W., Henry, G.N., and Larson, W.J. (Eds), McGraw-Hill, New York, 1995.
4. Gordon, S. and McBride, S., "Computer Program for Calculation of Complex Chemical Equilibrium Compositions and Applications, Vol. 1: Analysis," October 1994 and "Vol. 2: User Manual and Program Description," NASA Reference Publication 1311, 1996.
5. Heiser, H.W., Pratt, D.T., Daley, D.H., and Mehta, U.B., *Hypersonic Airbreathing Propulsion*, AIAA, Inc., Reston, VA, 1994.
6. Heister, S., "Solid Rocket Motors," Chapter 6 in *Space Propulsion Analysis and Design*, Humble, R.W., Henry, G.N., and Larson, W.J. (Eds), McGraw-Hill, New York, 1995.
7. Hill, P.G. and Peterson, C.R., *Mechanics and Thermodynamics of Propulsion*, 2nd edition, Addison-Wesley, Reading, MA, 1992.
8. Humble, R.W., Lewis, D., Bissell, W., and Sakheim, R., "Liquid Rocket Propulsion Systems," Chapter 5 in *Space Propulsion Analysis and Design*, Humble, R.W., Henry, G.N., and Larson, W.J. (Eds), McGraw-Hill, New York, 1995.
9. Huzel, D.K. and Huang, D.H., *Design of Liquid Propellant Rocket Engines*, AIAA, Inc., Reston, VA, 1992.
10. Isakowitz, S.J., *International Reference Guide to Space Launch Systems*, 2nd edition, AIAA, Inc., Reston, VA, 1995.

11. Kerrebrock, J.L., *Gas Turbines and Aircraft Engines*, 2nd edition, MIT Press, Cambridge, MA, 1992.
12. Kubota, N., "Survey of Rocket Propellants and their Combustion Characteristics," Chapter 1 in *Fundamentals of Solid Propellant Combustion*, Kuo, K.K. and Summerfield, M. (Eds), AIAA Progress Series in Astronautics and Aeronautics, Vol. 90, AIAA Inc., Reston, VA, 1984.
13. NASA SP-8089, "Liquid Rocket Engine Injectors," March 1976.
14. NASASP-8120, "Liquid Rocket Engine Nozzles," July 1976.
15. Olson, W.T., "Recombination and Condensation Processes in High Area Ratio Nozzles," *Journal of American Rocket Society*, Vol. 32, No. 5, May 1962, pp. 672–680.
16. Price, E.W., "Experimental Observations of Combustion Instability," Chapter 13 in *Fundamentals of Solid Propellant Combustion*, Kuo, K.K. and Summerfield, M. (Eds), AIAA Progress Series in Astronautics and Aeronautics, Vol. 90, AIAA Inc., Reston, VA, 1984.
17. Razdan, M.K. and Kuo, K.K., "Erosive Burning of Solid Propellants," Chapter 10, in *Fundamentals of Solid Propellant Combustion*. Kuo, K.K. and Summerfield, M. (Eds), AIAA Progress Series in Astronautics and Aeronautics, Vol. 90, AIAA Inc., Reston, VA, 1984.
18. Sutton, G.P. and Biblarz, O., *Rocket Propulsion Elements*, 7th edition, John Wiley & Sons, Inc., New York, 2001.
19. Witte, A.B. and Harper, E.Y., "Experimental Investigation and Empirical Correlation of Local Heat Transfer Rates in Rocket-Engine Thrust Chambers," Technical Report Number 32-244 Jet Propulsion Laboratory, California Institute of Technology, Pasadena, CA, March 1962.
20. Reaction Engines Ltd website: www.reactionengines.co.uk (last accessed 7 December 2013)
21. SpaceX Corporation website is www.spacex.com (last accessed 7 December 2013)
22. Varvill, R. and Bond, A., "A Comparison of Propulsion Concepts for SSTO Reusable Launchers," *Journal of British Interplanetary Society*, Vol. 56, pp. 108–117, 2003.

Problems

12.1 A booster stage produces 190,400 lb of thrust at sea level and 242,500 lb at altitude. Assuming the momentum thrust remains nearly constant with altitude, estimate the nozzle exit diameter D_2 for the booster.

12.2 RD-170 is a Russian launch vehicle booster. It has a nozzle throat diameter of 235.5 mm and exit diameter of 1430 mm. Propellant flow rate is 2393 kg/s and the nozzle exit static pressure is 7300 Pa. RD-170 develops a vacuum-specific impulse of 337 s. Calculate

- (a) nozzle area ratio, A_2/A_{th}
- (b) effective exhaust speed c in m/s
- (c) vacuum thrust in MN
- (d) pressure thrust in vacuum in kN

12.3 A rocket engine has a propellant mass flow rate of 1000 kg/s and an effective exhaust speed of $c = 3500$ m/s. Calculate

- (a) rocket thrust F in kN
- (b) specific impulse I_s in seconds

12.4 A rocket engine has a chamber pressure of $p_c = 1000$ psia and the throat area is $A_{th} = 1.5$ ft². Assuming that the nozzle is perfectly expanded with the gas ratio of specific heats $\gamma = 1.2$ and the ambient pressure of $p_0 = 14.7$ psia, calculate

- (a) optimum thrust coefficient $C_{F,opt}$
- (b) thrust F in lbf

- (c) nozzle exit Mach number M_2
- (d) nozzle area expansion ratio A_2/A_{th}

12.5 Consider a fuel-rich combustion of the hydrocarbon fuel known as RP-1 and oxygen in a liquid propellant rocket according to



Calculate

- (a) number of moles of oxygen n_{O_2}
- (b) the mixture ratio r , i.e., the oxidizer-to-fuel ratio
- (c) the molecular weight of the mixture of gases in the products of combustion

12.6 The average specific impulse of a chemical rocket is 360 s. The rocket is in a zero gravity vacuum flight. Calculate and graph vehicle terminal speed ΔV for the propellant fraction ζ , that ranges between 0.80 and 0.95.

12.7 A rocket is vertically launched and operates for 60 s and has a mass ratio of 0.05. The (mean) rocket-specific impulse is 375 s. Assuming the average gravitational acceleration over the burn period is 9.70 m/s², calculate the terminal velocity of the rocket with and without gravitational effects. Neglect the effect of aerodynamic drag in both cases.

12.8 A rocket has a mass ratio of $MR = 0.10$ and a mean specific impulse of 365 s. The flight trajectory is described by a constant dynamic pressure of $q_0 = 50$ kPa. The mean

drag coefficient is approximated to be 0.25, the vehicle initial mass is $m_0 = 100,000$ kg, and the vehicle (maximum) frontal cross-sectional area A_f is 5 m^2 . For a burn time of 100 s, calculate the rocket terminal speed while neglecting gravitational effect.

12.9 In comparing the flight performance of a single-stage with a two-stage rocket, let us consider the two rockets have the same initial mass m_0 , the same payload mass m_L , and the same overall structural mass m_s . The structural mass fraction ϵ , which is defined as the ratio of stage structural mass to the initial stage mass, is also assumed to be the same for the single-stage rocket and each of the two stages of the two-stage rocket. For the effective exhaust speed of 3500 m/s be constant for the single-stage and each stage of the two-stage rocket, calculate the terminal velocity for the two rockets in zero gravity and vacuum flight, for

$$\begin{aligned} m_0 &= 100,000 \text{ kg} \\ m_L &= 500 \text{ kg} \\ m_s &= 10,000 \text{ kg} \\ \epsilon_{\text{single-stage}} &= 0.1 \\ \epsilon_{\text{stage-1}} &= \epsilon_{\text{stage-2}} = 0.1 \end{aligned}$$

12.10 A liquid propellant rocket uses a hydrocarbon fuel and oxygen as propellant. The heat of reaction for the combustion is $Q_R = 18.7 \text{ MJ/kg}$. The specific impulse is 335 s and the flight speed is 2500 m/s. Neglecting the propellant kinetic power at the injector plate, calculate

- (a) effective exhaust speed c in m/s
- (b) propulsive efficiency η_p
- (c) overall efficiency η_o

12.11 An injector plate uses an unlike impingement design. The fuel and oxidizer orifice discharge coefficients are $C_{df} = 0.80$ and $C_{do} = 0.75$. The static pressure drop across the injector plate for both oxidizer and fuel jets is the same, $\Delta p_f = \Delta p_o = 180 \text{ kPa}$. The fuel and oxidizer densities are $\rho_f = 325 \text{ kg/m}^3$ and $\rho_o = 1200 \text{ kg/m}^3$ and the oxidizer-fuel mass ratio is $r = 3.0$. Calculate

- (a) oxidizer-to-fuel orifice area ratio A_o/A_f
- (b) oxidizer and fuel jet velocities v_o and v_f

12.12 A solid rocket motor has a design chamber pressure of 10 MPa, an end-burning grain with $n = 0.4$ and $r = 3$ cm/s at the design chamber pressure and design grain temperature of 15°C . The temperature sensitivity of the burning rate is $\sigma_p = 0.002/^\circ\text{C}$, and chamber pressure sensitivity to initial grain temperature is $\sigma_K = 0.005/^\circ\text{C}$. The nominal effective burn time for the rocket is 120 s, i.e., at design conditions. Calculate

- (a) the new chamber pressure and burning rate when the initial grain temperature is 75°C
- (b) the corresponding reduction in burn time Δt_b in seconds

12.13 Extract the erosive burning parameter k from the data of Figure 12.30 for the two solid propellants shown.

12.14 A regeneratively cooled rocket thrust chamber has its maximum heat flux of 15 MW/m^2 near its throat. The hot gas stagnation temperature is 3000 K and the local gas Mach number is assumed to be ~ 1.0 . The gas mean molecular weight is $MW = 23 \text{ kg/kmol}$ and the ratio of specific heats is $\gamma = 1.24$.

Calculate

- (a) gas static temperature T_g in K
- (b) gas speed near the throat in m/s
- (c) gas-side film coefficient h_g for $T_{wg} \sim 1000 \text{ K}$

12.15 A rocket combustion chamber is designed for a chamber pressure of $p_c = 50 \text{ MPa}$. The combustion gas has a ratio of specific heats $\gamma = 1.25$. If this rocket is to operate between sea level and 200,000 ft altitude, calculate the range of area ratios in the nozzle that will lead to perfect expansion at all altitudes. Assume isentropic flow in the nozzle.

12.16 The propellant flow rate in a chemical nozzle is 10,000 kg/s, the nozzle exhaust speed is 2200 m/s, and the nozzle exit pressure is $p_2 = 0.01 \text{ atm}$. Assuming the nozzle exit diameter is $D_2 = 2 \text{ m}$, calculate

- (a) the pressure thrust (in MN) at sea level
- (b) the effective exhaust speed c (in m/s) at sea level

12.17 A solid propellant rocket motor uses a composite propellant with 16% aluminum. The same propellant with 18% aluminum enhances the combustion temperature by 5.7%. Assuming in both cases that the solid particles are fully accelerated (i.e., $V_s = V_g$) in the nozzle but the solid temperature remains constant (i.e., $T_s = \text{constant}$), calculate the ratio of specific impulse in the two cases. Aluminum specific heat is $c_s = 903 \text{ J/kg} \cdot \text{K}$, and the specific heat at constant pressure for the gas is $c_{pg} = 2006 \text{ J/kg} \cdot \text{K}$.

12.18 The coefficient of linear thermal expansion for a solid propellant grain is $1.5 \times 10^{-4}/^\circ\text{C}$. Calculate the change of length ΔL for a 1 m long propellant grain that experiences a temperature change from -30°C to $+70^\circ\text{C}$.

12.19 A ramjet has a maximum temperature $T_{t4} = 2500 \text{ K}$. The inlet total pressure recovery π_d varies with flight Mach number according to

$$\pi_d = 1 - 0.075 (M_0 - 1)^{1.35}$$

The ramjet burns hydrogen fuel with $Q_R = 120,000 \text{ kJ/kg}$ and combustor efficiency and total pressure ratio are $\eta_b = 0.99$ and $\pi_b = 0.95$, respectively. The nozzle is perfectly expanded and has a total pressure ratio $\pi_n = 0.90$. Assuming a calorically perfect gas with $\gamma = 1.4$ and $R = 287 \text{ J/kg} \cdot \text{K}$, use a spreadsheet to calculate the ramjet (fuel)-specific impulse, propulsive, thermal, and overall efficiencies over a range of flight Mach number starting at $M_0 = 3$ up until ramjet ceases to produce any thrust. Altitude pressure and temperature are 15 kPa and 250 K, respectively.

12.20 Consider a scramjet in a Mach 6 flight. The fuel for this engine is hydrogen with $Q_R = 120,000$ kJ/kg. The inlet uses multiple oblique shocks with a total pressure recovery following MIL-E-5008B standards for $M_0 > 5$, i.e.,

$$\pi_d = 800 / (M_0^4 + 935)$$

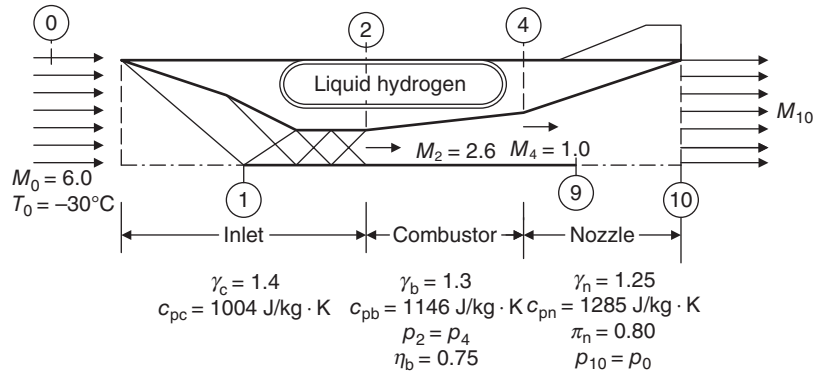
The combustor entrance Mach number is $M_2 = 2.6$. Use frictionless, constant-pressure heating, i.e., $C_f = 0$ and $p_4 = p_2$, to simulate the combustor with combustor exit Mach number $M_4 = 1.0$. All component parameters and gas constants are shown in the schematic drawing below.

Calculate

- (a) Inlet static temperature ratio T_2/T_0
- (b) combustor exit temperature T_4 in K

- (c) combustor static pressure ratio p_4/p_2
- (d) fuel-to-air ratio f
- (e) nozzle exit Mach number M_{10}
- (f) nondimensional ram drag $D_{ram}/\rho_0 A_1$ (note that $A_0 = A_1$)
- (g) nondimensional gross thrust $F_g/\rho_0 A_1$
- (h) fuel-specific impulse I_s in seconds
- (i) combustor area ratio A_4/A_2
- (j) nozzle area ratio A_{10}/A_4
- (k) thermal efficiency
- (l) propulsive efficiency

■ FIGURE P12.20



APPENDIX A

U.S. Standard Atmosphere

U.S. Standard Atmosphere U.S. Units

In this table **alt** is altitude in thousands of feet.
sigma is density divided by sea-level density.
delta is pressure divided by sea-level pressure.
theta is temperature divided by sea-level temperature.
temp is temperature in degrees Rankine.
press is pressure in pounds per square foot.
dens is density in slugs per cubic foot.
a is the speed of sound in feet per second.
visc is viscosity in 10^{-6} slugs per foot-second.
k.visc is kinematic viscosity in 10^{-6} square feet per second.
ratio is speed of sound divided by kinematic viscosity times 10^6 .
Sea-level density = 0.0023769 slugs per cubic foot
Sea-level temperature = 518.7 degree Rankine
Sea-level pressure = 2116.2 pounds per square foot

alt	sigma	delta	theta	temp	press	dens	a	visc	k.visc	ratio
-1	1.0296	1.0367	1.0069	522.2	2193.8	0.0024472	1120.3	0.376	1.54E-4	7.30
0	1.0000	1.0000	1.0000	518.7	2116.2	0.0023769	1116.5	0.374	1.57E-4	7.10
1	0.9711	0.9644	0.9931	515.1	2040.9	0.0023081	1112.6	0.372	1.61E-4	6.91
2	0.9428	0.9298	0.9863	511.5	1967.7	0.0022409	1108.7	0.370	1.65E-4	6.72
3	0.9151	0.8963	0.9794	508.0	1896.7	0.0021752	1104.9	0.368	1.69E-4	6.54
4	0.8881	0.8637	0.9725	504.4	1827.7	0.0021109	1101.0	0.366	1.73E-4	6.36
5	0.8617	0.8321	0.9656	500.8	1760.9	0.0020482	1097.1	0.364	1.78E-4	6.18
6	0.8359	0.8014	0.9588	497.3	1696.0	0.0019869	1093.2	0.362	1.82E-4	6.01
7	0.8107	0.7717	0.9519	493.7	1633.1	0.0019270	1089.3	0.360	1.87E-4	5.84
8	0.7861	0.7429	0.9450	490.2	1572.1	0.0018685	1085.3	0.358	1.91E-4	5.67
9	0.7621	0.7149	0.9381	486.6	1512.9	0.0018113	1081.4	0.355	1.96E-4	5.51
10	0.7386	0.6878	0.9313	483.0	1455.6	0.0017555	1077.4	0.353	2.01E-4	5.35
11	0.7157	0.6616	0.9244	479.5	1400.1	0.0017011	1073.4	0.351	2.07E-4	5.20
12	0.6933	0.6362	0.9175	475.9	1346.2	0.0016480	1069.4	0.349	2.12E-4	5.05
13	0.6715	0.6115	0.9107	472.3	1294.1	0.0015961	1065.4	0.347	2.18E-4	4.90
14	0.6502	0.5877	0.9038	468.8	1243.6	0.0015455	1061.4	0.345	2.23E-4	4.75
15	0.6295	0.5646	0.8969	465.2	1194.8	0.0014962	1057.4	0.343	2.29E-4	4.61
16	0.6092	0.5422	0.8901	461.7	1147.5	0.0014480	1053.3	0.341	2.35E-4	4.47
17	0.5895	0.5206	0.8832	458.1	1101.7	0.0014011	1049.2	0.339	2.42E-4	4.34
18	0.5702	0.4997	0.8763	454.5	1057.5	0.0013553	1045.1	0.337	2.48E-4	4.21
19	0.5514	0.4795	0.8695	451.0	1014.7	0.0013107	1041.0	0.335	2.55E-4	4.08
20	0.5332	0.4599	0.8626	447.4	973.3	0.0012673	1036.9	0.332	2.62E-4	3.95
21	0.5153	0.4410	0.8558	443.9	933.3	0.0012249	1032.8	0.330	2.70E-4	3.83
22	0.4980	0.4227	0.8489	440.3	894.6	0.0011836	1028.6	0.328	2.77E-4	3.71
23	0.4811	0.4051	0.8420	436.7	857.2	0.0011435	1024.5	0.326	2.85E-4	3.59
24	0.4646	0.3880	0.8352	433.2	821.2	0.0011043	1020.3	0.324	2.93E-4	3.48
25	0.4486	0.3716	0.8283	429.6	786.3	0.0010663	1016.1	0.322	3.02E-4	3.37
26	0.4330	0.3557	0.8215	426.1	752.7	0.0010292	1011.9	0.319	3.10E-4	3.26
27	0.4178	0.3404	0.8146	422.5	720.3	0.0009931	1007.7	0.317	3.19E-4	3.15
28	0.4031	0.3256	0.8077	419.0	689.0	0.0009580	1003.4	0.315	3.29E-4	3.05
29	0.3887	0.3113	0.8009	415.4	658.8	0.0009239	999.1	0.313	3.39E-4	2.95
30	0.3747	0.2975	0.7940	411.8	629.7	0.0008907	994.8	0.311	3.49E-4	2.85
31	0.3611	0.2843	0.7872	408.3	601.6	0.0008584	990.5	0.308	3.59E-4	2.76
32	0.3480	0.2715	0.7803	404.7	574.6	0.0008270	986.2	0.306	3.70E-4	2.66
33	0.3351	0.2592	0.7735	401.2	548.5	0.0007966	981.9	0.304	3.82E-4	2.57
34	0.3227	0.2474	0.7666	397.6	523.5	0.0007670	977.5	0.302	3.93E-4	2.48
35	0.3106	0.2360	0.7598	394.1	499.3	0.0007382	973.1	0.300	4.06E-4	2.40
36	0.2988	0.2250	0.7529	390.5	476.1	0.0007103	968.7	0.297	4.19E-4	2.31
37	0.2852	0.2145	0.7519	390.0	453.9	0.0006780	968.1	0.297	4.38E-4	2.21
38	0.2719	0.2044	0.7519	390.0	432.6	0.0006463	968.1	0.297	4.59E-4	2.11
39	0.2592	0.1949	0.7519	390.0	412.4	0.0006161	968.1	0.297	4.82E-4	2.01
40	0.2471	0.1858	0.7519	390.0	393.1	0.0005873	968.1	0.297	5.06E-4	1.91

alt	sigma	delta	theta	temp	press	dens	a	visc	k.visc	ratio
41	0.2355	0.1771	0.7519	390.0	374.7	0.0005598	968.1	0.297	5.30E-4	1.83
42	0.2245	0.1688	0.7519	390.0	357.2	0.0005336	968.1	0.297	5.56E-4	1.74
43	0.2140	0.1609	0.7519	390.0	340.5	0.0005087	968.1	0.297	5.84E-4	1.66
44	0.2040	0.1534	0.7519	390.0	324.6	0.0004849	968.1	0.297	6.12E-4	1.58
45	0.1945	0.1462	0.7519	390.0	309.4	0.0004623	968.1	0.297	6.42E-4	1.51
46	0.1854	0.1394	0.7519	390.0	295.0	0.0004407	968.1	0.297	6.74E-4	1.44
47	0.1767	0.1329	0.7519	390.0	281.2	0.0004201	968.1	0.297	7.07E-4	1.37
48	0.1685	0.1267	0.7519	390.0	268.1	0.0004005	968.1	0.297	7.41E-4	1.31
49	0.1606	0.1208	0.7519	390.0	255.5	0.0003817	968.1	0.297	7.78E-4	1.24
50	0.1531	0.1151	0.7519	390.0	243.6	0.0003639	968.1	0.297	8.16E-4	1.19
51	0.1460	0.1097	0.7519	390.0	232.2	0.0003469	968.1	0.297	8.56E-4	1.13
52	0.1391	0.1046	0.7519	390.0	221.4	0.0003307	968.1	0.297	8.98E-4	1.08
53	0.1326	0.0997	0.7519	390.0	211.0	0.0003153	968.1	0.297	9.42E-4	1.03
54	0.1264	0.0951	0.7519	390.0	201.2	0.0003006	968.1	0.297	9.88E-4	0.98
55	0.1205	0.0906	0.7519	390.0	191.8	0.0002865	968.1	0.297	1.04E-3	0.93
56	0.1149	0.0864	0.7519	390.0	182.8	0.0002731	968.1	0.297	1.09E-3	0.89
57	0.1096	0.0824	0.7519	390.0	174.3	0.0002604	968.1	0.297	1.14E-3	0.85
58	0.1044	0.0785	0.7519	390.0	166.2	0.0002482	968.1	0.297	1.20E-3	0.81
59	0.0996	0.0749	0.7519	390.0	158.4	0.0002367	968.1	0.297	1.25E-3	0.77
60	0.0949	0.0714	0.7519	390.0	151.0	0.0002256	968.1	0.297	1.32E-3	0.74
61	0.0905	0.0680	0.7519	390.0	144.0	0.0002151	968.1	0.297	1.38E-3	0.70
62	0.0863	0.0649	0.7519	390.0	137.3	0.0002050	968.1	0.297	1.45E-3	0.67
63	0.0822	0.0618	0.7519	390.0	130.9	0.0001955	968.1	0.297	1.52E-3	0.64
64	0.0784	0.0590	0.7519	390.0	124.8	0.0001864	968.1	0.297	1.59E-3	0.61
65	0.0747	0.0562	0.7519	390.0	118.9	0.0001777	968.1	0.297	1.67E-3	0.58

U.S. Standard Atmosphere SI Units

In this table **alt** is altitude in kilometers.

sigma is density divided by sea-level density.

delta is pressure divided by sea-level pressure.

theta is temperature divided by sea-level temperature.

temp is temperature in Kelvin.

press is pressure in Newtons per square meter (or Pa).

dens is density in kilograms per cubic meter.

a is the speed of sound in meters per second.

visc is viscosity in 10^{-6} kilograms per meter-second.

k.visc is kinematic viscosity in square meters per second.

Sea-level density = 1.225 kg per cubic meter

Sea-level temperature = 288.1 Kelvin

Sea-level pressure = $1.013 \times 100,000$ Pascal

alt km	sigma	delta	theta	temp K	press Pa	dens kg/m ³	a m/s	visc kg/m-s	k.visc m ² /s
-2	1.2067E+0	1.2611E+0	1.0451	301.2	1.278E+5	1.478E+0	347.9	18.51	1.25E-5
0	1.0000E+0	1.0000E+0	1.0000	288.1	1.013E+5	1.225E+0	340.3	17.89	1.46E-5
2	8.2168E-1	7.8462E-1	0.9549	275.2	7.950E+4	1.007E+0	332.5	17.26	1.71E-5
4	6.6885E-1	6.0854E-1	0.9098	262.2	6.166E+4	8.193E-1	324.6	16.61	2.03E-5
6	5.3887E-1	4.6600E-1	0.8648	249.2	4.722E+4	6.601E-1	316.5	15.95	2.42E-5
8	4.2921E-1	3.5185E-1	0.8198	236.2	3.565E+4	5.258E-1	308.1	15.27	2.90E-5
10	3.3756E-1	2.6153E-1	0.7748	223.3	2.650E+4	4.135E-1	299.5	14.58	3.53E-5
12	2.5464E-1	1.9146E-1	0.7519	216.6	1.940E+4	3.119E-1	295.1	14.22	4.56E-5
14	1.8600E-1	1.3985E-1	0.7519	216.6	1.417E+4	2.279E-1	295.1	14.22	6.24E-5
16	1.3589E-1	1.0217E-1	0.7519	216.6	1.035E+4	1.665E-1	295.1	14.22	8.54E-5
18	9.9302E-2	7.4662E-2	0.7519	216.6	7.565E+3	1.216E-1	295.1	14.22	1.17E-4
20	7.2578E-2	5.4569E-2	0.7519	216.6	5.529E+3	8.891E-2	295.1	14.22	1.60E-4
22	5.2660E-2	3.9945E-2	0.7585	218.6	4.047E+3	6.451E-2	296.4	14.32	2.22E-4
24	3.8316E-2	2.9328E-2	0.7654	220.6	2.972E+3	4.694E-2	297.7	14.43	3.07E-4
26	2.7964E-2	2.1597E-2	0.7723	222.5	2.188E+3	3.426E-2	299.1	14.54	4.24E-4
28	2.0470E-2	1.5950E-2	0.7792	224.5	1.616E+3	2.508E-2	300.4	14.65	5.84E-4
30	1.5028E-2	1.1813E-2	0.7861	226.5	1.197E+3	1.841E-2	301.7	14.75	8.01E-4
32	1.1065E-2	8.7740E-3	0.7930	228.5	8.890E+2	1.355E-2	303.0	14.86	1.10E-3
34	8.0709E-3	6.5470E-3	0.8112	233.7	6.634E+2	9.887E-3	306.5	15.14	1.53E-3
36	5.9245E-3	4.9198E-3	0.8304	239.3	4.985E+2	7.257E-3	310.1	15.43	2.13E-3
38	4.3806E-3	3.7218E-3	0.8496	244.8	3.771E+2	5.366E-3	313.7	15.72	2.93E-3
40	3.2615E-3	2.8337E-3	0.8688	250.4	2.871E+2	3.995E-3	317.2	16.01	4.01E-3
42	2.4445E-3	2.1708E-3	0.8880	255.9	2.200E+2	2.995E-3	320.7	16.29	5.44E-3
44	1.8438E-3	1.6727E-3	0.9072	261.4	1.695E+2	2.259E-3	324.1	16.57	7.34E-3
46	1.3992E-3	1.2961E-3	0.9263	266.9	1.313E+2	1.714E-3	327.5	16.85	9.83E-3
48	1.0748E-3	1.0095E-3	0.9393	270.6	1.023E+2	1.317E-3	329.8	17.04	1.29E-2
50	8.3819E-4	7.8728E-4	0.9393	270.6	7.977E+1	1.027E-3	329.8	17.04	1.66E-2
52	6.5759E-4	6.1395E-4	0.9336	269.0	6.221E+1	8.055E-4	328.8	16.96	2.10E-2
54	5.2158E-4	4.7700E-4	0.9145	263.5	4.833E+1	6.389E-4	325.4	16.68	2.61E-2
56	4.1175E-4	3.6869E-4	0.8954	258.0	3.736E+1	5.044E-4	322.0	16.40	3.25E-2
58	3.2344E-4	2.8344E-4	0.8763	252.5	2.872E+1	3.962E-4	318.6	16.12	4.07E-2
60	2.5276E-4	2.1668E-4	0.8573	247.0	2.196E+1	3.096E-4	315.1	15.84	5.11E-2
62	1.9647E-4	1.6468E-4	0.8382	241.5	1.669E+1	2.407E-4	311.5	15.55	6.46E-2
64	1.5185E-4	1.2439E-4	0.8191	236.0	1.260E+1	1.860E-4	308.0	15.26	8.20E-2
66	1.1668E-4	9.3354E-5	0.8001	230.5	9.459E+0	1.429E-4	304.4	14.97	1.05E-1
68	8.9101E-5	6.9593E-5	0.7811	225.1	7.051E+0	1.091E-4	300.7	14.67	1.34E-1
70	6.7601E-5	5.1515E-5	0.7620	219.6	5.220E+0	8.281E-5	297.1	14.38	1.74E-1
72	5.0905E-5	3.7852E-5	0.7436	214.3	3.835E+0	6.236E-5	293.4	14.08	2.26E-1
74	3.7856E-5	2.7635E-5	0.7300	210.3	2.800E+0	4.637E-5	290.7	13.87	2.99E-1
76	2.8001E-5	2.0061E-5	0.7164	206.4	2.033E+0	3.430E-5	288.0	13.65	3.98E-1
78	2.0597E-5	1.4477E-5	0.7029	202.5	1.467E+0	2.523E-5	285.3	13.43	5.32E-1
80	1.5063E-5	1.0384E-5	0.6893	198.6	1.052E+0	1.845E-5	282.5	13.21	7.16E-1
82	1.0950E-5	7.4002E-6	0.6758	194.7	7.498E-1	1.341E-5	279.7	12.98	9.68E-1
84	7.9106E-6	5.2391E-6	0.6623	190.8	5.308E-1	9.690E-6	276.9	12.76	1.32E+0
86	5.6777E-6	3.6835E-6	0.6488	186.9	3.732E-1	6.955E-6	274.1	12.53	1.80E+0

APPENDIX B

Isentropic Table

Isentropic tables are produced, for calorically perfect gas (i.e., constant γ), based on the following equations:

$$\frac{T_t}{T} = 1 + \left(\frac{\gamma - 1}{2}\right) M^2 \quad (\text{B.1})$$

$$\frac{p_t}{p} = \left(\frac{T_t}{T}\right)^{\frac{\gamma}{\gamma-1}} = \left[1 + \left(\frac{\gamma - 1}{2}\right) M^2\right]^{\frac{\gamma}{\gamma-1}} \quad (\text{B.2})$$

$$\frac{\rho_t}{\rho} = \left(\frac{p_t}{p}\right)^{\frac{1}{\gamma}} = \left[1 + \left(\frac{\gamma - 1}{2}\right) M^2\right]^{\frac{1}{\gamma-1}} \quad (\text{B.3})$$

$$\frac{A}{A^*} = \frac{1}{M} \left(\frac{1 + \frac{\gamma-1}{2} M^2}{\frac{\gamma+1}{2}}\right)^{\frac{\gamma+1}{2(\gamma-1)}} \quad (\text{B.4})$$

$$\frac{T}{T^*} = \frac{\frac{\gamma+1}{2}}{1 + \left(\frac{\gamma-1}{2}\right) M^2} \quad (\text{B.5})$$

$$\frac{p}{p^*} = \left[\frac{\frac{\gamma+1}{2}}{1 + \left(\frac{\gamma-1}{2}\right) M^2}\right]^{\frac{\gamma}{\gamma-1}} \quad (\text{B.6})$$

$$\frac{\rho}{\rho^*} = \frac{p}{p^*} / \frac{T}{T^*} \left[\frac{\frac{\gamma+1}{2}}{1 + \left(\frac{\gamma-1}{2}\right) M^2}\right]^{\frac{1}{\gamma-1}} \quad (\text{B.7})$$

We derived these equations in Chapter 2.

Isentropic Table $\gamma = 1.4$

M	T_1/T	p_1/p	ρ_1/ρ	A/A^*	T/T^*	p/p^*	ρ/ρ^*
0.02	1.0001E+00	1.0003E+00	1.0002E+00	2.8942E+01	1.1999E+00	1.8924E+00	1.5771E+00
0.04	1.0003E+00	1.0011E+00	1.0008E+00	1.4481E+01	1.1996E+00	1.8908E+00	1.5762E+00
0.06	1.0007E+00	1.0025E+00	1.0018E+00	9.6658E+00	1.1991E+00	1.8882E+00	1.5746E+00
0.08	1.0013E+00	1.0045E+00	1.0032E+00	7.2615E+00	1.1985E+00	1.8845E+00	1.5724E+00
0.10	1.0020E+00	1.0070E+00	1.0050E+00	5.8218E+00	1.1976E+00	1.8797E+00	1.5696E+00
0.12	1.0029E+00	1.0101E+00	1.0072E+00	4.8643E+00	1.1966E+00	1.8740E+00	1.5661E+00
0.14	1.0039E+00	1.0138E+00	1.0098E+00	4.1823E+00	1.1953E+00	1.8672E+00	1.5621E+00
0.16	1.0051E+00	1.0180E+00	1.0128E+00	3.6727E+00	1.1939E+00	1.8594E+00	1.5574E+00
0.18	1.0065E+00	1.0229E+00	1.0163E+00	3.2779E+00	1.1923E+00	1.8506E+00	1.5522E+00
0.20	1.0080E+00	1.0283E+00	1.0201E+00	2.9635E+00	1.1905E+00	1.8409E+00	1.5463E+00
0.22	1.0097E+00	1.0343E+00	1.0244E+00	2.7076E+00	1.1885E+00	1.8302E+00	1.5399E+00
0.24	1.0115E+00	1.0409E+00	1.0290E+00	2.4955E+00	1.1863E+00	1.8185E+00	1.5329E+00
0.26	1.0135E+00	1.0481E+00	1.0341E+00	2.3173E+00	1.1840E+00	1.8060E+00	1.5254E+00
0.28	1.0157E+00	1.0560E+00	1.0397E+00	2.1655E+00	1.1815E+00	1.7926E+00	1.5173E+00
0.30	1.0180E+00	1.0644E+00	1.0456E+00	2.0350E+00	1.1788E+00	1.7783E+00	1.5086E+00
0.32	1.0205E+00	1.0735E+00	1.0520E+00	1.9218E+00	1.1759E+00	1.7633E+00	1.4995E+00
0.34	1.0231E+00	1.0833E+00	1.0588E+00	1.8229E+00	1.1729E+00	1.7474E+00	1.4898E+00
0.36	1.0259E+00	1.0937E+00	1.0661E+00	1.7358E+00	1.1697E+00	1.7308E+00	1.4797E+00
0.38	1.0289E+00	1.1048E+00	1.0738E+00	1.6587E+00	1.1663E+00	1.7134E+00	1.4691E+00
0.40	1.0320E+00	1.1166E+00	1.0819E+00	1.5901E+00	1.1628E+00	1.6953E+00	1.4580E+00
0.42	1.0353E+00	1.1290E+00	1.0905E+00	1.5289E+00	1.1591E+00	1.6766E+00	1.4465E+00
0.44	1.0387E+00	1.1422E+00	1.0996E+00	1.4740E+00	1.1553E+00	1.6573E+00	1.4345E+00
0.46	1.0423E+00	1.1561E+00	1.1092E+00	1.4246E+00	1.1513E+00	1.6373E+00	1.4222E+00
0.48	1.0461E+00	1.1708E+00	1.1192E+00	1.3801E+00	1.1471E+00	1.6168E+00	1.4094E+00
0.50	1.0500E+00	1.1862E+00	1.1297E+00	1.3398E+00	1.1429E+00	1.5958E+00	1.3963E+00
0.52	1.0541E+00	1.2024E+00	1.1407E+00	1.3034E+00	1.1384E+00	1.5743E+00	1.3828E+00
0.54	1.0583E+00	1.2194E+00	1.1522E+00	1.2703E+00	1.1339E+00	1.5523E+00	1.3690E+00
0.56	1.0627E+00	1.2373E+00	1.1643E+00	1.2403E+00	1.1292E+00	1.5299E+00	1.3549E+00
0.58	1.0673E+00	1.2560E+00	1.1768E+00	1.2130E+00	1.1244E+00	1.5072E+00	1.3405E+00
0.60	1.0720E+00	1.2755E+00	1.1898E+00	1.1882E+00	1.1194E+00	1.4841E+00	1.3258E+00
0.62	1.0769E+00	1.2959E+00	1.2034E+00	1.1656E+00	1.1143E+00	1.4607E+00	1.3108E+00
0.64	1.0819E+00	1.3173E+00	1.2176E+00	1.1451E+00	1.1091E+00	1.4370E+00	1.2956E+00
0.66	1.0871E+00	1.3396E+00	1.2322E+00	1.1265E+00	1.1038E+00	1.4131E+00	1.2801E+00
0.68	1.0925E+00	1.3628E+00	1.2475E+00	1.1096E+00	1.0984E+00	1.3890E+00	1.2645E+00
0.70	1.0980E+00	1.3871E+00	1.2633E+00	1.0944E+00	1.0929E+00	1.3647E+00	1.2487E+00
0.72	1.1037E+00	1.4124E+00	1.2797E+00	1.0806E+00	1.0873E+00	1.3402E+00	1.2327E+00
0.74	1.1095E+00	1.4387E+00	1.2967E+00	1.0681E+00	1.0815E+00	1.3157E+00	1.2165E+00

M	T_t/T	p_t/p	ρ_t/ρ	A/A^*	T/T^*	p/p^*	ρ/ρ^*
0.76	1.1155E+00	1.4661E+00	1.3143E+00	1.0570E+00	1.0757E+00	1.2911E+00	1.2002E+00
0.78	1.1217E+00	1.4947E+00	1.3325E+00	1.0470E+00	1.0698E+00	1.2665E+00	1.1838E+00
0.80	1.1280E+00	1.5243E+00	1.3514E+00	1.0382E+00	1.0638E+00	1.2418E+00	1.1673E+00
0.82	1.1345E+00	1.5552E+00	1.3709E+00	1.0305E+00	1.0578E+00	1.2172E+00	1.1507E+00
0.84	1.1411E+00	1.5873E+00	1.3910E+00	1.0237E+00	1.0516E+00	1.1925E+00	1.1340E+00
0.86	1.1479E+00	1.6207E+00	1.4118E+00	1.0179E+00	1.0454E+00	1.1680E+00	1.1173E+00
0.88	1.1549E+00	1.6553E+00	1.4333E+00	1.0129E+00	1.0391E+00	1.1436E+00	1.1006E+00
0.90	1.1620E+00	1.6913E+00	1.4555E+00	1.0089E+00	1.0327E+00	1.1192E+00	1.0838E+00
0.92	1.1693E+00	1.7287E+00	1.4784E+00	1.0056E+00	1.0263E+00	1.0950E+00	1.0670E+00
0.94	1.1767E+00	1.7675E+00	1.5020E+00	1.0031E+00	1.0198E+00	1.0710E+00	1.0502E+00
0.96	1.1843E+00	1.8078E+00	1.5264E+00	1.0014E+00	1.0132E+00	1.0471E+00	1.0334E+00
0.98	1.1921E+00	1.8496E+00	1.5515E+00	1.0003E+00	1.0066E+00	1.0234E+00	1.0167E+00
1.00	1.2000E+00	1.8929E+00	1.5774E+00	1.0000E+00	1.0000E+00	1.0000E+00	1.0000E+00
1.02	1.2081E+00	1.9379E+00	1.6041E+00	1.0003E+00	9.9331E-01	9.7679E-01	9.8336E-01
1.04	1.2163E+00	1.9846E+00	1.6316E+00	1.0013E+00	9.8658E-01	9.5382E-01	9.6679E-01
1.06	1.2247E+00	2.0330E+00	1.6599E+00	1.0029E+00	9.7982E-01	9.3112E-01	9.5030E-01
1.08	1.2333E+00	2.0831E+00	1.6891E+00	1.0051E+00	9.7302E-01	9.0870E-01	9.3390E-01
1.10	1.2420E+00	2.1351E+00	1.7191E+00	1.0079E+00	9.6618E-01	8.8656E-01	9.1759E-01
1.12	1.2509E+00	2.1890E+00	1.7500E+00	1.0113E+00	9.5932E-01	8.6473E-01	9.0139E-01
1.14	1.2599E+00	2.2449E+00	1.7818E+00	1.0153E+00	9.5244E-01	8.4321E-01	8.8531E-01
1.16	1.2691E+00	2.3028E+00	1.8145E+00	1.0198E+00	9.4554E-01	8.2201E-01	8.6935E-01
1.18	1.2785E+00	2.3628E+00	1.8481E+00	1.0248E+00	9.3861E-01	8.0113E-01	8.5353E-01
1.20	1.2880E+00	2.4250E+00	1.8827E+00	1.0304E+00	9.3168E-01	7.8060E-01	8.3784E-01
1.22	1.2977E+00	2.4894E+00	1.9183E+00	1.0366E+00	9.2473E-01	7.6041E-01	8.2231E-01
1.24	1.3075E+00	2.5560E+00	1.9549E+00	1.0432E+00	9.1777E-01	7.4057E-01	8.0692E-01
1.26	1.3175E+00	2.6251E+00	1.9925E+00	1.0504E+00	9.1080E-01	7.2108E-01	7.9170E-01
1.28	1.3277E+00	2.6967E+00	2.0311E+00	1.0581E+00	9.0383E-01	7.0195E-01	7.7664E-01
1.30	1.3380E+00	2.7707E+00	2.0708E+00	1.0663E+00	8.9686E-01	6.8318E-01	7.6175E-01
1.32	1.3485E+00	2.8474E+00	2.1116E+00	1.0750E+00	8.8989E-01	6.6478E-01	7.4704E-01
1.34	1.3591E+00	2.9269E+00	2.1535E+00	1.0842E+00	8.8292E-01	6.4674E-01	7.3250E-01
1.36	1.3699E+00	3.0091E+00	2.1965E+00	1.0940E+00	8.7596E-01	6.2907E-01	7.1815E-01
1.38	1.3809E+00	3.0942E+00	2.2407E+00	1.1042E+00	8.6901E-01	6.1177E-01	7.0398E-01
1.40	1.3920E+00	3.1823E+00	2.2861E+00	1.1149E+00	8.6207E-01	5.9484E-01	6.9001E-01
1.42	1.4033E+00	3.2734E+00	2.3327E+00	1.1261E+00	8.5514E-01	5.7827E-01	6.7623E-01
1.44	1.4147E+00	3.3678E+00	2.3805E+00	1.1379E+00	8.4822E-01	5.6207E-01	6.6264E-01
1.46	1.4263E+00	3.4654E+00	2.4296E+00	1.1501E+00	8.4133E-01	5.4623E-01	6.4925E-01
1.48	1.4381E+00	3.5665E+00	2.4800E+00	1.1629E+00	8.3445E-01	5.3075E-01	6.3606E-01
1.50	1.4500E+00	3.6710E+00	2.5317E+00	1.1762E+00	8.2759E-01	5.1564E-01	6.2306E-01

(Continued)

M	T_t/T	p_t/p	ρ_t/ρ	A/A^*	T/T^*	p/p^*	ρ/ρ^*
1.52	1.4621E+00	3.7792E+00	2.5848E+00	1.1899E+00	8.2075E-01	5.0088E-01	6.1027E-01
1.54	1.4743E+00	3.8911E+00	2.6392E+00	1.2042E+00	8.1393E-01	4.8648E-01	5.9769E-01
1.56	1.4867E+00	4.0068E+00	2.6951E+00	1.2190E+00	8.0715E-01	4.7242E-01	5.8530E-01
1.58	1.4993E+00	4.1266E+00	2.7524E+00	1.2344E+00	8.0038E-01	4.5872E-01	5.7312E-01
1.60	1.5120E+00	4.2504E+00	2.8111E+00	1.2502E+00	7.9365E-01	4.4535E-01	5.6114E-01
1.62	1.5249E+00	4.3785E+00	2.8714E+00	1.2666E+00	7.8695E-01	4.3232E-01	5.4937E-01
1.64	1.5379E+00	4.5110E+00	2.9332E+00	1.2835E+00	7.8027E-01	4.1963E-01	5.3780E-01
1.66	1.5511E+00	4.6479E+00	2.9965E+00	1.3010E+00	7.7363E-01	4.0726E-01	5.2643E-01
1.68	1.5645E+00	4.7896E+00	3.0614E+00	1.3190E+00	7.6703E-01	3.9522E-01	5.1526E-01
1.70	1.5780E+00	4.9360E+00	3.1280E+00	1.3376E+00	7.6046E-01	3.8350E-01	5.0430E-01
1.72	1.5917E+00	5.0874E+00	3.1962E+00	1.3567E+00	7.5392E-01	3.7208E-01	4.9353E-01
1.74	1.6055E+00	5.2439E+00	3.2662E+00	1.3764E+00	7.4742E-01	3.6098E-01	4.8296E-01
1.76	1.6195E+00	5.4057E+00	3.3378E+00	1.3967E+00	7.4096E-01	3.5017E-01	4.7259E-01
1.78	1.6337E+00	5.5729E+00	3.4113E+00	1.4175E+00	7.3454E-01	3.3966E-01	4.6242E-01
1.80	1.6480E+00	5.7458E+00	3.4865E+00	1.4390E+00	7.2816E-01	3.2945E-01	4.5244E-01
1.82	1.6625E+00	5.9244E+00	3.5636E+00	1.4610E+00	7.2181E-01	3.1951E-01	4.4265E-01
1.84	1.6771E+00	6.1091E+00	3.6426E+00	1.4836E+00	7.1551E-01	3.0986E-01	4.3305E-01
1.86	1.6919E+00	6.2998E+00	3.7235E+00	1.5069E+00	7.0925E-01	3.0047E-01	4.2365E-01
1.88	1.7069E+00	6.4970E+00	3.8063E+00	1.5307E+00	7.0304E-01	2.9136E-01	4.1442E-01
1.90	1.7220E+00	6.7006E+00	3.8912E+00	1.5552E+00	6.9686E-01	2.8250E-01	4.0539E-01
1.92	1.7373E+00	6.9111E+00	3.9781E+00	1.5804E+00	6.9073E-01	2.7390E-01	3.9653E-01
1.94	1.7527E+00	7.1284E+00	4.0671E+00	1.6062E+00	6.8465E-01	2.6555E-01	3.8786E-01
1.96	1.7683E+00	7.3530E+00	4.1582E+00	1.6326E+00	6.7861E-01	2.5744E-01	3.7936E-01
1.98	1.7841E+00	7.5849E+00	4.2514E+00	1.6597E+00	6.7262E-01	2.4957E-01	3.7104E-01
2.00	1.8000E+00	7.8244E+00	4.3469E+00	1.6875E+00	6.6667E-01	2.4192E-01	3.6289E-01
2.02	1.8161E+00	8.0718E+00	4.4446E+00	1.7159E+00	6.6076E-01	2.3451E-01	3.5491E-01
2.04	1.8323E+00	8.3273E+00	4.5447E+00	1.7451E+00	6.5491E-01	2.2732E-01	3.4710E-01
2.06	1.8487E+00	8.5911E+00	4.6471E+00	1.7750E+00	6.4910E-01	2.2034E-01	3.3945E-01
2.08	1.8653E+00	8.8635E+00	4.7518E+00	1.8056E+00	6.4334E-01	2.1357E-01	3.3197E-01
2.10	1.8820E+00	9.1447E+00	4.8590E+00	1.8369E+00	6.3762E-01	2.0700E-01	3.2464E-01
2.12	1.8989E+00	9.4350E+00	4.9687E+00	1.8690E+00	6.3195E-01	2.0063E-01	3.1747E-01
2.14	1.9159E+00	9.7347E+00	5.0809E+00	1.9018E+00	6.2633E-01	1.9445E-01	3.1046E-01
2.16	1.9331E+00	1.0044E+01	5.1957E+00	1.9354E+00	6.2076E-01	1.8846E-01	3.0360E-01
2.18	1.9505E+00	1.0363E+01	5.3132E+00	1.9698E+00	6.1523E-01	1.8266E-01	2.9689E-01
2.20	1.9680E+00	1.0693E+01	5.4333E+00	2.0050E+00	6.0976E-01	1.7703E-01	2.9033E-01
2.22	1.9857E+00	1.1033E+01	5.5561E+00	2.0409E+00	6.0433E-01	1.7157E-01	2.8391E-01
2.24	2.0035E+00	1.1384E+01	5.6818E+00	2.0777E+00	5.9895E-01	1.6629E-01	2.7763E-01
2.26	2.0215E+00	1.1746E+01	5.8103E+00	2.1153E+00	5.9361E-01	1.6116E-01	2.7149E-01
2.28	2.0397E+00	1.2119E+01	5.9416E+00	2.1538E+00	5.8833E-01	1.5620E-01	2.6549E-01
2.30	2.0580E+00	1.2504E+01	6.0759E+00	2.1931E+00	5.8309E-01	1.5138E-01	2.5962E-01

M	T_t/T	p_t/p	ρ_t/ρ	A/A^*	T/T^*	p/p^*	ρ/ρ^*
2.32	2.0765E+00	1.2902E+01	6.2133E+00	2.2333E+00	5.7790E-01	1.4672E-01	2.5388E-01
2.34	2.0951E+00	1.3312E+01	6.3536E+00	2.2744E+00	5.7276E-01	1.4220E-01	2.4827E-01
2.36	2.1139E+00	1.3734E+01	6.4971E+00	2.3164E+00	5.6767E-01	1.3782E-01	2.4279E-01
2.38	2.1329E+00	1.4170E+01	6.6438E+00	2.3592E+00	5.6262E-01	1.3358E-01	2.3743E-01
2.40	2.1520E+00	1.4620E+01	6.7937E+00	2.4031E+00	5.5762E-01	1.2948E-01	2.3219E-01
2.42	2.1713E+00	1.5084E+01	6.9469E+00	2.4478E+00	5.5267E-01	1.2550E-01	2.2707E-01
2.44	2.1907E+00	1.5562E+01	7.1034E+00	2.4936E+00	5.4777E-01	1.2164E-01	2.2207E-01
2.46	2.2103E+00	1.6054E+01	7.2634E+00	2.5403E+00	5.4291E-01	1.1791E-01	2.1718E-01
2.48	2.2301E+00	1.6562E+01	7.4268E+00	2.5880E+00	5.3810E-01	1.1429E-01	2.1240E-01
2.50	2.2500E+00	1.7086E+01	7.5938E+00	2.6367E+00	5.3333E-01	1.1079E-01	2.0773E-01
2.52	2.2701E+00	1.7626E+01	7.7643E+00	2.6864E+00	5.2862E-01	1.0740E-01	2.0317E-01
2.54	2.2903E+00	1.8182E+01	7.9385E+00	2.7372E+00	5.2394E-01	1.0411E-01	1.9871E-01
2.56	2.3107E+00	1.8755E+01	8.1165E+00	2.7890E+00	5.1932E-01	1.0093E-01	1.9435E-01
2.58	2.3313E+00	1.9346E+01	8.2982E+00	2.8419E+00	5.1474E-01	9.7848E-02	1.9009E-01
2.60	2.3520E+00	1.9954E+01	8.4839E+00	2.8959E+00	5.1020E-01	9.4865E-02	1.8593E-01
2.62	2.3729E+00	2.0581E+01	8.6734E+00	2.9511E+00	5.0571E-01	9.1975E-02	1.8187E-01
2.64	2.3939E+00	2.1227E+01	8.8669E+00	3.0073E+00	5.0127E-01	8.9177E-02	1.7790E-01
2.66	2.4151E+00	2.1892E+01	9.0646E+00	3.0647E+00	4.9687E-01	8.6467E-02	1.7402E-01
2.68	2.4365E+00	2.2577E+01	9.2663E+00	3.1232E+00	4.9251E-01	8.3843E-02	1.7023E-01
2.70	2.4580E+00	2.3283E+01	9.4723E+00	3.1830E+00	4.8820E-01	8.1301E-02	1.6653E-01
2.72	2.4797E+00	2.4010E+01	9.6825E+00	3.2439E+00	4.8393E-01	7.8841E-02	1.6292E-01
2.74	2.5015E+00	2.4758E+01	9.8971E+00	3.3061E+00	4.7971E-01	7.6458E-02	1.5938E-01
2.76	2.5235E+00	2.5528E+01	1.0116E+01	3.3695E+00	4.7553E-01	7.4150E-02	1.5593E-01
2.78	2.5457E+00	2.6322E+01	1.0340E+01	3.4341E+00	4.7139E-01	7.1915E-02	1.5256E-01
2.80	2.5680E+00	2.7138E+01	1.0568E+01	3.5001E+00	4.6729E-01	6.9751E-02	1.4927E-01
2.82	2.5905E+00	2.7979E+01	1.0801E+01	3.5673E+00	4.6323E-01	6.7656E-02	1.4605E-01
2.84	2.6131E+00	2.8844E+01	1.1038E+01	3.6359E+00	4.5922E-01	6.5626E-02	1.4291E-01
2.86	2.6359E+00	2.9735E+01	1.1281E+01	3.7058E+00	4.5525E-01	6.3661E-02	1.3984E-01
2.88	2.6589E+00	3.0651E+01	1.1528E+01	3.7771E+00	4.5132E-01	6.1757E-02	1.3684E-01
2.90	2.6820E+00	3.1594E+01	1.1780E+01	3.8497E+00	4.4743E-01	5.9914E-02	1.3391E-01
2.92	2.7053E+00	3.2564E+01	1.2037E+01	3.9238E+00	4.4358E-01	5.8129E-02	1.3105E-01
2.94	2.7287E+00	3.3563E+01	1.2300E+01	3.9993E+00	4.3977E-01	5.6400E-02	1.2825E-01
2.96	2.7523E+00	3.4590E+01	1.2567E+01	4.0762E+00	4.3600E-01	5.4725E-02	1.2552E-01
2.98	2.7761E+00	3.5646E+01	1.2840E+01	4.1546E+00	4.3226E-01	5.3103E-02	1.2285E-01
3.00	2.8000E+00	3.6733E+01	1.3119E+01	4.2345E+00	4.2857E-01	5.1533E-02	1.2024E-01
3.05	2.8605E+00	3.9586E+01	1.3839E+01	4.4410E+00	4.1951E-01	4.7818E-02	1.1399E-01
3.10	2.9220E+00	4.2646E+01	1.4595E+01	4.6573E+00	4.1068E-01	4.4387E-02	1.0808E-01
3.15	2.9845E+00	4.5925E+01	1.5388E+01	4.8838E+00	4.0208E-01	4.1218E-02	1.0251E-01
3.20	3.0480E+00	4.9437E+01	1.6219E+01	5.1209E+00	3.9370E-01	3.8290E-02	9.7256E-02
3.25	3.1125E+00	5.3196E+01	1.7091E+01	5.3690E+00	3.8554E-01	3.5584E-02	9.2295E-02

(Continued)

M	T_t/T	p_t/p	ρ_t/ρ	A/A^*	T/T^*	p/p^*	ρ/ρ^*
3.30	3.1780E+00	5.7219E+01	1.8005E+01	5.6286E+00	3.7760E-01	3.3082E-02	8.7613E-02
3.35	3.2445E+00	6.1520E+01	1.8961E+01	5.9000E+00	3.6986E-01	3.0769E-02	8.3192E-02
3.40	3.3120E+00	6.6117E+01	1.9963E+01	6.1836E+00	3.6232E-01	2.8630E-02	7.9018E-02
3.45	3.3805E+00	7.1029E+01	2.1011E+01	6.4800E+00	3.5498E-01	2.6650E-02	7.5076E-02
3.50	3.4500E+00	7.6272E+01	2.2108E+01	6.7895E+00	3.4783E-01	2.4818E-02	7.1352E-02
3.55	3.5205E+00	8.1868E+01	2.3255E+01	7.1127E+00	3.4086E-01	2.3122E-02	6.7833E-02
3.60	3.5920E+00	8.7837E+01	2.4453E+01	7.4500E+00	3.3408E-01	2.1550E-02	6.4508E-02
3.65	3.6645E+00	9.4200E+01	2.5706E+01	7.8019E+00	3.2747E-01	2.0095E-02	6.1364E-02
3.70	3.7380E+00	1.0098E+02	2.7015E+01	8.1690E+00	3.2103E-01	1.8745E-02	5.8392E-02
3.75	3.8125E+00	1.0820E+02	2.8381E+01	8.5516E+00	3.1475E-01	1.7494E-02	5.5581E-02
3.80	3.8880E+00	1.1589E+02	2.9807E+01	8.9505E+00	3.0864E-01	1.6334E-02	5.2922E-02
3.85	3.9645E+00	1.2407E+02	3.1295E+01	9.3660E+00	3.0269E-01	1.5257E-02	5.0406E-02
3.90	4.0420E+00	1.3277E+02	3.2847E+01	9.7989E+00	2.9688E-01	1.4258E-02	4.8024E-02
3.95	4.1205E+00	1.4201E+02	3.4465E+01	1.0250E+01	2.9123E-01	1.3329E-02	4.5770E-02
4.00	4.2000E+00	1.5184E+02	3.6151E+01	1.0719E+01	2.8571E-01	1.2467E-02	4.3634E-02
4.05	4.2805E+00	1.6227E+02	3.7908E+01	1.1207E+01	2.8034E-01	1.1666E-02	4.1612E-02
4.10	4.3620E+00	1.7334E+02	3.9739E+01	1.1715E+01	2.7510E-01	1.0920E-02	3.9695E-02
4.15	4.4445E+00	1.8509E+02	4.1644E+01	1.2243E+01	2.7000E-01	1.0227E-02	3.7879E-02
4.20	4.5280E+00	1.9755E+02	4.3628E+01	1.2791E+01	2.6502E-01	9.5821E-03	3.6157E-02
4.25	4.6125E+00	2.1075E+02	4.5692E+01	1.3362E+01	2.6016E-01	8.9817E-03	3.4523E-02
4.30	4.6980E+00	2.2475E+02	4.7839E+01	1.3955E+01	2.5543E-01	8.4225E-03	3.2974E-02
4.35	4.7845E+00	2.3957E+02	5.0072E+01	1.4570E+01	2.5081E-01	7.9014E-03	3.1504E-02
4.40	4.8720E+00	2.5526E+02	5.2392E+01	1.5210E+01	2.4631E-01	7.4158E-03	3.0108E-02
4.45	4.9605E+00	2.7186E+02	5.4804E+01	1.5873E+01	2.4191E-01	6.9630E-03	2.8783E-02
4.50	5.0500E+00	2.8941E+02	5.7310E+01	1.6562E+01	2.3762E-01	6.5406E-03	2.7525E-02
4.55	5.1405E+00	3.0798E+02	5.9912E+01	1.7276E+01	2.3344E-01	6.1463E-03	2.6329E-02
4.60	5.2320E+00	3.2759E+02	6.2614E+01	1.8018E+01	2.2936E-01	5.7783E-03	2.5193E-02
4.65	5.3245E+00	3.4832E+02	6.5418E+01	1.8786E+01	2.2537E-01	5.4345E-03	2.4113E-02
4.70	5.4180E+00	3.7020E+02	6.8328E+01	1.9583E+01	2.2148E-01	5.1133E-03	2.3086E-02
4.75	5.5125E+00	3.9330E+02	7.1346E+01	2.0408E+01	2.1769E-01	4.8130E-03	2.2110E-02
4.80	5.6080E+00	4.1766E+02	7.4477E+01	2.1263E+01	2.1398E-01	4.5322E-03	2.1180E-02
4.85	5.7045E+00	4.4337E+02	7.7722E+01	2.2149E+01	2.1036E-01	4.2695E-03	2.0296E-02
4.90	5.8020E+00	4.7046E+02	8.1086E+01	2.3067E+01	2.0683E-01	4.0236E-03	1.9454E-02
4.95	5.9005E+00	4.9901E+02	8.4571E+01	2.4017E+01	2.0337E-01	3.7934E-03	1.8652E-02
5.00	6.0000E+00	5.2909E+02	8.8182E+01	2.5000E+01	2.0000E-01	3.5777E-03	1.7889E-02
5.10	6.2020E+00	5.9410E+02	9.5792E+01	2.7069E+01	1.9349E-01	3.1862E-03	1.6467E-02
5.20	6.4080E+00	6.6608E+02	1.0395E+02	2.9283E+01	1.8727E-01	2.8419E-03	1.5176E-02
5.30	6.6180E+00	7.4566E+02	1.1267E+02	3.1649E+01	1.8132E-01	2.5386E-03	1.4000E-02
5.40	6.8320E+00	8.3352E+02	1.2200E+02	3.4174E+01	1.7564E-01	2.2710E-03	1.2930E-02
5.50	7.0500E+00	9.3038E+02	1.3197E+02	3.6869E+01	1.7021E-01	2.0346E-03	1.1953E-02

M	T_t/T	p_t/p	ρ_t/ρ	A/A^*	T/T^*	p/p^*	ρ/ρ^*
5.60	7.2720E+00	1.0370E+03	1.4260E+02	3.9740E+01	1.6502E-01	1.8253E-03	1.1062E-02
5.70	7.4980E+00	1.1543E+03	1.5394E+02	4.2797E+01	1.6004E-01	1.6399E-03	1.0247E-02
5.80	7.7280E+00	1.2830E+03	1.6602E+02	4.6049E+01	1.5528E-01	1.4754E-03	9.5014E-03
5.90	7.9620E+00	1.4242E+03	1.7888E+02	4.9507E+01	1.5072E-01	1.3291E-03	8.8186E-03
6.00	8.2000E+00	1.5789E+03	1.9255E+02	5.3179E+01	1.4634E-01	1.1989E-03	8.1925E-03
6.10	8.4420E+00	1.7481E+03	2.0707E+02	5.7076E+01	1.4215E-01	1.0829E-03	7.6180E-03
6.20	8.6880E+00	1.9329E+03	2.2248E+02	6.1209E+01	1.3812E-01	9.7930E-04	7.0901E-03
6.30	8.9380E+00	2.1347E+03	2.3884E+02	6.5589E+01	1.3426E-01	8.8673E-04	6.6047E-03
6.40	9.1920E+00	2.3547E+03	2.5617E+02	7.0227E+01	1.3055E-01	8.0389E-04	6.1578E-03
6.50	9.4500E+00	2.5942E+03	2.7452E+02	7.5133E+01	1.2698E-01	7.2966E-04	5.7461E-03
6.60	9.7120E+00	2.8548E+03	2.9395E+02	8.0322E+01	1.2356E-01	6.6306E-04	5.3664E-03
6.70	9.9780E+00	3.1380E+03	3.1449E+02	8.5804E+01	1.2026E-01	6.0323E-04	5.0158E-03
6.80	1.0248E+01	3.4454E+03	3.3620E+02	9.1592E+01	1.1710E-01	5.4941E-04	4.6920E-03
6.90	1.0522E+01	3.7787E+03	3.5913E+02	9.7701E+01	1.1405E-01	5.0095E-04	4.3925E-03
7.00	1.0800E+01	4.1398E+03	3.8332E+02	1.0414E+02	1.1111E-01	4.5725E-04	4.1152E-03
7.10	1.1082E+01	4.5307E+03	4.0883E+02	1.1093E+02	1.0828E-01	4.1780E-04	3.8584E-03
7.20	1.1368E+01	4.9533E+03	4.3572E+02	1.1808E+02	1.0556E-01	3.8216E-04	3.6203E-03
7.30	1.1658E+01	5.4098E+03	4.6405E+02	1.2560E+02	1.0293E-01	3.4991E-04	3.3993E-03
7.40	1.1952E+01	5.9026E+03	4.9386E+02	1.3352E+02	1.0040E-01	3.2070E-04	3.1941E-03
7.50	1.2250E+01	6.4339E+03	5.2522E+02	1.4184E+02	9.7959E-02	2.9421E-04	3.0034E-03
7.60	1.2552E+01	7.0064E+03	5.5819E+02	1.5058E+02	9.5602E-02	2.7017E-04	2.8260E-03
7.70	1.2858E+01	7.6227E+03	5.9283E+02	1.5976E+02	9.3327E-02	2.4833E-04	2.6608E-03
7.80	1.3168E+01	8.2855E+03	6.2922E+02	1.6940E+02	9.1130E-02	2.2846E-04	2.5070E-03
7.90	1.3482E+01	8.9979E+03	6.6740E+02	1.7951E+02	8.9008E-02	2.1038E-04	2.3636E-03
8.00	1.3800E+01	9.7629E+03	7.0745E+02	1.9011E+02	8.6957E-02	1.9389E-04	2.2297E-03
8.10	1.4122E+01	1.0584E+04	7.4945E+02	2.0121E+02	8.4974E-02	1.7885E-04	2.1048E-03
8.20	1.4448E+01	1.1464E+04	7.9345E+02	2.1284E+02	8.3056E-02	1.6512E-04	1.9881E-03
8.30	1.4778E+01	1.2407E+04	8.3954E+02	2.2502E+02	8.1202E-02	1.5257E-04	1.8789E-03
8.40	1.5112E+01	1.3416E+04	8.8778E+02	2.3776E+02	7.9407E-02	1.4109E-04	1.7768E-03
8.50	1.5450E+01	1.4496E+04	9.3826E+02	2.5108E+02	7.7670E-02	1.3058E-04	1.6812E-03
8.60	1.5792E+01	1.5651E+04	9.9104E+03	2.6501E+02	7.5988E-02	1.2095E-04	1.5917E-03
8.70	1.6138E+01	1.6884E+04	1.0462E+03	2.7956E+02	7.4359E-02	1.1211E-04	1.5077E-03
8.80	1.6488E+01	1.8201E+04	1.1039E+03	2.9476E+02	7.2780E-02	1.0400E-04	1.4290E-03
8.90	1.6842E+01	1.9605E+04	1.1641E+03	3.1063E+02	7.1250E-02	9.6551E-05	1.3551E-03
9.00	1.7200E+01	2.1103E+04	1.2269E+03	3.2719E+02	6.9767E-02	8.9698E-05	1.2857E-03
9.10	1.7562E+01	2.2699E+04	1.2925E+03	3.4445E+02	6.8329E-02	8.3392E-05	1.2204E-03
9.20	1.7928E+01	2.4398E+04	1.3609E+03	3.6246E+02	6.6934E-02	7.7584E-05	1.1591E-03
9.30	1.8298E+01	2.6207E+04	1.4322E+03	3.8122E+02	6.5581E-02	7.2231E-05	1.1014E-03
9.40	1.8672E+01	2.8130E+04	1.5065E+03	4.0077E+02	6.4267E-02	6.7292E-05	1.0471E-03
9.50	1.9050E+01	3.0174E+04	1.5839E+03	4.2113E+02	6.2992E-02	6.2734E-05	9.9590E-04

(Continued)

M	T_t/T	p_t/p	ρ_t/ρ	A/A^*	T/T^*	p/p^*	ρ/ρ^*
9.60	1.9432E+01	3.2345E+04	1.6645E+03	4.4232E+02	6.1754E-02	5.8523E-05	9.4767E-04
9.70	1.9818E+01	3.4650E+04	1.7484E+03	4.6436E+02	6.0551E-02	5.4629E-05	9.0220E-04
9.80	2.0208E+01	3.7096E+04	1.8357E+03	4.8730E+02	5.9382E-02	5.1027E-05	8.5930E-04
9.90	2.0602E+01	3.9690E+04	1.9265E+03	5.1114E+02	5.8247E-02	4.7693E-05	8.1880E-04
10.00	2.1000E+01	4.2439E+04	2.0209E+03	5.3593E+02	5.7143E-02	4.4603E-05	7.8056E-04
10.10	2.1402E+01	4.5351E+04	2.1190E+03	5.6168E+02	5.6070E-02	4.1739E-05	7.4442E-04
10.20	2.1808E+01	4.8435E+04	2.2210E+03	5.8843E+02	5.5026E-02	3.9082E-05	7.1025E-04
10.30	2.2218E+01	5.1697E+04	2.3268E+03	6.1621E+02	5.4010E-02	3.6616E-05	6.7794E-04
10.40	2.2632E+01	5.5148E+04	2.4367E+03	6.4504E+02	5.3022E-02	3.4324E-05	6.4736E-04
10.50	2.3050E+01	5.8796E+04	2.5508E+03	6.7495E+02	5.2061E-02	3.2195E-05	6.1841E-04
10.60	2.3472E+01	6.2651E+04	2.6692E+03	7.0599E+02	5.1125E-02	3.0214E-05	5.9099E-04
10.70	2.3898E+01	6.6721E+04	2.7919E+03	7.3816E+02	5.0213E-02	2.8371E-05	5.6500E-04
10.80	2.4328E+01	7.1019E+04	2.9192E+03	7.7152E+02	4.9326E-02	2.6654E-05	5.4036E-04
10.90	2.4762E+01	7.5553E+04	3.0512E+03	8.0609E+02	4.8461E-02	2.5054E-05	5.1700E-04
11.00	2.5200E+01	8.0334E+04	3.1879E+03	8.4190E+02	4.7619E-02	2.3563E-05	4.9483E-04
11.10	2.5642E+01	8.5375E+04	3.3295E+03	8.7899E+02	4.6798E-02	2.2172E-05	4.7378E-04
11.20	2.6088E+01	9.0687E+04	3.4762E+03	9.1739E+02	4.5998E-02	2.0873E-05	4.5379E-04
11.30	2.6538E+01	9.6281E+04	3.6280E+03	9.5714E+02	4.5218E-02	1.9661E-05	4.3479E-04
11.40	2.6992E+01	1.0217E+05	3.7852E+03	9.9828E+02	4.4458E-02	1.8527E-05	4.1674E-04
11.50	2.7450E+01	1.0837E+05	3.9478E+03	1.0408E+03	4.3716E-02	1.7468E-05	3.9957E-04
11.60	2.7912E+01	1.1489E+05	4.1160E+03	1.0848E+03	4.2992E-02	1.6477E-05	3.8324E-04
11.70	2.8378E+01	1.2174E+05	4.2900E+03	1.1303E+03	4.2286E-02	1.5549E-05	3.6770E-04
11.80	2.8848E+01	1.2895E+05	4.4698E+03	1.1774E+03	4.1597E-02	1.4680E-05	3.5291E-04
11.90	2.9322E+01	1.3651E+05	4.6557E+03	1.2260E+03	4.0925E-02	1.3866E-05	3.3882E-04
12.00	2.9800E+01	1.4446E+05	4.8478E+03	1.2762E+03	4.0268E-02	1.3103E-05	3.2540E-04
12.10	3.0282E+01	1.5281E+05	5.0462E+03	1.3281E+03	3.9628E-02	1.2388E-05	3.1260E-04
12.20	3.0768E+01	1.6157E+05	5.2511E+03	1.3816E+03	3.9002E-02	1.1716E-05	3.0040E-04
12.30	3.1258E+01	1.7075E+05	5.4626E+03	1.4369E+03	3.8390E-02	1.1086E-05	2.8877E-04
12.40	3.1752E+01	1.8038E+05	5.6810E+03	1.4940E+03	3.7793E-02	1.0494E-05	2.7767E-04
12.50	3.2250E+01	1.9048E+05	5.9064E+03	1.5529E+03	3.7209E-02	9.9376E-06	2.6707E-04
12.60	3.2752E+01	2.0106E+05	6.1390E+03	1.6136E+03	3.6639E-02	9.4146E-06	2.5696E-04
12.70	3.3258E+01	2.1215E+05	6.3788E+03	1.6762E+03	3.6082E-02	8.9227E-06	2.4729E-04
12.80	3.3768E+01	2.2375E+05	6.6262E+03	1.7408E+03	3.5537E-02	8.4599E-06	2.3806E-04
12.90	3.4282E+01	2.3590E+05	6.8812E+03	1.8074E+03	3.5004E-02	8.0242E-06	2.2924E-04
13.00	3.4800E+01	2.4862E+05	7.1441E+03	1.8761E+03	3.4483E-02	7.6139E-06	2.2080E-04
13.10	3.5322E+01	2.6191E+05	7.4150E+03	1.9468E+03	3.3973E-02	7.2273E-06	2.1274E-04
13.20	3.5848E+01	2.7582E+05	7.6942E+03	2.0196E+03	3.3475E-02	6.8629E-06	2.0502E-04
13.30	3.6378E+01	2.9036E+05	7.9817E+03	2.0947E+03	3.2987E-02	6.5193E-06	1.9763E-04
13.40	3.6912E+01	3.0555E+05	8.2779E+03	2.1719E+03	3.2510E-02	6.1951E-06	1.9056E-04
13.50	3.7450E+01	3.2143E+05	8.5828E+03	2.2515E+03	3.2043E-02	5.8892E-06	1.8379E-04

M	T_1/T	p_1/p	ρ_1/ρ	A/A^*	T/T^*	p/p^*	ρ/ρ^*
13.60	3.7992E+01	3.3800E+05	8.8967E+03	2.3334E+03	3.1586E-02	5.6003E-06	1.7731E-04
13.70	3.8538E+01	3.5531E+05	9.2198E+03	2.4177E+03	3.1138E-02	5.3275E-06	1.7109E-04
13.80	3.9088E+01	3.7338E+05	9.5523E+03	2.5044E+03	3.0700E-02	5.0697E-06	1.6514E-04
13.90	3.9642E+01	3.9223E+05	9.8944E+03	2.5936E+03	3.0271E-02	4.8260E-06	1.5943E-04
14.00	4.0200E+01	4.1190E+05	1.0246E+04	2.6854E+03	2.9851E-02	4.5956E-06	1.5395E-04
14.10	4.0762E+01	4.3241E+05	1.0608E+04	2.7797E+03	2.9439E-02	4.3776E-06	1.4870E-04
14.20	4.1328E+01	4.5379E+05	1.0980E+04	2.8767E+03	2.9036E-02	4.1714E-06	1.4366E-04
14.30	4.1898E+01	4.7608E+05	1.1363E+04	2.9764E+03	2.8641E-02	3.9761E-06	1.3883E-04
14.40	4.2472E+01	4.9930E+05	1.1756E+04	3.0789E+03	2.8254E-02	3.7912E-06	1.3418E-04
14.50	4.3050E+01	5.2349E+05	1.2160E+04	3.1842E+03	2.7875E-02	3.6160E-06	1.2972E-04
14.60	4.3632E+01	5.4868E+05	1.2575E+04	3.2924E+03	2.7503E-02	3.4500E-06	1.2544E-04
14.70	4.4218E+01	5.7491E+05	1.3002E+04	3.4035E+03	2.7138E-02	3.2926E-06	1.2133E-04
14.80	4.4808E+01	6.0221E+05	1.3440E+04	3.5177E+03	2.6781E-02	3.1433E-06	1.1737E-04
14.90	4.5402E+01	6.3061E+05	1.3890E+04	3.6349E+03	2.6431E-02	3.0017E-06	1.1357E-04
15.00	4.6000E+01	6.6016E+05	1.4351E+04	3.7552E+03	2.6087E-02	2.8674E-06	1.0992E-04
16.00	5.2200E+01	1.0277E+06	1.9687E+04	5.1445E+03	2.2989E-02	1.8420E-06	8.0127E-05
17.00	5.8800E+01	1.5589E+06	2.6512E+04	6.9204E+03	2.0408E-02	1.2143E-06	5.9499E-05
18.00	6.5800E+01	2.3110E+06	3.5121E+04	9.1592E+03	1.8237E-02	8.1911E-07	4.4915E-05
19.00	7.3200E+01	3.3557E+06	4.5843E+04	1.1946E+04	1.6393E-02	5.6409E-07	3.4409E-05
20.00	8.1000E+01	4.7830E+06	5.9049E+04	1.5377E+04	1.4815E-02	3.9576E-07	2.6714E-05
21.00	8.9200E+01	6.7031E+06	7.5147E+04	1.9558E+04	1.3453E-02	2.8240E-07	2.0991E-05
22.00	9.7800E+01	9.2509E+06	9.4590E+04	2.4606E+04	1.2270E-02	2.0462E-07	1.6677E-05
23.00	1.0680E+02	1.2589E+07	1.1788E+05	3.0650E+04	1.1236E-02	1.5036E-07	1.3382E-05
24.00	1.1620E+02	1.6913E+07	1.4555E+05	3.7832E+04	1.0327E-02	1.1192E-07	1.0838E-05
25.00	1.2600E+02	2.2454E+07	1.7821E+05	4.6304E+04	9.5238E-03	8.4302E-08	8.8517E-06
26.00	1.3620E+02	2.9486E+07	2.1649E+05	5.6235E+04	8.8106E-03	6.4197E-08	7.2864E-06
27.00	1.4680E+02	3.8330E+07	2.6110E+05	6.7806E+04	8.1744E-03	4.9385E-08	6.0414E-06
28.00	1.5780E+02	4.9360E+07	3.1280E+05	8.1211E+04	7.6046E-03	3.8350E-08	5.0430E-06
29.00	1.6920E+02	6.3009E+07	3.7239E+05	9.6662E+04	7.0922E-03	3.0042E-08	4.2360E-06
30.00	1.8100E+02	7.9777E+07	4.4075E+05	1.1438E+05	6.6298E-03	2.3728E-08	3.5790E-06
31.00	1.9320E+02	1.0024E+08	5.1882E+05	1.3462E+05	6.2112E-03	1.8885E-08	3.0404E-06
32.00	2.0580E+02	1.2504E+08	6.0759E+05	1.5763E+05	5.8309E-03	1.5138E-08	2.5962E-06
33.00	2.1880E+02	1.5494E+08	7.0814E+05	1.8369E+05	5.4845E-03	1.2217E-08	2.2276E-06
34.00	2.3220E+02	1.9077E+08	8.2159E+05	2.1309E+05	5.1680E-03	9.9224E-09	1.9200E-06
35.00	2.4600E+02	2.3349E+08	9.4916E+05	2.4614E+05	4.8780E-03	8.1070E-09	1.6619E-06
40.00	3.2100E+02	5.9261E+08	1.8461E+06	4.7853E+05	3.7383E-03	3.1942E-09	8.5446E-07
45.00	4.0600E+02	1.3485E+09	3.3214E+06	8.6063E+05	2.9557E-03	1.4038E-09	4.7494E-07
50.00	5.0100E+02	2.8147E+09	5.6182E+06	1.4554E+06	2.3952E-03	6.7252E-10	2.8078E-07
100.00	2.0010E+03	3.5840E+11	1.7911E+08	4.6365E+07	5.9970E-04	5.2816E-12	8.8072E-09
1000.00	2.0000E+05	3.5778E+18	1.7889E+13	4.6296E+12	6.0000E-06	5.2908E-19	8.8181E-14

Isentropic Table $\gamma = 1.3$

M	T_t/T	p_t/p	ρ_t/ρ	A/A^*	T/T^*	p/p^*	ρ/ρ^*
0.02	1.0001E+00	1.0003E+00	1.0002E+00	2.9268E+01	1.1499E+00	1.8319E+00	1.5931E+00
0.04	1.0002E+00	1.0010E+00	1.0008E+00	1.4644E+01	1.1497E+00	1.8305E+00	1.5921E+00
0.06	1.0005E+00	1.0023E+00	1.0018E+00	9.7740E+00	1.1494E+00	1.8281E+00	1.5905E+00
0.08	1.0010E+00	1.0042E+00	1.0032E+00	7.3423E+00	1.1489E+00	1.8248E+00	1.5883E+00
0.10	1.0015E+00	1.0065E+00	1.0050E+00	5.8860E+00	1.1483E+00	1.8206E+00	1.5855E+00
0.12	1.0022E+00	1.0094E+00	1.0072E+00	4.9174E+00	1.1475E+00	1.8154E+00	1.5820E+00
0.14	1.0029E+00	1.0128E+00	1.0098E+00	4.2275E+00	1.1466E+00	1.8093E+00	1.5779E+00
0.16	1.0038E+00	1.0167E+00	1.0129E+00	3.7118E+00	1.1456E+00	1.8022E+00	1.5732E+00
0.18	1.0049E+00	1.0212E+00	1.0163E+00	3.3123E+00	1.1444E+00	1.7943E+00	1.5679E+00
0.20	1.0060E+00	1.0263E+00	1.0201E+00	2.9940E+00	1.1431E+00	1.7855E+00	1.5619E+00
0.22	1.0073E+00	1.0318E+00	1.0244E+00	2.7349E+00	1.1417E+00	1.7759E+00	1.5554E+00
0.24	1.0086E+00	1.0380E+00	1.0291E+00	2.5202E+00	1.1401E+00	1.7654E+00	1.5484E+00
0.26	1.0101E+00	1.0447E+00	1.0342E+00	2.3396E+00	1.1385E+00	1.7540E+00	1.5407E+00
0.28	1.0118E+00	1.0520E+00	1.0397E+00	2.1859E+00	1.1366E+00	1.7419E+00	1.5325E+00
0.30	1.0135E+00	1.0598E+00	1.0457E+00	2.0537E+00	1.1347E+00	1.7290E+00	1.5237E+00
0.32	1.0154E+00	1.0683E+00	1.0521E+00	1.9389E+00	1.1326E+00	1.7153E+00	1.5145E+00
0.34	1.0173E+00	1.0773E+00	1.0590E+00	1.8385E+00	1.1304E+00	1.7009E+00	1.5047E+00
0.36	1.0194E+00	1.0870E+00	1.0663E+00	1.7502E+00	1.1281E+00	1.6857E+00	1.4943E+00
0.38	1.0217E+00	1.0973E+00	1.0740E+00	1.6719E+00	1.1256E+00	1.6699E+00	1.4836E+00
0.40	1.0240E+00	1.1082E+00	1.0823E+00	1.6023E+00	1.1230E+00	1.6534E+00	1.4723E+00
0.42	1.0265E+00	1.1198E+00	1.0910E+00	1.5401E+00	1.1204E+00	1.6363E+00	1.4606E+00
0.44	1.0290E+00	1.1321E+00	1.1001E+00	1.4843E+00	1.1175E+00	1.6186E+00	1.4484E+00
0.46	1.0317E+00	1.1450E+00	1.1098E+00	1.4341E+00	1.1146E+00	1.6004E+00	1.4358E+00
0.48	1.0346E+00	1.1586E+00	1.1199E+00	1.3888E+00	1.1116E+00	1.5815E+00	1.4228E+00
0.50	1.0375E+00	1.1730E+00	1.1306E+00	1.3479E+00	1.1084E+00	1.5622E+00	1.4094E+00
0.52	1.0406E+00	1.1880E+00	1.1417E+00	1.3107E+00	1.1052E+00	1.5424E+00	1.3956E+00
0.54	1.0437E+00	1.2038E+00	1.1534E+00	1.2770E+00	1.1018E+00	1.5221E+00	1.3815E+00
0.56	1.0470E+00	1.2204E+00	1.1656E+00	1.2464E+00	1.0983E+00	1.5015E+00	1.3670E+00
0.58	1.0505E+00	1.2378E+00	1.1783E+00	1.2186E+00	1.0948E+00	1.4804E+00	1.3523E+00
0.60	1.0540E+00	1.2560E+00	1.1916E+00	1.1932E+00	1.0911E+00	1.4590E+00	1.3372E+00
0.62	1.0577E+00	1.2750E+00	1.2055E+00	1.1702E+00	1.0873E+00	1.4372E+00	1.3218E+00
0.64	1.0614E+00	1.2948E+00	1.2199E+00	1.1492E+00	1.0834E+00	1.4152E+00	1.3062E+00
0.66	1.0653E+00	1.3156E+00	1.2349E+00	1.1302E+00	1.0795E+00	1.3929E+00	1.2903E+00
0.68	1.0694E+00	1.3372E+00	1.2505E+00	1.1129E+00	1.0754E+00	1.3703E+00	1.2742E+00
0.70	1.0735E+00	1.3598E+00	1.2667E+00	1.0972E+00	1.0713E+00	1.3476E+00	1.2579E+00
0.72	1.0778E+00	1.3833E+00	1.2835E+00	1.0831E+00	1.0670E+00	1.3246E+00	1.2414E+00
0.74	1.0821E+00	1.4079E+00	1.3010E+00	1.0703E+00	1.0627E+00	1.3016E+00	1.2247E+00

M	T_t/T	p_t/p	ρ_t/ρ	A/A^*	T/T^*	p/p^*	ρ/ρ^*
0.76	1.0866E+00	1.4334E+00	1.3191E+00	1.0589E+00	1.0583E+00	1.2784E+00	1.2079E+00
0.78	1.0913E+00	1.4600E+00	1.3379E+00	1.0486E+00	1.0538E+00	1.2551E+00	1.1910E+00
0.80	1.0960E+00	1.4877E+00	1.3574E+00	1.0395E+00	1.0493E+00	1.2317E+00	1.1739E+00
0.82	1.1009E+00	1.5165E+00	1.3775E+00	1.0315E+00	1.0446E+00	1.2083E+00	1.1567E+00
0.84	1.1058E+00	1.5464E+00	1.3984E+00	1.0245E+00	1.0399E+00	1.1849E+00	1.1394E+00
0.86	1.1109E+00	1.5776E+00	1.4200E+00	1.0185E+00	1.0352E+00	1.1615E+00	1.1221E+00
0.88	1.1162E+00	1.6100E+00	1.4424E+00	1.0134E+00	1.0303E+00	1.1382E+00	1.1047E+00
0.90	1.1215E+00	1.6436E+00	1.4655E+00	1.0092E+00	1.0254E+00	1.1149E+00	1.0872E+00
0.92	1.1270E+00	1.6786E+00	1.4895E+00	1.0058E+00	1.0204E+00	1.0917E+00	1.0698E+00
0.94	1.1325E+00	1.7149E+00	1.5142E+00	1.0032E+00	1.0154E+00	1.0685E+00	1.0523E+00
0.96	1.1382E+00	1.7526E+00	1.5397E+00	1.0014E+00	1.0103E+00	1.0455E+00	1.0349E+00
0.98	1.1441E+00	1.7917E+00	1.5661E+00	1.0004E+00	1.0052E+00	1.0227E+00	1.0174E+00
1.00	1.1500E+00	1.8324E+00	1.5934E+00	1.0000E+00	1.0000E+00	1.0000E+00	1.0000E+00
1.02	1.1561E+00	1.8746E+00	1.6216E+00	1.0003E+00	9.9476E-01	9.7748E-01	9.8263E-01
1.04	1.1622E+00	1.9184E+00	1.6506E+00	1.0014E+00	9.8947E-01	9.5516E-01	9.6533E-01
1.06	1.1685E+00	1.9639E+00	1.6806E+00	1.0030E+00	9.8413E-01	9.3304E-01	9.4809E-01
1.08	1.1750E+00	2.0111E+00	1.7116E+00	1.0054E+00	9.7876E-01	9.1115E-01	9.3093E-01
1.10	1.1815E+00	2.0600E+00	1.7436E+00	1.0083E+00	9.7334E-01	8.8950E-01	9.1386E-01
1.12	1.1882E+00	2.1108E+00	1.7766E+00	1.0119E+00	9.6788E-01	8.6809E-01	8.9690E-01
1.14	1.1949E+00	2.1635E+00	1.8106E+00	1.0160E+00	9.6239E-01	8.4695E-01	8.8005E-01
1.16	1.2018E+00	2.2182E+00	1.8457E+00	1.0208E+00	9.5687E-01	8.2608E-01	8.6332E-01
1.18	1.2089E+00	2.2749E+00	1.8818E+00	1.0262E+00	9.5131E-01	8.0549E-01	8.4672E-01
1.20	1.2160E+00	2.3337E+00	1.9192E+00	1.0321E+00	9.4572E-01	7.8520E-01	8.3026E-01
1.22	1.2233E+00	2.3947E+00	1.9576E+00	1.0386E+00	9.4011E-01	7.6520E-01	8.1395E-01
1.24	1.2306E+00	2.4579E+00	1.9973E+00	1.0457E+00	9.3447E-01	7.4551E-01	7.9779E-01
1.26	1.2381E+00	2.5235E+00	2.0381E+00	1.0533E+00	9.2881E-01	7.2614E-01	7.8180E-01
1.28	1.2458E+00	2.5915E+00	2.0802E+00	1.0616E+00	9.2313E-01	7.0709E-01	7.6597E-01
1.30	1.2535E+00	2.6620E+00	2.1236E+00	1.0703E+00	9.1743E-01	6.8836E-01	7.5032E-01
1.32	1.2614E+00	2.7351E+00	2.1683E+00	1.0797E+00	9.1171E-01	6.6997E-01	7.3485E-01
1.34	1.2693E+00	2.8108E+00	2.2144E+00	1.0896E+00	9.0598E-01	6.5191E-01	7.1956E-01
1.36	1.2774E+00	2.8894E+00	2.2619E+00	1.1001E+00	9.0024E-01	6.3418E-01	7.0446E-01
1.38	1.2857E+00	2.9708E+00	2.3107E+00	1.1111E+00	8.9448E-01	6.1680E-01	6.8956E-01
1.40	1.2940E+00	3.0552E+00	2.3611E+00	1.1227E+00	8.8872E-01	5.9976E-01	6.7486E-01
1.42	1.3025E+00	3.1427E+00	2.4129E+00	1.1349E+00	8.8294E-01	5.8306E-01	6.6036E-01
1.44	1.3110E+00	3.2334E+00	2.4663E+00	1.1477E+00	8.7717E-01	5.6670E-01	6.4606E-01
1.46	1.3197E+00	3.3275E+00	2.5213E+00	1.1610E+00	8.7138E-01	5.5069E-01	6.3198E-01
1.48	1.3286E+00	3.4249E+00	2.5779E+00	1.1750E+00	8.6560E-01	5.3502E-01	6.1810E-01
1.50	1.3375E+00	3.5259E+00	2.6362E+00	1.1895E+00	8.5981E-01	5.1970E-01	6.0443E-01

(Continued)

M	T_t/T	p_t/p	ρ_t/ρ	A/A^*	T/T^*	p/p^*	ρ/ρ^*
1.52	1.3466E+00	3.6306E+00	2.6962E+00	1.2046E+00	8.5403E-01	5.0471E-01	5.9098E-01
1.54	1.3557E+00	3.7390E+00	2.7579E+00	1.2203E+00	8.4825E-01	4.9007E-01	5.7775E-01
1.56	1.3650E+00	3.8515E+00	2.8215E+00	1.2367E+00	8.4247E-01	4.7577E-01	5.6473E-01
1.58	1.3745E+00	3.9680E+00	2.8869E+00	1.2536E+00	8.3669E-01	4.6180E-01	5.5194E-01
1.60	1.3840E+00	4.0887E+00	2.9543E+00	1.2712E+00	8.3092E-01	4.4816E-01	5.3936E-01
1.62	1.3937E+00	4.2138E+00	3.0236E+00	1.2895E+00	8.2517E-01	4.3486E-01	5.2699E-01
1.64	1.4034E+00	4.3435E+00	3.0949E+00	1.3083E+00	8.1942E-01	4.2188E-01	5.1485E-01
1.66	1.4133E+00	4.4778E+00	3.1682E+00	1.3279E+00	8.1368E-01	4.0922E-01	5.0293E-01
1.68	1.4234E+00	4.6170E+00	3.2437E+00	1.3481E+00	8.0795E-01	3.9688E-01	4.9122E-01
1.70	1.4335E+00	4.7612E+00	3.3214E+00	1.3690E+00	8.0223E-01	3.8486E-01	4.7974E-01
1.72	1.4438E+00	4.9107E+00	3.4013E+00	1.3906E+00	7.9653E-01	3.7315E-01	4.6847E-01
1.74	1.4541E+00	5.0655E+00	3.4835E+00	1.4128E+00	7.9085E-01	3.6174E-01	4.5741E-01
1.76	1.4646E+00	5.2259E+00	3.5680E+00	1.4359E+00	7.8518E-01	3.5064E-01	4.4657E-01
1.78	1.4753E+00	5.3921E+00	3.6550E+00	1.4596E+00	7.7952E-01	3.3983E-01	4.3595E-01
1.80	1.4860E+00	5.5643E+00	3.7445E+00	1.4841E+00	7.7389E-01	3.2931E-01	4.2553E-01
1.82	1.4969E+00	5.7427E+00	3.8365E+00	1.5093E+00	7.6827E-01	3.1908E-01	4.1533E-01
1.84	1.5078E+00	5.9274E+00	3.9311E+00	1.5353E+00	7.6268E-01	3.0914E-01	4.0533E-01
1.86	1.5189E+00	6.1189E+00	4.0284E+00	1.5621E+00	7.5711E-01	2.9947E-01	3.9554E-01
1.88	1.5302E+00	6.3171E+00	4.1284E+00	1.5897E+00	7.5156E-01	2.9007E-01	3.8596E-01
1.90	1.5415E+00	6.5225E+00	4.2313E+00	1.6181E+00	7.4603E-01	2.8093E-01	3.7658E-01
1.92	1.5530E+00	6.7353E+00	4.3371E+00	1.6474E+00	7.4052E-01	2.7206E-01	3.6739E-01
1.94	1.5645E+00	6.9556E+00	4.4458E+00	1.6775E+00	7.3504E-01	2.6344E-01	3.5841E-01
1.96	1.5762E+00	7.1838E+00	4.5576E+00	1.7085E+00	7.2958E-01	2.5507E-01	3.4961E-01
1.98	1.5881E+00	7.4202E+00	4.6725E+00	1.7404E+00	7.2415E-01	2.4695E-01	3.4102E-01
2.00	1.6000E+00	7.6650E+00	4.7906E+00	1.7732E+00	7.1875E-01	2.3906E-01	3.3261E-01
2.02	1.6121E+00	7.9185E+00	4.9121E+00	1.8069E+00	7.1337E-01	2.3140E-01	3.2438E-01
2.04	1.6242E+00	8.1811E+00	5.0369E+00	1.8415E+00	7.0802E-01	2.2398E-01	3.1635E-01
2.06	1.6365E+00	8.4529E+00	5.1651E+00	1.8772E+00	7.0270E-01	2.1677E-01	3.0849E-01
2.08	1.6490E+00	8.7345E+00	5.2970E+00	1.9138E+00	6.9741E-01	2.0979E-01	3.0081E-01
2.10	1.6615E+00	9.0260E+00	5.4324E+00	1.9514E+00	6.9215E-01	2.0301E-01	2.9331E-01
2.12	1.6742E+00	9.3278E+00	5.5716E+00	1.9901E+00	6.8691E-01	1.9644E-01	2.8598E-01
2.14	1.6869E+00	9.6403E+00	5.7147E+00	2.0298E+00	6.8171E-01	1.9008E-01	2.7883E-01
2.16	1.6998E+00	9.9638E+00	5.8616E+00	2.0706E+00	6.7653E-01	1.8390E-01	2.7183E-01
2.18	1.7129E+00	1.0299E+01	6.0126E+00	2.1125E+00	6.7139E-01	1.7792E-01	2.6501E-01
2.20	1.7260E+00	1.0646E+01	6.1678E+00	2.1555E+00	6.6628E-01	1.7213E-01	2.5834E-01
2.22	1.7393E+00	1.1005E+01	6.3271E+00	2.1997E+00	6.6120E-01	1.6651E-01	2.5184E-01
2.24	1.7526E+00	1.1376E+01	6.4908E+00	2.2450E+00	6.5615E-01	1.6107E-01	2.4548E-01
2.26	1.7661E+00	1.1761E+01	6.6590E+00	2.2916E+00	6.5114E-01	1.5581E-01	2.3928E-01
2.28	1.7798E+00	1.2159E+01	6.8317E+00	2.3394E+00	6.4615E-01	1.5070E-01	2.3324E-01
2.30	1.7935E+00	1.2571E+01	7.0091E+00	2.3884E+00	6.4120E-01	1.4576E-01	2.2733E-01

M	T_t/T	p_t/p	ρ_t/ρ	A/A^*	T/T^*	p/p^*	ρ/ρ^*
2.32	1.8074E+00	1.2997E+01	7.1913E+00	2.4388E+00	6.3629E-01	1.4098E-01	2.2157E-01
2.34	1.8213E+00	1.3439E+01	7.3784E+00	2.4904E+00	6.3140E-01	1.3635E-01	2.1595E-01
2.36	1.8354E+00	1.3895E+01	7.5705E+00	2.5434E+00	6.2655E-01	1.3187E-01	2.1047E-01
2.38	1.8497E+00	1.4368E+01	7.7678E+00	2.5977E+00	6.2174E-01	1.2753E-01	2.0513E-01
2.40	1.8640E+00	1.4857E+01	7.9703E+00	2.6535E+00	6.1695E-01	1.2334E-01	1.9992E-01
2.42	1.8785E+00	1.5363E+01	8.1783E+00	2.7107E+00	6.1220E-01	1.1928E-01	1.9483E-01
2.44	1.8930E+00	1.5886E+01	8.3918E+00	2.7693E+00	6.0749E-01	1.1535E-01	1.8987E-01
2.46	1.9077E+00	1.6428E+01	8.6110E+00	2.8295E+00	6.0281E-01	1.1154E-01	1.8504E-01
2.48	1.9226E+00	1.6988E+01	8.8360E+00	2.8912E+00	5.9816E-01	1.0786E-01	1.8033E-01
2.50	1.9375E+00	1.7567E+01	9.0670E+00	2.9544E+00	5.9355E-01	1.0431E-01	1.7574E-01
2.52	1.9526E+00	1.8167E+01	9.3040E+00	3.0193E+00	5.8897E-01	1.0086E-01	1.7126E-01
2.54	1.9677E+00	1.8787E+01	9.5473E+00	3.0857E+00	5.8443E-01	9.7536E-02	1.6689E-01
2.56	1.9830E+00	1.9428E+01	9.7970E+00	3.1539E+00	5.7992E-01	9.4317E-02	1.6264E-01
2.58	1.9985E+00	2.0091E+01	1.0053E+01	3.2238E+00	5.7544E-01	9.1203E-02	1.5850E-01
2.60	2.0140E+00	2.0777E+01	1.0316E+01	3.2954E+00	5.7100E-01	8.8193E-02	1.5446E-01
2.62	2.0297E+00	2.1486E+01	1.0586E+01	3.3688E+00	5.6660E-01	8.5282E-02	1.5052E-01
2.64	2.0454E+00	2.2219E+01	1.0863E+01	3.4440E+00	5.6223E-01	8.2467E-02	1.4668E-01
2.66	2.0613E+00	2.2978E+01	1.1147E+01	3.5211E+00	5.5789E-01	7.9746E-02	1.4295E-01
2.68	2.0774E+00	2.3761E+01	1.1438E+01	3.6001E+00	5.5359E-01	7.7115E-02	1.3930E-01
2.70	2.0935E+00	2.4572E+01	1.1737E+01	3.6810E+00	5.4932E-01	7.4572E-02	1.3576E-01
2.72	2.1098E+00	2.5410E+01	1.2044E+01	3.7639E+00	5.4509E-01	7.2113E-02	1.3230E-01
2.74	2.1261E+00	2.6276E+01	1.2358E+01	3.8489E+00	5.4089E-01	6.9736E-02	1.2893E-01
2.76	2.1426E+00	2.7171E+01	1.2681E+01	3.9359E+00	5.3672E-01	6.7439E-02	1.2565E-01
2.78	2.1593E+00	2.8096E+01	1.3012E+01	4.0251E+00	5.3259E-01	6.5218E-02	1.2246E-01
2.80	2.1760E+00	2.9052E+01	1.3351E+01	4.1164E+00	5.2849E-01	6.3072E-02	1.1935E-01
2.82	2.1929E+00	3.0040E+01	1.3699E+01	4.2099E+00	5.2443E-01	6.0997E-02	1.1631E-01
2.84	2.2098E+00	3.1061E+01	1.4056E+01	4.3057E+00	5.2040E-01	5.8992E-02	1.1336E-01
2.86	2.2269E+00	3.2116E+01	1.4422E+01	4.4038E+00	5.1640E-01	5.7054E-02	1.1049E-01
2.88	2.2442E+00	3.3206E+01	1.4797E+01	4.5043E+00	5.1244E-01	5.5181E-02	1.0769E-01
2.90	2.2615E+00	3.4333E+01	1.5181E+01	4.6072E+00	5.0851E-01	5.3371E-02	1.0496E-01
2.92	2.2790E+00	3.5496E+01	1.5576E+01	4.7125E+00	5.0462E-01	5.1622E-02	1.0230E-01
2.94	2.2965E+00	3.6698E+01	1.5980E+01	4.8204E+00	5.0075E-01	4.9931E-02	9.9714E-02
2.96	2.3142E+00	3.7939E+01	1.6394E+01	4.9308E+00	4.9692E-01	4.8297E-02	9.7194E-02
2.98	2.3321E+00	3.9222E+01	1.6818E+01	5.0439E+00	4.9313E-01	4.6718E-02	9.4741E-02
3.00	2.3500E+00	4.0546E+01	1.7254E+01	5.1596E+00	4.8936E-01	4.5192E-02	9.2351E-02
3.05	2.3954E+00	4.4049E+01	1.8389E+01	5.4611E+00	4.8009E-01	4.1598E-02	8.6648E-02
3.10	2.4415E+00	4.7845E+01	1.9596E+01	5.7806E+00	4.7102E-01	3.8298E-02	8.1311E-02
3.15	2.4884E+00	5.1954E+01	2.0879E+01	6.1190E+00	4.6215E-01	3.5269E-02	7.6316E-02
3.20	2.5360E+00	5.6403E+01	2.2241E+01	6.4774E+00	4.5347E-01	3.2487E-02	7.1643E-02
3.25	2.5844E+00	6.1215E+01	2.3687E+01	6.8569E+00	4.4498E-01	2.9933E-02	6.7270E-02

(Continued)

<i>M</i>	T_1/T	p_1/p	ρ_1/ρ	A/A^*	T/T^*	p/p^*	ρ/ρ^*
3.30	2.6335E+00	6.6420E+01	2.5221E+01	7.2584E+00	4.3668E-01	2.7588E-02	6.3177E-02
3.35	2.6834E+00	7.2045E+01	2.6849E+01	7.6833E+00	4.2856E-01	2.5433E-02	5.9347E-02
3.40	2.7340E+00	7.8123E+01	2.8575E+01	8.1326E+00	4.2063E-01	2.3455E-02	5.5763E-02
3.45	2.7854E+00	8.4687E+01	3.0404E+01	8.6076E+00	4.1287E-01	2.1637E-02	5.2407E-02
3.50	2.8375E+00	9.1771E+01	3.2342E+01	9.1096E+00	4.0529E-01	1.9967E-02	4.9267E-02
3.55	2.8904E+00	9.9415E+01	3.4395E+01	9.6399E+00	3.9787E-01	1.8431E-02	4.6326E-02
3.60	2.9440E+00	1.0766E+02	3.6569E+01	1.0200E+01	3.9063E-01	1.7020E-02	4.3573E-02
3.65	2.9984E+00	1.1654E+02	3.8869E+01	1.0791E+01	3.8354E-01	1.5722E-02	4.0994E-02
3.70	3.0535E+00	1.2612E+02	4.1303E+01	1.1416E+01	3.7662E-01	1.4529E-02	3.8579E-02
3.75	3.1094E+00	1.3643E+02	4.3876E+01	1.2074E+01	3.6985E-01	1.3431E-02	3.6316E-02
3.80	3.1660E+00	1.4752E+02	4.6596E+01	1.2769E+01	3.6323E-01	1.2421E-02	3.4196E-02
3.85	3.2234E+00	1.5946E+02	4.9471E+01	1.3501E+01	3.5677E-01	1.1491E-02	3.2209E-02
3.90	3.2815E+00	1.7230E+02	5.2508E+01	1.4273E+01	3.5045E-01	1.0634E-02	3.0346E-02
3.95	3.3404E+00	1.8611E+02	5.5714E+01	1.5087E+01	3.4427E-01	9.8457E-03	2.8599E-02
4.00	3.4000E+00	2.0094E+02	5.9099E+01	1.5944E+01	3.3824E-01	9.1191E-03	2.6962E-02
4.05	3.4604E+00	2.1686E+02	6.2670E+01	1.6846E+01	3.3233E-01	8.4494E-03	2.5425E-02
4.10	3.5215E+00	2.3396E+02	6.6437E+01	1.7796E+01	3.2657E-01	7.8320E-03	2.3984E-02
4.15	3.5834E+00	2.5230E+02	7.0408E+01	1.8795E+01	3.2093E-01	7.2626E-03	2.2631E-02
4.20	3.6460E+00	2.7197E+02	7.4594E+01	1.9847E+01	3.1541E-01	6.7373E-03	2.1361E-02
4.25	3.7094E+00	2.9306E+02	7.9004E+01	2.0953E+01	3.1003E-01	6.2525E-03	2.0169E-02
4.30	3.7735E+00	3.1565E+02	8.3649E+01	2.2115E+01	3.0476E-01	5.8050E-03	1.9049E-02
4.35	3.8384E+00	3.3985E+02	8.8540E+01	2.3337E+01	2.9961E-01	5.3916E-03	1.7996E-02
4.40	3.9040E+00	3.6575E+02	9.3687E+01	2.4621E+01	2.9457E-01	5.0098E-03	1.7008E-02
4.45	3.9704E+00	3.9347E+02	9.9103E+01	2.5970E+01	2.8965E-01	4.6568E-03	1.6078E-02
4.50	4.0375E+00	4.2312E+02	1.0480E+02	2.7386E+01	2.8483E-01	4.3305E-03	1.5204E-02
4.55	4.1054E+00	4.5482E+02	1.1079E+02	2.8872E+01	2.8012E-01	4.0287E-03	1.4383E-02
4.60	4.1740E+00	4.8870E+02	1.1708E+02	3.0432E+01	2.7552E-01	3.7494E-03	1.3609E-02
4.65	4.2434E+00	5.2488E+02	1.2369E+02	3.2069E+01	2.7101E-01	3.4909E-03	1.2882E-02
4.70	4.3135E+00	5.6352E+02	1.3064E+02	3.3785E+01	2.6660E-01	3.2516E-03	1.2197E-02
4.75	4.3844E+00	6.0475E+02	1.3793E+02	3.5584E+01	2.6230E-01	3.0299E-03	1.1552E-02
4.80	4.4560E+00	6.4875E+02	1.4559E+02	3.7470E+01	2.5808E-01	2.8244E-03	1.0944E-02
4.85	4.5284E+00	6.9566E+02	1.5362E+02	3.9447E+01	2.5395E-01	2.6340E-03	1.0372E-02
4.90	4.6015E+00	7.4566E+02	1.6205E+02	4.1517E+01	2.4992E-01	2.4573E-03	9.8329E-03
4.95	4.6754E+00	7.9894E+02	1.7088E+02	4.3685E+01	2.4597E-01	2.2934E-03	9.3245E-03
5.00	4.7500E+00	8.5569E+02	1.8015E+02	4.5954E+01	2.4211E-01	2.1413E-03	8.8451E-03
5.10	4.9015E+00	9.8040E+02	2.0002E+02	5.0815E+01	2.3462E-01	1.8690E-03	7.9662E-03
5.20	5.0560E+00	1.1215E+03	2.2182E+02	5.6134E+01	2.2745E-01	1.6338E-03	7.1833E-03
5.30	5.2135E+00	1.2810E+03	2.4570E+02	6.1947E+01	2.2058E-01	1.4304E-03	6.4851E-03
5.40	5.3740E+00	1.4608E+03	2.7183E+02	6.8294E+01	2.1399E-01	1.2543E-03	5.8617E-03
5.50	5.5375E+00	1.6634E+03	3.0039E+02	7.5216E+01	2.0767E-01	1.1015E-03	5.3044E-03

M	T_t/T	p_t/p	ρ_t/ρ	A/A^*	T/T^*	p/p^*	ρ/ρ^*
5.60	5.7040E+00	1.8913E+03	3.3157E+02	8.2756E+01	2.0161E-01	9.6883E-04	4.8056E-03
5.70	5.8735E+00	2.1471E+03	3.6556E+02	9.0963E+01	1.9579E-01	8.5337E-04	4.3587E-03
5.80	6.0460E+00	2.4341E+03	4.0259E+02	9.9885E+01	1.9021E-01	7.5277E-04	3.9578E-03
5.90	6.2215E+00	2.7554E+03	4.4288E+02	1.0958E+02	1.8484E-01	6.6499E-04	3.5978E-03
6.00	6.4000E+00	3.1147E+03	4.8668E+02	1.2009E+02	1.7969E-01	5.8827E-04	3.2740E-03
6.10	6.5815E+00	3.5160E+03	5.3422E+02	1.3149E+02	1.7473E-01	5.2114E-04	2.9826E-03
6.20	6.7660E+00	3.9635E+03	5.8579E+02	1.4383E+02	1.6997E-01	4.6230E-04	2.7201E-03
6.30	6.9535E+00	4.4619E+03	6.4168E+02	1.5718E+02	1.6538E-01	4.1066E-04	2.4832E-03
6.40	7.1440E+00	5.0163E+03	7.0217E+02	1.7162E+02	1.6097E-01	3.6527E-04	2.2692E-03
6.50	7.3375E+00	5.6322E+03	7.6759E+02	1.8721E+02	1.5673E-01	3.2533E-04	2.0758E-03
6.60	7.5340E+00	6.3156E+03	8.3828E+02	2.0403E+02	1.5264E-01	2.9012E-04	1.9008E-03
6.70	7.7335E+00	7.0729E+03	9.1458E+02	2.2216E+02	1.4870E-01	2.5906E-04	1.7422E-03
6.80	7.9360E+00	7.9112E+03	9.9688E+02	2.4169E+02	1.4491E-01	2.3161E-04	1.5984E-03
6.90	8.1415E+00	8.8380E+03	1.0856E+03	2.6271E+02	1.4125E-01	2.0732E-04	1.4678E-03
7.00	8.3500E+00	9.8615E+03	1.1810E+03	2.8532E+02	1.3772E-01	1.8580E-04	1.3492E-03
7.10	8.5615E+00	1.0991E+04	1.2837E+03	3.0961E+02	1.3432E-01	1.6672E-04	1.2412E-03
7.20	8.7760E+00	1.2235E+04	1.3941E+03	3.3569E+02	1.3104E-01	1.4976E-04	1.1430E-03
7.30	8.9935E+00	1.3604E+04	1.5126E+03	3.6366E+02	1.2787E-01	1.3469E-04	1.0534E-03
7.40	9.2140E+00	1.5109E+04	1.6398E+03	3.9365E+02	1.2481E-01	1.2127E-04	9.7169E-04
7.50	9.4375E+00	1.6763E+04	1.7762E+03	4.2578E+02	1.2185E-01	1.0931E-04	8.9708E-04
7.60	9.6640E+00	1.8577E+04	1.9223E+03	4.6017E+02	1.1900E-01	9.8631E-05	8.2890E-04
7.70	9.8935E+00	2.0566E+04	2.0787E+03	4.9695E+02	1.1624E-01	8.9093E-05	7.6652E-04
7.80	1.0126E+01	2.2744E+04	2.2461E+03	5.3626E+02	1.1357E-01	8.0562E-05	7.0941E-04
7.90	1.0362E+01	2.5126E+04	2.4250E+03	5.7825E+02	1.1099E-01	7.2923E-05	6.5708E-04
8.00	1.0600E+01	2.7731E+04	2.6161E+03	6.2308E+02	1.0849E-01	6.6075E-05	6.0908E-04
8.10	1.0842E+01	3.0574E+04	2.8201E+03	6.7089E+02	1.0607E-01	5.9929E-05	5.6502E-04
8.20	1.1086E+01	3.3676E+04	3.0377E+03	7.2185E+02	1.0373E-01	5.4409E-05	5.2454E-04
8.30	1.1334E+01	3.7057E+04	3.2697E+03	7.7614E+02	1.0147E-01	4.9444E-05	4.8732E-04
8.40	1.1584E+01	4.0740E+04	3.5169E+03	8.3394E+02	9.9275E-02	4.4975E-05	4.5307E-04
8.50	1.1838E+01	4.4746E+04	3.7800E+03	8.9544E+02	9.7149E-02	4.0948E-05	4.2153E-04
8.60	1.2094E+01	4.9102E+04	4.0600E+03	9.6082E+02	9.5088E-02	3.7316E-05	3.9246E-04
8.70	1.2354E+01	5.3834E+04	4.3578E+03	1.0303E+03	9.3091E-02	3.4036E-05	3.6565E-04
8.80	1.2616E+01	5.8969E+04	4.6741E+03	1.1041E+03	9.1154E-02	3.1072E-05	3.4090E-04
8.90	1.2882E+01	6.4538E+04	5.0102E+03	1.1824E+03	8.9275E-02	2.8390E-05	3.1803E-04
9.00	1.3150E+01	7.0573E+04	5.3668E+03	1.2655E+03	8.7452E-02	2.5963E-05	2.9690E-04
9.10	1.3422E+01	7.7108E+04	5.7451E+03	1.3536E+03	8.5683E-02	2.3762E-05	2.7735E-04
9.20	1.3696E+01	8.4179E+04	6.1462E+03	1.4469E+03	8.3966E-02	2.1766E-05	2.5925E-04
9.30	1.3973E+01	9.1823E+04	6.5712E+03	1.5458E+03	8.2299E-02	1.9954E-05	2.4248E-04
9.40	1.4254E+01	1.0008E+05	7.0213E+03	1.6504E+03	8.0679E-02	1.8308E-05	2.2694E-04
9.50	1.4537E+01	1.0900E+05	7.4977E+03	1.7611E+03	7.9106E-02	1.6810E-05	2.1252E-04

(Continued)

M	T_t/T	p_t/p	ρ_t/ρ	A/A^*	T/T^*	p/p^*	ρ/ρ^*
9.60	1.4824E+01	1.1862E+05	8.0016E+03	1.8781E+03	7.7577E-02	1.5447E-05	1.9913E-04
9.70	1.5113E+01	1.2899E+05	8.5345E+03	2.0018E+03	7.6091E-02	1.4205E-05	1.8670E-04
9.80	1.5406E+01	1.4016E+05	9.0976E+03	2.1324E+03	7.4646E-02	1.3073E-05	1.7514E-04
9.90	1.5701E+01	1.5218E+05	9.6924E+03	2.2703E+03	7.3241E-02	1.2040E-05	1.6440E-04
10.00	1.6000E+01	1.6513E+05	1.0320E+04	2.4159E+03	7.1875E-02	1.1096E-05	1.5439E-04
10.10	1.6301E+01	1.7904E+05	1.0983E+04	2.5694E+03	7.0546E-02	1.0234E-05	1.4508E-04
10.20	1.6606E+01	1.9399E+05	1.1682E+04	2.7313E+03	6.9252E-02	9.4452E-06	1.3640E-04
10.30	1.6913E+01	2.1004E+05	1.2419E+04	2.9019E+03	6.7993E-02	8.7233E-06	1.2831E-04
10.40	1.7224E+01	2.2727E+05	1.3195E+04	3.0815E+03	6.6767E-02	8.0621E-06	1.2076E-04
10.50	1.7537E+01	2.4575E+05	1.4013E+04	3.2707E+03	6.5574E-02	7.4559E-06	1.1371E-04
10.60	1.7854E+01	2.6555E+05	1.4873E+04	3.4698E+03	6.4411E-02	6.8999E-06	1.0713E-04
10.70	1.8173E+01	2.8676E+05	1.5779E+04	3.6792E+03	6.3279E-02	6.3894E-06	1.0098E-04
10.80	1.8496E+01	3.0948E+05	1.6732E+04	3.8993E+03	6.2176E-02	5.9205E-06	9.5230E-05
10.90	1.8821E+01	3.3378E+05	1.7734E+04	4.1308E+03	6.1100E-02	5.4894E-06	8.9850E-05
11.00	1.9150E+01	3.5977E+05	1.8787E+04	4.3739E+03	6.0052E-02	5.0929E-06	8.4815E-05
11.10	1.9481E+01	3.8754E+05	1.9893E+04	4.6293E+03	5.9030E-02	4.7279E-06	8.0099E-05
11.20	1.9816E+01	4.1721E+05	2.1054E+04	4.8973E+03	5.8034E-02	4.3916E-06	7.5680E-05
11.30	2.0153E+01	4.4889E+05	2.2274E+04	5.1786E+03	5.7062E-02	4.0817E-06	7.1537E-05
11.40	2.0494E+01	4.8269E+05	2.3553E+04	5.4737E+03	5.6114E-02	3.7959E-06	6.7652E-05
11.50	2.0837E+01	5.1874E+05	2.4895E+04	5.7831E+03	5.5189E-02	3.5321E-06	6.4005E-05
11.60	2.1184E+01	5.5717E+05	2.6302E+04	6.1074E+03	5.4286E-02	3.2885E-06	6.0582E-05
11.70	2.1533E+01	5.9812E+05	2.7776E+04	6.4472E+03	5.3405E-02	3.0634E-06	5.7366E-05
11.80	2.1886E+01	6.4172E+05	2.9321E+04	6.8031E+03	5.2545E-02	2.8552E-06	5.4343E-05
11.90	2.2241E+01	6.8812E+05	3.0939E+04	7.1757E+03	5.1705E-02	2.6627E-06	5.1502E-05
12.00	2.2600E+01	7.3749E+05	3.2632E+04	7.5657E+03	5.0885E-02	2.4844E-06	4.8829E-05
12.10	2.2961E+01	7.8999E+05	3.4405E+04	7.9738E+03	5.0084E-02	2.3193E-06	4.6313E-05
12.20	2.3326E+01	8.4579E+05	3.6260E+04	8.4006E+03	4.9301E-02	2.1663E-06	4.3944E-05
12.30	2.3693E+01	9.0507E+05	3.8199E+04	8.8468E+03	4.8537E-02	2.0244E-06	4.1713E-05
12.40	2.4064E+01	9.6801E+05	4.0227E+04	9.3133E+03	4.7789E-02	1.8928E-06	3.9611E-05
12.50	2.4437E+01	1.0348E+06	4.2346E+04	9.8006E+03	4.7059E-02	1.7706E-06	3.7628E-05
12.60	2.4814E+01	1.1057E+06	4.4560E+04	1.0310E+04	4.6345E-02	1.6571E-06	3.5759E-05
12.70	2.5193E+01	1.1809E+06	4.6872E+04	1.0841E+04	4.5647E-02	1.5516E-06	3.3995E-05
12.80	2.5576E+01	1.2606E+06	4.9287E+04	1.1396E+04	4.4964E-02	1.4535E-06	3.2329E-05
12.90	2.5961E+01	1.3450E+06	5.1807E+04	1.1975E+04	4.4296E-02	1.3623E-06	3.0757E-05
13.00	2.6350E+01	1.4344E+06	5.4436E+04	1.2579E+04	4.3643E-02	1.2774E-06	2.9271E-05
13.10	2.6741E+01	1.5291E+06	5.7179E+04	1.3210E+04	4.3004E-02	1.1983E-06	2.7867E-05
13.20	2.7136E+01	1.6292E+06	6.0040E+04	1.3866E+04	4.2379E-02	1.1246E-06	2.6539E-05
13.30	2.7533E+01	1.7352E+06	6.3022E+04	1.4551E+04	4.1767E-02	1.0559E-06	2.5283E-05
13.40	2.7934E+01	1.8473E+06	6.6130E+04	1.5265E+04	4.1168E-02	9.9186E-07	2.4095E-05
13.50	2.8337E+01	1.9657E+06	6.9368E+04	1.6008E+04	4.0582E-02	9.3210E-07	2.2970E-05

M	T_1/T	p_1/p	ρ_1/ρ	A/A^*	T/T^*	p/p^*	ρ/ρ^*
13.60	2.8744E+01	2.0908E+06	7.2740E+04	1.6782E+04	4.0008E-02	8.7631E-07	2.1905E-05
13.70	2.9153E+01	2.2230E+06	7.6252E+04	1.7588E+04	3.9446E-02	8.2421E-07	2.0896E-05
13.80	2.9566E+01	2.3626E+06	7.9908E+04	1.8426E+04	3.8896E-02	7.7552E-07	1.9940E-05
13.90	2.9981E+01	2.5099E+06	8.3713E+04	1.9299E+04	3.8357E-02	7.3001E-07	1.9034E-05
14.00	3.0400E+01	2.6652E+06	8.7672E+04	2.0207E+04	3.7829E-02	6.8745E-07	1.8174E-05
14.10	3.0821E+01	2.8291E+06	9.1790E+04	2.1151E+04	3.7312E-02	6.4763E-07	1.7359E-05
14.20	3.1246E+01	3.0019E+06	9.6072E+04	2.2133E+04	3.6805E-02	6.1036E-07	1.6585E-05
14.30	3.1673E+01	3.1839E+06	1.0052E+05	2.3153E+04	3.6308E-02	5.7546E-07	1.5851E-05
14.40	3.2104E+01	3.3758E+06	1.0515E+05	2.4213E+04	3.5821E-02	5.4276E-07	1.5153E-05
14.50	3.2537E+01	3.5778E+06	1.0996E+05	2.5315E+04	3.5344E-02	5.1211E-07	1.4491E-05
14.60	3.2974E+01	3.7905E+06	1.1495E+05	2.6459E+04	3.4876E-02	4.8338E-07	1.3861E-05
14.70	3.3413E+01	4.0143E+06	1.2014E+05	2.7648E+04	3.4417E-02	4.5642E-07	1.3263E-05
14.80	3.3856E+01	4.2498E+06	1.2553E+05	2.8881E+04	3.3967E-02	4.3113E-07	1.2694E-05
14.90	3.4301E+01	4.4975E+06	1.3112E+05	3.0162E+04	3.3526E-02	4.0739E-07	1.2152E-05
15.00	3.4750E+01	4.7579E+06	1.3692E+05	3.1490E+04	3.3094E-02	3.8509E-07	1.1637E-05
16.00	3.9400E+01	8.1991E+06	2.0810E+05	4.7777E+04	2.9188E-02	2.2347E-07	7.6570E-06
17.00	4.4350E+01	1.3693E+07	3.0874E+05	7.0781E+04	2.5930E-02	1.3381E-07	5.1610E-06
18.00	4.9600E+01	2.2235E+07	4.4828E+05	1.0265E+05	2.3185E-02	8.2403E-08	3.5545E-06
19.00	5.5150E+01	3.5208E+07	6.3840E+05	1.4603E+05	2.0852E-02	5.2039E-08	2.4959E-06
20.00	6.1000E+01	5.4497E+07	8.9339E+05	2.0417E+05	1.8852E-02	3.3620E-08	1.7835E-06
21.00	6.7150E+01	8.2630E+07	1.2305E+06	2.8101E+05	1.7126E-02	2.2173E-08	1.2949E-06
22.00	7.3600E+01	1.2295E+08	1.6706E+06	3.8125E+05	1.5625E-02	1.4901E-08	9.5381E-07
23.00	8.0350E+01	1.7984E+08	2.2382E+06	5.1048E+05	1.4312E-02	1.0188E-08	7.1193E-07
24.00	8.7400E+01	2.5891E+08	2.9624E+06	6.7532E+05	1.3158E-02	7.0764E-09	5.3788E-07
25.00	9.4750E+01	3.6738E+08	3.8773E+06	8.8350E+05	1.2137E-02	4.9872E-09	4.1095E-07
26.00	1.0240E+02	5.1432E+08	5.0226E+06	1.1440E+06	1.1230E-02	3.5623E-09	3.1724E-07
27.00	1.1035E+02	7.1112E+08	6.4443E+06	1.4673E+06	1.0421E-02	2.5764E-09	2.4726E-07
28.00	1.1860E+02	9.7192E+08	8.1950E+06	1.8653E+06	9.6965E-03	1.8851E-09	1.9444E-07
29.00	1.2715E+02	1.3141E+09	1.0335E+07	2.3518E+06	9.0444E-03	1.3942E-09	1.5417E-07
30.00	1.3600E+02	1.7590E+09	1.2934E+07	2.9424E+06	8.4559E-03	1.0416E-09	1.2320E-07
31.00	1.4515E+02	2.3324E+09	1.6069E+07	3.6548E+06	7.9228E-03	7.8552E-10	9.9161E-08
32.00	1.5460E+02	3.0655E+09	1.9829E+07	4.5089E+06	7.4386E-03	5.9766E-10	8.0359E-08
33.00	1.6435E+02	3.9957E+09	2.4312E+07	5.5274E+06	6.9973E-03	4.5852E-10	6.5539E-08
34.00	1.7440E+02	5.1677E+09	2.9631E+07	6.7355E+06	6.5940E-03	3.5454E-10	5.3775E-08
35.00	1.8475E+02	6.6342E+09	3.5909E+07	8.1612E+06	6.2246E-03	2.7616E-10	4.4373E-08
40.00	2.4100E+02	2.0989E+10	8.7092E+07	1.9781E+07	4.7718E-03	8.7289E-11	1.8296E-08
45.00	3.0475E+02	5.8033E+10	1.9043E+08	4.3233E+07	3.7736E-03	3.1570E-11	8.3675E-09
50.00	3.7600E+02	1.4423E+11	3.8360E+08	8.7061E+07	3.0585E-03	1.2702E-11	4.1538E-09
100.00	1.5010E+03	5.8105E+13	3.8711E+10	8.7770E+09	7.6616E-04	3.1530E-14	4.1162E-11
1000.00	1.5000E+05	2.6889E+22	1.7926E+17	4.0630E+16	7.6666E-06	6.8124E-23	8.8889E-18

APPENDIX C

Normal Shock Table

Normal shock relations that are used in calculating the jump conditions, for a calorically perfect gas (i.e., $\gamma = \text{constant}$), are summarized below:

$$M_2^2 = \frac{2 + (\gamma - 1)M_1^2}{2\gamma M_1^2 - (\gamma - 1)} \quad (\text{C.1})$$

$$\frac{\rho_2}{\rho_1} = \frac{(\gamma + 1)M_1^2}{2 + (\gamma - 1)M_1^2} \quad (\text{C.2})$$

$$\frac{p_2}{p_1} = 1 + \frac{2\gamma}{\gamma + 1} (M_1^2 - 1) \quad (\text{C.3})$$

$$\frac{T_2}{T_1} = \left[1 + \frac{2\gamma}{\gamma + 1} (M_1^2 - 1) \right] \left[\frac{2 + (\gamma - 1)M_1^2}{(\gamma + 1)M_1^2} \right] \quad (\text{C.4})$$

$$\frac{p_{t2}}{p_{t1}} = \left[1 + \frac{2\gamma}{\gamma + 1} (M_1^2 - 1) \right] \left[\frac{1 + \frac{\gamma - 1}{2} \left(\frac{2 + (\gamma - 1)M_1^2}{2\gamma M_1^2 - (\gamma - 1)} \right)}{1 + \frac{\gamma - 1}{2} M_1^2} \right]^{\frac{\gamma}{\gamma - 1}} \quad (\text{C.5})$$

$$\Delta s/R = -\ln(p_{t2}/p_{t1}) \quad (\text{C.6})$$

$$\frac{p_2}{p_1} = \frac{p_{t2}}{p_{t1}} \frac{p_{t1}}{p_1} = \left[1 + \frac{2\gamma}{\gamma + 1} (M_1^2 - 1) \right] \left[+ \frac{\gamma - 1}{2} \left(\frac{2 + (\gamma - 1)M_1^2}{2\gamma M_1^2 - (\gamma - 1)} \right) \right]^{\frac{\gamma}{\gamma - 1}} \quad (\text{C.7})$$

We have derived these expressions in Chapter 2.

Normal Shock Table $\gamma = 1.4$

M_1	M_2	T_2/T_1	p_2/p_1	ρ_2/ρ_1	p_{02}/p_{01}	p_{02}/p_1	$\Delta s/R$
1	1	1	1	1	1	1.8929	0
1.02	0.9805	1.0132E+00	1.0471E+00	1.0334E+00	9.9999E-01	1.9379E+00	9.9554E-06
1.04	0.9620	1.0263E+00	1.0952E+00	1.0671E+00	9.9992E-01	1.9844E+00	7.6696E-05
1.06	0.9444	1.0393E+00	1.1442E+00	1.1009E+00	9.9975E-01	2.0325E+00	2.4928E-04
1.08	0.9277	1.0522E+00	1.1941E+00	1.1349E+00	9.9943E-01	2.0819E+00	5.6942E-04
1.1	0.9118	1.0649E+00	1.2450E+00	1.1691E+00	9.9893E-01	2.1328E+00	1.0725E-03
1.12	0.8966	1.0776E+00	1.2968E+00	1.2034E+00	9.9821E-01	2.1851E+00	1.7885E-03
1.14	0.8820	1.0903E+00	1.3495E+00	1.2378E+00	9.9726E-01	2.2388E+00	2.7426E-03
1.16	0.8682	1.1029E+00	1.4032E+00	1.2723E+00	9.9605E-01	2.2937E+00	3.9559E-03
1.18	0.8549	1.1154E+00	1.4578E+00	1.3069E+00	9.9457E-01	2.3500E+00	5.4461E-03
1.2	0.8422	1.1280E+00	1.5133E+00	1.3416E+00	9.9280E-01	2.4075E+00	7.2276E-03
1.22	0.8300	1.1405E+00	1.5698E+00	1.3764E+00	9.9073E-01	2.4663E+00	9.3122E-03
1.24	0.8183	1.1531E+00	1.6272E+00	1.4112E+00	9.8836E-01	2.5263E+00	1.1709E-02
1.26	0.8071	1.1657E+00	1.6855E+00	1.4460E+00	9.8568E-01	2.5875E+00	1.4427E-02
1.28	0.7963	1.1783E+00	1.7448E+00	1.4808E+00	9.8268E-01	2.6500E+00	1.7469E-02
1.3	0.7860	1.1909E+00	1.8050E+00	1.5157E+00	9.7937E-01	2.7136E+00	2.0842E-02
1.32	0.7760	1.2035E+00	1.8661E+00	1.5505E+00	9.7575E-01	2.7784E+00	2.4547E-02
1.34	0.7664	1.2162E+00	1.9282E+00	1.5854E+00	9.7182E-01	2.8444E+00	2.8585E-02
1.36	0.7572	1.2290E+00	1.9912E+00	1.6202E+00	9.6758E-01	2.9115E+00	3.2958E-02
1.38	0.7483	1.2418E+00	2.0551E+00	1.6549E+00	9.6304E-01	2.9798E+00	3.7665E-02
1.4	0.7397	1.2547E+00	2.1200E+00	1.6897E+00	9.5819E-01	3.0492E+00	4.2704E-02
1.42	0.7314	1.2676E+00	2.1858E+00	1.7243E+00	9.5306E-01	3.1198E+00	4.8074E-02
1.44	0.7235	1.2807E+00	2.2525E+00	1.7589E+00	9.4765E-01	3.1915E+00	5.3772E-02
1.46	0.7157	1.2938E+00	2.3202E+00	1.7934E+00	9.4196E-01	3.2643E+00	5.9795E-02
1.48	0.7083	1.3069E+00	2.3888E+00	1.8278E+00	9.3600E-01	3.3382E+00	6.6139E-02
1.5	0.7011	1.3202E+00	2.4583E+00	1.8621E+00	9.2979E-01	3.4133E+00	7.2800E-02
1.52	0.6941	1.3336E+00	2.5288E+00	1.8963E+00	9.2332E-01	3.4894E+00	7.9775E-02
1.54	0.6874	1.3470E+00	2.6002E+00	1.9303E+00	9.1662E-01	3.5667E+00	8.7057E-02
1.56	0.6809	1.3606E+00	2.6725E+00	1.9643E+00	9.0970E-01	3.6450E+00	9.4644E-02
1.58	0.6746	1.3742E+00	2.7458E+00	1.9981E+00	9.0255E-01	3.7244E+00	1.0253E-01
1.6	0.6684	1.3880E+00	2.8200E+00	2.0317E+00	8.9520E-01	3.8050E+00	1.1071E-01
1.62	0.6625	1.4018E+00	2.8951E+00	2.0653E+00	8.8765E-01	3.8866E+00	1.1917E-01
1.64	0.6568	1.4158E+00	2.9712E+00	2.0986E+00	8.7992E-01	3.9693E+00	1.2792E-01
1.66	0.6512	1.4299E+00	3.0482E+00	2.1318E+00	8.7201E-01	4.0531E+00	1.3695E-01
1.68	0.6458	1.4440E+00	3.1261E+00	2.1649E+00	8.6394E-01	4.1379E+00	1.4625E-01
1.7	0.6405	1.4583E+00	3.2050E+00	2.1977E+00	8.5572E-01	4.2238E+00	1.5581E-01
1.72	0.6355	1.4727E+00	3.2848E+00	2.2304E+00	8.4736E-01	4.3108E+00	1.6563E-01
1.74	0.6305	1.4873E+00	3.3655E+00	2.2629E+00	8.3886E-01	4.3989E+00	1.7571E-01

(Continued)

M_1	M_2	T_2/T_1	p_2/p_1	ρ_2/ρ_1	P_{c2}/P_{c1}	P_{c2}/P_1	$\Delta s/R$
1.76	0.6257	1.5019E+00	3.4472E+00	2.2952E+00	8.3024E-01	4.4880E+00	1.8604E-01
1.78	0.6210	1.5167E+00	3.5298E+00	2.3273E+00	8.2151E-01	4.5782E+00	1.9661E-01
1.8	0.6165	1.5316E+00	3.6133E+00	2.3592E+00	8.1268E-01	4.6695E+00	2.0741E-01
1.82	0.6121	1.5466E+00	3.6978E+00	2.3909E+00	8.0376E-01	4.7618E+00	2.1845E-01
1.84	0.6078	1.5617E+00	3.7832E+00	2.4224E+00	7.9476E-01	4.8552E+00	2.2971E-01
1.86	0.6036	1.5770E+00	3.8695E+00	2.4537E+00	7.8569E-01	4.9497E+00	2.4120E-01
1.88	0.5996	1.5924E+00	3.9568E+00	2.4848E+00	7.7655E-01	5.0452E+00	2.5290E-01
1.9	0.5956	1.6079E+00	4.0450E+00	2.5157E+00	7.6736E-01	5.1418E+00	2.6480E-01
1.92	0.5918	1.6236E+00	4.1341E+00	2.5463E+00	7.5812E-01	5.2394E+00	2.7691E-01
1.94	0.5880	1.6394E+00	4.2242E+00	2.5767E+00	7.4884E-01	5.3381E+00	2.8922E-01
1.96	0.5844	1.6553E+00	4.3152E+00	2.6069E+00	7.3954E-01	5.4378E+00	3.0173E-01
1.98	0.5808	1.6713E+00	4.4071E+00	2.6369E+00	7.3021E-01	5.5386E+00	3.1442E-01
2	0.5774	1.6875E+00	4.5000E+00	2.6667E+00	7.2087E-01	5.6404E+00	3.2729E-01
2.02	0.5740	1.7038E+00	4.5938E+00	2.6962E+00	7.1153E-01	5.7433E+00	3.4034E-01
2.04	0.5707	1.7203E+00	4.6885E+00	2.7255E+00	7.0218E-01	5.8473E+00	3.5357E-01
2.06	0.5675	1.7369E+00	4.7842E+00	2.7545E+00	6.9284E-01	5.9523E+00	3.6696E-01
2.08	0.5643	1.7536E+00	4.8808E+00	2.7833E+00	6.8351E-01	6.0583E+00	3.8051E-01
2.1	0.5613	1.7705E+00	4.9783E+00	2.8119E+00	6.7420E-01	6.1654E+00	3.9422E-01
2.12	0.5583	1.7875E+00	5.0768E+00	2.8402E+00	6.6492E-01	6.2735E+00	4.0809E-01
2.14	0.5554	1.8046E+00	5.1762E+00	2.8683E+00	6.5567E-01	6.3827E+00	4.2210E-01
2.16	0.5525	1.8219E+00	5.2765E+00	2.8962E+00	6.4645E-01	6.4929E+00	4.3626E-01
2.18	0.5498	1.8393E+00	5.3778E+00	2.9238E+00	6.3727E-01	6.6042E+00	4.5056E-01
2.2	0.5471	1.8569E+00	5.4800E+00	2.9512E+00	6.2814E-01	6.7165E+00	4.6500E-01
2.22	0.5444	1.8746E+00	5.5831E+00	2.9784E+00	6.1905E-01	6.8298E+00	4.7956E-01
2.24	0.5418	1.8924E+00	5.6872E+00	3.0053E+00	6.1002E-01	6.9442E+00	4.9426E-01
2.26	0.5393	1.9104E+00	5.7922E+00	3.0319E+00	6.0105E-01	7.0597E+00	5.0908E-01
2.28	0.5368	1.9285E+00	5.8981E+00	3.0584E+00	5.9214E-01	7.1762E+00	5.2401E-01
2.3	0.5344	1.9468E+00	6.0050E+00	3.0845E+00	5.8329E-01	7.2937E+00	5.3906E-01
2.32	0.5321	1.9652E+00	6.1128E+00	3.1105E+00	5.7452E-01	7.4122E+00	5.5423E-01
2.34	0.5297	1.9838E+00	6.2215E+00	3.1362E+00	5.6581E-01	7.5319E+00	5.6950E-01
2.36	0.5275	2.0025E+00	6.3312E+00	3.1617E+00	5.5718E-01	7.6525E+00	5.8487E-01
2.38	0.5253	2.0213E+00	6.4418E+00	3.1869E+00	5.4862E-01	7.7742E+00	6.0035E-01
2.4	0.5231	2.0403E+00	6.5533E+00	3.2119E+00	5.4014E-01	7.8969E+00	6.1592E-01
2.42	0.5210	2.0595E+00	6.6658E+00	3.2367E+00	5.3175E-01	8.0207E+00	6.3159E-01
2.44	0.5189	2.0788E+00	6.7792E+00	3.2612E+00	5.2344E-01	8.1455E+00	6.4734E-01
2.46	0.5169	2.0982E+00	6.8935E+00	3.2855E+00	5.1521E-01	8.2713E+00	6.6318E-01
2.48	0.5149	2.1178E+00	7.0088E+00	3.3095E+00	5.0707E-01	8.3982E+00	6.7911E-01
2.5	0.5130	2.1375E+00	7.1250E+00	3.3333E+00	4.9901E-01	8.5261E+00	6.9512E-01
2.52	0.5111	2.1574E+00	7.2421E+00	3.3569E+00	4.9105E-01	8.6551E+00	7.1120E-01
2.54	0.5092	2.1774E+00	7.3602E+00	3.3803E+00	4.8318E-01	8.7851E+00	7.2736E-01

M_1	M_2	T_2/T_1	p_2/p_1	ρ_2/ρ_1	p_{t2}/p_{t1}	P_{t2}/P_{t1}	$\Delta s/R$
2.56	0.5074	2.1976E+00	7.4792E+00	3.4034E+00	4.7540E-01	8.9161E+00	7.4360E-01
2.58	0.5056	2.2179E+00	7.5991E+00	3.4263E+00	4.6772E-01	9.0482E+00	7.5990E-01
2.6	0.5039	2.2383E+00	7.7200E+00	3.4490E+00	4.6012E-01	9.1813E+00	7.7626E-01
2.62	0.5022	2.2590E+00	7.8418E+00	3.4714E+00	4.5263E-01	9.3155E+00	7.9269E-01
2.64	0.5005	2.2797E+00	7.9645E+00	3.4937E+00	4.4522E-01	9.4506E+00	8.0918E-01
2.66	0.4988	2.3006E+00	8.0882E+00	3.5157E+00	4.3792E-01	9.5869E+00	8.2573E-01
2.68	0.4972	2.3217E+00	8.2128E+00	3.5374E+00	4.3071E-01	9.7241E+00	8.4233E-01
2.7	0.4956	2.3429E+00	8.3383E+00	3.5590E+00	4.2359E-01	9.8624E+00	8.5899E-01
2.72	0.4941	2.3642E+00	8.4648E+00	3.5803E+00	4.1657E-01	1.0002E+01	8.7570E-01
2.74	0.4926	2.3858E+00	8.5922E+00	3.6015E+00	4.0965E-01	1.0142E+01	8.9245E-01
2.76	0.4911	2.4074E+00	8.7205E+00	3.6224E+00	4.0283E-01	1.0283E+01	9.0925E-01
2.78	0.4896	2.4292E+00	8.8498E+00	3.6431E+00	3.9610E-01	1.0426E+01	9.2610E-01
2.8	0.4882	2.4512E+00	8.9800E+00	3.6636E+00	3.8946E-01	1.0569E+01	9.4298E-01
2.82	0.4868	2.4733E+00	9.1111E+00	3.6838E+00	3.8293E-01	1.0714E+01	9.5991E-01
2.84	0.4854	2.4955E+00	9.2432E+00	3.7039E+00	3.7649E-01	1.0859E+01	9.7687E-01
2.86	0.4840	2.5179E+00	9.3762E+00	3.7238E+00	3.7014E-01	1.1006E+01	9.9387E-01
2.88	0.4827	2.5405E+00	9.5101E+00	3.7434E+00	3.6389E-01	1.1154E+01	1.0109E+00
2.9	0.4814	2.5632E+00	9.6450E+00	3.7629E+00	3.5773E-01	1.1302E+01	1.0280E+00
2.92	0.4801	2.5861E+00	9.7808E+00	3.7821E+00	3.5167E-01	1.1452E+01	1.0451E+00
2.94	0.4788	2.6091E+00	9.9175E+00	3.8012E+00	3.4570E-01	1.1603E+01	1.0622E+00
2.96	0.4776	2.6322E+00	1.0055E+01	3.8200E+00	3.3982E-01	1.1754E+01	1.0793E+00
2.98	0.4764	2.6555E+00	1.0194E+01	3.8387E+00	3.3404E-01	1.1907E+01	1.0965E+00
3	0.4752	2.6790E+00	1.0333E+01	3.8571E+00	3.2834E-01	1.2061E+01	1.1137E+00
3.02	0.4740	2.7026E+00	1.0474E+01	3.8754E+00	3.2274E-01	1.2216E+01	1.1309E+00
3.04	0.4729	2.7264E+00	1.0615E+01	3.8935E+00	3.1723E-01	1.2372E+01	1.1481E+00
3.06	0.4717	2.7503E+00	1.0758E+01	3.9114E+00	3.1180E-01	1.2529E+01	1.1654E+00
3.08	0.4706	2.7744E+00	1.0901E+01	3.9291E+00	3.0646E-01	1.2687E+01	1.1827E+00
3.1	0.4695	2.7986E+00	1.1045E+01	3.9466E+00	3.0121E-01	1.2846E+01	1.1999E+00
3.12	0.4685	2.8230E+00	1.1190E+01	3.9639E+00	2.9605E-01	1.3006E+01	1.2172E+00
3.14	0.4674	2.8475E+00	1.1336E+01	3.9811E+00	2.9097E-01	1.3167E+01	1.2345E+00
3.16	0.4664	2.8722E+00	1.1483E+01	3.9981E+00	2.8597E-01	1.3329E+01	1.2519E+00
3.18	0.4654	2.8970E+00	1.1631E+01	4.0149E+00	2.8106E-01	1.3492E+01	1.2692E+00
3.2	0.4643	2.9220E+00	1.1780E+01	4.0315E+00	2.7623E-01	1.3656E+01	1.2865E+00
3.22	0.4634	2.9471E+00	1.1930E+01	4.0479E+00	2.7148E-01	1.3821E+01	1.3039E+00
3.24	0.4624	2.9724E+00	1.2081E+01	4.0642E+00	2.6681E-01	1.3987E+01	1.3212E+00
3.26	0.4614	2.9979E+00	1.2232E+01	4.0803E+00	2.6222E-01	1.4155E+01	1.3386E+00
3.28	0.4605	3.0234E+00	1.2385E+01	4.0963E+00	2.5771E-01	1.4323E+01	1.3559E+00
3.3	0.4596	3.0492E+00	1.2538E+01	4.1120E+00	2.5328E-01	1.4492E+01	1.3733E+00
3.32	0.4587	3.0751E+00	1.2693E+01	4.1276E+00	2.4892E-01	1.4662E+01	1.3906E+00
3.34	0.4578	3.1011E+00	1.2848E+01	4.1431E+00	2.4463E-01	1.4834E+01	1.4080E+00

(Continued)

M_1	M_2	T_2/T_1	p_2/p_1	ρ_2/ρ_1	p_{t2}/p_{t1}	p_{t2}/p_1	$\Delta s/R$
3.36	0.4569	3.1273E+00	1.3005E+01	4.1583E+00	2.4043E-01	1.5006E+01	1.4253E+00
3.38	0.4560	3.1537E+00	1.3162E+01	4.1734E+00	2.3629E-01	1.5180E+01	1.4427E+00
3.4	0.4552	3.1802E+00	1.3320E+01	4.1884E+00	2.3223E-01	1.5354E+01	1.4600E+00
3.42	0.4544	3.2069E+00	1.3479E+01	4.2032E+00	2.2823E-01	1.5530E+01	1.4774E+00
3.44	0.4535	3.2337E+00	1.3639E+01	4.2179E+00	2.2431E-01	1.5706E+01	1.4947E+00
3.46	0.4527	3.2607E+00	1.3800E+01	4.2323E+00	2.2045E-01	1.5884E+01	1.5121E+00
3.48	0.4519	3.2878E+00	1.3962E+01	4.2467E+00	2.1667E-01	1.6062E+01	1.5294E+00
3.5	0.4512	3.3151E+00	1.4125E+01	4.2609E+00	2.1295E-01	1.6242E+01	1.5467E+00
3.52	0.4504	3.3425E+00	1.4289E+01	4.2749E+00	2.0929E-01	1.6423E+01	1.5640E+00
3.54	0.4496	3.3701E+00	1.4454E+01	4.2888E+00	2.0570E-01	1.6604E+01	1.5813E+00
3.56	0.4489	3.3978E+00	1.4619E+01	4.3026E+00	2.0218E-01	1.6787E+01	1.5986E+00
3.58	0.4481	3.4257E+00	1.4786E+01	4.3162E+00	1.9871E-01	1.6971E+01	1.6159E+00
3.6	0.4474	3.4537E+00	1.4953E+01	4.3296E+00	1.9531E-01	1.7156E+01	1.6332E+00
3.62	0.4467	3.4819E+00	1.5122E+01	4.3429E+00	1.9197E-01	1.7341E+01	1.6504E+00
3.64	0.4460	3.5103E+00	1.5291E+01	4.3561E+00	1.8869E-01	1.7528E+01	1.6677E+00
3.66	0.4453	3.5388E+00	1.5462E+01	4.3692E+00	1.8547E-01	1.7716E+01	1.6849E+00
3.68	0.4446	3.5674E+00	1.5633E+01	4.3821E+00	1.8230E-01	1.7905E+01	1.7021E+00
3.7	0.4439	3.5962E+00	1.5805E+01	4.3949E+00	1.7919E-01	1.8095E+01	1.7193E+00
3.72	0.4433	3.6252E+00	1.5978E+01	4.4075E+00	1.7614E-01	1.8286E+01	1.7365E+00
3.74	0.4426	3.6543E+00	1.6152E+01	4.4200E+00	1.7314E-01	1.8478E+01	1.7536E+00
3.76	0.4420	3.6836E+00	1.6327E+01	4.4324E+00	1.7020E-01	1.8671E+01	1.7708E+00
3.78	0.4414	3.7130E+00	1.6503E+01	4.4447E+00	1.6731E-01	1.8865E+01	1.7879E+00
3.8	0.4407	3.7426E+00	1.6680E+01	4.4568E+00	1.6447E-01	1.9060E+01	1.8050E+00
3.82	0.4401	3.7723E+00	1.6858E+01	4.4688E+00	1.6168E-01	1.9256E+01	1.8221E+00
3.84	0.4395	3.8022E+00	1.7037E+01	4.4807E+00	1.5895E-01	1.9454E+01	1.8392E+00
3.86	0.4389	3.8323E+00	1.7216E+01	4.4924E+00	1.5626E-01	1.9652E+01	1.8562E+00
3.88	0.4383	3.8625E+00	1.7397E+01	4.5041E+00	1.5362E-01	1.9851E+01	1.8733E+00
3.9	0.4377	3.8928E+00	1.7578E+01	4.5156E+00	1.5103E-01	2.0051E+01	1.8903E+00
3.92	0.4372	3.9233E+00	1.7761E+01	4.5270E+00	1.4848E-01	2.0253E+01	1.9073E+00
3.94	0.4366	3.9540E+00	1.7944E+01	4.5383E+00	1.4598E-01	2.0455E+01	1.9243E+00
3.96	0.4360	3.9848E+00	1.8129E+01	4.5494E+00	1.4353E-01	2.0658E+01	1.9412E+00
3.98	0.4355	4.0158E+00	1.8314E+01	4.5605E+00	1.4112E-01	2.0863E+01	1.9581E+00
4	0.4350	4.0469E+00	1.8500E+01	4.5714E+00	1.3876E-01	2.1068E+01	1.9750E+00
4.1	0.4324	4.2048E+00	1.9445E+01	4.6245E+00	1.2756E-01	2.2111E+01	2.0592E+00
4.2	0.4299	4.3666E+00	2.0413E+01	4.6749E+00	1.1733E-01	2.3179E+01	2.1427E+00
4.3	0.4277	4.5322E+00	2.1405E+01	4.7229E+00	1.0800E-01	2.4273E+01	2.2256E+00
4.4	0.4255	4.7017E+00	2.2420E+01	4.7685E+00	9.9481E-02	2.5393E+01	2.3078E+00
4.5	0.4236	4.8751E+00	2.3458E+01	4.8119E+00	9.1698E-02	2.6539E+01	2.3893E+00
4.6	0.4217	5.0523E+00	2.4520E+01	4.8532E+00	8.4587E-02	2.7710E+01	2.4700E+00

M_1	M_2	T_2/T_1	p_2/p_1	ρ_2/ρ_1	p_{t2}/p_{t1}	p_{t2}/p_1	$\Delta s/R$
4.7	0.4199	5.2334E+00	2.5605E+01	4.8926E+00	7.8086E-02	2.8907E+01	2.5499E+00
4.8	0.4183	5.4184E+00	2.6713E+01	4.9301E+00	7.2140E-02	3.0130E+01	2.6291E+00
4.9	0.4167	5.6073E+00	2.7845E+01	4.9659E+00	6.6699E-02	3.1379E+01	2.7076E+00
5	0.4152	5.8000E+00	2.9000E+01	5.0000E+00	6.1716E-02	3.2653E+01	2.7852E+00
5.1	0.4138	5.9966E+00	3.0178E+01	5.0326E+00	5.7151E-02	3.3954E+01	2.8621E+00
5.2	0.4125	6.1971E+00	3.1380E+01	5.0637E+00	5.2966E-02	3.5280E+01	2.9381E+00
5.3	0.4113	6.4014E+00	3.2605E+01	5.0934E+00	4.9126E-02	3.6632E+01	3.0134E+00
5.4	0.4101	6.6097E+00	3.3853E+01	5.1218E+00	4.5601E-02	3.8009E+01	3.0878E+00
5.5	0.4090	6.8218E+00	3.5125E+01	5.1489E+00	4.2361E-02	3.9412E+01	3.1615E+00
5.6	0.4079	7.0378E+00	3.6420E+01	5.1749E+00	3.9383E-02	4.0841E+01	3.2344E+00
5.7	0.4069	7.2577E+00	3.7738E+01	5.1998E+00	3.6643E-02	4.2296E+01	3.3065E+00
5.8	0.4059	7.4814E+00	3.9080E+01	5.2236E+00	3.4120E-02	4.3777E+01	3.3779E+00
5.9	0.4050	7.7091E+00	4.0445E+01	5.2464E+00	3.1795E-02	4.5283E+01	3.4484E+00
6	0.4042	7.9406E+00	4.1833E+01	5.2683E+00	2.9651E-02	4.6815E+01	3.5183E+00
6.1	0.4033	8.1760E+00	4.3245E+01	5.2893E+00	2.7672E-02	4.8373E+01	3.5873E+00
6.2	0.4025	8.4153E+00	4.4680E+01	5.3094E+00	2.5845E-02	4.9957E+01	3.6556E+00
6.3	0.4018	8.6584E+00	4.6138E+01	5.3287E+00	2.4156E-02	5.1566E+01	3.7232E+00
6.4	0.4011	8.9055E+00	4.7620E+01	5.3473E+00	2.2594E-02	5.3201E+01	3.7901E+00
6.5	0.4004	9.1564E+00	4.9125E+01	5.3651E+00	2.1148E-02	5.4862E+01	3.8562E+00
6.6	0.3997	9.4113E+00	5.0653E+01	5.3822E+00	1.9808E-02	5.6549E+01	3.9217E+00
6.7	0.3991	9.6700E+00	5.2205E+01	5.3987E+00	1.8566E-02	5.8261E+01	3.9864E+00
6.8	0.3985	9.9326E+00	5.3780E+01	5.4145E+00	1.7414E-02	5.9999E+01	4.0505E+00
6.9	0.3979	1.0199E+01	5.5378E+01	5.4298E+00	1.6345E-02	6.1763E+01	4.1138E+00
7	0.3974	1.0469E+01	5.7000E+01	5.4444E+00	1.5351E-02	6.3553E+01	4.1765E+00
7.1	0.3968	1.0744E+01	5.8645E+01	5.4586E+00	1.4428E-02	6.5368E+01	4.2386E+00
7.2	0.3963	1.1022E+01	6.0313E+01	5.4722E+00	1.3569E-02	6.7209E+01	4.3000E+00
7.3	0.3958	1.1304E+01	6.2005E+01	5.4853E+00	1.2769E-02	6.9076E+01	4.3608E+00
7.4	0.3954	1.1590E+01	6.3720E+01	5.4980E+00	1.2023E-02	7.0969E+01	4.4209E+00
7.5	0.3949	1.1879E+01	6.5458E+01	5.5102E+00	1.1329E-02	7.2887E+01	4.4804E+00
7.6	0.3945	1.2173E+01	6.7220E+01	5.5220E+00	1.0680E-02	7.4831E+01	4.5393E+00
7.7	0.3941	1.2471E+01	6.9005E+01	5.5334E+00	1.0075E-02	7.6801E+01	4.5977E+00
7.8	0.3937	1.2772E+01	7.0813E+01	5.5443E+00	9.5102E-03	7.8797E+01	4.6554E+00
7.9	0.3933	1.3078E+01	7.2645E+01	5.5550E+00	8.9819E-03	8.0818E+01	4.7125E+00
8	0.3929	1.3387E+01	7.4500E+01	5.5652E+00	8.4878E-03	8.2865E+01	4.7691E+00
8.1	0.3925	1.3700E+01	7.6378E+01	5.5751E+00	8.0254E-03	8.4938E+01	4.8251E+00
8.2	0.3922	1.4017E+01	7.8280E+01	5.5847E+00	7.5924E-03	8.7037E+01	4.8806E+00
8.3	0.3918	1.4338E+01	8.0205E+01	5.5940E+00	7.1866E-03	8.9162E+01	4.9355E+00
8.4	0.3915	1.4662E+01	8.2153E+01	5.6030E+00	6.8061E-03	9.1312E+01	4.9899E+00

(Continued)

M_1	M_2	T_2/T_1	p_2/p_1	ρ_2/ρ_1	p_{t2}/p_{t1}	p_{t2}/p_1	$\Delta s/R$
8.5	0.3912	1.4991E+01	8.4125E+01	5.6117E+00	6.4492E-03	9.3488E+01	5.0438E+00
8.6	0.3909	1.5324E+01	8.6120E+01	5.6201E+00	6.1141E-03	9.5689E+01	5.0972E+00
8.7	0.3906	1.5660E+01	8.8138E+01	5.6282E+00	5.7994E-03	9.7917E+01	5.1500E+00
8.8	0.3903	1.6000E+01	9.0180E+01	5.6361E+00	5.5036E-03	1.0017E+02	5.2023E+00
8.9	0.3901	1.6345E+01	9.2245E+01	5.6437E+00	5.2255E-03	1.0245E+02	5.2542E+00
9	0.3898	1.6693E+01	9.4333E+01	5.6512E+00	4.9639E-03	1.0475E+02	5.3056E+00
9.1	0.3895	1.7045E+01	9.6445E+01	5.6584E+00	4.7175E-03	1.0708E+02	5.3565E+00
9.2	0.3893	1.7401E+01	9.8580E+01	5.6653E+00	4.4856E-03	1.0944E+02	5.4069E+00
9.3	0.3891	1.7760E+01	1.0074E+02	5.6721E+00	4.2669E-03	1.1182E+02	5.4569E+00
9.4	0.3888	1.8124E+01	1.0292E+02	5.6787E+00	4.0608E-03	1.1423E+02	5.5064E+00
9.5	0.3886	1.8492E+01	1.0513E+02	5.6850E+00	3.8664E-03	1.1666E+02	5.5554E+00
9.6	0.3884	1.8863E+01	1.0735E+02	5.6912E+00	3.6828E-03	1.1912E+02	5.6041E+00
9.7	0.3882	1.9238E+01	1.0961E+02	5.6972E+00	3.5095E-03	1.2161E+02	5.6523E+00
9.8	0.3880	1.9617E+01	1.1188E+02	5.7031E+00	3.3458E-03	1.2412E+02	5.7000E+00
9.9	0.3878	2.0001E+01	1.1418E+02	5.7088E+00	3.1911E-03	1.2665E+02	5.7474E+00
10	0.3876	2.0388E+01	1.1650E+02	5.7143E+00	3.0448E-03	1.2922E+02	5.7943E+00
11	0.3859	2.4471E+01	1.4100E+02	5.7619E+00	1.9451E-03	1.5626E+02	6.2425E+00
12	0.3847	2.8943E+01	1.6783E+02	5.7987E+00	1.2866E-03	1.8587E+02	6.6557E+00
13	0.3837	3.3805E+01	1.9700E+02	5.8276E+00	8.7709E-04	2.1806E+02	7.0389E+00
14	0.3829	3.9055E+01	2.2850E+02	5.8507E+00	6.1380E-04	2.5282E+02	7.3958E+00
15	0.3823	4.4694E+01	2.6233E+02	5.8696E+00	4.3953E-04	2.9016E+02	7.7298E+00
16	0.3817	5.0722E+01	2.9850E+02	5.8851E+00	3.2119E-04	3.3008E+02	8.0435E+00
17	0.3813	5.7138E+01	3.3700E+02	5.8980E+00	2.3899E-04	3.7257E+02	8.3391E+00
18	0.3810	6.3944E+01	3.7783E+02	5.9088E+00	1.8072E-04	4.1763E+02	8.6186E+00
19	0.3806	7.1139E+01	4.2100E+02	5.9180E+00	1.3865E-04	4.6527E+02	8.8836E+00
20	0.3804	7.8722E+01	4.6650E+02	5.9259E+00	1.0777E-04	5.1548E+02	9.1355E+00
21	0.3802	8.6694E+01	5.1433E+02	5.9327E+00	8.4778E-05	5.6827E+02	9.3755E+00
22	0.3800	9.5055E+01	5.6450E+02	5.9387E+00	6.7414E-05	6.2364E+02	9.6047E+00
23	0.3798	1.0381E+02	6.1700E+02	5.9438E+00	5.4140E-05	6.8158E+02	9.8239E+00
24	0.3796	1.1294E+02	6.7183E+02	5.9484E+00	4.3877E-05	7.4209E+02	1.0034E+01
25	0.3795	1.2247E+02	7.2900E+02	5.9524E+00	3.5859E-05	8.0519E+02	1.0236E+01
30	0.3790	1.7594E+02	1.0498E+03	5.9669E+00	1.4531E-05	1.1593E+03	1.1139E+01
35	0.3788	2.3914E+02	1.4290E+03	5.9756E+00	6.7571E-06	1.5777E+03	1.1905E+01
40	0.3786	3.1206E+02	1.8665E+03	5.9813E+00	3.4771E-06	2.0606E+03	1.2569E+01
45	0.3784	3.9469E+02	2.3623E+03	5.9852E+00	1.9339E-06	2.6078E+03	1.3156E+01
50	0.3784	4.8706E+02	2.9165E+03	5.9880E+00	1.1438E-06	3.2194E+03	1.3681E+01

Normal Shock Table $\gamma = 1.3$

M_1	M_2	T_2/T_1	p_2/p_1	ρ_2/ρ_1	p_{t2}/p_{t1}	p_{t2}/p_1	$\Delta s/R$
1	1	1	1	1	1	1.8324	0
1.02	0.9805	1.0104E+00	1.0457E+00	1.0349E+00	9.9999E-01	1.8746E+00	9.7482E-06
1.04	0.9619	1.0206E+00	1.0922E+00	1.0702E+00	9.9992E-01	1.9183E+00	7.7203E-05
1.06	0.9442	1.0307E+00	1.1397E+00	1.1058E+00	9.9975E-01	1.9634E+00	2.5262E-04
1.08	0.9273	1.0407E+00	1.1881E+00	1.1416E+00	9.9942E-01	2.0099E+00	5.7916E-04
1.1	0.9112	1.0506E+00	1.2374E+00	1.1777E+00	9.9891E-01	2.0578E+00	1.0938E-03
1.12	0.8958	1.0605E+00	1.2876E+00	1.2141E+00	9.9817E-01	2.1070E+00	1.8282E-03
1.14	0.8810	1.0703E+00	1.3387E+00	1.2507E+00	9.9719E-01	2.1575E+00	2.8094E-03
1.16	0.8669	1.0801E+00	1.3907E+00	1.2876E+00	9.9595E-01	2.2092E+00	4.0603E-03
1.18	0.8533	1.0898E+00	1.4436E+00	1.3246E+00	9.9442E-01	2.2622E+00	5.6003E-03
1.2	0.8403	1.0995E+00	1.4974E+00	1.3618E+00	9.9258E-01	2.3164E+00	7.4458E-03
1.22	0.8278	1.1092E+00	1.5521E+00	1.3993E+00	9.9044E-01	2.3718E+00	9.6103E-03
1.24	0.8159	1.1189E+00	1.6077E+00	1.4368E+00	9.8797E-01	2.4283E+00	1.2105E-02
1.26	0.8043	1.1286E+00	1.6642E+00	1.4746E+00	9.8517E-01	2.4861E+00	1.4939E-02
1.28	0.7932	1.1383E+00	1.7217E+00	1.5125E+00	9.8204E-01	2.5450E+00	1.8120E-02
1.3	0.7825	1.1480E+00	1.7800E+00	1.5505E+00	9.7858E-01	2.6050E+00	2.1653E-02
1.32	0.7722	1.1578E+00	1.8392E+00	1.5886E+00	9.7478E-01	2.6661E+00	2.5542E-02
1.34	0.7623	1.1676E+00	1.8994E+00	1.6268E+00	9.7065E-01	2.7283E+00	2.9791E-02
1.36	0.7527	1.1774E+00	1.9604E+00	1.6651E+00	9.6618E-01	2.7917E+00	3.4402E-02
1.38	0.7435	1.1872E+00	2.0224E+00	1.7035E+00	9.6139E-01	2.8561E+00	3.9374E-02
1.4	0.7346	1.1971E+00	2.0852E+00	1.7419E+00	9.5628E-01	2.9217E+00	4.4709E-02
1.42	0.7260	1.2070E+00	2.1490E+00	1.7804E+00	9.5084E-01	2.9883E+00	5.0405E-02
1.44	0.7176	1.2170E+00	2.2136E+00	1.8189E+00	9.4510E-01	3.0560E+00	5.6461E-02
1.46	0.7096	1.2271E+00	2.2792E+00	1.8574E+00	9.3906E-01	3.1247E+00	6.2874E-02
1.48	0.7018	1.2372E+00	2.3457E+00	1.8960E+00	9.3273E-01	3.1945E+00	6.9644E-02
1.5	0.6942	1.2473E+00	2.4130E+00	1.9346E+00	9.2611E-01	3.2654E+00	7.6765E-02
1.52	0.6869	1.2575E+00	2.4813E+00	1.9731E+00	9.1921E-01	3.3373E+00	8.4236E-02
1.54	0.6799	1.2678E+00	2.5505E+00	2.0117E+00	9.1206E-01	3.4103E+00	9.2052E-02
1.56	0.6730	1.2782E+00	2.6206E+00	2.0502E+00	9.0465E-01	3.4843E+00	1.0021E-01
1.58	0.6664	1.2886E+00	2.6916E+00	2.0887E+00	8.9700E-01	3.5593E+00	1.0870E-01
1.6	0.6599	1.2991E+00	2.7635E+00	2.1272E+00	8.8911E-01	3.6354E+00	1.1753E-01
1.62	0.6537	1.3097E+00	2.8363E+00	2.1656E+00	8.8101E-01	3.7125E+00	1.2668E-01
1.64	0.6476	1.3204E+00	2.9100E+00	2.2039E+00	8.7270E-01	3.7906E+00	1.3616E-01
1.66	0.6417	1.3311E+00	2.9846E+00	2.2422E+00	8.6420E-01	3.8697E+00	1.4595E-01
1.68	0.6360	1.3419E+00	3.0601E+00	2.2804E+00	8.5551E-01	3.9499E+00	1.5606E-01
1.7	0.6304	1.3529E+00	3.1365E+00	2.3185E+00	8.4665E-01	4.0311E+00	1.6647E-01
1.72	0.6250	1.3638E+00	3.2138E+00	2.3565E+00	8.3762E-01	4.1133E+00	1.7719E-01

(Continued)

M_1	M_2	T_2/T_1	p_2/p_1	ρ_2/ρ_1	p_{t2}/p_{t1}	p_{t2}/p_1	$\Delta s/R$
1.74	0.6198	1.3749E+00	3.2921E+00	2.3944E+00	8.2845E-01	4.1965E+00	1.8820E-01
1.76	0.6146	1.3861E+00	3.3712E+00	2.4322E+00	8.1914E-01	4.2808E+00	1.9950E-01
1.78	0.6097	1.3974E+00	3.4512E+00	2.4698E+00	8.0970E-01	4.3660E+00	2.1109E-01
1.8	0.6048	1.4087E+00	3.5322E+00	2.5074E+00	8.0015E-01	4.4523E+00	2.2296E-01
1.82	0.6001	1.4201E+00	3.6140E+00	2.5448E+00	7.9049E-01	4.5396E+00	2.3510E-01
1.84	0.5955	1.4317E+00	3.6968E+00	2.5821E+00	7.8074E-01	4.6278E+00	2.4752E-01
1.86	0.5911	1.4433E+00	3.7804E+00	2.6193E+00	7.7090E-01	4.7171E+00	2.6019E-01
1.88	0.5867	1.4550E+00	3.8650E+00	2.6563E+00	7.6100E-01	4.8074E+00	2.7313E-01
1.9	0.5825	1.4668E+00	3.9504E+00	2.6932E+00	7.5103E-01	4.8987E+00	2.8631E-01
1.92	0.5784	1.4788E+00	4.0368E+00	2.7299E+00	7.4101E-01	4.9909E+00	2.9975E-01
1.94	0.5744	1.4908E+00	4.1241E+00	2.7664E+00	7.3094E-01	5.0842E+00	3.1342E-01
1.96	0.5704	1.5029E+00	4.2122E+00	2.8028E+00	7.2084E-01	5.1785E+00	3.2733E-01
1.98	0.5666	1.5151E+00	4.3013E+00	2.8390E+00	7.1072E-01	5.2738E+00	3.4148E-01
2	0.5629	1.5274E+00	4.3913E+00	2.8750E+00	7.0058E-01	5.3700E+00	3.5585E-01
2.02	0.5592	1.5398E+00	4.4822E+00	2.9108E+00	6.9043E-01	5.4673E+00	3.7043E-01
2.04	0.5557	1.5523E+00	4.5740E+00	2.9465E+00	6.8029E-01	5.5656E+00	3.8524E-01
2.06	0.5522	1.5650E+00	4.6667E+00	2.9820E+00	6.7015E-01	5.6648E+00	4.0025E-01
2.08	0.5488	1.5777E+00	4.7603E+00	3.0173E+00	6.6003E-01	5.7651E+00	4.1548E-01
2.1	0.5455	1.5905E+00	4.8548E+00	3.0524E+00	6.4993E-01	5.8663E+00	4.3090E-01
2.12	0.5423	1.6034E+00	4.9502E+00	3.0873E+00	6.3985E-01	5.9685E+00	4.4651E-01
2.14	0.5391	1.6165E+00	5.0465E+00	3.1219E+00	6.2982E-01	6.0718E+00	4.6232E-01
2.16	0.5361	1.6296E+00	5.1437E+00	3.1564E+00	6.1983E-01	6.1760E+00	4.7831E-01
2.18	0.5331	1.6428E+00	5.2418E+00	3.1907E+00	6.0988E-01	6.2812E+00	4.9449E-01
2.2	0.5301	1.6562E+00	5.3409E+00	3.2248E+00	5.9999E-01	6.3873E+00	5.1084E-01
2.22	0.5272	1.6696E+00	5.4408E+00	3.2587E+00	5.9016E-01	6.4945E+00	5.2736E-01
2.24	0.5244	1.6832E+00	5.5416E+00	3.2923E+00	5.8039E-01	6.6027E+00	5.4406E-01
2.26	0.5217	1.6969E+00	5.6434E+00	3.3257E+00	5.7069E-01	6.7118E+00	5.6091E-01
2.28	0.5190	1.7106E+00	5.7460E+00	3.3590E+00	5.6106E-01	6.8220E+00	5.7792E-01
2.3	0.5163	1.7245E+00	5.8496E+00	3.3920E+00	5.5151E-01	6.9331E+00	5.9509E-01
2.32	0.5138	1.7385E+00	5.9540E+00	3.4248E+00	5.4204E-01	7.0452E+00	6.1241E-01
2.34	0.5112	1.7526E+00	6.0594E+00	3.4573E+00	5.3266E-01	7.1583E+00	6.2987E-01
2.36	0.5088	1.7668E+00	6.1656E+00	3.4896E+00	5.2336E-01	7.2724E+00	6.4748E-01
2.38	0.5064	1.7812E+00	6.2728E+00	3.5218E+00	5.1416E-01	7.3874E+00	6.6523E-01
2.4	0.5040	1.7956E+00	6.3809E+00	3.5536E+00	5.0505E-01	7.5035E+00	6.8310E-01
2.42	0.5017	1.8101E+00	6.4898E+00	3.5853E+00	4.9603E-01	7.6205E+00	7.0111E-01
2.44	0.4994	1.8248E+00	6.5997E+00	3.6167E+00	4.8712E-01	7.7385E+00	7.1925E-01
2.46	0.4972	1.8395E+00	6.7105E+00	3.6479E+00	4.7830E-01	7.8575E+00	7.3751E-01
2.48	0.4950	1.8544E+00	6.8222E+00	3.6789E+00	4.6959E-01	7.9775E+00	7.5589E-01

M_1	M_2	T_2/T_1	p_2/p_1	ρ_2/ρ_1	p_{t2}/p_{t1}	P_{t2}/P_{t1}	$\Delta s/R$
2.5	0.4929	1.8694E+00	6.9348E+00	3.7097E+00	4.6099E-01	8.0985E+00	7.7438E-01
2.52	0.4908	1.8845E+00	7.0483E+00	3.7402E+00	4.5249E-01	8.2204E+00	7.9299E-01
2.54	0.4888	1.8997E+00	7.1627E+00	3.7705E+00	4.4410E-01	8.3433E+00	8.1171E-01
2.56	0.4868	1.9150E+00	7.2780E+00	3.8005E+00	4.3582E-01	8.4672E+00	8.3053E-01
2.58	0.4848	1.9304E+00	7.3942E+00	3.8304E+00	4.2765E-01	8.5921E+00	8.4945E-01
2.6	0.4829	1.9459E+00	7.5113E+00	3.8600E+00	4.1959E-01	8.7180E+00	8.6847E-01
2.62	0.4810	1.9616E+00	7.6293E+00	3.8894E+00	4.1165E-01	8.8449E+00	8.8759E-01
2.64	0.4791	1.9774E+00	7.7482E+00	3.9185E+00	4.0381E-01	8.9727E+00	9.0680E-01
2.66	0.4773	1.9932E+00	7.8681E+00	3.9474E+00	3.9609E-01	9.1015E+00	9.2610E-01
2.68	0.4755	2.0092E+00	7.9888E+00	3.9761E+00	3.8849E-01	9.2313E+00	9.4549E-01
2.7	0.4738	2.0253E+00	8.1104E+00	4.0045E+00	3.8100E-01	9.3621E+00	9.6496E-01
2.72	0.4721	2.0415E+00	8.2330E+00	4.0328E+00	3.7362E-01	9.4938E+00	9.8451E-01
2.74	0.4704	2.0578E+00	8.3564E+00	4.0608E+00	3.6636E-01	9.6266E+00	1.0041E+00
2.76	0.4687	2.0743E+00	8.4808E+00	4.0885E+00	3.5921E-01	9.7603E+00	1.0238E+00
2.78	0.4671	2.0908E+00	8.6060E+00	4.1161E+00	3.5218E-01	9.8950E+00	1.0436E+00
2.8	0.4655	2.1075E+00	8.7322E+00	4.1434E+00	3.4526E-01	1.0031E+01	1.0635E+00
2.82	0.4639	2.1243E+00	8.8592E+00	4.1705E+00	3.3845E-01	1.0167E+01	1.0834E+00
2.84	0.4624	2.1412E+00	8.9872E+00	4.1973E+00	3.3175E-01	1.0305E+01	1.1034E+00
2.86	0.4609	2.1582E+00	9.1161E+00	4.2240E+00	3.2517E-01	1.0444E+01	1.1234E+00
2.88	0.4594	2.1753E+00	9.2458E+00	4.2504E+00	3.1870E-01	1.0583E+01	1.1435E+00
2.9	0.4580	2.1925E+00	9.3765E+00	4.2766E+00	3.1234E-01	1.0724E+01	1.1637E+00
2.92	0.4565	2.2099E+00	9.5081E+00	4.3026E+00	3.0609E-01	1.0865E+01	1.1839E+00
2.94	0.4551	2.2273E+00	9.6406E+00	4.3283E+00	2.9995E-01	1.1008E+01	1.2041E+00
2.96	0.4538	2.2449E+00	9.7740E+00	4.3538E+00	2.9392E-01	1.1151E+01	1.2245E+00
2.98	0.4524	2.2626E+00	9.9083E+00	4.3792E+00	2.8799E-01	1.1296E+01	1.2448E+00
3	0.4511	2.2804E+00	1.0043E+01	4.4043E+00	2.8217E-01	1.1441E+01	1.2652E+00
3.02	0.4498	2.2983E+00	1.0180E+01	4.4291E+00	2.7646E-01	1.1588E+01	1.2857E+00
3.04	0.4485	2.3164E+00	1.0317E+01	4.4538E+00	2.7085E-01	1.1735E+01	1.3062E+00
3.06	0.4472	2.3345E+00	1.0455E+01	4.4783E+00	2.6534E-01	1.1883E+01	1.3267E+00
3.08	0.4460	2.3528E+00	1.0593E+01	4.5025E+00	2.5994E-01	1.2033E+01	1.3473E+00
3.1	0.4448	2.3711E+00	1.0733E+01	4.5265E+00	2.5463E-01	1.2183E+01	1.3679E+00
3.12	0.4436	2.3896E+00	1.0874E+01	4.5503E+00	2.4943E-01	1.2334E+01	1.3886E+00
3.14	0.4424	2.4082E+00	1.1015E+01	4.5739E+00	2.4432E-01	1.2487E+01	1.4093E+00
3.16	0.4412	2.4270E+00	1.1158E+01	4.5973E+00	2.3932E-01	1.2640E+01	1.4300E+00
3.18	0.4401	2.4458E+00	1.1301E+01	4.6205E+00	2.3440E-01	1.2794E+01	1.4507E+00
3.2	0.4389	2.4648E+00	1.1445E+01	4.6435E+00	2.2958E-01	1.2950E+01	1.4715E+00
3.22	0.4378	2.4838E+00	1.1590E+01	4.6663E+00	2.2486E-01	1.3106E+01	1.4923E+00
3.24	0.4368	2.5030E+00	1.1736E+01	4.6889E+00	2.2023E-01	1.3263E+01	1.5131E+00
3.26	0.4357	2.5223E+00	1.1883E+01	4.7113E+00	2.1568E-01	1.3421E+01	1.5339E+00
3.28	0.4346	2.5417E+00	1.2031E+01	4.7335E+00	2.1123E-01	1.3580E+01	1.5548E+00

(Continued)

M_1	M_2	T_2/T_1	p_2/p_1	ρ_2/ρ_1	P_{t2}/P_{t1}	p_{t2}/p_{t1}	$\Delta s/R$
3.3	0.4336	2.5613E+00	1.2180E+01	4.7555E+00	2.0687E-01	1.3740E+01	1.5757E+00
3.32	0.4326	2.5809E+00	1.2330E+01	4.7772E+00	2.0259E-01	1.3901E+01	1.5966E+00
3.34	0.4316	2.6007E+00	1.2480E+01	4.7988E+00	1.9839E-01	1.4064E+01	1.6175E+00
3.36	0.4306	2.6206E+00	1.2632E+01	4.8202E+00	1.9428E-01	1.4227E+01	1.6384E+00
3.38	0.4296	2.6406E+00	1.2784E+01	4.8415E+00	1.9026E-01	1.4391E+01	1.6594E+00
3.4	0.4287	2.6607E+00	1.2937E+01	4.8625E+00	1.8631E-01	1.4556E+01	1.6803E+00
3.42	0.4277	2.6809E+00	1.3092E+01	4.8833E+00	1.8245E-01	1.4722E+01	1.7013E+00
3.44	0.4268	2.7012E+00	1.3247E+01	4.9039E+00	1.7866E-01	1.4889E+01	1.7223E+00
3.46	0.4259	2.7217E+00	1.3403E+01	4.9244E+00	1.7495E-01	1.5057E+01	1.7433E+00
3.48	0.4250	2.7423E+00	1.3560E+01	4.9447E+00	1.7131E-01	1.5225E+01	1.7643E+00
3.5	0.4241	2.7630E+00	1.3717E+01	4.9648E+00	1.6775E-01	1.5395E+01	1.7853E+00
3.52	0.4232	2.7838E+00	1.3876E+01	4.9847E+00	1.6427E-01	1.5566E+01	1.8063E+00
3.54	0.4224	2.8047E+00	1.4036E+01	5.0044E+00	1.6085E-01	1.5738E+01	1.8273E+00
3.56	0.4215	2.8257E+00	1.4196E+01	5.0239E+00	1.5751E-01	1.5911E+01	1.8483E+00
3.58	0.4207	2.8469E+00	1.4358E+01	5.0433E+00	1.5423E-01	1.6085E+01	1.8693E+00
3.6	0.4199	2.8681E+00	1.4520E+01	5.0625E+00	1.5102E-01	1.6259E+01	1.8903E+00
3.62	0.4191	2.8895E+00	1.4683E+01	5.0815E+00	1.4788E-01	1.6435E+01	1.9113E+00
3.64	0.4183	2.9110E+00	1.4847E+01	5.1004E+00	1.4481E-01	1.6612E+01	1.9324E+00
3.66	0.4175	2.9327E+00	1.5012E+01	5.1190E+00	1.4180E-01	1.6790E+01	1.9534E+00
3.68	0.4167	2.9544E+00	1.5178E+01	5.1375E+00	1.3885E-01	1.6968E+01	1.9744E+00
3.7	0.4160	2.9763E+00	1.5345E+01	5.1559E+00	1.3596E-01	1.7148E+01	1.9954E+00
3.72	0.4152	2.9982E+00	1.5513E+01	5.1741E+00	1.3314E-01	1.7328E+01	2.0164E+00
3.74	0.4145	3.0203E+00	1.5682E+01	5.1921E+00	1.3037E-01	1.7510E+01	2.0374E+00
3.76	0.4138	3.0425E+00	1.5851E+01	5.2099E+00	1.2766E-01	1.7693E+01	2.0583E+00
3.78	0.4130	3.0648E+00	1.6022E+01	5.2276E+00	1.2501E-01	1.7876E+01	2.0793E+00
3.8	0.4123	3.0873E+00	1.6193E+01	5.2451E+00	1.2242E-01	1.8061E+01	2.1003E+00
3.82	0.4116	3.1098E+00	1.6365E+01	5.2625E+00	1.1988E-01	1.8246E+01	2.1212E+00
3.84	0.4109	3.1325E+00	1.6539E+01	5.2797E+00	1.1740E-01	1.8433E+01	2.1422E+00
3.86	0.4103	3.1553E+00	1.6713E+01	5.2967E+00	1.1496E-01	1.8620E+01	2.1631E+00
3.88	0.4096	3.1782E+00	1.6888E+01	5.3136E+00	1.1258E-01	1.8809E+01	2.1841E+00
3.9	0.4089	3.2012E+00	1.7063E+01	5.3303E+00	1.1025E-01	1.8998E+01	2.2050E+00
3.92	0.4083	3.2243E+00	1.7240E+01	5.3469E+00	1.0797E-01	1.9188E+01	2.2259E+00
3.94	0.4076	3.2476E+00	1.7418E+01	5.3634E+00	1.0574E-01	1.9380E+01	2.2467E+00
3.96	0.4070	3.2710E+00	1.7597E+01	5.3796E+00	1.0356E-01	1.9572E+01	2.2676E+00
3.98	0.4064	3.2944E+00	1.7776E+01	5.3958E+00	1.0142E-01	1.9765E+01	2.2885E+00
4	0.4058	3.3181E+00	1.7957E+01	5.4118E+00	9.9330E-02	1.9960E+01	2.3093E+00
4.1	0.4028	3.4378E+00	1.8872E+01	5.4896E+00	8.9525E-02	2.0946E+01	2.4132E+00
4.2	0.4000	3.5605E+00	1.9810E+01	5.5639E+00	8.0727E-02	2.1956E+01	2.5167E+00
4.3	0.3975	3.6862E+00	2.0771E+01	5.6350E+00	7.2834E-02	2.2991E+01	2.6196E+00
4.4	0.3950	3.8147E+00	2.1755E+01	5.7029E+00	6.5752E-02	2.4050E+01	2.7219E+00

M_1	M_2	T_2/T_1	p_2/p_1	ρ_2/ρ_1	P_{c2}/P_{c1}	P_{c2}/P_1	$\Delta s/R$
4.5	0.3927	3.9462E+00	2.2761E+01	5.7678E+00	5.9398E-02	2.5134E+01	2.8235E+00
4.6	0.3906	4.0806E+00	2.3790E+01	5.8299E+00	5.3695E-02	2.6241E+01	2.9244E+00
4.7	0.3886	4.2180E+00	2.4841E+01	5.8893E+00	4.8574E-02	2.7374E+01	3.0247E+00
4.8	0.3867	4.3583E+00	2.5915E+01	5.9461E+00	4.3976E-02	2.8530E+01	3.1241E+00
4.9	0.3849	4.5015E+00	2.7011E+01	6.0005E+00	3.9844E-02	2.9711E+01	3.2228E+00
5	0.3832	4.6476E+00	2.8130E+01	6.0526E+00	3.6129E-02	3.0917E+01	3.3207E+00
5.1	0.3816	4.7967E+00	2.9272E+01	6.1025E+00	3.2788E-02	3.2147E+01	3.4177E+00
5.2	0.3801	4.9488E+00	3.0437E+01	6.1503E+00	2.9780E-02	3.3401E+01	3.5139E+00
5.3	0.3786	5.1038E+00	3.1623E+01	6.1961E+00	2.7072E-02	3.4679E+01	3.6093E+00
5.4	0.3773	5.2617E+00	3.2833E+01	6.2400E+00	2.4630E-02	3.5982E+01	3.7038E+00
5.5	0.3760	5.4225E+00	3.4065E+01	6.2822E+00	2.2428E-02	3.7309E+01	3.7974E+00
5.6	0.3747	5.5863E+00	3.5320E+01	6.3226E+00	2.0441E-02	3.8661E+01	3.8902E+00
5.7	0.3736	5.7531E+00	3.6597E+01	6.3614E+00	1.8646E-02	4.0037E+01	3.9821E+00
5.8	0.3725	5.9228E+00	3.7897E+01	6.3986E+00	1.7023E-02	4.1437E+01	4.0732E+00
5.9	0.3714	6.0954E+00	3.9220E+01	6.4344E+00	1.5555E-02	4.2862E+01	4.1634E+00
6	0.3704	6.2710E+00	4.0565E+01	6.4688E+00	1.4226E-02	4.4311E+01	4.2527E+00
6.1	0.3694	6.4495E+00	4.1933E+01	6.5018E+00	1.3021E-02	4.5785E+01	4.3412E+00
6.2	0.3685	6.6309E+00	4.3323E+01	6.5336E+00	1.1929E-02	4.7282E+01	4.4288E+00
6.3	0.3676	6.8153E+00	4.4737E+01	6.5641E+00	1.0937E-02	4.8804E+01	4.5156E+00
6.4	0.3668	7.0027E+00	4.6172E+01	6.5935E+00	1.0037E-02	5.0351E+01	4.6015E+00
6.5	0.3660	7.1930E+00	4.7630E+01	6.6218E+00	9.2182E-03	5.1922E+01	4.6866E+00
6.6	0.3652	7.3862E+00	4.9111E+01	6.6491E+00	8.4733E-03	5.3517E+01	4.7708E+00
6.7	0.3645	7.5824E+00	5.0615E+01	6.6753E+00	7.7950E-03	5.5137E+01	4.8543E+00
6.8	0.3638	7.7815E+00	5.2141E+01	6.7006E+00	7.1768E-03	5.6781E+01	4.9369E+00
6.9	0.3631	7.9836E+00	5.3690E+01	6.7250E+00	6.6129E-03	5.8449E+01	5.0187E+00
7	0.3625	8.1886E+00	5.5261E+01	6.7485E+00	6.0982E-03	6.0142E+01	5.0998E+00
7.1	0.3619	8.3966E+00	5.6855E+01	6.7712E+00	5.6280E-03	6.1859E+01	5.1800E+00
7.2	0.3613	8.6075E+00	5.8471E+01	6.7931E+00	5.1981E-03	6.3600E+01	5.2595E+00
7.3	0.3607	8.8214E+00	6.0110E+01	6.8142E+00	4.8047E-03	6.5366E+01	5.3382E+00
7.4	0.3601	9.0382E+00	6.1772E+01	6.8346E+00	4.4444E-03	6.7156E+01	5.4161E+00
7.5	0.3596	9.2579E+00	6.3457E+01	6.8543E+00	4.1142E-03	6.8970E+01	5.4933E+00
7.6	0.3591	9.4806E+00	6.5163E+01	6.8733E+00	3.8114E-03	7.0809E+01	5.5698E+00
7.7	0.3586	9.7063E+00	6.6893E+01	6.8917E+00	3.5334E-03	7.2672E+01	5.6455E+00
7.8	0.3581	9.9348E+00	6.8645E+01	6.9095E+00	3.2780E-03	7.4560E+01	5.7205E+00
7.9	0.3577	1.0166E+01	7.0420E+01	6.9267E+00	3.0433E-03	7.6472E+01	5.7948E+00
8	0.3573	1.0401E+01	7.2217E+01	6.9434E+00	2.8273E-03	7.8408E+01	5.8684E+00
8.1	0.3568	1.0638E+01	7.4037E+01	6.9595E+00	2.6285E-03	8.0369E+01	5.9414E+00
8.2	0.3564	1.0879E+01	7.5880E+01	6.9751E+00	2.4453E-03	8.2354E+01	6.0136E+00
8.3	0.3560	1.1122E+01	7.7745E+01	6.9902E+00	2.2764E-03	8.4363E+01	6.0852E+00
8.4	0.3557	1.1368E+01	7.9633E+01	7.0048E+00	2.1205E-03	8.6397E+01	6.1561E+00

(Continued)

M_1	M_2	T_2/T_1	p_2/p_1	ρ_2/ρ_1	p_{t2}/p_{t1}	p_{t2}/p_1	$\Delta s/R$
8.5	0.3553	1.1618E+01	8.1543E+01	7.0190E+00	1.9767E-03	8.8455E+01	6.2263E+00
8.6	0.3549	1.1870E+01	8.3477E+01	7.0327E+00	1.8437E-03	9.0537E+01	6.2960E+00
8.7	0.3546	1.2125E+01	8.5432E+01	7.0461E+00	1.7208E-03	9.2644E+01	6.3650E+00
8.8	0.3543	1.2383E+01	8.7410E+01	7.0590E+00	1.6071E-03	9.4775E+01	6.4333E+00
8.9	0.3539	1.2644E+01	8.9411E+01	7.0715E+00	1.5018E-03	9.6931E+01	6.5011E+00
9	0.3536	1.2908E+01	9.1435E+01	7.0837E+00	1.4043E-03	9.9111E+01	6.5682E+00
9.1	0.3533	1.3175E+01	9.3481E+01	7.0954E+00	1.3138E-03	1.0132E+02	6.6348E+00
9.2	0.3530	1.3445E+01	9.5550E+01	7.1069E+00	1.2300E-03	1.0354E+02	6.7008E+00
9.3	0.3528	1.3717E+01	9.7641E+01	7.1180E+00	1.1521E-03	1.0580E+02	6.7662E+00
9.4	0.3525	1.3993E+01	9.9755E+01	7.1288E+00	1.0798E-03	1.0807E+02	6.8310E+00
9.5	0.3522	1.4272E+01	1.0189E+02	7.1393E+00	1.0126E-03	1.1038E+02	6.8953E+00
9.6	0.3520	1.4554E+01	1.0405E+02	7.1495E+00	9.5006E-04	1.1270E+02	6.9590E+00
9.7	0.3517	1.4838E+01	1.0623E+02	7.1594E+00	8.9190E-04	1.1505E+02	7.0222E+00
9.8	0.3515	1.5126E+01	1.0844E+02	7.1690E+00	8.3775E-04	1.1743E+02	7.0848E+00
9.9	0.3513	1.5416E+01	1.1066E+02	7.1784E+00	7.8730E-04	1.1983E+02	7.1469E+00
10	0.3510	1.5710E+01	1.1291E+02	7.1875E+00	7.4028E-04	1.2225E+02	7.2085E+00
11	0.3491	1.8806E+01	1.3665E+02	7.2663E+00	4.1085E-04	1.4782E+02	7.7973E+00
12	0.3476	2.2198E+01	1.6265E+02	7.3274E+00	2.3840E-04	1.7583E+02	8.3416E+00
13	0.3464	2.5884E+01	1.9091E+02	7.3757E+00	1.4380E-04	2.0628E+02	8.8471E+00
14	0.3455	2.9865E+01	2.2143E+02	7.4145E+00	8.9725E-05	2.3916E+02	9.3188E+00
15	0.3448	3.4141E+01	2.5422E+02	7.4460E+00	5.7683E-05	2.7448E+02	9.7606E+00
16	0.3442	3.8712E+01	2.8926E+02	7.4721E+00	3.8077E-05	3.1223E+02	1.0176E+01
17	0.3436	4.3578E+01	3.2657E+02	7.4938E+00	2.5735E-05	3.5242E+02	1.0568E+01
18	0.3432	4.8739E+01	3.6613E+02	7.5121E+00	1.7765E-05	3.9505E+02	1.0938E+01
19	0.3429	5.4194E+01	4.0796E+02	7.5277E+00	1.2499E-05	4.4011E+02	1.1290E+01
20	0.3426	5.9945E+01	4.5204E+02	7.5410E+00	8.9464E-06	4.8761E+02	1.1624E+01
21	0.3423	6.5990E+01	4.9839E+02	7.5525E+00	6.5046E-06	5.3754E+02	1.1943E+01
22	0.3421	7.2331E+01	5.4700E+02	7.5625E+00	4.7972E-06	5.8991E+02	1.2247E+01
23	0.3419	7.8966E+01	5.9787E+02	7.5713E+00	3.5846E-06	6.4471E+02	1.2539E+01
24	0.3417	8.5896E+01	6.5100E+02	7.5789E+00	2.7108E-06	7.0196E+02	1.2818E+01
25	0.3415	9.3121E+01	7.0639E+02	7.5858E+00	2.0729E-06	7.6163E+02	1.3087E+01
30	0.3410	1.3367E+02	1.0173E+03	7.6103E+00	6.2331E-07	1.0966E+03	1.4288E+01
35	0.3406	1.8159E+02	1.3847E+03	7.6252E+00	2.2492E-07	1.4924E+03	1.5308E+01
40	0.3404	2.3688E+02	1.8086E+03	7.6349E+00	9.2847E-08	1.9491E+03	1.6192E+01
45	0.3403	2.9955E+02	2.2890E+03	7.6415E+00	4.2498E-08	2.4667E+03	1.6974E+01
50	0.3401	3.6959E+02	2.8260E+03	7.6463E+00	2.1110E-08	3.0452E+03	1.7674E+01

APPENDIX D

Rayleigh Flow

The parameters corresponding to a Rayleigh line, for a calorically perfect gas (i.e., $\gamma = \text{constant}$), are summarized below:

$$\frac{p}{p^*} = \frac{\gamma + 1}{1 + \gamma M^2} \quad (\text{D.1})$$

$$\frac{T}{T^*} = M^2 \left(\frac{\gamma + 1}{1 + \gamma M^2} \right)^2 \quad (\text{D.2})$$

$$\frac{\rho}{\rho^*} = \frac{1}{M^2} \left(\frac{1 + \gamma M^2}{\gamma + 1} \right) \quad (\text{D.3})$$

$$\frac{T_t}{T_t^*} = M^2 \left(\frac{\gamma + 1}{1 + \gamma M^2} \right)^2 \left(\frac{1 + \frac{\gamma - 1}{2} M^2}{\frac{\gamma + 1}{2}} \right) \quad (\text{D.4})$$

$$\frac{p_t}{p_t^*} = \left(\frac{\gamma + 1}{1 + \gamma M^2} \right) \left(\frac{1 + \frac{\gamma - 1}{2} M^2}{\frac{\gamma + 1}{2}} \right)^{\frac{\gamma}{\gamma - 1}} \quad (\text{D.5})$$

$$\frac{\Delta s}{R} = \frac{s^* - s}{R} = - \left(\frac{\gamma}{\gamma - 1} \right) \ell n \left(\frac{T}{T^*} \right) + \ell n \left(\frac{p}{p^*} \right) \quad (\text{D.6})$$

We have derived these expressions in Chapter 2.

Rayleigh Flow $\gamma = 1.4$

M	p/p^*	T/T^*	ρ/ρ^*	T_t/T_t^*	p_t/p_t^*	$\Delta s/R$
0.10	2.3669E+00	5.6020E-02	4.2250E+01	4.6777E-02	1.2591E+00	1.0949E+01
0.12	2.3526E+00	7.9698E-02	2.9519E+01	6.6606E-02	1.2554E+00	9.7088E+00
0.14	2.3359E+00	1.0695E-01	2.1842E+01	8.9471E-02	1.2510E+00	8.6724E+00
0.16	2.3170E+00	1.3743E-01	1.6859E+01	1.1511E-01	1.2461E+00	7.7865E+00
0.18	2.2959E+00	1.7078E-01	1.3443E+01	1.4324E-01	1.2406E+00	7.0169E+00
0.20	2.2727E+00	2.0661E-01	1.1000E+01	1.7355E-01	1.2346E+00	6.3402E+00
0.22	2.2477E+00	2.4452E-01	9.1921E+00	2.0574E-01	1.2281E+00	5.7395E+00
0.24	2.2209E+00	2.8411E-01	7.8171E+00	2.3948E-01	1.2213E+00	5.2023E+00
0.26	2.1925E+00	3.2496E-01	6.7470E+00	2.7446E-01	1.2140E+00	4.7193E+00
0.28	2.1626E+00	3.6667E-01	5.8980E+00	3.1035E-01	1.2064E+00	4.2828E+00
0.30	2.1314E+00	4.0887E-01	5.2130E+00	3.4686E-01	1.1985E+00	3.8870E+00
0.32	2.0991E+00	4.5119E-01	4.6523E+00	3.8369E-01	1.1904E+00	3.5271E+00
0.34	2.0657E+00	4.9327E-01	4.1877E+00	4.2056E-01	1.1822E+00	3.1989E+00
0.36	2.0314E+00	5.3482E-01	3.7984E+00	4.5723E-01	1.1737E+00	2.8992E+00
0.38	1.9964E+00	5.7553E-01	3.4688E+00	4.9346E-01	1.1652E+00	2.6250E+00
0.40	1.9608E+00	6.1515E-01	3.1875E+00	5.2903E-01	1.1566E+00	2.3740E+00
0.42	1.9247E+00	6.5346E-01	2.9454E+00	5.6376E-01	1.1480E+00	2.1439E+00
0.44	1.8882E+00	6.9025E-01	2.7355E+00	5.9748E-01	1.1394E+00	1.9331E+00
0.46	1.8515E+00	7.2538E-01	2.5525E+00	6.3007E-01	1.1308E+00	1.7397E+00
0.48	1.8147E+00	7.5871E-01	2.3918E+00	6.6139E-01	1.1224E+00	1.5624E+00
0.50	1.7778E+00	7.9012E-01	2.2500E+00	6.9136E-01	1.1141E+00	1.3998E+00
0.52	1.7409E+00	8.1955E-01	2.1243E+00	7.1990E-01	1.1059E+00	1.2509E+00
0.54	1.7043E+00	8.4695E-01	2.0122E+00	7.4695E-01	1.0979E+00	1.1145E+00
0.56	1.6678E+00	8.7227E-01	1.9120E+00	7.7249E-01	1.0901E+00	9.8977E-01
0.58	1.6316E+00	8.9552E-01	1.8219E+00	7.9648E-01	1.0826E+00	8.7577E-01
0.60	1.5957E+00	9.1670E-01	1.7407E+00	8.1892E-01	1.0753E+00	7.7174E-01
0.62	1.5603E+00	9.3584E-01	1.6673E+00	8.3983E-01	1.0682E+00	6.7696E-01
0.64	1.5253E+00	9.5298E-01	1.6006E+00	8.5920E-01	1.0615E+00	5.9078E-01
0.66	1.4908E+00	9.6816E-01	1.5399E+00	8.7708E-01	1.0550E+00	5.1260E-01
0.68	1.4569E+00	9.8144E-01	1.4844E+00	8.9350E-01	1.0489E+00	4.4187E-01
0.70	1.4235E+00	9.9290E-01	1.4337E+00	9.0850E-01	1.0431E+00	3.7807E-01
0.72	1.3907E+00	1.0026E+00	1.3871E+00	9.2212E-01	1.0376E+00	3.2072E-01
0.74	1.3585E+00	1.0106E+00	1.3442E+00	9.3442E-01	1.0325E+00	2.6940E-01
0.76	1.3270E+00	1.0171E+00	1.3047E+00	9.4546E-01	1.0278E+00	2.2370E-01
0.78	1.2961E+00	1.0220E+00	1.2682E+00	9.5528E-01	1.0234E+00	1.8324E-01

M	p/p^*	T/T^*	ρ/ρ^*	T_t/T_t^*	p_t/p_t^*	$\Delta s/R$
0.80	1.2658E+00	1.0255E+00	1.2344E+00	9.6395E-01	1.0193E+00	1.4767E-01
0.82	1.2362E+00	1.0276E+00	1.2030E+00	9.7152E-01	1.0157E+00	1.1668E-01
0.84	1.2073E+00	1.0285E+00	1.1738E+00	9.7807E-01	1.0124E+00	8.9953E-02
0.86	1.1791E+00	1.0283E+00	1.1467E+00	9.8363E-01	1.0095E+00	6.7220E-02
0.88	1.1515E+00	1.0269E+00	1.1214E+00	9.8828E-01	1.0070E+00	4.8217E-02
0.90	1.1246E+00	1.0245E+00	1.0977E+00	9.9207E-01	1.0049E+00	3.2700E-02
0.92	1.0984E+00	1.0212E+00	1.0756E+00	9.9506E-01	1.0031E+00	2.0444E-02
0.94	1.0728E+00	1.0170E+00	1.0549E+00	9.9729E-01	1.0017E+00	1.1237E-02
0.96	1.0479E+00	1.0121E+00	1.0354E+00	9.9883E-01	1.0008E+00	4.8812E-03
0.98	1.0236E+00	1.0064E+00	1.0172E+00	9.9971E-01	1.0002E+00	1.1930E-03
1.00	1.0000E+00	1.0000E+00	1.0000E+00	1.0000E+00	1.0000E+00	0.0000E+00
1.02	9.7698E-01	9.9304E-01	9.8382E-01	9.9973E-01	1.0002E+00	1.1412E-03
1.04	9.5456E-01	9.8554E-01	9.6857E-01	9.9895E-01	1.0008E+00	4.4660E-03
1.06	9.3275E-01	9.7755E-01	9.5417E-01	9.9769E-01	1.0017E+00	9.8337E-03
1.08	9.1152E-01	9.6913E-01	9.4056E-01	9.9601E-01	1.0031E+00	1.7112E-02
1.10	8.9087E-01	9.6031E-01	9.2769E-01	9.9392E-01	1.0049E+00	2.6179E-02
1.12	8.7078E-01	9.5115E-01	9.1550E-01	9.9148E-01	1.0070E+00	3.6917E-02
1.14	8.5123E-01	9.4169E-01	9.0394E-01	9.8871E-01	1.0095E+00	4.9219E-02
1.16	8.3222E-01	9.3196E-01	8.9298E-01	9.8564E-01	1.0124E+00	6.2984E-02
1.18	8.1374E-01	9.2200E-01	8.8258E-01	9.8230E-01	1.0157E+00	7.8116E-02
1.20	7.9576E-01	9.1185E-01	8.7269E-01	9.7872E-01	1.0194E+00	9.4525E-02
1.22	7.7827E-01	9.0153E-01	8.6328E-01	9.7492E-01	1.0235E+00	1.1213E-01
1.24	7.6127E-01	8.9108E-01	8.5432E-01	9.7092E-01	1.0279E+00	1.3085E-01
1.26	7.4473E-01	8.8052E-01	8.4578E-01	9.6675E-01	1.0328E+00	1.5061E-01
1.28	7.2865E-01	8.6988E-01	8.3765E-01	9.6243E-01	1.0380E+00	1.7135E-01
1.30	7.1301E-01	8.5917E-01	8.2988E-01	9.5798E-01	1.0437E+00	1.9299E-01
1.32	6.9780E-01	8.4843E-01	8.2247E-01	9.5341E-01	1.0497E+00	2.1548E-01
1.34	6.8301E-01	8.3766E-01	8.1538E-01	9.4873E-01	1.0561E+00	2.3876E-01
1.36	6.6863E-01	8.2689E-01	8.0861E-01	9.4398E-01	1.0629E+00	2.6277E-01
1.38	6.5464E-01	8.1613E-01	8.0212E-01	9.3914E-01	1.0701E+00	2.8747E-01
1.40	6.4103E-01	8.0539E-01	7.9592E-01	9.3425E-01	1.0777E+00	3.1281E-01
1.42	6.2779E-01	7.9469E-01	7.8997E-01	9.2931E-01	1.0856E+00	3.3874E-01
1.44	6.1491E-01	7.8405E-01	7.8427E-01	9.2434E-01	1.0940E+00	3.6522E-01
1.46	6.0237E-01	7.7346E-01	7.7880E-01	9.1933E-01	1.1028E+00	3.9221E-01
1.48	5.9018E-01	7.6294E-01	7.7356E-01	9.1431E-01	1.1120E+00	4.1968E-01
1.50	5.7831E-01	7.5250E-01	7.6852E-01	9.0928E-01	1.1215E+00	4.4758E-01
1.52	5.6676E-01	7.4215E-01	7.6368E-01	9.0424E-01	1.1315E+00	4.7589E-01
1.54	5.5552E-01	7.3189E-01	7.5902E-01	8.9920E-01	1.1419E+00	5.0458E-01
1.56	5.4458E-01	7.2173E-01	7.5455E-01	8.9418E-01	1.1527E+00	5.3361E-01
1.58	5.3393E-01	7.1168E-01	7.5024E-01	8.8917E-01	1.1640E+00	5.6295E-01

(Continued)

M	p/p^*	T/T^*	ρ/ρ^*	T_t/T_t^*	p_t/p_t^*	$\Delta s/R$
1.60	5.2356E-01	7.0174E-01	7.4609E-01	8.8419E-01	1.1756E+00	5.9259E-01
1.62	5.1346E-01	6.9190E-01	7.4210E-01	8.7922E-01	1.1877E+00	6.2250E-01
1.64	5.0363E-01	6.8219E-01	7.3825E-01	8.7429E-01	1.2002E+00	6.5265E-01
1.66	4.9405E-01	6.7259E-01	7.3454E-01	8.6939E-01	1.2131E+00	6.8303E-01
1.68	4.8472E-01	6.6312E-01	7.3096E-01	8.6453E-01	1.2264E+00	7.1360E-01
1.70	4.7562E-01	6.5377E-01	7.2751E-01	8.5971E-01	1.2402E+00	7.4436E-01
1.72	4.6677E-01	6.4455E-01	7.2418E-01	8.5493E-01	1.2545E+00	7.7529E-01
1.74	4.5813E-01	6.3545E-01	7.2096E-01	8.5019E-01	1.2692E+00	8.0636E-01
1.76	4.4972E-01	6.2649E-01	7.1785E-01	8.4551E-01	1.2843E+00	8.3757E-01
1.78	4.4152E-01	6.1765E-01	7.1484E-01	8.4087E-01	1.2999E+00	8.6889E-01
1.80	4.3353E-01	6.0894E-01	7.1193E-01	8.3628E-01	1.3159E+00	9.0031E-01
1.82	4.2573E-01	6.0036E-01	7.0912E-01	8.3174E-01	1.3324E+00	9.3183E-01
1.84	4.1813E-01	5.9191E-01	7.0640E-01	8.2726E-01	1.3494E+00	9.6342E-01
1.86	4.1072E-01	5.8359E-01	7.0377E-01	8.2283E-01	1.3669E+00	9.9507E-01
1.88	4.0349E-01	5.7540E-01	7.0122E-01	8.1845E-01	1.3849E+00	1.0268E+00
1.90	3.9643E-01	5.6734E-01	6.9875E-01	8.1414E-01	1.4033E+00	1.0585E+00
1.92	3.8955E-01	5.5941E-01	6.9636E-01	8.0987E-01	1.4222E+00	1.0903E+00
1.94	3.8283E-01	5.5160E-01	6.9404E-01	8.0567E-01	1.4417E+00	1.1221E+00
1.96	3.7628E-01	5.4392E-01	6.9180E-01	8.0152E-01	1.4616E+00	1.1539E+00
1.98	3.6988E-01	5.3636E-01	6.8962E-01	7.9742E-01	1.4821E+00	1.1858E+00
2.00	3.6364E-01	5.2893E-01	6.8750E-01	7.9339E-01	1.5031E+00	1.2176E+00
2.05	3.4866E-01	5.1087E-01	6.8248E-01	7.8355E-01	1.5579E+00	1.2971E+00
2.10	3.3454E-01	4.9356E-01	6.7782E-01	7.7406E-01	1.6162E+00	1.3764E+00
2.15	3.2122E-01	4.7696E-01	6.7347E-01	7.6493E-01	1.6780E+00	1.4555E+00
2.20	3.0864E-01	4.6106E-01	6.6942E-01	7.5613E-01	1.7434E+00	1.5342E+00
2.25	2.9675E-01	4.4582E-01	6.6564E-01	7.4768E-01	1.8128E+00	1.6126E+00
2.30	2.8551E-01	4.3122E-01	6.6210E-01	7.3954E-01	1.8860E+00	1.6905E+00
2.35	2.7487E-01	4.1723E-01	6.5878E-01	7.3173E-01	1.9634E+00	1.7679E+00
2.40	2.6478E-01	4.0384E-01	6.5567E-01	7.2421E-01	2.0451E+00	1.8448E+00
2.45	2.5522E-01	3.9100E-01	6.5275E-01	7.1699E-01	2.1311E+00	1.9211E+00
2.50	2.4615E-01	3.7870E-01	6.5000E-01	7.1006E-01	2.2218E+00	1.9968E+00
2.55	2.3754E-01	3.6691E-01	6.4741E-01	7.0340E-01	2.3173E+00	2.0718E+00
2.60	2.2936E-01	3.5561E-01	6.4497E-01	6.9700E-01	2.4177E+00	2.1463E+00
2.65	2.2158E-01	3.4478E-01	6.4267E-01	6.9084E-01	2.5233E+00	2.2200E+00
2.70	2.1417E-01	3.3439E-01	6.4049E-01	6.8494E-01	2.6343E+00	2.2931E+00
2.75	2.0712E-01	3.2442E-01	6.3843E-01	6.7926E-01	2.7508E+00	2.3655E+00
2.80	2.0040E-01	3.1486E-01	6.3648E-01	6.7380E-01	2.8731E+00	2.4373E+00
2.85	1.9399E-01	3.0568E-01	6.3463E-01	6.6855E-01	3.0014E+00	2.5083E+00
2.90	1.8788E-01	2.9687E-01	6.3288E-01	6.6350E-01	3.1359E+00	2.5787E+00
2.95	1.8205E-01	2.8841E-01	6.3121E-01	6.5865E-01	3.2768E+00	2.6483E+00

M	p/p^*	T/T^*	ρ/ρ^*	T_t/T_t^*	p_t/p_t^*	$\Delta s/R$
3.00	1.7647E-01	2.8028E-01	6.2963E-01	6.5398E-01	3.4245E+00	2.7173E+00
3.10	1.6604E-01	2.6495E-01	6.2669E-01	6.4516E-01	3.7408E+00	2.8532E+00
3.20	1.5649E-01	2.5078E-01	6.2402E-01	6.3699E-01	4.0871E+00	2.9863E+00
3.30	1.4773E-01	2.3766E-01	6.2159E-01	6.2940E-01	4.4655E+00	3.1168E+00
3.40	1.3966E-01	2.2549E-01	6.1938E-01	6.2236E-01	4.8783E+00	3.2446E+00
3.50	1.3223E-01	2.1419E-01	6.1735E-01	6.1580E-01	5.3280E+00	3.3699E+00
3.60	1.2537E-01	2.0369E-01	6.1548E-01	6.0970E-01	5.8173E+00	3.4926E+00
3.70	1.1901E-01	1.9390E-01	6.1377E-01	6.0401E-01	6.3488E+00	3.6128E+00
3.80	1.1312E-01	1.8478E-01	6.1219E-01	5.9870E-01	6.9256E+00	3.7307E+00
3.90	1.0765E-01	1.7627E-01	6.1073E-01	5.9373E-01	7.5505E+00	3.8463E+00
4.00	1.0256E-01	1.6831E-01	6.0938E-01	5.8909E-01	8.2268E+00	3.9595E+00
4.10	9.7823E-02	1.6086E-01	6.0812E-01	5.8473E-01	8.9579E+00	4.0706E+00
4.20	9.3400E-02	1.5388E-01	6.0695E-01	5.8065E-01	9.7473E+00	4.1796E+00
4.30	8.9266E-02	1.4734E-01	6.0587E-01	5.7682E-01	1.0599E+01	4.2865E+00
4.40	8.5397E-02	1.4119E-01	6.0486E-01	5.7322E-01	1.1516E+01	4.3914E+00
4.50	8.1772E-02	1.3540E-01	6.0391E-01	5.6982E-01	1.2502E+01	4.4944E+00
4.60	7.8370E-02	1.2996E-01	6.0302E-01	5.6663E-01	1.3563E+01	4.5955E+00
4.70	7.5174E-02	1.2483E-01	6.0220E-01	5.6362E-01	1.4702E+01	4.6948E+00
4.80	7.2167E-02	1.2000E-01	6.0142E-01	5.6078E-01	1.5923E+01	4.7923E+00
4.90	6.9336E-02	1.1543E-01	6.0069E-01	5.5809E-01	1.7232E+01	4.8881E+00
5.00	6.6667E-02	1.1111E-01	6.0000E-01	5.5556E-01	1.8634E+01	4.9822E+00
5.20	6.1767E-02	1.0316E-01	5.9874E-01	5.5088E-01	2.1734E+01	5.1658E+00
5.40	5.7383E-02	9.6019E-02	5.9762E-01	5.4667E-01	2.5268E+01	5.3432E+00
5.60	5.3447E-02	8.9584E-02	5.9662E-01	5.4288E-01	2.9281E+01	5.5150E+00
5.80	4.9900E-02	8.3765E-02	5.9572E-01	5.3944E-01	3.3822E+01	5.6814E+00
6.00	4.6693E-02	7.8487E-02	5.9491E-01	5.3633E-01	3.8946E+01	5.8427E+00
6.50	3.9900E-02	6.7263E-02	5.9320E-01	5.2970E-01	5.4683E+01	6.2256E+00
7.00	3.4483E-02	5.8264E-02	5.9184E-01	5.2438E-01	7.5414E+01	6.5824E+00
7.50	3.0094E-02	5.0943E-02	5.9074E-01	5.2004E-01	1.0229E+02	6.9162E+00
8.00	2.6490E-02	4.4910E-02	5.8984E-01	5.1647E-01	1.3662E+02	7.2298E+00
8.50	2.3495E-02	3.9883E-02	5.8910E-01	5.1349E-01	1.7992E+02	7.5254E+00
9.00	2.0979E-02	3.5650E-02	5.8848E-01	5.1098E-01	2.3388E+02	7.8048E+00
9.50	1.8846E-02	3.2053E-02	5.8795E-01	5.0885E-01	3.0041E+02	8.0698E+00
10.00	1.7021E-02	2.8972E-02	5.8750E-01	5.0702E-01	3.8161E+02	8.3217E+00
15.00	7.5949E-03	1.2979E-02	5.8519E-01	4.9752E-01	2.6488E+03	1.0325E+01

Rayleigh Flow $\gamma = 1.3$

M	p/p^*	T/T^*	ρ/ρ^*	T_t/T_t^*	p_t/p_t^*	$\Delta s/R$
0.10	2.2705E+00	5.1551E-02	4.4043E+01	4.4894E-02	1.2471E+00	1.3669E+01
0.12	2.2577E+00	7.3402E-02	3.0758E+01	6.3966E-02	1.2437E+00	1.2132E+01
0.14	2.2429E+00	9.8596E-02	2.2748E+01	8.5987E-02	1.2397E+00	1.0847E+01
0.16	2.2259E+00	1.2684E-01	1.7549E+01	1.1072E-01	1.2351E+00	9.7477E+00
0.18	2.2070E+00	1.5782E-01	1.3984E+01	1.3790E-01	1.2300E+00	8.7922E+00
0.20	2.1863E+00	1.9120E-01	1.1435E+01	1.6726E-01	1.2245E+00	7.9514E+00
0.22	2.1639E+00	2.2662E-01	9.5483E+00	1.9849E-01	1.2185E+00	7.2046E+00
0.24	2.1398E+00	2.6373E-01	8.1135E+00	2.3131E-01	1.2121E+00	6.5363E+00
0.26	2.1142E+00	3.0216E-01	6.9969E+00	2.6541E-01	1.2053E+00	5.9347E+00
0.28	2.0873E+00	3.4156E-01	6.1109E+00	3.0050E-01	1.1983E+00	5.3908E+00
0.30	2.0591E+00	3.8159E-01	5.3961E+00	3.3629E-01	1.1909E+00	4.8971E+00
0.32	2.0298E+00	4.2189E-01	4.8111E+00	3.7250E-01	1.1834E+00	4.4476E+00
0.34	1.9995E+00	4.6217E-01	4.3263E+00	4.0886E-01	1.1756E+00	4.0374E+00
0.36	1.9684E+00	5.0213E-01	3.9200E+00	4.4512E-01	1.1677E+00	3.6624E+00
0.38	1.9365E+00	5.4150E-01	3.5762E+00	4.8106E-01	1.1596E+00	3.3190E+00
0.40	1.9040E+00	5.8002E-01	3.2826E+00	5.1647E-01	1.1515E+00	3.0043E+00
0.42	1.8710E+00	6.1748E-01	3.0300E+00	5.5115E-01	1.1434E+00	2.7156E+00
0.44	1.8375E+00	6.5369E-01	2.8110E+00	5.8494E-01	1.1352E+00	2.4506E+00
0.46	1.8038E+00	6.8849E-01	2.6200E+00	6.1769E-01	1.1271E+00	2.2073E+00
0.48	1.7699E+00	7.2173E-01	2.4523E+00	6.4928E-01	1.1191E+00	1.9840E+00
0.50	1.7358E+00	7.5329E-01	2.3043E+00	6.7960E-01	1.1111E+00	1.7791E+00
0.52	1.7018E+00	7.8310E-01	2.1731E+00	7.0858E-01	1.1033E+00	1.5911E+00
0.54	1.6678E+00	8.1108E-01	2.0562E+00	7.3614E-01	1.0957E+00	1.4188E+00
0.56	1.6339E+00	8.3719E-01	1.9516E+00	7.6224E-01	1.0882E+00	1.2610E+00
0.58	1.6002E+00	8.6140E-01	1.8577E+00	7.8684E-01	1.0809E+00	1.1166E+00
0.60	1.5668E+00	8.8370E-01	1.7729E+00	8.0993E-01	1.0739E+00	9.8476E-01
0.62	1.5336E+00	9.0410E-01	1.6963E+00	8.3151E-01	1.0671E+00	8.6447E-01
0.64	1.5008E+00	9.2263E-01	1.6267E+00	8.5158E-01	1.0605E+00	7.5499E-01
0.66	1.4684E+00	9.3930E-01	1.5633E+00	8.7015E-01	1.0543E+00	6.5555E-01
0.68	1.4365E+00	9.5417E-01	1.5055E+00	8.8726E-01	1.0483E+00	5.6550E-01
0.70	1.4050E+00	9.6728E-01	1.4525E+00	9.0294E-01	1.0426E+00	4.8418E-01
0.72	1.3740E+00	9.7870E-01	1.4039E+00	9.1722E-01	1.0373E+00	4.1102E-01
0.74	1.3436E+00	9.8849E-01	1.3592E+00	9.3016E-01	1.0323E+00	3.4548E-01
0.76	1.3136E+00	9.9671E-01	1.3180E+00	9.4180E-01	1.0276E+00	2.8706E-01
0.78	1.2843E+00	1.0034E+00	1.2799E+00	9.5219E-01	1.0233E+00	2.3529E-01

M	p/p^*	T/T^*	ρ/ρ^*	T_t/T_t^*	p_t/p_t^*	$\Delta s/R$
0.80	1.2555E+00	1.0088E+00	1.2446E+00	9.6139E-01	1.0193E+00	1.8974E-01
0.82	1.2272E+00	1.0127E+00	1.2118E+00	9.6944E-01	1.0157E+00	1.5001E-01
0.84	1.1996E+00	1.0154E+00	1.1814E+00	9.7642E-01	1.0124E+00	1.1572E-01
0.86	1.1726E+00	1.0169E+00	1.1531E+00	9.8238E-01	1.0095E+00	8.6524E-02
0.88	1.1461E+00	1.0173E+00	1.1267E+00	9.8736E-01	1.0070E+00	6.2098E-02
0.90	1.1203E+00	1.0166E+00	1.1020E+00	9.9143E-01	1.0049E+00	4.2138E-02
0.92	1.0951E+00	1.0150E+00	1.0789E+00	9.9465E-01	1.0031E+00	2.6359E-02
0.94	1.0704E+00	1.0124E+00	1.0573E+00	9.9707E-01	1.0018E+00	1.4496E-02
0.96	1.0464E+00	1.0090E+00	1.0370E+00	9.9873E-01	1.0008E+00	6.3002E-03
0.98	1.0229E+00	1.0049E+00	1.0179E+00	9.9969E-01	1.0002E+00	1.5407E-03
1.00	1.0000E+00	1.0000E+00	1.0000E+00	1.0000E+00	1.0000E+00	0.0000E+00
1.02	9.7768E-01	9.9446E-01	9.8312E-01	9.9971E-01	1.0002E+00	1.4748E-03
1.04	9.5591E-01	9.8833E-01	9.6720E-01	9.9885E-01	1.0008E+00	5.7748E-03
1.06	9.3470E-01	9.8165E-01	9.5217E-01	9.9748E-01	1.0018E+00	1.2722E-02
1.08	9.1403E-01	9.7448E-01	9.3797E-01	9.9563E-01	1.0032E+00	2.2148E-02
1.10	8.9390E-01	9.6686E-01	9.2454E-01	9.9334E-01	1.0049E+00	3.3897E-02
1.12	8.7429E-01	9.5883E-01	9.1182E-01	9.9065E-01	1.0071E+00	4.7821E-02
1.14	8.5518E-01	9.5045E-01	8.9977E-01	9.8759E-01	1.0097E+00	6.3784E-02
1.16	8.3658E-01	9.4175E-01	8.8833E-01	9.8420E-01	1.0127E+00	8.1654E-02
1.18	8.1847E-01	9.3276E-01	8.7747E-01	9.8050E-01	1.0161E+00	1.0131E-01
1.20	8.0084E-01	9.2353E-01	8.6715E-01	9.7653E-01	1.0199E+00	1.2264E-01
1.22	7.8367E-01	9.1408E-01	8.5733E-01	9.7231E-01	1.0241E+00	1.4553E-01
1.24	7.6695E-01	9.0444E-01	8.4798E-01	9.6786E-01	1.0288E+00	1.6989E-01
1.26	7.5068E-01	8.9465E-01	8.3908E-01	9.6322E-01	1.0338E+00	1.9562E-01
1.28	7.3484E-01	8.8473E-01	8.3059E-01	9.5840E-01	1.0392E+00	2.2263E-01
1.30	7.1942E-01	8.7470E-01	8.2249E-01	9.5342E-01	1.0451E+00	2.5083E-01
1.32	7.0442E-01	8.6458E-01	8.1475E-01	9.4830E-01	1.0514E+00	2.8016E-01
1.34	6.8980E-01	8.5440E-01	8.0736E-01	9.4306E-01	1.0581E+00	3.1052E-01
1.36	6.7558E-01	8.4417E-01	8.0029E-01	9.3772E-01	1.0653E+00	3.4186E-01
1.38	6.6173E-01	8.3392E-01	7.9352E-01	9.3229E-01	1.0728E+00	3.7411E-01
1.40	6.4825E-01	8.2365E-01	7.8705E-01	9.2679E-01	1.0809E+00	4.0721E-01
1.42	6.3513E-01	8.1339E-01	7.8084E-01	9.2122E-01	1.0893E+00	4.4109E-01
1.44	6.2235E-01	8.0314E-01	7.7489E-01	9.1561E-01	1.0982E+00	4.7571E-01
1.46	6.0990E-01	7.9292E-01	7.6919E-01	9.0996E-01	1.1075E+00	5.1101E-01
1.48	5.9779E-01	7.8274E-01	7.6371E-01	9.0428E-01	1.1173E+00	5.4694E-01
1.50	5.8599E-01	7.7261E-01	7.5845E-01	8.9858E-01	1.1275E+00	5.8347E-01
1.52	5.7449E-01	7.6253E-01	7.5340E-01	8.9287E-01	1.1382E+00	6.2053E-01
1.54	5.6330E-01	7.5253E-01	7.4855E-01	8.8716E-01	1.1494E+00	6.5810E-01
1.56	5.5240E-01	7.4259E-01	7.4388E-01	8.8145E-01	1.1611E+00	6.9614E-01
1.58	5.4177E-01	7.3274E-01	7.3938E-01	8.7576E-01	1.1732E+00	7.3460E-01

(Continued)

M	p/p^*	T/T^*	ρ/ρ^*	T_t/T_t^*	p_t/p_t^*	$\Delta s/R$
1.60	5.3142E-01	7.2297E-01	7.3505E-01	8.7008E-01	1.1858E+00	7.7346E-01
1.62	5.2134E-01	7.1330E-01	7.3089E-01	8.6443E-01	1.1989E+00	8.1269E-01
1.64	5.1151E-01	7.0372E-01	7.2687E-01	8.5880E-01	1.2125E+00	8.5224E-01
1.66	5.0193E-01	6.9424E-01	7.2300E-01	8.5321E-01	1.2266E+00	8.9211E-01
1.68	4.9260E-01	6.8486E-01	7.1926E-01	8.4766E-01	1.2412E+00	9.3225E-01
1.70	4.8350E-01	6.7560E-01	7.1566E-01	8.4215E-01	1.2563E+00	9.7264E-01
1.72	4.7463E-01	6.6644E-01	7.1218E-01	8.3668E-01	1.2719E+00	1.0133E+00
1.74	4.6598E-01	6.5739E-01	7.0882E-01	8.3125E-01	1.2881E+00	1.0541E+00
1.76	4.5754E-01	6.4846E-01	7.0558E-01	8.2588E-01	1.3049E+00	1.0951E+00
1.78	4.4931E-01	6.3964E-01	7.0244E-01	8.2056E-01	1.3222E+00	1.1363E+00
1.80	4.4129E-01	6.3095E-01	6.9941E-01	8.1529E-01	1.3400E+00	1.1776E+00
1.82	4.3346E-01	6.2236E-01	6.9648E-01	8.1008E-01	1.3584E+00	1.2190E+00
1.84	4.2582E-01	6.1390E-01	6.9364E-01	8.0492E-01	1.3775E+00	1.2606E+00
1.86	4.1837E-01	6.0556E-01	6.9089E-01	7.9983E-01	1.3971E+00	1.3022E+00
1.88	4.1110E-01	5.9733E-01	6.8823E-01	7.9479E-01	1.4173E+00	1.3440E+00
1.90	4.0400E-01	5.8922E-01	6.8566E-01	7.8982E-01	1.4381E+00	1.3858E+00
1.92	3.9708E-01	5.8124E-01	6.8316E-01	7.8490E-01	1.4595E+00	1.4276E+00
1.94	3.9031E-01	5.7337E-01	6.8074E-01	7.8005E-01	1.4816E+00	1.4695E+00
1.96	3.8371E-01	5.6562E-01	6.7839E-01	7.7526E-01	1.5043E+00	1.5114E+00
1.98	3.7726E-01	5.5798E-01	6.7612E-01	7.7053E-01	1.5277E+00	1.5533E+00
2.00	3.7097E-01	5.5047E-01	6.7391E-01	7.6587E-01	1.5518E+00	1.5953E+00
2.05	3.5586E-01	5.3218E-01	6.6868E-01	7.5449E-01	1.6150E+00	1.7001E+00
2.10	3.4160E-01	5.1461E-01	6.6381E-01	7.4350E-01	1.6826E+00	1.8047E+00
2.15	3.2814E-01	4.9773E-01	6.5928E-01	7.3290E-01	1.7551E+00	1.9091E+00
2.20	3.1541E-01	4.8151E-01	6.5505E-01	7.2269E-01	1.8324E+00	2.0130E+00
2.25	3.0338E-01	4.6595E-01	6.5110E-01	7.1285E-01	1.9150E+00	2.1165E+00
2.30	2.9199E-01	4.5101E-01	6.4741E-01	7.0339E-01	2.0031E+00	2.2194E+00
2.35	2.8120E-01	4.3668E-01	6.4395E-01	6.9428E-01	2.0970E+00	2.3217E+00
2.40	2.7097E-01	4.2293E-01	6.4070E-01	6.8551E-01	2.1970E+00	2.4233E+00
2.45	2.6127E-01	4.0973E-01	6.3765E-01	6.7709E-01	2.3033E+00	2.5242E+00
2.50	2.5205E-01	3.9707E-01	6.3478E-01	6.6898E-01	2.4164E+00	2.6243E+00
2.55	2.4330E-01	3.8492E-01	6.3208E-01	6.6119E-01	2.5367E+00	2.7236E+00
2.60	2.3498E-01	3.7326E-01	6.2953E-01	6.5370E-01	2.6644E+00	2.8221E+00
2.65	2.2707E-01	3.6207E-01	6.2713E-01	6.4649E-01	2.7999E+00	2.9198E+00
2.70	2.1953E-01	3.5133E-01	6.2486E-01	6.3956E-01	2.9438E+00	3.0165E+00
2.75	2.1235E-01	3.4101E-01	6.2271E-01	6.3290E-01	3.0964E+00	3.1125E+00
2.80	2.0550E-01	3.3110E-01	6.2067E-01	6.2649E-01	3.2582E+00	3.2075E+00
2.85	1.9897E-01	3.2158E-01	6.1875E-01	6.2033E-01	3.4296E+00	3.3016E+00
2.90	1.9274E-01	3.1243E-01	6.1692E-01	6.1440E-01	3.6113E+00	3.3949E+00
2.95	1.8679E-01	3.0364E-01	6.1518E-01	6.0869E-01	3.8037E+00	3.4872E+00

M	p/p^*	T/T^*	ρ/ρ^*	T_t/T_t^*	p_t/p_t^*	$\Delta s/R$
3.00	1.8110E-01	2.9518E-01	6.1353E-01	6.0320E-01	4.0073E+00	3.5786E+00
3.10	1.7046E-01	2.7923E-01	6.1046E-01	5.9282E-01	4.4507E+00	3.7588E+00
3.20	1.6070E-01	2.6446E-01	6.0768E-01	5.8319E-01	4.9466E+00	3.9354E+00
3.30	1.5175E-01	2.5076E-01	6.0514E-01	5.7424E-01	5.5003E+00	4.1085E+00
3.40	1.4350E-01	2.3804E-01	6.0283E-01	5.6592E-01	6.1179E+00	4.2782E+00
3.50	1.3589E-01	2.2622E-01	6.0071E-01	5.5818E-01	6.8059E+00	4.4444E+00
3.60	1.2887E-01	2.1522E-01	5.9877E-01	5.5096E-01	7.5712E+00	4.6074E+00
3.70	1.2236E-01	2.0497E-01	5.9698E-01	5.4423E-01	8.4216E+00	4.7671E+00
3.80	1.1633E-01	1.9540E-01	5.9533E-01	5.3794E-01	9.3652E+00	4.9237E+00
3.90	1.1072E-01	1.8646E-01	5.9380E-01	5.3206E-01	1.0411E+01	5.0772E+00
4.00	1.0550E-01	1.7810E-01	5.9239E-01	5.2656E-01	1.1569E+01	5.2277E+00
4.10	1.0064E-01	1.7027E-01	5.9108E-01	5.2139E-01	1.2850E+01	5.3754E+00
4.20	9.6106E-02	1.6293E-01	5.8986E-01	5.1655E-01	1.4264E+01	5.5202E+00
4.30	9.1864E-02	1.5604E-01	5.8873E-01	5.1201E-01	1.5824E+01	5.6624E+00
4.40	8.7894E-02	1.4956E-01	5.8768E-01	5.0773E-01	1.7544E+01	5.8018E+00
4.50	8.4172E-02	1.4347E-01	5.8669E-01	5.0370E-01	1.9436E+01	5.9388E+00
4.60	8.0679E-02	1.3773E-01	5.8576E-01	4.9991E-01	2.1517E+01	6.0732E+00
4.70	7.7397E-02	1.3232E-01	5.8490E-01	4.9633E-01	2.3802E+01	6.2053E+00
4.80	7.4309E-02	1.2722E-01	5.8409E-01	4.9296E-01	2.6308E+01	6.3350E+00
4.90	7.1400E-02	1.2240E-01	5.8333E-01	4.8976E-01	2.9055E+01	6.4624E+00
5.00	6.8657E-02	1.1784E-01	5.8261E-01	4.8675E-01	3.2061E+01	6.5877E+00
5.20	6.3620E-02	1.0945E-01	5.8130E-01	4.8118E-01	3.8939E+01	6.8319E+00
5.40	5.9114E-02	1.0190E-01	5.8013E-01	4.7617E-01	4.7127E+01	7.0680E+00
5.60	5.5066E-02	9.5092E-02	5.7908E-01	4.7166E-01	5.6835E+01	7.2966E+00
5.80	5.1417E-02	8.8935E-02	5.7814E-01	4.6757E-01	6.8300E+01	7.5181E+00
6.00	4.8117E-02	8.3349E-02	5.7729E-01	4.6386E-01	8.1790E+01	7.7329E+00
6.50	4.1127E-02	7.1461E-02	5.7551E-01	4.5595E-01	1.2641E+02	8.2427E+00
7.00	3.5549E-02	6.1922E-02	5.7409E-01	4.4961E-01	1.9131E+02	8.7179E+00
7.50	3.1029E-02	5.4156E-02	5.7295E-01	4.4443E-01	2.8385E+02	9.1625E+00
8.00	2.7316E-02	4.7754E-02	5.7201E-01	4.4017E-01	4.1338E+02	9.5803E+00
8.50	2.4230E-02	4.2416E-02	5.7124E-01	4.3661E-01	5.9167E+02	9.9740E+00
9.00	2.1637E-02	3.7921E-02	5.7059E-01	4.3361E-01	8.3332E+02	1.0346E+01
9.50	1.9438E-02	3.4100E-02	5.7003E-01	4.3106E-01	1.1562E+03	1.0699E+01
10.00	1.7557E-02	3.0826E-02	5.6957E-01	4.2888E-01	1.5822E+03	1.1035E+01
15.00	7.8365E-03	1.3817E-02	5.6715E-01	4.1752E-01	2.0348E+04	1.3706E+01

Fanno Flow

The equations used to tabulate Fanno flow functions, for a calorically perfect gas, are summarized below:

$$4C_f \frac{L^*}{D_h} = \frac{1 - M^2}{\gamma M^2} + \frac{\gamma + 1}{2\gamma} \ln \left[\frac{(\gamma + 1)M^2}{2 \left(1 + \frac{\gamma - 1}{2} M^2\right)} \right] \quad (\text{E.1})$$

$$\frac{T}{T^*} = \frac{\gamma + 1}{2 \left(1 + \frac{\gamma - 1}{2} M^2\right)} \quad (\text{E.2})$$

$$\frac{\rho}{\rho^*} = \frac{1}{M} \sqrt{\frac{2 \left(1 + \frac{\gamma - 1}{2} M^2\right)}{\gamma + 1}} \quad (\text{E.3})$$

$$\frac{p}{p^*} = \frac{1}{M} \sqrt{\frac{\gamma + 1}{2 \left(1 + \frac{\gamma - 1}{2} M^2\right)}} \quad (\text{E.4})$$

$$\frac{I}{I^*} = \frac{p(1 + \gamma M^2)}{p^*(1 + \gamma)} = \frac{1}{M} \sqrt{\frac{\gamma + 1}{2 [1 + (\gamma - 1)M^2/2]}} \left(\frac{1 + \gamma M^2}{\gamma + 1} \right) \quad (\text{E.5})$$

$$\frac{p_t}{p_t^*} = \frac{1}{M} \left(\frac{1 + \frac{\gamma - 1}{2} M^2}{\frac{\gamma + 1}{2}} \right)^{\frac{\gamma + 1}{2(\gamma - 1)}} \quad (\text{E.6})$$

$$\frac{\Delta s}{R} = \frac{s^* - s}{R} = - \left(\frac{\gamma}{\gamma - 1} \right) \ell n \left(\frac{T}{T^*} \right) + \ell n \left(\frac{p}{p^*} \right) \quad (\text{E.7})$$

We derived these expressions in Chapter 2.

Fanno Flow $\gamma = 1.4$

M	$4C_f L^*/D$	T/T^*	p/p^*	ρ/ρ^*	p_1/p_1^*	I/I^*	$\Delta s/R$
0.10	6.6922E+01	1.1976E+00	1.0944E+01	9.1378E+00	5.8218E+00	4.6236E+00	1.7616E+00
0.12	4.5408E+01	1.1966E+00	9.1156E+00	7.6182E+00	4.8643E+00	3.8747E+00	1.5819E+00
0.14	3.2511E+01	1.1953E+00	7.8093E+00	6.5333E+00	4.1824E+00	3.3432E+00	1.4309E+00
0.16	2.4198E+01	1.1939E+00	6.8291E+00	5.7200E+00	3.6727E+00	2.9474E+00	1.3009E+00
0.18	1.8543E+01	1.1923E+00	6.0662E+00	5.0879E+00	3.2779E+00	2.6422E+00	1.1872E+00
0.20	1.4533E+01	1.1905E+00	5.4554E+00	4.5826E+00	2.9635E+00	2.4004E+00	1.0864E+00
0.22	1.1596E+01	1.1885E+00	4.9554E+00	4.1694E+00	2.7076E+00	2.2046E+00	9.9606E-01
0.24	9.3866E+00	1.1863E+00	4.5383E+00	3.8255E+00	2.4956E+00	2.0434E+00	9.1451E-01
0.26	7.6877E+00	1.1840E+00	4.1851E+00	3.5347E+00	2.3173E+00	1.9088E+00	8.4040E-01
0.28	6.3573E+00	1.1815E+00	3.8820E+00	3.2857E+00	2.1656E+00	1.7950E+00	7.7268E-01
0.30	5.2993E+00	1.1788E+00	3.6191E+00	3.0702E+00	2.0351E+00	1.6979E+00	7.1053E-01
0.32	4.4468E+00	1.1759E+00	3.3887E+00	2.8818E+00	1.9219E+00	1.6144E+00	6.5329E-01
0.34	3.7520E+00	1.1729E+00	3.1853E+00	2.7158E+00	1.8229E+00	1.5420E+00	6.0042E-01
0.36	3.1802E+00	1.1697E+00	3.0042E+00	2.5684E+00	1.7358E+00	1.4789E+00	5.5146E-01
0.38	2.7055E+00	1.1663E+00	2.8420E+00	2.4367E+00	1.6587E+00	1.4236E+00	5.0603E-01
0.40	2.3086E+00	1.1628E+00	2.6958E+00	2.3184E+00	1.5901E+00	1.3749E+00	4.6382E-01
0.42	1.9744E+00	1.1591E+00	2.5634E+00	2.2115E+00	1.5289E+00	1.3318E+00	4.2455E-01
0.44	1.6916E+00	1.1553E+00	2.4428E+00	2.1145E+00	1.4740E+00	1.2937E+00	3.8798E-01
0.46	1.4510E+00	1.1513E+00	2.3326E+00	2.0261E+00	1.4246E+00	1.2598E+00	3.5391E-01
0.48	1.2454E+00	1.1471E+00	2.2313E+00	1.9451E+00	1.3801E+00	1.2296E+00	3.2215E-01
0.50	1.0691E+00	1.1429E+00	2.1381E+00	1.8708E+00	1.3398E+00	1.2027E+00	2.9255E-01
0.52	9.1747E-01	1.1384E+00	2.0519E+00	1.8024E+00	1.3034E+00	1.1786E+00	2.6497E-01
0.54	7.8667E-01	1.1339E+00	1.9719E+00	1.7391E+00	1.2703E+00	1.1571E+00	2.3927E-01
0.56	6.7362E-01	1.1292E+00	1.8975E+00	1.6805E+00	1.2403E+00	1.1378E+00	2.1535E-01
0.58	5.7572E-01	1.1244E+00	1.8282E+00	1.6260E+00	1.2130E+00	1.1205E+00	1.9310E-01
0.60	4.9086E-01	1.1194E+00	1.7634E+00	1.5753E+00	1.1882E+00	1.1050E+00	1.7244E-01
0.62	4.1723E-01	1.1143E+00	1.7026E+00	1.5279E+00	1.1656E+00	1.0912E+00	1.5328E-01
0.64	3.5333E-01	1.1091E+00	1.6456E+00	1.4836E+00	1.1451E+00	1.0788E+00	1.3553E-01
0.66	2.9788E-01	1.1038E+00	1.5919E+00	1.4421E+00	1.1265E+00	1.0678E+00	1.1915E-01
0.68	2.4980E-01	1.0984E+00	1.5413E+00	1.4032E+00	1.1097E+00	1.0579E+00	1.0405E-01
0.70	2.0817E-01	1.0929E+00	1.4935E+00	1.3665E+00	1.0944E+00	1.0492E+00	9.0181E-02
0.72	1.7217E-01	1.0873E+00	1.4482E+00	1.3320E+00	1.0806E+00	1.0414E+00	7.7490E-02
0.74	1.4114E-01	1.0815E+00	1.4054E+00	1.2994E+00	1.0681E+00	1.0345E+00	6.5923E-02
0.76	1.1449E-01	1.0757E+00	1.3647E+00	1.2686E+00	1.0570E+00	1.0284E+00	5.5434E-02
0.78	9.1691E-02	1.0698E+00	1.3261E+00	1.2395E+00	1.0471E+00	1.0231E+00	4.5979E-02
0.80	7.2306E-02	1.0638E+00	1.2893E+00	1.2119E+00	1.0382E+00	1.0185E+00	3.7517E-02
0.82	5.5946E-02	1.0578E+00	1.2542E+00	1.1858E+00	1.0305E+00	1.0145E+00	3.0009E-02

(Continued)

M	$4C_f L^*/D$	T/T^*	p/p^*	ρ/ρ^*	p_t/p_t^*	I/I^*	$\Delta s/R$
0.84	4.2269E-02	1.0516E+00	1.2208E+00	1.1609E+00	1.0237E+00	1.0112E+00	2.3419E-02
0.86	3.0976E-02	1.0454E+00	1.1889E+00	1.1373E+00	1.0179E+00	1.0083E+00	1.7713E-02
0.88	2.1804E-02	1.0391E+00	1.1583E+00	1.1148E+00	1.0129E+00	1.0059E+00	1.2858E-02
0.90	1.4520E-02	1.0327E+00	1.1291E+00	1.0934E+00	1.0089E+00	1.0040E+00	8.8238E-03
0.92	8.9194E-03	1.0263E+00	1.1011E+00	1.0730E+00	1.0056E+00	1.0025E+00	5.5815E-03
0.94	4.8199E-03	1.0198E+00	1.0743E+00	1.0535E+00	1.0031E+00	1.0014E+00	3.1035E-03
0.96	2.0601E-03	1.0132E+00	1.0485E+00	1.0348E+00	1.0014E+00	1.0006E+00	1.3636E-03
0.98	4.9614E-04	1.0066E+00	1.0238E+00	1.0170E+00	1.0003E+00	1.0001E+00	3.3708E-04
1.00	0.0000E+00	1.0000E+00	1.0000E+00	1.0000E+00	1.0000E+00	1.0000E+00	0.0000E+00
1.02	4.5728E-04	9.9331E-01	9.7711E-01	9.8369E-01	1.0003E+00	1.0001E+00	3.2967E-04
1.04	1.7657E-03	9.8658E-01	9.5507E-01	9.6805E-01	1.0013E+00	1.0005E+00	1.3043E-03
1.06	3.8337E-03	9.7982E-01	9.3383E-01	9.5306E-01	1.0029E+00	1.0012E+00	2.9032E-03
1.08	6.5792E-03	9.7302E-01	9.1335E-01	9.3868E-01	1.0051E+00	1.0020E+00	5.1061E-03
1.10	9.9283E-03	9.6618E-01	8.9359E-01	9.2486E-01	1.0079E+00	1.0031E+00	7.8941E-03
1.12	1.3815E-02	9.5932E-01	8.7451E-01	9.1159E-01	1.0113E+00	1.0043E+00	1.1249E-02
1.14	1.8179E-02	9.5244E-01	8.5608E-01	8.9883E-01	1.0153E+00	1.0057E+00	1.5152E-02
1.16	2.2967E-02	9.4554E-01	8.3826E-01	8.8655E-01	1.0198E+00	1.0073E+00	1.9587E-02
1.18	2.8130E-02	9.3861E-01	8.2103E-01	8.7473E-01	1.0248E+00	1.0090E+00	2.4537E-02
1.20	3.3625E-02	9.3168E-01	8.0436E-01	8.6335E-01	1.0304E+00	1.0108E+00	2.9986E-02
1.22	3.9412E-02	9.2473E-01	7.8822E-01	8.5238E-01	1.0366E+00	1.0128E+00	3.5919E-02
1.24	4.5456E-02	9.1777E-01	7.7258E-01	8.4181E-01	1.0432E+00	1.0149E+00	4.2321E-02
1.26	5.1723E-02	9.1080E-01	7.5743E-01	8.3161E-01	1.0504E+00	1.0170E+00	4.9177E-02
1.28	5.8185E-02	9.0383E-01	7.4274E-01	8.2176E-01	1.0581E+00	1.0193E+00	5.6474E-02
1.30	6.4814E-02	8.9686E-01	7.2848E-01	8.1226E-01	1.0663E+00	1.0217E+00	6.4199E-02
1.32	7.1588E-02	8.8989E-01	7.1465E-01	8.0308E-01	1.0750E+00	1.0241E+00	7.2338E-02
1.34	7.8484E-02	8.8292E-01	7.0122E-01	7.9421E-01	1.0842E+00	1.0267E+00	8.0878E-02
1.36	8.5482E-02	8.7596E-01	6.8818E-01	7.8563E-01	1.0940E+00	1.0292E+00	8.9808E-02
1.38	9.2565E-02	8.6901E-01	6.7551E-01	7.7734E-01	1.1042E+00	1.0319E+00	9.9115E-02
1.40	9.9716E-02	8.6207E-01	6.6320E-01	7.6931E-01	1.1149E+00	1.0346E+00	1.0879E-01
1.42	1.0692E-01	8.5514E-01	6.5122E-01	7.6154E-01	1.1262E+00	1.0373E+00	1.1882E-01
1.44	1.1416E-01	8.4822E-01	6.3958E-01	7.5402E-01	1.1379E+00	1.0401E+00	1.2919E-01
1.46	1.2144E-01	8.4133E-01	6.2825E-01	7.4673E-01	1.1501E+00	1.0430E+00	1.3989E-01
1.48	1.2873E-01	8.3445E-01	6.1722E-01	7.3967E-01	1.1629E+00	1.0458E+00	1.5092E-01
1.50	1.3602E-01	8.2759E-01	6.0648E-01	7.3283E-01	1.1762E+00	1.0487E+00	1.6226E-01
1.52	1.4332E-01	8.2075E-01	5.9602E-01	7.2619E-01	1.1899E+00	1.0516E+00	1.7391E-01
1.54	1.5060E-01	8.1393E-01	5.8583E-01	7.1975E-01	1.2042E+00	1.0546E+00	1.8584E-01
1.56	1.5787E-01	8.0715E-01	5.7591E-01	7.1351E-01	1.2190E+00	1.0575E+00	1.9807E-01
1.58	1.6511E-01	8.0038E-01	5.6623E-01	7.0745E-01	1.2344E+00	1.0605E+00	2.1057E-01

M	$4C_f L^*/D$	T/T^*	p/p^*	ρ/ρ^*	p_t/p_t^*	III^*	$\Delta s/R$
1.60	1.7233E-01	7.9365E-01	5.5679E-01	7.0156E-01	1.2502E+00	1.0635E+00	2.2333E-01
1.62	1.7950E-01	7.8695E-01	5.4759E-01	6.9584E-01	1.2666E+00	1.0665E+00	2.3636E-01
1.64	1.8664E-01	7.8027E-01	5.3862E-01	6.9029E-01	1.2836E+00	1.0695E+00	2.4963E-01
1.66	1.9373E-01	7.7363E-01	5.2986E-01	6.8489E-01	1.3010E+00	1.0725E+00	2.6315E-01
1.68	2.0078E-01	7.6703E-01	5.2131E-01	6.7965E-01	1.3190E+00	1.0755E+00	2.7690E-01
1.70	2.0777E-01	7.6046E-01	5.1297E-01	6.7455E-01	1.3376E+00	1.0785E+00	2.9088E-01
1.72	2.1471E-01	7.5392E-01	5.0482E-01	6.6959E-01	1.3567E+00	1.0815E+00	3.0508E-01
1.74	2.2158E-01	7.4742E-01	4.9686E-01	6.6476E-01	1.3764E+00	1.0845E+00	3.1949E-01
1.76	2.2840E-01	7.4096E-01	4.8909E-01	6.6007E-01	1.3967E+00	1.0875E+00	3.3411E-01
1.78	2.3516E-01	7.3454E-01	4.8149E-01	6.5550E-01	1.4175E+00	1.0905E+00	3.4893E-01
1.80	2.4185E-01	7.2816E-01	4.7407E-01	6.5105E-01	1.4390E+00	1.0935E+00	3.6394E-01
1.82	2.4847E-01	7.2181E-01	4.6681E-01	6.4672E-01	1.4610E+00	1.0965E+00	3.7913E-01
1.84	2.5503E-01	7.1551E-01	4.5972E-01	6.4250E-01	1.4836E+00	1.0995E+00	3.9450E-01
1.86	2.6152E-01	7.0925E-01	4.5278E-01	6.3839E-01	1.5069E+00	1.1024E+00	4.1005E-01
1.88	2.6794E-01	7.0304E-01	4.4600E-01	6.3439E-01	1.5308E+00	1.1054E+00	4.2576E-01
1.90	2.7429E-01	6.9686E-01	4.3936E-01	6.3048E-01	1.5553E+00	1.1083E+00	4.4164E-01
1.92	2.8057E-01	6.9073E-01	4.3287E-01	6.2668E-01	1.5804E+00	1.1112E+00	4.5767E-01
1.94	2.8677E-01	6.8465E-01	4.2651E-01	6.2297E-01	1.6062E+00	1.1141E+00	4.7385E-01
1.96	2.9291E-01	6.7861E-01	4.2029E-01	6.1935E-01	1.6326E+00	1.1170E+00	4.9018E-01
1.98	2.9897E-01	6.7262E-01	4.1421E-01	6.1582E-01	1.6597E+00	1.1198E+00	5.0665E-01
2.00	3.0495E-01	6.6667E-01	4.0825E-01	6.1237E-01	1.6875E+00	1.1227E+00	5.2325E-01
2.05	3.1961E-01	6.5200E-01	3.9388E-01	6.0412E-01	1.7600E+00	1.1297E+00	5.6531E-01
2.10	3.3381E-01	6.3762E-01	3.8024E-01	5.9635E-01	1.8369E+00	1.1366E+00	6.0810E-01
2.15	3.4756E-01	6.2354E-01	3.6728E-01	5.8902E-01	1.9185E+00	1.1434E+00	6.5157E-01
2.20	3.6086E-01	6.0976E-01	3.5494E-01	5.8210E-01	2.0050E+00	1.1500E+00	6.9563E-01
2.25	3.7374E-01	5.9627E-01	3.4319E-01	5.7557E-01	2.0964E+00	1.1565E+00	7.4024E-01
2.30	3.8618E-01	5.8309E-01	3.3200E-01	5.6938E-01	2.1931E+00	1.1628E+00	7.8533E-01
2.35	3.9821E-01	5.7021E-01	3.2133E-01	5.6353E-01	2.2953E+00	1.1690E+00	8.3085E-01
2.40	4.0984E-01	5.5762E-01	3.1114E-01	5.5798E-01	2.4031E+00	1.1751E+00	8.7676E-01
2.45	4.2107E-01	5.4533E-01	3.0141E-01	5.5272E-01	2.5168E+00	1.1810E+00	9.2300E-01
2.50	4.3193E-01	5.3333E-01	2.9212E-01	5.4772E-01	2.6367E+00	1.1867E+00	9.6954E-01
2.55	4.4241E-01	5.2163E-01	2.8323E-01	5.4298E-01	2.7630E+00	1.1923E+00	1.0163E+00
2.60	4.5253E-01	5.1020E-01	2.7473E-01	5.3846E-01	2.8960E+00	1.1978E+00	1.0633E+00
2.65	4.6232E-01	4.9906E-01	2.6658E-01	5.3417E-01	3.0359E+00	1.2031E+00	1.1105E+00
2.70	4.7176E-01	4.8820E-01	2.5878E-01	5.3007E-01	3.1830E+00	1.2083E+00	1.1578E+00
2.75	4.8089E-01	4.7761E-01	2.5131E-01	5.2617E-01	3.3377E+00	1.2133E+00	1.2053E+00
2.80	4.8971E-01	4.6729E-01	2.4414E-01	5.2245E-01	3.5001E+00	1.2182E+00	1.2528E+00
2.85	4.9823E-01	4.5723E-01	2.3726E-01	5.1890E-01	3.6707E+00	1.2230E+00	1.3004E+00
2.90	5.0646E-01	4.4743E-01	2.3066E-01	5.1551E-01	3.8498E+00	1.2277E+00	1.3480E+00
2.95	5.1441E-01	4.3788E-01	2.2431E-01	5.1227E-01	4.0376E+00	1.2322E+00	1.3957E+00

(Continued)

M	$4C_f L^*/D$	T/T^*	p/p^*	ρ/ρ^*	p_t/p_t^*	III^*	$\Delta s/R$
3.00	5.2210E-01	4.2857E-01	2.1822E-01	5.0918E-01	4.2346E+00	1.2366E+00	1.4433E+00
3.10	5.3672E-01	4.1068E-01	2.0672E-01	5.0337E-01	4.6573E+00	1.2450E+00	1.5384E+00
3.20	5.5038E-01	3.9370E-01	1.9608E-01	4.9804E-01	5.1210E+00	1.2530E+00	1.6333E+00
3.30	5.6317E-01	3.7760E-01	1.8621E-01	4.9314E-01	5.6286E+00	1.2605E+00	1.7279E+00
3.40	5.7515E-01	3.6232E-01	1.7704E-01	4.8862E-01	6.1837E+00	1.2676E+00	1.8219E+00
3.50	5.8637E-01	3.4783E-01	1.6851E-01	4.8445E-01	6.7896E+00	1.2743E+00	1.9154E+00
3.60	5.9689E-01	3.3408E-01	1.6055E-01	4.8059E-01	7.4501E+00	1.2807E+00	2.0082E+00
3.70	6.0677E-01	3.2103E-01	1.5313E-01	4.7701E-01	8.1691E+00	1.2867E+00	2.1004E+00
3.80	6.1605E-01	3.0864E-01	1.4620E-01	4.7368E-01	8.9506E+00	1.2924E+00	2.1917E+00
3.90	6.2478E-01	2.9688E-01	1.3971E-01	4.7059E-01	9.7990E+00	1.2978E+00	2.2823E+00
4.00	6.3300E-01	2.8571E-01	1.3363E-01	4.6771E-01	1.0719E+01	1.3029E+00	2.3720E+00
4.10	6.4074E-01	2.7510E-01	1.2793E-01	4.6502E-01	1.1715E+01	1.3077E+00	2.4608E+00
4.20	6.4804E-01	2.6502E-01	1.2257E-01	4.6250E-01	1.2792E+01	1.3123E+00	2.5488E+00
4.30	6.5492E-01	2.5543E-01	1.1753E-01	4.6015E-01	1.3955E+01	1.3167E+00	2.6358E+00
4.40	6.6142E-01	2.4631E-01	1.1279E-01	4.5794E-01	1.5210E+01	1.3208E+00	2.7219E+00
4.50	6.6757E-01	2.3762E-01	1.0833E-01	4.5587E-01	1.6562E+01	1.3247E+00	2.8071E+00
4.60	6.7338E-01	2.2936E-01	1.0411E-01	4.5393E-01	1.8018E+01	1.3285E+00	2.8914E+00
4.70	6.7888E-01	2.2148E-01	1.0013E-01	4.5210E-01	1.9583E+01	1.3320E+00	2.9747E+00
4.80	6.8410E-01	2.1398E-01	9.6371E-02	4.5037E-01	2.1264E+01	1.3354E+00	3.0570E+00
4.90	6.8904E-01	2.0683E-01	9.2812E-02	4.4875E-01	2.3067E+01	1.3386E+00	3.1384E+00
5.00	6.9373E-01	2.0000E-01	8.9443E-02	4.4721E-01	2.5000E+01	1.3416E+00	3.2189E+00
5.20	7.0242E-01	1.8727E-01	8.3220E-02	4.4439E-01	2.9283E+01	1.3473E+00	3.3770E+00
5.40	7.1028E-01	1.7564E-01	7.7611E-02	4.4186E-01	3.4175E+01	1.3525E+00	3.5315E+00
5.60	7.1741E-01	1.6502E-01	7.2540E-02	4.3959E-01	3.9740E+01	1.3572E+00	3.6824E+00
5.80	7.2389E-01	1.5528E-01	6.7941E-02	4.3754E-01	4.6050E+01	1.3615E+00	3.8297E+00
6.00	7.2980E-01	1.4634E-01	6.3758E-02	4.3568E-01	5.3180E+01	1.3655E+00	3.9737E+00
6.50	7.4247E-01	1.2698E-01	5.4823E-02	4.3173E-01	7.5134E+01	1.3740E+00	4.3193E+00
7.00	7.5273E-01	1.1111E-01	4.7619E-02	4.2857E-01	1.0414E+02	1.3810E+00	4.6458E+00
7.50	7.6114E-01	9.7959E-02	4.1731E-02	4.2601E-01	1.4184E+02	1.3867E+00	4.9547E+00
8.00	7.6812E-01	8.6957E-02	3.6860E-02	4.2390E-01	1.9011E+02	1.3915E+00	5.2476E+00
8.50	7.7397E-01	7.7670E-02	3.2787E-02	4.2214E-01	2.5109E+02	1.3955E+00	5.5258E+00
9.00	7.7891E-01	6.9767E-02	2.9348E-02	4.2066E-01	3.2719E+02	1.3989E+00	5.7905E+00
9.50	7.8313E-01	6.2992E-02	2.6419E-02	4.1940E-01	4.2113E+02	1.4019E+00	6.0429E+00
10.00	7.8676E-01	5.7143E-02	2.3905E-02	4.1833E-01	5.3594E+02	1.4044E+00	6.2840E+00
15.00	8.0577E-01	2.6087E-02	1.0768E-02	4.1276E-01	3.7552E+03	1.4177E+00	8.2309E+00

Fanno Flow $\gamma = 1.3$

M	$4C_f L^*/D$	T/T^*	p/p^*	ρ/ρ^*	p_t/p_t^*	II^*	$\Delta s/R$
0.10	7.2202E+01	1.1483E+00	1.0716E+01	9.3320E+00	5.8860E+00	4.7196E+00	1.7726E+00
0.12	4.9020E+01	1.1475E+00	8.9269E+00	7.7793E+00	4.9174E+00	3.9539E+00	1.5928E+00
0.14	3.5120E+01	1.1466E+00	7.6486E+00	6.6705E+00	4.2275E+00	3.4102E+00	1.4417E+00
0.16	2.6157E+01	1.1456E+00	6.6895E+00	5.8393E+00	3.7118E+00	3.0053E+00	1.3116E+00
0.18	2.0058E+01	1.1444E+00	5.9432E+00	5.1932E+00	3.3123E+00	2.6929E+00	1.1977E+00
0.20	1.5732E+01	1.1431E+00	5.3459E+00	4.6765E+00	2.9940E+00	2.4452E+00	1.0967E+00
0.22	1.2562E+01	1.1417E+00	4.8569E+00	4.2540E+00	2.7349E+00	2.2445E+00	1.0061E+00
0.24	1.0177E+01	1.1401E+00	4.4491E+00	3.9022E+00	2.5202E+00	2.0792E+00	9.2438E-01
0.26	8.3414E+00	1.1385E+00	4.1038E+00	3.6047E+00	2.3396E+00	1.9411E+00	8.5004E-01
0.28	6.9035E+00	1.1366E+00	3.8076E+00	3.3499E+00	2.1859E+00	1.8242E+00	7.8207E-01
0.30	5.7595E+00	1.1347E+00	3.5507E+00	3.1293E+00	2.0537E+00	1.7244E+00	7.1966E-01
0.32	4.8370E+00	1.1326E+00	3.3257E+00	2.9364E+00	1.9389E+00	1.6385E+00	6.6215E-01
0.34	4.0848E+00	1.1304E+00	3.1271E+00	2.7663E+00	1.8385E+00	1.5639E+00	6.0900E-01
0.36	3.4653E+00	1.1281E+00	2.9503E+00	2.6153E+00	1.7502E+00	1.4989E+00	5.5974E-01
0.38	2.9507E+00	1.1256E+00	2.7920E+00	2.4804E+00	1.6719E+00	1.4418E+00	5.1401E-01
0.40	2.5200E+00	1.1230E+00	2.6493E+00	2.3591E+00	1.6023E+00	1.3915E+00	4.7149E-01
0.42	2.1572E+00	1.1204E+00	2.5202E+00	2.2494E+00	1.5401E+00	1.3470E+00	4.3190E-01
0.44	1.8499E+00	1.1175E+00	2.4026E+00	2.1499E+00	1.4843E+00	1.3075E+00	3.9500E-01
0.46	1.5882E+00	1.1146E+00	2.2951E+00	2.0591E+00	1.4341E+00	1.2724E+00	3.6059E-01
0.48	1.3645E+00	1.1116E+00	2.1965E+00	1.9760E+00	1.3888E+00	1.2410E+00	3.2849E-01
0.50	1.1724E+00	1.1084E+00	2.1056E+00	1.8997E+00	1.3479E+00	1.2130E+00	2.9855E-01
0.52	1.0071E+00	1.1052E+00	2.0217E+00	1.8293E+00	1.3107E+00	1.1880E+00	2.7062E-01
0.54	8.6433E-01	1.1018E+00	1.9438E+00	1.7642E+00	1.2770E+00	1.1655E+00	2.4457E-01
0.56	7.4082E-01	1.0983E+00	1.8715E+00	1.7039E+00	1.2464E+00	1.1454E+00	2.2030E-01
0.58	6.3377E-01	1.0948E+00	1.8040E+00	1.6478E+00	1.2186E+00	1.1273E+00	1.9771E-01
0.60	5.4087E-01	1.0911E+00	1.7409E+00	1.5956E+00	1.1932E+00	1.1112E+00	1.7670E-01
0.62	4.6018E-01	1.0873E+00	1.6818E+00	1.5468E+00	1.1702E+00	1.0966E+00	1.5720E-01
0.64	3.9008E-01	1.0834E+00	1.6264E+00	1.5011E+00	1.1492E+00	1.0836E+00	1.3913E-01
0.66	3.2919E-01	1.0795E+00	1.5742E+00	1.4583E+00	1.1302E+00	1.0720E+00	1.2241E-01
0.68	2.7632E-01	1.0754E+00	1.5250E+00	1.4181E+00	1.1129E+00	1.0616E+00	1.0700E-01
0.70	2.3049E-01	1.0713E+00	1.4786E+00	1.3802E+00	1.0972E+00	1.0524E+00	9.2820E-02
0.72	1.9082E-01	1.0670E+00	1.4347E+00	1.3446E+00	1.0831E+00	1.0441E+00	7.9830E-02
0.74	1.5658E-01	1.0627E+00	1.3931E+00	1.3109E+00	1.0703E+00	1.0369E+00	6.7977E-02
0.76	1.2713E-01	1.0583E+00	1.3536E+00	1.2790E+00	1.0589E+00	1.0304E+00	5.7215E-02
0.78	1.0192E-01	1.0538E+00	1.3161E+00	1.2489E+00	1.0486E+00	1.0248E+00	4.7501E-02
0.80	8.0447E-02	1.0493E+00	1.2804E+00	1.2203E+00	1.0395E+00	1.0199E+00	3.8796E-02
0.82	6.2305E-02	1.0446E+00	1.2464E+00	1.1932E+00	1.0315E+00	1.0156E+00	3.1063E-02

(Continued)

M	$4C_f L^*/D$	T/T^*	p/p^*	ρ/ρ^*	p_t/p_t^*	I/I^*	$\Delta s/R$
0.84	4.7118E-02	1.0399E+00	1.2140E+00	1.1674E+00	1.0246E+00	1.0120E+00	2.4266E-02
0.86	3.4562E-02	1.0352E+00	1.1831E+00	1.1429E+00	1.0185E+00	1.0089E+00	1.8372E-02
0.88	2.4350E-02	1.0303E+00	1.1535E+00	1.1195E+00	1.0134E+00	1.0064E+00	1.3350E-02
0.90	1.6230E-02	1.0254E+00	1.1251E+00	1.0973E+00	1.0092E+00	1.0043E+00	9.1719E-03
0.92	9.9783E-03	1.0204E+00	1.0980E+00	1.0760E+00	1.0058E+00	1.0027E+00	5.8086E-03
0.94	5.3962E-03	1.0154E+00	1.0720E+00	1.0557E+00	1.0032E+00	1.0015E+00	3.2342E-03
0.96	2.3076E-03	1.0103E+00	1.0470E+00	1.0363E+00	1.0014E+00	1.0006E+00	1.4236E-03
0.98	5.5556E-04	1.0052E+00	1.0231E+00	1.0178E+00	1.0004E+00	1.0002E+00	3.5312E-04
1.00	0.0000E+00	1.0000E+00	1.0000E+00	1.0000E+00	1.0000E+00	1.0000E+00	0.0000E+00
1.02	5.1576E-04	9.9476E-01	9.7782E-01	9.8297E-01	1.0003E+00	1.0001E+00	3.4258E-04
1.04	1.9908E-03	9.8947E-01	9.5646E-01	9.6664E-01	1.0014E+00	1.0006E+00	1.3602E-03
1.06	4.3247E-03	9.8413E-01	9.3588E-01	9.5097E-01	1.0030E+00	1.0013E+00	3.0329E-03
1.08	7.4272E-03	9.7876E-01	9.1604E-01	9.3592E-01	1.0054E+00	1.0022E+00	5.3418E-03
1.10	1.1217E-02	9.7334E-01	8.9689E-01	9.2146E-01	1.0083E+00	1.0033E+00	8.2685E-03
1.12	1.5622E-02	9.6788E-01	8.7840E-01	9.0755E-01	1.0119E+00	1.0047E+00	1.1796E-02
1.14	2.0574E-02	9.6239E-01	8.6054E-01	8.9417E-01	1.0160E+00	1.0063E+00	1.5906E-02
1.16	2.6017E-02	9.5687E-01	8.4327E-01	8.8129E-01	1.0208E+00	1.0080E+00	2.0584E-02
1.18	3.1894E-02	9.5131E-01	8.2657E-01	8.6887E-01	1.0262E+00	1.0099E+00	2.5813E-02
1.20	3.8159E-02	9.4572E-01	8.1040E-01	8.5691E-01	1.0321E+00	1.0119E+00	3.1578E-02
1.22	4.4766E-02	9.4011E-01	7.9475E-01	8.4538E-01	1.0386E+00	1.0141E+00	3.7866E-02
1.24	5.1677E-02	9.3447E-01	7.7958E-01	8.3425E-01	1.0457E+00	1.0165E+00	4.4660E-02
1.26	5.8854E-02	9.2881E-01	7.6488E-01	8.2350E-01	1.0533E+00	1.0189E+00	5.1949E-02
1.28	6.6266E-02	9.2313E-01	7.5062E-01	8.1313E-01	1.0616E+00	1.0215E+00	5.9718E-02
1.30	7.3882E-02	9.1743E-01	7.3679E-01	8.0310E-01	1.0703E+00	1.0241E+00	6.7955E-02
1.32	8.1675E-02	9.1171E-01	7.2336E-01	7.9341E-01	1.0797E+00	1.0269E+00	7.6647E-02
1.34	8.9622E-02	9.0598E-01	7.1032E-01	7.8403E-01	1.0896E+00	1.0297E+00	8.5782E-02
1.36	9.7699E-02	9.0024E-01	6.9765E-01	7.7497E-01	1.1001E+00	1.0327E+00	9.5349E-02
1.38	1.0589E-01	8.9448E-01	6.8534E-01	7.6619E-01	1.1111E+00	1.0357E+00	1.0534E-01
1.40	1.1416E-01	8.8872E-01	6.7337E-01	7.5769E-01	1.1227E+00	1.0387E+00	1.1573E-01
1.42	1.2252E-01	8.8294E-01	6.6173E-01	7.4945E-01	1.1349E+00	1.0419E+00	1.2652E-01
1.44	1.3093E-01	8.7717E-01	6.5040E-01	7.4148E-01	1.1477E+00	1.0451E+00	1.3771E-01
1.46	1.3939E-01	8.7138E-01	6.3937E-01	7.3374E-01	1.1610E+00	1.0483E+00	1.4926E-01
1.48	1.4788E-01	8.6560E-01	6.2863E-01	7.2624E-01	1.1750E+00	1.0516E+00	1.6119E-01
1.50	1.5639E-01	8.5981E-01	6.1817E-01	7.1896E-01	1.1895E+00	1.0549E+00	1.7347E-01
1.52	1.6492E-01	8.5403E-01	6.0798E-01	7.1190E-01	1.2046E+00	1.0583E+00	1.8610E-01
1.54	1.7344E-01	8.4825E-01	5.9805E-01	7.0505E-01	1.2203E+00	1.0617E+00	1.9907E-01
1.56	1.8196E-01	8.4247E-01	5.8837E-01	6.9839E-01	1.2367E+00	1.0651E+00	2.1237E-01
1.58	1.9047E-01	8.3669E-01	5.7893E-01	6.9193E-01	1.2536E+00	1.0686E+00	2.2600E-01

M	$4C_f L^*/D$	T/T^*	p/p^*	ρ/ρ^*	p_t/p_t^*	III^*	$\Delta s/R$
1.60	1.9895E-01	8.3092E-01	5.6972E-01	6.8564E-01	1.2712E+00	1.0721E+00	2.3993E-01
1.62	2.0740E-01	8.2517E-01	5.6073E-01	6.7954E-01	1.2895E+00	1.0756E+00	2.5417E-01
1.64	2.1581E-01	8.1942E-01	5.5196E-01	6.7360E-01	1.3083E+00	1.0791E+00	2.6870E-01
1.66	2.2419E-01	8.1368E-01	5.4340E-01	6.6783E-01	1.3279E+00	1.0826E+00	2.8352E-01
1.68	2.3252E-01	8.0795E-01	5.3504E-01	6.6222E-01	1.3481E+00	1.0861E+00	2.9863E-01
1.70	2.4081E-01	8.0223E-01	5.2687E-01	6.5675E-01	1.3690E+00	1.0897E+00	3.1400E-01
1.72	2.4904E-01	7.9653E-01	5.1889E-01	6.5143E-01	1.3906E+00	1.0933E+00	3.2964E-01
1.74	2.5721E-01	7.9085E-01	5.1109E-01	6.4626E-01	1.4129E+00	1.0968E+00	3.4554E-01
1.76	2.6532E-01	7.8518E-01	5.0347E-01	6.4122E-01	1.4359E+00	1.1004E+00	3.6169E-01
1.78	2.7338E-01	7.7952E-01	4.9601E-01	6.3631E-01	1.4596E+00	1.1039E+00	3.7808E-01
1.80	2.8136E-01	7.7389E-01	4.8873E-01	6.3152E-01	1.4841E+00	1.1075E+00	3.9471E-01
1.82	2.8928E-01	7.6827E-01	4.8160E-01	6.2686E-01	1.5093E+00	1.1111E+00	4.1157E-01
1.84	2.9713E-01	7.6268E-01	4.7463E-01	6.2232E-01	1.5353E+00	1.1146E+00	4.2866E-01
1.86	3.0491E-01	7.5711E-01	4.6781E-01	6.1789E-01	1.5621E+00	1.1182E+00	4.4596E-01
1.88	3.1262E-01	7.5156E-01	4.6113E-01	6.1357E-01	1.5897E+00	1.1217E+00	4.6347E-01
1.90	3.2025E-01	7.4603E-01	4.5459E-01	6.0935E-01	1.6181E+00	1.1252E+00	4.8119E-01
1.92	3.2781E-01	7.4052E-01	4.4820E-01	6.0524E-01	1.6474E+00	1.1287E+00	4.9911E-01
1.94	3.3529E-01	7.3504E-01	4.4193E-01	6.0123E-01	1.6775E+00	1.1322E+00	5.1722E-01
1.96	3.4269E-01	7.2958E-01	4.3579E-01	5.9732E-01	1.7085E+00	1.1357E+00	5.3552E-01
1.98	3.5002E-01	7.2415E-01	4.2978E-01	5.9350E-01	1.7404E+00	1.1392E+00	5.5401E-01
2.00	3.5727E-01	7.1875E-01	4.2390E-01	5.8977E-01	1.7732E+00	1.1427E+00	5.7267E-01
2.05	3.7506E-01	7.0536E-01	4.0969E-01	5.8082E-01	1.8592E+00	1.1513E+00	6.2006E-01
2.10	3.9235E-01	6.9215E-01	3.9617E-01	5.7238E-01	1.9514E+00	1.1597E+00	6.6845E-01
2.15	4.0915E-01	6.7912E-01	3.8330E-01	5.6440E-01	2.0501E+00	1.1681E+00	7.1776E-01
2.20	4.2546E-01	6.6628E-01	3.7103E-01	5.5686E-01	2.1555E+00	1.1763E+00	7.6791E-01
2.25	4.4130E-01	6.5364E-01	3.5932E-01	5.4973E-01	2.2682E+00	1.1844E+00	8.1885E-01
2.30	4.5665E-01	6.4120E-01	3.4815E-01	5.4297E-01	2.3884E+00	1.1923E+00	8.7050E-01
2.35	4.7154E-01	6.2897E-01	3.3748E-01	5.3656E-01	2.5167E+00	1.2001E+00	9.2282E-01
2.40	4.8598E-01	6.1695E-01	3.2728E-01	5.3047E-01	2.6535E+00	1.2078E+00	9.7573E-01
2.45	4.9997E-01	6.0514E-01	3.1751E-01	5.2469E-01	2.7992E+00	1.2153E+00	1.0292E+00
2.50	5.1352E-01	5.9355E-01	3.0817E-01	5.1920E-01	2.9544E+00	1.2226E+00	1.0831E+00
2.55	5.2665E-01	5.8217E-01	2.9922E-01	5.1397E-01	3.1196E+00	1.2298E+00	1.1375E+00
2.60	5.3937E-01	5.7100E-01	2.9063E-01	5.0899E-01	3.2954E+00	1.2368E+00	1.1924E+00
2.65	5.5169E-01	5.6005E-01	2.8240E-01	5.0424E-01	3.4823E+00	1.2437E+00	1.2475E+00
2.70	5.6362E-01	5.4932E-01	2.7450E-01	4.9972E-01	3.6810E+00	1.2504E+00	1.3030E+00
2.75	5.7518E-01	5.3880E-01	2.6692E-01	4.9540E-01	3.8921E+00	1.2570E+00	1.3588E+00
2.80	5.8637E-01	5.2849E-01	2.5963E-01	4.9127E-01	4.1164E+00	1.2634E+00	1.4148E+00
2.85	5.9721E-01	5.1840E-01	2.5263E-01	4.8733E-01	4.3545E+00	1.2697E+00	1.4710E+00
2.90	6.0771E-01	5.0851E-01	2.4590E-01	4.8356E-01	4.6072E+00	1.2758E+00	1.5274E+00
2.95	6.1788E-01	4.9883E-01	2.3942E-01	4.7995E-01	4.8753E+00	1.2817E+00	1.5840E+00

(Continued)

M	$4C_f L^*/D$	T/T^*	p/p^*	ρ/ρ^*	p_t/p_t^*	III^*	$\Delta s/R$
3.00	6.2774E-01	4.8936E-01	2.3318E-01	4.7650E-01	5.1596E+00	1.2876E+00	1.6407E+00
3.10	6.4653E-01	4.7102E-01	2.2139E-01	4.7002E-01	5.7806E+00	1.2988E+00	1.7543E+00
3.20	6.6419E-01	4.5347E-01	2.1044E-01	4.6406E-01	6.4774E+00	1.3095E+00	1.8681E+00
3.30	6.8077E-01	4.3668E-01	2.0025E-01	4.5857E-01	7.2584E+00	1.3196E+00	1.9819E+00
3.40	6.9636E-01	4.2063E-01	1.9075E-01	4.5349E-01	8.1326E+00	1.3293E+00	2.0956E+00
3.50	7.1103E-01	4.0529E-01	1.8189E-01	4.4880E-01	9.1096E+00	1.3385E+00	2.2091E+00
3.60	7.2484E-01	3.9063E-01	1.7361E-01	4.4444E-01	1.0200E+01	1.3472E+00	2.3221E+00
3.70	7.3784E-01	3.7662E-01	1.6586E-01	4.4040E-01	1.1416E+01	1.3555E+00	2.4347E+00
3.80	7.5010E-01	3.6323E-01	1.5860E-01	4.3664E-01	1.2769E+01	1.3634E+00	2.5467E+00
3.90	7.6166E-01	3.5045E-01	1.5179E-01	4.3313E-01	1.4273E+01	1.3709E+00	2.6581E+00
4.00	7.7258E-01	3.3824E-01	1.4539E-01	4.2986E-01	1.5944E+01	1.3781E+00	2.7687E+00
4.10	7.8289E-01	3.2657E-01	1.3938E-01	4.2681E-01	1.7796E+01	1.3849E+00	2.8786E+00
4.20	7.9263E-01	3.1541E-01	1.3372E-01	4.2395E-01	1.9847E+01	1.3914E+00	2.9877E+00
4.30	8.0185E-01	3.0476E-01	1.2838E-01	4.2126E-01	2.2115E+01	1.3975E+00	3.0959E+00
4.40	8.1058E-01	2.9457E-01	1.2335E-01	4.1875E-01	2.4621E+01	1.4034E+00	3.2032E+00
4.50	8.1885E-01	2.8483E-01	1.1860E-01	4.1638E-01	2.7386E+01	1.4090E+00	3.3096E+00
4.60	8.2669E-01	2.7552E-01	1.1411E-01	4.1416E-01	3.0432E+01	1.4143E+00	3.4151E+00
4.70	8.3413E-01	2.6660E-01	1.0986E-01	4.1207E-01	3.3785E+01	1.4194E+00	3.5196E+00
4.80	8.4119E-01	2.5808E-01	1.0584E-01	4.1009E-01	3.7470E+01	1.4243E+00	3.6231E+00
4.90	8.4790E-01	2.4992E-01	1.0202E-01	4.0823E-01	4.1517E+01	1.4289E+00	3.7257E+00
5.00	8.5427E-01	2.4211E-01	9.8408E-02	4.0647E-01	4.5954E+01	1.4333E+00	3.8272E+00
5.20	8.6611E-01	2.2745E-01	9.1715E-02	4.0323E-01	5.6134E+01	1.4416E+00	4.0273E+00
5.40	8.7686E-01	2.1399E-01	8.5666E-02	4.0032E-01	6.8294E+01	1.4492E+00	4.2234E+00
5.60	8.8663E-01	2.0161E-01	8.0181E-02	3.9770E-01	8.2756E+01	1.4561E+00	4.4154E+00
5.80	8.9554E-01	1.9021E-01	7.5195E-02	3.9533E-01	9.9885E+01	1.4624E+00	4.6035E+00
6.00	9.0369E-01	1.7969E-01	7.0649E-02	3.9318E-01	1.2009E+02	1.4683E+00	4.7877E+00
6.50	9.2121E-01	1.5673E-01	6.0906E-02	3.8861E-01	1.8721E+02	1.4809E+00	5.2317E+00
7.00	9.3547E-01	1.3772E-01	5.3016E-02	3.8494E-01	2.8532E+02	1.4914E+00	5.6530E+00
7.50	9.4721E-01	1.2185E-01	4.6544E-02	3.8196E-01	4.2578E+02	1.5000E+00	6.0533E+00
8.00	9.5698E-01	1.0849E-01	4.1172E-02	3.7950E-01	6.2308E+02	1.5073E+00	6.4340E+00
8.50	9.6519E-01	9.7149E-02	3.6669E-02	3.7745E-01	8.9544E+02	1.5134E+00	6.7966E+00
9.00	9.7215E-01	8.7452E-02	3.2858E-02	3.7573E-01	1.2655E+03	1.5186E+00	7.1425E+00
9.50	9.7809E-01	7.9106E-02	2.9606E-02	3.7426E-01	1.7611E+03	1.5231E+00	7.4729E+00
10.00	9.8322E-01	7.1875E-02	2.6810E-02	3.7300E-01	2.4159E+03	1.5270E+00	7.7890E+00
15.00	1.0102E+00	3.3094E-02	1.2128E-02	3.6647E-01	3.1490E+04	1.5476E+00	1.0356E+01

APPENDIX F

Prandtl–Meyer Function and Mach Angle

In sonic and supersonic flows, Mach waves are formed. The local Mach wave angle is called a Mach angle μ , and it is related to the local Mach number via

$$\sin \mu = \frac{1}{M} \text{ or } \mu = \sin^{-1} \left(\frac{1}{M} \right) \quad (\text{F.1})$$

Each Mach wave causes an infinitesimal turn of the flow and a corresponding infinitesimal change in fluid pressure, temperature, density, and Mach number. Through infinitely many such waves, that is, Mach waves, flow can turn a finite angle and attain a finite change in static pressure, static temperature, static density, and Mach number. The Prandtl–Meyer function $v(M)$ defines an angle (in radians) that a sonic flow has to turn in order to achieve a supersonic Mach number M .

$$v(M) = \sqrt{\frac{\gamma+1}{\gamma-1}} \tan^{-1} \sqrt{\frac{\gamma-1}{\gamma+1}(M^2-1)} - \tan^{-1} \sqrt{M^2-1} \quad (\text{F.2})$$

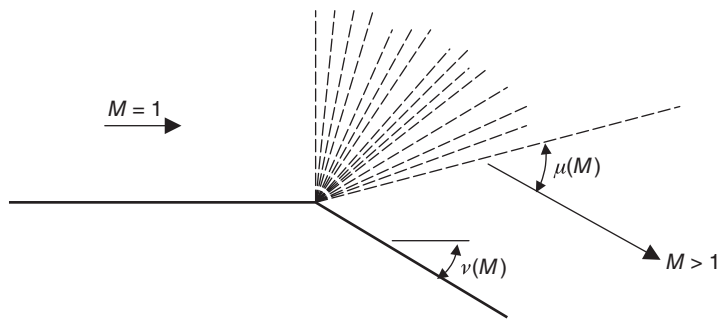
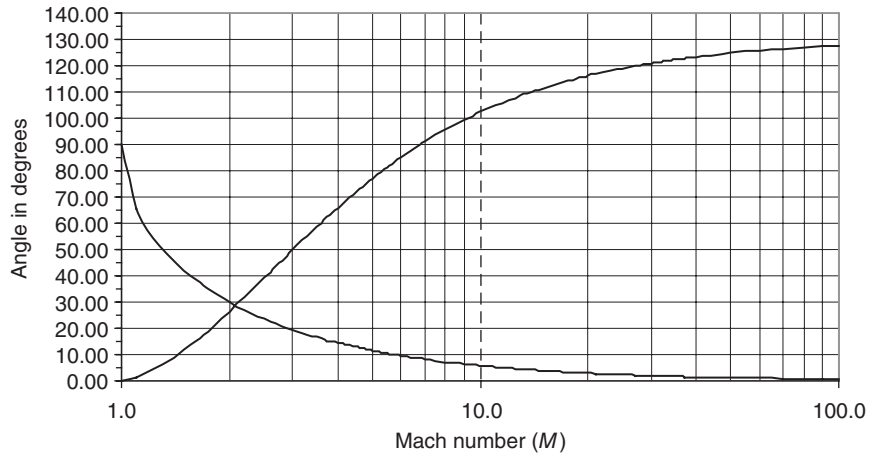
A graphical representation of the Prandtl–Meyer function and the Mach angle is shown.

Note: $v(M)$ in equation F.2 is in Radians

$$v(M \rightarrow \infty) = \sqrt{\frac{\gamma+1}{\gamma-1}} \frac{\pi}{2} - \frac{\pi}{2} = \frac{\pi}{2} \left[\sqrt{\frac{\gamma+1}{\gamma-1}} - 1 \right], \text{ which is } 130.4^\circ$$

M	ν (deg)	μ (deg)	M	ν (deg)	μ (deg)	M	ν (deg)	μ (deg)
1.0	0.00	90.00	5.4	80.43	10.67	28	120.2	2.05
1.1	1.34	65.38	5.5	81.25	10.48	29	120.6	1.98
1.2	3.56	56.44	5.6	82.03	10.29	30	120.9	1.91
1.3	6.17	50.28	5.7	82.80	10.10	31	121.2	1.85
1.4	8.99	45.58	5.8	83.54	9.93	32	121.5	1.79
1.5	11.91	41.81	5.9	84.26	9.76	33	121.8	1.74
1.6	14.86	38.68	6	84.96	9.59	34	122.0	1.69
1.7	17.81	36.03	6.2	86.30	9.28	35	122.3	1.64
1.8	20.73	33.75	6.4	87.56	8.99	36	122.5	1.59
1.9	23.59	31.76	6.6	88.76	8.71	37	122.7	1.55
2.0	26.38	30.00	6.8	89.90	8.46	38	122.9	1.51
2.1	29.10	28.44	7	90.97	8.21	39	123.1	1.47
2.2	31.73	27.04	7.5	93.44	7.66	40	123.3	1.43
2.3	34.28	25.77	8	95.63	7.18	50	124.7	1.15
2.4	36.75	24.62	8.5	97.57	6.76	60	125.7	0.95
2.5	39.12	23.58	9	99.32	6.38	70	126.4	0.82
2.6	41.42	22.62	9.5	100.89	6.04	80	126.9	0.72
2.7	43.62	21.74	10	102.32	5.74	90	127.3	0.64
2.8	45.75	20.92	10.5	103.61	5.47	100	127.6	0.57
2.9	47.79	20.17	11	104.80	5.22			
3.0	49.76	19.47	11.5	105.88	4.99			
3.1	51.65	18.82	12	106.88	4.78			
3.2	53.47	18.21	12.5	107.80	4.59			
3.3	55.22	17.64	13	108.65	4.41			
3.4	56.91	17.10	13.5	109.44	4.25			
3.5	58.53	16.60	14	110.18	4.10			
3.6	60.09	16.13	14.5	110.87	3.95			
3.7	61.60	15.68	15	111.51	3.82			
3.8	63.05	15.26	15.5	112.11	3.70			
3.9	64.44	14.86	16	112.68	3.58			
4.0	65.79	14.48	16.5	113.21	3.47			
4.1	67.08	14.12	17	113.71	3.37			
4.2	68.33	13.77	17.5	114.18	3.28			
4.3	69.54	13.45	18	114.63	3.18			
4.4	70.71	13.14	18.5	115.05	3.10			
4.5	71.83	12.84	19	115.45	3.02			
4.6	72.92	12.56	20	116.2	2.87			
4.7	73.97	12.28	21	116.9	2.73			
4.8	74.99	12.02	22	117.5	2.61			
4.9	75.97	11.78	23	118.0	2.49			
5	76.92	11.54	24	118.6	2.39			
5.1	77.84	11.31	25	119.0	2.29			
5.2	78.73	11.09	26	119.5	2.20			
5.3	79.60	10.88	27	119.9	2.12			

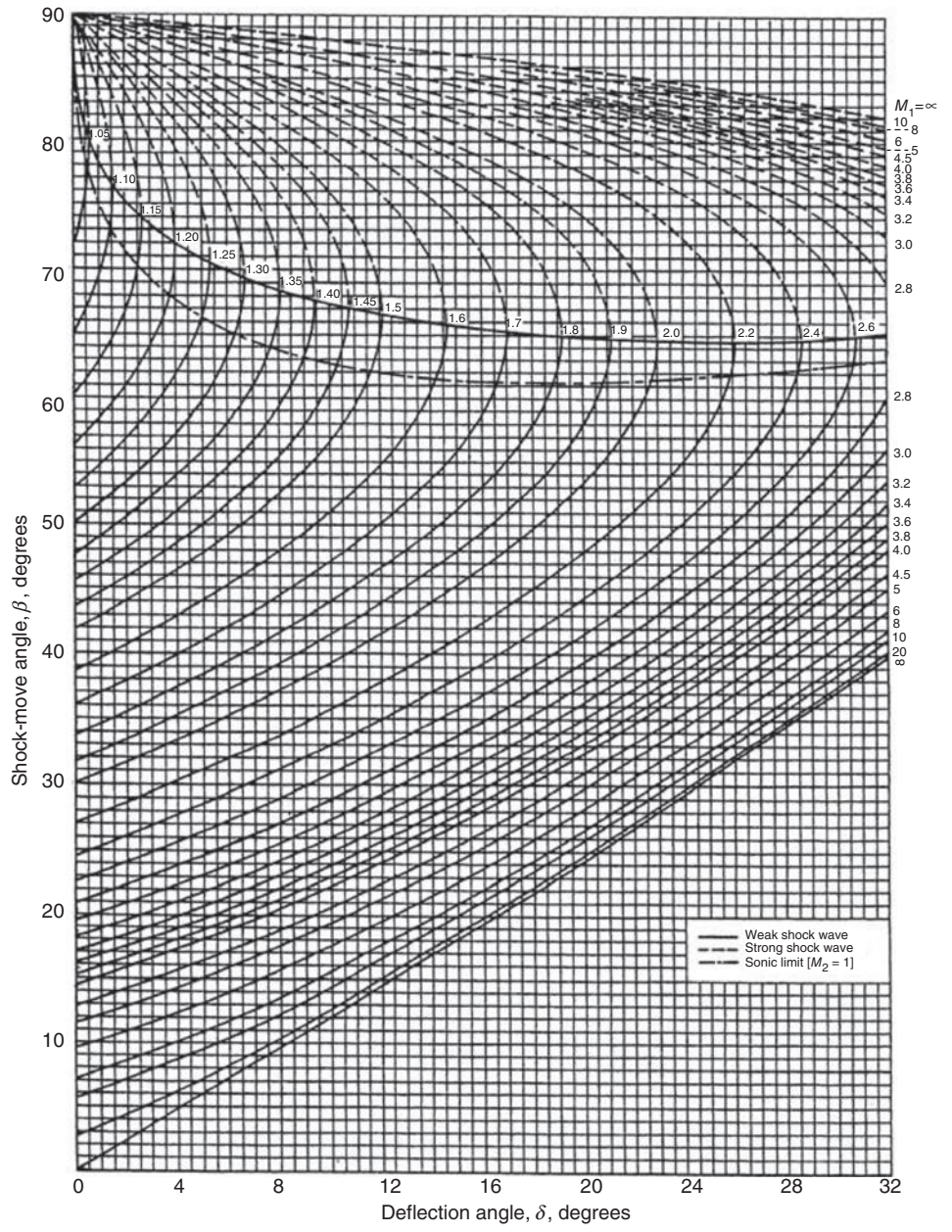
Prandtl–Meyer function and Mach angle
for $\gamma = 1.4$

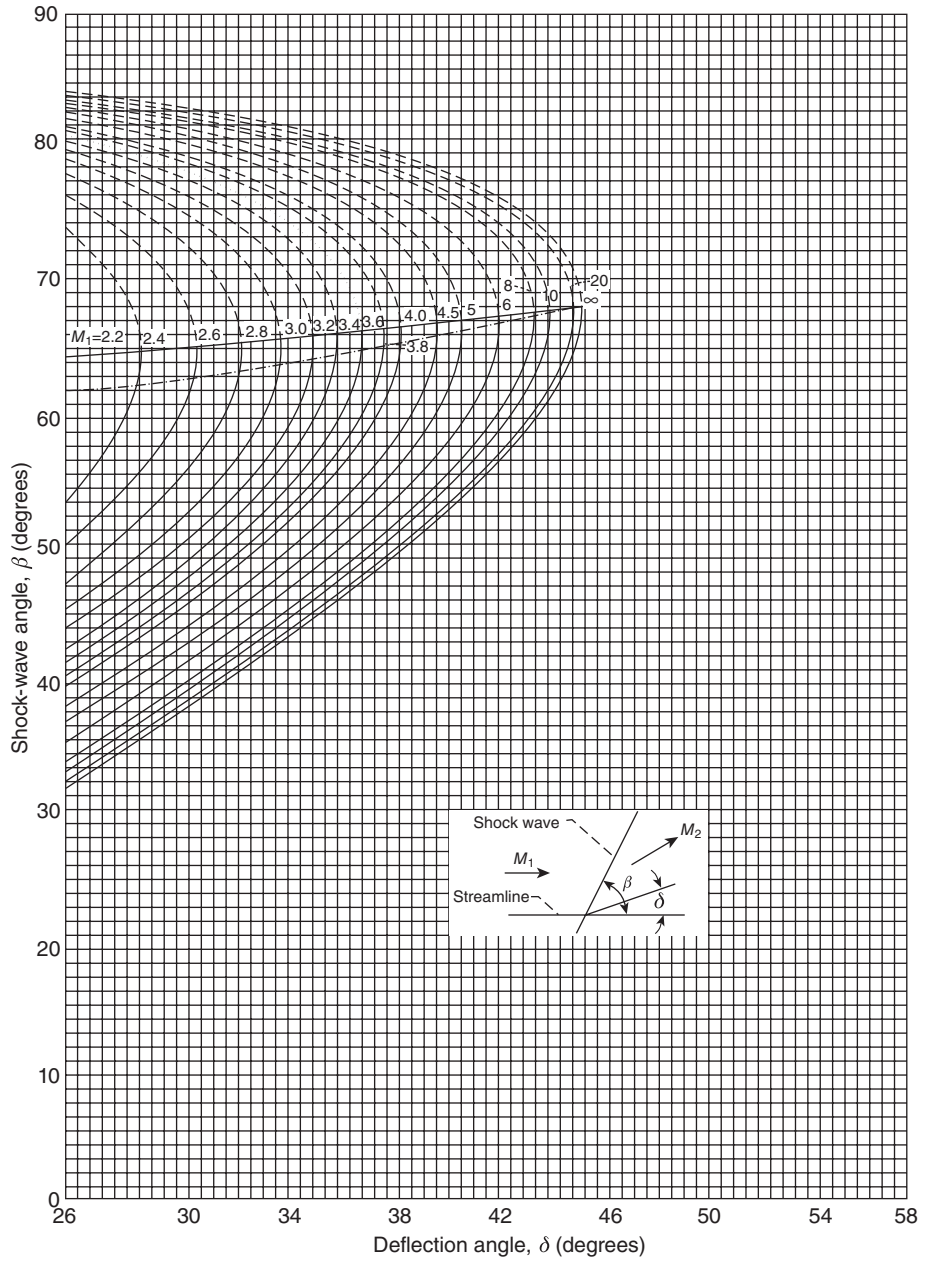


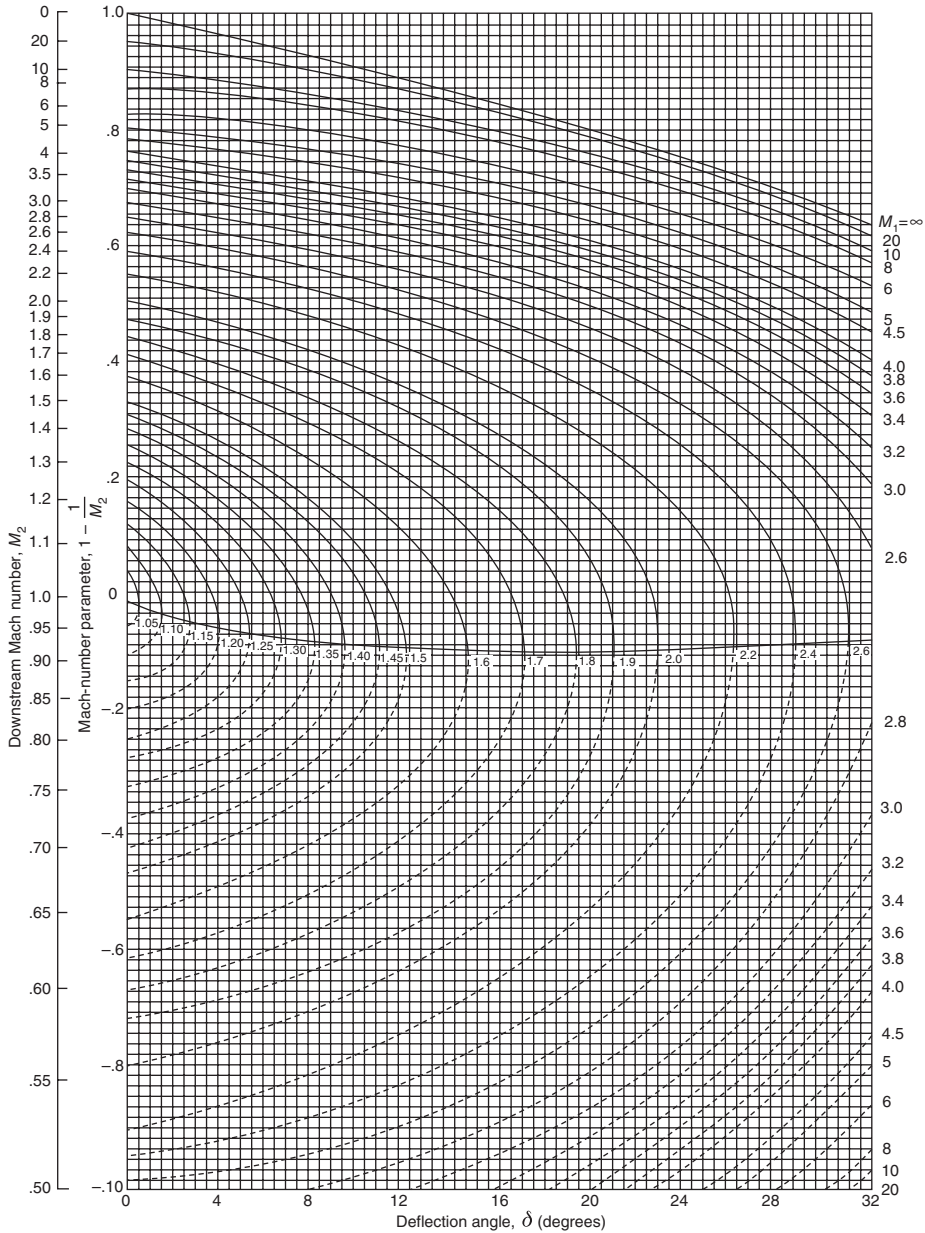
APPENDIX G

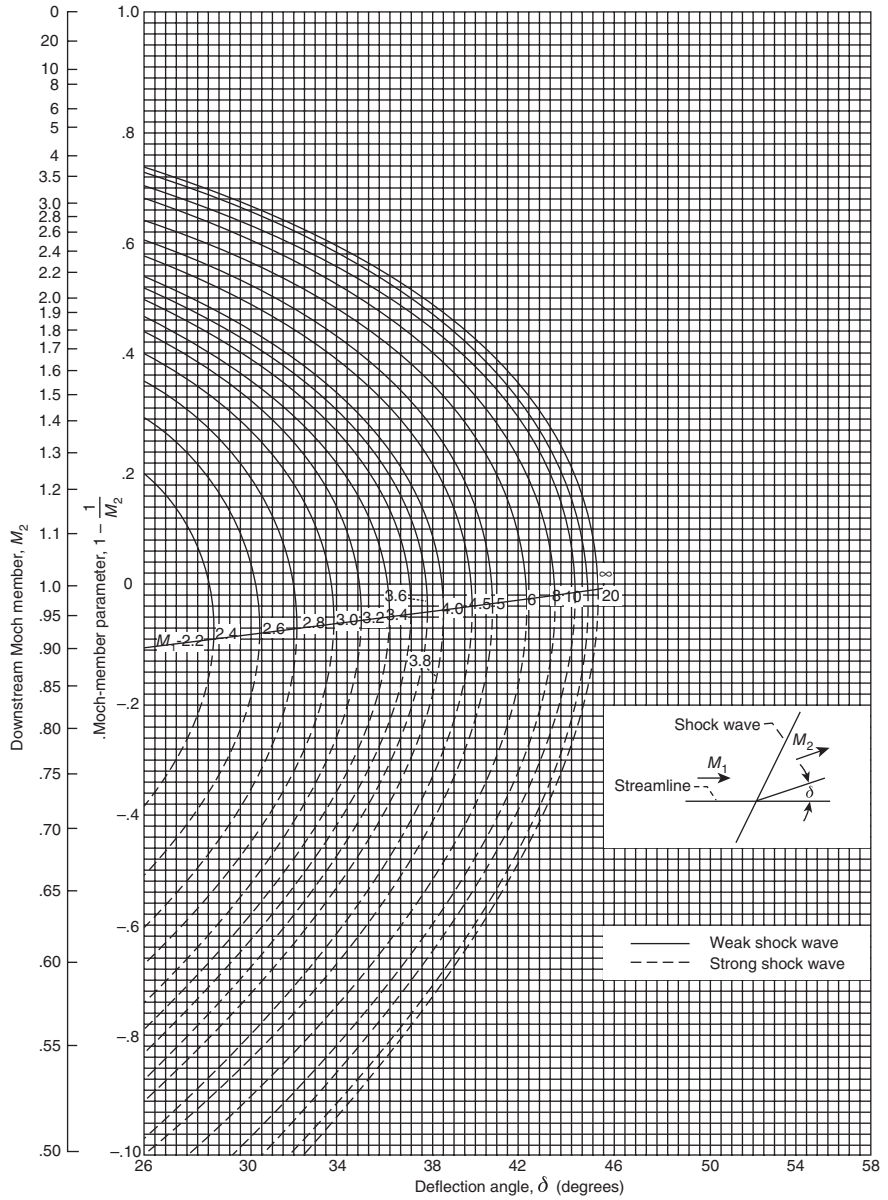
Oblique Shock Charts

Oblique Shock Charts $\gamma = 1.4$







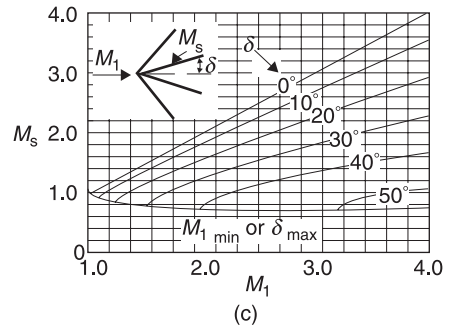
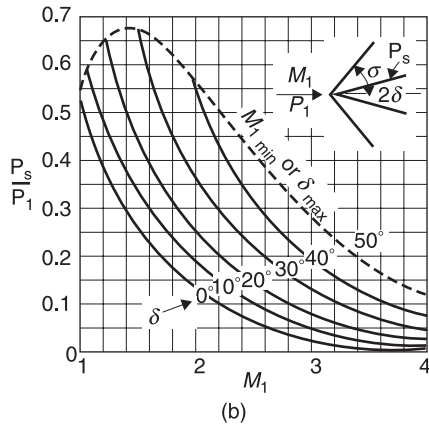
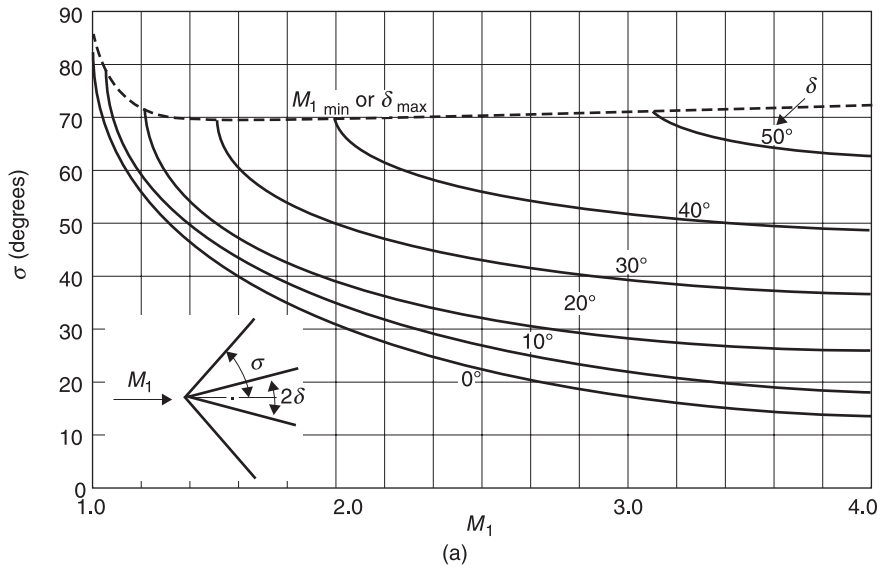


The oblique shock charts are from NACA Report 1135, *Equations, Tables, and Charts for Compressible Flow*, Ames Research Staff, 1953

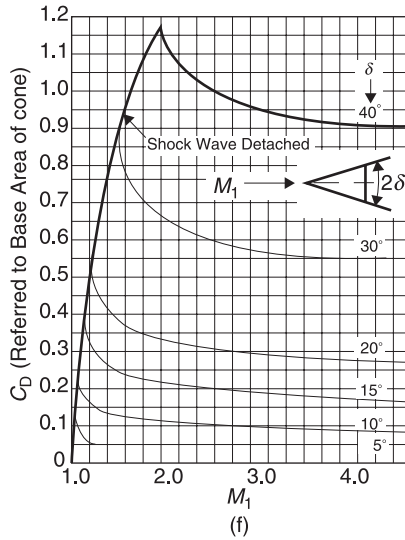
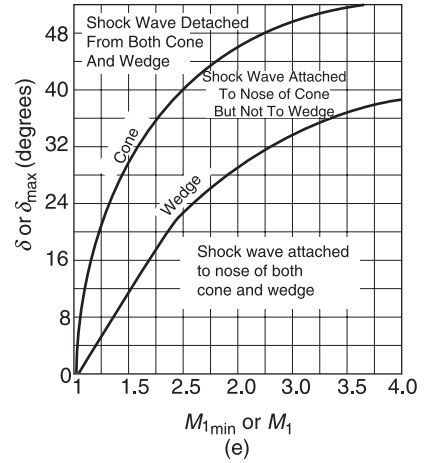
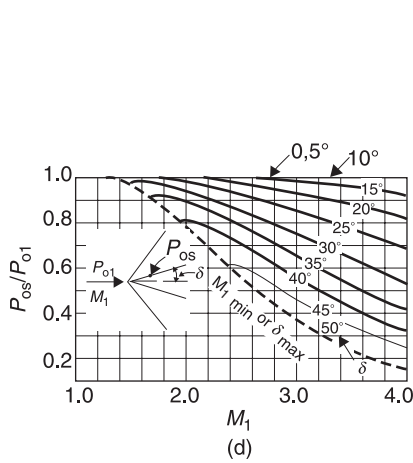
APPENDIX H

Conical Shock Charts

Conical Shock Charts $\gamma = 1.4$



- (a) Shock angle versus approach Mach number, with cone angle as parameter.
- (b) Ratio of surface pressure to free stream stagnation pressure versus free stream Mach number.
- (c) Surface Mach number versus free stream Mach number, with cone angle as parameter.



- (d) Ratio of surface stagnation pressure to free stream stagnation pressure, with cone angle as parameter.
- (e) Regions of shock attachment and detachment for cone and wedge.
- (f) Pressure drag coefficient based on projected frontal area.

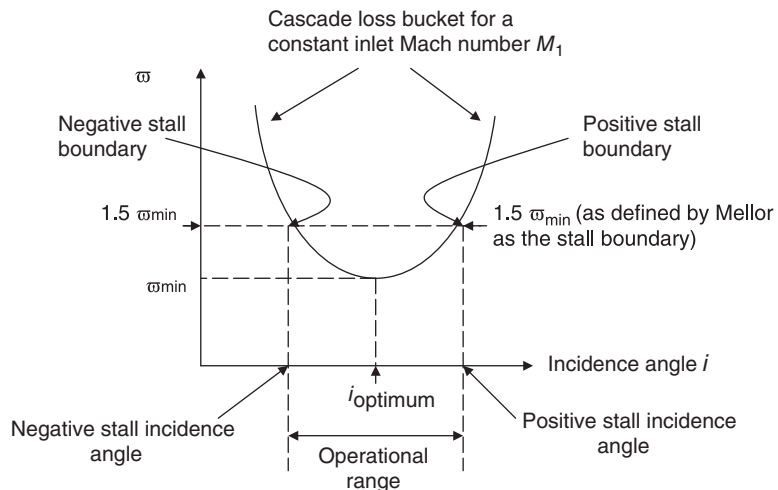
From: A. H. Shapiro, *The Dynamics and Thermodynamics of Compressible Fluid Flow*, Vol. II, The Ronald Press Company, 1954.

APPENDIX I

Cascade Data

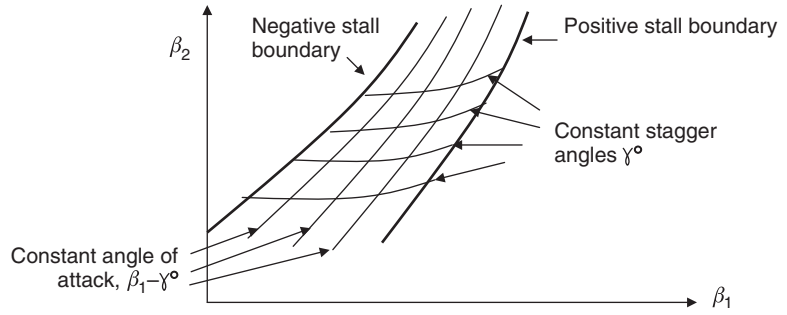
NACA-65 Series Cascade Data

Cascade total pressure loss data are plotted in the shape of a “bucket” in terms of incidence angle. A definition sketch is shown.



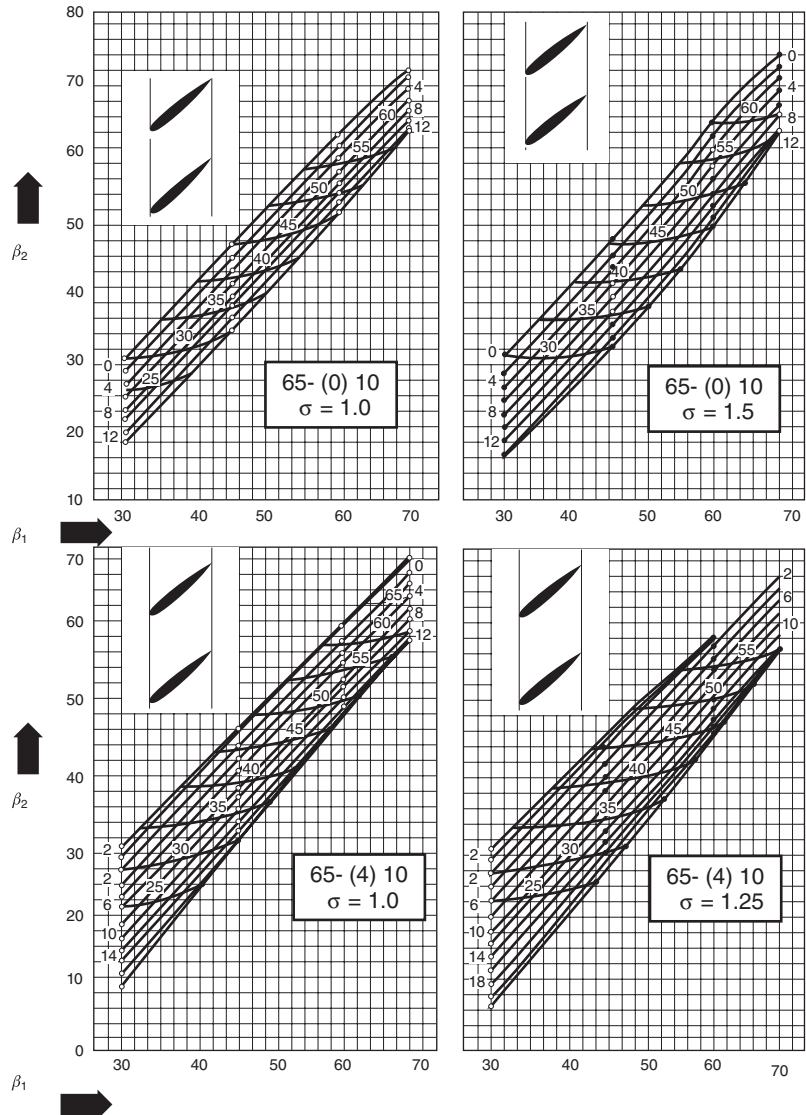
Definition sketch for the cascade stall boundaries, according to Mellor

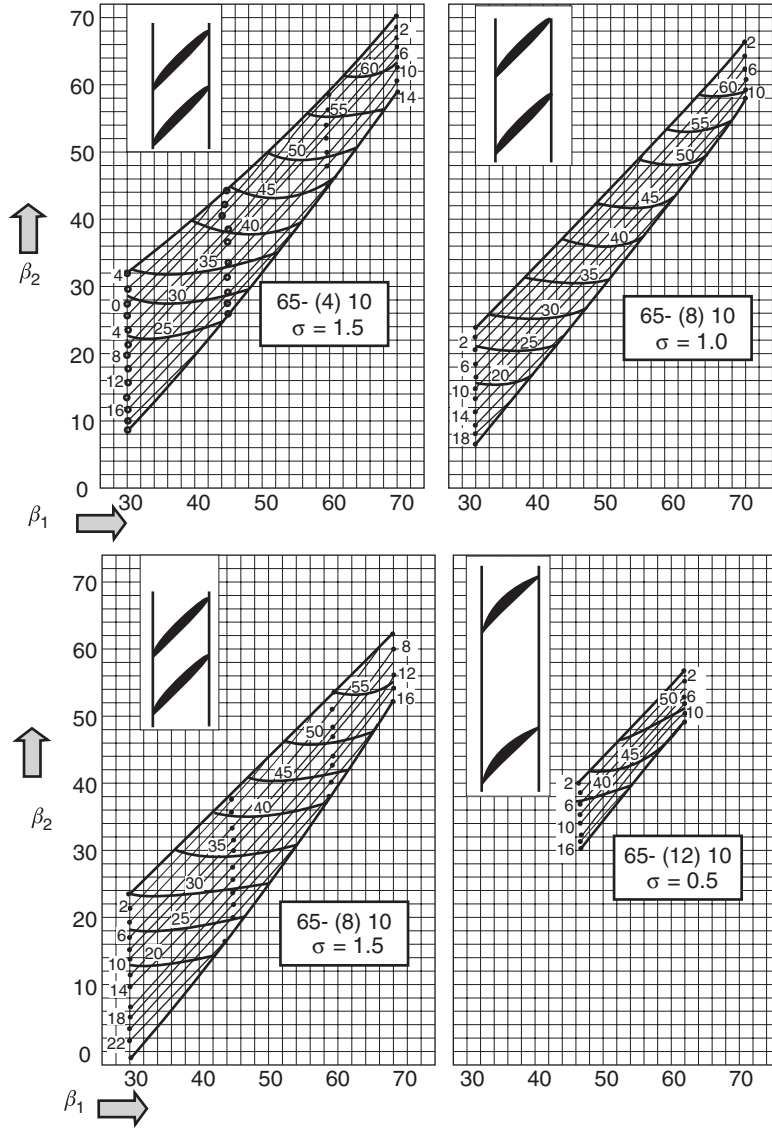
Mellor presents the operational range of each 65-series airfoils in various cascade arrangements that are very useful for preliminary design purposes. Mellor's unpublished graphical correlations (originated at MIT's Gas Turbine Laboratory) were published by Horlock (1973), Hill and Peterson (1992), among others. In this appendix, Mellor's cascade data presentation is graphed according to the following definition sketch.

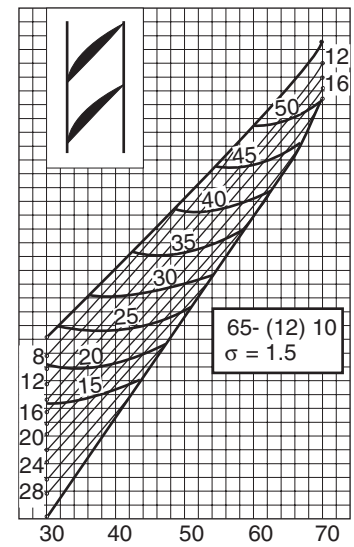
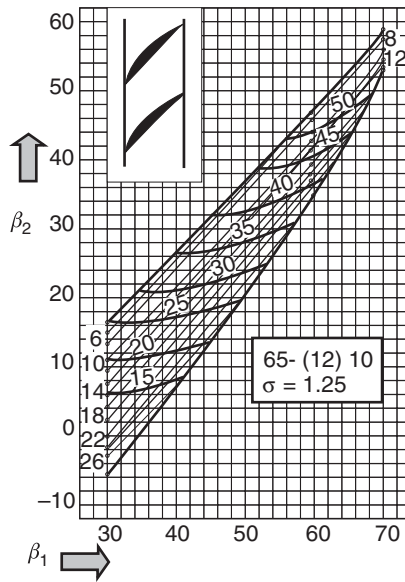
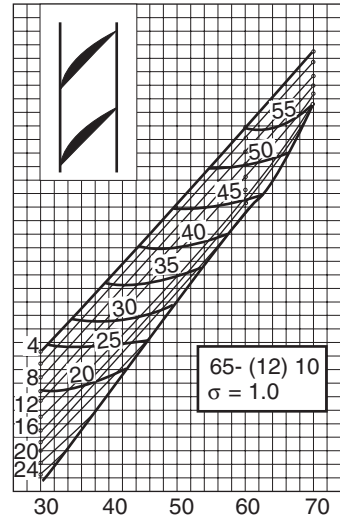
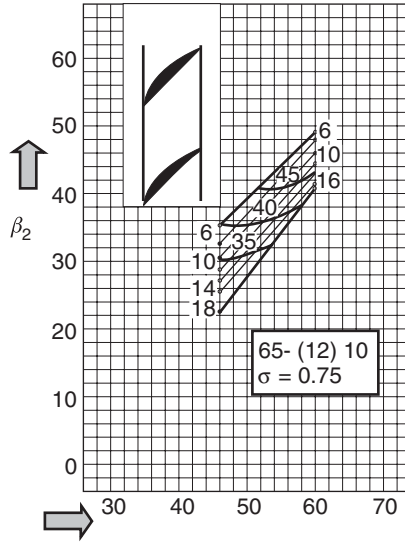


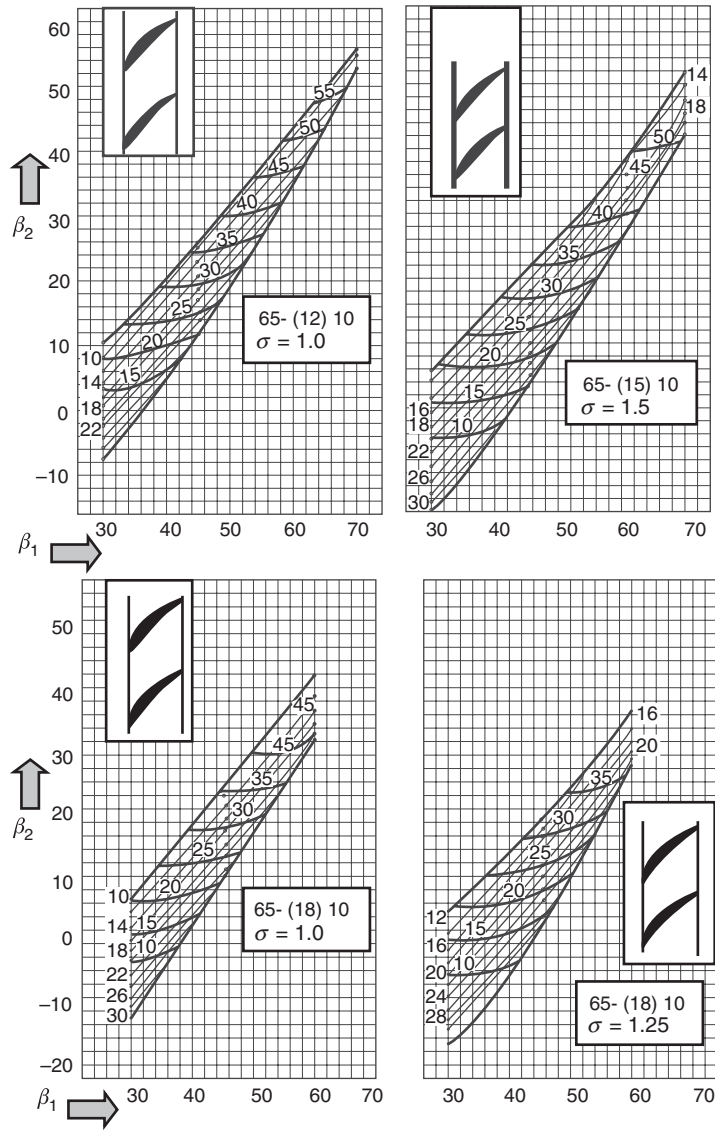
Definition sketch for the 65-series cascade data as presented by Mellor

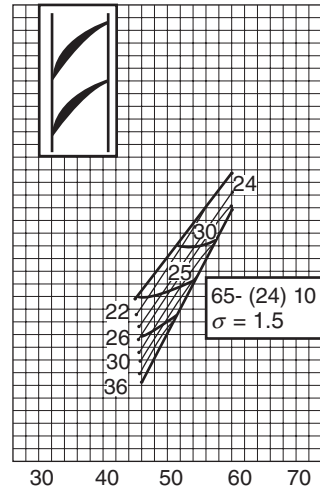
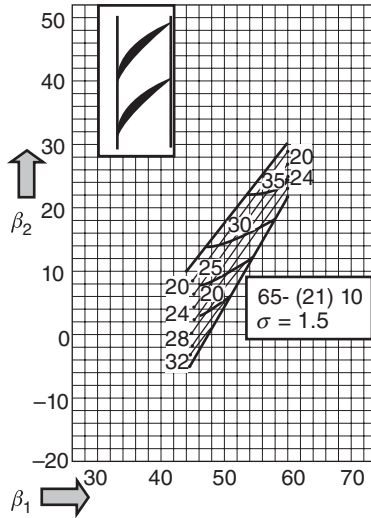
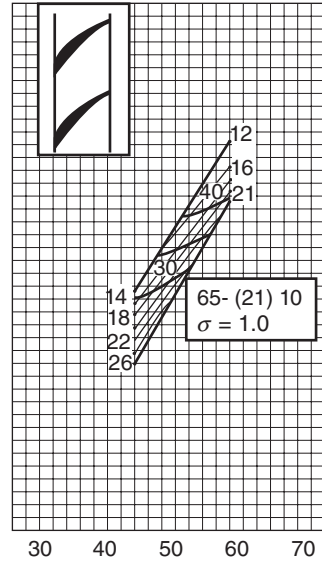
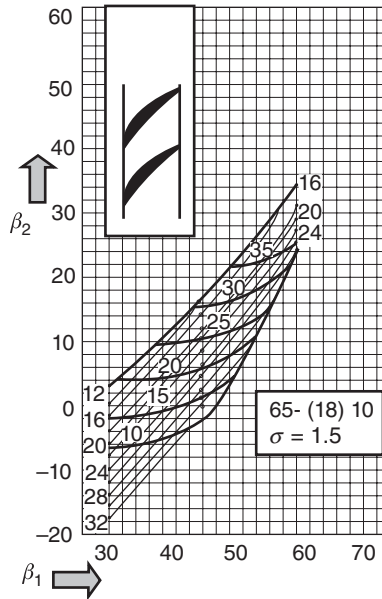
Cascade Data











APPENDIX J

Websites

The websites of NASA and major aircraft engine manufacturers are listed for reference (all websites were last accessed in December 2013).

www.hq.nasa.gov
www.grc.nasa.gov
www.pw.utc.com
www.pwc.ca
www.ge.com
www.mtu.de
www.rolls-royce.com
www.snecma.com
www.enginealliance.com
www.cfm56.com
www.geae.com
www.V2500.com
www.williams-int.com

APPENDIX K

10-Minute Quiz

Closed books and notes

Quiz No. 1

1. Draw a complete *Rayleigh line* on a T-s diagram and identify its branches, Mach numbers.
2. Draw a complete *Fanno line* on a T-s diagram and identify its branches, Mach numbers.
3. Draw an ideal *Brayton cycle* on a T-s diagram and write its thermal efficiency.
4. Draw an ideal *Carnot cycle* on a T-s diagram and write its thermal efficiency.

Quiz No. 2

1. Write the *perfect gas* equation and define the variables/constants in the equation.
2. What is the density of air at sea level (give a ballpark value in any unit)? What is the absolute static pressure at sea level (give the value in any unit)?
3. Define a *calorically perfect* gas.
4. Define a *thermally perfect* gas.
5. Write the *Bernoulli equation* and identify its terms and limitations.

Quiz No. 3

1. Write the *first law of thermodynamics* for a system.
2. What are the *dimensions of specific heat at constant pressure, c_p* ?
3. What are the dimensions of the *coefficient of viscosity, μ* ?
4. Define *Newton's law of friction* in a fluid.
5. Define a *Newtonian fluid*.
6. What do we mean by *continuum*?
7. What is the definition of "*mean-free path*" in a gas?
8. How does the *mean-free path* in air vary with altitude?

Quiz No. 4

1. What is the definition of *Reynolds number* and what does it mean?
2. What is the definition of *Mach number* and what does it mean?
3. What are the dimensions of the *gas constant, R* ?
4. How do gas constants, R_1 and R_2 , in two different (perfect) gases relate to each other?
5. How does *speed of sound* (wave) propagation in a gas relate to the gas molecular weight?
6. Is *sound propagation* in a gas, such as air, adiabatic or isentropic?
7. What happens at/near Mach 0.3 that is considered to be the boundary between the incompressible and compressible flow in air?

Quiz No. 5

1. Draw a schematic of a gas generator and identify its components.
2. Write an expression for the *gross thrust, F_g* .
3. Write an expression for *ram drag* of an airbreathing engine, D_r .
4. Write an expression for pressure thrust.
5. Define a *perfectly-expanded nozzle*.
6. Draw a schematic of a *turbojet engine* and identify its station numbers.

Quiz No. 6

1. Write an expression for the *thermal power input* in a gas turbine engine.
2. Write the definition of *thermal efficiency* for a gas turbine engine.
3. Write the definition of *propulsive efficiency* for an aircraft jet engine.
4. Define *thrust-specific fuel consumption* for an aircraft jet engine.
5. Define specific thrust and compare the specific thrust of a turbojet to a turbofan engine.

6. Define an underexpanded nozzle and the thrust penalty associated with that.
7. Relate temperature ratio to pressure ratio for an isentropic process.
8. Write a *general, that is, compressible*, form of the Bernoulli equation for a perfect gas.

Quiz No. 7

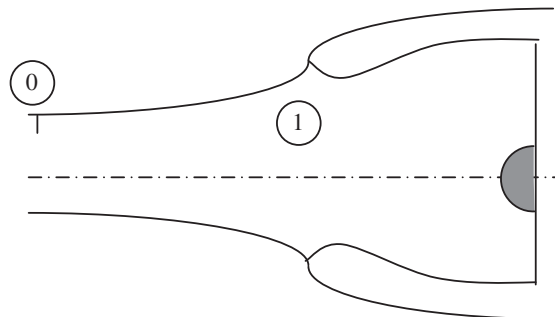
1. Draw static and stagnation states of a gas, on a T-s diagram, on the two sides of a normal or oblique shock.
2. Draw static and stagnation states, on a T-s diagram, for an *inlet* for both *real* and *ideal* conditions.
3. Draw static and stagnation states, on a T-s diagram, for a *compressor* for both *real* and *ideal* conditions.
4. Draw static and stagnation states, on a T-s diagram, for a *burner or afterburner* for both *real* and *ideal* conditions.
5. Draw static and stagnation states, on a T-s diagram, for a *turbine* for both *real* and *ideal* conditions.
6. Draw static and stagnation states, on a T-s diagram, for a *nozzle* for both *real* and *ideal* conditions.

Quiz No. 8

1. Define *installed thrust* in a turbojet engine.
2. Define *bypass ratio* in a turbofan engine.
3. At what nozzle flow condition will the gross thrust achieve its maximum?
4. Write an expression for the *uninstalled thrust* of a turbofan engine with separate exhausts. Assume the bypass ratio is α .

Quiz No. 9

1. Define *inlet additive drag*, D_{add} .



2. Define *inlet spillage drag*, D_{spillage} .
3. Define *cowl lip suction force*.
4. Draw a T-s diagram of a gas turbine engine with a regenerator. Identify the regenerator path on the diagram.

Quiz No. 10

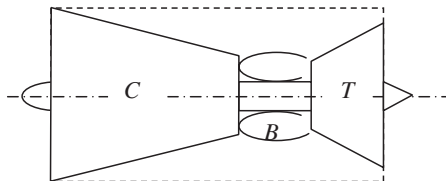
1. Define *specific thrust* for a turbofan engine.
2. Are there any penalties on engine performance with the afterburner in the off position? Briefly explain.
 - Case 1: Ideal engine
 - Case 2: Real engine
3. Define *thrust specific fuel consumption* in an airbreathing engine.
4. Draw a T-s diagram for the fan stream (assuming ideal processes) from the flight state 0 to the fan nozzle exit, 19.

Quiz No. 11

1. What is the definition of *burner efficiency*, η_b ?
2. What are the factors that cause *total pressure loss* in a combustor?
3. What are combustor-generated *pollutants*? Name four!
4. Write the chemical reaction of the stoichiometric combustion of methane and oxygen.
5. Write the molar composition of *theoretical air*.

Quiz No. 12

1. Write the power balance equation between the turbine and compressor in a gas generator.



2. Relate π_c to τ_c for an ideal compressor.
3. Write an equation for the compressor shaft power, $\dot{\varphi}_c$.
4. Write an equation for the energy balance across the burner.

5. What is the customary unit for the heating value of fuel, Q_R , in the metric and English systems of units?
6. What is a common unit for the thrust-specific fuel consumption of an aircraft engine in the English system of units?
7. Define the two limit temperatures in an afterburning turbojet engine.

Quiz No. 13

1. Define propeller efficiency, η_{prop} .
2. Define the boundary condition imposed at the fan duct exit lip in a mixed-flow turbofan engine.
3. Define overall efficiency for a turboprop engine.
4. Write an equation for the thrust produced by the core stream in a turboprop engine.
5. Why can $\tau_{\lambda\text{AB}}$ be greater than τ_{λ} in an engine with an afterburner? Briefly explain.
6. Write an energy balance for the mixer in a mixed-flow turbofan engine.

Quiz No. 14

1. Write the gross thrust equation for the fan nozzle in a turbofan engine.
2. Write an equation for the shaft power of the fan in a turbofan engine.
3. Write an energy balance equation for, that is, across, an afterburner.
4. Where do we apply the “Kutta” condition in a turbofan engine?
5. What is the effect of bypass ratio on propulsive efficiency?
6. What is the effect of compressor pressure ratio on thermal efficiency?

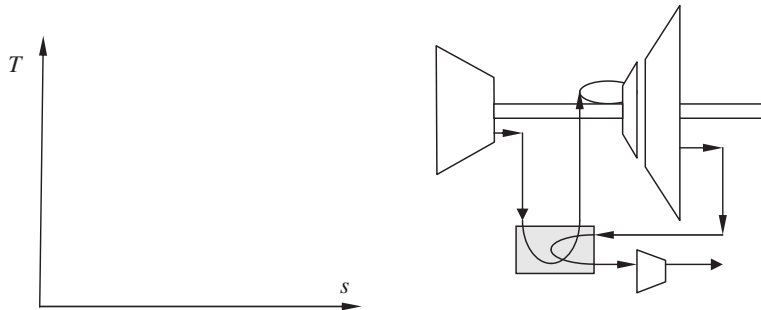
Quiz No. 15

1. Use a T-s diagram to show the total pressure loss in a burner.
2. Use a T-s diagram to define the total pressure loss in an inlet.
3. Graph *the trend* of compressor adiabatic efficiency, η_c , as a function of compressor pressure ratio, π_c .
4. Graph *the trend* of turbine adiabatic efficiency, η_t , as a function of turbine pressure ratio, $1/\pi_t$.
5. Define afterburner efficiency, η_{AB} .
6. Use a T-s diagram to define nozzle adiabatic efficiency, η_n .

Quiz No. 16

1. In an ideal turboprop engine at takeoff, the “optimum” power split between the propeller and the core nozzle sets the engine core thrust at what level?

- Draw the T-s diagram of an ideal *turboshaft engine with regeneration*. Label all stations.



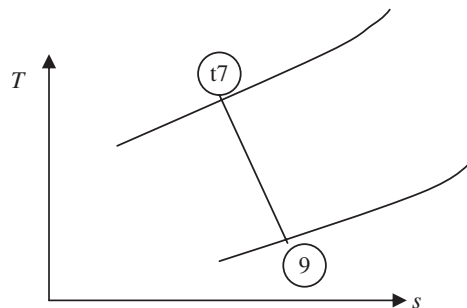
- The flow in a real inlet is irreversible, yet adiabatic. What are the implications on π_d and τ_d ?
- The flow in a real nozzle is assumed to be adiabatic. What are the implications on π_n and τ_n ?

Quiz No. 17

- Draw an ideal and a real combustion process on a T-s diagram and identify $(\Delta p_t)_{\text{burner}}$ on the graph.



- Identify the nozzle exit total condition, that is, t_9 , based on the exit static condition, 9, as shown. Label the exhaust kinetic energy on the graph.

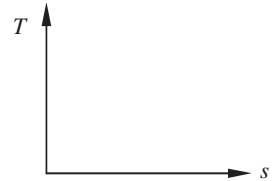


- Write the energy balance equation across a real combustion chamber.

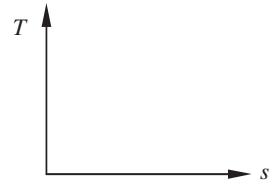
4. What is mechanical efficiency, η_m , that is used in power balance in a gas turbine engines?
5. Write the actual power balance between a compressor, fan and a turbine in a turbofan engine.

Quiz No. 18

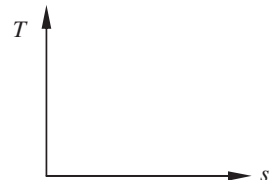
1. Define inlet adiabatic efficiency, η_d .
(First draw the thermodynamic process)



2. Define compressor adiabatic efficiency, η_c .
(First draw the thermodynamic process)



3. Define compressor polytropic efficiency, e_c .
(First draw the thermodynamic process)



4. Define turbine adiabatic efficiency, η_t .
(First draw the thermodynamic process)

5. Define burner efficiency, η_b .

Quiz No. 19

1. Define the *static pressure recovery coefficient*, C_{PR} , in a subsonic diffuser.
2. What is meant by *transitory stall* in a diffuser flow?
3. Define *inlet blockage*, B , in a diffuser.
4. What is *jet flow* regime in a diffuser?
5. What is meant by the *fully-developed stall* in a diffuser?
6. Draw a *dump diffuser*.
7. Draw an *annular diffuser*.

Quiz No. 20

1. What is the maximum (mean) *throat Mach number* that we use in a subsonic inlet design?

2. What is the definition of *critical flight Mach number* for a subsonic inlet?
3. How can we reduce *nacelle drag* in subsonic/transonic flight? Name two methods!
4. How does local skin friction coefficient, c_f , relate to the friction drag coefficient, C_f ?
5. How does *skin friction coefficient*, c_f , vary with *Reynolds number* for laminar and turbulent boundary layer flows?
6. What is the effect of *Mach number*, that is, compressibility, on skin friction and why?
7. What is the *transition Reynolds number* for a flat plate?

Quiz No. 21

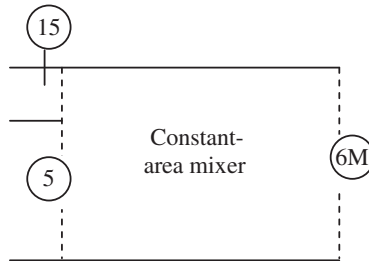
1. Write an expression for (the time rate of change of) angular momentum at the inlet to a blade row, say at the pitchline.
2. Write the *Euler turbine equation*.
3. Write an expression for *stator torque*, based on angular momentum.
4. What flow condition has to be satisfied for a *repeated stage*?
5. Define blade *solidity*, σ .
6. Define *degree of reaction*, $^{\circ}R$, for a compressor stage.
7. What is a typical maximum value of D-factor for a compressor blade section?

Quiz No. 22

1. What do we mean by an *underexpanded* nozzle flow?
2. What do we mean by an *overexpanded* nozzle flow?
3. What are the boundary conditions on a *slipstream* or *free shear layer*?
4. What is the definition of *Nozzle Pressure Ratio*?
5. What do we mean by “critical” nozzle pressure ratio?
6. Is a subsonic jet that emerges from a nozzle into atmosphere always perfectly expanded?

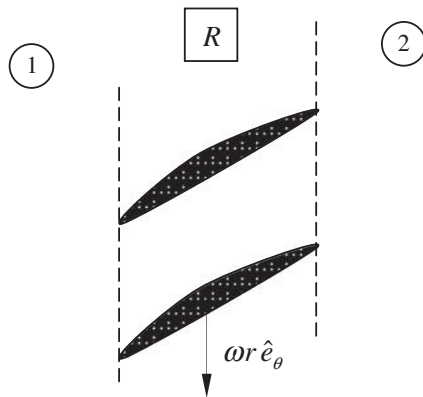
Quiz No. 23

1. Define *mechanical efficiency*, η_m , in a gas turbine engine.
2. Define the *gearbox efficiency*, η_{gb} .
3. Define *propeller efficiency*, η_{pr} .
4. Relate π_c to τ_c using polytropic efficiency, e_c .
5. Relate π_t to τ_t using the turbine polytropic efficiency, e_t .
6. Write the *energy balance equation* for a mixer; use stations 5, 15 and 6M as the two entrances and one exit stations, respectively, as shown.

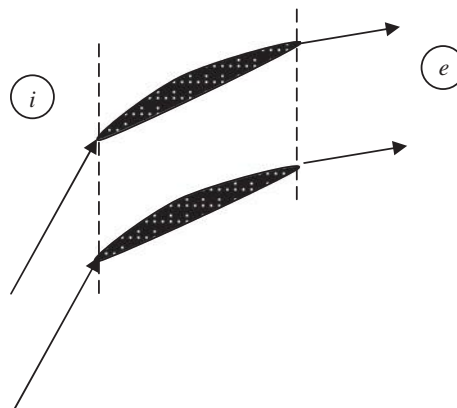


Quiz No. 24

1. Draw velocity triangles in stations 1 and 2 across the rotor and identify the absolute and relative flow angles.



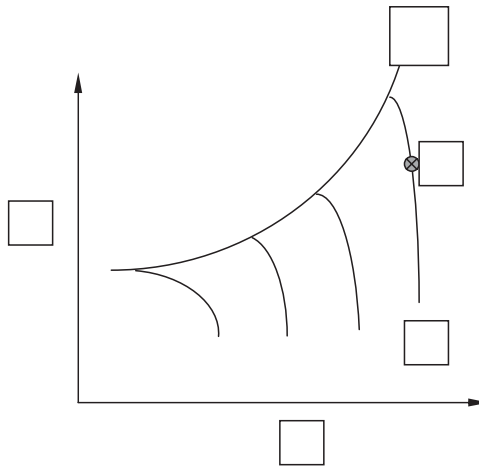
2. Define *stage loading coefficient*, ψ , and *flow coefficient*, ϕ , in turbomachinery.
3. On the following cascade, draw and identify the incidence angle, deviation angle and camber angle.



4. Define *de Haller criterion* for the flow diffusion limit across a compressor blade.
5. What is a typical (relative) *tip Mach number* in a modern transonic fan?
6. What is a typical transonic *fan pressure ratio*?

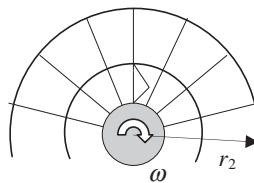
Quiz No. 25

1. Define *corrected mass flow rate* at the engine face, \dot{m}_{c2} .
2. Define *corrected shaft speed*, N_c .
3. Define *corrected thrust*, F_c .
4. On the following compressor map, fill in the boxes.



Quiz No. 26

1. Define slip factor, ϵ , in a centrifugal compressor.
2. Draw a velocity triangle at the exit of the centrifugal compressor impeller, shown.



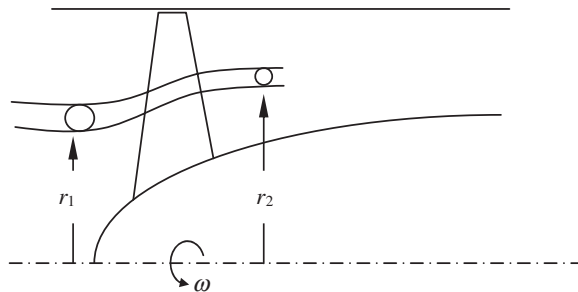
3. First, draw three turbine nozzle blade profiles (cascade), then, draw the exit velocity triangle.
4. Define the diffusion factor for a compressor blade rotor.

Quiz No. 27

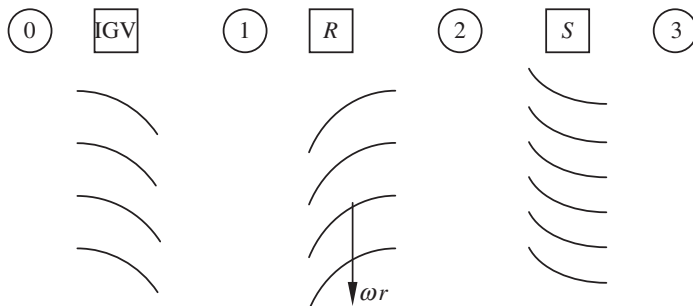
1. Describe the physical mechanism for *inlet buzz instability*.
2. Describe the physical mechanism for *rotating stall* in a compressor.
3. Describe the *instability of a shock* in the converging section of a C-D inlet and how it relates to *inlet start* and *unstart*.

Quiz No. 28

1. Write an equation for the *torque* acting on the fluid streamtube shown in a turbomachinery.

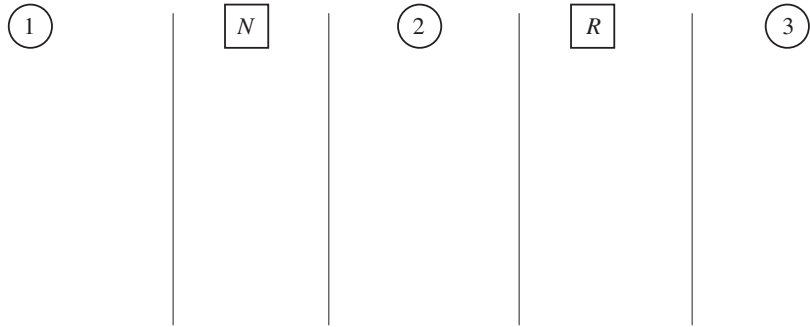


2. Write a vector equation for the velocity triangle relating the absolute and the rotating frames of reference.
3. Write the *specific work* of a rotor blade, that is, the Euler turbine equation.
4. Among stations 0, 1, 2 and 3 which has the *highest absolute swirl* and which has no swirl?

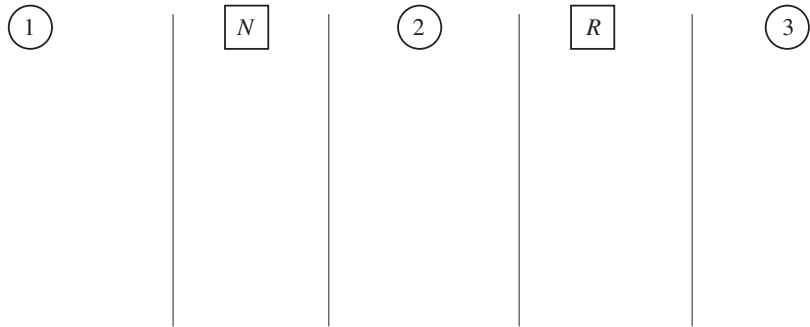


Quiz No. 29

1. Draw blade profiles and velocity triangles in stations 2 and 3 of an axial-flow turbine stage, for a 50% degree of reaction, °R.



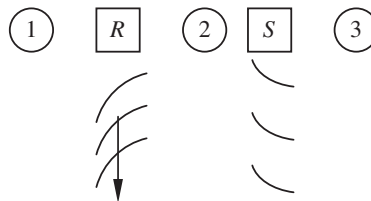
2. Draw blade profiles and velocity triangles in stations 2 and 3 of an axial-flow turbine stage, for a 0% degree of reaction, $^{\circ}R$, that is, an impulse stage.



3. Write an equation for h_{t2R} in terms of flow velocity components.
 4. Relate h_{t2R} to h_{t3R} in a turbine.

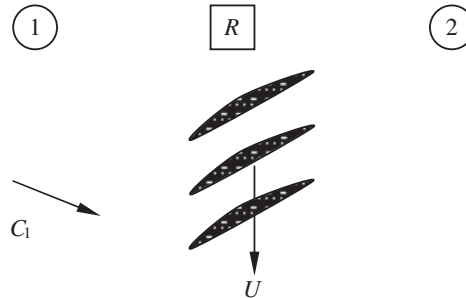
Quiz No. 30

1. Define *degree of reaction*, $^{\circ}R$, in an axial-flow compressor stage.



2. Define the *stage loading coefficient*, ψ .
 3. Define the *flow coefficient*, ϕ .

4. Define blade solidity, σ .
5. Draw the velocity triangles in stations 1 and 2 across the rotor.



Quiz No. 31

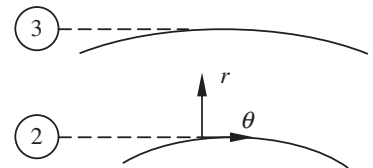
1. What kind of supersonic inlet has a *starting problem*?
2. How can we *start* such inlets?
3. What does “the best back pressure” mean in an inlet?
4. Briefly describe the “*buzz*” *instability* for an external-compression inlet.
5. What kind of an inlet is the *Kantrowitz–Donaldson* inlet?
6. What establishes the position of the *normal shock* in an inlet?
7. Where can a *normal shock* be stabilized in a convergent–divergent inlet?
8. What is a suitable *Mach number range* for an internal-compression inlet?
9. What is a suitable *Mach number range* for an external-compression inlet?
10. Define *equivalence ratio*, ϕ , in a combustion chamber.

Quiz No. 32

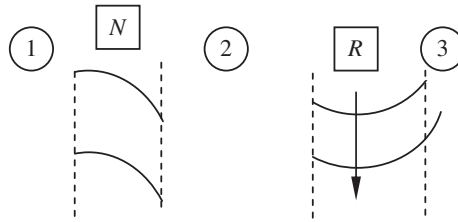
1. Define *slip factor*, ϵ , for a centrifugal compressor.
2. In a radial diffuser following a centrifugal compressor rotor, assuming ideal flow, how does swirl and radial velocity vary with radius?

$$C_\theta(r) \sim$$

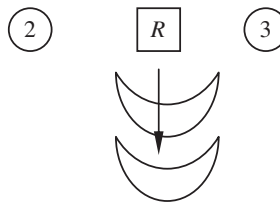
$$\rho C_r(r) \sim$$



3. Draw a velocity triangle in stations 2 and 3 of the axial-flow turbine shown and label flow angles.



4. What is an *upper limit* for the exit flow angle, α_2 , in a turbine nozzle?
5. Draw the velocity triangles in stations 2 and 3 of an *impulse turbine* (i.e., $\circ R = 0$) rotor.



Quiz No. 33

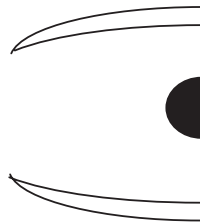
1. Define “*angularity*” loss for an exhaust nozzle.
2. Define *gross thrust coefficient*, C_{fg} , for a nozzle.
3. Define *velocity coefficient*, C_v , for a nozzle.
4. Define *discharge coefficient*, C_d , for a nozzle.
5. What physical condition is required for a perfectly expanded nozzle?
6. What does an *underexpanded* nozzle mean?
7. What does an *overexpanded* nozzle mean?
8. Where is the *normal shock* in an external-compression inlet in subcritical mode?
9. Where can a *normal shock* be stabilized in a C–D inlet?
10. Draw a *normal shock inlet* with the backpressure lower than the “best back pressure”.

Quiz No. 34

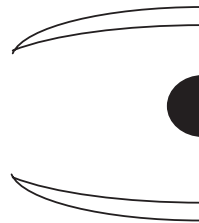
1. Draw a *typical* performance map for an axial-flow compressor.
2. Draw a *typical* performance map for an axial-flow turbine.
3. Define *corrected thrust*, *corrected rpm*, and *corrected mass flow rates*.
4. What is a typical *axial Mach number*, M_z , at the compressor face?
5. Is the corrected mass flow rate (in a fixed-area turbine) constant if the flow in that station remains choked? Explain.
6. Relate \dot{m}_{c4} to \dot{m}_{c8} in a turbojet engine, assuming stations 4 and 8 are choked.

Quiz No. 35

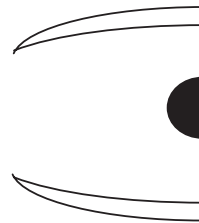
1. Identify a suitable flight *Mach number range* for the following supersonic inlets:
 - (a) a normal shock inlet
 - (b) an external-compression inlet
 - (c) a mixed-compression inlet
 - (d) an internal-compression inlet.
2. Identify three possible methods of “*starting*” a supersonic, convergent–divergent (C–D) inlet.
 - (a) Method 1:
 - (b) Method 2:
 - (c) Method 3:
3. In a C–D inlet operating in a supersonic flow,
 - (a) Where can a normal shock be *stabilized*?
 - (b) What establishes the position of the *terminal (i.e., the normal) shock* inside the inlet?
4. For the following normal shock inlet, place the NS according to the *inlet’s mode of operation*.



Critical mode



Subcritical mode



Supercritical mode

5. About the throat section of a Kantrowitz–Donaldson C–D inlet, answer the following questions:
 - (a) Is it choked in the started mode?
 - (b) Is it choked in the unstarted mode?

Quiz No. 36

1. Distinguish between *surge* and *rotating stall*.
2. Describe the effect of *inlet distortion* on compressor instability.
3. What is meant by *free-vortex design* of a turbomachinery blade?
4. What is the definition of *degree of reaction* in a turbomachinery stage?
5. What do we mean by *radial equilibrium* in turbomachinery flows?

Quiz No. 37

1. What is the definition of *incidence angle* in a compressor blade?
2. What is the definition of *deviation angle* in a compressor?
3. Define *camber angle* for a compressor blade profile.
4. What is *stagger angle* in a compressor cascade?
5. What is the *minimum Reynolds number based on chord* for a compressor blade section?

Quiz No. 38

1. How does the HHV of a fuel relate to the LHV in a combustion reaction?
2. What is *Avagadro's number* and what does it mean?
3. What is a *mole* in chemistry?
4. What is an exothermic reaction? Give an example.
5. What is an endothermic reaction? Give an example.
6. Describe the *chemical composition* of air in standard sea-level conditions.

Quiz No. 39

1. What do we mean by *chemical equilibrium* in a combustion process?
2. What is the *reaction time scale* in a combustor and how should it relate to *residence time*?
3. What is *soot*?
4. What are the *greenhouse gases* and what do they do in the atmosphere?
5. What does the Federal Aviation Regulation (FAR) say about *aircraft noise* in landing and takeoff?
6. What is *sonic boom*?
7. What does the Federal Aviation Regulation (FAR) say about engine *combustion-related pollutants* as in NO_x , CO, and UHC?
8. Describe the impact of NO on the *ozone layer* in the upper atmosphere.

Quiz No. 40

1. Define the *standard heat of formation* for a chemical compound.
2. What is the standard heat of formation of gaseous oxygen?
3. What is the definition of *partial pressure* in a mixture of gases and what is Dalton's Law of additive pressures?
4. Maximum *flame temperature* in a combustion process occurs near a particular fuel-air mixture ratio. What is the fuel-air mixture ratio that leads to maximum flame temperature?

5. The *flame temperature* in combustion of fuel in oxygen is higher than the same fuel combusting in air. Why?
6. What is meant by the *spontaneous ignition temperature* in common fuels?
7. Why is there an *autoignition delay time*? What factors impact the delay?

Quiz No. 41

1. What is the *effect of humidity* on engine mass flow rate?
2. Is the molecular weight of *dry air* higher or lower than air with humidity? Why?
3. What is the impact of a *hot day* at a high-altitude airport (e.g., Denver) on engine takeoff thrust?
4. What is the impact of *water injection* into inlet on a hot day?
5. How does *latent heat of vaporization* of water impact the engine mass flow rate?

Quiz No. 42

1. What is the *Reynolds analogy* between skin friction and heat transfer?
2. Write the *Fourier law* of heat conduction.
3. What are the dimensions of the coefficient of thermal conductivity, κ ?
4. Name three kinds of *heat transfer*.
5. How does *radiation heat transfer* scale with (absolute) temperature?
6. What is *adiabatic wall temperature*? How does it relate to stagnation temperature?

Quiz No. 43

1. What are the factors that influence *boundary layer transition*?
2. Relate curvature to the *stability of viscous flow*.
3. What is a Görtler vortex and how does it impact the *heat transfer* on a turbine blade?
4. How does heating or cooling a wall impact boundary layer transition?
5. What is the effect of *Mach number*, that is, compressibility, on boundary layer transition?
6. How does coefficient of *viscosity*, μ , *change with temperature* in a gas or liquid and why?
7. What is the definition of *Prandtl number*, Pr ?

Quiz No. 44

1. Define *specific impulse*, I_s , and *total impulse*, I_t , for a rocket engine.
2. Would a rocket engine produce more thrust in vacuum or at launch? Why?

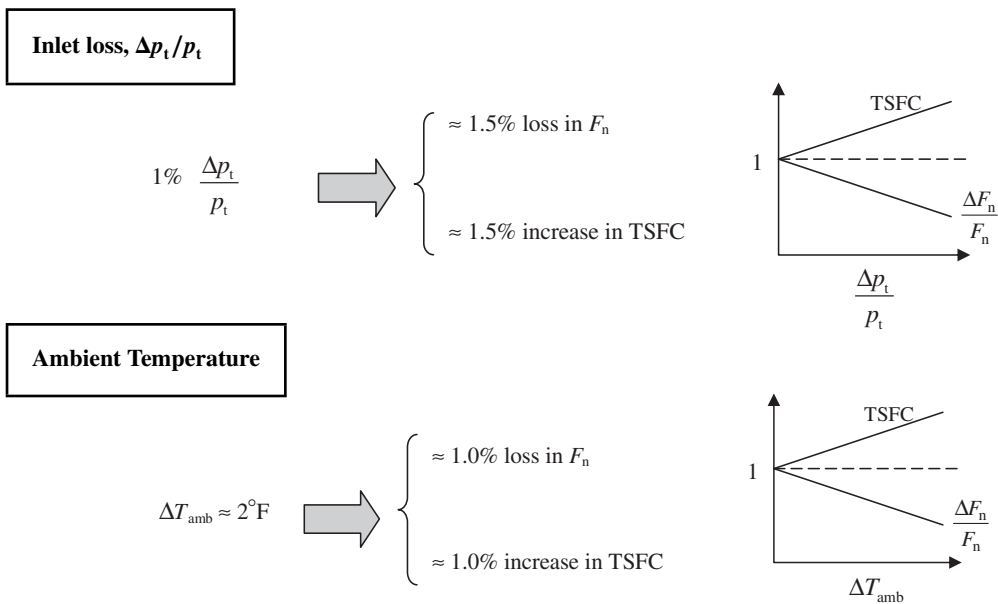
3. What is a typical *flight Mach number* for a conventional ramjet that it starts to exceed the performance of a turbojet engine?
4. What is the typical *flight Mach number* where a scramjet is more efficient than a conventional ramjet?
5. What is the *flight Mach number* in a circular orbit (in LEO)?
6. A figure of merit in rocket design is *Mass Ratio*, MR. Define MR!

Quiz No. 45

1. Define *thrust coefficient*, C_F , for a rocket engine.
2. What is roughly the *mean radius of the Earth* (in km or miles)?
3. What is “chugging” instability in a liquid propellant chemical rocket engine and what is the solution to avoid this problem?
4. What is “screaming” or “screeching” instability in a chemical rocket engine?
5. What are the advantages of having metal oxides or metal additives in solid propellants?
6. Describe the process of regenerative cooling in a rocket thrust chamber.
7. Write Newton’s law of cooling and define the variables in the equation.
8. “Inhibitors” are used in the design of solid propellant rocket motors. What is an inhibitor and what does it do?

APPENDIX L

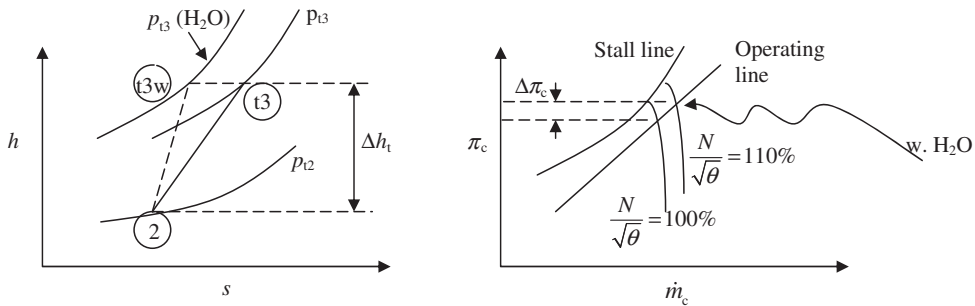
Some "Rules of Thumb" and Trends in Aircraft Propulsion



Example: Takeoff thrust at the standard ambient temperature of 59°F will suffer ~20% drop at an ambient temperature of 99°F!

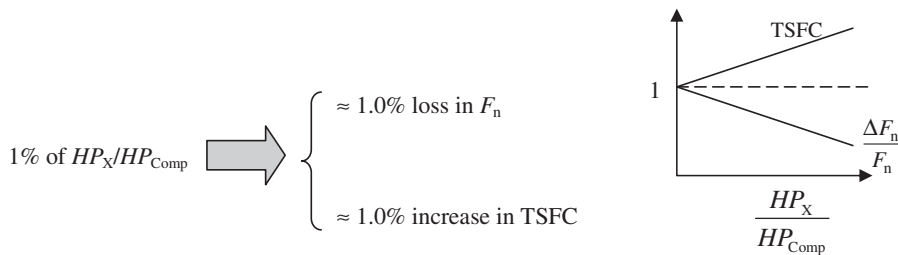
Solution: Water or water–alcohol injection in the compressor

- Advantages {
- Evaporative cooling increases \dot{m} and p_t
 - \dot{m} increase due to injection itself
 - Alcohol (if used) burns in combustor as fuel



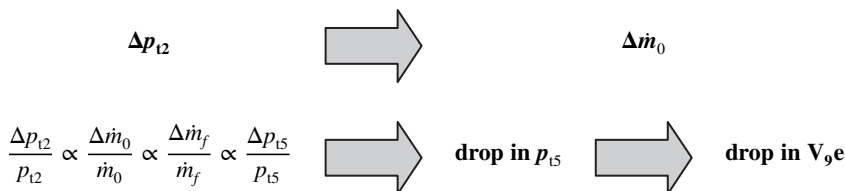
- Heat absorbed to evaporate the water leads to a lower Δs , higher pressure and density
- Increased mass flow rate is not shown, since the h - s diagram is per unit mass
- Compressor pressure ratio increases as the corrected shaft speed increases with lower temperature
- Latent heat of evaporation of water is higher than alcohol, therefore it takes more alcohol for the same cooling effect.

Power Extraction HP_X/HP_{Comp} (varies between 0 and 10%)



Airflow Rate

At any engine speed, airflow rate varies directly with density at the compressor face, therefore p_{t2}



Example:

We can use this quick rule to estimate the engine mass flow rate at off-design altitude and Mach number. For example, the total pressure at the engine face in takeoff (SSL) is ~100 kPa, for example, at design point. The engine at 40 kft (U.S. Standard Atmosphere) at flight Mach number of 0.8 creates an engine face *total pressure* of ~28 kPa. Therefore, the “ball park” value of air mass flow rate in this flight condition is about 28% of its SSL value.

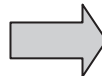
Supersonic Inlets

Normal shock inlets are suitable for Mach number



$$(M_D)_{NS-Inlet} < 1.6$$

External-compression inlets are suitable for



$$(M_D)_{External-Compression} < 2.6$$

Mixed-compression inlets are suitable for



$$(M_D)_{Mixed-Compression} < 5$$

Internal-compression inlets



$$(M_D)_{Internal-Compression} > 5$$

Inlet Instabilities

External-compression inlets exhibit



“Buzz” instability in subcritical mode

All supersonic inlets with internal throat exhibit



Starting Problem/Unstart

Subsonic Inlets

Limit on the mean throat Mach number



$$\bar{M}_{th} < 0.75$$

Limit nacelle drag rise at transonic speeds by



“Slimline”, supercritical nacelle design

Inlet total pressure recovery at cruise

$$\pi_d \sim 0.995$$

Axial-Flow Compressor

Interblade row spacing is typically one quarter of *average* stage axial chord length, namely,

$$\Delta z_{blade\ row} \approx \frac{1}{4} \bar{c}_{stage}$$

Reynolds number based on chord

$$Re_c > 500,000$$

Modern transonic fan (stage) pressure ratio

$$\pi_{stage} \sim 2$$

Modern transonic fan aspect ratio

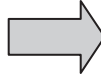
$$(AR)_{fan} \sim 1$$

Compressor pressure ratio, per spool

$$(\pi_c)_{spool} < 20$$

Fan Casing Treatment

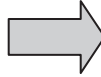
Circumferential groove in the casing



$\Delta(\text{Stall Margin}) = +3 \text{ to } +5\% \text{ increase}$
 $\eta_{fan} \sim \text{unchanged}$

Compressor Blade Tip Coating

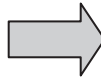
Cubic boron nitride (CBN) tip coating effectively reduces tip clearance



$\Delta\eta_{fan} + 1\% \text{ increase}$

Compressor Discharge Temperature Limit

This is the creep-rupture limit temperature of nickel-based superalloys, namely:

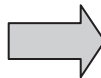


$(T_{t3})_{max} \sim 900 \text{ K}$

This limits the compressor pressure ratio to about 45–50.

Compressor Face Axial Mach Number

In a conventional turbofan engine, axial Mach number at the engine face has a design value of about 0.5. The current trend is in increasing M_{z2} to ~ 0.6 .



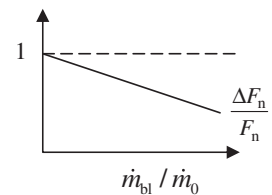
$M_{z2} \approx 0.5 - 0.6$

Compressor Bleed, \dot{m}_{bl}/\dot{m}_0 (for cockpit a/c)

1% of \dot{m}_{bl}/\dot{m}_0



$\approx 2\% \text{ loss in } F_n$



Rotating Stall

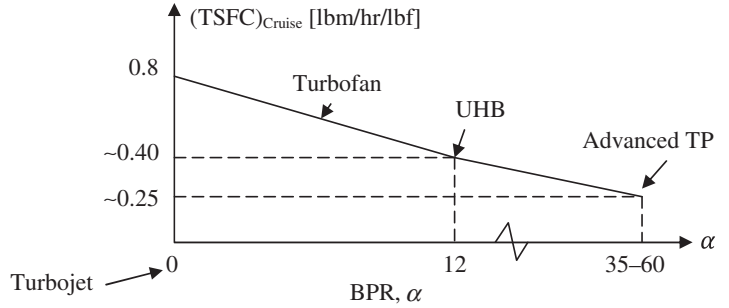
Rotating stall cell spins at $1/2$ the rotor angular speed, in the opposite direction, in the relative (i.e., rotor) frame of reference.



$\omega_{\text{Rotating stall}} \sim \frac{1}{2} \omega_{\text{shaft}}$

Cruise TSFC versus Bypass Ratio

Cruise TSFC drops dramatically with BPR
The TSFC numbers are “ballpark” values.

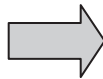


Primary Burner

Typical burner efficiency at takeoff
Typical burner efficiency at cruise

Flow deceleration in the burner prediffuser

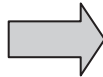
Typical combustor total pressure ratio



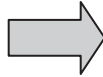
Burner efficiency drops with altitude (since pressure drops)

$(\eta_b)_{takeoff} \sim 0.995$

$(\eta_b)_{cruise} \sim 0.95$



$(M_{burner})_{inlet} < 0.1$



$\pi_b \approx 0.95$

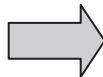
Since η_b drops with altitude, fuel-related parameters (e.g., f , TSFC) do not exactly follow the corrected parameters defined for TSFC_c

Stoichiometric fuel-to-air ratio for typical hydrocarbon or JP fuels

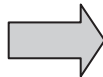
Fuel-to-air ratio in primary burner

Hydrogen versus hydrocarbon or JP fuel

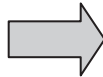
Combustor liner cooling effectiveness



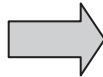
$f_{stoich} \sim 6.7\%$



$f \sim 3\%$ at takeoff
 $f \sim 2\%$ at cruise

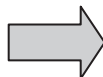


$(Q_R)_{H_2} \sim 3(Q_R)_{HC-Fuel}$



$\Phi \sim 0.8$

Afterburner



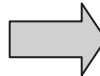
TSFC doubles, while thrust increases by 50–80%
Low-frequency oscillation: “Rumble”, $f \sim 50\text{--}100$ Hz
High-frequency instability: “Screech”, $f \sim 1\text{--}5$ kHz

Turbine

Temperatures

Gas path temperature in nozzle	$(T_t)_n < 2500 \text{ K}$
Gas path temperature in rotor frame of reference	$(T_t)_r \approx (T_t)_n - 150 \text{ K}$
Blade service temperature	$T_{\text{metal}} \sim 80\%(T_{\text{melt}})_{\text{superalloys}} \sim 1200\text{--}1400 \text{ K}$
Adiabatic wall temperature	$T_{\text{aw}} \approx (T_t)_g$
Coolant temperature at the rotor blade root (preswirl)	$(T_{\text{tc}})_r \approx (T_{\text{t3}})_{\text{compressor}} - 100 \text{ K}$
Coolant mass fraction in the first nozzle blade row	$\epsilon_{\text{N1}} \approx 10\%$
Coolant mass fraction in the first rotor	$\epsilon_{\text{R1}} \approx 4\%$
Thermal barrier coating (TBC) offers protection	$(T_w)_{\text{TBC}} \sim T_w - 100 \text{ K}$

Cooling Effectiveness



$$\eta \equiv \frac{T_g - T_m}{T_g - T_c} \sim 0.65\text{--}0.70$$

Creep Life

In a turbine component, for example, blades, the blade life is reduced by 50% for each 10 K rise in material temperature

Mach Numbers

First nozzle, per spool is choked		$(M_{\text{exit}})_{\text{N1, per spool}} \sim 1.0\text{--}1.1$
All rotor exits in relative frame unchoked		$(M_{\text{exit}})_R, \text{ relative frame} < 1.0$
Turbine Exit Mach number		$(M_{\text{exit}})_{\text{turbine}} \leq 0.50$

Max Exit Flow Angle



$$(\alpha_2)_{\text{noz}} \leq 70^\circ$$

Turbine Exit Swirl



$$(C_\theta)_{\text{exit}} \sim 0$$

Turbine Tip Clearance



$$\frac{\Delta\eta}{\eta_0} \sim 1.5\text{--}3\% \text{ Loss}$$

Turbine efficiency loss per percentage increase in tip clearance is between 1.5 and 3%.

Exhaust Nozzle

Critical Nozzle Pressure Ratio, $(NPR)_{crit}$

$$NPR_{crit} \sim 2$$

Gross thrust is maximized when perfectly expanded

$$(F_g)_{max} \text{ when } p_9 = p_0$$

A subsonic jet is always perfectly expanded

$$\text{Always } p_9 = p_0 \text{ if } M_9 < 1$$

Penalty of convergent nozzle versus C–D nozzle

$$\frac{\Delta F_g}{F_g} > 5\% \text{ when } NPR > 6$$

Benefit of mixing the fan and core flows in TF engines

$$\frac{\Delta F_g}{F_g} \sim 2\text{--}3\%$$

Thrust reverser effectiveness in separate flow TF

$$\text{Reverser Effectiveness} \sim 10\%$$

Thrust reverser effectiveness in mixed flow TF

$$\text{Reverser Effectiveness} \sim 30\%$$

Chevron nozzle jet noise reduction benefit

$$\Delta EPNL \sim 2.5 \text{ dB in flyover or community noise}$$

Chevron nozzle penalty on cruise gross thrust

$$\frac{\Delta F_g}{F_g} < \frac{1}{2}\% \text{ in cruise}$$

Throat area scheduled with afterburner

$$\frac{A_g - AB - ON}{A_g - AB - OFF} \approx \sqrt{\frac{(T_{tg})AB - ON}{(T_{tg})AB - OFF}}$$

NPR grows exponentially with flight Mach number, for example, in hypersonic regime we have

$$NPR \sim 1000 \text{ for } M_0 = 5.0$$

INDEX

A

Acoustic absorption, treatment, 328, 350, 407, 515
Activation energy, 430, 459
Actuator disk theory, 242. *See also* Propeller
Adiabatic, flow, 34, 38, 41, 43, 46, 47, 50, 71, 77, 82, 83, 88, 97, 101, 153, 156, 157, 158, 160, 163, 173, 181, 184, 211, 224, 231, 235, 250, 339, 350, 351, 376, 395, 402, 572, 581, 669, 770, 783, 808
Adiabatic wall temperature, definition, 720
Aerodynamic forces, 247, 526, 527, 528, 541, 563
Aerothermodynamics, 22, 151, 685
Afterburner, *see* Combustor
Air
 dry, 23
 humidity, 802, 803, 804, 807
 quality standards, 448, 498, 517. *See also* Environmental Protection Agency
Airbreathing engines, 144, 411, 473, 516, 822, 827, 843, 870, 884, 897
Aircraft
 flight envelope, 156
 noise, 199, 221. *See also* Noise
Airfoil, 49, 180, 225, 247, 319, 549, 567
 controlled diffusion, 552, 553, 554
 double circular arc, 552, 556, 627, 632
 J-profile, 627
 multiple circular arc, 627
 parabolic arc, 552, 553, 556
Area scheduling, 389–392, 411
Ariane-4 rocket, 847
Arrhenius equation, rule, 459
Aspect ratio (duct), 348
Atmosphere
 aerodynamic drag, *see* Rockets
 US standard-, 903–906
Attitude control, 827
AV-8B, 399

Aviation fuels, *see* Fuels
Avogadro's number, 430

B

B1-B aircraft, 322, 333
Batteries
 advanced, 316
 fuel cells, 318, 319, 324
 Li-ion, 316, 317, 323
Bearing, radial, axial or thrust, 172, 771
Bellmouth, *see* Gas turbine engine performance testing, 156, 802–810
Bending stress, 625
Bernoulli equation, 93, 94, 243, 330, 476, 555, 566, 714, 809, 850
Blade, *see* Compressor, turbine
Bladed-disk, Blisk, 8, 638
Bladed-ring, Bling, 8
Blade loss sources, 702
Blade setting angle, *see* Stagger angle
Bleed, 168, 310, 369, 394, 615, 617, 719, 747
Blockage, 336, 349, 379, 399, 480, 494, 495, 605, 670, 673, 674, 737, 806. *See also* Inlets and nozzles
Blocker, 398
Blowout, 462, 466, 493, 494
Boattail, 124, 178, 387, 391, 392, 411
Boiling point, 166, 309, 509–511, 514, 865–867
Boltzmann factor, 459
Boundary layer, 5, 41, 42, 74, 92, 97, 153, 157, 163, 169, 177, 222, 228, 249, 327, 328, 330, 331, 333, 338, 340, 341, 348, 350, 359, 367–371, 379, 387, 399, 411, 490, 532, 535, 545, 549, 558, 585, 591, 595, 605, 606, 612, 615, 616, 622, 632, 633, 636, 674, 685, 690, 691, 702, 704–706, 715, 721, 725, 757, 806, 874
 displacement thickness, 336, 379, 806
 momentum deficit thickness, 553, 554, 567, 591

- Brake-specific fuel consumption, 287, 295
 Brayton cycle, *see* Cycle
 Breguet range equation, 137, 138, 139
 Buckingham Π theorem, 91
 Buffet, definition, 596
 Burner, 113, 125, 133, 151–153, 164–168, 192, 250, 260.
 See also Combustor
 Burning rate (solid propellant), 825, 856–861, 879
 Buzz, instability cycle, 367–371, 812, 855
 Bypass ratio, 10, 130, 144, 195, 209, 210, 212–217, 221,
 226, 229, 231, 232, 241, 344, 397, 405, 407, 794,
 796, 797, 799, 800, 824
- C**
- Campbell diagram, *see* Compressor and turbine
 Capture, area, streamtube, 121, 122, 123, 126, 153, 156,
 242, 244, 339, 340, 344–347, 349, 352, 359, 362,
 770, 771, 809, 891
 Carbon-carbon, 395, 396, 741. *See also* Material
 Carbon monoxide, 458, 488, 499, 500. *See also* Combustion
 Carburetion, 310
 Carnot cycle, 134, 144, 186, 190, 194. *See also* Cycle
 Carter's rule, 556
 Cascade, 397, 398, 399, 549–557, 559, 560, 563, 567, 568,
 587, 590, 591, 595, 601, 626, 634, 637, 703, 711,
 735, 736, 751
 Cascade total pressure loss, definition, 559, 560, 563, 567
 Ceramic matrix composite, 487, 507. *See also* Material
 Characteristic Mach number, definition, 51
 Chemical
 composition, *see* Combustion
 equilibrium, 445
 kinetics, 445, 459, 470, 472, 488, 883
 reaction, 434, 440, 445
 rockets, 824, 826, 855, 870
 Choking
 frictional-, 83, 85, 479, 480
 length, 83, 85, 86, 88, 89
 Choked throat, 98, 198, 353, 694, 799, 830
 Circulation, definition, 546
 Combined cycle, 10, 11, 15, 18
 Combustion
 activation energy, 430, 459
 adiabatic flame temperature, 436, 442, 443, 444, 456,
 457, 487, 516, 518–523
 Arrhenius rule, 459
 chamber, gas turbine, 151, 164, 165, 166, 429, 431, 439,
 440, 444, 456, 473
 chamber, rocket, 824, 826, 829, 833, 849, 851, 853, 855,
 862, 869
 chemical composition, 445
 chemical equilibrium, 445, 516
 chemical kinetics, 429, 445, 459, 470, 472, 488, 517
 chemical reaction, 429, 430, 434, 435, 436, 440, 442,
 443, 445, 456, 459–470, 474, 485, 488, 492–494,
 500, 516, 518–524
 constant-pressure, 13
 constant-volume, 12–14
 delay or ignition delay, 470–472, 488, 517, 519
 detonation, 14
 effective collisions, 429
 efficiency, 229, 461, 462, 488, 490, 503, 505, 849, 850,
 894
 endothermic, 434, 435, 438
 equilibrium constant, 446–451, 454, 455, 519
 equivalence ratio, 435, 436, 444, 456, 457, 461, 464, 465,
 467, 470, 473, 488, 489, 503, 505, 506, 516, 518,
 519, 521–523
 exothermic, 164, 434, 435, 438
 flammability limit, 461, 462, 520
 flameout limit, 488
 flame speed, 464–467
 flame temperature, 434–444, 456, 457, 487, 503, 505,
 516, 518–523
 fuel droplets, 430, 470, 513, 516
 fuel lean, 435, 436, 456, 494, 499
 fuel rich, 435, 436, 442, 456, 501
 -generated pollutants, 498
 carbon monoxide, 439, 441, 458, 488, 499, 500, 521,
 523
 greenhouse gases, 498, 499, 513, 516
 impact on ozone layer, 507, 508
 oxides of nitrogen, NO_x , 498, 500, 501, 505
 oxides of sulfur, SO_x , 498
 smoke, soot, 459, 498, 501–504
 -number, 502
 unburned hydrocarbon, UHC, 488, 498
 heat of formation, 436–440, 442
 ignition, 429, 460, 462–464, 470–472, 488, 494, 497,
 510, 512, 513, 516, 517, 519
 -relight envelope, 460
 instability, 199, 515
 resonance frequency, 515
 rumble, 515
 screech, screech damper, 497, 498, 515
 isothermal, 438–440
 law of mass action, 445, 446, 447, 459, 516
 molar concentration, 443, 445, 499
 molar specific heats, 442, 444, 520, 522, 523
 mole fraction, 432, 433, 445, 447, 448, 518, 519
 pollutants, 472, 488, 498, 500, 516
 rate of reaction, 430, 445, 446
 forward-, 446
 reverse-, 446

- reaction time scale, 461, 470, 471
- reverse reaction, 444, 446, 459
- sensible enthalpy, 436
- spontaneous ignition delay, 470, 472, 488, 517
- stable, stability, 462, 473, 485, 503, 849, 850
- staged, 6, 503, 504
- standard heats of formation, 439–441, 521, 522
- stoichiometric, 436, 443, 455, 456, 461, 851, 862
- timescale, 429, 459, 461, 464, 466, 470, 471, 488, 492, 494, 513, 519
- turbulence intensity, 430, 464, 466
- vaporization rate, 430, 513
- Comburntor
 - afterburner, 461, 468, 469, 470, 477, 479–483, 493, 494, 497, 498, 515, 516, 517, 519, 520, 521, 523
 - choking, 479, 480, 483
 - dry mode, 477, 480, 481, 519, 520, 523
 - reheat or wet mode, 477, 481, 482, 483, 497, 517, 519, 521
 - stability criterion; marginal stability criterion, 494–496
 - total pressure loss, 479, 480, 482, 483
 - cooling methods and effectiveness, 485, 486, 507, 723
 - dilution zone, 483, 485
 - flameholder
 - axisymmetric, 496, 497
 - blockage, 480, 481, 495
 - bluff body, 469, 479–481, 493, 495, 518
 - drag, 477–483, 493, 521, 523
 - ring, 497
 - wake-width, 493–497
 - flow pattern, 483
 - ignition, 460
 - liner, 485–488, 499, 516
 - cooling effectiveness, 487
 - loading parameter, CLP, 470, 488
 - low emission, 6, 503
 - pattern factor, 483
 - primary zone, 461, 468, 469, 473, 483, 485, 488, 489, 498–503, 505, 509
 - profile factor, 484
 - relight, 460, 488
 - residence time, 459, 461, 488, 491, 496, 499, 505, 506, 509, 516
 - reverse-flow, 468
 - scaling laws, 489
 - scramjet, 461, 468
 - secondary zone, 498
 - sizing, 489
 - scramjet, 15, 72, 371, 461, 468, 823, 852, 891, 892, 894.
 - See also* Scramjet
 - temperature profile, 483
 - total pressure loss, 473, 474, 475, 476, 477
 - ultra-low NO_x combustor, 459, 505, 506
- Component matching, 768
- Compressor, 152, 157
 - adiabatic efficiency, 158, 160, 161, 162, 163
 - aerodynamic forces, 526, 527, 533, 541, 563
 - annulus design, 627
 - axial-flow, 163, 525, 526, 532, 535, 541, 545, 558, 590, 605, 607, 610, 611, 620, 625, 635, 651, 653, 659, 670, 674
 - blade aspect ratio, 606, 622, 633
 - blade design-blade selection, 626
 - blade forces, definition, 526
 - blade vortex design, 573
 - buffet, 596
 - camber angle, 551, 556, 605, 606, 627, 633
 - Campbell diagram, 625, 626, 633
 - casing, 173
 - centrifugal, 314, 473, 525, 531, 651
 - channel diffuser, 670
 - efficiency, 674
 - backswept or backward-leaning, 654, 656–658, 661, 680, 682
 - blockage effect, 670, 673, 674, 681
 - forward-leaning, 654, 656–658, 690
 - loading, 656, 657
 - radial, 654–656, 658, 660, 674, 679, 680–682
 - specific work, 657, 680
 - wake, 675
 - flow coefficient, 657
 - impeller, 651–683
 - inducer, 651–658, 670
 - D-factor, 671
 - design parameters, 672
 - solidity, 671, 672, 679
 - inlet guide vanes (IGV), 673
 - Kutta condition, 670
 - logarithmic spiral, 667, 668
 - Mach index, 658, 659, 662, 680, 681
 - pressure ratio, 663, 672, 677, 678
 - radial diffuser, 654, 660, 662–664, 666–670, 679, 680–683
 - slip factor, 655–657, 660, 661, 680, 681
- circulation, 546–548, 563, 566, 570, 571, 588, 639, 641, 643
- constant-work rotor, 573, 574, 576, 578, 584
- controlled diffusion blade, 552–554, 639
- corrected flow, 618
- corrected shaft speed, 594, 595
- degree of reaction, definition, 543
- De Haller criteria, 558, 560, 625, 628, 632, 639, 641, 645–650

Compressor (*Continued*)

- design, 546, 620
 - deviation angle, 549, 556, 557, 626, 627, 633
 - diffusion factor, 544–546, 548, 549, 553, 554, 556, 557, 582, 637, 639, 643, 645, 646, 649, 650
 - distortion effect on compressor stability, 599, 616, 618
 - double-circular arc blade (DCA), 556, 632, 633
 - end-bender, 587
 - flow angles, 534
 - flutter, 596
 - forced vibration, 596
 - forced-vortex design, 582
 - free-vortex design, 574–577, 579, 645
 - Greitzer B-parameter, 597–599
 - high-pressure, HPC, 113, 143, 185, 793
 - hybrid, 526
 - incidence angle, 538, 549, 551–553, 589, 595–597, 605, 618, 626, 633, 637, 644
 - inlet guide vane (IGV), 532, 533, 539, 540, 543, 544, 556, 574, 576, 577, 579, 583, 644
 - instability, 595
 - intermediate-pressure, 421
 - lift and drag, definition, 565
 - loading coefficient, 628, 641, 645
 - losses, 566, 568
 - cascade-, 549, 552, 554, 560, 626
 - due to unsteadiness; vortex shedding, 563, 566, 568, 585, 589, 638
 - end wall-, 557, 558, 563, 567, 568, 585, 587, 606, 635, 645
 - profile, 549, 563, 570, 571, 589, 626
 - secondary flow-, 585, 588, 591, 616, 640
 - shock-, 539, 541, 558, 563, 568, 585, 586, 591, 592, 633, 639, 643
 - tip clearance losses, 585
 - turbulent mixing, 568, 585, 589
 - low-pressure, LPC, 113, 143, 173
 - multiple circular arc profile (MCA), 556, 627
 - multi-stage, 587, 591, 599, 604, 611, 612, 626, 635, 638, 652
 - NACA-65 series profiles, 553, 628, 639
 - operating line, 599
 - optimum pressure ratio, 208
 - parabolic-arc blade, 552, 553, 556
 - performance map, 593, 595, 599, 600, 602, 614, 675, 772, 776, 777, 781, 782, 802
 - polytropic efficiency, 158, 160, 161, 162, 163, 170, 223, 224, 229, 250, 256, 541, 570, 582, 600, 628, 663
 - pressure ratio, optimum, 208
 - radial equilibrium, 531, 560, 571–573, 578, 638, 645
 - relative Mach number, 556, 560–562, 577, 628, 642, 644, 647–650
 - Reynolds number effect, 590
 - upper critical Reynolds number, 591, 643
 - rotating stall, 596–599, 639
 - rotor, 526
 - rotor centrifugal stress, definition, 622
 - shaft power, 168
 - solidity, definition of, 546
 - stability, 563, 612, 615–617, 640
 - stage efficiency, 540, 541, 560, 563, 643
 - stage, and stage parameters, 536
 - Stagger angle, 549, 551, 556, 558, 633, 644, 645
 - stall and surge, 595, 597, 686, 771, 812
 - stalling pressure rise, 545, 557–559, 590, 591, 604–613, 628, 639
 - stall margin, 599, 604, 605, 609, 610, 611, 618, 628, 634
 - diffuser analogy, 605, 611
 - starting problem, 612, 614
 - intercompressor bleed, 615
 - Multispool, 615, 638
 - variable stator, 615, 621
 - stator, 686
 - supersonic, 5, 10
 - swirl profile, 563, 572–580, 582–585, 638
 - three-dimensional flow, 558, 571, 670
 - torque, 526, 529, 531, 533, 534, 545, 603, 604, 640–643, 646
 - transonic, 591, 593, 637
 - unsteady flow, 585, 589, 638
 - velocity triangle, 528, 540, 618
- Computational fluid dynamics, CFD, 6, 14, 120, 338, 571, 638
- Conservation principles, 28
- Continuity equation, 28, 29, 30, 35, 43, 50, 67, 96, 99, 198, 228, 237, 242, 330, 340, 345, 352, 389, 477, 489, 490, 491, 575, 629, 856, 893
- Control surface, 29, 95, 114, 115, 121, 122, 123, 124, 342, 397, 564
- Control volume, 24, 28, 50, 54, 114, 115, 120, 121, 122, 226, 341, 342, 344, 477, 547
- Convective cooling, *see* Turbine cooling
- Corrected fuel flow rate, definition, 769
- Corrected mass flow rate, definition, 593, 769
- Corrected shaft speed, definition, 594, 769
- Corrected thrust, definition, 769
- Corrected thrust-specific fuel consumption, 769
- Convergent-divergent inlets, 350
- Creep rupture strength, 636, 742, 744
- Crew Exploration Vehicle, CEV, 826
- Cycle
 - Brayton, 1, 12, 13, 20, 185, 186, 188, 190–193, 258, 271
 - Carnot, 20, 186, 190, 193, 194, 266
 - Diesel, 286–289, 295, 299, 300, 306–308, 323, 325

Four-stroke, 284, 291, 292, 294, 299, 324
 Humphrey, 12–14, 20
 Otto, 284, 285, 290
 regenerative, 271
 two-stroke, 287, 288, 290, 292, 299
 Variable Cycle Engine (VCE), 407. *See also* Engine
 Cryogenic, *see* Fuels

D

D'Arcy friction factor, 91
 Degree of reaction, definition, *see* Compressor and turbine
 De Haller criterion, 558. *See also* Compressor
 Deviation angle, definition, 556
 Diffuser, 329
 annular, 335, 336
 axisymmetric, conical, 329, 336
 channel-, 670
 -cone, 481, 497
 conical, 429, 335–338
 dump-, 490, 491
 ideal, 330
 optimum performance, 336, 338
 parallel, 338
 performance charts, 337
 planar, 336–338
 radial, 654, 660, 666, 667, 668
 real, 331
 splitter plates, 338
 static pressure recovery, 96, 330, 335, 610, 669
 subsonic, 45, 96, 98, 329, 331, 333, 336, 351, 359, 362, 366, 668
 supersonic, 45, 328, 370, 668
 Diffusion factor, definition, *see* Compressor
 Dimensionless parameters, 91
 Direct operating cost (DOC), 221
 Discharge coefficient, 379, 399, 411, 710, 806, 852, 869.
 See also Nozzle
 Distortion, *see* Inlets
 dynamic, 327, 350, 619, 771
 steady-state, 619
 Drag
 additive or pre-entry, 123, 124, 126, 127, 344, 349
 aft-end, 125, 144
 aircraft, 120, 124, 294
 boattail, 392, 411
 divergence, 156, 341, 350
 flameholder, 477–480, 482, 483, 493
 friction, 79, 227, 591
 installation, 120, 124, 127, 210, 214, 328, 373
 interference, 120
 nacelle, 222, 341, 347

 pylon, 120, 124
 ram, 117, 118, 119, 128, 144, 214, 225, 259, 398, 803, 822, 848
 spillage, 124, 125, 347, 349, 353, 357, 359, 366
 Durability requirement, 487

E

Earth

 atmosphere, *see* US Standard Atmosphere, 903–906
 average radius, 824
 gravitational force on surface, 824, 835–837, 843
 low-earth orbit, (LEO), 823, 824, 826
 Eckert-Livingood correlation, 727
 Effective exhaust speed, definition, 216, 219, 833
 Efficiency
 adiabatic, 155–163, 170, 171, 176, 181–184, 211, 229, 230, 252, 253, 257, 258, 261, 262, 267, 268, 270, 278, 279
 afterburner, 200, 229
 burner, 165, 166, 212, 216, 773, 894
 carnot, 20, 186, 190, 193, 194, 266
 centrifugal compressor, 674
 component, 152
 gearbox, 249
 mechanical, 172, 229, 251, 256, 294, 775
 overall, 137, 138, 139, 196, 615, 848
 polytropic, 158, 160–168, 170, 176, 211, 218, 223, 224, 229, 236, 250, 251, 256, 257, 261, 262, 270, 271, 274, 277–280
 propeller, 137, 245, 246, 247, 248, 295, 350
 propulsive, 10, 133, 134, 135, 144, 194, 210, 216, 407, 793, 847, 848, 887
 stage, definition, 540
 thermal, 10, 11, 131, 132, 133, 134, 135, 144, 169, 185, 186, 187, 215, 216, 254, 258, 284, 295, 314, 831, 832, 888
 volumetric, 166
 Ejector, *see* Nozzles
 Electric motor, 316, 323
 AC motor, 315, 316
 DC motor, 312, 315, 316
 Emission index, 499, 500, 505
 Emission standards, 503, 502
 Emissivity, 863, 864, 868
 Endurance, 137, 139, 140, 300, 316, 591
 Energy, law of conservation, 29, 32, 115, 132, 174, 227, 244, 431, 432, 436, 445, 768, 770, 774, 775, 783, 852
 Engine, *see also* Gas turbine
 air-cooled, 284, 287, 299, 308, 314
 brake horsepower (BHP), 293–295, 314, 324
 brake-mean effective pressure (BMEP), 294, 324

Engine (*Continued*)

carburetor
 float-type, 310, 311
 icing, 288, 310
 pressure injection-, 311
 compression ignition, 290, 295, 300
 compression ratio, 284, 294, 295, 324
 crankshaft, 286, 292, 295–298, 313, 314, 322, 324
 cylinder, 284, 286, 288, 290, 291–298, 300, 305, 307, 308, 309, 311, 312, 314, 324, 325
 diesel, 286, 287, 299, 306, 307, 325
 displacement, 292, 305
 electric, *see* Electric motor
 emission standards, 292, 308
 exhaust port or valve, 290, 291
 friction horsepower (FHP), 293–295, 324
 indicated horsepower (IHP), 293–295, 324
 indicated mean effective pressure (IMEP), 294, 324
 intake port or valve, 290–292, 314
 kickback, 313
 knock, 308
 liquid-cooled, 299
 lubrication system, 313
 materials, 284, 295, 324
 oil cooler, 313, 314
 air-cooled, 314
 fuel-cooled, 314
 piston, 284, 288, 290, 292, 294–296, 298, 300, 303, 306, 308, 313, 314, 321, 322
 reciprocating, 283, 284, 290–292, 295, 296, 298, 300–307, 315, 324
 remotely-controlled (RC), 300
 Rotary or Wankel, 289, 290–293, 298, 300, 303
 scaling, 300–308, 325
 spark-ignition, 284, 287, 295, 300, 324
 stroke, *see* Two-stroke and four-stroke cycle
 sump, 313, 314
 supercharging, 284, 287, 314
 thrust horsepower (THP), 294, 295, 320, 324
 variable-cycle, 407
 weight, 283, 288, 289, 292, 293, 295, 300–309, 315, 317, 319, 322, 324, 325
 windmilling, 320

Environmental Protection Agency (EPA), 459, 488, 498, 500, 502–504, 521

Equilibrium constant, 446, 447, 448, 449, 450, 451, 454, 455, 516

Equivalence ratio, 435, 436, 444, 456, 458, 461, 464, 465, 467, 473, 488, 503, 833

Erosive burning, 860, 861

Euler turbine equation, 529, 530, 536, 541, 542, 572, 637, 652, 656, 686

Eurojet, EJ200, 8, 9, 20

Exhaust cone, *see* Diffuser cone

Exhaust mixer, *see* Mixer

Exhaust nozzles, *see* Nozzle

Exhaust systems, *see* Nozzle

Exhaust velocity, *see* Nozzle

Exothermic, 164, 434, 474. *See also* Combustion

Expansion corner, 67

F

F119 engine, 8

F135 engine, 142

F-22 Raptor, 8

F-35 Joint Strike Fighter, 8

Fan

adiabatic efficiency, 211

nozzle, 118, 119, 210, 214, 215, 408, 795

polytropic efficiency, 211

total pressure ratio, 224, 399

transonic, 5, 6

unducted fan (UDF), 10, 221

Fanno, -flow, -line, -function, 77, 78, 80, 81, 83, 84, 85, 86, 87, 88, 89, 90, 91

Fatigue, low-cycle, high-cycle, 332, 741, 742

Federal Aviation Administration (FAA), 221

Film coefficient, 169

Film cooling, 485, 486, 487, 723, 729, 730, 731, 732.

See also Turbine cooling

Flame

diffusion-, 464

laminar, 464–466

pre-mixed flame, 464–469, 503, 505, 506

speed, laminar, turbulent, 464, 465, 466, 467

stability, 76, 429, 466, 470, 483, 493, 494

-loop, 467, 470, 519

temperature, adiabatic, *see* Combustion

turbulent-, 464, 466

wrinkled-, 465, 466

Flameholder, flameholding, *see* Combustor

Flammability limits, 461, 462, 473, 510, 511

Flashpoint, 510, 513

Flow angles, definition, 534

Flow coefficient, definition, 536

Flutter, definition, 596

Force coefficient, 92

Foreign object damage, FOD, 328

Fourier's law of heat conduction, 722, 863

Friction coefficient

skin-, 78, 725

wall-, -drag, 79, 88, 91, 227, 591

Frozen equilibrium, *see* Rocket thrust chamber

Fuel

alternative jet fuels (AJF), 514, 515, 516
 Commercial Aviation Alternative Fuels Initiative (CAAFI), 515
 life cycle assessment (LCA), 514
 aromatics, 513
 avgas (aviation gasoline), 284, 286, 287, 295, 308, 309, 316, 324
 aviation, 139, 288, 308, 498, 509, 511, 513
 boiling characteristics, 509, 510, 511, 514
 butane, 441, 463, 522
 consumption, thrust-specific, 130, 139, 196, 197, 203, 207, 208, 219, 221, 223, 225, 238, 258, 260, 769, 788, 802
 consumption, power-specific, 257, 258
 cryogenic, 166, 169, 396, 511, 853
 decane, 463, 522
 ethanol, 513, 523
 gasoline, 461–463, 494, 510, 511, 513, 520
 heating value
 higher heating value (HHV), 440, 441, 522, 523
 lower heating value (LHV), 440, 441, 512, 522, 523
 heptane, 458, 463, 464
 hexane, 463
 hexadecane, 463
 hydrazine, 834, 866, 867, 870
 hydrocarbon, 132, 165, 166, 168, 430, 435, 459, 460, 461, 465, 471, 487, 488, 498, 499, 512, 513, 768, 822, 826, 834, 851, 892
 hydrogen, 166, 822, 823, 824
 injection system, 296
 continuous flow, 311
 direct, 311
 iso-octane, 463
 Jet-A, 287, 288, 457
 JP-3, 441, 463
 JP-4, 439, 441, 463, 472, 510, 511, 512, 513, 514, 884
 JP-5, 463, 510, 511, 513, 514
 JP-8, 463, 511, 513, 514
 kerosene, 319, 462, 463, 510, 512, 513, 834, 867
 latent heat of vaporization, 440
 leaded, 308, 309
 methane, 169, 396, 431, 441, 444, 458, 462, 464, 465, 511, 512, 834, 866
 nonane, 463
 octane, 166, 284, 286, 292, 308, 309, 435, 441, 463
 olefins, 513
 propane, C₃H₈, 441, 462, 463, 465, 511, 512, 517, 519, 522
 pump, 128, 129, 200, 288, 511, 513
 RP-1, 826, 834, 851, 852, 866, 870

spontaneous ignition temperature (SIT), 463

spray ring, 199, 497

tank, 166, 513

viscosity, 513

Fuselage, 331, 350, 403, 411, 596, 652

G

Gas

calorically-perfect, 23, 25, 27, 28, 34, 38, 39, 40, 48, 55, 62, 73, 77, 81, 231

-constant, 22

degrees of freedom, 26, 27

diatomic, 26, 27, 37, 39, 47, 65, 81, 803

emissivity, 863, 864

inert, 432, 884

mixture of gases

 Dalton's law, 431

 Gibbs–Dalton law, 432

 mole fraction, 432, 433, 445, 447, 448, 518, 519

 partial pressure, 431, 433, 518

 volume fraction, 433, 499, 513, 518

molecular weight, 22, 37, 166, 390, 430, 433, 434, 437, 464, 802, 851, 879

monatomic, 26, 27

perfect, 22, 25, 36, 44, 46, 53, 67, 70, 82

thermally-perfect, 22, 236, 801

Gas generator, 133, 151, 157, 169, 171, 185, 200, 209, 241, 253, 411, 652, 685, 746, 768, 774, 777, 779, 781, 784, 785, 811, 812, 824, 863, 874, 895, 897

Gas turbine engine

component matching, 768–818

 combustor-turbine matching, 773, 774

 compressor-combustor matching, 771, 772

 compressor-turbine matching, 773–775, 792

 inlet-compressor matching, 769–771

 turbine-afterburner-nozzle matching, 783

corrected parameters, 768, 769, 776, 777, 811, 813

installed performance, 120, 143

internal performance, 120, 128, 143

off-design analysis, 768–811

performance testing, 802–810

 altitude testing facility, 803

 bellmouth, 802–810

 flight testing: flying test bed, 803, 806

 ground testing facility, 803, 807

 icing test, 803, 805

 ram air facility, 803

single-spool, 802, 803, 811

three-spool, 133, 615

throttle line, 599, 602, 772

thrust stand, 803–810. *See also* Performance testing
 turbofan, 793–797, 799, 811, 815, 817, 818

Gas turbine engine (*Continued*)
 turbojet, 132, 151, 153, 182, 185, 194
 two-spool, 9, 173, 210, 768, 793, 811
 Gearbox, 222
 GE-36 engine, 10
 General aviation (GA), 283–324
 Gibbs–Dalton law, 432
 Gibbs equation, *see* Thermodynamics
 GP7000 engine, 6, 142
 Greenhouse gases, 498, 499, 513, 516
 Ground clearance, 123, 215, 344

H

Heat flux, critical, 74, 76, 867
 Heat of formation, standard, molar, 436, 437, 438, 439
 Heat sink, 396
 Heat Transfer
 ablative-, 868
 conduction-, 862–864
 convective-, 863
 radiation-, 862, 863, 868, 869
 Heat of vaporization, latent, 396, 440, 862, 866, 868
 Heating value. *See also* Fuel
 higher, 440
 lower, 75, 440, 512, 513
 Helmholtz resonator, 407, 515
 High-cycle fatigue (HCF), 472
 High-speed civil transport, HSCT, 505, 507
 Hot streak, 401
 Human space exploration, 826
 Humphrey cycle, 12, 13, 14
 Hydraulic actuator, 368
 Hydraulic diameter, 78, 85, 89, 91, 677, 865, 868
 Hydrazine, 834, 866, 867, 870
 Hydrogen, *see* Fuel
 Hypersonic, flight, propulsion, vehicle, 16, 96, 327, 371, 395, 402, 411, 843, 891, 896, 897
 Hysteresis, 334, 597

I

Ignition, 460
 battery, 311, 312
 boosters, 312
 full authority digital engine control, 310–314. *See also* FADEC
 high tension, 311, 312
 low tension, 312
 minimum ignition energy, 464
 spontaneous-, 462, 463, 470, 472, 488, 510, 512, 517
 Impeller, *see* Centrifugal compressor
 Impingement cooling, *see* Turbine cooling

Impulse

fluid-, 50, 67, 78, 80, 88, 95–102
 specific-, 130, 131, 196, 225, 822, 823, 827, 828, 829, 838, 851, 874, 879
 total-, definition, 827
 Incidence angle, definition, 538
 Inducer, 652, 658, 663, 670, 671, 673, 675
 Inducer-less impellers, 673
 Inhibitor, 862, 868
 Injector plate, 128, 824, 848, 849, 850, 852, 854, 855
 Inlet
 additive drag, 344–349, 414, 422, 425, 426. *See also* Drag
 adiabatic efficiency, 155, 156, 229, 328
 AIA standards, 372
 backpressure, 353–371, 389, 404, 416, 417, 419
 blockage, 336, 337, 349
 buzz instability, 367–371
 capture ratio, 343, 346
 contraction ratio, 356
 convergent-divergent, C-D, 350, 353, 358
 distortion, 327, 332, 335, 341, 348, 350, 359–361, 367–369, 371, 415
 dynamic-, 327, 350
 steady-state, 327, 350
 external-compression, 362, 365, 366, 368, 370, 812
 variable ramps, 368
 foreign object damage (FOD), 328
 guide vanes, 539, 587, 654, 673
 internal-compression C-D, 352, 371
 isentropic C-D, 356
 Kantrowitz–Donaldson, K–D, 356, 358
 lip bluntness, 349
 lip contraction ratio, 340, 341, 349, 414, 415
 low observables, 328, 373
 mass flow ratio (MFR), 339, 343, 344, 415, 423
 mixed-compression, 368
 MIL-E-5008B standards, 372, 412
 normal-shock, 359, 360, 361, 362, 372
 optimum ramp angle, 365
 recovery (standard), supersonic, 371
 spillage, 342, 347, 349, 353, 355–361, 366, 367, 415–417, 421, 423
 subsonic, cruise, 338, 347, 349
 supercritical nacelle, 342, 350. *See also* Nacelle
 supersonic, 41, 84, 350, 359, 368, 370, 891
 stability margin, 367, 369–371
 stall characteristics, 331–334. *See also* Diffuser
 starting a supersonic C-D inlet, 358
 over-speeding, 355, 356, 417
 variable throat, 355, 358, 369
 Kantrowitz–Donaldson (K–D), 356–358, 412, 416, 422, 426

stealth, 328, 331, 333
 throat, 340, 358
 unstart, 812
 variable geometry, 8, 153, 198, 199, 357, 358, 368, 371, 374, 392, 411, 540
 variable-ramps, 368
 variable-throat, 355, 358, 369
 International Traffic in Arms Regulation, ITAR, 140
 Isentropic compression, supersonic, 153, 350
 Isentropic flow, process, 27, 36, 44, 47, 184, 340, 343, 344, 352, 356, 359, 361, 581, 833
 Isolator, 891, 896. *See also* Supersonic combustion ramjet

J

J-31 engine, 4
 J57 engine, 144
 Jet propulsion, 122, 128, 821
 JT3D engine, 144
 JT8D engine, 145
 JT9D engine, 147
 Jumo 004B, 3–8, 19

K

Kantrowitz–Donaldson inlet, 356, 358
 Knudsen number, 92
 Kutta condition, 180, 225, 227, 229, 233, 670

L

Law of mass action, 446
 Leibnitz rule, 29, 31, 32
 Lift, 138
 Lift-drag ratio, 104, 138, 149
 Losses
 annulus, 705
 secondary flow, 704
 Low-earth-orbit, LEO, definition, 823

M

Mach angle, 37, 63, 64, 65, 350
 Mach-area relation, 44
 Mach cone, 49
 Mach number, definition, 37
 Mach index, definition, 658
 Mass action, law of, 446
 Mass flow parameter, 49, 77
 Mass flow ratio, MFR, 339
 Mass ratio, definition, 828
 Matching
 combustor-turbine, 773
 compressor-combustor, 771
 compressor-turbine, 774

inlet-compressor, 769
 turbine-afterburner-nozzle, 783
 Mean-free path, 63, 92
 Mixer, 210, 225, 227–229, 237, 264, 268, 404, 406, 411
 Mixing layer, *see* Shear layer
 Mixture of gases, 225, 390, 431–434, 883
 Mixture ratio (in rockets), definition, 851
 Mollier diagram, 40
 Momentum equation, 30, 31, 36, 44, 50, 52, 53, 67–71, 78, 79, 83, 95, 116, 121, 227, 342, 345, 476, 564, 853, 877
 Moody diagram, 91, 92
 Multispool configuration, 4

N

Nacelle, 120–128, 144, 154, 156, 157, 222, 223, 299, 328, 339, 341–344, 347, 350, 391, 392, 784
 slimline-, 144, 344
 supercritical-, 342, 350
 wave drag, 366
 Navier–Stokes equations, 338
 Newton's law of cooling, 723, 863
 Nitrogen oxides, 498, 501–508, 513, 516
 Noise, engine, fan, 328
 Nozzle, 8, 177, 373
 adiabatic efficiency, 181–184, 252, 252, 253, 373, 376
 angularity, exit flow, 350, 370, 381–384, 393, 411
 area scheduling, 389–393, 411
 bell-, 874, 884
 boundary layer, 379
 conical, 329, 331, 335–338, 381, 384, 872
 convergent, 178, 373, 375–379, 389, 409, 410, 784, 785, 793, 799
 convergent-divergent, De Laval, 45, 46, 97, 179, 198, 350–358, 376–378, 411, 786, 799
 cooling, 373, 394
 ejector, 15, 895
 exhaust systems, 24, 152, 177, 198, 327, 333, 373, 394, 399, 410
 exhaust velocity, effective, 216
 extendable, 871
 gross thrust coefficient, 385, 386, 388, 389
 hypersonic, 373, 895
 overexpanded, 117, 120, 183, 373, 386–389
 perfectly-expanded, 117, 135, 144, 178, 180, 183, 184, 188, 191–195, 197, 204, 215–217, 256, 373, 376, 386, 403, 404, 831, 832, 880
 plug- or aerospike-, 872–874, 885
 pressure ratio, NPR, critical NPR, 179, 182, 184, 224, 374–378, 380, 386, 388, 399, 403, 408, 799, 832, 870

Nozzle (*Continued*)

- rectangular, 2D-CD, 329, 331–336
- subsonic, 45, 177
- supersonic, 45, 179, 180
- thrust vectoring, 396, 399, 884
- total pressure ratio, 181, 182, 374, 378
- turbine integration, 409, 410
- unchoked, 737, 798
- under-expanded, 117, 120, 183, 375, 376
- variable-geometry, 198
- velocity coefficient, 379

Nusselt number, 864

O

- Oblique shock, *see* Shocks
- Off-design, 161, 260, 335, 360, 366–367, 389, 540, 543, 601, 700, 767, 785–802, 873
- Optimum ramp angles, 365
- Optimum total pressure recovery, 365
- Orbital speed, circular, 823
- Overall efficiency, *see* Efficiency
- Overspeeding; inlets, 355, 356
- Ozone, layer, 507–509

P

- Partial pressure, 431, 433, 446, 447, 450. *See also* Mixture of gases
- Periodic shock cell, 375
- Photochemical cycle, 508
- Pitchline, definition, 530
- Plank's constant, 507
- Pollutants, *see* Combustion
- Power split, turboprops, 254
- Prandtl–Meyer expansion waves, function, angle, 49, 65, 66, 351
- Prandtl number, 92, 721, 724, 864, 865
- Prandtl relation, 52
- Pressure coefficient, critical, 92, 342
- Pressure gradient
 - adverse, 153, 177
 - favorable, 177, 327
 - streamwise, 97, 331, 558
 - transverse, 97
- Pressure recovery, static-, 96
- Propellant mass fraction, definition, 828
- Propeller, 241–249
- Propeller efficiency, *see* Efficiency
- Propulsive efficiency, *see* Efficiency
- Pulse detonation engine, PDE, 14
- Pumping characteristics, gas generator, 774, 777
- Pylon, 114, 120, 121

Q

Quasi-one-dimensional flow, 41

R

- Radial equilibrium, 531
- Radiation cooling, 723
- Ram drag, *see* Drag
- Ramjet, 15, 151, 189, 208, 822–824
- Range factor, 139
- Rayleigh, -flow, -line, 67–84, 476, 479, 892, 893
- Reaction timescale, 461, 464, 466, 471, 492, 494, 870
- Recovery factor, definition, 708
- Regenerative cooling, 166, 169, 396, 461, 862, 863, 892
- Residence time, 459, 461, 488, 491, 492, 496, 499, 505, 506, 509
- Reynolds number, 42, 78, 91, 92, 247, 336, 471, 481, 490, 553, 590–592, 606, 607, 610, 612, 622, 628, 703, 710, 724, 725, 738, 850, 864–865

Rocket

- aerodynamics, 841
- based airbreathing propulsion, 15, 895
- based combined cycle, RBCC, 15, 131
- characteristic velocity, 833
- chemical, 821
- combustion chamber, 849, 863, 869
- combustion instabilities, 855, 862
- combustor volume, 869
- flight performance, 835, 847, 861, 869
- hybrid, 825
- liquid-propellant, 128, 169, 435
- multistage, 826, 838, 845
- multiphase flow, 874–882
- nozzles, performance, 869
- overall efficiency, 887, 888
- payload mass, 847
- propulsion, 821, 827
- propulsive efficiency, 847, 848
- solid-propellant, grain, 821, 825, 834, 855–862
- thrust, *see* Thrust
- thrust chamber, 849–851, 855, 862–868, 896, 897
- thrust coefficient, 830–833, 884
- thrust vectoring nozzles, 884

Rotating stall, *see* Compressor stall

S

- Schlieren, 21, 702
- Scramjet, 15, 16, 18, 371, 461, 468, 823, 824, 852, 891–896
- Screech, 199, 497, 498, 515–516
- Screech damper, 515
- S-duct, 332

- Secondary flow, 97, 331, 332, 348, 350, 371, 483, 585, 588, 591, 616, 703–705
- Shaft power, 33, 133, 134, 135, 137, 168, 172, 174, 209, 241–249, 525, 531, 604, 653, 654
- Shear layer, mixing layer, 98, 226, 367, 387, 388, 490, 497, 700, 874, 894
- Shifting equilibrium, *see* Rocket thrust chamber
- Shock
- boundary layer interaction, 6, 350, 360, 367, 369, 563, 585, 591, 702, 757
 - bow-, 60, 353, 359, 368, 468, 539, 586
 - conical-, 60–63, 362, 363
 - cowl-, 359, 360, 362, 366, 404, 886
 - lambda-, 387, 388
 - normal-, 49, 68, 71, 83–87, 180, 353–363, 365, 370, 387, 415, 885, 891
 - oblique-, 49, 54–60, 180, 184, 362, 365, 366, 368, 387, 700, 891, 892
 - plume-, 404
 - starting-, 353–358
 - terminal-, 356, 362, 366, 369
 - trap, 370
- Signature, radar, thermal, IR, noise, 177, 328, 373, 411
- Silicon carbide, 488, 741
- Single crystal, 8, 624, 741, 745, 755
- Single-stage to orbit, SSTO, 10, 131, 824
- Slip, slip factor, definition, 655–657
- Slipstream, 49, 387
- Small disturbance, 37, 38
- Smoke, smoke number, 498, 501, 502
- Solidity, definition, 546, 549
- Solidity, optimum solidity, 685
- Sonic bubble, 340, 342, 344
- Sonic throat, 45, 329, 354, 375
- Soot, 459, 501
- Space Shuttle Main Engine, SSME, 821, 826
- Speed of sound, 35–38
- Spillage, spilled flow, 72, 77, 83, 86, 124, 342, 347, 353, 356
- Spool, multi-spool, 158, 209
- Stability margin, 369
- Stage loading, definition, 542
- Stall margin, 599
- Stagger angle, definition, 551
- Stagnation state, 38
- Stanton number, 92, 724, 725
- Stefan-Boltzmann constant, 863
- Stodola's model, 708
- Stoichiometric, *see* Combustion
- Superalloy, 719, 745. *See also* Material
- Supermaneuverability, 396, 397
- Supersonic combustion ramjet, 823, 891
- Swirl, 158, 242, 243, 244, 468, 515, 526, 528, 531, 534, 542, 544, 560, 563, 565, 572, 573, 576, 577, 585, 616, 630, 636, 652, 661, 667, 686, 698, 715, 736, 747, 750, 753, 850
- T**
- Takeoff, 119, 123, 152, 186, 187, 224, 256, 289, 306, 346, 396, 401, 629, 719, 727, 767, 823, 895
- Temperature gradient, 153, 722
- TF30-P-3 Turbofan engine, 497
- Thermal barrier or protection, 723, 740, 755, 757. *See also* Turbine cooling
- Thermal ceiling, 892
- Thermal conductivity, 721–723, 727, 740, 746, 749, 757, 762
- Thermal efficiency, *see* Efficiency
- Thermal limit, 152, 167, 188, 203
- Thermal protection coating, TPC, 7
- Thermal stresses, 625, 635, 745
- Thermodynamics
- brief review, 22
 - first law, 23, 32, 530, 652
 - Gibbs equation, 24, 25, 27, 39, 69, 70, 81, 154, 573
 - second law, 24, 134, 154, 160, 173, 181
- Three-dimensional relieving effect, 496
- Throat, sonic, 45
- Throttle station, 773
- Thrust
- core, 219, 225, 249, 258
 - gross, 118, 119, 125, 128, 144, 177, 184, 214, 218, 224, 249, 259, 373, 376, 377, 381, 385, 388, 404, 406, 784, 803, 810, 829
 - growth, 328, 340
 - installed, 119, 120, 124, 127, 135, 194, 768
 - internal-, 126, 127
 - lip-, 123, 124, 127
 - load cell, 803, 807, 809, 810
 - net-, 96, 117, 124, 139, 219, 258, 399, 889
 - power, 134, 135, 137, 138, 194, 242, 247, 253, 847
 - pressure-, 118, 124, 128, 129, 177, 194, 214, 829
 - propeller, 137, 242, 244, 249, 254, 320
 - reversing, reverser, 8
 - cascade, 398
 - clamshell thrust reverser, 396, 397
 - effectiveness, 397–399
 - fan, 398, 399
 - rocket, 128, 830, 837, 849, 851, 864, 884, 896
 - specific-, 129, 196, 203, 207, 214, 219, 788, 851, 880
 - specific fuel consumption, *see* Fuel
 - stand, 803–807, 809, 810
 - takeoff, 119, 823, 895

- Thrust (*Continued*)
 uninstalled, 18, 117, 118, 119, 120, 124, 128, 135, 194, 214, 822
 vectoring, 8, 9, 373, 396, 399, 884
- Torque, 158, 174, 242, 244, 293, 315, 526, 529, 603, 652, 667, 686, 736
- Transition ducts, 332, 348, 350
- Transonic compressor, *see* Compressor
- Transpiration cooling, *see* Turbine cooling
- Trent 1000 engine, 5
- Turbine
 adiabatic efficiency, 170, 176, 733, 753, 782, 801
 adiabatic wall temperature, 720–722, 727, 731, 749, 761–763, 765
 annulus losses, 702, 705, 757
 axial-flow, 101, 685, 687, 746
 blade
 angles, definition, 736
 -cooling, 725, 734, 735, 749, 751, 752
 -life, 686, 691, 737
 losses, 702
 material selection, 742
 profile design, 735, 738
 -service temperature, 685, 719
 allowable, 744
 centrifugal-, 685, 743, 744, 763
 thermal-, 740, 746
 vibratory-, 743
 throat Reynolds number, 738, 763
 -tip configuration, 709, 711, 712
 tip discharge coefficient, 710, 711, 713, 714, 761
 bending or flap mode, 739, 740, 743, 746
 Campbell diagram, 739, 740
 combined bending and torsional-, 739, 740
 torsional-, 739, 740
- casing, 164, 173
- cascade, 702, 703, 706, 711, 735, 736, 751, 757, 758
- cooling, 7, 169, 173, 718, 719, 720, 747, 757, 773, 862, 864
 convective-, 723, 757
 film-, 723, 729–732, 758
 -fraction, 727, 734, 750
 impingement-, 723, 724, 728, 729, 762
 radiation-, 723
 regenerative-, 862, 863, 892
 transpiration-, 723, 732, 757, 758
- degree of reaction, definition, 543, 544
- design, 685, 689, 741, 746
- disks, 742, 746
- efficiency, 225, 685, 692, 707, 710, 734, 773, 801
- end wall, 705, 713
- fatigue, 740–742
 high-cycle – (HCF), 742
 low-cycle- (LCF), 742
- “Fishtail” shock formation, 701
- free-, or power-, 241, 251, 252, 253
- heat transfer, *see* Turbine cooling
- high-pressure, HPT, 113, 168, 172, 175, 209, 251, 256, 719, 726, 732, 793
- impulse-, 686, 689–691, 693, 699, 712, 747, 755, 756
- jet-wake
- losses
 annulus-, 702
 cooling-, 685
 profile-, 703, 737, 757
 secondary-flow, 702, 703, 757
 tip-clearance, 702, 706–708, 757, 758
- low-pressure, LPT, 113, 173, 209, 221, 249, 389, 691, 768, 793
- material, 743
 carbon–carbon, 395–396
 ceramics, 740, 741
 conventionally cast, 742, 765
 creep, 741–744
 directionally solidified, 741, 742, 765
 high-strength nickel alloy, 719, 727, 740, 745, 746
 Larson-Miller parameter, 742
 single crystal, 745, 755
 strength-to-weight ratio, 745
 superalloys, 719, 741
 wrought nickel alloy, 624
 yield strength, 742
- nozzle, 173, 175, 483, 492, 601, 685, 694, 698, 704, 718, 737, 748, 752, 772, 773, 793, 800
- operating line, 777
- optimum solidity, 685, 703, 714–716, 718, 748, 751, 757
- optimal swirl Mach number, 698–700
- performance map, 733, 776, 811
- polytropic efficiency, 170, 236, 251, 786
- recovery factor, 708, 721
- rotor, 484, 530, 687, 691, 706, 707, 720, 750, 755
- scraping vortex, 706, 707
- shaft power, 171, 176, 224, 747, 768, 784, 800
- stage, 133, 143, 164, 169, 174, 209, 686, 689, 698, 711, 714, 756, 768
- swirl
 absolute-, 686, 753, 764
 relative-, 686, 709, 750
- tip clearance, loss, 757
- unchoked nozzle, 737, 798
- velocity triangle, 688, 755
- wall
 cooled-, 723, 727
 heated-, 723

- insulated-, 720, 722, 724
 - jet, 708
 - Zweifel loading parameter, 716, 717
 - Turbofan**
 - geared turbofan (GTF), 10, 11, 222, 223, 225
 - mixed-exhaust, 151, 225–239, 264, 271
 - separate exhaust, 210, 212, 214, 217, 220, 264, 275, 277
 - Turbojet**, *see* Gas turbine engine
 - Turbomachinery**, *see* Compressor and turbine
 - Turboprop**
 - advanced turboprop (ATP), 10, 221, 249
 - cycle analysis, 249, 260
 - optimum power split, 254, 256, 258
 - Turboshaft**, 12, 133, 685
 - Two-phase flow**, *see* Rocket
- U**
- Ultra-high bypass, UHB, 10, 144, 220, 221, 407
 - Ultraviolet (UV) radiation, 509
 - Unburned hydrocarbons, UHC, 6, 488, 498, 499, 503, 513, 803
 - Unmanned aerial vehicle, UAV, 16, 260, 283, 290, 316
 - Unmanned combat air vehicle, UCAV, 16
 - Upwash, 49, 350
 - U.S. Standard Atmosphere, 903–906
- V**
- V-2 rocket, 841
 - V2500 engine, 140
 - Variable cycle engine (VCE), 407
 - Variable gas properties, 801, 812
 - Variable stator, 5, 615, 638
 - Variable throat, 358, 369
 - Vector thrust, *see* Thrust vectoring
 - Velocity triangle, definition, 528
 - Velocity vectors, absolute and relative, 248, 349, 466, 528, 534, 535, 548, 570, 609, 636, 697, 714
 - Volatility, 511
 - Von O'Hain's jet engine, 3
- Vortex breakdown, 467, 564
 - Vortex, vortices, 158, 169, 335, 338, 348, 367, 387, 406, 490, 546, 558, 563, 572, 573, 577, 584, 625, 637, 670, 702, 713, 894
- W**
- W1; Whittle jet engine, 1, 2
 - Wake, 700, 702, 757
 - Wall jet, 708. *See also* Turbine
 - Wall static pressure taps, 805, 807
 - Wave**
 - acoustic-, 35, 515
 - envelope, 66
 - expansion-, 49, 63, 375, 403, 586, 700, 702, 872
 - helical-, 515
 - instability, 335, 515, 563
 - Mach-, 37, 57, 60, 63, 66, 350, 585
 - rotor, 12
 - shock, *see* Shock
 - supersonic-, 64, 894
 - Whittle jet engine, 2
 - Windmilling, 320, 346, 349, 614
- X**
- X-planes, 16
 - X-15, 21
 - X-36, 16
 - X-43, 16, 17
 - X-45, 16
 - X-47, 16
 - X-48, 16
 - XB-70, 372
 - XRS-2200 aerospike linear rocket, 873
- Y**
- Yield strength, *see* Material
- Z**
- Zweifel loading parameter, definition, 715, 717

Conversion factors

Energy:	1 kWh	= 3412.76 BTU
	1 BTU	= 778.16 ft-lbf
		= 1054.9 J
		= 0.29302 Wh
	1 J	= 1 W · s = 0.7376 ft-lbf
	1 cal	= 4.1868 J
	1 kcal	= 3.969 BTU
Power:	1 ft-lbf	= 1.355817 J
	1 kW	= 0.947989 BTU/s
	1 hp	= 0.7456 kW
		= 550 ft · lbf/s
	1 BTU/s	= 1.415 hp
Specific heat:	1 BTU/lbm · °R	= 4.187 kJ/kg · K
Torque:	1 ft-lbf	= 1.3558 N · m
Mass:	1 lbm	= 0.45359 kg
		= 16 oz
	1 slug	= 32.174 lbm = 14.593 kg
	1 kg	= 2.205 lbm = 1000 g
	1 ton	= 2000 lbm
Length:	1 (metric) ton	= 1000 kg = 1.103 tons
	1 in	= 25.40 mm
	1 ft	= 304.8 mm
		= 12 in = 0.3333 yd
	1 mile	= 1.609 km
		= 5280 ft
	1 nautical mile	= 1852.0 m
	1 mil	= 1.0×10^{-3} in = 0.0000254 m
	1 micron (μm)	= 10^{-6} m
	1 angstrom (\AA)	= 10^{-10} m
1 astronomical unit (au)	= 1.496×10^{11} m	
Area:	1 ft ²	= 0.09290 m ²
	1 m ²	= 1550 in ² = 10.7639 ft ²
Volume:	1 ft ³	= 0.02832 l m ³
		= 28.32 liters
	1 l	= 0.001 m ³
	1 gal (U.S.)	= 3.785 l = 0.003785 m ³
		= 4 qt = 8 pt = 32 fl oz
	1 gal (BR)	= 4.546 l
Force:	1 lbf	= 4.44822 N
		= 16.0 oz
		= 32.174 lbm · ft/s ²
	1 N	= 10 ⁵ dyne
	1 kg (force)	= 9.80665 N

Conversion factors

Pressure (and stress):	1 lbf/in ²	= 6.895 kPa (kPa \equiv kN/m ²)
	1 lbf/ft ²	= 47.88 Pa
	1 atm	= 1.01×10^5 Pa
		= 760 mm Hg
		= 2116.2 lbf/ft ²
		1 bar = 10^5 Pa
	1 mm Hg = 13.3322 Pa	
Density:	1 lbm/ft ³	= 16.0166 kg/m ³
	1 kg/m ³	= 6.243×10^{-2} lbm/ft ³
		= 1.9404×10^{-3} slug/ft ³
Thermal conductivity:	1 BTU/ft · h · °R	= 1.73073 W/m · K
Velocity:	1 mi/h	= 1.467 ft/s = 1.609 km/h = 0.4470 m/s
	1 knot	= 1.15155 mile/h
	1 km/h	= 0.2278 m/s = 0.6214 mile/h
		= 0.9113 ft/s
		1 ft/s = 0.3048 m/s = 12.0 in/s
Temperature:	1 K	= 1.8 °R
		= °C + 273.15
	1 · °R	= °F + 459.67
	T(°F)	= 1.8T(°C) + 32
	T(°C)	= 5/9[T(°F) – 32]
	0°C	= 273.15 K
	0°F = 459.67 °R	
Viscosity:	1 kg/m · s	= 0.67197 lbm/ft · s
	1 centipoise	= 0.001 Pa · s = 0.001 kg/m · s
		= 6.7197×10^{-4} lbm/ft · s
	1 stoke	= 1.0×10^{-4} m ² /s (kinematic viscosity)
	1 lbf-s/ft ²	= 47.88025 kg/m · s
	1 lbm/ft · s	= 1.48817 N · s/m ²
Thrust-specific fuel consumption (TSFC):	1 lbm/h/lbf	= 28.33 mg/N · s
Specific thrust:	1 lbf/lbm/s	= 9.807 N · s/kg
Gas constant R:	1 ft ² /s ² · °R	= 0.1672 m ² /s ² · K
Specific enthalpy:	1 BTU/lbm	= 2.326 kJ/kg

Constants

Universal gas constant:	8314.219 J/kg-mol · K 4.97×10^4 ft-lbf/slug-mol · °R 1.98592 BTU/lb-mol · °R
Gas constant R for air:	286.96 J/kg · K 1716 ft · lbf/slug · °R 0.068549 BTU/lbm · °R
Air pressure at sea level (standard):	1.01325×10^5 Pa = 2116.22 lbf/ft ²
Air temperature at sea level (standard):	288.15 K = 518.67 °R
Air density at sea level (standard):	1.2250 kg/m ³ = 0.002377 slug/ft ³
Coefficient of viscosity μ of air (at sea level):	1.7894×10^{-5} kg/m · s 3.7373×10^{-7} slug/ft · s 1.2024×10^{-5} lbm/ft · s
Avogadro's number N_A :	6.023×10^{23} /mol
Boltzmann constant k :	1.38×10^{-23} J/K 0.565×10^{-23} ft-lbf/°R
Earth's gravitational acceleration (sea level) g_0	9.80665 m/s ² 32.174 ft/s ²
Earth's mean radius R_E	6371 km, 3960 mi
Newton's universal gravitational constant G	6.670×10^{-11} m ³ /kg · s ²
Stefan-Boltzmann constant σ	5.67×10^{-8} W/m ² · K ⁴
